

# APPLIED GEOPHYSICS

SECOND

دانشگاه صنعتی شهرود — کتابخانه مرکزی  
Shahrood Univ. - Central Library



0-114713

ON

**W. M. Telford**

**L. P. Geldart**

**R. E. Sheriff**

# *Applied Geophysics*

## *Second Edition*

**W. M. Telford**

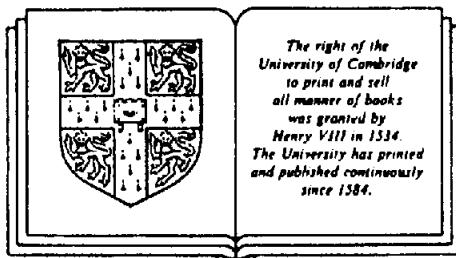
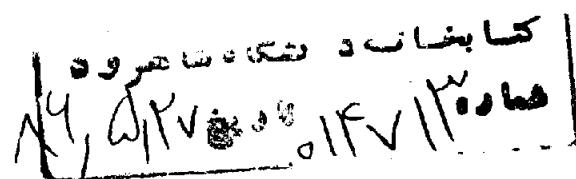
*McGill University*

**L. P. Geldart**

*Former Canadian International Development Agency Program  
Director for Brazil*

**R. E. Sheriff**

*University of Houston*



**Cambridge University Press**

*Cambridge*

*New York Port Chester Melbourne Sydney*

QC

806

T4A6  
c.2

Published by the Press Syndicate of the University of Cambridge  
The Pitt Building, Trumpington Street, Cambridge CB2 1RP  
40 West 20th Street, New York, NY 10011, USA  
10 Stamford Road, Oakleigh, Melbourne 3166, Australia

© Cambridge University Press 1990

First published 1990

**Library of Congress Cataloging-in-Publication Data**

Telford, W. M. (William Murray), 1917-  
Applied geophysics/W. M. Telford, L. P. Geldart, R. E. Sheriff. —  
2nd ed.

p. cm.

Includes bibliographies and index.

ISBN 0-521-32693-1 — ISBN 0-521-33938-3 (pbk)

1. Prospecting — Geophysical methods. I. Geldart, L. P.  
II. Sheriff, Robert E. III. Title.

TN269.T44 1990

622'.15—dc19

88-38761

CIP

**British Library Cataloguing in Publication Data**

Telford, W. M. (William Murray)

Applied geophysics. — 2nd ed.

I. Mineral deposits. Prospecting. Applications of  
geophysics

I. Title II. Geldart, L. P. III. Sheriff, R. E. (Robert  
Edward), 1922-

622'.15

ISBN 0-521-32693-1 hardback

ISBN 0-521-33938-3 paperback

Transferred to digital printing 2004

# *Contents*

<b>Preface to the Second Edition / xv</b>	
<b>Excerpts from Preface to the First Edition / xvii</b>	
<b>Mathematical Conventions / xix</b>	
<b>1. Introduction / 1</b>	2.4.3. Relative Measurement of Gravity / 20
Reference / 5	2.5. Field Operations / 23
<b>2. Gravity Methods / 6</b>	2.5.1. Land Surveys / 23
2.1. Introduction / 6	2.5.2. Drift Correction / 24
2.1.1. General / 6	2.5.3. Marine Surveys / 24
2.1.2. History of Gravity Exploration / 6	2.5.4. Airborne Gravity / 26
2.2. Principles of Gravity / 7	2.6. Gravity Data Processing / 26
2.2.1. Newton's Law of Gravitation / 7	2.6.1. Noise, Regionals, and Residuals / 26
2.2.2. Acceleration of Gravity / 7	2.6.2. Graphical Residualizing / 27
2.2.3. Gravitational Potential / 7	2.6.3. Surface-Fitting Residualizing Methods / 27
2.2.4. Potential-Field Equations / 9	2.6.4. Empirical Gridding Methods / 27
2.2.5. Derivatives of the Potential / 9	2.6.5. Second Vertical Derivative Methods / 32
2.3. Gravity of the Earth / 10	2.6.6. Wavelength Filtering / 32
2.3.1. Figure of the Earth / 10	2.6.7. Field Continuation / 32
2.3.2. Gravity Reduction / 11	2.7. Gravity Interpretation / 34
2.3.3. Densities of Rocks and Minerals / 15	2.7.1. General / 34
2.3.4. Density Estimates from Field Results / 18	2.7.2. Gravity Effect of a Sphere / 35
2.4. Gravity Instruments / 19	2.7.3. Gravity Effect of a Horizontal Rod / 36
2.4.1. General / 19	2.7.4. Gravity Effect of a Vertical Cylinder / 37
2.4.2. Absolute Measurement of Gravity / 20	2.7.5. Gravity Effect of a Thin Dipping Sheet / 39
	2.7.6. Gravity Effect of Horizontal Sheets, Slabs, Dikes, and Faults / 40
	2.7.7. Applying Simple Models to Actual Anomalies / 44
	2.7.8. Gravity Effects of Complex Shapes / 44
	2.7.9. The Direct and Inverse

Problems of Interpretation / 46	3.4.5. Gradiometers / 80
2.7.10. Excess Mass / 47	3.4.6. Instrument Recording / 80
2.7.11. Overburden Effects / 48	3.4.7. Calibration of Magnetometers / 80
2.7.12. Maximum-Depth Rules / 48	
<b>2.8. Field Examples / 48</b>	<b>3.5. Field Operations / 80</b>
<b>2.9. Problems / 52</b>	3.5.1. General / 80
<b>References / 60</b>	3.5.2. Airborne Magnetic Surveys / 81
<b>3. Magnetic Methods / 62</b>	3.5.3. Shipborne Magnetic Surveys / 83
<b>3.1. Introduction / 62</b>	3.5.4. Ground Magnetic Surveys / 83
3.1.1. General / 62	3.5.5. Gradiometer Surveys / 84
3.1.2. History of Magnetic Methods / 62	
<b>3.2. Principles and Elementary Theory / 63</b>	<b>3.6. Magnetic Effects of Simple Shapes / 84</b>
3.2.1. Classical versus Electromagnetic Concepts / 63	3.6.1. General / 84
3.2.2. B-H Relations: The Hysteresis Loop / 64	3.6.2. The Isolated Pole (Monopole) / 85
3.2.3. Magnetostatic Potential for a Dipole Field / 65	3.6.3. The Dipole / 87
3.2.4. The General Magnetic Anomaly / 66	3.6.4. Two-Dimensional Features / 88
3.2.5. Poisson's Relation / 67	3.6.5. Dipping Dike (Prism) / 92
<b>3.3. Magnetism of the Earth / 67</b>	3.6.6. Dipping Sheet / 97
3.3.1. Nature of the Geomagnetic Field / 67	3.6.7. Horizontal Sheet (Plate) / 100
3.3.2. The Main Field / 68	3.6.8. Semiinfinite Horizontal Sheet: Fault Approximation / 100
3.3.3. The External Magnetic Field / 72	3.6.9. Contact between Beds of Different Susceptibilities / 103
3.3.4. Local Magnetic Anomalies / 72	3.6.10. Demagnetization / 104
3.3.5. Magnetism of Rocks and Minerals / 72	
3.3.6. Remanent Magnetism / 73	<b>3.7. Processing and Interpretation / 106</b>
3.3.7. Magnetic Susceptibilities of Rocks and Minerals / 73	3.7.1. General / 106
3.3.8. Magnetic Susceptibility Measurements / 73	3.7.2. Crude Interpretation and Structural Aspects / 106
<b>3.4. Field Instruments for Magnetic Measurements / 75</b>	3.7.3. Data Processing Operations: The Fourier Transform / 107
3.4.1. General / 75	3.7.4. Derivatives / 107
3.4.2. Flux-gate Magnetometer / 75	3.7.5. Continuation / 107
3.4.3. Proton-Precession Magnetometer / 77	3.7.6. Spectral Analysis / 108
3.4.4. Optically Pumped Magnetometer / 78	3.7.7. Reduction to the Pole / 109
	3.7.8. Use of Master Curves for Dikes of Great Depth Extent / 109
	3.7.9. Matched Filtering / 112
	3.7.10. Werner Deconvolution / 112
	3.7.11. Depth Estimates / 113
	<b>3.8. Field Examples / 114</b>
	3.8.1. Ground Surveys / 114
	3.8.2. Airborne Surveys / 117
	<b>3.9. Problems / 124</b>
	<b>References / 134</b>

<b>4. Seismic Methods / 136</b>	
<b>4.1. Introduction / 136</b>	
<b>4.1.1. Importance of Seismic Work / 136</b>	
<b>4.1.2. History of Seismic Exploration / 137</b>	
<b>4.1.3. Outline of the Seismic Reflection Method / 139</b>	
<b>4.2. Seismic Theory / 140</b>	
<b>4.2.1. Theory of Elasticity / 140</b>	
<b>4.2.2. Wave Equation and Its Solutions / 143</b>	
<b>4.2.3. Body Waves: <math>P</math> and <math>S</math> Waves / 147</b>	
<b>4.2.4. Surface Waves / 149</b>	
<b>4.2.5. Energy of Waves / 149</b>	
<b>4.2.6. Wave Motion / 151</b>	
<b>4.2.7. Partitioning of Energy at an Interface / 155</b>	
<b>4.2.8. Seismic Velocity / 158</b>	
<b>4.3. Geometry of Seismic Wavepaths / 162</b>	
<b>4.3.1. Reflection Paths in a Constant Velocity Layer / 162</b>	
<b>4.3.2. Velocity Gradient and Raypath Curvature / 167</b>	
<b>4.3.3. Geometry of Refraction Paths / 169</b>	
<b>4.4. Characteristics of Seismic Events / 175</b>	
<b>4.4.1. Distinguishing Features of Events / 175</b>	
<b>4.4.2. Reflections and Refractions / 175</b>	
<b>4.4.3. Diffractions / 176</b>	
<b>4.4.4. Multiples / 178</b>	
<b>4.4.5. Surface Waves / 182</b>	
<b>4.4.6. Effects of Reflector Curvature / 182</b>	
<b>4.4.7. Types of Seismic Noise / 184</b>	
<b>4.4.8. Attenuation of Noise / 185</b>	
<b>4.5. Reflection Field Methods and Equipment / 186</b>	
<b>4.5.1. Field Methods for Land Surveys / 186</b>	
<b>4.5.2. Field Layouts / 187</b>	
<b>4.5.3. Field Equipment for Land Surveys / 192</b>	
<b>4.5.4. Marine Equipment and Methods / 202</b>	
<b>4.5.5. Measurement of Velocity / 207</b>	
<b>4.6. Refraction Field Methods and Equipment / 209</b>	
<b>4.6.1. Comparison of Refraction and Reflection Methods / 209</b>	
<b>4.6.2. In-Line Refraction / 209</b>	
<b>4.6.3. Broadside Refraction and Fan Shooting / 210</b>	
<b>4.6.4. Engineering Surveys on Land / 211</b>	
<b>4.6.5. Marine Refraction Work / 212</b>	
<b>4.6.6. Refraction Data Reduction / 212</b>	
<b>4.7. Data Processing / 214</b>	
<b>4.7.1. Data Reduction / 214</b>	
<b>4.7.2. Introduction to Digital Processing: Fourier Transforms / 216</b>	
<b>4.7.3. Convolution / 217</b>	
<b>4.7.4. Correlation / 222</b>	
<b>4.7.5. Phase Considerations / 226</b>	
<b>4.7.6. Frequency Filtering / 226</b>	
<b>4.7.7. Velocity Analysis / 229</b>	
<b>4.7.8. Common-Midpoint Stacking / 229</b>	
<b>4.7.9. Apparent-Velocity (Apparent-Dip) Filtering / 229</b>	
<b>4.7.10. The <math>p</math>-<math>\tau</math> Transform / 230</b>	
<b>4.7.11. Relative-Amplitude Processing / 230</b>	
<b>4.7.12. Migration or Imaging / 230</b>	
<b>4.7.13. Measures of Coherence / 232</b>	
<b>4.7.14. Other Types of Processing / 233</b>	
<b>4.8. Basic Geological Concepts in Petroleum Exploration / 233</b>	
<b>4.8.1. Basic Concepts / 233</b>	
<b>4.8.2. Objectives of Interpretation / 235</b>	
<b>4.9. Refraction Interpretation / 235</b>	
<b>4.9.1. Interpretation of Refraction Records / 235</b>	
<b>4.9.2. Refraction Interpretation Methods / 237</b>	
<b>4.9.3. Delay-Time Methods / 237</b>	
<b>4.9.4. Wavefront Methods / 240</b>	
<b>4.9.5. Engineering Applications / 242</b>	

<b>4.10. Reflection Interpretation / 243</b>	<b>5.4. Typical Values of Electrical Constants of Rocks and Minerals / 289</b>
4.10.1. Interpretation Techniques / 243	5.4.1. Resistivities of Rocks and Minerals / 289
4.10.2. Modeling: Synthetic Seismograms / 245	5.4.2. Dielectric Constants of Rocks and Minerals / 291
4.10.3. Evidences of Faulting / 248	5.4.3. Magnetic Permeability of Minerals / 292
4.10.4. Fold and Flow Structures / 250	
4.10.5. Reefs / 257	
4.10.6. Unconformities and Seismic Facies Patterns / 262	
4.10.7. Use of Velocity Information / 262	
4.10.8. Hydrocarbon Indicators / 262	
<b>4.11. Specialized Methods / 264</b>	<b>References / 292</b>
4.11.1. Profiling / 264	
4.11.2. Three-Dimensional Methods / 267	
4.11.3. Use of Channel Waves / 270	
4.11.4. Vertical Seismic Profiling / 270	
4.11.5. Shear Waves in Exploration / 271	
4.11.6. Variation of Amplitude with Offset / 271	
4.11.7. Cross-Hole Methods / 271	
<b>4.12. Problems / 273</b>	
<b>References / 280</b>	
<b>5. Electrical Properties of Rocks and Minerals / 283</b>	<b>6. Methods Employing Natural Electrical Sources / 293</b>
<b>5.1. Classification of Electrical Methods / 283</b>	<b>6.1. Self-Potential Method / 293</b>
<b>5.2. Electrical Properties of Rocks and Minerals / 283</b>	6.1.1. Origin of Potentials / 293
5.2.1. Electrical Potentials / 283	6.1.2. Self-Potential Field Equipment / 296
5.2.2. Electrical Conductivities / 284	6.1.3. Field Procedure / 296
5.2.3. Magnetic Permeability / 287	6.1.4. Interpretation of Self-Potential Data / 297
5.2.4. Polarization Potentials / 287	
<b>5.3. Measurement of Electrical Properties of Rocks and Minerals / 288</b>	<b>6.2. Telluric and Magnetotelluric Methods / 302</b>
5.3.1. Laboratory Measurement of Resistivity / 288	6.2.1. Origin and Characteristics of Magnetotelluric Fields and Telluric Currents / 302
5.3.2. Measurement of Dielectric Constant / 288	6.2.2. Elementary Electromagnetic Theory / 306
	6.2.3. Attenuation of EM Fields / 307
	6.2.4. Boundary Conditions / 309
	6.2.5. Magnetotelluric Fields / 309
	6.2.6. Field Equipment and Operations / 311
	6.2.7. Interpretation of Telluric Data / 314
	6.2.8. Interpretation of Magnetotelluric Data / 317
	<b>6.3. Field Examples / 327</b>
	6.3.1. Self-Potential / 327
	6.3.2. Tellurics and Magnetotellurics / 327
	<b>6.4. Problems / 335</b>
	<b>References / 342</b>

<b>7. Electromagnetic Methods / 343</b>	<b>7.6. EM Field Procedures / 383</b>
7.1. <i>Introduction and Historical Background / 343</i>	7.7. <i>Interpretation / 383</i>
7.2. <i>Electromagnetic Theory / 343</i>	7.7.1. <i>Introduction / 383</i>
7.2.1. <i>Vector and Scalar Potentials / 343</i>	7.7.2. <i>General Interpretation Procedure / 385</i>
7.2.2. <i>Description of EM Fields; Biot-Savart Law / 344</i>	7.7.3. <i>Ground Systems; FDEM over Dipping Sheet / 385</i>
7.2.3. <i>Field in the Frequency Domain / 345</i>	7.7.4. <i>Ground Systems; TDEM over Dipping Sheet / 409</i>
7.2.4. <i>Combination of FD Fields / 350</i>	7.7.5. <i>The Sphere Model in FD and TD Ground Systems / 436</i>
7.2.5. <i>Mutual Inductance / 353</i>	7.7.6. <i>Layered Structure: EM Depth Sounding / 441</i>
7.2.6. <i>Fields in the Time Domain / 355</i>	7.7.7. <i>Interpretation of Airborne EM Data / 450</i>
7.3. <i>EM Equipment / 361</i>	7.7.8. <i>Turair / 454</i>
7.3.1. <i>General / 361</i>	7.7.9. <i>Airborne VLF / 454</i>
7.3.2. <i>Power Sources / 361</i>	7.7.10. <i>Phase-Component AEM / 456</i>
7.3.3. <i>Transmitter Loops / 362</i>	7.7.11. <i>Resistivity Mapping / 460</i>
7.3.4. <i>Receiver Coils / 362</i>	7.7.12. <i>Input AEM / 464</i>
7.3.5. <i>Receiver Amplifiers / 362</i>	
7.3.6. <i>Indicators / 363</i>	<b>7.8. Field Examples / 477</b>
7.3.7. <i>Compensating Networks / 363</i>	<b>7.9. Problems / 504</b>
<b>7.4. EM Field Systems for Ground Surveys / 364</b>	<b>References / 519</b>
7.4.1. <i>General / 364</i>	<b>8. Resistivity Methods / 522</b>
7.4.2. <i>Frequency-Domain Systems; Dip-Angle Measurements / 364</i>	8.1. <i>Introduction / 522</i>
7.4.3. <i>FD Systems for Phase-Component Measurements / 370</i>	8.2. <i>Elementary Theory / 522</i>
7.4.4. <i>Time-Domain EM Ground Systems / 372</i>	8.2.1. <i>Potentials in Homogeneous Media / 522</i>
7.4.5. <i>Measurement of <math>H</math> / 376</i>	8.2.2. <i>Single Current Electrode at Depth / 523</i>
7.4.6. <i>Assessment of EM Ground Methods / 377</i>	8.2.3. <i>Single Current Electrode at Surface / 523</i>
<b>7.5. Airborne EM Systems / 377</b>	8.2.4. <i>Two Current Electrodes at Surface / 524</i>
7.5.1. <i>General / 377</i>	8.2.5. <i>Current Distribution / 525</i>
7.5.2. <i>Quadrature Method / 377</i>	8.3. <i>Effect of Inhomogeneous Ground / 527</i>
7.5.3. <i>Turair System / 377</i>	8.3.1. <i>Introduction / 527</i>
7.5.4. <i>Airborne VLF / 378</i>	8.3.2. <i>Distortion of Current Flow at a Plane Interface / 527</i>
7.5.5. <i>Phase-Component Measurements / 378</i>	8.3.3. <i>Distortion of Potential at a Plane Interface / 527</i>
7.5.6. <i>Transient (Input) Method / 379</i>	8.3.4. <i>Surface Potential due to Horizontal Beds / 529</i>
7.5.7. <i>Cryogenic EM System / 383</i>	
7.5.8. <i>Assessment of Airborne EM / 383</i>	

8.3.5.	Potential Due to Buried Sphere / 530	9.3.	<i>Induced Polarization Measurements / 581</i>
8.3.6.	Effect of Anisotropic Ground / 531	9.3.1.	General / 581
8.3.7.	Effect of Topography / 532	9.3.2.	Time-Domain Measurements / 581
8.4.	<i>Equipment for Resistivity Field Work / 532</i>	9.3.3.	Frequency-Domain Measurements / 582
8.4.1.	Power Sources / 532	9.3.4.	Relative Phase Shift and Phase Components / 582
8.4.2.	Meters / 534	9.3.5.	Magnetic Induced Polarization (MIP) Measurements / 583
8.4.3.	Electrodes and Wire / 535	9.3.6.	Relation between Time- and Frequency-Domain IP Measurements / 583
8.5.	<i>Electrode Layouts and Field Procedure / 535</i>	9.3.7.	IP Response Examples / 583
8.5.1.	General / 535	9.4.	<i>IP Field Operations / 584</i>
8.5.2.	Apparent Resistivity / 535	9.4.1.	General / 584
8.5.3.	Electrode Arrays (Spreads) / 535	9.4.2.	Field Equipment / 584
8.5.4.	Resistivity Field Procedures / 538	9.4.3.	Field Procedures / 588
8.6.	<i>Interpretation / 539</i>	9.4.4.	Noise Sources / 589
8.6.1.	Introduction / 539	9.5.	<i>Interpretation / 591</i>
8.6.2.	Resistivity Modeling / 539	9.5.1.	Plotting Methods / 591
8.6.3.	Vertical Sounding; Two Horizontal Beds / 539	9.5.2.	General Interpretation / 595
8.6.4.	Vertical Sounding; Multiple Horizontal Beds / 544	9.5.3.	Theoretical and Model Work / 596
8.6.5.	Lateral Mapping; Vertical Contact / 554	9.6.	<i>Field Examples / 602</i>
8.6.6.	The Vertical Dike / 559	9.7.	<i>Problems / 604</i>
8.6.7.	Mapping Three-Dimensional Anomalies / 561	References / 609	
8.6.8.	Measuring Overburden Depth and Resistivity / 562	10.	<b>Radioactivity Method / 611</b>
8.7.	<i>Field Examples / 565</i>	10.1.	<i>Introduction / 611</i>
8.8.	<i>Problems / 570</i>	10.2.	<i>Principles of Radioactivity / 611</i>
	<i>References / 577</i>	10.2.1.	Constituents of the Nucleus / 611
9.	<b>Induced Polarization / 578</b>	10.2.2.	Nuclear Disintegrations / 612
9.1.	<i>Introduction / 578</i>	10.2.3.	Radioactive Decay Processes / 614
9.2.	<i>Sources of the Induced Polarization Effects / 578</i>	10.2.4.	Radioactive Equilibrium / 617
9.2.1.	General / 578	10.2.5.	Units / 618
9.2.2.	Membrane Polarization / 579	10.2.6.	Radioactivity of Rocks and Minerals / 619
9.2.3.	Electrode Polarization / 579	10.2.7.	Age Determination Using Radioisotopes / 619
9.2.4.	Equivalent Electrical Circuits / 581	10.3.	<i>Instruments / 620</i>
		10.3.1.	Introduction / 620
		10.3.2.	Geiger-Müller Counter / 620

10.3.3. Scintillation Meter / 621	11.7. Elastic-Wave (Acoustic) Methods / 665
10.3.4. Gamma-Ray Spectrometer / 622	11.7.1. Elastic Waves in Boreholes / 665
10.3.5. Miscellaneous Instruments / 627	11.7.2. Sonic Log / 667
10.3.6. Calibration of Instruments / 628	11.7.3. Amplitude and Full-Waveform Logs / 670
10.4. Field Operations / 628	11.7.4. Borehole Televiewer / 672
10.5. Interpretation / 629	11.8. Nuclear Methods / 673
10.6. Field Examples / 634	11.8.1. Nuclear Processes / 673
10.7. Problems / 637	11.8.2. Gamma-Ray Logging / 675
References / 644	11.8.3. Density Log / 676
11. Geophysical Well Logging / 645	11.8.4. Neutron Logging / 677
11.1. Introduction / 645	11.9. Gravity, Magnetic, and Thermal Methods / 681
11.1.1. Uses of Well Logging / 645	11.9.1. Gravity and Magnetic Field Logging / 681
11.1.2. History of Well Logging / 645	11.9.2. Susceptibility Log / 681
11.1.3. General Aspects of Well Logging / 646	11.9.3. Nuclear Magnetic-Resonance Log / 682
11.1.4. Rock Property Measurements / 647	11.9.4. Thermal Logging / 683
11.2. Resistivity Methods / 648	11.10. Well-Log Interpretation / 683
11.2.1. Introduction to Resistivity Logging / 648	11.10.1. General / 683
11.2.2. Normal Resistivity Logging / 649	11.10.2. Combining Measurements from Several Logs / 683
11.2.3. Lateral Arrangement / 650	11.11. Field Examples / 684
11.2.4. Microlog / 650	11.11.1. Analysis of an Oil Sand / 684
11.2.5. Focused-Current Logs / 651	11.11.2. Analysis of Carbonate Section / 684
11.2.6. Induction Log / 652	11.11.3. Coal Identification / 684
11.2.7. Resistivity Logging in Mineral Search / 654	11.11.4. Evaporites / 685
11.3. Self-Potential (SP) Logging / 654	11.11.5. Sulfur / 687
11.3.1. Sources of SP / 654	11.11.6. Slate and Chert / 687
11.3.2. Instrumentation / 655	11.11.7. Mineral Exploration / 687
11.3.3. Uses of SP Curves in Oil-Well Logging / 656	11.11.8. Borehole Methods in the USSR / 689
11.3.4. Uses of SP Curves in Mineral Logging / 658	11.12. Problems / 690
11.3.5. Geological Interpretation of SP / 658	References / 698
11.4. The Dipmeter / 659	12. Integrated Geophysical Problems / 700
11.5. Electromagnetic Wave Propagation Method / 663	12.1. Introduction / 700
11.6. Induced Polarization Logging / 665	12.2. Examples and Problems / 701

**Appendix A. Mathematical Background / 727****A.1. Determinants / 727****A.2. Matrices / 728****A.3. Vector Analysis / 729****A.3.1. Basic Theory / 729****A.3.2. Vector Products / 730****A.3.3. The Vector Operator  $\nabla$  / 731****A.3.4. Vector Theorems / 731****A.4. Curvilinear Coordinates / 733****A.5. Taylor's Series; Maclaurin's Series / 735****A.6. Binomial Expansion / 736****A.7. Complex Numbers / 736****A.8. Method of Least Squares / 737****A.9. Fourier Series and Transforms / 738****A.9.1. Fourier Series / 738****A.9.2. Fourier Integral; Fourier Transforms / 738****A.9.3. Digital Functions; z Transforms / 740****A.10. Convolution / 740****A.11. Correlation / 741****A.11.1. Cross-Correlation / 741****A.11.2. Autocorrelation / 741****A.12. Laplace Transforms / 741****A.12.1. Basic Theory / 741****A.12.2. Calculation of Laplace Transforms / 742****A.12.3. Transforms of the Error Function and its Derivatives / 742****A.13. Linear Systems / 743****References / 744****Appendix B. Location Determination / 745****B.1. Direction Determination / 745****B.2. Distance Measurement / 745****B.3. Elevation Measurement / 745****B.4. Angle Measurement / 746****B.5. Doppler Measurement of Velocity / 746****B.6. Radionavigation / 746****B.7. Acoustic and Inertial Positioning / 748****B.8. Satellite Positioning / 749****Reference / 750****Index / 751**

Dr. David A. Keys, the fourth author of the first edition, died in 1978. He was one of the authors of *Applied Geophysics in the Search for Minerals* by Eve and Keys, first published in 1929, which made it one of the earliest texts in applied geophysics. It served several generations of geophysicists in the course of four editions. In the mid-1960s, Dr. Keys suggested to the senior author that they collaborate in preparing a fifth edition; this was the starting point for what turned out to be an entirely new book with the shorter title *Applied Geophysics*.

Dr. Keys is remembered with great affection and esteem by his coauthors, two of whom (WMT, LPG) knew him well at McGill University and later as Vice-President (Scientific), National Research Council of Canada, Chalk River.

We express our gratitude to the companies, individuals, and other publishers who contributed information and illustrations. In particular, we wish to extend our sincere thanks to Alex Becker, Jerry Roth, and Bill Gore for their invaluable help in the preparation of Chapters, 5 to 10, 3, and 11, respectively. We owe special gratitude to John E. Riddell who provided many examples of mineral exploration drawn from his 35 years of experience in this area.

**June 1990**

**W. M. Telford**

**L. P. Geldart**

**R. E. Sheriff**

# Chapter

## 1

### *Introduction*

Geophysics, as its name indicates, has to do with the physics of the earth and its surrounding atmosphere. Gilbert's discovery that the earth behaves as a great and rather irregular magnet and Newton's theory of gravitation may be said to constitute the beginning of geophysics. Mining and the search for metals date from the earliest times, but the scientific record began with the publication in 1556 of the famous treatise *De re metallica* by Georgius Agricola, which for many years was the authoritative work on mining. The initial step in applying geophysics to the search for minerals probably was taken in 1843, when Von Wrede pointed out that the magnetic theodolite, used by Lamont to measure variations in the earth's magnetic field, might also be employed to discover bodies of magnetic ore. However, this idea was not acted on until the publication in 1879 of Professor Robert Thalén's book *On the Examination of Iron Ore Deposits by Magnetic Methods*. The Thalén-Tiberg magnetometer manufacture in Sweden, and later the Thomson-Thalén instrument, furnished the means of locating the strike, dip, and depth below surface of magnetic dikes.

The continued expansion in the demand for metals of all kinds and the enormous increase in the use of petroleum products since the turn of the century have led to the development of many geophysical techniques of ever-increasing sensitivity for the detection and mapping of unseen deposits and structures. Advances have been especially rapid since World War II because of major improvements in instrumentation and the widespread application of the digital computer in the processing and interpretation of geophysical data.

Because the great majority of mineral deposits are beneath the surface, their detection depends on those characteristics that differentiate them from the surrounding media. Methods based on variations in the elastic properties of rocks have been developed for determining structures associated with oil and gas, such as faults, anticlines, and synclines several kilometers below the surface. The variation in electrical

conductivity and natural currents in the earth, rates of decay of artificial potential differences introduced into the ground, local changes in gravity, magnetism, and radioactivity – all these provide information about the nature of the structures below the surface, thus permitting geophysicists to determine the most favorable places to search for the mineral deposits they seek.

Several of the devices used by geophysicists were derived from methods used for locating gun emplacements, submarines, and aircraft during the two world wars. Attempts were made to locate artillery batteries during World War I by measuring the arrival times of the elastic waves generated in the earth by their recoil; this led directly to the refraction method of seismic prospecting. Submarines were located by transmitting sonar pulses underwater and measuring the interval between the emission and the return of reflected pulses; knowing the velocity of sound in seawater, one can calculate the distance to the reflecting object. Sonar is now used widely for navigation in marine geophysical surveys. Radar, developed during World War II, utilized radio pulses in a similar manner to track aircraft and ships. Ships, submarines, and mines were also detected in both wars by their magnetic properties.

It should be pointed out that geophysics techniques can detect only a discontinuity, that is, where one region differs sufficiently from another in some property. This, however, is a universal limitation, for we cannot perceive that which is homogeneous in nature; we can discern only that which has some variation in time and/or space.

Geophysics deals with all aspects of the physics of the earth, its atmosphere, and space. Geophysical measurements were made by the men who landed on the moon, and the atmospheres, magnetic fields, and other properties of planets are studied using geophysical data obtained by unmanned spacecraft.

The principal subdivisions of geophysics are as follows; some of these have been investigated for many years simply because of their scientific

Table 1.1. Total 1987 worldwide expenditures by survey type and objective (in thousands of U.S. dollars).

Type	Land	Transition zone	Marine	Airborne	Drill hole	Total
Petroleum						
Exploration	809,394	10,091	541,053	13,405	1,504	1,375,447
Development	20,161	25	9,657	32	294	30,169
Minerals	13,076		62	13,705	58	26,901
Environmental	443			92	91	626
Engineering	2,100		8,580		235	10,914
Geothermal	1,095				30	1,125
Groundwater	1,505				283	1,788
Oceanography			1,458	300		1,758
Research	3,217		6,190	802	184	10,393
Total	850,990	10,116	556,999	28,336	2,679	1,459,120

interest:

Seismology

Thermal properties of the earth

Terrestrial magnetism

Telluric currents

Geodesy and gravitation

Radioactivity of the earth, sea, and atmosphere; cosmic rays

Atmospheric electricity

Meteorology

Radioactivity

Well logging

Miscellaneous chemical, thermal, and other methods

Our knowledge of the Earth has been developed by combining information from all these fields. This holds also for investigations in applied geophysics as well; combining several different approaches may help us to determine more accurately the location of a structure or deposit. Purely scientific investigation of such subjects as the rate of evaporation of water from lakes, the chemical compositions of different rocks and waters from streams and ponds, the measurement of natural earth currents, potential variations, and impurities in the atmosphere - all these influence methods of locating deposits that the applied geophysicist seeks. For example, the concentrations of radon in the air or streams may give indications of deposits of uranium. Electromagnetic waves caused by distant thunderstorms are used to locate conducting ores at great depths below the surface.

Applied geophysics in the search for minerals, oil, and gas may be divided into the following methods of exploration:

Gravitational

Magnetic

Seismic

Electrical

Electromagnetic

Certain geological conditions generally are associated with metallic ores, others with gas and oil. Ore deposits usually are found in areas where extensive igneous activity occurred, after which the rocks may or may not have been metamorphosed. Ultimately the area was eroded sufficiently to bring the deposits close enough to the surface to be discovered and exploited. Coal is the result of the rapid burial of vegetation that existed near a sea or large lake, and gas and oil usually are due to the deposition and subsequent burial of marine organisms. The search for metallic ores generally is concentrated in areas of known igneous and metamorphic rocks, such as the Rocky Mountains, the Andes, the Alps, and the Urals. However, important exceptions occur because (1) minerals can be transported away from the place of original formation, perhaps by mechanical transport, as in the case of alluvial gold, perhaps in solution, and (2) some minerals such as salt and gypsum are deposited originally from aqueous solution and hence occur in sedimentary areas. The search for coal, oil, and gas is confined to sedimentary basins, except for rare instances in which oil or gas has migrated into fractured igneous or metamorphic rocks.

The choice of techniques to locate a certain mineral depends on the nature of the mineral and of the surrounding rocks. Sometimes a method may give a direct indication of the presence of the mineral being sought, for example, the magnetic method when used to find magnetic ores of iron or nickel; at other times the method may indicate only whether or not conditions are favorable to the occurrence of the mineral

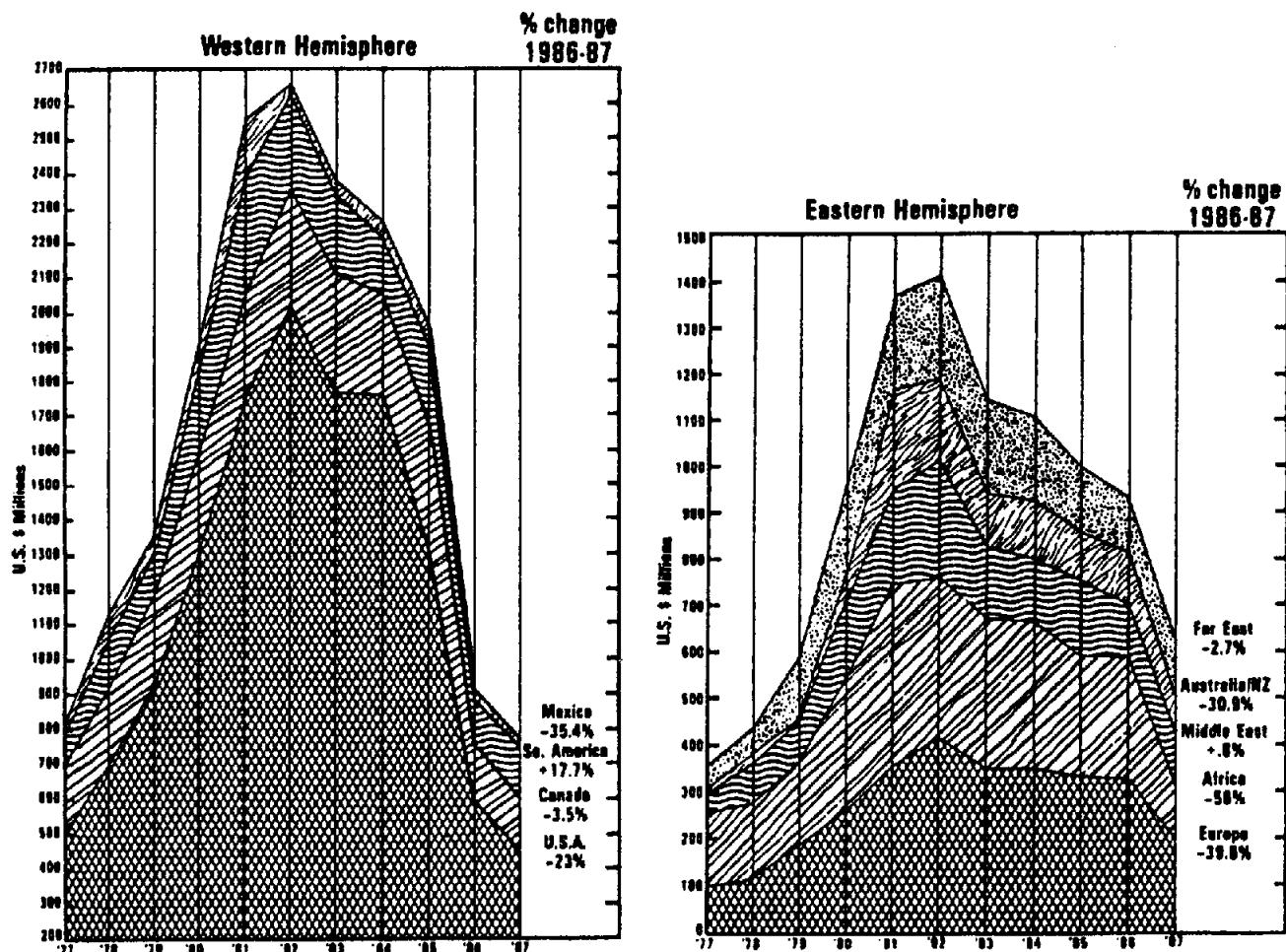


Figure 1.1. Total expenditures on petroleum exploration and development, 1977-87  
(From Senti, 1988.)

sought. For example, the magnetic method is used in petroleum exploration as a reconnaissance tool to determine the depth to the basement rocks and thus determine where the sediments are thick enough to warrant exploration.

Surveys using aircraft carrying magnetic, electromagnetic, and other devices are the most rapid methods of finding geophysical anomalies. Such areal surveys are also the most inexpensive for covering large areas and hence are frequently used for reconnaissance; anomalies of interest are later investigated using more detailed ground techniques. Seismic exploration is another method that has been used to explore large areas, both on land and offshore, though at considerably greater cost, in both time and money.

Table 1.1 shows world expenditures for acquisition of geophysical data during the year 1987. The total expenditure of about \$1.5 billion (U.S.)<sup>1</sup> does not include work in the Soviet Union, Eastern Europe, or China. This figure is only 30% of the 1982 figure and is below those of all the years since 1977 (Fig. 1.1), reflecting the low prices for petroleum and minerals. There seems to be a rather widespread

feeling that the sharp decline seen in Figure 1.1 has leveled out, although statistical data are not yet available to support this. Many (including the authors) expect a gradual increase in activity over the next several years.

Figure 1.1 also shows major shifts in the locales of geophysical work. The proportions of the different geophysical methods and unit costs are shown in Table 1.2. Cost figures are sensitive to many factors such as the supply and demand of particular commodities, economic conditions, governmental regulations, technological advances, and exploration philosophy, as well as operational environment, length and nature of surveys, and other factors.

Tables 1.1 and 1.2 are based on the latest annual survey carried out by the Society of Exploration Geophysicists (Senti, 1988); this survey depends on voluntary reporting by a multitude of organizations, who do not necessarily report on the same bases nor in the same units. Nevertheless, the perturbations

1 All figures in this book are U.S. dollars.

Table 1.2. Geophysical expenditures and unit costs, 1987.

	Cost basis	Unit costs	
<b>Petroleum exploration</b>			
Land seismic (2-D, P wave)	72.1%	\$207 × 10 <sup>3</sup> /mo	\$2,206/km <sup>2</sup>
Transition zone seismic	0.4	198	1930*
Marine seismic	20.5	479	283*
Seismic processing			280
Seismic refraction	0.6	91	51
Land S wave	0.3	170	
Land 3-D	2.8		\$7,589/km <sup>3</sup>
Marine 3-D	2.3	380	
VSP	0.2		
Land gravity	0.2	12	61/stn
Marine gravity	<0.1	20	46/km
Magnetotellurics	<0.1	30	1,548/stn
Airborne magnetics	1.0		11/km
Other airborne	0.1		
Other	0.1		
<b>Seismic sources</b>			
Land	Dynamite	41.6% (line-kilometers)	
	Air gun	1.4	
	Weight drop	1.5	
	Vibroseis	50.4	
	S wave	0.3	
Marine	Air gun	96.9%	
	Sparker	0.1	
	Expenditures	Unit costs	
<b>Airborne work</b>			
Gravity	\$283 × 10 <sup>3</sup>	\$48/km	
Magnetics	16,575	9	
Mag. + Time-domain EM	1,660	24	
Frequency-domain EM	5,759	45	
VLF EM	1,608	20	
Radiometric	991	19	
<b>Land mining</b>			
Seismic reflection	\$3,875	\$1,606/km	
Seismic refraction	77	2,810	
Gravity	1,298	\$24/stn	
Magnetics	1,070	1	149
Resistivity	267	10	132
SP	401		310
Time-domain EM	417		1,169
Frequency-domain EM	250		136
VLF EM	71		165
Mag. + time-domain EM	133		362
Mag. + frequency-domain EM	801		197
Mag. + VLF EM	224		351
Time-domain IP	1,645		564
Frequency-domain IP	197		862
Complex resistivity IP	25		
Magnetotelluric natural field	7		51
Magnetotellurics controlled source	353		120
Gamma ray	6		30
Drill hole	58		
<b>Gravity-magnetic surveys by objective</b>			
Petroleum		61.9%	
Mineral exploration		24.6	
Environmental		0.4	
Engineering		0.9	
Geothermal		0.4	
Groundwater		0.6	
Oceanographic		1.1	
Research		9.9	

\*Excluding processing.

because the data are not homogeneous are probably small.

Comparing 1987 data with that for previous years shows an important change in seismic petroleum work: a shift from exploration, the finding of hydrocarbons, to reservoir studies, detailing oil/gas finds with the objectives of exploiting the finds more economically and increasing the oil/gas recoverable from the finds.

Applied geophysics is a relatively new science and the design of instruments, field techniques, and interpretation of the data are undergoing rapid develop-

ment. The following chapters will provide the reader with a survey of the different methods currently employed to acquire and interpret geophysical data as an aid in the exploration for minerals and petroleum and in the planning of large construction projects.

## REFERENCE

- Senti, R. J. 1988. Geophysical activity in 1987. *Geophysics, The Leading Edge of Exploration* 7, No. 8, 33-56.

# Chapter

## 2

# *Gravity Methods*

### 2.1. INTRODUCTION

#### 2.1.1. General

Gravity prospecting involves measurements of variations in the gravitational field of the earth. One hopes to locate local masses of greater or lesser density than the surrounding formations and learn something about them from the irregularities in the earth's field. It is not possible, however, to determine a unique source for an observed anomaly. Observations normally are made at the earth's surface, but underground surveys also are carried out occasionally.

Gravity prospecting is used as a reconnaissance tool in oil exploration; although expensive, it is still considerably cheaper than seismic prospecting. Gravity data are also used to provide constraints in seismic interpretation. In mineral exploration, gravity prospecting usually has been employed as a secondary method, although it is used for detailed follow-up of magnetic and electromagnetic anomalies during integrated base-metal surveys. Gravity surveys are sometimes used in engineering (Arzi, 1975) and archaeological studies.

Like magnetics, radioactivity, and some electrical techniques, gravity is a natural-source method. Local variations in the densities of rocks near the surface cause minute changes in the gravity field. Gravity and magnetics techniques often are grouped together as the *potential methods*, but there are basic differences between them. Gravity is an inherent property of mass, whereas the magnetic state of matter depends on other factors, such as the inducing fields and/or the orientations of magnetic domains. Density variations are relatively small, and the gravity effects of local masses are very small compared with the effect of the background field of the Earth as a whole (often of the order of 1 part in  $10^6$  to  $10^7$ ), whereas magnetic anomalies often are large relative to the main field. The time variation of the magnetic field is complex, whereas the gravity field is constant (ignoring "earth tides"). Corrections to gravity read-

ings are more complicated and more important than in magnetic or other geophysical methods. Gravity field operations are more expensive than magnetic operations, and field work is slower and requires more highly skilled personnel.

#### 2.1.2. History of Gravity Exploration

Galileo Galilei, in about 1589, so legend tells us, dropped light and heavy weights from the Leaning Tower of Pisa in an attempt to determine how weight affects the speed at which a given object falls. Johann Kepler worked out the laws of planetary motion, and this enabled Sir Isaac Newton to discover the universal law of gravitation (*Mathematical Principles of Natural Philosophy*, 1685-87).

The expeditions of the French Academy of Sciences to Lapland and Peru (Ecuador) in 1735-45 gave Pierre Bouguer the opportunity to establish many of the basic gravitational relationships, including variations of gravity with elevation and latitude, the horizontal attraction due to mountains, and the density of the Earth.

Captain Henry Kater, in 1817, introduced the compound pendulum, with interchangeable centers of oscillation and suspension, which became the major tool for gravity investigation for over a century. Because the variations in gravitational attraction are so small, Baron Roland von Eötvös set out to measure derivatives rather than total magnitudes. He completed his first torsion balance (a modification of the Coulomb balance) in 1890 and made the first gravity survey on the ice of Lake Balaton in 1901. F. A. Vening Meinesz, in 1923, measured gravity with pendulums on board a Dutch submarine and demonstrated gravity variations over various areas of the oceans, especially the large gravity effects near the Indonesian trench.

In December 1922, a torsion-balance survey of the Spindletop oil field initiated geophysical exploration for oil. In late 1924, a test well on the Nash salt dome in Brazoria County, Texas, verified the

gravity interpretation, becoming the first geophysical hydrocarbon discovery, although the first producing oil well did not come in until January 1926.

The last half of the 1920s saw extensive gravity surveys with the torsion balance. In 1929 the portable pendulum began to be used, followed in 1932 by the stable gravimeter (and the unstable gravimeter, which was not publicly described until 1937). By 1940, gravimeters had become so stable and convenient that torsion balances and portable pendulums disappeared from use. LaCoste (1934) described the zero-length spring, but the first workable LaCoste gravimeter did not appear until 1939. In subsequent years, gravimeters have been adapted (LaFehr, 1980) to measurements under water, on moving ships and aircraft, and in boreholes.

The major addition to our knowledge of gravity in recent years has come from observations of satellite paths (Kahn, 1983). These have considerably increased our knowledge of the detailed shape of the Earth, but this has not changed gravity exploration significantly.

In the 1940s, graphic and grid methods of isolating anomalies were developed, and the anomalies that result from simple shapes were calculated. The computing power made available by digital computers since the 1960s has considerably increased our interpretation capabilities, the ultimate goal being solution of the *inverse problem* (§2.7.9).

## 2.2. PRINCIPLES OF GRAVITY

### 2.2.1. Newton's Law of Gravitation

The force of gravitation is expressed by *Newton's law*: The force between two particles of masses  $m_1$  and  $m_2$  is directly proportional to the product of the masses and inversely proportional to the square of the distance between the centers of mass:

$$\mathbf{F} = \gamma(m_1 m_2 / r^2) \mathbf{r}_1 \quad (2.1)$$

where  $\mathbf{F}$  is the force on  $m_2$ ,  $\mathbf{r}_1$  is a unit vector directed from  $m_2$  toward  $m_1$ ,  $r$  is the distance between  $m_1$  and  $m_2$ , and  $\gamma$  is the universal gravitational constant. Note that the force  $\mathbf{F}$  is always attractive. In SI units the value of  $\gamma$  is  $6.672 \times 10^{-11}$  N m<sup>2</sup>/kg<sup>2</sup> or in cgs units  $6.672 \times 10^{-8}$  dyne cm<sup>2</sup>/g<sup>2</sup>.

### 2.2.2. Acceleration of Gravity

The acceleration of  $m_2$  due to the presence of  $m_1$  can be found by dividing  $\mathbf{F}$  by  $m_2$  in Equation (2.1), that is,

$$\mathbf{g} = (\gamma m_1 / r^2) \mathbf{r}_1 \quad (2.2a)$$

The acceleration  $\mathbf{g}$  is equal to the gravitational force per unit mass due to  $m_1$ . If  $m_1$  is the mass of the Earth,  $M_e$ ,  $\mathbf{g}$  becomes the *acceleration of gravity* and is given by

$$\mathbf{g} = (\gamma M_e / R_e^2) \mathbf{r}_1 \quad (2.2b)$$

$R_e$  being the radius of the Earth and  $\mathbf{r}_1$  extending downward toward the center of the Earth. (It is customary to use the same symbol  $\mathbf{g}$  whether it is due to the Earth or a mass  $m$ .) The acceleration of gravity was first measured by Galileo in his famous experiment at Pisa. The numerical value of  $\mathbf{g}$  at the Earth's surface is about 980 cm/s<sup>2</sup>. In honor of Galileo, the unit of acceleration of gravity, 1 cm/s<sup>2</sup>, is called the galileo or Gal.

Gravimeters used in field measurements have a sensitivity of about  $10^{-5}$  Gal or 0.01 mGal, although the reading accuracy is generally only 0.03 to 0.06 mGal. As a result, they are capable of distinguishing changes in the value of  $\mathbf{g}$  with a precision of one part in  $10^8$ . Microgravimeters are available with measuring accuracy of about 5  $\mu$ Gal.

### 2.2.3. Gravitational Potential

(a) *Newtonian or three-dimensional potential*. Gravitational fields are conservative; that is, the work done in moving a mass in a gravitational field is independent of the path traversed and depends only on the end points (§A.3.4). If the mass is eventually returned to its original position, the net energy expenditure is zero, regardless of the path followed. Another way of expressing this is to say that the sum of kinetic (motion) energy and potential (position) energy is constant within a closed system.

The gravitational force is a vector whose direction is along the line joining the centers of the two masses. The force giving rise to a conservative field may be derived from a scalar potential function  $U(x, y, z)$ , called the *Newtonian or three-dimensional potential*, by finding the gradient [Eqs. (A.17), (A.30), and (A.31)]:

$$\begin{aligned} \nabla U(x, y, z) &= -\mathbf{F}(x, y, z)/m_2 \\ &= -\mathbf{g}(x, y, z) \end{aligned} \quad (2.3a)$$

In spherical coordinates (Fig. A.4b) this becomes

$$\begin{aligned} \nabla U(r, \theta, \phi) &= -\mathbf{F}(r, \theta, \phi)/m_2 \\ &= -\mathbf{g}(r, \theta, \phi) \end{aligned} \quad (2.3b)$$

Alternatively, we can solve this equation for the

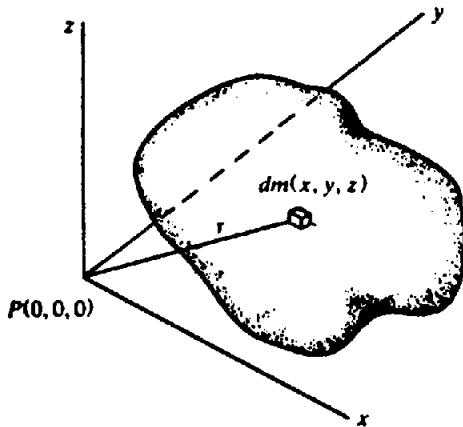


Figure 2.1. Potential of three-dimensional mass.

gravitational potential in the form [Eq. (A.16)]

$$\begin{aligned} U(r, \theta, \phi) &= \int_{\infty}^r (\nabla U) \cdot dr \\ &= - \int_{\infty}^r \mathbf{g} \cdot dr \end{aligned} \quad (2.4)$$

which is a statement of the work done in moving a unit mass from infinity (that is, a very distant point), by any path, to a point distant  $r$  from the point mass producing the gravitational field. Using Equation (2.2a) in scalar form, we get

$$U(r) = -\gamma \int_{\infty}^r m(1/r^2) dr = \gamma m/r \quad (2.5)$$

It is often simpler to solve gravity problems by calculating the scalar potential  $U$  rather than the vector  $\mathbf{g}$  and then to obtain  $\mathbf{g}$  from Equation (2.3).

Considering a three-dimensional mass of arbitrary shape as in Figure 2.1, the potential and acceleration of gravity at a point outside the mass can be found by dividing the mass into small elements and integrating to get the total effect. From Equation (2.5), the potential due to an element of mass  $dm$  at the point  $(x, y, z)$  a distance  $r$  from  $P(0, 0, 0)$  is

$$dU = \gamma dm/r = \gamma \rho dx dy dz / r$$

where  $\rho(x, y, z)$  is the density, and  $r^2 = x^2 + y^2 + z^2$ . Then the potential of the total mass  $m$  is

$$U = \gamma \int_x \int_y \int_z (\rho/r) dx dy dz \quad (2.6a)$$

Because  $\mathbf{g}$  is the acceleration of gravity in the  $z$  direction (positive vertically downward), and assuming  $\rho$  constant,

$$\begin{aligned} g &= -(\partial U / \partial z) \\ &= \gamma \rho \int_x \int_y \int_z (z/r^3) dx dy dz \end{aligned} \quad (2.7a)$$

Sometimes it is more convenient to use cylindrical coordinates (Figure A.4a). Because  $dx dy dz = r_0 dr_0 d\theta dz$  and  $r^2 = r_0^2 + z^2$ ,  $r_0^2 = x^2 + y^2$ , the potential becomes

$$U = \gamma \rho \int_{r_0} \int_{\theta} \int_z (r_0/r) dr_0 d\theta dz \quad (2.6b)$$

and the acceleration in the  $z$  direction is

$$g = \gamma \rho \int_{r_0} \int_{\theta} \int_z (r_0 z/r^3) dr_0 d\theta dz \quad (2.7b)$$

In spherical coordinates,

$$dx dy dz = r^2 \sin \theta dr d\theta d\phi$$

hence,

$$U = \gamma \rho \int_r \int_{\theta} \int_{\phi} r \sin \theta dr d\theta d\phi \quad (2.6c)$$

Taking the  $z$  axis along the polar axis,

$$\begin{aligned} g &= -\partial U / \partial z \\ &= -\gamma \rho \int_r \int_{\theta} \int_{\phi} (z/r) \sin \theta dr d\theta d\phi \\ &= -\gamma \rho \int_r \int_{\theta} \int_{\phi} \sin \theta \cos \theta dr d\theta d\phi \end{aligned} \quad (2.7c)$$

because  $z/r = \cos \theta$ . (The minus sign indicates that  $\mathbf{g}$  is directed toward the mass  $dm$  at the center of the sphere.)

(b) *Logarithmic or two-dimensional potential.* If the mass is very long in the  $y$  direction and has a uniform cross section of arbitrary shape in the  $xz$  plane, the gravity attraction derives from a logarithmic (rather than Newtonian) potential. Then Equation (2.6a) becomes

$$U = \gamma \rho \int_x \int_z dx dz \int_{-\infty}^{\infty} (1/r) dy$$

With some manipulation (see problem 1), the logarithmic potential becomes

$$U = 2\gamma \rho \int_x \int_z \ln(1/r') dx dz \quad (2.8)$$

where  $r'^2 = x^2 + z^2$ . The gravity effect for the two-dimensional body is

$$g = -\partial U / \partial z = 2\gamma \int_x \int_z \rho(z/r'^2) dx dz \quad (2.9)$$

## 2.2.4. Potential-Field Equations

The divergence theorem [Gauss's theorem; Eq. (A.27)] states that the integral of the divergence of a vector field  $\mathbf{g}$  over a region of space  $V$  is equivalent to the integral of the outward normal component of the field  $\mathbf{g}$  over the surface enclosing the region. We have

$$\int_V \nabla \cdot \mathbf{g} dv = \int_S g_n ds \quad (2.10)$$

If there is no attracting matter within the volume, the integrals are zero and  $\nabla \cdot \mathbf{g} = 0$ . But from Equation (2.3a) the gravitational force is the gradient of the scalar potential  $U$ , so that

$$-\nabla \cdot \mathbf{g} = \nabla \cdot \nabla U = \nabla^2 U = 0 \quad (2.11a)$$

that is, the potential in free space satisfies Laplace's equation. In cartesian coordinates, Laplace's equation is

$$\nabla^2 U = \frac{\partial^2 U}{\partial x^2} + \frac{\partial^2 U}{\partial y^2} + \frac{\partial^2 U}{\partial z^2} = 0 \quad (2.11b)$$

[see Eq. (A.37) for Laplace's equation in spherical coordinates]. Also, because  $\mathbf{g} = -\partial U/\partial \mathbf{z}$ , and any derivative of a solution of a differential equation is also a solution, we have

$$\nabla^2 \mathbf{g} = 0 \quad (2.11c)$$

If, on the other hand, there is a particle of mass at the center of a sphere of radius  $r$ , then

$$\begin{aligned} \int_S g_n ds &= -(\gamma m/r^2)(4\pi r^2) \\ &= -4\pi\gamma m \end{aligned} \quad (2.12a)$$

the minus meaning that  $g_n$  is opposite to  $\mathbf{n}$ , the outward-drawn normal. It can be shown (see problem 2) that this result holds regardless of the shape of the surface and the position and size of the mass within the surface. If the surface encloses several masses of total mass  $M$ , we can write

$$\int_V \nabla \cdot \mathbf{g} dv = \int_S g_n ds = -4\pi\gamma M \quad (2.12b)$$

If the volume  $V$  is very small, enclosing only a point, we can remove the integral sign to give

$$\nabla \cdot \mathbf{g} = -4\pi\gamma\rho \quad (2.13a)$$

where  $\rho$  is the density at the point. Then, from

Equation (2.3a),

$$\nabla^2 U = 4\pi\gamma\rho \quad (2.13b)$$

which is *Poisson's equation*.

Equations (2.11a) and (2.13b) state that the gravity potential satisfies Laplace's equation in free space and Poisson's equation in a region containing mass.

These equations imply that various distributions of mass can produce the same potential field over a surface (Skeels, 1947); this is sometimes called the "inherent ambiguity" of gravity interpretation. Sometimes it is convenient to substitute for masses distributed throughout a volume  $V$  a fictitious *surface density* of mass over a surface  $S$  enclosing  $V$  such that the effect outside  $S$  is the same. From Equations (2.12b) and (2.13a) we have

$$\int_V (-4\pi\gamma\rho) dv = \int_S g_n ds \quad (2.14)$$

that is, the component of gravity perpendicular to the surface gives the equivalent surface density. For an equipotential surface, this is merely the total gravitational field.

## 2.2.5. Derivatives of the Potential

Quantities useful in gravity analysis may be obtained by differentiating the potential in various ways. We have already noted in Equation (2.7a) that vertical gravity  $g = -\partial U/\partial z$ . This is the quantity measured by gravimeters.

The first vertical derivative of  $g$  [from Eq. (2.7a)] is

$$\begin{aligned} \partial g / \partial z &= -\partial^2 U / \partial z^2 \\ &= -U_{zz} \\ &= \gamma\rho \int_x \int_y \int_z (1/r^3 - 3z^2/r^5) dx dy dz \end{aligned} \quad (2.15)$$

where subscripts indicate derivatives of  $U$ . Measurements occasionally are made of the vertical gradient (Falkiewicz, 1976; Jordan, 1978; Ager and Lilard, 1982; Butler, 1984).

The second vertical derivative is

$$\begin{aligned} \partial^2 g / \partial z^2 &= -\partial^3 U / \partial z^3 \\ &= -U_{zzz} \\ &= 3\gamma\rho \int_x \int_y \int_z (5z^3/r^7 - 3z/r^5) dx dy dz \end{aligned} \quad (2.16)$$

This derivative frequently is employed in gravity interpretation for isolating anomalies (§2.6.5) and for upward and downward continuation (§2.6.7).

Derivatives tend to magnify near-surface features by increasing the power of the linear dimension in the denominator. That is, because the gravity effect varies inversely as the distance squared, the first and second derivatives vary as the inverse of the third and fourth powers, respectively (for three-dimensional bodies).

By taking the derivatives of  $g$  in Equation (2.7a) along the  $x$  and  $y$  axes, we obtain the components of the *horizontal gradient of gravity*:

$$\begin{aligned} U_{xx} &= -\partial g / \partial x \\ &= 3\gamma\rho \int_x \int_y \int_z (xz/r^5) dx dy dz \quad (2.17) \end{aligned}$$

and similarly for the  $y$  component  $U_{yy}$ . The horizontal gradient can be determined from gravity profiles or map contours as the slope or rate of change of  $g$  with horizontal displacement. The horizontal gradient is useful in defining the edges and depths of bodies (Stanley, 1977).

The *differential curvature* (or *horizontal directive tendency*, HDT) is a measure of the warped or curved shape of the potential surface. From Equation (2.6a),

$$U_{xx} = \gamma\rho \int_x \int_y \int_z (3x^2/r^5 - 1/r^3) dx dy dz \quad (2.18)$$

Other components are  $U_{yy}$  and  $U_{xy}$ . The differential curvature (HDT) is given by

$$\begin{aligned} \text{HDT} &= \left\{ (U_{yy} - U_{xx})^2 + (2U_{xy})^2 \right\}^{1/2} \\ &= 3\gamma\rho \int_x \int_y \int_z \left\{ (x^2 + y^2)/r^5 \right\} dx dy dz \quad (2.19) \end{aligned}$$

It is not possible to measure  $U_{xx}$ ,  $U_{yy}$ ,  $U_{xy}$ , or HDT directly. Differential curvature can be obtained from torsion-balance measurements.

## 2.3. GRAVITY OF THE EARTH

### 2.3.1. Figure of the Earth

(a) *General.* Gravity prospecting evolved from the study of the Earth's gravitational field, a subject of interest to geodesists for determining the shape of the Earth. Because the Earth is not a perfect homogeneous sphere, gravitational acceleration is not constant over the Earth's surface.

The magnitude of gravity depends on five factors: latitude, elevation, topography of the surrounding terrain, earth tides, and density variations in the subsurface. Gravity exploration is concerned with

anomalies due to the last factor, and these anomalies generally are much smaller than the changes due to latitude and elevation, although larger than the anomalies due to tidal and (usually) topographic effects. The change in gravity from equatorial to polar regions amounts to about 5 Gal, or 0.5% of the average value of  $g$  (980 Gal), and the effect of elevation can be as large as 0.1 Gal, or 0.01% of  $g$ . A gravity anomaly considered large in oil exploration, on the other hand, would be 10 mGal, or 0.001% of  $g$ , whereas in mineral exploration a large anomaly would be 1 mGal. Thus, variations in  $g$  that are significant in prospecting are small in comparison with the magnitude of  $g$  and also in comparison with latitude and elevation effects. Fortunately, we can, with good accuracy, remove most of the effects of factors that are not of interest in prospecting.

(b) *The reference spheroid.* The shape of the Earth, determined by geodetic measurements and satellite tracking, is nearly spheroidal, bulging at the equator and flattened at the poles. The *polar flattening* is  $(R_{eq} - R_p)/R_{eq} = 1/298.25$ , where  $R_{eq}$  and  $R_p$  are the Earth's equatorial and polar radii, respectively.

The *reference spheroid* is an oblate ellipsoid that approximates the mean sea-level surface (*geoid*), with the land above it removed. In 1930 the International Union of Geodesy and Geophysics adopted a formula (Nettleton, 1976, p. 17) for the theoretical value of gravity  $g_i$ , but this has been superseded (Woolard, 1979) by the Geodetic Reference System 1967 (GRS67):

$$\begin{aligned} g_i &= 978,031.846(1 + 0.005,278,895 \sin^2 \phi \\ &\quad + 0.000,023,462 \sin^4 \phi) \text{ mGal} \quad (2.20) \end{aligned}$$

where  $\phi$  is latitude.

(c) *The geoid.* Mean continental elevations are about 500 m, and maximum land elevations and ocean depressions are of the order of 9,000 m referred to sea level. Sea level is influenced by these variations and other lateral density changes. We define mean sea level (the equipotential for the Earth's gravity plus centrifugal effects), called the *geoid*, as the average sea level over the oceans and over the surface of sea water that would lie in canals if they were cut through the land masses.

The simplified *figure of the Earth* allows for increasing density with depth, but not for lateral variations, which are the objects of gravity exploration. Because of the lateral variations, the geoid and reference spheroid do not coincide. Local mass anomalies warp the geoid as in Figure 2.2a. We might expect

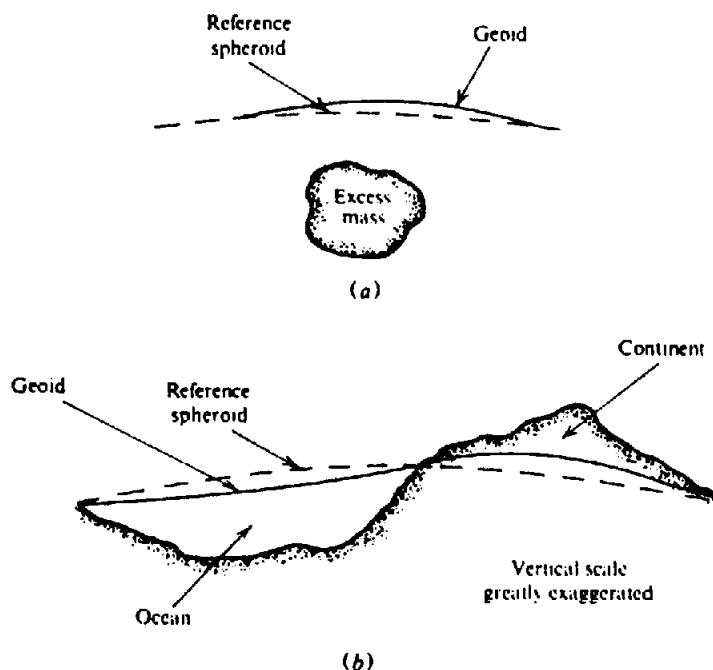


Figure 2.2. Comparison of reference spheroid and geoid. (a) Warping of the geoid by a local mass. (b) Large-scale warping.

the geoid to be warped upward under the continents because of attracting material above, and downward over the ocean basins because of the low density of water (Figure 2.2b). However, deviations from the spheroid do not correlate with the continents nor with the lithospheric plates, suggesting that density differences exist below the lithosphere. The deviations between the two surfaces (Kahn, 1983) are as much as 100 m.

### 2.3.2. Gravity Reduction

(a) *General.* Gravity readings are generally influenced by the five factors listed in Section 2.3.1a, hence we must make corrections to reduce gravity readings to the values they would have on a datum equipotential surface such as the geoid (or a surface everywhere parallel to it).

(b) *Latitude correction.* Both the rotation of the Earth and its equatorial bulge produce an increase of gravity with latitude. The centrifugal acceleration due to the rotating Earth is maximum at the equator and zero at the poles; it opposes the gravitational acceleration, while the polar flattening increases gravity at the poles by making the geoid closer to the Earth's center of mass. The latter effect is counteracted partly by the increased attracting mass at the equator. A *latitude correction*  $\Delta g_L$  is obtained by

differentiating Equation (2.20):

$$\begin{aligned}\Delta g_L/\Delta s &= (1/R_e)\Delta g_i/\Delta\phi \\ &= 0.811 \sin 2\phi \text{ mGal/km} \quad (2.21a)\end{aligned}$$

$$= 1.305 \sin 2\phi \text{ mGal/mile} \quad (2.21b)$$

where  $\Delta s$  = N-S horizontal distance =  $R_e$ ,  $\Delta\phi$  and  $R_e$  is the radius of the Earth ( $\approx 6368$  km). The correction is a maximum at latitude  $45^\circ$  where it amounts to  $0.01 \text{ mGal}/(13 \text{ m})$  and it is zero at the equator and poles. The correction is added to  $g$  as we move toward the equator.

(c) *Free-air correction.* Since gravity varies inversely with the square of distance, it is necessary to correct for changes in elevation between stations to reduce field readings to a datum surface. The *free air correction* does not take account of the material between the station and the datum plane. It is obtained by differentiating the scalar equation equivalent to Equation (2.2b); the result is (dropping the minus sign)

$$\begin{aligned}\Delta g_{FA}/\Delta R &= 2\gamma M_e/R_e^3 = 2g/R_e \\ &= 0.3086 \text{ mGal/m} \quad (2.22a)\end{aligned}$$

$$= 0.09406 \text{ mGal/ft} \quad (2.22b)$$

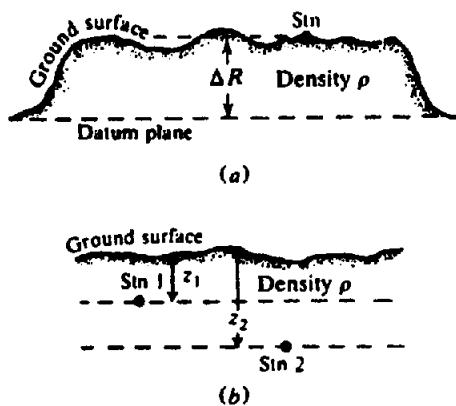


Figure 2.3. Bouguer correction. (a) Station on a broad plateau. (b) Underground stations.

at 45° latitude. The free-air correction is added to the field reading when the station is above the datum plane and subtracted when below it.

To make latitude and free-air corrections, station position must be known precisely. For an accuracy of 0.01 mGal, the usual accuracy of the gravimeter, N-S location (at 45° latitude) must be known to within 13 m (40 ft) and elevation to 3 cm (1 in.).

(d) *Bouguer correction.* The *Bouguer correction* accounts for the attraction of material between the station and datum plane that was ignored in the free-air calculation. If the station were centrally located on a plateau of large horizontal extent and uniform thickness and density (Fig. 2.3a), the gravity reading would be increased by the attraction of this slab between the station and the datum. The Bouguer correction is given by

$$\begin{aligned}\Delta g_B / \Delta R &= 2\pi\gamma\rho \\ &= 0.04192\rho \text{ mGal/m} \quad (2.23a) \\ &= 0.01278\rho \text{ mGal/ft} \quad (2.23b)\end{aligned}$$

where  $\rho$  is the slab density in grams per cubic centimeter [see Eq. (2.57)]. If we assume an average density for crustal rocks of 2.67 g/cm³, the numerical value is

$$\begin{aligned}\Delta g_B / \Delta R &= 0.112 \text{ mGal/m} \quad (2.24a) \\ &= 0.0341 \text{ mGal/ft} \quad (2.24b)\end{aligned}$$

The Bouguer correction is applied in the opposite sense to free air, that is, it is subtracted when the station is above the datum and vice versa.

When gravity measurements are made at underground stations, as in Figure 2.3b, the slab between stations at depths  $z_1$  and  $z_2$  exerts an attraction downward on station 1 and upward on 2. Thus the difference in gravity between them is  $4\pi\gamma\rho(z_2 - z_1)$  mGal, that is, the Bouguer correction is doubled.

The Bouguer and free-air corrections are often combined into an *elevation correction*. From Equations (2.22) and (2.23) the result is

$$\Delta g_E / \Delta R = \Delta g_{FA} / \Delta R - \Delta g_B / \Delta R$$

$$= (0.3086 - 0.0419\rho) \text{ mGal/m} \quad (2.25a)$$

$$= (0.0941 - 0.0128\rho) \text{ mGal/ft} \quad (2.25b)$$

The elevation correction is applied in the same way as the free-air correction.

Two assumptions were made in deriving the Bouguer correction: (1) The slab is of uniform density and (2) it is of infinite horizontal extent; neither is really valid. To modify the first, one needs considerable knowledge of local rock types and densities. The second is taken care of in the next reduction.

(e) *Terrain correction.* The terrain correction allows for surface irregularities in the vicinity of the station. Hills above the elevation of the gravity station exert an upward pull on the gravimeter, whereas valleys (lack of material) below it fail to pull downward on it. Thus both types of topographic undulations affect gravity measurements in the same sense and the *terrain correction* is added to the station reading.

There are several methods for calculating terrain corrections, all of which require detailed knowledge of relief near the station and a good topographical map (contour interval ~ 10 m or 50 ft or smaller) extending considerably beyond the survey area. The usual procedure is to divide the area into compartments and compare the elevation within each compartment with the station elevation. This can be done by outlining the compartments on a transparent sheet overlying a topographic map. The most common template used concentric circles and radial lines, making sectors whose areas increased with distance from the station. The gravity effect of a single sector was calculated from the following for-

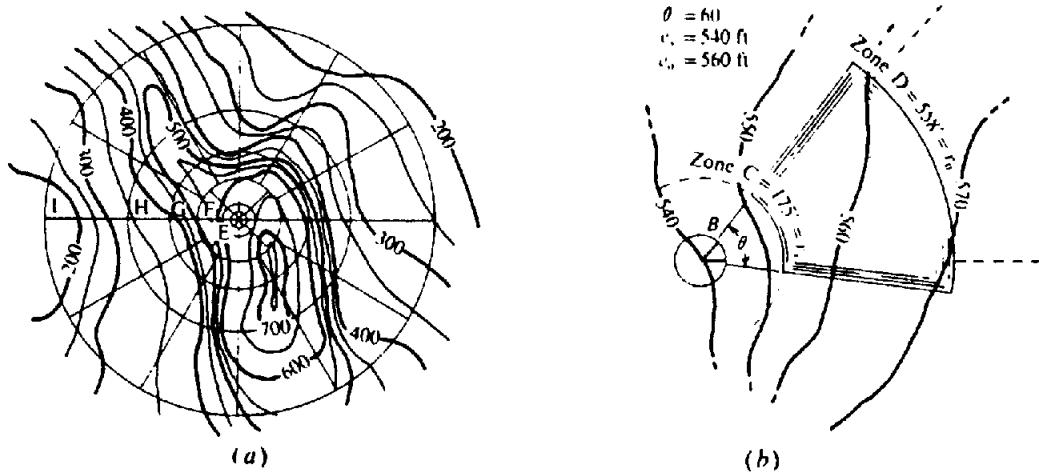


Figure 2.4. Use of terrain chart with topographic map. (a) Terrain chart overlying map. (b) Enlarged view of a single zone.

mula [Eq. (2.58)]:

$$\delta g_T(r, \theta) = \gamma \rho \theta \left\{ (r_o - r_i) + (r_o^2 + \Delta z^2)^{1/2} - (r_i^2 + \Delta z^2)^{1/2} \right\} \quad (2.26)$$

where  $\theta$  is the sector angle (radians),  $\Delta z = |z_s - z_a|$ ,  $z_s$  is the station elevation,  $z_a$  is the average elevation in the sector, and  $r_o$  and  $r_i$  are the outer and inner sector radii. The terrain correction  $\Delta g_T$  is the sum of the contributions of all sectors:

$$\Delta g_T = \sum_r \sum_\theta \delta g_T(r, \theta) \quad (2.27)$$

The use of a terrain chart of this type is illustrated in Figure 2.4. The transparent template is placed over the topographic map with the center of the circles at the gravity station. The average elevation within a single compartment is estimated from the contours within it and subtracted from the known station elevation. The difference is  $\Delta z$  in Equation (2.26), from which the contribution to  $\Delta g_T$  is calculated for the compartment. Tables of terrain corrections such as Table 2.1 facilitated this operation. [Hammer (1982) gives corrections for subdivisions of the inner zones required in microgravity surveys for engineering and archaeological surveys.] Note that there was no provision for relief within 2 m of the station, that is, it has to be flat for a 2 m distance from the station. It can be seen from Table 2.1 that the correction is small if  $r > 20z$ ,  $r$  being the average distance from the compartment to the station.

Other methods for segmenting the topographic map occasionally were applied; for instance, when contours were practically linear, there was no advantage in using circular sectors. An alternative scheme

used elementary areas so proportioned that the gravity effect of each was the same regardless of distance.

Terrain corrections for outer zones are often made on a computer using elevations on a regular grid (Krohn, 1976). Regardless of the approach, the topographic reduction is a slow and tedious task. Furthermore, in areas of steep and erratic slopes, it usually is not very accurate, particularly for relief in the vicinity of the station itself. At the edge of a steep cliff or gorge, the terrain correction is almost inevitably in error. A better solution is to move the gravity station away from sharp relief features if this is possible.

Bouguer anomalies (§2.3.2h) for marine surface and airborne surveys require a different terrain correction from that discussed earlier. The Bouguer correction is calculated (for marine data) as if the water depth were everywhere constant, and hence it is discontinuous over abrupt elevation changes. The terrain correction is made discontinuous to compensate for the Bouguer correction discontinuities. To the left of a two-dimensional vertical step in the sea floor (Fig. 2.5), the terrain correction is positive due to the deeper water on the right (analogous to a nearby valley in land work), and it is negative to the right of the step.

(f) Earth-tide correction. Instruments for measuring gravity are sensitive enough to record the changes in  $g$  caused by movement of the Sun and Moon, changes that depend on latitude and time. Their range is about 0.3 mGal. Figure 2.6 shows calculated and measured tidal variations for a stationary gravimeter.

The correction can be calculated from knowledge of the locations of the Sun and Moon. However, because the variation is smooth and relatively slow,

Table 2.1. Terrain corrections

Zone B		Zone C		Zone D		Zone E		Zone F		Zone G		Zone H		Zone I	
4 sectors	6 sectors	4.6' - 175'	54.6' - 175'	6 sectors	175' - 558'	8 sectors	558' - 1280'	8 sectors	1280' - 2936'	12 sectors	2936' - 5018'	12 sectors	5018' - 8578'	12 sectors	8578' - 14612'
$\pm z$	$d\mathfrak{g}_T$	$\pm z$	$d\mathfrak{g}_T$	$\pm z$	$d\mathfrak{g}_T$	$\pm z$	$d\mathfrak{g}_T$	$\pm z$	$d\mathfrak{g}_T$	$\pm z$	$d\mathfrak{g}_T$	$\pm z$	$d\mathfrak{g}_T$	$\pm z$	$d\mathfrak{g}_T$
0.0 - 1.1	0.00000	0.0 - 4.3	0.00000	0.0 - 7.7	0.00000	0 - 18	0.00000	0 - 27	0.00000	0 - 58	0.00000	0 - 75	0.00000	0 - 99	0.00000
1.1 - 1.9	0.00133	4.3 - 7.5	0.00133	7.7 - 13.4	0.00133	18 - 30	0.00133	27 - 46	0.00133	58 - 100	0.00133	75 - 131	0.00133	99 - 171	0.00133
1.9 - 2.5	0.00267	7.5 - 9.7	0.00267	13.4 - 17.3	0.00267	30 - 39	0.00267	46 - 60	0.00267	100 - 129	0.00267	131 - 169	0.00267	171 - 220	0.00267
2.5 - 2.9	0.0040	9.7 - 11.5	0.0040	17.3 - 20.5	0.0040	39 - 47	0.0040	60 - 71	0.0040	129 - 153	0.0040	169 - 200	0.0040	220 - 261	0.0040
2.9 - 3.4	0.0053	11.5 - 13.1	0.0053	20.5 - 23.2	0.0053	47 - 53	0.0053	71 - 80	0.0053	153 - 173	0.0053	200 - 226	0.0053	261 - 296	0.0053
3.4 - 3.7	0.0067	13.1 - 14.5	0.0067	23.2 - 25.7	0.0067	53 - 58	0.0067	80 - 88	0.0067	173 - 191	0.0067	226 - 250	0.0067	296 - 327	0.0067
3.7 - 7	0.0133	14.5 - 24	0.0133	25.7 - 43	0.0133	58 - 97	0.0133	88 - 146	0.0133	191 - 317	0.0133	250 - 414	0.0133	327 - 540	0.0133
7 - 9	0.0267	24 - 32	0.0267	43 - 56	0.0267	97 - 126	0.0267	146 - 189	0.0267	317 - 410	0.0267	414 - 535	0.0267	540 - 698	0.0267
9 - 12	0.040	32 - 39	0.040	56 - 66	0.040	126 - 148	0.040	189 - 224	0.040	410 - 486	0.040	535 - 633	0.040	698 - 827	0.040
12 - 14	0.053	39 - 45	0.053	66 - 76	0.053	148 - 170	0.053	224 - 255	0.053	486 - 552	0.053	633 - 719	0.053	827 - 938	0.053
14 - 16	0.067	45 - 51	0.067	76 - 84	0.067	170 - 189	0.067	255 - 282	0.067	552 - 611	0.067	719 - 796	0.067	938 - 1038	0.067
16 - 19	0.080	51 - 57	0.080	84 - 92	0.080	189 - 206	0.080	282 - 308	0.080	611 - 666	0.080	796 - 866	0.080	1038 - 1129	0.080
19 - 21	0.0935	57 - 63	0.0935	92 - 100	0.0935	206 - 222	0.0935	308 - 331	0.0935	666 - 716	0.0935	866 - 931	0.0935		
21 - 24	0.107	63 - 68	0.107	100 - 107	0.107	222 - 238	0.107	331 - 353	0.107	716 - 754	0.107	931 - 992	0.107		
24 - 27	0.120	68 - 74	0.120	107 - 114	0.120	238 - 252	0.120	353 - 374	0.120	764 - 809	0.120	992 - 1050	0.120		
27 - 30	0.133	74 - 80	0.133	114 - 120	0.133	252 - 266	0.133	374 - 394	0.133	809 - 852	0.133	1050 - 1105	0.133		
80 - 86	0.147	120 - 127	0.147	266 - 280	0.147	394 - 413	0.147			852 - 894	0.147				
86 - 91	0.160	127 - 133	0.160	280 - 293	0.160	413 - 431	0.160			894 - 933	0.160				
91 - 97	0.174	133 - 140	0.174	293 - 306	0.174	431 - 449	0.174			933 - 972	0.174				
97 - 104	0.187	140 - 146	0.187	306 - 318	0.187	449 - 466	0.187			972 - 1009	0.187				
104 - 110	0.200	146 - 152	0.200	318 - 331	0.200	466 - 483	0.200			1009 - 1046	0.200				

Note:  $d\mathfrak{g}_T = \theta \gamma p \{ \epsilon_0 - \epsilon_1 + \sqrt{(\epsilon_0^2 + z^2)} - \sqrt{(\epsilon_1^2 + z^2)} \}$ ,  $\epsilon_0, \epsilon_1$  = inner, outer sector radii,  $\gamma = 6.67 \times 10^{-6}$ ,  $d\mathfrak{g}_T$  in milligals,  $z, r, \epsilon_0$  in feet, and  $z$  = average sector elevation.

Source: From Hammer (1939), but based on average density  $\rho = 2.67 \text{ g/cm}^3$ .

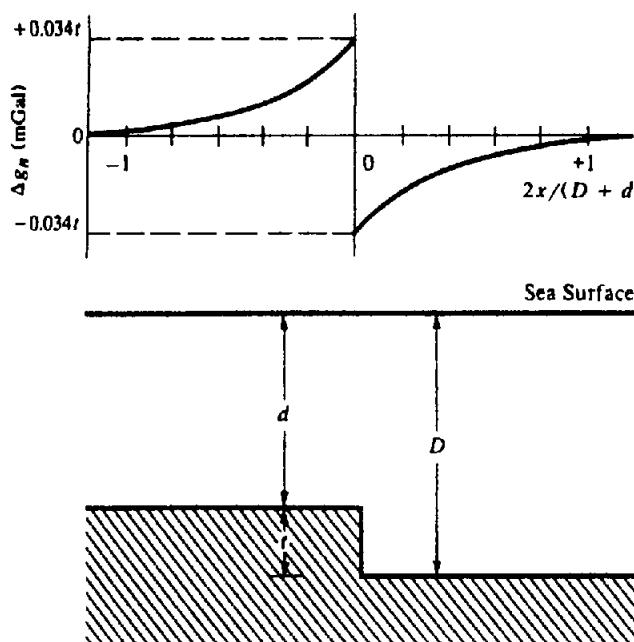


Figure 2.5. Marine terrain correction for vertical sea-floor step.  $\rho_w = 1.03$ ,  $\rho_{rock} = 2.67$ ,  $t$  = meters. (After Nettleton, 1971.)

usually it is included in the instrument drift correction (§2.5.2).

(g) *Isostatic correction.* The worldwide average of Bouguer anomalies on land near sea level is approximately zero. In regions of large elevation they are generally negative, while in oceanic regions mainly positive. These large-scale effects are due to density variations in the crust, indicating denser material beneath the ocean and less dense material in regions of elevated land.

In 1855, two hypotheses were put forward to account for the density variations. Airy proposed a crust of uniform density but variable thickness floating on a liquid substratum of higher density, whereas

Pratt suggested a crust where the density varies with topography, being lower in mountain regions and higher beneath the oceans. Both hypotheses appear to be true to some extent. An *isostatic correction* occasionally is necessary in large-scale surveys to compensate for crustal variations.

(h) *Bouguer and free-air anomalies.* When all of the preceding corrections have been applied to the observed gravity reading, we obtain the value of the *Bouguer anomaly*  $g_B$  for the station:

$$g_B = g_{\text{obs}} - g_i + (\Delta g_L + \Delta g_{FA} - \Delta g_B + \Delta g_T) \quad (2.28)$$

where  $g_{\text{obs}}$  is the station reading,  $g_i$  is the theoretical gravity,  $\Delta g_L$  is the latitude correction,  $\Delta g_{FA}$  is the free-air correction,  $\Delta g_B$  is the Bouguer correction, and  $\Delta g_T$  is the terrain correction. The correction terms in Equation (2.28) correspond to a station south of the reference latitude (in the northern hemisphere) and above the datum. Sometimes, rather than the value from Equation (2.20), some particular station value in the survey area is used for  $g_i$ . Note that the signs of  $\Delta g_{FA}$  and  $\Delta g_B$  change when the station is below the datum plane.

Another quantity that is sometimes used (especially with marine data) is the *free-air anomaly*, the value of  $g_B$  when  $\Delta g_B$  (and often  $\Delta g_T$ ) is omitted from Equation (2.28).

If the Earth had no lateral variations in density, after corrections for the preceding effects, gravity readings would be identical. The Bouguer and free-air anomalies result from lateral variations in density (see also Ervin, 1977).

### 2.3.3. Densities of Rocks and Minerals

The quantity to be determined in gravity exploration is local lateral variation in density. Generally density

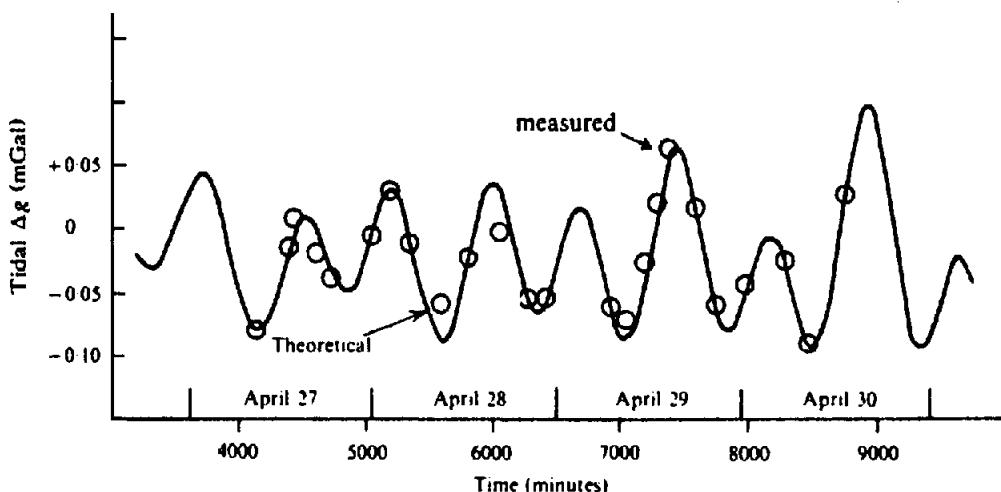


Figure 2.6. Earth-tide variations, Montreal, April 1969. Gravity readings have been corrected for instrument drift.

Table 2.2. Densities.

Rock type	Range (g/cm <sup>3</sup> )	Average (g/cm <sup>3</sup> )	Mineral	Range (g/cm <sup>3</sup> )	Average (g/cm <sup>3</sup> )
<b>Sediments (wet)</b>					
Overburden		1.92	<b>Metallic minerals</b>		
Soil	1.2 – 2.4	1.92	Bauxite	2.3 – 2.55	2.45
Clay	1.63 – 2.6	2.21	Limonite	3.5 – 4.0	3.78
Gravel	1.7 – 2.4	2.0	Siderite	3.7 – 3.9	3.83
Sand	1.7 – 2.3	2.0	Rutile	4.18 – 4.3	4.25
Sandstone	1.61 – 2.76	2.35	Manganite	4.2 – 4.4	4.32
Shale	1.77 – 3.2	2.40	Chromite	4.3 – 4.6	4.36
Limestone	1.93 – 2.90	2.55	Ilmenite	4.3 – 5.0	4.67
Dolomite	2.28 – 2.90	2.70	Pyrolusite	4.7 – 5.0	4.82
<b>Sedimentary rocks (av.)</b>			Magnetite	4.9 – 5.2	5.12
<b>Igneous rocks</b>					
Rhyolite	2.35 – 2.70	2.52	Franklinite	5.0 – 5.22	5.12
Andesite	2.4 – 2.8	2.61	Hematite	4.9 – 5.3	5.18
Granite	2.50 – 2.81	2.64	Cuprite	5.7 – 6.15	5.92
Granodiorite	2.67 – 2.79	2.73	Cassiterite	6.8 – 7.1	6.92
Porphyry	2.60 – 2.89	2.74	Wolframite	7.1 – 7.5	7.32
Quartz diorite	2.62 – 2.96	2.79	<b>Sulfides, arsenides</b>		
Diorite	2.72 – 2.99	2.85	Sphalerite	3.5 – 4.0	3.75
Lavas	2.80 – 3.00	2.90	Malachite	3.9 – 4.03	4.0
Diabase	2.50 – 3.20	2.91	Chalcopyrite	4.1 – 4.3	4.2
Basalt	2.70 – 3.30	2.99	Stannite	4.3 – 4.52	4.4
Gabbro	2.70 – 3.50	3.03	Stibnite	4.5 – 4.6	4.6
Peridotite	2.78 – 3.37	3.15	Pyrrhotite	4.5 – 4.8	4.65
Acid igneous	2.30 – 3.11	2.61	Molybdenite	4.4 – 4.8	4.7
Basic igneous	2.09 – 3.17	2.79	Marcasite	4.7 – 4.9	4.85
<b>Metamorphic rocks</b>					
Quartzite	2.5 – 2.70	2.60	Pyrite	4.9 – 5.2	5.0
Schists	2.39 – 2.9	2.64	Bornite	4.9 – 5.4	5.1
Graywacke	2.6 – 2.7	2.65	Chalcocite	5.5 – 5.8	5.65
Marble	2.6 – 2.9	2.75	Cobaltite	5.8 – 6.3	6.1
Serpentine	2.4 – 3.10	2.78	Arsenopyrite	5.9 – 6.2	6.1
Slate	2.7 – 2.9	2.79	Bismuththinitite	6.5 – 6.7	6.57
Gneiss	2.59 – 3.0	2.80	Galena	7.4 – 7.6	7.5
Amphibolite	2.90 – 3.04	2.96	Cinnabar	8.0 – 8.2	8.1
Eclogite	3.2 – 3.54	3.37	<b>Non-metallic minerals</b>		
Metamorphic	2.4 – 3.1	2.74	Petroleum	0.6 – 0.9	—
			Ice	0.88 – 0.92	—
			Sea Water	1.01 – 1.05	—
			Lignite	1.1 – 1.25	1.19
			Soft coal	1.2 – 1.5	1.32
			Anthracite	1.34 – 1.8	1.50
			Chalk	1.53 – 2.6	2.01
			Graphite	1.9 – 2.3	2.15
			Rock salt	2.1 – 2.6	2.22
			Gypsum	2.2 – 2.6	2.35
			Kaolinite	2.2 – 2.63	2.53
			Orthoclase	2.5 – 2.6	—
			Quartz	2.5 – 2.7	2.65
			Calcite	2.6 – 2.7	—
			Anhydrite	2.29 – 3.0	2.93
			Biotite	2.7 – 3.2	2.92
			Magnesite	2.9 – 3.12	3.03
			Fluorite	3.01 – 3.25	3.14
			Barite	4.3 – 4.7	4.47

is not measured *in situ*, although it can be measured by borehole logging tools (see §11.8.3). Density can also be estimated from seismic velocity (§4.2.8a). Often density measurements are made in the laboratory on small outcrop or drill-core samples. However, laboratory results rarely give the true bulk

density because the samples may be weathered, fragmented, dehydrated, or altered in the process of being obtained. Consequently, density is often not very well known in specific field situations.

Density data are given in Table 2.2. Sedimentary rocks are usually less dense than igneous and meta-

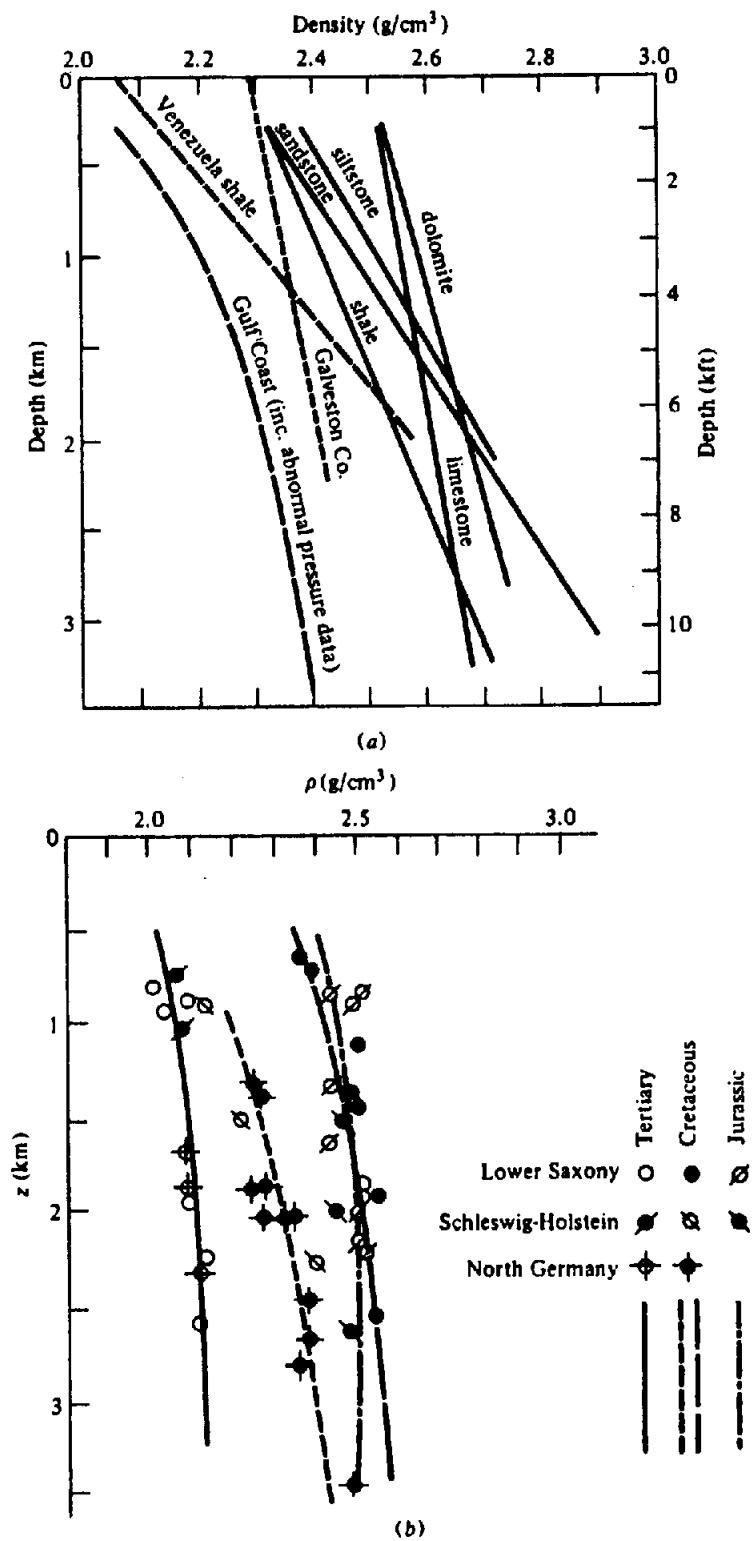


**Figure 2.7.** Density versus depth. (a) Western Hemisphere data: Venezuelan data from Hedberg (1936), Gulf Coast data from Dickenson (1953), Galveston County data from Bible (1964), and remaining data (Canadian) from Maxant (1980). (b) North Europe data from Hermes (1986).

morphic rocks. The wide range of density of sedimentary rocks is primarily due to variations in porosity. The nature of the pore fluids also affects the bulk density. Sedimentary rock density is also influenced by age, previous history, and depth of burial. Obviously a porous rock will be compacted when buried. In general, density increases with depth

(Fig. 2.7) and time. The density contrast between adjacent sedimentary formations in the field is seldom greater than  $0.25 \text{ g/cm}^3$  (except for the near-surface; §2.7.11).

Although igneous rocks generally are denser than sedimentary rocks, there is considerable overlap. Volcanics, particularly lavas, may have high porosi-

ties and, hence, low density. Generally, basic igneous rocks are heavier than acidic ones. Porosity, which affects the density of sediments so greatly, is of minor significance in most igneous and metamorphic rocks unless they are highly fractured.

Density usually increases with the degree of metamorphism because the process tends to fill pore spaces and recrystallize the rock in a denser form. Thus metamorphosed sediments, such as marble, slate, and quartzite, generally are denser than the original limestone, shale, and sandstone. The same is true for the metamorphic forms of igneous rocks, gneiss versus granite, amphibolite versus basalt, and so on.

With few exceptions, nonmetallic minerals have lower densities than the average for rocks ( $2.67 \text{ g/cm}^3$ ). Metallic minerals, on the other hand, mainly are heavier than this average, but since they rarely occur in pure form in large volumes, their effect normally is not great.

### 2.3.4. Density Estimates from Field Results

(a) *Density from underground measurements.* Sometimes it is feasible to make gravity measurements underground. If readings are taken at points directly below one another (for example, at the surface and in an underground opening), then the difference between these values is given by [see Eqs. (2.22) and (2.23)]

$$\Delta g = (0.3086 - 0.0838\rho) \Delta z + \epsilon_T \text{ mGal}$$

$$\Delta g = (0.0941 - 0.0256\rho) \Delta z' + \epsilon_T \text{ mGal}$$

where  $\Delta z$  is the elevation difference in meters,  $\Delta z'$  in feet,  $\rho$  is in grams per cubic centimeter, and  $\epsilon_T$  is the difference in terrain corrections (due to air-filled mine tunnels) in milligals. (Note that the Bouguer correction has been doubled; see §2.3.2d.) Hence the average bulk density in the intervening rock is

$$\rho = 3.68 - 11.93(\Delta g - \epsilon_T)/\Delta z \text{ g/cm}^3 \quad (2.29a)$$

or

$$\rho = 3.68 - 39.06(\Delta g - \epsilon_T)/\Delta z' \text{ g/cm}^3 \quad (2.29b)$$

Because  $\epsilon_T$  depends upon  $\rho$ , Equations (2.29) are usually solved by successive approximations.

Hussain, Walach, and Weber (1981) discuss underground surveys.

(b) *Density from borehole gravimeter measurements.* Borehole gravimeters (§11.9.1) are able to make gravity measurements to an accuracy of about  $5 \mu\text{Gal}$  (Schmoker, 1978; LaFehr, 1983). Terrain corrections are not necessary in borehole measurements. Differentiating Equations (2.29) keeping  $\Delta z$  and  $\Delta z'$  fixed gives

$$\Delta\rho = 0.0119\Delta(\Delta g/\Delta z) \text{ g/cm}^3 \quad (2.30a)$$

$$\Delta\rho = 0.0391\Delta(\Delta g/\Delta z') \text{ g/cm}^3 \quad (2.30b)$$

where  $\Delta g$  is in microgals. With meter accuracy of  $\pm 5 \mu\text{Gal}$ , the error in  $\Delta(\Delta g)$  can be as large as  $\pm 10 \mu\text{Gal}$ , and measuring density to  $\pm 0.01 \text{ g/cm}^3$  requires readings 12 m (40 ft) or more apart.

The volume contributing most to borehole gravity measurements is the portion closest to the borehole. Half of the effect is produced by rocks within a radius of  $0.7\Delta z$ , 80% from  $2.45\Delta z$  (the *radius of investigation*) and 90% from within  $5\Delta z$ . Borehole gravity measurements (LaFehr, 1983) permit determination of the density sufficiently far from the borehole so that invasion and alteration by the drilling process are unimportant, in contrast to the few inches of effective penetration achieved by other density logging tools. The main objective of borehole gravity measurements usually is to determine porosity, which is directly related to density.

(c) *Nettleton's method.* A reasonably satisfactory method of estimating near-surface density uses a gravity profile over topography that is not correlative with density variations (Nettleton, 1976). For example, a profile across an erosional valley that is not structure-controlled would probably be suitable, but a profile across a structure-controlled ridge might be suspect because density changes associated with the structure may correlate with elevation. Field readings are reduced to Bouguer gravity profiles assuming different values of  $\rho$  for the Bouguer and terrain corrections. The profile that reflects the topography the least is the one with the best estimate of the density. The method is illustrated in Figure 2.8; incorrect density assumptions result in profiles either following or inverting the topography. Obviously the density involved is that between the elevations of the highest and lowest stations.

(d) *Parasnis' method.* An analytical approach somewhat similar to Nettleton's graphical method has been developed by Parasnis (1962, p. 40). Rearranging Equation (2.28) and using Equation (2.25),

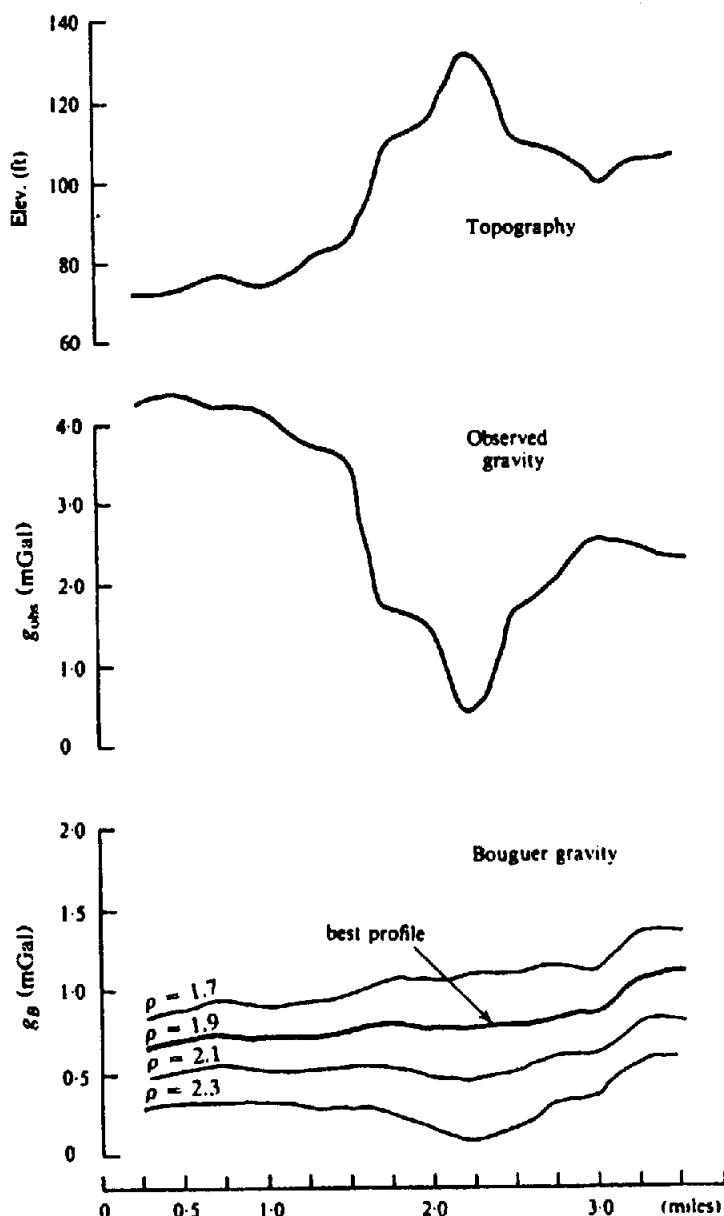


Figure 2.8. Method for estimating surface density.

we obtain

$$(g_{\text{obs}} - g_t + \Delta g_L + 0.3086z) - g_B \\ = (0.0419z - \Delta g_T/\rho)\rho \quad (2.31a)$$

$$(g_{\text{obs}} - g_t + \Delta g_L + 0.0941z') - g_B \\ = (0.0128z' - \Delta g_T/\rho)\rho \quad (2.31b)$$

where  $z$  is in meters and  $z'$  is in feet. We wish to determine the average bulk density for the data set by considering the Bouguer anomaly  $g_B$  to be a random error of mean value zero. If we plot

$$(g_{\text{obs}} - g_t + \Delta g_L + 0.3086z)$$

versus  $(0.0419z - \Delta g_T/\rho)$  (or the equivalent in terms

of  $z'$ ), the slope of the best-fit straight line through the origin will be  $\rho$ .

## 2.4. GRAVITY INSTRUMENTS

### 2.4.1. General

The absolute measurement of gravity is usually carried out at a fixed installation by the accurate timing of a swinging pendulum or of a falling weight.

Relative gravity measurements may be made in various ways. Three types of instruments have been used: the torsion balance, the pendulum and the gravimeter (or gravity meter). The latter is the sole instrument now used for prospecting, the others having only historical interest.

### 2.4.2. Absolute Measurement of Gravity

Although the timing of a freely falling body was the first method of measuring  $g$ , the accuracy was poor because of the difficulty in measuring small time intervals. The method has been revived as a result of instrumentation improvements and elaborate free-fall installations are now located at several national laboratories. It is necessary to measure time to about  $10^{-8}$  s and distance to  $< \frac{1}{2} \mu\text{m}$  to obtain an accuracy of 1 mGal with a fall of 1 or 2 m.

Until recently, the standard method for measuring  $g$  employed a modified form of the *reversible Kater pendulum*. The value of  $g$  was obtained by timing a large number of oscillations.

### 2.4.3. Relative Measurement of Gravity

(a) *Portable pendulum*. The pendulum has been used for both geodetic and prospecting purposes. Since  $g$  varies inversely as the square of the period  $T$ , we have

$$T^2 g = \text{constant}$$

Differentiating, we get

$$\begin{aligned}\Delta g &= -2g \Delta T/T \\ &= -2g(T_2 - T_1)/T_1\end{aligned}\quad (2.32)$$

Thus if we can measure the periods at two stations to about 1  $\mu\text{s}$ , the gravity difference is accurate to 1 mGal. This is not difficult with precise clocks such as quartz crystal, cesium, or rubidium.

The pendulum has been used extensively for geodetic work, both on land and at sea (in submarines). Portable pendulums used in oil exploration during the early 1930s had a sensitivity of about 0.25 mGal. Pendulum apparatus was complex and bulky. Two pendulums, swinging in opposite phase, were used to reduce sway of the mounting; they were enclosed in an evacuated, thermostatically controlled chamber to eliminate pressure and temperature effects. To get the required accuracy, readings took about  $\frac{1}{2}$  hr.

(b) *Torsion balance*. A fairly complete account of the salient features of the torsion balance can be found in Nettleton (1976). Figure 2.9 is a schematic of the torsion balance. Two equal masses  $m$  are separated both horizontally and vertically by rigid bars, the assembly being supported by a torsion fiber with an attached mirror to measure rotation by the deflection of a light beam. Two complete beam assemblies were used to reduce the effects of support sway. Readings were taken at three azimuth posi-

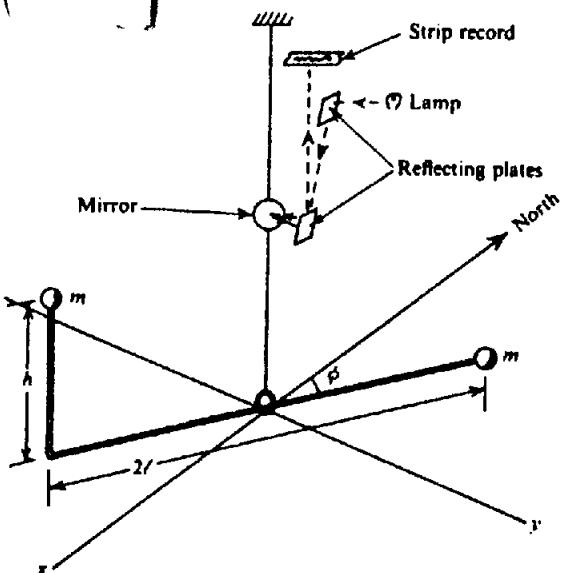


Figure 2.9. Torsion balance (schematic).

tions of the beam assemblies, normally  $120^\circ$  apart, to get sufficient data to calculate the required results. Elaborate precautions were required to minimize extraneous effects such as temperature and air convection. Each station had to be occupied for approximately one hour so that daily production was only 8 to 10 stations.

The deflection of the torsion balance beam is due to horizontal and vertical changes in the gravity field resulting from curvature of the equipotential surfaces. Torsion-balance measurements permitted calculation of  $U_{xy}$ ,  $U_{xx}$ ,  $U_{yy}$ , and  $|U_{yy} - U_{xx}|$ . The plotted values are usually the *horizontal gradient* [the vector  $(U_{xx}\mathbf{i} + U_{yy}\mathbf{j})$ ] and the *differential curvature* [a vector with magnitude given by Equation (2.19) and direction relative to the  $x$  axis of  $(1/2)\tan^{-1}(2U_{xy}/|U_{yy} - U_{xx}|)$ ]. Measurements were usually in Eötvös units (EU) equal to  $10^{-6}$  mGal/cm.

(c) *Stable-type gravimeters*. The first gravimeters dating from the early 1930s were of the stable type but these have now been superceded by more sensitive unstable meters. Nettleton (1976) describes a number of different gravimeters. All gravimeters are essentially extremely sensitive mechanical balances in which a mass is supported by a spring. Small changes in gravity move the weight against the restoring force of the spring.

The basic elements of a stable gravimeter are shown in Figure 2.10. Whereas the displacement of the spring is small, Hooke's law applies, that is, the change in force is proportional to the change in length; hence,

$$\Delta F = M \delta g = k \delta s \quad \text{or} \quad \delta g = k \delta s/M \quad (2.33)$$

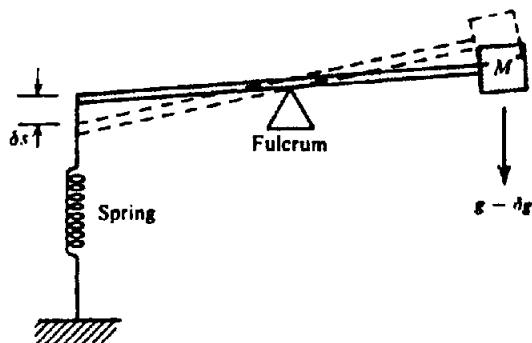


Figure 2.10. Basic principle of the stable gravimeter.

where  $k$  is the spring constant in dynes per centimeter. To measure  $g$  to 0.1 mGal, we must detect a fractional change in spring length of  $1/10^7$  (because  $Mg \approx ks$ ,  $\delta g/g \approx \delta s/s$ ), hence the need for considerable magnification. Mechanically we can make  $k/M$  small by using a large mass and a weak spring, but this method of enhancing sensitivity is limited. The period of oscillation of this system is

$$T = 2\pi(M/k)^{1/2}$$

Substituting for  $M$  in Equation (2.33), we get

$$\delta g = 4\pi^2 \delta s/T^2 \quad (2.34)$$

Thus for good sensitivity, the period is very large and measurement of  $\delta g$  requires considerable time. Stable gravimeters are extremely sensitive to other physical effects, such as changes in pressure, temperature, and small magnetic and seismic variations.

(d) *Unstable-type gravimeters*. Also known as *labilized or astatized gravimeters*, these instruments have an additional negative restoring force operating against the restoring spring force, that is, in the same sense as gravity. They essentially are in a state of unstable equilibrium and this gives them greater sensitivity than stable meters. Their linear range is less than for stable gravimeters so they are usually operated as null instruments.

The *Thyssen gravimeter*, although now obsolete, illustrates very clearly the astatic principle (Fig. 2.11). The addition of the mass  $m$  above the pivot raises the center of gravity and produces the instability condition. If  $g$  increases, the beam tilts to the right and the moment of  $m$  enhances the rotation; the converse is true for a decrease in gravity.

At present the Worden and LaCoste-Romberg meters are the only types used for exploration.

(e) *LaCoste-Romberg gravimeter*. The LaCoste-Romberg gravimeter was the first to employ a zero-length spring, now used by almost all gravimeters

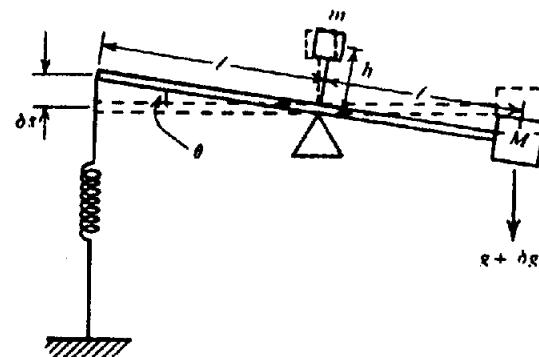


Figure 2.11. Basic principle of the unstable (Thyssen) gravimeter. (After Dobrin, 1960.)

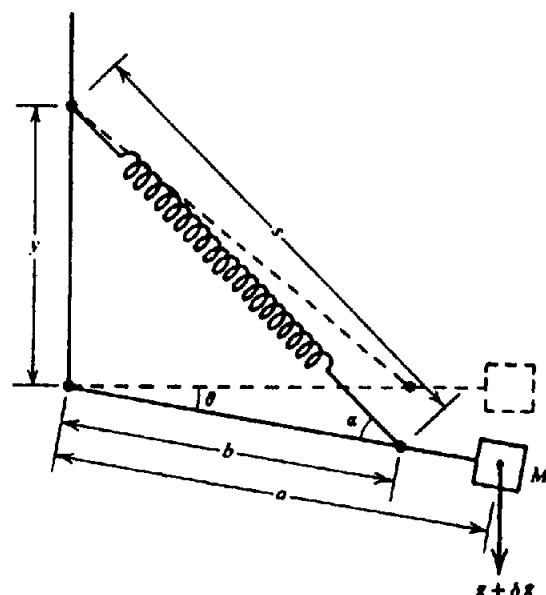


Figure 2.12. Lacoste-Romberg gravimeter.

(Askania, Frost, Magnolia, and North American). A *zero-length spring* is one in which the tension is proportional to the actual length of the spring, that is, if all external forces were removed the spring would collapse to zero length. The advantage of the zero-length spring is that if it supports the beam and mass  $M$  (see Fig. 2.12) in the horizontal position, it will support them in any position (note that  $\cos \theta$  in Eq. (2.35) cancels out, and  $g = K(1 - c/s)$ , which always has a solution since  $g$  is finite). Zero-length-springs are built with initial tension so that a threshold force is required before spring extension begins (as with a door spring).

To derive the expression for the sensitivity of the LaCoste-Romberg gravimeter, we write  $k(s - c)$  for the tension in the spring when its length is  $s$ ; thus,  $c$  is a small correction for the fact that the spring is not truly zero length. Taking moments about the pivot in Figure 2.12, we get

$$\begin{aligned} Mga \cos \theta &= k(s - c)b \sin \alpha \\ &= k(s - c)b(y \cos \theta)/s \quad (2.35) \end{aligned}$$



Figure 2.13. Reading a Worden gravimeter.

using the law of sines. Thus

$$g = (k/M)(b/a)(1 - c/s)y$$

When  $g$  increases by  $\delta g$ , the spring length increases by  $\delta s$  where

$$\delta g = (k/M)(b/a)(c/s)(y/s) \delta s \quad (2.36)$$

For a given change in gravity  $\delta g$ , we can make  $\delta s$  as large as we wish by decreasing one or more of the factors on the right-hand side; moreover, the closer the spring is to the zero-length spring, the smaller  $c$  is and the larger  $\delta s$  becomes.

In operation this is a null instrument, a second spring being used, which can be adjusted to restore the beam to the horizontal position. The sensitivity of gravimeters in use in surface exploration is generally 0.01 mGal. The instrument requires a constant-temperature environment, usually achieved by keeping it at a constant temperature that is higher than the surroundings.

(f) *Worden gravimeter.* The Worden gravimeter (Fig. 2.13) is especially portable and fast to operate. It uses small, very light weight parts of quartz (for example, the mass  $M$  weighs only 5 mg) with small inertia so that it is not necessary to clamp the movement between stations. Sensitivity to temperature and pressure changes is reduced by enclosing the system in a vacuum flask. The meter also employs an automatic temperature-compensating arrangement. The Worden meter is small (instrument dimensions are a few centimeters, the outer case is

about 25 cm high and 12 cm in diameter) and weighs about 2.5 kg. Its only power requirement is two penlight cells for illuminating the scale.

A simplified schematic is shown in Figure 2.14. The moving system is similar to the LaCoste-Romberg meter. The arm  $OP'$  and beam  $OM$  are rigidly connected and pivot about  $O$ , changing the length of the main spring  $P'C$ , which is fixed at  $C$ . We have the following relations:

$$\angle OCP' = \angle OP'C = \pi/2 - (\alpha + \theta/2)$$

$$RP \perp CP \quad P'P \perp OP$$

so

$$\angle RPP' = \pi/2 - \alpha$$

$$s = CP \quad \delta s = CP' - CP \approx b\theta \sin(\pi/2 - \alpha)$$

so

$$\theta = \delta s / (b \cos \alpha)$$

The correction factor  $c$  that appeared in the treatment of the LaCoste-Romberg meter is negligible for the Worden meter. Taking moments about the pivot for the case where  $\theta = 0$ , we get

$$Mga = ksh \cos \alpha$$

When  $g$  increases to  $(g + \delta g)$ ,  $P$  moves along the

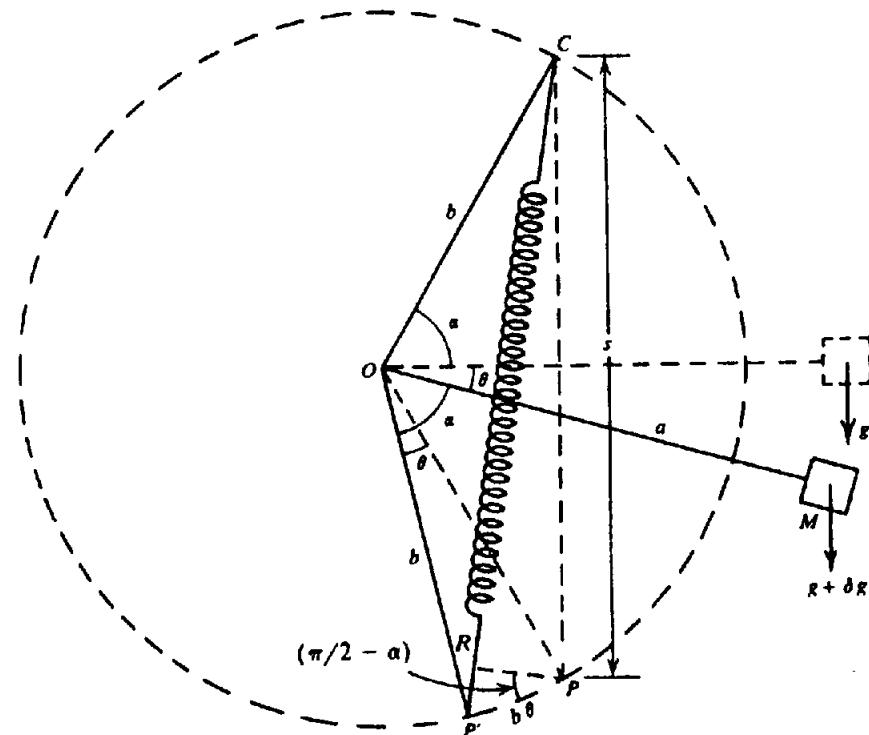


Figure 2.14. Basic principle of the Worden gravimeter.

circle to  $P'$  and

$$M(g + \delta g)a \cos \theta = kb(s + \delta s) \cos(\alpha + \theta/2)$$

When  $\theta \approx 0$ , to the first approximation this becomes

$$\begin{aligned} M(g + \delta g)a &= kb(s + \delta s)\{\cos \alpha - (\theta/2)\sin \alpha\} \\ &= kb(s + \delta s)\{\cos \alpha - (\delta s/2b)\tan \alpha\} \\ &= kb\{s \cos \alpha - \delta s(s/2b)\tan \alpha + \delta s \cos \alpha\} \end{aligned}$$

Subtracting the first moment equation to eliminate  $g$ , we get

$$Ma \delta g = kb\{\cos \alpha - (s/2b)\tan \alpha\} \delta s$$

Using the relation  $\sin \alpha = s/2b$ , we finally get

$$\delta g = (k/M)(b/a)(\cos 2\alpha/\cos \alpha) \delta s \quad (2.37)$$

As in the LaCoste-Romberg meter, the sensitivity can be increased by decreasing the factors  $(k/M)$  and  $(b/a)$ ; in addition the factor  $(\cos 2\alpha/\cos \alpha)$  approaches zero when  $\alpha$  approaches  $45^\circ$ , thus furnishing another method of obtaining high sensitivity. In practice the sensitivity is about 0.01 mGal.

Like the LaCoste-Romberg instrument, the Worden meter is read by measuring the force required to restore the beam to the horizontal position.

(g) Calibration of gravimeters. Both the Worden and LaCoste-Romberg meters are null instruments and changes in gravity are shown as arbitrary scale

divisions on a micrometer dial. There are several methods for converting these scale readings to gravity units.

Theoretically calibration can be carried out by tilting because a precise geometrical system is involved, but this is not the usual procedure. Generally, readings are taken at two or more stations where values of  $g$  are already known. If the value of  $\delta g$  between the stations is large enough to cover a reasonable fraction of the instrument range, a linear response is usually assumed between them. However, one should occupy several additional stations if possible.

## 2.5. FIELD OPERATIONS

### 2.5.1. Land Surveys

Gravity exploration is carried out both on land and at sea. Although some attempts have been made to develop an airborne instrument, this mode of operation is not yet practical (Paterson and Reeves, 1985).

The distinction between reconnaissance and detailed field work is based on the objective, that is, whether the purpose is to find features of interest or to map them. Station spacings in field work with the gravimeter vary from 20 km to as little as 5 m. The station interval is usually selected on the basis of assumed depth and size of the anomalies sought. For oil exploration, one station per 2 to 4 km<sup>2</sup> is desirable because structures associated with oil accumulation are usually larger than this and hence their

anomalies would not be missed with such spacing. While a more-or-less uniform grid of stations is desirable, stations are often run on loops that are operationally easier. Stations 0.5 to 1.0 km apart on loops roughly  $6 \times 6$  km in size might be typical for a petroleum survey.

In mineral exploration, gravity is normally employed as a secondary detail method for confirmation and further analysis of anomalies already outlined by magnetic and/or electrical techniques. The spacing is determined mainly by knowledge gained from the earlier surveys. Measurements are usually made at the same locations as the magnetic or electrical stations, commonly 15 to 30 m apart.

*Microgravity* engineering and archaeological surveys (for example, searching for cavities or bedrock) sometimes involve station spacing as close as 1 m (Arzi, 1975).

Field measurements with modern gravimeters are straightforward. The gravimeter must be leveled precisely for each reading. It may be difficult to get a stable null in swampy ground and when the wind is strong, but extra care and time generally give an acceptable measurement. Similar problems arise in marine gravity work using instruments that rest on the sea floor. For reasonable speed of operation, a vehicle normally is used for getting from station to station.

Precision is required in surveying gravity stations. Achieving the required precision (10 cm in elevation and about 30 m in latitude for 0.03 mGal accuracy) often involves the major cost of field work. Gravity measurements typically proceed much faster than the surveying, and three or four survey teams may be required to keep ahead of one meter operator.

*Inertial navigation* sometimes cuts the cost of determining location and elevation, especially where helicopter transport is used in areas of difficult access (LaFehr, 1980). An inertial navigation system (§B.7) senses acceleration by means of three orthogonal accelerometers mounted on a gyroscopically stabilized platform; changes in horizontal and vertical position are determined by integrating twice over time. Very small errors tend to accumulate rapidly to produce large errors, but these can be reduced to acceptable amounts if the helicopter stops every 3 to 5 min during which time the drift rate can be determined. This time interval is compatible with the travel time from station to station. Lynch and King (1983) claim 0.8 m elevation accuracy and 15 m horizontal accuracy in a survey in the mountainous overthrust belt of the Rocky Mountains, to yield Bouguer values with 0.3 mGal accuracy. In a high-precision survey of a limited area in northern Canada checked by leveling, elevations were determined to

0.9 m and horizontal positioning to 0.43 m, so inertial navigation can achieve remarkable accuracy. With a helicopter survey, stations can be located on a more uniform grid than with land surveys (which are usually run around the perimeter on traverses), so that interpolation errors are considerably reduced.

### 2.5.2. Drift Correction

Gravimeters change their null reading value gradually with time. This *drift* results mainly from creep in the springs and is usually unidirectional. Modern instruments, however, have very little drift. Gravity readings also change with time because of tidal effects (§2.3.2f).

The net result of drift and tidal effects is that repeated readings at one station give different values. *Drift correction* is accomplished by reoccupying some stations. The maximum time between repeat readings depends on the accuracy desired, but is usually 3 or 4 hr. A drift curve is shown in Figure 2.15. Its oscillatory shape is determined by tidal effects. It is not necessary to use the same station for checking drift because any station can be reoccupied. Intermediate gravity stations occupied only once can then be corrected for the drift that occurred.

If the meter movement is not clamped between readings or is subjected to sudden motion or jarring (as during transport), somewhat erratic changes (called *tears* or *tares*) may be produced. If the instrument is bumped, it is wise to reread a known station immediately. Since there is no way of allowing for erratic changes, we can only correct those points occupied while the drift curve is smooth.

### 2.5.3. Marine Surveys

(a) *Locating marine stations.* Considerable gravity work has been done on the surface of water-covered areas and also on the sea floor. Locating the station is usually done by using a radionavigation system such as Shoran, Raydist, or RPS (see §B.6). The accuracy of offshore location is usually lower than on land but elevation determination is not a problem if appropriate allowance is made for tidal variations.

(b) *Remote control systems.* Standard gravimeters have been adapted for operation on the sea floor to depths of 200 m. This method of measurement is suitable for most inland waters and coastal areas. The meter is enclosed in a pressure housing that is supported on a squat tripod with disk feet. About

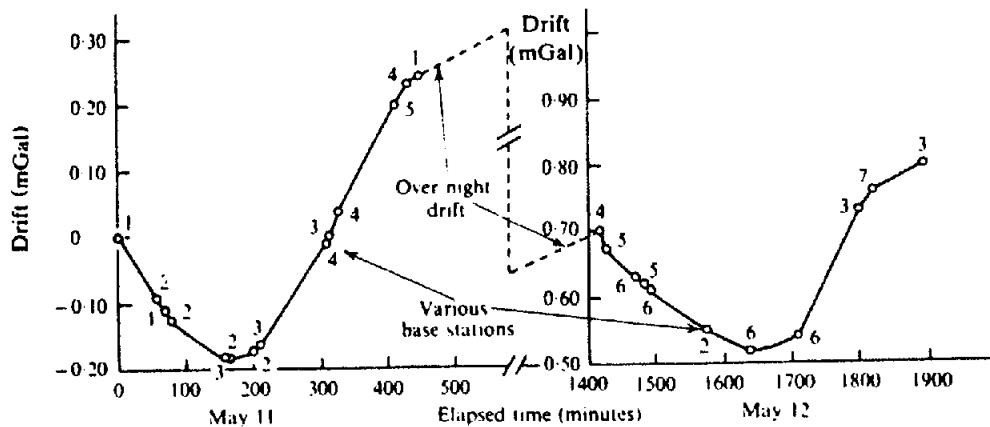


Figure 2.15. Gravimeter drift during a field survey.

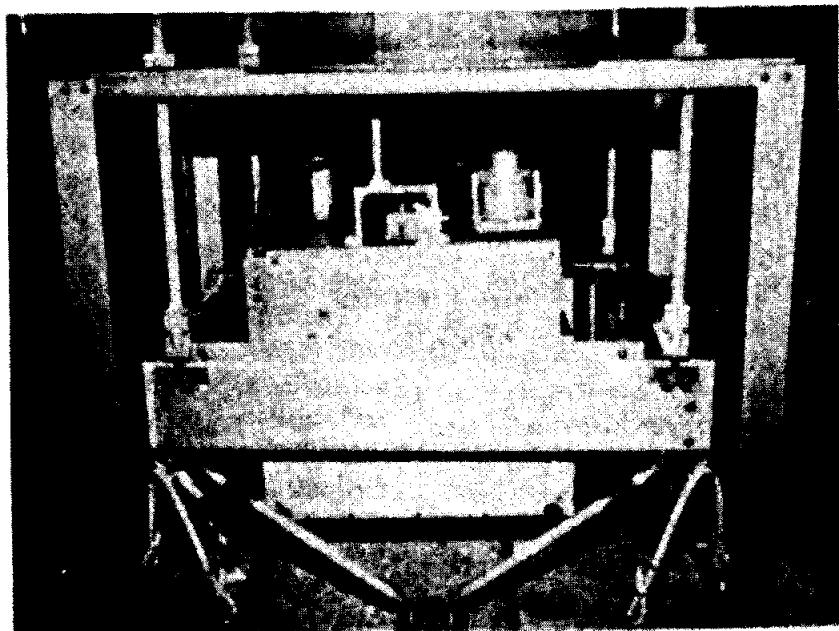


Figure 2.16. Photograph of a shipboard gravimeter.

half the total weight of the assembly is in the tripod in order to provide maximum stability when it is resting on the bottom; the overall weight of one model is 300 kg. The assembly is connected to a ship by a cable from which it is lowered into position on the bottom. Leveling is achieved by small motors that raise or lower the disk feet.

Although the high sensitivity of this equipment is an advantage, operation in deep water is slow because the assembly must be raised to the surface between stations. A problem in reoccupying stations is that the sea floor location may be different from that previously occupied, even when the surface location is identical. This method is now little used.

(c) *Shipboard operations and the Eötvös correction.* Shipboard gravimeters (Fig. 2.16) are used for most gravity measurements at sea. Shipboard gravimeters are mounted on an elaborate gyro-stabilized platform (Valliant and LaCoste, 1976) located in the part of a ship where there is minimum movement due to roll and pitch.

If a gravimeter has a velocity during a measurement, the centrifugal force acting on the meter is different from that when it is at rest. An eastward component of velocity adds to the velocity owing to the rotation of the Earth and hence increases the centrifugal force and decreases the gravity reading. A westward component of velocity has the opposite

effect. A northward component creates a new component of centrifugal force, which is added vectorially to the first. The correction for the velocity of the meter,  $\Delta g_V$ , called the *Eötvös correction*, is given by

$$\Delta g_V = 4.040V \cos \phi \sin \alpha + 0.001211V^2 \text{ mGal} \quad (2.38a)$$

$$\Delta g_V = 7.503V' \cos \phi \sin \alpha + 0.004154V'^2 \text{ mGal} \quad (2.38b)$$

where  $V$  is in kilometers per hour,  $V'$  in knots,  $\phi$  is the latitude, and  $\alpha$  is the course direction with respect to true north. The accuracy of shipboard gravity depends mainly on the accuracy of the Eötvös correction.

The error in the Eötvös correction due to errors in  $V$  and  $\alpha$  is

$$\begin{aligned} d(\Delta g_V) &= (0.0705V \cos \phi \cos \alpha) d\alpha \\ &\quad + (4.040 \cos \phi \sin \alpha + 0.002422V) dV \end{aligned} \quad (2.39)$$

with  $V$  and  $dV$  in kilometers per hour and  $d\alpha$  in degrees. Thus the sensitivity to velocity error is greatest for an east-west course and the sensitivity to course-direction error is greatest for a north-south course. Assuming that the velocity at the moment of gravity reading involves an uncertainty of 0.2 km/hr and instantaneous heading error of  $1^\circ$ ,  $\phi = 40^\circ$ , and  $V = 10$  km/hr, then  $d(\Delta g_V) = 0.62$  mGal for an east-west course and 0.54 mGal for a north-south course.

#### 2.5.4. Airborne Gravity

The main difficulty with airborne gravity surveys arises from very large and rapid changes in  $g_{obs}$ , caused by changes in the aircraft altitude, linear acceleration, roll, and heading. These effects can be corrected for in shipborne gravity work because changes are slow and the velocity is low.

Hammer (1983) tells of using a helicopter flying (in the middle of the night to avoid air turbulence) at a speed of 50 to 100 km/hr at elevations of 300 to 4,000 m using an autopilot directed by a navigation-system computer (a human pilot is not sufficiently precise). His data, smoothed over a 2 min window (2 to 4 km), suggest that airborne gravity would be

useful for regional studies and reconnaissance of large anomalies. Brozena (1984) achieved an accuracy of 5 mGal averaged over 20 km.

## 2.6. GRAVITY DATA PROCESSING

### 2.6.1. Noise, Regionals, and Residuals

Because a Bouguer map shows horizontal differences in the acceleration of gravity, only horizontal changes in density produce anomalies. Purely vertical changes in density produce the same effect everywhere and so no anomalies result.

The gravity field is a superposition of anomalies resulting from density changes (anomalous masses) at various depths. Some anomalous masses lie at depths in the zone of interest, some result from deeper masses, and some from shallower ones. As the source of an anomaly deepens, the anomaly becomes more spread out and its amplitude decreases. The smoothness (or apparent wavelength) of anomalies is generally roughly proportional to the depth of the lateral density changes.

The depth range we wish to emphasize depends on the objectives of the interpretation. Shallow anomalies are of interest in mineral exploration but are usually regarded as undesirable noise in petroleum exploration. As in any geophysical technique, the most useful factor in interpretation is knowledge of the local geology.

Whereas it is possible for a distributed anomalous mass to give an anomaly that appears to originate from a more concentrated deeper mass, a concentrated mass cannot appear to originate deeper. The horizontal extent and smoothness of an anomaly is therefore usually a measure of the depth of the anomalous mass, and this property can be used to partially separate the effects of anomalous masses that lie within a depth zone of interest from the effects of both shallower and deeper masses.

The effects of shallow masses (*near-surface noise*) are usually of short wavelength. They can be removed largely by filtering out (smoothing) short-wavelength anomalies. The effects of deep masses are called the *regional*. The gravity field after near-surface noise and the regional have been removed is called the *residual*; it presumably represents effects of the intermediate zone of interest.

The major problem in gravity interpretation is separating anomalies of interest from the overlapping effects of other features; usually the main obscuring effects result from deeper features. *Residualizing* attempts to remove the regional so as to emphasize the residual. However, the separation usu-

ally is not complete; both regional and residual are distorted by the effects of each other.

Residualizing can also be thought of as predicting the values expected from deep features and then subtracting them from observed values, so as to leave the shallower effects. The expected value of the regional is generally determined by averaging values in the area surrounding the station. Several methods of removing the unwanted regional are described in the next section. Gupta and Ramani (1982) discuss the application of different residualizing methods.

Gravity station locations should be shown on the final map to aid in distinguishing residuals that are well controlled from those possibly resulting from interpolation.

The result obtained by smoothing profiles or contours is inevitably biased by the interpreter, but this is not necessarily bad. If the interpreter is experienced and uses additional geologic knowledge to guide him, it may be a decided advantage. It should be noted that nonsmoothing methods of residualizing also involve subjective elements, such as the choice of order for surface fitting, of grid dimensions in grid residualizing, and so on.

### 2.6.2. Graphical Residualizing

Graphical residualizing is done by smoothing either profiles or maps. A simple example of removing the regional by smoothing is illustrated in Figure 2.17. The profile in Figure 2.17a shows disturbances of different sizes; the smooth, nearly linear slope is the regional. In Figure 2.17b, the regional contours are regular and the residual obtained by subtracting the smoothed contours from the map values should be reliable.

The emphasis in drawing a smooth regional should be on "smooth" and most of the errors or failures in residualizing are caused by the regional not being sufficiently smooth. "Smooth" implies both smooth in shape and systematic in contour interval. Often profiles are plotted for several parallel lines, generally in the dip direction. Smooth regionals are then drawn on these parallel lines, making certain that they are consistent on all profiles. Often cross profiles are drawn linking the parallel lines into a grid to ensure that the regional is consistent over the grid. This approach is especially suitable when the regional trend is mainly unidirectional. If the survey has been carried out with close, uniform spacing of stations and lines, the station values themselves can be used instead of contour values to plot the profiles, thereby reducing errors because of contour interpolation.

Once the regional has been contoured, the residuals are obtained by subtracting the regional from the Bouguer map, either graphically or numerically. Graphical residualizing is sometimes done by drawing contours of constant difference through the points where regional and observed contours intersect.

When the regional is so irregular that the directional trend is not immediately apparent or when there are several superimposed regional systems, residualizing may be done iteratively, that is, one first determines and removes the most obvious regional and then finds a second-order regional from the first-order residual, and so on.

### 2.6.3. Surface-Fitting Residualizing Methods

The regional is sometimes represented by a low-order analytic surface. The parameters of the analytic surface are usually determined by a least-squares fit (Agocs, 1951) or some similar operation. How closely the surface fits the data depends on the order of the surface and the magnitude of the area being fitted. Nettleton (1976) illustrates orders of fit for a one-dimensional case (Fig. 2.18). The regional surface is often that given by a polynomial or the low-order components of a 2D-Fourier surface [Eq. (A.52a)]. The selection of order is usually made by examination of trial fits of several different orders.

Surface fitting is sometimes done to isolate and emphasize trends. Results from Coons, Woolard, and Hershey (1967) are shown in Figure 2.19. The trend becomes more evident as the order increases up to some point, about tenth order for the data of Figure 2.19. The residual for low order still contains appreciable regional trend and thus low orders are not very effective in separating the regional from the residual. Likewise, high-order surfaces are not effective because much of the sought-after anomaly is mixed with the regional in the surface fit.

### 2.6.4. Empirical Gridding Methods

Gridding provides a simple way of predicting the regional by regarding it as the average value of gravity in the vicinity of the station (Griffin, 1949). Usually the values averaged are those on the circumference of a circle centered at the station:

$$\overline{g(r)} = (1/2\pi) \int_0^{2\pi} g(r, \theta) d\theta \quad (2.40)$$

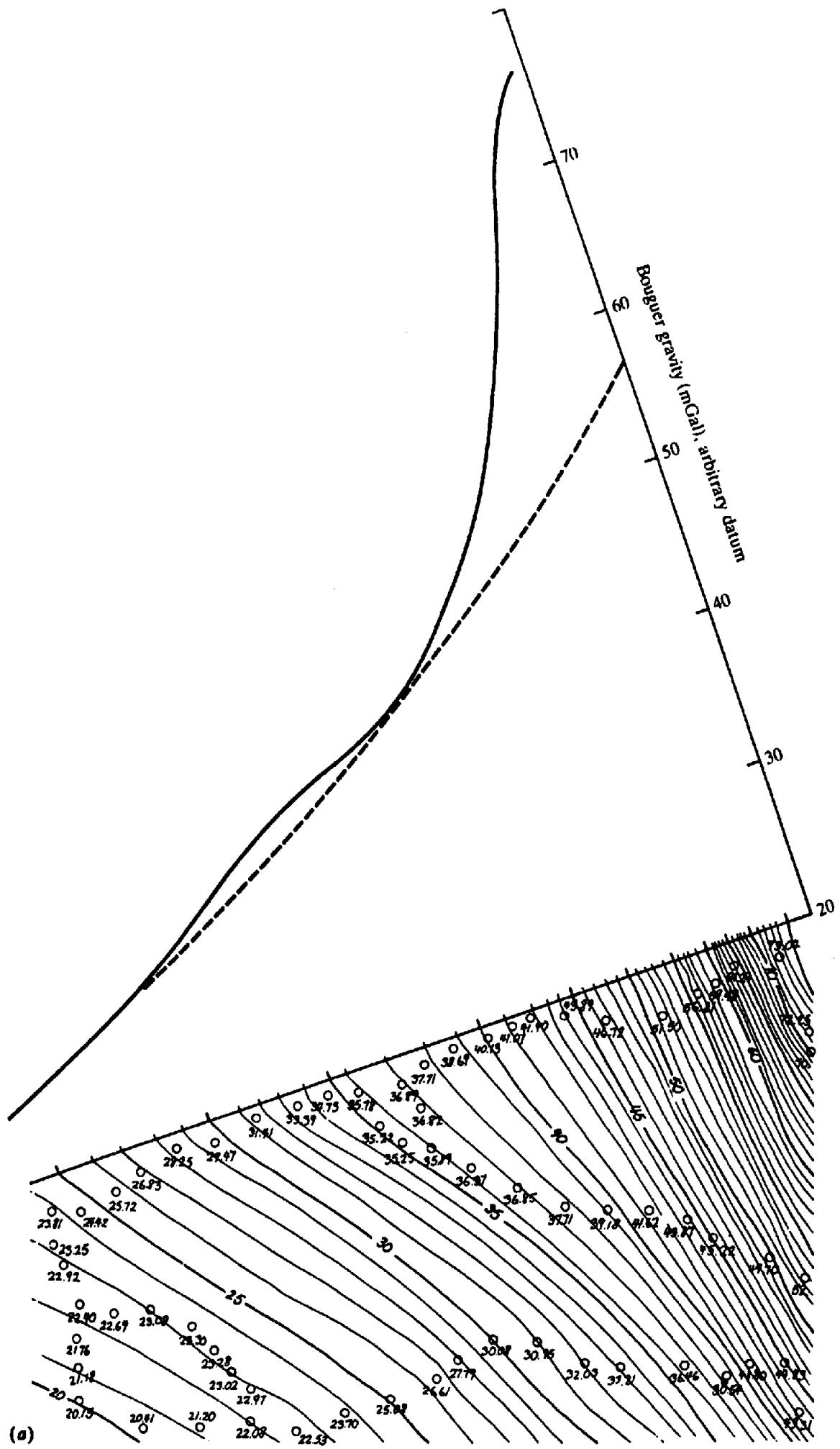


*Figure 2.17. Graphical residualizing (After Sheriff, 1978). (a) Removing the regional on a profile across a local uplift and a fault.*

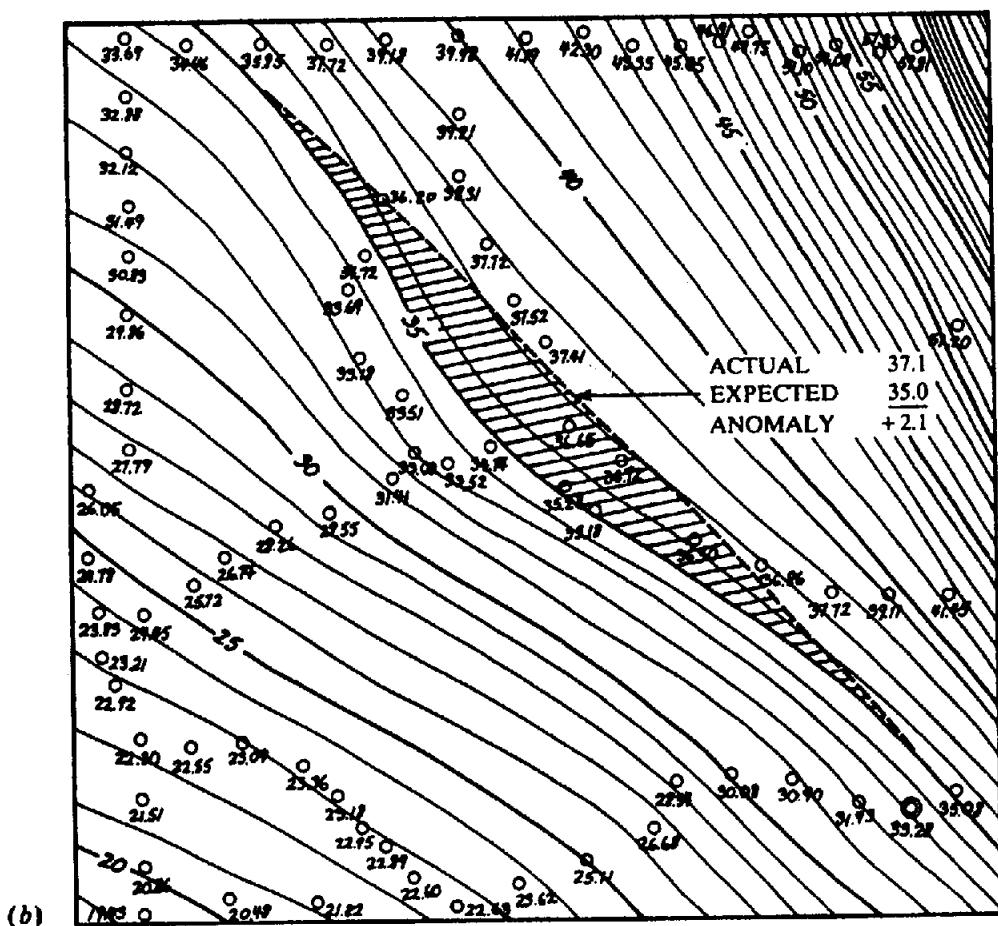


Figure 2.17. (Continued) (b) Removing the regional by contour smoothing.

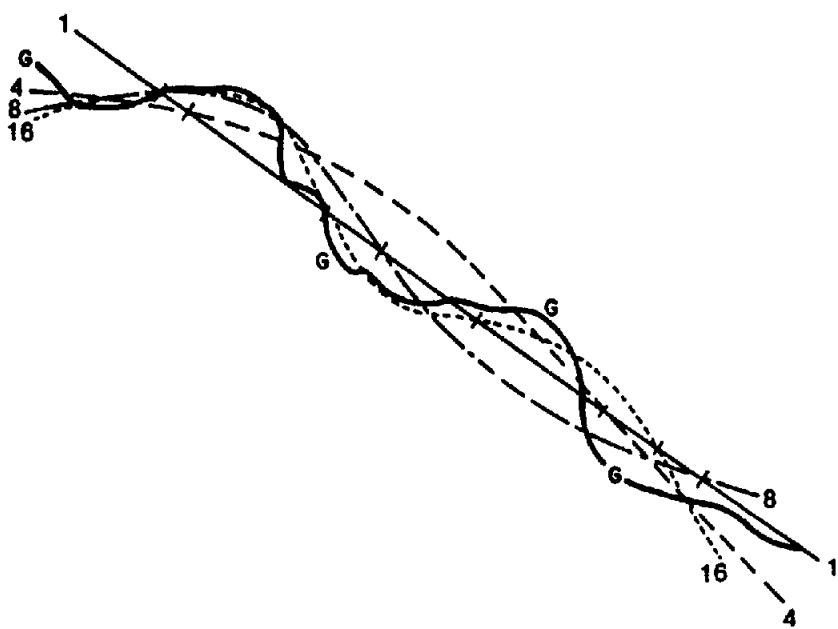


Figure 2.18. Illustrating least-squares surface-fitting. Curve G represents a gravity profile and curves 1, 4, 8, 16 represent fits of the respective orders. The surface fit, and hence the residual, depends on the dimensions that are fitted (from Nettleton, 1976).

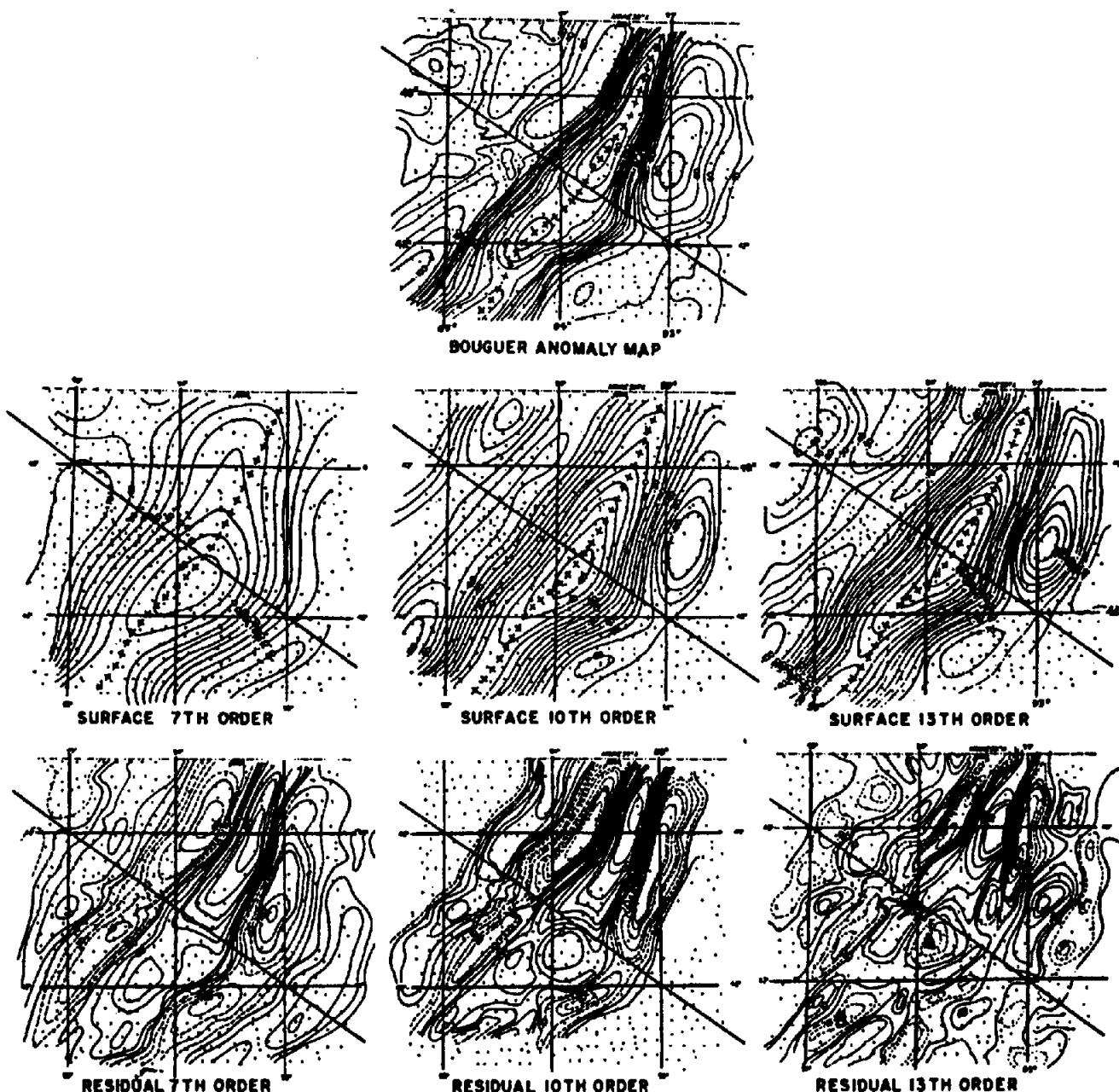


Figure 2.19. Fits of surfaces of different order and the respective residuals. (After Coons, Woolard, and Hershey, 1967.)

In actual practice the integral is generally replaced by a sum of discrete values (as in Fig. 2.20a):

$$\bar{g}(r) = \{g(r, 0) + g(r, \theta_1) + \dots + g(r, \theta_{n-1})\} / n \quad (2.41)$$

where  $\theta_m = m(2\pi/n)$ . The residual is then

$$g_r = g_B - \bar{g}(r) \quad (2.42)$$

where  $g_B$  is the Bouguer anomaly value. Usually the values of  $g(r, \theta_m)$  are obtained by interpolation from the gravity map contours. The result depends somewhat on the number of points selected but even more on the radius of the circle. If the radius is so small

that part of the anomaly is included on the circle, then the anomaly magnitude will be too small; if the radius is too large, the average may be biased by other anomalies. The radius is usually of the same order of magnitude as the depth of the anomaly to be emphasized, but both shallower and deeper anomalies will still contribute to the results. The grid spacing for points to be calculated is generally about half the radius used for averaging.

Sometimes averages over several circles of different radii  $r_i$  are used; successive circles are assigned different weights,  $w_i$ :

$$g_r = (c/s^2) \{ g_0 + w_1 \bar{g}(r_1) + w_2 \bar{g}(r_2) + \dots \} \quad (2.43)$$

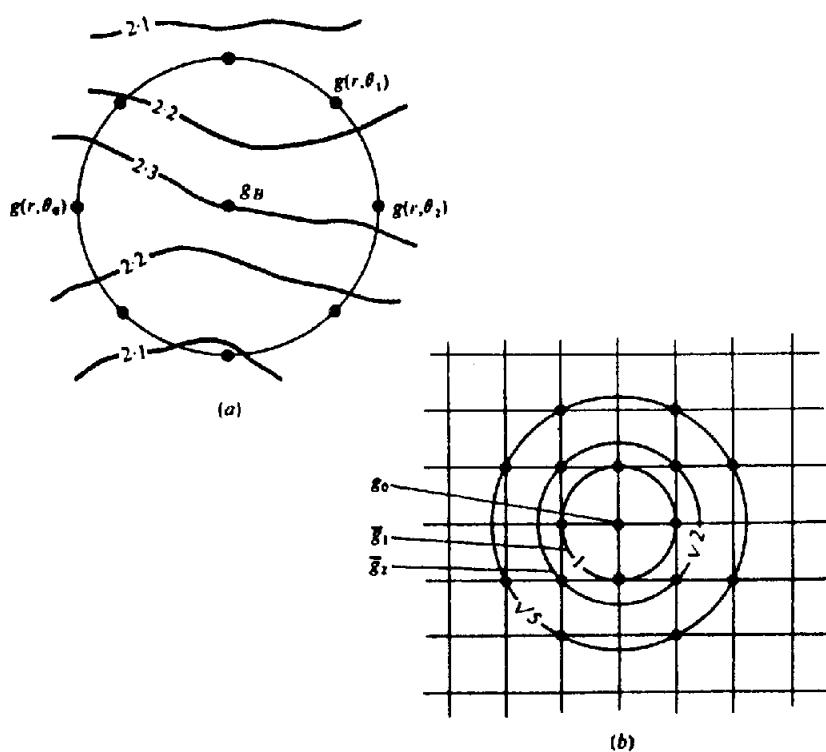


Figure 2.20. Analytical separation of the residual and the regional. (a) Griffin method. (b) Second-derivative method.

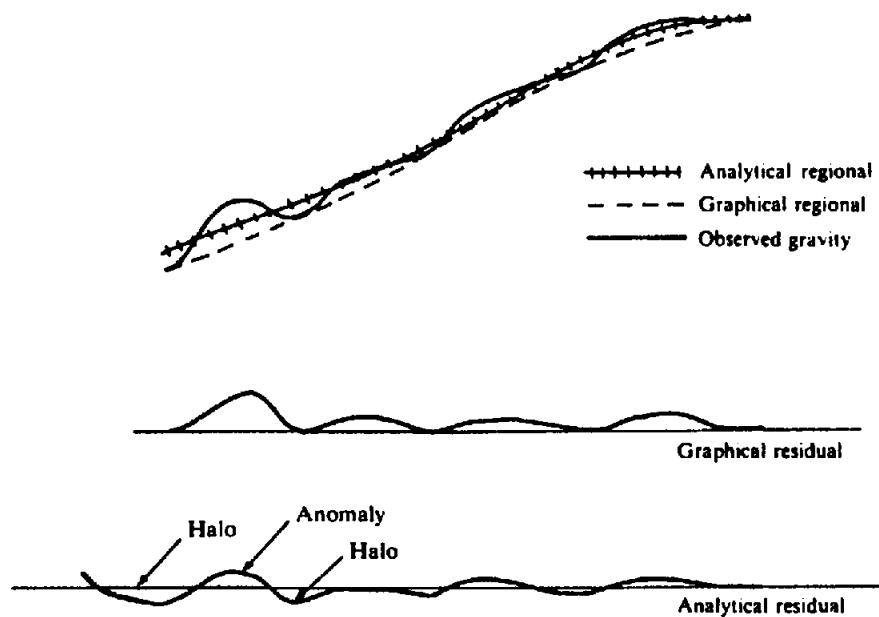


Figure 2.21. Comparison of graphical and analytical methods of removing regional gravity.

where  $c$  is a constant,  $s$  is a scale factor, and  $\sum w_i = -1$ . Usually the values on the various circles are read at grid points as in Figure 2.20b. Equation (2.43) is simply the expression for a 2-D convolution, and residualizing can be thought of as a convolution or filtering operation.

In graphical methods the interpreter usually draws the regional so that all residuals are either positive or

negative according to his concept of the density contrast expected to cause the anomaly. However, in nongraphical methods, the average value of the residual is usually set at zero so that both positive and negative residuals result. This is illustrated in Figure 2.21. A consequence of this is that each anomaly is surrounded by a "halo" of opposite sign, which does not indicate a separate anomaly.

### 2.6.5. Second Vertical Derivative Methods

The second vertical derivative enhances near-surface effects at the expense of deeper anomalies. Second derivatives are a measure of curvature, and large curvatures are associated with shallow anomalies.

The second vertical derivative can be obtained from the horizontal derivatives because the gravity field satisfies Laplace's equation

$$\nabla^2 g = \partial^2 g / \partial x^2 + \partial^2 g / \partial y^2 + \partial^2 g / \partial z^2 = 0$$

$$\partial^2 g / \partial z^2 = -(\partial^2 g / \partial x^2 + \partial^2 g / \partial y^2) \quad (2.44)$$

For the one-dimensional case, the first derivative can be estimated by dividing the difference between readings at two nearby locations,  $x_1$  and  $x_2$ , separated by the distance  $\Delta x$ :

$$dg(x_{1.5})/dx = \{g(x_2) - g(x_1)\}/\Delta x$$

The second derivative is obtained from the difference between nearby first derivatives:

$$\begin{aligned} d^2 g(x_2)/dx^2 &\approx \{dg(x_{2.5})/dx - dg(x_{1.5})/dx\}/dx \\ &\approx [\{g(x_3) - g(x_2)\}/\Delta x \\ &\quad - \{g(x_2) - g(x_1)\}/\Delta x]/\Delta x \\ &\approx \{g(x_3) - 2g(x_2) \\ &\quad + g(x_1)\}/(\Delta x)^2 \quad (2.45) \end{aligned}$$

Equation (2.45) has the same form as Equation (2.43) (a weighted sum of the values at nearby points), and Equation (2.43) yields an estimate of the second vertical derivative for appropriate values of  $w_i$ .

A number of mathematical treatments have been developed (Henderson and Zietz, 1949; Elkins, 1951; Dean, 1958) to extract the vertical second derivative from the average values at various distances from the station. Generally values over concentric circles are weighted to produce an expression of the form [compare with Eq. (2.43)]

$$\partial^2 g / \partial z^2 = (c/s^2)(w_0 g_0 + w_1 \bar{g}_1 + w_2 \bar{g}_2 + \dots) \quad (2.46a)$$

where  $g_0$  is the gravity at the station where the second derivative is being determined,  $g_1, g_2, \dots$  are averages over surrounding circles of various radii,  $w_0, w_1, \dots$  are weighting coefficients such that  $\sum w_i = 0$ ,  $c$  is a numerical factor, and  $s$  is the grid spacing. For example, if the survey is on a square grid and the successive radii are  $s$ ,  $s\sqrt{2}$ , and  $s\sqrt{5}$  (as in Fig. 2.20b), one form of equation (2.46a) is

$$\partial^2 g / \partial z^2 = 2(3g_0 - 4\bar{g}_1 + \bar{g}_2)/s^2 \quad (2.46b)$$

(Henderson and Zietz, 1949). Gupta and Ramani (1982) show an application to mineral exploration.

### 2.6.6. Wavelength Filtering

The foregoing methods of separating residuals from the regional are based on the degree of smoothness (or wavelength = 1/wavenumber; see §4.2.2d) of anomalies. Filtering can also be done by transforming map data to a wavenumber-wavenumber domain using a two-dimensional Fourier transform [Eqs. (A.57)], removing certain wavenumber components (that is, filtering), and then doing an inverse transformation to reconstitute the map, but with certain wavelengths removed. What are removed are usually the small wavenumbers (large wavelengths) of the regional, so that the wavenumber components involved in the inverse transform are the large ones which correspond to the short wavelengths of the residual.

Wavenumber filtering encounters the same problem as other residualizing schemes. The wavenumber spectra of most features are broadband, so spectra of features at different depths overlap and consequently the features cannot be separated completely by filtering.

### 2.6.7. Field Continuation

The fact that gravity fields obey Laplace's equation permits us to determine the field over an arbitrary surface if the field is known completely over another surface and no masses are located between the two surfaces. This process is called *continuation*.

Following the method of Grant and West (1965, pp. 216–21), we let the plane  $z = 0$  separate free space ( $z < 0$ ) from the region containing masses ( $z > 0$ ) (Fig. 2.22a);  $P$  is a point in free space,  $Q$  locates a point mass, and  $R$  is the distance  $PQ$ . If  $U_p$

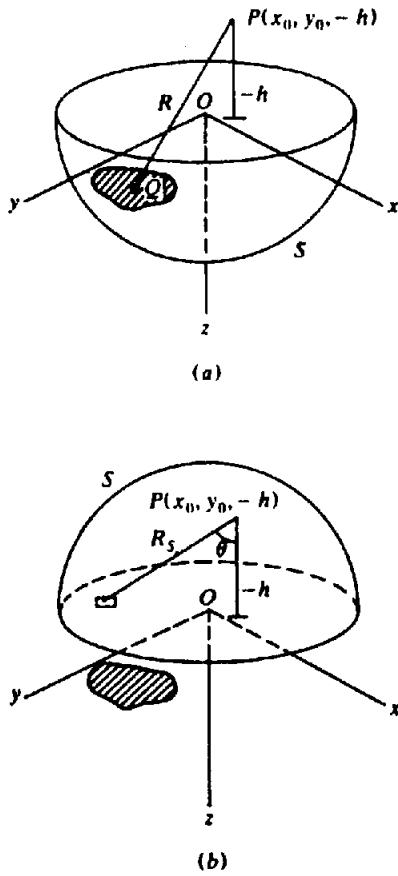


Figure 2.22. The continuation theorem. (After Grant and West, 1965.) (a) Hemisphere  $S$  on positive side of  $xy$  plane. (b) Hemisphere on negative side of  $xy$  plane.

and  $U_Q$  are the potentials at  $P$  and  $Q$ . Equations (2.6a) and (2.13b) give

$$U_P = \gamma \int_V (\rho / R) dv$$

$$\nabla^2 U_Q = -4\pi \gamma \rho$$

Eliminating  $\rho$ , we have

$$U_P = -(1/4\pi) \int_V (1/R) \nabla^2 U_Q dv$$

We now apply Green's theorem [Eq. (A.28)] to the hemisphere in Figure 2.22a with  $W = 1/R$ ,  $U = U_Q$  inside  $S$ , and  $U = U_S$  on the surface. Since  $\nabla^2(1/R) = 0$ , we get

$$-\int_V (1/R) \nabla^2 U_Q dv = 4\pi U_P - \int_S \{ U_S \nabla (1/R_S)$$

$$-(1/R_S) \nabla U_S \} \cdot ds$$

$$= \int_S \{ U_S \partial/\partial n (1/R_S)$$

$$-(1/R_S) \partial U_S / \partial n \} ds$$

The derivatives within the braces are the components of the gradients normal to the surface  $ds$ . Setting the radius of the hemisphere equal to infinity causes the contribution of the curved surface to vanish because of the factor  $1/R_S$ , and the integral reduces to

$$4\pi U_P = \int_{x,y} \{ U_S (\partial/\partial n) (1/R_S)$$

$$-(1/R_S) \partial U_S / \partial n \} dx dy \quad (2.47a)$$

The integration is taken over that portion of the  $xy$  plane where the anomalous field is significantly larger than zero.

We now follow the same procedure using the hemisphere in Figure 2.22b. Because  $\nabla^2 U_Q = 0$  within the hemisphere [Eq. (2.11a)], we get

$$0 = \int_{x,y} \{ U_S (\partial/\partial n) (1/R_S)$$

$$-(1/R_S) \partial U_S / \partial n \} dx dy \quad (2.47b)$$

The right-hand sides of Equations (2.47a) and (2.47b) appear to be the same, but, in fact, they are different because  $n$ , the outward unit normal to the surface  $ds$ , is upward ( $-z$  direction) in Equation (2.47a) and downward ( $+z$  direction) in Equation (2.47b). Thus,  $\partial U_S / \partial n = -g$  in Equation (2.47a) and  $+g$  in Equation (2.47b). Also,  $R_S^2 = (x - x_0)^2 + (y - y_0)^2 + (z + h)^2$ , so, on the  $xy$  plane,

$$(\partial/\partial n)(1/R_S) = \lim_{z \rightarrow 0} (\partial/\partial z)(1/R_S)$$

$$= \lim_{z \rightarrow 0} \{ -(z + h)/R_S^3 \}$$

$$= -h/R_S^3$$

which is independent of the direction of  $n$ . Thus, subtracting Equation (2.47b) from (2.47a), we obtain

$$U_P = (1/2\pi) \int_{x,y} (g/R_S) dx dy$$

where  $R_S^2 = (x - x_0)^2 + (y - y_0)^2 + h^2$ . To get  $\partial U_P / \partial z$  at  $P$ , we replace  $h^2$  in  $R_S^2$  with  $z^2$ , differentiate, and then replace  $z$  with  $(-h)$  (note that  $g$  on the  $xy$  plane is not a function of  $z$ ). The result is

$$\partial U_P / \partial z = g_P = (1/2\pi) h \int_{x,y} (g/R_S^3) dx dy \quad (2.48)$$

Since  $(h/R_S) = \cos \theta$  in Figure 2.22b,  $(g/2\pi)$  can be regarded as a surface density of mass replacing the mass below the  $xy$  plane [compare with Eq. (2.14)]. Equation (2.48) is the *upward continuation* equation that allows us to calculate the gravitational acceleration anywhere in free space from a knowledge of its values over the surface. Upward continuation is effectively smoothing. Although upward continuation is not done much in gravity analysis, it is used in magnetic interpretation to compare measurements made at different flight elevations.

If we can calculate the gravity field over a surface closer to the anomaly sources, the anomaly should be sharper and less confused by the effects of deeper features. This process, called *downward continuation*, was described by Peters (1949). It involves calculating a gravity value at depth from gravity values and derivatives on a shallower surface. The derivatives are usually evaluated by averaging over circles of different radii as described in Section 2.6.5. The main theoretical limitation on the method is singularities associated with masses through which the continuation process is carried. The main practical limitation is imposed by uncertainty in the measured field; because derivatives involve differences, their calculation magnifies uncertainties. The result is that minor noise is increased in the downward-continued field and this noise may outweigh the benefits of sharpening anomalies.

We begin with Laplace's equation (2.11b) (thus implicitly assuming that we will not continue through any masses) and the expressions for second derivatives calculated by finite differences [Eq. (2.45)]. For the point  $(x_0, y_0, 0)$  and station spacing  $s$ , we write

$$\frac{\partial^2 g}{\partial x^2} = \{ g(x_0 + s, y_0, 0) - 2g(x_0, y_0, 0) \\ + g(x_0 - s, y_0, 0) \} / s^2$$

$$\frac{\partial^2 g}{\partial y^2} = \{ g(x_0, y_0 + s, 0) - 2g(x_0, y_0, 0) \\ + g(x_0, y_0 - s, 0) \} / s^2$$

$$\frac{\partial^2 g}{\partial z^2} = \{ g(x_0, y_0, +s) - 2g(x_0, y_0, 0) \\ + g(x_0, y_0, -s) \} / s^2$$

If we take  $z$  to be positive downward, then  $g(x_0, y_0, +s)$  is the gravity value a distance  $s$  below the station  $g(x_0, y_0, 0)$ . Substituting into Laplace's

equation, we get

$$g(x_0, y_0, +s) = 6g(x_0, y_0, 0) \\ - \{ g(x_0 + s, y_0, 0) \\ + g(x_0 - s, y_0, 0) \\ + g(x_0, y_0 + s, 0) \\ + g(x_0, y_0 - s, 0) \\ + g(x_0, y_0, -s) \} \quad (2.49)$$

All of these terms can be found from the gravity values read from a grid except for the last term, which can be found from Equation (2.48). Similar but more complicated procedures use concentric circles passing through grid stations. Other methods employ Fourier transform theory (see Grant and West, 1965, p. 218).

## 2.7. GRAVITY INTERPRETATION

### 2.7.1. General

After the camouflaging interference effects of other features have been removed to the best of our ability, the interpretation problem usually is finding the mass distribution responsible for the residual anomaly. This often is done by *iterative modeling* (Bhattacharyya, 1978). The field of a model mass distribution is calculated and subtracted from the residual anomaly to determine the effects for which the model cannot account. Then the model is changed and the calculations repeated until the remaining effects become smaller than some value considered to be "close enough." To limit the number of possible changes, we include some predetermined constraints, for example, we might change only the upper surface of the mass distribution.

Before iterative modeling became practical, interpreters generally compared residual anomalies to anomalies associated with simple shapes, and this procedure is still useful in many situations. Simple shapes can be modeled with a microcomputer (Reeves and MacLeod, 1983). A gravity anomaly is not especially sensitive to minor variations in the shape of the anomalous mass, so that simple shapes often yield results that are close enough to be useful. Study of the gravity effect of simple shapes also helps in understanding the types of information that can be

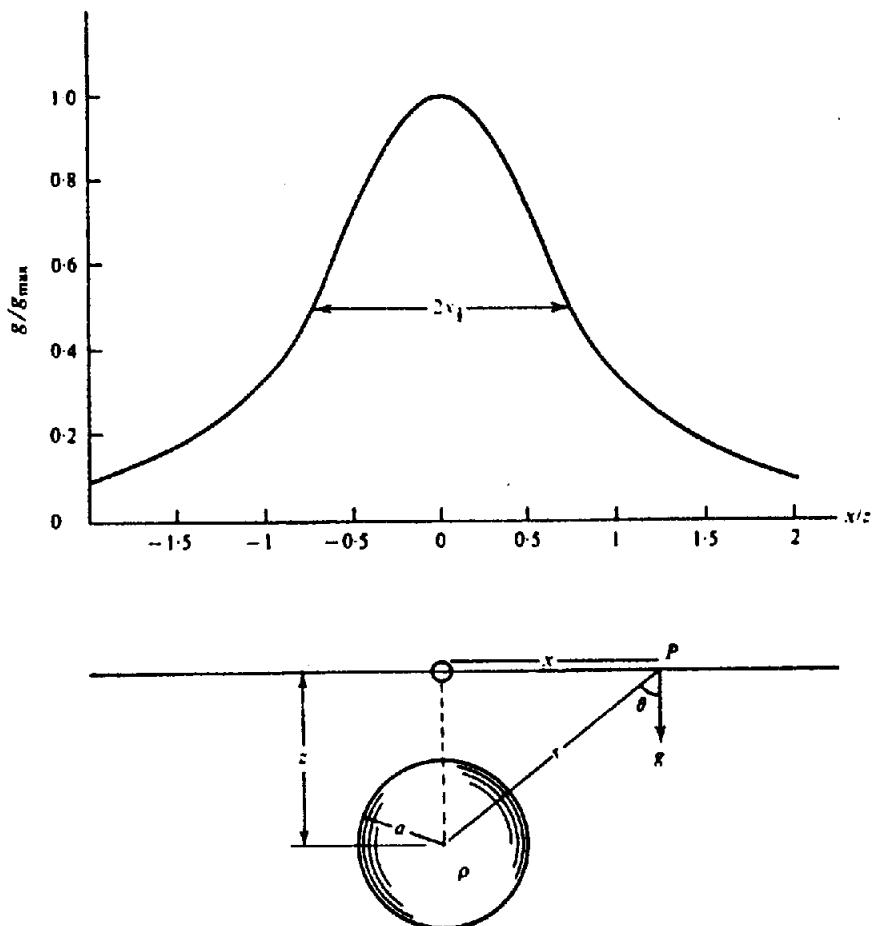


Figure 2.23. Gravity effect of a sphere.

learned, for example, in determining what aspects of an anomaly indicate the depth, shape, density contrast, total mass, and so forth.

In the following examples, the density symbol  $\rho$  is the density contrast with respect to the laterally equivalent material (in numerical relations,  $\rho$  is the difference in specific gravity because density is usually given in grams per cubic centimeters even where linear dimensions are given in English units).

### 2.7.2. Gravity Effect of a Sphere

The gravity effect of a sphere at a point  $P$  (Fig. 2.23), directed along  $r$ , is  $g_r = \gamma M/r^2$ . The vertical component is

$$\begin{aligned} g &= g_r \cos \theta = \gamma M z / r^3 \\ &= k \rho a^3 z / (x^2 + z^2)^{3/2} \text{ mGal} \quad (2.50) \end{aligned}$$

where

$$k = 4\pi\gamma/3$$

$= 27.9 \times 10^{-3}$  when  $a, x, z$  are in meters

$= 8.52 \times 10^{-3}$  when  $a, x, z$  are in feet

Note that  $z$  is the depth to the sphere center rather than to the top of the sphere and that the profile is symmetrical about the origin taken directly above the center. The maximum value of  $g$  is

$$g_{\max} = 27.9 \times 10^{-3} \rho a^3 / z^2 \quad \text{when } a, z \text{ in meters} \quad (2.51a)$$

$$= 8.52 \times 10^{-3} \rho a^3 / z^2 \quad \text{when } a, z \text{ in feet} \quad (2.51b)$$

The depth of the center of the sphere,  $z$ , can be found from a profile. When  $g = g_{\max}/2$ ,  $z = 1.3x_{1/2}$ ,

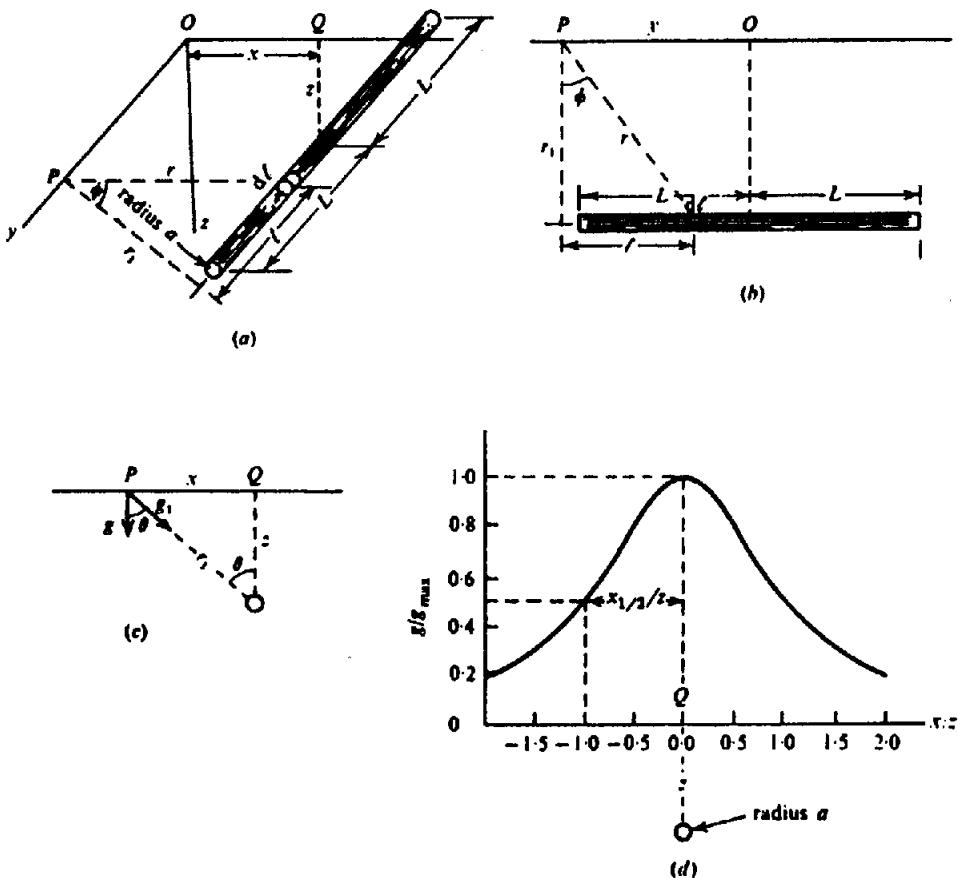


Figure 2.24. Gravity effect of a horizontal rod. (a) Three-dimensional view. (b) Projection on the plane containing the rod and the  $y$  axis. (c) Projection on the  $xz$  plane. (d) Gravity profile along the  $x$  axis ( $L = \infty$ ).

where  $x_{1/2}$  is the *half-width* of the profile, that is, half the width at the half-maximum value. We can also express the mass of the sphere,  $M$ , in terms of  $x_{1/2}$  and  $g_{\max}$ :

$$M = 25.5 g_{\max} (x_{1/2})^2 \text{ tonnes} \quad (2.52a)$$

where  $x_{1/2}$  is in meters, or, where  $x'_{1/2}$  is in feet,

$$M = 2.61 g_{\max} (x'_{1/2})^2 \text{ short tons} \quad (2.52b)$$

The spherical shape is particularly useful as a first approximation in the interpretation of three-dimensional anomalies that are approximately symmetrical.

### 2.7.3. Gravity Effect of a Horizontal Rod

The effect at  $P(x, y, 0)$  of a segment of length  $dl$  of a horizontal rod perpendicular to the  $x$  axis at a depth  $z$  (Fig. 2.24) with mass  $m$  per unit length is

$$dg_r = \gamma m dl / r^2 = \gamma m (r_1 d\phi / \cos^2 \phi) / r^2 = \gamma m d\phi / r_1$$

where  $dl = (r_1 d\phi / \cos^2 \phi)$ . The component along  $r_1$

is

$$dg_1 = dg_r \cos \phi = \gamma m \cos \phi d\phi / r_1$$

and the vertical component is

$$dg = dg_1 \cos \theta = dg_1 (z/r_1) = \gamma m z \cos \phi d\phi / r_1^2$$

Integrating from  $\tan^{-1}((y-L)/r_1)$  to  $\tan^{-1}((y+L)/r_1)$ , we get

$$\begin{aligned} g &= \left( \frac{\gamma m z}{r_1^2} \right) \left[ \frac{y+L}{\{(y+L)^2 + r_1^2\}^{1/2}} \right. \\ &\quad \left. - \frac{y-L}{\{(y-L)^2 + r_1^2\}^{1/2}} \right] \\ &= \frac{\gamma m}{z(1+x^2/z^2)} \left[ \frac{1}{\{1+(x^2+z^2)/(y+L)^2\}^{1/2}} \right. \\ &\quad \left. - \frac{1}{\{1+(x^2+z^2)/(y-L)^2\}^{1/2}} \right] \quad (2.53) \end{aligned}$$

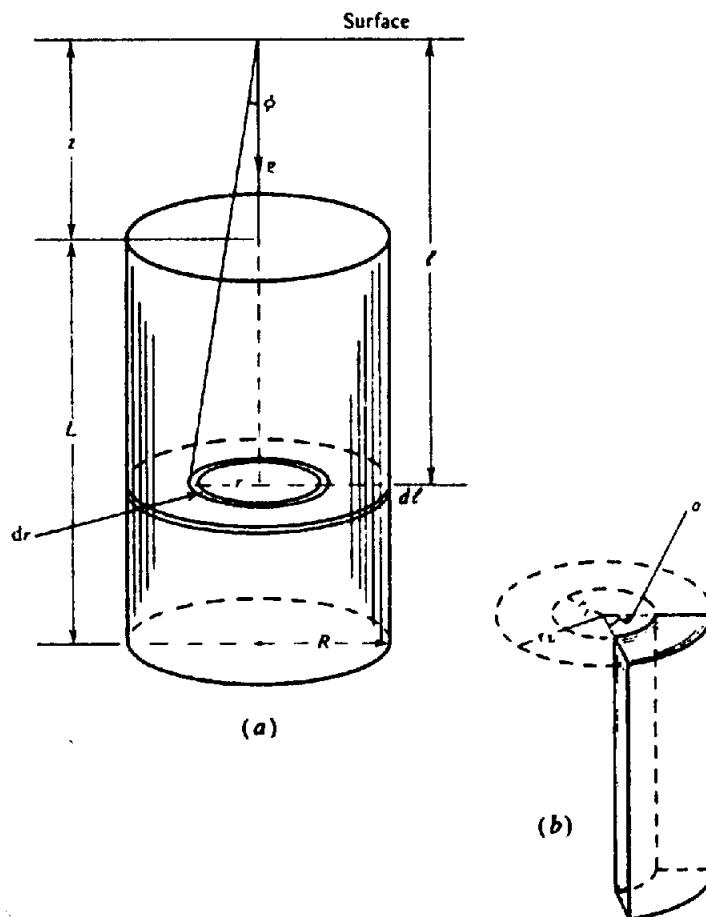


Figure 2.25. Gravity effect of a vertical cylinder. (a) Calculation of gravity over the axis. (b) Geometry of a cylindrical slice.

If the rod is infinite in length, the limits of integration would have been  $\pm\pi/2$  and the result would be

$$g = 2\gamma m/z(1 + x^2/z^2) \quad (2.54)$$

This is usually a good approximation when  $L > 10z$ . The depth  $z$  to the center of the rod in Equation (2.54) can be found from the half-width  $x_{1/2}$ :

$$z = x_{1/2} \quad (2.55)$$

If the rod is expanded into a cylinder of radius  $a$ , the only change in Equations (2.53) and (2.54) is that  $m = \pi a^2 \rho$ .

#### 2.7.4. Gravity Effect of a Vertical Cylinder

The gravity effect on the axis of a vertical cylinder (which is the maximum value) can easily be calculated. First we find  $g$  on the axis for a disk of thickness  $d\ell$  (Fig. 2.25a). We start with an elementary ring of width  $dr$  whose mass is  $\delta m = 2\pi\rho r dr d\ell$ ,

so that its gravity effect is

$$\begin{aligned} \delta g &= \gamma \delta m \cos \phi / (r^2 + \ell^2) \\ &= (2\pi\rho\gamma d\ell) r dr \cos \phi / (r^2 + \ell^2) \\ &= 2\pi\gamma\rho d\ell \sin \phi d\phi \end{aligned}$$

on eliminating  $r$ . Integrating first from  $\phi = 0$  to  $\tan^{-1}(R/\ell)$  for the disk and then from  $\ell = z$  to  $z + L$ , we get, for the whole cylinder,

$$\begin{aligned} g &= 2\pi\gamma\rho \int_z^{z+L} \left\{ 1 - \ell / (\ell^2 + R^2)^{1/2} \right\} d\ell \\ &= 2\pi\gamma\rho \left[ L + (z^2 + R^2)^{1/2} \right. \\ &\quad \left. - \{(z + L)^2 + R^2\}^{1/2} \right] \quad (2.56) \end{aligned}$$

where

$$2\pi\gamma = 41.9 \times 10^{-3} \text{ when } z, R, L \text{ are in meters}$$

$$= 12.77 \times 10^{-3} \text{ when } z, R, L \text{ are in feet}$$

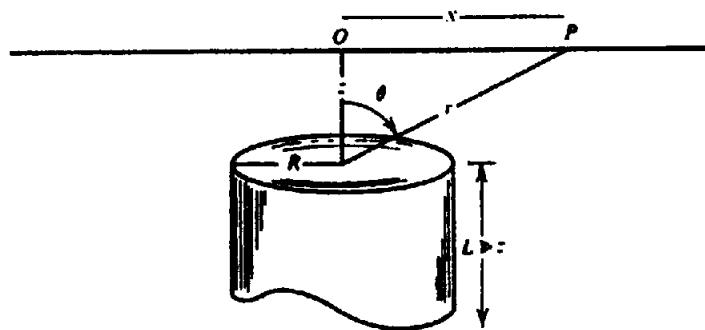
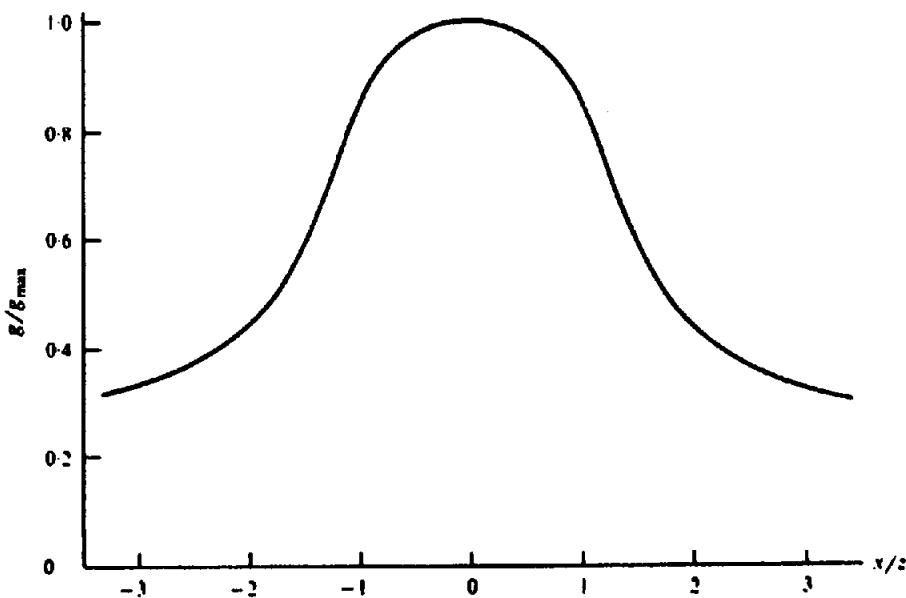


Figure 2.26. Gravity effect off the axis of a vertical cylinder.

There are several cases of special significance:

1. If  $R \rightarrow \infty$ , we have an infinite horizontal slab and

$$g = 2\pi\gamma\rho L \quad (2.57)$$

This is the Bouguer correction given in Section 2.3.2d. Note that  $g$  is independent of the depth of the slab and varies only with its thickness.

2. The terrain correction can be obtained using a sector of the cylinder as shown in Figure 2.25b. We have  $\delta m = \rho(r\theta) dr d\ell$  so that

$$\delta g = \gamma(\rho r\theta dr d\ell) \cos\phi / (r^2 + \ell^2)$$

$$= \gamma\rho\theta d\ell \sin\phi d\phi$$

on eliminating  $r$ . We integrate from  $\phi = \tan^{-1}(r_1/\ell)$  to  $\tan^{-1}(r_2/\ell)$  and from  $\ell = 0$  to  $L$ .

The result is

$$\delta g_T = \gamma\rho\theta \left\{ (r_2 - r_1) + (r_1^2 + L^2)^{1/2} - (r_2^2 + L^2)^{1/2} \right\} \quad (2.58)$$

which is Equation (2.26) with  $L$  replacing  $\Delta z$ .

3. When  $z = 0$ , the cylinder outcrops and we get

$$g = 2\pi\gamma\rho \left\{ L + R - (L^2 + R^2)^{1/2} \right\} \quad (2.59)$$

4. If  $L \rightarrow \infty$ , we have

$$g = 2\pi\gamma\rho \left\{ (z^2 + R^2)^{1/2} - z \right\} \quad (2.60)$$

If, in addition,  $z = 0$ , we have

$$g = 2\pi\gamma\rho R \quad (2.61)$$

When  $L \gg z$ , we can use Equation (2.60) to get the gravity off-axis (see MacRobert, 1948:151–5 or Pipes and Harvill, 1970:348–9). Because  $g$  satisfies Laplace's equation, we can express it in a series of

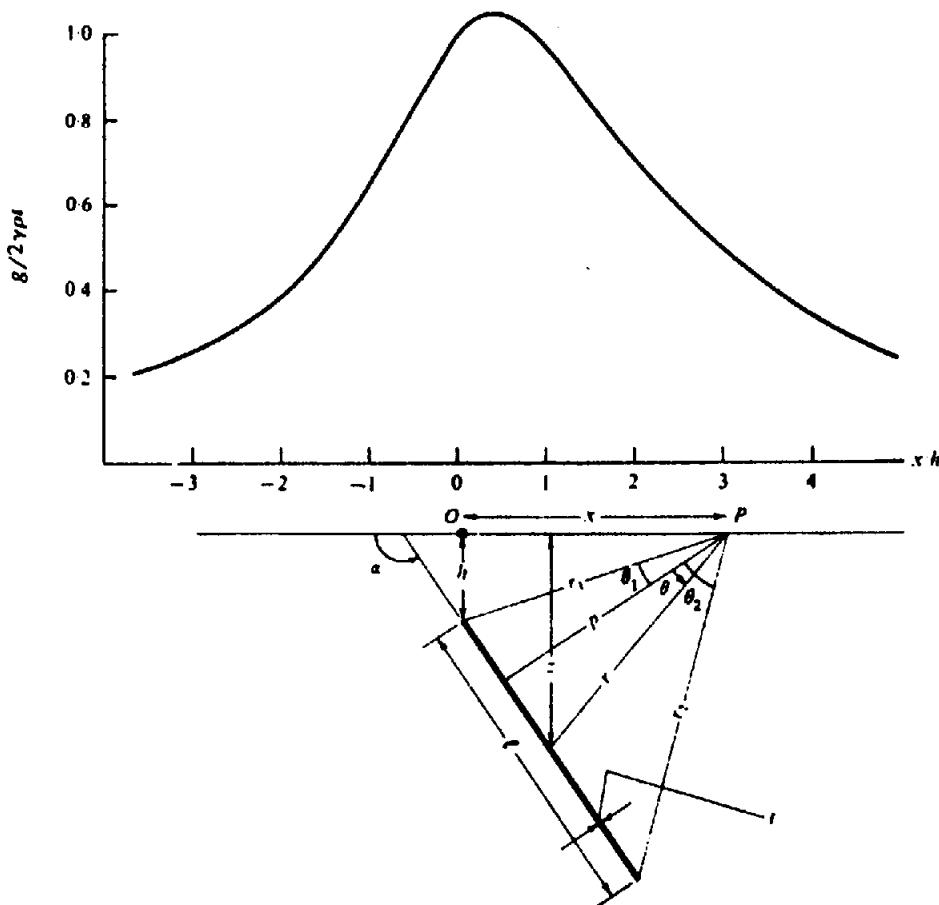


Figure 2.27. Gravity effect of a thin sheet of infinite strike length.

Legendre polynomials  $P_n(\mu)$  where  $\mu = \cos \theta$  (Pipes and Harvill, 1970:799–805). Taking  $r > z$  in Figure 2.26, we have three cases to consider:  $r > z > R$ ,  $R > r > z$ , and  $r > R > z$ . For the first case, we get (see problem 3)

$$g(r, \theta) = 2\pi\gamma\rho R \left\{ (R/2r) - (R/2r)^3 P_2(\mu) + 2(R/2r)^5 P_4(\mu) + \dots \right\} \quad (2.62)$$

For the second case,  $R > r > z$ , the result is

$$g(r, \theta) = 2\pi\gamma\rho R \left\{ 1 - 2(r/2R) P_1(\mu) + 2(r/2R)^2 P_2(\mu) - 2(r/2R)^4 P_4(\mu) + \dots \right\} \quad (2.63)$$

The result for the third case,  $r > R > z$ , is the same as Equation (2.62), showing that Equation (2.62) is valid whenever  $r > R$ . From Equations (2.62) and (2.63) we get the curve in Figure 2.26.

## 2.7.5. Gravity Effect of a Thin Dipping Sheet

Considerable simplification can be effected when a body can be considered two-dimensional. In general,

this holds when the strike length is about 20 times the other dimensions (including depth).

Referring to Figure 2.27, we have the following relations:

$$p = (x - h \cot \alpha) \sin \alpha = x \sin \alpha - h \cos \alpha,$$

$$r = p \sec \theta$$

$$z = r \sin(\alpha + \theta - \pi/2) = p(\sin \alpha \tan \theta - \cos \alpha)$$

$$dz = p \sin \alpha \sec^2 \theta d\theta$$

$$r_1 = (x^2 + h^2)^{1/2}$$

$$r_2 = \{(x + \ell \cos \alpha)^2 + (h + \ell \sin \alpha)^2\}^{1/2}$$

Now we apply Equation (2.9) for a two-dimensional structure. The product  $dx dz$  in Equation (2.9) represents an element of area of the cross section, that is,

$$dx dz = \ell d\ell = \ell \csc \alpha dz = \ell p \sec^2 \theta d\theta$$

Equation (2.9) now gives (note that  $r'$  is the same as

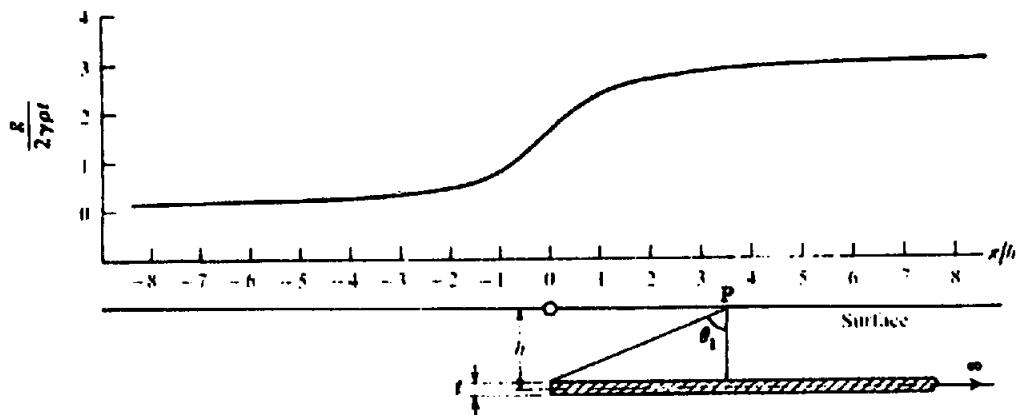


Figure 2.28. Gravity effect of a semiinfinite horizontal sheet.

r here)

horizontal sheet,

$$\begin{aligned}
 g &= 2\gamma\rho t \int_{-\theta_1}^{\theta_2} (z/r^2) \sec^2 \theta d\theta \\
 &= 2\gamma\rho t \int_{-\theta_1}^{\theta_2} (\sin \alpha \tan \theta - \cos \alpha) d\theta \\
 &= 2\gamma\rho t \{ \sin \alpha \ln(\cos \theta_1 / \cos \theta_2) - (\theta_2 + \theta_1) \cos \alpha \} \\
 &= 2\gamma\rho t \{ \sin \alpha \ln(r_2/r_1) - (\theta_2 + \theta_1) \cos \alpha \}
 \end{aligned} \quad (2.64)$$

If the sheet is vertical, Equation (2.64) simplifies to

$$g = 2\gamma\rho t \ln \left\{ ((h + t)^2 + x^2) / (x^2 + h^2) \right\} \quad (2.65)$$

The thin sheet is a good approximation to a prism unless the thickness of the prism is somewhat greater than  $h$ , the depth to the top. When the dip is steep ( $> 60^\circ$ ), the depth can be roughly estimated from the half-width, for example, when  $h \approx t$ ,  $h \approx 0.7x_{1/2}$ . However, when  $t$  is large or when the dip is small it is not possible to get a reliable estimate.

### 2.7.6. Gravity Effect of Horizontal Sheets, Slabs, Dikes, and Faults

(a) *Horizontal thin sheet.* When the sheet in Equation (2.64) is horizontal,  $\alpha = \pi$  and we have

$$\begin{aligned}
 g &= 2\gamma\rho t (\theta_1 + \theta_2) \\
 &= 2\gamma\rho t [\tan^{-1}\{(\ell - x)/h\} + \tan^{-1}(x/h)]
 \end{aligned} \quad (2.66)$$

If, in addition,  $\ell \rightarrow \infty$ , we have, for a semiinfinite

$$g = 2\gamma\rho t \{ \pi/2 + \tan^{-1}(x/h) \} \quad (2.67)$$

and if the sheet extends to infinity in the other direction (that is,  $x$  goes to infinity as well) we have the Bouguer correction as in Equation (2.57) with  $t$  replacing  $L$ .

The profile for a semiinfinite horizontal sheet is shown in Figure 2.28. The thin sheet result can be used to approximate a horizontal slab with an error less than 2% when  $h > 2t$ . A fault often can be approximated by two semiinfinite horizontal sheets, one displaced above the other as in Figure 2.29.

(b) *Horizontal slab.* Equation (2.67) can be used to find the gravity effect of a semiinfinite horizontal slab terminating at a plane dipping at the angle  $\alpha$  (Fig. 2.30). We use Equation (2.67) to get the effect of the thin sheet of thickness  $dz$  and then integrate to find the result for the slab (Geldart, Gill, and Sharma, 1966).

We must replace  $x$  in Equation (2.67) with  $(x + z \tan \beta)$ , so  $\tan^{-1}(x/h)$  becomes  $\tan^{-1}((x + z \tan \beta)/z) = \theta$ . Equation (2.67) now gives

$$g = 2\gamma\rho \int_{z_1}^{z_2} (\pi/2 + \theta) dz = 2\gamma\rho \left( \pi t/2 + \int_{z_1}^{z_2} \theta dz \right)$$

We now have:

$$\begin{aligned}
 \tan \theta &= (x + z \tan \beta)/z = (x/z) + \tan \beta \\
 z &= x/(\tan \theta - \tan \beta) \\
 dz &= -x \sec^2 \theta d\theta / (\tan \theta - \tan \beta)^2 \\
 &= -x \cos^2 \beta d\theta / \sin^2(\theta - \beta) \\
 &= -x \cos^2 \beta d\psi / \sin^2 \psi
 \end{aligned}$$

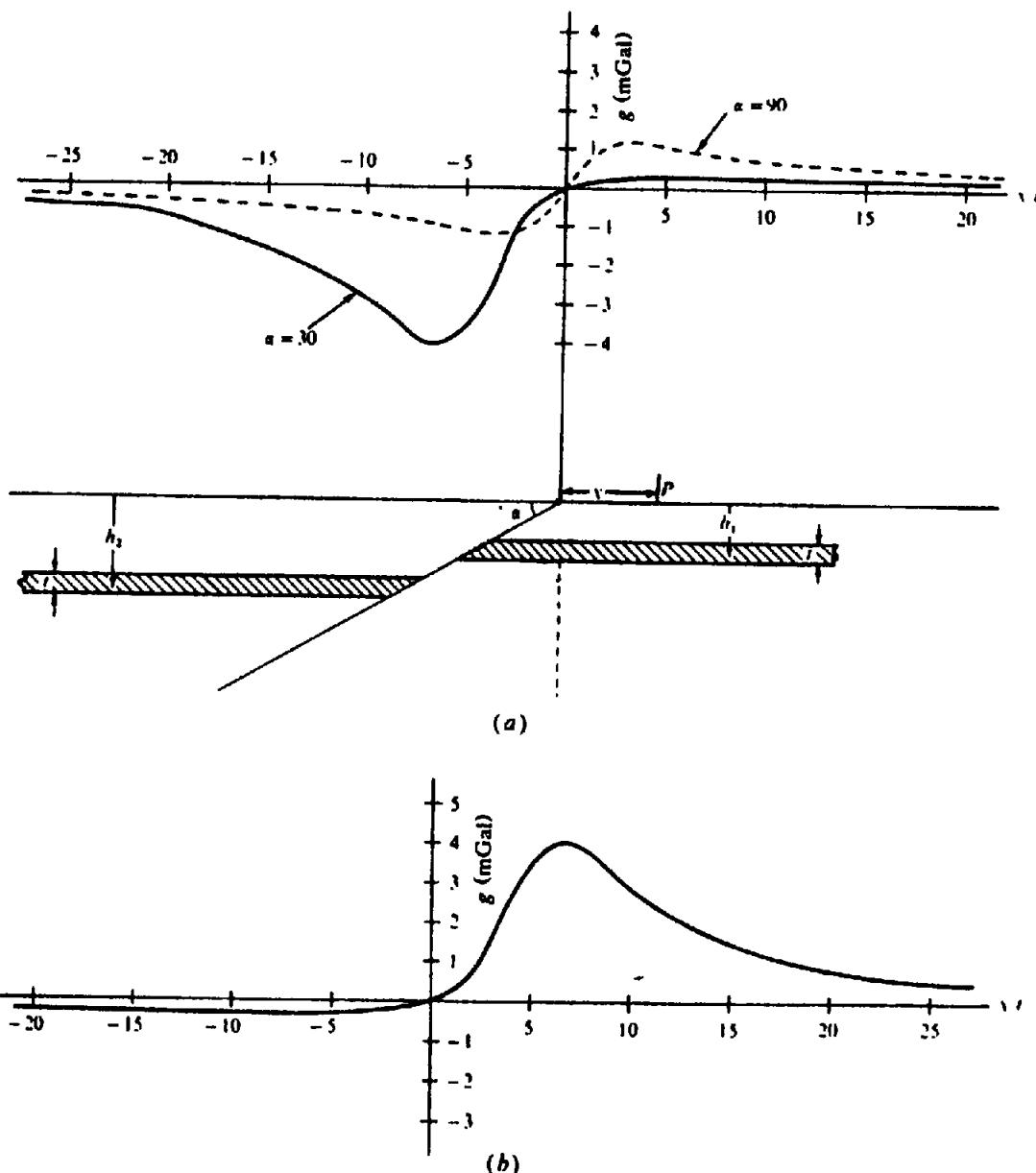


Figure 2.29. Gravity effect of a faulted horizontal sheet;  $t = 300$  m,  $h_1 = 750$  m,  $h_2 = 1350$  m, and  $\rho = 1 \text{ g/cm}^3$ . (a) Normal fault dipping  $\alpha = 30$  and  $90^\circ$ . (b) Reverse fault,  $\alpha = -30^\circ$ .

where  $\psi = \theta - \beta$ . Substituting for  $dz$ , we get

$$g = 2\gamma\rho \left\{ \pi t/2 - x \cos^2 \beta \int_{\psi_1}^{\psi_2} (\psi + \beta) d\psi / \sin^2 \psi \right\}$$

Using the relation  $\int dx / \sin^2 x = -\cot x$ , we can integrate the first term by parts, that is,

$$\begin{aligned} \int \psi d\psi / \sin^2 \psi &= -\psi \cot \psi + \int \cot \psi d\psi \\ &= -\psi \cot \psi + \ln(\sin \psi) \end{aligned}$$

Thus,

$$\begin{aligned} g &= 2\gamma\rho \left[ \pi t/2 - x \cos^2 \beta \left\{ -\psi \cot \psi + \ln(\sin \psi) \right. \right. \\ &\quad \left. \left. - \beta \cot \psi \right\} \Big|_{\psi_1}^{\psi_2} \right] \\ &= 2\gamma\rho \left[ \pi t/2 + x \cos^2 \beta \left\{ (\psi + \beta) \cot \psi \right. \right. \\ &\quad \left. \left. - \ln(\sin \psi) \right\} \Big|_{\psi_1}^{\psi_2} \right] \\ &= 2\gamma\rho \left[ \pi t/2 + x \cos^2 \beta \left\{ (\psi_2 + \beta) \cot \psi_2 \right. \right. \\ &\quad \left. \left. - (\psi_1 + \beta) \cot \psi_1 \right. \right. \\ &\quad \left. \left. - \ln(\sin \psi_2 / \sin \psi_1) \right\} \right] \end{aligned}$$

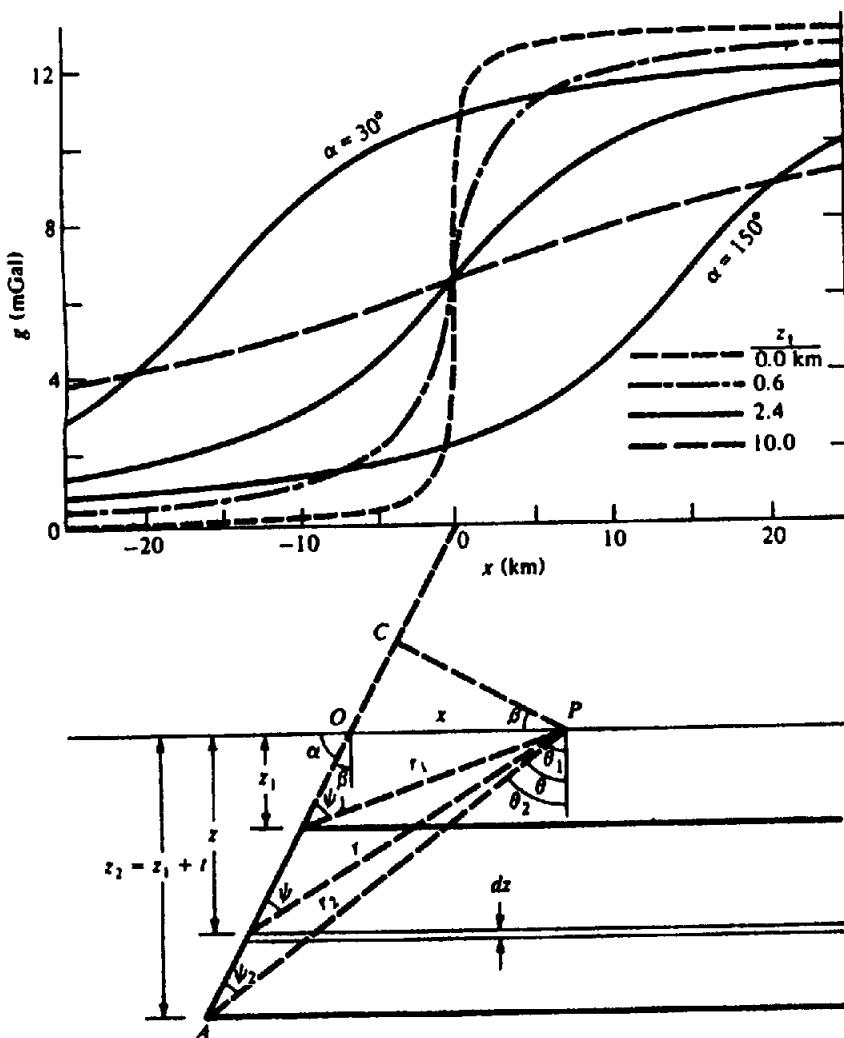


Figure 2.30. Gravity effect of a semiinfinite slab.  $t = 300$  m,  $\alpha = 90^\circ$  except where otherwise noted on the curves,  $\rho = 1 \text{ gm/cm}^3$ .

Figure 2.30 shows that

$$\begin{aligned}\beta(\cot \psi_2 - \cot \psi_1) &= \beta(AC/CP - BC/CP) \\ &= \beta(AB/CP) \\ &= \beta(t/\cos \beta)/(x \cos \beta) \\ &= \beta t/(x \cos^2 \beta)\end{aligned}$$

so

$$(\sin \psi_2 / \sin \psi_1) = r_1 / r_2$$

Also,

$$\begin{aligned}\cot \psi_i &= \{(z_i / \cos \beta) + x \sin \beta\} / x \cos \beta \\ &= (z_i + x \sin \beta \cos \beta) / x \cos^2 \beta\end{aligned}$$

so that we finally get

$$g = 2\gamma\rho \left\{ (\pi/2 + \beta)t + x \cos^2 \beta (F_2 - F_1) \right\} \quad (2.68)$$

Substituting in Equation (2.68) and noting that  $t = (z_2 - z_1)$ , we obtain

$$g = 2\gamma\rho \left\{ (\pi/2 + \beta)t + (\theta_2 - \beta) \right\}$$

$$\times (z_2 + x \sin \beta \cos \beta)$$

$$- (\theta_1 - \beta)(z_1 + x \sin \beta \cos \beta)$$

$$+ x \cos^2 \beta \ln(r_2/r_1) \}$$

where

$$\begin{aligned}F_i &= \psi_i \cot \psi_i - \ln(\sin \psi_i) \quad \psi_i = \theta_i - \beta_i \\ \theta_i &= \tan^{-1} \{ (x/z_i) + \tan \beta_i \}\end{aligned}$$

Equation (2.68) is sometimes given in another form. From Figure 2.30 we have

$$x/\sin \psi_1 = r_1/\sin(\pi/2 + \beta) = r_1/\cos \beta$$

$$x/\sin \psi_2 = r_2/\cos \beta$$

$$= 2\gamma\rho \left\{ (\pi t/2) + (z_2 \theta_2 - z_1 \theta_1) \right\}$$

$$+ x(\theta_2 - \theta_1) \sin \beta \cos \beta$$

$$+ x \cos^2 \beta \ln(r_2/r_1) \} \quad (2.69)$$

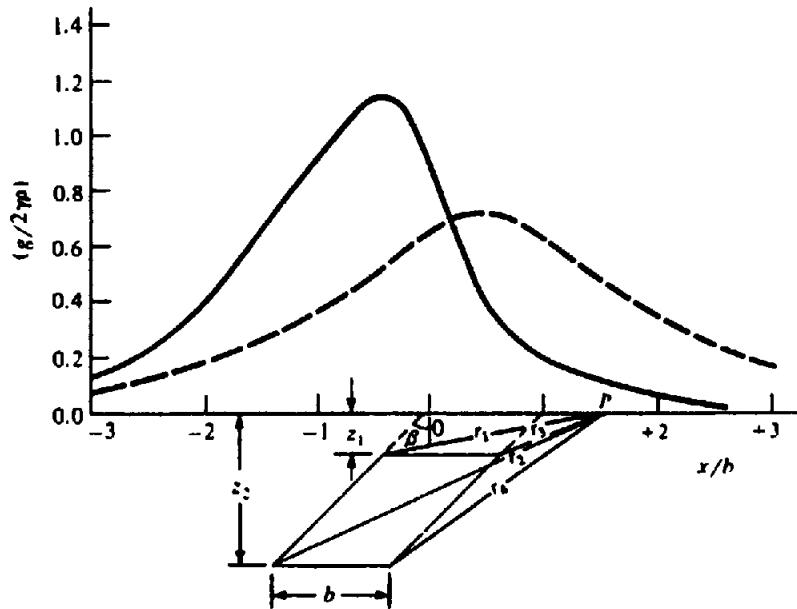


Figure 2.31. Gravity effect of a dike. Profiles are perpendicular to the dike.  $L = \infty$ ,  $b = 1$ ,  $z_1 = 1/3$ ,  $z_2 = 4/3$ ,  $\beta = 45^\circ$  (solid line),  $0^\circ$  (dashed line).

If the end of the slab is vertical,  $\beta = 0$  and this is Equation (2.69) gives

$$g = 2\gamma\rho \{ (\pi t/2) + (z_2\theta_2 - z_1\theta_1) + x \ln(r_2/r_1) \} \quad (2.70)$$

If the slab outcrops,  $z_1 = 0$ ,  $z_2 = t$ ,  $\theta_1 = \pi/2$ ,  $r_1 = x$ , and

$$g = 2\gamma\rho \{ (\pi t/2) + \theta_2 t + x(\theta_2 - \pi/2)\sin\beta\cos\beta + x\cos^2\beta\ln(r_2/x) \} \quad (2.71)$$

Figure 2.30 shows curves for a semiinfinite slab. The slope is quite sensitive to the depth of the slab but not to the dip of the end.

(c) Thick two-dimensional dike. The result for the dike in Figure 2.31 can be obtained by subtracting two slabs, one being displaced horizontally with respect to the other. The result is

$$g = 2\gamma\rho \cos^2\beta \{ x(F_2 - F_1) - (x - b)(F_4 - F_3) \} \quad (2.72)$$

using Equation (2.68). In terms of Equation (2.69),

$$\begin{aligned} g &= 2\gamma\rho [z_2(\theta_2 - \theta_4) - z_1(\theta_1 - \theta_3) \\ &\quad + \sin\beta\cos\beta \{ x(\theta_2 - \theta_1) \\ &\quad - (x - b)(\theta_4 - \theta_3) \} \\ &\quad + \cos^2\beta \{ x\ln(r_2/r_1) \\ &\quad - (x - b)\ln(r_4/r_3) \}] \\ &= 2\gamma\rho [z_2(\theta_2 - \theta_4) - z_1(\theta_1 - \theta_3) \\ &\quad + \sin\beta\cos\beta \{ x(\theta_2 + \theta_3 - \theta_4 - \theta_1) \\ &\quad + b(\theta_4 - \theta_3) \} \\ &\quad + \cos^2\beta \{ x\ln(r_2r_3/r_4r_1) \\ &\quad + b\ln(r_4/r_3) \}] \end{aligned} \quad (2.73)$$

When the sides of the dike are vertical,  $\beta = 0$  and

$$g = 2\gamma\rho \{ z_2(\theta_2 - \theta_4) - z_1(\theta_1 - \theta_3) + x\ln(r_2r_3/r_4r_1) + b\ln(r_4/r_3) \} \quad (2.74)$$

If the dike outcrops,  $z_1 = 0$ ,  $r_1 = x$ ,  $r_3 = (x - b)$ ,  $\theta_1 = \pi/2 = \theta_3$ , and the result is

$$\begin{aligned} g &= 2\gamma\rho [z_2(\theta_2 - \theta_4) + \sin\beta\cos\beta \\ &\quad \times \{ x(\theta_2 - \theta_4) - b(\pi/2 - \theta_4) \} \\ &\quad + x\cos^2\beta\ln\{ r_2(x - b)/r_4x \} \\ &\quad + b\cos^2\beta\ln\{ r_4/(x - b) \}] \end{aligned} \quad (2.75)$$

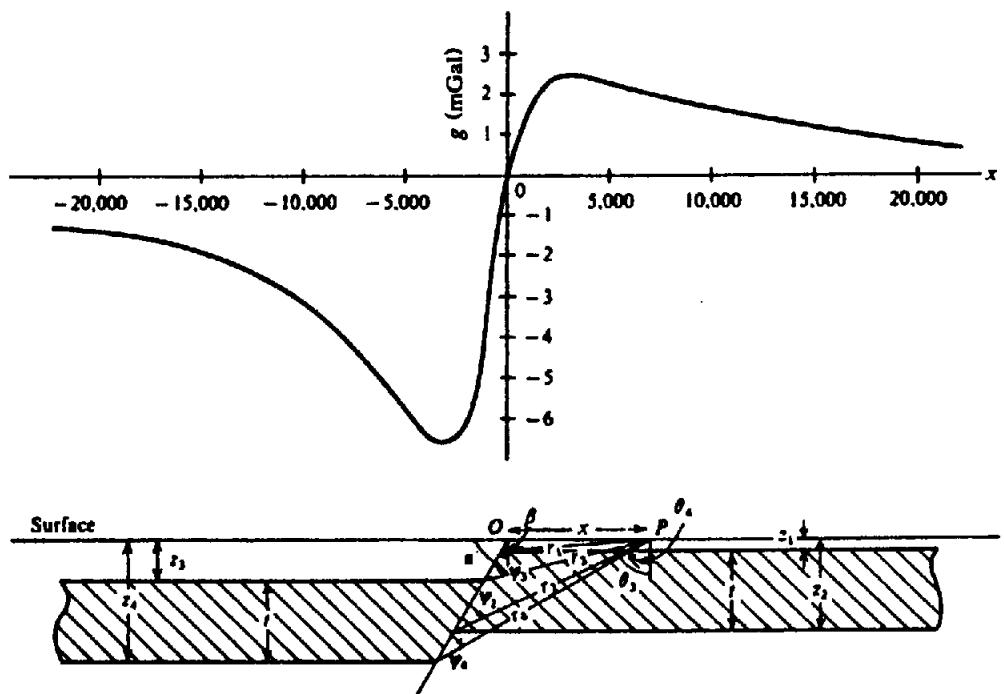


Figure 2.32. Gravity effect of a faulted horizontal bed;  $t = 1,200 \text{ m}$ ,  $z_1 = 150 \text{ m}$ ,  $z_2 = 1,350 \text{ m}$ ,  $z_3 = 600 \text{ m}$ ,  $z_4 = 1,800 \text{ m}$ ,  $\alpha = 60^\circ$ , and  $\rho = 1 \text{ g/cm}^3$ . (From Geldart, Gill, and Sharma, 1966.)

If the dike is also vertical, this reduces further to

$$g = 2\gamma\rho [z_2(\theta_2 - \theta_1) + x \ln(r_2(x-b)/r_4x) + b \ln(r_4/(x-b))] \quad (2.76)$$

An estimate of  $z_1$ , the depth to the top of the dike, is not very satisfactory in terms of  $x_{1/2}$ . When  $z_1 = b$ , we find that  $z_1 = 0.67x_{1/2}$  when  $z_2 = 2b$ , and  $z_1 = 0.33x_{1/2}$  when  $z_2 = 10b$ , that is, a factor of 2 depending on the depth extent. In general, the curves become sharper as both  $z_1$  and  $z_2$  get smaller. Also, it is impossible to make a good estimate of the width of the dike from the shape of the curve.

(d) Fault. The gravity effect of the fault shown in Figure 2.32 can be obtained by adding the effects of:

- (i) A near-surface semiinfinite slab.
- (ii) A deeper infinite slab of the same thickness.
- (iii) A semiinfinite slab of negative density contrast to wipe out the part of the infinite slab under the near-surface slab.

The result is

$$g = 2\gamma\rho [\pi t + x \cos^2 \beta ((F_2 - F_1) - (F_4 - F_3))] \quad (2.77)$$

A typical curve is shown in Figure 2.32 (note that the

constant term  $2\pi\gamma\rho t$  has been omitted). Obviously one can extend Equation (2.77) to include a series of horizontal beds at increasing depths.

### 2.7.7. Applying Simple Models to Actual Anomalies

Most of the formulas for simple shapes are far from easy to apply. Even when we can assume that a field result can be matched by a specific geometry, it is still tedious to plot profiles from expressions that contain a number of geometrical unknowns in addition to the density contrast. Use of a collection of characteristic curves reduces the labor involved.

We first establish some significant features associated with the profiles. Usually the number of parameters is reduced by measuring in terms of one of them, preferably the one that influences the significant features the least. Grant and West (1965, pp. 273–80) discussed how to construct curves for the thin dipping sheet model. They concluded that symmetry and sharpness are the most diagnostic features, and thus they developed curves in terms of ratios that depend principally on these properties.

### 2.7.8. Gravity Effects of Complex Shapes

The gravity effects of complex shapes are usually calculated by subdividing the body into rectangular cells, calculating the effect of each with a digital

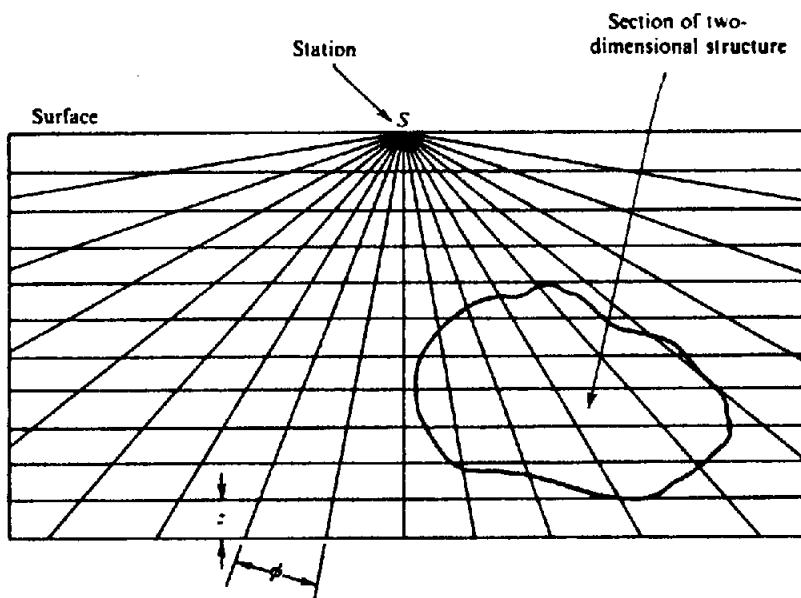


Figure 2.33. Template for calculating the gravity effect of two-dimensional bodies of irregular cross section. (From Hubbert, 1948).

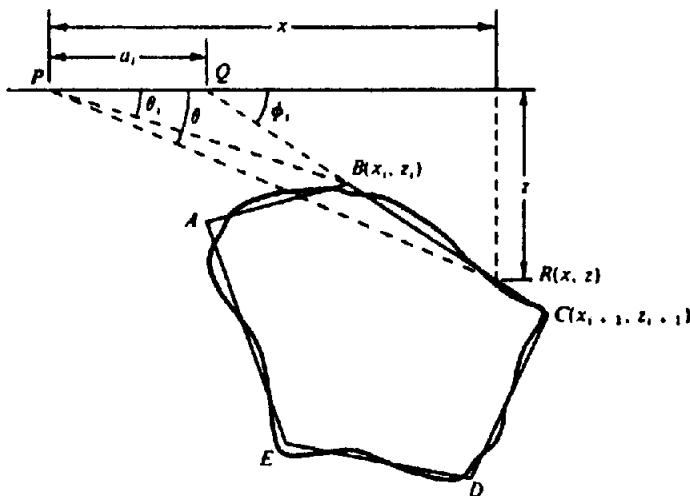


Figure 2.34. Polygon approximation of an irregular vertical section of a two-dimensional body.

computer, and then summing. This procedure is sometimes carried out graphically using templates superimposed on a cross section to divide it into elementary areas, each of which contributes the same effect at a surface station.

A template of this type is shown in Figure 2.33. The gravity effect at the chart apex is

$$g = K \times 10^{-5} \rho N \phi z \text{ mGal} \quad (2.78)$$

where  $N$  is the number of segments covering the cross section,  $\phi$  is the angular separation of radial lines,  $z$  is the separation of horizontal lines,  $K = 23$  for  $z$  in meters and 7.1 for  $z$  in feet.

When the structure is not really two dimensional, the finite length can be taken into account by applying a correction. For a point in the plane of the cross section of a finite structure at a distance  $r$  from the section's center of gravity, the correction is

$$\frac{g}{g_m} = \frac{1}{2} \left\{ \frac{1}{(1 + r^2/Y_1^2)^{1/2}} + \frac{1}{(1 + r^2/Y_2^2)^{1/2}} \right\} \quad (2.79)$$

where  $g$  is the actual gravity of the finite body,  $g_m$  is the gravity for a body of the same cross section and of infinite length, and  $Y_1, Y_2$  are the distances from the cross section to the ends of the body.

Graphical methods have also been employed on three-dimensional bodies by placing templates over

contours of the body in a horizontal plane. In effect, the body is broken up into a stack of horizontal slabs whose thickness is determined by the contour interval. This approach is more difficult than the two-dimensional procedure because the chart must have a variable scale parameter to allow for different slab depths.

One can calculate the gravity effect of a 2-D body of arbitrary cross section by using an  $n$ -sided polygon to approximate the outline of the vertical section (Talwani, Worzel, and Landisman, 1959). A simple section is illustrated in Figure 2.34. The gravity effect of this section is equal to a line integral around the perimeter (Hubbert, 1948). The relation is

$$g = 2\gamma\rho \oint z d\theta$$

From the geometry of Figure 2.34 we have the following relations:

$$z = x \tan \theta = (x - a_i) \tan \phi_i$$

or

$$z = (a_i \tan \theta \tan \phi_i) / (\tan \phi_i - \tan \theta)$$

The line integral for the side  $BC$  is

$$\int_{BC} z d\theta = \int_B^C \frac{a_i \tan \theta \tan \phi_i}{\tan \phi_i - \tan \theta} d\theta = Z_i$$

Thus,

$$g = 2\gamma\rho \sum_{i=1}^n Z_i \quad (2.80)$$

In the most general case,  $Z_i$  is given by

$$Z_i = a_i \sin \phi_i \cos \phi_i \left[ (\theta_i - \theta_{i+1}) + \tan \phi_i \cdot \ln \left\{ \frac{\cos \theta_i (\tan \theta_i - \tan \phi_i)}{\cos \theta_{i+1} (\tan \theta_{i+1} - \tan \phi_i)} \right\} \right] \quad (2.81)$$

where

$$\theta_i = \tan^{-1} \left( \frac{z_i}{x_i} \right), \quad \phi_i = \tan^{-1} \left( \frac{z_{i+1} - z_i}{x_{i+1} - x_i} \right)$$

$$a_i = x_{i+1} - z_{i+1} \cot \phi_i$$

$$= x_{i+1} + z_{i+1} \left( \frac{x_{i+1} - x_i}{z_i - z_{i+1}} \right)$$

This technique has also been used for three-dimensional bodies by replacing the contours in the horizontal plane with  $n$ -sided polygons. The solution, from line integrals of the polygons, is essentially a more complicated version of Equation (2.81).

### 2.7.9. The Direct and Inverse Problems of Interpretation

The interpretation techniques outlined in previous sections employ models with simplified shapes. Calculating the effects of models is the *direct* or *forward approach* to interpretation (the same procedure is used in other geophysical methods). The initial selection of a reasonable model is made with the aid of geological information and the experience of the interpreter. Interpretation in terms of simple models, a more-or-less force-fit to the data, is commonly used when data and control are incomplete. Detailed analysis is complicated by the fact that model fits are not unique. Ambiguity is well illustrated in the classic paper of Skeels (1947), who shows a gravity profile that could be produced by a number of mass distributions.

The inverse problem involves determining the geometry and physical properties of the source from measurements of the anomaly, rather than simply selecting a model and determining the parameters that match the anomaly approximately. The inherent nonuniqueness may make such a task appear to be a waste of time; however, with additional constraints and a computer, this type of analysis becomes increasingly useful.

We outline here a typical least-squares procedure for the inverse method. First, assume some mathematical model based on prior knowledge of the geology and/or of the geometry plus additional information gleaned from the general appearance of profiles and contours. Next, limit the number of parameters allowed to vary, for example, some subset of strike, length, attitude, depth, and depth extent; this makes the inverse problem more tractable. Next, linearize the problem (because the mathematical model is often essentially nonlinear) to simplify computations. Matrices (§A.2) are generally used. The solution is obtained by using the model and a given set of parameters to calculate simulated data (called the *model response*), comparing the model response with the values given by the observed data, and then varying the parameters to fit the data more closely. We illustrate this procedure as follows:

1. The model gives a relation between  $m$  parameters  $p_j$ . For each set of values of  $p_j$ , we get a model response  $f(p_1, p_2, p_3, \dots, p_m)$ , which has a value  $f_i(p_1, p_2, p_3, \dots, p_m)$  at each of the  $n$  data points.

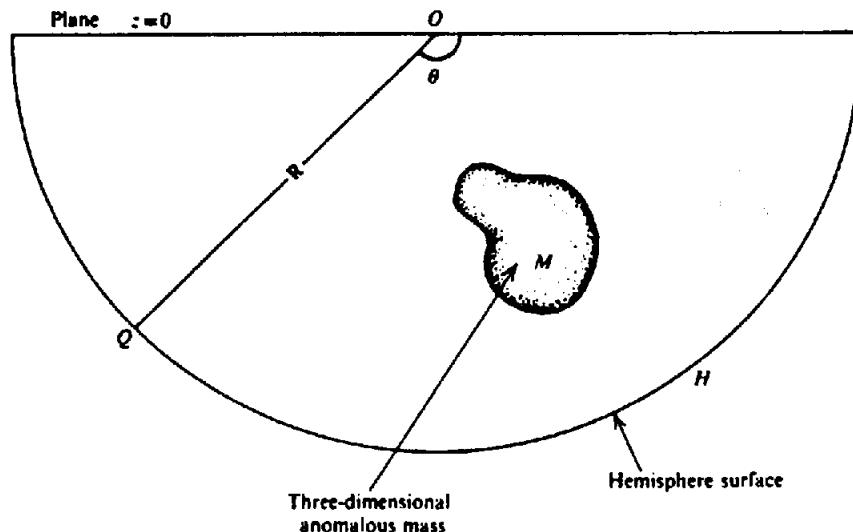


Figure 2.35. Calculation of excess mass.

We write

$$e_i = f_i(p_1, p_2, p_3, \dots, p_m) - c_i \quad i = 1, 2, \dots, n \quad (2.82)$$

where  $c_i$  are the observed data that  $f_i$  are intended to match and  $e_i$  are the errors between the observed data and the model response. We begin with an estimate of  $p_j$ .

2. Because  $f(p_1, p_2, p_3, \dots, p_m)$  generally involves nonlinear relations between the parameters, we simplify calculations by using a first-order Taylor-series expansion to get equations that are linear with respect to the derivatives. Differentiating Equation (2.82), we get

$$\sum (\partial f_i / \partial p_j) \delta p_j = \delta e_i \quad (2.83a)$$

where each derivative is evaluated using the current set of  $p_j$  values. In matrix notation Equation (2.83a) becomes

$$\mathcal{D}\mathcal{P} = \mathcal{E} \quad (2.83b)$$

where  $\mathcal{D}$  is an  $(n \times m)$  matrix whose elements are  $\partial f_i / \partial p_j$ ,  $\mathcal{P}$  is an  $(m \times 1)$  column matrix of the sought-for parameter changes  $\delta p_j$ , and  $\mathcal{E}$  is an  $(n \times 1)$  column matrix whose elements are  $\delta e_i$ .

3. In the usual overdetermined case,  $n \gg m$  and  $\mathcal{D}$  is not square; we use Equation (A.5b) to solve Equation (2.83b):

$$\mathcal{P} = (\mathcal{D}^T \mathcal{D})^{-1} \mathcal{D}^T \mathcal{E} \quad (2.84)$$

This solution is equivalent to  $n$  equations in the

$m$  increments  $\delta p_j$ . Since  $n > m$ , we apply the method of least squares (Sheriff and Geldart, 1983, §10.1.5) to obtain the values of  $\delta p_j$ . The  $p_j$  are then replaced by  $p_j + \delta p_j$ , and the calculations are repeated. Iteration is stopped when  $\sum e_i^2$  is smaller than some acceptable (prespecified) value.

Many modifications of the preceding procedure exist, notably methods that stabilize the procedure. If  $\mathcal{D}$  is too large to be efficiently handled by the computer, procedures such as steepest descent or conjugate gradient methods, may be employed. Marquardt (1963) employs an adjustable damping factor, whereas Jackson (1979) and Tarantola and Valette (1982) introduce a priori information to constrain the problem (see §3.8.2, example 3, for a similar magnetic procedure). If the model is highly nonlinear, these methods may not work well and Monte Carlo methods may be appropriate.

## 2.7.10. Excess Mass

Although there is no unique solution to a set of potential field data, it is possible to determine uniquely the total anomalous mass, regardless of its geometrical distribution. Sometimes this is a useful calculation (although potentially dangerous) in estimating ore tonnage in mineral exploration.

To find the *excess mass*, we start with Equation (2.12). Dropping the minus sign, we have

$$\int_S g_n ds = 4\pi\gamma M$$

We surround the mass by a hemisphere whose upper face is the datum plane  $z = 0$ . The surface integral can be separated into two parts: the integral over the

circular base in the  $xy$  plane and the surface of the half-sphere. From Figure 2.35, we have

$$\int_S g_n \, ds = \iint_{z=0} g_n \, dx \, dy + \iint_H g_n R^2 \sin \theta \, d\theta \, d\phi = 4\pi \gamma M$$

where  $g_n$  in the integral over the datum plane  $z = 0$  is the residual anomaly  $g(x, y)$  and  $R$  is the radius of the hemisphere. We take  $R$  large enough that  $M$  is in effect a point mass at the origin and  $g_n = \gamma M/R^2$  at the hemispherical surface. Integration over this surface as  $\phi$  goes from 0 to  $2\pi$  and  $\theta$  from  $\pi/2$  to  $\pi$  leads to the value  $2\pi\gamma M$ , so that

$$\int_{-\infty}^{\infty} \int_{-\infty}^{\infty} g(x, y) \, dx \, dy = 2\pi\gamma M$$

or

$$M = (1/2\pi\gamma) \int_{-\infty}^{\infty} \int_{-\infty}^{\infty} g(x, y) \, dx \, dy \quad (2.85)$$

In practice, the integral is evaluated by numerical integration using the relation

$$M = K \sum g(x, y) \Delta x \Delta y \quad (2.86)$$

where  $m$  is in metric tons or short tons according as  $K = 26.3$  for  $\Delta x, \Delta y$  in meters, or  $K = 2.44$  for  $\Delta x, \Delta y$  in feet. The actual mass producing the anomaly can be determined if we know its density  $\rho_a$  and density contrast  $\Delta\rho$ . This multiplies Equation (2.86) by the factor  $(\rho_a/\Delta\rho)$ :

$$\text{actual mass} = (\rho_a/\Delta\rho) \times \text{excess mass} \quad (2.87)$$

If the regional has not been properly removed, or if other residual anomalies are included, the estimate obviously will be in error.

### 2.7.11. Overburden Effects

In many field situations, the effects of variations in the depth of the overburden may be larger than the effects of different rocks at depth, and so variations in overburden thickness can produce significant gravity anomalies. The average density for an assortment of overburden materials is about  $1.92 \text{ g/cm}^3$  when wet and  $1.55 \text{ g/cm}^3$  when dry, and the averages for wet and dry sedimentary rocks are  $\sim 2.50$  and  $\sim 2.20 \text{ g/cm}^3$ , respectively. Thus a contrast of  $0.6 \text{ g/cm}^3$  is possible.

As a rough estimate, we expect the overburden to be thicker in valleys and low-lying flat land than on steep hillsides and elevated plateaus. Abrupt changes in overburden thickness, however, are common enough. In any gravity survey, and particularly in mineral exploration, it is worthwhile to consider the extent to which gravity anomalies may be caused by variations in overburden thickness.

From the Bouguer correction given in Equation (2.23) and the effect of a semiinfinite horizontal slab, we can get some idea of the magnitude of the overburden effect. The maximum gravity variation that results from a sudden change  $\Delta h$  in overburden thickness, where the density contrast is  $\Delta\rho$ , is given by

$$\Delta g_{\max} = 41.9 \times 10^{-3} \Delta\rho \Delta h \quad (2.88a)$$

$$= 12.8 \times 10^{-3} \Delta\rho \Delta h' \quad (2.88b)$$

where  $\Delta h$  is in meters,  $\Delta h'$  is in feet, and  $\Delta g_{\max}$  is in milligals.

The maximum horizontal gradient of gravity will, of course, be large if overburden irregularity is the source. For abrupt depth changes of 10 m or more in a horizontal distance of 10 m and  $\Delta\rho = 0.6 \text{ g/cm}^3$ , the value of  $(dg_{\max}/dx)$  will be about  $0.03 \text{ mGal/m}$ . In fact, this steep gradient is more diagnostic than the magnitude of  $g_{\max}$ . Clearly the depth of overburden should be measured in areas of shallow gravity anomalies. This is best done by small-scale refraction or surface resistivity measurements.

### 2.7.12. Maximum-Depth Rules

Smith (1959) gives several formulas for maximum depths of gravity distributions whose shapes are not known, provided that the anomalous bodies have a density contrast with the host rock that is either entirely positive or entirely negative. If  $|g_{\max}|$  and  $|(\partial g/\partial x)_{\max}|$  are the maximum values of gravity and of the horizontal derivative, respectively, the depth to the upper surface has a limiting value given by

$$z \leq 0.86 |g_{\max}| / |(\partial g/\partial x)_{\max}| \quad (2.89)$$

If the anomaly is two dimensional, the factor 0.86 becomes 0.65 in Equation (2.89). However, this expression is not particularly accurate.

## 2.8. FIELD EXAMPLES

(1) Figure 2.36a shows a Bouguer gravity contour map compiled from a survey in the vicinity of Portland Creek Pond in northern Newfoundland. This was an exploration program for oil and gas in

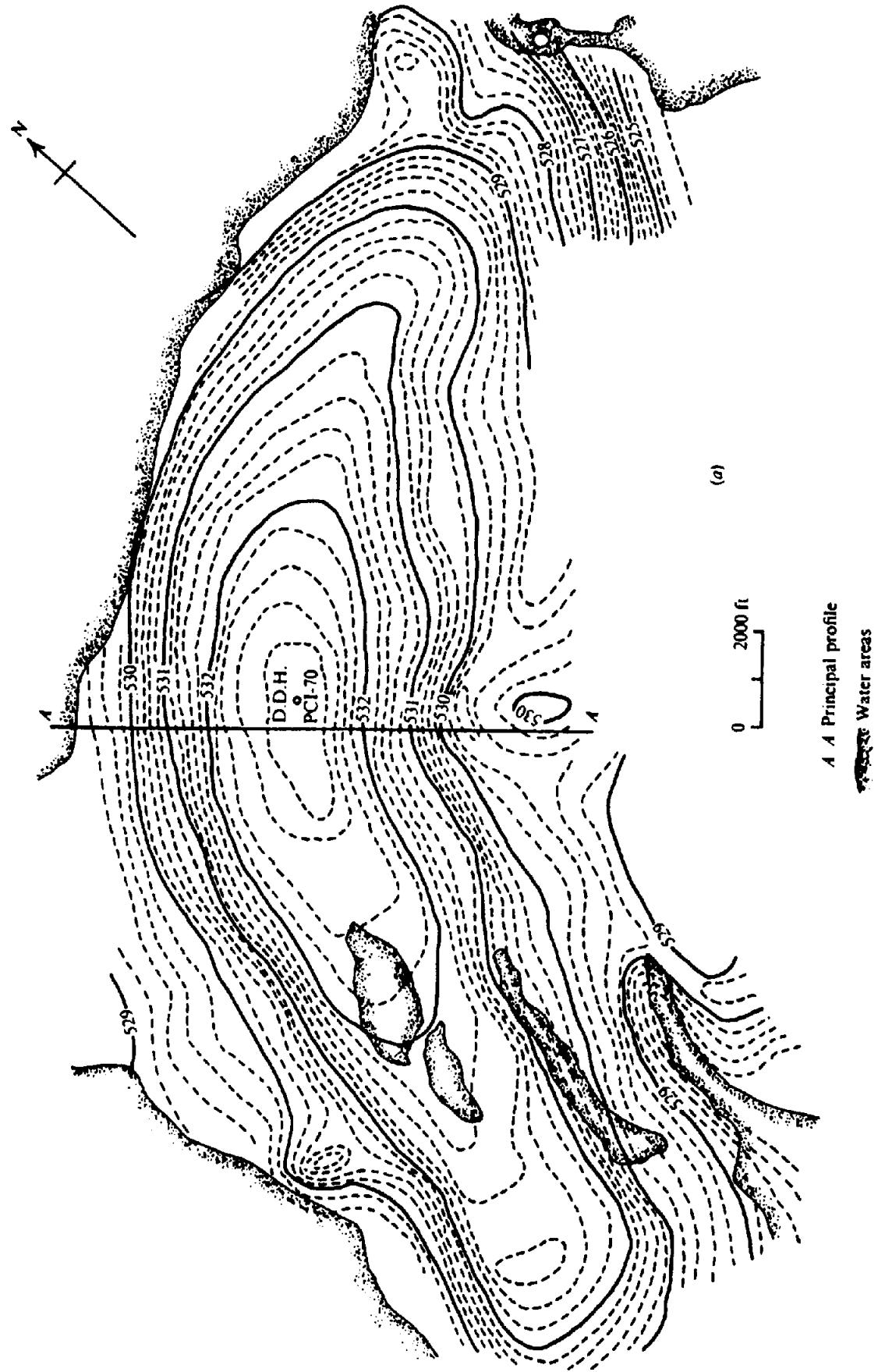


Figure 2.36. Gravity survey, Portland Creek Pond, Newfoundland. (a) Bouguer gravity map, contour interval (C.I.) = 0.2 mGal.

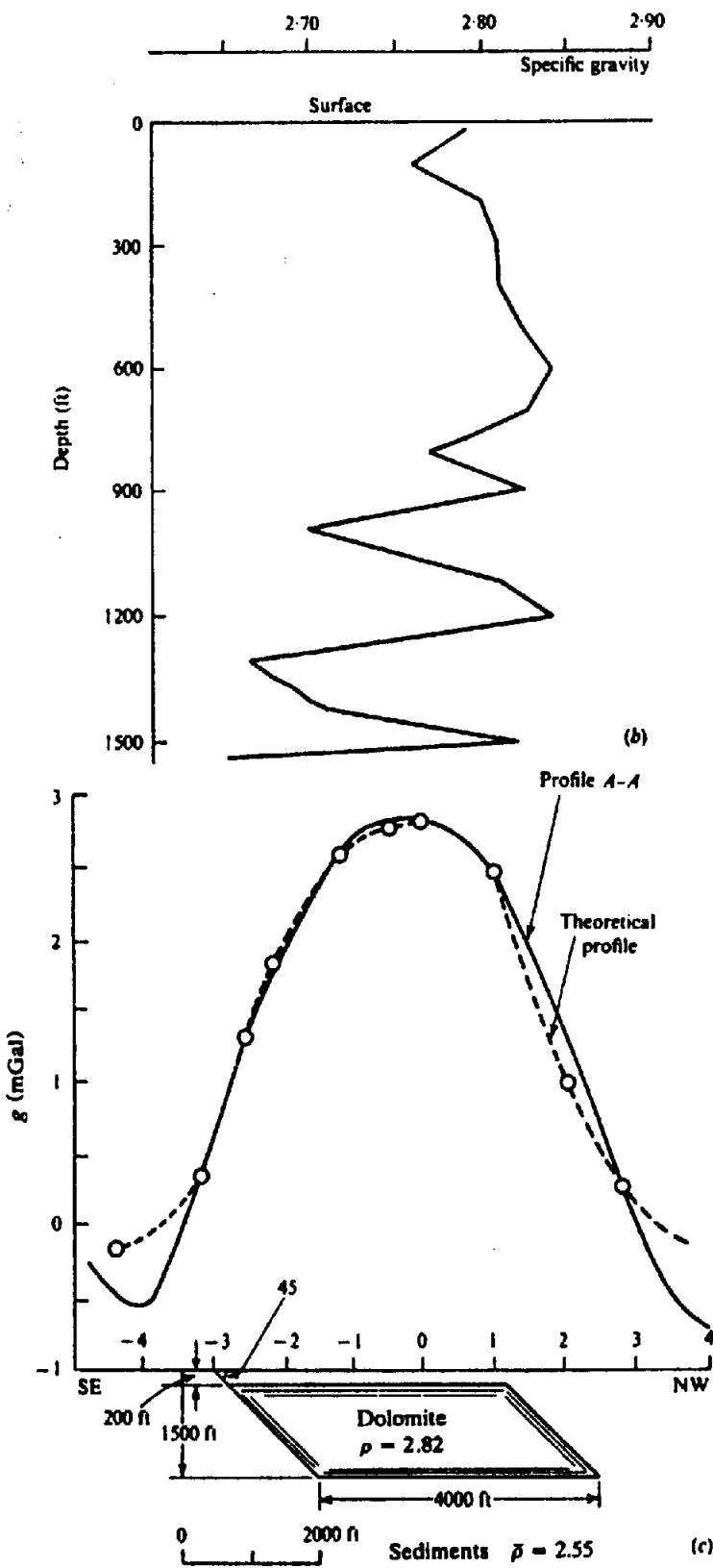


Figure 2.36. (Continued) (b) Density log in borehole DDH PCI-70. (c) Comparison with calculated profile for a 2-D dipping prism.

an area of sedimentary rocks whose thickness, a few miles south, is known to be over 5,000 ft. The topography is reasonably flat and no terrain corrections were required.

It is evident that the large positive anomaly is not a reflection of deep basement structure because the

gradients are too steep. If we use Equation (2.68) to approximate a slab for profile AA' in Figure 2.36a, the values of  $g_{\max}$  and  $(\partial g / \partial x)_{\max}$  indicate that  $h$  is not greater than 650–800 ft. This indicates that the source is shallow and hence must be within the sediments. One possibility is an intrusive dike of

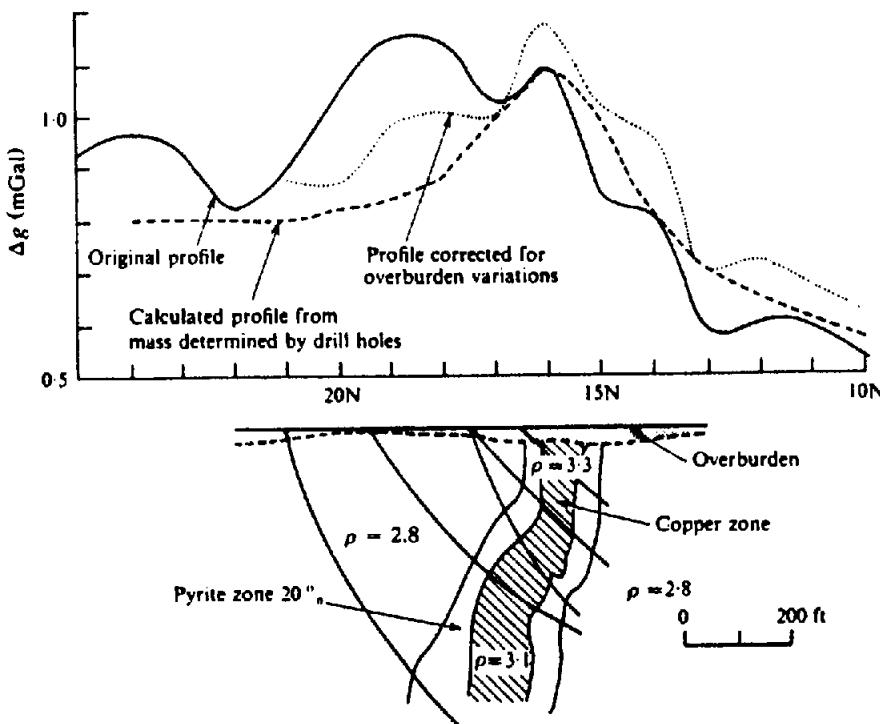


Figure 2.37. Gravity profiles over a copper deposit, Louvicourt, Quebec.

great linear extent, but Equation (2.74) shows that the flanks of the anomaly in this case would be much less steep than the field profile; this suggests that the source is of limited depth.

A 1,600 ft drill hole was put down in the center of this gravity anomaly; its location is shown in Figure 2.36a. Density measurements on core samples at 100 ft intervals are shown in Figure 2.36b. The local presence of dolomite from near surface to 1,000 ft and interbedded with dark shales from 1,000 to 1,600 ft accounts for the positive gravity. The average density of the dolomite samples was 2.82 g/cm<sup>3</sup>. If the surrounding sedimentary formations are assumed to have a density of about 2.55 g/cm<sup>3</sup>, it is possible to match the field profile reasonably well with the dipping prism shown in Figure 2.36c. This analysis is oversimplified since the actual structure is neither two dimensional ( $L \approx 9b$ ) nor homogeneous in the bottom 500 ft. Both factors would steepen the flanks on the profile.

(2) The profiles in Figure 2.37 illustrate the pronounced effect of overburden thickness on gravity results. This is the Louvicourt Township copper deposit near Val d'Or, Quebec. Discovery was made by drilling a weak Turam anomaly (§7.4.3b); the gravity survey was carried out immediately after.

The original Bouguer gravity profile indicated a weak anomaly of 0.15 mGal directly over the conductor and a much broader and larger magnitude anomaly about 75 m to the north. Obviously the small peak would not have aroused any great enthusiasm. Later, when it had been established that the overburden thickness increased appreciably immedi-

ately over the sulfide zone, it was possible to correct for this variable thickness, as discussed in Section 2.7.11, using a density contrast of about 0.08 g/cm<sup>3</sup> between the host rock and the overburden. This is equivalent to 0.03 mGal/m of overburden thickness. In the corrected field profile the larger anomaly to the north has practically disappeared and the small peak has been enhanced to 0.3 mGal. A third profile calculated from density measurements of diamond drill cores is also shown.

This example clearly indicates the importance of measuring the overburden thickness in conjunction with gravity applied to small-scale mineral exploration. This is particularly necessary in surveys for vein-type base-metal deposits that respond to EM methods. The overburden effect would be less pronounced in regions favorable for IP, that is, large-area low-grade disseminated mineralization.

(3) The Delson fault is a well-documented structural feature in the St. Lawrence lowlands. Striking roughly E-W, it is located east of the St. Lawrence River several kilometers southeast of Montreal. Although the area is generally covered by about 15 m of overburden, there are exposures of Utica shales and Chazy limestones in river beds to indicate the location and direction of the fault. The sedimentary beds of the lowlands are flat-lying shales, limestones, and dolomites of Paleozoic age underlain by Precambrian basement rocks at a depth usually greater than 750 m.

Figure 2.38 shows a Bouguer gravity profile taken across the Delson fault in a N-S direction, together with a geologic section. A linear regional trend of

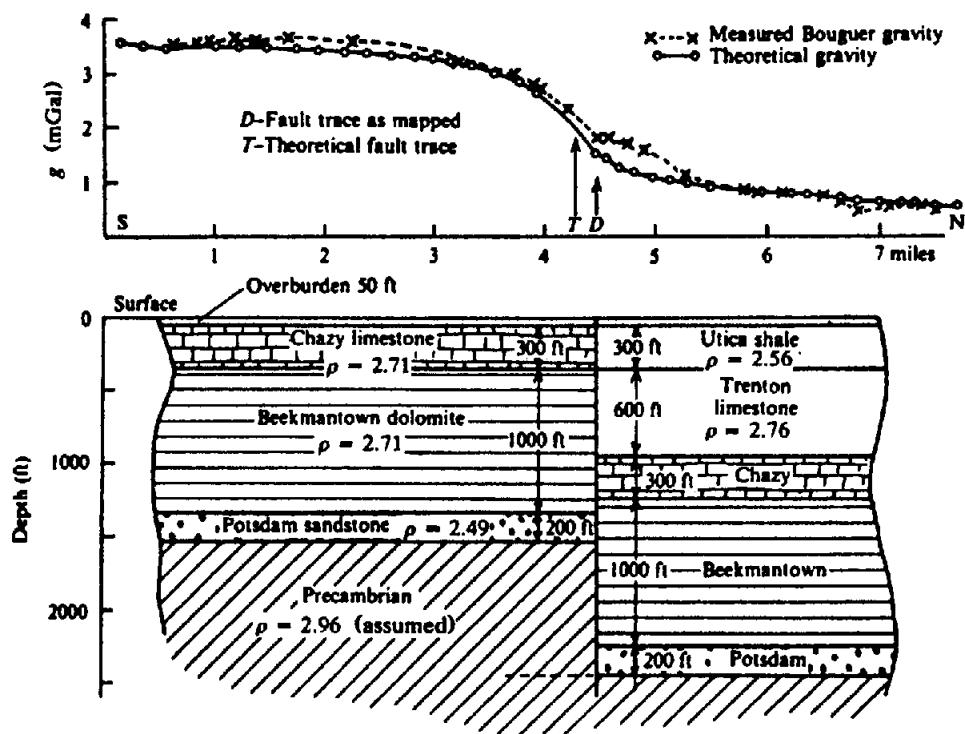


Figure 2.38. Gravity profile and geologic section across the Delson fault, St. Lawrence lowlands.

0.45 mGal/km positive to the south, has been removed.

The profile in Figure 2.38 resembles the gravity effect of a horizontal slab rather than a fault (compare with Figs. 2.28, 2.29, and 2.32). The only appreciable gravity effect from the sedimentary beds would be provided by the juxtaposition of the Chazy and Utica formations near surface and the displaced Potsdam layer (whose thickness is in some doubt) at greater depth. The first pair produces a gravity profile of the proper shape with a total variation of 0.57 mGal and maximum slope of 3.7 mGal/km; thus the total anomaly is too small and the slope too large to fit the field profile. The low-density Potsdam section, on the other hand, would tend to reduce the anomaly, since the bed nearer the surface lies on the south side of the fault; the total effect, however, is only about -0.1 mGal and maximum slope -0.15 mGal/km.

By postulating a density of 2.96 g/cm<sup>3</sup> in the Precambrian rocks and a step of 275 m on the fault down to the south, we obtain a total anomaly of 2.1 mGal with maximum slope of 1.2 mGal/km. The theoretical profile in Figure 2.38 is the result.

The theoretical profile is shifted about 300 m south of the mapped fault location. There are two explanations for this. First, the Delson fault is not vertical, but dips north about 80°. Second, faults very rarely show single clear-cut faces, that is, there is a faulted region of some width. The field profile also shows a small anomaly about 2½ miles north of

the Delson fault, although there is no supporting geological evidence.

## 2.9. PROBLEMS

1. Verify Equation (2.8). [Hint: Start with Equation (2.6a), integrate along the  $y$  axis between the limits  $\pm L$ , and subtract the potential at  $(x^2 + z^2) = a^2 - 1$  (this avoids  $U \rightarrow \infty$  as  $L \rightarrow \infty$ ). By setting  $L = \infty$ , we get Equation (2.8).]
2. Show that Equation (2.12a) holds for an arbitrary closed surface  $S$  regardless of the position of  $m$  within  $S$ . [Hint: Write the integrand in the form  $\gamma m(ds \cos \theta / r^2) = \gamma m d\Omega$ , where  $r$  is the distance from  $m$  to  $ds$ ,  $\theta$  is the angle between  $r$  and  $n$ , the outward-drawn normal to  $ds$ , and  $d\Omega$  is the element of solid angle subtended by  $ds$  at  $m$ . Consider the case where  $r$  cuts  $S$  more than once.]
3. Verify Equations (2.62) and (2.63). [Hint: A solution of Equation (2.11c) is (Pipes and Harvill, 1970, p. 348)]

$$g(r, \theta)$$

$$= 2\pi\gamma\rho \left\{ \sum_{n=0}^{\infty} a_n r^n + \sum_{n=0}^{\infty} b_n r^{-(n+1)} \right\} P_n(\mu)$$

where  $\mu = \cos \theta$ . When  $r > z > R$ , we use the

Table 2.3.

Stn	Time (hr)	$g_{\text{obs}}$ (mGal)	Stn	Time (hr)	$g_{\text{obs}}$ (mGal)	Stn	Time (hr)	$g_{\text{obs}}$ (mGal)
Aug. 31	Line 0							
0°53	13:55	182.78	42	14:29	182.95	31	15:07	184.48
52	14:00	182.77	41	14:31	183.06	32	15:10	184.81
51	14:04	182.73	40	14:35	183.15	33	15:12	184.53
50	14:07	182.92	0°39	14:37	183.13	34	15:14	184.33
49	14:10	183.05	25	14:50	183.82	35	15:16	184.17
48	14:15	183.19	26	14:52	183.97	36	15:19	184.03
47	14:17	182.99	27	14:55	183.99	37	15:22	183.73
46	14:20	182.88	28	14:59	183.96	38	15:25	183.38
45	14:22	182.89	29	15:01	184.25	0°39	15:27	183.35
44	14:25	182.85	30	15:05	184.48	0°53	15:45	183.01
43	14:27	182.91						
Sept. 6	Line 2S							
0°53	9:10	185.02	33	10:56	185.39	44	11:44	184.53
2S°53	9:20	185.11	34	11:00	185.39	45	11:47	184.56
2S°39	9:40	184.93	35	11:05	185.52	46	11:52	184.64
24	10:19	185.86	36	11:09	185.37	47	11:55	184.67
25	10:23	185.66	37	11:15	185.00	48	11:59	184.67
26	10:27	185.65	38	11:20	184.86	49	12:02	184.76
27	10:31	185.66	2S°39	11:25	184.86	50	12:05	184.76
28	10:34	185.59	40	11:29	184.79	51	12:08	184.80
29	10:38	185.47	41	11:32	184.69	52	12:12	184.90
30	10:41	185.51	42	11:35	184.67	2S°53	12:16	185.09
31	10:45	185.46	43	11:39	184.60	0°53	12:28	185.03
32	10:50	185.39						

right-hand series and compare it with the expansion of Equation (2.60) in terms of  $(R/z)$  [see Eq. (A.43)] for points on the axis where  $\mu = 1$ ,  $P_n(1) = 1$ , and  $r = z$ ; this gives the values of  $b_i$  and we get Equation (2.62). Doing the same for  $R > r > z$  and using the first series, we get Equation (2.63). Since  $r > z$  on physical grounds, there are, in fact, only two cases:  $r > R$  and  $R > r$ , so Equation (2.62) holds for the third case,  $r > R > z$ .]

4. The data in Table 2.3 were obtained over a 2 day period of gravity followup on a base-metal prospect. Stations marked ° were visited at least twice for drift correction. For example, station 53, line 0, was occupied at the beginning and end of each of the 2 days, station 53, line 2S, at the beginning and end of the second day's work and the stations 39 on both lines were used as base stations for checking drift at intermediate times.

Draw a drift curve for the 2 day period and correct all station readings. (Note that each of the four stations 53 and 39 must have the same gravity readings – or very nearly so – as a result of the drift corrections.)

5. The gravity data in Table 2.4 were obtained during a followup on a small sphalerite showing in eastern Ontario. Reduce the gravity readings

by taking out the drift, free-air (including height of instrument), Bouguer (assuming an average density of  $2.67 \text{ g/cm}^3$ ), and latitude corrections (lines are N–S). Plot the two profiles. Are there any indications of a small high-grade (10–15%) or larger low-grade (2–5%) sphalerite deposit? Can you suggest any reason for the general shape of the profiles?

6. Show that the gravity anomaly produced by a vertical cone at its apex is

$$\Delta g_{\text{max}} = 2\pi\gamma\rho h(1 - \cos \alpha)$$

where  $h$  is the vertical height and  $\alpha$  half the apex angle of the cone. Hence show that the terrain correction at the apex of a conical hill is

$$\delta g_i = 2\pi\gamma\rho h \cos \alpha$$

If  $h = 1000 \text{ ft}$ ,  $\alpha = 68^\circ$ , and  $\rho = 2.67 \text{ g/cm}^3$ , with the aid of a template and Table 2.1 determine the terrain correction required at various points on the sloping sides and on flat ground surrounding the cone (obviously the correction is the same at any particular elevation because of symmetry). How close to the base can gravity measurements be made without a significant terrain effect?

Table 2.4.

Stn L 8W	$g_{obs}$ (mGal)	Time (PM)	H.I. (ft)	Elev. (ft)	Stn L 8W	$g_{obs}$ (mGal)	Time (PM)	H.I. (ft)	Elev. (ft)
*3S	37.04	2.20	1.42	0.00	1 + 75	36.86	3.33	1.42	1.60
3 + 25	36.82	2.30	1.25	3.69	1 + 50	36.88	3.37	1.58	1.84
3 + 50	36.87	2.33	1.33	3.63	1 + 25	37.49	3.42	1.33	-5.81
3 + 75	36.84	2.36	1.33	4.78	15	37.77	3.45	1.08	-9.68
4S	36.80	2.40	1.33	5.85	0 + 75	38.00	3.49	1.10	-13.99
4 + 25	36.68	2.45	1.33	7.11	0 + 50	38.03	3.53	0.83	-14.93
4 + 50	36.63	2.48	1.50	8.26	0 + 25	38.07	3.59	0.83	-15.06
4 + 75	36.57	2.52	1.17	10.03	B.L.	38.03	4.02	1.17	-15.30
5S	36.47	2.55	1.33	11.42	L 10W				
5 + 25	36.56	2.57	1.25	10.19	B.L.	37.62	4.23	1.42	-3.06
5 + 50	36.67	3.00	1.33	8.91	15	37.94	4.34	1.08	-7.41
5 + 75	36.67	3.04	1.33	8.21	25	37.60	4.38	1.23	-9.14
6S	36.73	3.06	1.42	7.46	35	37.55	4.40	1.42	-8.20
*3S	37.06	3.13	1.33	0.00	45	37.27	4.46	1.42	-4.85
2 + 75	36.96	3.17	1.33	-0.76	55	37.45	4.50	1.17	1.04
2 + 50	36.74	3.23	1.42	1.18	65		4.53	1.42	-1.04
2 + 25	36.89	3.28	1.25	1.23	L 8W				
2S	36.86	3.30	1.42	1.39	*3S	37.10	5.00	1.17	0.00

Note: L = line; B.L. = base line = 0 ft on each line; 3S = 300 ft south of base line, 3 + 75 = 375 ft south of base line, and so on; H.I. = height of instrument (gravimeter) above the surface whose elevation is given. Lat. of B.L. = 46°25'N.

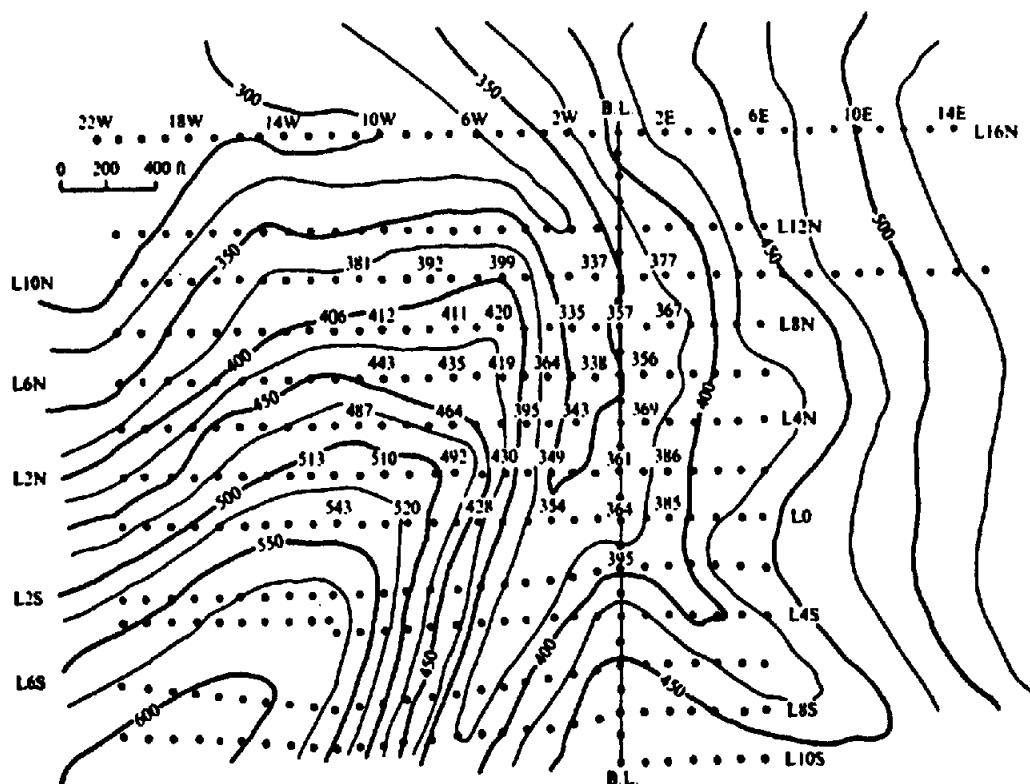


Figure 2.39. Topographic map for terrain correction.

7. The topographic map in Figure 2.39 was prepared in considerable detail to take out a terrain correction for a gravity survey. Make a template of appropriate scale for the first four or five zones of Table 2.1 (zones B-F) and calculate the terrain correction at several stations, such as (2N, 3W), (8N, 12W), (0, 9W), etc. Assuming that

the topography is reasonably flat in the area surrounding the section illustrated, how many additional zones would be necessary to make a complete terrain correction?

In fact, there is a steep ridge to the northwest, striking southwest-northeast. At a distance of about 2 miles from the center of the area the

elevations increase from 300 to 1,100 ft within 1/2 mile. There is also a lake, which is roughly 1 mile across and a maximum of 100 ft in depth, situated about 2 miles to the northeast. To what extent would these large topographic features affect the overall terrain correction?

8. The reduced gravity readings (Bouguer) in Table 2.5 were obtained from an east-west traverse with stations at 30 m intervals. An electromagnetic survey carried out earlier had outlined a conducting zone about 750 m long, striking roughly north-south, with a maximum width of 50 m in the central part of the area. The gravity work was done as an attempt to assess the metallic content of the conductor. Four additional parallel gravity traverses, on lines adjacent to line 81N, produced essentially similar results. No information is available on the depth of overburden. Plot the profile and make a qualitative interpretation of the nature of the conducting zone based on the gravity survey.
9. The Bouguer gravity readings in Table 2.6 are taken from a survey in the sedimentary Pine Point area of the Northwest Territories. Station spacing is 30 m on a N-S line.

Plot the profile and interpret the gravity anomaly, assuming it to be approximately two dimensional. Make two interpretations, assuming first that (a) below is valid, then assuming that (b) [but not (a)] is valid.

(a) A Turam survey has not located any conductors in the area, while soil geochemistry shows minor lead and zinc.

(b) The gravity anomaly coincides with a strong IP anomaly.

Attempt to match the gravity profile with a simple geometrical cross section with particular regard to its depth, depth extent, and width.

Table 2.5. Line 81N.

Stn	$g_B$ (mGal)	Stn	$g_B$ (mGal)
85E	1.35	93E	0.77
86	1.30	94	0.75
87	1.25	95	0.66
88	1.22	96	0.55
89	1.20	97	0.51
90	1.15	98	0.50
91	1.07	99	0.40
92	0.87		

Table 2.6.

Stn	$g_B$ (mGal)	Stn	$g_B$ (mGal)
8S	0.02	2N	0.62
7S	0.06	3N	0.79
6S	0.08	4N	0.82
5S	0.09	5N	0.82
4S	0.08	6N	0.67
3S	0.06	7N	0.33
2S	0.01	8N	0.22
1S	0.04	9N	0.20
B.L.	0.19	10N	0.18
1N	0.41	11N	0.16

10. Residual gravity contours obtained from a survey over a base-metal area are shown in Figure 2.40. A regional trend of about 0.8 mGal/1,000 ft was removed to produce this map. A profile along the south-north line has also been plotted. The gravity anomaly is obviously caused by a plug-type of structure of considerable positive density contrast. Make an interpretation of the source as precisely as possible with these data.

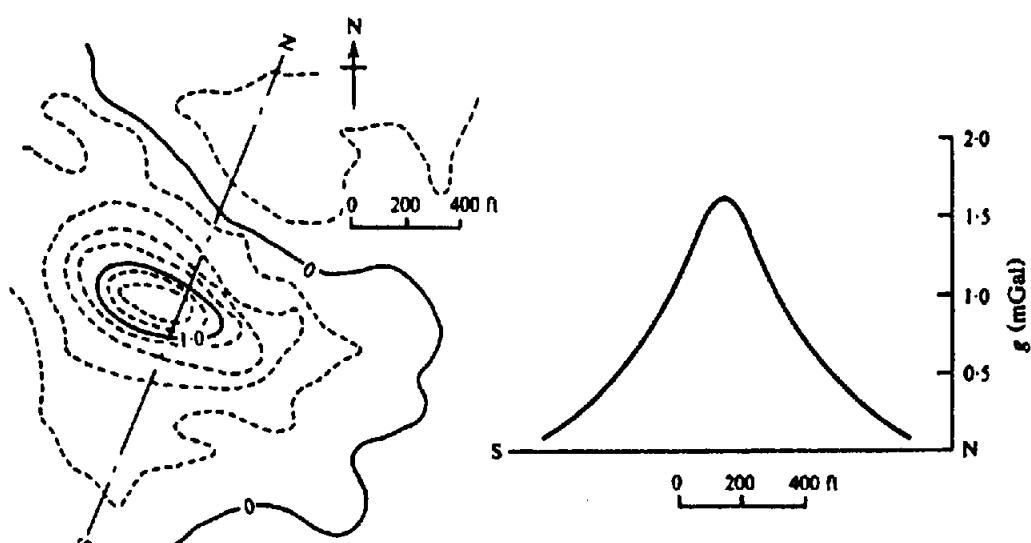


Figure 2.40. Residual gravity contours and principal profile, northwest Quebec.; C.I. = 0.2 mGal. (After Seigel, 1957.)

11. Table 2.7 gives Bouguer gravity readings from a survey made in the Bathurst area of northern New Brunswick. Station spacing is 100 ft and the line spacing is as noted. (L20N means 2,000 ft north of the base line.) Because of limited time and money, only four lines were selected for a followup of an earlier combined magnetic-electrical-geochemical survey. (Although this type of spot gravity work is used to some extent in base-metal exploration, it has obvious limitations.) There is a pronounced regional gradient, positive to the east, but it is not uniform, being stronger in the north lines and weakest on line 10N. Furthermore the large and irregular spacing between the lines makes it difficult to plot well-defined contours. On the other hand, if we attempt to remove the gradients from each line independently, it is not clear what background level should be selected; because we are looking for massive sulfides, the tendency is to overemphasize positive gravity areas. No measurements were made of overburden depth.

Try to remove the regional by graphical smoothing and by gridding (more sophisticated techniques are not warranted). Interpret any remaining residuals.

12. Additional data obtained in the gravity survey of problem 4 are given in Table 2.8. Lines are east-west, 200 m apart; stations are 50 m apart with the larger numbers to the west. For some reason the base line through Stn 0 was cut at an angle of 20° east of true north, so that each station on line 0 is displaced about 73 m east of its equivalent on line 2S. Obviously there is a small latitude correction,  $2\phi$  being  $\approx 93^\circ$ .

Using the data in problem 4 (corrected for drift), apply the appropriate reductions to obtain Bouguer gravity for all stations, using an average density of 2.67 g/cm<sup>3</sup> for the local formations which consist of gneiss on the western portion extending roughly to station 25 and ultrabasic rocks to the east. There are frequent large outcrops in the eastern region, while the gneiss is covered by a fairly uniform thin overburden of 1-2 m. Plot the gravity profiles and make an interpretation of the results.

13. Figure 2.41 shows Bouguer gravity values at 30 m intervals. The following methods of analysis are suggested:

- (i) Remove the regional by drawing contours and graphical smoothing.
- (ii) Remove the regional by gridding.
- (iii) Calculate the second derivative.
- (iv) Carry out downward continuation by any method you know.

Compare the results achieved with the different

methods and consider their relative advantages and limitations. Interpret the residual anomaly or anomalies, if any, and calculate the excess mass. Is the section large enough to give reasonable results?

Table 2.7.

Stn	L20N (mGal)	L16N (mGal)	L10N (mGal)	L2N (mGal)
4W	45.38	45.71	46.10	—
3W	45.47	45.94	46.10	46.43
2W	45.68	45.90	46.40	46.48
1W	45.79	45.97	46.22	46.60
BL	45.91	45.93	46.27	46.68
1E	46.09	46.14	46.31	47.00
2E	46.21	46.42	46.55	47.09
3E	46.08	46.40	46.72	47.00
4E	46.54	46.53	46.80	47.12
5E	46.62	46.75	46.66	47.50
6E	46.91	46.87	46.61	47.61

Table 2.8.

Line 0			Line 2S		
Stn	H.I. (m)	Elev. (m)	Stn	H.I. (m)	Elev. (m)
53	0.46	6.76	53	0.46	8.03
52	0.43	6.99	52	0.44	7.85
51	0.49	7.08	51	0.43	8.20
50	0.47	5.95	50	0.43	8.50
49	0.51	4.73	49	0.46	8.75
48	0.53	4.68	48	0.46	8.91
47	0.53	6.00	47	0.47	8.61
46	0.48	6.42	46	0.46	8.36
45	0.50	6.40	45	0.40	8.64
44	0.48	6.75	44	0.41	9.03
43	0.47	7.20	43	0.43	9.06
42	0.50	6.64	42	0.42	8.41
41	0.46	5.82	41	0.45	8.02
40	0.39	5.96	40	0.44	7.65
39	0.45	6.21	39	0.48	7.62
			24	0.44	3.84
25	0.50	2.59	25	0.46	4.74
26	0.46	3.15	26	0.41	4.88
27	0.40	3.78	27	0.42	4.69
28	0.50	3.17	28	0.42	5.69
29	0.43	1.96	29	0.45	6.15
30	0.45	1.31	30	0.46	6.03
31	0.40	2.22	31	0.42	6.51
32	0.43	0.00	32	0.42	7.01
33	0.42	1.04	33	0.45	6.89
34	0.48	1.55	34	0.45	6.34
35	0.47	2.50	35	0.44	5.39
36	0.47	3.00	36	0.45	6.58
37	0.49	4.06	37	0.46	7.80
38	0.47	5.38	38	0.46	7.67
39	0.48	6.21	39	0.45	7.62
53	0.45	6.76	53	0.43	8.03

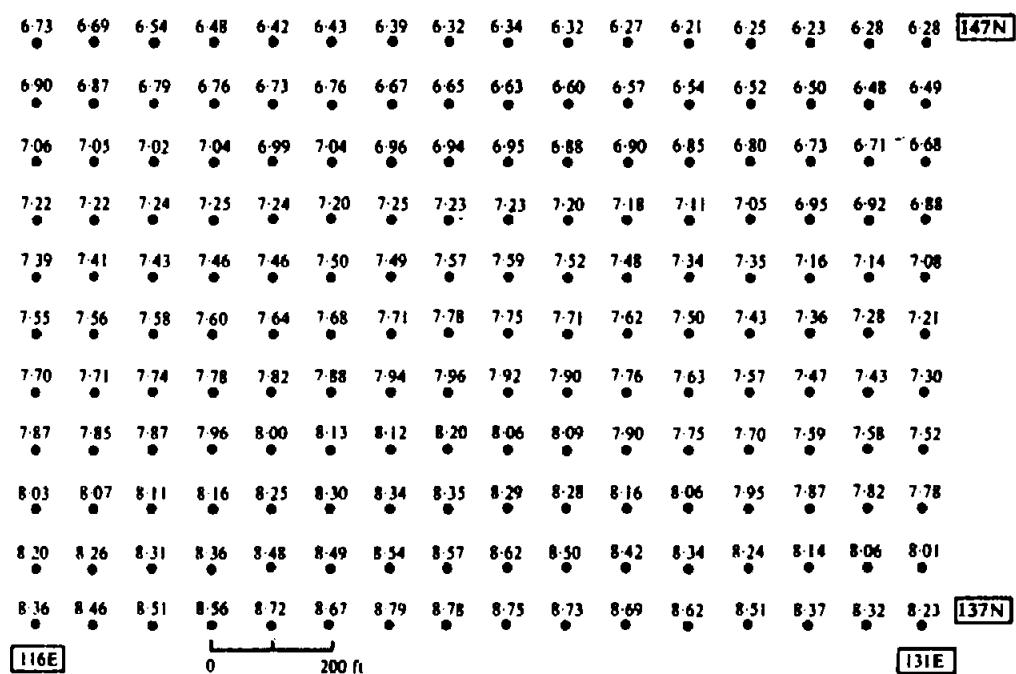


Figure 2.41. Bouguer gravity values on 30 m grid; values in milligals.

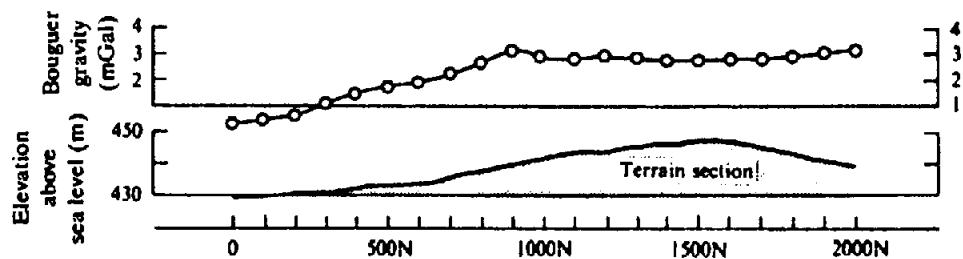


Figure 2.42. Bouguer gravity and topographic profiles, East Africa.

14. A topographic section and Bouguer gravity profile over a long east-west ridge are shown in Figure 2.42. Without other information, is it possible to answer the following questions with assurance?
  - (a) Was a terrain correction taken out in reducing the gravity readings?
  - (b) Is a terrain correction necessary?
  - (c) Is the gravity profile essentially a reflection of the topography?
  - (d) Is a regional gravity effect present that is independent of the topography?
  - (e) Assuming there is a gravity anomaly caused by a subsurface structure, can you locate it and estimate its approximate section? (As an aid to making this interpretation, it would be very helpful to replot the gravity profile on an expanded vertical scale.)
15. Figure 2.43 is a Bouguer gravity contour map of the area whose topography is shown in Figure 2.39. The geology is sedimentary, with sandstone and limestone beds that are known to be over 5,000 ft thick a few miles to the west. Within the

survey area the limestone-sandstone contact can be seen at the bottom of the hill just west of the base line. The limestone bed extends east from this contact at surface and appears to be less than 50 ft thick; because it does not continue west under the hill, a fault is indicated. Under normal circumstances, the sandstone would have the lower density; but in this area, because the limestone is thin and because there are underground streams flowing in it, the density contrast is probably insignificant and may even be in the opposite sense.

Problem 7, with which Figure 2.39 is connected, was an exercise in making terrain corrections in rugged ground. Preparation of the map in Figure 2.43 required more than 15 man-days of work, most of it spent on terrain corrections for about 400 gravity stations. The end result is a gravity map that appears to be a fair reproduction of the topography.

Do the two maps, Figures 2.39 and 2.43, resemble each other in spite of the elaborate terrain correction or because of it? If the latter is

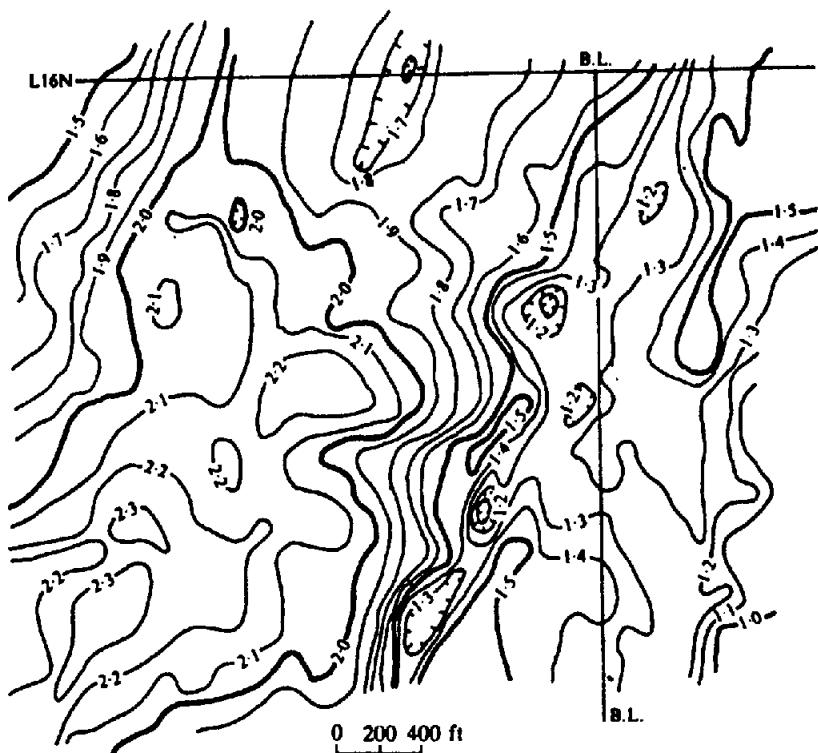


Figure 2.43. Bouguer gravity contours, eastern Nova Scotia; C.I. = 0.1 mGal.

true, would this be a fundamental argument against carrying out gravity surveys in regions where the topography is highly irregular? On the other hand, if the anomalous gravity is not due to topography, how do you explain it?

16. The reduced gravity contours in Figure 2.44 show a portion of a large survey made over a base-metal property in southern New Brunswick. Remove the regional. Given that there are ore-grade sulfides in the area, interpret the residual and estimate the excess mass.
17. Figure 2.45 shows residual Bouguer gravity across a three-dimensional structure of positive density contrast in the St. Lawrence lowlands east of Montreal. The contours are approximately circular. Drill logs from gas and oil exploration holes in the vicinity have indicated flat-lying sedimentary beds to a depth of over 4,000 ft. The maximum density contrast among the different sediments is not greater than 0.2 g/cm<sup>3</sup> and generally is closer to 0.1. Density of the Precambrian basement rocks is not known, but they are probably denser than the average sediments by 0.25–0.30 g/cm<sup>3</sup>.
- To interpret this anomaly, first consider the maximum gravity combined with the maximum slope of the flanks, with respect to the known depths and density contrasts in the area. This will indicate an approximate depth to the source. Then attempt to match the profile with a simple shape, such as the sphere, rod, cylinder, and so forth. (Note that it is possible to simulate a pillbox-type of structure by taking the difference between the gravity effects of two long cylinders with their tops at different depths.)
18. On the portion of the Bouguer anomaly map shown in Figure 2.46, the most negative values are found in the lower left corner. (The numerical values shown are with respect to an arbitrary datum.)
  - (a) A large fault strikes N20°W just east of AUS. Examine the shape of the fault anomaly by drawing the profile A'A.
  - (b) For a simple fault model, the point where the fault's gravity expression is half its maximum value locates the fault. What difficulties are encountered in the practical application of this rule? Another rule is that the fault is located at the inflection point on the fault profile. Locate the fault on this profile by applying these rules. What does the asymmetry of the fault profile indicate?
  - (c) The half-width rule states that the depth to the midpoint on a fault is equal to the distance between the points on the fault's gravity profile, where the fault's gravity expression is  $\frac{1}{4}$  and  $\frac{1}{2}$  (or  $\frac{1}{2}$  and  $\frac{3}{4}$ ) of its maximum expression. What depth does this give for this fault? What difficulties are encountered in the practical application of this rule?

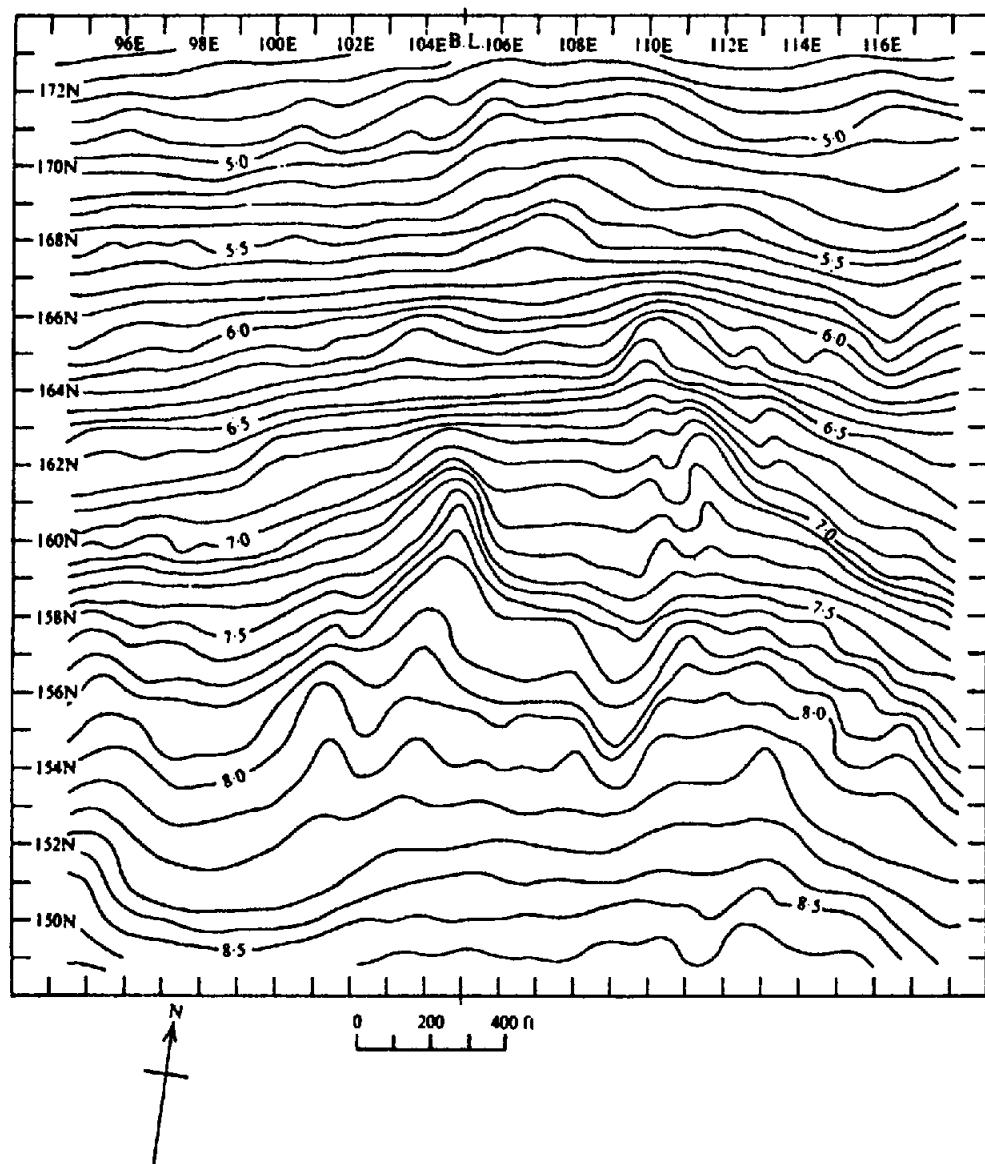


Figure 2.44. Bouguer gravity contours, southern New Brunswick; C.I. = 0.1 mGal.

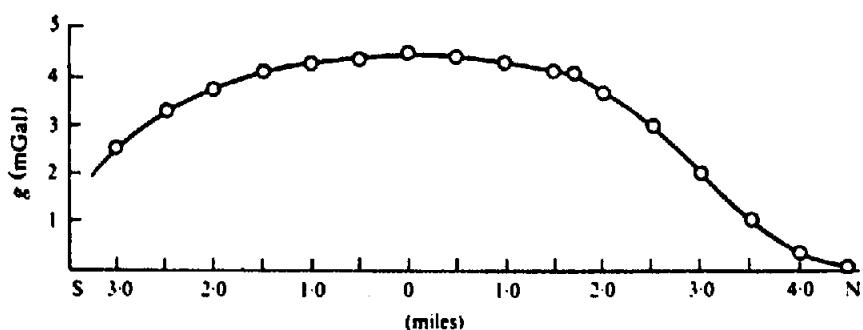


Figure 2.45. Residual gravity profile over three-dimensional structure, St. Lawrence lowlands.

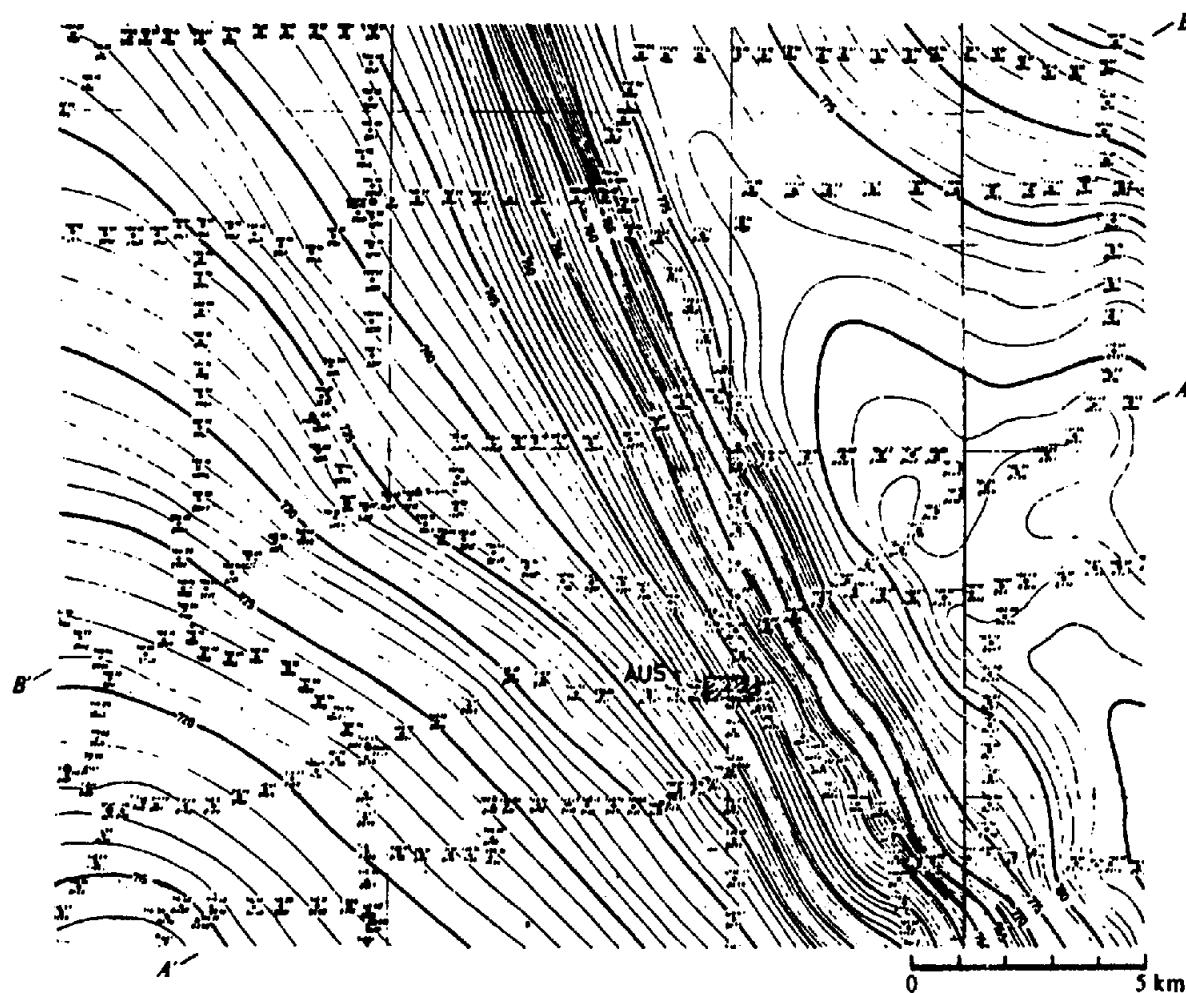


Figure 2.46. Bouguer gravity map, Western Australia; C.I. = 1.0 mGal. (Courtesy West Australian Petroleum.)

- (d) What is the magnitude of this fault in milligals? Assume that a uniform density contrast across the fault exists from the surface to twice the depth given in part (c). How much density contrast is implied?
19. On the Bouguer anomaly map of Figure 2.46, the bow in the contours about 9 km NW of AUS indicates a structure.
- Draw the profile  $B'B$  to separate this anomaly from the fault anomaly examined in problem 18. Where is the center of the anomaly?
  - Draw a profile at right angles to  $B'B$  through the center of the anomaly. Is the anomaly easier to see on this profile? Are the residual anomalies consistent with each other? What is the magnitude of the anomaly in milligals?
  - Assume that the anomaly can be approximated by a buried spherical mass (see Fig. 2.23). How deep must the center of the sphere be? If a density contrast of  $0.1 \text{ g/cm}^3$  is assumed, what would be the radius of the sphere?
  - The bow in the contours about 5 km SSW of AUS might be interpreted as a similar anomaly. What is unreliable about this anomaly?
20. A grid residual is one way of isolating anomalies from a regional background. Read the contour values on a 2 km grid over the Bouguer anomaly map of Figure 2.46. Assuming that the expected value at each grid station is the average of the four values, which are 2 km away, the residual is the difference between the observed and the expected values. Determine the residuals for all the grid points and contour the resulting map. Note how the fault studied in problem 18 and the anomaly studied in problem 19 are emphasized by this process.

## REFERENCES

- Ager, C. A., and Liard, L. O. 1982. Vertical gradient surveys: Field results and interpretation in British Columbia. *Geophysics* 47, 919–25.
- Agocs, W. B. 1951. Least-squares residual anomaly determination. *Geophysics* 16, 686–96.
- Arzi, A. A. 1975. Microgravity for engineering applications. *Geophys. Prosp.* 23, 408–25.
- Bhattacharyya, B. K. 1978. Computer modeling in gravity and magnetic interpretation. *Geophysics* 43, 912–29.
- Bible, J. L. 1964. Gravity for the geologist. *World Oil*, Oct. and Nov. issues.

- Brozena, J. M. 1984. A preliminary analysis of the NRL airborne gravimetry system. *Geophysics* 49, 1060-9.
- Butler, D. K. 1984. Microgravimetric and gravity gradient techniques for detection of subsurface cavities. *Geophysics* 49, 1084-96.
- Coons, R. L., Woolard, G. P., and Hershey, G. 1967. Structural significance of the mid-continent gravity high. *Bull. Am. Assoc. Petr. Geol.* 51, 2381-99.
- Dean, W. C. 1958. Frequency analysis for gravity and magnetic interpretation. *Geophysics* 23, 97-127.
- Dickenson, G. 1953. Geological aspects of abnormal reservoir pressure on Gulf Coast, Louisiana. *A. A. P. G. Bulletin* 37, 410-32.
- Dobrin, M. B. 1960. Introduction to Geophysical prospecting, 2nd ed. New York: McGraw-Hill.
- Elkins, T. A. 1951. The second derivative method of gravity interpretation. *Geophysics* 16, 29-50.
- Ervin, C. P. 1977. Theory of the Bouguer anomaly. *Geophysics* 42, 1468.
- Falkiewicz, Z. J. 1976. Gravity vertical gradient measurements for the detection of small geologic and anthropogenic forms. *Geophysics* 41, 1016-30.
- Geldart, L. P., Gill, D. E., and Sharma, B. 1966. Gravity anomalies of two-dimensional faults. *Geophysics* 31, 372-97.
- Grant, F. S., and West, G. F. 1965. *Interpretation Theory in Applied Geophysics*. New York: McGraw-Hill.
- Griffin, W. R. 1949. Residual gravity in theory and practice. *Geophysics* 14, 39-56.
- Gupta, V. K., and Ramani, N. 1982. Optimum second vertical derivatives in geological mapping and mineral exploration. *Geophysics* 47, 1706-15.
- Hammer, S. 1939. Terrain corrections for gravimeter stations. *Geophysics* 4, 184-94.
- Hammer, S. 1982. Critique of terrain corrections for gravity stations. *Geophysics* 47, 839-40.
- Hammer, S. 1983. Airborne gravity is here. *Geophysics* 48, 213-23.
- Hedberg, H. 1936. The gravitational compaction of clays and shales. *Am. J. Sci.* 31, 241-87.
- Henderson, R. G., and Zietz, I. 1949. The computation of second vertical derivatives of geomagnetic fields. *Geophysics* 14, 508-16.
- Hermes, H. J. 1986. Calculation of pre-Zechstein Bouguer anomaly in northwest Germany. *First Break* 4, No. 11, 13-22.
- Hubbert, M. K. 1948. A line integral method of computing gravimetric effects of two-dimensional masses. *Geophysics* 13, 215-25.
- Hussain, A., Walach, G., and Weber, F. 1981. Underground gravity survey in alpine regions. *Geophys. Prosp.* 29, 407-25.
- Jackson, D. D. 1979. The use of *a priori* data to resolve non-uniqueness in linear inversion. *Geophys. J. Roy. Astron. Soc.* 57, 137-57.
- Jordan, S. K. 1978. Moving-base gravity gradiometer surveys and interpretation. *Geophysics* 43, 94-101.
- Kahn, M. A. 1983. Satellite contributions to geophysical exploration at sea. In *CRC Handbook of Geophysical Exploration at Sea*, R. A. Geyer, ed., pp. 3-68. Boca Raton: CRC Press.
- Krohn, D. H. 1976. Gravity terrain corrections using multiquadratic equations. *Geophysics* 41, 266-75.
- LaCoste, L. J. B., Jr. 1934. A new type long period vertical seismograph. *Physics* 5, 178-80.
- LaFehr, T. R. 1980. History of geophysical exploration: Gravity method. *Geophysics* 45, 1634-9.
- LaFehr, T. R. 1983. Rock density from borehole gravity surveys. *Geophysics* 48, 341-56.
- Lynch, A. M., and King, A. R. 1983. A review of parameters affecting the accuracy and resolution of gravity surveys. *Bull. Aus. Soc. Explor. Geophys.* 14, 131-42.
- MacRobert, T. M. 1948. *Spherical Harmonics*. New York: Dover.
- Marquardt, D. W. 1963. An algorithm for least squares estimation of non-linear parameters. *J. Soc. Ind. and Appl. Math.* 11, 431-41.
- Maxant, J. 1980. Variation of density with rock type, depth, and formation in the Western Canada basin from density logs. *Geophysics* 45, 1061-76.
- Nettleton, L. L. 1971. *Elementary Gravity and Magnetics for Geologists and Seismologists*. Tulsa: Society of Exploration Geophysics.
- Nettleton, L. L. 1976. *Gravity and Magnetics in Oil Prospecting*. New York: McGraw-Hill.
- Parasnis, D. S. 1962. *Principles of Applied Geophysics*. London: Methuen.
- Paterson, N. R., and Reeves, C. V. 1985. Applications of gravity and magnetic surveys: The state of the art in 1985. *Geophysics* 50, 2558-94.
- Peters, L. J. 1949. The direct approach to magnetic interpretation and its practical application. *Geophysics* 14, 290-320.
- Pipes, L. A., and Harvill, L. R. 1970. *Applied Mathematics for Engineers and Physicists*. New York: McGraw-Hill.
- Reeves, C. V., and MacLeod, I. N. 1983. Modeling of potential field anomalies - Some applications for the microcomputer. *First Break* 1, No. 8, 18-24.
- Schmoker, J. W. 1978. Accuracy of borehole gravity data. *Geophysics* 43, 538-42.
- Seigel, H. O. 1957. Discovery of Mobrun Copper Ltd. sulfide deposit, Noranda Mining District, Quebec. In *Methods and Case Histories in Mining Geophysics. 6th Commonwealth Mining and Metallurgical Congress*. Montreal: Mercury Press.
- Sheriff, R. E. 1978. *First Course in Geophysical Exploration and Interpretation*. Boston: International Human Resources Development Co.
- Sheriff, R. E., and Geldart, L. P. 1983. *Exploration Seismology*, vol. II. Cambridge: Cambridge University Press.
- Skeels, D. C. 1947. Ambiguity in gravity interpretation. *Geophysics* 12, 43-56.
- Smith, R. A. 1959. Some depth formulae for local gravity and magnetic anomalies. *Geophys. Prosp.* 7, 55-63.
- Stanley, J. M. 1977. Simplified gravity interpretation by gradients - The geological contact. *Geophysics* 42, 1230-5.
- Talwani, M., Worzel, J. L., and Landisman, M. 1959. Rapid gravity computations for two-dimensional bodies with applications to the Mendocino submarine fracture zones. *J. Geophys. Res.* 64, 49-59.
- Tarantola, A., and Valette, B. 1982. Generalized nonlinear inverse problems solved using the least-squares criterion. *Rev. Geophys. and Space Phys.* 20-2, 219-32.
- Valliant, H. D., and LaCoste, L. J. B., Jr. 1976. Theory and evaluation of the LaCoste and Romberg three-axis inertial platform for marine gravimetry. *Geophysics* 41, 459-67.
- Woolard, G. P. 1979. The new gravity system - Changes in international gravity base values and anomaly values. *Geophysics* 44, 1352-66.

- Brozena, J. M. 1984. A preliminary analysis of the NRL airborne gravimetry system. *Geophysics* 49, 1060-9.
- Butler, D. K. 1984. Microgravimetric and gravity gradient techniques for detection of subsurface cavities. *Geophysics* 49, 1084-96.
- Coons, R. L., Woolard, G. P., and Hershey, G. 1967. Structural significance of the mid-continent gravity high. *Bull. Am. Assoc. Petr. Geol.* 51, 2381-99.
- Dean, W. C. 1958. Frequency analysis for gravity and magnetic interpretation. *Geophysics* 23, 97-127.
- Dickenson, G. 1953. Geological aspects of abnormal reservoir pressure on Gulf Coast, Louisiana. *A. A. P. G. Bulletin* 37, 410-32.
- Dobrin, M. B. 1960. Introduction to Geophysical prospecting, 2nd ed. New York: McGraw-Hill.
- Elkins, T. A. 1951. The second derivative method of gravity interpretation. *Geophysics* 16, 29-50.
- Ervin, C. P. 1977. Theory of the Bouguer anomaly. *Geophysics* 42, 1468.
- Falkiewicz, Z. J. 1976. Gravity vertical gradient measurements for the detection of small geologic and anthropogenic forms. *Geophysics* 41, 1016-30.
- Geldart, L. P., Gill, D. E., and Sharma, B. 1966. Gravity anomalies of two-dimensional faults. *Geophysics* 31, 372-97.
- Grant, F. S., and West, G. F. 1965. *Interpretation Theory in Applied Geophysics*. New York: McGraw-Hill.
- Griffin, W. R. 1949. Residual gravity in theory and practice. *Geophysics* 14, 39-56.
- Gupta, V. K., and Ramani, N. 1982. Optimum second vertical derivatives in geological mapping and mineral exploration. *Geophysics* 47, 1706-15.
- Hammer, S. 1939. Terrain corrections for gravimeter stations. *Geophysics* 4, 184-94.
- Hammer, S. 1982. Critique of terrain corrections for gravity stations. *Geophysics* 47, 839-40.
- Hammer, S. 1983. Airborne gravity is here. *Geophysics* 48, 213-23.
- Hedberg, H. 1936. The gravitational compaction of clays and shales. *Am. J. Sci.* 31, 241-87.
- Henderson, R. G., and Zietz, I. 1949. The computation of second vertical derivatives of geomagnetic fields. *Geophysics* 14, 508-16.
- Hermes, H. J. 1986. Calculation of pre-Zechstein Bouguer anomaly in northwest Germany. *First Break* 4, No. 11, 13-22.
- Hubbert, M. K. 1948. A line integral method of computing gravimetric effects of two-dimensional masses. *Geophysics* 13, 215-25.
- Hussain, A., Walach, G., and Weber, F. 1981. Underground gravity survey in alpine regions. *Geophys. Prosp.* 29, 407-25.
- Jackson, D. D. 1979. The use of *a priori* data to resolve non-uniqueness in linear inversion. *Geophys. J. Roy. Astron. Soc.* 57, 137-57.
- Jordan, S. K. 1978. Moving-base gravity gradiometer surveys and interpretation. *Geophysics* 43, 94-101.
- Kahn, M. A. 1983. Satellite contributions to geophysical exploration at sea. In *CRC Handbook of Geophysical Exploration at Sea*, R. A. Geyer, ed., pp. 3-68. Boca Raton: CRC Press.
- Krohn, D. H. 1976. Gravity terrain corrections using multiquadratic equations. *Geophysics* 41, 266-75.
- LaCoste, L. J. B., Jr. 1934. A new type long period vertical seismograph. *Physics* 5, 178-80.
- LaFehr, T. R. 1980. History of geophysical exploration: Gravity method. *Geophysics* 45, 1634-9.
- LaFehr, T. R. 1983. Rock density from borehole gravity surveys. *Geophysics* 48, 341-56.
- Lynch, A. M., and King, A. R. 1983. A review of parameters affecting the accuracy and resolution of gravity surveys. *Bull. Aus. Soc. Explor. Geophys.* 14, 131-42.
- MacRobert, T. M. 1948. *Spherical Harmonics*. New York: Dover.
- Marquardt, D. W. 1963. An algorithm for least squares estimation of non-linear parameters. *J. Soc. Ind. and Appl. Math.* 11, 431-41.
- Maxant, J. 1980. Variation of density with rock type, depth, and formation in the Western Canada basin from density logs. *Geophysics* 45, 1061-76.
- Nettleton, L. L. 1971. *Elementary Gravity and Magnetics for Geologists and Seismologists*. Tulsa: Society of Exploration Geophysics.
- Nettleton, L. L. 1976. *Gravity and Magnetics in Oil Prospecting*. New York: McGraw-Hill.
- Parasnis, D. S. 1962. *Principles of Applied Geophysics*. London: Methuen.
- Paterson, N. R., and Reeves, C. V. 1985. Applications of gravity and magnetic surveys: The state of the art in 1985. *Geophysics* 50, 2558-94.
- Peters, L. J. 1949. The direct approach to magnetic interpretation and its practical application. *Geophysics* 14, 290-320.
- Pipes, L. A., and Harvill, L. R. 1970. *Applied Mathematics for Engineers and Physicists*. New York: McGraw-Hill.
- Reeves, C. V., and MacLeod, I. N. 1983. Modeling of potential field anomalies - Some applications for the microcomputer. *First Break* 1, No. 8, 18-24.
- Schmoker, J. W. 1978. Accuracy of borehole gravity data. *Geophysics* 43, 538-42.
- Seigel, H. O. 1957. Discovery of Mobrun Copper Ltd. sulfide deposit, Noranda Mining District, Quebec. In *Methods and Case Histories in Mining Geophysics. 6th Commonwealth Mining and Metallurgical Congress*. Montreal: Mercury Press.
- Sheriff, R. E. 1978. *First Course in Geophysical Exploration and Interpretation*. Boston: International Human Resources Development Co.
- Sheriff, R. E., and Geldart, L. P. 1983. *Exploration Seismology*, vol. II. Cambridge: Cambridge University Press.
- Skeels, D. C. 1947. Ambiguity in gravity interpretation. *Geophysics* 12, 43-56.
- Smith, R. A. 1959. Some depth formulae for local gravity and magnetic anomalies. *Geophys. Prosp.* 7, 55-63.
- Stanley, J. M. 1977. Simplified gravity interpretation by gradients - The geological contact. *Geophysics* 42, 1230-5.
- Talwani, M., Worzel, J. L., and Landisman, M. 1959. Rapid gravity computations for two-dimensional bodies with applications to the Mendocino submarine fracture zones. *J. Geophys. Res.* 64, 49-59.
- Tarantola, A., and Valette, B. 1982. Generalized nonlinear inverse problems solved using the least-squares criterion. *Rev. Geophys. and Space Phys.* 20-2, 219-32.
- Valliant, H. D., and LaCoste, L. J. B., Jr. 1976. Theory and evaluation of the LaCoste and Romberg three-axis inertial platform for marine gravimetry. *Geophysics* 41, 459-67.
- Woolard, G. P. 1979. The new gravity system - Changes in international gravity base values and anomaly values. *Geophysics* 44, 1352-66.

# Chapter

## 3

# *Magnetic Methods*

### 3.1. INTRODUCTION

#### 3.1.1. General

Magnetic and gravity methods have much in common, but magnetics is generally more complex and variations in the magnetic field are more erratic and localized. This is partly due to the difference between the dipolar magnetic field and the monopolar gravity field, partly due to the variable direction of the magnetic field, whereas the gravity field is always in the vertical direction, and partly due to the time-dependence of the magnetic field, whereas the gravity field is time-invariant (ignoring small tidal variations). Whereas a gravity map usually is dominated by regional effects, a magnetic map generally shows a multitude of local anomalies. Magnetic measurements are made more easily and cheaply than most geophysical measurements and corrections are practically unnecessary. Magnetic field variations are often diagnostic of mineral structures as well as regional structures, and the magnetic method is the most versatile of geophysical prospecting techniques. However, like all potential methods, magnetic methods lack uniqueness of interpretation.

#### 3.1.2. History of Magnetic Methods

The study of the earth's magnetism is the oldest branch of geophysics. It has been known for more than three centuries that the Earth behaves as a large and somewhat irregular magnet. Sir William Gilbert (1540–1603) made the first scientific investigation of terrestrial magnetism. He recorded in *de Magnete* that knowledge of the north-seeking property of a magnetite splinter (a *lodestone* or leading stone) was brought to Europe from China by Marco Polo. Gilbert showed that the Earth's magnetic field was roughly equivalent to that of a permanent magnet lying in a general north-south direction near the Earth's rotational axis.

Karl Frederick Gauss made extensive studies of the Earth's magnetic field from about 1830 to 1842, and most of his conclusions are still valid. He concluded from mathematical analysis that the magnetic field was entirely due to a source within the Earth, rather than outside of it, and he noted a probable connection to the Earth's rotation because the axis of the dipole that accounts for most of the field is not far from the Earth's rotational axis.

The terrestrial magnetic field has been studied almost continuously since Gilbert's time, but it was not until 1843 that von Wrede first used variations in the field to locate deposits of magnetic ore. The publication, in 1879, of *The Examination of Iron Ore Deposits by Magnetic Measurements* by Thalén marked the first use of the magnetic method.

Until the late 1940s, magnetic field measurements mostly were made with a magnetic balance, which measured one component of the earth's field, usually the vertical component. This limited measurements mainly to the land surface. The fluxgate magnetometer was developed during World War II for detecting submarines from an aircraft. After the war, the fluxgate magnetometer (and radar navigation, another war development) made aeromagnetic measurements possible. Proton-precession magnetometers, developed in the mid-1950s, are very reliable and their operation is simple and rapid. They are the most commonly used instruments today. Optical-pump alkali-vapor magnetometers, which began to be used in 1962, are so accurate that instrumentation no longer limits the accuracy of magnetic measurements. However, proton-precession and optical-pump magnetometers measure only the magnitude, not the direction, of the magnetic field. Airborne gradiometer measurements began in the late 1960s, although ground measurements were made much earlier. The gradiometer often consists of two magnetometers vertically spaced 1 to 30 m apart. The difference in readings not only gives the vertical gradient, but also, to a large extent, removes the effects of tempo-

ral field variations, which are often the limiting factor on accuracy.

Digital recording and processing of magnetic data removed much of the tedium involved in reducing measurements to magnetic maps. Interpretation algorithms now make it possible to produce computer-drawn profiles showing possible distributions of magnetization.

The history of magnetic surveying is discussed by Reford (1980) and the state of the art is discussed by Paterson and Reeves (1985).

## 3.2. PRINCIPLES AND ELEMENTARY THEORY

### 3.2.1. Classical versus Electromagnetic Concepts

Modern and classical magnetic theory differ in basic concepts. Classical magnetic theory is similar to electrical and gravity theory; its basic concept is that point magnetic poles are analogous to point electrical charges and point masses, with a similar inverse-square law for the forces between the poles, charges, or masses. Magnetic units in the centimeter-gram-second and electromagnetic units (cgs and emu) system are based on this concept. Système International (SI) units are based on the fact that a magnetic field is electrical in origin. Its basic unit is the dipole, which is created by a circular electrical current, rather than the fictitious isolated monopole of the cgs-emu system. Both emu and SI units are in current use.

The cgs-emu system begins with the concept of magnetic force  $\mathbf{F}$  given by Coulomb's law:

$$\mathbf{F} = (p_1 p_2 / \mu r^2) \mathbf{r}_1 \quad (3.1)$$

where  $\mathbf{F}$  is the force on  $p_2$ , in dynes, the poles of strength  $p_1$  and  $p_2$  are  $r$  centimeters apart,  $\mu$  is the magnetic permeability [a property of the medium; see Eq. (3.7)], and  $\mathbf{r}_1$  is a unit vector directed from  $p_1$  toward  $p_2$ . As in the electrical case (but unlike the gravity case, in which the force is always attractive), the magnetostatic force is attractive for poles of opposite sign and repulsive for poles of like sign. The sign convention is that a positive pole is attracted toward the Earth's north magnetic pole; the term *north-seeking* is also used.

The magnetizing field  $\mathbf{H}$  (also called *magnetic field strength*) is defined as the force on a unit pole:

$$\mathbf{H}' = \mathbf{F}/p_2 = (p_1 / \mu r^2) \mathbf{r}_1 \quad (3.2)$$

(we use a prime to indicate that  $H$  is in cgs-emu

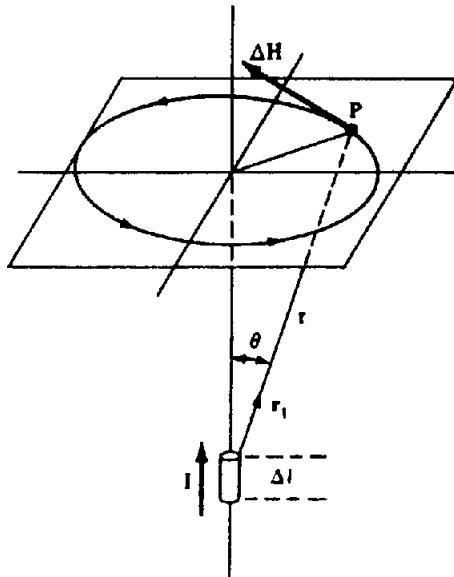


Figure 3.1. Ampère's law. A current  $I$  through a length of conductor  $\Delta l$  creates a magnetizing field  $\Delta H$  at a point  $P$ :

$$\Delta H = (I \Delta l) \times r_1 / 4\pi r^2$$

where  $\Delta H$  is in amperes per meter when  $I$  is in amperes and  $r$  and  $\Delta l$  are in meters.

units);  $H'$  is measured in oersteds (equivalent to dynes per unit pole).

A magnetic dipole is envisioned as two poles of strength  $+p$  and  $-p$  separated by a distance  $2l$ . The magnetic dipole moment is defined as

$$\mathbf{m} = 2lp\mathbf{r}_1 \quad (3.3)$$

$\mathbf{m}$  is a vector in the direction of the unit vector  $\mathbf{r}_1$  that extends from the negative pole toward the positive pole.

A magnetic field is a consequence of the flow of an electrical current. As expressed by Ampère's law (also called the Biot-Savart law), a current  $I$  in a conductor of length  $\Delta l$  creates, at a point  $P$  (Fig. 3.1), a magnetizing field  $\Delta H$  given by

$$\Delta H = (I \Delta l) \times r_1 / 4\pi r^2 \quad (3.4)$$

where  $H$  has the SI dimension amperes per meter [ $= 4\pi \times 10^{-3}$  oersted],  $r$  and  $\Delta l$  are in meters,  $I$  is in amperes, and  $\Delta H$ ,  $r_1$ , and  $I \Delta l$  have the directions indicated in Figure 3.1.

A current flowing in a circular loop acts as a magnetic dipole located at the center of the loop and oriented in the direction in which a right-handed screw would advance if turned in the direction of the current. Its dipole moment is measured in ampere-meter<sup>2</sup> ( $= 10^{10}$  pole-cm). The orbital motions of electrons around an atomic nucleus constitute circular currents and cause atoms to have magnetic mo-

ments. Molecules also have spin, which gives them magnetic moments.

A magnetizable body placed in an external magnetic field becomes magnetized by induction; the magnetization is due to the reorientation of atoms and molecules so that their spins line up. The magnetization is measured by the *magnetic polarization*  $M$  (also called *magnetization intensity* or *dipole moment per unit volume*). The lineup of internal dipoles produces a field  $M$ , which, within the body, is added to the magnetizing field  $H$ . If  $M$  is constant and has the same direction throughout, a body is said to be *uniformly magnetized*. The SI unit for magnetization is ampere-meter<sup>2</sup> per meter<sup>3</sup> [= ampere per meter ( $A/m$ )].

For low magnetic fields,  $M$  is proportional to  $H$  and is in the direction of  $H$ . The degree to which a body is magnetized is determined by its *magnetic susceptibility*  $k$ , which is defined by

$$M = kH \quad (3.5)$$

Magnetic susceptibility in emu differs from that in SI units by the factor  $4\pi$ , that is,

$$k_{SI} = 4\pi k'_{emu} \quad (3.6)$$

Susceptibility is the fundamental rock parameter in magnetic prospecting. The magnetic response of rocks and minerals is determined by the amounts and susceptibilities of magnetic materials in them. The susceptibilities of various materials are listed in Table 3.1, Section 3.3.7.

The *magnetic induction*  $B$  is the total field, including the effect of magnetization. It can be written

$$B = \mu_0(H + M) = \mu_0(1 + k)H = \mu\mu_0 H \quad (3.7a)$$

$$B' = H' + 4\pi M' = (1 + 4\pi k')H' = \mu H' \quad (3.7b)$$

when  $H$  and  $M$  ( $H'$  and  $M'$ ) are in the same direction, as is usually the case. The SI unit for  $B$  is the tesla = 1 newton/ampere-meter = 1 weber/meter<sup>2</sup> ( $Wb/m^2$ ). The electromagnetic unit for  $B'$  is the gauss [ $= 10^{-4}$  tesla ( $T$ )]. The permeability of free space  $\mu_0$  has the value  $4\pi \times 10^{-7}$   $Wb/A \cdot m$ . In vacuum  $\mu = 1$  and in air  $\mu \approx 1$ . Confusion sometimes results between  $H'$  and  $B'$  because the em units gauss and oersted are numerically equal and dimensionally the same, although conceptually different; both  $H'$  and  $B'$  are sometimes called the "magnetic field strength." In magnetic prospecting, we measure  $B$  to about  $10^{-4}$  of the Earth's main field (which is about  $50 \mu T$ ). The unit of magnetic induction generally used for geophysical work is the nanotesla (also

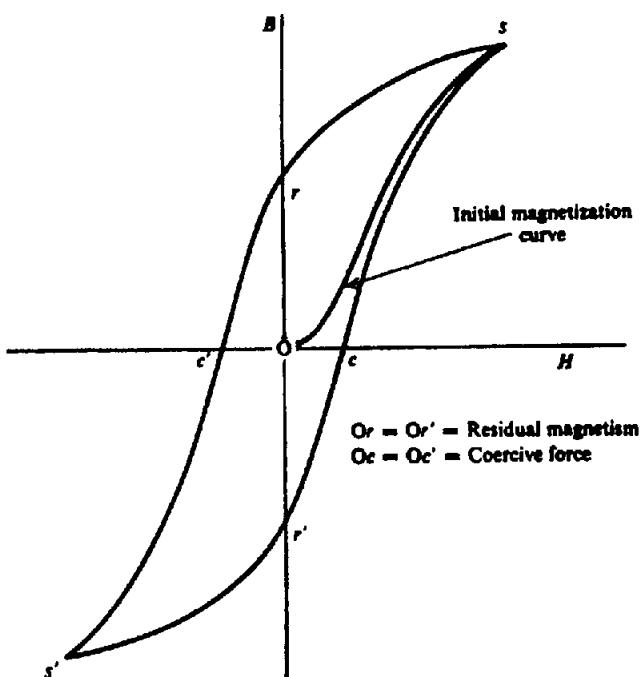


Figure 3.2. Hysteresis loop.  $s, s'$  = saturation,  $r$  and  $r'$  = remanent magnetism,  $c$  and  $c'$  = coercive force.

called the gamma,  $\gamma$ ):

$$1\gamma = 10^{-9} T = 1 nT$$

There is often confusion as to whether the quantity involved in magnetic exploration is  $B$  or  $H$ . Although we measure  $B_e$ , we are interested in the Earth's field  $H_e$ . However, because  $B$  and  $H$  are linearly related [Eq. (3.7)] and usually  $\mu \approx 1$ , we can (and do) treat a map of  $B_e$  as if it were a map of  $H_e$ .

We also speak of *magnetic flux* or *magnetic lines of force*  $\phi$ :

$$\phi = B \cdot A \quad (3.8)$$

where  $A$  is a vector area (§A.3.2). Thus  $|B| = \phi/|A|$  when  $A$  and  $B$  are parallel, that is,  $B$  is the density of magnetic flux. The SI unit for magnetic flux is the weber ( $= T \cdot m^2$ ) and the em unit is the maxwell ( $= 10^{-8} Wb$ ).

### 3.2.2. B-H Relations: The Hysteresis Loop

The relation between  $B$  and  $H$  can be complex in ferromagnetic materials (§3.3.5). This is illustrated by hysteresis (Fig. 3.2) in a cycle of magnetization. If a demagnetized sample is subjected to an increasing magnetizing field  $H$ , we obtain the first portion of the curve in which  $B$  increases with  $H$  until it flattens off as we approach the maximum value that  $B$  can have for the sample (*saturation*). When  $H$  is decreased, the curve does not retrace the same path, but it does show a positive value of  $B$  when  $H = 0$ ;

this is called *residual (remanent) magnetism*. When  $H$  is reversed,  $B$  finally becomes zero at some negative value of  $H$  known as the *coercive force*. The other half of the hysteresis loop is obtained by making  $H$  still more negative until reverse saturation is reached and then returning  $H$  to the original positive saturation value. The area inside the curve represents the energy loss per cycle per unit volume as a result of hysteresis (see Kip, 1962, pp. 235–7). Residual effects in magnetic materials will be discussed in more detail in Section 3.3.6. In some magnetic materials,  $B$  may be quite large as a result of previous magnetization having no relation to the present value of  $H$ .

### 3.2.3. Magnetostatic Potential for a Dipole Field

Conceptually the magnetic scalar potential  $A$  at the point  $P$  is the work done on a unit positive pole in bringing it from infinity by any path against a magnetic field  $\mathbf{F}(r)$  [compare Eq. (2.4)]. (Henceforth in this chapter  $\mathbf{F}$ ,  $F$  indicate magnetic field rather than force and we assume  $\mu = 1$ .) When  $\mathbf{F}(r)$  is due to a positive pole at a distance  $r$  from  $P$ ,

$$A(r) = - \int_{-\infty}^r \mathbf{F}(r) \cdot d\mathbf{r} = p/r \quad (3.9)$$

However, since a magnetic pole cannot exist, we consider a magnetic dipole to get a realistic entity. Referring to Figure 3.3, we calculate  $A$  at an external point:

$$\begin{aligned} A &= \left( \frac{p}{r_1} - \frac{p}{r_2} \right) \\ &= p \left\{ \frac{1}{(r^2 + l^2 - 2rl \cos \theta)^{1/2}} - \frac{1}{(r^2 + l^2 + 2rl \cos \theta)^{1/2}} \right\} \quad (3.10) \end{aligned}$$

We can derive the vector  $\mathbf{F}$  by taking the gradient of  $A$  [Eq. (A.17)]:

$$\mathbf{F}(r) = -\nabla A(r) \quad (3.11)$$

Its radial component is  $F_r = -\partial A / \partial r$  and its angular

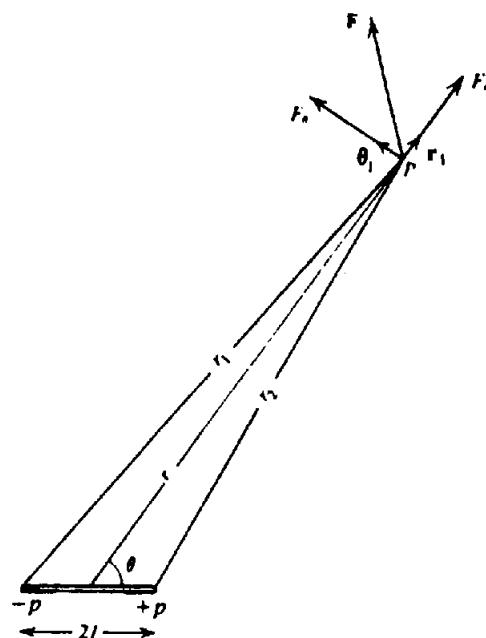


Figure 3.3. Calculating the field of a magnetic dipole.

lateral component is  $F_\theta = -\partial A / \partial \theta$ ; these are

$$F_r = -p \left\{ \frac{r + l \cos \theta}{(r^2 + l^2 + 2rl \cos \theta)^{3/2}} - \frac{r - l \cos \theta}{(r^2 + l^2 - 2rl \cos \theta)^{3/2}} \right\} \quad (3.12a)$$

$$F_\theta = p \left\{ \frac{l \sin \theta}{(r^2 + l^2 + 2rl \cos \theta)^{3/2}} + \frac{l \sin \theta}{(r^2 + l^2 - 2rl \cos \theta)^{3/2}} \right\} \quad (3.12b)$$

When  $r \gg l$ , Equation (3.10) becomes

$$A \approx |m| \cos \theta / r^2 \quad (3.13)$$

where  $m$  is the dipole moment of magnitude  $m = 2lp$ . Equations (3.11) and (3.13) give [§A.4 and Equation (A.33)]

$$\mathbf{F} \approx (m/r^3)(2 \cos \theta \mathbf{r}_1 + \sin \theta \mathbf{\theta}_1) \quad (3.14a)$$

where unit vectors  $\mathbf{r}_1$  and  $\mathbf{\theta}_1$  are in the direction of increasing  $r$  and  $\theta$  (counterclockwise in Fig. 3.3). The resultant magnitude is

$$F = |\mathbf{F}| \approx (m/r^3)(1 + 3 \cos^2 \theta)^{1/2} \quad (3.14b)$$

and the direction with respect to the dipole axis is

$$\tan \alpha = F_\theta / F_r = (1/2) \tan \theta \quad (3.14c)$$

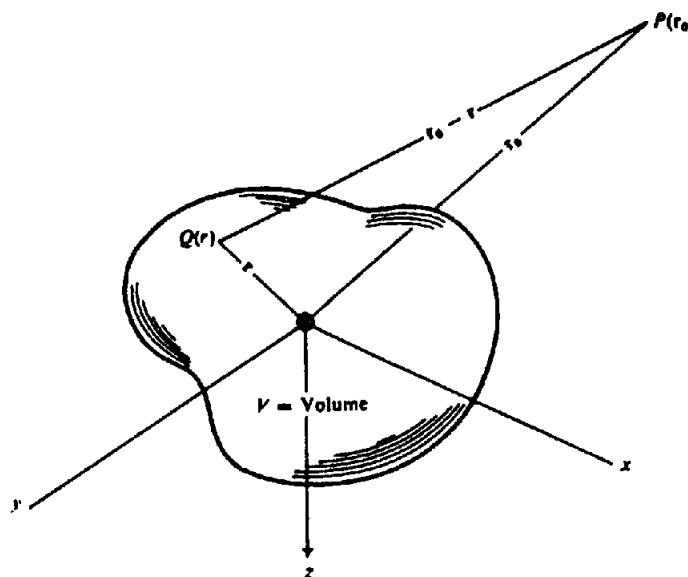


Figure 3.4. General magnetic anomaly.

Two special cases,  $\theta = 0$  and  $\pi/2$  in Equation (3.12), are called the *Gauss-A* (end-on) and *Gauss-B* (side-on) positions. From Equations (3.12) they are given by

$$F_r = 2mr/(r^2 - l^2)^2 \quad F_\theta = 0 \quad \theta = 0 \quad (3.15a)$$

$$F_r = 0 \quad F_\theta = m/(r^2 + l^2)^{3/2} \quad \theta = \pi/2 \quad (3.15b)$$

If  $r \gg l$ , these simplify to

$$\left. \begin{aligned} F_r &\approx 2m/r^3 & \theta &= 0 \\ F_\theta &\approx m/r^3 & \theta &= \pi/2 \end{aligned} \right\} \quad (3.15c)$$

### 3.2.4. The General Magnetic Anomaly

A volume of magnetic material can be considered as an assortment of magnetic dipoles that results from the magnetic moments of individual atoms and dipoles. Whether they initially are aligned so that a body exhibits residual magnetism depends on its previous magnetic history. They will, however, be aligned by induction in the presence of a magnetizing field. In any case, we may regard the body as a continuous distribution of dipoles resulting in a vector dipole moment per unit volume,  $M$ , of magnitude  $M$ . The scalar potential at  $P$  [see Fig. 3.3 and Eq. (3.13)] some distance away from a dipole  $M$  ( $r \gg l$ ) is

$$A = M(r)\cos\theta/r^2 = -M(r) \cdot \nabla(1/r) \quad (3.16)$$

The potential for the whole body at a point outside

the body (Fig. 3.4) is

$$A = - \int_V \mathbf{M}(\mathbf{r}) \cdot \nabla \left( \frac{1}{|\mathbf{r}_0 - \mathbf{r}|} \right) dv \quad (3.17)$$

The resultant magnetic field can be obtained by employing Equation (3.11) with Equation (3.17). This gives

$$\mathbf{F}(\mathbf{r}_0) = \nabla \int_V \mathbf{M}(\mathbf{r}) \cdot \nabla \left( \frac{1}{|\mathbf{r}_0 - \mathbf{r}|} \right) dv \quad (3.18)$$

If  $M$  is a constant vector with direction  $\alpha = \ell\mathbf{i} + m\mathbf{j} + n\mathbf{k}$ , then the operation

$$\mathbf{M} \cdot \nabla = M \frac{\partial}{\partial \alpha} = M \left( \ell \frac{\partial}{\partial x} + m \frac{\partial}{\partial y} + n \frac{\partial}{\partial z} \right) \quad (3.19)$$

[Eq. (A.18)] and

$$A = -M \frac{\partial}{\partial \alpha} \int_V \left( \frac{dv}{|\mathbf{r}_0 - \mathbf{r}|} \right) \quad (3.20)$$

The magnetic field in Equation (3.20) exists in the presence of the Earth's field  $\mathbf{F}_e$ , that is, the total field  $\mathbf{F}$  is given by

$$\mathbf{F} = \mathbf{F}_e + \mathbf{F}(\mathbf{r}_0)$$

where the directions of  $\mathbf{F}_e$  and  $\mathbf{F}(\mathbf{r}_0)$  are not necessarily the same. If  $\mathbf{F}(\mathbf{r}_0)$  is much smaller than  $\mathbf{F}_e$  or if the body has no residual magnetism,  $\mathbf{F}$  and  $\mathbf{F}_e$  will be in approximately the same direction. Where  $\mathbf{F}(\mathbf{r}_0)$  is an appreciable fraction (say, 25% or more) of  $\mathbf{F}_e$  and

has a different direction, the component of  $\mathbf{F}(r_0)$  in the direction of  $\mathbf{F}_e$ ,  $F_D$ , becomes [Eq. (3.20)]

$$F_D = -\mathbf{f}_1 \cdot \nabla A = -\frac{\partial A}{\partial f} = M \frac{\partial^2}{\partial \alpha \partial f} \int_V \frac{dv}{|\mathbf{r}_0 - \mathbf{r}|} \quad (3.21a)$$

where  $\mathbf{f}_1$  is a unit vector in the direction of  $\mathbf{F}_e$  (§3.3.2a). If the magnetization is mainly induced by  $\mathbf{F}_e$ , then

$$F_D(r_0) = M \frac{\partial^2}{\partial f^2} \int_V \frac{dv}{|\mathbf{r}_0 - \mathbf{r}|} = k F_e \frac{\partial^2}{\partial f^2} \int_V \frac{dv}{|\mathbf{r}_0 - \mathbf{r}|} \quad (3.21b)$$

The magnetic interpretation problem is clearly more complex than the gravity problem because of the dipolar field (compare §2.2.3).

The magnetic potential  $A$ , like the gravitational potential  $U$ , satisfies Laplace's and Poisson's equations. Following the method used to derive Equations (2.12) and (2.13), we get

$$\nabla \cdot \mathbf{F} = -\nabla^2 A = 4\pi\mu p$$

$p$  is the net positive pole strength per unit volume at a point. We recall that a field  $\mathbf{F}$  produces a partial reorientation along the field direction of the previously randomly oriented elementary dipoles. This causes, in effect, a separation of positive and negative poles. For example, the  $x$  component of  $\mathbf{F}$  separates pole strengths  $+q$  and  $-q$  by a distance  $\xi$  along the  $x$  axis and causes a net positive pole strength  $(q\xi) dy dz = M_x dy dz$  to enter the rear face in Figure A.2a. Because the pole strength leaving through the opposite face is  $\{M_x + (\partial M_x / \partial x) dx\} dy dz$ , the net positive pole strength per unit volume ( $p$ ) created at a point by the field  $\mathbf{F}$  is  $-\nabla \cdot \mathbf{M}$ . Thus,

$$\nabla^2 A = 4\pi\mu \nabla \cdot \mathbf{M}(r) \quad (3.22)$$

In a nonmagnetic medium,  $\mathbf{M} = 0$  and

$$\nabla^2 A = 0 \quad (3.23)$$

### 3.2.5. Poisson's Relation

If we have an infinitesimal unit volume with magnetic moment  $\mathbf{M} = M \mathbf{a}_1$  and density  $\rho$ , then at a distant point we have, from Equation (3.16),

$$A = -\mathbf{M} \cdot \nabla(1/r) = -M \nabla(1/r) \cdot \mathbf{a}_1 \quad (3.24)$$

From Equations (2.3a), (2.5), and (A.18), the compo-

$A$  = magnetic potential

$U$  = gravitational potential

$M$  = magnetic moment 67

nent of  $\mathbf{g}$  in the direction  $\mathbf{a}_1$  is

$f_1$  = density

$$g_\alpha = -dU/d\alpha = -\nabla U \cdot \mathbf{a}_1 = -\gamma\rho \nabla(1/r) \cdot \mathbf{a}_1 \quad (3.25)$$

Thus,

$$A = (M/\gamma\rho) g_\alpha \quad (3.26)$$

If we apply this result to an extended body, we must sum contributions for each element of volume. Provided that  $M$  and  $\rho$  do not change throughout the body, the potentials  $A$  and  $U$  will be those for the extended body. Therefore, Equations (3.24) to (3.26) are valid for an extended body with constant density and uniform magnetization.

In terms of fields,

$$\begin{aligned} \mathbf{F} &= -\nabla A = -(M/\gamma\rho) \nabla g_\alpha \\ &= (M/\gamma\rho) \nabla(\nabla U \cdot \mathbf{a}_1) \\ &= (M/\gamma\rho) \nabla U_\alpha \end{aligned} \quad (3.27a)$$

where  $U_\alpha = dU/d\alpha$ . For a component of  $\mathbf{F}$  in the direction  $\beta_1$ , this becomes

$$F_\beta = (M/\gamma\rho) U_{\alpha\beta} \quad (3.27b)$$

In particular, if  $M$  is vertical, the vertical component of  $\mathbf{F}$  is

$$Z = (M/\gamma\rho) U_{zz} = (M/\gamma\rho)(\partial g_z / \partial z) \quad (3.28)$$

These relations are used to make pseudogravity maps from magnetic data.

## 3.3. MAGNETISM OF THE EARTH

### 3.3.1. Nature of the Geomagnetic Field

As far as exploration geophysics is concerned, the geomagnetic field of the Earth is composed of three parts:

1. The main field, which varies relatively slowly and is of internal origin.
2. A small field (compared to the main field), which varies rather rapidly and originates outside the Earth.
3. Spatial variations of the main field, which are usually smaller than the main field, are nearly constant in time and place, and are caused by local magnetic anomalies in the near-surface crust of the Earth. These are the targets in magnetic prospecting.

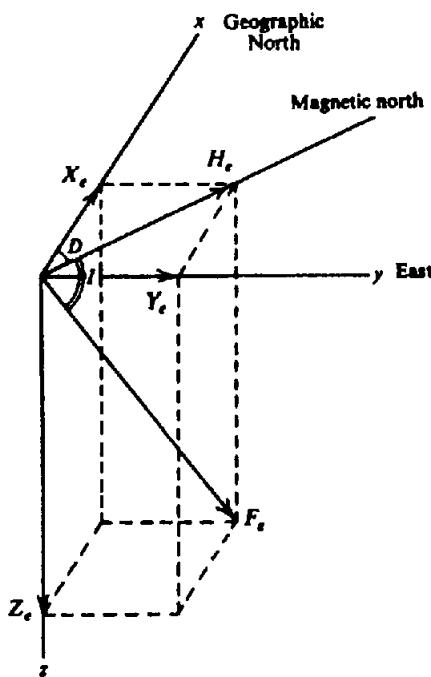


Figure 3.5. Elements of the Earth's magnetic field.

### 3.3.2. The Main Field

(a) *The Earth's magnetic field.* If an unmagnetized steel needle could be hung at its center of gravity, so that it is free to orient itself in any direction, and if other magnetic fields are absent, it would assume the direction of the Earth's total magnetic field, a direction that is usually neither horizontal nor in-line with the geographic meridian. The magnitude of this field,  $F_e$ , the *inclination* (or *dip*) of the needle from the horizontal,  $I$ , and the angle it makes with geographic north (the *declination*),  $D$ , completely define the main magnetic field.

The *magnetic elements* (Whitham, 1960) are illustrated in Figure 3.5. The field can also be described in terms of the vertical component,  $Z_e$ , reckoned positive downward, and the horizontal component,  $H_e$ , which is always positive.  $X_e$  and  $Y_e$  are the components of  $H_e$ , which are considered positive to the north and east, respectively. These elements are related as follows:

$$\left. \begin{aligned} F_e^2 &= H_e^2 + Z_e^2 = X_e^2 + Y_e^2 + Z_e^2 \\ H_e &= F_e \cos I \quad Z_e = F_e \sin I \\ X_e &= H_e \cos D \quad Y_e = H_e \sin D \\ \tan D &= Y_e/X_e \quad \tan I = Z_e/H_e \\ F_e &= F_e \mathbf{i}_1 = F_e (\cos D \cos I \mathbf{i}_1 \\ &\quad + \sin D \cos I \mathbf{j}_1 + \sin I \mathbf{k}_1) \end{aligned} \right\} (3.29)$$

As stated earlier, the end of the needle that dips downward in northern latitudes is the north-seeking

or positive pole; the end that dips downward in southern latitudes is the south-seeking or negative pole.

Maps showing lines of equal declination, inclination, horizontal intensity, and so on, are called *isomagnetic maps* (Fig. 3.6). *Isogonic*, *isoclinic*, and *isodynamic maps* show, respectively, lines of equal declination  $D$ , inclination  $I$ , and equal values of  $F_e$ ,  $H_e$ , or  $Z_e$ . Note that the inclination is large (that is,  $Z_e > H_e$ ) for most of the Earth's land masses, and hence corrections do not have to be made for latitude variations of  $F_e$  or  $Z_e$  ( $\approx 4$  nT/km) except for surveys covering extensive areas. The overall magnetic field does not reflect variations in surface geology, such as mountain ranges, mid-ocean ridges or earthquake belts, so the source of the main field lies deep within the Earth. The geomagnetic field resembles that of a dipole whose north and south magnetic poles are located approximately at  $75^\circ\text{N}, 101^\circ\text{W}$  and  $69^\circ\text{S}, 145^\circ\text{E}$ . The dipole is displaced about 300 km from the Earth's center toward Indonesia and is inclined some  $11.5^\circ$  to the Earth's axis. However, the geomagnetic field is more complicated than the field of a simple dipole. The points where a dip needle is vertical, the *dip poles*, are at  $75^\circ\text{N}, 101^\circ\text{W}$  and  $67^\circ\text{S}, 143^\circ\text{E}$ .

The magnitudes of  $F_e$  at the north and south magnetic poles are 60 and 70  $\mu\text{T}$ , respectively. The minimum value,  $\sim 25 \mu\text{T}$ , occurs in southern Brazil—South Atlantic. In a few locations,  $F_e$  is larger than 300  $\mu\text{T}$  because of near-surface magnetic features. The line of zero inclination (*magnetic equator*, where  $Z = 0$ ) is never more than  $15^\circ$  from the Earth's equator. The largest deviations are in South America and the eastern Pacific. In Africa and Asia it is slightly north of the equator.

(b) *Origin of the main field.* Spherical harmonic analysis of the observed magnetic field shows that over 99% is due to sources inside the Earth. The present theory is that the main field is caused by convection currents of conducting material circulating in the liquid outer core (which extends from depths of 2,800 to 5,000 km). The Earth's core is assumed to be a mixture of iron and nickel, both good electrical conductors. The magnetic source is thought to be a self-excited dynamo in which highly conductive fluid moves in a complex manner caused by convection. Paleomagnetic data show that the magnetic field has always been roughly along the Earth's spin axis, implying that the convective motion is coupled to the Earth's spin. Recent exploration of the magnetic fields of other planets and their satellites provide fascinating comparisons with the Earth's field.

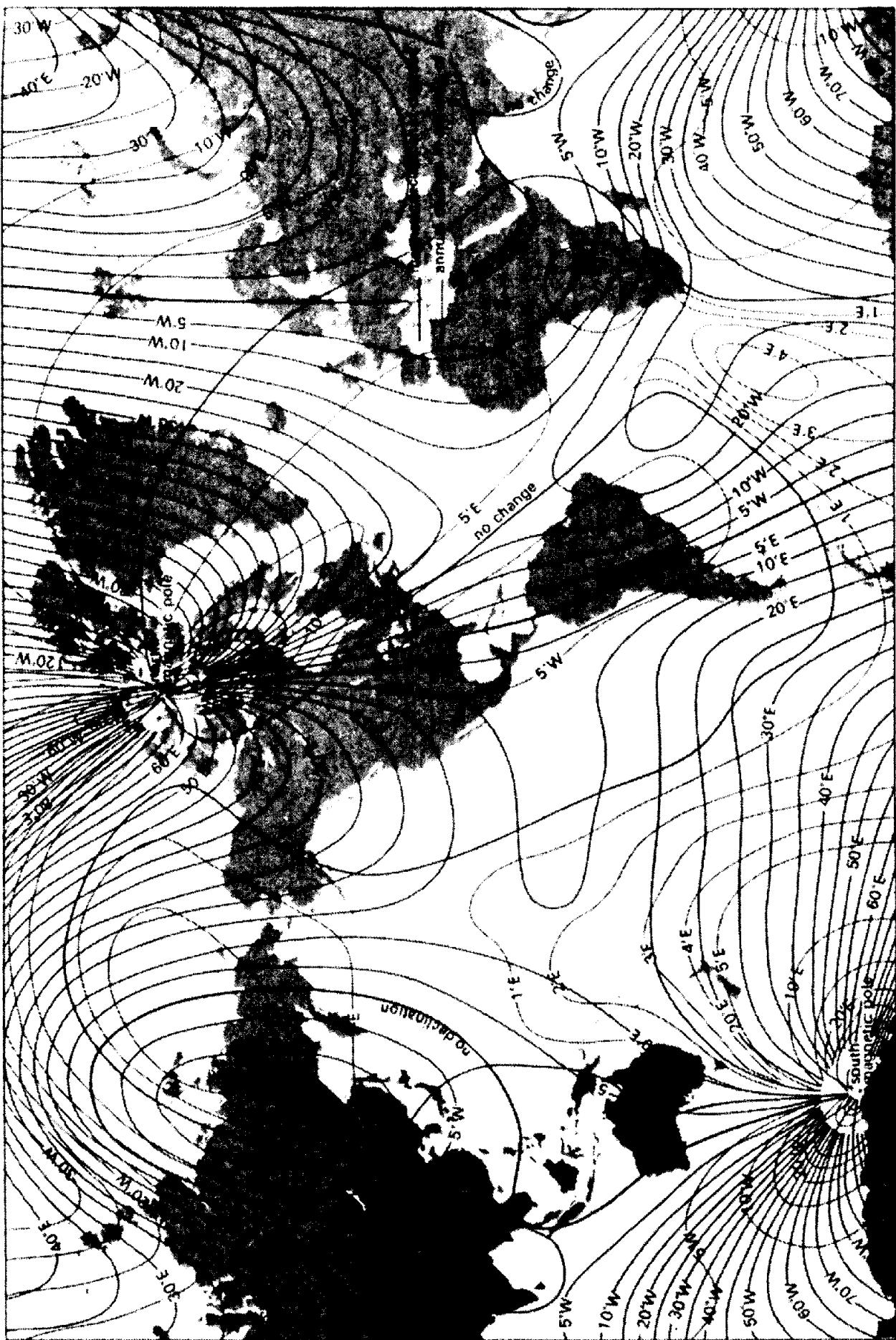


Figure 3.6. The Earth's magnetic field in 1975. (From Smith, 1982). (a) Declination (heavy lines) and annual rate of change in minutes/year (light lines)

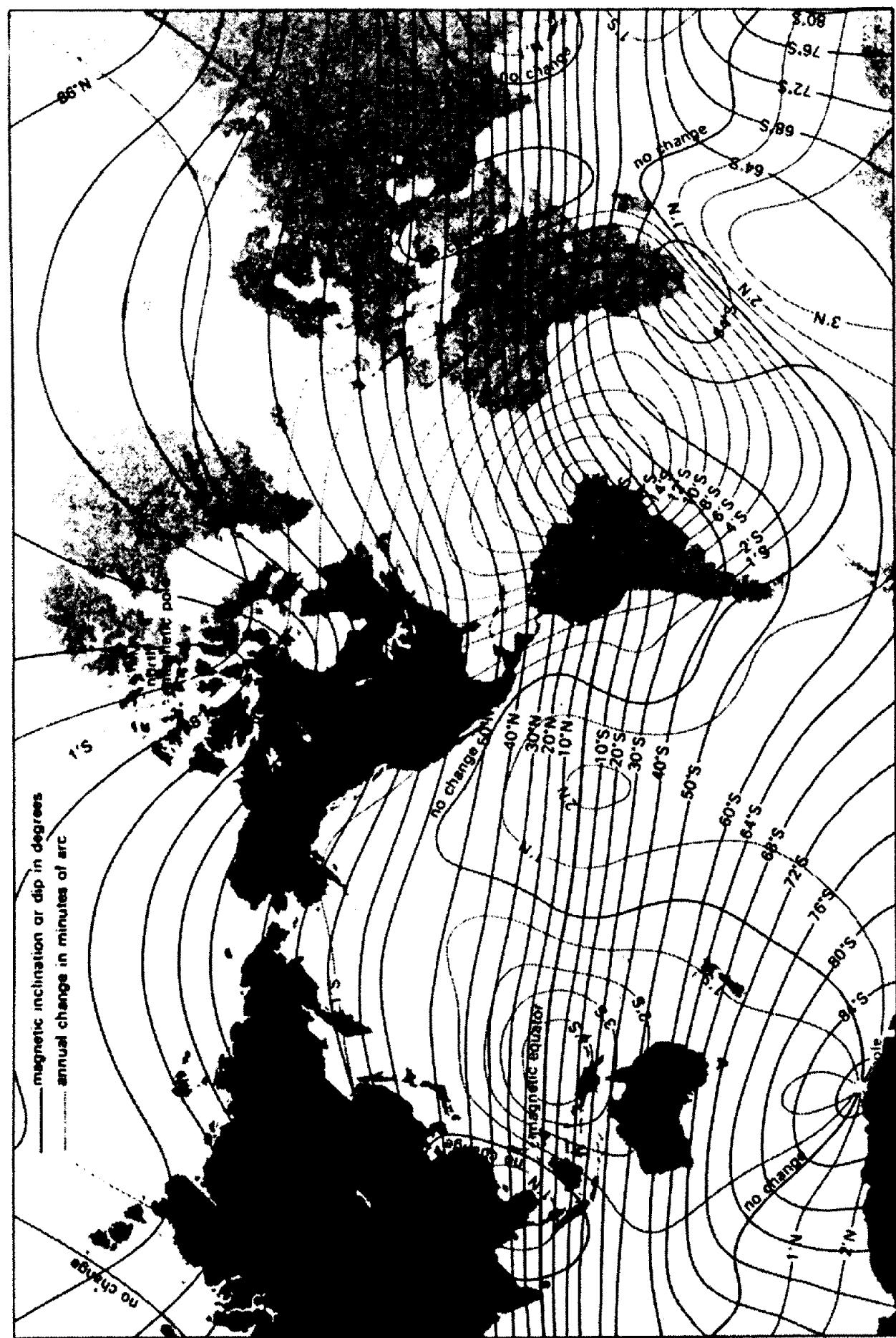


Figure 3.6. (Continued) (b) geomagnetic latitude (heavy lines) and annual rate of change in minutes/year (light lines)

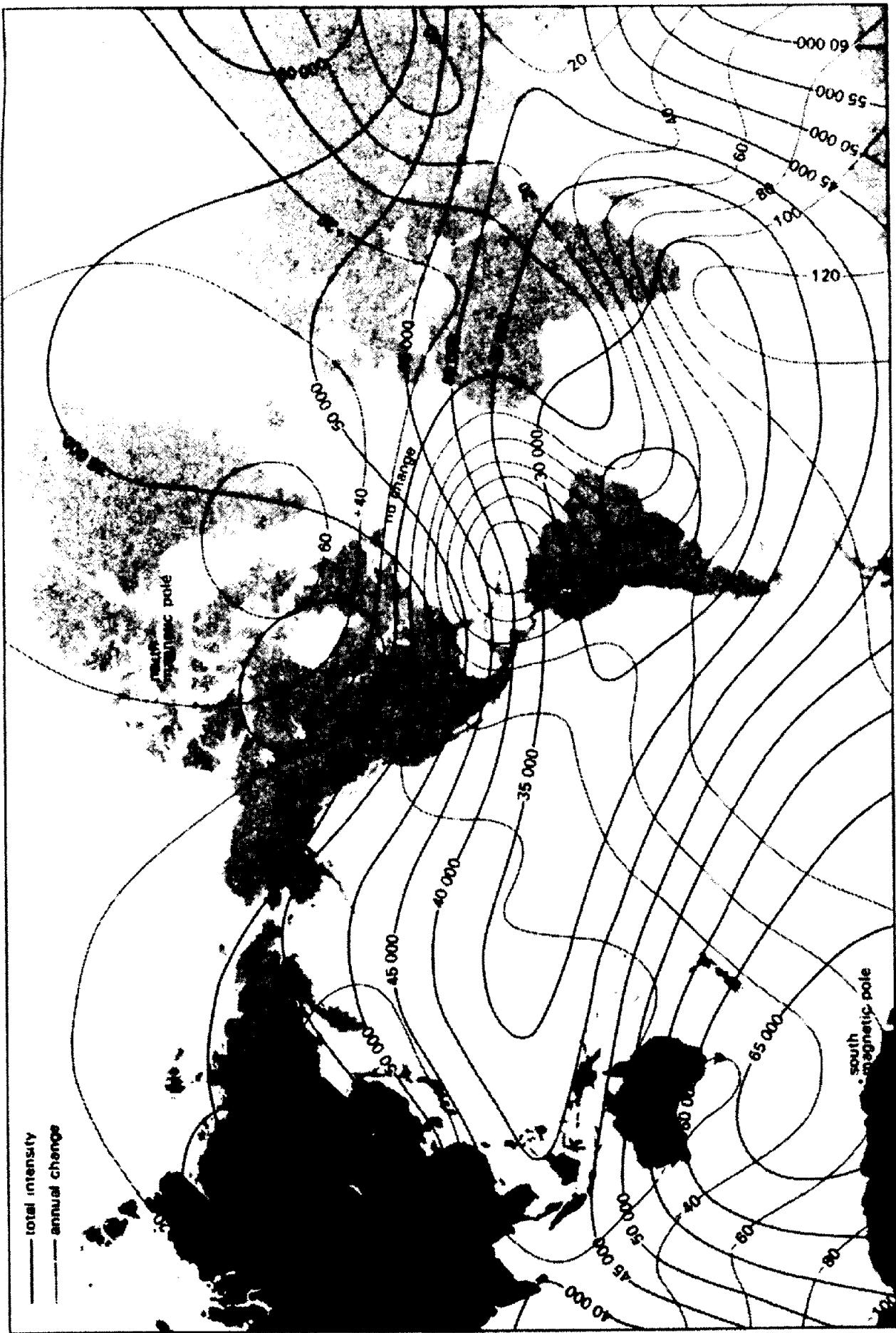


Figure 3.6. (Continued) (c) total field strength in nanotesla (heavy lines) and rate of change in nanotesla/year (light lines).

(c) *Secular variations of the main field.* Four hundred years of continuous study of the Earth's field has established that it changes slowly. The inclination has changed some  $10^\circ$  ( $75^\circ$  to  $65^\circ$ ) and the declination about  $35^\circ$  ( $10^\circ\text{E}$  to  $25^\circ\text{W}$  and back to  $10^\circ\text{W}$ ) during this period. The source of this wandering is thought to be changes in convection currents in the core.

The Earth's magnetic field has also reversed direction a number of times. The times of many of the periodic field reversals have been ascertained and provide a *magnetochronographic time scale*.

### 3.3.3. The External Magnetic Field

Most of the remaining small portion of the geomagnetic field appears to be associated with electric currents in the ionized layers of the upper atmosphere. Time variations of this portion are much more rapid than for the main "permanent" field. Some effects are:

1. A cycle of 11 years duration that correlates with sunspot activity.
2. Solar diurnal variations with a period of 24 h and a range of 30 nT that vary with latitude and season, and are probably controlled by action of the solar wind on ionospheric currents.
3. Lunar variations with a 25 h period and an amplitude 2 nT that vary cyclically throughout the month and seem to be associated with a Moon-ionosphere interaction.
4. Magnetic storms that are transient disturbances with amplitudes up to 1,000 nT at most latitudes and even larger in polar regions, where they are associated with aurora. Although erratic, they often occur at 27 day intervals and correlate with sunspot activity. At the height of a magnetic storm (which may last for several days), long-range radio reception is affected and magnetic prospecting may be impractical.

These time and space variations of the Earth's main field do not significantly affect magnetic prospecting except for the occasional magnetic storm. Diurnal variations can be corrected for by use of a base-station magnetometer. Latitude variations ( $\approx 4$  nT/km) require corrections only for high-resolution, high-latitude, or large-scale surveys.

### 3.3.4. Local Magnetic Anomalies

Local changes in the main field result from variations in the magnetic mineral content of near-surface rocks. These anomalies occasionally are large enough to double the main field. They usually do not persist over great distances; thus magnetic maps generally do not exhibit large-scale regional features (although

the Canadian Shield, for example, shows a magnetic contrast to the Western Plains). Many large, erratic variations often make magnetic maps extremely complex. The sources of local magnetic anomalies cannot be very deep, because temperatures below  $\sim 40$  km should be above the *Curie point*, the temperature ( $\approx 550^\circ\text{C}$ ) at which rocks lose their magnetic properties. Thus, local anomalies must be associated with features in the upper crust.

### 3.3.5. Magnetism of Rocks and Minerals

Magnetic anomalies are caused by magnetic minerals (mainly magnetite and pyrrhotite) contained in the rocks. Magnetically important minerals are surprisingly few in number.

Substances can be divided on the basis of their behavior when placed in an external field. A substance is *diamagnetic* if its field is dominated by atoms with orbital electrons oriented to oppose the external field, that is, if it exhibits negative susceptibility. Diamagnetism will prevail only if the net magnetic moment of all atoms is zero when  $H$  is zero, a situation characteristic of atoms with completely filled electron shells. The most common diamagnetic earth materials are graphite, marble, quartz, and salt. When the magnetic moment is not zero when  $H$  is zero, the susceptibility is positive and the substance is *paramagnetic*. The effects of diamagnetism and most paramagnetism are weak.

Certain paramagnetic elements, namely iron, cobalt, and nickel, have such strong magnetic interaction that the moments align within fairly large regions called *domains*. This effect is called *ferromagnetism* and it is  $\sim 10^6$  times the effects of diamagnetism and paramagnetism. Ferromagnetism decreases with increasing temperature and disappears entirely at the Curie temperature. Apparently ferromagnetic minerals do not exist in nature.

The domains in some materials are subdivided into subdomains that align in opposite directions so that their moments nearly cancel; although they would otherwise be considered ferromagnetic, the susceptibility is comparatively low. Such a substance is *antiferromagnetic*. The only common example is hematite.

In some materials, the magnetic subdomains align in opposition but their net moment is not zero, either because one set of subdomains has a stronger magnetic alignment than the other or because there are more subdomains of one type than of the other. These substances are *ferrimagnetic*. Examples of the first type are magnetite and titanomagnetite, oxides of iron and of iron and titanium. Pyrrhotite is a magnetic mineral of the second type. Practically all magnetic minerals are ferrimagnetic.

### 3.3.6. Remanent Magnetism

In many cases, the magnetization of rocks depends mainly on the present geomagnetic field and the magnetic mineral content. Residual magnetism (called *natural remanent magnetization*, NRM) often contributes to the total magnetization, both in amplitude and direction. The effect is complicated because NRM depends on the magnetic history of the rock. Natural remanent magnetization may be due to several causes. The principal ones are:

1. *Thermoremanent magnetization* (TRM), which results when magnetic material is cooled below the Curie point in the presence of an external field (usually the Earth's field). Its direction depends on the direction of the field at the time and place where the rock cooled. Remanence acquired in this fashion is particularly stable. This is the main mechanism for the residual magnetization of igneous rocks.
2. *Detrital magnetization* (DRM), which occurs during the slow settling of fine-grained particles in the presence of an external field. Varied clays exhibit this type of remanence.
3. *Chemical remanent magnetization* (CRM), which takes place when magnetic grains increase in size or are changed from one form to another as a result of chemical action at moderate temperatures, that is, below the Curie point. This process may be significant in sedimentary and metamorphic rocks.
4. *Isothermal remanent magnetization* (IRM), which is the residual left following the removal of an external field (see Fig. 3.2). Lightning strikes produce IRM over very small areas.
5. *Viscous remanent magnetization* (VRM), which is produced by long exposure to an external field; the buildup of remanence is a logarithmic function of time. VRM is probably more characteristic of fine-grained than coarse-grained rocks. This remanence is quite stable.

Studies of the magnetic history of the Earth (*paleomagnetism*) indicate that the Earth's field has varied in magnitude and has reversed its polarity a number of times (Strangway, 1970). Furthermore, it appears that the reversals took place rapidly in geologic time, because there is no evidence that the Earth existed without a magnetic field for any significant period. Model studies of a self-excited dynamo show such a rapid turnover. Many rocks have remanent magnetism that is oriented neither in the direction of, nor opposite to, the present Earth field. Such results support the plate tectonics theory. Paleomagnetism helps age-date rocks and determine past movements, such as plate rotations. Paleomagnetic

laboratory methods separate residual from induced magnetization, something that cannot be done in the field.

### 3.3.7. Magnetic Susceptibilities of Rocks and Minerals

Magnetic susceptibility is the significant variable in magnetics. It plays the same role as density does in gravity interpretation. Although instruments are available for measuring susceptibility in the field, they can only be used on outcrops or on rock samples, and such measurements do not necessarily give the bulk susceptibility of the formation.

From Figure 3.2, it is obvious that  $k$  (hence  $\mu$  also) is not constant for a magnetic substance; as  $H$  increases,  $k$  increases rapidly at first, reaches a maximum, and then decreases to zero. Furthermore, although magnetization curves have the same general shape, the value of  $H$  for saturation varies greatly with the type of magnetic mineral. Thus it is important in making susceptibility determinations to use a value of  $H$  about the same as that of the Earth's field.

Since the ferrimagnetic minerals, particularly magnetite, are the main source of local magnetic anomalies, there have been numerous attempts to establish a quantitative relation between rock susceptibility and  $\text{Fe}_3\text{O}_4$  concentration. A rough linear dependence ( $k$  ranging from  $10^{-3}$  to 1 SI unit as the volume percent of  $\text{Fe}_3\text{O}_4$  increases from 0.05% to 35%) is shown in one report, but the scatter is large, and results from other areas differ.

Table 3.1 lists magnetic susceptibilities for a variety of rocks. Although there is great variation, even for a particular rock, and wide overlap between different types, sedimentary rocks have the lowest average susceptibility and basic igneous rocks have the highest. In every case, the susceptibility depends only on the amount of ferrimagnetic minerals present, mainly magnetite, sometimes titanomagnetite or pyrrhotite. The values of chalcopyrite and pyrite are typical of many sulfide minerals that are basically nonmagnetic. It is possible to locate minerals of negative susceptibility, although the negative values are very small, by means of detailed magnetic surveys. It is also worth noting that many iron minerals are only slightly magnetic.

### 3.3.8. Magnetic Susceptibility Measurements

(a) *Measurement of  $k$ .* Most measurements of  $k$  involve a comparison of the sample with a standard. The simplest laboratory method is to compare the deflection produced on a tangent magnetometer by a

Table 3.1. Magnetic susceptibilities of various rocks and minerals.

Type	Susceptibility $\times 10^3$ (SI)	
	Range	Average
<i>Sedimentary</i>		
Dolomite	0–0.9	0.1
Limestones	0–3	0.3
Sandstones	0–20	0.4
Shales	0.01–15	0.6
Av. 48 sedimentary	0–18	0.9
<i>Metamorphic</i>		
Amphibolite		0.7
Schist	0.3–3	1.4
Phyllite		1.5
Gneiss	0.1–25	
Quartzite		4
Serpentine	3–17	
Slate	0–35	6
Av. 61 metamorphic	0–70	4.2
<i>Igneous</i>		
Granite	0–50	2.5
Rhyolite	0.2–35	
Dolerite	1–35	17
Augite-syenite	30–40	
Olivine-diabase		25
Diabase	1–160	55
Porphyry	0.3–200	60
Gabbro	1–90	70
Basalts	0.2–175	70
Diorite	0.6–120	85
Pyroxenite		125
Peridotite	90–200	150
Andesite		160
Av. acidic igneous	0–80	8
Av. basic igneous	0.5–97	25
<i>Minerals</i>		
Graphite		0.1
Quartz		-0.01
Rock salt		-0.01
Anhydrite, gypsum		-0.01
Calcite	-0.001 – - 0.01	
Coal		0.02
Clays		0.2
Chalcopyrite		0.4
Sphalerite		0.7
Cassiterite		0.9
Siderite	1–4	
Pyrite	0.05–5	1.5
Limonite		2.5
Arsenopyrite		3
Hematite	0.5–35	6.5
Chromite	3–110	7
Franklinite		430
Pyrrhotite	1–6000	1500
Ilmenite	300–3500	1800
Magnetite	1200–19200	6000

prepared sample (either a drill core or powdered rock in a tube) with that of a standard sample of magnetic material (often  $\text{FeCl}_3$  powder in a test tube) when the sample is in the Gauss-A position [Eq. (3.15a)]. The susceptibility of the sample is found from the ratio of deflections:

$$k_s = k_{std} d_s / d_{std}$$

$d_s$  and  $d_{std}$  are the deflections for the sample and standard, respectively. The samples must be of the same size.

A similar comparison method employs an inductance bridge (Hague, 1957) having several air-core coils of different cross sections to accommodate samples of different sizes. The sample is inserted into one of the coils and the bridge balance condition is compared with the bridge balance obtained when a standard sample is in the coil. The bridge may be calibrated to give susceptibility directly, in which case the sample need not have a particular geometry (although the calibration may not be valid for samples of highly irregular shape). This type of instrument with a large diameter coil is used in field measurements on outcrop. The bridge is balanced first with the coil remote from the outcrop and then lying on it. A calibration curve obtained with a standard relates  $k$  and the change in inductance.

(b) *Measurement of remanent magnetism.* Measurement of remanent susceptibility is considerably more complicated than that of  $k$ . One method uses an astatic magnetometer, which consists of two magnets of equal moment that are rigidly mounted parallel to each other in the same horizontal plane with opposing poles. The magnetic system is suspended by a torsion fiber. The specimen is placed in various orientations below the astatic system and the angular deflections are measured. This device, in effect, measures the magnetic field gradient, so that extraneous fields must either be eliminated or made uniform over the region of the sample. Usually the entire assembly is mounted inside a three-component coil system that cancels the Earth's field.

Another instrument for the analysis of the residual component is the *spinner magnetometer*. The rock sample is rotated at high speed near a small pickup coil and its magnetic moment generates alternating current (ac) in the coil. The phase and intensity of the coil signal are compared with a reference signal generated by the rotating system. The total moment of the sample is obtained by rotating it about different axes.

Cryogenic instruments for determining two-axes remanent magnetism have been developed (Zimmerman and Campbell, 1975; Weinstock and

Overton, 1981). They achieve great sensitivity because of the high magnetic moments and low noise obtainable at superconducting temperatures.

### 3.4. FIELD INSTRUMENTS FOR MAGNETIC MEASUREMENTS

#### 3.4.1. General

Typical sensitivity required in ground magnetic instruments is between 1 and 10 nT in a total field rarely larger than 50,000 nT. Recent airborne applications, however, have led to the development of magnetometers with sensitivity of 0.001 nT. Some magnetometers measure the absolute field, although this is not a particular advantage in magnetic surveying.

The earliest devices used for magnetic exploration were modifications of the mariner's compass, such as the Swedish mining compass, which measured dip  $I$  and declination  $D$ . Instruments (such as *magnetic variometers*, which are essentially dip needles of high sensitivity) were developed to measure  $Z_e$  and  $H_e$ , but they are seldom used now. Only the modern instruments, the fluxgate, proton-precession, and optical-pump (usually rubidium-vapor) magnetometers, will be discussed. The latter two measure the absolute total field, and the fluxgate instrument also generally measures the total field.

#### 3.4.2. Fluxgate Magnetometer

This device was originally developed during World War II as a submarine detector. Several designs have been used for recording diurnal variations in the Earth's field, for airborne geomagnetics, and as portable ground magnetometers.

The fluxgate detector consists essentially of a core of magnetic material, such as mu-metal, permalloy, or ferrite, that has a very high permeability at low magnetic fields. In the most common design, two cores are each wound with primary and secondary coils, the two assemblies being as nearly as possible identical and mounted parallel so that the windings are in opposition. The two primary windings are connected in series and energized by a low frequency (50 to 1,000 Hz) current produced by a constant current source. The maximum current is sufficient to magnetize the cores to saturation, in opposite polarity, twice each cycle. The secondary coils, which consist of many turns of fine wire, are connected to a *differential amplifier*, whose output is proportional to the difference between two input signals.

The effect of saturation in the fluxgate elements is illustrated in Figure 3.7. In the absence of an external magnetic field, the saturation of the cores is

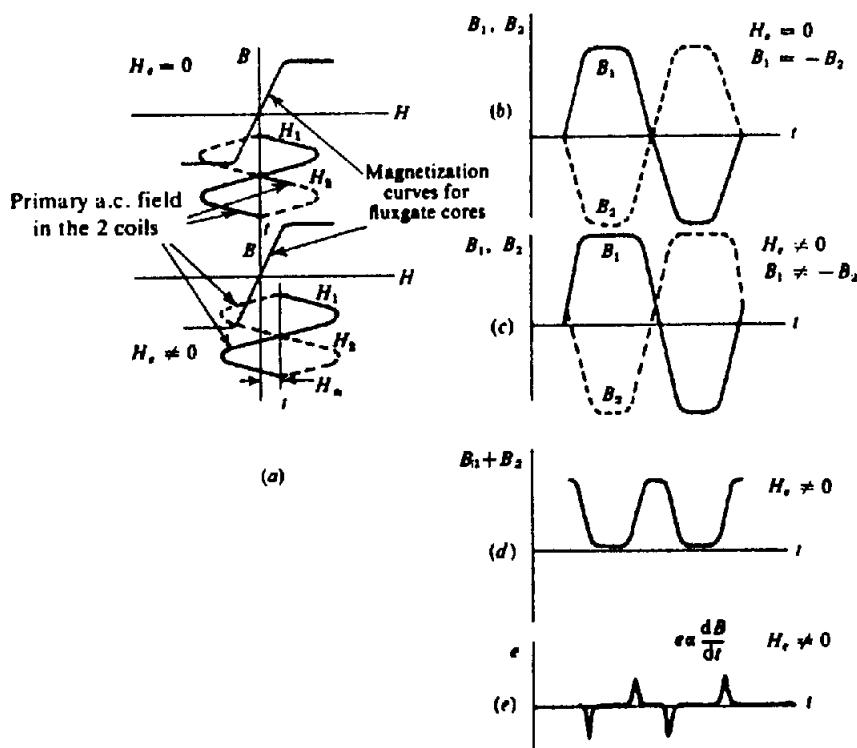


Figure 3.7. Principle of the fluxgate magnetometer. Note that  $H_e = F_e$ , etc. (From Whitham, 1960.) (a) Magnetization of the cores. (b) Flux in the two cores for  $F_e = 0$ . (c) Flux in the two cores for  $F_e \neq 0$ . (d)  $F_1 + F_2$  for  $F_e \neq 0$ . (e) Output voltage for  $F_e \neq 0$ .

symmetrical and of opposite sign near the peak of each half-cycle so that the outputs from the two secondary windings cancel. The presence of an external field component parallel to the cores causes saturation to occur earlier for one half-cycle than the other, producing an unbalance. The difference between output voltages from the secondary windings is a series of voltage pulses which are fed into the amplifier, as shown in Figure 3.7d. The pulse height is proportional to the amplitude of the biasing field of the Earth. Obviously any component can be measured by suitable orientation of the cores.

The original problem with this type of magnetometer – a lack of sensitivity in the core – has been solved by the development and use of materials having sufficient initial permeability to saturate in small fields. Clearly the hysteresis loop should be as thin as possible. There remains a relatively high noise level, caused by hysteresis effects in the core. The fluxgate elements should be long and thin to reduce eddy currents. Improvements introduced to increase the signal-to-noise ratio include the following:

1. By deliberately unbalancing the two elements, voltage spikes are present with or without an ambient field. The presence of the Earth's field increases the voltage of one polarity more than the other and this difference is amplified.
2. Because the odd harmonics are canceled fairly



Figure 3.8. Portable fluxgate magnetometer.

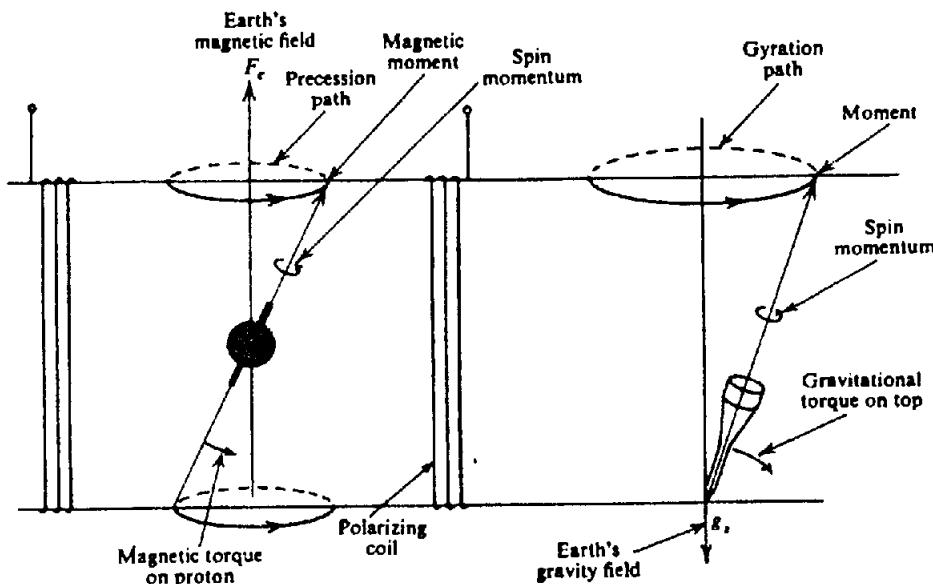


Figure 3.9. Proton precession and spinning-top analogy.

well in a reasonably matched set of cores, the even harmonics (generally only the second is significant) are amplified to appear as positive or negative signals, depending on the polarity of the Earth's field.

3. Most of the ambient field is canceled and variations in the remainder are detected with an extra secondary winding.
4. Negative feedback of the amplifier outputs is used to reduce the effect of the Earth's field.
5. By tuning the output of the secondary windings with a capacitance, the second harmonic is greatly increased; a phase-sensitive detector, rather than the difference amplifier, may be used with this arrangement.

There are several fundamental sources of error in the fluxgate instrument. These include inherent unbalance in the two cores, thermal and shock noise in cores, drift in biasing circuits, and temperature sensitivity ( $1 \text{ nT}/^\circ\text{C}$  or less). These disadvantages are minor, however, compared to the obvious advantages – direct readout, no azimuth orientation, rather coarse leveling requirements, light weight (2 to 3 kg), small size, and reasonable sensitivity. Another attractive feature is that any component of the magnetic field may be measured. No elaborate tripod is required and readings may be made very quickly, generally in about 15 s. A portable fluxgate instrument is shown in Figure 3.8.

### 3.4.3. Proton-Precession Magnetometer

This instrument grew out of the discovery, around 1945, of nuclear magnetic resonance. Some nuclei

have a net magnetic moment that, coupled with their spin, causes them to precess about an axial magnetic field.

The proton-precession magnetometer depends on the measurement of the free-precession frequency of protons (hydrogen nuclei) that have been polarized in a direction approximately normal to the direction of the Earth's field. When the polarizing field is suddenly removed, the protons precess about the Earth's field like a spinning top; the Earth's field supplies the precessing force corresponding to that of gravity in the case of a top. The analogy is illustrated in Figure 3.9. The protons precess at an angular velocity  $\omega$ , known as the *Larmor precession frequency*, which is proportional to the magnetic field  $F$ , so that

$$\omega = \gamma_p F \quad (3.30a)$$

The constant  $\gamma_p$  is the *gyromagnetic ratio of the proton*, the ratio of its magnetic moment to its spin angular momentum. The value of  $\gamma_p$  is known to an accuracy of 0.001%. Since precise frequency measurements are relatively easy, the magnetic field can be determined to the same accuracy. The proton, which is a moving charge, induces, in a coil surrounding the sample, a voltage that varies at the precession frequency  $v$ . Thus we can determine the magnetic field from

$$F = 2\pi v / \gamma_p \quad (3.30b)$$

where the factor  $2\pi/\gamma_p = 23.487 \pm 0.002 \text{ nT/Hz}$ . Only the total field may be measured.

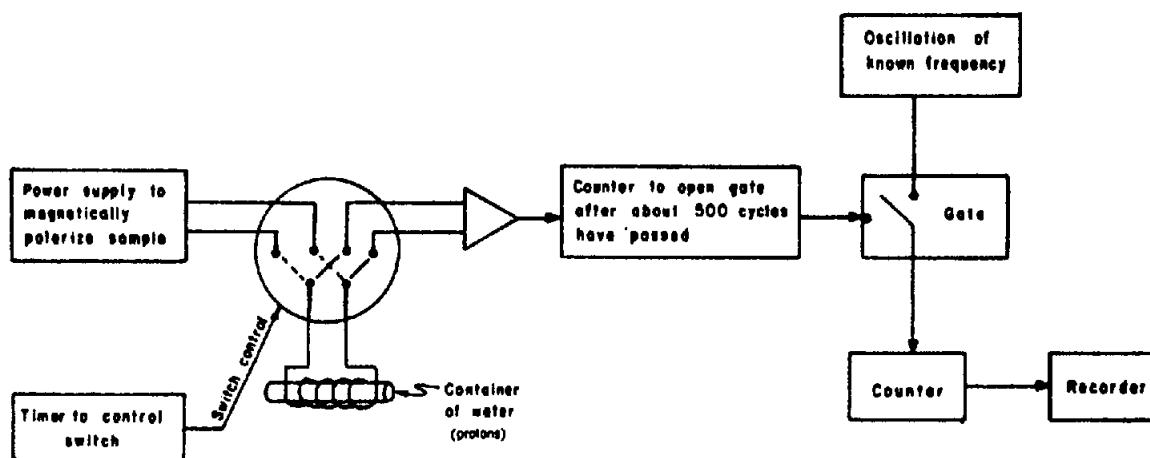


Figure 3.10. Proton-precession magnetometer. (From Sheriff, 1984.)

The essential components of this magnetometer include a source of protons, a polarizing magnetic field considerably stronger than that of the Earth and directed roughly normal to it (the direction of this field can be off by  $45^\circ$ ), a pickup coil coupled tightly to the source, an amplifier to boost the minute voltage induced in the pickup coil, and a frequency-measuring device. The latter operates in the audio range because, from Equation (3.30b),  $v = 2130$  Hz for  $F_e = 50,000$  nT. It must also be capable of indicating frequency differences of about 0.4 Hz for an instrument sensitivity of 10 nT.

The proton source is usually a small bottle of water (the nuclear moment of oxygen is zero) or some organic fluid rich in hydrogen, such as alcohol. The polarizing field of 5 to 10 mT is obtained by passing direct current through a solenoid wound around the bottle, which is oriented roughly east-west for the measurement. When the solenoid current is abruptly cut off, the proton precession about the Earth's field is detected by a second coil as a transient voltage building up and decaying over an interval of  $\sim 3$  s, modulated by the precession frequency. In some models the same coil is used for both polarization and detection. The modulation signal is amplified to a suitable level and the frequency measured. A schematic diagram is shown in Figure 3.10.

The measurement of frequency may be carried out by actually counting precession cycles in an exact time interval, or by comparing them with a very stable frequency generator. In one ground model, the precession signal is mixed with a signal from a local oscillator of high precision to produce low-frequency beats ( $\approx 100$  Hz) that drive a vibrating reed frequency meter. Regardless of the method used, the frequency must be measured to an accuracy of 0.001% to realize the capabilities of the method. Although this is not particularly difficult in

a fixed installation, it poses some problems in small portable equipment.

The proton-precession magnetometer's sensitivity ( $\approx 1$  nT) is high, and it is essentially free from drift. The fact that it requires no orientation or leveling makes it attractive for marine and airborne operations. It has essentially no mechanical parts, although the electronic components are relatively complex. The main disadvantage is that only the total field can be measured. It also cannot record continuously because it requires a second or more between readings. In an aircraft traveling at 300 km/hr, the distance interval is about 100 m. Proton-precession magnetometers are now the dominant instrument for both ground and airborne applications.

### 3.4.4. Optically Pumped Magnetometer

A variety of scientific instruments and techniques has been developed using the energy in transferring atomic electrons from one energy level to another. For example, by irradiating a gas with light or radio-frequency waves of the proper frequency, electrons may be raised to a higher energy level. If they can be accumulated in such a state and then suddenly returned to a lower level, they release some of their energy in the process. This energy may be used for amplification (masers) or to get an intense light beam, such as that produced by a laser.

The optically pumped magnetometer is another application. The principle of operation may be understood from an examination of Figure 3.11a, which shows three possible energy levels,  $A_1$ ,  $A_2$ , and  $B$  for a hypothetical atom. Under normal conditions of pressure and temperature, the atoms occupy ground state levels  $A_1$  and  $A_2$ . The energy difference between  $A_1$  and  $A_2$  is very small [ $\approx 10^{-8}$  electron volts (eV)], representing a fine structure due to atomic electron spins that normally are not all aligned in the

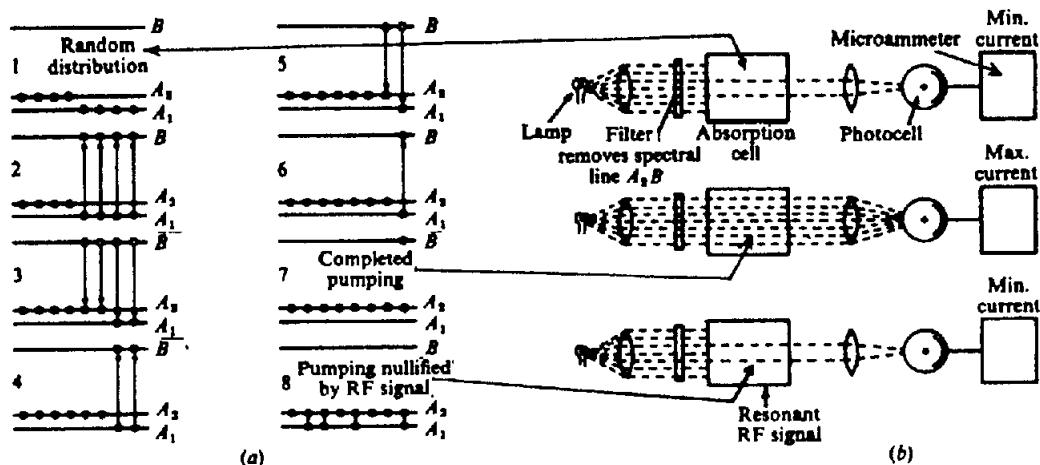


Figure 3.11. Optical pumping. (a) Energy level transitions. (b) Effect of pumping on light transmission.

same direction. Even thermal energies ( $\approx 10^{-2}$  eV) are much larger than this, so that the atoms are as likely to be in level  $A_1$  as in  $A_2$ .

Level  $B$  represents a much higher energy and the transitions from  $A_1$  or  $A_2$  to  $B$  correspond to infrared or visible spectral lines. If we irradiate a sample with a beam from which spectral line  $A_2B$  has been removed, atoms in level  $A_1$  can absorb energy and rise to  $B$ , but atoms in  $A_2$  will not be excited. When the excited atoms fall back to ground state, they may return to either level, but if they fall to  $A_1$ , they will be removed by photon excitation to  $B$  again. The result is an accumulation of atoms in level  $A_2$ .

The technique of overpopulating one energy level in this fashion is known as *optical pumping*. As the atoms are moved from level  $A_1$  to  $A_2$  by this selective process, less energy will be absorbed and the sample becomes increasingly transparent to the irradiating beam. When all atoms are in the  $A_2$  state, a photosensitive detector will register a maximum current, as shown in Figure 3.11b. If now we apply an RF signal, having energy corresponding to the transition between  $A_1$  and  $A_2$ , the pumping effect is nullified and the transparency drops to a minimum again. The proper frequency for this signal is given by  $\nu = E/h$ , where  $E$  is the energy difference between  $A_1$  and  $A_2$  and  $h$  is Planck's constant [ $6.62 \times 10^{-34}$  joule-seconds].

To make this device into a magnetometer, it is necessary to select atoms that have magnetic energy sublevels that are suitably spaced to give a measure of the weak magnetic field of the Earth. Elements that have been used for this purpose include cesium, rubidium, sodium, and helium. The first three each have a single electron in the outer shell whose spin axis lies either parallel or antiparallel to an external magnetic field. These two orientations correspond to

the energy levels  $A_1$  and  $A_2$  (actually the sublevels are more complicated than this, but the simplification illustrates the pumping action adequately), and there is a difference of one quantum of angular momentum between the parallel and antiparallel states. The irradiating beam is circularly polarized so that the photons in the light beam have a single spin axis. Atoms in sublevel  $A_1$  then can be pumped to  $B$ , gaining one quantum by absorption, whereas those in  $A_2$  already have the same momentum as  $B$  and cannot make the transition.

Figure 3.12 is a schematic diagram of the rubidium-vapor magnetometer. Light from the Rb lamp is circularly polarized to illuminate the Rb vapor cell, after which it is refocused on a photocell. The axis of this beam is inclined approximately  $45^\circ$  to the Earth's field, which causes the electrons to precess about the axis of the field at the Larmor frequency. At one point in the precession cycle the atoms will be most nearly parallel to the light-beam direction and one-half cycle later they will be more antiparallel. In the first position, more light is transmitted through the cell than in the second. Thus the precession frequency produces a variable light intensity that flickers at the Larmor frequency. If the photocell signal is amplified and fed back to a coil wound on the cell, the coil-amplifier system becomes an oscillator whose frequency  $\nu$  is given by

$$F = 2\pi\nu/\gamma_e \quad (3.31)$$

where  $\gamma_e$  is the gyromagnetic ratio of the electron.

For Rb, the value of  $\gamma_e/2\pi$  is approximately  $4.67$  Hz/nT whereas the corresponding frequency for  $F_e = 50,000$  nT is  $233$  kHz. Because  $\gamma_e$  for the electron is known to a precision of about 1 part in  $10^7$  and because of the relatively high frequencies involved, it

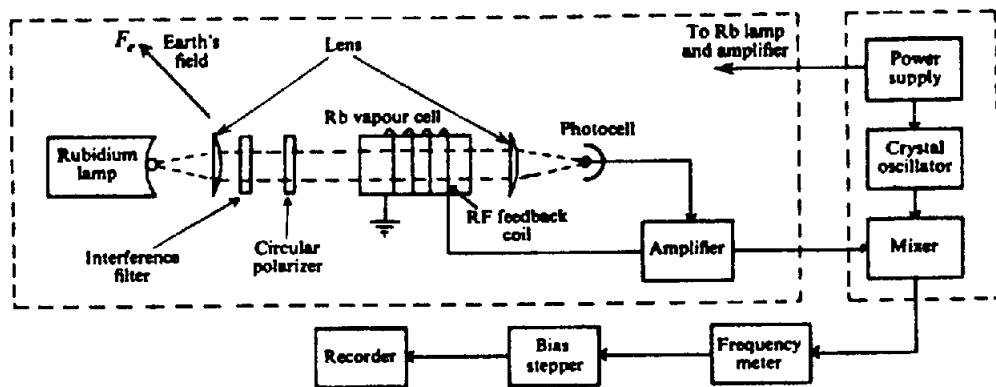


Figure 3.12. Rubidium-vapor magnetometer (schematic).

is not difficult to measure magnetic field variations as small as 0.01 nT with a magnetometer of this type.

### 3.4.5. Gradiometers

The sensitivity of the optically pumped magnetometer is considerably greater than normally required in prospecting. Since 1965, optically pumped rubidium- and cesium-vapor magnetometers have been increasingly employed in airborne gradiometers. Two detectors, vertically separated by about 35 m, measure  $dF/dz$ , the total-field vertical gradient. The sensitivity is reduced by pitch and yaw of the two birds. Major improvements by the Geological Survey of Canada involve reducing the vertical separation to 1 to 2 m and using a more rigid connection between the sensors. Gradient measurements are also made in ground surveys. The two sensors on a staff in the Scintrex MP-3 proton-magnetometer system, for example, measure the gradient to  $\pm 0.1$  nT/m. Gradiometer surveys are discussed further in Section 3.5.5.

### 3.4.6. Instrument Recording

Originally the magnetometer output in airborne installations was displayed by pen recorder. To achieve both high sensitivity and wide range, the graph would be "paged back" (the reference value changed) frequently to prevent the pen from running off the paper. Today recording is done digitally, but generally an analog display is also made during a survey. Some portable instruments for ground work also digitally record magnetometer readings, station coordinates, diurnal corrections, geological and terrain data.

### 3.4.7. Calibration of Magnetometers

Magnetometers may be calibrated by placing them in a suitably oriented variable magnetic field of known value. The most dependable calibration

method employs a *Helmholtz coil* large enough to surround the instrument. This is a pair of identical coils of  $N$  turns and radii  $a$  coaxially spaced a distance apart equal to the radius. The resulting magnetic field, for a current  $I$  flowing through the coils connected in series-aiding, is directed along the axis and is uniform within about 6% over a cylinder of diameter  $a$  and length  $3a/4$ , concentric with the coils. This field is given by

$$H = 9.0NI/a \quad (3.32a)$$

where  $I$  is in microamperes,  $H$  in nanoteslas, and  $a$  in meters. Because  $H$  varies directly with the current, this can be written

$$\Delta H = 9.0N\Delta I/a \quad (3.32b)$$

## 3.5. FIELD OPERATIONS

### 3.5.1. General

Magnetic exploration is carried out on land, at sea, and in the air. For areas of appreciable extent, surveys usually are done with the airborne magnetometer.

In oil exploration, airborne magnetics (along with surface gravity) is done as a preliminary to seismic work to establish approximate depth, topography, and character of the basement rocks. Since the susceptibilities of sedimentary rocks are relatively small, the main response is due to igneous rocks below (and sometimes within) the sediments.

Within the last few years it has become possible to extract from aeromagnetic data weak anomalies originating in sedimentary rocks, such as result from the faulting of sandstones. This results from (a) the improved sensitivity of magnetometers, (b) more precise determination of location with Doppler radar (§B.5), (c) corrections for diurnal and other temporal

field variations, and (d) computer-analysis techniques to remove noise effects.

Airborne reconnaissance for minerals frequently combines magnetics with airborne EM. In most cases of followup, detailed ground magnetic surveys are carried out. The method is usually indirect, that is, the primary interest is in geological mapping rather than the mineral concentration per se. Frequently the association of characteristic magnetic anomalies with base-metal sulfides, gold, asbestos, and so on, has been used as a marker in mineral exploration. There is also, of course, an application for magnetics in the direct search for certain iron and titanium ores.

### 3.5.2. Airborne Magnetic Surveys

(a) *General.* In Canada and some other countries, government agencies have surveyed much of the country and aeromagnetic maps on a scale of 1 mile to the inch are available at a nominal sum. Large areas in all parts of the world have also been surveyed in the course of oil and mineral exploration.

The sensitivity of airborne magnetometers is generally greater than those used in ground exploration – about 0.01 nT compared with 10 to 20 nT. Because of the initial large cost of the aircraft and availability of space, it is practical to use more sophisticated equipment than could be handled in portable instruments; their greater sensitivity is useful in making measurements several hundred meters above the ground surface, whereas the same sensitivity is usually unnecessary (and may even be undesirable) in ground surveys.

(b) *Instrument mounting.* Aside from stabilization, there are certain problems in mounting the sensitive magnetic detector in an airplane, because the latter has a complicated magnetic field of its own. One obvious way to eliminate these effects is to tow the sensing element some distance behind the aircraft. This was the original mounting arrangement and is still used. The detector is housed in a streamlined cylindrical container, known as a *bird*, connected by a cable 30 to 150 m long. Thus the bird may be 75 m nearer the ground than the aircraft. A photograph of a bird mounting is shown in Figure 3.13a.

An alternative scheme is to mount the detector on a wing tip or slightly behind the tail. The stray magnetic effects of the plane are minimized by permanent magnets and soft iron or permalloy shielding strips, by currents in compensating coils, and by metallic sheets for electric shielding of the eddy currents. The shielding is a cut-and-try process, since the magnetic effects vary with the aircraft and

mounting location. Figure 3.13b shows an installation with the magnetometer head in the tail.

(c) *Stabilization.* Since proton-precession and optically pumped magnetometers measure total field, the problem of stable orientation of the sensing element is minor. Although the polarizing field in the proton-precession instrument must not be parallel to the total-field direction, practically any other orientation will do because the signal amplitude becomes inadequate only within a cone of about 5°.

Stabilization of the fluxgate magnetometer is more difficult, because the sensing element must be maintained accurately in the *F* axis. This is accomplished with two additional fluxgate detectors that are oriented orthogonally with the first; that is, the three elements form a three-dimensional orthogonal coordinate system. The set is mounted on a small platform that rotates freely in all directions. When the sensing fluxgate is accurately aligned along the total-field axis, there is zero signal in the other two. Any tilt away from this axis produces a signal in the control elements that drive servomotors to restore the system to the proper orientation.

(d) *Flight pattern.* Aeromagnetic surveys almost always consist of parallel lines (Fig. 3.13c) spaced anywhere from 100 m to several kilometers apart. The heading generally is normal to the main geologic trend in the area and altitude usually is maintained at fixed elevations, the height being continuously recorded by radio or barometric altimeters. It is customary to record changes in the Earth's field with time (due to diurnal or more sudden variations) with a recording magnetometer on the ground. A further check generally is obtained by flying several cross lines, which verify readings at line intersections.

A *drape survey*, which approximates constant clearance over rough topography, is generally flown with a helicopter. It is often assumed that drape surveys minimize magnetic terrain effects, but Grauch and Campbell (1984) dispute this. Using a uniformly magnetized model of a mountain-valley system, four profiles (one level, the others at different ground clearance) all showed terrain effects. However, Grauch and Campbell recommend drape surveys over level-flight surveys because of greater sensitivity to small targets, particularly in valleys. The disadvantages of draped surveys are higher cost, operational problems, and less sophisticated interpretation techniques.

(e) *Effect of variations in flight path.* Altitude differences between flight lines may cause herringbone patterns in the magnetic data. Bhattacharyya (1970) studied errors arising from flight deviations

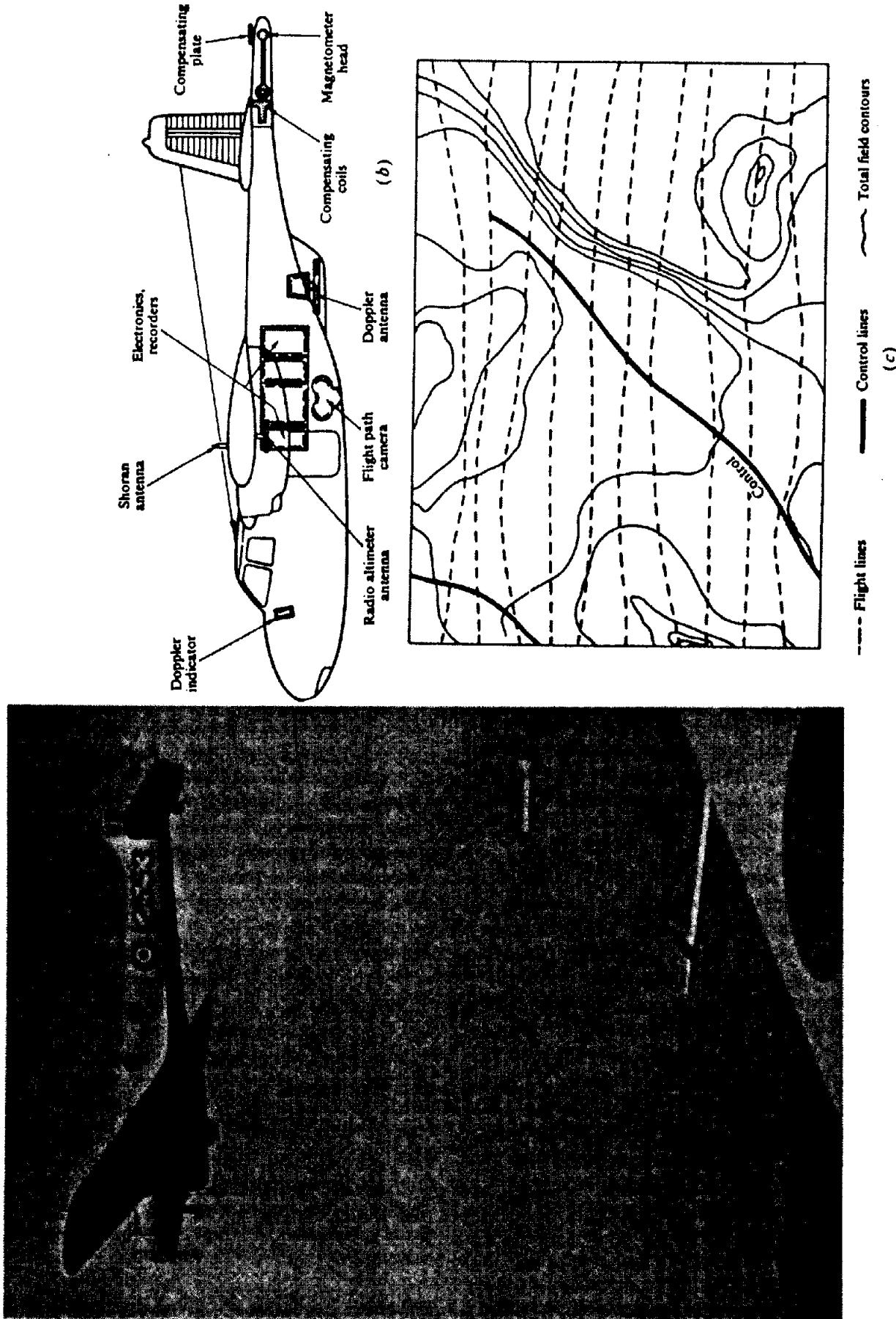


Figure 3.13. Airborne magnetics. (a) Magnetometer in a bird. (b) Magnetometer in a tail mounting. (c) Flight pattern and magnetic map.

over an idealized dike (prism) target. Altitude and heading changes produced field measurement changes that would alter interpretations based on anomaly shape measurements, such as those of slope. Such deviations are especially significant with high-resolution data.

(f) *Aircraft location.* The simplest method of locating the aircraft at all times, with respect to ground location, is for the pilot to control the flight path by using aerial photographs, while a camera takes photos on strip film to determine locations later. The photos and magnetic data are simultaneously tagged at intervals. Over featureless terrain, radio navigation (see §B.6) gives aircraft position with respect to two or more ground stations, or Doppler radar (§B.5) determines the precise flight path. Doppler radar increasingly is employed where high accuracy is required.

(g) *Corrections to magnetic data.* Magnetic data are corrected for drift, elevation, and line location differences at line intersections in a least-squares manner to force ties. Instrument drift is generally not a major problem, especially with proton and optically pumped magnetometers whose measurements are absolute values.

The value of the main magnetic field of the Earth is often subtracted from measurement values. The Earth's field is usually taken to be that of the *International Geomagnetic Reference Field* (IGRF) model.

A stationary base magnetometer is often used to determine slowly varying diurnal effects. Horizontal gradiometer arrangements help in eliminating rapid temporal variations; the gradient measurements do not involve diurnal effects. Usually no attempt is made to correct for the large effects of magnetic storms.

(h) *Advantages and disadvantages of airborne magnetics.* Airborne surveying is extremely attractive for reconnaissance because of low cost per kilometer (see Table 1.2) and high speed. The speed not only reduces the cost, but also decreases the effects of time variations of the magnetic field. Erratic near-surface features, frequently a nuisance in ground work, are considerably reduced. The flight elevation may be chosen to favor structures of certain size and depth. Operational problems associated with irregular terrain, sometimes a source of difficulty in ground magnetics, are minimized. The data are smoother, which may make interpretation easier. Finally, aeromagnetics can be used over water and in regions inaccessible for ground work.

The disadvantages in airborne magnetics apply mainly to mineral exploration. The cost for survey-

ing small areas may be prohibitive. The attenuation of near-surface features, apt to be the survey objective, become limitations in mineral search.

### 3.5.3. Shipborne Magnetic Surveys

Both the fluxgate and proton-precession magnetometers have been used in marine operations. There are no major problems in ship installation. The sensing element is towed some distance (150 to 300 m) astern (to reduce magnetic effects of the vessel) in a watertight housing called a *fish*, which usually rides about 15 m below the surface. Stabilization is similar to that employed in the airborne bird. Use of a ship rather than an aircraft provides no advantage and incurs considerable cost increase unless the survey is carried out in conjunction with other surveys, such as gravity or seismic. The main application has been in large-scale oceanographic surveying related to earth physics and petroleum search. Much of the evidence supporting plate tectonics has come from marine magnetics.

### 3.5.4. Ground Magnetic Surveys

(a) *General.* Magnetic surveying on the ground now almost exclusively uses the portable proton-precession magnetometer. The main application is in detailed surveys for minerals, but ground magnetics are also employed in the followup of geochemical reconnaissance in base-metal search. Station spacing is usually 15 to 60 m; occasionally it is as small as 1 m. Most ground surveys now measure the total field, but vertical-component fluxgate instruments are also used. Sometimes gradiometer measurements (§3.5.5) are made.

(b) *Corrections.* In precise work, either repeat readings should be made every few hours at a previously occupied station or a base-station recording magnetometer should be employed. This provides corrections for diurnal and erratic variations of the magnetic field. However, such precautions are unnecessary in most mineral prospecting because anomalies are large (> 500 nT).

Since most ground magnetometers have a sensitivity of about 1 nT, stations should not be located near any sizeable objects containing iron, such as railroad tracks, wire fences, drill-hole casings, or culverts. The instrument operator should also not wear iron articles, such as belt buckles, compasses, knives, iron rings, and even steel spectacle frames.

Apart from diurnal effects, the reductions required for magnetic data are insignificant. The vertical gradient varies from approximately 0.03 nT/m at the poles to 0.01 nT/m at the magnetic equator. The

latitude variation is rarely  $> 6 \text{ nT/km}$ . Thus elevation and latitude corrections are generally unnecessary.

The influence of topography on ground magnetics, on the other hand, can be very important. This is apparent when taking measurements in stream gorges, for example, where the rock walls above the station frequently produce abnormal magnetic lows. Terrain anomalies as large as 700 nT occur at steep ( $45^\circ$ ) slopes of only 10 m extent in formations containing 2% magnetite ( $k = 0.025 \text{ SI unit}$ ) (Gupta and Fitzpatrick, 1971). In such cases, a terrain correction is required, but it cannot be applied merely as a function of topography alone because there are situations (for example, sedimentary formations of very low susceptibility) in which no terrain distortion is observed.

A terrain smoothing correction may be carried out by reducing measurements from an irregular surface  $z = h(x, y)$  to a horizontal plane, say  $z = h$ , above it. This can be done approximately by using a Taylor series (§A.5) with two terms:

$$Z(x, y, 0) = Z(x, y, h) - h(\partial Z / \partial z)_{z=h} \quad (3.33)$$

### 3.5.5. Gradiometer Surveys

The gradient of  $F$  is usually calculated from the magnetic contour map with the aid of templates. There is, however, considerable merit in measuring the vertical gradient directly in the field. It is merely necessary to record two readings, one above the other. With instrument sensitivity of 1 nT, an elevation difference of  $\approx 1 \text{ m}$  suffices. Then the vertical gradient is given by

$$\partial F / \partial z = (F_2 - F_1) / \Delta z$$

where  $F_1$  and  $F_2$  are readings at the higher and lower elevations, and  $\Delta z$  is the separation distance.

Discrimination between neighboring anomalies is enhanced in the gradient measurements. For example, the anomalies for two isolated poles at depth  $h$  separated by a horizontal distance  $h$  yield separate peaks on a  $\partial F / \partial z$  profile but they have to be separated by  $1.4 h$  to yield separate anomalies on an  $F$  profile. The effect of diurnal variations is also minimized, which is especially beneficial in high magnetic latitudes. For most of the simple shapes discussed in Section 3.6 (especially for the isolated pole, finite-length dipole, and vertical contact of great depth extent), better depth estimates can be made from the first vertical-derivative profiles than from either the  $Z$  or  $F$  profiles. For features of the first two types, the width of the profile at  $(\partial Z / \partial z)_{\max} / 2$  equals the depth within a few per-

cent. For the vertical contact, half the separation between maximum and minimum values equals the depth. Gradiometer measurements are valuable in field continuation calculations (§3.7.5).

Ground gradiometer measurements (Hood and McClure, 1965) have recently been carried out for gold deposits in eastern Canada in an area where the overburden is only a few meters thick. The host quartz was located because of its slightly negative susceptibility using a vertical separation of 2 m and a station spacing of  $\approx 1 \text{ m}$ . Gradiometer surveys have also been used in the search for archeological sites and artifacts, mapping buried stone structures, forges, kilns, and so forth (Clark, 1986; Wynn, 1986).

Vertical gradient aeromagnetic surveys (Hood, 1965) are often carried out at 150 to 300 m altitude. Detailed coverage with 100 to 200 m line spacing is occasionally obtained at 30 m ground clearance.

Two magnetometers horizontally displaced from each other are also used, especially with marine measurements where they may be separated by 100 to 200 m. This arrangement permits the elimination of rapid temporal variations so that small spatial anomalies can be interpreted with higher confidence.

## 3.6. MAGNETIC EFFECTS OF SIMPLE SHAPES

### 3.6.1. General

Because ground surveys (until about 1968) measured the vertical-field component, whereas airborne surveys measured the total field, both vertical-component and total-field responses will be developed. Depth determinations are most important and lateral extent less so, whereas dip estimates are the least important and quite difficult. In this regard, aeromagnetic and electromagnetic interpretation are similar. In petroleum exploration the depth to basement is the prime concern, whereas in mineral exploration more detail is desirable. The potentialities of high resolution and vertical-gradient aeromagnetics are only now being exploited to a limited extent.

As in gravity and electromagnetics, anomalies are often matched with models. The magnetic problem is more difficult because of the dipole character of the magnetic field and the possibility of remanence. Very simple geometrical models are usually employed: isolated pole, dipole, lines of poles and dipoles, thin plate, dike (prism), and vertical contact. Because the shape of magnetic anomalies relates to the magnetic field, directions in the following sections are with respect to magnetic north (the  $x$  direction), magnetic east, and so forth, the  $z$  axis is positive downward, and we assume that locations are in the northern hemisphere. We use  $I$  for the field inclination,  $\xi$  for

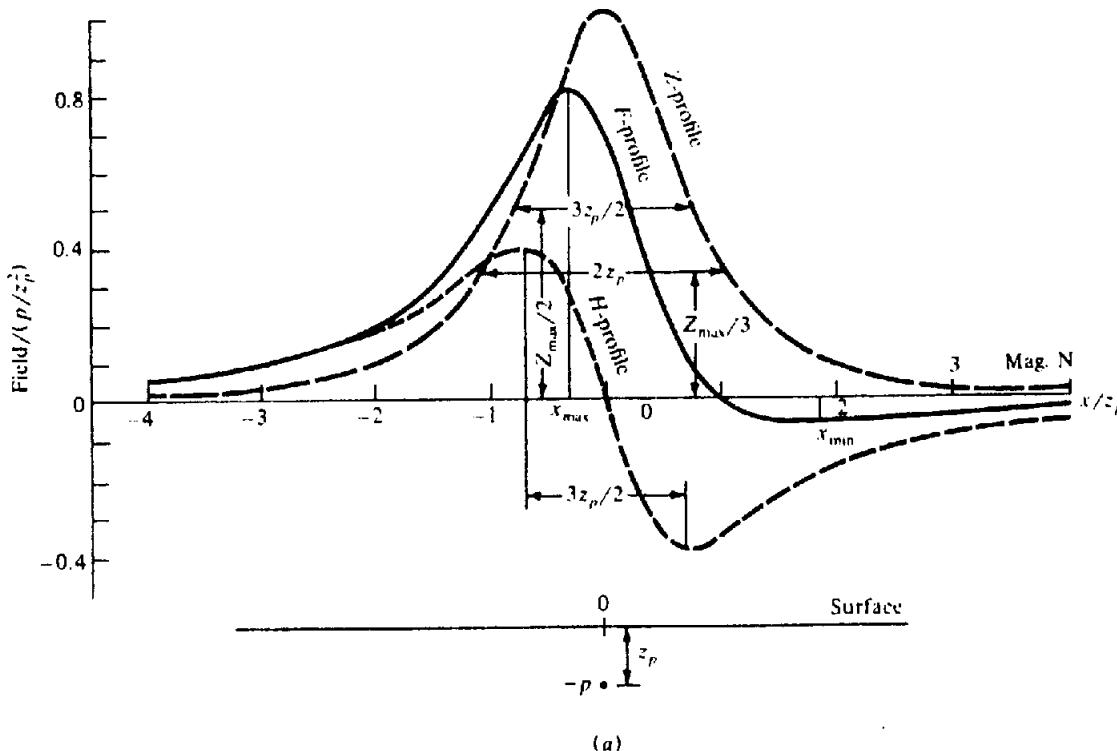


Figure 3.14. Magnetic effects of an isolated pole. (a)  $F$ ,  $Z$ , and  $H$  profiles for  $I = 45^\circ$ .

the dip of bodies and  $\beta$  for the strike angle relative to magnetic north ( $x$  axis). Note that depths are measured with respect to the measurement elevation (the aircraft elevation for aeromagnetic measurements).

### 3.6.2. The Isolated Pole (Monopole)

Although an isolated pole is a fiction, in practice it may be used to represent a steeply dipping dipole whose lower pole is so far away that it has a negligible effect. The induced magnetization in a long, slender, near-vertical body tends to be along the axis of the body except near the magnetic equator. If the length of the body is large, we have, in effect, a single negative pole  $-p$  located at  $(0, 0, z_p)$ .

From Equation (3.2) or Equations (3.9) and (3.11), we get for the field at  $P(x, y, 0)$ ,

$$\mathbf{F}_p = (-p/r^2)\mathbf{r}_1 = (p/r^3)(-xi - yj + z_p k)$$

where  $\mathbf{r}_1$  is a unit vector from  $P(x, y, 0)$  toward the pole  $-p$ . The vertical anomaly is

$$Z = (pz_p/r^3) \quad (3.34a)$$

Usually the field of the pole,  $\mathbf{F}_p$ , is much smaller than the field of the Earth,  $\mathbf{F}_e$ , and the total field

anomaly is approximately the component of  $\mathbf{F}_p$  in the  $\mathbf{F}_e$  direction. Using Equation (3.29),

$$F \approx \mathbf{F}_p \cdot \mathbf{f}_1 = (p/r^3)(-x \cos I + z_p \sin I) \quad (3.34b)$$

[Note that the total field anomaly  $F$ , which is only a component of  $\mathbf{F}_p$ , may be smaller than  $Z$ , and that in general  $F \neq (Z^2 + H^2)^{1/2}$ .]

Profiles are shown in Figure 3.14a for  $I = 45^\circ$ ;  $Z_{\max}$  is located directly over the pole. The  $H$  profile is perfectly asymmetric and its positive half intersects the  $Z$  profile nearly at  $Z_{\max}/3$ . The horizontal distance between positive and negative peaks of  $H$  is approximately  $3z_p/2$ . This profile is independent of the traverse direction only if the effect of the pole is much larger than the horizontal component of the Earth's field.

A set of total-field profiles for various values of  $I$  is shown in Figure 3.14c.  $F_{\max}$  occurs south of the monopole and  $F_{\min}$  north of it.  $F$  is zero north of the pole at  $x = z \tan I$ . The curves would be reflected in the vertical axis in southern latitudes. A total-field profile on a magnetic meridian becomes progressively more asymmetric as the inclination decreases (that is, as we move toward the magnetic equator). At the same time, the maximum decreases and the minimum increases and both are displaced progressively southward. The statement also applies

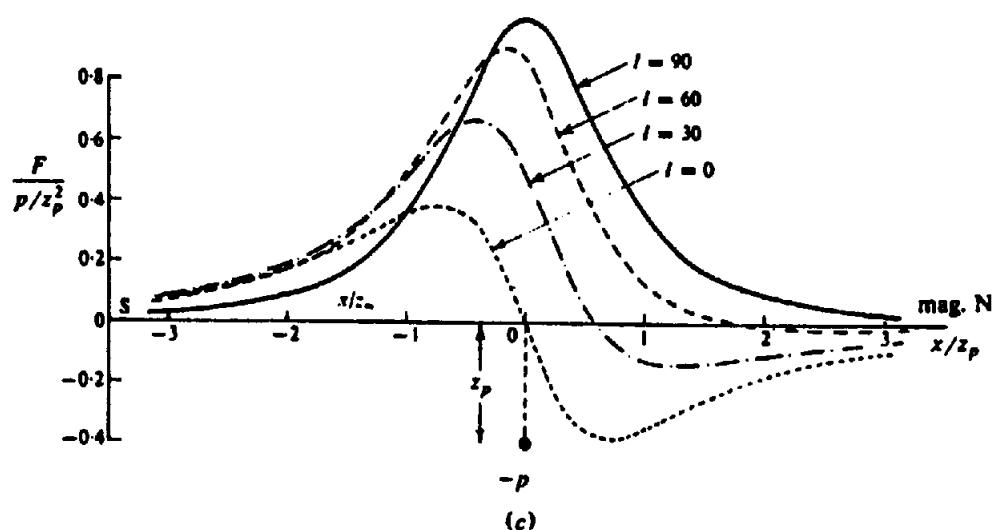
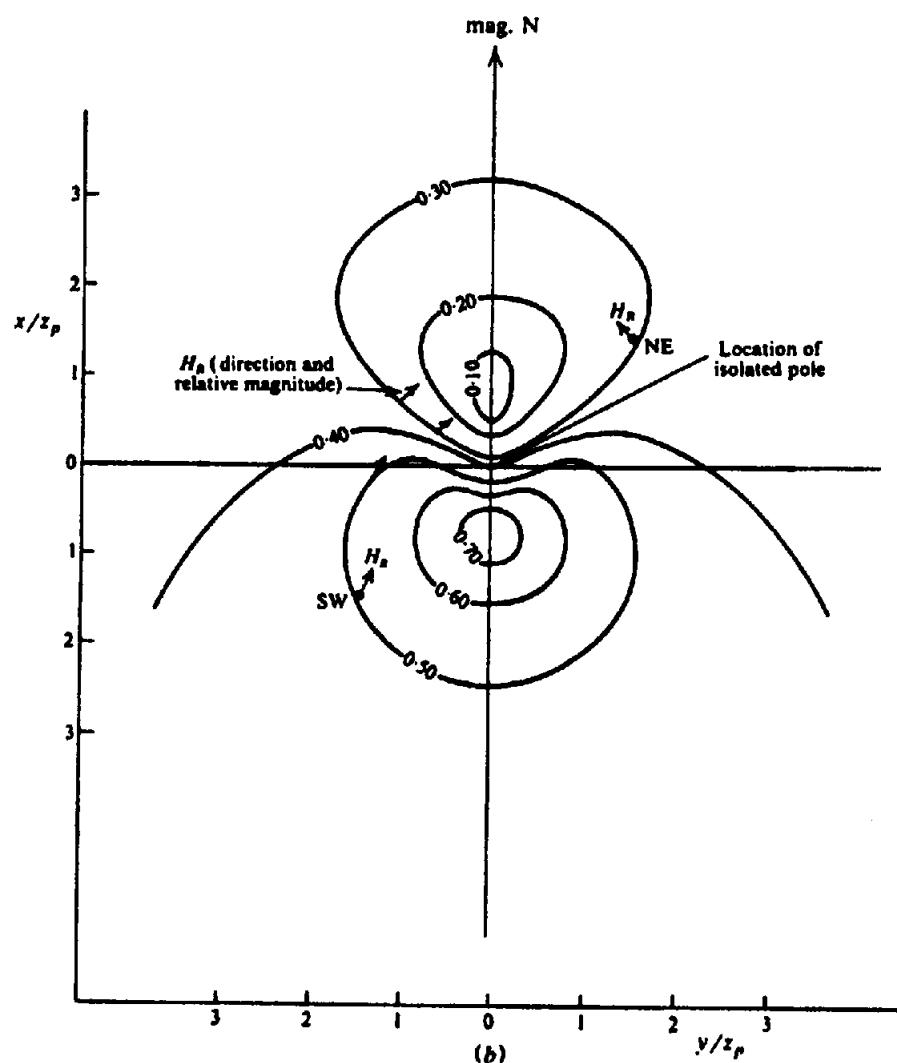


Figure 3.14. (Continued) (b) Contours of  $|H_B| = |H + H_e|$  for  $H_{\max} = H_e = 0.38$ . (c)  $F$  profiles for various inclinations. (After Smellie, 1967.)

to the southern hemisphere if we interchange maximum and minimum.

The maximum and minimum values of  $F$  in Equation (3.34b) occur at

$$x_{\max, \min} = z_p \left\{ 3 \pm (9 + 8 \cot^2 I)^{1/2} \right\} / 4 \cot I \quad (3.35a)$$

where the plus sign gives  $F_{\max}$ . The maximum and minimum values of  $F$  (recalling that the pole is  $-p$ , hence  $p$  is positive) are

$$F_{\max, \min} = \left( p \sin I / 4z_p^2 \right) \left\{ 1 \pm (9 + 8 \cot^2 I)^{1/2} \right\} / \left\{ 1 + (x_{\max, \min}/z_p)^2 \right\}^{3/2} \quad (3.35b)$$

There are several relations between the profile characteristics and the pole depth. When  $Z = Z_{\max}/2$ ,  $x_{1/2} = 0.75z_p$  (Fig. 3.14a), and when  $Z = Z_{\max}/3$ ,  $x_{1/3} = z_p$ , where  $x_{1/2}$  and  $x_{1/3}$  are the half-widths at  $Z_{\max}/2$  and  $Z_{\max}/3$ , respectively. Pole depth may also be estimated from Equations (3.35). For example,

$$z_p = 2(x_{\min} - x_{\max}) / (8 + 9 \tan^2 I)^{1/2} \quad (3.36a)$$

$$= 4(x_0 - x_{\max}) / \left\{ \tan I + (8 + 9 \tan^2 I)^{1/2} \right\} \quad (3.36b)$$

It may be difficult to locate  $x_{\min}$  and  $x_0$  in high latitudes, however, since the curves are practically symmetrical when  $I > 60^\circ$ . An alternative estimate, good within 10%, is given by  $z_p \approx 1.4x_{1/2}$ , where  $x_{1/2}$  is the half-width of the  $F$  profile.

A first vertical-derivative profile provides a good depth estimate. The width of the profile at  $(1/2)(\partial Z/\partial z)_{\max}$  is equal to  $z_p$  to within a few percent.

### 3.6.3. The Dipole

A small three-dimensional structure containing anomalous concentrations of magnetic materials and varying in section from rod-like to spherical often may be represented by a dipole model. The dipole field was developed in Section 3.2.3. Assuming that a structure is magnetized mainly by induction in the direction of the Earth's field, the dipole dip will be that of the inclination, and the magnetic response may be obtained from Equation (3.14). If the body's intrinsic field due to remanence is much larger than the external field (an unlikely case), the magnetic

response may also be obtained from these equations, replacing the inclination  $I$  with the dip of the dipole  $\xi$ .

Figure 3.15a shows the geometry. For a traverse in the dip direction, we find  $F$ ,  $H$ , and  $Z$  by resolving  $F_r$  and  $F_\theta$  in Equation (3.14a) along the dipole, the vertical, and the horizontal directions, respectively. Thus,

$$\begin{aligned} F &= F_r \cos \theta - F_\theta \sin \theta = (m/r^3) (3 \cos^2 \theta - 1) \\ &= (m/r^3) \{ 3 \cos^2(I + \phi) - 1 \} \\ &= (m/r^5) \{ (3 \cos^2 I - 1)x^2 - 6xz_m \sin I \cos I \\ &\quad + (3 \sin^2 I - 1)z_m^2 \} \quad (3.37a) \end{aligned}$$

$$\begin{aligned} Z &= -(F_r \sin \phi + F_\theta \cos \phi) \\ &= -(m/r^3) (2 \cos \theta \sin \phi + \sin \theta \cos \phi) \\ &= (m/r^5) \{ (2z_m^2 - x^2) \sin I - 3xz_m \cos I \} \quad (3.37b) \end{aligned}$$

$$\begin{aligned} H &= F_r \cos \phi - F_\theta \sin \phi \\ &= (m/r^3) (2 \cos \theta \cos \phi - \sin \theta \sin \phi) \\ &= (m/r^5) \{ (2x^2 - z_m^2) \cos I - 3xz_m \sin I \} \quad (3.37c) \end{aligned}$$

where  $m = 2pt$  and  $z_m$  is the depth of the dipole below the surface of measurement.

Profiles are shown in Figure 3.15b for  $I = 45^\circ$ . The dipole curves are somewhat sharper than for the monopole. The width,  $x^*$ , of the  $Z$  curves in Figure 3.15b at  $\sim Z_{\max}/2$  is  $x^* \approx z_m$ . The same relation holds for the  $F$  curves in Figure 3.15b, e in the range  $30^\circ \leq I \leq 90^\circ$ . For  $I = 0$ , however, the profile is sharper and  $x^* \approx 0.7z_m$  at  $F_{\max}/2$ . The  $F$  and  $Z$  profiles would be symmetrical on E-W traverses, with the flanks asymptotic to zero. The width of a gradiometer profile peak at  $(1/2)(\partial Z/\partial z)_{\max}$  gives a good estimate of  $z_m$ .

When the dipole is polarized approximately vertically, which would be the case where  $I \geq 70^\circ$ , we have

$$F \approx Z = m(2z_m^2 - x^2)/r^5 \quad \text{and} \quad H = -3mxz_m/r^5 \quad (3.38a)$$

Near the magnetic equator,  $I \approx 0$  and

$$F \approx H = m(2x^2 - z_m^2)/r^5 \quad \text{and} \quad Z = -3mxz_m/r^5 \quad (3.38b)$$

Curves for these limiting cases are shown in Figure 3.15c and d.

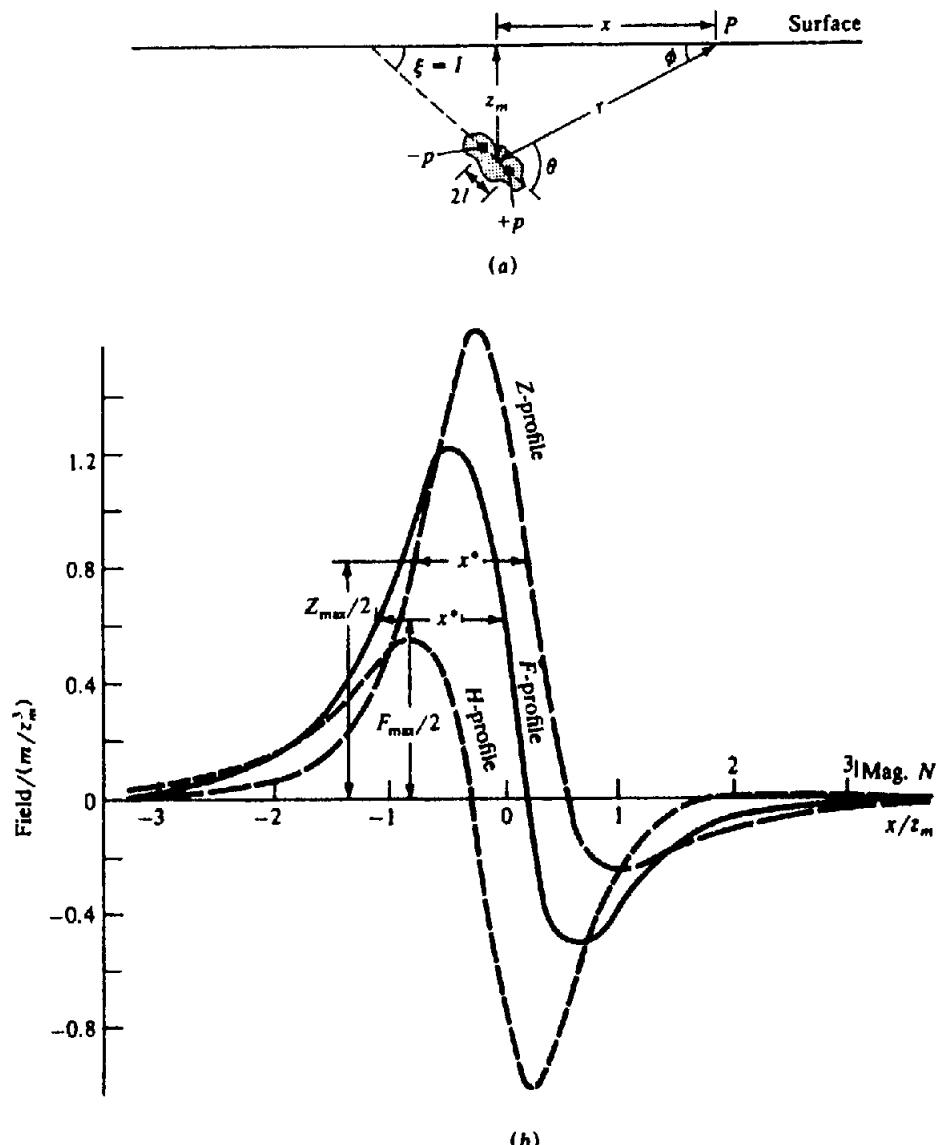


Figure 3.15. Magnetic effects of an isolated dipole. (a) Geometry. (b) Profiles for  $I = 45^\circ$ .

The following relations hold for the vertical dipole:

$$\left. \begin{array}{l} \text{At } x = 0, Z, F \text{ are maxima:} \\ Z_{\max} = F_{\max} = 2m/z_m^3 \\ \text{At } x = \pm 2z_m, Z, F \text{ are minima:} \\ Z_{\min} = F_{\min} = -0.036m/z_m^3 \\ \text{At } x = \pm z_m/\sqrt{2} \quad Z = F = 0 \end{array} \right\} (3.39a)$$

Similar relations hold for the horizontal dipole:

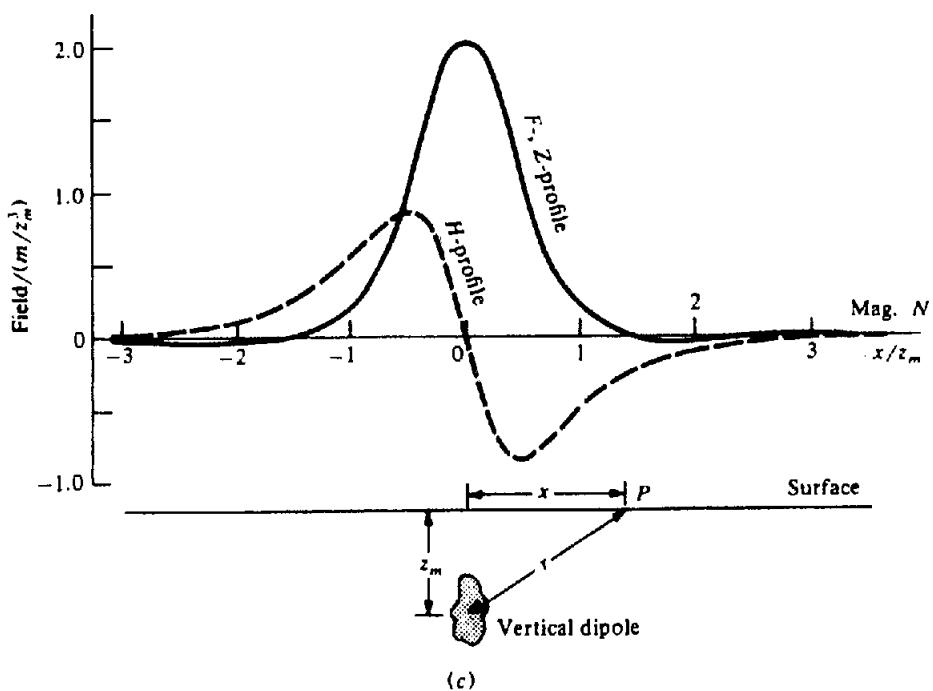
$$\left. \begin{array}{ll} \text{At } x = 0, & H_{\min} = F_{\min} = -m/z_m^3 \\ \text{At } x = \pm 1.2z_m, & H_{\max} = F_{\max} = 0.20m/z_m^3 \\ \text{At } x = \pm z_m/\sqrt{2}, & H = F = 0 \end{array} \right\} (3.39b)$$

The direction of dipole dip is toward the side of the  $Z$  profile that has the steeper slope and negative tail. This tail is not pronounced, however, unless the dip  $\xi < 50^\circ$ . The  $F$  profiles are even more diagnostic of dip. In Figure 3.15d the  $Z$  profile is asymmetrical, with peak and trough above the ends of a long dipole for  $z_m/l \ll 2$ . When  $z_m/l > 1$ , the peak and trough occur beyond the ends and depth cannot be estimated, although a steep slope at the zero crossover would indicate a shallow source.

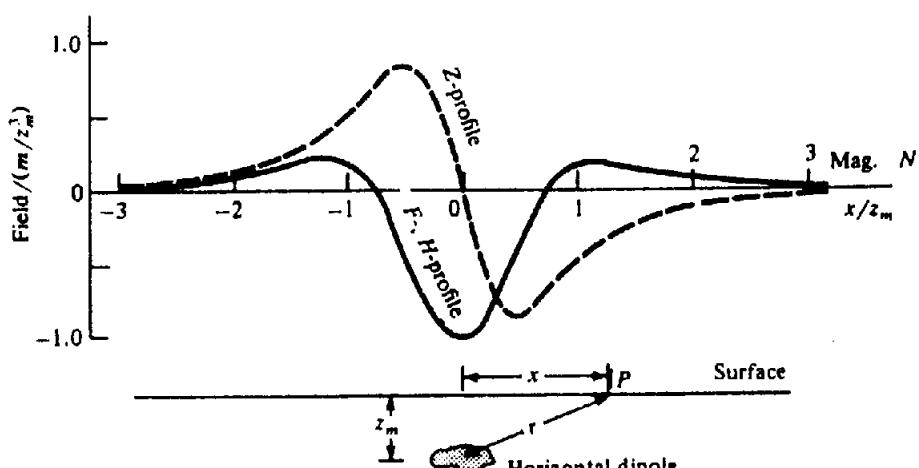
A finite dipole sometimes may be represented by a dipping sheet of finite length and depth extent [Eq. (3.58)] or by an infinite vertical dipping dike of finite strike length [Eq. (3.49)].

### 3.6.4. Two-Dimensional Features

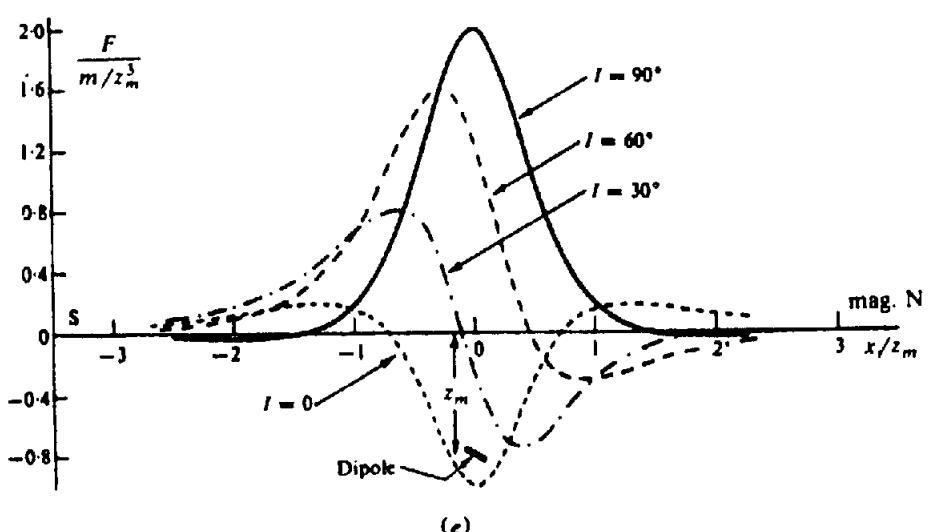
(a) General. Clearly the strike of a two-dimensional feature with respect to the earth's field will



(c)



(d)



(e)

Figure 3.15. (Continued) (c) Profiles for vertical dipole. (d) Profiles for horizontal dipole. (e)  $F$  profiles for different inclinations of field and dipole. (After Smellie, 1967.)

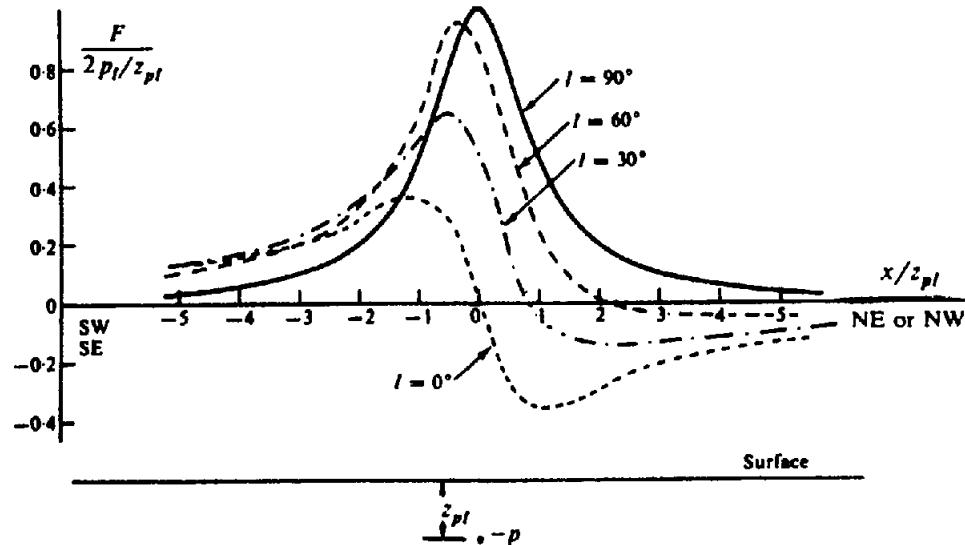


Figure 3.16. Total-field profiles normal to a line of poles striking NW-SE.

control induced magnetization, so the strike direction  $\beta$  will be incorporated in the expressions for various structures. Traverse direction is more critical in identifying a 2-D target. A profile approximately along strike will be unproductive. For 2-D models, it is customary to exhibit only *principal profiles* (normal to strike of the bodies). As in gravity, a magnetic body generally is considered to be 2-D when its strike length is at least 10 to 20 times larger than other dimensions. This situation is even less likely to be true in magnetics than it is in gravity, and formulas are often modified for finite strike length (Rasmussen and Pedersen, 1979).

In addition to using direct magnetic analysis, 2-D features may also be derived with relative ease from the corresponding gravity shapes by using Poisson's relation (§3.2.5).

(b) *Line of poles (thin vertical dike of infinite depth extent)*. An infinite horizontal line of poles is an approximation to a long shear or fracture zone or thin dike, which has appreciable susceptibility contrast and which extends to considerable depth. The magnetic potential is given by the logarithmic relation  $A = -2p_l \ln(1/r)$ , where  $-p_l$  is the pole intensity per unit length [this equation comes from Eq. (3.9) following the procedure in problem 1, Chapter 2, and assuming infinitesimal cross section in Eq. (2.8)]. We pass a vertical plane through  $P(x, y, 0)$  perpendicular to the line of poles and take  $x'$  and  $z'$  axes in this plane such that  $x'$  is horizontal,  $z' = z$ , and the line of poles intersects the  $z$  axis at a depth  $z_{pl}$ .  $\beta$  is the angle between the  $x$  and  $-y'$  axes. The field  $\mathbf{F}_{pl}$  is in this plane and is directed down from  $P$  toward the line of poles along the vector  $\mathbf{r} = (-x'l' + z_{pl}\mathbf{k})$ . To get derivatives of  $r$  at  $P$ , we write  $r^2$  in terms of the components of  $\mathbf{r}$  and

temporarily replace  $P(x', 0)$  with  $P'(x', z)$ . Then,  $r^2 = (-x')^2 + (z_{pl} - z)^2$ ,  $\partial r/\partial x = x'/r$ , and  $\partial r/\partial z = \lim_{z \rightarrow 0} \{-(z_{pl} - z)/r\} = -z_{pl}/r$ . Then,

$$\begin{aligned}\mathbf{F}_{pl} &= -\nabla A = -2p_l \nabla \{\ln r\} \\ &= (2p_l/r^2)(-x'l' + z_{pl}\mathbf{k}) \\ &= (2p_l/r^2)(-x' \sin \beta l + z_{pl}\mathbf{k})\end{aligned}\quad (3.40a)$$

Now the component along  $\mathbf{F}_e$  is

$$\begin{aligned}\mathbf{F} &= \mathbf{F}_{pl} \cdot \mathbf{f}_1 \\ &= (2p_l/r^2)(-x' \sin \beta l + z_{pl}\mathbf{k}) \\ &\quad \cdot (\cos I \mathbf{i} + \sin I \mathbf{k}) \\ &= (2p_l/r^2)(-x' \cos I \sin \beta + z_{pl} \sin I)\end{aligned}\quad (3.40b)$$

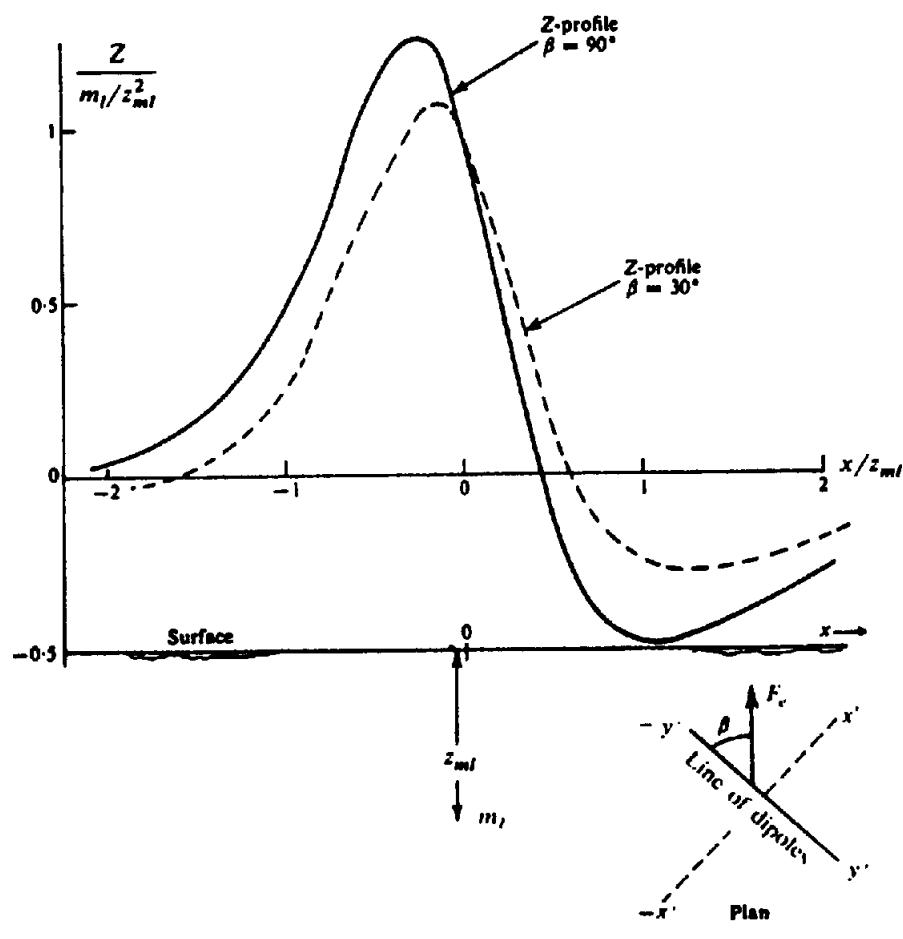
where  $r^2 = x'^2 + z_{pl}^2$ . The vertical component is

$$Z = 2p_l z_{pl}/r^2 \quad (3.40c)$$

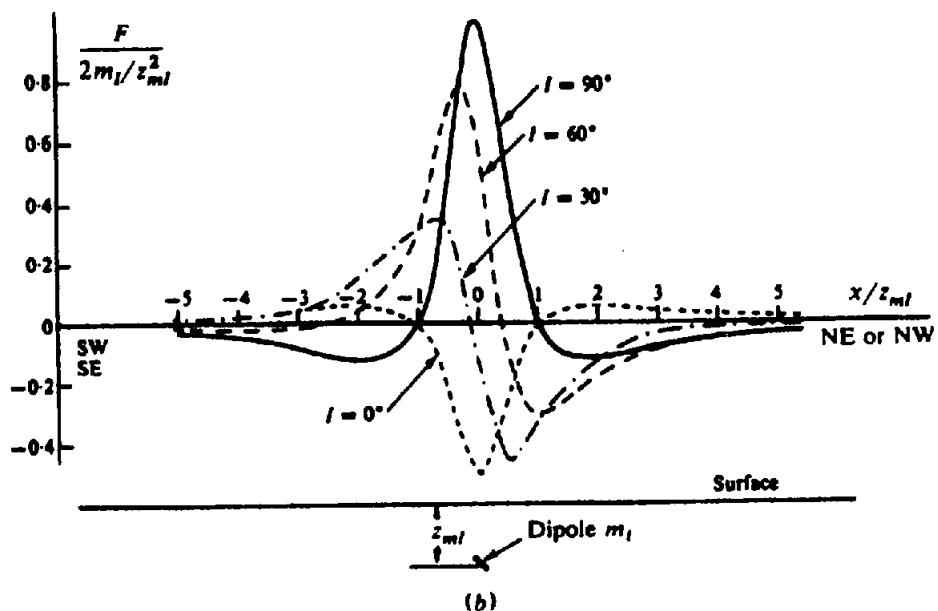
The north-south component of  $H$  is from Equation (3.40a):

$$H = -(2p_l/r^2)x' \sin \beta \quad (3.40d)$$

Total-field principal profiles (normal to strike) are shown in Figure 3.16 for several inclinations and strike  $\beta = 45^\circ$ . Obviously the  $Z$  profiles are the same for any strike direction. The  $F$  curves in Figure 3.16 have the same character as for the single pole, although they are somewhat broader. For  $I < 30^\circ$ , the half-width of the profile at  $F_{\max}/2$  is about equal to the depth. When  $I$  is smaller, the depth is roughly equal to half the horizontal distance between  $F_{\max}$  and  $F_{\min}$ .



(a)



(b)

Figure 3.17. Profiles normal to a horizontal line of dipoles. (a) Vertical-field profiles,  $i = 45^\circ$ . (b)  $F$  profiles for  $\beta = \pm 45^\circ$ .

(c) *Line of dipoles (ribbon)*. The opposite extreme to a line of poles is a magnetic stringer of limited depth extent, which can be modeled by a line (ribbon) of dipoles, sometimes called a thin horizontal cylinder. We take the  $y'$  axis along the strike and derive the magnetic response along the principal profile (in the  $I'$  direction) using Poisson's relation [Eq. (3.26)]:

$$A = (m_l/\gamma\rho_l) g_a = -(m_l/\gamma\rho_l) \nabla U \cdot \alpha_l$$

where  $\rho_l$  is the density per unit length and  $m_l$  is the dipole moment per unit length in the direction  $\alpha_l = \cos I \sin \beta i' + \sin I k$ . Then  $U = -2\gamma\rho_l \ln(r)$  for infinitesimal cross section [Eq. (2.8)]; we now write  $r^2 = x'^2 + (z_{ml} - z)^2$ , differentiate, then set  $z = 0$ . This gives

$$\nabla U = -2\gamma\rho_l(x'i' - z_{ml}k)/r^2$$

The magnetic potential becomes

$$\begin{aligned} A &= \{(-m_l/\gamma\rho_l)(-2\gamma\rho_l)(x'i' - z_{ml}k)/r^2\} \cdot \alpha_l \\ &= (2m_l/r^2)(x'i' - z_{ml}k) \\ &\quad \cdot (\cos I \sin \beta i' + \sin I k) \\ &= (2m_l/r^2)(x' \cos I \sin \beta - z_{ml} \sin I) \end{aligned}$$

The field components are found from this (noting that  $H$  is along the  $x'$  axis so that the component along the  $x$  axis is  $H \sin \beta$  – see Eq. (3.41c))

$$\begin{aligned} Z &= -\partial A / \partial z \\ &= (2m_l/r^4) \\ &\quad \times \{(z_{ml}^2 - x'^2) \sin I - 2x'z_{ml} \cos I \sin \beta\} \end{aligned} \quad (3.41a)$$

$$\begin{aligned} H &= -\partial A / \partial x' \\ &= (2m_l/r^4) \\ &\quad \times \{(x'^2 - z_{ml}^2) \cos I \sin \beta - 2x'z_{ml} \sin I\} \end{aligned} \quad (3.41b)$$

$$\begin{aligned} F &= (H \sin \beta) \cos I + Z \sin I \\ &= (2m_l/r^4) \\ &\quad \times \{(x'^2 - z_{ml}^2)(\cos^2 I \sin^2 \beta - \sin^2 I) \\ &\quad - 4x'z_{ml} \sin I \cos I \sin \beta\} \end{aligned} \quad (3.41c)$$

Two principal profiles for the vertical component are shown in Figure 3.17a, one where the dipole line strikes E-W ( $\beta = \pi/2$ ) and one for a strike N30°W ( $\beta = \pi/6$ ). When the dipole line is in the magnetic meridian,  $\beta = 0$ , the curve is symmetrical with  $Z_{\max}$

directly above the center. As in the case of the dipole, the depth to the center of the dipole line is approximately equal to the width of the profile at  $Z_{\max}/2$ .

Figure 3.17b displays total-field principal profiles for a line of dipoles striking NW (or NE) for inclinations  $I = 90^\circ, 60^\circ, 30^\circ, 0^\circ$ . When  $0^\circ \leq I \leq 15^\circ$  and  $45^\circ \leq I \leq 90^\circ$ , the full width of  $F_{\max}/2$  is roughly the depth, whereas for  $15^\circ \leq I \leq 45^\circ$ , the depth is approximately the distance between  $F_{\max}$  and  $F_{\min}$ . These profiles are also more diagnostic of dip than  $Z$  measurements are.

### 3.6.5. Dipping Dike (Prism)

(a) *General case*. Magnetic anomalies caused by intrusions, flows, or iron-rich sedimentary horizons are common features in regions favorable for mineral exploration, and there is frequently a contrast in the magnetic mineral content of such features with respect to the host rock. Such features may often be simulated by a two-dimensional dipping dike (prism). A vertical dike is also commonly used in making basement depth determinations in oil prospecting.

Direct application of Poisson's relation is difficult, so we proceed as follows. We assume a dike with dip  $\xi$  and strike  $\beta$ , and we take the  $y'$  axis along the strike direction. We assume that magnetic polarization is in the  $F_e$  direction, that is,  $M = kF_e$ . The geometry is illustrated in Figure 3.18a, from which we have the following relations:

$$\begin{aligned} r_1^2 &= d^2 + (x + d \cot \xi)^2 \\ r_2^2 &= D^2 + (x + D \cot \xi)^2 \\ r_3^2 &= d^2 + (x + d \cot \xi - b)^2 \\ r_4^2 &= D^2 + (x + D \cot \xi - b)^2 \\ \phi_1 &= \tan^{-1}\{d/(x + d \cot \xi)\} \end{aligned}$$

and so on. Starting with Equation (3.26), we have

$$A = (M/\gamma\rho) g_f = -(M/\gamma\rho) \nabla U \cdot f_1 \quad (3.42)$$

where  $f_1 = (\cos I \sin \beta i' + \sin I k)$ . Using Equation (3.27a) this becomes

$$\begin{aligned} F &= -\nabla A = (M/\gamma\rho) \nabla(\nabla U \cdot f_1) \\ &= (M/\gamma\rho) \nabla(U_x \cos I \sin \beta + U_z \sin I) \\ &= (kF_e/\gamma\rho) \{(U_{xx} \cos I \sin \beta + U_{xz} \sin I)i' \\ &\quad + (U_{xz} \cos I \sin \beta + U_{zz} \sin I)k\} \end{aligned} \quad (3.43)$$

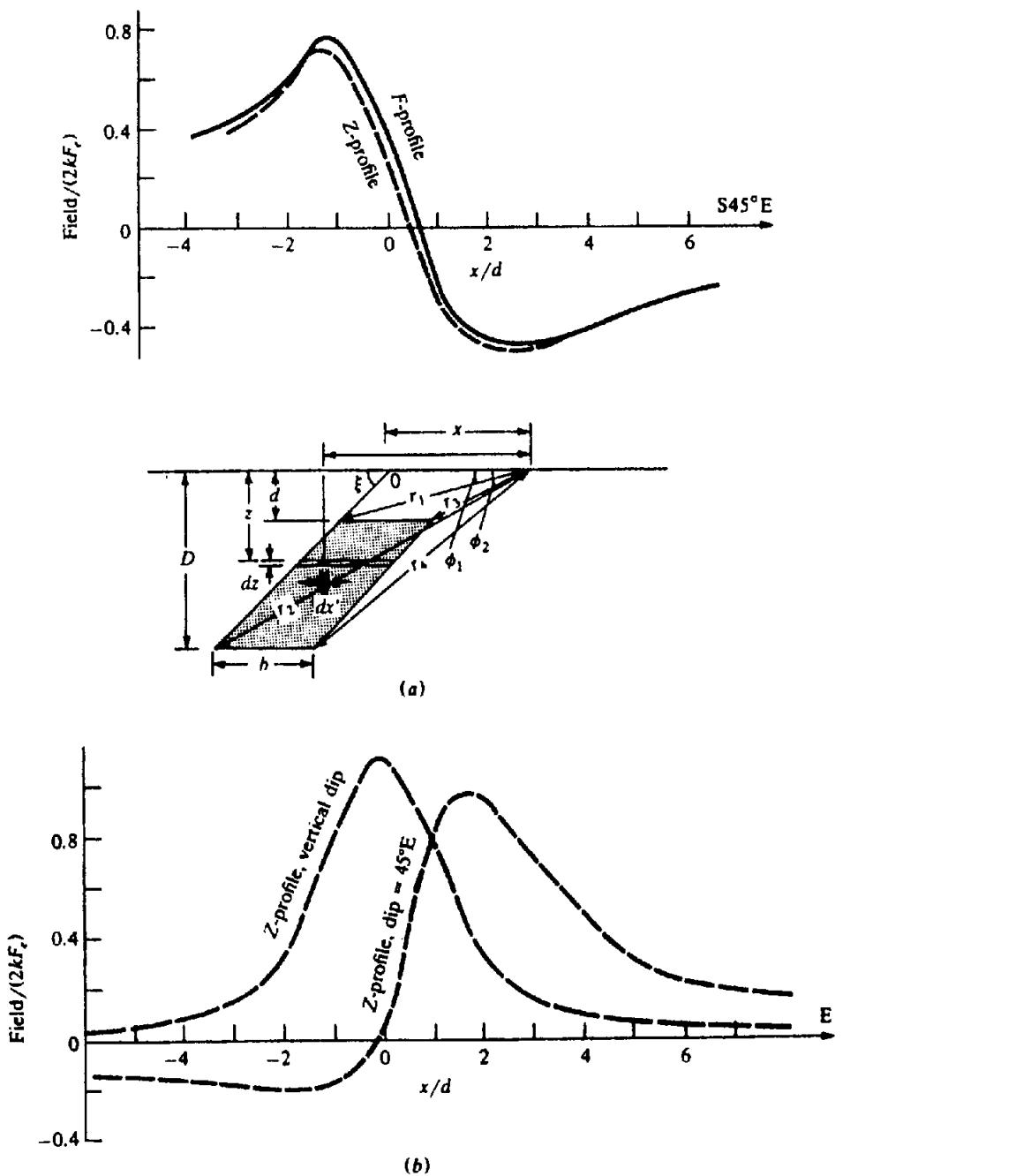


Figure 3.18. Profiles for dike model.  $l = \infty$  except for (d). (a)  $F, Z$  profiles for  $l = 60^\circ$ ,  $\beta = 45^\circ$ ,  $\xi = 45^\circ$ ,  $b = 2d$ ,  $D = 3.5d$ . (b)  $Z$  profiles for  $l = 75^\circ$ ,  $\beta = 0^\circ$ ,  $\xi = 45^\circ E$  and  $90^\circ$ ,  $b = 2d$ ,  $D = \infty$ .

Because  $U$  satisfies Laplace's equation (2.11a),  $U_{xx} = -U_{zz}$ . Differentiating Equation (2.9), we get

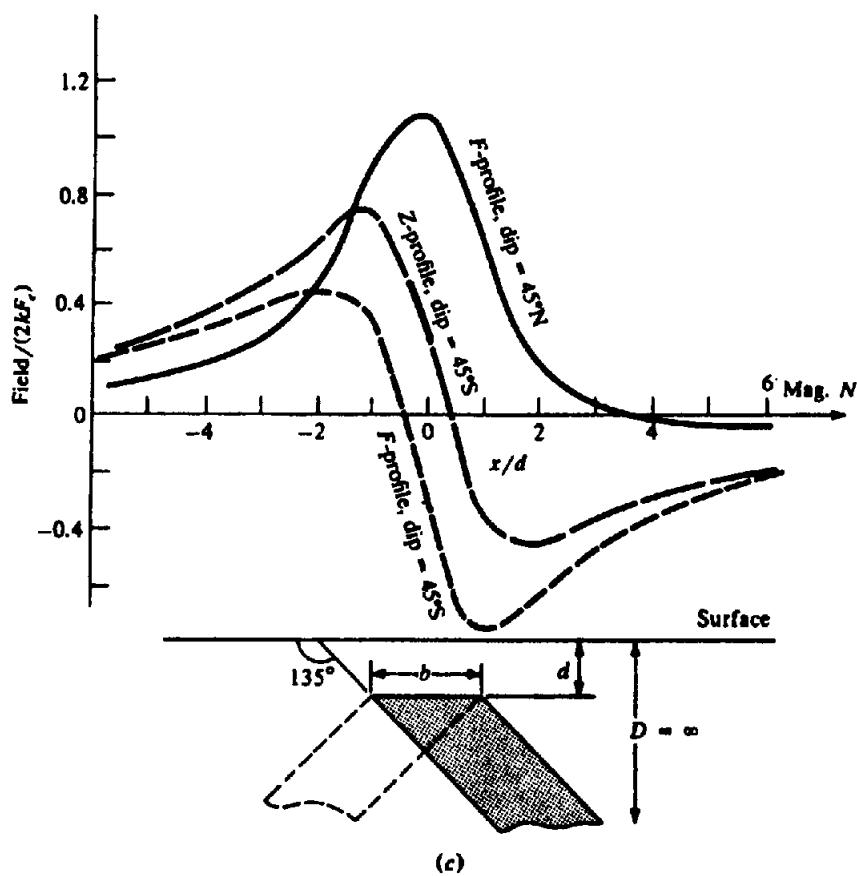
$$U_{xz} = 4\gamma\rho \int \int (xz/r^4) dx dz$$

$$U_{zz} = 2\gamma\rho \int \int ((z^2 - x^2)/r^4) dx dz$$

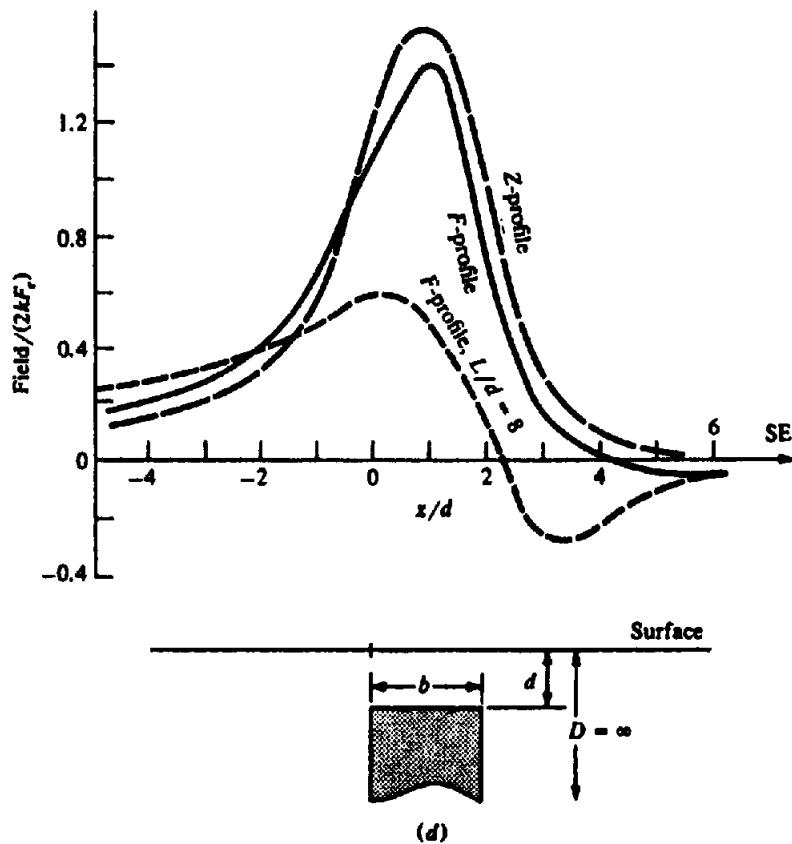
We change  $x$  and  $z$  to  $x'$  and  $z'$ , the coordinates of a point inside the dike.  $r^2$  becomes  $(x'^2 + z'^2)$ .

Then,

$$\begin{aligned} U_{xz} &= 4\gamma\rho \int_{x'} \int_{z'} \frac{x' z'}{r^4} dx' dz' \\ &= 4\gamma\rho \int z' dz' \int \frac{x' dx'}{(z'^2 + x'^2)^2} \\ &= 4\gamma\rho \int z' dz' \left\{ \frac{-1}{2(z'^2 + x'^2)} \right\} \Big|_{x+z' \cot \xi - b}^{x+z' \cot \xi - b} \\ &= 2\gamma\rho \int_d^D \left\{ \frac{z'}{z'^2 \csc^2 \xi + 2z' x \cot \xi + x^2} \right. \\ &\quad \left. - \frac{z'}{z'^2 \csc^2 \xi + 2z'(x-b) \cot \xi + (x-b)^2} \right\} dz' \end{aligned}$$



(c)



(d)

Figure 3.18. (Continued) (c)  $F$ ,  $Z$  profiles for  $I = 60^\circ$ ,  $\beta = 90^\circ$ ,  $\xi = 45^\circ N$  and  $S$ ,  $b = 2d$ ,  $D = \infty$ . (d)  $F$ ,  $Z$  profiles for  $I = 75^\circ$ ,  $\beta = 90^\circ$ ,  $\xi = 90^\circ$ ,  $b = 2d$ ,  $D = \infty$ ,  $2L = \infty$  and  $16d$ .

After some manipulation, this becomes

$$U_{xx} = 2\gamma\rho \sin \xi \{ \sin \xi \ln(r_2 r_3 / r_1 r_4) + \cos \xi (\phi_1 - \phi_2 - \phi_3 + \phi_4) \}$$

The value of  $U_{zz}$  can be found the same way; the result is

$$U_{zz} = 2\gamma\rho \sin \xi \{ \cos \xi \ln(r_2 r_3 / r_1 r_4) - \sin \xi (\phi_1 - \phi_2 - \phi_3 + \phi_4) \}$$

Substitution of the values of the derivatives in Equation (3.43) gives

$$\begin{aligned} Z = 2kF_e \sin \xi &\{ (\cos I \sin \xi \sin \beta \\ &+ \sin I \cos \xi) \ln(r_2 r_3 / r_4 r_1) \\ &+ (\cos I \cos \xi \sin \beta - \sin I \sin \xi) \\ &\times (\phi_1 - \phi_2 - \phi_3 + \phi_4) \} \end{aligned} \quad (3.44a)$$

$$\begin{aligned} H = 2kF_e \sin \xi \sin \beta &\times \{ (\sin I \sin \xi - \cos I \cos \xi \sin \beta) \ln(r_2 r_3 / r_4 r_1) \\ &+ (\cos I \sin \xi \sin \beta + \sin I \cos \xi) \\ &\times (\phi_1 - \phi_2 - \phi_3 + \phi_4) \} \end{aligned} \quad (3.44b)$$

$$\begin{aligned} F = 2kF_e \sin \xi &\{ [\sin 2I \sin \xi \sin \beta \\ &- \cos \xi (\cos^2 I \sin^2 \beta - \sin^2 I)] \\ &\times \ln(r_2 r_3 / r_4 r_1) \\ &+ \{ \sin 2I \cos \xi \sin \beta \\ &+ \sin \xi (\cos^2 I \sin^2 \beta - \sin^2 I) \} \\ &\times (\phi_1 - \phi_2 - \phi_3 + \phi_4) \} \end{aligned} \quad (3.44c)$$

The parameter values in these equations may sometimes be found from the interpretation of ground surveys, but generally this cannot be done for airborne work. Monopole- and dipole-line approximations (§3.6.4b, c) may occasionally be distinguished from dike-like models of considerable width in mineral exploration, but usually basement is so far removed from the aircraft in oil reconnaissance work that discrimination is impossible. The vertical dike is often used for basement depth determinations in the latter case.

(b) E-W or N-S strike. When the dike strikes E-W,  $\beta = 90^\circ$  and Equations (3.44a, c) become

$$Z = 2kF_e \sin \xi \{ \sin(I + \xi) \ln(r_2 r_3 / r_4 r_1) + \cos(I + \xi) (\phi_1 - \phi_2 - \phi_3 + \phi_4) \} \quad (3.45a)$$

$$\begin{aligned} F = 2kF_e \sin \xi &\{ -\cos(\xi + 2I) \ln(r_2 r_3 / r_4 r_1) \\ &+ \sin(\xi + 2I) \\ &\times (\phi_1 - \phi_2 - \phi_3 + \phi_4) \} \end{aligned} \quad (3.45b)$$

If, in addition, the dike has vertical sides,  $\xi = 90^\circ$  and Equations (3.45) are simplified to

$$Z = 2kF_e \{ \cos I \ln(r_2 r_3 / r_4 r_1) - \sin I (\phi_1 - \phi_2 - \phi_3 + \phi_4) \} \quad (3.46a)$$

$$F = 2kF_e \{ \sin 2I \ln(r_2 r_3 / r_4 r_1) + \cos 2I (\phi_1 - \phi_2 - \phi_3 + \phi_4) \} \quad (3.46b)$$

For N-S strike,  $\beta = 0$ , so

$$Z = 2kF_e \sin \xi \sin I \{ \cos \xi \ln(r_2 r_3 / r_4 r_1) - \sin \xi (\phi_1 - \phi_2 - \phi_3 + \phi_4) \} \quad (3.47a)$$

$$F = 2kF_e \sin \xi \sin^2 I \{ (\cos \xi) \ln(r_2 r_3 / r_4 r_1) - \sin \xi (\phi_1 - \phi_2 - \phi_3 + \phi_4) \} \quad (3.47b)$$

For a vertical dike with N-S strike, Equations (3.47) become

$$Z = -2kF_e \sin I (\phi_1 - \phi_2 - \phi_3 + \phi_4) \quad (3.48a)$$

$$F = -2kF_e \sin^2 I (\phi_1 - \phi_2 - \phi_3 + \phi_4) \quad (3.48b)$$

(c) Dike of limited length. Dike anomalies rarely satisfy the criteria for two-dimensionality (strike length  $\geq 10b$ , where  $b$  is width). For a more realistic model (sometimes called a prism model) having a strike length  $2L$ ,  $D = \infty$ , and  $\xi = 90^\circ$ , equation (3.44c) becomes

$$\begin{aligned} F = kF_e &\left\{ \sin 2I \sin \beta \left[ \ln \left\{ (r_1^2 + L^2)^{1/2} + L \right\} \right. \right. \\ &- \ln \left\{ (r_1^2 + L^2)^{1/2} - L \right\} \\ &+ \ln \left\{ (r_3^2 + L^2)^{1/2} - L \right\} \\ &- \ln \left\{ (r_3^2 + L^2)^{1/2} + L \right\} \left. \right] \\ &- (\cos^2 I \sin \beta - \sin^2 I) \\ &\times \left[ \tan^{-1} \left( \frac{L}{x} \right) - \tan^{-1} \left( \frac{L}{x-b} \right) \right. \\ &- \tan^{-1} \left\{ \frac{Ld}{x(r_1^2 + L^2)^{1/2}} \right\} \\ &+ \tan^{-1} \left\{ \frac{Ld}{(x-b)(r_3^2 + L^2)^{1/2}} \right\} \left. \right] \end{aligned} \quad (3.49)$$

(d) Discussion of principal profiles. Principal profiles are shown in Figure 3.18. In Figure 3.18a, the

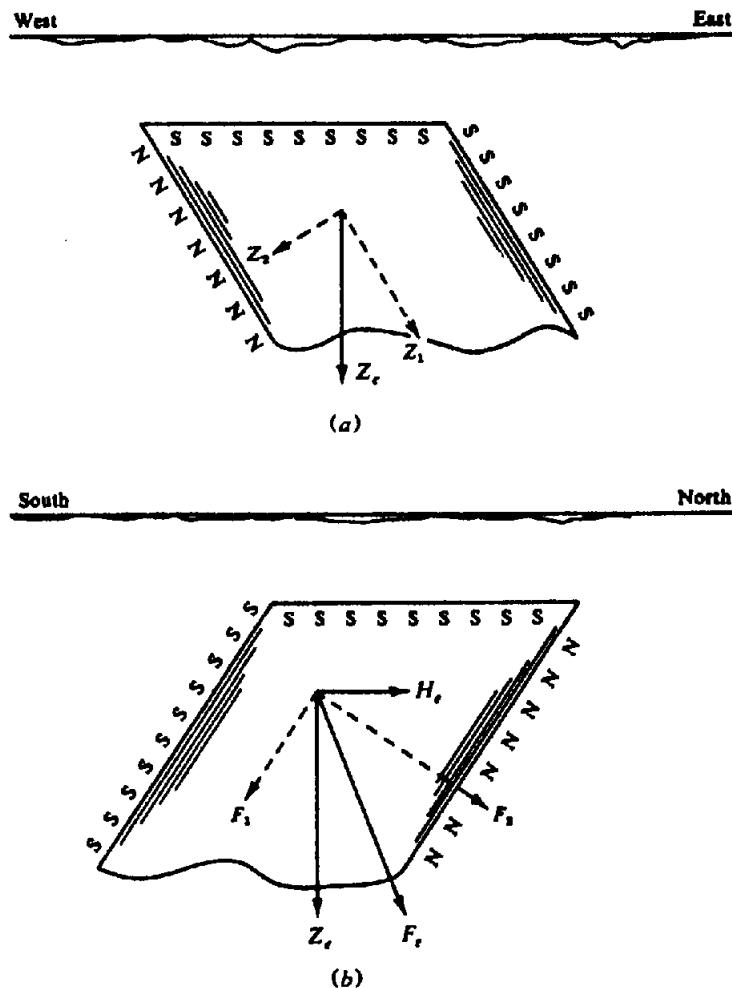


Figure 3.19. Pole distribution in a dike.

dike strikes NE-SW and dips  $45^\circ$  SE. In high magnetic latitudes where the  $H$  component is small, strike direction is relatively unimportant. This is clear from Equations (3.44a, c) where, if  $I \approx 90^\circ$ , the expressions for  $Z$  and  $F$  are practically independent of the strike direction  $\beta$ .

Figure 3.18b displays profiles for N-S strike. Figure 3.18c is for E-W strike. The asymmetry is less pronounced for north dips than for south dips. In high latitudes a dike with E-W strike and dip  $I$  gives a symmetrical  $Z$  profile and a nearly symmetrical  $F$  profile.

Figure 3.18d is for a vertical dike with NW or NE strike;  $Z$  and  $F$  profiles for  $L = \infty$  are similar because the vertical component of  $F$  predominates. Gay (1967) takes advantage of these similarities and obtains a single family of curves for  $F$ ,  $Z$ , and  $H$  over the whole range of dips and inclinations, defined by an index response parameter.

Figure 3.18d also shows the total field response over a short dike. The shape is similar to the other two curves but with lower amplitude. This profile is across the center of the dike and normal to the strike.

It is useful to provide a qualitative explanation for the character of the profiles in Figure 3.18 based on pole distribution where the magnetization is mainly induced by the Earth's field. For a dike dipping east and striking N-S as in Figure 3.19a,  $Z_e$  will produce N and S poles along the footwall and hanging wall, respectively, as can be seen by resolving  $Z_e$  into components parallel and normal to the dip. A similar explanation (Fig. 3.19b) accounts for the more pronounced asymmetry in the profile of the E-W dike dipping south in Figure 3.18c; the N poles on the footwall are produced by components of both  $H_e$  and  $Z_e$ . In fact, such a dike tends to be magnetized transversely because  $F_e$  is practically normal to the dip axis.

Depth estimates based on width of profiles are not particularly useful unless the profiles are symmetrical and the width is no greater than the depth to the top face. Under these restrictions the rule for half-width at half-maximum gives the depth to within 20%, that is,  $x_{1/2} \approx d$  at  $Z = Z_{\max}/2$ . Several techniques based on profile slopes are effective for depth determination for the dike model (§3.7.11b). Direction of dip is usually fairly obvious from the profiles

since we know the total-field direction. The situation is complicated, however, because we cannot determine in advance the presence and direction of remanent magnetism and we have difficulty in determining the zero line for a field profile, that is, in isolating a single anomaly. A solution to finding the zero line for the dike model is given in Section 3.7.8.

The dike profiles in Figure 3.18b, c, and d were simplified by assuming infinite depth extent ( $D = \infty$ ). They are not greatly changed for finite depth extent unless the depth extent is less than five times the width of the top face, in which case the positive tails are pulled down slightly. For very shallow dip, short strike length, and small depth extent (effectively a flat-lying plate magnetized transversely), the profiles becomes more symmetrical, with a broad maximum of small magnitude above the plate and negative tails at the flanks.

### 3.6.6. Dipping Sheet

The expressions for  $Z$  and  $F$  profiles over a thin sheet may be derived from Equation (3.44) by replacing the horizontal width  $b$  of the dipping dike model with  $t \csc \xi$ , where  $t$  is the thickness of the sheet. The principal reason for considering the thin sheet is that the expressions are simpler than for the dike and are sufficiently accurate provided the thickness  $t$  is not greater than the depth to the top  $d$ . The thin sheet geometry is also common in mineral exploration areas.

For the geometry shown in Figure 3.20a, the result is

$$\begin{aligned} Z = & 2ktF_e \left[ \left( \frac{1}{r_2} \right) \left\{ \cos I \sin \beta \sin(\xi + \theta_2) \right. \right. \\ & + \sin I \cos(\xi + \theta_2) \} \\ & - \left( \frac{1}{r_1} \right) \left\{ \cos I \sin \beta \sin(\xi + \theta_1) \right. \\ & \left. \left. + \sin I \cos(\xi + \theta_1) \right\} \right] \quad (3.50a) \end{aligned}$$

$$\begin{aligned} F = & 2ktF_e \left[ \left( \frac{1}{r_2} \right) \left\{ \sin 2I \sin \beta \sin(\xi + \theta_2) \right. \right. \\ & - (\cos^2 I \sin^2 \beta - \sin^2 I) \\ & \times \cos(\xi + \theta_2) \} \\ & - \left( \frac{1}{r_1} \right) \left\{ \sin 2I \sin \beta \sin(\xi + \theta_1) \right. \\ & \left. \left. - (\cos^2 I \sin^2 \beta - \sin^2 I) \right. \right. \\ & \times \cos(\xi + \theta_1) \} \right] \quad (3.50b) \end{aligned}$$

When the strike is E-W ( $\beta = 90^\circ$ ), Equations (3.50) become

$$\begin{aligned} Z = & 2ktF_e \left\{ \sin(\xi + I + \theta_2)/r_2 \right. \\ & - \sin(\xi + I + \theta_1)/r_1 \} \quad (3.51a) \end{aligned}$$

$$\begin{aligned} F = & -2ktF_e \left\{ \cos(\xi + 2I + \theta_2)/r_2 \right. \\ & - \cos(\xi + 2I + \theta_1)/r_1 \} \quad (3.51b) \end{aligned}$$

and when the strike is N-S ( $\beta = 0^\circ$ ),

$$Z = 2ktF_e \sin I \left\{ \cos(\xi + \theta_2)/r_2 - \cos(\xi + \theta_1)/r_1 \right\} \quad (3.52a)$$

$$\begin{aligned} F = & 2ktF_e \sin^2 I \left\{ \cos(\xi + \theta_2)/r_2 \right. \\ & - \cos(\xi + \theta_1)/r_1 \} \quad (3.52b) \end{aligned}$$

If the sheet is vertical,  $\xi = 90^\circ$  and Equations (3.50b), (3.51b), and (3.52b) simplify to

$$\begin{aligned} F = & 2ktF_e \left[ \left( \frac{1}{r_2} \right) \left\{ \sin 2I \sin \beta \cos \theta_2 \right. \right. \\ & + (\cos^2 I \sin^2 \beta - \sin^2 I) \sin \theta_2 \} \\ & - \left( \frac{1}{r_1} \right) \left\{ \sin 2I \sin \beta \cos \theta_1 \right. \\ & \left. \left. + (\cos^2 I \sin^2 \beta - \sin^2 I) \sin \theta_1 \right\} \right] \quad (3.53a) \end{aligned}$$

$$F = 2ktF_e \left\{ \sin(2I + \theta_2)/r_2 - \sin(2I + \theta_1)/r_1 \right\} \quad (3.53b)$$

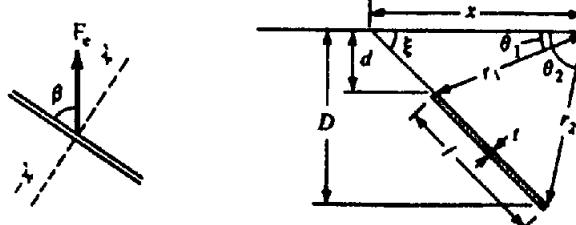
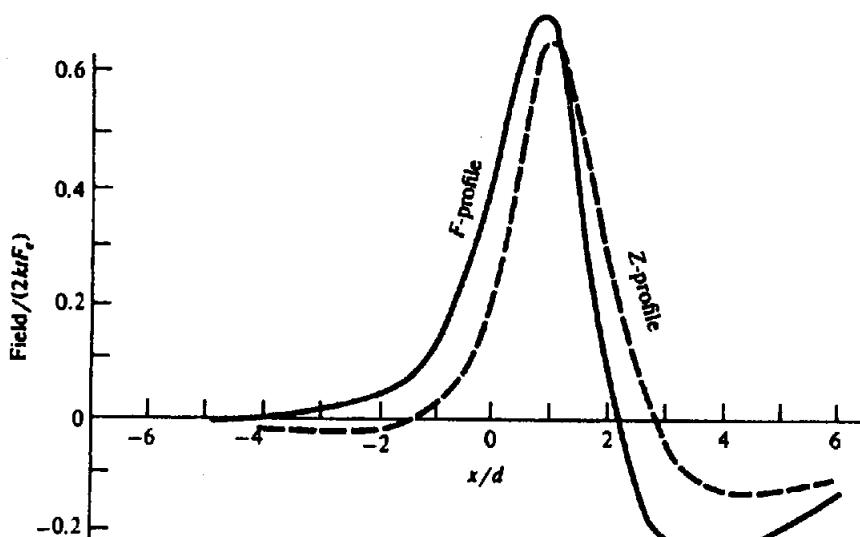
$$F = -2ktF_e \sin^2 I \left( \sin \theta_2/r_2 - \sin \theta_1/r_1 \right) \quad (3.53c)$$

The profiles in Figure 3.20 for  $I = 60^\circ$  are similar to, although sharper than, those for the dike. Rough dip estimates are possible when the strike of the body and total-field direction are known. Depth estimates from curve widths are fairly good when the curves are roughly symmetrical, but not practical when the sheet extends to great depth. The half-widths at  $Z_{\max}/2$  for the short vertical and dipping models give  $x_{1/2} \approx 1.7d$ .

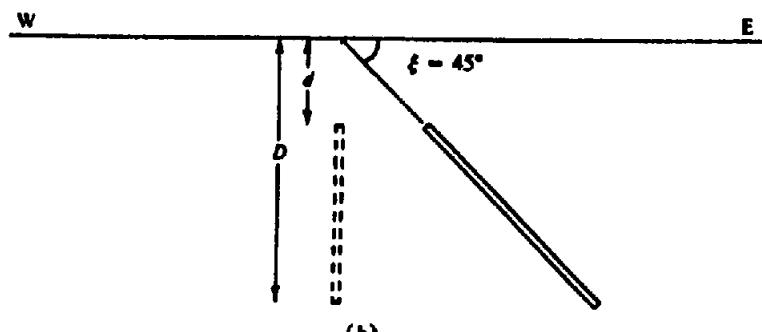
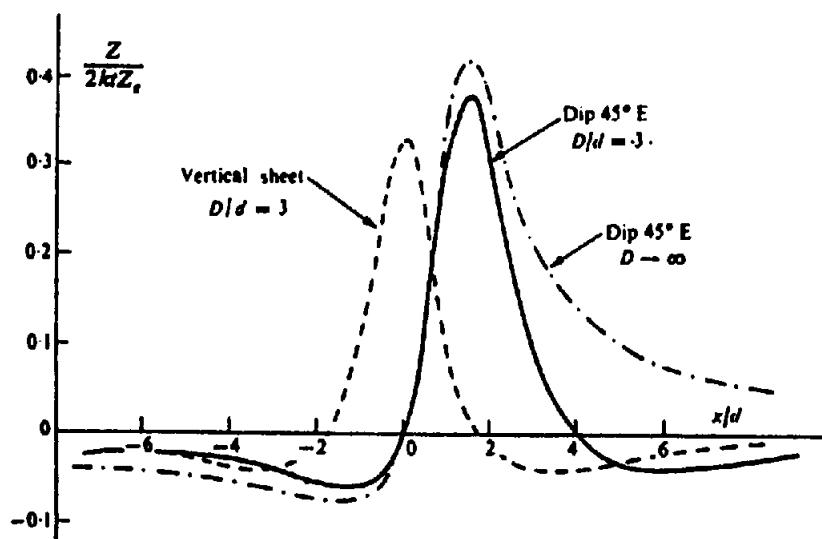
When the depth extent is very great,  $r_2 \approx \infty$  and the sheet is effectively a half-plane. Then for  $Z$  and  $F$  we have from Equations (3.50),

$$\begin{aligned} Z = & -(2ktF_e/r_1) \left\{ \cos I \sin \beta \sin(\xi + \theta_1) \right. \\ & + \sin I \cos(\xi + \theta_1) \} \quad (3.54a) \end{aligned}$$

$$\begin{aligned} F = & -(2ktF_e/r_1) \left\{ \sin 2I \sin \beta \sin(\xi + \theta_1) \right. \\ & - (\cos^2 I \sin^2 \beta - \sin^2 I) \cos(\xi + \theta_1) \} \quad (3.54b) \end{aligned}$$

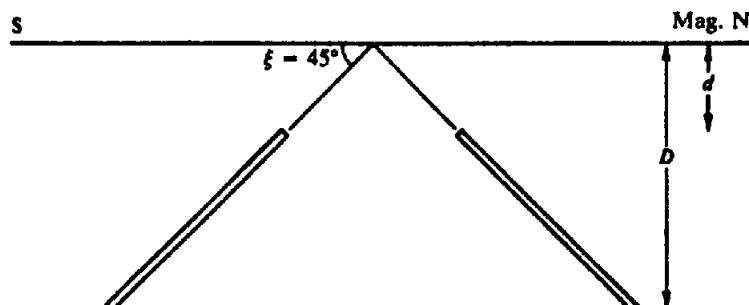
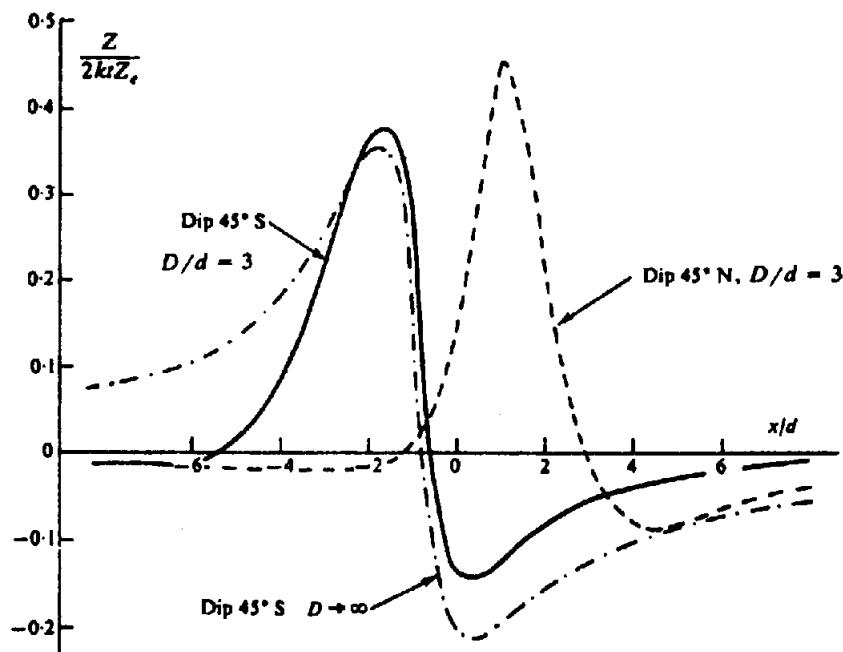


(a)



(b)

Figure 3.20. Thin sheet;  $I = 60^\circ$ ,  $D/d = 3$ . (a)  $F$ ,  $Z$  profiles for  $\xi = 45^\circ NE$ ,  $\beta = 60^\circ$ . (b)  $Z$  profiles for N-S strike ( $\beta = 0^\circ$ ),  $\xi = 45^\circ N$  and  $90^\circ$ , and effect of depth extent.



(c)

Figure 3.20. (Continued) (c) Z profiles for E-W strike,  $\xi = 45^\circ N$  and  $45^\circ S$ ,  $\beta = 90^\circ$ .

For this limiting case we can determine the depth and dip uniquely. Setting  $dZ/dx = dF/dx = 0$ , we obtain the  $x$  values for the maximum and minimum values for  $Z$  and  $F$ . This yields the following relations for  $Z$ :

$$x_m/d = 2(\cos^2 I \sin^2 \beta + \sin^2 I)^{1/2} / (\cos I \sin \beta \sin \xi + \sin I \cos \xi) \quad (3.55a)$$

$$x_{1/2}/d = \{\cos^2 I \sin^2 \beta + \sin^2 I\}^{1/2} / (\cos I \sin \beta \cos \xi + \sin I \sin \xi) \quad (3.55b)$$

where  $x_m = x_{\max} - x_{\min}$  and  $x_{1/2}$  is the full width at half-maximum. Likewise, writing  $x'_m$ ,  $x'_{1/2}$  for the

$F$  curve, we have

$$\begin{aligned} x'_m/d &= 2 \left\{ \sin^2 2I \sin^2 \beta + (\sin^2 I - \cos^2 I \sin^2 \beta)^2 \right\}^{1/2} / \{ \sin 2I \sin \beta \sin \xi + (\sin^2 I - \cos^2 I \sin^2 \beta) \cos \xi \} \quad (3.56a) \\ x'_{1/2}/d &= \left\{ \sin^2 2I \sin^2 \beta + (\sin^2 I - \cos^2 I \sin^2 \beta)^2 \right\}^{1/2} / \{ \sin 2I \sin \beta \cos \xi + (\sin^2 I - \cos^2 I \sin^2 \beta) \sin \xi \} \quad (3.56b) \end{aligned}$$

Combining Equations (3.55), we obtain the dip

angle  $\xi$ ,

$$\begin{aligned} \tan \xi = & (-2x_{1/2} \cos I \sin \beta + x_m \sin I) \\ & /(2x_{1/2} \sin I - x_m \cos I \sin \beta) \end{aligned} \quad (3.57a)$$

and the depth,

$$d = x_m x_{1/2} / (x_m^2 + 2x_{1/2}^2)^{1/2} \quad (3.57b)$$

When the sheet is not two dimensional, we can modify Equations (3.50) for a length  $2L$ . Then the principal profiles for  $Z$  and  $F$  become

$$Z = 2ktLF_e \{ (Q + R) \cos I \sin \beta + (S + T) \sin I \} \quad (3.58a)$$

$$F = 2ktLF_e \{ (Q + R) \sin 2I \sin \beta \\ - (S + T) (\cos^2 I \sin^2 \beta - \sin^2 I) \} \quad (3.58b)$$

where

$$\left. \begin{aligned} Q &= \sin(\xi + \theta_2) / \{ r_2(r_2^2 + L^2)^{1/2} \} \\ &\quad - \sin(\xi + \theta_1) / \{ r_1(r_1^2 + L^2)^{1/2} \} \\ R &= \{ x \sin^2 \xi \cos \xi / (x^2 \sin^2 \xi + L^2) \} \\ &\quad \times \{ \cot(\xi - \theta_2) / (r_2^2 + L^2)^{1/2} \\ &\quad - \cot(\xi - \theta_1) / (r_1^2 + L^2)^{1/2} \} \\ S &= \cos(\xi + \theta_2) / \{ r_2(r_2^2 + L^2)^{1/2} \} \\ &\quad - \cos(\xi + \theta_1) / \{ r_1(r_1^2 + L^2)^{1/2} \} \\ T &= \{ x \cos^2 \xi \sin \xi / (x^2 \sin^2 \xi + L^2) \} \\ &\quad \times \{ \cot(\xi - \theta_2) / (r_2^2 + L^2)^{1/2} \\ &\quad - \cot(\xi - \theta_1) / (r_1^2 + L^2)^{1/2} \} \end{aligned} \right\} \quad (3.58c)$$

The profile is reduced in magnitude but otherwise unchanged in shape.

### 3.6.7. Horizontal Sheet (Plate)

When the sheet is horizontal (see Fig. 3.21a),  $\xi = 0$ ,  $d$  becomes the depth of the sheet, and Equations (3.50) give

$$\begin{aligned} Z &= -2ktF_e \{ (1/r_1)(\cos I \sin \beta \sin \theta_1 + \sin I \cos \theta_1) \\ &\quad - (1/r_2)(\cos I \sin \beta \sin \theta_2 + \sin I \cos \theta_2) \} \end{aligned}$$

$$\begin{aligned} F &= -2ktF_e \{ (1/r_1) \{ \sin 2I \sin \beta \sin \theta_1 \\ &\quad - (\cos^2 I \sin^2 \beta - \sin^2 I) \cos \theta_1 \} \\ &\quad - (1/r_2) \{ \sin 2I \sin \beta \sin \theta_2 \\ &\quad - (\cos^2 I \sin^2 \beta - \sin^2 I) \cos \theta_2 \} \} \end{aligned}$$

where  $r_1^2 = x^2 + d^2$ ,  $r_2^2 = (x - l)^2 + d^2$ ,  $\sin \theta_1 =$

$d/r_1$ ,  $\cos \theta_1 = x/r_1$ ,  $\sin \theta_2 = d/r_2$ , and  $\cos \theta_2 = (x - l)/r_2$ . Eliminating  $\theta_1$  and  $\theta_2$ , we get

$$\begin{aligned} Z &= -2ktF_e \{ (1/r_1)^2 (d \cos I \sin \beta + x \sin I) \\ &\quad - (1/r_2)^2 (d \cos I \sin \beta + (x - l) \sin I) \} \end{aligned} \quad (3.59a)$$

$$\begin{aligned} F &= -2ktF_e \{ (1/r_1)^2 (d \sin 2I \sin \beta \\ &\quad - x(\cos^2 I \sin^2 \beta - \sin^2 I)) \\ &\quad - (1/r_2)^2 (d \sin 2I \sin \beta - (x - l) \\ &\quad \times (\cos^2 I \sin^2 \beta - \sin^2 I)) \} \end{aligned} \quad (3.59b)$$

Figure 3.21 shows profiles for horizontal plates. In Figure 3.21a, a shallow plate striking north-south produces a symmetrical  $Z$  profile. The  $F$  profile (not shown) is the same as the  $Z$  profile but reduced in magnitude by the multiplier  $\sin I$ . It is not possible to make good depth estimates from the width of these curves, but other techniques are available (see §3.7.8 and §3.7.11).

Over a horizontal thin sheet of finite strike length  $2L$ , Equation (3.59b) becomes

$$\begin{aligned} F &= -2ktF_e \{ (d \sin 2I \sin \beta \\ &\quad - x(\cos^2 I \sin^2 \beta - \sin^2 I)) \\ &\quad / r_1(1 + r_1^2/L^2)^{1/2} \\ &\quad - (d \sin 2I \sin \beta - (x - l) \\ &\quad \times (\cos^2 I \sin^2 \beta - \sin^2 I)) \\ &\quad / r_2(1 + r_2^2/L^2)^{1/2} \} \end{aligned} \quad (3.60)$$

Total-field profiles for the thin plate, illustrated in Figure 3.21b for infinite strike length and for  $2L = 4l$ , are remarkably similar. (This is also true for gravity profiles over a thin plate.) Unless  $L < l$ , the finite length does not affect the curve more than 20%.

Use of both the bottomless dike and the thin sheet models yields minimum and maximum depths, respectively, for  $d$ . Sharpness of the peak is characteristic of a shallow plate compared with the dike.

### 3.6.8. Semiinfinite Horizontal Sheet: Fault Approximation

If  $r_2$  (or  $r_1$ ) approaches infinity,  $l$  becomes very large and Equations (3.59) reduce to one term for a semi-infinite sheet. Profiles for vertical component and total field are illustrated in Figure 3.22. In Figure 3.22a, the strike is N-S with  $I = 60^\circ$ ; both curves

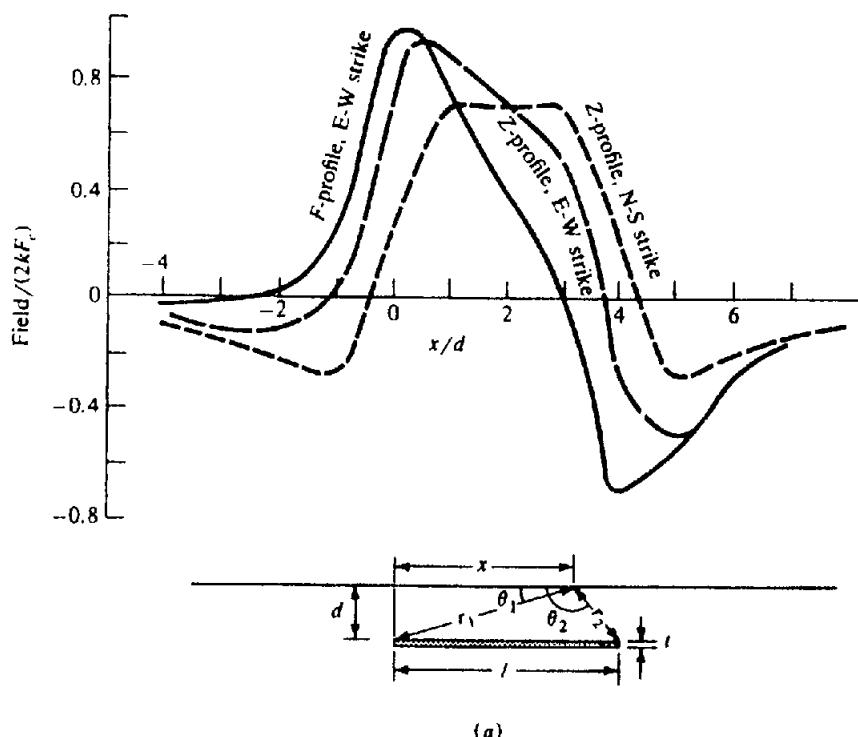


Figure 3.21. Thin horizontal plate of finite width,  $t/l = 0.125$ . (a) Profiles for  $I = 60^\circ$ ,  $\beta = 0^\circ$  and  $90^\circ$ ,  $d/l = 0.25$ .

are antisymmetrical. The response in Figure 3.22b is similar to those from targets with steep dip. Both E-W profiles provide good depth estimates;  $d$  equals half the horizontal distance between  $Z_{\max}$  and  $Z_{\min}$  (or  $F_{\max}$  and  $F_{\min}$ ). This measurement is 25% too large for the N-S profile (Fig. 3.22a).

It is necessary to traverse a considerable distance before the magnetic background is reached. For example, when  $d = 30$  m, the survey should extend at least 800 m either way from the edge of the sheet. In practical situations this often cannot be done because there are likely to be other magnetic features in the vicinity.

If we introduce another semiinfinite sheet at a different depth, as shown in Figure 3.23, we have an approximation to a fault. When the fault plane has dip  $\xi$ , Equations (3.59) give

$$\begin{aligned} Z = & -2ktF_e \left[ \left( 1/r_1^2 \right) \left( d \cos I \sin \beta \right. \right. \\ & + \left. \left. (x + d \cot \xi) \sin I \right) \right. \\ & - \left. \left( 1/r_2^2 \right) \left( D \cos I \sin \beta \right. \right. \\ & + \left. \left. (x + D \cot \xi) \sin I \right) \right] \quad (3.61a) \end{aligned}$$

$$\begin{aligned} F = & -2ktF_e \left[ \left( 1/r_1^2 \right) \left( d \sin 2I \sin \beta \right. \right. \\ & - \left. \left. (x + d \cot \xi) (\cos^2 I \sin^2 \beta - \sin^2 I) \right) \right. \\ & - \left. \left( 1/r_2^2 \right) \left( D \sin 2I \sin \beta \right. \right. \\ & - \left. \left. (x + D \cot \xi) (\cos^2 I \sin^2 \beta - \sin^2 I) \right) \right] \quad (3.61b) \end{aligned}$$

where

$$r_1^2 = d^2 + (x + d \cot \xi)^2$$

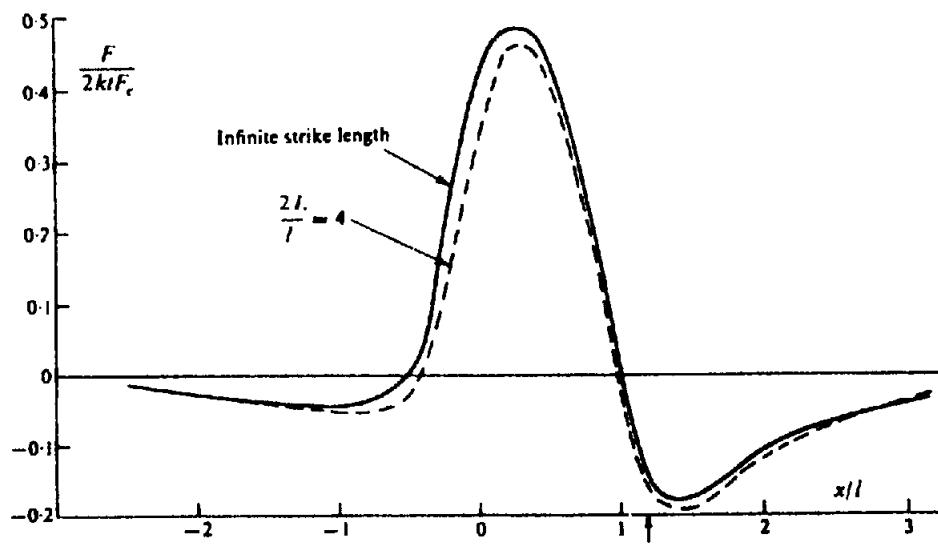
$$r_2^2 = D^2 + (x + D \cot \xi)^2$$

For a vertical fault,  $Z$  and  $F$  profiles are shown in Figure 3.23a. Responses from normal faults are similar to these examples regardless of strike, but a profile over a reverse fault reflects the concentration of anomalous material in the area of overlap and resembles the response of a steeply dipping target. An estimate of the depth to the upper bed can be made in terms of  $x_{1/2}$ , half the distance between  $Z_{\max}$  and  $Z_{\min}$ :  $0.5 \leq x_{1/2}/d \leq 1.25$ . The lower limit applies when the lower bed is only slightly displaced; the upper limit applies when  $D/d$  is large. When the fault-plane dip  $\xi$  is fairly steep,  $\xi \approx 90^\circ$  and  $D$  can be estimated from

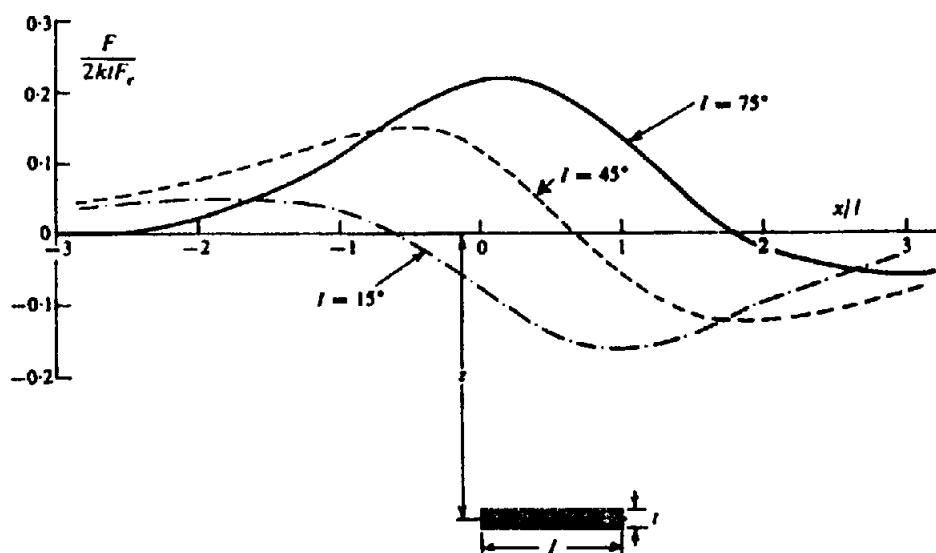
$$\begin{aligned} D \approx x_{1/2} & \left[ Z_m \left( 1 + x_{1/2}^2/d^2 \right) \right. \\ & / \left( 2x_{1/2} (dZ/dx)_{\max} \right. \\ & \left. \left. - Z_m \left( 1 + x_{1/2}^2/d^2 \right) \right) \right], \quad (3.62) \end{aligned}$$

where  $Z_m = Z_{\max} - Z_{\min}$  and  $(dZ/dx)_{\max}$  is the maximum slope.

The fault approximation in Equations (3.61) is accurate to within a few percent provided  $d$  is larger



(b)



(c)

Figure 3.21. (Continued) (b) Profiles for  $l = 75^\circ$ ,  $\beta = 45^\circ$ ,  $d/l = 0.5$ . (c) Profiles for  $l = 15^\circ$ ,  $\beta = 45^\circ$ ,  $d/l = 2$ .

than  $2t$ . When this assumption is not valid, it is necessary to use the dike model (§3.6.5). With  $r_3 = r_4 = \infty$  and  $\phi_3 = \phi_4 = \pi$ , the  $Z$  and  $F$  expressions for the horizontal slab are identical to Equations (3.44) to (3.48) with the terms in  $r_3$ ,  $r_4$ ,  $\phi_3$ , and  $\phi_4$  omitted (see Fig. 3.24). Figure 3.24 shows  $F$  profiles over a single horizontal bed with N-S strike and face angles of  $45^\circ$  and  $135^\circ$ . The curves are reflections of each other in both axes.

To simulate a fault, we add a similar slab at a different depth (as in Fig. 2.32), for example, for

E-W strike and strike length  $2L$ , we get

$$Z = 2kF_r \sin \xi [Q \ln(r_2r_7/r_1r_8) + R(\phi_1 - \phi_2 - \phi_7 + \phi_8)] \quad (3.63a)$$

$$F = 2kF_r \sin \xi [S \ln(r_2r_7/r_1r_8) + T(\phi_1 - \phi_2 - \phi_7 + \phi_8)] \quad (3.63b)$$

where  $Q$ ,  $R$ ,  $S$ , and  $T$  are as in Equations (3.58c). [Note that  $\xi$  in Eqs. (3.63) and in the factors  $Q$ ,  $R$ ,  $S$ , and  $T$  is the slope of the fault plane.]

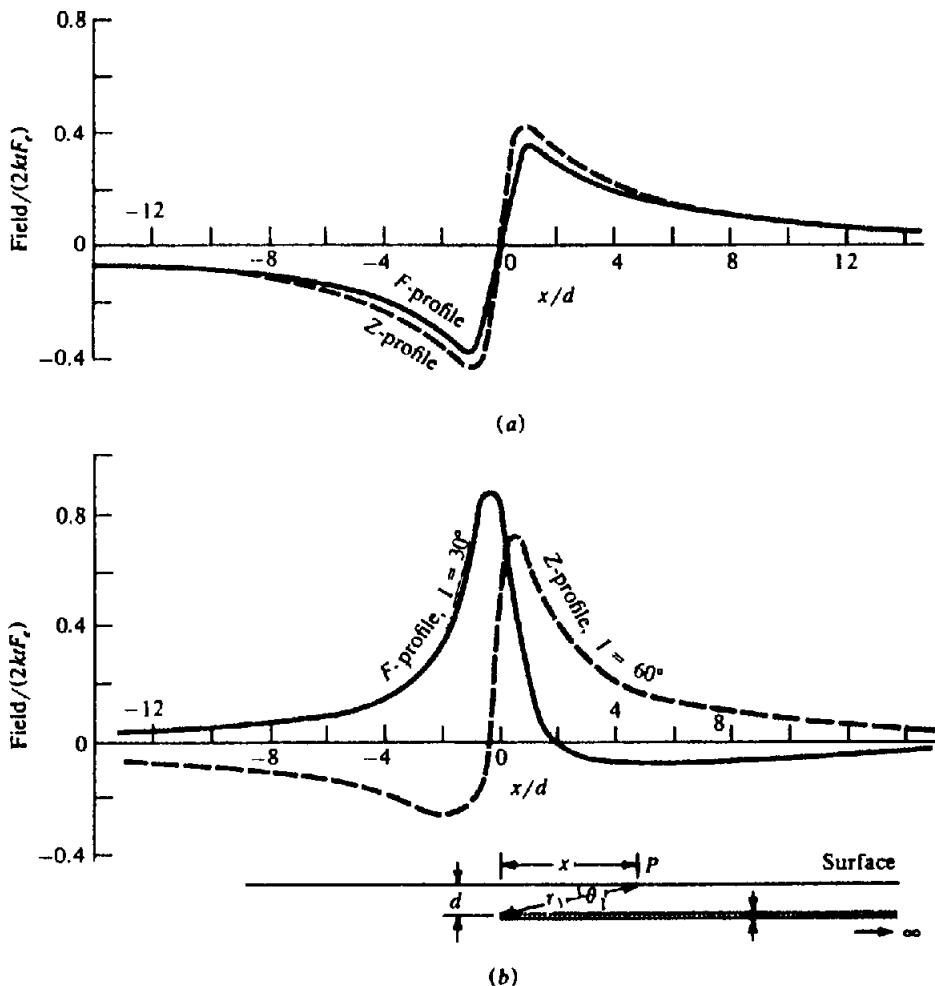


Figure 3.22. Semiinfinite horizontal sheet. F, Z profiles for (a) N-S strike,  $I = 60^\circ$ ; (b) E-W strike,  $I = 60$  and  $30^\circ$ .

### 3.6.9. Contact between Beds of Different Susceptibilities

A common magnetic structure results from the contact of two slabs with contrasting susceptibility values (see Fig. 3.25). Because a uniform continuous slab creates no magnetic anomaly, the effect of the contact is the same as that of the semiinfinite slab to the left with susceptibility  $\Delta k = k' - k$ . From Equation (3.44), we have

$$\begin{aligned} Z = 2 \Delta k F_e \sin \xi &\{ (\cos I \sin \xi \sin \beta \\ &+ \sin I \cos \xi) \ln(r_2/r_1) \\ &+ (\cos I \cos \xi \sin \beta \\ &- \sin I \sin \xi) (\phi_1 - \phi_2) \} \quad (3.64a) \end{aligned}$$

$$\begin{aligned} F = 2 \Delta k F_e &\{ \sin \xi \{ \sin 2I \sin \xi \sin \beta \\ &- \cos \xi (\cos^2 I \sin^2 \beta - \sin^2 I) \} \ln(r_2/r_1) \\ &+ (\sin 2I \cos \xi \sin \beta \\ &+ \sin \xi (\cos^2 I \sin^2 \beta - \sin^2 I)) (\phi_1 - \phi_2) \} \quad (3.64b) \end{aligned}$$

Figure 3.25 shows profiles over vertical and dipping contacts of considerable depth extent. When  $\phi_2 = \pi/2$ , Equation (3.64b) becomes, for a vertical contact striking N-S

$$\begin{aligned} F &= 2 \Delta k F_e \sin^2 I \{ \pi/2 - \tan^{-1}(d/x) \} \\ &= 2 \Delta k F_e \sin^2 I \tan^{-1}(x/d) \quad (3.65) \end{aligned}$$

The difference between the limiting value of  $F$  at  $x = \pm \infty$  is

$$\Delta F = F_{\max} - F_{\min} = 2\pi \Delta k F_e \sin^2 I$$

The maximum slope occurs over the contact and is given by  $(dF/dx)_{x=0} = 2 \Delta k F_e \sin^2 I / d$ . We can calculate the susceptibility contrast and depth of the bed:

$$\Delta k = \Delta F \sin^2 I / 2\pi F_e \quad \text{and} \quad d = \Delta F / \pi (dF/dx)_{x=0} \quad (3.66)$$

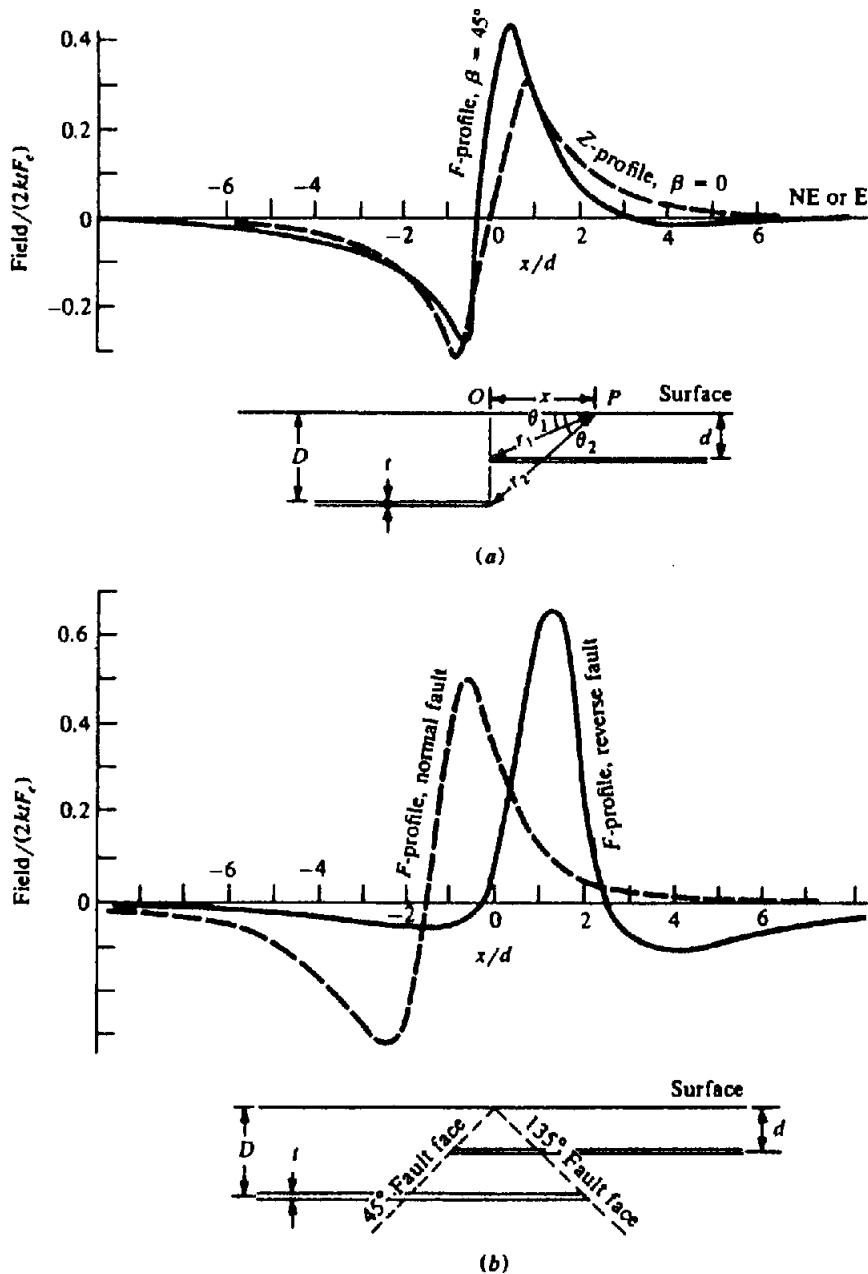


Figure 3.23. Thin-sheet fault approximation;  $D = 2d$ ,  $I = 60^\circ$ . (a)  $F$ ,  $Z$  profiles for vertical faults striking N-S and SE-NW ( $\beta = 0^\circ$ ,  $45^\circ$ ). (b)  $F$  profiles for normal and reverse faults striking E-W; fault dip  $45$ ,  $135^\circ$ .

This calculation is not simple in practice because long traverses are required to locate  $F_{\max}$  and  $F_{\min}$  and they are usually obscured by other anomalies.

The curve in Figure 3.25a for E-W strike is similar to profiles over dikes dipping east (Figures 3.18b and 3.20b) and it would be difficult to recognize that it represents a steeply dipping contact. In Figure 3.25b, a contact with a slant face produces a curve that gives some indication of the model. One curve (broken line) also resembles a dipping sheet; the other resembles a dipping dike.

A gradiometer profile of  $dF/dx$  defines the location of a vertical contact better than either  $Z$  or  $F$

profiles. The depth is equal to the separation of maximum and minimum values.

### 3.6.10. Demagnetization

In the preceding examples, we assumed that the induced magnetization is the product of  $k$ , the volume susceptibility of the body, and the external field  $\mathbf{F}_e$ . In fact this is true only for rod-like shapes magnetized along the axis and having a cross section small in comparison to their length, such as the dipole of Equations (3.37). In general, the resultant field inside the body is different from  $\mathbf{F}_e$ . This is

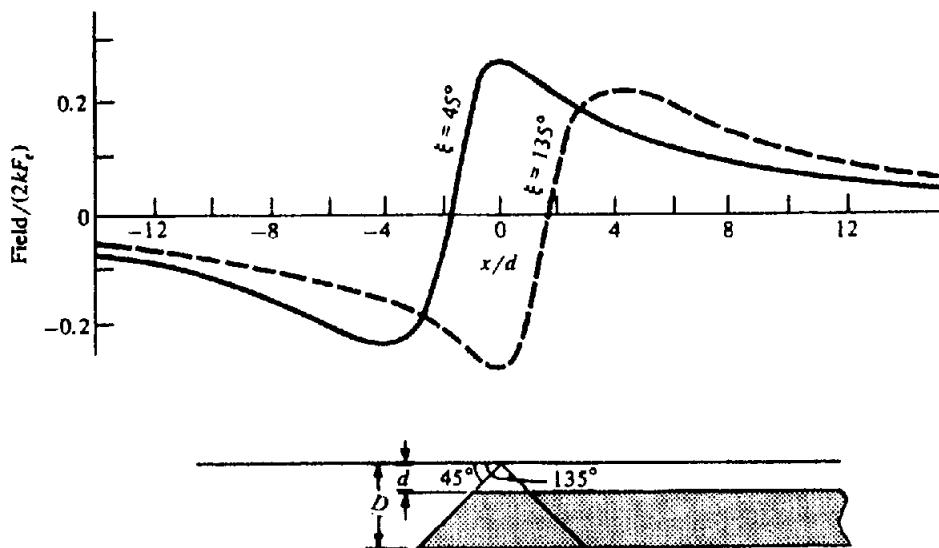
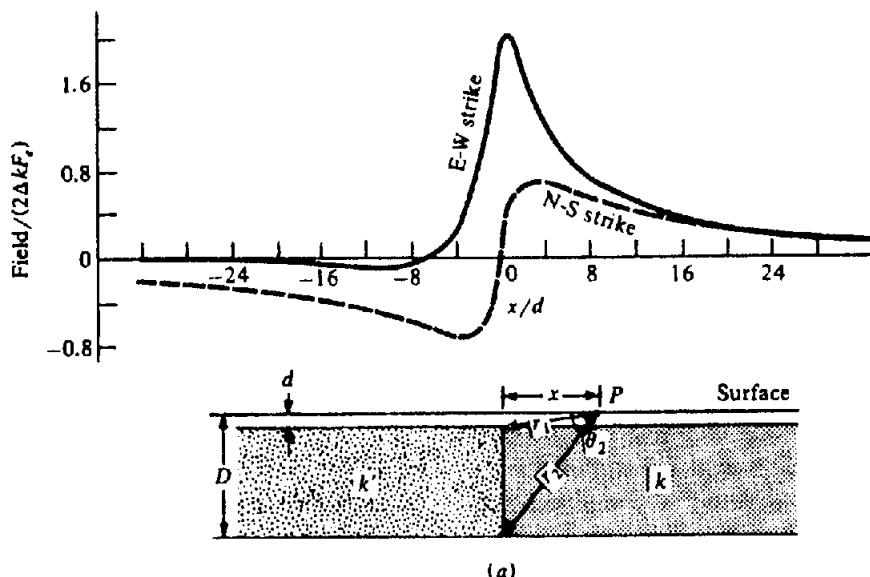
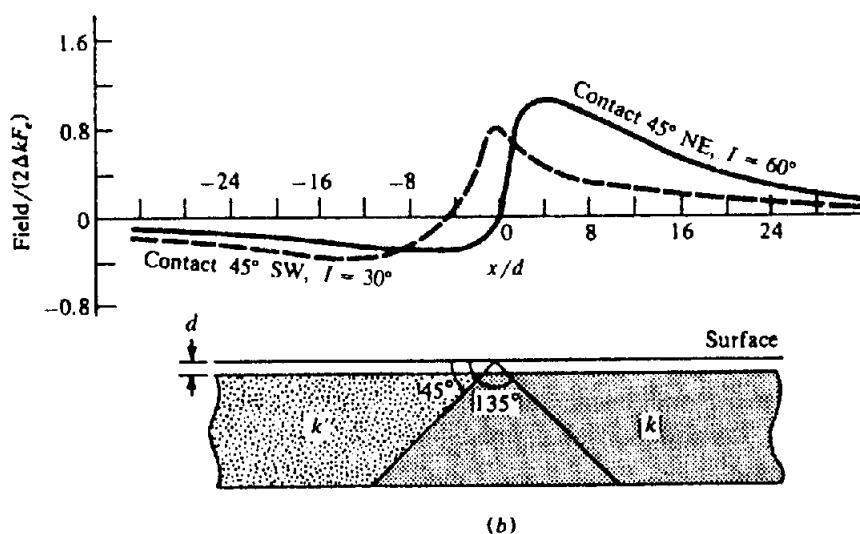


Figure 3.24.  $F$  profiles for a semi-infinite horizontal slab striking N-S.  $I = 45^\circ$ , dip of slab terminus 45 and  $135^\circ$ ,  $D = 3d$ .



(a)



(b)

Figure 3.25.  $F$  profiles for contact between two horizontal slabs of different susceptibilities;  $\Delta k = k - k'$ ,  $D = 10d$ . (a) Vertical contact ( $\xi = 90^\circ$ ),  $I = 60^\circ$ ,  $\beta = 0$  and  $90^\circ$ . (b) Sloping contact ( $\xi = 45^\circ$ ) for  $I = 30$  and  $60^\circ$ ,  $\beta = 45^\circ$ .

usually called *demagnetization*. The effect can be accommodated by replacing the susceptibility  $k$  by an *apparent susceptibility*  $k_a$ :

$$k_a = k/(1 + Nk) \quad 0 < N < 4\pi \quad (3.67)$$

Maximum demagnetization occurs in thin sheets magnetized normal to the face; in this case,  $N = 4\pi$ . For the sphere  $N = 4\pi/3$ . The effect is quite small unless  $k \geq 0.1$  SI units. Demagnetization is significant only in massive pyrrhotite and in rocks containing  $> 5\text{--}10\%$  magnetite. Sometimes an additional factor of  $(1 - \cos^2 D \cos^2 \Delta I)$  is included to allow for the resultant magnetization being in a different direction from  $\mathbf{I}$ ;  $\Delta I$  is the difference in inclination and  $D$  is the declination.

### 3.7. PROCESSING AND INTERPRETATION

#### 3.7.1. General

Magnetic survey results are displayed as a set of profiles or a magnetic contour map. In sedimentary areas there may be some similarity between magnetic and gravity maps, but in general magnetic anomalies are more numerous, more erratic, less persistent, and of larger magnitude than gravity anomalies. Consequently, regional-residual separation is much more complex. Considerable success has been achieved with bandpass, matching, and nonlinear filter operators. Downward continuation is not suitable in areas of complex shallow magnetics, characteristic of mineral exploration regions. It might be used for estimating the thickness of sediments in petroleum surveys, but it is not used much for this purpose. Instead, depths are determined by semiempirical depth rules or techniques like Werner deconvolution. Second-derivative analysis is useful in mineral prospecting to enhance small-scale features near the surface, whereas upward continuation may be used to suppress them. Upward continuation may also be used to reduce topographic effects in ground magnetic work. Equation (3.33) is a crude form of upward continuation.

Aeromagnetic data are often treated as follows:

1. Reduction of data to a uniform grid by one-dimensional interpolation perpendicular to flight direction.
2. Preprocessing, which might involve continuation, calculation of derivatives, extraction of the vertical component, and so forth.
3. Summation of several profiles to attenuate background noise.
4. Filtering and setting a threshold to locate anomalous areas.

5. Analyzing the profiles for the locations and orientations of anomalies.
6. Interpolating profiles normal to strike and centered on anomalies, for more detailed analysis.
7. Comparing profiles with curves developed from models.

Comparing field measurements with the results expected for simple models, such as discussed in Section 3.6, is done to determine the location, depth, size, shape, attitude, and, possibly, the susceptibility of the magnetic bodies responsible for the anomalies. Although simplified both geometrically and with regard to magnetization, matching curves (*parametric analysis*) with model curves provides reasonably rapid analysis and may be sufficient, especially where data are poor and/or incomplete.

Considerable effort has been expended to develop workable inversion procedures for magnetics, and, in spite of the nonunique nature of the problem, several effective algorithms have been developed, to which numerous references in the literature attest (Bhattacharyya, 1964; Hartman, Teskey, and Friedberg, 1971; Al-Chalabi, 1971; McGrath and Hood, 1973; Barnett, 1976; Teskey, 1980). Werner deconvolution (§3.7.10) is one such algorithm. The conventional starting point for magnetic data inversion might be a least-squares fit, ridge regression (Leite and Leao, 1985), and so on, as in Section 2.7.9, but magnetic inversion is more complex than gravity inversion because there are more variables.

#### 3.7.2. Crude Interpretation and Structural Aspects

Because of the erratic and complex character of magnetic maps, interpretation is often only qualitative. Indeed, interpretation is something of a fine art. An interpreter experienced in magnetics can usually see structure merely by looking at a magnetic map, much as one can visualize surface features from the contours of a topographic map. Frequently magnetic features are rather directly related to surface outcrops and a magnetic map may be a fair substitute for a surface geology map where surface features are obscured by alluvium. Often there is a connection between magnetism and topography, as well as with buried geologic structures, particularly in mineral exploration areas. A visual study of the magnetic maps can be fruitful for preliminary interpretation. In this regard, experience is essential. Remanent magnetization, however, can produce significant effects and lead to incorrect interpretation if overlooked.

In sedimentary regions, particularly where the basement depth exceeds 1,500 m, the magnetic con-

tours are normally smooth and variations are small, reflecting the basement rocks rather than near-surface features. The larger anomalies usually are caused by susceptibility variations rather than basement relief. Consequently, anomaly magnitude is not of much value in finding basement depth, and depth calculations are usually based upon anomaly shape measurements, especially sharpness.

Regions where igneous and metamorphic rocks predominate, like the Precambrian Canadian Shield and the Appalachians, usually exhibit complex magnetic variations. Deep features are frequently camouflaged by higher frequency magnetic effects originating nearer the surface. Techniques for separating deep and shallow anomalies are similar to those discussed for gravity features in Section 2.6.

Magnetic anomalies often lie in trends. From a study of aeromagnetic maps of primarily sedimentary areas in western and central North America and Venezuela, Affleck (1963) found that the dominant direction within single magnetic-tectonic provinces is usually NE-SW or NW-SE and the trend normally terminates at the province boundaries. Moderate to weak features trending E-W or N-S often are superimposed on these. These weaker trends frequently extend across province boundaries and are probably of more recent origin. A cursory study of the Canadian Appalachian region (the Maritime provinces and eastern Quebec south of the St. Lawrence) and northern Saskatchewan and Alberta appears to confirm the trends. Large-scale northeast trends are obvious on the east and west flanks of the Canadian Shield.

### 3.7.3. Data Processing Operations: The Fourier Transform

As with gravity and seismic data processing, mathematical operations, such as convolution and correlation, can accomplish filtering, residualizing, continuation, and so on. Operations can be performed in the spatial, or wavenumber, domain (often called the frequency domain because wavenumber is spatial frequency). Fourier transforms (§A.9) are particularly useful in magnetics for (i) resolution of specific anomalies by downward or upward continuation, (ii) changing the effective field inclination (reduction to the pole) or conversion of total-field data to vertical-component data, (iii) calculation of derivatives, (iv) general filtering – separating anomalies caused by sources of different size and depth, and (v) modeling (Bhattacharyya and Navolio 1976). For literature on transformations of potential field data, see Dean (1958), Bhattacharyya (1965, 1966), Gunn (1975), and Spector and Grant (1985).

We usually write relations using two-dimensional Fourier transforms  $f(x, y) \leftrightarrow F(u, v)$  (Eq. (A.57)) in the form

$$f(x, y) = (1/2\pi)^2 \int \int F(u, v) e^{j2\pi(ux+vy)} du dv \quad (3.68a)$$

$$F(u, v) = \int \int f(x, y) e^{-j2\pi(ux+vy)} dx dy \quad (3.68b)$$

$(x, y)$  are spatial coordinates and  $(u, v)$  are wave-number coordinates.

The important characteristic of transformations is that information is not lost in the process, and in many cases operations are easier to perform in the transform domain. For example, the output-input expression  $g(x, y) \rightarrow f(x, y) * w(x, y)$  for convolution in the spatial domain is (§A.10)

$$g(x, y) = \int \int f(x - \alpha, y - \beta) w(\alpha, \beta) d\alpha d\beta \quad (3.69a)$$

where  $w(\alpha, \beta)$  is the convolution operator (also called a *weighting function* or *filter*). In the wave-number domain, this becomes simple multiplication:

$$G(u, v) = F(u, v) W(u, v) \quad (3.69b)$$

The relations between sources and their potential fields may be considered convolution operations, and transforms can be used to determine source characteristics from field operations, as discussed in the following sections.

### 3.7.4. Derivatives

Derivatives tend to sharpen the edges of anomalies and enhance shallow features. First and second vertical derivative maps are the most common ones made. Derivative maps may be made by the same techniques used for gravity data (§2.6.5). The first vertical derivative is also measured in gradiometer surveys.

### 3.7.5. Continuation

Field continuation was discussed in Section 2.6.7 as it applies to gravity. Adapting Equation (2.48) to magnetics, we have, for upward continuation (where  $z$  is positive downward),

$$F(x', y', -h) = \frac{h}{2\pi} \int \int \frac{F(x, y, 0) dx dy}{\{(x - x')^2 + (y - y')^2 + h^2\}^{1/2}} \quad (3.70)$$

Table 3.2. Coefficients for upward continuation.

$i$	$r_i$	$K(r_i, 1)$	$K(r_i, 2)$	$K(r_i, 3)$	$K(r_i, 4)$	$K(r_i, 5)$
0	0	0.11193	0.04034	0.01961	0.01141	0.00742
1	1	0.32193	0.12988	0.06592	0.03908	0.02566
2	$\sqrt{2}$	0.06062	0.07588	0.05260	0.03566	0.02509
3	$\sqrt{5}$	0.15206	0.14559	0.10563	0.07450	0.05377
4	$\sqrt{8}$	0.05335	0.07651	0.07146	0.05841	0.04611
5	$\sqrt{13}$	0.06586	0.09902	0.10226	0.09173	0.07784
6	$\sqrt{5}$	0.06650	0.11100	0.12921	0.12915	0.11986
7	$\sqrt{50}$	0.05635	0.10351	0.13635	0.15474	0.16159
8	$\sqrt{136}$	0.03855	0.07379	0.10322	0.12565	0.14106
9	$\sqrt{274}$	0.02273	0.04464	0.06500	0.08323	0.09897
10	25	0.03015	0.05998	0.08917	0.11744	0.14458

The left side is the total field at the point  $P(x', y', -h)$  above the surface on which  $F(x, y, 0)$  is known. The calculation procedure is to replace the integral with a weighted sum of values taken on a regular grid.

The empirical formula of Henderson (1960) gives the field at the elevation  $h$  above the surface in terms of values  $F(r_i)$ , the average value  $\bar{F}(r_i)$  over a circle of radius  $r_i$  centered at the point  $(x, y, 0)$ :

$$F(x, y, -h) = \sum \bar{F}(r_i) K(r_i, -h) \quad (3.71)$$

where  $K(r_i, -h)$  are weighting coefficients (listed in Table 3.2 for  $h = 1$  to 5). These coefficients give the upward continued field within 2%.

Another solution for continuation (in either direction) is by means of a Maclaurin expansion [Eq. (A.40)]:

$$\begin{aligned} F(x, y, h) &= F(x, y, 0) + h \partial F(x, y, 0) / \partial z \\ &\quad + (h^2/2!) \partial^2 F(x, y, 0) / \partial z^2 \\ &\quad + (h^3/3!) \partial^3 F(x, y, 0) / \partial z^3 + \dots \end{aligned} \quad (3.72)$$

[compare with Eq. (3.33)]. For a first approximation, the first two terms involving  $F$  and  $\partial F / \partial z$  are often sufficient, and the simultaneous measurement of total field and vertical gradient provides these values. The  $\partial^2 F / \partial z^2$  term can be found from maps of  $F$ , as indicated in Section 2.6.5, and, if necessary, the  $\partial^3 F / \partial z^3$  term can be found in a similar manner from maps of  $\partial F / \partial z$ .

The Fourier transform provides another technique for field continuation. The integrand in Equation (3.70) is the product of  $F(x, y, 0)$  and  $(h/2\pi)\{(x - x')^2 + (y - y')^2 + h^2\}^{-3/2}$ . Using the symmetry theorem [Eq. (A.60)] and the convolution theorem [Eq. (A.67a)], we get

$$\begin{aligned} X(t) Y(t) &\leftrightarrow 2\pi x(-\omega) * y(-\omega) \\ &= 2\pi x(\omega) * y(\omega) \end{aligned}$$

Thus, applying this result and Equation (A.62), we obtain for the transform of Equation (3.70),

$$\mathcal{F}_h(u, v) = (-2\pi/uv) \mathcal{F}_0(u, v) * \mathcal{W}(u, v) \quad (3.73)$$

where  $\mathcal{F}_h(u, v) \leftrightarrow F(x', y', -h)$ ,  $\mathcal{F}_0(u, v) \leftrightarrow F(x, y, 0)$ , and  $\mathcal{W}(u, v) \leftrightarrow w(x, y) = (h/2\pi)(x^2 + y^2 + h^2)^{-3/2}$ .

The continuation filter is

$$\begin{aligned} \mathcal{W}(u, v) &= (h/2\pi) \int \int (x^2 + y^2 + h^2)^{-3/2} \\ &\quad \times e^{-j2\pi(ux+vy)} dx dy \\ &= (h/2\pi) e^{-2\pi h(u^2 + v^2)^{1/2}} \end{aligned} \quad (3.74)$$

For upward continuation, we know  $F_0(x, y, 0)$  and the unknown is  $F_h(x, y, -h)$ , whose transform is

$$\begin{aligned} \mathcal{F}_h(u, v) &= \mathcal{F}_0(u, v)(h/2\pi) \\ &\quad \times \exp\{-2\pi h(u^2 + v^2)^{1/2}\} \end{aligned} \quad (3.75)$$

Thus the calculation of  $\mathcal{F}_h(u, v)$  is straightforward.

Hanson and Miyazaki (1984) use a continuation method that is effective where surface relief is large and rocks are highly magnetic. As in gravity, upward continuation smooths the data, whereas downward continuation emphasizes high frequencies.

### 3.7.6. Spectral Analysis

The Fourier transform expresses a magnetic field as an integral of sine and/or cosine waves, each defining a wave of amplitude  $A(\kappa)$  and phase  $\phi(\kappa)$ , where  $\kappa/2\pi = 1/\lambda$  is the wavenumber. Plotting  $A(\kappa)$  gives the amplitude spectrum and  $A^2(\kappa)$  gives the power spectrum.

The expression for the field of an anomalous body often can be written as the product of three functions in the wavenumber domain (their convolution in the spatial domain):

- (i)  $f_a$ , amplitude factor, which is equal to  $(4\pi M)^2$ , where  $M$  is the magnetic moment/unit volume.
- (ii)  $f_h$ , the depth factor,  $\exp\{-2h(u^2 + v^2)^{1/2}\}$ , where  $h$  is the pole depth.
- (iii)  $f_\beta$ , the field-orientation factor,  $\{l \cos \beta + m \sin \beta\}^2 + n^2 = (lu + mv)^2/(u^2 + v^2) + n^2$ , where  $\beta$  is the angle between the body's orientation and magnetic north and  $l$ ,  $m$ , and  $n$  are the direction cosines of the field  $\mathbf{F}_e$ .

For bodies that are large compared to their depth, we require two additional factors:

- (iv) The size factor: for a rectangular prism,  $(\sin ua \sin vb)/(ua vb)^2$ , where  $2a$  and  $2b$  are the prism dimensions.
- (v) The polarization-orientation factor involving the direction cosines of the polarization vector.

We thus write the field of a point pole or dipole in terms of factors (i) to (iii) as

$$F(x, y, 0) = f_a(x, y) * f_h(x, y, h) * f_\beta(x, y) \quad (3.76a)$$

or, in the wavenumber domain,

$$\mathcal{F}(u, v, 0) = \mathcal{F}_a(u, v) \mathcal{F}_h(u, v, h) \mathcal{F}_\beta(u, v) \quad (3.76b)$$

The effect of any of these factors may be removed by deconvolving in the space domain or by dividing in the wavenumber domain.

Numerous other filter operations can be used to separate deep from shallow, large from small, and three-dimensional from two-dimensional effects. Gunn (1975) discusses a solution for the magnetized rectangular prism. Hahn, Kind, and Mishra (1976) estimate depth from Fourier spectra.

### 3.7.7. Reduction to the Pole

This operation changes the actual inclination to the vertical. It can be performed (Baranov, 1957; Spector and Grant, 1985) by convolving the magnetic field with a filter whose wavenumber response is the product of a polarization-orientation factor and the field-orientation factor in items (v) and (iii) of Section 3.7.6. This transformation simplifies total-field maps and is a relatively easy operation at high magnetic latitudes where  $Z \approx F$ , but becomes more difficult near the magnetic equator (Silva, 1986).

### 3.7.8. Use of Master Curves for Dikes of Great Depth Extent

It is often difficult to establish a background or datum level for magnetic measurements and to locate a dike with respect to the profile. Hence, matching field results with profiles obtained from simple shapes can be difficult. An analysis (Koulomzine, Lamontagne, and Nadeau, 1970) for prisms and dikes of infinite depth extent solves this problem with master (or characteristic) curves that give depth, dip, and width of a prism or dike.

We rewrite Equation (3.44a) making the width  $2b$  instead of  $b$  (Fig. 3.18a) and shifting the origin to a

point above the midpoint of the top of the dike. If we assume infinite depth extent so that  $r_2 = r_4 = \infty$ ,  $\phi_2 = \phi_4$ , we have

$$\begin{aligned} Z = 2kF_e \sin \xi &\{ (\cos I \sin \xi \sin \beta \\ &+ \sin I \cos \xi) \ln(r_3/r_1) \\ &+ (\cos I \cos \xi \sin \beta \\ &- \sin I \sin \xi)(\phi_1 - \phi_3) \} \end{aligned}$$

where  $r_1^2 = d^2 + (x + b)^2$ ,  $r_3^2 = d^2 + (x - b)^2$ ,  $\phi_1 = \cot^{-1}(x + b)/d$ , and  $\phi_3 = \cot^{-1}(x - b)/d$ . Dividing by  $d$  to obtain the dimensionless parameters  $X = x/d$  and  $B = b/d$ , we obtain

$$\begin{aligned} Z = M &\{ \cot^{-1}(X + B) - \cot^{-1}(X - B) \} \\ &+ (N/2) \ln \left[ \left\{ (X - B)^2 + 1 \right\} \right. \\ &\left. / \left\{ (X + B)^2 + 1 \right\} \right] \quad (3.77) \end{aligned}$$

where

$$M = 2kF_e \sin \xi \{ (\cos I \sin \beta \cos \xi - \sin I \sin \xi) \}$$

and

$$N/2 = 2kF_e \sin \xi \{ (\cos I \sin \beta \sin \xi + \sin I \cos \xi) \}$$

The first term is the symmetric component  $S$  and the second term is the antisymmetric component  $A$ . Over the center of the dike,  $S$  has a maximum and  $A = 0$ .

If we chose two conjugate points  $X_1$  and  $X_2$  on the dike profile such that the sum of the  $Z$  values is equal to  $Z_0$ , the value of  $Z$  at  $X = 0$ , that is,

$$Z_1 + Z_2 = Z_0 \quad (3.78)$$

Then, because

$$(S_1 + A_1) + (S_2 + A_2) = (S_0 + A_0) = S_0$$

we have

$$S_1 + S_2 = S_0 = Z_0 \quad A_1 + A_2 = 0 \quad (3.79)$$

For the antisymmetric component,

$$\begin{aligned} \ln \left[ \left\{ (X_1 - B)^2 + 1 \right\} / \left\{ (X_1 + B)^2 + 1 \right\} \right] \\ + \ln \left[ \left\{ (X_2 - B)^2 + 1 \right\} \right. \\ \left. / \left\{ (X_2 + B)^2 + 1 \right\} \right] = 0 \\ \{ (X_1 - B)^2 + 1 \} \{ (X_2 - B)^2 + 1 \} \\ = \{ (X_1 + B)^2 + 1 \} \{ (X_2 + B)^2 + 1 \} \end{aligned}$$

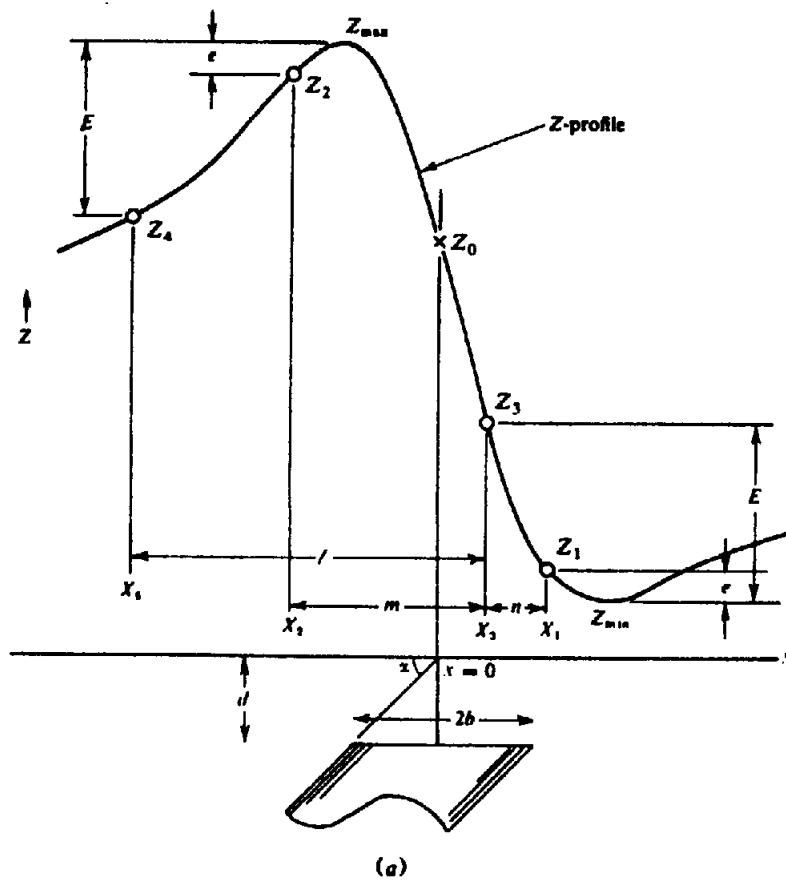


Figure 3.26. Two-dimensional dike of infinite depth extent. (a) Location of conjugate points and  $X = 0$ .

Solving for  $X_1 X_2$ , this gives

$$X_1 X_2 = -(1 + B^2) \quad (3.80)$$

Initially we do not know either the location of the dike center,  $X = x = 0$ , or the datum level  $Z = 0$ . Two pairs of conjugate points,  $X_1, X_2$  and  $X_3, X_4$ , are chosen such that Equation (3.78) is satisfied, and, in addition,  $Z_{\max} - Z_2 = Z_1 - Z_{\min} = e$  and  $Z_{\max} - Z_4 = Z_3 - Z_{\min} = E$  (Fig. 3.26a). Writing  $l = X_3 - X_4$ ,  $m = X_3 - X_2$ ,  $n = X_1 - X_3$ , and using the relation  $X_1 X_2 = X_3 X_4$  [Eq. (3.74)], we find that

$$\left. \begin{aligned} X_1 &= n(n+l)/(l-m+n) \\ X_2 &= -m(l-m)/(l-m+n) \\ X_3 &= mn/(l-m+n) \\ X_4 &= (m-l)(n+l)/(l-m+n) \end{aligned} \right\} \quad (3.81)$$

We can now locate the point  $X = 0$  and get  $Z_0$ . For the best accuracy,  $X_3$  and  $X_4$  should be located close to the midpoint of the anomaly, and  $X_1$  and  $X_2$  near the maximum and minimum.  $Z(0)$  is the point on the profile located a horizontal distance  $X_3$  from  $Z_3$ ,  $X_2$  from  $Z_2$ , and so forth. Thus the datum line  $Z = 0$  can be drawn at a distance above  $Z_{\min}$  equal to the vertical distance between  $Z_{\max}$  and  $Z_0$ . This

follows from Equation (3.78) if we put  $Z_1 = Z_{\max}$  and  $Z_2 = Z_{\min}$ , that is,  $-Z_{\min} = Z_{\max} - Z_0$ .

The analysis may now be carried further to establish the dike parameters. First, from the definitions of symmetric and antisymmetric functions,

$$\text{and } \left. \begin{aligned} S(X) &= (1/2)\{Z(X) + Z(-X)\} \\ A(X) &= (1/2)\{Z(X) - Z(-X)\} \end{aligned} \right\} \quad (3.82)$$

we can plot  $S(X)$  and  $A(X)$  by taking points that are equidistant either side of  $X = 0$ . On these profiles we mark points  $S_{3/4}$ ,  $S_{1/2}$ , and  $A_{1/2}$  with corresponding abscissae  $X_{3/4}$ ,  $X_{1/2}$ , and  $X_{e/2}$ ; also  $X_e$  (Fig. 3.26b). By a development similar to that used for Equation (3.81), it can be shown that

$$\left. \begin{aligned} d &= x_{1/2}(\phi^2 - 1)/2 = 2x_{1/2}D \\ 2b &= x_{1/2}\{4 - (\phi^2 - 1)^2\}^{1/2} = 2x_{1/2}W \\ d &= x_e(1 - \mu)^2/2\mu = 2x_e\mathcal{D} \\ 2b &= x_e\{4\mu^2 - (1 - \mu)^4\}^{1/2}/\mu = 2x_e\mathcal{W} \end{aligned} \right\} \quad (3.83)$$

where  $\phi = x_{1/2}/x_{3/4}$ ,  $\mu = x_e/x_{e/2}$ ,  $D = (\phi^2 - 1)/4$ ,  $\mathcal{D} = (1 - \mu)^2/4\mu$ ,  $W = \{4 - (\phi^2 - 1)^2\}^{1/2}/2$ ,  $\mathcal{W} = (1/2\mu)\{4\mu^2 - (1 - \mu)^4\}^{1/2}$ ,  $x_{1/2} = X_{1/2}d$ , and so forth. Finally, we can find the dip angle  $\xi$

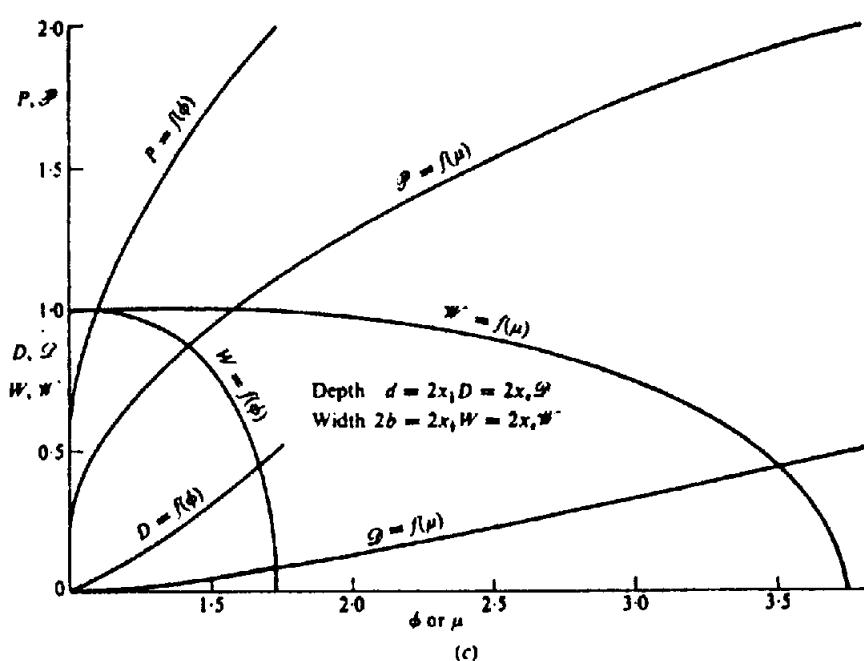
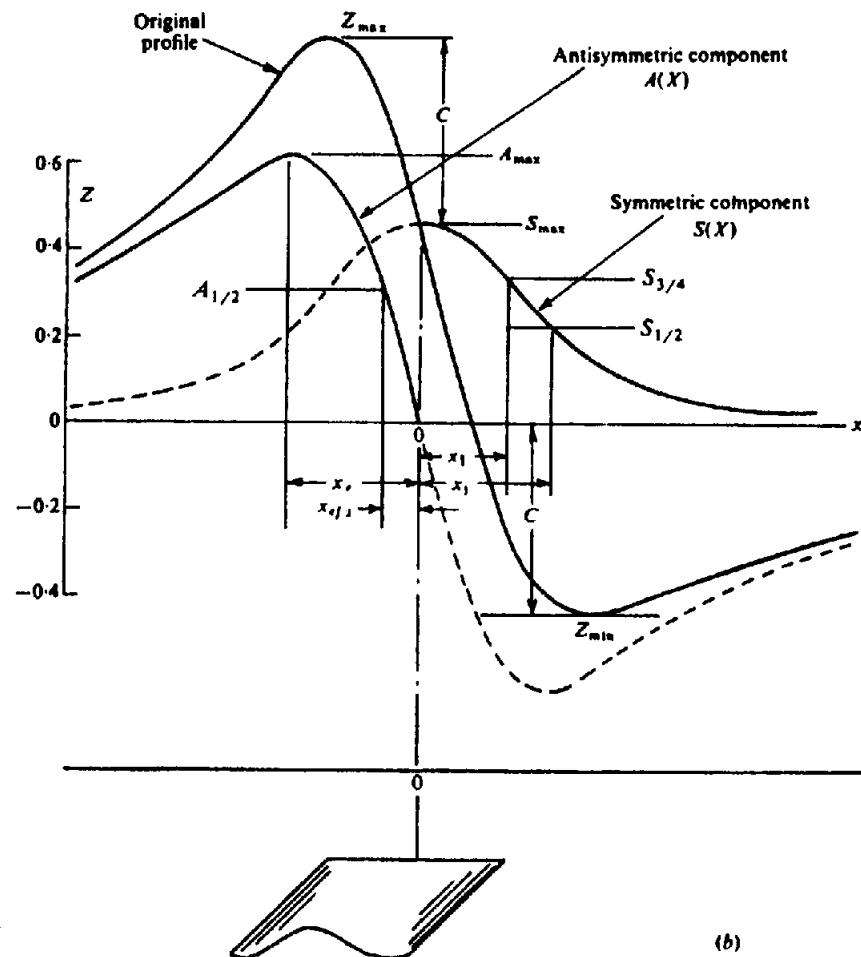


Figure 3.26. (Continued) (b) Symmetric and antisymmetric components. (c) Master curves.

from the relation

$$\xi = \pi - \cot^{-1} \left( \frac{H_e \sin \beta}{Z_e} \right) + \tan^{-1} \left\{ \frac{A(X)_{\max}}{S(X)_{\max}} \cdot \frac{4 \tan^{-1} B}{\ln \{ (x_e - B)/(x_e + B) \}} \right\} \quad (3.84a)$$

or

$$\xi = \pi - \cot^{-1} \left( \frac{H_e \sin \beta}{Z_e} \right) + \tan^{-1} \left\{ \frac{A(X)_{\max}}{S(X)_{\max}} \cdot \frac{4 \tan^{-1} B}{\ln \{ (x_{1/2} - B)/(x_{1/2} + B) \}} \right\}. \quad (3.84b)$$

Six master curves involving functions of  $d$ ,  $b$ , and  $\xi$  for the symmetric and antisymmetric components of the dike profile are shown in Figure 3.26c. The dip-angle functions  $P$  and  $\mathcal{P}$  in Figure 3.26 are related to known quantities in the following expansions of Equation (3.84):

$$\xi = \{ \pi - \cot^{-1}(H_e \sin \beta / Z_e) \} - \tan^{-1}(\mathcal{E}P) \text{ or } \tan^{-1}(\mathcal{E}\mathcal{P}), \quad (3.85a)$$

where  $\mathcal{E} = A(X)_{\max} / S(X)_{\max}$ ,

$$P = \frac{4 \tan^{-1}(W/2D)}{\ln \{ (1 - W)/(1 + W) \}} \quad (3.85b)$$

$$\mathcal{P} = \frac{4 \tan^{-1}(\mathcal{W}/2\mathcal{D})}{\ln \{ (1 - \mathcal{W})/(1 + \mathcal{W}) \}}$$

Because Equation (3.83) gives  $W$ ,  $D$ ,  $\mathcal{W}$ , and  $\mathcal{D}$  in terms of  $\phi$  and  $\mu$ , and these in turn can be found from the curves,  $P$  and  $\mathcal{P}$  are fully determined.

We can solve for the total-field anomaly in similar fashion. The analysis for the dike of infinite depth extent has been extended to cover a prism of finite length and depth extent. Because of the extra terms, it is necessary to provide more master curves, but the procedure is similar. Master curves for other models are also available (Grant and Martin, 1966; Martin, 1966; Gay, 1967). The second reference contains the following models, in addition to the prism: horizontal slab, plate, rod, and dipping sheet. (The method can be extended to dikes or prisms in gravity interpretation.)

### 3.7.9. Matched Filtering

Where the problem is locating a signal in a data set, matched filtering provides a powerful method if the

spectrum of the sought-for signal is known. A *matched filter* is a filter that has the same spectrum as the sought-for signal. One way to carry out matched filtering involves using the Hilbert transform (Sheriff and Geldart, 1983: §10.3.11) to separate the symmetric and antisymmetric anomaly components (§3.7.8). Both total-field and gradient data may be processed in this way (Naudy, 1971; Nabighian, 1984).

### 3.7.10. Werner Deconvolution

Werner (1953) proposed a method for isolating a magnetic anomaly from the interference produced by nearby anomalies. This led to automated procedures for interpreting magnetic data, now known as *Werner deconvolution* (Hartman, Teskey, and Friedberg, 1971; Jain, 1976; Kilty, 1983).

The magnetic anomaly for a dipping dike can be written in empirical form as

$$F(x) = \{ M(x - x_0) + Nz \} / \{ (x - x_0)^2 + z^2 \} \quad (3.86a)$$

where  $x_0$  is the surface point directly above the center of the top of the dike,  $z$  is the depth to the top,  $x$  is the point of measurement, and the  $x$  axis is normal to the strike.  $M$  and  $N$  are unknown functions of the dike geometry and mineralization. Rearranging Equation (3.86a) in the form

$$x^2 F(x) = a_0 + a_1 x + b_0 F(x) + b_1 x F(x) \quad (3.86b)$$

where  $a_0 = -Mx_0 + Nz$ ,  $a_1 = M$ ,  $b_0 = -x_0^2 - z^2$ , and  $b_1 = 2x_0$ , we find that  $x_0 = b_1/2$  and  $z = (-4b_0 - b_1^2)^{1/2}/2$ . Thus we can determine  $x_0$  and  $z$  by measuring  $F$  at four stations and solving Equation (3.86b) for  $a_0$ ,  $a_1$ ,  $b_0$ , and  $b_1$ .

Extending the problem beyond an isolated anomaly, Werner assumed that the noise or interference caused by neighboring magnetic anomalies could be taken into account by extending the polynomial, so that the measured field  $\mathcal{F}$  becomes

$$\mathcal{F} = F(x) + c_0 + c_1 x + \cdots + c_n x^n \quad (3.87)$$

where  $F(x)$  is given by Equation (3.86a) so that  $(n + 5)$  unknown quantities are involved. Usually the polynomial is first or second order only, so that six or seven stations are sufficient for a solution.

The scope of this analysis has been enlarged to include models other than dikes: basement topography, magnetic interfaces (which use  $dF/dx$  rather

Table 3.3. Empirical depth estimation methods for magnetic anomalies.

Method	Half-width	Peak-to-Zero	Vertical grad.	Flank slope
Component measured	$F, Z$	$F, Z, H$	$F, \partial F/\partial z,$ $Z, \partial Z/\partial z$	$F, Z$
<i>Model</i>				
Monopole	$1.3x_{1/2}$	$1.3x_{p0}$	$-2F/(\partial F/\partial z)$	
Dipole	$2x_{1/2}$	$1.3/x_{p0} \leq 2$	$-3F/(\partial F/\partial z)$	
Monopole line	$x_{1/2}$	$x_{p0}$	$-F/(\partial F/\partial z)$	
Dipole line	$2x_{1/2}$	$x_{p0}$	$-2F/(\partial F/\partial z)$	
General	$0.7 \leq x_{1/2} \leq 1.3$	$x_{p0}$	$-nF/(\partial F/\partial z)$	$0.5 \leq x_f \leq 1.5$

Note:  $x_{1/2}$  is the full width at half-peak amplitude,  $x_{p0}$  is the horizontal distance from peak to zero-crossing,  $n$  is an empirically determined index factor, and  $x_f$  is the horizontal distance over which slope is straight line.

than  $F$ ), faults, and contacts. This type of analysis is also suitable for gravity interpretation.

There are limitations to Werner deconvolution, such as resolution between neighboring bodies and lack of discrimination among parameters, leading to a relation between, say, dip angle and susceptibility. The data are sensitive to geological and measurement noise (signal/noise = 100 produces 20% scatter in depth and position estimates). However, the technique is attractive because of ease of access to the computer and consequent speed in handling large quantities of data.

### 3.7.11. Depth Estimates

(a) *Smith rules for maximum depth.* As in Section 2.7.12, which dealt with depth estimates for gravity anomalies, there are corresponding limiting values in magnetics derived by Smith (1961). If the magnetization  $M$  is parallel throughout a body, though not necessarily uniform or even in the same sense, and if  $|M|_{\max}$ ,  $|\partial Z/\partial x|_{\max}$ , and  $|\partial Z^2/\partial x^2|_{\max}$  are absolute values of the maxima of  $M$  and the first and second derivatives of  $F$  or  $Z$  along the  $x$  profile, then the depth  $z_u$  to the upper surface is given by

$$\left. \begin{aligned} z_u &\leq 5|M|_{\max}/|\partial F/\partial x|_{\max} \\ z_u^2 &\leq 30|M|_{\max}/|\partial F^2/\partial x^2|_{\max} \end{aligned} \right\} \quad (3.88a)$$

For  $Z$  profiles, where  $M$  is everywhere vertical and in the same direction (down or up), the numerical factors are reduced to 2.6 and 3.1, respectively.

For two-dimensional magnetic features having infinite length in the  $y$  direction, in which the total magnetization is parallel throughout, the equivalent expressions become

$$\left. \begin{aligned} z &\leq 4|M|_{\max}/|\partial F/\partial x|_{\max} \\ z^2 &\leq 5|M|_{\max}/|\partial F^2/\partial x^2|_{\max} \end{aligned} \right\} \quad (3.88b)$$

Where the body is uniformly magnetized by induction, we may replace  $M_{\max}$  by  $kF_e$  or  $kF_e/(1 + Nk)$  as in Equation (3.67).

Because we do not normally have a value of  $M_{\max}$ , estimates obtained by combining the two limits are even cruder than the equivalent relations for gravity. For a semiinfinite thin sheet, the result is within 50%, but it appears to be even poorer for three-dimensional features.

(b) *Empirical depth rules.* A number of rules-of-thumb for depth estimation have developed from practical experience in magnetic interpretation. These relate to profile shapes; for example, they often use horizontal widths at some fraction of the peak value for symmetrical curves and horizontal distances from peak-to-zero values for asymmetric curves. Peters (1949) was probably the first to relate depth to the horizontal extent of portions of sloping flanks, and variations of slope techniques are among the most popular. The vertical gradient is also used in such rules (Barongo, 1985). A summary of such rules is given in Table 3.3.

Slope methods are widely used, especially for aeromagnetic interpretation. Graphical techniques use the sloping flanks of profiles to estimate depth (Nettleton, 1971; Spector, 1979). In Figure 3.27a,  $S$  is the horizontal extent of the portion of the curve that is nearly linear at the maximum slope. Two additional line segments have been drawn tangent to the profile at half the maximum slope; the distance between the points of tangency is  $P$ . The depth of the source beneath these portions of the curve is given by

$$h = k_1 S \quad 1.67 \leq k_1 \leq 2.0 \\ (\text{generally } k_1 \approx 1.82) \quad (3.89a)$$

$$h = k_2 P \quad (\text{generally } k_2 \approx 0.63) \quad (3.89b)$$

The use of both methods provides a check on the

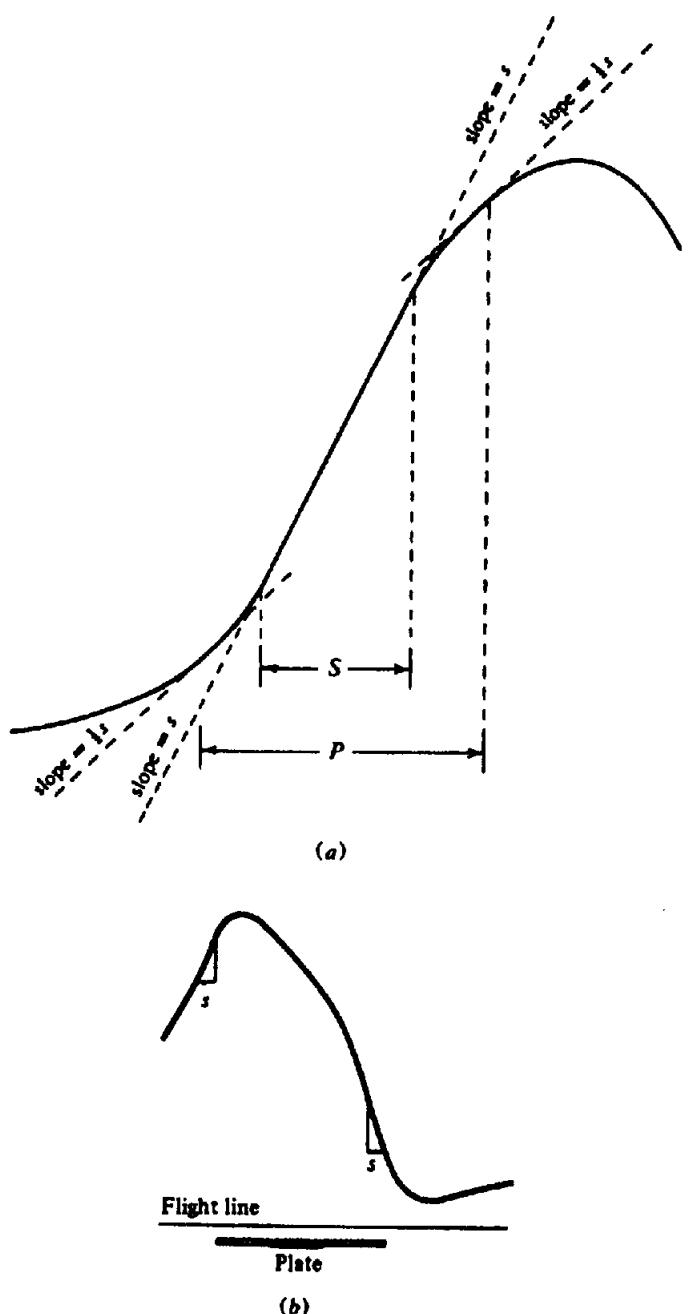


*Figure 3.27. Determining anomaly depth from the slope of a magnetic profile. (a) Maximum-slope ( $S$ ) and half-slope ( $P$ ) measurements. (b) Maximum-slope measurements on a thin plate anomaly.*

depth estimates and the care with which the graphical analysis is done. This method generally yields reasonable results for horizontal basement models with steeply dipping contacts; thus, it is suitable in the analysis of airborne data. It is much simpler and faster and provides more depth estimates than analysis by model curve fitting. It can be carried out on original field profiles and so need not wait on map preparation; it can also be applied to analysis of maps (Rao and Babu, 1984).

Use of slope techniques requires corrections. When flight lines are not normal to the local geological strike, horizontal distances are too large and

should be multiplied by a cosine factor. Correction also has to be made for the flight elevation to give values with respect to sea level (or to an arbitrary datum).

### 3.8. FIELD EXAMPLES

#### 3.8.1. Ground Surveys

(1) The first example shows the inherent complexity of ground magnetic data and the difficulties in accurately interpreting them. Figure 3.28 displays magnetic contours and two vertical component profiles

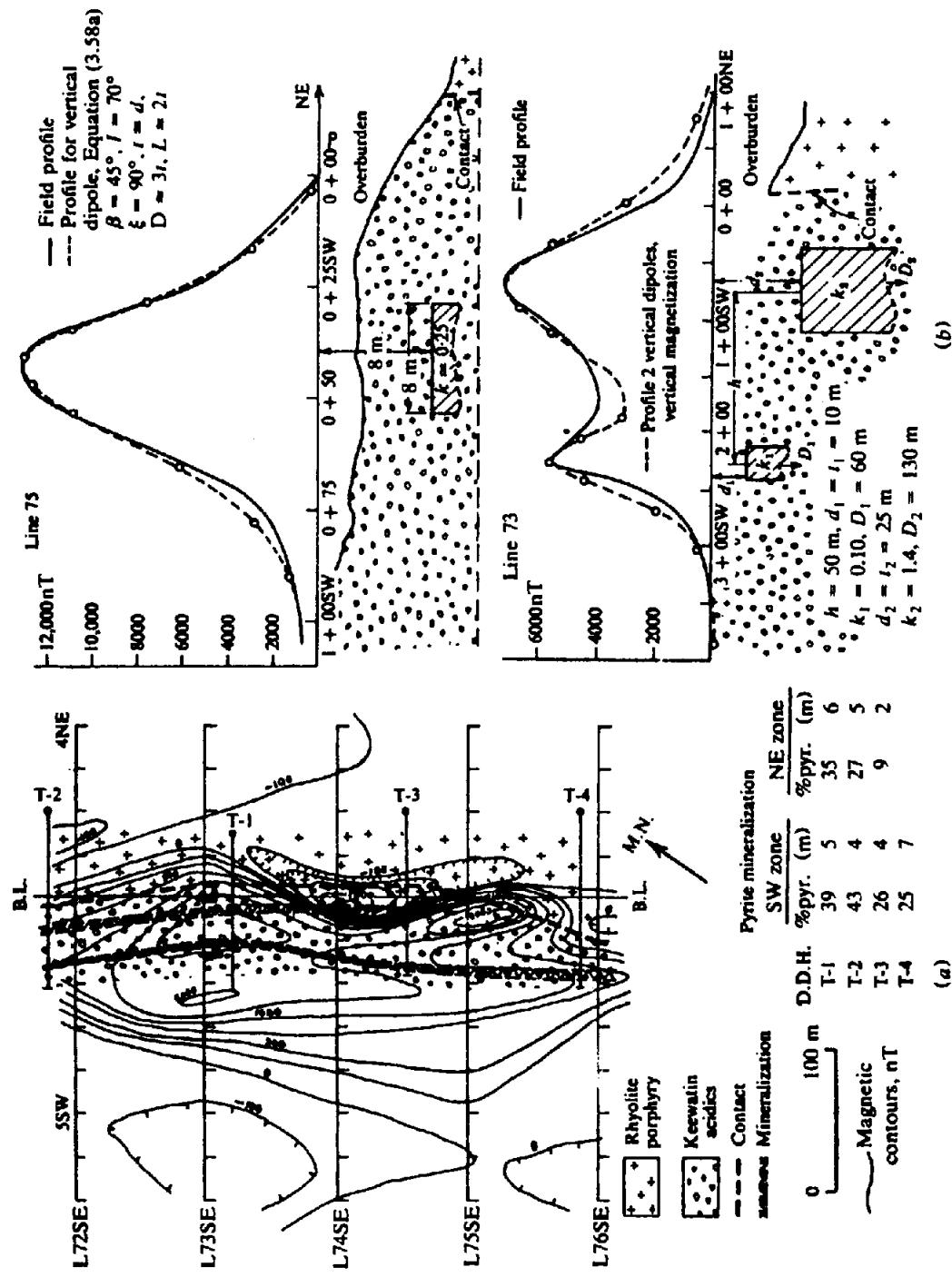


Figure 3.28. Ground magnetic survey over pyrite mineralization, Barraute, northwest Quebec. (a) Magnetic map. (b) Attempt to match profiles on lines 75SE and 73SE.

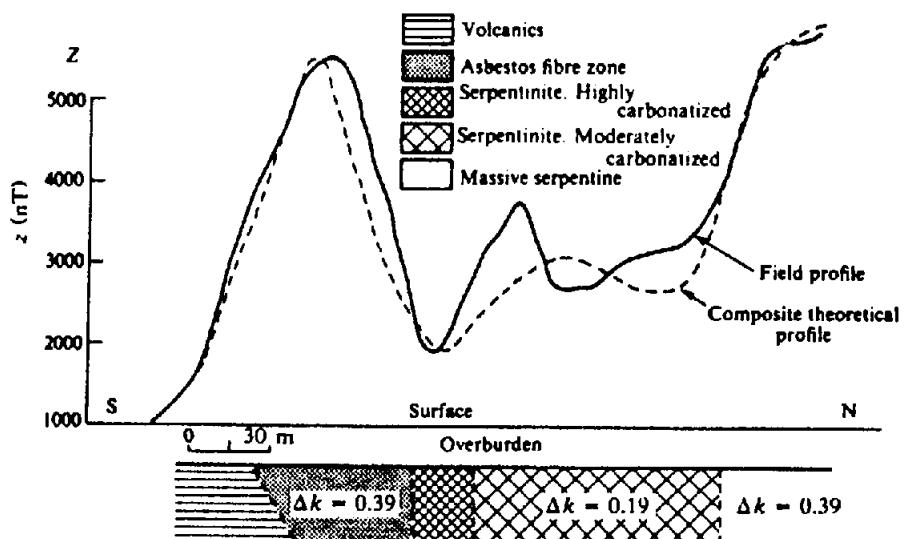


Figure 3.29. Vertical component ground magnetic profile in an area of asbestos mineralization near Matheson, Ontario.

normal to the strike of pyrite mineralization. There are two parallel pyrite zones in acidic flows, near a contact between the latter and rhyolite porphyry. Both have a strike length greater than 300 m and the zone nearer the contact appears to pinch out on line 75.

Although the pyrite mineralization is clearly associated with a magnetic trend in the area, the large magnetic anomalies on lines 73 and 75 could only be due to magnetite or possibly pyrrhotite, since the susceptibility of pyrite is relatively low (Table 3.1). However, there is no specific indication of these minerals in the drill logs of holes 1 to 4.

Because the overburden near the diamond drill holes was generally quite thick (25 m at T-1, for example), it was originally assumed to be at least 15 m throughout the grid. However, a shallow seismic refraction survey carried out later on line 75 showed bedrock only 1.5 to 3 m below the surface in the vicinity of the pyrite zones, dropping off abruptly to 15 to 25 m northeast of the acidic flow-rhyolite contact. Thus the magnetite sources may be very close to the surface and of small depth extent.

The source for the single 13  $\mu$ T peak on line 75 appears to be a finite steeply dipping sheet at very shallow depth. Using Equation (3.58a) with  $\beta = 45^\circ$ ,  $I = 70^\circ$ ,  $\xi = 90^\circ$ , and  $Z_e = 36 \mu$ T, and fitting the profiles at three points (including the maximum), we obtain a reasonable fit with  $t \approx d \approx 8$  m,  $D \approx 25$  m,  $2L \approx 30$  m, and  $k = 3$  SI unit (See Fig. 3.28b). However, when we try to match the double peak profile on line 73 by assuming two vertical sheets of identical cross section separated by 50 m and inductively magnetized in the earth's field, Equation (3.58a) produces the following parameters:  $d \approx t \approx 2.5$  m,

$D = 70$  m,  $2L = 90$  m,  $k_1 = 1.3$  SI, and  $k_2 = 1.9$  SI. This results in a reasonable match of the central trough and the northeast flank, but the southwest flank is much too large. A better fit (shown in Fig. 3.28b) was obtained with the two vertical sheets illustrated, but the trough between them is too deep. Also, the depth extent must be less than 120 m because the bodies were not encountered in holes T-1 and T-3. Although this interpretation is certainly not definitive, it is clear that the magnetic sources are shallow, have limited strike length, steep dip, and large susceptibility contrast. This last fact indicates high magnetite content and possibly large remanence, which may be responsible for the disagreements (Green, 1960).

(2) The magnetic method is particularly useful in exploring for asbestos because of its occurrence in ultrabasic intrusive rocks rich in magnetite. When olivine ( $Mg_2SiO_4$ ) is altered to serpentine ( $Mg_2SiO_5(OH)_4$ ) and magnesite ( $MgCO_3$ ) by the addition of water and carbon dioxide, the asbestos is associated with high magnetic susceptibility and massive serpentinite. Figure 3.29 shows a vertical component profile over an asbestos prospect near Matheson in northern Ontario and the geologic section under a 15 m overburden. High magnetic responses correspond to the asbestos and massive serpentinite zones with lows over the volcanics and highly carbonized serpentite. A reasonable match to the field profile was obtained by assuming dikes of considerable depth extent using Equation (3.44a) with  $r_2 \approx r_4$ ,  $\phi_2 \approx \phi_4$ ,  $\beta = \pi/2$ , and all contacts vertical except the left one, which dips  $30^\circ$ . The presence of asbestos in the massive serpentinite zones can only be established by drilling.

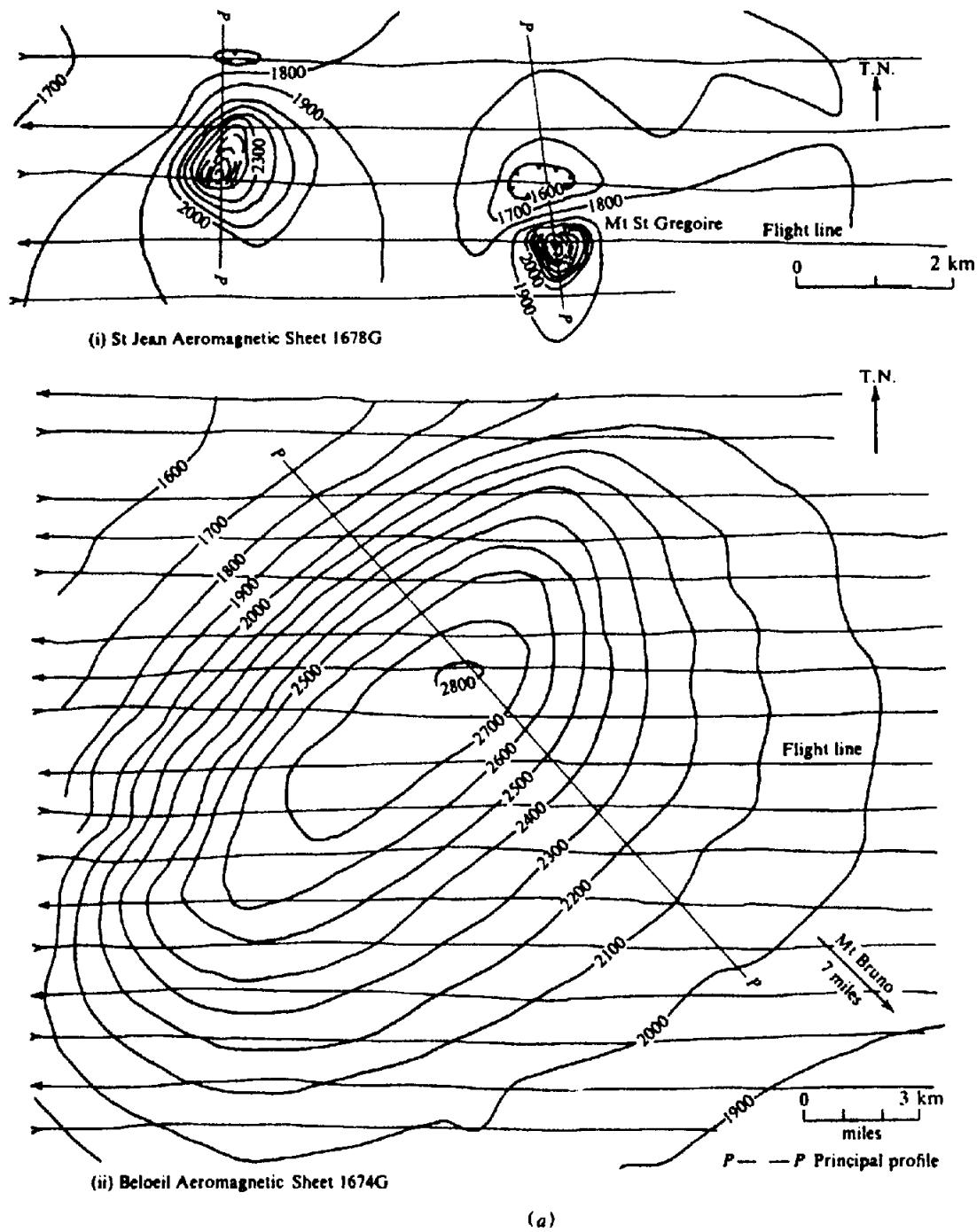


Figure 3.30. Magnetic data for three anomalous areas in the St. Lawrence lowlands.  
(a) Maps, C.I. = 100 nT.

### 3.8.2. Airborne Surveys

(1) The Montréalian hills of the St. Lawrence lowland region near Montréal were formed by igneous intrusions into sedimentary rocks. These hills are magnetic as well as topographic anomalies because of their contrast with the low susceptibility sediments. Aeromagnetic maps (Canadian Government Aeromagnetic Series, St. Jean and Beloeil) show this clearly for Mt. Bruno, Mt. St. Hilaire, Mt. Rougemont, and Mt. St. Gregoire. On the same sheets we

also see two well-defined magnetic highs that are not topographic features: one about 5 km west of Mt. St. Gregoire and a larger one 11 km northwest of Mt. Bruno. One assumes that they are igneous plugs that failed to reach the eminence of the Montréalian hills.

These two features and Mt. St. Gregoire provide excellent examples of the vertical-prism model commonly employed in aeromagnetic interpretation. Figure 3.30 shows the total-field contours, whereas profiles are displayed in Figure 3.30b. Two methods

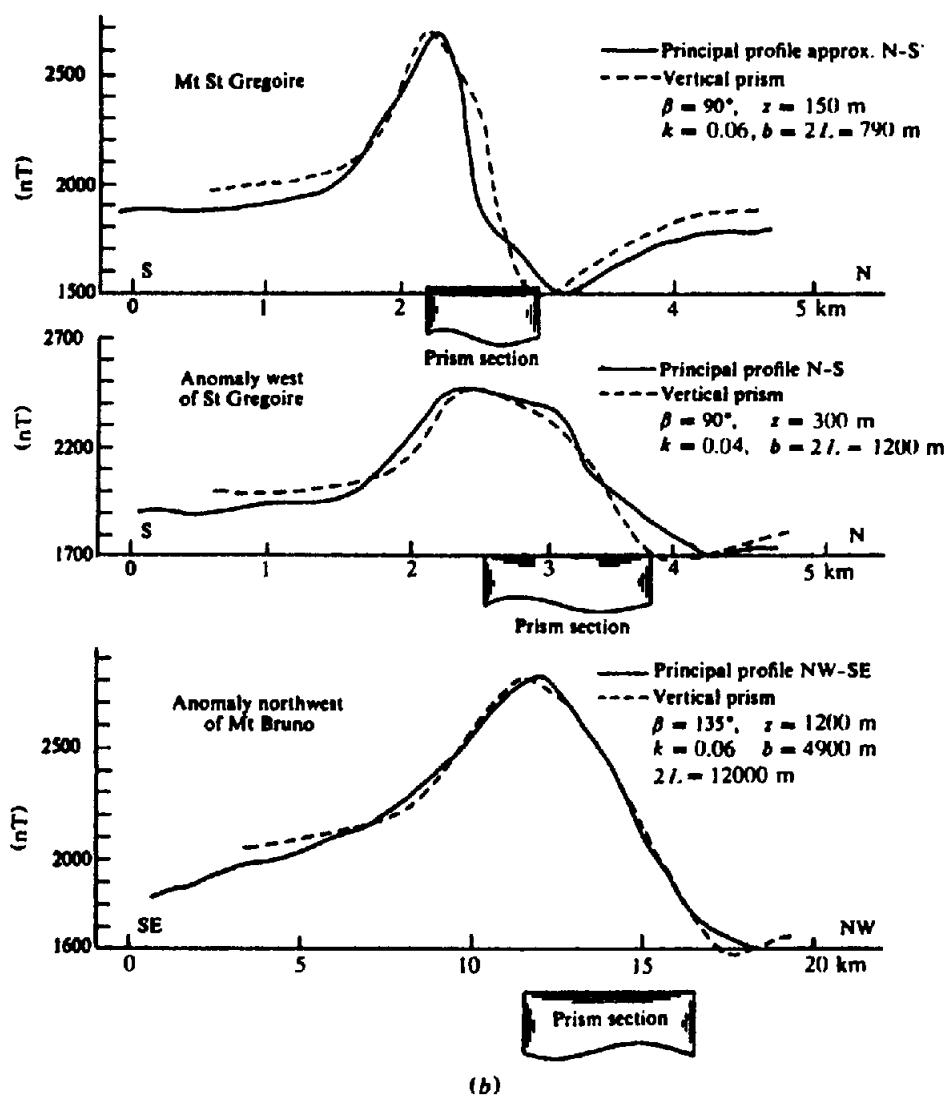


Figure 3.30. (Continued) (b) Principal profiles,  $I = 60^\circ$  and  $F_e = 60 \mu T$ .

Table 3.4. Interpretation of anomalies in the St. Lawrence lowlands.

Anomaly	$I$ (deg)	$k$ (SI)	$z$ (m)	$b$ (m)	$2L$ (m)	Source
St. Gregoire	60	0.04	110	880	880	Vacquier (Fig. A60)
	75	0.05	110	880	670	Vacquier (Fig. A70)
	60	0.06	150	790	790	Equation (3.44c)
Anomaly near St. Gregoire	60	0.025	230	1,700	1,700	Vacquier (Fig. A60)
	75	0.03	230	1,700	1,250	Vacquier (Fig. A70)
	60	0.04	300	1,220	1,220	Equation (3.44c)
Anomaly near Bruno	75	0.08	1,130	3,660	9,140	Vacquier (Fig. A75)
	60	0.055	1,220	4,880	12,200	Equation (3.44c)

were employed to assess the magnetic characteristics. One used the models of Vacquier et al. (1951) and the other used Equation (3.44c) for a vertical prism. This allowed calculation of the susceptibility contrast  $k$ , the depth  $z$ , strike length  $2L$ , and width  $b$  by matching the principal profiles. The results, which fit reasonably well, are shown in Table 3.4 and in Figure 3.30b. If we assume  $I = 75^\circ$  instead of  $60^\circ$ ,

the curves have steeper slopes on the south or southeast flanks and it is necessary to increase the lateral dimensions to match the field profiles. In practical interpretations, the depth to the top of the prism is the most significant dimension. Because flight elevation was 300 m, Table 3.4 puts the St. Gregoire plug about 150–190 m above ground (Mt. St. Gregoire rises to a height of 180 m above ground). The top of

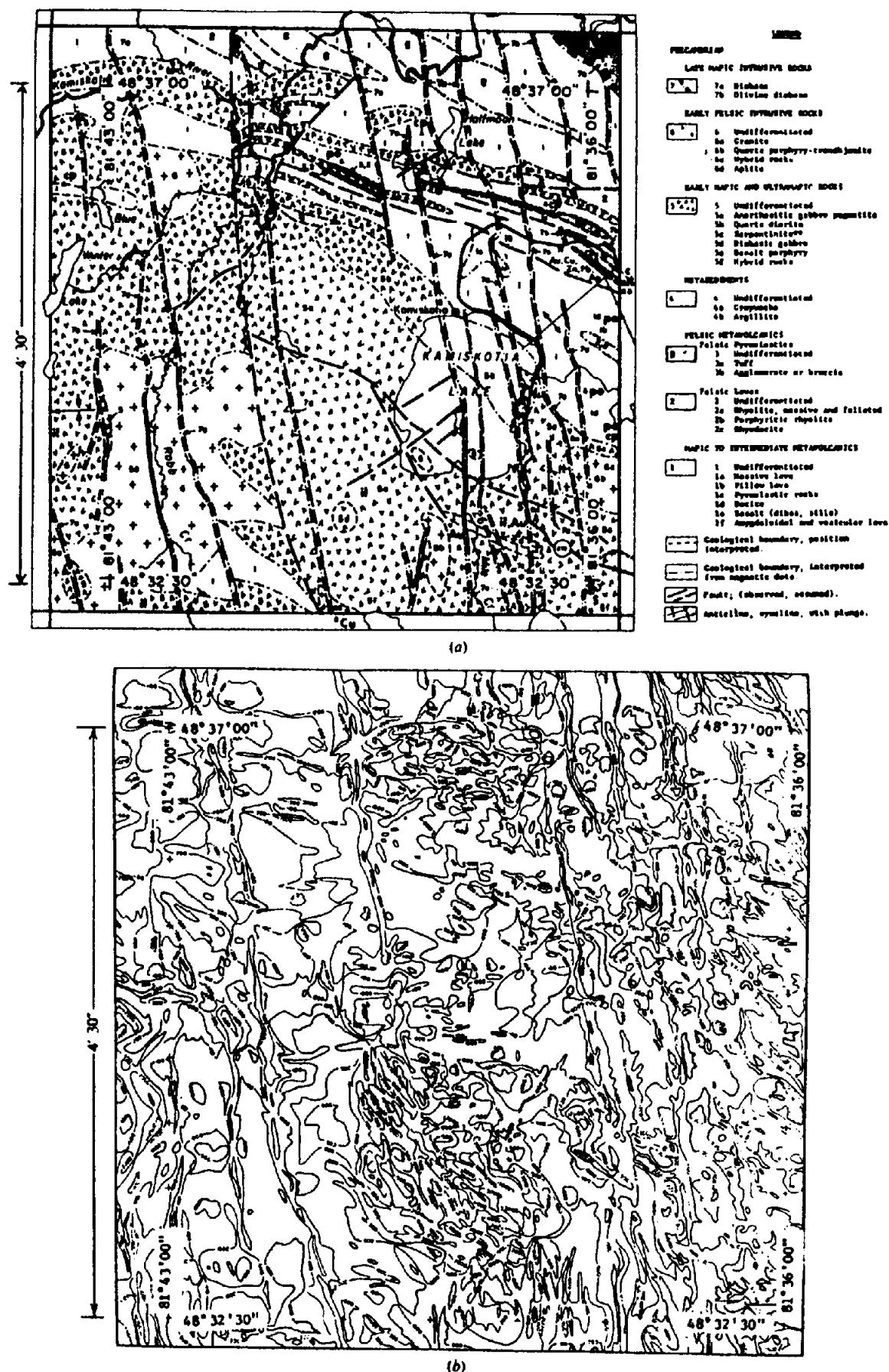


Figure 3.31. High-resolution aeromagnetic survey, Timmins area, Ontario. (From Bhattacharyya, 1971.) (a) Geological map. (b) Ground vertical-intensity map.

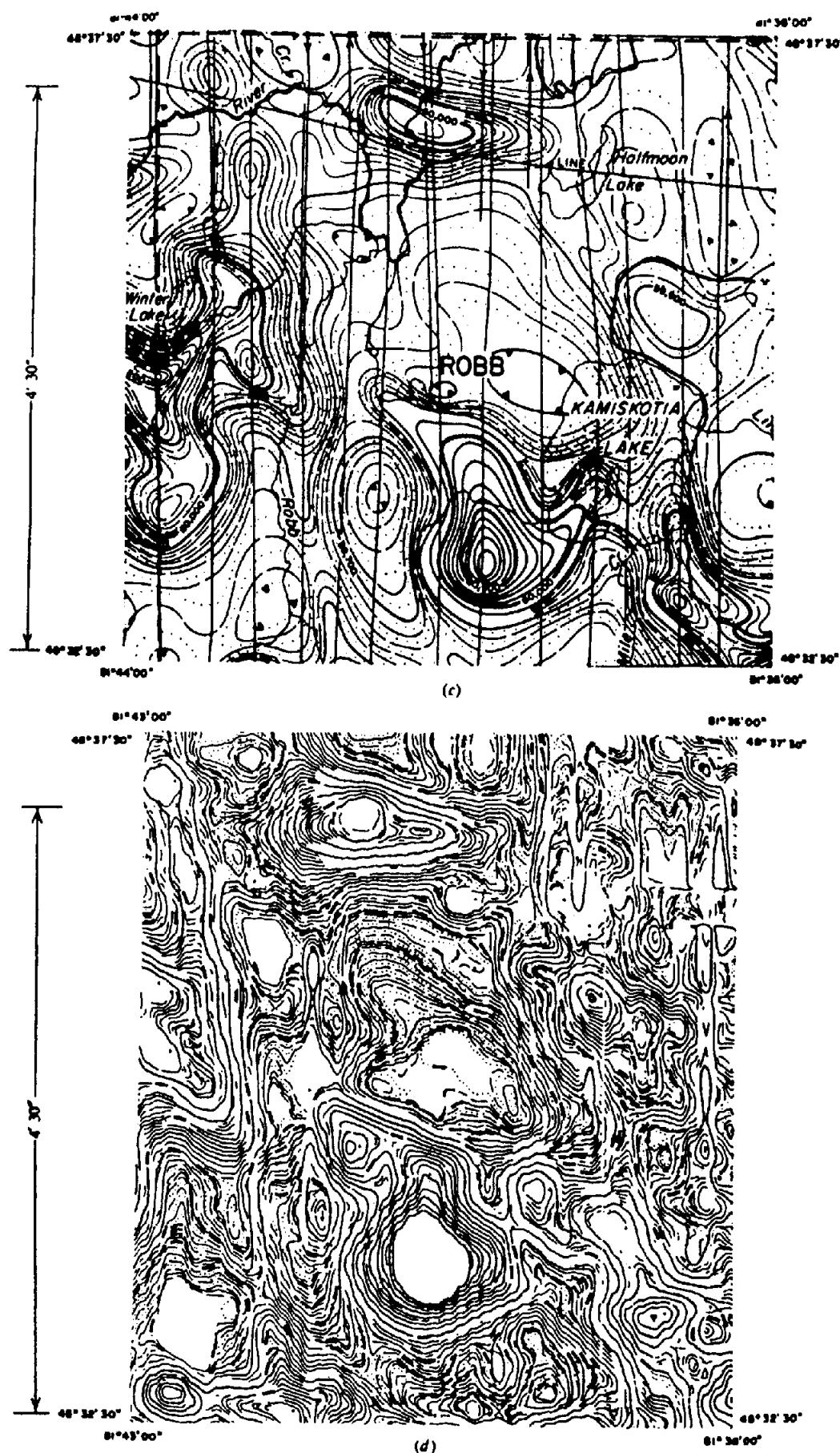


Figure 3.31. (Continued) (c) Conventional aeromagnetic map. (d) High-resolution aeromagnetic map.

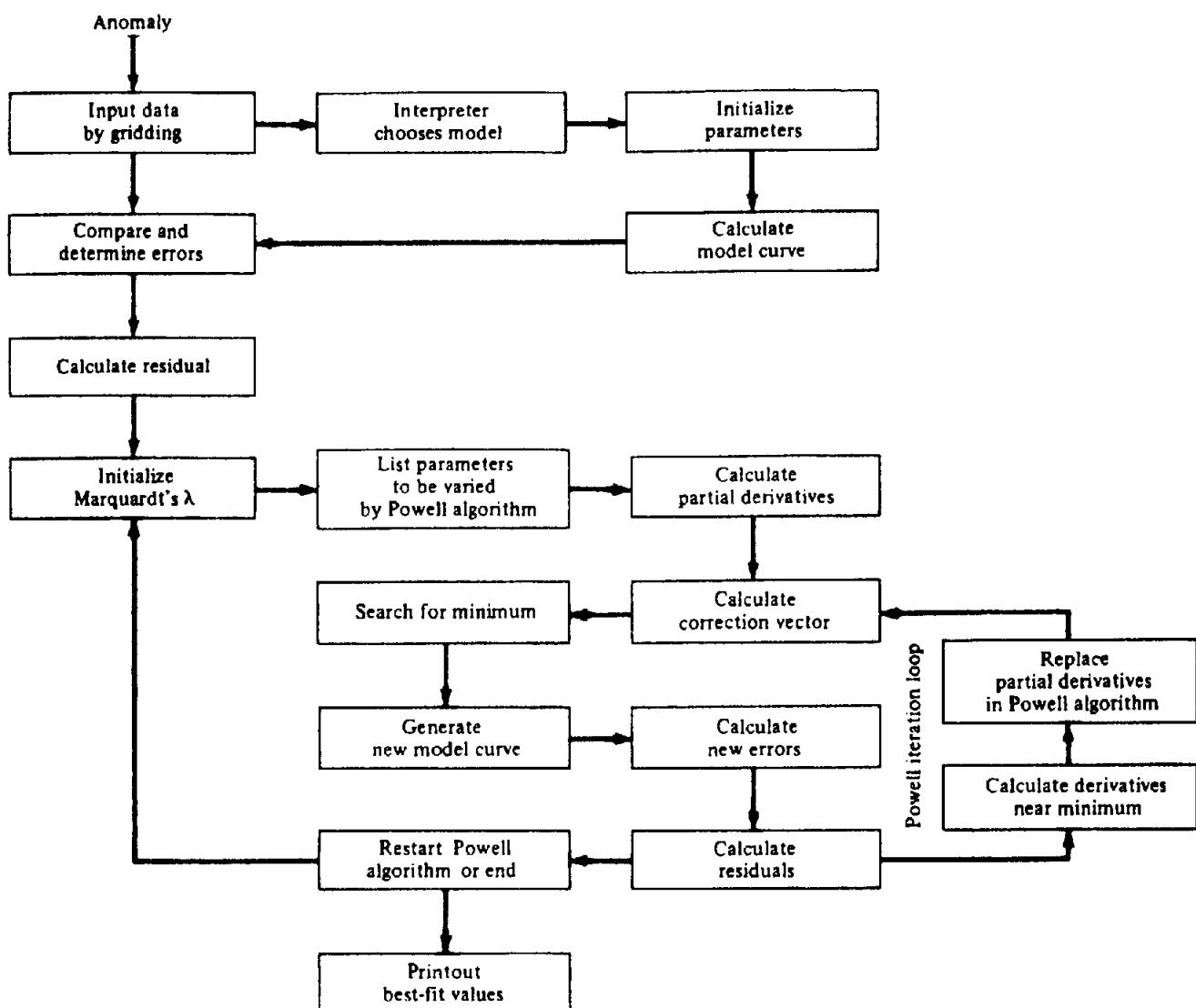


Figure 3.32. Generalized flow chart of computerized interpretation. (From McGrath and Hood, 1973.)

the anomaly near Mt. St. Gregoire is just above the surface whereas the one near Mt. Bruno is about 870 m below the surface.

(2) The use of high sensitivity aeromagnetic data has been described by Bhattacharyya (1971). In 1969, the Geological Survey of Canada arranged an experimental high-resolution survey in the Precambrian shield of northern Ontario near Timmins that used a cesium-vapor magnetometer with a sensitivity of 0.02 nT. Control of the survey was much tighter than in conventional work at the time. Line spacing was 300 m at an average altitude of 250 m and flight paths were straight within 100 m over 24 km. Double baselines perpendicular to these were flown in opposite directions every 8 km. The total field was continuously recorded at a ground station. The following were recorded on the aircraft:

1. Total magnetic field in units of 0.02 nT.
2. Total field vertical gradient in units of 0.005 nT.

3. Terrain clearance in units of 60 cm.
4. Barometric altitude in units of 3 m.
5. Doppler-radar along-track and cross distances in units of 50 m.
6. Time in seconds.

Data compilation involved the following:

1. Check of in-flight digital data and necessary corrections.
2. Calculation of coordinates.
3. Location of traverse and baseline intersections.
4. Adjustment of intersection points.
5. Calculation of, and correction for, drift.
6. Reduction of data to a common datum.
7. Reduction of corrected values for contouring.

A map of a 10 × 10 km portion of this survey is shown in Figure 3.31d.

Figure 3.31a, a provisional geological map, was prepared with help from an earlier ground vertical-

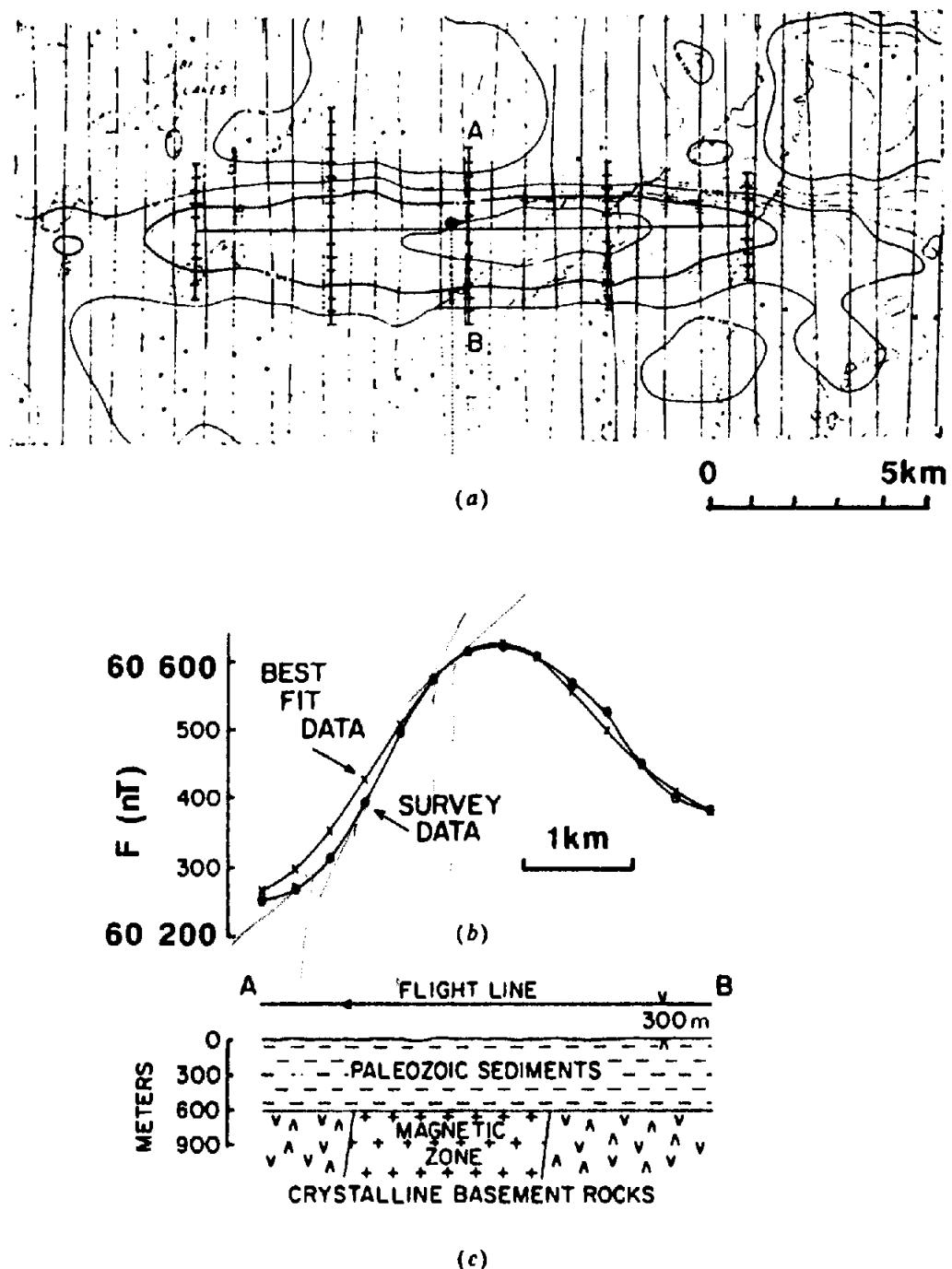


Figure 3.33. Belec Lake anomaly, Ontario. (From McGrath and Hood, 1973.) (a) Aeromagnetic map of the anomaly. (b) Profile AB and the anomaly computed from the model. (c) Inferred geological cross section.

intensity map (Fig. 3.32b). The bedrock in this area, cut by numerous N-S diabase dikes, is an Archean complex of gabbro, granite, and mafic and felsic volcanics. There are three major fault systems: The one striking N30°W is the main control for the diabase dikes, whereas the other two, trending WNW and NE, appear to have affected the dikes by shearing and deflection.

The ground survey map shows much detail, but the trends are broken up. The map from a conventional survey, Figure 3.31c, flown with a proton-pre-

cession instrument (sensitivity 0.1 nT) at 300 m with 800 m line spacing, obviously shows much less detail than the high-resolution magnetic map in Figure 3.31d. Several pronounced anomalies, probably due to gabbro, are obvious on both aeromagnetic maps, whereas the ground map does not show them clearly. The cost of the high-resolution survey was about six times greater than the conventional aeromagnetic survey, but the difference would be much less today; an equivalent ground survey on 120 m spacing would cost five to six times as much.

(3) An example of computer modeling followed the procedure diagrammed in Figure 3.32. This modeling minimizes  $E$ , the difference between observed,  $D(x, y)$ , and model anomalies  $T(x, y)$ , at  $m$  points through an iterative adjustment of  $n$  model parameters,  $q_1, q_2, \dots, q_n$ :

$$E(q_1, q_2, \dots, q_n) = \sum [D(x, y) - T(x, y, q_1, q_2, \dots, q_n)]^2$$

The minimum of  $E$  may be found by the method of Gauss, least squares, steepest descent, or other techniques. Here it was found by a combination of the Marquart and Powell algorithms (McGrath and Hood, 1973). [See §2.7.9 for a similar gravity procedure.]

This example is of modeling a basement anomaly in the Moose River basin of the Hudson Bay lowlands in northern Ontario, which is shown in Figure 3.33. The model was a thick, steeply dipping plate. The Moose River basin contains about 600 m of nonmagnetic Paleozoic sediments overlying a Precambrian crystalline basement (based on seismic and

drilling measurements). The best-fit model showed an intrabasement magnetic zone at a depth of 900 m, which corresponds to 600 m of sediment. The magnetic body is 1.730 m thick with a strike length of 14 km and dips 82° north; the susceptibility contrast is 0.029 SI, which is typical of igneous rocks. The body has its polarization vector dipping 64° with declination 107°. The local magnetic inclination is 79°, which means that the body possesses significant remanent magnetization.

Table 3.5. Vertical-component readings in serpentine zone.

Stn.	Z (nT)	Stn.	Z (nT)
ON	275	8N	-40
1	220	9	-10
2	224	10	-15
3	230	11	+100
4	185	12	150
5	185	13	220
6	155	14	220
7	35		

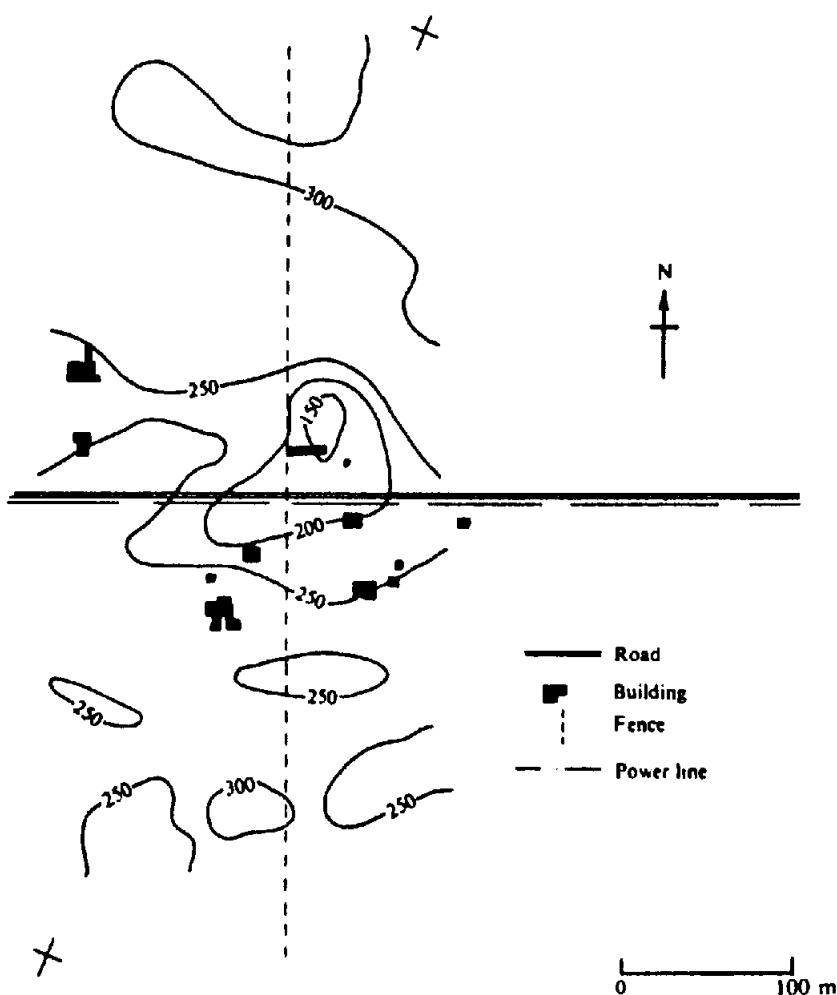


Figure 3.34. Vertical magnetic ground survey, Noranda area: C.I. = 50 nT. (After Seigel, 1957.)

Table 3.6. Traverse in Quebec Eastern Townships.

Stn.	Z (nT)	Stn.	Z (nT)
17W	2,040	8W	-7,000
16	2,320	7	-1,060
15	2,080	6	2,720
14	2,080	5	5,140
13	1,800	4	4,260
12	3,280	3	2,680
11	9,200	2	2,220
10	3,400	1	2,240
9	-9,500	0	1,940

Table 3.7. Vertical-component readings across zinc property.

Stn. (ft)	Z (nT)	Stn. (ft)	Z (nT)
6 + 00S	45	0 + 50S	130
5 + 00	50	0 + 00	95
4 + 50	52	0 + 50N	75
4 + 00	50	1 + 00	40
3 + 50	45	2 + 00	8
3 + 00	50	3 + 00	0
2 + 00	90	4 + 00	-5
1 + 00	135		

### 3.9. PROBLEMS

1. Chromite is found in serpentine in a certain district. A magnetic analysis of several specimens indicates that there is less magnetite in the chromite-bearing serpentine than in barren serpentine. The Z-component readings in Table 3.5 were taken on a N-S line at 8 m stations. Assuming a two-dimensional E-W zone of min-

eralization, estimate the depth and cross-section of the body causing magnetic anomaly from this profile.

2. Figure 3.34 shows Z-component contours obtained from a detailed ground magnetic survey in the Noranda district, an area rich in sulfides and graphite. The rocks to the south are rhyolites, rhyolitic breccias, and tuffs. To the north we find basic volcanics and tuffs with occasional rhyolite. Where would you expect to find anomalous sulfides and/or graphite? Are they shallow or deep? If they are sulfides, what varieties can be ruled out? Have the fence and power line affected the readings to any extent?
3. Table 3.6 shows Z-component readings made 3 m apart on an E-W traverse in the Quebec Eastern Townships region. The large anomaly was originally detected during a pace-and-compass exercise when the magnetic declination suddenly changed by about  $110^\circ$ , an effect that did not persist for any appreciable distance. Interpret the source with regard to location, depth, dip, lateral extent, and possible mineral character.
4. Use a dipping sheet model of considerable strike length to calculate and plot the total field  $F$  and vertical gradient  $\partial F/\partial z$ , given that  $D = b = 10d$  and that the structure strikes (a) N-S and (b) E-W, in a region where  $I = 60^\circ$ . By neglecting small terms, calculate the approximate maximum and minimum values of  $F$  and  $\partial F/\partial z$  in (a) to check the N-S profile.
5. The vertical component magnetometer readings in Table 3.7 are from a detailed survey of an old mining property where the primary metal was zinc, with some low-grade copper and minor silver. Assume that the source of the weak mag-

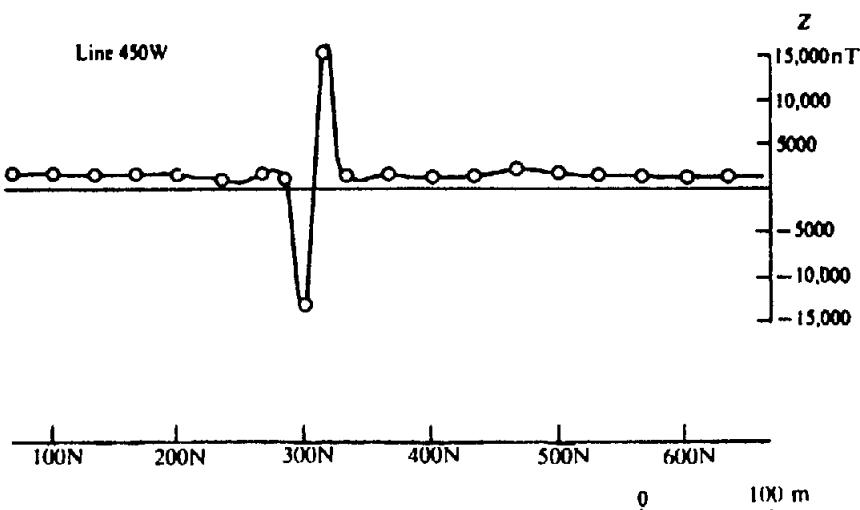
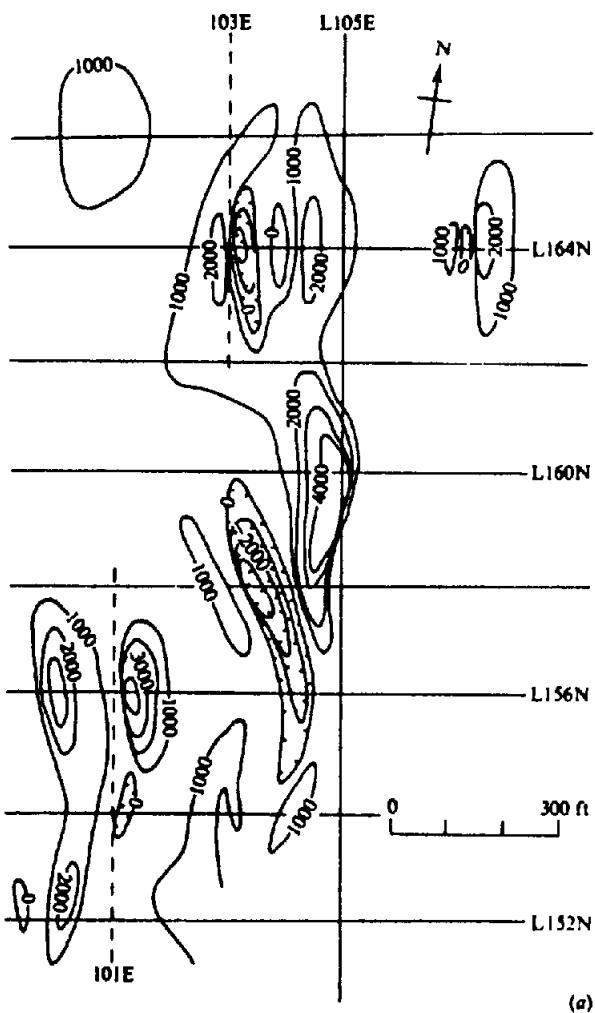
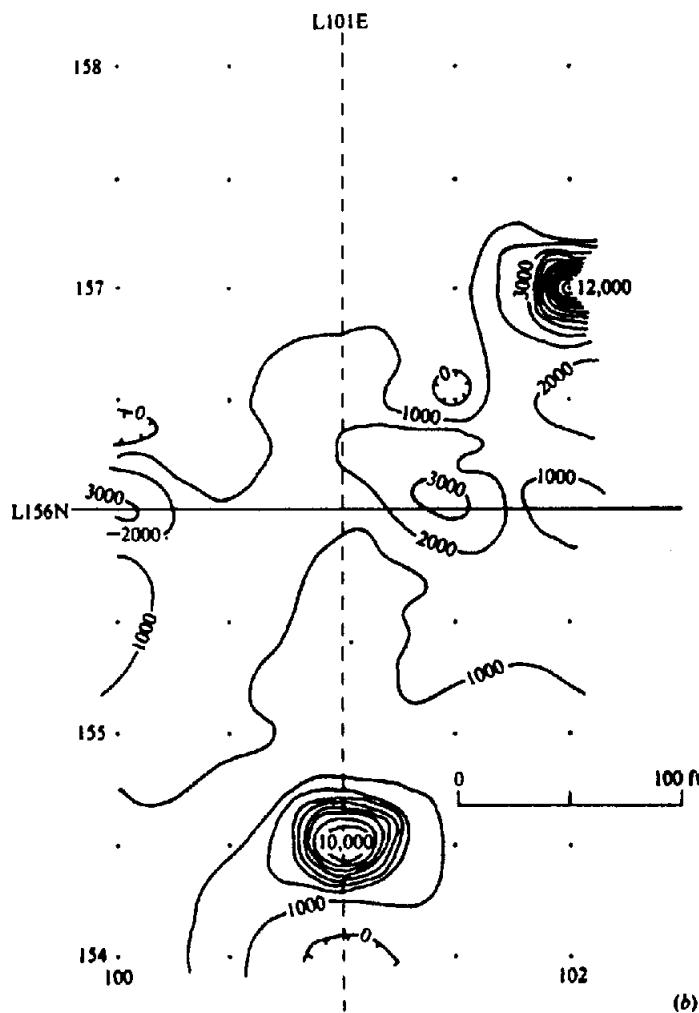


Figure 3.35. Vertical-component ground magnetic profile, East Africa.



(a)



(b)

**Figure 3.36.** Effect of line spacing on magnetic data. (a) Conventional magnetic map. C.I. = 1,000 nT. (b) Detailed magnetic map centered at 156N, 101E.

netic anomaly is a dike of large strike length and depth extent and use the method of Section 3.7.8 to determine its parameters.

6. The vertical-component ground profile shown in Figure 3.35 is from a large-scale multiple-method survey for base metals in Tanzania. The geology is generally Precambrian metamorphosed sediments and volcanics associated with granite. In this region,  $F_e \approx 0.35 \mu\text{T}$ , the declination is  $4^\circ\text{W}$ , and the inclination is  $I \approx 31^\circ\text{N}$ . Sulfide bodies with large E-W extent are known in the vicinity. Interpret the anomaly.
7. The magnetic contours in Figure 3.36 show the effect of line spacing (see also Bhattacharyya, Sweeney, and Godson, 1979). A small section from what would normally be considered a detailed ground survey is shown in Figure 3.36a. Lines were spaced 200 ft apart N-S with station readings every 50 ft (reduced to 20 ft near anomalous values). The contours of Figure 3.36a are elongated N-S because the line spacing is greater than the station spacing. Some of the

zones were resurveyed in followup work on 50 ft grids with occasional readings 5 to 10 ft apart because of the small lateral extent of the anomalies. Three of these detailed grids are shown in Figure 3.36b, c, d.

- The differences, particularly in lateral extent, strike axis, magnitude, and anomaly location, are very apparent. What are they? Other surveys have indicated massive sulfides at the centers of Figure 3.36b, d but not at 164N, 103E. Given this additional information, would you conclude that the magnetic anomalies are directly or indirectly related to the sulfides? Do they have any association with the sulfides? Would you reach the same conclusion if only Figure 3.36a were available? Estimate the depth, lateral extent, attitude, susceptibility, and probable content of a few of the anomalies in all four diagrams. Do they show evidence of strong remanent magnetization?
8. The vertical-component ground magnetic contours in Figure 3.37 were from a survey over a

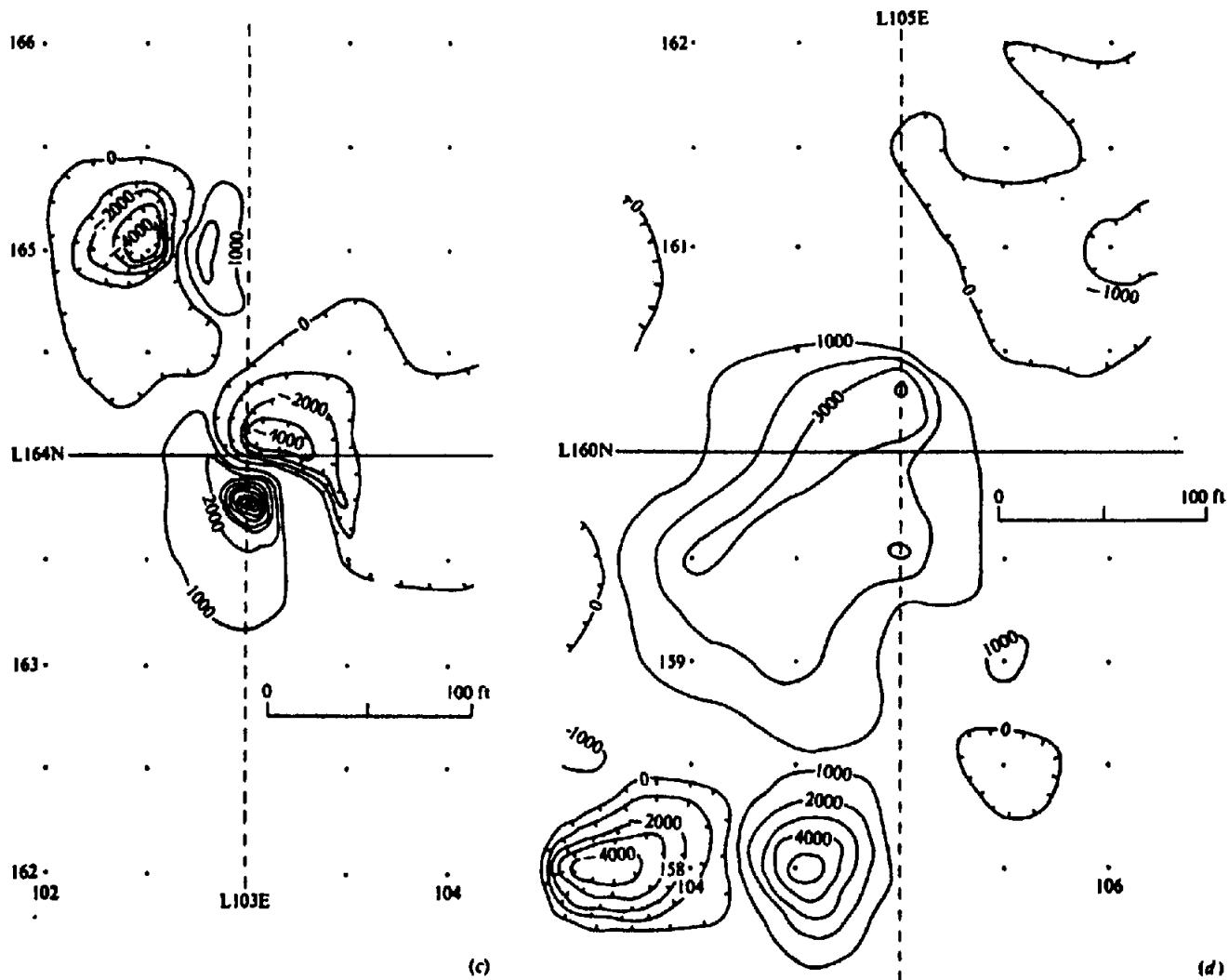


Figure 3.36. (Continued) (c) Detailed magnetic map centered at 164N, 103E.  
(d) Detailed magnetic map centered at 160N, 105E.

nickel prospect in northern Manitoba. Zone C is approximately 4 km NE of zone A. There is considerable overburden throughout the area. Electromagnetic surveys showed that both zones were good conductors. One of them contained ore-grade nickel sulfides, the other was barren of sulfides and graphite. Is it possible to distinguish the economic mineralization solely from the magnetic results? Estimate the depths of the main magnetic anomalies in the two zones.

9. A copper deposit of limited extent in the Rouyn district of Quebec produced the Z profiles in Figure 3.38. Match the profiles to an appropriate model given that the E-W strike is very limited and the inclination  $I = 75^\circ$ . What is the probable magnetic mineral?
10. Figure 3.39 shows four vertical-component magnetic profiles from the Manitoba Nickel Belt, obtained during large-scale base-metal exploration programs. Sulfides and graphite occur in the Precambrian rocks below Paleozoic sedi-

ments and thick overburden; the mineralized zones frequently extend for miles.

Diamond drilling has established that the mineralization associated with two of these profiles is pyrite and pyrrhotite, a third is graphite and pyrite, and the fourth graphite and pyrrhotite, and that they are located at four different depths. With this information, use the magnetic data to locate the mineralized sections as precisely as you can.

11. The two ground magnetic contour maps in Figure 3.40 illustrate the effect of irregular topography on magnetic measurements (Oliver and Hinze, 1985). The areas surveyed in Figure 3.40 are only 60 miles apart. The terrain is quite rugged in both, as can be seen from the dotted contours, but the geology is entirely different. In the former, the rocks are sedimentary to great depth; at the latter site, there are granites in most of the north and west parts of the map and sediments in the lower ground at the south. It is

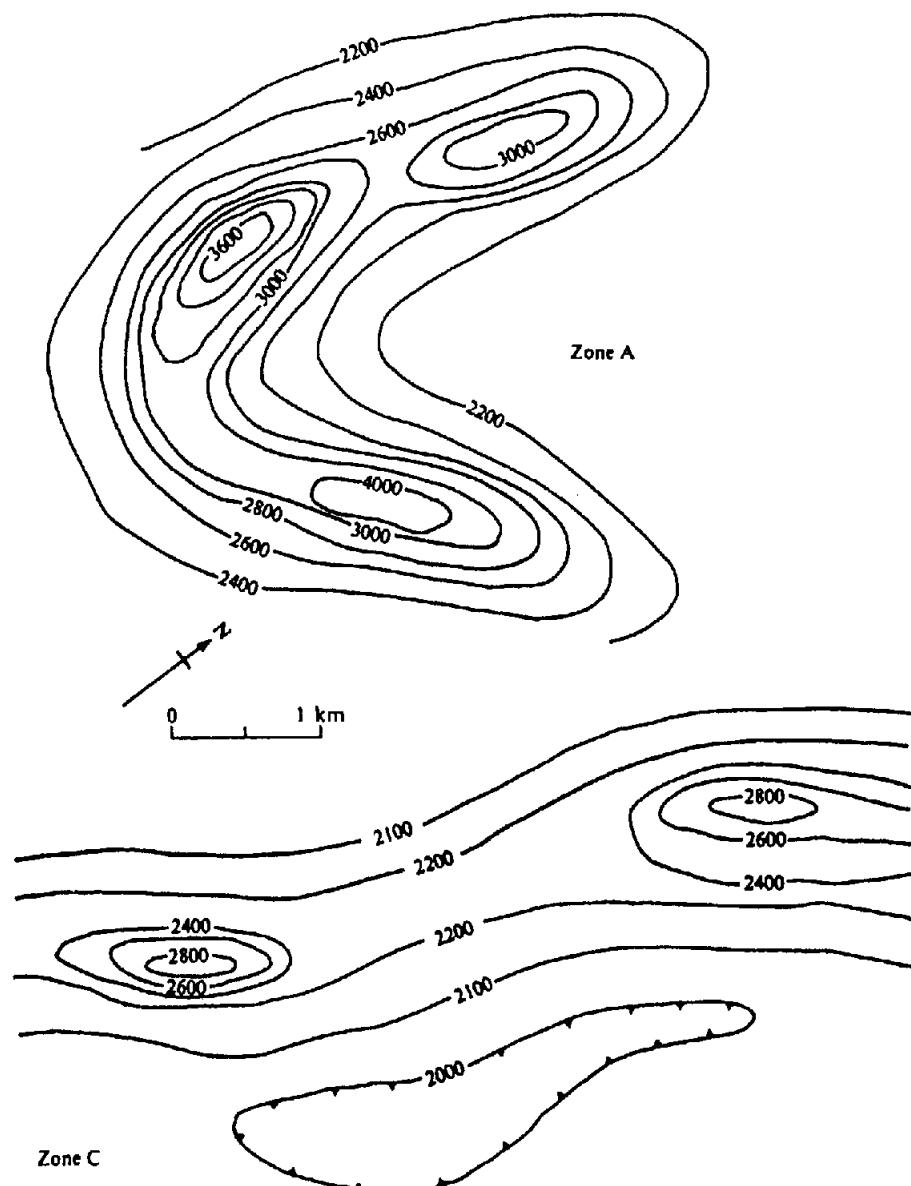


Figure 3.37. Ground magnetic contours, northern Manitoba. C.I. = 100 nT.

thought that the sediments extend for some distance up the hill in the lower left corner and the assumed contact between the granites and volcanic formations is somewhere in the upper left portion of the map.

The uniform magnetic response over the sediments in Figure 3.40a (about 300 nT maximum) is to be expected because of the low susceptibility of sandstone and limestones. There is no particular correlation between the topographic and magnetic contours, hence no need for a topographic correction.

In Figure 3.40b the situation is quite different. A definite magnetic contrast exists between the granites and the sedimentary area, although the map does not extend far enough south and

southeast to indicate this clearly. However, a pronounced magnetic low follows the topography from north to south, then west to east, starting in the upper left area. This is a clear reflection of the terrain effect on ground magnetics.

Using Equations (3.33) and (3.71), apply the terrain correction at a few selected points on the map of Figure 3.40a. For example, the 100 nT low on the steep slope near the bottom of the map, midway between the east-west boundaries, lies on the 425 ft contour; if we choose the 600 ft elevation for  $z = 0$ , the value of  $h$  will be 175 ft. Reasonable values for circle radii would be  $r_1 = 100$  ft,  $r_2 = 200$  ft, and so forth. For other stations, one might select one at the top of the

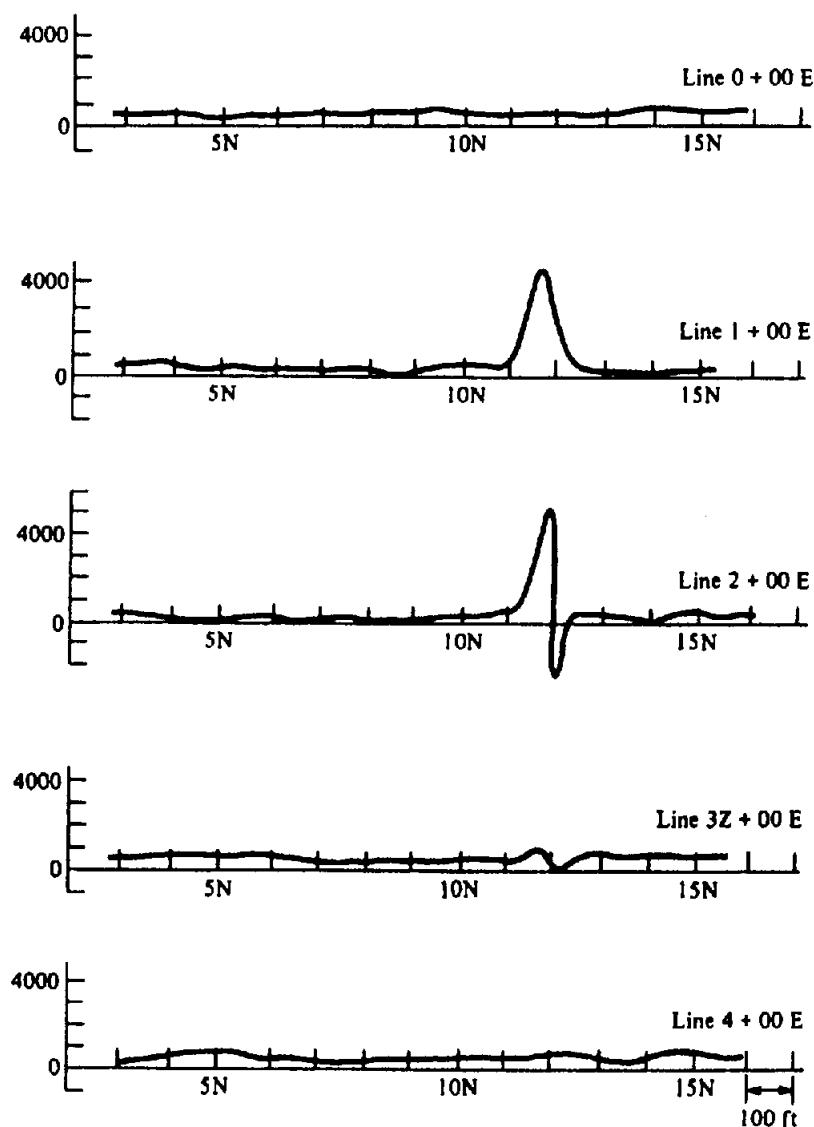


Figure 3.38. Vertical-component magnetic profiles, Rouyn-Noranda district, Quebec.

hill, one in the northwest corner, and one to the southeast. Do these modified Z values aid the magnetic interpretation in any way?

Repeat the procedure for several strategically located stations on the map of Figure 3.40b, particularly in the area of the magnetic lows following the stream gorge. (Obviously the best method for handling analysis of this type would be to digitize the contoured data and use a computer.) Are the terrain corrections significant? Would they be more reliable if vertical gradients had been measured? Why?

12. The two sets of contours shown in Figure 3.41 illustrate the differences between airborne total-field and ground vertical-component survey results. Only the relative values are significant because there is no relation between the absolute magnitudes. The airborne results show the ef-

fects of smoothing with altitude. The ground survey indicates five distinct maxima, compared with a single symmetrical anomaly in the airborne contours. Furthermore, the largest of these ground maxima is displaced about 650 m from the center of the total-field anomaly. The altitude of the aircraft was 300 m and the ground is flat. The magnetic inclination in the area is  $75^\circ$ . Calculate the depths and approximate lateral extents of the 6,000 nT and the larger of the 2,000 nT ground anomalies as well as the airborne anomaly.

With the aid of Equation (3.71) and Table 3.2, carry out an upward continuation of the ground data to 300 m by choosing  $r_1 = 100$  m and  $h = 5$ .

13. Figure 3.42 shows a  $9.5 \times 6.5$  km section from a Canadian government aeromagnetic survey in

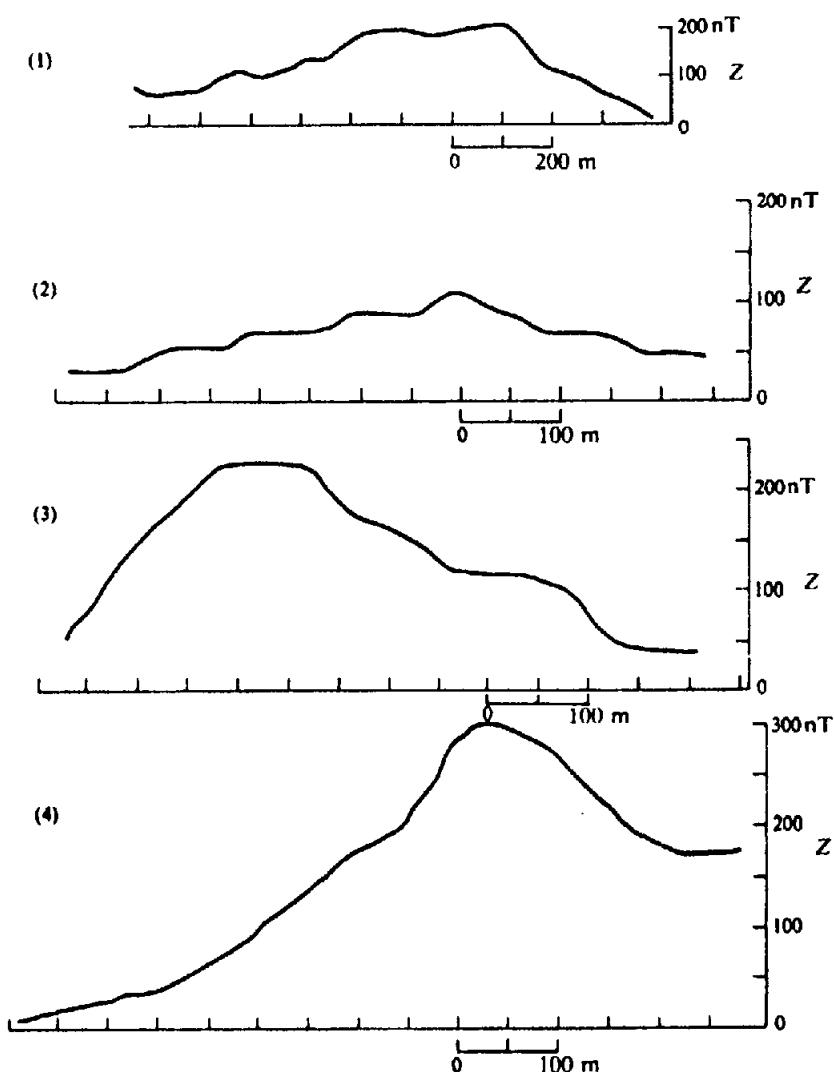


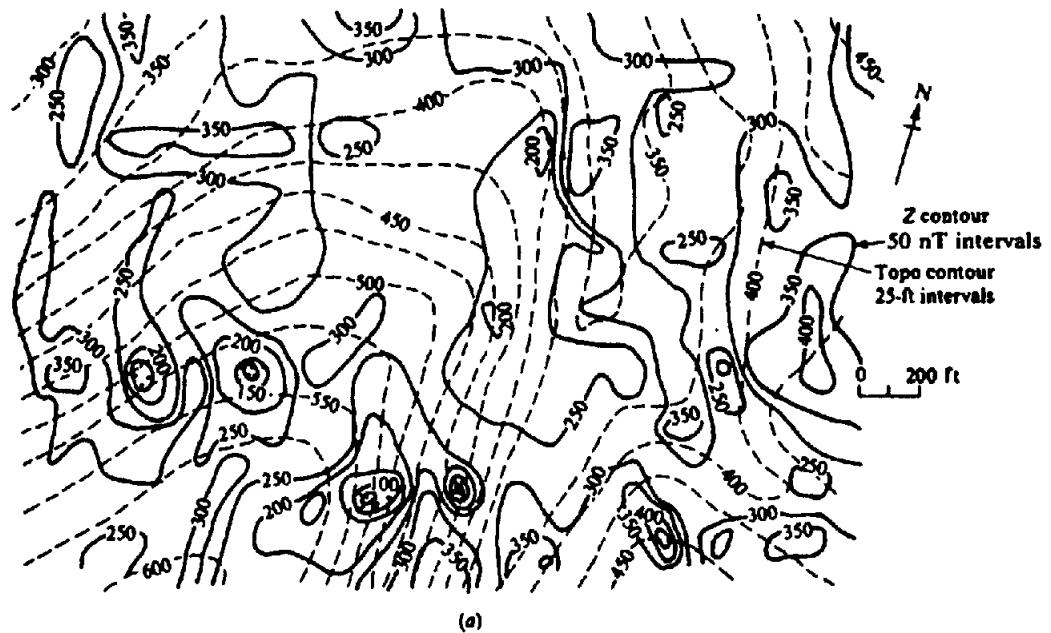
Figure 3.39. Vertical-component magnetic profiles, Manitoba Nickel Belt.

northwest Newfoundland. The rocks in the area are sedimentary, consisting of sandstones, shales, and limestones with some dolomite. In the upper half and the lower left quarter of the section the topography is flat; the average elevation is  $\sim 100$  m. A steep escarpment, in the shape of an inverted U with apex to the north, occupies the lower middle portion of the figure. It follows the closed 200 nT contour on the left, continues north and east to overlap the east half of the 100 nT low, and then turns southeast between the 300 nT contours on the lower right. This scarp rise about 200 m, in places having a slope of nearly  $30^\circ$ . As a result, the magnetic high in the lower part of the diagram is on a 300 m plateau. Flight lines were east-west, 300 m above ground level.

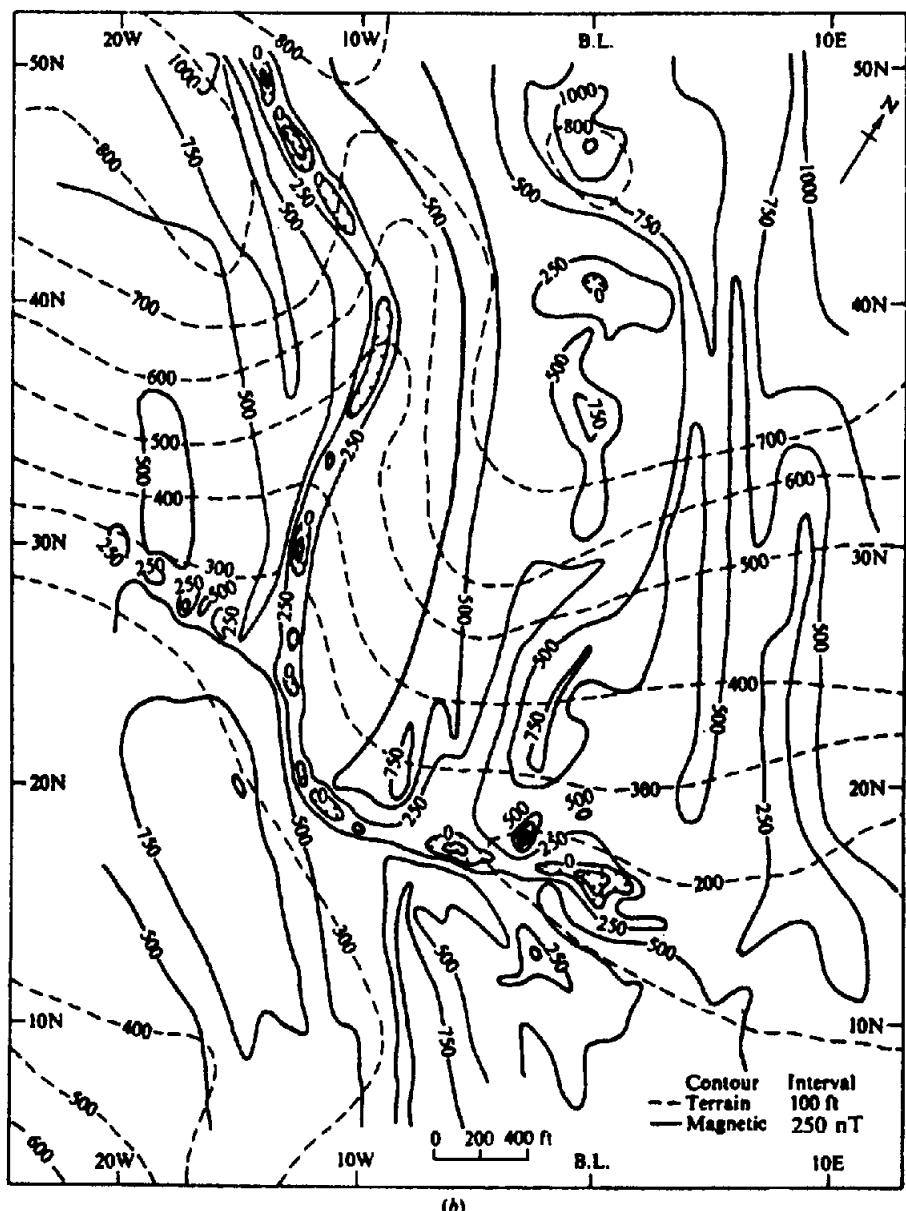
With this information, make an interpretation of the magnetic anomaly in the lower central

part of the section. Could it be entirely or partly the result of topography? Is it the reflection of a single magnetic structure? Is it possible that the larger magnetic low area, contained in the 200 nT contour striking roughly east-west, might represent a distinctly different structure?

14. The Z-component data in Table 3.8 constitute airborne and ground profiles along approximately the same line crossing a strong magnetic anomaly of great length, striking roughly E-W. The airborne magnetometer was a heavily damped vertical-component instrument at elevations of 300 to 400 ft above ground. The ground instrument was a conventional fluxgate magnetometer. Station intervals are in feet and airborne station 800N corresponds approximately to a point between 400 and 500N on the ground traverse. Determine the depth, cross section, approximate susceptibility, and direction of mag-



(a)



(b)

**Figure 3.40. Effect of topography on magnetic measurements.** (a) Elevation (dashed) and Z-component (solid) contours in an area of sedimentary rocks. (b) Elevation and Z-component contours in an area of granitic and sedimentary rocks.

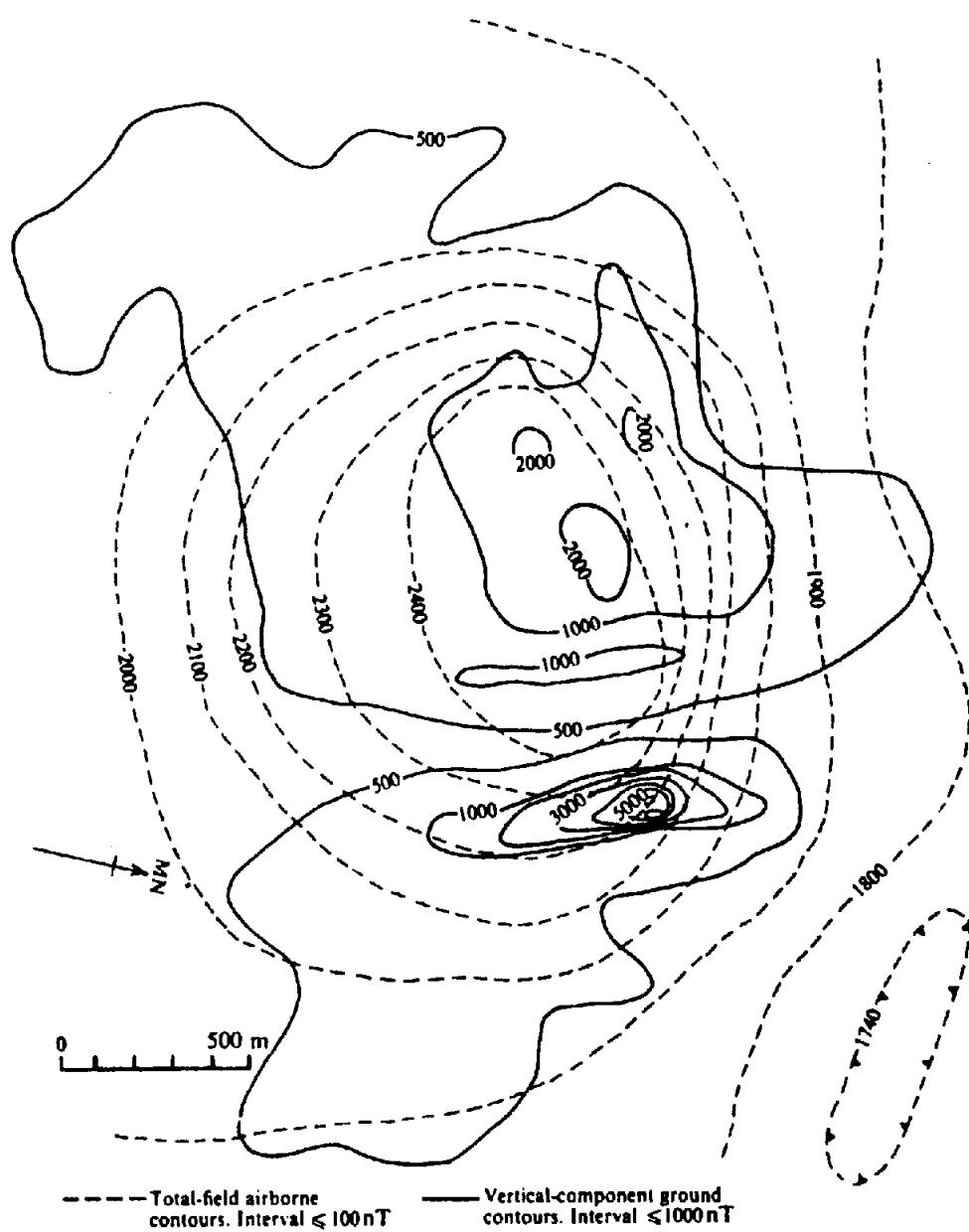


*Figure 3.41. Comparison of ground vertical-component data with airborne total-field data.*

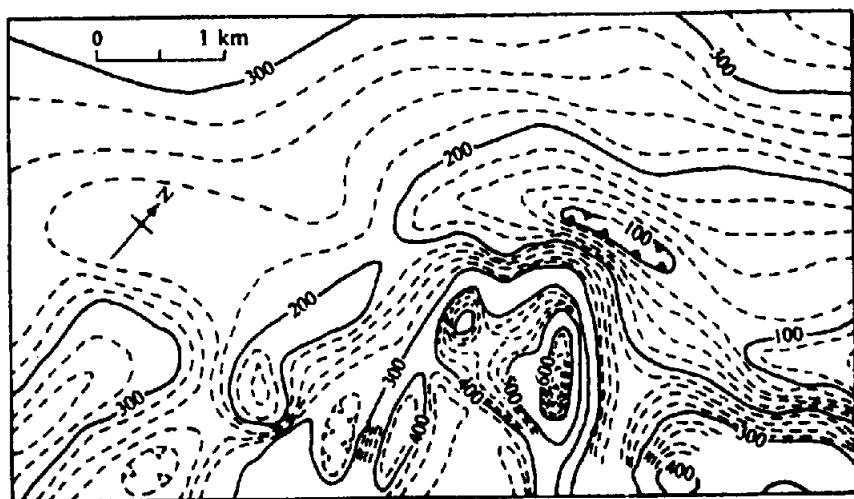


*Figure 3.42. Total-field aeromagnetic contours, northwest Newfoundland. C.I. = 20 nT and flight altitude 300 m.*

Table 3.8. Ground and airborne vertical-component survey.

Airborne		Ground			
Stn.	Z (nT)	Stn.	Z (nT)	Stn.	Z (nT)
ON	600	ON	4,600	600N	36,000
400	2,600	100	7,400	700	28,600
600	4,100	200	13,700	800	16,000
800	5,700	300	28,600	900	8,000
1,000	4,050	400	40,000	1,000	4,600
1,200	2,760	500	40,000		
1,500	750				

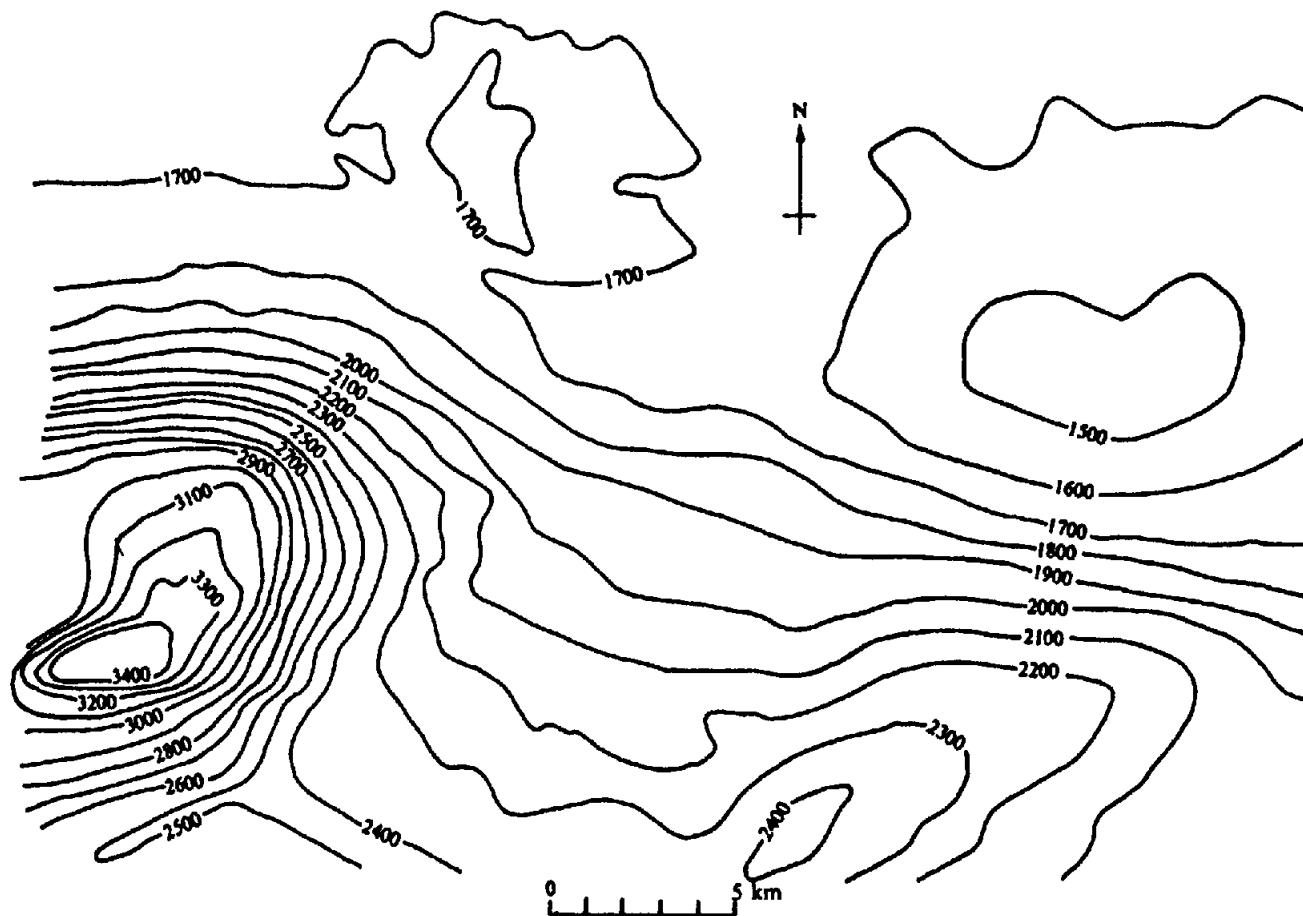


Figure 3.43. Total-field aeromagnetic contours, St. Lawrence lowlands. C.I. = 100 nT.

netization of the source from each traverse. As a check on the results, continue the ground profile upward to find out if it matches the airborne profile.

15. A section from Canadian government aeromagnetic maps of the St. Lawrence lowlands sedimentary region is reproduced in Figure 3.43. There are at least three large structural features producing the magnetic anomalies. Two are well documented geologically. Can you distinguish any fault zones? Any domes or plugs? Are these

anomalies produced by structures in the sediments or in the underlying basement rocks? Analyze this aeromagnetic section as precisely as possible, with particular emphasis on depths to the sources. Altitude of the aircraft was 300 m above ground level and the flight lines were E-W. The topography is essentially flat throughout.

16. Figure 3.44 shows a portion of an E-W aeromagnetic profile. The fiducial marks (numbers at the bottom) are 2 km apart and the aircraft was

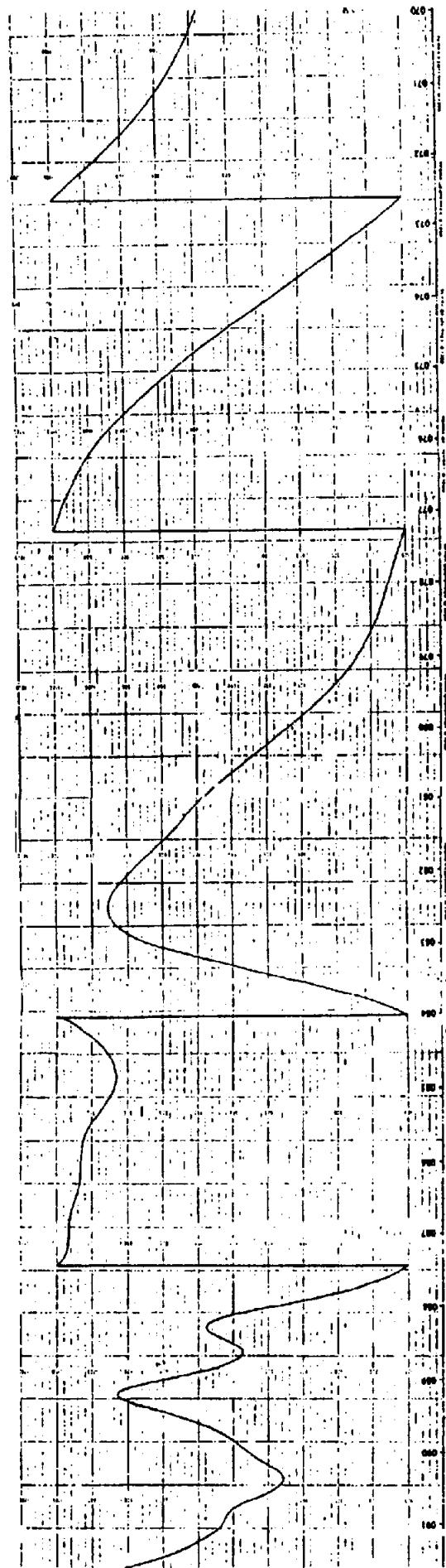


Figure 3.44. E-W aeromagnetic profile, East Texas. Full scale 600 nT. (Courtesy Chevron Oil Co.)

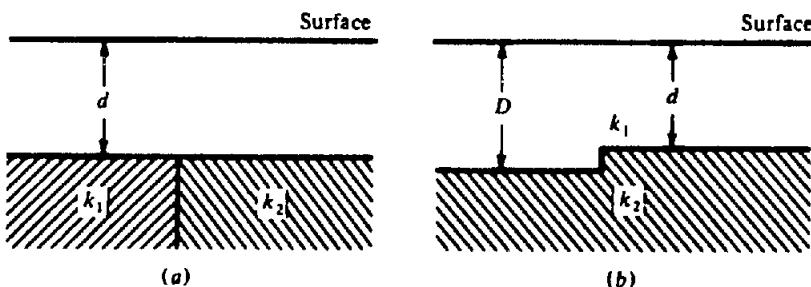


Figure 3.45. Basement structures. (a) Contact between slabs of different susceptibility. (b) Uniform bed with a step.

- flown at a constant barometric elevation of 750 m. Analyze the profile using the methods of Section 3.7.11 and Equations (3.89).
17. The schematics shown in Figure 3.45 represent two relatively common basement structures: (a) a contact between beds of great strike length and depth extent and (b) a uniform bed with a step. Assume  $D/d = 1.1$  and a N-S strike for both features. Plot both profiles and compare the maximum anomalies.

## REFERENCES

- Affleck, J. 1963. Magnetic anomaly trend and spacing patterns. *Geophysics* 28, 379–95.
- Al-Chalabi, M. 1971. Some studies relating to non-uniqueness in the gravity and magnetic inverse problem. *Geophysics* 36, 835–54.
- Baranov, V. 1957. A new method for interpretation of aeromagnetic maps: Pseudogravimetric anomalies. *Geophysics* 22, 359–83.
- Barnett, C. T. 1976. Theoretical modeling of the magnetic and gravitational fields of an arbitrarily shaped 3-D body. *Geophysics* 41, 1353–64.
- Barongo, J. O. 1985. Method for depth estimation on aeromagnetic vertical gradient anomalies. *Geophysics* 50, 963–8.
- Bhattacharyya, B. K. 1964. Magnetic anomalies due to prism-shaped bodies with arbitrary polarization. *Geophysics* 29, 517–31.
- Bhattacharyya, B. K. 1965. Two-dimensional harmonic analysis as a tool for magnetic interpretation. *Geophysics* 30, 829–57.
- Bhattacharyya, B. K. 1966. Continuous spectrum of total magnetic-field anomaly due to a rectangular prismatic body. *Geophysics* 31, 97–121.
- Bhattacharyya, B. K. 1970. Some important considerations in the acquisition and treatment of high-resolution aeromagnetic data. *Bulletino di Geofisica Teorica e di Applicata* 12, 21–44, 45–6.
- Bhattacharyya, B. K. 1971. An automatic method of compilation and mapping of high-resolution aeromagnetic data. *Geophysics* 36, 695–716.
- Bhattacharyya, B. K., and Navolio, M. E. 1976. A fast-Fourier transform method for rapid computation of gravity and magnetic anomalies due to arbitrary bodies. *Geophys. Prosp.* 24, 633–49.
- Bhattacharyya, B. K., Sweeney, R. E., and Godson, R. H. 1979. Integration of aeromagnetic data acquired at different times with varying elevations and line spacings. *Geophysics* 44, 742–52.
- Clark, A. J. 1986. Archaeological geophysics in Britain. *Geophysics* 51, 1403–13.
- Dean, W. C. 1958. Frequency analysis for gravity and magnetic interpretation. *Geophysics* 23, 97–127.
- Gay, S. P. 1967. Standard curves for interpretation of magnetic anomalies over long tabular bodies. In *Mining Geophysics*, vol. 2, pp. 512–48. Tulsa: Society of Exploration Geophysicists.
- Grant, F. S., and Martin, L. 1966. Interpretation of aeromagnetic anomalies by the use of characteristic curves. *Geophysics* 31, 135–48.
- Grauch, V. J. S., and Campbell, D. L. 1984. Does draping aeromagnetic data reduce terrain-induced effects? *Geophysics* 49, 75–80.
- Green, R. 1960. Remanent magnetization and the interpretation of magnetic anomalies. *Geophys. Prosp.* 8, 98–110.
- Gunn, P. J. 1975. Linear transformations of gravity and magnetic fields. *Geophys. Prosp.* 23, 300–12.
- Gupta, V. K., and Fitzpatrick, M. M. 1971. Evaluation of terrain effects in ground magnetic surveys. *Geophysics* 36, 582–9.
- Hague, B. 1957. *Alternating Current Bridge Methods*. New York: Putnam.
- Hahn, A., Kind, E. G., and Mishra, D. G. 1976. Depth estimation of magnetic sources by means of Fourier amplitude spectra. *Geophys. Prosp.* 24, 287–308.
- Hanson, R. D. and Miyazaki, Y. 1984. Continuation of potential fields between arbitrary surfaces. *Geophysics* 49, 789–95.
- Hartman, R. R., Teskey, D. J., and Friedberg, J. L. 1971. A system for rapid digital aeromagnetic interpretation. *Geophysics* 36, 891–918.
- Henderson, R. G. 1960. A comprehensive system of automatic computation in magnetic and gravity interpretation. *Geophysics* 25, 569–85.
- Hood, P. J. 1965. Gradient measurements in aeromagnetic surveying. *Geophysics* 30, 891–902.
- Hood, P., and McClure, D. J. 1965. Gradient measurements in ground magnetic prospecting. *Geophysics* 30, 403–10.
- Jain, S. 1976. An automatic method of direct interpretation of magnetic profiles. *Geophysics* 41, 531–41.
- Kilty, K. T. 1983. Werner deconvolution of profile potential field data. *Geophysics* 48, 234–7.
- Kip, A. F. 1962. *Fundamentals of Electricity and Magnetism*. New York: McGraw-Hill.
- Koulomzine, T., Lamontagne, Y., and Nadeau, A. 1970. New methods for direct interpretation of magnetic anomalies caused by inclined dikes of infinite length. *Geophysics* 35, 812–30.
- Leite, L. W. B., and Leao, J. W. D. 1985. Ridge regression applied to the inversion of two-dimensional aeromagnetic anomalies. *Geophysics* 50:1294–306.

- Martin, L. 1966. *Manual of Magnetic Interpretation*. Toronto: Computer Applications and Systems Engineering.
- McGrath, P. H., and Hood, P. J. 1973. An automatic least-squares multimodel method for magnetic interpretation. *Geophysics* 38, 349-58.
- Nabighian, M. N. 1984. Toward a three-dimensional automatic interpretation of potential field data via generalized Hilbert transforms: Fundamental relations. *Geophysics* 49, 780-6.
- Naudy, H. 1971. Automatic interpretation of depth on aeromagnetic profiles. *Geophysics* 36, 717-22.
- Nettleton, L. L. 1971. *Elementary Gravity and Magnetics for Geologists and Seismologists*. Tulsa: Society of Exploration Geophysicists.
- Oliver, R., and Hinze, W. J. 1985. Potential fields in rugged topography. *Geophysics, the Leading Edge of Exploration* 4, No. 4, 14-17.
- Paterson, N. R., and Reeves, C. V. 1985. Applications of gravity and magnetic surveys: the state-of-the-art in 1985. *Geophysics* 50, 2558-94.
- Peters, L. J. 1949. The direct approach to magnetic interpretation and its practical application. *Geophysics* 14, 290-320.
- Rao, D. A., and Babu, H. V. R. 1984. On the half-slope and straight-slope methods of basement depth determination. *Geophysics* 49, 1365-8.
- Rasmussen, R., and Pederson, L. B. 1979. End corrections in potential field modeling. *Geophys. Prosp.* 27, 749-60.
- Reford, M. S. 1980. History of geophysical exploration, magnetic method. *Geophysics* 45, 1640-58.
- Seigel, H. O. 1957. Discovery of Mobrun Copper Ltd. sulfide deposit, Noranda Mining District, Quebec. In *Methods and Case Histories in Mining Geophysics, 6th Commonwealth Mining and Metallurgical Congress*. Montreal: Mercury Press.
- Sheriff, R. E. 1984. *Encyclopedic Dictionary of Exploration Geophysics*. Tulsa: Society of Exploration Geophysicists.
- Sheriff, R. E., and Geldart, L. P. 1983. *Exploration Seismology*, vol. 2. Cambridge: Cambridge University Press.
- Silva, J. B. C. 1986. Reduction to the pole as an inverse problem and its application to low-latitude anomalies. *Geophysics* 51, 369-82.
- Smellie, D. W. 1967. Elementary approximations in aeromagnetic interpretation. In *Mining Geophysics*, vol. 2, pp. 474-89. Tulsa: Society of Exploration Geophysicists.
- Smith, P. J. 1982. The Earth as a Magnet. In *Cambridge Encyclopaedia of Earth Sciences*. D. G. Smith, ed., pp. 109-23. Cambridge: Cambridge University Press.
- Smith, R. A. 1961. Some theorems concerning local magnetic anomalies. *Geophys. Prosp.* 9, 399-410.
- Spector, A. 1979. paper presented at the Canadian Institute of Mining and Metallurgy, Montreal, April.
- Spector, A., and Grant, F. S. 1985. Statistical models for interpreting aeromagnetic data. *Geophysics* 50, 1951-60.
- Strangway, D. W. 1970. *History of the Earth's Magnetic Field*. New York: McGraw Hill.
- Teskey, D. J. 1980. Computer based system for interpretation of airborne gradiometer data with application to Key Lake area, Saskatchewan. Current Research, B, Geol. Surv. Canada paper 80-18, pp. 59-67.
- Vacquier, V., Steenland, N. C., Henderson, R. G., and Zeitz, I. 1951. Interpretation of aeromagnetic maps. *Geol. Soc. Am. Memoir* 47.
- Weinstock, H., and Overton, W. C. 1981. *Squid Applications to Geophysics*. Tulsa: Society of Exploration Geophysicists.
- Werner, S. 1953. Interpretation of aeromagnetic anomalies at sheet-like bodies. *Sver. Geol. Undersok. Ser. C, Arshok* 43, No. 6.
- Whitham, K. 1960. Measurement of the geomagnetic elements. In *Methods and Techniques in Geophysics*, vol. 1, S. K. Runcorn, ed., pp. 134-48. New York: Interscience.
- Wynn, J. . 1986. Geophysics in archaeology. *Geophysics* 51, 533-634.
- Zimmerman, J. E., and Campbell, W. H. 1975. Tests of cryogenic squid for geomagnetic field measurements. *Geophysics* 40, 269-84.

# Chapter

## 4

# *Seismic Methods*

### 4.1. INTRODUCTION

#### 4.1.1. Importance of Seismic Work

The seismic method is by far the most important geophysical technique in terms of expenditures (see Table 1.1) and number of geophysicists involved. Its predominance is due to high accuracy, high resolution, and great penetration. The widespread use of seismic methods is principally in exploring for petroleum: the locations for exploratory wells rarely are made without seismic information. Seismic methods are also important in groundwater searches and in civil engineering, especially to measure the depth to bedrock in connection with the construction of large buildings, dams, highways, and harbor surveys. Seismic techniques have found little application in direct exploration for minerals where interfaces between different rock types are highly irregular. However, they are useful in locating features, such as buried channels, in which heavy minerals may be accumulated.

Exploration seismology is an offspring of earthquake seismology. When an earthquake occurs, the earth is fractured and the rocks on opposite sides of the fracture move relative to one another. Such a rupture generates seismic waves that travel outward from the fracture surface and are recorded at various sites using seismographs. Seismologists use the data to deduce information about the nature of the rocks through which the earthquake waves traveled.

Exploration seismic methods involve basically the same type of measurements as earthquake seismology. However, the energy sources are controlled and movable, and the distances between the source and the recording points are relatively small. Much seismic work consists of *continuous coverage*, where the response of successive portions of earth is sampled along lines of profile. Explosives and other energy sources are used to generate the seismic waves, and arrays of seismometers or geophones are used to

detect the resulting motion of the earth. The data usually are recorded digitally on magnetic tape so that computer processing can be used to enhance the signals with respect to the noise, extract the significant information, and display it for geological interpretation.

The basic technique of seismic exploration consists of generating seismic waves and measuring the time required for the waves to travel from the sources to a series of geophones, usually disposed along a straight line directed toward the source. From a knowledge of traveltimes and the velocity of the waves, one attempts to reconstruct the paths of the seismic waves. Structural information is derived principally from paths that fall into two main categories: *headwave* or *refracted* paths, in which the principal portion of the path is along the interface between two rock layers and hence is approximately horizontal, and *reflected* paths, in which the wave travels downward initially and at some point is reflected back to the surface, the overall path being essentially vertical. For both types of path, the traveltimes depend on the physical properties of the rocks and the attitudes of the beds. The objective of seismic exploration is to deduce information about the rocks, especially about the attitudes of the beds, from the observed arrival times and (to a lesser extent) from variations in amplitude, frequency, phase, and wave shape.

Despite the indirectness of the method – most seismic work results in the mapping of geological structure rather than finding petroleum directly – the likelihood of a successful venture is improved more than enough to pay for the seismic work. Likewise, engineering surveys, mapping of water resources, and other studies requiring accurate knowledge of subsurface structure derive valuable information from seismic data.

We shall first give a brief outline of the history of seismic exploration and of the field methods used for acquiring seismic data. This will be followed by a

brief discussion of seismic methods that will provide a background for the following sections. The subsequent sections will then discuss the theory of seismic wave propagation, the geometry of seismic raypaths, and the characteristics of seismic events. We shall then examine, in more detail, the recording instrumentation and field techniques used for land and marine reflection and refraction surveys. Finally, we shall describe the processing of seismic data and conclude with a discussion of interpretation techniques.

#### 4.1.2. History of Seismic Exploration

Much of seismic theory was developed prior to the availability of instruments that were capable of sufficient sensitivity to permit significant measurements. Earthquake seismology preceded exploration applications. In 1845, Mallet experimented with "artificial earthquakes" in an attempt to measure seismic velocities. Knott developed the theory of reflection and refraction at interfaces in a paper in 1899 and Zoeppritz and Wiechert published on wave theory in 1907. During World War I, both the Allies and Germany carried out research directed toward locating heavy guns by recording the arrival of seismic waves generated by the recoil. Although this work was not very successful, it was fundamental in the development of exploration seismology, and several workers engaged in this research later pioneered the development of seismic prospecting techniques and instruments. Among these researchers, Mintrop in Germany and Karcher, McCollum, and Eckhardt in the United States were outstanding.

In 1919, Mintrop applied for a patent on the refraction method and, in 1922, Mintrop's Seismos Company furnished two crews to do refraction seismic prospecting in Mexico and the Gulf Coast area of the United States using a mechanical seismograph of rather low sensitivity. The discovery, in 1924, of the Orchard salt dome in Texas led to an extensive campaign of refraction shooting during the next six years, the emphasis being principally on the location of salt domes. By 1930 most of the shallow domes had been discovered and the refraction method began to give way to the reflection method. Whereas refraction techniques were ideal for locating salt domes, reflection techniques are more suitable for mapping other types of geologic structures commonly encountered.

Reflection seismic prospecting stemmed principally from the pioneering work of Reginald Fessenden about 1913. This work was directed toward measuring water depths and detecting icebergs using sound waves. In the early 1920s, Karcher de-

veloped a reflection seismograph that saw field use in Oklahoma. It was not until 1927, however, that commercial utilization of the reflection method began with a survey by the Geophysical Research Corporation of the Maud field in Oklahoma, which used a vacuum tube amplifier. Oklahoma proved to be particularly suitable for the application of reflection methods, just as the Gulf Coast had been suitable for refraction techniques, and the reflection method rapidly grew in popularity until it virtually displaced the refraction method. Although reflection has continued to be the principal seismic method, there are certain areas and types of problems where refraction techniques enjoy advantages over reflection shooting, and so they continue to be used to a modest degree.

A distinctive reflection was characteristic of the first reflection application in Oklahoma. Hence the first reflection work utilized the *correlation method* whereby a map was constructed by recognizing the same event on isolated individual records. However, most areas are not characterized by such a distinctive reflector and so, in general, the correlation method has little application.

In 1929, the calculation of dip from the time differences across several traces of a seismic record permitted the successful application of reflection exploration in the Gulf Coast area where reflections were not distinctive of a particular lithologic break and could not be followed for long distances. This method proved to be much more widely applicable than correlation shooting and so led to rapid expansion of seismic exploration.

As the capability of recording the data from more geophones grew, recordings became spaced so closely that reflections could be followed continuously along lines of profile, and continuous coverage became the standard seismic reflection method. Reflections from interfaces were interpreted on photographic recordings (Fig. 4.1) to map structure features.

In 1936, Rieber published the idea of processing seismic data using variable-density records and photocells for reproduction; however, widespread use of playback processing did not begin until magnetic tape became commercially available in 1953. Magnetic tape recording spread rapidly in the next few years, especially after digital recording and processing were introduced in the 1960s. Magnetic tape recording made it possible to combine the data from several recordings made at different times and this made the use of weaker energy sources feasible. Introduction, in 1953, of a dropped weight as a source of seismic energy was the forerunner of a series of different kinds of seismic sources.

Radar was one of the outstanding technological advances of World War II and it was widely used in

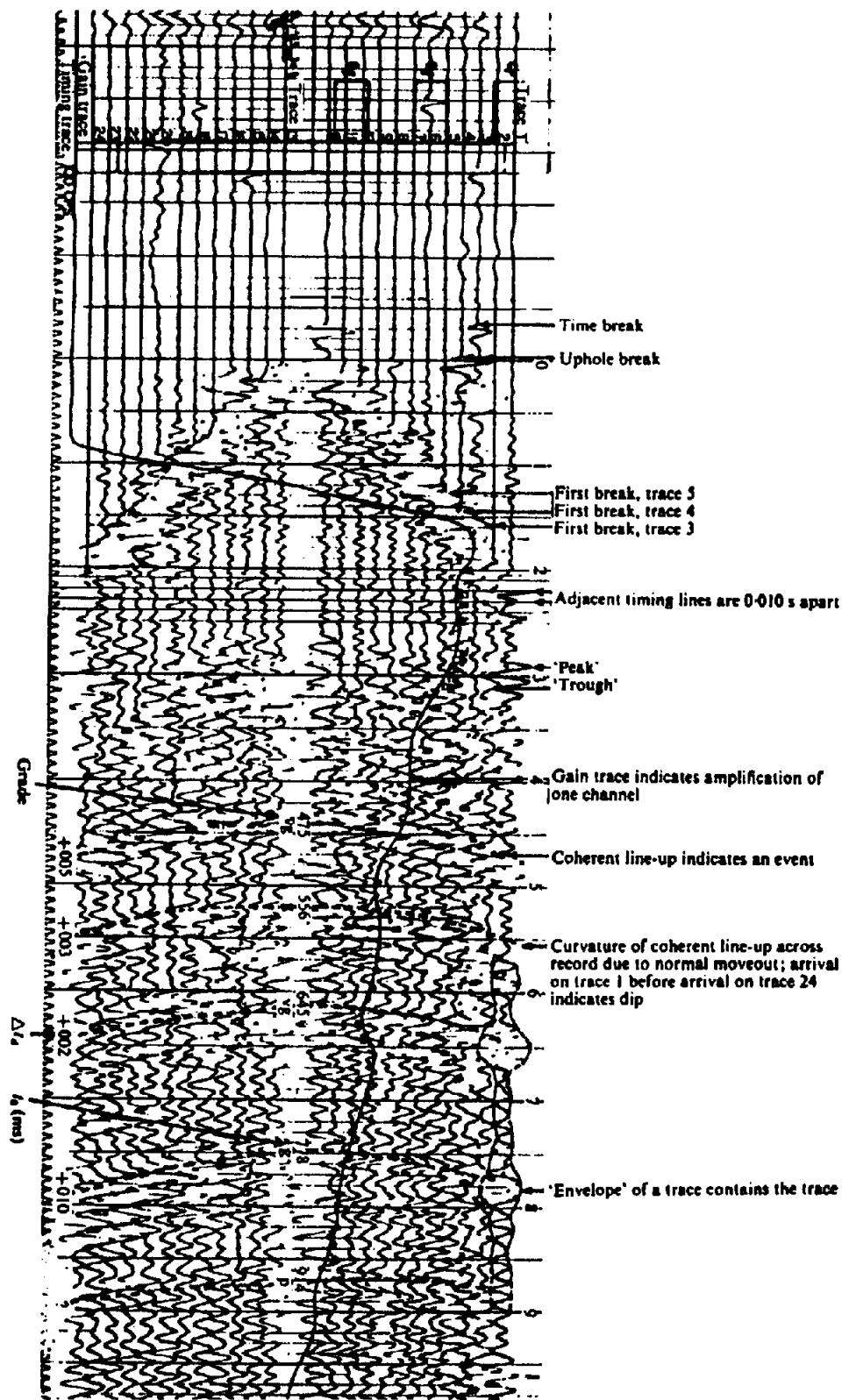


Figure 4.1. 24-trace seismic record for 12 geophone groups on either side of the sourcepoint. The trace spacing is 50 m, the heavy timing lines are 0.1 s apart, and the finer timing lines 0.01 s apart. Traces 12 and 13 are 50 m from the shotpoint. (Courtesy Chevron Oil Co.)

the detection of aircraft. However, noise frequently interfered with the application of radar and considerable theoretical effort was devoted to the detection of signals in the presence of noise. The result was the birth of a new field of mathematics – information theory. Early in the 1950s a research group at the Massachusetts Institute of Technology studied its application to seismic exploration problems (Flinn, Robinson, and Treitel, 1967). Simultaneously with this development, rapid advances in digital computer technology made extensive calculations feasible for the first time (Robinson, 1985). These two developments had a great impact on seismic exploration in the early 1960s and before the end of the decade, data processing (as the application is called) had changed seismic exploration dramatically, so much so that it came to be referred to as the "digital revolution." Most seismic recording is now done in digital form and most data are subjected to data processing before being interpreted.

The common-midpoint method (also called common-depth-point and common-reflection-point) was patented in 1956. This method involves recording data from the same subsurface a number of times with varied source and geophone locations and then combining the data in processing. The redundancy of data achieved with this method made practical a number of schemes for the attenuation of noise (including multiple reflections) and improved data quality so much that most areas were remapped with the new techniques.

Most seismic sources are impulsive, that is, they develop a short, sharp waveform. In contrast, the Vibroseis method, developed in 1953 but not applied extensively until much later, generates a wavetrain that is so long that reflections overlap extensively. Processing effectively collapses the wavetrain back to that achieved with an impulsive source. About half of the land data is now acquired with the Vibroseis method.

Because of continual improvements in instrumentation and processing, many areas have been resurveyed or reprocessed repeatedly; each time better quality of data is achieved. New acquisition techniques, such as vertical profiling and the use of *S* waves, have been developed. In areas of special interest, three-dimensional acquisition techniques are employed that cover an area rather than merely along occasional profile lines. Interpretation techniques also have been improved continually. Rather than being limited merely to mapping structural features, interpretation now involves studies of velocity, amplitude, frequency, and waveform variations so that information can be determined about the lithology, stratigraphic features, and hydrocarbon accumulations. Applications are extending beyond lo-

cating hydrocarbons to helping guide oil-field development and monitoring production.

More on the history of seismic exploration is given in Allen (1980), Bates, Gaskell, and Rice (1982), and Sheriff and Geldart (1982, pp. 3–27).

#### 4.1.3. Outline of the Seismic Reflection Method

To provide a background for the following sections, a brief outline of one of the many variations of seismic reflection technique will be given at this point (although the reasons for various steps will only be given later).

Assume that a land crew uses an explosive as the energy source. The first step in the field work is to drill a vertical hole at the *sourcepoint* (*shotpoint*), the hole diameter being perhaps 10 cm and the depth between 6 and 30 m. A *charge* of 2 to 25 kg of explosive is armed with an electric blasting *cap* and placed near the bottom of the hole. Two wires extend from the cap to the surface where they are connected to a *blaster* that is used to send an electrical current through the wires to the cap, which then explodes and detonates the main explosive (*shot*). Sourcepoints are usually spaced at equal intervals of 50 to 400 m. *Cables* are laid out in a straight line extending away from the sourcepoint; each cable contains many pairs of electrical conductors. Each pair of wires is connected to an outlet and the outlets are spaced at intervals of 25 to 100 m along the cable. Several *geophones* (*seismometers*) are connected to each of these outlets so that each pair of wires carries the output energy of a group of geophones back to the recording instruments. Because of the small spacing between the geophones attached to one pair of wires, the group is approximately equivalent to a single large geophone located at the center of the group. Often 96 or more geophone groups are used. When seismic waves from the explosion arrive, each geophone group generates a signal that depends on the motion of the ground in the vicinity of the group. The net result is signals furnishing information about the ground motion at a number of regularly spaced points along a straight line passing through the sourcepoint.

The electrical signals go to amplifiers that increase the signal strength and partially eliminate (*filter out*) parts of the signal deemed undesirable. This information along with accurate timing signals are recorded on magnetic tape. Thus the recorded data consist of a number of *traces*, each showing how the motion of the ground at one geophone group varied with time after the source instant (*time-break*).

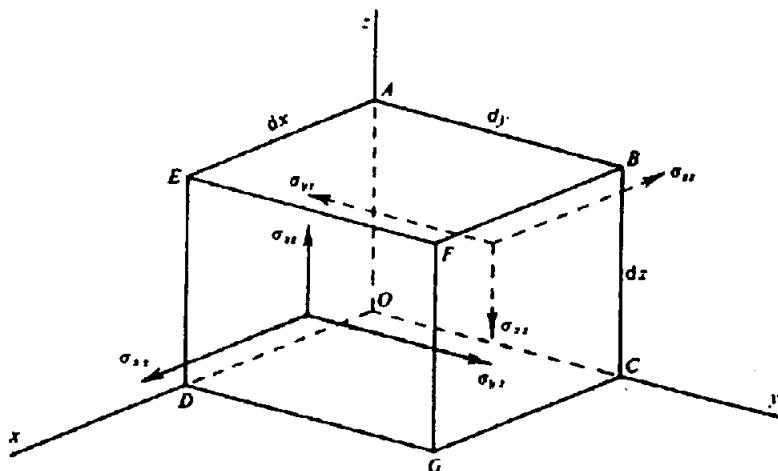


Figure 4.2. Components of stress.

The arrival of seismic waves produces systematic variations from trace to trace (*events*). The *travel-times*, the intervals between the source instant and the arrivals of the seismic energy (also known as the *arrival times*), of events believed to be reflections are measured. The location and attitude of the interface that gave rise to each reflection event are calculated from the traveltimes. The results from various source locations are combined into cross sections and contour maps to represent the structure of geological interfaces. The presence of hydrocarbons or other minerals is inferred mainly from the structural information (see, however, § 4.8.7).

We have introduced a number of terms (indicated by italics) used in a specialized sense in seismic work. We shall follow the definitions for such terms given by Sheriff (1984).

## 4.2. SEISMIC THEORY

### 4.2.1. Theory of Elasticity

(a) *General.* The seismic method utilizes the propagation of waves through the earth. Because this propagation depends on the elastic properties of the rocks, we briefly shall discuss the basic concepts of elasticity.

The size and shape of a solid body can be changed by applying forces to the external surface of the body. These external forces are opposed by internal forces that resist the changes in size and shape. As a result, the body tends to return to its original condition when the external forces are removed. Similarly, a fluid resists changes in size (volume) but not changes in shape. This property of resisting changes in size or shape and of returning to the undeformed condition when the external forces are removed is called *elasticity*. A perfectly elastic body is one that

recovers completely after being deformed. Many substances including rocks can be considered perfectly elastic without appreciable error, provided the deformations are small, as is the case for seismic waves except near a seismic source.

The theory of elasticity relates the applied forces to the resulting changes in size and shape. The relations between the applied forces and the deformations are expressed in terms of the concepts, stress and strain.

(b) *Stress.* *Stress* is defined as force per unit area. When a force is applied to a body, the stress is the ratio of the force to the area on which the force is applied. If the force varies from point to point, the stress also varies and its value at any point is found by taking an infinitesimally small element of area centered at the point and dividing the total force acting on this area by the magnitude of the area. If the force is perpendicular to the area, the stress is said to be a *normal stress* (or *pressure*). In this book, positive values correspond to tensile stresses (the opposite convention of signs is also used frequently). When the force is tangential to the element of area, the stress is a *shearing stress*. When the force is neither parallel nor perpendicular to the element of area, it can be resolved into components parallel and perpendicular to the element. Hence any stress can be resolved into normal and shearing components.

If we consider a small element of volume, the stresses acting on each of the six faces of the element can be resolved into components, as shown in Figure 4.2 for the two faces perpendicular to the *x* axis. Subscripts denote the *x*, *y*, and *z* axes, respectively, and  $\sigma_{xy}$  denotes a stress parallel to the *x* axis acting on a surface perpendicular to the *y* axis. When the two subscripts are the same (as with  $\sigma_{xx}$ ), the stress is a normal stress; when the subscripts are different (as with  $\sigma_{xy}$ ), the stress is a shearing stress.

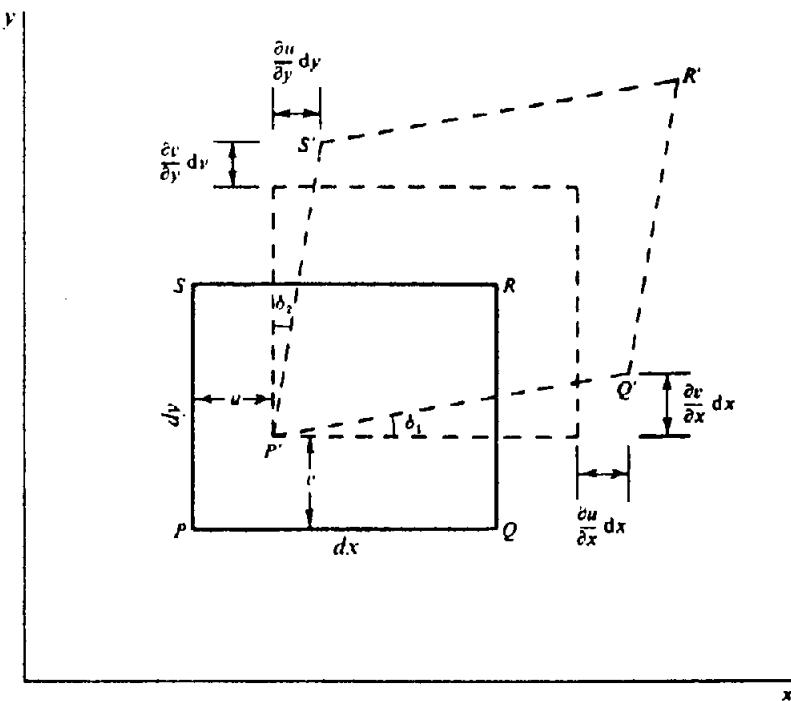


Figure 4.3. Analysis of two-dimensional strain.

When the medium is in static equilibrium, the forces must be balanced. This means that the three stresses  $\sigma_{xx}$ ,  $\sigma_{yx}$ , and  $\sigma_{xy}$  acting on the face  $OABC$  must be equal and opposite to the corresponding stresses shown on the opposite face  $DEFG$ , with similar relations for the remaining four faces. In addition, a pair of shearing stresses, such as  $\sigma_{yx}$ , constitute a *couple* tending to rotate the element about the  $z$  axis. The magnitude of the couple is

$$(\text{force} \times \text{lever arm}) = (\sigma_{yx} dy dz) dx$$

If we consider the stresses on the other four faces, we find that this couple is opposed solely by the couple due to the pair of stresses  $\sigma_{xy}$  with magnitude  $(\sigma_{xy} dx dz) dy$ . Because the element is in equilibrium, the total moment must be zero; hence  $\sigma_{xy} = \sigma_{yx}$ . In general, we must have

$$\sigma_{ij} = \sigma_{ji}$$

(c) *Strain*. When an elastic body is subjected to stresses, changes in shape and dimensions occur. These changes, which are called *strains*, can be resolved into certain fundamental types.

Consider a rectangle  $PQRS$  in the  $xy$  plane (see Fig. 4.3). When the stresses are applied, let  $P$  move to  $P'$ ;  $PP'$  have components  $u$  and  $v$ . If the other vertices  $Q$ ,  $R$ , and  $S$  have the same displacement as  $P$ , the rectangle is merely displaced as a whole by the amounts  $u$  and  $v$ . In this case, there is no change in size or shape and no strain exists. However, if  $u$  and  $v$  are different for the different vertices, the rectangle

will undergo changes in size and/or shape, and strains will exist.

Let us assume that  $u = u(x, y)$  and  $v = v(x, y)$ . Then the coordinates of the vertices of  $PQRS$  and  $P'Q'R'S'$  are

$$P(x, y), Q(x + dx, y);$$

$$S(x, y + dy), R(x + dx, y + dy);$$

$$P'(x + u, y + v);$$

$$Q'\left(x + dx + u + \frac{\partial u}{\partial x} dx, y + v + \frac{\partial v}{\partial x} dx\right);$$

$$S'\left(x + u + \frac{\partial u}{\partial y} dy, y + dy + v + \frac{\partial v}{\partial y} dy\right);$$

$$R'\left(x + dx + u + \frac{\partial u}{\partial x} dx + \frac{\partial u}{\partial y} dy,$$

$$y + dy + v + \frac{\partial v}{\partial x} dx + \frac{\partial v}{\partial y} dy\right)$$

In general, the changes in  $u$  and  $v$  are much smaller than the quantities  $dx$  and  $dy$ . Accordingly, we assume that the terms  $(\partial u / \partial x)$ ,  $(\partial u / \partial y)$ , and so on, are small enough that powers and products can be neglected. With this assumption, we see that:

1.  $PQ$  increases in length by the amount  $(\partial u / \partial x) dx$  and  $PS$  increases by the amount  $(\partial v / \partial y) dy$ . Hence,  $\partial u / \partial x$  and  $\partial v / \partial y$  are the fractional increases in length in the direction of the axes.
2. The infinitesimal angles  $\delta_1$  and  $\delta_2$  are equal to  $\partial v / \partial x$  and  $\partial u / \partial y$ , respectively.

3. The right angle at  $P$  decreases by the amount  $(\delta_1 + \delta_2) = (\partial v / \partial x + \partial u / \partial y)$ .
4. The rectangle as a whole is rotated counterclockwise through the angle  $(\delta_1 - \delta_2)/2 = (\partial v / \partial x - \partial u / \partial y)/2$ .

Strain is defined as the relative change (that is, the fractional change) in a dimension or shape of a body. The quantities  $\partial u / \partial x$  and  $\partial v / \partial y$  are the relative increases in length in the directions of the  $x$  and  $y$  axes and are referred to as *normal strains*. The quantity  $(\partial v / \partial x + \partial u / \partial y)$  is the amount by which a right angle in the  $xy$  plane is reduced when the stresses are applied; hence, it is a measure of the change in shape of the medium, which is known as a *shearing strain* and is denoted by the symbol  $\epsilon_{xy}$ . The quantity  $(\partial v / \partial x - \partial u / \partial y)/2$ , which represents a rotation of the body about the  $z$  axis, does not involve change in size or shape and hence is not a strain; we denote it by the symbol  $\theta_z$ .

Extending the above analysis to three dimensions, we write  $(u, v, w)$  as the components of displacement of a point  $P(x, y, z)$ . The elementary strains thus are

$$\text{Normal strains } \left. \begin{aligned} \epsilon_{xx} &= \frac{\partial u}{\partial x} \\ \epsilon_{yy} &= \frac{\partial v}{\partial y} \\ \epsilon_{zz} &= \frac{\partial w}{\partial z} \end{aligned} \right\} \quad (4.1)$$

$$\text{Shearing strains } \left. \begin{aligned} \epsilon_{xy} &= \epsilon_{yx} = \frac{\partial v}{\partial x} + \frac{\partial u}{\partial y} \\ \epsilon_{yz} &= \epsilon_{zy} = \frac{\partial w}{\partial y} + \frac{\partial v}{\partial z} \\ \epsilon_{zx} &= \epsilon_{xz} = \frac{\partial u}{\partial z} + \frac{\partial w}{\partial x} \end{aligned} \right\} \quad (4.2)$$

In addition to these strains, the body is subjected to simple rotation about the three axes, which is given by

$$\left. \begin{aligned} \theta_x &= \frac{1}{2} \left( \frac{\partial w}{\partial y} - \frac{\partial v}{\partial z} \right) \\ \theta_y &= \frac{1}{2} \left( \frac{\partial u}{\partial z} - \frac{\partial w}{\partial x} \right) \\ \theta_z &= \frac{1}{2} \left( \frac{\partial v}{\partial x} - \frac{\partial u}{\partial y} \right) \end{aligned} \right\} \quad (4.3)$$

The changes in dimensions given by the normal strains result in volume changes; the change in volume per unit volume is called the *dilatation* and is

represented by  $\Delta$ . If we start with a rectangular parallelepiped with edges  $dx$ ,  $dy$ , and  $dz$  in the unstrained medium, the dimensions in the strained medium are  $dx(1 + \epsilon_{xx})$ ,  $dy(1 + \epsilon_{yy})$ , and  $dz(1 + \epsilon_{zz})$ ; hence the increase in volume is approximately  $(\epsilon_{xx} + \epsilon_{yy} + \epsilon_{zz}) dx dy dz$ . Because the original volume was  $(dx dy dz)$ , we see that

$$\begin{aligned} \Delta &= \epsilon_{xx} + \epsilon_{yy} + \epsilon_{zz} \\ &= \frac{\partial u}{\partial x} + \frac{\partial v}{\partial y} + \frac{\partial w}{\partial z} \end{aligned} \quad (4.4)$$

(d) *Hooke's law.* In order to calculate the strains when the stresses are known, we must know the relationship between stress and strain. When the strains are small, this relation is given by *Hooke's law*, which states that a given strain is directly proportional to the stress producing it. When several stresses exist, each produces strains independently of the others; hence the total strain is the sum of the strains produced by the individual stresses. This means that each strain is a linear function of all of the stresses and vice versa. In general, Hooke's law leads to complicated relations but when the medium is *isotropic*, that is, when properties do not depend on direction, it can be expressed in the relatively simple form

$$\sigma_{ii} = \lambda' \Delta + 2\mu \epsilon_{ii} \quad i = x, y, z \quad (4.5)$$

$$\sigma_{ij} = \mu \epsilon_{ij} \quad i, j = x, y, z, i \neq j \quad (4.6)$$

Equation (4.5) states that a normal stress may produce stress in directions other than the direction of the stress; Equation (4.6) states that a shearing stress produces only a shearing strain (no normal strains).

The quantities  $\lambda'$  and  $\mu$  are known as *Lamé constants*. If we write  $\epsilon_{ij} = (\sigma_{ij}/\mu)$ , it is evident that  $\epsilon_{ij}$  is smaller the larger  $\mu$  is. Hence  $\mu$  is a measure of the resistance to shearing strain and is often referred to as the *modulus of rigidity* or *shear modulus*.

When the stress is increased beyond an *elastic limit*, Hooke's law no longer holds and strains increase more rapidly. Strains resulting from stresses that exceed this limit do not entirely disappear when the stresses are removed.

(e) *Elastic constants.* Although Lamé constants are convenient at times, other elastic constants are also used. Consider a medium in which all stresses are zero except  $\sigma_{xx}$ . Assuming  $\sigma_{xx}$  is positive (that is, a tensile stress), dimensions parallel to  $\sigma_{xx}$  will increase whereas dimensions normal to  $\sigma_{xx}$  will decrease. This means that  $\epsilon_{xx}$  is positive (elongation in the  $x$  direction) whereas  $\epsilon_{yy}$  and  $\epsilon_{zz}$  are negative. From symmetry we can see that  $\epsilon_{yy} = \epsilon_{zz}$ . We now

define Young's modulus and Poisson's ratio by the relations [see problem 1(a) and (b)].

$$\text{Young's modulus } E = \frac{\sigma_{xx}}{\epsilon_{xx}} = \frac{\mu(3\lambda' + 2\mu)}{\lambda' + \mu} \quad (4.7)$$

$$\begin{aligned} \text{Poisson's ratio } \sigma &= -\frac{\epsilon_{yy}}{\epsilon_{xx}} \\ &= -\frac{\epsilon_{zz}}{\epsilon_{xx}} = \frac{\lambda'}{2(\lambda' + \mu)} \end{aligned} \quad (4.8)$$

The minus signs are inserted to make  $\sigma$  positive. (The symbol  $\sigma$  is more-or-less standard for Poisson's ratio; the subscripts should prevent any confusion with a stress  $\sigma_{ij}$ .)

Consider a medium subjected only to a hydrostatic pressure  $p$ , which is equivalent to the statements

$$\sigma_{xx} = \sigma_{yy} = \sigma_{zz} = -p \quad \sigma_{xy} = \sigma_{yz} = \sigma_{zx} = 0$$

Then,  $k$  is the ratio of the pressure to the dilatation:

$$\text{bulk modulus } k = \frac{-p}{\Delta} = \frac{3\lambda' + 2\mu}{3} \quad (4.9)$$

The minus sign is inserted to make  $k$  positive.

By eliminating different pairs of constants, many different relations can be derived to express one of the five constants in terms of two others (see Sheriff and Geldart, 1982, p. 74).

The preceding theory assumes an isotropic medium, but sedimentary and metamorphic rocks are frequently not isotropic; differences of 20 to 25% have been reported. If one does not assume isotropy, the mathematics becomes complicated and physical insight is more difficult. Fortunately the assumption of isotropy usually provides a reasonable explanation of actual results. The next simplest situation after isotropy is *transverse isotropy*, where properties are the same in two orthogonal directions (usually the bedding-plane directions) but different in the third. This situation is discussed by Sheriff and Geldart (1982, pp. 36–7 and 52–3). It can be shown that a layered medium composed of isotropic layers behaves like a transversely isotropic medium when the seismic wavelengths are large compared to the bed thicknesses. Interest in anisotropy is growing because fracturing of rocks induces anisotropy and because fracture porosity markedly affects hydrocarbon production.

The elastic constants are defined in such a way that they are positive numbers. As a consequence,  $\sigma$  must have values between 0 and 0.5 [because in Eq.

(4.8)  $\lambda' / (\lambda' + \mu)$  is less than unity]. Values range from 0.05 for very hard, rigid rocks to about 0.45 for soft, poorly consolidated materials. Liquids have no resistance to shear and hence for them  $\mu = 0$  and  $\sigma = 0.5$ . For most rocks,  $E$ ,  $k$ , and  $\mu$  lie in the range from 10 to 200 gigapascal (GPa) [10 to  $200 \times 10^9$  newton/meter<sup>2</sup> (N/m<sup>2</sup>)];  $E$  generally is the largest and  $\mu$  the smallest of the three. Extensive tables of elastic constants of rocks have been given by Birch (1966, pp. 107–73).

#### 4.2.2. Wave Equation and its Solutions

(a) *Wave equation*. Up to this point we have been discussing a medium in static equilibrium. We shall now remove this restriction and consider what happens when the stresses are not in equilibrium. In Figure 4.2 we now assume that the stresses on the rear face of the element of volume are as shown in the diagram, but that the stresses on the front face are, respectively,

$$\sigma_{xx} + \frac{\partial \sigma_{xx}}{\partial x} dx \quad \sigma_{yx} + \frac{\partial \sigma_{yx}}{\partial x} dx \quad \sigma_{zx} + \frac{\partial \sigma_{zx}}{\partial x} dx$$

Because these stresses are opposite to those acting on the rear face, the net (unbalanced) stresses are

$$\frac{\partial \sigma_{xx}}{\partial x} dx \quad \frac{\partial \sigma_{yz}}{\partial x} dx \quad \frac{\partial \sigma_{zx}}{\partial x} dx$$

These stresses act on a face that has an area ( $dy dz$ ) and they affect the volume ( $dx dy dz$ ); hence we get for the net forces per unit volume in the directions of the  $x$ ,  $y$ , and  $z$  axes the values

$$\frac{\partial \sigma_{xx}}{\partial x} \quad \frac{\partial \sigma_{yz}}{\partial x} \quad \frac{\partial \sigma_{zx}}{\partial x}$$

respectively. Similar expressions hold for the other faces; hence we find for the total force per unit volume in the direction of the  $x$  axis the expression

$$\left( \frac{\partial \sigma_{xx}}{\partial x} + \frac{\partial \sigma_{xy}}{\partial y} + \frac{\partial \sigma_{xz}}{\partial z} \right)$$

Newton's second law of motion states that the unbalanced force equals the mass times the acceleration; thus we obtain the equation of motion along the  $x$  axis:

$$\rho \frac{\partial^2 u}{\partial t^2} = \text{unbalanced force per unit volume}$$

in the  $x$  direction

$$= \frac{\partial \sigma_{xx}}{\partial x} + \frac{\partial \sigma_{xy}}{\partial y} + \frac{\partial \sigma_{xz}}{\partial z} \quad (4.10)$$

where  $\rho$  is the density. Similar equations can be written for motion along the  $y$  and  $z$  axes.

Equation (4.10) relates the displacements to the stresses. We can obtain an equation involving only displacements by using Hooke's law to replace the stresses with strains and then expressing the strains in terms of the displacements, using Equations (4.1), (4.2), (4.4), (4.5), and (4.6):

$$\begin{aligned} \rho \frac{\partial^2 u}{\partial t^2} &= \frac{\partial \sigma_{xx}}{\partial x} + \frac{\partial \sigma_{xy}}{\partial y} + \frac{\partial \sigma_{xz}}{\partial z} \\ &= \lambda' \frac{\partial \Delta}{\partial x} + 2\mu \frac{\partial \epsilon_{xx}}{\partial x} + \mu \frac{\partial \epsilon_{xy}}{\partial y} + \mu \frac{\partial \epsilon_{xz}}{\partial z} \\ &= \lambda' \frac{\partial \Delta}{\partial x} + \mu \left( 2 \frac{\partial^2 u}{\partial x^2} + \left( \frac{\partial^2 v}{\partial x \partial y} + \frac{\partial^2 u}{\partial y^2} \right) \right. \\ &\quad \left. + \left( \frac{\partial^2 u}{\partial z^2} + \frac{\partial^2 w}{\partial x \partial z} \right) \right) \\ &= \lambda' \frac{\partial \Delta}{\partial x} + \mu \nabla^2 u + \mu \frac{\partial}{\partial x} \left( \frac{\partial u}{\partial x} + \frac{\partial v}{\partial y} + \frac{\partial w}{\partial z} \right) \\ &= (\lambda' + \mu) \frac{\partial \Delta}{\partial x} + \mu \nabla^2 u \end{aligned} \quad (4.11)$$

where  $\nabla^2 u = \text{Laplacian}$  of  $u = (\partial^2 u / \partial x^2 + \partial^2 u / \partial y^2 + \partial^2 u / \partial z^2)$ . By analogy we can write the equations for  $v$  and  $w$ :

$$\rho \frac{\partial^2 v}{\partial t^2} = (\lambda' + \mu) \frac{\partial \Delta}{\partial y} + \mu \nabla^2 v \quad (4.12)$$

$$\rho \frac{\partial^2 w}{\partial t^2} = (\lambda' + \mu) \frac{\partial \Delta}{\partial z} + \mu \nabla^2 w \quad (4.13)$$

To obtain the wave equation, we differentiate these three equations with respect to  $x$ ,  $y$ , and  $z$ , respectively, and add the results together. This gives

$$\begin{aligned} \rho \frac{\partial^2}{\partial t^2} \left( \frac{\partial u}{\partial x} + \frac{\partial v}{\partial y} + \frac{\partial w}{\partial z} \right) \\ - (\lambda' + \mu) \left( \frac{\partial^2 \Delta}{\partial x^2} + \frac{\partial^2 \Delta}{\partial y^2} + \frac{\partial^2 \Delta}{\partial z^2} \right) \\ + \mu \nabla^2 \left( \frac{\partial u}{\partial x} + \frac{\partial v}{\partial y} + \frac{\partial w}{\partial z} \right) \end{aligned}$$

that is,

$$\rho \frac{\partial^2 \Delta}{\partial t^2} = (\lambda' + 2\mu) \nabla^2 \Delta$$

or

$$\frac{1}{\alpha^2} \frac{\partial^2 \Delta}{\partial t^2} = \nabla^2 \Delta \quad \alpha^2 = \frac{\lambda' + 2\mu}{\rho} \quad (4.14)$$

By subtracting the derivative of Equation (4.12) with respect to  $z$  from the derivative of Equation (4.13) with respect to  $y$ , we get

$$\rho \frac{\partial^2}{\partial t^2} \left( \frac{\partial w}{\partial y} - \frac{\partial v}{\partial z} \right) = \mu \nabla^2 \left( \frac{\partial w}{\partial y} - \frac{\partial v}{\partial z} \right)$$

that is

$$\frac{1}{\beta^2} \frac{\partial^2 \theta_x}{\partial t^2} = \nabla^2 \theta_x \quad \beta^2 = \frac{\mu}{\rho} \quad (4.15)$$

By subtracting appropriate derivatives, we obtain similar results for  $\theta_y$  and  $\theta_z$ . These equations are different examples of the *wave equation*, which we can write in the general form

$$\frac{1}{V^2} \frac{\partial^2 \psi}{\partial t^2} = \nabla^2 \psi \quad (4.16)$$

The wave equation relates a time derivative of a displacement (the left side) to spatial derivatives (the right side); the constant of proportionality is  $V^2$ .

(b) *Plane-wave solutions*. Let us consider first the case where  $\psi$  is a function only of  $x$  and  $t$ , so that Equation (4.16) reduces to

$$\frac{1}{V^2} \frac{\partial^2 \psi}{\partial t^2} = \frac{\partial^2 \psi}{\partial x^2} \quad (4.17)$$

Any function of  $(x - Vt)$ ,

$$\psi = f(x - Vt) \quad (4.18)$$

is a solution of Equation (4.17) (see problem 2) provided that  $\psi$  and its first two derivatives have no discontinuities. This solution (known as *d'Alembert's solution*), furnishes an infinite number of particular solutions [for example,  $e^{k(x-Vt)}$ ,  $\sin(x - Vt)$ ,  $(x - Vt)^3$ ]. The answer to a specific problem consists of selecting a combination of solutions that also satisfies the boundary conditions for the problem.

A *wave* is a "disturbance" that travels through the medium. In our notation, the disturbance  $\psi$  is a volume change when  $\psi = \Delta$  and a rotation when  $\psi = \theta_x$ . Obviously the disturbance in Equation (4.18) is traveling along the  $x$  axis. We shall now show that it travels with a speed equal to the quantity  $V$ .

In Figure 4.4, a certain part of the wave has reached the point  $P_0$  at the time  $t_0$ . If the coordinate

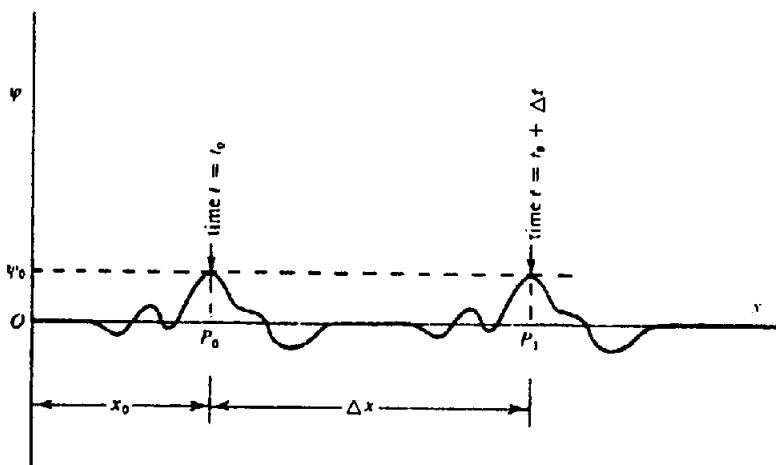


Figure 4.4. Illustrating the velocity of a wave.

of  $P_0$  is  $x_0$ , then the value of  $\psi$  at  $P_0$  is  $\psi_0 = f(x_0 - Vt_0)$ . If this same portion of the wave reaches  $P_1$  at the time  $t_0 + \Delta t$ , then we have for the value of  $\psi$  at  $P_1$ ,

$$\psi_1 = f\{x_0 + \Delta x - V(t_0 + \Delta t)\}$$

But, because this is the same portion of the wave that was at  $P_0$  at time  $t_0$ , we must have  $\psi_0 = \psi_1$ , that is,

$$x_0 - Vt_0 = x_0 + \Delta x - V(t_0 + \Delta t)$$

Thus, the quantity  $V$  is equal to  $\Delta x / \Delta t$  and is therefore the speed with which the disturbance travels in the positive  $x$  direction.

A function of  $(x \pm Vt)$  denotes a wave traveling in the negative  $x$  direction. The general solution of Equation (4.17)

$$\psi = f(x - Vt) + g(x + Vt) \quad (4.19)$$

represents two waves traveling along the  $x$  axis in opposite directions with velocity  $V$ . Because the value of  $\psi$  is independent of  $y$  and  $z$ , the disturbance must be the same everywhere in a plane perpendicular to the  $x$  axis. This type of wave is called a *plane wave*.

The quantity  $(x \pm Vt)$  is known as the *phase*. The surfaces on which the wave motion is the same, that is, surfaces on which the phase is constant, are known as *wavefronts*. In the case we are considering, the wavefronts are planes perpendicular to the  $x$  axis and the wave is traveling in the direction normal to the wavefront. This holds for all waves in isotropic media. A line denoting the direction of travel of the wave energy is called a *raypath*.

It is convenient to have an expression for a plane wave that is not traveling parallel to an axis. Assume

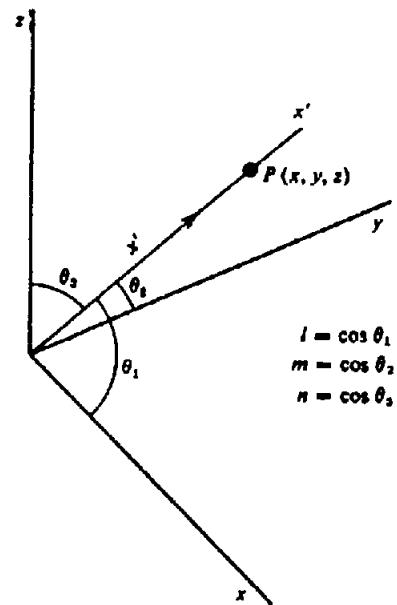


Figure 4.5. Wave direction not along an axis.

that the wave is traveling along the  $x'$  axis that has direction cosines  $(l, m, n)$  (§ A.3.1.) relative to the  $x$ ,  $y$ , and  $z$  axes (Fig. 4.5). Then, at a point  $P$  on the  $x'$  axis at a distance  $x'$  from the origin, we have

$$x' = lx + my + nz$$

where the coordinates of  $P$  are  $(x, y, z)$ . Then,

$$\begin{aligned} \psi &= f(lx + my + nz - Vt) \\ &+ g(lx + my + nz + Vt) \end{aligned} \quad (4.20)$$

(c) *Spherical-wave solutions.* In addition to plane waves, we often use *spherical waves* where the wavefronts are a series of concentric spherical surfaces. We express the wave equation [Eq. (4.16)] in spherical coordinates  $(r, \theta, \phi)$ , where  $\theta$  is the colatitude

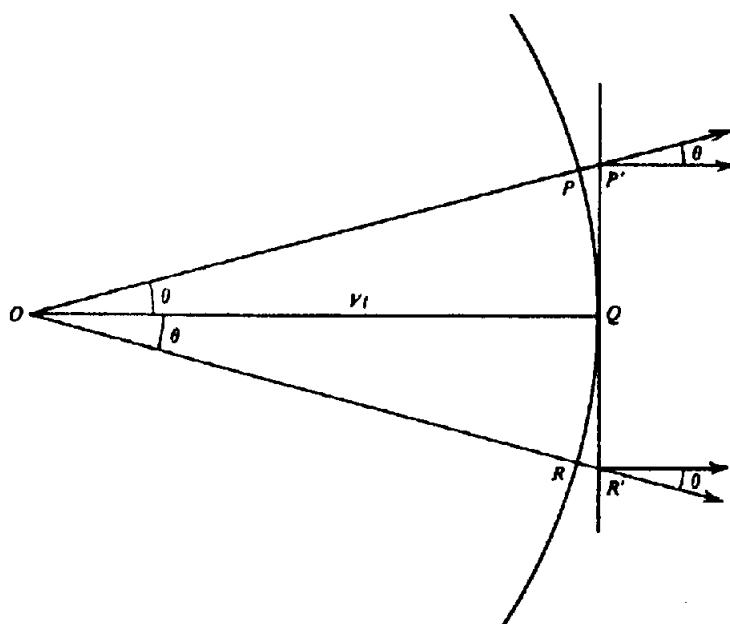


Figure 4.6. Relation between spherical and plane waves.

and  $\phi$  is the longitude [Eq. (A.37)]:

$$\frac{1}{V^2} \frac{\partial^2 \psi}{\partial t^2} = \frac{1}{r^2} \left\{ \frac{\partial}{\partial r} \left( r^2 \frac{\partial \psi}{\partial r} \right) + \frac{1}{\sin \theta} \frac{\partial}{\partial \theta} \left( \sin \theta \frac{\partial \psi}{\partial \theta} \right) + \frac{1}{\sin^2 \theta} \frac{\partial^2 \psi}{\partial \phi^2} \right\} \quad (4.21)$$

We consider only the special case when the wave motion is independent of  $\theta$  and  $\phi$ , hence is a function only of  $r$  and  $t$ . Then we get the simplified equation

$$\frac{1}{V^2} \frac{\partial^2 \psi}{\partial t^2} = \frac{1}{r^2} \frac{\partial}{\partial r} \left( r^2 \frac{\partial \psi}{\partial r} \right) \quad (4.22)$$

Solutions of this equation are

$$\psi = \frac{1}{r} f(r \pm Vt)$$

and the general solution is

$$\psi = \frac{1}{r} f(r - Vt) + \frac{1}{r} g(r + Vt) \quad (4.23)$$

in which the first term represents a wave expanding outward from a central point and the second term a wave collapsing toward the central point.

When  $r$  and  $t$  are fixed,  $(r - Vt)$  is constant and hence  $\psi$  is constant. Thus, at the instant  $t$  the wave has the same value at all points on the spherical surface of radius  $r$ . The spherical surfaces are therefore wavefronts and the radii are rays. Obviously the rays are normal to the wavefronts.

As the wave progresses outward from the center, the radius increases and eventually the portion of the wavefront near any particular point will be approximately plane. The error that we introduce when we replace the spherical wavefront  $PQR$  in Figure 4.6 with the plane wavefront  $P'QR'$  is due to the divergence between the true direction of propagation (the direction of the radius) and the direction normal to the plane. By taking the radius very large and/or the portion of the wavefront being considered very small, we can make the error as small as desired. Because plane waves are easy to visualize and also the simplest to handle mathematically, we generally assume plane waves. Also, curved wavefronts can be thought of as a superposition of plane waves, which often allows us to treat curved-wave problems in terms of plane waves.

(d) *Harmonic waves.* So far we have discussed only the spatial aspects of waves, that is, the way in which waves depend on space coordinates. However,  $\psi$  is also a function of the time  $t$ .

The simplest form of time variation is that of a *harmonic wave*, that is, a wave involving sine or cosine expressions, such as

$$\left. \begin{aligned} \psi &= A \cos \kappa(x - Vt) \\ \psi &= A \sin \kappa(lx + my + nz + Vt) \end{aligned} \right\} \quad (4.24)$$

$$\psi = (B/r) \cos \kappa(r - Vt) \quad (4.25)$$

At a fixed point,  $\psi$  varies as the sine or cosine of the time, and so the motion is *simple harmonic*. The values of  $\psi$  range from  $+A$  to  $-A$  for the plane waves of Equation (4.24) and from  $+B/r$  to  $-B/r$  for

for the spherical wave in Equation (4.25). The value  $|A|$  or  $|B/r|$  is known as the *amplitude* of the wave  $\psi$ .

For a fixed value of  $t$ , whenever  $x$  in Equation (4.24) increases by  $(2\pi/\kappa)$ , the argument of the sine or cosine increases by  $2\pi$  and hence the value of  $\psi$  repeats. The distance  $(2\pi/\kappa)$  is called the *wavelength*, which is usually represented by the symbol  $\lambda$ . The quantity  $(\kappa/2\pi)$  is the *wave number*, the number of wavelengths per unit length.

If the space coordinates in Equations (4.24) and (4.25) are kept fixed and  $t$  allowed to increase, the value of  $\psi$  repeats each time that  $t$  increases by the amount  $T$  where  $\kappa VT = 2\pi = 2\pi(VT/\lambda)$ . Consequently,

$$T = \lambda/V \quad \nu = (1/T) = V/\lambda \quad V = \nu\lambda \quad (4.26)$$

where  $T$  is the period and  $\nu$  is the frequency of the wave. Another frequently used quantity is the angular frequency  $\omega$ , where  $\omega = 2\pi\nu = \kappa V$ . Using the preceding symbols, we can write Equation (4.24) in the equivalent forms

$$\left. \begin{aligned} \psi &= A \cos \kappa(x - Vt) = A \cos \frac{2\pi}{\lambda}(x - Vt) \\ &= A \cos(\kappa x - \omega t) = A \cos \omega \left( \frac{x}{V} - t \right) \\ &= A \cos 2\pi \left( \frac{x}{\lambda} - \nu t \right) = A \cos(\kappa x - 2\pi\nu t) \end{aligned} \right\} \quad (4.27)$$

#### 4.2.3. Body Waves: *P* and *S* Waves

Up to this point our discussion of wave motion has been based on Equation (4.16). The quantity  $\psi$  has not been defined; we have merely inferred that it is some disturbance that is propagated from one point to another with the speed  $V$ . However, in a homogeneous isotropic medium, Equations (4.14) and (4.15) must be satisfied. We can identify the functions  $\Delta$  and  $\theta_x$  with  $\psi$  and conclude that two types of waves can be propagated in a homogeneous isotropic medium, one corresponding to changes in the dilatation  $\Delta$ , the other to changes in one or more components of the rotation given in Equation (4.3). These waves, which travel in the interior of a medium, are called *body waves*.

The first type is variously known as a *dilational*, *longitudinal*, *irrotational*, *compressional*, or *P wave*, the latter name being due to the fact that this type is usually the first (primary) event on an earthquake recording. The second type is referred to as the *shear*, *transverse*, *rotational*, or *S wave* (be-

cause it is usually the second event observed on earthquake records). The *P* wave has the velocity  $\alpha$  in Equation (4.14) and the *S* wave has the velocity  $\beta$  in Equation (4.15) where

$$\left. \begin{aligned} \alpha &= \{(\lambda + 2\mu)/\rho\}^{1/2} \\ \beta &= (\mu/\rho)^{1/2} \end{aligned} \right\} \quad (4.28)$$

Because the elastic constants are positive,  $\alpha$  is always greater than  $\beta$ . Writing  $\gamma$  for the ratio  $\beta/\alpha$ , we see that

$$\gamma^2 = \frac{\beta^2}{\alpha^2} = \frac{\mu}{\lambda + 2\mu} = \frac{\frac{1}{2} - \sigma}{1 - \sigma} \quad (4.29)$$

using Equation (4.8). As  $\sigma$  decreases from 0.5 to zero,  $\gamma$  increases from zero to its maximum value  $1/\sqrt{2}$ ; thus, the velocity of the *S* wave ranges from zero up to 70% of the velocity of the *P* wave.

For fluids,  $\mu$  is zero and hence  $\beta$  and  $\gamma$  are also zero. Therefore *S* waves do not propagate through fluids.

Let us investigate the nature of the motion of the medium corresponding to the two types of wave motion. Consider a spherical *P* wave of the type given by Equation (4.25). Figure 4.7 shows wavefronts drawn at quarter-wavelength intervals. The arrows represent the direction of motion of the medium at the wavefront. The medium is undergoing maximum compression at *B* (that is, the dilatation  $\Delta$  is a minimum) and minimum compression (maximum  $\Delta$ ) at the wavefront *D*.

We can visualize the plane-wave situation by imagining that the radius in Figure 4.7 has become so large that the wavefronts are practically plane surfaces. The displacements are perpendicular to these planes so that there is no convergence or divergence of the particles of the medium as they move back and forth parallel to the direction of propagation. Such a displacement is longitudinal, which explains why *P* waves are sometimes called longitudinal waves. *P* waves are the dominant waves involved in seismic exploration.

To determine the motion of a medium during the passage of an *S* wave, we return to Equation (4.15) and consider the case where a rotation  $\theta_z(x, t)$  is being propagated along the  $x$  axis. We have

$$\frac{1}{\beta^2} \frac{\partial^2 \theta_z}{\partial t^2} = \frac{\partial^2 \theta_z}{\partial x^2}$$

Because

$$\theta_z = \frac{\partial v}{\partial x} - \frac{\partial u}{\partial y} = \frac{\partial v}{\partial x}$$

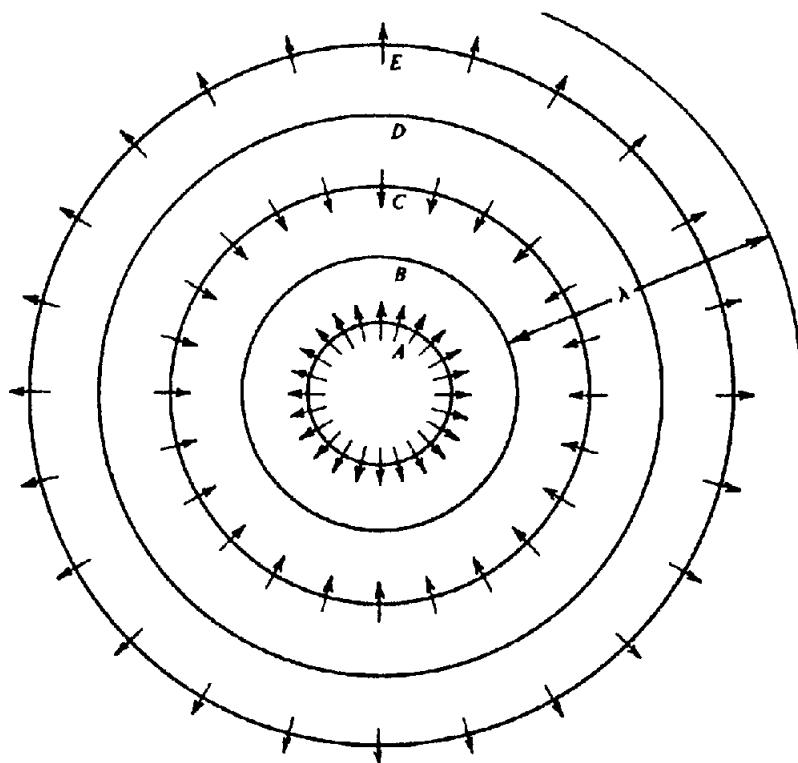


Figure 4.7. Displacements for a spherical P wave.

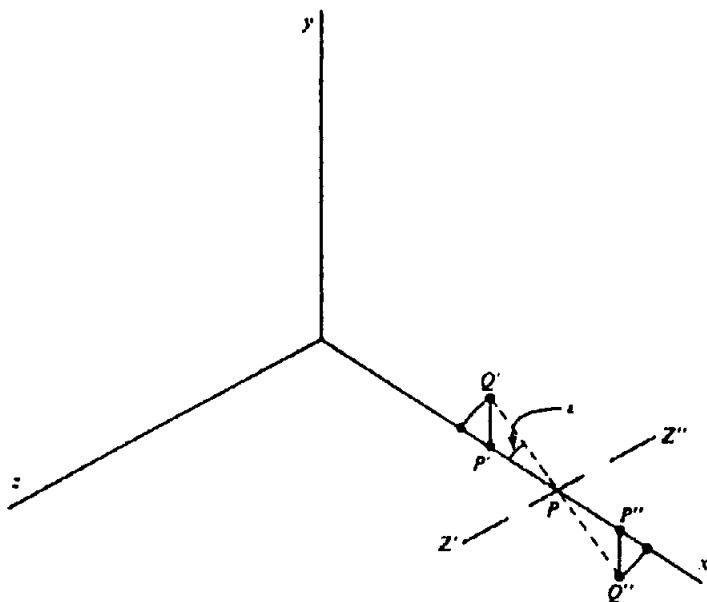


Figure 4.8. Motion during passage of an S wave.

from Equation (4.3), we see that the wave motion consists solely of a displacement  $v$  of the medium in the  $y$  direction;  $v$  is a function of both  $x$  and  $t$ . Because  $v$  is independent of  $y$  and  $z$ , the motion is everywhere the same in a plane perpendicular to the  $x$  axis, that is, we are discussing a plane S wave traveling along the  $x$  axis. By Equation (4.19) the displacement  $v$  must have the form

$$v = f(x - \beta t) + g(x + \beta t)$$

We can visualize the preceding relations by using Figure 4.8. When the wave arrives at  $P$ , it causes the medium in the vicinity of  $P$  to rotate about the axis  $Z'Z''$  (parallel to the  $z$  axis) through an angle  $\epsilon$ . Since we are dealing with infinitesimal strains, we can ignore the curvature of the displacements and consider that points such as  $P'$  and  $P''$  are displaced parallel to the  $y$  axis to the points  $Q'$  and  $Q''$ . Thus, as the wave travels along the  $x$  axis, the medium is displaced transversely to the direction of propagation, hence the name *transverse wave*. Moreover,

because the rotation varies from point to point at any given instant, the medium is subjected to varying shearing stresses as the wave moves along. This accounts for the name *shear wave*.

Because we might have chosen to illustrate  $\theta_y$  in Figure 4.8 instead of  $\theta_x$ , it is clear that shear waves have 2 degrees of freedom—unlike *P* waves that have only 1—along the radial direction. In practice, *S*-wave motion is usually resolved into components parallel and perpendicular to the surface of the ground, which are known, respectively, as *SH* and *SV* waves.

Because the 2 degrees of freedom of *S* waves are independent, we can have an *S* wave that involves motion in only one plane, for example, *SH* or *SV* motion; such a wave is said to be *plane polarized*. We can also have a wave in which the *SH* and *SV* motion have the same frequency and a fixed phase difference; such a wave is *elliptically polarized*. However, polarization of *S* waves usually is not important in seismic exploration.

In the case of a medium that is not homogeneous and isotropic, it may not be possible to resolve wave motion into separate *P* and *S* waves. However, inhomogeneities and anisotropy in the earth are small enough that assumption of separate *P* and *S* waves is valid for practical purposes.

#### 4.2.4. Surface Waves

(a) *Rayleigh waves*. In an infinite homogeneous isotropic medium, only *P* and *S* waves exist. However, when the medium does not extend to infinity in all directions, other types of waves can be generated. These waves are called *surface waves* because they are confined to the vicinity of one of the surfaces that bound the medium.

In exploration seismology, the main type of surface wave of importance is the *Rayleigh wave*, often called *ground roll*. This wave travels along the surface of the earth and involves a combination of longitudinal and transverse motion with a definite phase relation to each other. The amplitude of this wave motion decreases exponentially with depth. The particle motion is confined to the vertical plane, which includes the direction of propagation of the wave. During the passage of the wave, a particle traverses an elliptical path and the major axis of the ellipse is vertical (near the surface). The direction of particle motion around the ellipse is called *retrograde* (Fig. 4.9) because it is opposite to the more familiar direction of motion of particles in waves on the surface of water. The velocity of Rayleigh waves depends upon the elastic constants near the surface and is always less than the *S* wave velocity  $\beta$ . When  $\sigma = \frac{1}{4}$ , the Rayleigh wave velocity is  $0.92\beta$ . The

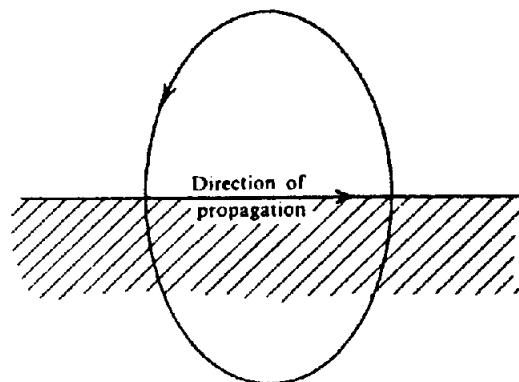


Figure 4.9. Motion during passage of a Rayleigh wave.

exponential decrease in amplitude with depth depends on the wavelength of the waves. Because the elastic constants change with depth, the velocity of Rayleigh waves varies with wavelength. A variation of velocity with wavelength (or frequency) is called *dispersion* and it results in a change of the shape of the wave train with distance (§ 4.2.6d).

(b) *Love waves*. When a surface layer overlies a half-space, another type of surface wave, called a *Love wave*, may exist. A Love wave involves transverse motion parallel to the surface of the ground and sometimes it is called an *SH* wave. Love waves have velocities intermediate between the *S*-wave velocity at the surface and that in deeper layers, and they exhibit dispersion. Energy sources used in seismic work do not generate Love waves to a significant degree and hence Love waves are unimportant in ordinary seismic exploration. Also, modern geophones designed to respond only to vertical motion of the surface would not detect any Love waves that might exist.

Surface waves, including Rayleigh, Love, tube, Stoneley, and channel waves are discussed in more detail in Sheriff and Geldart (1982, pp. 48–52 and 70–3).

#### 4.2.5. Energy of Waves

(a) *Energy density; intensity*. Probably the single most important feature of any wave is the energy associated with the motion of the medium as the wave passes through it. Usually we are not concerned with the total energy of a wave, but rather with the energy in the vicinity of the point where we observe it. The *energy density* is the energy per unit volume in the neighborhood of a point.

Consider a spherical harmonic *P* wave for which the radial displacement for a fixed value of  $r$  is given by

$$u = A \cos(\omega t + \phi)$$

where  $\phi$  is a *phase angle*. The displacement  $u$  ranges from  $-A$  to  $+A$ . Since the displacement varies with time, each element of the medium has a velocity  $\partial u / \partial t$  and an associated kinetic energy. The kinetic energy  $\delta L$  contained within each element of volume  $\delta v$  is

$$\delta L = \frac{1}{2} (\rho \delta v) (\partial u / \partial t)^2$$

The kinetic energy per unit volume is

$$\frac{\delta L}{\delta v} = \frac{1}{2} \rho \left( \frac{\partial u}{\partial t} \right)^2 = \frac{1}{2} \rho \omega^2 A^2 \sin^2(\omega t + \phi)$$

This expression varies from zero to a maximum of  $\rho \omega^2 A^2 / 2$ .

The wave also involves potential energy resulting from the elastic strains created during the passage of the wave. As the medium oscillates back and forth, the energy is converted back and forth from kinetic to potential form and the total energy remains fixed. When a particle is at zero displacement, the potential energy is zero and the kinetic energy is a maximum, and when the particle is at its extreme displacement, the energy is all potential. Because the total energy equals the maximum value of the kinetic energy, the energy density  $E$  for a harmonic wave is

$$E = \frac{1}{2} \rho \omega^2 A^2 = 2 \pi^2 \rho v^2 A^2 \quad (4.30)$$

Thus we see that the energy density is proportional to the first power of the density of the medium and to the second powers of the frequency and amplitude of the wave.

We are interested also in the rate of flow of energy and we define the *intensity* as the quantity of energy that flows through a unit area normal to the direction of wave propagation in unit time. Take a cylinder of infinitesimal cross section area  $\delta \omega$ , whose axis is parallel to the direction of propagation and whose length is equal to the distance traveled in the time  $\delta t$ . The total energy inside the cylinder at any instant  $t$  is  $EV\delta t \delta \omega$ . At the time  $t + \delta t$ , all of this energy has left the cylinder through one of the ends. Dividing by the area of the end of the cylinder  $\delta \omega$  and by the time interval  $\delta t$ , we get the intensity  $I$ , the amount of energy passing through unit area in unit time:

$$I = EV \quad (4.31)$$

For a harmonic wave, this becomes

$$I = \frac{1}{2} \rho V \omega^2 A^2 \quad (4.32)$$

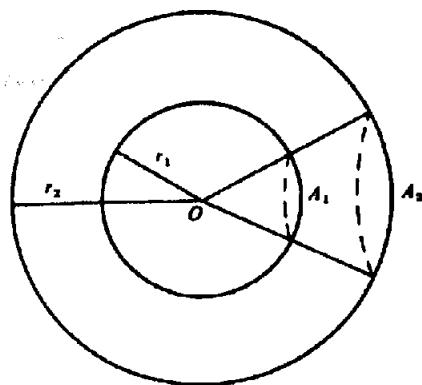


Figure 4.10. Dependence of intensity on distance.

In Figure 4.10 we show a spherical wavefront diverging from a center  $O$ . By drawing sufficient radii we can define two portions of wavefronts,  $A_1$  and  $A_2$ , of radii  $r_1$  and  $r_2$ , such that the energy that flows outward through the spherical cap  $A_1$  in 1 s must be equal to that passing outward through the spherical cap  $A_2$  in 1 s (because the energy is moving only in the radial direction). The flow of energy per second is the product of the intensity and the area, hence

$$I_1 \omega_1 = I_2 \omega_2$$

Since the areas  $\omega_1$  and  $\omega_2$  are proportional to the square of their radii, we get

$$\frac{I_2}{I_1} = \frac{\omega_1}{\omega_2} = \left( \frac{r_1}{r_2} \right)^2$$

Moreover, it follows from Equation (4.31) that  $E$  is proportional to  $I$  and hence

$$\frac{I_2}{I_1} = \frac{E_2}{E_1} = \left( \frac{r_1}{r_2} \right)^2 \quad (4.33)$$

Thus, geometrical spreading causes the intensity and the energy density of spherical waves to decrease inversely as the square of the distance from the source (Newman, 1973). This is called *spherical divergence*.

(b) *Absorption*. We shall also consider two other mechanisms, absorption and partition at interfaces, which cause the energy density of a wave to decrease. In the preceding section we considered variations of the energy distribution as a function of geometry. Implicit in the discussion was the assumption that none of the wave energy disappeared, that is, was transformed into other forms of energy. In

reality this assumption is always incorrect because, as the wave passes through the medium, the elastic energy associated with the wave motion is gradually absorbed by the medium and reappears ultimately in the form of heat. This process is called *absorption* and is responsible for the eventual complete disappearance of the wave motion.

The mechanisms by which the elastic energy is transformed into heat are not understood clearly (Toksoz and Johnston, 1981). During the passage of a wave, heat is generated during the compressive phase and absorbed during the expansive phase. The process is not perfectly reversible because the heat conducted away during the compression is not equal to the heat flowing back during the expansion. Internal friction is undoubtedly involved, and many other mechanisms may contribute, such as loss of energy involved in the creation of new surfaces (fracturing near an explosion), piezoelectric and thermoelectric effects, and viscous losses in the fluids filling the rock pores.

The measurement of absorption is very difficult. Absorption varies with frequency, and laboratory measurements, which are invariably made at high frequencies, may not be applicable to actual seismic waves. Field measurements must be corrected for reflection or refraction effects, and the entire path should be through the same homogeneous medium. Measurement difficulties have resulted in wide divergence in absorption measurements.

The loss of energy by absorption appears to be exponential with distance for elastic waves in rocks. Thus, we can write

$$I = I_0 e^{-\eta x} \quad (4.34)$$

where  $I$  and  $I_0$  are values of the intensity at two points a distance  $x$  apart and  $\eta$  is the absorption coefficient.

Other measures of absorption are also used, such as the quality factor  $Q = \pi/\eta\lambda$ , where  $\lambda$  is the wavelength. Experimental evidence indicates that the absorption coefficient is proportional to frequency, that is,  $\eta\lambda$  and  $Q$  are roughly constant for a particular rock. The increase in absorption with frequency provides one mechanism for the loss of high frequencies with distance. The consensus is that for rocks,  $\eta$  is of the order of 0.16 to 0.02 dB per wavelength (or that  $Q$  is in the range 20 to 150).

To compare the loss by absorption with the loss of intensity by spherical divergence, we calculate the losses in going from a point 200 m from the source to various distances from the source assuming  $\eta = 0.10 \text{ dB}/\lambda$  and  $V = 2 \text{ km/s}$ . The results shown in Table 4.1 were calculated using the following rela-

Table 4.1. Energy losses by absorption and spreading.  
 $\eta = 0.10 \text{ dB/wavelength}$ ;  $V = 2,000 \text{ m/s}$ .

Frequency $\nu$ (Hz)	Distance from sourcepoint ( $x_s$ )			
	1,200 m (dB)	2,200 m (dB)	4,200 m (dB)	8,200 m (dB)
Absorption	1	0.22	0.43	0.86
	3	0.64	1.3	2.6
	10	2.2	4.3	8.6
	30	6.4	13	26
	100	22	43	86
Spreading	all	16	21	26
				32

tions:

#### Absorption:

$$\begin{aligned} \text{Loss in dB} &= 10 \log(I_0/I) \\ &= 4.3 \ln(e^{0.10x/\lambda}) \\ &= 0.43(x_s - 200)/\lambda \\ &= 0.43\nu(x_s - 200)/2000 \end{aligned}$$

#### Spreading:

$$\begin{aligned} \text{Loss in dB} &= 10 \log(I_0/I) \\ &= 20 \log(x_s/200) \end{aligned}$$

where  $x_s$  is the distance from the shotpoint,  $x = x_s - 200$ .

Table 4.1 shows that losses by spreading are more important than losses by absorption for low frequencies and short distances. As the frequency and distance increase, absorption losses increase more rapidly than spreading losses, and eventually become dominant. The more rapid loss of higher frequencies results in change of wave shape with distance.

In addition to absorption and spreading, the partitioning of energy at interfaces is also responsible for the decrease in the energy of a wave with distance. This is discussed in Section 4.2.7.

#### 4.2.6. Wave Motion

(a) *Huygens' principle*. This principle is important in understanding wave travel and is frequently useful in drawing successive positions of wavefronts. *Huygens' principle* states that every point on a wavefront can be regarded as a new source of waves. Given the location of a wavefront at a certain instant, future positions of the wavefront can be found by considering each point on the first wavefront as a new wave source. In Figure 4.11,  $AB$  is the wavefront at the time  $t_0$  and we wish to find the wavefront at a later time  $(t_0 + \Delta t)$ . During the interval  $\Delta t$ , the wave will advance a distance  $V\Delta t$  where  $V$  is the velocity (which may vary from point to point). We select points on the wavefront,  $P_1$ ,  $P_2$ ,  $P_3$ , and

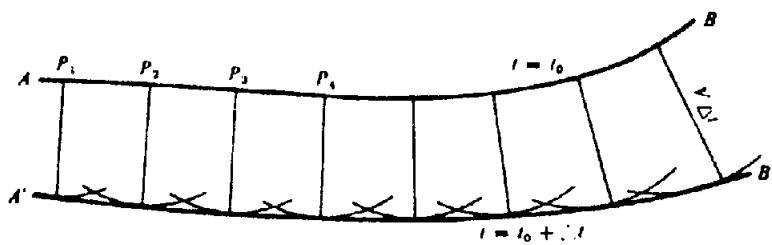


Figure 4.11. Using Huygens' principle to locate new wavefronts.

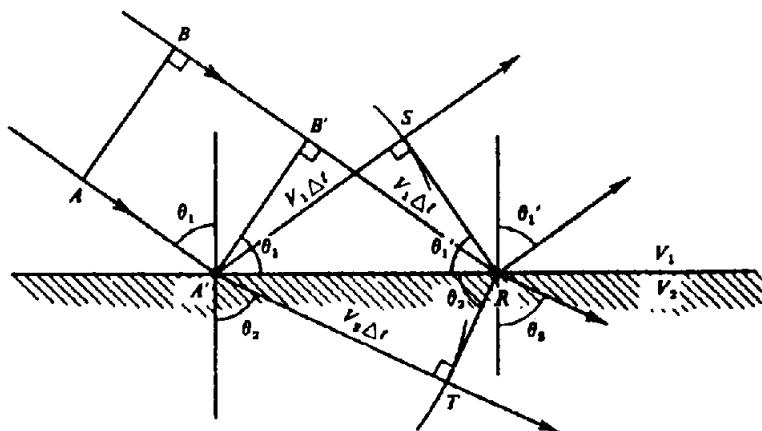


Figure 4.12. Reflection and refraction of a plane wave.

so on, from which we draw arcs of radius  $V\Delta t$ . Provided we select enough points, the envelope of the arcs ( $A'B'$ ) will define as accurately as we wish the position of the wavefront at the time  $(t + \Delta t)$ . Except on the envelope, the elemental waves interfere destructively so that their effects cancel.

(b) *Reflection and refraction.* Whenever a wave encounters an abrupt change in the elastic properties, as when it arrives at a surface separating two beds, part of the energy is *reflected* and remains in the same medium as the original energy. The balance of the energy is *refracted* into the other medium with an abrupt change in the direction of propagation.

We can derive the familiar laws of reflection and refraction using Huygens' principle. Consider a plane wavefront  $AB$  incident on a plane interface as in Figure 4.12 (if the wavefront is curved, we merely take  $A$  and  $B$  sufficiently close together that  $AB$  is a plane to the required degree of accuracy).  $AB$  occupies the position  $A'B'$  when  $A$  arrives at the surface, and at this instant, the energy at  $B'$  still must travel the distance  $B'R$  before arriving at the interface. If  $B'R = V_1 \Delta t$ , then  $\Delta t$  is the time interval between the arrival of the energy at  $A'$  and at  $R$ . By Huygens' principle, during the time  $\Delta t$  the energy that reached  $A'$  will have traveled either upward a distance  $V_1 \Delta t$  or downward a distance  $V_2 \Delta t$ . By drawing arcs with center  $A'$  and lengths equal to  $V_1 \Delta t$  and  $V_2 \Delta t$ , and then drawing the tangents from

$R$  to these arcs, we locate the new wavefronts  $RS$  and  $RT$  in the upper and lower media. The angle at  $S$  is a right angle and  $A'S = V_1 \Delta t = B'R$ . Therefore, the triangles  $A'B'R$  and  $A'SR$  are equal with the result that the *angle of incidence*  $\theta_1$  is equal to the *angle of reflection*  $\theta_1'$ . This is the *law of reflection*. For the refracted wave, the angle at  $T$  is a right angle and we have

$$V_2 \Delta t = A'R \sin \theta_2$$

and

$$V_1 \Delta t = A'R \sin \theta_1$$

Hence

$$\frac{\sin \theta_1}{V_1} = \frac{\sin \theta_2}{V_2} = p \quad (4.35)$$

The angle  $\theta_2$  is called the *angle of refraction* and Equation (4.35) is the *law of refraction*, also known as *Snell's law*. The angles are usually measured between the raypaths and a normal to the interface, but these angles are the same as those between the interface and the wavefronts in isotropic media. The laws of reflection and refraction can be combined in single statement: At an interface the quantity  $p = (\sin \theta_i)/V_i$  has the same value for the incident, reflected, and refracted waves. This generalized form of Snell's law will be understood in future references to Snell's law. The quantity  $p$  is called the *raypath parameter*.

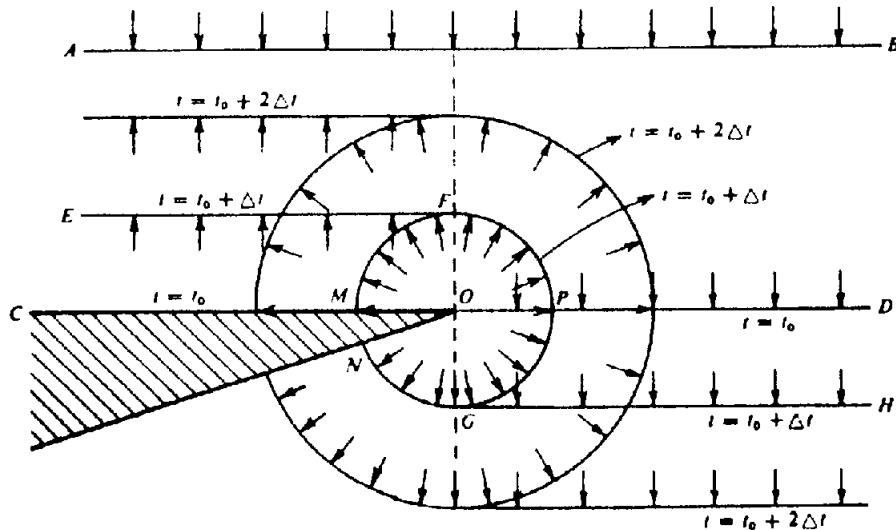


Figure 4.13. Diffracted wavefronts. Diffraction allows seismic energy to reach regions forbidden by ray theory, such as the shadow zone underneath the wedge.

When the medium consists of a number of parallel beds, Snell's law requires that the quantity  $p$  have the same value everywhere for all reflected and refracted rays resulting from a given initial ray.

When  $V_2$  is less than  $V_1$ ,  $\theta_2$  is less than  $\theta_1$ . However, when  $V_2$  is greater than  $V_1$ ,  $\theta_2$  reaches  $90^\circ$  when  $\theta_1 = \sin^{-1}(V_1/V_2)$ . For this value of  $\theta_1$ , the refracted ray is traveling along the interface. The angle of incidence for which  $\theta_2 = 90^\circ$  is the *critical angle*  $\theta_c$ ; obviously,  $\sin \theta_c = V_1/V_2$ . For angles of incidence greater than  $\theta_c$ , it is impossible to satisfy Snell's law (because  $\sin \theta_2$  cannot exceed unity) and *total reflection* occurs (that is, the refracted ray does not exist). This situation is discussed in Section 4.2.7.

Snell's law is very useful in determining raypaths and traveltimes and in deriving reflector position from observed traveltimes, but it does not give information about the amplitudes of the reflected and transmitted waves. This subject is also taken up in Section 4.2.7.

(c) *Diffraction phenomena.* Seismic energy travels along other paths besides those given by Snell's law. Whenever a wave encounters a feature whose radius of curvature is comparable to or smaller than the wavelength, the ordinary laws of reflection and refraction no longer apply. In such cases, the energy is *diffracted* rather than reflected or refracted. Because seismic wavelengths are large (often 100 m or more) compared with many geologic dimensions, diffraction is an important process. The laws of diffraction are complex, but at distances greater than several wavelengths from the diffracting source, the diffracted wavefront is essentially that given by Huygens' construction (Troyer, 1970).

Figure 4.13 illustrates the method of constructing diffracted wavefronts produced by a faulted bed. We assume a plane wavefront  $AB$  incident normally on the faulted bed  $CO$ ; the position of the wavefront when it reaches the surface of the bed at  $t = t_0$  is  $COD$ . At  $t = t_0 + \Delta t$ , the portion to the right of  $O$  has advanced to the position  $GH$ , whereas the portion to the left of  $O$  has been reflected and has reached the position  $EF$ . We might have constructed the wavefronts  $EF$  and  $GH$  by selecting a large number of centers in  $CO$  and  $OD$  and drawing arcs of length  $V\Delta t$ .  $EF$  and  $GH$  would then be determined by the envelopes of these arcs. However, for the portion  $EF$  there would be no centers to the right of  $O$  to define the envelope, whereas for the portion  $GH$  there would be no centers to the left of  $O$  to define the envelope. Thus,  $O$  marks the transition point between centers that give rise to the upward-traveling wavefront  $EF$  and centers that give rise to the downward-traveling wavefront  $GH$ . The arc  $FPG$  with center  $O$  is the diffracted wavefront originating at  $O$  and connecting the two wavefronts  $EF$  and  $GH$ . The diffracted wavefront also extends into the geometrical shadow area  $GN$  and into the region  $FM$ . Diffraction events will be discussed in Section 4.4.3. Sheriff and Geldart (1982, pp. 59–64) give an analytic treatment of diffraction.

(d) *Dispersion: group velocity.* The velocity  $V$ ,  $a$ , or  $\beta$ , which appears in Equations (4.14) to (4.29), is known as the *phase velocity* because it is the distance traveled per unit time by a point of constant phase, such as a peak or trough. This is not necessarily the same as the speed with which a pulse of energy travels, which is the *group velocity* and will be

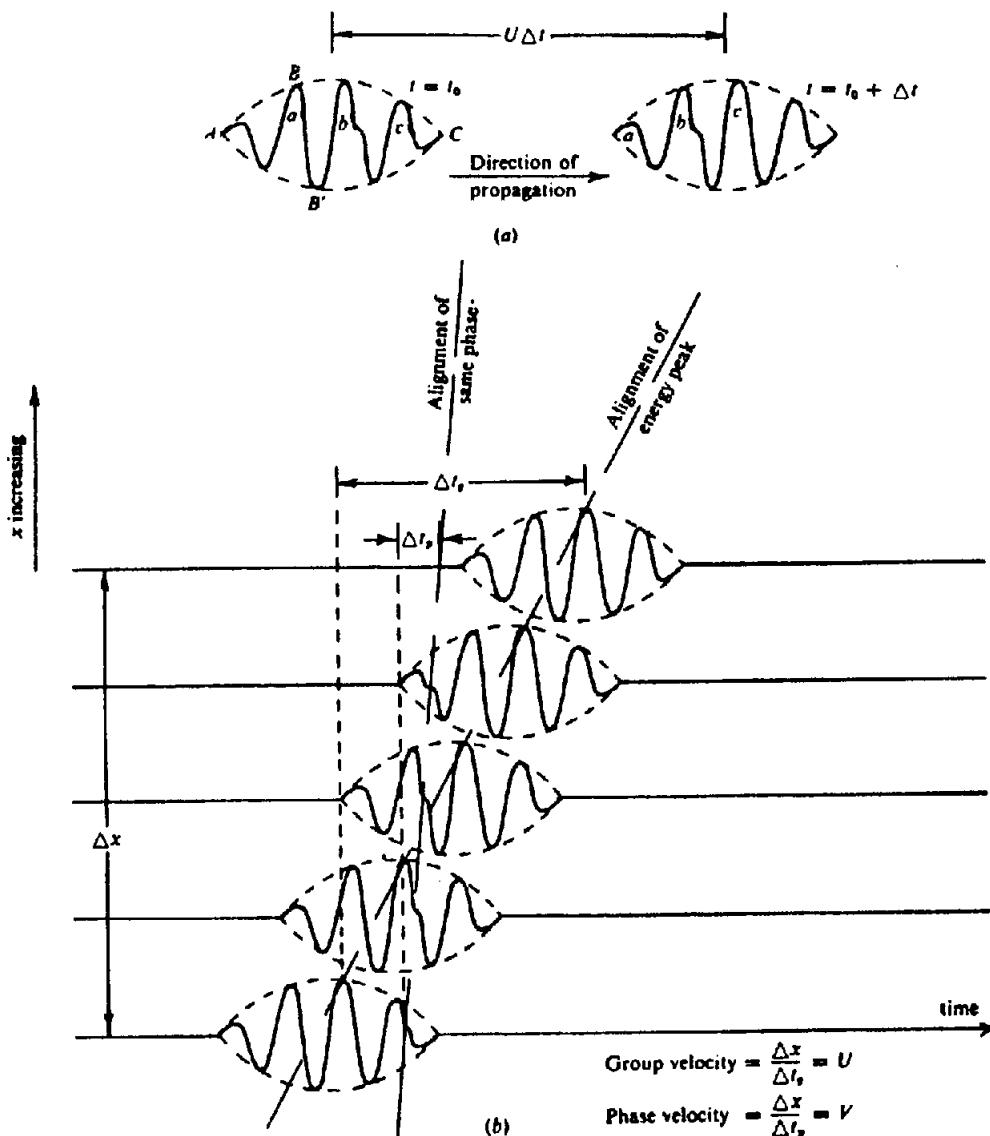


Figure 4.14. Comparison of group and phase velocities. (a) Definition of group velocity  $U$ . (b) Arrival of a dispersive wave at successive geophones.

denoted by  $U$ . Consider, for example, the wave train shown in Figure 4.14a. We could determine the group velocity  $U$  by drawing the envelope of the pulse (the double curve  $ABC$ ,  $AB'C$ ) and measuring the distance that the envelope travels in unit time. The relation between  $U$  and  $V$  is shown in Figure 4.14b, where  $V$  is given by the rate of advance of a certain phase (such as a trough), whereas  $U$  is measured by the speed of the maximum amplitude of the envelope.

If we decompose a pulse into its component frequencies by Fourier analysis, we find a spectrum of frequencies. If the velocity is the same for all frequencies, the pulse shape will remain the same and the group velocity will be the same as the phase velocity. However, if the velocity varies with frequency, the pulse changes shape as it travels and the group velocity is different from the phase velocity, that is, the medium is dispersive. It can be shown

(see problem 3c) that the group velocity  $U$  is

$$U = V - \lambda \frac{dV}{d\lambda} = V + v \frac{dV}{dv} \quad (4.36)$$

where  $V$ ,  $\lambda$ ,  $\omega$ ,  $dV/d\lambda$ , and  $dV/dv$  are average values for the range of frequencies that makes up the principal part of the pulse.

When  $V$  decreases with frequency,  $V$  is larger than  $U$ . This is called *normal dispersion* and is illustrated in Figure 4.14 where the envelope travels slower than the individual cycles, which overtake and pass through the envelope and disappear as they reach the leading edge. When  $V$  increases with frequency, the opposite is true.

Dispersion is not a dominant feature of exploration seismology because most rocks exhibit little variation of velocity with frequency in the seismic frequency range. However, dispersion is important in

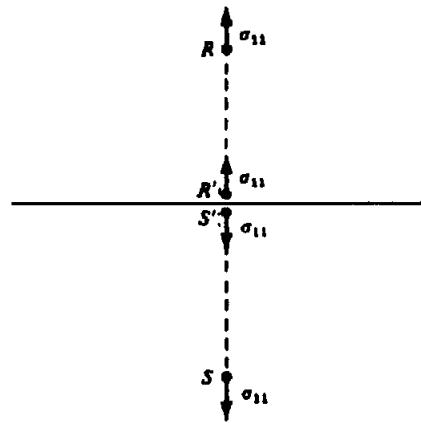


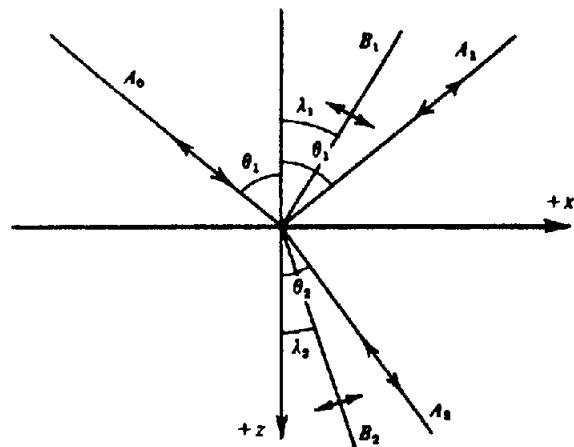
Figure 4.15. Continuity of normal stress.

connection with surface waves and certain other phenomena.

#### 4.2.7. Partitioning of Energy at an Interface

When a wave arrives at a surface separating two media having different elastic properties, it gives rise to reflected and refracted waves as previously described. At the boundary, the stresses and displacements must be continuous. Two neighboring points  $R$  and  $S$ , which lie on opposite sides of the boundary as shown in Figure 4.15, will in general have different values of normal stress. This difference results in a net force that accelerates the layer between them. However, if we choose points closer and closer together, the stress values must approach each other, and in the limit when the two points coincide on the boundary, the two stresses must be equal. If this were not so, the infinitesimally thin layer at the boundary would be acted on by a finite force and hence have an acceleration that would approach infinity as the two points approach each other. Because the same reasoning applies to a tangential stress, we see that the normal and tangential components of stress must be continuous (cannot change abruptly) at the boundary. Likewise the normal and tangential components of displacement must be continuous. If the normal displacement were not continuous, one medium would either separate from the other, leaving a vacuum in between, or else would penetrate into the other so that the two media would occupy the same space. If the tangential displacement were not continuous, the two media would move differently on opposite sides of the boundary and one would slide over the other. We rule out such motion for rocks, and so displacement must be continuous at the boundary.

The continuity of normal and tangential stresses and displacements at the boundary can be expressed by means of four equations (*boundary conditions*)

Figure 4.16. Waves generated at an interface by an incident  $P$  wave.

that the wave motion must obey at the interface. Assume a plane  $P$  wave with amplitude  $A_0$  incident on the boundary between two solid media. Snell's law fixes the angles of reflection and refraction whereas the amplitudes of the reflected and refracted waves are fixed by the four boundary conditions. However, to satisfy four equations we must have four unknown amplitudes; hence four waves must be generated at the boundary. These correspond to reflected and refracted  $P$  waves and reflected and refracted  $S$  waves. This is illustrated in Figure 4.16 where  $A_1$ ,  $A_2$ ,  $\theta_1$ , and  $\theta_2$  are the amplitudes and angles of the reflected and refracted  $P$  waves and  $B_1$ ,  $B_2$ ,  $\lambda_1$ , and  $\lambda_2$  are the amplitudes and angles of the reflected and refracted  $S$  waves.

Snell's law tells us that

$$\frac{\sin \theta_1}{\alpha_1} = \frac{\sin \theta_2}{\alpha_2} = \frac{\sin \lambda_1}{\beta_1} = \frac{\sin \lambda_2}{\beta_2} = p \quad (4.37)$$

[This more general statement of Snell's law can be derived following the same reasoning used to derive Eq. (4.35).] The equations governing the amplitudes were first given by Knott (1899), but he expressed them in terms of potential functions from which the displacements must be found by differentiation. The corresponding equations in terms of amplitudes were given by Zoeppritz (1919) in the following form [see Sheriff and Geldart (1982, pp. 65–6) for derivations of Zoeppritz's and Knott's equations]:

$$A_1 \cos \theta_1 - B_1 \sin \lambda_1 + A_2 \cos \theta_2 + B_2 \sin \lambda_2 \\ = A_0 \cos \theta_1 \quad (4.38)$$

$$A_1 \sin \theta_1 + B_1 \cos \lambda_1 - A_2 \sin \theta_2 + B_2 \cos \lambda_2 \\ = -A_0 \sin \theta_1 \quad (4.39)$$

$$A_1 Z_1 \cos 2\lambda_1 - B_1 W_1 \sin 2\lambda_1 - A_2 Z_2 \cos 2\lambda_2 \\ - B_2 W_2 \sin 2\lambda_2 = -A_0 Z_1 \cos 2\lambda_1 \quad (4.40)$$

$$A_1 \gamma_1 W_1 \sin 2\theta_1 + B_1 W_1 \cos 2\lambda_1 + A_2 \gamma_2 W_2 \sin 2\theta_2 \\ - B_2 W_2 \cos 2\lambda_2 = A_0 \gamma_1 W_1 \sin 2\theta_1 \quad (4.41)$$

Table 4.2. Energy reflected at the interface between two media.

Interface	First medium		Second medium		$Z_1/Z_2$	$R$	$E_R$
	Velocity	Density	Velocity	Density			
Sandstone on limestone	2.0	2.4	3.0	2.4	0.67	0.20	0.040
Limestone on sandstone	3.0	2.4	2.0	2.4	1.5	-0.20	0.040
Typical shallow interface	2.1	2.4	2.3	2.4	0.91	0.045	0.0021
Typical deeper interface	4.3	2.4	4.5	2.4	0.96	0.023	0.0005
"Soft" ocean bottom	1.5	1.0	1.5	2.0	0.50	0.33	0.11
"Hard" ocean bottom	1.5	1.0	3.0	2.5	0.20	0.67	0.44
Surface of ocean (from below)	1.5	1.0	0.36	0.0012	35.00	-0.9994	0.9988
Base of weathering	0.5	1.5	2.0	2.0	0.19	0.68	0.47

Note: All velocities are in km/s and densities are in g/cm<sup>3</sup>.

where

$$\gamma_i = \beta_i/\alpha_i \quad Z_i = \rho_i\alpha_i \quad W_i = \rho_i\beta_i \quad i = 1, 2$$

These equations govern the amplitudes of all the waves that result from an interface, but they involve so many parameters that it is difficult to generalize from them.

The products of density and velocity ( $Z_i$  and  $W_i$ ) are known as *acoustic impedances*. To apply these equations at an interface, we must know the density and velocity in each of the media, hence  $Z_1$ ,  $Z_2$ ,  $W_1$ ,  $W_2$ ,  $\gamma_1$ , and  $\gamma_2$  are known. For a given  $A_0$  and  $\theta_1$ , we can calculate  $\theta_2$ ,  $\lambda_1$ , and  $\lambda_2$  from Equation (4.37) and the four amplitudes,  $A_1$ ,  $A_2$ ,  $B_1$ , and  $B_2$ , from Equations (4.38) to (4.41).

Zoeppritz's equations reduce to a very simple form for normal incidence. Because the curves change slowly for small angles of incidence (say up to 20°), the results for normal incidence have wide application. For a *P* wave at normal incidence, the tangential stresses and displacements are zero; hence  $B_1 = B_2 = 0$  and  $\theta_1 = \theta_2 = 0$ , so Equations (4.38) to (4.41) reduce to

$$\begin{aligned} A_1 + A_2 &= A_0 \\ Z_1 A_1 - Z_2 A_2 &= -Z_1 A_0 \end{aligned}$$

The solution of these equations is

$$\left. \begin{aligned} R &= \frac{A_1}{A_0} = \frac{Z_2 - Z_1}{Z_2 + Z_1} \\ T &= \frac{A_2}{A_0} = \frac{2Z_1}{Z_2 + Z_1} \end{aligned} \right\} \quad (4.42)$$

These ratios usually are called the *normal reflection* and *transmission coefficients*, but the fractions of the incident energy that are reflected and refracted are

also sometimes called by these names. Writing  $E_R$  and  $E_T$  for the fractions of the incident energy reflected and transmitted, we find, from Equations (4.32) and (4.42),

$$\left. \begin{aligned} E_R &= \frac{\frac{1}{2}\alpha_1\rho_1\omega^2 A_1^2}{\frac{1}{2}\alpha_1\rho_1\omega^2 A_0^2} = \left( \frac{Z_2 - Z_1}{Z_2 + Z_1} \right)^2 \\ E_T &= \frac{\frac{1}{2}\alpha_2\rho_2\omega^2 A_2^2}{\frac{1}{2}\alpha_1\rho_1\omega^2 A_0^2} = \frac{4Z_1 Z_2}{(Z_2 + Z_1)^2} \end{aligned} \right\} \quad (4.43)$$

$$E_R + E_T = 1 \quad (4.44)$$

For a wave incident on an interface from the opposite direction, we interchange  $Z_1$  and  $Z_2$ . This will change the sign of  $R$  and the value of  $T$ , but leave  $E_R$  and  $E_T$  unchanged. Hence the partition of energy does not depend on which medium contains the incident wave. When the impedance contrast vanishes,  $E_R = 0$  and all the energy is transmitted (note that this does not require that  $\rho_1 = \rho_2$  and  $\alpha_1 = \alpha_2$ ). As the impedance contrast approaches 0 or  $\infty$ ,  $T$  approaches zero and  $R$  approaches unity; thus, the farther the impedance contrast is from unity, the stronger the reflected energy.

Table 4.2 shows how the reflected energy varies for impedance contrasts such as might be expected within the earth. Because both density and velocity contrasts are small for most of the interfaces encountered, only a small portion of the energy is reflected at any one interface; this is illustrated by the first four lines in Table 4.2. The sandstone-on-limestone interface is about as large a contrast as is apt to be encountered, whereas the typical shallow interface and the typical deep interface figures are more representative of most interfaces in the earth. Hence, usually appreciably less than 1% of the energy is reflected at any interface. The major exceptions involve the bottom and surface of the ocean and the

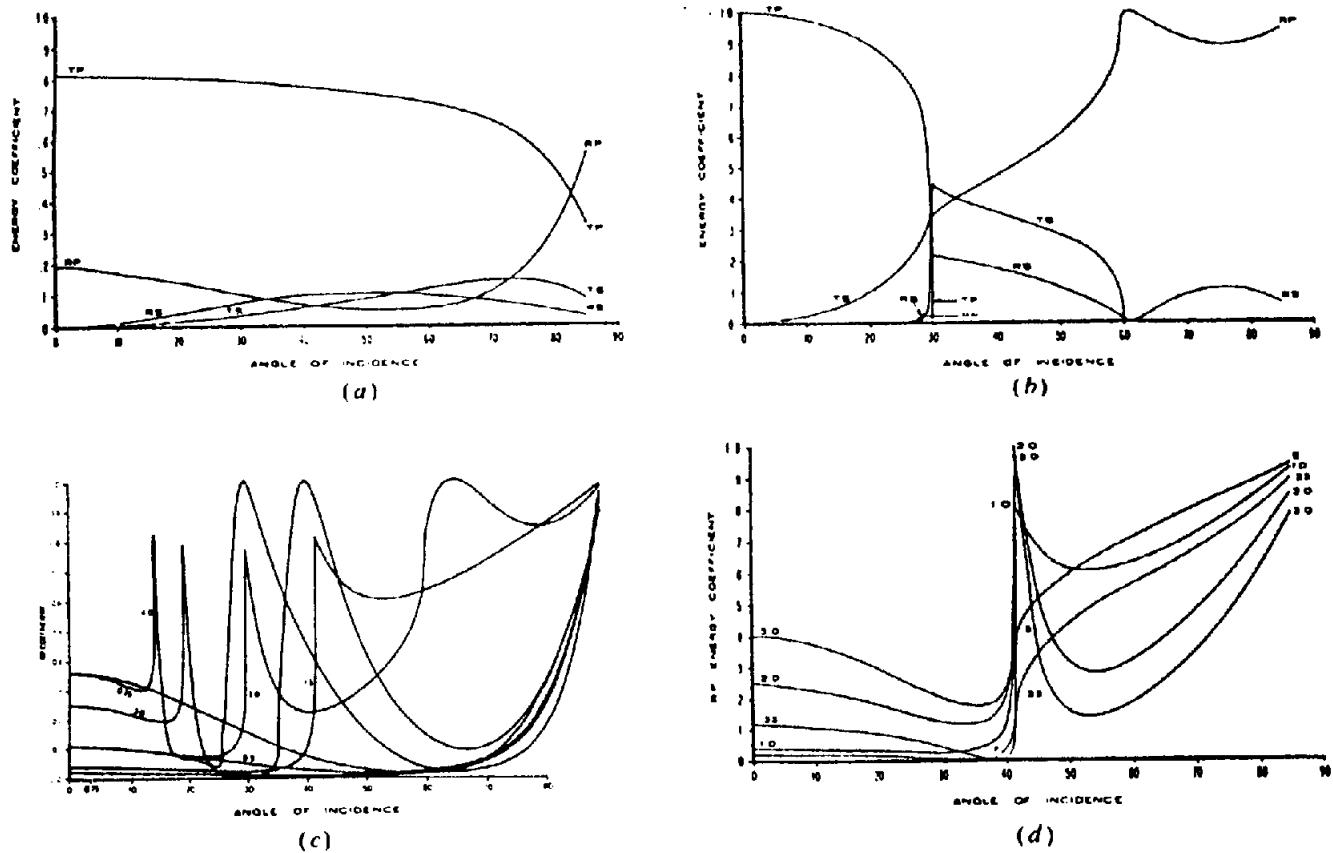


Figure 4.17. Partitioning of energy between transmitted and reflected waves as a function of angle of incidence for the case of an incident  $P$  wave.  $TP$  = fraction of energy in transmitted  $P$  wave,  $RP$  = fraction in reflected  $P$  wave,  $TS$  = fraction in transmitted  $S$  wave, and  $RS$  = fraction in reflected  $S$  wave. (From Tooley, Spencer, and Sagoci, 1965.) (a) Case where velocity in the incident medium is larger:  $\alpha_2/\alpha_1 = 0.5$ ,  $\rho_2/\rho_1 = 0.8$ ,  $\sigma_1 = 0.3$ , and  $\sigma_2 = 0.25$ . (b) Case where velocity in the incident medium is smaller:  $\alpha_2/\alpha_1 = 2.0$ ,  $\rho_2/\rho_1 = 0.5$ ,  $\sigma_1 = 0.3$ , and  $\sigma_2 = 0.25$ . (c) Fraction of energy reflected as  $P$  wave for various  $P$ -wave velocity ratios and  $\rho_2/\rho_1 = 1.0$ ,  $\sigma_1 = \sigma_2 = 0.25$  (from Denham and Palmeira, 1984). (d) Fraction of energy reflected as a  $P$  wave for various density ratios and  $\alpha_2/\alpha_1 = 1.5$ ,  $\sigma_1 = \sigma_2 = 0.25$ .

base of the weathering (§ 4.2.8b). A much larger proportion of the energy can be reflected from these and hence they are especially important in the generation of multiple reflections and other phenomena that we shall deal with later. The land surface is usually of less importance than the base of the weathering for multiple generation because increased travel in the weathered layer involves appreciable absorption.

A negative value of  $R$  means that the reflected wave is  $180^\circ$  out of phase with the incident wave. Thus, for an incident wave  $A_0 \cos \omega t$ , the reflected wave is  $A_1 \cos(\omega t + \pi)$ . Phase reversal occurs when  $Z_1$  exceeds  $Z_2$  (see Table 4.2).

Turning now to the general case where the angle of incidence is not necessarily zero, we illustrate solutions of Zoeppritz's equations with graphs that show the energy partition as functions of the angle of incidence for certain values of parameters. Many curves would be required to show the variations of energy partitioning as a function of incident angle

because of the many parameters that can be varied: incident  $P$ ,  $SH$ , or  $SV$  wave,  $P$  wave velocity ratio, density ratio, and Poisson ratio for each medium or equivalent values (such as  $S$ - to  $P$ -wave velocity ratios). Figure 4.17 shows several cases representative of the variety of results possible.

Figure 4.17a shows the partitioning of energy when a  $P$  wave is incident on a medium of lower velocity. For small incident angles, almost all of the energy is in the reflected and transmitted  $P$  waves and hence hardly any  $S$  waves are generated. As the incident angle increases, some of the energy goes into reflected and transmitted  $S$  waves, and at intermediate angles the reflected  $S$  wave carries more energy than the reflected  $P$  wave. Such *converted waves* (waves resulting from the conversion of  $P$  waves to  $S$  waves or vice versa at an interface) are sometimes recorded at long offsets (§ 4.5.2b) where they are evidenced by alignments that disappear as one tries to follow them to shorter offsets. As grazing incidence is approached, the energy of the reflected

*P* wave increases until at 90° all of the energy stays in the *P* wave in the incident medium.

The opposite situation is shown in Figure 4.17b where a *P* wave is incident in the low-velocity medium. Because the change in density is opposite to the change in velocity such that  $Z_1 = Z_2$ , the *P*-wave reflection coefficient is essentially zero for small incident angles. As the incident angle increases, *S*-wave energy increases. As the critical angle for *P* waves is approached, the transmitted *P*-wave energy falls rapidly to zero and no transmitted *P* wave exists for larger incident angles. Also as the critical angle is approached, reflected *P* and *S* waves become very strong; such a buildup of reflection strength near the critical angle is called *wide-angle reflection*. Sometimes offsets are increased to take advantage of this phenomenon to map reflectors that cannot be followed at short offsets (Meissner, 1967). As the critical angle for *S* waves is approached, the transmitted *S* wave falls to zero.

Figure 4.17c shows the *P*-wave reflection coefficient for various *P*-wave velocity ratios when there is no density or Poisson-ratio contrast. The reflected energy is zero for a velocity ratio of unity (no impedance contrast) and increases as the velocity ratio increases or decreases. The peaks for  $\alpha_2/\alpha_1 > 1$  occur at the critical angles for the *P* and *S* waves, respectively. Figure 4.17d shows the energy of the reflected *P* wave for various density contrasts.

The graphs in Figure 4.17 generally show that the reflected amplitude decreases slightly as the angle of incidence increases, which is equivalent to saying that the *P*-wave amplitude decreases as the offset (source-to-geophone distance) increases. However, Shuey (1985) shows theoretically that the amplitude may increase if Poisson's ratio changes appreciably. Such a change may occur when gas fills the pore space in a rock. Ostrander (1984) observed on field records such behavior associated with gas reservoirs. This behavior of amplitude with offset is used as an indicator of hydrocarbon gas (§ 4.10.8).

#### 4.2.8. Seismic Velocity

(a) *Factors affecting velocity.* Equation (4.28) shows that the velocity of *P* waves in a homogeneous solid is a function only of the elastic constants and the density. One might expect that the elastic constants, which are properties of the intermolecular forces, would be relatively insensitive to pressure, whereas the density should increase with pressure because rocks are moderately compressible. This would lead one to expect that the numerator in the expression for velocity would not change very much with increasing pressure whereas the denominator would get larger so that velocity would decrease with

depth of burial in the earth. In fact, this is contrary to actual observations.

Birch (1966) shows wide ranges in the velocity of any given rock type, as illustrated in Figure 4.18. Whereas most rocks are mixtures of different minerals, even if we were to consider only relatively "pure" rocks, such as sandstones composed mainly of quartz or limestones that are almost pure calcite, we would encounter a wide range of velocity values, almost all of them lower than the values for quartz or calcite.

The most important aspect in which sedimentary rocks differ from homogeneous solids is in having granular structure with voids between the grains. These voids are responsible for the porosity of rocks (§ 11.1.4) and porosity is the important factor in determining velocity. Sheriff and Geldart (1983, Chap. 7) discuss this and other factors that affect velocity.

Gassmann (1951) derived an expression for the velocity in a model consisting of tightly packed elastic spherical particles under pressure such that the contacts between the spheres become areas rather than points. The elastic constants of such a pack vary with pressure, and the effect is to make the *P*-wave velocity vary as the 1/6th power of the pressure. Faust (1953) found an empirical formula for velocity in terms of the depth of burial *Z* and the formation resistivity *R*:

$$V = 2 \times 10^3 (ZR)^{1/6} \quad (4.45)$$

*V* is in feet per second when *Z* is in feet and *R* is in ohm-feet. However, the deviations of individual measurements were very large, which indicates the presence of other factors that this equation does not take into account.

An earlier form of Faust's law (Faust, 1951) also included the age of the rock as a factor in determining velocity. An older rock might be expected to have a higher velocity, having been subjected for a longer time to pressures, cementation, and other factors that might increase its velocity.

In actual rocks, the pore spaces are filled with a fluid whose elastic constants and density also affect the seismic velocity. Oil is slightly more compressible than water, so oil-filled pores result in slightly lower velocity than water-filled pores. Gas is considerably more compressible than water and so gas-filled pores often result in much lower velocity. Even a small amount of gas may lower velocity appreciably (Domenico, 1977). These effects are used as hydrocarbon indicators (§ 4.10.8).

The fluid in rock pore spaces is under a pressure that usually is different from that due to the weight of the overlying rocks. In this situation, the effective pressure on the granular matrix is the difference

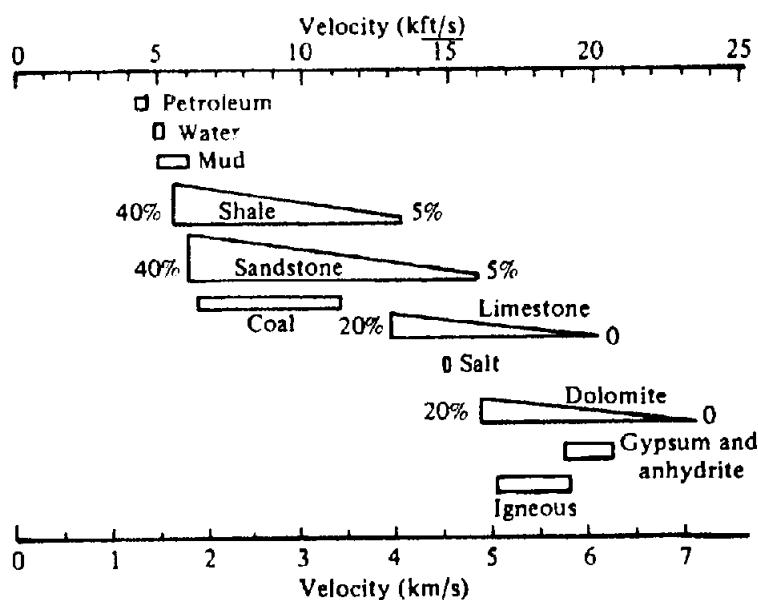


Figure 4.18. Measurement of velocity in different rock types reported by Birch (1966). (From Sheriff and Geldart, 1983.)

between the overburden and fluid pressures. Where formation fluids are under abnormally high pressures, sometimes approaching the overburden pressure, the seismic velocity is exceptionally low, a fact that is sometimes used to predict *abnormal fluid pressure* from velocity measurements (Bilgeri and Ademeno, 1982).

Subjecting a porous rock to high pressure results in both reversible and irreversible changes in porosity, that is, when the pressure is removed, a small part of the original porosity is regained whereas most is permanently lost, perhaps because of crushing of the grains, alteration of the packing, or other permanent structural changes. Empirical data suggest that the maximum depth to which a rock has been buried is a measure of the irreversible effect on porosity. In summary, porosity appears to be the dominant variable in determining the velocity in sedimentary rocks, and porosity in turn is determined principally by the existing differential pressure and the maximum depth of burial.

The variation of velocity with depth (Fig. 4.19), referred to as the *velocity function*, is frequently a reasonably systematic increase as we go to greater depths. Areas of moderately uniform geology, such as the U.S. Gulf Coast, exhibit relatively little horizontal variation in velocity from area to area. Because of seaward dip, as one goes seaward, younger section is encountered at a given depth but the velocity does not vary greatly horizontally; the maximum pressures to which the rocks have been subjected are the existing pressures, which depend mainly on depth, not age. On the other hand, areas subject to recent structural deformation and uplift, such as California, exhibit rapid horizontal variation

of velocity from area to area. Many of the California rocks have been buried to greater depths and subjected to greater stresses than exist at present, resulting in rapid lateral changes in velocity, which profoundly affect seismic interpretation.

The variation of velocity with density is shown in Figure 4.20. The large range of velocity for any given lithology (for example, shale velocities range from 1.6 to 4.0 km/s) tells the same story as Figure 4.18. The overlap of ranges of velocity makes it impossible to tell the lithology of a sample merely from its velocity. The range of density values results mainly from different porosities, and the curves would look very similar if velocity had been plotted against porosity. The dotted line in Figure 4.20 is sometimes used when a relation between velocity and density is needed, as in synthetic seismogram manufacture, seismic log calculation, and other situations.

The empirical *time-average equation* is often used to relate velocity  $V$  and porosity  $\phi$ . It assumes that the traveltimes per unit path length in a fluid-filled porous rock is the average of the traveltimes per unit path length in the matrix material  $1/V_m$  and in the fluid  $1/V_f$ , where the traveltimes are weighted in proportion to their respective volumes:

$$\frac{1}{V} = \frac{\phi}{V_f} + \frac{(1 - \phi)}{V_m} \quad (4.46)$$

This relationship is used extensively in well-log interpretation.

Whereas the velocity of  $S$  waves is generally about half that of  $P$  waves, the factor relating the two velocities varies with the lithology and is

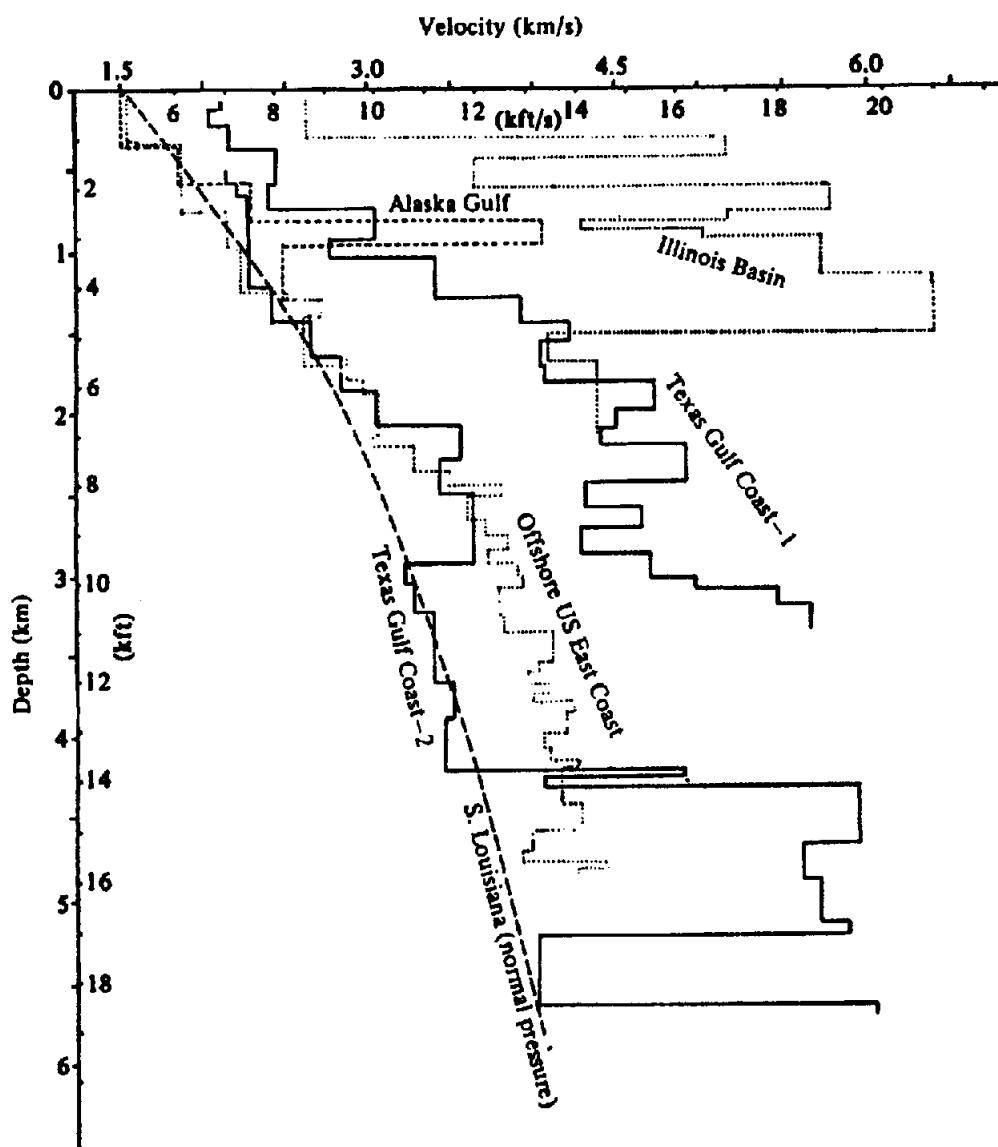


Figure 4.19. Velocity–depth relationships from selected wells. (From Sheriff and Geldart, 1983.)

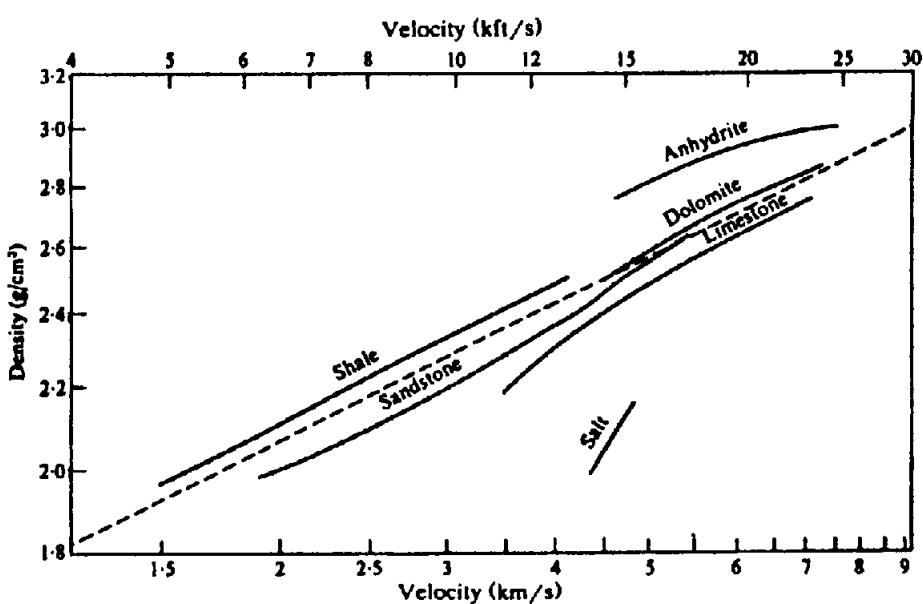


Figure 4.20. P-wave velocity–density relationships for different lithologies (log–log scale). The dotted line represents Gardner's rule:  $\rho = aV^{1/4}$ . (From Gardner, Gardner, and Gregory, 1974.)

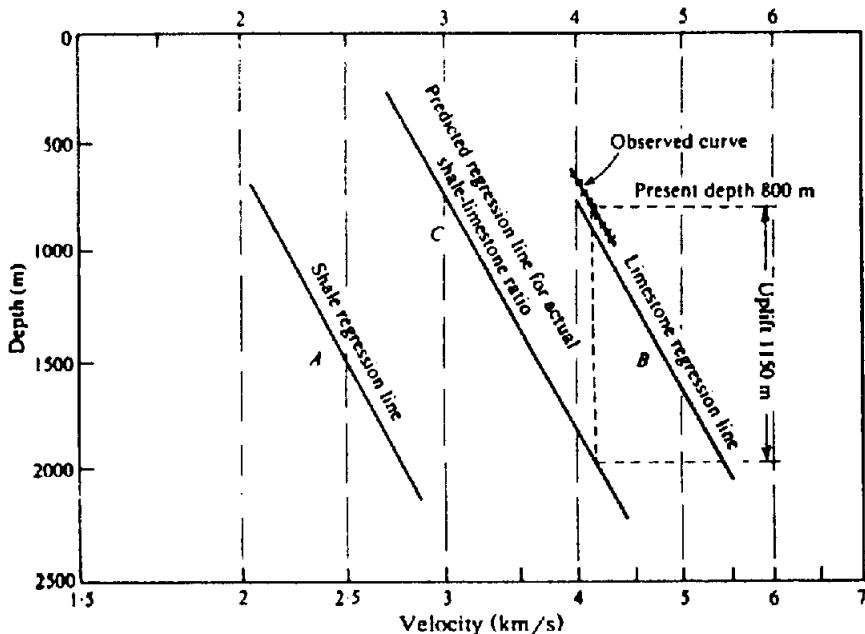


Figure 4.21. Finding maximum depth of burial from velocity. The shale and limestone regression lines represent rocks believed to have not been uplifted. (From Jankowsky, 1970.)

occasionally used to determine lithology (Domenico, 1984). The velocity of *S* waves is relatively insensitive to the nature of the fluid filling rock pore spaces, in contrast to that of *P* waves. Thus a local change in the *S*-wave to *P*-wave velocity ratio constitutes another hydrocarbon indicator (§ 4.10.8).

The irreversible change in porosity (and consequently in velocity) with depth of burial has been used to determine the maximum depth at which a section formerly lay. If the velocity-depth relationship for a given lithology can be established in an area not subjected to uplift, the maximum depth of burial can be ascertained from the observed velocity-depth relationship, and hence the amount of the uplift can be inferred. In Figure 4.21 the shale and limestone regression lines (curves *A* and *B*) represent measurements on "pure" shales and limestones that are believed to be at their maximum depth of burial. Curve *C*, which is obtained from these curves by interpolation, is the predicted curve based on the relative amounts of shale and limestone actually present and assuming the rocks to be at their maximum depth of burial. The displacement in depth required to fit this curve to the actual measurements is presumed to indicate the amount of uplift that has occurred.

Velocity and its effects are discussed more thoroughly in Sheriff and Geldart (1983, pp. 2–16) and Cordier (1985).

(b) *The weathered or low-velocity layer.* Seismic velocities that are lower than the velocity in water usually imply that gas (air or methane, probably

resulting from the decomposition of vegetation) fills at least some of the pore space (Watkins, Walters, and Godson, 1972). Such low velocities are usually found only near the surface in a zone called the *weathered layer* or the *low-velocity layer*, often abbreviated LVL. This layer, usually 4 to 50 m thick, is characterized by seismic velocities that are not only low (usually between 250 and 1000 m/s) but at times highly variable. Frequently the base of the LVL coincides roughly with the water table, indicating that the low-velocity layer corresponds to the aerated zone above the water-saturated zone, but this is not always the case. Obviously the term "weathering" as used by geophysicists differs from the geologist's "weathering," which denotes the disintegration of rocks under the influence of the elements.

The importance of the low-velocity layer is four-fold: (1) The absorption of seismic energy is high in this zone, (2) the low velocity and the rapid changes in velocity have a disproportionately large effect on traveltimes, (3) the marked velocity change at the base of the LVL sharply bends seismic rays so that their travel through the LVL is nearly vertical regardless of their direction of travel beneath the LVL, and (4) the very high impedance contrast at the base of the LVL makes it an excellent reflector, important in multiple reflections and in wave conversion. Because of the first factor, records from shots in this layer often are of poor quality and efforts are made to locate the shot below the LVL. Methods of investigating the low-velocity layer are discussed in Section 4.5.2e and methods of correcting for it in Section 4.7.1.

(c) *Permafrost.* Because the thermal conductivity of most rocks is so small, seasonal changes in the surface temperature do not significantly affect temperatures below a few meters, where the temperature approximates the average surface temperature. The result in arctic regions is a zone of permanently frozen rocks called *permafrost*. Frozen rocks generally have very high velocities, often 3.0 to 3.8 km/s or higher. The permafrost may be very irregular in thickness and often disappears completely under lakes that do not freeze solidly during the winter. The laterally variable nature of the permafrost results in time shifts and distortions that are often very difficult to remove. The very upper portion that is affected by surface temperature variations is called the active layer, and its velocity and other physical properties change seasonally by large amounts. Permafrost may even be present under the ocean, presumably having formed during a time of lowered sea level.

### 4.3. GEOMETRY OF SEISMIC WAVEPATHS

#### 4.3.1. Reflection Paths in a Constant-Velocity Layer

(a) *General.* The basic problem in reflection seismic surveying is to determine the position of a bed that gives rise to a reflection on a seismic record. In general, this is a problem in three dimensions. However, the dip is often very gentle and the direction of profiling is frequently nearly along either the direction of dip or the direction of strike. In such cases 2-D solution is generally used. We shall discuss the 2-D problem in the next two sections and then the more general problem.

The exact interpretation of reflection data requires a knowledge of the velocity at all points along the reflection paths. However, even if we had such detailed knowledge, the calculations would be tedious and often we would assume a simple distribution of velocity that is close enough to give usable results. The simplest assumption is that the velocity is constant between the surface and the reflecting bed. Although this assumption is rarely even approximately true, it leads to simple formulas that give answers that are within the required accuracy in many instances.

(b) *Horizontal reflector: normal moveout.* The simplest 2-D problem is that of zero dip, illustrated in the lower part of Figure 4.22. The reflecting bed *AB* is at a depth *h* below the source *S*. Energy leaving *S* will be reflected in such a direction that the angle of reflection equals the angle of incidence.

Although the reflected ray *CR* can be determined by laying off an angle equal to  $\alpha$  at *C*, it is easier to make use of the image point *I*, which is located on the same normal to the reflector as *S* and as far below the bed as *S* is above. If we join *I* to *C* and prolong the straight line to *R*, *CR* is the reflected ray (since *CD* is parallel to *SI*, making all the angles marked  $\alpha$  equal).

Denoting the velocity by *V*, the travel time *t* for the reflected wave is  $(SC + CR)/V$ . However,  $SC = CI$  so that *IR* is equal in length to the actual path *SCR*. Therefore,  $t = IR/V$  and in terms of *x*, the source-to-geophone distance (*offset*), we can write

$$\text{or } \left. \begin{aligned} V^2 t^2 &= x^2 + 4h^2 \\ \frac{V^2 t^2}{4h^2} - \frac{x^2}{4h^2} &= 1 \end{aligned} \right\} \quad (4.47)$$

Thus the traveltime curve is a hyperbola as shown in the upper part of Figure 4.22.

The geophone at *R* will also record the *direct wave* that travels along the path *SR*. Because *SR* is always less than  $(SC + CR)$ , the direct wave arrives first. The traveltime is  $t_D = x/V$  and the traveltime curves are the straight lines *OM* and *ON* passing through the origin with slopes of  $\pm 1/V$ .

When the distance *x* becomes very large, the difference between *SR* and  $(SC + CR)$  becomes small and the reflection traveltime approaches the direct wave traveltime asymptotically.

The location of the reflecting bed is determined by measuring *t<sub>0</sub>*, the traveltime for a geophone at the source. Setting *x* = 0 in Equation (4.47), we see that

$$h = \frac{1}{2} V t_0 \quad (4.48)$$

Equation (4.47) can be written

$$t^2 = \frac{x^2}{V^2} + \frac{4h^2}{V^2} = \frac{x^2}{V^2} + t_0^2 \quad (4.49)$$

If we plot *t*<sup>2</sup> against *x*<sup>2</sup> (instead of *t* versus *x* as in Fig. 4.22), we obtain a straight line of slope  $(1/V^2)$  and intercept *t<sub>0</sub>*<sup>2</sup>. This forms the basis of a well-known scheme for determining *V*, the "*X*<sup>2</sup> – *T*<sup>2</sup>" method, which will be described in Section 4.5.5c.

We can solve Equation (4.49) for *t*, the traveltime measured on the seismic record. Generally *2h* is appreciably larger than *x* so that we can use a binomial expansion as follows:

$$\begin{aligned} t &= \frac{2h}{V} \left\{ 1 + \left( \frac{x}{2h} \right)^2 \right\}^{1/2} = t_0 \left\{ 1 + \left( \frac{x}{Vt_0} \right)^2 \right\}^{1/2} \\ &= t_0 \left\{ 1 + \frac{1}{2} \left( \frac{x}{Vt_0} \right)^2 - \frac{1}{8} \left( \frac{x}{Vt_0} \right)^4 + \dots \right\} \quad (4.50) \end{aligned}$$

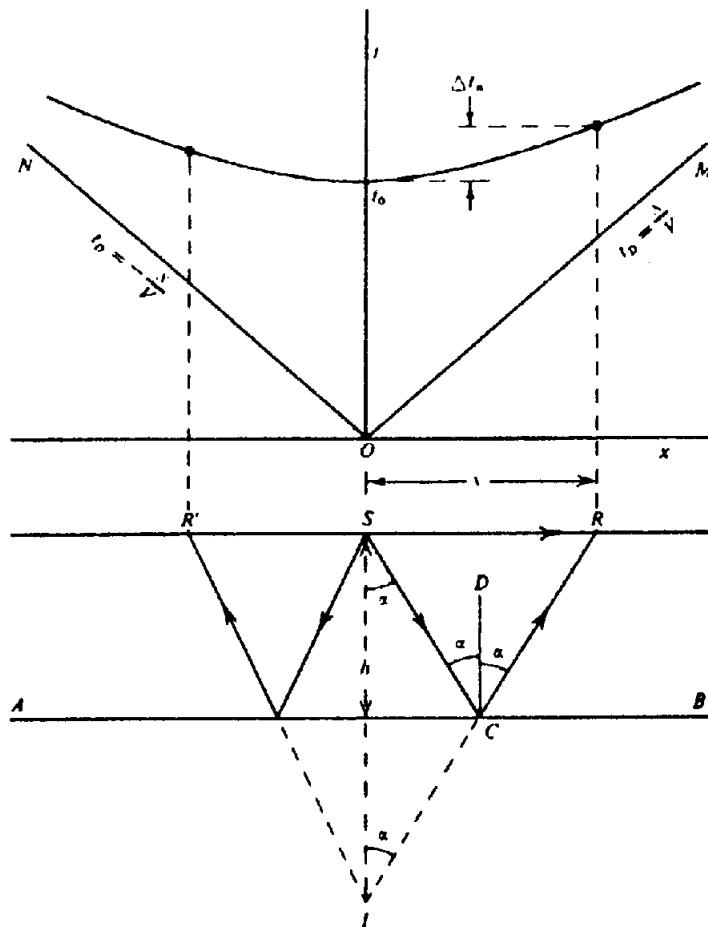


Figure 4.22. Geometry and traveltime curve for horizontal reflector.

The difference in traveltime for a given reflection for two geophone locations is known as *moveout* and it is represented by  $\Delta t$ . If  $t_1$ ,  $t_2$ ,  $x_1$ , and  $x_2$  are the traveltimes and offsets, we have to the first approximation

$$\Delta t = t_2 - t_1 = \frac{x_2^2 - x_1^2}{2V^2 t_0} \quad (4.51)$$

In the special case where one geophone is at the source,  $\Delta t$  is known as the *normal moveout*, which we shall denote by  $\Delta t_n$ . Then,

$$\Delta t_n = \frac{x^2}{2V^2 t_0} \quad (4.52)$$

At times we retain another term in the expansion:

$$\Delta t_n \approx \frac{x^2}{2V^2 t_0} - \frac{x^4}{8V^4 t_0^3} = \frac{x^2}{2V^2 t_0} \left\{ 1 - \left( \frac{x}{4h} \right)^2 \right\} \quad (4.53)$$

From Equation (4.52) we note that the normal moveout increases as the square of the offset  $x$ , inversely as the square of the velocity, and inversely

as the first power of the traveltime [or depth; see Eq. (4.48)]. Thus reflection curvature increases rapidly as we go to more distant geophones and, at the same time, the curvature becomes progressively less with increasing record time.

The concept of normal moveout is extremely important. It is the principal criterion by which we decide whether an event observed on a seismic record is a reflection or not. If the normal moveout differs from the value given by Equation (4.52) by more than the allowable experimental error, we are not justified in treating the event as a reflection. One of the most important quantities in seismic interpretation is the change in arrival time caused by dip. To find this quantity, we must correct for normal moveout. Normal moveout must also be eliminated before "stacking" (adding together) common-midpoint records (§ 4.7.8). Finally, Equation (4.52) can be used to find  $V$  by measuring  $x$ ,  $t_0$ , and  $\Delta t_n$ . This forms the basis of velocity analysis (§ 4.7.7).

(c) *Dipping reflector: dip moveout.* When the bed is dipping in the direction of the profile, we have the situation shown in Figure 4.23, where  $\xi$  is the dip and  $h$  is the depth (normal to the bed). To draw the raypath for the reflection arriving at the geophone  $R$ ,

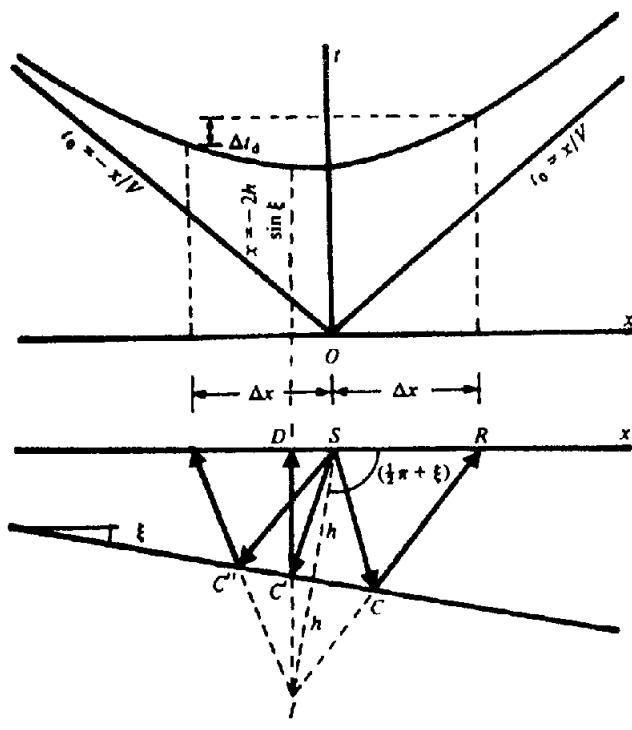


Figure 4.23. Geometry and traveltime curve for dipping reflector.

we join the image point  $I$  to  $R$  by a straight line cutting the bed at  $C$ . The path is then  $SCR$  and  $t = (SC + CR)/V$ . Because  $(SC + CR) = IR$ , application of the cosine law to the triangle  $SIR$  gives

$$\begin{aligned} V^2 t^2 &= IR^2 \\ &= x^2 + 4h^2 - 4hx \cos\left(\frac{\pi}{2} + \xi\right) \\ &\doteq x^2 + 4h^2 + 4hx \sin \xi \end{aligned} \quad (4.54)$$

On completing the squares, we obtain

$$\frac{V^2 t^2}{(2h \cos \xi)^2} - \frac{(x + 2h \sin \xi)^2}{(2h \cos \xi)^2} = 1$$

Thus, as before, the traveltime curve is a hyperbola, but the axis of symmetry is now the line  $x = -2h \sin \xi$  instead of the  $t$  axis. This means that  $t$  has different values for geophones symmetrically placed on opposite sides of the source, unlike the case for zero dip.

Setting  $x = 0$  in Equation (4.54) gives the same value for  $h$  as in Equation (4.48). Note, however, that  $h$  is not the vertical depth here as it was in the earlier result.

To obtain the dip  $\xi$ , we solve for  $t$  in Equation (4.54) by assuming that  $2h$  is greater than  $x$  and expanding as in the derivation of Equation (4.50).

Then

$$\begin{aligned} t &= \frac{2h}{V} \left\{ 1 + \left( \frac{x^2 + 4hx \sin \xi}{4h^2} \right) \right\}^{1/2} \\ &\approx t_0 \left( 1 + \frac{x^2 + 4hx \sin \xi}{8h^2} \right) \end{aligned} \quad (4.55)$$

using only the first term of the expansion. The simplest method of finding  $\xi$  is from the difference in traveltimes for two geophones equally distant from, and on opposite sides of, the source. Letting  $x$  have the values  $+\Delta x$  for the downdip geophone and  $-\Delta x$  for the updip geophone and denoting the equivalent traveltimes by  $t_1$  and  $t_2$ , we get

$$\begin{aligned} t_1 &\approx t_0 \left\{ 1 + \frac{(\Delta x)^2 + 4h \Delta x \sin \xi}{8h^2} \right\} \\ t_2 &\approx t_0 \left\{ 1 + \frac{(\Delta x)^2 - 4h \Delta x \sin \xi}{8h^2} \right\} \\ \Delta t_d &= t_1 - t_2 \approx t_0 \left( \frac{\Delta x \sin \xi}{h} \right) \approx \frac{2 \Delta x}{V} \sin \xi \end{aligned}$$

The quantity  $(\Delta t_d/\Delta x)$  is the *dip moveout* (this term is also used with a different meaning in some seismic processing). The dip is found from the equation

$$\sin \xi \approx \frac{V}{2} \left( \frac{\Delta t_d}{\Delta x} \right) \quad (4.56)$$

For small angles,  $\xi \approx \sin \xi$  so that the dip is directly proportional to  $(\Delta t_d/\Delta x)$  under these circumstances. To obtain the dip as accurately as possible, we use as large a value of  $\Delta x$  as the data quality permits. For symmetrical spreads, we measure dip moveout between the geophone groups at opposite ends of the spread.

It should be noted that normal moveout was eliminated in the derivation of Equation (4.56). The terms in  $(\Delta x)^2$  that disappeared in the subtraction represent the normal moveout.

Figure 4.24 illustrates diagrammatically the relation between normal moveout and dip moveout. The diagram at the left represents a reflection from a dipping bed; the alignment is curved and unsymmetrical about the source. Diagram (B) shows what would have been observed if the bed had been horizontal; the alignment is curved symmetrically about the source position owing to the normal moveout. The latter ranges from 0 to 29 ms (1 millisecond =  $10^{-3}$  s = 1 ms, the unit of time commonly used in seismic work) at an offset of 600 m. Diagram (C) was obtained by subtracting the normal moveouts shown in (B) from the arrival times in (A). The resulting alignment shows the effect of dip alone; it is straight

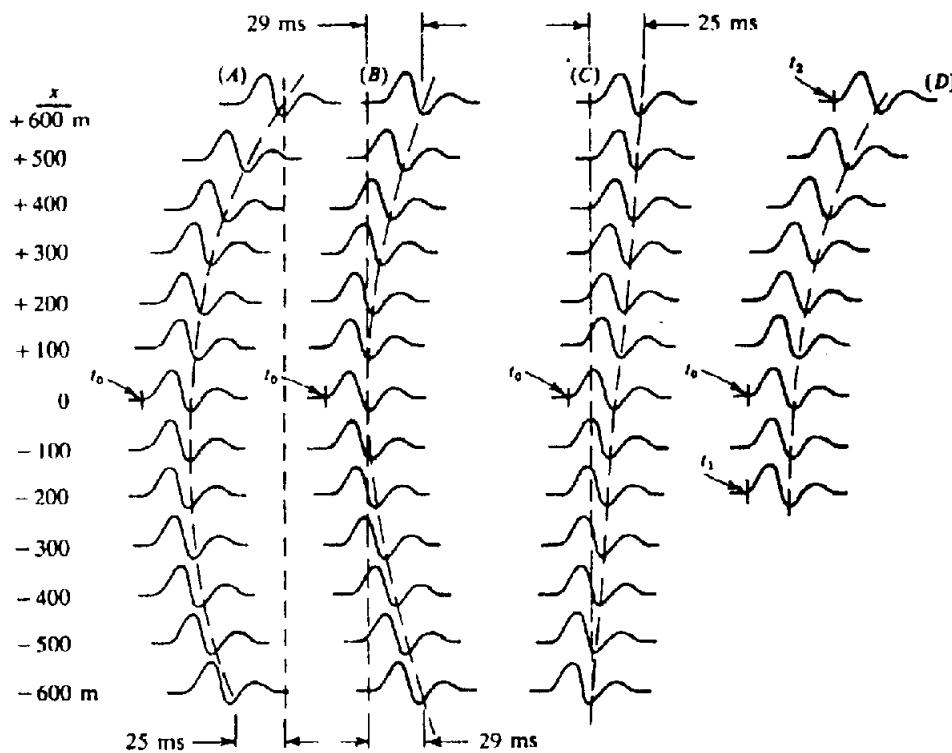


Figure 4.24. Relation between normal moveout and dip moveout;  $t_0 = 1.000$  s,  $V = 2,500$  m/s.

and has a time difference between the outside curves of 25 ms, that is,  $\Delta t_d/\Delta x = 0.042$  ms/m. Thus we find that the dip is  $\sin^{-1}(2,500 \times 0.021/1,000) = 0.052$  rad =  $3.0^\circ$ .

The method of normal-moveout removal illustrated in Figure 4.24 was used solely to demonstrate the difference between normal moveout and dip moveout. If we require only the dip moveout  $\Delta t_d$ , we merely subtract the traveltimes for the two outside geophones in (A).

We may not have a symmetrical spread and we find the dip moveout by removing the effect of normal moveout. As an example, refer to Figure 4.24, curve (D), which shows a reflection observed on a spread extending from  $x = -200$  to  $x = +600$  m. Let  $t_0 = 1.000$  s,  $t_1 = 0.997$  s,  $t_2 = 1.025$  s,  $V = 2,800$  m/s. From Equation (4.52) we get, for  $\Delta t_n$  at offsets of 200 and 600 m, respectively, the values 3 and 23 ms (rounded off to the nearest millisecond because this is usually the precision of measurements on seismic records). Subtracting these values, we obtain, for the corrected traveltimes,  $t_1 = 0.994$  s and  $t_2 = 1.002$  s. Hence, the dip moveout is  $8/400 = 0.020$  ms/m. The corresponding dip is  $\sin^{-1}(\frac{1}{2} \times 2,800 \times 0.020/1,000) \approx 0.03$  rad  $\approx 2^\circ$ .

An alternative to the preceding method is to use the arrival times at  $x = -200$  and  $x = +200$  m, thus obtaining a symmetrical spread and eliminating the need for calculating normal moveout. However, doing this would decrease the effective spread length

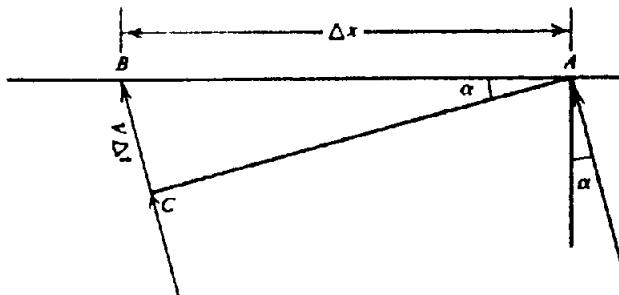


Figure 4.25. Finding the angle of approach of a wave.

from 800 to 400 m and thereby reduce the accuracy of the ratio ( $\Delta t_d/\Delta x$ ).

Equation (4.56) is similar to the equation that gives the angle of approach of a plane wave as it reaches the surface. In Figure 4.25,  $AC$  represents an upward-traveling plane wave at the instant when it arrives at the end of the spread,  $A$ . After a further interval  $\Delta t$ , the same wave reaches the other end of the spread,  $B$ . Then,  $BC = V\Delta t$  and

$$\sin \alpha = \frac{BC}{BA} = V \frac{\Delta t}{\Delta x} \quad (4.57)$$

This result, although similar in form to Equation (4.56) has a different significance because it gives the direction of travel of a plane wave as it reaches the spread.  $V$  is the average velocity between  $C$  and the surface. In Equation (4.56),  $V$  is the average velocity down to the reflector and  $\xi$  is the angle of dip. The

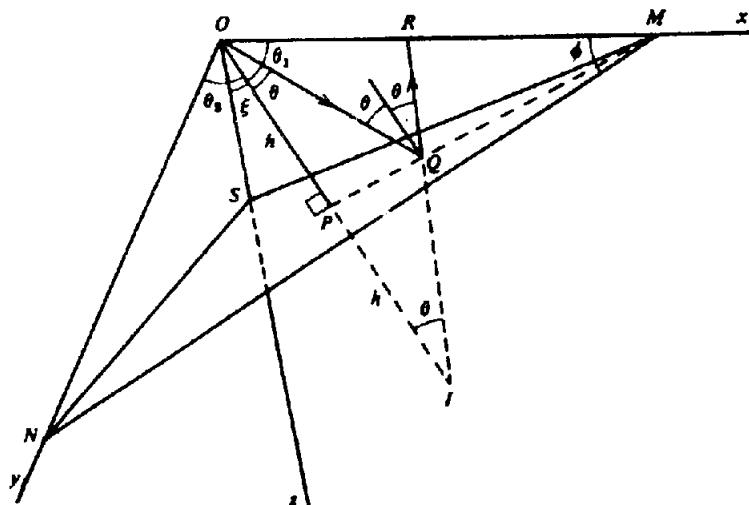


Figure 4.26. Three-dimensional view of a reflection path for a dipping bed.

two formulas give the same angle because  $V$  is constant down to the reflector and  $2\Delta x$  in Equation (4.56) is the same as  $\Delta x$  in Equation (4.57). Often  $V$  will not be constant, as we shall see presently.

(d) *Cross dip.* When the profile is not perpendicular to the strike, the determination of dip becomes a 3-D problem. In Figure 4.26 we take the  $xy$  plane as horizontal with the  $z$  axis extending vertically downward. The line  $OP$  of length  $h$  is perpendicular to a dipping plane bed that outcrops (that is, intersects the  $xy$  plane) along the line  $MN$  if sufficiently extended.

We write  $\theta_1$ ,  $\theta_2$ , and  $\xi$  for the angles between  $OP$  and  $x$ ,  $y$ , and  $z$  axes. The cosines of these angles (the direction cosines of  $OP$ ) have the values  $\ell$ ,  $m$ , and  $n$ . Equation (A.8) states that

$$\ell^2 + m^2 + n^2 = 1$$

The angle  $\phi$  between  $MN$  and the  $x$  axis is the direction of strike of the bed whereas  $\xi$  is the angle of dip.

The path of a reflected wave arriving at a geophone  $R$  on the  $x$  axis can be found using the image point  $I$ . The line joining  $I$  to  $R$  cuts the reflector at  $Q$ ; hence  $OQR$  is the path. Since  $OQ = QI$ , the line  $IR = Vt$  where  $t$  is the traveltime for the geophone at  $R$ . The coordinates of  $I$  and  $R$  are, respectively,  $(2h\ell, 2hm, 2hn)$  and  $(x, 0, 0)$ . Hence we have

$$\begin{aligned} V^2 t^2 &= IR^2 \\ &= (x - 2h\ell)^2 + (0 - 2hm)^2 + (0 - 2hn)^2 \\ &= x^2 + 4h^2(\ell^2 + m^2 + n^2) - 4h\ell x \\ &= x^2 + 4h^2 - 4h\ell x \end{aligned}$$

When  $x = 0$ , we obtain the same relation between  $h$  and  $t_0$  as in Equation (4.48). Proceeding as

in the derivation of Equation (4.55), we get, for the approximate value of  $t$ ,

$$t \approx t_0 \left( 1 + \frac{x^2 - 4h\ell x}{8h^2} \right)$$

By subtracting the arrival times at two geophones located on the  $x$  axis at  $x = \pm \Delta x$ , we find

$$\begin{aligned} \Delta t_x &\approx t_0 \left( \frac{\ell \Delta x}{h} \right) \\ &\approx \frac{2\ell \Delta x}{V} \\ \ell &= \cos \theta_1 \approx \frac{V}{2} \left( \frac{\Delta t_x}{\Delta x} \right) \quad (4.58) \end{aligned}$$

If we also have a spread along the  $y$  axis (cross spread; see § 4.5.2b), we get

$$m = \cos \theta_2 \approx \frac{V}{2} \left( \frac{\Delta t_y}{\Delta y} \right) \quad (4.59)$$

where  $\Delta t_y$  is the time difference (cross dip) between geophones a distance  $2\Delta y$  apart and symmetrical about the shotpoint. Because

$$\begin{aligned} n &= \cos \xi = \{1 - (\ell^2 + m^2)\}^{1/2} \\ \sin \xi &= (1 - n^2)^{1/2} = (\ell^2 + m^2)^{1/2} \\ &= \frac{V}{2} \left\{ \left( \frac{\Delta t_x}{\Delta x} \right)^2 + \left( \frac{\Delta t_y}{\Delta y} \right)^2 \right\}^{1/2} \quad (4.60) \end{aligned}$$

When the profile lines are not perpendicular, for example, when one is along the  $x$  axis and the other along the  $y'$  axis at an angle  $\beta$  to the  $x$  axis, the solution is more complicated. Taking the length of a

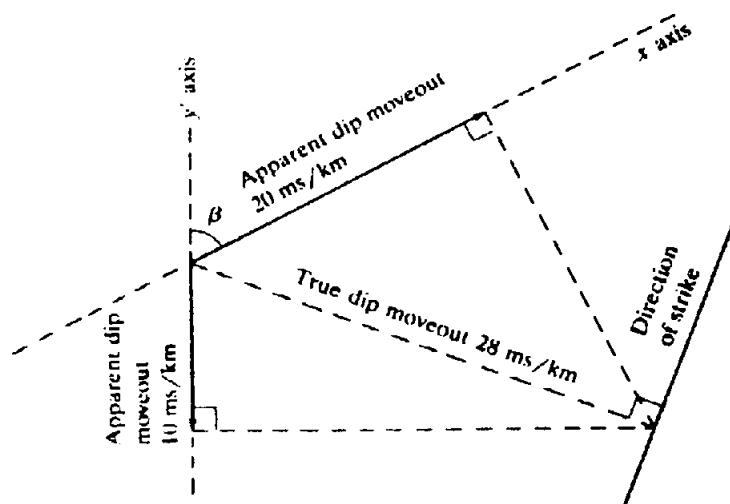


Figure 4.27. Resolution of cross-spread information.

symmetrical spread along the  $y'$  axis as  $2 \Delta y'$ , the coordinates of the ends of this spread (relative to the  $x$ ,  $y$ , and  $z$  axes) are  $(\Delta y' \cos \beta, \Delta y' \sin \beta, 0)$  and  $(-\Delta y' \cos \beta, -\Delta y' \sin \beta, 0)$ . Then

$$\begin{aligned} V^2 t_{\pm}^2 &= (2h\ell \pm \Delta y' \cos \beta)^2 \\ &\quad + (2hm \pm \Delta y' \sin \beta)^2 + (2hn)^2 \\ &= (\Delta y')^2 + 4h^2 \pm 4h \Delta y' (\ell \cos \beta + m \sin \beta) \end{aligned}$$

The moveout becomes

$$\Delta t' = \frac{2 \Delta y'}{V} (\ell \cos \beta + m \sin \beta)$$

or

$$(\ell \cos \beta + m \sin \beta) = \frac{V}{2} \left( \frac{\Delta t'}{\Delta y'} \right) \quad (4.61)$$

The measured moveouts,  $\Delta t_x$  and  $\Delta t'$ , give the values of  $\ell$  and  $(\ell \cos \beta + m \sin \beta)$  using Equations (4.58) and (4.61). Because  $\beta$  is known,  $m$  can be found using Equation (4.60). The solution can also be found graphically as shown in Figure 4.27 (see also problem 5).

To find the strike  $\phi$ , we start from the equation of a plane (that is, the reflector) that has a perpendicular from the origin of length  $h$  and direction cosines  $(\ell, m, n)$ , namely

$$\ell x + my + nz = h$$

Setting  $z = 0$  gives the equation of the line of intersection of the reflector and the surface ( $MN$  in Fig. 4.26 or 4.28). This strike line has the equation

$$\ell x + my = h$$

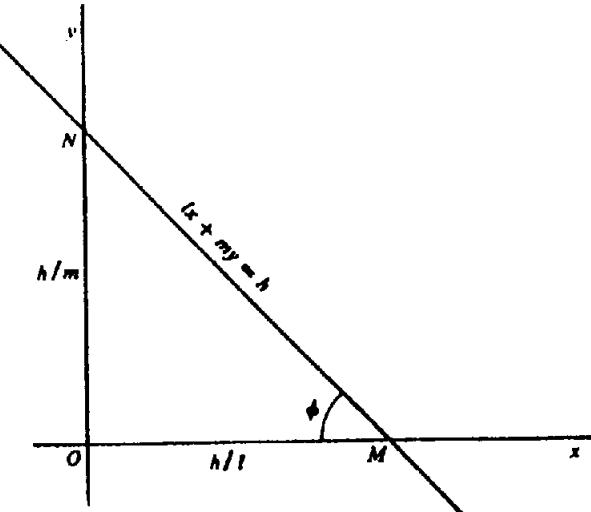


Figure 4.28. Determination of strike.

The intercepts of this line on the  $x$  and  $y$  axes are  $h/\ell$  and  $h/m$ . Referring to Figure 4.28, we find that

$$\tan \phi = \frac{h}{m} \div \frac{h}{\ell} = \frac{\ell}{m} = \left( \frac{\Delta t_x}{\Delta x} \right) \left( \frac{\Delta y}{\Delta t_y} \right) = \left( \frac{\Delta t_x}{\Delta t_y} \right) \quad (4.62)$$

when  $\Delta x = \Delta y$ . The strike can also be found using the construction shown in Figure 4.27.

#### 4.3.2. Velocity Gradient and Raypath Curvature

(a) *Effect of velocity variations.* The assumption of constant velocity is not valid, in general, because the velocity usually changes as we go from one point to another. In petroleum exploration we are usually dealing with more-or-less flat-lying bedding, and the changes in seismic velocity as we move horizontally are, for the most part, the result of slow changes in

density and elastic properties of the beds. These horizontal variations are generally much less rapid than the variations in the vertical direction where we are going from bed to bed with consequent lithological changes and increasing pressure with increasing depth. Because the horizontal changes are gradual, they can often be taken into account by dividing the survey area into smaller areas within each of which the horizontal variations can be ignored and the same vertical velocity distribution can be used. Such areas often are large enough to include several structures of the size of interest in oil exploration so that changes from one velocity function to another do not impose a serious burden on the interpreter.

(b) *Equivalent average velocity.* Vertical variations in velocity can be taken into account in various ways. One of the simplest is to use a modification of the constant velocity model. We assume that the actual section existing between the surface and a certain reflecting horizon can be replaced with an equivalent single layer of constant velocity  $V$  equal to the average velocity between the surface and the reflecting horizon. This velocity is usually given as a function of depth (or of  $t_0$ , which is nearly the same except when the dip is large). Thus the section is assigned a different constant velocity for each of the reflectors below it. Despite this inconsistency, the method is useful and is extensively applied. The variation of the average velocity with  $t_0$  is found using one of the methods described in Section 4.5.5. For the observed values of the arrival time  $t_0$ , we select the average velocity  $V$  corresponding to this reflector. Using the values of  $t_0$ , the dip moveout  $\Delta t_d/\Delta x$ , and  $V$ , we calculate the depth  $h$  and the dip  $\xi$  using Equations (4.48) and (4.56).

(c) *Velocity layering.* A method that is commonly used to take into account velocity variations is to replace the actual velocity distribution with an approximate one that corresponds to a number of horizontal layers of different velocities; the velocity is constant within each layer. Simple equations such as (4.48) and (4.56) are no longer appropriate because rays bend at each layer interface. We often replace the actual raypaths with a series of line segments that are straight within each layer but undergo abrupt changes in direction at the boundaries between layers. Dix (1955) shows that the effect of this for a series of horizontal parallel layers is to replace the average velocity  $V$  in Equation (4.49) by its root-mean-square (rms) value  $V_{\text{rms}}$ , so that

$$t^2 = t_0^2 + x^2/V_{\text{rms}}^2 \quad (4.63)$$

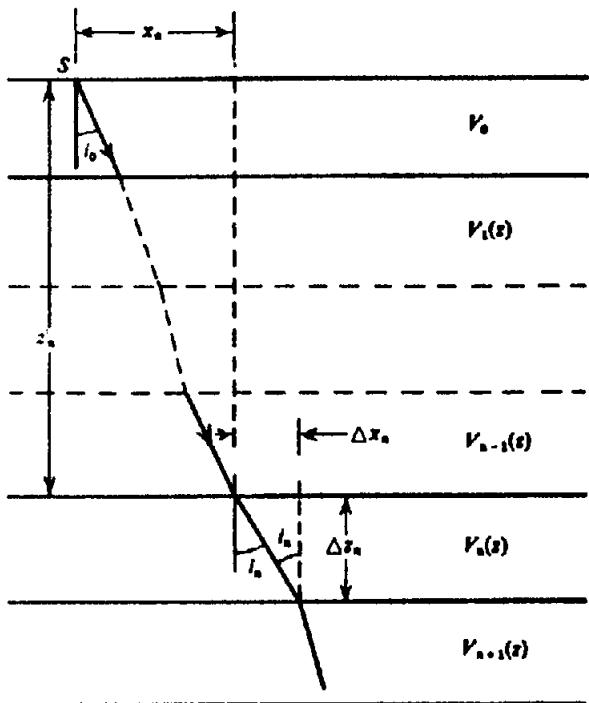


Figure 4.29. Raypath where velocity varies with depth.

where

$$V_{\text{rms}} = \left( \sum_i^n V_i^2 t_i / \sum_i^n t_i \right)^{1/2} \quad (4.64)$$

$V_i$  and  $t_i$  are, respectively, the average velocity in and the traveltime through, the  $i$ th layer (see also Shah and Levin, 1973).

(d) *Velocity functions.* At times the assumption is made that the velocity varies in a systematic continuous manner and therefore can be represented by a velocity function. The actual velocity usually varies extremely rapidly over short intervals, as shown by sonic logs (§ 11.7.2). However, if we integrate these changes over distances of a wavelength or so (30 to 100 m), we obtain a function, which is generally smooth except for discontinuities at marked lithological changes. If the velocity discontinuities are small, we are often able to represent the velocity distribution with sufficient accuracy by a smooth velocity function. The path of a wave traveling in such a medium is then determined by two integral equations.

To derive the equations, we assume that the medium is divided into a large number of thin horizontal beds in each of which the velocity is constant. When we let the number of beds go to infinity, the thickness of each bed becomes infinitesimal and the velocity distribution becomes a continuous function of depth. Referring to Figure 4.29, we have, for the

*n*th bed.

$$\frac{\sin i_n}{V_n} = \frac{\sin i_0}{V_0} = p$$

$$V_n = V_n(z)$$

$$\Delta x_n = \Delta z_n \tan i_n$$

$$\Delta t_n = \frac{\Delta z_n}{V_n \cos i_n}$$

The raypath parameter  $p$  (§ 4.2.6b) is a constant that depends on the direction in which the ray left the shotpoint, that is, upon  $i_0$ . In the limit when  $n$  becomes infinite, we get

$$\left. \begin{aligned} \frac{\sin i}{V} &= \frac{\sin i_0}{V_0} = p & V &= V(z) \\ \frac{dx}{dz} &= \tan i & \frac{dt}{dz} &= \frac{1}{V \cos i} \\ x &= \int_0^z \tan i dz & t &= \int_0^z \frac{dz}{V \cos i} \end{aligned} \right\} \quad (4.65)$$

hence

$$\left. \begin{aligned} x &= \int_0^z \frac{pV dz}{\{1 - (pV)^2\}^{1/2}} \\ t &= \int_0^z \frac{dz}{V\{1 - (pV)^2\}^{1/2}} \end{aligned} \right\} \quad (4.66)$$

Since  $V$  is a function of  $z$ , Equation (4.66) furnishes two integral equations relating  $x$  and  $t$  to the depth  $z$ . These equations can be solved by numerical methods when we have a table of values of  $V$  at various depths.

### 4.3.3. Geometry of Refraction Paths

(a) Headwaves. In refraction seismology we make use of waves that have been refracted at the critical angle; these waves are often called *headwaves*. In Figure 4.30a we see a  $P$  wave incident on the refracting horizon at the critical angle  $\theta_c$ . After refraction it travels along the interface in the lower medium. This produces an oscillatory motion parallel to and immediately below the interface (as shown by the double-headed arrow just below the interface). Because relative motion between the two media is not possible, the upper medium is forced to move in phase with the lower medium. The disturbance in the upper medium travels along the interface with the same velocity  $V_2$  as the refracted wave just below the

interface. Let us assume that these disturbances represented by the arrows reach the point  $P$  in Figure 4.30b at the time  $t$ . According to Huygens' principle,  $P$  then becomes a center from which a wave spreads out into the upper medium. After a further time interval  $\Delta t$ , this wave has a radius of  $V_1 \Delta t$  whereas the wave moving along the refractor has reached  $Q$ ,  $PQ = V_2 \Delta t$ . Drawing the tangent from  $Q$  to the arc of radius  $V_1 \Delta t$ , we obtain the wavefront  $RQ$ . Hence the passage of the refracted wave along the interface in the lower medium generates a plane wave traveling upward in the upper medium at the angle  $\theta$ , where

$$\sin \theta = \frac{V_1 \Delta t}{V_2 \Delta t} = \frac{V_1}{V_2} = \sin \theta_c \quad (4.67)$$

Thus we see that  $\theta = \theta_c$ , so that the two inclined portions of the path are symmetrically disposed with respect to the normal to the refractor.

The preceding discussion of the geometry of headwaves ignores an important point, which the alert reader may already have noted, namely that the transmitted energy, which is the product of the intensity and the beam width, is zero at  $\theta_c$  because the beam width becomes zero (the amplitude does not become zero). Consequently, the headwave carries no energy. However, at angles slightly smaller than  $\theta_c$ , the narrow beams do carry finite energy. Because the velocity below the interface usually increases slightly with depth below the interface, the refracted energy will be bent back toward the surface, as in Figure 4.30c, and its travelpath will be almost the same as that along the interface, so that the result is nearly the same as if energy had been refracted along the interface. Headwaves do exist and frequently are very strong. A more exact theory based on curved wavefronts (Grant and West, 1965, Chap. 6) predicts the existence of headwaves with nonzero intensities and the same geometrical relations as those predicted by plane-wave theory.

Obviously the headwave will not be observed at offsets less than  $ON$  in Figure 4.30b where

$$\begin{aligned} x_c &= ON = 2z \tan \theta_c \\ &= 2z \tan \left\{ \sin^{-1} \left( \frac{V_1}{V_2} \right) \right\} = 2z \left\{ \left( \frac{V_2}{V_1} \right)^2 - 1 \right\}^{-1/2} \end{aligned} \quad (4.68)$$

$x_c$  is called the *critical distance*. As the ratio  $V_2/V_1$  increases,  $x_c$  decreases. When  $V_2/V_1 = 1.4$ ,  $x_c = 2z$ .

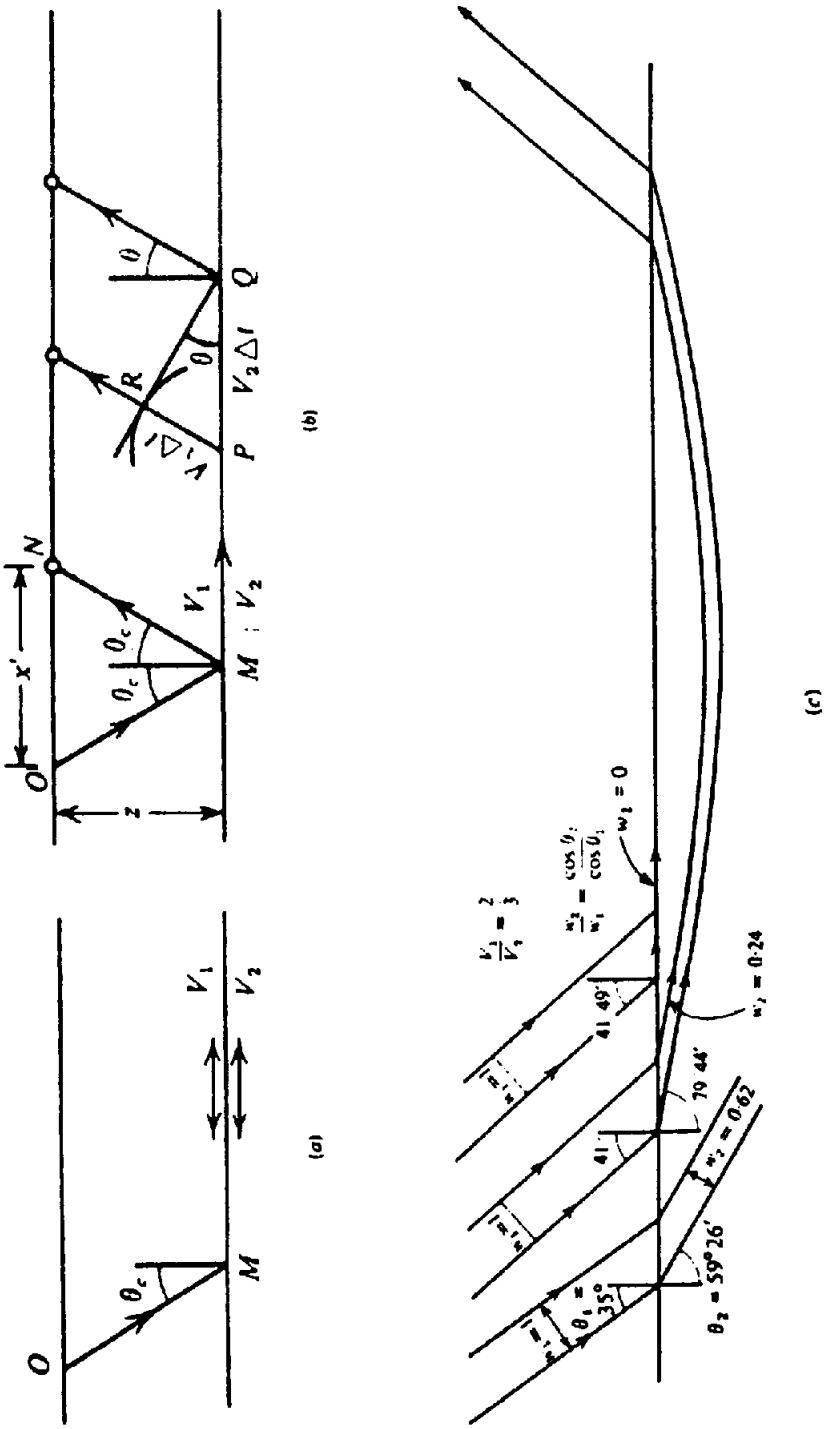


Figure 4.30. Headwaves. (a) Motion at the interface. (b) Wavefront emerging from refractor at critical angle. (c) Changes in beam width upon refraction and bending of refracted raypaths because of the velocity gradient in the high-velocity medium.

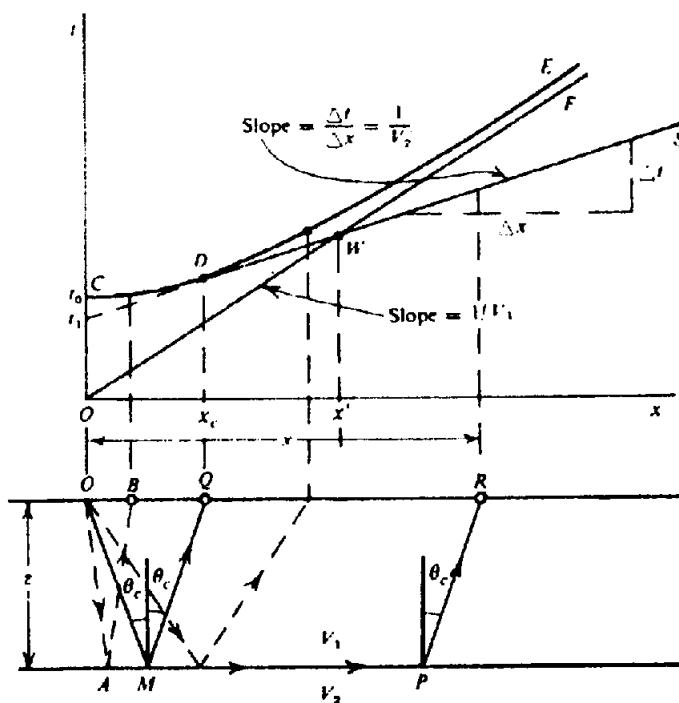


Figure 4.31. Relation between reflection and refraction raypaths and traveltime curves.

Hence as a rule of thumb, refractions are observed only at offsets greater than twice the depth to the refractor.

(b) Single horizontal refractor. In the case of a single horizontal refracting horizon, we can readily derive a formula expressing the arrival time in terms of the offset, the depth, and the velocities. In Figure 4.31, the lower part shows a horizontal plane refractor separating two beds of velocities  $V_1$  and  $V_2$ , where  $V_2 > V_1$ . For a geophone at  $R$ , the path of the refracted wave is  $OMPR$ . The traveltime  $t$  can be written

$$\begin{aligned} t &= \frac{OM}{V_1} + \frac{MP}{V_2} + \frac{PR}{V_1} = \frac{MP}{V_2} + 2 \frac{OM}{V_1} \\ &= \frac{x - 2z \tan \theta_c}{V_2} + \frac{2z}{V_1 \cos \theta_c} \\ &= \frac{x}{V_2} + \frac{2z}{V_1 \cos \theta_c} \left( 1 - \frac{V_1}{V_2} \sin \theta_c \right) \\ &= \frac{x}{V_2} + \frac{2z \cos \theta_c}{V_1} \end{aligned} \quad (4.69)$$

where we have used the relation  $\sin \theta_c = V_1/V_2$  in the last step. This equation can also be written

$$t = \frac{x}{V_2} + t_i \quad (4.70)$$

where

$$t_i = (2z \cos \theta_c)/V_1$$

or

$$z = \frac{1}{2} V_1 t_i / \cos \theta_c$$

Equation (4.70) represents a straight line of slope  $1/V_2$  and intercept time  $t_i$ . This is illustrated in Figure 4.31 where  $OMQ$  and  $OMPR$  are two of a series of refraction paths and  $DWS$  is the corresponding time-distance curve. Note that this straight-line equation does not have physical meaning for offsets less than  $x_c$  because the refracted wave does not exist in this region. Nevertheless, we can project the line back to the time axis to find  $t_i$ .

The problem to be solved usually is to find the depth  $z$  and the two velocities  $V_1$  and  $V_2$ . The slope of the direct-wave time-distance curve is the reciprocal of  $V_1$  and the same measurement for the refraction event gives  $V_2$ . We can then calculate the critical angle  $\theta_c$  from the relation  $\theta_c = \sin^{-1}(V_1/V_2)$ , and use the intercept time  $t_i$  to calculate  $z$  from Equation (4.70).

In Figure 4.31 the time-distance curves for the reflection from the interface  $AP$  and for the direct path are represented by the hyperbola  $CDE$  and the straight line  $OF$ , respectively. Since the path  $OMQ$  can be regarded either as a reflection or as the beginning of the refracted wave, the reflection and refraction time-distance curves must coincide at  $x = x_c$ , that is, at the point  $D$ . Moreover, differentiating Equation (4.47) to obtain the slope of the

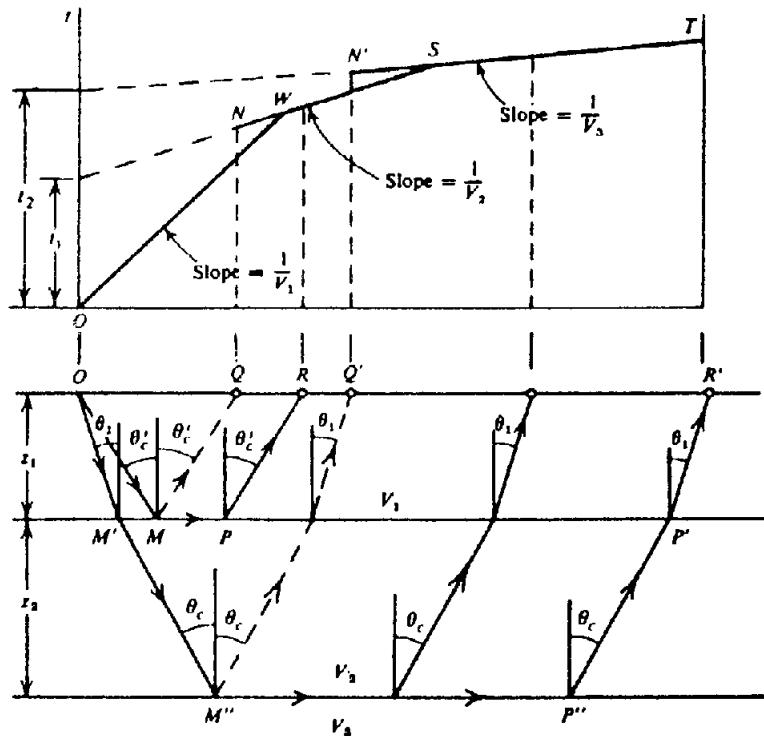


Figure 4.32. Raypaths and traveltime curves for the two-refractor case.

reflection time-distance curve at  $x = x_c$ , we find

$$\begin{aligned} \left[ \frac{dt}{dx} \right]_{x=x_c} &= \left[ \frac{x}{V_1^2 t} \right]_{x=x_c} \\ &= \frac{1}{V_1} \left[ \frac{OQ}{OM + MQ} \right] \\ &= \frac{1}{V_1} \left( \frac{\frac{1}{2} OQ}{OM} \right) \\ &= \frac{1}{V_1} \sin \theta_c = \frac{1}{V_2} \end{aligned}$$

We see therefore that the reflection and refraction curves have the same slope at  $D$ , and consequently the refraction curve is tangent to the reflection curve at  $x = x_c$ .

Comparing reflected and refracted waves from the same horizon and arriving at the same geophone, we note that the refraction arrival time is always less than the reflection arrival time (except at  $D$ ). The intercept time  $t_i$  for the refraction is less than the arrival time  $t_0$  for the reflection at the shotpoint because

$$t_i = \frac{2z}{V_1} \cos \theta_c \quad t_0 = \frac{2z}{V_1} \quad \text{hence } t_i < t_0$$

Starting at the point  $Q$ , we see that the direct wave arrives ahead of the reflected and refracted waves because its path is the shortest of the three.

However, part of the refraction path is traversed at velocity  $V_2$ , so that as  $x$  increases, eventually the refraction wave will overtake the direct wave. In Figure 4.31 these two traveltimes are equal at the point  $W$ . If the offset corresponding to  $W$  is  $x'$ , we have

$$\begin{aligned} \frac{x'}{V_1} &= \frac{x'}{V_2} + \frac{2z}{V_1} \cos \theta_c \\ z &= \frac{x'}{2} \left( 1 - \frac{V_1}{V_2} \right) / \cos \theta_c \\ &= \frac{x'}{2} \left( \frac{V_2 - V_1}{V_2} \right) \frac{V_2}{(V_2^2 - V_1^2)^{1/2}} \\ z &= \frac{x'}{2} \left( \frac{V_2 - V_1}{V_2 + V_1} \right)^{1/2} \end{aligned} \quad (4.71)$$

This relation sometimes is used to find  $z$  from measurements of the velocities and the *crossover distance*  $x'$ . However, usually we can determine  $t_i$  more accurately than  $x'$  and hence Equation (4.70) provides a better method of determining  $z$ .

(c) *Several horizontal refractors.* Where all beds are horizontal, Equation (4.70) can be generalized to cover the case of more than one refracting horizon. Consider the situation in Figure 4.32 where we have three beds of velocities  $V_1$ ,  $V_2$ , and  $V_3$ . Whenever  $V_2 > V_1$ , we have the refraction path  $OPR$  and

corresponding time-distance curve  $WS$ , just as we had in Figure 4.31. If  $V_3 > V_2 > V_1$ , the deeper refraction will eventually overtake the shallower refraction. The refraction paths such as  $OM'M''P''P'R'$  are fixed by Snell's law:

$$\frac{\sin \theta_1}{V_1} = \frac{\sin \theta_c}{V_2} = \frac{1}{V_3}$$

where  $\theta_c$  is the critical angle for the lower horizon whereas  $\theta_1$  is less than the critical angle  $\theta'_c$  for the upper horizon. The expression for the traveltime curve  $ST$  is obtained as before:

$$\begin{aligned} t &= \frac{OM' + R'P'}{V_1} + \frac{M'M'' + P'P''}{V_2} + \frac{M''P''}{V_3} \\ &= \frac{2z_1}{V_1 \cos \theta_1} + \frac{2z_2}{V_2 \cos \theta_c} \\ &\quad + \frac{x - 2z_1 \tan \theta_1 - 2z_2 \tan \theta_c}{V_3} \\ &= \frac{x}{V_3} + \frac{2z_2}{V_2 \cos \theta_c} \left( 1 - \frac{V_2}{V_3} \sin \theta_c \right) \\ &\quad + \frac{2z_1}{V_1 \cos \theta_1} \left( 1 - \frac{V_1}{V_3} \sin \theta_1 \right) \\ &= \frac{x}{V_3} + \frac{2z_2}{V_2} \cos \theta_c + \frac{2z_1}{V_1} \cos \theta_1 \\ &= \frac{x}{V_3} + t_2 \end{aligned} \quad (4.72)$$

Thus the time-distance curve for this refraction is also a straight line whose slope is the reciprocal of the velocity just below the refracting horizon and whose intercept is the sum of terms of the form  $(2z_i/V_i \cos \theta_i)$ ; each bed above the refracting horizon contributes one term. We can generalize for  $n$  beds:

$$t = \frac{x}{V_n} + \sum_{i=1}^{n-1} \frac{2z_i}{V_i} \cos \theta_i \quad (4.73)$$

where  $\theta_i = \sin^{-1}(V_i/V_n)$  (note that  $\theta_i$  are not critical angles except for  $\theta_{n-1}$ ). This equation can be used to find the velocities and thicknesses of each of a series of horizontal refracting beds of constant velocity, provided each bed contributes enough of the time-distance curve to permit it to be analyzed correctly. Then we can find all of the velocities (hence the angles  $\theta_i$  also) by measuring the slopes of the various sections of the time-distance curve and get the thicknesses of the beds from the intercepts.

(d) Effect of refractor dip. The simple situations on which Equations (4.68) to (4.73) are based are frequently not valid. One of the most serious defects is the neglect of dip because dip changes the refraction time-distance curve drastically. The lower part of Figure 4.33 shows a vertical dip section through a refracting horizon. Let  $t$  be the traveltime for the refraction path  $AMPB$ . Then, we have

$$\begin{aligned} t &= \frac{AM + BP}{V_1} + \frac{MP}{V_2} \\ &= \frac{z_A + z_B}{V_1 \cos \theta_c} + \frac{AQ - (z_A + z_B) \tan \theta_c}{V_2} \\ &= \frac{x \cos \xi}{V_2} + \frac{z_A + z_B}{V_1} \cos \theta_c \end{aligned} \quad (4.74)$$

If we place the shotpoint at  $A$  and a detector at  $B$ , we are "shooting downdip." In this case it is convenient to have  $t$  in terms of the distance from the shotpoint to the refractor  $z_A$ , hence we eliminate  $z_B$  using the relation

$$z_B = z_A + x \sin \xi$$

Writing  $t_d$  for the downdip traveltime, we obtain

$$\begin{aligned} t_d &= \frac{x \cos \xi}{V_2} + \frac{x}{V_1} \cos \theta_c \sin \xi + \frac{2z_A}{V_1} \cos \theta_c \\ &= \frac{x}{V_1} \sin(\theta_c + \xi) + \frac{2z_A}{V_1} \cos \theta_c \\ &= \frac{x}{V_1} \sin(\theta_c + \xi) + t_A \end{aligned} \quad (4.75)$$

where

$$t_A = \frac{2z_A}{V_1} \cos \theta_c$$

The result for shooting in the updip direction is similarly obtained by eliminating  $z_A$ :

$$t_u = \frac{x}{V_1} \sin(\theta_c - \xi) + t_B \quad (4.76)$$

where

$$t_B = \frac{2z_B}{V_1} \cos \theta_c$$

Note that the downdip traveltime from  $A$  to  $B$  is equal to the updip traveltime from  $B$  to  $A$ . This shotpoint-to-shotpoint traveltime is called the *reciprocal time* and is denoted by  $t_r$ .

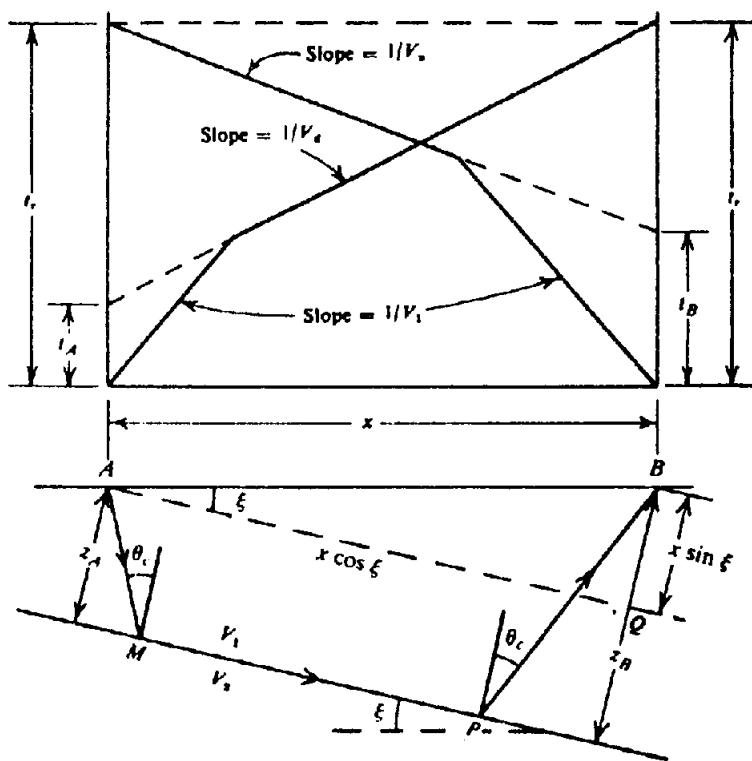


Figure 4.33. Raypaths and traveltime curves for a dipping refractor.

These equations can be expressed in the same form as Equation (4.70):

$$\left. \begin{aligned} t_d &= \frac{x}{V_d} + t_A \\ t_u &= \frac{x}{V_u} + t_B \end{aligned} \right\} \quad (4.77)$$

where

$$V_d = \frac{V_1}{\sin(\theta_c + \xi)} \quad V_u = \frac{V_1}{\sin(\theta_c - \xi)} \quad (4.78)$$

$V_d$  and  $V_u$  are known as *apparent velocities* and are given by the reciprocals of the slopes of the time-distance curves.

For reversed profiles such as shown in Figure 4.33, Equation (4.78) can be solved for the dip  $\xi$  and the critical angle  $\theta_c$  (and hence for the refractor velocity  $V_2$ ):

$$\left. \begin{aligned} \theta_c &= \frac{1}{2} \left( \sin^{-1} \left( \frac{V_1}{V_d} \right) + \sin^{-1} \left( \frac{V_1}{V_u} \right) \right) \\ \xi &= \frac{1}{2} \left( \sin^{-1} \left( \frac{V_1}{V_d} \right) - \sin^{-1} \left( \frac{V_1}{V_u} \right) \right) \end{aligned} \right\} \quad (4.79)$$

The distances to the refractor,  $z_A$  and  $z_B$ , can then

be found from the intercepts using Equations (4.75) and (4.76).

Equation (4.78) can be simplified when  $\xi$  is small enough that we can approximate by letting  $\cos \xi \approx 1$  and  $\sin \xi \approx \xi$ . With this simplification, Equation (4.78) becomes

$$\frac{V_1}{V_d} = \sin(\theta_c + \xi) \approx \sin \theta_c + \xi \cos \theta_c$$

$$\frac{V_1}{V_u} = \sin(\theta_c - \xi) \approx \sin \theta_c - \xi \cos \theta_c$$

hence

$$\sin \theta_c = \frac{V_1}{V_2} \approx \frac{V_1}{2} \left( \frac{1}{V_d} + \frac{1}{V_u} \right)$$

so that

$$\frac{1}{V_2} = \frac{1}{2} \left( \frac{1}{V_d} + \frac{1}{V_u} \right) \quad (4.80)$$

An even simpler approximate formula for  $V_2$  (although slightly less accurate) can be obtained by applying the binomial theorem (§ A.6) to Equation (4.78) and assuming that  $\xi$  is small enough that

higher powers of  $\xi$  are negligible:

$$\begin{aligned} V_d &= \frac{V_1}{\sin \theta_c} (\cos \xi + \cot \theta_c \sin \xi)^{-1} \\ &\approx V_2(1 - \xi \cot \theta_c) \\ V_u &\approx V_2(1 + \xi \cot \theta_c) \end{aligned}$$

hence

$$V_2 \approx \frac{1}{2}(V_d + V_u) \quad (4.81)$$

Equations similar to Equations (4.75) and (4.76) can be derived for a number of beds that have the same dip and strike or other specific situations, but such equations are of limited value in practice. Not only do they involve a large amount of computation, but also one usually is not sure that they are applicable to a specific real situation. Moreover, where there are more than two refracting horizons, it is often difficult to identify equivalent updip and downdip segments, especially if the refractors are not plane or if the dip and strike change.

## 4.4. CHARACTERISTICS OF SEISMIC EVENTS

### 4.4.1. Distinguishing Features of Events

The basic task of interpreting reflection sections is that of selecting those events on the record that represent primary reflections, translating the traveltimes of these reflections into depths and dips, and mapping the reflecting horizons. In addition, the interpreter must be alert to other types of events that may yield valuable information, such as multiple reflections and diffractions.

Recognition and identification of seismic events are based upon five characteristics: (a) coherence, (b) amplitude standout, (c) character; (d) dip moveout, and (e) normal moveout. The first of these is by far the most important in recognizing an event. Whenever a wave recognizable as such reaches a spread, it produces approximately the same effect on each geophone. If the wave is strong enough to override other energy arriving at the same time, the traces will look more-or-less alike during the interval in which this wave is arriving. This similarity in appearance from trace to trace is called *coherence* (Fig. 4.34) and is a necessary condition for the recognition of any event. *Amplitude standout* refers to an increase of amplitude such as results from the arrival of coherent energy. It

is not always marked, especially when AGC (§ 4.5.3e) is used. *Character* refers to a distinctive appearance of the waveform that identifies a particular event, something that makes one event look different from another event. It involves the shape of the envelope, the number of cycles showing amplitude standout, and irregularities in phase resulting from interference among components of the event. *Moveout*, which refers to a systematic difference in the trace-to-trace traveltimes of an event, has been discussed in Section 4.3.1b, c.

Coherence and amplitude standout tell us whether or not a strong seismic event is present, but they say nothing about the type of event. Moveout is the most distinctive criterion for identifying the nature of events.

### 4.4.2. Reflections and Refractions

Reflections exhibit normal moveouts that must fall within certain limits set by the velocity distribution. The apparent velocity (distance between two geophones divided by the difference in traveltimes) is very large for reflections, usually greater than 50 km/s. Reflection events rarely involve more than two or three cycles and are often rich in frequency components in the range 15 to 50 Hz. Deep reflections may have considerable energy below this range.

Refractions are relatively low frequency events and they usually oscillate for more cycles and have much smaller apparent velocities than reflections. In-line refractions and *reflected refractions* (refracted waves that are reflected back toward the spread; see Fig. 4.35a) generally have straight alignments (prior to normal-moveout correction) in contrast with the curved alignments of reflections and diffractions. Broadside reflected refractions (Fig. 4.35c) have normal moveout appropriate to the refractor velocity. Refractions from deep refractors are not observed on reflection records except where the offsets are unusually long or when the occasional reflected refraction is recorded. Reflected refractions of the type shown in Figure 4.35b are one of the reasons why refraction wavetrains are so long.

A powerful technique for distinguishing between reflections, diffractions, reflected refractions, and multiples is to examine gathers (§ 4.7.8) after correcting for (a) weathering and elevation (*static corrections*, because the correction is the same for all arrival times on a given trace (see § 4.7.1), and (b) normal moveout (*dynamic corrections*, because the amount of correction decreases with increasing traveltime). Provided the correct normal moveout was removed, reflections appear (Fig. 4.36) as straight

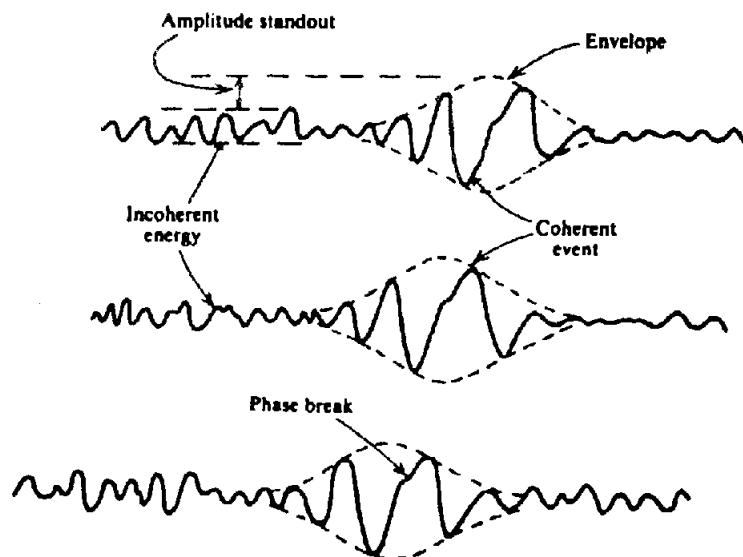


Figure 4.34. Characteristics of seismic events.

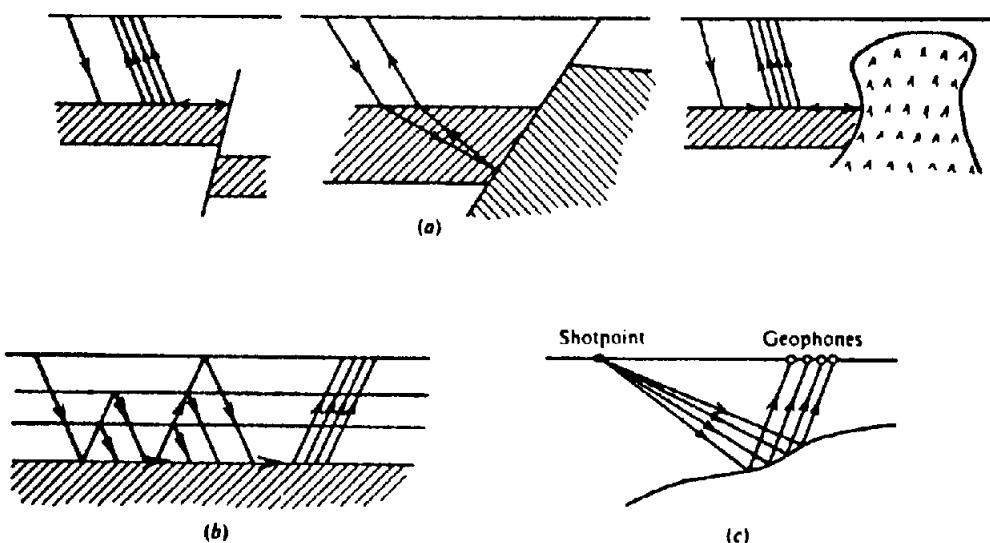


Figure 4.35. Reflected refractions. (a) Reflected refractions from faults and salt dome. (b) Multiply reflected refraction. (c) Broadside reflected refraction (plan view).

alignments whereas diffractions and multiples still have some curvature (because their normal moveouts are larger than those of primary reflections), and refractions and other formerly straight alignments have inverse curvature.

#### 4.4.3. Diffractions

Diffractions are indistinguishable from reflections on the basis of character. The amplitude of a diffraction is a maximum at some point along the diffraction curve, that is, where a reflection event terminates (where the reflection is tangent to the diffraction).

The amplitude decreases rapidly as we go away from this point. Diffractions usually exhibit distinctive moveout. In Figure 4.37, for all shotpoint and geophone positions such that the point of reflection  $R$  is to the left of  $A$ , the reflection travelttime curve is given by Equation (4.49), that is,

$$t_r = \frac{1}{V} (x^2 + 4h^2)^{1/2} \approx \frac{2h}{V} + \frac{x^2}{4Vh} = t_0 + \Delta t_n$$

assuming that  $x$  is smaller than  $h$ . The reflection travelttime curve is a hyperbola as shown in Figure

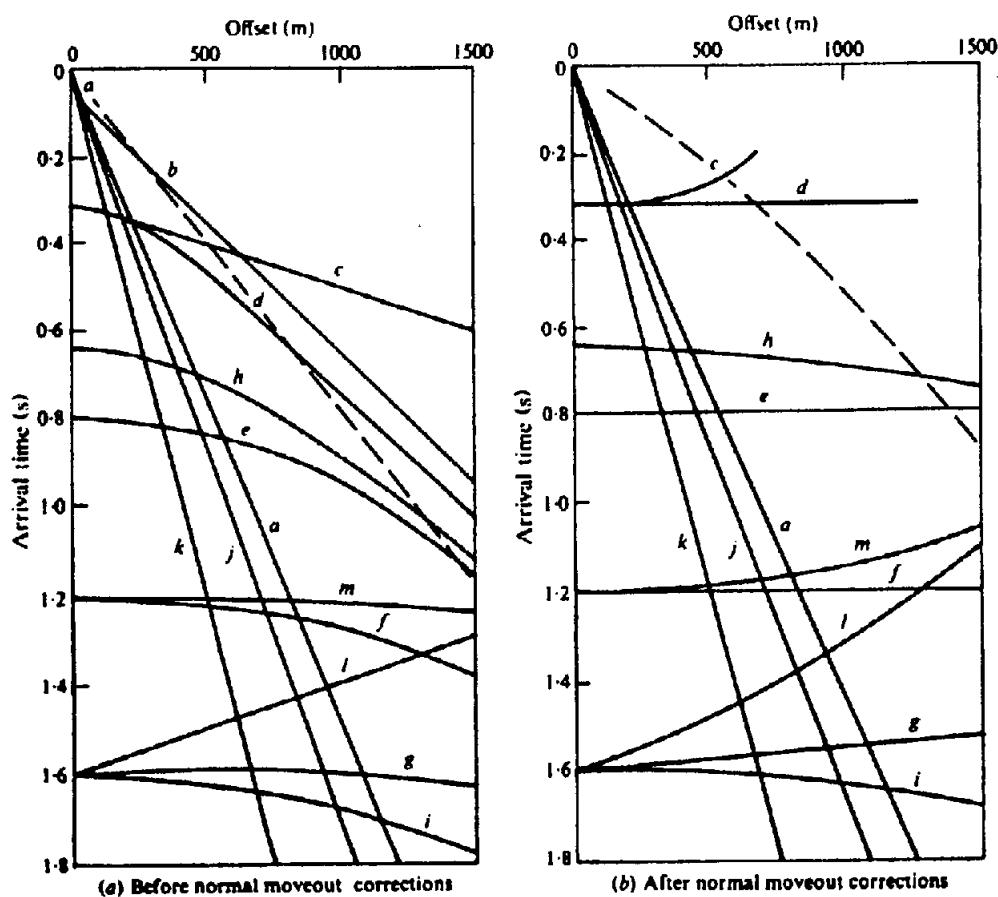


Figure 4.36. Types of events on a seismic record. Identities of events are: a = direct wave,  $V = 650 \text{ m/s}$ ; b = refraction at base of weathering,  $V_H = 1.640 \text{ m/s}$ ; c = refraction from flat refractor,  $V_R = 4.920 \text{ m/s}$ ; d = reflection from refractor c,  $V_{av} = 1.640 \text{ m/s}$ ; e = reflection from flat reflector,  $V_{av} = 1.970 \text{ m/s}$ ; f = reflection from flat reflector,  $V_{av} = 2.300 \text{ m/s}$ ; g = reflection from dipping reflector,  $V_{av} = 2.630 \text{ m/s}$ ; h = multiple of d; i = multiple of c; j = ground roll,  $V = 575 \text{ m/s}$ ; k = air wave,  $V = 330 \text{ m/s}$ ; l = reflected refraction from in-line disruption of the refractor c; m = reflected refraction from broadside disruption of refractor c. After normal-moveout correction, primary reflections are straight. In processing, data are usually muted, that is, data earlier than that indicated by the dashed lines are set to zero so that the data in the upper right corner do not appear.

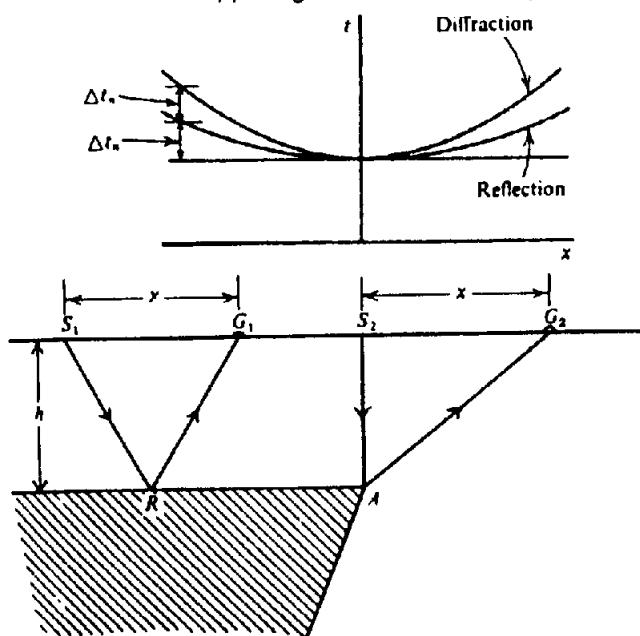


Figure 4.37. Diffraction traveltimne curve.

4.22. For the case where the shotpoint is directly above the diffraction source A, the diffraction traveltimne curve is given by the equation

$$\begin{aligned}
 t_d &= \frac{1}{V} \left( h + (x^2 + h^2)^{1/2} \right) \\
 &\approx \frac{2h}{V} + \frac{x^2}{2Vh} \\
 &= t_0 + 2 \Delta t_n
 \end{aligned} \tag{4.82}$$

Thus, the diffraction curve is also a hyperbola, but with twice the normal moveout of a reflection. The reflection corresponds to a virtual source at a depth of  $2h$  whereas the diffraction comes from a source at depth  $h$ . The earliest traveltimne on a diffraction curve is for the trace that is recorded directly over

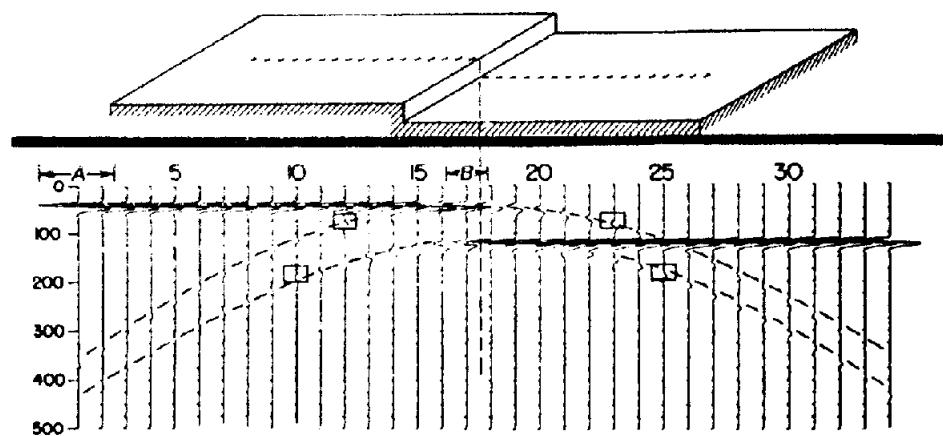


Figure 4.38 Reflection and diffraction response of a step for sources and receivers coincident. (After Hilterman, 1970.)

the diffracting point (except for situations with unusual velocity distributions).

Figure 4.38 shows the response of a model that demonstrates the major properties of diffraction events. The crest of the diffraction curves locates the discontinuities (in the absence of velocity complications), reflections that terminate at the diffracting point are tangent to the diffraction curve, the reflection amplitude decreases as the end of the reflection is approached, and the reflection is continuous with the diffraction. The "forward branch" of the diffraction (the branch that tends to carry the reflection forward) is of opposite polarity to the "backward branch" that lies underneath the reflection, and the amplitude of forward and backward branches is equal at equal distances from the point where the reflection is tangent to the diffraction curves.

Diffractions are very important in determining the appearance of reflections where the reflectors are not continuous or plane. Figure 4.39 shows the events that are caused by a sharply bent reflector. The reflection to the right of  $x = 10,000$  gives rise to  $BP'$ ; the reflection to the left of  $x = 10,000$  gives  $AP$ . Diffraction fills in the gap  $PP'$  and makes the seismic event continuous without a sharp break.

#### 4.4.4. Multiples

Multiples are events that have undergone more than one reflection. Because the amplitude of multiples is proportional to the product of the reflection coefficients for each of the reflectors involved and because these are very small for most interfaces, only the strongest impedance contrasts generate multiples strong enough to be recognized as events.

We may distinguish between two classes of multiples, which we call long path and short path. A

*long-path multiple* is one whose travelpath is long compared with primary reflections from the same deep interfaces and hence long-path multiples appear as separate events on a seismic record. A *short-path multiple*, on the other hand, arrives so soon after the associated primary reflection that it interferes with and adds tail to the primary reflection; hence its effect is that of changing wave shape rather than producing a separate event. Possible raypaths for these two classes are shown in Figure 4.40.

The only important long-path multiples are those that have been reflected once at the surface or base of the LVL (§4.2.8b) and twice at deeper interfaces with relatively large acoustic impedance contrasts. Because  $E_R$  is about 50% at the base of the LVL and perhaps 5% for the strongest interfaces at depth, the maximum effective  $E_R$  for such multiples will be of the order of  $0.05 \times 0.5 \times 0.05 = 0.001$ . This value is in the range of typical reflection coefficients so that such multiples may have sufficient energy to be confused with primary events. Note that the relative amplitudes of these multiples depend mainly on the reflection coefficients at depth. The principal situation where weaker long-path multiples may be observable is where primary energy is nearly absent at the time of arrival of the multiple energy so that the gain of the recording system is very high.

Short-path multiples that have been reflected successively from the top and base of thin reflectors (Fig. 4.41a), often called *peg-leg multiples*, are important in altering wave shape. A peg-leg multiple delays part of the energy, thus lengthening the wavelet. Most peg-leg multiples tend to have the same polarity as the primary (because successive large impedance contrasts tend to be in opposite directions; otherwise the successive large changes in velocity would cause the velocity to exceed its allowable range). This effectively lowers the signal

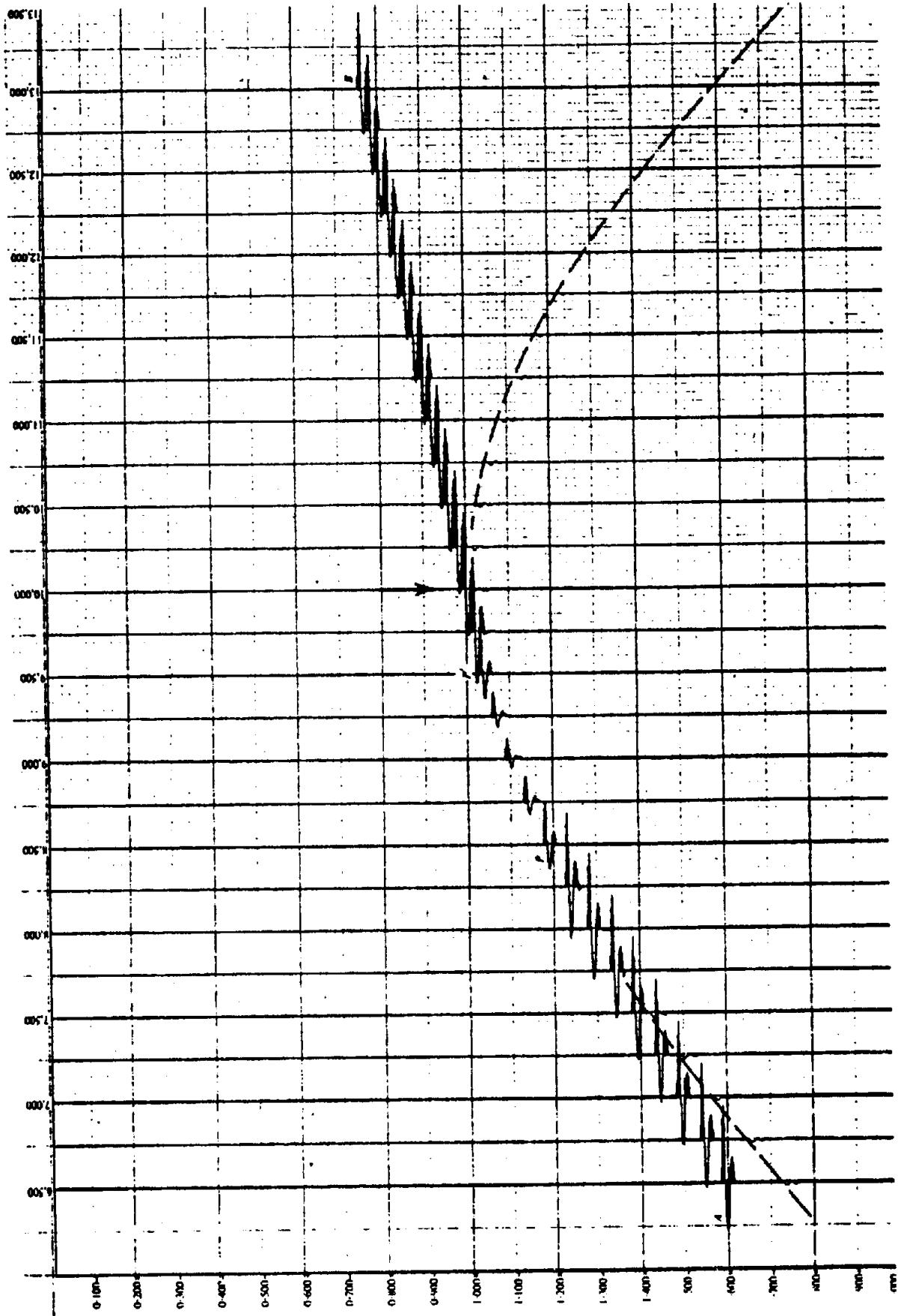


Figure 4.39. Reflections and diffractions from a sharply bent reflector. The reflector dips 3 parts in 5 to the left of  $x = 10,000$ , 1 part in 5 to the right.  
(Courtesy Chevron Oil Co.)

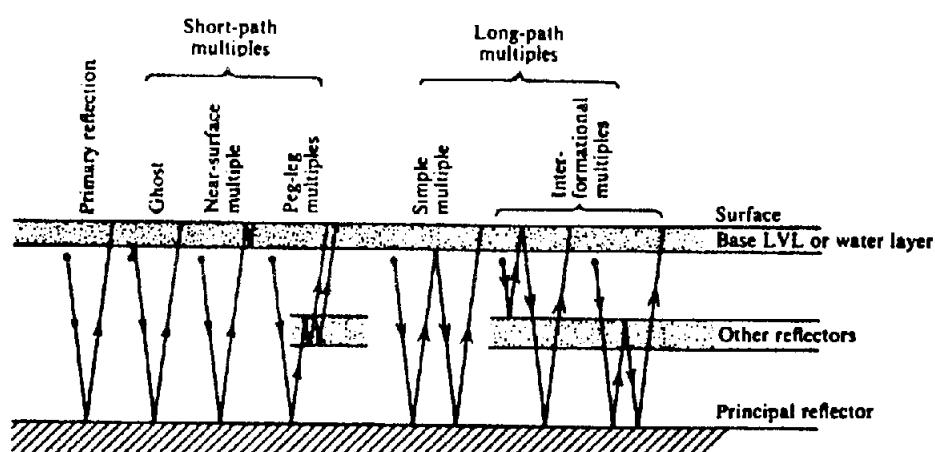


Figure 4.40. Types of multiples.

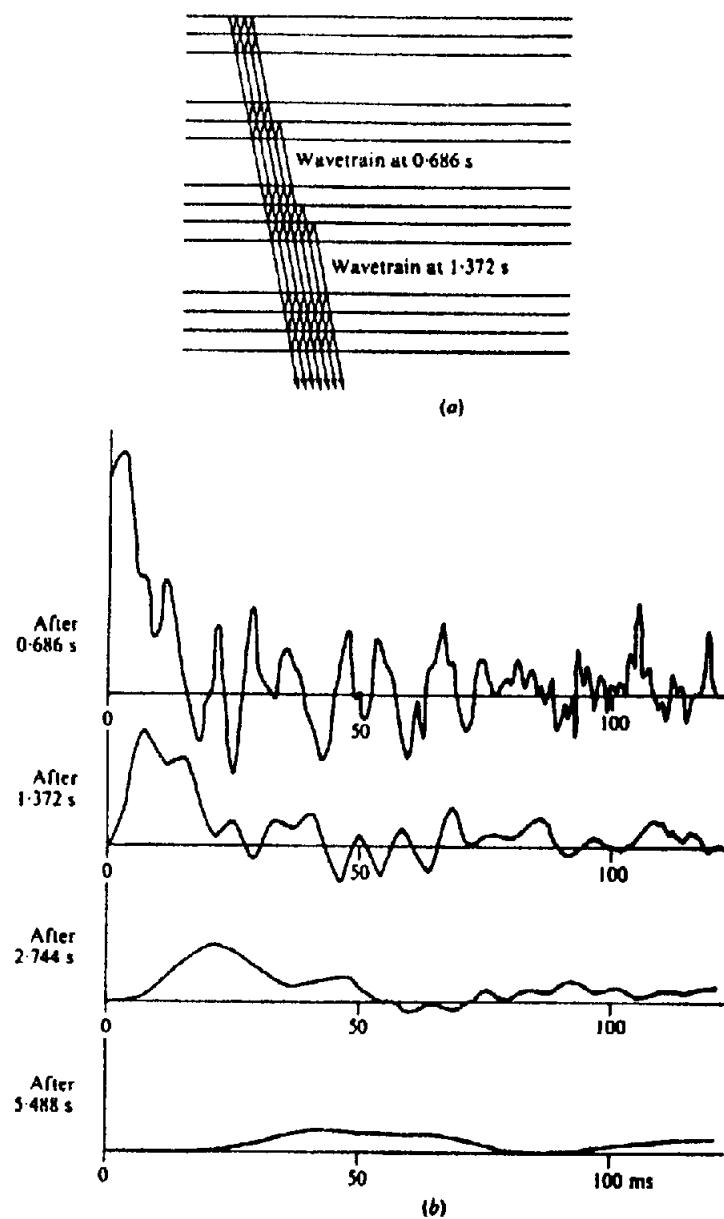


Figure 4.41. Changes in waveshape resulting from passage through a layered sequence. (After O'Doherty and Anstey, 1971.) (a) Schematic diagram showing peg-leg multiples. (b) Wavetrains after different traveltimes.

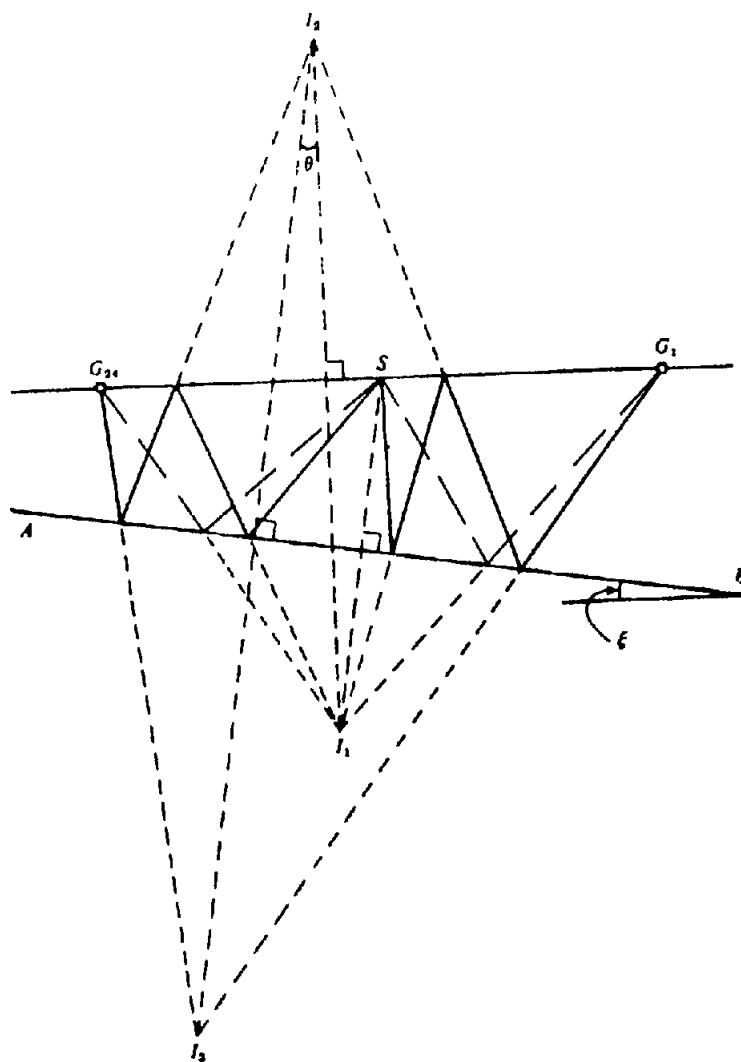


Figure 4.42. Raypath of a multiple from a dipping bed.

frequency as time increases (O'Doherty and Anstey, 1971). Figure 4.41b shows how a simple impulse becomes modified as a result of passing it through a sequence of interfaces.

The reflection-seismic technique is based on the assumption of simple waves such as those in Figures 4.22 and 4.23. Thus it is important that long-path multiples be recognized as such so that they will not be interpreted as reflections from deeper horizons.

Because velocity generally increases with depth, multiples usually exhibit more normal moveout than primary reflections with the same traveltimes. This is the basis of the attenuation of multiples in common-midpoint processing that will be discussed in Section 4.7.8. However, the difference in normal moveout often is not large enough to identify multiples.

The effect of dip on multiples that involve the surface or the base of the LVL can be seen by tracing rays using the method of images. In Figure 4.42, we trace a multiple arriving at symmetrically

disposed geophones  $G_1$  and  $G_{24}$ . The first image point  $I_1$  is on the perpendicular from  $S$  to  $AB$  as far below  $AB$  as  $S$  is above. We next draw the perpendicular from  $I_1$  to the surface of the ground where the second reflection occurs and place  $I_2$  as far above the surface as  $I_1$  is below. Finally, we locate  $I_3$  on the perpendicular to  $AB$  as far below as  $I_2$  is above. We can now draw the rays from the source  $S$  to the geophones (working backward from the geophones). The dip moveout is the difference between the path lengths  $I_3G_{24}$  and  $I_1G_1$ . It is about double that of the primary ( $I_3G_{24} - I_1G_1$ ). The multiple at the shotpoint will appear to come from  $I_3$ , which is updip from  $I_1$ , the image point for the primary, and  $I_3S$  is slightly less than twice  $I_1S$ . Hence we can see that if the reflector dips, the multiple involves a slightly different portion of the reflector than the primary and has a traveltimes slightly less than double the traveltimes of the primary. The latter fact makes identifying multiples by merely doubling the arrival time of the primary imprecise whenever

appreciable dip is present. The arrival time of the multiple will be approximately equal to that of a primary reflection from a bed at the depth of  $I_1$ . If the actual dip at  $I_1$  is not double that at  $AB$  (and one would not, in general, expect such a dip), then the multiple will appear to have anomalous dip. If the multiple should be misidentified as a primary, one might incorrectly postulate an unconformity or up-dip thinning that might lead to erroneous geologic conclusions.

*Ghosts* are the special type of multiple illustrated in Figure 4.40. The energy traveling downward from the shot has superimposed on it energy that initially traveled upward and was then reflected downward at the base of the LVL (in land surveys) or at the surface of the water (in marine surveys). A 180° phase shift, equivalent to half a wavelength, occurs at the additional reflection, and hence the effective path difference between the direct wave and the ghost is  $(\lambda/2 + 2d)$ , where  $d$  is the depth of the shot below the reflector producing the ghost. The interference between the ghost and the primary depends on the fraction of a wavelength represented by the difference in effective path length. Because the seismic wavelet is made up of a range of frequencies, the interference effect will vary for the different components. Thus, the overall effect on the wavelet shape will vary as  $d$  is varied. Relatively small changes in shot depth can result in large variations in reflection character, creating serious problems for the interpreter. Therefore the depth of the shot below the base of the weathering or the surface of the water is maintained as nearly constant as possible.

Ghosts are especially important in marine surveys because the surface of the water is almost a perfect reflector and consequently the ghost interference will be strong. If  $d$  is small in comparison with the dominant wavelengths, appreciable signal cancellation will occur. At depths of 10 to 15 m, interference is constructive for frequencies of 25 to 40 Hz, which is in the usual seismic range. The same effect occurs with respect to hydrophones at depth. Hence marine sources and detectors are often operated at such depths.

A particularly troublesome type of multiple produces the coherent noise known as *singing* (also called *ringing* or *water reverberation*) that is frequently encountered in marine work (and occasionally on land). This is due to multiple reflections in the water layer. The large reflection coefficients at the top and bottom of this layer result in considerable energy being reflected back and forth repeatedly; the reverberating energy is reinforced periodically by reflected energy. Depending on the water depth, certain frequencies are enhanced, and as a result the record looks very sinusoidal (Fig. 4.43).

Not only is the picking of reflections difficult, but measured traveltimes and dip moveouts will probably be in error. This type of noise and its attenuation are discussed in Section 4.7.3d.

#### 4.4.5. Surface Waves

Surface waves (often called *ground roll*) are usually present on reflection records. For the most part, these are Rayleigh waves with velocities ranging from 100 to 1000 m/s or so. Ground roll frequencies usually are lower than those of reflections and refractions, often with the energy concentrated below 10 Hz. Ground roll alignments are straight, just as refractions are, but they represent lower velocities. The envelope of ground roll builds up and decays very slowly and often includes many cycles. Ground roll energy generally is high enough even in the reflection band to override all but the strongest reflections. However, because of the low velocity, different geophone groups are affected at different times so that only a few groups are affected at any one time. Sometimes there is more than one ground roll wave train, each with different velocities. Occasionally where ground roll is exceptionally strong, in-line offsets are used so that desired reflections can be recorded before the surface waves reach the spread.

#### 4.4.6. Effects of Reflector Curvature

Geometric focusing as a result of curvature of a reflector affects the amplitude of a reflection. Over anticlinal curvature reflected ray paths diverge, which results in reduced energy density. Strengthening of reflections occurs over gentle synclines. Energy focusing as a result of the concave-mirror effect makes more of the reflector surface effective for producing a reflection. If the center of curvature of a reflector lies on the surface of the ground, the amplitude may be so large that the event will not be passed by the recording system.

If the curvature of a synclinal reflector is great enough, the energy focuses below the surface of the ground (see the two deeper reflections in Fig. 4.44) and a *buried focus* occurs. For a given surface location, reflections may be obtained from more than one part of the reflector; the time-distance curve is no longer a simple curve, but has several branches, most commonly three. The two deeper reflections in Figure 4.44 involve buried foci; each shows branches from each flank of the syncline plus a *reverse branch* from the curved bottom of the syncline. Obviously the likelihood of occurrence of a buried focus increases with reflector depth.

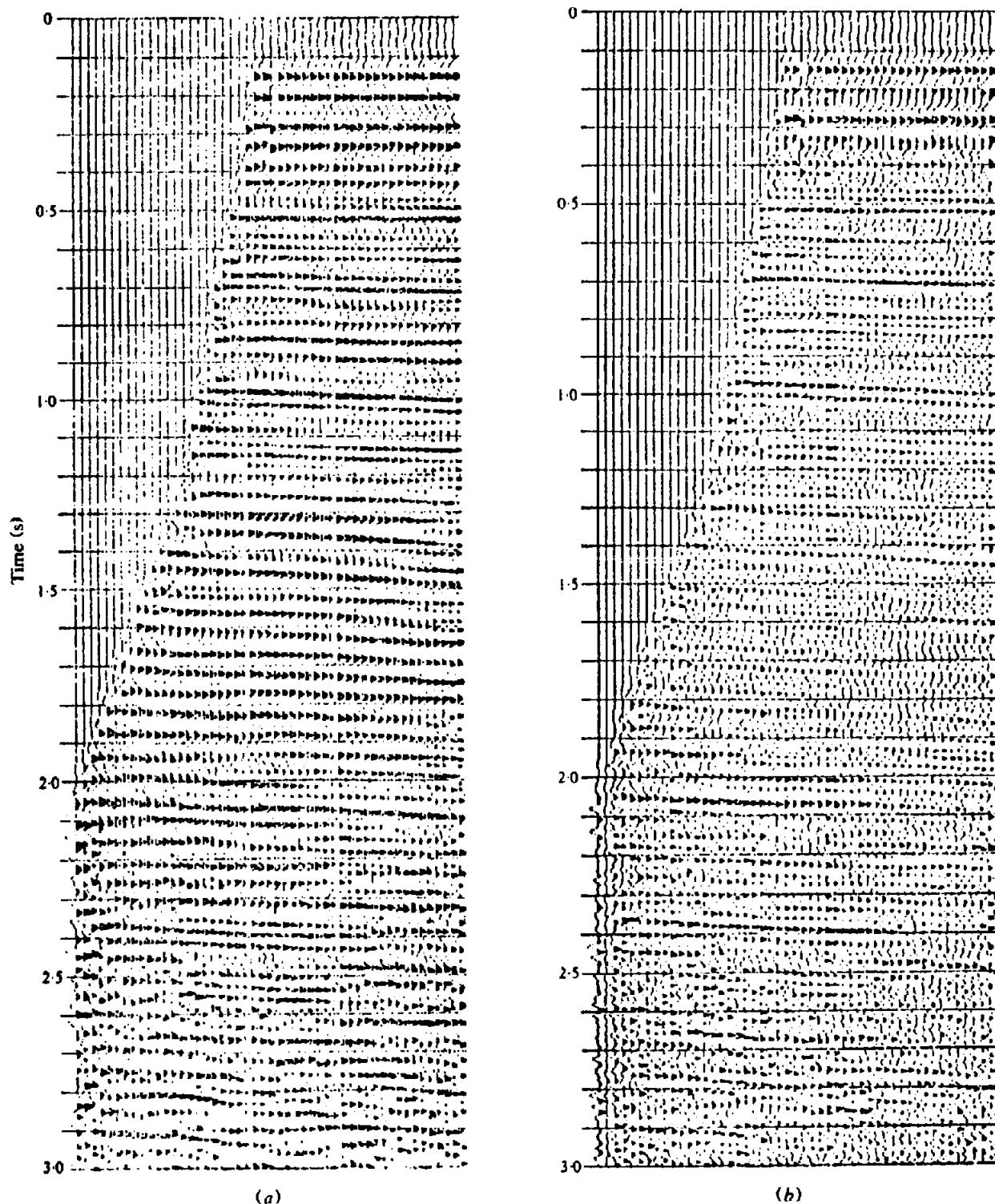


*Figure 4.43. Seismic record showing singing. (Courtesy Geosource Inc.) (a) Field record. (b) Same after singing has been removed by deconvolution processing (§4.7.3d).*

The waves producing the reverse branch pass through a focus, which results in a  $90^\circ$  phase shift relative to waves that do not pass through the focus (Sheriff and Geldart, 1982, p. 116); however, this phase shift is rarely useful in identifying buried-focus effects. Nevertheless, it would affect calculations of reflector depth in the syncline if picking were done systematically on the same phase, for example, al-

ways in the troughs. The reverse branch is so named because the point of reflection traverses the reflector in the opposite direction from the surface traverse. Thus, in Figure 4.44, as one moves from left to right on the surface, the reflection point for the reverse branch moves from right to left.

Just as light can be focused by passing through a lens, seismic waves can also be focused by curved

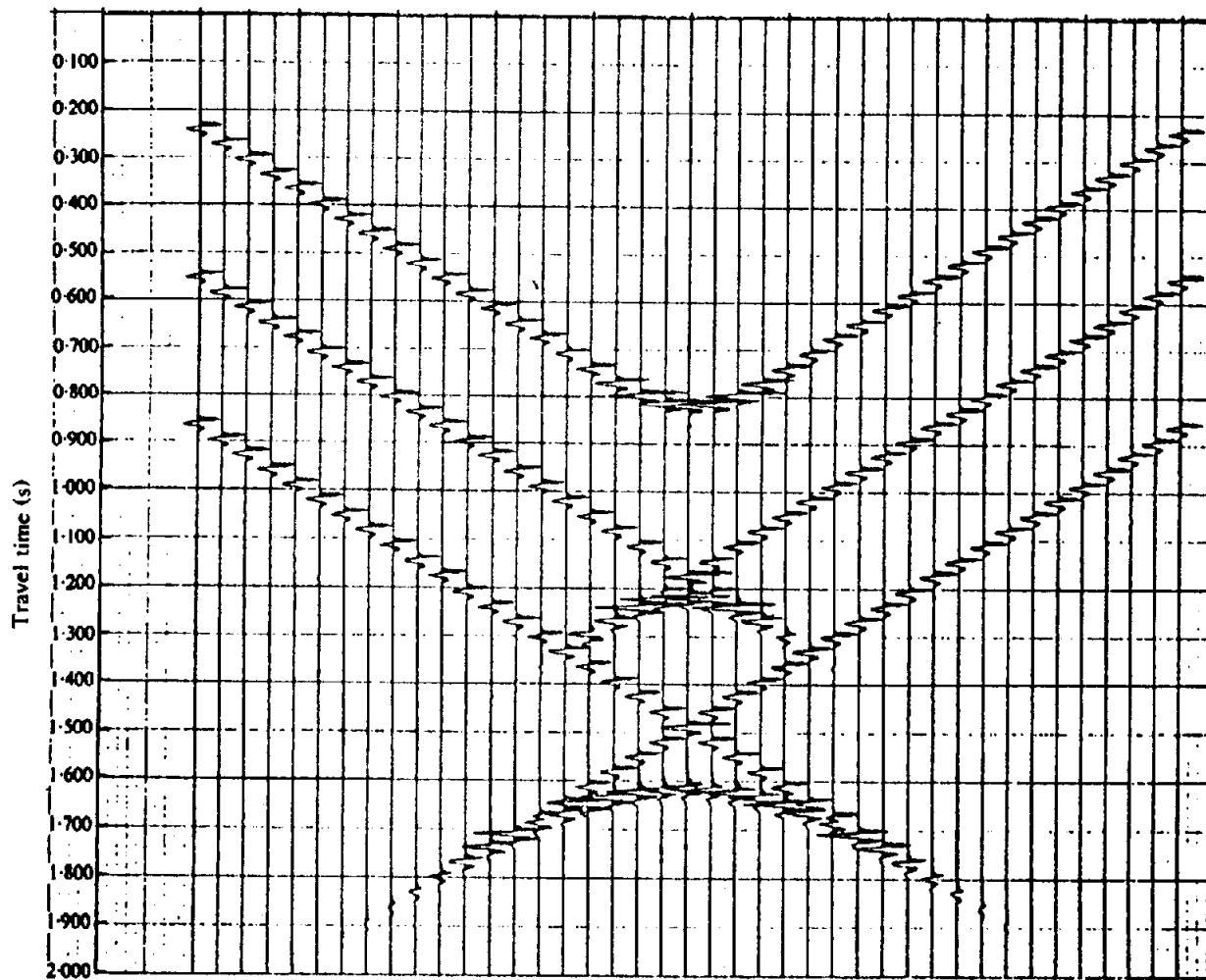


Figure 4.44. Reflections from curved reflector. In all cases, reflector radius of curvature = 1,000 m,  $V = 2,000$  m/s. Depths to the bottom of the syncline are 800, 1,200, and 1,600 m, respectively, for the three reflectors. The traces are 100 m apart. (Courtesy Chevron Oil Co.)

velocity surfaces, which results in seismic rays being bent by refraction; such situations are often very complex. Curvature at the base of the weathering can be especially important because of the large velocity contrast usually associated with this surface. Variations in permafrost thickness especially cause lens-type effects.

#### 4.4.7. Types of Seismic Noise

The reliability of seismic mapping is strongly dependent on the quality of the records. However, the quality of seismic data varies tremendously. At one extreme we have areas where excellent reflections (or refractions) are obtained without any special measures being taken; at the other extreme are those areas in which the most modern equipment, extremely complex field techniques, and sophisticated data processing methods do not yield usable data (often called *NR areas*, that is, areas of no reflections). In between these extremes lie the vast majority of areas in which useful results are obtained but

the quantity and quality of the data could be improved with beneficial results.

We use the term *signal* to denote any event on the seismic record from which we wish to obtain information. Everything else is *noise*, including coherent events that interfere with the observation and measurement of signals. The *signal-to-noise ratio*, abbreviated  $S/N$ , is the ratio of the signal energy in a specified portion of the record to the total noise energy in the same portion. Poor records result whenever the signal-to-noise ratio is small; just how small is, to some extent, a subjective judgment. Nevertheless, when  $S/N$  is less than unity, the record quality is usually marginal and deteriorates rapidly as the ratio decreases further.

Seismic noise may be either (a) coherent or (b) incoherent. *Coherent noise* can be followed across at least a few traces, unlike incoherent noise where we cannot predict what a trace will be like from a knowledge of nearby traces. Often the difference between coherent and incoherent noise is merely a matter of scale and, if we had geophones more

closely spaced, incoherent noise would be seen as coherent. Nevertheless, incoherent noise is defined with respect to the records being used without regard for what closer spacing might reveal.

Incoherent noise is often referred to as *random noise* (spatially random), which implies not only nonpredictability but also certain statistical properties. More often than not the noise is not truly random. (It should be noted that spatial randomness and time randomness may be independent; the usual seismic trace is apt to be random in time because we do not know when a reflection will occur on the basis of what the trace has shown previously, with the exception of multiples.)

Coherent noise is sometimes subdivided into (a) energy that travels essentially horizontally and (b) energy that reaches the spread more or less vertically. Another important distinction is between (a) noise that is repeatable and (b) noise that is not; in other words, whether the same noise is observed at the same time on the same trace when a shot is repeated. The three properties – coherence, travel direction, and repeatability – form the basis of most methods of improving record quality.

Coherent noise includes surface waves, reflections or reflected refractions from near-surface structures such as fault planes or buried stream channels, refractions carried by high-velocity stringers, noise caused by vehicular traffic or farm tractors, multiples, and so forth. All of the preceding except multiples travel essentially horizontally and all except vehicular noise are repeatable on successive shots.

Incoherent noise, which is spatially random and also repeatable, is due to scattering from near-surface irregularities and inhomogeneities such as boulders, small-scale faulting, and so forth. Such noise sources are so small and so near the spread that the outputs of two geophones will only be the same when the geophones are placed almost side by side. Nonrepeatable random noise may be due to wind shaking a geophone or causing the roots of trees to move, which generates seismic waves, stones ejected by the shot and falling back to the earth near a geophone, ocean waves beating on a seashore, distant earthquakes, a person walking near a geophone, and so on.

#### 4.4.8. Attenuation of Noise

If the noise has appreciable energy outside the principal frequency range of the signal, frequency filtering can be used to advantage. Very low-frequency components (such as high-energy surface waves rich in low frequencies) may be attenuated during the initial recording provided the low frequencies are

sufficiently separated from the reflection frequencies. However, the spectrum of the noise often overlaps the signal spectrum and then frequency filtering is of limited value in improving record quality. With modern digital recording, the only low-frequency filtering used in the field is often that resulting from the low-frequency response of the geophones.

If we add several random noises together, there will be some cancellation because they will be out of phase with each other. If they are truly random in the statistical sense, the sum of  $n$  random signals will be proportional to  $\sqrt{n}$ , whereas the sum of  $n$  coherent in-phase signals will be proportional to  $n$  so that the signal-to-noise ratio will be improved by the factor  $\sqrt{n}$  (Sheriff and Geldart, 1982, p. 126). This principle is the basis of the use of multiple geophones or multiple sources (called *geophone* or *source arrays*; see §4.5.2c) to cancel noise. If we connect together, for example, 16 geophones that are spaced far enough apart that the noise is spatially random but still close enough together that reflected energy traveling almost vertically is essentially in phase at all 16 geophones, the sum of the 16 outputs will have a signal-to-noise ratio 4 times greater than the output when the 16 geophones are placed side by side. If, on the other hand, we are attenuating coherent noise and the 16 geophones are spread evenly over one wavelength of a coherent noise wavetrain (for example, ground roll), then the coherent noise will be greatly reduced.

Noise can also be attenuated by adding together traces shot at different times or different places or both. This forms the basis of several *stacking* techniques including vertical stacking, common-midpoint stacking, uphole stacking, and several more complicated methods (§4.7.9 and §4.7.13a). The gain in record quality often is large because of a reduction of both random and coherent noise. Provided the static and dynamic corrections are accurately made, signal-to-noise improvements for random noise should be about 5 for 24-fold stacking.

*Vertical stacking* involves combining several records for which both the source and geophone locations remain the same. It is extensively used with weak surface energy sources (§4.5.3c). Vertical stacking usually implies that no trace-to-trace corrections are applied but that corresponding traces on separate records are merely added to each other. The effect, therefore, is essentially the same as simultaneously using multiple shots or multiple source units. In difficult areas, both multiple source units and vertical stacking may be used. In actual practice, the surface source is moved somewhat (3 to 10 m) between the shots. Up to 20 or more separate records may be vertically stacked; the stacking is often done in the field, sometimes in subsequent processing.

Marine vertical stacking rarely involves more than 4 records because at normal ship speeds the ship moves so far that data would be *smeared* when stacked. Smearing means that changes in the reflecting points affect the arrival times so much that the signal may be adversely affected by summing (the effect is similar to using a very large geophone or source array).

The *common-midpoint* technique is very effective in attenuating several kinds of noise. The summation traces comprise energy from several shots using different geophone and sourcepoint locations. The field technique will be discussed in Section 4.5.2a and the processing (which is almost always done in a processing center rather than in the field) in Section 4.7.8.

## 4.5. REFLECTION FIELD METHODS AND EQUIPMENT

### 4.5.1. Field Methods for Land Surveys

(a) *The program.* Usually the seismic crew receives the *program* in the form of lines on a map that indicate where data are to be obtained.

Before beginning a survey the following question should be asked: "Is it probable that the proposed lines will provide the required information?" Data migration (§4.7.12) may require that lines be located elsewhere than directly on top of features in order to measure critical aspects of a structure. Crestal areas may be so extensively faulted that lines across them are nondefinitive. The structures being sought may be beyond seismic resolving power. Near-surface variations may be so large that the data are difficult to interpret whereas moving the seismic line a short distance may improve data quality. Obstructions along a proposed line may increase difficulties unnecessarily, whereas moving the line slightly may achieve the same objectives at reduced cost. Where the dip is considerable, merely running a seismic line to a wellhead may not tie the seismic data to the well data. Lines may not extend sufficiently beyond faults and other features to establish the existence of such features unambiguously or to determine fault displacements. Lines may cross features such as faults so obliquely that their evidences are not readily interpretable. Lack of cross control may result in features located below the seismic line being confused by features to the side of the line.

(b) *Permitting.* Once the seismic program has been decided on, it is usually necessary to secure permission to enter the land to be traversed. Permission to enter may involve a payment, often a fixed sum per source location, as compensation in advance for "damages that may be incurred." Even where the

surface owners do not have the right to prevent entry, it is advantageous to explain the nature of the impending operations. Of course, a seismic crew is responsible for damages resulting from their actions whether or not permission is required to carry out the survey.

(c) *Laying out the line.* The survey crew lays out the lines to be shot, usually by a transit-and-chain survey that determines the positions and elevations of both the sourcepoints and the centers of geophone groups. The *chain* is often a wire equal in length to the geophone group interval. Successive group centers are laid out along the line, and each center is marked by means of brightly colored plastic ribbon called *flagging*. The transit is used to keep the line straight and to obtain the elevation of each group center by sighting on a rod carried by the lead chainman.

Many variations from the above procedures are used depending on the sort of terrain being traversed. Electronic distance measuring (EDM) instruments are generally used (§B.2; also Sheriff and Geldart, 1982, pp. 134–5). Plane tables and alidades are occasionally used. Ties to benchmarks and well-heads are often made by transit theodolite and rod rather than by chaining. Side features are often tied in by triangulation. The surveyor should indicate in his data and maps the locations of all important features, such as streams, buildings, roads, and fences. The surveyor also plans access routes so that drills, recording trucks, and so forth, can get to their required locations most expeditiously.

In areas of difficult terrain or heavy vegetation, trail-building or trail-cutting crews may be required. These often precede the survey crew but usually are under the supervision of the surveyor, who is therefore responsible for the preparation of a straight trail in the proper location.

(d) *Shothole drilling.* The next unit on the scene is the drilling crew (when explosives are used as the energy source). Depending on the number and depth of holes required and the ease of drilling, a seismic crew will generally have from one to four drilling crews. Whenever conditions permit, the drills are truck-mounted. Water trucks are often required to supply the drills with water for drilling. In areas of rough terrain, the drills may be mounted on tractors or portable drilling equipment may be used. In swampy areas, the drills are often mounted on amphibious vehicles. Usually the drilling crew places the explosive in the holes before leaving the site.

(e) *Recording.* The drilling crews are followed by the recording unit. This unit can be divided into

three groups on the basis of primary function: the shooting crew, who are responsible for loading the shotholes (if the drillers have not already loaded them) and for setting off the explosive, the jug hustlers, who lay out the cables, place the geophones in their proper locations, and connect them into the cables, and the recording crew, who do the actual recording of the signals.

With common-midpoint recording, shotpoints are about 100 m apart, so high production and high efficiency are needed to achieve a low cost per kilometer. Redundancy of coverage has lessened the dependence on any individual record so that occasional missed records can be tolerated. Also, the broad dynamic range of digital recording has removed much of the need for filtering in the field and the need to tailor instrument settings to particular local conditions. Cost considerations dictate that the recording operation must not wait on other units. Shotholes may be drilled for the entire line before the recording crew begins so that it need never wait on the drills. Extra cables and geophones are laid out and checked in advance of the recording unit. A *roll-along switch* is used, which makes it possible for the recording unit to be physically located at a different place than where it is located electrically. The recording unit connects to the seismic cable at any convenient location, for example, the intersection of a road and the seismic line. The roll-along switch is adjusted so that the proper geophones are connected and the shooters are instructed to operate the blaster. Following the shot, the shooters move on to the next shothole (which is not very far away) and the *observer* (instrument operator) adjusts the roll-along switch so that the next geophones are connected. The time between shots may be only a few minutes and the recording truck may not move all day long. Holes where misfires occur are not reloaded and reshot. The shooting unit often walks the line because they need no equipment except the blaster and firing line and perhaps shovels to fill in the shothole after the shot. Damages are reduced because less equipment traverses the line. Thus other benefits accrue besides increased recording efficiency.

When a seismic crew uses a surface energy source, the source units move into place and a signal from the recording truck activates the source trucks so that the energy is introduced into the ground at the proper time. Despite the fact that an explosive may not be involved, terms such as "shot" and "shot-point" are still used. The energy from each surface source usually is small compared to the energy from a dynamite explosion so that many records are made for each source location and vertically stacked to make a single record. The source units may advance

a few meters between the component subshots, which will be combined to make one record. It is not uncommon to use 3 or 4 source trucks and combine 30 or so component subshots.

A monitor record is usually made in the field, either in parallel with the recording or by playback of the magnetic tape. These monitor records are checked to make certain that the equipment is functioning properly and also to determine weathering corrections (discussed in §4.7.1).

The magnetic tapes are shipped to a data processing center where corrections are applied and various processing techniques are used, for example, velocity analysis, filtering, stacking, and migration (§4.7). The end result of the data processing is usually record sections from which an interpretation is made.

#### 4.5.2. Field Layouts

(a) *Split-dip and common-midpoint recording.* Virtually all routine seismic work consists of *continuous coverage (profiling)*, that is, the cables and sourcepoints are arranged so that there are no gaps in the data other than those due to the fact that the geophone groups are spaced at intervals rather than continuously spaced. Single coverage implies that each reflecting point is sampled only once, in contrast to common-midpoint, or *redundant*, coverage where each reflecting point is sampled more than once. Areal or cross coverage indicates that the dip components perpendicular to the seismic line have been measured as well as the dip components along the line. Each of these methods can employ various relationships between sources and geophone groups.

Single coverage split-dip shooting is illustrated in Figure 4.45. Sourcepoints are laid out at regular intervals along the line of profiling, often 400 to 540 m apart. A seismic cable is laid on the ground with provision for connecting groups of geophones at regular intervals (called the *group interval*). Thus, with sourcepoints 400 m apart and 24 groups, the group centers are 36.4 m apart. With the cable stretched from  $O_1$  to  $O_{24}$ , source (shot)  $O_2$  is fired, which gives subsurface control (for flat dip) between  $A$  and  $B$ . The portion of cable between  $O_1$  and  $O_2$  is then moved between  $O_3$  and  $O_4$  and source  $O_3$  is shot; this gives subsurface coverage between  $B$  and  $C$ . The travelpath for the last group from source  $O_{24}$  is the reversed path for the first group from source  $O_2$  so that the subsurface coverage is continuous along the line.

Common-midpoint (CMP) or roll-along shooting is illustrated in Figure 4.46a (Mayne, 1962, 1967). We have evenly spaced geophone groups that we number by their sequence along the seismic line rather than by the trace that they represent on the

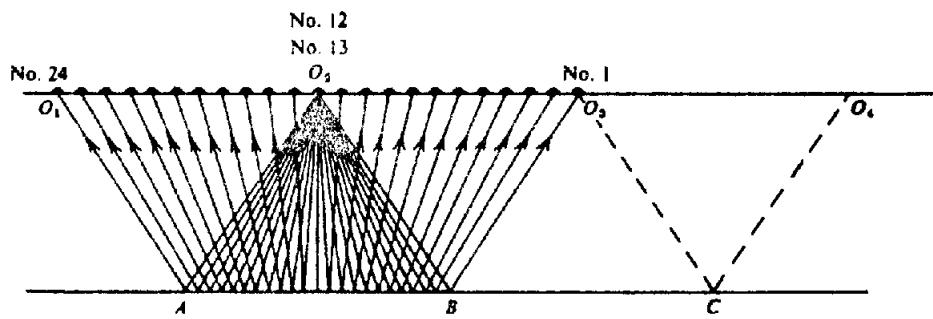
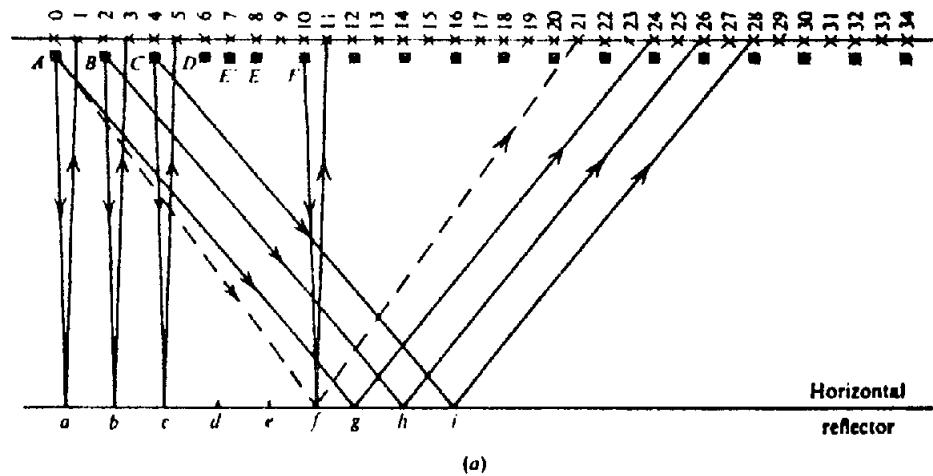
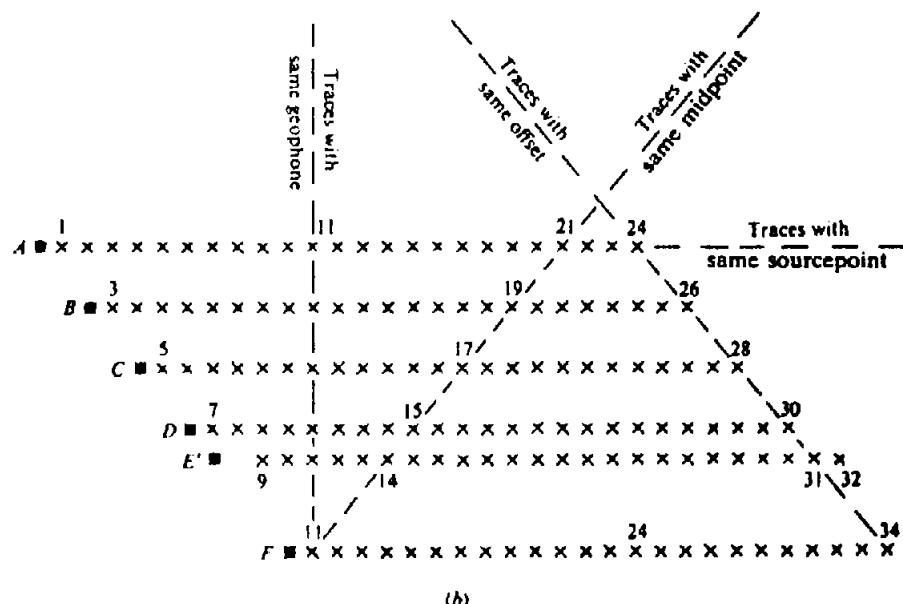


Figure 4.45. Symmetrical spread with continuous subsurface coverage.



(a)



(b)

Figure 4.46. Common-midpoint profiles. The symbols  $x$  and  $O$  represent geophone groups and sourcepoints, respectively. (a) Vertical section illustrating common-midpoint profiling. (b) Stacking chart.

seismic record. Geophone groups 1 to 24 are connected to the amplifier inputs in the recording truck and shot  $A$  is fired. Assuming a horizontal reflector, this gives subsurface coverage from  $a$  to  $g$ . Geophone groups 3 to 26 are then connected to the amplifier inputs; the change is made by means of the roll-along switch rather than by physically moving

the seismic cable. Shot  $B$  is then fired, which gives subsurface coverage from  $b$  to  $h$ . Shot  $C$  is now fired into geophones 5 to 28, which gives coverage from  $c$  to  $i$ , and so on down the seismic line. Note that the reflecting point for the energy from shot  $A$  into geophone group 21 is point  $f$ , which is also the reflecting point for the energy from  $B$  into geophone

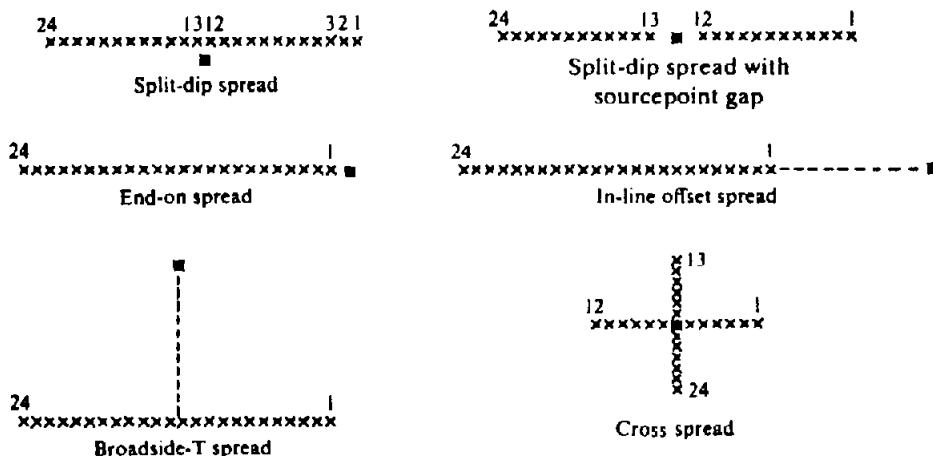


Figure 4.47. Types of reflection spreads. The symbols  $x$  and  $\square$  represent geophone groups and sourcepoints, respectively.

group 19, from *C* into 17, from *D* into 15, from *E* into 13 and from *F* into 11. After normal-moveout removal using a *stacking velocity* (§4.5.5c), these traces will be combined (*stacked*) in a subsequent data processing operations. Thus reflecting point *f* is sampled six times and the coverage is called sixfold recording. Obviously, the multiplicity tapers off at each end of the line. Most present-day recording uses 96 or more geophone groups and 24- to 48-fold multiplicity.

Occasionally one of the regularly spaced locations will not be a suitable place for a shothole (perhaps because of risk of damage to nearby buildings) and an irregularly spaced shotpoint will be used. Thus if shotpoint *E* (Fig. 4.46a) could not be used, a shot might be taken at *E'* instead and then geophone group 14 (instead of 13) would receive the energy reflected at *f*. To help keep track of the many traces involved, *stacking charts* are used (Morgan, 1970). Figure 4.46b shows the stacking chart when *E'* is shot instead of *E*. Note how the six traces which have the common midpoint *f* line up along a diagonal; points along the opposite diagonal have a common offset whereas points on a horizontal line have the same shotpoint and points on a vertical line represent traces from a common geophone group. Stacking charts are useful in making static and dynamic corrections and to ensure that the traces are properly stacked.

(b) *Spread types.* By *spread* we mean the relative locations of the sourcepoint and the centers of the geophone groups used to record the energy from the source. Several spread types are shown in Figure 4.47. In split-dip shooting the sourcepoint is at the center of a line of regularly spaced geophone groups. Placing the source close to a geophone group often results in a noisy trace (because of ground roll or truck noise with a surface source, or gases escaping

from the shothole and ejection of tamping material); hence the source may be moved 15 to 50 m perpendicular to the seismic line. Often the geophone groups nearest the source are not used, which creates a *sourcepoint (shotpoint) gap*.

Often the source is at the end of the spread of active geophone groups to produce an *end-on spread*, and in areas of exceptionally heavy ground roll the sourcepoint is offset an appreciable distance (often 500 to 700 m) along the line from the nearest active geophone group to produce an *in-line offset spread*. Alternatively, the sourcepoint may be offset in the direction normal to the cable, either at one end of the active part to produce a *broadside-L* or opposite the center to give a *broadside-T spread*. End-on and in-line offset spreads often employ sources off each end to give continuous coverage and two records for each spread. The in-line and broadside offsets permit recording reflection energy before the ground-roll energy arrives at the spread. *Cross spreads*, which consist of two lines of geophone groups roughly at right angles to each other, are used to record three-dimensional dip information.

(c) *Arrays.* The term *array* refers either to the pattern of geophones that feeds a single channel or to a distribution of shotholes or surface energy sources that are fired simultaneously; it also includes the different locations of sources for which the results are combined by vertical stacking. A wave approaching the surface in the vertical direction will affect each geophone or an array simultaneously so that the outputs will combine constructively whereas a wave traveling horizontally will affect the various geophones at different times so that there will be a certain degree of destructive interference. Similarly, waves traveling vertically downward from a source array will add constructively whereas waves traveling horizontally away from the source array will arrive at

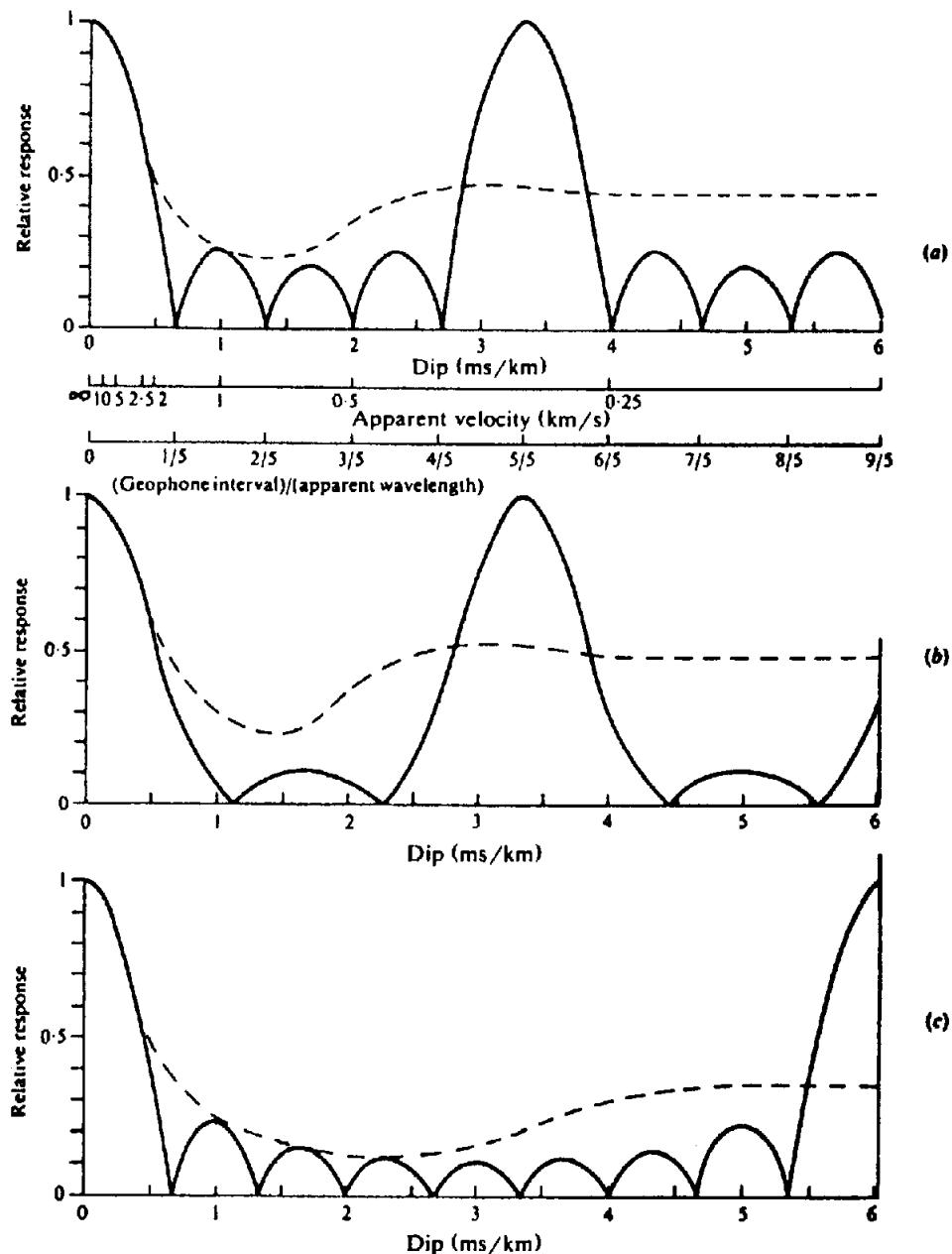


**Figure 4.48.** Response of arrays to 30 Hz signal. The overall length of the array, which is the factor controlling the width of the first peak, is the same for all three arrays. The location of the principal secondary (alias) peak is controlled by the element spacing. Weighting increases the attenuation in the reject region. The dotted curves indicate the array response to a bell-shaped frequency spectrum peaked at 30 Hz with a width of 30 Hz. (Courtesy Chevron Oil Co.) (a) Five in-line geophones spaced 10 m apart. (b) Geophones spaced 10 m apart and weighted 1, 2, 3, 2, 1. (c) Nine geophones spaced 5.5 m apart.

a geophone with different phases and will be partially cancelled. Thus, arrays provide a means of discriminating between waves arriving from different directions.

Arrays are *linear* when the elements are spread along the seismic line or *areal* when the group is distributed over an area. The response of a geophone array is usually illustrated by a graph (such as Fig. 4.48) that shows the output of the array compared to the output of the same number of geophones concen-

trated at one location. The response is usually given for a sine-wave input and plotted against a dimensionless variable, such as the ratio of the apparent wavelength to the element spacing (or some other key dimension of the array).

Theoretically we get the same results by using 1 sourcepoint and 16 geophones as by using 1 geophone and 16 sourcepoints spaced in the same manner; however, we use multiple geophones much more than multiple sources because the cost is less, al-

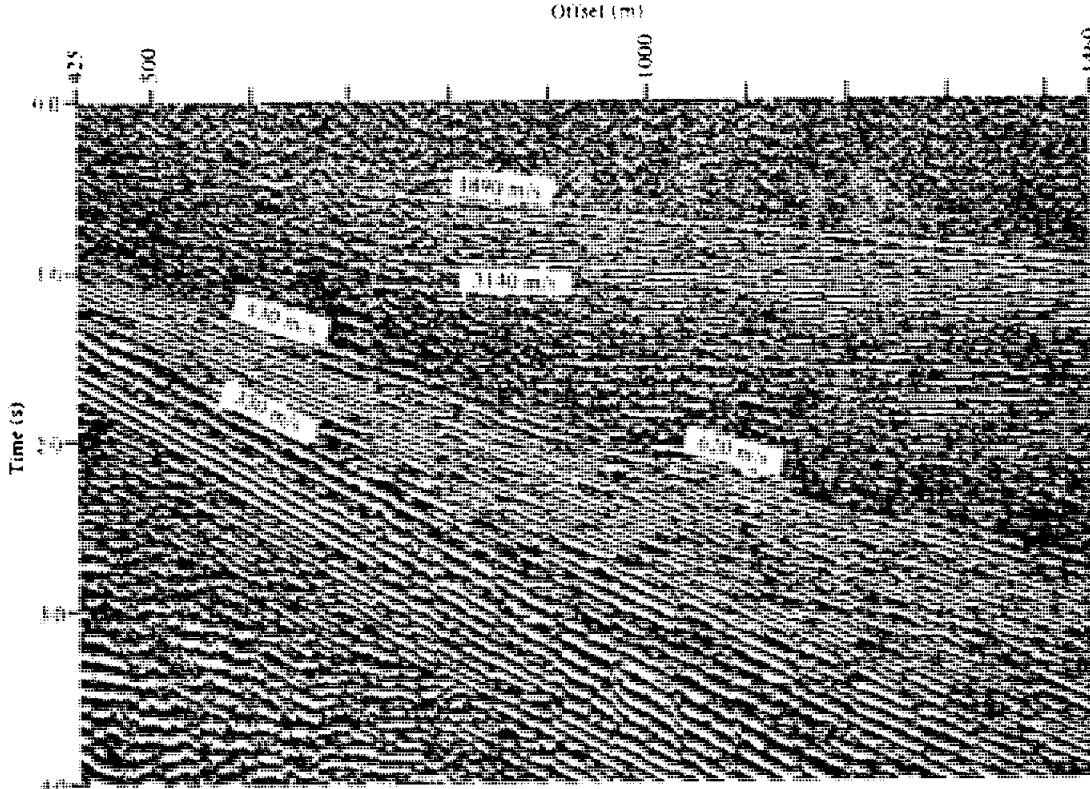


**Figure 4.49.** Noise analysis or walkaway. The vibroseis source with geophones spaced 1.5 m apart, is offset 425 m to the first geophone. Identification of events: 1,890 m/s arrival = refraction from base of weathering; 530 and 620 m/s = ground-roll modes; 330 m/s = air wave; 3,140 m/s = refraction event. (After Sheriff, 1984).

though in exceptionally difficult areas, both multiple sources and multiple geophones are used at the same time.

The canceling of horizontally traveling coherent noise by using geophone and source arrays presents a more challenging array design problem than the cancellation of random noise. In the case of random noise, the locations of the elements of the array are unimportant provided they are not so close that the noise is identical. For coherent noise the size, spacing, and orientation of the array must be selected on the basis of the properties of the noise to be canceled (Schoenberger, 1970). If the noise is a long sinusoidal wavetrain, an array consisting of  $n$  elements spaced along the direction of travel of the wave at intervals of  $\lambda/n$ , where  $\lambda$  is the apparent wavelength, will provide cancellation. However, actual noise often consists of several types that arrive from different directions; each type invariably comprises a range of wavelengths. Moreover, the nature of the noise may change from point to point along the line. One can apply the principles of antenna design to obtain maximum cancellation for a band of frequencies approaching the spread from an arbitrary direction, and numerous articles have been written on the subject of arrays. A review paper by McKay (1954)

shows examples of the improvement in record quality for different arrays.

In addition to the difficulties in defining the noise wavelengths to be attenuated, actual field layouts rarely correspond with their theoretical design (Newman and Mahoney, 1973). Measuring the location of individual geophones is not practicable because of the time required. In heavy brush one may have to detour when laying out successive geophones and often one cannot see from one geophone to another, so that even the orientation of lines of geophones can be irregular. In rough topography maintaining an array design might require that geophones be at different elevations, which may produce far worse effects than those that the array is intended to eliminate. Similar problems arise where the conditions for planting the geophones vary within a group (Lamer, 1970), perhaps as a result of loose sand, mucky soil, or scattered rock outcrops. The best rules for array design are often (1) to determine the maximum size that can be permitted without discriminating against events with the maximum anticipated dip and (2) to distribute as many geophones as field economy will permit more-or-less uniformly over an area a little less than the maximum size permitted, maintaining all geophone plants and

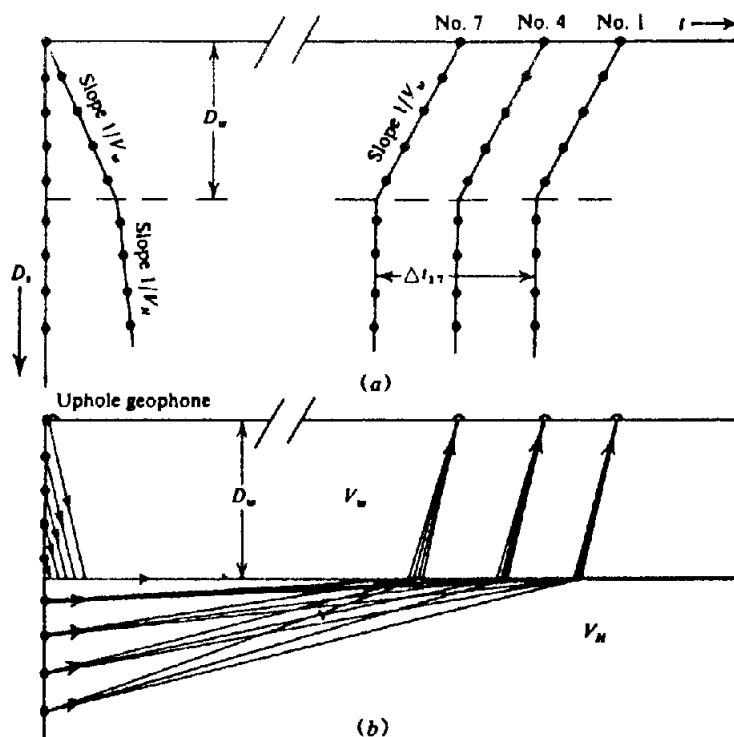


Figure 4.50. Uphole survey. (a) Traveltime versus shot depth. (b) Vertical section showing raypaths.

elevations as nearly constant as possible even if this requires severe distortion of the layout.

(d) **Noise analysis.** Systematic investigation of coherent noise often begins with shooting a *noise profile* (also called a *microspread* or *walkaway*). This is a small-scale profile with a single geophone per trace, the geophones being spaced as closely as 1 to 3 m over a total spread length of the order of 300 m or more. If the weathering or elevation is variable, corrections should be made for each trace. The corrected data, such as shown in Figure 4.49, are studied to determine the nature of the coherent events, their frequencies and apparent velocities, *windows* between noise trains where reflection data would not be overridden by such noise, and so on. Once we have some indications of the types of noises present, we can design arrays or other field techniques to attenuate the noise and then field-test our techniques to see if the desired effect is achieved.

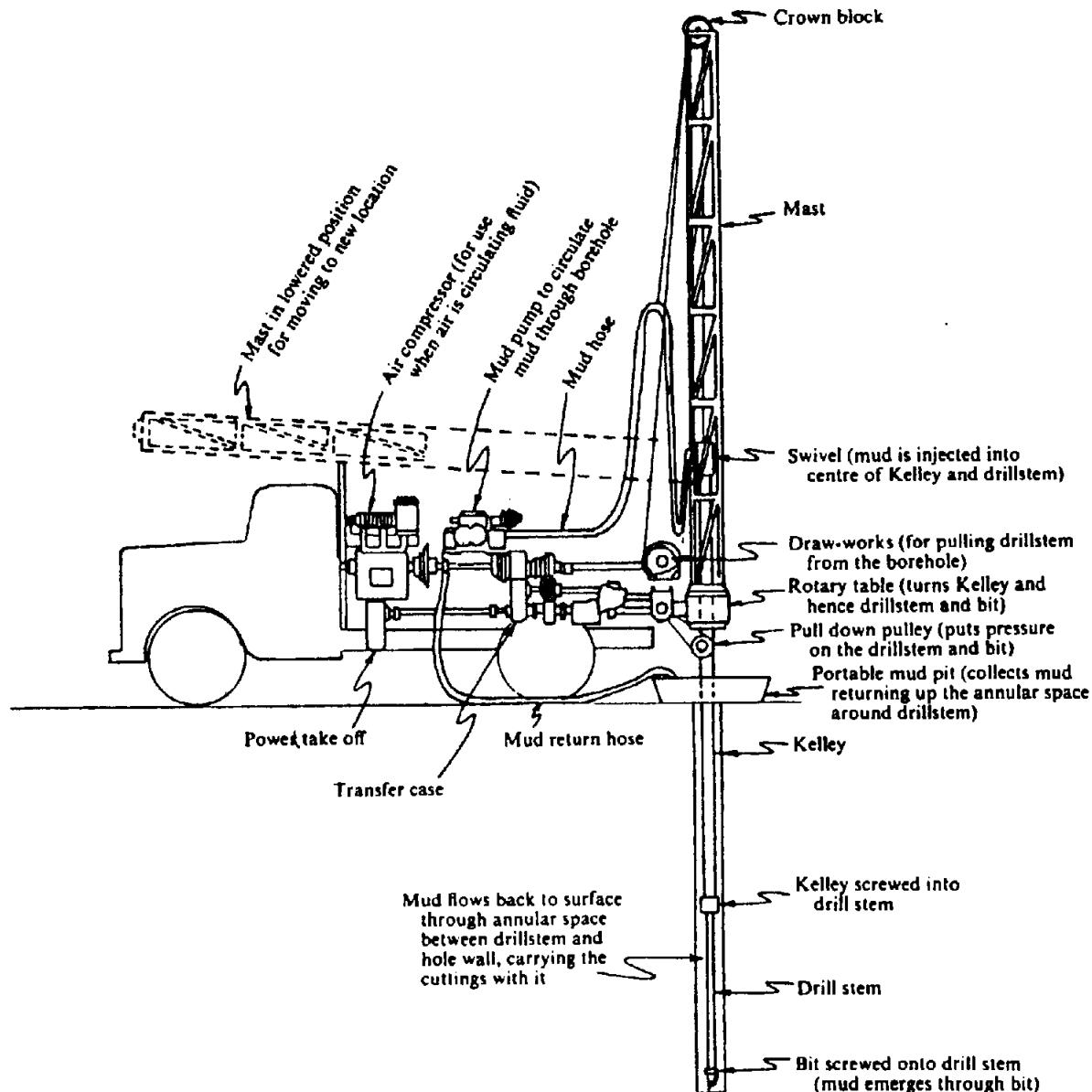
(e) **Uphole surveys.** An *uphole survey* is one of the best methods of investigating the near-surface and finding the thickness and velocity of the low-velocity layer (LVL),  $D_w$  and  $V_w$ , and the subweathering velocity  $V_h$ . An upheole survey requires a shothole deeper than the base of the LVL, a complete spread of geophones, plus an *uphole geophone* (a geophone usually within 3 m of the shothole). Shots are fired at various depths in the hole, as shown in Figure 4.50, beginning at the bottom and continuing until the shot is just below the surface of the ground. Travel-

times are plotted against shot depth for the upheole geophone (that is, the upheole time  $t_{ub}$ ) as well as for several distant geophones, including two or more spaced 200 m or more apart, as shown in Figure 4.50. The plot for the upheole geophone changes abruptly where the shot enters the LVL; the slope of the portion above the base of the LVL gives  $V_w$  and the break in slope usually defines  $D_w$  clearly.

For the distant geophones the plot is almost vertical at first because the path length changes very little as long as the shot is in the high-speed layer. However, when the shot enters the LVL there is an abrupt change in slope and the traveltimes increases rapidly as the path length in the LVL increases. The refraction velocity at the base of the LVL,  $V_h$ , is obtained by dividing the time interval between the vertical portions of the curves for two widely separated geophones ( $\Delta t_{17}$  in Figure 4.50a) into the distance between the geophones. This velocity measurement may be different from that given by the slope of the deeper portion of the upheole geophone curve, partly because the latter is less accurate (since the time interval is less than  $\Delta t_{17}$ ), partly because the layering of beds of different velocities has little effect on  $\Delta t_{17}$  but may affect  $t_{ub}$  substantially.

#### 4.5.3. Field Equipment for Land Surveys

(a) **Drilling.** When explosives are used as the energy source, holes are drilled so that the explosive can be placed below the low-velocity layer. The holes are usually about 8 to 10 cm in diameter and 6 to



### ROTARY DRILL

Figure 4.51. Rotary drill. (From Sheriff, 1984.)

30 m in depth, although depths of 80 m or more are used occasionally. Normally the holes are drilled with a rotary drill, usually mounted on a truck bed, but sometimes on a tractor or amphibious vehicle for working in difficult areas. Some light drills can be broken down into units small enough that they can be carried. Augers are used occasionally. In work in soft marshes, holes are sometimes jetted down with a hydraulic pump. Typical rotary-drilling equipment is shown in Figure 4.51.

Rotary drilling is accomplished with a drill bit at the bottom of a drill pipe, the top of which is turned so as to turn the bit. Fluid is pumped down through the drill pipe, passes out through the bit and returns to the surface in the annular region around the drill pipe. The functions of the drilling fluid are to bring the cuttings to the surface, to cool the bit, and to plaster the drill hole to prevent the walls from caving

and formation fluids from flowing into the hole. The most common drilling fluid is *mud*, which consists of a fine suspension of bentonite, lime and/or barite in water. Sometimes water alone is used and sometimes air is the circulating fluid. Drag bits are used most commonly in soft formations; these tear out pieces of the earth. Hard rock is usually drilled with roller bits or cone bits, which cause pieces of rock to chip off because of the pressure exerted by teeth on the bits. In areas of exceptionally hard rock, diamond drill bits are used.

(b) Explosive energy sources. Explosives were the sole source of energy used in seismic exploration until weight dropping was introduced in 1953. Explosives continue to be an important seismic energy source in land work. Most explosives have a *velocity of detonation* (that is, the velocity with which the

explosion travels away from the point of initiation in the explosive) around 6 to 7 km/s. Consequently, the seismic pulses generated have very steep fronts. This high concentration of energy is desirable from the point of view of seismic wave analysis but detrimental from the viewpoint of damage to nearby structures.

Ammonium nitrate and nitrocarbonitrite (NCN) are the dominant explosives used today. Explosives are packaged in tins or in tubes of cardboard or plastic about 5 cm in diameter that usually contain 1 to 10 lb (0.5 to 5 kg) of explosive. The tubes and tins are constructed so that they can be easily joined together end-to-end to obtain various quantities of explosives.

Electric blasting caps are used to initiate an explosion. These consist of small metal cylinders, roughly 0.6 cm in diameter and 4 cm long. They contain a resistance wire imbedded in a mixture of powder charges, one of which ignites at a relatively low temperature. By means of two wires issuing from the end of the cap, a large current is passed through the resistance wire and the heat generated thereby initiates the explosion. The cap has previously been placed inside one of the explosive charges so that the explosion of the cap detonates the entire charge. The current that causes the blasting cap to explode is derived from a *blaster*, which is basically a device for charging a capacitor to a high voltage by means of either batteries or a hand-operated generator, and then discharging the capacitor through the cap at the desired time. Incorporated in the blaster is a device that generates an electrical pulse at the instant that the explosion begins. This *timebreak* pulse fixes the instant of the explosion,  $t = 0$ . The timebreak pulse is transmitted to the recording equipment where it is recorded along with the seismic data.

Several techniques are used at times to concentrate the energy traveling downward from an explosion. The detonating front in an explosive usually travels much faster than the seismic wave in the formation, so that the seismic wave originating from the top of a long explosive charge lags behind the wave from the bottom of the charge even where the explosive is detonated at the top (which is the usual method). Explosives with low detonating velocity are sometimes used, but they are made in long flexible tubes that are difficult to load. Delay units are sometimes used between several concentrated explosive charges to allow the wave in the formation to catch up with the explosive front; they may consist of delay caps (which introduce a fixed delay between the time the detonating shock initiates them and the time they themselves explode) or helically wound detonating cord (so that the detonating front has to travel a longer distance). Expendable impact blasters

have also been used; they detonate when they are actuated by the shock wave from another explosion.

Although explosives provide the most compact high-energy source, they have many disadvantages that often preclude their use: high cost, the time and expense involved in drilling holes, potential damage to nearby buildings, wells, and so forth, as well as restrictions about where holes can be drilled and explosives detonated.

(c) *Surface energy sources.* Many alternative energy sources have been developed for use in both land and marine work (Laster, 1985). Discussion of those that are used primarily at sea and infrequently on land will be postponed until Section 4.5.4c.

Without exception, the surface energy sources are less powerful than explosives and their use on a large scale has been made feasible by vertical stacking methods that permit adding the effects of a large number of weak impulses to obtain a usable result.

Some surface methods use explosive detonating cords buried 10 to 40 cm. A 100 m of cord may be buried, often in a pattern, using a special plow, and then exploded by means of caps placed at intervals along the cord. Occasionally, in remote areas, explosive charges on sticks 1 to 2 m above the ground are used; this procedure is called *air shooting*. Aside from raising a cloud of dust, it does no damage to the vegetation. However, it generates a strong air-wave that can damage the ears of animals within 100 m or so of the explosion.

The earliest nonexplosive source to gain wide acceptance was the *thumper* or *weight dropper*. A rectangular steel plate weighing about 3,000 kg is dropped from a height of about 3 m. The instant of impact is determined by a sensor on the plate. Weights often are dropped every few meters and the results of 50 or more drops composited into a single field record. The time between release of the weight and impact on the ground is not constant enough to permit simultaneous use of more than one source. Often two or three units are used in succession, one dropping its weight while the others lift their weights into the armed position and move ahead to the next drop point. The use of weight dropping is now largely restricted to desert or semidesert areas where the massive trucks can move about relatively freely. Several variations of mechanical sources are used in shallow-penetration work for coal exploration or engineering objectives (McCann, Andrew, and McCann, 1985).

Whereas the foregoing are primarily surface sources, gas guns, air guns (Brede et al., 1970), and other devices are sometimes used in boreholes, especially in soft marsh where there is little risk of being unable to recover the equipment from the hole. The



Figure 4.52. Vibrators mounted for off-road survey. (Courtesy Conoco.)

air guns used on land are modifications of the guns designed for marine use, which are discussed in Section 4.5.4c. Air guns are sometimes used in bags of water set on the surface of the ground; the coupling with the ground is generally good (Montgomery, 1984).

Unlike other energy sources that try to deliver energy to the ground in the shortest time possible, the Vibroseis source passes energy into the ground for 7 s or more. A vibrator (usually hydraulic) actuates a steel plate pressed firmly against the ground (Fig. 4.52). The output wavetrain consists of a sine wave whose frequency increases continuously from 6 to ~ 50 Hz during the 7 to 21 s "sweep." Each returning reflection event is a similar wave train of about 7 to 21 s duration. Because reflections occur much closer together than this, the result is a superposition of many wavetrains. Subsequent data processing (discussed in §4.7.4e) is necessary to resolve the data. In effect, the processing compresses each returning wavetrain into short wavelets, thus removing much of the overlap (see Fig. 4.82).

Vibroseis sources, like most surface sources, produce low-energy density; as a result they can be used in cities and other areas where explosives and other sources would cause extensive damage. Vibroseis is now the most popular land seismic source.

(d) Geophones. Seismic energy arriving at the surface of the ground is detected by geophones, frequently referred to as seismometers, detectors, or jugs. Although many types have been used in the past, modern geophones are almost entirely of the

moving-coil electromagnetic type for land work and the piezoelectric type for marsh and marine work. The former will be described briefly here (for a more complete discussion, see Sheriff and Geldart, 1982, pp. 161–6); the latter will be discussed in Section 4.5.4d in connection with marine equipment.

The schematic diagram of a moving-coil electromagnetic geophone in Figure 4.53 shows a permanent magnet in the form of a cylinder into which a circular slot has been cut. The slot separates the central S pole from the outer annular N pole. A coil consisting of a large number of turns of very fine wire is suspended centrally in the slot by means of light leaf springs A, B, and C. The geophone is placed on the ground in an upright position. When the ground moves vertically, the magnet moves with it but the coil, because of its inertia, tends to stay fixed. The relative motion between the coil and the magnetic field generates a voltage between the terminals of the coil. The geophone output for horizontal motion is essentially zero because the coil is supported in such a way that it stays fixed relative to the magnet during horizontal motion.

The output voltage of the geophone is directly proportional to the strength of the magnetic field of the permanent magnet, the number of turns in the coil, the radius of the coil, and the velocity of the coil relative to the magnet. Modern high sensitivity geophones have an output of 0.5 to 0.7 V for a velocity of 1 cm/s of the ground.

The geophone coil and springs constitute an oscillatory system with natural frequency in the range from 7 to 30 Hz for reflection work and 4 to 10 Hz

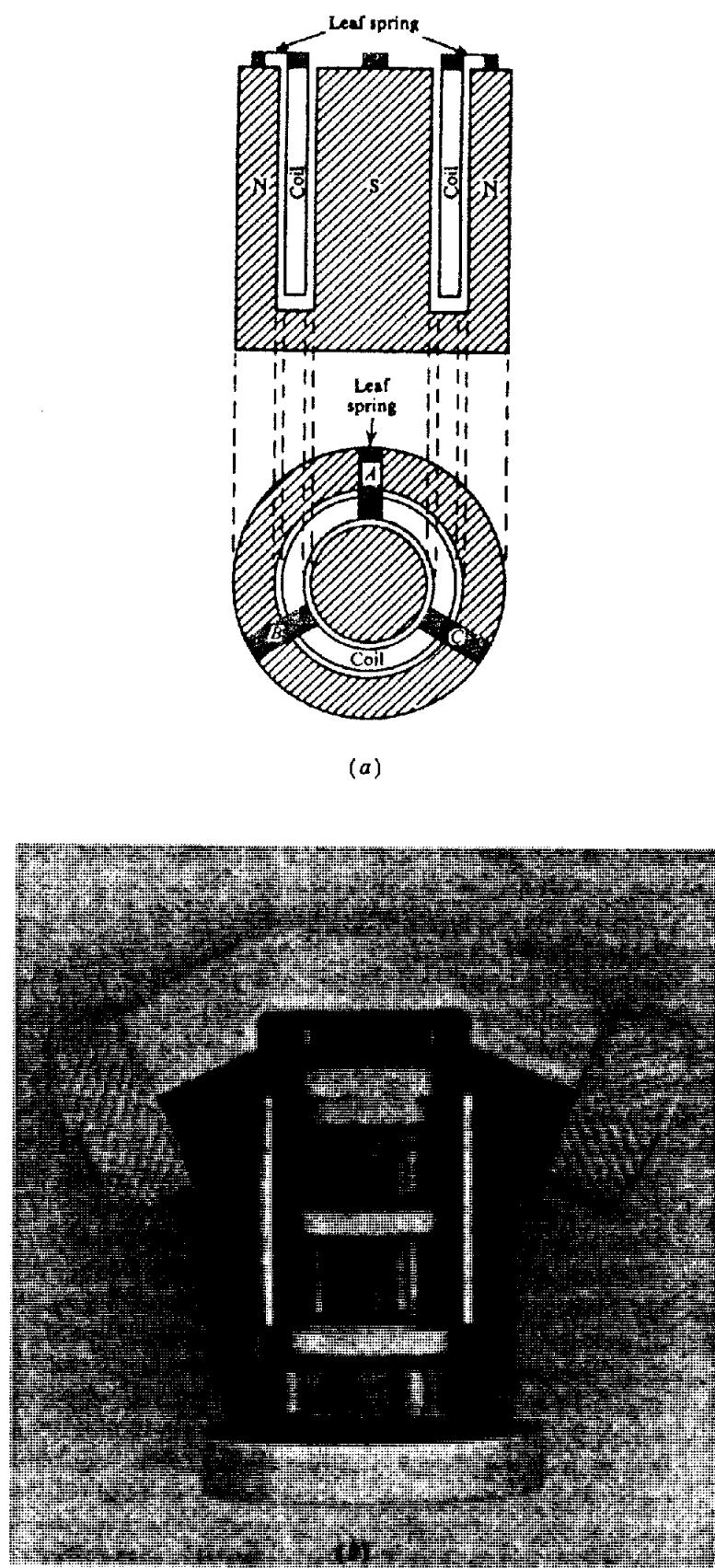


Figure 4.53. Moving-coil geophone. (a) Schematic. (b) Cutaway of a digital-grade geophone. (Courtesy Geo Space Corp.)

for refraction work. Because the coil tends to oscillate after the ground motion dies away, it is necessary to dampen (attenuate) the motion. This is achieved in part by winding the coil on a metal "former"; eddy currents induced in the latter when it moves in the magnetic field oppose the motion and hence produce damping. Additional damping is obtained by connecting a shunt resistance across the coil of the geophone; when a current flows through the coil the interaction between the magnetic fields of the current and the permanent magnet further slows down the motion of the coil (the input impedance of the recording system is so large that it does not significantly affect the current and hence the damping). The geophone damping can be adjusted by varying the shunt resistance because this changes the current through the geophone. A geophone with a high resistance shunt will oscillate for some time after being tapped lightly. As the shunt resistance is decreased, the number of oscillations will decrease because of the increased damping until finally a point will be reached where a tap will just fail to produce an oscillation. At this point, the geophone is *critically damped*.

The response of a geophone to a harmonic signal depends on the relation between the frequency of the signal and the natural frequency of the geophone as well as the degree of damping. Figure 4.54a shows curves of the amplitude of the output current as a function of frequency. The maximum velocity of the geophone is the same for all curves. Often the output is normalized with respect to (that is, expressed as a fraction of) the output for high frequencies. The various curves correspond to different values of the damping;  $h$  is the ratio of the amount of damping relative to critical damping ( $h = 1$ ). For zero damping ( $h = 0$ ), the output becomes infinite at the natural frequency; obviously this is merely a theoretical result since zero damping can never be achieved. As  $h$  increases, the output peak decreases in magnitude and moves slowly toward higher frequencies. Somewhere between  $h = 0.5$  and 0.7 the peak disappears and the range of flat response has its maximum extent. As  $h$  increases beyond this value, the low-frequency response gradually falls off. The generally accepted choice of 70% of critical damping for geophones results in more-or-less optimum operating conditions with respect to amplitude distortion in the geophone output.

The output of a geophone is shifted in phase with respect to the input by the amounts shown in Figure 4.54b. Phase shift is important because the seismic signal comprises a range of frequencies; if the phase shift does not vary properly with frequency, phase distortion occurs. The optimum phase shift is linear with frequency and with an intercept of  $n\pi$ , that is,

the shift is equal to  $(k\omega + n\pi)$  where  $k$  is a constant and  $n$  an integer. To show this, we note that an input signal of the form  $A \cos \omega t$  will appear in the output as

$$B \cos(\omega t + k\omega + n\pi) = \pm B \cos \omega(t + k)$$

Thus, the net effect is to shift all frequencies in time by the amount  $k$  and to invert the pulse when  $n$  is odd, neither of which results in change of wave shape.

Usually several closely spaced geophones are connected in a series-parallel arrangement to produce a single composite output. The entire geophone group is considered to be equivalent to a single geophone located at the center of the group. However, the damping of each geophone will be affected by the presence of the other geophones because of the change in resistance of the circuit. An exception is an arrangement of  $n$  parallel branches, each containing  $n$  identical geophones in series, which has the same resistance as a single geophone and hence the same damping.

The geophone signals are usually transmitted to the recorder by many pairs of wires in cables. Increasingly, the geophone output is digitized at the geophone group by a remote digitization unit (RDU) and the digital signal transmitted to the recorder. The signal may be stored temporarily where it is digitized and subsequently transmitted to the recorder, perhaps along with the signals from other digitizing boxes, in a coded fashion over twin-lead cable, coaxial cable, or fiber-optic cable; sometimes the transmission is by radio. At times the output for an entire day is stored on a magnetic tape in the digitizing box, to be collected and combined with the data from other digitizing boxes at the end of the day's work.

(e) *Analog recording.* Except for very strong signals arriving soon after the shot is fired, the output of the geophone is too weak to be recorded without amplification. Also, the useful range of amplitudes of the geophone output extends from a few tenths of a volt at the beginning of the recording to about  $1 \mu\text{V}$  near the end of the recording several seconds after the shot, weaker signals being lost in the system noise, a relative change or *dynamic range* of about  $10^5$  (100 dB). Besides amplifying weak signals, the amplifier usually is called on to compress the range of signals as well as filter signals. Seismic amplifiers generally employ solid state circuitry, which allows them to be very compact. Although they are usually mounted in a recording truck or other vehicle, they can also be carried where necessary. A block diagram of an analog amplifier is shown in Figure 4.55.

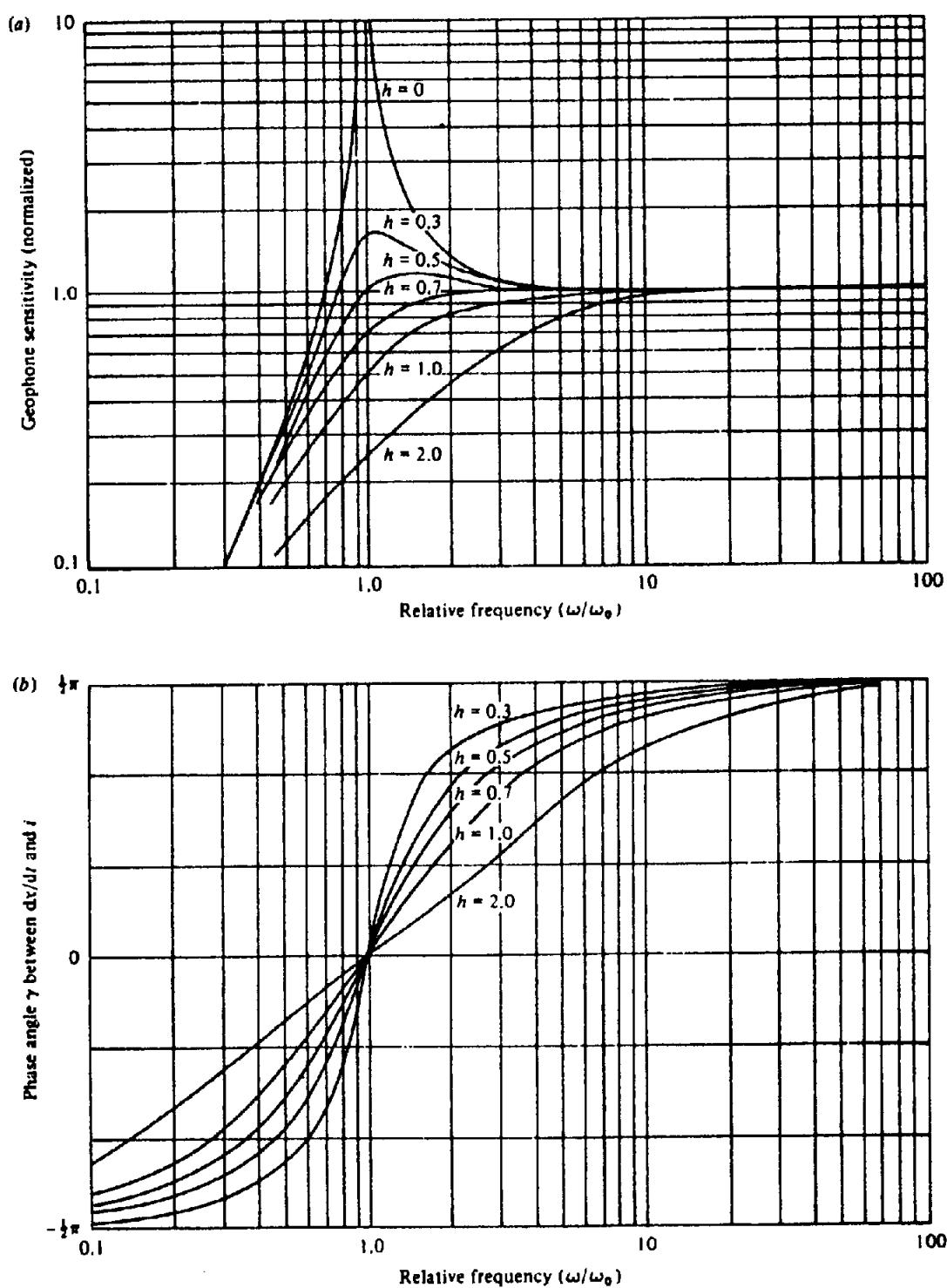


Figure 4.54. Geophone response curves. (After Dennison, 1953) (a) Amplitude of output relative to input. (b) Phase of output relative to input.

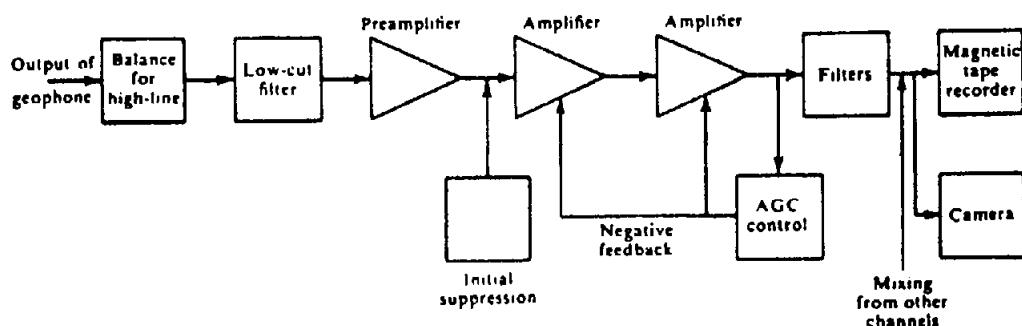


Figure 4.55. Block diagram of analog seismic amplifier.

The cable from the geophones may be connected to a balance circuit that permits adjustment of the impedance to ground so as to minimize the coupling with nearby power lines, thus reducing pickup of noise at the power-line frequency (*high-line pickup*). The next circuit element usually is a filter to attenuate the low frequencies that arise from strong ground roll and that otherwise might overdrive the first amplification stage and introduce distortion.

Seismic amplifiers are multistage and have very high maximum gain, usually of the order of  $10^5$  (100 dB), sometimes as much as  $10^7$  (140 dB); 100 dB means that an input of 5  $\mu$ V amplitude appears in the output with an amplitude of 0.5 V. Lower amplification can be obtained by means of a master gain switch, which reduces the gain in steps.

The amplifier gain may be varied during the recording interval starting with low amplification during the arrival of strong signals at the early part of the record and ending up with the high gain value fixed by the master gain setting. This variation of gain with time (signal compression) can be accomplished with *automatic gain (volume) control*, usually abbreviated AGC or AVC, which utilizes a negative feedback loop to measure the average output signal level over a short interval and adjust the gain to keep the output more-or-less constant regardless of the input level.

It is important in making corrections for near-surface effects that we be able to observe clearly the *first breaks*, the first arrivals of energy at the different geophone groups. (For a geophone near the shot-point, the first arrival travels approximately along the straight line from the shot to the geophone; for a distant geophone the first arrival is a headwave refracted at the base of the low-velocity layer – see Fig. 4.76 and the discussion of weathering corrections, §4.7.1.)

If we allow the AGC to determine the gain prior to the first arrivals, the low input level (which is entirely noise) results in very high gain; the output may then be noise amplified to the point where it becomes difficult to observe the exact instant of arrival of the first breaks. This problem is solved by using *initial suppression* or *presuppression*. A high-frequency oscillator signal (about 3 kHz) is fed into the AGC circuit, which reacts by reducing the gain so that the noise is barely perceptible; the high-frequency signal is subsequently removed by filtering so that it does not appear in the output. With the reduced gain, the relatively strong first breaks stand out clearly. As soon as the first breaks have all been recorded, the oscillator signal is removed, usually by a relay triggered by one of the first breaks. Thereafter, the AGC adjusts the gain in accordance with the seismic signal level.

Seismic amplifiers are intended to reproduce the input with a minimum of distortion and hence the gain (without filters) should be constant for the entire frequency spectrum of interest. For reflection work this range is about 10 to 100 Hz and for refraction work the range is about 2 to 50 Hz; accordingly most amplifiers have flat response for all frequencies from ~1 to 200 Hz or more.

*Frequency filtering* refers to the discrimination against certain frequencies relative to others. Seismic amplifiers have a number of filter circuits, which permit us to reduce the range of frequencies that the amplifier passes. Although details vary, most permit the selection of the upper and the lower limits of the passband. Often it is possible to select also the sharpness of the *cutoff* (the rate at which the gain decreases as we leave the passband). Figure 4.56 shows typical filter response curves. The curves are specified by the frequency values at which the gain has dropped by 3 dB (30% of amplitude, 50% of power); the curve marked "Out" is the response curve of the amplifier without filters.

Seismic amplifiers may include circuitry for *mixing* or *compositing*, that is, combining two or more signals to give a single output. Mixing in effect increases the size of the geophone group and is sometimes used to attenuate surface waves. The commonest form, called 50% mixing, is the addition of equal fractions of the signals from adjacent geophone groups. Magnetic tape recording has virtually eliminated the need to mix during recording because we can always mix in playback.

The timebreak signal often is superimposed on one of the amplifier outputs where it appears as a sharp pulse that marks the point  $t = 0$  for the record. When explosives are being used, the uphole signal (§4.5.2e) is also superimposed on one of the outputs;  $t_{uh}$  is important in correcting for near-surface effects.

*High resolution* or HR amplifiers are used in engineering and mining problems to map the top 200 m or so. To get resolution of a few meters, we must use short wavelengths; accordingly these amplifiers have essentially uniform response up to 300 Hz, sometimes to 500 Hz, and the AGC time constants are correspondingly short. To permit recording very shallow reflections, small offsets are used and the initial suppression permits recording events within 0.050 s or so after the first break.

The recorded data must be presented in visual form for monitoring and for interpretation. This is done most commonly by an electrostatic *camera*. A small motor moves a strip of paper at constant speed (about 30 cm/s) during the recording period and a series of galvanometers, one for each geophone group, transforms the electrical signals coming out of the amplifiers into spots of light moving in accordance

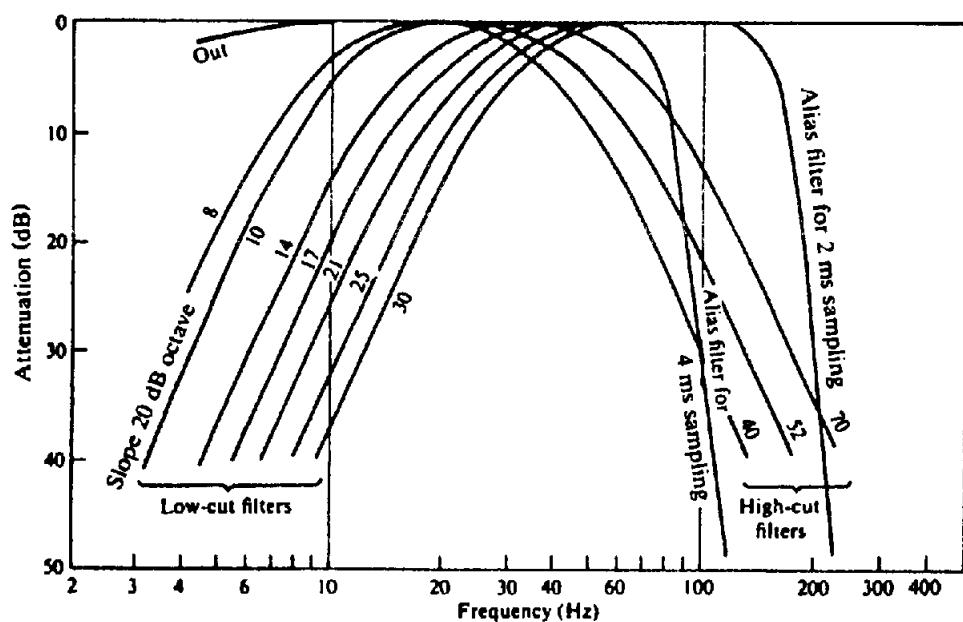


Figure 4.56. Response of seismic filters.

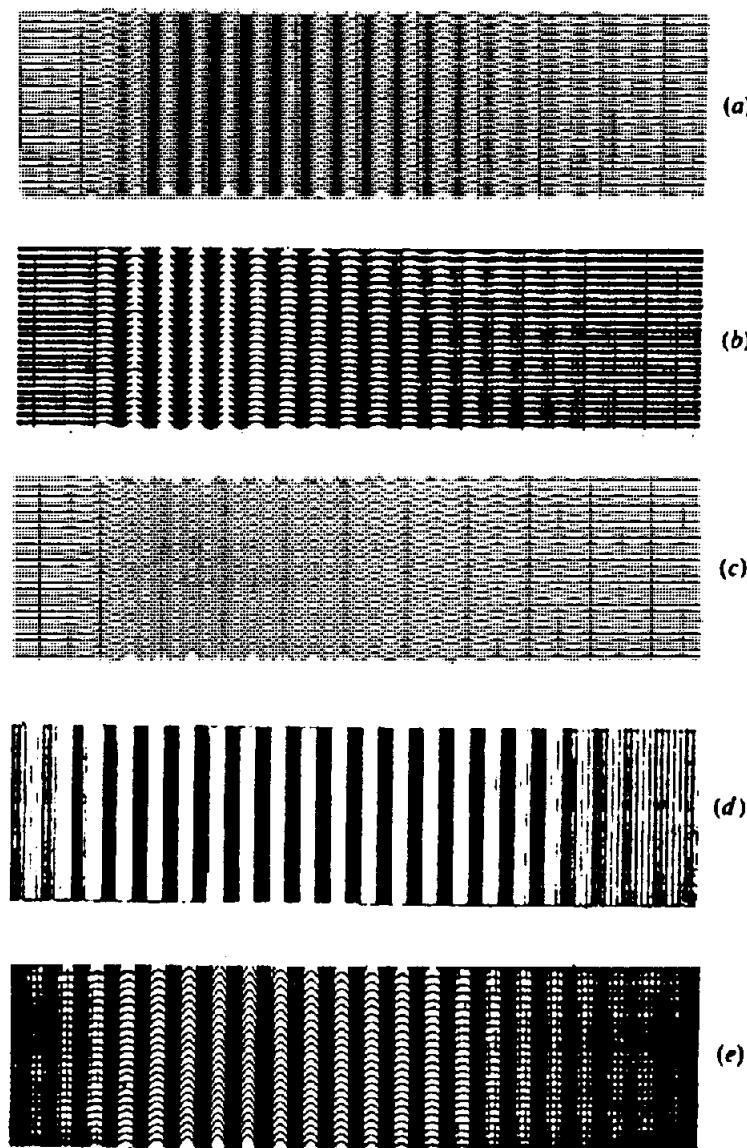


Figure 4.57. Modes of displaying seismic data. (Courtesy Geo Space Corp.) (a) Wiggle superimposed on variable area. (b) Variable area. (c) Wiggle. (d) Variable density. (e) Wiggle superimposed on variable density.

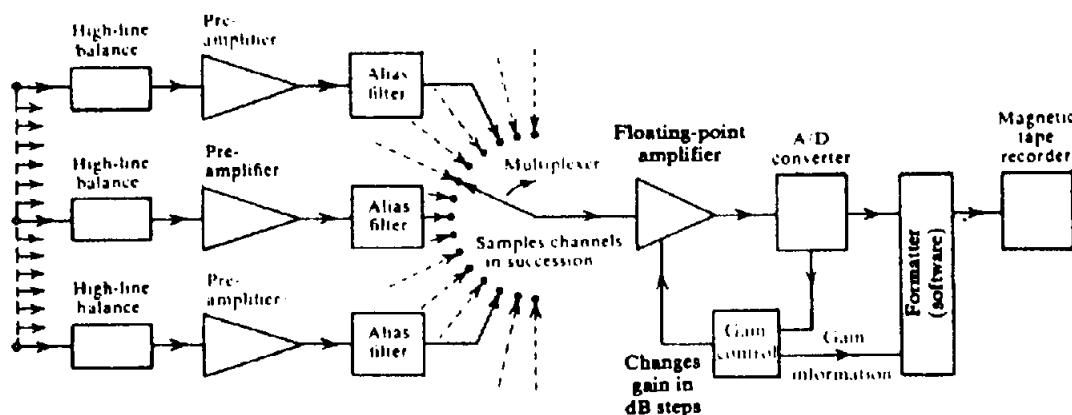


Figure 4.58. Block diagram of digital seismic amplifier.

with the signals, producing "wiggly" lines on the paper. A timing device records accurate timing marks on the record; the heart of the timing system is an oscillating electric circuit whose frequency is accurately controlled by a crystal. Timing lines are usually placed every 10 ms.

Each individual graph, which represents the output of a geophone group, is called a *trace*. Modes of representation are compared in Figure 4.57. The *variable-area* trace can be pictured as the result of passing the light from a galvanometer through a cylindrical lens whose axis would be vertical to give the result shown in the figure. This lens produces a vertical line of light instead of a point, as for the wiggly trace. As this line moves up and down with the signal variations, the lower part is cut off by a stop. The *variable-density* trace is obtained by using a light source whose intensity is varied in accordance with the signal variations. For example, the intensity might increase during signal peaks and decrease during signal troughs; the photographic record will then be darker for peaks and lighter for troughs. Figures 4.57a, e show the wiggly trace superimposed on variable area and variable density, respectively; these have the advantage of retaining the fine detail afforded by the wiggly trace and at the same time obtaining the graphic effects of the variable-area or variable-density displays.

(f) *Digital recording.* Digital recording was first introduced in seismic work in the 1960s and is now almost universally used. Whereas analog devices represent the signal as a voltage (usually) that varies continuously with time, digital recording represents the signal by a series of numbers that denotes the geophone output at regular intervals, usually every 2 ms. Digital recording is capable of higher fidelity than analog recording and permits numerical processing of the data without adding appreciably to the distortion. However, the beginning (geophone response) and end (display) of the recording process

continue to be analog. Anstey (1970) discusses instrument requirements for digital recording and Pieuchot (1984) gives a comprehensive review of seismic instrumentation.

We shall discuss digital representations in the binary scale of 2. The binary scale uses only two digits, 0 and 1; hence only two different conditions are required to represent binary numbers, for example, a switch opened or closed. Binary arithmetic operations are much like decimal ones, for example, Decimal:

$$20873 = 2 \times 10^4 + 8 \times 10^2 + 7 \times 10^1 + 3 \times 10^0$$

Binary:

$$1011011 = 1 \times 2^6 + 1 \times 2^4 + 1 \times 2^3 + 1$$

$$\times 2^1 + 1 \times 2^0$$

= decimal number 91

Each pulse representing 1 or 0 is called a *bit* and the series of bits, which give the value of a quantity, is called a *word*.

The block diagram of a digital recorder in Figure 4.58 can be compared with that of the analog recorder shown in Figure 4.55. Digital amplifiers usually have enough dynamic range so that they do not require low-cut filtering prior to the first amplification stage. Digital amplifiers are usually of the instantaneous floating-point type: they measure the magnitude of each sample; each value is expressed as a certain number of significant figures times 2 raised to the proper power, where both the significant figures and the power are recorded.

The output of each preamplifier passes through an alias filter whose function will be explained in Section 4.7.3b. From the alias filter the signal passes to a *multiplexer*, which is in essence a high-speed electric switch. From the multiplexer onward, we require only one channel - one amplifier, one A/D (*analog-to-digital*) converter, and so forth, instead of one for each trace.

The multiplexer connects each channel in turn to the amplifier. Here the amplifier is connected to a

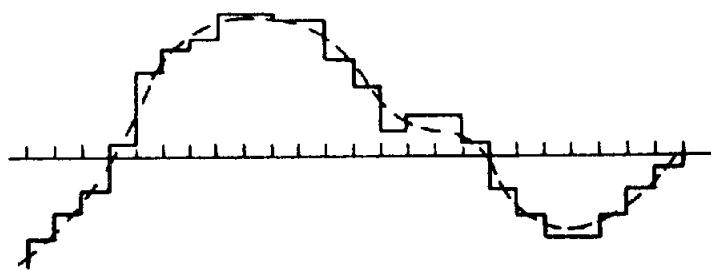


Figure 4.59. Conversion from digital to analog form.

**sample-and-hold** unit for about  $1\ \mu\text{s}$  which is sufficient time to charge a capacitor to the same voltage as the amplifier output at that instant. The amplifier is then disconnected and the A/D converter compares the capacitor voltage with a series of standard voltages. The result of this comparison is a series of pulses that gives the polarity and the value of the amplifier output voltage (in the binary scale) at the sampling instant. Processing the data for each trace requires so little time that there is ample time to read each trace even at the fastest sampling rate ( $1\ \text{ms}$ ) ordinarily used. (For very large numbers of traces, digitization is usually done at the geophone so that these considerations are irrelevant.) The output of the A/D converter is a word containing 14 bits (usually), the first of which gives the sign (plus or minus) of the signal and the remaining bits the magnitude.

The series of pulses from the A/D converter passes to the *formatter*, the device that controls the sequence in which the various bits and words are recorded on the magnetic tape. In addition to the data from the A/D converter, the formatter also receives data identifying the profile, the timebreak, uphole information, a word to mark the end of a record, and so on (all of this information is in digital form). This series of numbers is written on half-inch tape by nine recording heads. The formatter distributes the various bits among the heads in a fixed pattern known as the *format* (SEG 1980). The tape speed is adjusted so that the density of data along a single track is constant (often 6,250 bits/in.).

Digital recording (and processing) involves a series of operations that take place sequentially on a time scale measured in microseconds. The entire sequence is controlled by an electronic "clock," a crystal-controlled oscillator that operates in the megacycle range, which furnishes a continuous series of pulses whose shape and spacing are accurately maintained. Time is measured by counting these pulses and the operating cycles of the component units (such as the multiplexer and the formatter) are controlled by circuits that count the clock pulses and operate electronic switches when the count reaches predetermined values.

Although digital data are ideal for versatile data processing, analog data are more suitable for interpretation and for monitoring the recording system to ensure that all units are functioning properly. Accordingly, digital systems provide for reconverting the digital data to analog form for recording by a camera. The D/A (digital-to-analog) conversion is carried out by reversing the recording process. The bits coming off the tape are rearranged by a deformatter before going to the D/A converter. Usually only the seven or eight "most significant" bits specifying a signal value are used because the camera unit has a resolution of only about 1% (or 1 part in 1100100 in binary). Smaller amplitude changes are undetectable on paper records. The D/A converter can be regarded as a series of batteries with voltages proportional to  $2^6, 2^5, 2^4, 2^3, 2^2, 2^1, 2^0$  units (when seven bits are used). The batteries are connected in series so that the total voltage is 1111111 (that is, 127 in the decimal system). Each "zero" disconnects the corresponding battery. The bit giving the polarity of the signal controls the polarity of the output. The result is a voltage at the output of the D/A converter equal in magnitude and sign to the original signal at the instant of sampling.

The output from the D/A converter goes then to a demultiplexer that connects each voltage to a sample-and-hold circuit in the proper channel. The sample-and-hold output has a staircase form such as shown in Figure 4.59. The output goes through a low-pass filter that smooths out the steps and is then amplified to the voltage level required by the camera.

Computers are part of most recording equipment, taking over many test and diagnostic functions as well as simple processing operations, such as vertical stacking and correlation (Walker and Crouse, 1985).

#### 4.5.4. Marine Equipment and Methods

(a) *Marine operations.* Marine seismic operations usually imply water that is sufficiently deep to allow freedom of movement for ships that are 30 to 70 m in length (Fig. 4.60). Such operations differ from operations on land and in shallow water primarily because of the speed with which they take place.

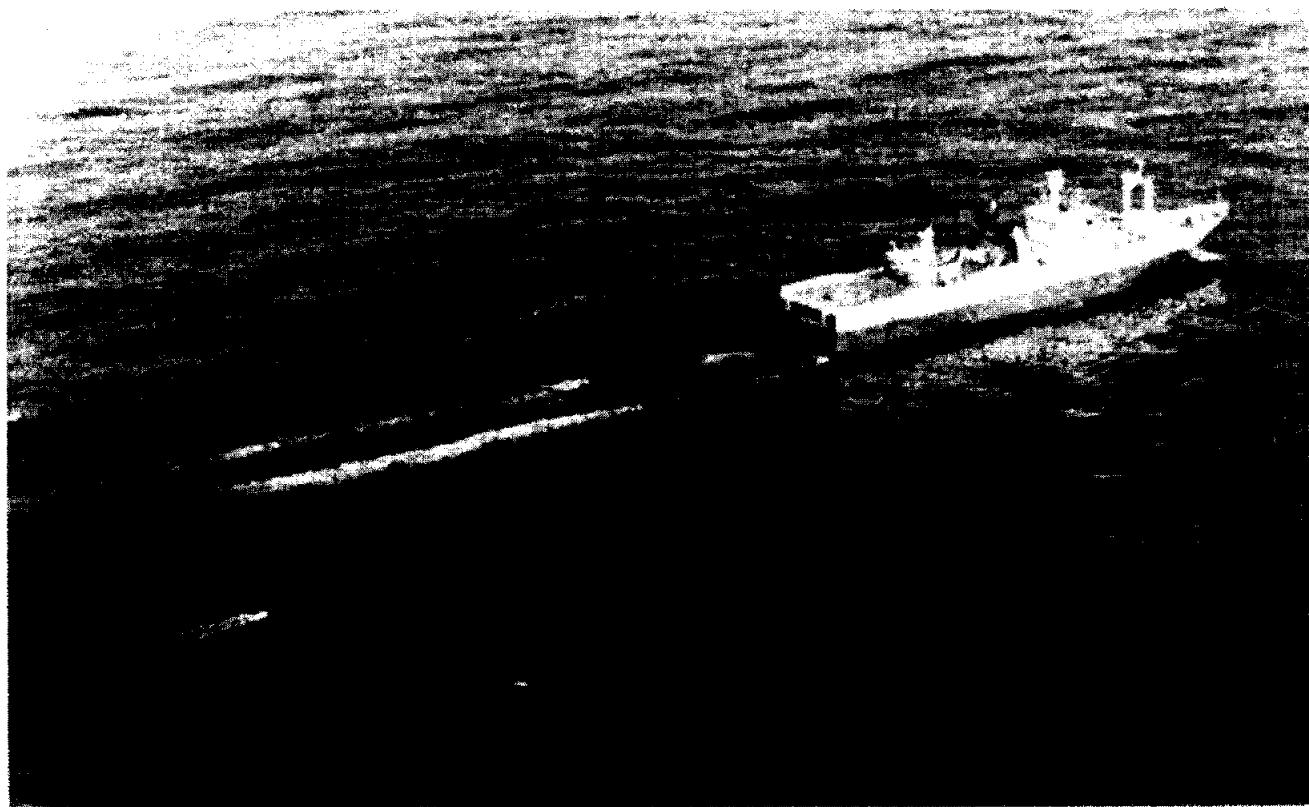


*Figure 4.60. Seismic ship towing two streamers and two air-gun arrays. The outer wakes are produced by paravanes that pull streamers off to each side and the inner two wakes are produced by the two air-gun arrays. (Courtesy Western Geophysical Co.)*

Normal production shooting takes place at a speed of the order of 6 knots and can proceed on a 24 hour per day basis. Coverage of 250 km/day would be possible if all the time were spent recording. This much production is never achieved because time is spent traveling to the line or from the end of one line to the start of the next, waiting for good weather, or because of other factors. Production rates may be of the order of 2 records/minute, each consisting of 2 to 4 component subshots which are then vertically stacked.

The monthly cost of a marine crew is large, but the high production cuts the unit cost of marine seismic data to about 10% of that of land data. The high production rate requires special emphasis on efficiency in operations. Source and receiver units are towed into place and forward travel does not stop during a recording. Although detailed monitoring of data quality is not possible, the relatively constant water environment surrounding the sources and receivers and the general absence of a low-velocity weathering layer such as is usually present on land lessen variations in data quality.

(b) *Bubble effect.* An underwater bubble of gases at high pressure, such as an explosion produces, tends to alternately expand and contract. As long as

the gas pressure exceeds the hydrostatic pressure of the surrounding water, the net force will accelerate the water outward. The net force decreases as the bubble expands and becomes zero when the bubble expansion reduces the gas pressure to the value of the hydrostatic pressure. However, at this point the water has acquired its maximum outward velocity and so continues to move outward while decelerating because the net force is now directed inward. Eventually the water comes to rest and the net inward force now causes a collapse of the bubble with a consequent sharp increase in gas pressure, in effect a new energy release, and the process repeats itself. Seismic waves will be generated by each oscillation. With explosive charges of 7.5 kg, the effect is that of additional seismic records every 0.2 to 0.4 s superimposed on each other so that one cannot tell from which oscillation a reflection event comes. Although explosives are no longer used in marine operations, other types of sources also generate bubbles.

(c) *Marine energy sources.* Marine seismic reflection work consists mostly of two types, common-midpoint and profiler work. These differ considerably in cost, size of energy source, effective penetration, and various other aspects. We shall discuss here the larger energy sources commonly used

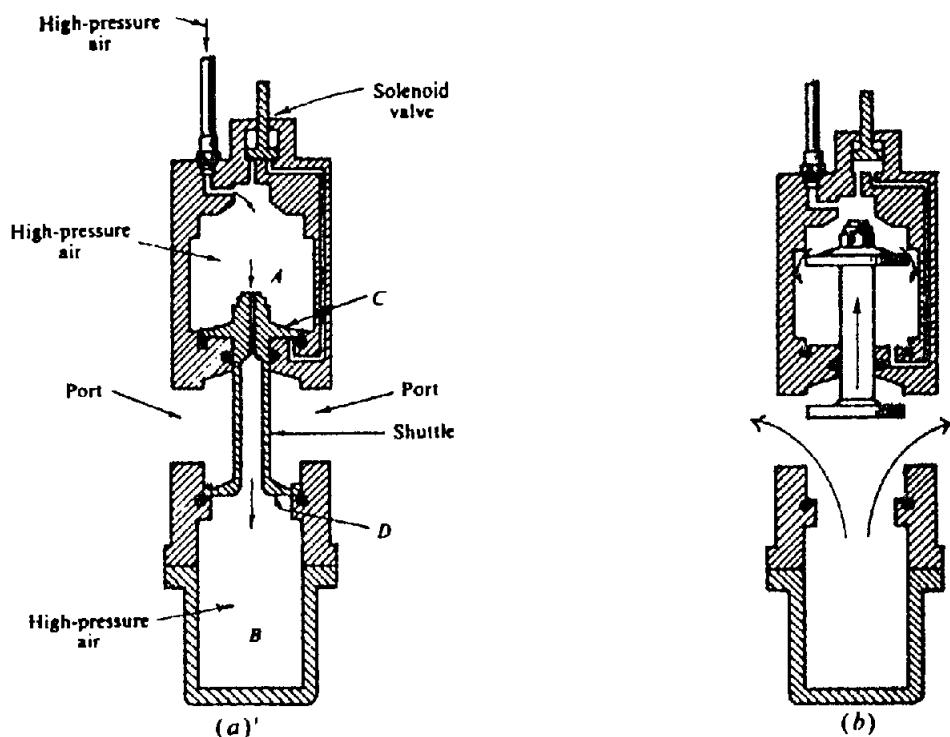


Figure 4.61. Air gun. (Courtesy Bolt Associates.) (a) Ready for firing. (b) Firing.

in common-midpoint recording: The smaller energy sources used in profiling will be described in Section 4.5.5f.

The most widely used large energy source is the *air gun*, a device that discharges air under very high pressure into the water (Giles, 1968; Schulze-Gattermann, 1972). Pressures up to 10,000 psi are used, although 2,000 psi is most common. The gun in Figure 4.61a is shown in the armed position, ready for firing. Chambers *A* and *B* are filled with high pressure air, which entered *A* at the top left and passed into *B* through an axial opening in the "shuttle." The latter is held in the closed position by the air pressure (because flange *C* is larger than flange *D*, resulting in a net downward force). To fire the gun, the solenoid at the top opens a valve that allows high pressure air to reach the underside of flange *C*. This produces an upward force that is large enough to overcome the force holding the shuttle in the closed position and, consequently, the shuttle opens rapidly. This allows the high pressure air in the lower chamber to rush out through ports into the water. The bubble of high-pressure air oscillates at a frequency in the seismic range and so lengthens the source pulse (rather than generating new pulses).

The upward motion of the shuttle is arrested before it strikes the top of chamber *A* because the upward force falls off rapidly as the air enters the water and the downward force of the air in the upper chamber increases. The shuttle then returns to the armed position and the lower chamber again fills with air. The explosive release of the air occurs in 1 to 4 ms and the entire discharge cycle requires about

25 to 40 ms. Usually several air guns are used in parallel. Because the dominant frequency of the pulse depends on the energy (that is, on the product of the pressure and volume of air discharged), mixtures of gun sizes (the gun size is the volume of the lower chamber) from 10 to 2,000 in.<sup>3</sup> are usually used to give a broader frequency spectrum. One variation of the air gun (Mayne and Quay, 1971) allows air flow into the bubble for some time after the initial discharge to retard the violent collapse of the bubble. This is achieved by dividing the lower chamber into two parts connected by a small orifice. The air in the lowermost chamber is delayed in passing through this orifice before discharging into the water.

Several types of imploders are sometimes used. *Imploders* operate by creating a region of very low pressure; the collapse of water into the region generates a seismic shock wave. Water guns (Fig. 4.62) are the most common imploders. Space inside the gun is divided between an upper firing chamber, which is filled with compressed air, and a lower chamber, which is filled with water (Safar, 1984). On firing the gun, the compressed air forces the shuttle downward, expelling the water into the surrounding water. The "slugs" of water leaving the ports create voids behind them and the collapse of water into these voids generates a seismic wave. Often three water guns are used vertically above one another to decrease ghosting effects.

With the Flexichoc†, an adjustable-volume chamber is evacuated while the walls of the chamber are

† Trademark of Compagnie Générale de Géophysique.

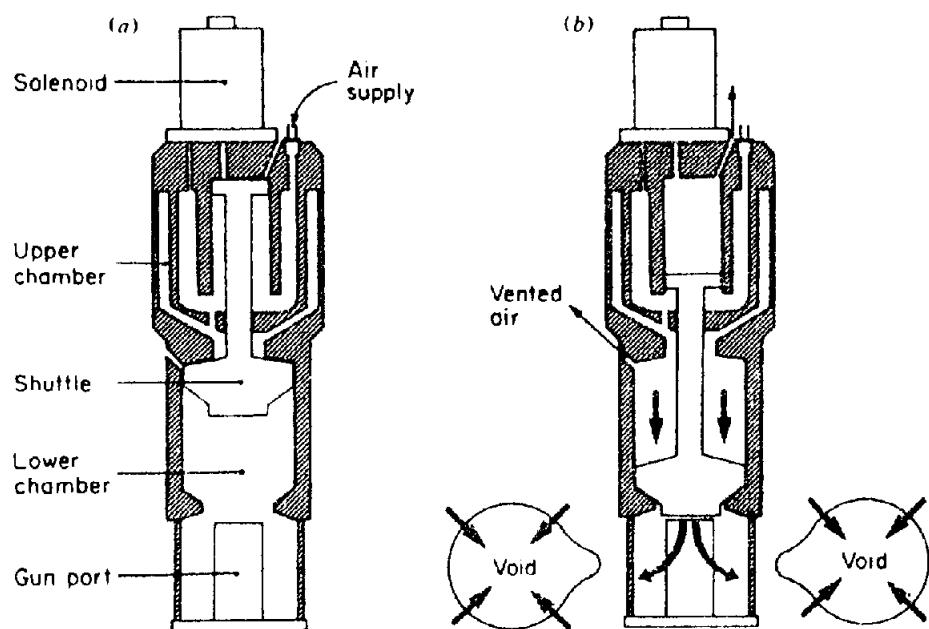


Figure 4.62. Water-gun schematic. (From Safar, 1985.) (a) At beginning of firing cycle. (b) At end of firing cycle.

kept fixed by mechanical restraint. On removal of the restraint, the hydrostatic pressure collapses the chamber and so generates a seismic pulse free of spurious bubbles. Air is then pumped into the chamber to expand it again, whereupon the mechanical restraint holds it open while the air is evacuated, ready for the next collapse. With the Hydroseint†, two plates are driven apart suddenly by a pneumatic piston, creating between them a very low pressure region into which the water rushes. With the Boomer‡, two plates are forced apart suddenly by a heavy surge of electrical current through a coil on one of the plates that generates eddy currents in the other plate, resulting in its being suddenly repelled. The Boomer produces less energy than Flexichoc or Hydrosein.

Many other types of marine sources have been used. Comparison may be made on the basis of energy or waveform shape (*signature*). Rayleigh (1917), while studying the sounds emitted by oscillating steam bubbles, related bubble frequency to bubble radius, pressure, and fluid density, and Willis (1941), while studying underwater explosions, expressed the relationship in terms of source energy (the Rayleigh-Willis formula). The relationship is illustrated in Figure 4.63. In general, large energy involves low frequency and vice versa.

(d) Marine detectors. *Hydrophones* or marine pressure geophones are usually of the piezoelectric

type, that is, they depend on the fact that application pressure to certain substances produces an electric potential difference between two surfaces. Synthetic piezoelectric materials, such as barium zirconate, barium titanate, or lead metaniobate, are generally used. Hydrophones are often arranged in pairs so that their outputs cancel for translational accelerations but add for pressure pulses. Because hydrophones have high electrical impedance, impedance-matching transformers often are included for each group.

The hydrophones are mounted in a long *streamer* towed behind the seismic ship at a depth between 10 and 20 m (Bedenbender, Johnston, and Neitzel, 1970; Berni, 1983). Figures 4.64 and 4.65 show a schematic diagram of a streamer and a photograph of a portion of a streamer. Twenty or more hydrophones spaced at intervals of ~1 m are connected in series (so the generated voltages add up) to form a single equivalent geophone 10 to 50 m in length. The hydrophones and other sensors, connecting wires, and a stress member (to take the strain of towing) are placed inside a plastic tube up to 7 cm in diameter that is filled with sufficient lighter-than-water oil to make the streamer neutrally buoyant, that is, so that its average density equals that of seawater. A lead-in section about 200 m in length is left between the stern of the ship and the first group of hydrophones to reduce pickup of ship noises. Dead sections are sometimes included between the different hydrophone groups to give the spread length desired. The last group is often followed by a tail section to which a buoy is attached. Visual or radar sighting on this buoy is used to determine the amount of drift of the streamer away from the track of the seismic ship

† Trademark of EG & G International.

‡ Trademark of Compagnie Générale de Géophysique.

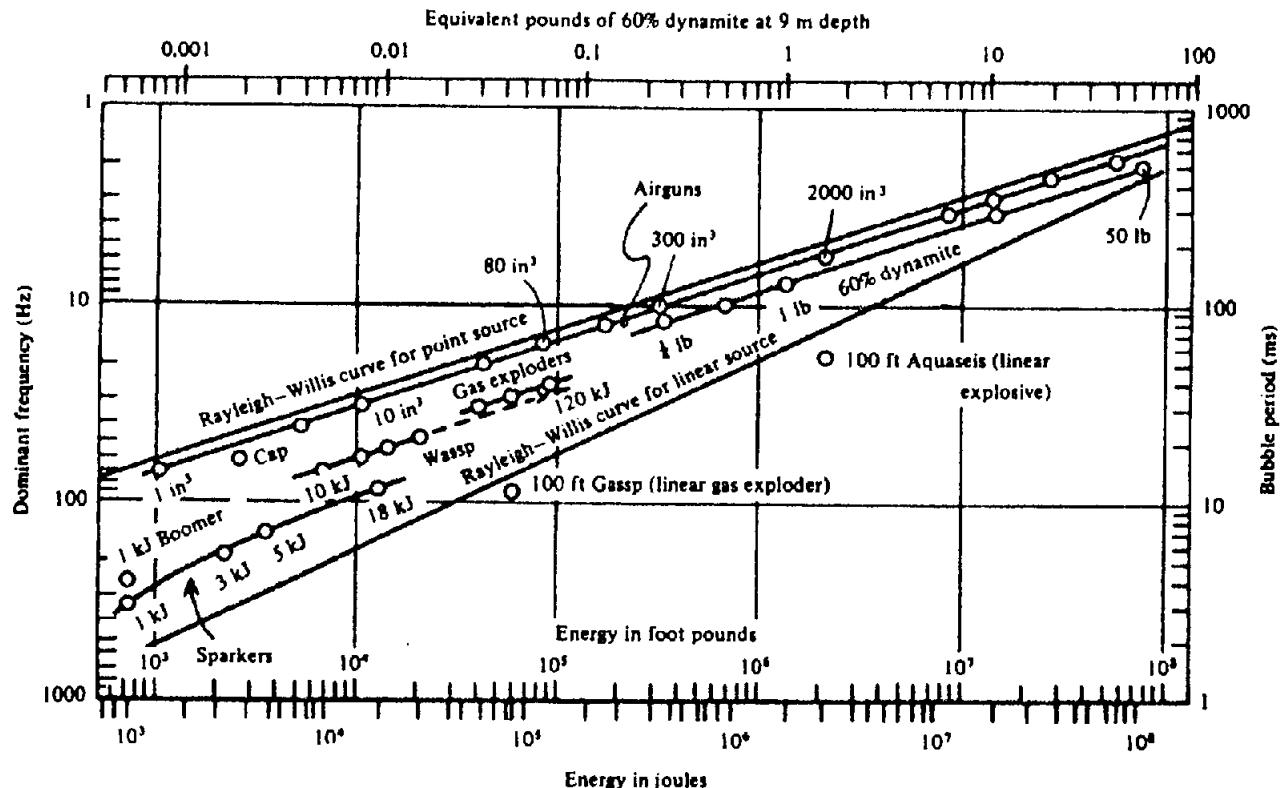


Figure 4.63. Energy-frequency relationships for marine sources at 10 m depth. (From Kramer, Peterson, and Walter, 1968.)

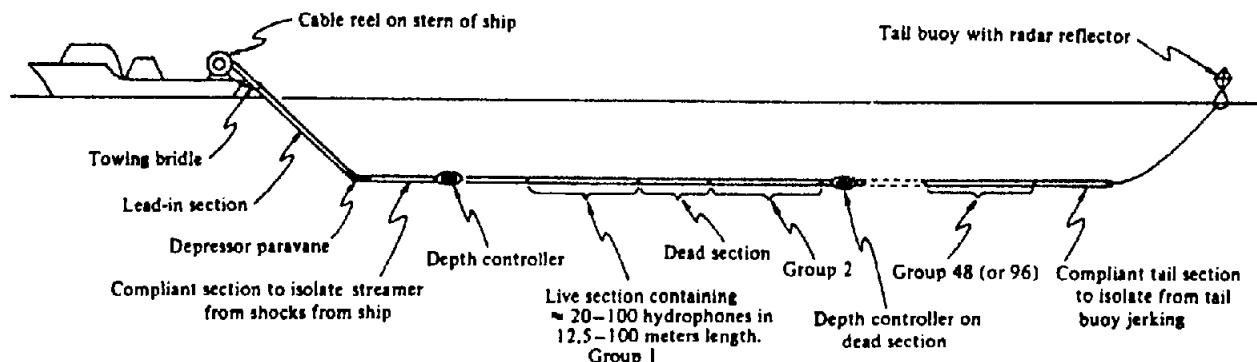


Figure 4.64. Streamer. (After Sheriff, 1984.)

(caused by water currents). This buoy also helps retrieve the streamer if it should be broken accidentally. The total length of streamer in the water is 1 to 5 km and may include up to 500 hydrophone groups. Some streamers digitize the signals at various locations within the streamer so that the signals transmitted to the ship are in digitized form.

When not in use, the streamer is stored on a large motor-driven reel on the stern of the ship. When the streamer is being towed, depth controllers and other devices keep the active part of the cable horizontal at the proper depth. Depth detectors may be included at several places within the streamer to verify that the depth is correct. Water-break detectors are also included at several places along the streamer; these are high-frequency (500 to 5,000 Hz) hydrophones

that detect energy from the source traveling through the water. Knowing the velocity of sound in the water permits converting the water-break traveltimes into the offset distance. Magnetic compasses are also included to give the streamer's orientation. The signals from the sensors in the streamer may be digitized in the streamer and the digital signals relayed to the boat via wires or fiber optics.

When towing a streamer, a seismic ship must avoid stopping, making sharp turns, or even drastic reductions in speed; otherwise the streamer tends to drift, which may allow it to get into dangerous locations such as into the ship's propellers. The depth controllers raise or depress the cable by virtue of water flowing by their vanes and thus they become ineffective when the streamer is not in motion.

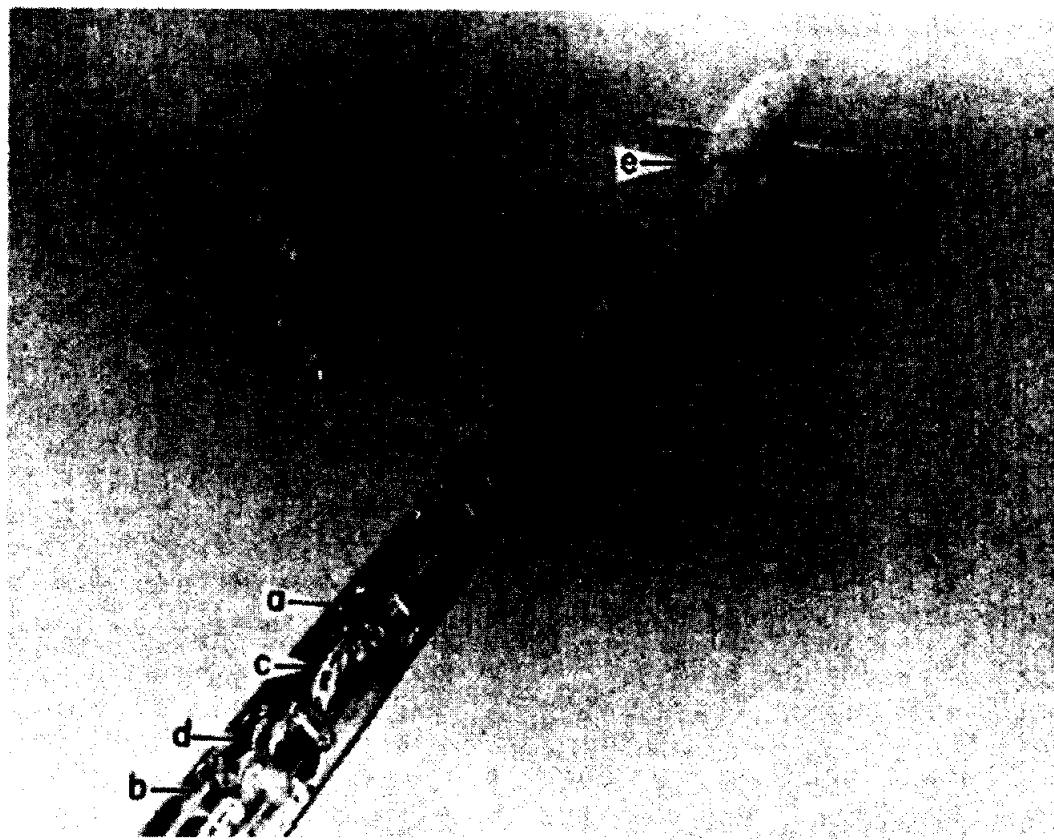


*Figure 4.65. Photo of seismic streamer. Plastic spacers (a) are connected by three tensile cables (b). A bundle of electrical conductors (c) passes through holes in the centers of the spacers. A hydrophone is at (d). A depth controller (e) is clamped over the streamer (Courtesy Seismic Engineering).*

Consequently, if a shot is missed for any reason, it cannot be repeated because the ship will have passed the location. If too many shots are missed, the ship must circle with a diameter larger than the streamer length in order to get the streamer in proper location to make up the missed shots. This is very time consuming and consequently very expensive.

(e) *Marine positioning.* Marine seismic navigation involves two aspects: (a) placing the ships at a desired position and (b) determining the actual location afterward so that the data can be processed and mapped properly. Absolute accuracy is important in tying marine surveys to land surveys and in returning to a certain point later, for example, to locate an offshore well. Relative accuracy is important, primarily to ensure the proper location of one seismic profile relative to the next. Relative accuracies of  $\pm 10$  m are desirable whereas absolute accuracies of  $\pm 50$  m are often sufficient. The actual accuracies obtained in a survey depend upon the system and equipment used, the configuration of shore stations, the position of the mobile station with respect to the shore stations, variations in the propagation of radio waves, instrument malfunctioning, operator error, and so on. Systems capable of giving adequate accu-

racy under good conditions may not realize such accuracy unless considerable care is exercised at all times. Many types of navigation methods are used, including radiolocation, sonic devices, observation of navigation satellites, and so forth. Usually combinations of systems are used so that the advantages of one system compensate for the disadvantages of another. Positioning methods are discussed in Sections B.6 to B.8.

#### 4.5.5. Measurement of Velocity

(a) *Conventional well surveys.* The most accurate methods of determining velocity require the use of a deep borehole. Three types of well surveys are used: "shooting" a well, sonic logging, and vertical profiling (§4.11.4).

*Shooting a well* consists of suspending a geophone or hydrophone in the well by means of a cable and recording the time required for energy to travel from a source near the well down to the geophone (Fig. 4.66). The geophone is specially constructed to withstand immersion under the high temperatures and pressures encountered in deep wells. The cable supports the geophone, serves to measure the depth of the geophone, and brings the geophone output to the

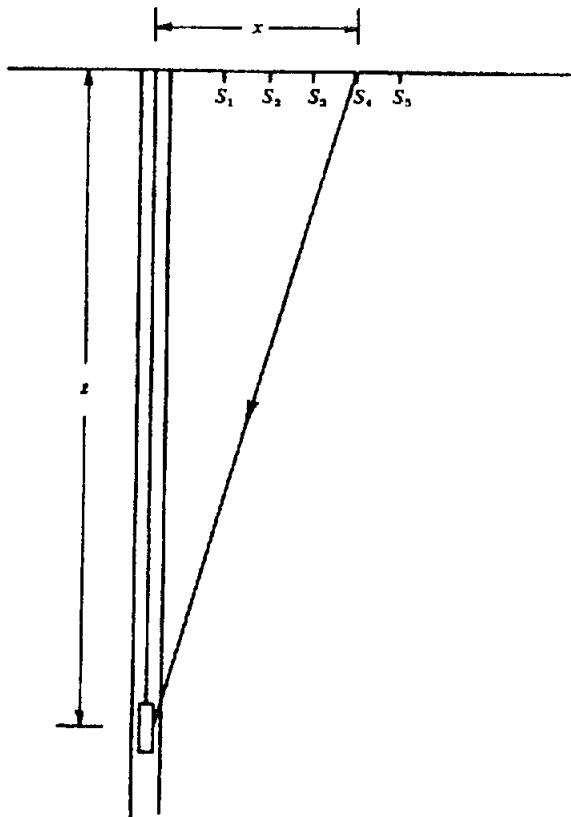


Figure 4.66. Shooting a well for velocity.

surface where it is recorded. The geophone is moved between shots so that the results are a set of traveltimes from the surface down to various depths. The geophone depths are chosen to include the most important geological markers, such as tops of formations and unconformities, and also intermediate locations, so that the interval between successive measurements is small enough to give reasonable accuracy (often 200 m apart).

Results of a well survey are shown in Figure 4.67. The vertical traveltime,  $t$ , to the depth  $z$  is obtained by multiplying the observed time by the factor  $\{z/(z^2 + x^2)^{1/2}\}$  to correct for the slant distance. The average velocity between the surface and the depth  $z$  is then given by  $z/t$ . If we subtract the depths and times for two shots, we find the *interval velocity*  $V_i$ , the average velocity in the interval  $(z_m - z_n)$ , by means of the formula

$$V_i = \frac{z_m - z_n}{t_m - t_n} \quad (4.83)$$

Shooting a well gives the average velocity with good accuracy of measurement. It is, however, expensive because the cost includes not only the one-half to one day's time of the seismic crew but also the cost of standby time for the well (which often exceeds the seismic cost). Potential damage to the well is another factor that discourages shooting wells;

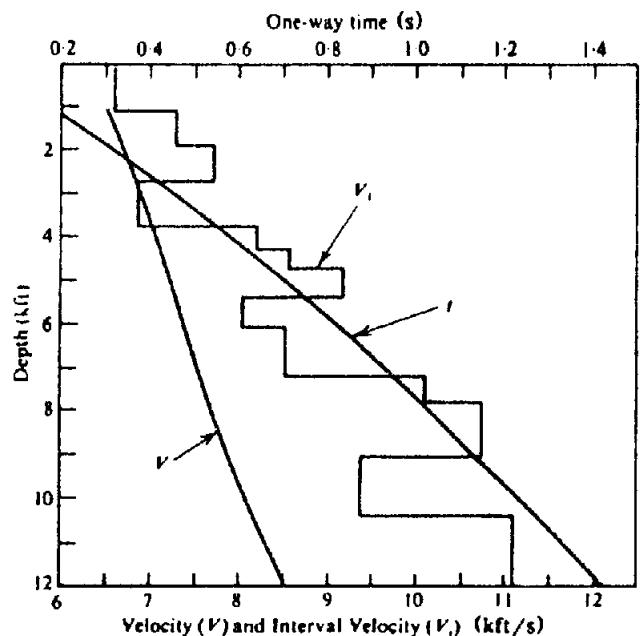


Figure 4.67. Plot of average velocity from datum to depth ( $V$ ) and interval velocity ( $V_i$ ) for a well-velocity survey.

while the survey is being run, the well must stand without drill stem in the hole and hence is vulnerable to cave-in, blow-out, or other damage.

For marine well surveys, air gun energy sources are used (Kennett and Ireson, 1971). The air guns may be merely hung over the side of the drill platform or drill ship and hence only a small crew is required to obtain data at many depths.

(b) *Sonic logging*. *Sonic logging* (§11.7.2), also called *velocity logging*, yields a continuous-velocity survey. The sonic log measures the traveltimes of a  $P$  wave between two sensors 2 ft (60 cm) apart to give the velocity, and the traveltimes are integrated to give a time-depth relation. The sonic log is rarely run all the way to the surface. The traveltimes to the top of the sonic log and to a number of other depths (including total depth) are often determined by direct measurement from the surface to a borehole geophone (as discussed in §4.5.5a). The results of these *check shots* are used to remove the cumulative and other errors involved in integrating the sonic log.

(c)  $X^2-T^2$  method. The traveltime of reflected energy depends not only on the reflector depth and the velocity above the reflector, but also on offset distance, a dependence that permits measuring the velocity. Equation (4.63) can be written

$$t^2 = x^2/V_s^2 + t_0^2 \quad (4.84)$$

If we plot  $t^2$  as a function of  $x^2$ , we get a straight line whose slope is  $1/V_s^2$  and whose intercept is  $t_0^2$ , from which we can determine the reflector depth.

The quantity  $V_s$  is the stacking velocity (§4.5.2a) because it is used for normal-moveout removal in stacking. Velocity analyses (§4.7.7) are based on the normal-moveout concept. Sometimes special long-offset profiles are used to give better accuracy. An  $X^2 \cdot T^2$  survey can give velocities accurate within a few percent where (1) the data are of good quality and have a moderate number of reflections from nearly horizontal, parallel reflectors, (2) accurate near-surface corrections are applied, and (3) the velocity distribution is simple (that is, there is no lateral variation of velocity or complexity of structure).

For horizontal velocity layering,  $V_s \approx V_{rms}$  and the interval velocity can be found between parallel reflectors. Writing  $V_L$  for the velocity to the  $n$ th reflector and  $V_U$  for the velocity to the reflector above it, Equation (4.64) gives

$$\sum_1^n V_i^2 t_i = \sum_1^{n-1} V_i^2 t_i + V_n^2 t_n = V_L^2 \sum_1^n t_i$$

$$\sum_1^{n-1} V_i^2 t_i = V_U^2 \sum_1^{n-1} t_i$$

Subtracting, we get the *Dix formula* for the interval velocity in the  $n$ th bed:

$$V_n^2 = \left( V_L^2 \sum_1^n t_i - V_U^2 \sum_1^{n-1} t_i \right) / t_n \quad (4.85)$$

Note that this equation requires parallel horizontal reflectors. The measurement of velocity is discussed by Hubral and Krey (1980).

## 4.6. REFRACTION FIELD METHODS AND EQUIPMENT

### 4.6.1. Comparison of Refraction and Reflection Methods

Refraction and reflection work are similar in many aspects and reflection field crews sometimes do refraction profiling, though often not with the efficiency of a crew specifically designed for refraction. The differences between reflection and refraction field work mostly result from the long source-to-geophone distances employed in refraction. The energy input to the ground must be larger for refraction shooting, and explosives continue to be the dominant energy source, although other sources are also used. The longer travelpaths result in the higher frequencies being mostly absorbed so that refraction data are generally of low frequency. Consequently refraction geophones have lower natural frequencies than re-

flection geophones, although the response of the latter is often adequate for satisfactory refraction recording. Most digital seismic equipment can be used for refraction. Refraction shooting is usually slower than reflection shooting because the large offset distances involve more moving time and create problems of communications and logistics. However, refraction profiles are often not as closely spaced as reflection lines and hence the cost of mapping an area is not necessarily greater.

### 4.6.2. In-Line Refraction

The basic refraction field method involves shooting reversed refraction profiles, a long linear spread of many geophone groups shot from each end; the distance is great enough that the dominant portion of the travelpath is as a headwave in the refractor or refractors being mapped. Usually it is not practical to simultaneously record many geophone groups spread over such a long distance, and hence refraction profiles are shot in segments. Referring to Figure 4.68a, which shows a single refractor, the spread of geophone groups might be laid out between  $C$  and  $D$  and shots at  $C$  and  $G$  fired to give two records; the spread then might be moved between  $D$  and  $E$  and shots fired at  $C$  and  $G$  as before, and so on, to develop the complete reversed profile  $CDEFG$ . The charge size is often varied for the different segments because larger charges are required when the offset becomes greater. Usually one or two groups will be repeated for successive segments to increase the reliability of the time tie between segments.

The shothole at  $C$  can also be used to record a profile to the left of  $C$  and the shothole at  $G$  to record a profile to the right of  $G$ . Note that the reciprocal time  $t_r$  is the same for the reversed profiles and that the intercept times for profiles shot in different directions from the same shotpoint are equal. These equalities are exceedingly valuable in identifying segments of complex time-distance curves where several refractors are present. In simple situations, the reverse profile can be constructed without having to actually shoot it by using the reciprocal time and intercept time information. However, usually situations of interest are sufficiently complicated that this procedure cannot be carried out reliably.

The *reversed profiles* shot from  $C$  and  $G$  allow the mapping of the refractor from  $L$  to  $M$ . The reversed profile to the left of  $C$  permits mapping as far as  $K$ , but no coverage is obtained for the portion  $KL$ . Hence continuous coverage on the refractor requires an overlap of the reversed profiles; a reversed profile between  $A$  and  $E$  (shown dashed in Fig. 4.68a) would provide coverage between  $U$  and  $V$ , thus

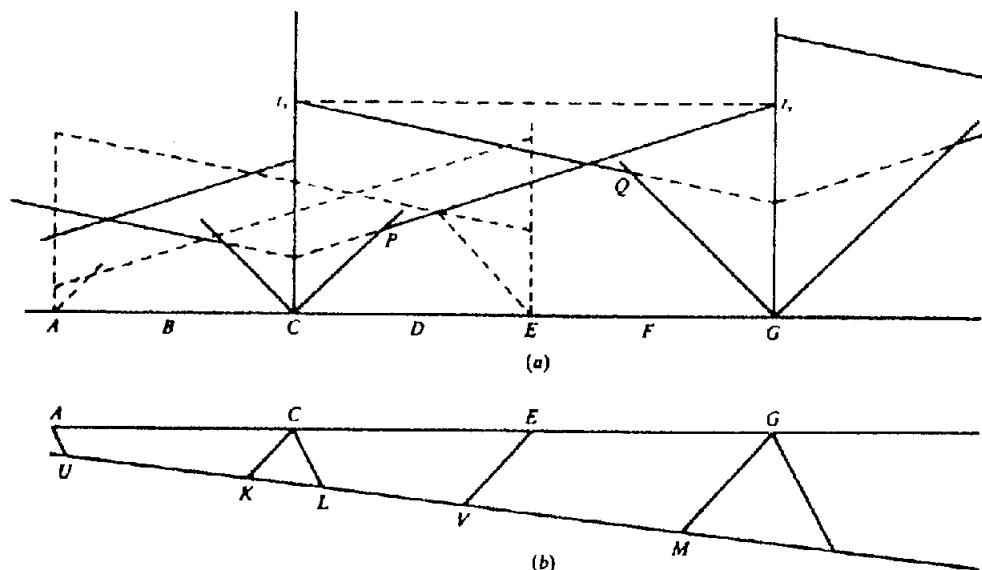


Figure 4.68. Reversed refraction profiles. (a) Time-distance plot for continuous reversed profiling. (b) Section showing raypaths for single refractor.

including the gap *KL* as well as duplicating the coverage *UK* and *LV*. Duplicate coverage does not yield new information but in actual profiling it provides valuable checks that increase the reliability of interpretation.

If we have the two-refractor situation in Figure 4.69, first break coverage on the shallow refractor is obtained from *L* to *K* and from *M* to *N* when the shots are at *C* and *G*. The corresponding coverage on the deeper refractor is from *Q* to *S* and from *R* to *P*.

If we are able to resolve the refraction events that arrive later than the first breaks, called *second arrivals* or *secondary refractions*, we can increase the coverage obtained with a single profile. However, it is difficult with analog equipment to adjust the gain to optimize both first breaks and second arrivals at the same time. If the gain is too low, the first breaks may be weak and ambiguities in timing may result, whereas if the gain is too high, the secondary refractions may be unpickable. Because of this difficulty, prior to magnetic-tape recording, refraction mapping was generally based on first breaks only. With magnetic-tape recording, each event can be displayed under optimum conditions.

The portions of the time-distance curves that do not add information necessary to map the refractor of interest often are not shot where they can be predicted reasonably accurately. Thus, the portions *CP* and *GQ* of the reversed profile in Figure 4.68a can be omitted.

Where a single refractor is being followed, a series of short refraction profiles is often shot rather than a long profile. In Figure 4.70 geophones from *C* to *E* are used with shotpoint *C*, from *E* to *F* with

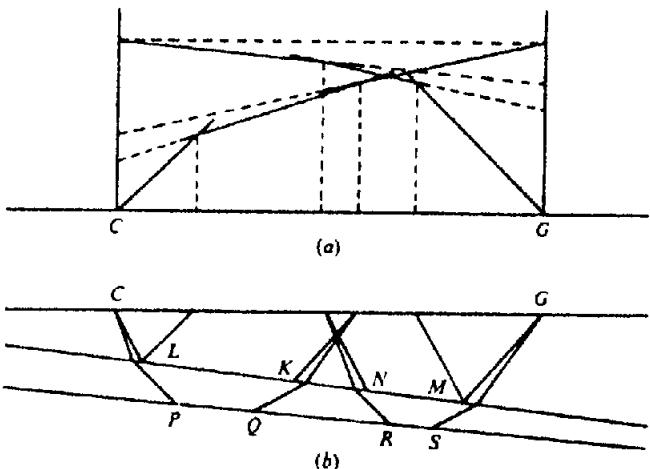


Figure 4.69. Reversed refraction profiles for two-refractor case. (a) Time-distance plot. (b) Section showing raypaths for two refractors.

shotpoint *D*, *F* to *G* with shotpoint *E*, etc. The portions of the time-distance curves attributable to the refractor being mapped are then translated parallel to themselves until they connect to make a composite time-distance curve such as that shown by the dashed line. The composite curve may differ from the curve that would actually have been obtained for a long profile from shotpoint *C* because of refraction events from other horizons.

#### 4.6.3. Broadside Refraction and Fan Shooting

In *broadside refraction* shooting, shotpoints and spreads are located along two parallel lines (Fig. 4.71) selected so that the desired refraction event can be mapped with a minimum of interference from other events. Where the refraction event can be

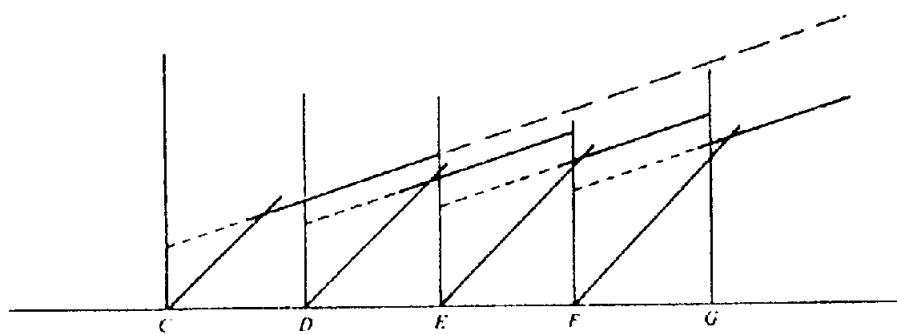


Figure 4.70. Unreversed refraction profiles for a single refractor, showing projections back to the intercept time (short dashes) and compositing for shot C by upward translation of segments of the curves.

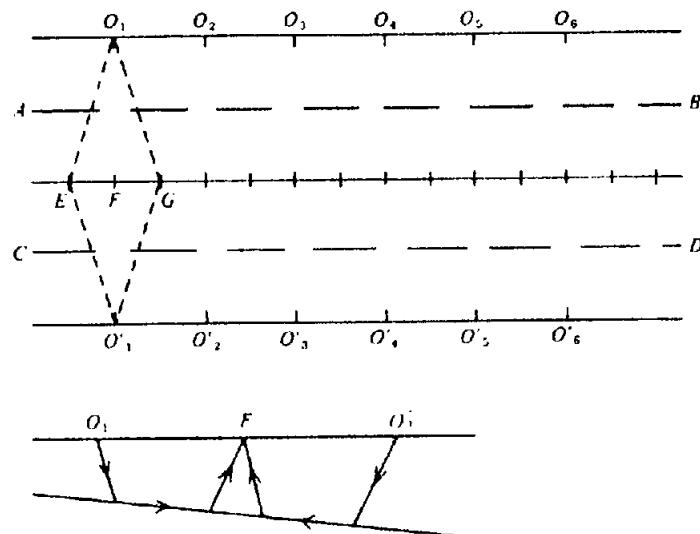


Figure 4.71. Broadside refraction profiling.

clearly distinguished from other arrivals, it provides a very economical method of profiling because all the data yield information about the refractor. However, usually the criteria for identifying the refraction event are based on in-line measurements (such as the apparent velocity or the relationship to other events), and these criteria are not available on broadside records where the offset distance is essentially constant. Thus if the refractor should unexpectedly change its depth or if another refraction arrival should appear, one might end up mapping the wrong horizon. Consequently, broadside refraction shooting is often combined with occasional in-line profiles to check the identity of the horizon being mapped.

The first extensive use of refraction was in searching for salt domes by the fan-shooting technique. A salt dome inserts a high-velocity mass into an otherwise low-velocity section so that horizontally traveling energy arrives earlier than if the salt dome were not present; the difference in traveltimes between that actually observed and that expected with no salt dome present is called a *lead*. In *fan shooting* (Fig. 4.72), geophones are located in different directions from the shotpoint at roughly the same offset dis-

tances. The desire to maintain constant offset distance usually is sacrificed in favor of locations that are more readily accessible. The leads shown by overlapping fans then roughly locate the high-velocity mass. This method is not used for precise shape definition.

#### 4.6.4. Engineering Surveys on Land

The shallow refractions used in engineering applications, such as in determining the depth to bedrock, do not require large energy sources or complex instrumentation. Energy sources are usually very simple, for example, a hammer striking a steel plate on the ground. The instant of impact is determined by an inertial switch on the hammer. Sometimes the energy is obtained by a hand-operated tamper, by a weight dropped on the ground (§4.5.3c), or by a small explosion. Such sources are also used for reflection engineering surveys (Meidav, 1969).

The energy is usually detected by moving-coil geophones similar to those already described. Often only a few channels are used, perhaps six, because otherwise the spread layout becomes complicated.

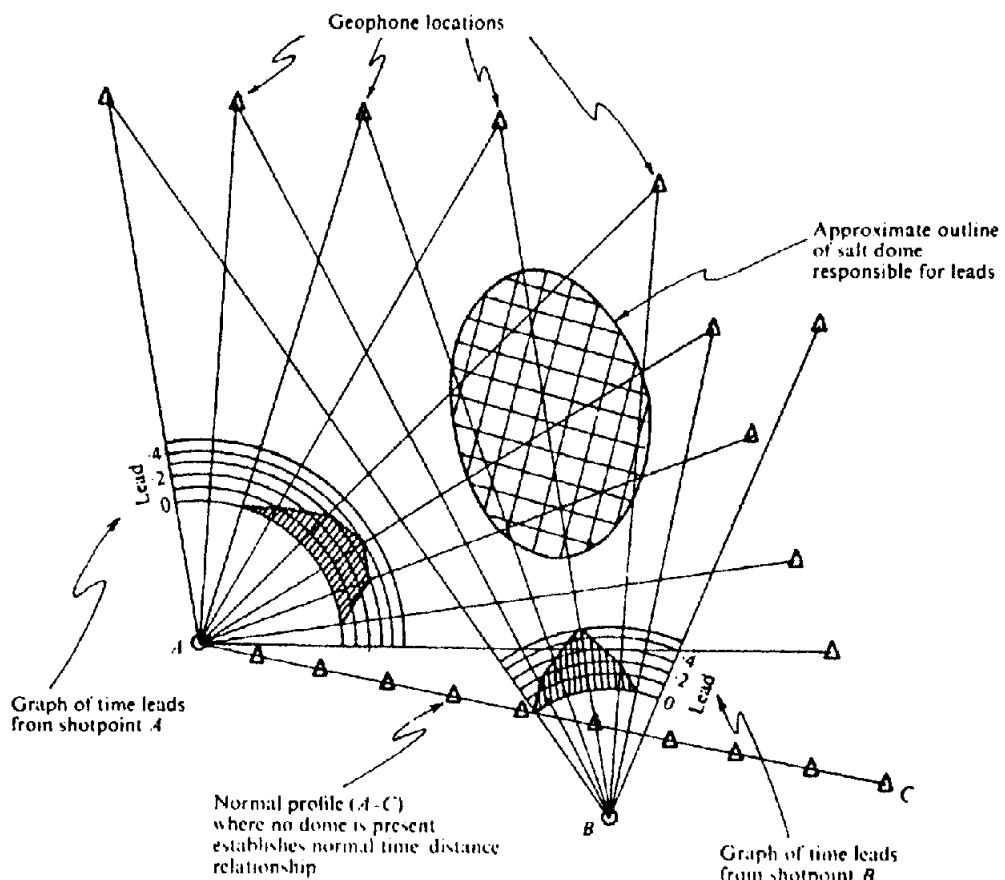


Figure 4.72. Fan shooting. (After Nettleton, 1940.)

The amplifiers and the camera generally weigh only a few pounds and often are contained in a small metal suitcase. In some systems, the recorded data are displayed on a small oscilloscope tube and photographed with a Polaroid camera so that a permanent record is obtained. In other systems, time counters are started at the instant the energy is delivered to the ground and stopped when the first-break energy arrives at the geophones, thus giving direct readings of traveltimes.

#### 4.6.5. Marine Refraction Work

Because refraction recording requires that there be appreciable distance between the source and the recording locations, two ships have usually been required for marine refraction recording. To shoot a reversed refraction profile in one traverse requires three ships - a shooting ship at each end and a recording ship that travels between them. For the shooting ships to travel the considerable distances between shotpoints takes appreciable time because of the relatively low maximum speed of ships, and hence the high production rates that make marine reflection work economical are not realized in marine refraction.

The *sonobuoy* (Fig. 4.73) permits recording a refraction profile with only one ship. The sonobuoy is

an expendable listening station that radios the information it receives back to the shooting ship. The sonobuoy is merely thrown overboard. The salt water activates batteries in the sonobuoy as well as other devices that cause a radio antenna to be extended upward and one or two hydrophones to be suspended beneath the buoy. As the ship travels away from the buoy, shots are fired and the signals received by the hydrophones are radioed back to the ship where they are recorded. The arrival time of the wave that travels directly through the water from the shot to the hydrophone is used to give the offset distance. After a given length of time the buoy sinks itself and is not recovered. Sonobuoys make it practical to record unreversed refraction profiles while carrying out reflection profiling. The only additional equipment cost is that of the sonobuoys.

#### 4.6.6. Refraction Data Reduction

Refraction data have to be corrected for elevation and weathering variations, as with reflection data. The correction methods (§4.7.1) are essentially the same except that often geophones are too far from the shotpoint to record the refraction at the base of the LVL and thus there may be no weathering data along much of the line. Additional shots may be taken for weathering information.

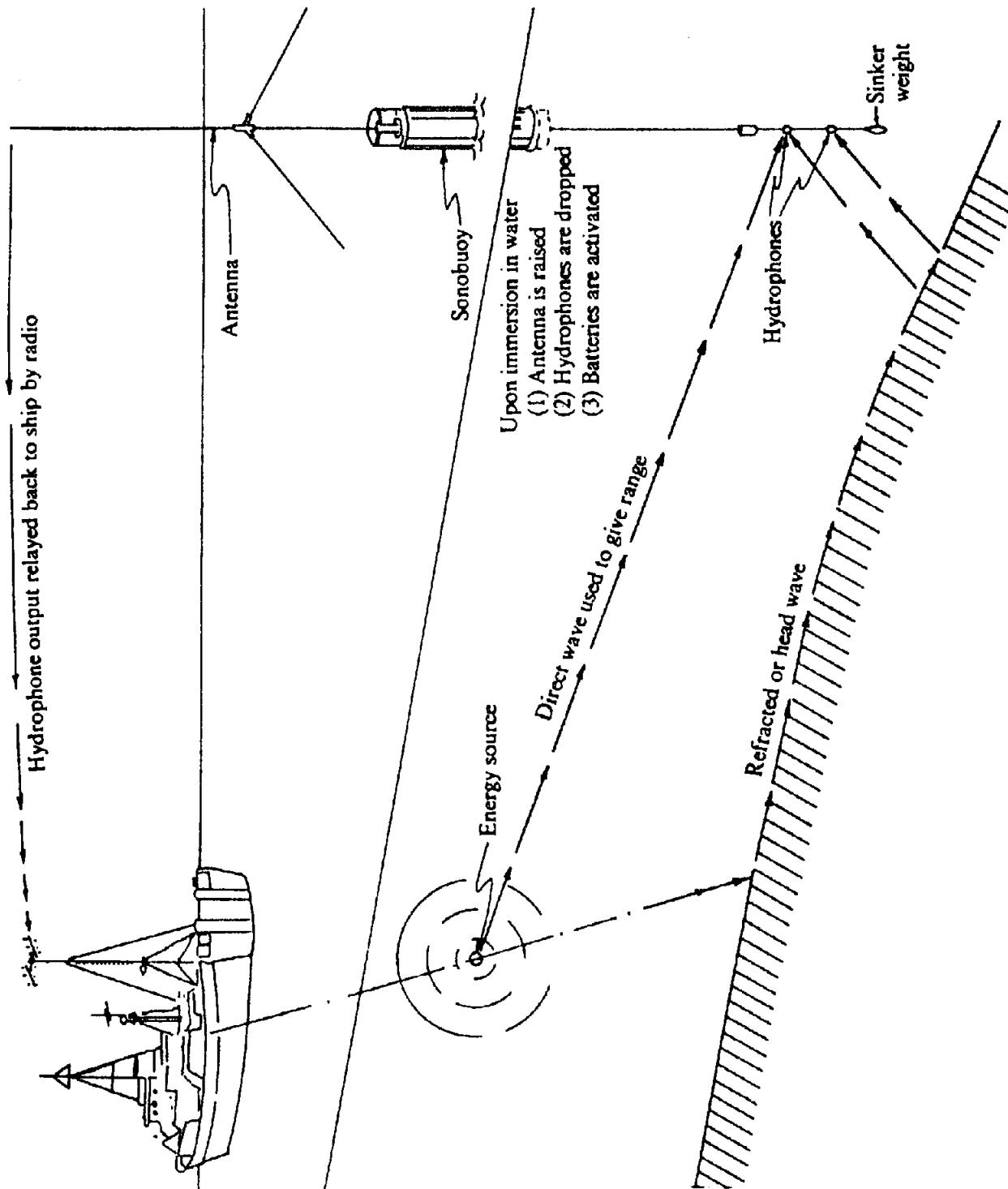


Figure 4.73. Sonobuoy operation.

Where complete refraction profiles from zero offset to large offsets are available, playback of the data with judicious selections of filters and AGC may allow one to correlate reflection events with refraction events, thus adding useful information to each type of interpretation. Often the most prominent reflections will not correspond to the most prominent refractions.

Another useful technique is to display the data as a *reduced refraction section* where arrival times have been shifted by the amount  $x/V_R$ , where  $V_R$  is near the refractor velocity. If  $V_R$  were exactly equal to the refractor velocity, the residual times would be the delay times (which will be discussed in §4.9.3), and relief on the reduced refraction section would correlate with refractor relief (although displaced from the subsurface location of the relief). However, even if  $V_R$  is only approximately correct, the use of reduced sections considerably improves the pickability of refraction events, especially secondary refractions.

## 4.7. DATA PROCESSING

### 4.7.1. Data Reduction

Variations in the elevation of the surface affect traveltimes and it is necessary to correct for such variations as well as for changes in the near-surface low-velocity-layer (LVL). Usually a *reference datum* is selected and corrections are calculated so that, in effect, the shotpoints and geophones are located on the datum surface, and it is assumed that conditions are uniform and that there is no LVL material below the datum level. The reference datum is usually horizontal, but where elevation variations are large, a *tilted datum* or a *floating datum* (one having the generalized relief of the surface but with smaller magnitude) may be used.

Many methods exist for correcting for near-surface effects. These schemes are usually based on (1) uphole times, (2) refractions from the base of the LVL, or (3) the smoothing of reflections. We shall describe several of these methods that are simple to apply and adequate to cover most situations. Automatic statics-correction schemes, which usually involve statistical methods of smoothing reflections, will be discussed in Section 4.7.5d. We shall assume that  $V_w$  and  $V_H$ , the velocities in the LVL and in the layer just below it, are known; they can be found from an uphole survey or the refraction first breaks, as will be discussed later in the section. In what follows we assume that the shot is placed below the base of the LVL; if this is not true, modifications have to be made in the equations in this section (see problem 10).

Figure 4.74 illustrates a method of obtaining the correction for  $t_0$ , the shotpoint arrival time.  $E_d$  is the elevation of the datum,  $E_s$  the elevation of the surface at the shotpoint,  $D_s$  the depth of the shot below the surface, and  $t_{uh}$  is the uphole time (§4.5.2e). The deviation of reflection paths from the vertical is usually small enough that we can regard the paths as vertical. Therefore, the time required for the wave to travel from the source down to the datum is  $\Delta t_s$ , where

$$\Delta t_s = \frac{(E_s - D_s - E_d)}{V_H} \quad (4.86)$$

Similarly, the time for the wave to travel up from the datum to a geophone on the surface at  $B$  is  $\Delta t_g$  where

$$\Delta t_g = \Delta t_s + t_{uh} \quad (4.87)$$

The correction  $\Delta t_0$  for the traveltime for a geophone at the sourcepoint is then

$$\begin{aligned} \Delta t_0 &= \Delta t_s + \Delta t_g = 2\Delta t_s + t_{uh} \\ &= \frac{2(E_s - D_s - E_d)}{V_H} + t_{uh} \end{aligned} \quad (4.88)$$

Subtraction of  $\Delta t_0$  from the arrival time  $t_0$  is equivalent to placing the shot and the shotpoint geophone group on the datum plane, thereby eliminating the effect of the low-velocity layer if the shot is beneath the LVL. At times the shot may be so far below the datum plane that  $\Delta t_s$  will be negative.

When Equation (4.56) is used to calculate dip, the dip moveout must be corrected for elevation and weathering. The correction to the dip moveout,  $\Delta t_c$ , often called the *differential weathering correction*, is the difference in traveltimes at opposite ends of a split-dip spread for a reflection from a horizontal bed. Referring to Figure 4.74, the raypaths from the shot  $B$  down to a horizontal bed and back to geophones at  $A$  and  $C$  have identical traveltimes except for the portions  $A'A$  and  $C'C$  from the datum to the surface. Assuming as before that  $A'A$  and  $C'C$  are vertical, we get for  $\Delta t_c$  the expression

$$\begin{aligned} \Delta t_c &= (\Delta t_g)_C - (\Delta t_g)_A \\ &= (\Delta t_s + t_{uh})_C - (\Delta t_s + t_{uh})_A \end{aligned} \quad (4.89)$$

If we take the positive direction of dip to be down from  $A$  toward  $C$ , then  $(\Delta t_c/\Delta x)$  must be subtracted algebraically from the observed moveout to obtain the true dip moveout.

The following calculation illustrates the effect of the correction. We take as datum a horizontal plane

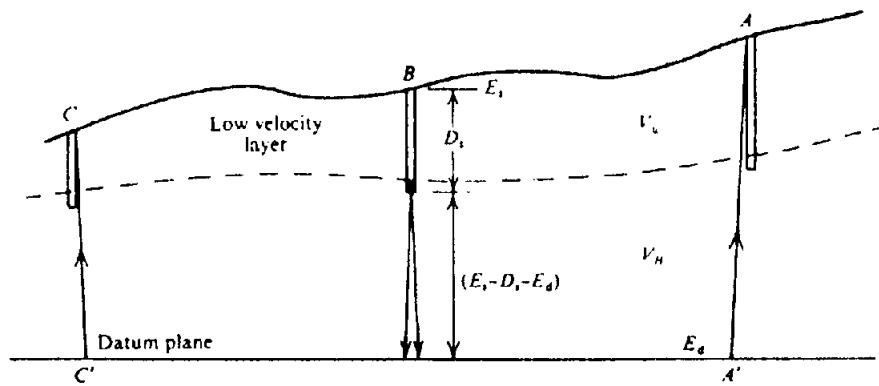


Figure 4.74. Calculation of weathering corrections.

Table 4.3. Calculation of differential weathering correction.

	Shotpoint C	Shotpoint B	Shotpoint A	
Measured	$E_c$ (m) $D_s$ (m) $t_{uh}$ (ms)	248 15 48	244 13 44	257 20 53
Calculated	$\Delta t_s$ (ms) $\Delta t_g$ (ms) $\Delta t_0$ (ms) $\Delta t_c$ (ms)	16 64 80 -7	15 59 74	18 71 89

200 m above sea level;  $V_H$  is 2,075 m/s. Table 4.3 gives data for three successive shotpoints, A, B, and C, at intervals of 500 m (such as those in Fig. 4.74).

Let us suppose that a reflection on a split profile from shotpoint B gives the following data:  $t_0 = 2.421$  s,  $t_A = 2.419$  s, and  $t_C = 2.431$  s. Then the corrected value of  $t_0$  is  $2.421 - 0.074 = 2.347$  s and the corrected dip moveout is

$$\Delta t_d/\Delta x = \{2.431 - 2.419 - (-0.007)\}/0.5$$

$$= 38 \text{ ms/km}$$

If  $(t_C - t_A)$  had been negative, for example -10 ms, then the dip moveout would be  $(-10 - (-7))/0.5 = -6 \text{ ms/km}$ , so that the correction can change the direction of dip as well as its magnitude. Therefore accurate corrections are essential.

Corrections are often required for geophones in between shotpoints, hence uphole times are not available and the first breaks are frequently used in this case. In Figure 4.75 G is a geophone intermediate between adjacent shotpoints A and B. Let  $t_{AG}$  and  $t_{BG}$  be the first-break times for the paths A'C'G and B'C''G. Almost always GC' and GC'' are within 20° of the vertical and C'C'' is therefore small. Thus,

we can write the approximate relation

$$t_{AG} + t_{BG} \approx \frac{A'B'}{V_H} + 2t_w = \frac{AB}{V_H} + 2t_w$$

where  $t_w$  is the traveltime through the weathered layer at G. Thus,

$$t_w \approx \{t_{AG} + t_{BG} - (AB/V_H)\}/2 \quad (4.90)$$

Subtracting  $t_w$  from the arrival times in effect places the geophone at the base of the LVL. To correct to datum we must subtract the additional amount  $(E_g - E_d - D_w)/V_H$ , where  $E_g$  is the elevation of the geophone group and  $D_w$  is found by multiplying  $t_w$  by  $V_w$ .

Occasionally special refraction profiles are shot to obtain data for making corrections for intermediate geophones. These profiles may be of the standard type using small charges placed near the surface or a nondynamite source on the surface; they are interpreted using standard methods such as Wyrobek's (§4.9.3c) to find the depth and traveltime to the base of the LVL. Alternatively, a shot may be placed just below the LVL as in Figure 4.75, in which event we must modify Equation (4.69) because the shot is at the base rather than the top of the upper layer. Thus,

$$t = \frac{x - D_w \tan \theta_c}{V_H} + \frac{D_w}{V_w \cos \theta_c} = \frac{x}{V_H} + \frac{D_w \cos \theta_c}{V_w} \quad (4.91)$$

Most near-surface correction methods require a knowledge of  $V_H$  and sometimes of  $V_w$  as well. The former can be determined by: (1) an uphole survey as described in Section 4.5.2e, (2) a special refraction survey as described above, or (3) analysis of the first breaks for distant geophone groups (because these are equivalent to a refraction profile such as that shown in Fig. 4.76). The weathering velocity  $V_w$  can be found by (1) measuring the slope of a plot of the first breaks for geophones near the shotpoint (correcting distances for obliquity), (2) dividing  $D_w$  by

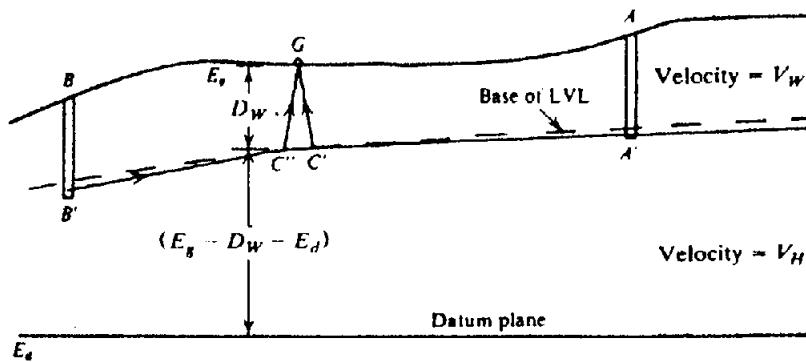


Figure 4.75. Datum correction for geophone between shotpoints.

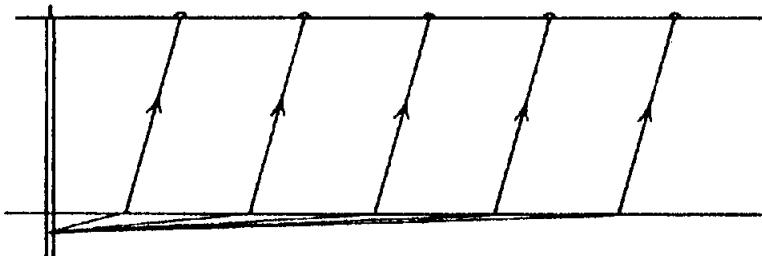


Figure 4.76. Refraction weathering profile.

$t_{ab}$  for a shot placed near the base of the LVL, (3) an uphole survey, or (4) firing a cap at the surface and measuring the velocity of the direct wave. Of these, (3) is clearly superior.

#### 4.7.2. Introduction to Digital Processing: Fourier Transforms

Most seismic processing is done in digital form (Robinson and Treitel, 1973; Schultz, 1985) and in the following we treat seismic data as time series (whereas Appendix A treats much of the same material as continuous functions). Data processing is based on the application of information theory and we present here a simplified version of its concepts; a more complete account is given in Sheriff and Geldart (1983, Chap. 10).

Usually we think of seismic data as the variation with time (measured from the source instant) of the amplitudes of various geophone outputs. When we take this viewpoint, we are thinking in the *time domain*, that is, time is the independent variable. We also sometimes find it convenient to regard a seismic wave as a superposition of many sinusoidal waves differing in frequency, amplitude, and phase. Then the relative amplitudes and phases are functions of frequency and we are thinking in the *frequency domain*. The frequency domain approach is illustrated by electrical systems that are specified by their effects on the amplitude and phases of sinusoidal signals of different frequencies. For example, graphs of filter characteristics usually show amplitude ratios

or phase shifts as ordinates with frequency along the abscissa.

A *Fourier transform* (§A.9.2) in our context involves transforming functions from the time domain to the frequency domain and an *inverse Fourier transform* transforming from the frequency domain to the time domain. The important point with transforms is that no information is lost in transforming. We can, thus, start with a waveform in the time domain, transform it into the frequency domain, and then transform the frequency-domain representation into a waveform that is identical with the original waveform. This makes it possible to do part of our processing in the time domain and part in the frequency domain, taking advantage of the fact that some processes can be executed more economically in one domain than in the other. We also gain additional understanding from having the viewpoints of both domains.

If we have a reasonably "well-behaved" function  $g_i$  and its transform  $G_i$ , then [compare with Eq. (A.53)]

$$g_i = \sum_j G_j e^{j2\pi f_j t} \quad (4.92)$$

$$G_i = \sum_j g_j e^{-j2\pi f_j t} \quad (4.93)$$

Equation (4.93) gives the Fourier transform of  $g_i$ , whereas Equation (4.92) gives the inverse transform  $g_i$ . [Eqs. (4.92) and (4.93) are often written in other equivalent forms.] We refer to  $g_i$  and  $G_i$  as a *trans-*

form pair and the relation is expressed in the form

$$g_t \leftrightarrow G_s$$

For actual waveforms,  $g_t$  is real and usually causal (§A.9.3). In general,  $G_s$  is complex [Eq. (A.56)], so

$$G_s = A_s e^{j\phi_s} \quad (4.94)$$

where  $A_s$  is real and positive and is called the *amplitude spectrum*;  $\phi_s$  is also real and is called the *phase spectrum*. Substitution in Equation (4.92) gives

$$g_t = \sum_s A_s e^{j(2\pi s t + \phi_s)} \quad (4.95)$$

When  $g_t$  is real (the usual case), it equals the real part of Equation (4.95):

$$g_t = \sum_s A_s \cos(2\pi s t + \phi_s) \quad (4.96)$$

#### 4.7.3. Convolution

(a) *The convolution operation.* Let us now consider the time-domain operation called *convolution* (§A.10). Assume that we feed into a system data sampled at regular intervals, for example, a digital seismic trace. The output of the system can be calculated if we know the *impulse response* (§A.13) of the system, that is, the response of the system when the input is a *unit impulse*  $\delta_t$  (§A.9.3). The impulse response of the system will be zero prior to  $t = 0$  and then will have the values  $f_0, f_1, f_2, \dots$  at successive sampling intervals. We represent this process diagrammatically thus:

$$\delta_t \rightarrow \boxed{\text{system}} \rightarrow f_t = [f_0, f_1, f_2, \dots]$$

Most systems with which we deal are linear (§A.13) and time-invariant (or very nearly so). A *linear system* is one in which the output is directly proportional to the input whereas a *time-invariant system* is one in which the output is independent of the time when the input occurred. Writing  $\delta_{t-n}$  for a unit impulse that occurs at  $t = n\Delta$ , where  $\Delta$  is the sampling interval, we can illustrate linear and time-invariant systems as follows:

Linear:

$$k \delta_t \rightarrow \boxed{\text{system}} \rightarrow k f_t = [kf_0, kf_1, kf_2, \dots]$$

Time invariant:

$$\begin{aligned} \delta_{t-n} &\rightarrow \boxed{\text{system}} \rightarrow f_{t-n} \\ &= \left[ \underbrace{0, 0, 0, \dots, 0}_{n \text{ zeros}}, f_0, f_1, f_2, \dots \right] \end{aligned}$$

In the last bracket on the right, the first output different from zero is  $f_0$  and occurs at the instant  $t = n\Delta$ .

Obviously any input that consists of a series of sampled values can be represented by a series of unit impulses multiplied by appropriate amplitude factors. We can then use the above two properties to find the output for each input impulse and by superimposing these we get the output for the arbitrary input. This process is called *convolution*.

We shall illustrate convolution by considering the output for a filter whose impulse response  $f_t$  is  $[f_0, f_1, f_2] = [1, -1, \frac{1}{2}]$ . When the input  $x_t$  is  $[x_0, x_1, x_2] = [1, \frac{1}{2}, -\frac{1}{2}]$ , we apply to the input the series of impulses  $[\delta_t, \frac{1}{2}\delta_{t-1}, -\frac{1}{2}\delta_{t-2}]$  (the last two subscripts mean that the impulses are delayed by one and two sampling intervals, respectively) and obtain the output

$$\begin{aligned} \delta_t &\rightarrow [1, -1, \frac{1}{2}] \\ \frac{1}{2}\delta_{t-1} &\rightarrow [0, \frac{1}{2}, -\frac{1}{2}, \frac{1}{4}] \\ -\frac{1}{2}\delta_{t-2} &\rightarrow [0, 0, -\frac{1}{2}, \frac{1}{2}, -\frac{1}{4}] \end{aligned}$$

By summing we find the output

$$[\delta_t + \frac{1}{2}\delta_{t-1} - \frac{1}{2}\delta_{t-2}] \rightarrow [1, -\frac{1}{2}, -\frac{1}{2}, \frac{3}{4}, -\frac{1}{4}]$$

Convolution is illustrated in Figure 4.77. This operation is equivalent to replacing each element of the input by an appropriately scaled version of the impulse response and then summing elements that occur at the same times. If we call the output  $z_t$  and denote the operation of taking the convolution by an asterisk, we can express this as

$$z_t = x_t * f_t = \sum_k x_{t-k} f_k \quad (4.97a)$$

$$= [x_0 f_0, x_1 f_0 + x_0 f_1, x_2 f_0 + x_1 f_1 + x_0 f_2, \dots] \quad (4.97b)$$

Note that we would have obtained the same result if we had input  $f_t$  into a filter whose impulse response is  $x_t$ ; in other words, convolution is commutative:

$$x_t * f_t = f_t * x_t = \sum_k x_{t-k} f_k = \sum_k f_{t-k} x_k \quad (4.98)$$

The convolution theorem states that the Fourier transform of the convolution of two functions is

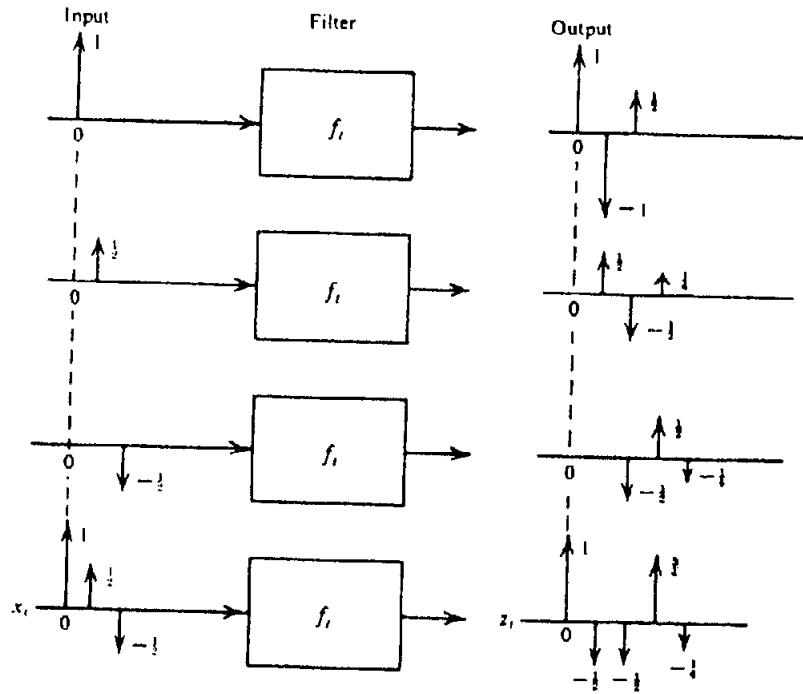


Figure 4.77. Filtering as an example of convolution.

equal to the product of the transforms of the individual functions. We can state the theorem as

$$\begin{aligned} x_t &\leftrightarrow X(\nu) = |X(\nu)| e^{j\phi_x(\nu)} \\ f_t &\leftrightarrow F(\nu) = |F(\nu)| e^{j\phi_f(\nu)} \\ x_t * f_t &\leftrightarrow X(\nu) F(\nu) \\ &= [|X(\nu)| e^{j\phi_x(\nu)}] [|F(\nu)| e^{j\phi_f(\nu)}] \\ &\leftrightarrow |X(\nu)| |F(\nu)| e^{j[\phi_x(\nu) + \phi_f(\nu)]} \end{aligned} \quad (4.99)$$

where  $|X(\nu)|$  and  $|F(\nu)|$  are the amplitude spectra, and  $\phi_x(\nu)$  and  $\phi_f(\nu)$  are the phase spectra. This means that if two sets of data are convolved in the time domain, the effect in the frequency domain is to multiply their amplitude spectra and to add their phase spectra. Because of symmetry properties of the Fourier transform [Eq. (A.60)], it can be shown that

$$x_t f_t \leftrightarrow X(\nu) * F(\nu) \quad (4.100)$$

(b) *Sampling and aliasing.* In the analog-to-digital conversion, we replace the continuous signal with a series of values at fixed intervals. It would appear that we are losing information by discarding the data between the sampling instants. The transform relationship in Equations (4.92) and (4.93) can be used to understand sampling and the situations in which information is not lost.

We make use of the *comb* or *sampling function*, which consists of an infinite set of regularly spaced unit impulses (§A.9.3 and Fig. 4.78b). The transform

of a comb is also a comb:

$$\text{comb}(t) \leftrightarrow k_1 \text{comb}(\nu) \quad (4.101)$$

where  $k_1$  depends upon the sampling interval (see problem 12b). If the comb in the time domain has elements every 4 ms, that is, the sampling frequency is  $1/0.004 = 250$  Hz, the transform is a comb with spacing 250 Hz. We shall also make use of the boxcar (Fig. 4.78d), a function that has a constant value over the range  $\pm\nu_0$  and is zero everywhere else. The transform of a boxcar is a *sinc function*:

$$\text{boxcar}(\nu) \leftrightarrow k_2 \text{sinc}(2\pi\nu_0 t) = k_2 \frac{\sin 2\pi\nu_0 t}{2\pi\nu_0 t} \quad (4.102)$$

where  $k_2$  is the area of the boxcar (see problem 12c).

Figure 4.78a shows a continuous, real, causal function  $y(t)$  and its amplitude spectrum  $|Y(\nu)|$ ; the latter is symmetric about zero, so negative frequencies give the same values as positive frequencies.

The sampled data that represent  $y(t)$  can be found by multiplying the continuous function by the comb (hence the name "sampling function"). If we are sampling every 4 ms we use a comb with elements every 4 ms. According to Equation (4.100),

$$\text{comb}(t) y(t) \leftrightarrow k_1 \text{comb}(\nu) * Y(\nu).$$

Convolution is equivalent to replacing each data element [each impulse in  $\text{comb}(\nu)$  in this instance] with the other function  $Y(\nu)$  (properly scaled). This is illustrated in Figure 4.78c. Note that the frequency

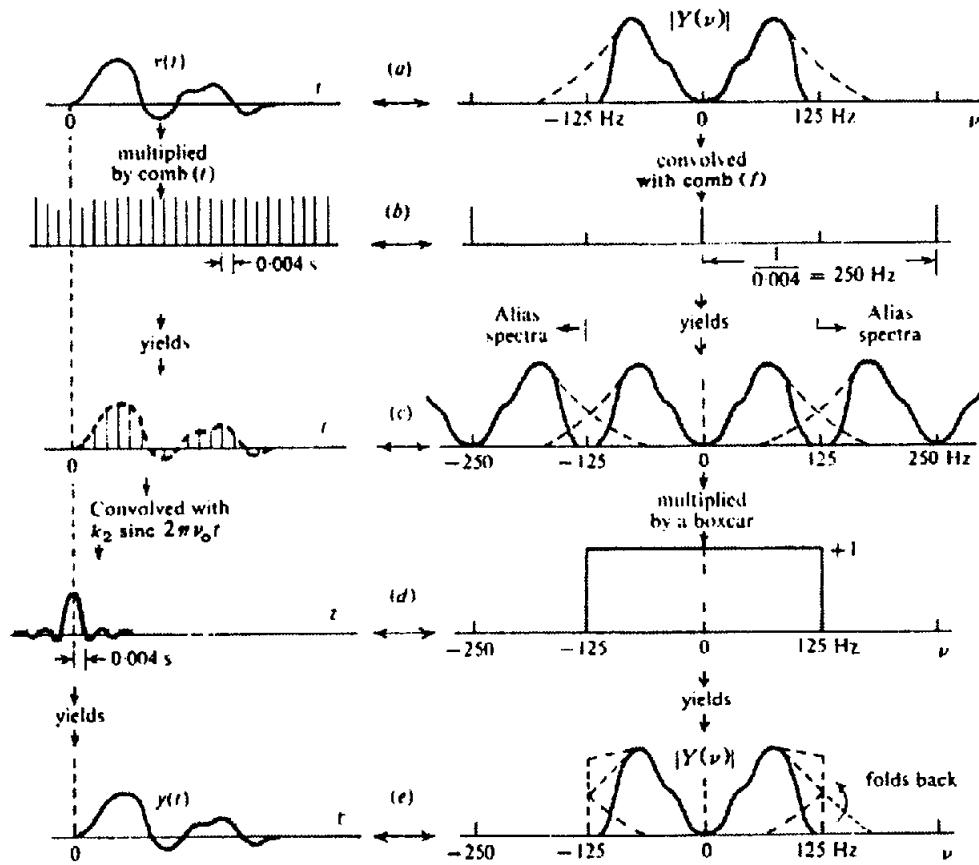


Figure 4.78. Sampling and reconstituting.

spectrum of the sampled function differs from the spectrum of the continuous function by the repetition of the spectrum every 250 Hz.

We can recover the spectrum of the original function by multiplying the spectrum of the sampled function by a boxcar. The equivalent time-domain operation [Eq. (4.99)] is to convolve the sample data with the sinc function. As shown in Figure 4.78e, this restores the original function in every detail. The sinc function thus provides the precise "operator" for interpolating between sample values.

In the above instance no information whatsoever was lost in the process of sampling and interpolating. However, if the continuous function had had a spectrum (shown dotted in Fig. 4.78a) that included frequency components higher than 125 Hz (in this example), then the time-domain multiplication by the sampling function would have produced an overlap of frequency spectra (dotted curves in Fig. 4.78c) and no longer would we be able to recover the original spectrum from the spectrum of the sampled data; hence we would not be able to recover the original waveform. Whether or not the original waveform is recoverable depends, therefore, on whether or not the original waveform contains frequencies higher than half of the sampling frequency.

The relationships demonstrated in the foregoing text are summarized by the *sampling theorem*: No

information is lost by regular sampling provided that the sampling frequency is greater than twice the highest frequency component in the waveform being sampled. This is equivalent to saying that there must be more than two samples per cycle for the highest frequency. The sampling theorem thus determines the minimum sampling we can use. Because this minimum sampling allows complete recovery of the waveform, we can further conclude that nothing is gained by using a finer sampling. Thus, sampling rates of 2 and 4 ms permit us to record data faithfully provided none of the signal spectrum lies above 250 and 125 Hz, respectively.

Half the sampling frequency is called the *Nyquist frequency*. Any frequency present in the signal that is greater than the Nyquist frequency  $v_n$  by the amount  $\Delta v$  will be indistinguishable from the lower frequency  $v_n - \Delta v$ . In Figure 4.79 we see that a sampling rate of 4 ms (that is, 250 samples/s) will allow perfect recording of a 75 Hz signal but 175 and 250 Hz signals will appear as (that is, will alias as) 75 and 0 Hz (which is the same as a direct current), respectively. Alias signals that fall within the frequency band in which we are primarily interested will appear to be legitimate signals. To avoid this, *aliasing filters* are used before sampling to remove frequency components higher than the Nyquist frequency. With filters having 72 dB/octave slope, we

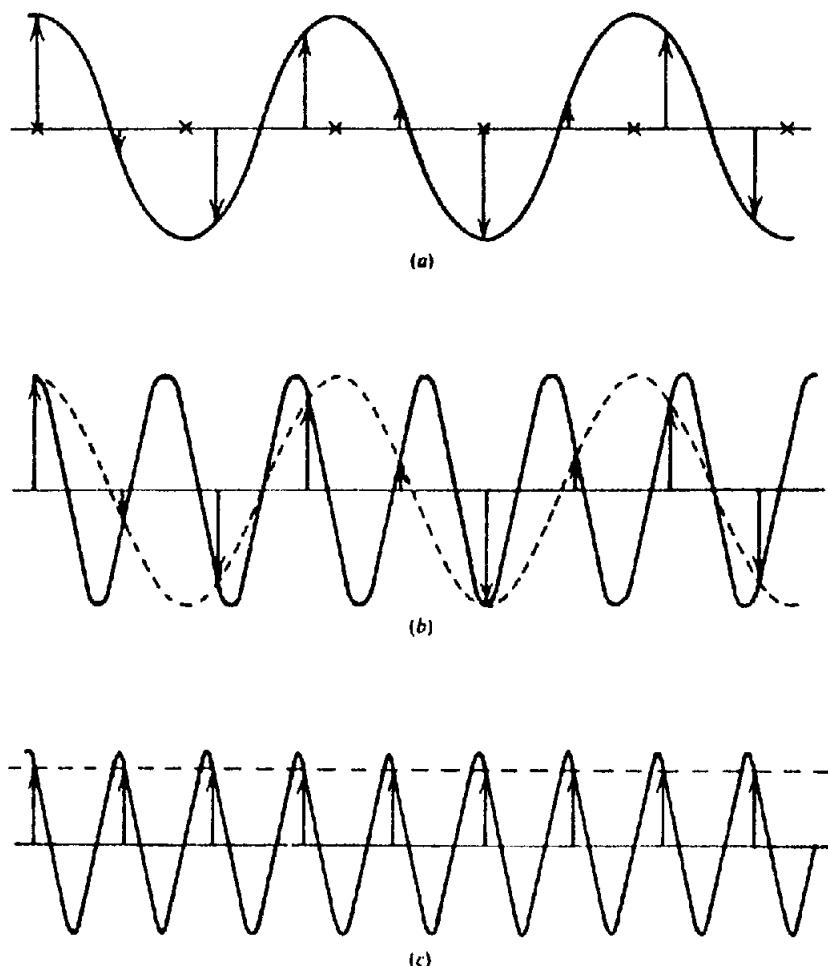


**Figure 4.79. Sampling and aliasing.** Different frequencies sampled at 4 ms intervals (250 times per second). (a) 75 Hz signal. (b) The 175 Hz signal yields the same sample values as 75 Hz. (c) The 250 Hz signal yields samples of constant value (dc).

must begin filtering an octave lower than the Nyquist frequency to be sure that frequencies that might otherwise alias are reduced by at least 72 dB before sampling (Fig. 4.56). This must be done before sampling because afterward the alias signals cannot be distinguished. Alias filtering also has to be done before any resampling operation that may be performed during data processing. Aliasing is an inherent property of all systems that sample and thus applies not only to time sampling but also to other situations, such as where we use geophones to sample the earth motion (spatial sampling).

(c) *Filtering by the earth.* We can think of the earth as a filter of seismic energy. We might consider the wave resulting from an explosion as an impulse  $k\delta_r$ , that is, the wave motion at the source of the explosion is zero both before and after the explosion and differs from zero only in an extremely short interval (essentially at  $t = 0$ ) and during this infinitesimal interval the motion is very large. Ideally, the signal that we record would be simply  $k\delta(t)$  convolved with the impulse response of the earth.

The result would be zero except for sharp pulses corresponding to the arrivals of different reflections. If this were so, we could determine easily from the recorded data the complete solution to the seismic problem. However, in practice, the waveform is strung out and modified by filtering due to absorption and other causes so that reflection waveforms overlap, and several types of coherent noise and random noise are superimposed.

The waveform that we finally record as a seismic record is the result of the successive convolutions of the shot impulse with the impulse response of the various portions of the earth through which the wave travels. We can arrive at an approximate picture by considering the earth to be divided into zones:

1. The zone near the shot where stress levels and the absorption of the highest frequencies are very severe. We write  $s_1$  for the impulse response of this zone.
2. The reflecting sequence of beds whose impulse response  $e_i$  is the "message" information that we are seeking to discover by our seismic exploration.

3. Changes in propagating through the section ( $p_t$ ) because of absorption, peg-leg multiples, and other causes.
4. The near-surface zone that exercises considerable filtering action in changing the waveshape. We write  $n_t$  for the impulse response of this last zone.

Neglecting additional filtering effects, we thus write the seismic trace  $z_t$  as the expression

$$z_t = k \delta_t * s_t * e_t * p_t * n_t = (k \delta_t * s_t * p_t * n_t) * e_t \quad (4.103)$$

The factor  $(k \delta_t * s_t * p_t * n_t)$  is called the *embedded wavelet*.

When we use a Vibroseis source, the input to the earth is a long wavetrain  $v_t$ , and the seismic trace  $z'_t$ , which results is

$$z'_t = (v_t * s'_t * p_t * n_t) * e_t \quad (4.104)$$

(where we write  $s'_t$  rather than  $s_t$ , because the filtering processes near the Vibroseis source may be different from those near a shot owing to the different magnitude of the stresses involved).

(d) Water reverberation and deconvolution. Let us examine the effect of multiples resulting from reflection at the bottom and top of a water layer (Backus, 1959). We write  $n\Delta$  for the round trip traveltime from top to bottom of the water and back where  $n$  is an integer and  $\Delta$  is the sampling interval. We assume that the reflection coefficients at the surface and bottom of the water layer are such that the ratios of the reflected to incident amplitudes are  $-1$  and  $+r$ , respectively, where the minus sign denotes phase reversal at the water-air interface. We assume also that the amplitude of a wave returning directly to a hydrophone after reflection at a certain horizon (without a "bounce" round trip between top and bottom of the water layer) is unity and that its traveltime is  $t$ . A wave that is reflected at the same horizon and suffers a bounce either before or after its travel down to the reflector, will arrive at time  $t + n\Delta$  with the amplitude  $-r$ . Because there are two ray-paths with the same traveltime for a single-bounce wave, one that bounced before traveling downward and one that bounced after returning from depth, we have in effect a wave arriving at time  $t + n\Delta$  with amplitude  $-2r$ . There will be three waves that suffer two bounces: One that bounces twice before going downward to the reflector, one that bounces twice on return to the surface, and one that bounces once before and once after its travel downward; each of these is of amplitude  $r^2$  so that their sum is a wave of amplitude  $3r^2$  arriving at time  $t + 2n\Delta$ . Continu-

ing thus, we see that a hydrophone will detect successive signals of amplitudes  $1, -2r, 3r^2, -4r^3, 5r^4, \dots$  arriving at intervals of  $n\Delta$ . We can therefore write for the impulse response of water layers of depths  $d = (n\Delta)V/2$ , where  $V$  is the velocity in the water and  $n = 1, 2, 3$ , respectively:

$$\left. \begin{aligned} w_t &= [1, -2r, 3r^2, -4r^3, 5r^4, \dots] \\ &= [1, 0, -2r, 0, 3r^2, 0, -4r^3, \dots] \\ &= [1, 0, 0, -2r, 0, 0, 3r^2, \dots] \end{aligned} \right\} \quad (4.105)$$

If we transform this to the frequency domain, we find a large peak (the size of the peak increasing with increasing  $r$ ) at the frequency  $2/n\Delta$  and at multiples of this frequency. These are the frequencies that are reinforced at this water depth (that is, the frequencies for which interference is constructive). The result of passing a wavetrain through a water layer is the same as multiplying the amplitude spectrum of the waveform without the water layer by the spectrum of the impulse response of the water layer. Whenever the reflection coefficient is large (and hence  $r$  is large) and the frequency ( $2/n\Delta$ ) (or one of its harmonics) lies within the seismic spectrum, the seismic record will appear very sinusoidal with hardly any variation in amplitude throughout the recording period (Fig. 4.43b). Because of the overriding oscillations, it will be difficult to interpret the primary reflections.

A filter  $i_t$  that has the property that

$$w_t * i_t = \delta_t \quad (4.106)$$

is called the *inverse filter* of  $w_t$ . If we pass the reverberatory output from the hydrophones through the inverse filter (in a data processing center), we will remove the effect of the water-layer filter. The inverse of the water-layer filter is a simple filter with only three nonzero terms, for example,

$$\left. \begin{aligned} i_t &= [1, 2r, r^2] & n = 1 \\ &= [1, 0, 2r, 0, r^2] & n = 2 \\ &= [1, 0, 0, 2r, 0, 0, r^2] & n = 3 \end{aligned} \right\} \quad (4.107)$$

and so forth (see problem 13). Figure 4.36b shows the result of applying such a filter.

The process of convolving with an inverse filter is called *deconvolution* and is one of the most important operations in seismic data processing (Middleton and Whittlesey, 1968; Webster, 1978; Ziolkowski, 1984). Whereas we have illustrated deconvolution as removing the singing effect of a water layer, if we know enough about the filters and the

signal, we could also deconvolve for other filters whose effects we wish to remove.

#### 4.7.4. Correlation

(a) *Cross-correlation*. The *cross-correlation function* is a measure of the similarity between two data sets. One set is displaced relative to the other, corresponding values of the two sets are multiplied together, and the products are summed to give the value of the cross-correlation. Wherever the two sets are nearly the same, the products will usually be positive and hence the cross-correlation is large; wherever the sets are unlike, some of the products will be positive and some negative, and hence the sum will be small. If the cross-correlation function has a large negative value, it means that the two data sets would be similar if one were inverted (that is, they are similar except that they are out of phase). Obviously, the cross-correlation is a function of the relative shift between the sets. By convention we call a shift positive if it involves moving the second function to the left with respect to the first function.

We express the cross-correlation of two data sets  $x_t$  and  $y_t$  as

$$\phi_{xy}(\tau) = \sum_k x_k y_{k+\tau} \quad (4.108)$$

where  $\tau$  is the displacement of  $y_t$  relative to  $x_t$ . [Note that  $\phi_{xy}(\tau)$  is a data set rather than a continuous function, because  $x$  and  $y$  are data sets.] Let us illustrate cross-correlation by correlating the two functions  $x_t = [1, -1, \frac{1}{2}]$  and  $y_t = [1, \frac{1}{2}, -\frac{1}{2}]$ , shown in Figure 4.80. Figure 4.80c shows the two functions in their normal positions. Figure 4.80a shows  $y_t$  shifted two units to the right; corresponding coordinates are multiplied and summed as shown below the diagram to give  $\phi_{xy}(-2)$ . Figures 4.80b, c, d, e show  $y_t$  shifted varying amounts whereas Figure 4.80f shows the graph of  $\phi_{xy}(\tau)$ . The cross-correlation has its maximum value (the functions are most similar) when  $y_t$  is shifted one unit to the left ( $\tau = 1$ ). Obviously, we get the same results if we shift  $x_t$  one space to the right. In other words,

$$\phi_{xy}(\tau) = \phi_{yx}(-\tau) \quad (4.109)$$

The similarity between Equation (4.108) and the convolution equation (4.98) should be noted. We may rewrite Equation (4.108) in the form

$$\begin{aligned} \phi_{xy}(\tau) &= \phi_{yx}(-\tau) = \sum_k y_k x_{k-\tau} \\ &= \sum_k y_k x_{-(\tau-k)} = y_\tau * x_{-\tau} \quad (4.110) \end{aligned}$$

Hence cross-correlation can be performed by reversing the first data set and convolving.

If two data sets are cross-correlated in the time domain, the effect in the frequency domain is the same as multiplying the complex spectrum of the first data set by the conjugate of the complex spectrum of the second set. Because forming the complex conjugate involves only reversing the sign of the phase, cross-correlation is equivalent to multiplying the amplitude spectra and subtracting the phase spectra. In mathematical terms,

$$\begin{aligned} x_t &\leftrightarrow X(\nu) = |X(\nu)| e^{j\Phi_x(\nu)} \\ y_t &\leftrightarrow Y(\nu) = |Y(\nu)| e^{j\Phi_y(\nu)} \\ x_{-\tau} &\leftrightarrow \overline{X(\nu)} = |X(\nu)| e^{-j\Phi_x(\nu)} \\ \phi_{xy}(\tau) &\leftrightarrow \overline{X(\nu)} Y(\nu) = |X(\nu)| |Y(\nu)| e^{j(\Phi_y - \Phi_x)} \end{aligned} \quad (4.111)$$

We note that changing the sign of a phase spectrum is equivalent to reversing the trace in the time domain.

(b) *Autocorrelation*. The special case where a data set is being correlated with itself is called *autocorrelation*. In this case, Equation (4.108) becomes

$$\phi_{xx}(\tau) = \sum_k x_k x_{k+\tau} \quad (4.112)$$

Autocorrelation functions are symmetrical because a time shift to the right is the same as a shift to the left, that is, from Equation (4.112),

$$\phi_{xx}(\tau) = \phi_{xx}(-\tau) \quad (4.113)$$

The autocorrelation has its peak value at zero time shift (that is, a data set is most like itself before it is time-shifted). If the autocorrelation should have a large value at some time shift  $\Delta t \neq 0$ , it indicates that the set tends to be periodic with the period  $\Delta t$ . Hence the autocorrelation function may be thought of as a measure of the repetitiveness of a function.

(c) *Normalized correlation*. The autocorrelation value at zero shift is called the *energy* of the trace:

$$\phi_{xx}(0) = \sum_k x_k^2 \quad (4.114)$$

(This terminology is justified on the basis that  $x_t$  is usually a voltage, current, or velocity, and hence  $x_t^2$  is proportional to energy.) For the autocorrelation

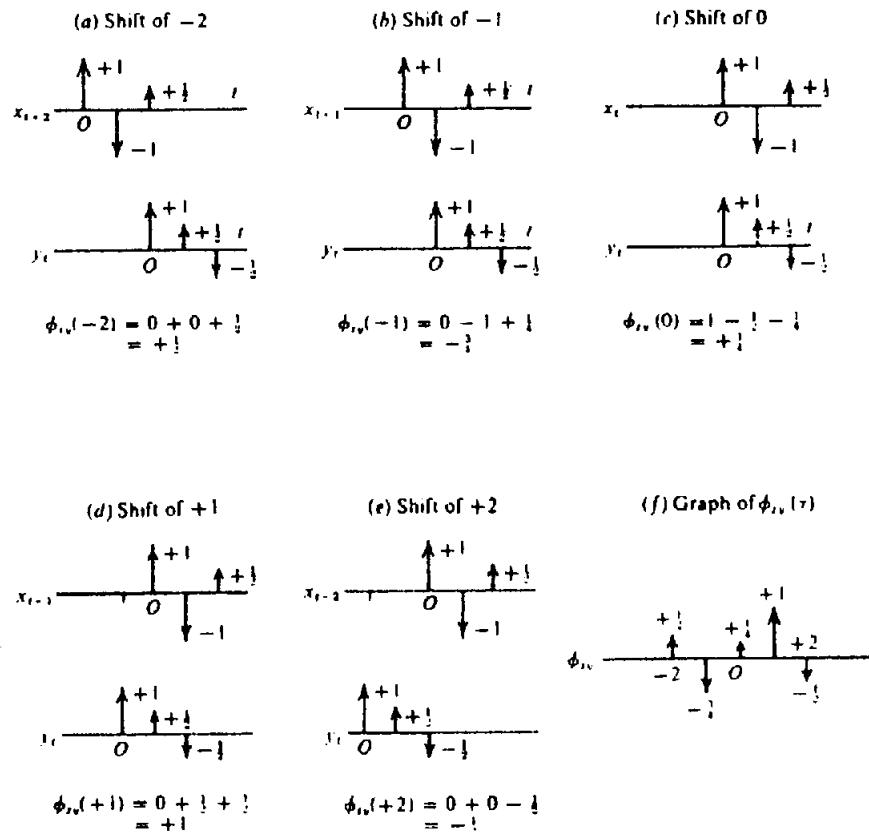


Figure 4.80. Calculating the cross-correlation of two functions.

function, Equation (4.111) becomes

$$\phi_{xx}(\tau) \leftrightarrow |X(\nu)|^2 \quad (4.115)$$

Because the zero-shift value of the autocorrelation function is the energy of the trace,  $[x(t)]^2$  is the energy per unit of time or the *power* of the trace and  $|X(\nu)|^2$  is the energy per increment of frequency, usually called the *energy density*.

We often normalize the autocorrelation function by dividing by the energy:

$$\phi_{xx}(\tau)_{\text{norm}} = \frac{\phi_{xx}(\tau)}{\phi_{xx}(0)} \quad (4.116)$$

The cross-correlation function is normalized in a similar manner by dividing by the geometric mean of the energy of the two traces:

$$\phi_{xy}(\tau)_{\text{norm}} = \frac{\phi_{xy}(\tau)}{[\phi_{xx}(0)\phi_{yy}(0)]^{1/2}} \quad (4.117)$$

Normalized correlation values lie between  $\pm 1$ . A value of  $+1$  indicates perfect copy; a value of  $-1$  indicates perfect copy if one of the traces is inverted.

(d) *Automatic statics.* Cross-correlation affords us a means of determining the amount of time shift that

will result in the optimum alignment of two seismic traces. If one trace has been delayed with respect to another, for example, in passing through the near-surface layers, the delay equals the shift that maximizes the cross-correlation, that is, that produces the optimum alignment (match) of the two traces. The magnitude of the cross-correlation indicates quantitatively how much improvement such a shift will produce. Cross-correlation is a powerful tool and is especially useful when the data quality is poor. It is used in many processes to determine static corrections and the amount of normal moveout to introduce to align traces from different offsets before stacking (Hileman, Embree, and Pfeiffer, 1968; Dishner and Naquin, 1970). Criteria can be set that permit such shifts to be determined and applied automatically, provided tests are incorporated to ensure that the shifts so introduced are consistent (for example, to ensure that the same corrections are always assumed for the weathering beneath any particular location). Figure 4.81 illustrates the improvement in a CMP stack resulting from the use of an automatic statics program.

(e) *Vibroseis analysis.* The signal  $z'_t$  that the system records when we use a Vibroseis source [Eq. (4.104)] bears little resemblance to  $e_t$ , the impulse response of the earth. To obtain a meaningful record, the data are correlated with the Vibroseis sweep

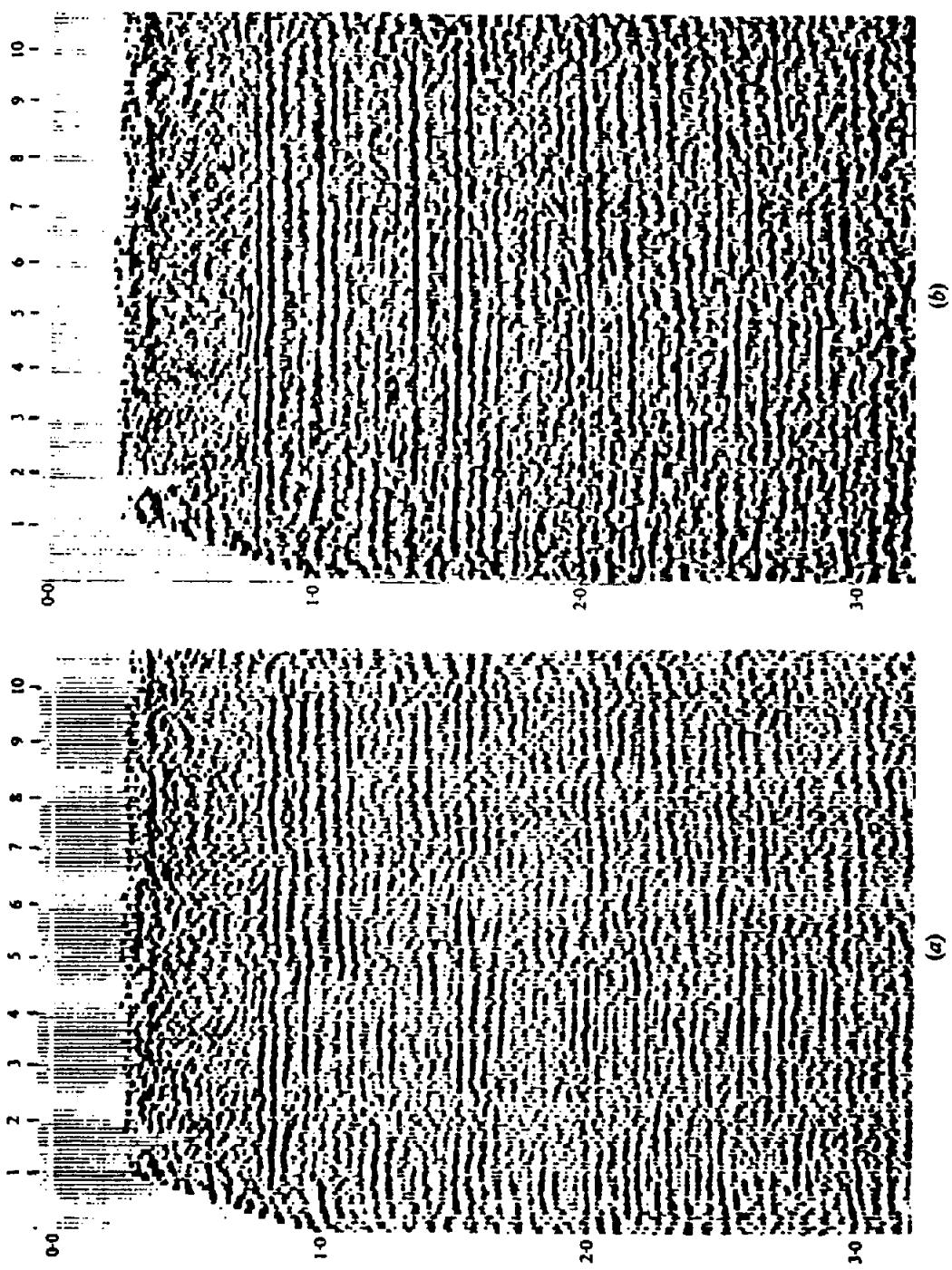


Figure 4.81. Example of automatic statics correction. (Courtesy Regional Surveys.) (a) Before statics correction. (b) After statics correction.

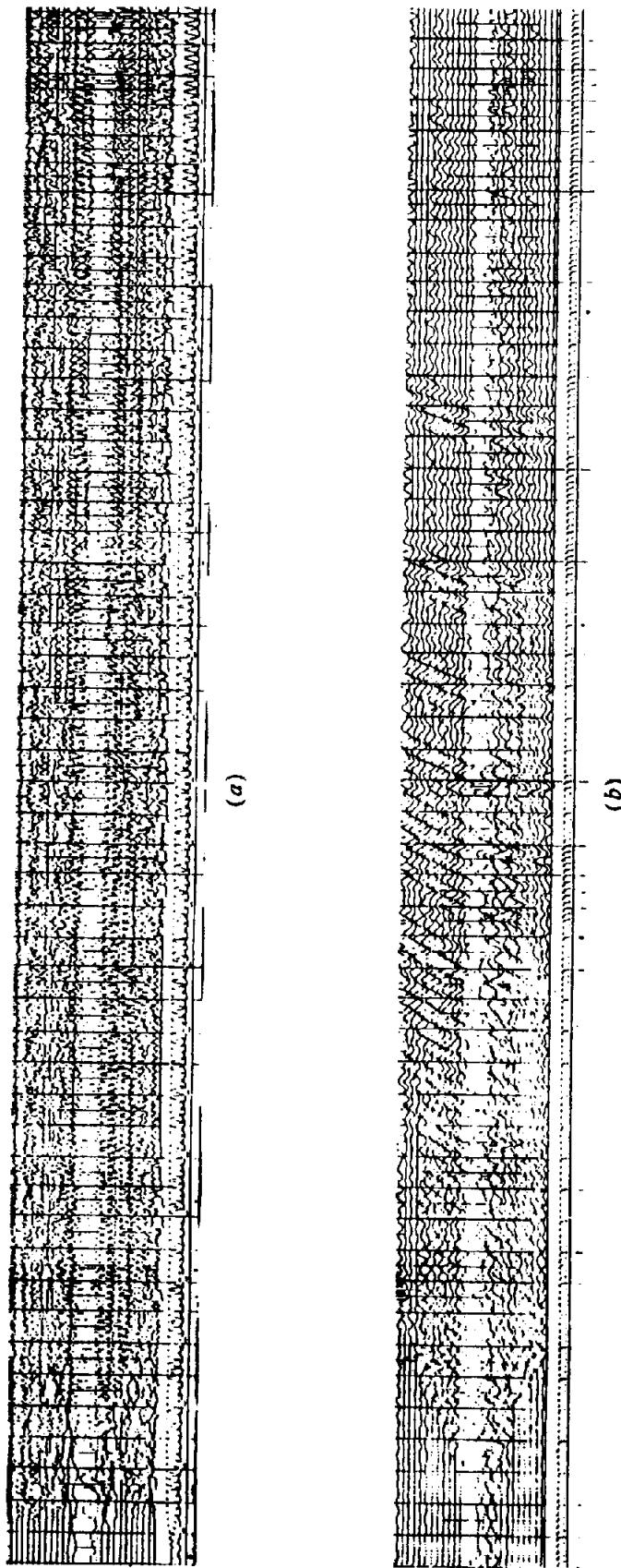


Figure 4.82. Vibroseis record. (Courtesy Grant-Nopac.) (a) Before correlation (only the first portion of the very long uncorrelated record is shown). (b) After correlation.

signal  $v_t$ . The recorded signal  $z'_t$  is

$$z'_t = v_t * e'_t$$

where we let  $e'_t = s'_t * e_t * p_t * n_t$ , in Equation (4.104). Using Equation (4.110), we find, for the cross-correlation of the sweep and the recorded signal,

$$\begin{aligned}\phi_{vz}(t) &= z'_t * v_{-t} = (v_t * e'_t) * v_{-t}, \\ &= e'_t * (v_t * v_{-t}) \\ &= e'_t * \phi_{vv}(t)\end{aligned}\quad (4.118)$$

(The next to the last step is possible because convolution is commutative.) Hence the overall effect is that of convolving the earth function with the autocorrelation of the Vibroseis sweep signal. The autocorrelation function  $\phi_{vv}(t)$  is quite sharp and has sizable values only over a very narrow range of time shifts. Therefore, the overlap produced by the passage of a long sweep through the earth has been eliminated almost entirely. This is shown in Figure 4.82, where (a) and (b) are the same Vibroseis record before and after cross-correlation.

#### 4.7.5. Phase Considerations

Equation (4.96) represents the adding together of cosine waves of different frequencies and different phases. If the same components are added together with different phase relations, different waveforms result. Changing the waveform changes the location of a particular peak or trough, and hence measurements of traveltimes are affected by variations in the phase spectra. Because seismic exploration primarily involves determining the traveltimes of events, preservation of proper phase relationships during data processing is essential.

Out of all possible wavelets with the same amplitude spectrum, the wavelet whose energy builds up the fastest is called the *minimum-delay* wavelet. Its phase is always less than the other wavelets with the same amplitude spectrum, and hence it is also called *minimum phase*. The simplest wavelet (except for an impulse) is a data set that contains only two elements, the set  $[a, b]$ . The amplitude spectrum of this data set is identical with that of the set  $[b, a]$ , but no other data set has the same spectrum. If  $|a| > |b|$ , energy is concentrated earlier in the wavelet in the set  $[a, b]$  than in the set  $[b, a]$ , and hence  $[a, b]$  is minimum phase (or minimum delay). Larger wavelets can be expressed as the successive convolution of two-element wavelets; a large wavelet is minimum

phase if all of its component wavelets are minimum phase. The impulse response of many of the natural filtering processes in the earth are minimum phase.

Some filtering processes require that assumption be made about the phase of the signal; generally minimum phase is assumed (Sherwood and Troprey, 1965). Thus deconvolution based on autocorrelation information has to assume the phase because the phase information of the waveform was lost when its autocorrelation was formed. This can be seen from Equation (4.115) where we note that the autocorrelation function  $\phi_{xx}(t)$  has the transform  $|X(\nu)|^2$  with zero phase for all values of frequency. Thus all of the phase information present in  $X(\nu)$  has been lost in the autocorrelation.

#### 4.7.6. Frequency Filtering

(a) *Least-squares (Wiener) filtering.* Sometimes we wish to determine the filter that will do the best job of converting an input into a desired output. The filter that most nearly accomplishes this objective in the least-squares sense (§A.8) is called the *least-squares filter* or the *Wiener filter*, occasionally the *optimum filter* (Robinson and Treitel, 1967).

Let the input data set be  $x_i$ , the filter that we have to determine be  $f_i$ , and the desired output set be  $z_i$ . The actual result of passing  $x_i$  through this filter is  $x_i * f_i$  and the "error", or difference, between the actual and the desired outputs is  $(z_i - x_i * f_i)$ . With the least-squares method, we add together the squares of the errors, find the partial derivatives of the sum with respect to the variables  $f_i$  (the elements of  $f_i$ ), and set these derivatives equal to zero. This gives the simultaneous equations where  $z_i$  and  $x_i$  are known:

$$\frac{\partial}{\partial f_i} \sum_t (z_i - x_i * f_i)^2 = 0 \quad i = 0, 1, 2, \dots, n \quad (4.119)$$

One such equation is obtained for each of the  $n + 1$  elements in  $f_i$ , and solving for the unknowns  $f_i$ , we find the filter  $f_i$  that minimizes the sum of the errors squared. Manipulation leads to the so-called *normal equations* (Sheriff and Geldart, 1983, pp. 41 and 151), which are more convenient than Equation (4.119):

$$\sum_{j=0}^n \phi_{xx}(\tau - j) f_j = \phi_{xz}(\tau) \quad \tau = 0, 1, 2, \dots, n \quad (4.120)$$

These equations can be used to cross-equalize traces, that is, to make traces as nearly alike as possible. Suppose we have a group of traces to be stacked, such as the components of a common-mid-point stack. After the normal-moveout corrections have been made, the traces may still differ from each other because they have passed through different portions of the near surface. The normal equations can be used to find filters that will make all the traces as nearly as possible like some *pilot trace*, such as the sum of the traces. This procedure will improve the quality of the stacked result.

The normal equations are also used to design deconvolution operators. The earth impulse response  $e_r$  is assumed to be random, that is, knowledge of shallow reflections does not help to predict deeper primary reflections. Consequently, the autocorrelation of  $e_r$  is negligibly small except for a shift of zero time and we can write

$$\phi_{ee}(\tau) \approx k\delta_\tau \quad (4.121)$$

The geophone input  $g_t$  is regarded [Eq. (4.103)] as the convolution of  $e_r$  with various filters (the most important of which usually results from near-surface effects), and the overall effect is represented by the single equivalent filter  $n'_r$ :

$$g_t = e_r * n'_r$$

The desired output  $z_t$  is the earth's impulse response  $e_r$  (which can be shown to be minimum phase); hence using Equation (4.110) we can write

$$\begin{aligned} \phi_{gz}(\tau) &= z_r * g_{-\tau} \\ &= e_r * (e_{-\tau} * n'_{-\tau}) \\ &= (e_r * e_{-\tau}) * n'_{-\tau} \\ &= k\delta_\tau * n'_{-\tau} \\ &= kn'_r, \end{aligned} \quad (4.122)$$

The filter  $n'_r$  is causal, that is, it does not yield an output until after there has been an input; hence  $n'_r = 0$  for  $\tau < 0$ . Thus

$$\phi_{gz}(\tau) = 0 \quad \text{for } \tau < 0 \quad (4.123)$$

Therefore, if we concern ourselves only with positive values of  $\tau$ , we have the values required to solve Equation (4.120) for the deconvolution filter.

(b) *Frequency filtering and deconvolution.* The use of deconvolution to remove the filtering effect of a water layer and the near surface has already been discussed. Although the water-layer filter was presented in a deterministic way, the proper choice of parameters is usually not obvious. Statistical and empirical ways of choosing filter parameters are sometimes used (Kunetz and Fourmann, 1968). Deconvolution by Wiener filtering [using Eq. (4.123)]

has also been discussed (Peacock and Treitel, 1969; Robinson, 1972).

One deconvolution assumption is that the amplitude spectrum should be flat, that is, all frequency components should be present in equal amounts. It is argued that the Earth's reflectivity is effectively random [the same argument that justified Eq. (4.121)] and hence should contain equal amounts of all frequencies. This assumption is called *whitening*, in analogy to white light, which contains all frequencies in equal magnitude. It is also called *spiking deconvolution* because the amplitude spectrum of a spike ( $\delta_\tau$ ) is white. Whitening can be accomplished by Fourier transforming a trace, flattening the amplitude spectrum but not changing the phase spectrum, and then inverse transforming. Whitening can also be done in analog processing by passing the signal through a number of narrow bandpass filters, making their outputs equal in magnitude, and then recombining. Whitening tends to increase the noise if the signal level is below the noise level for any frequency components.

The values of a correlation function for  $\tau \neq 0$  measure the predictability involved. If a trace were nonpredictable (that is, random), Equation (4.123) would hold. If all reflections involve the same embedded waveshape [as implied by Eq. (4.103)] and it is known, then the early part of a reflection can be used to predict the values that follow. If the reflection waveshape has the length  $n$  and if this waveshape is the only predictable element, the autocorrelation will have nonzero values between  $\pm n$  and the autocorrelation spectrum will be the square of the spectrum of the wavelet.

If multiples are generated by a reflector associated with the traveltimes  $m$ , then the traveltimes of the multiples can be predicted, which will cause the trace autocorrelation to have nonzero values for  $\tau > m$ . Predictive deconvolution utilizes these facts. Setting  $\phi_{gg}(\tau) = 0$  for  $\tau > m$  effectively shortens the waveshape to the length  $n$ . Using the values of  $\phi_{gg}(\tau)$  for  $\tau > m$  gives the predictable effect of the multiples, which can be subtracted from the trace to produce a result that should be free of the multiples. This is called *gapped deconvolution* because the autocorrelation values in the gap  $\tau < m$  are not involved.

Wavelet processing is a type of deconvolution that attempts to achieve a short wavelet of symmetrical waveshape, a waveshape that facilitates interpretation. The spectrum of the embedded wavelet can be found from the spectrum of the trace autocorrelation, as previously indicated. Usually the autocorrelations of a number of traces are summed to average out trace-to-trace noise differences. If the wavelet phase spectrum can be assumed or determined, then the embedded wavelet is given by the inverse Fourier

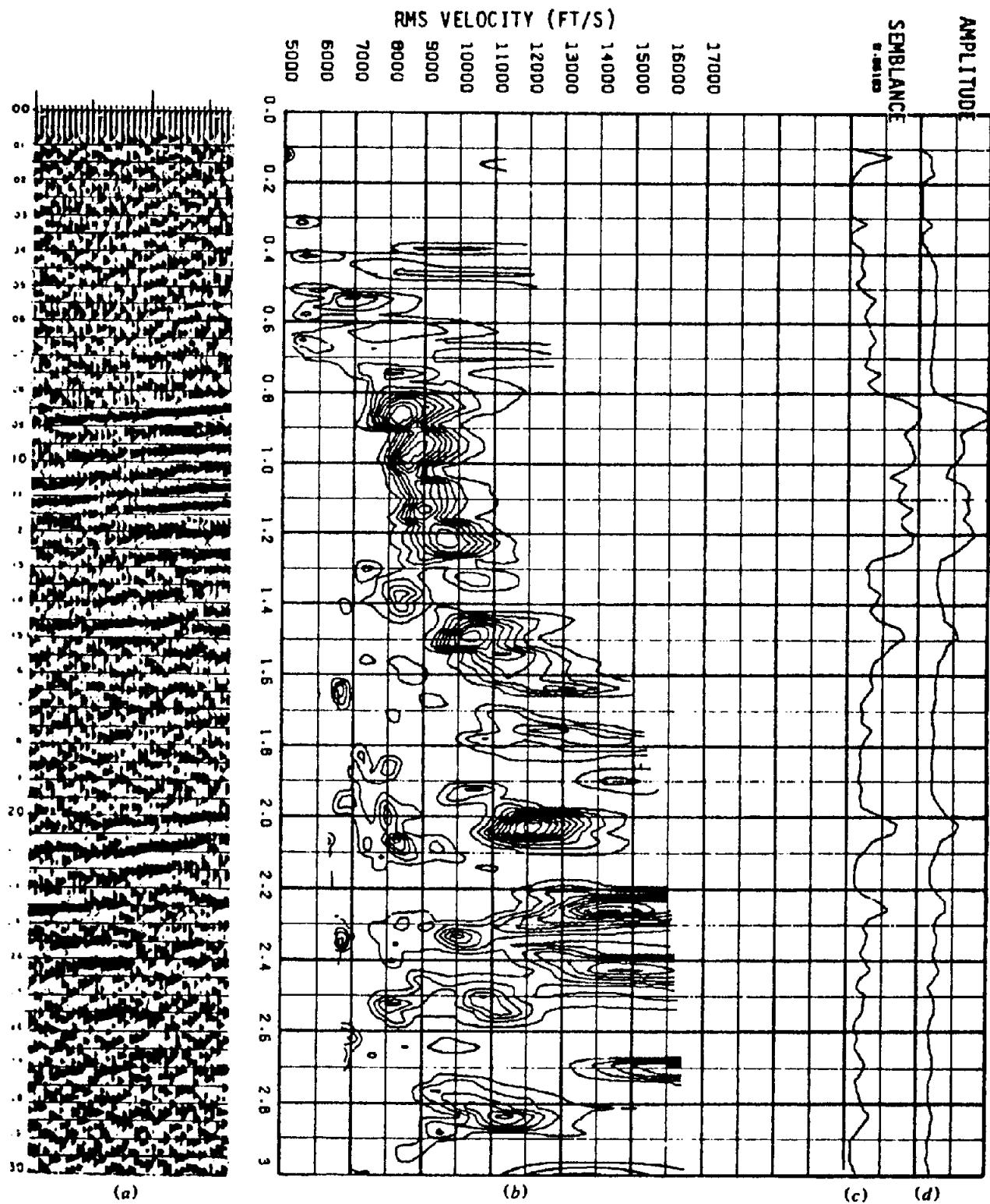


*Figure 4.83. Velocity analysis. (Courtesy Grant-Norpac.) (a) Portion of seismic section. (b) Velocity analysis of data at right side of (a). (c) Maximum semblance at each record time. (d) Peak amplitude at each record time.*

transform. Once the embedded wavelet is known, an operator can be found to replace it with some other desired waveshape.

(c) *Time-variant filtering.* Deeper reflections have a higher percentage of low-frequency energy than shallow reflections because of the greater attenuation of

the higher frequencies as a result of absorption and other filtering mechanisms. Hence, time-variant filtering is used in which the passband moves toward lower frequencies as record time increases. One method of achieving time-variant filtering is to use separate gates (time intervals), for example, shallow and deep, so that the deconvolution operator varies with record time (Clarke, 1968).

#### 4.7.7. Velocity Analysis

The variation of normal moveout with velocity and record time has already been discussed in connection with Equation (4.52). Several techniques utilize the variation of normal moveout with record time to find velocity (Garotta and Michon, 1967; Schneider and Backus, 1968; Cook and Taner, 1969; Taner and Koehler, 1969). Most assume a stacking velocity [ $V_s$  in Eq. (4.84)], apply normal-moveout corrections as a function of arrival time and offset, and then measure the coherence (degree of match) among all the traces available to be stacked. Several measures of coherence may be used and they are discussed further in Section 4.7.13 [Eqs. (4.125) and (4.126)]. Another stacking velocity is then assumed and the calculations repeated, and so on, until the coherence has been determined as a function of both stacking velocity and arrival time. (Sometimes normal moveout is the variable rather than stacking velocity.)

A velocity-analysis display is shown in Figure 4.83. This is a good analysis because the data involved are good. Highs on the contour plot correspond to events. The locations of the highs yield the velocities (or normal moveouts), that optimize the stack (hence the name stacking velocity for  $V_s$ ). Multiples as well as primaries give rise to peaks and hence the results have to be interpreted to determine the best values to be used to stack the data (Robinson, 1983a). In many areas where the velocity more-or-less monotonically increases with depth, the peaks associated with the highest reasonable stacking velocities are assumed to represent primary reflections and the peaks associated with lower velocities are attributed to multiples of various sorts. In other areas the relationships are not as obvious, and even where the velocity relationships are generally regular, difficulties will be encountered.

The major objective of velocity analysis is to ascertain the amount of normal moveout that should be removed to maximize the stacking of events that are considered to be primaries. This does not necessarily optimize the primary-to-multiple energy ratio and better stacks can be achieved with respect to identifiable multiples. This is not often done, however. An auxiliary objective of velocity analysis is identifying lithology; this is discussed in Section 4.10.7.

#### 4.7.8. Common-Midpoint Stacking

Common-midpoint stacking is probably the most important application of data processing for improving data quality. The principles involved have already been discussed along with the field procedures used to acquire the data. The component data are sometimes displayed as a *gather*: a common-midpoint

*gather* has the components for the same midpoint arranged side by side and a *common-offset gather* has the components for which the offset is the same arranged side by side. After correcting for normal moveout, the data are stacked into a single output trace for each midpoint.

If reflectors dip, the reflecting point is not common for common-midpoint traces and consequently the stacking result involves smearing and degradation of data quality. The degradation can be avoided by migrating before stacking (which is expensive) or approximately but relatively cheaply by several methods. Sometimes partial stacks, each of traces over a limited offset range, are made and migrated to cut down on the amount of data to be migrated.

Dip-moveout (DMO) processing transforms a set of prestack common-midpoint gathers so that each gather contains events from the same reflecting point (Deregowski, 1986). If the velocity is constant, the locus for equal traveltimes is an ellipse with the source and receiver locations as foci; all reflectors, dipping as well as horizontal, are tangent to such an ellipse. DMO uses the differences between the midpoint and the points where perpendiculars to the ellipse intercept the surface to create common-reflecting point gathers. These gathers can then be stacked and migrated without reflecting-point smear. The constant-velocity assumption provides a reasonably satisfactory approximation where velocity varies vertically.

First-break data and the refraction wavetrains that follow the first breaks usually are so strong that they have to be excluded from the stack to avoid degrading the quality of shallow reflections. This is done by *muting*, which involves arbitrarily assigning zero values to traces during the period when the first breaks and following wavetrains are arriving. Thus the multiplicity of a stack increases by steps, with the shallowest data often being only a twofold stack, slightly deeper data being a fourfold stack, and so on, until the full multiplicity of the stack is achieved after the muted events have passed beyond the most distant geophones.

#### 4.7.9. Apparent-Velocity (Apparent-Dip) Filtering

The apparent velocity of an event,  $V_A$ , is found by dividing the distance between two points on the surface of the ground by the difference in traveltime for the same event at geophones located at the points. It is thus the reciprocal of the quantity  $\Delta t/\Delta x$  in Equation (4.57):

$$V_A = \Delta x/\Delta t = V/\sin \alpha \quad (4.124)$$

where  $V$  is the velocity with which a wavefront

approaches the spread and  $\alpha$  is the angle between the wavefront and the spread. Apparent velocity is an entirely different quantity from the stacking velocity or the velocity used to convert traveltimes to reflector depths. A reflection that arrives from vertically beneath the spread has an infinite apparent velocity (after correction for normal moveout) without regard for the depth of the reflector or the velocity with which the reflection energy has traveled in the earth. Apparent velocity generally decreases for dipping reflectors, becoming smaller as the dip increases, but usually it is still much larger than seismic velocities. Horizontally traveling wavetrains (mainly ground-roll and refractions) have low apparent velocities compared with reflections and so can be discriminated against on this basis. This forms the basis of velocity-filtering methods (Treitel, Shanks, and Frasier, 1967; Sengbush and Foster, 1968; Christie, Hughes, and Kennett, 1983). The filtering can be achieved in the time domain by mixing signals in such a way that events with certain apparent velocities are added out of phase and so cancelled. Filtering can also be done in the  $(\omega, \kappa)$  domain (Christie, Hughes, and Kennett, 1983) after two-dimensional Fourier transformation [Eq. (A.57)]. Apparent-velocity filtering is sometimes done before stacking but usually afterward.

#### 4.7.10. The $p$ - $\tau$ Transform

The axes of a seismic record (or section) are offset (location) and travelttime. The same data can also be represented by a plot of the slope of events  $p$  against the intercept on the time axis  $\tau$  (Diebold and Stoffa, 1981). [For reflections,  $p$  is the raypath parameter of Eq. (4.65)]. Whereas the Fourier transform represents data as a superposition of harmonics, the  $p$ - $\tau$  plot represents the same data as a superposition of straight-line events; curved wavefronts become a superposition of plane wavefronts. Straight-line events, such as the direct wave, headwave events, ground roll, and air waves, transform into points whereas hyperbolic reflections become ellipses in the  $p$ - $\tau$  domain. As with other transforms, one can transform back into the time-space domain without loss of information except that due to the interpolation between sampled values and to boundary effects. Filtering and other operations can be done in the  $p$ - $\tau$  domain as with apparent-velocity and frequency-domain processing.

#### 4.7.11. Relative-Amplitude Processing

Most of the information for structural interpretation is determined from the traveltimes of events, and it is desirable to see as many events as possible. This is

better achieved by minimizing amplitude differences between events, and so sections for structural interpretation objectives often do not preserve relative amplitude. However, for stratigraphic interpretation and hydrocarbon indicator purposes, maintaining correct relative trace-to-trace amplitudes for each event is important. Some amplitude variations, such as spherical divergence, can be corrected based on theory. Some, such as absorption and peg-leg multiple effects, vary so slowly that they can be approximated by gradual exponential amplitude correction. Some, such as variations near the source or geophone, can be corrected by a surface-consistent amplitude model where the corrections are statistically determined from the redundancy in data (Taner and Koehler, 1981). After correcting for as many factors as possible, remaining amplitude variations are usually attributed to reflectivity variations. Relative amplitude data are sometimes displayed at very low gain so that only the strongest events are apparent; these then are considered as possible hydrocarbon indicators (§4.10.8).

#### 4.7.12. Migration or Imaging

Common-midpoint seismic sections show reflections (and other) data oriented with respect to midpoints, that is, with respect to where the equivalent coincident sources and geophones are located. Our goal, however, is to locate reflectors and diffracting points in the subsurface. The process of moving data elements from midpoint locations to subsurface locations is called *migration*. It is also called *imaging* because its objective is to produce a clear image of the subsurface (Robinson, 1983b; Brower, Douma, and Helbig, 1985).

Migration implies that the seismic data being migrated are either primary reflections or diffractions. Migration of other types of events as if they were reflections or diffractions smears them out and creates noise (*migration noise*). Large local bursts of energy get smeared into *smiles*, which have the general shape of wavefronts (Fig. 4.84). Almost every migrated section shows some smiles, especially deep in the section and near the ends of the sections where noise is high and data are incomplete.

Migration to the correct location requires knowledge of the velocity distribution but, in structurally complex areas where migration is most required, velocity information is apt to have large uncertainty. However, migration is fairly tolerant of errors in vertical variations in velocity so that migration with the wrong velocity usually helps to clarify structure even though events are not located correctly. Changes in velocity in the horizontal direction produce distortions unless they are allowed for correctly. Migration

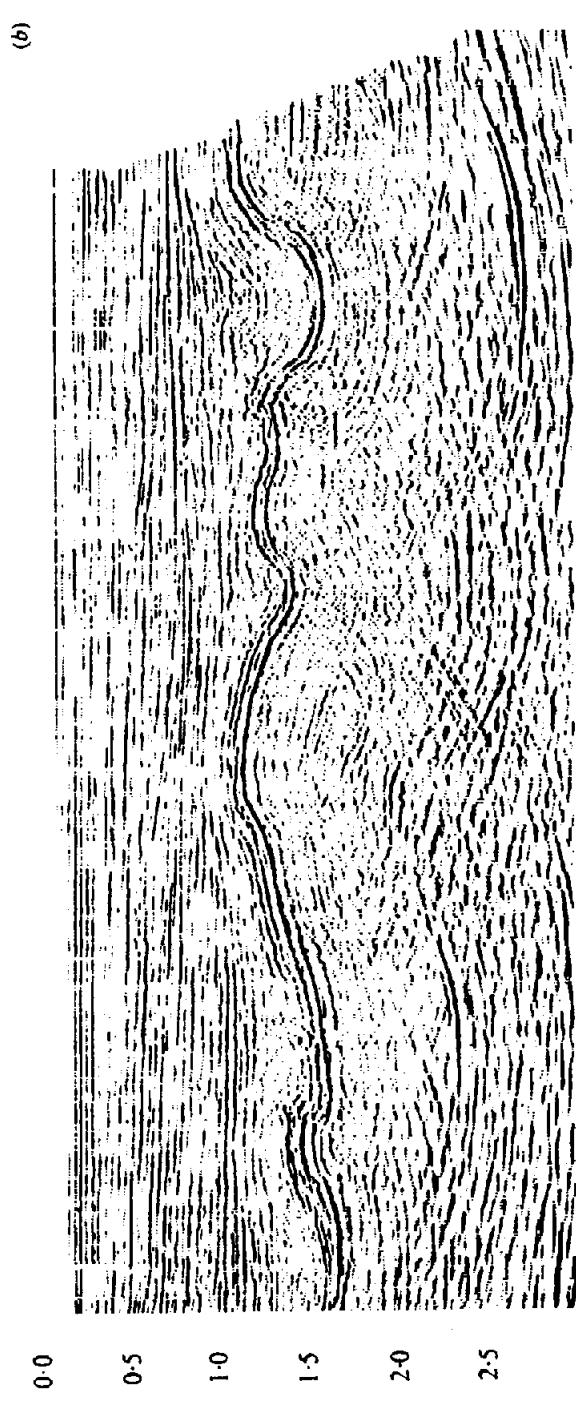
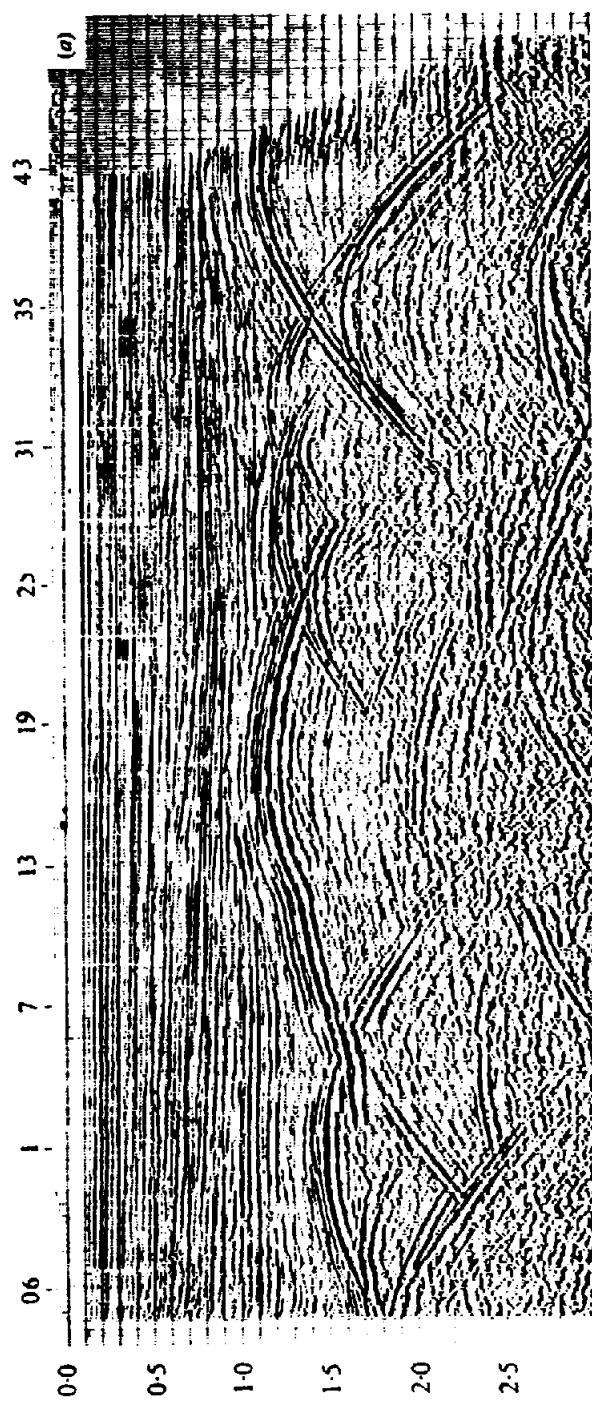


Figure 4.84. Unmigrated and migrated seismic sections. (Courtesy A.G.I.P. and Western Geophysical.) (a) Before migration. (b) After migration. Multiple-branch reflection events migrate into a relatively continuous reflector. Deeper data, which are principally multiples, are not migrated properly.

that attempts to allow for horizontal velocity changes is called *depth migration* (Larner et al., 1981). Iterative ray tracing may be used in complex areas; the model of velocity and dip values resulting from one iteration provide the input information for the next iteration.

Events from off to the side of the line generally are migrated incompletely because the migration deals only with the apparent dip in the in-line direction. Thus diffractions from faults that are not perpendicular to the line will collapse only partially. However, even if some events may be undermigrated, interpretation is usually made easier by the migration.

When velocity varies only with depth (that is, not laterally), the traveltimes for a diffraction (*diffraction curve*) depends only on the velocity above the diffracting point and the depth of the diffracting point. (The situation for sources off the line, diffracted reflections, diffracted refractions, and other more complicated paths, is more complex.) The energy diffracted by a point can be found by summing the energy along the diffraction curve for which that point is at the apex (Hagedoorn, 1954). If the apex is not at an actual diffracting point, the values along the diffraction curve will not be systematic, and negative and positive values will tend to cancel. If the section is searched along all possible diffraction curves and the sums of the energy found along each is positioned at the crests of the curves, all diffractions will be migrated correctly. Because the same physical processes are involved in generating reflections and diffractions, one can think of a reflector as many closely spaced diffracting points and a reflection as the interference composite of their diffractions (Huygens' principle). Thus if reflection elements are migrated as if they were diffraction elements, the reflections will be migrated correctly (providing the cross-dip is zero). This principle forms the basis of some computer migration processes (*Kirchhoff migration*). A result is shown in Figure 4.84.

The wave equation expresses how waves move in space and time and can be used to "move waves backward." If we assume coincident source and geophone (as a common-midpoint section implies), then a wave moved backward to where it was at half the traveltimes should be located at the reflector or diffracting point. This concept forms the basis for wave-equation methods of migration. The migration is sometimes done in the time domain using finite differences to approximate the derivatives in the wave equation, continuing the wavefield downward step by step (Berkhout, 1981). It is sometimes solved in the frequency-wave-number domain after a two-dimensional Fourier transform [Eq. (A.57)] converts

the data to the new domain; then the frequency-domain equivalents of downward continuation are performed (Chun and Jacewitz, 1981), after which the data are transformed back to the space-time domain for display of the migrated results. Sometimes combinations of domains are used or operations are performed partially in one domain and partially in another. The results of all types of migration are conceptually equivalent, but in practice, weaknesses in one type (mainly because of the approximations involved) or the ease of accommodating special considerations may favor one method or another. More information on migration can be found in Gardner (1985) and in Claerbout (1985).

#### 4.7.13. Measures of Coherence

Trace-to-trace coherence as defined in Section 4.4.1 can be given a quantitative significance in several ways. For two traces, one could use the cross-correlation as a measure of coherence. For a large number of traces, we could make use of the fact that when we stack several channels together the resulting amplitude is generally large where the individual channels are similar (coherent) so that they stack in-phase and small where they are unlike (incoherent). The ratio of the energy of the stack compared to the sum of the energies of the individual components would therefore be a measure of the degree of coherence.

If we let  $x_{it}$  be the amplitude of the individual channel  $i$  at the time  $t$ , then the amplitude of the stack at time  $t$  will be  $\sum_i x_{it}$  and the square of this will be the energy. If we call  $E_t$  the ratio of the output energy to the sum of the energies of the input traces, we may write

$$E_t = \frac{(\sum_i x_{it})^2}{\sum_i (x_{it}^2)} \quad (4.125)$$

We expect a coherent event to extend over a time interval; hence a more meaningful quantity than  $E_t$  is the *semblance*  $S_t$  (Neidell and Taner, 1971), which denotes the ratio of the total energy of the stack of  $N$  traces within a gate of length  $\Delta t$  to  $N$  times the sum of the energy of the component traces within the same time gate. Using the same terminology as before we can write.

$$S_t = \frac{\sum_{t-\Delta t}^{t+\Delta t} (\sum_i x_{it})^2}{N \sum_{t-\Delta t}^{t+\Delta t} \sum_i (x_{it}^2)} \quad (4.126)$$

The semblance will not only tend to be large when a coherent event is present but the magnitude of the semblance is also sensitive to whether or not all traces contribute equally. Thus strong events will

exhibit large semblance and weak events will exhibit moderate values of semblance whereas incoherent data will have very low semblance.

Semblance and other coherence measures are used to determine the values of parameters that will optimize a stack. The semblance is calculated for various combinations of time shifts between the component channels, and the optimum time shifts are taken to be those that maximize the semblance. Semblance therefore can be used to determine static corrections or normal-moveout corrections.

#### 4.7.14. Other Types of Processing

(a) *Diversity stacking*. Much data processing is far less exotic than suggested by the mathematical relationships expressed in the foregoing pages. Some of these processes merely involve excluding certain elements of the data, such as the muting operation, which has already been discussed.

*Diversity stacking* is another technique used to achieve improvement by excluding noise. Records in high-noise areas, such as in cities, often show bursts of large amplitude noise whereas other portions of the records display relatively little noise distortion. Under such circumstances, amplitude can be used as a discriminant to determine which portions are to be excluded. This can take the form of merely excluding all data where the amplitude exceeds some threshold, or perhaps some form of inverse weighting might be used. Such noise bursts often are randomly located on repeated recordings so that sufficient vertical stacking after the weighting tends to produce records relatively free from the high-amplitude noise.

(b) *First-break statics*. The first arrivals (or first breaks) on a seismic record are usually a headwave from the base of the weathered layer for geophones some distance from the sourcelpoint. The first-break traveltimes are often interpreted by standard refraction methods to give the thickness and traveltime through the weathered layer for the purpose of making static corrections. The first breaks may be picked automatically and static time shifts may be calculated (Hatherly, 1982; Farrell and Euwema, 1984). This is usually done to give first-order static corrections, and second-order corrections (*residual statics*) are made by a surface-consistent program that relies on cross-correlation between elements of a common-midpoint gather.

(c) *Specialized processing*. A variety of other types of seismic processing are performed for special purposes. Attributes (measurements based on seismic data such as amplitude of the trace envelope, instantaneous phase, or instantaneous frequency) are

sometimes calculated and displayed superimposed on the seismic data (Taner, Koehler, and Sheriff, 1979). Amplitude data are sometimes converted to acoustic impedance or synthetic sonic-log forms (the processing is called *inversion*) (Lindseth, 1979). Modeling (§4.10.2) of both stratigraphic and structural features is done to aid in interpretation (Hilterman, 1970, 1982).

### 4.8. BASIC GEOLOGIC CONCEPTS IN PETROLEUM EXPLORATION

#### 4.8.1. Basic Concepts

Before discussing the objectives of seismic interpretation, we shall review some basic concepts that are fundamental in petroleum exploration.

Petroleum is the result of the deposition of plant or animal matter in areas that are slowly subsiding. These areas are usually in the sea or along its margins in coastal lagoons or marshes and occasionally in lakes or inland swamps. Sediments are deposited along with the organic matter, and the rate of deposition of the sediments must be sufficiently rapid that at least part of the organic matter is preserved by burial before being destroyed by decay. As time goes on and the area continues to sink slowly [because of the weight of sediments deposited or because of regional (tectonic) forces], the organic material is buried deeper and hence is exposed to higher temperatures and pressures. Eventually chemical changes result in the generation of petroleum, a complex, highly variable mixture of hydrocarbons, including both liquids and gases (part of the gas is in solution because of the high pressure). Ultimately the subsidence will stop and may even reverse.

Sedimentary rocks are porous; *porosity* is the fractional volume of the rock occupied by cavities or pores. Petroleum collects in these cavities and intermingles with the remaining water that was buried with the sediments. When a significant fraction of the pores is interconnected so that fluids can pass through the rock, the rock is *permeable*. Permeability permits the gas, oil, and water to separate partially because of their different densities. The oil and gas tend to rise, and they eventually reach the surface of the earth and are dissipated unless they encounter a barrier that stops their upward migration. Such a barrier produces a *trap*. Figure 4.85 illustrates the most important types of traps.

The anticline shown in vertical cross section in Figure 4.85a is a common type of trap and often the easiest to map. In the diagram, bed A is impermeable whereas the reservoir rock B is permeable. Oil and gas can collect in the reservoir rock of the

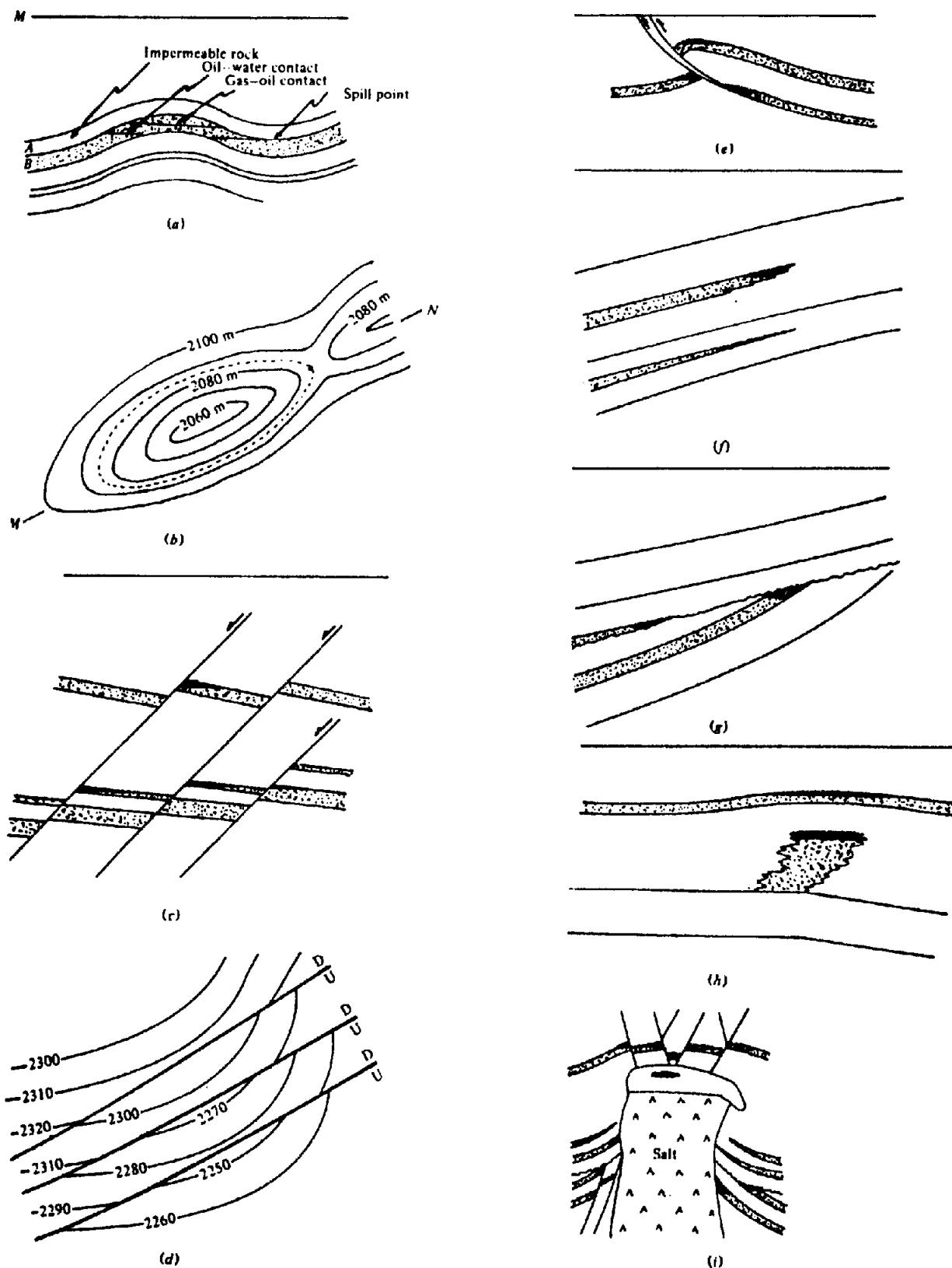


**Figure 4.85.** Sedimentary structures that produce hydrocarbon traps. Permeable beds are dotted; hydrocarbon accumulations are in black. (a) Vertical section through anticline along line MN in (b). (b) Map of the top of the permeable bed in (a) with the spill-point contour dashed. (c) Vertical section through fault traps. (d) Map of the lower permeable bed in (c). (e) Possible traps associated with thrust faulting. (f) Stratigraphic traps produced by lithologic change and pinchout. (g) Unconformity traps. (h) Trap in a reef and in draping over the reef. (i) Traps associated with a salt dome.

anticline until the anticline is filled to the *spill point*. Although the diagram is two-dimensional, similar conditions must hold for the third dimension, the structure forming an inverted bowl. The contour through the spill point, the *closing contour* (-2,085 m in Fig. 4.85b), defines the maximum area of hydrocarbon accumulation.

Figure 4.85c shows a *fault trap* in which permeable beds overlain by impermeable beds are faulted against impermeable beds. A trap exists if there is also closure parallel to the fault; an example is shown by the contours in Figure 4.85d. Obviously faults do not constitute traps if the rocks across the fault are permeable or if hydrocarbons can percolate up the fault plane. *Pinchouts* and *unconformities* (Figs. 4.85f and g) provide traps only when the adjacent rocks are impermeable and there is closure at right angles to the diagram.

Figure 4.85h shows a limestone *reef* that grew upward on a slowly subsiding platform (§4.10.5). The reef is composed of coral or other marine animals with calcareous shells, which grow prolifically under the proper conditions of water temperature and depth. As the reef subsides, sediments are deposited around it. Eventually the reef stops growing, perhaps because of a change in the water temperature or the rate of subsidence, and the reef may be buried. The reef material is usually highly porous and often covered and surrounded by impermeable sediments. Hence the reef may form a trap for petroleum generated in the reef itself or flowing into it from another bed.

Figure 4.85i represents a *salt dome* formed when a mass of salt flows upward under the pressure resulting from the weight of the overlying sediments. The salt dome bows up sedimentary beds and seals off disrupted beds and so provides traps over and around the sides of the dome.

#### 4.8.2. Objectives of Interpretation

The primary objective of a seismic survey for hydrocarbons usually is to locate structures such as those shown in Figure 4.85. However, many structures that provide excellent traps do not contain oil or gas in economic quantities. Because drilling wells is very costly, we try to derive from the seismic data as much information as possible about the geological history of the area and about the nature of the rocks in an effort to form an opinion about the probability of encountering petroleum in the structures that we map.

Unconformities often show up clearly on seismic sections, especially on long regional lines that give sufficient sense of perspective to allow an interpreter to distinguish between regional and local features

and between reasonably consistent geologic information and superimposed noise. Unconformities often indicate changes of eustatic sea level that can be correlated with specific times in geologic history; their recognition thus provides information for age-dating sediments. Patterns in the seismic data sometimes indicate the environment in which the rocks were deposited. The velocities of rocks are sometimes a clue to their lithology and origin. Drawing conclusions from these types of observations is an objective of seismic stratigraphy (§4.10.6).

The velocity, reflectivity, and other properties of a rock are sometimes altered noticeably because of changes in the fluid that fills the rock pores. Thus the effects of hydrocarbon accumulations can sometimes be seen (§4.10.8).

Seismic methods are also increasingly used for nonhydrocarbon objectives (Dobecki and Romig, 1985). Water resources are sometimes controlled by earlier topography or by faulting. Heavy minerals sometimes accumulate in channels on old topography, and minerals may be associated with rock contacts. Faulting that interrupts coal seams affect the planning of mining operations. In many mining areas, old mine drifts are not mapped accurately and knowing their location is essential to avoid cutting into one that is water-filled. Nuclear waste disposal requires reasonably detailed knowledge of faults and other geologic features. Seismic methods often provide the cheapest way of mapping such features with reasonable resolution.

Seismic methods are also used increasingly for engineering purposes. The integrity of foundation rocks must be established; cavities in the rocks or zones of weakness due to faulting or fracturing need to be known before large structures are constructed. In planning road cuts and other engineering projects involving earth removal, the cost of excavating depends to a significant degree on rock hardness; this can be estimated from seismic velocity.

### 4.9. REFRACTION INTERPRETATION

#### 4.9.1. Interpretation of Refraction Records

The identification of headwave events is usually simpler than for reflection events. traveltimes are usually available for a relatively long range of offsets, and hence it is easy to separate reflections and diffractions with their curved alignments from the direct wave, surface waves, and headwaves with their relatively straight alignments. The direct wave and surface waves are easily distinguished from headwaves because of the lower velocities of the former. Usually the only problem is in identifying the different headwaves when several refractors are present.

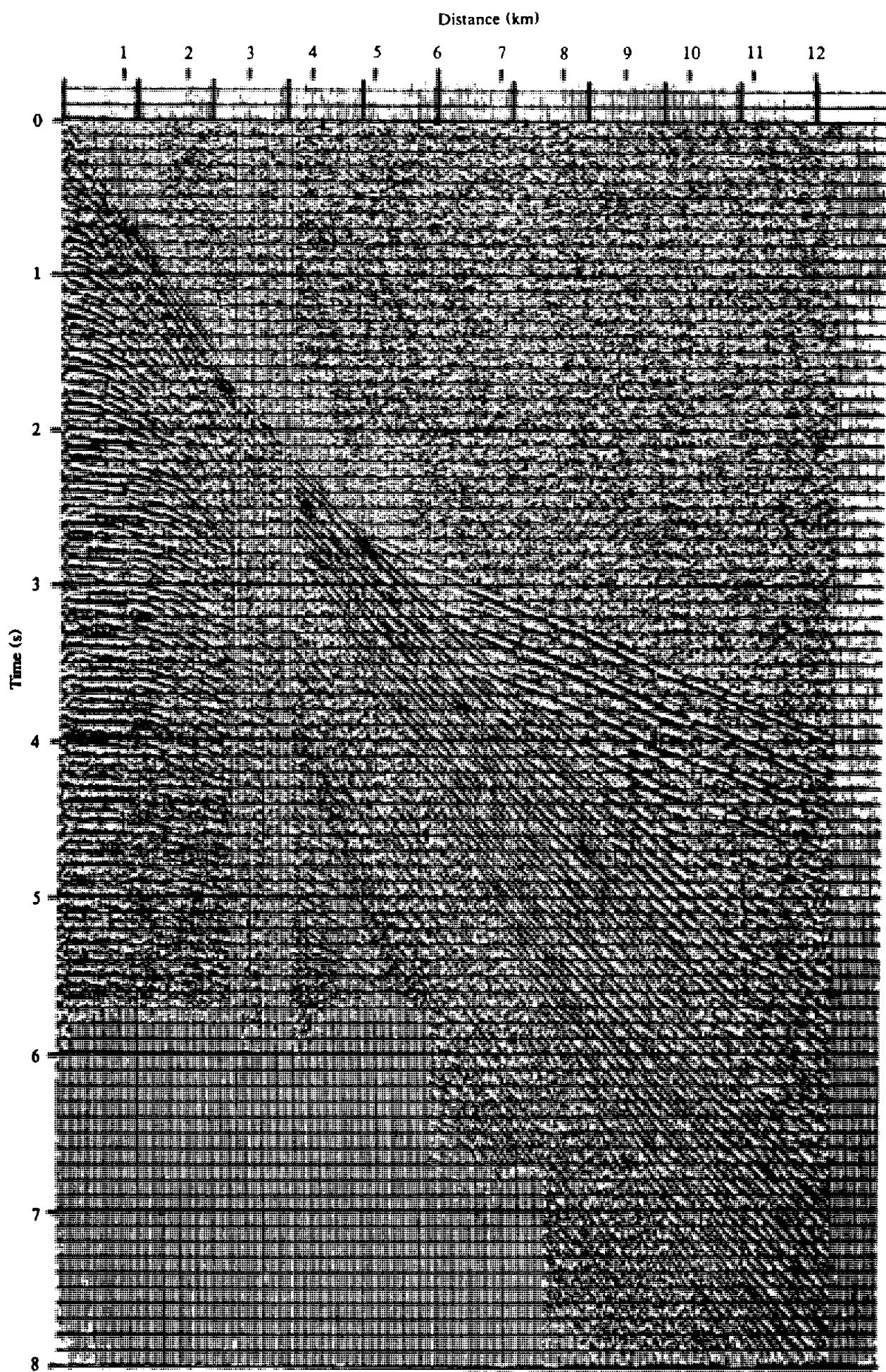


Figure 4.86. Marine refraction profile. (Courtesy Compagnie Générale de Géophysique.)

Record sections are especially useful in studying second arrivals. The *refraction record section* (also called a *refraction profile*) in Figure 4.86 shows the direct wave as the first arrival near the shotpoint; refractions from successively deeper refractors become the first arrivals as the offset distance increases. Following the first arrivals, the continuations of various events are seen after each has been overtaken by a deeper event. Numerous other events are also seen in the zone of second arrivals; most of these are either refractions that never became first arrivals or multiply-reflected refractions (see Fig. 4.35b).

The simple equations (4.68) through (4.81) can be used when the data are easy to interpret and limited in quantity. Often the chief failure of these equations (and of most refraction interpretation techniques) is in the assumption of  $V_1$ , the velocity of the section above the refractor. Most methods assume straight-line raypaths from the refractor upward to the surface. This is usually not true because the overburden velocity is rarely constant. The biggest improvement in the results obtained when using the simple equations to calculate refractor depths often is the result of using a more realistic assumption for  $V_1$  based on information other than that obtainable from the refraction data themselves (Laski, 1973).

Problems sometimes result from a *hidden zone*, a layer whose velocity is lower than that of the overlying bed so that it never carries a headwave. Energy that would approach it at the critical angle cannot get through the shallower refractors and hence there is no indication of its presence in the headwave arrivals. The low velocity of the hidden layer, however, increases the arrival times of deeper headwaves relative to what would be observed if the hidden zone had the same velocity as the overlying bed, which results in exaggeration of the depths of deeper refractors. Another situation, which is also referred to at times as a "hidden zone," is that of a layer whose velocity is higher than those of the overlying beds but that never produces first arrivals despite this because the layer is too thin and/or its velocity is not sufficiently greater than those of the overlying beds. Such a bed creates a second arrival but the second arrival may not be recognized as a distinct event.

Refraction interpretation often is based solely on first arrivals, primarily because this permits accurate determination of the traveltimes. When we use second arrivals we usually have to pick a later cycle in the wavetrain and estimate travelttime from the measured time. However, velocities based on second arrivals will be accurate, and much useful information is available through their study.

Several additional considerations affect refraction interpretation. Refraction traveltimes are corrected

to datum in the same manner as reflection traveltimes. There is one difference, however: Travelpaths above the refractor are inclined and so the datum should be near the surface to minimize the effects of the inclined paths on the corrections and the effective shotpoint-geophone distance.

If enough data are available, interpretational ambiguities often can be resolved. However, in an effort to keep survey costs down, only the minimum amount of data may be obtained (or less than the minimum), and some of the checks that increase certainty and remove ambiguities may not be possible.

#### 4.9.2. Refraction Interpretation Methods

Three types of approach are made to refraction interpretation:

1. Application of Equations (4.68) to (4.81).
2. Delay-time methods.
3. Wavefront reconstruction methods.

Simple multiple-layer equations are generalizations of Equations (4.69), (4.75), and (4.76). These equations generally demand that the refractors be nearly planar over the area being studied, that is, the refractor relief can be ignored in calculations of depth, dip, and velocity.

Refraction interpretation often involves "stripping," which is in effect the removal of one layer at a time. In this method the problem is solved for the first refractor, after which the portions of the time-distance curve for the deeper refractors are adjusted to give the result that would have been obtained if the shotpoint and geophones had been located on the first refracting horizon. The adjustment consists of subtracting the traveltimes along the slant paths from shotpoint down to the refractor and up from the refractor to the geophones, and also decreasing the offsets by the components of the slant paths parallel to the refractor. The new time-distance curve is now solved for the second refracting layer after which this layer can be stripped off and the process continued for deeper refractors.

#### 4.9.3. Delay-Time Methods

(a) *General.* The concept of delay time, introduced by Gardner (1939), is widely used in routine refraction interpretation, mainly because the various schemes based on the use of delay times are less susceptible to the difficulties encountered when we attempt to use Equations (4.69) to (4.81) with refractors that are curved or irregular. Assuming that the refraction times have been corrected for elevation and weathering, the *delay time*  $\delta$  associated with the path SMNG in Figure 4.87 is the observed refraction

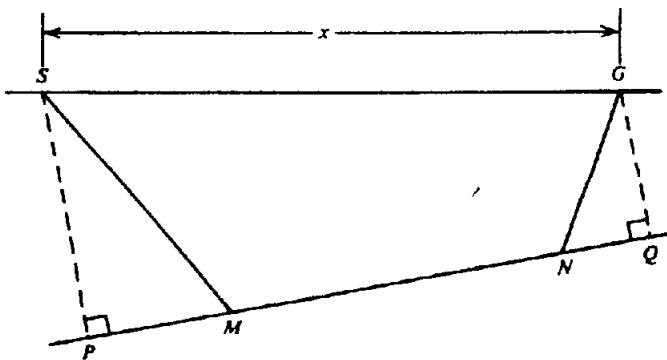


Figure 4.87. Illustrating delay time.

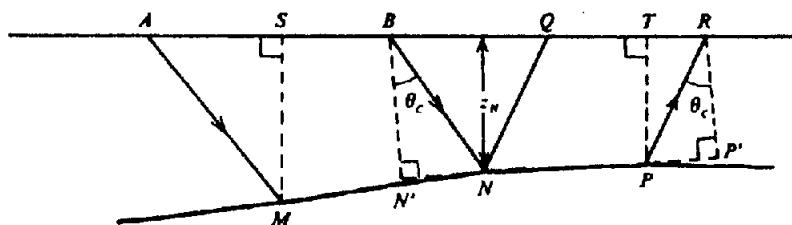


Figure 4.88. Determining sourcepoint and geophone delay times.

time at  $G$ ,  $t_g$ , minus the time required for the wave to travel from  $P$  to  $Q$  (the projection of the path on the refractor) at the velocity  $V_2$ . Writing  $\delta$  for the delay time, we have

$$\begin{aligned} \delta &= t_g - \frac{PQ}{V_2} \\ &= \left( \frac{SM + NG}{V_1} + \frac{MN}{V_2} \right) - \frac{PQ}{V_2} \\ &= \left( \frac{SM + NG}{V_1} \right) - \left( \frac{PM + NQ}{V_2} \right) \\ &= \left( \frac{SM}{V_1} - \frac{PM}{V_2} \right) + \left( \frac{NG}{V_1} - \frac{NQ}{V_2} \right) \\ &= \delta_s + \delta_g \end{aligned} \quad (4.127)$$

where  $\delta_s$  and  $\delta_g$  are known as the *shotpoint delay time* and the *geophone delay time* because they are associated with the portions of the path down from the shot and up to the geophone.

An approximate value of  $\delta$  can be found by assuming that the dip is small enough that  $PQ$  is approximately equal to the geophone offset  $x$ . In this case,

$$\delta = \delta_s + \delta_g \approx t_g - \frac{x}{V_2} \quad (4.128)$$

Provided the dip is less than about  $10^\circ$ , this relation is sufficiently accurate for most purposes. If we substitute the value of  $t_g$  obtained from Equations (4.70), (4.75), and (4.76), we see that  $\delta$  is equal to the

intercept time for a horizontal refractor but not for a dipping refractor.

Delay-time methods are subject to certain errors that must be guarded against. As the shotpoint to geophone distance increases, the refraction wavetrain becomes longer and energy peak shifts to later cycles. There is thus the danger that different cycles will be picked on different profiles and that the error will be interpreted as an increase in shot delay time. If sufficient data are available, the error is usually obvious. Variations in refractor velocity manifest themselves in local divergences of the offset total-delay-time curves for pairs of reversed profiles. However, if some data that do not represent refraction travel in the refractor under consideration are accidentally included, the appearance is apt to be the same as if the refractor velocity were varying. In situations where several refractors that have nearly the same velocities are present, unambiguous interpretation may not be possible.

Many interpretation schemes using delay time have been given in the literature, for example, Gardner (1939, 1967), Barthelmes (1946), Tarrant (1956), Wyrobek (1956), and Barry (1967). We shall describe only the latter two. The method described by Wyrobek is suitable for unreversed profiles whereas that of Barry works best with reversed profiles.

(b) *Barry's method.* The scheme described by Barry, like many based on delay times, requires that we resolve the total delay time  $\delta$  into its component parts  $\delta_s$  and  $\delta_g$ . In Figure 4.88 we show a geophone

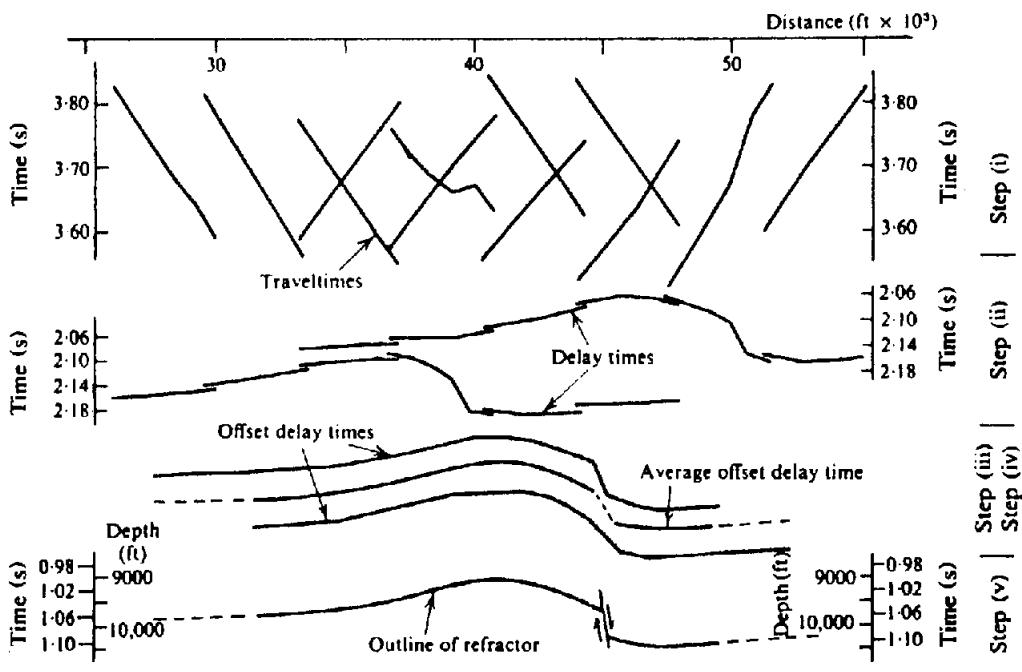


Figure 4.89. The delay-time method of interpreting reversed profiles. (After Barry, 1967.)

$R$  for which data are recorded from shots at  $A$  and  $B$ . The ray  $BN$  is reflected at the critical angle, and hence  $Q$  is the first geophone to record the head-wave from  $B$ . Let  $\delta_{AM}$  be the shotpoint delay time for shot  $A$ ,  $\delta_{NQ}$  and  $\delta_{PR}$  the geophone delay times for geophones at  $Q$  and  $R$ , and  $\delta_{AQ}$  and  $\delta_{AR}$  the total delay times for the paths  $AMNQ$  and  $AMPR$ . Then

$$\delta_{AQ} = \delta_{AM} + \delta_{NQ}$$

$$\delta_{AR} = \delta_{AM} + \delta_{PR}$$

$$\Delta\delta = \delta_{AQ} - \delta_{AR}$$

$$= \delta_{NQ} - \delta_{PR}$$

For the shot at  $B$ , the shot delay time  $\delta_{BN}$  is approximately equal to  $\delta_{NQ}$  provided the dip is small. In this case,

$$\delta_{BR} = \delta_{BN} + \delta_{PR} \approx \delta_{NQ} + \delta_{PR}$$

The geophone delay times are now given by

$$\left. \begin{aligned} \delta_{NQ} &\approx \frac{1}{2}(\delta_{BR} + \Delta\delta) \\ \delta_{PR} &\approx \frac{1}{2}(\delta_{BR} - \Delta\delta) \end{aligned} \right\} \quad (4.129)$$

Thus, it is possible to find the geophone delay time at  $R$  provided we have data from two shots on the same side and we can find point  $Q$ . If we assume that the bed is horizontal at  $N$  and is at a depth  $z_N$

we have

$$z_N = \frac{V_1 \delta_{BN}}{\cos \theta_c} \quad (4.130)$$

$$\begin{aligned} BQ &= 2z_N \tan \theta_c \\ &= 2V_1 \delta_{BN} \left( \frac{\tan \theta_c}{\cos \theta_c} \right) \\ &= 2V_2 \delta_{BN} \tan^2 \theta_c \end{aligned} \quad (4.131)$$

The shot delay time  $\delta_{BN}$  is assumed to be equal to half the intercept time at  $B$ ; this allows us to calculate an approximate value of  $BQ$  and thus determine the delay times for all geophones to the right of  $Q$  for which data from  $A$  and  $B$  were recorded.

The interpretation involves the following steps, which are illustrated in Figure 4.89:

- (i) The corrected traveltimes are plotted.
- (ii) The total delay times are calculated and plotted at the geophone positions.
- (iii) The geophone offset distances ( $PP'$  in Fig. 4.88) are calculated using Equation (4.131), and, assuming  $PP' = \frac{1}{2}BQ$ , the delay times in (ii) are shifted toward the shotpoint by these amounts.
- (iv) The shifted curves in (iii) for the reversed profiles should be parallel. Any divergence is due to an incorrect value of  $V_2$ , hence the value of  $V_2$  is adjusted and steps (ii) and (iii) are repeated until the curves are parallel (with practice only one adjustment is usually necessary).
- (v) The total delay times are separated into shotpoint and geophone delay times; the latter are plotted at the points of entry and emergence

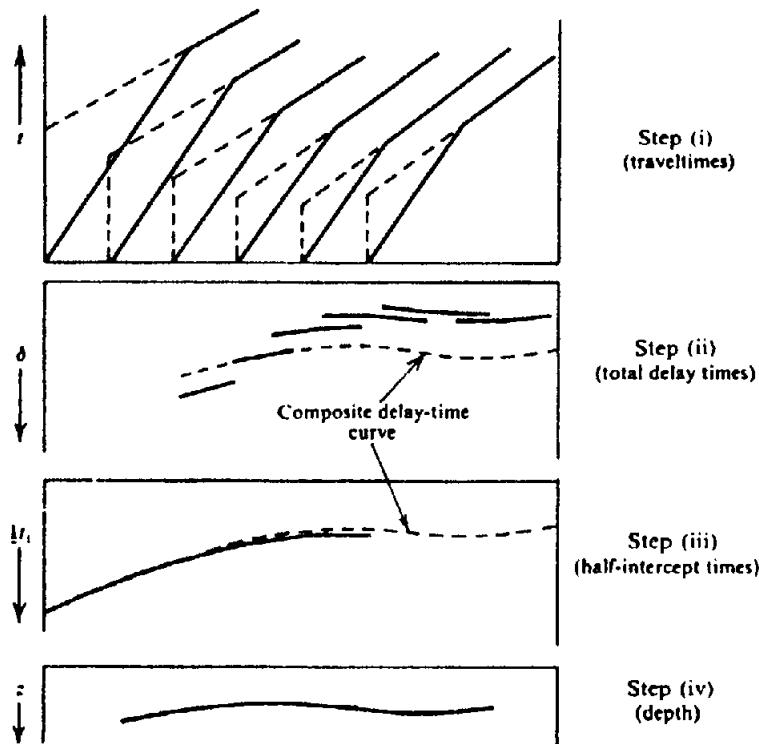


Figure 4.90. Wyrobek's method using unreversed profiles. (After Wyrobek, 1956).

from the refractor ( $S$  and  $T$  in Fig. 4.88). The delay-time scale can be converted into depth if required using Equations (4.130) with  $\delta_{PR}$  in place of  $\delta_{BN}$ .

(c) *Wyrobek's method.* To illustrate Wyrobek's method we assume a series of unreversed profiles as in the upper part of Figure 4.90. The various steps in the interpretation are as follows:

- The corrected traveltimes are plotted and the intercept times measured.
- The total delay time  $\delta$  is calculated for each geophone position for each shot and the values are plotted at the geophone position (if necessary, a value of  $V_2$  is assumed). By moving the various segments up or down, a composite curve similar to a phantom horizon is obtained.
- The intercept times divided by 2 are plotted and compared with the composite delay-time curve. Divergence between the two curves indicates an incorrect value of  $V_2$  (see below); hence the value used in step (ii) is varied until the two curves are "parallel," after which the half-intercept time curve is completed by interpolation and extrapolation to cover the same range as the composite delay-time curve.
- The half-intercept time curve is changed to a depth curve by using Equation (4.70), namely,

$$z = \frac{1}{2} V_1 t_i / \cos \theta_c$$

(Note that we are ignoring the difference between the vertical depth  $z$  and the slant depths  $z_A$  and  $z_B$  in Fig. 4.33.)

Wyrobek's method depends on the fact that the curve of  $\delta$  is approximately parallel to the half-intercept time curve (see problem 15). Wyrobek's method does not require reversed profiles because the intercept at a shotpoint does not depend on the direction in which the cable is laid out.

#### 4.9.4. Wavefront Methods

(a) *General.* Wavefront reconstruction, usually by graphical means, forms the basis of several refraction interpretation techniques. The classic paper is one by Thornburgh (1930); other important articles are those by Gardner (1949), Baumgarte (1955), Hales (1958), Hagedoorn (1959), Rockwell (1967), and Schenck (1967).

Figure 4.91 illustrates the basic method of reconstructing wavefronts. The refraction wavefront that reached  $A$  at  $t = 1.600$  s reached  $B, C, \dots$  at the times  $1.600 + \Delta t_B, 1.600 + \Delta t_C, \dots$ . By drawing arcs with centers  $B, C, \dots$  and radii  $V_1 \Delta t_B, V_1 \Delta t_C, \dots$ , we can establish the wavefront for  $t = 1.600$  s ( $AZ$ ) as accurately as we wish. Similarly, other refraction wavefronts, such as that shown for  $t = 1.400$  s, can be constructed at any desired traveltime interval. The direct wavefronts from the shot  $S$  are of course the circles shown in the diagram.

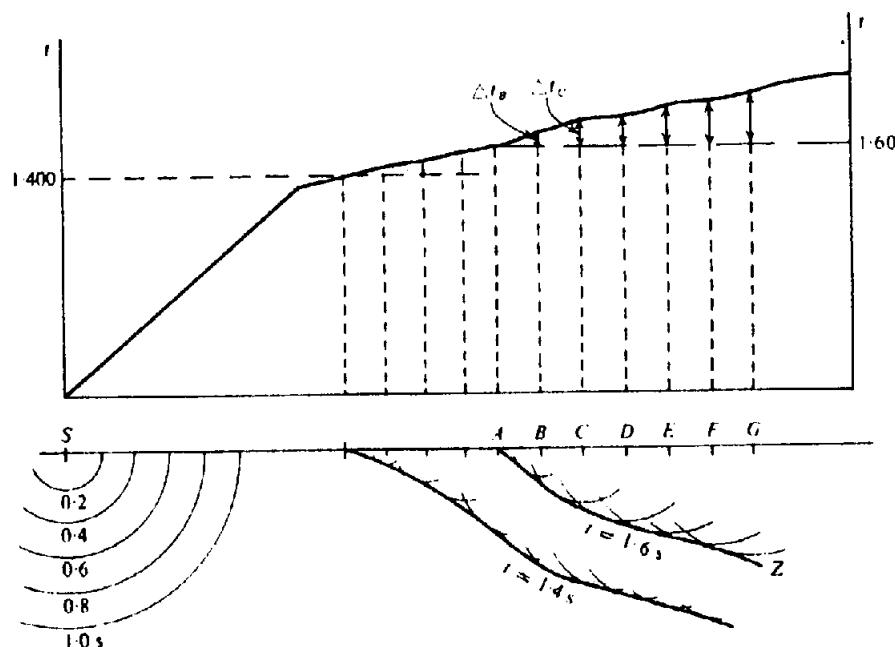


Figure 4.91. Reconstruction of wavefronts.

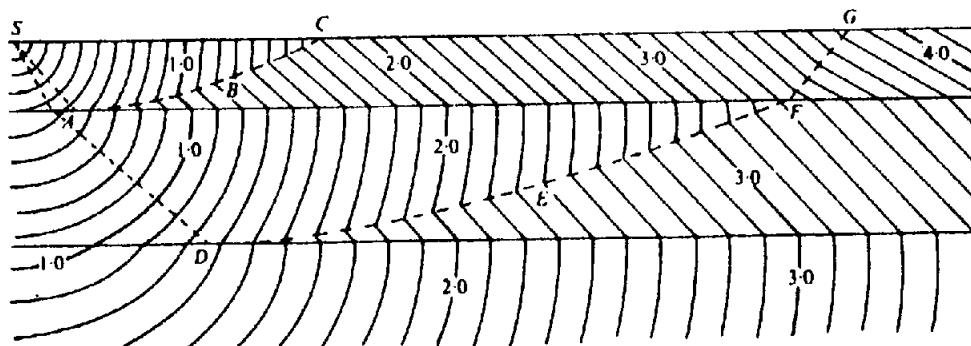


Figure 4.92. First-arrival wavefronts. Coincident-time curves are dotted. (After Thornburgh, 1930.)

In Figure 4.92 we show a series of wavefronts chosen so that only waves that will be first arrivals are shown (all secondary arrivals have been eliminated in the interest of simplicity). Between the shotpoint *S* and the crossover point *C* [Eq. (4.71)] the direct wave arrives first. To the right of *C*, the wave refracted at the first horizon arrives first until, to the right of *G*, the refraction from the deeper horizon overtakes the shallower refraction.

The two systems of wavefronts representing the direct wave and the refracted wave from the shallow horizon, intersect along the dotted line *ABC*. This line, called the *coincident-time line* by Thornburgh, passes through the points where the intersecting wavefronts have the same traveltimes. The curve *DEFG* is a coincident-time curve for the deeper horizon. The coincident-time curves are tangent to the refractors at *A* and *D* where the incident ray reaches the critical angle (see problem 16) whereas the points at which the coincident-time curves meet

the surface are marked by abrupt changes in the slopes of the time-distance plot.

Since the coincident-time curve is tangent to the refractor, the latter can be found when we have one profile plus other data - such as the dip, depth, critical angle - or a second profile (not necessarily reversed) because we now have two coincident-time curves and the refractor is the common tangent to the curves.

When reversed profiles are available, the construction of wavefronts provides an elegant method of locating the refractor. The basic principle is illustrated in Figure 4.93, which shows two wavefronts, *MCD* and *PCE*, from shots at *A* and *B* intersecting at an intermediate point *C*. Obviously the sum of the two traveltimes from *A* and *B* to *C* is equal to the reciprocal time between *A* and *B*,  $t_c$ . If we had reconstructed the two wavefronts from the time-distance curve without knowing where the refractor *RS* was located, we would draw the wavefronts as *MCN*

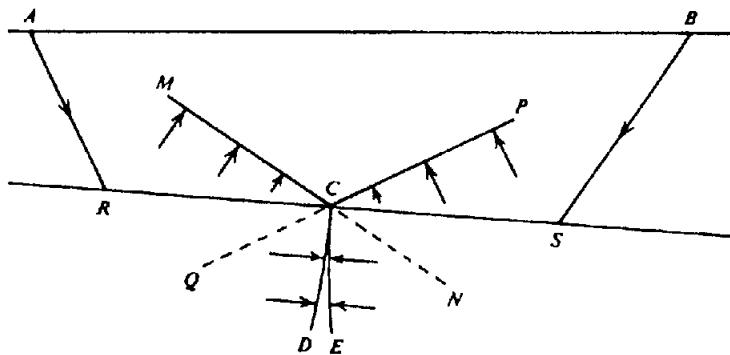


Figure 4.93. Determining refractor position from wavefront intersections.

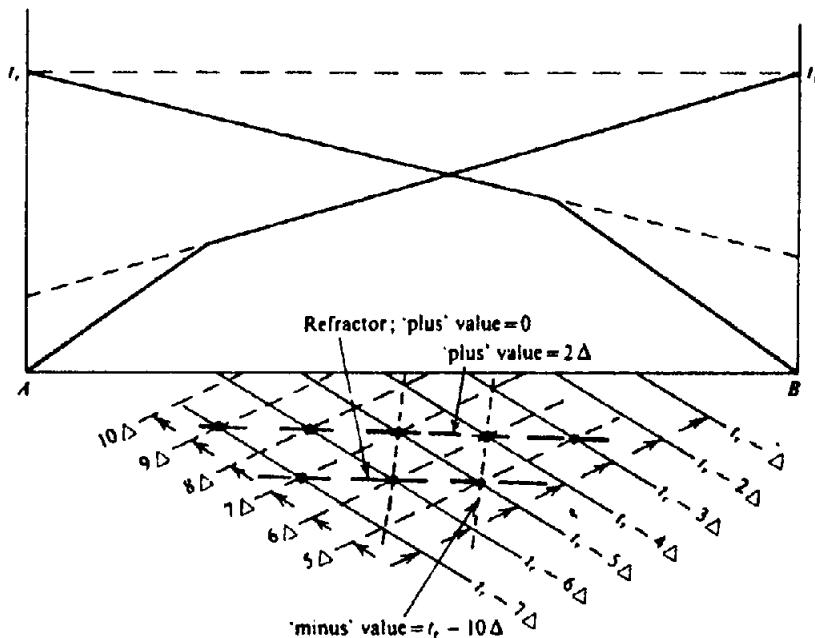


Figure 4.94. The plus-minus method. (After Hagedoorn, 1959.)

and  $PCQ$ , not  $MCD$  and  $PCE$ . Therefore, if we draw pairs of wavefronts from  $A$  and  $B$  such that the sum of the traveltimes is  $t_r$ , the refractor must pass through the points of intersection of the appropriate pairs of wavefronts in Figure 4.93.

(b) *Plus minus method.* The plus-minus method, devised by Hagedoorn (1959), utilizes a construction similar to that just described. When the refractor is horizontal, the intersecting wavefronts drawn at intervals of  $\Delta$  ms form diamond-shaped figures (Fig. 4.94) whose horizontal and vertical diagonals are equal to  $V_2\Delta$  and  $V_1\Delta/\cos \theta_c$ , respectively. If we add together the two traveltimes at each intersection and subtract  $t_r$ , the resulting "plus" values equal 0 on the refractor,  $+2\Delta$  on the horizontal line through the first set of intersections vertically above those defining the refractor,  $+4\Delta$  on the next line up, and so on. Because the distance between each pair of adjacent lines is  $V_1\Delta/\cos \theta_c$ , we can use any of the plus lines to plot the refractor. The difference between

two traveltimes at an intersection is called the "minus" value; it is constant along vertical lines passing through the intersections of wavefronts. The distance between successive minus lines as shown in Figure 4.94 is  $V_2\Delta$ ; hence a continuous check on  $V_2$  is possible. Although dip alters the preceding relations, the changes are small for moderate dip, and the assumption is made that the plus lines are still parallel to the refractor and the minus lines do not converge or diverge.

#### 4.9.5. Engineering Applications

Refraction methods are commonly applied in mineral-exploration and civil-engineering work to measure depth of bedrock. With the arrangement shown in Figure 4.95, shots are fired from the end points of the spread,  $A$  and  $B$ , and the midpoint  $C$ . (The "shot" is usually a hammer blow for shallow overburden or a blasting cap for deeper.) Let  $t_{AB}$  be the surface-to-surface traveltime from  $A$  to  $B$ , and so

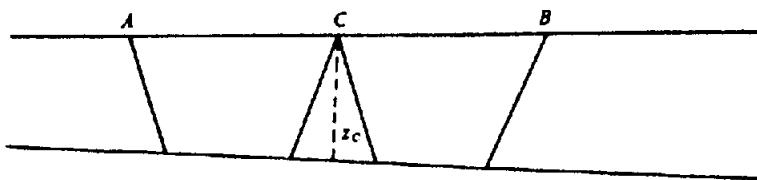


Figure 4.95. Refraction profile for determining depth to bedrock.

forth. Then (see problem 17)

$$z_C = \left( \frac{t_{CA} + t_{CB} - t_{AB}}{2} \right) \frac{V_1 V_2}{(V_2^2 - V_1^2)^{1/2}} \quad (4.132)$$

where  $V_1$  is the overburden and  $V_2$  is the bedrock velocity. Frequently  $V_2 \gg V_1$  and we can replace the velocity terms by  $V_1$ :

$$z_C = \frac{1}{2} V_1 (t_{CA} + t_{CB} - t_{AB}) \quad (4.133)$$

The error in  $z_C$  is less than 6% if  $V_2 > 3V_1$ . This method assumes that the overburden is essentially homogeneous, the depth variation is smooth, the dip is small, and the velocity contrast is so large that the perpendicular distance to bedrock is roughly equal to the vertical distance. Depth calculations by this technique are generally good because they depend on the measurement of only one velocity,  $V_1$ , and three traveltimes.

## 4.10. REFLECTION INTERPRETATION

### 4.10.1. Interpretation Techniques

(a) *Mapping reflecting horizons.* Reflections are usually identified with bedding planes based on correlations with observations in boreholes, velocity information, synthetic seismograms (§4.10.2), or previous experience in the area.

The horizons that we draw on seismic sections provide us with two-dimensional pictures only. A three-dimensional picture is necessary to determine whether closure exists, the area within the closing contour, the location of the highest point on the structure, and so on. To obtain three-dimensional information, we usually shoot a number of lines, and most reflection surveys are carried out along a more-or-less rectangular grid of lines.

Horizons are first mapped on cross sections and the sections are compared at line intersections to identify the same horizons on all lines; identification is made on the basis of character and traveltimes. The horizons are carried along all lines in the prospect area to the extent that the quality of the data permit.

When a horizon is carried all the way around a closed loop, we should end up with the same traveltime with which we started. This *closing of loops* provides an important check on reliability. When a loop fails to close within a reasonable error (which depends mainly on the record quality and the accuracy of the statics corrections), the cause of the misclosure should be investigated carefully. Migrated sections have to be tied by finding the same reflection on intersecting sections. Such tie points will be displaced from the vertical through the sourcepoint by the amount of the migration on each of the lines. Often misclosure is due to an error in correlating from line to line, possibly because of inaccurate corrections, change in reflection character, or error in correlating across faults. When the dip is different on the two sides of a fault or the throw varies along the fault, an incorrect correlation across the fault may result in misclosures (but not necessarily). After the sources of misclosure have been carefully examined and the final misclosure reduced to an acceptable level, the remaining misclosure is distributed around the loop.

After horizons have been carried on the sections, maps are prepared. For example, we might map a shallow horizon, an intermediate horizon at roughly the depth at which we expect to encounter oil if any is present, and a deep horizon. We map on a *base map*, which shows the locations of the seismic lines (usually by means of small circles representing sourcepoints) plus other features, such as oil wells, rivers, shorelines, roads, land and political boundaries, and so on. Values representing the depth of the horizon below the datum plane are placed on the map (*posted*), usually at each sourcepoint. Other information relevant to the horizon being mapped (depths in wells, locations of gravity anomalies, relevant geologic information, etc.) is also posted. Faults that have been identified on the records or cross sections are drawn on the map and depth values are then contoured.

*Isopach maps*, which show the thickness of sediments between two horizons, are useful in studying structural growth. They can be prepared by overlaying maps of the two horizons and subtracting the contour values wherever the contours on one map

cross the contours on the other. The differences are recorded on a blank map and then contoured. If the contours show a trend toward increased thickness in a certain direction, it may suggest that the region was tilted downward in this direction during the period of deposition or that the source of the sediments is in this direction. Uniform thickness of a folded bed indicates that the folding came after the deposition whereas if the thickness increases away from the crest of an anticline, deposition probably was contemporaneous with the growth of the structure. Growth during deposition is usually more favorable for petroleum accumulation because it is more likely for reservoir sands to be deposited on the flanks of structures with even slight relief.

(b) *Structural style.* Structural traps, such as anticlines and fault traps, and structural leads (possibilities of traps that require more work to define them completely) are usually evident from examination of the maps. Traps resulting from pinchouts and unconformities are more difficult to recognize and nonseismic evidence often must be combined with seismic data to define such features. Nevertheless, careful study of the maps, sections, and records plus broad experience and ample imagination may disclose variations of dip or other effects that help locate traps of these types.

The orientation and type of structural features depend on the stress fields to which they have been subjected. The underlying system of structure is called structural or tectonic style. The structural style of an area provides a guide for interpreting what otherwise might be ambiguous definition of structural features, especially where data are scarce. For example, if a well-defined fault is seen on one horizon but is not clear on other horizons, it might not be evident whether the fault movement was normal, reverse, or strike-slip and what the attitude of the fault plane is. However, the structural style, if known, helps to decide the most probable type of faulting, fault plane dip and orientation, and so on. Examples of structural style in seismic data are shown in Bally (1983-4).

(c) *Working out geological history.* After the structural information has been extracted, the next step is to work out as much as possible of the geological history of the area. Fundamental in this connection is the determination of the ages of the different horizons, preferably according to the geological time scale, but at least relative to one another. Often seismic lines pass close enough to wells to permit correlating the seismic horizons with geological horizons in the wells. Refraction velocities (if available) may help to identify certain horizons. Un-

conformities associated with major time gaps are apt to be among the most prominent reflectors. Occasionally a particular reflection has a distinctive character that persists over large areas, permitting identification not only of it but also of other events by their relation to it. Notable examples of persistent identifiable reflections are the low-frequency reflections sometimes associated with massive basement and the prominent reflection from the top of the Ellenburger, a limestone encountered in Northern Texas.

The unraveling of the geological history of the area is important in answering questions such as: (a) Was the trap formed prior to, during, or subsequent to the generation of the oil and gas? (b) Has the trap been tilted sufficiently to allow trapped oil to escape? (c) Did displacement of part of a structure by faulting occur before or after possible emplacement of oil? Whereas the seismic data rarely give unambiguous answers to such questions, often clues can be obtained that, when combined with other information, such as surface geology and well data, permit the interpreter to make intelligent guesses that improve the probability of finding oil. Alertness to such clues is the "art" of seismic interpretation and often the distinction between an "oil finder" and a routine interpreter.

(d) *Drawing conclusions from reflection data.* Deducing geological significance from the aggregate of many minor observations not only tests the ingenuity of an interpreter, it also tests his in-depth understanding of physical principles. For example, downdip thinning of reflection intervals might result from a normal increase of velocity with depth as well as from thinning of the sediments, and flow of salt or shale may cause illusory structure on deeper horizons. Geometric focusing produced by reflector curvature can produce various effects, especially if the migration is not correct, and energy that comes from a source located off to one side of the line can interfere with the patterns of other reflection events to produce effects that might be interpreted erroneously unless their true nature is recognized. Improper processing likewise can create opportunities for misinterpreting data (Tucker and Yorsten, 1973).

When the interpretation is finally completed, a report is usually prepared, often both for submission in writing and for oral presentation. In some ways this is the most difficult and most important task of the interpreter. He must present his findings in such a way that the appropriate course of action is defined as clearly as possible. The important aspects should not be obscured by presenting a mass of details nor should they be distorted by presenting carefully selected but nonrepresentative maps and

sections. Evidence to support significant conclusions should be given. Alternate interpretations should be presented and an estimate given of the reliability of the results and conclusions. Finally the interpreter should recommend what further action should be undertaken.

Good references on seismic interpretation include Sheriff and Geldart (1983), Bally (1983–4), McQuillin, Bacon, and Barclay (1984), Badley (1985), and Gries and Dyer (1985).

#### 4.10.2. Modeling: Synthetic Seismograms

(a) *General.* The effects of passage through a sequence of layers with given velocities and densities is expressed by  $e_r$  (Eq. (4.103)), in effect a list of the traveltimes and reflection coefficients for each reflecting interface. The embedded wavelet,  $k\delta_r * s_r * p_r * n_r$ , in Equation (4.103), can be used along with  $e_r$  to calculate a *synthetic seismogram*, that is, what the recorded waveform should theoretically be. A wave is assumed to impinge on the first interface where its energy is partitioned among transmitted and reflected waves. Each of these waves is then followed as it travels to other interfaces where additional waves are generated, and so on. The resulting seismic record is simply the superposition of those waves that are ultimately observed at the recording station. Because Snell's law determines raypaths and Zoeppritz's equations determine energy relationships, the problem is completely determined and the solution is straightforward if we know the spatial distribution of the elastic properties and densities. However, actually solving the problem is a formidable task, even for modern computers, because of the tremendous number of waves generated for a realistic sequence of layers; thus, simplifications must be made.

(b) *Normal incidence synthetic seismograms.* Often horizontal bedding is assumed and only the raypath normal to the reflecting interfaces is tracked. Density variations are frequently ignored or assumed to have a definite relation to velocity so that the reflection and transmission coefficients can be based on velocity changes only. Often small velocity variations are ignored and only the major contrasts are considered, or else the small changes are lumped together into larger steps. Often multiples, especially short-path multiples, are ignored.

In many areas the synthetic seismogram is a reasonable approximation to actual seismic records and is therefore useful in correlating reflection events with particular horizons. Comparison of the actual and synthetic seismograms may also help to determine which events represent primary reflections and

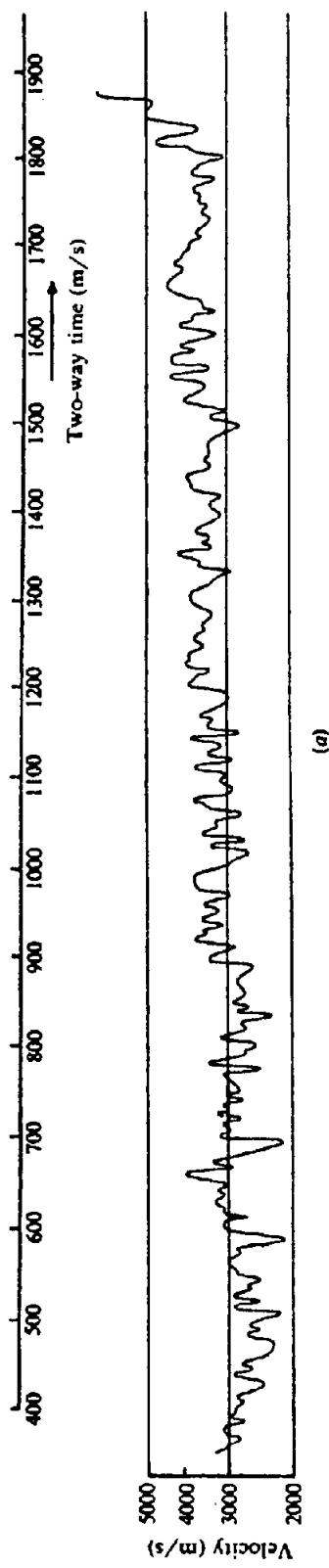
which represent multiples. Figure 4.96a shows a sonic log plotted to a time scale (rather than the usual depth scale) and Figure 4.96b shows the synthetic seismogram that would result, assuming a certain initial wave shape and neglecting multiples and changes in density. Figure 4.96c is a field recording made in the same area; some events, such as *B*, *D*, and *J*, correlate well with synthetic events but elsewhere the correlation ranges from fair to poor. Figure 4.96d differs from Figure 4.96b in that simple multiples are included; the principal differences are the appearance of a strong multiple at *K* and considerable reduction in the amplitude of *F*, presumably because of interference with multiples. This synthetic seismogram was made without shallow information; sonic logs are often not run in the upper part of a borehole, and consequently many of the most important effects cannot be modeled correctly.

A sonic log and a synthetic seismogram fail to have a one-to-one correspondence not only because of the approximations made in the calculation, but also because the seismic wavelengths are so much longer than the distances over which the acoustic properties can be assumed to be constant that the actual seismic waveform is the interference composite of many small events, and because the sonic log used to calculate the reflectivity is also subject to errors.

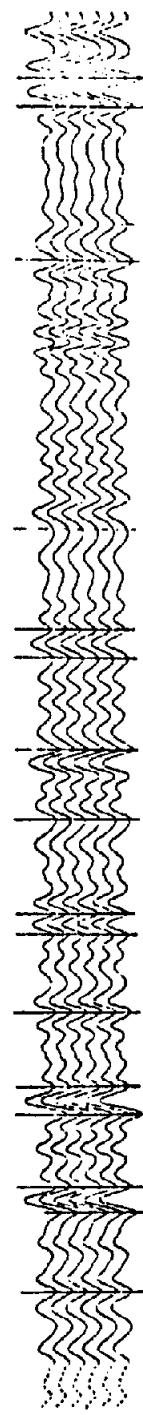
An important use of synthetic seismograms is in studying the effect of changes in the layering on the seismic record. One might, for example, assume that a shale passes laterally into a sand and determine how such a change would affect events on the record, possibly altering the number of legs in a reflection event or changing some other characteristic. This might then provide a clue in looking for ancient stream channels or other features of interest. Synthetic seismograms are important in indicating the features that may help to identify stratigraphic traps.

(c) *Two-dimensional synthetic seismograms.* A series of one-dimensional synthetic seismograms are often made where the model is modified slightly for successive traces in order to simulate stratigraphic or structural changes along a seismic line, and the result is displayed as a two-dimensional synthetic section. A true two-dimensional section to simulate unmigrated seismic data would show dipping features in different locations and diffractions. Such synthetic seismograms are sometimes made using a wave-theory algorithm according to the scalar wave equation (which does not allow for mode conversion).

(d) *Raypath modeling.* Where the structure and/or horizontal velocity variations are complicated, iterative ray tracing through a model may be used to



(a)



(b)



(c)



(d)

Figure 4.96. Synthetic seismograms. (Courtesy Compagnie Générale de Géophysique.) (a) Sonic log plotted in time. (b) Synthetic seismogram of primary reflections only. (c) Synthetic seismogram with simple multiples added. (d) Field record after normal-moveout correction.

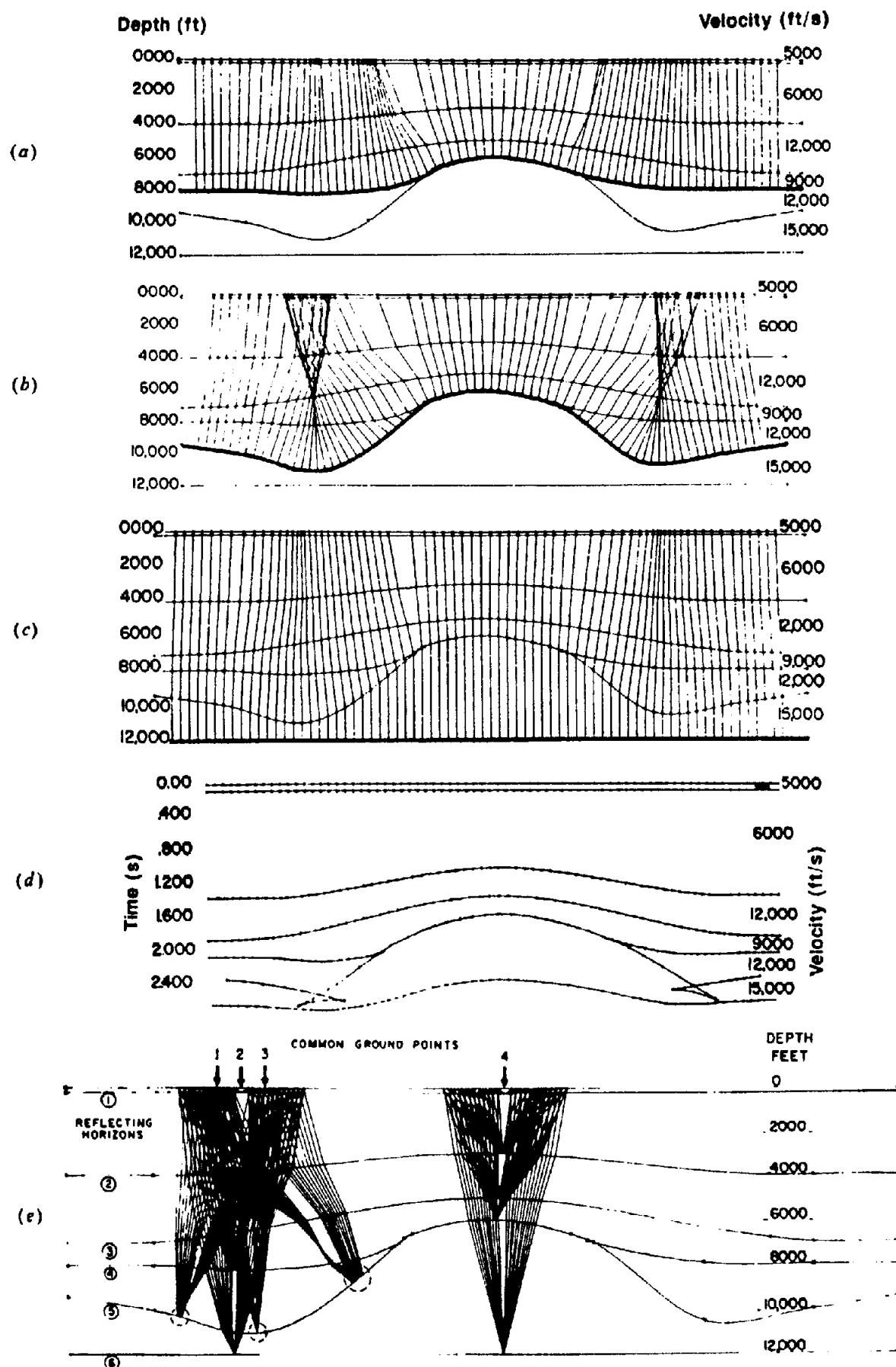


Figure 4.97. Ray-trace modeling of a CMP section. Rays perpendicular to reflectors are bent according to Snell's law as they pass through intervening interfaces. (From Taner, Cook, and Neidell, 1970.) (a), (b), (c) Tracing three reflectors for a North Sea model; (b)/(c) are the top/base of a salt layer. (d) The predicted CMP section. (e) Ray tracing to determine stacking velocity values.

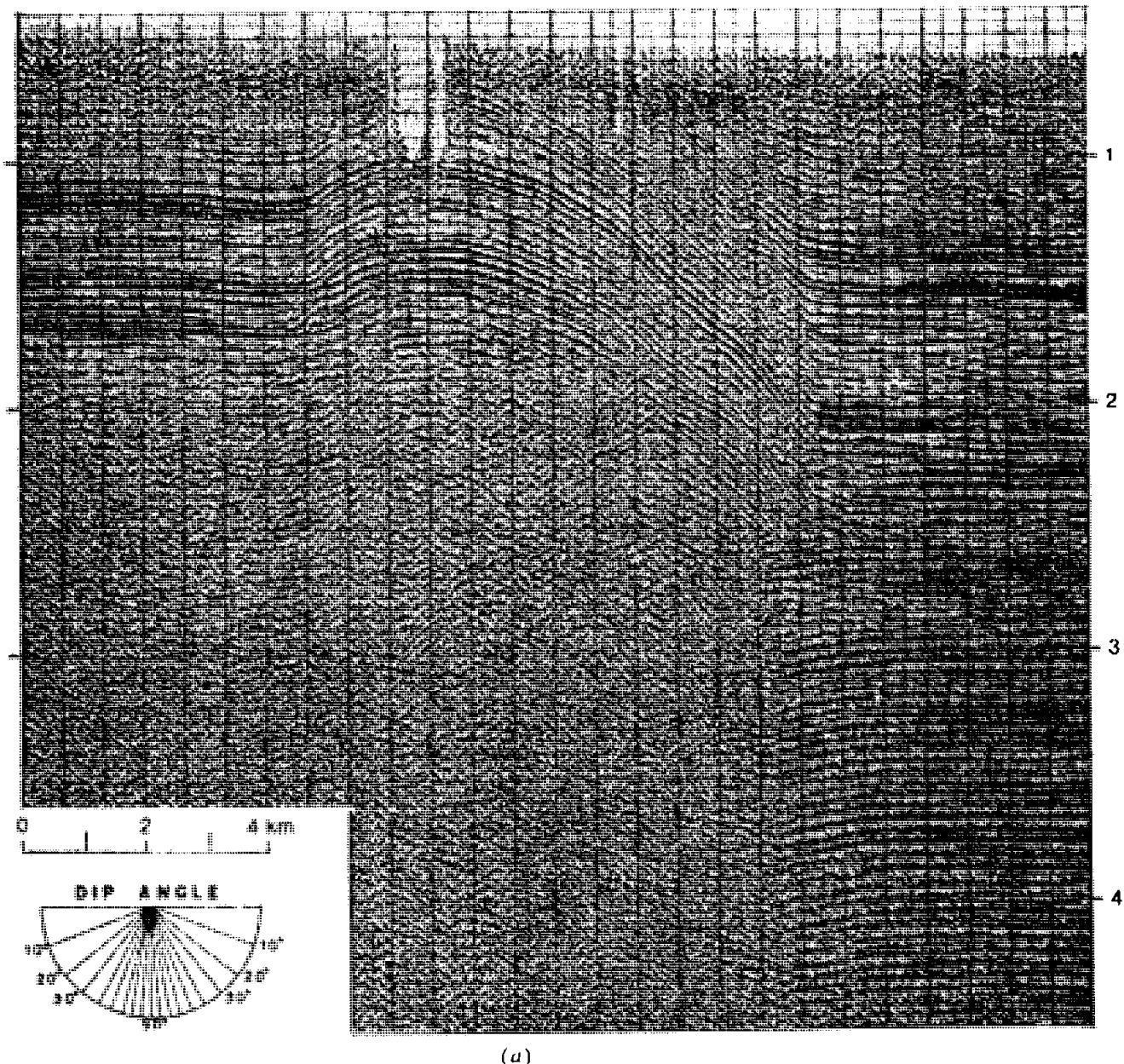


Figure 4.98. Section across a thrust fault in the Oregon Basin, part of the Big Horn Basin of Wyoming. (After Stone, 1985.) (a) Seismic section.

determine a model that is compatible with the seismic observations. The usual assumption is that reflections mark the boundaries between layers, each of which has constant velocity. The procedure often is to first map a shallow reflector, assuming a laterally constant velocity function. One then maps the reflection that marks the second interface, between layers 2 and 3, by tracing rays obeying Snell's law at the first interface. The interface and raypaths are varied iteratively so that the model time section matches the actual time section for each successive interface. The process is repeated at each interface. Examples of ray-trace modeling are shown in Figures 4.97 and 4.98.

Irregularities on one interface will distort stacking velocity measurements for deeper reflections, and a

further check on ray-trace modeling is provided by matching the model stacking-velocity calculations with those observed (Fig. 4.97e).

#### 4.10.3. Evidence of Faulting

Ideally reflection events terminate sharply as the point of reflection reaches the fault plane and resume again in displaced positions on the other side of the fault, the reflections having sufficiently distinctive character that the portions on opposite sides of the fault can be recognized and the fault throw determined. In practice, diffractions usually prolong events so that the location of the fault plane is not clearly evident, although occasionally it is possible to observe sharp terminations. Sometimes the same re-

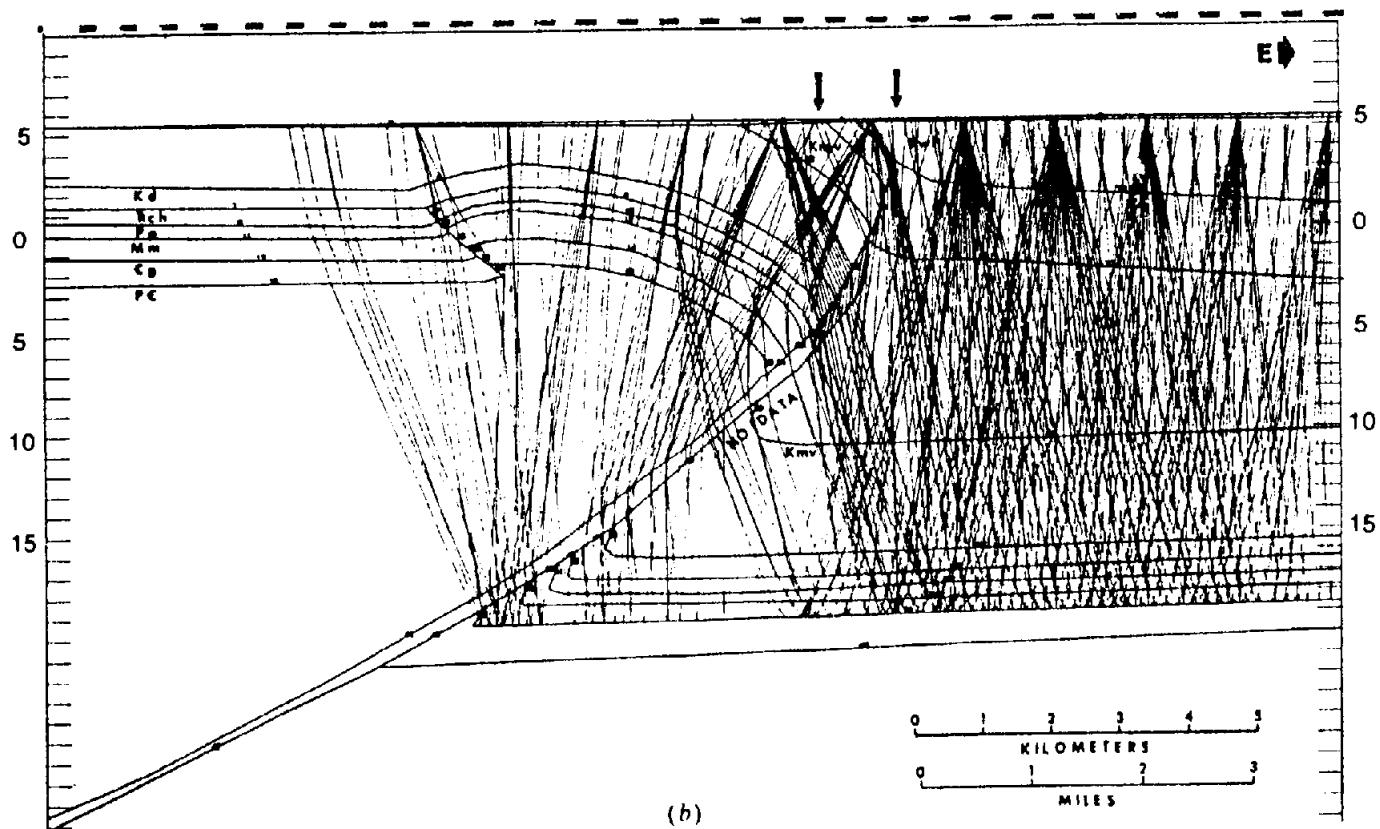


Figure 4.98. (Continued) (b) Ray tracing through a depth model (depths in  $\text{ft} \cdot 10^3$ ).

lection can be identified unequivocally on opposite sides of the fault, but in the majority of cases we can make only tentative correlations.

The two record sections in Figure 4.99 join at their north and west ends at right angles. On the N-S section, the reflection band, which consists of four strong "legs" (cycles) marked  $\Sigma$ , can be readily correlated across the normal fault, which is down-thrown to the south by about 65 ms at 1.6 s. At a velocity of 2,300 m/s, this represents a vertical throw of about 75 m. The event near 2.3 s (marked  $\chi$ ) indicates a throw of about 120 ms. At a velocity of 3,000 m/s, this represents 180 m of throw so that the fault appears to be growing rapidly with depth. Although the evidence suggests that the fault is a simple break in the shallow section, at greater depths there seems to be a fault zone or a subsidiary fault (shown dashed in the figure). If the deeper correlations across the fault(s) are correct, the downthrown event  $\Omega$  at 3.5 s is found around 2.9 s on the upthrown side, and assuming a velocity of 3,500 m/s at this depth, we get a vertical throw of 1,000 m.

The correlation across the fault for the shallow event is based on reflection character; for the deeper event, it is based on intervals between strong reflections, systematic growth of throw with depth, and time ties around loops. Sometimes the displacement of an unconformity or other recognizable feature will indicate the amount of throw. Often, however, the

throw cannot be determined clearly from the seismic data.

The component of fault-plane dip in Figure 4.99a is around  $53^\circ$  [using Eq. (4.56)]. A fault that is nearly straight on a *depth section* (a record section whose vertical scale is linear in depth) is concave upward on a *time section* (whose vertical scale is linear in traveltime for a vertically traveling wave) because of the increase in velocity with depth. If the fault surface is actually concave upward (the usual situation), the curvature will be accentuated on a time section.

The fault has not completely died out by the north end of the line, and hence the fault should appear on the intersecting line (Fig. 4.99b). As picked on the E-W section, the fault offsets the event  $\Sigma$  at 1.6 s by only about 30 m, which indicates that the fault is dying out rapidly toward the east. The fault plane has nearly as much dip in the E-W section, so the strike of the fault near the intersection of the two lines is NE and the fault plane dips about  $60^\circ$  to the southeast. The apparent dip on sections is always less than the true dip. Fault indications are not evident below 2.0 s on the E-W section, so the fault appears to have died out at depth.

Several diffractions can be seen along the fault trace in Figure 4.99a between 1.9 and 2.5 s, and changes in the reflection dip are seen on both sides of the fault trace; these are common evidences of

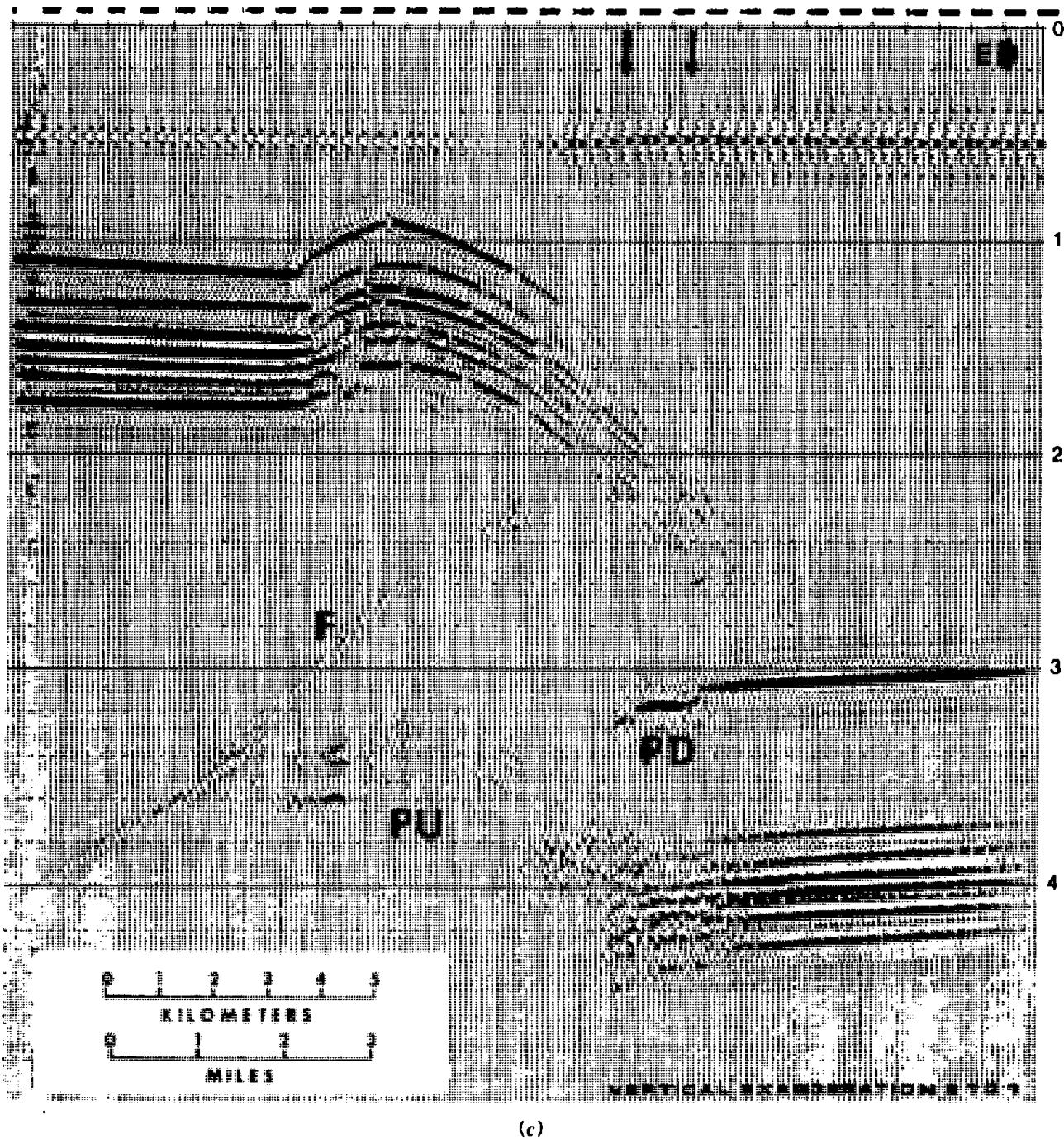


Figure 4.98. (Continued) (c) Seismic section predicted from the model.

faulting. Another feature that is often observed (but which is not clearly evident on these sections) is distortion of events whose raypaths passed through the fault plane and experienced bending at the fault plane. The effect is often accompanied by deterioration in data quality that sometimes is so great that reflections may be almost entirely absent beneath the fault, which causes a shadow zone. Occasionally the fault plane itself generates a reflection, but unless the data are migrated it may not be clear that the fault-plane reflection is associated with the fault.

The normal fault in Figure 4.99 is the most common type of fault encountered; it is associated with

extension. The fault in Figure 4.98 is a thrust fault, which is produced by compression. Figure 4.100 shows three successive thrusts buried beneath the plain of the Po River. Folding associated with the faulting provides traps for several oil fields.

#### 4.10.4. Fold and Flow Structures

When subjected to stresses, rocks may fault, fold, or flow, depending on the magnitude and duration of the stresses, the strength of the rocks, the nature of adjacent rocks, and so forth. The folding of rocks

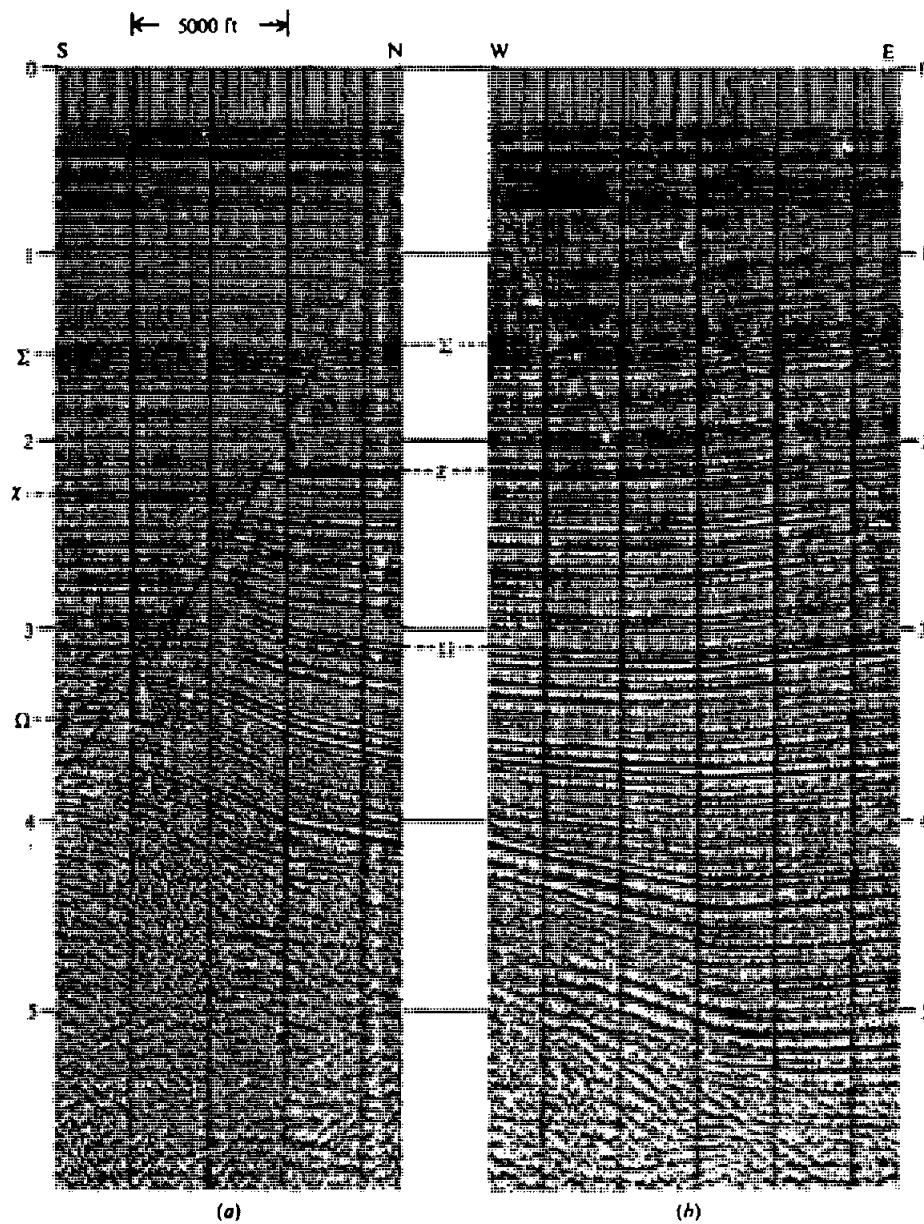


*Figure 4.99. Intersecting sections showing faulting. (Courtesy Geophysical Service Inc.)*  
*(a) N-S section. (b) E-W section.*

into anticlines and domes provides many of the traps in which oil and gas are found.

Figure 4.101 shows a migrated seismic section across an anticline. Some portions, such as *A*, that are composed of the more competent rocks (for example limestones and consolidated sandstones), tend to maintain their thickness as they fold. Other portions, such as *B*, that contain less competent rocks (often shales and evaporites), tend to flow and slip along the bedding, resulting in marked variations in thickness within short distances. Geometry places limits on the amount of folding that is possible and folded structures almost always involve faulting. Note at *C* how a fault is involved with the folding. Arching places sediments under tension so that often they break along normal faults and pro-

duce graben-type features on the top. Anticlinal curvature tends to make seismic reflections weaker as well as increase the likelihood of faulting and flow, so that data quality commonly deteriorates over anticlines.

Salt flow often produces anticlines and domes. In many parts of the world thick salt deposits have been buried fairly rapidly beneath relatively unconsolidated sediments. The sediments compact with depth and so increase their density, whereas the salt density remains nearly constant. Thus, below some critical depth the salt is less dense than the overlying sediments. Salt behaves like a very viscous fluid under sufficient pressure, and buoyancy may result in the salt flowing upward to form a salt dome, arching the overlying sediments and sometimes

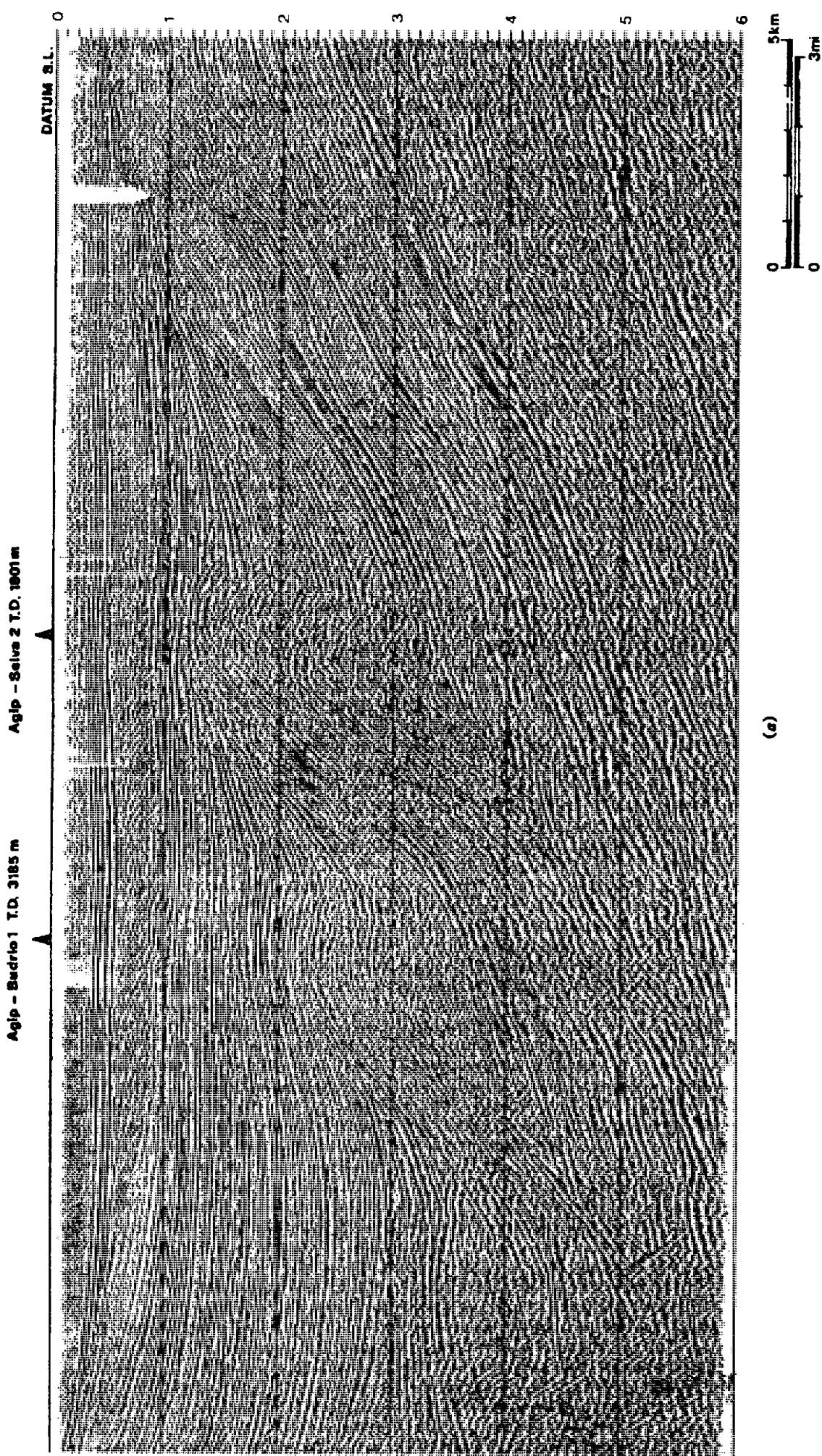


Figure 4.100. Seismic profile in the Po Valley. Thrust faulting from the north produced a series of folds. The Budrio thrust appears to have been relatively quiet in the Middle Pliocene, the Selva thrust quiet since the late Pliocene, and the thrust only partially seen at the right active into the Quaternary. (From Pieri, 1983.) (a) Migrated seismic section.

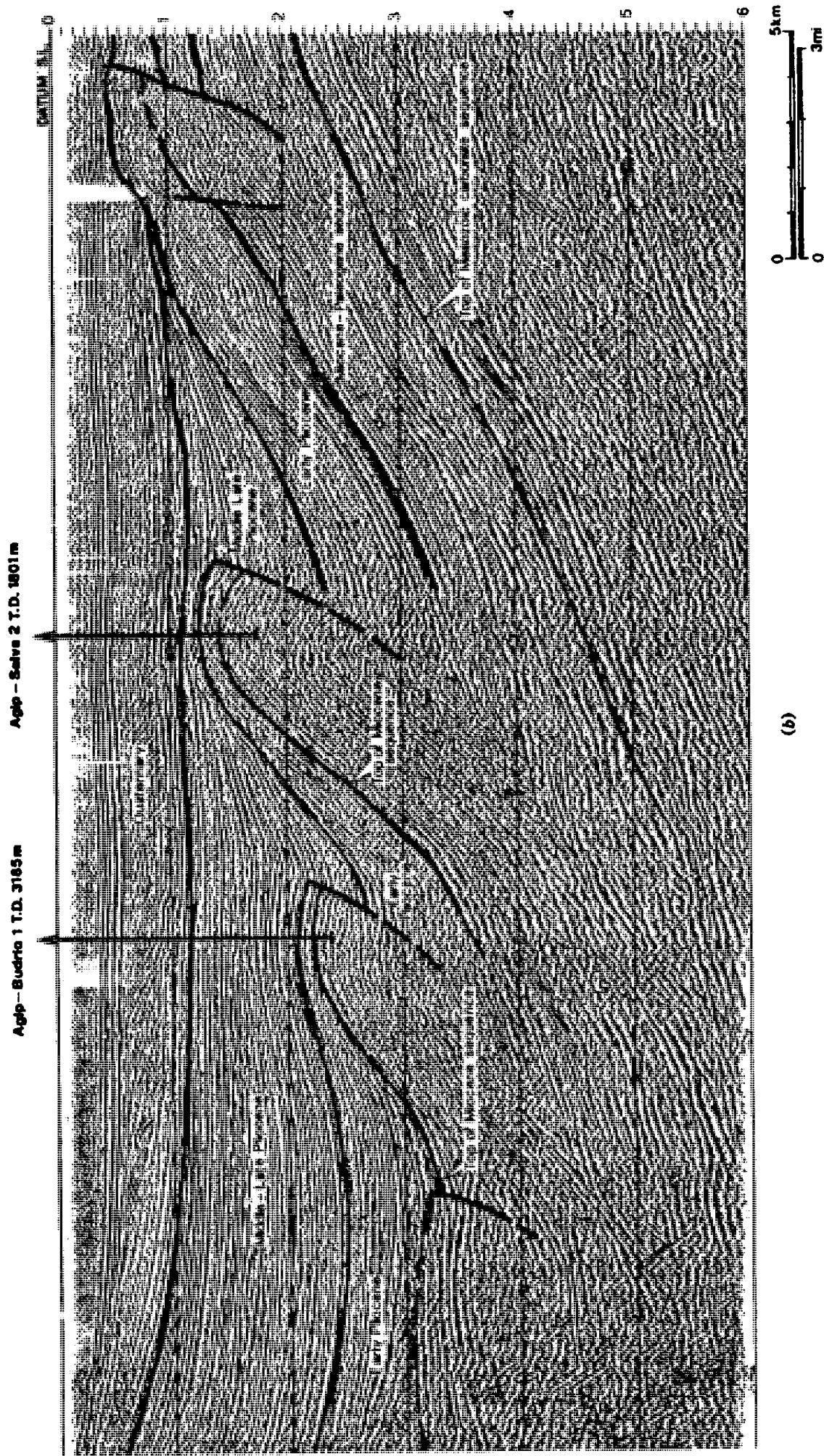
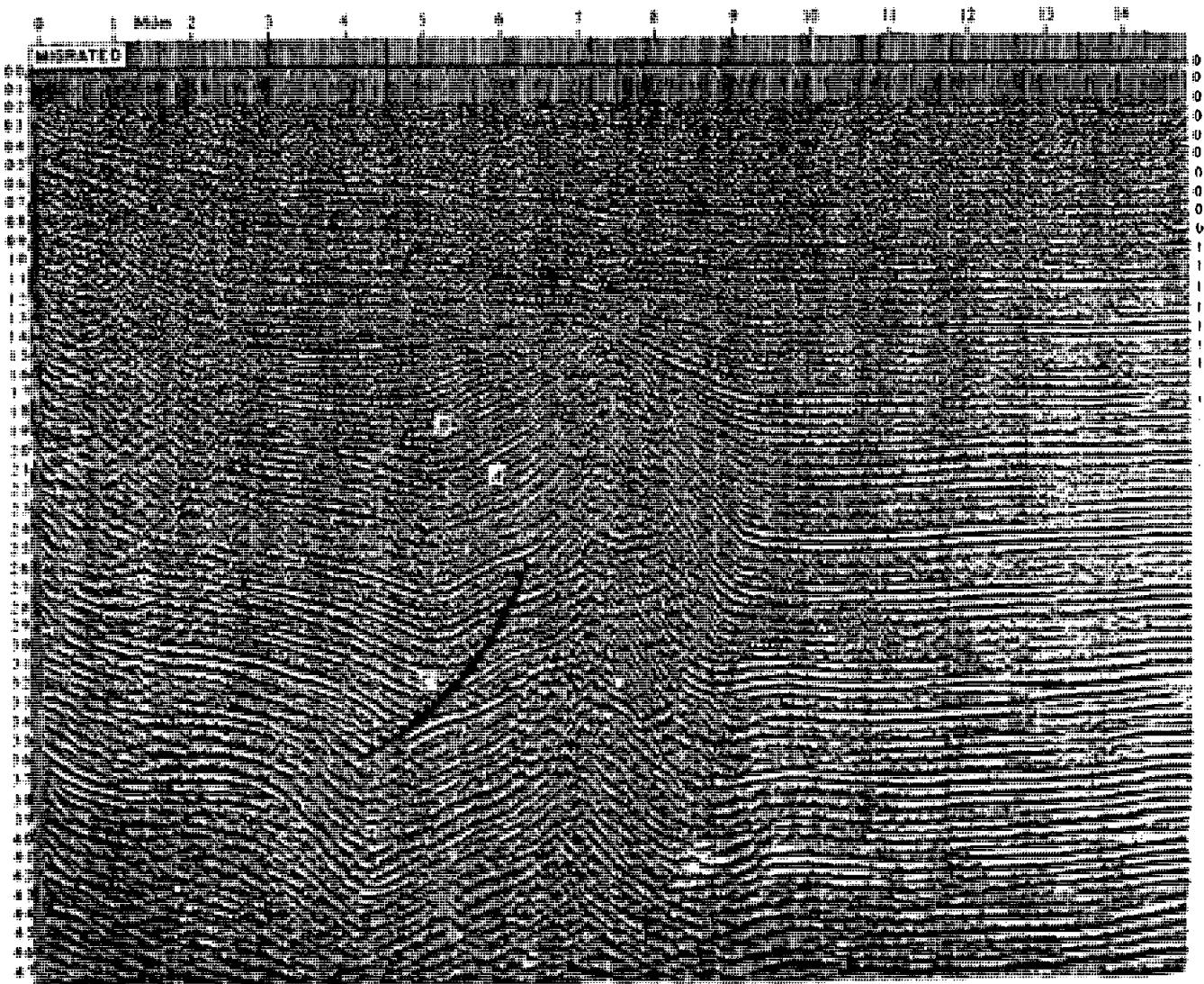


Figure 4.100. (Continued) (b) Interpretation of (a).



*Figure 4.101. Migrated section across a faulted anticline in the San Joaquin Valley of California. The main anticline is associated with a nearly vertical reverse fault. (Courtesy Texaco.)*

piercing through them. Grabens and radial normal faults (whose throw decreases away from the dome) often result from such arching of the overlying sediments, thus relieving the stretching that accompanies the arching. Salt domes tend to form along zones of weakness in the sediments.

Figure 4.102 exhibits several portions of a seismic line in the North Sea. The horizontal scale has been compressed so as to display a long line on a short section, which produces considerable vertical exaggeration. This line shows deep salt swells that have not pierced through the overlying sediments (Fig. 4.102a), salt that has pierced through some of the sedimentary section (Fig. 4.102b), and also salt that has pierced all the way to the sea floor (Fig. 4.102c). The reflection from the base of the salt is generally continuous and unbroken, but distortions produced by the variable salt thickness above it at times interrupt this reflection. Because the salt velocity is greater

than that of the adjacent sediments, the base of the salt event appears to be pulled up where the salt is thicker. In other areas where the salt velocity is lower than that of the surrounding sediments, flat reflectors beneath the salt may appear to be depressed where the overlying salt is thicker.

Shallow salt domes are apt to be so evident that they can scarcely be misidentified. Because of the large impedance contrast, the top of the salt dome (or the cap rock on top of the dome) is often a strong reflector. Steep dips may be seen in the sediments adjacent to the salt dome as a result of these sediments having been dragged up with the salt as it flowed upward. The salt itself is devoid of primary reflections, although multiples may obscure this feature. Defining the flank of a salt dome precisely is often economically important but seismically difficult. Hydrocarbons may be accumulated in a narrow belt adjacent to the flank of the dome, but because

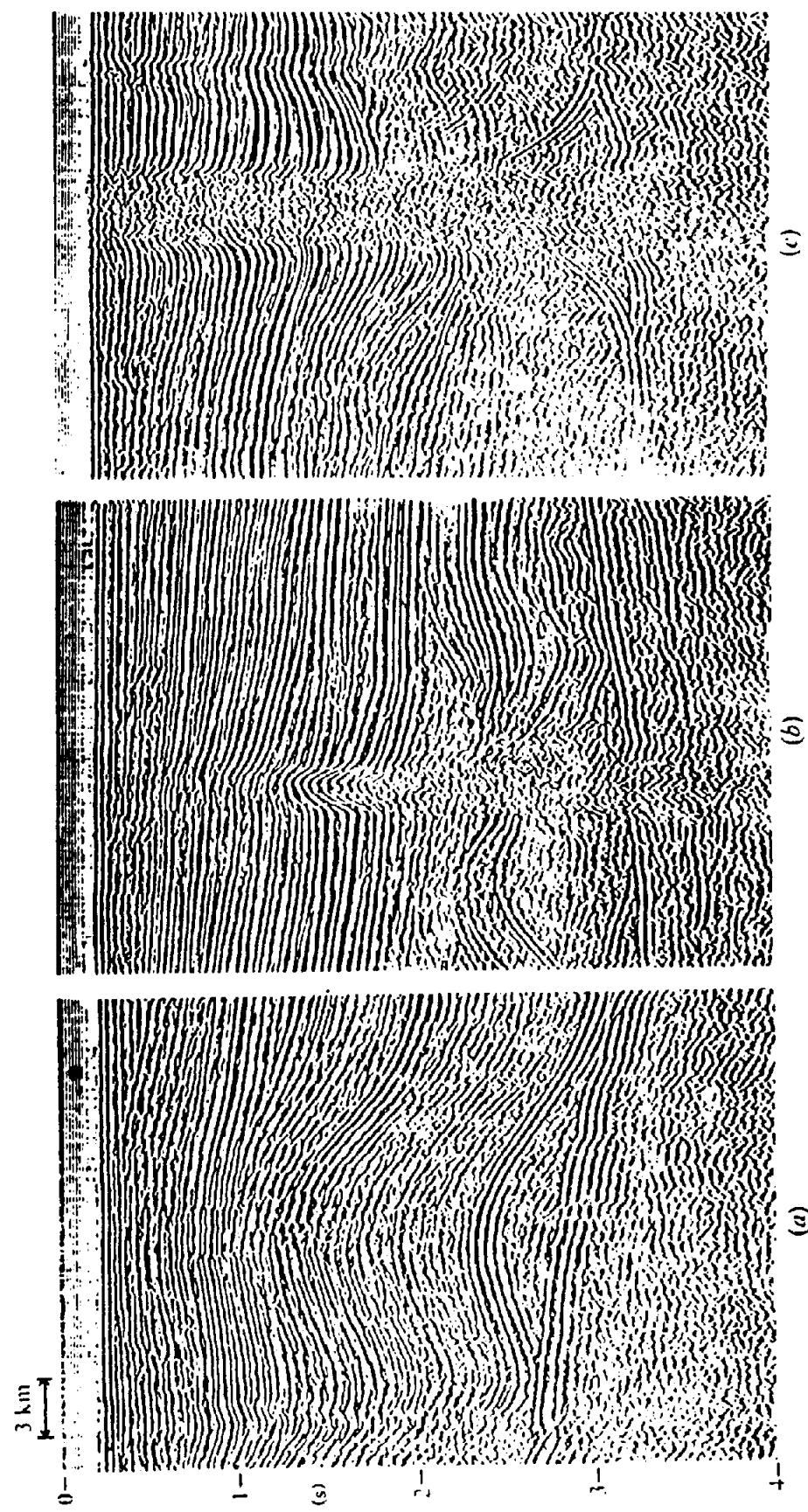


Figure 4.102. Portions of horizontally compressed sections in the North Sea. (Courtesy Grant-Norpac.) (a) Deep salt swell. (b) Salt dome that has pierced some of the sediments. (c) Salt dome that has pierced to the sea floor.

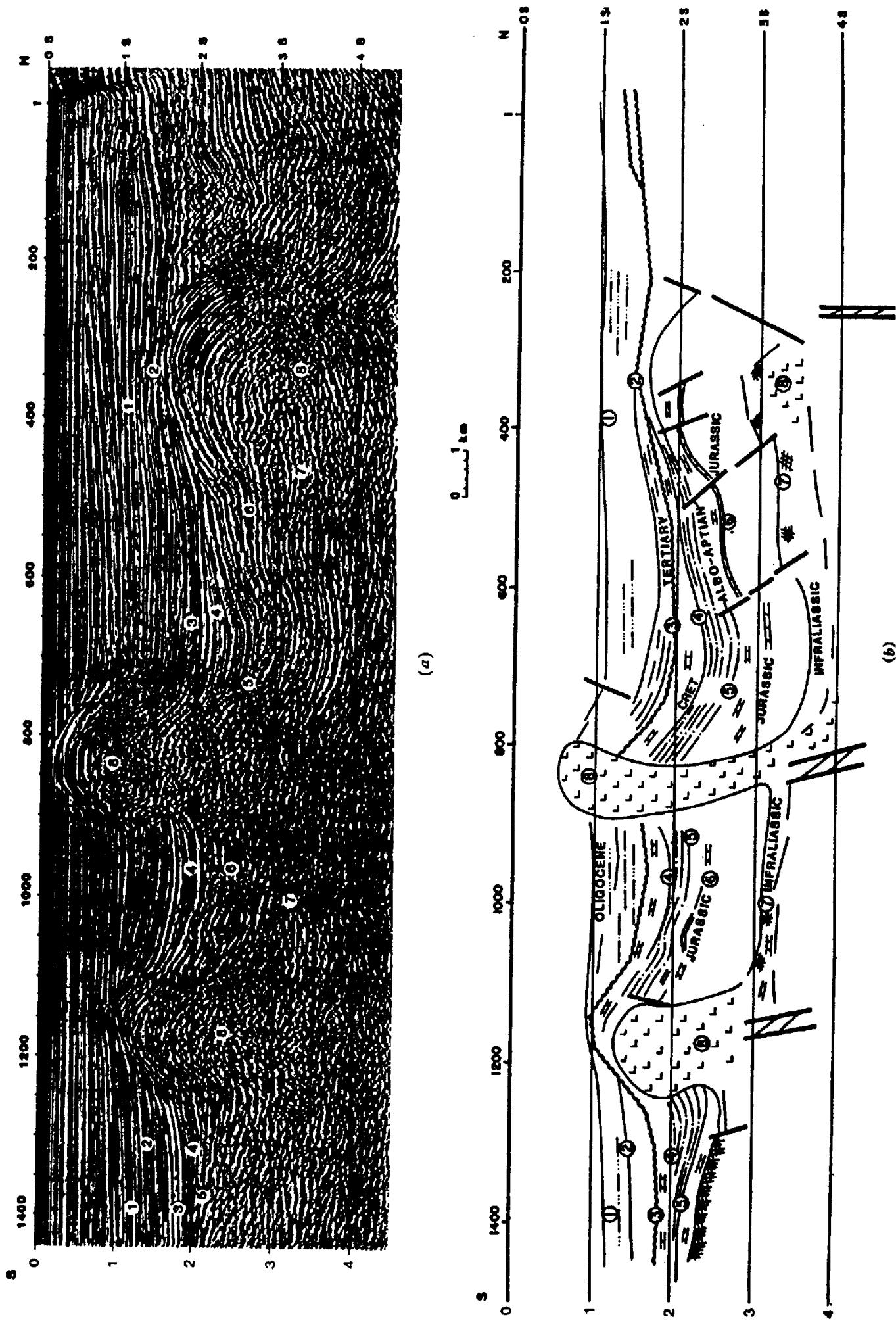


Figure 4.103. Seismic section in the offshore Aquitaine Basin, France. (From Curnelle and Marco, 1983.) (a) Unmigrated section. (b) Interpretation. 1 = Oligocene, 2 = Paleocene unconformity, 3 = base Tertiary unconformity, 4 = base Upper Cretaceous, 5 = Albo-Aptian unconformity, 6 = top Jurassic, 7 = top Infraclassic, 8 = salt.

the flank is usually nearly vertical, it rarely gives rise to a recognizable reflection. Fortunately the velocity distribution is often only slightly affected by the growth of the dome (except for the velocity in the salt and the cap rock) so that the steep dips of the sediments adjacent to the flanks can be migrated fairly accurately and the flank outlined by the terminations of these reflections. Nevertheless, there remains much art and experience in defining salt-dome flanks.

Three salt domes can be seen in Figure 4.103. The salt in a salt dome generally has come from the immediately surrounding region. The removal of the salt from under the sediments around the dome has thus allowed them to subside, which produces a rim syncline. Local thickening of portions of the section in the withdrawal synclines indicates when the salt was moving out from underneath and can be used to date the salt movement. Withdrawal synclines, which show fairly clearly in Figure 4.103, also help to provide closure in neighboring areas where the sediments continue to be supported by the residual salt.

Occasionally shale or other substances also form flow structures that resemble salt domes. Overpressured shale is an especially common diapiric material. The water laid down with clays (or shales) needs to escape as the clay comes under greater pressure because of additional rock deposited on top of them, but the very low permeability may prevent such escape. In this situation, the interstitial fluids become overpressured, the shale loses its shear strength, and it behaves like a viscous liquid. Often the instability that results produces growth faulting with shale moving from underneath the downthrown side of the fault and up on the upthrown side. Overpressured shale is often found on the upthrown side of normal faults in young sediments; it usually shows as a zone relatively devoid of reflections, and it can be confused with the shadow zone that is often seen because of the erratic bending of raypaths as they pass through the fault.

#### 4.10.5. Reefs

The term "reef" as used by petroleum geologists comprises a wide variety of types, including both extensive barrier reefs that cover large areas and small isolated pinnacle reefs. It includes carbonate structures built directly by organisms and aggregates comprising limestone and other related carbonate rocks, as well as banks of interstratified carbonate (and sometimes also noncarbonate) sediments. Reef dimensions range from a few tens of meters to several kilometers; large reefs are tens of kilometers in length, a few kilometers wide, and 200 to 400 m or more in vertical extent. Because reefs vary so widely,

the evidence for reefs shown by seismic data is extremely varied.

We shall describe a model reef so that we may develop the general criteria by which reefs can be recognized in seismic data, keeping in mind that deviations from the model may result in large variations from these criteria. Our model reef develops in a tectonically quiet area characterized by flat-lying bedding that is more-or-less uniform over a large area. The uniformity of the section makes it possible to attribute significance to subtle changes produced by the reef, which might go unnoticed in more active areas. The reef is the result of the buildup of marine organisms living in the zone of wave action where the water, light, and temperature are suitable for sustaining active growth. The site of the reef is usually a topographic high that provides the proper depth. The topographic high may be due to a hinge line or structure in the underlying beds, such as a tilted fault block, but more often it is provided by a previous reef. As a result, reefs tend to grow vertically, sometimes achieving thicknesses of 400 m or more, thereby accentuating their effects on the seismic data. For the reef to grow upward, the base must subside as the reef builds upward, maintaining its top in the wave zone as the sea transgresses. The reef may provide a barrier between a lagoonal area (the *backreef*) and the ocean basin (the *forereef*), so that sedimentation (and consequently the reflection pattern) may be different on opposite sides of the reef. The surrounding basin may be *starved*, that is, not have sufficient sediments available to keep it filled at the rate at which it is subsiding. At times only one side, more often the ocean side of the reef, may be starved. Alternatively, the reef may not be a barrier to movement of sediments, and in this case it will be surrounded by the same sediments on both sides. Erosion of the reef often provides detritus for deposition adjacent to the reef, resulting in *foreset beds* with dips up to 20°. Eventually the environment for the reef organisms will change so that they can no longer continue to live and build the reef; this might come about because of changes in the water temperature, an increase in the rate of subsidence so that the organic buildup cannot keep pace (called *drowning* of the reef), or various combinations of circumstances. Subsequently the reef may become buried by deep-water shales, which may provide both an impermeable cap to the porous reef and sufficient hydrocarbons so that the reef becomes a petroleum reservoir. Additional sediments may continue to be deposited; their weight compacts the sediments that surround the reef more than they compact the relatively rigid reef and thus the overlying sediments that were deposited flat may develop a drape over the reef.

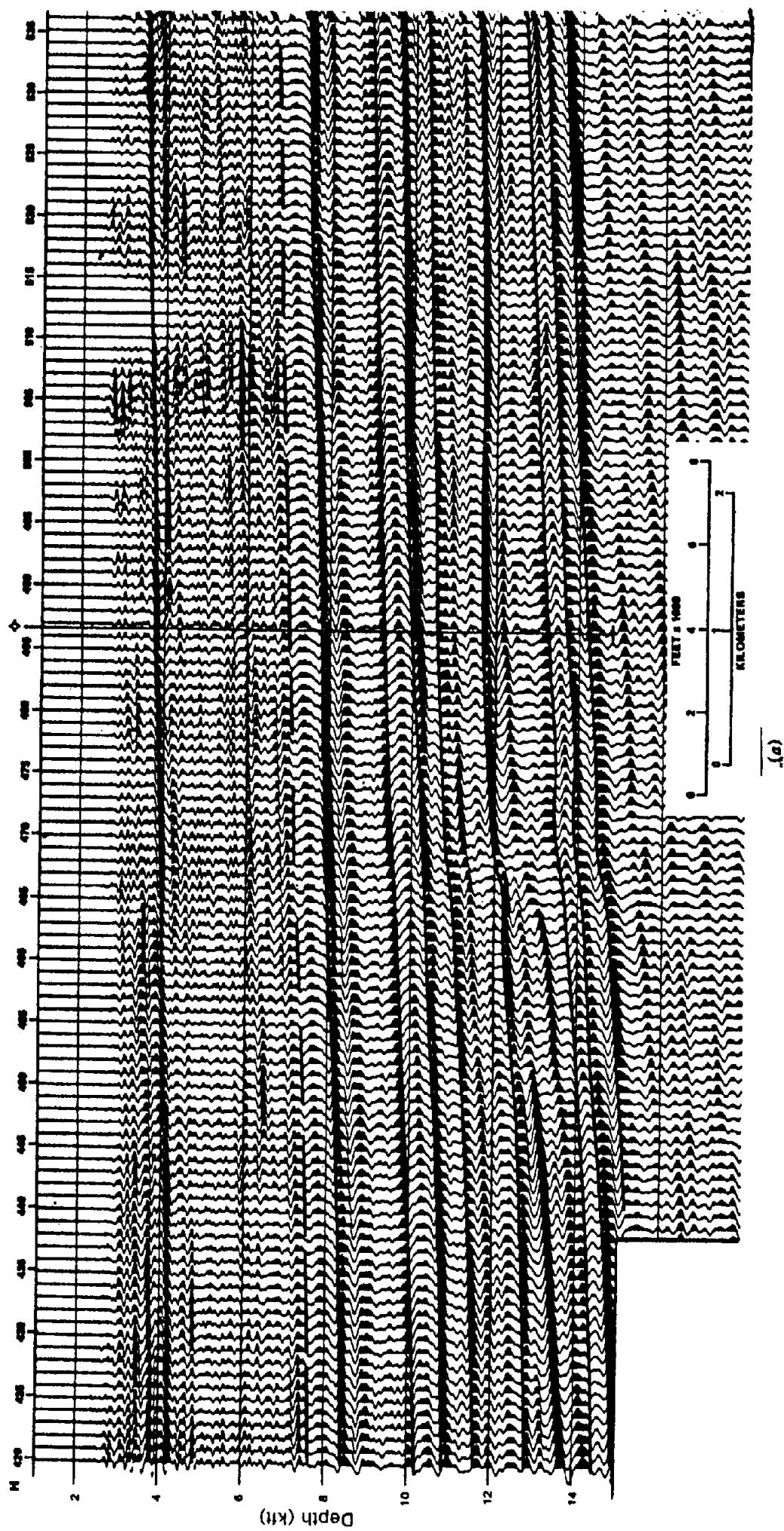
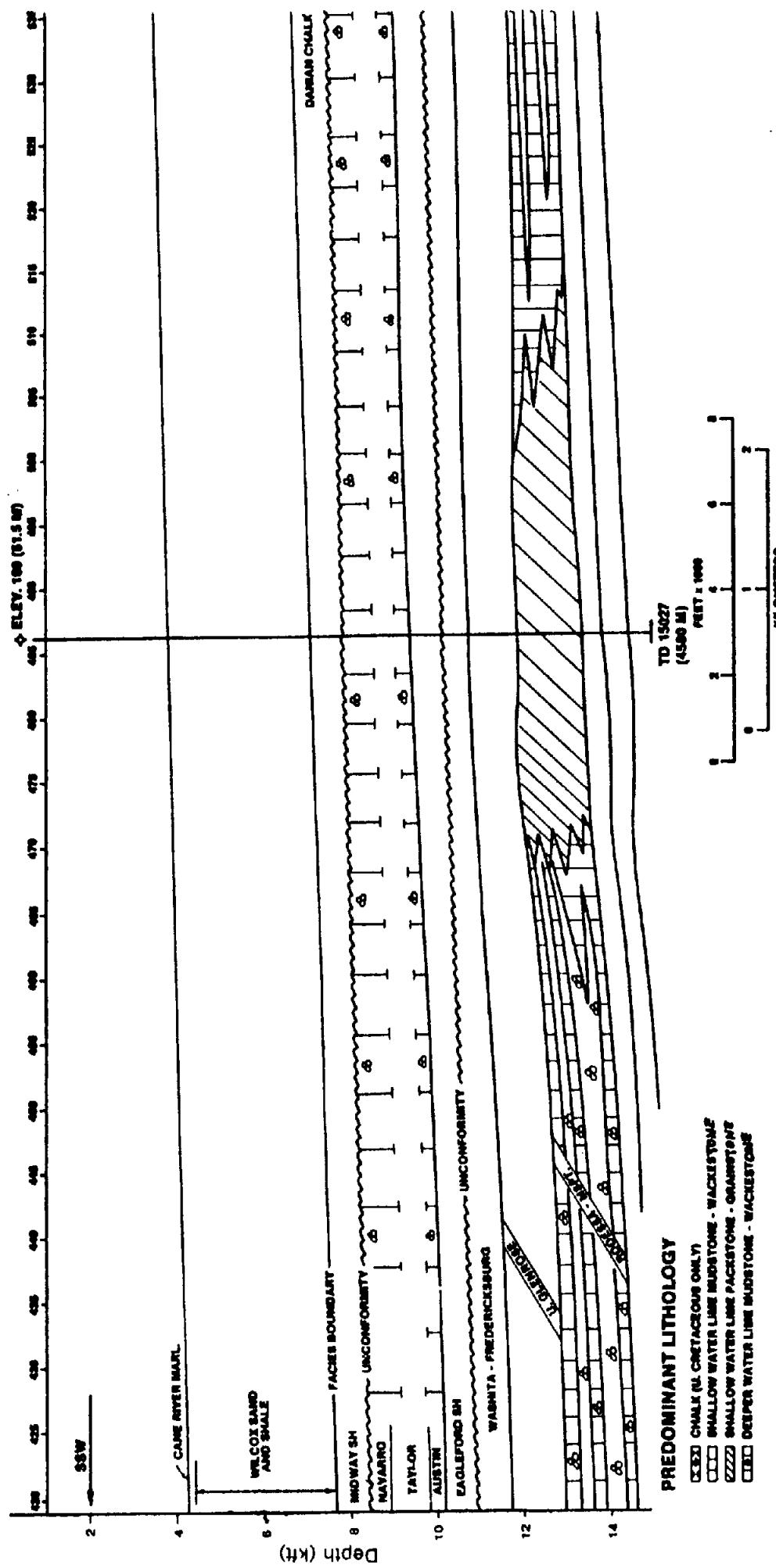


Figure 4.104. Section across a Louisiana reef. (From Phelps and Ronipaugh, 1983.) (a) Seismic section where the vertical scale is linear with depth.



*Figure 4.104. (Continued) (b) Interpretation.*

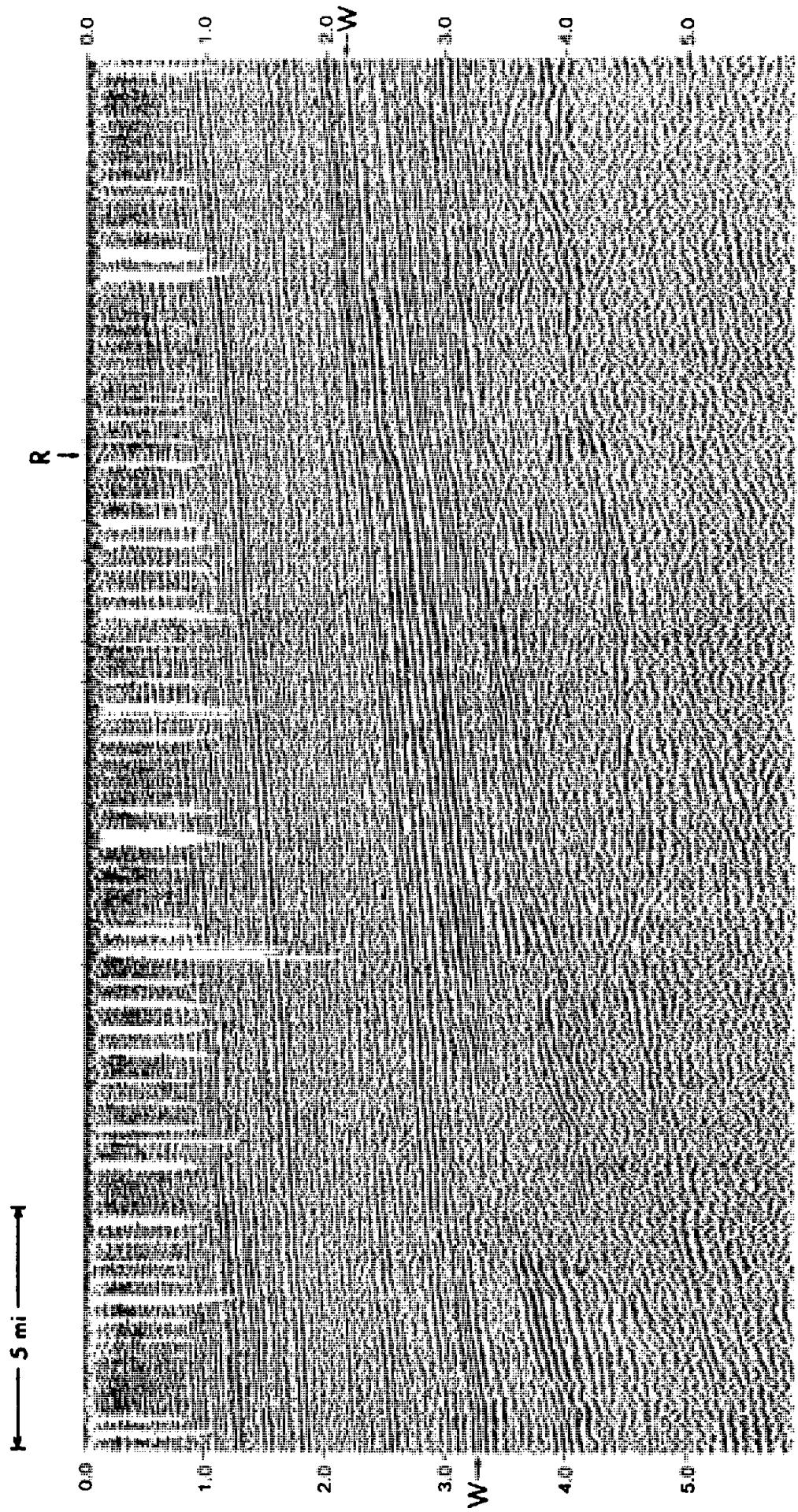
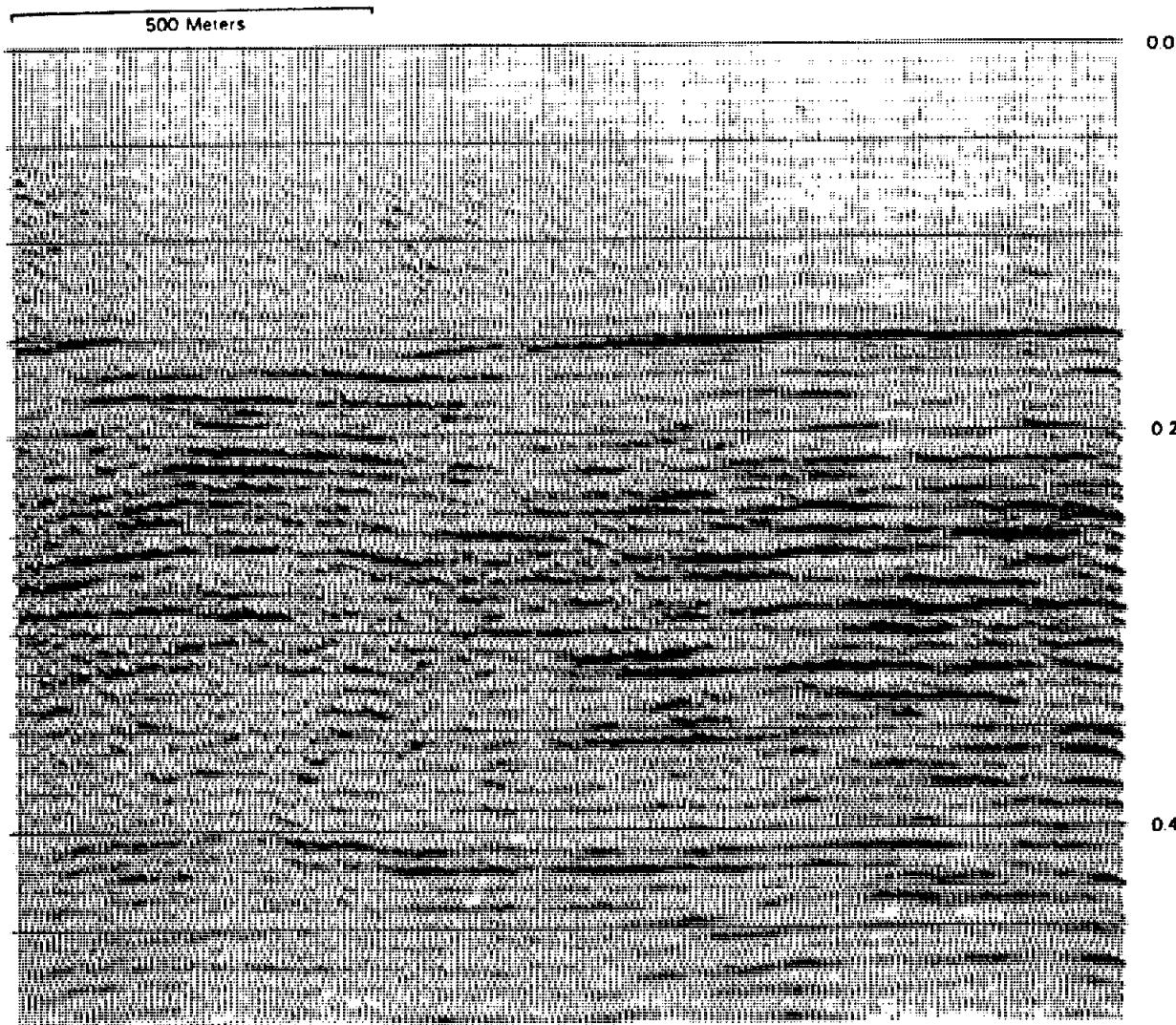


Figure 4.105. East Texas section showing a reef (just below event W with reef edge under R). (From Sheriff, 1973.)



*Figure 4.106. High-resolution seismic line showing a channel cut into a coal seam.  
(From Chapman and Schafers, 1985.)*

Based on the foregoing model, we might hope to see diffractions from the top and/or flanks of the reef. Abrupt termination of reflections from the surrounding sediments may indicate the location of the reef. If the reef provided a barrier to sedimentation, the entire reflection pattern may differ on the two sides of the reef, reflecting the different sedimentary environments. Overlying reflections may show small relief (usually only a few milliseconds in magnitude) because of the differential compaction. The velocity difference between the reef materials and the surrounding sediments may produce pseudostructure on reflecting horizons below the reef. Usually the velocity in the reef limestone will be greater than that in the surrounding shales so that there will be a pseudohigh under the reef, often less than 20 ms. Sometimes, however, the reef will be surrounded by calcareous shale, anhydrite, or other rock that has a higher velocity than the porous reef limestone, so that the time anomaly is reversed.

Figure 4.104a shows a barrier reef. The reef lies on a hinge in the underlying sediments; this can be seen by laying a straight edge along reflections from underneath the reef. The place to look for a reef is often above some underlying feature that might have provided the setting where a reef could grow. Some drape can also be seen above the reef. This is produced by differential compaction because the sediments around the reef compacted more under the weight of overlying sediments than did the relatively strong reef. The reflection patterns on opposite sides of the reef are different, showing that the reef was a barrier separating different depositional environments. Somewhat similar evidences indicate the reef on Figure 4.105.

Reef evidences are often so small and subtle that seismic mapping of reefs is feasible only in good record areas. Of first importance is geological information about the nature of the sediments and transgressive periods of deposition, so that one knows

beforehand in what portion of the section reefs are more likely to occur.

Similarities between reefs and salt features cause problems at times. The lagoonal areas behind reefs may provide conditions for evaporite deposition so that salt may be present in the same portion of the sedimentary column. Differential solution of salt beds followed by the collapse of the overlying sediments into the void thus created may produce seismic features that are similar in many ways to those that indicate reefs.

#### 4.10.6. Unconformities and Seismic Facies Patterns

Unconformities are often among the best seismic reflectors. They often are fairly easy to spot because of an angularity between families of reflections. An unconformity reflection may result from erosion or nondeposition, and angularities may occur above and/or below the unconformity. The nature of such a reflection may change laterally as different beds subcrop against the unconformity or onlap onto it, and consequently the reflection often changes character along a line, sometime even completely reversing the polarity.

Channels cut into unconformities sometimes provide channel sand or point-bar sand deposits that represent one type of stratigraphic trap. Channels are also sometimes filled with impermeable clay to seal the movement of hydrocarbons. A channel can be seen on Figure 4.106. This channel is cut into the coal bed that produces the strong reflection at about 0.150 s. Coal beds often have lower velocity and density than the overlying or underlying rocks, and consequently often produce strong reflections.

Unconformities subdivide a section into depositional units that are often different from adjacent units and are distinguished by distinctive seismic character (*seismic facies*). Certain patterns characterize depositional environments so that deltas, foreset bedding, reefs, sandbars, turbidite fans, periods of nondeposition, periods of tectonic activity, and so on, may be identified by the aggregate of subtle evidences. From seismic facies studies one may be able to suggest the environment of deposition of the rocks and hence something about the stratigraphy. Usually seismic data of excellent quality are required for facies analysis.

The amplitudes of reflections, especially lateral changes in amplitude, provide information for stratigraphic interpretation (Payton, 1977; Sheriff, 1980; Berg and Woolverton, 1985). Strong amplitudes result from large changes in acoustic impedance, such as may occur at basement or an unconformity, or because of a change from clastic to carbonate rocks. Strong amplitudes may also be the result of inter-

ence, focusing, and other causes. Gas accumulations may appreciably lower the density and velocity in porous sediments and hence may be located through amplitude effects (see Fig. 4.107).

#### 4.10.7. Use of Velocity Information

With common-midpoint data, which have a high degree of redundancy, and velocity-analysis programs (§4.7.7), interval velocities can be calculated from Equation (4.85) at many points in the section – in fact, almost on a continuous basis. After due allowance for uncertainties in the measurements, systematic variations might be interpreted in stratigraphic terms (Hofer and Varga, 1972). Carbonate and evaporite velocities are sufficiently higher than clastic velocities (especially in Tertiary basins) so that they can often be distinguished.

The analysis of velocity data constitutes an important interpretation problem. As with other interpretation problems, some interpretations can be ruled out because they imply impossible or highly improbable situations. From experience we know that velocity does not vary in a “capricious” manner. It is unreasonable to expect the velocity to vary other than in a slow systematic way unless the seismic section shows significant structural or other changes that suggest why the velocity should change rapidly. Two velocity analyses might show some differences between portions of the section that are separated by a fault, whereas one expects little velocity variation in portions that appear to be continuous.

One must be cautious about interpreting velocity data. Small errors in normal-moveout measurements can produce sizable errors in stacking velocities, and these in turn cause large errors in interval-velocity calculations when the intervals are small. Where the reflectors are not parallel, interval-velocity calculations are meaningless (Taner, Cook, and Neidell, 1970). Velocity measurements sometimes are severely distorted by interference effects, noise of various kinds, distortions produced by shallow velocity anomalies, or weathering variations, and care must be exercised that such effects are not taken as indications of actual changes in the velocity of the rocks.

#### 4.10.8. Hydrocarbon Indicators

Hydrocarbons in the pore space of a rock lower the velocity and the density compared to water in the pore spaces. Oil lowers the velocity and density slightly, but gas has a considerable effect. A small percentage of gas may lower the velocity more than either a larger percentage of gas or zero gas. Hydrocarbons thus change the contrast in acoustic impedance with the overlying and underlying rock and hence the reflectivity. The consequent change in am-

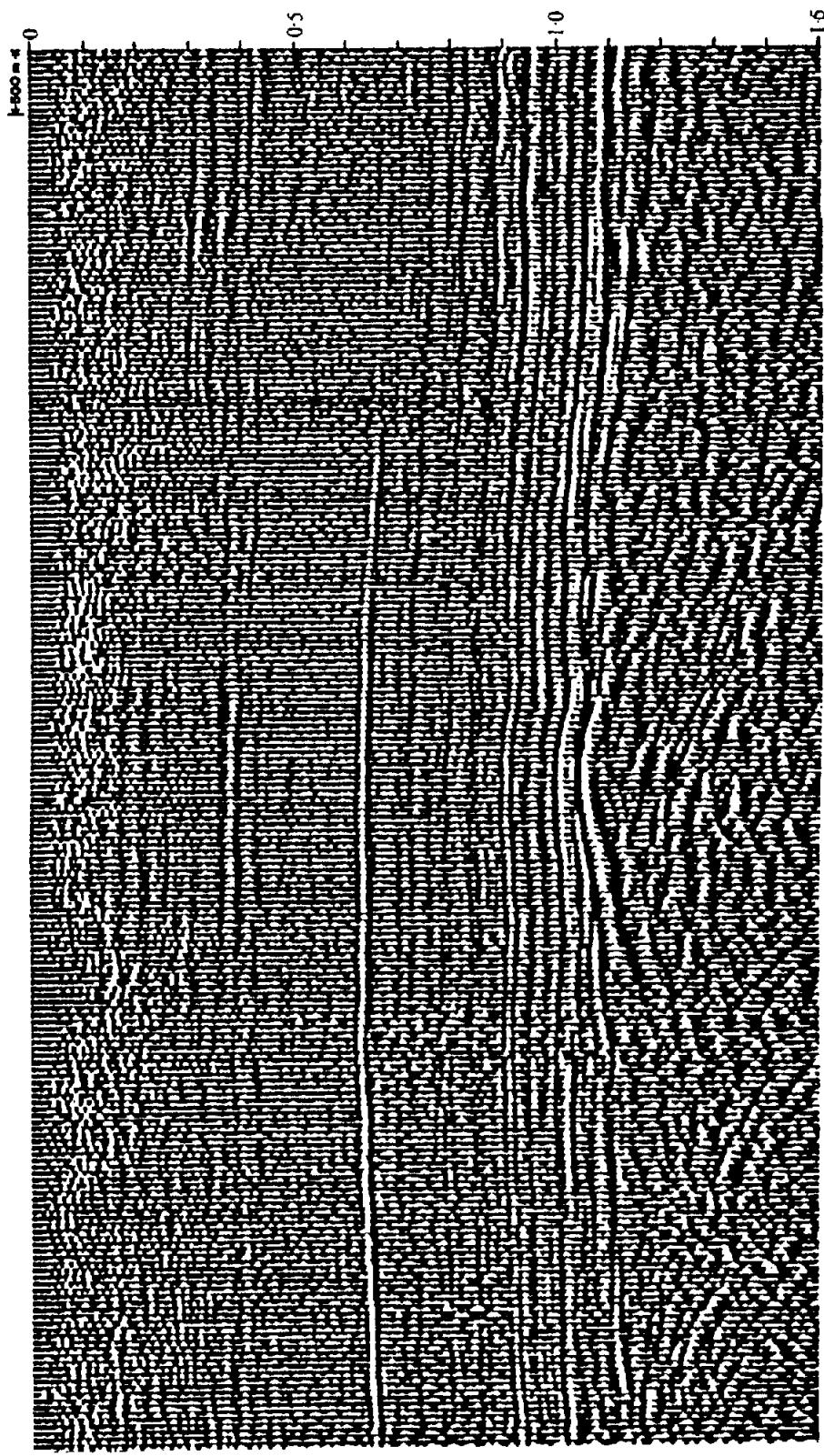


Figure 4.107. Seismic section with relative amplitudes preserved. The local increased amplitude of the reflection just below 0.6 s results from a gas accumulation. Such a "bright spot" is one of several hydrocarbon indicators. (Courtesy Chevron Oil Co.)

plitude (and sometimes of polarity) of the reflections from the reservoir rock often is large enough to be seen. In clastic sections, the lowering of the acoustic impedance of a reservoir often produces a high-amplitude reflection called a *bright spot*, which is the most common *hydrocarbon indicator* (HCl). Seismic sections are sometimes displayed with low gain so that only the bright spots stand out.

When the acoustic impedance of a water-filled reservoir is appreciably larger than that of the adjacent rock, as in a limestone reservoir capped by shale, the lowering of the acoustic impedance by hydrocarbons produces a *dim spot*. Where a water-filled reservoir's acoustic impedance is only slightly larger than the adjacent rock, the lowering by hydrocarbons may reverse the reflection polarity. Thus a bright spot HCl, a dim spot HCl, and a *polarity reversal* HCl all have the same cause. The lowering of velocity also increases the traveltimes of deeper reflections, producing a *velocity sag*, another HCl.

A horizontal gas-oil, gas-water, or oil-water contact may produce a distinct reflection, especially where the reservoir is thick; such a reflection is called a *flat spot* HCl. Overlying changes in gas column thickness may tilt a flat spot so that it is no longer horizontal. Almost all section displays employ an equalizing scheme whereby the gain on a trace is adjusted so that its average is the same as the average for adjacent traces. The increased amplitude of a bright spot which causes the gain of a trace to decrease lowers the amplitude of deeper and shallower reflections and produces an *amplitude shadow*. Sometimes immediately underneath a reservoir the dominant frequency is lowered. Gas leaking from a reservoir may permeate overlying formations enough to affect their velocities and transmission qualities, producing *gas-chimney* effects.

HCl effects usually indicate gas, and most effects attributable to oil accumulation are too weak to be observable. Virtually all the HCl effects can be produced by situations other than hydrocarbons so that observation of any one HCl may not indicate a hydrocarbon accumulation. The case for an accumulation is strengthened considerably when several indicators are present. HCl may be sufficiently weak that none are detectable. In general, HCl are useful in young (Tertiary) clastic sediments and become less useful with increasing age, consolidation, cementation, or depth of burial of the rocks.

## 4.11. SPECIALIZED METHODS

### 4.11.1. Profiling

Marine profiling may employ as few as one hydrophone group, and shooting and recording may take place at such short intervals that a continuous

record section is obtained. The technique is similar to the continuous recording of water depth using a fathometer (echo sounder). It differs from conventional marine surveying in that it employs smaller ships and weaker energy sources, and hence is much cheaper. Profilers also have relatively small penetration and cannot discriminate between events on the basis of normal moveout where only a single hydrophone group is used. Profiling is extensively used in engineering studies (Fig. 4.108) to map the bottom sediments and to locate bedrock. It is also widely used in oceanographic work to survey large areas cheaply (Fig. 4.109), to locate pipelines buried in mud, and so on.

The energy sources most commonly used are high-powered transducers, electric arcs, air guns, and imploders. High-powered transducers are usually piezoelectric devices that employ barium titanate or lead zirconate. Such materials not only generate electric fields when compressed (as when used as hydrophones), but they also change dimensions when subjected to an electric field, that is, they transform electrical energy to acoustic energy and vice versa. Profiling transducers operate at lower frequencies and higher power levels than fathometers used for water-depth measurements; frequencies in the range 2 to 10 kHz and power levels of roughly 100 W are commonly used. A repetition rate of 2 s and penetration of 20 to 100 m are generally achieved. Reflection character can sometimes be interpreted to indicate the nature of the sediments, for example, to find sand layers that can support structures erected on pilings.

Electric arcs (*sparkers*) utilize the discharge of a large capacitor to create a spark between two electrodes located in the water. The heat generated by the discharge vaporizes the water, creating an effect equivalent to a small explosion. Several sparker units are often used in parallel. Modern sparker arrays deliver as much as 200 kJ at 50 to 2,000 Hz and achieve penetrations of 600 m or so. A variation of the sparker often used in fresh water involves connecting the electrodes by a thin wire that is vaporized in the discharge. This increases the duration of the bubble and consequently its low-frequency content.

The air guns used in profiling are similar to those used in conventional marine work except that they are smaller; they involve as little as 1 in.<sup>3</sup> of air at 1,000 psi and a dominant frequency of 250 Hz. Imploders used in profiling include the Boomer already described, which delivers about 200 J of energy from 50 Hz to a few kilohertz.

Profiler data are sometimes recorded on electro-sensitive paper using a strip recorder, but most commonly they are recorded on magnetic tape, often in digital form.

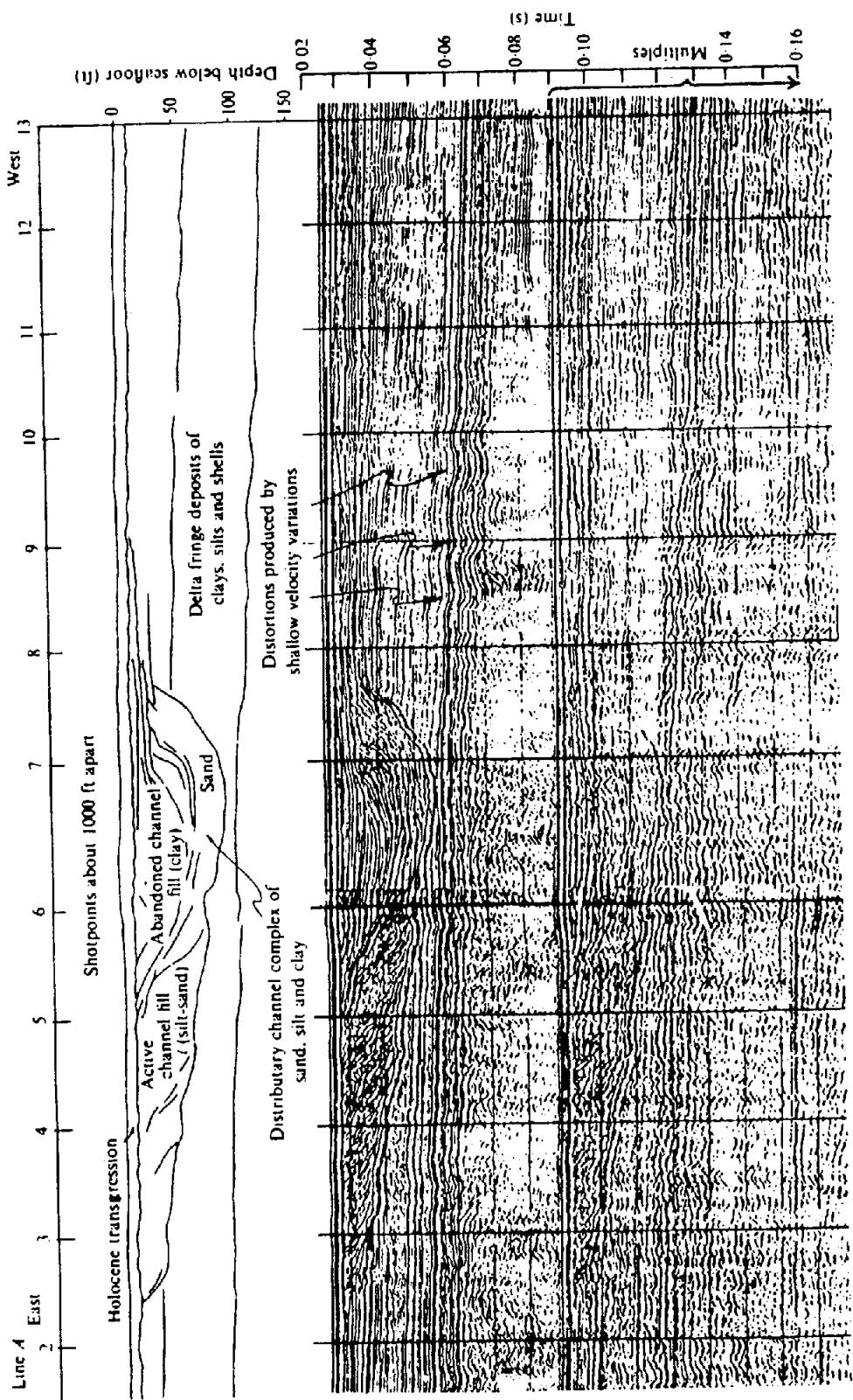
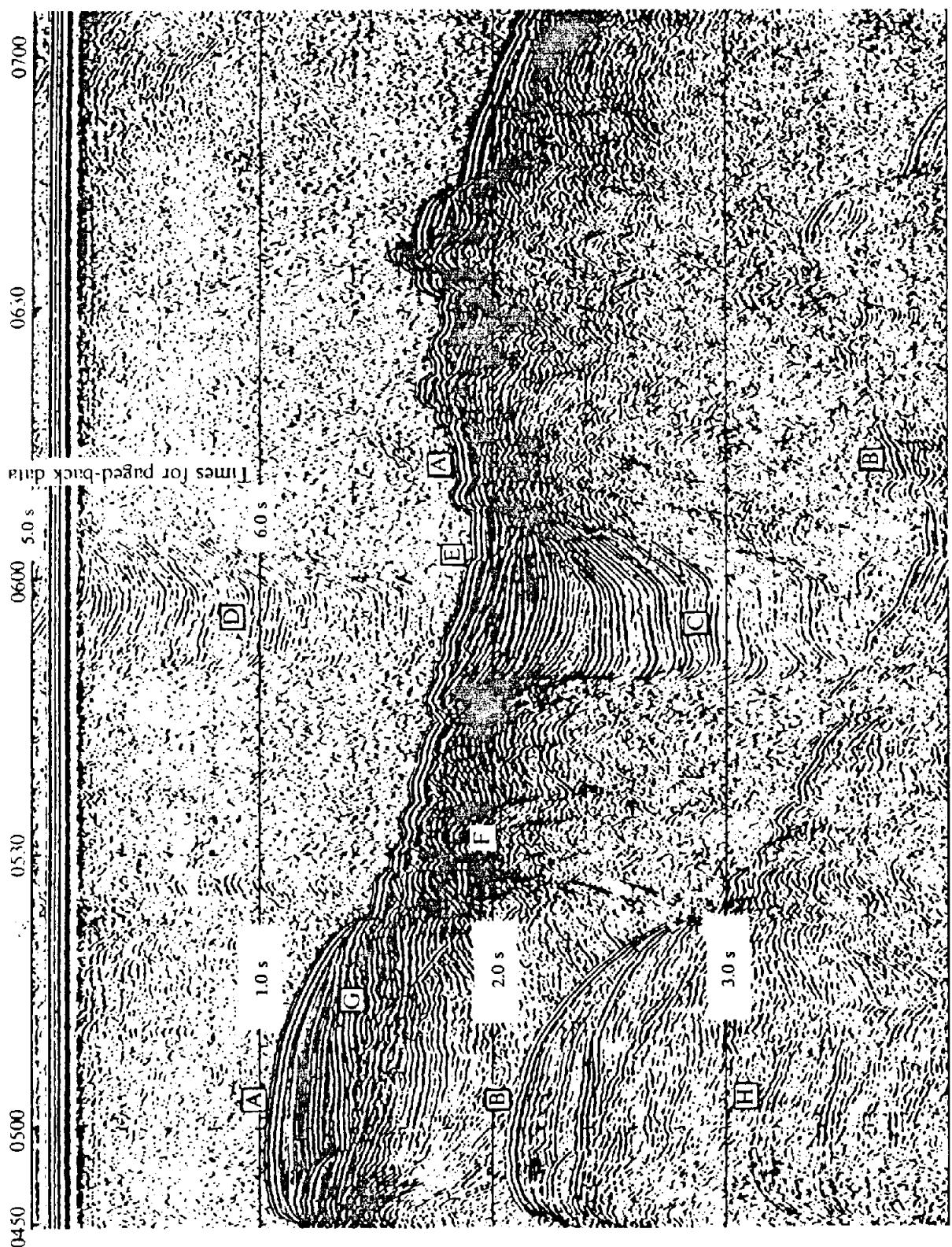
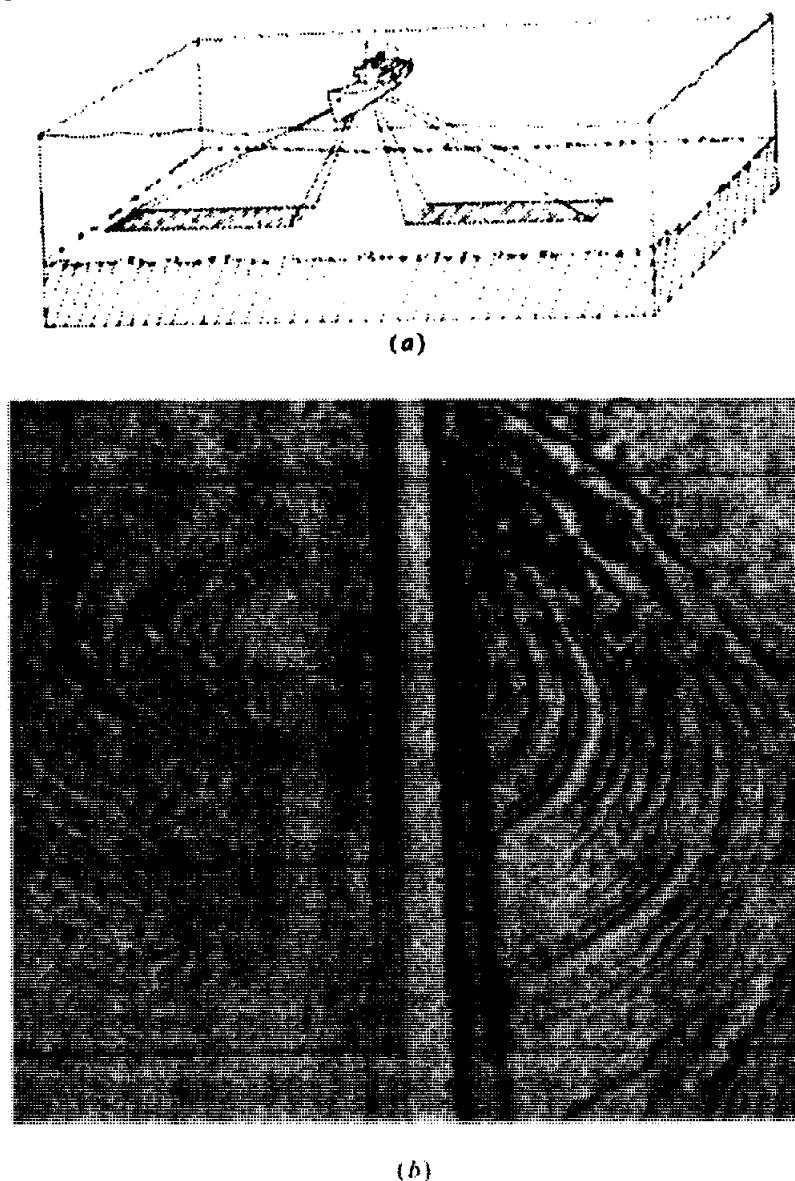


Figure 4.108. Profiler record showing subbottom deposits. (From King, 1973.)



**Figure 4.109.** Profiler record offshore Japan. The water-bottom reflection (A) with traveltimes of 1.0 to 2.0 s indicates water depths of 750 to 1,500 m. The ship traveled 8,500 m between the 30 min marks shown at the top of the record. Most primary reflections are obscured below the water-bottom multiple (B) and subsequent multiples. Over 1,000 m of sediments are indicated in the vicinity of C; multiples of these appear paged-back at D. E indicates a fault scarp on the ocean floor. F are diffractions, probably from sea floor relief slightly offset to the line. Note the onlap and thinning above G. H is a second multiple of the ocean floor. (Courtesy Teledyne.)



*Figure 4.110. Side-scan sonar. (Courtesy Compagnie Générale de Géophysique.) (a) Schematic diagram. (b) Record showing reflections from sea-floor relief. There is a blind zone under the ship's track.*

Multiples of the sea floor often are very strong and make data arriving after them unusable (Allen, 1972). In engineering work where interest is concentrated in the relatively thin layer of unconsolidated sediments overlying bedrock, such as shown in Fig. 4.108, this usually does not create a problem; where the unconsolidated sediments are thick, the sea bottom is apt to be soft (not involving a large acoustic impedance contrast) and hence the bottom multiple is relatively weak. In deep-water oceanographic work, a long period of time (a wide *window*) elapses before the ocean-bottom multiple arrives (as in Fig. 4.109) so that appreciable data are recorded without ambiguity.

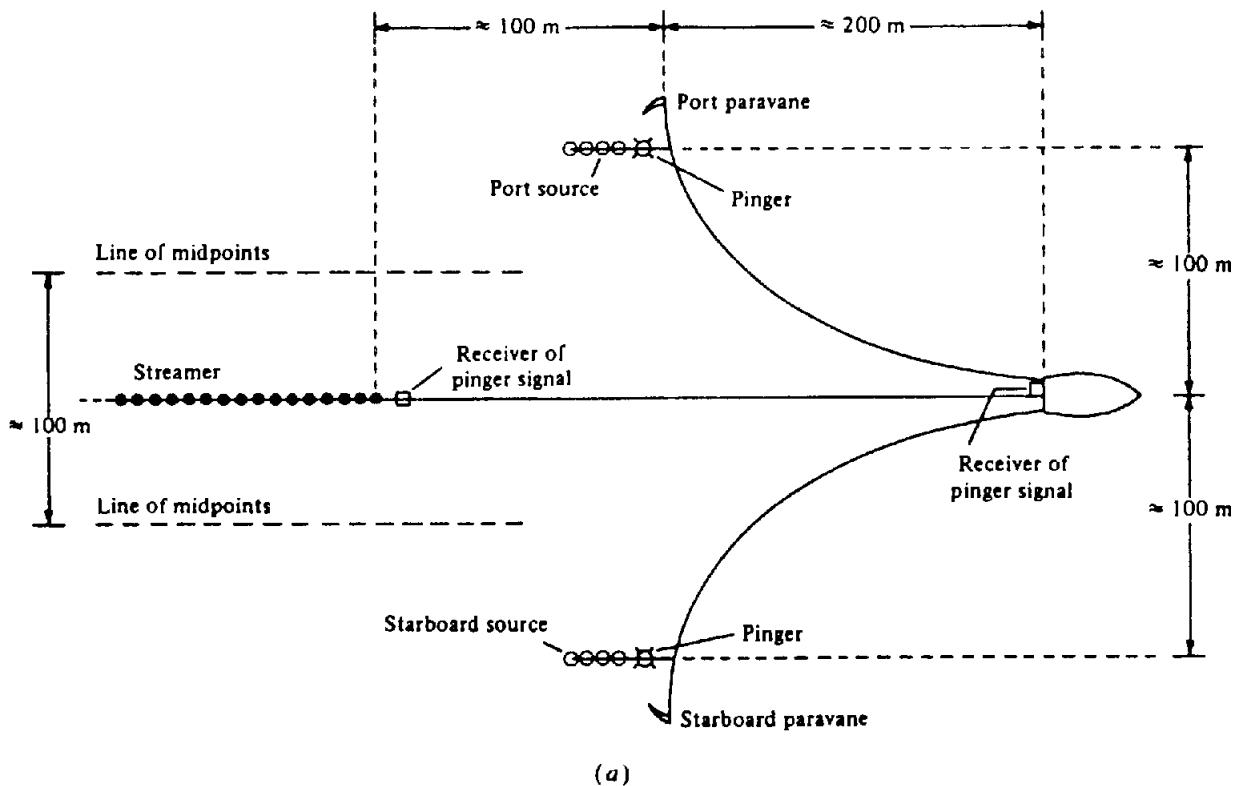
The power and complexity of profilers are sometimes increased to such an extent that the difference from conventional marine methods virtually disappears. They may employ arrays of sources, streamers

containing many hydrophone groups, and common-midpoint methods.

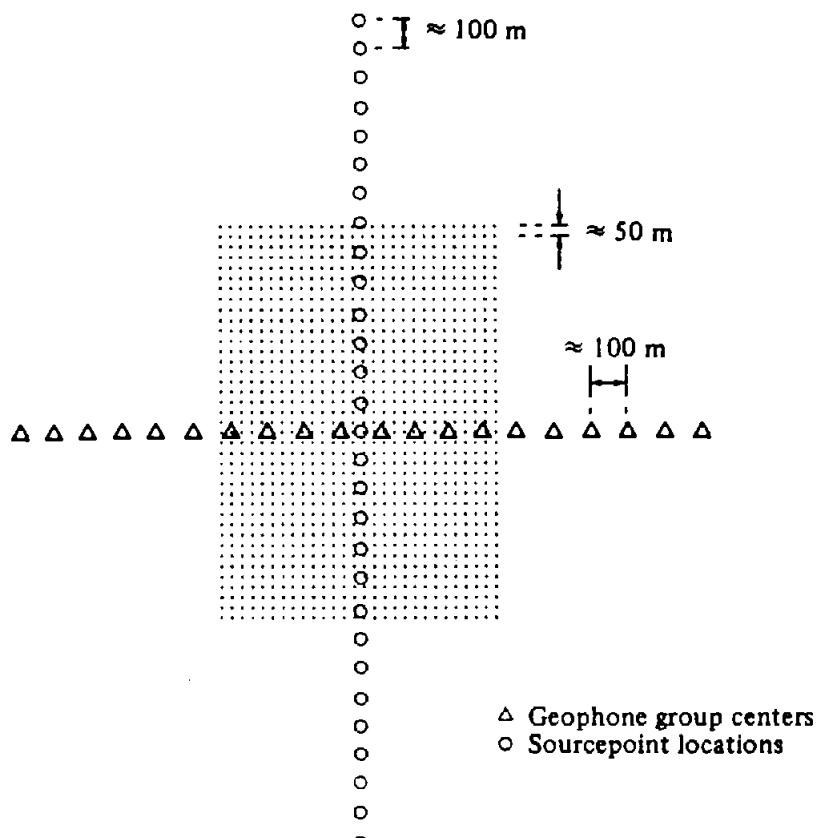
Profiler surveys often employ several types of sensors, possibly towing magnetometers and *sniffers* (devices that sample and analyze the seawater for hydrocarbons or other materials). Side-scan sonar (Fig. 4.110) is sometimes used, which utilizes high-frequency transducers to record energy reflected back from sea-floor relief to the side of the ship. Sometimes the deep-tow method is employed, that is, sources and sensors are towed near the sea floor in deep water.

#### 4.11.2. Three-Dimensional Methods

(a) *Acquisition.* Most seismic data are recorded along lines of traverse, and variations perpendicular to the seismic line are inferred from comparison with



(a)



(b)

*Figure 4.111. Arrangements for three-dimensional surveying. (From Sheriff and Geldart, 1982.) (a) Use of paravanes to pull source units to the side of the ship's track so that two parallel lines of coverage can be obtained by alternating sources. Paravanes are also used to record with two streamers simultaneously. (b) Land three-dimensional data are usually recorded with lines of geophones (usually with several parallel geophone lines used simultaneously) perpendicular to the line of sourcepoints.*

parallel lines or cross lines. This is often done during contouring, after interpreting the individual lines in a grid of lines. Three-dimensional methods involve acquiring data over an area rather than in linear fashion. Obviously 3-D data cost more than 2-D data, but the added cost will be justified if the removal of interpretation ambiguities is sufficiently important. Most 3-D data have been acquired after hydrocarbons have been discovered in an area and before field development. Most often the increased costs are more than offset by savings due to fewer dry development holes. Also, more precise maps of a field may result in locating wells so as to leave less hydrocarbons in the ground, which effectively increases the reserves discovered.

Ideally, element spacing in both directions should be the same – that dictated by spatial-aliasing considerations. These depend on the maximum dip to be recorded without ambiguity. The required spatial-sampling interval is often less than 50 m, but such small spacings are rarely used because of cost considerations, and typical spacing is about 100 m. Complete uniformity also requires that each element of data have the same multiplicity and be composed of the same mix of offset distances, so that it will have the same signal/noise ratio. Although uniformity is usually not achieved, interpretability is still improved because 3-D data elements have more neighboring values than linear data and so do not require the same uniformity.

In the marine environment most equipment is towed into place and usually the ship cannot stop without losing control of the towed equipment. This constrains marine 3-D acquisition to a series of closely spaced parallel lines. Towing dual streamers offset to the side, and/or the use of dual sources (Figs. 4.60 and 4.111a), also offset to the side, make it possible to obtain two or more lines of midpoints on a single traverse. Long streamers do not necessarily track the ship, however. Magnetic compasses located throughout the streamer and radar sighting on the tail buoy help determine the streamer's orientation, and water-break detectors help determine distances from the source locations. Streamer drift to the side because of a cross-current is sometimes used as a device to obtain areal coverage, though at the price of a nonuniform mix of offset distances.

Land 3-D acquisition is most often achieved using lines of geophones and sources at right angles to each other (Fig. 4.111b). This arrangement provides coverage over a *block*. Often several lines of geophones are used, especially with systems that can record large numbers of separate traces, to produce a *swath* of coverage. However, distortion is introduced because the directivity of arrays is usually different in the in-line and cross directions. Another arrange-

ment sometimes used, especially where the center of an area cannot be reached because of hills, lakes, and so on, is the *loop* method wherein both geophones and sourcepoints are arranged completely around a loop. Other systems are used to adapt to specific local access restrictions.

(b) *Processing.* Data must be located on a regular grid for almost all processing applications, so the area of coverage is divided up into rectangular cells called *bins* and traces are put into the bins in which the midpoints lie. Displays may be made of the number of traces in each bin as a check on the uniformity of coverage. Data may be interpolated from neighboring bins when bins have insufficient traces.

With land 3-D, many bins are not along lines of traverse where near-surface data are available and because the multiplicity within each bin is apt to be small and irregular, poorer control on static time shifts may result. Likewise the control for velocity analysis is apt to be poorer than with CMP data. Often CMP data in the area are used as the starting point for corrections, and additional CMP lines may be shot in connection with a 3-D survey to provide this information.

Migration is usually approximated by first doing a 2-D migration of the data in one direction and then migrating this intermediate result in the direction at right angles. The result is nearly the same as would be achieved by a true 3-D migration and it is considerably cheaper.

(c) *Display.* The 3-D data set can be thought of as a volume of data (Fig. 4.112) that can then be sliced in various ways. The data can be sliced vertically in various directions to provide cross sections in any direction; they can even be sliced along zig-zag lines to provide fence diagrams to connect well locations. The data can also be sliced horizontally to provide *time slices* (Fig. 4.112b), which are especially useful because a phase lineup on a time slice represents the same event at the same traveltime, that is, a time contour, and tracing the sequence of phase alignments on successive time slices generates directly a time-contour map. The data may also be sliced along reflecting horizons (a *horizon slice*; see Fig. 4.112c), so that variations in amplitude can be studied. This is a useful tool in studying stratigraphic changes and in mapping hydrocarbon accumulations where the hydrocarbons change the horizon's reflectivity.

Sections and slices are often displayed in color, using one color (often black or blue) to indicate peaks and another color (often red) to indicate troughs. Such a display usually makes significantly more information available to the interpreter than

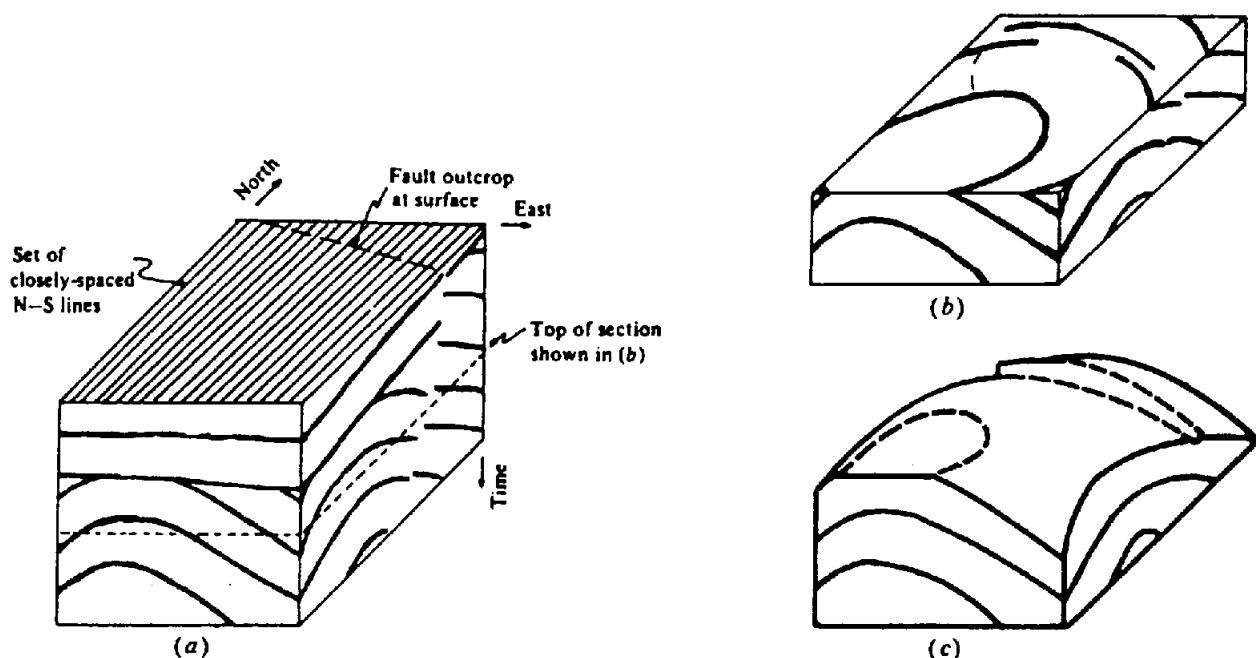


**Figure 4.112.** Three-dimensional data obtained from a set of closely spaced N-S lines. (a) Isometric diagram of the volume these data occupy. The easternmost N-S section is shown along with an E-W section made from the southernmost traces on each N-S line. (b) The data set with the top portion removed. The top now constitutes a time-slice. (c) The data sliced along one reflection constitutes a horizon-slice. Such maps show reflectivity variations along the same horizon such as may indicate stratigraphic or fluid-content changes.

does the common variable area display where often the trough information is lost. Sometimes an additional color border is used with slice displays to clarify which direction is down- or up-dip. Color codes are also used to indicate amplitude or other attribute measurements (Sheriff and Geldart, 1983, pp. 73-4).

(d) *Interpretation.* The major problems in the interpretation of 2-D data sets often involve deciding what goes on between the lines of traverse, how to connect up-fault evidences, whether there is a local high between lines, and so on. The interpreter's imagination is exercised trying to figure out the most optimistic possibilities in between the lines of coverage. With 3-D data, questions of this sort usually do not arise because the answers are clear from the data, and the questions for the interpreter deal with more subtle matters. Horvath (1985) and Brown (1988) show many examples of the interpretation of 3-D data.

#### 4.11.3. Use of Channel Waves

Seismic energy can sometimes be trapped within a low-velocity layer. Then the energy from a point source will decrease with distance according to cylindrical rather than spherical divergence, that is, at a slower rate. This will happen when total or near-total

reflection occurs at the layer boundaries; this may happen if the velocity contrast is exceptionally high (as at a free surface) or if the angle of incidence exceeds the critical angle (Sheriff and Geldart, 1982, pp. 70-3). *Channel waves* (also called *guided* or *normal-mode waves*) can travel in a water layer overlying a high-velocity sea floor and in low-velocity members, such as coal, that are sandwiched between high-velocity members.

Channel waves are used to determine the continuity of beds in coal exploration (Buchanan et al., 1981). A source in a gallery generates waves in a coal seam that can be detected in neighboring galleries if the coal seam is continuous, that is, not interrupted by intervening faulting. Sometimes source and geophones are located in the same gallery to detect reflections from fault faces.

Channel waves are generally dispersive, with different frequency components traveling at different velocities. The result is that an impulsive input becomes a long wavetrain (as in Fig. 4.113) after traveling for some distance.

#### 4.11.4. Vertical Seismic Profiling

Velocity surveys in boreholes (§4.5.5a) involve placing a geophone at several depths and measuring the traveltimes of the first energy from a source near the wellhead. The geometry for vertical seismic profiling

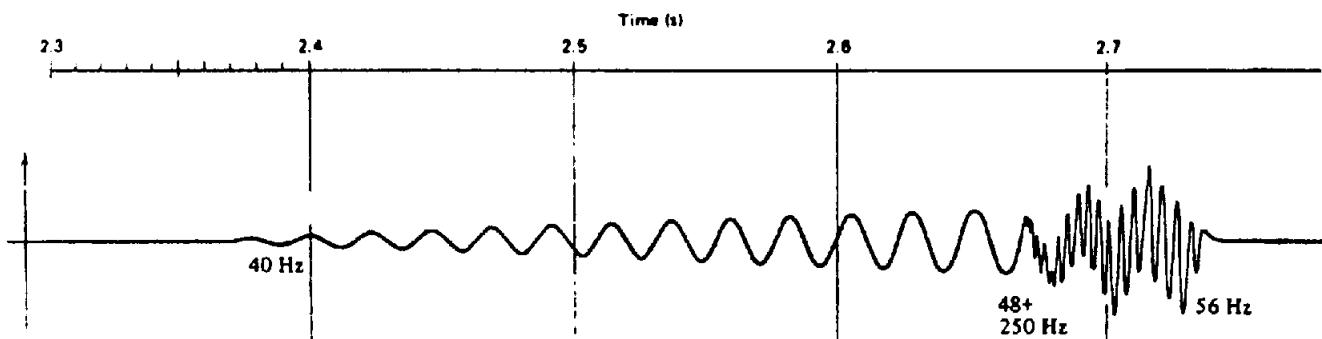


*Figure 4.113. Dispersion wavetrain such as that produced by channel waves. The burst of high-frequency energy starting about 2.66 s is superimposed on the low-frequency wave, both ending abruptly at about 2.73 s; this is known as the **Airy phase**. (From Clay and Medwin, 1977.)*

(VSP) is similar except that the entire wavetrain is recorded (Balch and Lee, 1984; Cassell, 1984; Hardage, 1985). The geophone locations in the boreholes are usually closely spaced, typically about every 50 m, and the results are usually displayed as in Figure 4.114. The wavetrains include not only direct waves, but also reflections and multiples of various types. The downward- and upward-traveling wavetrains can be separated almost completely in processing. The downward-traveling wavetrain provides the information needed for deconvolution. The upward-traveling wavetrain after deconvolution usually shows predominantly primary reflections and is useful in correlating reflection events with well horizons. The VSP is also useful in "seeing ahead of the bit," that is, in showing reflecting horizons that the well has not yet penetrated. These show up with greater clarity than in surface data because the waves have not had as far to travel.

If the source is moved some distance from the wellhead, then reflecting points will be located farther from the well, the farther the reflecting horizon is from the well geophone. Having recordings at many geophone depths results in a profile to the side of the wellbore. VSP records are thus useful in seeing features that the borehole missed, such as faults or other changes in reflectors. VSP surveys are also used in directional holes and in other situations as interpretational aids.

#### 4.11.5. Shear Waves in Exploration

Although most exploration is done with *P* waves, *S* waves depend on different elastic parameters and thus provide independent information. Appreciable effort has been expended in recent years to use *S*-wave data in conjunction with *P*-wave data to define lithology, as a hydrocarbon indicator (Ensley, 1985), and in fracture detection. The ratio of *S*-wave to *P*-wave velocities differs with lithology, and hydrocarbon accumulations, especially gas, often

change the *P*-wave velocity significantly but have little effect on the *S*-wave velocity (Tatham, 1982). Fractures affect velocities differently depending on the raypath orientation with respect to the fractures.

Several methods preferentially generate *S* waves, and geophones oriented to detect horizontal motion can be used as *S*-wave detectors. *P* waves generate *SV* waves upon conversion at interfaces and vice versa, which leads to confusion in interpreting results. However, most *S*-wave exploration is done with *SH* waves that do not convert.

#### 4.11.6. Variation of Amplitude with Offset

Reflections generally decrease in amplitude with increasing angle of incidence, that is, with increasing offset. However, when gas fills the pore spaces, the amplitude may increase with offset (Ostrander, 1984). Although the situation is complicated, the variation of amplitude with offset may be useful as a hydrocarbon indicator.

#### 4.11.7. Cross-hole Methods

Placing a seismic source in one borehole and geophones at various depths in another borehole provides data for a number of raypaths, the more so if the source is successively located at a number of depths. The traveltimes and amplitudes of the multitude of raypaths provide tomographic data that hopefully can be used to discover how velocities and factors causing amplitude loss are distributed throughout the region between the boreholes (Peterson, Paulsson, and McEvilly, 1985). Cross-hole methods are presently handicapped by limitations of the strength of the source that can be placed in a borehole; this limits the distance over which signals can be detected. However, the method offers promise as a field-development and production-monitoring tool.

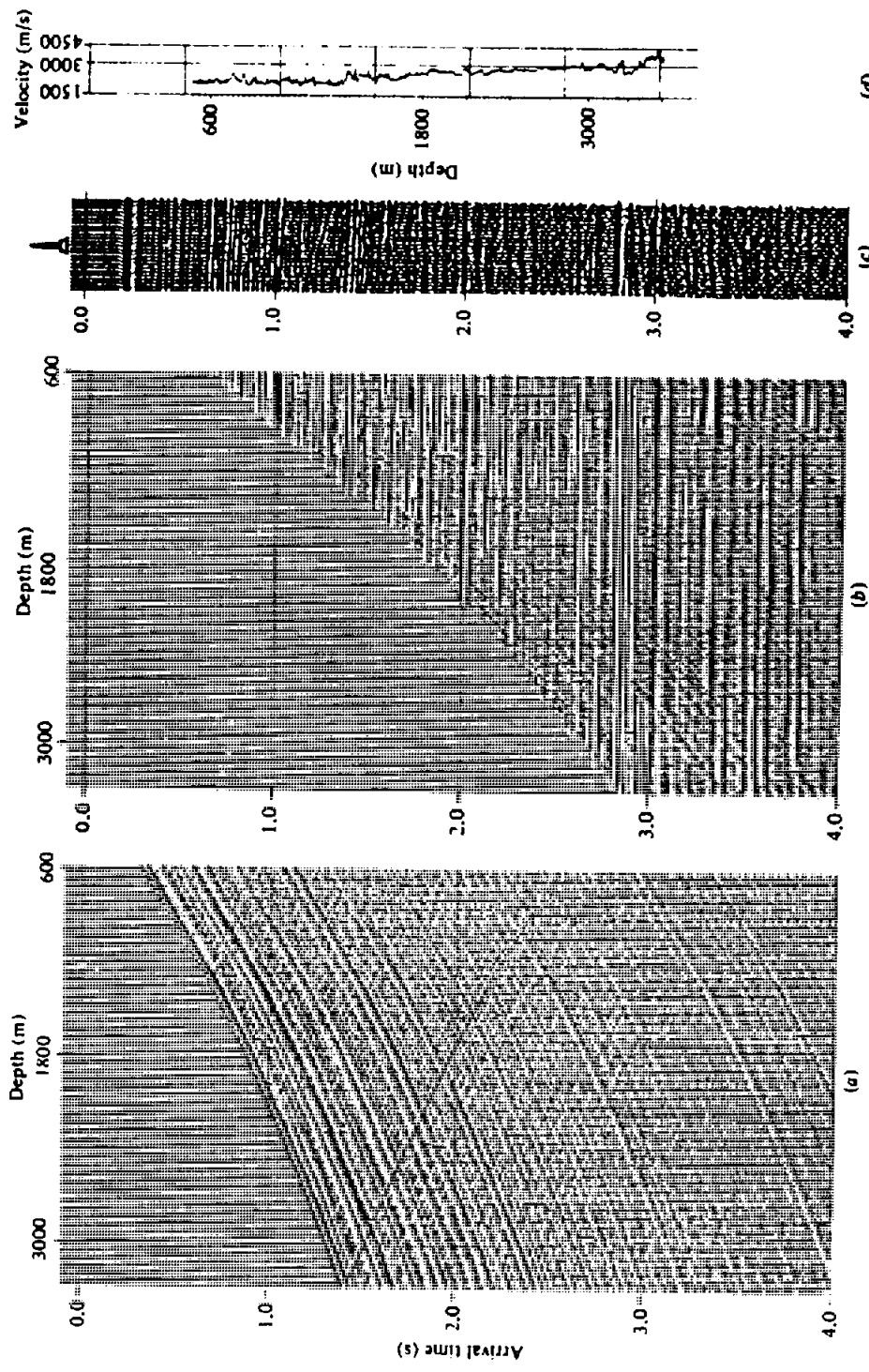


*Figure 4.114. Vertical seismic profile. (Courtesy SSC.) (a) Each trace is recorded at a station in a borehole using an air gun source at the surface. (b) Same except each trace has been shifted by the one-way traveltime to the surface, thus aligning reflections (upcoming events) horizontally. (c) Portion of reflection record shot across the wellhead. (d) Sonic log in the well.*

## 4.12. PROBLEMS

- (a) By substituting  $\sigma_{xx} > 0$  and  $\sigma_{yy} = \sigma_{zz} = 0$  in Equation (4.5), show that  $\epsilon_{yy} = \epsilon_{zz}$  and verify the relation for Poisson's ratio, Equation (4.8).  
 (b) By adding the three equations for  $\sigma_{xx}$ ,  $\sigma_{yy}$ , and  $\sigma_{zz}$ , derive the relation for Young's modulus, Equation (4.7).  
 (c) Substituting  $\sigma_{xx} = \sigma_{yy} = \sigma_{zz} = -p$  in Equation (4.5), derive the relation for the bulk modulus, Equation (4.9).
- (a) Verify that  $\psi$  in Equation (4.18) is a solution of the one-dimensional wave equation [Eq. (4.17)]. [Hint: Let  $\xi = (x - Vt)$  and show that  $\partial\psi/\partial x = (df/d\xi)(\partial\xi/\partial x) = df/d\xi = f'$ , and so on.]  
 (b) Verify that  $\psi$  in Equation (4.20) is a solution of the wave equation, Equation (4.16).  
 (c) Using the same technique as in parts (a) and (b), show that  $\psi = (1/r)f(r \pm Vt)$  satisfies the spherical wave equation, Equation (4.22).
- A pulse consists of two frequency components,  $\nu_0 \pm \Delta\nu$ , of equal amplitudes. For the two components we write

$$A \cos 2\pi(k_1 x - \nu_1 t) \quad A \cos 2\pi(k_2 x - \nu_2 t)$$

where  $\nu_1 = \nu_0 + \Delta\nu$ ,  $\nu_2 = \nu_0 - \Delta\nu$ ,  $k_0 = 1/\lambda_0 = \nu_0/V$ ,  $k_1 \approx k_0 + \Delta k \approx (\nu_0 + \Delta\nu)/V$ , and  $k_2 \approx k_0 - \Delta k \approx (\nu_0 - \Delta\nu)/V$ .

(a) Show that the pulse is given approximately by the expression

$$B \cos 2\pi(k_0 x - \nu_0 t)$$

where  $B = 2A \cos 2\pi\Delta k(x - (\Delta\nu/\Delta k)t)$ .

(b) Why do we regard  $B$  as the amplitude? Show that the envelope of the pulse is the graph of  $B$  plus its reflection in the  $x$  axis.

(c) Show that the envelope moves with the group velocity  $U$  where

$$U = \frac{\Delta\nu}{\Delta k} \approx \frac{d\nu}{dk} \approx V - \lambda \frac{dV}{d\lambda} \approx V + \omega \frac{dV}{d\omega}$$

- Assume three geophones oriented so that one records only the vertical component of a seismic wave, another records only the horizontal component in the direction of the shot, and the third records only the horizontal component at right angles to this. Assume a simple wave shape and draw the responses of the three geophones for the following cases: (i) a  $P$  wave traveling directly from the shot to the geophones; (ii) a  $P$

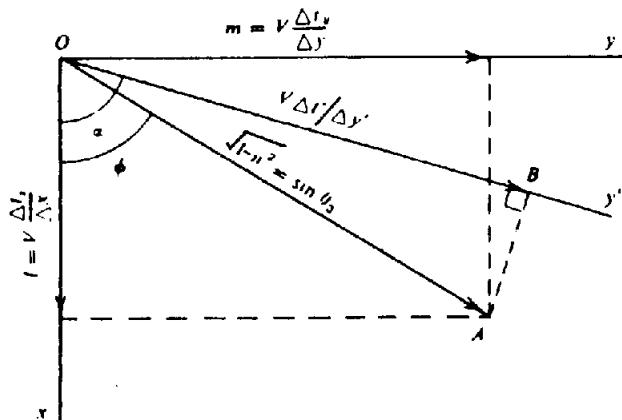


Figure 4.115. Combining dip components.

Table 4.4.

Depth (m)	Two-way time (s)
1,000	1.0
2,500	2.0
2,800	2.1
4,800	3.1

wave reflected from a deep horizon; (iii) an  $S$  wave generated by reflection of a  $P$  wave at an interface; (iv) a Rayleigh wave generated by the shot.

- Using Figure 4.115, show that the construction of Fig. 4.27 gives the same result as Equation (4.61). [Hint: Express  $OB$  in terms of  $n = \sin \theta_3$  and use equation (4.61).]
- (a) Given the time-depth information in Table 4.4, calculate interval velocities and average velocity to each depth. Plot velocity against depth and velocity against time, and determine the equations of straight lines that approximate interval velocity and average velocity against time and depth (four equations). What are some of the problems involved in making functional fits to data?  
 (b) Using the function derived in (a) for the average velocity as a function of time, calculate the depth of reflections with zero-dip moveout and traveltimes of 1.0, 2.0, 2.1, and 3.1 s. How much error has been introduced by approximating the velocity by a function?
- (a) Assuming equivalent average velocity as indicated in Section 4.3.2b, the results from part (a) of problem 6, and a dip moveout of 50 ms per 1,000 m, calculate the dip of reflectors corresponding to traveltimes of 1.0, 2.0, and 3.0 s. Plot the locations of the reflecting points.

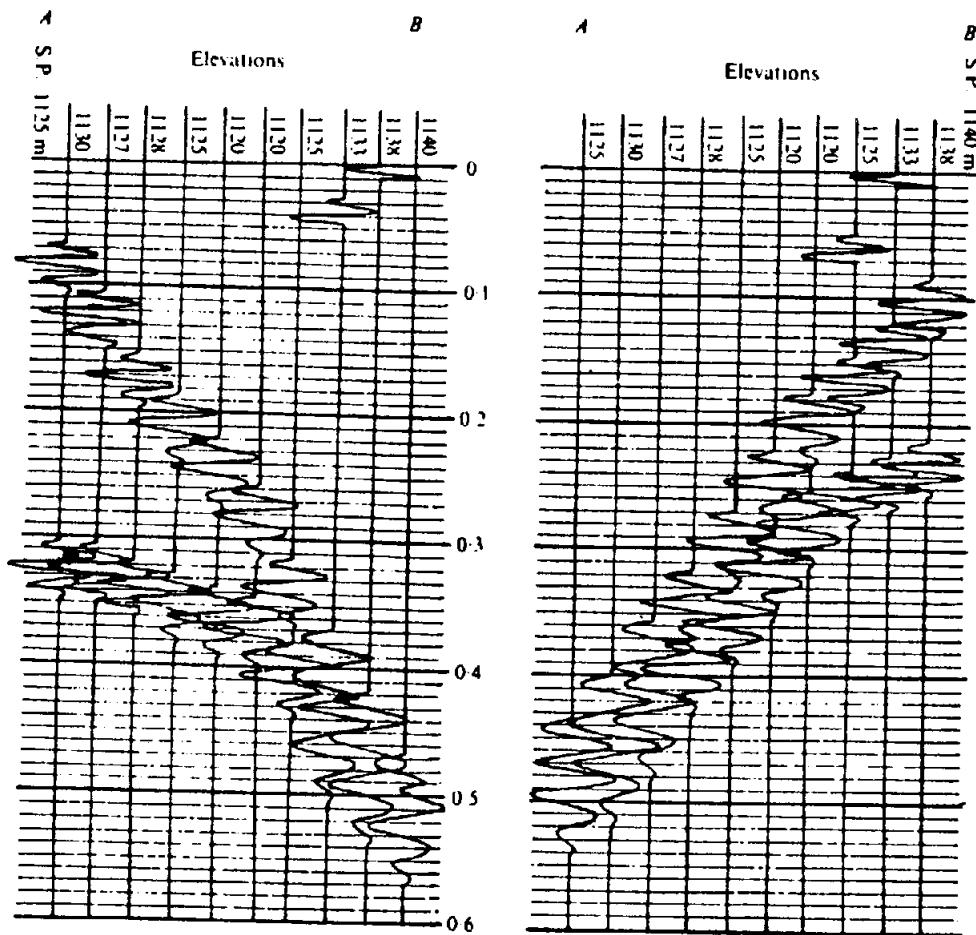


Figure 4.116. First breaks and a reflection on reversed end-on spreads.

(b) Assume constant-velocity layers as follows:

0 to 1,000 m	2,000 m/s
1,000 to 2,500 m	3,000 m/s
2,500 to 2,800 m	6,000 m/s
2,800 to 4,800 m	4,000 m/s

Verify that this gives the time-depth data of Table 4.4. By ray-tracing through these layers for a dip moveout of 50 ms per 1,000 m, find the dip and reflecting points for reflectors for which the arrival times are 1.0, 2.0, and 3.0 s. Compare with the results for part (a).

8. The correction methods discussed in Section 4.7.1 assume that the shot is below the base of the LVL. What changes are required in the equations of this section if this is not the case?
9. Figure 4.116 shows the first arrivals at geophone stations 100 m apart from shots 25 m deep at each end of the spread. (There are actually 11 geophone stations with the shotpoints at the first and eleventh stations; however, the geophone group at each shotpoint is not recorded because of hole noise.) The uphole geophone is recorded on the third trace from the right. The weathering velocity is 500 m/s.

(a) Estimate the subweathering velocity  $V_H$  by averaging the slopes of lines approximating the first breaks. The valley midway between the shotpoints produces a change in the first-break slopes, as if two refractors are involved, which is not the case. How can one be sure of the latter?

(b) Determine the weathering thicknesses at the two shotpoints from the uphole times.

(c) What corrections  $\Delta t_0$  should be applied to reflection times at the two shotpoints for a datum of 1,100 m?

(d) Calculate the weathering thickness and the static time correction for each geophone station.

10. (a) Two intersecting seismic spreads have bearings N10°E and N140°E. If the first spread shows an event at  $t_0 = 1.760$  s with dip moveout of 56 ms per 1,000 m while the same event on the second spread has a dip moveout of 32 ms per 1,000 m, find the true dip, depth, and the strike, assuming that (i) both dips are down to the south and west and (ii) dip on the first spread is down to the south while the other is down to the southeast. Take the average velocity as 3 km/s.
- (b) Calculate the migrated position for each spread as if the cross-information had not been

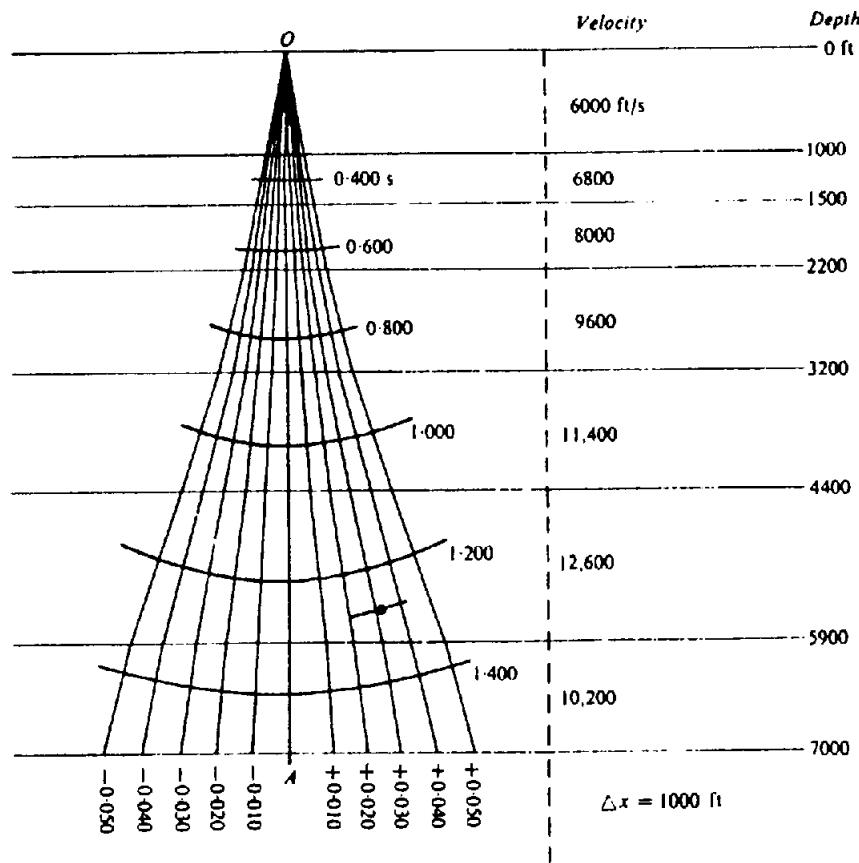


Figure 4.117. Simplified wavefront chart formerly used to plot cross sections on a transparent overlay. Chart shows rays traced through a series of constant-velocity layers for  $\Delta t_d$  values of  $0, \pm 0.010, \dots, \pm 0.050$  s.  $\Delta x = 1000$  ft. Wavefronts are shown for  $t_0 = 0.4$  to  $1.4$  s assuming that the rays are reflected upward along the downward paths. Plotted reflector is for  $t_0 = 1.28$  s,  $\Delta t_d = 0.033$  s.

- available and each had been assumed to indicate total moveout. Compare with the results of part (a).
11. Consider a reflection with an arrival time at the shotpoint of 1.200 s and arrival times at geophones 1,000 m away on opposite sides of the shotpoint equal to 1.162 and 1.237 s, respectively, where static and dynamic corrections have been applied to all traveltimes.
    - (a) Using the simplified wavefront chart and velocity distribution shown in Figure 4.117, plot the migrated position of the reflection.
    - (b) If straight-ray plotting were used at the angle of approach, where would the reflection be plotted? Velocity just below datum = 5,500 ft/s.
    - (c) Using straight-ray plotting and assuming that  $V_{av} = 12,600$  ft/s, the velocity at the reflector, what is the migrated position?
    - (d) The average velocity for a vertical traveltime of 1.200 s is 8,600 ft/s. How can this be determined from the data given in Figure 4.117?
    - (e) Assuming the average velocity 8,600 ft/s and straight-ray travel, what is the migrated position?
  - (f) On the adjoining record, which has a shot-point 1,500 ft away, what is the arrival time of this reflection for a geophone at the shotpoint (assume a plane reflector)?
  12. (a) Because  $\delta(t)$  is zero except for  $t = 0$  where it equals +1. Equation (4.93) now gives
- $$\delta(t) \leftrightarrow +1$$
- show that
- $$\delta(t - t_0) \leftrightarrow e^{-j2\pi vt_0}$$
- (b) The comb can be written
- $$\text{comb}(t) = \sum_{n=-\infty}^{+\infty} \delta(t - nt_0)$$
- the transform of this expression is clearly
- $$\text{comb}(t) \leftrightarrow S(v) = \sum_{n=-\infty}^{+\infty} e^{-j2\pi nt_0 v}$$

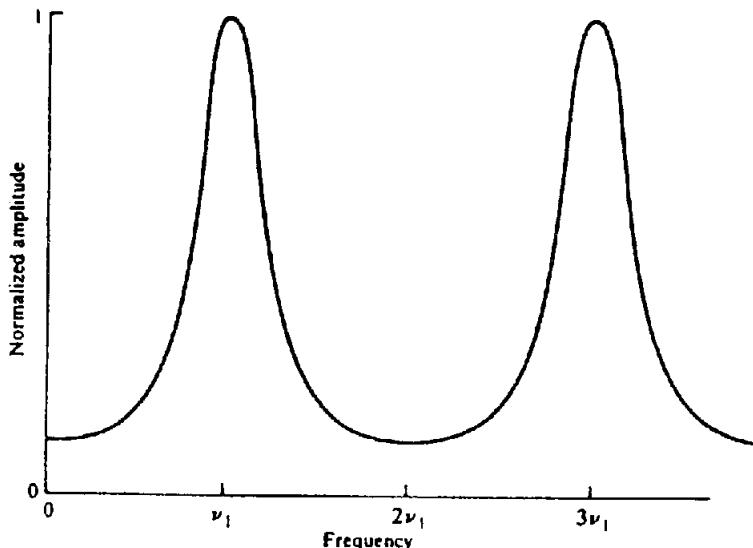


Figure 4.118. Spectrum of water-layer filter for water-bottom reflection coefficient of 0.5. If  $h$  = water depth and  $V$  = water velocity,  $\nu_1 = V/2h$ .

Show (Papoulis, 1962, p. 44) that this represents an infinite series of impulses of height  $2\pi/t_0$  spaced  $2\pi/t_0$  apart, that is,

$$\sum_{n=-\infty}^{+\infty} \delta(t - nt_0) \leftrightarrow \left( \frac{2\pi}{t_0} \right) \sum_{m=-\infty}^{+\infty} \delta\left( 2\pi\nu - \frac{2\pi m}{t_0} \right)$$

or

$$\text{comb}(t) \leftrightarrow \omega_0 \text{comb}(\omega)$$

(c) Show that a boxcar of height  $h$  and extending from  $-\nu_0$  to  $+\nu_0$  in the frequency domain has the transform

$$\text{boxcar}(\nu) \leftrightarrow A \text{sinc}(2\pi\nu_0 t) = A \frac{\sin 2\pi\nu_0 t}{2\pi\nu_0 t}$$

where  $A = 2h\nu_0$  = area of the boxcar.

13. (a) Verify that Equation (4.107) is the inverse filter for water reverberation by convolving Equation (4.105) with (4.107), that is, by substituting the expressions given by Equations (4.105) and (4.107) in Equation (4.106).  
 (b) The spectrum of the water-layer filter is shown in Figure 4.118; the large peaks occur at

the “singing frequency.” Sketch the amplitude spectrum of the inverse filter. [Hint: Time-domain convolution such as shown in Equation (4.106) corresponds to frequency-domain multiplication [Eq. (4.99)]; the frequency spectrum of the unit impulse is +1, i.e., flat.]

(c) Verify your sketch of the water-reverberation inverse filter by transforming Equation (4.107):

$$[1, 2r, r^2] \leftrightarrow 1 + 2re^{-j2\pi\nu\Delta} + r^2e^{-j4\pi\nu\Delta}$$

14. (a) Convolve [2, 5, -2, 1] with [6, -1, -1].  
 (b) Cross-correlate [2, 5, -2, 1] with [6, -1, -1]. For what shift are these functions most nearly alike?  
 (c) Convolve [2, 5, -2, 1] with [-1, -1, 6] and compare with the answer in (b). Explain the difference.  
 (d) Autocorrelate [6, -1, -1] and [3, -5, -2]. The autocorrelation of a function is not unique to that function, for example, other wavelets that have the same autocorrelations as the preceding are [-1, -1, 6] and [-2, -5, 3]. Which member of the set is the minimum delay wavelet?  
 (e) What is the normalized autocorrelation of [6, -1, -1]? What is the normalized cross-correlation in (b)? What do you conclude from the magnitude of the largest value of this normalized cross-correlation?  
 15. Prove that the half-intercept curve referred to in the discussion of Wyrobek's method in Section 4.9.3c is parallel to the curve of the total delay time  $\delta$  (Fig. 4.119). Note that the reciprocal time

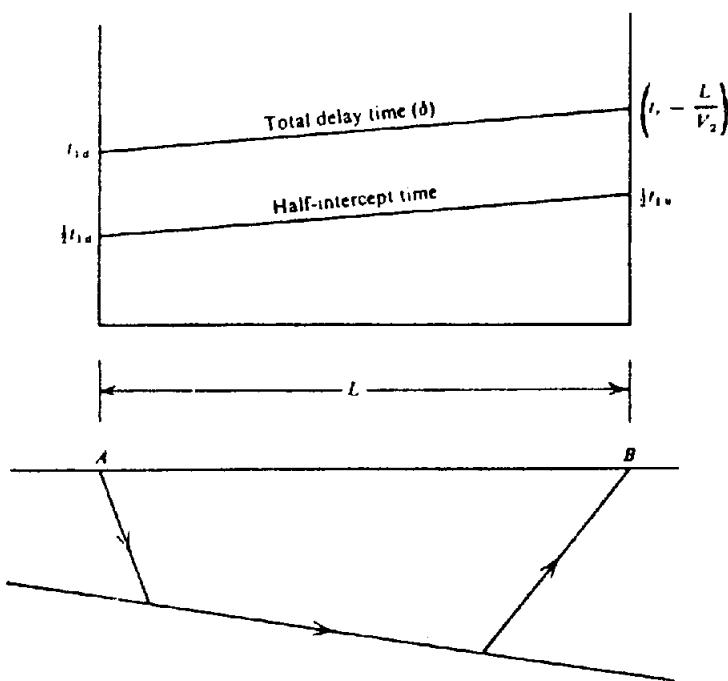


Figure 4.119. Demonstrating the parallelism of total-delay and half-intercept time curves.

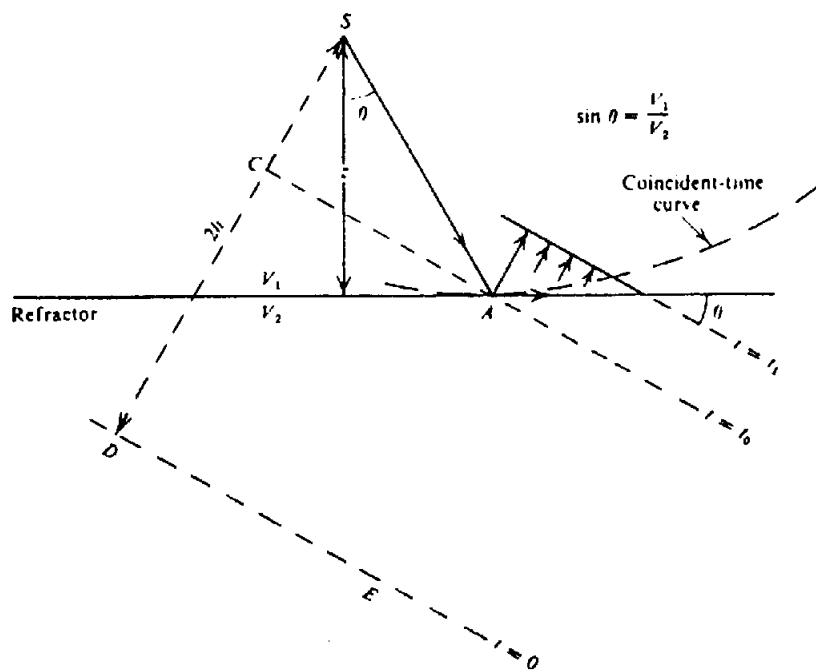


Figure 4.120. Deriving the properties of the coincident-time curve.

can be written [Eqs. (4.77)]

$$t_r = \frac{1}{2} \left\{ \left( \frac{L}{V_d} + t_{1d} \right) + \left( \frac{L}{V_u} + t_{1u} \right) \right\}$$

16. Using Figure 4.120 show that: (i)  $DE$ , the wavefront for  $t = 0$ , is at a depth of  $2h = SD =$

$2z \cos \theta$  (note that  $CD = SA = z/\cos \theta$ ); (ii) each point on the coincident-time curve is equidistant from  $S$  and  $DE$ , that is, the curve is a parabola; (iii) taking  $DE$  and  $SD$  as the  $x$  and  $y$  axes, the coincident-time curve has the equation  $4hy = x^2 + 4h^2$ ; (iv) the slope of the coincident-time curve at  $A$  is  $\tan \theta$ , hence the curve is tangent to the refractor at  $A$ .

Table 4.5.

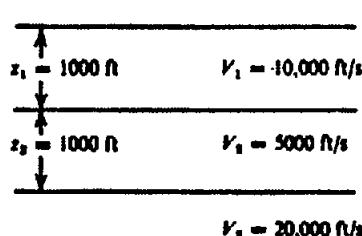
$x$ (m)	$t$ (ms)	$x$ (m)	$t$ (ms)
15	19	105	65
30	29	120	68
45	39	135	72
60	50	150	76
75	59	165	78
90	62	180	83

17. Prove Equation (4.132) assuming that the surface is horizontal and the refractor is plane between the two shotpoints.
18. To find the depth to bedrock in a dam-site survey, traveltimes were measured from the shotpoint to 12 geophones laid out at 15 m intervals along a straight line through the shotpoint. The offsets  $x$  range from 15 to 180 m. Determine the depth of overburden from the data in Table 4.5.
19. To determine the thickness of the surface layer in a certain area, the readings in Table 4.6 were obtained from refraction records. Shotpoints  $A$  and  $B$  are located at the end of a 180 m east-west spread of 13 geophones where  $A$  is west of  $B$  and  $t_A$  and  $t_B$  are the traveltimes at shotpoints  $A$  and  $B$ . The ground surface is flat. No data were obtained from the geophone at the shotpoint. Using the data in Table 4.6, find the velocities in the upper and lower beds, the dip, and the vertical depths to the refractor at  $A$  and  $B$ .
20. Show that the two geological sections illustrated in Figure 4.121 produce the same refraction time-distance curve. What is the apparent depth to the lower interface (obtained from the refraction data) if  $V_3 \approx V_1$  in the section at the left, for example,  $V_1 = 8.20$  kft/s,  $V_3 = 8.60$  kft/s, and  $V_2 = 4.10$  kft/s, and the bed thicknesses are as shown in the figure?
21. The time-distance observations in Figure 4.122 constitute an engineering refraction problem.
- (a) Using Equations (4.77) and (4.79), show that the first layer dips about  $1^\circ$  and ranges in thickness from 9 to 11 ft between points 63 and 69.

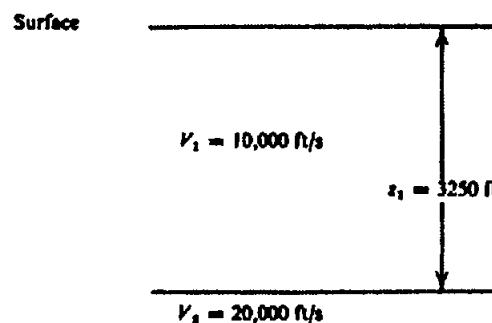
Table 4.6.

$x$ (m)	$t_A$ (ms)	$t_B$ (ms)
15	10	10
30	20	20
45	30	30
60	40	40
75	50	46
90	60	51
105	65	57
120	69	63
135	73	69
150	77	74
165	81	80
180	85	85

- (b) Show that the second and third layers have velocities of about 11,500 and 18,000 ft/s respectively, with the interface between the two layers dipping about  $6^\circ$ .
- (c) Determine the thickness of the second layer by stripping off the shallow layer (§4.9.2).
22. Assume horizontal layering as shown in Figure 4.123 with a shot at interface  $A$  that generates a wave that has amplitude 1 when it reaches interface  $B$ .
- (a) Calculate the amplitudes of the reflections observed at the surface from (i) interface  $B$ , (ii) interface  $C$ , (iii) multiple  $ABABS$ , and (iv) multiple  $ACBCS$ , assuming that processing has compensated for spherical divergence.
- (b) What were the amplitudes before compensating for spherical divergence?
23. Assume that the embedded wavelet is the minimum-phase wavelet shown in Figure 4.124 whose digital representation at 4 ms intervals is  $[10, 9, -8, -9, 0, 5, 3, 0, \dots]$ .
- (a) What is the wave shape reflected from a sand layer 12 m thick whose velocity is 2,000 m/s. Let the shale-to-sand reflection coefficient be 0.05.
- (b) Repeat for sand layer thicknesses of 20 and 28 m.
- (c) Assume that the upper 8 m of pore space in the 28 m thick sand is filled with gas so that its velocity is reduced to 1,500 m/s, and that this



(a)



(b)

Figure 4.121. Two different geologic sections that give the same refraction time-distance curve.

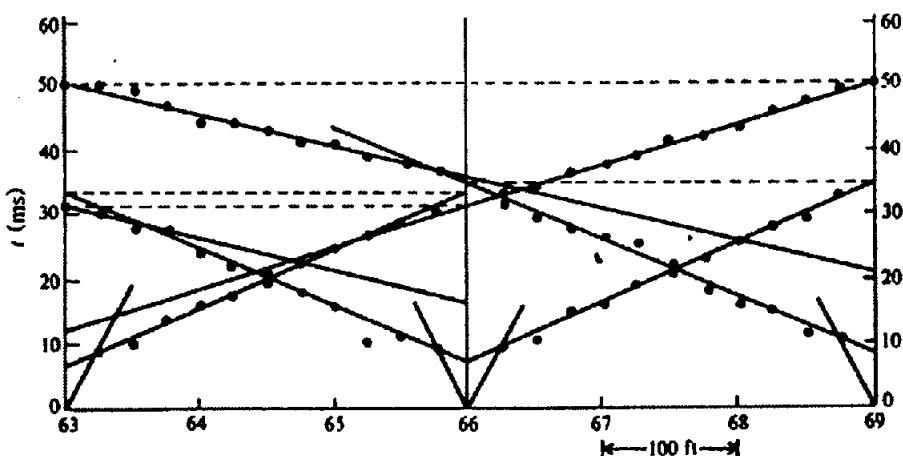


Figure 4.122. Engineering refraction profile.

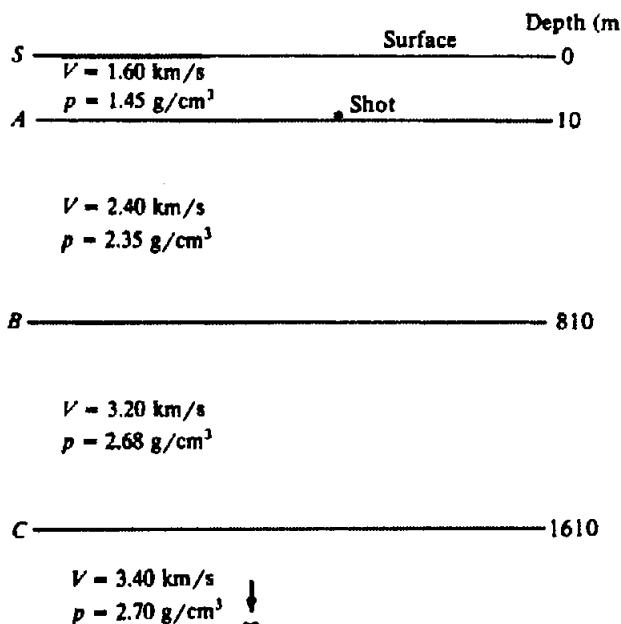


Figure 4.123. Horizontal layering situation.

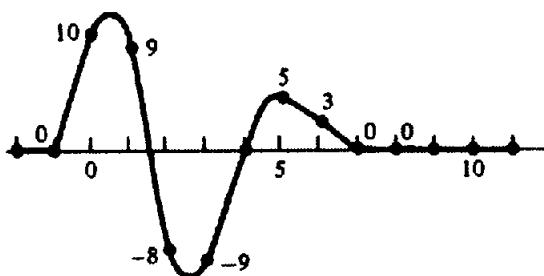


Figure 4.124. A minimum-phase wavelet.

- makes the shale-to-gas sand reflection coefficient  $-0.15$  and the gas-to-water sand reflection coefficient  $+0.20$ . What is the reflected wave shape?
- (d) Repeat (c) where  $20$  m of the sand is filled with gas.
24. Tabulate time-velocity pairs for the velocity analysis shown in Figure 4.83.  
 (a) Calculate the velocities for the intervals between reflections.

- (b) Assume that your time-velocity pairs are picked to an accuracy of  $2\%$ . What is the maximum error in the calculated interval-velocity values?
25. From the seismic record shown in Figure 4.1, determine the following:  
 (a) The depth of shot, assuming a near-surface velocity of  $500$  m/s.  
 (b) The velocity of the subweathering by plotting the first breaks.  
 (c) The stacking velocity from the measured normal moveout for three reflections.  
 (d) The depth and dip of the three reflections.
26. Pick unconformities in Figure 4.84. List problems likely to be encountered in picking seismic events. Can any depositional patterns be seen? What depositional patterns show in Figure 4.100a?
27. Interpret for yourself the section in Figure 4.100a. Explain the variations in thickness of the different units. How does this help date the underlying thrust faults?
28. Can you correlate events on opposite sides of the structure in Figure 4.101? In Figure 4.98?
29. List seismic evidences in support of reefing in Figure 4.104. Which of these also show in Figure 4.105? Where is another reef (in a different part of the section) on Figure 4.105?
30. Note the anticline just below  $0.4$  s on Figure 4.106. Its location coincides so closely with that of the channel cut in the coal that it suggests that it may be a velocity anomaly. Attempt to reconcile it as a velocity anomaly. Assume that the coal thickness is about  $10$  m and its velocity is  $1,200$  m/s, that the velocity of the section below the coal is  $1,800$  m/s, and that of the channel fill is  $700$  m/s.
31. How did the structure at about  $1.055$  s on Figure 4.107 affect shallower features? Explain the locally strong reflection at about  $0.3$  s.

## REFERENCES

- Allen, F. T. 1972. Some characteristics of marine sparker seismic data. *Geophysics* 37, 462–70.
- Allen, S. J. 1980. History of geophysical exploration: Seismic method. *Geophysics* 45, 1619–33.
- Anstey, N. A. 1970. Signal characteristics and instrument specifications. In *Seismic Prospecting Instruments*, vol. I. Berlin: Gebruder Borntraeger.
- Backus, M. M. 1959. Water reverberations – their nature and elimination. *Geophysics* 24, 233–61.
- Badley, M. E. 1985. *Practical Seismic Interpretation*. Boston: International Human Resources Development Co.
- Balch, A. H., and Lee, M. W. 1984. *Vertical Seismic Profiling: Technique, Applications, and Case Histories*. Boston: International Human Resources Development Co.
- Bally, A. W. 1983–4. *Seismic Expression of Structural Styles* (in 3 volumes), *Studies in Geology* 15. Tulsa: American Association of Petrological Geology.
- Barry, K. M. 1967. Delay time and its application to refraction profile interpretation. In *Seismic Refraction Prospecting*, A. W. Musgrave, ed., pp. 348–62. Tulsa: Society of Exploration Geophysicists.
- Barthelmes, A. J. 1946. Application of continuous profiling to refraction shooting. *Geophysics* 11, 24–42.
- Bates, C. C., Gaskell, T. F., and Rice, R. B. 1982. *Geophysics in the Affairs of Man*. London: Pergamon.
- Baumgarte, J. 1955. Konstruktive darstellung von seismischen horizonten unter berücksichtigung der strahlenbrechung im raum. *Geophys. Prosp.* 3, 126–62.
- Bedenbender, J. W., Johnston, R. C., and Neitzel, E. B. 1970. Electroacoustic characteristics of marine seismic streamers. *Geophysics* 35, 1054–72.
- Berg, O. R., and Woolverton, D. G. 1985. Seismic stratigraphy II. *Am. Assoc. Petr. Geol. Memoir* 39.
- Berkhout, A. J. 1981. Wave field extrapolation techniques in seismic migration, a tutorial. *Geophysics* 46, 1638–56.
- Berni, A. J. 1983. Hydrophone cables for seismic exploration. In *CRC Handbook of Geophysical Exploration at Sea*, R. A. Geyer, ed., pp. 293–316. Boca Raton: CRC Press.
- Bilgeri, D., and Ademeno, E. B. 1982. Predicting abnormally pressured sedimentary rocks. *Geophys. Prosp.* 30, 608–21.
- Birch, F. 1966. Compressibility; elastic constants. In *Handbook of Physical Constants*, Geological Society of America Memoir 97, S. P. Clark, ed., pp. 97–173.
- Bolt, B. A. 1976. *Inside the Earth*. San Francisco: Freeman.
- Brede, E. C., Johnston, R. C., Sullivan, L. B., and Viger, H. L. 1970. A pneumatic energy source for shallow water/marsh areas. *Geophys. Prosp.* 18, 581–99.
- Brower, J., Douma, J., and Helbig, K. 1985. A new look at migration. *First Break* 3, no. 12, 9–15.
- Brown, A. R. 1988. Interpretation of three-dimensional seismic data. *Am. Assoc. Petr. Geol. Memoir* 42.
- Buchanan, D. J., Davis, R., Jackson, P. J., and Taylor, P. M. 1981. Fault location by channel wave seismology in United Kingdom coal seams. *Geophysics* 46, 994–1002.
- Cassell, B. 1984. Vertical seismic profiles – an introduction. *First Break* 2, no. 11, 9–19.
- Chapman, W. L., and Schafers, C. J. 1985. Shallow sand channel, coal exploration, Illinois Basin. In *Seismic Expression of Structural Styles*, vol. I, *AAPG Studies in Geology* 15-1, A. W. Bally, ed., pp. 1.2.1.33–34. Tulsa: American Association of Petroleum Geology.
- Christie, P. A. F., Hughes, V. J., and Kennett, B. L. N. 1985. Velocity filtering of seismic reflection data. *First Break* 1, no. 33, 9–24.
- Chun, J. H., and Jacewitz, C. A. 1981. Fundamentals of frequency domain migration. *Geophysics* 46, 717–33.
- Claerbout, J. F. 1985. *Imaging the Earth's Interior*. Oxford: Blackwell Scientific Publications.
- Clarke, G. K. C. 1968. Time-varying deconvolution filters. *Geophysics* 33, 936–44.
- Clay, C. S., and Medwin, H. 1977. *Acoustical Oceanography*. New York: Wiley.
- Cook, E. E., and Taner, M. T. 1969. Velocity spectra and their use in stratigraphic and lithologic differentiation. *Geophys. Prosp.* 17, 433–48.
- Cordier, J. P. 1985. *Velocities in Reflection Seismology*. Dordrecht: Reidel.
- Curnelle, R., and Marco, R. 1983. Reflection profiles across the Aquitaine basin (salt tectonics). In *Seismic Expression of Structural Styles*, vol. 2, *AAPG Studies in Geology* 15-2, A. W. Bally, ed., pp. 2.3.2.11–17. Tulsa: American Association of Petroleum Geology.
- Denham, L. R., and Palmeira, R. A. R. 1984. On reflection and transmission of plane compressional waves. *Geophysics* 49, 2195.
- Dennison, A. T. 1953. The design of electromagnetic geophones. *Geophys. Prosp.* 1, 3–28.
- Deregowski, S. M. 1986. What is DMO? *First Break* 4, no. 7, 7–24.
- Diebold, J. B., and Stoffa, P. L. 1981. The traveltimes equation, tau-p mapping, and inversion of common-midpoint data. *Geophysics* 46, 238–54.
- Disher, D. A., and Naquin, P. J. 1970. Statistical automatic statics analysis. *Geophysics* 35, 574–85.
- Dix, C. H. 1955. Seismic velocities from surface measurements. *Geophysics* 20, 68–86.
- Dobecki, T. L., and Romig, P. R. 1985. Geotechnical and groundwater geophysics. *Geophysics* 50, 2621–36.
- Domenico, S. N. 1977. Elastic properties of unconsolidated porous sand reservoirs. *Geophysics* 42, 1339–68.
- Domenico, S. N. 1984. Rock lithology and porosity determination from shear and compressional wave velocity. *Geophysics* 49, 1188–95.
- Ensley, R. A. 1985. Evaluation of direct hydrocarbon indicators through comparison of compressional- and shear-wave seismic data: a case study of the Myrnam gas field, Alberta. *Geophysics* 50, 37–48.
- Farrell, R. C., and Euwema, R. N. 1984. Refraction statics. *Proc. Inst. Electr. Electron. Engrs.* 72, 1316–29.
- Faust, L. Y. 1951. Seismic velocity as a function of depth and geologic time. *Geophysics* 16, 192–206.
- Faust, L. Y. 1953. A velocity function including lithological variation. *Geophysics* 18, 271–88.
- Flinn, E. A., Robinson, E. A., and Treitel, S., eds. 1967. Special issue on the MIT Geophysical Analysis Group reports. *Geophysics* 32, 411–525.
- Gardner, G. H. F., ed. 1985. *Migration of Seismic Data*. Tulsa: Society of Exploration Geophysicists.
- Gardner, G. H. F., Gardner, L. W., and Gregory, A. R. 1974. Formation velocity and density – the diagnostic basics for stratigraphic traps. *Geophysics* 39, 770–80.
- Gardner, L. W. 1939. An areal plan of mapping subsurface structure by refraction shooting. *Geophysics* 4, 247–59.
- Gardner, L. W. 1949. Seismograph determination of salt-dome boundary using well detector deep on dome flank. *Geophysics* 14, 29–38.
- Gardner, L. W. 1967. Refraction seismograph profile interpretation. In *Seismic Refraction Prospecting*,

## References

- A. W. Musgrave, ed., pp. 338–47. Tulsa: Society of Exploration Geophysicists.
- Garotta, R., and Michon, D. 1967. Continuous analysis of the velocity function and of the moveout correction. *Geophys. Prosp.* 15, 584–97.
- Gassman, F. 1951. Elastic waves through a packing of spheres. *Geophysics* 16, 673–85.
- Giles, B. F. 1968. Pneumatic acoustic energy source. *Geophys. Prosp.* 16, 21–53.
- Grant, F. S., and West, G. F. 1965. *Interpretation Theory in Applied Geophysics*. New York: McGraw-Hill.
- Gries, R. R., and Dyer, R. C., eds. 1985. *Seismic Exploration of the Rocky Mountain Region*. Denver: Rocky Mountain Association of Geologists and Denver Geophysical Society.
- Hagedoorn, J. G. 1954. A process of seismic reflection interpretation. *Geophys. Prosp.* 2, 85–127.
- Hagedoorn, J. G. 1959. The plus-minus method of interpreting seismic refraction sections. *Geophys. Prosp.* 7, 158–82.
- Hales, F. W. 1958. An accurate graphical method for interpreting seismic refraction lines. *Geophys. Prosp.* 6, 285–314.
- Hardage, B. A. 1985. Vertical seismic profiling: A. Principles. In *Handbook of Geophysical Exploration*, vol. 14A, K. Helbig and S. Treitel, eds. Amsterdam: Geophysical Press.
- Hatherly, P. J. 1982. A computer method for determining seismic first arrival times. *Geophysics* 47, 1431–6.
- Hileman, J. A., Embree, P., and Pfeiffer, J. C. 1968. Automated static corrections. *Geophys. Prosp.* 16, 326–58.
- Hilterman, F. J. 1970. Three-dimensional seismic modeling. *Geophysics* 35, 1020–37.
- Hilterman, F. J. 1982. Interpretative lessons from three-dimensional modeling. *Geophysics* 47, 784–808.
- Hofer, H., and Varga, W. 1972. Seismogeologic experience in the Beaufort Sea. *Geophysics* 37, 605–19.
- Horvath, P. S. 1985. The effectiveness of offshore three-dimensional seismic surveys – case histories. *Geophysics* 50, 2411–30.
- Hubral, P., and Krey, T. 1980. *Interval Velocities from Seismic Reflection Time Measurements*. Tulsa: Society of Exploration Geophysicists.
- Jankowsky, W. 1970. Empirical investigation of some factors affecting elastic wave velocities in carbonate rocks. *Geophys. Prosp.* 18, 103–18.
- Kennett, P., and Ireson, R. L. 1971. Recent developments in well velocity surveys and the use of calibrated acoustic logs. *Geophys. Prosp.* 19, 395–411.
- King, V. L. 1973. Sea bed geology from sparker profiles, Vermillion Block 321, offshore Louisiana. Dallas: *Offshore Technology Conference Paper* 1802.
- Knott, C. G. 1899. Reflexion and refraction of elastic waves, with seismological applications. *Phil. Mag.*, 5th ser. 48, 64–87.
- Kramer, F. S., Peterson, R. A., and Walter, W. C., eds. 1968. *Seismic Energy Sources – 1968 Handbook*. Pasadena: Bendix United Geophysical.
- Kunetz, G., and Fourmann, J. M. 1968. Efficient deconvolution of marine seismic records. *Geophysics* 33, 412–23.
- Lamer, A. 1970. Coupling sol-geophone. *Geophys. Prosp.* 18, 300–19.
- Larner, K. L., Hatton, L., Gibson, B. S., and Hsu, I. 1981. Depth migration of imaged time sections. *Geophysics* 46, 734–50.
- Laski, J. D. 1973. Computation of the time-distance curve for a dipping refractor and velocity increasing with depth in the overburden. *Geophys. Prosp.* 21, 366–78.
- Laster, S. J. 1985. The present state of seismic data acquisition—one view. *Geophysics* 50, 2443–51.
- Lindseth, R. O. 1979. Synthetic sonic logs – a process for stratigraphic interpretation. *Geophysics* 44, 3–26.
- Mayne, W. H. 1962. Common-reflection-point horizontal data-stacking techniques. *Geophysics* 27, 927–38.
- Mayne, W. H. 1967. Practical considerations in the use of common reflection point techniques. *Geophysics* 32, 225–9.
- Mayne, W. H., and Quay, R. G. 1971. Seismic signatures of large air guns. *Geophysics* 36, 1162–73.
- McCann, D. M., Andrew, E. M., and McCann, C. 1985. Seismic sources for shallow reflection surveying. *Geophys. Prosp.* 33, 943–55.
- McKay, A. E. 1954. Review of pattern shooting. *Geophysics* 19, 420–37.
- McQuillin, R., Bacon, M., and Barclay, W. 1984. *An Introduction to Seismic Interpretation*. London: Graham and Trotman.
- Meidav, T. 1969. Hammer reflection seismics in engineering geophysics. *Geophysics* 34, 383–95.
- Meissner, R. 1967. Exploring deep interfaces by seismic wide-angle measurements. *Geophys. Prosp.* 15, 598–617.
- Middleton, D., and Wittlesey, J. R. B. 1968. Seismic models and deterministic operators for marine reverberation. *Geophysics* 33, 557–83.
- Montgomery, S. 1984. The land air gun–marine technology comes ashore. *Geophysics, The Leading Edge of Exploration* 3, no. 7, 34–7.
- Morgan, N. A. 1970. Wavelet maps – a new analysis tool for reflection seismograms. *Geophysics* 35, 447–60.
- Neidell, N. S., and Taner, M. T. 1971. Semblance and other coherency measures for multichannel data. *Geophysics* 36, 482–97.
- Nettleton, L. L. 1940. *Geophysical Prospecting for Oil*. New York: McGraw-Hill.
- Newman, P. 1973. Divergence effects in a layered earth. *Geophysics* 38, 481–8.
- Newman, P., and Mahoney, J. T. 1973. Patterns – with a pinch of salt. *Geophys. Prosp.* 21, 197–219.
- O'Doherty, R. F., and Anstey, N. A. 1971. Reflections on amplitudes. *Geophys. Prosp.* 19, 430–58.
- Ostrander, W. J. 1984. Plane-wave reflection coefficients for gas sands at nonnormal angles of incidence. *Geophysics* 49, 1637–48.
- Papoulis, A. 1962. *The Fourier integral and its applications*. New York: McGraw-Hill.
- Payton, C. E., ed. 1977. Seismic stratigraphy – applications to hydrocarbon exploration. *Am. Assoc. Petr. Geol. Memoir* 26.
- Peacock, K. L., and Treitel, S. 1969. Predictive deconvolution – theory and practice. *Geophysics* 34, 155–69.
- Peterson, J. E., Paulsson, B. N. P., and McEvilly, T. V. 1985. Applications of algebraic reconstruction techniques to crosshole seismic data. *Geophysics* 50, 1566–80.
- Phelps, E. H., and Roripaugh, C. C. 1983. Carbonate shelf, central Louisiana. In *Seismic Expression of Structural Styles*, vol. I, AAPG Studies in Geology 15-1, A. W. Bally, ed., pp. 1.2.4.1–5. Tulsa: American Association of Petroleum Geology.
- Pieri, M. 1983. Three seismic profiles through the Po plain. In *Seismic Expressions of Structural Styles*, vol. 3, AAPG Studies in Geology 15-3, A. W. Bally, ed., pp.

- 3.4.1.8-26. Tulsa: American Association of Petroleum Geology.
- Pieuchot, M. 1984. Seismic instrumentation. In *Handbook of Geophysical Exploration*, vol. 2, K. Helbig, and S. Treitel, eds. London: Geophysical Press.
- Rayleigh, L. 1917. On the pressure developed in a liquid during the collapse of a spherical cavity. *Philosophical Magazine* 34, 94-8.
- Robinson, E. A. 1983a. *Seismic Velocity Analysis and the Convolution Model*. Boston: International Human Resources Development Co.
- Robinson, E. A. 1983b. *Migration of Geophysical Data*. Boston: International Human Resources Development Co.
- Robinson, E. A. 1985. A historical account of computer research in seismic data processing—1949–1954. *Geophysics, The Leading Edge of Exploration* 4, no. 2, 40-5.
- Robinson, E. A., and Treitel, S. 1967. Principles of digital Wiener filtering. *Geophys. Prosp.* 15, 311-33.
- Robinson, E. A., and Treitel, S. 1973. *The Robinson-Treitel Reader*. Tulsa: Seismograph Service.
- Robinson, J. C. 1972. Computer-designed Wiener filters for seismic data. *Geophysics* 37, 235-59.
- Rockwell, D. W. 1967. A general wavefront method. In *Seismic Refraction Prospecting*, A. W. Musgrave, ed., pp. 363-415. Tulsa: Society of Exploration Geophysicists.
- Safar, M. H. 1984. On the S80 and P400 water guns: A performance comparison. *First Break* 2, no. 2, 20-4.
- Schenck, F. L. 1967. Refraction solutions and wavefront targeting. In *Seismic Refraction Prospecting*, A. W. Musgrave, ed., pp. 416-25. Tulsa: Society of Exploration Geophysicists.
- Schneider, W. A., and Backus, M. M. 1968. Dynamic correlation analysis. *Geophysics* 33, 105-26.
- Schoenberger, M. 1970. Optimization and implementation of marine seismic arrays. *Geophysics* 35, 1038-53.
- Schultz, P. S. 1985. Seismic data processing: current industry practice and new directions. *Geophysics* 50, 2452-7.
- Schulze-Gattermann, R. 1972. Physical aspects of the airpulser as a seismic energy source. *Geophys. Prosp.* 20, 155-92.
- SEG 1980. *Digital Tape Standards*. Tulsa: Society of Exploration Geophysicists.
- Sengbush, R. L., and Foster, M. R. 1968. Optimum multichannel velocity filters. *Geophysics* 33, 11-35.
- Shah, P. M., and Levin, F. K. 1973. Gross properties of time-distance curves. *Geophysics* 38, 643-56.
- Sheriff, R. E. 1976. Inferring stratigraphy from seismic data. *Bull. A. A. P. G.* 60, 528-42.
- Sheriff, R. E. 1980. *Seismic Stratigraphy*. Boston: International Human Resources Development Co.
- Sheriff, R. E. 1984. *Encyclopedic Dictionary of Exploration Geophysics*. 2nd ed. Tulsa: Society of Exploration Geophysicists.
- Sheriff, R. E., and Geldart, L. P. 1982-3. *Exploration Seismology* (in 2 volumes). New York: Cambridge University Press.
- Sherwood, J. W. C., and Torey, A. W. 1965. Minimum-phase and related properties of the response of a horizontally stratified absorptive earth to plane acoustic waves. *Geophysics* 30, 191-7.
- Shuey, R. T. 1985. A simplification of the Zoeppritz equations. *Geophysics* 50, 609-14.
- Stone, D. S. 1985. Geologic interpretation of seismic profiles, Big Horn Basin, Wyoming. In *Seismic Exploration of the Rocky Mountain Region*, R. R. Gries, and R. C. Dyer, eds., pp. 165-86. Denver: Rocky Mountain Association of Geologists and Denver Geophysical Society.
- Taner, M. T., Cook, E. E., and Neidell, N. S. 1970. Limitations of the reflection seismic method; lessons from computer simulations. *Geophysics* 35, 551-73.
- Taner, M. T., and Koehler, F. 1969. Velocity spectra—digital computer derivation and applications of velocity functions. *Geophysics* 34, 859-81.
- Taner, M. T., and Koehler, F. 1981. Surface consistent corrections. *Geophysics* 46, 17-22.
- Taner, M. T., Koehler, F., and Sheriff, R. E. 1979. Complex seismic trace analysis. *Geophysics* 44, 1041-63.
- Tarrant, L. H. 1956. A rapid method of determining the form of a seismic refractor from line profile results. *Geophys. Prosp.* 4, 131-9.
- Tatham, R. H. 1982.  $V_p/V_s$  and lithology. *Geophysics* 47, 336-44.
- Thornburgh, H. R. 1930. Wavefront diagrams in seismic interpretation. *Bull. A. A. P. G.* 14, 185-200.
- Toksoz, M. N., and Johnston, D. H. 1981. *Seismic Wave Attenuation*. Tulsa: Society of Exploration Geophysicists.
- Tooley, R. D., Spencer, T. W., and Sagoci, H. F. 1965. Reflection and transmission of plane compressional waves. *Geophysics* 30, 552-70.
- Treitel, S., Shanks, J. L., and Frasier, C. W. 1967. Some aspects of fan filtering. *Geophysics* 32, 789-800.
- Torey, A. W. 1970. A simple theory for seismic diffractions. *Geophysics* 35, 762-84.
- Tucker, P. M., and Yorston, H. J. 1973. *Pitfalls in Seismic Interpretation*. Tulsa: Society of Exploration Geophysicists.
- Walker, C., and Crouse, B. J. 1985. Field processing in the '80s. *Geophysics, The Leading Edge of Exploration* 4, no. 3, 41-70.
- Watkins, J. S., Walters, L. A., and Godson, R. H. 1972. Dependence of in-situ compressional-wave velocity on porosity in unsaturated rocks. *Geophysics* 37, 29-35.
- Webster, G. M. (ed.) 1978. *Deconvolution* (in 2 volumes). Tulsa: Society of Exploration Geophysicists.
- Willis, H. F. 1941. Underwater explosions—time interval between successive explosions. British Report Wa-47-21.
- Wyrobek, S. M. 1956. Application of delay and intercept times in the interpretation of multilayer refraction time distance curves. *Geophys. Prosp.* 4, 112-30.
- Ziolkowski, A. 1984. *Deconvolution*. Boston: International Human Resources Development Co.
- Zoeppritz, K. 1919. Über reflexion und durchgang seismischer wellen durch Unstetigerlsflaschen. *Berlin, Über Erdbebenwellen VII B, Nachrichten der Königlichen Gesellschaft der Wissenschaften zu Göttingen, math-phys. Kl.* pp. 57-84.

# Chapter

## 5

# *Electrical Properties of Rocks and Minerals*

### 5.1. CLASSIFICATION OF ELECTRICAL METHODS

Electrical prospecting involves the detection of surface effects produced by electric current flow in the ground. There is a much greater variety of techniques available than in the other prospecting methods, where one makes use of a single field of force or anomalous property – gravitation, magnetism, elasticity, radioactivity. Using electrical methods, one may measure potentials, currents, and electromagnetic fields that occur naturally – or are introduced artificially – in the earth. Furthermore, the measurements can be made in a variety of ways to determine a variety of results. Basically, however, it is the enormous variation in electrical conductivity found in different rocks and minerals that makes these techniques possible.

Electrical methods include self-potential (SP), telluric currents and magnetotellurics (MT), resistivity, including mise-à-la-masse, electromagnetic (EM), including AFMAG, and induced polarization (IP). They are often classified by the type of energy source involved, that is, natural or artificial. On this basis the first three and AFMAG above are grouped under natural sources and the remainder as artificial. Such a classification can be made for prospecting methods in general. Hence gravity, magnetics, and radioactivity are included in the natural source methods, whereas seismic requires artificial energy.

In the following chapters we shall study the electrical methods in a slightly different sequence, grouping three natural source methods together but considering AFMAG with EM, because the field techniques are quite similar. For the same reason IP will be considered immediately after resistivity.

### 5.2. ELECTRICAL PROPERTIES OF ROCKS AND MINERALS

#### 5.2.1. Electrical Potentials

(a) *General.* Several electrical properties of rocks and minerals are significant in electrical prospecting. They are natural electrical potentials, electrical conductivity (or the inverse, electrical resistivity), and the dielectric constant. Magnetic permeability is also an indirect factor. Of these, electrical conductivity is by far the most important, whereas the others are of minor significance.

Certain natural or spontaneous potentials occurring in the subsurface are caused by electrochemical or mechanical activity. The controlling factor in all cases is underground water. These potentials are associated with weathering of sulfide mineral bodies, variation in rock properties (mineral content) at geological contacts, bioelectric activity of organic material, corrosion, thermal and pressure gradients in underground fluids, and other phenomena of similar nature. There are four principal mechanisms producing these potentials; the first is mechanical, the latter three chemical.

(b) *Electrokinetic potential.* Also known as *streaming potential*, this is observed when a solution of electrical resistivity  $\rho$  and viscosity  $\eta$  is forced through a capillary or porous medium. The resultant potential difference between the ends of the passage is

$$E_k = - \frac{\zeta \Delta P k \rho}{4\pi \eta} \quad (5.1)$$

where  $\zeta$  is the *adsorption (zeta) potential*,  $\Delta P$  is the pressure difference, and  $k$  is the solution dielectric constant.

The quantity  $\zeta$  is the potential of a double layer (solid-liquid) between the solid and solution. Although generally of minor importance, the streaming effect may be the cause of occasional large anomalies associated with topography. It is also observed in self-potential well logging, where the drilling fluid penetrates porous formations (§11.3.1).

(c) *Liquid-junction (diffusion) potential*. This is due to the difference in mobilities of various ions in solutions of different concentrations. The value is given by

$$E_d = - \frac{R\theta(I_a - I_c)}{Fn(I_a + I_c)} \ln\left(\frac{C_1}{C_2}\right) \quad (5.2a)$$

where  $R$  is the gas constant ( $8.31 \text{ J}/^\circ\text{C}$ ),  $F$  is the Faraday constant ( $9.65 \times 10^4 \text{ C/mol}$ ),  $\theta$  is the absolute temperature,  $n$  is the valence,  $I_a$  and  $I_c$  are the mobilities of anions and cations, and  $C_1$  and  $C_2$  are the solution concentrations. In NaCl solutions,  $I_a/I_c = 1.49$ , hence at  $25^\circ\text{C}$ ,

$$E_d = - 11.6 \log(C_1/C_2) \quad (5.2b)$$

$E_d$  is in millivolts.

(d) *Shale (Nernst) potential*. When two identical metal electrodes are immersed in a homogeneous solution, there is no potential difference between them. If, however, the concentrations at the two electrodes are different, there is a potential difference given by

$$E_s = - \frac{R\theta}{Fn} \ln\left(\frac{C_1}{C_2}\right) \quad (5.3a)$$

For  $n = 1$ ,  $\theta = 298 \text{ K}$ , this becomes ( $E_s$  in millivolts)

$$E_s = - 59.1 \log(C_1/C_2) \quad (5.3b)$$

The combined diffusion and Nernst potentials are known as the *electrochemical, or static, self-potential*. For NaCl at  $T^\circ\text{C}$ , the electrochemical self-potential (in millivolts) is

$$E_e = - 70.7 \frac{(T + 273)}{273} \log\left(\frac{C_1}{C_2}\right) \quad (5.4)$$

When the concentrations are in the ratio 5 : 1,  $E_e = \pm 50 \text{ mV}$  at  $25^\circ\text{C}$ .

(e) *Mineralization potential*. When two dissimilar metal electrodes are immersed in a homogeneous solution, a potential difference exists between the electrodes. This *electrolytic contact potential*, along with the static self-potential, considered in Section 5.2.1 b, c, d is undoubtedly among the basic causes of the large potentials associated with certain mineral zones and known as *mineralization potentials*. These potentials, which are especially pronounced in zones containing sulfides, graphite, and magnetite, are much larger than those described in the preceding sections; values of several hundred millivolts are common and potentials greater than 1 V have been observed in zones of graphite and alunite. Because of the large magnitude, mineralization potentials cannot be attributed solely to the electrochemical potentials described earlier. The presence of metallic conductors in appreciable concentrations appears to be a necessary condition; nevertheless, the exact mechanism is not entirely clear, as will be seen in the more detailed discussion of mineralization potentials in Section 6.1.1 in connection with the self-potential prospecting method.

Other sources of electrical potentials in the earth should be mentioned. From Equations (5.2a) and (5.3a) it can be seen that the magnitude of the static self-potential depends on temperature; this thermal effect is analogous to the pressure difference in streaming potential and is of minor importance. Obviously metal corrosion – of underground pipes, cables, etc. – is a local source of electrochemical potential. Large-scale earth currents (§6.2.1) induced from the ionosphere, nuclear blasts, thunderstorms (see AFMAG, §7.4.2e), and the like create small, erratic earth potentials. Currents of bioelectric origin flowing, for instance, in plant roots are also a source of earth potentials. Negative potentials of 100 mV have been reported in this connection, in passing from cleared ground to wooded areas.

Most of the earth potentials discussed above are relatively permanent in time and place. Of the variable types, only telluric and AFMAG sources have been employed in prospecting. When measuring static potentials these fluctuations cause a background noise and may be a nuisance.

## 5.2.2. Electrical Conductivities

(a) *General*. Electric current may be propagated in rocks and minerals in three ways: electronic (ohmic), electrolytic, and dielectric conduction. The first is the normal type of current flow in materials containing free electrons such as the metals. In an electrolyte the current is carried by ions at a comparatively slow rate. Dielectric conduction takes place in poor conductors or insulators, which have very few free carri-

Table 5.1. Resistivities of minerals

Mineral	Formula	Resistivity ( $\Omega\text{m}$ )	
		Range	Average
Bismuthinite	$\text{Bi}_2\text{S}_3$	18–570	
Covellite	$\text{CuS}$	$3 \times 10^{-7}–8 \times 10^{-5}$	$2 \times 10^{-5}$
Chalcocite	$\text{Cu}_2\text{S}$	$3 \times 10^{-5}–0.6$	$10^{-4}$
Chalcopyrite	$\text{CuFeS}_2$	$1.2 \times 10^{-5}–0.3$	$4 \times 10^{-3}$
Bornite	$\text{Cu}_5\text{FeS}_4$	$2.5 \times 10^{-5}–0.5$	$3 \times 10^{-3}$
Pyrite	$\text{FeS}_2$	$2.9 \times 10^{-5}–1.5$	$3 \times 10^{-1}$
Pyrrhotite	$\text{Fe}_{n,m}\text{S}$	$6.5 \times 10^{-6}–5 \times 10^{-2}$	$10^{-4}$
Cinnabar	$\text{HgS}$		$2 \times 10^7$
Molybdenite	$\text{MoS}_2$	$10^{-3}–10^6$	10
Galena	$\text{PbS}$	$3 \times 10^{-5}–3 \times 10^2$	$2 \times 10^{-3}$
Millerite	$\text{NiS}$		$3 \times 10^{-7}$
Stannite	$\text{Cu}_2\text{FeSnS}_2$	$10^{-3}–6 \times 10^3$	
Stibnite	$\text{Sb}_2\text{S}_3$	$10^5–10^{12}$	$5 \times 10^6$
Sphalerite	$\text{ZnS}$	$1.5–10^7$	$10^2$
Cobaltite	$\text{CoAsS}$	$3.5 \times 10^{-4}–10^{-1}$	
Arsenopyrite	$\text{FeAsS}$	$2 \times 10^{-5}–15$	$10^{-3}$
Niccolite	$\text{NiAs}$	$10^{-7}–2 \times 10^{-3}$	$2 \times 10^{-5}$
Bauxite	$\text{Al}_2\text{O}_3 \cdot n\text{H}_2\text{O}$	$2 \times 10^2–6 \times 10^3$	
Cuprite	$\text{Cu}_2\text{O}$	$10^{-3}–300$	30
Chromite	$\text{FeCr}_2\text{O}_4$	$1–10^6$	$6 \times 10^{-3}$
Specularite	$\text{Fe}_2\text{O}_3$	$3.5 \times 10^{-3}–10^7$	
Hematite	$\text{Fe}_2\text{O}_3$	$10^3–10^7$	
Limonite	$2\text{Fe}_2\text{O}_3 \cdot 3\text{H}_2\text{O}$	$5 \times 10^{-5}–5.7 \times 10^3$	
Magnetite	$\text{Fe}_3\text{O}_4$	$10^{-3}–50$	
Ilmenite	$\text{FeTiO}_3$		
Wolframite	$\text{Fe, Mn, WO}_4$	$10–10^5$	
Pyrolusite	$\text{MnO}_2$	$5 \times 10^{-3}–10$	
Quartz	$\text{SiO}_2$	$4 \times 10^{10}–2 \times 10^{14}$	
Cassiterite	$\text{SnO}_2$	$4 \times 10^{-4}–10^4$	0.2
Rutile	$\text{TiO}_2$	$30–1000$	500
Uraninite (pitchblende)	$\text{UO}_2$	1–200	
Anhydrite	$\text{CaSO}_4$		$10^9$
Calcite	$\text{CaCO}_3$		$2 \times 10^{12}$
Fluorite	$\text{CaF}_2$		$8 \times 10^{13}$
Siderite	$\text{Fe}_2(\text{CO}_3)_3$		70
Rock salt	$\text{NaCl}$	$30–10^{13}$	
Sylvite	$\text{KCl}$	$10^{11}–10^{12}$	
Diamond	C	$10–10^{14}$	
Serpentine		$2 \times 10^2–3 \times 10^3$	
Hornblende		$2 \times 10^2–10^6$	
Mica		$9 \times 10^2–10^{14}$	
Biotite		$2 \times 10^2–10^6$	
Bitum. coal		$0.6–10^5$	
Anthracite		$10^{-3}–2 \times 10^5$	
Lignite		9–200	
Fire clay		$30–10^3$	30
Meteoric waters			
Surface waters (ign. rocks)		$0.1–3 \times 10^3$	
Surface waters (sediments)		10–100	100
Soil waters			
Natural waters (ign. rocks)		0.5–150	9
Natural waters (sediments)		1–100	3
Sea water			0.2
Saline waters, 3%			0.15
Saline waters, 20%			0.05

ers or none at all. Under the influence of an external varying electric field, the atomic electrons are displaced slightly with respect to their nuclei; this slight relative separation of negative and positive charges is known as dielectric polarization of the material and it produces a current known as the *displacement current*.

(b) *Electronic conduction.* The *electrical resistivity* of a cylindrical solid of length  $L$  and cross section  $A$ , having resistance  $R$  between the end faces, is given by

$$\rho = RA/L \quad (5.5)$$

If  $A$  is in square meters,  $L$  in meters, and  $R$  in ohms, the resistivity unit is the ohm-meter ( $\Omega\text{m}$ ). For dimensions in centimeters the unit becomes the ohm-centimeter ( $\Omega\text{cm}$ ):  $1 \Omega\text{m} = 100 \Omega\text{cm}$ .

The resistance  $R$  is given in terms of the voltage  $V$  applied across the ends of the cylinder and the resultant current  $I$  flowing through it, by Ohm's law:

$$R = V/I$$

where  $R$  is in ohms and the units of  $V$  and  $I$  are volts and amperes.

The reciprocal of resistivity is the *conductivity*  $\sigma$ , where the units are siemens per meter ( $\text{S}/\text{m}$ ). Then

$$\sigma = 1/\rho = L/RA = (I/A)/(V/L) = J/E \quad (5.6)$$

where  $J$  is the current density ( $\text{A}/\text{m}^2$ ) and  $E$  is the electric field ( $\text{V}/\text{m}$ ).

(c) *Electrolytic conduction.* Because most rocks are poor conductors, their resistivities would be extremely large were it not for the fact that they are usually porous and the pores are filled with fluids, mainly water. As a result the rocks are *electrolytic conductors*, whose effective resistivity may be defined as in Equation (5.5), where the propagation of current is by ionic conduction – by molecules having an excess or deficiency of electrons. Hence the resistivity varies with the mobility, concentration, and degree of dissociation of the ions; the latter depends on the dielectric constant of the solvent. As mentioned previously, the current flow is not only slow compared to ohmic conduction, but represents an actual transport of material, usually resulting in chemical transformation.

The conductivity of a porous rock varies with the volume and arrangement of the pores and even more with the conductivity and amount of contained water. According to the empirical formula due to Archie (1942),

$$\rho_e = a\phi^{-m}S^{-n}\rho_w \quad (5.7)$$

where  $\phi$  is the fractional pore volume (porosity),  $S$  is the fraction of the pores containing water,  $a, m$  are constants,  $0.5 \leq a \leq 2.5$ ,  $1.3 \leq m \leq 2.5$ . For example, suppose  $S = 1$ ,  $a = 1.5$ , and  $m = 2$ , then  $\rho_e/\rho_w = 1.5/\phi^2$  and for values of  $\phi = 0.01, 0.1, 0.3, 0.5$ ,  $\rho_e/\rho_w$  becomes  $1.5 \times 10^4, 150, 17$ , and 6, respectively.

Water conductivity varies considerably (see Table 5.1), depending on the amount and conductivity of dissolved chlorides, sulfates, and other minerals present.

The geometrical arrangement of the interstices in the rock has a less pronounced effect, but may make the resistivity anisotropic, that is, having different magnitudes for current flow in different directions. Anisotropy is characteristic of stratified rock that is generally more conductive in the bedding plane. The anisotropy effect depends on the ratio of maximum to minimum resistivity, may be as large as 2 in some graphitic slates, and varies from 1 to 1.2 in rocks such as limestone, shale, and rhyolite.

As an example, consider the layered formation shown in Figure 5.1, having resistivities  $\rho_1$  and  $\rho_2$  whose respective fractional volumes are  $v$  and  $1 - v$ . Here the resistivity in the horizontal direction – a stack of beds effectively in parallel – is

$$\rho_h = \rho_1\rho_2 / \{ \rho_1(1 - v) + \rho_2v \} \quad (5.8)$$

In the vertical direction, the beds are in series so that

$$\rho_v = \rho_1v + \rho_2(1 - v) \quad (5.9)$$

Then the ratio is

$$\frac{\rho_v}{\rho_h} = (1 - 2v + 2v^2) + \left( \frac{\rho_1}{\rho_2} + \frac{\rho_2}{\rho_1} \right) v(1 - v)$$

If  $v \ll 1$  and  $\rho_2/\rho_1 \gg 1$ , this simplifies to

$$\frac{\rho_v}{\rho_h} \approx 1 + \frac{\rho_2}{\rho_1}v \quad (5.10)$$

If the layer of resistivity  $\rho_1$  is for water-saturated beds, this ratio might be quite large.

(d) *Dielectric conduction.* The mechanism of dielectric conduction – the displacement current – was described briefly at the beginning of this section, where it was pointed out that the displacement current flows only in nonconductors when the external electric field changes with time. The significant parameter in dielectric conduction is the *dielectric constant*  $k$ , sometimes called the *specific inductive*

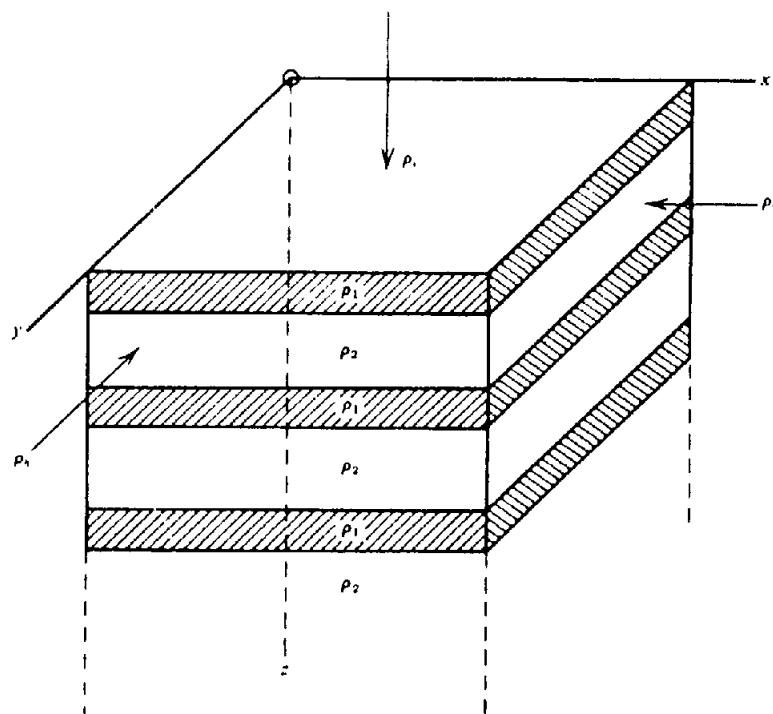


Figure 5.1. Anisotropic resistivity as a result of horizontal bedding.

capacity of the medium. In analogy with magnetic quantities  $M$ ,  $H$ ,  $k$ ,  $B$ , and  $\mu$  (§3.2.1) we have an electrostatic set: *electric polarization* (*electric dipole moment/unit volume*)  $P$ , *electric field strength*  $E$ , *electric susceptibility*  $\eta$ , *electric displacement* (*flux/unit area*)  $D$ , and *dielectric constant*  $k$ . In electrostatic units, the relations between these are

$$P = \eta E \quad D = E + 4\pi P = E(1 + 4\pi\eta) = kE \quad (5.11)$$

whereas in mks units,

$$P = \eta E \quad D = \epsilon_0 E + P = E(\epsilon_0 + \eta) = \epsilon E \quad (5.12)$$

and the dielectric constant  $k = 1 + \eta/\epsilon_0 = \epsilon/\epsilon_0$ .

In electrostatic units,  $P$ ,  $E$  and  $D$  are volts per centimeter and  $\eta$  and  $k$  are dimensionless. In mks units  $\epsilon$ ,  $\epsilon_0$ , and  $\eta$  are in farads per meter,  $P$ ,  $D$  are in coulombs per square meter,  $E$  is in volts per meter, and  $k$  is again dimensionless and the same in either system.

The dielectric constant is similar to the conductivity in porous formations in that it varies with the amount of water present (note that water has a very large dielectric constant; see Table 5.5). We shall see in Section 6.2.3 that displacement currents are of secondary importance in earth materials because electrical prospecting methods generally employ low frequencies.

### 5.2.3. Magnetic Permeability

Where EM sources are employed, the voltage induced in a subsurface conductor varies not only with the rate of change of magnetic field, but also with the magnetic permeability of the conductor. From Maxwell's equation,

$$\nabla \times \mathbf{E} = -\mu \frac{\partial \mathbf{H}}{\partial t}$$

we see that currents induced in the ground are enhanced by the factor  $\mu$ . Practically, however, the permeability rarely is appreciably greater than unity, except for a few magnetic minerals (§5.4.3); consequently it is of no particular significance in electrical work, except when  $\text{Fe}_2\text{O}_3$  is present in large concentration.

### 5.2.4. Polarization Potentials

Where a steady current is passed through an electrolytic conductor containing mineral particles it is possible, as described in Section 5.3.1, to determine the effective resistivity. If a current is suddenly switched on or off in a circuit containing an electrolyte, a finite time elapses before the potential increases to a fixed value or drops to zero. The delayed buildup or decay of current is characteristic of electrolytic conduction, and is due to accumulation of ions at interfaces between the electrolyte and mineral particles. As a result, a potential opposing

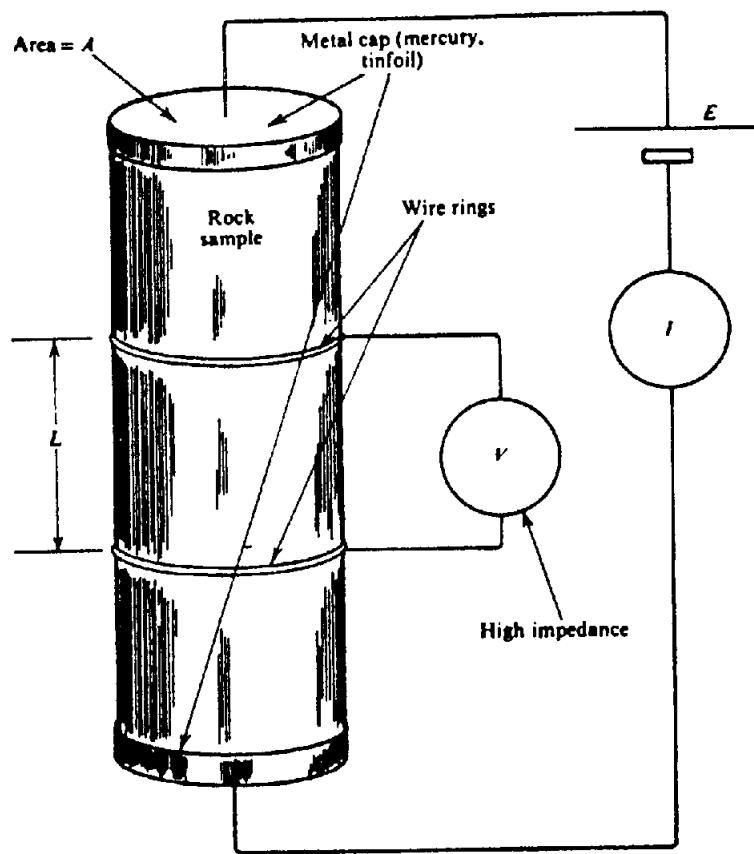


Figure 5.2. Simplified schematic of equipment for measuring resistivity of core samples.

the normal current flow is developed across the interface. A similar effect is observed at the contact between electrolytes and clay particles. These are known as *polarization potentials*; the process is called the *induced polarization effect*. Induced polarization (IP) prospecting involves these interface potentials. They will be considered in more detail in Section 9.2.

### 5.3. MEASUREMENT OF ELECTRICAL PROPERTIES OF ROCKS AND MINERALS

#### 5.3.1. Laboratory Measurement of Resistivity

In order to measure directly the true resistivity of a rock, mineral, electrolyte, and so forth, it is necessary to shape the sample in some regular form, such as a cylinder, cube, or bar of regular cross section. An experimental arrangement is shown in Figure 5.2. The main difficulty is in making good electrical contact, particularly for the current electrodes. For this purpose tinfoil or mercury electrodes may be used and it is generally necessary to apply pressure to the current electrodes; sometimes the ends of the sample are dipped in soft solder. From Figure 5.2 and Equation (5.6) the resistivity is given by

$$\rho = AV/LI$$

The power source may be dc or preferably low frequency ac (400 Hz or less). The possibility of anisotropy can be checked by measuring the resistivity in two directions, provided the shape is suitable for this.

Obviously one can make these measurements in the field as well, on drill core, grab samples, even outcrop, if the electrode contact is reasonably good. Estimates of resistivity, made on samples by using an ohmmeter and merely pressing or scraping the terminals of the leads against the surface however, are not very trustworthy.

#### 5.3.2. Measurement of Dielectric Constant

An ac bridge may also be used to measure the resistivity of soils and electrolytes. At audio frequencies any reactive component – normally capacitive – must be accounted for in order to get a good bridge balance. Consequently the measurement determines the effective capacitance, as well as resistivity, of the specimen. Since capacitance varies with the dielectric constant of the material, it is thus possible to determine the latter by substitution. The Schering capacitance bridge is suitable for this measurement in the laboratory (Hague, 1957).

Table 5.2. Resistivities of various ores

Ore	Other minerals	Gangue	$\rho$ ( $\Omega\text{m}$ )
Pyrite			
18%	2% (chalco)	80%	300
60%	5% (ZnS) + 15%	20%	0.9
95%	5% (ZnS)		1.0
Pyrrhotite			
41%		59%	$2.2 \times 10^{-4}$
79%		21%	$1.4 \times 10^{-5}$
95%		5%	$1.4 \times 10^{-5}$
SbS <sub>2</sub> in quartz			$4 \times 10^3 - 3 \times 10^7$
FeAsS 60%	FeS 20%	20% SiO <sub>2</sub>	0.39
FeAsS			$10^{-4} - 10^{-2}$
Cu <sub>5</sub> FeS <sub>4</sub>			$3 \times 10^{-3}$
Cu <sub>5</sub> FeS <sub>4</sub> 40%		60% SiO <sub>2</sub>	$7 \times 10^{-2}$
Fe, Mn, WO <sub>4</sub>	CoAsS		$10^3 - 10^7$
PbS, near massive			0.8
Fe <sub>2</sub> O <sub>3</sub>			$0.1 - 300$
Fe <sub>2</sub> O <sub>3</sub> , massive			$2.5 \times 10^3$
Iron			
Fe <sub>3</sub> O <sub>4</sub> 60%			45
75% brown iron oxide		25%	$2 \times 10^4 - 8 \times 10^5$
Fe <sub>3</sub> O <sub>4</sub>			$5 \times 10^3 - 8 \times 10^3$
Zinc			
30%	5% PbS, 15% FeS	50%	0.75
80%	10% PbS, 10% FeS		$1.7 \times 10^3$
90%	5% PbS	5%	130
Graphitic slate			0.13
Graphite, massive			$10^{-4} - 5 \times 10^{-3}$
MoS <sub>2</sub>			$2 \times 10^2 - 4 \times 10^3$
MnO <sub>2</sub> colloidal ore			1.6
Cu <sub>2</sub> S			$3 \times 10^{-2}$
CuFeS <sub>2</sub>			$10^{-4} - 1$
CuFeS <sub>2</sub> 90%	2% FeS	8% SiO <sub>2</sub>	0.65
FeCr <sub>2</sub> O <sub>4</sub>			$10^3$

## 5.4. TYPICAL VALUES OF ELECTRICAL CONSTANTS OF ROCKS AND MINERALS

### 5.4.1. Resistivities of Rocks and Minerals

Of all the physical properties of rocks and minerals, electrical resistivity shows the greatest variation. Whereas the range in density, elastic wave velocity, and radioactive content is quite small, in magnetic susceptibility it may be as large as  $10^5$ . However, the resistivity of metallic minerals may be as small as  $10^{-5} \Omega\text{m}$ , that of dry, close-grained rocks, like gabbro as large as  $10^7 \Omega\text{m}$ . The maximum possible range is even greater, from native silver ( $1.6 \times 10^{-8} \Omega\text{m}$ ) to pure sulfur ( $10^{16} \Omega\text{m}$ ).

A *conductor* is usually defined as a material of resistivity less than  $10^{-5} \Omega\text{m}$ , whereas an *insulator* is one having a resistivity greater than  $10^7 \Omega\text{m}$ . Between these limits lie the *semiconductors*. The metals and graphite are all conductors; they contain a large number of free electrons whose mobility is very great. The semiconductors also carry current by mobile electrons but have fewer of them. The insulators

are characterized by ionic bonding so that the valence electrons are not free to move; the charge carriers are ions that must overcome larger barrier potentials than exist either in the semiconductors or conductors.

A further difference between conductors and semiconductors is found in their respective variation with temperature. The former vary inversely with temperature and have their highest conductivities in the region of 0 K. The semiconductors, on the other hand, are practically insulators at low temperatures.

In a looser classification, rocks and minerals are considered to be good, intermediate, and poor conductors within the following ranges:

- (a) Minerals of resistivity  $10^{-8}$  to about  $1 \Omega\text{m}$ .
- (b) Minerals and rocks of resistivity  $1$  to  $10^7 \Omega\text{m}$ .
- (c) Minerals and rocks of resistivity above  $10^7 \Omega\text{m}$ .

Group (a) includes the metals, graphite, the sulfides except for sphalerite, cinnabar and stibnite, all the arsenides and sulfo-arsenides except SbAs<sub>2</sub>, the antimonides except for some lead compounds, the

Table 5.3. Resistivities of various rocks and sediments

Rock type	Resistivity range ( $\Omega\text{m}$ )
Granite porphyry	$4.5 \times 10^3$ (wet) – $1.3 \times 10^6$ (dry)
Feldspar porphyry	$4 \times 10^3$ (wet)
Syenite	$10^2$ – $10^6$
Diorite porphyry	$1.9 \times 10^3$ (wet) – $2.8 \times 10^4$ (dry)
Porphyrite	$10$ – $5 \times 10^4$ (wet) – $3.3 \times 10^3$ (dry)
Carbonatized porphyry	$2.5 \times 10^3$ (wet) – $6 \times 10^4$ (dry)
Quartz diorite	$2 \times 10^4$ – $2 \times 10^6$ (wet) $-1.8 \times 10^5$ (dry)
Porphyry (various)	$60$ – $10^4$
Dacite	$2 \times 10^4$ (wet)
Andesite	$4.5 \times 10^4$ (wet) – $1.7 \times 10^3$ (dry)
Diabase (various)	$20$ – $5 \times 10^7$
Lavas	$10^2$ – $5 \times 10^4$
Gabbro	$10^3$ – $10^6$
Basalt	$10$ – $1.3 \times 10^7$ (dry)
Olivine norite	$10^3$ – $6 \times 10^4$ (wet)
Peridotite	$3 \times 10^3$ (wet) – $6.5 \times 10^3$ (dry)
Hornfels	$8 \times 10^3$ (wet) – $6 \times 10^7$ (dry)
Schists (calcareous and mica)	$20$ – $10^4$
Tuffs	$2 \times 10^3$ (wet) – $10^5$ (dry)
Graphite schist	$10$ – $10^2$
Slates (various)	$6 \times 10^2$ – $4 \times 10^7$
Gneiss (various)	$6.8 \times 10^4$ (wet) – $3 \times 10^6$ (dry)
Marble	$10^2$ – $2.5 \times 10^6$ (dry)
Skarn	$2.5 \times 10^2$ (wet) – $2.5 \times 10^8$ (dry)
Quartzites (various)	$10$ – $2 \times 10^8$
Consolidated shales	$20$ – $2 \times 10^3$
Argillites	$10$ – $8 \times 10^2$
Conglomerates	$2 \times 10^3$ – $10^4$
Sandstones	$1$ – $6.4 \times 10^8$
Limestones	$50$ – $10^7$
Dolomite	$3.5 \times 10^2$ – $5 \times 10^3$
Unconsolidated wet clay	20
Marls	3 – 70
Clays	1 – 100
Oil sands	4 – 800

tellurides, and some oxides such as magnetite, manganese, pyrolusite, and ilmenite. Most oxides, ores, and porous rocks containing water are intermediate conductors. The common rock-forming minerals, silicates, phosphates and the carbonates, nitrates, sulfates, borates, and so forth, are poor conductors.

The following tables list characteristic resistivities for various minerals and rocks. The data are from various sources, including Heiland (1940, Ch. 10), Jakosky (1950, Ch. 5), Parasmis (1956, 1966, Ch. 6), Keller (1966), and Parkhomenko (1967).

Resistivities of the various metals in pure form, from antimony to zinc, vary by only about 2 orders of magnitude. ( $\text{Bi} \approx 1.2 \times 10^{-6} \Omega\text{m}$ ,  $\text{Ag} \approx 1.6 \times 10^{-8} \Omega\text{m}$ ). Tellurium is an exception ( $\approx 10^{-3} \Omega\text{m}$ ). Two other elements of common occurrence are

Table 5.4. Variation of rock resistivity with water content

Rock	% $\text{H}_2\text{O}$	$\rho$ ( $\Omega\text{m}$ )
Siltstone	0.54	$1.5 \times 10^4$
Siltstone	0.38	$5.6 \times 10^8$
Coarse grain SS	0.39	$9.6 \times 10^5$
Coarse grain SS	0.18	$10^8$
Medium grain SS	1.0	$4.2 \times 10^3$
Medium grain SS	0.1	$1.4 \times 10^8$
Graywacke SS	1.16	$4.7 \times 10^3$
Graywacke SS	0.45	$5.8 \times 10^4$
Arkoseic SS	1.0	$1.4 \times 10^3$
Organic limestone	11	$0.6 \times 10^3$
Dolomite	1.3	$6 \times 10^3$
Dolomite	0.96	$8 \times 10^3$
Peridotite	0.1	$3 \times 10^3$
Peridotite	0	$1.8 \times 10^7$
Pyrophyllite	0.76	$6 \times 10^6$
Pyrophyllite	0	$10^{11}$
Granite	0.31	$4.4 \times 10^3$
Granite	0.19	$1.8 \times 10^6$
Granite	0	$10^{10}$
Diorite	0.02	$5.8 \times 10^5$
Diorite	0	$6 \times 10^6$
Basalt	0.95	$4 \times 10^4$
Basalt	0	$1.3 \times 10^8$
Olivine-pyrox.	0.028	$2 \times 10^4$
Olivine-pyrox.	0	$5.6 \times 10^7$

graphite ( $5 \times 10^{-7}$  to  $10 \Omega\text{m}$  range,  $\approx 10^{-3} \Omega\text{m}$  average) and sulfur ( $10^7$ – $10^{16} \Omega\text{m}$  range,  $\approx 10^{14} \Omega\text{m}$  average).

The variation in resistivity of particular minerals is enormous, as can be seen from Table 5.1. Among the more common minerals, pyrrhotite and graphite appear to be the most consistent good conductors, whereas pyrite, galena, and magnetite are often poor conductors in bulk form, although the individual crystals have high conductivity. Hematite and sphalerite, in pure form, are practically insulators, but when combined with impurities may have resistivities as low as  $0.1 \Omega\text{m}$ . Graphite is often the connecting link in mineral zones, which makes them good conductors.

The range of resistivities of various waters is notably smaller than for solid minerals; the actual resistivities are also lower than those of a great many minerals.

Table 5.2 from Parkhomenko (1967) lists resistivities for a variety of ores. In general it appears that pyrrhotite in massive form has the lowest resistivity, that the resistivity of zinc ores is surprisingly low (possibly due to the presence of lead and copper fractions), and that molybdenite, chromite, and iron ores have values in the range of many rocks.

Table 5.3 lists typical values for rocks and unconsolidated sediments. The ranges are quite similar to that for water, which is the controlling factor in many rocks.

Very roughly, igneous rocks have the highest resistivity, sediments the lowest, with metamorphic rocks intermediate. However, there is considerable overlapping, as in other physical properties. In addition, the resistivities of particular rock types vary with age and lithology, because the porosity of the rock and salinity of the contained water are affected by both. For example, the resistivity range of Precambrian volcanics is 200–5,000 Ωm, whereas for Quaternary rocks of the same kind it is 10–200 Ωm.

The effect of water content on the bulk resistivity of rocks is evident from Table 5.3. Further data are listed in Table 5.4, where samples with variable amounts of water are shown. In most cases a small change in the percentage of water affects the resistivity enormously.

As the depth of penetration of electrical methods is increased with new and refined equipment, it is found that the significance of water in lowering bulk resistivity of crustal rocks gradually decreases with increasing depth, whereas that of temperature and pressure increases. Hermance (1973) carried out deep sounding resistivity and magnetotelluric surveys in Iceland that indicated crust resistivities decreasing from 100 to 10 Ωm in the depth range 2 to 12 km. Because this is a geothermal area straddling the Atlantic Ridge, one would expect anomalous low resistivities at shallow (< 2 km) depth. However, modeling of the data suggested that water persisted to 8 to 10 km depth, whereas solid conduction in dry crustal rocks at high temperatures (700 to 1,000°C) and pressures (1 to 4 kb) became dominant below this.

Subsequent laboratory studies on dry granites, basalts, and gabbros in the temperature range 500 to 1,000°C by Kariya and Shankland (1983) provided rough agreement with the results of Hermance and showed a 2-order decrease in resistivity over the 500°C temperature change.

#### 5.4.2. Dielectric Constants of Rocks and Minerals

As mentioned previously, the dielectric constant is a measure of the electrical polarization resulting from an applied electric field. This polarization may be electronic, ionic, or molecular. The first type is characteristic of all nonconductors. Ionic displacement occurs in many rock-forming minerals, whereas water and the hydrocarbons are the only common materials that exhibit molecular polarization.

Because of the relatively slow mobilities of the charge carriers, molecular polarization – the largest of the three effects – and ionic polarization are insignificant at very high frequencies. Thus the dielectric constant, which is proportional to the degree of

Table 5.5. Dielectric constants of rocks and minerals

Rock, mineral	Dielectric const.
Galena	18
Sphalerite	7.9–69.7
Cassiterite	23
Hematite	25
Fluorite	6.2–6.8
Calcite	7.8–8.5
Apatite	7.4–11.7
Barite	7–12.2
Peridotite	8.6
Norite	61
Quartz porphyry	14–49.3
Diabase	10.5–34.5
Trap	18.9–39.8
Dacite	6.8–8.2
Obsidian	5.8–10.4
Sulphur	3.6–4.7
Rock salt	5.6
Anthracite	5.6–6.3
Gypsum	5–11.5
Biotite	4.7–9.3
Epidote	7.6–15.4
Plagioclase feldspar	5.4–7.1
Quartz	4.2–5
Granite (dry)	4.8–18.9
Gabbro	8.5–40
Diorite	6.0
Serpentine	6.6
Gneiss	8.5
Sandstone (dry to moist)	4.7–12
Packed sand (dry to moist)	2.9–105
Soil (dry to moist)	3.9–29.4
Basalt	12
Clays (dry to moist)	7–43
Petroleum	2.07–2.14
Water (20°C)	80.36
Ice	3–4.3

Table 5.6. Magnetic permeabilities

Mineral	Permeability
Magnetite	5
Pyrrhotite	2.55
Titanomagnetite	1.55
Hematite	1.05
Pyrite	1.0015
Rutile	1.0000035
Calcite	0.999987
Quartz	0.999985
Hornblende	1.00015

polarization, varies inversely with frequency. It is also indicative of the amount of water present, because water has a dielectric constant of 80 at low frequencies.

Table 5.5 lists dielectric constants for various minerals and rocks. Most of the measurements have been made at frequencies of 100 kHz and up. For very low frequencies the values would be generally

higher by about 30%. In exceptional cases – one example being certain ice samples – the results have been larger by several orders of magnitude.

#### 5.4.3. Magnetic Permeability of Minerals

The effect of  $\mu$  on electrical measurements is very slight except in the case of concentrated magnetite, pyrrhotite, and titanomagnetite. From Equation (3.7), magnetic permeability is related to susceptibility by the expression

$$\mu' = 1 + 4\pi k' \text{ in cgs units}$$

$$\mu = 1 + k \text{ in SI units}$$

$\mu$  and  $\mu'$  are dimensionless. Generally  $k$  is too small to change  $\mu$  appreciably from unity. Table 5.6 lists maximum permeabilities of some common minerals.

#### REFERENCES

- Archie, G. E. 1942. The electric resistivity log as an aid in determining some reservoir characteristics. *Trans. AIME* 146, 54–62.
- Hague, B. 1957. *Alternative Current Bridge Methods*. London: Pitman.
- Heiland, C. A. 1940. *Geophysical Exploration*. New York: Prentice-Hall.
- Hermance, J. F. 1973. An electrical model for the sub-Icelandic crust. *Geophysics* 38, 3–13.
- Jakosky, J. J. 1950. *Exploration Geophysics*. Newport Beach, CA: Trija.
- Kariya, K. A., and Shankland, T. J. 1983. Electrical conductivity of dry lower crustal rocks. *Geophysics* 48, 52–61.
- Keller, G. V. 1966. In *Handbook of Physical Constants*, S. P. Clark, Jr., ed. *Geol. Soc. Am. Memoir* 97, 553–76.
- Parasnis, D. S. 1956. The electrical resistivity of some sulphide and oxide minerals and their ores. *Geophys. Prosp.* 4, 249–79.
- Parasnis, D. S. 1966. *Mining Geophysics*. Amsterdam: Elsevier.
- Parkhomenko, E. I. 1967. *Electrical Properties of Rocks*, G. V. Keller, transl. New York: Plenum.

# Chapter

## 6

# *Methods Employing Natural Electrical Sources*

### 6.1. SELF-POTENTIAL METHOD

#### 6.1.1. Origin of Potentials

Various spontaneous ground potentials were discussed in Section 5.2.1. Only two of these have been considered seriously in surface exploration, although the self-potential method is used in a variety of ways in well logging (§11.3). Mineralization potentials produced mainly by sulfides have long been the main target of interest, although recently exploration for geothermal sources has included self-potential surveys as well. The remainder of these spontaneous potentials may be classified as background or noise. This also means that geothermal anomalies become noise if they occur in the vicinity of a sulfide survey and vice versa (§6.1.4). A more detailed description of these sources follows.

*Background potentials* are created by fluid streaming, bioelectric activity in vegetation, varying electrolytic concentrations in ground water, and other geochemical action. Their amplitudes vary greatly but generally are less than 100 mV. On the average, over intervals of several thousand feet, the potentials usually add up to zero, because they are as likely to be positive as negative.

In addition there are several characteristic regional background potentials. One is a gradient of the order of 30 mV/km, which sometimes extends over several kilometers and may be either positive or negative. It is probably due to gradual changes in diffusion and electrolytic potentials in ground water. Sometimes a more abrupt change will result in a baseline shift of background potential. Another regional gradient of similar magnitude seems to be associated with topography. It is usually negative going uphill and is probably caused by streaming

potential. These background effects are not difficult to recognize.

Potentials arising from bioelectric activity of plants, trees, and so forth, sometimes are as large as several hundred millivolts. They have been observed as sharp negative anomalies - when passing from open ground into bush - that are quite similar to those appearing over sulfide zones.

Long period telluric currents ( $> 1$  min) may also produce background potentials, as large as several hundred millivolts per kilometer over resistive ground, which are more difficult to detect, because the self-potential readings are made at a much faster rate.

Self-potential (SP) anomalies apparently generated by thermoelectric and/or electrokinetic coupling processes have been reported in the course of surveys for geothermal sources, an application of the method which has become attractive since the late 1970s (Corwin and Hoover, 1979). The thermal mechanism is not well understood, but may result from differential thermal diffusion of ions in pore fluids and electrons with donor ions in the rock matrix. The ratio of voltage to temperature difference  $\Delta V/\Delta T$  is known as the *thermoelectric coupling coefficient*. The *electrokinetic coupling coefficient*,  $E_k/\Delta P$  in Equation (5.1), depends on fluid flow, which may be due to the thermal as well as the pressure gradient. Analysis of the coupling processes is presently not developed sufficiently to provide quantitative comparison of the two effects.

Corwin and Hoover (1979) describe two SP surveys over geothermal sources produced by shallow coal fires. At Marshall, Colorado, a well-defined negative anomaly of 140 mV peak was centered over the burn area, which was overlain by 10 m of sandstone. At the second site, Acme, Wyoming, a 30 mV

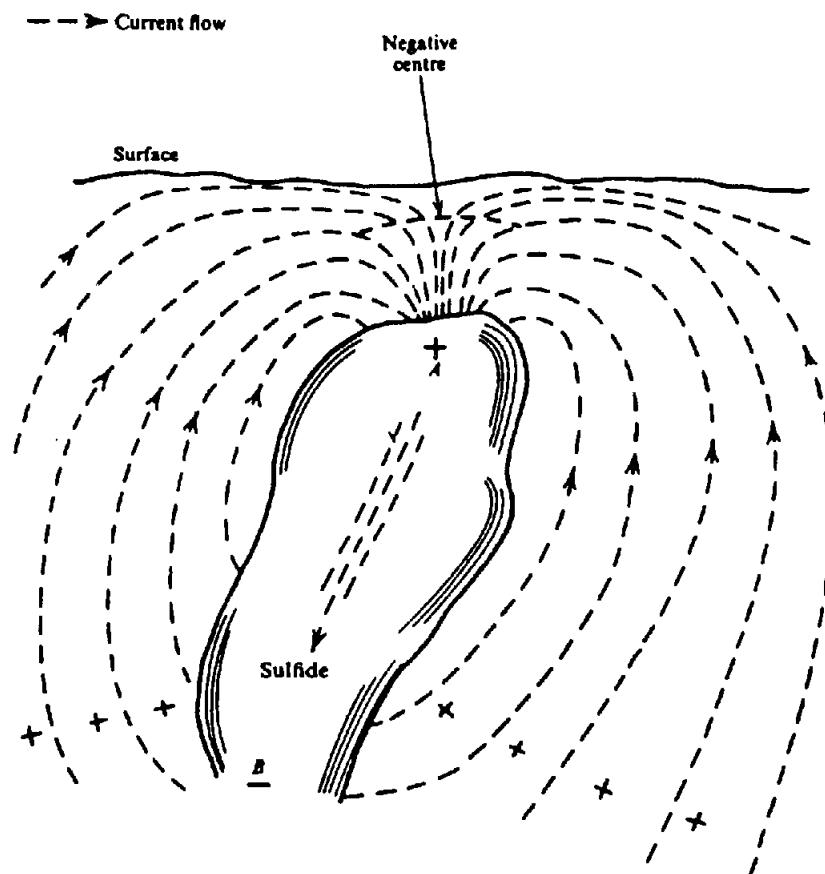


Figure 6.1. Oxidizing sulfide zone as a galvanic cell.

positive anomaly was recorded where the burn was about 3 m below surface. Larger potentials were measured over thicker overburden nearby; they suggest that electrokinetic effects were increasing the response.

Mineralization potentials have usually been the main interest when prospecting with the self-potential method. They are associated with the sulfides of the metals, with graphite, and sometimes with the metal oxides such as magnetite. The most common mineralization potential anomalies occur over pyrite, chalcopyrite, pyrrhotite, sphalerite, galena, and graphite. Amplitudes range from a few millivolts to 1 V; 200 mV would be considered a good SP anomaly. The potentials are almost always negative near the upper end of the body and are quite stable in time.

The mechanism of spontaneous polarization in mineral zones, like the geothermal effect, is not completely understood, although several hypotheses have been developed to explain it. Field measurements indicate that some part of the mineral must be in a zone of oxidation in order that SP anomalies may appear at the surface. The original explanation, based on this evidence, was that the body behaved like a galvanic cell with a potential difference being created between the oxidizing zone (generally the upper sur-

face) and the remainder. The action of this cell is illustrated in Figure 6.1.

There are several weaknesses in this explanation. Graphite frequently is the source of large SP anomalies, although it does not oxidize appreciably. On the other hand, extensive oxidation, such as could occur in most metal sulfides, would leave the upper surface of the body with a net positive charge due to the loss of electrons. In fact the charge is negative.

Another hypothesis suggests that pH variations above and below the water table could provide the current flowing around the source. There is considerable evidence that the solutions above sulfide bodies, and within the water table, are highly acidic ( $\text{pH} = 2-4$ ), whereas those below the table are slightly basic ( $\text{pH} = 7-9$ ). There is probably a close relation between pH and mineralization potentials, but a difference in pH alone is not sufficient to move electrons in and out of the mineral zone and maintain the flow of current.

A reasonably complete explanation of mineralization potentials is that proposed by Sato and Mooney (1960). They postulate two electrochemical half-cell reactions of opposite sign, one cathodic above the water table, the other anodic at depth. In the cathode half-cell there is chemical reduction of the

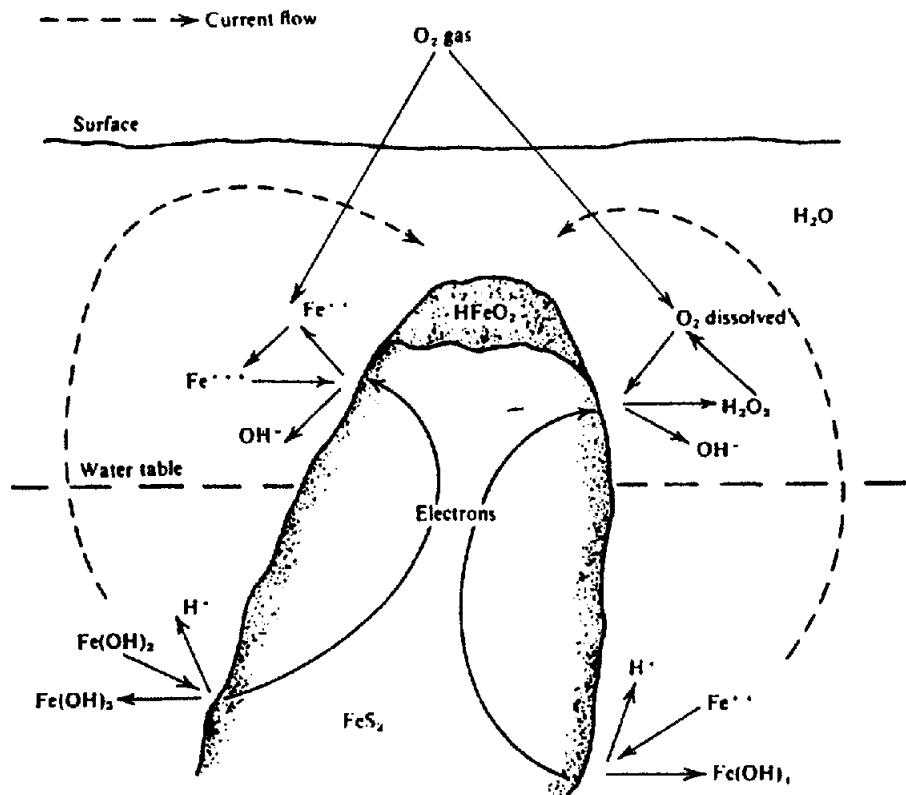


Figure 6.2. Self-potential mechanism in pyrite. (From Sato and Mooney, 1960.)

substances in solution – that is, they gain electrons – while in the anode cell an oxidation reaction takes place and electrons are lost. The mineral zone itself functions only to transport electrons from anode to cathode. The magnitude of the overall SP effect is determined by the difference in oxidation potential (Eh) between the solutions at the two half-cells. This mechanism is illustrated in Figure 6.2, showing the flow of electrons and ions that leave the upper surface negatively charged, the lower positively.

This hypothesis, although a considerable improvement on previous explanations, still fails to account for some observed anomalies. For instance, Sato and Mooney give maximum possible potentials for various sources, such as graphite (0.78 V), pyrite (0.73 V), and galena (0.33 V). For surface measurements this would imply a maximum no greater than these values, even when the body outcrops. Potentials as large as 1.5 V, however, have been reported over graphite. A field study in which potentials were measured in drill holes penetrating a sulfide zone, as well as on the surface over the zone, gave surface anomalies of approximately the same size as those encountered in the sulfide itself, even though the latter was well below the surface. These abnormally large SP results may be due to combinations of anomalies from adjacent mineralized zones, or enhancement by coincident background potentials.

Other unusual field results are discussed in Section 6.1.4.

Most of the sulfides are good conductors, with the exception of sphalerite, cinnabar, and stibnite. Self-potential anomalies have, however, been observed over sphalerite and in drill holes that passed through sphalerite bodies. The Sato–Mooney theory assumes that the sulfide zone must be a good conductor to transport electrons from depth to the oxidizing zone near surface. Thus the case of sphalerite is puzzling, although it may behave as a semiconductor and in many occurrences it is closely associated with other conductive sulfides.

Recent reports by Roy (1984) and Corry (1985) disagree with the Sato and Mooney hypothesis of mineralization potentials. Both authors show field results that indicate the measured potential is simply  $\Delta E$ , the oxidation potential difference between the electronic conductor (sulfides) and either the bore-hole fluid or a surface electrode outside the mineral zone. That is, without the borehole or a wire connecting the surface electrodes, no current will flow. There are additional arguments for this mechanism and against the Sato Mooney version; these include the obvious long time stability of sulfide deposits in various climates, the lack of evidence for a positive pole in their vicinity, the absence of surface SP anomalies over highly oxidized mineralization, the presence of unusually large surface SP (in excess of

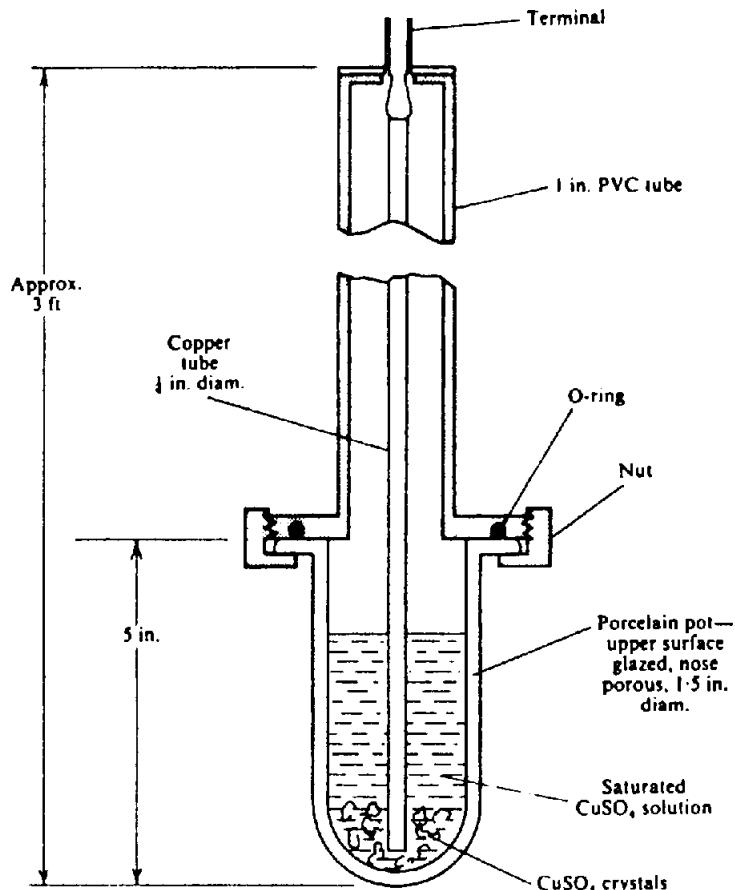


Figure 6.3. Walking-stick SP electrode.

1 V negative), and large depth of penetration ( $\geq 1$  km).

#### 6.1.2. Self-Potential Field Equipment

The SP method goes back to 1830, when Robert Fox used copper-plate electrodes and a string galvanometer as a detector in an attempt to find extensions of underground copper deposits in Cornwall. Since 1920 it has been employed in base-metal search, usually as a secondary method. The equipment required is extremely simple, consisting merely of a pair of electrodes connected by wire to a millivoltmeter. There are, however, two restrictions on the electrodes and detector that are most important.

If one were to use metal stakes driven into the ground as SP electrodes, the resultant electrochemical action at the ground contacts would create spurious potentials of the same size as those being measured. Furthermore these contact potentials are quite erratic in different ground and at different times, so that it would not be possible to make a fixed correction. Consequently nonpolarizing electrodes are essential. These consist of a metal immersed in a saturated solution of its own salt, such as Cu in  $\text{CuSO}_4$ , Ag in  $\text{AgCl}$ , and so on, and contained in a porous pot that allows the solution to leak slowly

and make contact with the ground. A good electrode of this type is the walking stick arrangement shown in Figure 6.3.

The main requirement of the millivoltmeter is that its input impedance should be large enough that negligible current will be drawn from the ground during the measurement. This was formerly achieved by using a potentiometer, now a small digital dc meter with an input impedance greater than  $10^8 \Omega$ . Such instruments, with ranges from 10 mV to 20 V full scale, are readily available. It is sometimes necessary to enclose the meter in a shield can to prevent erratic readings caused by contact of the instrument case with the body or ground.

#### 6.1.3. Field Procedure

The two porous pots should be filled from a uniform batch of salt solution. Otherwise the pots can be partly filled with salt crystals and water added; the first method is obviously preferable. When the loaded pots are standing side by side in a hole in the ground with the meter connected between them, the reading should be less than 2 mV. If not, the pots should be cleaned and recharged with fresh solution. Generally they can be used for a couple of days before running dry.

Where possible, traverses are carried out normal to the strike of suspected SP anomalies. Station intervals are usually not greater than 30 m and may be as small as 3 m. One of two electrode spreads may be employed: either one electrode is fixed at a base station while the other moves to successive stations along the line, or both electrodes are moved while maintaining a fixed interval between them.

The first arrangement, recommended for long traverses, requires a reel with several kilometers of cable. The meter may be at either electrode, but is usually at the base station. The advantages of this layout are that the potential is measured continually with respect to a fixed point, located, if possible, in a barren area; at the same time small zero errors between the electrodes do not accumulate. The only disadvantage is the long cable that inevitably slows down the measurements.

The fixed-electrode spread is maintained by moving the rear electrode up to the front pot hole and the forward electrode to a new station after each measurement. If the interval is small this is essentially a measurement of potential gradient,  $dV/ds$ , at a point midway between stations, where  $ds$  is the electrode spacing. Alternately the successive values of  $dV$  may be added algebraically to give the same potential profile as in the first method. This arrangement is faster than the other electrode layout, but has the disadvantage that the zero errors add up as the traverse progresses. To reduce this cumulative error the pots should be checked side by side in the same hole every 300 m or so.

An alternative procedure for the fixed-electrode spread is to leapfrog the electrodes in moving from station to station. If the rear pot is carried beyond the forward pot to the new station, cumulative zero errors are eliminated. The relative polarities are reversed at successive stations in the process; this must be kept in mind to produce the potential profile.

Since the potential between the electrodes will be randomly positive and negative, the use of a center-zero meter is a great advantage. At the same time it is essential to maintain a sign convention between the pots, that is, forward pot with respect to rear, or moving pot with respect to base pot. On completion of a closed grid, the algebraic sum of potentials should be zero. This is obviously easy with a fixed base station, but may require some care in measuring with two moving electrodes. In all SP field work the individual traverse lines must be tied together by measuring the potentials between each line.

In general, the procedures outlined in the foregoing text are sufficient for sulfide exploration, where anomalies are frequently large and distinct. In geothermal surveys more care is required, because the sources may be deeper and more extensive. Sev-

eral additional background effects may be troublesome in these circumstances, such as variations in soil moisture caused by watering the electrodes for better ground contact, spurious polarization from electrode contamination, differential drift, and temperature. The Ag-AgCl electrodes are better than the usual Cu types in these situations. With care, reading errors may be held within  $\pm 5$  mV.

#### 6.1.4. Interpretation of Self-Potential Data

The end result of an SP survey is a set of profiles and possibly a contour map of equipotentials. A typical profile and set of contours are illustrated in Figure 6.4. Note that the negative maximum lies directly over the sulfide mass; where the topography is steep, the center may be displaced somewhat.

It is possible to calculate the potential distributions around polarized bodies of simple shape, such as the dipole, sphere, and ellipsoid, by making some simplifications and assumptions concerning the potentials on the surfaces of the sources themselves. For example, consider the polarized rod in Figure 6.5. The potential at a point  $P$  on the ground above is given by

$$V = q(1/r_1 - 1/r_2) \quad (6.1)$$

where  $\pm q$  is the charge at either end of the rod. Because  $r_1 = (x^2 + z_1^2)^{1/2}$  and  $r_2 = ((x - a)^2 + z_2^2)^{1/2}$ , where  $a = l \cos \alpha$ ,  $l$  is the length of rod, and  $\alpha$  is the dip angle, this expression becomes

$$V = q \left[ 1/(x^2 + z_1^2)^{1/2} - 1/\{(x - a)^2 + z_2^2\}^{1/2} \right] \quad (6.2)$$

Because of the air-ground interface, the rod has an electrical image above surface, which could make this potential twice as large (§8.3.3 and §8.3.4). Typical profiles are plotted in Figure 6.5. It is apparent that the characteristic SP curve is fairly symmetrical unless the dip angle is quite shallow.

The polarized sphere is illustrated in Figure 6.6. To simplify the analysis, the sphere is assumed to be sliced in two with a constant potential  $-V_0$  on the upper half and zero on the lower. To calculate the potentials off the vertical axis it is necessary to employ Legendre polynomials (§2.7.4 and §8.3.5).

Although these simple shapes give results that are similar to profiles obtained in the field, they are seldom used in SP interpretation, which is mainly qualitative. The shape of an anomaly and its extent are indicated by the contour map or by a set of profiles normal to strike. An estimate of depth can be made from the shape of the profile. If  $x_{1/2}$  is the

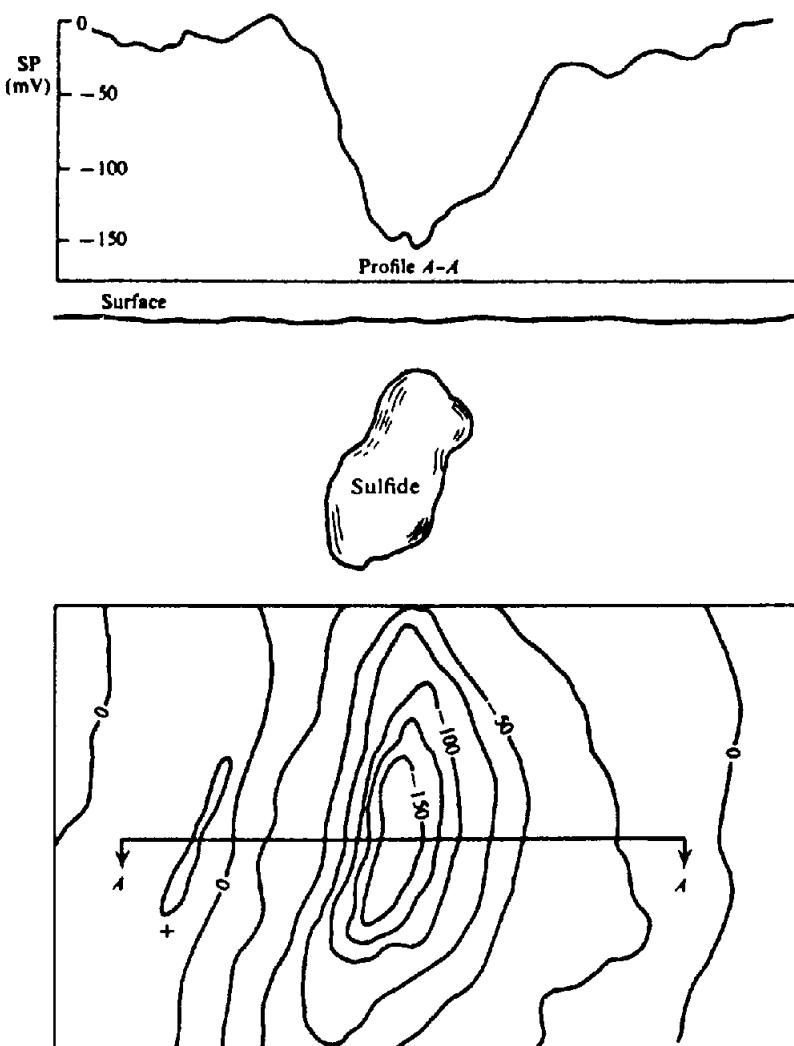


Figure 6.4. Typical SP profile and contours over sulfide body.

total width of the profile at half the (negative) maximum, then the depth to the top of the body is of the order of half this distance. From the sphere in Figure 6.6, this is obviously a very crude rule, and judging from half a dozen random field examples, the estimate may be within  $\pm 100\%$ . In particular, if the anomalous profile is wide, the source is also wide, rather than deep, because the depth of detection in SP is usually not greater than 60 m.

A rough idea of the attitude of the body may also be obtained from the lack of symmetry of the profile, that is, the steep slope and positive tail should be on the down-dip side. It is often desirable to remove regional effects from the SP profiles in order to clarify the anomaly shapes. This can be done by inspection, to take out large-scale gradients, baseline shifts, effects of surface vegetation, known geologic structure, and the like.

The type of overburden apparently has a pronounced effect on surface SP. Figures 6.7a, b show surface SP profiles over two sulfide bodies. Both have been drilled and the SP and core logs are also

illustrated. In Figure 6.7a sulfides at 300 ft gave a good surface SP anomaly, whereas in Figure 6.7b the mineralization at 300 and 4–500 ft did not show up at all on surface. The topsoil in the vicinity of the first was sand, in the second clay. From other examples as well, the absence of surface SP seems to be associated with a clay cover.

Figure 6.7a is also surprising for another reason. No sulfides were encountered above a depth of 300 ft; the surface SP anomaly is presumably due to mineralization between 300 and 500 ft. This is well below the water table in the area.

Self-potential measurements have occasionally been made offshore, to locate deposits in shallow water, to determine whether a known land anomaly extends offshore, and to locate unknown deposits in rugged shoreline terrain. Corwin (1976) describes a survey carried out by boat in Penobscot Bay, Maine, where sulfides had produced near-shore SP anomalies. Although the saline water generally reduces the SP amplitude, noise level is also greatly reduced at the same time ( $< 0.3$  mV), so that anomalies of a

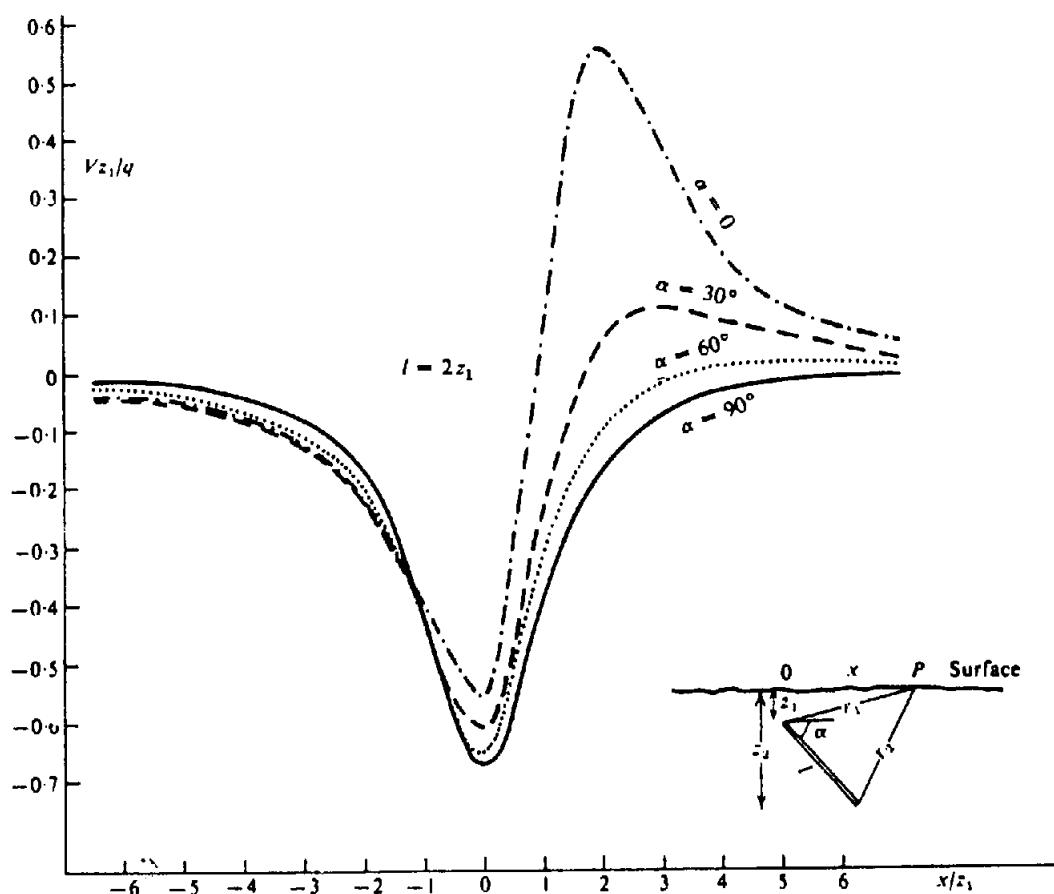


Figure 6.5. SP profiles over buried polarized rod.

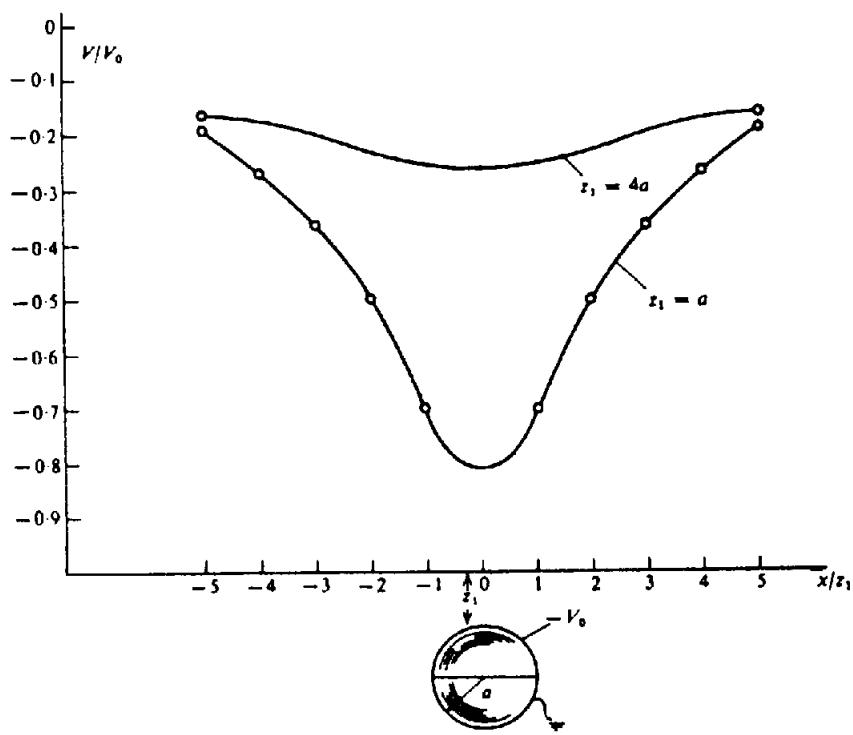


Figure 6.6. SP profiles over buried polarized sphere.

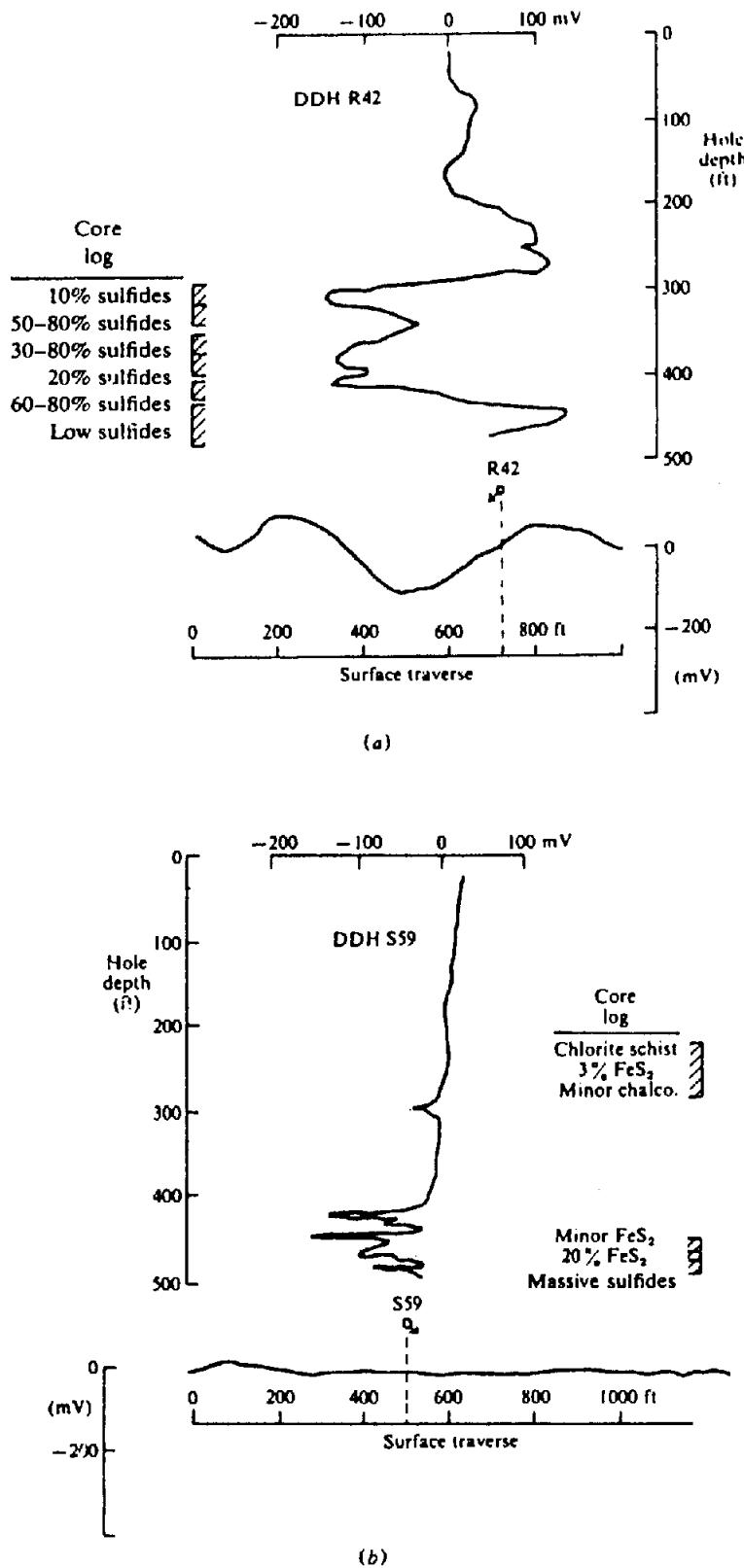


Figure 6.7. Surface and drill-hole SP for different overburdens. (a) Sand overburden.  
(b) Clay overburden.

few millivolts were clearly detected below 12 m of water. Special Ag-AgCl electrodes are necessary for this type of work, in which the near electrode is located one or two boat lengths astern and the other 10 to 100 m beyond this. The larger electrode separation produces better sensitivity, but increases the

noise level, particularly in the vicinity of irregular shorelines.

The discussion of background or noise potentials in Section 6.1.1 and elsewhere was based on the assumption that any potentials not generated by the target source constituted noise. This is correct as far

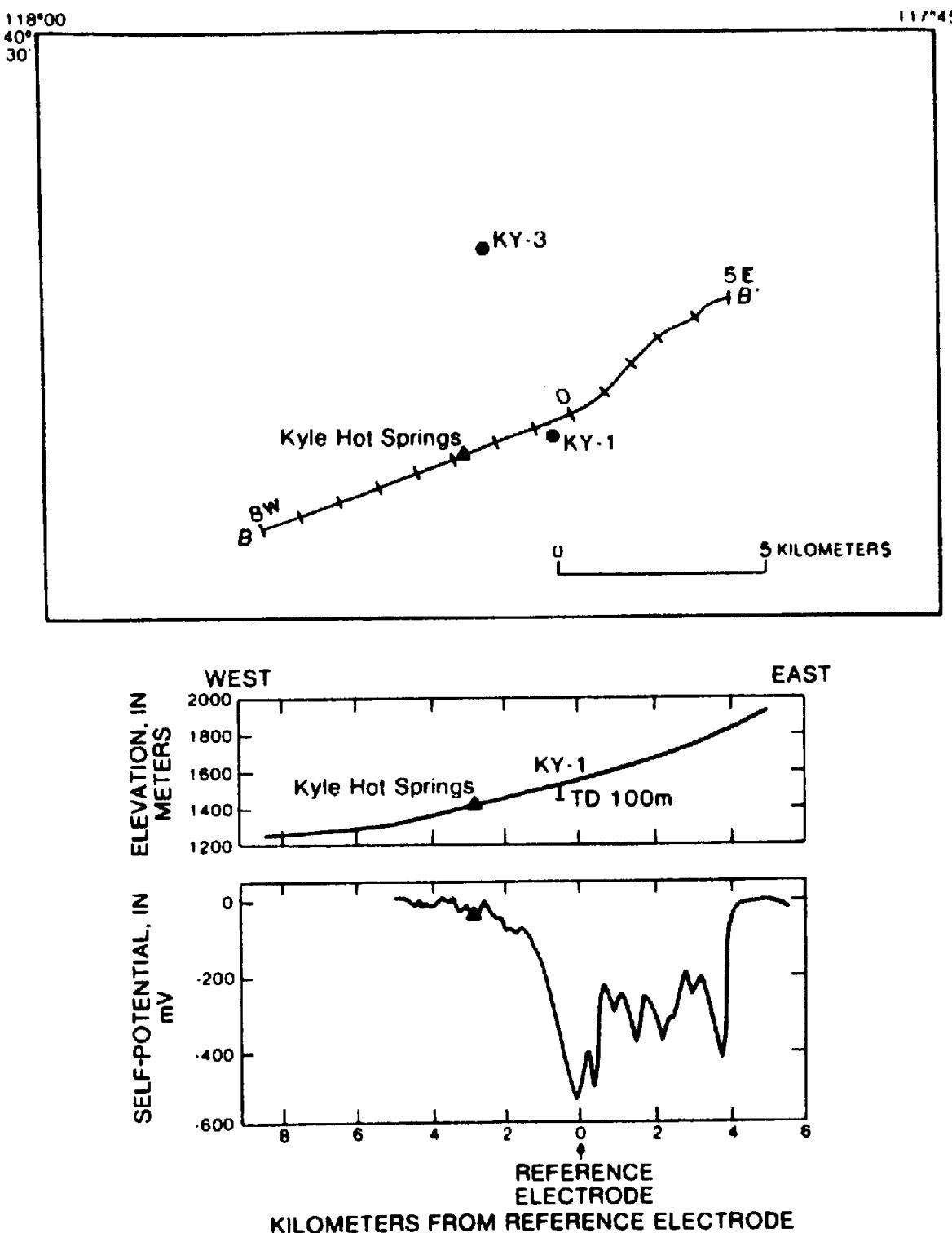


Figure 6.8. SP profile, line B-B', Kyle Hot Springs, Buena Vista Valley, Nevada. KY-1 and KY-3 are drill-hole locations. (After Corwin and Hoover, 1979.)

as it goes, but the recent use of SP in geothermal exploration has sometimes relegated mineralization potentials to the category of noise. Although the converse is also true, the resultant noise effect is less of a problem, because mineral anomalies are usually larger. The first situation is illustrated in Figure 6.8, which shows a huge negative anomaly of 550 mV peak extending over some 5 km of a 14 km profile measured on sloping ground at Kyle Hot Springs in

Nevada. Originally thought to be produced either by a geothermal source associated with the hot spring or a streaming potential due to the 800 m slope, or a combination of the two, the test holes KY-1 and KY-3 penetrated an extensive section of conductive graphite with pyrite, continuing downward from 40 m depth. Furthermore, the heat flow in the holes was normal for the area. In this context the mineralization represents an extremely large source of noise.

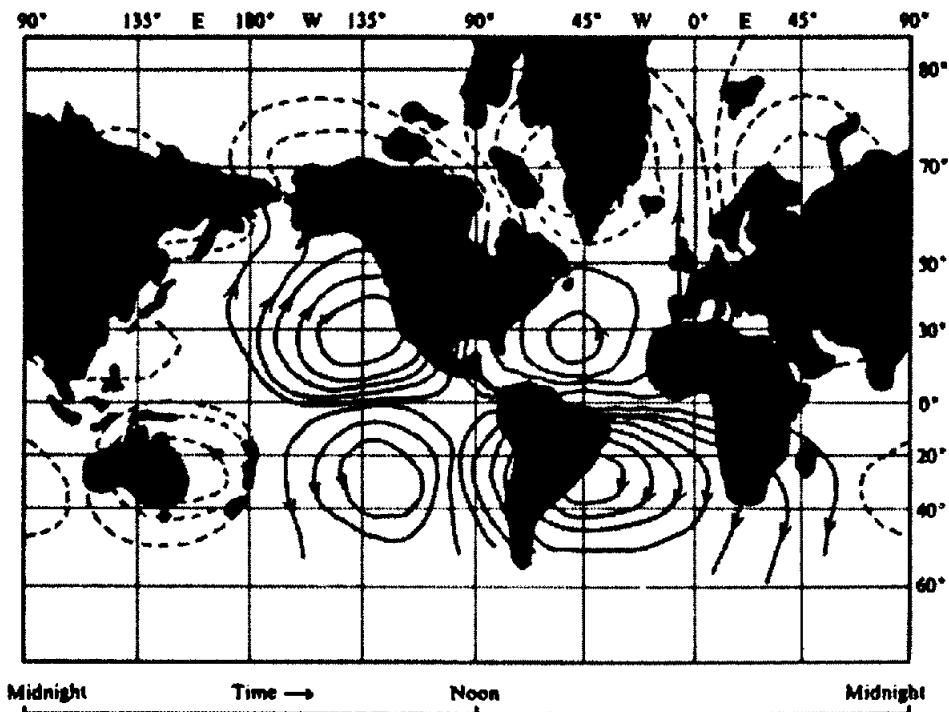


Figure 6.9. Worldwide telluric-current system on Mercator's projection. (After Dobrin, 1960.)

Self-potential has played a minor role in geophysical exploration. This is mainly due to the difficulty in making significant interpretation of the results - which are frequently quite erratic - and partly because the depth of penetration has generally been assumed to be shallow, although this matter is not at all clear. It is, however, a simple, fast, and cheap method that is useful in rapid ground reconnaissance for base metals when accompanied by magnetics, EM, and geochemistry. Aside from the possibility of detecting sulfides, it is useful in mapping shallow structures like faults, shear and fracture zones, and contacts, and appears to have some application in the search for geothermal sources.

## 6.2. TELLURIC AND MAGNETOTELLURIC METHODS

### 6.2.1. Origin and Characteristics of Magnetotelluric Fields and Telluric Currents

In this section we shall consider techniques that employ certain large-scale (generally low-frequency) magnetic fields and the terrestrial current systems induced by these fields. The terms "magnetotelluric" and "telluric" are generally used to designate these fields and currents, respectively. These topics are included in this chapter because they are natural-source electrical methods, like self-potential. Such magnetic fields, however, are identical with those discussed in Section 7.2.

The existence of natural large-scale earth currents was first established by Barlow in 1847 in the course of studies on the first British telegraph system. Long-term records of telluric currents were made at Greenwich, Paris, and Berlin in the late nineteenth century; nowadays they are recorded at various observatories around the world.

The source of these currents has been fairly definitely located outside the earth. Periodic and transient fluctuations can be correlated with diurnal variations in the earth's magnetic field, caused by solar emission, aurora, and so forth. These activities have a direct influence on currents in the ionosphere; it is thought that the telluric currents are induced in the earth by ionospheric currents.

The inductive mechanism is an electromagnetic field propagated with slight attenuation over large distances in the space between the ionosphere and earth surface, somewhat in the manner of a guided wave between parallel conducting plates. That is to say, it proceeds by bouncing back and forth between these boundaries and hence has a large vertical component. At large distances from the source this is a plane wave of variable frequency (from about  $10^{-5}$  Hz up to the audio range at least). Obviously these magnetotelluric (MT) fields can penetrate the earth's surface to produce the telluric currents.

The pattern of these terrestrial current systems is shown in Figure 6.9. The huge whorls cover millions of square kilometers, are fixed with respect to the Sun, and rotate alternately clockwise and counter-clockwise. In mid-latitudes there are two maxima

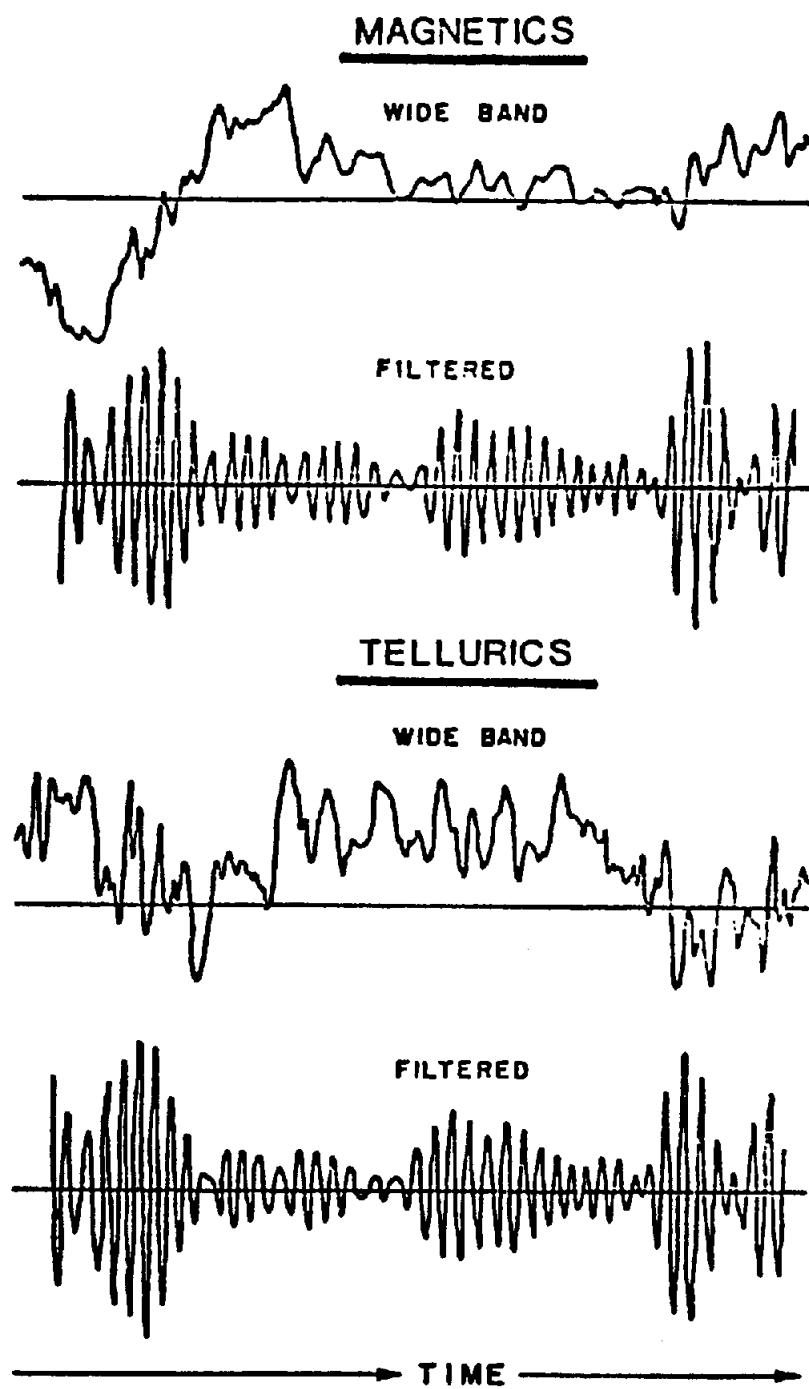


Figure 6.10. Magnetic and telluric field data before and after filtering.

and two minima per day, the average direction being mainly in the magnetic meridian. Near the equator (Peru, Madagascar), on the other hand, there appear to be only one maximum and one minimum per day, the amplitudes are considerably smaller, and the average direction is east-west. For signals in the period range 10 to 40 s ( $P_c$  type), the current intensity is much larger on the daylight side of Earth, as well as in aurora latitudes compared to temperate. The electric fields related to these currents are of the order of 10 mV/km, whereas the associated magnetic fields are in the milligamma (picotesla) range.

Superimposed on this average telluric field are random fluctuations whose intensities vary with elec-

trical disturbances in the ionosphere. These pulsations occur at frequencies as high as 100 kHz, although most are much lower. As a result the telluric record consists of erratic variations in potential, as illustrated in Figure 6.10, which also shows the raw signals after filtering.

One source of the higher-frequency current fluctuations is electric storms. Although their location is to some extent random, there are three major storm centers, all located in equatorial regions - Brazil, Central Africa, and Malaya. Some of the thunderstorm energy is converted to electromagnetic fields that are propagated in the ionosphere-Earth inter-space. The weak currents induced by these fields in

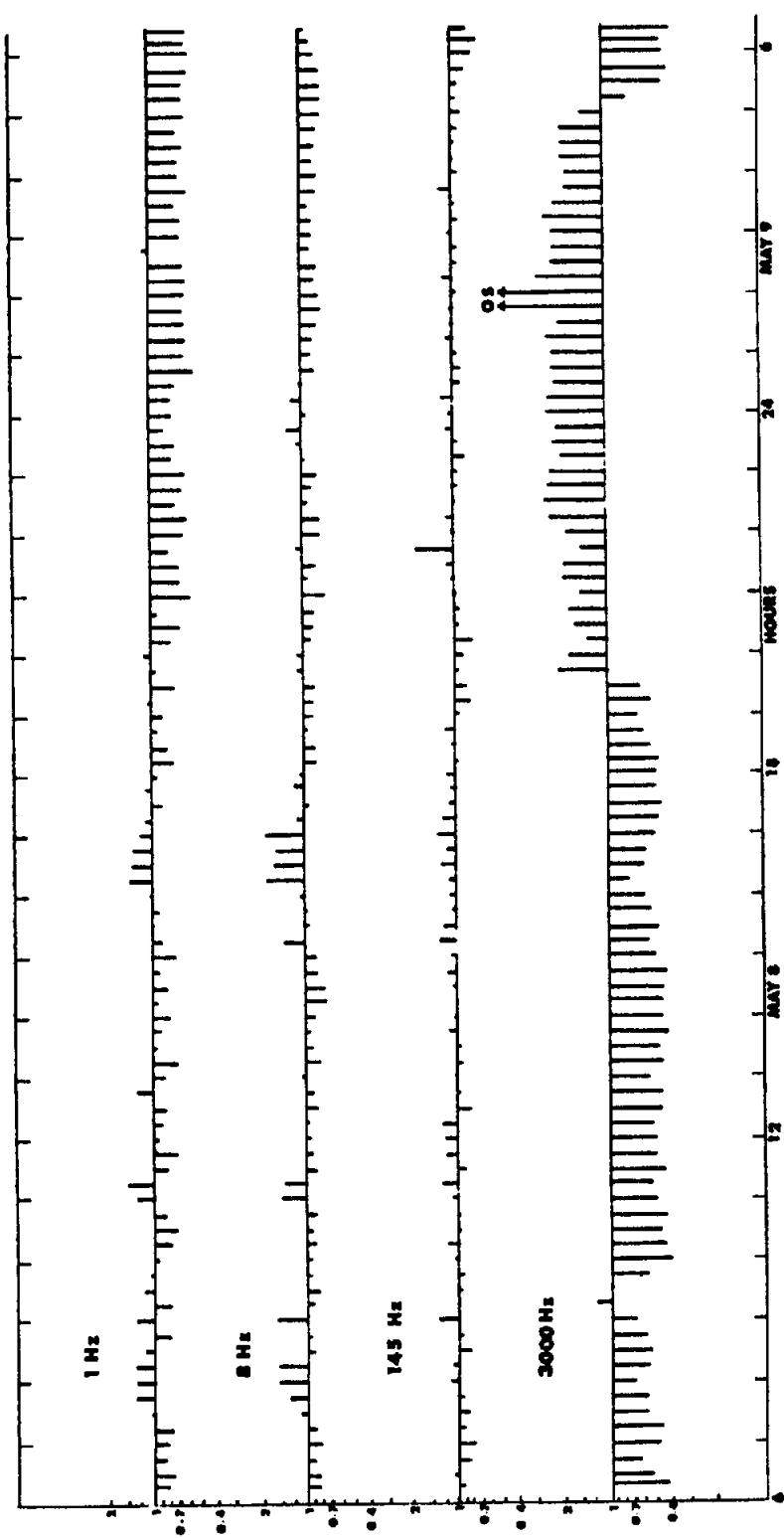
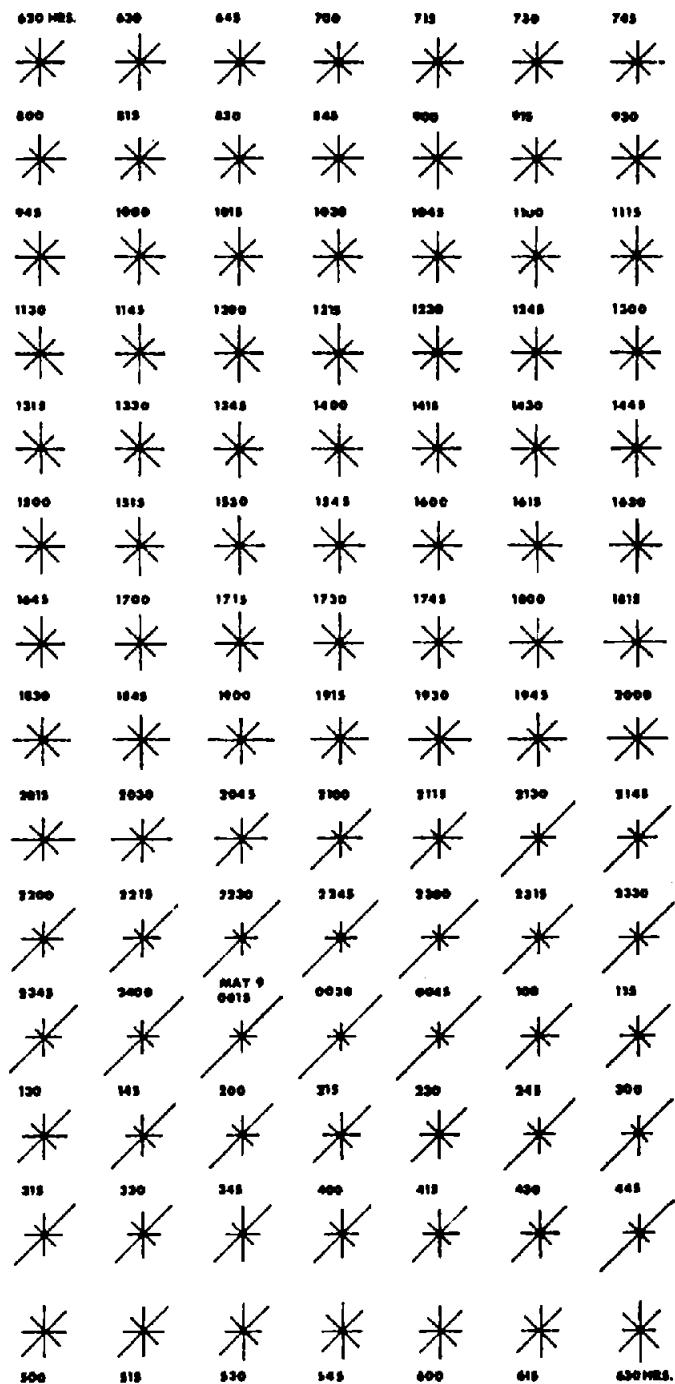


Figure 6.11. Telluric response, Vale Perkins, Quebec, May 8-9, 1975. Electrodes are north-south.



**Figure 6.12.** Anisotropic telluric response, Vale Perkins, Quebec, May 8-9, 1975. Frequency 145 Hz.

the subsurface are useful in telluric and magnetotelluric prospecting, particularly because they have amplitude peaks at several distinct frequencies – 8, 14, 760 Hz, and so on. These same electromagnetic fields are also employed in the AFMAG method (§7.4.2e).

Information concerning audio and subaudio teluric and MT signals may be found in several reports (Slankis, Telford, and Becker, 1972; Strangway, Swift, and Holmer, 1973; Goldstein and Strangway, 1975; Hoover, Long, and Senterfit, 1978). To investi-

gate the diurnal amplitude and azimuthal variations of telluric signals at 1, 8, 145, and 3,000 Hz, four telluric receivers connected to four pairs of electrodes were set up at a site free from power-line disturbances in the Appalachian region about 150 km east of Montreal (Telford, 1977). Each electrode pair spacing was 30 m, the orientations being approximately  $343^\circ$ ,  $28^\circ$ ,  $73^\circ$ ,  $118^\circ$  with respect to true north. The telluric units, described in Section 6.2.6a, with their gains equalized, were simultaneously read

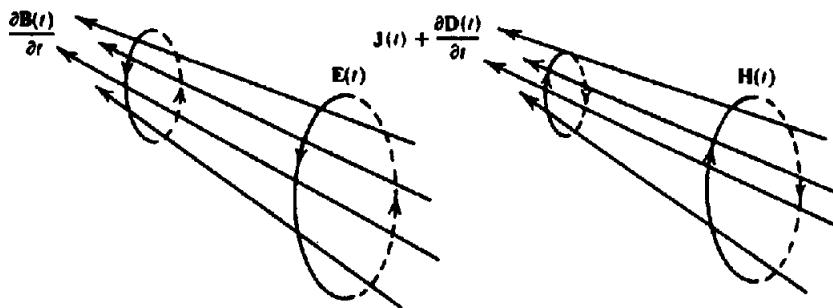


Figure 6.13. Electric and magnetic fields of Equations (6.3) and (6.4). (After Grant and West, 1965.)

every quarter hour for the four frequencies over a 24 hour period.

Figure 6.11 illustrates the telluric response from the north-south electrodes; the data have been normalized for each frequency and plotted on a log scale. The 3,000 Hz signal abruptly increases and decreases at sunset and sunrise, respectively, on all four orientations; in the 28° (~ NNE) azimuth the lower three frequencies are very similar to this. However, for the north, northwest, and east electrodes, the 1, 8, and 145 Hz levels are generally low from 21:00 hours through the night. In this respect these frequencies resemble the  $P_c$  signals mentioned previously, whereas the response in the north-northeast azimuth is reversed. The explanation for this is not clear, although the general regional strike (Sutton anticlinorium) is approximately north-northeast.

Figure 6.12 shows the directional response at 145 Hz, which is practically isotropic during daylight hours and becomes stronger north-northeast from about sundown to sunrise, that is, 20:45 to 5:15 hr (these signals have been normalized at each frequency and measurement time for the four orientations). For the other frequencies 3,000 Hz is strongly maximum along the 28° axis throughout the entire day, 1 and 8 Hz only during the night.

## 6.2.2. Elementary Electromagnetic Theory

An elementary development of electromagnetic theory can be employed to describe magnetotelluric wave propagation. To understand the propagation and attenuation of such waves it is necessary to use Maxwell's equations in a form relating the electric and magnetic field vectors:

$$\nabla \times \mathbf{E} = -\frac{\partial \mathbf{B}}{\partial t} \quad (6.3)$$

$$\nabla \times \mathbf{H} = \mathbf{J} + \frac{\partial \mathbf{D}}{\partial t} \quad (6.4)$$

where  $\mathbf{J}$  is the current density ( $\text{A}/\text{m}^2$ ),  $\mathbf{E}$  is the electric field intensity ( $\text{V}/\text{m}$ ),  $\mathbf{B}$  is the magnetic flux

density [teslas ( $\text{T}$ )],  $\mathbf{H}$  is the magnetic field intensity ( $\text{A}/\text{m}$ ), and  $\mathbf{D}$  is the electric displacement ( $\text{C}/\text{m}^2$ ).

Equation (6.3) is a mathematical statement of Faraday's law that an electric field exists in the region of a time-varying magnetic field, such that the induced emf is proportional to the negative rate of change of magnetic flux. Equation (6.4) is a mathematical statement of Ampere's law (taking into account Maxwell's displacement current  $\partial D/\partial t$ ), namely, that a magnetic field is generated in space by current flow and that the field is proportional to the total current (conduction plus displacement) in the region (Fig. 6.13).

Using the vector identity  $\nabla \cdot \nabla \times \mathbf{A} = 0$  [Eq. (A.24)] we get for time-varying fields

$$\nabla \cdot \nabla \times \mathbf{E} = -\nabla \cdot \frac{\partial \mathbf{B}}{\partial t} = -\frac{\partial}{\partial t}(\nabla \cdot \mathbf{B}) = 0 \quad (6.5a)$$

that is

$$\nabla \cdot \mathbf{B} = 0 \quad (6.5b)$$

Similarly,

$$\nabla \cdot \mathbf{J} + \nabla \cdot \frac{\partial \mathbf{D}}{\partial t} = \nabla \cdot \mathbf{J} + \frac{\partial}{\partial t}(\nabla \cdot \mathbf{D}) = 0 \quad (6.5c)$$

We also know that the divergence of current density is equivalent to the rate of accumulation of charge density,  $Q$ , or from Equation (6.5c),

$$\nabla \cdot \mathbf{J} = -\frac{\partial Q}{\partial t} = -\frac{\partial}{\partial t}(\nabla \cdot \mathbf{D}) \quad (6.6a)$$

hence

$$\nabla \cdot \mathbf{D} = Q \quad (6.6b)$$

In regions of finite conductivity, charge does not accumulate to any extent during current flow (omit-

ting electrolytic conductors), hence  $\mathbf{Q} = 0$  so that

$$\nabla \cdot \mathbf{J} = 0 \quad \nabla \cdot \mathbf{D} = \epsilon \epsilon_0 \nabla \cdot \mathbf{E} = 0 \quad (6.7)$$

Besides the relation between displacement and electric field, we also have the following relation between  $\mathbf{B}$  and  $\mathbf{H}$  [Eq. (3.7a)]:

$$\mathbf{B} = \mu \mu_0 \mathbf{H} \quad (6.8)$$

In Equations (6.7) and (6.8),  $\mu$  is the relative magnetic permeability of the medium,  $\epsilon$  is the relative dielectric permittivity,  $\mu_0$  is the permeability of free space  $= 4\pi \times 10^{-7}$  H/m (Tm/A), and  $\epsilon_0$  is the permittivity of free space  $= 8.85 \times 10^{-12}$  (F/m). Furthermore, in homogeneous isotropic media, we can express these relations, together with Ohm's law, as

$$\mathbf{B} = \mu \mathbf{H} \quad \mathbf{D} = \epsilon \mathbf{E} \quad \mathbf{J} = \sigma \mathbf{E} \quad (6.9)$$

where  $\sigma$  is the conductivity and we have eliminated  $\mu_0$ ,  $\epsilon_0$  for convenience by using mks units. We can simplify Equations (6.3) and (6.4) as

$$\nabla \times \mathbf{E} = -\mu \frac{\partial \mathbf{H}}{\partial t} \quad (6.10)$$

$$\nabla \times \mathbf{H} = \sigma \mathbf{E} + \epsilon \frac{\partial \mathbf{E}}{\partial t} \quad (6.11a)$$

If, as in some situations, there are independent current sources  $\mathbf{J}_0$ , not related to the magnetic field (from SP, power devices, etc.), Equation (6.11a) becomes

$$\nabla \times \mathbf{H} = \mathbf{J}_0 + \sigma \mathbf{E} + \epsilon \frac{\partial \mathbf{E}}{\partial t} \quad (6.11b)$$

Taking the curl of Equations (6.10) and (6.11a) and using Equation (A.25), we finally get [note that  $\nabla \cdot \mathbf{H} = 0 = \nabla \cdot \mathbf{E}$  from Eqs. (6.5b) and (6.7)]

$$\nabla^2 \mathbf{E} - \mu \frac{\partial}{\partial t} (\nabla \times \mathbf{H}) = \mu \sigma \frac{\partial \mathbf{E}}{\partial t} + \mu \epsilon \frac{\partial^2 \mathbf{E}}{\partial t^2} \quad (6.12a)$$

$$\begin{aligned} \nabla^2 \mathbf{H} &= -\sigma (\nabla \times \mathbf{E}) - \epsilon \frac{\partial}{\partial t} (\nabla \times \mathbf{E}) \\ &= \mu \sigma \frac{\partial \mathbf{H}}{\partial t} + \mu \epsilon \frac{\partial^2 \mathbf{H}}{\partial t^2} \end{aligned} \quad (6.12b)$$

If we choose sinusoidal time variations – which is generally done in MT work – we can write

$$\mathbf{E}(t) = \mathbf{E}_0 e^{j\omega t}$$

$$\mathbf{H}(t) = \mathbf{H}_0 e^{j\omega t}$$

$$\frac{\partial \mathbf{E}}{\partial t} = j\omega \mathbf{E}$$

$$\frac{\partial \mathbf{H}}{\partial t} = j\omega \mathbf{H}$$

where  $\omega = 2\pi f$  is the angular frequency of the field. Thus Equations (6.12) are simplified to

$$\nabla^2 \mathbf{E} = j\omega \mu \sigma \mathbf{E} - \omega^2 \mu \epsilon \mathbf{E} \quad (6.13a)$$

$$\nabla^2 \mathbf{H} = j\omega \mu \sigma \mathbf{H} - \omega^2 \mu \epsilon \mathbf{H} \quad (6.13b)$$

the first and second terms on the right-hand side being related to the conduction and displacement currents, respectively. These are the electromagnetic equations for propagation of electric and magnetic field vectors in an isotropic homogeneous medium having conductivity  $\sigma$ , relative permeability  $\mu$ , and relative dielectric permittivity  $\epsilon$ .

### 6.2.3. Attenuation of EM Fields

The wave is attenuated in traveling through some media but not in free space. This can be shown as follows. Considering the relative magnitudes of the parameters  $\epsilon$ ,  $\mu$ ,  $\omega$ , and  $\sigma$ , we can say that the maximum normal value of  $\epsilon$  occurs in water where  $\epsilon = 80$ ; for rocks,  $\epsilon$  is generally less than 10. Similarly,  $\mu \leq 3$ , even in ferromagnetic minerals; normally the value is unity. Thus we have

$$\epsilon \approx 10\epsilon_0 \approx 9 \times 10^{-11} \text{ F/m}$$

$$\mu \approx \mu_0 \approx 1.3 \times 10^{-6} \text{ H/m}$$

The periodic frequencies employed in MT work (and in EM methods as well, as we shall see in Ch. 7) are usually less than 3,000 Hz, hence  $\omega \leq 2 \times 10^4$ . The corresponding wavelengths, which are given by

$$\lambda = 2\pi c/\omega = 2\pi \times 3 \times 10^8 / \omega \text{ m}$$

are greater than 90 km. Because the distances involved in field layouts are usually less than 1 to 2 km, the phase variation resulting from propagation is negligible.

In the air  $\sigma = 0$ ,  $\epsilon = \epsilon_0$ , and  $\mu = \mu_0$ . Thus the factor  $\omega^2 \mu \epsilon$  in Equations (6.13) is of the order of  $5 \times 10^{-9}$ , that is, there is no attenuation of the wave in air.

The conductivity of rocks and minerals, however, varies enormously, as we have seen in Section 5.4.1. In rocks of low conductivity we might have  $\epsilon = 10\epsilon_0$ ,  $\mu = \mu_0$ , and  $\sigma \approx 10^{-3}$  S/m, so that, for  $\omega = 2 \times 10^4$ ,

$$\nabla^2 \mathbf{E} = (-4 \times 10^{-8} + 2.5 \times 10^{-5} j) \mathbf{E} \approx 0$$

However, in regions of high-conductivity (massive sulfides, graphite, and the like)  $\sigma \approx 10^3$  S/m and

$$\nabla^2 \mathbf{E} \approx (-4 \times 10^{-8} + 25j) \mathbf{E} \approx 25j \mathbf{E}$$

Comparison of Equations (6.13) shows that identical relations hold for  $H$  also. Thus in all cases the real part of the right-hand side of the equation (which corresponds to the displacement current) is negligible. As a result, in air and in poorly conducting rocks, we have

$$\nabla^2 E \approx 0 \quad \nabla^2 H \approx 0 \quad (6.14)$$

whereas within a good conductor the imaginary part of the expression is significant, and Equations (6.12) then are written

$$\nabla^2 E \approx \mu\sigma \frac{\partial E}{\partial t} \approx j\omega\mu\sigma E \quad (6.15a)$$

$$\nabla^2 H \approx \mu\sigma \frac{\partial H}{\partial t} \approx j\omega\mu\sigma H \quad (6.15b)$$

This is the diffusion equation, which reduces to Laplace's equation [Eq. (6.14)] in the air and in rocks of low conductivity. Equations (6.15) are generally difficult to solve; however, there is one important case in which a solution is readily obtained, that in which the wave is plane polarized. Assume the wave is propagating along the  $z$  axis so that the  $xy$  plane is the plane of polarization. We can then solve Equation (6.15b) by assuming the form

$$H = H_y(z, t) = H_0 e^{j\omega t + mz}$$

where  $H$  is the magnitude of  $H$ . Then,

$$\nabla^2 H = (\partial^2 H_y / \partial z^2) = m^2 H$$

and

$$(\partial H_y / \partial t) = j\omega H$$

Substitution in Equation (6.15) shows that we must have

$$m^2 = j\omega\mu\sigma$$

or

$$m = \pm(1+j)\sqrt{\omega\mu\sigma/2} = \pm(1+j)a$$

where  $a = (\omega\mu\sigma/2)^{1/2}$ . Because  $H$  must be finite when  $z = +\infty$ , we discard the plus sign and obtain the solution

$$H_y = H_0 e^{j\omega t - (1+j)a z} = H_0 e^{-az + j(\omega t - az)} \quad (6.16a)$$

Taking the real part as the required solution, we have

$$H_y = H_0 e^{-az} \cos(\omega t - az) \quad (6.16b)$$

The second part of the expression represents simple harmonic motion with a phase shift whereas the exponential is the attenuation of the wave with propagation distance. This attenuation term may be written (taking  $\mu = \mu_0 = 4\pi \times 10^{-7}$ )

$$|H_y/H_0| \approx e^{-2 \times 10^{-3} z_f (\Omega/\rho)} \quad (6.16c)$$

Taking a few numerical examples, we get values as in Tables 6.1 and 6.2.

A commonly used criterion for the penetration of electromagnetic waves is the *skin depth*, the distance

Table 6.1. Attenuation of EM waves.

$f$ (Hz)	$\rho$ ( $\Omega\text{m}$ )	$ H_y/H_0 $ for $z = 30 \text{ m}$	$z$ for $ H_y/H_0  = 0.1$ (m)
$10^3$	$10^{-4}$	0.00	0
$10^3$	$10^{-2}$	0.00	0
$10^3$	1	0.15	37
$10^3$	$10^2$	0.83	370
$10^3$	$10^4$	0.98	3,700
$10^4$	10	0.94	1,160
$10^2$	10	0.83	370
$10^4$	10	0.15	37
$10^6$	10	0.00	3.7

Table 6.2. Skin depth variation with frequency and resistivity.

$f$ (Hz)	$\rho = 10^{-4} \Omega\text{m}$ $z_s$ (m)	$10^{-2} \Omega\text{m}$ $z_s$ (m)	$10^0 \Omega\text{m}$ $z_s$ (m)	$10^2 \Omega\text{m}$ $z_s$ (m)	$10^4 \Omega\text{m}$ $z_s$ (m)
$10^{-3}$	160	1,600	$1.6 \times 10^4$	$1.6 \times 10^5$	$1.6 \times 10^6$
$10^{-2}$	50	500	$5 \times 10^4$	$5 \times 10^5$	$5 \times 10^6$
$10^{-1}$	16	160	$1.6 \times 10^4$	$1.6 \times 10^4$	$1.6 \times 10^5$
1	5	50	500	5,000	$5 \times 10^4$
10	1.6	16	160	1,600	$1.6 \times 10^4$
$10^2$	0.5	5	50	500	5,000
$10^3$	0.16	1.6	16	160	1,600
$10^4$	0.05	0.5	5	50	500
$10^6$	0.005	0.05	0.5	5	50
$10^8$	—	0.005	0.05	0.5	5

in which the signal is reduced by  $1/e$ , that is, to 37%. This is given by  $z_s = 1/a$  in Equation (6.16b), that is,

$$z_s \approx 500 (\rho/f)^{1/2} \text{ m} \quad (6.17)$$

From these tables it is quite obvious that if the resistivity is low, or the frequency high, or both, the magnetic field will not penetrate the ground to any extent. As a crude rule of thumb we can say that if

$$z_s(f/\rho) > 10^3$$

the attenuation will be large and vice versa.

For the same plane polarized wave in Equation (6.16b) we can also find the current, using Equations (6.9) and (6.11a). Thus we have (neglecting the term  $\partial E / \partial t$  because  $\omega \ll \sigma$ )

$$\nabla \times H = \sigma E = J$$

Hence

$$J_y = J_z = 0$$

and

$$\begin{aligned} J_x &= -\frac{\partial H_y}{\partial z} = -\frac{\partial}{\partial z} \{ H_0 e^{-az} \cos(\omega t - az) \} \\ &= aH_0 e^{-az} \{ \cos(\omega t - az) - \sin(\omega t - az) \} \\ &= \sqrt{2} aH_0 e^{-az} \cos\left(\omega t - az + \frac{\pi}{4}\right) \\ &= (\omega \mu \sigma)^{1/2} H_0 e^{-z/(\omega \mu \sigma/2)} \\ &\quad \times \cos\left(\omega t - z \left(\frac{\omega \mu \sigma}{2}\right)^{1/2} + \frac{\pi}{4}\right) \quad (6.18) \end{aligned}$$

This shows that the amplitude of the current is  $(\omega \mu \sigma)^{1/2}$  times that of the magnetic field at all points. Also, because  $J_x$  is proportional to  $H_y$ , the current flux exhibits the same skin effect as the magnetic field and in a good conductor, therefore, it is concentrated near the surface.

The physical result is that when  $(\omega \mu \sigma/2)^{1/2}$  is small, the magnetic field will propagate through the medium without much attenuation and in the process will fail to induce any appreciable current flow in it. Consequently there will be very little secondary magnetic field generated. On the other hand, when  $(\omega \mu \sigma/2)^{1/2}$  is large, the large surface current creates a large secondary magnetic field, out of phase with the original, which partially or completely cancels the primary field.

When the medium has intermediate conductivity there will be some secondary magnetic field developed. Even here the current density will not be

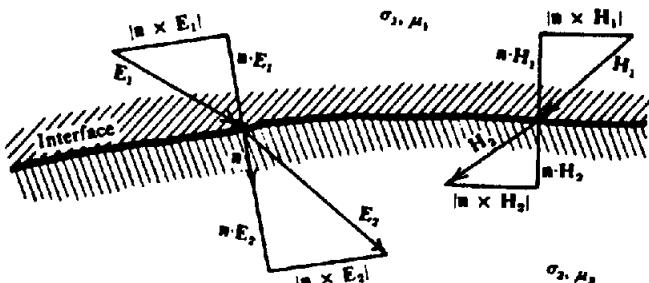


Figure 6.14. Boundary conditions on EM fields at an interface.

uniform throughout the volume of the conductor but will be concentrated toward the outside. Because it is not generally possible to determine this current distribution, even for simple shapes, the analytical solution of most problems by electromagnetic theory is out of the question.

#### 6.2.4. Boundary Conditions

As in dc resistivity there are several boundary conditions for EM fields that must hold at interfaces where  $\sigma$  (and possibly  $\mu$ ) change abruptly. These can be derived from Equations (6.3), (6.4), (6.7), and (6.9) as follows (Fig. 6.14):

$$n \times (E_1 - E_2) = 0$$

electric field tangential to interface is continuous.

$$n \times (H_1 - H_2) = 0$$

magnetic field tangential to interface is continuous.

$$n \cdot (\sigma_1 E_1 - \sigma_2 E_2) = 0$$

current density normal to interface is continuous.

$$n \cdot (\mu_1 H_1 - \mu_2 H_2) = 0$$

magnetic flux normal to interface is continuous.

These four conditions are valid when there is no free charge or current on the interface. For this case, the potential  $V$  is also continuous across the interface, because no work is done in carrying a charge from one side of it to the other. All electromagnetic fields must satisfy the preceding conditions at all interfaces.

#### 6.2.5. Magnetotelluric Fields

To adapt the wave equations to magnetotellurics, it is necessary to make certain simplifying assumptions. Certainly the frequencies are so low that displacement currents are negligible. Next, for plane waves of this type, it is clear that horizontal variations in  $E$  and  $H$  are small compared with vertical variations. Furthermore, we will consider only periodic frequency variations, because the fields are so

erratic that it would be difficult to do otherwise. Taking the  $xy$  plane as horizontal and  $z$  positive downward, these conditions can be expressed mathematically in the form

$$\frac{\partial D}{\partial t} = 0 \quad \frac{\partial}{\partial x} = 0 = \frac{\partial}{\partial y}$$

$$E \propto e^{-j\omega t} \quad H \propto e^{-j\omega t} \quad \frac{\partial}{\partial t} = -j\omega$$

If the wave is polarized in the  $xy$  plane and traveling in the  $z$  direction, we taken the magnetic vector as  $H_0$  at an angle  $\theta$  to the  $x$  axis so that the magnitudes of the magnetic components are  $H_{x0} = H_0 \cos \theta$  and  $H_{y0} = H_0 \sin \theta$ . We can write

$$\left. \begin{aligned} H_x &= (H_0 \cos \theta) e^{-az} \cos(\omega t - az) \\ H_y &= (H_0 \sin \theta) e^{-az} \cos(\omega t - az) \end{aligned} \right\} \quad (6.19a)$$

From Equation (6.11a),

$$\begin{aligned} E_x &= \frac{1}{\sigma} (\text{x component of } \nabla \times \mathbf{H}) = \frac{1}{\sigma} \left( -\frac{\partial H_y}{\partial z} \right) \\ &= -\frac{1}{\sigma} (H_0 \sin \theta) e^{-az} (-a \cos(\omega t - az) \\ &\quad + a \sin(\omega t - az)) \\ &= \sqrt{2} \frac{a}{\sigma} (H_0 \sin \theta) e^{-az} \cos\left(\omega t - az + \frac{\pi}{4}\right) \end{aligned} \quad (6.19b)$$

Similarly,

$$E_y = \sqrt{2} \frac{a}{\sigma} (H_0 \cos \theta) e^{-az} \cos\left(\omega t - az + \frac{\pi}{4}\right) \quad (6.19c)$$

Dividing Equations (6.19b) and (6.19c) by Equation (6.19a), the squares of the ratios of the amplitudes become

$$\left| \frac{E_y}{H_x} \right|^2 = \left| \frac{E_x}{H_y} \right|^2 = 2 \left( \frac{a}{\sigma} \right)^2 = \omega \mu \rho \quad (6.20)$$

If we assume  $\sigma$  to be the effective conductivity in a penetration depth  $\mathcal{D}$ , we can find approximate values of  $\mathcal{D}$  and  $\sigma$  by replacing  $\partial/\partial z$  by  $1/\mathcal{D}$  and  $\omega$  by  $2\pi/T$ ; Equations (6.19) and (6.20) then give

$$\mathcal{D} \approx \frac{1}{\sigma} \left| \frac{H_y}{E_x} \right| \approx \frac{1}{\sigma (\omega \mu \rho)^{1/2}} = \frac{(2\pi \mu \rho)^{1/2}}{\omega \mu} = \frac{T}{2\pi \mu} \left| \frac{E_x}{H_y} \right| \quad (6.21a)$$

and

$$\rho \approx \frac{T}{2\pi \mu} \left| \frac{E_x}{H_y} \right|^2 \quad (6.22a)$$

Clearly the  $x$  and  $y$  axes can be interchanged, hence these expressions can be stated in the more general form

$$\mathcal{D} \approx \frac{T}{2\pi \mu} \left| \frac{\mathcal{E}}{\mathcal{H}} \right| \quad (6.21b)$$

$$\rho \approx \frac{T}{2\pi \mu} \left| \frac{\mathcal{E}}{\mathcal{H}} \right|^2 \quad (6.22b)$$

where  $\mathcal{E}/\mathcal{H}$  is equal to either  $E_x/H_y$  or  $E_y/H_x$ .

Setting  $\mu = \mu_0 = 4\pi \times 10^{-7}$ , substituting Equation (6.22b) in Equation (6.12b), and changing units to millivolts per kilometers for  $\mathcal{E}$ , gammas (nT) for  $\mathcal{H}$ , and kilometers for  $\mathcal{D}$ , we get finally

$$\mathcal{D} \approx \frac{1}{2\pi} (5\rho T)^{1/2} \text{ km} \quad (6.21c)$$

$$\rho \approx 0.2T \left| \frac{\mathcal{E}}{\mathcal{H}} \right|^2 \Omega \text{m} \quad (6.22c)$$

The application of magnetotelluric theory to determine the electrical conductivity within the earth was originally described by Cagniard (1953). These relations are similar, except that the penetration depth is 70% of Cagniard's value.

By measuring the amplitudes of orthogonal horizontal components of the electric and magnetic fields at the surface, for various frequencies, one can determine the variation of resistivity with depth. This is an apparent resistivity (§8.5.2).

The potential advantages in using these natural fields and currents are immediately obvious. With a relatively small electrode separation (100 to 600 m) it should be possible to determine the depth and resistivity of horizontal beds. Furthermore the depth of penetration can be very great if low frequencies are selected. In practice, however, the possibilities are limited by the nonuniformity of the subsurface and by the fact that the signal is rarely sinusoidal so that measurements of  $E$  and  $H$  for a particular value of  $T$  are not easily achieved.

The magnetotelluric survey requires detection of both magnetic and electric field components. In the telluric method it is only necessary to measure the electric field associated with the earth currents. Thus the latter technique is simpler and requires less equipment. However, the amount of information derived from tellurics is considerably less than from MT work.

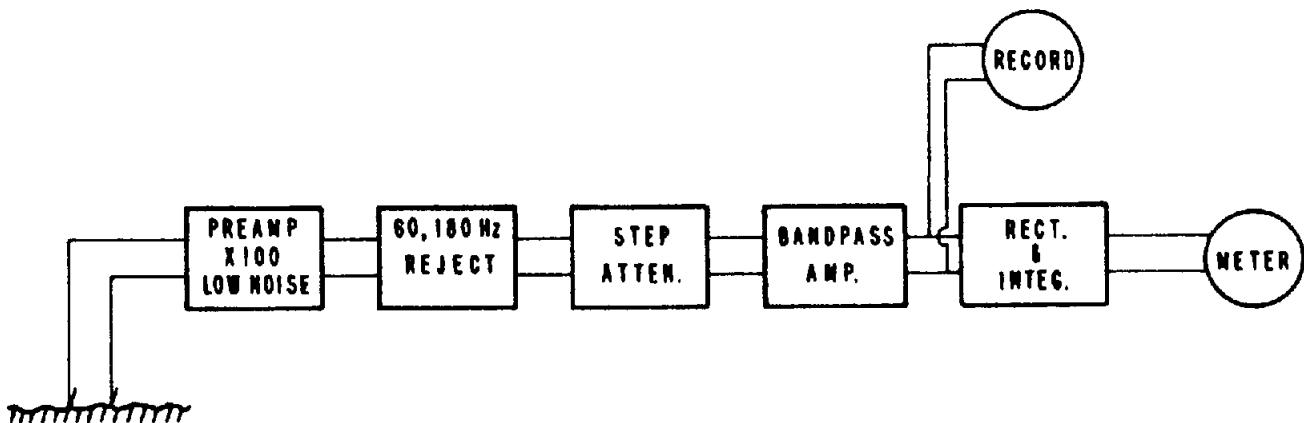


Figure 6.15. Schematic of telluric unit for audio and subaudio frequencies.

### 6.2.6. Field Equipment and Operations

(a) *Telluric current equipment.* Because the currents cannot be measured directly, it is necessary to measure the potential gradients between electrodes planted on surface or possibly in drill holes. As in SP work, nonpolarizing electrodes should be used to reduce erratic potentials at the surface contact; lead plates, which are fairly inert chemically, might be suitable. However, metal (stainless steel, brass) stakes driven into the ground are more commonly used and are quite acceptable at frequencies above 1 Hz. The electrodes are connected to an amplifier (bandwidth dc to 100 Hz, gain 2,000) that will drive a strip chart or magnetic tape recorder. If specific frequencies are of interest, various bandpass and reject filters are incorporated in the amplifier section. Also, static potentials between the electrodes, which may be several hundred millivolts, must be balanced out; this is done with a potentiometer, or capacitance input, the latter having a time constant considerably longer than the maximum period to be recorded.

Because of large variations of signal amplitude, with time, two electrode spreads are necessary, one as a base station monitor, the other for the moving station. Because the signals also vary in direction with time, the base and field stations normally have two pairs of electrodes each, laid out perpendicular to each other, say north-south and east-west, or parallel and normal to regional strike, if the latter is known. Thus continuous records of two horizontal components are obtained at each station.

With this arrangement one can – at least in theory – compare the horizontal components of electric field variations between the base and field station, with regard to frequency, phase, and amplitude. This is the method used in oil exploration applications.

A simpler field method may be used when tellurics (usually in the subaudio and audio range) is applied to mineral exploration. A single pair of electrodes is set up at each station (one fixed base, the other moving), all electrodes being in a traverse

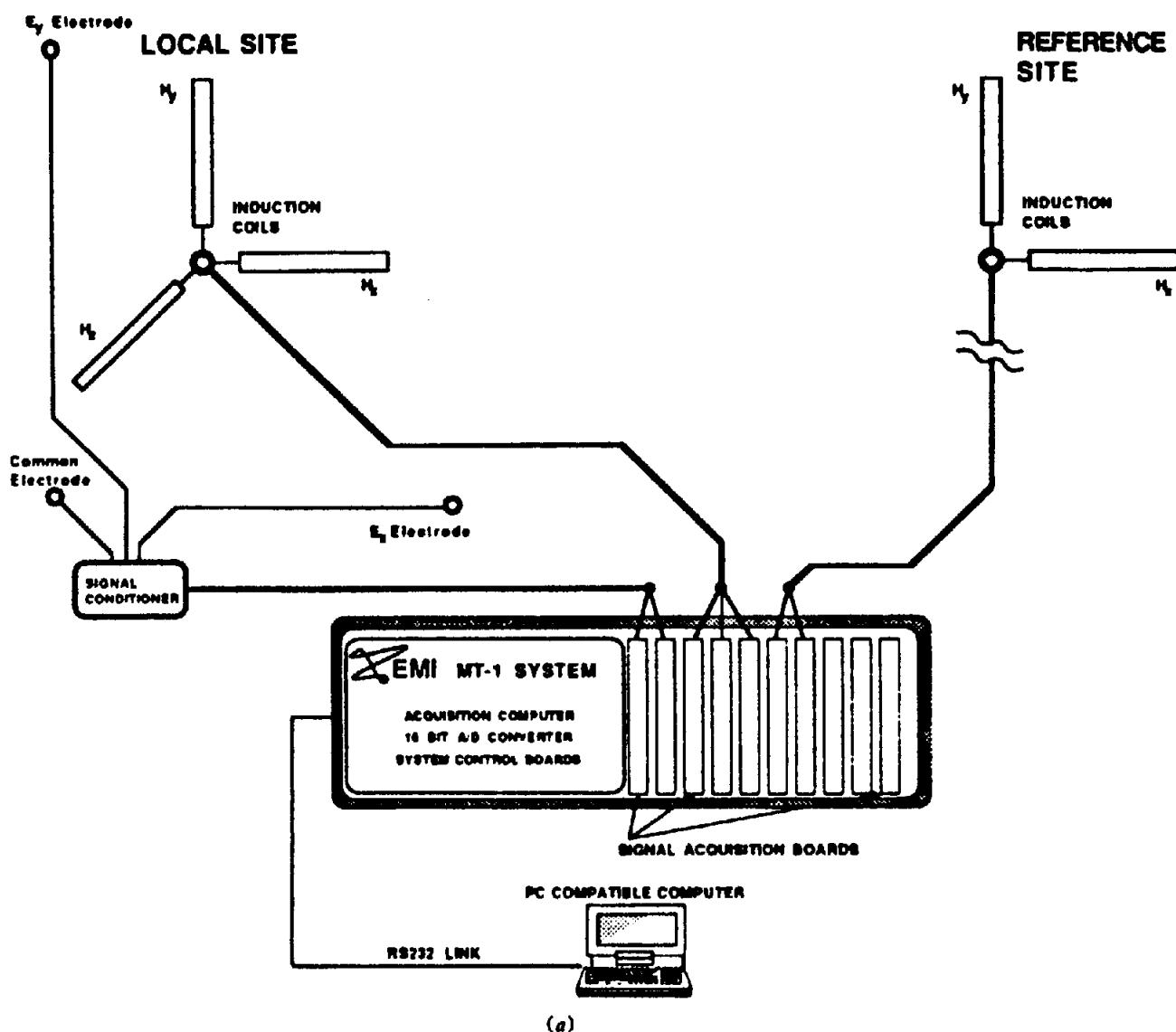
line or perpendicular to it. The signals at the two stations are integrated over the same time intervals, using an integrating circuit and meter readout in place of the recorder, and the two compared for amplitude. In addition the amplifier has a narrow passband, for example,  $(8 \pm 0.5)$  Hz.

A block diagram of the telluric unit of this type is displayed in Figure 6.15. The preamplifier gain is 100 to 200, with a bandwidth sufficient for the desired overall frequency range. The fundamental difference between this receiver and the wide band sets used for deep sounding is that the former contains several narrow-band channels to amplify, rectify, and integrate selected frequencies whose outputs are read from a meter or recorded. For signals at frequencies 8 Hz and higher, an integration time of about 30 s is sufficient. Signals are normally averaged for three or more successive measurements at each station.

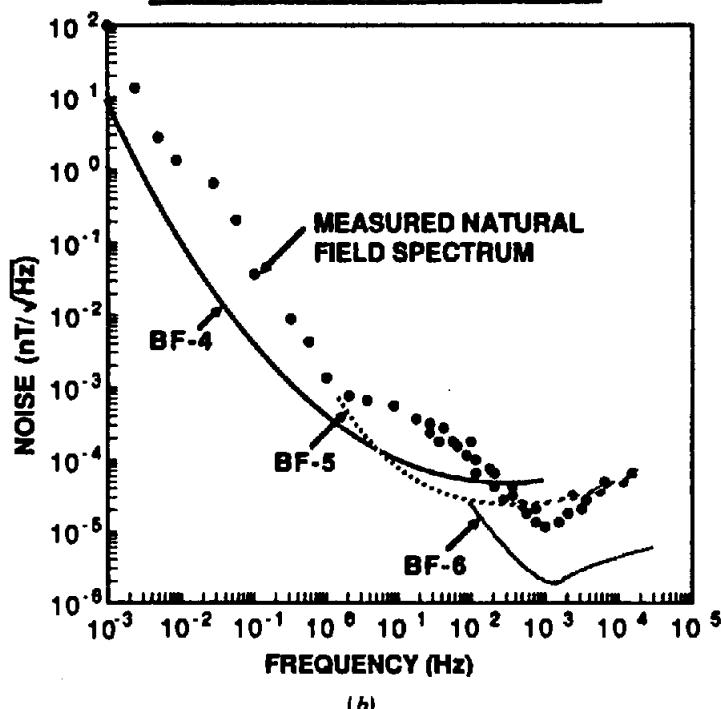
Looking again at Figures 6.11 and 6.12, it is evident that fluctuations in signal amplitude and direction are relatively small ( $\pm 50\%$ ) during a 6 to 8 h period centered about midday. (Of course when there are local thunderstorms, signal strength increases and fluctuates greatly so that work generally must be suspended.) Since we are looking for conductivity variations in the subsurface much larger than this, it was possible to dispense with the base station entirely in most surveys. This increases the speed of operations to a point where the method is faster than resistivity and induced polarization and comparable to ground electromagnetic methods.

Electrode spacings for deep sounding structural studies and oil exploration are usually 100 to 600 m. For mineral search the spread can be much smaller, 30 m or less being reasonable. In both cases the field station is moved with respect to the base, if the latter is used.

(b) *Magnetotelluric equipment.* Equipment for MT work is more complicated than for tellurics alone. The electric field detector is similar to that described in Section 6.2.6a; two components are



(a)

**FIELD NOISE TEST OF BF SENSORS.**

(b)

Figure 6.16. Magnetotelluric field equipment. (After Nichols, 1987.) (a) Schematic. (b) Frequency response of sensors.

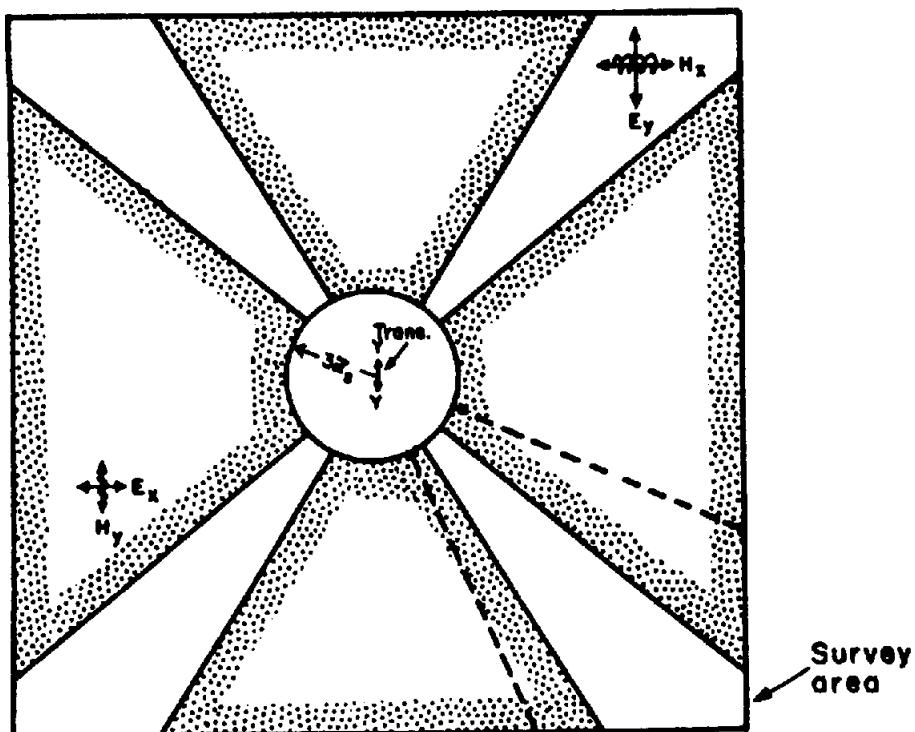


Figure 6.17. AMT survey with dipole source. Shaded areas represent areas with minimum coupling between Y-oriented transmitter (center) and  $E_x$ - $H_y$  receiver orientation; dotted lines show approximate limits of strong coupling for  $E_y$ - $H_x$  receiver directions. (After Goldstein and Strangway, 1975.)

measured at each station, but no base station is required. A schematic of an MT set is seen in Figure 6.16a; the block diagram is shown in Figure 6.21.

Although at extremely long periods it is possible to measure the magnetic field with a fluxgate magnetometer, the sensor for this purpose is normally a coil of many turns ( $\geq 50,000$ ) on a large frame, or a long solenoid wound on ferrite or other high permeability core. The coil, or several sections of it, must be able to detect the complete frequency band desired, say 0.00001 to 1 Hz. Three magnetic components are measured at each station: two horizontal, in the same directions as the telluric components, plus the vertical as an indicator of two-dimensional structures.

MT equipment designed for the frequency range 1 Hz to 10 kHz requires smaller coils with fewer turns to reduce the self-capacitance and permit resonant tuning to the frequencies selected in the band-pass sections described in Section 6.2.6a. Alternatively a coil with wider passband (1 to 1,000 Hz) has been used successfully. Because the magnetic variations are in the milligamma (pT) range, the sensitivity requirements for the magnetic unit are higher than for the telluric section.

The coil is a critical component in MT work. Generally it is necessary to install it in a shallow trench, because very slight motions create noise voltages, particularly troublesome in wooded areas. The coil actually records  $\partial H / \partial t$  rather than variations

of  $H$ ; a portable ac magnetometer would be an improvement, but no suitable instrument is presently available.

A further modification of the MT technique in the audio range (AMT) was produced with the introduction of a controlled grounded electric dipole source (Goldstein and Strangway, 1975), similar to that formerly used in the grounded Turam transmitter (§7.4.3b), although considerably shorter. This 50 ft (15 m) source produced 1.5 A at various frequencies up to 10 kHz.

To simulate normal conditions for MT work (plane wave from a remote source), various theoretical, model, and field tests were carried out. Clearly over a homogeneous area the  $|E/H|$  ratio must be reasonably constant for the plane-wave assumption to be correct [Eqs. (6.22)]. This was found to be so, provided the distance between transmitter and receiver was at least three skin depths (§6.2.3, Table 6.2) relative to the highest ground resistivity in the area, for two orthogonal orientations of the receiver sensors with respect to the transmitter.

The geometry involved is clarified in Figure 6.17, where the large square represents a uniform area to be surveyed and the inner circle radius is three skin depths. With the dipole source centered along the  $y$  axis, the shaded segments correspond to areas that may be surveyed with the receiver oriented  $E_x$ - $H_y$ . Response within the circle varies as  $1/r$  rather than  $1/r^3$  and is too large, whereas in the corners of the

square it becomes too small with the  $E_x$ - $H_y$  alignment. The corner segments are mapped successfully with the receiver oriented  $E_y$ - $H_x$  and there is some overlap of the  $E_x$ - $H_y$  data.

With these restrictions MT surveys may be performed over complex ground with good results, which may be analyzed using standard interpretation techniques.

(c) *Field operations.* Until recently most MT field work, intended for crustal sounding and oil exploration, has been done on a large scale using very low frequencies ( $\ll 1$  Hz) as mentioned elsewhere (§6.3.2, Example 2). As a result the survey work is slow (as few as one station per day) and expensive (comparable to seismic operations). In this application the traditional telluric deep sounding technique is considerably faster than MT, but of course provides much less data, generally of qualitative character.

Apart from the longer setup time for MT work, the magnetic signals generally require more time to record than the telluric field, being of lower amplitude and quality. Hermance and Thayer (1975) proposed a modification of the conventional MT technique, which they called a *telluric-magnetotelluric method*, in which telluric measurements are made simultaneously at both base and field stations, as is normal practice in low-frequency surveys ( $\leq 1$  Hz), whereas magnetic data are recorded only at the base site and only in sufficient detail, over the whole survey time, to determine the impedance tensor [Eq. (6.27a)] for the base station. This procedure results in the recording of better quality data (from the electric field and selectively from the magnetic field) and speeds up the work considerably in the process. There may be an additional advantage in recording  $H$ -field data only at the base station; because the horizontal magnetic field is more homogeneous than the  $E$  field in the vicinity of lateral discontinuities, the base station location is not as critical as in the conventional telluric method (Boissonnas and Leonardon, 1948).

Field operations at the higher frequencies are simpler, faster, and cheaper than for deep sounding. Multifrequency telluric surveys, with and without a base station, as well as MT of the same type have been carried out for base-metal exploration in various parts of Canada, Brazil, and Chile over the past 25–30 years (Slankis, 1970; Slankis, Telford and Becker, 1972; Doborzynski, 1973; Pham Van Ngoc, Boyer, and Chouteau, 1978). Usually profiles are made across geologic strike with the electrodes along the traverse at 15 or 30 m spacing; occasionally in open ground the electrode pair straddles the profile line. The situation in Chile was strangely anomalous,

because huge erratic signals at random times prevented operation without a base station. These were certainly not due to local thunderstorms, nor did they appear to be associated with seismic activity.

Obviously the simple telluric equipment of this type can be improved by the addition of another channel with coil input for AMT surveys (Strangway, Swift, and Holmer, 1973; Strangway and Koziar, 1979) with or without an artificial source. The  $H$ -field measurement slows the survey somewhat, but the extra quantitative data are well worth this disadvantage. AMT reconnaissance surveys have been carried out in a number of geothermal areas (Hoover, Frischknecht, and Tippens, 1976; Hoover, Long, and Senterfit, 1978; Sandberg and Hohmann, 1982), recording two orthogonal  $E$ - and  $H$ -field responses, with a frequency range 7.5 Hz to 18.6 kHz. The geothermal sources are resistivity lows, produced by high temperature and salinity of the water, usually surrounded by a conductive zone of larger volume. In one area where double-dipole resistivity surveys had also been performed, the AMT proved somewhat less expensive, faster, and provided better resolution. However, there were problems with natural source signals falling to low levels in the frequency range 250 to 5,000 Hz during the winter season.

### 6.2.7. Interpretation of Telluric Data

If the ground were quite homogeneous at both base and field stations, the only difference in electric field signals between the two could be a slight phase shift, if they were far enough apart. However, any nonuniform geologic structure that distorts the current flow at one station will produce an anomaly in this field. An anticline or dome of high resistivity in the basement would cause such distortion by crowding the current lines over the apex, as shown in Figure 6.18.

The effect of certain simple geological structures on the electric field can be computed theoretically. These include two-dimensional structures, such as the anticline, basement step, and horizontal cylinder, and three-dimensional shapes like the sphere and ellipsoid. Examples of the first three, solved by using conformal transformations, are given in Keller and Frischknecht (1966).

In these examples the current flow is assumed to be normal to the anomaly strike. In field situations, however, the currents tend to flow parallel to strike, that is, they flow in the good conductor rather than across it. Furthermore, because most rock structures are anisotropic, the flow will not usually be uniform in any case. The records may be further complicated by near-surface effects of overburden and erratic electrode contacts.

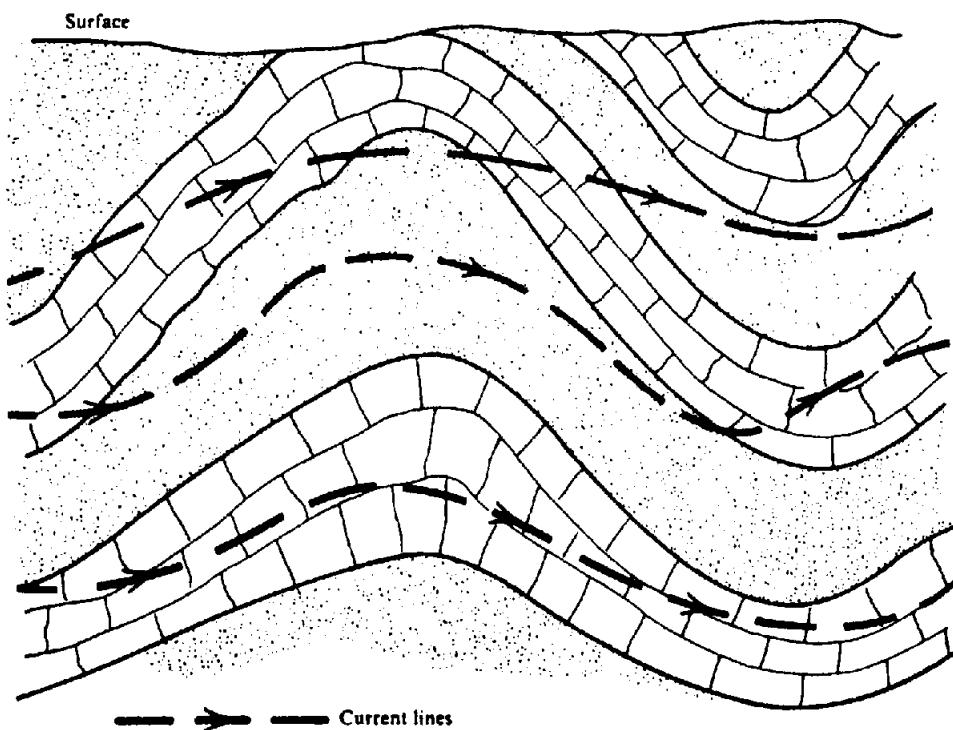


Figure 6.18. Distortion of telluric current flow by anticline. (After Boissonnas and Leonardon, 1948.)

Model profiles over a vertical dike of finite depth extent in a uniform host rock are shown in Figure 6.19a. The  $E$  field measured normal to strike is defined as the  $E_{\perp}$  or  $H$  polarization; when the electrodes are maintained parallel to strike along the same traverse, we have the  $E_{\parallel}$  or  $E$  polarization, as in Figure 6.19b. Signals are normalized and plotted on a log scale. Both diagrams have been plotted for two frequencies, 100 Hz and 10 kHz. There is only a 30% difference between the minima in the  $E_{\perp}$  examples, the lower frequency being larger; the contrast in  $E_{\parallel}$  response is considerably greater, the higher frequency being more pronounced.

Although the  $E_{\parallel}$  arrangement produces twice the anomaly of the other in this example, it does not define the thin conductor as well. Furthermore, the electrode arrangement (parallel to strike while traversing across strike) would be quite difficult except in open ground. Figure 6.19c shows the  $E_{\perp}$  response at 8 Hz over the same type of dikes dipping 60 and 30°. The profiles clearly become asymmetric over bodies with shallow dip, with a more pronounced minimum down dip and positive overshoot on the footwall side.

The model curves in Figure 6.19 may be produced by several numerical methods: finite difference, impedance network, finite element (Forsythe and Wasow 1960; Swift 1967; Silvester and Haslam 1972). These techniques are well suited to analysis of two-dimensional structures. Taking the  $y$  axis parallel to strike ( $\partial/\partial y = 0$ ) and  $z$  axis positive down-

ward, Equations (6.10) and (6.11a) become, for  $E_{\perp}$  polarization ( $E_y = \text{const.}$ ),

$$\begin{aligned}\partial E_x / \partial x - \partial E_x / \partial z &= j\omega\mu_0 H_y \\ -\partial H_y / \partial z &= \sigma E_x \\ \partial H_y / \partial x &= \sigma E_x\end{aligned}$$

which may be combined to give the scalar diffusion equation in  $H_y$ , analogous to Equation (6.15):

$$\frac{\partial^2 H_y}{\partial x^2} + \frac{\partial^2 H_y}{\partial z^2} - j\omega\mu_0\sigma H_y = 0 \quad (6.23a)$$

The boundary conditions at the air-ground interface come from the facts that  $\sigma = 0$  in air and displacement currents are negligible. Thus  $J_z|_{z=0} = 0$  and  $E_x|_{z=0} = \partial H_y / \partial x|_{z=0} = 0$ , which means that  $H_y$  is invariant along the ground surface. Thus if we measure  $E_x$  and  $H_y$  simultaneously at two stations, Equation (6.22b) gives us  $\rho_i = T|E_x/H_y|^2/2\pi\mu_0$ , where  $i = 1, 2$ ; from this we find that

$$\rho_1/\rho_2 = |E_{x_1}/E_{x_2}|^2 \quad (6.24)$$

Hence for this orientation we obtain relative values of  $\rho_a$  without measuring  $H$  at all.

Similarly, for  $E_{\parallel}$  polarization we have

$$\frac{\partial^2 E_y}{\partial x^2} + \frac{\partial^2 E_y}{\partial z^2} - j\omega\mu_0\sigma E_y = 0 \quad (6.23b)$$

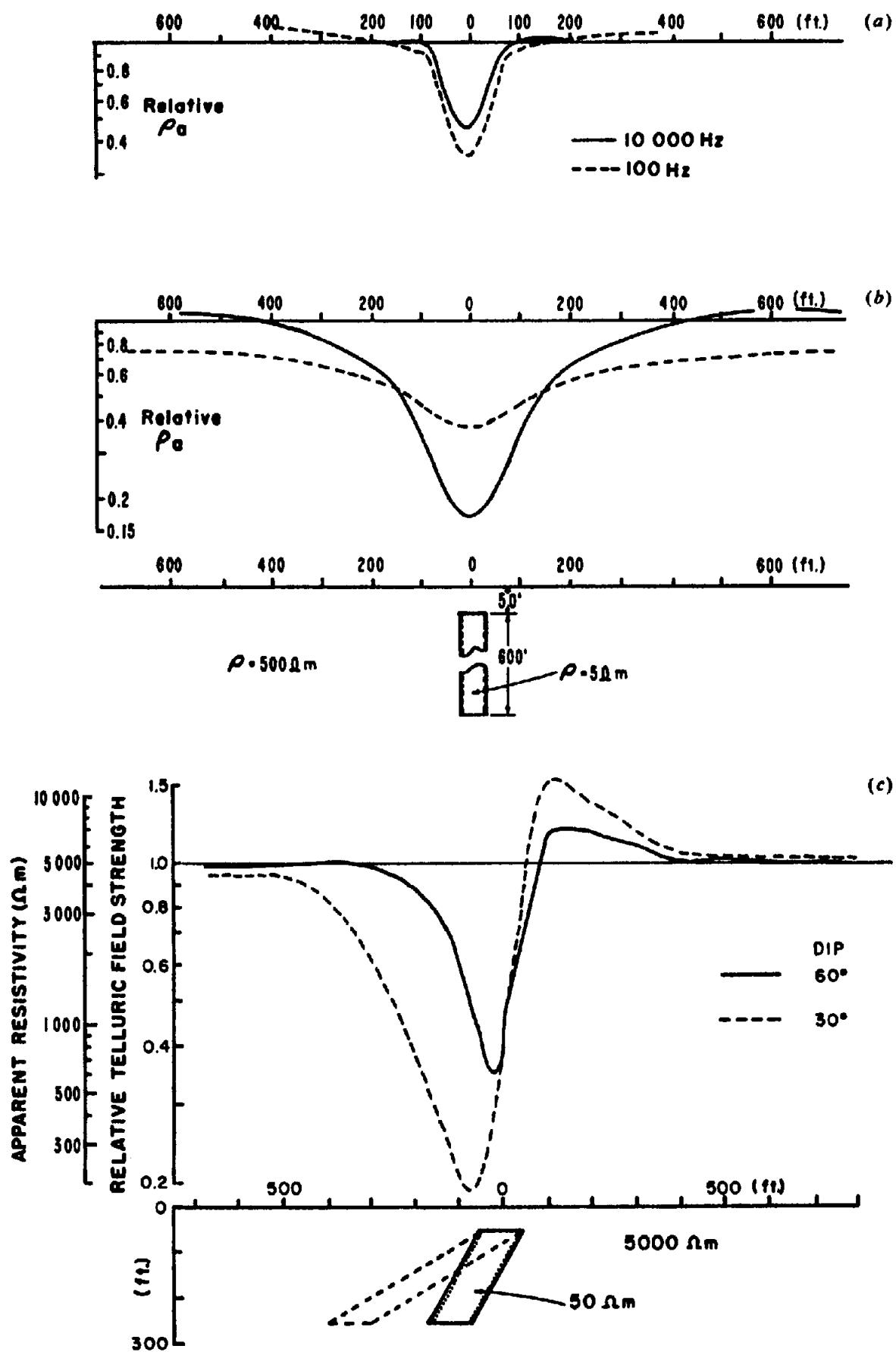


Figure 6.19. Theoretical resistivity profiles over vertical dike [(a) and (b)] and dipping dike (c). (a)  $E_{\perp}$  polarization. (b)  $E_{\parallel}$  polarization. (c)  $E_{\perp}$  polarization.

The boundary conditions are not as simple for  $E$  polarization, because  $H_x$ ,  $H_z$ , and  $E_y$  are all continuous across the air-ground interface. Consequently, the horizontal  $H$  field is not constant everywhere above ground in the vicinity of a lateral inhomogeneity. Thus it is necessary to consider the air layer as well as the subsurface structure in attempting to get numerical solutions for  $E$  polarization. This requires an upward extension of the model cross section to the air-ionosphere interface, which has no lateral changes in conductivity. Then  $H_z = 0$  and  $E_y$  is constant, because  $\partial E_y / \partial x = -j\omega\mu_0 H_z$ .

Equations (6.23) may be solved numerically using finite differences by dividing the geologic section into a nonuniform mesh whose spacing is small in the vicinity of conductivity discontinuities – zones where the MT or telluric fields change rapidly – and increases with distance from these interfaces until the mesh sections are undisturbed in homogeneous isotropic host rock. Using appropriate boundary conditions, values of  $H_y$  and  $E_y$  at interior mesh points are computed iteratively, using overrelaxation factors (Wachspress, 1966) to calculate their real and imaginary components by successive sweeps through the mesh, with values adjusted after each pass to bring the expressions closer to zero. The impedance network numerical version introduces voltages and currents, in a five-element (four impedances  $Z$ , one admittance  $Y$ ) circuit, as analogs to the parameters in Equations (6.23). Apart from using a matrix solution rather than the iterative procedure, the subsequent operation is similar to the other techniques and has certain advantages. In the finite element numerical technique, the section mesh is divided into triangles of various sizes, which permit better matching of irregular boundaries, a particular advantage when computing complex shapes.

The flexibility of the numerical methods thus allows solutions for a wide range of geometrical sections. Because only a limited number of models can be solved analytically, the technique is a powerful tool for interpretation in tellurics and MT; it is used frequently in resistivity and IP as well.

Equations (6.19) tell us that in homogeneous ground the electric field leads the magnetic component in phase by  $45^\circ$ . The presence of anomalous structures will change this value. It may be shown that the conductor geometry has more effect on the phase than on amplitude response in certain cases. Figure 6.20 illustrates this feature. The amplitude response at 10 kHz over the block model is negligible because the skin depth in the host material is only about 25% of the depth to its top. From Figure 6.20b we see that the phase shift varies from about  $1^\circ$  at 10 Hz to a maximum of roughly  $7.5^\circ$  at 1,000 Hz and then decreases at higher frequencies. Figure 6.20c

emphasizes the phase sensitivity still more clearly by showing the sharp dependence on skin depth in the host rock. Thus it would be useful to measure phase as well as amplitude in MT work. Although this might be difficult with natural source fields, it would be an attractive test with a controlled source. The phase measurement might also help to explain sudden large phase shifts – up to  $180^\circ$  as reported by Slankis (1970) and others – when crossing highly conductive zones during  $E_\perp$  surveys.

Although developed and employed before MT, the telluric method has not been used to any extent in petroleum prospecting in America, in spite of considerable application and some successes in Western Europe, North Africa, and the USSR, nor has much been done with the relatively speedy and simple audiofrequency telluric technique in mineral prospecting, although it has produced some promising and interesting results.

### 6.2.8. Interpretation of Magnetotelluric Data

(a) General. The end result of a conventional low-frequency MT survey is a paper and/or magnetic tape record of two electric and three magnetic component field variations, similar to the examples shown in Figure 6.10. To determine the general type of structure (1-D, 2-D, anisotropic, and so on) plus the impedance  $Z$  and resistivity  $\rho$  values associated with it requires that we perform a complicated analysis of the raw data. The processing involves power-spectrum analysis and various forms of filtering.

A typical up-to-date instrumentation system for MT data analysis is shown in the block diagram of Figure 6.21. This represents a single acquisition board of the 10 illustrated in Figure 6.16. Input from one of the sensors passes by one of two routes through the various blocks to be filtered, amplified, and deposited in the sample-hold amplifier. The low-frequency path receives signal data at 0.001 to 100 Hz, the other from 100 to 20,000 Hz, with heterodyne demodulation to reduce higher frequencies to 100 Hz. The multiplexer-A/D converter digitizes the signal, after which the digital computer develops the power spectra by standard methods, followed by analysis to determine the MT parameters. Several MT systems are now available equipped with a computer, eliminating the necessity for storing raw data; these are evaluated and may even be interpreted in the field.

Various other information, such as station and sensor locations and calibration data, is also fed into the computer. The analysis, of course, becomes more complex with the type of structure that has been

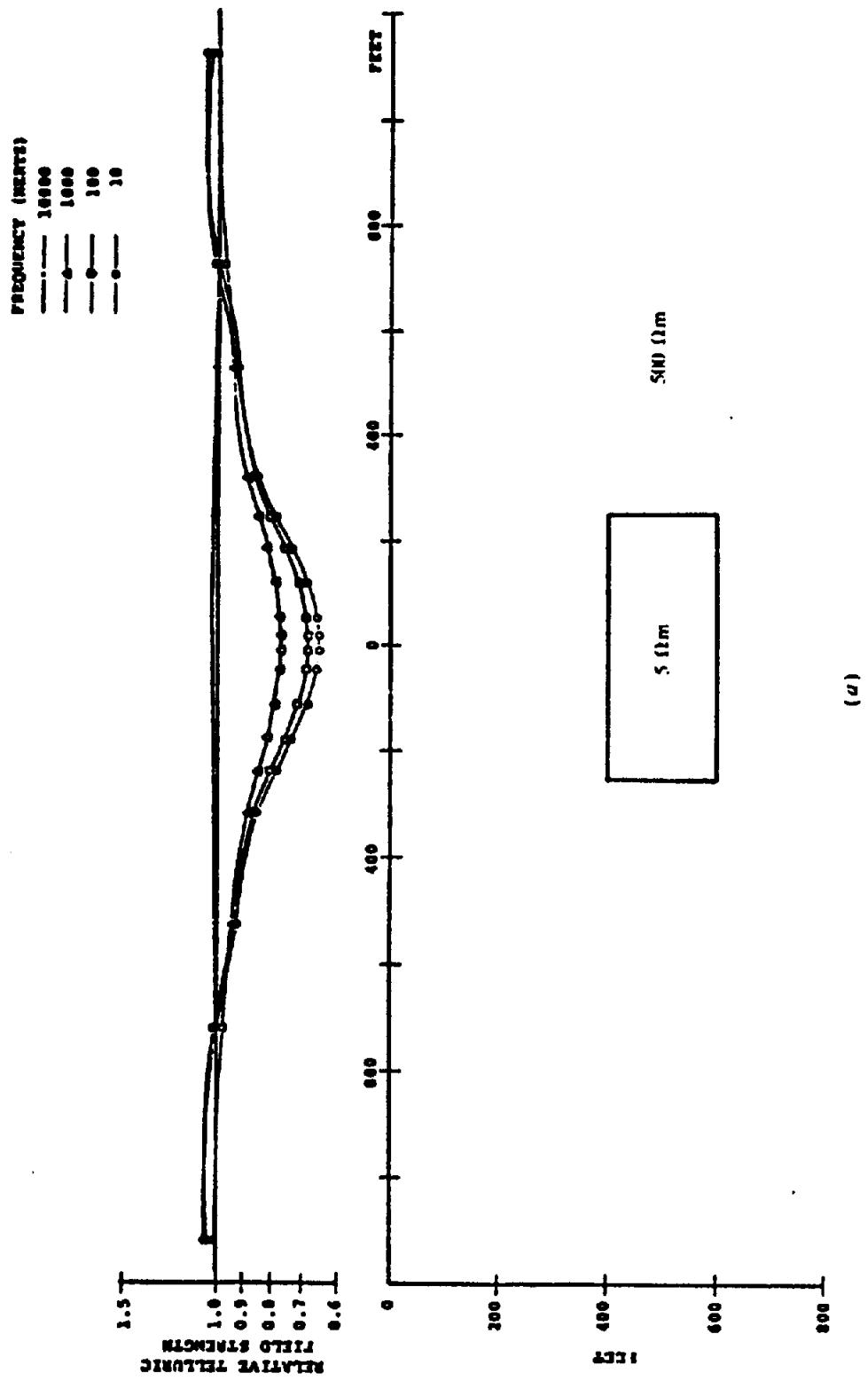


Figure 6.20. Theoretical amplitude and phase curves for a deeply buried slab. (a) Amplitude profiles.

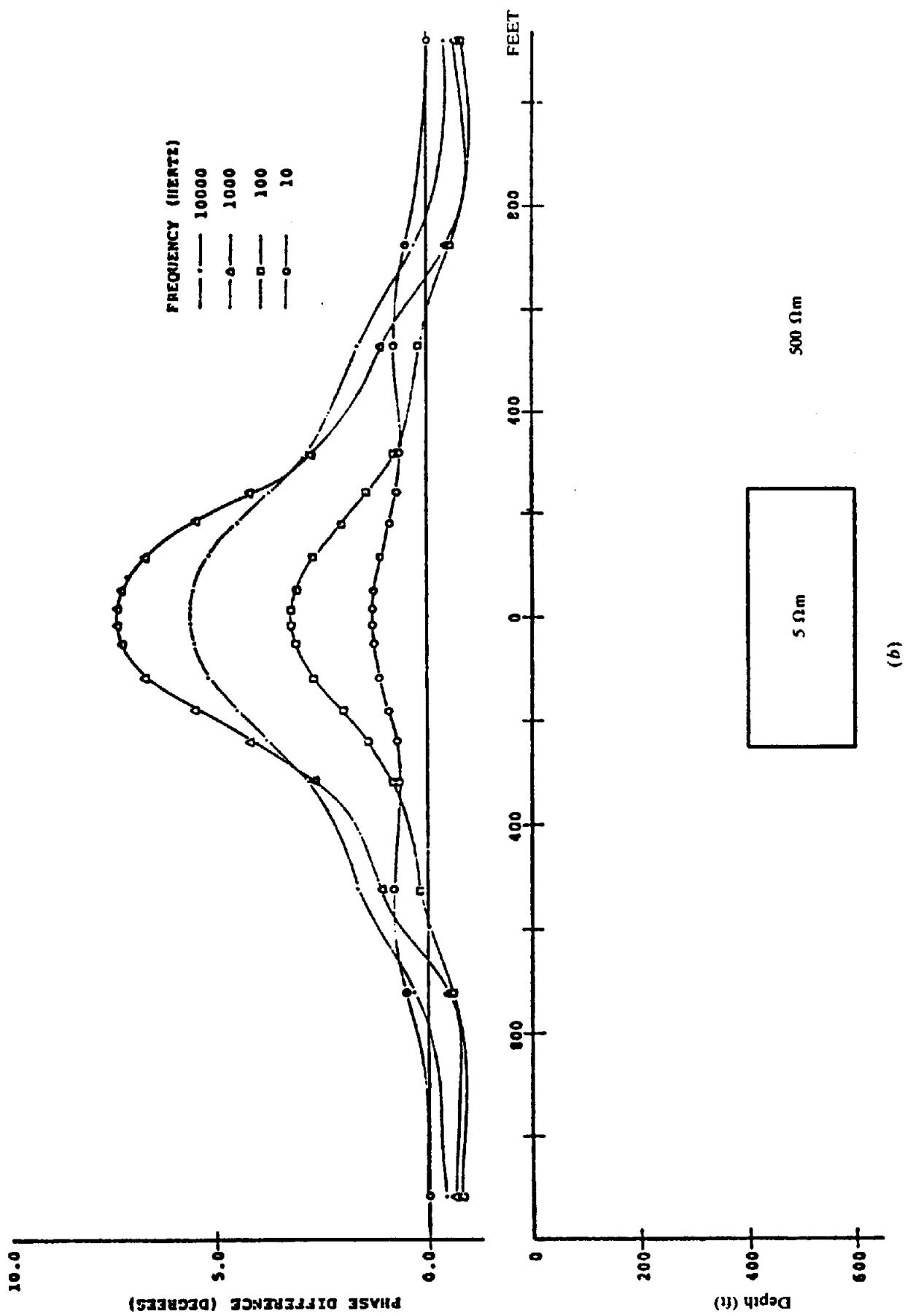


Figure 6.20. (Continued) (b) Phase difference profiles.

(b)

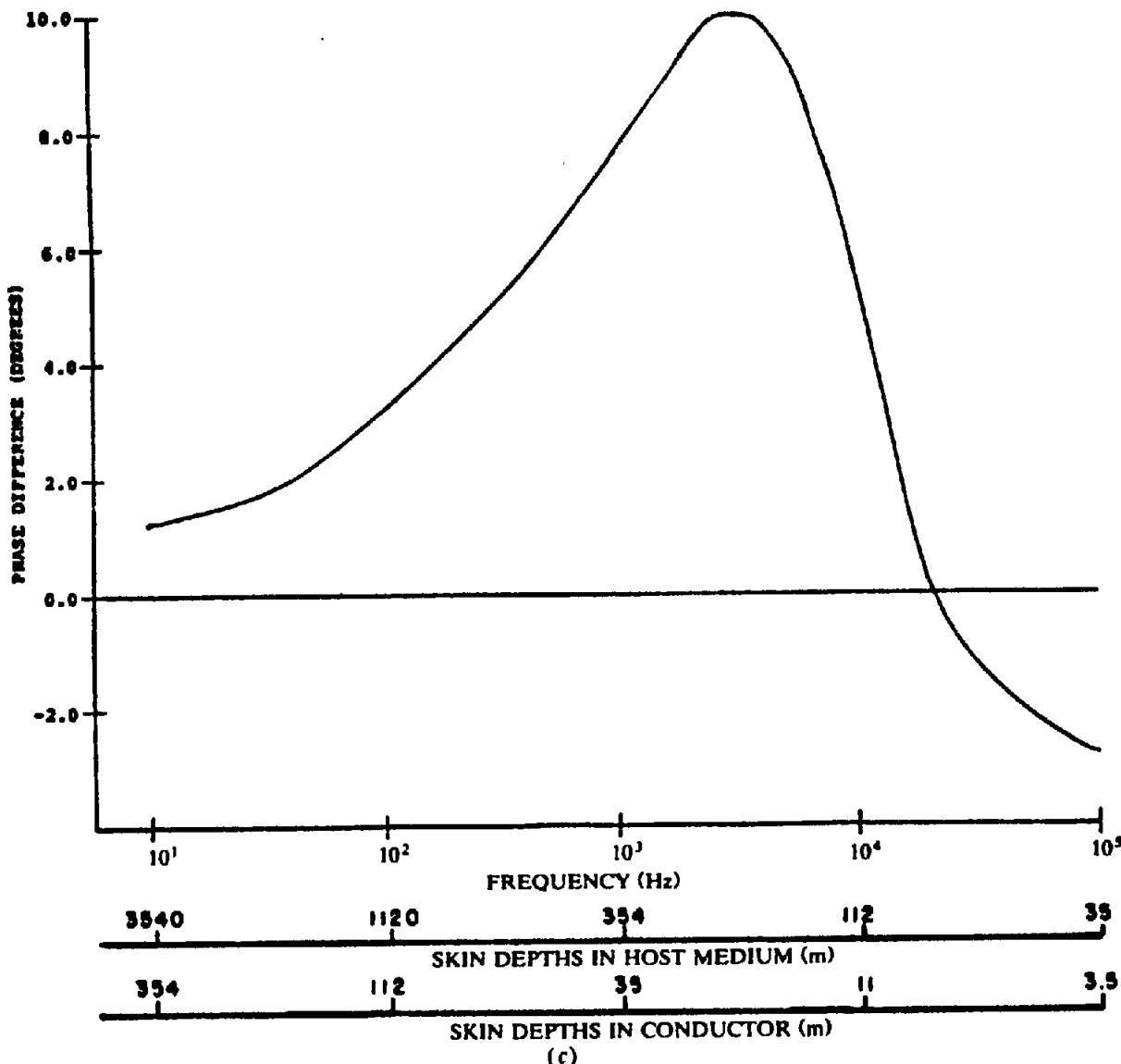


Figure 6.20. (Continued) (c) Phase difference versus frequency.

surveyed and should be done step by step, particularly where there are several routines available between input and solution (Hermance, 1973). It is also advisable to monitor the original data along the way.

(b) One-dimensional structures. The MT method should perform best over uniform, isotropic, more or less horizontal layers in which the resistivity varies only with depth. An expression for apparent resistivity measured above two beds, such as a top layer over basement with resistivities  $\rho_1$  and  $\rho_2$  and thicknesses  $z$  and  $\infty$ , respectively, was given by Cagniard (1953). Somewhat modified, this relation becomes

$$\frac{\rho_a}{\rho_1} = \frac{\alpha^2 e^{2\gamma} + 2\alpha e^\gamma \cos \gamma + 1}{\alpha^2 e^{2\gamma} - 2\alpha e^\gamma \cos \gamma + 1} \quad (6.25a)$$

where

$$\alpha = (\rho_2 + \rho_1)/(\rho_2 - \rho_1),$$

$$\gamma = 2z(\omega\mu_0/2\rho_1)^{1/2} \approx 0.004z(f/\rho_1)^{1/2} = 2z/z,$$

$f$  is the frequency, and  $z$ , is the skin depth in the upper bed. The phase angle, representing the lag of  $H$  with respect to  $E$ , is

$$\tan \phi = \frac{\alpha^2 e^{2\gamma} - 2\alpha e^\gamma \sin \gamma - 1}{\alpha^2 e^{2\gamma} + 2\alpha e^\gamma \sin \gamma - 1} \quad (6.25b)$$

Master curves in  $\rho_a$  and  $\phi$ , developed from Equations (6.25) for a two-layer earth, are shown in Figure 6.22. The phase curves are not much used, except for verification of results from the resistivity data; this is mainly due to the difficulties in acquiring reliable phase measurements. This is unfortunate because MT phase information is quite useful in resistivity, just as it is in EM and IP work. It should be easier to obtain with controlled-source equipment.

The original master curves of this type, which may be found in Cagniard's paper and elsewhere,

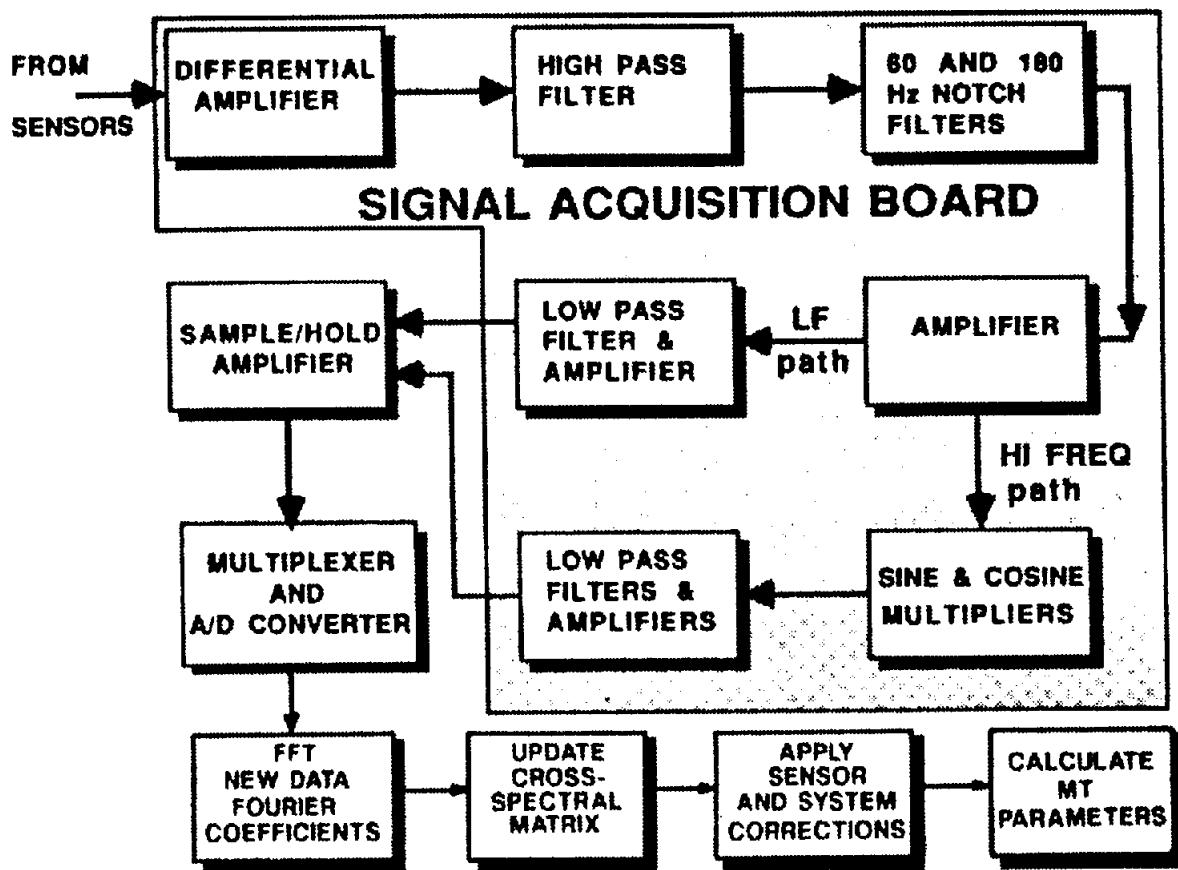


Figure 6.21. Block diagram of a wide-band MT system with computerized data processing. (After Nichols, 1987.)

were plotted with  $(\rho_a/\rho_1)$  or  $\phi$  as ordinate and  $\sqrt{T}$  ( $T$  = signal period) as abscissa, both on log scales, for  $\rho_1 = 1 \Omega\text{m}$ ,  $z = 1 \text{ km}$ , and a large range of values of  $\rho_2$ .

The master curves in Figure 6.22 are more suitable for AMT and certain EM survey work (§7.7.6b), because the horizontal-axis log scale is frequency (Hz) corresponding to an expansion of the left-hand portion of the  $\sqrt{T}$  scale in the originals, whereas  $\rho_1$  is  $100 \Omega\text{m}$  and  $z$  only  $10 \text{ m}$ . However, they perform the same function, for shallow rather than deep sounding.

To use either version of such curves, it is necessary to plot field results in the form  $\rho_a$  versus  $f$  or  $\sqrt{T}$  on the same scale log paper as the master curve and match the plot to one of the theoretical curves of the master, maintaining the ordinate and baseline axes parallel. Sometimes it may be necessary to interpolate between two of the latter.

When the superposition has been made, we obtain a value of  $\rho_a$  on the field plot overlying or corresponding to  $\rho_a = 1 \Omega\text{m}$  on the Cagniard curve or  $\rho_a = 100 \Omega\text{m}$  on the curves of Figure 6.22, whichever are being used. This gives the value of  $\rho_1$  for the survey, whereas  $\rho_2/\rho_1$  on the master yields the value of  $\rho_2$  for the bottom layer. Finally, the thickness of the top layer may be calculated. From

Equation (6.25a) we see that when  $\rho_a = \rho_1$ ,  $\cos \gamma = 0$ , and  $\gamma = \pi/2$ . Thus we can write

$$z = 250\gamma(\rho_1/f)^{1/2} \approx 400(\rho_1/f)^{1/2}$$

where  $f$  is the frequency at which  $\gamma = \pi/2$  (marked with a vertical bar at  $154 \text{ kHz}$  in Fig. 6.22). For the Cagniard curve it is necessary to substitute  $T$  for  $1/f$  in the above relation and use the corresponding abscissa point  $A$  marked on the master curves.

Theoretically it is possible to extend the 1-D problem to  $n$  beds. The procedure is to start from the bottom interface and work upward, one layer at a time, using a recursion formula given by

$$(\rho_a/\rho)^{1/2} e^{-j\theta} = (1 + \lambda e^{2az})/(1 - \lambda e^{2az}) \quad (6.26)$$

where

$$\begin{aligned} \lambda &= \left\{ (\rho_a/\rho)^{1/2} e^{-j\theta} - 1 \right\} e^{-2az} / \\ &\quad \left\{ (\rho_a/\rho)^{1/2} e^{-j\theta} + 1 \right\}, \\ \alpha &= (\omega\mu_0\sigma/2)^{1/2}(1 - j), \end{aligned}$$

and  $\theta = \phi - \pi/4$ .

The parameter  $\lambda$  is constant for any bed. Also the boundary conditions (§6.2.4) for  $E$  and  $H$  across each interface must hold. Consequently the value of

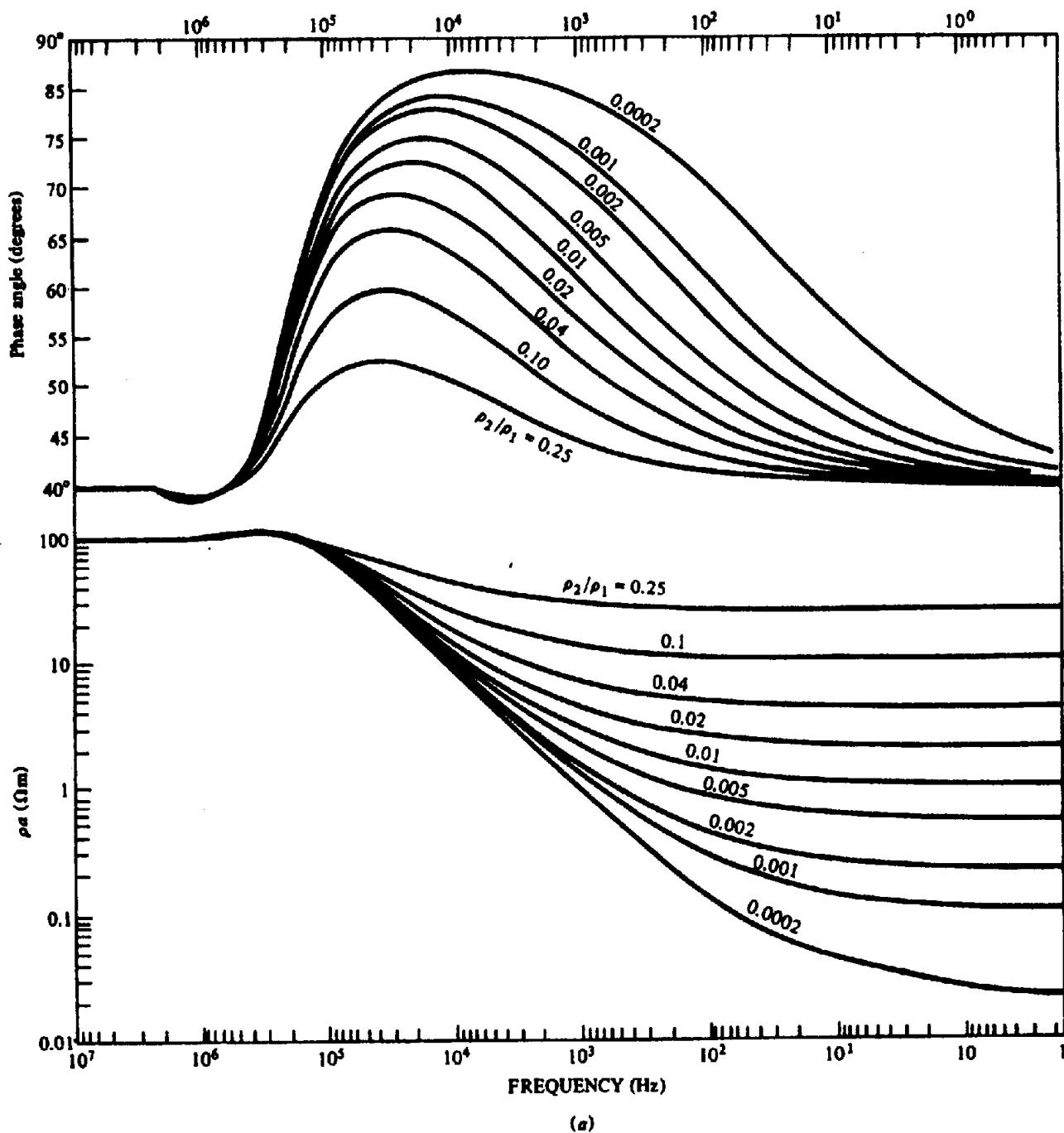


Figure 6.22. Master curves for MT sounding over two-layer earth.  $\rho_1 = 100 \Omega\text{m}$  and  $z_1 = 10 \text{ m}$ . (a)  $\rho_2 < \rho_1$ .

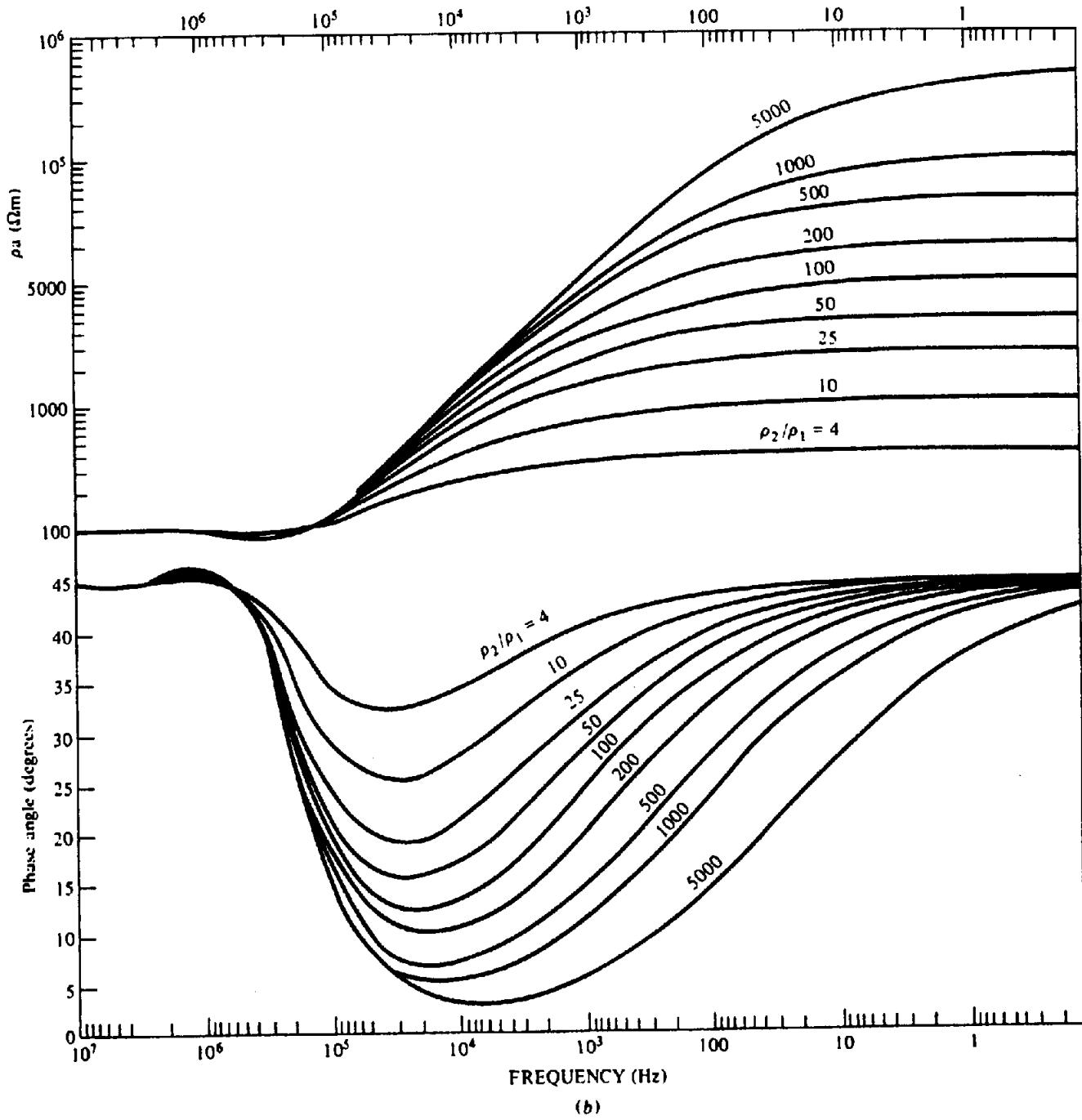
$\rho_a$  at the bottom of a layer must be the same as that at the top of the layer below it. Figure 6.23 shows the geometry and parameters for the multilayer section, together with an example of a typical MT sounding curve, which appears to have a relatively shallow resistive bed, an intermediate conductive section, and a resistive basement.

Thus the successive  $\rho_a$  and  $\phi$  values may be found from Equation (6.26) by equating the real and imaginary parts at each interface, beginning at the top of the basement, where  $\phi = \pi/4$  ( $\theta_n = 0$ ) and  $\rho_{a_n} = \rho_n$ . Proceeding upward to the next and shallower interfaces, it is necessary to establish values for  $\rho_{a(n-1)}$ ,  $\theta_{n-1}$ , and so forth, using data from the

sounding curve. Generally this is best done by an inversion process.

Practically the preparation of master curves for more than three beds is a formidable task, just as in resistivity soundings (§8.6.4), because of the enormous range of possible  $z$  and  $\rho$  combinations. Three-layer master curves, however, are available (Srivastava, 1967). The matching procedure is analogous to that used in resistivity interpretation, although not as highly developed.

(c) Two-dimensional structures. In dealing with tabular geometries in Section 6.2.7, whether of one or more layers, we found that the horizontal electric

Figure 6.22. (Continued) (b)  $\rho_2 > \rho_1$ .

and magnetic field components were laterally invariant ( $\partial/\partial x = \partial/\partial y = 0$ ) and the vertical components  $E_z$  and  $H_z$  were zero [Eqs. (6.21) and (6.22)]. If we define an impedance  $Z = E_x/H_y$ , it is clear that  $Z$  is complex (because of the phase difference between  $E$  and  $H$ ), that it has units of ohms, and that in tabular structures it is independent of the measurement direction, that is, it may also be written  $Z = E_y/H_x$  or whatever.

In the presence of 2- or 3-D structures (faults, veins, etc.), however, the impedance  $Z$  is not invariant, but depends on the distance of the point of measurement from the structure and the angles between the strike and the coordinate axes. Thus,  $E_x$

varies not only with  $H_y$  but is affected by the  $H_x$  component as well; the same holds for  $E_y$ . Therefore, the scalar impedance  $Z$  for the 1-D structures becomes a tensor impedance for 2-D structures; the tensor relation can be written

$$\left. \begin{aligned} E_x &= Z_{xx}H_x + Z_{xy}H_y \\ E_y &= Z_{yx}H_x + Z_{yy}H_y \end{aligned} \right\} \quad (6.27a)$$

The simple impedance  $Z$  is changed to four tensor components  $Z_{ij}$ . To determine these, the first step is to record two horizontal  $E$  and  $H$  compo-

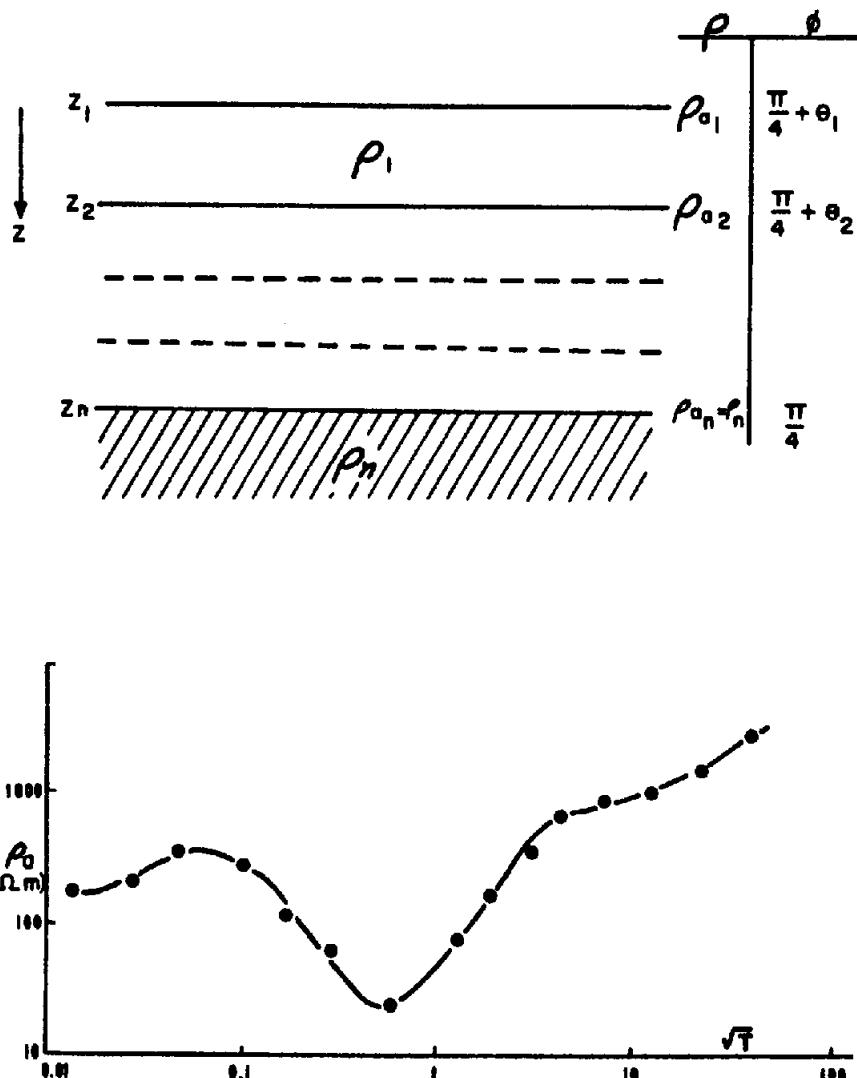


Figure 6.23. Magnetotelluric sounding over multiple beds.

nents. (This is normally done in MT surveys, but obviously it is not necessary when surveying a structure known to be one-dimensional. However this operation is still not sufficient to solve Equations (6.27a) because we have four unknown quantities.

A common procedure for processing the recorded data to get the tensor impedance components is: (a) manual editing to discard noisy data; (b) Fourier transformation of the five field components to the frequency domain to get in-phase and quadrature values for each; (c) cross-multiplication of each  $E_x$  and  $E_y$  equation by  $H_x$  and  $H_y$  and filtering (smoothing) the results, hence obtaining estimates of the four tensor components in Equation (6.27a) which are averages over frequency bands. Two assumptions are made here: The impedances change little with frequency and the  $H$  components are independent; both are reasonably correct.

Impedance estimates obtained by such an averaging process, however, are frequently biased by noise.

A marked improvement in this regard was recently obtained by using a remote source, located a few kilometers from the survey station, which records reference fields  $H_{rx}$ ,  $H_{ry}$  simultaneously (Gamble, Goubau, and Clarke, 1979; Labson, et al., 1985). Although these measurements also contain noise, it is not generally correlated with the  $H$  and  $E$  fields at the MT station: if we mix the data from the latter with the remote station data, the  $Z_{ij}$  values ( $i, j = x, y$ ) emerge almost free of autospectral noise bias.

Alternative procedures have been used in calculating the tensor elements, such as replacing the Fourier transforms by autocorrelation and cross-correlation spectra, further bandpass filtering of the original MT time series, and optimization of the estimates when large amounts of data are available.

The next step in the analysis is to establish the geometry and electrical characteristics of the structure, first its strike, then the impedances and resistivities parallel and normal to strike. Because initially it

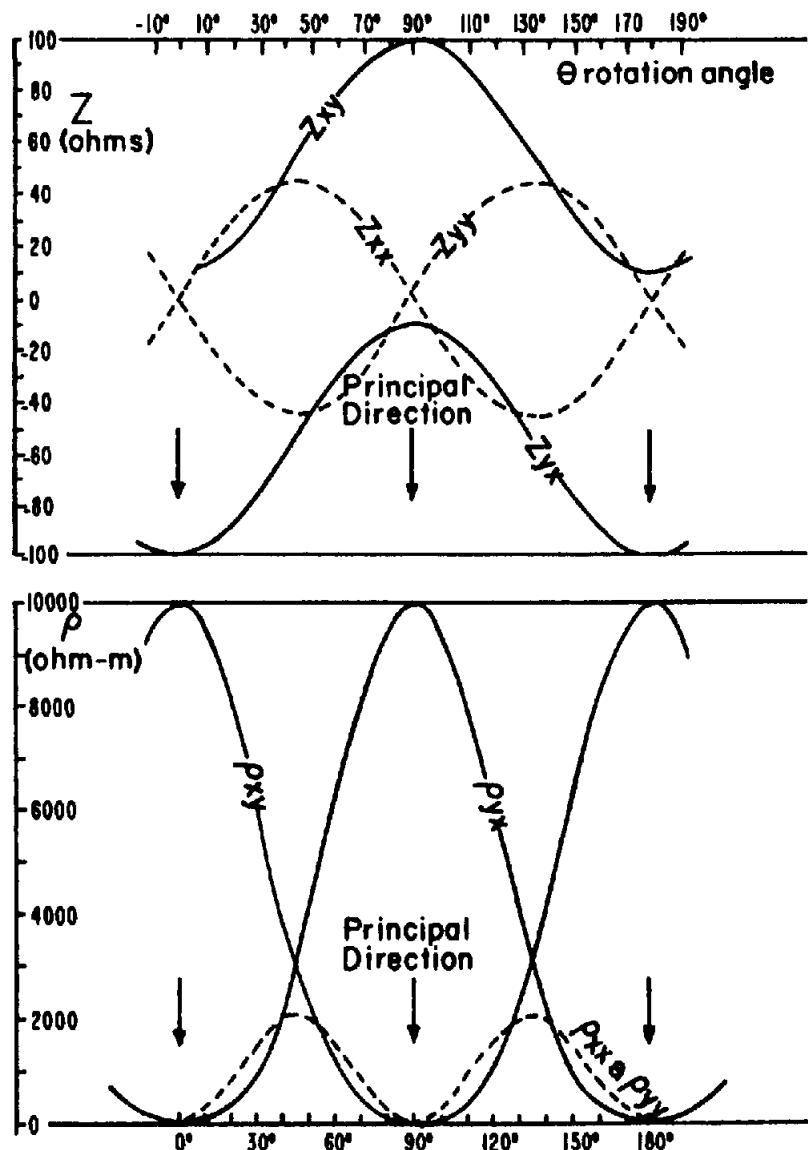


Figure 6.24. Rotation of axes for two-dimensional model with  $Z'_{xy} = 100 \Omega$  and  $Z'_{yx} = 10 \Omega$ .

is unlikely that we would know the azimuth of either the source wave or the structure, the survey axes will normally be at an arbitrary angle to both. The series of measurements produces data to fit Equations (6.27a). By an analytical rotation of the survey axes we now align the components in Equations (6.27a) parallel and normal to the structure. This procedure, known as *location of the principal axes*, produces relations similar to Equation (6.24) by decoupling the four tensor impedances so that Equations (6.27a) become

$$\left. \begin{aligned} E'_x &= Z'_{xy} H'_y \\ E'_y &= Z'_{yx} H'_x \end{aligned} \right\} \quad (6.27b)$$

where the primes define the axes parallel and perpendicular to strike and the *principal impedances*  $Z'_{xy}$ ,

$Z'_{yx}$  are related to the tensor impedances as follows:

$$\left. \begin{aligned} Z_{xx} &= \frac{1}{2}(Z'_{xy} + Z'_{yx}) \sin 2\theta \\ Z_{yy} &= -\frac{1}{2}(Z'_{xy} + Z'_{yx}) \sin 2\theta \end{aligned} \right\} \quad (6.27c)$$

$$\left. \begin{aligned} Z_{xy} &= Z'_{xy} - (Z'_{xy} + Z'_{yx}) \sin^2 \theta \\ Z_{yx} &= Z'_{yx} - (Z'_{xy} + Z'_{yx}) \sin^2 \theta \end{aligned} \right\} \quad (6.27d)$$

where  $\theta$  is the clockwise rotation angle between the survey and the principal axes. Clearly we have

$$\left. \begin{aligned} Z_{xx} + Z_{yy} &= 0 \\ Z_{xy} - Z_{yx} &= Z'_{xy} - Z'_{yx} \\ &= \text{constant for all } \theta \end{aligned} \right\} \quad (6.27e)$$

During a rotation of  $180^\circ$ , the off-diagonal elements  $Z_{xy}$  and  $Z_{yx}$  each go through two maxima

(0°, 180°) and one minimum (90°). The diagonal element  $Z_{xx}$  has two minima (-45°, 135°) with a maximum at 45°, whereas  $Z_{yy}$  is the exact converse. When the axes of measurement are parallel to and normal to strike,  $Z_{xx} = Z_{yy} = 0$ . The condition that  $Z_{xx} = -Z_{yy}$  [Eq. (6.27e)] has been shown to hold also for a stack of anisotropic horizontal beds (Vozoff, 1972). Sims and Bostick (1969) have reported that Equation (6.27e) is also valid for 3-D structures; however, the analysis is very difficult for such features.

Figure 6.24 illustrates the axial rotation plot for a 2-D model having principal impedances  $Z'_{xy} = 100 \Omega$  and  $Z'_{yx} = 10 \Omega$ . One of the principal directions is obviously  $\theta = 90^\circ$ , where  $Z_{xx} = Z_{yy} = 0$  and  $Z_{xy}, Z_{yx}$  are minima; the other is normal to this, at  $\theta = 0^\circ$ . In a practical case, using best estimates of the impedances from generally noisy data, the values of  $\theta$  will not be exactly 0° and 90°, that is,  $(Z_{xx} + Z_{yy}) \neq 0$ , nor will  $(Z_{xy} - Z_{yx})$  be constant over the range of  $\theta$ . A measure of this discrepancy, called the *skewness* or *skew ratio*, is

$$S = |Z_{xx} + Z_{yy}| / |Z_{xy} - Z_{yx}|$$

$S$  should be minimum (theoretically  $S = 0$ ). Deviations from zero indicate the reliability of the results. A large skew ratio may also be an indication that the structure is not truly 2-D, at least not in the frequency range chosen for the  $Z$  estimates.

Another parameter that serves as a check on the proper rotation angle  $\theta$  is called the *tipper* (see the summary at the end of this section, also §6.3.2, Example 3).

We may now determine the apparent resistivities in the principal directions from the corresponding impedances; thus,

$$\rho'_{xy} = 0.2T|E_x/H_y|^2 = 0.2T|Z'_{xy}|^2 (\Omega\text{m}) \quad (6.28a)$$

$$\rho'_{yx} = 0.2T|E_y/H_x|^2 = 0.2T|Z'_{yx}|^2 (\Omega\text{m}) \quad (6.28b)$$

These  $\rho$  values are scalars,  $\rho'_{xy}$  being the resistivity for  $H$  polarization and  $\rho'_{yx}$  for  $E$  polarization.

We can summarize the preceding discussion of the interpretation of telluric and MT data over various structures as follows, keeping in mind Equations (6.21) and (6.27).

*1-D structures.* If the ground is isotropic, orientation problems are eliminated in the survey work (because  $\partial/\partial x = \partial/\partial y = 0$ ) and the parameters of the subsurface bed(s) may be determined either by telluric or MT soundings carried out over a range of frequencies in any horizontal direction. Tensor impedances are reduced to scalars and  $Z_{xx} = Z_{yy} = 0$  and  $Z_{xy} = -Z_{yx}$ .

If the beds are randomly anisotropic, the survey results resemble those for a 2-D structure to some extent and analysis involves tensor impedances  $Z_{ij}$ ; thus, the direction in which  $E$  and  $H$  components are measured is significant. However,  $Z_{xx} = -Z_{yy}$ ,  $H_z = 0$ , and  $Z_{xy} \neq Z_{yx}$ .

*2-D structures.* Lateral discontinuities produce the same effect as random anisotropy, and, in general,  $\rho_a$  varies with measurement direction as well as frequency. If the structure is known reasonably well, the survey (telluric or MT) may be performed on traverses normal to strike. This allows measurements to be made either in the  $H$  polarization ( $E_\perp$ ) or  $E$  polarization ( $E_\parallel$ ) orientation, the first being more practical. Only scalar impedances need be considered, regardless of the source-field direction, because  $E$  and  $H$  fields may be resolved into components normal and parallel to strike ( $\partial/\partial y = 0$ ). This setup allows us to find resistivities using Equations (6.28) and then solve Equations (6.23) by the various numerical methods outlined in Section 6.2.7a.

If the strike is not known, the survey of necessity is carried out at an arbitrary orientation. Five components must be measured, namely,  $E_x, E_y, H_x, H_y$ , and  $H_z$ , to provide data for estimating the four tensor impedances  $Z_{ij}$  in Equation (6.27a). It is then possible to determine the strike by an analytic rotation of the survey axes (this could be done physically, but only with great effort) until one of them coincides more or less with a principal direction normal to or parallel to strike. We can then use Equations (6.28) to calculate the scalar principal impedances and resistivities. If noisy data and/or complex structure obscure the precise orientation of the principal axes, we may indicate the deviation by means of the skew ratio mentioned earlier. A second check is provided by a transfer tensor relation between vertical and horizontal magnetic components. The *tipper*,  $T$ , defined by the relation

$$H_z(\omega) = T_x(\omega)H_x(\omega) + T_y(\omega)H_y(\omega) \quad (6.29)$$

is a complex function of frequency (Vozoff, 1972; Labson et al., 1985) related to the ratios  $H_z/H_x$  and  $H_z/H_y$  for 2-D structures (Fig. 6.28). It is also a good indicator of noise sources (Labson et al., 1985, p. 657).

*3-D structures.* Apart from features with pronounced symmetry like the sphere and ellipsoid, no entirely successful interpretation procedures have been developed to date.  $E$ -polarization end effects on a slab of limited strike length are particularly troublesome; apparently the 2-D approximations for this model with  $H$  polarization are more reliable.

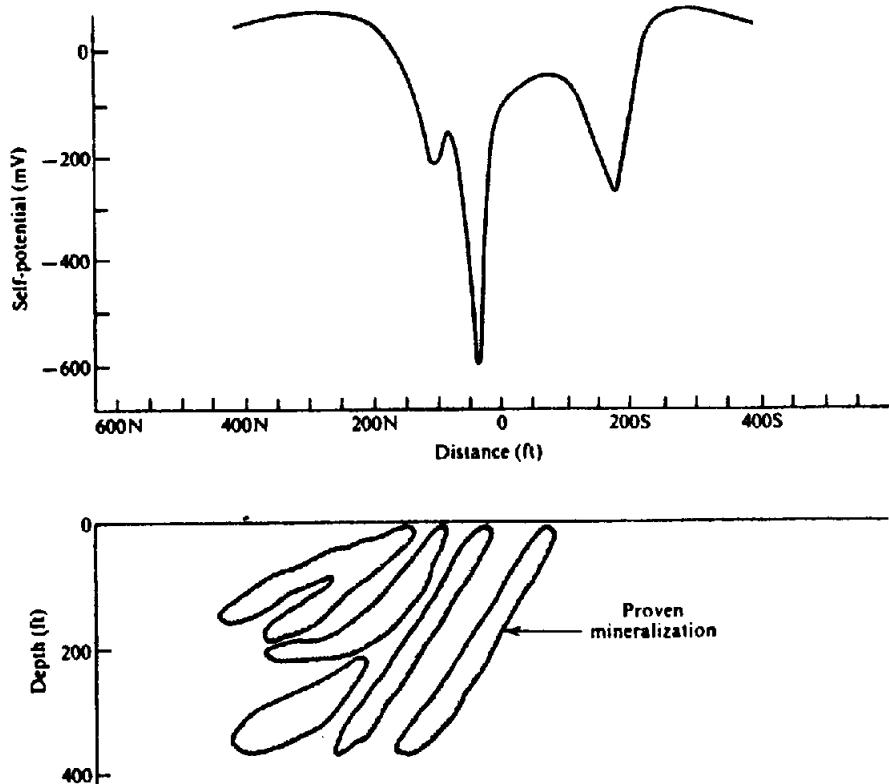


Figure 6.25. SP profile across massive sulfides, Senneterre Area, Quebec.

### 6.3. FIELD EXAMPLES

#### 6.3.1. Self-Potential

Figure 6.25 shows an SP profile obtained over a massive sulfide body in the Senneterre area of Quebec. The mineralization is pyrite and pyrrhotite, averaging about 30% for the entire zone, 40 to 70% in the more strongly mineralized sections. The host rocks are metasedimentary breccias and tuffs, interbedded with lava flows. Twenty-five diamond drill holes outline the sulfides in some detail.

Although the maximum SP anomaly is very large (600 mV), it is also surprisingly narrow, appearing to reflect one of the sulfide zones, rather than a combined effect. North of this peak the two shallow sulfides produce very little surface potential, whereas the one to the south is not detected at all. The negative peak at 200S coinciding with a low swampy surface is not explained.

#### 6.3.2. Tellurics and Magnetotellurics

1. Results of an 8 Hz telluric survey made over a massive sulfide body in northern New Brunswick are shown in Figure 6.26. The zone, located in diorite-rhyolite host rock, has been well outlined by diamond drilling. It subcrops below the overburden to the south and plunges gently to a depth of 400 ft at the north end.

Contours are apparent resistivity values determined from relative telluric field strength measurements as in Equation (6.24). The sulfide zone is clearly indicated, with the lowest resistivities at the south end. The extension of the contours beyond the southern extremity of the sulfide outline is due to further shallow mineralization between lines  $T_3$  and  $T_4$ . The telluric anomaly extends to line 1930S in the northern part of the mineralized zone, which is over 200 ft deep at this point.

2. An example of magnetotelluric deep sounding in a relatively simple geologic area is given by Reddy and Rankin (1971), who carried out measurements in the period range 1 to 1,000 s (1 to 0.001 Hz) at 16 stations in Alberta. Their results are summarized in Figure 6.27, which shows a geologic section for a southwest-northeast line through Edmonton extending from the Rocky Mountains for 350 miles to the Saskatchewan border. Sediments in the central Alberta plain vary in thickness from 4,000 ft in the east to more than 15,000 ft where they abut the deep-rooted, deformed Precambrian mountain sediments in the southwest. The basement is composed of crystalline rocks of Precambrian age.

The magnetotelluric fields are controlled by the strike of the contacts of these plains sediments with the other two sections, both of which have relatively high resistivities. As a result the currents at depth in the more conductive sedimentary basin are polarized northwest-southeast to produce a pronounced

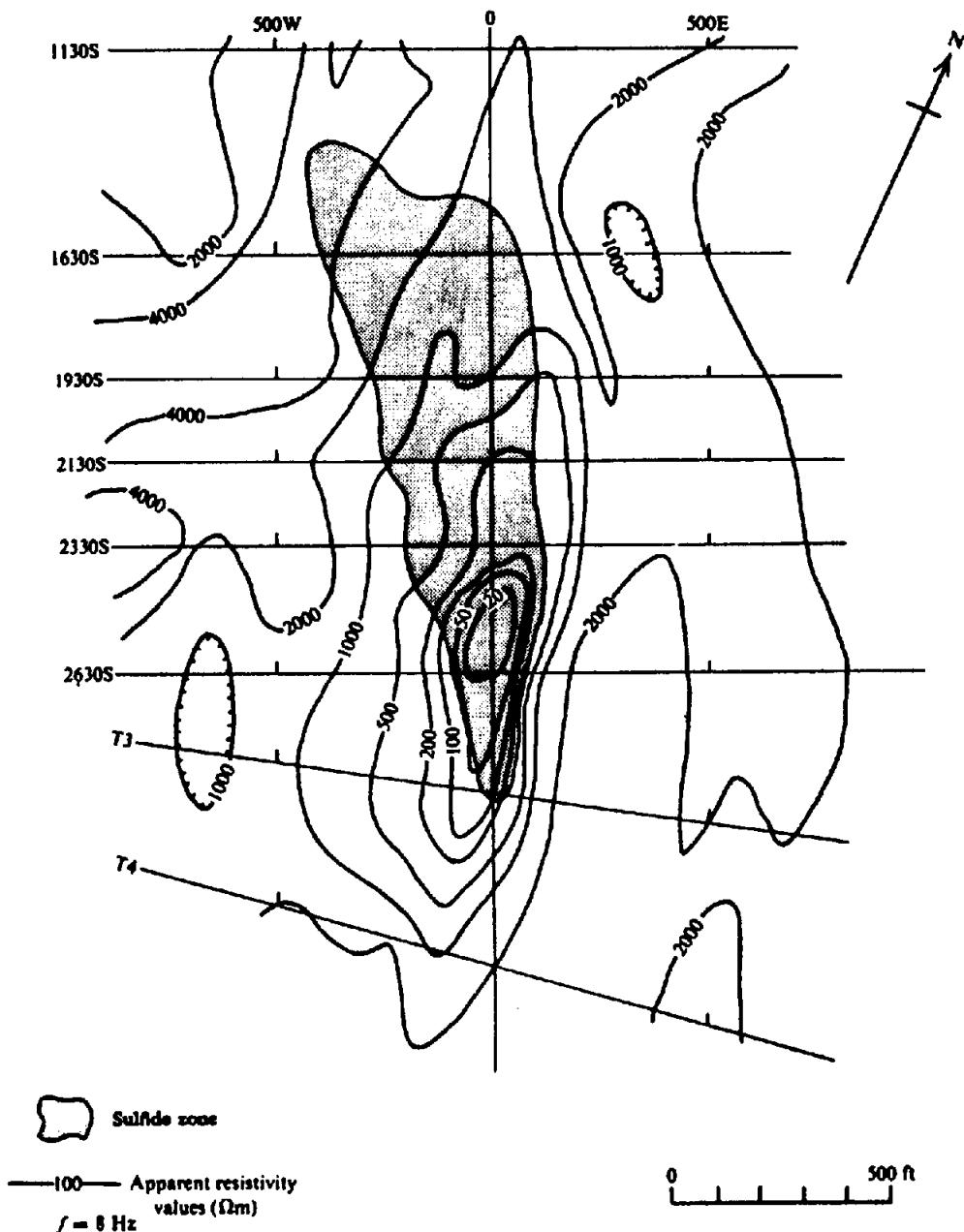


Figure 6.26. Telluric data from 8 Hz survey over massive sulfides, New Brunswick.

anisotropy in the apparent resistivities, that is, the maximum values are generally parallel to strike for the longer period signals. The fact that there is no apparent anisotropy at short periods (10 s or so), on the other hand, would indicate that the basin sediments are reasonably homogeneous.

Figure 6.27 shows a set of smoothed curves of  $\rho_a$  versus period from the 16 stations, taken along the major axis of anisotropy, as well as theoretical curves for a two-layer earth model in which the thickness ( $z_1$ ) and resistivity ( $\rho_1$ ) of the top layer are varied. Clearly both parameters are variable in the field area. It is possible to produce more complex three- and four-layer sections for individual stations that match the measured results very well, although these models are not unique.

Although the results are satisfactory in the example of Figure 6.27, in general the agreement between field results and simple layer theory has not been particularly good. Discrepancies are often caused by anisotropic ground and lateral discontinuities in conductivity. The theory assumes vertical currents to be negligible. In fact large vertical current components extending over distances of more than 130 km have been reported in the literature.

3. Figure 6.28 shows an 8 Hz magnetotelluric profile over a contact between Precambrian metasediments and Paleozoic shales, sandstones, limestones, and dolomites. The area is about 20 miles west of Ottawa, north of the Ottawa river. The apparent resistivities in Figure 6.28a are obtained from the ratio  $E_{\perp}/H_{\parallel}$ , that is, the telluric field was measured

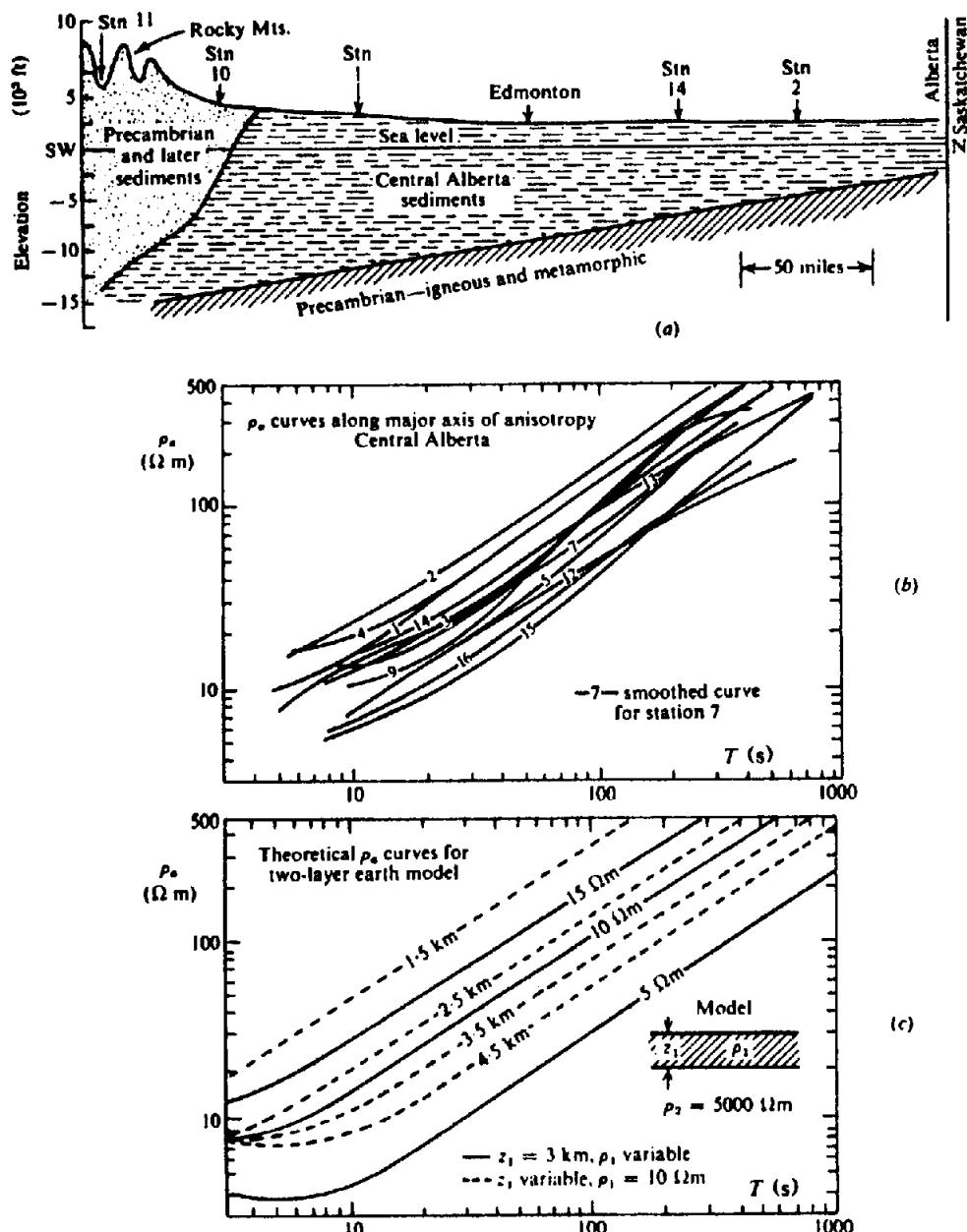


Figure 6.27. Magnetotelluric deep soundings in Central Alberta. (After Reddy and Rankin, 1971.) (a) Geological section. (b)  $\rho_a$  curves along major axis of anisotropy. (c) Theoretical  $\rho_a$  curves for two-layer earth.

roughly normal to the contact, the magnetic field parallel to it. The agreement between the measured profiles and the theoretical ones, originally derived from a vertical contact of great depth with resistivity contrast of 100, is fair. The actual geologic profile is not so simple because the Paleozoic sediments (the low resistivity section) are only 600 ft thick as illustrated in Figure 6.28f. The MT profile, however, reflects the contact clearly.

Measurement of the telluric field at several azimuth angles other than  $E_{\perp}$  showed that the apparent resistivity became progressively more anisotropic as the contact was approached from the north and that the minimum  $\rho_a$  was parallel to strike (Fig. 6.28b).

The Precambrian-Paleozoic contact is indicated on all profiles except that in Figure 6.28c, where the  $H_{\parallel}$  field theoretically should remain invariant. The field components change gradually across the contact, suggesting a zone of variable resistivity between the resistive igneous and conductive sedimentary rocks; in fact there is an outcrop of Precambrian age about 0.5 mile south of the main contact. The model tipper profile in Figure 6.28e is a reasonable match with the vertical contact model, considering the shallow character of the actual section.

The next two examples show several pseudodepth plots from subaudio and audiofrequency MT surveys, a type of display popular for IP data (§9.5.1). It may also be employed in resistivity, tellurics, MT,

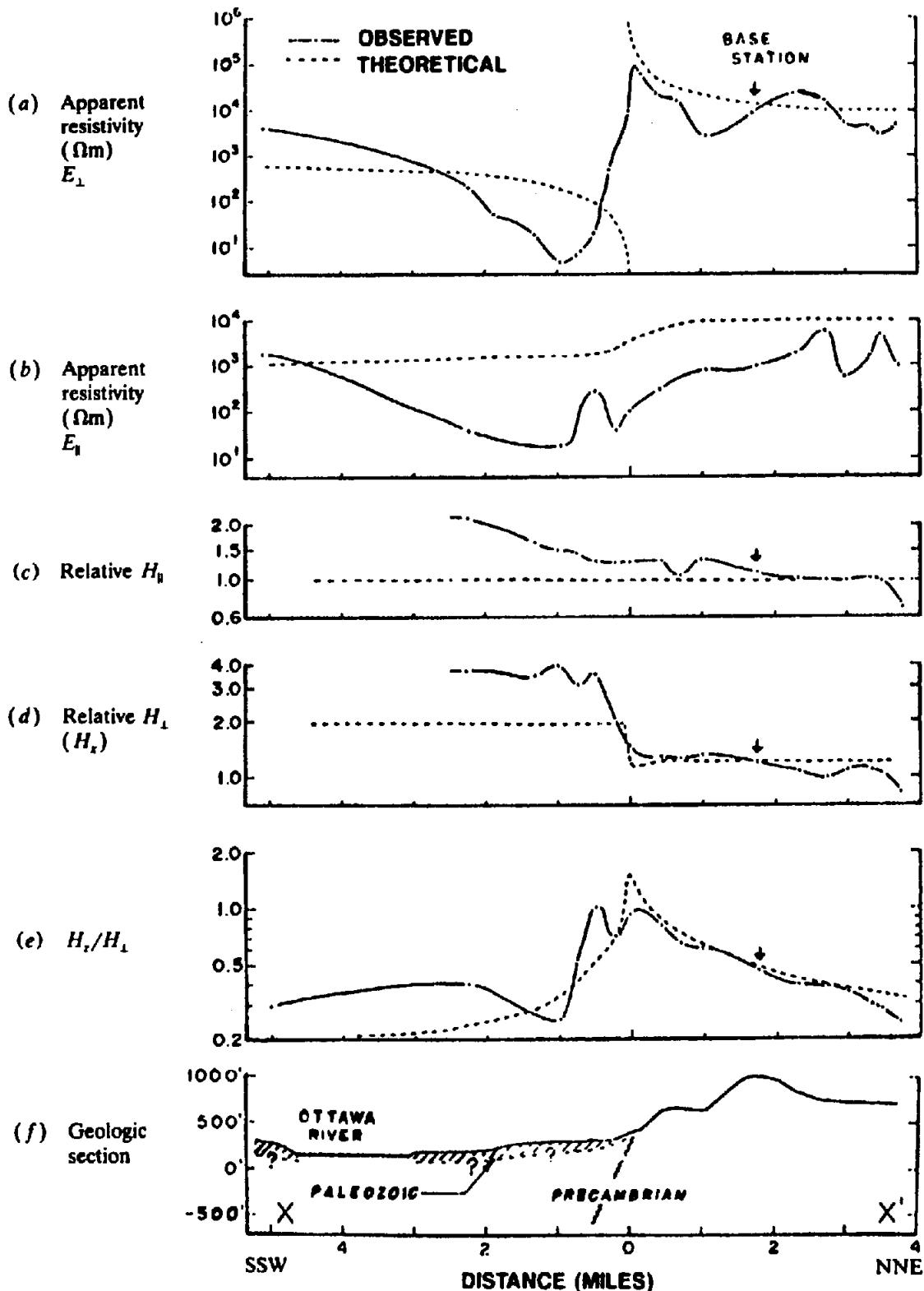


Figure 6.28. MT profiles over Precambrian-Paleozoic contact, near Ottawa. (a)  $\rho_a$  based on  $E_\perp$ . (b)  $\rho_a$  based on  $E_\parallel$ . (c) Relative  $H_\parallel$ . (d) Relative  $H_\perp$ . (e)  $H_z/H_\perp$ . (f) Geologic section.

and certain types of EM work. The only difference between the MT and IP plots is in the vertical scale; this is logarithmic in period or frequency for MT, linear in distance for IP. Thus the depth of penetration in the first is related to skin depth, in the second primarily to electrode spacing. Readings for the pro-

file and contour plots in Figures 6.29 and 6.30 are reckoned at the midpoints of the electrodes.

4. Figure 6.29 shows a pseudodepth MT plot over a conductive zone bounded by two outcropping faults, ( $F_1$  and  $F_2$ ), seen in the geologic section below. This illustration is taken from a survey car-

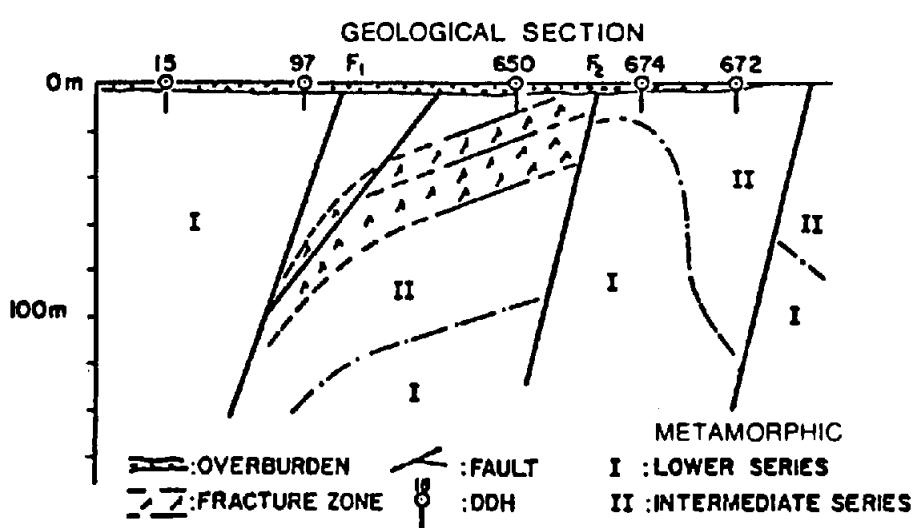
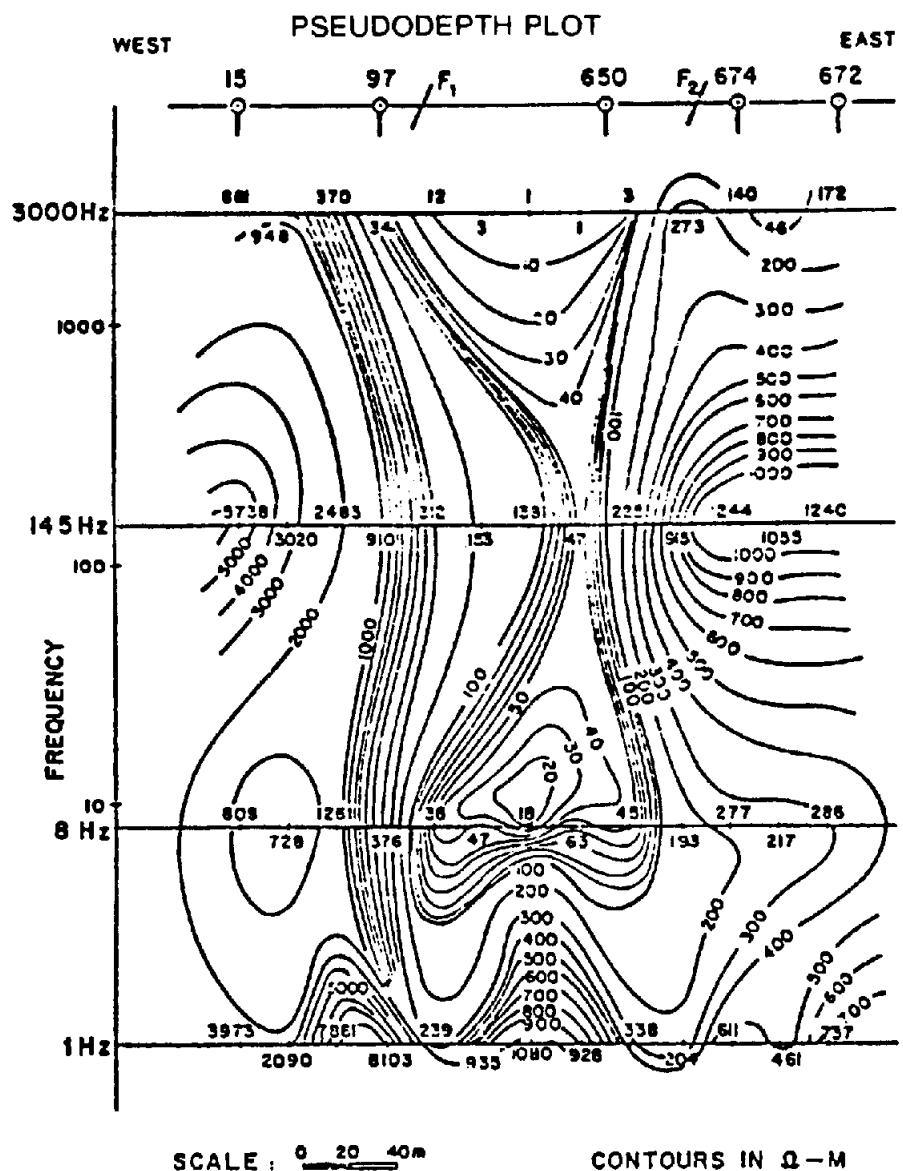
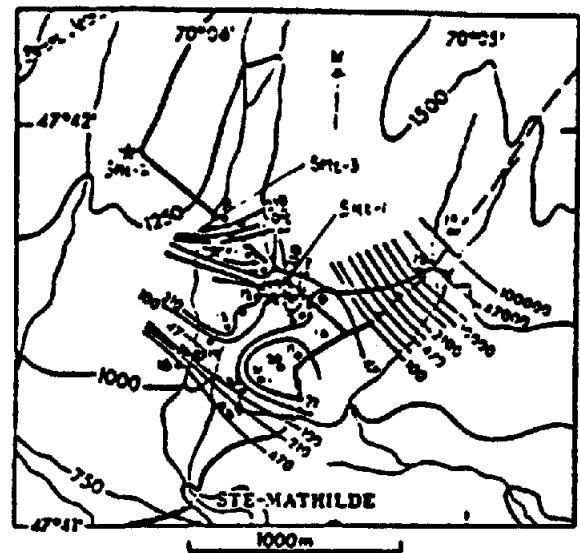


Figure 6.29. Magnetotelluric pseudodepth plot for conductive fracture zone, Northern Saskatchewan.



(a)

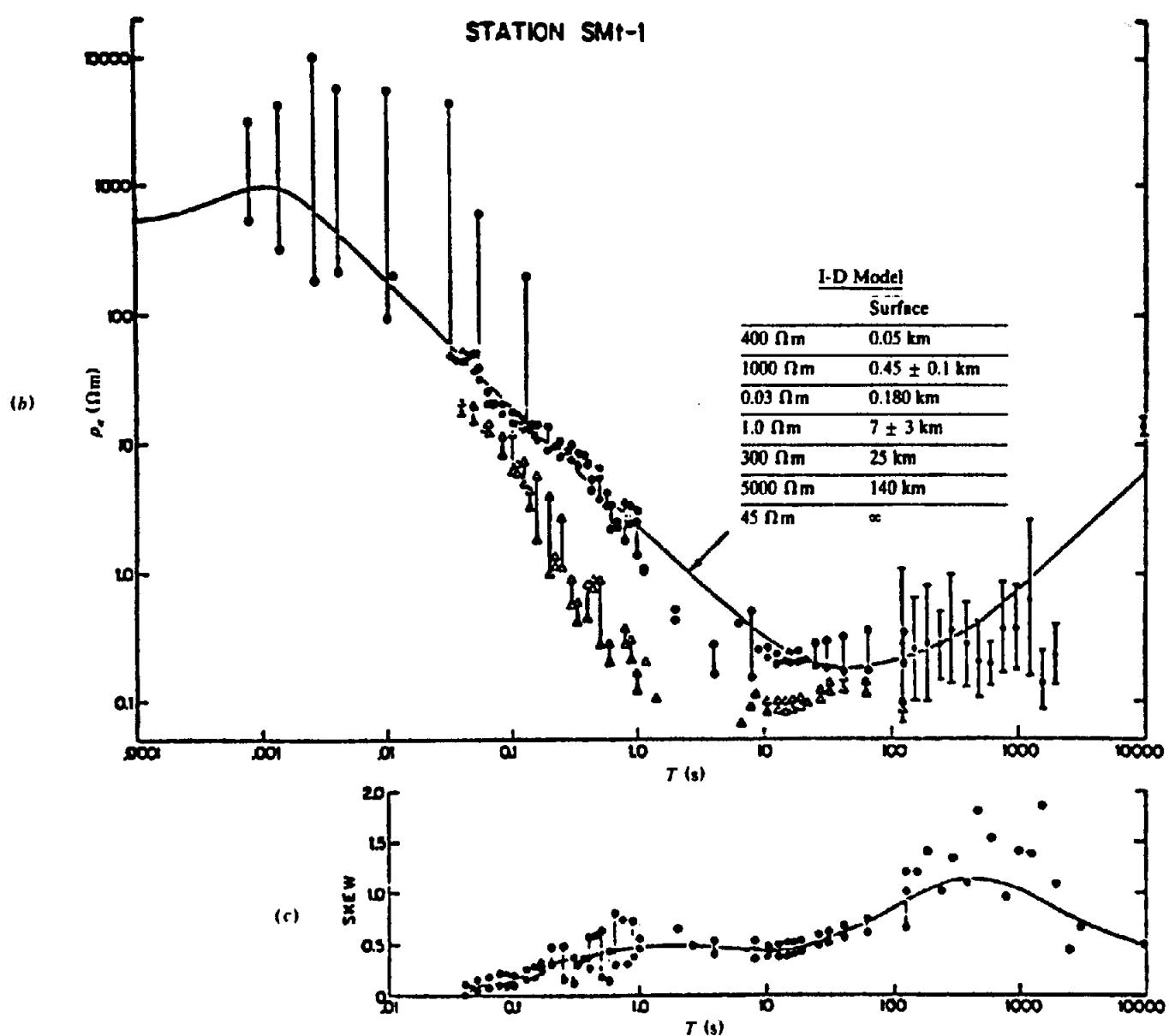


Figure 6.30.  $\rho_s$  results near Ste. Mathilde, Quebec. (a) Map showing elevations, locations of profiles 1–3 plus  $\rho_s$  contours. (b) Results for station SMT-1:  $\rho_s$  curve, tensor data in the principal axis of anisotropy from 0.03 to 10,000 s, and scalar data from 0.0008 to 0.13 s; dots and triangles are  $\rho_s$  values for the major and minor axes of anisotropy, respectively; error bars show maximum scatter from 0.0008 to 100 s, two standard deviations from 100 to 10,000 s; solid curve is for the 1-D model. (c) Skew ratios.

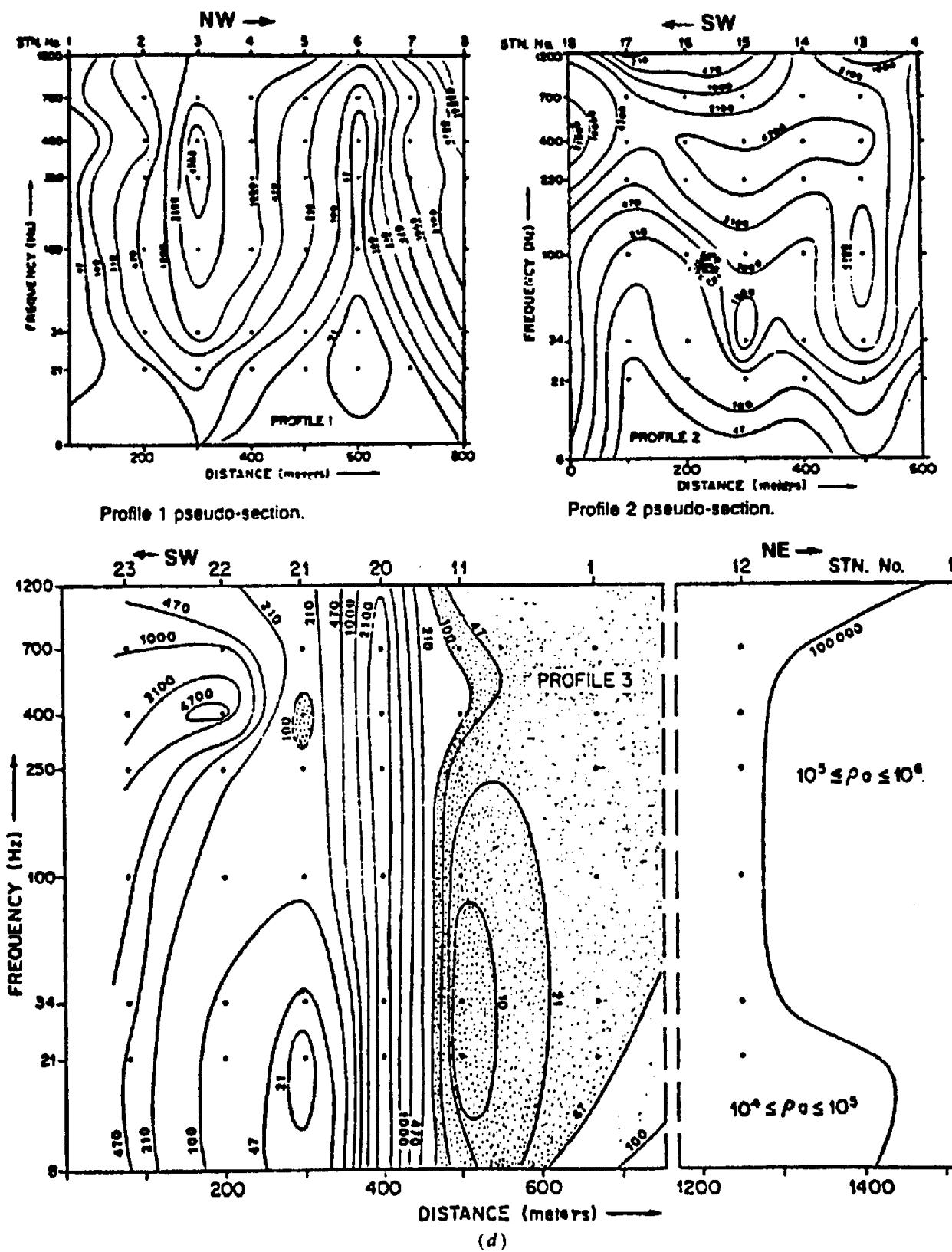


Figure 6.30. (Continued) (d) AMT pseudodepth plots from profiles 1, 2, and 3.

ried out in northern Saskatchewan in the area of Coxwell Dome, where uranium mineralization is sometimes associated with conductive fracture zones within the resistive Precambrian formations. The low resistivity section is more clearly evident from this form of MT plot, both horizontally and vertically, than from conventional MT or resistivity profiles.

5. Figure 6.30a shows an anomalous high conductivity zone of limited lateral extent located near the village of Ste. Mathilde, Quebec, on the lower north shore of the St. Lawrence River. This feature is in a region of highly complex geology, within a few kilometers of Logan's Line, a major thrust fault separating the Grenville Province from the Appalachian;

Table 6.3.

Station	SP (mV)
0W	0
1	-37
2	-100
3	-108
4	-158
5	-236
6	-138
7	-210
8	-290
9	-335
10	-258
11	-170
12	-120
13	-73
14	-40
15	-21
16	-17
17	-7

the zone is adjacent to the east rim of a large Paleozoic impact crater and near the northeast edge of an active seismic zone along the St. Lawrence. On a smaller scale a granite body about 2 km by 0.6 km, surrounded by a wide migmatite zone injected by pegmatites and overlain by frequent outcrops of Precambrian rock, appears to be roughly centered on the anomalous zone. The cause of this extremely conductive feature is not known. It is thought to be a volume of highly fractured rock filled with conductive aqueous solutions, possibly including graphitic, sulfide, or ferrous mineralization (although there is no particular indication of the latter on local aeromagnetic maps; see Kurtz et al., 1980).

The depth to the top of this feature, determined from 1-D modeling, is between 0.25 and 1.0 km, the vertical extent being 4 to 7 km. The structure, no more than a few square kilometers in cross section, trends northwest-southeast and plunges northwest. Figure 6.30a shows a map of the area plus  $\rho_a$  con-

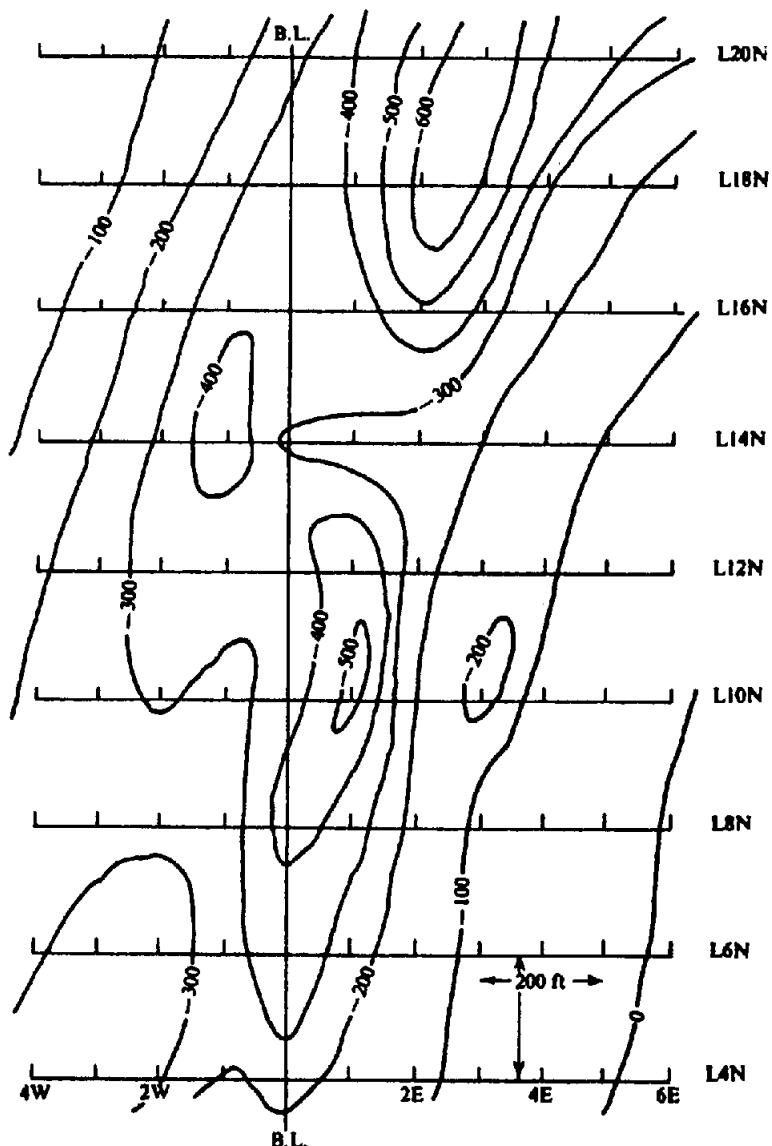


Figure 6.31. SP survey in Northern New Brunswick. Contour values in millivolts.

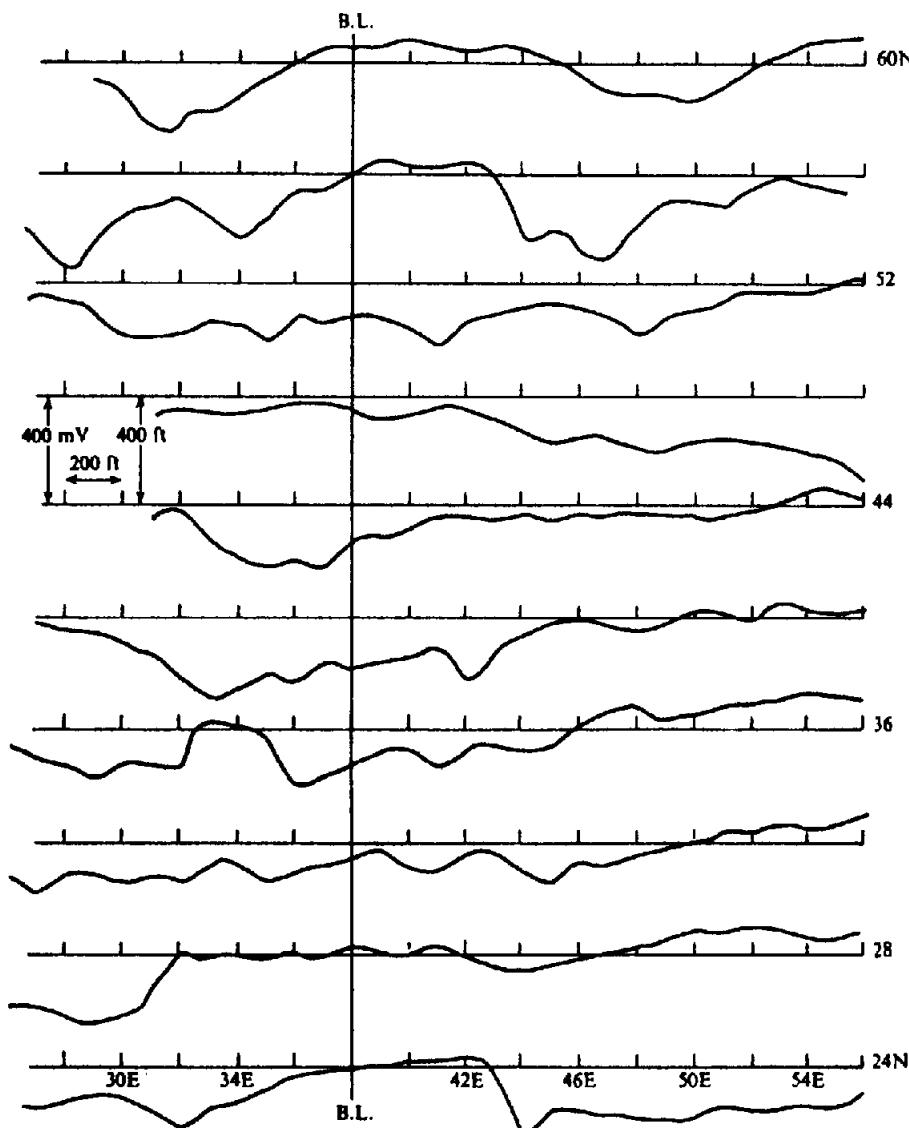


Figure 6.32. SP survey in Eastern Nova Scotia.

tours. Figure 6.30b shows  $\rho_a$  values obtained from the field data plus a sounding curve for the 1-D model shown. Figure 6.30c gives skew ratios for (b). Figure 6.30d displays three AMT pseudodepth plots from profiles 1 to 3 (Fig. 6.30a). The pseudodepth plots, like the  $\rho_a$  contours in Figure 6.30a, enhance the small dimensions and sharp boundaries of this odd feature.

#### 6.4. PROBLEMS

1. The self-potential readings in Table 6.3 were obtained on a detailed traverse. Stations are 10 ft apart and SP readings are given with reference to station 0. Make an interpretation of this anomaly based on the limited data available.
2. Figure 6.31 shows a set of SP contours for a prospect in northern New Brunswick. The area is

mainly wooded with some open ground roughly parallel to, and slightly west of, the baseline between lines 10N and 20N. What interpretation can be made of this prospect – particularly the large SP negative centers – from the data? Is any additional work warranted and if so what would you recommend?

3. The SP profiles shown in Figure 6.32 were the result of a survey carried out on a large geochemical anomaly in eastern Nova Scotia. These profiles are part of a much larger SP survey, extending further in all directions except east, in which the general background SP is 140 mV more positive than the zero values shown. Convert the profiles into contours by adding -140 mV to all readings and make any interpretations you can of the result.
4. Readings from a self-potential survey made over suspected sulfide mineralization in southeastern

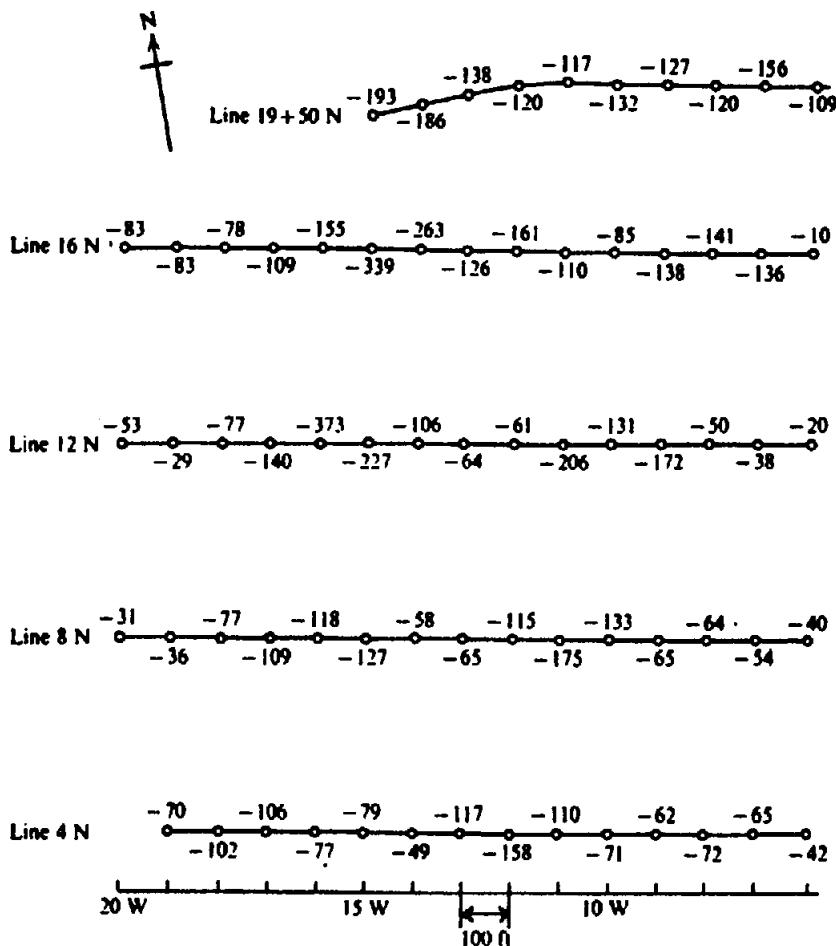


Figure 6.33. SP survey in Southeastern Ontario. Readings in millivolts.

Table 6.4.

Stn	1 Hz	8 Hz	32 Hz	145 Hz
20W	120	110	282	655
19	69	140	270	590
18	97	140	265	550
17	81	155	307	763
16	62	126	243	607
15	37	56	117	256
14	37	40	88	242
13	46	39	81	242
12	45	44	70	127
11	62	84	133	190
10	29	71	140	305
9	48	92	160	205
8	143	257	393	660
7	156	375	565	970
6	207	510	845	1700
5	223	445	715	1580

Ontario are shown in Fig. 6.33. By drawing profiles and contouring these data, make an interpretation for the area.

5. The telluric field strength readings in Table 6.4 were obtained during a traverse over a prospect in eastern Nova Scotia. Four frequencies, 1, 8, 32, and 145 Hz, are measured by integrating

signals, obtained from 100 ft electrode spreads, for 30 s.

Normalize these readings for each channel, by taking the averages of all stations to obtain a common background of unity, plot on a log scale, and interpret the result. (Note: Presumably one can make use of the fact that depth of

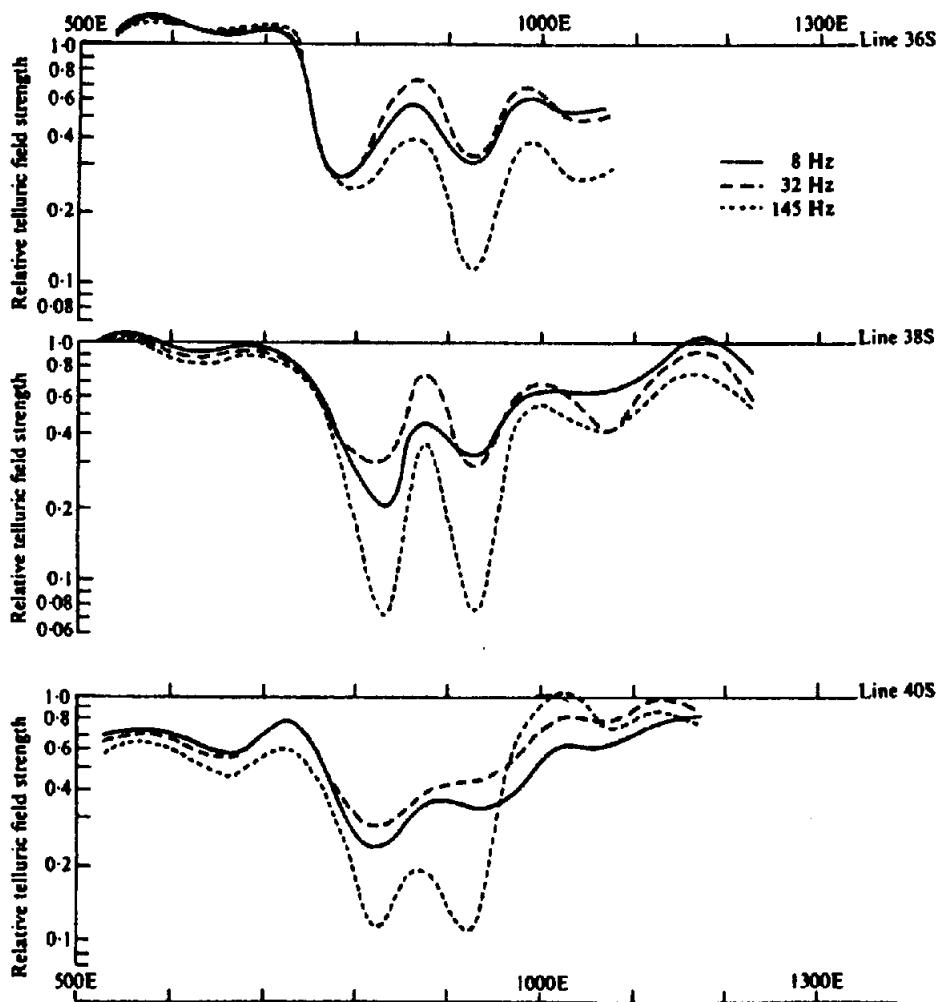


Figure 6.34. Multifrequency telluric profiles from Southeastern Quebec. Electrode spacing 50 ft.

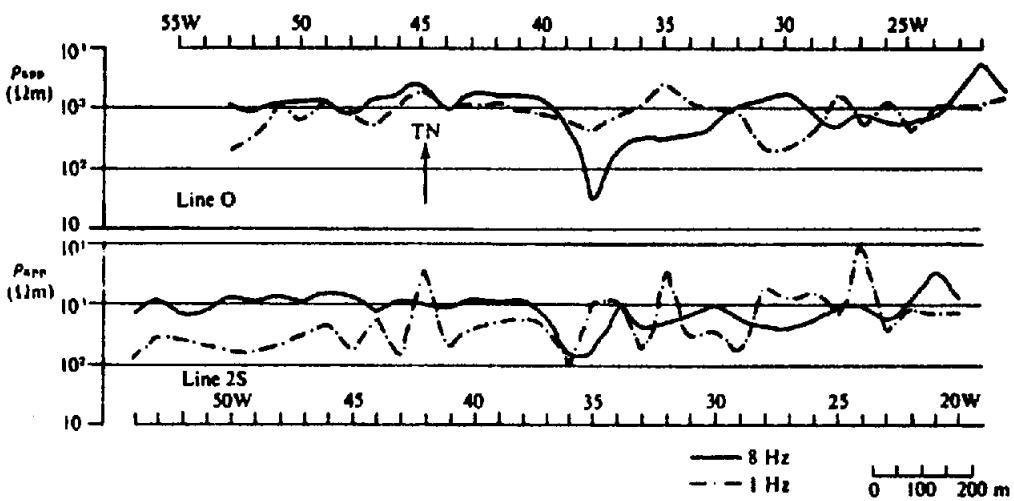


Figure 6.35. Telluric profiles at 1 and 8 Hz, Northeastern Brazil.

- penetration varies inversely with frequency in some fashion.)
- Figure 6.34 shows three profiles of multifrequency (8, 32, and 145 Hz) telluric field strength over a zone of sulfide mineralization in southeastern Quebec. As in problem 5, the signals were integrated for 30 s, while the electrode separation was 50 ft. Make an interpretation of the results based on tellurics alone.
  - The profiles shown in Figure 6.35 were part of a multifrequency reconnaissance telluric survey. Only two of the four frequencies measured

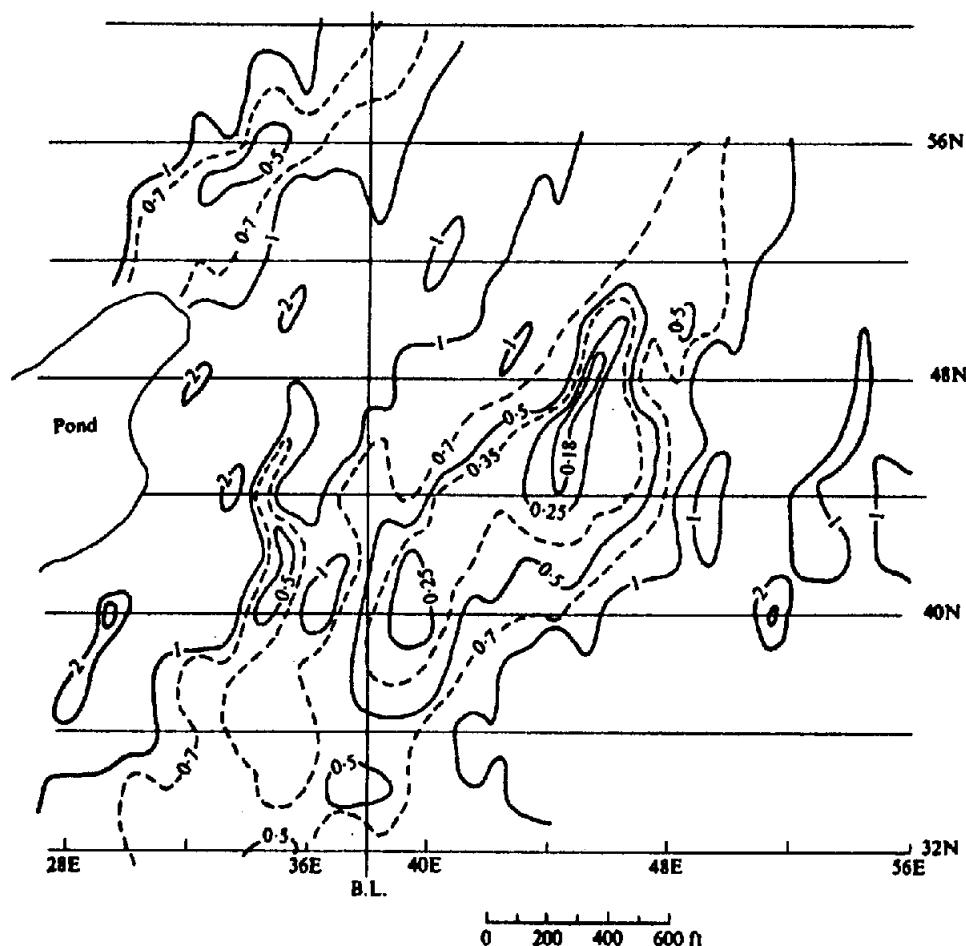


Figure 6.36. 8 Hz telluric data, normalized and contoured for large-scale interpretation.

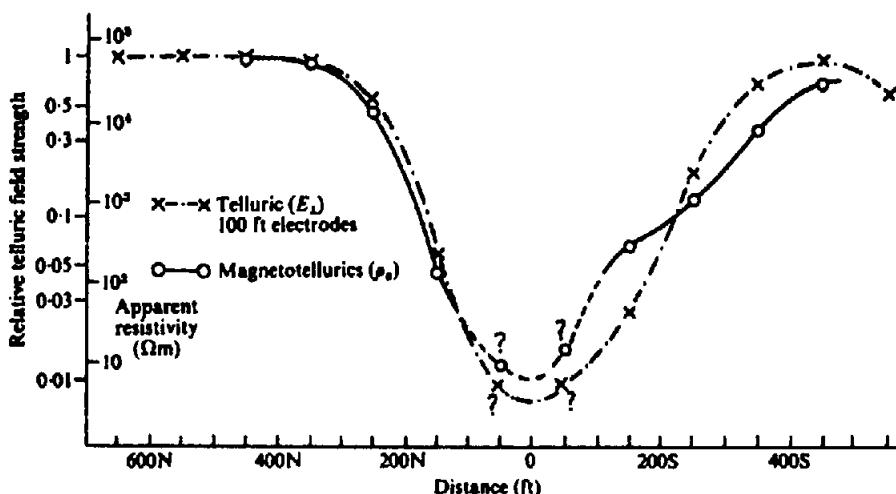


Figure 6.37. 8 Hz magnetotelluric profile, Northern Quebec.

- (1 and 8 Hz) are reproduced here. Spacing between the two lines shown is 400 m. Relative telluric field readings have been converted to apparent resistivities, based on resistivity measurements made at several stations in the area. Make an interpretation of these limited data.
8. An experimental 8 Hz telluric survey was made over an area previously covered by IP in eastern

Canada. The relative telluric field contours are shown in Figure 6.36. Interpret the broad features of this area with no other data available.

9. The magnetotelluric profile illustrated in Figure 6.37 was obtained by measuring  $E_{\perp}$  and  $H_{\parallel}$  (electric field roughly normal, magnetic field parallel, to strike of the mineralization) at 8 Hz over a sulfide showing in northern Quebec. The tel-

Table 6.5.

Stn	8 Hz	145 Hz	1,000 Hz	3,000 Hz	SP
050	0.83	1.00	—	—	20
100	1.00	1.10	1.40	1.50	10
150	1.20	1.25	1.28	1.30	6
200	1.28	1.30	1.10	1.14	7
250	1.50	1.40	1.00	1.06	+8
300	1.26	1.07	0.94	0.96	-74
350	1.05	0.90	0.90	0.92	-119
400	0.83	0.57	0.55	0.55	-50
450	0.72	0.38	0.30	0.29	-7
500	0.80	0.37	0.24	0.23	+25
550	0.80	0.38	0.22	0.19	33
600	0.78	0.40	0.23	0.16	33
650	0.73	0.43	0.22	0.15	31
700	0.77	0.42	0.25	0.12	19
750	0.78	0.40	0.27	0.11	0
800	0.67	0.36	0.22	0.14	24
850	0.62	0.35	0.21	0.17	34
900	0.72	0.37	0.25	0.18	31
1,000	1.00	0.42	0.26	0.18	35
1,100	0.93	0.47	0.27	0.22	20
1,200	0.80	0.78	0.78	0.75	33
1,300	0.85	1.00	1.28	1.40	37
1,400	0.82	0.72	0.96	1.00	25
1,450	0.81	0.63	0.74	0.81	19
1,500	0.82	0.82	1.00	1.26	40
1,600	1.00	1.22	1.50	1.70	62

luric profile for  $E_{\perp}$  is also shown. It indicates that the telluric measurement corresponds very closely to the magnetotelluric result, although the apparent resistivity values, of course, cannot be determined. What crude interpretation can be made from this profile?

10. During a routine reconnaissance ground survey with four-frequency tellurics and SP in eastern Nova Scotia, the readings in Table 6.5 were obtained over a part of a long traverse. Station readings are in feet, SP in millivolts, and the telluric readings have been normalized (as in problem 5) to produce a relative telluric field strength (RTFS).

The upper layer of overburden carries anomalous lead and zinc values. Overburden depth is not generally known, but appears to be as much as 50 ft from nearby trenches; it also contains numerous fractured boulders laced with sulfides.

Plot these profiles and interpret them with regard to possible base-metal anomalies and their depths, geometry, and commercial interest.

11. Figure 6.38 shows an area of potential base-metal mineralization on the Canadian east coast; earlier prospecting had exposed promising Cu showings and  $\text{MoS}_2$  samples were common along the rocky shoreline. An extensive geochemical soil survey had also established a large-scale anomalous zone that included Pb and Zn. Ear-

lier, magnetic and IP surveys were carried out to establish structural trends and disseminated sulfide mineralization, without marked success. MT and telluric work were done in an attempt to determine whether the latter, cheap and rapid compared to MT and IP, was a suitable substitute method.

The MT profiles displayed in the upper section of Figure 6.38b were obtained several years after the telluric results shown below and simultaneously with EM16R measurements of apparent resistivity (§7.4.2f; §7.7.6b), shown dotted in the upper half of Figure 6.38b.

Consider the multifrequency MT and telluric profiles carefully. Do they correlate sufficiently that you would employ tellurics with confidence for faster and cheaper coverage? Is this correlation as good between EM16R (17,800 Hz) and tellurics at 3,000 Hz? Are there visible trends in conductive and resistive structure, both horizontally and vertically? Is the EM16 source (Cutler, Maine, roughly west of the area) well located for the horizontal trends?

12. A novel expression of ground geophysical measurements over a well-mapped working-mine subsurface is displayed in Figure 6.39. The steep profile line, striking roughly east-west, passes over a large section of the ore body, including the edge of the worked-out "Glory Hole" around

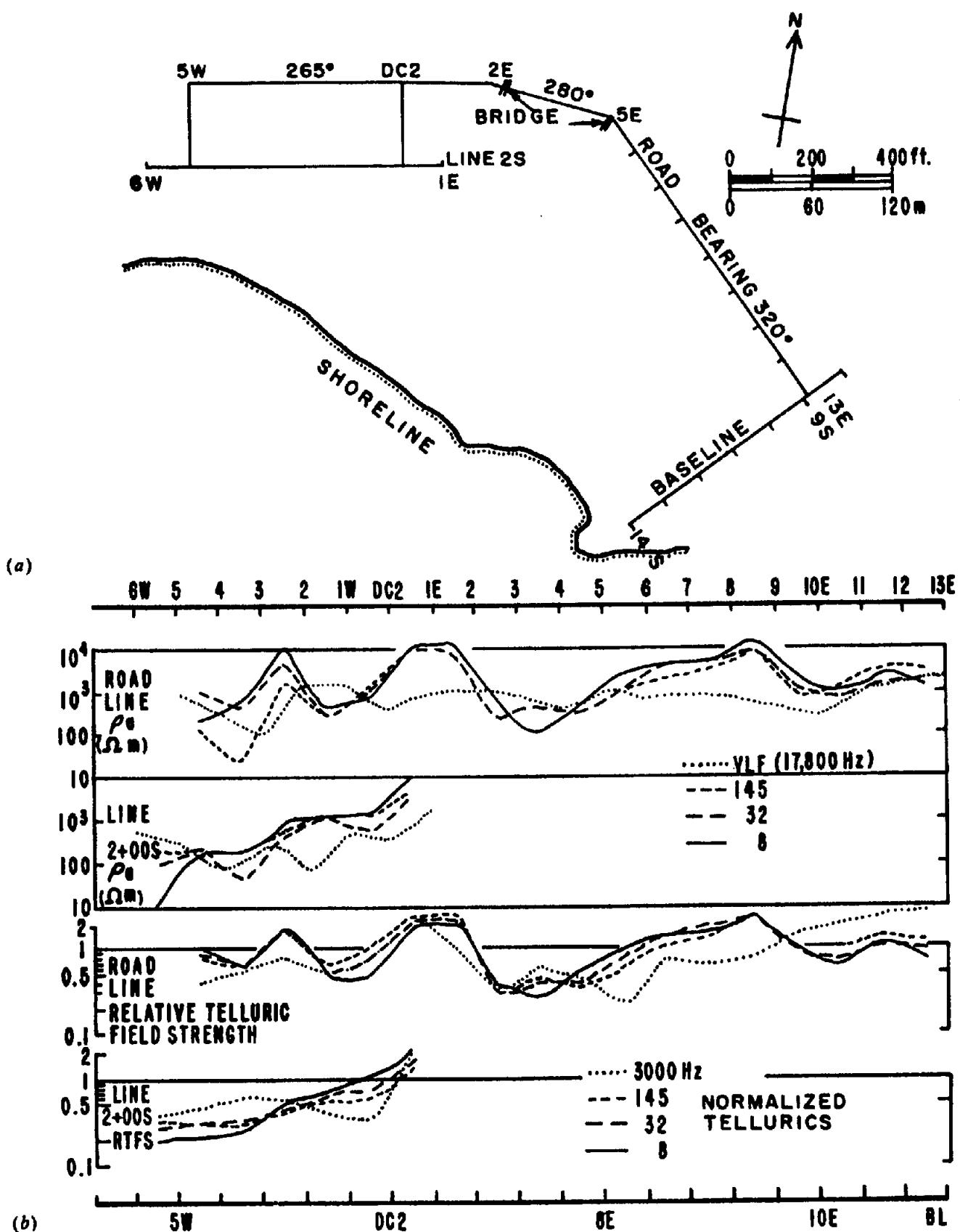


Figure 6.38. Telluric, MT, and VLF results, Canadian east coast. (a) Plan of survey area. (b) Top two sets of curves:  $\rho_a$  profiles from MT and VLF (EM16R) measurements; bottom two sets: relative telluric field strength (RTFS) profiles.

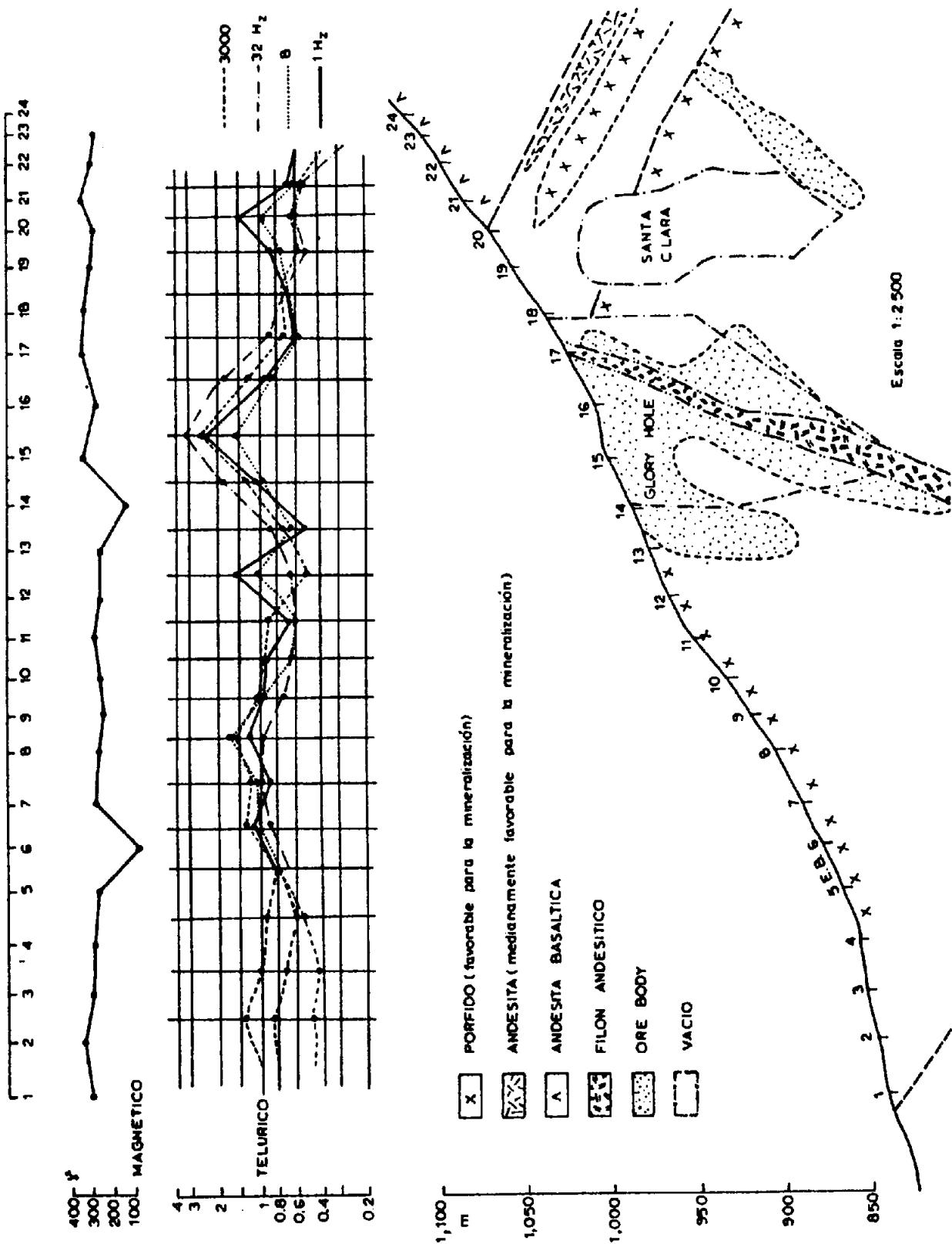


Figure 6.39. Geologic section with magnetic and telluric surface profiles over mine area, Chile.

station 15. A telluric base located near station 5 was occupied during the traverse to reduce noise caused by erratic signals.

Study the magnetic and four-frequency telluric responses throughout the profiles. Do they reflect the known section properly? Draw a telluric pseudodepth plot, as in field Examples 4 and 5, and compare it with the geologic section seen here. Does this display enhance the telluric response with respect to frequency versus penetration depth? Is there evidence for a terrain effect in any of the diagrams?

## REFERENCES

- Self-Potential**
- Corry, C. E. 1985. Spontaneous polarization associated with porphyry sulfide mineralization. *Geophysics* 50, 1020-34.
- Corwin, R. F. 1976. Offshore use of the self-potential method. *Geophys. Prosp.* 24, 79-90.
- Corwin, R. F., and Hoover, D. B. 1979. The self-potential method in geothermal exploration. *Geophysics* 44, 226-45.
- Roy, J. 1984. Electrical methods in mineral well logging. Ph.D. thesis, McGill Univ., Montreal.
- Sato, M., and Mooney, H. M. 1960. The electrochemical mechanism of sulfide self potentials. *Geophysics* 25, 226-49.
- Tellurics**
- Boissonnas, E., and Leonardon, E. G. 1948. Geophysical exploration by telluric currents with special reference to a survey of the Haynesville Salt Dome, Wood County, Texas. *Geophysics* 13, 387-403.
- Doborzynski, Z. B. 1973. Prospecting with multi-frequency tellurics. M.Eng. thesis, McGill Univ., Montreal.
- Dobrin, M. B. 1960. *Introduction to Geophysical Prospecting*. New York: McGraw-Hill.
- Gamble, T. D., Goubaud, W. M., and Clarke, J. 1979. Magnetotellurics with a remote reference. *Geophysics* 44, 53-68.
- Keller, G. V., and Frischknecht, F. C. 1966. *Electrical Methods in Geophysical Prospecting*. Oxford: Pergamon.
- Slankis, J. A. 1970. Telluric and magnetotelluric surveys at 8 Hz. Ph.D. thesis, McGill Univ., Montreal.
- Slankis, J. A., Telford, W. M., and Becker, A. 1972. 8 Hz telluric and magnetotelluric prospecting. *Geophysics* 37, 862-78.
- Telford, W. M. 1977. Characteristics of audio and sub-audio telluric signals. *Geophys. Prosp.* 25, 321-33.
- Magnetotellurics**
- Cagniard, L. 1953. Basic theory of the magneto-telluric method of geophysical prospecting. *Geophysics* 18, 605-35.
- Forsythe, G. E., and Wasow, W. R. 1960. *Finite Difference Methods for Partial Differential Equations*. New York: Wiley.
- Goldstein, M. A., and Strangway, D. W. 1975. Audio frequency magnetotellurics with a grounded electrical dipole source. *Geophysics* 40, 669-83.
- Grant, F. S., and West, G. F. 1965. *Interpretation Theory in Applied Geophysics*. New York: McGraw-Hill.
- Hermance, J. F. 1973. Processing of magnetotelluric data. *Phys. Earth and Planet. Inter.* 7, 349-64.
- Hermance, J. F., and Thayer, R. E. 1975. The telluric-magnetotelluric method. *Geophysics* 40, 664-8.
- Hoover, D. B., Frischknecht, F. C., and Tippens, C. 1976. Audio-magnetotelluric soundings as a reconnaissance exploration technique in Long Valley, Calif. *J. Geophys. Res.* 81, 801-9.
- Hoover, D. B., Long, C. L., and Senterfit, R. M. 1978. Audiomagnetotelluric investigations in geothermal areas. *Geophysics* 43, 1501-14.
- Kurtz, R. D., Niblett, E. R., Chouteau, M., Scott, W. J., and Newitt, L. R. 1980. An anomalous electrical resistivity zone near Ste. Mathilde, Quebec. *J. Canadian Soc. Explor. Geophysics*, 56-67.
- Labson, V. F., Becker, A., Morrison, H. F., and Conti, U. 1985. Geophysical exploration with audiofrequency natural magnetic fields. *Geophysics* 50, 656-64.
- Nichols, E. 1987. Personal communication.
- Pham Van Ngoc, Boyer, D., and Chouteau, M. 1978. Cartographie des "pseudo-resistivités apparentes" par profilage tellurique-tellurique associé à la magneto-tellurique. *Geophys. Prosp.* 26, 218-46.
- Reddy, I. K., and Rankin, D. 1971. Magnetotelluric measurements in central Alberta. *Geophysics* 36, 739-53.
- Sandberg, S. K., and Hohmann, G. W. 1982. Controlled source audiomagnetotellurics in geothermal exploration. *Geophysics* 47, 100-16.
- Silvester, P., and Haslam, C. R. S. 1972. Magnetotelluric modeling by the finite element method. *Geophys. Prosp.* 20, 872-91.
- Sims, W. E., and Bostick, F. X., Jr. 1969. Methods of magnetotelluric analysis. EGRL Tech. Rep. #58, Univ. of Texas, Austin.
- Srivastava, S. P. 1967. Magnetotelluric two and three layer master curves. Dom. Observ. (Ottawa, Canada) Pub. 35, No. 7.
- Strangway, D. W., and Koziar, A. 1979. Audiofrequency magnetotelluric sounding - a case history at the Cavendish geophysical test range. *Geophysics* 44, 1429-46.
- Strangway, D. W., Swift, C. M., Jr., and Holmer, R. C. 1973. The application of AMT to mineral exploration. *Geophysics* 38, 1159-75.
- Swift, C. M., Jr. 1967. A magnetotelluric investigation of an electrical conductivity anomaly in the southwestern United States. Ph.D. thesis, Dept. of Geol. and Geophys., MIT, Cambridge, MA.
- Vozoff, K. 1972. The magnetotelluric method in the exploration of sedimentary basins. *Geophysics* 37, 98-141.
- Wachspress, E. L. 1966. *Iterative Solutions of Elliptic Systems*. Englewood Cliffs, NJ: Prentice-Hall.

# Chapter

## 7

# *Electromagnetic Methods*

### 7.1. INTRODUCTION AND HISTORICAL BACKGROUND

With the exception of magnetics, the electromagnetic (EM) prospecting technique is the most commonly used in mineral exploration. In its usual form the equipment is not suitable for oil search, because it responds best to good electrical conductors at shallow depth. Nor has it been much employed in civil engineering work, although it is used occasionally to locate buried pipe and cable, for the detection of land mines, and for mapping surficial areas infiltrated by contaminants.

As the name implies, the method involves the propagation of continuous-wave or transient electromagnetic fields in and over the earth. There is a close analogy between the transmitter, receiver, and buried conductor in the EM field situation, and a trio of electric circuits coupled by electromagnetic induction. In a few EM ground systems the source energy may be introduced into the ground by direct contact, although generally inductive coupling is used; invariably the detector receives its signal by induction.

The EM ground method was developed during the 1920s in Scandinavia, the United States, and Canada, regions where the detection of conductive base-metal deposits was facilitated by their large contrast with the resistive host rock and generally thin overburden. The airborne version was introduced some 30 years later.

Until the early 1960s, practically all EM equipment transmitted and received continuously on one frequency at a time. Such a continuous wave system is said to be operating in the frequency domain (FEM or FDEM). Although several attempts were made, dating back to the 1930s, to transmit transient pulses and detect the ground response during off-time (Statham, 1936; Hawley, 1938), the first successful applications of this type did not appear until 1962. These were the airborne Input (Barringer, 1962), the MPPO-1 ground transient system in the USSR, and the EMP pulse ground equipment of Newmont Ex-

ploration (Dolan, 1970). Since the early 1970s, there has been a dramatic increase in the development of such time-domain systems (TEM or TDEM).

Almost all EM field sets include a portable power source. However, limited use has also been made of radio transmission stations in the frequency range 100 kHz to 10 MHz and particularly in the very low frequency range (VLF), 15 to 25 kHz. One other field method that can be included with EM, AF-MAG, makes use of atmospheric energy resulting from worldwide thunderstorm activity (§6.2.1).

A great advantage of the inductive coupling is that it permits the use of EM systems in aircraft. Airborne EM, usually in combination with other aeromagnetic methods, has been widely applied in mineral exploration reconnaissance and recently in detailed surveys.

### 7.2. ELECTROMAGNETIC THEORY

#### 7.2.1. Vector and Scalar Potentials

The propagation and attenuation of electromagnetic waves were discussed in Sections 6.2.2 to 6.2.5 in connection with the magnetotelluric method. Although the frequencies employed in EM prospecting are somewhat higher than in most MT work, the general theory, limiting assumptions (negligible displacement current and spatial phase shift), and boundary conditions are identical in the two methods.

In general potential theory it is usually easier to solve problems by starting with the potential and obtaining the field vectors by appropriate differentiation. The same rule applies in electromagnetics, where it is convenient to introduce certain potentials from which both electric and magnetic field vectors may be derived. We define the *vector magnetic potential A* in terms of the magnetic induction

$$\nabla \times \mathbf{A} = \mathbf{B} \quad (7.1)$$

Then from Equation (6.3) we have

$$\nabla \times (\mathbf{E} + \partial \mathbf{A} / \partial t) = 0$$

The vector inside the bracket is irrotational [see Eq. (A.31)] and can be expressed as the gradient of a scalar potential  $\phi$ :

$$\mathbf{E} + \partial \mathbf{A} / \partial t = -\nabla \phi$$

or

$$\mathbf{E} = -(\partial \mathbf{A} / \partial t + \nabla \phi) \quad (7.2)$$

The term  $-\partial \mathbf{A} / \partial t$  is the induced emf portion of  $\mathbf{E}$  while  $-\nabla \phi$  is the potential gradient due to current flow in a resistive medium.

Using Equations (7.1) and (7.2) along with Equations (6.4) and (6.9), we have

$$\nabla \times \nabla \times \mathbf{A} + \mu \epsilon \{ \partial^2 \mathbf{A} / \partial t^2 + \nabla (\partial \phi / \partial t) \} = \mu \mathbf{J} \quad (7.3a)$$

[If external sources are present,  $\mathbf{J}$  must be replaced by  $\mathbf{J} + \mathbf{J}_0$ —see Eq. (6.11b).] The electric field  $\mathbf{E}$  in Equation (7.2) produces a current in a conducting medium such that (see Eq. (6.9))

$$\mathbf{J} = \sigma \mathbf{E} = -\sigma (\partial \mathbf{A} / \partial t + \nabla \phi)$$

Substituting for  $\mathbf{J}$  in Equation (7.3a) and using Equation (A.25), we obtain

$$\begin{aligned} \nabla (\nabla \cdot \mathbf{A}) - \nabla^2 \mathbf{A} + \mu \epsilon \{ \partial^2 \mathbf{A} / \partial t^2 + \nabla (\partial \phi / \partial t) \} \\ + \mu \sigma (\partial \mathbf{A} / \partial t + \nabla \phi) = 0 \end{aligned} \quad (7.3b)$$

Equation (6.6b) states that  $\nabla \cdot \mathbf{D} = Q$ ,  $Q$  being the charge density. Using this to eliminate  $\mathbf{E}$  in Equation (7.2) gives

$$\nabla^2 \phi + \nabla \cdot (\partial \mathbf{A} / \partial t) = -Q/\epsilon \quad (7.4)$$

We now make use of the Lorentz condition (Ward, 1967):

$$\nabla \cdot \mathbf{A} = -(\mu \epsilon \partial \phi / \partial t + \mu \sigma \phi) \quad (7.5)$$

(this forces both  $\mathbf{A}$  and  $\phi$  to satisfy the same wave equation as  $H$  and  $E$ ). Substituting Equation (7.5) into Equations (7.3b) and (7.4) we get

$$\nabla^2 \mathbf{A} - \mu \epsilon \partial^2 \mathbf{A} / \partial t^2 - \mu \sigma \partial \mathbf{A} / \partial t = 0 \quad (7.6)$$

$$\nabla^2 \phi - \mu \epsilon \partial^2 \phi / \partial t^2 - \mu \sigma \partial \phi / \partial t = -Q/\epsilon \quad (7.7)$$

Thus we have a pair of potentials, one vector and the other scalar, that in homogeneous media satisfy the same wave equation as the fields.

Still another potential, the *Hertz vector potential*  $\Pi$ , is available to define the EM field. It is defined in terms of  $\mathbf{A}$  and  $\phi$  thus:

$$\left. \begin{aligned} \mathbf{A} &= \mu \epsilon \partial \Pi / \partial t + \mu \sigma \Pi \\ \phi &= -\nabla \cdot \Pi \end{aligned} \right\} \quad (7.8)$$

Following manipulation similar to that for  $\mathbf{A}$  and  $\phi$ , we arrive at the expression (Ward, 1967)

$$\nabla^2 \Pi - \mu \epsilon \partial^2 \Pi / \partial t^2 - \mu \sigma \partial \Pi / \partial t = \mathbf{K} \quad (7.9)$$

where  $\mathbf{K} = -\mathbf{P}/\epsilon$ , or  $-\mathbf{M}$ , or zero.  $\mathbf{P}$ ,  $\mathbf{M}$  are the respective electric and magnetic-dipole moments per unit volume. The value of  $\mathbf{K}$  depends on the conditions of the system.

Although these potentials do not have the physical significance of the scalar potential in gravity or electrostatics, they provide convenient mathematical tools for determining various EM fields, as we shall see in the following sections. The similarity in form between Equations (7.6), (7.7), (7.9), and (6.13) is worth noting.

### 7.2.2. Description of EM Fields; Biot – Savart Law

(a) *General.* The primary or source fields used in EM prospecting are normally generated by passing alternating or pulsed current through long wires or coils. For simple geometric configurations such as these the resultant fields can be calculated exactly for points in the surrounding region, although this is not generally possible. With FDEM one must measure the disturbing field in the presence of the original primary field, hence it is often necessary to calculate the latter at the receiver in order to eliminate, or at least reduce, its effect. With TDEM the primary field is eliminated by source cutoff. In both cases the secondary fields of interest are small in comparison with the primary fields.

(b) *Biot – Savart law; magnetic field of a long wire.* Originally stated for static magnetic fields, this law is valid also for low-frequency ac, provided the linear distances involved are much less than the wavelength (§6.2.3). From Equation (3.4) and Figure 7.1 we have

$$\Delta \mathbf{H} = (I dl) \times \mathbf{r}_1 / 4\pi r^2$$

In scalar form this becomes

$$\begin{aligned} \Delta H &= I \rho \{ \sec^2 \phi \sin(\pi/2 - \phi) \} d\phi / 4\pi r^2 \sec^2 \phi \\ &= I \cos \phi d\phi / 4\pi r \end{aligned} \quad (7.10a)$$

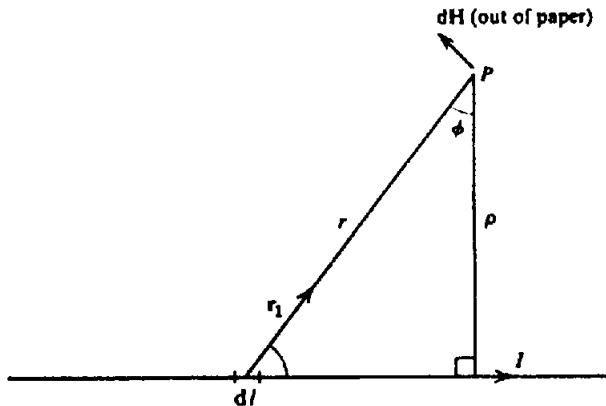


Figure 7.1. Illustrating the Biot-Savart law.

Integrating over a straight wire, the result is

$$H = (I/4\pi\rho)(\sin\phi_2 - \sin\phi_1) \quad (7.10b)$$

If the wire is extremely long (infinite length),  $\phi_2 = \pi/2$ ,  $\phi_1 = -\pi/2$ , and

$$H = I/2\pi\rho \quad (7.10c)$$

(c) *Vector potential of a current element.* To get the potential  $\mathbf{A}$  for a current element  $I dl$ , we simplify Equation (7.3a) by neglecting all currents (including displacement currents) except those induced in the conductor. Thus, we set  $\mu\epsilon\partial^2\mathbf{A}/\partial t^2 = 0$  (this eliminates displacement currents—see discussion of eqs. (6.13b) and (6.14)), and we also set  $\phi = 0$ . This reduces eq. (7.3a) to

$$\nabla \times \nabla \times \mathbf{A} = \mu\mathbf{J}$$

But  $\nabla \cdot \mathbf{A} = 0$  from Equation (7.5) when  $\phi = 0$ , hence Equation (A.25) gives

$$\nabla^2\mathbf{A} = -\mu\mathbf{J}$$

This equation resembles Poisson's equation in gravity and magnetics. It has the following solution for a current element  $I dl$

$$\mathbf{A} = (\mu/4\pi) \int_V \mathbf{J} dv/r = (\mu/4\pi) \oint I dl/r \quad (7.11)$$

where the line integral (§A.3.4) is over a closed path encircling the element  $dl$  or its prolongation,  $\mathbf{A}$  is the potential at  $P(x, y, z)$ , and  $r$  is the distance from  $P$  to  $dl$ .

### 7.2.3. Fields in the Frequency Domain

(a) *General.* In this section we consider propagation of alternating fields from several common trans-

mitter sources in free space and over a conductive half-space. The assumption of free space is generally valid because the host rocks surrounding the conductor often are highly resistive.

Ward and Hohmann (1988) give an excellent theoretical treatment of electromagnetic fields in EM prospecting. The discussion in Section 7.2.3 is based largely on their paper.

(b) *Long straight horizontal wire.* We take the  $y$  axis along the wire. The field is now given by Equation (7.10c) where  $\rho^2 = x^2 + z^2$ , and  $\mathbf{H}$  is a vector perpendicular to  $\rho$  at the point  $P(x, y, z)$  in the direction given by the righthand rule (Fig. 7.1). The  $x$  and  $z$  components are

$$H_x = Iz/2\pi\rho^2 \quad H_z = Ix/2\pi\rho^2 \quad (7.10d)$$

There is also an electric component (Ward and Hohmann, 1988) given by

$$E_y = -j\omega\mu I K_0(jk\rho)/2\pi \quad (7.10e)$$

where  $K_0(jk\rho)$  is the modified Bessel function of the second kind of order zero and  $k$  is the propagation constant given by

$$k^2 = \omega^2\mu\epsilon - j\omega\mu\sigma;$$

in free space  $\sigma = 0$  and

$$k^2 = \omega^2\mu_0\epsilon_0 = \omega^2/c^2 = (2\pi/\lambda)^2,$$

$c$  being the velocity of light in free space. When  $k\rho$  is small,  $K_0(jk\rho) \approx -\ln(jk\rho/2)$  (Abramowitz and Stegun, 1964: 375) and Equation (7.10e) reduces to

$$E_y \approx j\omega\mu I \ln(jk\rho/2)/2\pi \quad (7.10f)$$

while Equation (7.10d) is unchanged.

When the long-wire source lies on the ground (the usual case), Equations (7.10d, e, f) are modified because the propagation constant becomes  $k^2 = -j\omega\mu\sigma$  (Ward and Hohmann, 1988). For  $(k\rho)$  small, the components become

$$\left. \begin{aligned} H_x &= jkI/2\sqrt{2}\pi, \\ H_z &= -(I/\pi x)\ln(jkx/2) \quad E_y \approx 0 \end{aligned} \right\} \quad (7.10g)$$

When the current is alternating,  $I$  in Equations (7.10) should be replaced with  $Ie^{-j\omega t}$  but in practice the exponential factor is understood and not written out (however it must be taken into account when time derivatives are involved). Also, we assume that the FDEM fields are  $H(\omega)$ ,  $E(\omega)$  in contrast to the

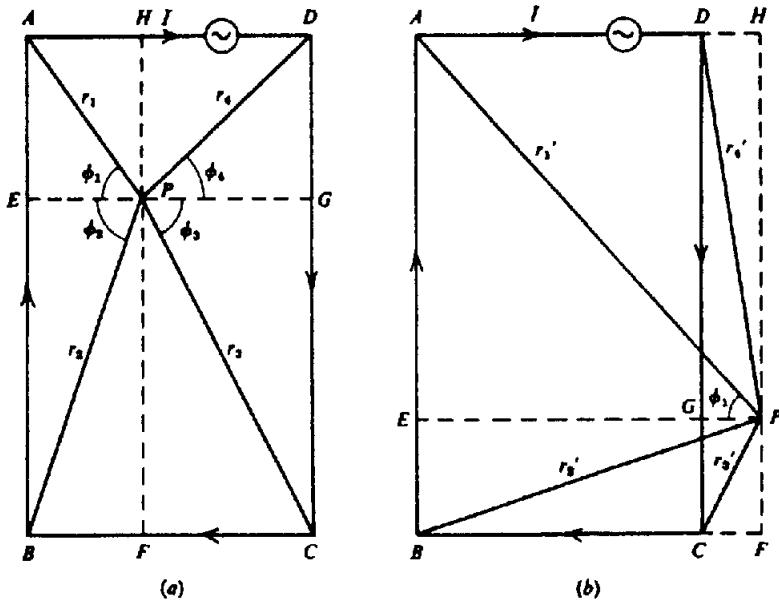


Figure 7.2. Geometrical parameters involved in calculating the magnetic field of a rectangular loop. (a) Calculating the field at an internal point; (b) Calculating the field at an external point.

TDEM fields  $H(t)$ ,  $E(t)$  to be considered later (§7.2.6).

(c) Large rectangle. The geometry is shown in Figure 7.2. Inside the rectangle the field (which is normal to the paper) at  $P$ , produced by the current in segment  $AE$ , is from Equation (7.10b) with  $\phi_1 = 0$ ,

$$H(AE) = I \sin \phi_1 / 4\pi (EP) = I(HP)^2 / 4\pi r_1 \mathcal{A}_1$$

where  $\mathcal{A}_1$  is the area of the rectangle with diagonal  $r_1$ . Adding the field  $H(AH)$ ,

$$\begin{aligned} H(AE) + H(AH) &= (I/4\pi r_1 \mathcal{A}_1) \{(HP)^2 + (EP)^2\} \\ &= (I/4\pi)(r_1/\mathcal{A}_1) \end{aligned}$$

Adding the fields of the four subrectangles, we get the total field

$$H = (I/4\pi) \sum_{n=1}^4 (r_n/\mathcal{A}_n) \quad (7.12a)$$

When  $P$  is outside the rectangle, we find

$$\begin{aligned} H' &= (I/4\pi)(r'_1/\mathcal{A}'_1 + r'_2/\mathcal{A}'_2 \\ &\quad - r'_3/\mathcal{A}'_3 - r'_4/\mathcal{A}'_4) \quad (7.12b) \end{aligned}$$

Within the loop the field varies about 40% over a rectangle concentric with ABCD and one-quarter the area, being a minimum at the center. Outside the loop the field will be mainly determined by the near side of the rectangle, provided the distance from it is

considerably less than the distance to the far side. It is important to note that the field in the neighborhood of the long wire, or outside a large rectangle and close to one side, falls off inversely as the distance, a relatively slow decrease in intensity.

The preceding analysis is for a loop in free space. The case of a rectangle lying on a homogeneous half-space has not been solved up to the present (see also §7.2.6d).

Both the long wire with and without the ends grounded and the large rectangle or square have been extensively used for generating EM primary fields in FD systems such as Turam, and also for pulse transmission (UTEM, Newmont EMP, SIROTEM, etc.). Dimensions are generally several hundred meters.

(d) Small horizontal circular coil (vertical magnetic dipole). By using the vector potential we can calculate the field at a point in the neighborhood of the loop, not necessarily in its plane or on the axis. The cylindrical coordinate system is shown in Figure 7.3. The cross section of the winding on the loop is assumed to be very small with respect to its radius. Because the current is confined to a circular path there is only one component of  $A$ ,  $A_\phi$ . Then  $dv = ad\phi d\rho dz$ ,  $J_\phi = I/d\rho dz$ , and Equation (7.11) simplifies to

$$\begin{aligned} A_\phi &= \frac{\mu}{4\pi} \int_V \frac{\cos \phi J_\phi(\rho) dv}{R} \\ &= \frac{\mu I}{4\pi} \oint_0^{2\pi} \frac{a \cos \phi d\phi}{(\rho^2 + z^2 + a^2 - 2ap \cos \phi)^{1/2}} \end{aligned}$$

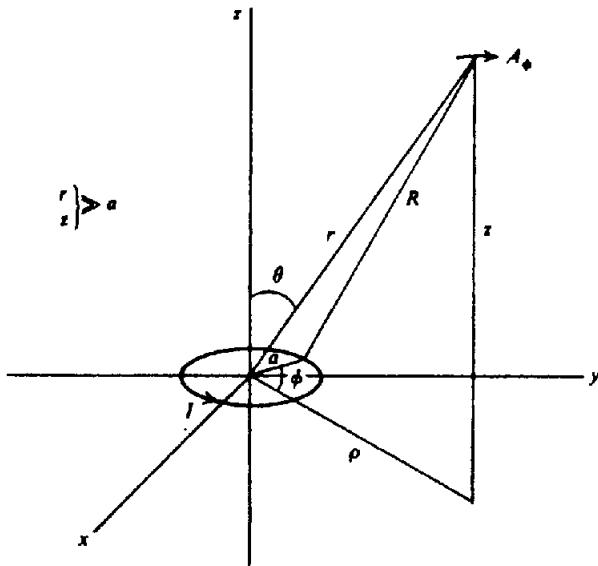


Figure 7.3. Field of a small circular coil at a point outside the plane of the loop.

If we assume that  $\rho^2 + z^2 \gg a^2$  and expand the denominator, we obtain

$$\begin{aligned} A_\phi &= \frac{\mu I}{4\pi} \int_0^{2\pi} \frac{a \cos \phi}{(\rho^2 + z^2)^{1/2}} \\ &\quad \times \left\{ 1 - \frac{a^2}{2(\rho^2 + z^2)} + \frac{a\rho \cos \phi}{(\rho^2 + z^2)} \dots \right\} d\phi \\ &= \frac{\mu I a^2 \rho}{4(\rho^2 + z^2)^{3/2}} \end{aligned} \quad (7.13)$$

Now we can get the magnetic field using Equation (A.36) (see §A.4)

$$\begin{aligned} \mathbf{H} &= \frac{\nabla \times \mathbf{A}}{\mu} = \frac{1}{\mu} \left\{ -\frac{\partial A_\phi}{\partial z} \mathbf{i}_\rho + \frac{1}{\rho} \frac{\partial (\rho A_\phi)}{\partial \rho} \mathbf{i}_z \right\} \\ &= \frac{Ia^2}{4(\rho^2 + z^2)^{5/2}} \{ 3\rho z \mathbf{i}_\rho + (2z^2 - \rho^2) \mathbf{i}_z \} \end{aligned} \quad (7.14a)$$

where  $\mathbf{i}_\rho$  and  $\mathbf{i}_z$  are unit vectors along the  $\rho$  and  $z$  axes. Thus the magnetic field has two components: one in the  $\rho$  direction and the other in the  $z$  direction:

$$H_\rho = 3I\delta\mathcal{A}\rho z / 4\pi(\rho^2 + z^2)^{5/2} \quad (7.14b)$$

$$H_z = I\delta\mathcal{A}(2z^2 - \rho^2) / 4\pi(\rho^2 + z^2)^{5/2} \quad (7.14c)$$

where  $\delta\mathcal{A} = \pi a^2$ , the area of the loop.

There is also an electric field component  $E_\phi$ , obtained from Equation (7.2) with the potential  $\phi =$

0; inserting the time factor  $\exp(-j\omega t)$ , we have

$$\begin{aligned} E_\phi &= -\partial A_\phi / \partial t \\ &= j\omega\mu I \delta\mathcal{A} \rho e^{-j\omega t} / 4\pi (\rho^2 + z^2)^{3/2} \end{aligned} \quad (7.14d)$$

However, its effect is small compared to the magnetic fields.

All three components may also be expressed in spherical coordinates as  $H_r$ ,  $H_\theta$ , and  $E_\phi$  [the last being identical to  $E_\phi$  in Eq. (7.14d)]. Because  $H_r^2 + H_\theta^2 = H_\rho^2 + H_z^2$  and  $z = r \cos \theta$ ,  $\rho = r \sin \theta$ , we get

$$H_r = 2H_z / (2 \cos \theta - \sin \theta \tan \theta) = 2H_z / 3 \sin \theta$$

$$H_\theta = H_z / (2 \cos \theta \cot \theta - \sin \theta) = H_z / 3 \cos \theta$$

Thus,

$$H_r = I \delta\mathcal{A} \cos \theta / 2\pi r^3 \quad (7.14e)$$

$$H_\theta = I \delta\mathcal{A} \sin \theta / 4\pi r^3 \quad (7.14f)$$

$$E_\phi = j\omega\mu I \delta\mathcal{A} \sin \theta / 4\pi r^2 \quad (7.14g)$$

There are three limiting cases of interest in regard to the  $H$  fields:

(i)  $\rho = 0$ , so  $\theta = 0$  and the field is axial:

$$H_z = H_r = I \delta\mathcal{A} / 2\pi z^3 \quad (7.14h)$$

(ii)  $z = 0$ , so  $\theta = \pi/2$  and the loop and field are coplanar:

$$H_z = -H_\theta = -I \delta\mathcal{A} / 4\pi \rho^3 \quad (7.14i)$$

These are approximations because we took  $(\rho^2 + z^2) \gg a^2$ ; the error, however, is less than 3% if either  $z$  or  $\rho$  is larger than  $7a$ . Replacing the latter in the original expression for  $A_\phi$  and setting  $\rho = z = 0$ , we find the field at the coil center to be

$$(iii) \quad H_z = I/2a \quad H_r = 0 \quad (7.14j)$$

Clearly the small coil is equivalent to an oscillating magnetic dipole lying in the  $z$  axis at the origin with magnetic moment given by  $m = I \delta\mathcal{A} e^{-j\omega t}$ . Furthermore its shape is not significant, provided  $a < 0.14\rho$  (or  $0.14z$ ); for a square loop  $(H_z)_{z=0} \approx I \delta\mathcal{A} / 4\pi \rho^3$ . It is also of interest that the  $z$  components in Equations (7.14h) and (7.14i) resemble the Gauss A and B positions (§3.2.3) with  $m$  in Equation (3.15c) replaced with  $I \delta\mathcal{A} / 4\pi$ .

The dipole field intensity, then, falls off with the inverse cube of the distance; compared to the long-wire systems, the intensity decreases much faster. However, it should be kept in mind that both are approximations. The straight wire is assumed to be considerably longer than the perpendicular distance to the station at which the field is measured, whereas

the closed-loop dimensions are considerably smaller than its distance from the field station.

If the source loop, instead of being in free space, is lying on homogeneous ground, the field components in Equations (7.14b, c, d) become (Ward and Hohmann, 1988:211-2) in cylindrical coordinates

$$H_\rho = -(I \delta \omega k^2 / 4\pi\rho) \{ I_1(\frac{1}{2}jk\rho) K_1(\frac{1}{2}jk\rho) - I_2(\frac{1}{2}jk\rho) K_2(\frac{1}{2}jk\rho) \} \quad (7.14k)$$

$$H_z = (I \delta \omega / 2\pi k^2 \rho^3) \{ 9 - (9 + 9jk\rho - 4k^2 \rho^2 - jk^3 \rho^3) e^{-jk\rho} \} \quad (7.14l)$$

$$E_\phi = -(I \delta \omega / 2\pi \sigma \rho^4) \{ 3 - (3 + 3jk\rho - k^2 \rho^2) e^{-jk\rho} \} \quad (7.14m)$$

where the propagation constant (§7.2.3b)  $k = (\omega^2 \mu \epsilon - j\omega \mu \sigma)^{1/2} = (-j\omega \mu \sigma)^{1/2}$  over homogeneous ground,  $I_n(\frac{1}{2}jk\rho)$  and  $K_n(\frac{1}{2}jk\rho)$  are modified Bessel functions of the first and second kinds of order  $n$  (Pipes and Harvill, 1970). For  $(k\rho) \approx 0$ , the above equations become

$$H_\rho \approx -(I \delta \omega k^2 / 16\pi\rho) \quad (7.14n)$$

$$H_z \approx -(I \delta \omega / 4\pi\rho^3) \quad (7.14o)$$

$$E_\phi \approx (I \delta \omega k^2 / 4\pi \sigma \rho^2) \quad (7.14p)$$

Using reasonable values such as  $\rho = 100$  m,  $\sigma = 0.01$  S/m, we find that the magnitudes of all three components in Equations (7.14n, o, p) are smaller than those in free space by a factor of about  $10^{-4}$ . The vertical magnetic dipole is widely used in ground systems.

*(e) Horizontal magnetic dipole.* This type of source is commonly used in vertical-loop fixed-transmitter and broadside ground units (§7.4.2b, c) and in airborne systems. The results for propagation in free space are easily obtained. We take the coil in the  $xz$  plane with its center at the origin; the expressions for the components are then obtained by replacing  $z$  in Equations (7.14b, c, d) with  $y$ .

When the coil is on homogeneous ground, the components are (Ward and Hohmann, 1988)

$$H_x = 3I \delta \omega xy / 4\pi \rho^3 \quad (7.14q)$$

$$H_y = I \delta \omega (2y^2 - x^2) / 4\pi \rho^5 \quad (7.14r)$$

$$H_z = -j\omega \mu_0 \sigma I \delta \omega y / 16\pi \rho^2 \quad (7.14s)$$

where  $\rho^2 = x^2 + z^2$ .

In all the preceding magnetic field sources we have also assumed only one turn of wire. If there are

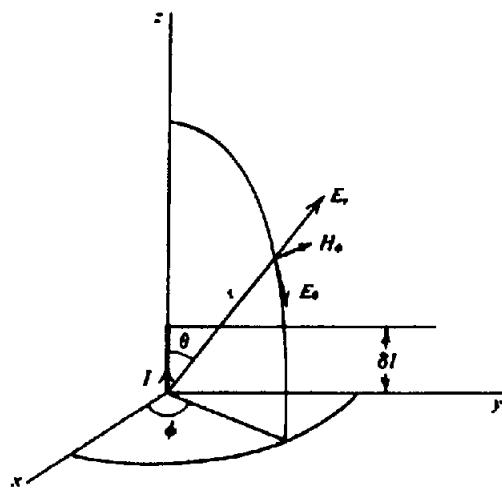


Figure 7.4. Field of a short vertical wire at a distant point.

$n$  turns, the calculated fields are increased by a factor of  $n$  in all cases.

*(f) Vertical straight wire (vertical electric dipole).* One other artificial source of EM waves that has been employed in prospecting should be considered here. This is the high power VLF (very-low-frequency) transmission in the range 15 to 25 kHz, which is normally used for air and marine navigation. There are, of course, many RF stations available as well, but the frequencies are considerably higher (500 kHz and up) and the power lower than the VLF sources, so that the range and depth of penetration are limited.

The VLF antenna is effectively a grounded vertical wire, several hundred meters high. Consequently it is much shorter than a transmission wavelength, which, for a frequency of 20 kHz, is 15 km. Whereas the small loop is equivalent to a magnetic dipole, the short wire behaves as an electric dipole.

There are several possible modes of radiation from this type of antenna, but in the low-frequency range and at distances considerably greater than a wavelength, the propagation is a combination of ground wave and sky wave. The former travels over the earth's surface, whereas the sky wave is refracted and reflected by the ionized layers in the upper atmosphere (50 km and higher) to return to ground. At large distances from the antenna the VLF waves appear to be propagated in the space between the spherical reflecting shell formed by the earth surface and the lower ionosphere. The attenuation is comparatively small in both surfaces.

From Figure 7.4 it is apparent that the electric dipole is quite like the magnetic dipole if we interchange the  $E$  and  $H$  components of the wave, that is, there are two components of electric field,  $E_r$  and  $E_\phi$ , in spherical coordinates, and one magnetic com-

ponent  $H_\phi$  in the azimuth. The vector potential of a current element  $I\delta l$  can be found from Equation (7.11); in spherical coordinates,

$$\begin{aligned} \mathbf{A} &= \mu I \delta l e^{-j\omega t^*} \mathbf{i}_z / 4\pi r \\ &= \mu I \delta l e^{-j\omega t^*} (\cos \theta \mathbf{i}_r - \sin \theta \mathbf{i}_\theta) / 4\pi r \end{aligned}$$

where the current flow in the dipole length  $\delta l$  is along the  $z$  axis,  $t^* = t - r/c = t - r(\mu\epsilon)^{1/2}$ , and  $c$  is the velocity of light =  $3 \times 10^8$  m/s. The scalar portion,  $\phi'$ , composed of the scalar potential plus an extra term caused by phase difference in the time-varying potential, becomes

$$\phi' = I\delta l \cos \theta (\omega/cr + 1/r^2) e^{-j\omega t^*} / 4\pi\epsilon\omega.$$

Using Equations (7.1), (7.2), and (A.38), we find

$$\left. \begin{aligned} \mathbf{E} &= -\nabla\phi' - \partial\mathbf{A}/\partial t \\ &= -(\partial\phi'/\partial r + \partial A_r/\partial t)\mathbf{i}_r - (\partial\phi'/\partial\theta + \partial A_\theta/\partial t)\mathbf{i}_\theta \\ \mathbf{H} &= (\nabla \times \mathbf{A})/\mu \\ &= [\partial(rA_\theta)/\partial r - \partial A_r/\partial\theta]\mathbf{i}_\phi/\mu r \end{aligned} \right\} \quad (7.15a)$$

These expressions produce one magnetic and two electric components:

$$H_\phi = I\delta l \sin \theta e^{-j\omega t^*} (\omega/cr + 1/r^2) / 4\pi \quad (7.15b)$$

$$\begin{aligned} E_r &= I\delta l \cos \theta e^{-j\omega t^*} \\ &\times (1/cr^2 - j/\omega r^3) / 2\pi\epsilon \end{aligned} \quad (7.15c)$$

$$\begin{aligned} E_\theta &= I\delta l \sin \theta e^{-j\omega t^*} \\ &\times (\omega/c^2 r + 1/cr^2 - j/\omega r^3) / 4\pi\epsilon \end{aligned} \quad (7.15d)$$

The three components may be converted to cylindrical coordinates as in Section 7.2.3d. For example, using Equation (A.36) and neglecting terms in  $1/r^2$ ,  $1/r^3$  (note that  $r^2 = \rho^2 + z^2$  in Fig. 7.3),

$$E_\rho \approx 3j\omega\mu I \delta l \rho e^{-j\omega t^*} / 4\pi (\rho^2 + z^2)^{3/2} \quad (7.15e)$$

$$E_z \approx 0 \quad (7.15f)$$

$$H_\phi \approx j\omega(\mu\epsilon)^{1/2} I \delta l \rho e^{-j\omega t^*} / 4\pi (\rho^2 + z^2) \quad (7.15g)$$

These formulas are more complete and more complex than those for the magnetic dipole, and they contain terms in  $1/r$ ,  $1/r^2$  as well as  $1/r^3$ . Clearly the VLF system is designed for long-distance transmission; the so-called *radiation fields* or *far fields*, varying as  $1/r$ , are significant when the *induction* and *static fields* (*near fields*), varying as  $1/r^2$  and  $1/r^3$ , have become negligible. Consequently, we

consider only the first term inside the brackets in Equations (7.15b, d) and assume that  $E_r \approx E_z \approx 0$  at great distance.

The preceding development may be carried out for Equations (7.14c, f, g) (Stratton, 1941; Smythe, 1950). Apart from the dipole moments and a phase shift of  $\pm\pi/2$  (indicated by  $\pm j$ ; see §A.7), for all terms, Equations (7.14g) and (7.15b) are identical, and Equations (7.15c) and (7.15d) are the same as Equations (7.14e) and (7.14f) if the latter are multiplied by  $(1/\omega\epsilon)$  and  $H$  and  $E$  interchanged. However, because the magnetic dipole is very rarely used for transmission beyond a few kilometers, only the near-field term is significant.

Because the amplitude of VLF fields decreases only as  $1/r$  and the station output power is large (100 to 1,000 kW), it is possible to detect these sources over continental distances, occasionally nearly half way around the world.

At great distances from the source,  $E_r$  is negligible and  $E$  would appear to be nearly vertical; at the ground-air boundary, however, there is a considerable horizontal component in the direction of propagation. The magnetic field lines are horizontal circles concentric about the antenna; at distances of several hundred kilometers this field is practically uniform over, say, a few square kilometers, and is at right angles to the station direction.

Figure 7.5 compares the magnitude of primary fields from the various sources described in this section: VLF transmitter, long wire, square loop, and circular coil. These were calculated from Equations (7.10b), (7.14), and a modification of Equation (7.15b), following, that allows for attenuation:

$$H = \frac{I \delta l}{2\lambda r} e^{-1.5 \times 10^{-3} r/\lambda} \quad (7.15h)$$

where  $\lambda$ ,  $r$ , and  $\delta l$  are in kilometers. The curves are drawn for the following parameters:

1. VLF transmitter power =  $10^6$  W, frequency = 20 kHz, antenna current = 5,000 A, and height = 300 ft (100 m).
2. Long-wire power = 1,000 W, current = 3 A, and length = 4,000 ft (1,200 m).
3. Square-loop power = 300 W, current = 3 A, section area =  $36 \text{ ft}^2$ , ( $3.3 \text{ m}^2$ ), and turns of wire = 100.
4. Circular-loop power = 5 W, current = 100 mA, diameter = 3 ft (1 m), and turns of wire = 1,000.

These values correspond roughly to (1) VLF, (2) Turam, (3) vertical-loop dip-angle, and (4) horizontal-loop systems used in EM field work.

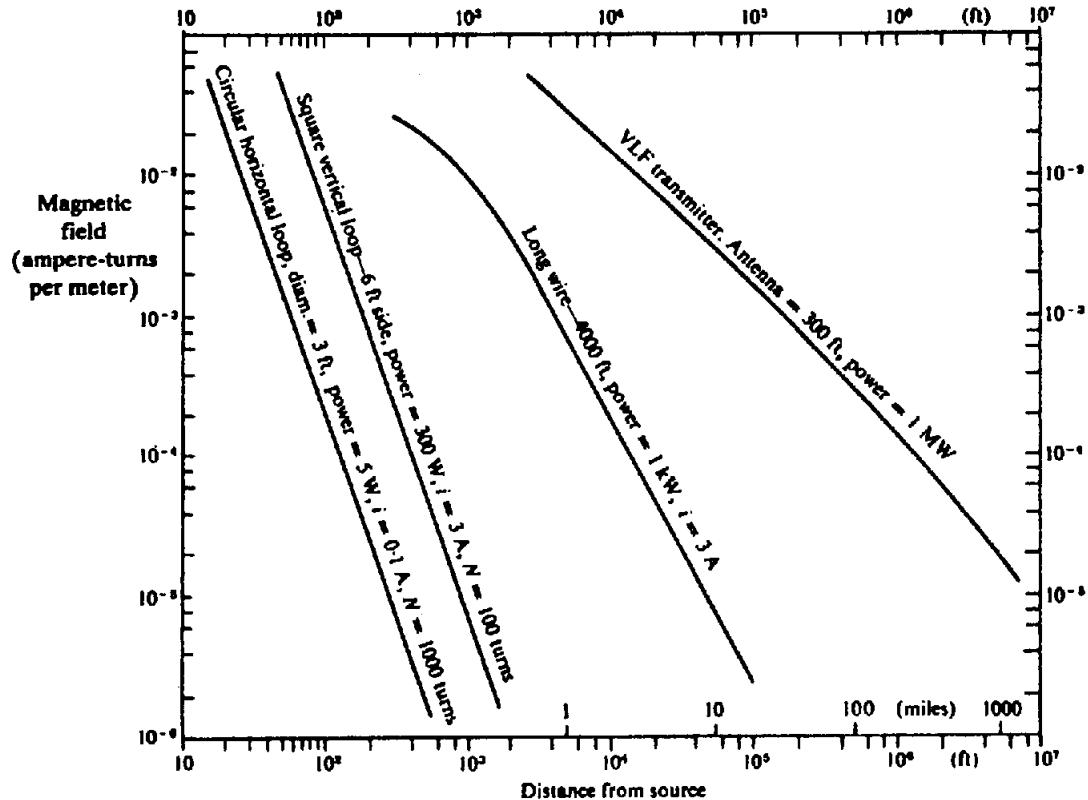


Figure 7.5. Comparison of magnetic fields produced by various sources.

#### 7.2.4. Combination of FD Fields

(a) *General.* So far we have described the propagation, attenuation, and generation of alternating magnetic fields. We have seen that such fields can be initiated by various current configurations and attenuated more or less depending on their frequency and the conductivity (and permeability) of the medium through which they travel.

In Section 6.2.3 it was also noted that the EM field was shifted in phase on encountering a relatively good conductor. In fact, this conductor becomes the source of a secondary field, which differs in phase from the primary field, while having the same frequency. Hence a suitable detector in the vicinity will be energized by both the primary and secondary fields simultaneously. The existence of the secondary field, indicating the presence of a subsurface conductor, may be established with respect to the primary field by a change of amplitude and/or phase in the normal detector signal. Some EM systems measure both quantities; some respond to one or the other.

(b) *Amplitude and phase relations.* The character of the secondary magnetic field is best illustrated by a consideration of the coupling between ac circuits. We assume a trio of coils having inductance and resistance and negligible capacitance; the first is the primary source, the second is equivalent to the con-

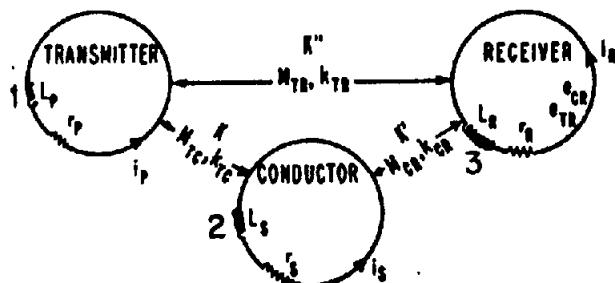


Figure 7.6. Electric-circuit analogy for EM system.

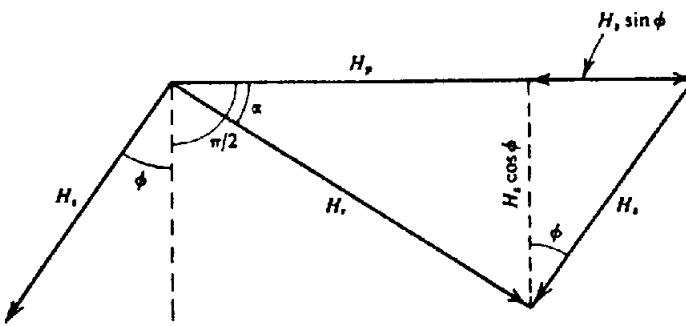
ductor, and the third is the detector (Fig. 7.6). The primary EM field at a point near the conductor (coil 2), resulting from a current  $i_p$  flowing in the first coil, is given by

$$H_p = Ki_p = KI_p \sin \omega t$$

where  $K$  depends on the geometry of the system, the area and number of turns of the primary coil, and attenuation of the wave.

As a result of this field, coil 2 has an emf induced in it that lags behind the primary field by  $\pi/2$ ; thus,

$$\begin{aligned} e_s &= -M \frac{di_p}{dt} = -\omega M I_p \cos \omega t \\ &= \omega M I_p \sin(\omega t - \pi/2) \\ &= -j\omega M H_p / K \end{aligned}$$

Figure 7.7. Vector diagram showing phase shift between  $H_s$  and  $H_p$ .

(§A.7) where  $M = M_{TC}$  = mutual inductance (see §7.2.5) between coils 1 and 2. Then the current flowing in coil 2 will be

$$i_s = e_s/z_s = e_s/(r_s + j\omega L_s)$$

where  $z_s = (r_s + j\omega L_s)$  is the effective impedance of the conductor of resistance  $r_s$ , and inductance  $L_s$ . The secondary field near the detector (coil 3) as a result of this current will be

$$\begin{aligned} H_s &= K'i_s = \frac{-K'j\omega MH_p}{K(r_s + j\omega L_s)} \\ &= \frac{-K'MH_p(j\omega r_s + \omega^2 L_s)}{K(r_s^2 + \omega^2 L_s^2)} \\ &= \frac{-K'MH_p(Q^2 + jQ)}{KL_s(1 + Q^2)} \end{aligned} \quad (7.16a)$$

where  $K'$  is a constant similar to  $K$  and  $Q = \omega L_s/r_s$  is the figure of merit.

The primary field at the detector coil will be

$$H'_p = K''i_p = K''I_p \sin \omega t = K''H_p/K$$

where  $K''$  is similar to  $K$  and  $K'$ .

Thus the relative magnitude of the fields at the detector is

$$\begin{aligned} \left| \frac{H_s}{H'_p} \right| &= \frac{K'i_s}{K''i_p} \\ &= \frac{K'M}{K''L_s} \left\{ \frac{Q^4}{(1 + Q^2)^2} + \frac{Q^2}{(1 + Q^2)^2} \right\}^{1/2} \\ &= \frac{K'M}{K''L_s} \frac{1}{(1 + 1/Q^2)^{1/2}} \end{aligned} \quad (7.16b)$$

Because the ratio  $K'M/K''L_s$  is generally very small, the ratio  $H_s/H'_p$  is small, regardless of the value of  $Q$ .

The phase difference between primary and secondary fields is

$$\theta_p - \theta_s = \left( \frac{\pi}{2} + \tan^{-1} \frac{\omega L_s}{r_s} \right) - \left( \frac{\pi}{2} + \phi \right) \quad (7.17)$$

where  $\tan \phi = \omega L_s/r_s$ . The lag in phase of  $\pi/2$  is due to the inductive coupling between coils 1 and 2, whereas the additional phase lag  $\phi$  is determined by the properties of the conductor as an electrical circuit. That is,

$$\begin{aligned} H_s &= K'I_s \sin(\omega t - (\pi/2 + \phi)) \\ &= -K'I_s \cos(\omega t - \phi) \end{aligned}$$

The phase shift is most clearly illustrated by the vector diagram in Figure 7.7. (In this diagram the magnitude of  $H_s$  with respect to  $H_p$  is greatly exaggerated.) The resultant of  $H_p$  and  $H_s$  is  $H_r$ .

From this diagram and Equation (7.17), it can be seen that when we have a very good conductor,  $Q = \omega L_s/r_s \rightarrow \infty$  and  $\phi \rightarrow \pi/2$ . In this case, the phase of the secondary field is practically  $180^\circ$  ( $\pi$ ) behind the primary field. For a very poor conductor  $\omega L_s/r_s \rightarrow 0$  and  $\phi \rightarrow 0$ ; the secondary field lags  $\pi/2$  behind the primary. Generally  $H_s$  is somewhere between  $\pi/2$  and  $\pi$  ( $90^\circ$  and  $180^\circ$ ) out of phase with  $H_p$ .

The component of  $H_s$   $180^\circ$  out of phase with  $H_p$  is  $H_s \sin \phi$ , whereas the component  $90^\circ$  out of phase is  $H_s \cos \phi$ . In EM parlance, the  $180^\circ$  out-of-phase fraction of  $H_s$  is called the *real* or *in-phase* component. The  $90^\circ$  out-of-phase fraction of  $H_s$  is called the *imaginary*, *out-phase*, or *quadrature* component. These terms originated in ac circuit theory and, in fact, there is nothing imaginary about the quadrature component. From Figure 7.7 we get the important relation [see Eq. (A.47a)]

$$\tan \phi = [\mathcal{I}_m\{H_s\}/\mathcal{R}_s\{H_s\}] \quad (7.18)$$

(c) **Elliptic polarization.** The detector in an EM field system, generally a small coil with many turns of fine wire, measures the secondary field produced by a subsurface conductor, in the presence of the primary field. Consequently, the detected signal is a combination of the primary and one or more secondary fields. In general the combination is a magnetic field that is elliptically polarized. From the previous section we can write

$$H_p = A \sin \omega t \quad \text{and} \quad H_s = B \cos(\omega t - \phi)$$

where  $A$  and  $B$  are functions of the geometry of the transmitter, conductor and detector. Because

$$\begin{aligned} \cos(\omega t - \phi) &= \cos \omega t \cos \phi + \sin \omega t \sin \phi \\ &= (1 - H_p^2/A^2)^{1/2} \cos \phi \\ &\quad + H_p \sin \phi / A \\ &= H_s / B \end{aligned}$$

we get

$$\frac{H_p^2}{A^2} + \frac{H_s^2}{B^2} - \frac{2H_p H_s \sin \phi}{AB} = \cos^2 \phi$$

that is,

$$\frac{H_p^2}{A^2 \cos^2 \phi} + \frac{H_s^2}{B^2 \cos^2 \phi} - \frac{2H_p H_s \sin \phi}{AB \cos^2 \phi} = 1 \quad (7.19)$$

This equation is of the form

$$Lx^2 - 2Mxz + Nx^2 = 1$$

which is the equation of an ellipse.

We have made two simplifying assumptions in obtaining the equation. The first is that  $H_p$  and  $H_s$  are orthogonal in space, which is not generally true. However, if the angle between  $H_p$  and  $H_s$  is  $\alpha \neq \pi/2$ , these vectors may be resolved in two orthogonal components, say

$$H_s = H_p + H_s \cos \alpha \quad \text{and} \quad H_x = H_s \sin \alpha$$

in which case the expression for  $H_p$  and  $H_x$  is more complicated and has constant terms, but is still the equation of an ellipse.

The second assumption was that  $H_s$  is due to the current in only one conductor. This is not necessarily the case; however, a combination of vectors of different amplitudes, directions, and phases, resulting from currents in several conductors, can be resolved into a single resultant for  $H_s$ .

Consequently the superposition of fields produces a single field that is elliptically polarized, the vector being finite at all times [although  $H_p$  and  $H_s$  become zero at  $\omega t = n\pi$  and  $(2n+1)\pi/2$ , respectively] and rotating in space with continuous amplitude change. Its extremity sweeps out an ellipse.

This ellipse may lie in any space plane, although the plane will normally be only slightly tilted off horizontal or vertical. This is because the major axis of the ellipse is determined by  $H_p$  – because it is usually much larger than  $H_s$  – and the primary field is normally either horizontal or vertical in EM systems.

There are two special cases of Equation (7.19) of considerable importance. Figure 7.7 is again helpful in visualizing these situations.

(i)  $\phi = \pi/2$ . Equation (7.19) then reduces to

$$\left( \frac{H_p}{A} - \frac{H_s}{B} \right)^2 = 0 \quad \text{or} \quad BH_p - AH_s = 0$$

which is a straight line through the origin of the coordinates, having a slope  $+B/A$ . This case corresponds to a very good conductor, because

$$\phi = \tan^{-1} \omega L_s / r_s = \pi/2$$

or, because  $\tan \phi = \infty$ ,

$$r_s = 0$$

The ellipse of polarization has collapsed into a straight line.

(ii)  $\phi = 0$ . The ellipse equation simplifies to

$$\frac{H_p^2}{A^2} + \frac{H_s^2}{B^2} = 1$$

which signifies a poor conductor because  $r_s \gg \omega L_s$ , when  $\phi = 0$ . In the unlikely event that  $A = B$  as well, the combination of  $H_p$  and  $H_s$  results in circular polarization.

Obviously a detector coil can always be oriented so that it lies in the plane of polarization, when a true null signal would be obtained. Some of the early EM methods were based on this fact; the dip and azimuth of the polarization ellipse and its major and minor axes were measured.

On the other hand, if the detector coil is rotated about its vertical or horizontal diameter, it will not always be possible to find a perfect null position, because the plane of the coil will not, in general, coincide with the plane of the ellipse. There will, however, be a minimum signal at one coil orientation.

### 7.2.5. Mutual Inductance

(a) *General theory.* It was noted in the discussion of phase shift that the inductive coupling between electrical circuits is proportional to the coefficient of mutual inductance  $M$ . This parameter can be used to some effect in determining the signal amplitude at the receiver due to both the transmitter and conductor. It has already been employed to estimate the current induced in the conductor as the result of the primary field.

If we can simulate the transmitter and receiver coils and the conductor by simple electric circuits, it may be possible to calculate the mutual inductances that couple them. Consider the coil system illustrated in Figure 7.6, in which the mutual inductances between transmitter and conductor, conductor and receiver, and transmitter and receiver are, respectively,  $M_{TC}$ ,  $M_{CR}$ , and  $M_{TR}$ .

It was shown previously (§7.2.4b) that the current  $i_p$  induced in the conductor by the transmitter is related to the transmitter current by the expression

$$i_s = -\frac{j\omega M_{TC} i_p}{r_s + j\omega L_s} = -\frac{M_{TC}}{L_s} \frac{(Q^2 + jQ) i_p}{1 + Q^2}$$

where  $Q = \omega L_s / r_s$  was a figure of merit for the conductor circuit.

Current  $i_s$ , in turn, will induce an emf in the receiver coil given by

$$e_{CR} = -j\omega M_{CR} \cdot i_s = \frac{j\omega M_{CR} M_{TC}}{L_s} \frac{(Q^2 + jQ) i_p}{1 + Q^2}$$

At the same time the primary field induces an emf in the receiver

$$e_{TR} = -j\omega M_{TR} i_p$$

Because the secondary or anomalous field is measured in the presence of the primary field, we have

$$\frac{e_{CR}}{e_{TR}} = -\frac{M_{CR} M_{TC}}{M_{TR} L_s} \left( \frac{Q^2 + jQ}{1 + Q^2} \right) \quad (7.20a)$$

Mutual inductance may also be written in terms of the coupled self-inductances:

$$M_{CR} = k_{CR} (L_s L_R)^{1/2}$$

$$M_{TC} = k_{TC} (L_s L_T)^{1/2}$$

$$M_{TR} = k_{TR} (L_T L_R)^{1/2}$$

where  $k_{CR}$  is the coupling coefficient between conductor and receiver and so forth,  $L_T$  is the transmit-

ter loop inductance, and  $L_R$  is the receiver loop inductance. Then we can write Equation (7.20a) in the form

$$\frac{e_{CR}}{e_{TR}} = -\frac{k_{CR} k_{TC}}{k_{TR}} \left( \frac{Q^2 + jQ}{1 + Q^2} \right) \quad (7.20b)$$

Although this eliminates  $L_s$  in the first part of the expression, it does not simplify the first ratio much because the  $k$  values, like the  $M$  values, involve complicated geometry of the system. Equation (7.20b) does indicate, however, that this ratio, sometimes called the *coupling parameter*, is usually a very small quantity because  $k_{TR}$  will tend to be much larger than the two coefficients in the numerator. That is to say, the transmitter and receiver are coupled through air, which means the attenuation is practically zero. In some FDEM field layouts, the source and detector coils are purposely oriented to reduce the direct coupling, whereas in others the decoupling is accomplished by electrical means.

In any case, the mutual inductances between the various components within the range of the magnetic field are a controlling factor in EM systems. Consequently it would be useful to determine  $M$  for simple geometrical configurations that simulate field situations, as an aid in interpretation.

The mutual inductance  $M_{12}$  between two circuits 1 and 2 is defined as the total flux  $\Phi_{12}$  through circuit 1, produced by unit current in circuit 2. Thus,

$$M_{12} = \frac{\Phi_{12}}{i_2} = \int_{S_1} \frac{\mathbf{B}_2 \cdot d\mathbf{s}_1}{i_2} = \int_{S_1} \frac{\nabla \times \mathbf{A}_2 \cdot d\mathbf{s}_1}{i_2}$$

$$= \oint_{C_1} \frac{\mathbf{A}_2 \cdot d\ell_1}{i_2}$$

where  $S_1$  is any surface terminating on circuit  $C_1$ , and the last result came from Stokes' theorem [Eq. (A.29c)]. From Equation (7.11) we have

$$\mathbf{A}_2 = \frac{\mu i_2}{4\pi} \oint \frac{d\ell_2}{r}$$

This gives the general *Neumann formula* for mutual inductance:

$$M_{12} = \oint \frac{\mathbf{A}_2 \cdot d\ell_1}{i_2} = \frac{\mu}{4\pi} \oint \oint \frac{d\ell_1 \cdot d\ell_2}{r}$$

$$= \frac{\mu}{4\pi} \oint \oint \frac{\cos \theta}{r} d\ell_1 d\ell_2 \quad (7.21a)$$

where  $d\ell_1$ ,  $d\ell_2$  are elements of length in circuits 1 and 2,  $r$  is the distance between  $d\ell_1$  and  $d\ell_2$ , and  $\theta$  is the angle between  $d\ell_1$  and  $d\ell_2$ .

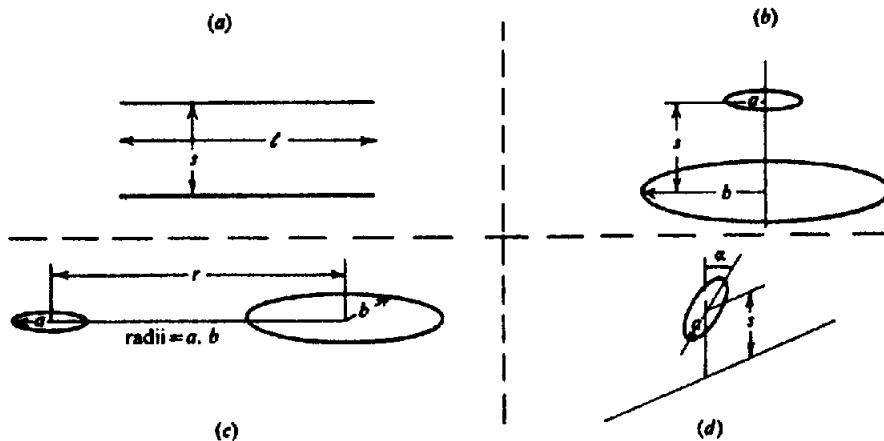


Figure 7.8. Calculating mutual inductance of various geometrical figures. (a) Two parallel straight lines. (b) Coaxial circles. (c) Coplanar circles. (d) Circle and long straight wire.

In many cases it is necessary to integrate numerically to get a particular answer from this general formula. However, several simple circuits can be worked out exactly. These are illustrated in Figure 7.8 and the formulas are given in the following text. Units are microhenrys and meters.

(i) *Two parallel wires of equal length.* Let the length be  $\ell$  and the distance apart  $s$ . Then,

$$M = 0.2\ell \left[ \ln \left\{ \frac{\ell}{s} + \left( 1 + \frac{\ell^2}{s^2} \right)^{1/2} \right\} - \left( 1 + \frac{s^2}{\ell^2} \right)^{1/2} + \frac{s}{\ell} \right] \quad (7.21b)$$

When  $\ell/s > 1$ , this can be modified to give

$$M = 0.2\ell \left[ \ln \left( \frac{2\ell}{s} \right) - 1 + \frac{s}{\ell} \left\{ 1 - \left( \frac{s}{2\ell} \right)^2 + \frac{1}{2} \left( \frac{s}{2\ell} \right)^4 - \frac{2}{3} \left( \frac{s}{2\ell} \right)^6 \dots \right\} \right]$$

More complicated forms of straight conductors may be found in Grover (1962).

(ii) *Two coaxial circles.*  $M$  is a function of  $a$ ,  $b$ , and  $s$ , the radii and separation, which varies with a parameter  $k$ , given by

$$k^2 = [(a - b)^2 + s^2]/[(a + b)^2 + s^2]$$

which is found in tables (Grover, 1962). When  $s \geq 10a$  or  $10b$ ,

$$M = 0.2\pi a^2 \pi b^2 / s^3 = 0.2\mathcal{A}\mathcal{B} / s^3 = 2a^2 b^2 / s^3 \quad (7.21c)$$

$\mathcal{A}$ ,  $\mathcal{B}$  being areas of the circles.

(iii) *Two coplanar circles.* When  $r \gg a, b$ ,

$$M \approx -0.1\pi a^2 \pi b^2 / r^3 \approx -0.1\mathcal{A}\mathcal{B} / r^3 = -a^2 b^2 / r^3 \quad (7.21d)$$

Again, more complicated arrangements of the circles are dealt with in Grover.

(iv) *Circle and long straight wire.* Let a long straight wire intersect at right angles the extension of a diameter of the circle of radius  $a$ . If the plane of the circle makes an acute angle  $\alpha$  with the plane through the diameter and the long wire, and if  $s$  is the distance between the wire and the center of the circle, then

$$M = 4\pi \times 10^{-3} \left\{ s \sec \alpha - (s^2 \sec^2 \alpha - a^2)^{1/2} \right\} \quad (7.21e)$$

and when  $s/a \geq 5$ , this is simplified to

$$M \approx \frac{2\pi \times 10^{-3} a^2}{s \sec \alpha} = \frac{0.002\mathcal{A}}{s \sec \alpha} \quad (7.21f)$$

(b) *Self-inductance.* Values of  $L$  for the straight wire and circle are given by

$$L_w = 0.2\ell [\ln(2\ell/\rho) - 0.75] \quad (7.22a)$$

$$L_c \approx 4\pi \times 10^{-3} a [\ln(8a/\rho) - 2] \quad (7.22b)$$

where  $\rho$  is the wire radius, and  $\ell$ ,  $a$  are as shown in Figure 7.8. Self-inductance for several regular figures may be written

$$L = 0.2l_e [\ln(4l_e/\rho) - x] \quad (7.22c)$$

where  $l_e$  is the perimeter of the figure and  $x$  is a constant related to the shape; generally  $x < 3$ .

In all these formulas the values of  $M$  are increased by  $N_1 N_2$  and  $L$  by  $N^2$  if these are the number of turns on the various circuits. Although  $M$  and  $L$  are easily determined for the regular figures of the transmitter and receiver antennae, it is a difficult problem to simulate the conductor. Because we normally do not know the current-flow cross section, it is necessary to oversimplify the equivalent circuit.

(c) *Numerical example.* To illustrate the magnitude of the coupling factor,  $(M_{CR} M_{TC})/(M_{TR} L_s)$ , in Equation (7.20a), consider the case of a horizontal-loop system (§7.4.3c) straddling a long, thin vertical conducting sheet that outcrops at the surface as in Figure 7.9. We assume that the transmitter and receiver coils are identical (cross section =  $A$ ), the distance  $l$  between their centers being less than  $\ell$ , the length of the sheet, and that the ratio  $\ell/p \approx 2,500$ . The principal effect of the sheet is due to its upper edge; hence to a first approximation we can consider the sheet as a horizontal wire of length  $\ell$  at the surface. Using Equations (7.21d, f), and (7.22a), we get for the coupling factor in Equation (7.20a)

$$\begin{aligned}\frac{M_{TC} M_{CR}}{M_{TR} L_s} &= \left( \frac{0.002\alpha}{l/2} \right)^2 \left( \frac{l^3}{0.1\alpha^2} \right) \\ &\times \left( \frac{1}{0.2\ell \{ \ln(2\ell/p) - 3/4 \}} \right) \\ &\approx 10^{-4} (l/\ell) < 10^{-4}\end{aligned}$$

Thus the signal response has been reduced by the factor  $10^4$  or more.

(d) *Conductor response.* Returning to Equation (7.20b), the second factor on the right-hand side depends only on the conductor and the frequency (because  $Q = \omega L_s/r_s$ ). In this situation  $Q$  is known as the *response parameter* of the conductor, whereas the complex ratio  $(Q^2 + jQ)/(1 + Q^2)$  is called the *response function* or *induction number*.

Plotting the response function against  $Q$ , we get two curves for the real and imaginary parts of the function:

$$A = Q^2/(1 + Q^2)$$

and

$$B = Q/(1 + Q^2)$$

where  $A$  and  $B$  are real. This plot is shown in Figure 7.10.

This example, of course, is oversimplified because it represents a wire loop. However, more realistic models of a sphere, thin sheet, or half-space are quite similar.

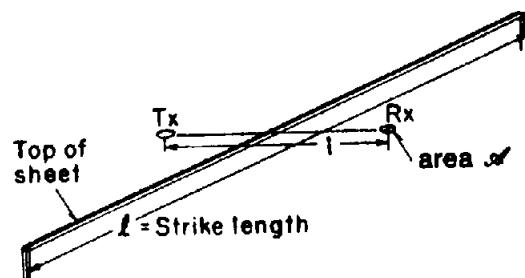


Figure 7.9. Coupling factor of horizontal-loop system over a long vertical sheet conductor.

When  $Q$  is very small, both real and imaginary parts of the function are very small. The ratio of secondary to primary response in the receiver will be

$$\frac{e_{CR}}{e_{TR}} \approx - \frac{jQk_{CR}k_{TC}}{k_{TR}}$$

This is the case of a poor conductor. As  $Q$  increases, the imaginary part increases at a faster rate at first and its magnitude is larger than the real fraction until  $Q = 1$ , when they are both equal to 0.5. Beyond this point the imaginary part decreases until, at large values of  $Q$ , it is again zero. Meanwhile, the value of  $A$  increases to an upper limit of unity when  $Q$  is large, or

$$\left| \frac{e_{CR}}{e_{TR}} \right| = \frac{k_{CR}k_{TC}}{k_{TR}}$$

which is the maximum value for a very good conductor.

When the value of  $Q$  is quite small the phase angle of this function is  $\pi/2$ ; when  $Q = 1$ , it is  $3\pi/4$  after which it increases to  $\pi$  for a very good conductor, that is, the secondary signal is opposed to the primary.

In the range  $0 \leq Q \leq 1$  the imaginary or quadrature component is larger than the real component, whereas from  $1 \leq Q \leq \infty$  the reverse is true. Thus the ratio of in-phase to quadrature components is somewhat diagnostic of the conductor. It is also clear that if one measures only the imaginary component in an EM system, a very good conductor will give a very poor response.

## 7.2.6. Fields in the Time Domain

(a) *General.* The time-domain EM transmitter generates repetitive signals of a transient or pulse character in various forms: half sine-wave, step, ramp functions, and so forth. All of these have a broad frequency spectrum that results in a secondary field time-decay curve beginning immediately following

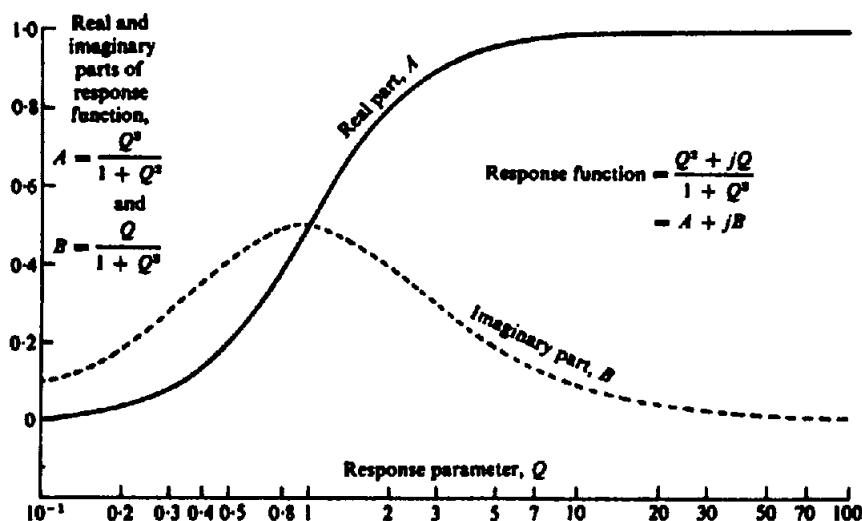


Figure 7.10. Response function of a conductor in an ac field. (After Grant and West, 1965).

the transmitter cutoff and in which the frequency decreases with time.

Material for Section 7.2.6 is taken, to a great extent, from Ward and Hohmann (1988) and from the classic papers of Wait (1951a, c; 1960a; 1971). It is interesting that the theoretical work was done so long before the serious development of TDEM.

In Section 7.2.3 we denoted FDEM fields by  $H$  and  $E$ ; in this section we use  $h$  and  $e$  for TDEM fields.

(b) *Method of TD analysis.* Development in the time domain analogous to that in Section 7.2.3 for the frequency domain is best accomplished by using Laplace transforms (§A.12) which are well suited to discussion of transient fields.

Taking Laplace transforms of Equations (6.3) and (6.4), and using Equation (A.78a) with  $n = 1$ , we obtain

$$\nabla \times e(s) = -\mu s h(s) \quad (7.23a)$$

$$\nabla \times h(s) = (\sigma + es)e(s), \quad (7.23b)$$

where  $e(s) \leftrightarrow e(t)$ , and so forth. Generally, potential functions such as those discussed in Section 7.2.1 are used. If we use the Hertz vector potential, we write for Equation (7.9) (Wait, 1951a),

$$\{ \nabla^2 - (\mu es^2 + \mu\sigma s) \} \pi(s) = -j(s)/(\sigma + es) \quad (7.24a)$$

Equations (7.2) and (7.8) give  $e(s)$  whereas  $h(s)$  is given by Equations (7.1) and (7.8); the results are

$$e(s) = \nabla \cdot \pi(s) - (\mu\sigma s + \mu es^2) \pi(s) \quad (7.25a)$$

$$h(s) = (\sigma + es) \nabla \times \pi(s) \quad (7.25b)$$

From here on we shall neglect displacement currents because we are considering propagation in a conducting medium; this eliminates terms in  $\epsilon$  in all the equations above, producing a diffusion equation as discussed in Section 6.2.3. Then a solution for Equation (7.24a) is (Stratton, 1941, Section 8.3)

$$\pi(s) = (1/4\pi\sigma) \int_V j(s) [\exp\{-r(\mu\sigma s)^{1/2}\}/r] dv \quad (7.24b)$$

where the integration is performed over a volume  $V$  containing the source of current, whereas  $\pi(s)$  is determined at a point at a distance  $r$  outside it. The source is a step function given by  $J(t) = Ju(t)$  [Equation (A.79)]. From Equation (A.80) we have  $Ju(t) \leftrightarrow J/s$ .

Having found  $\pi(s)$  from Equation (7.24b), we find  $e(s)$ ,  $h(s)$  from Equations (7.25), then transform back to the time domain to get  $e(t)$  and  $h(t)$  for a step input.

A simplified version of the above approach is given by Ward and Hohmann (1988); they consider the FD field relations as Fourier transforms, then translate these into Laplace transforms of the TD response to a step input. This method will be discussed in Section 7.2.6e.

(c) *Long straight horizontal wire.* Ward and Hohmann (1988) give relations for the TDEM field for this source in free space. When the wire is along the  $y$  axis,

$$e_y = -\mu_0 I e^{-\theta^2 r^2} / 4\pi t \quad (7.26a)$$

$$h = I e^{-\theta^2 r^2} (z\mathbf{i} - x\mathbf{k}) / 2\pi r^2 \quad (7.26b)$$

$$\partial h / \partial t = I \theta^2 e^{-\theta^2 r^2} (z\mathbf{i} - x\mathbf{k}) / 2\pi t \quad (7.26c)$$

where  $\theta = (\mu_0\sigma/4t)^{1/2}$ ,  $\rho^2 = x^2 + z^2$ , and  $t$  is the decay time of the transient after current shutoff. [The time derivative of  $\mathbf{h}$  is given here because it is frequently the measured parameter in TD surveys.] The  $x$  and  $z$  components of  $\mathbf{h}$  and  $\partial \mathbf{h} / \partial t$  are easily found from Equations (7.26b, c). Strictly speaking,  $\sigma = 0$  so that the exponentials in Equations (7.26) are unity.

When the wire lies on homogeneous ground, the formulas are modified and we have

$$e_y = I(1 - e^{-\theta^2 x^2})/\pi\sigma x^2 \quad (7.27a)$$

$$h_x = I\{\theta^2 x^2 F(\theta x) - \theta x\}/\pi^{3/2} x \quad (7.27b)$$

$$h_z = -I\{1 + \theta^2 x^2(e^{-\theta^2 x^2} - 1)\}/2\pi x \quad (7.27c)$$

$$\partial h_x / \partial t = I\{(1 + 1/\theta^2 x^2)F(\theta x) - 1/\theta x\}/\pi^{3/2} x t \quad (7.27d)$$

$$\partial h_z / \partial t = I\left\{\sum_1^{\infty} (-1)^{n+1} n(\theta x)^{2n}/(n+1)!\right\}/2\pi x t \quad (7.27e)$$

where  $F(\theta x)$  is Dawson's integral (Abramowitz and Stegun, 1964). Retaining only the first term in the series expansions of Equations (7.27d, e), the expressions for the time derivatives become

$$\partial h_x / \partial t \approx (\mu_0\sigma)^{1/2} I / 6(\pi t)^{3/2}$$

$$\partial h_z / \partial t \approx \mu_0\sigma I x / 16\pi t^2$$

TD fields for the long straight insulated wire lying on a conductive half-space have been discussed in several reports (Wait, 1971; Kauahikaua, 1978; Oristaglio, 1982). The second paper quoted discusses the effect of grounding the ends of the wire; obviously this introduces galvanic currents into the half-space. According to Kauahikaua, this affects various field components:  $e_y$  and  $h_x$  are modified,  $h_y$ ,  $e_x$ , and  $e_z$  components are introduced by the grounded ends, while only the  $h_z$  field is entirely due to the insulated length.

(d) Large rectangle. This geometry, much used in TDEM systems as well as in Turam, is discussed in Section 7.2.3c. Fundamentally it is similar to the magnetic dipole in Section 7.2.3d, apart from the dimensions of the loop relative to its distance from the detector. Nevertheless the equations are so difficult to solve that no analytical solution is currently available for the general case of a Turam-type loop on homogeneous ground. However, a solution is available for the transient response when the receiver

is at the center of a circular transmitter loop of radius  $a$  similar to that used in the Sirotem coincident-loop equipment (§7.4.4.d) and in EM depth sounding (§7.7.6). We have for the field at the center (Ward and Hohmann, 1988)

$$h_z = (I/2a)\left\{3e^{-\theta^2 a^2}/\sqrt{\pi}\theta a + (1 - 3/2\theta^2 a^2)\operatorname{erf}(\theta a)\right\} \quad (7.28a)$$

$$\begin{aligned} \partial h_z / \partial t = & -\left(I/\mu_0\sigma a^3\right)\left\{3\operatorname{erf}(\theta a)\right. \\ & \left.-\left(\frac{2\theta a}{\sqrt{\pi}}\right)e^{-\theta^2 a^2}(3 + 2\theta^2 a^2)\right\} \end{aligned} \quad (7.28b)$$

where  $\operatorname{erf}(\theta a)$  is the error function (§A.12.3).

At late times of the transient response, for  $\sigma \approx 0$ , these expressions become

$$h_z \approx I(\mu_0\sigma)^{3/2} a^2 / 30(\pi t^3)^{1/2} \quad (7.28c)$$

$$\partial h_z / \partial t \approx I(\mu_0\sigma)^{3/2} a^2 / 20(\pi t^5)^{1/2} \quad (7.28d)$$

In a well-known paper, Nabighian (1979) described the downward and outward diffusion from the dipole of a transient EM field through a conducting half-space, the velocity and amplitude decreasing with time very much like a smoke ring in air.

Oristaglio (1982), using two parallel line sources, illustrated a similar effect in which the two current patterns move away from each line at an angle of about 25°. Three sections drawn for current densities at successive times in the ratio 1 : 2 : 4 are displayed in Figure 7.11. Nabighian and Oristaglio (1984) noted that at late decay times the response fell off as  $t^{-2.5}$  in both systems, provided the rectangular source was of reasonable size.

The velocity  $V$ , radius  $R$ , and diffusion distance  $d$  (the TD equivalent of the skin depth—see §6.2.3) of the current whorls are of considerable significance. They are given by the relations

$$V = 2/(\pi\mu_0\sigma t)^{1/2} = 1/\sqrt{\pi}\theta t \quad (7.29)$$

$$R = (4.37t/\mu_0\sigma)^{1/2} = 1.05/\theta \quad (7.30)$$

$$d = 2\pi(2t/\mu_0\sigma)^{1/2} = \sqrt{2\pi}/\theta \quad (7.31)$$

The diffusion distance locates the center of a whorl in terms of the decay time and conductivity. At late times the eddy currents reach large distances from the source; for a fixed time interval, the increase in  $d$  will be less, the larger  $\sigma$  is, hence the whorls take longer to travel a given distance, that is, they remain longer in high conductivity beds.

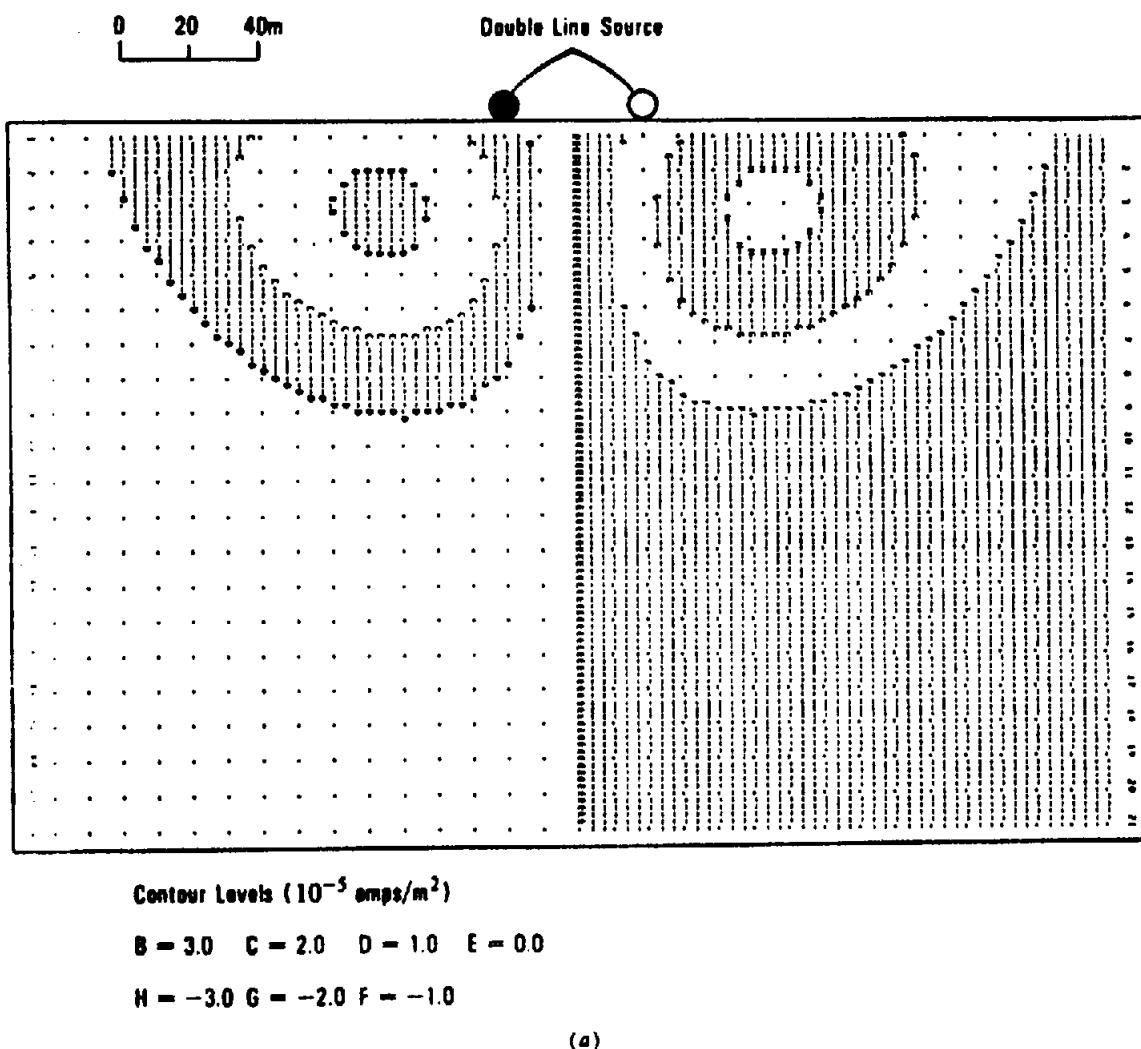


Figure 7.11. Plots of subsurface current density. Current flow 1 A, into page at ●, out at ○. Current shut-off time  $t = 0$ . Contour intervals  $10^{-5} \text{ A/m}^2$  in (a) and (b),  $10^{-6} \text{ A/m}^2$  in (c). (After Oristaglio, 1982). (a) Plot for  $t/\sigma\mu = 10^3 \text{ m}^2$ .

(e) Small horizontal coil (vertical magnetic dipole). There is no airborne TD source of this type in current use. As for ground systems, although Input uses a horizontal-loop transmitter, the shape is roughly triangular and the loop is considerably larger than the conventional small horizontal loop. However, PEM and SIROTEM Slingram-type ground equipment use relatively small vertical magnetic dipoles (see §7.7.4b and Table 7.3).

The TD field response in free space for this source can be written (Ward and Hohmann, 1988)

$$h_\rho = (3I\delta\omega\rho z / 4\pi r^5) (1 + 4\theta^3 r^3 / 3\sqrt{\pi}) \quad (7.32a)$$

$$h_z = (I\delta\omega / 4\pi r^5) (2z^2 - \rho^2) \\ \times \{1 - 4\theta^3 r^3 \rho^2 / \sqrt{\pi} (2z^2 - \rho^2)\} \quad (7.32b)$$

$$e_\phi = (j\omega\mu_0 I\delta\omega\rho / 4\pi r^3) \\ \times \{1 - \operatorname{erf}(\theta r) + 2\theta r e^{-\theta^2 r^2 / \sqrt{\pi}}\} \quad (7.32c)$$

where  $r^2 = \rho^2 + z^2 = x^2 + y^2 + z^2$ .

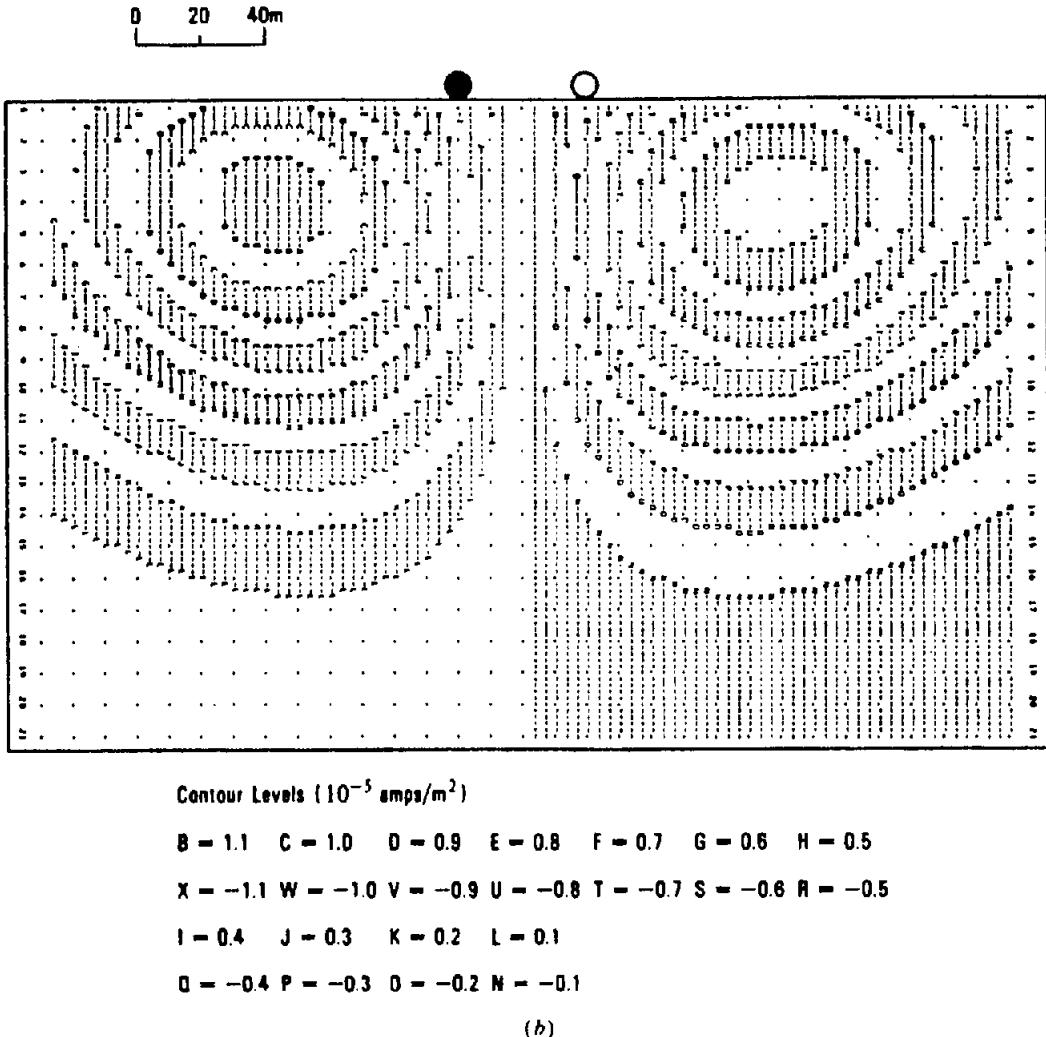
Over homogeneous ground the TD components can be obtained from Equations (7.14k, l, m). For a homogeneous conducting medium,  $k = (-j\omega\mu\sigma)^{1/2}$  where  $\mu$  and  $\sigma$  are constant. Thus, at a fixed point (that is,  $\rho$  also constant), the right hand sides of Equations (7.14k, l, m) are functions of  $j\omega$ , that is, they are Fourier transforms of the field responses. Assuming the system is linear (§A.13) we see from the discussion of Equation (A.87a) that these expressions are transforms of the unit impulse responses. Moreover, for the functions involved in these equations, we can set the convergence factor  $\sigma$  in Equation (A.75b) equal to zero, that is,  $s = j\omega$ . When we replace  $j\omega$  with  $s$ , the Fourier transforms become Laplace transforms (§A.12).

Writing  $\alpha = (\mu\sigma)^{1/2}\rho$ , we have

$$jk\rho = j(-j\omega\mu\sigma)^{1/2}\rho = (j\omega)^{1/2}\alpha = as^{1/2};$$

$$k^2\rho^2 = -\alpha^2 s; \quad jk^3\rho^3 = -\alpha^3 s^{3/2}$$

Substituting these relations in Equations (7.14k, l,

Figure 7.11. (Continued) (b)  $t/\sigma\mu = 2 \times 10^3$  m $^2$ .

m), we get the Laplace transforms of the unit impulse responses. Dividing by  $s$  gives us the transforms of the unit step responses (Sheriff and Geldart, 1983:174–5) in the form

difficult; details are given in Ward and Hohmann (1988:216). The final results are

$$h_p = (I \delta \mathcal{A} \theta^2 / 2\pi\rho) e^{-\theta^2 \rho^2 / 2} \times \left\{ I_1\left(\frac{1}{2}\theta^2 \rho^2\right) - I_2\left(\frac{1}{2}\theta^2 \rho^2\right) \right\} \quad (7.32d)$$

$$h_z = -\left( I \delta \mathcal{A} / 2\pi\mu\sigma\rho^3 \right) \left\{ (9/2\theta^2 \rho^2) \operatorname{erf}(\theta\rho) + \operatorname{erfc}(\theta\rho) - (4\theta\rho + 9/\theta\rho) e^{-\theta^2 \rho^2 / \sqrt{\pi}} \right\} \quad (7.32e)$$

$$h_\phi = -\left( I \delta \mathcal{A} / 2\pi\sigma\rho^4 \right) \left\{ 3 \operatorname{erf}(\theta\rho) - (2\theta\rho/\sqrt{\pi})(3 + 2\theta^2 \rho^2) e^{-\theta^2 \rho^2} \right\} \quad (7.32f)$$

where  $\operatorname{erfc}(\theta\rho) = 1 - \operatorname{erf}(\theta\rho)$  (§A.12).

To get the time derivatives of the field responses, we multiply the Laplace transforms by  $s$  (see Eq. (A.78a) with  $n = 1$ ,  $g(0+) = 0$ ), then transform to the time domain. The results for the magnetic field

The last two are readily transformed to the time domain using Equations (A.84b) and (A.85a, b, c, d). Transformation of the first expression is more dif-

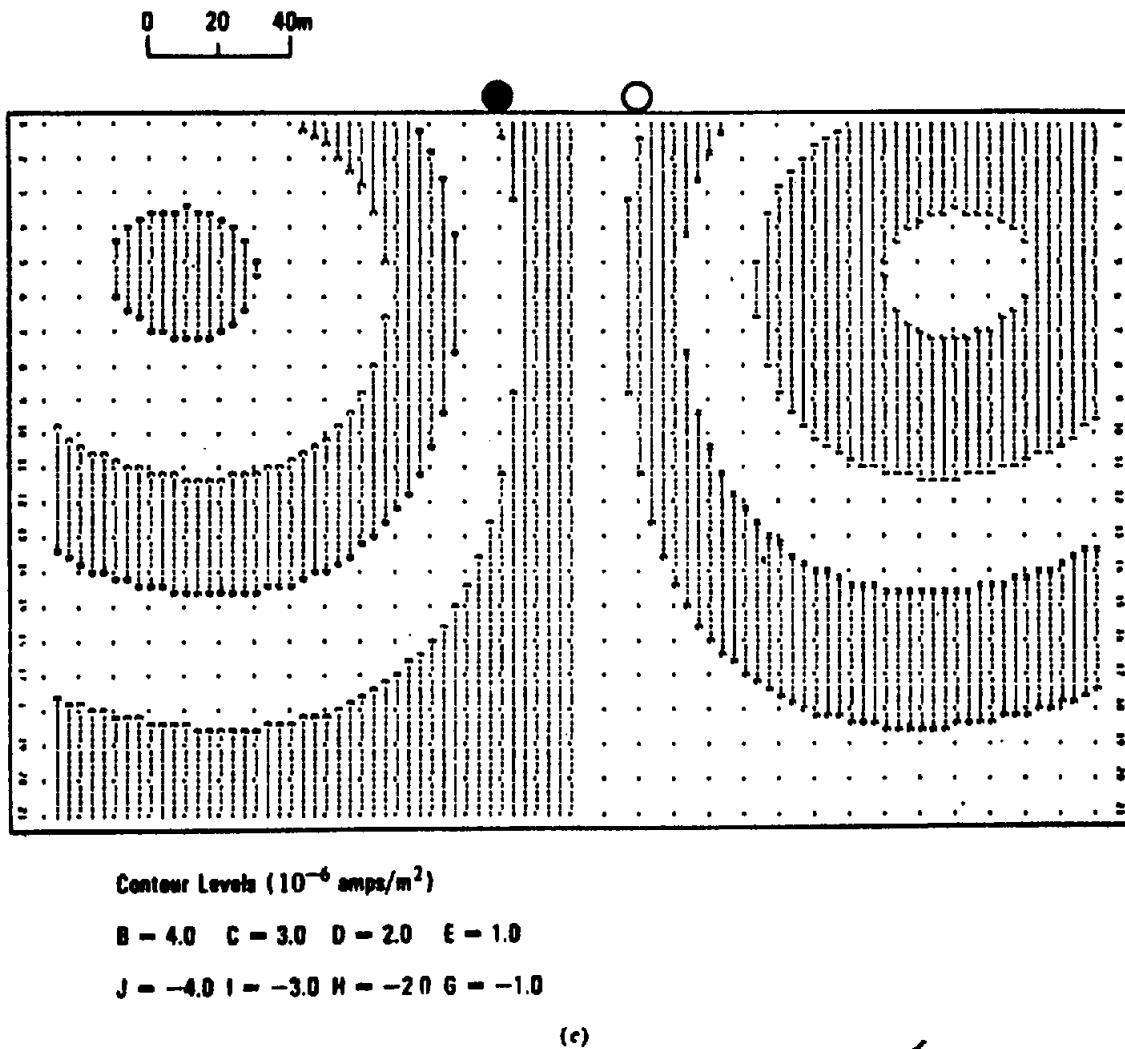


Figure 7.11. (Continued) (c)  $t/\sigma\mu = 4 \times 10^3$  m $^2$ .

are (Ward and Hohmann, 1988)

$$\begin{aligned} \partial h_p / \partial t &= \left( I \delta \mathcal{A} \theta^2 / 2 \pi \rho t \right) e^{-\theta^2 \rho^2 / 2} \\ &\times \left\{ (1 + \theta^2 \rho^2) I_0 \left( \frac{1}{2} \theta^2 \rho^2 \right) \right. \\ &\left. - (2 + \theta^2 \rho^2 + 4/\theta^2 \rho^2) I_1 \left( \frac{1}{2} \theta^2 \rho^2 \right) \right\} \quad (7.32g) \end{aligned}$$

$$\begin{aligned} \partial h_s / \partial t &= - \left( I \delta \mathcal{A} / 2 \pi \mu \sigma \rho^5 \right) \left\{ 9 \operatorname{erf}(\theta \rho) \right. \\ &\left. - (2 \theta \rho / \sqrt{\pi}) (9 + 6\theta^2 \rho^2 + 4\theta^4 \rho^4) e^{-\theta^2 \rho^2} \right\} \quad (7.32h) \end{aligned}$$

At late time, Equations (7.32d, e, g, h) become

$$\left. \begin{aligned} h_p &\approx - \left( I \delta \mathcal{A} \rho \mu^2 \sigma^2 / 128 \pi t^2 \right) \\ h_s &\approx \left( I \delta \mathcal{A} / 30 \right) \left( \mu \sigma / \pi t \right)^{3/2} \end{aligned} \right\} \quad (7.32i)$$

$$\left. \begin{aligned} \partial h_p / \partial t &\approx \left( I \delta \mathcal{A} \rho \mu^2 \sigma^2 / 64 \pi t^3 \right) \\ \partial h_s / \partial t &\approx - \left( I \delta \mathcal{A} / 20t \right) \left( \mu \sigma / \pi t \right)^{3/2} \end{aligned} \right\} \quad (7.32j)$$

Figure 7.12 illustrates theoretical responses for  $h_p$  and  $h_s$ , and their time derivatives for the vertical magnetic dipole. The decay amplitude is the value at a point 100 m from the transmitter over a 100  $\Omega$ m homogeneous earth. Thus the curves show maximum values of  $h$  and  $\partial h / \partial t$  at the surface for the circular currents or "smoke rings" (Nabighian, 1979) as they diffuse during the decay cycle (Fig. 7.11). Note also that the currents change sign on 3 of the 4 plots, following a sharp cusp or crossover.

In Figure 7.12a the  $h_p$  curve is positive throughout with a peak of  $\sim 10^{-7}$  A/m at about 10  $\mu$ s after current cutoff. At later time  $h_p$  decays at  $t^{-1}$ , the curve being at an angle of about 63° to the horizontal. The  $\partial h_p / \partial t$  curve changes sign abruptly at  $\sim 10$   $\mu$ s and subsequently falls off as  $t^{-3}$  at 72°. From Figure 7.12b it is seen that the early-time maximum of  $h_s$  ( $10^{-7}$   $\mu$ A/m) persists to  $\sim 10$   $\mu$ s where it changes sign and decays as  $t^{-3/2}$  at an angle of 56°;  $\partial h_s / \partial t$  also is constant ( $-10$  mA/m.s) through early time to  $\sim 20$   $\mu$ s after which it decays as  $t^{-5/2}$  at an angle of 68° (Oristaglio, 1982).

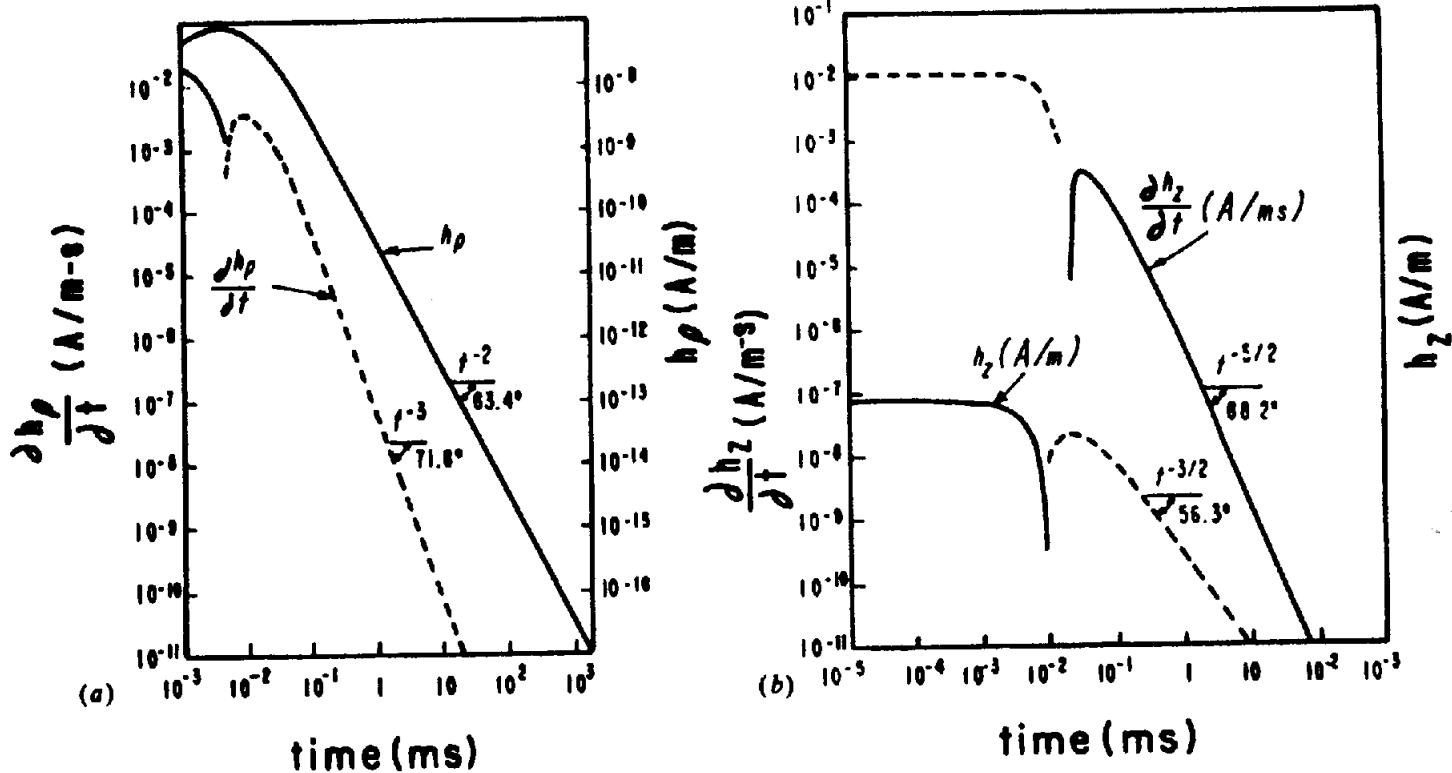


Figure 7.12. TD transient decay curves at a point 100 m from a vertical magnetic dipole on 100  $\Omega\text{m}$  homogeneous earth. (From Ward and Hohmann, 1988.) (a)  $h_p$  and  $\partial h_p/\partial t$ . (b)  $h_z$  and  $\partial h_z/\partial t$ .

(f) Horizontal magnetic dipole; vertical electric dipole. Although Wait (1951a) has discussed the TD version of the electric dipole on homogeneous ground, neither of these sources has been developed for either airborne or ground TD surveys.

VLF and AFMAG, make use of remote power sources and consequently do not need a transmitter.

### 7.3. EM EQUIPMENT

#### 7.3.1. General

The measuring equipment for EM systems includes a local ac power source operating at one or several recurrence frequencies, transmitter and receiver coils (which may be one and the same in some TD sets), receiver amplifier tuned to the transmitter frequency (FD units) or wide-band ( $\sim 40$  kHz in TD receivers), and an indicator, such as headphones, meter, digital readout, or recorder. Some FD field sets require in addition an ac potentiometer (or phase and amplitude compensator) for comparison of primary and secondary field signals. There is very little difference in these components whether they are used for ground or airborne sets, except that the latter are more elaborate and bulky. Two field methods that properly come under the heading of EM, namely

#### 7.3.2. Power Sources

Formerly the power supply for EM transmitters was normally either a gas-driven alternator or a small, light battery-powered oscillator with a power amplifier having a low impedance output. The choice between these depended on the type of field set, that is, whether the transmitter was only semiportable or continually moving. In the long-wire, the large horizontal-loop, and the vertical-loop fixed-transmitter systems the larger power source would be used, whereas for the various completely mobile transmitters, such as horizontal-loop and vertical-loop broadside, the small unit was necessary.

Actual output from the semiportable power supplies varies between 250 and 2,500 W. The moving sources range from 1 to 10 W. Weight of the equipment, of course, increases with the power output and may be anywhere from 2 to 100 kg.

In recent EM equipment power supplies have been modified to reduce weight and size. For portable units the transmitter coil is an integral part of the

oscillator, eliminating the low-efficiency power amplifier. High-power sets employ a type of "flip-flop" switching unit to feed the coil directly for the same purpose.

The transmitter output, sinusoidal in FD equipment, is in the lower audio range, 100 to 5,000 Hz. With TDEM the periodic transient frequencies are low (3 to 300 Hz), consisting of half-sine, square-wave, or ramp-type (sawtooth) pulses, all of alternating polarity. The off time may be equal to or several times longer than the on time. One TDEM unit, the UTEM system (West, Macnae, and Lamontagne, 1984), uses a triangular waveform with zero off time. Formerly some FD power sources were dual frequency, one low and one relatively high, for example, 875 and 2,200, 1,000 and 5,000, and 400 and 2,200 Hz. Recent ground FDEM equipment has a range from 111 to 3,555 Hz in steps of 2 (approximately). Frequency range in one operating airborne system is 900 to 35,000 Hz. The advantage in using two or more frequencies lies in discriminating between shallow and deep conductors and/or an indication of conductivity of the anomaly and the surrounding medium.

### 7.3.3. Transmitter Loops

In order to generate the desired electromagnetic field, the output of the power source must energize the ground by passing a current through some wire system. In the semiportable field sets this is done by coupling power into a long straight wire grounded at each end, a large (usually a single turn) rectangle or square laid out on the ground, or a relatively large vertical loop supported on a tripod or hung from a tree. In the first two arrangements, the dimensions are 0.5 km or more. The vertical loop, which may be single- or multiple-turn winding, may be triangular, square, or circular, and of necessity has an area of only a few square meters. Some means must be provided for orienting this coil in any desired azimuth.

The completely mobile FDEM transmitters often employ multiple-turn coils (100 turns or more) wound on insulating frames of 1 m diameter or less. Sometimes the coil may be merely a single turn of heavy conductor; in this case, a matching transformer may be necessary in the source output. An alternative to this type of aircore coil, in which the wire is wound as a solenoid on a ferrite or other high-permeability core, is now used in many EM systems. If the winding is distributed properly, it is possible to generate a field equivalent to a coil wound on a much larger frame, because the value of  $H$  increases with core permeability to compensate for the small

area enclosed. Because the value of  $\mu$  for certain ferrites is about 1,000, the cross section can be greatly reduced.

Many FD transmitter systems have a capacitance in series with the coil, the value being chosen to resonate approximately with the coil inductance at the source frequency. Because the coil has low resistance, this permits maximum current (within the limits of the power supply) to flow in the coil.

### 7.3.4. Receiver Coils

In FD systems, these are generally small enough to be entirely portable, that is, 3 ft (1 m) diameter or less, and have many turns of fine wire. Smaller coils with high-permeability cores are also used. The coil may be shunted by an appropriate capacitance to give parallel resonance at the source frequency. The resulting high impedance across the amplifier input acts as a bandpass filter to enhance the signal-to-noise ratio.

Receiver loops, and usually the portable transmitter loops as well, are electrostatically shielded to eliminate capacitive coupling between coil and ground and between coil and operator. The shielding is obtained by conductive paint or strips of conductive foil over the winding; the shield, which is split around the perimeter to permit emission and reception of the signal field, is then connected to the main circuit ground.

Generally the receiver coil must be oriented in a certain direction relative to the detected field. In some ground systems this merely means that the loop is maintained approximately horizontal or vertical. In others it is necessary to measure inclination and/or azimuth at each station. In airborne EM systems it is often a difficult problem to maintain a fixed orientation between transmitter and receiver coils.

In some TDEM systems the same coil may be employed both for transmitting and receiving (obviously this is not possible with continuous transmission). In such cases the loop size may vary from a few meters to several hundred; hence the coil is not completely portable.

### 7.3.5. Receiver Amplifiers

Amplifiers are of fairly standard design. The overall voltage gain is usually between  $10^4$  and  $10^5$ . One or more narrow bandpass filters, tuned to the source frequency or frequencies, are incorporated in the FD amplifier. A network of this type, called the *Twin-T*, which uses only resistors and capacitors, is illus-

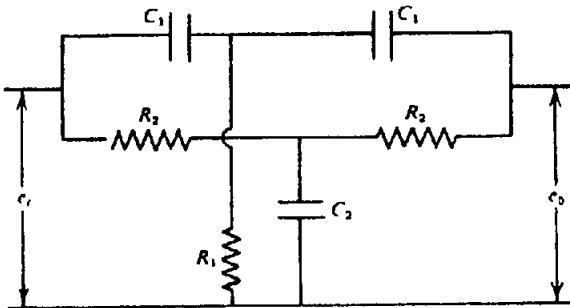


Figure 7.13. Twin-T network for EM receivers.  $\omega^2 = 1/(2C_1^2R_1R_2) = 2/(C_1C_2R_2^2)$ . Generally  $R_2 \approx 2R_1$ ,  $C_2 \approx 2C_1$  for convenience in design.

trated in Figure 7.13. This circuit presents very high impedance at either end to a single frequency  $\omega$  given by the formula in the legend. When the Twin-T is connected across an amplifier stage, the feedback is practically zero at this frequency and increases rapidly either side of it. Sometimes band-reject filters, particularly for power line frequencies, are included in both FD and TD receiver systems.

The amplifier used in time-domain sets has a large bandwidth to handle the frequencies from below the transient recurrence rate up to 30 to 40 kHz at the high frequency limit. This introduces noise problems from power lines and their harmonics, VLF, and other manmade signals, as well as sferic noise (due mainly to lightning discharge; see §6.2.1 and §7.4.2e) over the amplifier spectrum. The artificial noise sources may be greatly reduced by suitable digital band-reject filters, whereas synchronous detection and signal averaging (stacking) enhances the signal-to-noise ratio by reducing sferics and other natural sources as well as the cultural interference. Thus the wide-band TD receiver, although susceptible to noise not present in FD equipment, performs quite as well as the latter (Macnae, Lamontagne, and West, 1984; McCracken, Oristaglio, and Hohmann, 1986; Becker and Cheng, 1988).

### 7.3.6. Indicators

In many ground FDEM sets measurement is made by nulling or at least reducing the receiver signal to a minimum – sometimes by changing the orientation of the receiver loop, sometimes by manipulation of electrical components as in balancing an ac bridge. The indicator is normally a set of sensitive headphones on the output of the amplifier. Occasionally a suitable meter may be used, but in the audio range there is no particular advantage in the visual indicator. In any case, the significant parameters are noted when the minimum signal is obtained. These parameters might be the dip or azimuth angle of the receiver loop in degrees or percent of a maximum

value, or they could be the percentage change in amplitude and phase required to null the signal, this change being compared to a normal or background null.

Because the readings are continuous in airborne EM, a recorder of some type is required. These were formerly of the strip-chart type, but digital recording is now widely used as well. As in other geophysical methods, the computer revolution has led far beyond this to digitized EM systems, particularly airborne versions, in which the processing and presentation of data are automatic.

### 7.3.7. Compensating Networks

Unless the receiver loop is purposely oriented to minimize coupling of the primary wave in FD equipment, the secondary signal will be swamped by the primary as we have seen from the numerical example in Section 7.2.5c. Because many EM systems, both ground and airborne, use transmitter-receiver loop geometry in which the coupling is maximum, it is necessary to cancel the primary signal by some other means. This is accomplished by introducing at the receiver input an artificial signal of the same frequency and amplitude but opposite in phase.

Compensation of this sort would be sufficient to permit measurement of an amplitude, that is, the real component, of the secondary field. However, from Section 7.2.4 and Figure 7.7, it is apparent that  $H_p$  and  $H_s$  generally differ in phase as well as amplitude and that, furthermore, this phase shift is diagnostic of the conductor. Thus some provision for changing phase should also be included in the compensator.

The primary-field cancellation is achieved by a signal derived from the transmitter current, for example, by means of a small single-turn coil on or near the transmitter loop. The amplitude and phase shift may be adjusted for minimum in a barren or background region. Relative amplitude and phase changes caused by secondary fields at other locations may then be measured directly, by using a synchronous detector with digital readout.

Referring again to Figure 7.7 we see that a vector equal in amplitude and opposite in direction to  $H_p$  will cancel the receiver signal. From the geometry of the vector triangle, when  $H_s/H_p \ll 1$ , it is easily shown that

$$H_r \approx H_p \left( 1 - \frac{H_s}{H_p} \sin \phi + \frac{H_s^2}{2H_p^2} \right)$$

and

$$\sin \alpha \approx \frac{H_s}{H_p} \cos \phi$$

Thus the required vector has approximately the same amplitude as  $H_p$  and is shifted in phase by  $(\pi - \alpha)$ . For a very good conductor,

$$H_r \approx (H_p - H_s) \quad \text{and} \quad \alpha \approx 0$$

whereas for a very poor one,

$$H_r = H_p \left( 1 + \frac{H_s^2}{2H_p^2} \right) \approx H_p \quad \text{and} \quad \alpha \approx \frac{H_s}{H_p}$$

## 7.4. EM FIELD SYSTEMS FOR GROUND SURVEYS

### 7.4.1. General

A great variety of methods is available for EM fieldwork. These can be divided into ground and airborne systems and subdivided according to type, FD or TD, and actual measurement made, such as polarization ellipse, intensity and phase components, and so on. There are in addition many techniques developed 30 or 40 years ago that have gone out of style or have been superseded by improved versions; these will not be considered to any extent. An enormous amount of information on state-of-the-art EM equipment may be found in the annual summaries by Peter Hood in the *Canadian Mining Journal* since the late 1960s (Hood, 1967 and following years).

### 7.4.2. Frequency-Domain Systems; Dip-Angle Measurements

(a) *General.* There are several field systems that measure, in effect, the direction of the combined primary and secondary fields at a receiver station. Whether they employ a natural or artificial source for the primary field and whether this source is fixed or movable, they all come under the heading of dip-angle measurements, because the tilt of the detector coil about a horizontal axis is recorded as the station reading. Furthermore, all the systems employ a primary field that is approximately horizontal.

The dip-angle systems remain very popular in EM work, in spite of their limitations, primarily because the equipment is inexpensive and simple to operate and the technique is rapid and works quite well over steeply dipping sheet-like conductors, which are common geological features. The fixed-transmitter unit and AFMAG are also capable of a reasonably large penetration depth.

(b) *Fixed vertical-loop transmitter.* This is the oldest of the methods, developed in the 1920s and still used quite widely. The transmitter coil, which may

be square, triangular, or circular, usually has a few hundred turns with effective area of the order of  $2 \text{ m}^2$ . The coil stands vertical and is free to rotate in the azimuth. The power source usually delivers several hundred watts.

The receiver coil, consisting of many turns of fine wire wound either on an open frame 50 cm in diameter or on a ferrite core, is connected to a tuned high-gain amplifier with headphones, or occasionally a meter, in the output. Provision is made for measuring the tilt angle of the coil.

Figure 7.14 shows the operating procedure. Traverses are made by moving the receiver along lines approximately normal to geologic strike. Station intervals are usually 15 to 60 m. For each receiver setup, the transmitter coil is rotated to point at the receiver station (that is, its plane is in the transmitter-receiver line so that the primary field at the receiver is horizontal), either on a prearranged time schedule or on receipt of a signal given by shouting or by walkie-talkie. The receiver is then tilted about the T-R axis for a minimum signal and the tilt angle is recorded. Operations may be speeded up by having two receiver sets; in this event, the second operator must occupy a station on the same axis at the same time as the first receiver (Fig. 7.14).

It is apparent that in the absence of conductors the minimum will be obtained with the receiver coil horizontal, because this represents zero-coupling geometry with respect to the transmitter coil. This would also be true when the receiver coil was directly over a rather narrow conductive zone, because the secondary field would have no vertical component. Characteristic profiles over this type of conductor are shown in Figures 7.30 and 7.31a. The tilt angle either side of the conductor is such that the coil axis points toward the conductor until the receiver has moved a considerable distance away from it.

Range of receiver operation depends mainly on the size of the transmitter loop and power source. In practice the maximum T-R separation may be 200 to 400 m. There is also a minimum separation of about 60 to 120 m; at smaller spacing it is difficult to obtain a minimum signal. Obviously there will be other situations as well when the minimum will be poorly defined, because there is no arrangement for balancing out the quadrature component.

The profiles in Figure 7.30 contain considerable information about the conductor. The *crossover point* (that is, the point where the dip angle changes sign) locates the top of the body, the slope near the crossover is an indication of its depth, as is the maximum dip angle, plus or minus. The symmetry of the profile is a clue to its dip, as can be seen in Figure 7.30.

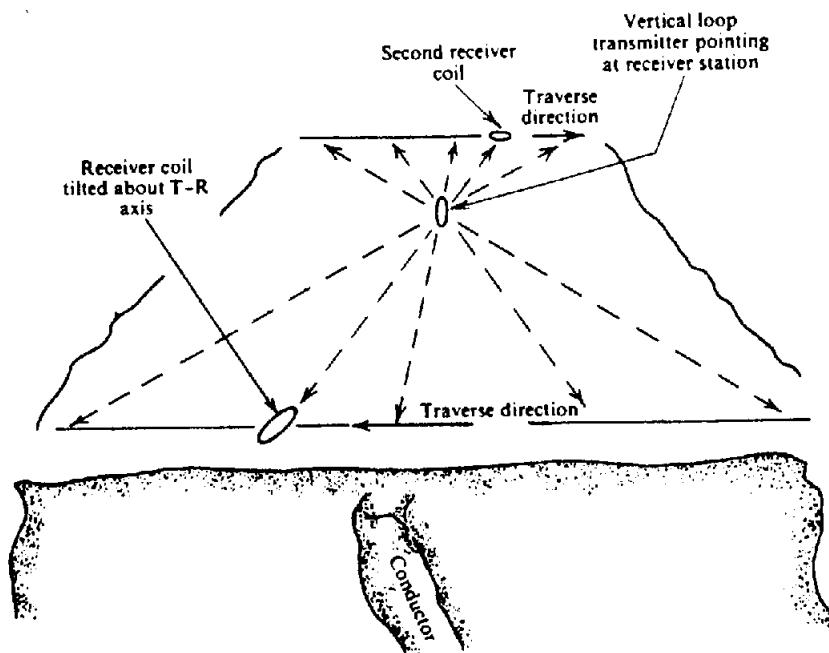


Figure 7.14. Dip-angle system, fixed transmitter.

For reconnaissance and ground followup of airborne EM, particularly where the strike is not known, the fixed-transmitter field procedure is modified. First the transmitter is set up roughly in the center of the area of interest and pointed at successive receiver positions along the perimeter of the area. Dip angles are recorded at, say, 50 m intervals in this fashion.

When a proper crossover (§7.7.3b) is found, the transmitter is moved to this station and dip angles measured on a traverse approximately across the center of the area with the transmitter loop lined up on each station. If a second crossover is located, the transmitter is moved to this station and the original crossover checked. Usually this point will be changed somewhat from the original perimeter crossover, unless the first transmitter location was fortuitously on top of the conductor.

When, as is often the case, more than one crossover has been found during reconnaissance, several interchanges of the transmitter and receiver may be necessary to establish the strike. Having clearly defined the latter, detailed dip-angle or other EM surveys may be carried out on suitable lines. If multiple conductors are present, usually the sharpest crossover (that is, the steepest slope or largest maximum tilt angle) will be obtained when the receiver is on the conductor nearest to or directly below the transmitter, because the coupling is then a maximum.

(c) *Broadside (parallel-line) method.* The transmitter is completely portable and is moved simultaneously with the receiver, the two proceeding along parallel lines. Readings are taken at intervals of 15 to

60 m, with the transmitter coil pointed at the receiver for each station reading. The receiver coil, normally horizontal, is then rotated about the *T-R* (also written *Tx-Rx*) axis to obtain a null. The transmitter-receiver line is maintained approximately parallel to geologic strike where possible, the *T-R* spacing being usually 100 to 200 m.

This arrangement is shown in Figure 7.15, and typical profiles are given in Figures 7.32 and 7.33. As in the fixed-transmitter method, two or more receivers can be used provided all are kept in line with the transmitter. The source power is inevitably lower than in the fixed-transmitter arrangement and is normally a battery-driven solid state oscillator of 1 to 10 W output.

Comparing the profiles of Figures 7.30 and 7.32, we see that the crossover is above the top of the conductor in both instances, whereas the slope of the curve near the crossover is somewhat steeper in Figure 7.32. The maximum dip angle is much more clearly defined by the parallel-line layout, because, as might be expected, the dip angle becomes zero again a relatively short distance off the conductor axis.

A modification of this field method is often used in preliminary ground reconnaissance work. The transmitter and receiver are moved along the same traverse line with the transmitter coil pointing at the receiver station 60 to 120 m away. Dip-angle measurements are recorded as described previously. The traverse lines are not usually perpendicular to strike, but rather at about 45°, because the purpose is merely to locate the conductor and perhaps get an idea of its extent. One of the standard dip-angle (or other) EM surveys is then carried out in detail.

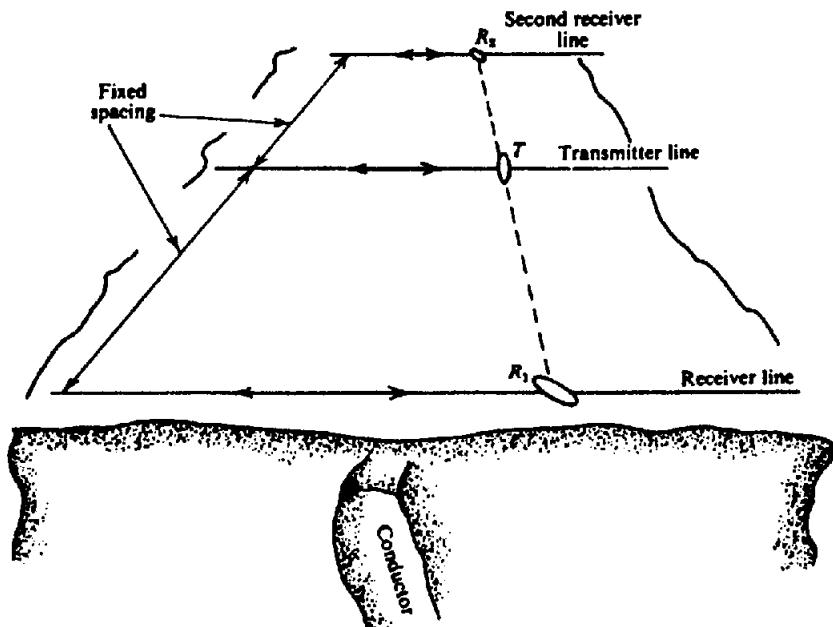


Figure 7.15. Dip-angle system, broadside orientation.

(d) *Shoot-back method.* In very hilly terrain it is difficult to maintain correct alignment of the transmitter and receiver coils, and, as a result, false dip angles are often obtained. The *shoot-back method*, developed by Crone Geophysics, was intended to overcome this problem. The coil configuration resembles a modification of an early method of Mason (1927) [see also Eve and Keys, 1956: p. 176] rather than the present dip-angle sets.

The field procedure is the same as that described in the preceding text for reconnaissance with the portable transmitter. However, the shoot-back system requires a receiver and transmitter at each station; for this purpose the coils are convertible. The spacing is usually 50 to 60 m and the axis, rather than the plane, of the transmitter coil is pointed toward the receiver station.

Consider the situation shown schematically in Figure 7.16a. With unit 1 transmitting, the axis of coil 1 is directed toward coil 2 but dipping 15° below horizontal. Coil 2 is then rotated about a horizontal axis normal to the traverse line to get a minimum. Then a second reading is taken for the same station with transmitter and receiver interchanged. Coil 2, now the transmitter, is oriented so that its axis is directed at coil 1, but inclined 15° above the horizontal, while coil 1 is tilted for a minimum. In both setups, the possibility of misalignment and of obtaining an incorrect dip angle are eliminated by the relative orientation of the two coils; the axis of the transmitter coil, rather than its plane, determines the rotation of the receiver coil about an axis normal to, rather than coaxial with, the T-R line.

In homogeneous ground the difference between the two tilt angles will be zero. This will be true

regardless of the relative elevations of the two coils. However, with a conductor present, the secondary field will affect the tilt angles at the two receiver positions in the opposite sense, as can be seen better from the distorted field lines in Figure 7.16b. A profile obtained over a sheet-like conductor is also illustrated in Figure 7.16c. Normally the difference between the two dip angles is plotted at the midpoint of the two coils.

The equipment uses two frequencies, 480 and 1,800 Hz. The latter is used alone for reconnaissance work. The profile in Figure 7.16c shows the resultant ( $\alpha_2 - \alpha_1$ ) positive over the conductor. A dipping sheet results in an asymmetric profile that is positive over the upper end and crosses zero to a negative maximum down dip. Flat-lying conductors produce a negative anomaly symmetric about the midpoint.

(e) *AFMAC method.* The initials denote audiofrequency magnetic fields. This is a natural-source dip-angle method, introduced by Ward (1959b). The main origin of the primary field is lightning discharge (sferics) associated with worldwide thunderstorm activity as in audiofrequency MT work (§6.2.1). There are other minor sources of energy such as corpuscular radiation interaction with the earth's magnetic field and manmade noise. This EM energy is propagated between the earth surface and the lower ionosphere as in a waveguide. The frequencies associated with AFMAG are in the ELF range, from 1 to 1,000 Hz, with the best reception apparently between 100 and 500 Hz.

Because the sferic sources are random, the signal is effectively noise with seasonal, diurnal, and short-period variations in intensity. Over the ELF range an

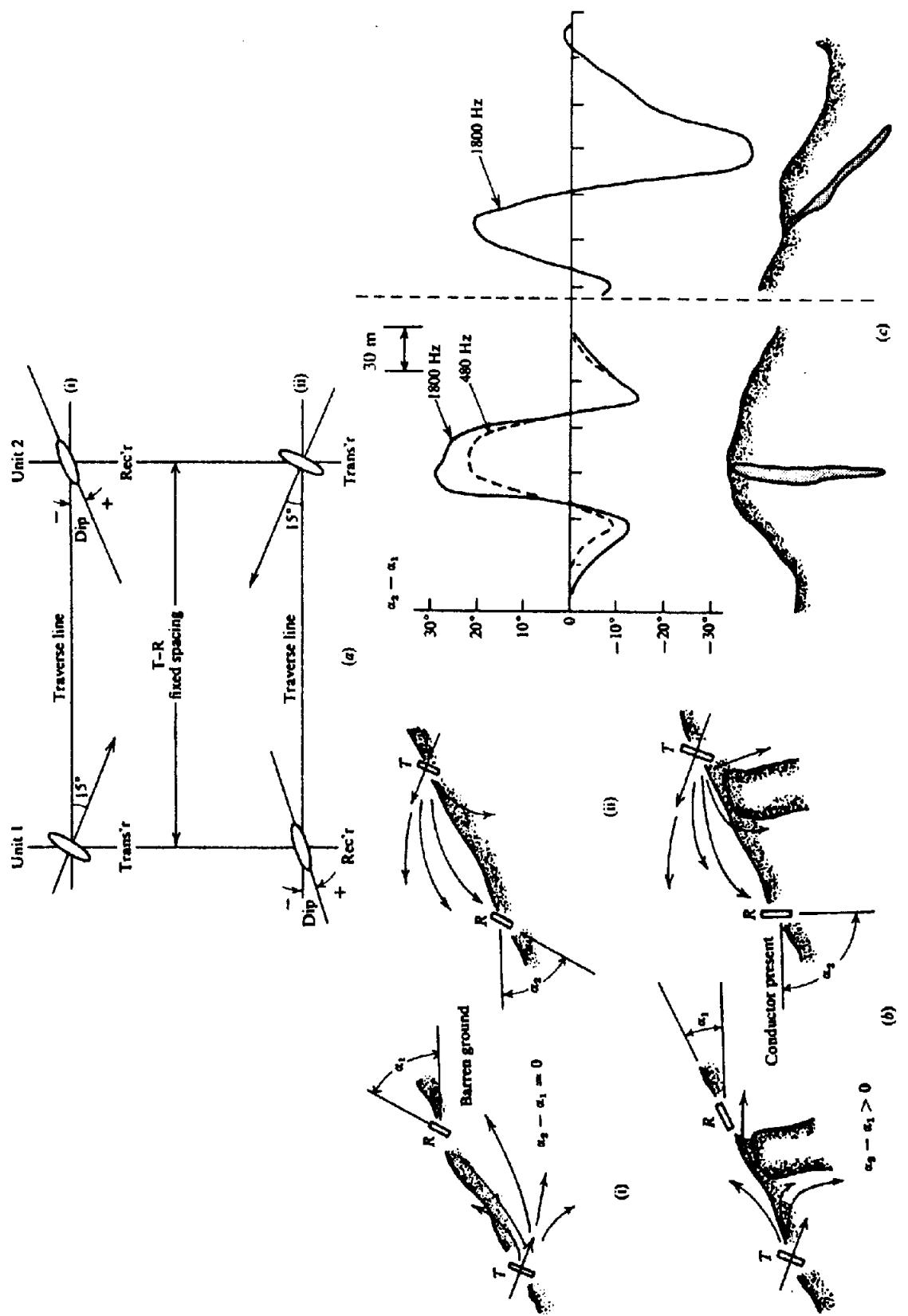


Figure 7.16. Crane shootback system. (After Grant and West, 1965). (a) Transmitter-receiver arrangements, (i) and (ii) representing interchanged positions of the transmitter and receiver for successive measurements at the same station. (b) Operation in rugged terrain. (c) Typical profiles with T-R spacing of 50 to 60 m.

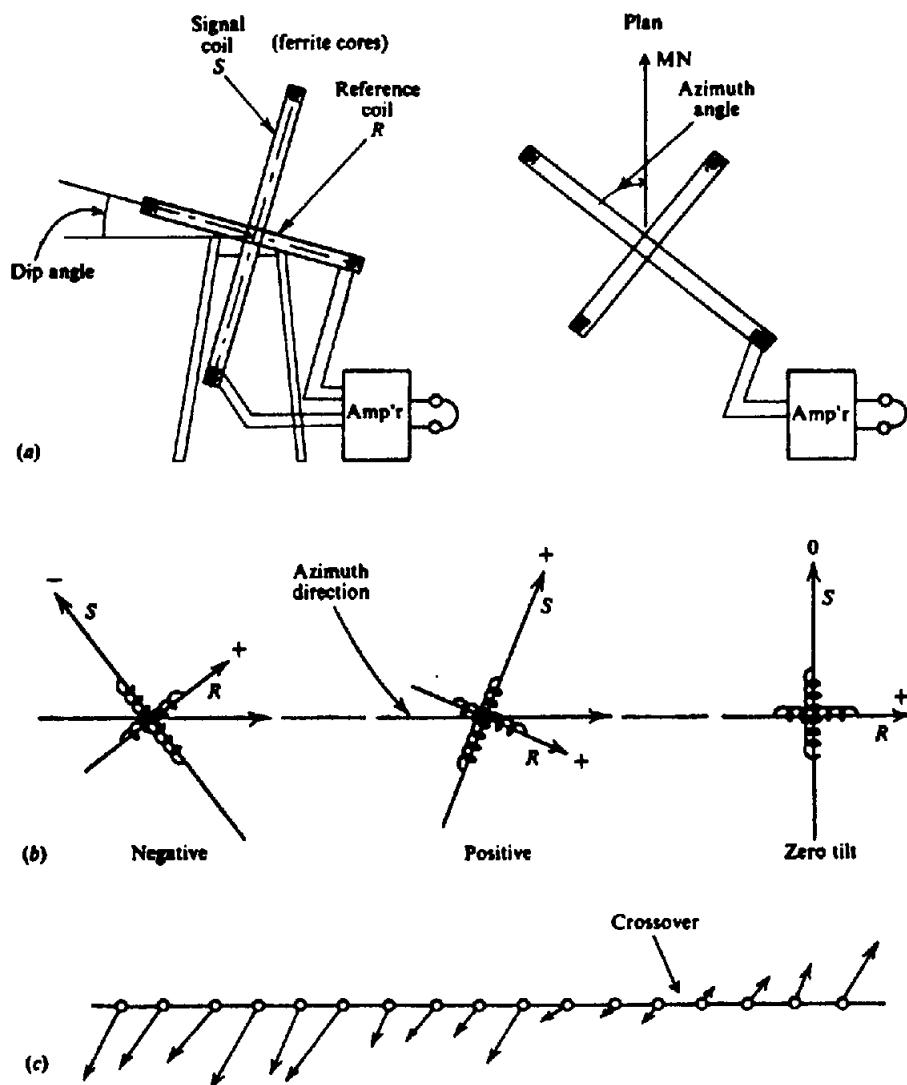


Figure 7.17. AFMAG system. (a) AFMAG equipment (schematic) and measurement of azimuth. (b) Measurement of tilt. (c) Vector plot where azimuth is not in traverse line.

AFMAG record is quite similar to the telluric current record shown in Figure 6.10.

Generally the vertical component is small compared to the horizontal, except in the vicinity of a good conductor. Hence the AFMAG field may be detected by a tilt-angle technique. The receiver, however, is modified from the conventional dip-angle detector because the random variations in primary field intensity make it impossible to locate the minimum with a single coil.

Two mutually perpendicular coils, wound on an insulating frame or ferrite core, are mounted on a stand that allows rotation about vertical and horizontal axes. One of the coils is first connected to the receiver amplifier and rotated about a vertical axis to find the rough azimuth of the horizontal field (Fig. 7.17a). This azimuth, of course, is the direction of the horizontal component and is often quite fuzzy and erratic.

One of the orthogonal coils supplies a reference signal in the tilt-angle measurement. Using ferrite-core coils, as in the illustration of Figure 7.17, this

reference coil is usually nearly horizontal and in the azimuth direction. The other (vertical) coil is now connected to the amplifier along with the reference coil and the pair are tilted about a horizontal axis normal to the main azimuth to get a minimum. Positive and negative tilt convention is illustrated.

Measurements are generally made at two frequencies, 140 and 510 Hz, with two narrow-band filters in the amplifier. The field procedure is otherwise quite similar to the fixed-transmitter method, with the transmitter considered to be at an infinite distance. Traverses are made at right angles to geologic strike where possible. If the AFMAG azimuth is not roughly along the traverse line, it is preferable to measure the tilt angles in the azimuth direction. The resultant crossover profiles may be plotted exactly as in the fixed-transmitter method, or they may be plotted as vectors (Fig. 7.17c) if the minimum azimuth direction is distinctly different from that of the traverse line or if the azimuth varies appreciably over a short time interval. In the plot shown the length of each vector is proportional to the dip angle

and the direction is that of the azimuth minimum with respect to the traverse. The crossover is then indicated by the reversal of the arrows.

AFMAG has several real and potential advantages over the artificial source methods. No transmitter is required. The frequency is comparatively low and hence the depth of penetration is probably greater than for a local source. Because the primary field is uniform, at least instantaneously, over the survey area, all the conductors are energized uniformly. At times this may be a disadvantage, however, because it may emphasize large-scale, relatively poor conductors at the expense of smaller concentrated bodies.

There are two specific disadvantages with AFMAG. The first is the effect of large random changes in the amplitude and direction of the inducing field, that produce corresponding variations in the signal strength as well as changes in anomaly shape and size. The second is that the random fluctuations in direction may make it very difficult to locate the azimuth of the horizontal field.

Recent work with more sophisticated equipment and controls (Labson et al., 1985) appears to have reduced or eliminated these limitations in AFMAG. They constructed new field sensors (coils) sensitive enough to make year-round measurements (the AFMAG signal is weak in winter and at high latitudes) and incorporated digital acquisition and processing to provide results in the field, reducing noise by a remote reference source (Gamble, Goubau, and Clarke, 1979). These improvements produced relatively stable noise-free measurements of the ratio of vertical-to-horizontal  $H$ -field components (the "tipper" in MT work; see §6.2.8c).

(f) *VLF method.* The use of VLF signals broadcast by certain marine and air navigation systems as sources for EM exploration has been mentioned in Section 7.2.3f. The main magnetic-field component is horizontal like the AFMAG signal and theoretically is tangent to circles concentric about the antenna mast. Hence it is much less erratic in direction than AFMAG.

A worldwide network of high-power VLF stations was planned for marine navigation. The sites are arranged so that at least two stations can be detected anywhere over the Earth's surface. At present suitable transmissions for EM prospecting in North America are located at Cutler, ME, Annapolis, MD, Boulder, CO, Seattle, WA, and Hawaii. The useful ranges are surprisingly large, because the Seattle station is easily detected on the east coast of Canada. However, the coverage is much less complete in the Eastern Hemisphere, where only three large transmitters – Rugby, England, North Cape, Australia, and Moscow (undependable) – are currently avail-

able. The reception is best in the morning, but adequate all day.

The receiver for detecting VLF signals measures a tilt angle and a quadrature component by means of two mutually perpendicular coils wound on ferrite cores. The coil whose axis is normally vertical is first held in a horizontal position and rotated in azimuth to find a minimum. This direction is in line with the transmitter station and is usually well defined.

The same coil is next held vertically and tilted about a horizontal axis parallel to the direction of propagation. The second coil, which is rigidly mounted at right angles to the first and so is approximately horizontal initially, is similar to the reference coil in the AFMAG receiver. Its signal is shifted in phase by 90° and, connected in series with the vertical coil signal, is fed into the receiver. The amplitude of this signal is adjustable on the quadrature dial, which reads percent plus or minus. A clinometer on the instrument allows tilt angle measurement. By tilt and quadrature adjustments, a good minimum is obtained.

The receiver amplifier incorporates two plug-in units tuned to frequencies of two VLF stations that can be detected in the survey area. (It is useful to have extra units for other stations available, in case a particular station either is not operating, or its signal is weak, or the station direction is such that the azimuth minimum is not roughly normal to the direction of the traverse.) The minimum signal indication is obtained on headphones or from a small speaker (the transmitter carriers are audiomodulated).

The receiver is illustrated schematically in Figure 7.18a. An addition to the VLF instrument manufactured by Geonics (EM16), shown in Figure 7.18b, appeared about 1973. Known as the EM16R, it is mounted on the EM16 unit and coupled electrically to it, while a pair of 5 m leads terminating in two high impedance electrodes pushed into the ground are connected to the R-unit box. The orientation is clarified in Figure 7.18b. The combined unit, resting on the ground, permits measurement of apparent resistivity  $\rho_a$  of the subsurface and relative phase angle between the observed electric and magnetic fields by adjusting the  $\rho_a$  dial (identical to the quadrature dial in EM16 operation) and a phase dial for minimum. The values of  $\rho_a$  and  $\phi$  obtained by detecting  $E_{hor}$  and  $H_\phi$  (§7.2.3f) are essentially equivalent to those in Equations (6.25), using an artificial source at higher frequency. This additional information increases the usefulness of the instrument considerably.

Clearly the VLF tilt-angle system is similar to AFMAG, with the advantage that the primary field direction is fixed and the signal level fairly uniform. The depth of penetration is not too well established,

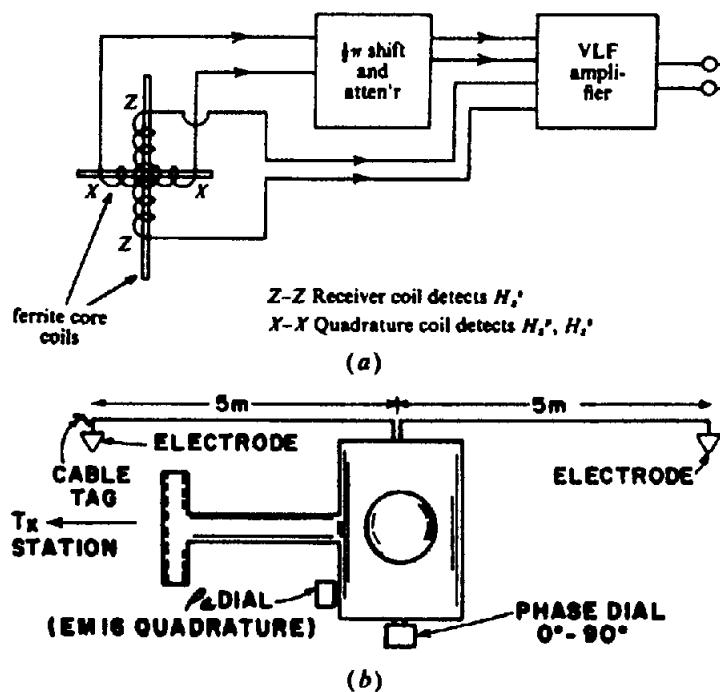


Figure 7.18. VLF receivers. (a) Schematic. (b) Schematic of the EM16R unit.

but seems to be somewhat less than that of dip-angle units using local power.

The field procedure and profile plotting are identical with AFMAG. The equipment is small, light, and conveniently made, and readings can be taken rapidly. The fact that the source is at infinity provides the same advantages and disadvantages in energizing the conductors in the survey area as described for AFMAG in the previous section. One drawback seems to be that it is not always possible to use a transmitting station approximately on geologic strike in the area, thus obtaining a primary field vector approximately across strike (that is, maximum coupling). The high frequency of the source is also an inherent weakness.

All the dip-angle methods have certain attractive features: simplicity, speed, and relatively low price. They have one common disadvantage as well: The distinction between anomaly conductivity and depth is often difficult. Measurement at two frequencies should help in this regard. However, the higher frequency seems to enhance surface features (conductive overburden, groundwater concentration, and the like) more than would be expected.

#### 7.4.3. FD Systems for Phase-Component Measurements

(a) General. All the ground EM sets discussed so far record only a part of the available information. As we saw in Section 7.2.5d a measurement of both in-phase and quadrature components of the secondary field would provide us with some knowledge

of the electrical properties of the conductor itself whereas the methods described so far are capable only of locating and outlining it. To record the additional data, it is necessary not only to cancel most of the primary field but to measure the phase as well as amplitude of the secondary field with respect to the primary. This is done with some form of compensating or ratiometer network. Two ground units of this type will be described.

(b) Turam method. The transmitter system consists of a 1 to 2 kVA source operating at 220 or 660 Hz feeding a long grounded wire or a large rectangle as shown in Figure 7.19. The long-wire transmitter is seldom used now because it introduces terrain current-channeling effects and other complications (see also §7.2.6c). Traverses are made normal to the long dimension with a receiver unit consisting of two identical coils spaced 15 to 60 m apart, joined by cable.

Measurements of amplitude ratio and phase difference between the two coils are made at each station (the midpoint of the two coils is reckoned as the station location). With no conductor present the phase difference will be zero, while the amplitude ratio  $e_1/e_2$  decreases with distance from the transmitter wire; multiplying the amplitude ratio at each station by  $d_2/d_1$ , the ratio of the distances to the far and near coils, one obtains a constant amplitude of unity and a constant  $\Delta\phi$  of zero for all stations under these conditions.

With a conductor near the receiver system, both parameters are changed - see Figures 7.37 and 7.38

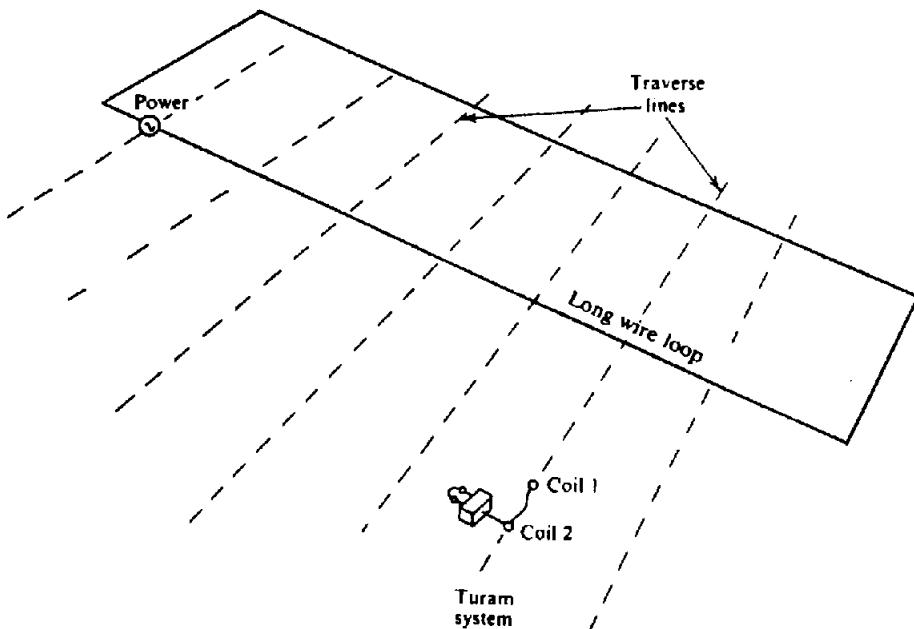


Figure 7.19. Turam field layout.

in Section 7.7.3g. The amplitude ratio is plotted in values greater or less than unity and the phase in degrees plus or minus. The profile is typical of a conductor of steep dip, its long axis roughly in line with the transmitter cable. Because the two receiver coils measure, in effect, the horizontal gradient of amplitude and phase of the vertical component of the secondary field, the profiles are horizontal derivatives of those obtained with the compensator equipment. Sensitivity is about 0.5% for the amplitude ratio, 0.2° in phase. Thus Turam provides the extra information available when both real and imaginary components are measured, achieving a good null balance in the process.

An alternative mode of Turam operation has been described by Duckworth and Bays (1984) in which the transmitter is rotated 90° to lie on the conductor, roughly normal to its strike, rather than adjacent to the conductor and parallel to its strike. The receiver system is then moved parallel to the transmitter-loop long axis, that is, across strike. The orientation is said to have several advantages over the original Turam layout:

1. a larger area of operation for one setup, hence the possibility of reconnaissance as well as detail surveys;
2. larger receiver coil spacing resulting in greater depth of penetration;
3. reduction of conductive host-rock and overburden effects because the receiver traverses are parallel, rather than normal, to the transmitter loop;
4. consistent indication of target dip (§7.7.3g);
5. conversion of original readings to reduced amplitude ratios and zero phase differences is unnecessary because they are already unity and zero, respectively, except over an anomaly.

In this orientation, however, coupling of the primary field to the sheet conductor should be very weak compared to the standard layout.

*(c) Moving source (horizontal-loop) method.*

Known also as *Slingram* and *Ronka* EM, this system, like so many others, was developed in Sweden and has been popular in North America since about 1958. The field layout is illustrated in Figure 7.20.

Both transmitter and receiver are moved, a fixed spacing of 100 to 1,200 ft (30 to 360 m) between them being maintained by a cable. The transmitter is low power (1 to 10 W) and the transmitter coil is about the same size as the receiver. In some sets the coils are wound on insulating frames ~ 1 m in diameter; in others, ferrite-core coils are employed. The coils are coplanar and almost always oriented to detect the vertical component, although this is not a necessary requirement. In at least one model, the connecting cable is replaced by a radio link; but the cable serves the additional purpose, on reasonably level ground, of maintaining correct spacing, which is quite critical.

Following procedures outlined in Section 7.3.7, after obtaining primary-field compensation in a barren area, the in-phase and quadrature components expressed as percent of the secondary field may be read off visual indicators. Sensitivity of both measurements is about 1 to 2%.

Traverses are made perpendicular to strike where possible and the readings plotted for the midpoint of the system. Typical profiles are shown in Figures

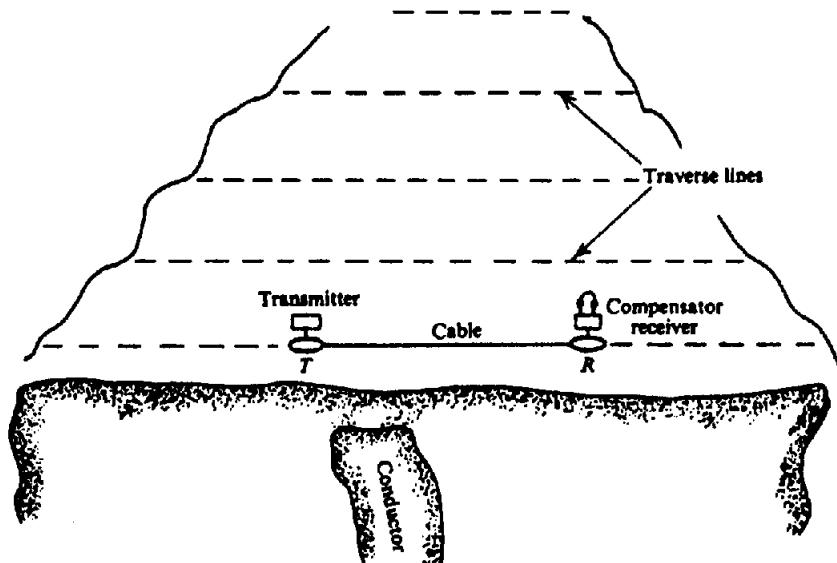


Figure 7.20. Horizontal-loop system.

7.36 and 7.41 in Sections 7.7.3f and 7.7.3i. As discussed later, the interpretation of anomalies with horizontal-loop (HLEM) systems is generally simpler than with other EM field sets. However, the chief advantage is that the fixed relative positions of the receiver and transmitter maintain a constant mutual inductance  $M_{TR}$  [Eq. (7.21d)]. Thus the direction of traverse is immaterial, that is, we can interchange the receiver and transmitter and get the same reading at the same station.

There are also some drawbacks to the horizontal-loop unit. The depth of penetration is inevitably limited by the portable low-power transmitter. Maximum depth for detecting a good conductor is often considered to be half the coil spacing; although separations as large as 350 m are available, it is unlikely that the corresponding depth would be 175 m.

Both the spacing and orientation of the coils also are critical. Decreasing a 60 m interval by 1 m will produce an appreciable in-phase anomaly (6%), and a relative tilt of 10° between the coils will give a 1.5% error or greater, depending on whether the measurement is made in the presence of a good conductor. Care must be taken in hilly ground to maintain both proper spacing and tilt. For instance, on a slope the coils must be parallel rather than horizontal, because their elevations are different. Correction may be necessary in this case because the total vertical component is not being measured. Again if the coils straddle a steep hilltop, the correct spacing may not be maintained.

Some horizontal-loop sets operate at two frequencies (e.g., 875 and 2,200 Hz) with a view to distinguishing shallow anomalies that may mask better conductors at depth. One popular unit, MaxMin, provides six frequencies.

#### 7.4.4. Time-Domain EM Ground Systems

(a) *General.* The USSR, very active in electrical prospecting since early connections with the Schlumbergers, pioneered in transient EM techniques for ground and downhole work from the early 1960s. Development and use of TDEM ground systems has increased in the Western world only since about 1973. Their popularity is based on several advantages over FDEM. It appears that both the maximum depth of penetration and ability to detect targets through conductive overburden are superior to the latter; the first feature is attractive anywhere and the second particularly so in tropical regions where surface terrain is often highly conductive. Results from FDEM base-metal surveys in Australia, for example, were disappointing prior to about 1976 and led to the development of the SIROTEM equipment in that country (Buselli and O'Neill, 1977).

All TDEM systems (except UTEM—see §7.4.4f) use a transmitter that produces a sharply terminated primary-field pulse and a detector that samples any resultant secondary-field transient at a number of preset time intervals (channels) after the primary field cutoff. All systems detect the time rate of change of the secondary field ( $dH/dt$ ) because an induction coil is used as the sensor (but see §7.4.5). We will outline several ground TD systems in the following sections.

(b) *MPP-4.* Developed by VITR Leningrad and operational since 1981, this is a Soviet ground and borehole TDEM system that may be used either with a single square loop (usually 200 × 200 m maximum) for transmitting and receiving or with a portable multturn ferrite-core receiver coil linked by radio to the transmitter for synchronization and

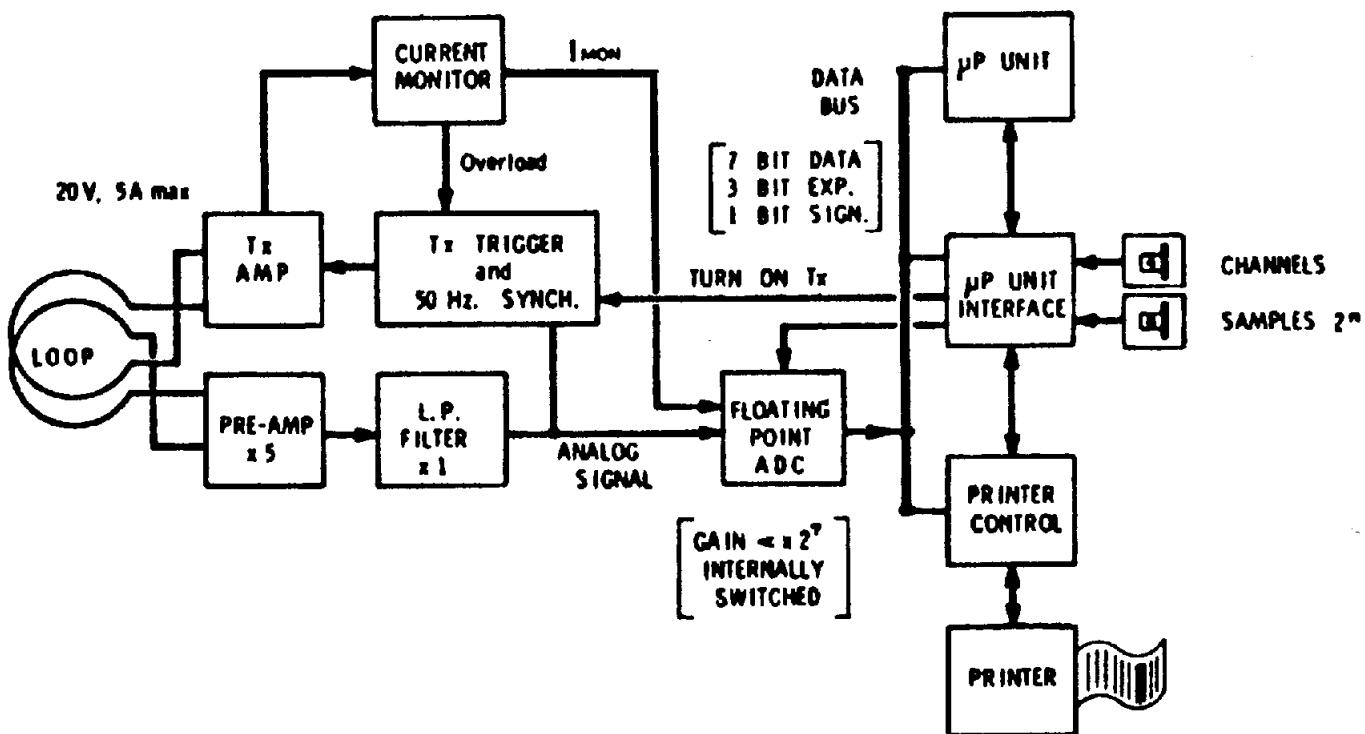


Figure 7.21. Simplified block diagram of SIROTEM. (After Buselli and O'Neill, 1977.)

communication. Transmitter current is about 20 A maximum, the square pulse being 20 to 40 ms duration with the same off time. Transient decay is sampled and averaged in 10 to 20 channels, commencing about 1 ms after current cutoff; the output is read on a meter.

The portable receiver is used for more detailed targeting by traversing grid lines either inside or outside the large transmitter loop. Whether this survey method is more sensitive to conductors of limited dimensions is not clear; the single-loop arrangement is said to be rather insensitive to small conductors, deep or shallow, giving best response for bodies whose dimensions are roughly the same as or greater than the large loop (Kleinkopf et al., 1974; Zietz et al., 1976; Buselli, 1980).

(c) PEM ("Pulse" EM). Originally designed by Crone Geophysics and Newmont Exploration, this equipment first appeared in 1972 as a semiportable horizontal-loop unit. The multturn transmitter coil is 6 to 15 m in diameter laid out in a rough circle on the ground. The recurrence frequency is either ~ 23 Hz for a 10.8 ms pulse with equal off time or ~ 12 Hz for 20.9 ms pulses with equal off time. In the original model the pulse turn-off was a 1.4 ms portion of a cosine wave, later changed to linear ramps of 0.5, 1.0, and 1.5 ms duration; the turn-on was exponential with 1.0 ms time constant.

This model was subsequently modified several times. In 1975 a larger Turam-type transmitter loop

was introduced along with a small receiver coil used for surface coverage outside the transmitter loop; a borehole receiver unit was included as well. Another version called Deepem appeared in 1977 with a 100 × 100 m transmitter loop. The receiver, which traversed outside the loop at distances of 50 to 350 m from the loop edge, measured the vertical and one horizontal component of  $H$ . About 1979 this system was provided with more transmitter power (2.5 kW, 20 A), energizing larger loops of 1,000 × 300 m.

The PEM system has been widely used in Arabia and Australia as well as in North America, and appears to have good depth of penetration. For example, in the logging mode the receiver is capable of detecting large conductors 150 m to one side of the borehole or 300 m below it. Surface surveys over resistive ground have defined conductor depth, position, and strike as well as partial shape. On conductive overburden, surface currents tend to disguise the target geometry and two transmitter loop positions are usually necessary to define it better. However, the penetration is said to be at least 200 m in resistive rock and 150 m under conductive overburden. The equipment now incorporates a field computer for data storage and analysis.

(d) SIROTEM. This time-domain equipment was developed during the period 1972 to 1977 by the Commonwealth Scientific Industrial Research Organization (CSIRO) in Australia (§7.4.4a). The decision to switch from FDEM to TDEM was taken in

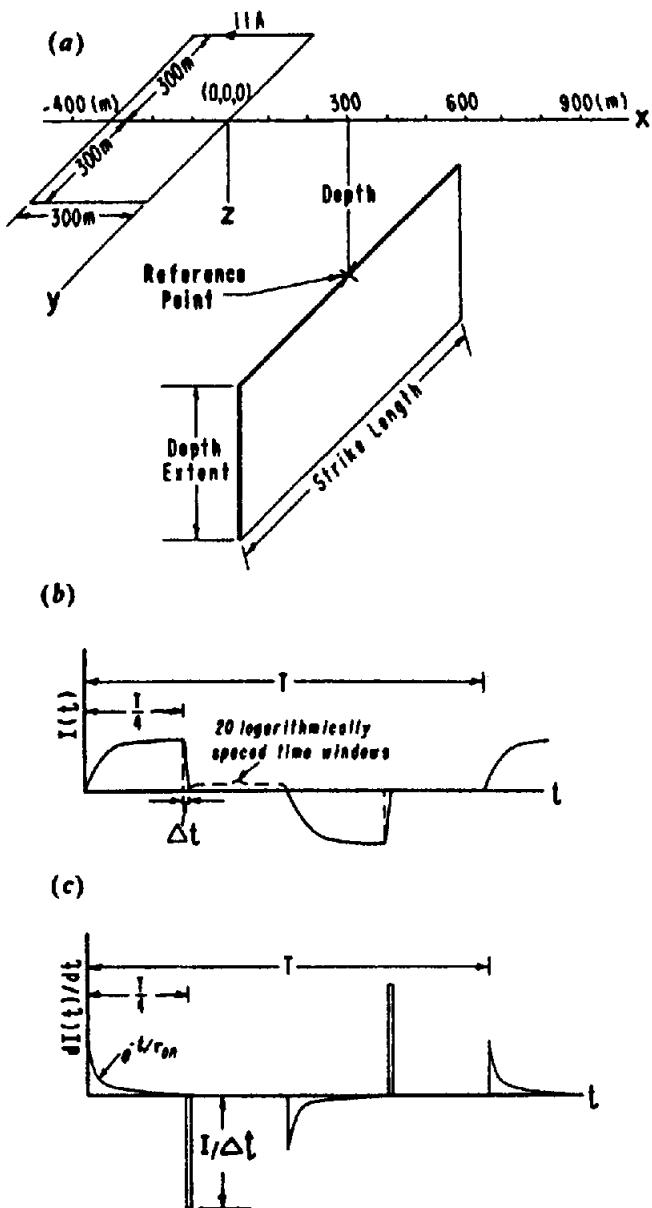


Figure 7.22. EM37 TDEM system. (After Gallagher, Ward, and Hohmann, 1985.) (a) Field layout. (b) Transmitter-current waveform. (c) Time derivative of current waveform.

spite of the difficulties in data inversion encountered in the latter (more troublesome at that time) and because of the practical advantages resulting from elimination of the large primary fields during measurement, superior extraction of small signals from noise, and less sensitivity to topography. A block diagram of the SIROTEM set is shown in Figure 7.21. The unit incorporates a microprocessor with 4K memory and PDP-8 language, controlling the transmitter, storage and averaging of data, measurement, and output sequence, and it will print out data as  $\mu\text{V}/\text{A}$ , apparent resistivity, or other suitable parameter.

Several additional improvements over earlier TDEM systems are the following: up to 32 channels

over the range 0.25 to 150 ms are available with widths from 400  $\mu\text{s}$  (early time) to 25.6 ms (late time); up to 4,096 pulses may be stacked in digital memory, maximum measuring time is 4 min/station, low noise level for small signals, suppression of power line and VLF interference, simultaneous measurement of channels, and common-mode suppression of 1,000 : 1.

The complete battery-operated instrument weighs 16 kg, operates 10 hours on one charge, and will deliver 10 A maximum to the transmitter coil. Either a coincident loop,  $100 \times 100$  m, or two loops, each  $25 \times 25$  m with two turns and 100 m separation between centers, may be used for field measurements. As in the PEM system, the two loops provide much better target definition than the single version. In 1979 a 4.3 kg logging probe was added.

(e) **EM37.** Manufactured by Geonics Ltd., this system is similar to the Crone PEM with a Turam-style transmitter loop of variable size up to  $300 \times 600$  m and a 1 m diameter air-core receiver coil. The latter will measure three components of  $\partial H / \partial t$  both inside and outside the transmitter layout over a range of 10 to 1,500 m (Fig. 7.22a). It first appeared about 1980.

The transmitter has a bipolar 30 A maximum output and operates at three recurrence frequencies, 3, 7.5, and 30 Hz, with equal on-off times. Figure 7.22b shows the current waveforms, with a slow exponential turn-on and fast ramp shutoff; the time derivative,  $dI/dt$  is displayed in Figure 7.22c.

Transient response is measured at the receiver (which has a 40 kHz bandwidth) in 20 logarithmically spaced windows, the first of these coming on 800, 320, or 80  $\mu\text{s}$  after cutoff, corresponding to the respective 3, 7.5, and 30 Hz repetition frequencies. The receiver output may be read on a digital meter with a 20-position rotary switch; T-R synchronization is obtained with a quartz crystal oscillator, direct wire link, or from the primary field.

(f) **UTEM.** Lamontagne and West developed this TEM system at the University of Toronto over the period 1972 to 1980 (West, Macnae, and Lamontagne, 1984). It uses a conventional Turam field layout with a transmitter loop of  $1 \times 2$  km in resistive terrain,  $300 \times 300$  m over conductive ground, with corresponding receiver distances up to twice the loop dimension. Measurements are made of  $H_r$ , sometimes of  $H_{\text{hor}}$  and  $E_{\text{hor}}$  also, the latter by means of grounded electrodes about 25 m apart. The geometry is shown in Figure 7.23a.

Unlike the other time-domain systems, the UTEM transmitter generates a continuous triangular waveform with no off time (§7.3.2). Thus the receiver

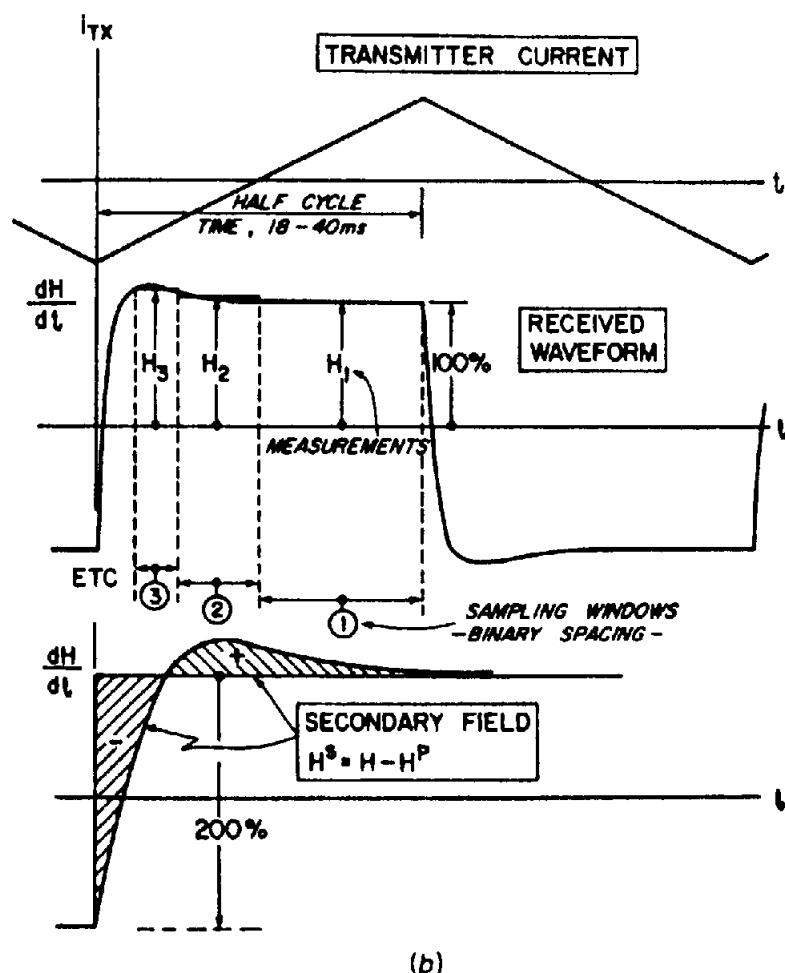
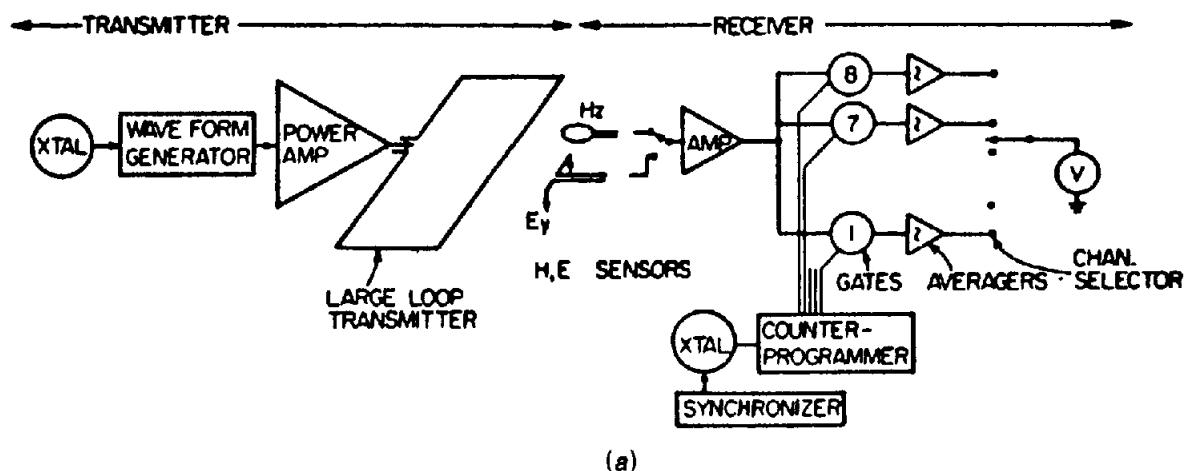


Figure 7.23. UTEM time-domain system. (After West, Macnae, and Lamontagne, 1984.)  
(a) Block diagram. (b) Transmitter and receiver waveforms.

response in free space would be exactly a square wave; in the vicinity of conductors the square wave is distorted. The UTEM receiver measures average amplitudes over 10 delay times spaced in a binary geometric progression between discontinuities on the triangular waveform. Hence the distortions are revealed in the various windows. Effectively then, UTEM measures the magnetic-field step response (response to a step in the primary field), whereas all

other TDEM systems measure impulse response (§A.13).

Transmitter and receiver waveforms are displayed in Figure 7.23b together with a few sampling windows. The latter are numbered in reverse, the first window being  $\frac{1}{4}$  cycle duration, the second  $\frac{1}{8}$ , the third  $\frac{1}{16}$ , and so on.

Differences in response of the UTEM system, compared to those from step-function transmitter

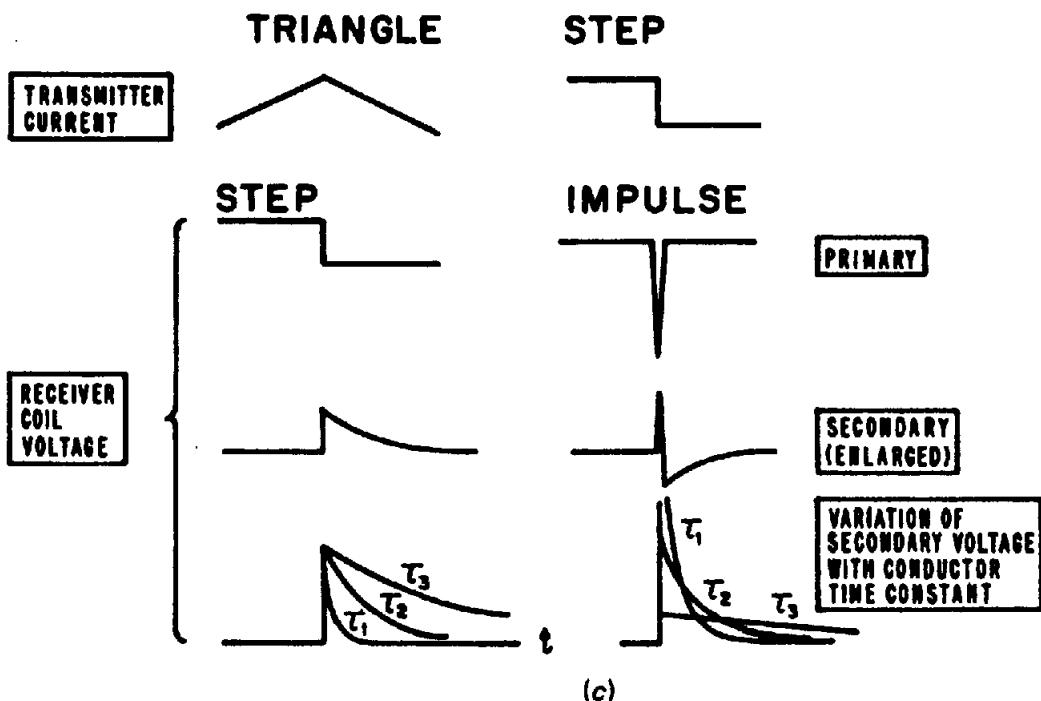


Figure 7.23. (Continued) (c) Comparison of signals for triangular and step-function inputs.

systems, are further illustrated in Figure 7.23c. The decay labeled  $\tau_1$  has a short time constant compared to  $\tau_2$  and  $\tau_3$ , associated with early time or high amplitude, characteristic of overburden anomalies. Although target response of this type is much larger for both step and triangular wave inputs than that caused by long time constant features, the effect is more pronounced with the step source.

Recurrence frequency of the UTEM transmitter is variable but usually is 30 or 15 Hz, and the ground response is measured from about  $25 \mu\text{s}$  to  $12.8 \text{ ms}$  for 30 Hz; twice these values for 15 Hz. These frequencies are chosen to minimize 60 Hz interference (because the waveform contains only odd harmonics). Receiver-transmitter synchronization is obtained by the crystal oscillator seen in Figure 7.23a. Maximum transmitter current is about 5 A.

(g) Megasource transient EM. Recent development of a novel EM source producing extremely high current suggests the possibility of very deep penetration by time-domain EM. The generator is a solid-fuel rocket motor, pulsed to produce short bursts of ionized gas expanding at supersonic velocities through a magnetic field. Pulses of 3 s duration delivering  $10^4$  A have been used during a test in southern California (Lawrence Berkeley Laboratory Research Review, 1986). The transmitter system is completed by feeding the current into a wire loop of conventional dimensions (100 to 200 m), while the decay fields are detected by high sensitivity magne-

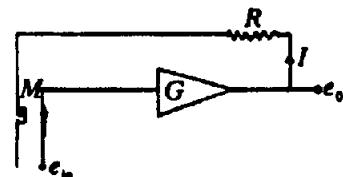


Figure 7.24. Feedback circuit to convert  $\partial H / \partial t$  signal to  $H$ .

tometers. It is expected that the maximum current may be increased by a factor of 10.

#### 7.4.5. Measurement of $H$

EM systems invariably employ a coil to detect secondary signals for the receiver. This is no problem in FD, but because the coil measures  $\partial H / \partial t$ , it enhances short time-constant response for TD signals. A wide-band ac magnetometer, measuring  $H_s(\omega)$ , would make a better sensor, but none is available at present (1988). An alternative approach is provided by heavy feedback in a receiver-amplifier stage. Figure 7.24 shows a circuit for this purpose; the receiver coil is coupled to the input and we have for the receiver output  $k \partial H / \partial t = j\omega kH = e_{in}$ .

With negative feedback across the stage whose gain is  $G$ , the feedback voltage is  $-j\omega MI = -j\omega Me_0/R$ . The input is now  $j\omega(kH - Me_0/R)$ , so

$$e_0 = j\omega G(kH - Me_0/R)$$

and

$$e_0 = j\omega kH / (1/G + j\omega M/R)$$

If  $G$  is very large, we have

$$e_0 \approx (kR/M) H$$

Thus the time derivative of  $H$  at the input is converted to a direct measurement of  $H$ .

#### 7.4.6. Assessment of EM Ground Methods

(a) *Frequency domain.* It would be attractive to compare the various frequency-domain EM ground sets in a sequence of increasing sophistication, so that we would arrive at the best possible equipment for field work, after consideration of simpler versions. This is not really possible, however, because there are inherent advantages and weaknesses in all the presently used systems. The criteria for judging the worth of a particular set include source power, reliability, speed and simplicity in field operation, information obtained, and ease of interpreting the results. In a rough summary we can say that the depth of penetration increases with source power and hence the large transmitting loop systems have an advantage. By the same token they are less attractive for fast reconnaissance; in this area the numerous dip-angle techniques are particularly suitable. Finally the units that measure both in-phase and quadrature components provide more information about the anomalies, but at the same time are more expensive, usually slower, and require more competent operators.

(b) *Time domain.* It is very difficult to rate the presently available TD ground systems, particularly on the same basis as in the preceding section, because there is considerably less variety among them. For example, the apparent advantage in using a single loop for transmitter and receiver is greatly reduced by its lack of mobility and poor discrimination, nor is the superiority of UTEM's continuous triangular waveform over pulse input clearly established.

There are, however, several obvious differences between time- and frequency-domain systems. The former have the advantage of wider frequency range, greater depth of penetration, and ability to see through conductive overburden. On the other hand, FD is more suitable for fast reconnaissance and detail with light-weight, portable, cheap units, probably produces better anomaly resolution, and the interpretation of field data is better developed. Because TD applications are relatively new, however, and are being actively investigated, some of these comparisons will soon be out of date.

### 7.5. AIRBORNE EM SYSTEMS

#### 7.5.1. General

A prime attraction of EM prospecting, as mentioned before, is that reconnaissance exploration can be done from the air. Only magnetism and radioactivity, among the other methods, can be used in this way. A great variety of airborne EM systems has been developed to take advantage of this fact. They will be considered in the order in which they appeared, an order that corresponds roughly to the development of more complete and complex equipment.

The frequencies employed in FD systems are the same as in ground EM, lower frequencies generally being used with higher power and greater altitude. The height of flight also determines the line spacing, which may vary from 300 ft to  $\frac{1}{2}$  mile (100 to 800 m). Position of the aircraft is usually determined from continuous strip photography, occasionally by radio navigation, which, of course, adds considerably to the cost. Recording of data is continuous, now generally digital. Originally airborne EM surveys were performed with small fixed-wing aircraft. Now both FD and TD systems have been modified for helicopter, which is more suitable for detailed work and rugged terrain. With either carrier they are normally combined with airborne magnetism, sometimes with airborne radiometrics and/or additional EM surveys.

#### 7.5.2. Quadrature Method

The first airborne installation used on any scale, this system measured only phase shift between primary and secondary fields. It was updated in the mid 1970s as the McPhar Quadrem to be carried by fixed-wing aircraft or helicopter; it had five frequencies (instead of two) to extend the range of conductor response. Otherwise, it suffered from the same limitations as the earlier models, and is no longer used to any extent.

#### 7.5.3. Turair System

Originally used in Russia and Western Europe, this is essentially a ground Turam transmitter unit with two helicopter-borne receiver loops measuring the gradient of either horizontal or vertical  $H$  fields on flight lines normal to the long dimension of the loop. The North American version is the Scintrex Turair. Parameters measured are the same as with the ground equipment.

There are two attractive features of this arrangement, one being a greater depth of penetration from

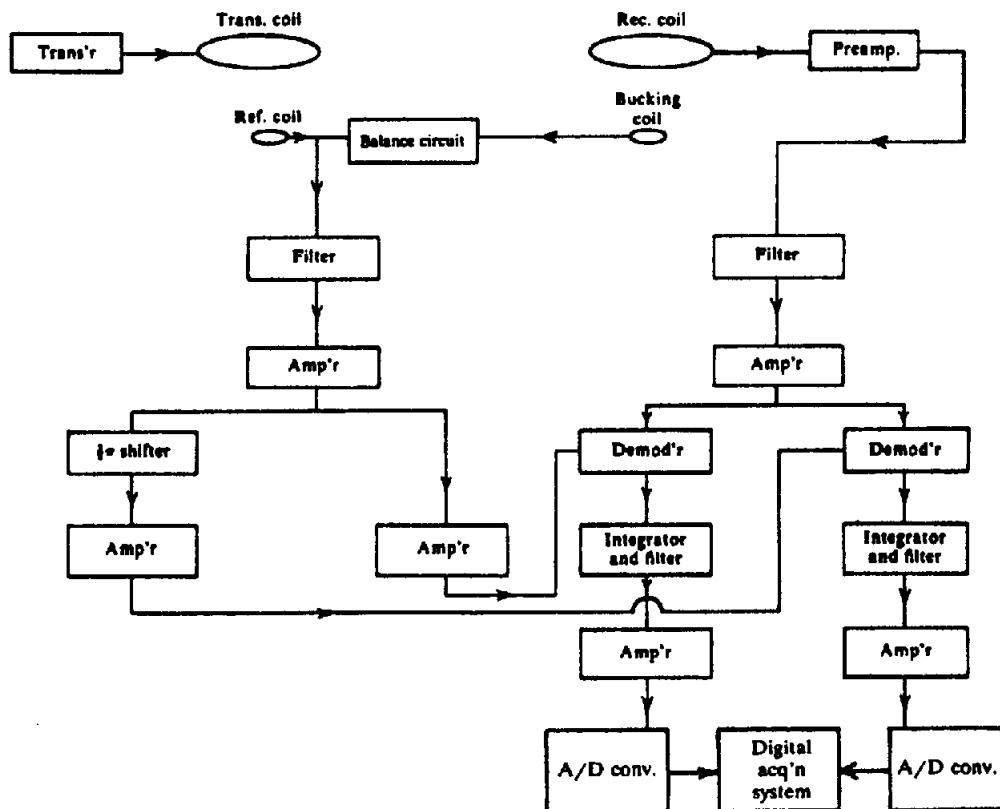


Figure 7.25. Block diagram of the airborne phase-component system. (From Keller and Frischknecht, 1966.)

the ground transmitter, the other that immediate ground followup may be carried out in more detail.

#### 7.5.4. Airborne VLF

Numerous versions of airborne VLF equipment have become available since about 1970; these include sets manufactured by Barringer, McPhar, Geonics, Scintrex, Sander, and Herz. The Barringer Radio-phase and  $E$  phase, among the earliest of these, appeared around 1970 (Barringer, 1970; Arcone, 1978). A pair of whip antennas (orthogonally mounted dipoles) mounted on an extension of the aircraft nose cone measure  $E_z$  and  $E_x$ , with the line of flight normal to transmitter direction. Only the quadrature phase component of  $E_x$  with respect to  $E_z$  is measured, the latter being the phase reference. This gives the wave tilt in the presence of ground conductors in the form  $W_q = E_{xq}/E_{zi}$ , where  $q$  and  $i$  refer to quadrature and in-phase components, respectively. Hence it is possible to determine ground apparent resistivity from the relation  $\rho_q = 2(E_{xq}/E_{zi})^2/\omega\epsilon_0$ .

The McPhar KEM system carries a pair of orthogonal coils underneath the wing tip to measure total-field tilt angle ( $\pm 30^\circ$  max) and displays horizontal-component  $H$  field and tilt angle on conventional meters, with provision for analog recording.

Geonics EM-18 and Scintrex SE-99 equipment both measure in-phase and quadrature components of  $H_z$  with respect to total horizontal  $H$  field in a similar fashion to the earlier airborne AFMAG unit (Becker, 1979). The Herz Totem-1A (Hood, 1979), a lightweight 5 kg unit, appears to be otherwise similar to these.

Sander's EM-11 VLF system, reported in Hood (1978), incorporated three orthogonal receiver coils to provide all amplitude and phase components. A later 1982 Herz model, Totem-2A, measures multiple parameters on two channels simultaneously, including amplitude of the total field and vertical quadrature. It uses advanced circuitry to achieve lower noise; for example, the system automatically corrects for aircraft pitch, yaw, and roll.

VLF systems at their present stage of development seem capable of performing fairly detailed shallow resistivity mapping, particularly in resistive environments, and have been used extensively in indirect exploration for uranium and gold.

#### 7.5.5. Phase-Component Measurements

There is a variety of these airborne systems, mounted either on a light aircraft or helicopter. They include the Kenting-Scintrex Tridem, Geonics EM-33, Barringer Aerodat, Dighem, and others. All are similar

to the horizontal-loop moving-source ground set, except that the coils more often are vertical, sometimes null-coupled; several frequencies are available. Flexure of the coil mountings caused by turbulent air is quite serious with this type of equipment. For a coil separation of 15 m, a change in distance of a fraction of a millimeter is sufficient to change the receiver loop signal by 10 ppm, although only the in-phase component is affected. Introduction in 1977 of the Aerodat low-noise bird or boom structure, made of light, high-rigidity plastic, reduced these mechanical problems. This type of button-on mounting holds the transmitter and receiver coils at a fixed spacing of 7 to 10 m and reduces noise level to  $\sim 1$  ppm.

The block diagram of a phase-component airborne unit is shown in Figure 7.25. Obviously it is much more complex than the ground unit. The primary field and the fixed anomaly of the aircraft are cancelled at the receiver as completely as possible; any additional signals above noise level are recorded as anomalous conductors. In effect we are detecting  $H_T$ , which is made up of all the signals arriving at the receiver loop: the primary dipole field, the effect of the aircraft, and whatever secondary field may also be present; that is,

$$H_T = H_S + H_P + H_A = H_S + H'_P$$

Cancellation of the last term,  $H'_P$ , by means of the bucking coil at the receiver, gives us  $H_S$ , which is measured in terms of  $H'_P$ . That is,

$$\frac{H_S}{H'_P} = \frac{H_T}{H'_P} - 1$$

where the ratio is generally expressed in parts per million.

Figure 7.26 illustrates three coil arrangements used on aircraft and helicopters. The coils are either coplanar or coaxial with their axes in the line of flight. All three configurations are basically similar, because the primary field at the receiver is given by Equations (7.14h, i) in Section 7.2.3d. That is, for either of the coaxial mounts on the helicopter,

$$H_P = Nia^2/2I^3$$

and for the coplanar system on the wing tips,

$$H_P = -Nia^2/4I^3$$

where  $N$ ,  $i$ , and  $a$  are the number of turns, current, and radius of the transmitter coil and  $I$  is the distance between centers of the two coils, which varies from 20 to 80 ft (6 to 24 m), depending on the aircraft.

Frequencies used in the fixed-separation systems range from 300 to 50,000 Hz, the choice having to do with the aircraft type, which in turn determines the flight altitude. Helicopter carriers can fly as low as 30 m and generally use the higher frequencies. Fixed-wing aircraft maintain an altitude of 300 to 600 ft (90 to 180 m) depending on the terrain. Noise (other than mechanical) may be filtered out with the aid of digital signal processing. Depth of penetration is lower for in-board and helicopter boom mounting than with towed bird systems, but more data are obtained.

The Dighem helicopter-borne equipment produces a large amount of data from three orthogonal receiver coils shown in Figure 7.26d. These are maximum-coupled (MC), null-coupled horizontal (NH), null-coupled vertical (NV); the first records in-phase and quadrature components at 2 and 5 ppm sensitivity, whereas the others show quadrature only at 2 ppm. The Aerodat AEM system includes two vertical coaxial pairs at 955 and 4,536 Hz and two horizontal coplanar pairs at 4,132 and 33,000 Hz. The latest Dighem unit carries three coil pairs, two coaxial and one coplanar.

Dighem data from an area containing numerous conductors are shown in Figure 7.27. All channels respond over the southern conductors, while the null-coupled pair are weak on the northern features. Model sets of curves for half-space, horizontal and vertical sheets, and two layers have been prepared for interpretation. MC data are analyzed for complex conductivity, assuming a superposed dipole system ( $\text{altitude} \gg T\text{-}R$  spacing).

The NV coil is sensitive to flight direction and may be used to correct the MC anomaly for oblique strike, whereas the NH coil indicates target dip. Profiles and contours of apparent resistivity may also be developed from the models.

### 7.5.6. Transient (Input) Method

As we have seen from the previous descriptions, the fundamental problem in airborne EM is the isolation of very small secondary responses in the presence of a very large primary field. This difficulty, of course, applies to ground systems as well, but to a much lesser degree. One way of getting around the problem is to use a pulsed – rather than continuous – primary field and attempt to measure secondary response during transmitter off-time. This principle is the basis of the Input (induced pulse transient) system (formerly called INPUT) developed by Barringer (1962). This was the original airborne time-domain system, and the transmitting and receiving method had some resemblance to the induced-polarization time-domain operation.

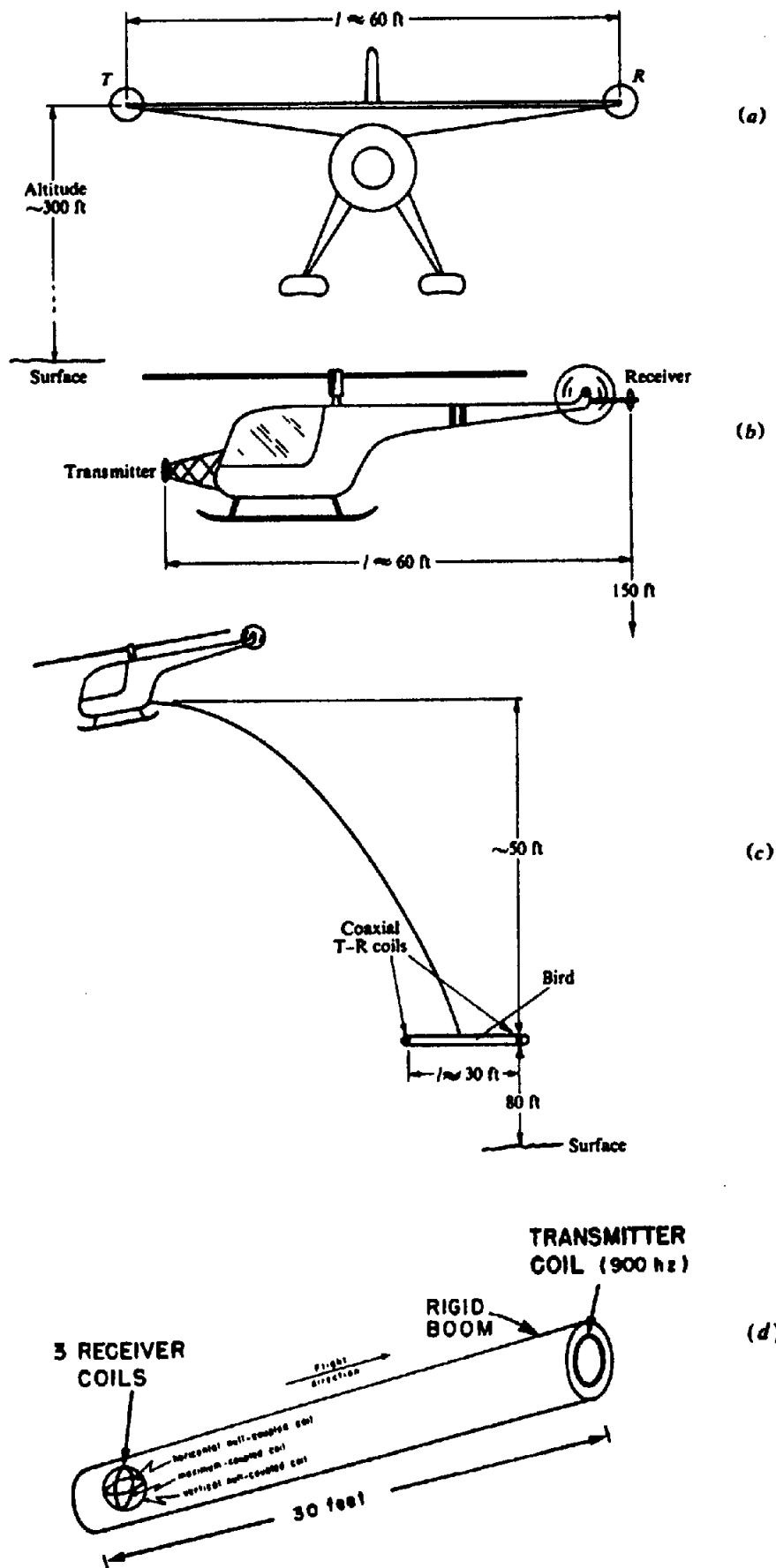


Figure 7.26. Airborne double-dipole EM systems. (a) Fixed-wing, coplanar. (b) Helicopter on-board coaxial mounting. (c) Helicopter boom mounting. (d) Digham multi-coil bird.

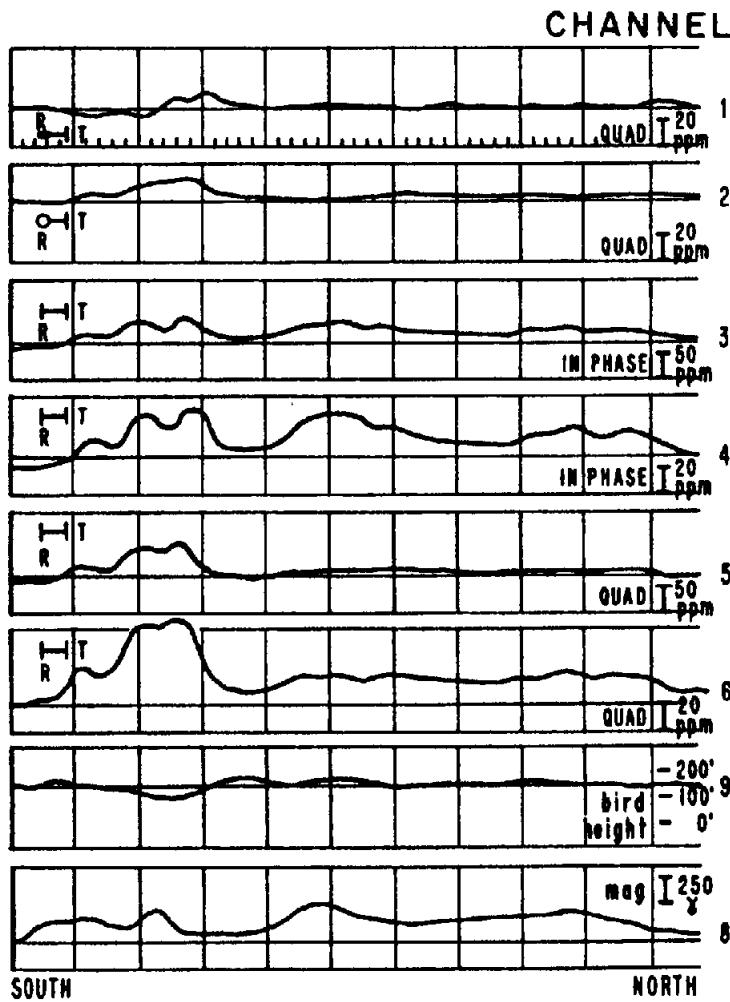


Figure 7.27. Dighem multicoil record over widespread conductors. (After Fraser, 1978.)

The transmitter loop, strung horizontally about a relatively large aircraft, is energized by half-sine-wave pulses of alternately opposite polarity. The on- and off-times were 1.5 and 2 ms, respectively, in an early model, resulting in a recurrence frequency of about 285 Hz; these parameters have since been modified over a small range for various applications. Large peak transmitter currents produce dipole moments of roughly  $2-5 \times 10^5 \text{ Am}^2$ . The receiver loop is usually vertical with its axis in the flight line; it may also be mounted with a vertical axis, particularly for resistivity mapping surveys. In either orientation it may be towed in a bird at the end of a 330 ft (100 m) cable in fixed-wing Input, or carried in the boom for a more recent helicopter version.

During transmitter-off periods the receiver amplifier samples the decay curve at several points (four in the first Input system, six and eleven in later models) for intervals of 100  $\mu\text{s}$  or longer, as seen in Figure 7.28d. These signals are integrated and recorded, formerly on a multichannel strip chart, now in digital form for automatic data processing. The sequence of magnetic field and voltage pulses is shown in Figure 7.28.

The 11-channel results in Figure 7.28e are from a test survey in the vicinity of Ottawa, Ontario (Dyck, Becker, and Collett, 1974), which was performed with the receiver coil horizontal. Minimum T-R coupling is obtained when the line between aircraft and bird is about  $36^\circ$  (Fig. 7.26). The first channel comes on about 220  $\mu\text{s}$  after current shutoff; the widths of successive gate intervals become progressively larger, with no off-time between them.

The chief source of noise is the spurious secondary field from the aircraft. The effect of this field is eliminated to a large extent by introducing a reference signal from the primary field voltage in the receiver coil, to cancel this signal in each channel of the receiver; relative motion of the bird is compensated at the same time. Other noise sources, such as atmospherics and power lines, are more difficult to suppress, although data processing in recent models has improved this.

The Input method has certain attractive features. The depth of penetration appears to be larger (possibly as great as 300 m) than most airborne EM, and the multichannel record reveals the character of conductors. Multichannel recording, however, is a neces-

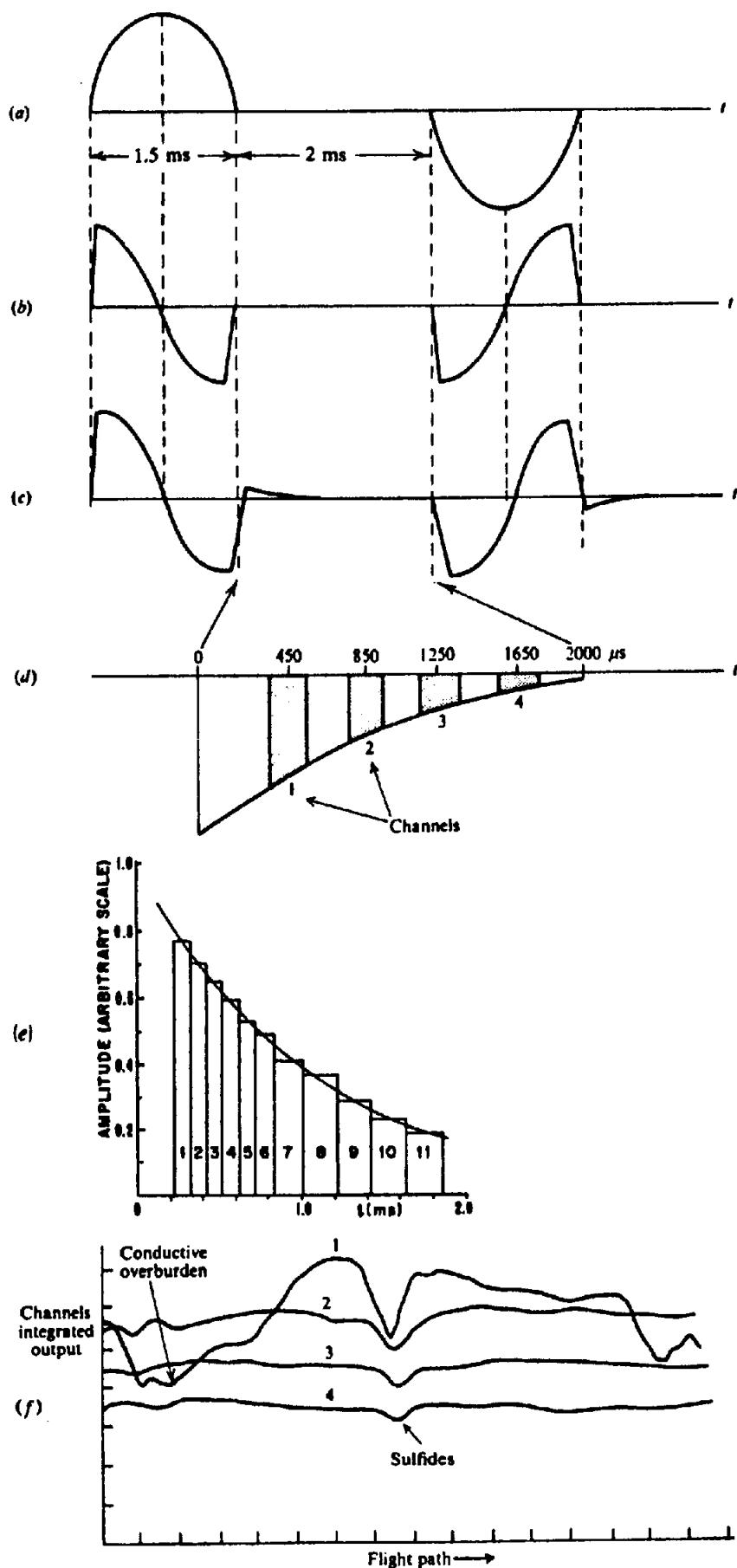


Figure 7.28. Input airborne EM system. (a) Primary magnetic field,  $H_p$ . (b) Receiver-coil voltage due to  $H_p$  when  $H_s = 0$ . (c) Receiver-coil voltage due to  $H_p + H_s$ . (d) Decay signals in the four sampling channels. (e) 11-channel sampling with zero off-time between. (f) Four-channel record over Texas Gulf Sulphur, Timmins, Ontario.

sity as well as an inherent advantage, because in a pulsed system the coil detector, which records  $dH_x/dt$ , enhances the fast decay fields, whereas good conductors usually produce a secondary field that decays slowly (however, see Section 7.4.5).

Being the only TD airborne system available and having established a highly successful record over 25 years, Input is used widely in a variety of applications. The latest units flown by Questor and Geotrex incorporate digital acquisition directly at the receiver-coil preamplifier, so that all subsequent signal processing becomes digital. This results in rejection of sferics and improved ease of computation.

### 7.5.7. Cryogenic EM System

A highly interesting single-coil airborne EM system (Morrison, Dolan, and Dey, 1976) detects minute changes in resistance of a large coil (~ 3 m diameter) immersed in liquid helium in a doughnut-shaped cryostat hanging vertically from a helicopter. Because the coil winding is superconducting and energized at a low frequency of 40 Hz, it responds to variable ground conductivity by mutual coupling and should have a large depth of penetration. Unfortunately, development is presently suspended on this novel equipment.

### 7.5.8. Assessment of Airborne EM

It is apparent from the discussion that airborne EM is considerably different in detail from ground methods, although the fundamental principles are the same. The equipment is more elaborate, there is more of it, the requirements for background noise reduction are much more stringent, depth of penetration and discrimination between conductors are reduced, and the interpretation possibilities restricted. The survey price, of course, is much increased, although not the unit cost (about \$60/km in 1987). In spite of these limitations, reconnaissance EM is invariably done from the air whenever the survey area is large enough and finances permit it. For fairly large-scale search, especially when accompanied by aeromagnetics, it becomes quite inexpensive per line-kilometer and is a powerful tool in mineral exploration.

There are, however, clear-cut differences among the present AEM systems. The VLF method is simple, cheap compared to other air surveys, and provides limited data for shallow depth. The semiairborne Turair furnishes phase-component data to considerable depth, but with higher mobilization costs. Input, the most popular airborne method for some years, yields rather rudimentary data with good

depth of penetration. Phase-component systems supply the most detailed information with some loss of penetration. Finally, there is an obvious choice between fixed and rotary wing carriers, the latter having an advantage in rugged terrain, in detail and discrimination, but at higher cost.

## 7.6. EM FIELD PROCEDURES

The standard field procedure is profiling along straight lines. Except in some ground reconnaissance, the surveying is done across geologic strike with the line and station spacing dictated by the amount of detail required. Procedures for the various ground and airborne systems have already been discussed in the previous sections.

EM may be used for vertical (depth) sounding in a manner similar to vertical resistivity sounding (§8.5.4b, §8.6.3, §8.6.4). This can be accomplished either by increasing the transmitter-receiver separation while maintaining a constant frequency, or by varying the frequency with fixed spacing. The latter has the advantage that lateral changes in resistivity do not affect the readings. As in resistivity, however, if there are several horizontal layers of different conductivity, more than one spacing may be necessary even when the frequency is varied.

Several of the ground EM methods have been used for depth sounding. The long-wire transmitter systems have a greater depth potential than, say, the horizontal-loop set; however, the latter is more attractive for interpretation because of the symmetry.

Apart from the use of several frequencies and T-R spacings in Slingram surveys, however, there were no EM sounding applications until about 1973. The growth of TDEM has since provided a stimulus, and the technique, discussed in Section 7.7.6, has developed considerably.

EM methods have been used to some extent in drill hole logging, particularly with TD equipment; this application is found in Section 11.5.

## 7.7. INTERPRETATION

### 7.7.1. Introduction

(a) *General.* As in other geophysical methods, the interpretation of EM field results is done by comparison with the calculated and/or measured response of the same type of equipment to conductors of various simple shapes and conductivities.

Theoretical calculations for this purpose are limited to very elementary geometry. For instance, it is possible to solve the following configurations (Grant

and West, 1965):

1. Conducting sphere (cylinder) in uniform ac and dipole field.
2. Conducting infinite horizontal thin sheet in uniform and dipole field.
3. Conducting infinite half-space in uniform and dipole field.
4. Conducting semiinfinite half-plane in dipole field.

This is a limited set of anomalies and the solutions are not at all simple. An alternative and more elementary theoretical approach is to assume the conductor to be a lumped circuit having resistance, self-inductance, and mutual inductance with respect to transmitter and receiver. Here again the number of geometrical shapes is quite limited, being confined to circular and straight line elements – in effect the edges of thin conductors. The solutions, however, are comparatively simple.

(b) *Analog model systems.* For more complex geometry and variable conductivity, it was formerly necessary to resort to analog model measurements to match field results. This technique was used more in EM interpretation than for other geophysical methods. We shall discuss briefly the theory of scaling for model systems.

From Equation (6.15), Section 6.2.3, we had the diffusion equation, which described the propagation of EM waves in the form

$$\nabla^2 H = \mu\sigma \frac{\partial H}{\partial t} = j\omega\mu\sigma H$$

In order that a model system may exactly simulate the field situation, both must satisfy this equation. Using subscripts *m* and *f* for model and field parameters, if *l* is a length and *f* a frequency and we scale distance and time linearly, then the following relations must hold:

$$l_m/l_f = x_m/x_f = y_m/y_f = z_m/z_f$$

and

$$t_m/t_f = f_f/f_m$$

Also,

$$\nabla^2 H_m = 2\pi j f_m \sigma_m \mu_m H_m$$

$$\nabla^2 H_f = 2\pi j f_f \sigma_f \mu_f H_f$$

hence

$$\nabla^2 H_m = \left(\frac{l_f}{l_m}\right)^2 \nabla^2 H_f = \left(\frac{f_m \mu_m \sigma_m}{f_f \mu_f \sigma_f}\right) \nabla^2 H_f$$

Therefore,

$$\frac{\rho_m}{\rho_f} = \frac{f_m \mu_m}{f_f \mu_f} \left(\frac{l_m}{l_f}\right)^2 \quad (7.33a)$$

Thus, the ratio  $\rho/\mu f^2$  has the same value in both systems. Now we generally measure EM effects in dimensionless form, for instance, the response ratio  $H_s/H_p$  or something similar to it; thus if the ratio  $\rho/\mu f^2$  has the same value in the two systems, the response ratio will be reproduced in going from one to the other. Practically, we may dispense with the permeability ratio, because magnetic permeabilities do not vary to any extent. Thus if we put  $(l_m/l_f) = 1/n$ , where  $n \gg 1$ , we get

$$\left(\frac{\rho_f}{\rho_m}\right) \left(\frac{f_m}{f_f}\right) = n^2 \quad (7.33b)$$

This relation means that we can vary either  $\rho$  or  $f$ , or both, to satisfy the above requirements. As an example, suppose we want to model a massive sulfide conductor (say  $\rho_f = 10^{-3} \Omega\text{m}$ ) on a dimensional scale of 1/500. We can make  $f_m/f_f = \rho_f/\rho_m = 500$ .

If the field equipment has a frequency of 1,000 Hz, the model parameters would be

$$10 \text{ cm} = 50 \text{ m}$$

$$f_m = 500 \text{ kHz}$$

$$\rho_m = 2 \times 10^{-6} \Omega\text{m}$$

These values, however, are unsatisfactory for a practical model, partly because the frequency is too high, but mainly because it is difficult to vary the resistivities of suitable model conductor materials more than 2 or 3 orders of magnitude. In fact, it is preferable to choose the  $\rho_m$  value first and, if possible, to maintain the same frequency in the model as the field system, because the field-set receiver may be used for the model measurements (much higher frequencies may introduce unwanted capacitive effects, hence displacement currents). In this case, if the model conductor is aluminum ( $\rho \approx 2.8 \times 10^{-8} \Omega\text{m}$ ), we have

$$n = (10^{-3}/2.8 \times 10^{-8})^{1/2} = 190$$

which makes the dimensional scale 10 cm ≈ 20 m.

As previously mentioned, the choice of model conductors is limited. Resistivities range through aluminum, brass to stainless steel ( $7 \times 10^{-7} \Omega\text{m}$ ). The only other solid material useful for models is commercial graphite ( $10^{-6}$  to  $10^{-5} \Omega\text{m}$ ). Closed loops of copper or aluminum wire may be used as models for

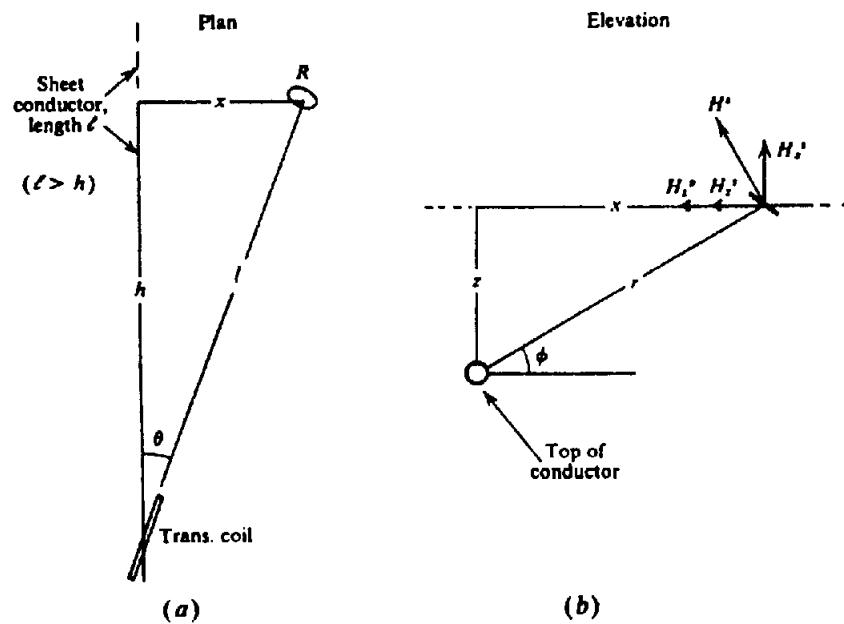


Figure 7.29. Dip-angle fixed transmitter over steeply dipping sheet. (a) Plan view. (b) Elevation showing receiver signals.

good conductors, as well as solid metal, because the induced currents do not penetrate the solid conductor to any extent. The wire loops have the additional advantage that the geometry may be changed easily.

If the host rock is a poor conductor it is permissible to measure the model conductor in air. To simulate the effect of a conductive overburden, horizontal sheets of aluminum foil may be placed over the model orebody, possibly with an electrical connection between the two. Where the long-wire transmitter – which introduces currents directly into the ground – is being used, or where the host rock has appreciable conductivity, the EM model may be immersed in a water tank (§8.6.2). The conductivity of the liquid is variable over a wide range by the addition of salt or acid. In the tank model it will usually be necessary to increase the frequency to maintain the scaling ratio.

Obviously the EM model equipment should be scaled the same as the conductor. Practically this may not be possible, because a 1 m diameter receiver coil becomes impractically small when scaled 1,000/1. But if the model coil is very large with respect to the station spacing, or receiver-transmitter spacing, it is preferable to adopt a smaller scale ratio. Coils may be conveniently wound on small diameter (2 to 5 mm) ferrite rods for model work; theoretically this limits the dimension ratio to about 200. However, considerable latitude is permissible in this respect.

(c) *Numerical modeling.* As a result of computer advances, the application of inversion techniques and other approaches have created small libraries of EM data for more complicated models. Several pro-

grams have been developed for determining EM response over 2-D structures. Digital-analysis methods include finite difference, transmission-line analog, and finite-element modeling (§6.2.7). Integral-equation methods require solutions of the equations for the EM fields or their current distributions (Parry and Ward, 1971; Hohmann, 1971). Computer analysis has replaced scale modeling to a great extent, even though computer solutions for 3-D structures are extremely difficult, as in MT interpretation.

### 7.7.2. General Interpretation Procedure

In discussing interpretation of ground EM we shall limit the types of frequency-domain field methods to dip-angle (fixed-transmitter, broadside, shootback, AFMAG, and VLF) and phase-component (Slingsham and Turam). Time-domain systems include PEM, SIROTEM, EM37, and UTEM. For airborne methods, we will describe elementary interpretation applied to data from quadrature, VLF, phase-component, and Input surveys.

The models that are amenable to interpretation are simple and few in number. By far the most popular is the conductive sheet in various attitudes, because it is a common and excellent target for EM. Response from spherical (3-D) and layered (1-D) structures will be considered more briefly.

### 7.7.3. Ground Systems; FDEM over Dipping Sheet

(a) *General.* A common configuration for conductive zones is a thin sheet, long in the strike direction, with variable dip and depth extent. If the conductiv-

ity is large or the frequency high, the induced current might be assumed to flow mainly along the top edge, vertically at the ends, and return at depth. That it does not follow this path has been shown by model studies (Koefoed and Kegge, 1968; Koefoed and Struyk, 1969; Annan et al., 1975). However, model work has proved a great aid for interpreting the response of common ground EM systems to this target.

(b) *Dip-angle measurement; fixed vertical-loop transmitter.* The coil geometry with this type of conductor is shown in Figure 7.29. The transmitter coil, located if possible at a point directly over the top of the conductor, is pointed at successive receiver stations and a minimum is obtained by tilting the receiver coil about the *T-R* axis. This measurement is the ratio of the vertical component to the total horizontal component at the detector. The former is entirely due to the secondary field, whereas the horizontal is the sum of the secondary component and the primary field (which of course is horizontal). Then we have

$$\tan \delta = H'_z / (H'_x + H'_y) = H'_z / H'_x \quad (7.34)$$

where  $H'_x$  is the total horizontal component. Because  $H'_z$  will be zero when the receiver coil is directly over the top of the sheet and will change sign as we move in either direction across strike (Fig. 7.29), it is clear that the dip angle profile is asymmetric. Using the sign convention that the dip angle is positive to the left, negative to the right, of the sheet as the traverse proceeds from left to right, we obtain profiles as in Figure 7.30a. The slope of these, positive to negative from left to right, defines a *real* or *proper crossover* at the zero dip angle; the latter marks quite accurately the location of a thin dipping conductive body surrounded by resistive host rock. (The sign convention for this definition could as easily be in the opposite sense, but must be consistent to avoid confusion.)

Figure 7.30b displays several profiles over vertical sheet models; these are perfectly asymmetric, the dip angle increasing to two peaks equal and opposite in sign either side of the crossover, then tailing off gradually for larger  $x/z$ . As the dip of the sheet decreases from  $90^\circ$  to  $30^\circ$  in Figure 7.30a, the positive peak to the left (footwall or updip side) increases, whereas the negative on the right (hanging wall or downdip side) decreases. Beyond these peaks the footwall-side dip angle falls off at about the same rate as the vertical sheet, whereas on the hanging wall the decrease is more rapid and may cross zero, indicating a *false* or *reverse crossover*, which in this example is merely a reflection of the bottom of the

sheet. Reverse crossovers, however, may also be produced by resistive structures and multiple conductors. It should be noted that the real crossover is displaced slightly downdip as the sheet lies more nearly horizontal.

Thus the deviation of the type curve from perfect asymmetry is diagnostic of the conductor dip. Similarly, the curve slope near the crossover tells us something of its depth and/or conductivity. The latter quantity is contained in the response parameter (§7.2.5d, §7.7.7a), which for the thin sheet is given by  $\mu\omega\sigma t l$ , where  $\sigma t$  is the thickness-conductivity product (TCP), also called *conductance*, and  $l$  is the *T-R* spacing. Consequently the conductor response should increase for profiles obtained on traverses further removed from the transmitter, provided the sheet is long enough and the eddy currents induced in it are less than saturation. That this is so is apparent from the pair of curves in Figure 7.30c, for profiles obtained at two *T-R* separations over the same model conductor. The scale ratio is 1/200. The upper profile, carried out  $\sim 250$  m from the transmitter, shows a positive peak some 30% larger than the one below it which was 125 m away; in fact, the entire upper curve is shifted upward with respect to the lower one.

The dip-angle curves in Figure 7.30b, obtained with a model vertical half-plane conductor, illustrate the effect of variable depth. Over a range of 50 for  $z$ , the peak values of  $\delta$  change from 3 to  $\sim 43^\circ$  and the peaks practically disappear at deep and very shallow depths. Depth extent of the sheet conductor is not very significant, except for some spreading of the profiles on the hanging wall side for different dip angles.

If the transmitter is offset with respect to the top edge of a dipping sheet, the crossover is still located almost exactly above the top (rather than slightly downdip) but the profiles are changed considerably, as can be seen in Figure 7.31a. The offset reduces peak dip angles in all locations. When it is downdip, the positive and negative maxima are more nearly equal than in figure 7.30a and again are more sharply defined downdip. If the transmitter is updip, response is almost zero on that side.

When the sheet is horizontal (Fig. 7.31b), transmitter location produces still greater changes in dip-angle response. The profile from a centrally located transmitter is similar to that from a thick horizontal slab (Fig. 7.31c). If it is near one edge, there are large peaks in the same sense with steep slopes near each edge of the sheet and no crossover at all. For an offset completely beyond the sheet, the dip angles are extremely small.

EM systems often use two frequencies, say 1,000 and 5,000 Hz, to aid in assessing conductor geometry

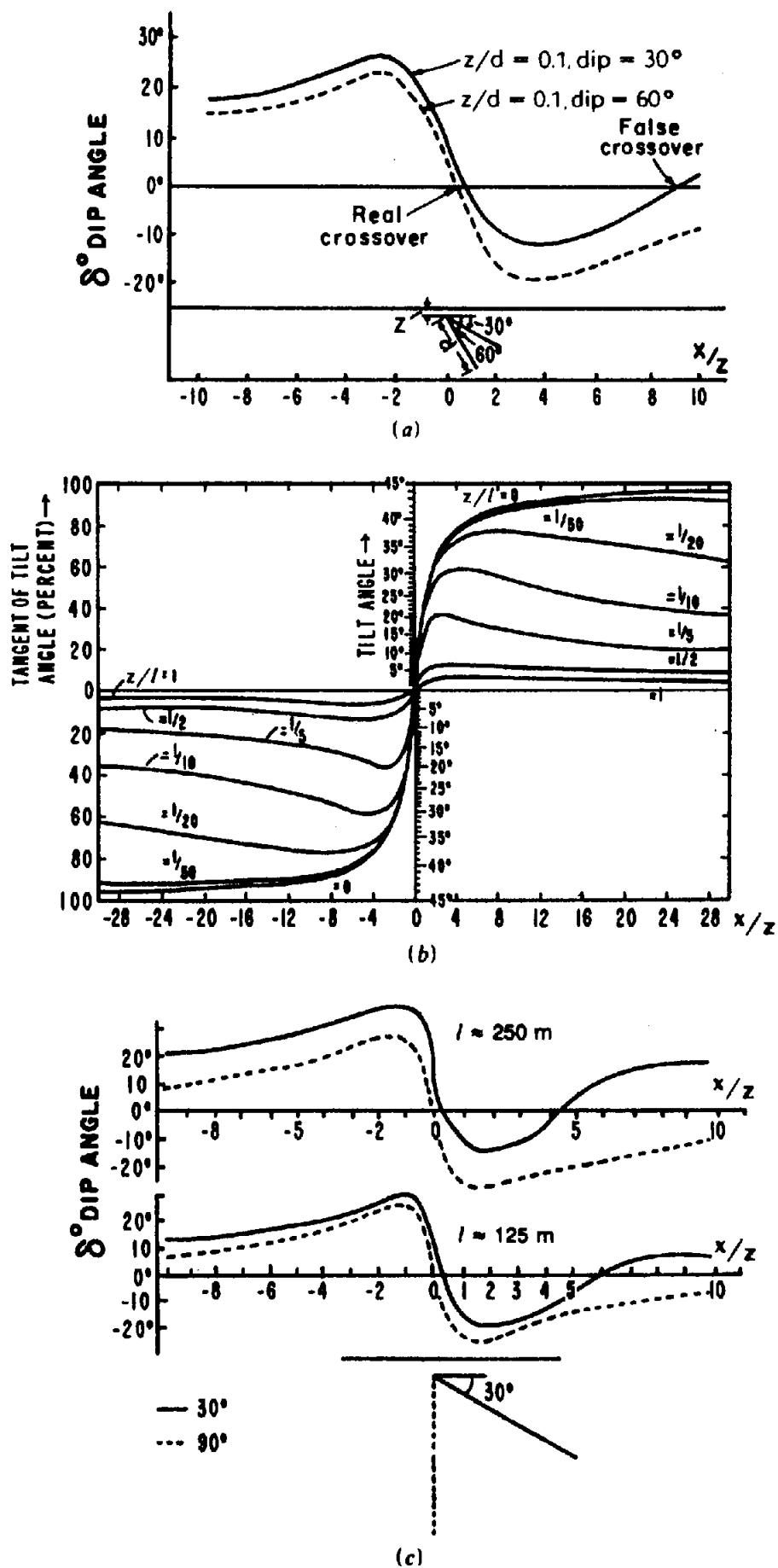


Figure 7.30. Response of dip-angle fixed-transmitter system to dipping sheets.  $l = \text{T-R}$ . (After Ward, 1967.) (a) Sheets of depth extent  $d$  dipping  $30^{\circ}$  and  $60^{\circ}$ . (b) Effect of variable depth of vertical sheet. (c) Effect of T-R separation.

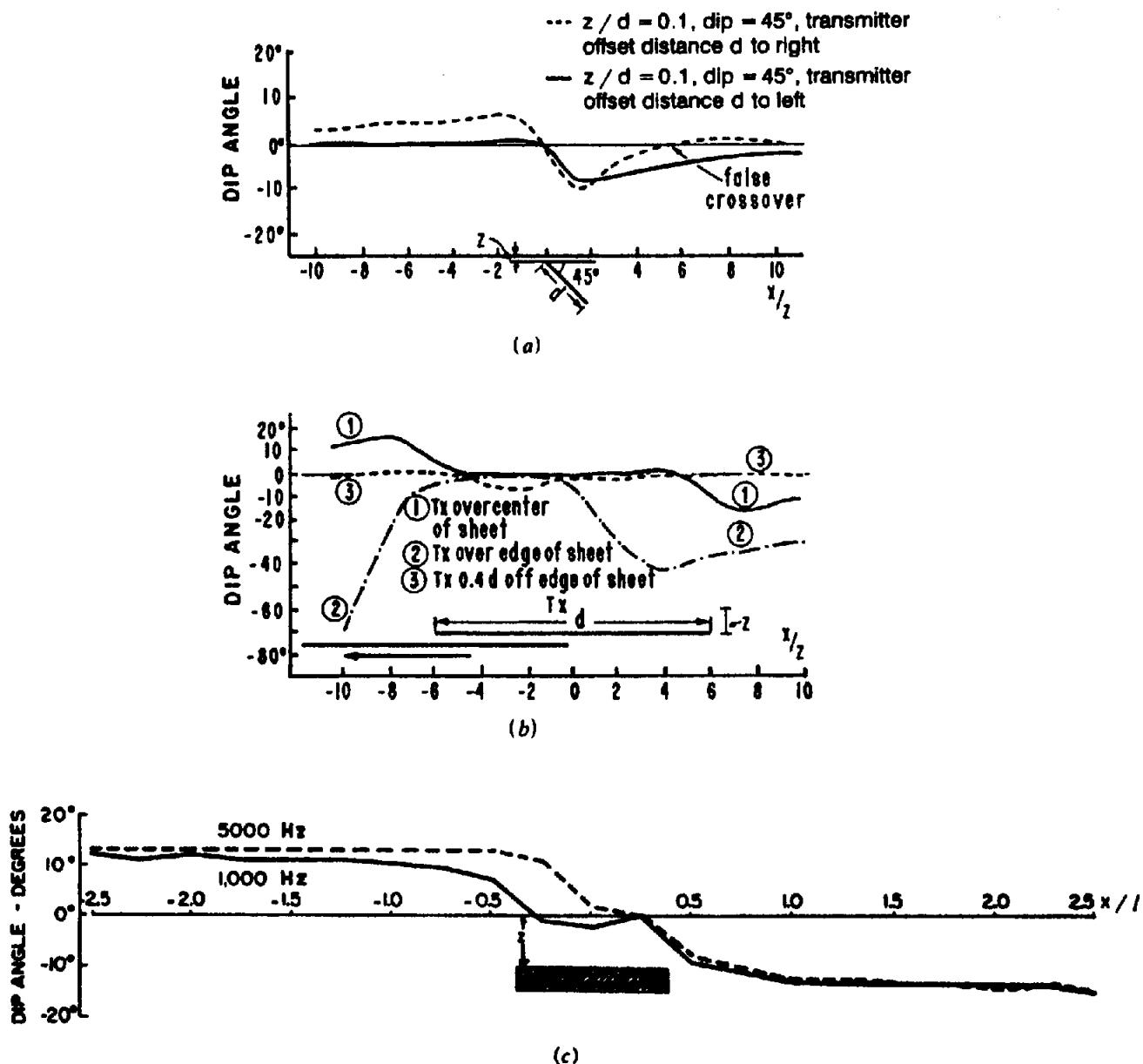


Figure 7.31. Effect of transmitter location and frequency on dip-angle fixed-transmitter results.  $l = T-R$ . (After Ward, 1967.) (a) Sheet of depth extent  $d$  dipping  $45^\circ$ . (b) Horizontal sheets of width  $d$ , various Tx locations;  $z/l = 0.1, d/l = 1.2$ . (c) Responses at 1,000 and 5,000 Hz to a conducting slab of finite width (graphite in the model).

and discriminating between depth and conductivity. Figure 7.31c displays two such profiles for the fixed-transmitter unit over an inhomogeneous slab. Although both frequencies give about the same size maxima and indicate a wide body, the shape of the curve for 5,000 Hz suggests a width less than half that for 1,000 Hz.

The strike of a long sheet conductor is fairly well determined by joining crossovers on successive dip-angle profiles. In the presence of broad or multiple conductors, this is never as simple as it sounds. Additional knowledge of the geology is essential.

Because the fixed-transmitter system will give anomalous profiles on traverses beyond the ends of the conductor, it is necessary to relocate the trans-

mitter on strike, but several hundred meters beyond the end of the conductor, to determine its strike length. The traverses near the transmitter will then be barren until the end of the conductor is crossed. With other EM sets, strike length is quite well marked by the absence of the anomaly on traverses beyond the ends of the conductor.

The effect of conductive host rock and overburden can be very significant in reducing response with all EM systems, particularly FD types. In all discussions hitherto the assumption has been that the conductors were immersed in a medium of very high resistivity. If the host rock and overlay are homogeneous and of relatively good conductivity, the attenuation will be appreciable, resulting in profiles of

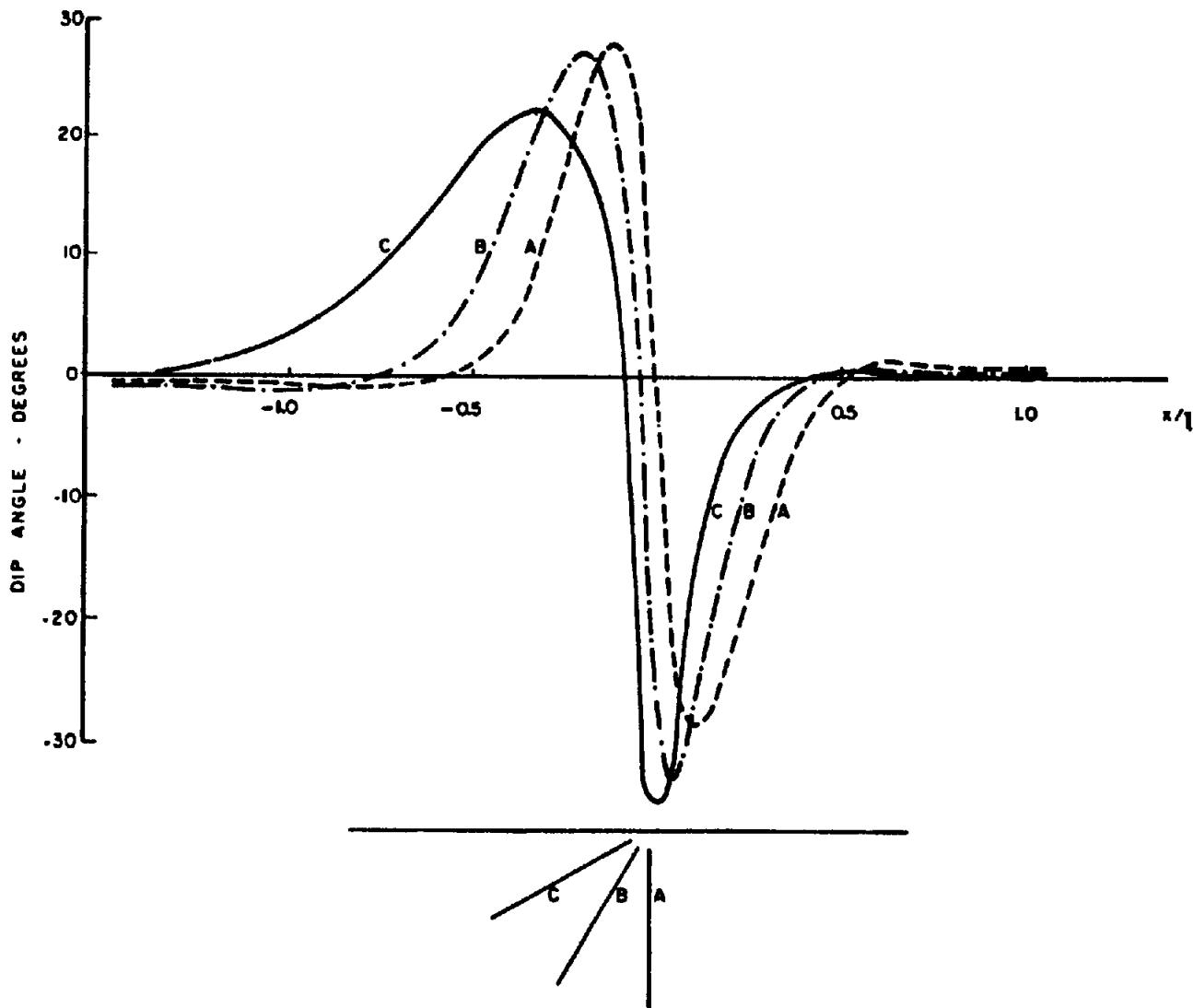


Figure 7.32. Response of the dip-angle broadside system over dipping sheets of finite depth extent. (After Ward, 1967.)

decreased amplitude. As mentioned before, this situation may be simulated in model work by making the measurements in a tank of suitable liquid; theoretically the homogeneous conducting medium can be allowed for as well.

However, when the overburden is a good conductor, lying as a horizontal slab over the anomaly source, the problem is more complicated. Field situations exist where swampy overburden of good conductivity (1 to 50  $\Omega\text{m}$ ) has apparently masked out any response from metallic conductors lying no more than 15 m below surface. In one location of this type in northern Quebec dip-angle, horizontal-loop, and Turam EM, as well as induced-polarization methods, all failed to give any significant response.

It is possible to test the effect of overburden in a model. The result of placing a conductive slab over the conductor of interest is to decrease the amplitude and shift the phase of the profiles, so that the anomaly appears to be deeper and of different conductivity than it actually is. Where two frequencies are employed, the ratio (that is, of dip angle, quadrature,

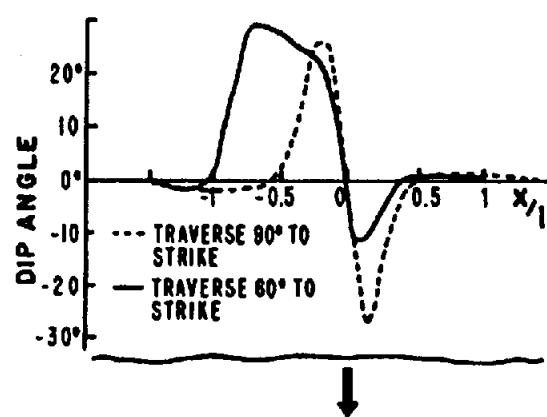
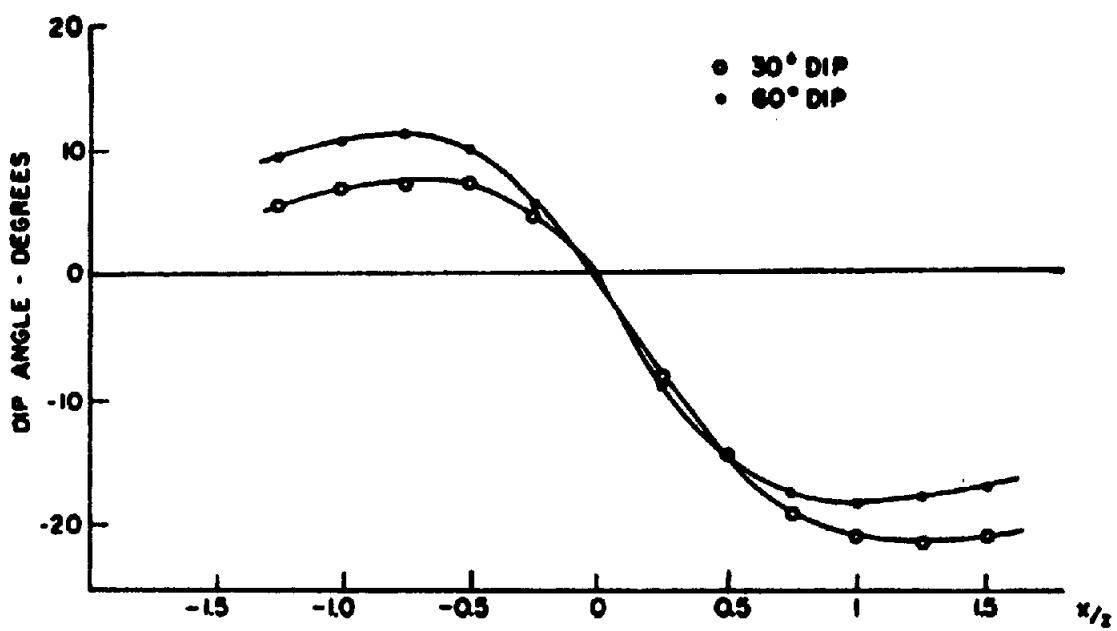
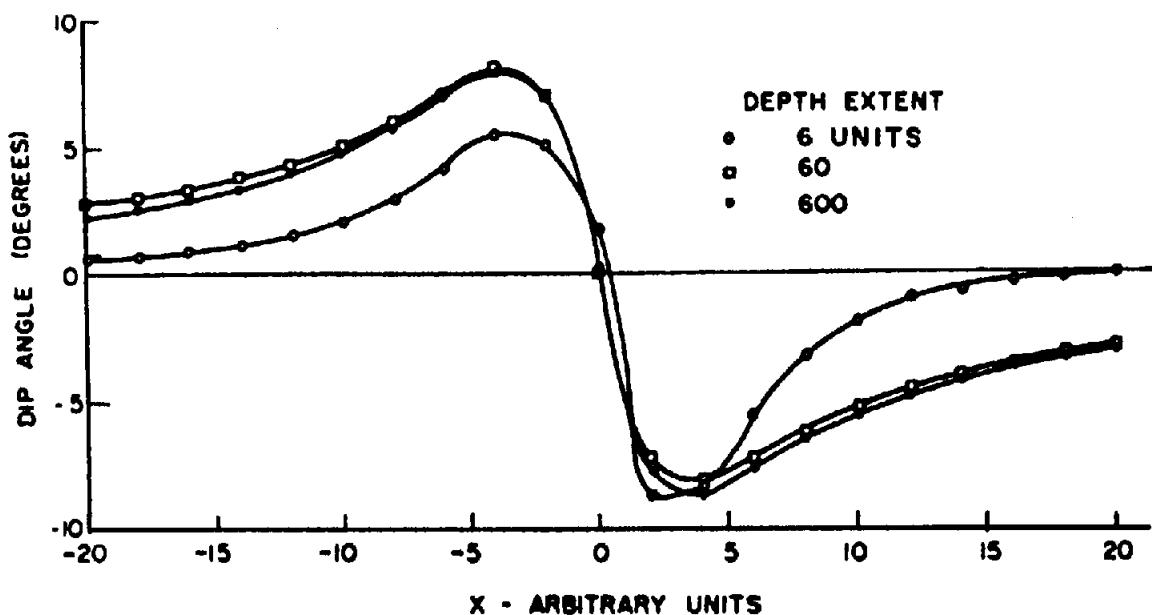


Figure 7.33. Effect of skew traverse direction on response of dip-angle broadside array.

amplitude, whatever the method) between them is decreased. Of course, if the overlying slab is of limited lateral extent, it will also introduce an anomaly of its own, as for a horizontal sheet; such overburden anomalies are, unfortunately, quite common.



(a)



(b)

Figure 7.34. Variations of AFMAG profiles with different parameters. (After Ward, 1967.)  
 (a) Effect of dip (b) Effect of depth extent

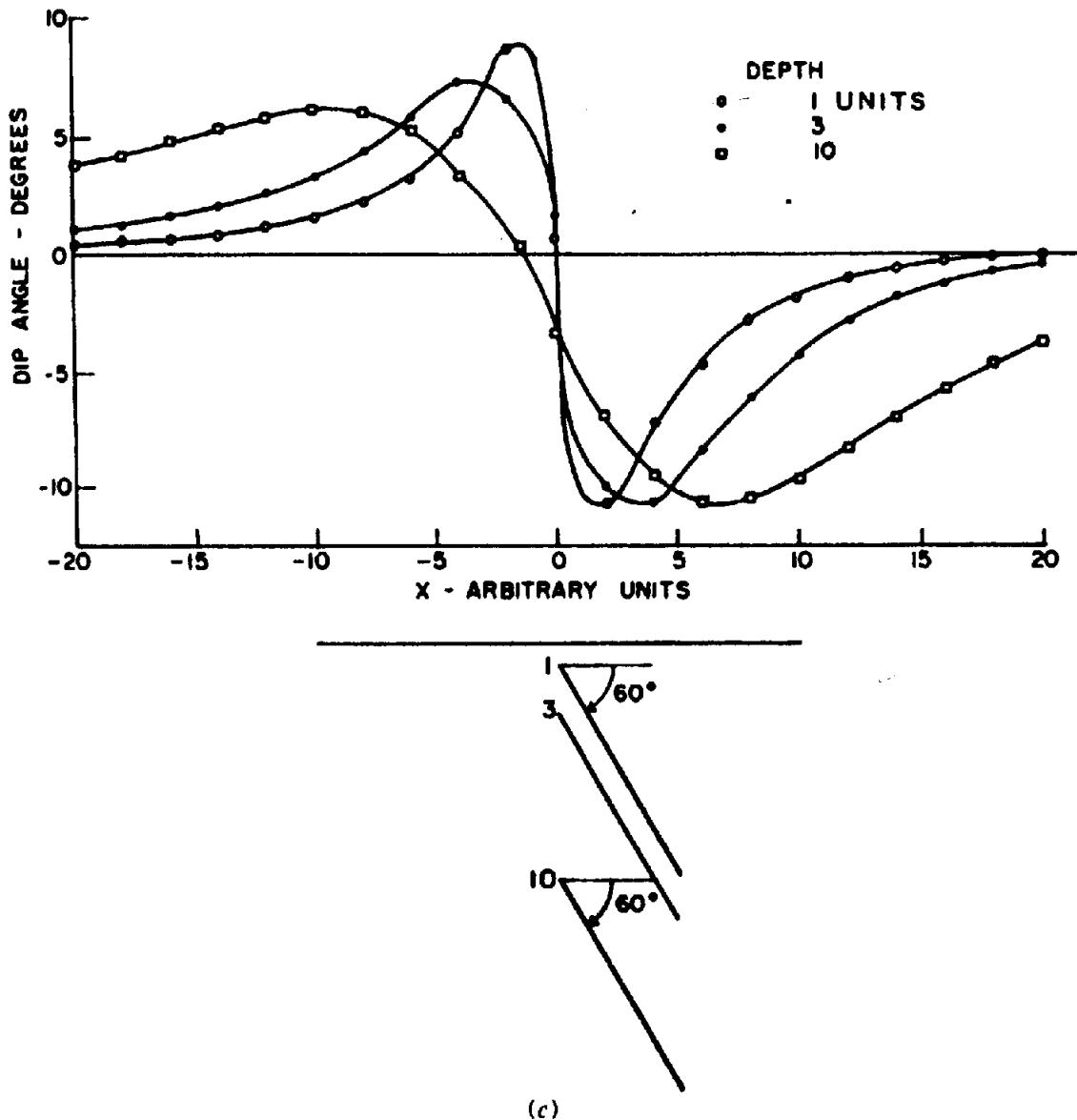


Figure 7.34. (Continued) (c) Effect of depth.

(c) Dip angle measurement; broadside (parallel line). Geometry of the unit is seen in Figure 7.15. The expressions for secondary-field components are the same as for the fixed-transmitter system. The  $T-R$  coupling remains constant, however, whereas the transmitter-conductor coupling is obviously variable. Otherwise the dip-angle measurement is expressed as in Equation (7.34). With the same sign convention as in Section 7.7.3b, the dip angle profile will again be asymmetric, but with sharper peaks and steeper tail slopes.

A trio of broadside curves is shown in Figure 7.32 over sheets dipping 30, 60, and 90°. The effect of decreasing dip is most obvious on the hanging wall side, where the reduced peak is broader and tails off more gradually than the updip peak. This EM system resolves multiple conductors much better than the fixed transmitter array. However, it is very sensitive

to off-normal traverse direction; deviations result in highly distorted profiles (Fig. 7.33). Otherwise it is similar to the fixed transmitter in regard to effects of depth, depth extent, and conductivity.

(d) AFMAG and VLF results. With both these ground methods, the results over sheet conductors are similar to the fixed transmitter. We have the same secondary-field components, whereas the remote source provides a uniform primary field over the entire survey area. In general the dip-angle curves are intermediate between parallel-line and fixed-transmitter response, with rather better defined peaks than the latter and tail slopes more gradual than the former.

There are, however, several specific differences in the AFMAG and VLF profiles with respect to the controlled source units of Sections 7.7.3b, c. For

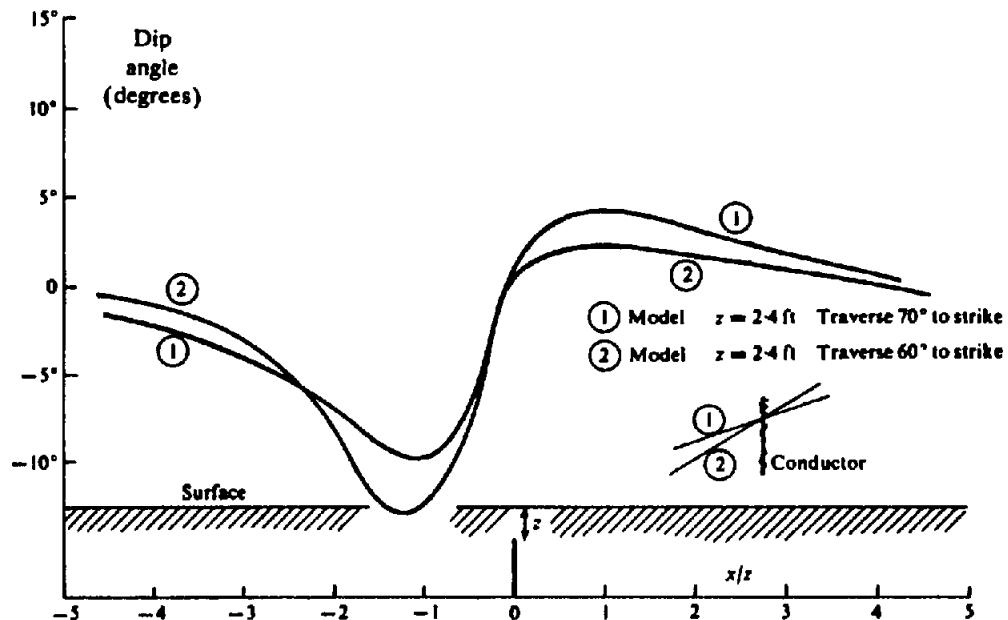


Figure 7.35. Effect of traverse direction on VLF profiles over a semiinfinite vertical sheet.

dipping sheets of finite depth extent the AFMAG and VLF curves become unbalanced, like the latter, but the larger dip-angle peak lies on the hanging wall side, that is, opposite to both other methods. As the depth extent increases, however, the peaks become more nearly equal again and the flanks increase on both sides. With constant depth extent, the effect of increasing depth to the top is to lower and spread the peaks, decrease the crossover slope, and lift the flanks.

The preceding features are illustrated in Figure 7.34. The explanation for these deviations from controlled-source dip-angle response lies in the uniform field from AFMAG and VLF, which makes the assumption of long-line currents (§7.7.3a) approximately correct. Thus the secondary field from current flow along the top of the sheet predominates for a shallow model, whereas the reverse field from the bottom becomes more significant at deeper burial.

As mentioned in Section 7.4.2e, f, the VLF and AFMAG systems, which have little or no control over the primary field direction, frequently do not permit measurement of the dip angle in the direction of traverse. Although the profiles may be plotted as vectors, as shown in Figure 7.17c, the results are inevitably distorted when the primary field is nearly parallel to conductor strike. This is a fundamental disadvantage of both methods.

Figure 7.35 shows two results of skew traverses ( $70^\circ$  and  $60^\circ$  to strike) across a vertical sheet. The crossover point is not shifted, but the asymmetry increases as the angle between strike axis and profile decreases, which would give a false indication of a dipping sheet.

(e) *Shootback results.* This system, described in Section 7.4.2d, was designed to overcome problems in measuring dip angles over rugged terrain. Profiles in Figure 7.16c show the response over vertical and dipping thin conductors. The first produces a symmetrical curve with a central positive peak over the top and equal negative tails on each flank. The dipping sheet enhances the hanging-wall negative while decreasing the other flank.

(f) *Measurement of phase components; horizontal loop.* This system (§7.4.3c), with coplanar horizontal receiver and transmitter coils, measures the ratio of vertical secondary to vertical primary magnetic fields at the receiver for the in-phase and quadrature components, that is,

$$\left. \begin{aligned} \% \text{ in-phase} &= R_s \{ H'_s / H'_p \} \\ \% \text{ quadrature} &= S_m \{ H'_s / H'_p \} \end{aligned} \right\} \quad (7.35)$$

Readings are plotted at the T-R midpoint.

Horizontal-loop profiles over half-planes dipping  $90^\circ$ ,  $60^\circ$ ,  $30^\circ$  and  $0^\circ$  are illustrated in Figure 7.36. The vertical-model profiles have the following general characteristics (see Fig. 7.36a): There is a single negative peak when the T-R spread straddles the conductor, two zeroes when either coil is directly over it (zero coupling), and two smaller positive peaks at approximately  $0.7l$ , after which the flanks tail off to zero. The curves are entirely symmetrical, that is, the receiver and transmitter and/or the direction of traverse could be reversed without affecting the shape. The sizes of the maxima and hence the steepness of the curves are an indication of the depth of conductor. Maximum depth of conductor that can

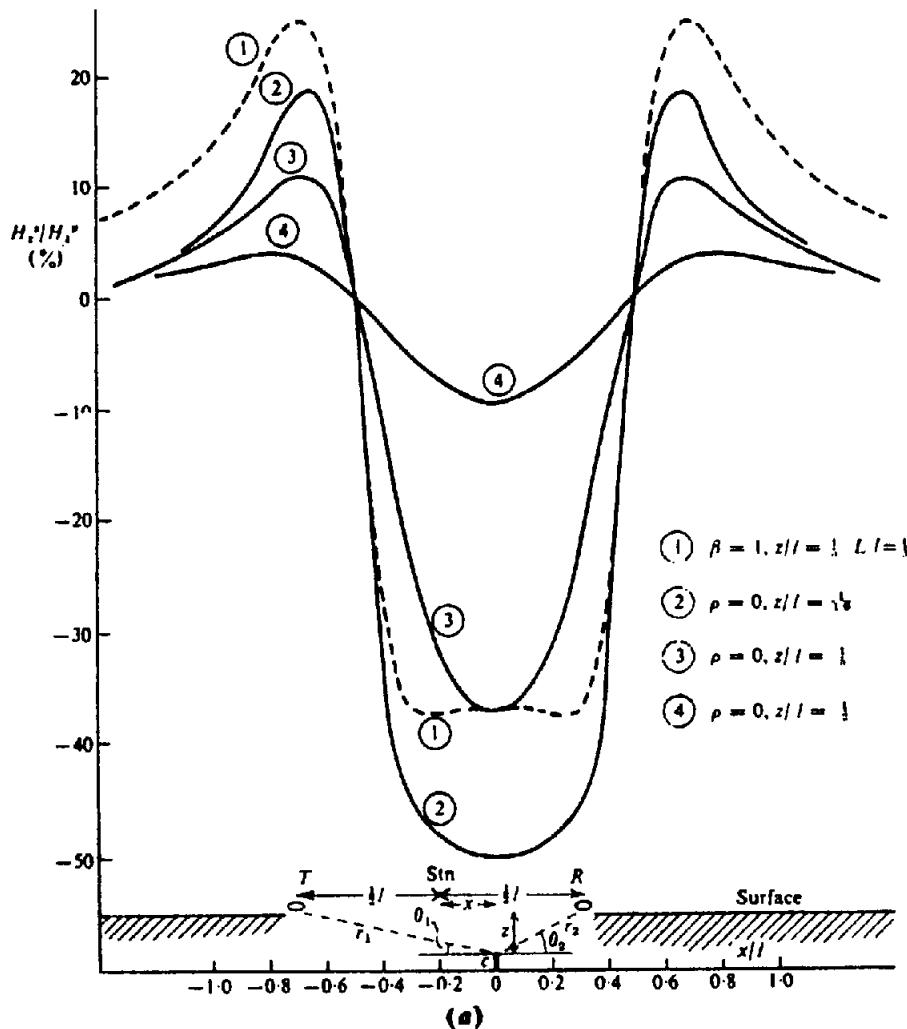


Figure 7.36. Effect of various parameters on horizontal-loop profiles over dipping sheets. (a) Effect of depth of a semiinfinite vertical sheet.

be detected is controlled by the coil separation, although the small power available in the portable transmitter is also a practical limitation. A rule of thumb frequently used for the horizontal-loop method is that the maximum detectable depth is one-half the coil separation.

The quadrature and in-phase profiles in Figure 7.36b are very similar and the former may be either much larger or smaller than the in-phase curve for a very poor or good conductor. The addition of the quadrature component clarifies greatly the ambiguity between conductivity and depth of burial, characteristic of dip-angle measurements. Some horizontal-loop field sets use two or more frequencies as a further aid in estimating depth.

With dip, the profile becomes asymmetric, although this is not very pronounced for dip angles larger than  $45^\circ$ . The in-phase peak negative response is increased as the dip angle decreases, the values being 57, 30 and 25% for angles of 30, 60, and  $90^\circ$ , respectively (Fig. 7.36c). At the same time, as the dip decreases, the negative peak is displaced toward the

hanging-wall side, as are the zero crossover points, while the positive peak on the same side is enhanced and the positive peak on the footwall decreased. The result is an in-phase curve that has a steeper slope on the down-dip side.

The quadrature response is also asymmetric. The negative peak increases slightly as the dip angle decreases, the zero crossover points are shifted down-dip, but there is little significant change in the positive peaks. The negative peak, however, is shifted toward the footwall – just the opposite to the in-phase curve. Thus the steep slope on the quadrature profile is on the up-dip side. The direction and the approximate dip of the conductor can be estimated from the characteristics of the two curves.

The effect of a horizontal sheet, seen in Figure 7.36c, is to split the in-phase profile into two equal negative peaks, located in the interval  $-1 \leq x/l \leq 1$ , with a positive maximum over the center of the sheet. The magnitudes of these peaks are greatly affected by the depth of the sheet as well as its width. For instance, when  $z/l = \frac{1}{10}$ , the negative peaks go

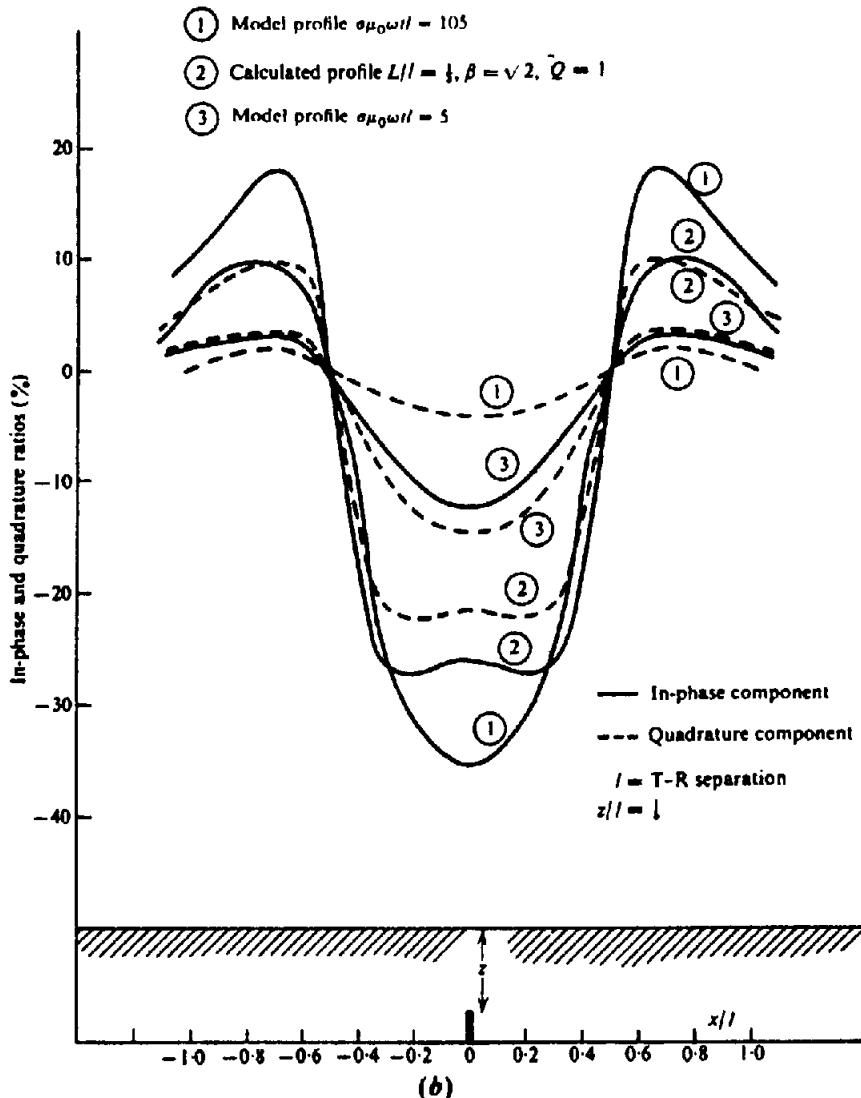


Figure 7.36. (Continued) (b) Effect of conductivity of a semiinfinite vertical sheet.

to 110%, while the positive is 75% (but still negative); for  $z/l = \frac{1}{2}$ , the negatives are about 4% and the center peak is 20% positive. For a narrower sheet ( $0.3/l$ ) the negative maxima are only 7%, while the center is 5% positive and practically flat.

The quadrature profile shows three minor negative maxima, the outside pair being closer to the edge of the sheet than the corresponding in-phase maxima, and the center peak is also negative. Again, this profile is largely influenced by the depth of the conductor, while the width has less effect.

The horizontal sheet could easily be mistaken for a pair of vertical conductors if the in-phase profile were considered alone. The quadrature curve, however, is generally different.

The depth extent of the conductor influences the horizontal-loop profiles only if it is small; if the depth extent is greater than  $2l$ , the profile is practically that of an infinite sheet. Depth to the top affects both component profiles in about the same

ratio, that is, a depth increase of six reduces both peaks by roughly the same amount (Figure 7.44).

Skew traverses have little effect on HLEM profile shape unless the angle with strike is less than  $30^\circ$ . Even then the profiles show little symmetrical distortion, although the negative peak decreases while the positive flanks grow larger and broader.

Conductive overburden has somewhat the same effect on HLEM response as that described for the fixed-transmitter, dip-angle system.

(g) Measurements of phase components; Turam. This ground method, like VLF and AFMAG, is suitable for energizing the sheet model as a long rectangular current loop with flow along the top edge and return at depth. We obtain the in-phase vertical component in the form of a reduced ratio, because there are two receiver coils (§7.4.3b), whereas the quadrature can be found from the difference in phase angle between them [Eq. (7.18)]. Thus we are

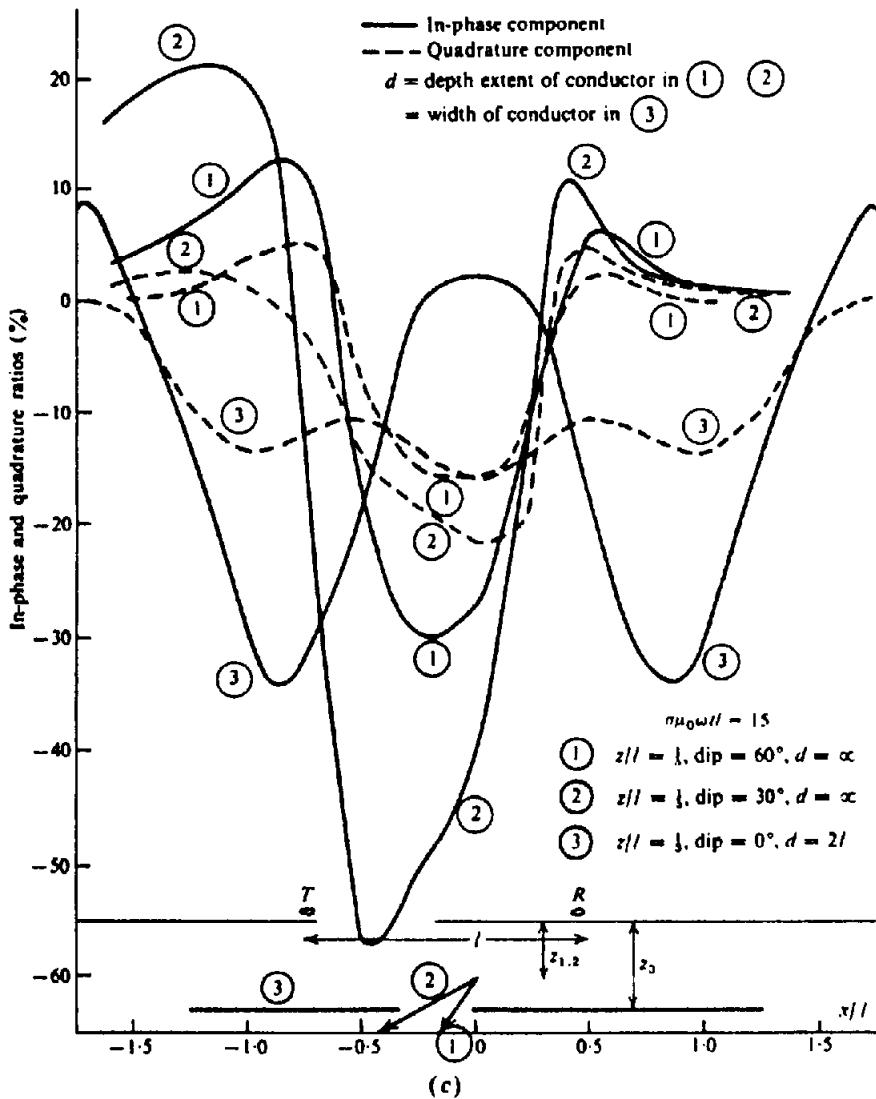


Figure 7.36. (Continued) (c) Effect of dip and depth extent.

measuring the total vertical fields at the two coils  $H_t^P(x - \delta x/2)$  and  $H_t^S(x + \delta x/2)$  (Fig. 7.37a), in the reduced ratio

$$\begin{aligned}
 & \left\{ \frac{H_t^P(x - \delta x/2) + H_t^S(x - \delta x/2)}{H_t^P(x + \delta x/2) + H_t^S(x + \delta x/2)} \right\} \\
 & \times \left\{ \frac{H_t^P(x + \delta x/2)}{H_t^P(x - \delta x/2)} \right\} \\
 & = \left( \frac{H_t^P + H_t^S}{H_t^P + H_t^S} \right) \left( \frac{H_t^P}{H_t^P} \right) = \frac{1 + H_t^S/H_t^P}{1 + H_t^S/H_t^P} = \frac{R}{p}
 \end{aligned} \tag{7.36a}$$

where  $R$  is the measured ratio,  $p$  is the normal ratio, and the difference in phase  $\Delta\phi = \phi_1 - \phi_2$  (see §7.7.3j for details).

Several Turam curves for model sheets of essentially infinite conductivity are shown in Figure 7.37; these illustrate the effect of varying depth and conductivity. The vertical scale is amplitude ratio or phase difference whereas the horizontal scale is made dimensionless by dividing the coil-cable distance by the conductor-cable separation. In Figure 7.37a it is apparent that the profile is slightly asymmetric over the vertical half-plane (because of the transmitter cable location) unless the sheet is quite deep. The amplitude peak locates the thin sheet quite accurately. Lateral extent of a thick conductor may be established by repeating the traverse with the loop on the opposite side.

For an increase in depth by the factor 2.5, Figure 7.37a indicates a decrease in the reduced ratio of about 55%. Because this is a model with zero resistivity ( $\sigma_1 = \infty$ ), the reduced ratio is the in-phase component. Figure 7.37b illustrates the effect of changing conductivity for essentially the same vertical

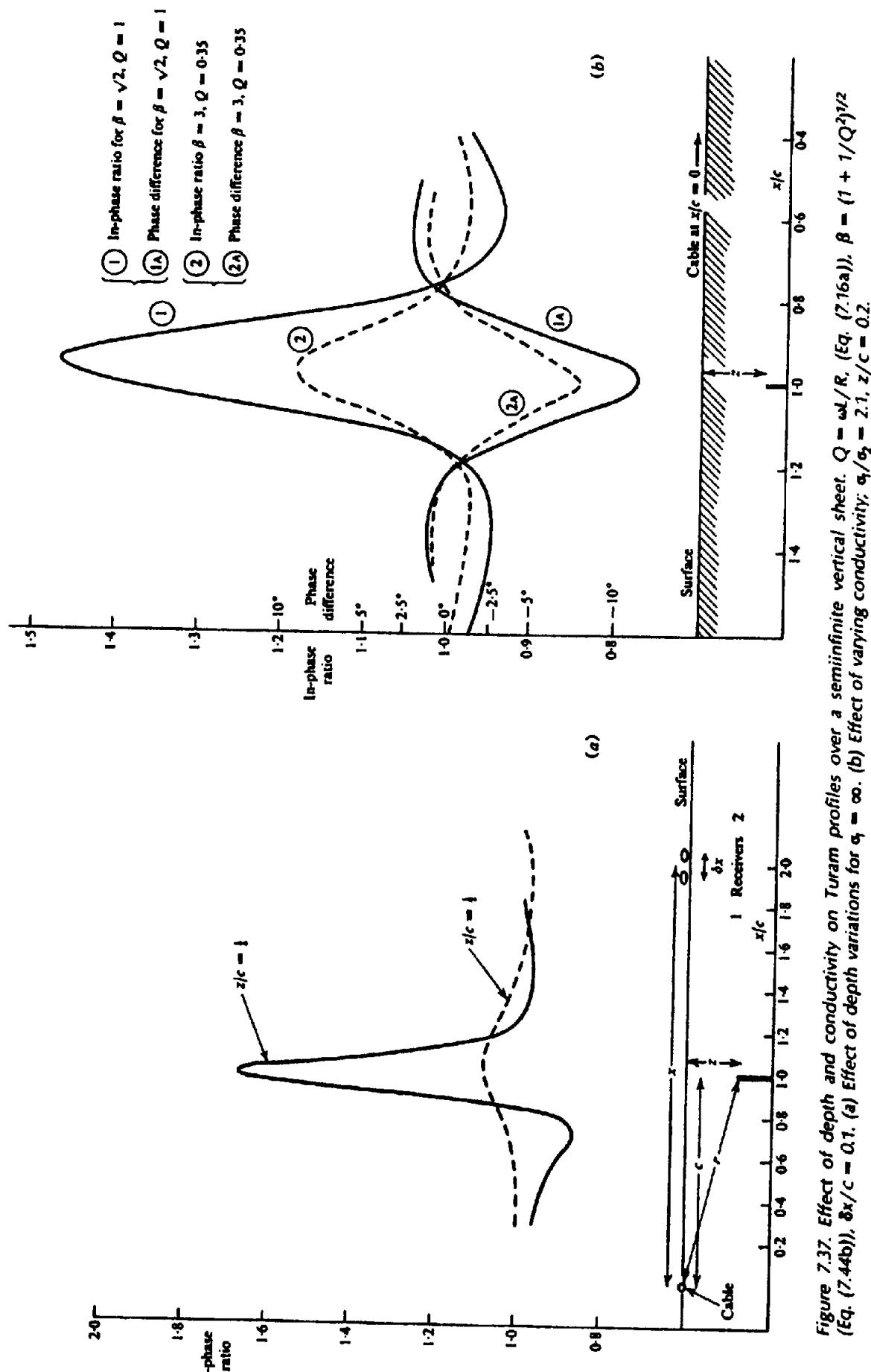


Figure 7.37. Effect of depth and conductivity on Turam profiles over a semi-infinite vertical sheet.  $Q = \omega_1/R$  (Eq. (7.16a)),  $\beta = (1 + 1/Q)^{1/2}$  (Eq. (7.44b)).  $\sigma_x/c = 0.1$ . (a) Effect of depth variations for  $\sigma_1 = \infty$ . (b) Effect of varying conductivity;  $\sigma_1/\sigma_2 = 2.1$ ,  $z/c = 0.2$ .

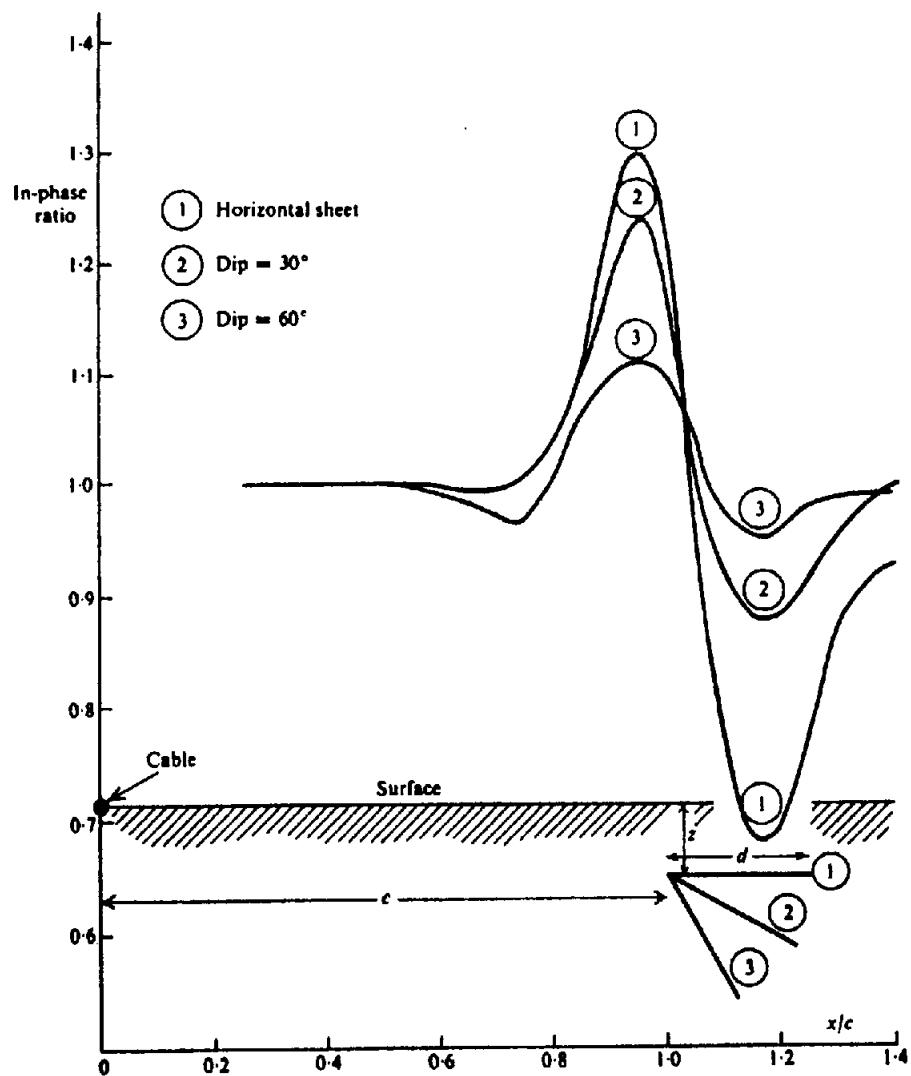


Figure 7.38. Effect of dip on Turam profiles over sheet of finite depth extent.  $z/d = \frac{1}{3}$ ;  $z/c = \frac{1}{6}$ .

sheet. Here we find that as the conductivity contrast is reduced to  $\sigma_1/\sigma_2 = 2.1$ , the in-phase component is increased by about 24%, and the phase difference by about 37%.

The effect of dip on Turam response is shown in Figure 7.38 for highly conductive sheets of small depth extent. Curve symmetry is not much affected until the dip angle is less than 45°, although the positive peak decreases steadily with increasing dip; a vertical sheet of the same dimension and depth produces a maximum of 1.09 (compare this with the half-plane in Fig. 7.37a). The negative peak is on the downdip side, whereas the positive is slightly displaced toward the cable.

When the sheet dips toward the cable, rather than away from it, the maxima are reduced, although the general shape is similar. In fact there is a particular geometry of thin dipping sheet and Turam cable for which the uniform primary field is parallel to the conductor face, when the resultant induced currents are practically zero, because they would have to flow

across the narrow dimension. This situation can be demonstrated in model measurements and has also been found in the field. The dip for this unfortunate location is known as the *extinction angle*; it also occurs in TDEM surveys that employ the Turam-type of fixed-transmitter loop (§7.7.4c; also Gallagher, Ward, and Hohmann, 1985). For dip angles even shallower than this, the sheet still dipping toward the cable, the curves are inverted. In such cases it may be difficult to determine the attitude of the conductor.

The sheet depth may be estimated from the width of the profile at half-peak value. However, for the examples shown in Figure 7.38 and in Figure 7.37b, the depth estimates are too large by as much as 40%, so that better methods of estimating depth should be used.

The masking effect of conductive overburden on several electrical survey methods, including Turam, was mentioned briefly in Section 7.7.3b. To aid in exposing conductive overburden effects, as well as

Table 7.1. Turam model data. Line 4 + 00; transmitter loop 1,600 × 1,200 ft; frequency 660 Hz.

Station (ft)	Rec'r coils (ft)	Station readings				$\Sigma \Delta\phi$ (degrees)	V	R =	I =
		FR	Phase ( $\Delta\phi$ )	NR	RR			$V \cos \phi$	$V \sin \phi$
	200					0°	1.0	1.0	0
250	300	1.77	0.25°	1.76	1.01	0.25	0.99	0.99	0.004
350	400	1.54	0.45	1.54	1.00	0.70	0.99	0.99	0.012
450	500	1.39	0.60	1.43	0.97	1.30	1.02	1.02	0.023
550	600	1.35	0.60	1.36	0.99	1.90	1.03	1.03	0.033
650	700	1.64	-0.25	1.31	1.25	1.65	0.83	0.83	0.023
750	800	1.39	1.45	1.27	1.10	3.10	0.75	0.75	0.041
850	900	1.26	1.50	1.25	1.01	4.60	0.74	0.74	0.059
950	1,000	1.24	1.65	1.22	1.02	6.25	0.73	0.73	0.084
1,050	1,100	1.23	1.80	1.21	1.02	8.05	0.70	0.70	0.098

discriminating between conductivity and conductor depth, Turam equipment is frequently operated at two frequencies, for example, 220 and 660 Hz.

Before concluding this section, we shall describe the procedure required to convert Turam field data for subsequent analysis.

As in Equation (7.35) we can separate the real and imaginary components in the practical situation when the conductivity is finite. The Turam system, however, measures the phase difference between the two receiver coils, rather than the imaginary component. Thus the respective phase angles may be found from the ratio of the imaginary to real parts of  $H'_x$  for each receiver coil, where [see Eq. (7.18)]

$$\tan \phi = \mathcal{F}_m \{ H^p + H' \} / \mathcal{R}_s \{ H^p + H' \} \quad (7.36b)$$

As in the horizontal-loop system, the conductivity can be estimated from the maximum values of ratios and phase differences. The usual method of plotting Turam results is not convenient for this, but it is relatively easy to determine the real and imaginary components of the resultant field from these values by converting the phase angle to a quadrature component. This procedure is explained with the aid of Table 7.1, which shows sample data taken from a laboratory Turam survey on a model conductor.

The first column gives the location of the receiver station (midway between the two coils);  $FR$  is the field ratio  $(H_n^p + H_n')/(H_{n+1}^p + H_{n+1}')$ , shown at the beginning of this section and the measured phase

difference is  $\Delta\phi = \phi_n - \phi_{n+1}$ . The normal ratio  $NR$  is  $H_n^p/H_{n+1}^p$ , or what would be measured over barren ground at the same two stations; this is calculated using Equation (7.10c) or (7.12b). Dividing  $FR$  by  $NR$ , we get the reduced ratio  $RR$ . In the next column  $\Sigma \Delta\phi$  is the sum of the phase differences, assuming zero values at the station adjacent to the near side of the transmitter loop. Note that station readings,  $NR$ , and  $RR$  values are referred to the station point, whereas in the remaining four columns the values are referred to the receiver coil nearer to the transmitter. This is because zero phase and unity total field are assumed to exist at the point of closest approach to the transmitter (presumably the latter has been located a reasonable distance from any conductors in the vicinity).

Total-field values  $V$  are calculated from the ratio  $V_n/RR_{n+1/2}$ , assuming  $V_1$  to be unity at the first station setup. Thus  $V_{300} = V_{200}/RR_{250}$ ,  $V_{400} = V_{300}/RR_{350}$ , and so forth. Finally, these are converted to real ( $R$ ) and imaginary ( $I$ ) components in the last two columns by calculating  $R = V \cos \phi$ ,  $I = V \sin \phi$ ,  $\phi$  being the corresponding  $\Sigma \Delta\phi$  value for each  $V$ . Note that  $R$  is always positive whereas  $I$  may be positive or negative.

By plotting the  $R$  and  $I$  curves, we can get additional estimates of conductor depth - half the horizontal distance between maxima and minima on either curve. The current center of the upper part of the conductor is located directly below the point of maximum slope of the  $R$  curve. Also the maximum

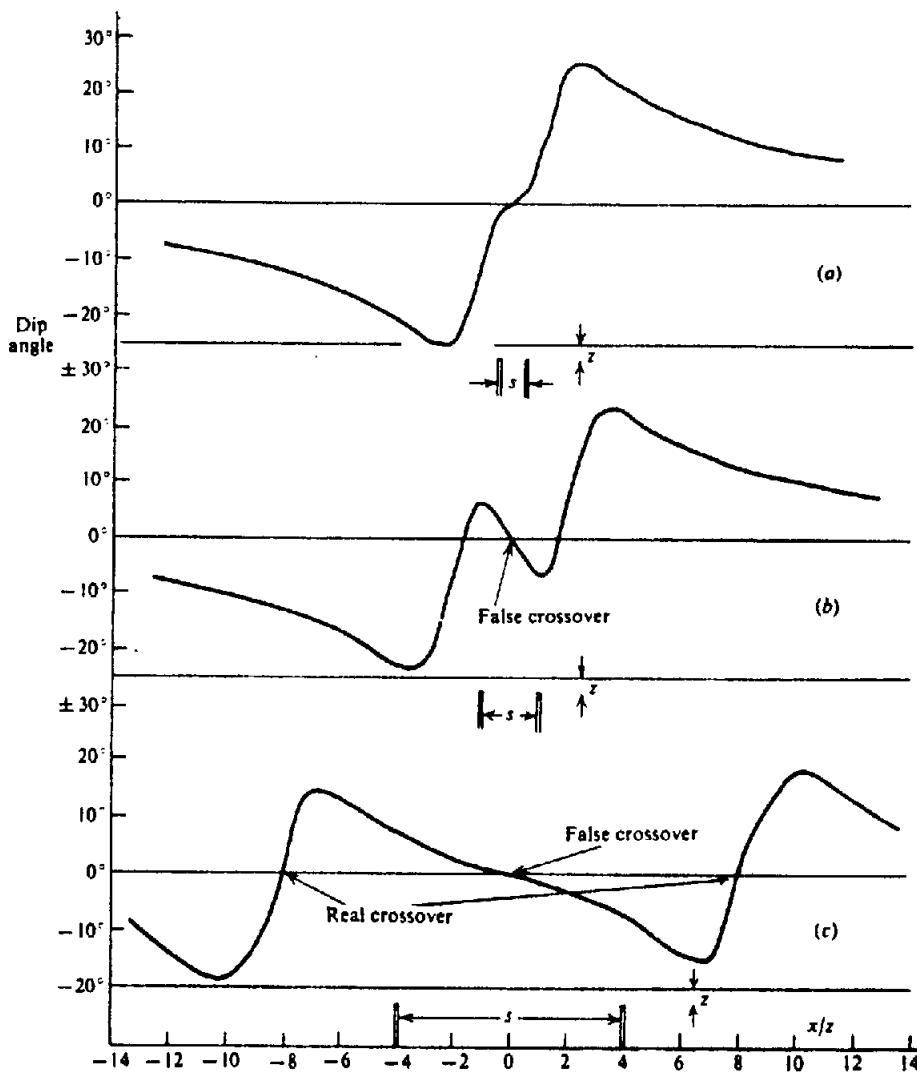


Figure 7.39. VLF profiles over two identical semiinfinite vertical sheets as a function of distance between the sheets. (a)  $s = 2z$ . (b)  $s = 4z$ . (c)  $s = 16z$ .

$R$  and  $I$  values may be used with characteristic curves to determine the thickness conductivity product. Field example 7 in Section 7.8 provides phase-component data determined from this procedure.

Clearly Turam interpretation requires much low-level calculation following data acquisition. The alternate spread described in Section 7.4.3b eliminates this work because the receiver coils are equidistant from the transmitter loop on each traverse. Unfortunately no published information is presently available with regard to this configuration.

#### (h) Sheet conductors; miscellaneous considerations.

**Two conductors.** Using an extension of the coupled-circuit analysis (§7.2.4b and §7.2.5a), Grant and West (1965: 532–6) have shown that the effect of

two conductors is not generally the sum of each one acting alone, but involves mutual coupling between them. This means that Equation (7.20b) becomes

$$\begin{aligned} \frac{e_s}{e_p} = & - \left( \frac{k_{C_1 R} k_{TC_1}}{k_{TR}} \right) \left( \frac{Q_1^2 + jQ_1}{1 + Q_1^2} \right) - \left( \frac{k_{C_1 R} k_{TC_2}}{k_{TR}} \right) \\ & \times \left( \frac{Q_2^2 + jQ_2}{1 + Q_2^2} \right) \\ & - \frac{k_{C_1 C_2}}{k_{TR}} (k_{C_1 R} k_{TC_1} + k_{C_1 R} k_{TC_2}) \\ & \times \left\{ \frac{Q_1 Q_2 (1 - Q_1 Q_2) - jQ_1 Q_2 (Q_1 + Q_2)}{(1 + Q_1^2)(1 + Q_2^2)} \right\} \end{aligned} \quad (7.37a)$$

where  $Q_1 = \omega L_1 / R_1$  for conductor  $C_1$ ,  $Q_2 =$

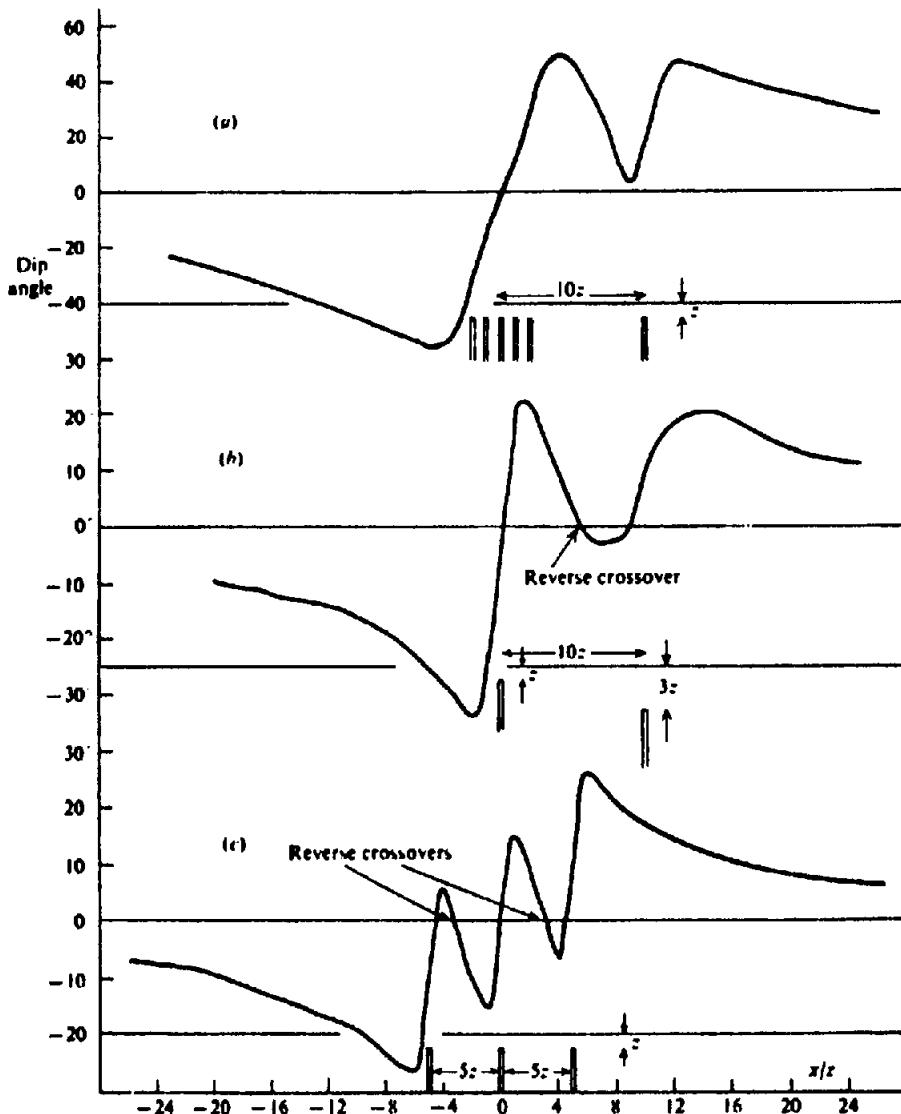


Figure 7.40. VLF profiles over multiple vertical-sheet conductors. (a) Five sheets spaced  $z$  apart plus one sheet distant  $10z$  from the midpoint of the five sheets, all at depth  $z$ . (b) Two sheets at depths of  $z$  and  $3z$ , spaced  $10z$  apart. (c) Three sheets at depth  $z$  and spaced  $5z$  apart.

$\omega L_2/R_2$  for conductor  $C_2$ , and terms in  $k_{C_1 C_2}^2$  are neglected because the coupling between the conductors is assumed to be relatively weak.

Two limiting cases arise. If the conductors are very far apart,  $k_{C_1 C_2} = 0$  and

$$\frac{e_s}{e_p} = - \left( \frac{k_{TC_1} k_{CR}}{k_{TR}} \right) \left( \frac{Q_1^2 + jQ_1}{1 + Q_1^2} \right) - \left( \frac{k_{TC_2} k_{CR}}{k_{TR}} \right) \left( \frac{Q_2^2 + jQ_2}{1 + Q_2^2} \right) \quad (7.37b)$$

which is the sum of the two conductors separately, as one might expect. On the other hand, if the two are

very close together,  $k_{C_1 C_2} \approx 1$ ,  $k_{TC_1} = k_{TC_2}$ ,  $k_{CR} = k_{CR}$ , and

$$\frac{e_s}{e_p} = - \left( \frac{k_{TC} k_{CR}}{k_{TR}} \right) \left( \frac{(Q_1 + Q_2)^2 + j(Q_1 + Q_2)}{1 + (Q_1 + Q_2)^2} \right) \quad (7.37c)$$

which is the response of a single loop having response parameter  $Q_1 + Q_2$ . The coupling between the two conductors may be positive or negative. Model studies have shown these expressions to be quite good approximations.

*Multiple conductors.* The various EM ground methods show different responses to multiple con-

ductors; clearly the differences are determined by the geometry of the particular system, as well as that of the conductors. The simplest dip-angle system to use as an illustration is VLF or AFMAG, in which the conductors are uniformly energized by the remote transmitter. Figures 7.39 and 7.40 show calculated profiles over several vertical-sheet configurations. Zero coupling is assumed between the conductors. When the spacing between the sheets is less than  $2z$ , these curves will not be exact, because the mutual coupling would make the maximum tilt angles somewhat larger.

From Figure 7.39 it can be seen that the proper crossovers are displaced to the flanks of the curves, beyond the actual locations of the sheets, unless their separation is less than twice the depth, in which case the profile indicates a single thick conductor. The examples (a) and (b) of Figure 7.40 show that a conductor that is deeper or smaller (or of lower conductivity, although this situation is not illustrated), than its neighbor will give a relatively weak response.

Discrimination among multiple conductors is even more difficult with the fixed-transmitter dip-angle technique. Unless the transmitter is located fairly well between two identical sheets, the more remote will hardly respond at all. In this case the two are not energized equally. Consequently it is more difficult to resolve multiple conductors with this type of EM.

The parallel-line dip-angle resolves adjacent conductors better than the fixed-transmitter unit, as might be expected. Furthermore the crossovers are in the right place. Even so, when the separation is less than twice the depth, the broadside traverse will not distinguish between two distinct sheets, a single thick one, or a flat sheet.

The horizontal-loop EM is perhaps slightly better than the broadside array in resolving two conductors. The in-phase profile shows two peaks at the proper location when the separation is twice the depth or greater, whereas the quadrature component is almost the same. These curves are shown in Figure 7.41. Coupling between the sheets affects the quadrature response particularly, so that the conductivity of two separate sheets would appear to be lower than when they are close together.

The resolving power of Turam over multiple conductors is probably not as good as with the horizontal-loop EM, because of the fixed transmitter, which would generally be located to one side. However, the fact that two receivers are used with fairly close spacing may help the resolution somewhat.

Discrimination between multiple and thick conductors varies with the different EM systems. From

Figure 7.41, the HLEM appears to have good resolution unless the width is greater than the  $T-R$  separation (see also Fig. 7.36c).

It is possible to get a fair idea of conductor width with the horizontal-loop set. Because the zero crossovers occur at  $x = \pm l/2$  for a thin sheet, any excess, greater than  $l$ , in the separation between these zeros is an estimate of conductor width. Here again the horizontal-loop EM has a distinct advantage over dip-angle EM.

As noted previously (§7.7.3g), the near-surface width of conductor may be estimated with the Turam unit by taking the same profile twice with the transmitter cable on alternate sides. With dip-angle EM equipment it is difficult to distinguish between a wide conductor and two thin sheets unless, as we have seen, the separation is appreciable.

One method of determining conductor width with the fixed-transmitter system is to offset the transmitter from the edges of the conductor 200 ft (60 m) or less and make several traverses normal to the conductor. As the receiver-transmitter separation increases, the crossovers shift toward the edge of the conductor remote from the transmitter. By repeating this measurement with the transmitter on either side of the conductor, a fairly good outline of its lateral extent is achieved.

The broadside array is theoretically better than the other methods for thick conductors, because the crossover at the center is reversed. Over separate thin sheets the center crossover is in the normal sense. However, these crossovers are usually quite small and the difference between normal and reverse may be difficult to distinguish.

#### (i) Sheet conductors - characteristic curves.

*General.* The usual procedure in EM interpretation - comparison of field profiles with theoretical and model results - requires a good-sized library of the latter type of curves. A considerable advantage is achieved by combining the theoretical and model data into characteristic curves that emphasize certain features of the EM profiles, such as maximum tilt angle and crossover slope for dip-angle measurements, or in-phase and quadrature response for phase-component systems.

*Dip-angle characteristic curves.* We have mentioned previously that the peak dip angle and the slope at the crossover are functions of both depth and conductivity. However, conductivity changes affect both parameters about the same, that is, the ratio of slope to peak response is approximately independent of conductivity. Thus a simple characteristic, which works fairly well for steeply dipping conductors, may be prepared by plotting this ratio

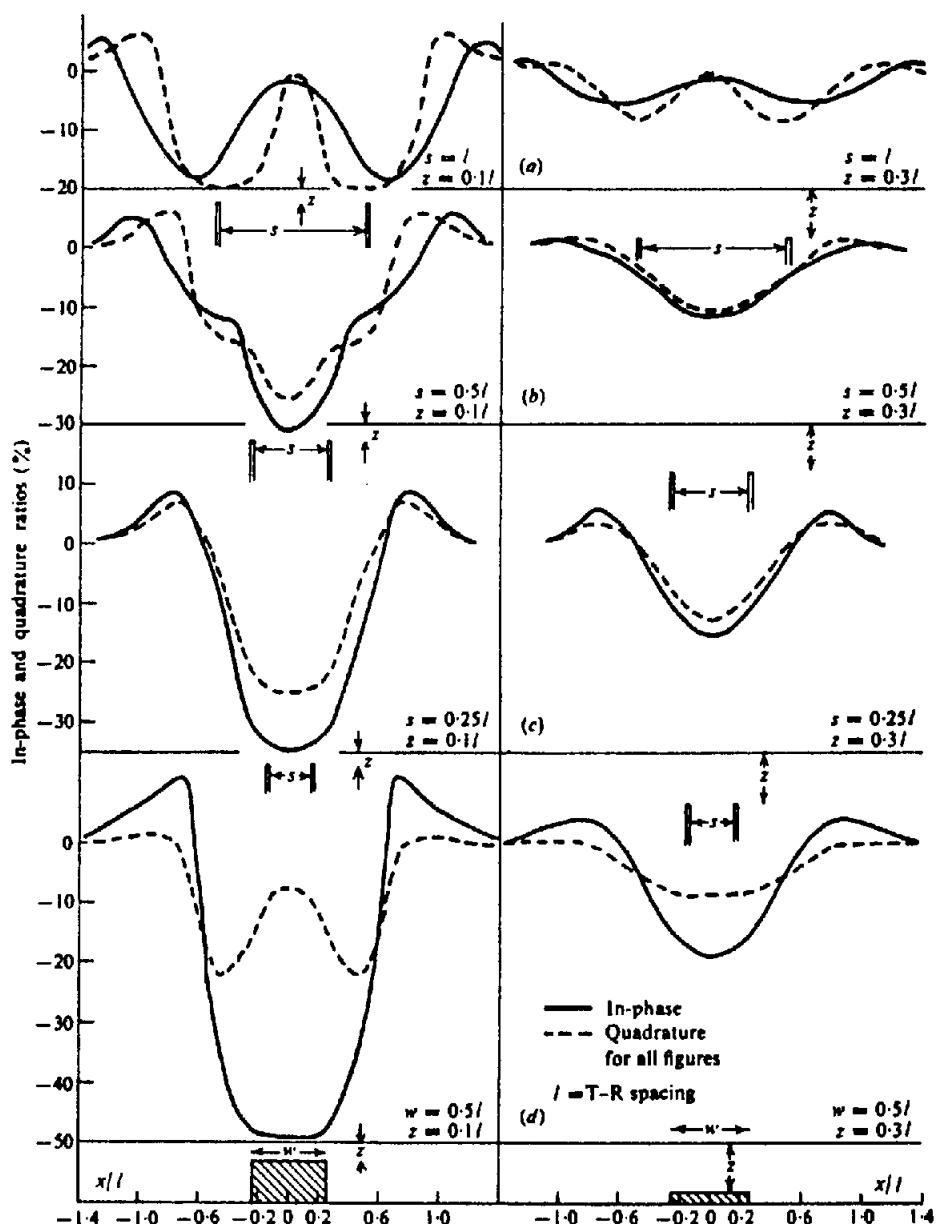


Figure 7.41. Horizontal-loop EM profiles over various conductors of great depth extent.  
 (a) Two thin sheets with spacing equal to the T-R spacing. (b) Two thin sheets with spacing equal to one-half the T-R spacing. (c) Two thin sheets with spacing equal to one-quarter the T-R spacing. (d) Conducting dike with width equal to half the T-R spacing.

against the known depth, or  $z/l$  ratio, taken from model results. An example is shown in Figure 7.42a; the slope near the zero crossover is plotted in the form of a ratio, degrees/ $(x/l)$ , against  $z/l$ .

A more useful characteristic curve, which provides both dip and depth for the semiinfinite sheet conductor, has been developed by Grant and West (1965, pp. 559–60) and is illustrated in Figure 7.42b. Here the ratio of peak tilt-angle magnitudes on either side of the crossover is plotted against their total amplitudes. If the resultant point falls reasonably on this diagram, the dip angle may be interpolated and the depth calculated from the relation  $z = kl \sin \alpha$ . This plot is developed for the fixed-transmitter set

and will give poor results if the sheet dimensions are less than the transmitter-receiver separation.

*Parameters for characteristic curves.* The response parameter  $Q$ , discussed in Section 7.2.5d and illustrated in Figure 7.10 for the simple electric circuit analogy, is a significant quantity in EM characteristic curves. Recalling the discussion of scale models in Section 7.7.1b, the ratio  $\mu f l^2 / \rho$  – or what is the same thing,  $\mu \omega \sigma l^2$  – is dimensionless and invariant in passing from a field to a model system. Similarly the response parameter  $Q$  is dimensionless and has the same form, a product of conductivity, permeability, frequency, and area (or linear dimension squared); this follows because  $L \propto \mu l$ ,  $R \propto \rho l/A$ ,

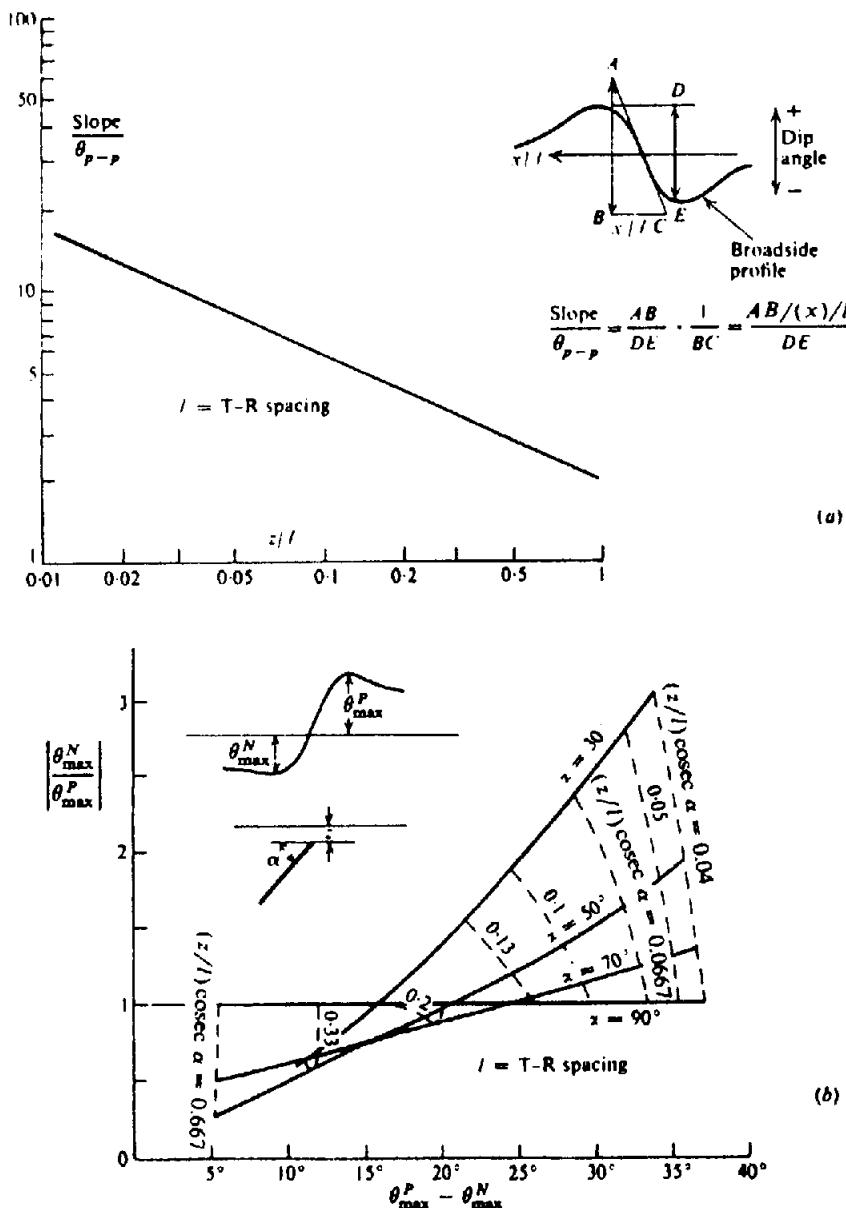


Figure 7.42. Characteristic curves for semiinfinite dipping-sheet conductor. (a) Depth to the top of a steeply dipping sheet from the crossover slope and peak tilt. Broadside array. (From Ward, 1967.) (b) Depth and dip using fixed-transmitter, dip-angle system. (From Grant and West, 1965.)

hence  $\omega L/R \propto \mu\omega\sigma A$  where  $A$  is the area, or product of two significant dimensions.

Employing a more sophisticated approach, electromagnetic theory gives the response parameters for several specific configurations. A few of these are:

Sphere	$\mu\omega\sigma a^2$	$a$ = radius
Disk	$\mu\omega\sigma a t$	$t$ = thickness
Thin sheet	$\mu\omega\sigma tc$	$c$ = conductor-EM unit spacing
Half space	$\mu\omega\sigma c^2$	

Note that the linear dimensions  $a$ ,  $t$ , and  $c$  appearing in these expressions are particularly signifi-

cant in determining the pattern and intensity of secondary current flow in the conductor. Frequently there are several dimensional parameters of this type, in which case we are free to choose any two of them. However, the effect of some of these parameters may vary with the conductor-EM system geometry; this is evidently true with moving source units.

In drawing up characteristic curves for thin sheet conductors, for example, it is customary to use as parameters the thickness and whichever fixed dimension of the EM system controls the response. Thus we would insert the transmitter-receiver spacing in artificial source dip-angle (Fig. 7.43), the height above ground in airborne double-dipole systems (Fig. 7.81c), or the horizontal distance between transmitter and conductor in Turam.

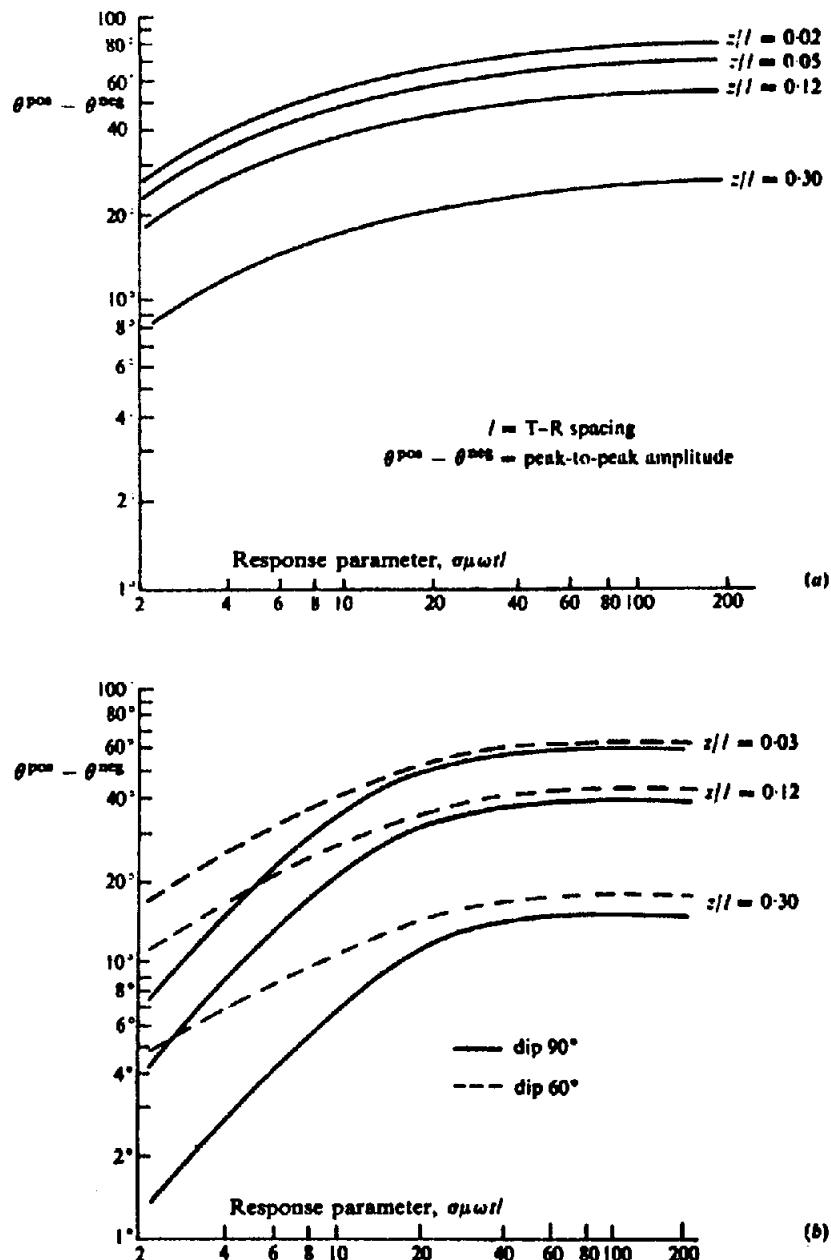


Figure 7.43. Characteristic curves for semiinfinite sheet. (From Ward, 1967).  
 (a) Fixed-transmitter dip-angle system, vertical sheet. (b) Broadside array, dipping sheet.

As mentioned in Section 2.7.7, we should try to minimize the number of variables in order to produce a reasonable number of curves. Because we are at liberty to employ one dimension as a scaling parameter, the number of unknowns is reduced by 1. This scaling unit may be either a length that has relatively little influence on the conductor response, or one that can be measured directly; for an example of the latter, we could use the transmitter-receiver separation or the aircraft height.

**Dip-angle curves.** At least two types of characteristic curves involving the response parameter have been developed from model measurements in dip-angle interpretation. In one of these, two source frequencies are required. The ratio of peak high-frequency response  $(\theta^{nec}/\theta^{pos})_{HF}$  is plotted against

low-frequency peak response  $(\theta^{nec}/\theta^{pos})_{LF}$  for various depth and dip angles. A large set of curves is required for different dip angles, each set being drawn for constant depth and constant response parameter.

The second type, for single frequency, consists of plotting peak-to-peak  $(\theta^{pos} - \theta^{neg})$  amplitude against response parameter for different depths, as illustrated in Figure 7.43, for fixed-transmitter and broadside array. The depth must be approximately known to use these curves. A complete catalogue again requires a characteristic curve for each dip angle. Presumably similar results could be developed for VLF.

From the plots illustrated in Figure 7.43, it is possible to find  $\mu\omega\sigma t/l$ , if we can obtain the depth by other means. We know  $\omega$  and  $l$  and can assume  $\mu$  to

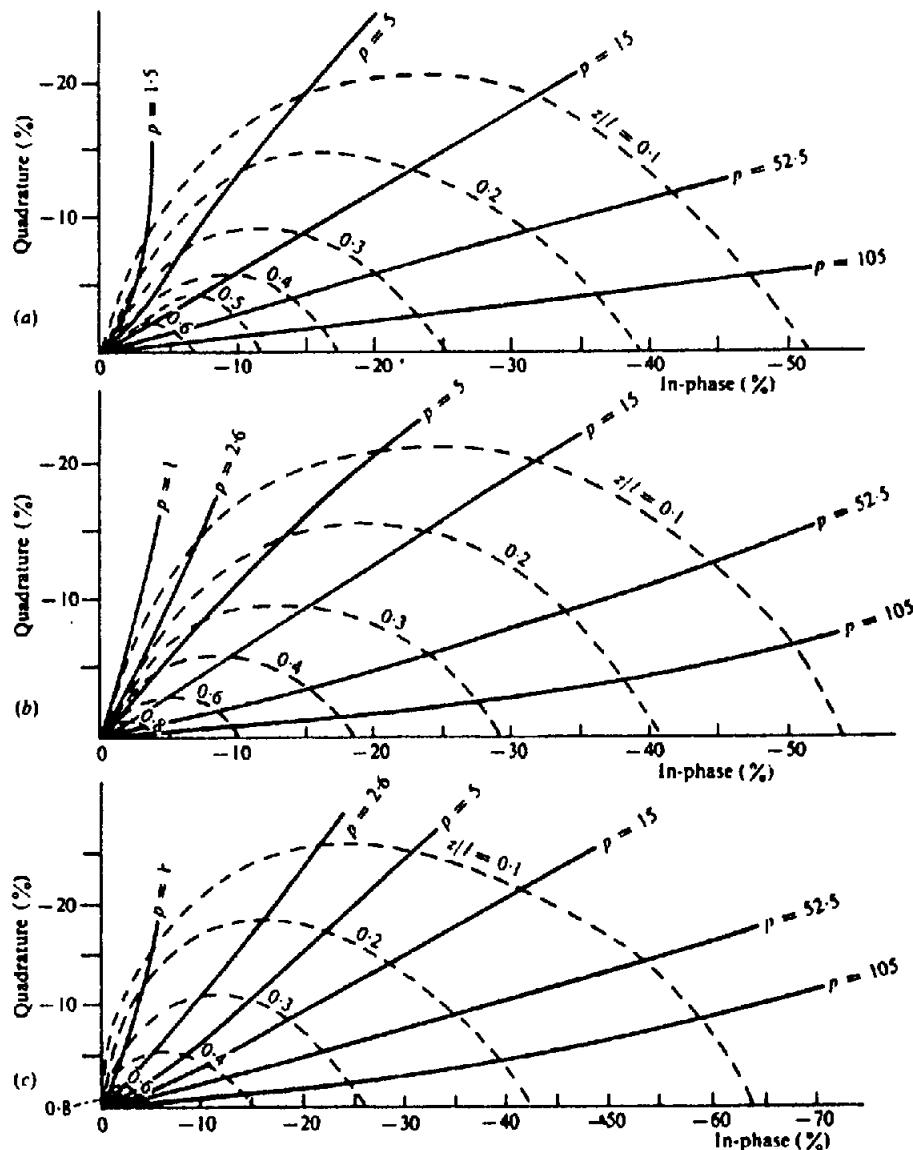


Figure 7.44. Characteristic curves for horizontal-loop system over a dipping sheet.  
 $p = \sigma \mu \text{wtl}$ . (From Strangway, 1966.) (a) Dip =  $90^\circ$ . (b) Dip =  $60^\circ$ . (c) Dip =  $30^\circ$ .

be the free-space value in most cases. If a reasonable estimate of the width  $t$  can be made, the approximate conductivity may be determined.

**Phase-component curves.** Standard characteristic curve sets for the thin sheet are illustrated in Figure 7.44 for the horizontal-loop EM. The ordinate and abscissa are, respectively, the quadrature and in-phase response taken midway between the zero crossovers. Three sets are shown, for dip angles of  $90^\circ$ ,  $60^\circ$ , and  $30^\circ$ . For the vertical sheet the responses are maximum values; this is not so for the dipping sheets, however, because of the asymmetry of the profiles. The depth and response parameter may be read off these curves. If the conductor width can be estimated by other means, it is then possible to get some idea of the conductivity.

There is some doubt, however, about the significance in separating the conductivity from the conductor width in the product  $\sigma t$ . The chances of a conductor being homogeneous over its entire width

are extremely small. As a result, the values obtained for conductivity of massive sulfides are an average and generally fall in quite a narrow range – something like 0.1 to 10 S/m – which is a few orders of magnitude smaller than the conductivities usually assigned to the majority of sulfides in tables (§5.4.1). Possibly the conductivity-thickness product is a more practical parameter and indeed it would give a rough estimate of volume or tonnage equally well.

Similar sets of curves are available for Turam, using peak quadrature and in-phase response. One of these, for a thin sheet dipping  $60^\circ$  and of 20 m depth, is shown in Figure 7.45 for different values of the parameter  $\lambda = 10^5 / \sigma t f$  and strike length  $f$  (note that, although the transmitter-coil dimensions affect the curve somewhat, they are fixed here).

It should be mentioned that, although these universal plots are extremely useful for interpretation, they should not be used alone without comparison of the field profiles with a standard catalogue of theo-

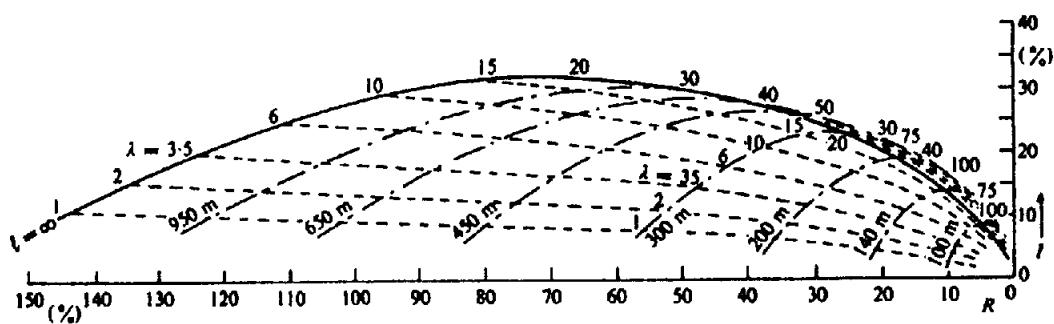


Figure 7.45. Characteristic curves for Turam system over dipping-sheet conductor of infinite depth extent and variable strike length  $l$ . Depth  $z = 20$  m, dip  $\phi = 60^\circ$ , Tx loop  $600 \times 1,200$  m,  $\lambda = 10^5/\sigma t f$ ,  $\mu = \mu_0$  (mks units).

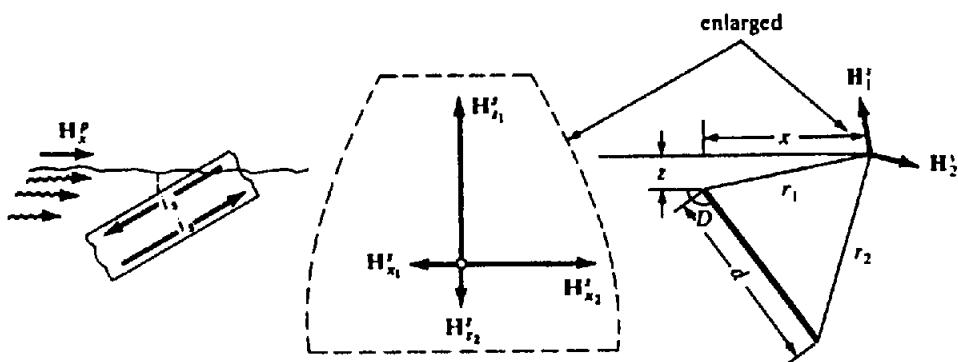


Figure 7.46. Geometry of dipping-sheet model energized by VLF source.

retical and model curves as well. That is, because the characteristic curves make use of only a couple of critical points on the standard profiles, the field plots should fit the latter reasonably well before the former may be used with confidence.

(j) FDEM systems; ac circuit analysis. In Sections 7.2.4b and 7.2.5d we made use of ac circuit parameters to illustrate amplitude, phase, and conductor response for EM analysis, and in Section 7.2.5a several relations were given for mutual inductance between circular and linear wire models. The ac analysis is attractive because the models can have finite conductivities, aside from the simplifications compared to EM theory. Because the coupling between conductors and transmitter and receiver loops is generally complex, however, this approach is greatly oversimplified. It will not produce useful results when the conductor dimensions are much larger than those of the transmitter, as with local-source dip-angle sets and Slingram, although it works reasonably well for uniform-field and long-wire systems like AFMAG, VLF, and Turam. We will consider the last two of these briefly for circuit analysis of the sheet conductor.

In performing VLF surveys, the azimuth of the transmitter station should be as nearly as possible on strike with the sheet target. From Figure 7.46 we find

the secondary field components in the form

$$\begin{aligned} H_x^S &= i_c x / 2\pi(x^2 + z^2) - i_c(x + d \cos D) \\ &/ 2\pi((x + d \cos D)^2 + (z + d \sin D)^2) \\ H_z^S &= i_c z / 2\pi(x^2 + z^2) - i_c(z + d \sin D) \\ &/ 2\pi((x + d \cos D)^2 + (z + d \sin D)^2) \end{aligned}$$

where  $i_c$  is the current in the conductor induced by the transmitter horizontal field  $H_x^P$ , and  $d$  and  $D$  are its depth extent and dip. The transmitter field may be taken as a constant. Because the dip angle  $\delta = \tan^{-1}(H_z^S/(H_x^P + H_x^S)) = \tan^{-1}(H_z^S/H_x^S)$  we have, following some manipulation,

$$\begin{aligned} \tan \delta &= |H_z^S/H_x^S| \\ &= \alpha / \{1 + K(1 + \alpha^2)\} - (\alpha + d \cos D/z) \\ &/ [K\{(1 + d \sin D/z)^2 \\ &+ (\alpha + d \cos D/z)^2\} \\ &- (1 + d \sin D/z)] \end{aligned} \quad (7.38a)$$

where  $\alpha = x/z$  and  $K = 2(z/i_c)H_x^P$ . The dimensionless parameter  $K$  may be used to obtain depth estimates.

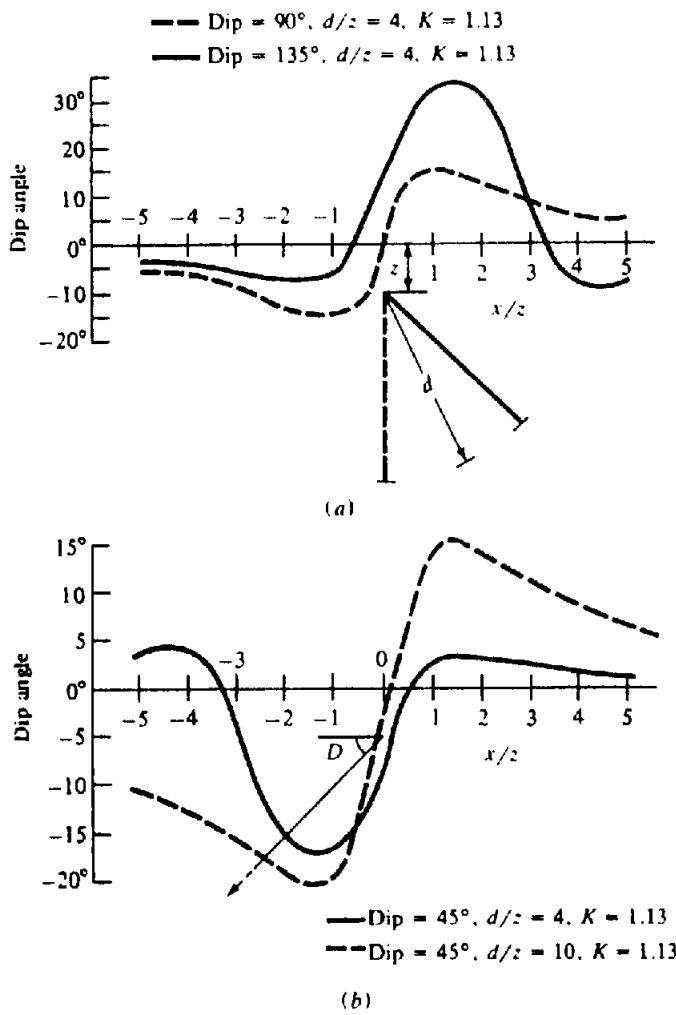


Figure 7.47. VLF profiles over dipping sheet obtained from ac circuit analysis. (a) Dip 90 and 135°,  $d/z = 4$ . (b) Dip 45°,  $d/z = 4$  and 10.

VLF profiles using the relation in Equation (7.38a) are displayed in Figure 7.47; the pronounced effect of dip for two models of limited depth extent ( $d/z = 4$ ), one vertical and the other dipping 135°, is shown by the change in the maximum dip angle by a factor of 2 as the dip changes from 90 to 135°. Note that the maximum lies over the hanging wall. Comparing this profile with the AFMAG profile in Figure 7.34a, we see that the peak-to-peak ratio is larger for VLF (however, the depth extent is also larger for the AFMAG example so that the comparison is not entirely valid).

Figure 7.47b demonstrates the effect of depth extent on VLF profiles. Two models, identical except that  $d/z$  changes from 4 to 10, produce entirely different curves; the peak-to-peak ratio is reduced from about 4 to 4/3 (see also Fig. 7.34b for a similar AFMAG example).

To work up the ac circuit analysis for Turam, we return to Equation (7.36a) (§7.7.3g). For the in-phase component the various fields are given by [Eq. (7.10c)

and Fig. 7.37a]

$$\begin{aligned} H_t^P &= \frac{i_p}{2\pi(x - \delta x/2)} \\ H_1^S &= \frac{i_c(x - c - \delta x/2)}{2\pi\{(x - c - \delta x/2)^2 + z^2\}} \\ &= \left(\frac{M}{\beta L}\right) \frac{i_p(x - c - \delta x/2)}{2\pi\{(x - c - \delta x/2)^2 + z^2\}} \\ H_2^S &= \frac{i_p}{2\pi(x + \delta x/2)} \\ H_2^S &= \left(\frac{M}{\beta L}\right) \frac{i_p(x - c + \delta x/2)}{2\pi\{(x - c + \delta x/2)^2 + z^2\}} \end{aligned}$$

where  $M$  is the mutual inductance between transmitter and the long wire conductor [Eq. (7.21b)],  $L$  is the conductor self-inductance [Eq. (7.22a), §7.2.5b], and  $\beta = (1 + Q^2)^{1/2}$ . Then we have

$$\begin{aligned} \frac{H_1^S}{H_t^P} &= \left(\frac{M}{\beta L}\right) \frac{(x - \delta x/2)(x - c - \delta x/2)}{z^2 + (x - c - \delta x/2)^2} \\ \frac{H_2^S}{H_t^P} &= \left(\frac{M}{\beta L}\right) \frac{(x + \delta x/2)(x - c + \delta x/2)}{z^2 + (x - c + \delta x/2)^2} \end{aligned}$$

Setting  $(M/\beta L) = W$ ,  $x/c = \alpha$ ,  $\delta x/c = \delta\alpha$ ,  $z/c = \gamma$ , and neglecting  $(\delta\alpha)^2$ , we get

$$\begin{aligned} \frac{R}{p} &= \left[ 1 + \frac{W\{\alpha(\alpha - 1) - \delta\alpha(\alpha - \frac{1}{2})\}}{(\alpha - 1)^2 - \delta\alpha(\alpha - 1) + \gamma^2} \right] / \\ &\quad \left[ 1 + \frac{W\{\alpha(\alpha - 1) + \delta\alpha(\alpha - \frac{1}{2})\}}{(\alpha - 1)^2 + \delta\alpha(\alpha - 1) + \gamma^2} \right] \quad (7.39a) \end{aligned}$$

This expression may be written in a simpler form if we assume  $H_2^S \ll H_t^P$  and  $\delta x \ll x$ ,  $\delta\alpha \ll \alpha$ , so that

$$\frac{R}{p} = 1 - \left( \frac{\delta x}{H_t^P} \right) \left( \frac{dH_2^S}{dx} \right) = 1 - \frac{2\pi x \delta x}{i_p} \left( \frac{dH_2^S}{dx} \right)$$

and

$$H_2^S = \frac{-Wi_p(x - c)}{2\pi\{z^2 + (x - c)^2\}}$$

This gives for the ratio  $R/p$  the approximate expression

$$\frac{R}{p} = 1 + W\alpha\delta\alpha \left\{ \frac{\gamma^2 - (\alpha - 1)^2}{\gamma^2 + (\alpha - 1)^2} \right\} \quad (7.39b)$$

The real component may be obtained by multiplying Equation (7.39a) or (7.39b) by  $Q^2/(1 + Q^2)$

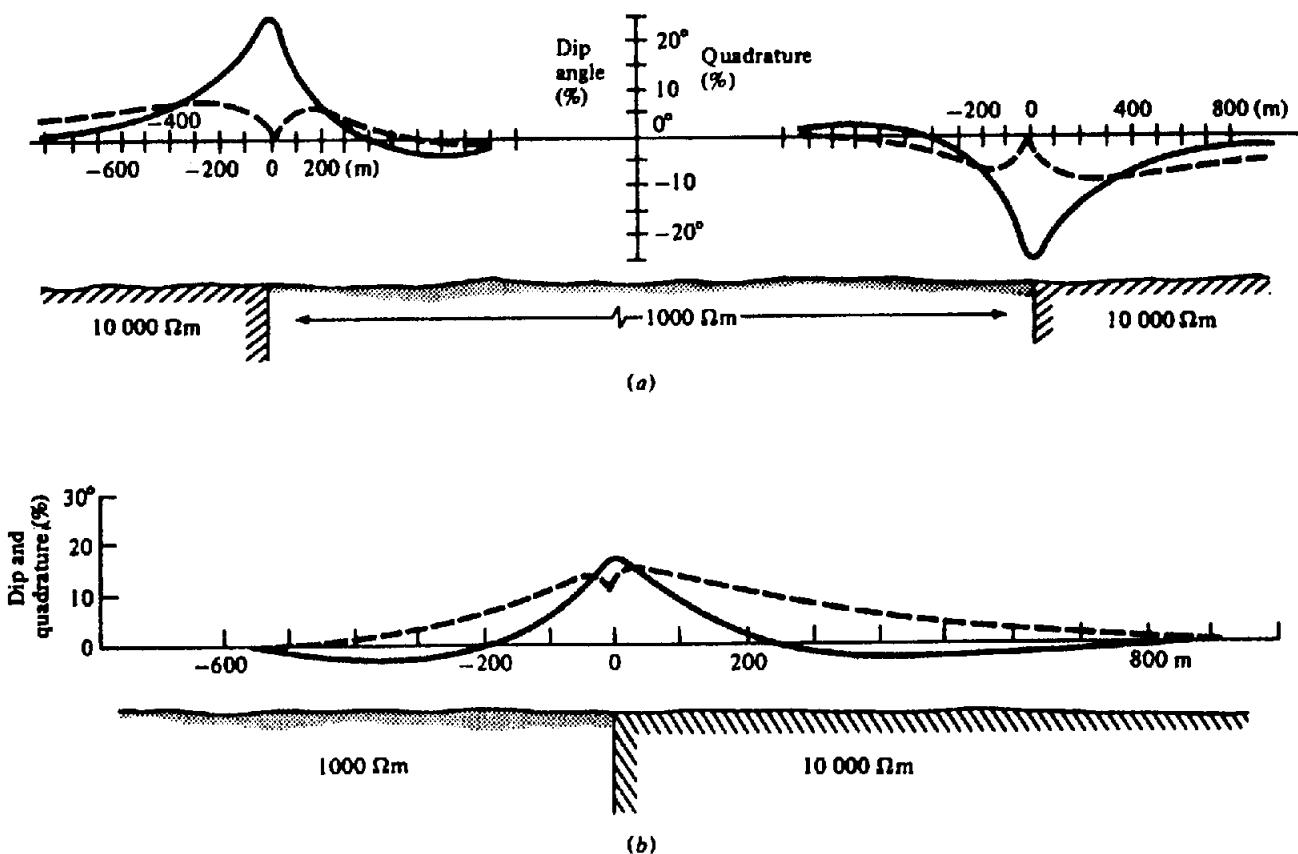


Figure 7.48. VLF profiles over vertical contacts between beds of different conductivities. (a) 1,000  $\Omega\text{m}$  bed between two half-spaces of 10,000  $\Omega\text{m}$ ; no overburden. (b) Same as (a) except overlain by 6 m of conductive overburden,  $\rho = 100 \Omega\text{m}$ .

[Eq. (7.16a)]. For the imaginary component we return to Equation (7.36b) and find the respective phase angles, using the same multiplier. Then we have

$$\tan \phi_1 = \left\{ (M/L)Q(1 - \alpha - \frac{1}{2}\delta\alpha)(\alpha + \frac{1}{2}\delta\alpha) \right\} / \left[ (1 + Q^2)\left\{ \gamma^2 + (1 - \alpha - \frac{1}{2}\delta\alpha)^2 \right\} + (M/L)Q^2(1 - \alpha - \frac{1}{2}\delta\alpha)(\alpha + \frac{1}{2}\delta\alpha) \right]$$

$$\tan \phi_2 = \left\{ (M/L)Q(1 - \alpha + \frac{1}{2}\delta\alpha)(\alpha - \frac{1}{2}\delta\alpha) \right\} / \left[ (1 + Q^2)\left\{ \gamma^2 + (1 - \alpha + \frac{1}{2}\delta\alpha)^2 \right\} + (M/L)Q^2(1 - \alpha + \frac{1}{2}\delta\alpha)(\alpha - \frac{1}{2}\delta\alpha) \right]$$

from which we get

$$\Delta\phi = \phi_1 - \phi_2. \quad (7.39c)$$

The expression for phase angle is much simpler if we use the approximation in Equation (7.39b), when we have

$$\tan \Delta\phi \approx \Delta\phi = \frac{\mathcal{J}_m\{R/p\}}{1 + \mathcal{R}_s\{R/p\}} \approx \mathcal{J}_m\left\{\frac{R}{p}\right\}$$

Thus,

$$\Delta\phi = -\frac{M}{L}(\alpha\delta\alpha) \frac{\{\gamma^2 - (\alpha - 1)^2\}}{\{\gamma^2 + (\alpha - 1)^2\}} \left( \frac{1}{Q} \right) \quad (7.39d)$$

Using Equation (7.39b), this can be written

$$\Delta\phi = \left( 1 - \frac{R}{P} \right) \frac{1}{(1 + Q^2)^{1/2}} = \left( 1 - \frac{R}{P} \right) \frac{1}{Q} \quad (Q \geq 3) \quad (7.39e)$$

The profiles of Figure 7.37 were plotted from these relations.

The VLF ground survey is attractive for mapping shallow geological structure because of its speed, simplicity, and low cost (Telford, King, and Becker, 1977; Fischer, Le Quang, and Müller, 1983). For example, the steeply dipping contact or single-bed fault produces a characteristic VLF signature when there is a conductivity contrast between the two sections (see §7.8, Example 4, for a classic case). Although this common structure may be treated by ac circuit modeling, it is more illuminating to use 2-D MT relations for  $E$  polarization (§6.2.7), because the  $E$  and  $H$  fields from the VLF source

produce  $E_y$  (on strike) and  $H_x$  (on traverse) components, whereas a vertical component  $H_z$  results from the conductivity contrast.

Equation (6.23b), the scalar diffusion equation in  $E_y$ , was derived from the 2-D relations for the VLF field in this orientation. These are

$$\begin{aligned}\partial H_x / \partial z - \partial H_z / \partial x &= \sigma E_y, \\ \partial E_y / \partial x &= -j\omega\mu_0 H_z, \\ \partial E_y / \partial z &= j\omega\mu_0 H_x.\end{aligned}$$

In the vicinity of the contact there is an  $H_z$  component which differs in phase from  $H_x$ . Thus the wave is elliptically polarized (§7.2.4c). With the VLF instrument we measure dip angle  $\delta$  (inclination of major axis) and ellipticity  $e$ , or quadrature (ratio of major to minor axis). These parameters are closely related to the values of  $H_z/H_x$  and  $\phi_z - \phi_x$ . Assuming  $H_z \ll H_x$  they are given approximately by

$$\left. \begin{aligned}\tan \delta &= |H_z/H_x| \cos(\phi_z - \phi_x) \\ e &= |H_z/H_x| \sin(\phi_z - \phi_x)\end{aligned} \right\} \quad (7.38b)$$

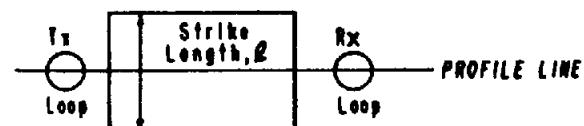
Figure 7.48 shows profiles obtained over a wide conductive outcropping slab model sandwiched between two resistive sections. There is no pronounced crossover associated with these curves, but they have two distinctive features: both dip angle and quadrature peak directly over the contact, the former positive, the quadrature a negative cusp, and both decay more rapidly to zero on the conductive side. As one would expect, the curves are reflected in the horizontal axis at the second contact.

Figure 7.48b shows that the effect of an overlying bed of conductive overburden is to decrease the dip readings and shrink the quadrature cusp.

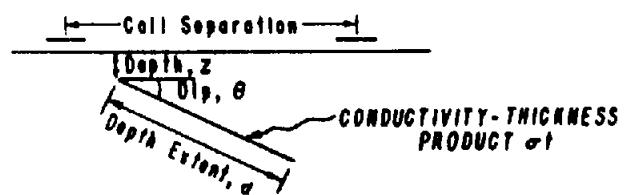
#### 7.7.4. Ground Systems; TDEM over Dipping Sheet

(a) General. Until the 1970s, most practical TD interpretation analysis was done on Input data because it was the only TD equipment in general use (Becker, 1969; Morrison, Phillips, and O'Brien, 1969; Palacky and West, 1973). At present there are at least six ground TDEM systems available. Compared to the diversity of FDEM ground units, however, there are no fundamental differences among them, except in transmitter waveform, loop(s) size, and portability. Initially interpretation was obtained from scale-model measurements, but since the late 1970s computer modeling has been refined and has become increasingly popular (Annan, 1974; Dyck, Bloor, and

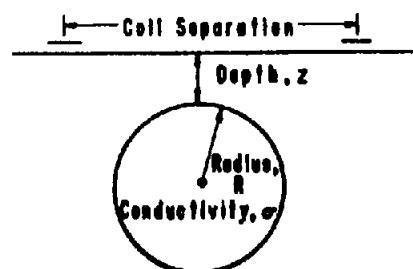
PLAN VIEW (i)



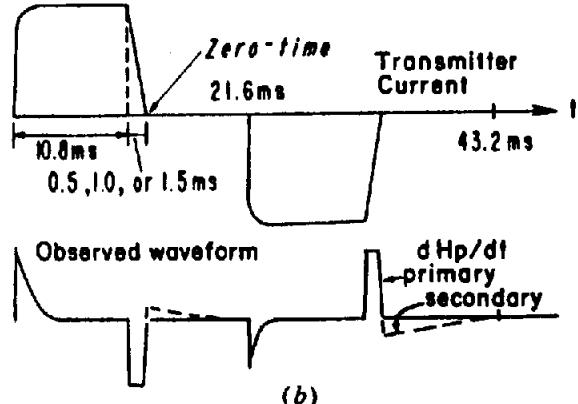
CROSS-SECTION



(ii)



(a)



(b)

Figure 7.49. PEM(1) moving-source TDEM. (After Bartel and Hohmann, 1985.) (a) Geometry of thin-plate and sphere models. (b) Waveform for 10.8 ms pulse.

Vallée, 1981). The PLATE model developed by Dyck, Bloor, and Vallée is now widely used for both TD and FDEM interpretation.

The PLATE computer package measures the response of a dimensionally and inductively thin sheet conductor in free space, that is, the thickness  $t \ll \ell$ ,  $d$ , where  $\ell$  is strike length and  $d$  is depth extent; at the same time  $t < 0.6\delta$ , where  $\delta$  is the skin depth (§6.2.3). Eddy currents induced in the sheet by the primary field are simulated by a set of so-called eigencurrents in the PLATE program, each having a different circulation pattern on the sheet. Their rate of decay increases with pattern complexity. Because

CHANNEL	10 ms PULSE		20 ms PULSE		GAIN FACTOR
	CENTER	WIDTH	CENTER	WIDTH	
PP	-0.05 ms	.1 ms	-0.1 ms	.2 ms	—
1	.15	.1	.3	.2	1.0
2	.3	.2	.6	.4	1.39
3	.55	.3	1.1	.6	1.93
4	.9	.4	1.8	.8	2.68
5	1.45	.7	2.9	1.4	3.73
6	2.4	1.2	4.8	2.4	5.18
7	4.0	2.0	8.0	4.0	7.20
8	6.4	2.8	12.8	5.6	10.0

(c)

Figure 7.49. (Continued) (c) Channel data; PP denotes  $H^P$ .

the response of each eigencurrent is independent of the others, the solution becomes a summation suitable for the computer. It may be obtained by computing the magnetic field impulse response (§A.13) and convolving it with the current waveform or its time derivative to obtain  $H^s$  or  $\partial H^s / \partial t$ .

(b) PEM. The geometry of the moving-source version of this system, traversing a sphere (to be discussed in §7.7.5) and a dipping sheet is shown in Figure 7.49a, and the 10.8 ms waveform and channel data in Figure 7.49b (Bartel and Hohmann, 1985). In the PEM 1 configuration (see Table 7.3), only  $\partial H_z^s / \partial t$  is measured usually, then normalized by dividing by the maximum value of  $\partial H_z^s / \partial t$  and displayed as parts per thousand (ppk) for each of the eight channels on an analog meter. Primary field is measured during the ramp turn-off.

The effect of dip is seen in Figure 7.50a for angles of 0, 30, 60, and 90°. A positive peak precisely marks the conductor edge (located below the zero distance) on the profiles of Figures 7.50 and 7.52 on the early channels, then drifts slightly inward on the sheet at later time; the latter is due to eddy current migration and decreases for steeper dip. There is a smaller negative side lobe off the conductor edge, which increases slightly with dip. The corresponding negative lobe to the right, considerably larger than the other at 30°, decreases with dip. Consequently the response indicates shallow dip but is not very sensitive to dips greater than 45°.

When the conductor depth is somewhat greater than the T-R separation there is insignificant response, as is evident in Figure 7.50b, c for models dipping 90 and 30°. If the presence of a sheet

conductor can be established at all, the slight negative anomaly over the 30° sheet at  $z = 200$  m might be interpreted as a shallow dip to the right, because the right-hand slope is more gradual. For the shallow dipping model, however, maximum detectable depth is little more than 100 m.

PEM profiles over a 30° sheet of variable conductance  $\sigma_t$  are shown in Figure 7.50d. All channels respond to the 100 S model, the response increasing slightly from channel 1 to 5, then decreasing. This minor peaking effect is caused by the gain factor in the receiver, shown in the right-hand column of the table in Figure 7.49c. When  $\sigma_t = 10$  S there is no significant response beyond channel 6 and for 3 S beyond 3; for  $\sigma_t \leq 1$  S no measurable anomaly is evident.

Decreasing the strike length of the model reduces late time response, much like the attenuation from a reduced conductance. Varying the depth extent gives similar results in addition to changing the horizontal extent of the profile for shallow dip.

All of the curves in Figure 7.50 are principal profiles over the center of a model plate 600 × 600 m. When the survey line passes over the end of the plate or beyond it, response is greatly attenuated or zero (§7.7.3b).

The change in target response produced by conductive overburden is perhaps more difficult to resolve for TDEM than FDEM. Using a model HLEM unit, Lowrie and West (1965) found that an overlying conductive sheet, not in galvanic contact with a vertical sheet below it, made the latter appear more conductive and more deeply buried than it actually was, thus rotating the curves of Figure 7.44 clockwise about the origin. The phase change, produced

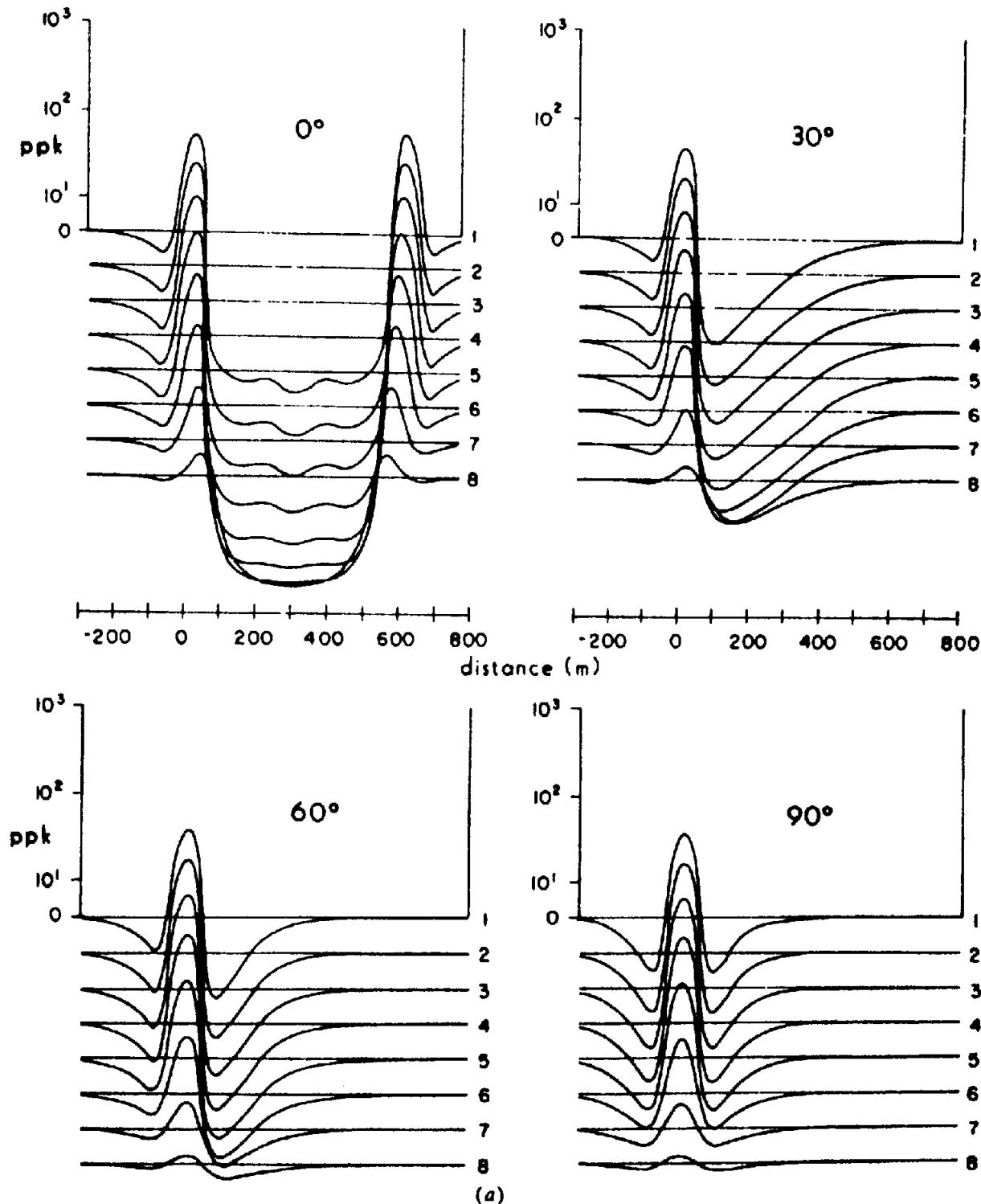


Figure 7.50. PFM(1) response to a dipping sheet as a function of dip, depth, and TCP.  $\ell = d = 600$  m, T-R = 100 m, TCP =  $\sigma t = 30$  S [except in (d)]. (After Bartel and Hohmann, 1985.) (a) Effect of dip;  $z = 50$  m.

by the primary and secondary fields going and returning through the overburden, becomes a time lag in TD measurements. Its effects may be approximated by adding the separate responses of overburden and target in the frequency domain, then transforming the sum into the time domain.

Using Nabighian's analogy (§7.2.6d) we may say that the smoke ring lingers in the overburden layer, to diffuse downward at a later time. Thus the ring may be beyond the receiver coil location at a delay time corresponding to, say, channel 1. The response by then is negative, producing a cancellation or

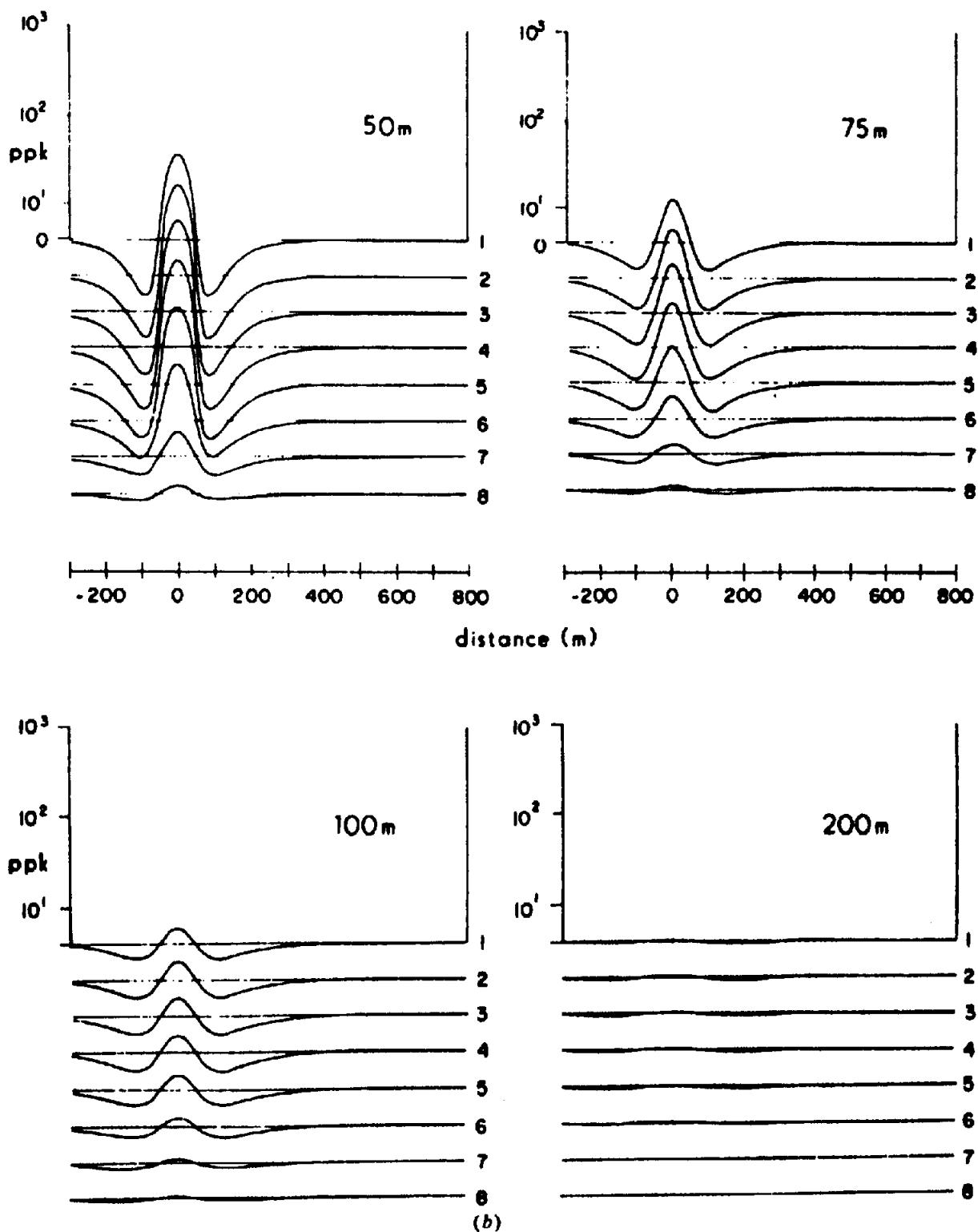


Figure 7.50. (Continued) (b) Effect of depth, dip = 90°.

reversal of the target signal; thus the latter may be detected in the proper sense only in late channels when the overburden signal has decayed sufficiently. Figure 7.51 shows the resultant effect on the primary field and the target response below the overburden.

Even if the smoke ring has arrived in time to produce a positive response in the receiver, at still

later times it may return a negative signal as a result of changes in overburden thickness and conductivity. Thus the profile may show positive and negative fluctuations, unlike those in the previous figures. This is illustrated in Figure 7.52b where the overburden effect has been simulated by tracking the smoke ring (Fig. 7.11) from surface down to the 30° sheet

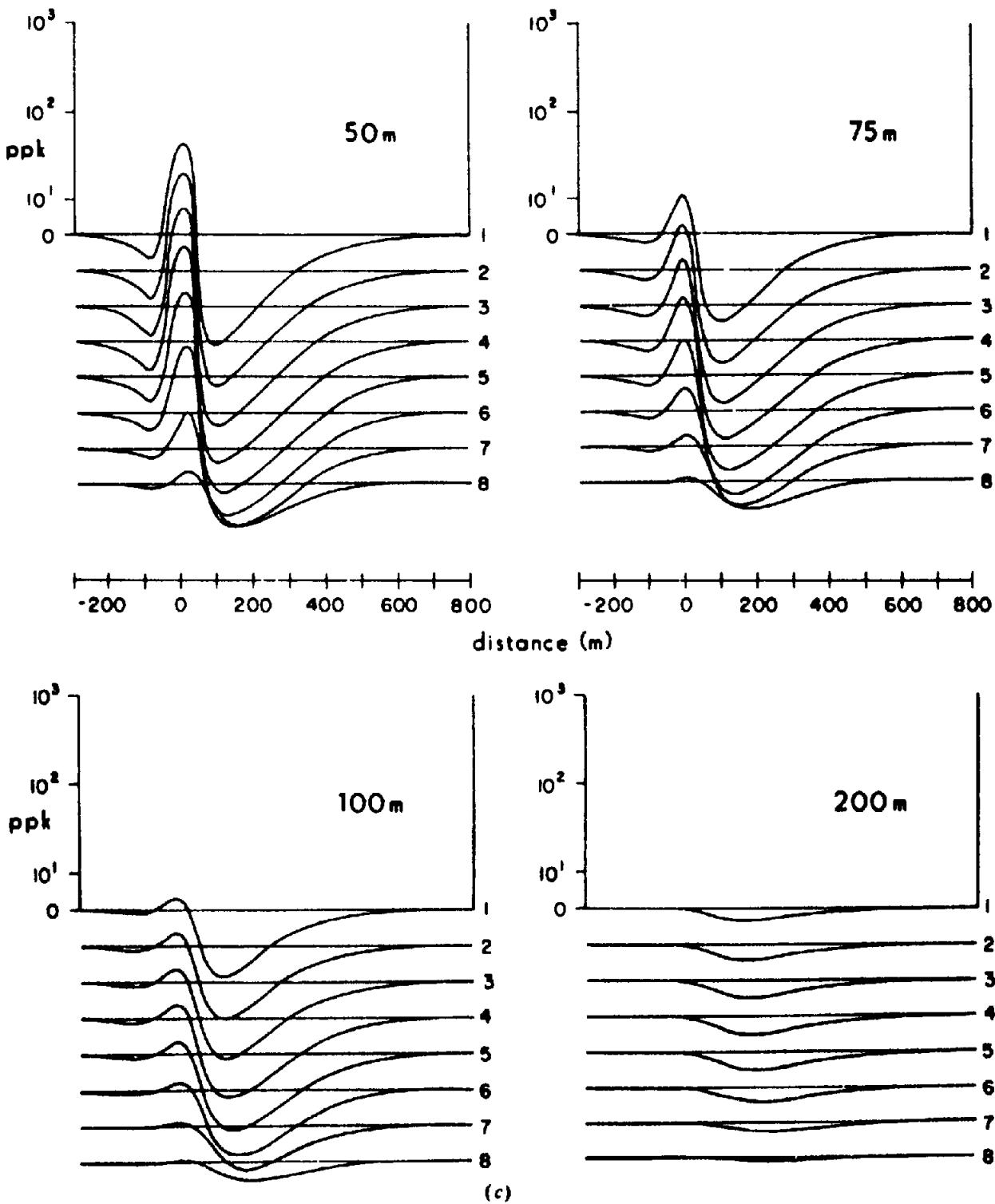


Figure 7.50. (Continued) (c) Same as (b) except dip = 30°.

model. To emphasize the profile changes caused by overburden, a curve set for no overburden is shown in Figure 7.52a.

(c) EM37. Model data for the EM37 TD system, obtained from the PLATE program, have been reported by Gallagher, Ward, and Hohmann (1985). Field procedure with EM37 is similar to Turam; the large  $T_x$  loop is fixed and off the target and only the

small  $Rx$  coil moves (§7.4.4e). Two of the three magnetic components,  $H_z$  and  $H_x$ , along traverse, were determined during the study, using a 30 Hz recurrence frequency (8 ms maximum window). For this frequency the window widths of the 20 channels ranged from 17  $\mu$ s at channel 1 to 1.56 ms for channel 20. Pertinent data for the channel on-off times  $t_1$  and  $t_2$  with respect to switch-off are given in Table 7.2.

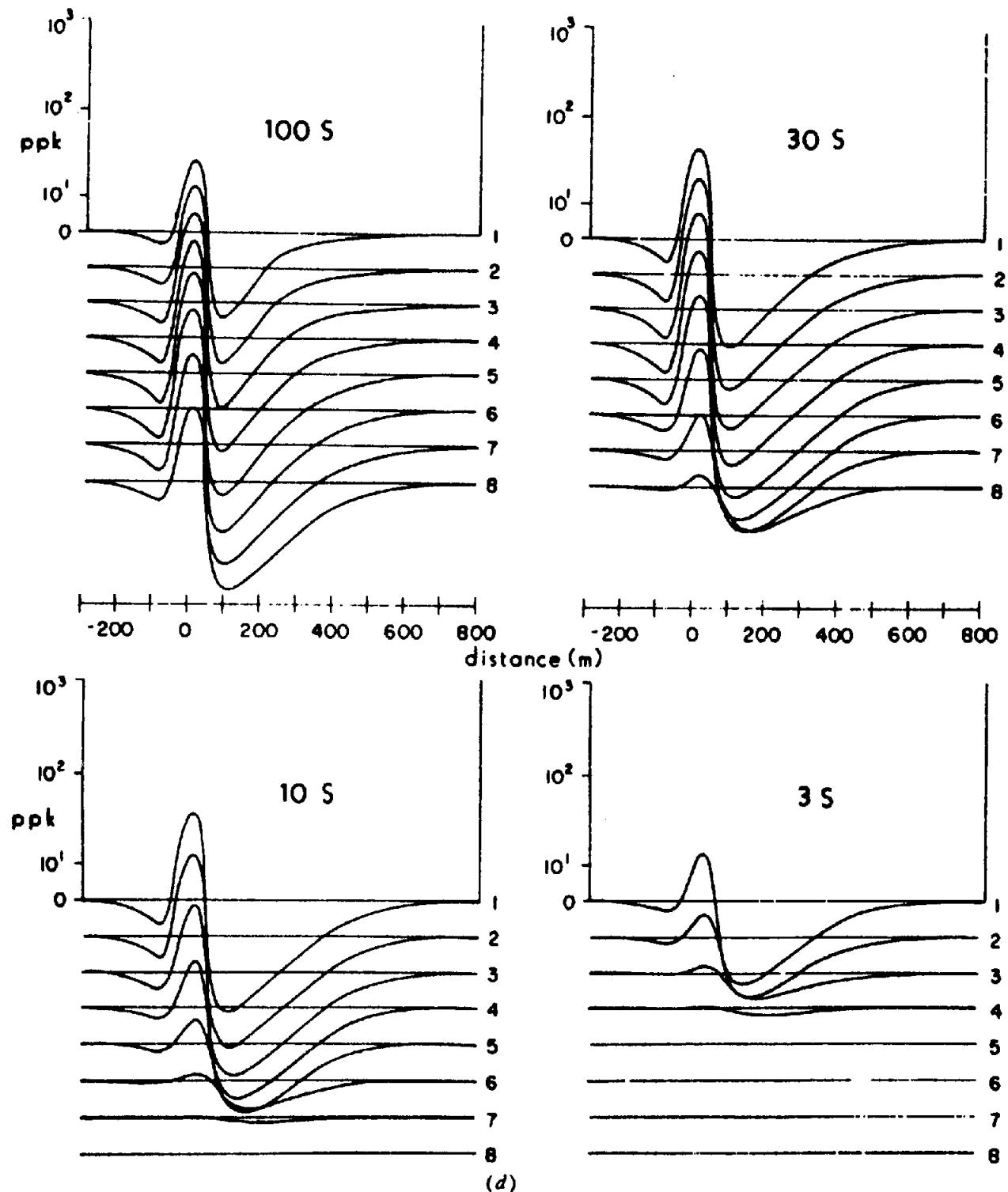


Figure 7.50. (Continued) (d) Variation with TCP;  $z = 50$  m, dip =  $30^\circ$ .

The model profiles that follow, similar to those for PEM, are in terms of the time derivative and plotted in nanovolts per square meter ( $\text{nV}/\text{m}^2$ ), converted from millivolt signal in the receiver by using the effective Rx coil area and the gain. Except where noted otherwise in figure legends, plate dimensions are  $\ell = 800$  m,  $d = 400$  m,  $\sigma t = 30$  S, and depth  $z = 100$  m. On the horizontal scales, zero represents the surface point coincident with the center point of

the near side of the Tx loop, whereas 300 lies over the top edge of the sheet, as shown in Figure 7.22a.

Figure 7.53a shows profiles of sheets dipping 0, 30, 90 and  $150^\circ$ . Dips less than  $90^\circ$  point away from the Tx loop and vice versa. Location of the Tx loop creates an asymmetry which appears greater in the  $H_z$  than the  $H_x$  curves. A vertical sheet produces symmetrical  $H_x$  profiles which develop a minor negative tail to the right as the dip angle decreases; this

asymmetry, as well as the peak-to-peak amplitude, is larger for dips in the opposite direction. The  $H_z$  curves, considered in the same sequence, are more asymmetric over the vertical sheet (compare with Turam curves in Fig. 7.37). As the dip decreases, so does the positive peak, whereas the negative peak increases. When the dip is toward the  $Tx$ , the opposite is true, the profiles becoming more symmetrical and the overall amplitude nearly doubling. In the latter orientation the possibility exists of vanishing primary field coupling (extinction angle; §7.7.3g). Response is reduced or completely suppressed for sheets of limited depth extent and a sign reversal may occur.

Dip direction may be indicated by the ratio of positive-to-negative peak amplitudes of the  $H_z$  curves. When  $\theta < 90^\circ$  the ratio is less than unity and vice versa. This estimator does not appear to hold for the  $H_x$  profiles where the positive peaks are larger throughout. For a horizontal sheet the negative  $H_z$  peak lies nearly over the center, whereas the edges are marked by the positive and negative  $H_x$  peaks.

The top edge of the sheet is roughly located by the positive peaks on the  $H_x$  profiles, although when  $\theta$  approaches  $180^\circ$  this is not so, because both  $H_x$  peaks drift toward the transmitter. Using the  $H_z$  curves, the top edge is more or less under the maximum slope for  $0^\circ < \theta < 135^\circ$ ; beyond this the same migration takes place.

When plate dimensions are  $< 800 \times 400$  m these curves are modified, particularly for peak-to-peak ratios. The same is true when plate-transmitter geometry is changed. More models are required for complete analysis. It is also apparent that the profiles are displaced laterally, from early to late time, unless  $45^\circ < \theta < 135^\circ$ , in which case interpretation may be refined by selecting particular profiles. To consolidate the data and simplify analysis, nomograms for dip estimates based on peak ratios are available (§7.7.4g).

Figure 7.53b displays vertical-component profiles over a vertical plate at depths of 50, 100, and 200 m. The vertical scales are adjusted to give reasonable response for each curve set. Amplitude increases nearly exponentially with increasing depth, producing a broader anomaly of smaller amplitude.

As in other geophysical methods, certain characteristics of the curves are used for depth estimate, such as change in slope, peak-to-peak distance, profile width at specific amplitude, and so on. One measure of the latter which is used is the horizontal width on the updip (positive) part of the  $H_z$  curve (which is less susceptible to dip and depth-extent variations) at two-thirds peak value. This estimate may also be made at early and late time without much error, unless the dip and depth are shallow.

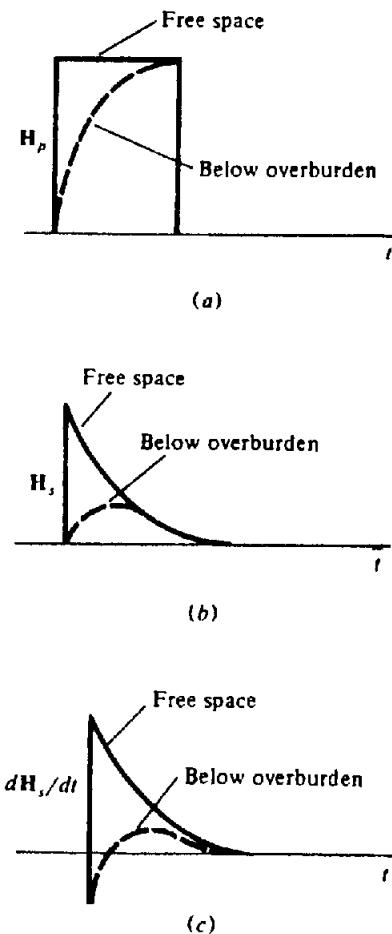


Figure 7.51. Effect of overburden (ob) on TDEM fields.  
(a) Primary field at target. (b) Secondary field at target.  
(c) Receiver response from target.

Another estimate is obtained from the horizontal distance between positive and negative peaks. It is not as reliable as the other because the apparent depth increases from early to late time due to current diffusion into the plate. It is also less accurate for sheets of shallow dip and is affected more by plate size and depth extent.

The effect of variable conductance  $\sigma t$  is illustrated in Figure 7.53c for vertical sheets of standard size and depth of 50 m. As mentioned earlier, there are practical limits on  $\sigma t$  for the sheet to be classified as thin for all channel widths available in a particular TDEM unit. Apart from this and other plate dimensions that influence the response of the system, the effect of variable conductivity is also significant. Because it is not possible usually to resolve  $\sigma$  and  $t$  separately (§7.7.3i), we must consider the  $\sigma t$  product (TCP) or conductance (siemens).

The physical explanation of the effects of variable conductivity and plate dimensions is that currents decay rapidly when  $\sigma t$  is small, slowly when it is

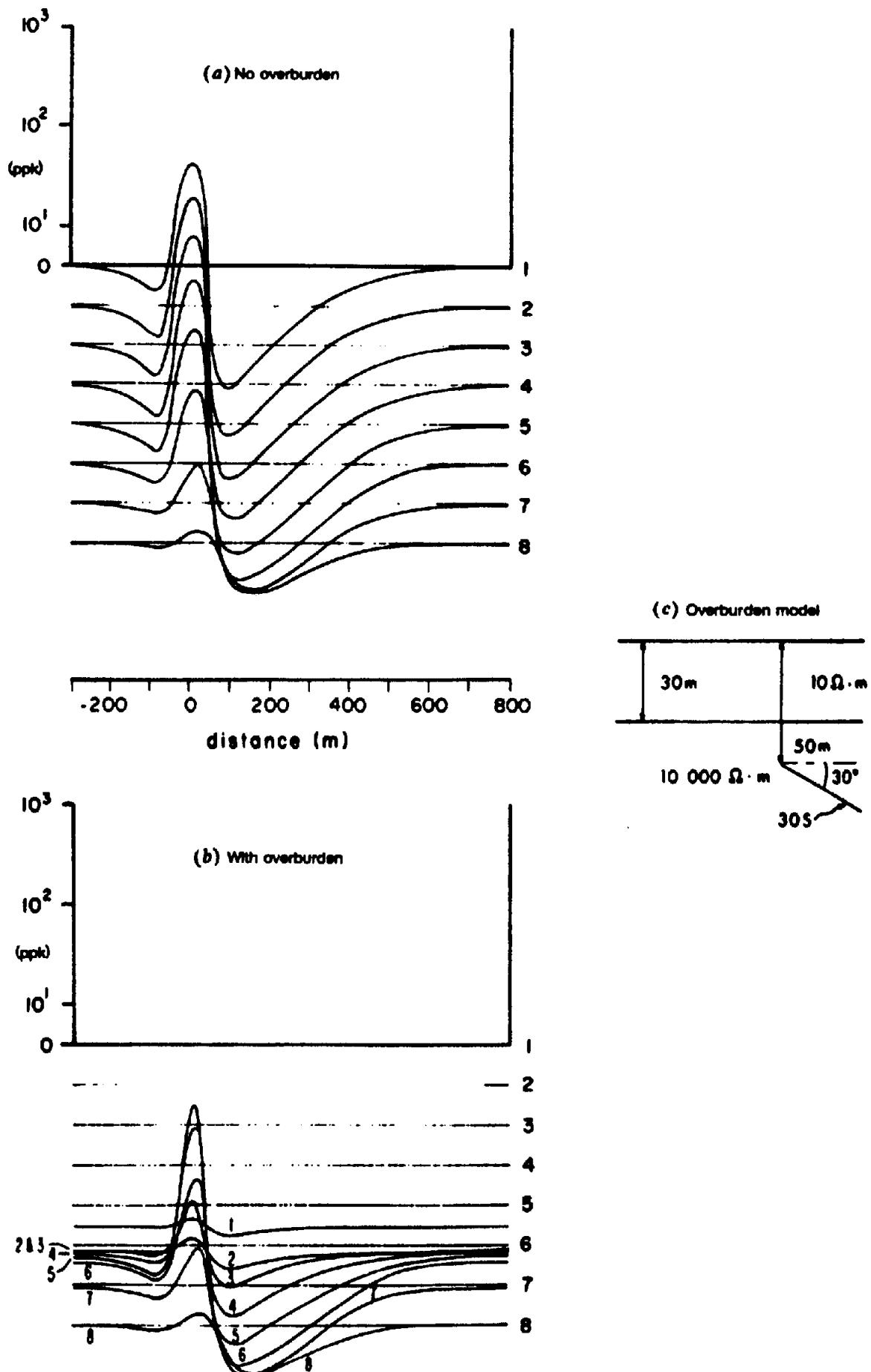


Figure 7.52. Approximate effect of conductive overburden.  $\ell = d = 600$  m,  $z = 50$  m,  $T-R = 100$  m,  $\sigma t = 30$  S, dip =  $30^\circ$ . Channel numbers are at the right in (a) and (b), channel response at the left. (After Bartel and Hohmann, 1985). (a) Response without overburden. (b) Response with overburden. (c) Overburden model.

large, whereas current diffusion from the perimeter toward the center of the plate takes less time in a small plate than in a large one.

Figure 7.53c shows the effect of varying  $\sigma t$  over a range of 10; the profiles show little response on the first 10 channels when the TCP is  $> 30$  S and practically zero signal through channels 10 to 20 when it is 3 S.

Depth extent is an important dimension because it affects proper estimates of other parameters; however, it may be difficult to determine. Examples of variable depth extent are shown in Figure 7.53d, e for vertical and horizontal field components, respectively, the first for  $30^\circ$  dip, the second for  $90^\circ$  dip. In both cases the profiles become sharper as depth extent decreases, the change in the  $H_z$  component being the more obvious. The signal decay rate is seen to decrease inversely with depth extent but this is also true for conductance. Only at shallow dip angles ( $\leq 30^\circ$ ) is the estimate of this parameter readily obtained.

Decrease in strike length is not as significant as for depth extent. Although the relations with decay rate are like the latter, they are less pronounced. Generally a smaller strike length merely reduces amplitude without much effect on the profile shapes.

(d) SIROTEM. Two TDEM field configurations have been considered in discussing PEM and EM37 interpretation. The Australian SIROTEM equipment uses one field layout, adapted from the USSR MPP series, which is unique in the Western World. Aside from variations in electrical and electronic details, mainly in the receiver, there are differences as well as similarities among the popular TD systems. These are summarized in Table 7.3.

Four of these units resemble Turam FDEM and two are somewhat like the horizontal loop. The novel SIROTEM(1) configuration has been identified by an astounding variety of names, including twin-, coincident-, single-, in-, and loop-loop, which all mean that it transmits and receives at the same station (the Russian equivalent transmits and receives on a single loop). We will use the names coincident-loop or SIROTEM(1). The other more conventional arrangement is called SIROTEM(2), twin-loop, or loop-loop. It is clear from the table that PEM(2), EM37, EMP, and UTEM resemble one another, as do PEM(1) and SIROTEM(2). Only SIROTEM(1) appears to be different from all other systems.

Several model examples of the coincident-loop system have been provided by Spies and Parker (1984). They all involve the effect of *current gathering* and *current channeling* on TDEM response. These terms are used interchangeably, although channeling

Table 7.2. On and off times ( $t_1, t_2$ ) for EM37 channel windows.

Channel	$t_1$ (ms)	$t_2$ (ms)
1	0.080	0.097
2	0.097	0.121
3	0.121	0.158
4	0.158	0.195
5	0.195	0.224
6	0.224	0.316
7	0.316	0.393
8	0.393	0.492
9	0.492	0.634
10	0.634	0.790
11	0.790	0.962
12	0.962	1.221
13	1.221	1.58
14	1.58	1.95
15	1.95	2.44
16	2.44	3.16
17	3.16	3.93
18	3.93	4.92
19	4.92	6.34
20	6.34	7.90

is a restriction of current flow caused by a resistive barrier, resembling dc current conduction. Gathering refers to a concentration of eddy currents or inductive flow. The distinction is clarified in the following figures.

Figure 7.54 shows large-loop (Turam-type) and coincident-loop profiles over a semiinfinite horizontal conducting slab 60 m thick, simulating conductive overburden of  $12 \Omega\text{m}$ . In part (a) the fixed loop lies on the overburden, in part (b) it is offset. Both curve sets appear to reflect the edge boundary strongly; the first is a slightly sharper version of Figure 7.54c, which was obtained over a 1-D sheet and inserted for comparison. That is, the lateral extent of the profiles is controlled by the smaller dimension of the Tx loop rather than its fortuitous distance ( $\sim 550$  m) from the overburden edge.

When, as in Figure 7.54b, the Tx loop is located  $\sim 350$  m off the sheet, the profiles mark the edge quite precisely, resembling the EM37 examples in Figure 7.53a, or Z- and F-magnetic curves over faulted thin sections in Figure 3.23.

Figure 7.54d displays coincident-loop profiles over the edge of the same overburden. Slopes are not as steep as in Figure 7.54a, although they mark the boundary very well. The curve shapes are also different, lacking peaks and zero crossovers entirely.

Large-loop and coincident-loop curves over a vertical sheet conductor are shown in Figure 7.55. In Figure 7.55a the response is similar to that obtained over the edge of overburden, with steep crossover slopes, and the flanks fall away more rapidly than in

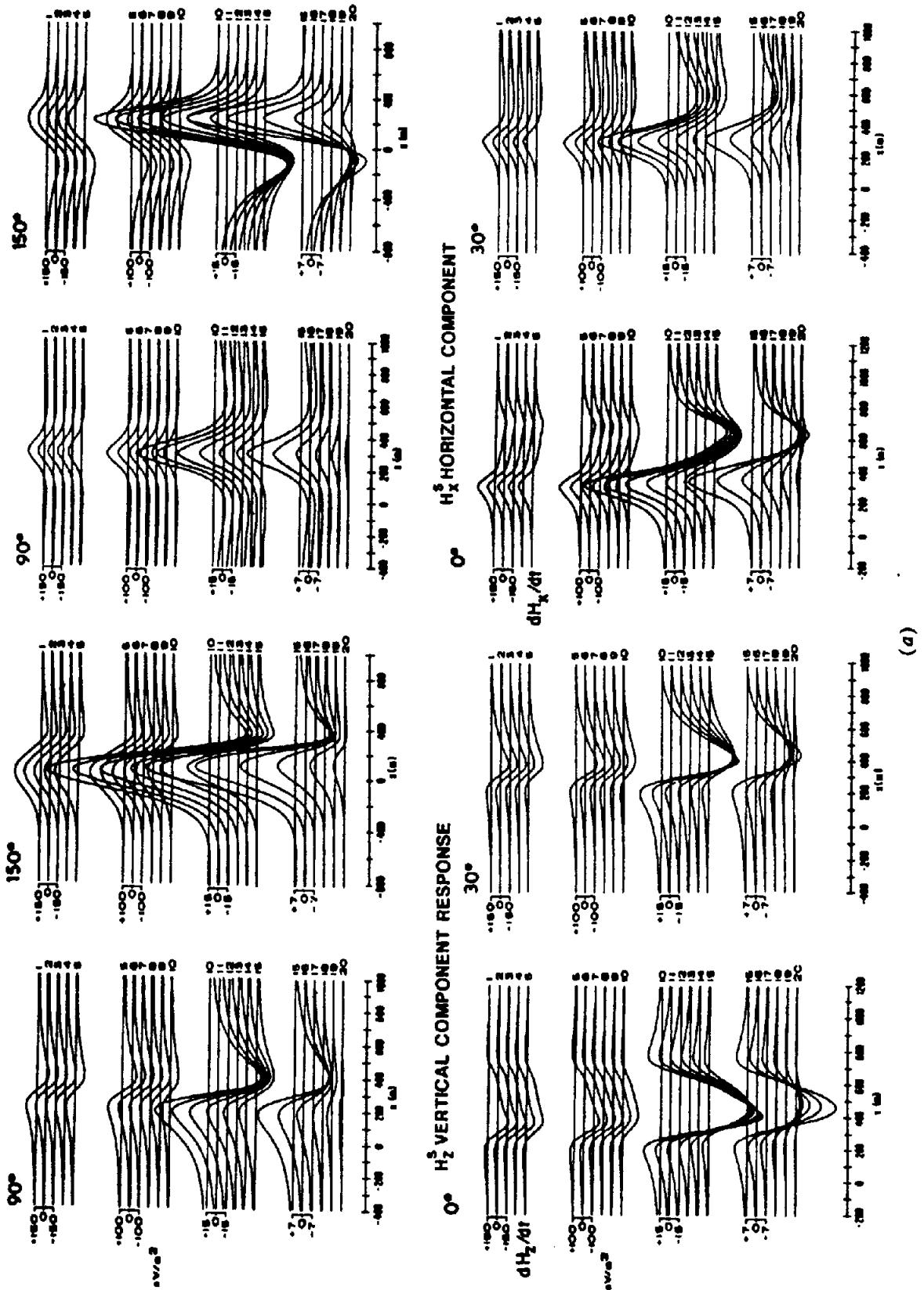


Figure 7.53. EM37 response over a plate model; curves show  $\partial H_x / \partial t$  and  $\partial H_z / \partial t$ .  $l' \times d = 800 \times 400$  m [except in (d) and (e)], TCP = 30 S [except in (c)]. (After Gallagher, Ward, and Hohmann, 1985.) (a) Effect of dip;  $z = -100$  m; left-hand half shows curves for  $H_x$ , right-hand half for  $H_z$ .

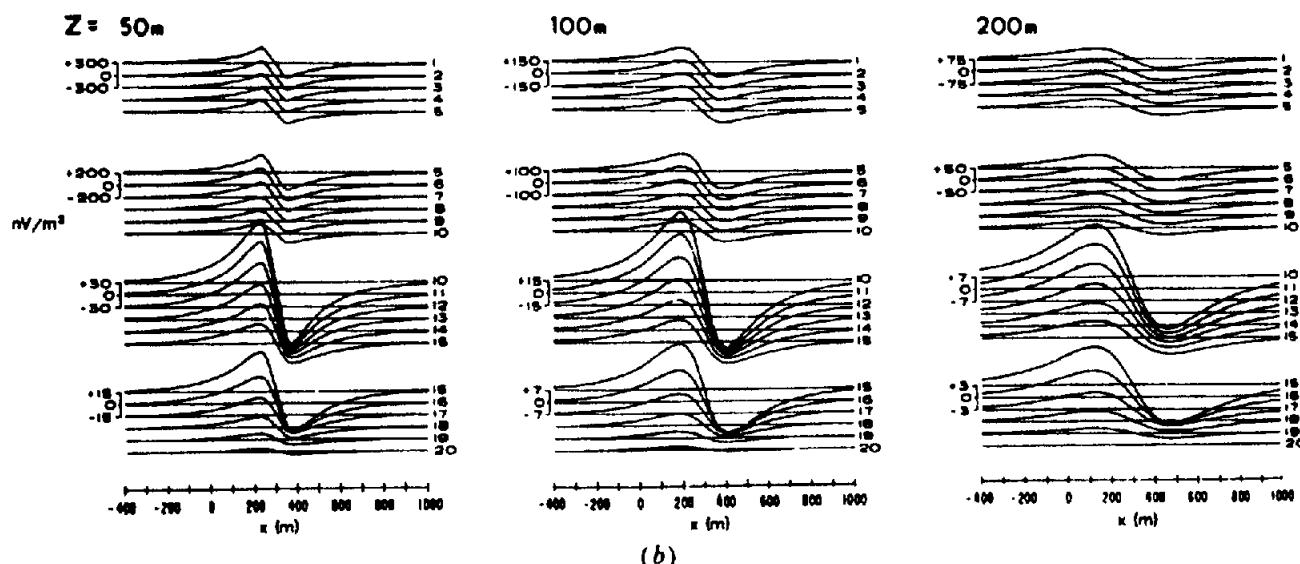


Figure 7.53. (Continued) (b) Variation in  $\partial H_x / \partial t$  with depth  $z$ ; dip =  $90^\circ$ .

Figure 7.54. The coincident-loop profiles, however, are quite different in Figure 7.55b.

From these examples it is clear that the coincident-loop TDEM system is superior to the Turam-type fixed transmitter in discriminating between two different model conductors. The vertical-sheet response in Figure 7.55a would be difficult to distinguish from that obtained at any large-loop location over the sheet (Fig. 7.54a); on the other hand there is no ambiguity between Figures 7.54d and 7.55b.

Further examples of distinctive coincident-loop response are given in the following figure. In Figure 7.56a, b the effect of a gap or resistive discontinuity in continuous overburden 60 m thick is shown for two positions of the Turam loop, whereas Figure 7.56c displays the SIROTEM(1) response; Figure 7.57 shows a set of curves for the same units over a vertical step that increases overburden thickness from 60 to 120 m. In both cases the coincident-loop response appears more realistic.

All the aforementioned anomalies are the result of current channeling, because the resistive underside of the overburden model produces a lateral diffusion of eddy currents away from the source. With the vertical-sheet model in a homogeneous ground the currents are able to move downward as well, to concentrate in the conductive sheet.

Field survey results from a fixed-loop system are illustrated in Figure 7.58. The section shows a thick overburden of 40 m with a step, from about 60 to 130 m left to right, which was thought to continue to a depth as a nearly vertical contact or shear. The latter feature is indicated by the dashed line. Two fixed-loop setups, one over the step, the other 350 m to the right, produced the profiles shown in the diagram. Those from loop A position are practically

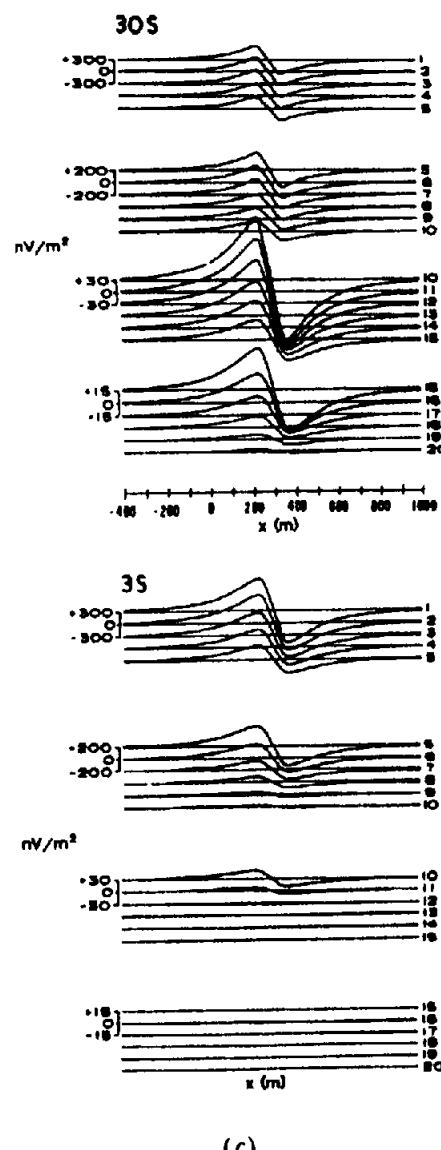
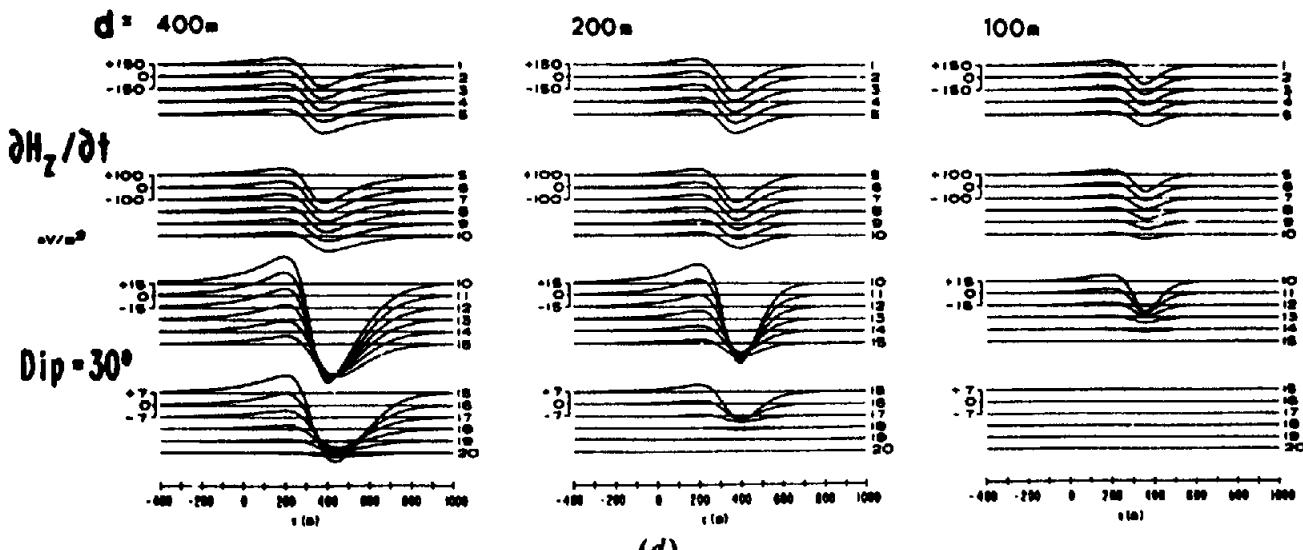
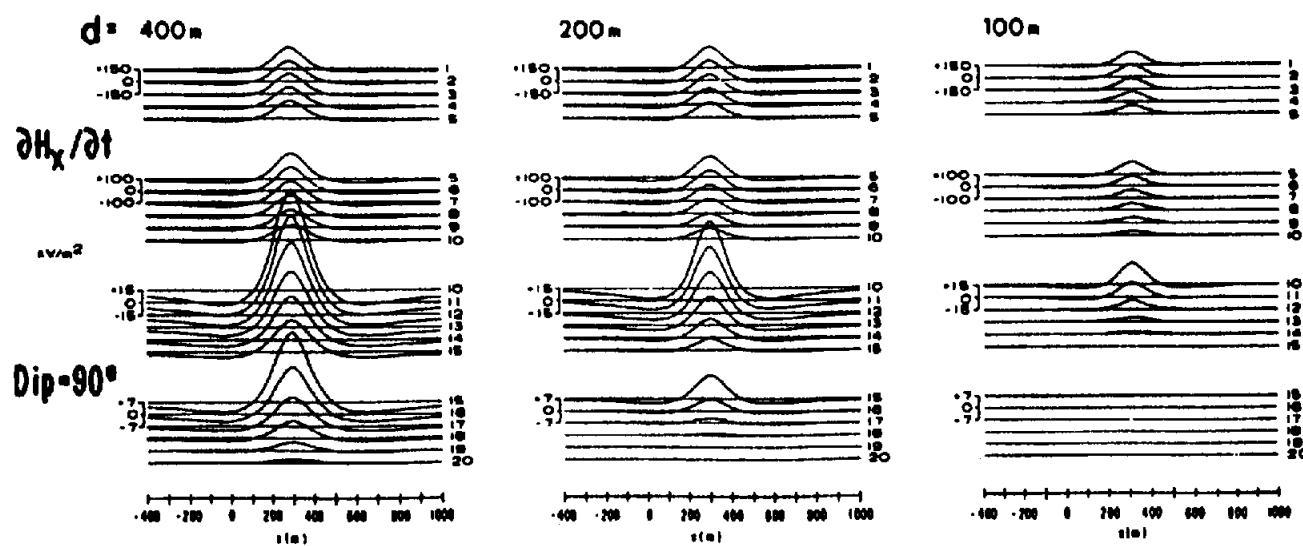


Figure 7.53. (Continued) (c) Variation in  $\partial H_x / \partial t$  with conductance;  $z = 50$  m, dip =  $90^\circ$ .



(d)



(e)

Figure 7.53. (Continued) (d) Effect of depth extent  $d$  on  $\partial H_z/\partial t$ ,  $z = 100 \text{ m}$ ,  $t = 800 \text{ m}$ , dip =  $30^\circ$ . (e) Same as (d) except for  $H_x$  and dip =  $90^\circ$ .

Table 7.3. Field layouts and data retrieval for TDEM ground systems.

Model	FDEM equiv.	Transmitter	Receiver	Measurement
PEM (1)	Slingram	Moving 6–15 m diam	Moving, small $Tx-Rx = 50\text{--}150 \text{ m}$	$H_x^s, H_y^s, 8 \text{ channels}$ $0.1\text{--}12.8 \text{ ms}^a$
	Turam	Fixed $100 \times 100 \text{ m}$	Moving, small $Tx-Rx = 50\text{--}350 \text{ m}$	Same as above
EM37	Turam	Fixed $300 \times 600 \text{ m}$	Moving, small <sup>b</sup> $Tx-Rx = 10\text{--}1,500 \text{ m}$	$H_x^s, H_y^s, H_z^s, 20 \text{ channels}$ $0.089\text{--}7.1 \text{ ms}^a$
EMP	Turam	Fixed $400 \times 800 \text{ m}$	Moving, small <sup>b</sup> $Tx-Rx = 10\text{--}1,500 \text{ m}$	$H_x^s, H_y^s, H_z^s, 28 \text{ channels}$ $1\text{--}75 \text{ ms}$
SIROTEM (1)	None	Moving 50 m, sq.	Moving, 50 m	$H_z^s, 32 \text{ channels}$ $0.25\text{--}150 \text{ ms}$
	Slingram	Moving 25 m diam	Coincident $Tx, Rx$ Moving, 25 m $Tx-Rx = 100 \text{ m}$	Same as above
UTEM	Turam	Fixed, $1 \times 2 \text{ km}$ Fixed, $300 \times 300 \text{ m}$	Moving, small $Tx-Rx = 2, 0.6 \text{ km}$	$H_x^s, H_y^s, H_z^s, E_{\text{hor}}^s$ $0.025\text{--}13 \text{ ms}, 10 \text{ channels}^a$

<sup>a</sup>Additional base frequencies available for channel range (§7.4.4c, e, f).

<sup>b</sup>Rx can be inside Tx loop.

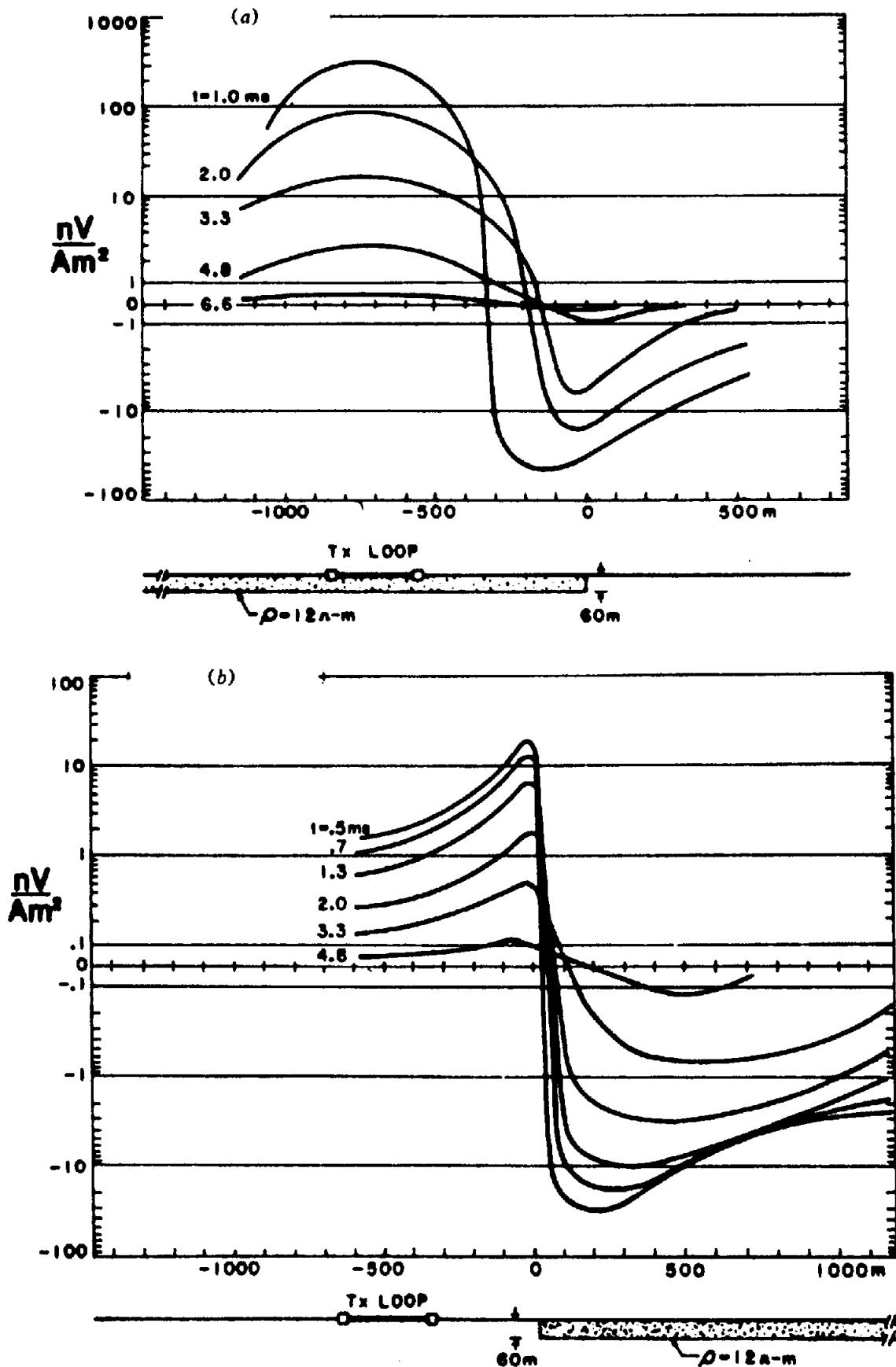


Figure 7.54. Comparison of responses of Turam-type (TDEM) and SIROTEM(1) over conductive overburden. Turam: Tx loop  $600 \times 300 \text{ m}$  in (a), (b), and (c). (After Spies and Parker, 1984.) (a) Tx on overburden  $\sim 550 \text{ m}$  from edge. (b) Tx offset  $\sim 350 \text{ m}$  from edge.

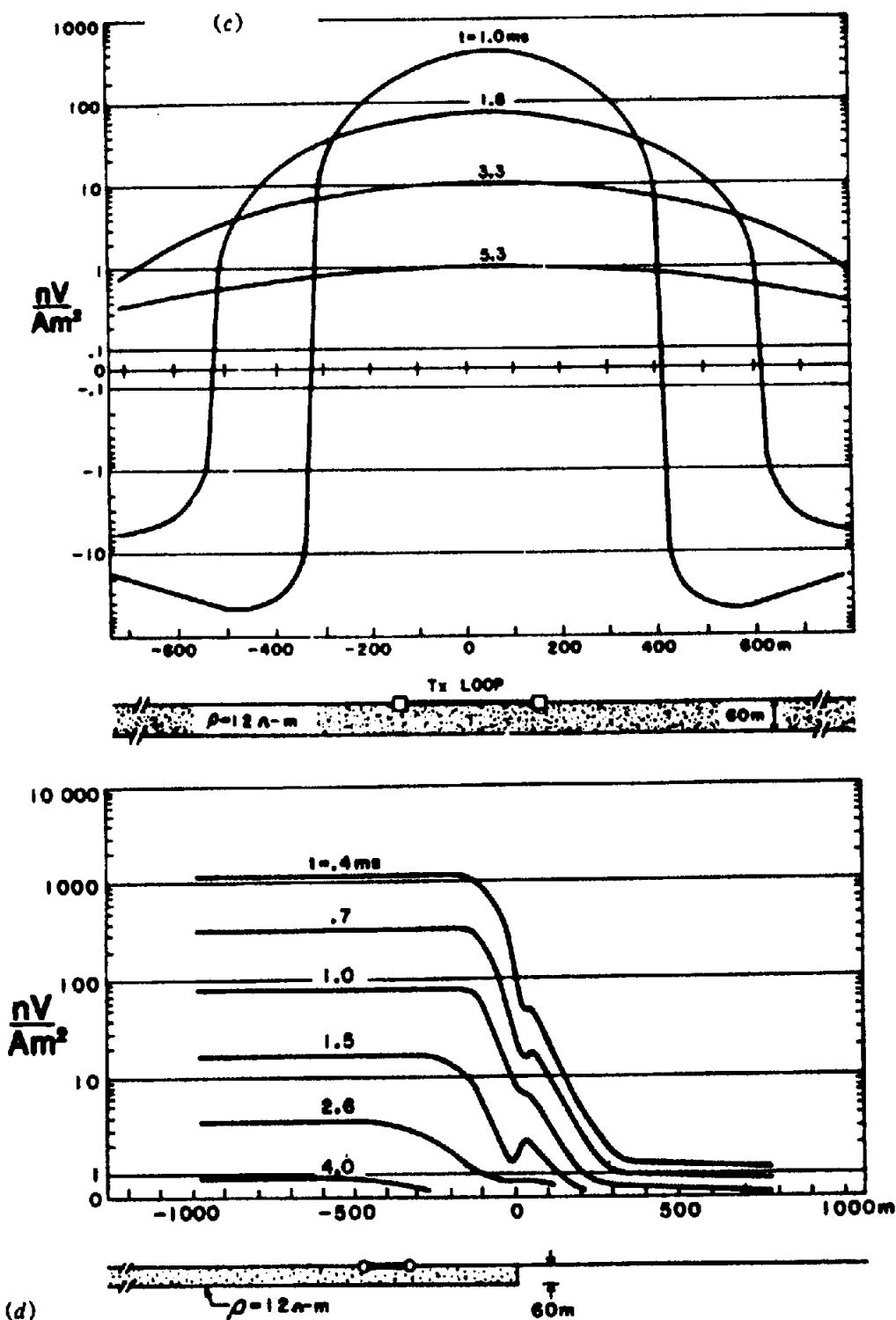


Figure 7.54. (Continued) (c) Tx on 1-D overburden. (d) SIROTEM(1) with 150 m diameter loop over overburden ~350 m from edge.

barren, whereas loop *B* gave a strong anomaly that resembles Figure 7.57c.

To explain the field data, the section was modeled using a conducting vertical sheet in contact with the overburden at the step. Three profile sets are seen in Figure 7.59, the first two for loop *A* and *B* positions and the last for a coincident-loop traverse. The fixed-loop models match the field profiles very well.

Figure 7.59c shows an entirely different response, as one would expect; the overburden step is reflected in all four decay curves, whereas the vertical plate anomaly increases at later time. Drilling subsequently located a mineralized shear zone under the overburden at the step.

Thus the Turam-type of TDEM field survey may give an incorrect indication in situations like those

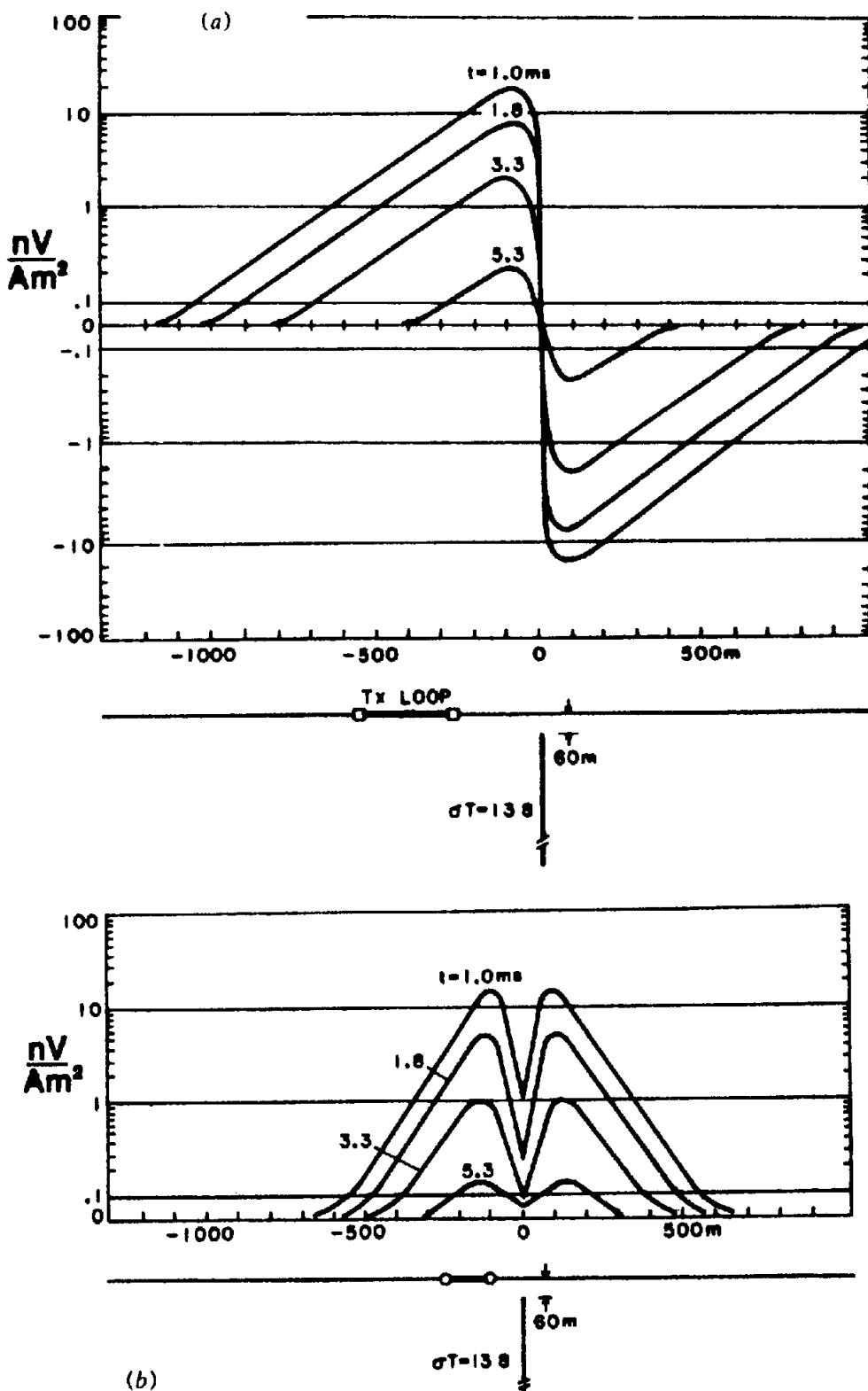


Figure 7.55. Large-loop Tx and coincident-loop responses over a vertical sheet. (After Spies and Parker, 1984.) (a) Large-loop Tx - 300 m from target. (b) Coincident-loop crossing sheet.

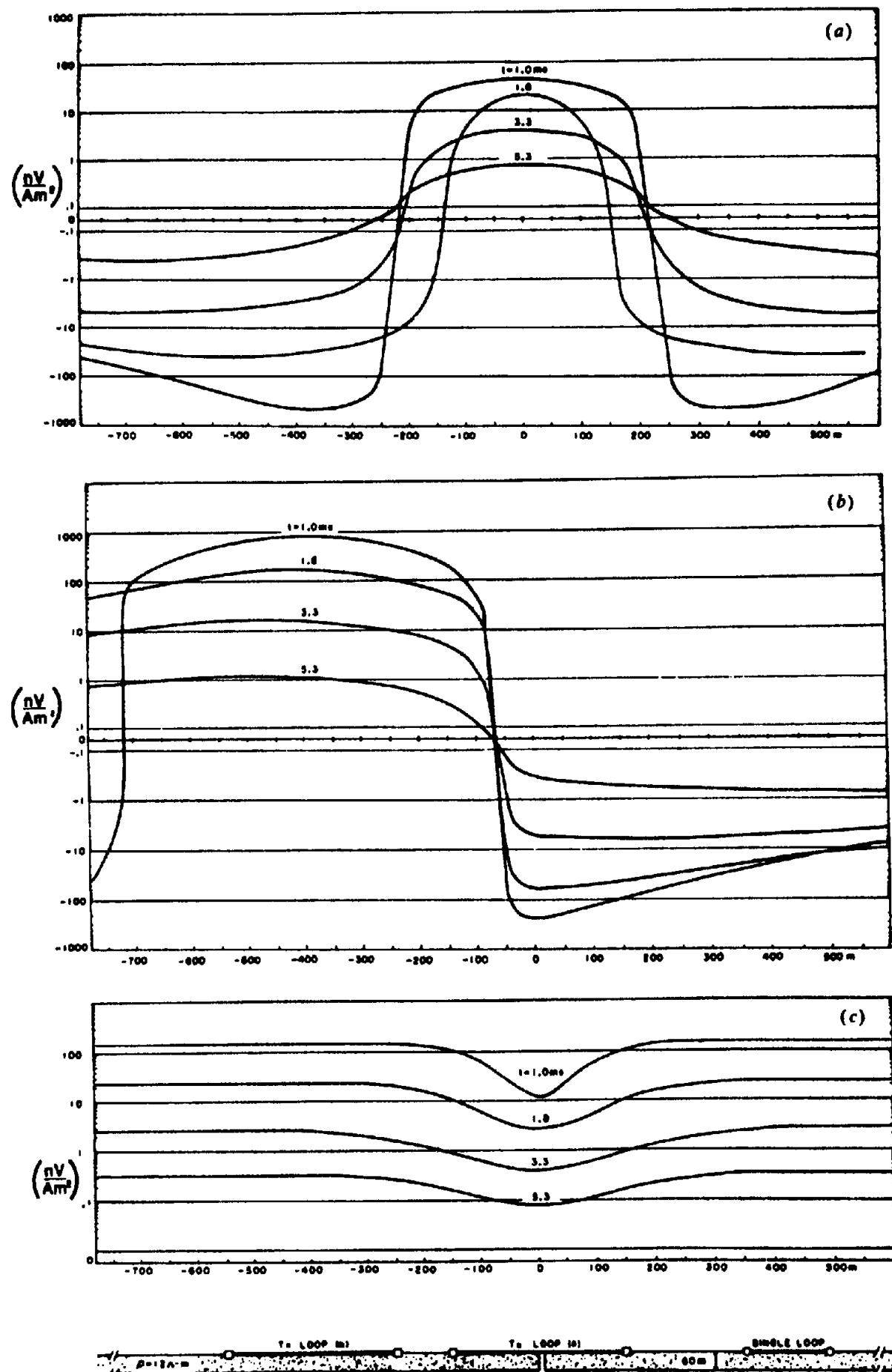
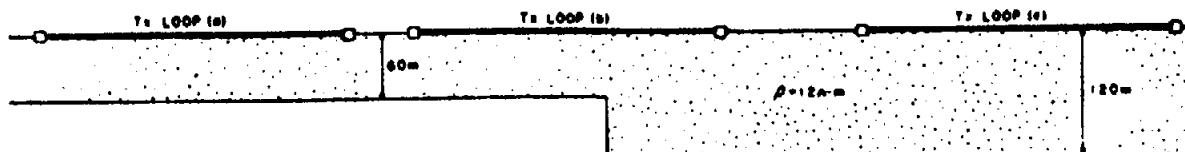
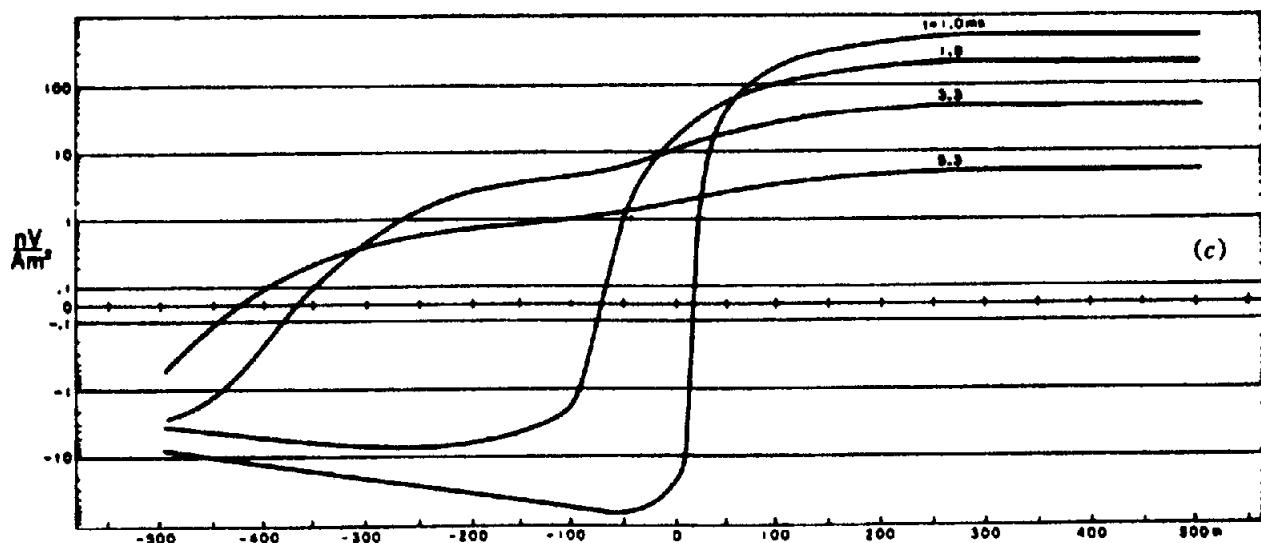
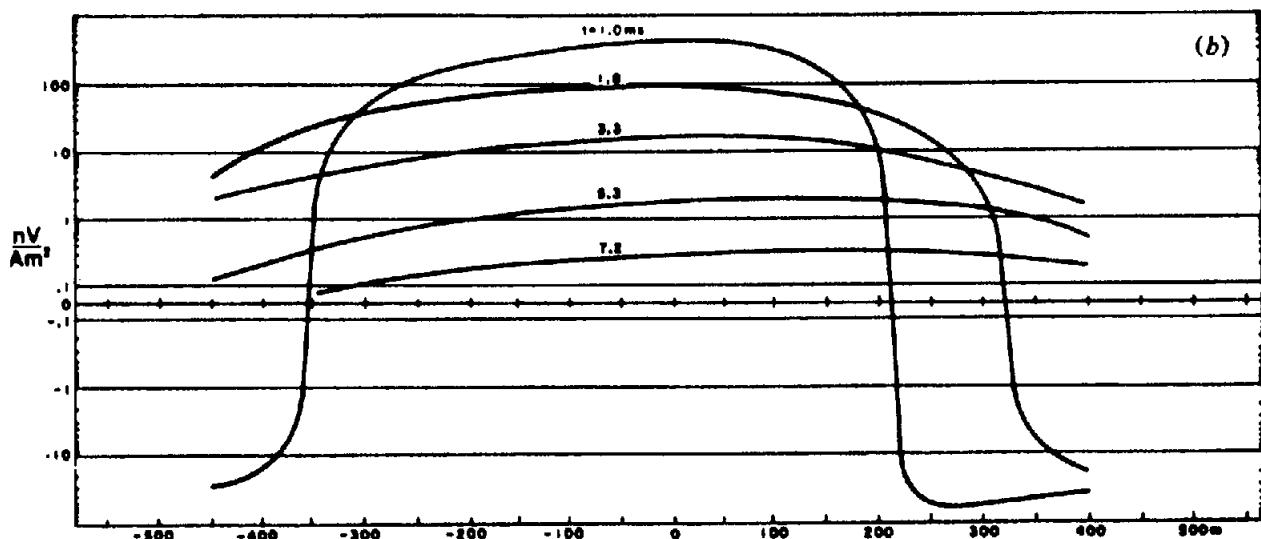
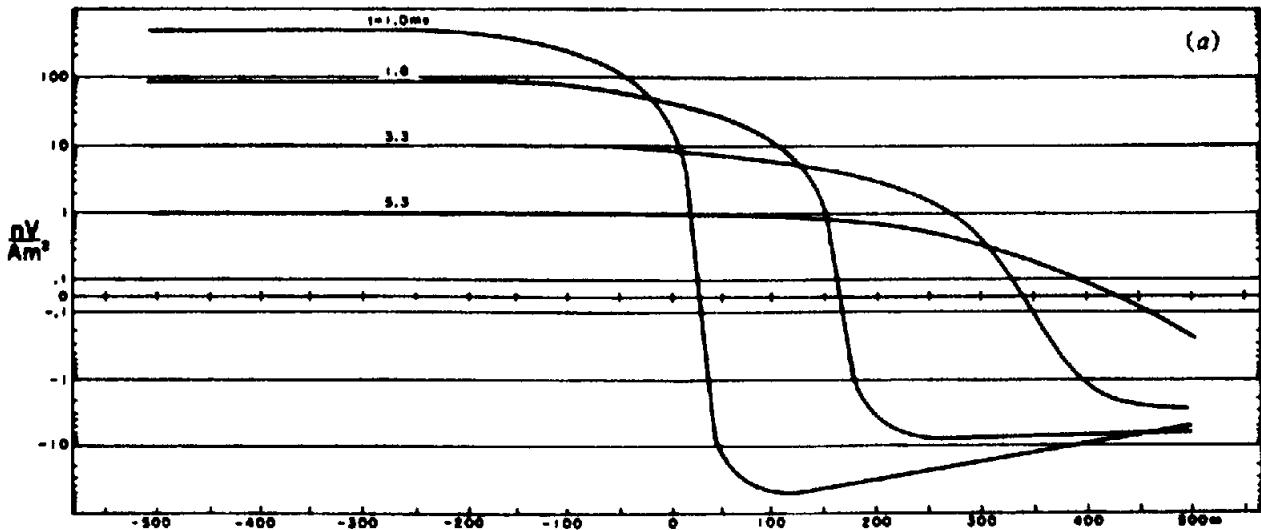


Figure 7.56. Turam and coincident-loop responses to a discontinuity in conductive overburden. (After Spies and Parker, 1984.) (a) Turam loop centered over the break. (b) Turam loop offset to left of break. (c) Coincident-loop traverse over the break.



**Figure 7.57.** Turam and coincident-loop responses to a step in conductive overburden. (After Spies and Parker, 1984.) (a) Turam Tx over 60 m section. (b) Tx centered over step. (c) Tx over 120 m section.

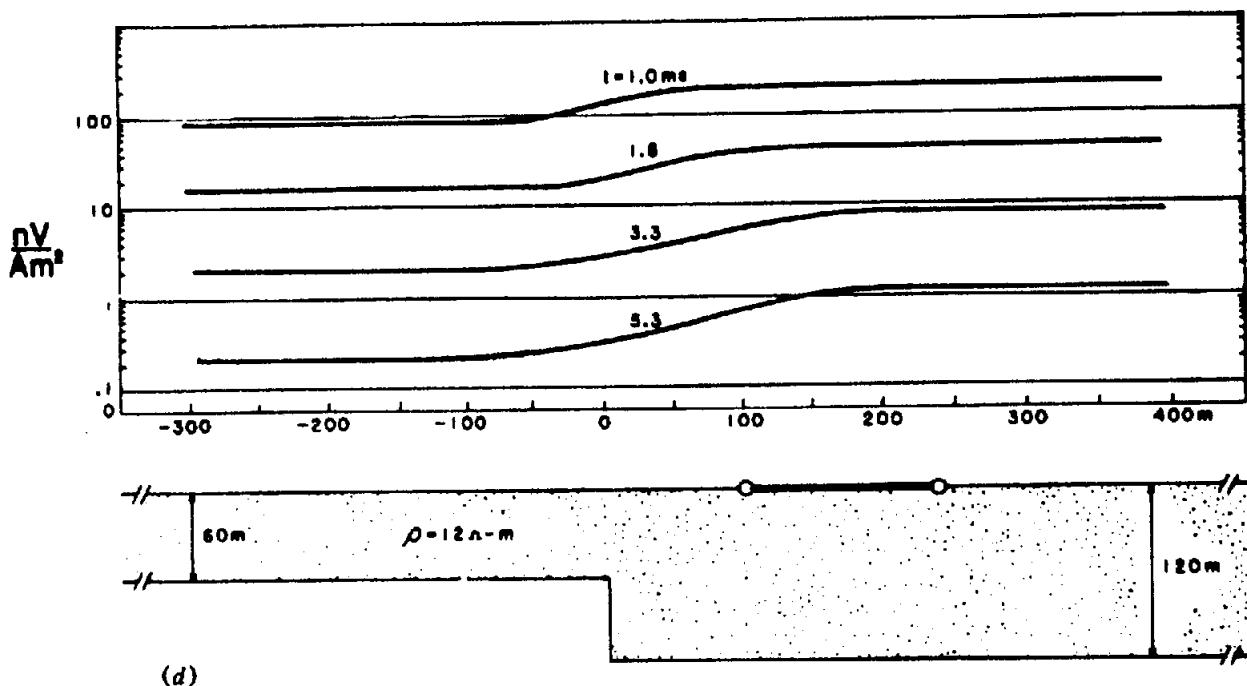


Figure 7.57. (Continued) (d) Coincident-loop traverse over step.

discussed, unless the  $T_x$  loop is relocated at least once and perhaps several times. This problem apparently does not arise with the coincident-loop system.

The latter system, however, is not the ideal array for all structures, specifically the familiar thin conductive sheet with steep dip. Consider the examples shown in Figure 7.60 from SIROTEM surveys in Australia. At each site both coincident- and twin-loop traverses were carried out. In Figure 7.60a the outcropping gossan containing pyrite at 320W produces a large anomaly on a half-dozen early-time channels of the twin-loop unit. Coincident-loop response in channels 10 to 14 in this vicinity is similar to Figure 7.55b. At the buried contact ( $\sim 100$  m) between graphitic siltstone and albitalite at 850W, the anomaly is clear on channels 2 to 13 of the coincident loop, but only on the first three of the twin loop.

A better example is found in Figure 7.60b. Ore in the form of a vertical sheet at about 120 m depth is well defined by twin-loop equipment on all six channels, poorly on the coincident-loop profiles.

Thus the coincident-loop system gives poor definition over steeply dipping sheets because of the wide double hump in the response. With such structures it is preferable to employ the twin-loop survey. For thin conductors of shallow dip, however, it appears to be superior to other TDEM systems.

(e) UTEM. The field layout and operation of this set is similar to the EM37, EMP, and PEM(2) units, because all employ a large Turam-type  $T_x$  loop usually located a few hundred meters off the target.

UTEM differs from the others in detail, particularly in regard to the continuous sawtooth transmitter waveform and in the capability of measuring the horizontal  $E$  field (generally  $E_y$ ) in addition to three  $H$  components.

Type curves for the sheet conductor, developed from the PLATE model, may be found in West, Macnae, and Lamontagne (1984). Field geometry of the system is seen in Figure 7.61a, together with a section showing sheets at various dip angles and the primary field vectors in their vicinity. This section indicates the location of the extinction angle (§7.7.3g) around 150 to 165° and the effect of sheet depth extent on the secondary response.

UTEM field readings, as in other TDEM methods, are normalized for plotting by dividing by the  $H_t^P$  field at each station. This procedure yields profiles that have the same general shape as those for EM37 (Fig. 7.53), but differ in relative amplitudes on the flanks and peaks; this is clear in comparing UTEM  $H_z$  and  $H_x$  profiles over a horizontal sheet (Fig. 7.61b) with the EM37 equivalents in Figure 7.53a. The  $H_z$  curves are quite symmetrical in both cases, but the positive overshoot, slightly larger in Figure 7.53a on the left, is clearly greater to the right in Figure 7.61b. Similarly the asymmetric shape for the  $H_x$  profiles has the peak amplitudes reversed from left to right. This is due to the normalization of the UTEM plots ( $H^P$  decreases with distance from the  $T_x$  loop).

Profiles of  $H_z^P$  over several model shapes are illustrated in Figure 7.62. Only early- and late-time response for each are shown, because changes over intermediate channels are smooth, as is apparent

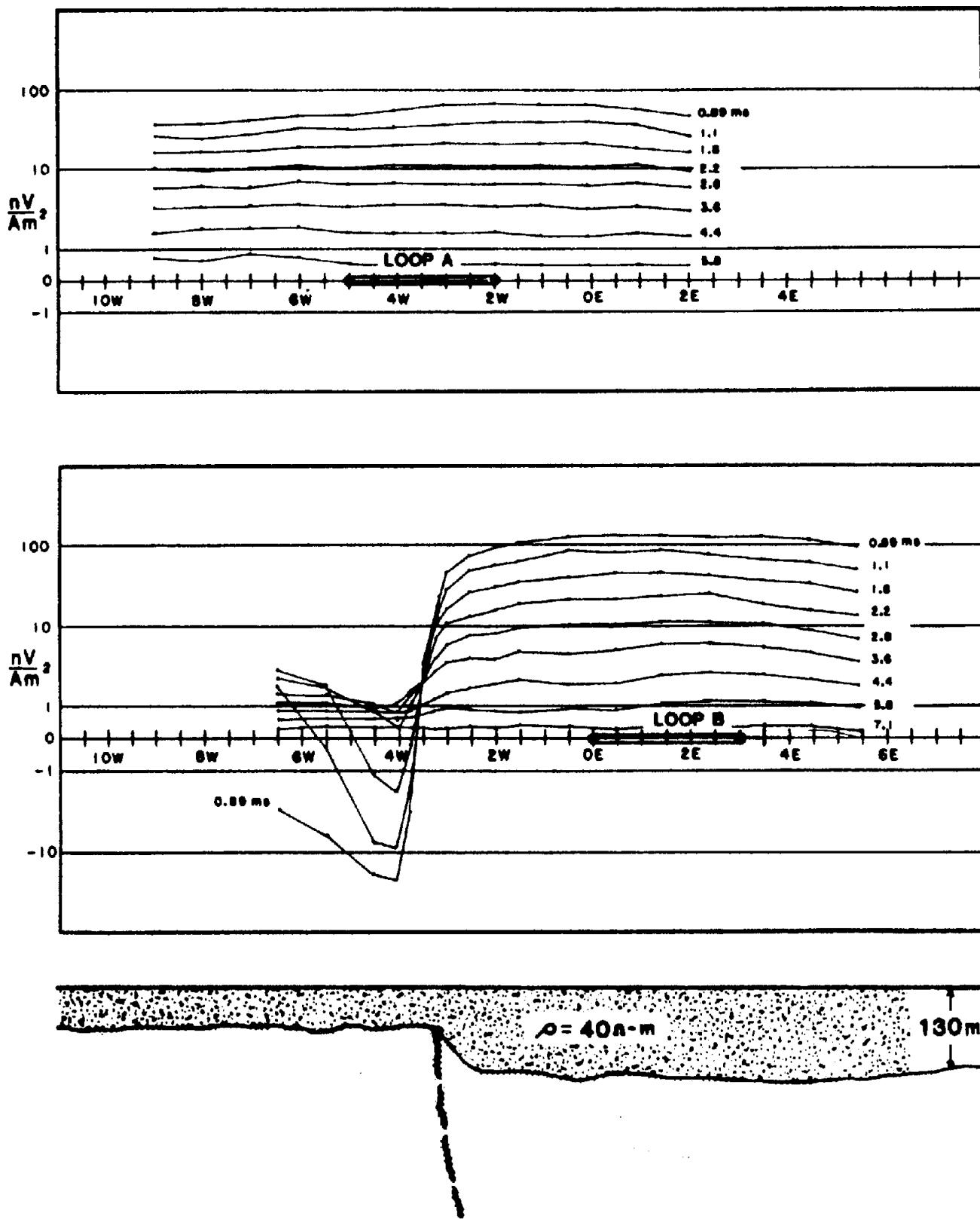


Figure 7.58. Field traverses obtained with a fixed-loop system for two different transmitter-loop positions. The strong anomaly recorded with loop B disappeared when loop A was used. (After Spies and Parker, 1984.)

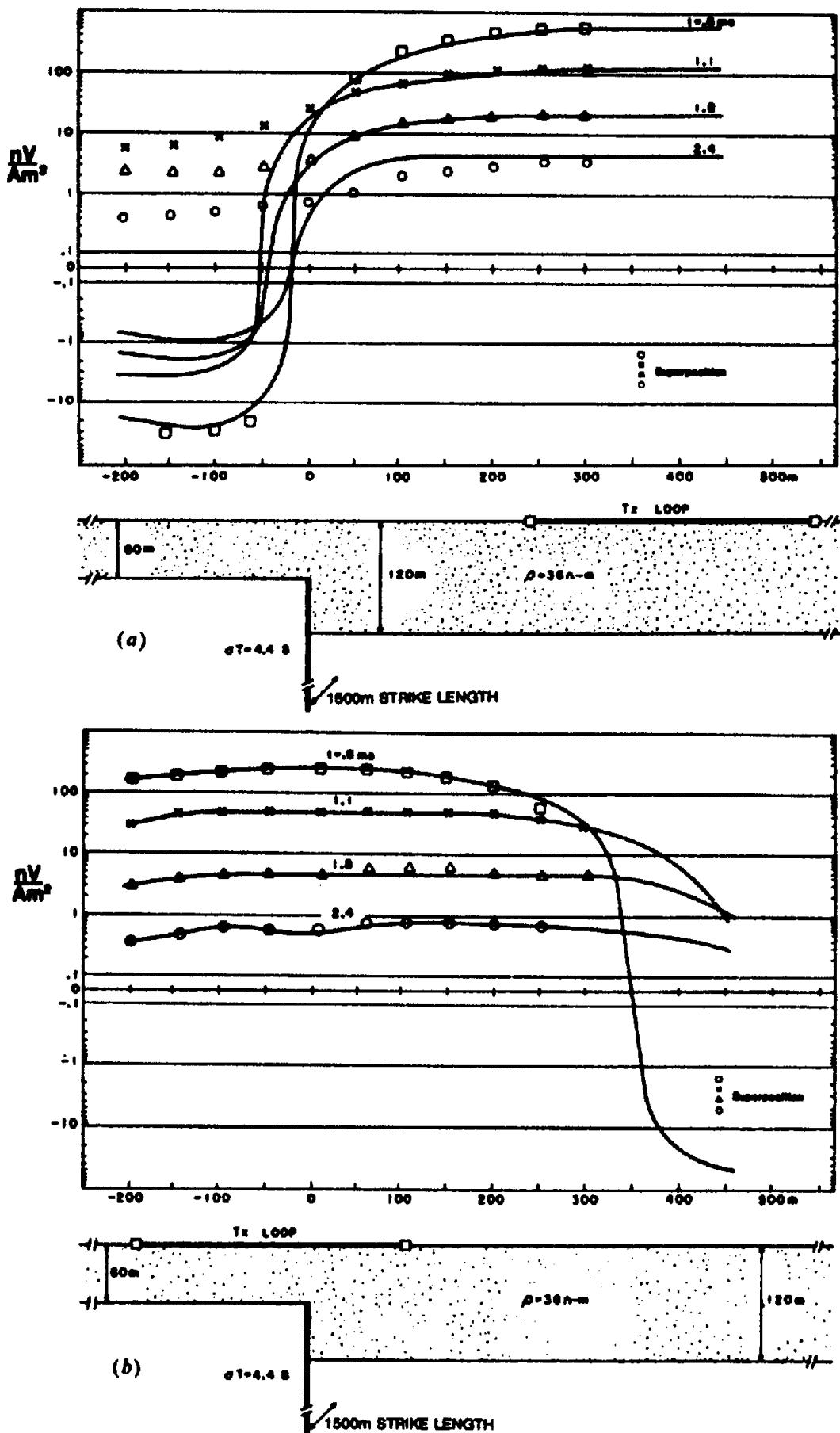


Figure 7.59. Comparison of fixed-loop and coincident loop results over a model consisting of a semiinfinite vertical-sheet conductor in contact with conducting overburden at a step in the latter. (After Spies and Parker, 1984.) (a) Fixed-loop system with Tx loop located several hundred meters from the step. (b) As in (a) except that the Tx loop straddles the step.

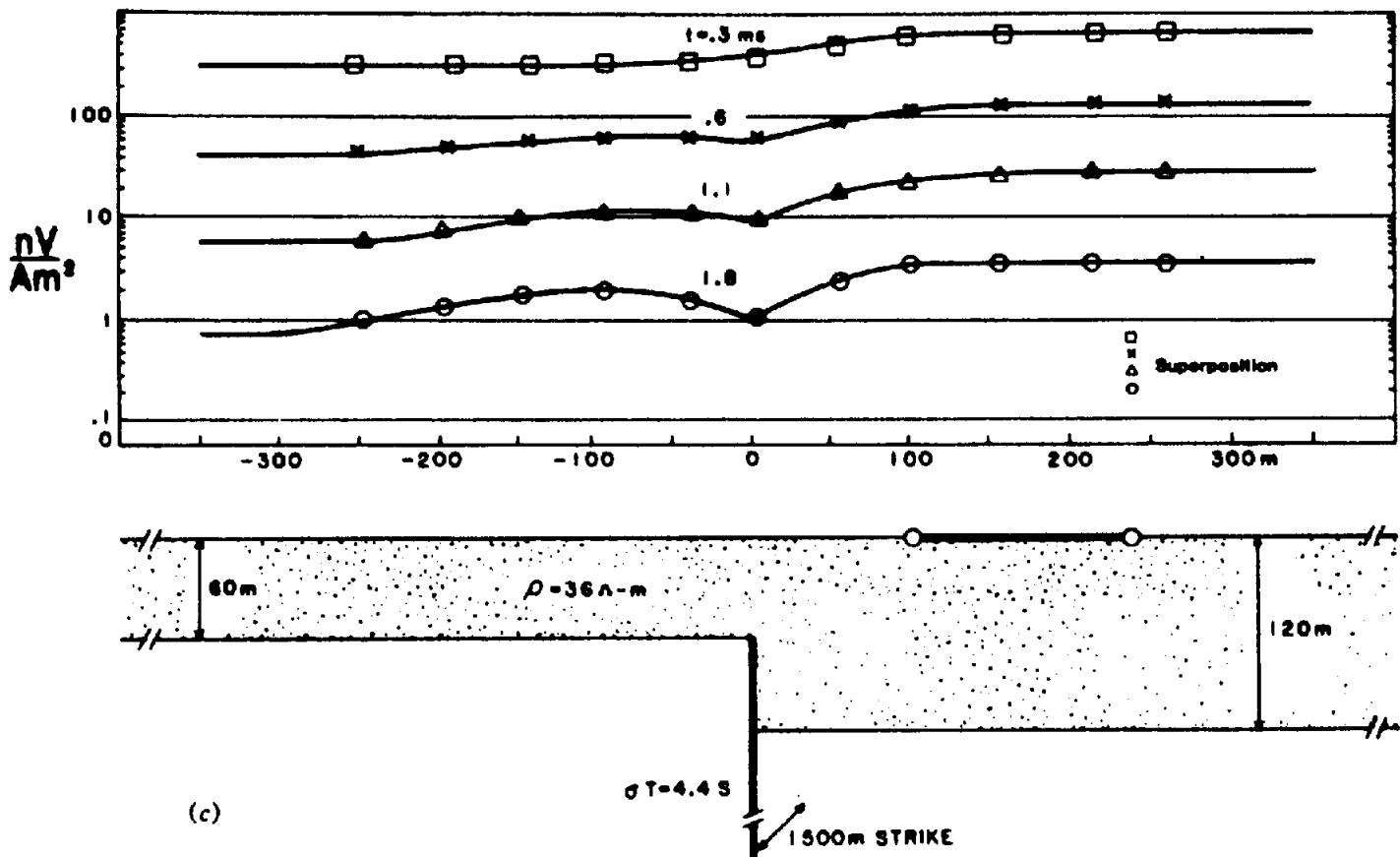


Figure 7.59. (Continued) (c) Coincident-loop traverse across the step.

from previous examples. In all models except (e) the transmitter loop (not shown) is offset left.

The thin conductive sheet of steep dip in model (a) produces a type of profile familiar in dip-angle FDEM, with nearly equal positive and negative peaks and a crossover, which, at early time, marks the top edge. In later time channels, amplitude decreases and the crossover slides downdip. A fair depth estimate is found at early time from half the horizontal distance between peaks; this estimate deteriorates as the profile becomes broader with decay time.

Response from the horizontal sheet in model (b) is a symmetrical curve with a low over the middle and positive flanks near the edges. At later time the curve shrinks as the flanks move inward. The example is similar to Figure 7.61b. The vertical block conductor in (c) has the same general symmetry as (b), although the center response is stronger and the positive shoulders reduced. Depth may be roughly indicated at early time from the horizontal projection of the steep slopes near the block edge.

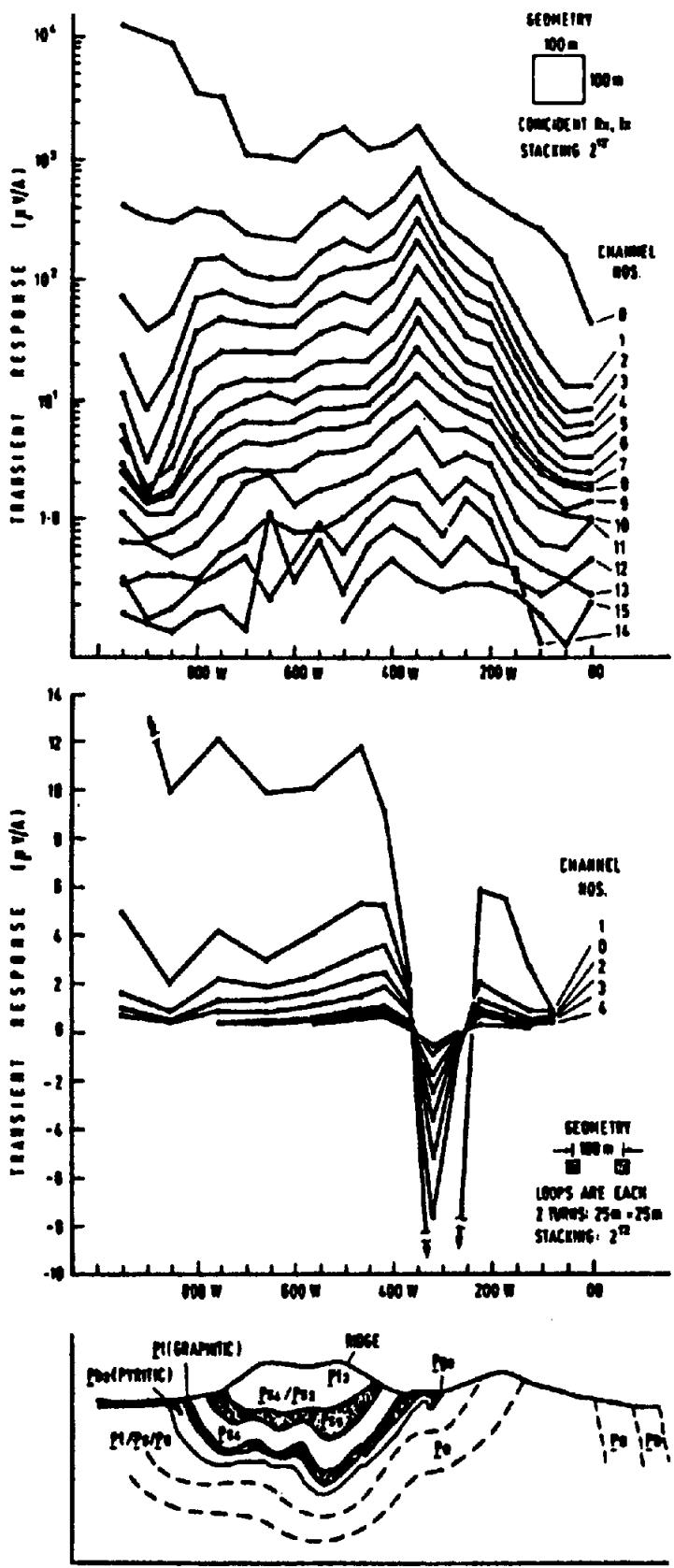
In model (a) eddy currents are concentrated mainly on the steep sides, whereas in (c) they are on the top face of the conductor. The dike in model (d) may support both current patterns; the top face

affects mainly the early time, whereas response from the vertical sides comes on later (particularly if the depth extent is appreciable), hence the different shapes of the early- and late-time profiles of model (d).

The 1-D shallow conducting layer in model (e) produces curves that are a slice of those in Figure 7.54c, that is, they are controlled by the Tx loop, not the model.

Effects of conductive overburden and current channeling are illustrated in Figure 7.63 with a vertical sheet-conductor model. When the overburden lies over the sheet in part (c), response is almost entirely from the overburden at early time, indicated by the curve labeled 8 on the left of part (c), which is almost identical to 8 in part (d) for overburden alone (recall UTEM channels are numbered in reverse order from other TEM equipment). This is because the "smoke rings" have not yet escaped from the overburden. At later time, channels 6 through 1, they have penetrated to the vertical sheet, when the response becomes more or less that of Figure 7.63a.

If the vertical conductor makes galvanic contact with the overburden, as in Figure 7.63b, the curves reflect the sheet through all channels, starting with



- (a)
- $\text{Pb}$  - ALBITELITE
  - $\text{Pb}$  - BOSSAN. SUBSURFACE IT CHARGES TO } CONDUCTIVE
  - $\text{Pb}$  WHICH CONTAINS PYRITE }
  - $\text{Pb}$  - GRAPHITE SCHIST } CONDUCTIVE
  - $\text{PbS}$  - CHIASTOLITE SCHIST }
  - $\text{AS}$  - ANDALUSITE SCHIST (OCCURS IN PATCHES)
  - $\text{QMS}$  - QUARTZ MUSCOWITE SCHIST (PREDOMINANT LITHOLOGY ON RIDGE)

Figure 7.60. Comparison of coincident-loop and separate Tx-Rx loop systems. (After Buselli and O'Neill, 1977.) (a) Traverse over the Mt. Bulga mineralization, New South Wales.

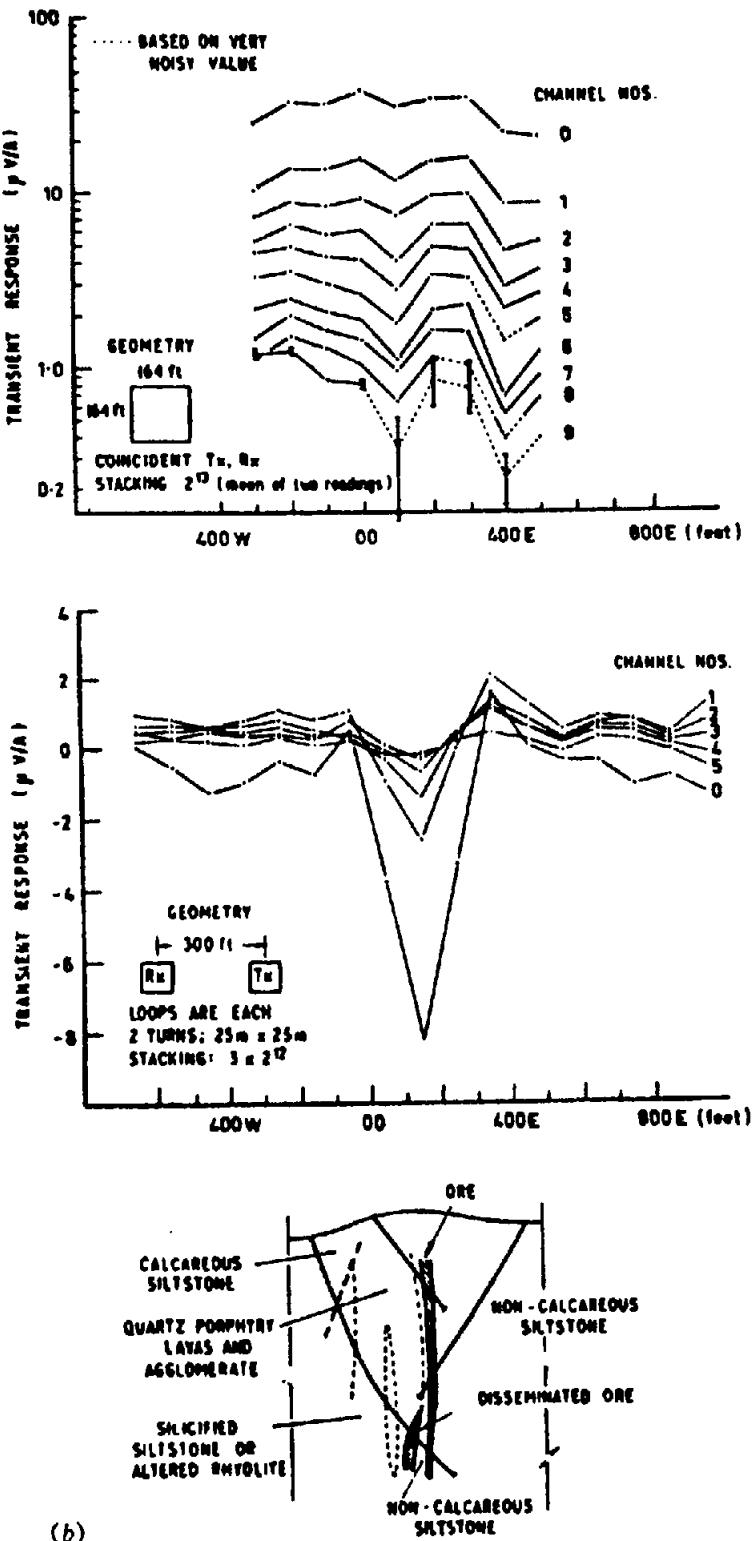


Figure 7.60. (Continued) (b) Traverse over a prospect in the Willyama Complex, South Australia.

enhanced response at early time and decreasing later to levels about the same as those in (a) and (c) on the left. This signal behavior is caused by current channeling.

These effects are further clarified in Figure 7.64, which shows the various data from Figure 7.63 in the form of decay curves over the complete channel

range. The left-hand plot indicates the signal enhancement caused by current channeling, when overburden eddy currents pass immediately into the more conductive dike; the right-hand plot illustrates the blanking or suppression of the dike signal when a resistive gap exists between the two. Both features take place at early time. When the same sheet is

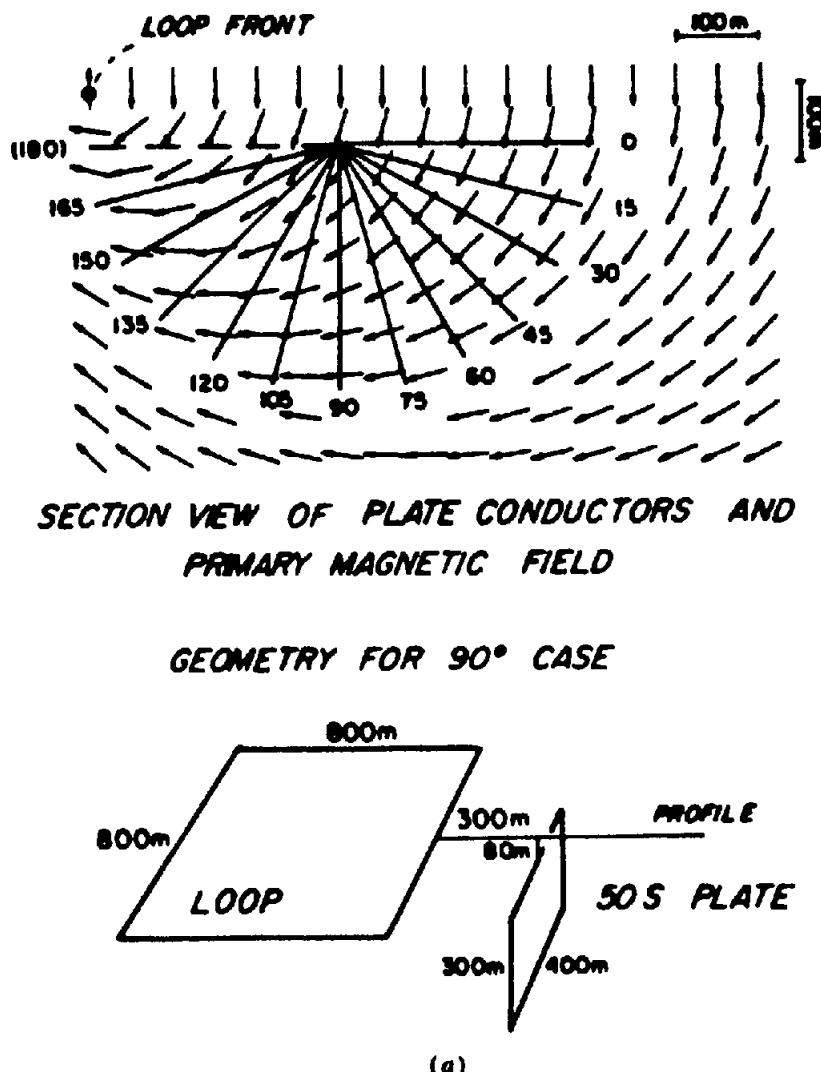


Figure 7.61. UTEM profiles over a dipping-plate model. (After West, Macnae, and Lamontagne, 1984.) (a) Geometry and dimensions of the model, and configuration of the primary field in the vicinity of the conductive plate.

contained in conductive host rock, both of the preceding effects are also evident, although at different times. Blanking again occurs at early time; gathering takes place later after an elapsed time, which varies with host rock conductivity.

An example of electric-field response, measured over a vertical plate with a Tx loop of  $1 \times 1$  km, is shown in Figure 7.65; the  $H_z'$  profiles are included for comparison. Because the  $E$ -field solution is difficult by numerical methods (§6.2.7), data were obtained by scale modeling. The  $E$ , curves are not useful. They do not locate the target, which is well marked by the crossovers in the  $H_z$  curves; they are also said to be highly susceptible to conductive overburden.

(f) Resolution of multiple conductors. Resolving power of TDEM systems has not been reported to any extent in the literature. Because four of the units listed in Table 7.3 are like Turam in geometry, one

would expect their discrimination to be much the same as that of FDEM Turam. Nor do the Slingram-type sets appear to be superior to their FDEM versions. Without any solid evidence, one may surmise that high resolution is not a great advantage of time-domain surveys.

(g) Characteristic curves. Several of these are available for rapid estimates of depth, dip, and conductance of sheet models. Gallagher, Ward, and Hohmann (1985) used the EM37 profiles of a plate conductor  $800 \times 400$  m, of variable dip and depth, to prepare early- and late-time nomograms. These are based on the ratio of small-to-large profile peaks and are shown in Figure 7.66a. From the dipping-sheet curves of Figure 7.53a it is apparent that the ratios are less than unity for all dips except  $90^\circ$ . The fact that the small peak decays faster than the larger one, producing early-time ratios larger than late-time, makes it necessary to plot two sets.

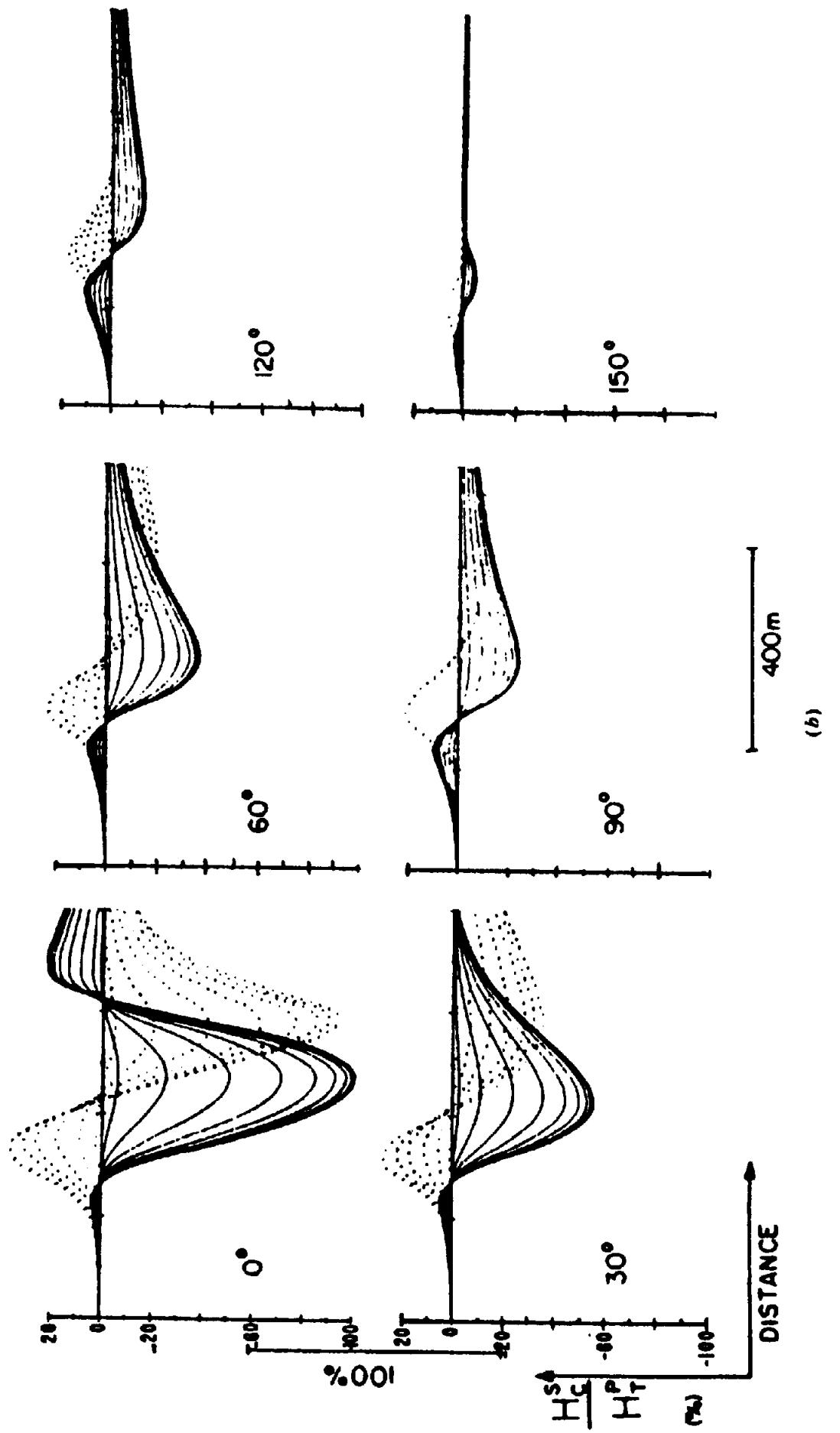


Figure 7.61. (Continued) (b) Profiles of  $H_z$  (solid) and  $H_x$  (dotted) as a function of dip.

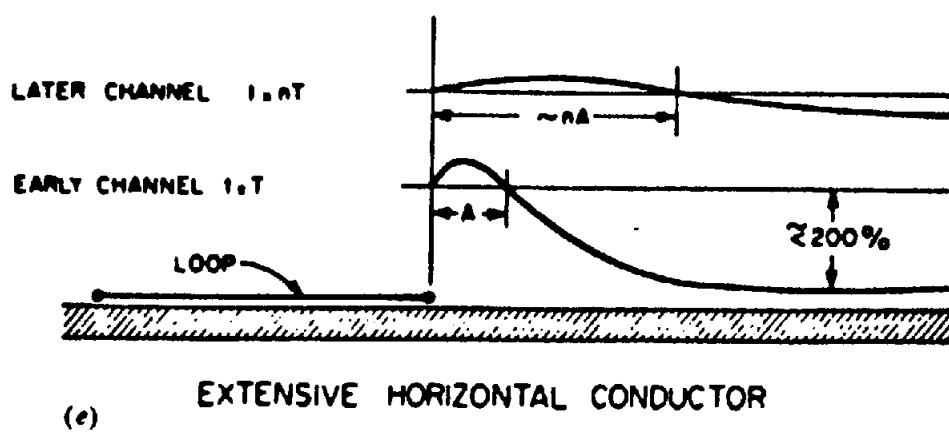
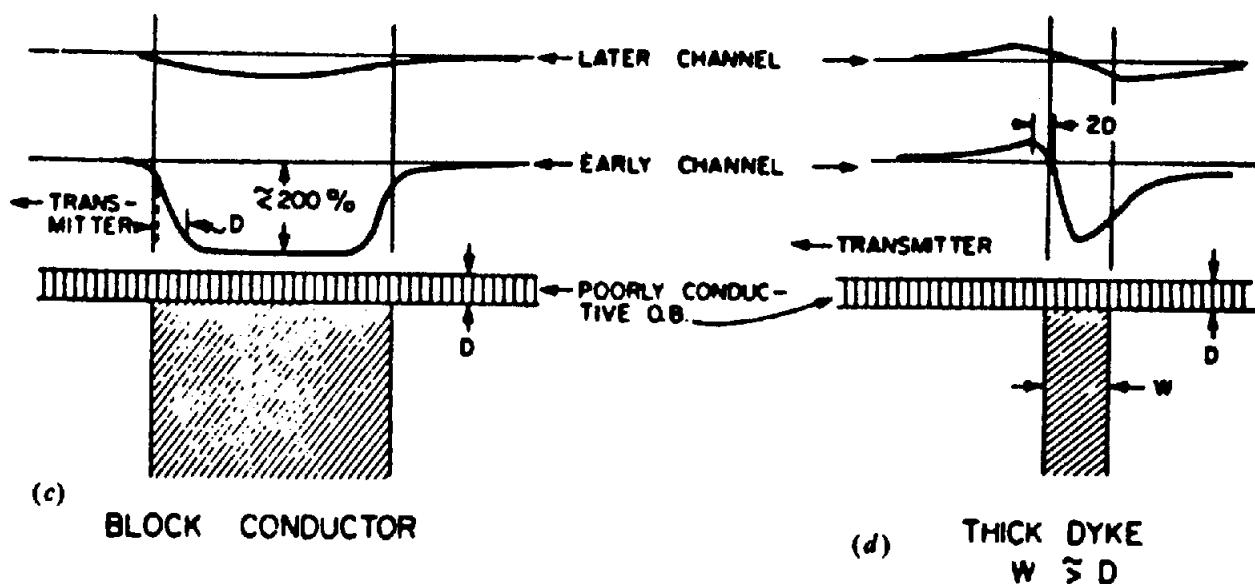
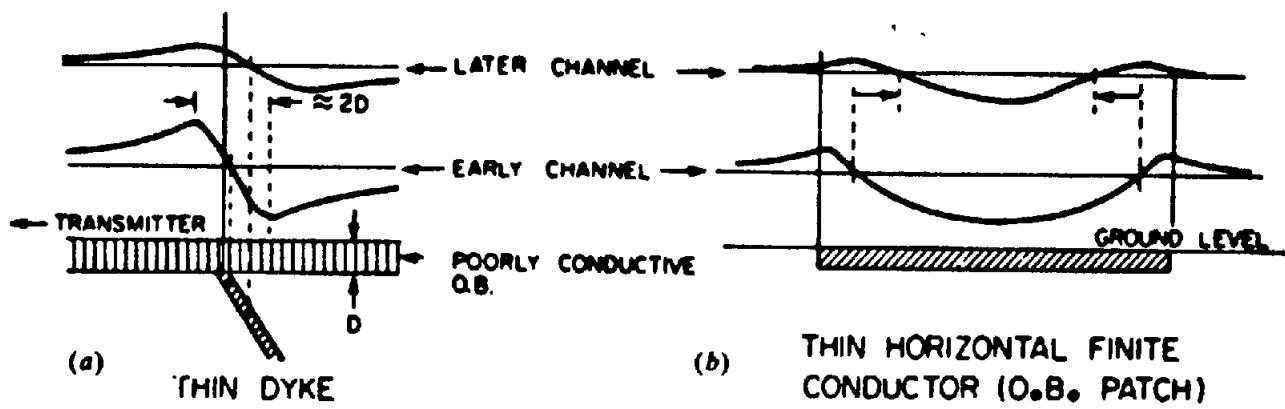
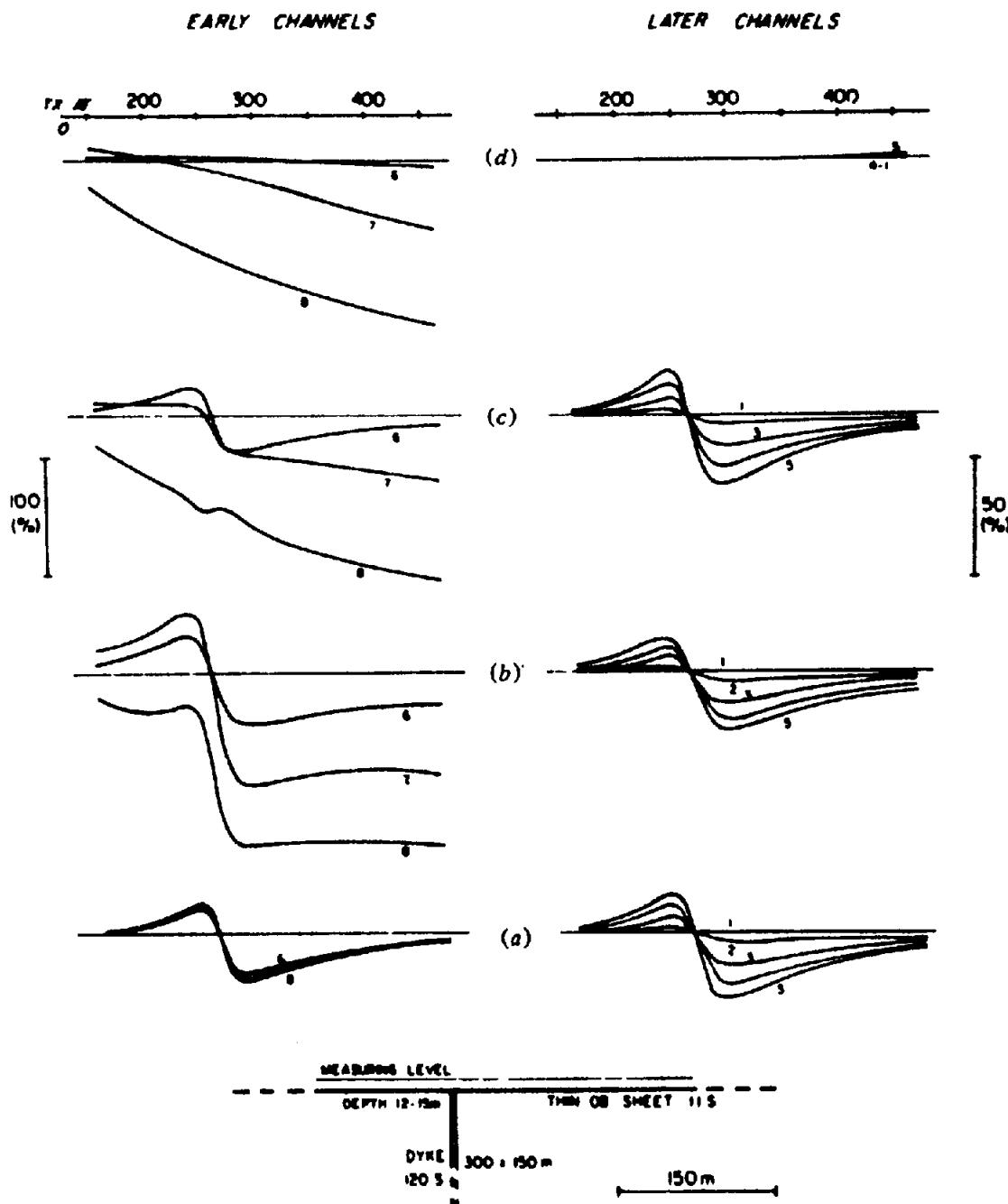


Figure 7.62. The form of continuously normalized UTEM  $H_z^s$  profiles over some simple shapes. All conductors are in free space. (After West, Macnae, and Lamontagne, 1984.)



**Figure 7.63.** Model UTEM  $H_z^s$  profiles over a vertical conductive sheet under a thin conductive overburden. (After West, Macnae, and Lamontagne, 1984.) (a) Effect of sheet alone. (b) Sheet in contact with the overburden. (c) Sheet not in contact with overburden. (d) Overburden alone.

Because it is possible to determine the direction ( $> 90^\circ$ ,  $< 90^\circ$ ) and approximate dips from the original profiles, it is only necessary to enter the two boxes in Figure 7.66a along the same peak-ratio lines and obtain from the vertical and horizontal axes of each box the depth and dip values that agree best.

A similar nomogram for PEM(1) data is given by Bartel and Hohmann (1985). It was noted in the discussion of dip (Fig. 7.50a) that the negative side lobe over the conductor was larger than the negative lobe off the edge. Ratio of the areas of these two

lobes is the variable in this case, with dip and ratio of depth to  $T-R$  separation as vertical and horizontal axes. The plot is shown in Figure 7.66b. Here an independent depth estimate is first found from the size of the positive peak at the updip edge of the sheet, seen in Figure 7.50b. When this peak is appreciable, which is so for  $z = 50, 75$  m, and marginally so for  $z = 100$  m, the horizontal scale ratio  $z/l \leq 1$ , that is, the depth is less than the coil separation. Having established these preliminary estimates, we proceed as for Figure 7.66a.

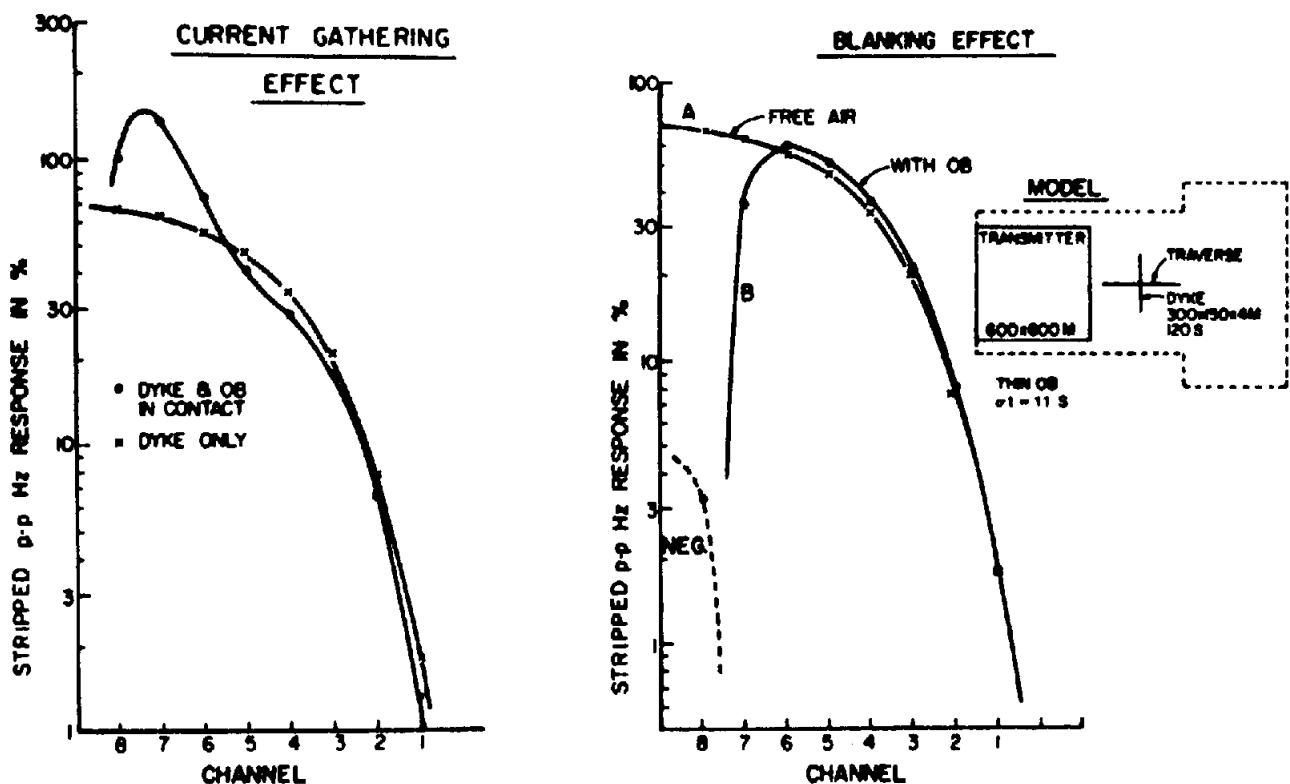


Figure 7.64. Decay plots for the  $H_x^s$  anomalies of Figure 7.63. (After West, Macnae, and Lamontagne, 1984.)

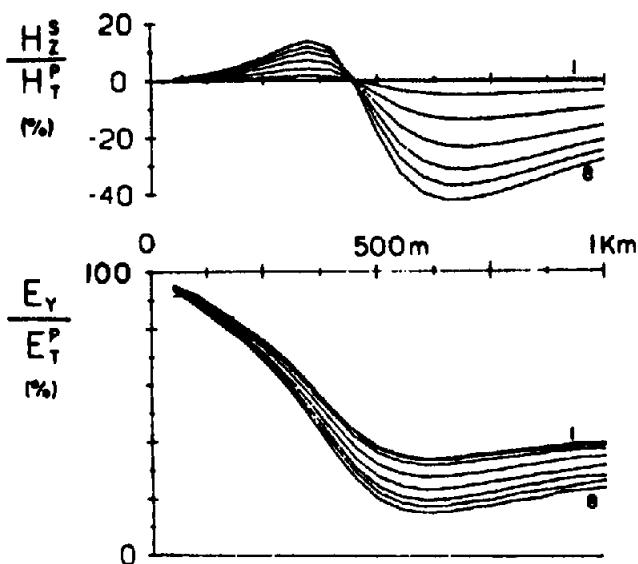


Figure 7.65. Model UTEM magnetic ( $H_x$ ) and electric ( $E_x$ ) responses over a vertical-plate conductor along the  $x$  axis. Tx loop = 1 × 1 km, conductor = 1 × 0.5 km, Tx 450 m to right of plate,  $z$  = 110 m, TCP = 20 S. (After West, Macnae, and Lamontagne, 1984.)

Depth estimates may also be made with data from EM37 and similar systems, using the horizontal distance between peaks and horizontal width at two-thirds of the positive peak, as discussed earlier. A depth nomogram from the latter measurement is displayed in Figure 7.66c for sheets dipping 60 and 90°.

Two conductance nomograms are shown in Figure 7.67. Both are based on signal decay rate, which varies inversely (roughly) with  $\sigma t$  as discussed in Section 7.7.4c. The plot in Figure 7.67a uses response ratios in successive channels of the PEM(1) unit, whereas figure 7.67b is obtained from EM37 decay curves for specific  $\sigma t$  models.

The response parameter, discussed in Section 7.7.3i in connection with frequency-domain characteristic curves, has an analog in time domain. For example, the thin sheet parameter in FD,  $\mu\omega\sigma tc$ , becomes  $\mu\sigma tc/\tau$ , where  $\mu$  is normally  $\mu_0$ ,  $c$  is a dimension – in this model the smaller of strike length or depth extent – and  $\tau$  is a time constant. The latter obviously depends on the eddy-current diffusion rate through the model and so is intimately related to the channel response at different times during the signal decay.

### 7.7.5. The Sphere Model in FD and TD Ground Systems

(a) General. The sphere and ellipsoid, simulating a model in the form of a conductive loop, are the only 3-D geometric shapes amenable to theoretical analysis. The sphere has been solved for both FD and TD systems when the source field is either uniform or dipolar (Wait, 1951b, 1960b; Ward, 1967). The solutions are in terms of Legendre polynomials, as in the

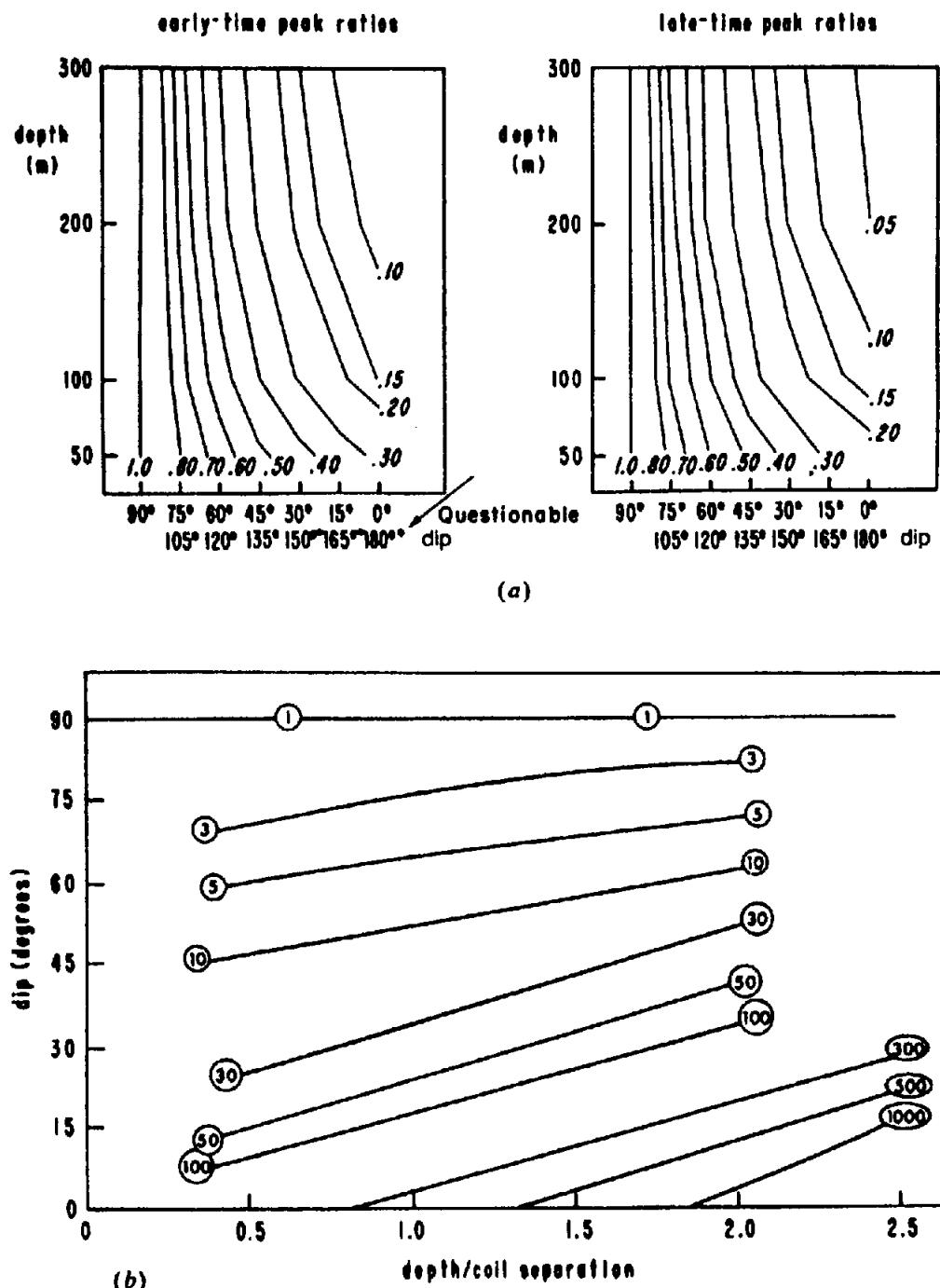
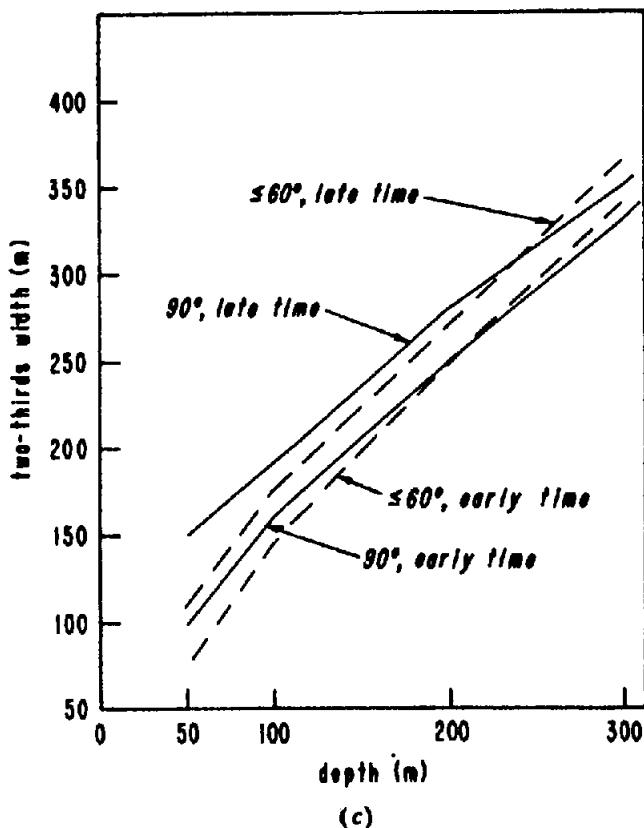


Figure 7.66. Characteristic curves for a dipping-model plate. (Parts a, c: After Gallagher, Ward, and Hohmann, 1985; part b: After Bartel and Hohmann, 1985.) (a) Early- and late-time peak ratio as a function of depth and dip, EM37; (b) Ratio of on-conductor side-lobe area to off-conductor side-lobe area as a function of dip and depth, PEM(1).

result for the sphere in resistivity (§8.3.5), but are considerably more complicated, particularly for the dipole field. The two solutions are the same when the dipole is remote from the sphere. A brief discussion follows.

(b) Frequency domain. The response parameter for the sphere is  $\mu\omega\sigma a^2$  (§7.7.3i) and the response function is a more complex form of  $A + jB$  shown

in Figure 7.10. When  $\mu = \mu_0$  the uniform field response function is similar to that for a circular loop. Reasonable profiles may be developed from the circuit analogy on this basis, mutual inductance being given by Equations (7.21c, d) for the dipole and Equation (7.21f) for long-wire coupling. The dipole coupling is suitable for analysis of airborne as well as ground double-dipole results; the source and detector, being close together, are considered common



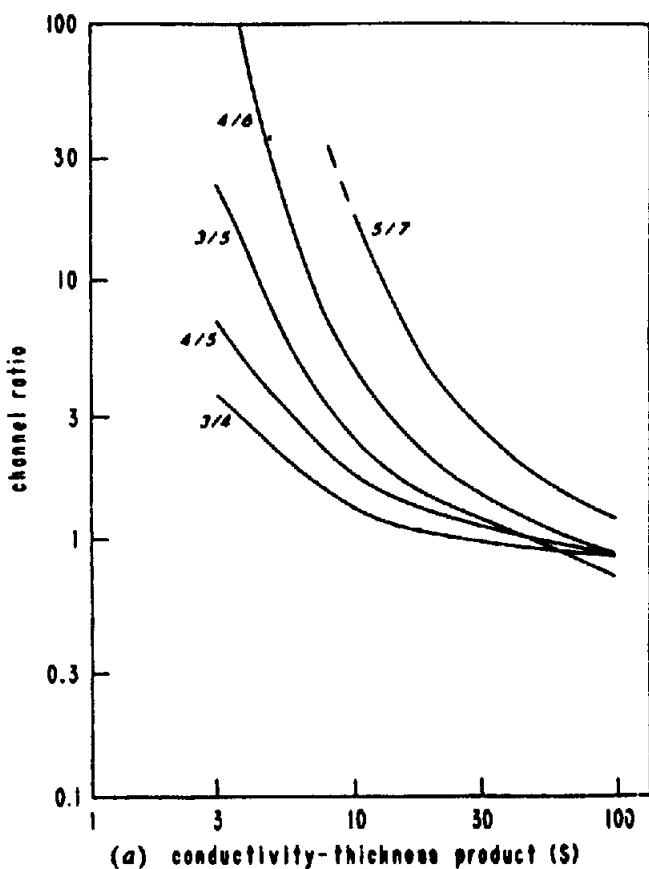
(c)

Figure 7.66. (Continued) (c) Two-thirds width versus depth for early and late times, dips 90 and  $\leq 60^\circ$ .

and the sphere is remote from both. Thus the interpretation of FD response from 3-D targets roughly simulated by a sphere may be carried out directly, or by using the ac circuit model.

Two sets of profiles over a spherical target at various depths are shown in Figure 7.68. The first is for HLEM, the second for the shootback method. In both examples dimensions are scaled to the T-R separation. Comparing the HLEM curves in Figure 7.68a with those of Figures 7.36c and 7.41 (and lacking the quadrature profiles in Fig. 7.68a), the sphere could be mistaken for a horizontal sheet of limited width, two vertical sheets of resolvable separation, or even a steeply dipping single sheet, all of rather shallow depth. This ambiguity applies to the shootback profiles of Figure 7.68b as well. The effect of conductive overburden on the spherical model appears to be similar to that of the thin sheet (§7.7.3b and §7.7.4b).

(c) Time domain. Eddy-current diffusion in the sphere during transmitter off-time is different from that on the thin sheet because of the different geometry. Although the vortex current motion is toward the center in both models, the 3-D sphere causes these currents to collapse from surface toward its center from early to late time; on the 2-D model they move inward from the edge, always in the plane of



(a) conductivity-thickness product (S)

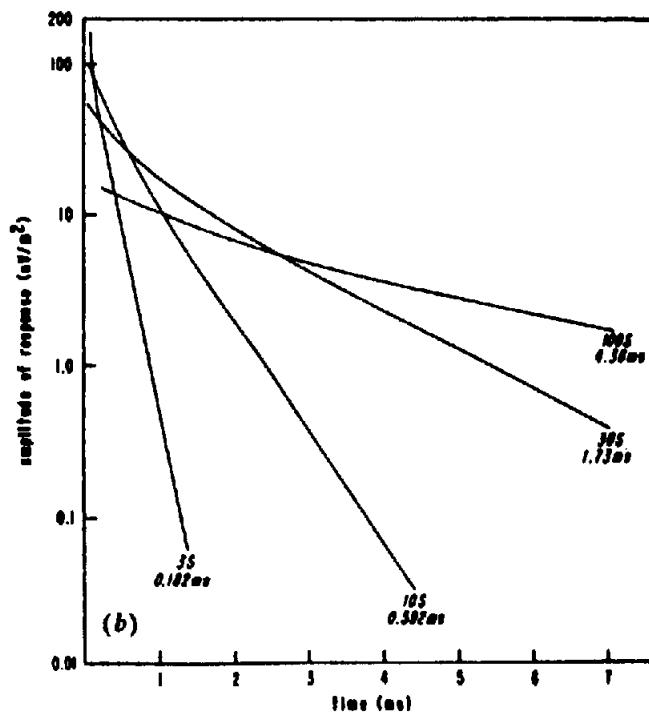


Figure 7.67. Nomograms for estimating  $\sigma t$  product. (a) PEM(1) system, channel ratios versus TCP (numbers at ends of curves denote channels); model plate 600  $\times$  600 m,  $z = 50$  m, dip =  $30^\circ$ , T-R = 100 m. (After Bartel and Hohmann, 1985.) (b) EM37 system, curves of response amplitude versus time for various values of TCP (or time constant); model plate 800  $\times$  400 m,  $z = 50$  m, dip =  $90^\circ$ . (After Gallagher, Ward, and Hohmann, 1985.)

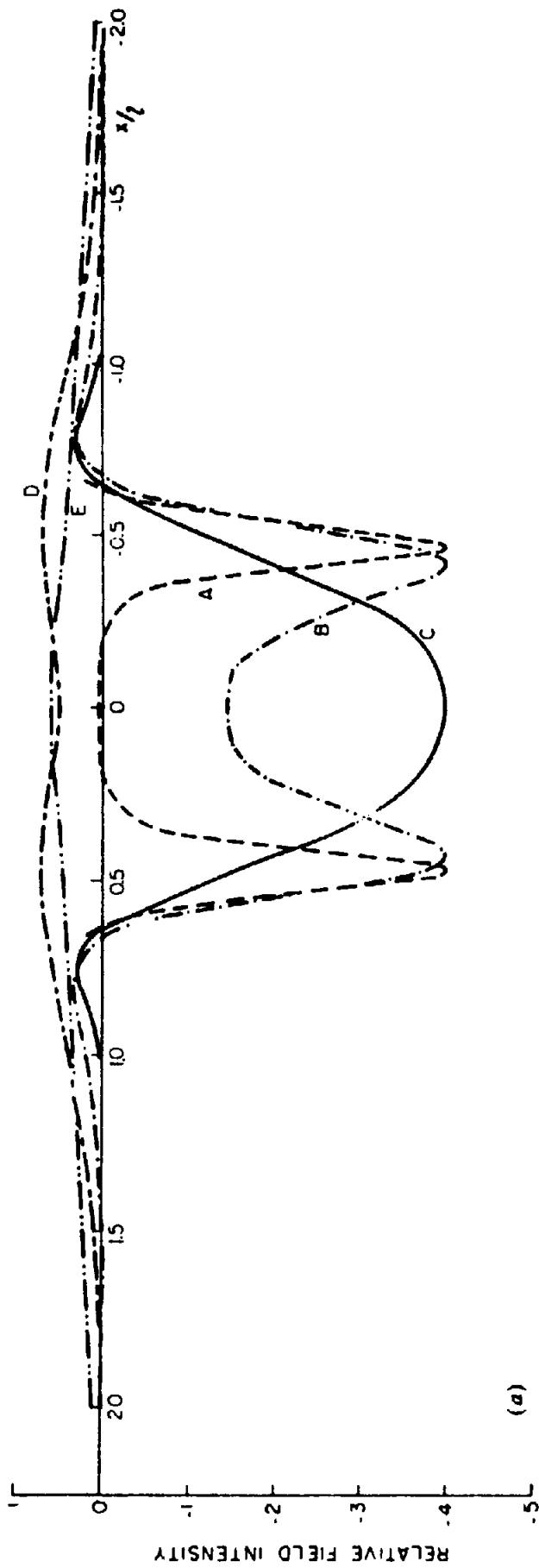


Figure 768. Response to a buried sphere. (a) HLEM profiles; 1 = T-R, depth to center of sphere is  $1/8, 1/4, 1/2, 1$ , and  $2l$  for curves A to E, respectively. (After Bhattacharya and Sinha, 1965.)

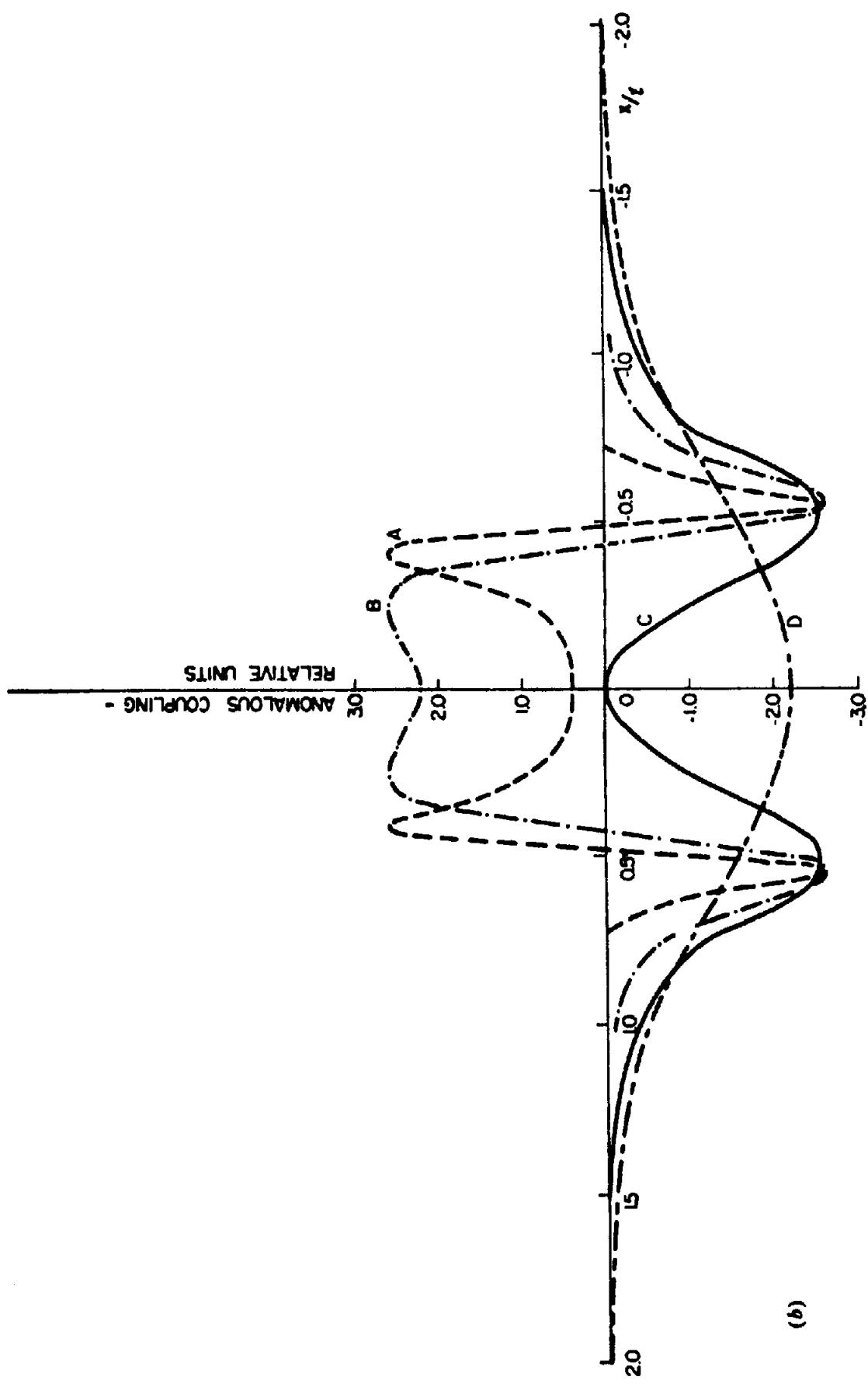


Figure 7.68. (Continued) (b) Shootback profiles, depths as in (a). (Based on data from Bhattacharya and Sinha, 1965.)

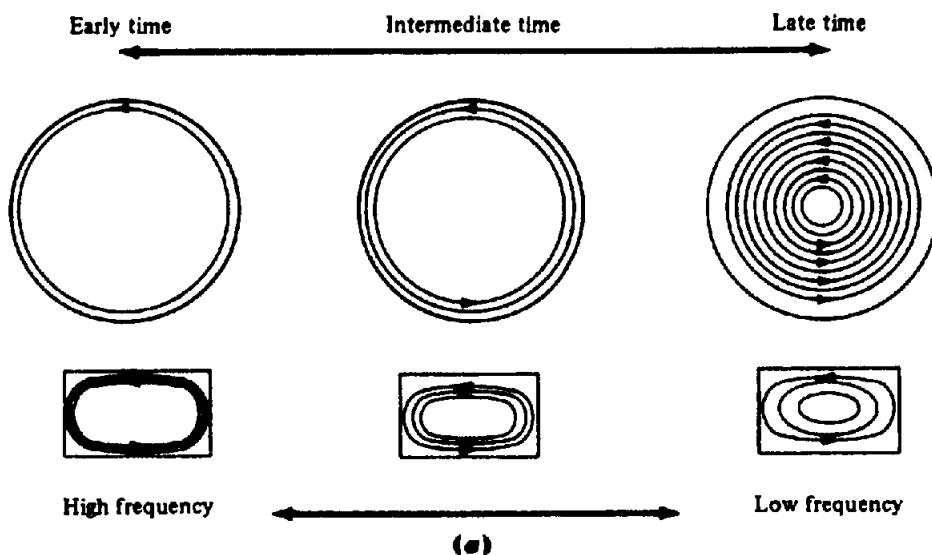


Figure 7.69. Time-domain eddy-current distribution in a spherical conductor. (a) Schematic comparing eddy-current diffusion in a sphere and a plate (After McNeill, 1980.)

the sheet. A schematic of the eddy-current diffusion in the thin plate and sphere is illustrated in Figure 7.69a; also included is a plot of current distribution versus time in the sphere (Fig. 7.69b).

The computer program SPHERE was developed by the same University of Toronto group that produced the PLATE program (§7.7.4a).

The SPHERE program was used to obtain Figure 7.70 which shows the effect of conductivity on PEM response over a sphere. Over early to late time the positive peak decays faster than the negative tails, compared to the vertical plate. This permits discrimination between thin and thick conductors.

### 7.7.6. Layered Structure: EM Depth Sounding

(a) *Introduction.* The use of EM methods for depth sounding was discussed briefly in Section 7.6. Until the early 1970s, this technique was little used, mainly because of the limited transmitter power and frequency range available with most ground equipment. Development of time-domain EM with its potential for greater depth of penetration provided a stimulus for this type of survey. Multifrequency continuous-wave systems have also been tested for the same purpose, on a much smaller scale. In both cases the practice has been to maintain fixed separation of transmitter and receiver as in magnetotellurics, rather than resistivity sounding. It may be necessary, however, to change *T-R* spacing several times when sounding over a number of beds stacked to appreciable depth. Detailed accounts of this application may be found in Keller and Frischknecht (1966) and Patra and Mallick (1980), as well as a more theoretical treatment in Kaufman and Keller (1983).

(b) *Frequency domain.* The VLF EM16R unit provides a fast and convenient shallow sounding measurement. As described in Section 7.4.2f, with the setup of Figure 7.18b we obtain values of apparent resistivity  $\rho_a$  and phase angle  $\phi$  (lag of  $H_\phi$  with respect to  $E_r$ ) by adjusting the corresponding instrument dials for minimum signal. The expressions are

$$\left. \begin{aligned} \rho_a &= |E_r/H_\phi|^2/\omega\mu_0 = |Z_s|^2/\omega\mu_0 \\ \phi &= \tan^{-1} Z_s \end{aligned} \right\} \quad (7.40a)$$

where  $E_r$  and  $H_\phi$  are the horizontal orthogonal components of electric and magnetic fields from the VLF transmitter, and  $Z_s$  is the complex surface impedance in the vicinity of the measuring station. Over homogeneous ground  $\rho_a$  is the actual resistivity and  $\phi = 45^\circ$ .

On a stratified ground, with several layers differing in thickness and resistivity,  $\rho_a$  is a function of these parameters (as in dc sounding), at least to the depth of penetration possible at VLF frequencies, and the phase angle generally will not be  $45^\circ$ . In practice multiple-layer structure will not be resolved with the EM16R sounding. In the vicinity of lateral discontinuities, the problem is even less tractable.

For two beds, however, a solution may be found from master curves. In this case we have three unknowns,  $\rho_1, z_1$  for the top bed,  $\rho_2$  for the basement and only two measured parameters  $\rho_a$  and  $\phi$ , for which the two-layer structure relations are

$$\left. \begin{aligned} \rho_a &= \rho_1 |Q_1|^2 \\ \phi &= 45^\circ + \tan^{-1}(Q_1) \end{aligned} \right\} \quad (7.40b)$$

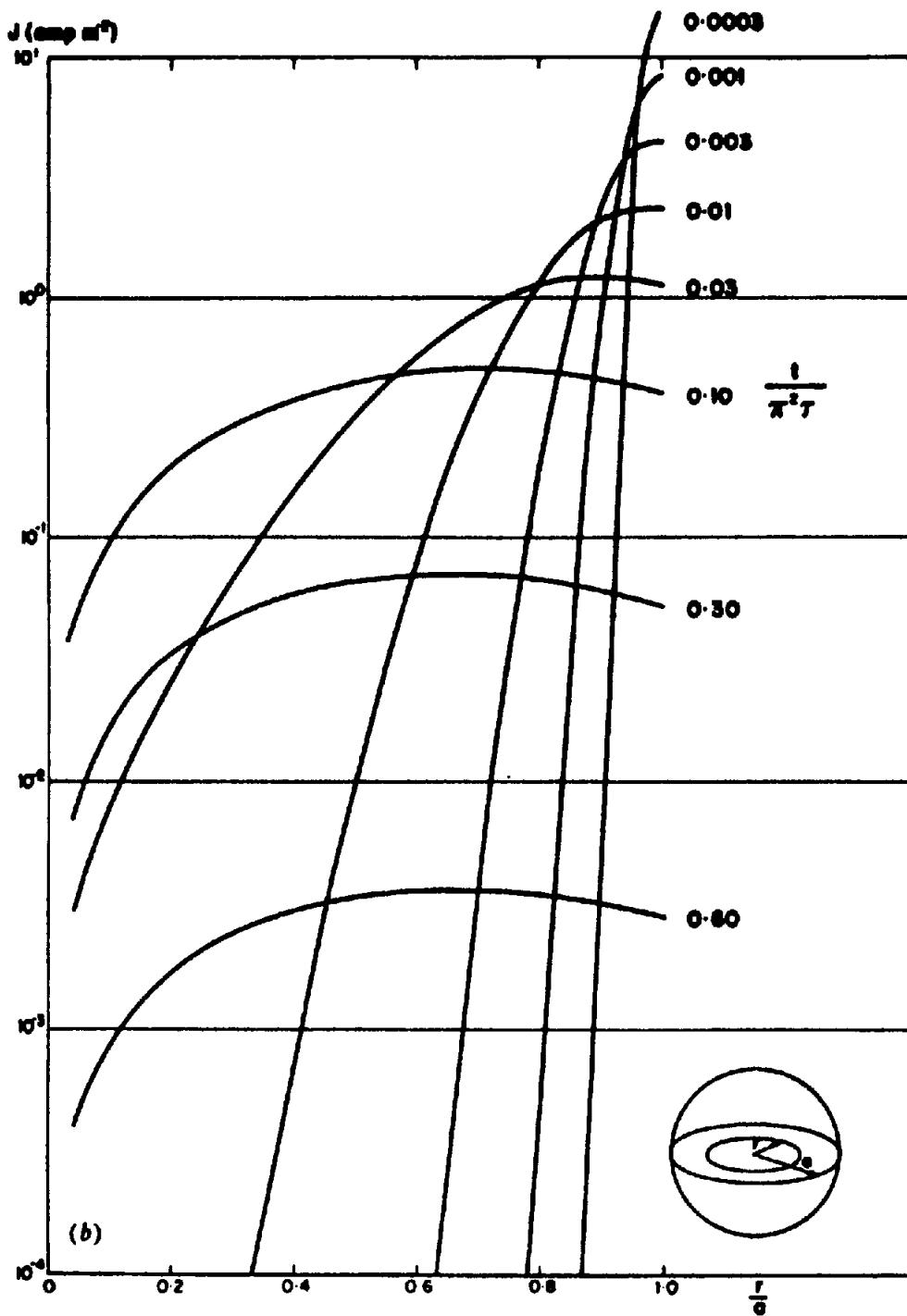


Figure 7.69. (Continued) (b) Radial distribution of current in a sphere for several values of  $(t/\pi^2\tau)$ . (After McNeill, 1980.)

where  $Q_1$  is a correction factor of the form

$$Q_1 = \left\{ \beta_1 + \tanh(j\alpha_1)^{1/2} \right\} / \left\{ 1 + \beta_1 \tanh(j\alpha_1)^{1/2} \right\} \quad (7.40c)$$

and  $\beta_1 = (\rho_2/\rho_1)^{1/2}$ ,  $\alpha_1 = (\omega\mu_0/\rho_1)^{1/2}z_1$ .

The master curves displayed in Figure 7.71 are plotted as  $\alpha_1$  versus  $\beta_1$  for various values of  $Q_1$  and  $\phi$ . It is still necessary to assume a value for either  $\rho_1$  or  $\rho_2/\rho_1$ , based on all available information. If we select  $\rho_1$ , the procedure is to compute  $|Q_1|$  from

Equation (7.40b), locate its intersection with  $\phi$  to get  $\alpha_1$  and  $\beta_1$  on the master, and calculate  $z_1$  from  $\alpha_1$ ,  $\rho_2$  from  $\beta_1$ .

When  $\beta_1 = (\rho_2/\rho_1)^{1/2}$  is the "known" parameter, we find its intersection with  $\phi$  to obtain  $|Q_1|$ , calculate  $\rho_1$  (from its relation with  $|Q_1|$ ),  $z_1$  from  $\alpha_1$ , and  $\rho_2$  from  $\beta_1$ . In this case two solutions for  $\alpha_1$  and  $Q_1$  are possible because of the shape of the  $Q_1$  curves.

Confidence in the results from this exercise may be greatly enhanced by including a portable dc resistivity unit in the field to measure  $\rho_1$  at small spacing for several stations.

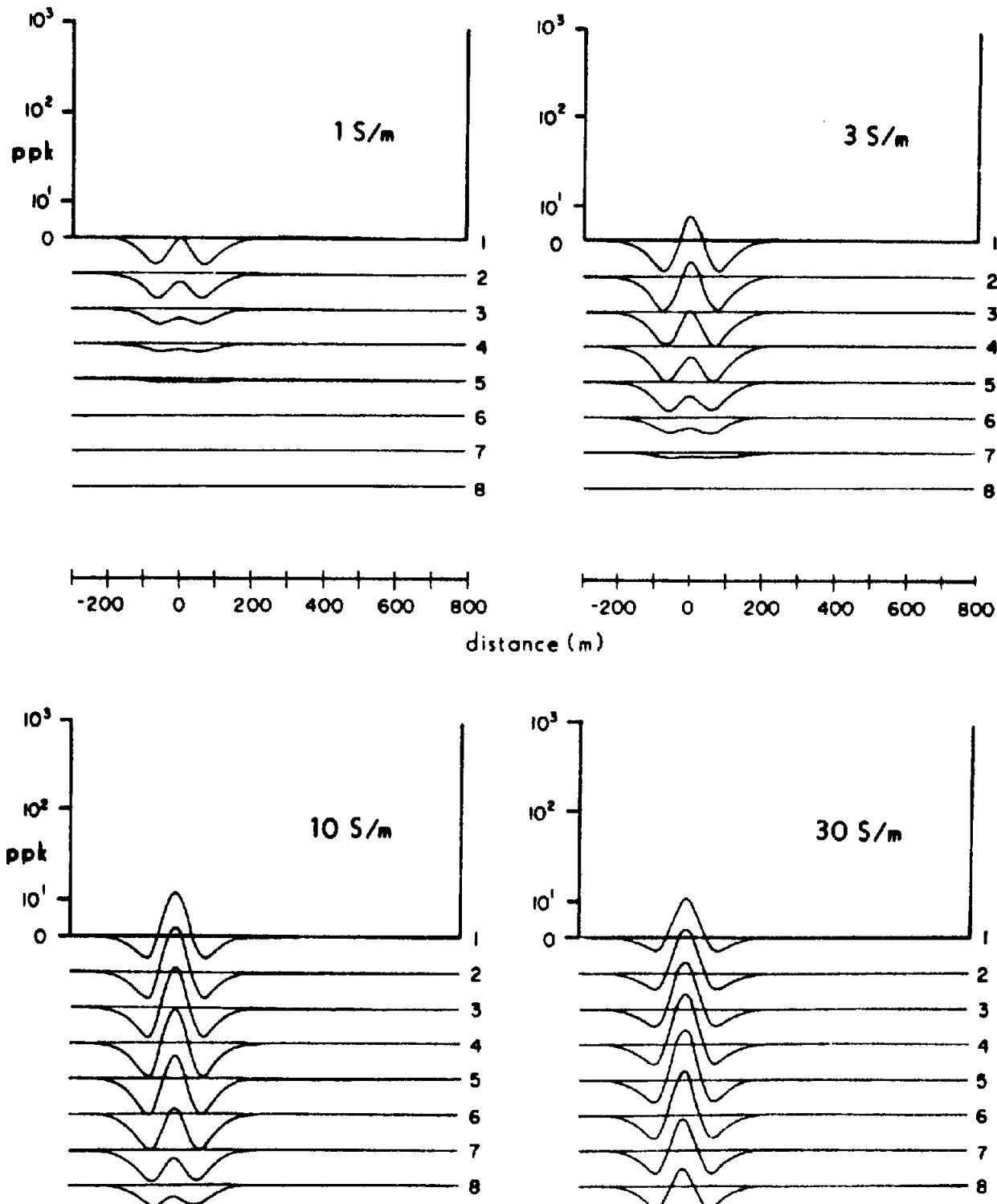


Figure 7.70. Response of PEM(1) system to a buried sphere as a function of conductivity. Radius of sphere = 50 m = depth to top,  $l = 100$  m. (After Bartel and Hohmann, 1985.)

Other standard EM systems are suitable for variable frequency sounding (Wait, 1955; Ward, 1967). These include (a) double-dipole (horizontal and vertical coplanar, vertical coaxial, and perpendicular), (b) large transmitter loop with small receiver at its center, (c) long grounded wire or Turam-type loop with small receiver coil located some distance from it. In (a) the dipole condition prevails if the T-R separation is  $\geq 5$  diameters of either loop; (b) is

used more in time-domain sounding, such as with the coincident-loop.

The mathematical treatment for interpretation is well developed, being somewhat similar to both dc resistivity and MT sounding analysis, that is, the procedure for determining FDEM response over multilayer ground requires that we calculate a complex ground impedance in terms of the mutual coupling (impedance) between transmitter and receiver

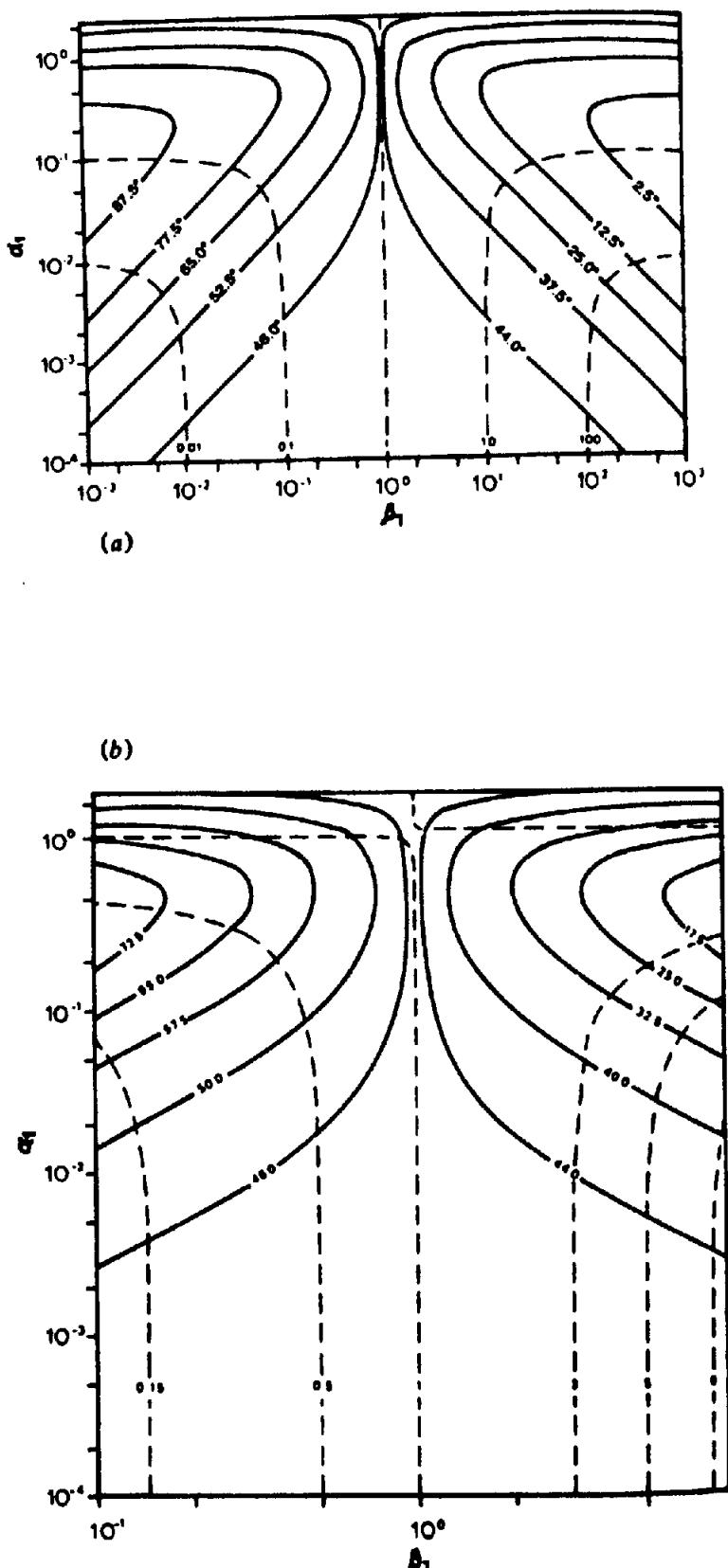


Figure 7.71. Master curves for two-layer VLF resistivity interpretation. (After Mathieson and Crossley, 1982.) (a) Contours of  $\phi$  (solid) and  $|Q_r|$  (dashed) as functions of  $\alpha_1$  and  $\beta_1$  [Eq. (7.40)]. (b) Enlargement of the central portion of (a).

in free space (§7.2.5). This involves successive solutions of the wave equation in two-layer structures from the basement up to surface; the solutions contain integrals like those appearing in resistivity sounding analysis [Eq. (8.47)].

The following examples for several EM systems over two layers should clarify the preceding general statement. The impedance ratio, related to the parameters of the beds, is given by an integral which varies with the type of FDEM.

(a) Horizontal coplanar loops:

$$(Z/Z_0)_a = 1 + B^3(T'_0 + T''_0) \quad (7.41a)$$

(b) Vertical coplanar loops:

$$(Z/Z_0)_b = 1 + B^2(T'_2 + T''_2) \quad (7.41b)$$

(c) Vertical coaxial loops:

$$(Z/Z_0)_c = 1 + \frac{1}{2}B^2\{(T'_1 + T''_1) - B(T'_0 + T''_0)\} \quad (7.41c)$$

(d) Perpendicular loops:

$$(Z/Z_0)_d = B^3(T'_1 + T''_1) \quad (7.41d)$$

(e) Long-wire horizontal loop:

$$(Z/Z_0)_e = 1 - B^2(T'_2 + T''_2) \quad (7.41e)$$

where  $Z_0$  and  $Z$  are the free-space  $T$ - $R$  mutual coupling and measured impedance, respectively,  $B = R/\delta$ , the ratio of  $T$ - $R$  spacing to the skin depth  $\delta = (2\rho_1/\omega\mu)^{1/2}$ , and

$$T'_0 = \int_0^\infty \{A(D, \lambda) - A(\infty, \lambda)\} \lambda^2 J_0(\lambda B) d\lambda$$

$$T''_0 = \int_0^\infty A(\infty, \lambda) \lambda^2 J_0(\lambda B) d\lambda$$

$$T'_1 = \int_0^\infty \{A(D, \lambda) - A(\infty, \lambda)\} \lambda^2 J_1(\lambda B) d\lambda$$

$$T''_1 = \int_0^\infty A(\infty, \lambda) \lambda^2 J_1(\lambda B) d\lambda$$

$$T'_2 = \int_0^\infty \{A(D, \lambda) - A(\infty, \lambda)\} \lambda J_1(\lambda B) d\lambda$$

$$T''_2 = \int_0^\infty A(\infty, \lambda) \lambda J_1(\lambda B) d\lambda$$

where  $D = 2z_1/\delta$  and  $z_1$  is the top bed thickness. The terms  $A(D, \lambda)$  and  $A(\infty, \lambda)$  are known as *kernel* or *input functions*. The function  $A(\infty, \lambda)$  is related to homogeneous ground, indicating that the

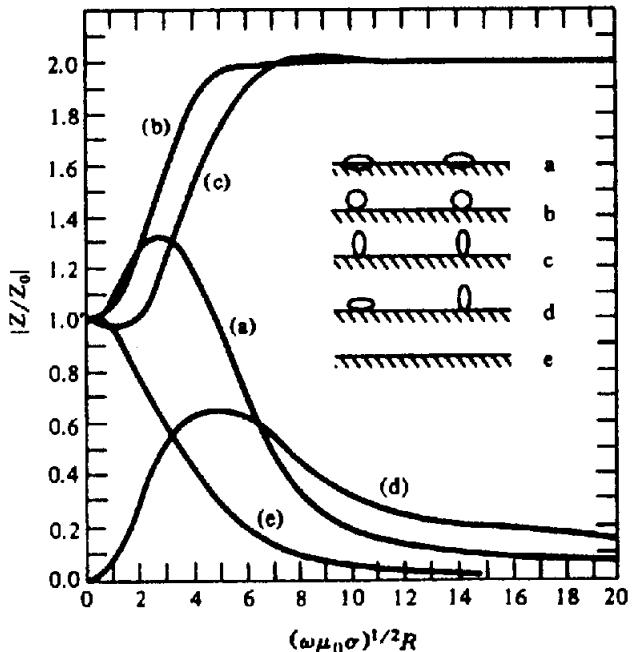


Figure 7.72. Mutual impedance ratios for systems (a) to (e) in Equation (7.41) as a function of  $(\omega\mu_0\sigma)^{1/2}R$ . (After Wait, 1955.)

integrals  $T''_0$ ,  $T''_1$ , and  $T''_2$  describe secondary fields over this simple structure and consequently may be solved analytically. Integrals  $T'_0$ ,  $T'_1$ , and  $T'_2$  are found by numerical integration in a variety of ways or by digital filtering (Koefoed, Ghosh, and Polman, 1972).

Equations (7.41c) and (7.41e) may be written in terms of Equations (7.41a) and (7.41b):

$$(Z/Z_0)_c = 1 + \frac{1}{2}\{(Z/Z_0)_b - (Z/Z_0)_a\}$$

$$(Z/Z_0)_e = 2 - (Z/Z_0)_b$$

so that we need only to determine the ratios for systems (a) and (b) to find solutions for (c) and (e).

A set of curves showing  $(Z/Z_0)$  versus  $(\omega\mu\sigma)^{1/2}R$  for systems (a) to (e) over homogeneous ground is illustrated in Figure 7.72. Note the similarity of the vertical loops (b) and (c), also the horizontal loop (a) and the long-wire transmitter in (e); the perpendicular loops of (d) produce a completely different response because of the minimum coupling.

Numerous curves and tables for the two-layer earth may be found in Frischknecht (1967). Because five FDEM systems are considered in terms of four forms of the coupling ratios (modulus, phase, real, and imaginary components) and five variables ( $\sigma_1$ ,  $\sigma_2$ ,  $z_1$ ,  $\omega$ ,  $R$ ), a great amount of data is presented, even for two beds, compared to dc resistivity soundings.

Several examples of two-layer curves in Figure 7.73 illustrate soundings using systems (a), (b), (d), and (e) [Eqs. (7.41)]. From top to bottom the first

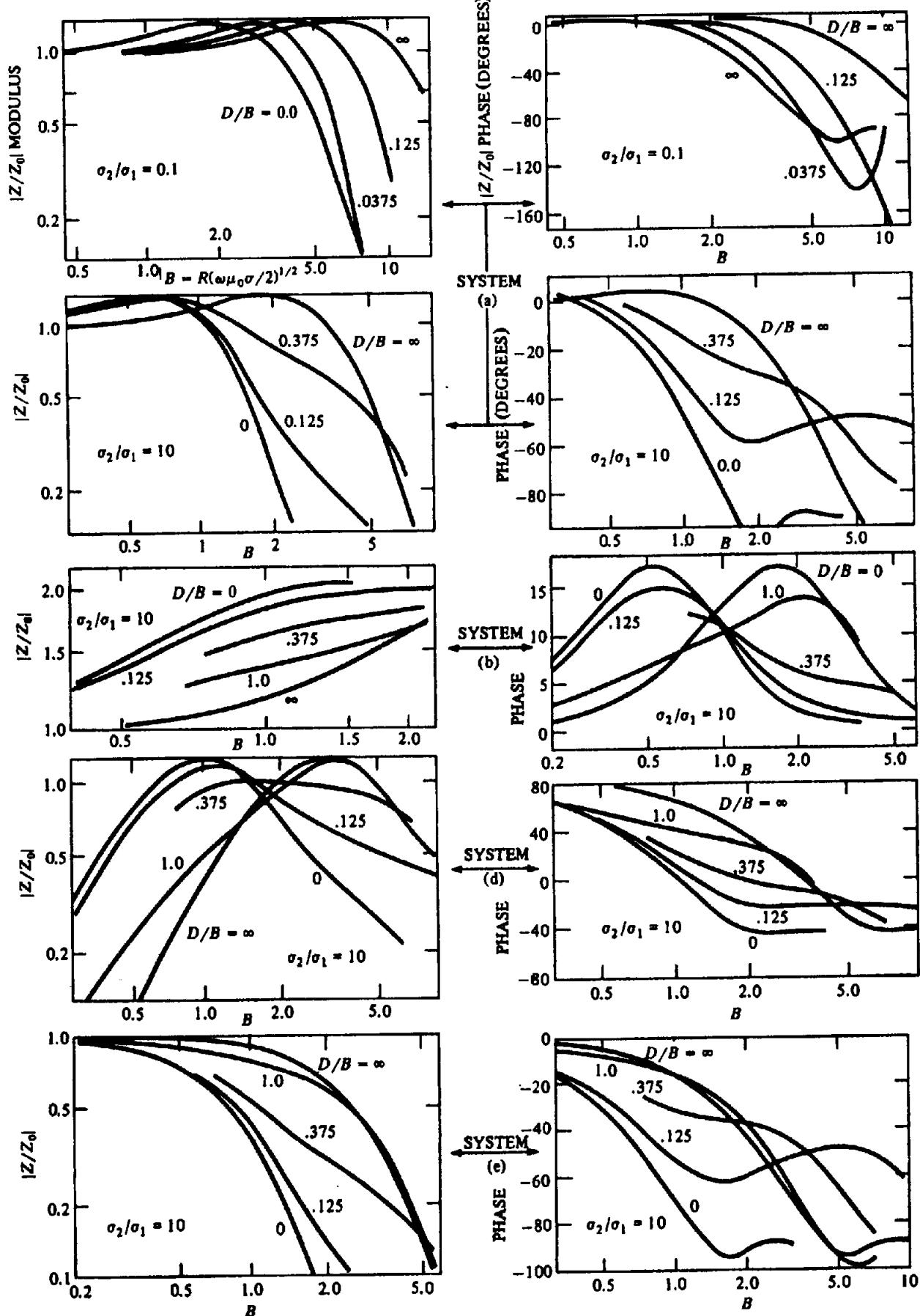


Figure 7.73. Modulus and phase of mutual coupling ratio ( $Z/Z_0$ ) for systems (a), (b), (d), and (e) in Equations (7.41) over a two-layer earth. (After Frischknecht, 1967.)

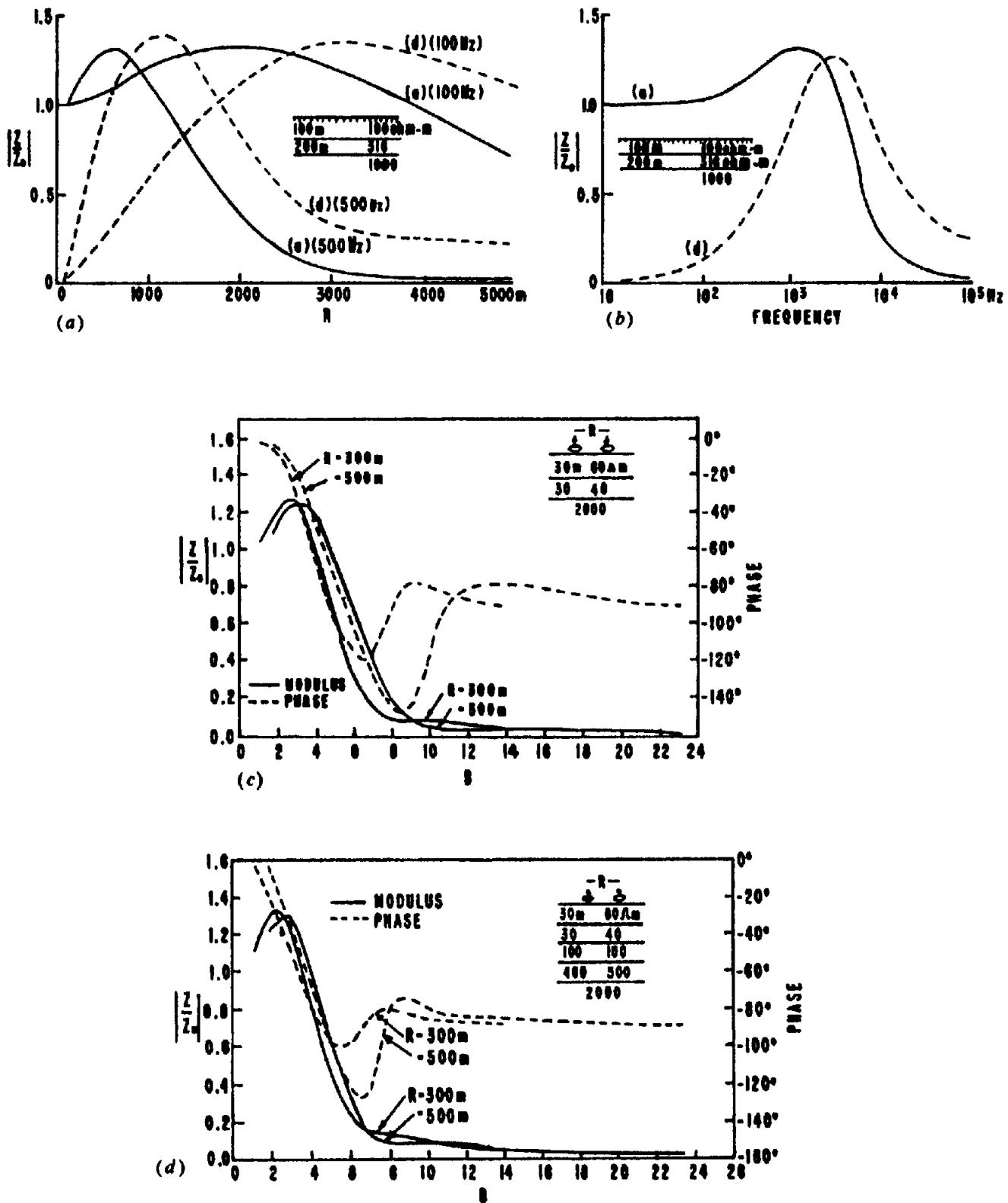


Figure 7.74. Mutual coupling ratio (modulus and phase) for systems (a) and (d) of Equation (7.41) over multilayer earth. (After Patra and Mallick, 1980.) (a) Modulus and phase for systems (a) and (d) over three-layer type-A earth (§8.6.4b), geometric sounding. (b) As in (a) except parametric sounding. (c) Modulus and phase as functions of  $B$  for a three-layer type-H earth, system (a). (d) As in (c) except for a five-layer earth.

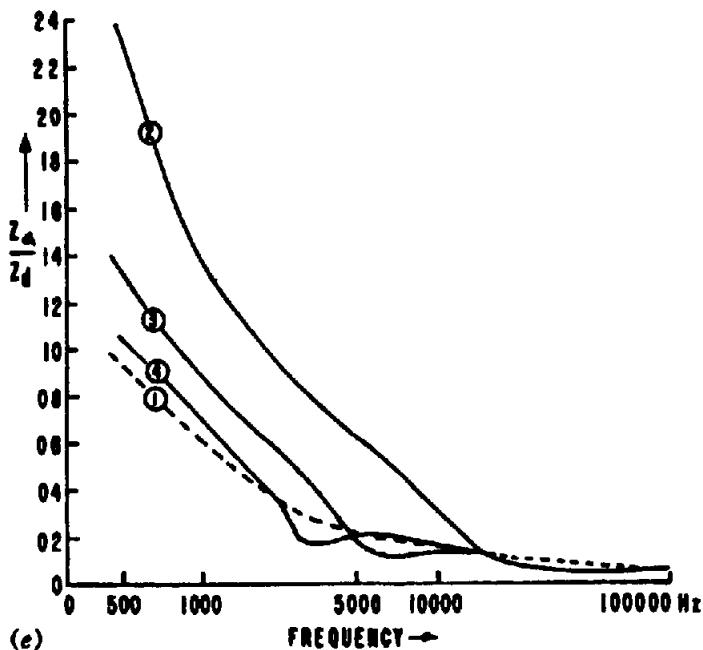


Figure 7.74. (Continued) (e) Ratio of moduli for systems (a) and (d) over one-, two-, three-, and four-layer earths.

pair represents a conductive top layer over resistive basement ( $\sigma_2/\sigma_1 = 0.1$ ), whereas the lower four portray a conductive basement ( $\sigma_2/\sigma_1 = 10.0$ ). In each paired set the left-hand box of curves displays the absolute value or modulus  $|Z/Z_0|$  of the mutual coupling ratio and the right-hand set shows the phase of  $Z/Z_0$ , all plotted against  $B$ .

Apart from a general left-to-right downward slope, which might be compared to a two-layer  $\rho_a$  curve over a conductive basement in dc soundings, these plots bear no resemblance to the latter; their decay merely represents an increase in frequency and/or  $T\text{-}R$  spacing on the horizontal axis. There are, however, certain similarities among them, for example, between systems (a) and (e) in both modulus and phase, and between systems (d) modulus and (b) phase. It is clear also that the FDEM sounding is more sensitive to a conductive than a resistive basement, as seen in comparing the upper two modulus and phase plots of system (a). This is also the case for the other systems.

As in Chapters 6 and 8, curve matching may be carried out successively on these master plots, provided the two-layer structure is actually present or that additional beds are deep enough to lie beyond the sounding range. Field data are plotted as  $\sqrt{f}$  versus  $V$ , voltage induced in the receiver coil, on log-log transparent paper with the same scale as the master, then moved about exactly as in MT and dc resistivity practice (§6.2.8b and §8.6.3g). When a reasonable match is obtained we find a horizontal-axis value of  $\sqrt{f}$  on  $B$ , from which we can calculate

$\sigma_1$ ; an estimate of  $D/B$  gives  $z_1$  and  $\sigma_2$  is determined from the  $k$  value for the particular master set.

It should be noted that the vertical scales,  $(Z/Z_0)$  on the master and  $V$  on the field plot, are relative rather than identical, that is,  $V = -j\omega\mu n_2 A_2 H = ZI$ , whereas  $(Z/Z_0) = m\pi R^3 H/n_1 A_1 I = H/H'$  [§7.2.5a, Eqs. (7.21c, d)], where  $m = 2$  or 4, depending on the loop system;  $n_1, n_2, A_1, A_2$  are the number of turns and areas of the transmitter and receiver loops,  $I$  the transmitter current,  $H'$  the primary field, and  $H$  the secondary field at the receiver in the presence of the earth. Thus  $V \propto H$ , hence  $V \propto Z$  also if  $I$  and  $R$  ( $\sim T\text{-}R$  spacing) are constant.

If the phase angle is measured, the curve matching may be performed on plots similar to Figure 7.73, the field curve being semilogarithmic. Additional master curves have been prepared for the same purpose, using the real and imaginary components of  $(Z/Z_0)$  and parameters of the polarization ellipse (tilt angle, ellipticity modulus, and phase). The latter, of course, require a different field measurement with the receiver coil.

It is not possible to use partial curve matching on EM sounding data over multiple layers. Figure 7.74 displays several examples of response from three beds and one from five beds.

In Figure 7.74a a theoretical geometric sounding (variable  $R$  and two values of  $f$ ) over a three-layer type-A structure ( $\rho_1 < \rho_2 < \rho_3$ ; §8.6.4b) for systems (a) and (d) is plotted for 100 and 500 Hz; the  $T\text{-}R$  spacing ranges from 100 to 5,000 m. The curves would be difficult to distinguish from two-layer or

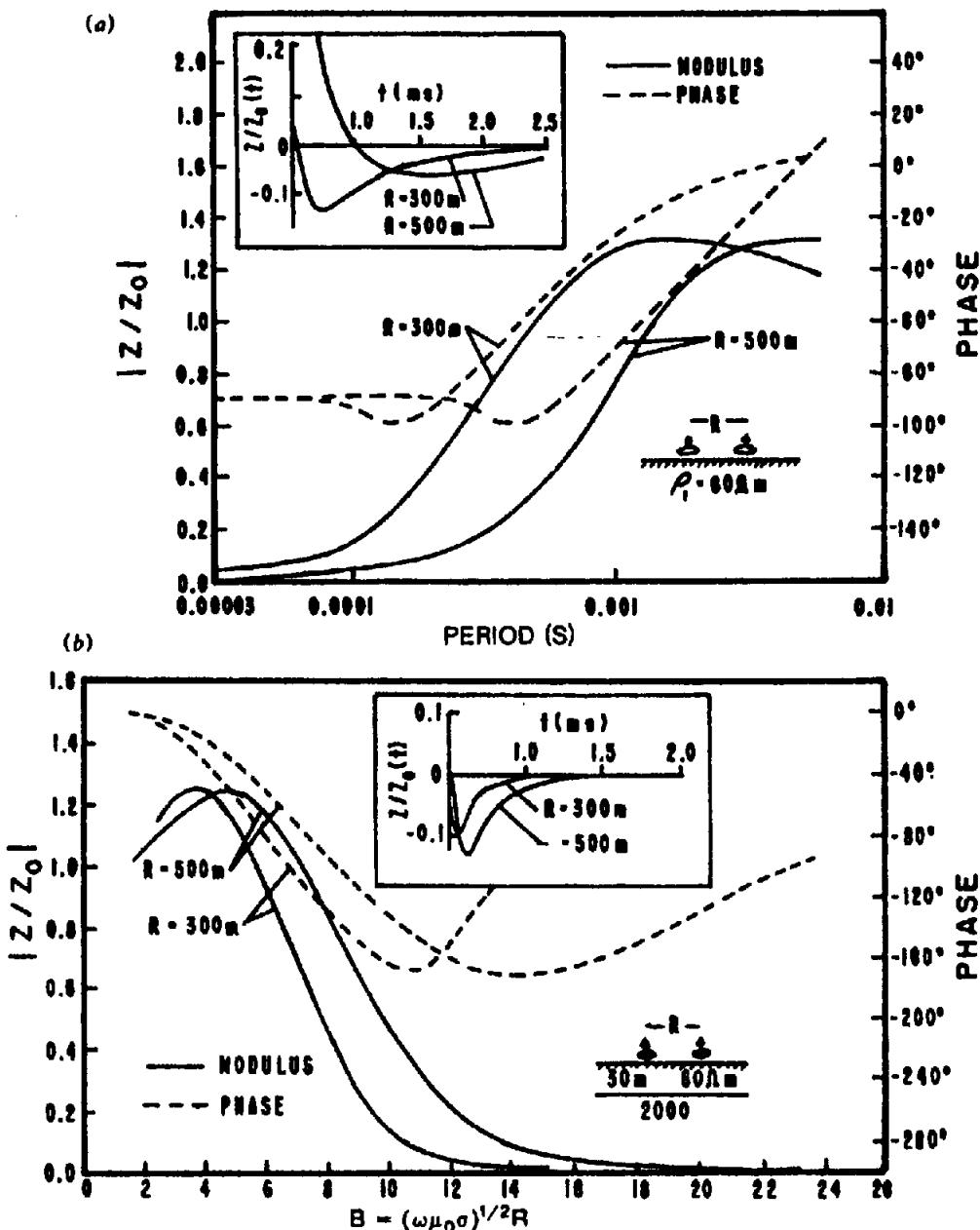


Figure 7.75. Modulus and phase of the mutual coupling ratio in the frequency domain and time domain (small insert) for the horizontal coplanar loop system [Eq. (7.41a)]. (After Patra and Mallick, 1980.) (a) Homogeneous earth. (b) Two-layer earth.

even homogeneous earth response. This is also true for the so-called *parametric sounding* in Figure 7.74b where the frequency is varied from 10 to  $10^5$  Hz. Figure 7.74c showing system (a) response over three-layer H-type beds ( $\rho_1 > \rho_2 < \rho_3$ ) is slightly more diagnostic, with a minimum around  $B = 6-8$ . However, the curves of Figure 7.74d for five layers show nothing of beds 3 and 4 and are practically identical to Figure 7.74c.

By calculating the response of both (a) and (d) systems and plotting the ratio, it appears possible to estimate the number of layers more successfully. Figure 7.74e illustrates this improved discrimination. Curves of  $(Z/Z_0)_a/(Z/Z_0)_d = Z_a/Z_d$  versus fre-

quency for one to four beds are increasingly complex, suggesting the performance of field surveys with two EM configurations.

Thus, the forward or curve-matching approach to EM sounding interpretation is clearly more difficult than for dc resistivity sounding. Solution of the inverse problem, as in other geophysical analysis, is increasingly used instead. Methods are similar and involve digital filtering, linearization, and least-squares minimization (§2.7.9).

(c) Time-domain sounding. The transient, or pulsed, EM system was long considered attractive for sounding, initially because of its similarity to the

seismic method. When suitable equipment became available about 1963, there still remained analytical difficulties. Then it was found that interpretation of the transient signal could be done by various transformations of frequency-domain response using Fourier series and Laplace and Fourier transforms (§7.2.6, §A.9, and §A.12). This analytical approach, however, has limitations when there are more than two layers; then it is necessary to use numerical methods for the FDEM response, as mentioned in Section 7.7.6b (Koefoed, Ghosh, and Polman, 1972).

To simplify the interpretation of TD sounding data it is desirable to convert the measured parameters from the field survey [normalized magnetic and electric fields in a variety of forms (§7.7.4)] into  $\rho_a$ , which is then plotted. It is not possible to produce a unique definition of  $\rho_a$ , as in dc sounding, because of the numerous expressions for EM coupling (Kaufman and Keller, 1983; Spies and Eggers, 1986). The resulting  $\rho_a$  curves, however, generally bear some resemblance to dc soundings whereas the original TD curves do not, as is apparent in Figure 7.75 where the TD curves, obtained by transformation from the FD (see the small inserts), are remarkably alike. They are also nearly identical to four- and five-layer curves (not shown).

Conversion of field data to resistivity curves is intimately related to the eddy-current diffusion in the ground. For two layers, the current at early time is entirely confined to the upper bed, whereas at late time it has penetrated to the basement. Thus the sounding measures  $\rho_1$  and  $\rho_2$  at the two limits. In between, the measurement is a combination of the two, depending on the thickness of the upper bed.

Mathematically, at late time the diffusion may be expressed as a relation between the measured parameter, say the vertical field component, time  $t$ , and the ground characteristics as follows:

$$\begin{aligned} H_z &\approx 2\mu M R^3 (\mu\sigma)^{3/2} / 4\pi R^3 \times 15\pi^{1/2} t^{3/2} \\ &= (\mu M / 30) (\mu\sigma / \pi t)^{3/2} \end{aligned}$$

where  $R = T-R$  spacing, and  $M$  is the transmitter dipole moment =  $IA$ . Because the receiver coil measures  $dH_z/dt = \dot{H}_z$ , we have

$$\dot{H}_z \approx \mu M (\mu\sigma)^{3/2} / 20\pi^{3/2} t^{5/2}$$

(ignoring the minus sign). Thus the signal decays as  $t^{-5/2}$ , whereas the apparent velocity of the diffusing current varies inversely with  $\sigma$ . We may obtain the apparent resistivity as a function of time from the preceding equations; because  $\sigma = 1/\rho \approx 1/\rho_a$ , so

$$\rho_a(t) \approx (\mu/\pi t) (\mu M / 20\dot{H}_z t)^{2/3} \quad (7.42)$$

Data from TD systems, which record other parameters such as  $H_x$ ,  $E_x$  components, may be converted to  $\rho_a$  in a similar fashion.

Several sets of  $\rho_a$  curves for two and three beds are shown in Figure 7.76. In all cases late-time response, which is most diagnostic of the structure, is plotted, as  $(\rho_a/\rho_1)$  versus  $(d/z_1)$ , where  $d = 2\pi(2t/\mu_0\sigma)^{1/2}$  [the diffusion distance given by Eq. (7.31)], and  $z_1$  is the surface bed thickness. Various values of  $R/z_1$  are included in each of the three-layer curve sets in Figure 7.76c, d, e, f.

The two-layer examples of Figures 7.76a, b, for resistive and conductive basements, respectively, resemble the equivalents in dc sounding. The set of three-layer  $H$ -type curves in Figure 7.76c are more characteristic of the bed sequence ( $\rho_1 = 16\rho_2$ ,  $\rho_3 = \infty$ ) than those for  $A$ -type in Figure 7.76d ( $\rho_1 = 0.25\rho_2 = 0.0625\rho_3$ ), which do not expose the intermediate resistive bed. Curve shapes for the  $K$ - and  $Q$ -type layering in Figure 7.76e, f, however, are quite diagnostic.

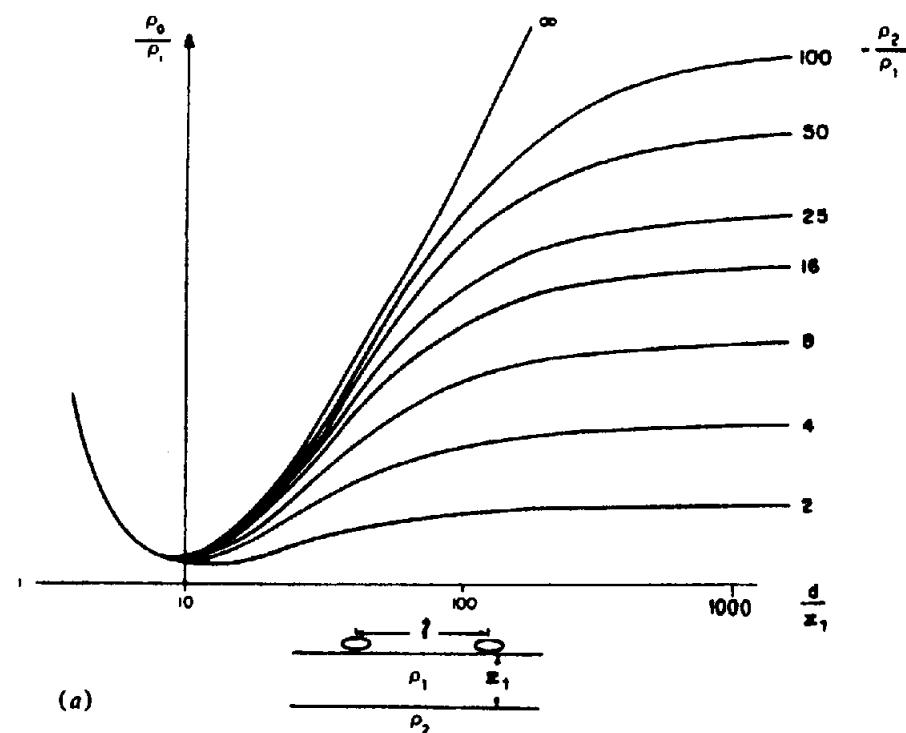
Curve matching is carried out by calculating  $\rho_a(t)$  from values of  $\dot{H}_z$  (or whatever component has been measured) and plotting it against  $t^{1/2}$  on semilog scales identical to the master curves. Then the field curves are fitted to the latter.

Summarizing the EM sounding technique and comparing it with dc resistivity, it is evident that both methods have a variety of standard field systems and are capable of great penetration depth, although transient EM has the greatest potential depth. Resistivity equipment and analysis are cheaper, simpler, and probably superior to EM at present in providing detailed results. However, EM is more convenient in the field, requiring fewer set-ups and no long wires, and is less sensitive to surficial variations including lateral discontinuities. Finally the EM sounding is insensitive to buried resistive beds, but both methods fail to resolve equivalent beds (§8.6.4f).

### 7.7.7. Interpretation of Airborne EM Data

(a) General. Although fundamentally the same as in ground work, the objective in airborne EM surveys is more modest. Generally, the airborne results locate conductors, outline their approximate extent, and perhaps provide enough information to estimate their characteristics. Ground followup is mandatory anyway, hence the airborne survey performs the function of rapid reconnaissance and elimination of barren ground.

The preceding statement was true when first written about 1970 but it is now unrealistic. Development of helicopter-borne systems, carrying automated EM and magnetic equipment and flying slowly



Two layer curves.

$$\frac{\rho_2}{\rho_1} > 1, \quad \frac{d}{z_1} = 1$$

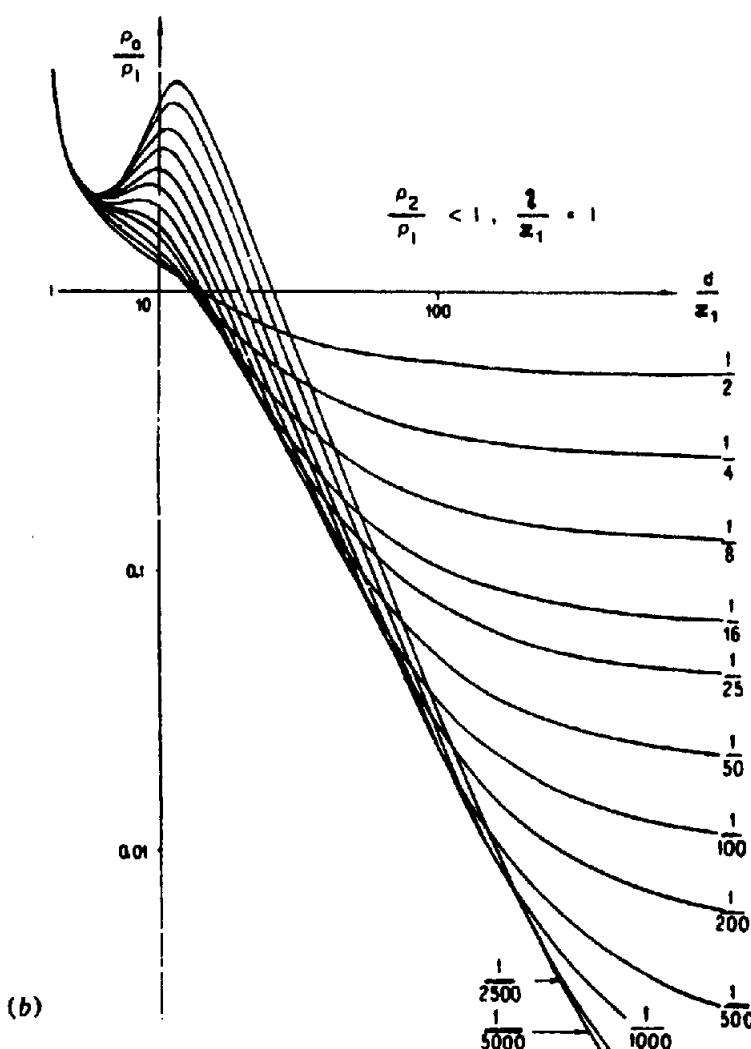


Figure 7.76. Master curves of late-time ( $\rho_0/\rho_1$ ) versus  $(d/z_1)$ . [Parts (a) and (b): After McNeill, 1980; parts (c) to (f): After Kaufmann and Keller, 1983.] (a) Two-layer curves for resistive basement. (b) Same as (a) except for conductive basement.

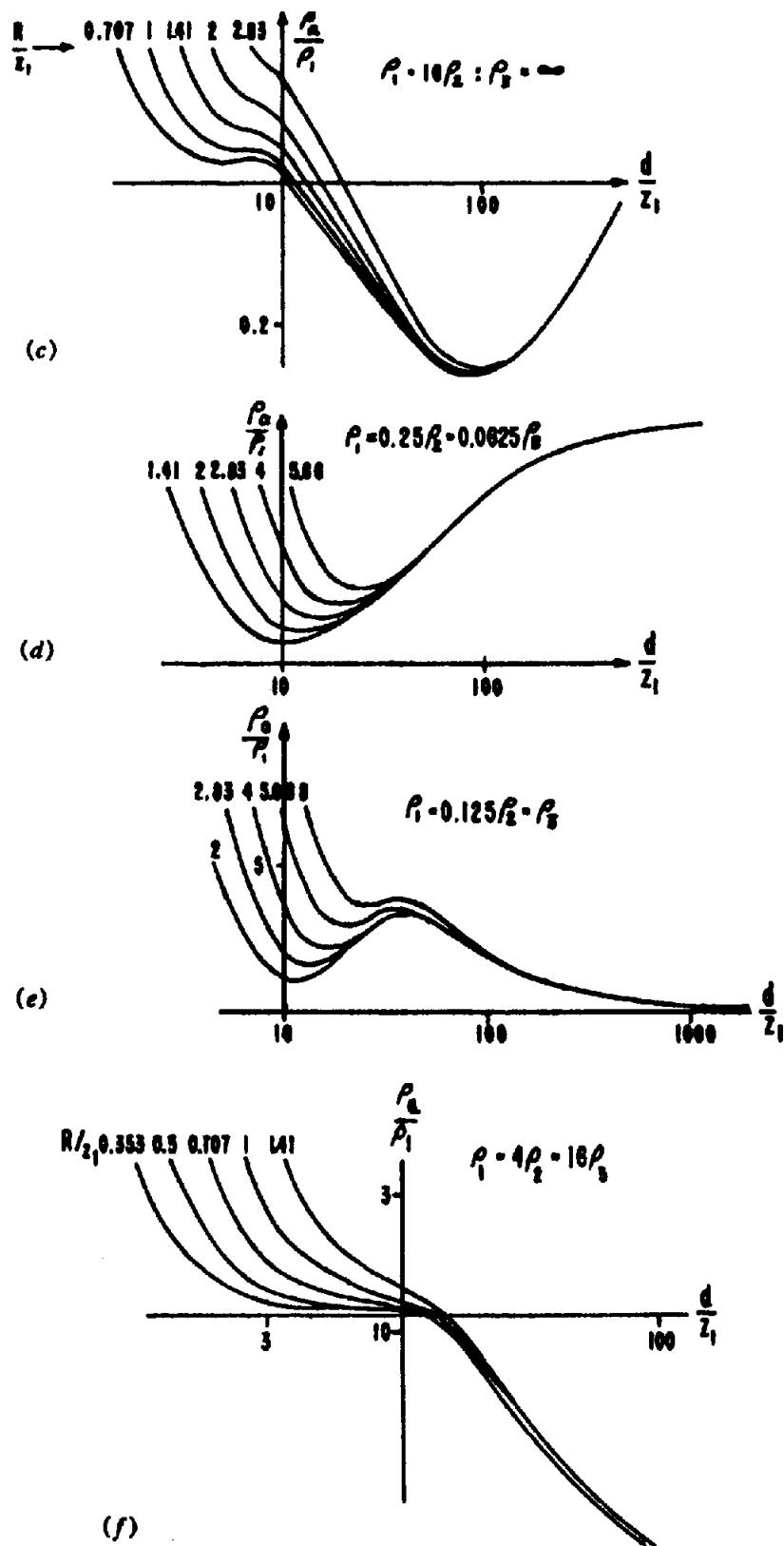


Figure 7.76. (Continued) (c) Three-layer curves for type-H structure. (d) Same as (c) except for type A. (e) Same as (c) except type K. (f) Same as (c) except type Q.

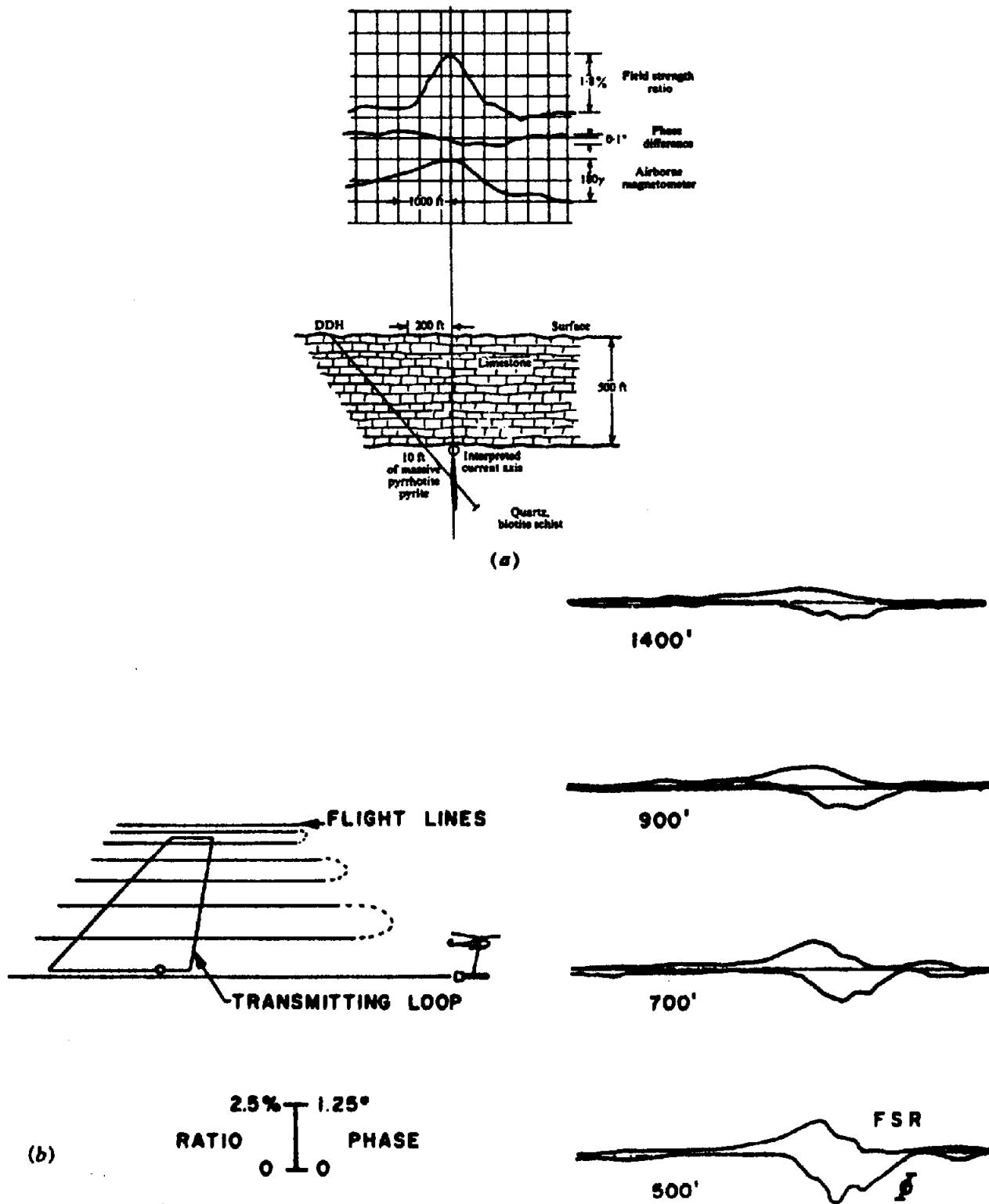


Figure 7.77. Examples of Turair responses. (a) Response over massive sulfide. (b) Effect of altitude over unknown conductor. FSR = Field strength ratio,  $\Phi$  = Phase.

at low ground clearance with sophisticated navigation aids, now make it possible to survey on 100 m line spacing. Coupled with the increasing cost of ground work and difficulties with environmental agencies, this improvement may in time reduce surface exploration in many areas to spotting drill sites, following surficial geology and geochemistry.

Large-scale reconnaissance airborne programs, however, still exist. As a rule, this type of AEM operation produces an excess of anomalies, because it detects without discrimination swamps, shear zones, faults, and similar large-scale features, as well as graphitic and metallic conductors. Airborne EM should be, and almost always is, carried out in

conjunction with airborne magnetics. Obviously the combination of two or more methods generally produces more than the information obtained from each separately; in airborne work the enhancement is even greater, because of the abundance of anomalies and because the geological knowledge is frequently limited in surveys of this type.

Scale modeling is very useful as an interpretation aid in airborne work. Three-dimensional (spherical) and sheet models are usually employed. However, computer-controlled interpretation is increasingly applied, following the production of profiles and contour plots from the automated data.

Height of the aircraft will normally replace  $T\text{-}R$  as the significant control dimension. As a result, the response parameters for the sphere and sheet become  $(\mu\omega\sigma a^2)$  and  $(\mu\omega\sigma th)$  where  $h$  is the aircraft height above the sheet.

*(b) Preliminary interpretation.* Because the classic asymmetric dip-angle curve is not recorded directly in airborne EM records (§7.5.4), the interpretation in various systems involves a consideration of peak amplitudes, width, and  $y$ -axis extent of a basically symmetric response. Consequently the initial step is to classify the anomaly as 3-D (limited  $x$ ,  $y$  extent), 2-D (long, thin, appreciable dip), or 1-D (large  $x$ ,  $y$  extent). This rough assessment may be made from the appearance of single profiles and correlation between adjacent flight lines.

Concurrently the interpreter notes the altitude and magnetic flight records to see if the anomaly may have been increased or created by changing height and whether there is any correlation between EM and magnetic profiles. This correlation is extremely useful, because with few exceptions most massive sulfides contain magnetic material, so that coincident or adjacent magnetic anomalies are particularly attractive. Having established the initial classification, quantitative interpretation will depend on the type of EM system used and the simplicity of the anomaly pattern.

The detailed data recorded with phase-component and VLF airborne systems make it possible to produce shallow structure resistivity maps of the survey area (Fraser, 1978; Seigel and Pitcher, 1978). These are a considerable aid in base-metal exploration to discriminate between bedrock conductors and host rock or overburden structural anomalies. The contour map is even more useful for engineering applications, such as nonmetallic deposits, ground-water sources, thickness of soil cover, and permafrost.

The mapping procedure is similar to that in Section 7.7.6c; an apparent resistivity is obtained from parameters of the coil system: receiver voltage  $V$ ,

transmitter dipole moment  $M$ , and  $T\text{-}R$  separation. In this application, an additional variable, height above ground of the AEM system, is also present as an important item and a potential source of error. Several computer programs have been devised to convert the data to  $\rho_a$ .

In the following we consider briefly the Turair and VLF systems; the interpretation of phase-component and Input AEM data are discussed in more detail.

### 7.7.8. Turair

This equipment, described in Section 7.5.3, consists of a Turam transmitter with a helicopter-borne receiver measuring gradients of vertical and horizontal field components. Information with regard to field results is limited. Two examples are shown in Figure 7.77, which emphasize the large exploration depth achieved with the ground transmitter. In Figure 7.77a, a 10 ft (3 m) section of massive pyrite and pyrrhotite, 500 ft (150 m) below limestone, in the Manitoba Nickel Belt, produces strong response, indicating a good conductor, accompanied by a clear magnetic anomaly. Height of the aircraft is not given. Figure 7.77b illustrates the Turair flight pattern in the field and response from different altitudes of an unknown structure, which appears to be less conductive than in Figure 7.77a because of the larger phase difference. Whatever its physical character, this anomaly is still visible at 1,400 ft (450 m) above surface.

The depth capability of this system appears sufficient almost to eliminate the need for ground followup, which was originally one of its advantages. Interpretation is like that in Turam ground surveys.

### 7.7.9. Airborne VLF

Various airborne versions of the VLF receiver were described in Section 7.5.4. Because of the small weight and size, any of these units may be mounted easily on any carrier. Thus the VLF measurement is frequently combined with airborne magnetometer and phase-component or other EM systems for routine surveying; occasionally airborne radiometrics are included as well.

Airborne VLF is not a carbon copy of the EM16-EM16R ground receiver (§7.4.2f, §7.5.4, and §7.7.6b), because it is impractical to measure tilt angle and more convenient to determine apparent resistivity from the wave-tilt  $W$  rather than from surface impedance  $Z_s$ . The latter was defined previously [Eqs. (6.22) and (7.41)] in terms of  $\rho_a$ , involving the ratio of horizontal electric to horizontal mag-

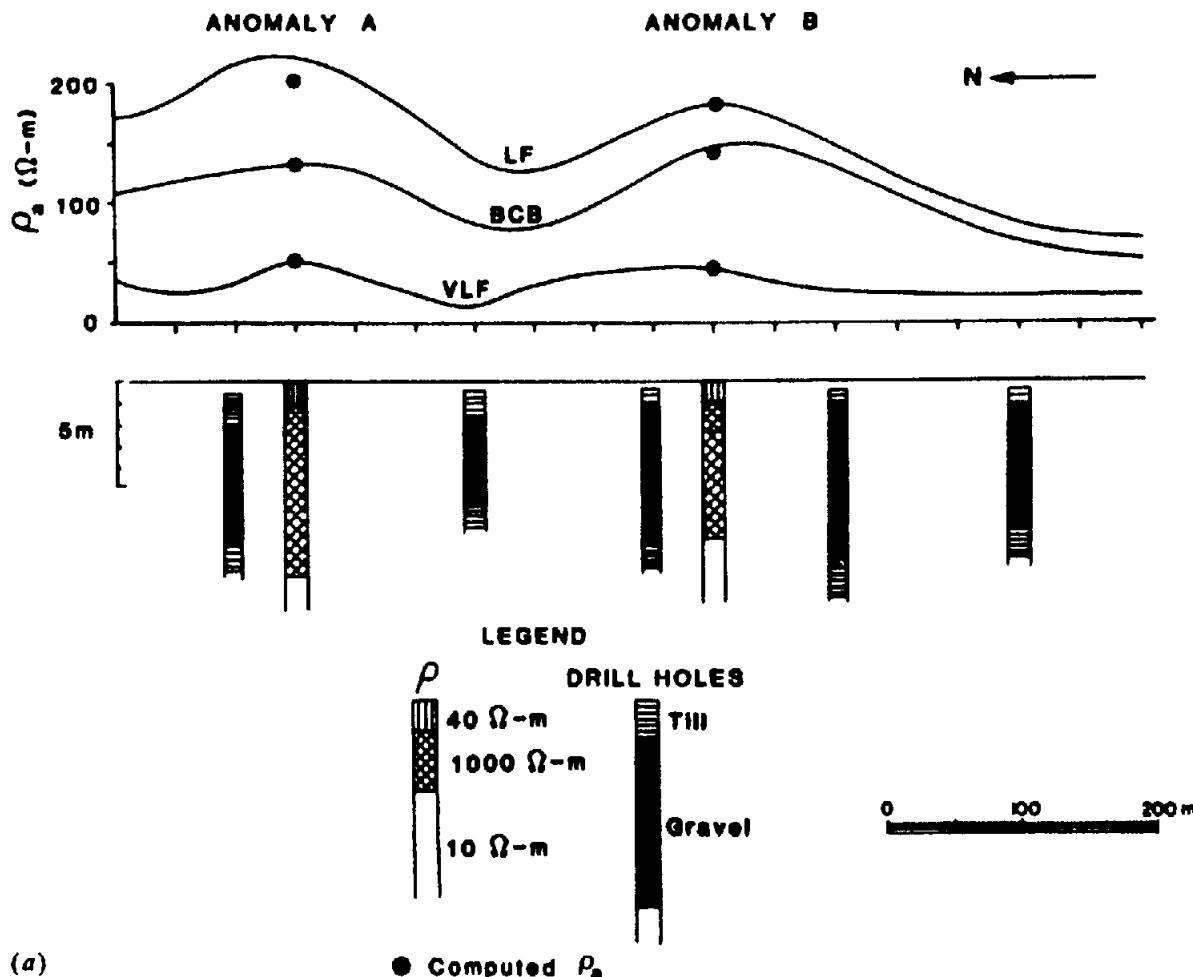


Figure 7.78. Results of an *E*-phase survey for gravel near Wadena, Saskatchewan. (From Palacky and Jagodits, 1975.) (a) Profile along line 47 [see map in (b)] for three frequencies plus interpretation of anomalies A and B based on  $\rho_a$  values and results of DDH logs. BCB = Broadcast band.

netic field components. The wave tilt is the ratio of horizontal to vertical electric fields,

$$W = E_r/E_t \quad (7.43a)$$

Over homogeneous ground this can be written

$$W = (j\omega\epsilon_0\rho)^{1/2} = (1+j)(\omega\epsilon_0\rho/2)^{1/2} \quad (7.43b)$$

[note that  $j = e^{j\pi/2}$ ,  $j^{1/2} = e^{j\pi/4}$ , and  $e^{-j3\pi/4}$ , so  $j^{1/2} = (\pm 1/\sqrt{2})(1+j)$ ; see §A.7] and so for a layered earth we have

$$\rho_a = |W|^2/\omega\epsilon_0 \quad (7.43c)$$

The Barringer *E*-phase VLF system measured only the quadrature component of  $W$  by phasing the receiver, to minimize the effects of terrain irregularity and aircraft pitch and roll on the antennas. The in-phase component is much more sensitive to such disturbances. Simultaneous measurement of VLF, LF (200 to 400 kHz), and broadcast band (550 to 1,500 kHz) frequencies at the receiver was also a help in this regard, while providing responses from

different depths. This was the first AEM equipment in which all the operations were automated, from digital recording, data correction, and conversion, to plotting resistivity sections.

An example of *E*-phase resistivity mapping is shown in Figure 7.78 for an area in Saskatchewan. Figure 7.78a shows three-frequency profiles along line 47; the two anomalies and their interpretation (aided by five drill-hole logs) located a gravel deposit. Figure 7.78b is the resistivity contour map, which outlines the gravel and sand section where  $\rho_a$  is somewhat larger than average background.

Presently available airborne VLF systems include Scintrex SE-99, Sander EM-11, and Herz Totem-1A and 2A, all described in Section 7.5.4. The first two incorporate automatic leveling devices to correct undesirable aircraft movement. The Totem units, recording total-field and vertical-quadrature components by means of three orthogonally mounted coils, require no other leveling controls. Furthermore, the total field is related to wave tilt and quadrature (§7.7.3); thus the  $\rho_a$  plot might be computed from these parameters, aided by direct measurements of

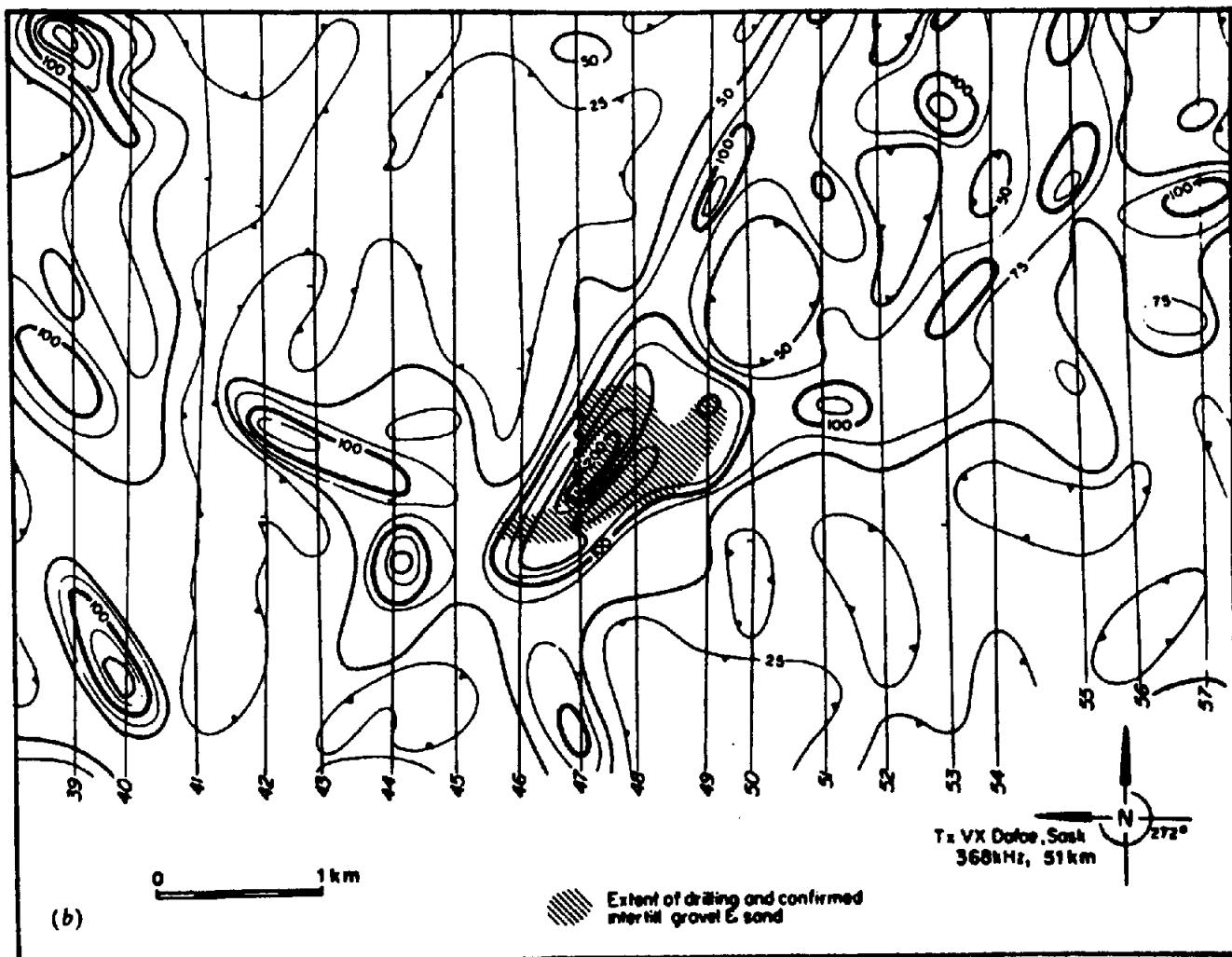


Figure 7.78. (Continued) (b) map showing flight lines and contours of  $\rho_a$  for frequency 368 kHz [LF in part (a)]; cross hatching indicates a gravel deposit located by the survey.

$\rho_a$ , such as EM16R or dc resistivity (because the  $\rho_a$  values are relative).

Contours of total-field response from a Totem-2A survey near Utik Lake Manitoba, in the Precambrian greenstone belt, are illustrated by the contour map of Figure 7.79. Conductors appear as long E-W strips; the superimposed circles are from a helicopter phase-component survey.

The Totem-2A unit is equipped to measure response from two VLF stations at once, which increases the possibility of signal enhancement. As noted in Section 7.4.2f, maximum coupling of the VLF plane wave is achieved when the transmitter is on strike with the conductor long axis. This advantage is not as great as it might seem because of the limited number of VLF stations and their global distribution. Except for North Cape, Australia, they are all located well north of the equator. In the Western Hemisphere the shutdown of Balboa Canal Zone has left the user with a compulsory preference for E-W strike.

Airborne VLF, like the ground method, is capable of detecting conductive structures with steeply

dipping boundaries. An example is shown in Figure 7.80a, obtained during a radiophase survey near Noranda, Quebec, where the Smoky Creek and Quesabe faults are marked by anomalies similar to Figure 7.48. Both this and an earlier airborne AFMAG survey outlined many well-known faults in the area. Detailed EM16 ground followup (Telford, King, and Becker, 1977) located Smoky Creek fault very precisely, as seen in Figure 7.80b, for the EM16 profile marked in Figure 7.80a. Although there is no lithological contrast across the contact, both sides being granodiorite, an abrupt 15 m increase in conductive overburden thickness was measured subsequently by shallow dc sounding. This accounted for the strong airborne and ground VLF anomalies.

#### 7.7.10. Phase-Component AEM

Although these FDEM systems are not capable of reaching depths as great as Turair or Input, they produce more data and are more suitable for de-

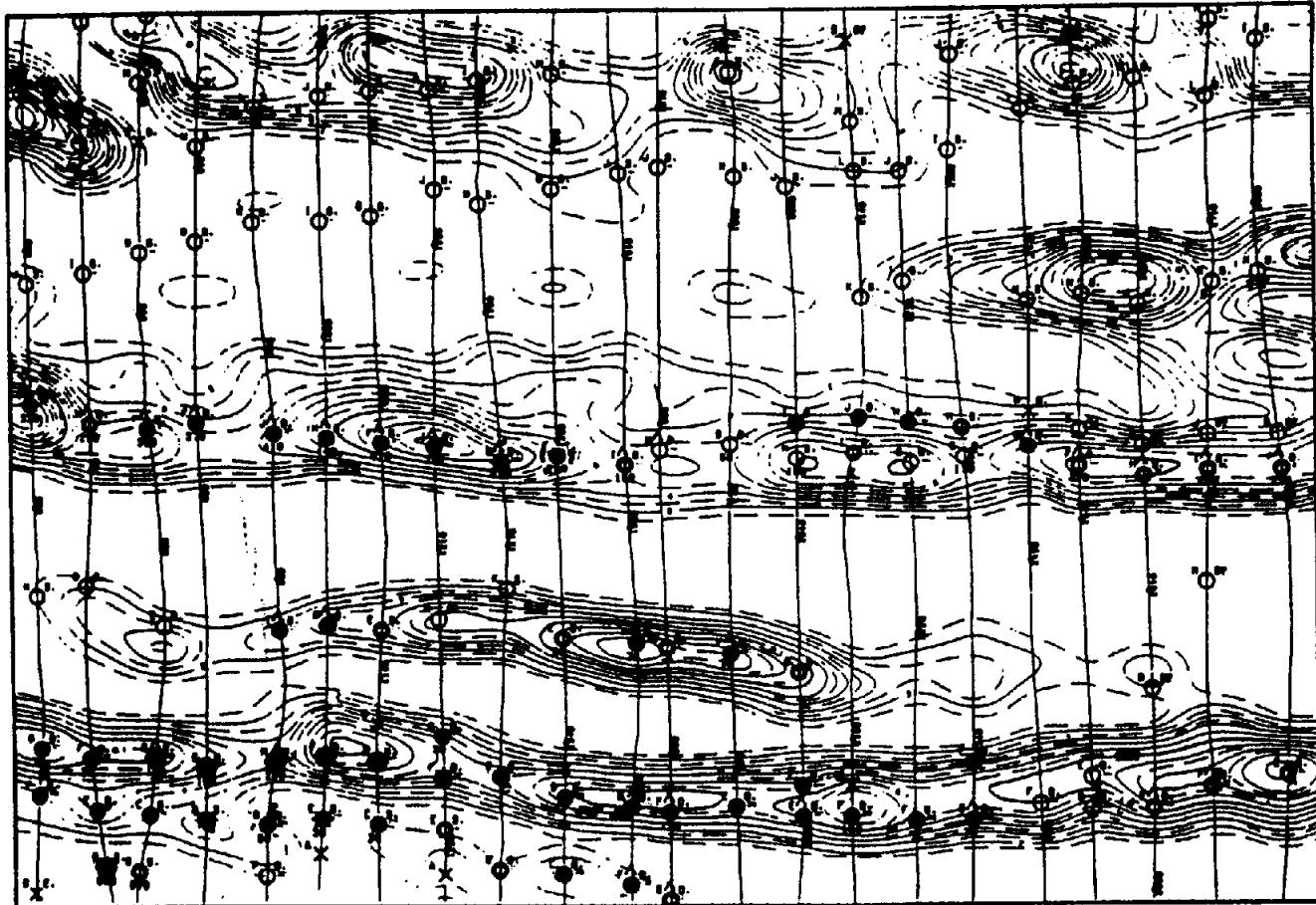


Figure 7.79. Total-field VLF contours from a Totem-2A survey near Utik Lake, Manitoba. Circles indicate conductors located by a helicopter phase-component survey. (After Herz, 1986.)

tailed surveys, detection and resolution of small-scale conductors, and mapping. We will consider the Tridem and Dighem versions of this type of equipment, both introduced in the early 1970s.

Tridem carries two vertical coplanar coils approximately 18 m apart on the wing tips of a De Havilland Otter aircraft (Fig. 7.26a), operating at 520, 2,020, and 8,020 Hz to provide six channels of simultaneous in-phase and quadrature data. The cutoff noise level is 50 ppm for a 2 s time constant on all channels. Use of these frequencies provides better discrimination in depth and between thick and thin conductors. Otherwise, Tridem is much like earlier phase-component airborne equipment.

The Dighem and Aerodat helicopter rigid-boom systems, described in Section 7.5.5, are multicoil as well as multifrequency methods. The former, illustrated in Figure 7.26d, shows the vertical transmitter coil with flight-line axis and three orthogonal receiver coils, two of which are minimum-coupled, known as fishtail and whaletail for obvious reasons. Formerly single frequency (900 Hz), there are two later models: Dighem III operates two horizontal coplanar coil pairs at 900 and 7,200 Hz and one vertical coaxial pair from 385 to 7,200 Hz; Dighem

IV carries a 56,000 Hz frequency. The Aerodat boom contains two vertical coaxial pairs at 955 and 4,536 Hz and two horizontal coplanar pairs at 4,132 and 33,000 Hz. Coil separation is 7 m and noise level 1 to 2 ppm in both. An attractive feature of phase-component AEM is its symmetry with respect to flight direction.

Data interpretation with these units is somewhat like the Slingram ground set, although the coils are mounted both horizontally and vertically. The latter orientation is more sensitive to conductors of steep dip when the ratio of  $z/l$  (Fig. 7.82) is large; with these AEM methods, particularly the helicopter system, such is the case. For example, the problem of a sphere or semiinfinite vertical sheet lends itself to an approximate solution using the lumped circuit analysis; for both models the loops are assumed to be superimposed. From the procedure used previously, we obtain for the sphere:

$$\Re_e \{ H_x^t / H_x^p \} \approx 0.8(a/h)^3(l/h)^3 \left( 1/\beta(1 + \alpha^2)^3 \right) \quad (7.44a)$$

$$\Im_m \{ H_x^t / H_x^p \} \approx \Re_e \{ H_x^t / H_x^p \} / Q \quad (7.44b)$$

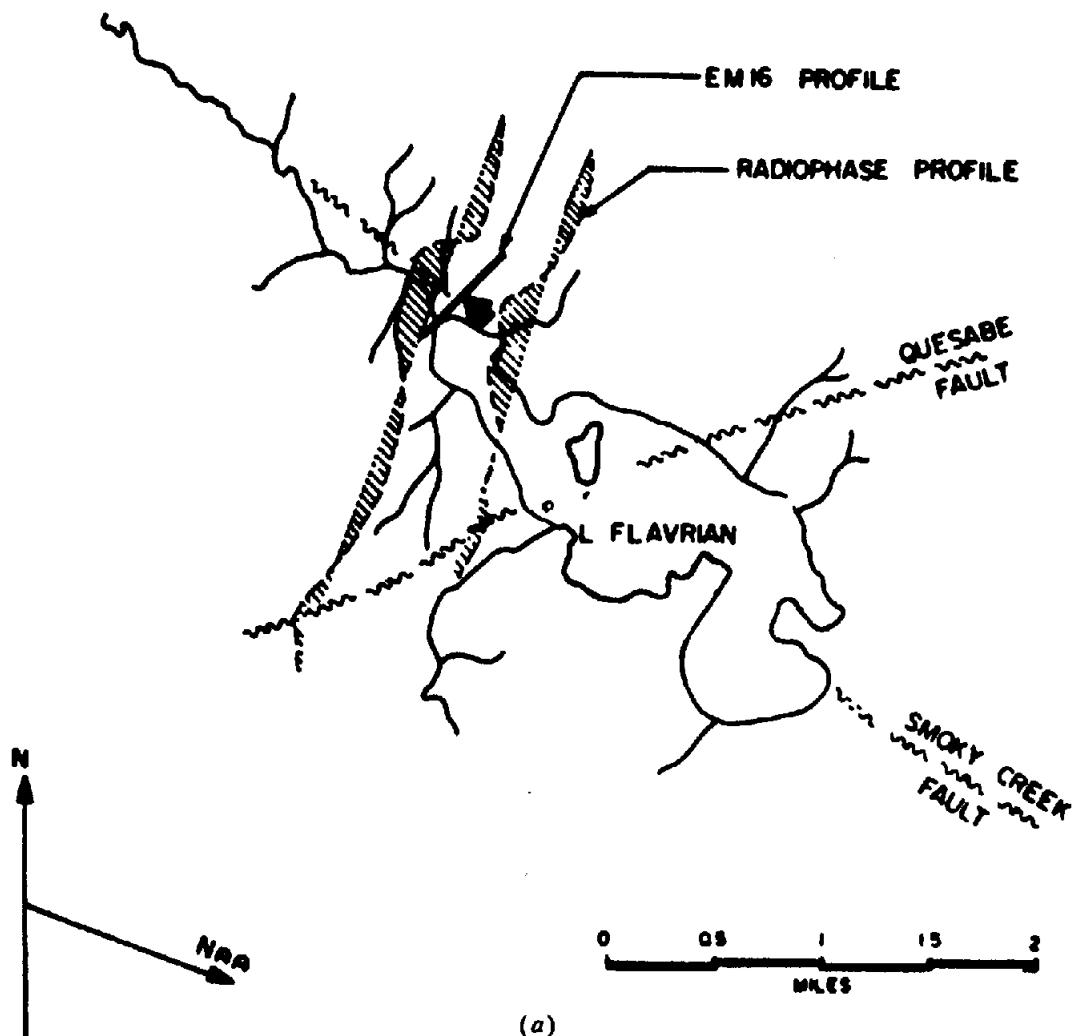


Figure 7.80. Airborne VLF (radiophase) and detailed EM16 ground survey, Smoky Creek fault area, near Lake Abitibi-Noranda, Quebec. (From Telford, King, and Becker, 1977.)  
(a) Map showing survey lines, fault traces, and profile locations.

where  $a$  is the sphere radius,  $h$  the distance between centers of the dipole and sphere,  $l = T-R$ ,  $\beta = (1 + 1/Q^2)^{1/2}$ , and  $\alpha = x/h$ .

For the vertical thin sheet, we have

$$H_x^s/H_x^p \approx 2 \times 10^{-4} (h/\ell)(l/h)^3 \left\{ 1/\beta(1 + \alpha^2)^2 \right\} \quad (7.44c)$$

where  $\ell$  is the effective conductor length energized along the top of the sheet and  $h$  is the distance from the dipole center to the top of the sheet.

Profiles for these models are sharper than those from AEM units with large  $T-R$  separations. Depth may be roughly estimated from the value of  $\alpha_{1/2}$  at half-maximum; for the sheet  $h = 0.8x_{1/2}$  whereas  $h = x_{1/2}$  for the sphere. Knowing the altitude of flight, one can get some idea of conductor geometry.

From Equations (7.44a, c) the sphere-model response decreases as  $h^{-3}$ , whereas the value for the thin sheet appears to be  $h^{-2}$  (although the correct value is said to be  $h^{-3.3}$  - and other powers ranging

from -2.6 up for equipment of this type). One might assume the 2-D geometry of the sheet should produce a slower falloff than the sphere, but the explanation is probably that the area of eddy-current induction is quite limited and that the effective inductance of the sheet also varies with height, possibly as  $1/h$ .

More satisfactory interpretation aids in the form of characteristic curves are available for phase-component systems. Using a semiinfinite vertical-sheet model and considering only the maximum response, when the sensors are directly over the top, we have (Grant and West, 1965, p. 526), assuming  $x = a = 0$ ,

$$H' = m_x \left\{ 1/3 - (l/2h)^2/5 + (l/2h)^4/7 - \dots \right\} / 16\pi^2 h^3$$

where  $m_x = 4\pi l^3 H^p / 2$  or  $-4\pi l^3 H^p$ , the transmitter dipole moment for coaxial and coplanar coils, re-

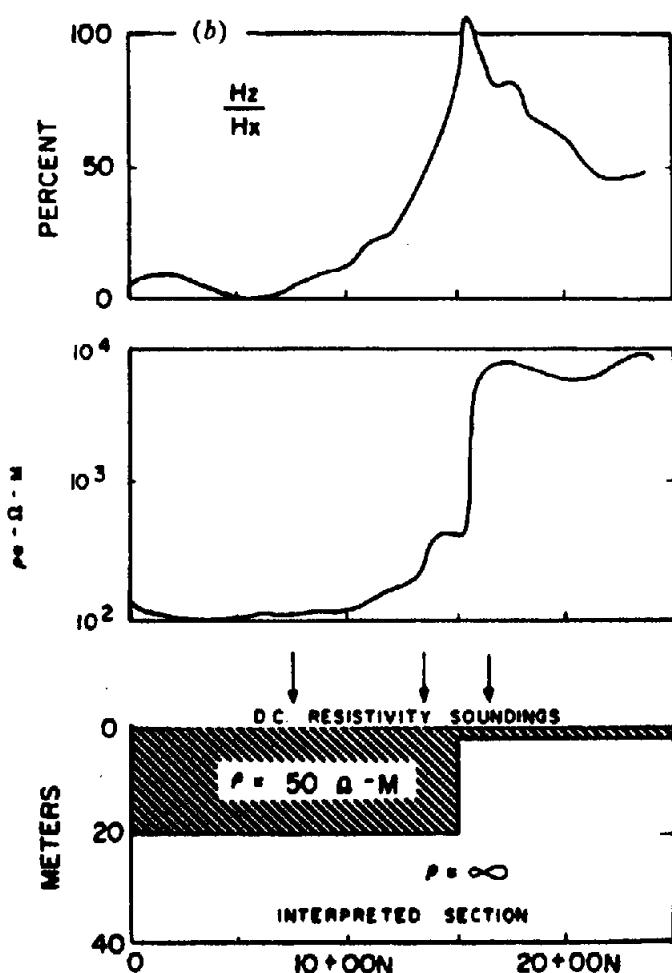


Figure 7.80. (Continued) (b) Curves of  $(H_z/H_x)$  and  $\rho_s$  on the EM16 profile, plus interpreted section.

spectively (§7.2.3d). When  $h \gg l$  this becomes

$$H'/H^p \approx (l/h)^3/24\pi \text{ or } -(l/h)^3/12\pi \quad (7.45a)$$

for the same configurations. Because Equation (7.45a) is derived for a model of infinite conductivity, these relations must be separated empirically into in-phase and quadrature components

$$R = M(l/h)^3 \quad Q = N(l/h)^3 \quad (7.45b)$$

and then plotted as  $R/Q$  versus induction number  $(\mu_0\omega\sigma h)^{1/2}$  (§7.7.3i), as shown in Figure 7.81a.

Because  $R/Q = M/N$ , we may now produce a response curve like that in Figure 7.10 for the  $M$  and  $N$  values of the vertical sheet, using the induction number as the second coordinate; see Figure 7.81b. Finally, the characteristic curves, with in-phase and quadrature maximum response for various values of  $\sigma$  and  $h$ , appear in Figure 7.81c. These are for

coaxial coils, but may be adapted for any maximum-coupled coil pair [e.g., §7.7.6b, systems (a), (b), and (c)] and frequency, provided the coil separation is small compared to flight height.

The flight heading is usually assumed normal to sheet strike; when it is oblique, the Dighem vertical null-coupled coil produces an anomaly. The angle may be determined from the relation

$$\alpha = \tan^{-1}(R_m/R_v)$$

where  $R_m$  and  $R_v$  are the respective responses in the maximum-coupled and vertical null-coupled channels. This leads to an azimuth correction

$$H^0 = H' \csc^2 \alpha \quad (7.45c)$$

where  $H^0$  is the signal normal to strike and  $H'$  the measured MC response at angle  $\alpha$ .

The Dighem horizontal NC coil indicates dipping conductors, useful in distinguishing near-surface conductive beds of shallow dip.

Response of the sheet target theoretically decreases as  $h^{-3}$  only for infinite conductivity in a resistive host rock. In a realistic situation,  $R/Q$  increases with flight altitude; from Figure 7.81c, at  $h = 100$  ft,  $R/Q = 1.2$ ; at 400 ft it is about 2.8. Effects of conductive overburden and host rock (§7.7.4e) are also quite as significant in airborne as in ground surveys.

AEM phase-component response over the spherical model has been well covered by Lodha and West (1976). Using the theoretical treatment available since the 1950s (e.g., Wait, 1960b), they computed the response function for a vertical coaxial-coil pair, helicopter-mounted on board or in a towed boom. Characteristic curves, with plots of  $(\mu\omega\sigma a^2)$  versus  $z/a$  for a range of  $z/l$ , are given in Figure 7.82 for a complete interpretation. In the diagram the rectangles mark the range of calculating the parameters for various vertical distances to the sphere center. (Note that all dimensions are measured in units of  $l$ .) Empirically it has been found that over a wide range of the parameters the half-peak widths of the field profiles are related to  $z$ :  $0.58W_{1/2} \leq z \leq 0.8W_{1/2}$ , and that  $W_{1/2} \approx 10l$ . The method is to select the average value,  $z = 0.7W_{1/2}$ , and find the point for the in-phase and quadrature peaks on the figure. This point will generally lie within the rectangle  $z/l = 7$ , from which  $z/a$ ,  $\mu\omega\sigma a^2$  (hence  $\sigma$  because  $z$  is assumed to be known) may be read directly. A second approximation may be obtained by changing  $z/l$  to 8 or 6 and then interpolating for a better result.

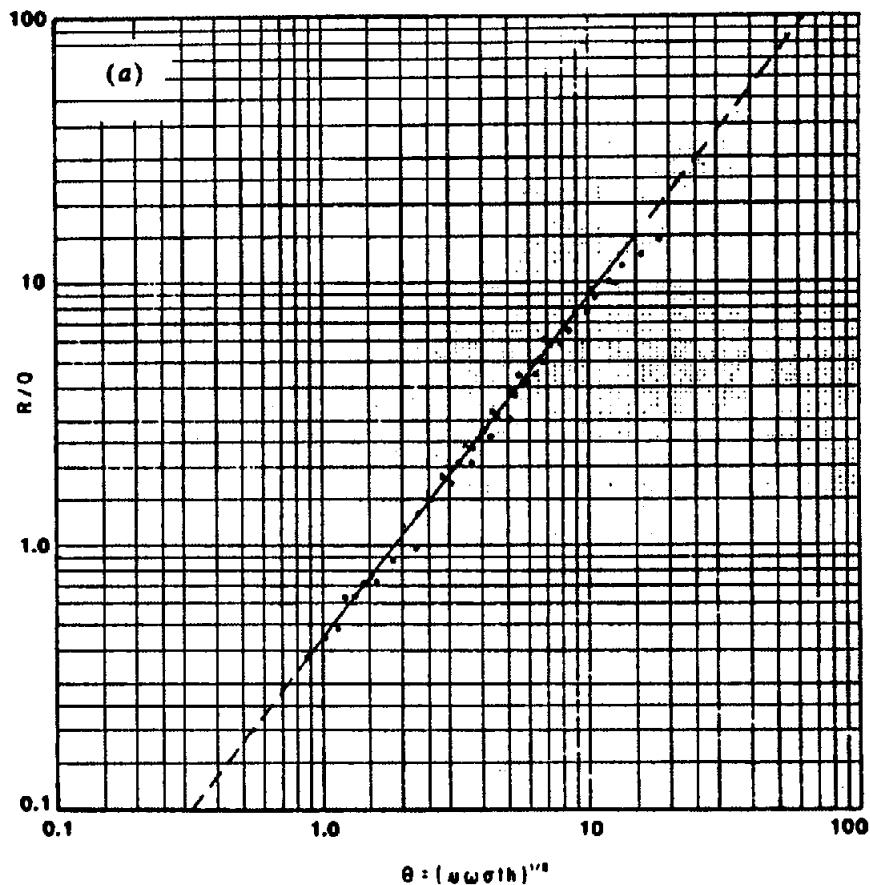


*Figure 7.81. Response of a maximum-coupled coil to a thin vertical dike. (After Fraser, 1972.) (a) Ratio of in-phase ( $R$ ) to quadrature ( $Q$ ) components as a function of the induction number  $\theta = (\mu_0 \sigma t)^{1/2}$ .*

Characteristic response of a horizontal thin-sheet conductor is another useful interpretation model, particularly for resistivity mapping. The analytical procedure is similar to but simpler than that for the sphere (Grant and West, 1965). Figure 7.83 shows this set of curves for Tridem. In general form it is like that for the vertical sheet in Figure 7.81c. However, the solid curves are plotted for various values of  $f\sigma t$ , permitting a determination of  $\sigma t$  at all frequencies used in the Tridem system.

The aforementioned model conductors may be analyzed by means of the computer programs PLATE and SPHERE (§7.7.4a and §7.7.5c) in both frequency and time domain.

### 7.7.11. Resistivity Mapping

Stagnation in base-metal prices and steady increase in exploration costs since 1978 have reduced the use of airborne EM from a peak of 600,000 line-kilometers in 1979 to less than half this figure in 1988. Activity in airborne magnetics and radiometrics, however, has not declined during the same period, the first because of its proven versatility and the second as a result of shallow mapping applications.

The message is clear enough: rather than detecting sulfide anomalies, airborne EM should be increasingly applied to structural mapping, preferably in combination with the other two techniques. This trend is already evident to some extent.

Development and interpretation of resistivity maps from AEM surveys have been discussed in several reports (Fraser, 1978; Seigel and Pitcher, 1978; Geological Survey of Canada Paper 86-22, 1986). To prepare these, flight data must be compared to zero or background-level response. This is achieved by periodically increasing altitude to about 200 m at the end of a flight line.

Various layer models have been employed for analysis in resistivity mapping. The recorded altitude of the system is a critical parameter in all cases, because the data are subject to errors caused by irregular terrain and dense tree cover. Correct or not, the addition of the altitude measurement to the other recorded quantities, in-phase and quadrature response (preferably at several frequencies for a layered section), is one parameter too many for unique determination of the apparent resistivity. The result is equivalent to simultaneous dc resistivity profiling and sounding, that is, a strong probability of more

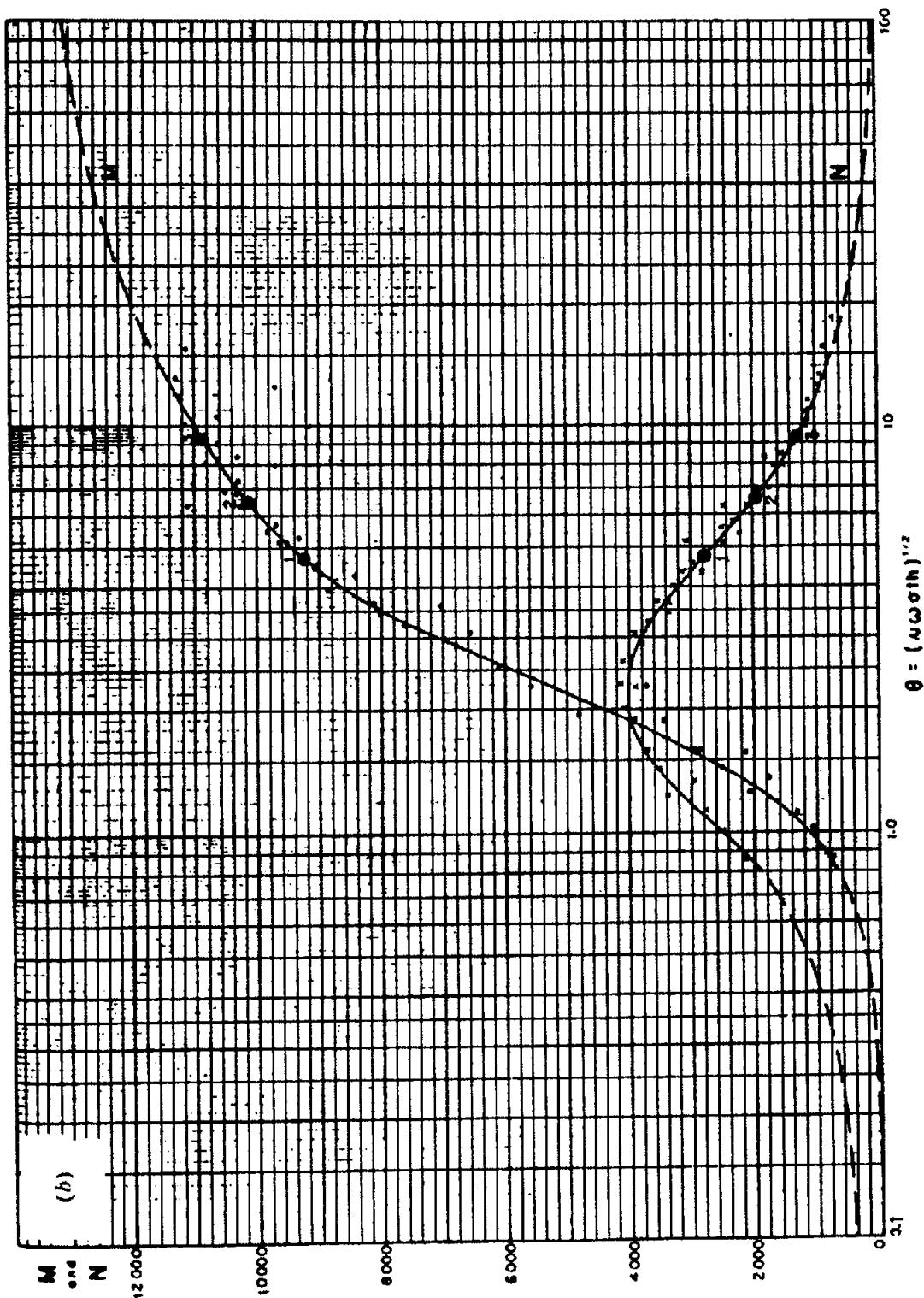


Figure 7.81. (Continued) (b)  $M$  and  $N$  as functions of  $\theta$ .

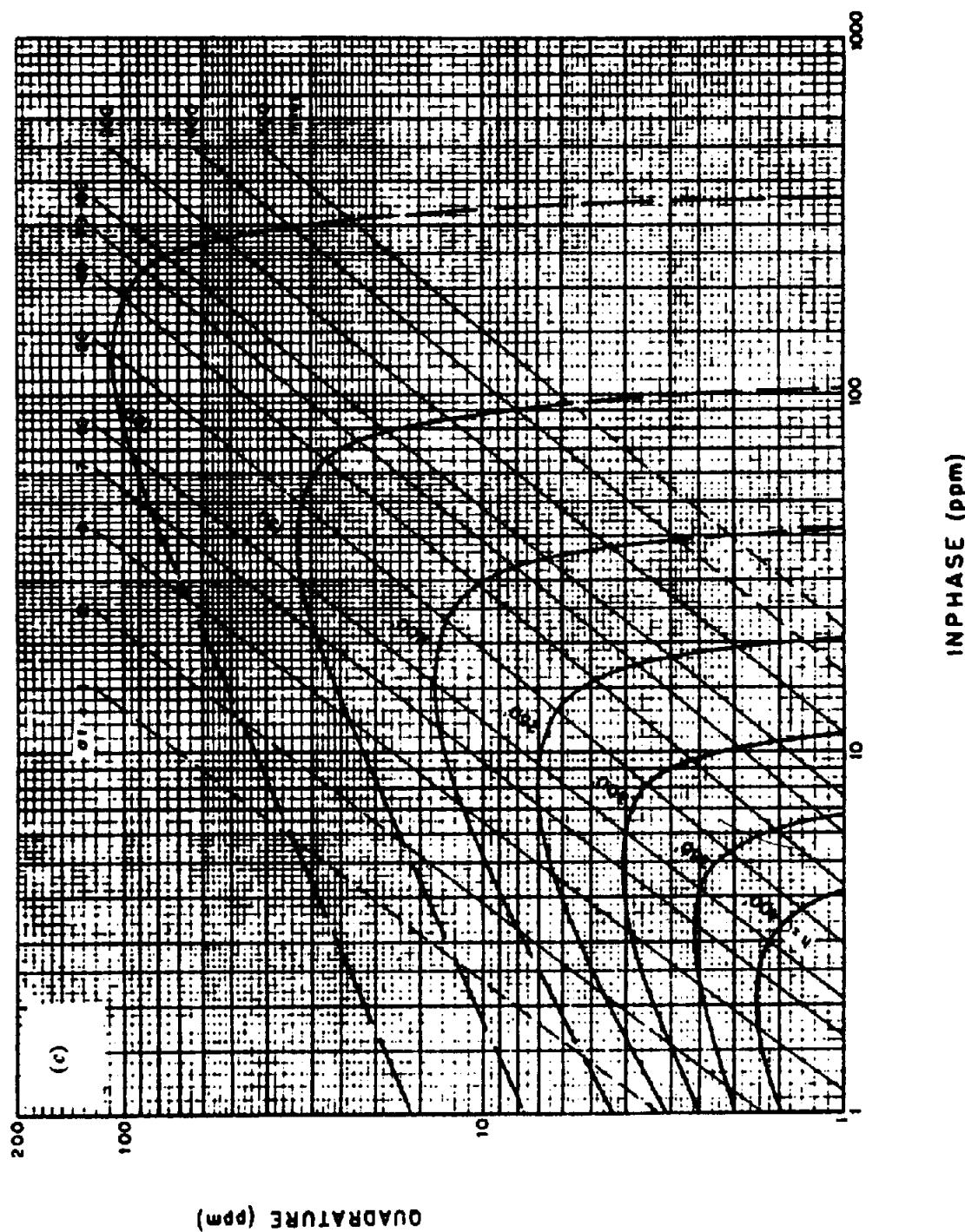


Figure 7.81. (Continued) (c) Nomogram giving  $h$  and  $\alpha$  in terms of  $R$  and  $Q$ .

## Practical AEM Interpretation

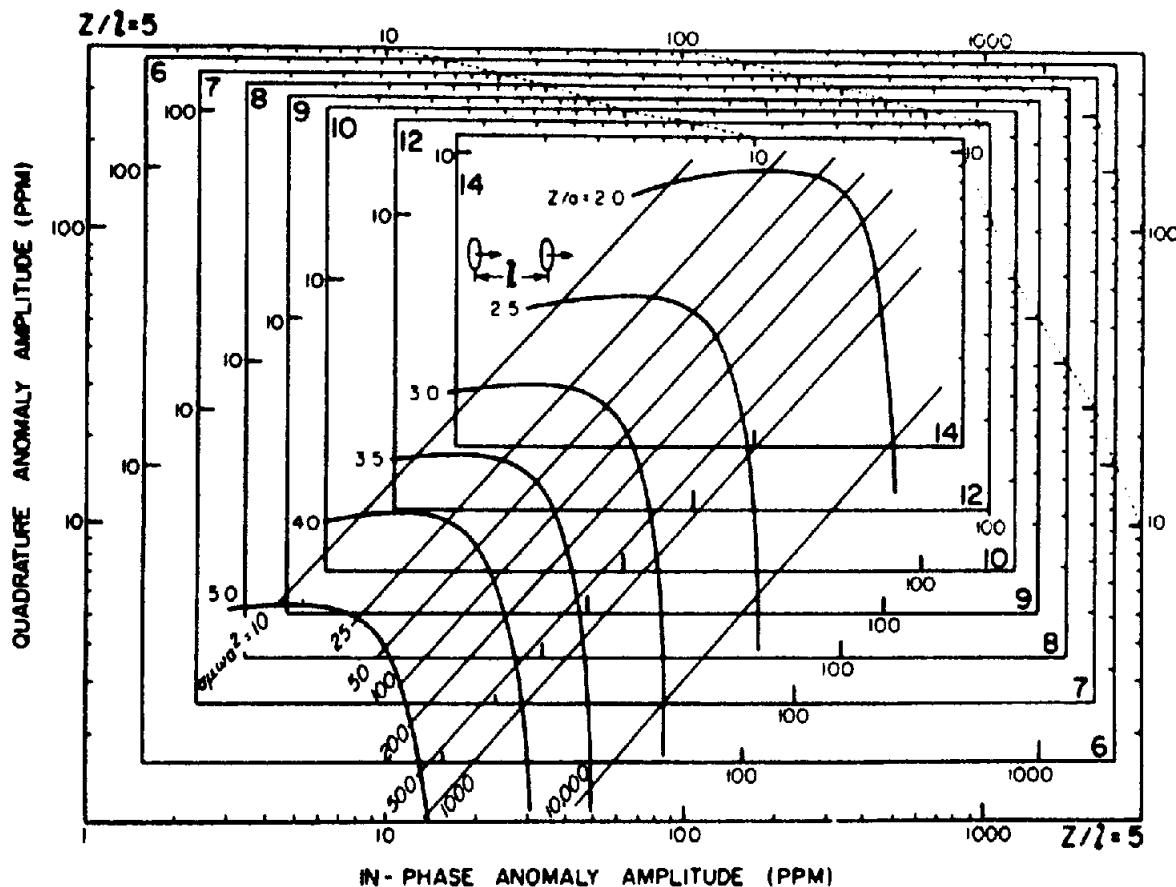


Figure 7.82. Interpretation diagram for a vertical coaxial-coil AEM system over a spherical conductor of radius  $a$  for  $z/l = 5, 6, 7, 8, 9, 10, 12$ , and  $14$ ;  $l = T-R$ . (After Lodha and West, 1976.)

than one solution, unless the ground is homogeneous and isotropic. For example, we may determine  $\rho_a$  as a function of (i) bird altitude and amplitude  $(R^2 + Q^2)^{1/2}$ , (ii) altitude and phase angle,  $\tan^{-1}(Q/R)$ , or (iii) amplitude and phase. The first two estimates will most likely be different and neither supplies any depth information. Solutions (i) and (iii) are shown in Figures 7.84a, b.

To avoid, or at least reduce, this difficulty, it has been the custom to assume a fictitious highly resistive layer of variable depth overlying either a half-space or two beds simulating overburden and bedrock. (Models with more layers are too complex for interpretation at present.) The first of these has been called the *pseudolayer half-space*, the second a *pseudolayer two-layer* or *three-layer model* (Fraser, 1986; Paterson and Reford, 1986). This resistive top layer is a device to absorb the difference between height of the boom recorded by the altimeter and the sensor-source distance determined from Figure 7.84b.

The two models are shown in Figure 7.84c and d, where  $a$  is the altimeter reading and  $h$  the computed vertical height. A positive value of  $(h - a)$  may be the result of tree cover, permafrost, glaciated overburden, and the like; it could be negative over treeless surfaces with a conductive top, or zero if the open ground is homogeneous to a depth greater than the penetration of the AEM system.

The ambiguity resulting when we attempt to match a two-layer model with half-space data from Figure 7.84a is illustrated in Figure 7.84e. The three-frequency AEM system produces three different  $\rho$  values as expected, but none is clearly related to  $\rho_1$  or  $\rho_2$ . Only the horizontal coplanar pair at 4,020 Hz determines  $h$  reasonably well, but  $h$  is already known (because it equals the aircraft altitude approximately; see Fig. 7.84d). Thus, no useful information is provided concerning the overburden.

The pseudolayer model of Figure 7.84c gives more reasonable results using the curves of Figure 7.84b, but only if the field geometry is at least approxi-

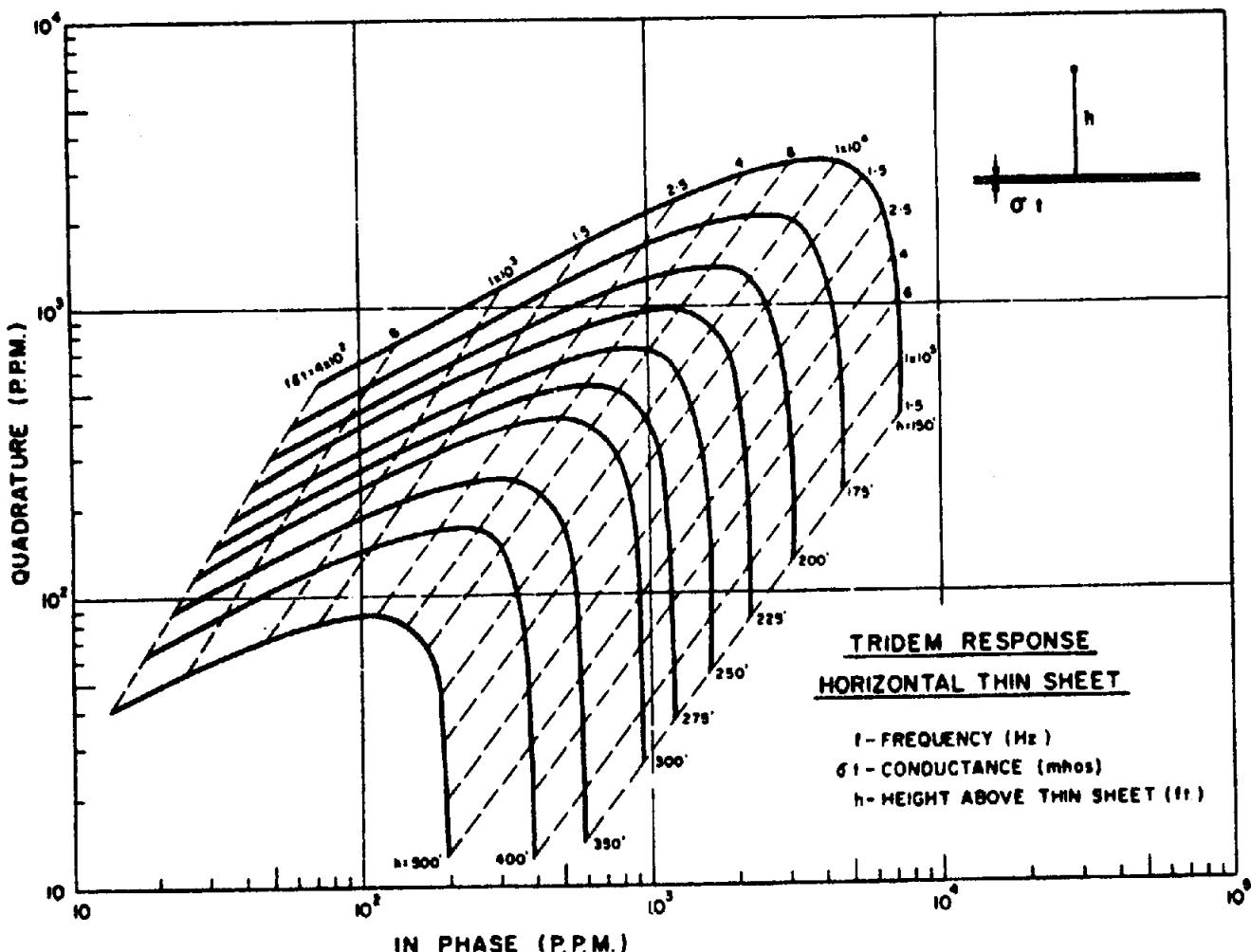


Figure 7.83. Characteristic curves for the Tridem system over a horizontal thin sheet. Solid-line curves are for constant  $f$  (ft), dashed are for constant  $h$ .

mately a half-space. However, the assumption of three layers, Figure 7.84d, to match two beds as in Figure 7.84e, is the most realistic model because it includes overburden in the four unknown parameters.

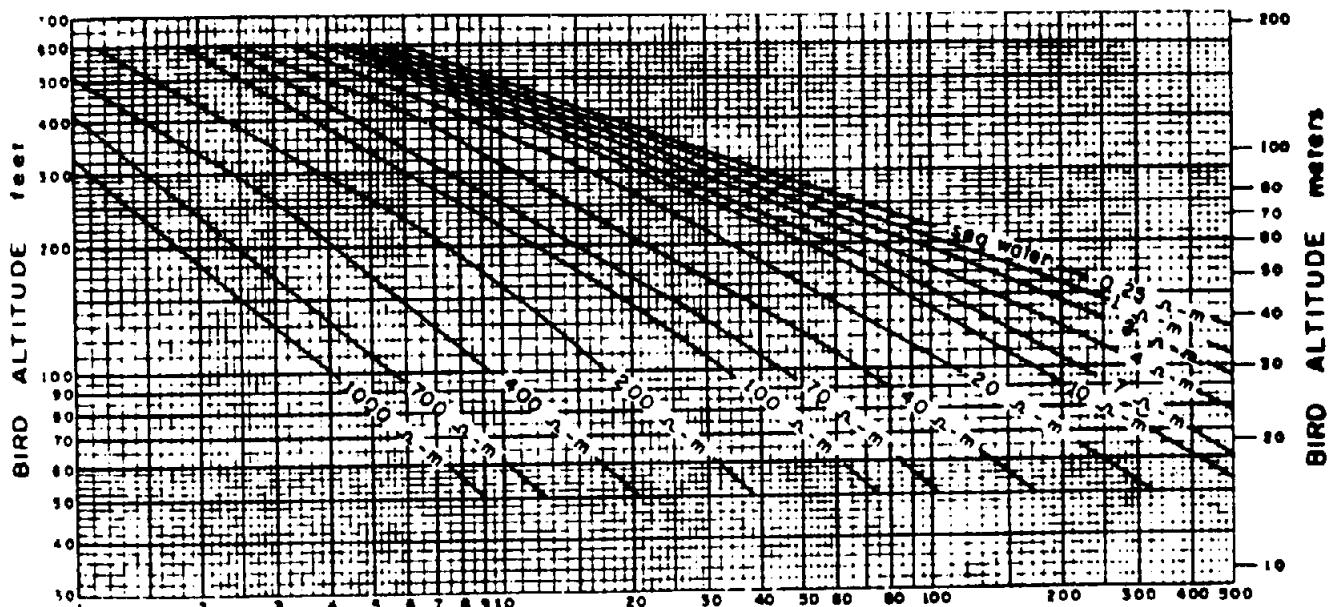
Analysis may be done with a *table lookup routine* (De Mouly and Becker, 1984; see also §7.7.12h), by comparing survey data with standard models, or by an inversion technique described for FDEM (Paterson and Reford, 1986) in which the fit between the model data and the field data is optimized (§2.7.9). In the latter analysis several routines are necessary to minimize the ambiguities in overdetermination. These include estimation of relative significance, error limits, and tolerance of each parameter for acceptable model fit, plus maximization of stability and economy because of the large amount of data. The procedure is known as *singular value decomposition* (SVD) or *eigenfunction analysis*.

The resistivity map can be a definite interpretation aid in base-metal surveys for distinguishing bedrock from overburden conductors. An example is shown in Figure 7.85. The original flight sheet in

Figure 7.85a locates anomalies with conductances marked on the flight lines, along with the interpreter's assessment of their character. Resistivity contours superimposed in Figure 7.85b locate two low zones of  $30 \Omega\text{m}$ , which could be identified with more confidence as bedrock sources because they were not associated with drainage. The ground IP-resistivity survey results, displayed in Figure 7.85c, plus later drilling confirmed this interpretation by exposing graphite with disseminated pyrite.

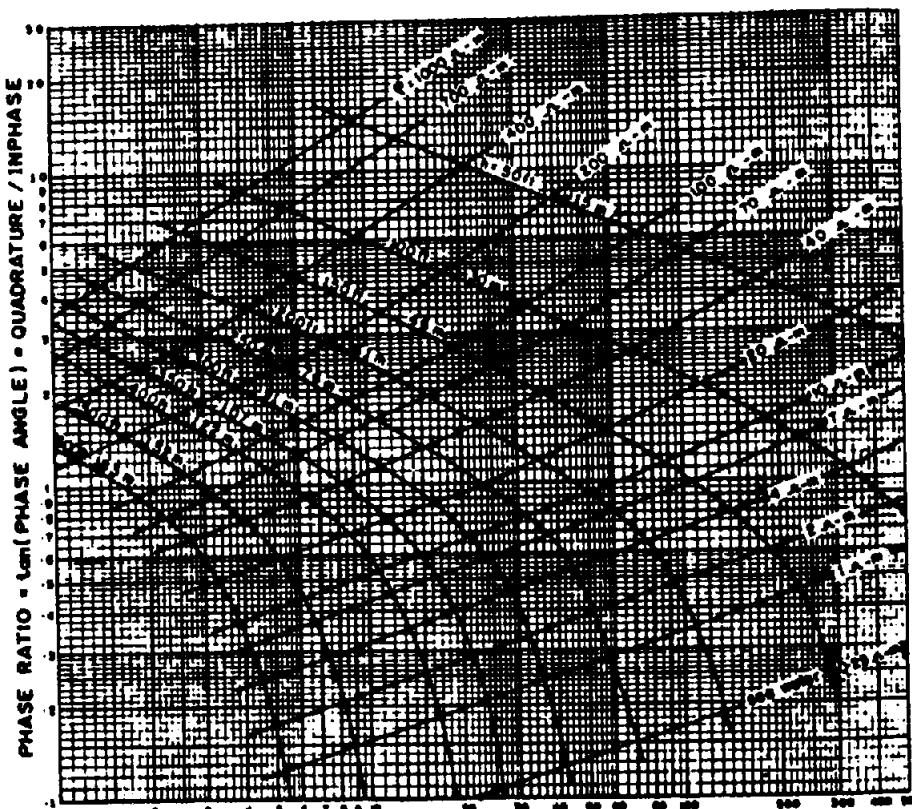
#### 7.7.12. Input AEM

(a) *General.* Since about 1963, this unique airborne time-domain technique has been the "bread and butter" reconnaissance EM system in base-metal exploration. Originally the interpretation procedure was quite elementary, but improvements in equipment – a 30% boost in transmitter power and more receiver channels – have greatly increased the signal-to-noise ratio and digital data acquisition and recording have provided higher quality data. Increased power allowed a shorter time constant, which in turn pro-



$$\text{AMPLITUDE (ppm)} = \left[ \text{INPHASE}^2 + \text{QUADRATURE}^2 \right]^{1/2}$$

(a)



$$\text{AMPLITUDE (ppm)} = \left[ \text{INPHASE}^2 + \text{QUADRATURE}^2 \right]^{1/2}$$

(b)

*Figure 7.84. Interpretation of airborne resistivity data over a multilayer half space. [Parts (a) and (b): After Fraser, 1978; parts (c) and (d): After Fraser, 1986; part (e): After Paterson and Reford, 1986.] (a) Altitude of bird versus amplitude for a maximum-coupled coil over a homogeneous half-space; frequency 900 Hz. (b)  $\tan\phi$  versus amplitude for maximum-coupled coil over the pseudolayer half-space model in (c); frequency 900 Hz.*

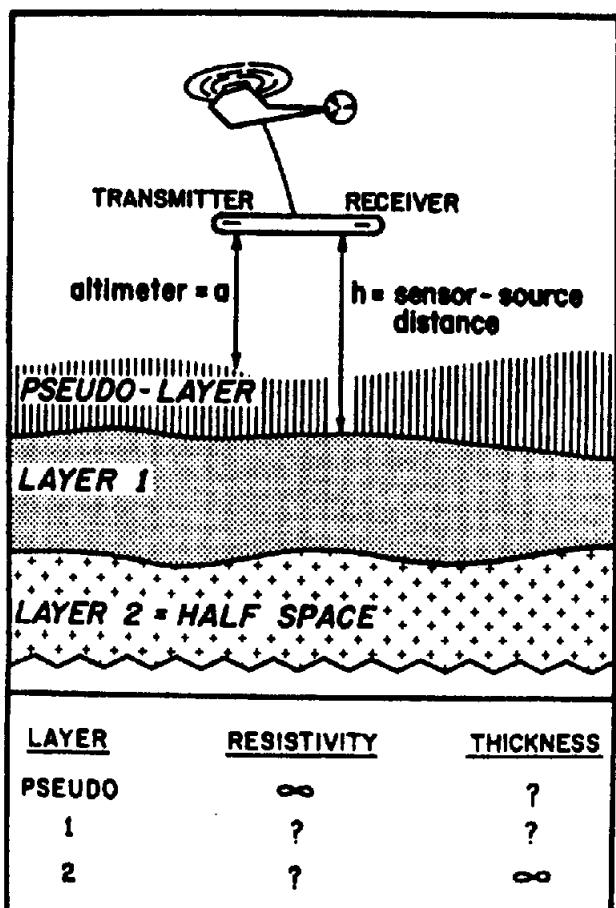
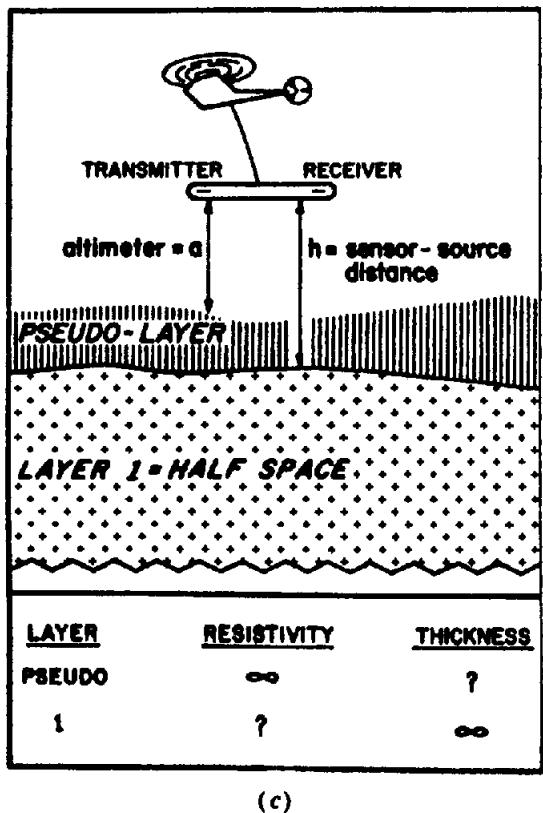


Figure 7.84. (Continued) (c) Configuration of the Dighem system with horizontal coplanar coil pair over pseudolayer half-space model. (d) As in (c) except pseudolayer plus two-layer model.

duced better anomaly resolution and greater depth of penetration. Development of more sophisticated scale models and digital data processing have also improved the interpretation, as in other airborne systems. Consequently Input may now be employed for mapping, as well as detecting bedrock conductors to considerable depth.

(b) *Vertical-sheet response.* In a pioneering report on TD interpretation, Becker (1969) simulated the transient response of the Input system to a thin conducting sheet. The procedure is carried out in the frequency domain; replacing the thin-sheet target with a loop conductor,  $L$  in series with  $R_L$  (§7.2.4b, §7.2.5d), the loop response function becomes

$$c(\omega) = G(Q^2 + jQ)/(1 + Q^2) \quad (7.46a)$$

where  $Q = \omega L/R_L = \omega\tau$ ,  $\tau$  is the loop time constant, and  $G$  is a multiplier relating to the transmitter-, receiver-, and conductor-loop geometries.

The conductor loop may be also simulated by the  $R$ - $C$  network, shown in Figure 7.86, whose transfer function is

$$\begin{aligned} c'(\omega) &= G'R_C/(R_C + 1/j\omega C) \\ &= G'(\omega^2 C^2 R_C^2 + j\omega CR_C)/(1 + \omega^2 C^2 R_C^2) \end{aligned} \quad (7.46b)$$

also  $CR_C = \omega\tau'$ . For an exact simulation, we must have, at all frequencies,  $c(\omega) = c'(\omega)$ , that is,  $G = G'$ , and  $\tau = \tau'$  or

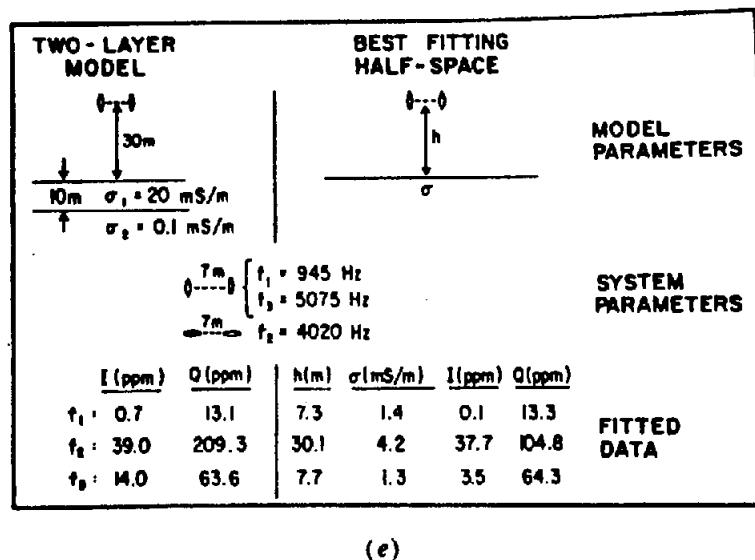
$$L/R_L = CR_C \quad (7.46c)$$

Standard Input field equipment, coupled to the circuit of Figure 7.86, may then be used as an equivalent analog model to simulate the transient response under various geometric conditions.

The preceding analog simulation, however, is not useful for conductor models other than the thin sheet. For different geometries, modeling is better done using a digital computer and convolution methods (§A.10, §A.13), provided the FD response is known.

Becker, Gauvreau, and Collett (1972) used a scale model to simulate Input four-channel response over vertical dikes of variable thickness and conductivity, as well as horizontal sheets as overburden. The scaling relation in Equation (7.33a), which can be written  $(\sigma_m/\sigma_f) = (f_f/f_m)(l_f/l_m)^2$ , was satisfied by taking  $f_m = 3f_f$ ,  $l_m = l_f/1560$ , and  $\sigma_m = 8.1 \times 10^3 \sigma_f$ .

As a result, aluminum, stainless steel, and graphite sheets ( $32 \times 10^6$ ,  $1.4 \times 10^6$ , and  $10^5$  S/m) correspond to field conductors of 40, 1.7, and 0.12 S/m,



(e)

Figure 7.84. (Continued) (e) Comparison of actual two-layer and best-fitting half-space response.

respectively. Both minimum and maximum  $T\text{-}R$  coupling were tested, the first with the receiver coil vertical, the second horizontal. It was found that sheets of 60 cm strike length and 15 cm depth extent, corresponding to  $900 \times 250$  m field dimensions, were sufficiently large to represent semiinfinite conductors, but unsuited as sheets of low  $\sigma t$ .

Examples of channel response for both couplings over the vertical sheet appear in Figure 7.87a. Amplitudes varied with the thickness-conductivity product (TCP) but the general shapes of curves were the same. Input response over thick vertical sheet models (not shown here) appeared to verify theoretical results of Paterson (1971), but both differ from field profiles, which are much wider and about half the maximum amplitude. A second discrepancy was noted between model and field results, namely, that the response decreased with altitude much faster for the models. However, this was thought to be caused by differences in the waveforms of the model system and the field equipment. Another set of profiles over the same target, simulating minimum coupling with the six-channel Input is shown in Figure 7.87b.

A nomogram for depth and conductance estimation is given in Figure 7.88a for the vertical half-plane conductor. Channel amplitudes are plotted against TCP on log-log scales. (These plots were developed by Palacky and West in 1973 from analog FD model measurements transformed to TD. They were useful only for the standard sensitivity of  $\sim 300$  ppm; the procedure is now automated for the computer.) Presumably the data may now be obtained via the PLATE program (Dyck, Bloore and Vallée, 1981). First the anomalous six-channel amplitudes are taken from the Input flight record and replotted to the log scale on the right of Figure 7.88a on a transparent

overlay; the  $10^5$  ppm point is also marked on this vertical scale. The transparency is then moved over the curves, maintaining parallel axes, to obtain the best fit for the six data points. Conductivity and depth below the aircraft are then read off the upper auxiliary grid at the location of the  $10^5$  ppm point, with respect to the slant and horizontal lines. An analogous nomogram for the conductive half-space is illustrated in Figure 7.88b.

(c) *Ribbon model.* Profiles over a ribbon, or thin sheet conductor of finite depth extent, show that amplitude varies with depth extent, but more for poor conductors than good ones. However, the channel ratios are practically unchanged, which is also true for limited strike length. Thus the conductivity estimates from the nomogram of Figure 7.88a are still valid. It is not possible to distinguish depth extent from depth to the top without additional geological or geophysical information.

(d) *Dipping half-plane.* Figure 7.87b displays model Input Mark VI profiles over a vertical half-plane, at two altitudes and for three  $\sigma t$  values. Comparing these with the maximum-coupled four-channel set in the upper part of Figure 7.87a, the six-channel Input clearly produces profiles with better definition, including a more obvious minor peak before (with respect to flight direction) the main anomaly. Initially, from field survey data, the minor peak was assumed to be a minor conductor; however, because it could not be found from ground followup and because it was also present on model profiles, such as Figure 7.87b, the small peak was seen to be an inherent feature of the Mark VI design.



Figure 7.85. Resistivity map as an aid in distinguishing bedrock from overburden anomalies. (After Fraser, 1978.) (a) Airborne EM map showing conductor pattern similar to that for conductive overburden.

Palacky and West (1973) have used the ratio of major-to-minor peak amplitudes to estimate dips of the half-plane conductor. From model and field data they found that the ratio was 10 for  $90^\circ$  dip, decreasing to about 1.5 for  $135^\circ$  dip. When flying updip, two distinct peaks are observed, the second over the

upper edge of the sheet. Downdip, only one peak of much larger amplitude appears on the profile plot.

Dip estimates may be made from Figure 7.89, which also includes an amplitude correction factor for modifying the conductor depth estimate. The procedure is to enter the righthand side of the figure

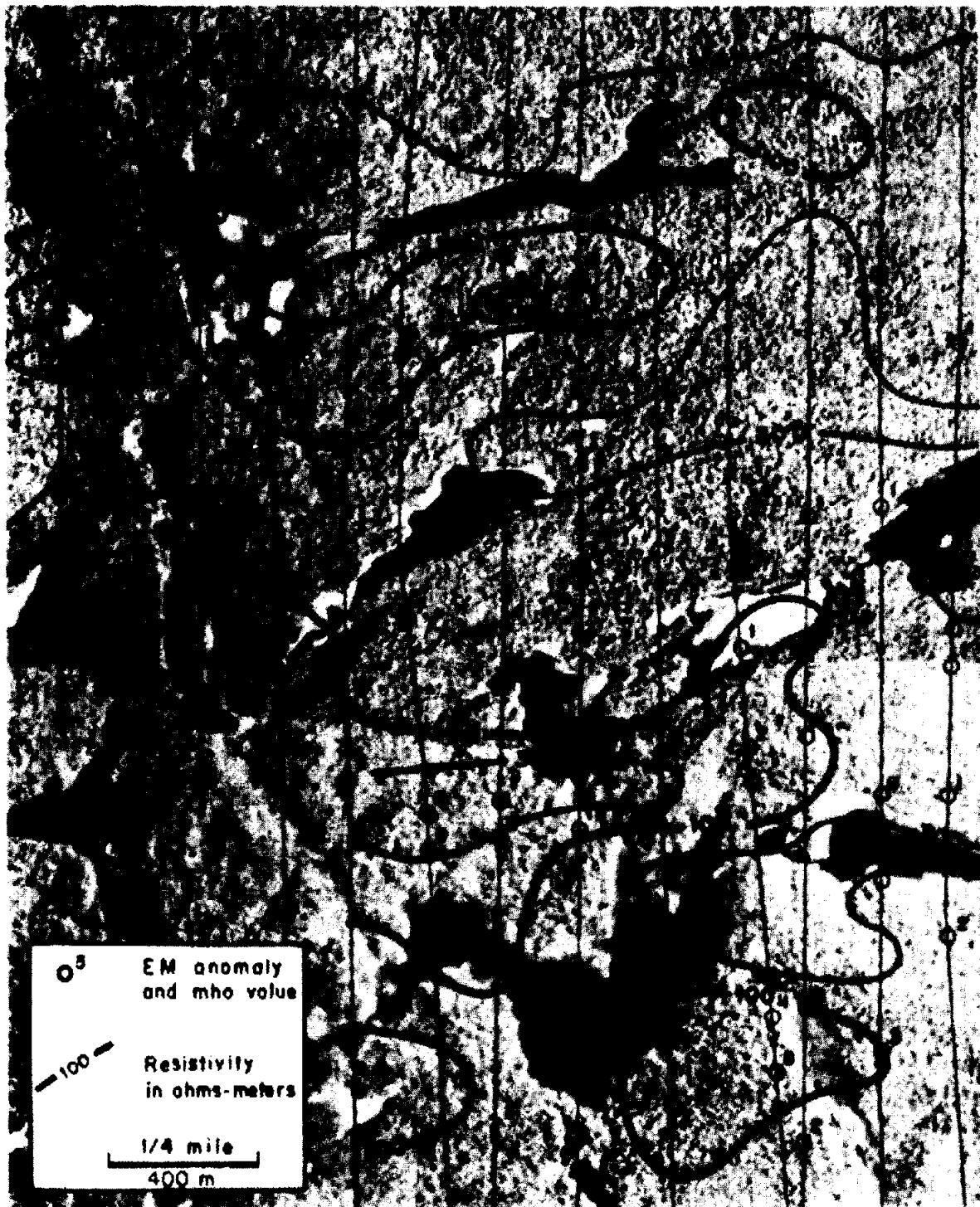


Figure 7.85. (Continued) (b) Pseudolayer resistivity map of the area in (a) showing two bedrock conductors.

at the measured value of the major/minor peak ratio (2 in this case), proceed left to intersect the slant line, then upward a distance 2 (using the lefthand scale), then left to the lefthand vertical scale where we obtain the amplitude correction ( $\sim 1.4$ ) for use in Figure 7.88a. Vertical lines through the two intersections with the slant line give the dip ( $120^\circ$  and  $65^\circ$  here).

(e) Conductive overburden. Figure 7.90 shows the modification of six-channel response from a half-plane model of  $\sigma t = 27 \text{ S}$  at 20 m depth due to conductive overburden. Background levels are increased in the first three channels and the overburden has a large, broad response, mainly confined to channel 1 when its lateral extent is limited. Only the amplitudes are reduced over a vertical plane whereas

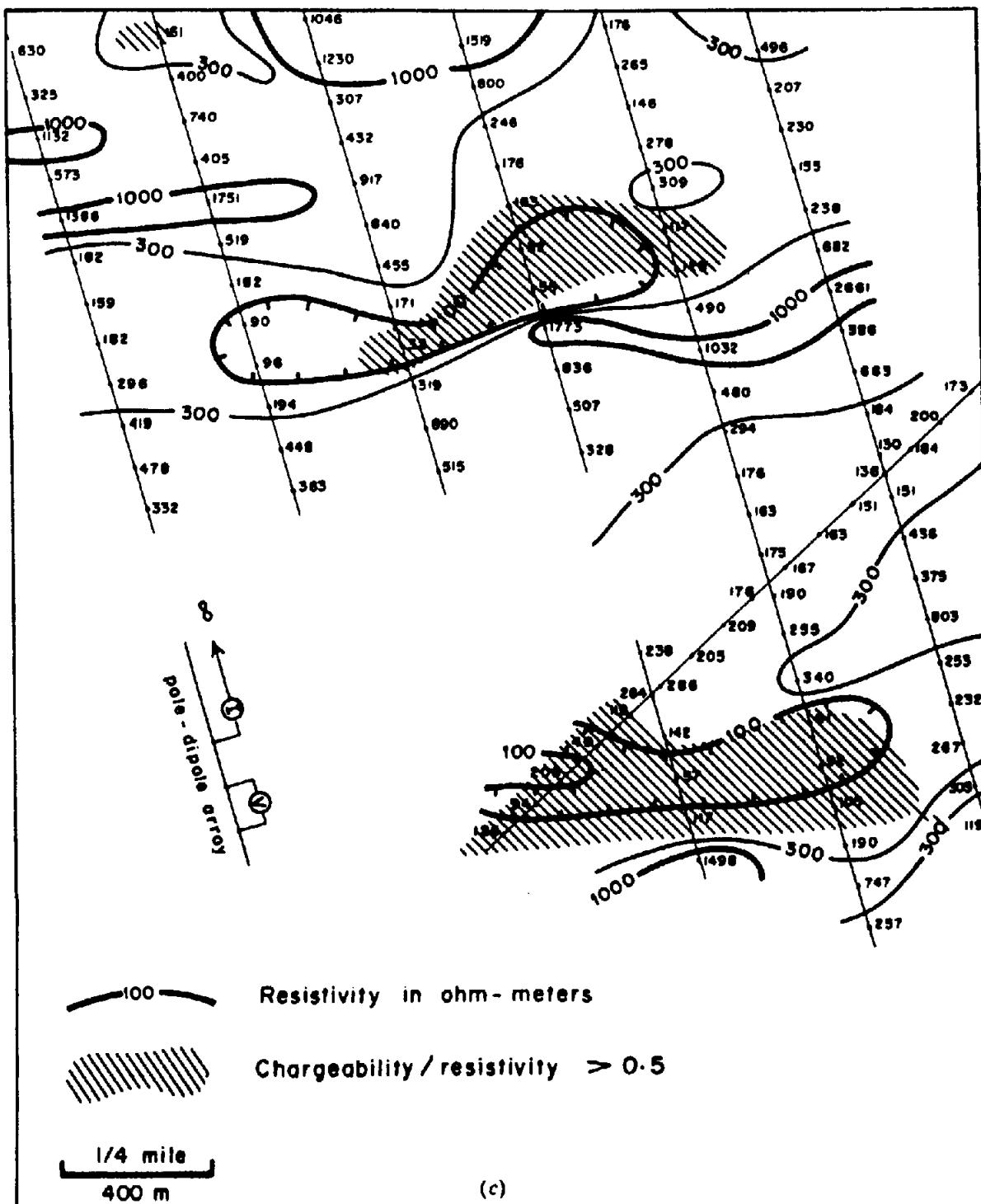
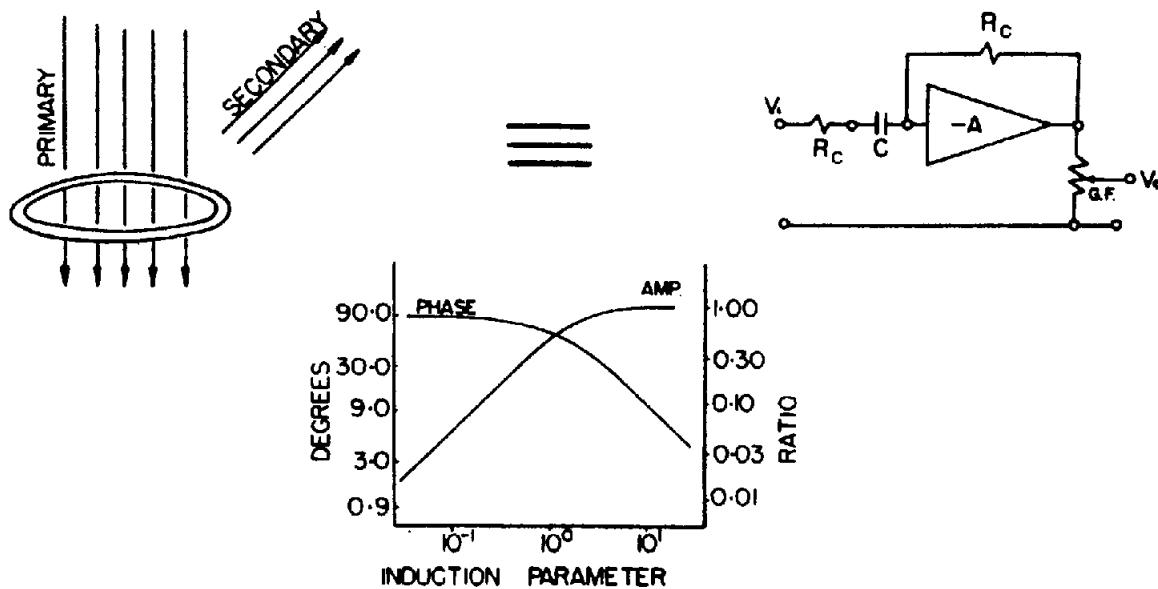


Figure 7.85. (Continued) (c) Ground IP resistivity map of the same area showing two anomalies.

dipping sheets also suffer shape distortion, which increases with the conductance of both the target and its cover. A combination of overburden and dip has changed the channel 1 negative peak to a positive trough over the two sheets dipping  $36^\circ$  and  $144^\circ$ .

(f) Conducting sphere. This model gives an Input profile that is perfectly asymmetric with a crossover

above the center, in contrast to the symmetric peak from 2-D sheet models (Mallick, 1972). Amplitude of the secondary-field positive and negative peaks either side of the crossover falls off as  $1/h^3$ ,  $h$  being the vertical distance between the sphere center and the receiver, and increases with the parameter  $\beta^2 = \mu\sigma a^2$ , where  $a$  is the sphere radius. However, when  $a$  goes to infinity, the theoretical transient response vanishes; this surprising result is related to the phase



$$c(\omega) = [G.F.] \frac{\alpha^2 + j\alpha}{\alpha^2 + 1}$$

$$c(\omega) = -[G.F.] \frac{b^2 + jb}{b^2 + 1}$$

$$\alpha = n\omega_0 L / R_L$$

$$b = n\omega_0 R_C C$$

G.F. = GEOMETRICAL FACTOR

Figure 7.86. Equivalence of electronic and electromagnetic transfer functions. (After Becker, 1969.)

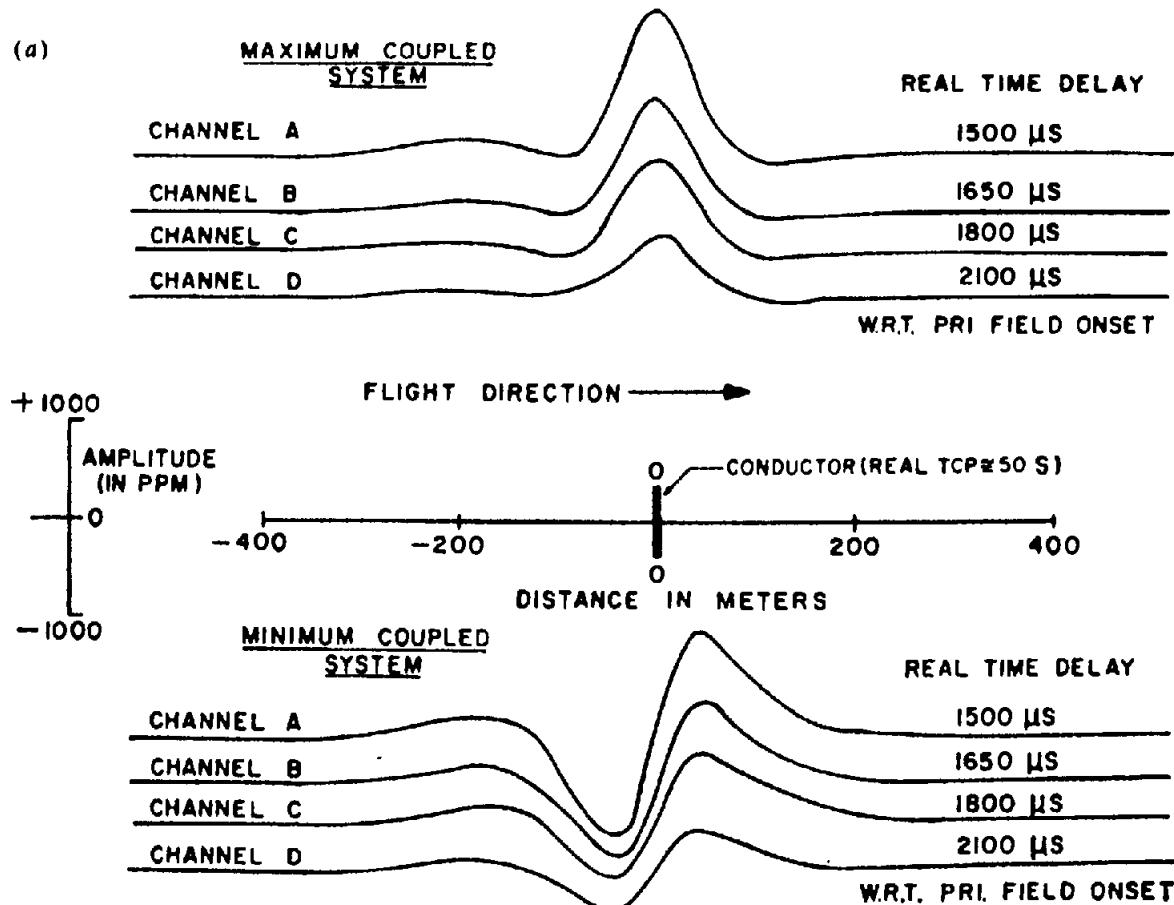


Figure 7.87. Model Input response to a thin vertical sheet. (a) Four-channel response for maximum- and minimum-coupled systems for various values of the real-time delay. (After Becker, Gavreau, and Collett, 1972.)

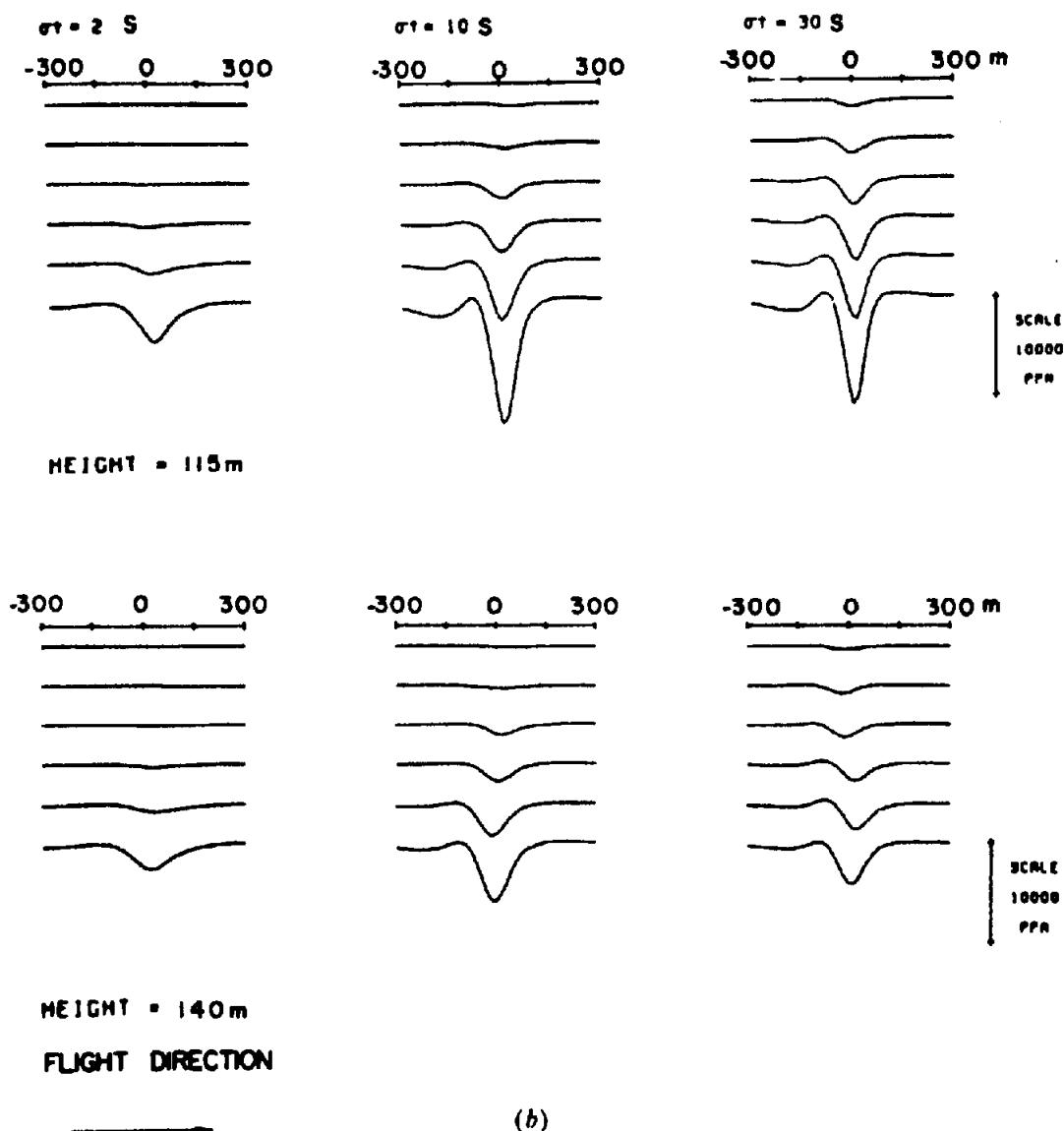


Figure 7.87. (Continued) (b) Six-channel response for two flight heights and several values of  $\sigma_t$ ; the top of the sheet is at zero height. (After Palacky and West, 1973.)

difference between primary and secondary fields, which decreases with increasing  $\beta^2$ .

(g) *Mapping shallow structure.* Input applications for outlining shallow geological structures and estimating overburden parameters have appeared in the literature since about 1975. Response from a fault containing conductive serpentinite, near Lake Wanipigow in southeastern Manitoba, is shown in Figure 7.91.

Data from a mapping program carried out by the Geological Survey of Canada over conductive overburden in the vicinity of Hawkesbury (near Ottawa) are displayed in Figure 7.92. The 11-channel vertical-axis Input receiver (Fig. 7.28e) was used for this test. Typical response from one flight line appears in Figure 7.92a. In the analysis, amplitudes and decay rates along the channel lines are averaged and en-

tered on a parameter interpretation chart seen in Figure 7.92b. (For large amounts of data this obviously requires a computer.) The output is an estimate of the TCP of the overburden.

Because the modeling routine assumes a three-layer structure as in Figure 7.84d, (§7.7.11), it is possible to separate these parameters only when the clay overburden is exposed at surface. In this event, its thickness and resistivity may be established independently. A comparison of the interpreted airborne data with ground dc resistivity is illustrated in Figure 7.92c. The 2 km spreads used for the ground survey resulted in less detail than that of the Input profile.

(h) *Bathymetry.* Input mapping of seawater depth in coastal regions has been described recently by Zollinger et al. (1987). Although frequency-domain AEM is also a possibility for this type of survey, the

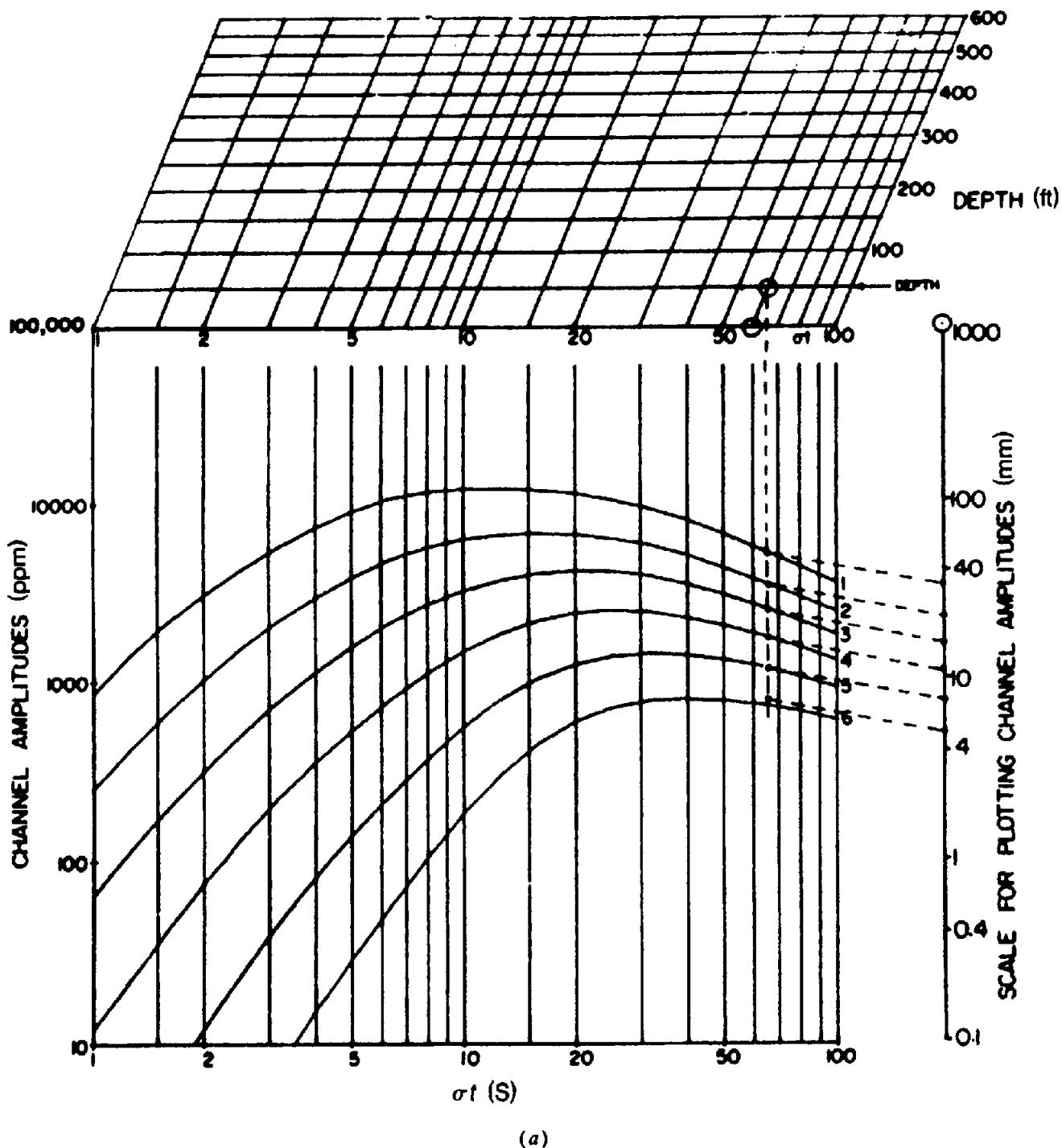


Figure 7.88. Nomograms for obtaining conductivity and depth. (a) Nomogram giving TCP and  $h$  for a vertical sheet. (After Palacky and West, 1973.)

maximum depth of penetration is not as great; both methods are doubtless suitable for freshwater areas.

Compared to mapping ground layers, the problem is greatly simplified, because the ground surface becomes sea level, overburden conductivity is constant ( $4 \text{ S/m}$ ) or practically so, and the only variable parameter is depth to the bottom, the latter being generally highly resistive. Interpretation is performed with an automatic curve-fitting algorithm to determine the depth from the recorded EM and altitude

data. The algorithm is essentially a stored set of models, judged to cover the maximum range of the survey data. Injected flight-path data points are compared with the stored models and the best fit is taken as the solution. Details of this procedure, known as a table lookup routine (§7.7.11), are given in Zollinger et al. (1987).

Two field examples are given, one line of 28 km over the E-W channel along the south shore of Cape Breton Island, Nova Scotia, the second heading

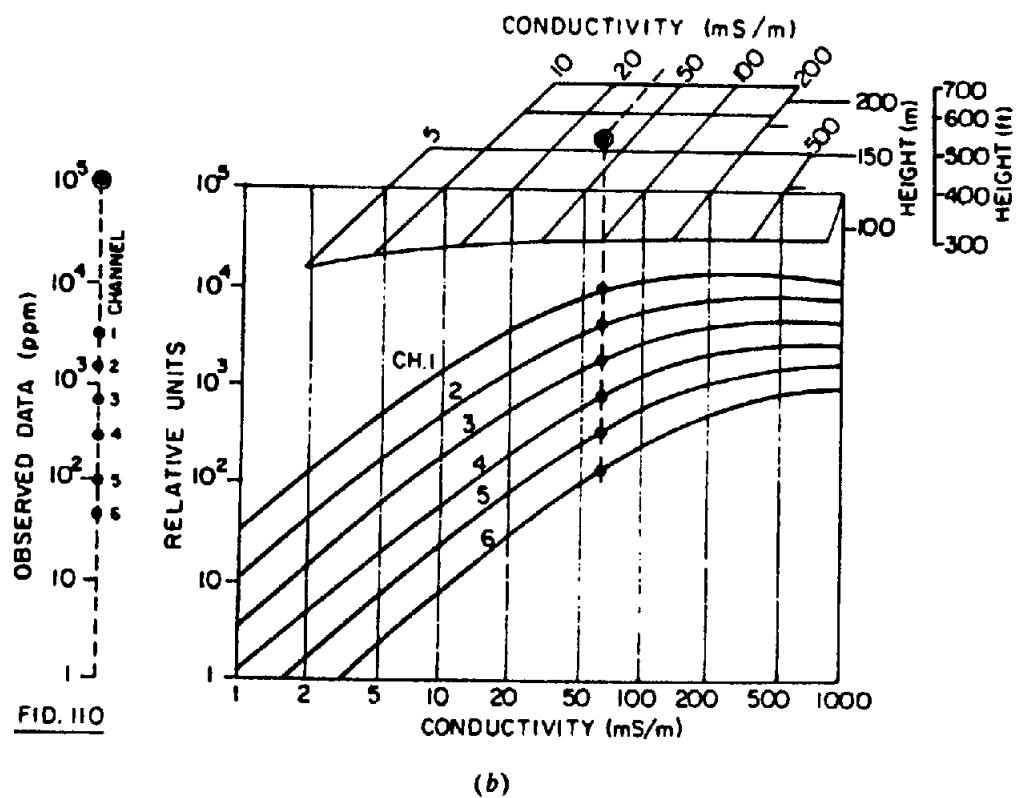


Figure 7.88. (Continued) (b) Palacky nomogram for interpreting conductivity and aircraft height (above the conductor) for a conductive half-space. (After De Mously and Becker, 1984.)

HALF PLANE  
AMPLITUDE CORRECTION FOR DIP

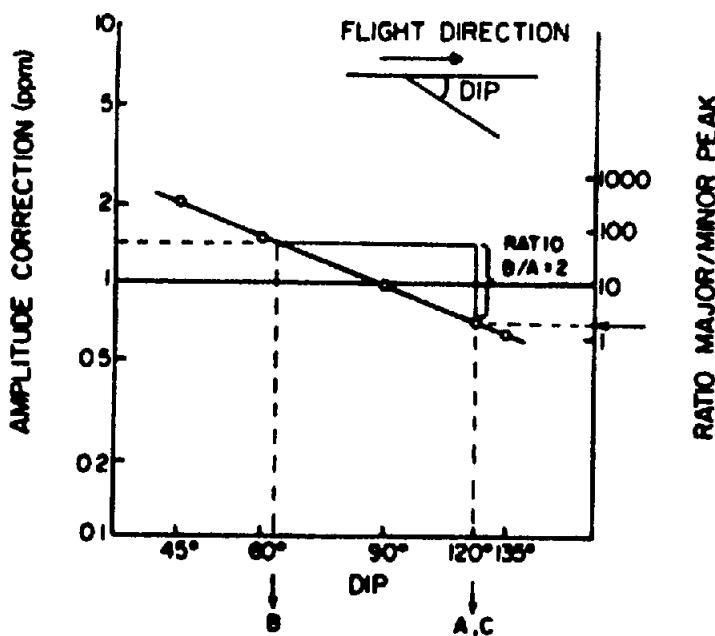


Figure 7.89. Estimating dip of a half-plane from the ratio of major-to-minor peak amplitudes. The amplitude correction (see left-hand vertical scale) corrects for the effect of dip on amplitude. (After Palacky and West, 1973.)

### Interpretation of AEM Measurements

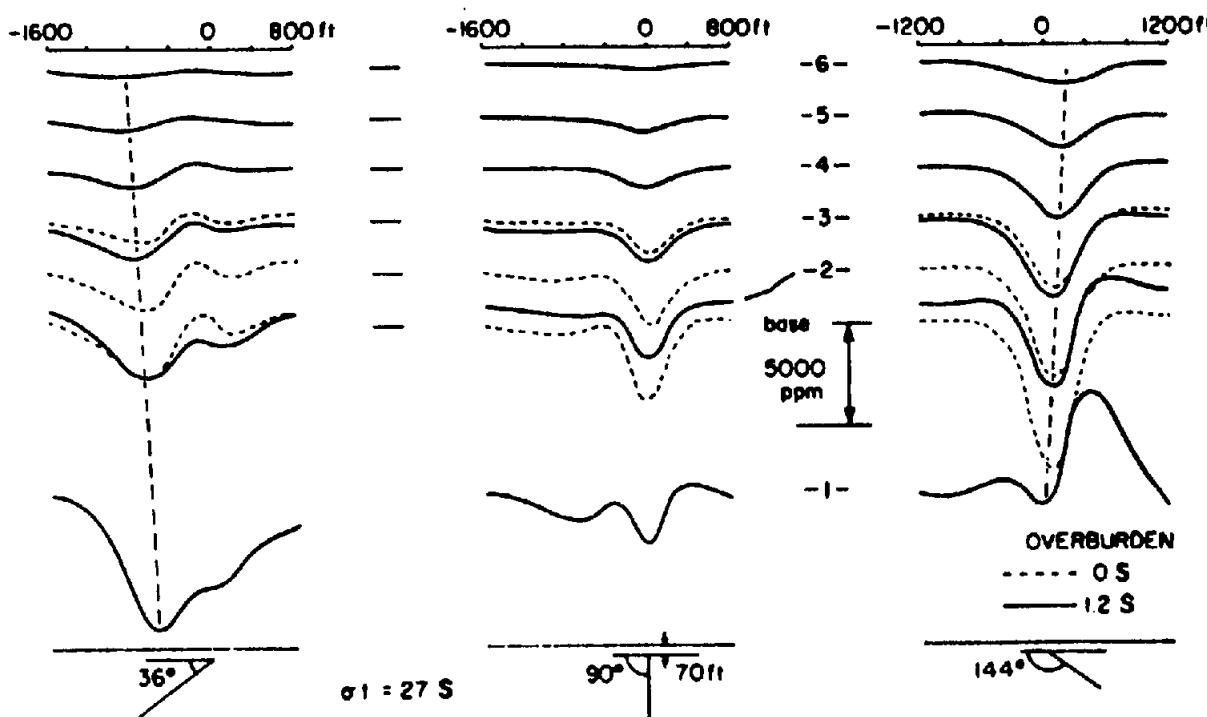


Figure 7.90. Model profiles over dipping half-plane ( $\sigma_1 = 27 \text{ S}$ , depth to top = 70 ft) under conductive overburden. Dashed line indicates shift of anomaly peak from early to late time. (After Palacky, 1975.)

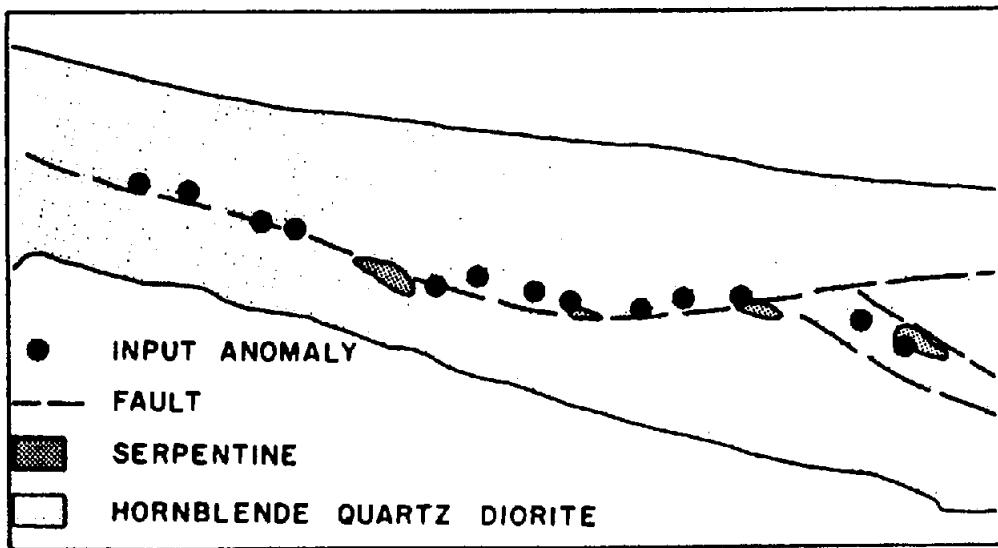


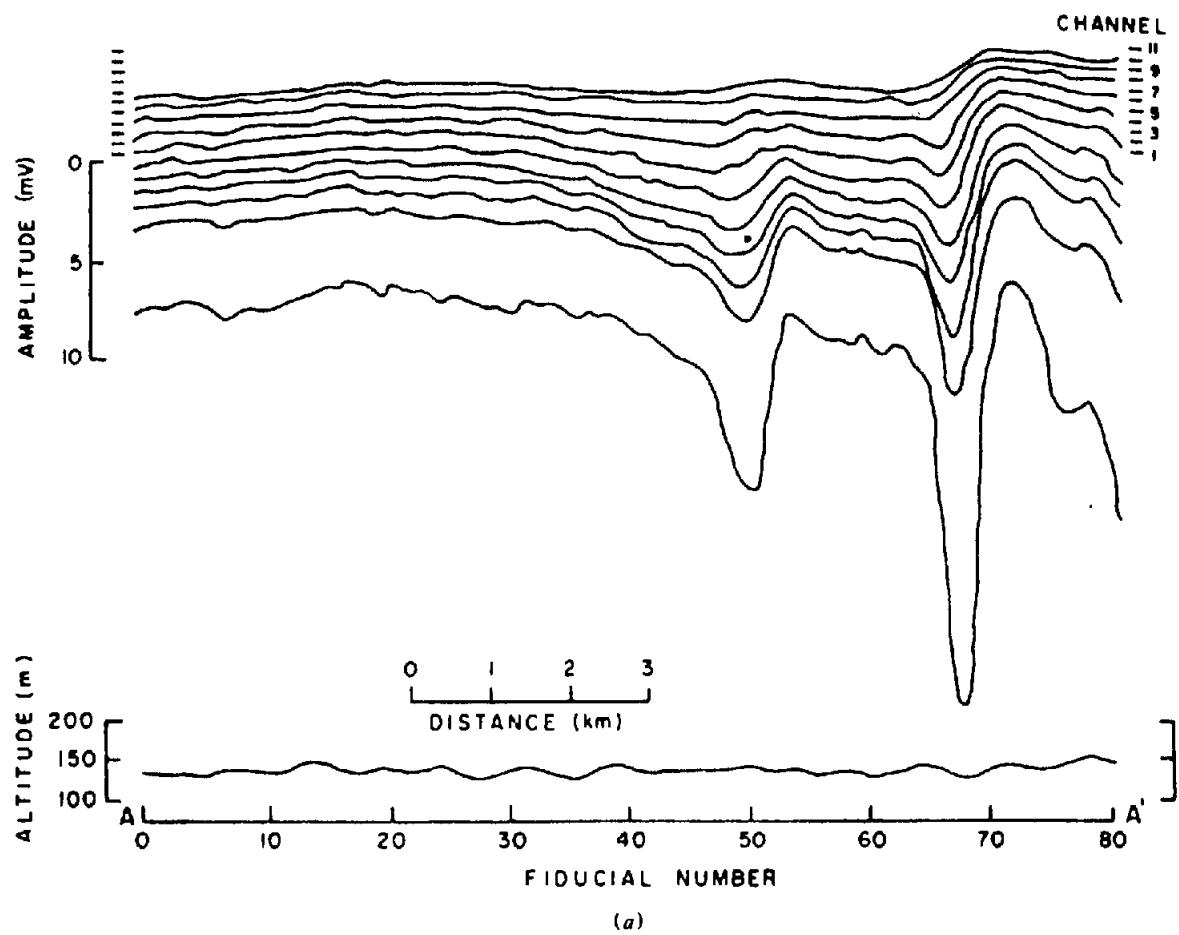
Figure 7.91. Structural mapping with Input system; Lake Wanipigow area, Southeastern Manitoba. (After Dyck, Becker, and Collett, 1975.)

N50°W for 19 km from coordinates 47°45'N, 64°39.5'W near New Brunswick, both on the Canadian east coast.

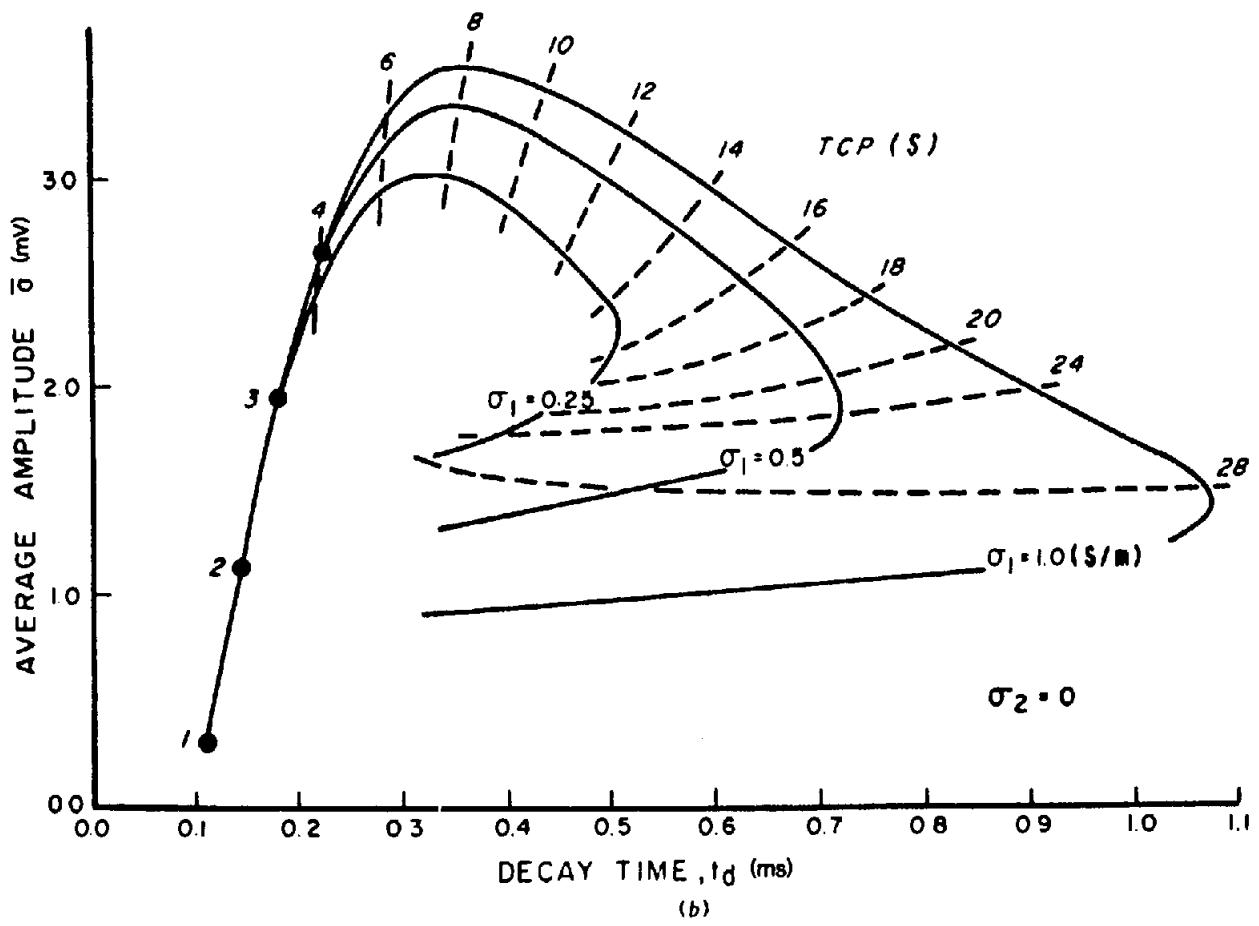
The Cape Breton line was flown six times both east and west on the same track at altitudes of 170, 200, and 230 m above sea level. The line is centered at 45°35'N, 60°50'W and crosses the mouth of Lennox Passage near this location. Figure 7.93a shows altitude, normalized amplitude response, and

depth for W-E flight at 230 m. Normalizing of the six-channel data was done by dividing each channel by the geometric-mean amplitude of channels 3 and 4, which were usually the most stable. Sea-bottom conductivity was assumed to be 0.001 S/m.

The bottom plot shows the interpreted depths to be within 2 m of the black dots taken from coastal charts, except for the deep break at Lennox Passage around 12 km. Results were poor here, indicating



(a)



(b)

Figure 7.92. Typical 11-channel vertical-axis receiver input response over conductive overburden, Hawkesbury area near Ottawa. (After Dyck, Becker, and Collett, 1974.) (a) Response curves. (b) Nomogram for finding TCP and  $t$  in terms of average amplitude and decay time.

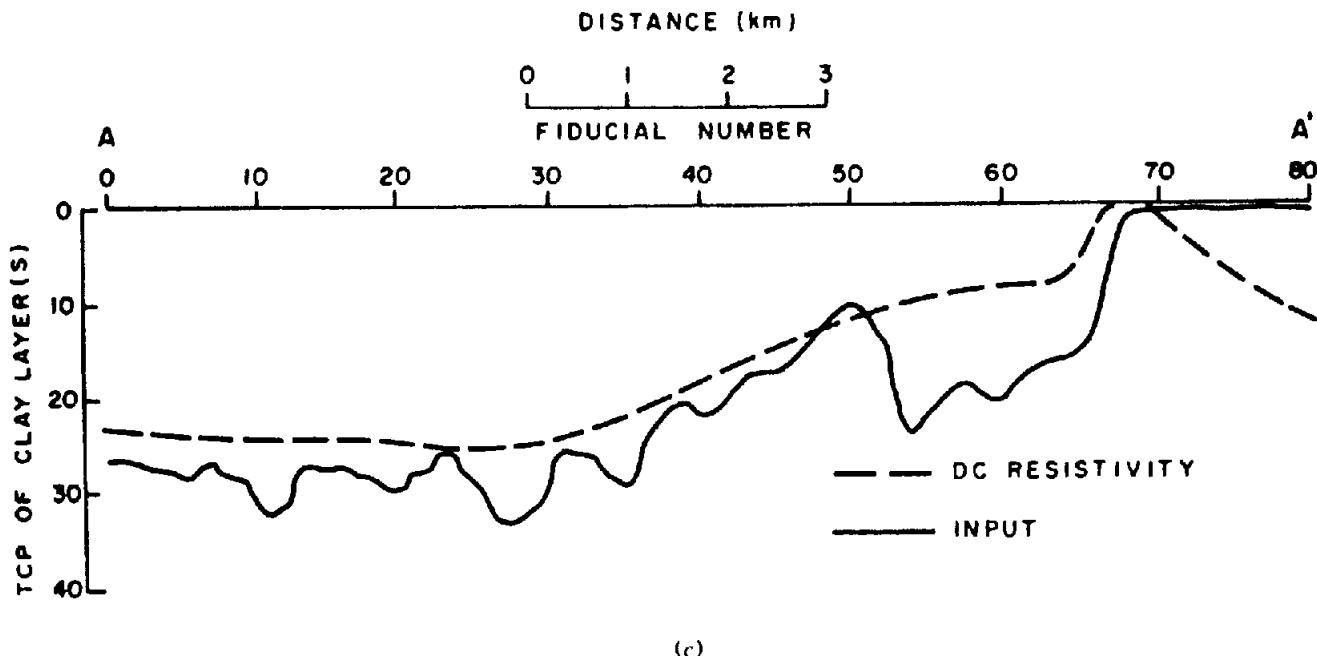


Figure 7.92. (Continued) (c) Comparison of TCP values for the overburden obtained using (b) and by dc resistivity surveys.

depths of 60 to 100 m; the chart depth was 43 m. Resolution below 40 m depth is thought to be greatly reduced with the present system. Apart from this small area, the several flights produced data within 2 m over most of the line.

Results from the New Brunswick test are illustrated in Figure 7.93b. Here the bottom falls away sharply to the NW and is mainly shallower than the first area over the rest of the line. However, the agreement with coastal chart values is quite good and persists over the ledge about 40 m deep between 26 and 28 km. Flight altitudes were a little higher (210 to 240 m) than at Cape Breton, which wiped out channels 5 and 6, leaving four channels for interpretation.

Sources of error considered troublesome in this type of sounding include atmospheric noise and effects of bird motion on the receiver, as well as use of incorrect conductivities for the model. Sea-water conductivity can vary because of changes in temperature and salinity, which are common in coastal waters. Changes in bottom conductivity were found to be negligible except where a thin conductive layer covered a resistive bottom; this may account for the Lennox Passage anomaly.

## 7.8. FIELD EXAMPLES

Because of the great variety of EM field methods, the number of case histories and problems is necessarily large. We have tried to provide examples of all of the techniques commonly used at present.

It should be noted here that many of the diagrams contain abbreviated names or acronyms for different types of EM ground equipment. Thus, VLEM, VEM, and JEM refer to vertical-loop units of various kinds, which employ a local transmitter (for the reader who is not familiar with the terms, it is necessary to specify also whether the transmitter is fixed or movable). As mentioned earlier, VLF refers to very low-frequency sets (generally EM16), which use remote transmitters. Likewise HLEM stands for horizontal-loop (or Slingram or phase-component) EM equipment.

1. An illustration of the vertical-loop fixed-transmitter method is shown in Figure 7.94. This is the well-documented Mobrun sulfide body, 10 miles northeast of Noranda, Quebec. The deposit, whose section is shown in the diagram, contains about 4 million tonnes of massive pyrite. This is a classical vertical-loop profile, obtained with the transmitter located 400 ft to the east, on the conductor strike axis. The large maximum dip angles on either side of the crossover are approximately equal, indicating a steeply dipping good conductor at shallow depth. Although the crossover appears to be displaced about 25 ft north of the geometrical center of the section, this is not significant because the body is 100 ft wide. Depth estimates are not very satisfactory; using the curves of Figure 7.42b, the conductor appears to outcrop.

2. Figure 7.95a is a good example of a vertical-loop broadside or parallel-line EM survey, carried out over the Uchi Lake sulfide body, some 50 miles east of the Red Lake gold area in northwestern

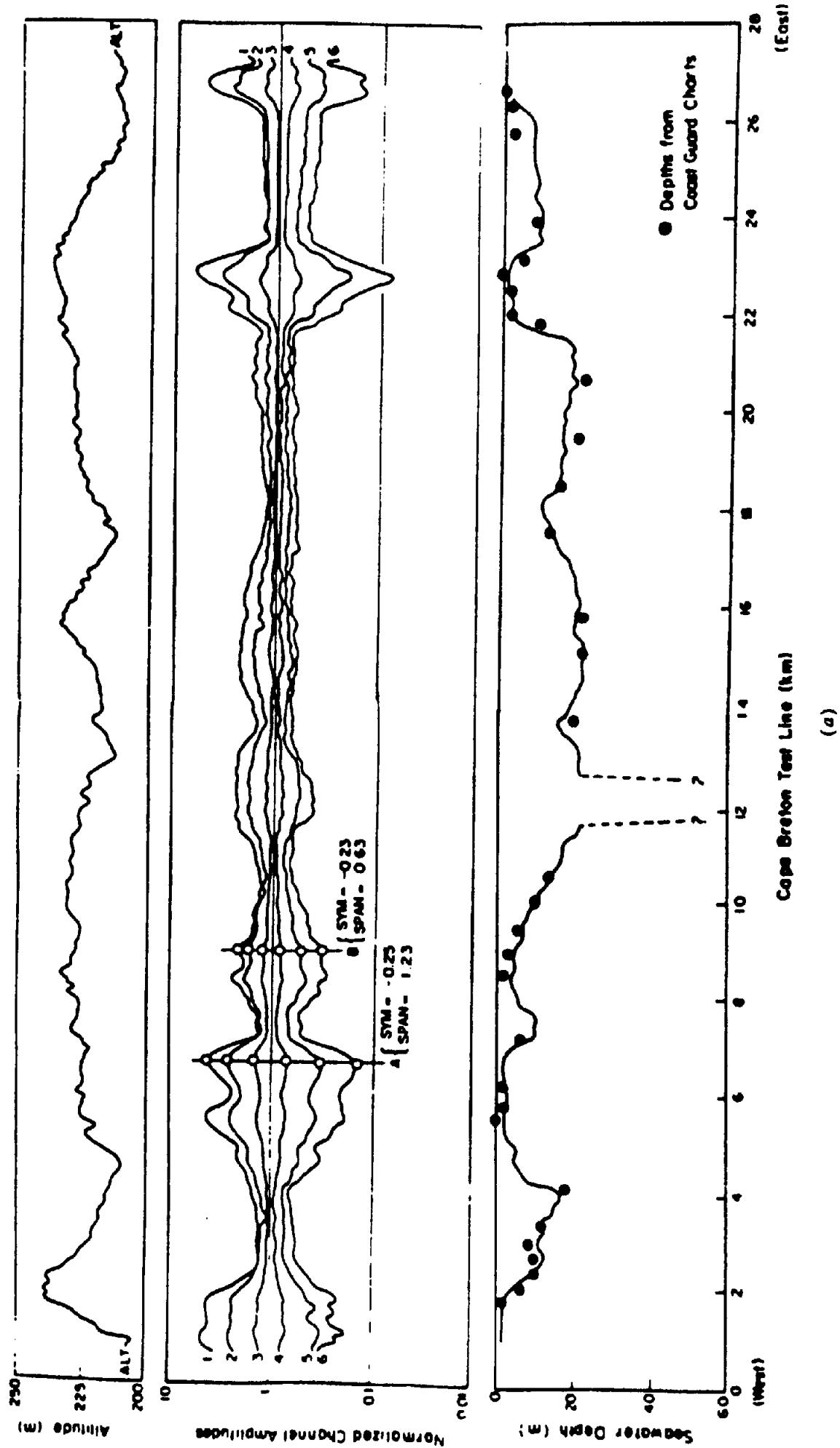


Figure 7.93. Bathymetry survey off the Canadian east coast using the Input system. (After Zollinger et al., 1987.) (a) Comparison of Input calculated depths and coastal charts, offshore Nova Scotia.

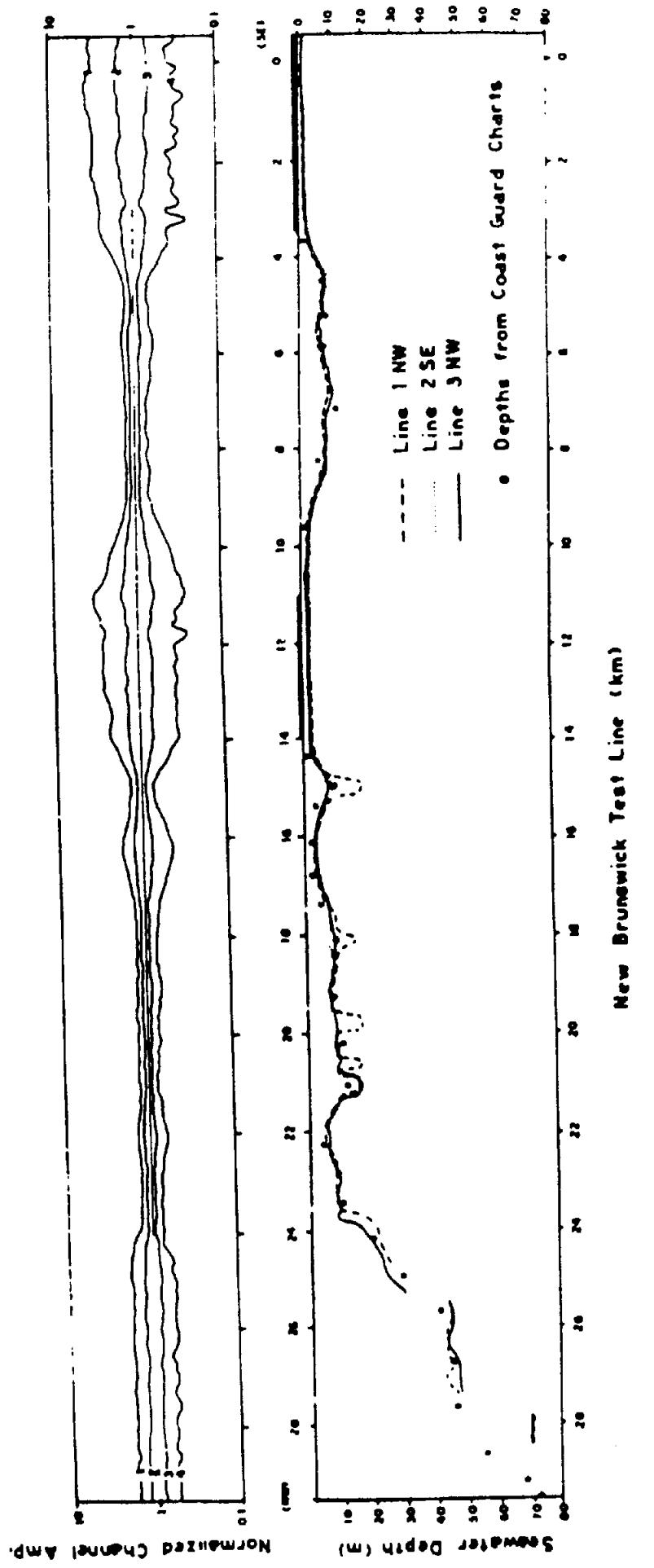


Figure 7.93. (Continued) (b) Same as (a) for offshore New Brunswick.  
(b)

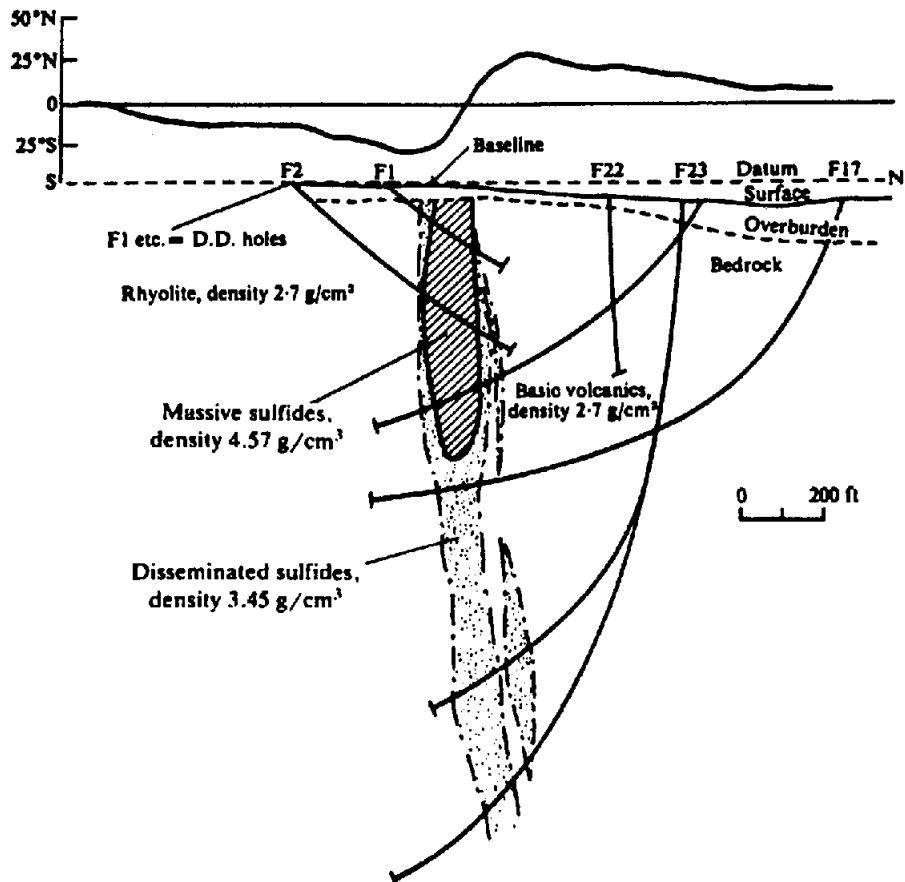


Figure 7.94. Vertical-loop fixed-transmitter profiles over Mobrun orebody. (After Seigel, 1957.)

Ontario. The mineralization, consisting of massive pyrite, chalcopyrite, and sphalerite, occurs in a complex of rhyolitic and dacitic rocks in the form of lenses striking, and probably plunging, northeast with nearly vertical dip.

The transmitter and receiver, separated by 400 ft, were moved along parallel lines crossing the strike axis; readings were taken every 25 ft. The strong crossovers on lines 2E and 4E coincide with a sub-outcrop of one of these lenses. Strike length is indicated by the small response on lines 0 and 6E. A second ore lens, about 100 ft northeast, mainly rich in sphalerite, was not detected, probably because of poor conductivity.

A single traverse on line 4E with a vertical-loop fixed-transmitter unit is shown in Figure 7.95b. For reference the broadside profile is included. The dual-frequency fixed transmitter (480, 1,800 Hz) was at station 1S on line 2E. The similar response at both frequencies shows a highly conductive zone. The profile asymmetry, which is surprisingly large, is probably due to the limited depth extent of the lens, because it is known to be approximately vertical.

3. The EM16 (VLF) profiles shown in Figure 7.96a are taken from a survey made on the Atlantic Nickel property near St. Stephen in southern New

Brunswick. The predominant geological feature in the area is a stock-like ultrabasic intrusive in metamorphosed sediments. The sulfide mineralization, consisting of pyrrhotite, chalcopyrite, and pentlandite, occurs close to contacts between the intrusive and the altered sediments.

The VLF source was the transmitter at Cutler, Maine, located 110 km to the south. Huge dip angles and steep crossovers on lines 160N and 162N are caused by a very good conductor, which outcrops on line 160N. On lines 158N and 156N the profiles indicate that the zone is either becoming wider or splitting in two, one leg continuing south, the other southwest. On the northern lines the dip appears to be steep and to the west.

A different method of displaying VLF data is illustrated in Figure 7.96b. The profiles have been converted to contours in such a way that proper crossovers are transformed to positive peak readings, whereas reverse crossovers become negative values; in the process there is also a smoothing effect that reduces the large geologic noise caused by the relatively high frequency of the transmitter (Cutler station operates at 24.0 kHz).

The procedure for conversion is very simple. If  $\theta_1, \dots, \theta_4$  are the dip angles obtained at stations

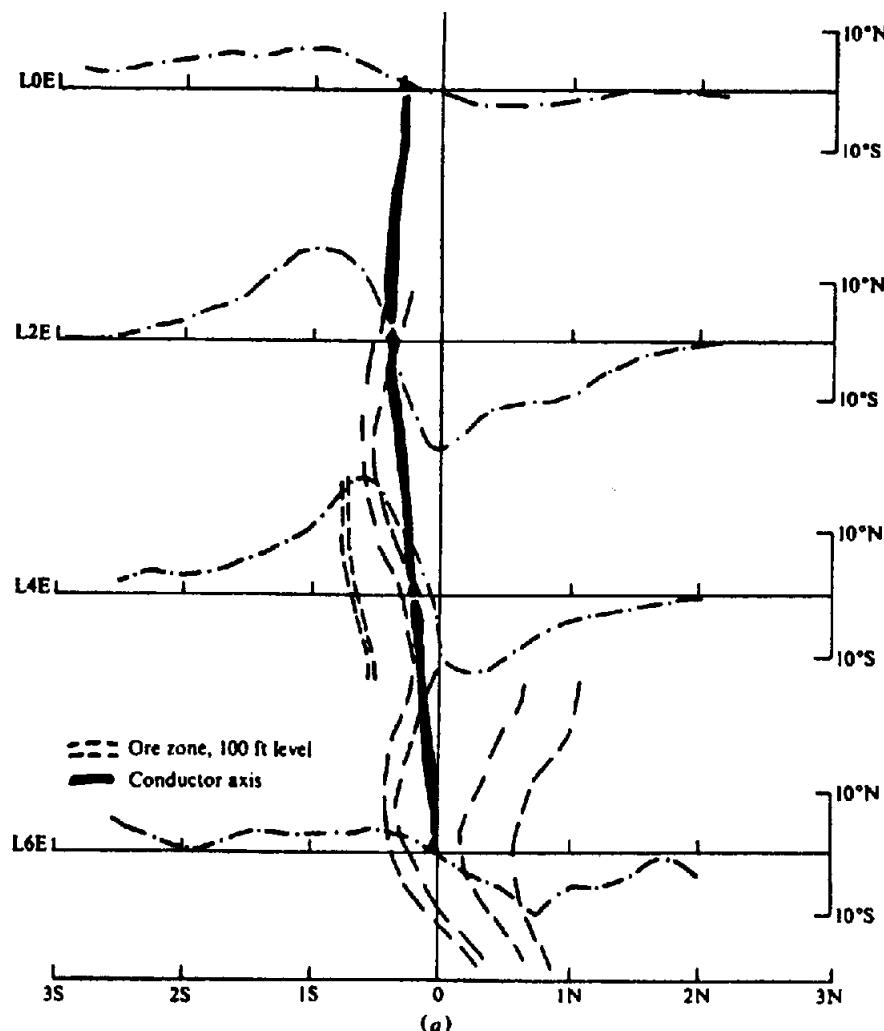


Figure 7.95. EM survey, Uchi Lake, northwest Ontario. (a) Dip-angle broadside profiles. Frequency 1,000 Hz,  $l = 400$  ft, station interval 25 ft.

1, ..., 4, the contour value  $C_{23}$  is

$$C_{23} = (\theta_3 + \theta_4) - (\theta_1 + \theta_2)$$

and is plotted midway between stations 2 and 3. The sign of  $C_{23}$  is positive in the vicinity of proper crossovers, negative for slopes in the opposite direction.

The contours in Figure 7.96b match the outline of the ore zone very well. The smaller anomaly in the vicinity of 109E, which is somewhat overshadowed on the profile display, is brought out more clearly in this plot. Negative contours, which represent higher resistivity zones, have been omitted here to clarify the conductive areas. In resistivity mapping they would be included.

4. The VLF method has been used for mapping shallow geologic structure, both on the ground and with the airborne version of the equipment. Contacts between beds of contrasting resistivity produce profiles that are quite different from the crossovers associated with the dipping-sheet conductor. This, of

course, is due to the fact that the profile over the contact corresponds to only half that over the sheet (see Fig. 7.48).

An EM16 survey, made over the Gloucester fault southeast of Ottawa, Ontario, illustrates this type of VLF response. Profiles and a typical geologic section are shown in Figure 7.97. The transmitter station was Cutler, Maine. This part of the Ottawa valley region is a sedimentary area well suited to such a technique because of the contrast between the low-resistivity Carlsbad shales and the Nepean and March formations upthrust by Precambrian rocks to the west.

The Gloucester fault is clearly displayed near the middle of Figure 7.97a, with the steeper slope on the east, over the low-resistivity beds. A second anomaly, parallel to the Gloucester fault and about 2,000 ft east of it, from 21 + 00S to 65 + 50S, indicates a contact with higher resistivity to the east. Still further east, from 32 + 00S to 60 + 50S, there appears to be a third feature, which has higher resistivity on the west. At 32 + 00S it is about 1,300 ft east of the

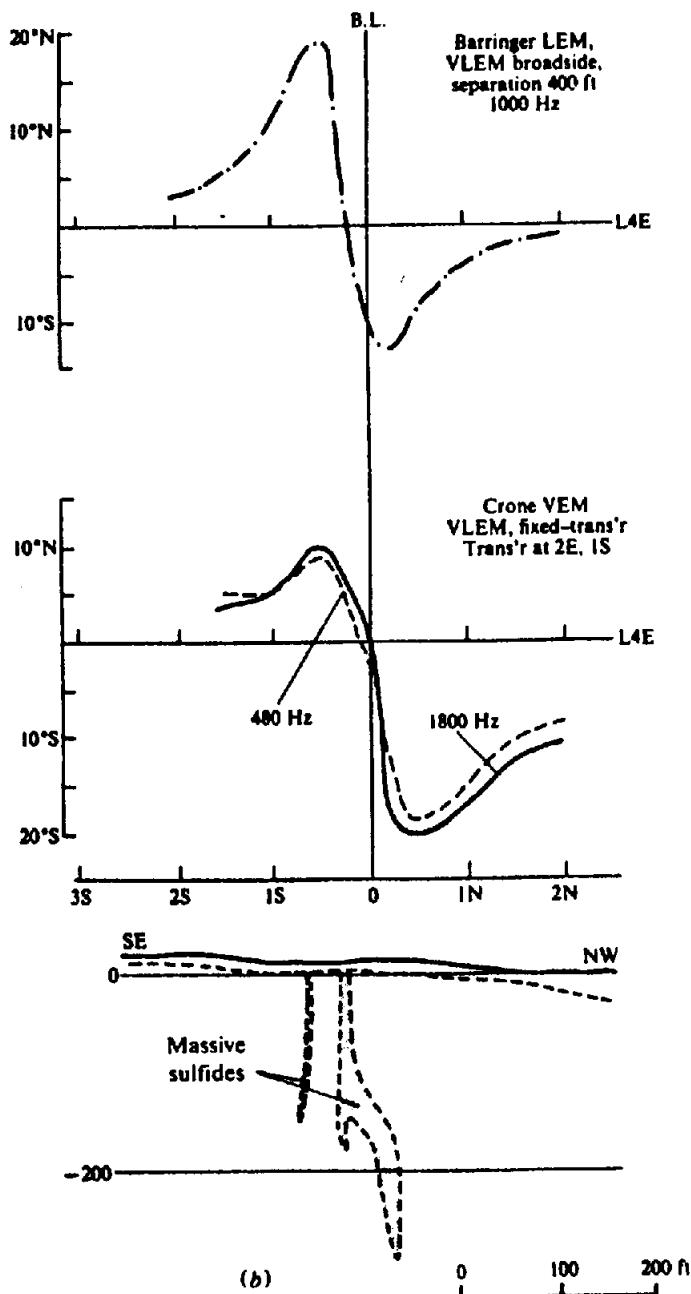


Figure 7.95. (Continued) (b) VLEM profiles and ore section.

second contact but, because of a more northerly strike, the separation is 800 ft at 60 + 50S, producing a crossover type of response on that line.

5. Figure 7.98a shows a pair of AFMAG profiles over the Mattagami Lake sulfide deposit at Watson Lake, about 90 miles north of Amos, Quebec. The ore zone, shown in rough outline, contains sphalerite, chalcopyrite, and pyrite, and is associated with basic rocks that have intruded the regional volcanics and sediments. A vertical section through line 4 + 00W is displayed in Figure 7.98b. Vectors drawn on the AFMAG profile give the azimuth direction of the field at various points of the traverse.

Both the high- and low-frequency anomalies are larger on line 1 + 00E than on 4 + 00W, because the zone plunges to the west; the depth of cover is about 35 ft on the east line and at least 300 ft on 4 + 00W. The 510 Hz response is greatly affected by the increased depth at 4 + 00W. It is difficult to get much quantitative information concerning the ore zone from these profiles. Their general shape indicates dip to the south, a widening of the zone to the west, and a depth greater than the actual depth, particularly on line 1 + 00E.

6. Three HLEM profiles, from a property near Woburn, Quebec, are shown in Figure 7.99. The

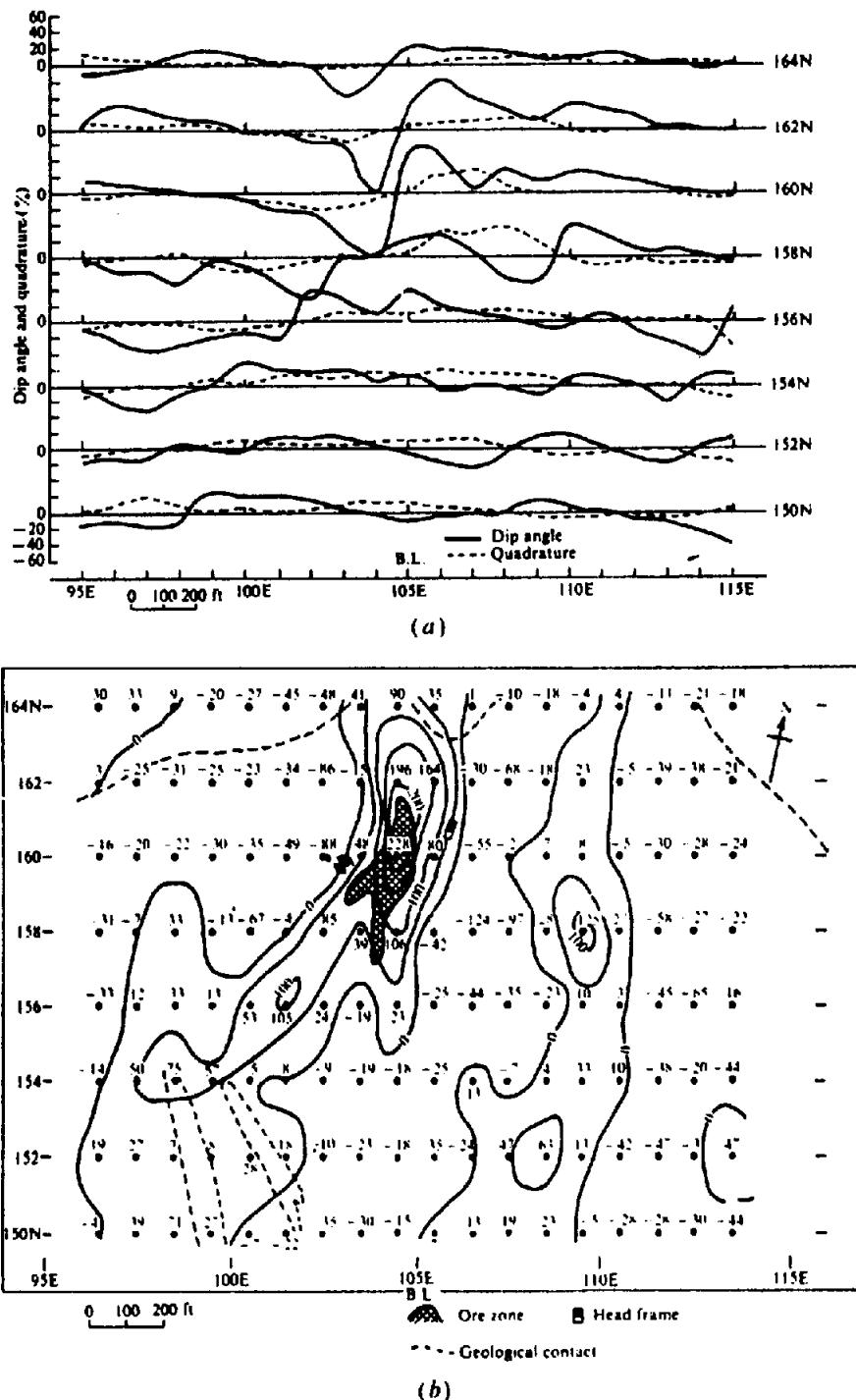


Figure 7.96. Results of VLF survey, Atlantic Nickel property, southern New Brunswick. Transmitter station: Cutler, Maine (24.0 kHz). (a) VLF profiles. (b) VLF contours.

mineralization consists of several dipping sulfide lenses located in a shear zone near a contact between volcanics and sediments. The sulfide content ranges from massive to disseminated, with considerable mineralization between the main zones.

Qualitatively, all three profiles indicate a single sheet-like conductor of shallow depth dipping west. In addition, it is probably a metallic conductor, because the ratio of peak in-phase to peak quadrature is about 4 in each case. Quantitatively, we can use the peak values with the characteristic curves of

Figure 7.44b, assuming the dip to be about  $60^\circ$ , to calculate some numerical results. For a transmitter-receiver separation of  $l = 200$  ft and frequency  $f = 800$  Hz, we find the data given in Table 7.4.

Obviously more information can be obtained from this type of EM survey than any discussed so far. Although the  $60^\circ$  dip angle is only an estimate, it is clear that there is dip to the west and the results would not be much different if we had assumed 90 or  $45^\circ$ , since HLEM is not particularly sensitive to dip. On the other hand, there is no indication of the

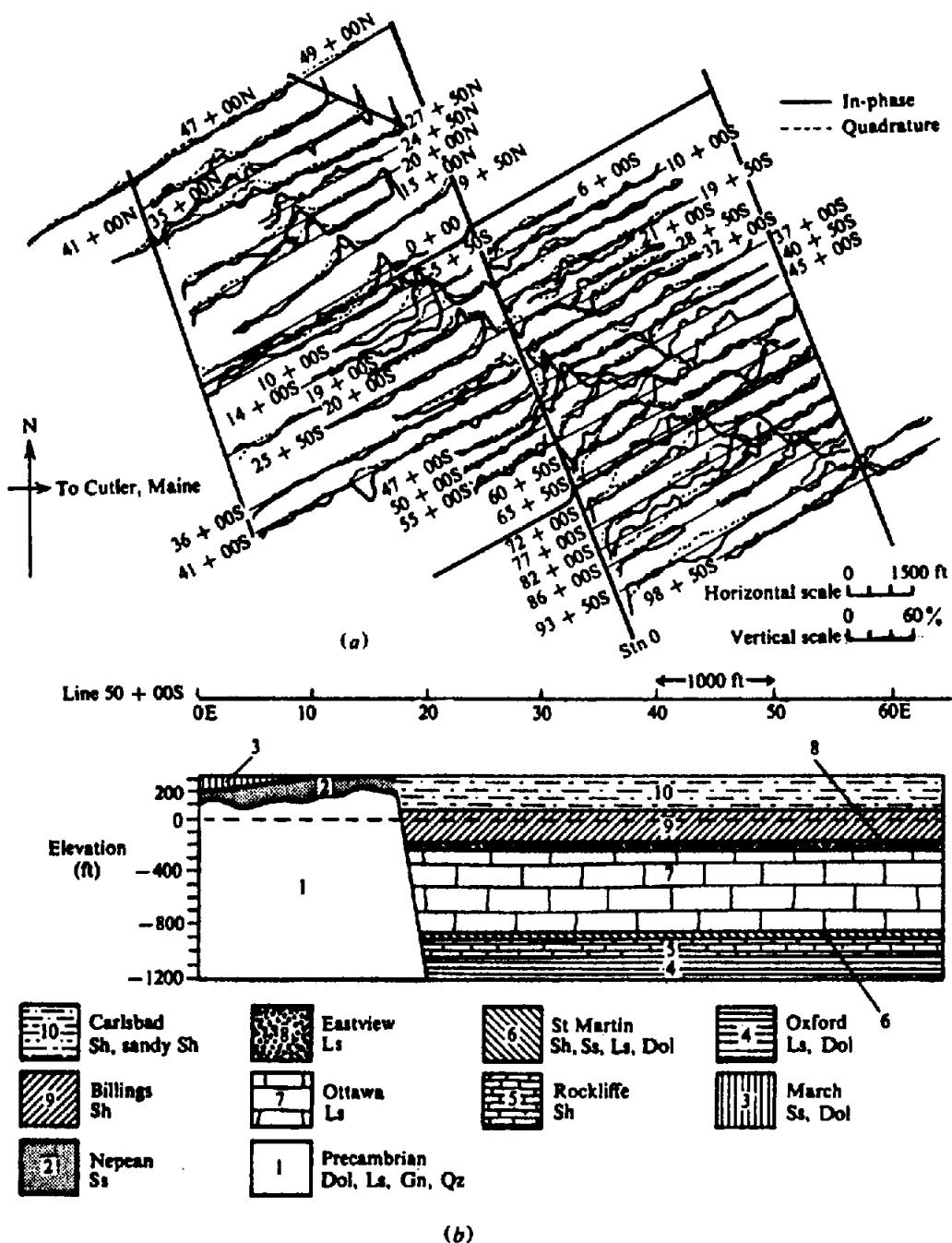


Figure 7.97. VLF survey across the Gloucester Fault, eastern Ontario. (a) Plot of the field data. (b) Geological section, line 50 + 00S.

disseminated sections, except perhaps on line 40S. A smaller separation ( $l = 100$  ft) might possibly have detected these zones.

7. The Murray sulfide deposit, in Restigouche County, northern New Brunswick, provides a good example of the Turam EM technique. This body, massive pyrite with sphalerite, galena, and chalcopyrite, occurs as a replacement in a chlorite schist along the axis of a reverse drag fold in Ordovician sediments. Considerable leaching and weathering of the near-surface mineralization has produced a heavy gossan cover, varying in thickness from 50 to 200 ft,

which masks detection of the main body by EM methods.

Turam field-strength ratios, shown in contour form in Figure 7.100a, correlate well with the outline of the sulfide body at 200 ft depth. The phase-shift contours are said to be similar. This is only a small part of the whole Turam survey, which covered an area about  $1\frac{1}{4}$  miles E-W by  $\frac{1}{2}$  mile N-S; extensive zones of graphitic schists also produced strong anomalies north and east of the sulfide body.

Figures 7.100b, c show a profile across the sulfide area on line 136E, as well as a shorter one on line

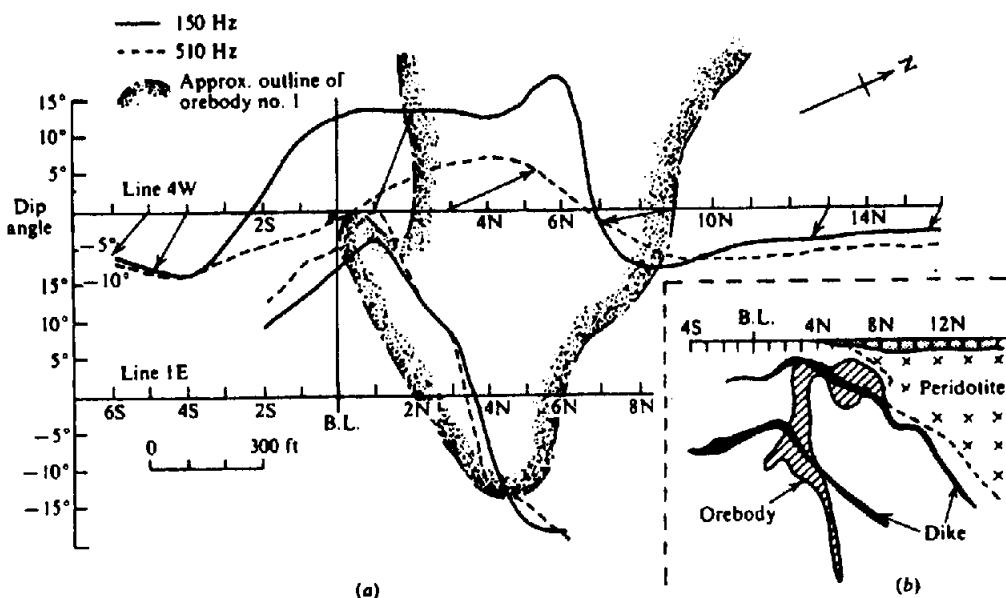


Figure 7.98. AFMAC survey, Mattagami Lake Mines, Quebec. (From Paterson, 1966.) (a) Profiles along lines 4W and 1E. (b) Cross section, line 4W.

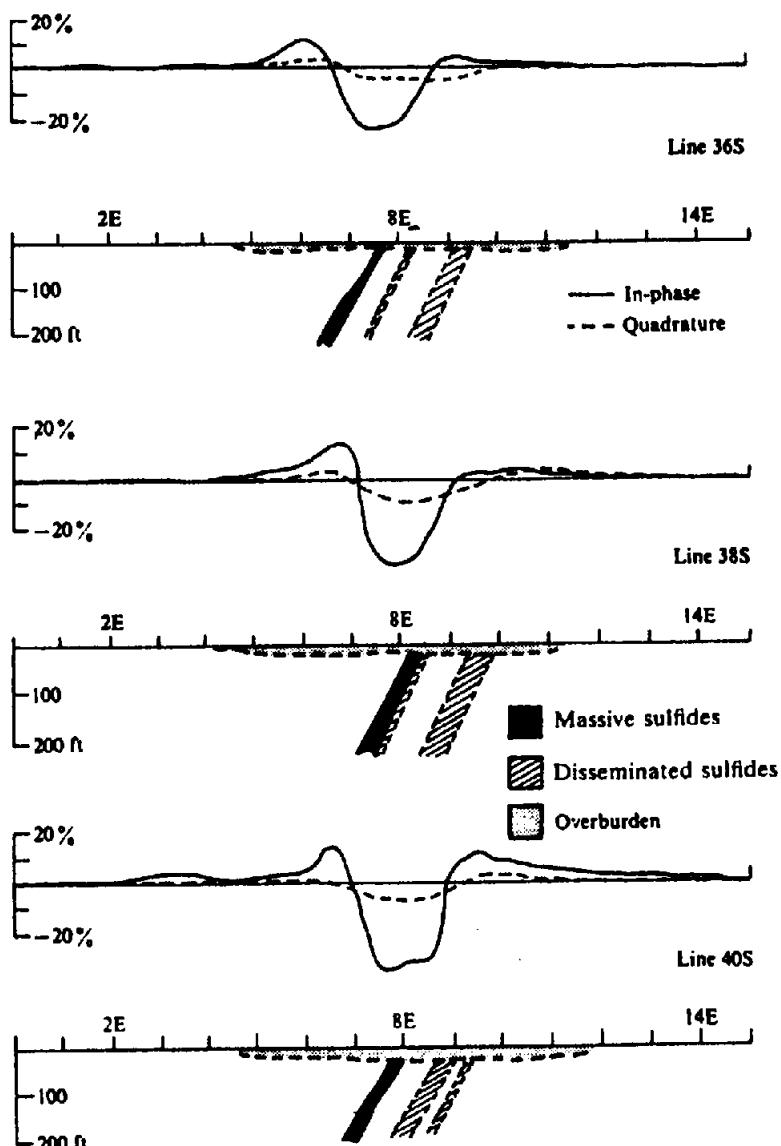


Figure 7.99. Horizontal-loop EM profiles, Woburn, Quebec.

Table 7.4.

Lines	Re (max) (%)	Im (max) (%)	Depth	$\mu_0 \omega \sigma l$	z (ft)	ot (S)
36S	-28	-7	0.27l	38	55	10
38S	-38	-11	0.17l	33	33	8.5
40S	-40	-9	0.16l	38	30	10

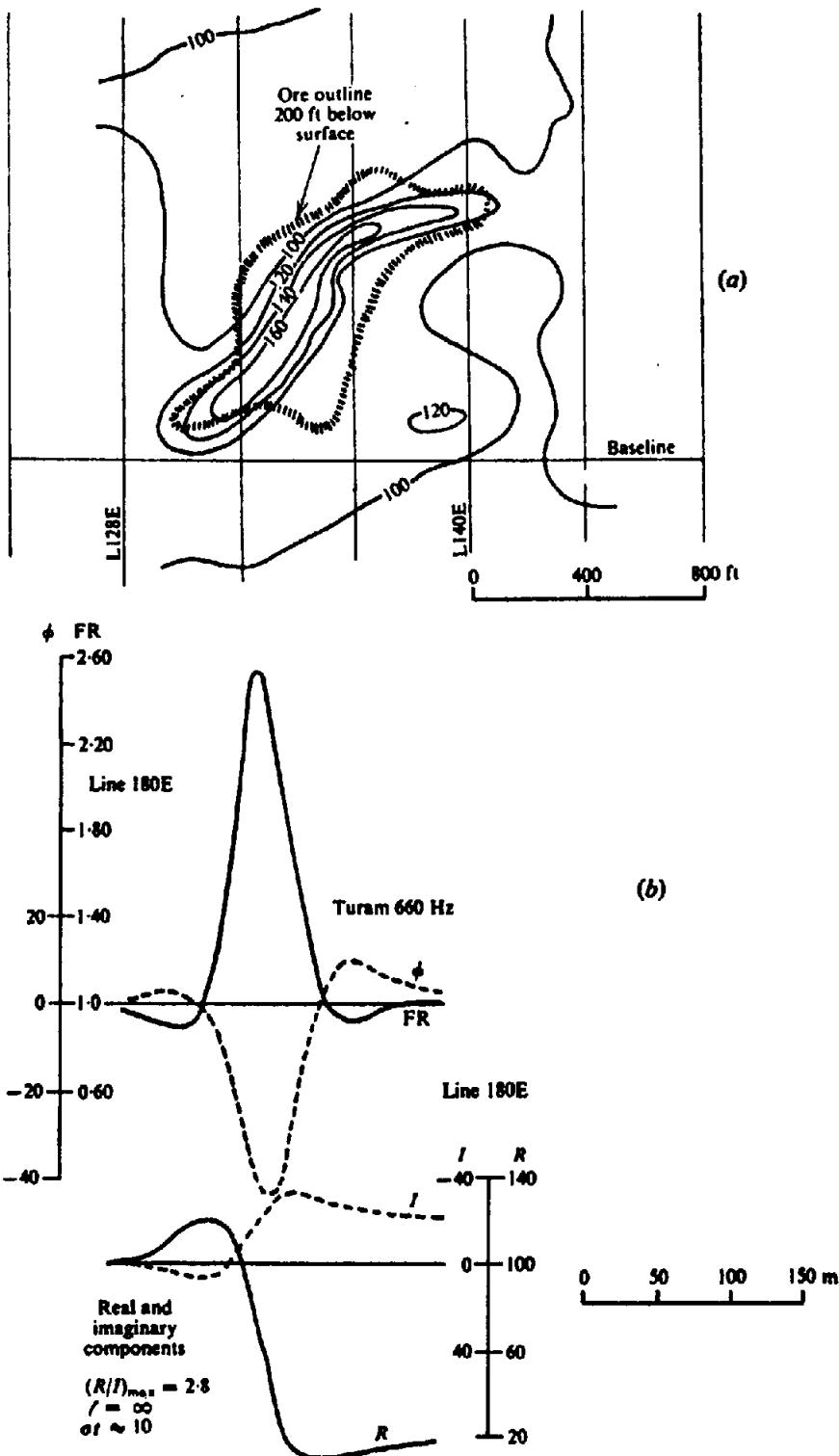


Figure 7.100. Turam survey over the Murray sulfide deposit, northern New Brunswick.  
(After Fleming, 1961.) (a) Field-strength contours. (b) Graphite response.

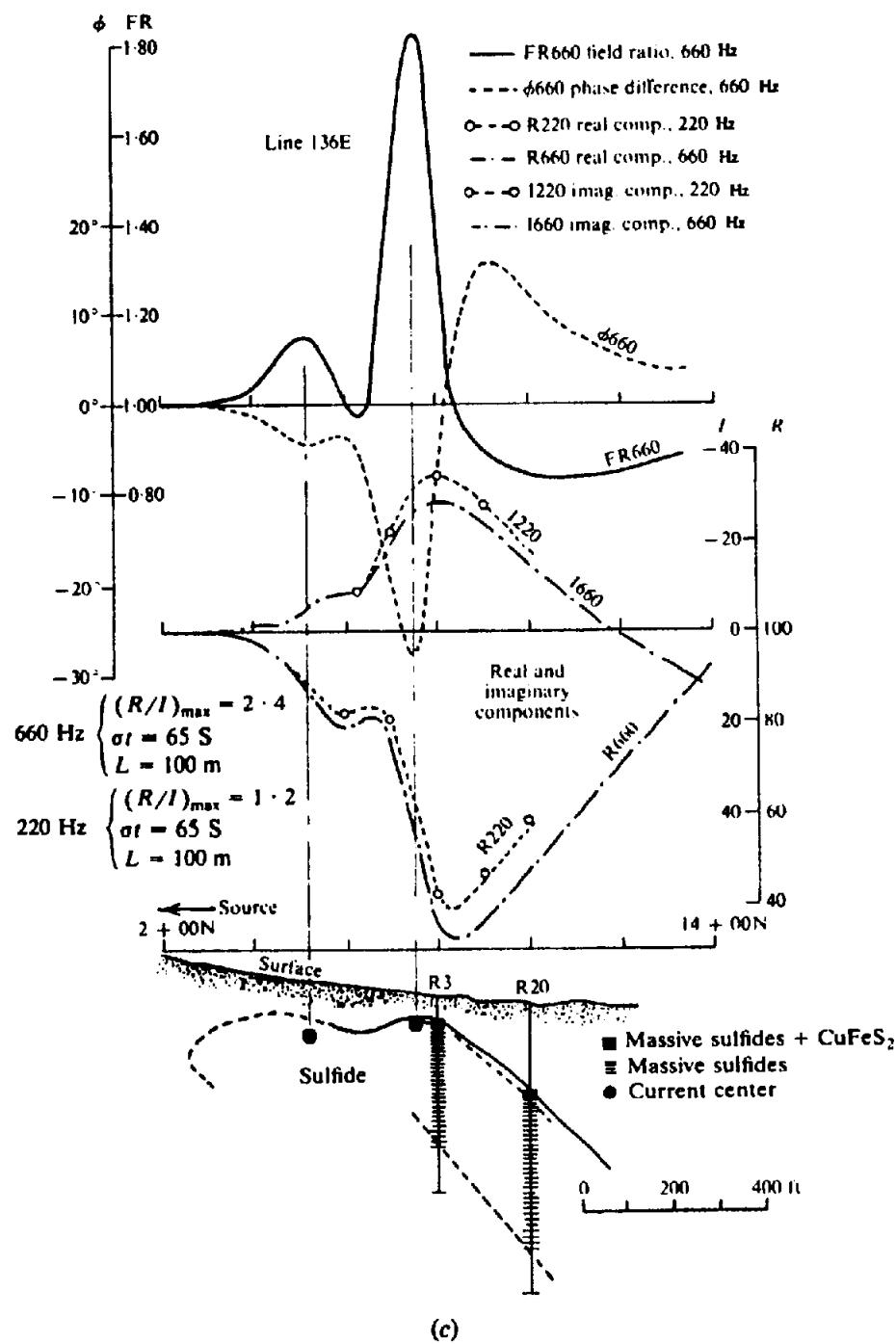


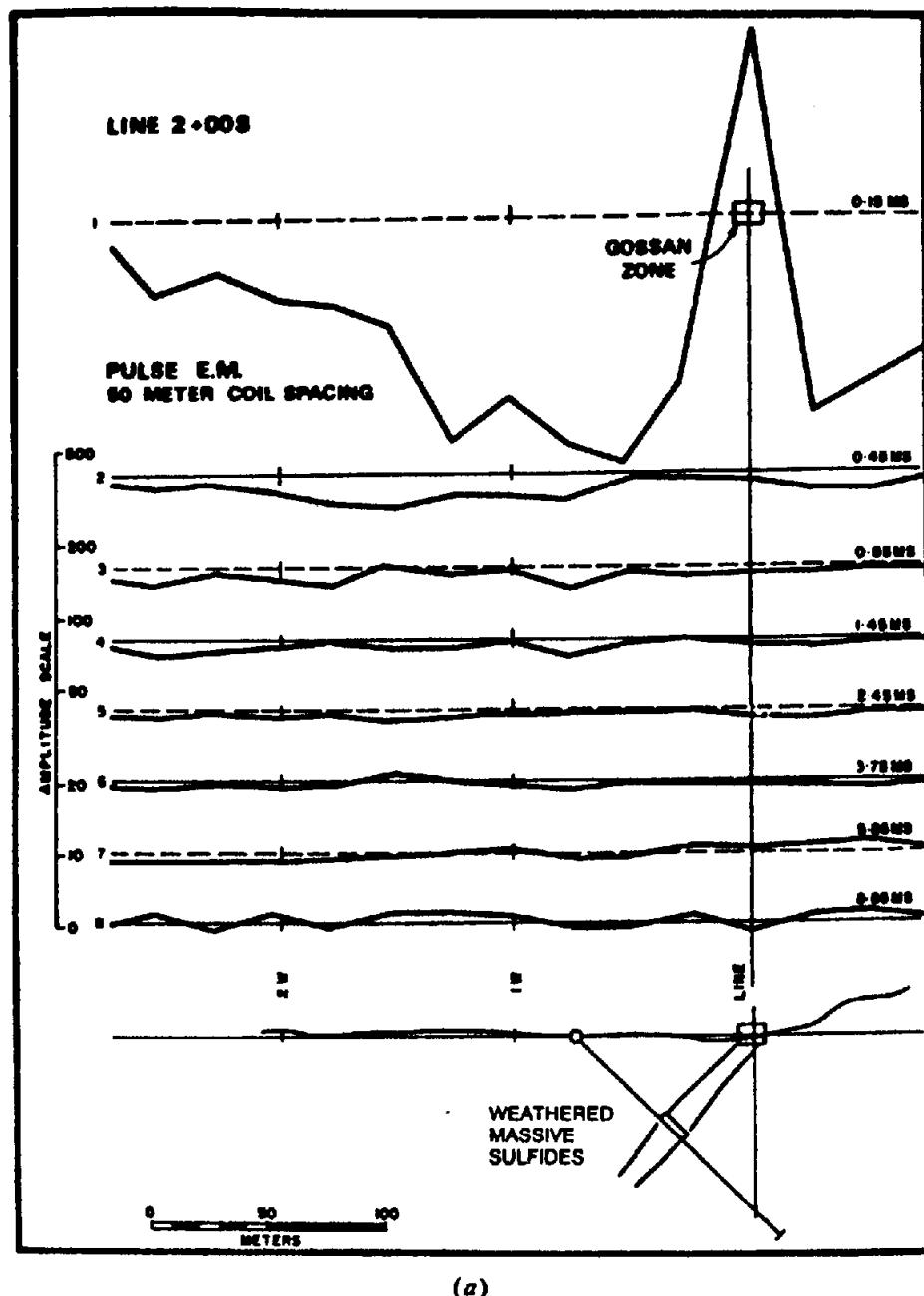
Figure 7.100. (Continued) (c) Sulfide response and interpreted section.

180E over the main graphite zone – which is continuous for at least  $1\frac{1}{2}$  miles NW–SE. Both components in the first profile indicate a shallow dip to the north (see Fig. 7.38) whereas the graphite zone appears to have a much steeper dip in the same direction. In both examples the response is strong. On line 136E there is, in addition, a minor anomaly 230 ft south of the main peak, which corresponds to the isolated 120 contour in Figure 7.100a. Apparently this is caused by the undulation in the top surface of the sulfides.

Although the sulfide deposit is massive and appears homogeneous throughout the body, which is about 300 ft thick at 136E, the Turam anomaly

resembles that of a thin conductor. Possibly this is explained by the core logs of drill holes R3 and R20, which show a high concentration of chalcopyrite in the first 15 ft of massive sulfides. The main bulk of the mineralization below this, mostly pyrite, appears to contribute little to the response. Massive pyrite is known to occur at times in a silicate matrix that isolates the sulfide particles from one another, reducing the conductivity greatly. Whether such a situation exists here is not known.

A very rough estimate of the depth of these conductors (the estimated value is invariably larger than the actual depth to the top) can be obtained



(a)

*Figure 7.101. Results of PEM base-metal survey in Sultanate of Oman using moving-coil method and interpretation using a model plate. [Parts (a) and (b): After Crone, 1979; parts (c) and (d): After Bartel and Hohmann, 1985.] (a) Profile over Chayth showing; 50 m coil spacing.*

from the width of the profile anomalies at half maximum. For the larger sulfide response we get 85 and 115 ft from the field-ratio and phase curves, respectively, for the smaller peak about 140 ft. Because the actual depths are about 40 and 75 ft, a better result is obtained by using the half width rather than the full width. However, there is probably a widening of both parts of the profile because the anomalies are close together. In the case of the graphite zone the depth estimate is about 150 ft.

Real and imaginary components, derived from the Turam field curves, are also displayed in Figures

7.100b, c for both zones. It is difficult to calculate the depth of the sulfide from these curves because they do not have well-defined minima, but for the graphite zone the estimates are about 125 and 90 ft from the real and imaginary components, respectively. The  $\sigma$  values are 65 S for the sulfide and 10 S for the graphite.

8. Several field examples of time-domain ground equipment follow. A large base-metal exploration program in the Sultanate of Oman was initiated in 1973, including airborne magnetics, Input, and ground followup with the Crone PEM system, using

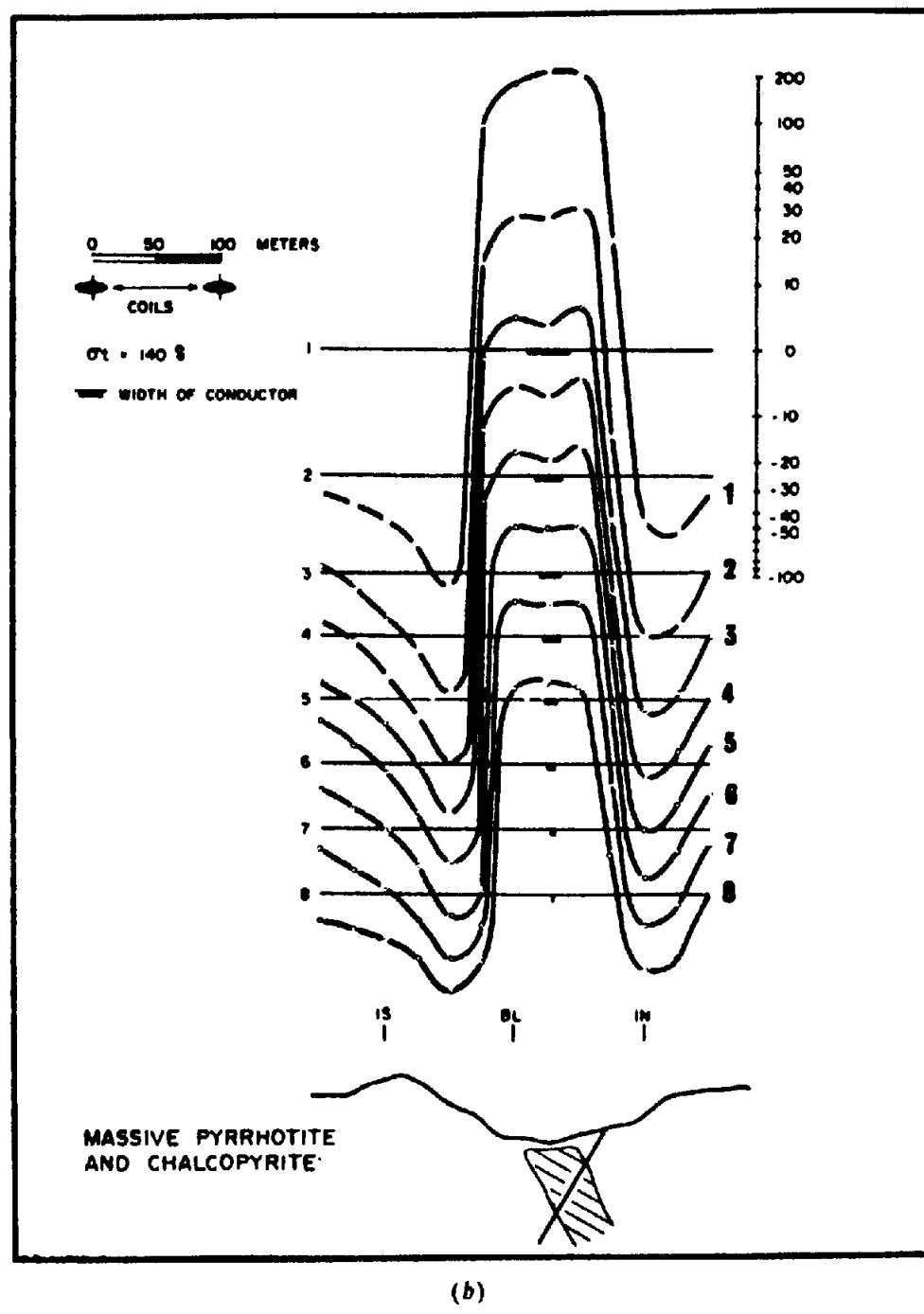


Figure 7.101. (Continued) (b) Profile over Maydan deposit; coil spacing 100 m.

the moving-coil method (Crone, 1979). In such arid areas, conductive surficial material produces background noise on all TD channels and the metallic anomaly may be further reduced by weathering to considerable depth. A saving feature of this weathering at depth is that it may produce for wide ( $> 10$  m) conductors an oxidized sheath surrounding a thinner core of high conductivity.

This process has occurred at the Maydan deposit, located in mountainous terrain, where the original 40 m wide massive sulfide body is weathered to a depth

of 10 m; as a result all eight channels in Figure 7.101b are active. On the other hand, in Figure 7.101a, which displays the Ghayth showing, only channel 1 is active because the zone was originally less than 3 m wide.

The Maydan deposit has been modeled by Bartel and Hohmann (1985), using their standard  $600 \times 600$  m plate. From the nomogram of Figure 7.67a they obtained estimate of TCP between 30 and 80 S and a steep north dip, deduced from the slight asymmetry of the side lobes plus geological and drilling infor-

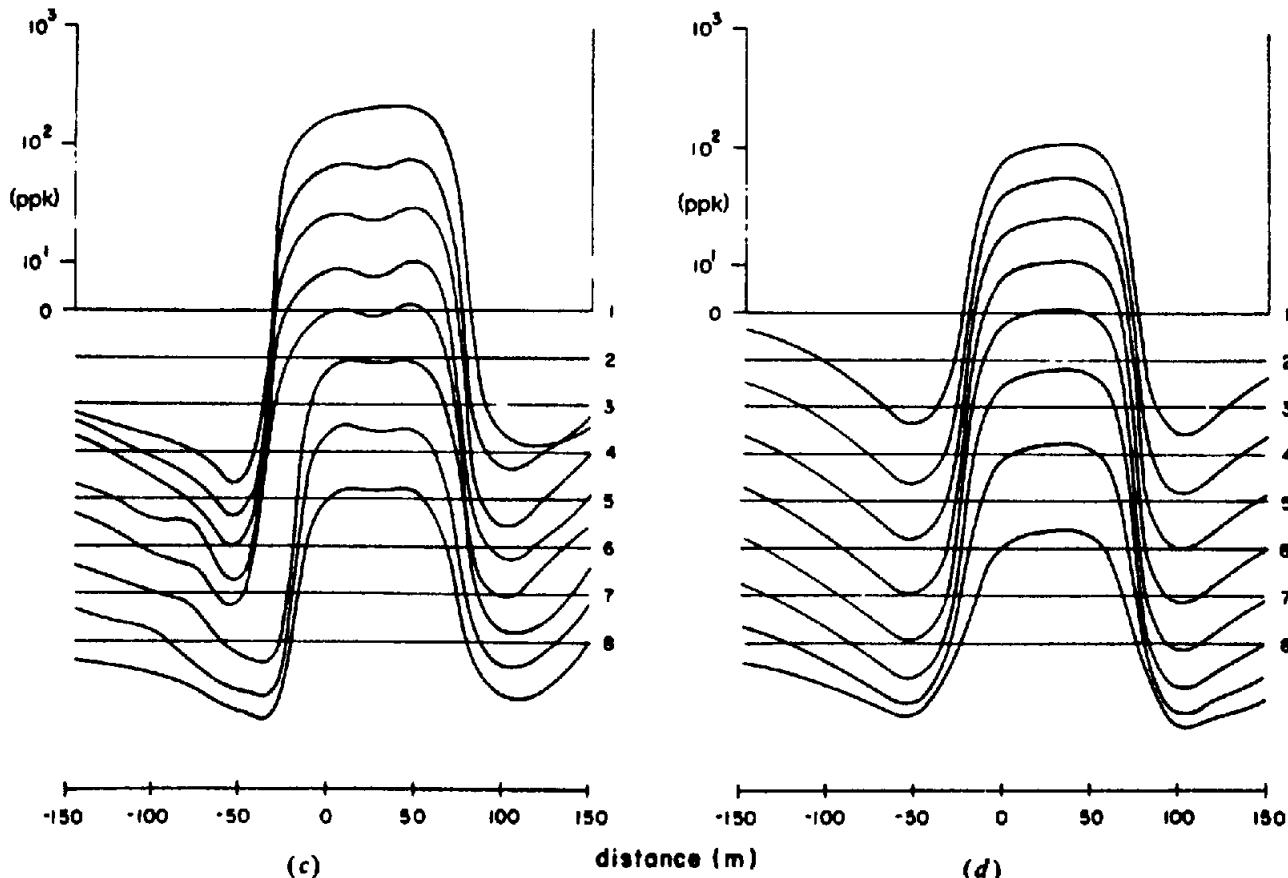


Figure 7.101. (Continued) (c) Field data over Maydan deposit; coil spacing 100 m. (d) Best-fit plate response to profile in (c);  $l = d = 600$  m,  $z = 20$  m, dip =  $80^\circ$ , TCP = 60 S.

mation. Field profiles were then matched by PLATE program modeling to produce the best-fit curves; see Figure 7.101c, d.

9. EM37 field results from the vicinity of the well-known Broken Hill ore deposit in New South Wales, Australia, are displayed in Figures 7.102 to 7.104. This is the White Leads Ag-Pb-Zn prospect (Smith, 1985). Gravity, magnetics, IP, and mise-à-la-masse surveys were carried out, as well as TDEM. Only the time-domain method was a success, after several attempts, when the double-dipole array spacing was reduced to 50 m. The pseudodepth plots and drill sections are shown in Figure 7.102a, where it is clear that the weathered zone of about 20 m is more conductive than the area containing massive sulfides.

A plan of the survey area with two locations of the EM37 Tx loop and grid lines is seen in Figure 7.102b. It also locates an earlier shaft and mapped "lode horizon." The successful IP survey line (100S) is seen to cross sulfides, which dip about  $75^\circ$ WNW.

The first EM37 survey was performed with the Tx loop in position 1, lying over the lode horizon with its SE corner directly above the sulfide zones. The resulting profiles, also on line 100S (Fig. 7.102a), are

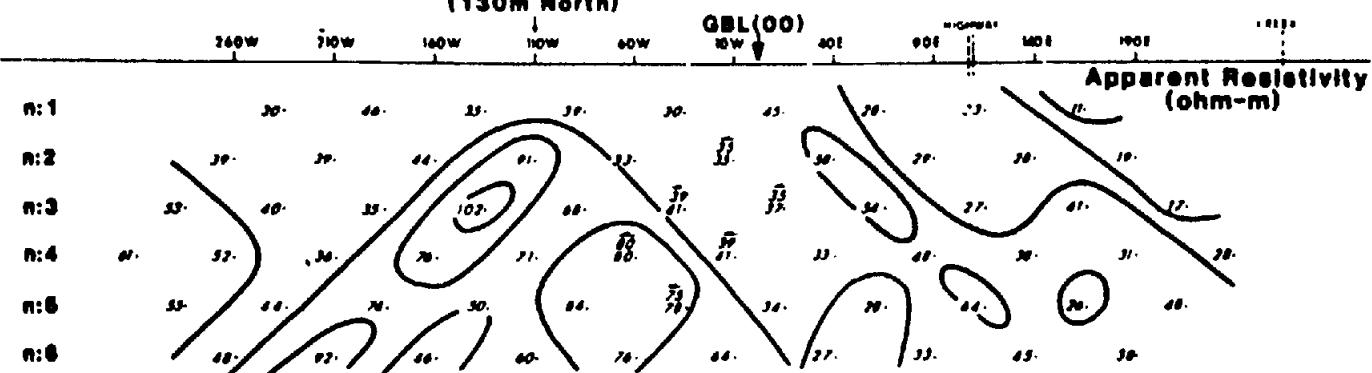
barren for both  $H_z$  and  $H_x$  in Figure 7.103. When the loop was relocated in position 3 roughly parallel and adjacent to the favorable horizon, there is a weak response over the sulfides and additional anomalies further west, as seen in Figure 7.104.

Failure of the EM37 to detect the sulfide mineralization is doubtless caused by two factors, the first being poor geometry of the field layout. Second and more critical is the positive resistivity contrast between the sulfide zone and its surroundings, as is obvious in Figure 7.102a.

10. An early test of the UTEM system was made in 1977 at the Izok Lake base-metal deposit some 400 km north of Yellowknife NWT in northern Canada. This is a  $12 \times 10^6$  tonne high grade massive Zn-Cu-Pb-Ag sulfide body that was used almost as a test area for geophysical methods; EM was particularly suitable because of the lack of surface cover and generally high resistivity. In this respect it is a complete contrast to the previous example.

Figure 7.105a shows the UTEM field layout and interpreted results in plan; a single profile for  $H_z$  from line 12E in Figure 7.105b sharply marks the conductive section. Conductance and depth of this

## NORTH-WEST

White Leads Shaft  
(130m North)

## SOUTH-EAST

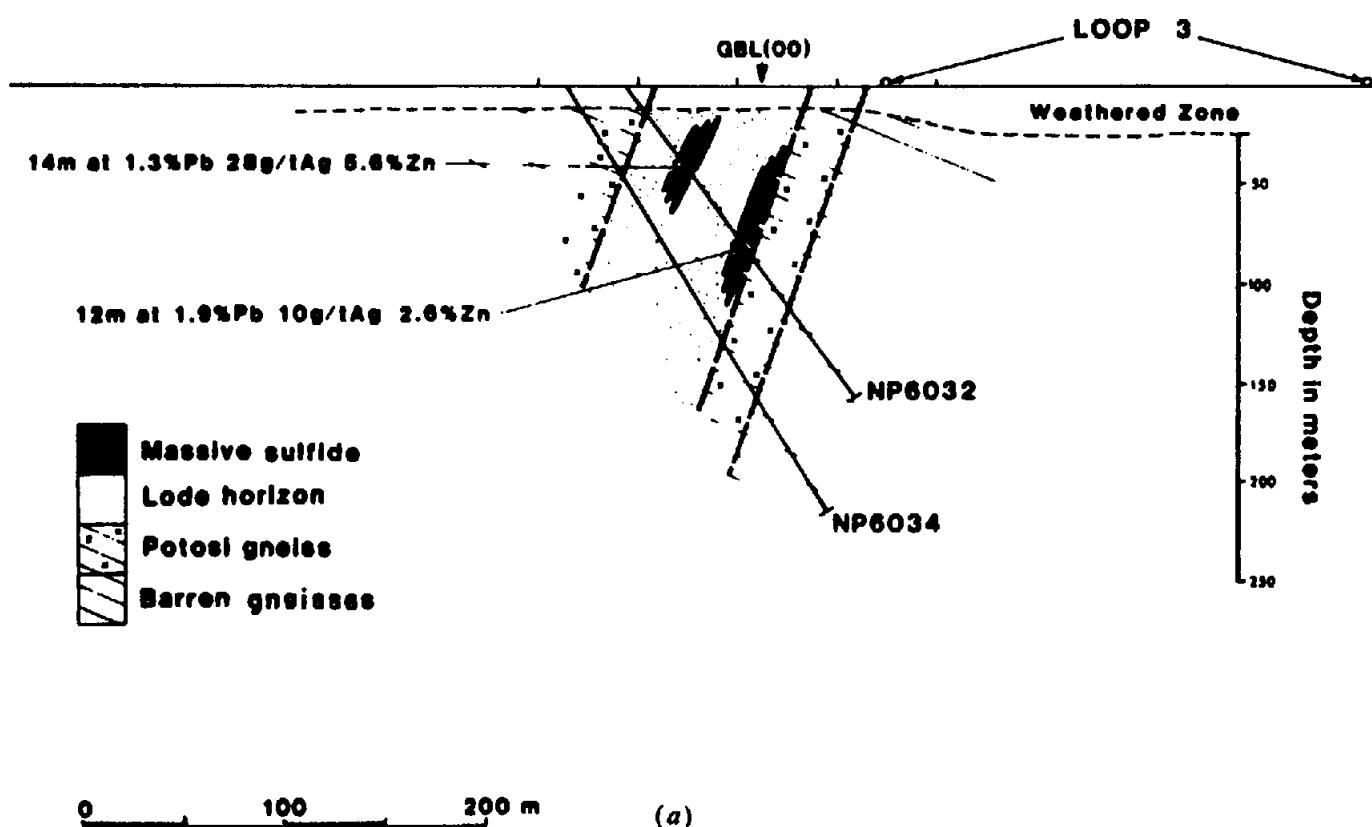
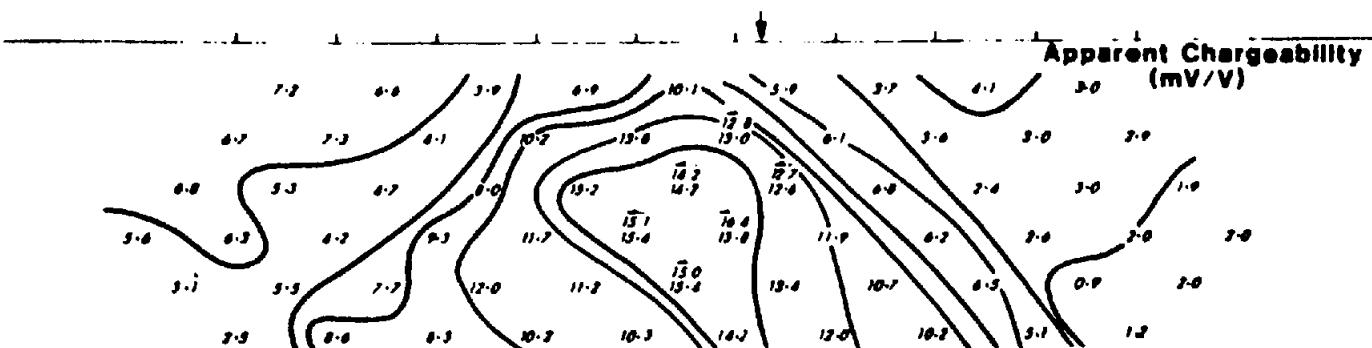
Apparent Resistivity  
(ohm-m)

Figure 7.102. Resistivity and IP results plus drill section, line 100 S, White Leads prospect, Broken Hill, New South Wales. (After Smith, 1985.) (a) IP and resistivity pseudodepth plots (dipole-dipole array, 50 m dipoles) with drill section.

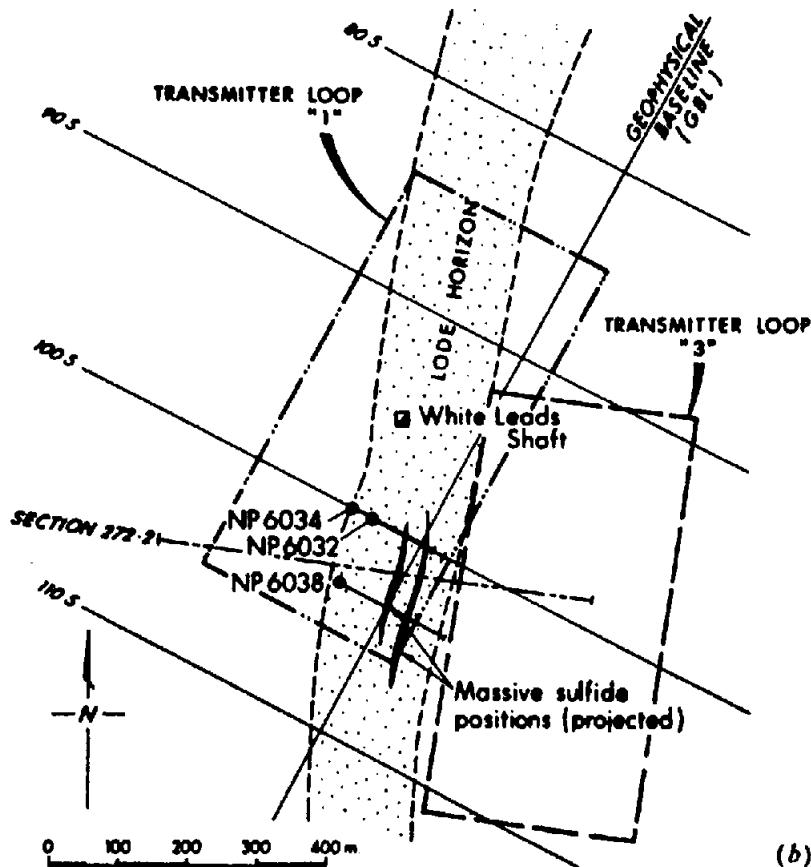


Figure 7.102. (Continued) (b) Plan showing lode horizon, geophysical grid, and drill hole locations.

anomaly were interpreted as 500 S at about 300 ft (90 m).

**Note:** Field examples for EMP and SIROTEM systems are not included here. The first is similar to EM37, the second is discussed in Section 7.7.4d, Figures 7.58 and 7.60.

11. Paterson (1967) has provided several good examples of the quadrature AEM system from surveys over the Canadian Shield. Typical profiles together with ground followup by various methods are illustrated in Figure 7.106. Figure 7.106a provides an estimate of the TCP from the airborne peak response ratio  $P$  in each example; it is quite large: 4.5 S in Figure 7.106b, 2.6 S in (c), and 3.7 S in (d), suggesting good conductors in all cases.

In Figure 7.106b the massive pyrite body is deeply buried, indicated by small quadrature response and 100 ft (30 m) of overburden on the drill section. The TCP is about 40 S. Both ground magnetic and gravity profiles appear to reflect the very massive pyrite. This is surprising in the case of the magnetic anomaly because pyrite is only weakly magnetic, and the section of 20% magnetite at the bottom of the hole has no apparent magnetic signature. The vertical-loop profile is typical of a conductor with shallow dip to the left. This is also peculiar in view of the drill hole inclination, which would not normally be downdip.

The HLEM profile in Figure 7.106c, apparently plotted upside down from the usual orientation, suggests a dip to the left as well, although steeper than in Figure 7.106b – which is reasonable. Ratio of real-to-imaginary peaks is only 1.5, indicating a poor conductor. Consulting the characteristic curves of Figure 7.44, we find the depth to be about 25 ft (7.5 m), with the TCP value 30 S, which agrees roughly with the airborne estimate of 20 S from Figure 7.106a. However, the validity of using the curves of Figure 7.44 is questionable because the graphite zone appears to be at least 200 ft (60 m) wide.

Correlation between airborne and ground data in Figure 7.106d over shallow low-grade sulfides is again rather poor. The VLEM profile suggests a broad conductor (400 ft or 120 m), possibly with shallow dip to the right. This is not in agreement with the gravity anomaly. The magnetic profile seems to mark the sulfides located by drilling, although the huge negative peak on the right is not explained. Quadrature peak ratios here give  $TCP \approx 35$  S.

12. The Whistle Mine, located on the northeast rim of the Sudbury basin, northeastern Ontario, is a favorite test site for airborne electromagnetic equipment. The massive steeply dipping sulfides, mainly pyrrhotite, are both conductive and magnetic. Figure 7.107 shows an assortment of profiles from several

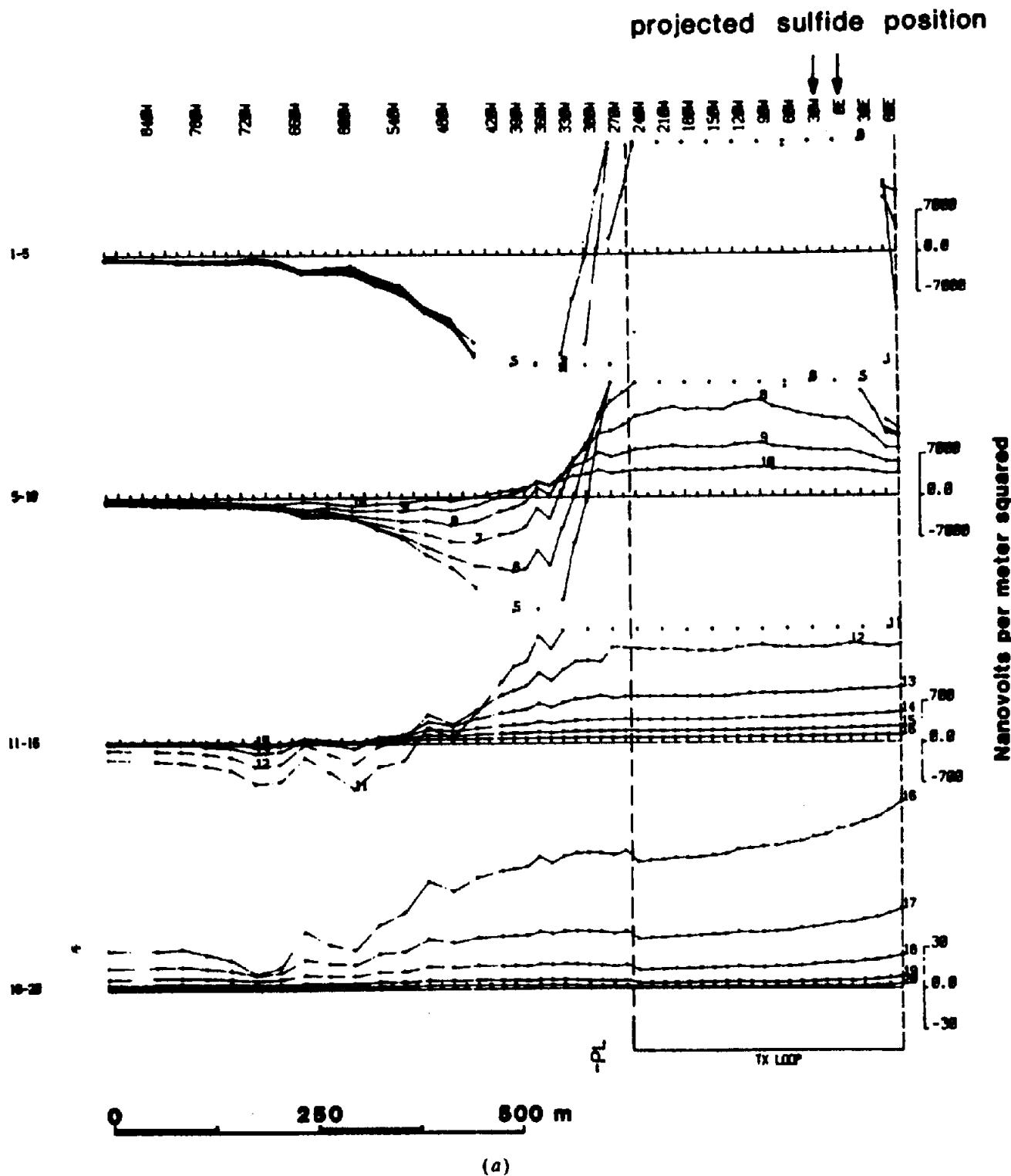


Figure 7.103. EM37 profiles, line 1005, White Leads prospect, Broken Hill, New South Wales. (After Smith, 1985.) (a) Vertical components.

airborne EM systems over this property. The upper three profiles in (a) include an airborne VLF (McPhar KEM), two-frequency quadrature (McPhar F-400), and aeromagnetics, for a single traverse. The next two in (b) show airborne AFMAG and a second airborne EM response, from a quadrature system, on the same flight line. The last set of three profiles in (c) is for a phase-component helicopter system

(Aero-Newmont) with aeromagnetics on the same line. The relative locations of these three traverses are not known.

In Figure 7.107a the ratio of peak low-frequency (340 Hz) to peak high-frequency (1,070 Hz) response is about 0.78, giving a  $\sigma f$  product of 4 from Figure 7.106d. This is a moderately good conductor. The distinct crossover and field strength peak from the

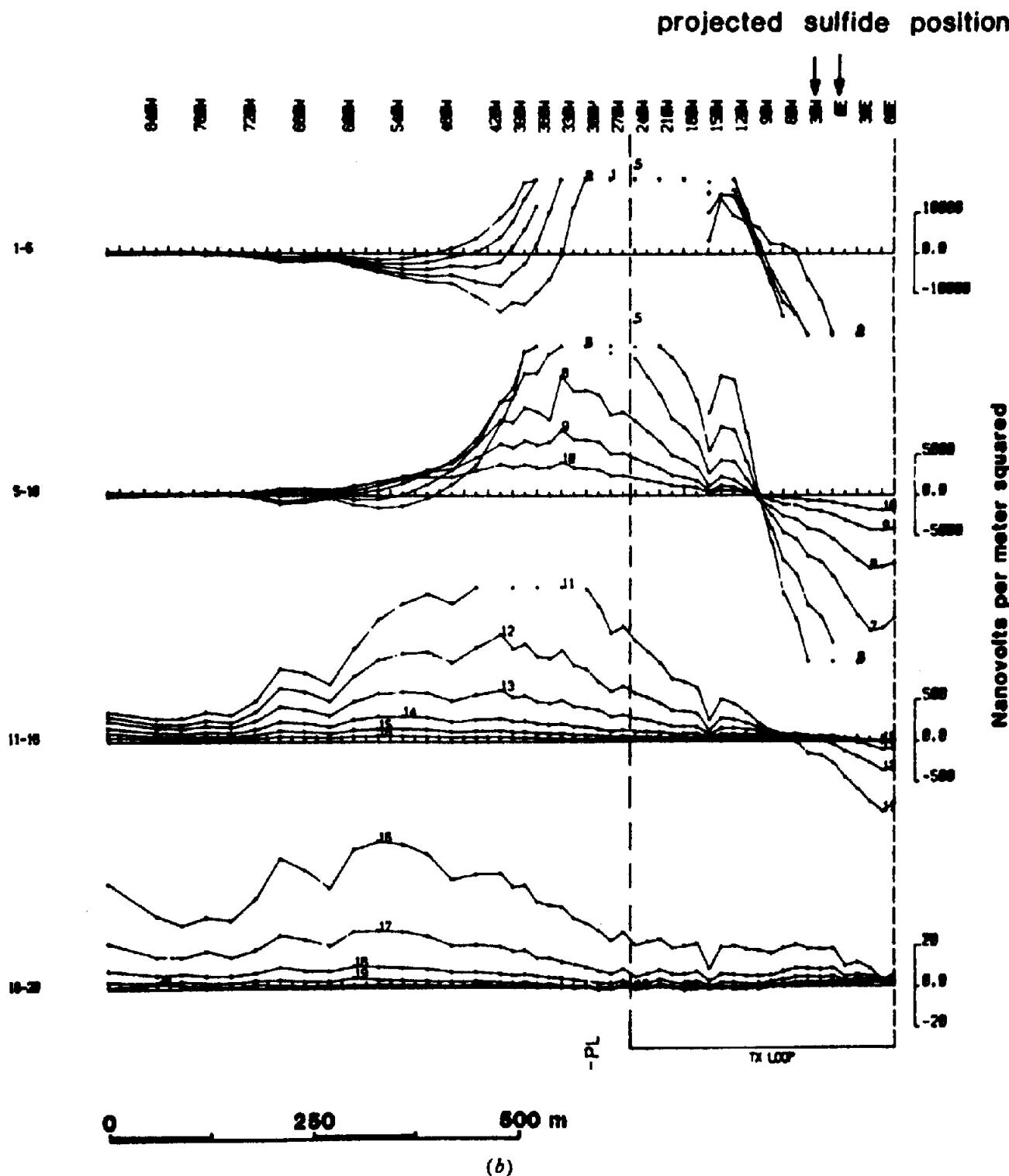


Figure 7.103. (Continued) (b) Horizontal component.

VLF trace correlates precisely with the quadrature peaks and indicates that the conductor is very shallow. There is in addition a large negative magnetic response to the south, whose north flank corresponds exactly to the electrical anomaly.

The AFMAG response in Figure 7.107b shows a strong crossover with steep slope on both frequencies. From these traces we may infer that the con-

ductor is near surface and has high conductivity, because the ratio of peak responses  $(\phi_{150}/\phi_{510})_{\max}$  is approximately unity.

The phase component system in Figure 7.107c produces a very strong in-phase peak of nearly 1,000 ppm. This is partly due to the high conductivity and shallow depth of the conductor, partly to the relatively low altitude which can be maintained by the

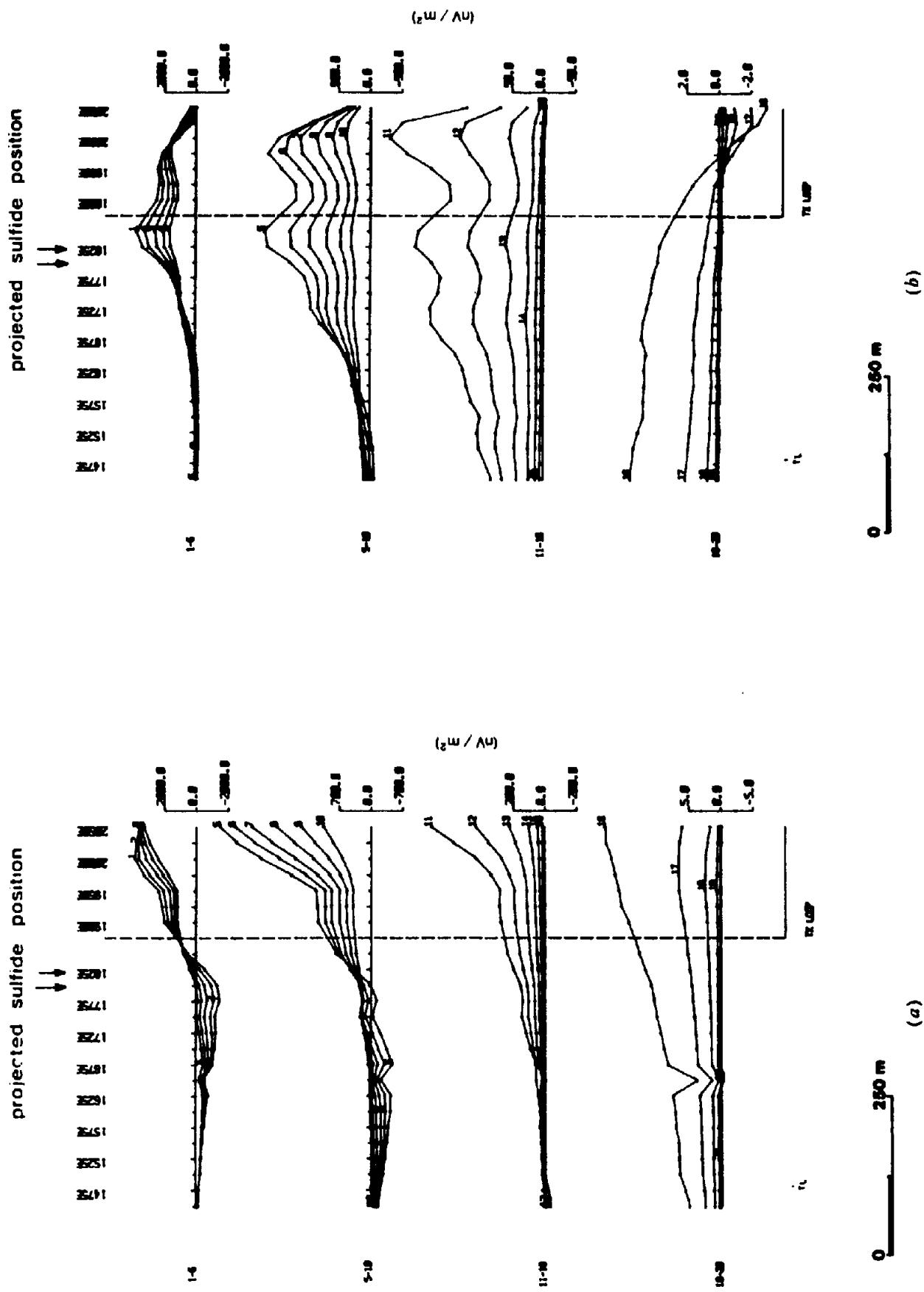


Figure 7.104. EM37 profiles, section 272.2, White Leads prospect, Broken Hill, New South Wales. (After Smith, 1985.) (a) Vertical component. (b) Horizontal component.

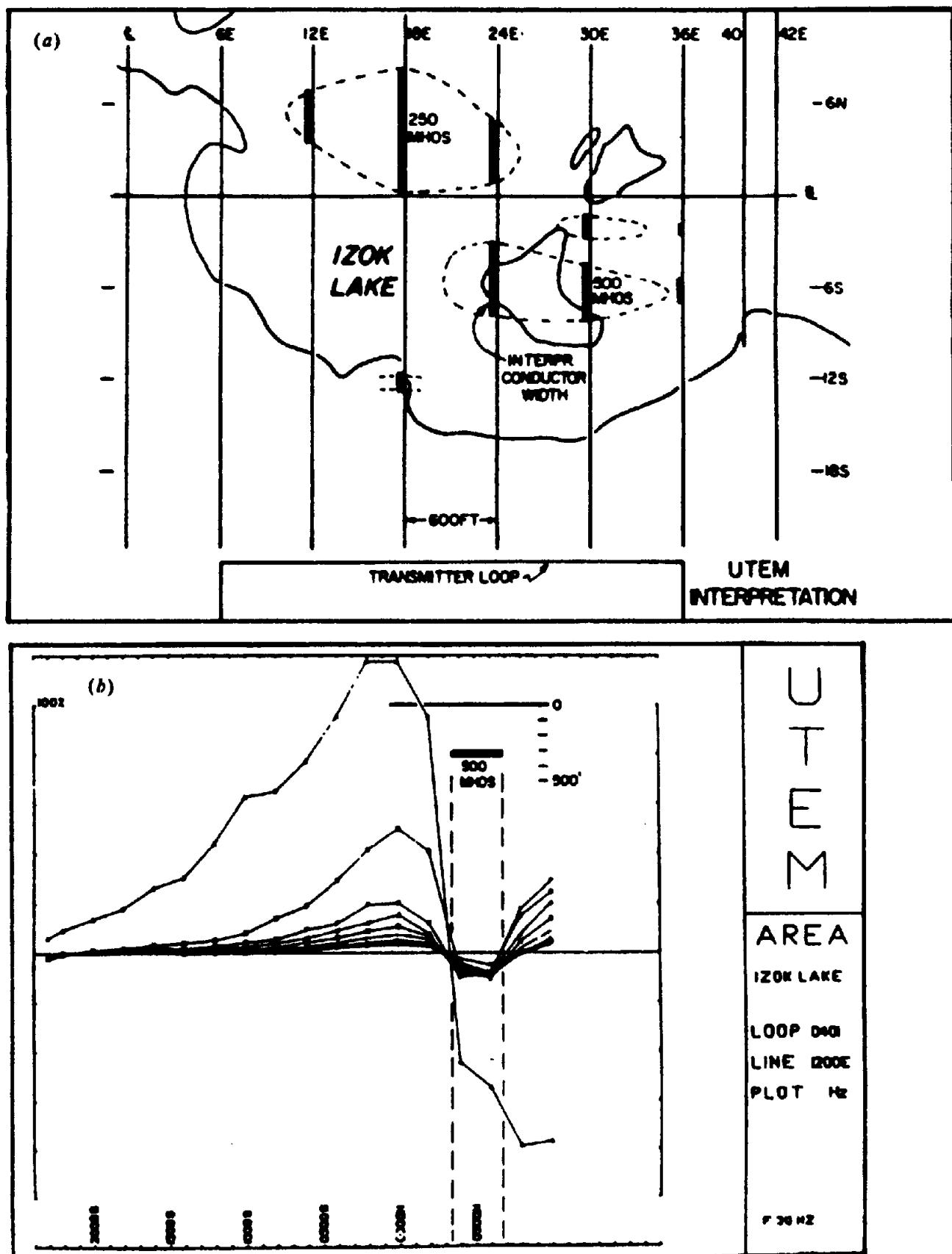
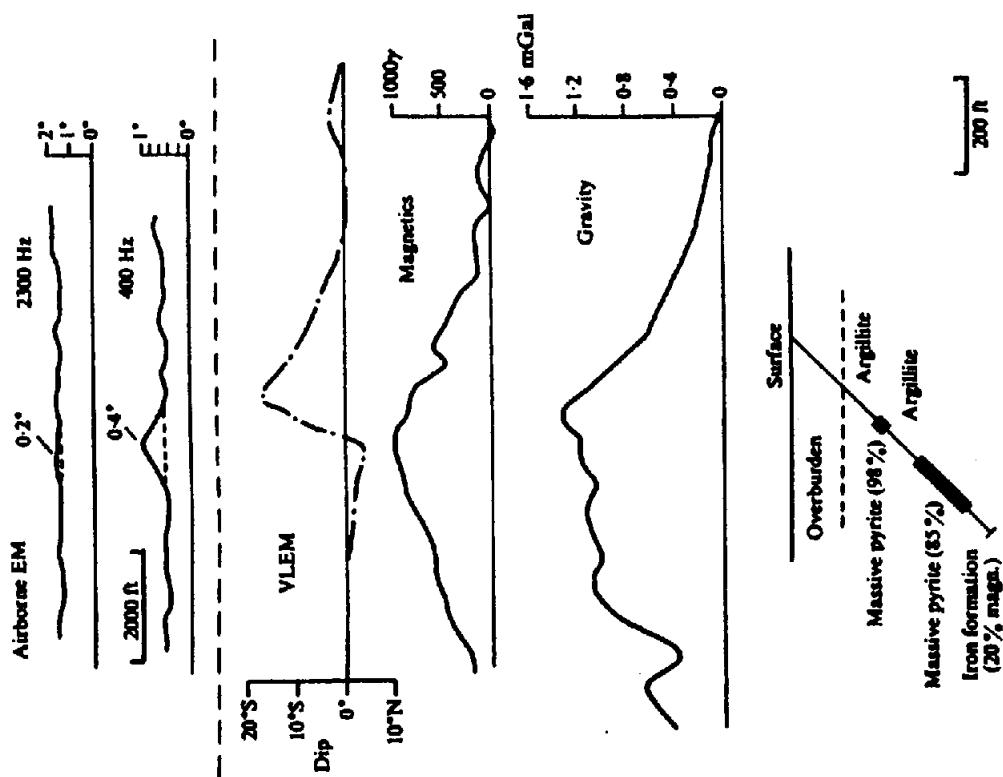
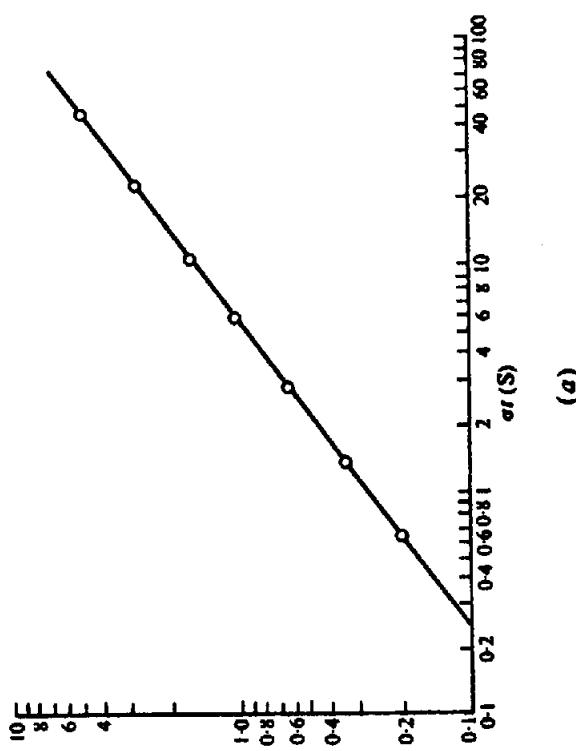


Figure 7.105. UTEM test over Izok Lake deposit, North West Territories, Canada. (After Podolsky and Slankis, 1979.) (a) Map of interpreted mineralization. (b) Profile along line 12E.



(b)



(a)

Figure 7.106. Comparison of airborne quadrature EM and several ground methods over various conductors. (After Paterson, 1967.)  
 (a) Curve of  $TCP$  versus  $P$ , the airborne peak-response ratio over vertical-sheet mode;  $P = (400 \text{ Hz peak})/(2,300 \text{ Hz peak})$ .  
 (b) Comparison with several methods over deep sulfides.

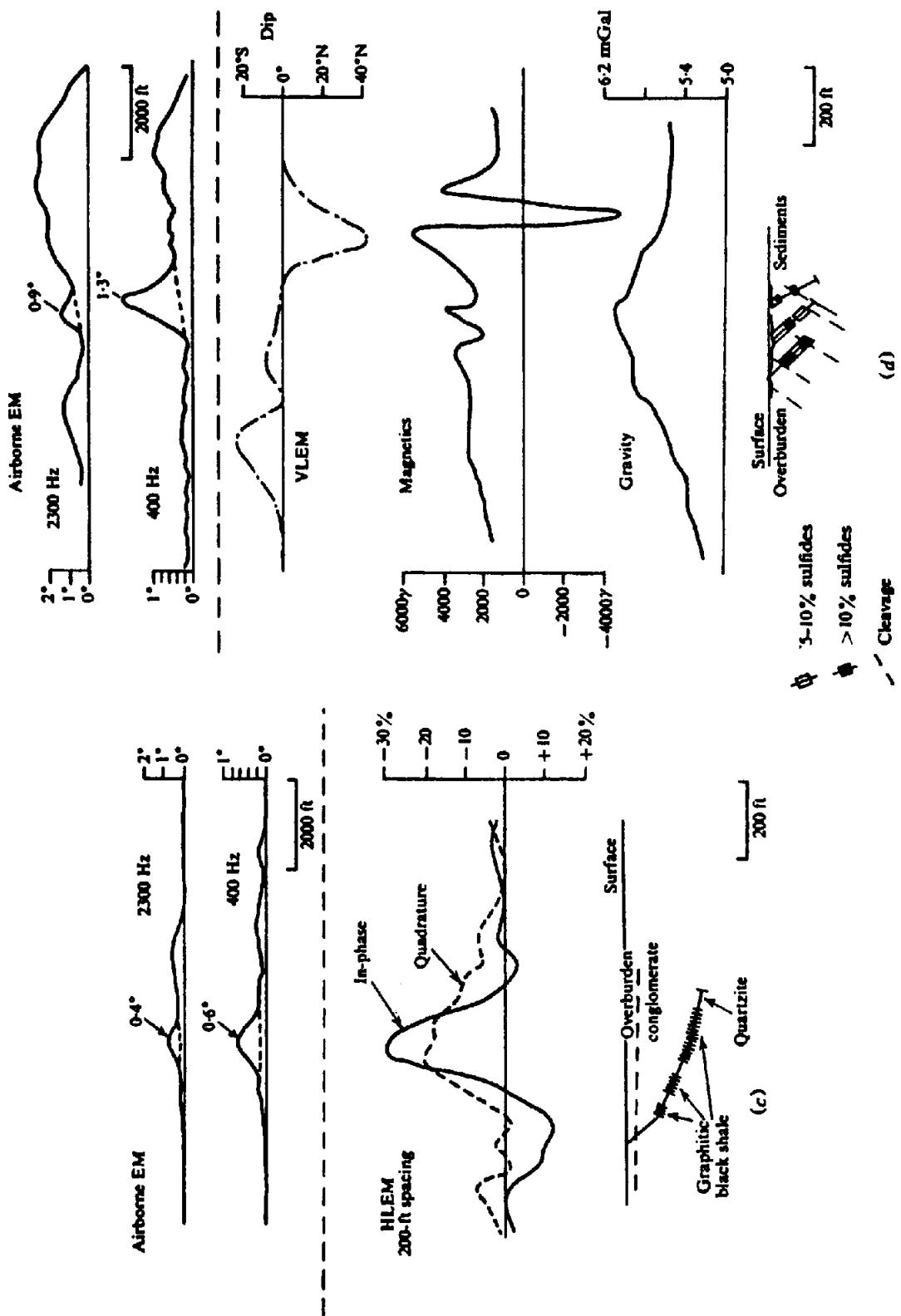


Figure 7.106. (Continued) (c) Comparison with HLEM over shallow graphite deposit. (d) Comparison with several methods over shallow sulfides.

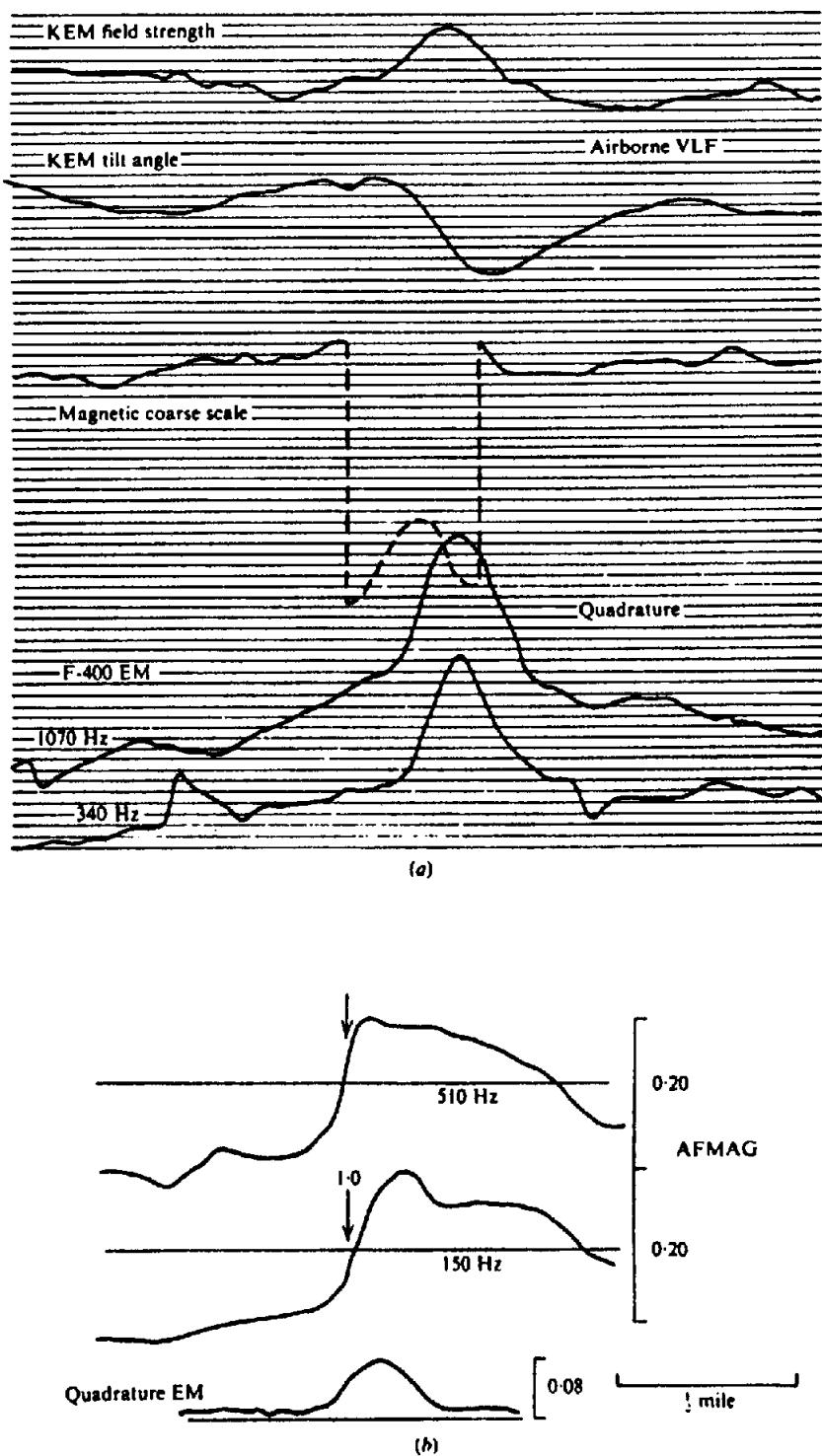
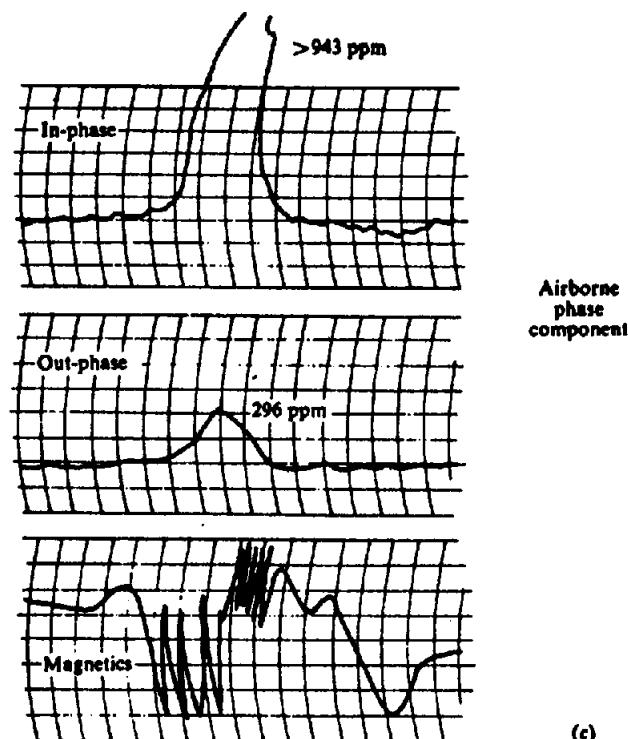


Figure 7.107. Comparison of various airborne EM systems and aeromagnetics, Whistle Mine, Sudbury, Ontario. (a) Comparison of VLF, quadrature EM, and aeromagnetics. (b) AFMAG and quadrature EM on the same line as (a). (From Ward, 1959b.)

helicopter. Using characteristic curves of the type shown in Figure 7.81c, the depth below the aircraft was found to be 115 ft (35 m) and the  $\sigma t$  product 140 S. As in Figure 7.107a, a large magnetic anomaly occurs with the EM anomaly.

13. Four examples from Input field surveys are illustrated in Figure 7.108. The first is taken from the

Manitoba Nickel Belt, northeast of Lake Winnipeg. This is an excellent test area for AEM because the electrical conductors, occurring in Precambrian rocks, are quite deeply buried beneath Paleozoic sandstone and dolomite, which are in turn generally covered with unconsolidated overburden. Sulfide zones, with and without nickel, occur in ultrabasics



**Figure 7.107. (Continued) (c) Phase-component EM and aeromagnetics. (From Ward, 1966.)**

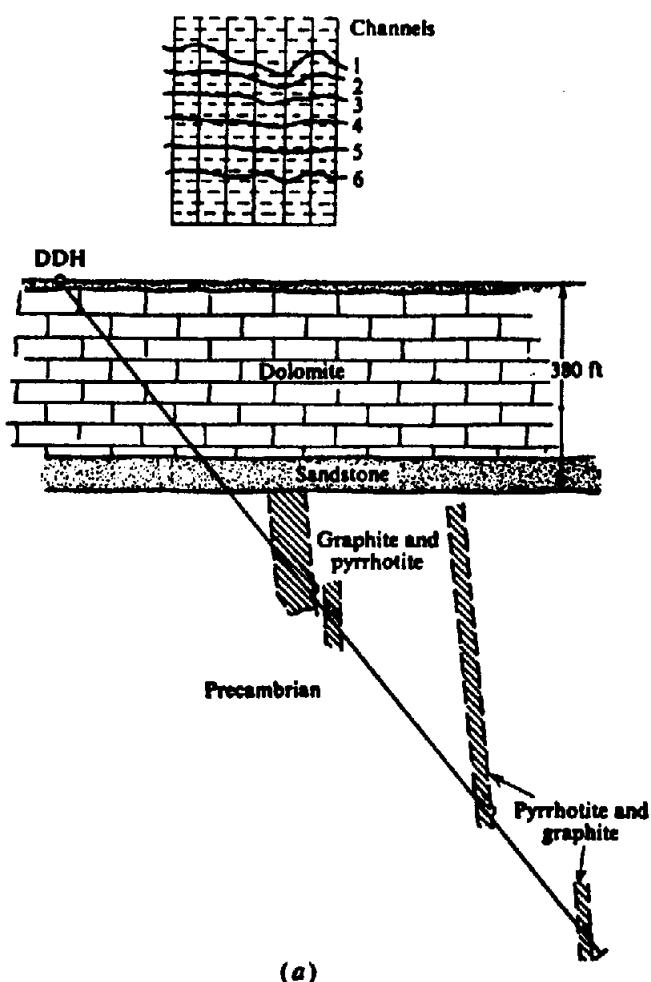


**Figure 7.108. Input response over various conductors. (a) Manitoba Nickel Belt, anomaly depth 115 m.**

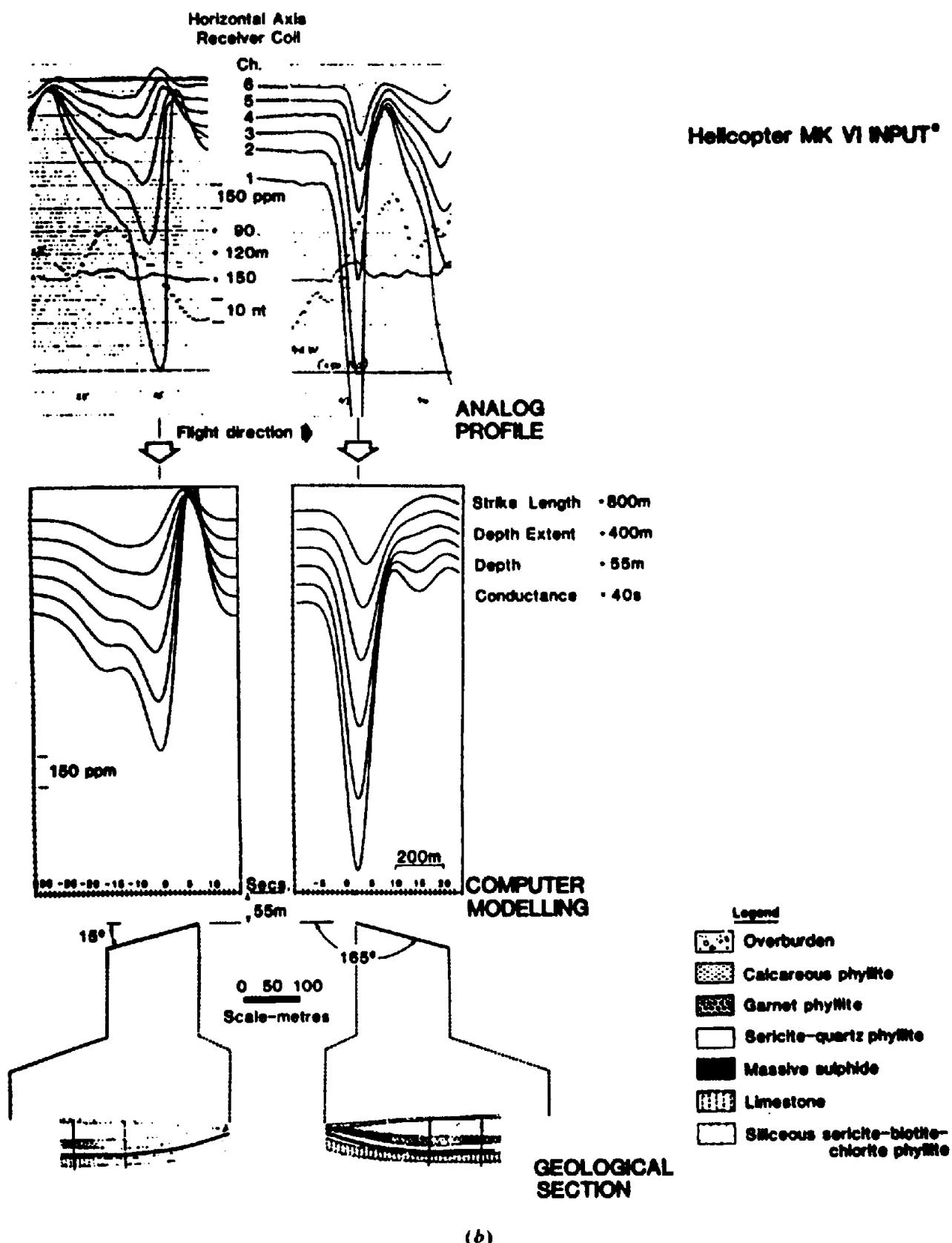


Figure 7.108. (Continued) (b) Goldstream sulfide body (Cu, Zn, Ag). In lower half of top set of profiles, solid line is elevation, dotted line is aeromagnetics.

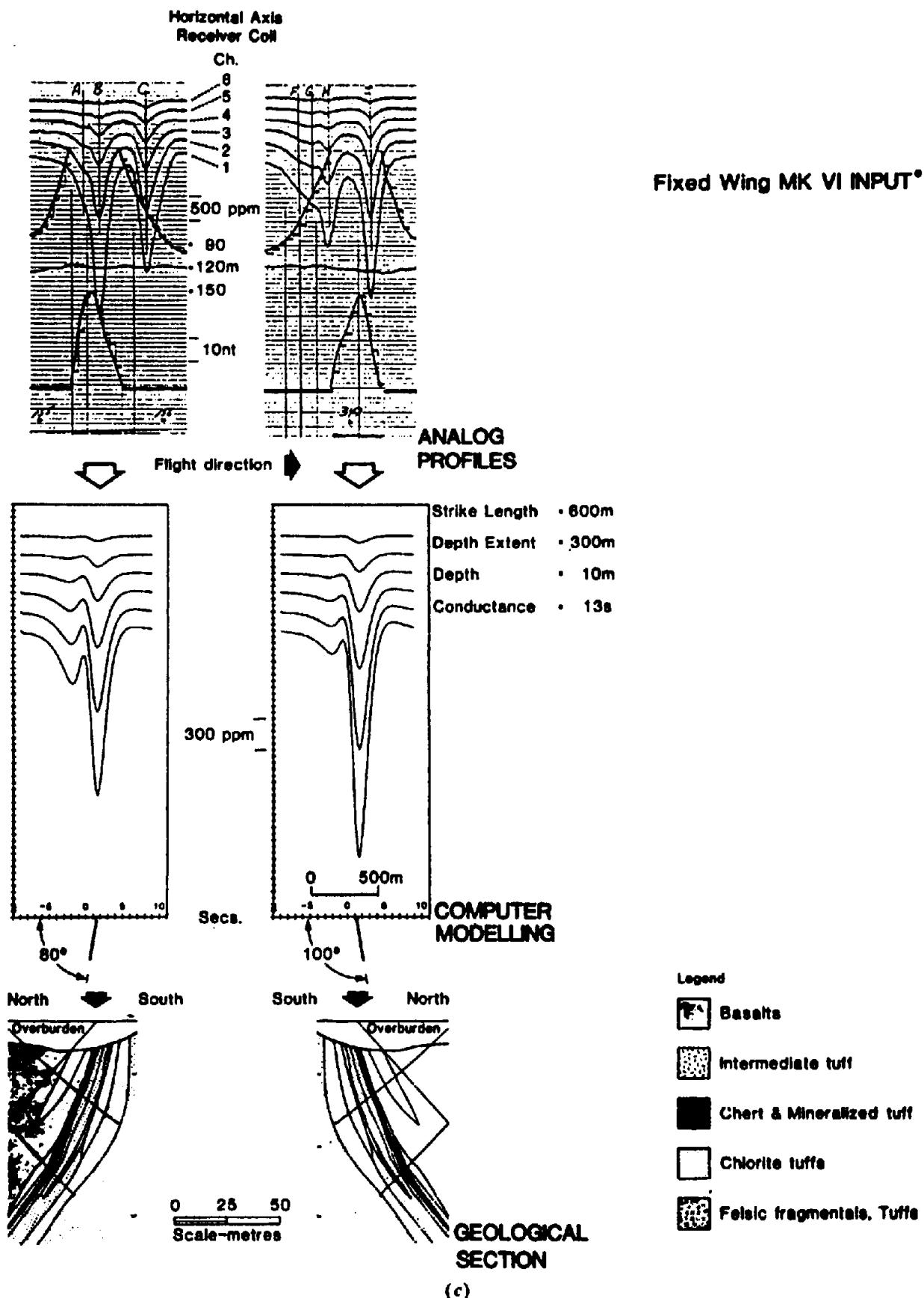
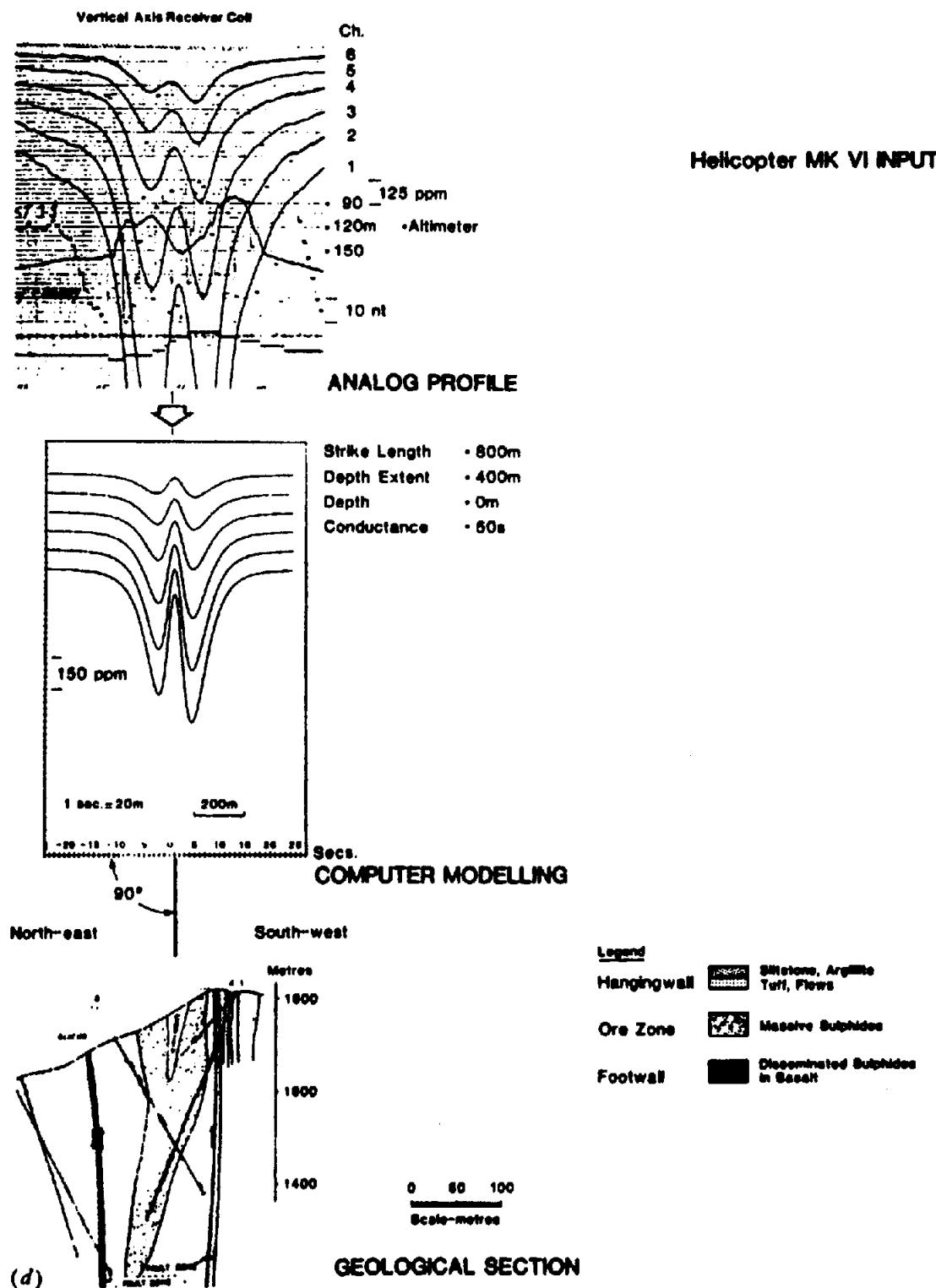


Figure 7.108. (Continued) (c) Detour Lake gold deposit.



•Figure 7.108. (Continued) (d) Windy Craggy sulfide body (Cu).

and gneisses, and frequently extend for kilometers. There is also considerable graphite with the sulfides.

The mineralization appears to be associated with a very large fault structure and is located in a highly resistive host rock. Although the analog record is comparatively quiet in Figure 7.108a, there are discernible responses on all six channels from a target ~ 380 ft (115 m) below surface, or ~ 800 ft (240 m)

below the Input receiver. This survey was performed with the fixed-wing Input system; the next three examples were obtained with the helicopter version in which the boom is much closer to the Tx coil strung around the helicopter.

Figures 7.108b, c display reverse profiles, on the same flight line, over two targets that may be modeled by thin plates of gentle (b) and steep (c) dip.

Table 7.5.

Station	Line 0			Station	Line 2S		
	$\phi(2,400)$ (deg)	$\phi(600)$ (deg)	$\phi(c)$ (deg)		$\phi(2,400)$ (deg)	$\phi(600)$ (deg)	$\phi(c)$ (deg)
42W	-28	-22	-28	43W	-15	-13	-13
41	-35	-26	-36	42	-22	-15	-15
40	-35	-30	-35	41	-24	-20	-20
39	-30	-25	-30	40	-12	-10	-10
38	-2	-2	-2	39	13	12	12
37	20	15	15	38	20	17	18
36	25	20	25	37	18	16	17
35	27	18	27				
34	15	10	20				

Reverse flight profiles are an aid in interpreting dip, as is evident from matching of the two views of each model (see also §7.7.12d and Figure 7.89).

Figure 7.108b is the stratiform Goldstream sulfide body, north of Revelstoke, British Columbia. It is contained in a thin layer dipping  $\sim 15^\circ$ , sandwiched between metasedimentary beds at a depth of  $\sim 50$  m. Ore reserves are estimated at  $3.2 \times 10^6$  tonne of 4.5% Cu, 3.1% Zn, and 12 g/tonne Ag. Response is strong on all channels. This example and the two following have been computer-modeled using the PLATE program and the resultant profiles here fit the analog data very well. (Model depth extent, given as 400 m, is essentially the plate width.) There is correlation with a 50 nT magnetic anomaly displaced 200 m from the Input peaks, although neither the host rock nor the mineralization appear to offer significant magnetic contrast.

Figure 7.108c displays data from the Detour Lake gold deposit. This target is of large extent and close to surface. It is readily modeled by a half-plane dipping  $80^\circ$ . The main gold concentration is in cherty tuff, which also contains sulfides (10 to 15% pyrrhotite-pyrite, up to 1% chalcopyrite). These produce both the EM and magnetic anomalies; the latter are much stronger than at Goldstream, as is evident from the scale change (1/100). Additional gold is found in the adjacent basalts and talc-carbonate rocks. Established gold reserves here are  $30 \times 10^6$  tonne, although the grade is rather low. Magnetic correlation with the mineralization is excellent.

In Figure 7.108d a huge, steeply dipping tabular pyrrhotite, pyrite, and chalcopyrite massive sulfide, which effectively outcrops, has produced a strong Input response on all channels, off scale on the first two. This enormous deposit is estimated to contain  $300 \times 10^6$  tonne of 1.5% Cu, with 0.08% Co. Again there is good correlation between EM and magnetics from the pyrrhotite. Extreme variations in altitude (60 m over  $\sim 200$  m horizontal) are seen in the

flight profile. These are the result of ground slope and atmospheric disturbance (the site is called Windy Craggy).

Note that the comparatively rare vertical-axis receiver coil was used in this survey. The change was made to reduce variations in the minimum T-R coupling, which are greatly increased when the Rx coil is carried in the boom rather than the remote bird. The problem arises in obtaining continuous normalization of secondary field in terms of primary (§7.7.4b, e). This ratio is highly sensitive to small changes from minimum-coupling position, compared to using approximate coplanar geometry. Thus signal stability was much improved. The profile shapes in Figure 7.108d are quite different from usual Input response and may be compared to coincident-loop curves in Figure 7.55b.

*Note:* There are numerous other AEM field examples not discussed here. These include Turair, Figure 7.77; structural mapping, Figures 7.80a and 7.91; resistivity mapping, Figures 7.78, 7.79, and 7.92; bedrock conductor location and resistivity mapping, Figure 7.85; bathymetry, Figure 7.93.

## 7.9. PROBLEMS

1. The VLEM readings in Table 7.5 were obtained during a fixed-transmitter ground survey in northeast Brazil. Stations are 50 m apart, the lines are 400 m apart; the transmitter was located on line 1S, midway between stations 38 and 39.

$\phi(2,400)$ ,  $\phi(600)$ , and  $\phi(c)$  are dip angles measured, respectively, at 2,400 Hz, 600 Hz, and both frequencies simultaneously. Plot the profiles. Estimate the depth, dip, possible strike length, and location of this anomaly, as well as its TCP. Do you see any advantages in the dip-angle measurement at two distinct frequencies? At two simultaneous frequencies?

2. The data in Table 7.6 are taken from a vertical-loop fixed-transmitter survey carried out in northern Quebec. The transmitter was located at 7 + 00S on line 4W. Station spacing was 100 ft and the two lines are 800 ft apart. Transmitter frequency was 1,000 Hz.

Make an interpretation, similar to that in problem 1, of these results with the aid of the following additional information. "...Geological mapping in the vicinity of the conductor shows that it lies in a band of amphibolite intruded by gabbro sills...this band, about 2,400 ft wide, is bounded north and south by andesitic volcanic rocks...outcrops of granite were located 2,600 ft NW of the west end of the conducting zone...The axis of the anomaly is parallel to the strike of surrounding rocks...Within the band a weak dissemination of chalcopyrite and pyrite has been observed in one outcrop."

3. Dip angles obtained with broadside VLEM equipment are given in Table 7.7. Four frequencies (600, 1,000, 2,400, and 5,000 Hz) were used in this survey. The receiver and transmitter were moved along parallel picket lines maintaining a fixed spacing of 400 ft and readings were taken every 100 ft.

Plot the profiles, preferably on two sheets by combining the 600 to 2,400 Hz and the 1,000 to 5,000 Hz dip angles, because these are the dual

Table 7.6.

Station	Line 8W		Line 0 + 00	
	Dip (deg)	Station	Dip (deg)	Station
B.L.	3	B.L.	12	
15	3	15	11	
2	2	2	14	
3	4	3	13	
4	4	4	12	
5	3	5	15	
6	5.5	6	9	
7	10	7	10	
7 + 50	13	8	-11	
8	9	9	-15	
9	-8	10	-11	
10	-22	11	-11	
11	-24	12	-9	
12	-26	13	-8	
13	-25			

frequencies on two different EM units. Locate any potential conductors and estimate their depth, dip, and, if possible, the TCP. Discuss the advantages of using two frequencies in this type of survey. Is there any point in employing four frequencies? Given a choice, how many or which of these would be preferable? Any other frequencies?

4. Figure 7.109 shows a set of VLF profiles, obtained with the EM16 unit, taken from a survey

Table 7.7.

Stn	Line 12N				Line 8N				Line 4N			
	600 (deg)	1,000 (deg)	2,400 (deg)	5,000 (deg)	600 (deg)	1,000 (deg)	2,400 (deg)	5,000 (deg)	600 (deg)	1,000 (deg)	2,400 (deg)	5,000 (deg)
20W	—	2	—	3	—	1	—	2	0	0	0	0
19	—	0.5	—	2	0	2	2	3	7	5.5	8.5	9.5
18	—	3	—	4	7.5	2	1.5	3	14	20	22	24.5
17	6	7	8.5	8	2	5	2	11	-11.5	-19.5	-19.5	-23.5
16	-12	-16.5	-15	-18.5	2	-7	-5	-16	-12	-13	-18.5	-18
15	-14	-18	-18	-22	-1.5	-6	-10	-14	-4.5	-3	-9.5	-12.5
14	-1	-7.5	-14	-12	0	-1	-2.5	-2.5	-1.5	0	-5	2
13	0	0	-4	-2.5	1	1	-1	3	0	2	0	3
12	0	-1.5	-1	-3	0	1	1	3	0	0	-1.5	-2
11	0	-2	0	-4	0	1	1	1.5	0	-2	-1.5	-7
10	0	4	1	6	0	0	-1	-8	-2	-1	-4.5	-4.5
9	0	-2	-1.5	-12	0	-2	-3.5	-10	1	0	0	-1
8	0	-5	-8	-10	-1	-1	-2.5	-4	0	2	0	3
7	0	-3	-5	-10	1	1	0	3	1	1	0	1.5
6	1	-2	1	-4	3	0	2	0	0	1	0	1.5
5	0	1	1	2	2	0	3	1.5	0	2	0	3
4	0	1	1	1.5	1	3	2	5	0	1	1	2
3	0	1	1	2	2	2	3	3.5	0	0	0	2
2	0	0	1	-1	1	2	1.5	2	-1.5	1.5	-2	3.5
1	3.5	0	5	0	2	1	0	3	0	1	-1	2.5
B.L.	1	0	2.5	0	-2	2	0	3	0	0	1	0

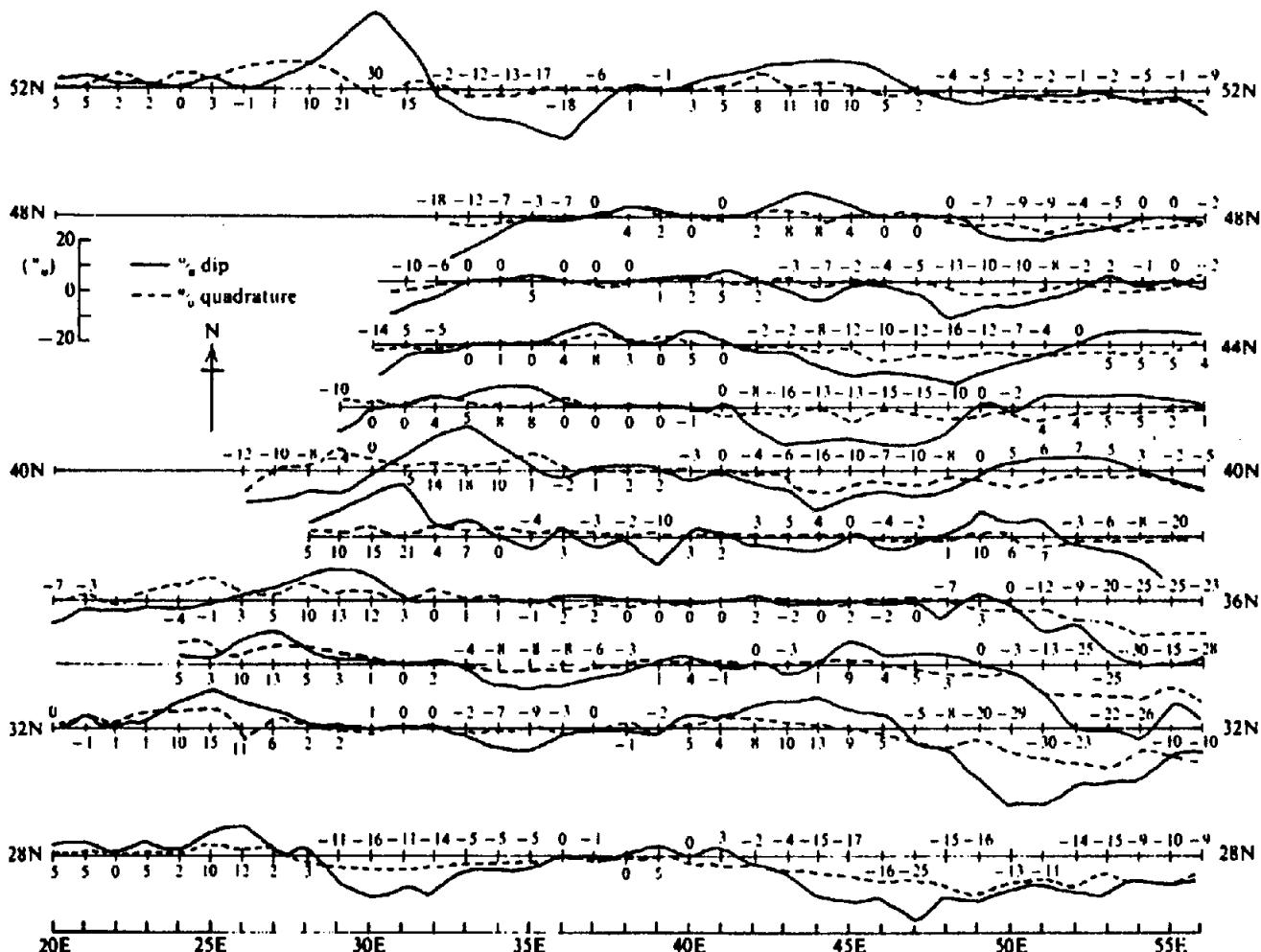


Figure 7.109. EM16 survey in eastern Nova Scotia.

in eastern Nova Scotia. The numerical values of percent dip angle are also shown for each station. The transmitter was Panama, roughly S30°W of the area. (This station no longer operates and its frequency, 24.0 kHz, is now transmitted from Cutler, Maine.) Real crossovers are in the sense of positive to negative going east, for example, near station 28E on line 28N.

At first glance there appears to be evidence both of steeply dipping contacts and flat-lying conductors here. The overburden varies between 8 and 20 ft in thickness and is known to have a resistivity of about 100 Ωm in one zone to the southwest, although generally it is thought to be higher than this over most of the area. Make what interpretation you can from the profiles. It is recommended that a contour plot, as described in Section 7.8, example 3, be made from the dip readings for clarification.

5. The EM16 readings in Table 7.8 were taken during a survey in Nova Scotia, using the Panama transmitter. The topography here is quite rugged;

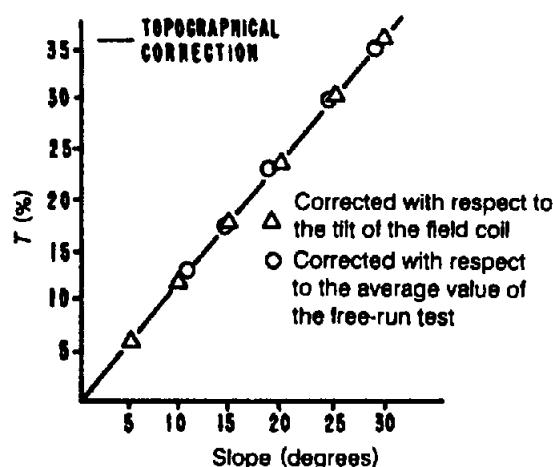
there is an increase in elevation of 250 ft between line 10N just east of the base line and the western portion of line 6S. This is the spine of a hill that has steep sides both east and west so that the terrain contours resemble the bowl of an inverted spoon. The hill is thought to be sandstone and there is a contact with limestone beds, which appear quite thin, on the east flank.

Stations are 100 ft apart, lines 400 ft. Real crossovers are positive to negative going east. Plot the profiles, contour the dip angles by the method of example 3, Section 7.8. In making an interpretation of the results, consider (a) overburden effects, (b) contacts between extensive beds of contrasting resistivity, (c) topographic effects, as well as the possibility of metallic conductors.

6. In making VLF measurements over irregular terrain it is found that the dip angle is affected by ground slope. This is because the secondary field tends to be parallel to the ground surface whereas the primary field remains horizontal. A simple

Table 7.8.

	Line 10N		Line 6N		Line 2N		Line 2S		Line 6S	
Str.	Dip	Quad.	Dip	Quad.	Dip	Quad.	Dip	Quad.	Dip	Quad.
20W	—%	—%	14%	—3%	20%	3%	20%	—2%	10%	—4%
19	2	—7	20	—7	20	4	18	—2	8	2
18	—12	2	15	0	18	3	20	0	10	—2
17	13	—8	15	—1	15	3	17	—2	5	4
16	9	—3	17	0	17	—3	10	—3	—5	2
15	5	1	18	2	22	—2	5	—2	—5	0
14	7	1	18	5	14	0	5	—3	—10	2
13	5	2	18	4	15	2	—4	—3	—20	0
12	8	3	23	3	10	—2	—3	—3	—25	—1
11	10	3	25	2	10	—3	—11	3	—37	2
10	23	0	14	2	10	0	—25	3	—29	—2
9	15	3	6	0	5	0	—38	3	—32	0
8	1	—2	5	0	—3	—2	—30	—2	—33	4
7	—1	1	1	—3	—16	0	—27	—2	—13	7
6	2	—3	—8	1	—25	—1	—32	3	0	—2
5	—2	—3	—12	0	—25	3	—20	3	17	—1
4	—2	2	—20	5	—15	0	1	—3	15	—5
3	—6	3	—20	3	—3	—2	18	—3	21	—3
2	—2	0	0	0	—12	—2	24	—5	22	—5
1	6	—2	6	—1	3	—3	13	3	15	—3
B.L.	8	—3	0	—6	8	—2	11	2	0	6
1E	5	—2	—10	1	11	5	5	2	3	0
2	7	0	3	0	19	—2	10	—1	0	0
3	12	0	15	—4	11	0	16	—5	—8	3
4	16	0	15	—2	9	0	5	—3	—2	—1
5	9	—1	11	2	7	1	0	—2	3	—1
6	2	—2	11	4	12	—2	10	—2	13	—2

Figure 7.110. Chart giving slope correction  $T$  in terms of slope. (From Baker and Myers, 1980.)

terrain correction has been developed by Baker and Myers (1980) from measurements in a tank model. The correction is directly proportional to the slope angle; it is added going downhill and vice versa.

Because elevation changes between successive field stations may readily be measured, it is convenient to consider the plotting point to be

halfway between. Then the corrected VLF dip angle is given by

$$\theta_c = (\theta_1 + \theta_2)/2 + T$$

where  $\theta_1, \theta_2$  are the dip angles at stations 1 and 2 and  $T$  is the correction for slope, all in percent. The value of  $T$  is read off the correction chart in Figure 7.110.

Given that the topographic map of Figure 2.39 is for the same area as the VLF data in problem 5, take off a terrain correction. Does this correction make a significant change in the profiles and contours plotted from problem 5? Does it lead to a more definite interpretation of the VLF survey?

7. The AFMAG profiles shown in Figure 7.111 are taken from a large-scale survey. Geologically the area is Precambrian with numerous outcrops of ultrabasic rocks in the eastern portion, and gneiss, generally covered by thin overburden, to the west; the exposed rocks are extremely metamorphosed.

Stations are 50 m apart and the lines 200 m; the AFMAG frequencies were 150 and 510 Hz. The predominant azimuth direction for these

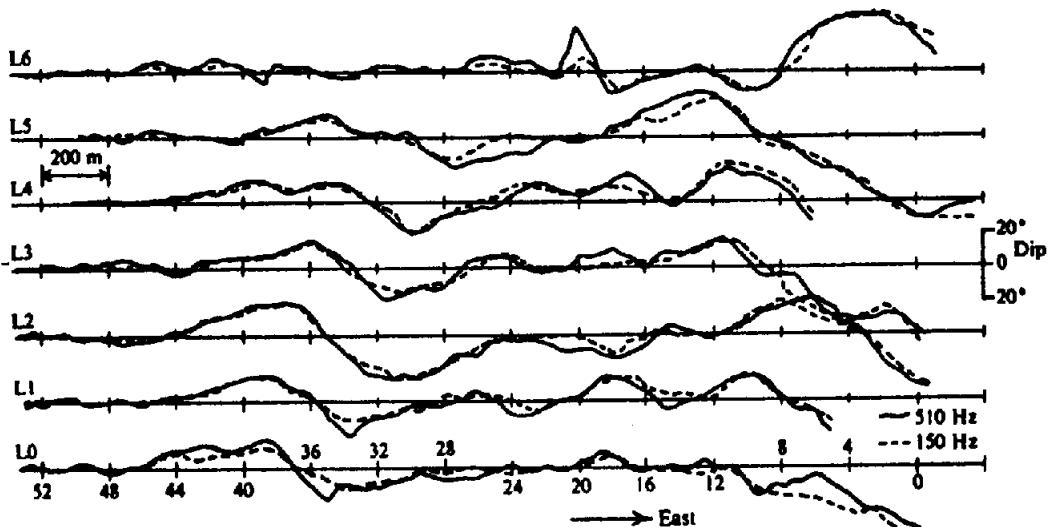


Figure 7.111. AFMAG profiles, northeastern Brazil.

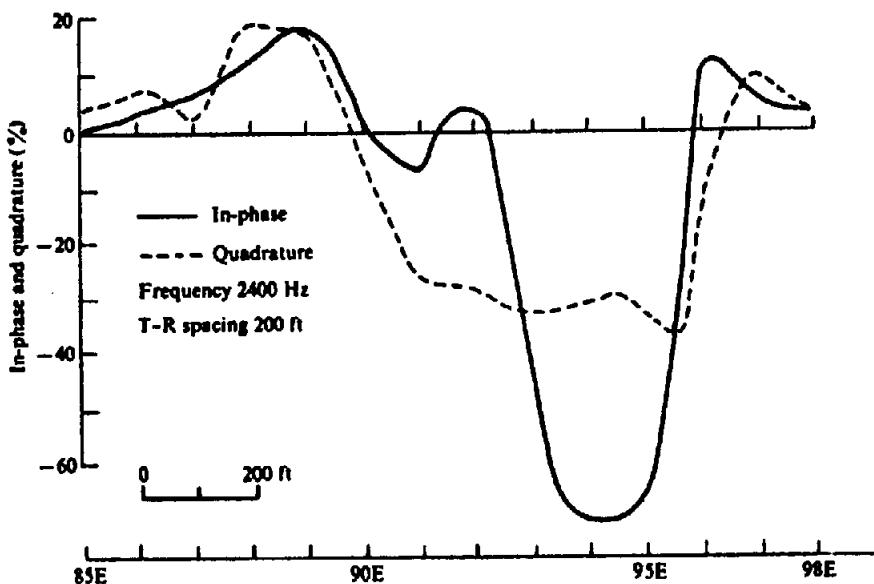


Figure 7.112. HLEM profiles, Eastern Townships, Quebec.

- signals was about N60°W, although this was quite erratic, and the tilt angle for minimum, particularly at the lower frequency, was often indeterminate over a considerable range. The effect of a high-voltage transmission line about 2 km to the east can be seen on the east end of several lines. Make an interpretation of these profiles with regard to location, depth, and dip of potential conductors.
8. Figure 7.112 is a single HLEM profile from a survey made in the Eastern Townships of Quebec. The main geological features consist of Ordovician and Cambrian slate, calcareous slate, greywacke, sandstone, and quartzite conglomerate; the general geological strike is slightly east of north. The anomaly, shown here for line 81N, has a strike length of at least 1,000 ft. Estimate its location, depth, dip, width, TCP, and conductivity. Is there evidence for more than one con-

Table 7.9.

Stn.	IN-PH. (%)	Quad. (%)
6S	2	1.5
5	0	0
4	0	1.0
3	0	0
2	-1.5	0
1	0	0
0	0	1.5
1N	0	1.0

ductor? With the limited information available, can you suggest the source? What further work would you do to verify the suggestion, possessing very limited finances?

9. As a contrast to problem 8, consider the HLEM readings in Table 7.9 below, taken from a survey

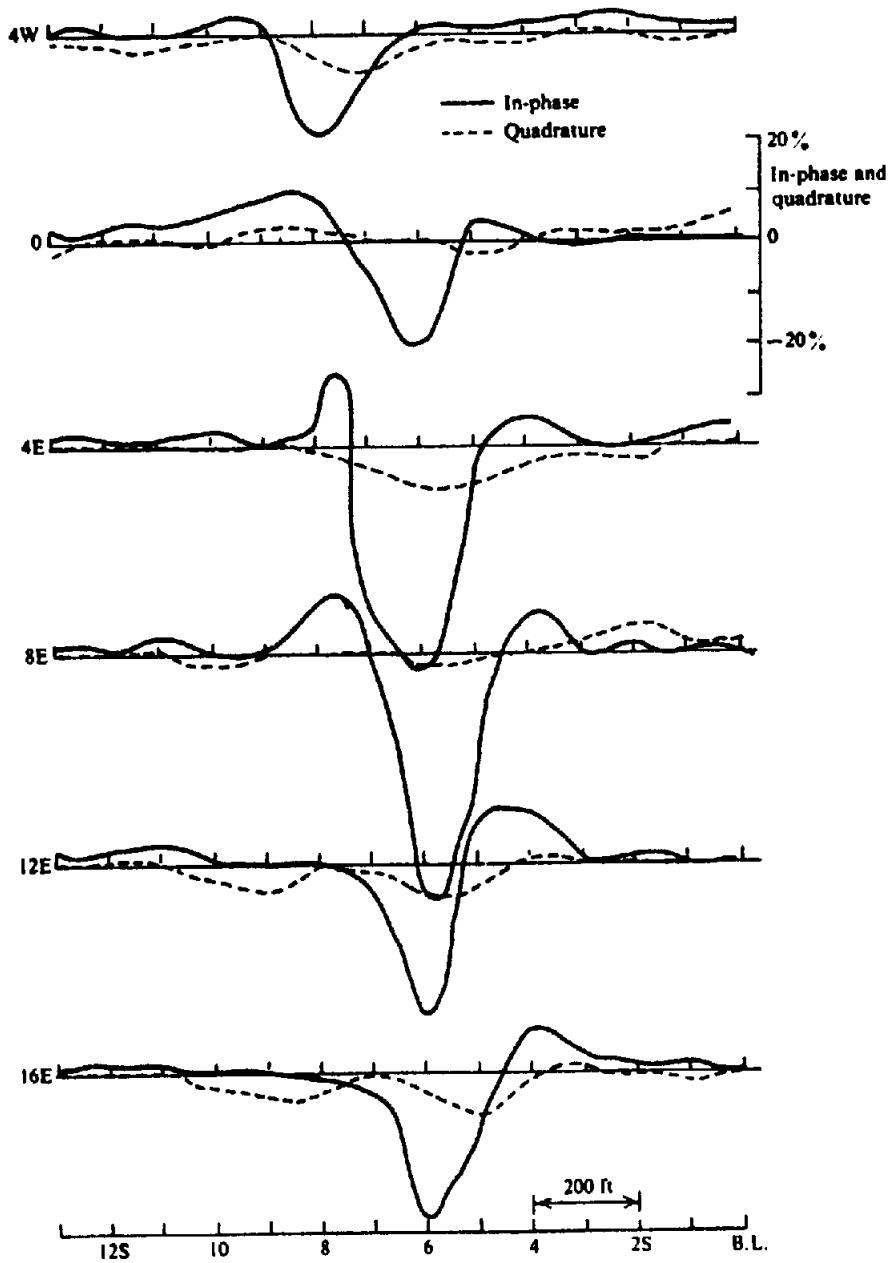


Figure 7.113. HLEM profiles, Chibougamau Area, Quebec.

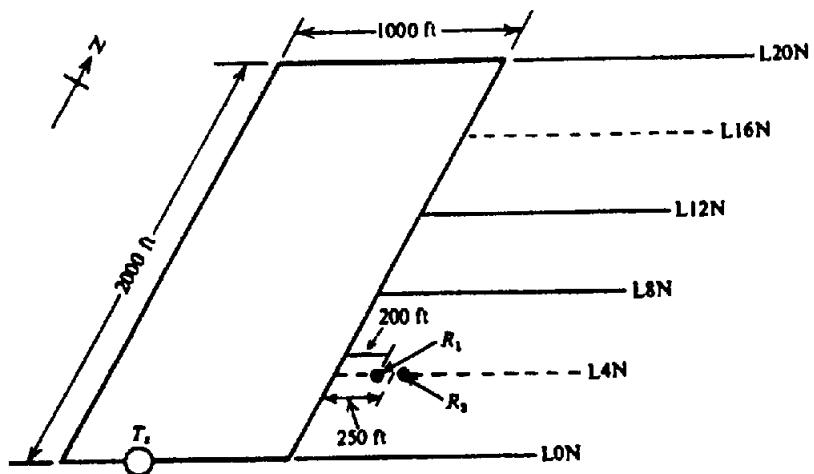


Figure 7.114. Model Turam configuration.

in Northern New Brunswick. The cable length ( $T$ - $R$  separation) was 200 ft and the frequency 2,400 Hz.

This traverse crosses a conductive zone that has a strike length of 1,100 ft. Is it possible to determine its properties from the horizontal-loop response? Would this response normally be considered significant? Would you recommend any further HLEM work or other geophysics on the basis of these results?

10. The profiles shown in Figure 7.113 were obtained during a HLEM survey in the Chibougamau area of Quebec. Geologically the region is Precambrian, typical of Northwestern Quebec, with metamorphosed, folded volcanics and sediments, intruded by acidic and basic rocks. Transmitter frequency was 880 Hz and cable length ( $T$ - $R$  spacing) 200 ft. Make an interpretation of these profiles, as complete as possible.
11. The Turam results given in Table 7.10 were obtained in a model survey over a sheet conductor in the laboratory. Figure 7.114 shows the "field" layout. The rectangular transmitting loop is  $2,000 \times 1,000$  ft and the field ratios and phase

Table 7.10.

Stn. (ft)	First coil (ft)	Line 4N Station readings		Line 16N Station readings	
		Phase ( $\Delta\phi$ )		Phase ( $\Delta\phi$ )	
		FR	(deg)	FR	(deg)
250	200	1.77	0	1.77	0.10
350	300	1.54	0.20	1.54	0.20
450	400	1.39	0.35	1.43	0.50
550	500	1.35	0.35	1.35	0.80
650	600	1.64	-0.50	1.30	1.0
750	700	1.39	1.20	1.30	-1.0
850	800	1.26	1.25	1.33	-4.25
950	900	1.24	1.40	1.27	-0.95
1050	1000	1.23	1.55	1.22	1.15

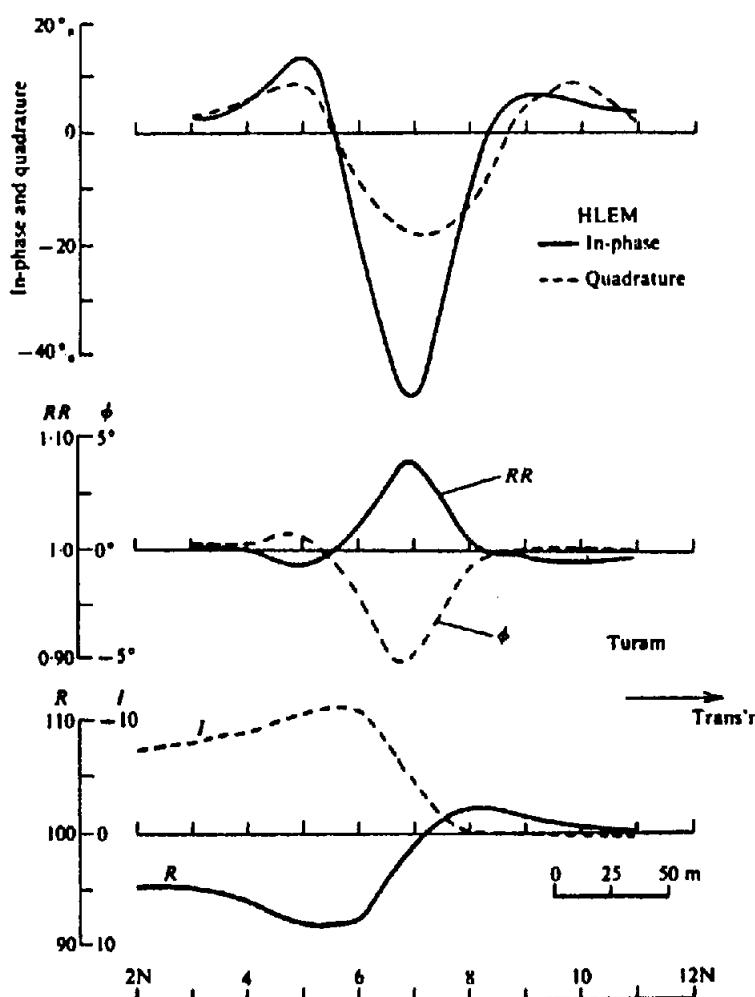


Figure 7.115. HLEM and Turam profiles, northern Quebec.

readings are for lines 4N and 16N, at stations 250W to 1050W in 100 ft steps. The transmitter frequency is 1,000 Hz and the receiver coils are 100 ft apart.

Calculate the  $NR$ ,  $RR$ ,  $\Sigma \Delta\phi$ ,  $V$ ,  $R$ , and  $I$  values from these data, using Equation (7.12b) and the routine outlined in Section 7.7.3g. Plot  $RR$ ,  $\phi$ ,  $R$ , and  $I$ , and determine the location, approximate depth, dip, and TCP for the conductor on each line.

12. Figure 7.115 shows HLEM and Turam profiles over a sulfide deposit in northern Quebec. The horizontal-loop survey was made first, and the Turam work was a followup in an attempt to increase the depth of investigation. The HLEM frequency was 3,600 Hz, with cable separation 50 m; the Turam frequency was 660 Hz. Interpret the results as completely as possible with this information. Why is the HLEM response so much larger than the Turam?
13. The readings in Table 7.11 are from a Turam survey over suspected sulfides on a property in

Table 7.11.

Stn	FR	Phase ( $\Delta\phi$ )	NR	RR	$\Sigma \Delta\phi$	V	R	I
350S	1.81	-0.75	1.80					
250S	1.58	-1.50	1.59					
150S	1.51	-2.00	1.47					
050S	1.44	-2.00	1.40					
050N	1.37	-1.50	1.35					
150N	1.32	-1.00	1.31					
250N	1.28	-0.50	1.28					
350N	1.25	0.00	1.25					
450N	1.23	0.00	1.23					

Abitibi Ouest, Quebec. Because the overburden was thought to be thick and of low resistivity, it was hoped that Turam would have better possibilities of penetrating to depth than other EM methods. The near leg of the transmitter rectangle, laid out E-W, was at station 6 + 00S and the dimensions of the rectangle were 1,200 × 1,000 ft. Transmitter frequency was 660 Hz and the receiver coils were 100 ft apart.

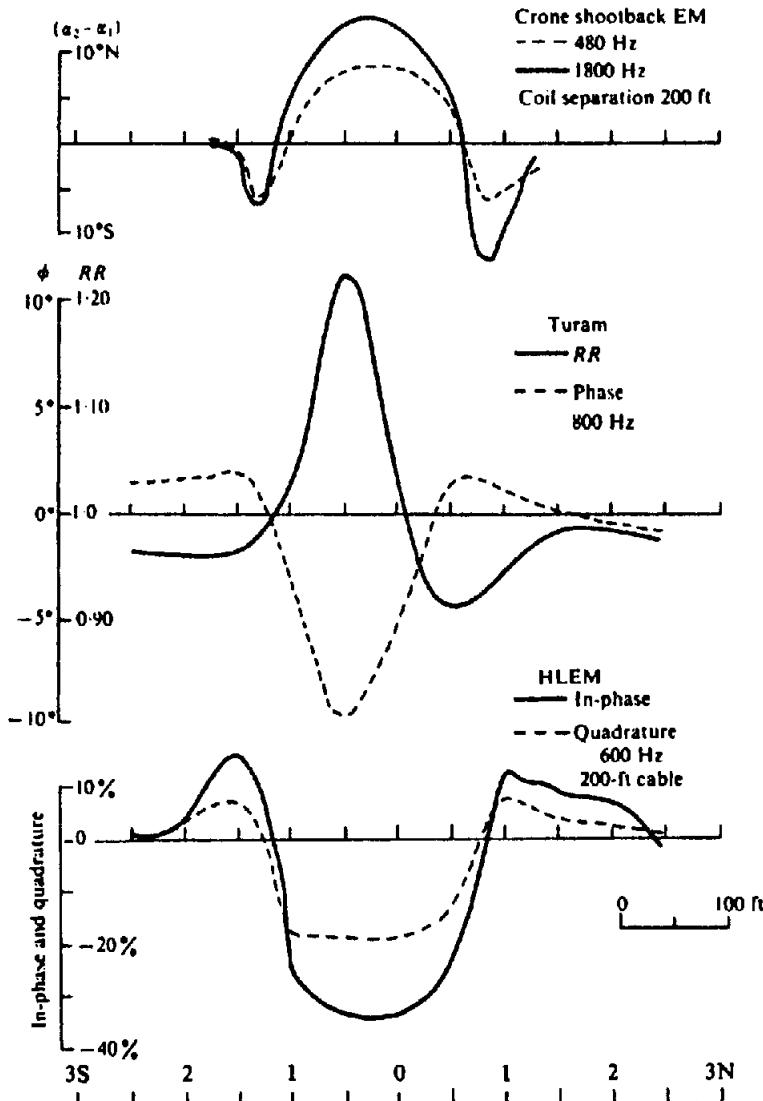


Figure 7.116. Shootback, Turam, and HLEM profiles, western Ontario.

Complete the table for  $RR$ ,  $\Sigma \Delta\phi$ ,  $V$ ,  $R$ , and  $I$  columns, plot  $RR$ ,  $\phi$ ,  $R$ , and  $I$  profiles, and interpret the results as completely as possible.

14. Figure 7.116 shows Crone-shootback, Turam, and horizontal-loop EM profiles over a sulfide deposit in western Ontario. Interpretation of shootback EM results is mainly qualitative (§7.7.3e); the ratio  $(\Phi_{450}/\Phi_{1800})_{\text{max}}$  is somewhat diagnostic of the type of conductor as in AFMAG and the quadrature AEM system. Use all three profiles to assess the various parameters of this deposit.
15. The readings in Table 7.12 were obtained from a survey over a copper prospect near Val d'Or, Quebec. The respective EM set frequencies were HLEM: 2,000 Hz, shoot-back: 1,800 Hz, VLEM: 1,800 Hz, and  $T$ - $R$  separations 200, 300, and 300 ft. (In the VLEM setup the transmitter was 300 ft east and on the conductor axis, which had been previously located by reconnaissance EM.) Plot these profiles and extract all the information you can from the data.
16. Figure 7.117 illustrates UTEM profiles from a single traverse over a test site in Ontario. The host rocks are mainly gneiss in dipping contact with crystalline limestone near the east end, both of high resistivity; overburden is generally thin. Seven of the 10 UTEM channels are seen in the

Table 7.12.

Stn. (ft)	HLEM			Shoot- back 2-1 (deg)	VLEM (deg)
	$R$ (%)	$I$ (%)			
7N	0	2.5	—	—	0
7 + 50	0	4	0	—	-0.5
8	-1	4	-1	-1	—
8 + 50	-0	3	-1	-2	—
9	-6.5	-3	3	-3	—
9 + 50	-13.0	-10	6.5	-2	—
10N	-14.5	-12	5	2	—
10 + 50	-12	-10	2.5	7	—
11N	-2.5	-1	0	6	—
11 + 50	1.5	5	-2.5	4	—
12N	1.0	4.5	-1.0	2	—
12 + 50	0.0	2.5	-0.5	2	—
13N	0.0	3.0	—	1	—

diagram. Make an interpretation of these with regard to conductors present, their relative depth, depth extent, dip, geometry, and TCP.

17. Figure 7.118a shows test survey profiles consisting of Turam, IP gradient and pole-dipole arrays, and Crone PEM, over a sulfide ore zone in southwest Africa. This was a difficult target for

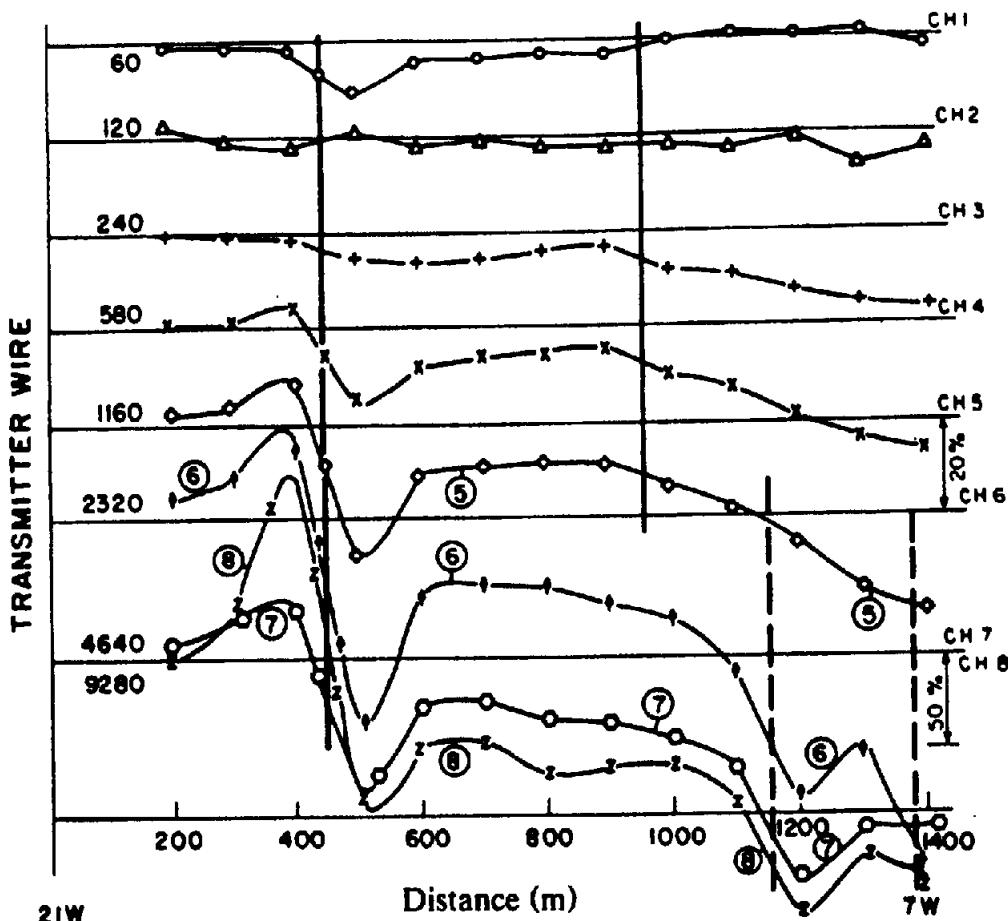
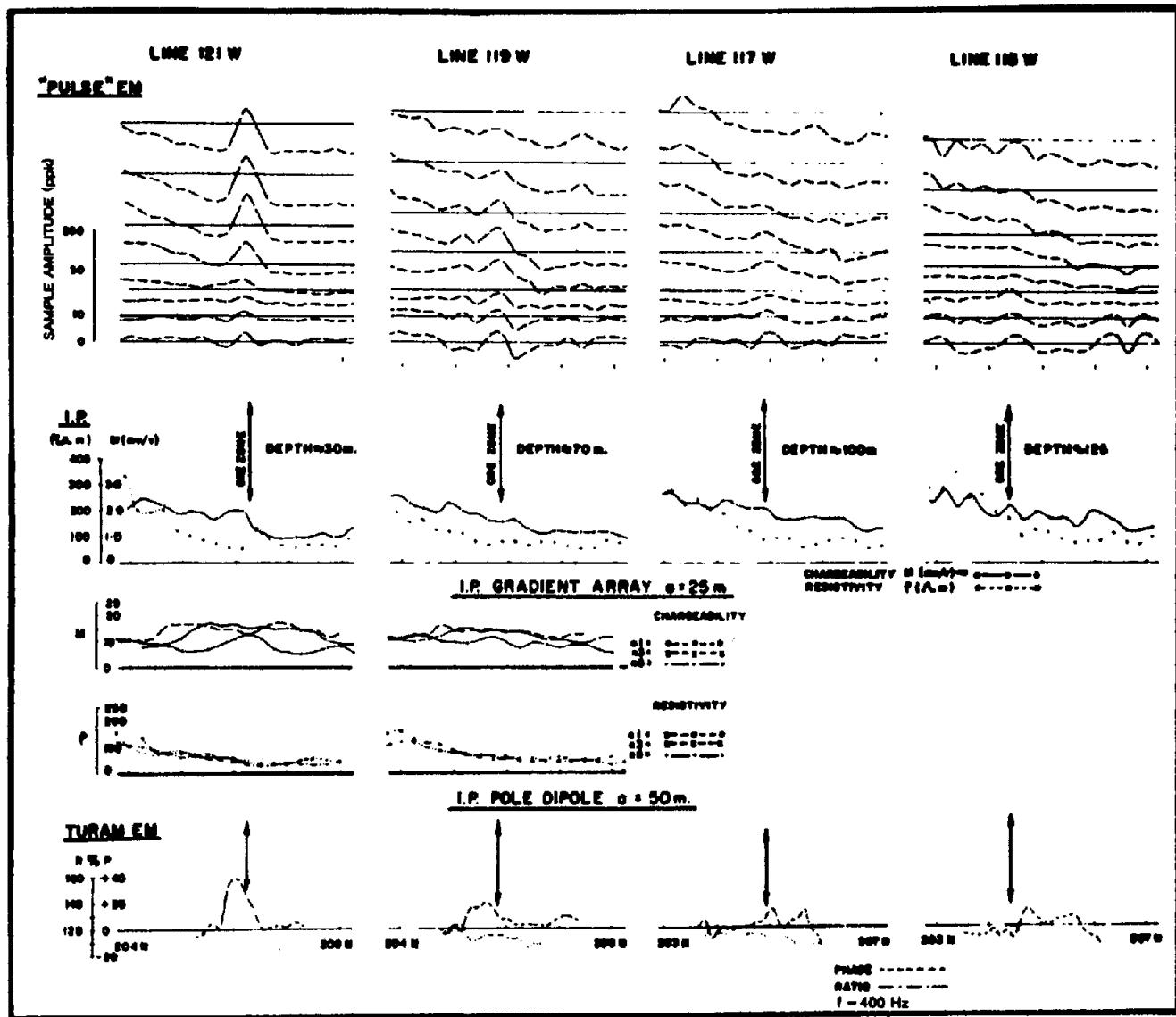


Figure 7.117. Profiles of seven-channel UTEM TD response, test site, Ontario.



(a)

Figure 7.118. Multimethod surveys over a sulfide ore body, southwest Africa. (a) PEM ("Pulse" EM), IP (gradient and pole-dipole arrays), Turam.

several reasons, including its relatively low conductivity with respect to the local country rocks. Data are shown for the four methods over four 400 m lines across strike, spaced 200 m apart. The sulfides lie along a synclinal axis striking N20W in a magnetite-quartzite host rock. The PEM unit used horizontal  $T_x$ - $R_x$  dipoles separated 75 m, whereas the Turam loop was 1,000  $\times$  1,000 m operating at 400 Hz, with a receiver coil pair whose spacing was 25 m. Dimensions of the IP array are given in the figure.

Make an assessment of the ore zone, employing as much of the data as possible, to obtain the following information: conductor model and depth, depth extent, cross section,  $\sigma t$  product; resistivity contrast with host rock; relative merits of the four surveys in this geological setting.

The two total-field magnetic profiles shown in Figure 7.118b were carried out on lines 118.50W and 115.25W. Given these additional data, can you add to or correct any of the conclusions reached from the interpretation of Figure 7.118a?

18. Quadrature airborne EM results over a test site in Ontario are illustrated in Figure 7.119. The location of VLEM and IP anomalies found in ground followup are illustrated for zones A and B in the upper diagram. This record is merely a small part of the airborne survey. It is obvious, as mentioned before, that airborne EM data do not suffer from a lack, but rather from a surplus, of anomalies; there are 17 marked in Figure 7.119a. These are loosely graded as "definite," "probable," and "possible," based partly on the maximum response amplitude, partly on the ra-

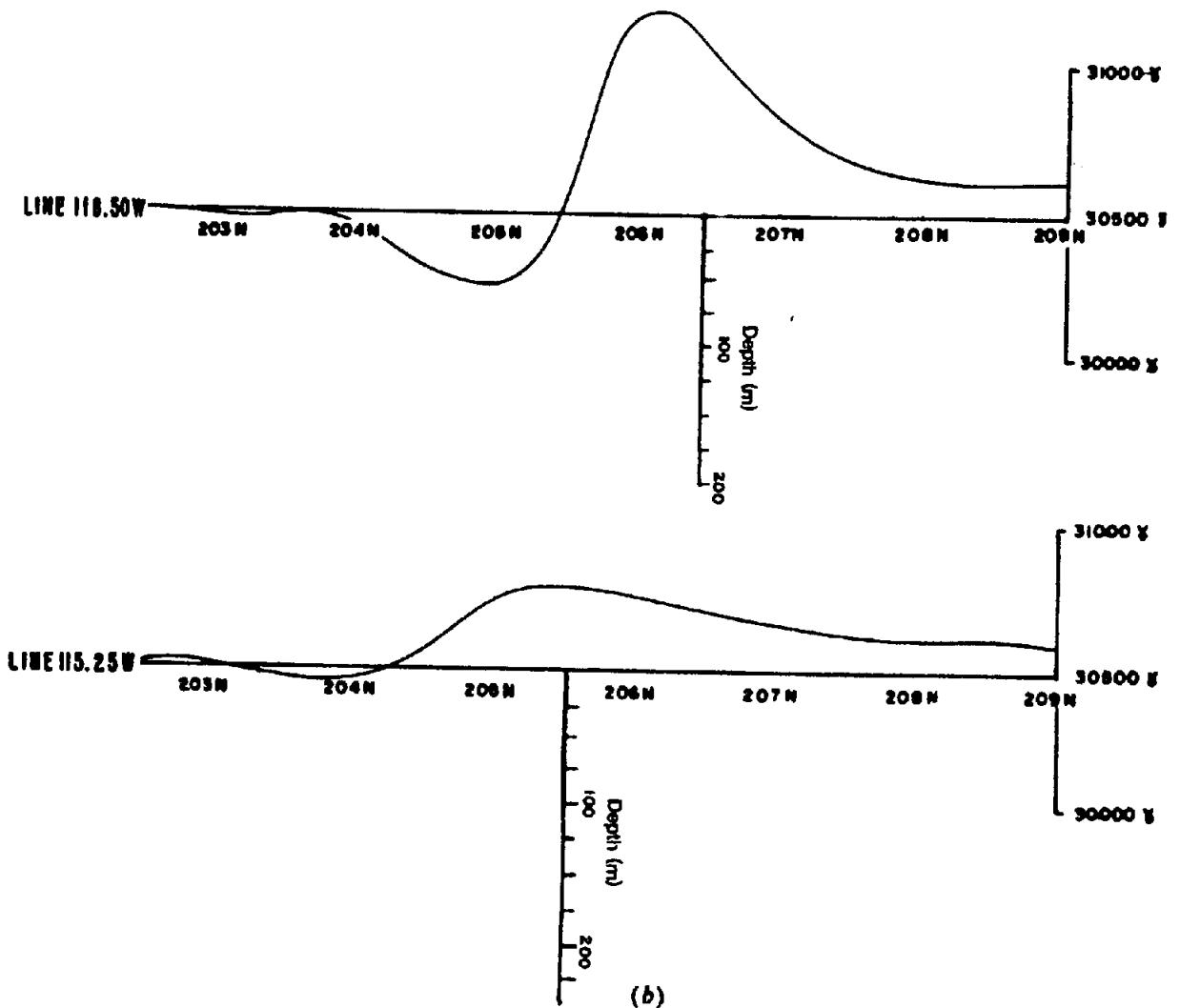


Figure 7.118. (Continued) (b) Total-field magnetics on lines 118.50W and 115.25W.

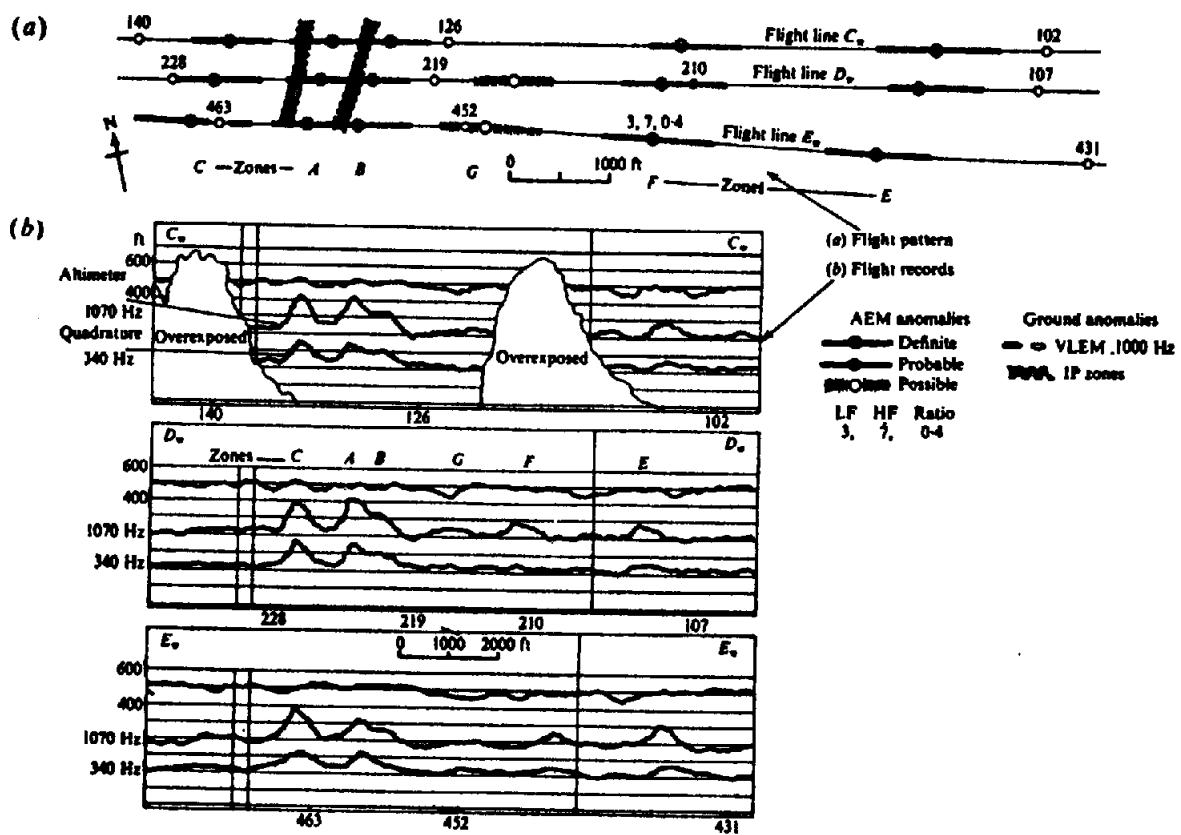
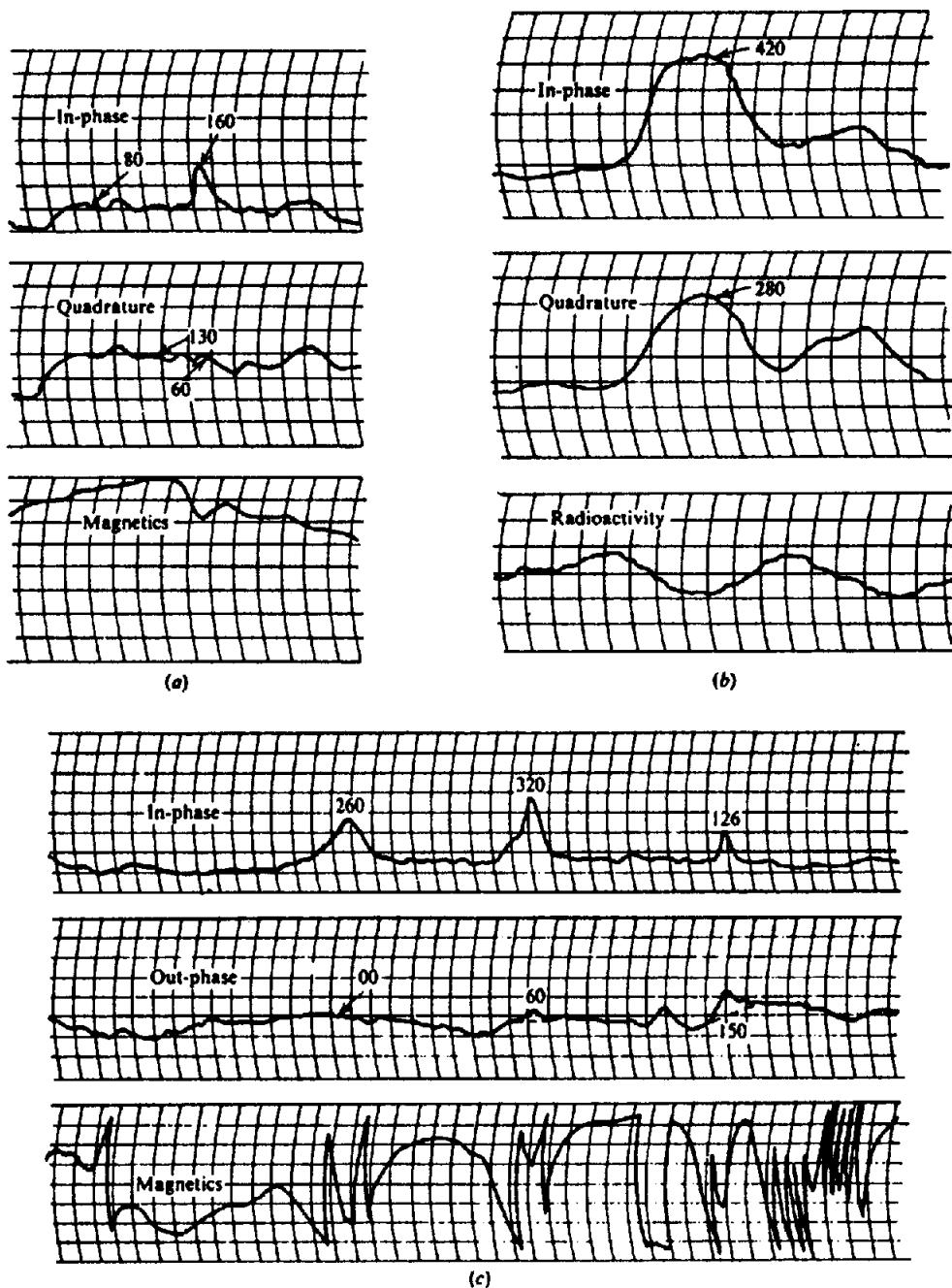


Figure 7.119. Quadrature airborne EM survey, Cavendish geophysical test site, Ontario.  
(a) Flight pattern. (b) Flight records.



*Figure 7.120. Typical response curves of the airborne phase-component EM system (Aero-Newmont) plus airborne magnetics and radiometric curves. (After Wieduwilt, 1962.) (a) Phase-component and magnetic curves. (b) Phase-component and radioactivity curves. (c) Same as in (a).*

tio of low to high-frequency maxima. These values are given for one "probable" zone *F* on line  $E_w$ .

From the flight records in Figure 7.119b, determine the low- and high-frequency response maxima and their ratios for the remaining 16 anomalies. Do you agree with the classifications in Figure 7.119a? Have they been influenced by response on adjacent flight lines, by altitude variations, by possible additional information

– airborne magnetics, terrain, geology, and so forth, not available here? What is the reason for the relative displacement of airborne and ground anomalies (about 200 ft) in zones *A* and *B*? Can you estimate other parameters of the conductive zones – depth, dip, width, strike extent, TCP – from the records?

19. Airborne EM data obtained with the Aero-Newmont phase-component system are shown in Figure 7.120. This equipment is mounted on a

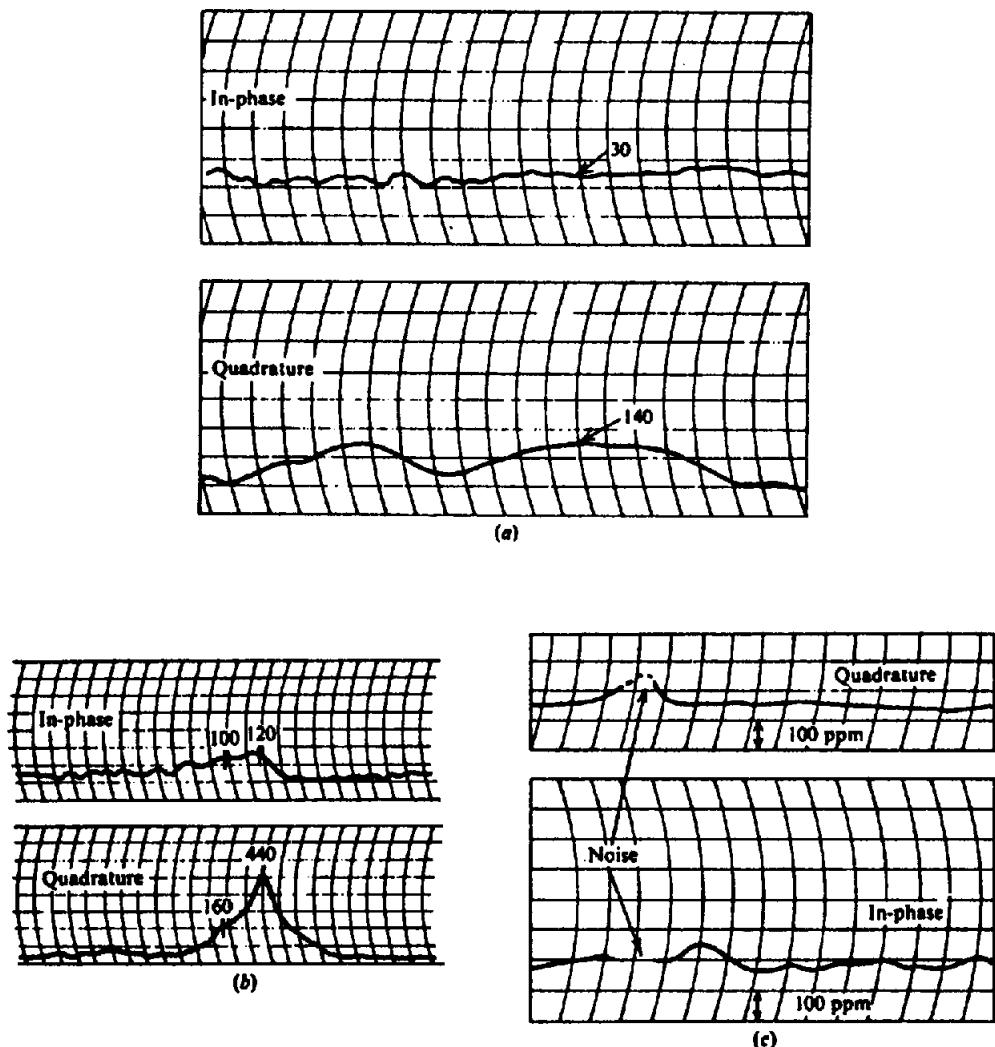


Figure 7.121. Airborne phase-component EM profiles. (a) Helicopter survey, transmitter frequency 400 Hz. (b) As in (a) for 320 Hz. (c) Fixed-wing aircraft, transmitter frequency 390 Hz.

Sikorsky S-55 helicopter. The coaxial transmitter and receiver coils are mounted fore and aft 18 m apart and the source frequency is 400 Hz.

In Figure 7.120a, note the sharp peak (160 ppm) on a broader anomaly of smaller amplitude. How would you model these two coincident anomalies? Estimate the depth and TCP of each, using appropriate characteristic curves from Section 7.7.10.

What do you make of the response in Figure 7.120b? Try modeling it as in Figure 7.120a for similar parameters. Does the radiometric channel provide any useful information?

Make a similar interpretation for the features in Figure 7.120c, with possibly extra aid from the magnetic record.

20. Three phase-component airborne EM profiles, each from a different area, are shown in Figure

7.121. Pertinent information with respect to each of these flight records is:

- Transmitter frequency, 400 Hz; T-R spacing, 60 ft; altitude, 140 ft.
- Transmitter frequency, 320 Hz; T-R spacing, 62 ft; altitude, 140 ft.
- Transmitter frequency, 390 Hz; T-R spacing, 60 ft; altitude, 140 ft.

One of these traverses was over a lake, one over a graphite zone, and one crossed a copper deposit of economic grade. By making as complete an interpretation as possible from these profiles, can you locate and identify the three sources? Can you suggest any reason why the record is so noisy in (c)?

21. Figure 7.122 shows two Input airborne EM records, the first from Northern Manitoba, the second Northwestern Ontario. At least four

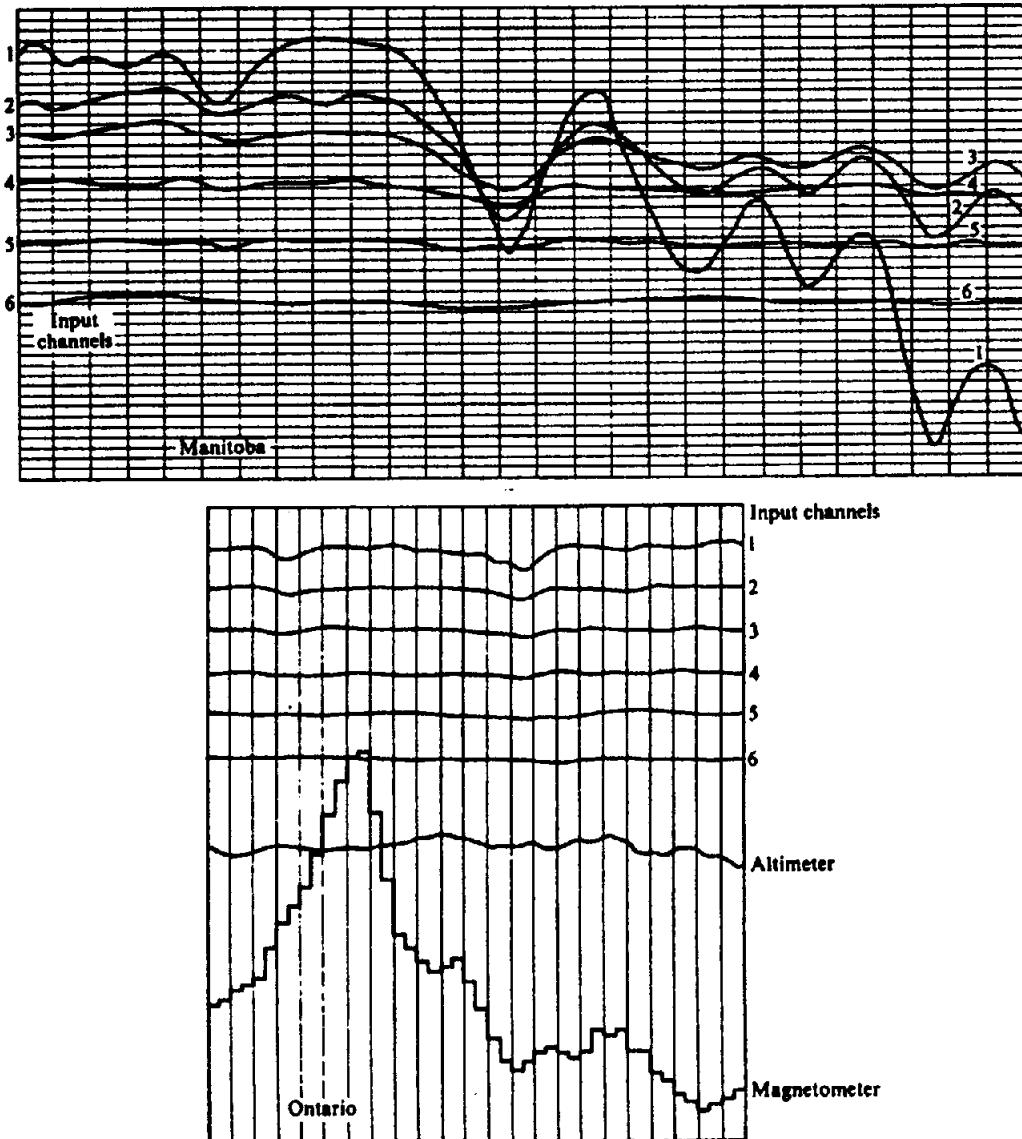


Figure 7.122. Airborne Input EM records.

- anomalies are evident on these two profiles. Given that they are caused by graphite, conductive overburden, pyrite and ore-grade massive sulfides – pyrite, chalcopyrite, sphalerite – at depths of 3, 75, 5, and 90 m (not necessarily in the same order), can you sort out these anomalies? Are there any others indicated?
22. The airborne EM anomaly map from a Dighem II (900 Hz, three coil pairs) survey, shown in Figure 7.123, was prepared on the basis that reasonable response from the coaxial coil pair could indicate bedrock metallic conductors. Circles locating these are marked with the conductance in siemens, determined from master curves for a vertical thin sheet. In some cases the interpreter, experienced at his work, has applied a label "s?", showing that the profile shape and other available information may suggest a surficial rather than a bedrock anomaly. He has also marked possible conductor axes with lines between several circle sets.
- Noting the area topography, does this map seem realistic? Could the conductors represent a large-scale shallow structure instead? What additional data are necessary to develop the alternative interpretation?
- Assuming a crude pseudolayer model with this limited information, contour a map of shallow resistivity for this purpose. Note that the "s?" anomalies lie mainly on the peripheral area of Figure 7.123 and that their  $\sigma$  values are small. Having completed this hypothetical map, make an interpretation. Are there indications of any bedrock conductors remaining?
23. The airborne data in Figure 7.124 were obtained in a test survey with the Dighem III system,



Figure 7.123. Airborne EM (Dighem II) map of an area in the Appalachians.

which uses two horizontal coplanar coil pairs at 900 and 7,200 Hz and one vertical coaxial pair (not shown), operating between 385 and 7,200 Hz, depending on the target and survey area. The test anomaly is a wide graphite conductor of irregular shape, somewhat resembling a thick dike. It is overlain by 85 m of glacial sands

averaging 300  $\Omega\text{m}$ ; host rock resistivity is probably greater than 3,000  $\Omega\text{m}$ .

Using the curves of Figure 7.84a, b, attempt to reproduce the 900 and 7,200 Hz resistivity profiles shown in the lower part of Figure 7.124.

24. Figure 7.125 displays profiles from the Input VI system recorded over four bedrock conductors

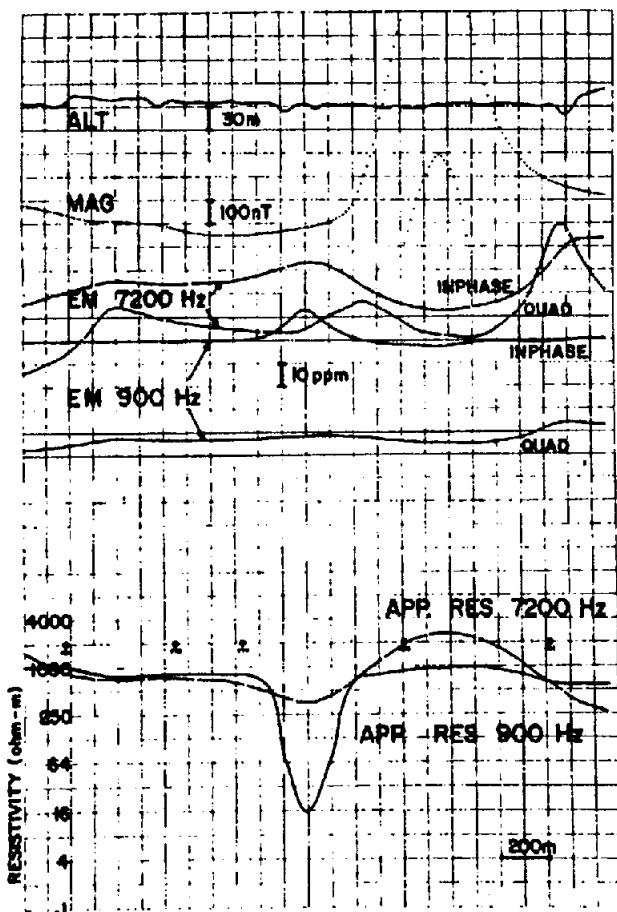


Figure 7.124. Results of Dighem III survey over a wide dike-like graphite conductor. EM curves are for two horizontal coplanar pairs of coils operating at 900 and 7,200 Hz. Curves are: altimeter, total-field magnetics, in-phase and quadrature components, and apparent resistivity calculated using a pseudolayer half-space model.

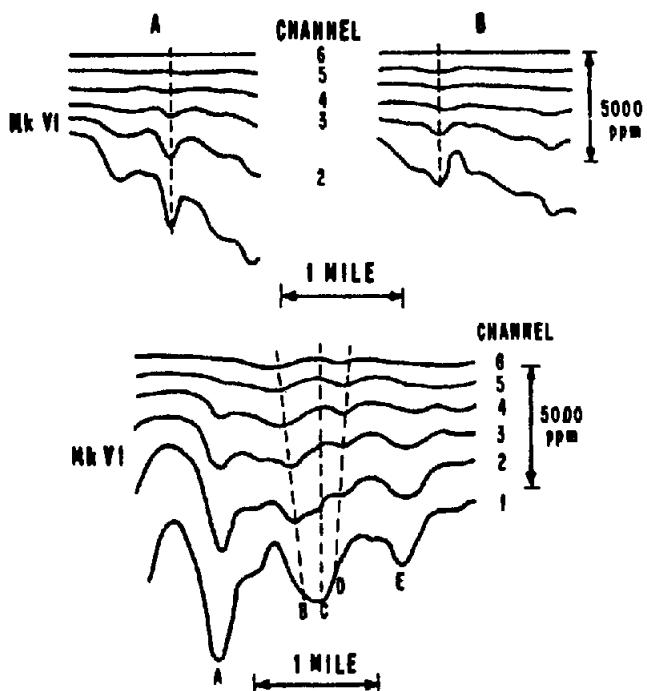


Figure 7.125. Input profiles over four bedrock conductors, Western Australia. Conductors are covered by varying thicknesses of conductive overburden.

covered by conductive overburden of variable thickness. Make as complete an interpretation of each as you can, with the aid of pertinent data from Section 7.7.12.

## REFERENCES

- Abramowitz, M. and Stegun, I. A. 1972. *Handbook of Mathematical Functions*. Nat. Bur. of Standards. U. S. Gov't Printing Office, Washington, D.C. 20402.
- Annan, A. P. 1974. The equivalent source method for electromagnetic source scattering analysis and its geophysical application. Ph.D. thesis, Memorial Univ., St. Johns, Newfoundland.
- Annan, A. P., Waller, W. M., Strangway, D. W., Rossiter, J. R., Redman, J. D., and Watts, R. D. 1975. The electromagnetic response of a low-loss, 2-layer dielectric earth for horizontal electric dipole excitation. *Geophysics* 40, 285–98.
- Arcone, S. A. 1978. An investigation of an airborne VLF resistivity survey conducted in northern Maine. *Geophysics* 43, 1399–417.
- Baker, H. A., and Meyers, J. C. 1980. A topographic correction for VLF-EM profiles based on model studies. *Geoexploration* 18, 135–49.
- Barringer, A. R. 1962. A new approach to exploration – the INPUT airborne-electrical pulse prospecting system. *Min. Cong. Jour.* 48, 49–52.
- Barringer, A. R. 1970. Regional reconnaissance techniques applied to exploration. In *Mining and Groundwater Geophysics*, Econ. Geol. Report 26, L. W. Morley, ed. Ottawa: Geol. Surv. Canada, pp. 202–12.
- Bartel, D. C., and Hohmann, G. W. 1985. Interpretation of Crone pulse electromagnetic data. *Geophysics* 50, 1488–99.
- Becker, A. 1969. Simulation of time-domain airborne electromagnetic system response. *Geophysics* 34, 739–52.
- Becker, A. 1979. Airborne electromagnetic methods. In *Geophysics and geochemistry in the search for metallic ores*, Econ. Geol. Report 31, P. J. Hood, ed. Ottawa: Geol. Surv. Canada, pp. 33–44.
- Becker, A., and Cheng, G. 1988. Detection of repetitive electromagnetic signals. In *Electromagnetic Methods in Applied Geophysics*, M. N. Nabighian, ed. Ch. 7, Tulsa: Society of Exploration Geophysicists.
- Becker, A., Gauvreau, C., and Collett, L. S. 1972. Scale model study of time-domain EM response of tabular conductors. *CIM Bull.* 65, 90–5.
- Bhattacharya, P. K. and Sinha, A. K. 1965. Response of a spherical conductor to an oscillating magnetic dipole and its use in geophysical prospecting, *Jour. Sci. and Eng. Res., Indian Inst. Tech., Kharag pur.* 9, pt. 1, 51–62.
- Buselli, G. 1980. Electrical geophysics in the USSR. *Geophysics* 45, 1551–62.
- Buselli, G., and O'Neill, B. 1977. SIROTEM: A new portable instrument for multichannel transient electromagnetic measurements. *Bull. Austral. Soc. Expl. Geophys.* 8, 82–7.
- Crone, D. 1979. Exploration for massive sulfides in desert areas using the ground pulse electromagnetic method. In *Geophysics and Geochemistry in the Search for Metallic Ores*, Econ. Geol. Report 31, P. J. Hood, ed. Geol. Surv. Canada. Ottawa: pp. 745–56.

- De Mouilly, G. T., and Becker, A. 1984. Automated interpretation of airborne electromagnetic data. *Geophysics* 49, 1301-12.
- Dolan, W. M. 1970. Geophysical detection of deeply buried sulfide bodies in weathered regions. In *Mining and Groundwater Geophysics, Econ. Geol. Report 26*, L. W. Morley, ed. Geol. Surv. Canada, pp. 336-44.
- Duckworth, K., and Bays, A. R. 1984. Modified mode of operation for the Turam electromagnetic exploration system with benefits for deep exploration. *Geophys. Prosp.* 32, 317-35.
- Dyck, A. V., Becker, A., and Collett, L. S. 1974. Surficial conductivity mapping with the airborne Input system. *CIM Bull.* 62, 104-9.
- Dyck, A. V., Becker, A., and Collett, L. S. 1975. Input AEM results from Project Pioneer, Manitoba. *Can. Jour. Earth Sci.* 12, 971-81.
- Dyck, A. V., Bloore, M., and Vallée, M. A. 1981. User manual for programs PLATE and SPHERE. *Research in Applied Geophysics*, 14, Toronto: Geophysics Lab., Dept. of Physics, Univ. of Toronto.
- Eve, A. S., and Keys, D. A. 1956. *Applied Geophysics*. Cambridge: Cambridge Univ. Press.
- Fischer, G., Le Quang, B. V., and Müller, I. 1983. Very-low frequency ground surveys, a powerful tool for the study of shallow two-dimensional structures. *Geophys. Prosp.* 31, 977-91.
- Fleming, H. W. 1961. The Murray deposit, Restigouche County, N. B., a geochemical-geophysical discovery. *Bull. Can. Inst. Min.* 54, 230-5.
- Fraser, D. C. 1972. A new multicoil electromagnetic prospecting system. *Geophysics* 37, 518-37.
- Fraser, D. C. 1978. Resistivity mapping with an airborne multicoil electromagnetic system. *Geophysics* 43, 144-72.
- Fraser, D. C. 1986. Dighem resistivity techniques in airborne electromagnetic mapping. In *Airborne Resistivity Mapping*, G. J. Palacky, ed., Geol. Surv. Canada paper 86-22, pp. 49-54.
- Frischknecht, F. C. 1967. Fields about an oscillating magnetic dipole over a two-layer earth and application to ground and airborne electromagnetic surveys. *Colorado School of Mines Quarterly* 62, 1-326.
- Gallagher, P. R., Ward, S. H., and Hohmann, G. W. 1985. A model study of a thin plate in free space for the EM37 transient electromagnetic system. *Geophysics* 50, 1002-19.
- Gamble, T. D., Goubaud, W. M., and Clarke, J. 1979. Magnetotellurics with a remote reference. *Geophysics* 44, 53-68.
- Geological Survey of Canada 1986. Airborne resistivity mapping. Paper 86-22. E. J. Palacky, ed.
- Grant F. S., and West, G. F. 1965. *Interpretation Theory in Applied Geophysics*. New York: McGraw-Hill.
- Grover, F. W. 1962. *Inductance Calculations*. New York: Dover.
- Hawley, P. F. 1938. Transients in electrical prospecting. *Geophysics* 3, 247-72.
- Herz, A. 1986. Airborne electromagnetic instruments operating at VLF and higher frequencies. In *Airborne Resistivity Mapping*, G. J. Palacky, ed. Geol. Surv. Canada paper 86-22, pp. 55-62.
- Hohmann, G. W. 1971. Electromagnetic scattering by conductors in the earth near a line source of current. *Geophysics* 36, 101-31.
- Hood, P. J. 1967. Mineral exploration trends and developments. *Can. Min. Jour.* 88 (appeared annually - in Feb. issue until 1972, in Jan. issue thereafter).
- Hood, P. J. 1978. See Hood (1967).
- Hood, P. J. 1979. See Hood (1967).
- Kauahikaua, J. 1978. The electromagnetic fields about a horizontal electric wire source of arbitrary length. *Geophysics* 43, 1019-22.
- Kaufman, A. A., and Keller, G. V. 1983. *Frequency and Transient Soundings*. Amsterdam: Elsevier.
- Keller, G. V., and Frischknecht, F. C. 1966. *Electrical Methods in Geophysical Prospecting*. London: Pergamon.
- Kleinkopf, M. D., Balch, A. H., Frischknecht, F. C., Hovey, R., and Savitt, C. H. 1974. Exploration geophysics in the U.S.S.R.. *Geophysics* 39, 697-711.
- Koefoed, O., Ghosh, D. P., and Polman, G. J. 1972. Computation of type curves for electromagnetic depth sounding with a horizontal transmitting coil by means of a digital linear filter. *Geophys. Prosp.* 20, 406-20.
- Koefoed, O., and Kegge, G. 1968. The electrical current pattern induced by an oscillating magnetic dipole in a semi-infinite thin plate of infinitesimal resistivity. *Geophys. Prosp.* 16, 144-58.
- Koefoed, O., and Struyk, A. P. 1969. The electrical current pattern induced by an oscillating magnetic dipole in a semi-infinite conducting thin plate. *Geophys. Prosp.* 17, 182-95.
- Labson, V. F., Becker, A., Morrison, H. F., and Conti, U. 1985. Geophysical exploration with audio frequency magnetic fields. *Geophysics* 50, 656-64.
- Lawrence Berkeley Laboratory Research Review. Winter 1986. Compact generator passes earth-sounding test. 11, no. 4, p. 92.
- Lodha, G. S., and West, G. F. 1976. Practical airborne EM interpretation using a sphere model. *Geophysics* 41, 1157-69.
- Lowrie, W., and West, G. F. 1965. The effect of a conducting overburden on electromagnetic prospecting measurements. *Geophysics* 30, 624-32.
- Macnae, J. C., Lamontagne, Y., and West, G. F. 1984. Noise processing techniques for time-domain electromagnetic systems. *Geophysics* 49, 934-48.
- Mallick, K. 1972. Conducting sphere in electromagnetic Input field. *Geophys. Prosp.* 20, 293-303.
- Mason, M. 1927. Geophysical exploration for ores. *Tech. Pub. Amer. Inst. Min. Eng.* no. 45.
- Mathieson, C. C., and Crossley, D. J. 1982. Interpretation of single frequency VLF data. In *Geophysical Applications of Surface Wave Impedance Measurements*, L. S. Collett and O. G. Jensen, eds. Geol. Surv. Canada, Ottawa, paper 81-15, Report IV, pp. 49-65.
- McCracken, K. G., Oristaglio, M. L., and Hohmann, G. W. 1986. Minimization of noise in electromagnetic exploration systems. *Geophysics* 49, 934-48.
- McNeill, J. D. 1980. *Applications of transient electromagnetic techniques*. Tech. Note TN-7, Geonics Ltd., Mississauga, Ontario.
- Morrison, H. F., Dolan, W. M., and Dey, A. 1976. Earth conductivity determination employing a single superconducting coil. *Geophysics* 41, 1184-1206.
- Morrison, H. F., Phillips, R. J., and O'Brien, D. P. 1969. Quantitative interpretation of transient electromagnetic fields over a layered half-space. *Geophys. Prosp.* 17, 82-101.
- Nabighian, M. N. 1979. Quasi-static transient response of a conducting half-space - an approximate representation. *Geophysics* 44, 1700-05.

- Nabighian, M. N. and Oristaglio, M. L. 1984. On the approximation of finite loop sources by two-dimensional line sources. *Geophysics* 49, 1027-29.
- Oristaglio, M. L. 1982. Diffusion of electromagnetic fields into the earth from a line source of current. *Geophysics* 47, 1585-92.
- Palacky, G. J. 1975. Interpretation of Input AEM measurements in areas of conductive overburden. *Geophysics* 40, 490-502.
- Palacky, G. J., and Jagodits, F. L. 1975. Computer data processing and quantitative interpretation of airborne resistivity surveys. *Geophysics* 40, 818-30.
- Palacky, G. J., and West, G. F. 1973. Quantitative interpretation of Input AEM measurements. *Geophysics* 38, 1145-58.
- Parry, J. R., and Ward, S. H. 1971. Electromagnetic scattering from cylinders of arbitrary cross-section in a conductive half-space. *Geophysics* 36, 67-100.
- Paterson, N. R. 1966. Mattagami Lake Mines - a discovery by geophysics. In *Mining Geophysics*, vol. 1, pp. 185-96. Tulsa: Society of Exploration Geophysicists.
- Paterson, N. R. 1967. Exploration for massive sulfides in the Canadian Shield. In *Mining and Groundwater Geophysics, Econ. Geol. Report 26*, L. W. Morley, ed. Ottawa: Geol. Surv. Canada, pp. 275-89.
- Paterson, N. R. 1971. Airborne electromagnetic methods as applied to search for sulfide deposits. *CIM Bull.* 74, 1-10.
- Paterson, N. R., and Reford, S. W. 1986. Inversion of airborne electromagnetic data for overburden mapping and groundwater exploration. In *Airborne Resistivity Mapping*, G. J. Palacky, ed., Geol. Surv. Canada paper 86-22, pp. 39-48.
- Patra, H. P., and Mallick, K. 1980. *Geosounding Principles 2 - Time-varying Geoelectric Soundings*. Amsterdam: Elsevier.
- Pipes, L. A. and Harvill, L. R. 1970. *Applied Mathematics for Engineers and Physicists*. New York: McGraw-Hill.
- Podolsky, G., and Slankis, J. A. 1979. Izok Lake deposit, North West Territories, Canada: a geophysical case history. In *Geophysics and Geochemistry in the Search for Metallic Ores, Econ. Geol. Report 31*, P. J. Hood, ed. Geol. Surv. Canada, pp. 641-52.
- Seigel, H. O. 1957. Discovery of Mobrun Copper Ltd. sulfide deposit, Noranda Mining District, Quebec. In *Methods and Case Histories in Mining Geophysics, 6th Commonwealth Mining and Met. Congress*. Montreal: Mercury Press.
- Seigel, H. O., and Pitcher, D. H. 1978. Mapping earth conductivities using a multifrequency airborne electromagnetic system. *Geophysics* 43, 563-75.
- Smith, R. J. 1985. Geophysics in Australian mineral exploration. *Geophysics* 50, 2637-65.
- Smythe, W. R. 1950. *Static and Dynamic Electricity*. New York: McGraw-Hill.
- Spies, B. R., and Eggers, D. B. 1986. The use and misuse of apparent resistivity in electromagnetic measurements. *Geophysics* 51, 1462-71.
- Spies, B. R., and Parker, P. D. 1984. Limitations of large loop transient electromagnetic surveys in conductive terrains. *Geophysics* 49, 902-12.
- Statham, L. 1936. Electric earth transients in geophysical prospecting. *Geophysics* 1, 271-7.
- Strangway, D. W. 1966. Electromagnetic parameters of some sulfide ore bodies. In *Mining Geophysics*, vol. 1, pp. 227-42. Tulsa: Society of Exploration Geophysicists.
- Stratton, J. A. 1941. *Electromagnetic Theory*. New York: McGraw-Hill.
- Telford, W. M., King, W. F., and Becker, A. 1977. VLF mapping of geological structure. *Geol. Surv. Canada Paper* 76-25.
- Wait, J. R. 1951a. Transient electromagnetic propagation in a conducting medium. *Geophysics* 16, 213-21.
- Wait, J. R. 1951b. A conducting sphere in a time varying magnetic field. *Geophysics* 16, 666-72.
- Wait, J. R. 1951c. The magnetic dipole over the horizontally stratified earth. *Can. Jour. Res.* 29, 577-92.
- Wait, J. R. 1955. Mutual electromagnetic coupling of loops over a homogeneous ground. *Geophysics* 20, 630-7.
- Wait, J. R. 1960a. Propagation of electromagnetic pulses in a homogeneous conducting earth. *App. Sci. Res. Sec. B*, 8, 215-53.
- Wait, J. R. 1960b. On the electromagnetic response of a conducting sphere to a dipole field. *Geophysics* 25, 649-58.
- Wait, J. R. 1971. Transient excitation of the earth by a line source of current. *Proc. IEEE Lett.* 59, 1287-8.
- Ward, S. H. 1959a. Unique determination of conductivity, susceptibility, size and depth in multifrequency electromagnetic exploration. *Geophysics* 24, 531-46.
- Ward, S. H. 1959b. AFMAG - airborne and ground. *Geophysics* 24, 761-89.
- Ward, S. H. 1966. The search for massive sulfides. Introduction. In *Mining Geophysics*, vol. 1, pp. 117-29. Tulsa: Society of Exploration Geophysicists.
- Ward, S. H. 1967. Electromagnetic theory for geophysical applications. (Also) The electromagnetic method. In *Mining Geophysics*, vol. 2, pp. 10-196, 224-372. Tulsa: Society of Exploration Geophysicists.
- Ward, S. H. and Hohmann, G. W. 1988. Electromagnetic theory for geophysical applications. In *Electromagnetic Methods in Applied Geophysics*, vol. 1, chap. 4, M. N. Nabighian, ed. Tulsa: Society of Exploration Geophysicists.
- Weir, G. J. 1980. Transient EM fields about an infinitesimally long grounded horizontal electric dipole on the surface of a uniform half-space. *Geophys. Jour. Roy Astron. Soc.* 61, 41-56.
- West, G. F., Macnae, J. C., and Lamontagne, Y. 1984. A time-domain electromagnetic system measuring the step response of the ground. *Geophysics* 49, 1010-26.
- Wieduwilt, W. G. 1962. Interpretation techniques for a single frequency airborne electromagnetic device. *Geophysics* 27, 493-506.
- Zietz, I., Eaton, G. P., Frischknecht, F. C., Kane, M. F., and Moss, C. K. 1976. A Western view of mining geophysics in the USSR. *Geophysics* 41, 310-23.
- Zollinger, R., Morrison, H. F., Lazenby, P. G., and Becker, A. 1987. Airborne electromagnetic bathymetry. *Geophysics* 52, 1127-37.

# Chapter 8

## *Resistivity Methods*

### 8.1. INTRODUCTION

All resistivity methods employ an artificial source of current, which is introduced into the ground through point electrodes or long line contacts; the latter arrangement is rarely used nowadays. The procedure is to measure potentials at other electrodes in the vicinity of the current flow. Because the current is measured as well, it is possible to determine an effective or apparent resistivity of the subsurface.

In this regard the resistivity technique is superior, at least theoretically, to all the other electrical methods, because quantitative results are obtained by using a controlled source of specific dimensions. Practically, as in other geophysical methods, the maximum potentialities of resistivity are never realized. The chief drawback is its high sensitivity to minor variations in conductivity near surface; in electronic parlance the noise level is high. An analogous situation would exist in ground magnetic surveys if one were to employ a magnetometer with sensitivity in the picotesla range.

This limitation, added to the practical difficulty involved in dragging several electrodes and long wires through rough wooded terrain, has made the electromagnetic method more popular than resistivity in mineral exploration. Nor is resistivity particularly suitable for oil prospecting. However, it is by no means obsolete, because the rapid development of the induced polarization technique, which includes resistivity data, guarantees its continued use. Furthermore the search for geothermal reservoirs normally involves resistivity surveying and it is also employed routinely in groundwater exploration, which is of increasing worldwide importance, and in civil engineering.

### 8.2. ELEMENTARY THEORY

#### 8.2.1. Potentials in Homogeneous Media

Consider a continuous current flowing in an isotropic homogeneous medium. (This analysis will also apply to ac if the frequency is low enough that displace-

ment currents are insignificant.) If  $\delta A$  is an element of surface and  $J$  the current density in amperes per square meters, then the current passing through  $\delta A$  is  $J \cdot \delta A$ . The current density  $J$  and the electric field  $E$  are related through Ohm's law:

$$J = \sigma E \quad (8.1)$$

where  $E$  is in volts per meter and  $\sigma$  is the conductivity of the medium in siemens per meter ( $S/m$ ).

The electric field is the gradient of a scalar potential,

$$E = -\nabla V \quad (8.2)$$

Thus we have

$$J = -\sigma \nabla V \quad (8.3)$$

From Equation (6.7),  $\nabla \cdot J = 0$ , so

$$\nabla \cdot (\sigma \nabla V) = 0 \quad (8.4)$$

Using Equation (A.21), we have

$$\nabla \sigma \cdot \nabla V + \sigma \nabla^2 V = 0 \quad (8.5)$$

If  $\sigma$  is constant throughout, the first term vanishes and we have Laplace's equation, that is, the potential is harmonic:

$$\nabla^2 V = 0 \quad (8.6)$$

There are two boundary conditions that must hold at any contact between two regions of different conductivity. In Section 6.2.4 we gave boundary conditions for interfaces where  $\sigma$  and  $\mu$  change abruptly. The first and third of these may be written in the form

$$E_{x_1} = E_{x_2} \quad \text{and} \quad \sigma_1 E_{x_1} = \sigma_2 E_{x_2} \quad (8.7a)$$

where the  $x$  and  $z$  axes are tangential and normal, respectively, to the interface,  $E_{x_1}$  being the tangen-

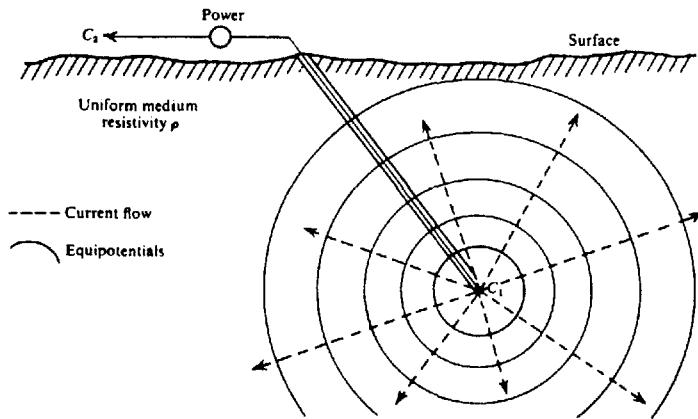


Figure 8.1. Buried point source of current in homogeneous ground.

tial component in medium 1, and so forth. In addition,

$$V_1 = V_2 \quad (8.7b)$$

surface is given by

$$I = 4\pi r^2 J = -4\pi r^2 \sigma \frac{dV}{dr} = -4\pi \sigma A$$

from Equations (8.3) and (8.9), so that

$$A = -\frac{Ip}{4\pi}$$

hence,

$$V = \left( \frac{Ip}{4\pi} \right) \frac{1}{r} \quad \text{or} \quad \rho = \frac{4\pi r V}{I} \quad (8.11)$$

The equipotentials, which are everywhere orthogonal to the current flow lines, will be spherical surfaces given by  $r = \text{constant}$ . These are illustrated in Figure 8.1.

### 8.2.2. Single Current Electrode at Depth

There are several field configurations used in resistivity that we will consider in turn. In the first of these we have an electrode of small dimensions buried in a homogeneous isotropic medium. This corresponds to the *mise-à-la-masse* method (see §8.5.4d) where the single electrode is down a drill hole or otherwise under the ground. The current circuit is completed through another electrode, usually at surface, but in any case far enough away that its influence is negligible.

From the symmetry of the system, the potential will be a function of  $r$  only, where  $r$  is the distance from the first electrode. Under these conditions Laplace's equation, in spherical coordinates, simplifies to

$$\nabla^2 V = d^2 V / dr^2 + (2/r) dV / dr = 0 \quad (8.8)$$

Multiplying by  $r^2$  and integrating, we get

$$\frac{dV}{dr} = \frac{A}{r^2} \quad (8.9)$$

integrating again, we have

$$V = -A/r + B \quad (8.10)$$

where  $A$  and  $B$  are constants. Because  $V = 0$  when  $r \rightarrow \infty$ , we get  $B = 0$ . In addition, the current flows radially outward in all directions from the point electrode. Thus the total current crossing a spherical

### 8.2.3. Single Current Electrode at Surface

If the point electrode delivering  $I$  amperes is located at the surface of the homogeneous isotropic medium and if the air above has zero conductivity, then we have the single probe or three-point system used in surface resistivity layouts. Again the return current electrode is at a great distance.

Because of the symmetry, Laplace's equation in spherical coordinates is applicable, the solution being given again by Equation (8.10) with  $B = 0$ . The boundary condition at the surface requires that  $E_z = \partial V / \partial z = 0$  at  $z = 0$  (because  $\sigma_{\text{air}} = 0$ ). This is already fulfilled because  $\partial V / \partial z = \partial(-A/r) / \partial z = -d/dr(A/r)(\partial r / \partial z) = Az/r^3 = 0$  at  $z = 0$ .

In addition all the current now flows through a hemispherical surface in the lower medium, or

$$A = -\frac{Ip}{2\pi}$$

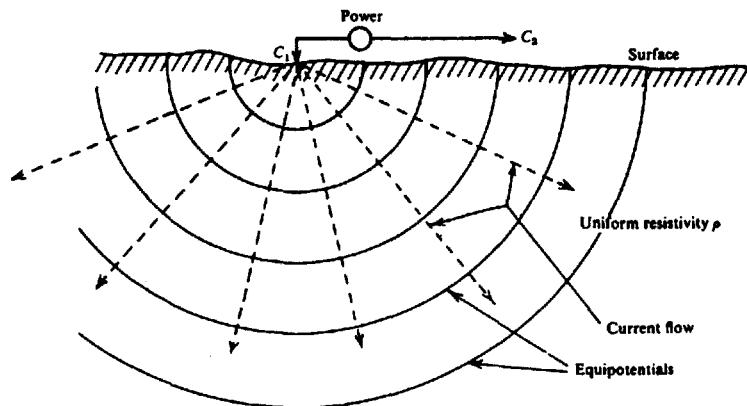


Figure 8.2. Point source of current at the surface of a homogeneous medium.

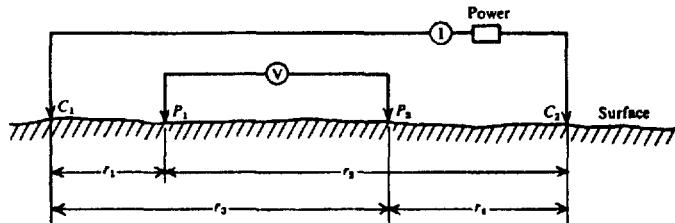


Figure 8.3. Two current and two potential electrodes on the surface of homogeneous isotropic ground of resistivity  $\rho$ .

so that in this case

$$V = \left( \frac{Ip}{2\pi} \right) \frac{1}{r} \quad \text{or} \quad \rho = \frac{2\pi r V}{I} \quad (8.12)$$

Here the equipotentials are hemispherical surfaces below ground as shown in Figure 8.2.

#### 8.2.4. Two Current Electrodes at Surface

When the distance between the two current electrodes is finite (Fig. 8.3), the potential at any nearby surface point will be affected by both current electrodes. As before, the potential due to  $C_1$  at  $P_1$  is

$$V_1 = -\frac{A_1}{r_1} \quad \text{where} \quad A_1 = -\frac{Ip}{2\pi}$$

Because the currents at the two electrodes are equal and opposite in direction, the potential due to  $C_2$  at  $P_1$  is

$$V_2 = -\frac{A_2}{r_2} \quad \text{where} \quad A_2 = \frac{Ip}{2\pi} = -A_1$$

Thus, we have

$$V_1 + V_2 = \frac{Ip}{2\pi} \left( \frac{1}{r_1} - \frac{1}{r_2} \right)$$

Finally, by introducing a second potential electrode at  $P_2$  we can measure the difference in potential between  $P_1$  and  $P_2$ , which will be

$$\Delta V = \frac{Ip}{2\pi} \left\{ \left( \frac{1}{r_1} - \frac{1}{r_2} \right) - \left( \frac{1}{r_3} - \frac{1}{r_4} \right) \right\} \quad (8.13)$$

Such an arrangement corresponds to the four-electrode spreads normally used in resistivity field work. In this configuration the current-flow lines and equipotentials are distorted by the proximity of the second current electrode  $C_2$ . The equipotentials and orthogonal current lines obtained by plotting the relations

$$\frac{1}{R_1} - \frac{1}{R_2} = \text{constant}$$

$$R_1^2 + R_2^2 - 2R_1R_2 \cos \theta = 4L^2$$

are shown in Figure 8.4. The distortion from spherical equipotentials is most evident in the regions between the current electrodes.

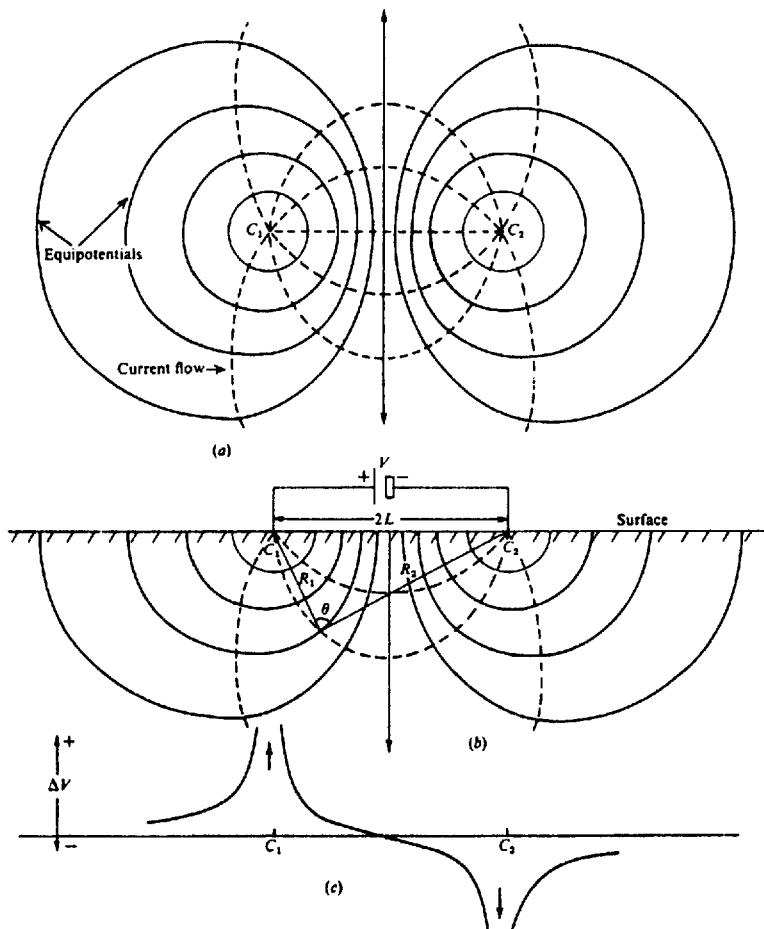


Figure 8.4. Equipotentials and current flow lines for two point sources of current on surface of homogeneous ground. (After Dobrin, 1960.) (a) Plan view. (b) Vertical section. (c) Potential variation at the surface along a straight line through the point sources.

### 8.2.5. Current Distribution

Figures 8.1, 8.2, and 8.4 illustrate, in a general way, the flow of current in homogeneous ground. Although they show that increasing the electrode spacing increases the penetration, the quantitative distribution in depth is not indicated. Consider the current flow in a homogeneous medium between two point electrodes  $C_1$  and  $C_2$  in Figure 8.5. The horizontal current density at point  $P$  is

$$\begin{aligned} J_x &= (-1/\rho) \partial V / \partial x \\ &= (-I/2\pi) \partial / \partial x (1/r_1 - 1/r_2) \\ &= (I/2\pi) \{ x/r_1^3 - (x-L)/r_2^3 \} \end{aligned}$$

and if this point is on the vertical plane midway between  $C_1$  and  $C_2$ , we have  $r_1 = r_2 = r$  and

$$J_x = \frac{I}{2\pi} \frac{L}{(z^2 + L^2/4)^{3/2}} \quad (8.14)$$

Figure 8.6 shows the variation in current density with depth across this plane when the electrode separation is maintained constant. If, on the other hand, the electrode spacing is varied, it is found that  $J_x$  is a maximum when  $L = \sqrt{2}z$ .

We can calculate the fraction of current flowing through a strip of this vertical plane, between depths  $z_1$  and  $z_2$ . Because  $r^2 = \{(L/2)^2 + y^2 + z^2\}$ , the

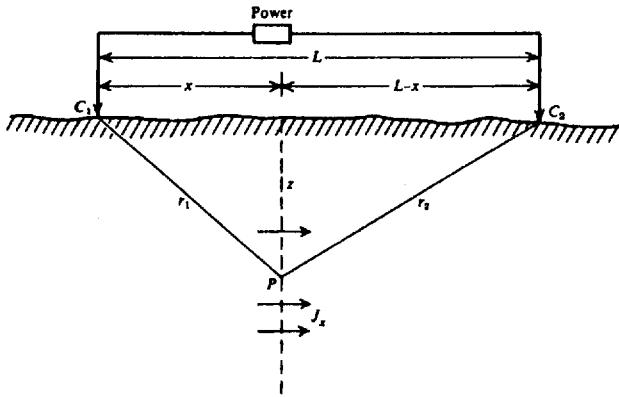


Figure 8.5. Determining the current density in uniform ground below two surface electrodes.

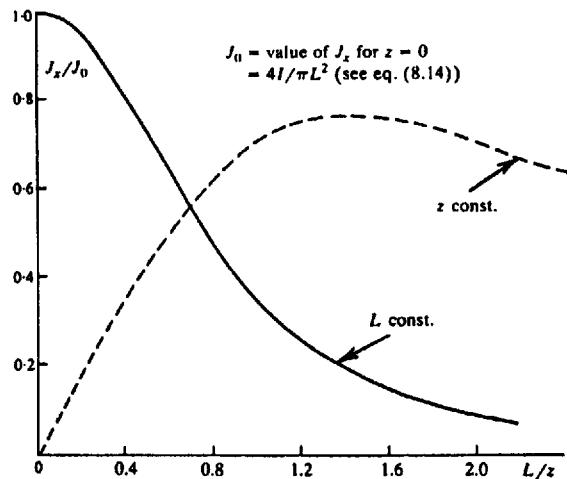


Figure 8.6. Current density versus depth (solid line) and electrode spacing (dashed line).

current through an element  $dy dz$  of the strip is

$$\delta I_z = J_x dy dz = \frac{I}{2\pi} \frac{L}{\{(L/2)^2 + y^2 + z^2\}^{3/2}} dy dz$$

the fraction of total current through a long strip ( $z_2 - z_1$ ) wide will be

$$\begin{aligned} \frac{I_x}{I} &= \frac{L}{2\pi} \int_{z_1}^{z_2} dz \int_{-\infty}^{\infty} \frac{dy}{\{(L/2)^2 + y^2 + z^2\}^{3/2}} \\ &= \frac{2}{\pi} \left( \tan^{-1} \frac{2z_2}{L} - \tan^{-1} \frac{2z_1}{L} \right) \end{aligned} \quad (8.15a)$$

This fraction has a broad maximum when  $L = 2(z_1 z_2)^{1/2}$ . Taking a numerical example, if  $z_1 = 180$

m,  $z_2 = 300$  m, the electrode spacing should be 420 m to get the maximum horizontal current density in the slab. The concentration, however, is not very significant.

Otherwise, if  $z_2 \rightarrow \infty$ , Equation (8.15a) becomes

$$\frac{I_x}{I} = 1 - \frac{2}{\pi} \tan^{-1} \frac{2z_1}{L} \quad (8.15b)$$

Figure 8.7 shows the electrode spacing necessary to force a given fraction of the current into the ground below a depth  $z_1$ . From this plot we see that, when  $L = 2z_1$ , half the current flows in the top layer, half below it.

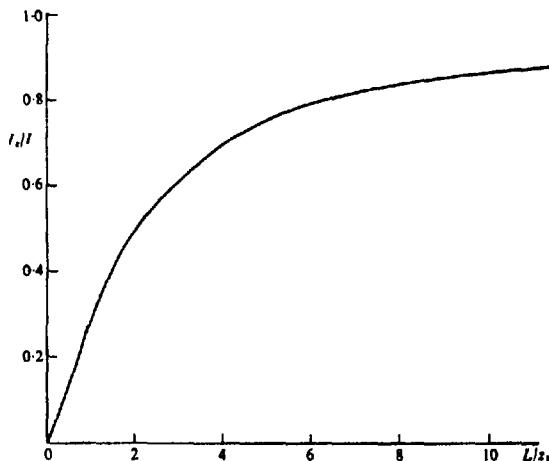


Figure 8.7. Fraction of current flowing below depth  $z_1$  for an electrode spacing  $L$ .

Because the variations in potential, measured at surface, are proportional to the current flow below, it is desirable to get as much current into the ground as possible. For good penetration we must use large enough spacing that sufficient current reaches the target depth; if the latter is 100 m, about one-third of the current will pass below this depth when the spacing is also 100 m. Compared to magnetotellurics, for instance, this places an inherent limitation on the resistivity method. However the controlled power source provides certain advantages.

### 8.3. EFFECT OF INHOMOGENEOUS GROUND

#### 8.3.1. Introduction

So far we have considered current flow and potential in and over homogeneous ground, a situation which is extremely rare in the field and which would be of no practical significance anyway. What we want to detect is the presence of anomalous conductivity in various forms, such as lumped (three-dimensional) bodies, dikes, faults, and vertical or horizontal contacts between beds. The resistivity method is most suitable for outlining horizontal beds and vertical contacts, less useful on bodies of irregular shape.

#### 8.3.2. Distortion of Current Flow at a Plane Interface

Consider two homogeneous media of resistivities  $\rho_1$  and  $\rho_2$  separated by a plane boundary as in Figure 8.8. Suppose that a current of density  $J_1$  is flowing in medium (1) in such a direction as to meet the boundary at an angle  $\theta_1$  to the normal. To determine the

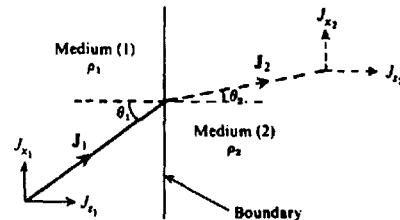


Figure 8.8. Distortion of current flow at a plane boundary when  $\rho_1 < \rho_2$ .

direction of this current in medium (2) we recall the conditions given in Equation (8.7); using Ohm's law to express these results in terms of the current density, we obtain

$$J_{x_1} \rho_1 = J_{x_2} \rho_2 \quad \text{and} \quad J_{z_1} = J_{z_2}$$

Dividing these expressions, we have

$$\rho_1 (J_{x_1}/J_{z_1}) = \rho_2 (J_{x_2}/J_{z_2}) \quad \text{or} \quad \rho_1 \tan \theta_1 = \rho_2 \tan \theta_2$$

so that

$$\tan \theta_2 / \tan \theta_1 = \rho_1 / \rho_2 \quad (8.16)$$

Thus the current lines are bent in crossing the boundary. If  $\rho_1 < \rho_2$ , they will be bent toward the normal and vice versa.

#### 8.3.3. Distortion of Potential at a Plane Interface

Clearly if the current flow is distorted in passing from a medium of one resistivity into another, the equipotentials also will be distorted. It is possible to

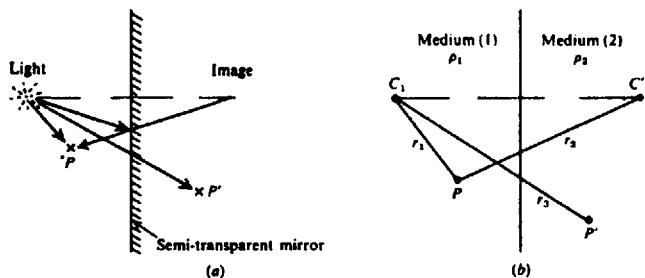


Figure 8.9. Analogy between optical and electrical images. (a) Optical image. (b) Electrical image.

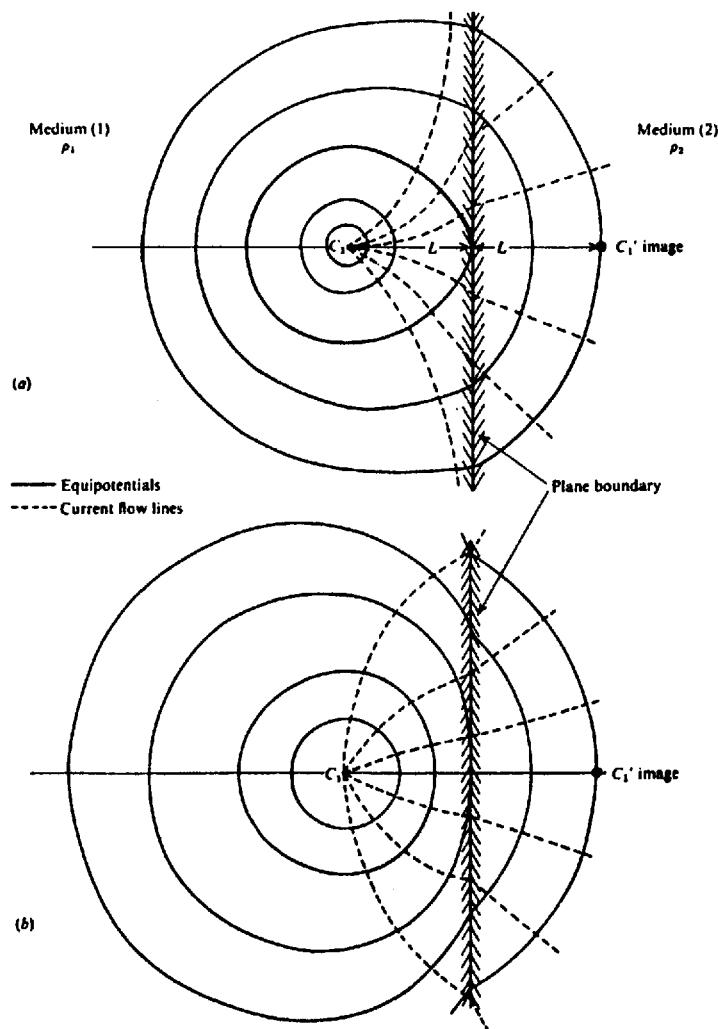


Figure 8.10. Distortion of equipotentials and current flow lines at a boundary between two media of different resistivities. (a)  $\rho_2/\rho_1 = 3$ ,  $k = 0.5$ . (b)  $\rho_2/\rho_1 = 1/3$ ,  $k = -0.5$ .

determine the potential field mathematically by solving Laplace's equation for the appropriate boundary conditions or by integrating it directly. Both methods require considerable mathematics. A much simpler approach employs electrical images, in analogy with geometrical optics. The use of images is valid in solving only a limited number of potential problems, including the plane boundary and the sphere (see Bewley, 1963, Ch. 5).

The analogy between the electrical situation and optics is based on the fact that current density, like light ray intensity, decreases with the inverse square of distance from a point source in a medium of resistivity  $\rho_1$ , separated from an adjacent medium  $\rho_2$  by a plane boundary.

In optics the analogous case would be a point source of light in one medium separated from another by a semitransparent mirror, having reflection and transmission coefficients  $k$  and  $1 - k$ . Then the light intensity at a point in the first medium is partly due to the point source and partly to its image in the second medium, the latter effect diminished by reflection from the mirror. On the other hand, the intensity at a point in the second medium is due only to the source in the first, diminished by transmission through the mirror (Fig. 8.9a).

If we replace the point source of light by a point source of current and the light intensity at a point by potential, the problem is now in the electrical domain. From Figure 8.9b we see that the potential at  $P$  in the first medium is

$$V = \frac{I\rho_1}{4\pi} \left( \frac{1}{r_1} + \frac{k}{r_2} \right) \quad (8.17)$$

and in the second medium at  $P'$  it is

$$V' = \frac{I\rho_2}{4\pi} \left( \frac{1-k}{r_3} \right) \quad (8.18)$$

Applying the boundary condition of Equation (8.7b), these potentials must be equal at the interface, when  $r_1 = r_2 = r_3$ . Thus we have

$$\frac{\rho_1}{\rho_2} = \frac{1-k}{1+k} \quad \text{or} \quad k = \frac{\rho_2 - \rho_1}{\rho_2 + \rho_1} \quad (8.19)$$

In this expression  $k$  is a *reflection coefficient* whose value lies between  $\pm 1$ , depending on the relative resistivities in the two media.

Figure 8.10 shows the traces of equipotential surfaces plotted from the relations in Equations (8.17) and (8.18) for  $k = \pm \frac{1}{2}$ . A few current flow lines are also drawn. This situation corresponds to the practical case of resistivity logging with respect to a plane

boundary underground or the measurement of surface potentials across a vertical contact.

### 8.3.4. Surface Potential Due to Horizontal Beds

If the current source and potential point are located on surface, above a horizontal boundary separating two media, the upper resistivity  $\rho_1$ , the lower  $\rho_2$ , the analysis is more complicated. Because of the ground surface there are now three media, separated by two interfaces. As a result there is an infinite set of images above and below the current electrode, as illustrated in Figure 8.11. The original image  $C_1'$ , at depth  $2z$  below surface, is reflected in the surface boundary to give an image  $C_1''$  a distance  $2z$  above  $C_1$ . This second image, reflected in the lower boundary, produces a third  $C_1'''$  at a depth  $4z$ , and so on.

The effect of each successive image on the potential at  $P$  is reduced by the reflection coefficient between the boundaries. For the current source and its first image below ground, the potential, is, as in Equation (8.17),

$$V' = \frac{I\rho_1}{2\pi} \left( \frac{1}{r} + \frac{k}{r_1} \right)$$

The effect of the second image at  $C_1''$ ,  $2z$  above ground, is

$$V'' = \frac{I\rho_1}{2\pi} \left( \frac{k \times k_a}{r_1} \right)$$

where  $k_a$  is the reflection coefficient at the surface boundary. Because  $\rho_a$  is essentially infinite this coefficient is unity, and from Equation (8.19),

$$V' + V'' = \frac{I\rho_1}{2\pi} \left( \frac{1}{r} + \frac{2k}{r_1} \right)$$

The potential due to the third image  $C_1'''$ ,  $4z$  below ground, will be further reduced, as will that of its image  $4z$  above ground, hence

$$V''' + V^{IV} = \frac{I\rho_1}{2\pi} \left( \frac{k \times k}{r_2} + \frac{k \times k \times k_a}{r_2} \right) \\ - \frac{I\rho_1}{2\pi} \left( \frac{2k^2}{r_2} \right)$$

The resultant total potential at  $P$  can thus be expressed as an infinite series of the form

$$V = \frac{I\rho_1}{2\pi} \left\{ \frac{1}{r} + \frac{2k}{r_1} + \frac{2k^2}{r_2} + \cdots + \frac{2k^m}{r_m} + \cdots \right\} \quad (8.20)$$

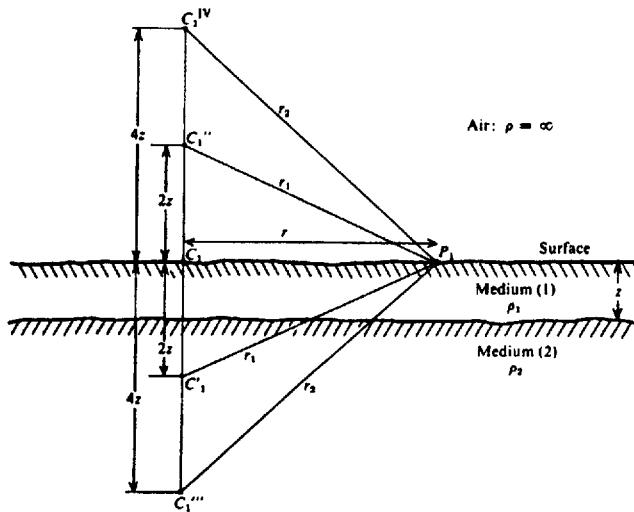


Figure 8.11. Images resulting from two horizontal beds.

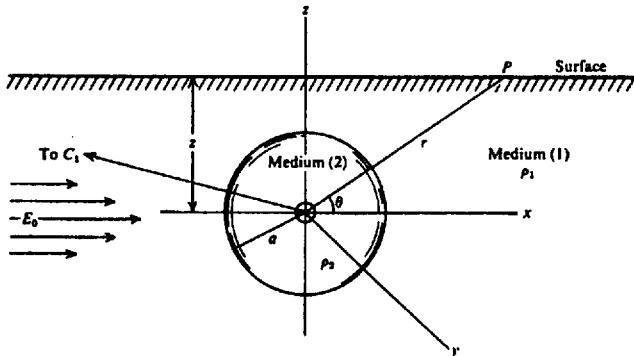


Figure 8.12. Buried conducting sphere in uniform field.

where

$$r_1 = \{ r^2 + (2z)^2 \}^{1/2}$$

$$r_2 = \{ r^2 + (4z)^2 \}^{1/2}$$

$$r_m = \{ r^2 + (2mz)^2 \}^{1/2}$$

This series can be written in the compact form

$$\begin{aligned} V &= \frac{I\rho_1}{2\pi} \left[ \frac{1}{r} + 2 \sum_{m=1}^{\infty} \frac{k^m}{\{ r^2 + (2mz)^2 \}^{1/2}} \right] \\ &= \frac{I\rho_1}{2\pi r} \left[ 1 + 2 \sum_{m=1}^{\infty} \frac{k^m}{\{ 1 + (2mz/r)^2 \}^{1/2}} \right] \quad (8.21) \end{aligned}$$

This series is convergent, because \$|k| < 1\$, whereas the denominator increases indefinitely. The number of terms necessary to get a reasonable answer depends mainly on the value of \$k\$ and partly on the ratio \$z/r\$. For a fixed value of \$r\$, the potential differs from that measured over uniform ground. The latter is given by the first term in the bracket of Equation (8.21) and is called the *normal potential*. The portion expressed by the infinite series is the *disturbing potential*. When \$k\$ is positive and approximately unity, the total potential at \$P\$ may be increased by a factor of 2 or more.

### 8.3.5. Potential Due to Buried Sphere

A three-dimensional body for which the external potential may be developed is the sphere. Figure 8.12 illustrates this case, in which we use spherical coordi-

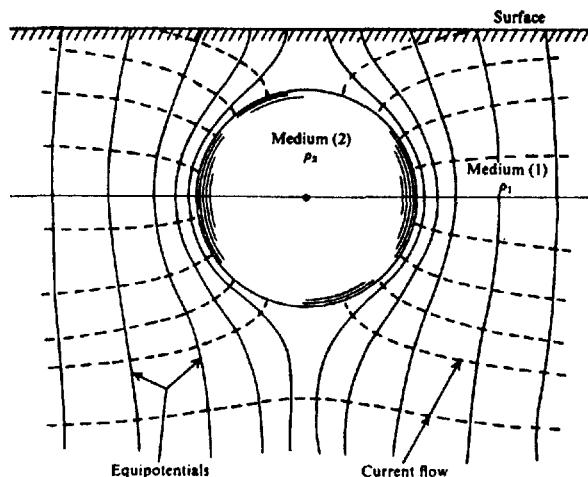


Figure 8.13. Equipotentials and current flow lines for buried conductive sphere.

nates with the sphere center as origin and the polar axis parallel to the  $x$  axis. The problem is to find solutions of Laplace's equation for particular boundary conditions; for simplicity we assume the sphere to be in a uniform field  $E_0$  parallel to the  $x$  axis. This is equivalent to having the current electrode at considerable distance from the sphere.

Using spherical coordinates and applying the boundary conditions of Equation (8.7), we can solve Laplace's equation in the form of a series of Legendre polynomials (§2.7.4), satisfying potential relations inside and outside the sphere. For  $r > a$ , we get

$$V_1 = -E_0 r \cos \theta \left\{ 1 - \frac{(\rho_1 - \rho_2)}{(\rho_1 + 2\rho_2)} \left( \frac{a}{r} \right)^3 \right\} \quad (8.22)$$

If the potential is measured at the ground surface, the sphere will have an image that will double the second term. In addition, if we consider the field to be generated by a current source  $C_1$  at a distance  $R$  from the origin, we can write

$$V_1 = -\frac{I\rho_1}{2\pi R^2} \left\{ 1 - 2 \frac{(\rho_1 - \rho_2)}{(\rho_1 + 2\rho_2)} \left( \frac{a}{r} \right)^3 \right\} r \cos \theta \quad (8.23)$$

As in Equation (8.21) we have two terms, the first being the normal potential, the second the disturbing potential caused by the sphere. Equipotential and current flow lines are illustrated in the section shown in Figure 8.13.

Note that we have made two assumptions here that are not necessarily valid, first that the external

or normal field is uniform and second that there is no interaction between the sphere and its image. Both are strictly true only when the sphere is a great distance from both the current source and surface, in which case the anomaly could not be detected anyway. However, if the distance between the sphere's center and the surface is not less than 1.3 times the radius, the approximation is reasonably good.

### 8.3.6. Effect of Anisotropic Ground

Most rock masses are anything but homogeneous and isotropic in the electrical sense because they are full of fractures. In particular, shales, slates, and frequently limestones and schists have a definite anisotropic character, especially with respect to the bedding planes.

As an example of this type of anisotropy, consider a point source at the surface of a semiinfinite medium in which the resistivity is uniform in the horizontal direction and has the value  $\rho_h$ ; in the vertical direction it is also constant and has a different magnitude  $\rho_v$ ,  $\rho_v$  almost invariably being larger than  $\rho_h$  (§5.2.2c).

Proceeding as in Section 8.2.3 with modifications to allow for the difference between horizontal and vertical directions, we find the equipotential surfaces to be ellipsoidal and symmetrical about the  $z$  axis. Mathematically this may be expressed by

$$V = -I\rho_h \lambda / 2\pi (x^2 + y^2 + \lambda^2 z^2)^{1/2} \quad (8.24)$$

where  $\lambda = (\rho_v / \rho_h)^{1/2}$  is the coefficient of anisotropy. This relation is similar to Equation (8.12) with

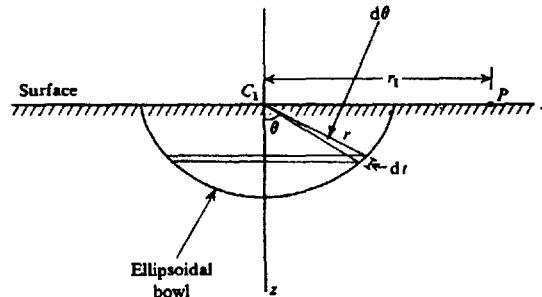


Figure 8.14. Point current source at the surface of anisotropic ground having resistivities  $\rho_h$  and  $\rho_v$  in the horizontal and vertical directions, respectively.

$\lambda/(x^2 + y^2 + \lambda^2 z^2)^{1/2}$  replacing  $r$  to represent the departure from spherical symmetry.

The potential at a surface point  $P$ , a distance  $r_1$  from the current electrode  $C_1$ , will be

$$V_p = \frac{-I\rho_h\lambda}{2\pi r_1} = \frac{-I(\rho_h\rho_v)^{1/2}}{2\pi r_1} \quad (8.25)$$

that is, the potential is equivalent to that for an isotropic medium of resistivity  $(\rho_h\rho_v)^{1/2}$ . Thus it is not possible to detect this type of anisotropy from field measurements.

From Equation (8.25) and Figure 8.14 it is obvious that the resistivity measured over horizontal beds is larger than the actual horizontal resistivity in the beds, but smaller than the vertical resistivity. On the other hand, if the beds have a steep dip and the measurement is made with a spread perpendicular to strike, the apparent resistivity will be smaller than the true resistivity normal to the bedding, just the opposite to the result over horizontal layers; this is known as the "paradox of anisotropy" (Bhattacharyya and Sen, 1981). If the array is parallel to the strike of the dipping beds, the apparent resistivity may be too large, depending on the current-electrode separation.

### 8.3.7. Effect of Topography

As mentioned earlier, resistivity measurements are strongly influenced by local variations in surface conductivity, caused by weathering and moisture content. Rugged topography will have a similar effect, because the current flow is concentrated or focused in valleys and dispersed or diverged beneath a hill. The equipotential surfaces are distorted as a result, producing false anomalies due to the topography alone. This effect may distort or mask a real anomaly.

Fox et al. (1980) made an analytical study of resistivity and IP response, obtained with a dipole-

dipole array (§8.5.3d) over common 2-D terrain features; slopes, ridges, valleys. This approach was extended to three dimensions by Holcombe and Jiracek (1984). In the former report, the finite-element numerical method was used for modeling, because it offers more flexibility for matching irregular boundaries. Potentials are assigned to each interior mesh, based on its boundary geometry and electrical properties, and recomputed by successive sweeps through the whole section until the residuals become insignificantly small. They found that at the surface of homogeneous ground, resistivity is anomalously low on hills and ridges, high in valleys and 3-D depressions. Figure 8.15a illustrates the finite-element mesh representing a 2-D ridge, whereas Figure 8.15b shows the distortion of a uniform field produced by the ridge.

The terrain effect increases with surface relief, being insignificant for slopes of less than 10°. Furthermore the resistivity array complicates the effect. A double-dipole system straddling a hill produces current focusing and a resistivity high, whereas a valley results in a low resistivity, just the opposite to the results of Fox et al. described above.

The response is also sensitive to the direction of the measuring array; for 2-D structures the anomaly is smaller if the spread is parallel, rather than normal, to strike. Analysis of the type described above allows us to reduce the field data to a flat earth by removing or at least minimizing the terrain anomaly.

## 8.4. EQUIPMENT FOR RESISTIVITY FIELD WORK

### 8.4.1. Power Sources

The necessary components for making resistivity measurements include a power source, meters for measuring current and voltage (which may be combined in one meter to read resistance), electrodes, cable, and reels. The power may be either dc or low frequency ac, preferably less than 60 Hz.

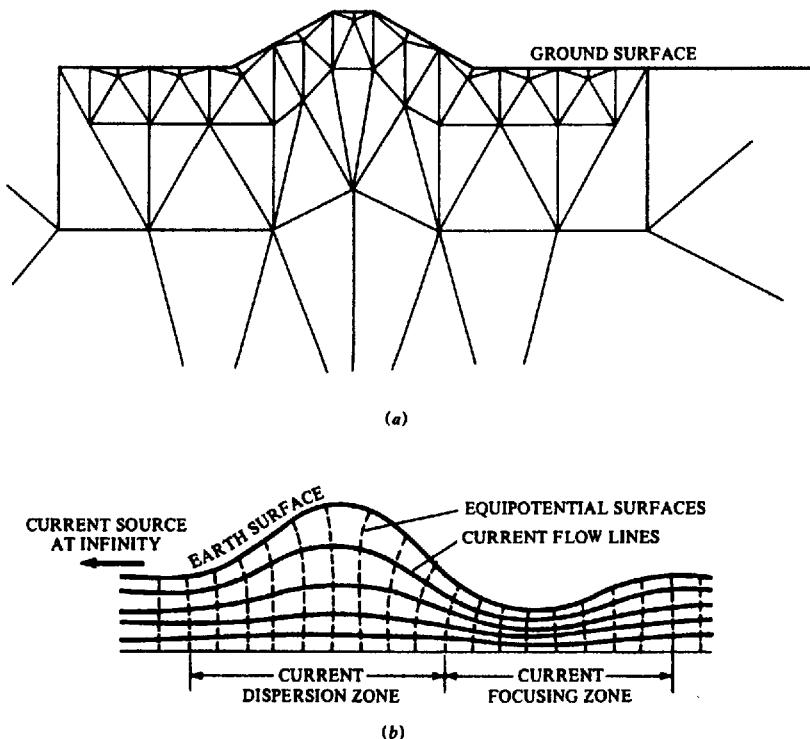


*Figure 8.15. Effect of a 2-D ridge on a uniform field. (After Fox et al. 1980.)  
(a) Finite-element mesh used to calculate terrain effect of ridge. (b) Distortion of uniform field by ridge.*

The power source is usually a motor generator of several hundred watts or a few kilowatts as in IP surveys. Equipment of this type, because of its bulk and weight, is only semiportable; it would not be moved each time the electrodes were shifted. When dc is used, one or more storage batteries or occasionally a set of B cells connected in series may be employed, although such sources are limited to small-scale work, such as overburden or engineering surveys.

To avoid the effects of electrolytic polarization caused by unidirectional current, the dc polarity should be reversed periodically, either by hand with a reversing switch, or by a mechanical commutator, relay system, or vibrator. The rate of commutation may range from three or four times a minute to 100 times per second.

Alternating current is also employed in place of commutated (effectively square-wave) dc. A low-frequency sine-wave transistor oscillator with transformer output of a few watts makes a convenient

portable source. Larger power can be obtained from a motor-driven alternator.

Each of these devices obviously has advantages and limitations. The dc source permits measurement of true dc resistivity – which is desirable – but it also measures spontaneous potentials. This requires that porous pots be used as potential electrodes; the SP effect must be noted before the source is turned on, and then subtracted, either directly or by means of a compensating voltage, from the potential measured when current is flowing.

The use of ac or rapidly interrupted dc eliminates the SP effect. In addition, narrow-band amplifiers tuned to the source frequency can be employed to increase the signal-to-noise ratio. However, the resistivity measured will generally be lower than the true dc value. More serious, inductive coupling between long current and adjacent potential leads, as well as leakage currents, particularly on wet ground, may give erratic readings. All these effects increase with the frequency (§9.4.4c).

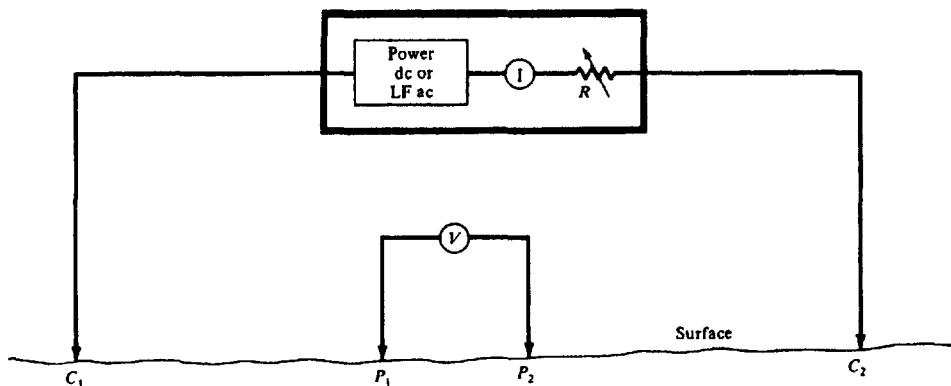


Figure 8.16. Schematic of equipment for measuring resistivity.

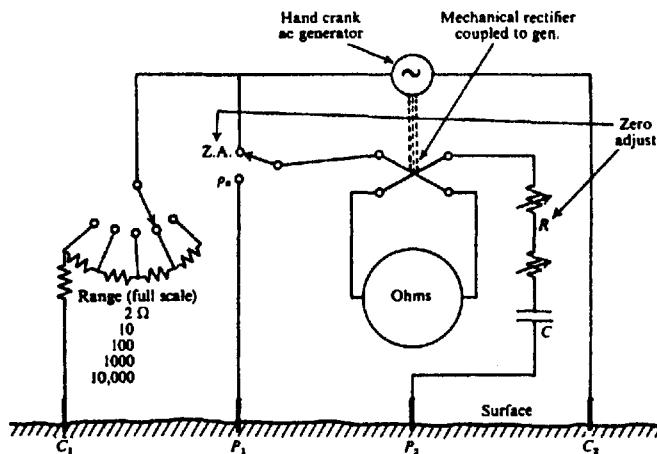


Figure 8.17. Portable equipment for measuring resistivity (schematic).

#### 8.4.2. Meters

With dc or long-period commutated dc sources, the current is measured with a dc milliammeter, whose range should be from about 5 to 500 mA, depending on the electrode spread, type of ground, and power used. Potential is normally measured with a dc voltmeter of high input impedance ( $1\ M\Omega$  or greater) and range 10 mV to perhaps 20 V. When ac sources are used, ac meters are of course necessary.

A typical resistivity set with voltage and current meters is illustrated schematically in Figure 8.16. In some resistivity equipment the current is maintained constant with a regulator, which eliminates the current measurement.

An instrument that measures the ratio of potential to current (that is, resistance) – usually associated with the trade name *Megger* – has been frequently employed for resistivity work. Originally

developed for testing cable insulation, this device was easily modified to measure ground resistance. Power is developed by hand cranking a dc generator or magneto; the output is  $\sim 100\text{ V}$  and a dc current coil is connected in series with one side. The output then is commutated on the generator shaft and applied to the current electrodes, the rate of reversal, being regulated by a governor. The potential electrodes are connected to a second commutator, synchronized with the other, which rectifies the ac potential and applies it to the potential coil. The latter is mounted with the current coil in such a way as to make the needle deflection proportional to  $V/I$ . This instrument is shown schematically in Figure 8.17.

Several other all-in-one resistivity instruments are also available, employing a vibrator powered by dry cells or low-frequency transistor oscillator. Such devices, like the *Megger*, necessarily have low power output. Furthermore, with some electrode spreads,

the combination of power source and both meters in one box may be a definite disadvantage. However, such instruments are compact and completely portable.

#### 8.4.3. Electrodes and Wire

With ac power sources, all the electrodes may be steel, aluminum, or brass; stainless steel is probably best for combined strength and resistance to corrosion. Metal electrodes should be at least  $\frac{1}{2}$  m long so they can be driven into the ground several centimeters for good electrical contact. In very dry surfaces this contact may be improved by watering the electrodes. If dc power is used the potential electrodes should be porous pots as in SP work.

Connecting wires, which must be insulated and as light as possible, are wound on portable reels. Plastic insulation is more durable than rubber against abrasion and moisture; however, some plastics deteriorate in cold weather and animals seem to find them very tasty in any season.

### 8.5. ELECTRODE LAYOUTS AND FIELD PROCEDURE

#### 8.5.1. General

An enormous number of electrode spreads have been used in resistivity at various times; not more than a half dozen have survived to any extent. In principle it is not necessary to use a collinear array. Practically, however, the electrodes are almost always in line; otherwise interpretation of results becomes difficult and the field work is complicated.

One drawback in resistivity work is the practical difficulty of moving stakes with great lengths of wire attached, a slow and expensive task in relation to magnetics, EM, and some other electrical survey methods. Thus it is an advantage to use electrode spreads that may require only one or two electrodes to be moved, and these at close spacing where possible.

#### 8.5.2. Apparent Resistivity

Before discussing the various electrode spreads, it is necessary to consider what is actually measured by an array of current and potential electrodes. We can rearrange the terms in Equation (8.13) to obtain

$$\rho = \frac{2\pi\Delta V}{I} \frac{1}{\{(1/r_1 - 1/r_2) - (1/r_3 - 1/r_4)\}} \\ = \left( \frac{2\pi\Delta V}{I} \right) p \quad (8.26)$$

where the parameter  $p$  has to do with the electrode geometry. By measuring  $\Delta V$  and  $I$  and knowing the electrode configuration, we obtain a resistivity  $\rho$ . Over homogeneous isotropic ground this resistivity will be constant for any current and electrode arrangement.

If the ground is inhomogeneous, however, and the electrode spacing is varied, or the spacing remains fixed while the whole array is moved, then the ratio will, in general, change. This results in a different value of  $\rho$  for each measurement. The magnitude is intimately related to the arrangement of electrodes. This measured quantity is known as the *apparent resistivity*,  $\rho_a$ . Although it is diagnostic, to some extent, of the actual resistivity of a zone in the vicinity of the electrode array, the apparent resistivity is definitely not an average value and only in the case of homogeneous grounds is it equal to the actual resistivity.

Another term that is frequently found in the literature is the so-called *surface resistivity*. This is the value of  $\rho_a$  obtained with small electrode spacing. Obviously it is equal to the true surface resistivity only when the ground is uniform over a volume roughly of the dimensions of the electrode separation.

#### 8.5.3. Electrode Arrays (Spreads)

(a) *Wenner array*. The most commonly used point-electrode systems are illustrated in Figure 8.18. The first two examples, the *Wenner* and *Schlumberger arrays*, were formerly most popular; since the development of the pseudodepth section (§9.5.1) in IP work, the double-dipole configuration has become equally so.

In the Wenner spread (Fig. 8.18a) the electrodes are uniformly spaced in a line. Setting  $r_1 = r_4 = a$  and  $r_2 = r_3 = 2a$ , in Equation (8.26), the apparent resistivity becomes

$$\rho_a = 2\pi a \Delta V / I \quad (8.27)$$

In spite of the simple geometry, this arrangement is often quite inconvenient for field work, and has some disadvantages from a theoretical point of view as well. For depth exploration using the Wenner spread, the electrodes are expanded about a fixed center, increasing the spacing  $a$  in steps. For lateral exploration or mapping, the spacing remains constant and all four electrodes are moved along the line, then along another line, and so on. In mapping, the apparent resistivity for each array position is plotted against the center of the spread.

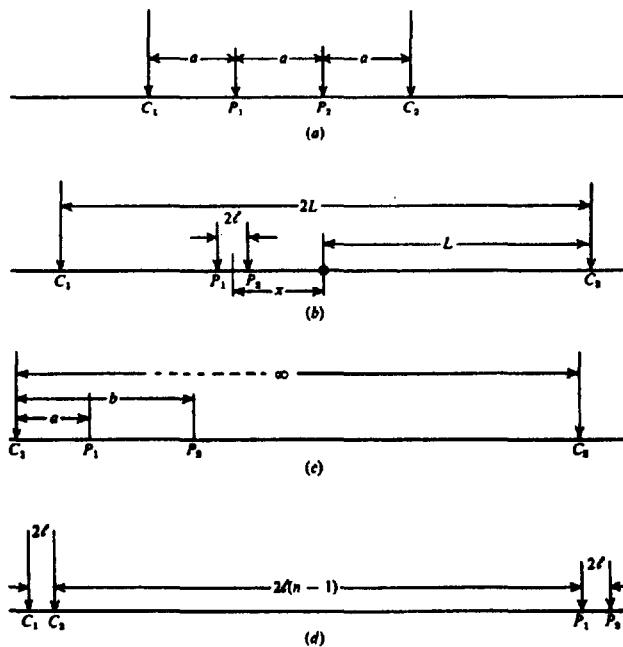


Figure 8.18. Electrode arrays in common use. (a) Wenner. (b) Schlumberger. (c) Pole-dipole. (d) Double-dipole.

(b) *Schlumberger (gradient) array*. For the Schlumberger array the current electrodes are spaced much further apart than the potential electrodes. From Figures 8.3 and 8.18b, we find that

$$r_1 = (L - x) - \ell$$

$$r_2 = (L + x) + \ell$$

$$r_3 = (L - x) + \ell$$

and

$$r_4 = (L + x) - \ell$$

Substituting these values in Equation (8.26), we get

$$\rho_a = \frac{2\pi\Delta V}{I} \left[ \left\{ \frac{1}{(L-x)-\ell} - \frac{1}{(L+x)+\ell} \right\} - \left\{ \frac{1}{(L-x)+\ell} - \frac{1}{(L+x)-\ell} \right\} \right]^{-1} \quad (8.28)$$

If the smallest current-potential electrode distance is always considerably greater than the distance between the two potential electrodes (by a factor of 10 or more), then  $(L - x) \gg 3\ell$  and we have to the first approximation

$$\rho_a \approx \frac{\pi}{2\ell} \frac{(L^2 - x^2)^2}{(L^2 + x^2)} \left( \frac{\Delta V}{I} \right) \quad (8.29a)$$

This array is often used symmetrically, that is,  $x = 0$ , in which case

$$\rho_a \approx \frac{\pi L^2}{2\ell} \left( \frac{\Delta V}{I} \right) \quad (8.29b)$$

Alternate symbols for the Schlumberger array are frequently found in the literature; for example, *A*, *B*, *M*, and *N* are used for *C*<sub>1</sub>, *C*<sub>2</sub>, *P*<sub>1</sub>, and *P*<sub>2</sub>, respectively; in this case  $L = \frac{1}{2}AB$ ,  $\ell = \frac{1}{2}MN$ .

In vertical sounding (§8.5.4b) the potential electrodes remain fixed while the current-electrode spacing is expanded symmetrically about the center of the spread. For large values of  $L$  it may be necessary to increase  $\ell$  also in order to maintain a measurable potential. Equation (8.29a) applies in this case. This procedure is more convenient than the Wenner expanding spread because only two electrodes need move. In addition, the effect of shallow resistivity variations is constant with fixed potential electrodes. Figures 8.42 and 8.44 illustrate vertical sounding results.

Lateral profiling (§8.5.4c) may be done in two ways. With a very large fixed separation of the current electrodes (300 m or more), the potential pair is moved between them, also with fixed spacing, subject to the limitation  $(L - x) \gg 3\ell$  [Eq. (8.29a)]. Apparent resistivity is plotted against the midpoint of the potential electrodes.

The other layout is similar to the Wenner in that the electrode spacing remains fixed ( $L \gg \ell$ ) and the whole array is moved along the line in suitable steps. This arrangement is less convenient than the first because it requires that all four electrodes be moved for each station.

In lateral profiling with the Schlumberger array (and with the pole-dipole array; see next section) it is permissible to measure potential somewhat off the line between fixed current electrodes, that is, to map the surface in two dimensions (because  $C_1$  and  $C_2$  are far apart, the current density is roughly uniform over a considerable lateral extent).

(c) *Pole-dipole (three-point) array.* One of the current electrodes is fixed at a great distance from the other three, all of which can have various spacings. The values in Equation (8.26) are now

$$\begin{aligned}r_1 &= a \\r_3 &= b \\r_2 = r_4 &= \infty\end{aligned}$$

so that

$$\rho_a = \frac{2\pi ab}{b-a} \left( \frac{\Delta V}{I} \right) \quad (8.30a)$$

When  $b = 2a$  this becomes

$$\rho_a = 4\pi a \left( \frac{\Delta V}{I} \right) \quad (8.30b)$$

or double the ratio in the Wenner array [Eq. (8.27)]. When the potential spacing is very small compared to the distance of either potential electrode from  $C_1$  ( $C_2$  still at  $\infty$ ), we write  $r_1 = a - \delta a/2$ ,  $r_3 = a + \delta a/2$ , and the apparent resistivity becomes

$$\rho_a \approx \frac{2\pi a^2}{I} \left( \frac{\partial V}{\partial a} \right) \quad (8.30c)$$

This arrangement is equivalent to a *half-Schlumberger array*. Equation (8.30c) is similar to Equation (8.34) with  $a = L$ ,  $\partial a = \Delta r$ , that is, both electrode configurations measure potential gradient.

Because the electrode  $C_2$  is remote, it is not necessary to have it in line with the other three. This permits lateral exploration on radial lines from a fixed position of  $C_1$ , by moving one or both potential electrodes, a particularly convenient method for resistivity mapping in the vicinity of a conductor of limited extent. This electrode arrangement is effectively the same as the *lateral spread* used in well logging, described in Section 11.2.3. It is also similar to the *mise-à-la-masse* method (§8.5.4d) in which the electrode  $C_1$  is in contact with the conducting zone.

A further variation on the pole-dipole array is obtained by moving one of the potential electrodes, say  $P_2$ , to a distant point, which is also remote from  $C_2$ . In this case,  $r_3 = b = \infty$  as well, and Equation (8.30a) is the same as Equation (8.27) for the Wenner spread, hence this array is known as the *half-Wenner array*. Although it is only necessary to move one potential electrode, the long connecting wire to the other is a disadvantage.

In field work the location of an electrode at infinity requires that it have very little influence on the rest of the array. For instance, when using a Wenner spread, the remote electrode or electrodes must be at least 10 times the spacing to reduce the effect to 10% or less. With the Schlumberger system, because the potential electrodes are close together, the far current electrode need only be about three times as far away as the one nearby to get the same result.

However, because the subsurface resistivity may vary laterally, these spacing estimates can be much too low and may have to be increased by a factor of 10 or more, depending on the resistivity contrast.

(d) *Double-dipole (dipole-dipole) system.* The potential electrodes are closely spaced and remote from the current electrodes, which are also close together. In this case, from Figure 8.18d and Equation (8.26) we get

$$\begin{aligned}r_1 = r_4 &= 2n\ell \\r_2 &= 2\ell(n-1) \\r_3 &= 2\ell(n+1) \quad \text{where } n \gg 1\end{aligned}$$

Then, dropping the minus,

$$\rho_a = 2\pi(n-1)n(n+1)\ell \Delta V/I \quad (8.31)$$

When  $n$  is 5 or less, this is the spread commonly used in IP work (§9.4.3). Inductive coupling between potential and current cables is reduced with this arrangement.

When the dipoles are widely separated,  $n \gg 1$  and we have

$$\rho_a = 2\pi n^3 \ell \Delta V/I \quad (8.32)$$

this is the approximation usually applied in resistivity surveys. The dipoles may also be placed broadside, bisected by the traverse line. In this case,

$$r_1 = r_4 = 2n\ell$$

$$r_2 = r_3 = 2\{(n\ell)^2 + \ell^2\}^{1/2} \approx 2n\ell(1 + 1/2n^2)$$

and

$$\rho_a \approx 4\pi n^3 \ell \Delta V/I \quad (8.33)$$

In all the above electrode layouts the potential and current electrodes may be interchanged. By the principle of reciprocity, the apparent resistivity should be the same in either case. The switching of current and potential electrodes could be desirable, for instance, in using high voltages with large spreads in Schlumberger and, possibly, Wenner layouts.

#### 8.5.4. Resistivity Field Procedures

(a) *Introduction.* Regardless of the specific electrode spread employed, there are really only two basic procedures in resistivity work. The particular procedure to be used depends on whether one is interested in resistivity variations with depth or with lateral extent. The first is called *vertical, electric, or vertical-electric (VES) sounding*, the second *lateral profiling or mapping*.

(b) *Vertical sounding.* Because the fraction of total current that flows at depth varies with the current-electrode separation, as described in §8.2.5, the field procedure is to use a fixed center with an expanding spread. Although the pole-dipole array is not suited to this technique, any of the other three configurations may be used, the Schlumberger having the advantages mentioned in Section 8.5.3b. The presence of horizontal or gently dipping beds of different resistivities is best detected by the expanding spread. Hence the method is useful in determining depth of overburden, depth, structure, and resistivity of flat-lying sedimentary beds and possibly of the basement also if it is not too deep.

It is frequently necessary to carry out this expansion procedure at several locations in an area, even when the main interest may be in lateral exploration, to establish proper electrode spacings for the lateral search.

(c) *Lateral profiling.* This method is particularly useful in mineral exploration, where the detection of isolated bodies of anomalous resistivity is required. Any of the electrode arrangements described in Section 8.5.3 may be used, the selection depending mainly on the field situation. In Wenner, Schlumberger, and pole-dipole surveys the apparent resistivity is plotted at the midpoint of the potential electrodes, except where one of these is effectively at infinity, as in the modified three-probe system, when the station is reckoned at the near potential electrode. For the double-dipole, the station is at the array midpoint.

When the potential electrodes are closely spaced with respect to the current spread, as in the Schlumberger and possibly the three-point system, the measurement is effectively of potential gradient

at the midpoint. This can be seen from Equation (8.29b) where, putting  $2\ell = \Delta r$ , we can write

$$\rho_a = \frac{\pi L^2}{I} \left( \frac{\Delta V}{\Delta r} \right) \quad (8.34)$$

If the current electrodes are close together and remote from the potential pair, the measurement is essentially that of the curvature of the field or the second derivative. For the double-dipole spread in Figure 8.18d, the potential gradient at the midpoint of  $P_1 P_2$  due to  $C_1$  only is  $\Delta V_1 / \Delta r$ , where  $\Delta r$  is the spacing of the potential electrodes. Similarly the potential gradient due to  $C_2$  only is  $\Delta V_2 / \Delta r$ . Then the measured potential gradient becomes, in the limit as  $\Delta r \rightarrow 0$ ,

$$\begin{aligned} \frac{\Delta V}{\Delta r} &= \frac{\Delta V_1 - \Delta V_2}{\Delta r} \rightarrow \left( \frac{\partial V}{\partial r} \right)_{C_1} - \left( \frac{\partial V}{\partial r} \right)_{C_2} \\ &= \Delta r \left( \frac{\partial^2 V}{\partial r^2} \right) \end{aligned}$$

or,

$$\Delta V = (\Delta r)^2 \frac{\partial^2 V}{\partial r^2} \quad (8.35)$$

Also, with  $r_1 = r_4 = r$ ,  $r_2 = r - \Delta r$ , and  $r_3 = r + \Delta r$ , we obtain from Equation (8.13),

$$\begin{aligned} \Delta V &= \frac{Ip_a}{2\pi} \left( \frac{1}{r} - \frac{1}{r - \Delta r} - \frac{1}{r + \Delta r} + \frac{1}{r} \right) \\ &= -\frac{Ip_a}{\pi} \frac{(\Delta r)^2}{r^3} \end{aligned}$$

using the second approximation (Eq. (A.44)). This gives

$$\rho_a \approx -\frac{\pi r^3}{(\Delta r)^2} \left( \frac{\Delta V}{I} \right) \approx -\frac{\pi r^3}{I} \left( \frac{\partial^2 V}{\partial r^2} \right) \quad (8.36)$$

Lateral exploration by resistivity measurements is best suited to detection of steeply dipping contacts and dikes of contrasting resistivity, that is, 2-D anomalies, and to a lesser extent for location of anomalous 3-D conductors such as could be roughly simulated by the sphere.

(d) *Mise-à-la-masse.* This is a variation on the three-point electrode system, used where some part of the conductive zone is already located and exposed, either as outcrop or in a drill hole. The near current electrode is embedded in the zone itself, the other being a large distance away on surface. The

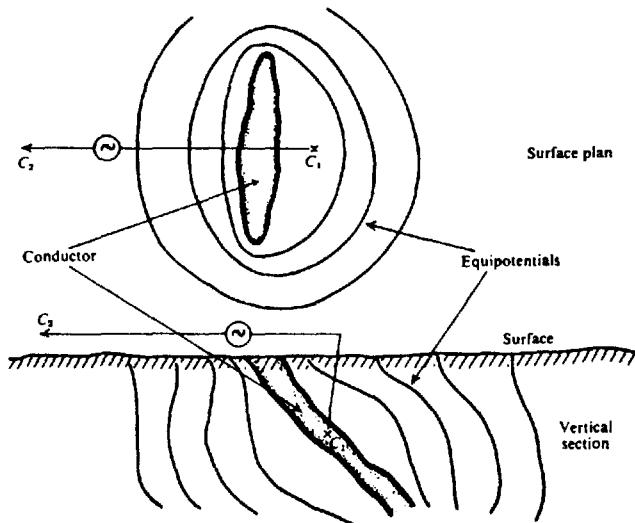


Figure 8.19. Distortion of the equipotentials around the near current electrode by a dipping conductor when using the mise-à-la-masse method.

potential electrodes are moved about, either on surface or in drill holes. The extent, dip, strike, and continuity of the zone will be better indicated by introducing the current directly into it than by the usual mapping techniques.

The effect of a dipping mineralized zone on the equipotentials is shown in Figure 8.19. Because the second current electrode is at infinity, it is possible to map the potentials in all directions around the zone without shifting the current stakes.

## 8.6. INTERPRETATION

### 8.6.1. Introduction

The mathematical analysis for quantitative interpretation of resistivity results is most highly developed for the vertical sounding technique, reasonably so for lateral profiling over large-scale contacts of steep dip, and least useful for the detection of 3-D anomalies. As in other geophysical methods where quantitative interpretation is possible, the assessment of results should progress from rough preliminary estimates made in the field toward more sophisticated methods of interpretation, eventually based on the complete survey. Such a procedure keeps the field work up-to-date, controls the day-by-day program, and indicates where more intensive work is warranted, both in the field survey and its interpretation. Van Nostrand and Cook (1966) give a very extensive bibliography of resistivity interpretation techniques.

### 8.6.2. Resistivity Modeling

The use of models, although not as common in resistivity as in EM, can be a useful aid in interpretation. Resistivity modeling is generally done in a water tank, the resistivity of the liquid being varied by the addition of salts such as NaCl or acids such as H<sub>2</sub>SO<sub>4</sub>. Sand may be used instead of liquid, provided reproducible contacts between the model electrodes and the surface can be made.

Various conducting or insulating sheets, cylinders, and blocks are immersed in the tank to simulate the field situation. The electrode spread is moved about laterally in a convenient jig mount on the surface of the tank; alternatively, in a liquid medium, the model anomaly may be moved past the electrode spread.

Scaling is not a problem in resistivity model work (§7.7.1b). The usual relation in resistivity is  $\Delta V/I \propto \rho/l$ , where  $l$  is scaled linearly. Rather than vary the resistivity  $\rho$ , it is simpler to change  $\Delta V$  or  $I$ . However, somewhat higher frequencies could conveniently be used in the model than in the field without introducing errors.

### 8.6.3. Vertical sounding; Two Horizontal Beds

(a) *Basic formula.* The method of images developed in Section 8.3.4 is useful in dealing with soundings on two horizontal layers, as well as profiling

over elementary 2-D structures. Its application to the former also provides some simple illustrations of limiting cases of the bed parameters.

Equation (8.21) relates the potential of a single electrode to the resistivity of the upper layer in terms of the electrode spacing, the depth to the interface, and the resistivity contrast between the two beds. We want this expression in the form of an apparent resistivity, which would be measured by a four-electrode system. Using the symbols of Figure 8.3 and Equation (8.13), Equations (8.19), (8.21), and (8.26) enable us to write, for the measured potential difference between  $P_1$  and  $P_2$ ,

$$\Delta V = V_1 - V_2 = \frac{I\rho_1}{2\pi} \left[ \left( \frac{1}{r_1} - \frac{1}{r_2} \right) - \left( \frac{1}{r_3} - \frac{1}{r_4} \right) + 2 \sum_{m=1}^{\infty} k^m \left\{ \frac{1}{(r_1^2 + 4m^2 z^2)^{1/2}} - \frac{1}{(r_2^2 + 4m^2 z^2)^{1/2}} - \frac{1}{(r_3^2 + 4m^2 z^2)^{1/2}} + \frac{1}{(r_4^2 + 4m^2 z^2)^{1/2}} \right\} \right] \quad (8.37)$$

(b) *Wenner spread.* Because  $r_1 = r_4 = a$ ,  $r_2 = r_3 = 2a$  (Fig. 8.18a), Equation (8.37) is simplified to give

$$\Delta V = \frac{I\rho_1}{2\pi a} \left[ 1 + \sum_{m=1}^{\infty} \frac{4k^m}{\{1 + (2mz/a)^2\}^{1/2}} - \sum_{m=1}^{\infty} \frac{4k^m}{\{4 + (2mz/a)^2\}^{1/2}} \right] = \frac{I\rho_1}{2\pi a} (1 + 4D_w)$$

where

$$D_w = \sum_{m=1}^{\infty} k^m \left[ \frac{1}{\{1 + (2mz/a)^2\}^{1/2}} - \frac{1}{\{4 + (2mz/a)^2\}^{1/2}} \right]$$

From Equation (8.26) we have

$$\begin{aligned} \rho_a &= 2\pi \Delta V p / I \\ &= 2\pi \Delta V / I (1/a - 1/2a - 1/2a + 1/a) \\ &= 2\pi a \Delta V / I \end{aligned}$$

so that the apparent resistivity is

$$\begin{aligned} \rho_a &= \rho_1 \left[ 1 + \sum_{m=1}^{\infty} \frac{4k^m}{\{1 + (2mz/a)^2\}^{1/2}} - \sum_{m=1}^{\infty} \frac{4k^m}{\{4 + (2mz/a)^2\}^{1/2}} \right] \\ &= \rho_1 (1 + 4D_w) \end{aligned} \quad (8.38)$$

(c) *Schlumberger spread.* When  $x = 0$ ,  $r_1 = r_4 = L - \ell$ ,  $r_2 = r_3 = L + \ell$  (Fig. 8.18b), and the potential is

$$\begin{aligned} \Delta V &= \frac{I\rho_1}{2\pi} \left[ \left( \frac{2}{L - \ell} - \frac{2}{L + \ell} \right) + 4 \sum_{m=1}^{\infty} k^m \times \left( \frac{1}{(L - \ell) \{1 + (2mz)^2/(L - \ell)^2\}^{1/2}} - \frac{1}{(L + \ell) \{1 + (2mz)^2/(L + \ell)^2\}^{1/2}} \right) \right. \\ &\quad \left. - \frac{I\rho_1 2\ell}{\pi(L^2 - \ell^2)} \left[ 1 + \left( \frac{L + \ell}{\ell} \right) \times \sum_{m=1}^{\infty} \frac{k^m}{\{1 + (2mz)^2/(L - \ell)^2\}^{1/2}} - \left( \frac{L - \ell}{\ell} \right) \sum_{m=1}^{\infty} \frac{k^m}{\{1 + (2mz)^2/(L + \ell)^2\}^{1/2}} \right] \right] \end{aligned}$$

When  $L \gg \ell$ , the terms inside the square brackets can be simplified; the potential difference then becomes

$$\begin{aligned} \Delta V &\approx \frac{I\rho_1 2\ell}{\pi L^2} \left[ 1 + 2 \sum_{m=1}^{\infty} \frac{k^m}{\{1 + (2mz/L)^2\}^{1/2}} \right] \\ &\approx \frac{I\rho_1 2\ell}{\pi L^2} (1 + 2D'_s) \end{aligned}$$

where

$$D'_s = \sum_{m=1}^{\infty} \frac{k^m}{\{1 + (2mz/L)^2\}^{3/2}}$$

The exact expression for apparent resistivity is

$$\begin{aligned}\rho_a &= \rho_1 \left[ 1 + \left( \frac{L+\ell}{\ell} \right) \right. \\ &\quad \times \sum_{m=1}^{\infty} \frac{k^m}{\{1 + (2mz)^2/(L-\ell)^2\}^{1/2}} \\ &\quad - \left( \frac{L-\ell}{\ell} \right) \\ &\quad \times \sum_{m=1}^{\infty} \frac{k^m}{\{1 + (2mz)^2/(L+\ell)^2\}^{1/2}} \left. \right] \\ &= \rho_1(1 + D_d)\end{aligned}\quad (8.39a)$$

where

$$\begin{aligned}D_d &= \left( \frac{L+\ell}{\ell} \right) \sum_{m=1}^{\infty} \frac{k^m}{\{1 + (2mz)^2/(L-\ell)^2\}^{1/2}} \\ &\quad - \left( \frac{L-\ell}{\ell} \right) \sum_{m=1}^{\infty} \frac{k^m}{\{1 + (2mz)^2/(L+\ell)^2\}^{1/2}}\end{aligned}$$

Approximately, we have

$$\begin{aligned}\rho_a &\approx \rho_1 \left[ 1 + 2 \sum_{m=1}^{\infty} \frac{k^m}{\{1 + (2mz/L)^2\}^{3/2}} \right] \\ &= \rho_1(1 + 2D'_d).\end{aligned}\quad (8.39b)$$

This result can also be obtained by differentiating Equation (8.21) with respect to  $r$ , multiplying the result by 2 (because there are two current electrodes), and applying Equation (8.34) to get  $\rho_a$ .

(d) Double-dipole spread. Because  $r_1 = r_4 = 2n\ell$ ,  $r_2 = 2(n-1)\ell$ ,  $r_3 = 2(n+1)\ell$  (Fig. 8.18d), the exact expression for the potential is

$$\begin{aligned}\Delta V &= - \frac{I\rho_1}{2\pi(n-1)n(n+1)\ell} \\ &\quad \times \left[ 1 + n(n+1) \right. \\ &\quad \times \sum_{m=1}^{\infty} \frac{k^m}{\{1 + (2mz)^2/\{2(n-1)\ell\}^2\}^{1/2}} \\ &\quad + n(n-1) \\ &\quad \times \sum_{m=1}^{\infty} \frac{k^m}{\{1 + (2mz)^2/\{2(n+1)\ell\}^2\}^{1/2}} \\ &\quad - 2(n-1)(n+1) \\ &\quad \times \left. \sum_{m=1}^{\infty} \frac{k^m}{\{1 + (2mz/2n\ell)^2\}^{1/2}} \right]\end{aligned}$$

The apparent resistivity is given by

$$\rho_a = \rho_1(1 + D_d) \quad (8.40a)$$

where  $(1 + D_d)$  is the expression inside the large square brackets above.

If we make  $n \gg 1$ , the preceding result is simplified and we can make use of Equation (8.21). Differentiating twice,

$$\begin{aligned}\frac{\partial^2 V}{\partial r^2} &= \frac{I\rho_1}{\pi r^3} \left[ 1 - \sum_{m=1}^{\infty} \frac{k^m}{\{1 + (2mz/r)^2\}^{3/2}} \right. \\ &\quad \left. + 3 \sum_{m=1}^{\infty} \frac{k^m}{\{1 + (2mz/r)^2\}^{5/2}} \right]\end{aligned}$$

and using Equation (8.36),

$$\begin{aligned}\rho_a &= \rho_1 \left[ 1 - \sum_{m=1}^{\infty} \frac{k^m}{\{1 + (2mz/r)^2\}^{3/2}} \right. \\ &\quad \left. + 3 \sum_{m=1}^{\infty} \frac{k^m}{\{1 + (2mz/r)^2\}^{5/2}} \right] \\ &= \rho_1(1 + D'_d)\end{aligned}\quad (8.40b)$$

(e) Discussion of theoretical results. Quantitatively we can see how the apparent resistivity varies from Equation (8.38) through (8.40) for the different electrode spreads. When the electrode spacing is very small, that is,  $r \ll z$ , the series terms in all cases tend to zero, so that we measure the resistivity in the upper formation. This is the surface resistivity defined in Section 8.5.2.

Because the reflection coefficient is less than unity, when the  $C-P$  electrode spacing is very large compared to  $z$ , the depth of the bed, the series expansions in all of the equations becomes the same (because the denominators  $\approx 1$  or 2):

$$\rho_a \approx \rho_1 \left( 1 + 2 \sum_{m=1}^{\infty} k^m \right) \quad (8.41)$$

Because  $k^2 < 1$ , the summation term is an infinite geometric progression with the value

$$\sum_{m=1}^{\infty} k^m = 1/(1-k) - 1$$

Substituting  $k = (\rho_2 - \rho_1)/(\rho_2 + \rho_1)$ , we get  $\rho_a = \rho_2$ . Thus at very large spacing, the apparent resistivity is practically equal to the resistivity in the lower formation.

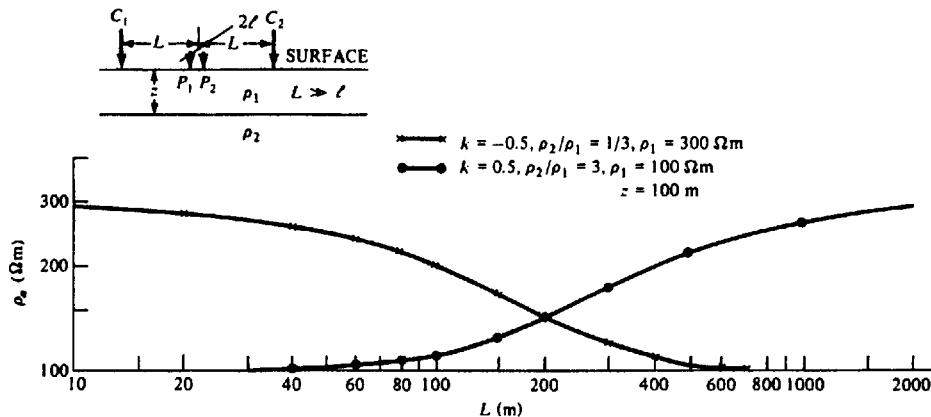


Figure 8.20. Plots of  $\rho_a$  versus  $L$  over two horizontal beds for a Schlumberger expanding spread. Curves were calculated from Equation (8.39b).

When the lower bed is an insulator,  $\rho_2 = \infty$  and  $k = 1$ . Then the apparent resistivity increases indefinitely with electrode spacing, as is obvious from Equation (8.41). Because all the current will flow in the upper bed, it is possible to determine the value of  $\rho_a$  when  $\rho_2 = \infty$  by calculating the electric field at the midpoint of the current electrodes. Because their separation is much larger than the thickness of the upper bed, it is reasonable to assume a uniform current density from top to bottom. Then the current from either electrode is found by integrating over a cylindrical equipotential surface of radius  $r$  and height  $z$ . Thus,

$$I = \int_0^{2\pi} \int_0^r J r d\theta dz = 2\pi r z J$$

From Equation (8.1) we have in this case (noting that the current is doubled because there are two current electrodes)

$$E = 2\rho_1 J = \rho_1 I / \pi r z$$

For the Wenner array, we get an apparent resistivity [Eq. (8.27)]

$$\begin{aligned} \rho_a &= \frac{2\pi a \Delta V}{I} = \frac{2\pi a}{I} \int_a^{2a} E dr = \left( \frac{2a\rho_1}{z} \right) \ln 2 \\ &= 1.39 \left( \frac{a\rho_1}{z} \right) \end{aligned} \quad (8.42a)$$

For the Schlumberger layout, using Equation (8.34) with  $L = r$ , we get

$$\rho_a = \frac{\pi L^2}{I} \frac{\partial V}{\partial r} = \frac{L\rho_1}{z} \quad (8.42b)$$

and for the double-dipole system, Equation (8.36) gives

$$\rho_a = - \left( \frac{\pi r^3}{I} \right) \frac{\partial^2 V}{\partial r^2} = \frac{r\rho_1}{2z} \quad (8.42c)$$

where  $r$  is the distance between centers of the current and potential dipoles.

In all three spreads we have

$$\rho_a/\rho_1 = c(\text{electrode spacing}/\text{depth to interface}) \quad (8.42d)$$

where the constant  $c$  varies with the type of spread. Thus if we plot  $\rho_a/\rho_1$  versus  $a/z$ ,  $L/z$ , or  $r/z$  under these conditions, the curve is a straight line.

On the other hand, if the lower bed is a very good conductor,  $\rho_2 \approx 0$  and  $k \approx -1$ . In this case  $\rho_a \approx \rho_2 \approx 0$  for large spacing.

(f) Crude interpretation. Before applying the more complicated methods of interpretation it is useful to consider a few rough ideas. Figure 8.20 shows a pair of resistivity curves for two layers with contrasts of 3 and  $\frac{1}{3}$ . The upper bed resistivity is 100 and 300  $\Omega\text{m}$  for the two cases (to put the two curves on the same ordinate scale), and the thickness is 100 m.

The curve for  $\rho_2/\rho_1 = \frac{1}{3}$  is clearly asymptotic to  $\rho_1$  and  $\rho_2$  at the limits of small and large spacing, and its point of maximum slope is approximately at 100 m. Thus we can estimate the depth and the resistivities of the two beds for this simple example.

The other curve gives the upper layer resistivity at small spacing, but it is not so clear what the value of  $\rho_2$  may be. If the spacing were increased to several kilometers, it would be asymptotic to 300  $\Omega\text{m}$ . The

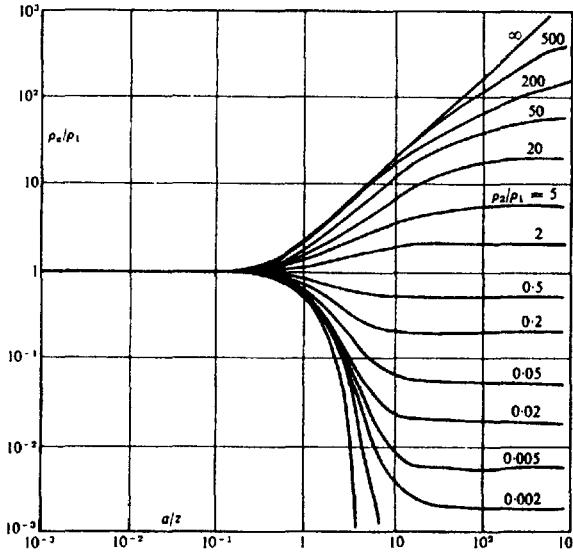


Figure 8.21. Wenner spread - master curves for two horizontal beds. (From Keller and Frischknecht, 1966.)

point of inflexion is not at 100 m but at a larger spacing.

Approximately then, we can get some idea of the unknown parameters  $\rho_1$  and  $\rho_2$  and  $z$  from the field curve, provided the resistivity contrast is not too great and particularly if the lower bed is the more conductive of the two.

(g) *Curve matching.* A much more accurate and dependable method of interpretation in electric sounding involves the comparison of field profiles with characteristic curves. It is quite similar to the interpretation from master curves in magnetotellurics, described in Section 6.2.8b.

The master curves are prepared with dimensionless coordinates. Equations (8.38) to (8.40) can be put in this form by dividing  $\rho_a$  by  $\rho_1$ . The ratios  $\rho_a/\rho_1$  are then plotted against  $a/z$ ,  $L/z$ , or  $r/z$ , that is, the electrode spacing divided by the depth of the upper bed for whatever electrode system is used. The curves are on logarithmic paper, usually six decades each way to provide a large range of both ratios on one sheet. Thus we are plotting  $(\log \rho_a - \log \rho_1)$  against  $(\log a - \log z)$ . If we make  $\rho_1 = 1 \Omega\text{m}$  and  $z = 1 \text{ km}$ , all the characteristic curves are preserved in shape. The sets of curves are constructed either for various values of  $k$  between  $\pm 1$  or for various ratios of  $\rho_2/\rho_1$  between 0 and  $+\infty$ . A typical set of curves is shown in Figure 8.21.

The characteristic curves are generally drawn on a transparency. To match a field result it is only neces-

sary to slide the master sheet around on the field profile until the latter coincides more or less with one of the master curves (or can be interpolated between adjacent master curves). The respective coordinate axes must be kept parallel. The point where  $\rho_a/\rho_1 = a/z = 1$  on the master sheet then determines the values of  $\rho_1$  and  $z$  on the field curve axes, while the actual curve fit gives the value of  $k$  and hence  $\rho_2$ .

(h) *Interpretation by asymptotes.* In the event that the lower bed has very large resistivity we saw in Section 8.6.3e that the characteristic two-layer curve becomes a straight line for large electrode spacing. In the logarithmic plots this line has a slope of  $45^\circ$  for all of the arrays considered, because we have made  $\rho_1$  and  $z$  unity.

The master curves are not necessary in this case. After plotting the field profile on log-log paper, a straight edge is placed horizontally as a best fit along the left-hand portion of the curve. The intersection of this straight edge with the  $\rho_a$  axis gives  $\rho_1$ . Next the hypotenuse of a  $45^\circ$  triangle is fitted to the sloping part of the curve on the right-hand side of the profile. The interface depth can then be found on the horizontal axis from the intersection of the triangle and the horizontal straight edge. This procedure is illustrated in Figure 8.22.

The asymptote method may also be used even when the maximum spacing has not been large enough to establish that the bottom layer has a very

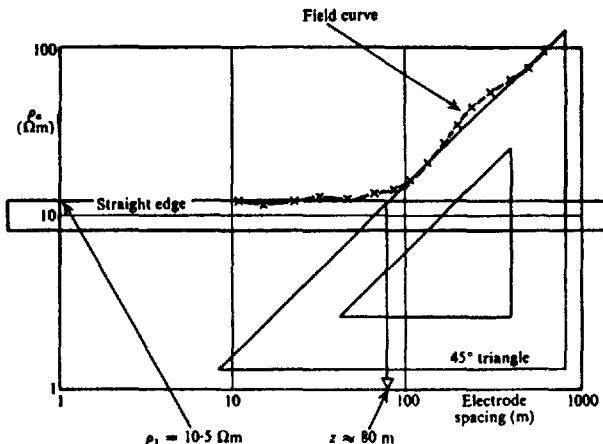


Figure 8.22. Estimate of  $\rho_a$  and  $z$  from the  $45^\circ$  asymptote. (After Keller and Frischknecht, 1966.)

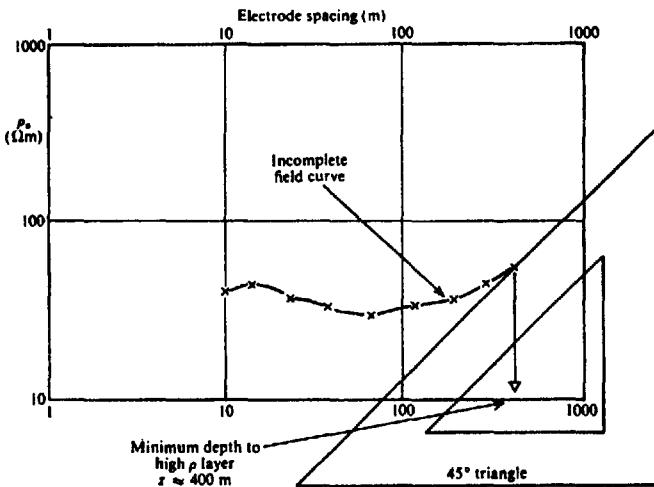


Figure 8.23. Asymptote method of estimating minimum depth.

high resistivity. In this case the  $45^\circ$  triangle is placed to intersect the point of maximum spacing as, for example, in Figure 8.23. In this case the depth estimate can only be a minimum.

#### 8.6.4. Vertical Sounding; Multiple Horizontal Beds

(a) *Introduction.* When there are more than two horizontal beds present, as is usually the case, the previously mentioned single overburden analysis is first used for relatively small electrode spacing. This gives the depth and resistivity of the upper layer.

Next it is possible to estimate the minimum conductance of all layers above the bottom by drawing

the  $45^\circ$  line through the point given for maximum electrode separation, as shown in Figure 8.23. The ratio of spacing to  $\rho_a$  for any point on this line will be a conductance representing all the rocks above an insulating layer; in Figure 8.23, for example, it is about 9 S. If the right-hand extreme of the field profile is itself a  $45^\circ$  line on the log-log plot, the bottom layer is highly resistive. In this case the actual, rather than minimum, conductance is determined.

(b) *Crude interpretation.* The overall shape of the middle portion of the profile will give us some idea of the character of the beds between surface and basement. Several shapes are illustrated in Figure

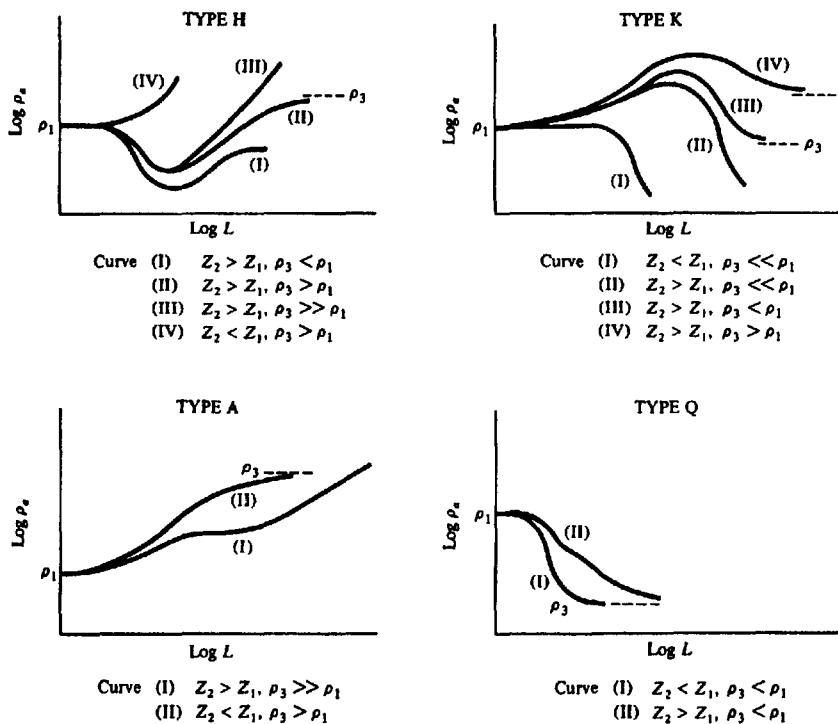


Figure 8.24. Various types of sounding curves over multilayer structures of three or more beds.

8.24. Types *H* and *K* have a definite minimum and maximum, indicating a bed, or beds, of anomalously low or high resistivity, respectively, at intermediate depth. Types *A* and *Q* show fairly uniform change in resistivity, the first increasing, the second decreasing with depth. Obviously these curves also may be combined. It is generally possible to tell from the shape of the adjacent parts of the profile which layer corresponds to the maximum or minimum on the first two curve types.

Although, in general, the characteristic sounding curves illustrated in Figure 8.24 represent multiple layers, in their crudest form they may be considered to be for two beds over a basement. On this assumption each of the four sets has particular properties that may be roughly classified. For *H*- and *K*-type curves  $\rho_1 > \rho_2 < \rho_3$  and  $\rho_1 < \rho_2 > \rho_3$ , respectively, and we may be able to draw some conclusions about the relative values of  $\rho_1$  and  $\rho_3$  if the spread has been extended sufficiently. The *A*- and *Q*-type curves correspond to  $\rho_1 < \rho_2 < \rho_3$  and  $\rho_1 > \rho_2 > \rho_3$ , respectively. Some idea of the relative bed thicknesses may be obtained from the horizontal extent of the

maxima and minima as well as the flanking portions in all cases.

(c) *Use of maximum and minimum points.* The coordinates of the extreme points in curves of types *H* and *K*, Figure 8.24 (i.e., maximum or minimum  $\rho_a$  and electrode separation) may be used with certain characteristic curves for three layers employing a particular electrode spread. Figure 8.25 shows a set for the Schlumberger array in which: (a)  $\rho_a(\text{max})/\rho_1$  is plotted against  $\rho_2/\rho_1$  for various values of  $z_2/z_1$  and (b) the ratio  $L(\text{max})/z_1$  is plotted against  $z_2/z_1$  for various values of  $\rho_2/\rho_1$ ,  $L(\text{max})$  being the electrode spacing at which  $\rho_a$  is a maximum or minimum.

Because we know the value of  $\rho_a(\text{max})/\rho_1$  and  $L(\text{max})/z_1$  (presumably  $\rho_1$  and  $z_1$  can be found from a two-layer curve match on the left of the profile), horizontal lines drawn across the characteristics in Figure 8.25a and b give two sets of possible values of  $\rho_2/\rho_1$  and  $z_2/z_1$ , corresponding to the intersections. If we now plot these values of  $z_2/z_1$  versus  $\rho_2/\rho_1$ , we get two curves which intersect at

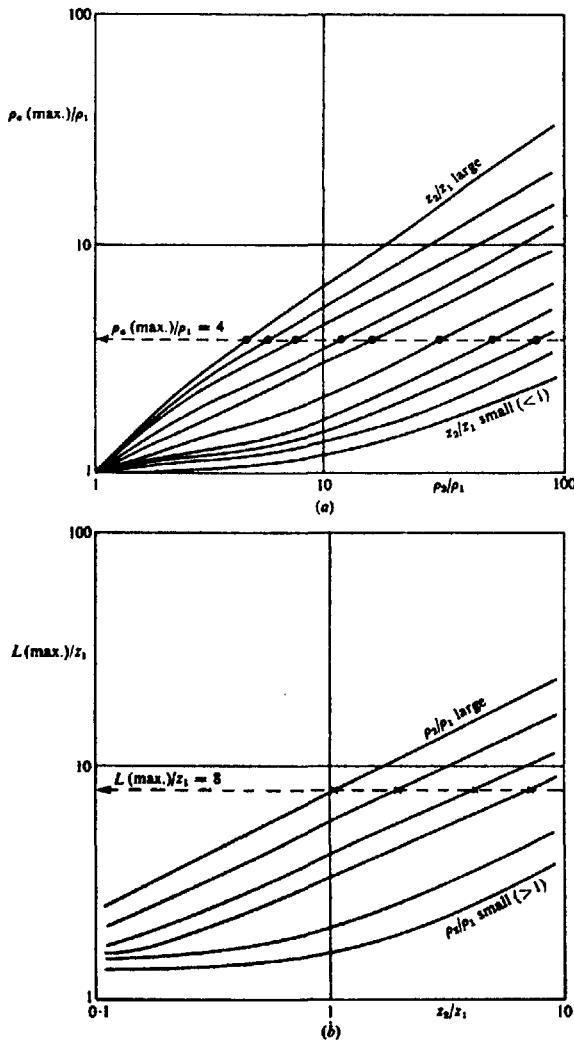


Figure 8.25. Schlumberger array - characteristic curves for three layers with type-K curves (see Fig. 8.24). (After Keller and Frischknecht, 1966.) (a) Plots of  $\rho_a(\text{max.})/\rho_1$  versus  $\rho_2/\rho_1$  for various  $z_2/z_1$  ratios. (b) Plots of  $L(\text{max.})/z_1$  versus  $z_2/z_1$  for various  $\rho_2/\rho_1$  ratios.

one point. This point represents the correct values of  $z_2$  and  $\rho_2$  for the layer in question as shown in Figure 8.26.

(d) *Partial curve matching.* This technique requires matching of small segments of the field profile with theoretical curves for two or, if possible, three horizontal layers. Generally one would start from the left-hand (small spacing) side of the profile and match successive segments toward the right (large spacing). When a portion of the field curve is reason-

ably matched in this way, all the layers in this segment are lumped together and assumed to have an effective resistivity  $\rho_e$  and depth  $z_e$ . This lumped layer is used as a surface layer and the next portion of the field curve is interpreted in a similar way.

It would be quite impractical to slide the field curve on the master randomly in attempting to find a reasonable fit between the segments of the curves. The process requires that we know where to locate the origin (for example, where  $\rho_a/\rho_1 = L/z_1 = 1$  on the master two- or three-layer curve) with respect to

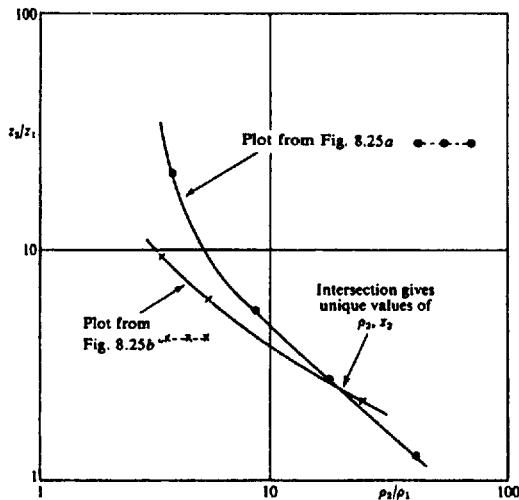


Figure 8.26. Determining second-layer parameters using data from Figure 8.25. (After Keller and Frischknecht, 1966.)

the field curve to obtain the best fit to successive portions of the latter as we progress from left to right. This interim origin is known as the *auxiliary point* or *cross* in the literature (Hummel, 1932; Zohdy, 1965; Bhattacharya and Patra, 1968). To illustrate the significance of these auxiliary points, consider a modification of Figure 5.1 and Equations (5.8) and (5.9). If we change Figure 5.1 so that it represents a vertical stack of beds with resistivities  $\rho_1, \rho_2, \dots, \rho_n$  and thicknesses  $z_1, z_2, \dots, z_n$  from top to bottom, and cross section  $1 \text{ m}^2$ , then  $v$  and  $1 - v$  in Equations (5.8) and (5.9) are proportional to the thicknesses.

Analogous to Equations (5.8) and (5.9) we have in the vertical direction a so-called *transverse unit resistance*

$$T = \rho_1 z_1 + \rho_2 z_2 + \dots + \rho_n z_n = \sum_{i=1}^n \rho_i z_i \quad (8.43a)$$

and in the horizontal direction a *longitudinal unit*

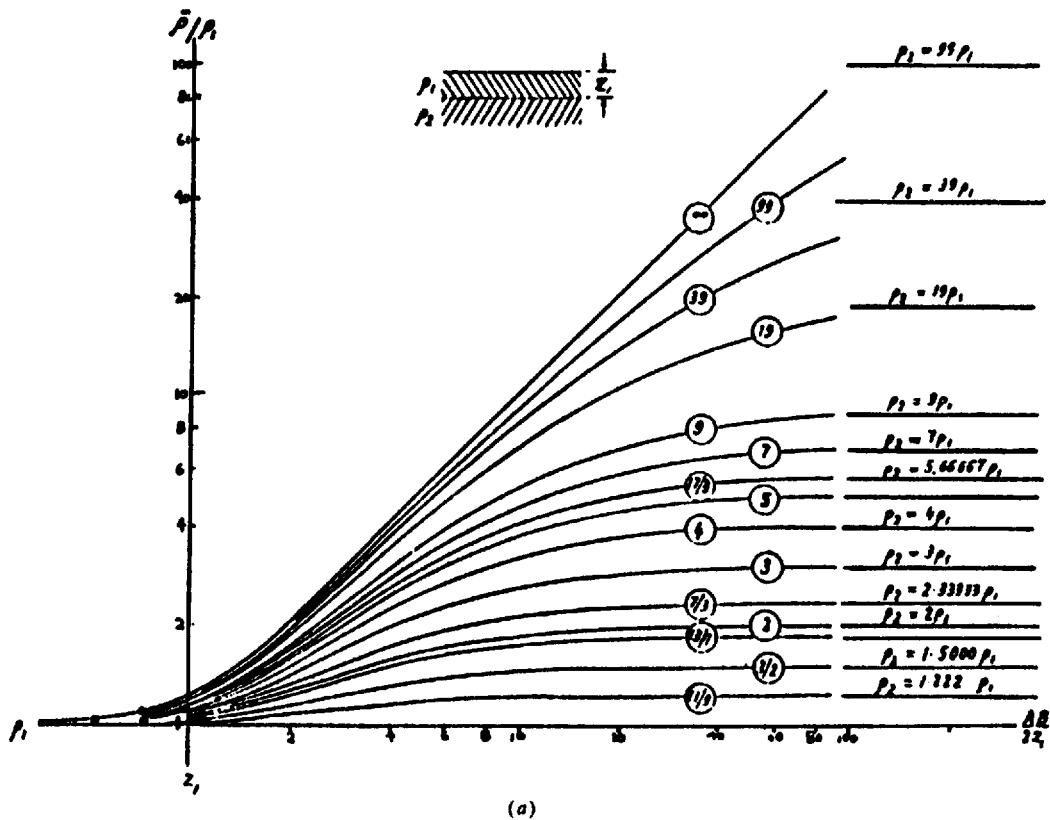


Figure 8.27. Two-layer Schlumberger master curves. (a) Ascending type ( $\rho_2 > \rho_1$ ).

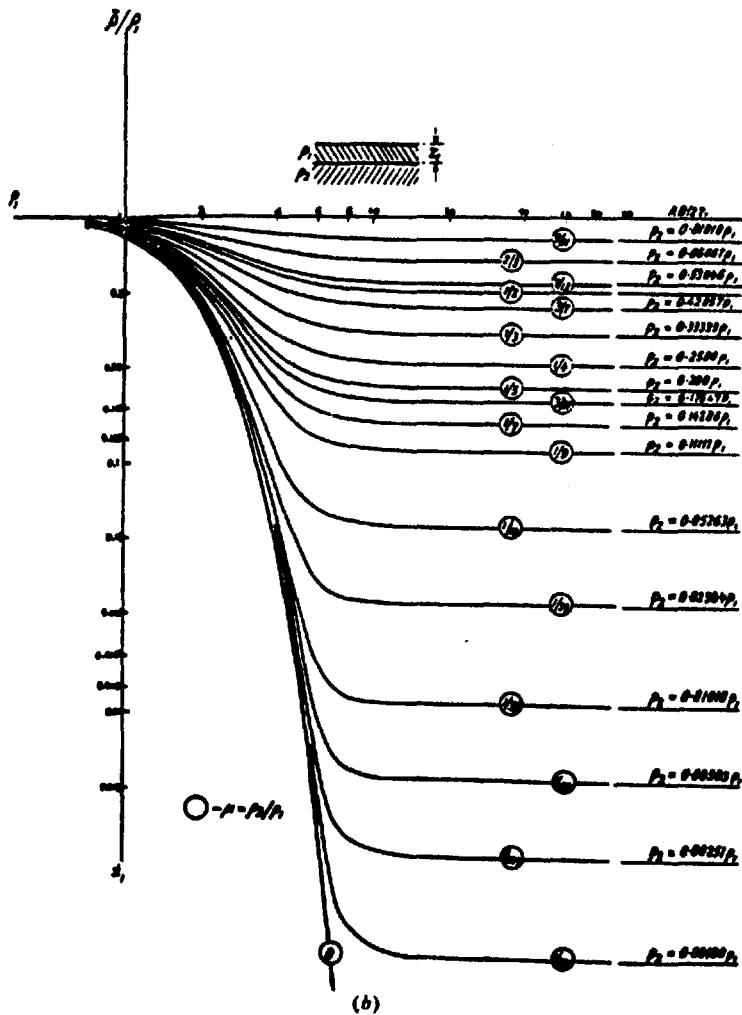


Figure 8.27. (Continued) (b) Descending type ( $\rho_2 < \rho_1$ ).

conductance

$$S = z_1/\rho_1 + z_2/\rho_2 + \cdots + z_n/\rho_n = \sum_{i=1}^n z_i/\rho_i \quad (8.43b)$$

The vertical and horizontal resistivities are

$$\rho_v = T/z_e \quad \rho_h = z_e/S \quad (8.44a)$$

where  $z_e = \sum z_i$ .

This column is indistinguishable from a single isotropic layer with resistivity and thickness  $\rho_m = (T/S)^{1/2}$ ,  $z_{eq} = z_e \lambda = (TS)^{1/2}$  [see Eq. (8.44b) below]. The quantities  $T$  and  $S$  are known as the *Dar Zarrouk parameters* and have many interesting properties (Maillet, 1947; Orellana, 1963). For example, the block can be considered anisotropic with an average square resistivity  $\rho_m$  and pseudoanisotropy  $\lambda$

given by [compare with Eqs. (8.24) and (8.25)]

$$\rho_m = (\rho_v \rho_h)^{1/2} \quad \lambda = (\rho_v / \rho_h)^{1/2} \quad (8.44b)$$

Applying the preceding results to the case of two beds, we change  $\rho_h$  to  $\rho_{e2}$ ,  $z_e$  to  $z_{e2}$  in Equation (8.44a) and get

$$S = z_{e2}/\rho_{e2} = z_1/\rho_1 + z_2/\rho_2 \quad (8.45)$$

This expression relating the parameters of two individual beds to those of a single equivalent bed allows us to prepare auxiliary charts to complement the master curves, by plotting  $(\rho_2/\rho_1)$  versus  $(z_e/z_1)$  on log-log scales identical to the master. These are shown in Figure 8.28; the first is used with *H*- and *A*-type, the second with *K*- and *Q*-type curves. A

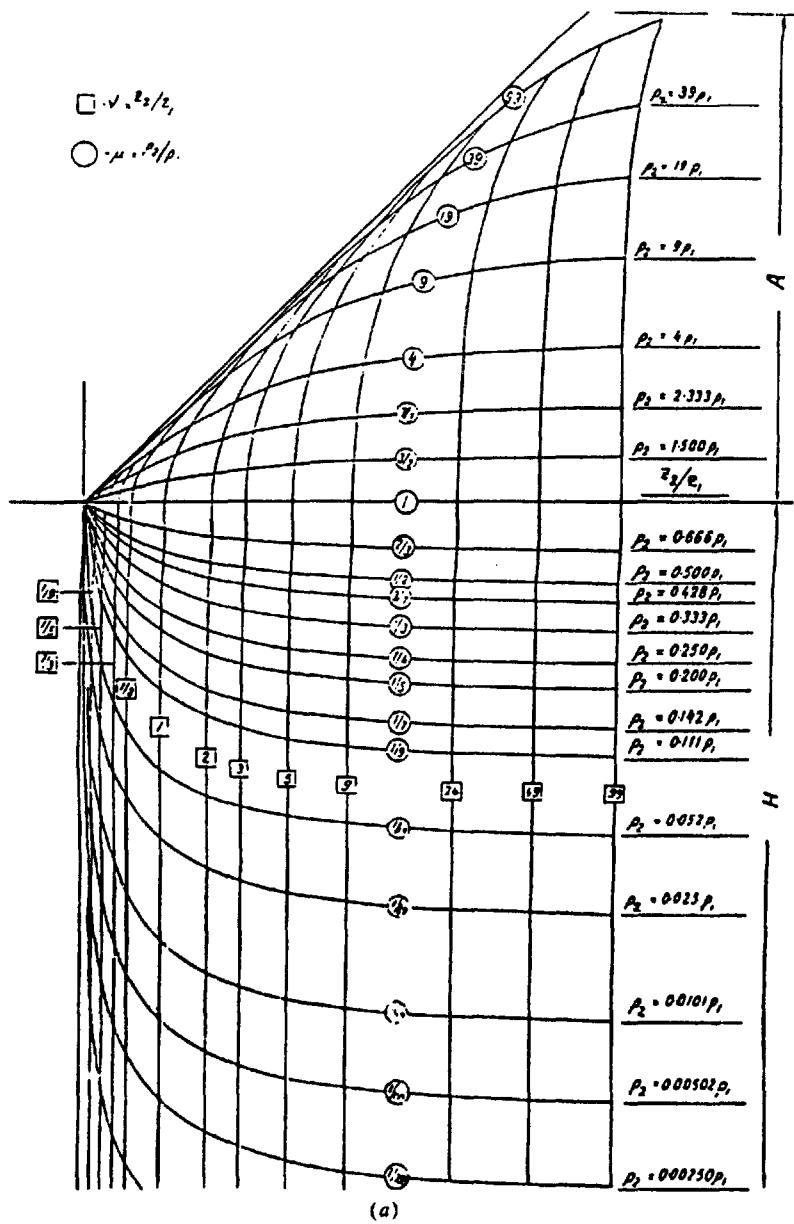


Figure 8.28. Auxiliary-point charts (a) for H- and A-type sounding curves.

pair of Schlumberger two-layer master curves on the same scale, shown in Figure 8.27, are included for reference. (Note the change in symbols:  $\bar{\rho} = \rho_a$ ,  $AB = 2L$ .)

The procedure for matching successive left-to-right segments of a field sounding is as follows:

1. The left-hand portion of the field sounding curve, plotted on a transparency of identical log-log scale, is fitted to as many points as possible on the

master, maintaining the respective axes parallel. This fit provides the location of the first cross or auxiliary point where the field sheet coincides with  $\rho_1 = L = 1$ , the origin on the master. Hence we obtain  $\rho_1$ ,  $z_1$ , whereas the best-fit segment gives  $(\rho_2/\rho_1)$  or  $\rho_2$ . [This segment may be extended beyond the fitted portion along the  $(\rho_2/\rho_1)$  line with pencil for a check on the next step.]

2. The sounding curve is transferred to the appropriate auxiliary curve set where the cross is placed at

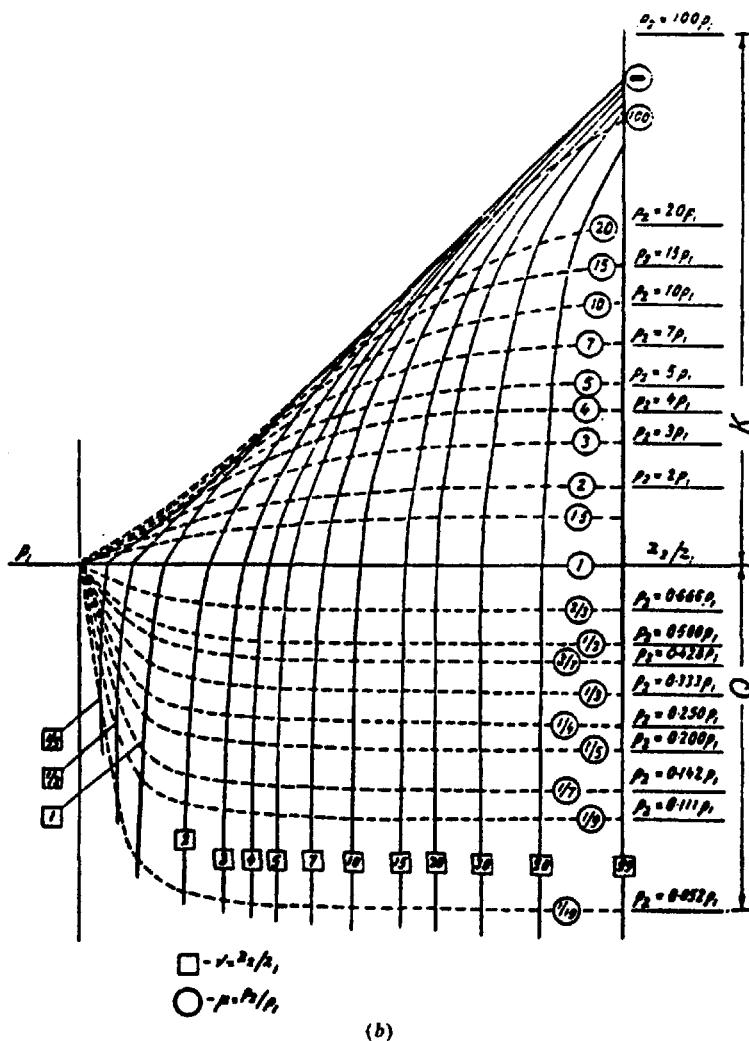


Figure 8.28. (Continued) Auxiliary-point charts (b) for K- and Q-type sounding curves.

the origin and the same  $(\rho_2/\rho_1)$  curve of the auxiliary as that in step 1 is drawn in pencil on the sounding.

3. Replacing the sounding curve on the master and maintaining the  $(\rho_2/\rho_1)$  line from step 2 on the master origin, a second master segment further to the right is fitted to the sounding curve. The second cross is marked over the master origin, giving  $\rho_{e2}$  and  $z_{e2}$  where  $z_{e2} = z_1 + z_2$  and  $\rho_{e2}$  is related to the other parameters by Equation (8.45), that is,

$$z_{e2}/\rho_{e2} = (z_1 + z_2)/\rho_{e2} = z_1/\rho_1 + z_2/\rho_2$$

(Clearly  $\rho_{e1} = \rho_1$  and  $z_{e1} = z_1$  at the first cross.)

We also obtain  $(\rho_3/\rho_{e2})$  and hence  $\rho_3$  from the fitted segment.

4. The sounding curve is returned to the auxiliary and step 2 is repeated.
5. Repeat step 3 to get  $\rho_{e3}$ ,  $z_{e3}$ , as well as  $\rho_4$  from the third cross.
6. Repeat steps 4 and 5 until the sounding curve is completely fitted.

[A check on the  $(\rho_e, z_e)$  values may be taken at any juncture, using the relation in step 3. Also the minimum conductance may be found (Fig. 8.23) and employed for the same purpose.]

If three-layer master curves are available (Compagnie Générale de Géophysique, 1955), it is preferable to use them if the field curve warrants this. The

procedure is similar to the steps 1 to 6, noting the following.

7. The first cross and match gives  $\rho_1$ ,  $\rho_2$ ,  $z_1$ ,  $z_{e2}$  (hence  $z_2$ ),  $\rho_{e2}$ .
8. The second cross, equivalent to the third in step 5, locates  $\rho_{e3}$ ,  $z_{e3}$ , from which  $\rho_3$  may be determined by the relation

$$z_{e3}/\rho_{e3} = z_1/\rho_1 + z_2/\rho_2 + z_3/\rho_3$$

$z_3$ ,  $z_{e4}$ ,  $z_4$ , and  $\rho_4$  are also obtained.

9. The third cross corresponds to the fifth, if it exists in the two-layer analysis, and so on.

It should be noted that this procedure gives good results only if the bed thicknesses increase rapidly with depth; in fact, each successive layer should be thicker than the total thickness above it ( $z_4 > z_{e3}$ , etc.). Correction factors for the auxiliary charts (Kunetz, 1966; Keller and Frischknecht, 1966) reduce the effect of this limitation considerably. For example, type-*A* curves require that  $z'_e = \lambda(z_1 + z_2)$ , that is, the lumped layer is thicker than the sum of the individuals (because  $\lambda = (\rho_e/\rho_h)^{1/2} > 1$ —see §8.3.6). For type-*K* curves the correction is still greater by a factor  $\eta$  which increases nonlinearly from 1 to 1.5 as  $\lambda$  increases from 1 to 3.

With *Q* curves we find that  $z'_e = (z_1 + z_2)/\eta$  and  $\rho'_e = \rho_e\eta$ ; the correction factor varies from 1 to 1.25 in the same sense as both  $z$  and  $\rho$ . Modifications for *H*-type curves appear to be unnecessary.

An example of partial curve matching is shown in Figure 8.29a from a groundwater sounding in Sri Lanka. Overall resistivity is unusually uniform and high. Subsequent drilling produced a dry well.

The crosses are marked on the sounding curve for both two- and three-layer analysis. The curve is erratic beyond 20 m which probably indicates noisy field readings. In any case, resistivity increases with depth.

The technique of partial curve matching, although rather crude compared to complete analysis of the sounding curve by computing methods, is quite useful in the field to keep abreast of daily measurements and as a control for the more sophisticated approach later.

(e) *Complete curve matching.* The expression for surface potential over two beds, Equation (8.21), may be expressed in integral form as

$$V = (I\rho_1/2\pi r) \left\{ 1 + 2r \int_0^\infty K(\lambda) J_0(\lambda r) d\lambda \right\} \quad (8.46)$$

where  $K(\lambda) = k \exp(-2\lambda z)/(1 - k \exp(-2\lambda z))$

and  $J_0$  is the zero order Bessel function. This expression is suitable for solving any number of layers (see Keller and Frischknecht, 1966; Zohdy, 1973). Employing the Schlumberger array (which is most convenient for vertical sounding and also measures potential gradient), we may write the resistivity relation in the form [see Eq. (8.39b)]

$$\rho_a = \rho_1 \left\{ 1 + 2L^2 \int_0^\infty K(\lambda) J_1(\lambda L) \lambda d\lambda \right\} \quad (8.47)$$

where  $J_1(\lambda L) = -J'_0(\lambda L)$  is the first order Bessel function.  $J'_0$  is the first derivative of  $J_0$  and we have replaced  $r$  by  $L$ , half the current electrode separation. The product  $K(\lambda)J_1(\lambda L)$  is known as the *Stefanescu function*.

The solution of this general expression may be obtained by expanding the integral as an infinite series or by numerical integration, both methods being suitable for computer programming. These and other methods are described in the literature (Ghosh, 1971; Inman, Ryu, and Ward, 1973; Johansen, 1975, 1977). Because an enormous number of theoretical models will fit the field data from an average sounding curve within  $\pm 5\%$  (which is quite within the data accuracy; see next section), some optimization technique for determining the limits on the parameters providing the curve match is necessary in practice. This additional feature is included in the methods of Inman, Ryu, and Ward, and Johansen. An example that employs a program somewhat similar to those is shown in Figure 8.29b.

(f) *Sounding interpretation errors.* Practically there are often erratic variations in field sounding measurements of  $\rho_a$  due to local resistivity changes near surface and poor electrode contacts. In addition, anisotropic ground and terrain effects will lead to errors in estimating both  $z$  and  $\rho$ .

An expanding spread, in homogeneous ground, parallel and adjacent to a vertical contact will give a profile that is somewhat similar to that obtained over horizontal layers, particularly if the bed on the other side of the contact has low resistivity (Fig. 8.34c, §8.6.5d). In all depth-probing operations the expanding spread should be carried out in at least two azimuths, a sound preliminary procedure in any case.

An example of pronounced topography effect is shown in Figure 8.30. Apparent resistivities were obtained from an expanding Wenner system over relatively homogeneous dolomite and limestone. The spread, however, is parallel to a 100 ft cliff, which produces a linearly increasing curve for  $\rho_a$  versus electrode separation. The bumps in curve *A* are probably the result of local variations in surface resistivity near the cliff edge. Obviously this is an

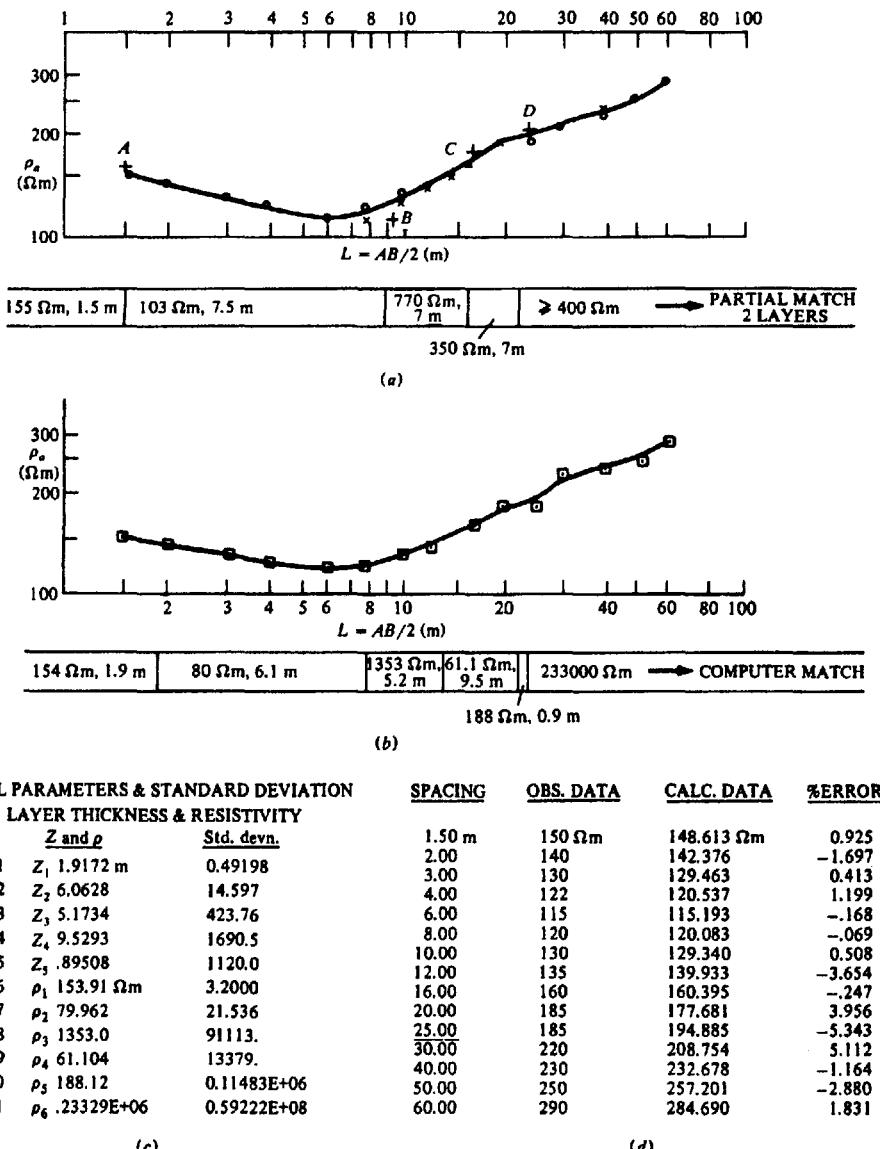


Figure 8.29. Examples of partial and complete curve matching of field soundings for groundwater, Sri Lanka. (a) Partial curve matching (two layers). (b) Complete curve matching. (c) Computer results for complete curve matching using six layers. (d) Comparison of observed  $\rho_s$  and  $\rho_a$  calculated from the data in (c).

extreme case, but the curves would be similar if the cliff face were a contact and the void filled with high resistivity rock. In the latter case the result could be erroneously interpreted as a subsurface layer of high resistivity.

The effect of dipping beds is not serious in sounding operations unless the sounding array is normal to

strike and particularly if the spread crosses over an outcrop of the dipping bed. Parallel to strike the  $z$  values will be those of the point directly below the array, and with a large enough separation of electrodes the response may become similar to that in Figure 8.30. The double-dipole array is said to be more sensitive to dipping beds than Schlumberger

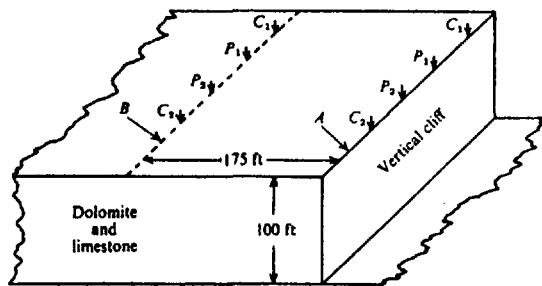
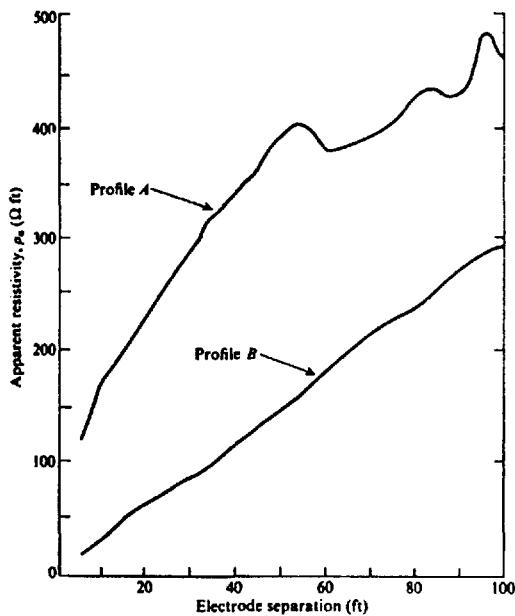


Figure 8.30. Effect of topography on expanding Wenner spread.

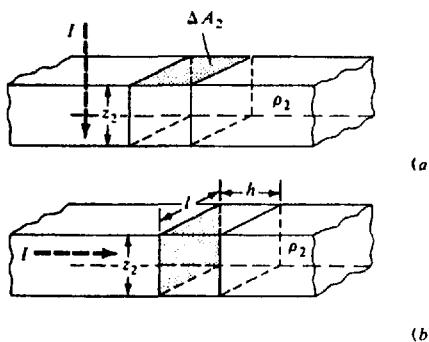


Figure 8.31. The equivalence principle (schematic). (a)  $\rho_1 < \rho_2 > \rho_3$ .  $\rho_2 z_2 = \text{constant}$ . (b)  $\rho_1 > \rho_2 < \rho_3$ .  $\rho_2/z_2 = \text{constant}$ .

and Wenner configurations. Again, to determine the dip it is necessary to measure  $\rho_a$  in two orthogonal directions.

Aside from the preceding errors which are related to the field work, ambiguity in sounding interpretation may arise owing to two factors. The first, known as the *principle of equivalence*, may be stated as follows: it is impossible to distinguish between two highly resistive beds of different  $z$  and  $\rho$  values if the product  $z\rho$  is the same, or between two highly conductive beds if the ratio  $z/\rho$  is the same. In Figure 8.31a the block of cross section  $\Delta A$  offers a resistance to vertical current flow given by  $R = \rho_2 z_2 / \Delta A$ ; thus layers having an identical product  $z\rho$  are equivalent and we cannot determine the two parameters separately. In the conductive bed of Figure 8.31b, the vertical current is deflected almost normal to the vertical stack, making  $R = \rho_2 h / z_2 l$ . Thus beds having the same ratio  $\rho/z$  are equivalent so that again  $\rho$  and  $z$  cannot be measured separately.

For either of these configurations the bed thickness and resistivity may vary within wide limits with respect to layers above and below it. However, these limits may be found by optimization methods as mentioned in Section 8.6.4e.

Some feeling for the wide limits of equivalence may be obtained from the examples of three-bed equivalent curves displayed in Figure 8.32, parts (a) and (b) being for types *A* and *H*, parts (c) and (d) for types *K* and *Q* sections analogous to the auxiliary curves in Figure 8.28. The dashed 45° slope lines represent equal  $S_2/S_1$  ratios, whereas the solid-line curves are limiting values of  $\rho_2/\rho_1$  and  $z_{\epsilon 2}/z_1$  for equivalence within  $\pm 5\%$ .

To illustrate the application consider the hatched area in the *H*-type section of Figure 8.32b. An approximate match produced the circle in the shaded square at  $\rho_2/\rho_1 = 1/39$ ,  $z_{\epsilon 2}/z_1 = 3$ . The minimum and maximum limits for the equivalence are at the corners of the square. Hence  $1.6 < z_{\epsilon 2}/z_1 < 4.2$ ,

$$\begin{aligned}
 &\text{(a)} \quad \begin{array}{l} \text{--- } 1m \quad \rho_1 = 1 \Omega m \\ \text{--- } 1m \quad \rho_2 = 20 \Omega m \\ \text{--- } \rho_3 = 0 \end{array} \quad \equiv \quad \begin{array}{l} \text{--- } \rho_1 = 1 \Omega m \quad \text{--- } 1m \\ \text{--- } \rho_2 = 40 \Omega m \quad \text{--- } 0.5m \\ \text{--- } \rho_3 = 0 \end{array} \\
 &\text{(b)} \quad \begin{array}{l} \text{--- } 1m \quad \rho_1 = 100 \Omega m \\ \text{--- } 1m \quad \rho_2 = 5 \Omega m \\ \text{--- } \rho_3 = \infty \end{array} \quad \equiv \quad \begin{array}{l} \text{--- } \rho_1 = 100 \Omega m \quad \text{--- } 1m \\ \text{--- } \rho_2 = 2.5 \Omega m \quad \text{--- } 0.5 \Omega m \\ \text{--- } \rho_3 = \infty \end{array}
 \end{aligned}$$

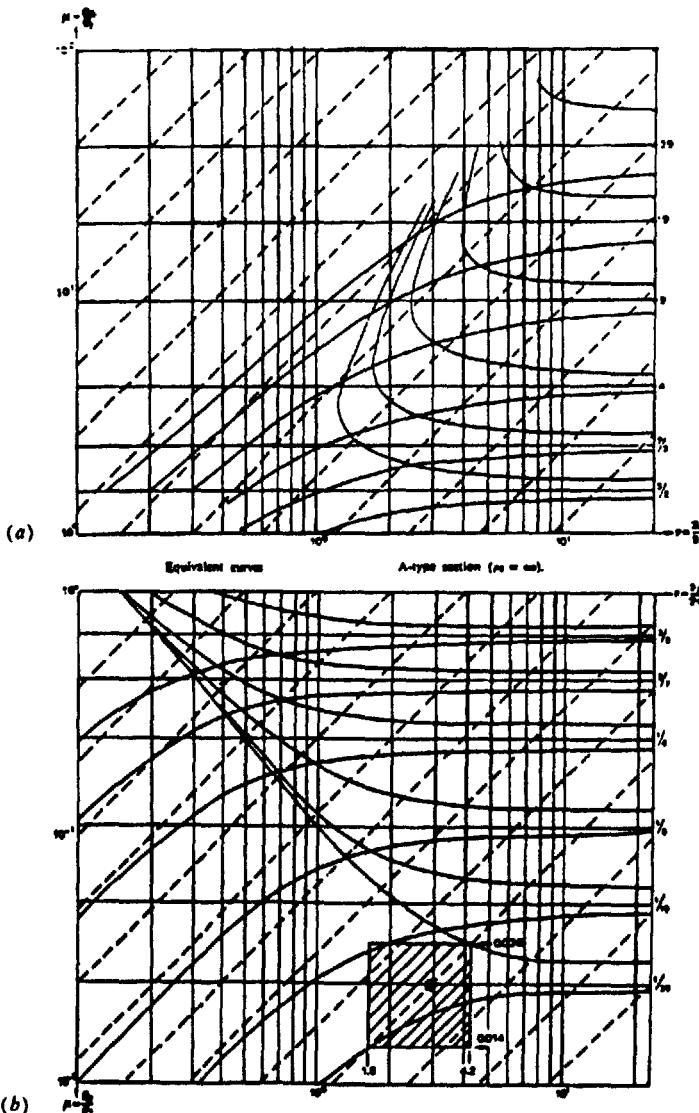


Figure 8.32. Equivalent curves. Solid-line curves are limiting values of  $\mu = \rho_2/\rho_1$  and  $\nu = z_2/z_1$  for equivalence; dashed lines are lines of equal  $S_2/S_1$  in (a) and (b), equal  $T_2/T_1$  in (c) and (d). (a) A-type section,  $\rho_3 = \infty$ . (b) H-type section,  $\rho_3 = \rho_1$ .

$0.014 < \rho_{z2}/\rho_1 < 0.038$ . Thus the same field curve section may be matched only within  $\pm 45\%$ . The limits are still wider in areas of the equivalent curves where the  $z$  ratios are smaller and/or  $\rho$  ratio estimates larger than this, as is clear from the open sections at the upper left.

The suppression principle states that if a bed is very thin compared to those above and below, its

effect on the sounding curve is insignificant unless its resistivity is extremely high or low.

#### 8.6.5. Lateral Mapping; Vertical Contact

(a) *General equations.* Also called lateral profiling, this technique is of considerable importance in mineral prospecting. It is also used for the measure-

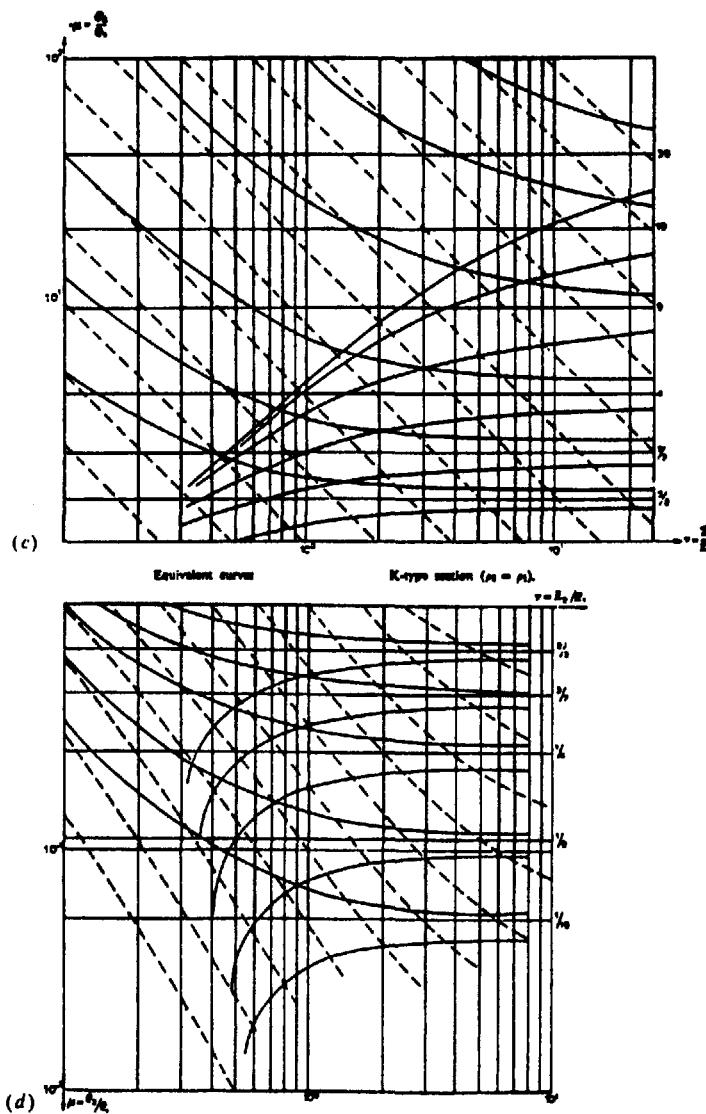


Figure 8.32. (Continued) (c) K-type section,  $\rho_2 = \rho_1$ . (d) Q-type section  $\rho_2 = 0$ .

ment of overburden depth in civil engineering work. The mineral exploration interpretation includes location of vertical contacts – faults, dikes, shear zones, and steeply dipping veins – and three-dimensional bodies of anomalous conductivity, such as massive sulfides.

In Section 8.3.3 the variation in potential crossing a plane interface was established for a single current and a single potential electrode system. Equation (8.17) gave the potential with both electrodes in the

same medium, Equation (8.18) when they were on opposite sides of the contact.

Any of the electrode arrays may be used for this type of mapping, but the profiles differ considerably from one to another. There is also a practical consideration: the traverse can be made faster and more easily if it is not necessary to move all the electrodes for each station measurement. It turns out also that the profiles are usually easier to understand as well in this case.

For the general case, with spacing  $r_1$ ,  $r_2$ ,  $r_3$ , and  $r_4$  we have five possible situations, depending on electrode positions with respect to the contact (Fig. 8.33):

(i) All electrodes on left-hand side:

$$\begin{aligned} V_1 &= \frac{I\rho_1}{2\pi} \left\{ \left( \frac{1}{r_1} + \frac{k}{2s - r_1} \right) \right. \\ &\quad \left. - \left( \frac{1}{r_2} + \frac{k}{2s - 2r_1 - r_2} \right) \right\} \\ V_2 &= \frac{I\rho_1}{2\pi} \left\{ \left( \frac{1}{r_3} + \frac{k}{2s - r_3} \right) \right. \\ &\quad \left. - \left( \frac{1}{r_4} + \frac{k}{2s - 2r_3 - r_4} \right) \right\} \\ \Delta V &= \frac{I\rho_1}{2\pi} \left[ \left( \frac{1}{r_1} - \frac{1}{r_2} \right) - \left( \frac{1}{r_3} - \frac{1}{r_4} \right) \right. \\ &\quad + k \left\{ \left( \frac{1}{2s - r_1} - \frac{1}{2s - 2r_1 - r_2} \right) \right. \\ &\quad \left. \left. - \left( \frac{1}{2s - r_3} - \frac{1}{2s - 2r_3 - r_4} \right) \right\} \right] \quad (8.48a) \end{aligned}$$

(ii)  $C_2$  on right-hand side (note that  $k$  changes sign for a current electrode to the right of the vertical contact and that there is no image of  $C_2$ ):

$$\begin{aligned} \Delta V &= \frac{I\rho_1}{2\pi} \left[ \left( \frac{1}{r_1} - \frac{1}{r_2} \right) - \left( \frac{1}{r_3} - \frac{1}{r_4} \right) \right. \\ &\quad + k \left\{ \left( \frac{1}{2s - r_1} - \frac{1}{r_2} \right) \right. \\ &\quad \left. \left. - \left( \frac{1}{2s - r_3} - \frac{1}{r_4} \right) \right\} \right] \quad (8.48b) \end{aligned}$$

(iii)  $C_2$ ,  $P_2$  on right-hand side:

$$\begin{aligned} V_1 &= \frac{I\rho_1}{2\pi} \left\{ \left( \frac{1}{r_1} + \frac{k}{2s - r_1} \right) - \frac{1+k}{r_2} \right\} \\ V_2 &= \frac{I\rho_2}{2\pi} \left\{ \frac{1-k}{r_3} - \left( \frac{1}{r_4} - \frac{k}{2r_3 + r_4 - 2s} \right) \right\} \end{aligned}$$

Using Equation (8.19) to express  $\rho_2$  in terms of  $\rho_1$ , and setting  $k^* = (1+k)/(1-k)$ , we obtain

$$\begin{aligned} \Delta V &= \frac{I\rho_1}{2\pi} \left[ \left( \frac{1}{r_1} - \frac{1}{r_2} \right) - k^* \left( \frac{1}{r_3} - \frac{1}{r_4} \right) \right. \\ &\quad + k \left\{ \left( \frac{1}{2s - r_1} - \frac{1}{r_2} \right) \right. \\ &\quad \left. \left. + k^* \left( \frac{1}{r_3} - \frac{1}{2r_3 + r_4 - 2s} \right) \right\} \right] \quad (8.48c) \end{aligned}$$

(iv)  $C_2$ ,  $P_2$ ,  $P_1$  on right-hand side:

$$\begin{aligned} V_1 &= \frac{I\rho_2}{2\pi} \left\{ \left( \frac{1}{r_1} - \frac{1}{r_2} \right) \right. \\ &\quad \left. - k \left( \frac{1}{r_1} - \frac{1}{2r_1 + r_2 - 2s} \right) \right\} \\ V_2 &= \frac{I\rho_2}{2\pi} \left\{ \left( \frac{1}{r_3} - \frac{1}{r_4} \right) \right. \\ &\quad \left. - k \left( \frac{1}{r_3} - \frac{1}{2r_3 + r_4 - 2s} \right) \right\} \\ \therefore \Delta V &= \frac{I\rho_1}{2\pi} \left[ k^* \left\{ \left( \frac{1}{r_1} - \frac{1}{r_2} \right) - \left( \frac{1}{r_3} - \frac{1}{r_4} \right) \right. \right. \\ &\quad \left. - k \left\{ \left( \frac{1}{r_1} - \frac{1}{2r_1 + r_2 - 2s} \right) \right. \right. \\ &\quad \left. \left. - \left( \frac{1}{r_3} - \frac{1}{2r_3 + r_4 - 2s} \right) \right\} \right] \quad (8.48d) \end{aligned}$$

(v) All electrodes on right-hand side:

$$\begin{aligned} V_1 &= \frac{I\rho_2}{2\pi} \left\{ \left( \frac{1}{r_1} - \frac{k}{2s + r_1} \right) \right. \\ &\quad \left. - \left( \frac{1}{r_2} - \frac{k}{2s + 2r_1 + r_2} \right) \right\} \\ V_2 &= \frac{I\rho_2}{2\pi} \left\{ \left( \frac{1}{r_3} - \frac{k}{2s + r_3} \right) \right. \\ &\quad \left. - \left( \frac{1}{r_4} - \frac{k}{2s + 2r_3 + r_4} \right) \right\} \\ \therefore \Delta V &= \frac{I\rho_1}{2\pi} \left[ k^* \left\{ \left( \frac{1}{r_1} - \frac{1}{r_2} \right) - \left( \frac{1}{r_3} - \frac{1}{r_4} \right) \right. \right. \\ &\quad \left. - k \left\{ \left( \frac{1}{2s + r_1} - \frac{1}{2s + 2r_1 + r_2} \right) \right. \right. \\ &\quad \left. \left. - \left( \frac{1}{2s + r_3} - \frac{1}{2s + 2r_3 + r_4} \right) \right\} \right] \quad (8.48e) \end{aligned}$$

If we ignore the existence of the contact, we can substitute for  $\Delta V/I$  in Equation (8.26) and get  $\rho_a$ . This gives

$$\rho_a/\rho_1 = p/p'$$

where  $1/p'$  is the quantity in square brackets in Equations (8.48) and  $p$  is the quantity in Equation (8.26) evaluated for the particular electrode spacing that holds for Equations (8.48).

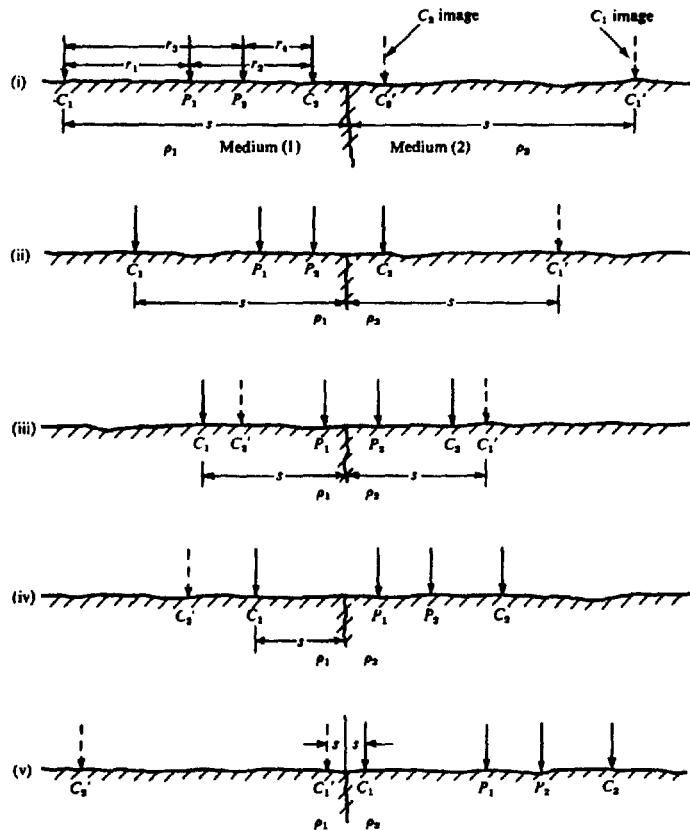


Figure 8.33. General resistivity spread over a vertical contact.

The expressions for  $\rho_a$  for the Wenner and Schlumberger arrays are cumbersome in general. We shall consider certain special cases in the following section.

(b) Half-Wenner array.  $r_1 = a$ ,  $r_2 = r_3 = r_4 = \infty$ . For the preceding configurations, the results are:

$$(i) \quad \frac{\rho_a}{\rho_1} = 1 + \{ka/(2s-a)\} \quad (8.49a)$$

$$(ii), (iii) \quad \text{Same as in (i)} \quad (8.49b, c)$$

$$(iv) \quad \frac{\rho_a}{\rho_1} = (1+k) \quad (8.49d)$$

$$(v) \quad \frac{\rho_a}{\rho_1} = k^* \left( 1 - \frac{ka}{2s+a} \right) \quad (8.49e)$$

(c) Half-Schlumberger array.  $r_1 = L - \ell$ ,  $r_3 = L + \ell$ ,  $r_2 = r_4 = \infty$ ,  $L \gg \ell$ .

$$(ii) \quad \text{Same as in (i)} \quad (8.50b)$$

$$(iii) \quad \frac{\rho_a}{\rho_1} = 1 + \frac{k(L-s)(L-\ell)}{\ell(2s-L+\ell)} \quad (8.50c)$$

$$(iv) \quad \frac{\rho_a}{\rho_1} = 1 + k \quad (8.50d)$$

$$(v) \quad \frac{\rho_a}{\rho_1} \approx k^* \left\{ 1 - \frac{kL^2}{(2s+L)^2} \right\} \quad (8.50e)$$

(d) Double-dipole array. (Potential electrodes to right of current pair.)  $r_1 = r_4 = r$ ,  $r_2 = r - \ell$ ,  $r_3 = r + \ell$ ,  $r \gg \ell$ .

(i) All four electrodes on left-hand side:

$$(i) \quad \frac{\rho_a}{\rho_1} \approx 1 - \frac{kL^2}{(2s-L)^2} \quad (8.50a)$$

$$\frac{\rho_a}{\rho_1} \approx 1 - \frac{kr^3}{(2s-r)^3} \quad (8.51a)$$

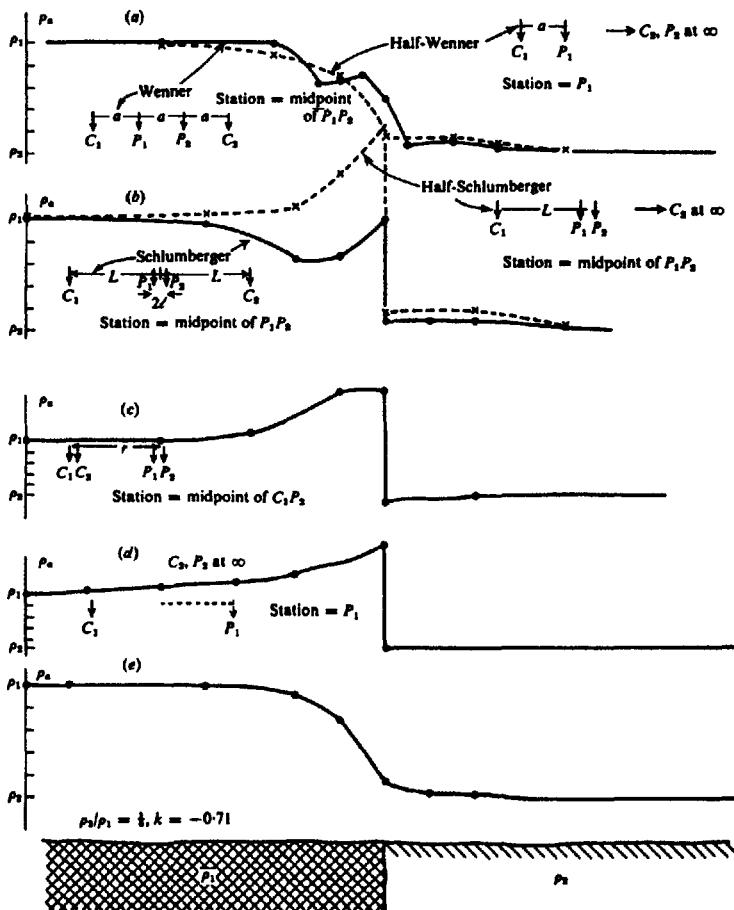


Figure 8.34. Profiles over a vertical contact using different electrode spreads.  
 (a) Wenner spread. (b) Schlumberger spread. (c) Double-dipole spread. (d) Spread with fixed  $C_1$ , movable  $P_2$ . (e) Schlumberger broadside spread.

(ii) Dipole straddles contact:

$$\frac{\rho_a}{\rho_1} = 1 + k \quad (8.51b)$$

(iii) All four on right-hand side:

$$\frac{\rho_a}{\rho_1} = k^* \left\{ 1 + \frac{kr^3}{(2s+r)^3} \right\} \quad (8.51c)$$

Profiles for these three electrode systems, plus some other possible arrangements, are shown in Figure 8.34. The profiles are characteristic of the array used. Except for Figure 8.34e, they all have discontinuities in the vicinity of the contact, related to the electrode spacing. In Figure 8.34e the electrodes are aligned parallel to the contact and are moved broad-

side, so that they all cross it simultaneously. The value of  $\rho_a/\rho_1$  can be obtained in this case by substitution in Equation (8.48a) and (8.48e). With the usual approximation ( $L \gg r$ ), we have:

Electrodes in medium (1):

$$\frac{\rho_a}{\rho_1} \approx 1 + k \left\{ 1 + \left( \frac{2s}{L} \right)^2 \right\}^{-3/2}$$

Electrodes in medium (2):

$$\frac{\rho_a}{\rho_1} \approx k^* \left[ 1 - k \left\{ 1 + \left( \frac{2s}{L} \right)^2 \right\}^{-3/2} \right]$$

This profile is by far the best for interpretation but it

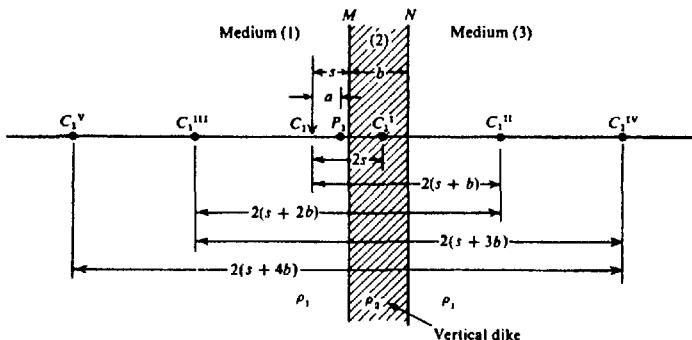


Figure 8.35. Locations of current images near a vertical dike.

is not very practical in the field. In some of the spreads the profile shape varies with the direction of traversing, that is, it depends on which electrode crosses the contact first.

### 8.6.6. The Vertical Dike

When a dike of anomalous resistivity and finite width is traversed, the profiles are even more affected by the electrode spacing than in the case of the vertical contact. The expressions for potential are as in Section 8.6.5 plus the effect of one or two sets of images caused by reflections in the two boundaries. The development is not fundamentally difficult, but is tedious. We will describe only one configuration in detail, that in which we have one current electrode and one potential electrode, both initially in medium (1) (fig. 8.35).

The current source  $I$  at  $C_1^V$  has an image in the dike at  $C_1^I$  (provided  $s < b$ ), caused by reflection in boundary  $M$ . Its strength is  $kI$  and it is located  $(2s - a)$  from  $P_1$ , the potential electrode.

There is a second image of  $C_1^V$  reflected in boundary  $N$  at  $C_1^{II}$ , which is located in medium (3) at a distance  $(2b + 2s - a)$  from  $P_1$ . This in turn causes an image in medium (1) at  $C_1^{III}$ ,  $(2b + a)$  from  $P_1$ . It is reflected in  $N$  to produce image  $C_1^{IV}$ , at  $(4b + 2s - a)$  from  $P_1$ . These reflections are repeated indefinitely in  $M$  and  $N$  to give two infinite series, of which only the set of images in medium (3) have any effect on the potential in medium (1).

When the potential electrode is in medium (2), the image at  $C_1^I$  does nothing, but both the series in medium (1) and (3) influence the potential. Finally when  $P_1$  is in medium (3), it is perturbed by  $C_1^I$  and all the images in medium (1). As a result we obtain the following potential expressions, for the different

locations of  $P_1$ :

Medium (1):

$$V_1 = \frac{Ip_1}{2\pi} \left\{ \frac{1}{a} + \frac{k}{2s - a} + A \sum_{m=0}^{\infty} \frac{(k^2)^m}{2(m+1)b + 2s - a} \right\} \quad (8.52a)$$

Medium (2):

$$V_2 = \frac{Ip_1}{2\pi} \left\{ B \sum_{m=0}^{\infty} \frac{(k^2)^m}{2(m+1)b + 2s - a} + C \sum_{m=0}^{\infty} \frac{(k^2)^m}{2mb + a} \right\} \quad (8.52b)$$

Medium (3):

$$V_3 = \frac{Ip_1}{2\pi} \left\{ D \sum_{m=0}^{\infty} \frac{(k^2)^m}{2mb + a} \right\} \quad (8.52c)$$

$A$ ,  $B$ ,  $C$ , and  $D$  are constants that are evaluated by applying the boundary condition of Equation (8.7b) at the boundaries  $M$  and  $N$ . They turn out to be

$$A = -k(1 - k^2) \quad B = -k(1 + k)$$

$$C = 1 + k \quad D = 1 - k^2$$

By a similar analysis, we can obtain the potentials when the current electrode is in the dike.

Medium (1):

$$V_1' = \frac{I\rho_1}{2\pi} (1 + k) \times \left\{ \sum_{m=0}^{\infty} \frac{k^{2m}}{2mb + a} - k \sum_{m=0}^{\infty} \frac{k^{2m}}{2(m+1)b + 2s + a} \right\} \quad (8.53a)$$

Medium (2):

$$V_2' = \frac{I\rho_1(1+k)}{2\pi(1-k)} \times \left[ \frac{1}{a} + k^2 \left\{ \sum_{m=0}^{\infty} \frac{k^{2m}}{2(m+1)b + a} + \sum_{m=0}^{\infty} \frac{k^{2m}}{2(m+1)b - a} \right. \right. \\ \left. \left. - k \left\{ \sum_{m=0}^{\infty} \frac{k^{2m}}{2(m+1)b + 2s \pm a} + \sum_{m=0}^{\infty} \frac{k^{2m}}{2mb - (2s \pm a)} \right\} \right] \right\} \quad (8.53b)$$

Medium (3):

$$V_3' = \frac{I\rho_1}{2\pi} (1 + k) \left\{ \sum_{m=0}^{\infty} \frac{k^{2m}}{2mb + a} - k \sum_{m=0}^{\infty} \frac{k^{2m}}{2mb - (2s - a)} \right\} \quad (8.53c)$$

In these equations the relative positions of the potential and current electrodes must be specified. In Equation (8.53a) the potential electrode is always to the left of the current electrode, whereas in Equation (8.53c) it is always to the right. In Equation (8.53b), however, it may be on either side of the current electrode. When it is on the left, one uses the upper signs for  $a$  in the denominators of the last bracket; when on the right, the lower sign.

Finally, when the current electrode is on the right-hand side in medium (3), and  $P_1$  is to the left

of  $C_1$ , the respective potentials are:

Medium (1):

$$V_1'' = \frac{I\rho_1}{2\pi} (1 - k^2) \sum_{m=0}^{\infty} \left( \frac{k^{2m}}{2mb + a} \right) \quad (8.54a)$$

Medium (2):

$$V_2'' = \frac{I\rho_1}{2\pi} (1 + k) \left\{ \sum_{m=0}^{\infty} \left( \frac{k^{2m}}{2mb + a} \right) - k \sum_{m=0}^{\infty} \frac{k^{2m}}{2mb - (2s + a)} \right\} \quad (8.54b)$$

Medium (3):

$$V_3'' = \frac{I\rho_1}{2\pi} \left\{ \frac{1}{a} + k \sum_{m=0}^{\infty} \frac{k^{2m}}{2(m-1)b - (2s + a)} - k \sum_{m=0}^{\infty} \frac{k^{2m}}{2mb - (2s + a)} \right\} \quad (8.54c)$$

From these relations one can obtain the value of  $\rho_a$  in terms of  $\rho_1$ , in the usual way, for complete profiles across the dike. In addition, the expressions can be made more general by assuming a resistivity  $\rho_3$  in medium (3).

The formulas are modified in all cases by differentiating the potentials for a half-Schlumberger array and by using the second derivative for the double dipole.

Profiles obtained with different spreads in traversing a thin dike are shown in Figure 8.36. On the whole the half-Schlumberger curve reproduces the shape of the dike best, particularly for thin dikes. The corresponding dipole profile has two peaks, the gap between being equal to the dipole spacing. This double anomaly could be quite misleading. On the other hand, the half-Wenner spread over a thin dike of high resistivity shows a "conductor" of width greater than the actual dike. The full-Wenner system, however, gives better results, although there are discontinuities near the edges of the dike, as illustrated in Figure 8.36c.

As in the case of the single vertical contact, better profiles would be obtained by moving the array broadside to the structure. In fact, the profiles are considerably better over thin dikes when the traverse is made at an oblique angle, although the anomalies will be wider than the actual dike.

Lateral exploration may also be applied to channels and filled sinks of anomalous resistivity when such features outcrop or lie very close to the surface. The profiles are similar to the dike, although the latter was assumed to have infinite depth in the previous discussions.

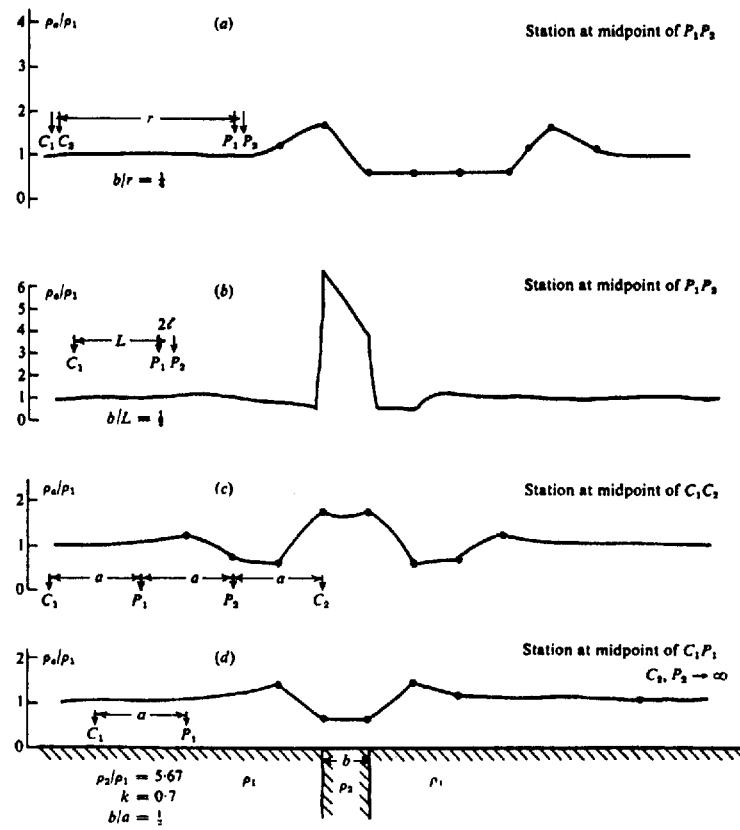


Figure 8.36. Profiles over a thin dike using different electrode spreads. (a) Double-dipole spread. (b) Half-Schlumberger spread. (c) Full-Wenner spread. (d) Half-Wenner spread.

### 8.6.7. Mapping Three-Dimensional Anomalies

The resistivity method is not particularly sensitive to 3-D anomalies for the same reason that it is ineffective over buried 2-D structures of finite width. This limitation is well illustrated by reference to the buried sphere considered in Section 8.3.5. Using a Schlumberger spread, the apparent resistivity can be calculated by differentiating Equation (8.22) with respect to  $x$  [note that  $E_0 = \rho_1 I$ ,  $x = r \cos \theta$ , and  $\rho_a = (1/I)(\partial V/\partial x)$ ] and assuming that the sphere is a very good conductor so that  $\rho_2 = 0$ , we obtain

$$\frac{\rho_a}{\rho_1} \approx 1 + \left(\frac{a}{z}\right)^3 \frac{(2x^2/z^2) - 1}{(1 + x^2/z^2)^{5/2}} \quad (8.55)$$

where  $x$  is the distance of the potential electrode from the surface point above the origin and  $z$  the depth to the sphere center. When  $z = 2a$  the maxi-

mum contrast between  $\rho_a$  and  $\rho_1$  is only 12%. Thus a sphere 30 m in diameter whose top lies only 15 m below surface probably would not be detected.

A similar limitation exists when the body outcrops, for instance, a hemispherical sink. Unless the traverse passes very close to the rim, the anomaly will be missed. These effects are illustrated in Figure 8.37. Note that when the survey line is over the center of the bowl ( $d = 0$ ), the ratio  $\rho_a/\rho_1$  remains zero until the potential electrodes are out of the sink, because  $\Delta V = 0$  for  $a \leq 2R$ .

It is not surprising that numerical methods like those described in Sections 6.2.7, 6.2.8, and 9.5.3 have been developed for resistivity modeling as well (Coggon, 1971; Lee, 1975; Snyder, 1976; Dey and Morrison, 1979). The models include 2-D and 3-D structures of the usual types. Again, the most striking feature of the resistivity results is the poor response of 3-D targets. Unless they are shallow and the width about the same as the depth, the anom-

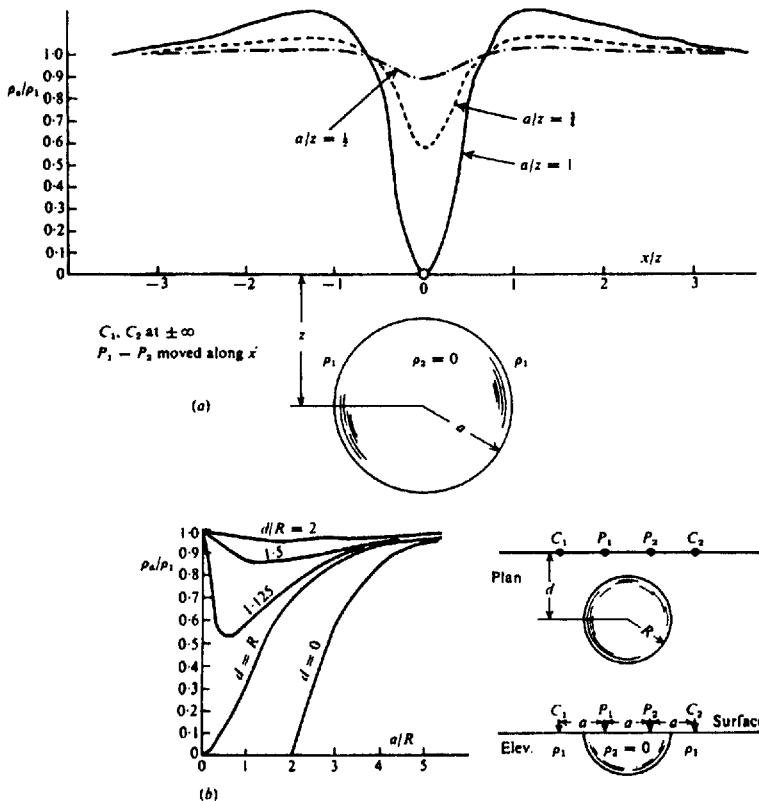


Figure 8.37. Resistivity profiles over three-dimensional conductors. (a) Schlumberger array over buried sphere. (b) Expanding Wenner array over outcropping hemispherical conductor.

is weak. Conductive overburden is also very effective in masking such structures. Figure 8.38 demonstrates these limitations with a display of profiles and pseudosections ( $\S 9.5.1$ ) over a vertical block with and without overburden cover.

#### 8.6.8. Measuring Overburden Depth and Resistivity

Obviously the depth of overburden can be found using an expanding spread. However, if the bedrock surface is irregular, many soundings will be necessary, entailing considerable time and expense. Where the overburden has much lower resistivity than bedrock, which is the usual case, good results may be obtained with three traverses, employing different electrode separations.

Obviously one small spread is necessary to measure  $\rho_1$ . This is achieved with a separation that is less than half the minimum overburden thickness; it should not be required at every profile station unless

$\rho_1$  varies rapidly. The conventional procedure has been to complete the profile at all stations with a second electrode spacing, which is somewhat larger than the maximum overburden depth. This gives a relation for  $z$  from Equation (8.42d):

$$z = c(\rho_1/\rho_a) \times (\text{electrode spacing}) \quad (8.56)$$

where  $c = 1.38, 1.0, 0.5$  and the spacing is  $a, L, r$  for the Wenner, Schlumberger, and double-dipole arrays, respectively. However, the value obtained is generally much larger than the correct value unless the spacing is large enough to make  $\rho_a \approx \rho_2$ . A better estimate may be obtained by taking two readings of  $\rho_a$  at two spreads larger than maximum overburden depth. Then the  $z$  values obtained from Equation (8.56) are plotted against the corresponding  $a, L$ , or  $r$  values; the straight line joining the two points, when extended to the ordinate axis, gives the correct depth. Figure 8.39 clarifies this procedure on linear  $z$  versus  $a, L$ , or  $r$  axes. Several additional

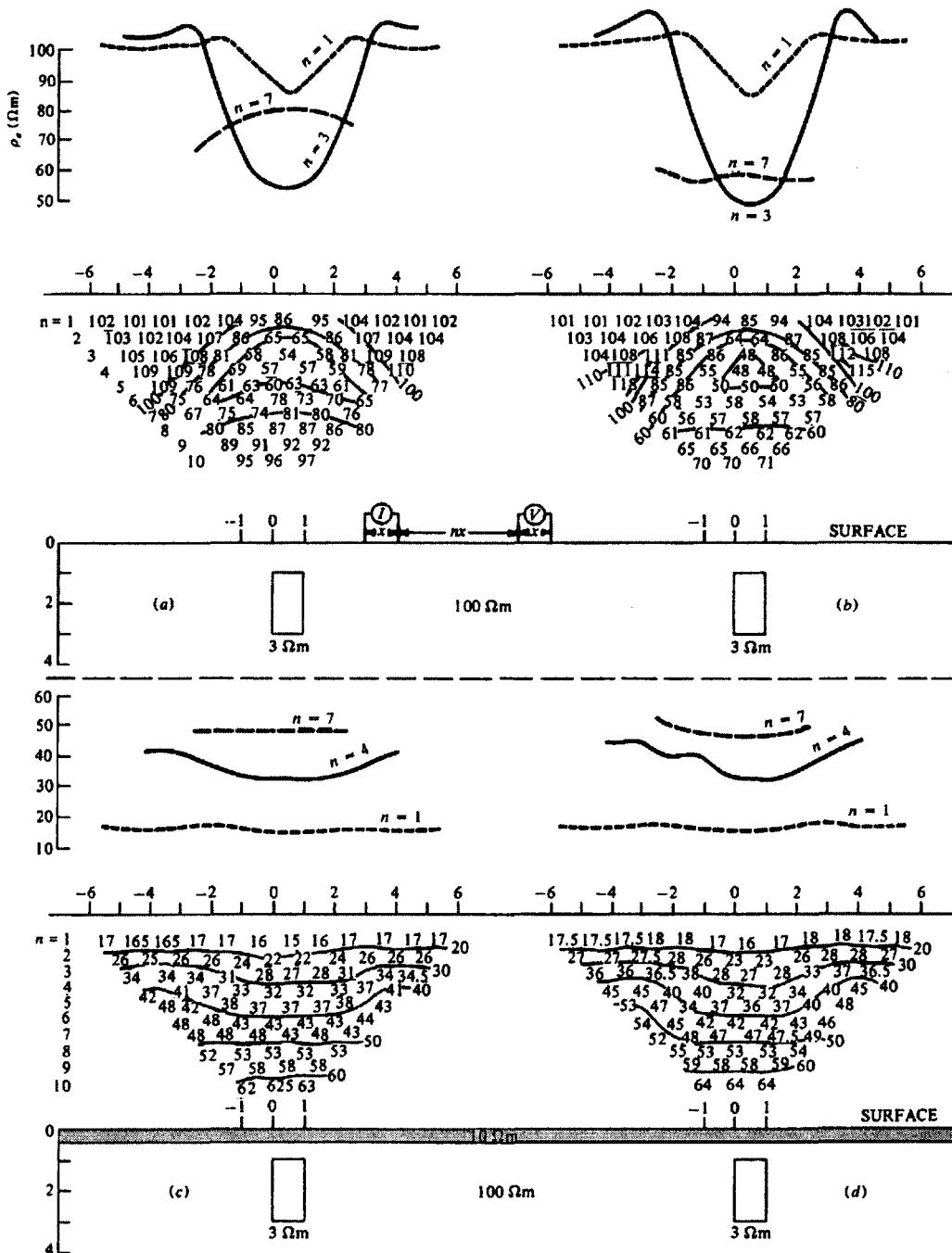


Figure 8.38. Resistivity finite-difference modeling: profiles and pseudodepth plots for the dipole-dipole array of Figure 9.8a. (After Dey and Morrison, 1979.) (a) 3-D block, strike length = 6 units. (b) 2-D block, infinite strike length. (c) and (d) same as (a) and (b) with conductive overburden 0.5 units thick,  $\rho = 10 \Omega\text{m}$ .

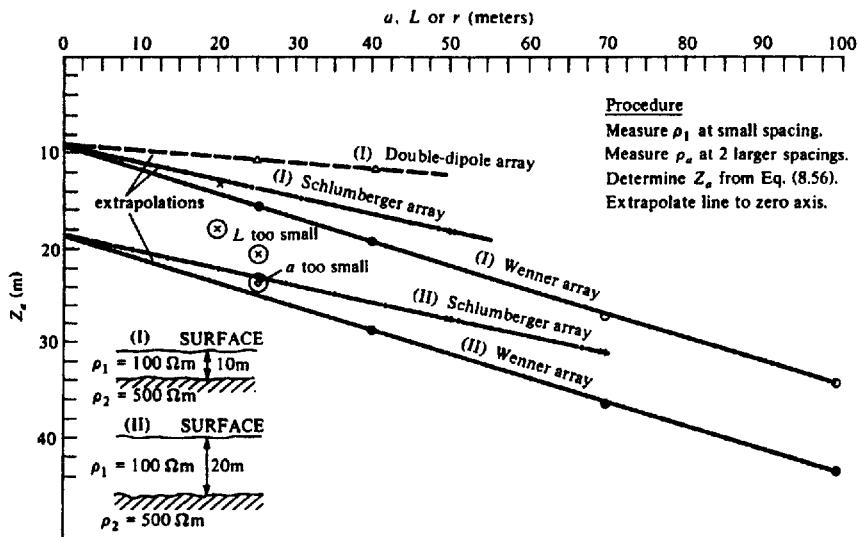


Figure 8.39. Graphical determination of overburden thickness using one small spread to get  $\rho_1$  and two large spreads to get  $z$ .

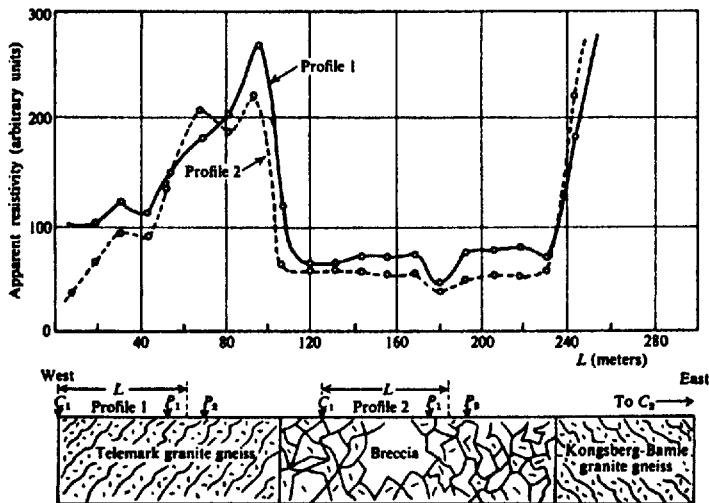


Figure 8.40. Mapping vertical contacts with the half-Schlumberger array, Kongsberg, Norway. (After Van Nostrand and Cook, 1966.)

points are included in the plot to indicate where the straight line extrapolation begins to fail. Because the relation appears to be linear, the usual log-log scale is not suitable. Alternatively the extrapolated  $z$  values may be calculated from  $z_s = ms + z_c$  where  $s$  is the separation,  $z_s$  is obtained from Equation (8.56), and  $z_c$  is the intercept on the ordinate.

If bedrock resistivity is lower than that of the overburden, it is necessary to use expanding spreads to get quantitative values for the depth, although the

electrode separation need not be as large as for  $\rho_2 > \rho_1$ . When  $\rho_2 < \rho_1$ , there is no relation between  $\rho_a$  and  $z$  equivalent to Equation (8.56), as can be seen from Figures 8.21 and 8.27b.

The cumulative- $\rho_a$  plot was formerly used to find depth of overburden and shallow resistivities. Although it has no sound theoretical basis, it works for soundings on thin beds but requires many constant increments of electrode spacing, which are small compared to bed thickness. The data are plotted by

summing successive  $\rho_a$  values for the ordinate, that is, if the readings were 100, 200, and 300  $\Omega\text{m}$  for spacings of 10, 20, and 30 m, one would plot 100, 300, and 600  $\Omega\text{m}$  versus 10, 20, and 30 m. An attempt is then made to find points where straight-line segments (drawn through as many points as possible) change slope, indicating depth to the interface.

## 8.7. FIELD EXAMPLES

In recent years most resistivity data related to mineral exploration are included in the results of IP surveys; the resistivity method is not much used as an independent technique in this application. It has, however, been employed to a considerable extent in ground water search and for engineering geology — preparation of dam sites, highway routes, building foundations, and so forth. Consequently the case histories and problems in this section include several examples not directly related to conventional prospecting. Further examples may be found in Chapter 9 of surveys where resistivity data were obtained in conjunction with IP data.

1. Apparent resistivity profiles obtained with a half-Schlumberger, or gradient, array traversing vertical contacts are shown in Figure 8.40. The two profiles correspond to different fixed locations of the current electrode  $C_1$ . The potential electrodes, which are close together compared to their separation from  $C_1$ , are moved together, whereas the second current electrode is effectively at infinity to the east. The contact with the low resistivity breccia is sharply defined in both profiles, which are quite similar to the theoretical result for the vertical contact shown in Figure 8.34b.

2. Resistivity data obtained in conjunction with an IP survey are shown in Figure 8.41. The area is the Cavendish Township test site, 100 miles northeast of Toronto. Unfortunately no detailed section is available for the subsurface.

The rocks are mainly metasedimentary with small areas of acidic and basic igneous types. The trend is northeast. Sulfides are present throughout the area, at least in trace amounts, and graphite occurs in a band of calcareous-siliceous rocks in the western part of the area.

Figure 8.41a shows apparent resistivities plotted in profile for four separations of the double-dipole electrode system ( $x = 200$  ft,  $n = 1, 2, 3, 4$ ) on line B; Figure 8.41b shows the usual pseudodepth plot employed in IP work (§9.5.1.) Clearly there is a low-resistivity zone, continuous at depth from 4W to 18W, which is capped by a higher-resistivity bowl near surface, located between 10W and 14W. A variety of EM surveys made on the Cavendish test

site agree with the shallow resistivity profiles, because they outline two distinct zones trending NE, located at 8W and 15W.

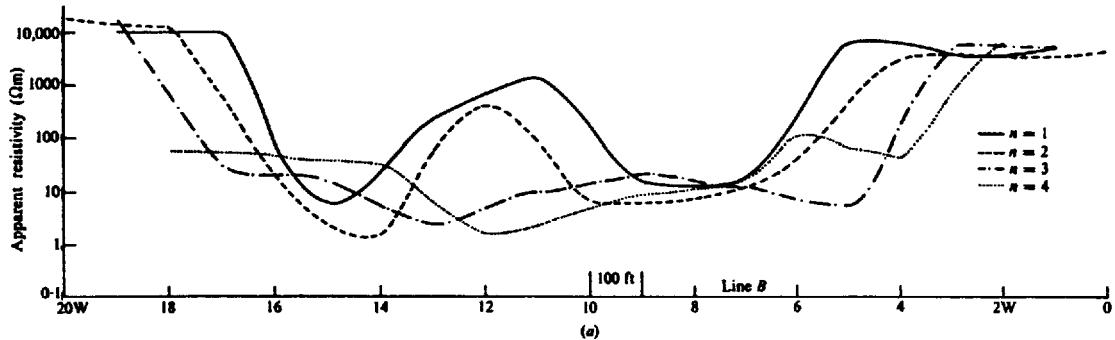
3. The search for groundwater normally requires resistivity surveys, both for regional mapping and for sounding. Frequently these are combined with gravity and seismic refraction, the former during reconnaissance and the latter to aid in identifying saturated beds containing fresh or salt water and to resolve the equivalence ambiguity between  $z$  and  $\rho$  by unique determination of bed thickness.

This problem is well illustrated by a groundwater survey carried out in the central Sudan savannah belt near the White Nile (van Overmeeren, 1981). Figure 8.42 displays vertical electric sounding (VES) data from three locations west of the river and includes a schematic of two interpretations of the basement section, assuming either fresh or saline water. Both versions fit the sounding curves, although only VES 13 suggests fresh water. However, the results from seismic refraction plus data from a well drilled earlier in the vicinity favored the shallower basement depths associated with salt water as shown in Figure 8.42d.

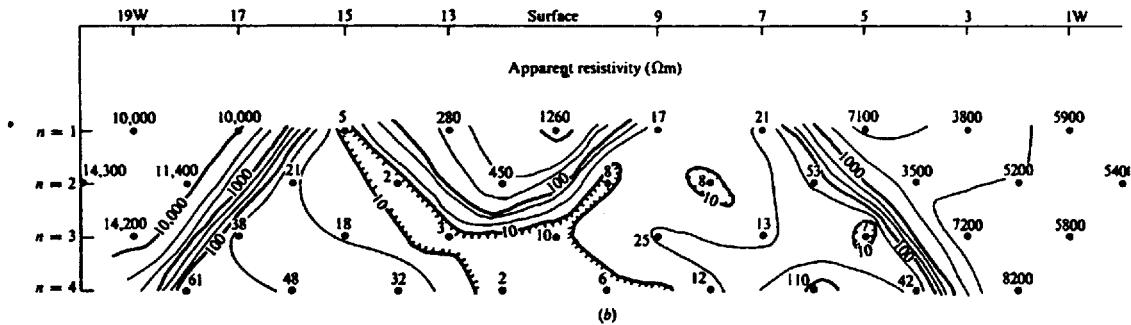
4. Resistivity is an important component of multiple-method geophysical surveys for geothermal sources. Geothermal targets are of two types: the more common hot-water systems characteristically have high concentrations of chlorides and if the subsurface temperatures are  $\sim 180^\circ\text{C}$  or higher they produce hot springs and deposit a sinter; the other type, vapor-dominated geothermals, is low in chlorides and rich in sulfate ions or alternatively in sodium bicarbonate.

The Mud Volcano area in Yellowstone Park, a typical vapor-dominated system, was surveyed in the late 1960s using IP, SP, resistivity lateral mapping, and resistivity soundings (Zohdy, Anderson, and Muffler, 1973). Three profiles of PFE (§9.3.3a), SP, and  $\rho_a$  are shown in Figure 8.43 together with a 6.7 km wide geoelectric section of the geothermal anomaly area. The profile line follows the Yellowstone River slightly SW of it. IP and resistivity profiles were carried out with a pole-dipole or half-Schlumberger array (Fig. 8.18) whose dimensions were  $(a + b)/2 = 1,000$  ft (300 m). The SP electrode spacing was 400 ft (120 m).

The IP profile is not very significant except for a strong PFE response about 2,000 ft (600 m) wide at the NW boundary of the geothermal area. The high IP background is attributed to widely distributed clay with some pyrite, whereas the anomaly is probably caused by pyrite concentration at depth, because a second profile with spacing  $AB/2 = 600$  ft (180 m) (not shown here) had a much reduced IP response in this vicinity.



(a)



(b)

Figure 8.41. Resistivity results, Cavendish Township, Ontario. (a) Resistivity profile using a double-dipole array with  $n = 1, 2, 3, 4$ . (b) Pseudodepth plot using the data in (a).

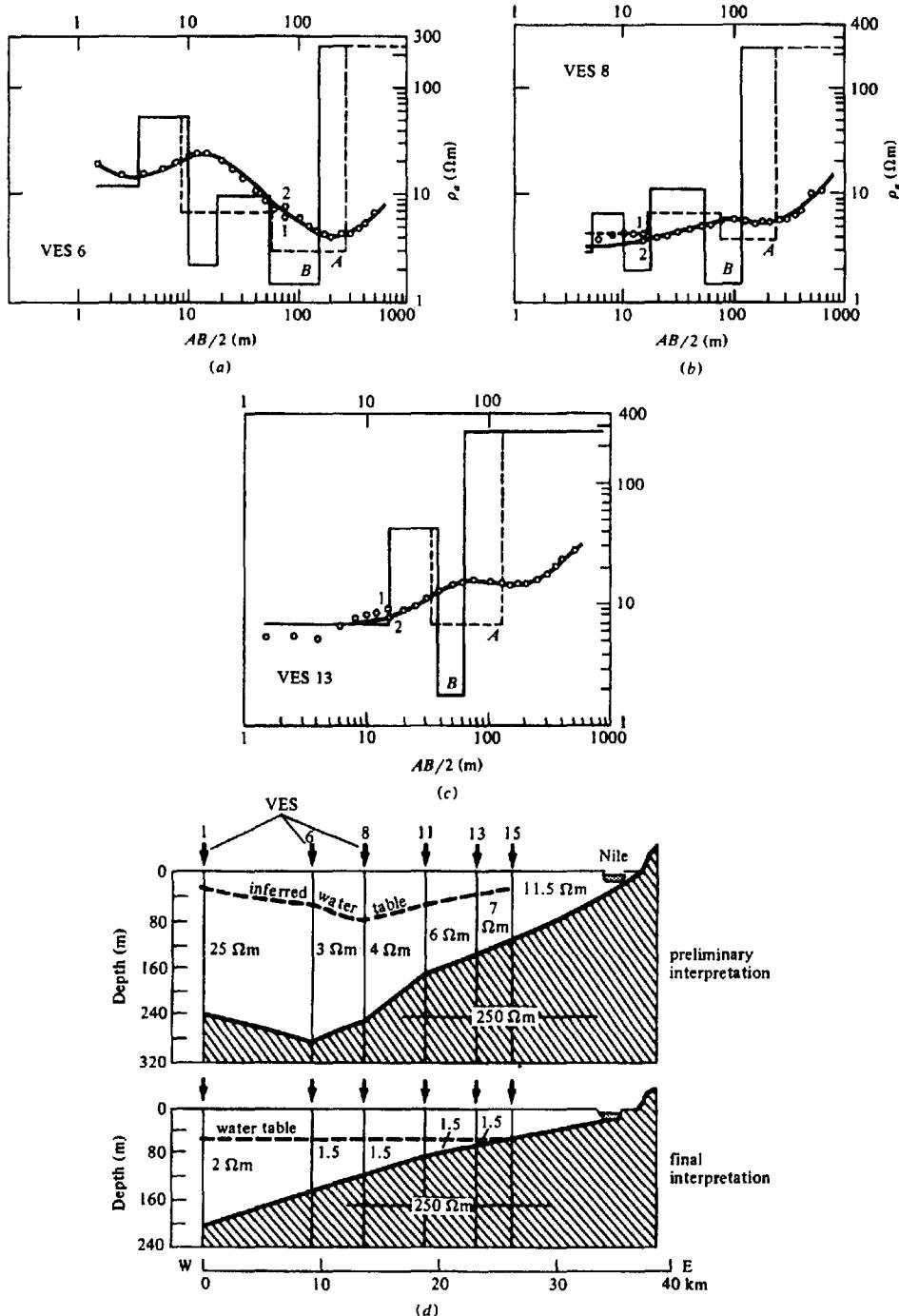


Figure 8.42. Results of vertical electric soundings, Sudan. (After van Overmeeren, 1981.) (a) Sounding VES 6 and two equivalent solutions, both for saline water. (b) Sounding VES 8 and two equivalent solutions. (c) Sounding VES 13 and equivalent solutions for fresh water (A) and saline water (B). (d) Preliminary and final interpretation.

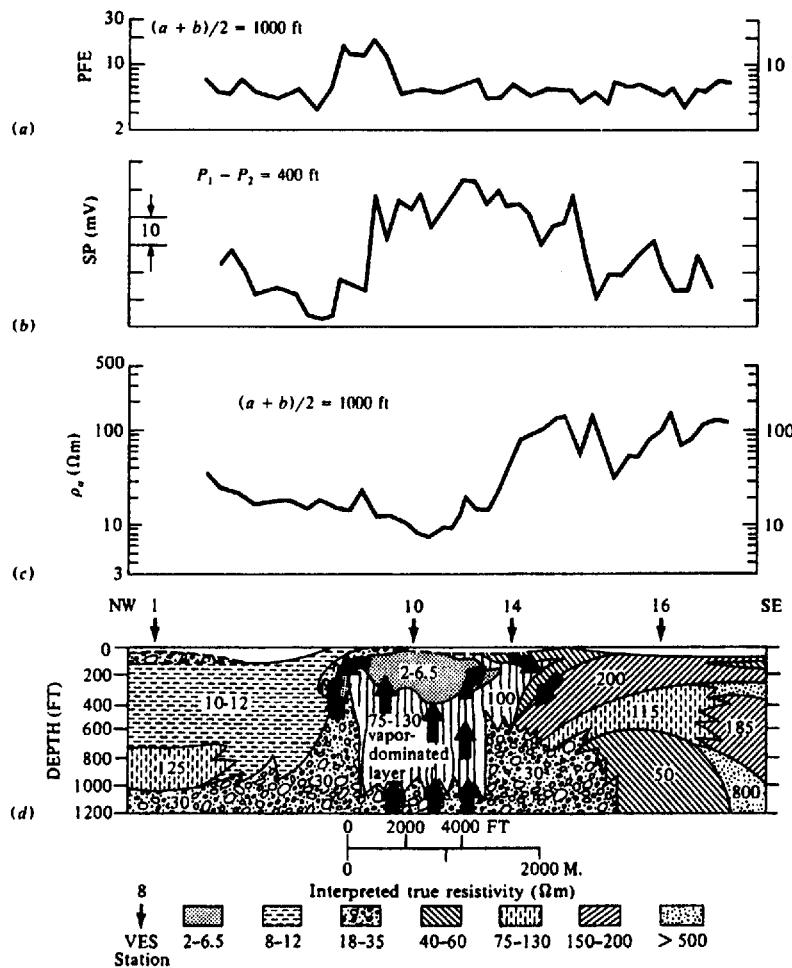


Figure 8.43. IP, SP, and resistivity profiles with geoelectric section, Mud Volcano, Yellowstone National Park geothermal zone. (After Zohdy, Anderson, and Muffler, 1973.)

There is a positive SP anomaly of  $\sim 60$  mV straddling the target and persisting for some 2,500 ft (760 m) beyond on the SE side. This anomaly is probably due to streaming or electrokinetic potential (§5.2.1b, §6.1.1), but the SE segment is not explained. The resistivity profile outlines the geothermal area best with a well-defined low directly above.

The results of 16 vertical soundings were used to produce the geoelectric section in Figure 8.43. Soundings VES 1, 10, 14, and 16 (see Fig. 8.43d for locations) are displayed in Figure 8.44, with the layer resistivities and thicknesses plotted along the Schlumberger horizontal axes. Interpretation of the sounding curves was done by two methods, one with partial master-curve matching and auxiliary-point

diagrams (VES 10, 14) and the other using an automatic technique for the complete curve (VES 16). Both interpretations are shown for VES 1, the first with a 6-bed model, the second with a 19-layer computer model.

5. It is worthwhile to summarize some rough rules for success in exploring for groundwater and geothermal sources:

- The most important is to assemble as much geological information as possible, with particular emphasis on any logs from old wells or drill holes in the area.
- Next is to do the same for geochemical and geophysical data.

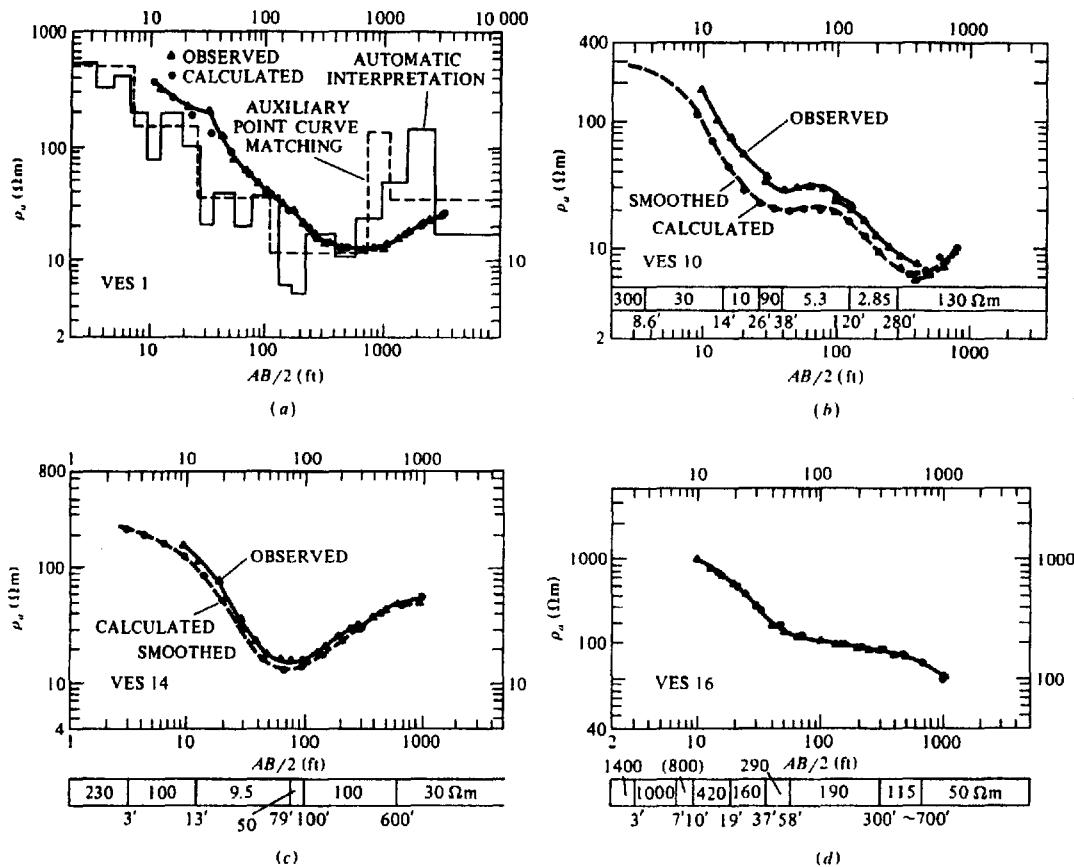


Figure 8.44. Soundings used to obtain geoelectric section in Figure 8.43. ▲ and ● denote observed and calculated values. (Note the alternative plotting methods used in (a) and (b); see also Figs. 8.29 and 8.42.) (After Zhody, Anderson, and Muffler, 1973.)  
 (a) VES 1 interpreted by partial curve matching (6-layer) and complete curve matching (19-layer). (b) VES 10, partial curve matching (7-layer). (c) VES 14, partial curve matching (6-layer). (d) VES 16, complete curve matching (9-layer).

Table 8.1. Sounding data.

Well	Min. $\rho_a$ (Ωm)	Max. $\rho_a$ (Ωm)	Avg. $\rho_a$ (Ωm)	Max/Min	Depth (m)	Yield (min.) (gal/min)
R161	55	120	80	2.2	2.5	Producer
R162	14	60	30	4.3	3	Producer
R102	25	60	39	2.4	30	10
R72	20	160	48	8.0	16	60
MH-10	60	100	89	1.7	10	25
Average	35	100	57	3.7	12	—
R163	35	100	57	2.9	30	Dry
R164	110	300	171	2.7	6	Dry
R166	110	210	172	1.9	25	Dry
Average	85	203	133	2.5	20	0

- (iii) Survey procedures should be similar to those described in field examples 3 and 4.
- (iv) On completion of resistivity profiling, it is desirable to select VES locations at resistivity lows taking into account (i) and (ii).
- (v) The shape of the sounding curve is certainly significant. The low-grade data from groundwater surveys given in Table 8.1 serve as an illustration of this.

The data in Table 8.1 are from various locations in Sri Lanka, whose geology is a continuation of the South India Decca platform, mainly Paleozoic and Precambrian with younger coastline sediments. The data in the table are not representative because the ratio of dry-to-producing wells drilled over the past five years (mainly less than 50 m deep) is less than 10%. However, it seems clear from the above and from other groundwater results in West Africa that, for a successful well, the sounding curve should have a fairly well defined minimum at reasonable depth, although, if this minimum is less than a few ohmmeters, the chances are increased that any water will be saline.

Although the same remarks apply to geothermal exploration, the problem is more complex. Depth of exploration is usually greater than that necessary in groundwater search and more geophysical methods are required. The resolution of saline from fresh sources, however, is not a factor.

## 8.8. PROBLEMS

1. In an investigation to determine the depth of a conducting layer of brine at Malagash, Nova Scotia, the readings in Table 8.2 were taken with a Megger using an expanding Wenner spread. The surface layer was found to have a resistivity of  $29 \Omega\text{m}$ . Determine the depth and resistivity of the brine layer.

Table 8.2.

	Separation (ft)	$\rho_s (\Omega\text{m})$
	40	28.5
	60	27.1
	80	25.3
	100	23.5
	120	21.7
	140	19.8
	160	18.0
	180	16.3
	200	14.5
	220	12.9
	240	11.3
	260	9.9
	280	8.7
	300	7.8
	320	7.1
	340	6.7
	360	6.5
	380	6.4

Table 8.3.

	Electrode separation (ft)	Resistivity ( $\Omega\text{m}$ )
	5	78.1
	10	56.0
	15	49.8
	20	47.1
	25	46.0
	30	51.2
	35	59.8
	40	76.0
	45	79.8
	50	72.2

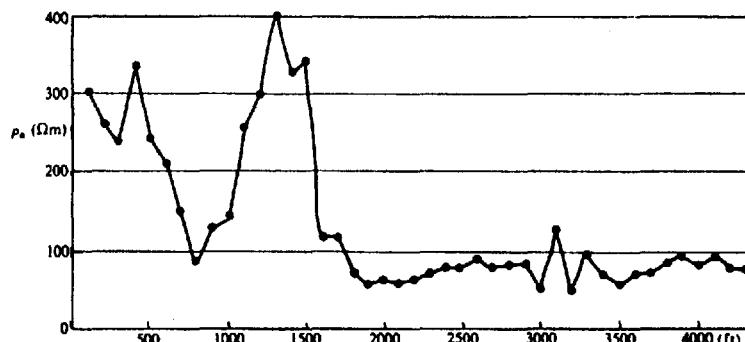


Figure 8.45. Resistivity mapping with Wenner spread over limestone and sandstone section separated by vertical contacts. Station interval 100 ft,  $a = 100$  ft. (After Van Nostrand and Cook, 1966.)

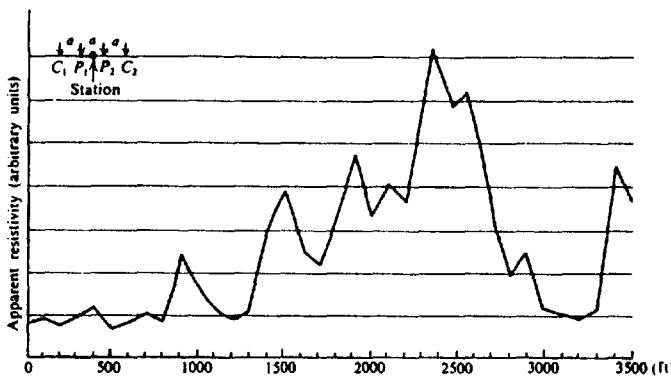


Figure 8.46. Resistivity mapping with Wenner spread over karst topography, Hardin County, Illinois. Station interval = 100 ft,  $a = 100$  ft. (After Van Nostrand and Cook, 1966.)

Table 8.4.

Station	Line 10 + 00S		Line 0 + 00		Line 10 + 00N	
	$\rho_a(n=1)$ ( $\Omega\text{m}$ )	$\rho_a(n=4)$ ( $\Omega\text{m}$ )	$\rho_a(n=1)$ ( $\Omega\text{m}$ )	$\rho_a(n=4)$ ( $\Omega\text{m}$ )	$\rho_a(n=1)$ ( $\Omega\text{m}$ )	$\rho_a(n=4)$ ( $\Omega\text{m}$ )
26W	2,750					
25	2,000					
24	1,700					
23	1,850					
22	2,250	1,450				
21	2,000	700				
20	1,000	450	1,700		500	1,500
19	400	250	3,000		150	1,900
18	250	200	2,150	500	400	2,000
17	200	150	850	300	850	1,600
16	150	200	350	500	1,500	800
15	250	150	250	500	1,700	2,400
14	400	100	250	450	1,200	5,300
13	600	20	200	50	3,800	10,000
12	900	150	150	100	8,900	12,700
11	1,000	350	250	450	9,300	13,500
10	150	200	450	850	9,200	12,700
9	550	50	650	1,100	6,650	12,000
8	4,100	20	1,750	550	2,460	10,900
7	3,600	25	2,350	800	5,750	7,800
6	2,800	100	3,800	1,550	6,600	5,700
5	1,000	350	1,000	850	4,000	5,500
4		700	950	1,250	2,250	5,200
3			1,000	850	4,000	5,500
2			1,100	2,000	7,400	4,300
1			1,600	2,850	7,000	6,500
B.L.			3,200	2,350	6,600	6,800

2. In a resistivity survey performed for highway construction, the readings in Table 8.3 were obtained with an expanding Wenner spread. Plot  $\rho_a$  versus  $a$ . How many layers are indicated by this curve? Can you use the method of partial curve matching for multiple layers and if so, do the results agree with those obtained by the

cumulative  $\rho$  plot and from the extrapolation described in Section 8.6.8? Find the depth of overburden by any or all of these methods.

3. Figure 8.45 shows a profile taken with a Wenner spread having a fixed spacing of 100 ft. Station intervals are 100 ft. The geologic section includes sandstone and limestone beds with practically

Table 8.5.

$L$ (m)	$\rho_a$ ( $\Omega\text{m}$ )
1.5	160
2	96
3	70
4	54
6	40
8	33
10	27
12.5	20
15	20
20	22
25	23
30	27
40	30
50	38
60	48
80	67

vertical contacts. Locate these beds and speculate on the source of the small positive anomaly at 3,100 ft.

- The profile of Figure 8.46 was obtained in exactly the same manner as that of problem 3; this is an area of karst topography in Hardin County, Illinois. The limestone contains numerous sinkholes and channels, most of which are filled with clay. There are occasional empty caverns as well. Make a rough interpretation of the near-surface section from the resistivity profile by locating the clay-filled sinks and/or caverns in the limestone host rock.
- Apparent resistivities in ohm-meters are given in Table 8.4 for portions of three lines from an area in eastern Nova Scotia where an IP survey was carried out. The topography is generally flat except for the west portion (line 0 + 00 has an elevation change of +250 ft between stations 13 and 20, line 10 + 00N has a change of +100 ft between stations 15 and 20, line 10 + 00S has a change of +75 ft between stations 21 and 26). The rocks are known to be sedimentary in the valley whereas the hills in the vicinity are mainly granitic. Lines are 1,000 ft apart and stations 100 ft. The double-dipole spread (Fig. 9.8a) was used with dipole spacings of  $x = 100$  ft; resistivities are given for  $n = 1$  and 4 only, i.e., the distances between the inner electrodes were 100 and 400 ft, respectively. Plot these profiles and interpret the results.
- The readings in Table 8.5 were obtained during a Schlumberger VES program for rural groundwater supply.  $L = AB/2$  is half the current electrode spacing. Potential electrode spacing was

Table 8.6.

Stn.	Resistivity		EM16	
	$\rho_a(10)$ ( $\Omega\text{m}$ )	$\rho_a(30)$ ( $\Omega\text{m}$ )	Dip (%)	Quad. (%)
- 4SW	—	—	-6	6
- 3	—	—	-5	4
- 2	135	—	-1	4
- 1	—	—	+1	4
0	135	225	0	3
1NE	160	180	-3	1
2	177	220	-4	1
3	—	210	0	0
4	105	190	4	-1
5	—	172	5	-2
6	75	—	3	-2
7	80	150	2	-3
8	80	—	-1	-5
9	87	168	-2	-2
10	87	130	-2	-2
11	90	137	-10	-3
12	100	168	-19	-7
13	150	165	-26	-7
14	300	245	-27	-13
15	460	355	-13	-15
16	250	270	+3	-13
17	204	242	17	-10
18	103	190	24	-12
19	90	197	22	-17
20	60	178	27	-19
21	—	86	28	-17
22	30	68	13	-17
23	32	67	7	-14
24	33	102	3	-14
25	—	60	2	-12
26	30	47	1	-7
27	—	48	-3	-4
28	30	50	-4	+1

increased three times during the sounding: at  $L = 8, 20$ , and  $30$  m; the resultant discontinuities have been eliminated by smoothing at these points.

Analyze the sounding using partial and complete curve matching with auxiliary-point curves plus two- and three-bed master curves and by computer, whatever is available. Compare the results.

- Although resistivity profiling has been carried out routinely for many years in groundwater exploration, it is a rather slow and expensive survey and the possibility of substituting a faster, cheaper technique is attractive.

The readings in Table 8.6 are from part of a Schlumberger profile done with two separations. The purpose was to locate an intrusive ledge of basement rock in a sedimentary section. At the same time a VLF profile was done with an

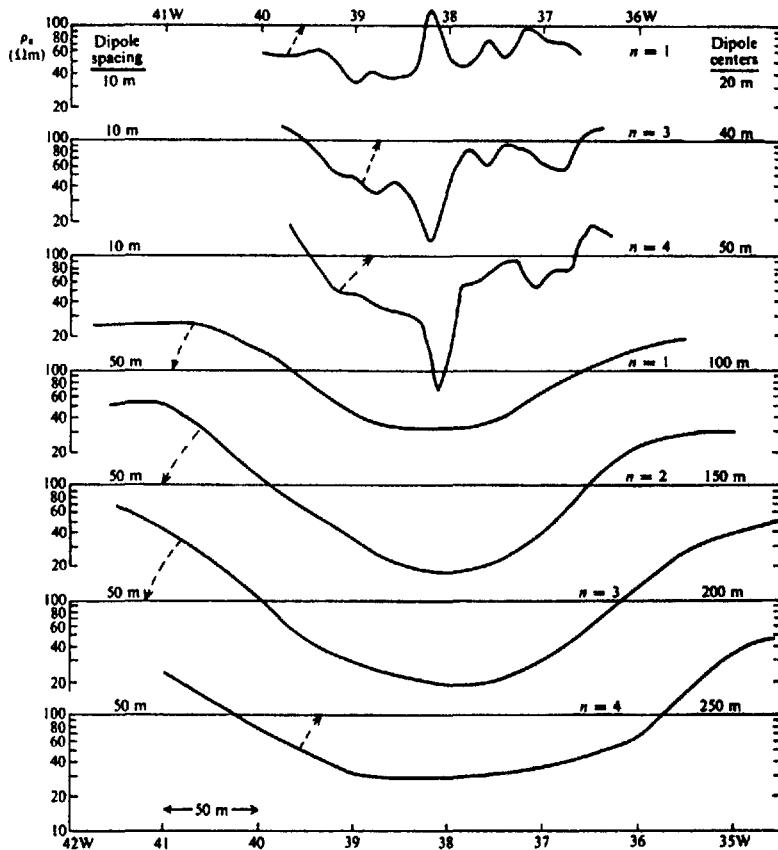


Figure 8.47. Apparent resistivities from IP survey, northeast Brazil.

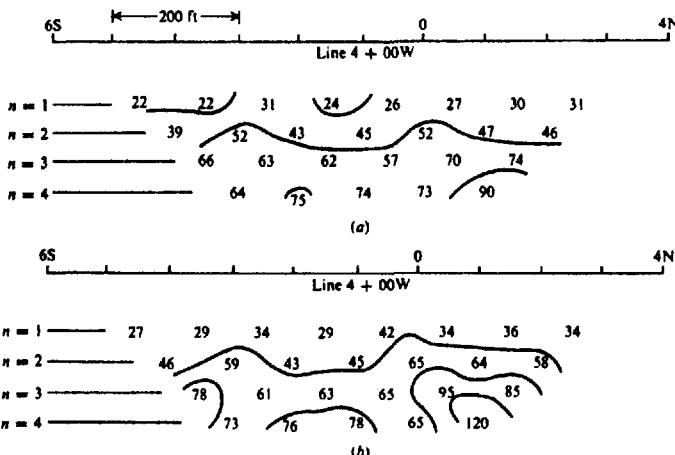


Figure 8.48. Apparent resistivities ( $\rho_a/2\pi \Omega\text{ft}$ ) from two IP surveys using a double-dipole array with separation 100 ft. (a) Data from frequency-domain IP. (b) Data from time-domain IP.

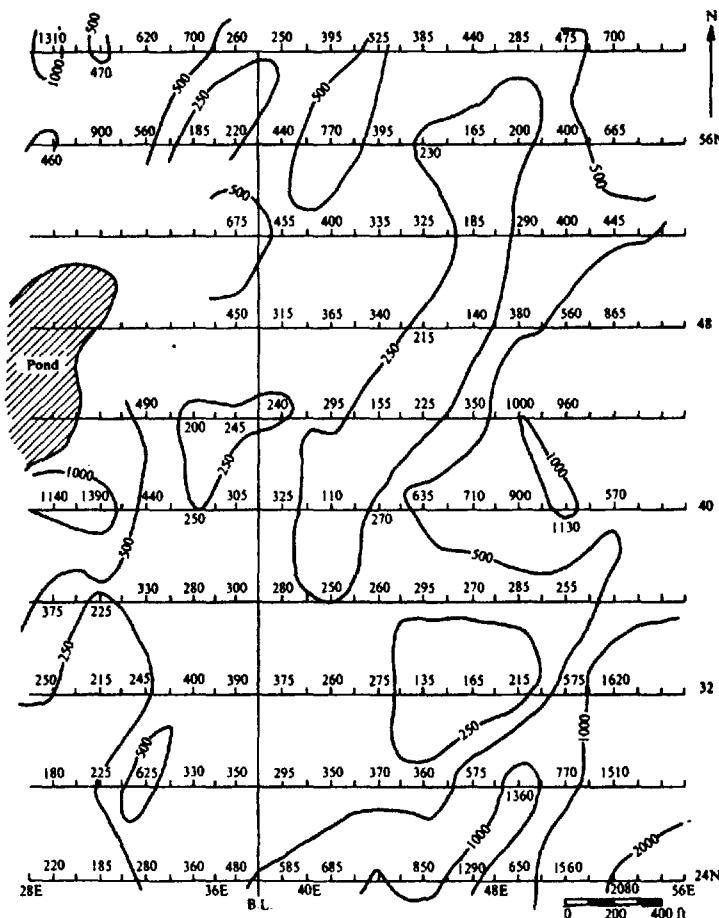


Figure 8.49. Apparent-resistivity contours ( $\Omega$ ft) for a base-metal zone, eastern Nova Scotia.

EM16 instrument (§7.4.2f; §7.8, examples 3, 4) which measured dip and quadrature associated with the secondary vertical EM field. These data are also given in Table 8.6.

Stations are 10 m apart. The resistivity columns are for Schlumberger spreads with  $AB/2 = 10$  m,  $MN/2 = 2$  m, and with  $AB/2 = 30$  m,  $MN/2 = 5$  m, respectively. Plot the resistivity and EM16 profiles on the same horizontal scales and compare them as to information derived and correlation.

Now plot the EM16 dip-angle data using the contouring relations given in Section 7.8, example 3. To maintain the proper polarity, the plotting is done from NE to SW (right to left with respect to the other profiles). Also the vertical scale should be chosen roughly the same length as the  $\rho_a$  scale to enhance the curve match. In

considering the possible correlation between the profiles, why should it exist? Is there any physical relation between the numbered vertical scale for the EM16 and the  $\rho_a$  scale of the resistivity profile? Hence what is the fundamental difference remaining between the two types of survey with respect to acquired data? The EM16 survey extended an additional 300 m SW and was performed by one man in 40 min; the resistivity profile occupied four men for nearly 3 h.

8. The resistivity profiles shown in Figure 8.47 are taken from an IP survey. The double-dipole spread was used with two dipole spacings:  $x = 10$  m for the top three profiles, 50 m for the remaining four. Distances between the dipole centers are noted on the right-hand column beside the profiles, corresponding to  $n = 1, 3$ , and 4 for  $x = 10$  m, and  $n = 1, 2, 3, 4$  for  $x = 50$  m.

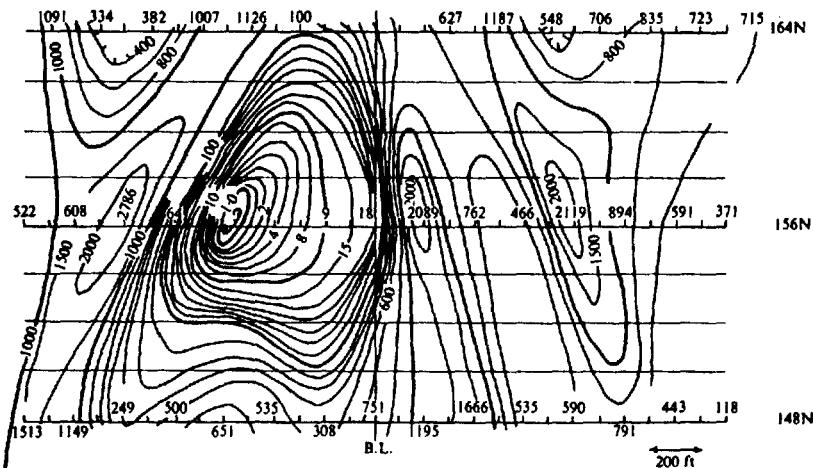


Figure 8.50. Apparent-resistivity contours ( $\Omega\text{m}$ ), southern New Brunswick.

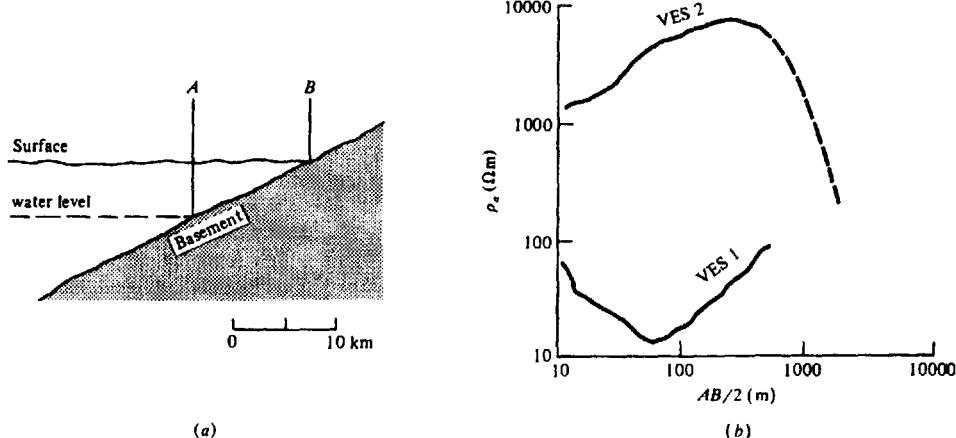


Figure 8.51. Example of "dry wedge" and related electric soundings for groundwater.  
(a) Vertical section. (b) Vertical sounding over the section.

- Apparent resistivities are plotted on a log scale and vary from a maximum of about  $700 \Omega\text{m}$  (west end of profile for  $x = 50 \text{ m}$ ,  $n = 3$ ) to a minimum of  $7 \Omega\text{m}$  (at  $38\text{W}$  on the profile for  $x = 10 \text{ m}$ ,  $n = 4$ ). The profiles represent successively larger depths of penetration from top to bottom of the figure. The overburden is considerably oxidized but is known to be thin, about 1–2 m. What interpretation can be made from these profiles? Would there be any advantage in plotting expanding spreads, that is, depth sounding profiles, for fixed station locations?
9. Two depth sections of apparent resistivity are shown in Figure 8.48 for an area in northern Quebec. Both employed the same double-dipole

electrode system with  $x = 100 \text{ ft}$  and  $n = 1, 2, 3, 4$ . One was done with a time-domain, the other with a frequency-domain, IP set. The traverse is in the vicinity of an old mining operation in which zinc, copper, lead, and some silver were recovered. Compare the results obtained by the two methods by plotting the profiles for  $n = 1$  to 4. Can you explain the difference? Are there any obvious interesting features in these plots? The survey was done during winter because of swampy terrain.

10. Figure 8.49 shows apparent resistivity contours obtained from an IP survey in eastern Nova Scotia. The electrode arrangement was double-dipole with  $x = 200 \text{ ft}$  and  $n = 1$ . The rocks in

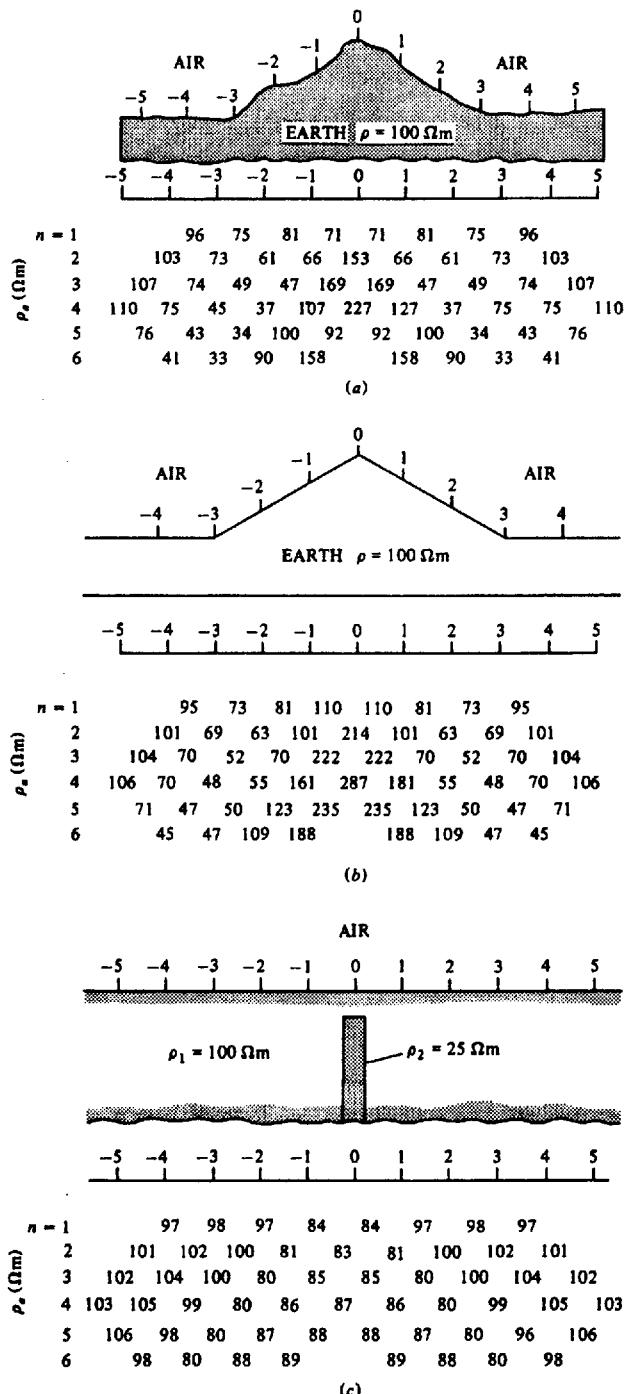


Figure 8.52. Effect of terrain on dipole-dipole resistivity survey. (a) Pseudodepth plot of  $\rho_e$  over 2-D ridge. (b) Model results for a 30° ridge. (c) Results over a buried vertical conductive dike.

- the area are generally volcanics, although in the section shown there are no outcrops; the overburden is not expected to be anywhere more than 25 ft deep and usually is less than 15 ft. There is a large-scale geochemical anomaly (Cu, Pb, Zn) associated with the area. Drainage is to the south whereas the glaciation direction is approximately northeast. With these data make an interpretation of the zone.
11. The contours of apparent resistivity illustrated in Figure 8.50 were developed from an IP survey in southern New Brunswick. The predominant geological feature in this area is a stock-like basic intrusive of gabbro-norite in an anticlinal structure of metasediments - argillite, slate, quartzitic mica schist, and gneiss. Note that the only lines actually surveyed are 148, 156, and 164N. Would you consider this coverage sufficient to interpolate contours of this type? Take off profiles from lines 156N and 160N and make an interpretation.
12. A problem encountered occasionally in groundwater search over large basin regions is called the "dry wedge." This is an area located above a relatively shallow section of inclined basement. As the name indicates, a well that reaches the impermeable basement above the water level in overlying sediments will be dry.
- The section shown in Figure 8.51a is a schematic of this situation from a groundwater program in West Africa. The dry wedge is between *A* and *B*. The two soundings shown in Figure 8.51b were carried out in the area. Interpret the geologic section below each and determine roughly where they were located in Figure 8.51a. What prior information about the region would be necessary to eliminate this difficulty?
13. The apparent-resistivity pseudodepth plot displayed in Figure 8.52a is from a dipole-dipole survey over the surface section above it. This was a 2-D feature that approximated a 30° ridge. The survey crew was supplied with a set of model cards for terrain corrections, of which Figure 8.52b was the closest match.
- Correct the data for topography and replot them. Compare the results with the dike anomaly in Figure 8.52c. Discuss any obvious differences between your corrected plot and Figure 8.52c.
- Bewley, L. V. 1963. *Two-Dimensional Fields in Electrical Engineering*. New York: Dover.
- Bhattacharya, P. K., and Patra, H. P. 1968. *Direct Current Electrical Sounding*. Amsterdam: Elsevier.
- Bhattacharyya, B. B., and Sen, M. K. 1981. Depth of investigation of colinear electrode arrays over homogeneous anisotropic half-space in direct current methods. *Geophysics* 46, 768-80.
- Coggon, J. H. 1971. Electromagnetic and electrical modeling by the finite element method. *Geophysics* 36, 132-55.
- Compagnie Générale de Géophysique. 1955. Abaque de sondage électrique. *Geophys. Prosp.* 3, Supp. no. 3.
- Dey, A., and Morrison, H. F. 1979. Resistivity modeling for arbitrarily shaped three-dimensional structures. *Geophysics* 44, 753-80.
- Dobrin, M. 1960. *Introduction to Geophysical Prospecting*. New York: McGraw-Hill.
- Fox, R. C., Hohmann, G. W., Killpack, T. J., and Rijo, L. 1980. Topographic effects in resistivity and induced polarization surveys. *Geophysics* 45, 75-93.
- Ghosh, D. P. 1971. The application of linear filter theory to the direct interpretation of geoelectric resistivity sounding measurements. *Geophys. Prosp.* 19, 192-217.
- Holcombe, H. T., and Jiracek, G. R. 1984. Three-dimensional terrain corrections in resistivity surveys. *Geophysics* 49, 439-52.
- Hummel, J. N. 1932. A theoretical study of apparent resistivity in surface potential methods. *Trans. A.I.M.E. Geophys. Prosp.* 97, 392-422.
- Inman, J. R., Ryu, J., and Ward, S. H. 1973. Resistivity inversion. *Geophysics* 38, 1088-1108.
- Johansen, H. K. 1975. Interactive computer-graphic-display-terminal system for interpretation of resistivity soundings. *Geophys. Prosp.* 23, 449-58.
- Johansen, H. K. 1977. A man/computer interpretation system for resistivity soundings over a horizontally stratified earth. *Geophys. Prosp.* 25, 667-91.
- Keller, G. V., and Frischknecht, F. C. 1966. *Electrical Methods in Geophysical Prospecting*. London: Pergamon.
- Kunetz, G. 1966. *Principles of Direct Current Resistivity Prospecting*. Berlin-Nikolaese: Gebruder Borntraeger.
- Lee, T. 1975. An integral equation and its solution for some two- and three-dimensional problems in resistivity and induced polarization. *Geophys. Jour. Roy. Astron. Soc.* 42, 81-95.
- Maitlet, R. 1947. The fundamental equations of electrical prospecting. *Geophysics* 12, 529-56.
- Orellana, E. 1963. Properties and drawing of the so-called Dar Zarrouk curves. *Geophysics* 28, 99-110.
- Snyder, D. D. 1976. A method for modeling the resistivity and IP response of two-dimensional bodies. *Geophysics* 41, 997-1015.
- Van Nostrand, R. G., and Cook, K. L. 1966. Interpretation of resistivity data. U.S.G.S. Prof. Paper No. 499.
- van Overmeeren, R. A. 1981. A combination of electrical resistivity, seismic refraction, and gravity measurements for groundwater exploration in Sudan. *Geophysics* 46, 1304-13.
- Zohdy, A. A. R. 1965. The auxiliary point method of electrical sounding interpretation and its relation to the Dar Zarrouk parameters. *Geophysics* 30, 644-60.
- Zohdy, A. A. R. 1973. Automatic interpretation of resistivity sounding curves using modified Dar Zarrouk functions. U.S.G.S. Report USGS-GD-74-017, PB-232703.
- Zohdy, A. A. R., Anderson, L. A., and Muffler, L. J. P. 1973. Resistivity, self-potential and induced polarization surveys of a vapor-dominated geothermal system. *Geophysics* 38, 1130-44.

## REFERENCES

- Bewley, L. V. 1963. *Two-Dimensional Fields in Electrical Engineering*. New York: Dover.
- Bhattacharya, P. K., and Patra, H. P. 1968. *Direct Current Electrical Sounding*. Amsterdam: Elsevier.

# Chapter

## 9

# *Induced Polarization*

### 9.1. INTRODUCTION

Induced polarization (IP) is a relatively new technique in geophysics, and has been employed mainly in base-metal exploration and to a minor extent in groundwater search. Although the Schlumberger brothers, the great pioneers in geophysical exploration, had recognized the phenomenon of induced polarization some 60 years ago, during their original work in self-potential, its popularity as a geophysical tool dates from the mid-1950s, following further development work from 1948 to 1953. One form of polarization, the overvoltage effect, has been familiar in the field of physical chemistry for an even longer time.

An illustration of induced polarization can be obtained with a standard four-electrode dc resistivity spread by interrupting the current abruptly. The voltage across the potential electrodes generally does not drop to zero instantaneously, but decays rather slowly, after an initial large decrease from the original steady-state value. This decay time is of the order of seconds or even minutes. If the current is switched on again, the potential, after a sudden initial increase, builds up over a similar time interval to the original dc amplitude.

In one type of IP detector the decay voltage is measured as a function of time in various ways; this method is known as *time-domain IP*. Because the buildup time is also finite, it is clear that the apparent resistivity (actually a complex impedance) must vary with frequency, decreasing as the latter increases. Thus the measurement of  $\rho_a$  at two or more frequencies, generally below 10 Hz, constitutes another method of detection. This is known as *frequency-domain IP*.

Superficially the decay and buildup time resembles the discharge and charge time of a capacitor through a finite resistance. But the charge and decay curves are logarithmic rather than exponential (as in the R-C circuit) and do not commence at the static potential limits, 0 and  $V_e$  (Fig. 9.1).

Because the equipment employed, although more elaborate, is similar to that used in resistivity, it is customary to measure apparent resistivity, in addition to the IP effect, at each station. However, induced polarization, being mainly electrochemical in origin, has more in common with spontaneous polarization than bulk resistivity. In order to understand IP we will consider these origins in the next section.

It is interesting to compare the growth of IP and EM techniques. At present it is possible to measure both in the time and frequency domain, and also to determine complex resistivity (amplitude and phase) with either method, although the timetable for development is surprisingly different. For example, EM frequency-domain surveys (Turam, Slingram) of amplitude and phase have been carried out in Scandinavia since the mid-1920s (Hedstrom, 1940), although they did not receive much attention in the United States and Canada until some 35 years later. Roughly another 10 years passed before the first time-domain EM equipment appeared (Newmont EMP, Input). On the other hand, time- and frequency-domain IP were developed within a few years of each other in the United States and Canada in the early 1950s, whereas the complex resistivity equipment was not available until two decades later.

### 9.2. SOURCES OF THE INDUCED POLARIZATION EFFECTS

#### 9.2.1. General

The decay curve shown in Figure 9.1 represents a return to the original state following the disturbance due to applied current. During the time of the original current flow, presumably some energy storage took place in the material. Although this stored energy theoretically could – and probably does – exist in several forms, for example, mechanical, electrical, and chemical, laboratory studies of polarization in various rock types have established that the chemical energy is by far the most important.

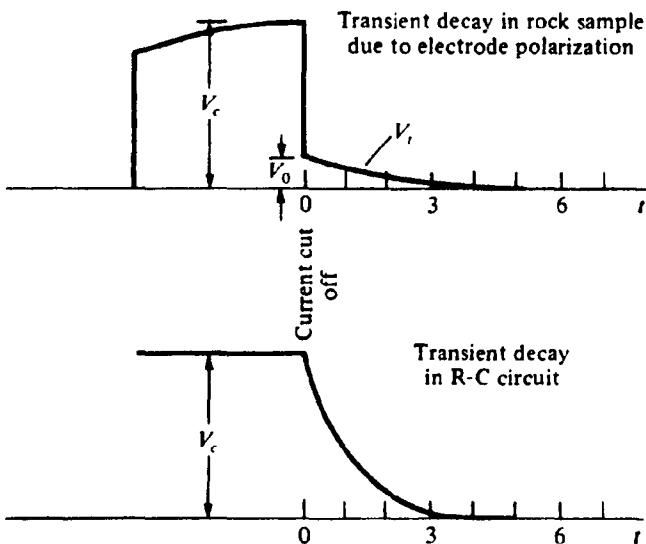


Figure 9.1. Comparison of IP and R-C decay curves.

This chemical energy storage is the result of (a) variations in the mobility of ions in fluids throughout the rock structure and (b) variations between ionic and electronic conductivity where metallic minerals are present. The first of these effects is known as *membrane* or *electrolytic polarization* and constitutes the background or so-called *normal IP effect*. It may occur in rocks that do not contain metallic minerals. The second is known as *electrode polarization* or *overvoltage*. It is generally larger in magnitude than the background IP and depends on the presence of metallic minerals in the rock. The two effects are indistinguishable by IP measurement. Furthermore, they appear to be independent of the atomic or molecular structure in rocks and minerals, that is, IP is a bulk effect.

## 9.2.2. Membrane Polarization

Electrolytic conduction is the predominating factor in most rocks (§5.2.2 and §5.2.4), being the only form of conduction when no minerals are present and the frequency is low. Thus a rock structure must be somewhat porous to permit current flow when metallic minerals are absent. Most rock minerals have a net negative charge at the interface between the rock surface and pore fluid. Consequently positive ions are attracted toward, negative repelled from, this interface; this positive ion concentration may extend into the fluid zone to a depth of about  $10^{-6}$  cm. If this is the order of width of the pore itself, negative ions will accumulate at one end of the zone and leave the other when a dc potential is applied across it. As a result of this polarized distribution, current flow is impeded. At a later time, when the current is switched off, the ions return to their origi-

nal positions, taking a finite time to do so. This situation is illustrated in Figure 9.2.

The membrane IP effect is most pronounced in the presence of clay minerals, in which the pores are particularly small. The magnitude of polarization, however, does not increase steadily with the clay mineral concentration, but reaches a maximum and then decreases again. This is because there must be alternate passages of larger cross section and very short length ( $\sim 10^{-3}$  cm) in the material where ion accumulation does not take place for appreciable time; otherwise both total current flow and polarization are reduced. Optimum concentration varies in different types of clay, being low in montmorillonite and higher in kaolinite. Shales, with a high percentage of clay minerals, have a relatively low polarization. The membrane effect also increases with the salinity of the pore fluid.

As a result of these factors, membrane polarization is generally a maximum in a rock containing clay materials scattered through the matrix in rather small ( $\leq 10\%$ ) concentration and in which the electrolyte has some salinity.

Other sources of background polarization include normal dielectric and electrokinetic effects, presence of conducting minerals in very small amounts, and possibly surface conduction on normally nonconducting material. Of these, the electrokinetic response due to variations in pore cross section affecting fluid flow is probably more significant than the others. None of these sources, however, is comparable in magnitude to membrane polarization.

The overall background polarization is about what one would expect from a rock containing 1 to 2% conducting minerals, but may vary from one-tenth to ten times this value. Because it cannot be distinguished from electrode polarization, the background provides a level of geological noise varying from place to place.

## 9.2.3. Electrode Polarization

This type, similar in principle to membrane polarization, exists when metallic material is present in the rock and the current flow is partly electronic, partly electrolytic. A chemical reaction occurs at the interface between the mineral and solution.

Consider the two pore passages shown in the rock section in Figure 9.2c. In the upper one the current flow is entirely electrolytic. In the lower, the presence of a metallic mineral, having net surface charges of opposite sign on either face, results in an accumulation of ions in the electrolyte adjacent to each. The action is that of electrolysis, when current flows and an electron exchange takes place between the metal

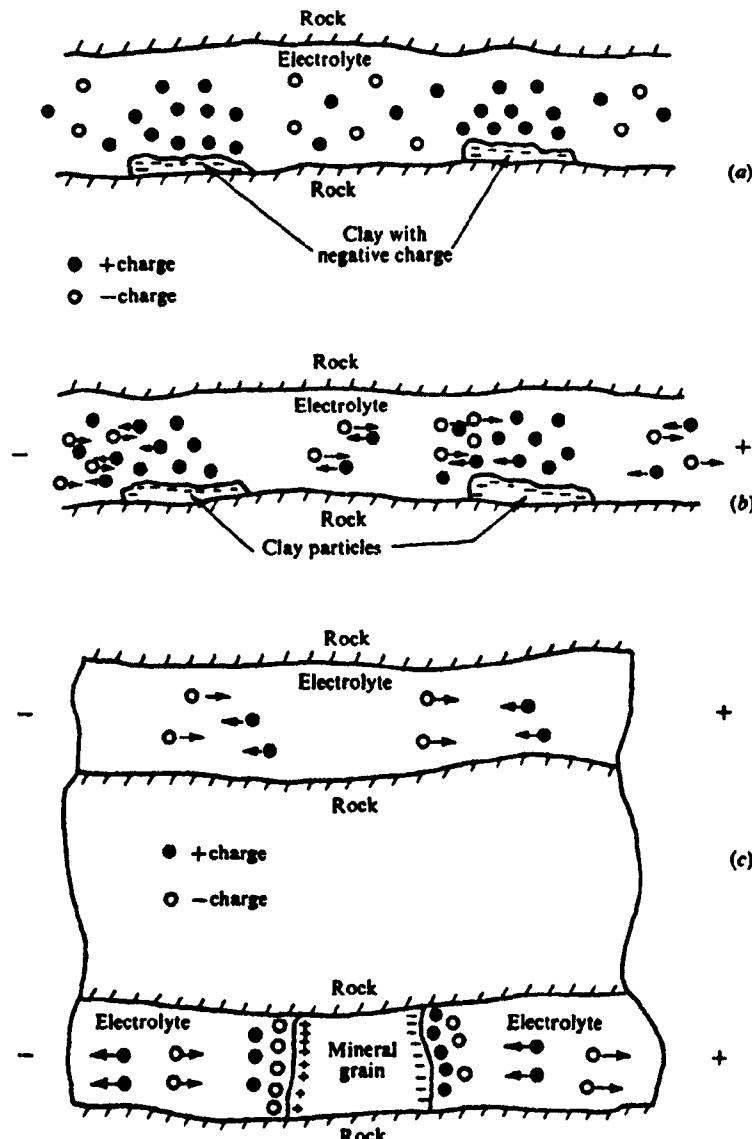


**Figure 9.2. Membrane and electrode polarization effects. (a) Normal distribution of ions in a porous sandstone; (b) Membrane polarization in a porous sandstone due to an applied dc voltage; (c) Electrolytic flow in upper pore, electrode polarization in lower pore.**

and the solution ions at the interface; in physical chemistry this effect is known as *overvoltage*.

Because the velocity of current flow in the electrolyte is much slower than in the metal, the pileup of ions is maintained by the external voltage. When the current is interrupted, the residual voltage decays as the ions diffuse back to their original equilibrium state.

Minerals that are electronic conductors exhibit electrode polarization. These include almost all the sulfides (excepting pure sphalerite and possibly cinnabar and stibnite), some oxides such as magnetite, ilmenite, pyrolusite, and cassiterite, and – unfortunately – graphite.

The magnitude of this electrode polarization depends, of course, on the external current source and

also on a number of characteristics of the medium. It varies directly with the mineral concentration, but because it is a surface phenomenon, it should be larger when the mineral is disseminated than when it is massive. Actually the situation is not as simple as this. The optimum particle size varies to some extent with the porosity of the host rock and its resistivity. Furthermore, so-called massive sulfides are generally not homogeneous, being interbedded with lower conductivity host rock. However, the fact that disseminated mineralization gives good IP response is a most attractive feature, because other electrical methods do not work very well in these circumstances.

Considerable careful sample testing was done in the early days of IP (Collett, 1959). Unfortunately it

is difficult to perform laboratory measurements at current density as low as those encountered in field work.

At low current density the overvoltage-current relation is known to be linear (Seigel, 1959a, b). Over a wider range, however, polarization varies inversely with current density, decreasing by a factor of 2 as the latter increases 10-fold. Thus laboratory and field results may not correspond, although the sampling work has provided additional useful information. For example, IP response decreases with increasing source frequency; this is true for membrane as well as electrode polarization, but the decrease is about 2 orders greater for the latter than for the former.

Other definite relations depend on type and condition of rocks. For a particular fluid concentration the polarization decreases with increasing rock porosity, because there is an increasing number of alternate paths for electrolytic conduction. Thus one would expect a larger IP effect in a disseminated sulfide occurring in dense igneous rocks than in a porous host rock (§9.3.7). Polarization also varies with the fluid content of the rock; from sample experiments, it has been shown that a maximum occurs when about 75% of the pore space is filled with water. Further laboratory investigations may be found in Fraser, Keevil, and Ward (1964), Zonge (1972), and Katsube and Collett (1973).

#### 9.2.4. Equivalent Electrical Circuits

It is attractive to replace the porous rock structure, with or without mineral and membrane zones, by an equivalent electrical circuit. We have already seen in Section 9.1 that a simple  $R$ - $C$  network will not explain the current flow and consequent IP effect. The circuit illustrated in Figure 9.3 provides a better analog for both types of polarization. The effective pore-fluid resistance is shown as  $R_1$  and  $R_0$ , the series section representing the solution resistance in the pore passages containing clay or metallic minerals ( $Z_m$ ), whereas the parallel section  $R_0$  simulates alternate zones that are purely resistive, with electrolytic conduction.

The impedance  $Z_m$  presumably represents a shortage or excess of ions in the vicinity of clay particles in the case of membrane polarization, or the metallic-ionic interface for electrode polarization. In early descriptions of the circuit,  $Z_m$  was known as a *Warburg impedance* whose magnitude varied inversely as the square root of frequency (Marshall and Madden, 1959). A more recent version, called the *Cole-Cole relaxation model* (Cole and Cole, 1941; Pelton et al., 1978), has the frequency exponent  $c$  in the range 0.25 to 0.35 (rather than 0.5) for most IP effects. However, the range has

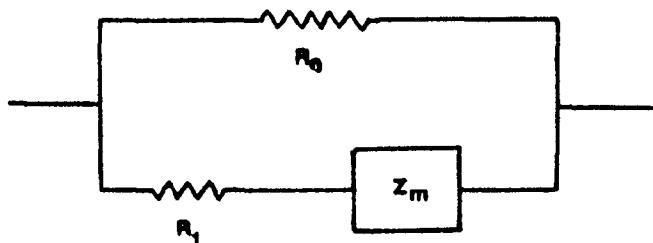


Figure 9.3. Equivalent electrical circuit to simulate the IP effect.

been extended upward to approximately 1.0 in dealing with EM coupling (§9.4.4c) and occasionally as low as 0.1 (Fig. 9.16c) for certain minerals. The theoretical limits for  $c$  are identical to those for the chargeability (§9.3.2c), that is, zero to unity. This circuit model, although still oversimplified, provides an improved match of IP response parameters.

### 9.3. INDUCED POLARIZATION MEASUREMENTS

#### 9.3.1. General

As mentioned in Section 9.1, measurements of IP may be made either in the time or the frequency domain. The former are known as *pulse transient measurements*, the latter as *frequency variations*. In both cases, the voltage is measured as a function either of time or frequency. In a recent development (§9.3.5) known as *magnetic IP (MIP)*, measurements are made of the magnetic field in either domain. The various units of measurement are defined in the next two sections.

#### 9.3.2. Time-Domain Measurements

(a) *Millivolts per volt (IP percent)*. The simplest way to measure IP effect with time-domain (T-D) equipment is to compare the residual voltage  $V(t)$  existing at a time  $t$  after the current is cut off with the steady voltage  $V_c$  during the current-flow interval (Fig. 9.4a). It is not possible to measure potential at the instant of cutoff because of large transients caused by breaking the current circuit. On the other hand,  $V(t)$  must be measured before the residual has decayed to noise level.

Because  $V(t)$  is much smaller than  $V_c$ , the ratio  $V(t)/V_c$  is expressed as millivolts per volt, or as a percent. The time interval  $t$  may vary between 0.1 and 10 s.

(b) *Decay-time integral*. Commercial IP sets generally measure potential integrated over a definite time interval of the transient decay, as shown in Figure 9.4b. If this integration time is very short and

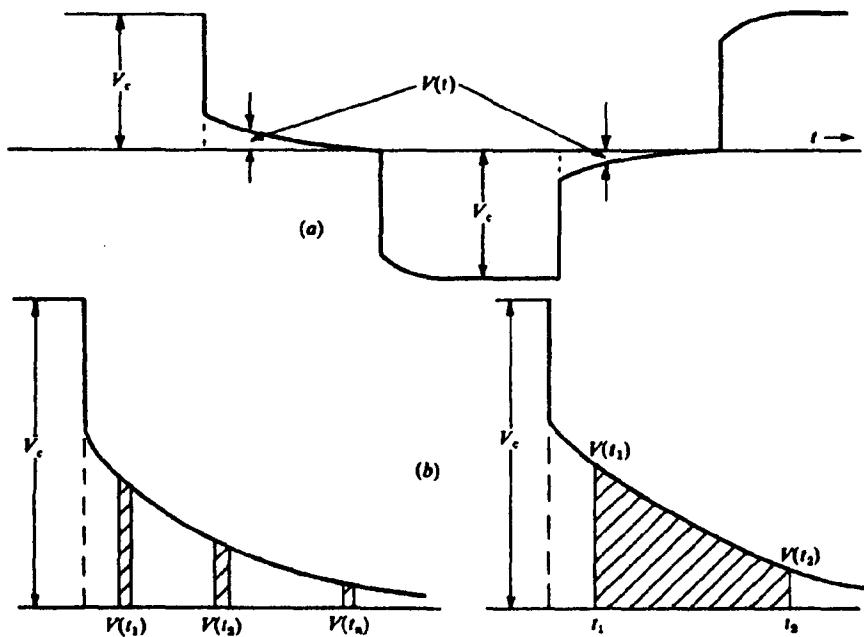


Figure 9.4. Different measures of the time-domain IP effect. (a) Comparison of  $V(t)$  with  $V_c$ . (b) Integral of  $V(t)$  over a time interval.

if the decay curve is sampled at several points, the values of the integral are effectively a measure of the potential existing at different times, that is,  $V(t_1), V(t_2), \dots, V(t_n)$ . This is an extension of the measurement in (a) from which one also obtains the decay curve shape.

(c) Chargeability. This is defined as

$$M = \frac{1}{V_c} \int_{t_1}^{t_2} V(t) dt \quad (9.1)$$

and is the most commonly used quantity in time-domain IP measurement. When  $V(t)$  and  $V_c$  have the same units, the chargeability  $M$  is in milliseconds.

### 9.3.3. Frequency-Domain Measurements

(a) Frequency effect. In frequency-domain (*F-D*) IP, one measures the apparent resistivity at two or more frequencies. The *frequency effect* is usually defined as

$$FE = (\rho_{dc} - \rho_{ac})/\rho_{ac} = (\rho_{dc}/\rho_{ac}) - 1 \quad (9.2a)$$

whereas the *percent frequency effect* is given by

$$PFE = 100(\rho_{dc} - \rho_{ac})/\rho_{ac} \quad (9.2b)$$

where  $\rho_{dc}, \rho_{ac}$  are apparent resistivities measured at dc and very high frequency. As we have seen in Section 9.2.4 and Figure 9.3,  $\rho_{dc}$  is determined by the alternate path  $R_0$  only, whereas  $\rho_{ac}$  depends on

$R_0$  shunted by  $R_1$  and  $Z_m$ . Hence  $\rho_{ac} < \rho_{dc}$ . In practice measurements are made at two or more frequencies in the range 0.1 to 10 Hz, or higher,  $\rho_{dc}$  being taken as the value obtained at the lowest frequency.

(b) Metal factor. We have mentioned that the IP effect varies with effective resistivity of the host rock, that is, the type of electrolyte, temperature, pore size, and so forth. The *metal-factor parameter*, originally suggested by Marshall and Madden (1959), corrects to some extent for this variation. It is a modification of the expression in Equation (9.2a):

$$\left. \begin{aligned} MF &= 2\pi \times 10^5 (\rho_{dc} - \rho_{ac}) / \rho_{dc} \rho_{ac} \\ &= 2\pi \times 10^5 FE / \rho_{dc} \end{aligned} \right\} \quad (9.3a)$$

Because apparent resistivities were frequently given in ohm-feet (actually in the form  $\rho_a/2\pi \Omega\text{ft}$ ) on frequency domain IP equipment, metal-factor values originally had units of mhos per foot, rather than mhos per meter (now siemens per meter). Thus, a more convenient form of Equation (9.3a) is

$$MF = 10^5 FE / (\rho_{dc}/2\pi) = 10^3 PFE / (\rho_{dc}/2\pi) \quad (9.3b)$$

### 9.3.4. Relative Phase Shift and Phase Components

The *relative phase shift (RPS)* is the phase angle or time shift between the transmitter current and receiver voltage. This is a measurement of considerable

significance in IP surveying, because there is a linear relation between phase and frequency effect in the form

$$\phi = k' \text{FE} \quad (9.4)$$

where  $\phi$  is the phase defined previously and  $k'$  is a constant for a particular sample or field situation, which appears to have an approximate range of  $-0.3$  to  $-0.5$  for different grades of mineralization (Scott 1971; see also Fig. 9.12b).

Measurements of RPS were originally carried out on rock samples to identify IP signatures for particular minerals in the laboratory (Fraser, Keevil, and Ward, 1964; Zonge, 1972). The study was extended shortly after to field work (Lambert, 1974; Zonge and Wynn, 1975). The phase measurement led directly to a determination of sample or ground impedance, because the measurement of  $R$ , the real component of the impedance, and the phase  $\phi$  enables us to find the impedance using Equation (7.18).

### 9.3.5. Magnetic Induced Polarization (MIP) Measurements

This method and another called *magnetometric resistivity (MMR)* appeared in the literature about the same time (Seigel, 1974; Edwards, 1974). The latter dates back to a patent of Jakosky in 1933 (Edwards, Lee, and Nabighian, 1978). In this paper it is stated that MIP is related to MMR in the same sense that IP resembles the resistivity method, although the similarities appear closer than this. For this reason we will concentrate on MIP, with reference to reports on both methods.

The MIP method utilizes a component of the magnetic, rather than the electric, field due to galvanic current (Seigel and Howland-Rose, 1983). Two quantities are usually measured: The first, the normalized primary magnetic field,  $H_N$ , is given by

$$H_N = H_p / H'_p \quad (9.5)$$

where  $H_p$  is the so-called *steady-state magnetic field amplitude* measured at a single transmitter frequency and  $H'_p$  is the  $H_p$  value calculated for uniform ground at the same location;  $H_N$  is expressed in percent. The second quantity is the magnetometric resistivity (MMR) (Edwards and Howell, 1976):

$$\text{MMR} = (H_p - H_{p0}) / H_{p0} \quad (9.6)$$

where  $H_{p0}$  is the predicted uniform-ground primary field at the midpoint between current electrodes.

The preceding are frequency-domain parameters. In the time domain we use chargeability  $M$  (§9.3.2c) averaged over preselected time intervals as in Figure 9.4b. For the selected  $i$ th time interval we obtain  $M_i$

from the voltage  $V_i(t)$ . During current on-time we measure  $H_p$  and calculate  $H_N$ ;  $M_i$  is then normalized by dividing by  $H_N$ . The magnetic fields considered here are very small, in the picotesla ( $10^{-12}$  T) range and require a sensitive low-noise fluxgate instrument (because components, not the total field, are measured).

### 9.3.6. Relation between Time- and Frequency-Domain IP Measurements

In theory, because both frequency and time measurements represent the same phenomenon, their results ought to be the same; practically the conversion of time domain to frequency domain and vice versa is quite difficult. The square wave used in time-domain IP contains all frequencies, assuming that the fronts are infinitely steep.

Seigel (1959a) defines the chargeability as

$$M = \left\{ \lim_{t \rightarrow \infty} V(t) - \lim_{t \rightarrow 0} V(t) \right\} / \lim_{t \rightarrow \infty} V(t)$$

By Laplace transform theory, it can be shown that

$$\lim_{t \rightarrow \infty} V(t) = J\rho_{dc} \quad \text{and} \quad \lim_{t \rightarrow 0} V(t) = J\rho_\infty$$

where  $\rho_\infty$  is the apparent resistivity at very high frequency and  $J$  is the current density. Consequently, using Equation (9.2a) and assuming that  $\rho_{ac} = \rho_\infty$ , we can write for the chargeability

$$\begin{aligned} M &= \frac{\rho_{dc} - \rho_\infty}{\rho_{dc}} = 1 - \frac{\rho_{ac}}{\rho_{dc}} \\ &= 1 - \frac{1}{1 + \text{FE}} = \frac{\text{FE}}{1 + \text{FE}} \approx \text{FE} \quad (9.7) \end{aligned}$$

when  $\text{FE} \ll 1$ .

In practical situations this simple relation is not valid, partly because an exact theoretical analysis of the IP effect is not available (that is, the basic premises of the two systems of measurements are only approximately valid), partly because the measurements are not made at dc and VHF in either IP system. Thus, in general, it is not possible to convert one result to the other (Fig. 9.11).

### 9.3.7. IP Response Examples

Although the type and grade of mineralization are not fixed by the values of the IP response, the following tables may be of some use in crude assessment of field results. Table 9.1 lists the chargeability of a variety of minerals at 1% volume concentration. The duration of the square-wave current was 3 s and

Table 9.1. Chargeability of minerals.

Mineral	Chargeability (ms)
Pyrite	13.4
Chalcocite	13.2
Copper	12.3
Graphite	11.2
Chalcopyrite	9.4
Bornite	6.3
Galena	3.7
Magnetite	2.2
Malachite	0.2
Hematite	0.0

Table 9.2. Chargeability of various minerals and rocks.

Material	Chargeability (ms)
20% sulfides	2,000 – 3,000
8 – 20% sulfides	1,000 – 2,000
2 – 8% sulfides	500 – 1,000
Volcanic tuffs	300 – 800
Sandstone, siltstone	100 – 500
Dense volcanic rocks	100 – 500
Shale	50 – 100
Granite, grandiorite	10 – 50
Limestone, dolomite	10 – 20

the decay was integrated over 1 s. These values appear high with respect to usual field measurements because it is not customary to employ such a long timing cycle or to integrate the complete decay curve. However, they do illustrate the variation between different IP sources.

Table 9.2 shows the response of a variety of mineralized and barren rocks. Here the charging time is long (~ 1 min) and the decay curve is integrated over its entire duration (excluding the initial transient and final noise).

Table 9.3 shows further values of chargeability for various materials. The charging time was 3 s and the integration time from 0.02 to 1 s of the decay curve.

Table 9.4 lists typical metal factors for a variety of igneous and metamorphic rocks.

Obviously because of the considerable overlap in values, it is not possible to distinguish between poorly mineralized rocks and several barren types, such as tuffs and clays.

## 9.4. IP FIELD OPERATIONS

### 9.4.1. General

As mentioned earlier, the equipment and field procedure for induced polarization surveys are similar to

Table 9.3. Chargeability of various materials.

Material	Chargeability (ms)
Ground water	0
Alluvium	1 – 4
Gravels	3 – 9
Precambrian volcanics	8 – 20
Precambrian gneisses	6 – 30
Schists	5 – 20
Sandstones	3 – 12
Argillites	3 – 10
Quartzites	5 – 12

Table 9.4. Metal factor of various rocks and minerals.

Material	Metal factor (mhos/cm)
Massive sulfides	10,000
Fracture-filling sulfides	1,000 – 10,000
Massive magnetite	3 – 3,000
Porphyry copper	30 – 1,500
Dissem. sulfides	100 – 1,000
Shale-sulfides	3 – 300
Clays	1 – 300
Sandstone – 1 – 2% sulfides	2 – 200
Finely dissem. sulfides	10 – 100
Tuffs	1 – 100
Graphitic sandstone and limestone	4 – 60
Gravels	0 – 200
Alluvium	0 – 200
Precambrian gneisses	10 – 100
Granites, monzonites, diorites	0 – 60
Various volcanics	0 – 80
Schists	10 – 60
Basic rocks (barren)	1 – 10
Granites (barren)	1
Groundwater	0

that used in resistivity exploration. This usually results in a combined resistivity-IP survey; sometimes SP may be measured as well. The equipment is relatively elaborate and bulky. Of the commonly used ground-exploration methods (excluding seismic), it is one of the most expensive, being roughly comparable to magnetotellurics and gravity in cost per month. The field work also is slow compared to magnetics, EM, and SP.

### 9.4.2. Field Equipment

(a) Transmitter. A block diagram of a conventional IP transmitter, which will function in either time or frequency mode, is illustrated in Figure 9.5. It consists of a motor generator whose output is converted to current-controlled (0.2 to 1%) high-voltage dc, followed by a switching system that produces square-wave output of various forms suitable for

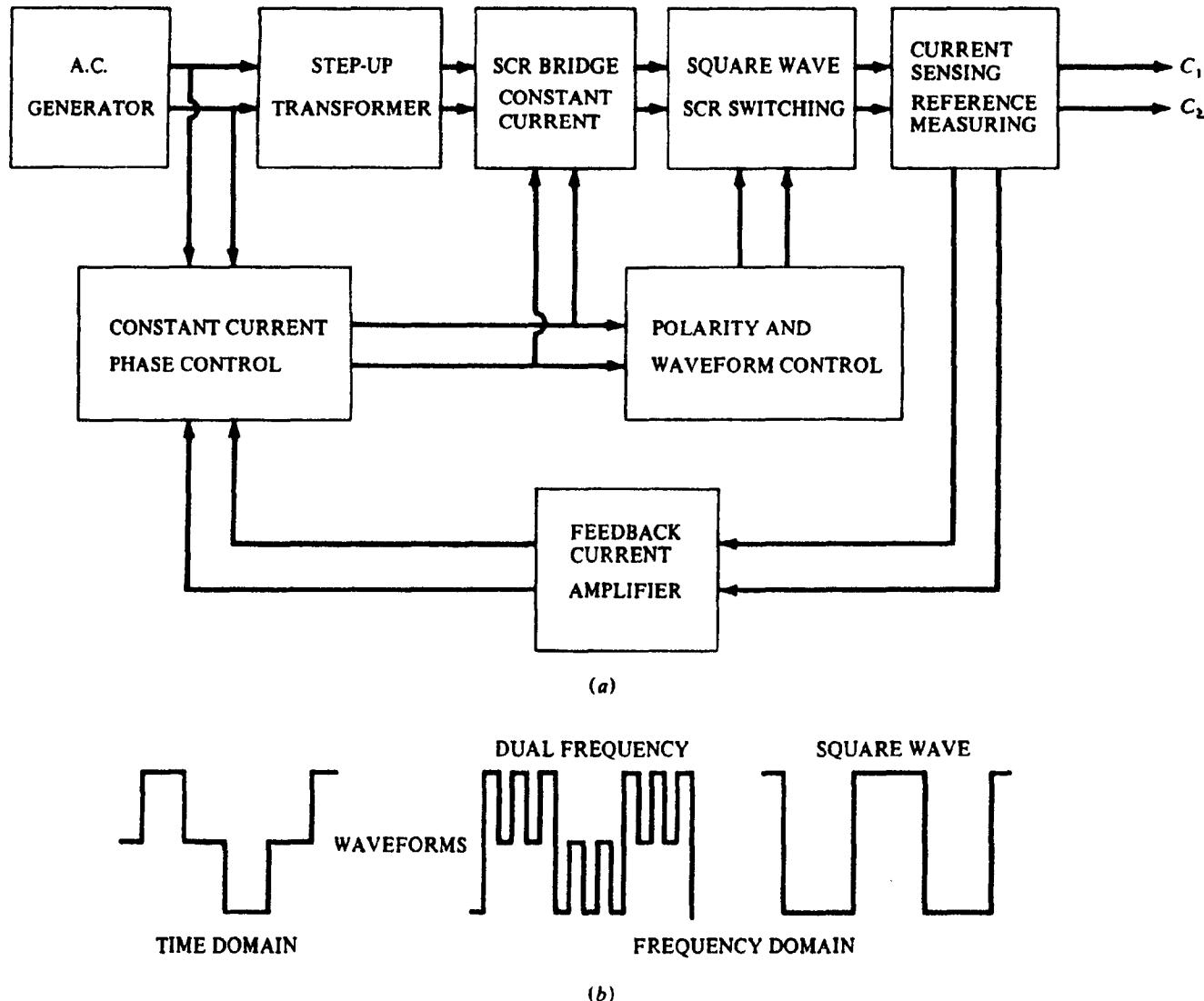


Figure 9.5. IP transmitter for time- and frequency-domain measurements. (After Sumner, 1976.) (a) Block diagram. (b) Typical waveforms.

either time- or frequency-domain operation, as shown in the diagram.

Most units use a gasoline-driven ac generator, generally 110 or 208 V, 400 Hz (to reduce weight), the power varying from 1 to 10 kVA, occasionally more. Several portable *T-D* transmitters are also available in the 100 W range. These employ battery-charged capacitors to produce the high-voltage pulse for shorter time periods and generally use signal stacking (§4.4.8). However, their range is limited, particularly in areas of conductive near-surface rocks and overburden. Large units are heavy, 70 to 350 kg.

The timing cycle may be 1 to 10 s on and off for *T-D* and 0.1 to 10 Hz with various intermediate frequencies for *F-D* equipment. Occasionally the ranges are considerably greater. Outputs vary from 1 to 5 A and up to 5,000 V in the larger units. Use of solid-state (SCR) switching has provided a great improvement in the control circuits so that a variety of output waveforms, sine- as well as square-wave,

may be produced. The sudden change to off-time during the *T-D* duty cycle requires a dummy load in the output or an automatic cutout device to minimize generator surges.

**(b) Receiver; general.** This half of the IP set measures the voltage at the potential electrodes. Formerly done with a simple voltmeter, it may now involve a miniature computer. Both *T-D* and *F-D* receivers require compensation for spurious SP and telluric signals. On older instruments SP was bucked out manually, later automatically, using a potentiometer control for dc offset at the receiver input. On some *F-D* receivers the SP was eliminated by capacitive input in the form of a high-pass filter, which also disposed of most of the telluric noise; however, the low-frequency cutoff for the IP signals was about 0.3 Hz. In *T-D* receivers the telluric effect may be reduced by averaging readings over several decay cycles.

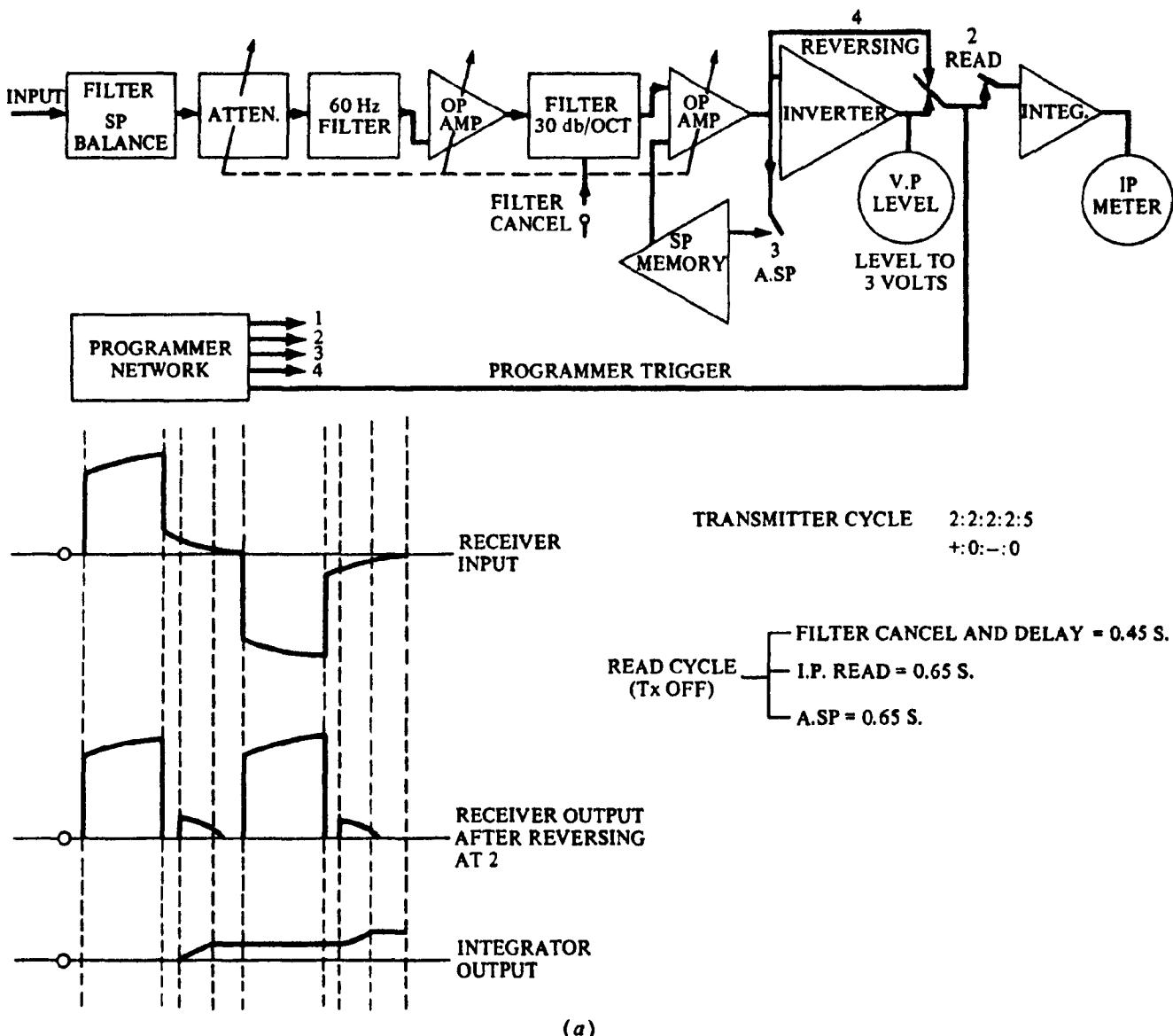


Figure 9.6. Block diagrams of typical IP receivers. (a) Newmont T-D receiver. (After Dolan and McLaughlin, 1967.)

(c) *Time-domain receiver.* Essentially an integrating voltmeter with a range from dc to very low-frequency ac, it measures decay voltage over a selected time interval following transmitter-current cutoff. This gives the chargeability  $M$  from Equation (9.1),  $V_c$  having been measured during current on-time. The integration time may typically be, as in the Newmont T-D receiver (Fig. 9.6a), from 0.45 to 1.1 s, during a 2 s on-off pulse. Obviously the character of the decay curve can be established by sampling and integrating the data in a series of windows to determine possible departure from logarithmic shape.

(d) *Frequency-domain receiver.* This also is a sensitive low-frequency voltmeter similar to the T-D version (Fig. 9.6b). Generally voltages at two or more frequencies are recorded separately, although in some units measurements may be made at two frequencies simultaneously; a McPhar instrument

achieves the latter by transmitting a dual frequency as shown in Figure 9.5 whereas a Scintrex model measures PFE between a fundamental and third harmonic of a single square-wave transmission. The Scintrex equipment also obtains the phase (RPS) between these components without the requirements listed in Section 9.4.2f.

(e) *Magnetic IP equipment.* The only addition to a standard IP instrument that is required for the MIP survey is a high-sensitivity vector magnetometer in place of the potential electrodes and receiver. The magnetometer must have flat frequency response from dc up to 1,000 Hz, resolution greater than 1 pT, and noise level less than  $(1/f)^{1/2}$  pT.

Magnetotelluric noise is a problem in MIP work; in equatorial regions this noise (caused mainly by thunderstorms) is of relatively high frequency whereas at higher latitudes it becomes troublesome

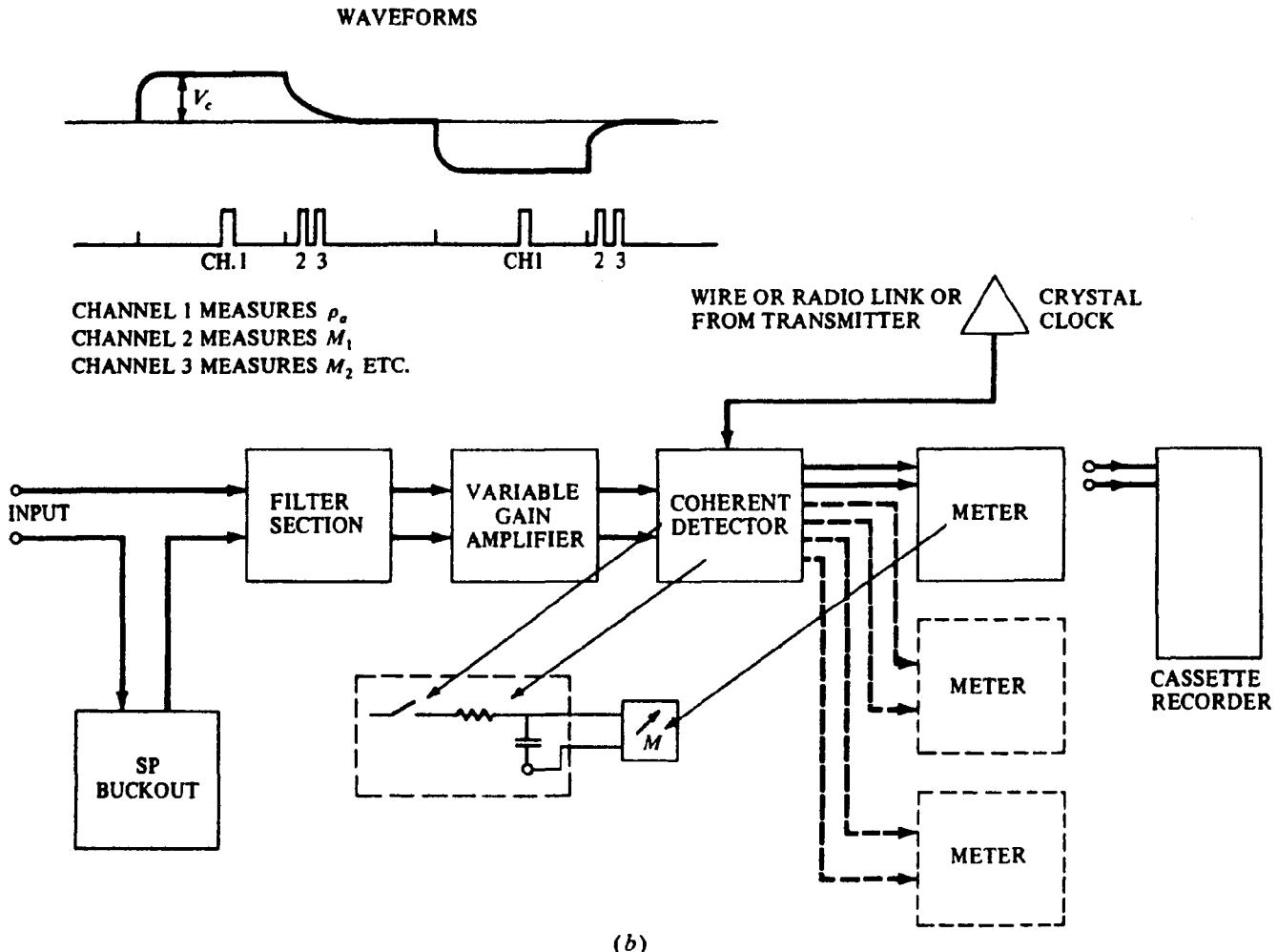


Figure 9.6. (Continued) (b) F-D receiver. (After Sumner, 1976.)

in the 0 to 10 Hz range. The situation is improved by (i) high-power IP transmitters to increase current density, (ii) narrow-band filters, particularly in *F-D* surveys, (iii) digital stacking and averaging in either domain, and (iv) a reference magnetometer at a base station located some distance away from the survey area, oriented parallel to the measuring instrument, and transmitting its signal by wire or radio to be mixed out-of-phase with the recorded signals.

The MIP technique may be performed in either time or frequency domain. The former allows measurement of broad-band response by recovery of the decay curve. In areas of high noise the *F-D* system with narrow-band filters produces better signal-to-noise ratios but less IP information per measurement.

(f) *Spectral-phase equipment.* Phase shift (RPS) and impedance were discussed in Section 9.3.4. There are several advantages gained from this measurement; (i) by obtaining amplitude and phase at a single frequency, one effects a saving in time over amplitude measured at two frequencies (although simultaneous transmission of dual frequencies is now available), (ii) improved signal-to-noise ratio

(Sumner, 1979), (iii) a means of removing EM coupling effects (Wynn and Zonge, 1975; Pelton et al., 1978; see also §9.4.4c), and (iv) determination of ground impedance.

The phase may be obtained from standard IP equipment in several ways: by a temporary *T-R* cable or radio link, by analysis of *T-R* data, or with a precise clock reference. There are drawbacks with each of these methods and they all work better with sinusoidal rather than square waveforms.

Recent computer-controlled systems, called *spectral-phase IP*, measure amplitude and phase over a wide frequency band which makes it possible to obtain the electrical impedance of the subsurface in the field. The computer control of frequency, transmitter current, and the linked receiver voltage provides, after digitizing, response spectra of  $\phi$ ,  $R$ , and  $X$ , as well as  $M$  (or FE) and  $\rho_a$ . Computer analysis may then be used to distinguish EM coupling from normal IP response (§9.4.4c) in order to remove the former. Finally, plots of phase versus frequency using field data may be matched by computer iterative processes for various models. A block diagram of a complex-resistivity IP (CRIP) system is shown in Figure 9.7.

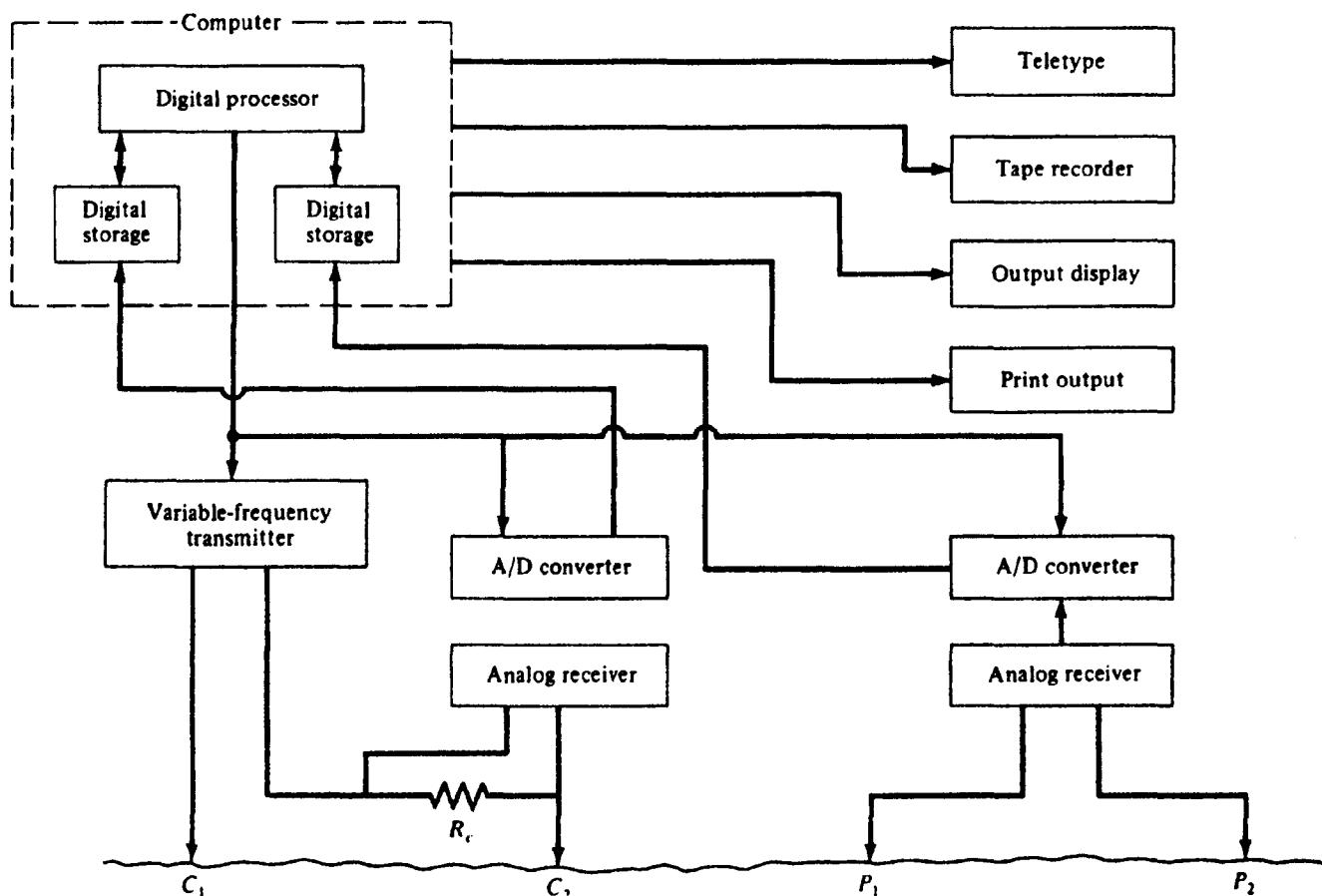


Figure 9.7. Block diagram of complex-resistivity system with double-dipole array. (After Sumner, 1979.)

(g) **Electrodes and cables.** Current electrodes are usually metal stakes as in resistivity work. Sometimes it is necessary to use aluminum foil in shallow holes. It may also be necessary to wet the electrodes with salt water to provide sufficiently good contact for the desired high currents. Porous pots are often used for the potential electrodes because of the low frequencies. The current wires must be capable of withstanding voltages of 5 to 10 kV.

#### 9.4.3. Field Procedures

Because the IP electrode system is identical to resistivity, theoretically one can use any of the field spreads described in Section 8.5.3. In practice the Schlumberger or gradient array, the pole-dipole in which one current electrode is removed a great distance, and the double-dipole, with a rather small value of  $n$ , are the three commonly used IP spreads, generally laid out across geologic or target strike.

The latter two configurations are illustrated in Figure 9.8. Using the dimensions as shown and Equation (8.26), the apparent resistivities for these two spreads, over homogeneous ground, are

**Double dipole:**

$$\rho_a = \pi n(n+1)(n+2)x \Delta V/I \quad (9.8)$$

**Pole dipole:**

$$\rho_a = 2\pi n(n+1)x \Delta V/I \quad (9.9)$$

Values of  $n$  range from 1 to 10, although 6 is usually the upper limit. The electrode spacing may be as small as 3 m and as large as 300 m. To reduce the work of moving the current electrodes and particularly the heavy transmitter unit, several pairs of current electrodes are often placed in suitable locations and wired to a fixed transmitter; the latter is then switched from one to the other.

Results are usually plotted at the midpoint of the spread (or in pole-dipole, the midpoint of  $C_1P_1$ ), although occasionally the midpoint of either current or potential pair is taken as the station location.

The larger electrode spacings are mainly for reconnaissance although, as in resistivity, the depth of penetration is controlled in part by the spacing. Frequently the same line is traversed several times with different spacings, for example,  $x = 30$  or 60 m and  $n = 1, 2, 3, 4$ , and so on; by so doing, one obtains a combination of lateral profiling and vertical sounding.

As mentioned previously, apparent resistivities are also obtained at each station. On older models self-potential may also be recorded by noting the

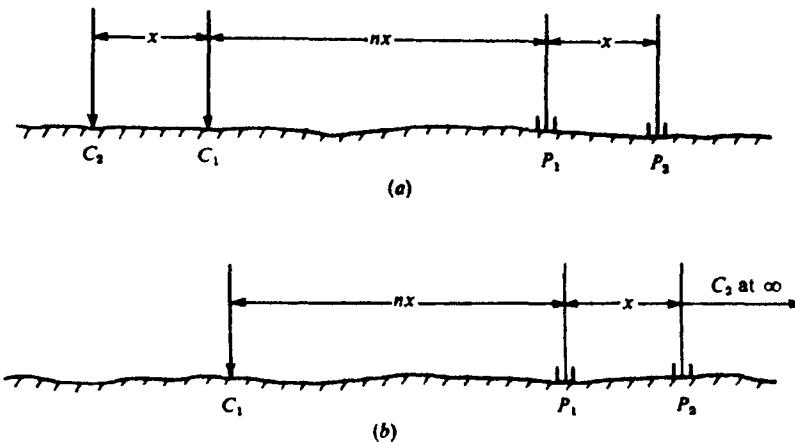


Figure 9.8. Typical IP spreads. (a) Double-dipole. (b) Pole-dipole.

bucking potential required before current is switched on.

Field arrays for MIP, two examples of which are shown in Figure 9.9, are considerably different from conventional IP and resistivity. The current electrodes are usually oriented along strike and located approximately over the target. The arrangement in Fig. 9.9a is used for reconnaissance;  $C_1$  and  $C_2$  are fixed and joined by a large U-shaped loop lying out of the area of interest. Magnetometer traverses are made on lines orthogonal to strike as shown, the horizontal component in this direction being measured at station intervals of 10 to 100 m, depending on target depth.

Another MIP array is shown in Figure 9.9b. The current electrodes are aligned along strike as before but with larger separation, whereas the cable lies directly between them. Several orthogonal traverse lines for the magnetometer are located off one end of the current pair. After surveying these,  $C_2$  is moved to  $C'_2$ , the traverse lines are moved one spacing to the right, and measurements are repeated. Several of these displacements produce data for pseudodepth plots as in conventional IP (§9.5.1). This type of array provides more lateral and depth control than the first, although signal strength is usually lower and more measurements are required.

#### 9.4.4. Noise Sources

(a) General. Besides SP, which is easily compensated, other sources of background noise are telluric currents, capacitive and electromagnetic coupling, and the IP effect from barren rocks (§9.2.2). The reduction of telluric noise has already been mentioned.

(b) Capacitive coupling. This may occur due to leakage currents between current electrodes and potential wires, or vice versa, or between current and

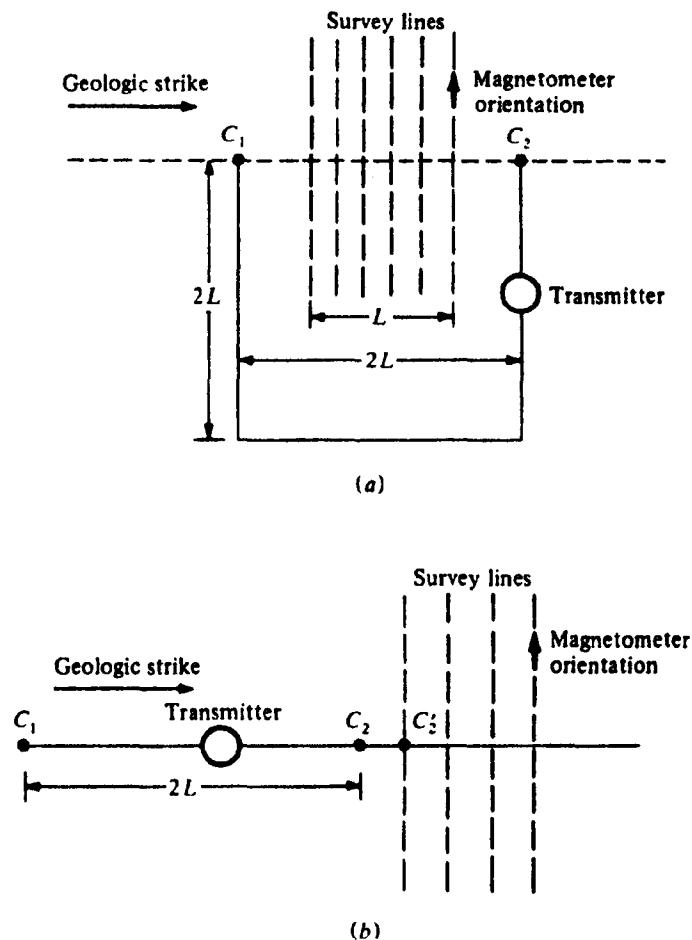


Figure 9.9. Magnetic IP arrays. (After Seigel, 1983.) (a) Horseshoe array for reconnaissance. (b) Linear array for detail surveying.

potential wires. The capacitive effect is usually small enough to be negligible, unless the insulation of the wires is defective or the wires lie very close to electrodes other than their own. In IP well logging, where the cables are side by side, it is necessary to use shielded wire.

(c) Electromagnetic coupling. This effect is extremely troublesome. It results from mutual induc-

tance between current and potential wires, both directly and through the ground in their vicinity. The EM effect can become quite large when long wire layouts or higher frequencies are used. Double-dipole and pole-dipole spreads are employed to reduce coupling due to long wires and the frequencies are usually kept below 10 Hz.

It is possible to calculate approximately the EM coupling between two wires in the presence of homogeneous ground (Millett, 1967). Resistivity variations in the vertical plane also influence the EM effect considerably. Coupling is generally in the sense of normal polarization when using the double-dipole array, although it may be the opposite, or negative, with the gradient system. Madden and Cantwell (1967) give a rule-of-thumb for limiting either the frequency or electrode spacing for a particular array to keep the EM coupling effect within background. For double-dipole electrode spreads the expression is

$$nx(f/\rho)^{1/2} < 200 \quad (9.10a)$$

for *F-D* measurements, where *x* is in meters and  $\rho$  in ohm-meters. For *T-D* measurements the limit is

$$t < 2\pi/f_c \quad (9.10b)$$

where

$$f_c \approx 10^4\rho/(nx)^2$$

Table 9.5 shows the maximum spreads permissible in *F-D* measurement for double-dipole spreads at various frequencies and ground resistivities. When pole-dipole spreads are used, the situation is somewhat better (longer spreads can be used), whereas for the Schlumberger or gradient array, the maximum *nx* is reduced by 2.

EM coupling may also be reduced in *T-D* IP surveys by using the later (low-frequency) portion of the decay curve to determine *M*, although sensitivity will be reduced in the process. The same improvement may be obtained with *F-D* units by measuring only low frequencies (< 3 Hz, say) in sine-wave rather than square-wave form if possible.

Development of spectral IP equipment, coupled with the use of the Cole-Cole model for interpretation, has produced a possible empirical method for separating EM coupling effects from normal IP response. The impedance of the equivalent Cole-Cole circuit for the latter, shown in Figure 9.3, may be written

$$Z(\omega) = R_0 \left[ 1 - M \left\{ 1 - \frac{1}{1 + (j\omega\tau)^c} \right\} \right] \quad (9.11)$$

Table 9.5. Maximum spreads for various frequencies and ground resistivities.

<i>f</i> (Hz)	$\rho$ ( $\Omega\text{m}$ )	<i>nx</i> (max) (m)
50	1,000	900
	100	300
	10	90
	1	30
10	1,000	2,000
	100	600
	10	200
	1	60
3	1,000	3,700
	100	1,100
	10	370
	1	110

where  $Z(\omega)$  is the complex impedance ( $\Omega$ ),  $\tau$  is the time constant (decay curve),  $R_0$  is the resistive component ( $\Omega$ ),  $c$  is the frequency exponent, and  $M$  is the chargeability.

The ranges of  $M$  and  $c$  are restricted, the upper and lower limits being unity and zero, the first by definition (Seigel, 1959b), the second because  $Z(\omega)$  decreases monotonically with frequency. Laboratory and field measurements on rocks indicate that  $c$  generally lies between 0.1 and 0.5 and typically is about 0.25, whereas  $\tau$  and  $R_0$  have a wide variation, the first from about  $10^{-3}$  to  $10^4$  s. Note that this discussion relates to both membrane and electrode polarization.

EM coupling values for these parameters, on the other hand, appear considerably different,  $\tau$  being very small ( $< 10^{-4}$  s) and  $c$  large (0.9 to 1.0). Under these conditions the phase spectra for typical porphyry copper mineralization and EM coupling are well separated, as can be seen from the phase versus frequency plots in Figure 9.10a. Values of  $c$  may be estimated from the slope of the asymptotes on the two curves, whereas the time constants are roughly related to the frequency maxima. Thus in situations where the phase curve contains more than one maximum or peaks at unusually high frequency, the Cole-Cole model may be modified to account for two (or more) distinct sources by including extra factors (called dispersion terms) of the form

$$\left[ 1 - M' \left\{ 1 - \frac{1}{1 + (j\omega\tau')^c} \right\} \right]$$

$$\text{or} \quad \left[ \frac{1}{1 + (j\omega\tau')^c} \right]$$

which multiply the right-hand side of Equation (9.11) (Pelton et al., 1978; Major and Silic, 1981).

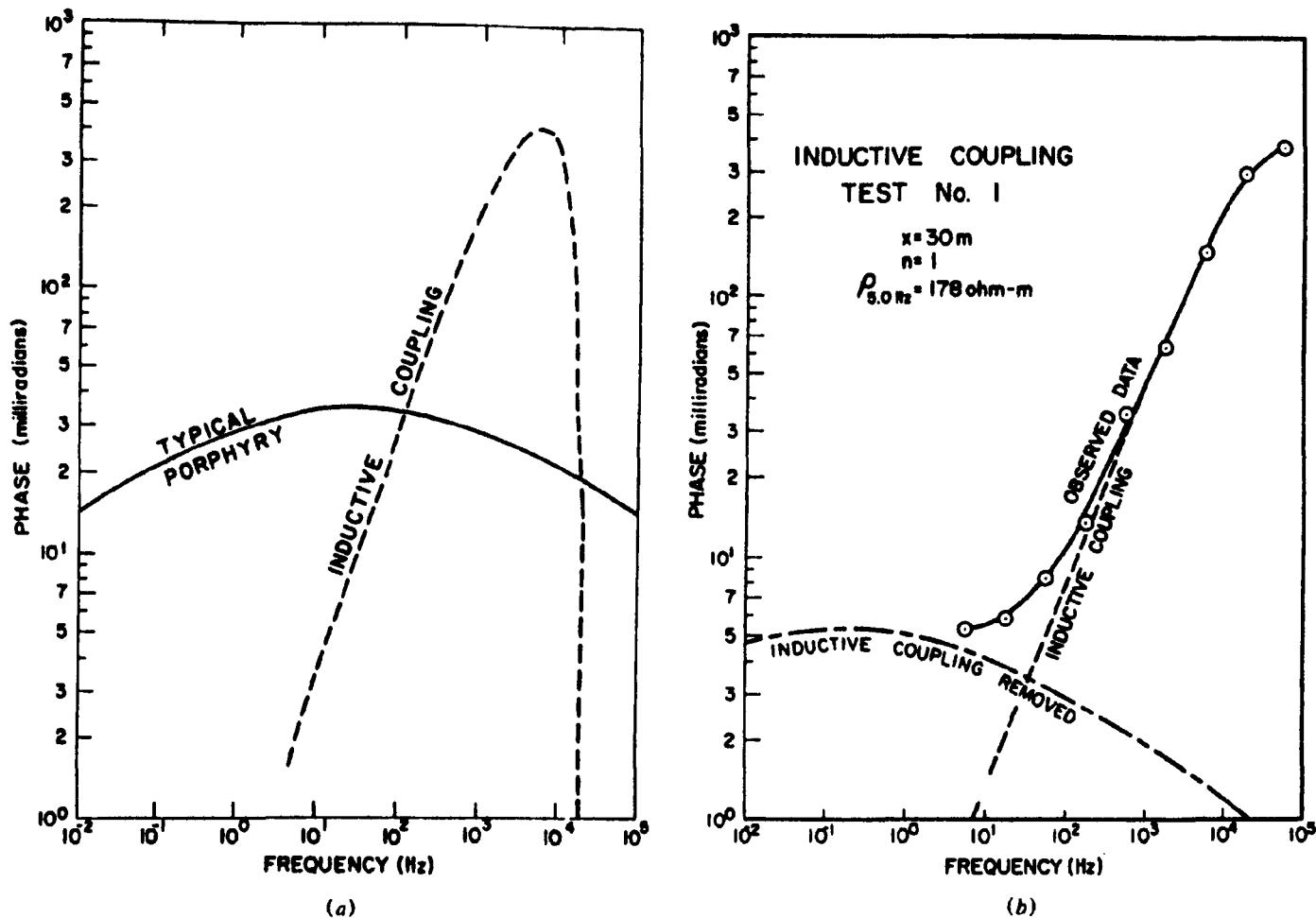


*Figure 9.10. Phase-angle spectra and their use in removing EM coupling effects. Double-dipole array:  $n = 1$ ,  $x = 30$  m. (After Pelton et al., 1978.) (a) Typical porphyry spectrum and EM coupling spectrum over homogeneous earth. (b) Observed data and curve (solid line) obtained using two Cole-Cole dispersion terms; dashed line is EM coupling spectrum calculated using the Cole-Cole parameters; the dash-dot line is the difference between the two previous curves.*

The curves in Figure 9.10b illustrate how the EM coupling may be removed. The complex resistivity measurements were made over relatively barren alluvium and the spectra extended to high frequencies to emphasize the inductive coupling component. Using two Cole-Cole dispersion terms the solid line was fitted to the data by an inversion process known as ridge regression (Inman, 1975; Petrick, Pelton, and Ward, 1977). Having acquired the various parameters for each term, the isolated coupling effect (dashed line) and IP response were calculated. Because there were no field data below 5 Hz, the IP response this is an extrapolation based partly on (a). The broad maximum around 0.1 Hz on the corrected curve is thought to be caused by polarizable clays in the alluvium.

Although this semianalytical technique for removing EM coupling is based on oversimplified modeling, it appears to be quite useful when spectral IP measurements are available with a wide frequency

band; it also has the advantage of using real field data.

## 9.5. INTERPRETATION

### 9.5.1. Plotting Methods

IP results are frequently displayed in simple profiles of chargeability, percent frequency effect, phase, and so forth, plotted against station location. The various MIP parameters may also be shown in this fashion. Several examples are given in Figure 9.11.

The profiles in Figure 9.11a show the same anomaly traversed with both time- and frequency-domain IP. There is little difference between the frequency-effect and metal-factor plots, and the chargeability profile is somewhat similar. However, the resistivity profiles are quite different for the two methods. This is probably due to the fact that the variable frequency IP used a double-dipole spread,

whereas the pulse system employed pole-dipole. These profiles are taken from line 29 + 00 on the contour plot of Figure 9.11c, which is a form of display occasionally used. From this illustration the two methods appear to give similar results.

Figure 9.11b shows a variable-frequency profile over a massive sulfide covered by some 80 ft of overburden (glacial till), which was a relatively good conductor. In the absence of this cover, the response would presumably be very much larger. It is also worth noting that the larger dipole separation gave slightly better response.

MIP data may be plotted in terms of  $H_s$ , the anomalous secondary field due to polarization, in such forms as  $H_s = H_p/I$  ( $I$  is the primary ground current) multiplied by PFE, RPS, MMR ( $F$ - $D$  systems), or by  $M$  ( $T$ - $D$  systems). Since the in-phase and quadrature components may be distinguished in  $F$ - $D$  measurements,  $H_s$  may also be converted to  $\Delta H_{sp}$  (change of in-phase component with frequency) and/or  $\Delta H_{sq}$  (quadrature).

Three MIP profiles of this type are displayed in Figure 9.11d. These were obtained over a zone of disseminated sulfides covered by conductive tailing sands ( $\sim 1 \Omega\text{m}$ ) and salt-lake material in the Kalgoorlie area of Western Australia. A vertical hole drilled on the anomaly peak encountered 47 m of tailing sands with overburden and weathered rock underlain by disseminated pyrite ( $\leq 10\%$ ) in black shales below 62 m. The parameters plotted are relative phase (RPS), magnetometric resistivity (MMR), and the normalized quadrature component of the anomalous secondary field,  $H_{sq}/I$ . The latter may be calculated from the measured phase angle and resistivity (§9.4.2f). This example, like that in Figure 9.11b, demonstrates the capability of MIP to detect targets beneath highly conductive cover.

Figure 9.12 has been included to illustrate the linear relation between phase angle and frequency effect. The data, from northern New Brunswick, were obtained over a shallow massive sulfide deposit in a diorite-rhyolite host rock of high resistivity (Scott, 1971). Almost perfect correlation between phase and frequency effect is evident in the profiles, producing an excellent linear relation with a slope of  $-0.37^\circ/\text{PFE}$  in the lower diagram. In the course of this study 10 sites with known mineralization were surveyed; of these, 3 gave negative results owing to high noise and conductivities beyond the transmitter capacity. The average slope of the remaining 7 was  $-0.38^\circ/\%$ ,  $\pm 20\%$ . However, it is not clear whether the slope should be constant or vary slightly for different types of minerals.

An alternative display method, which has been used in plotting IP to illustrate the effects of variable electrode spacing, was originally developed by

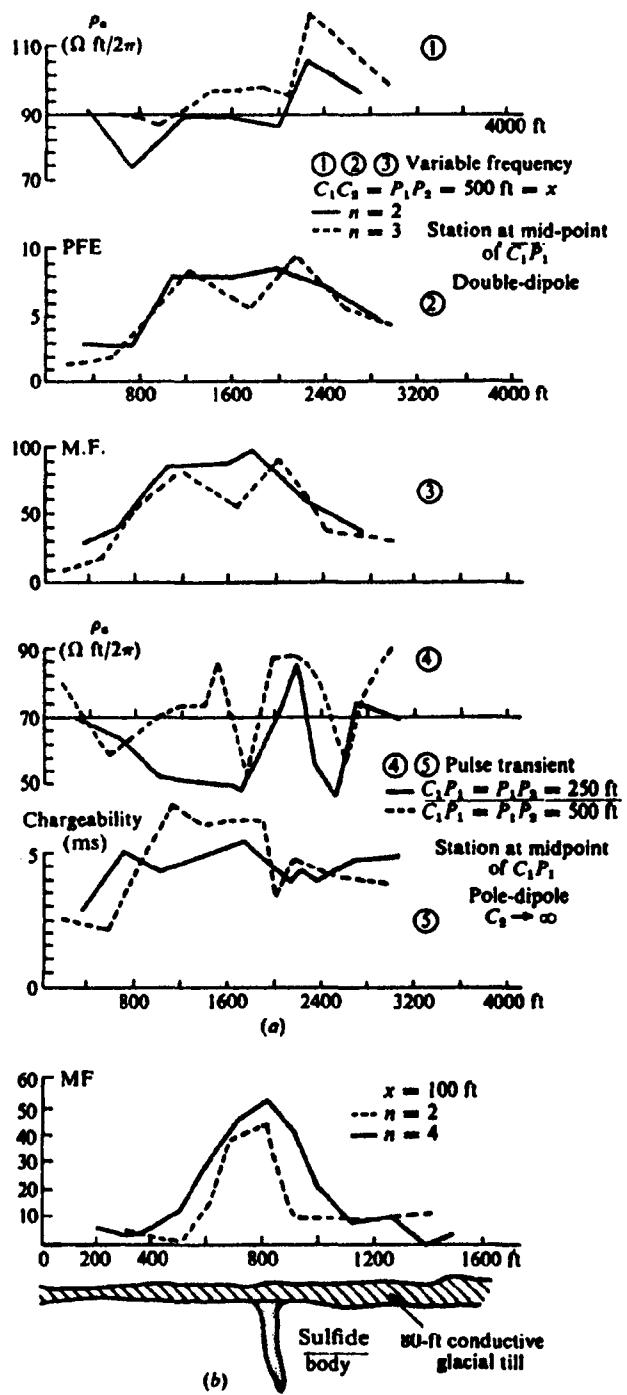


Figure 9.11. Display of IP results. (a) Comparison of time- and frequency-domain IP. (b) FD IP over massive sulfides.

Madden, Cantwell, and Hall (see Marshall and Madden (1959)). It is illustrated in Figure 9.13, for the sulfide deposit shown in Figure 9.11b. Values of frequency effect and apparent resistivity for each station are plotted on a vertical section at the points of intersection of  $45^\circ$  lines drawn from the base line or surface, starting at the midpoints of the current and potential electrodes (double-dipole array). In this way the PFE values appear at points directly below the center of the electrode spread, at a vertical distance from the ground surface that increases with

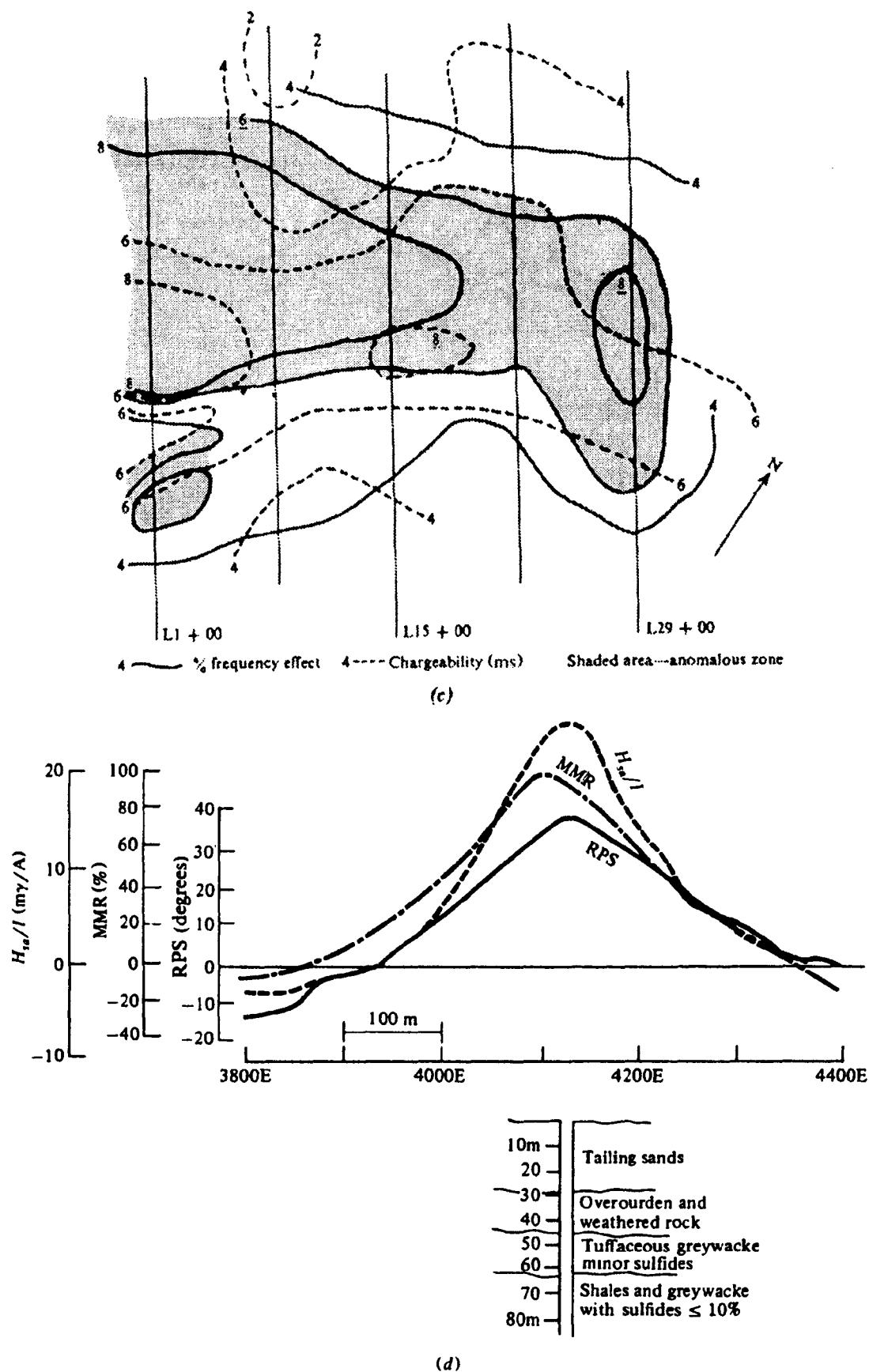


Figure 9.11. (Continued) (c) Contours for T-D and F-D IP. (d) FD MIP profiles, Kalgoorlie, Western Australia. (After Seigel and Howland-Rose, 1983.)

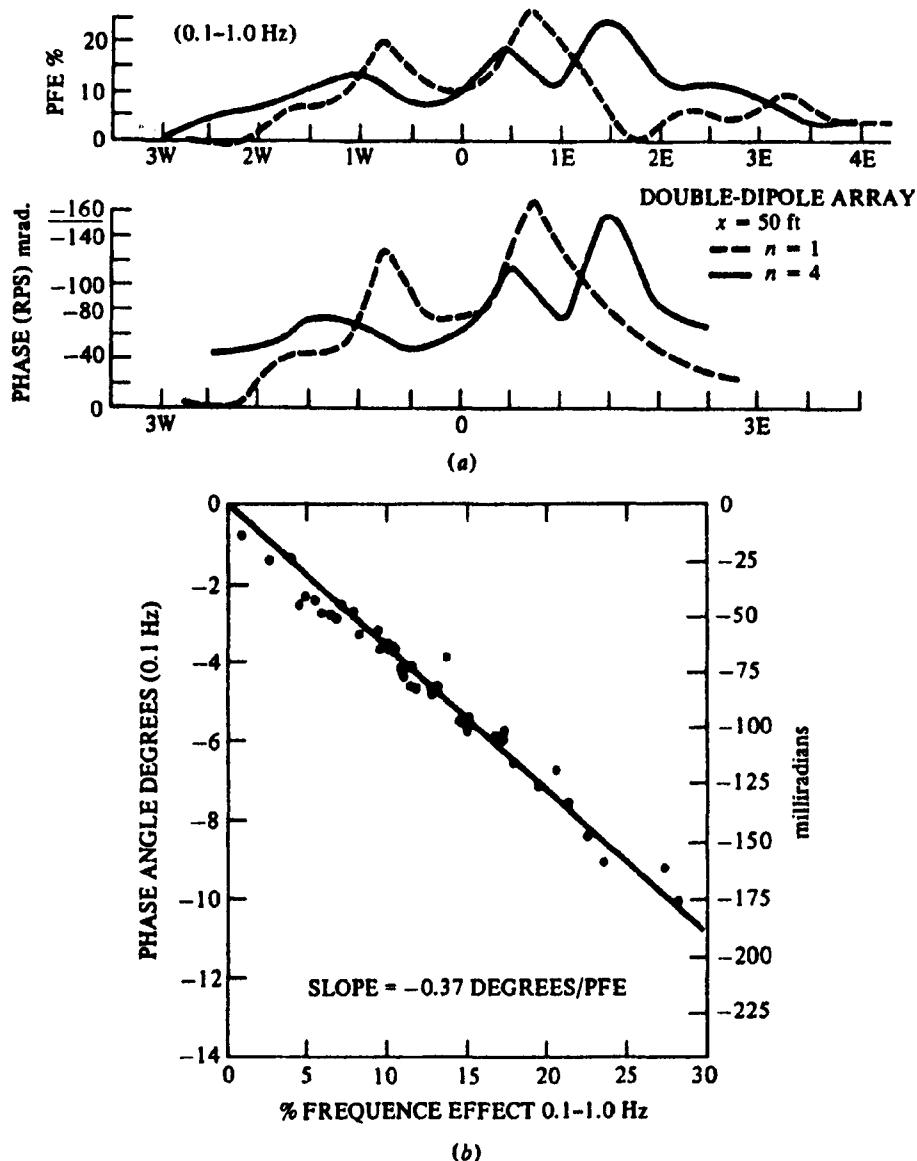


Figure 9.12. Relation between PFE and phase angle. (After Scott, 1971.) (a) PFE and phase angle curves over massive sulfides, northern New Brunswick. (b) Plot of PFE versus phase angle.

the  $n$  value for the spread. Similarly the  $\rho_a$  values are located at mirror image points above the center line. Finally contours of equal PFE and apparent resistivity are drawn on these vertical sections; the result is a form of 2-D plot in vertical section.

Clearly it is possible to display any of the IP parameters in this fashion provided the double-dipole array has been used for the survey; data from gradient and pole-dipole arrays have also been plotted in this way. Similar pseudodepth plots have been obtained from multiple  $T$ - $R$  spacing HLEM, MT, telluric, and variable-frequency EM data, where the vertical scale is logarithmic in frequency or period for the last three (§6.3.2, examples 4 and 5), rather than linear with depth.

The attractive feature of this display is that it gives some idea of the relative depths of anomalous conducting zones. The justification for such a plot is

that as the dipole separation is increased, the measured values are influenced by increasingly deeper zones. (For multifrequency MT, telluric, and EM plots, deeper penetration is obtained at lower frequencies.) The resultant contours may be misleading, however, because they appear to provide a vertical section of the ground conductivity. As pointed out in Section 8.5.2, the apparent resistivity is not in fact the actual resistivity in a volume of ground below the electrode array, but depends on the geometry of the electrodes as well as the surface resistivities. Consequently it should not be assumed that this type of plot is a representation of the actual subsurface.

Double-dipole pseudodepth plots, as is apparent from Figure 9.13 and several problems in Section 9.7, produce contours of a tent shape with  $45^\circ$  slope. This, of course, is a result of the plotting method. Pseudodepth plots developed from variable fre-

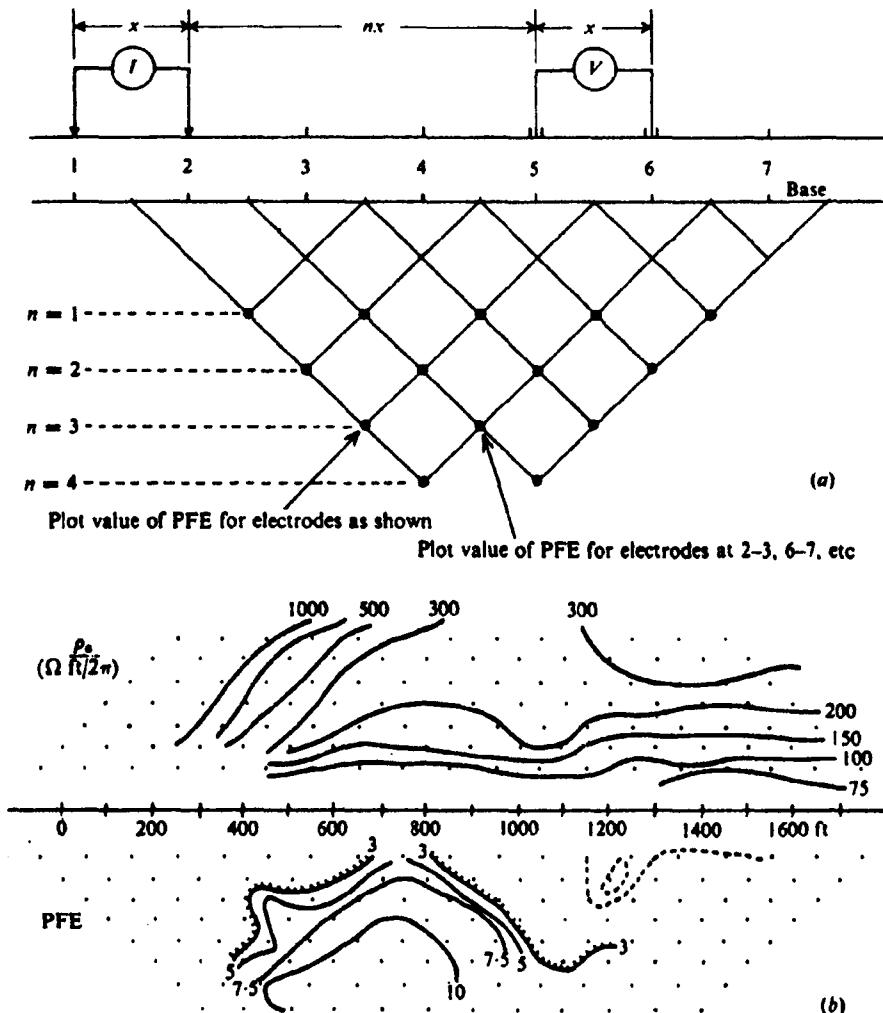


Figure 9.13. Variable-frequency IP pseudodepth plots. (After Marshall and Madden, 1959.) (a) Graphical construction for locating data points. (b) Pseudodepth plot of the data of Figure 9.11b.

quency soundings, on the other hand, have a pole-like appearance (see Figs. 6.29 and 6.30c) because the depth points are located virtually below surface stations.

### 9.5.2. General Interpretation

Until fairly recently IP interpretation was mainly qualitative. Location and lateral extent of anomalies were marked on profiles and pseudodepth plots by dark horizontal bars, solid for definite targets, stippled for probable or possible targets. The dimensions, along with depth and possibly dip, were generally estimated from the characteristics of the plots. The inherent advantages and weaknesses of resistivity (§8.1, §8.6.4f, §8.6.7) apply to IP as well. Among the former are good depth estimate and depth of penetration, whereas the latter include ambiguity as to location, effects of near-surface variations, and slow field operations.

Highly conductive overburden overlying mineral conductors may hamper detection of the latter by IP as well as by EM and resistivity, although IP is frequently more successful than the other methods in such terrain. Similarly, water-filled shear zones are generally indistinguishable from mineral zones; however, in special circumstances, for example, if the electrolytic effect is not as pronounced as the electrode polarization, it may be possible to distinguish between the two with IP.

At one time it was thought that massive sulfides should have a lower IP response than disseminated mineralization; this is theoretically reasonable, as discussed in Section 9.2.3. However, it is probable that the opposite is true. This may be due to the halo of disseminated mineralization that usually surrounds a massive zone. Another explanation is that truly homogeneous massive sulfide deposits do not exist; rather they are broken up into a great number of smaller conducting zones within a nonconducting,

or poorly conducting, matrix. Self-potential well logs generally indicate this internal subdivision for sections designated massive in the descriptive log.

The steeply dipping thin-sheet conductor, commonly used in EM modeling, is not a particularly good target for IP or resistivity surveys. The principal reason for this is that the electrode spacings are normally too large to respond strongly to such a structure. [In fact, an IP traverse made with small dipole separations of 8 and 15 m in one area produced a strong response directly above a sheet-like conductor.] Although a disadvantage, this is hardly a fundamental weakness of IP, because the technique would not usually be employed (and should not be necessary) to detect conductors of this nature. However, it does account for the lack of response directly over some of these structures and in certain cases, an apparently displaced IP anomaly on the flanks, the latter probably caused by the disseminated halo.

As a result of recent developments, IP surveying and interpretation techniques have become increasingly sophisticated. We may now use IP to measure complex impedance, possibly to determine various type of structure and forms of mineralization (vein-type, disseminated, massive), and potentially to discriminate between metals and graphite with broadband spectral IP. Thus the method appears to have outstripped the other electrical ground techniques and has become very popular in base-metal exploration (conceivably MIP might become airborne, but this is still in the future). This popularity is certainly not because it is cheap or fast. Average monthly coverage varies enormously, depending on terrain and other factors such as surface conductivity, but 10 to 40 line miles (15 to 70 km) per month is common. The price per line-kilometer is thus about \$500 to 800 (1988), which is considerably higher than magnetics or EM.

The popularity of IP is based on definite base-metal discoveries, particularly of large low-grade bodies, made with its aid. A study of various field results indicates that the IP and resistivity anomalies (generally IP highs and resistivity lows) very often occur together. One might argue, therefore, that the expense of the IP survey was not warranted. It is quite unlikely, however, that resistivity alone would provide enough information to justify itself. There are also numerous case histories of IP successes in areas of disseminated mineralization, such as porphyry coppers, where the resistivity anomaly is almost nonexistent (for example, see §7.8, example 9).

### 9.5.3. Theoretical and Model Work

(a) *Theoretical results.* IP response has been developed analytically for a few simple shapes like the

sphere, ellipsoid, and 2-D features such as a vertical contact and dike, as well as horizontal beds. These may be derived from resistivity formulas in simple cases (§8.3.5, §8.6.5, and §8.6.6) and for more complex shapes by the finite-element method (Coggon, 1971, 1973), somewhat similar to the analysis in Section 6.2.7. Figure 9.14 shows a set of theoretical IP profiles over each of these structures using several arrays. In examples (a) to (e) the chargeability is determined from the relation

$$M = \rho_2/\rho_a (\partial\rho_a/\partial\rho_2) \quad (9.12)$$

(Seigel 1959a). Numerical data for the models of Figure 9.14f to j are obtained from sets of equations for finite-element meshes in which the power dissipation due to ground current is minimized. In parts (a) to (e) the host rock is not polarizable, that is,  $M_1 = 0$ , whereas in the other five parts, (f) to (j), PFE = 1% in the host rock. Note that most horizontal scales in Figure 9.14 have no units. For pseudodepth plots and sometimes for profiles, units are generally equal to the potential-electrode spacing.

IP response is not always positive. Negative apparent IP may occur in the vicinity of 2-D and 3-D polarizable bodies (Bertin, 1968; Dieter, Paterson, and Grant, 1969; Coggon, 1971; Sumner, 1976). This is a geometrical effect related to the dipolar field and the position of the measuring electrodes (Figs. 9.14a, b, c, e, 9.21c, and 9.25). Certain 1-D structures also produce negative IP response [see model (d) in the following text].

We may summarize the salient features of these models as follows:

Models (a) to (c): For contrasts ( $\rho_1/\rho_2$ ) greater than those shown, the response does not change appreciably [this applies also to models (e) to (i)]. For an ellipsoid dipping less than 90°, the profile is not significantly different from those in parts (b) and (c).

Model (d): IP over two horizontal beds is quite conventional, but not necessarily so when there are more than two. For example, K- and Q-type structures ( $\rho_1 < \rho_2 > \rho_3$  and  $\rho_1 > \rho_2 > \rho_3$  respectively; see §8.6.4b) produce a negative IP response for the first layer which masks the effects of substrata, often causing an incorrect interpretation. Data must be analyzed with care with this possibility in mind to avoid errors in interpretation (Nabighian and Elliot, 1976). This, of course, assumes that the upper layer(s), unlike Figure 9.14a, b, c, d, are polarizable.

Model (e): The curves were obtained for the model shown below them by the method of images (§8.3.3), hence the sharp breaks in the flat portion. Otherwise the profiles would resemble gravity profiles for a semiinfinite horizontal slab (Fig. 2.30).

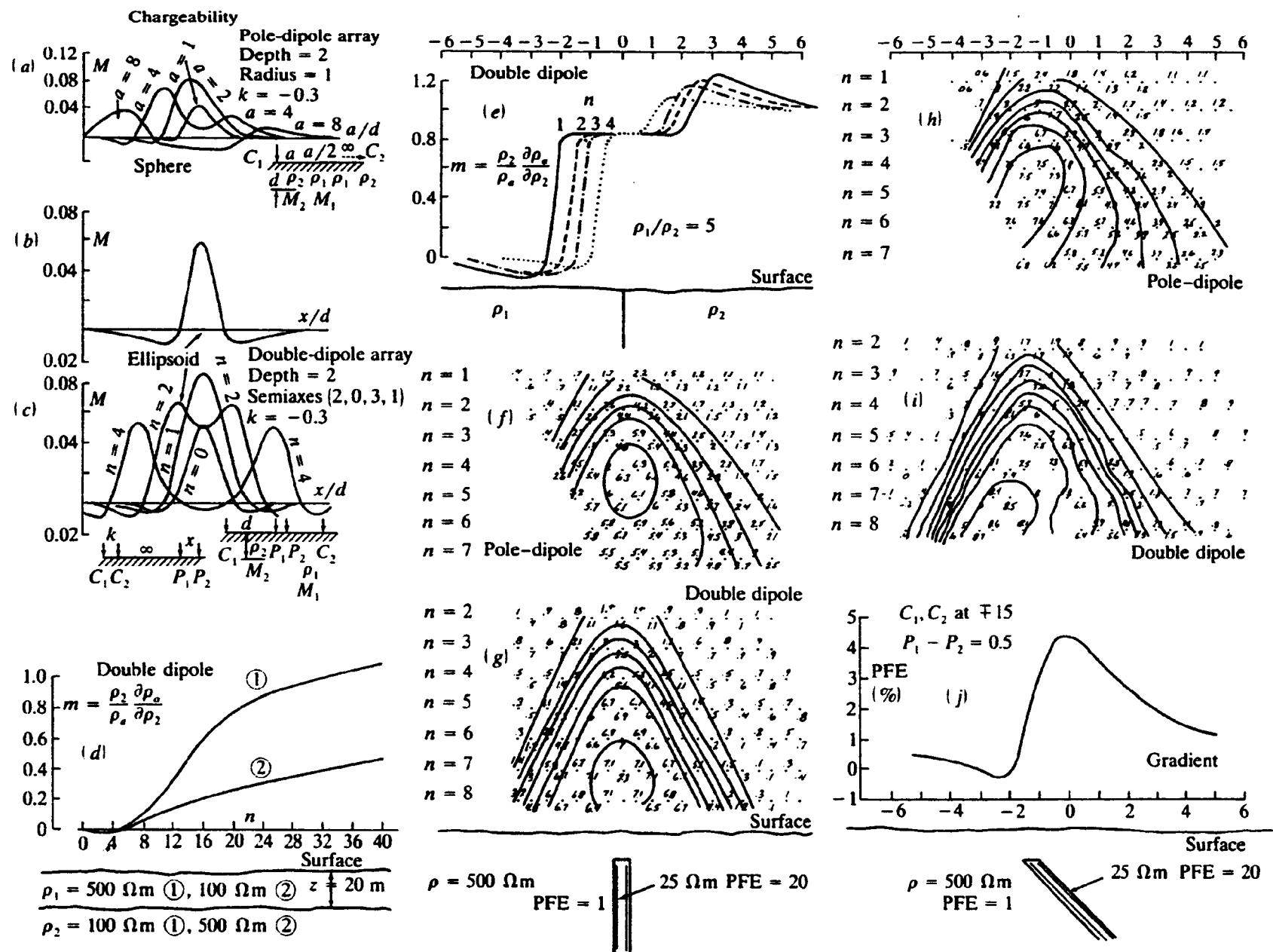


Figure 9.14. IP response from various theoretical models. (a) Sphere. (b) and (c) Ellipsoid. (d) Two beds. (e) Vertical contact. (f) and (g) Vertical dike. (h) to (j) Dipping dike.

Models (f) to (j): Double-dipole and pole-dipole arrays show appreciable response over the steeply dipping dikes whereas the gradient spread (not illustrated) is quite insensitive; when the dip is appreciable, the respective amplitudes are also in the preceding sequence. All three respond quite strongly to a horizontal slab. However, the gradient system is more sensitive to dip than the other two arrays, as is clear from Figure 9.14j.

Conductive overburden masks conductive structures in the bedrock because much of the current is short-circuited. The buried anomalies, when they are detected at all, appear deeper than they actually are, as in EM, for all three arrays. Lateral changes in overburden thickness and resistivity are best detected by the gradient spread, which also discriminates between multiple buried targets more successfully than the other two systems. The double-dipole, however, is considerably superior to the gradient array for depth resolution.

As mentioned previously the double-dipole array is affected least by EM coupling and the gradient array most.

(b) *Analogy between M and total-field magnetic anomaly.* Quick (1974) points out an interesting analogy between IP chargeability obtained with the gradient array over a 2-D dipping polarizable prism and the total-field magnetic anomaly due to the same target located at the magnetic equator and striking E-W. Because the gradient layout provides a uniform electric field in the otherwise homogeneous ground, the prism is horizontally polarized and the response is equivalent to the magnetic field. This permits a fast approximate estimate of dip and depth of the prism, because

$$x_{1/2} = 2d \csc \xi$$

$$M = 2d \sec \xi$$

or

$$\xi = \tan^{-1} (M/x_{1/2})$$

$$d = (x_{1/2} \sin \xi)/2 = (N \cos \xi)/2$$

where  $x_{1/2}$  is the full width at half-maximum amplitude,  $N$  the horizontal distance between profile maximum and minimum,  $d$  is depth to the top of the prism,  $M$  is chargeability, and  $\xi$  the dip. Examples of the sphere and horizontal cylinder are also discussed. Clearly the host material must be barren for IP.

(c) *Interpretation of spectral IP data.* Because of the recent development of the complex equipment, interpretation is still in a development stage. The main thrust, mentioned in the previous section, has

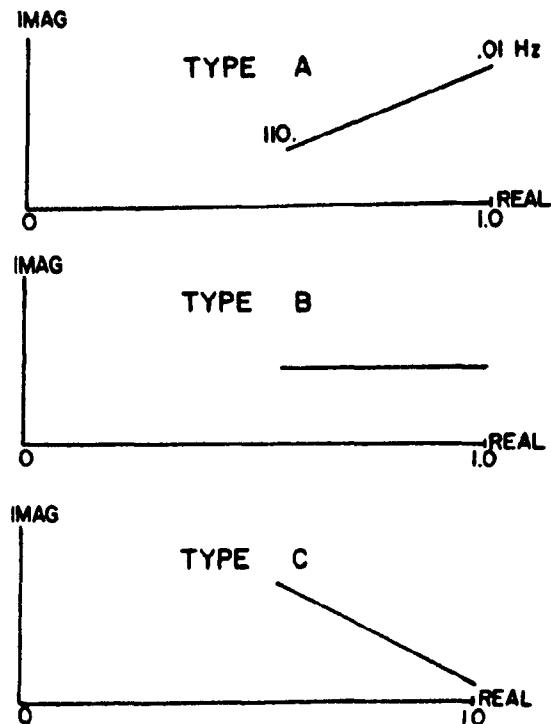


Figure 9.15. Idealized spectral IP response for three types of host rock. (After Zonge and Wynn, 1975.)

been to identify and discriminate between IP response characteristic of the host rock and various types of mineralization; it has already proved its usefulness in reducing the EM coupling effect (§9.4.4c).

Zonge and Wynn (1975), among others (§9.3.4), attempted to classify background rock signatures by laboratory and field measurements. Results are plotted as real and quadrature components ( $R, Q$ ) over a four-decade frequency range on a conventional Argand diagram (see Fig. A.5). Three idealized forms of response are shown in Figure 9.15. In types A and C the quadrature component varies inversely and directly, respectively, with frequency whereas it is constant over the spectrum for type B. Type A is said to be characteristic of strongly altered rocks, sulfide and graphitic mineralization, and some clays, whereas C usually represents weakly altered strata, chloritized fresh volcanic rocks, limestone, and alluvium; type B is intermediate and is associated with moderate alteration, low pyrite, and other mixed mineralization. This simple classification, however, is by no means all-embracing and the authors show several nonconforming examples in which the  $R-Q$  relation gyrates wildly instead of being roughly linear. Other authorities have criticized the general hypothesis on various grounds.

Distinctive IP signatures for different types of mineralization have been considered in a number of studies (§9.3.4). From spectral IP laboratory mea-

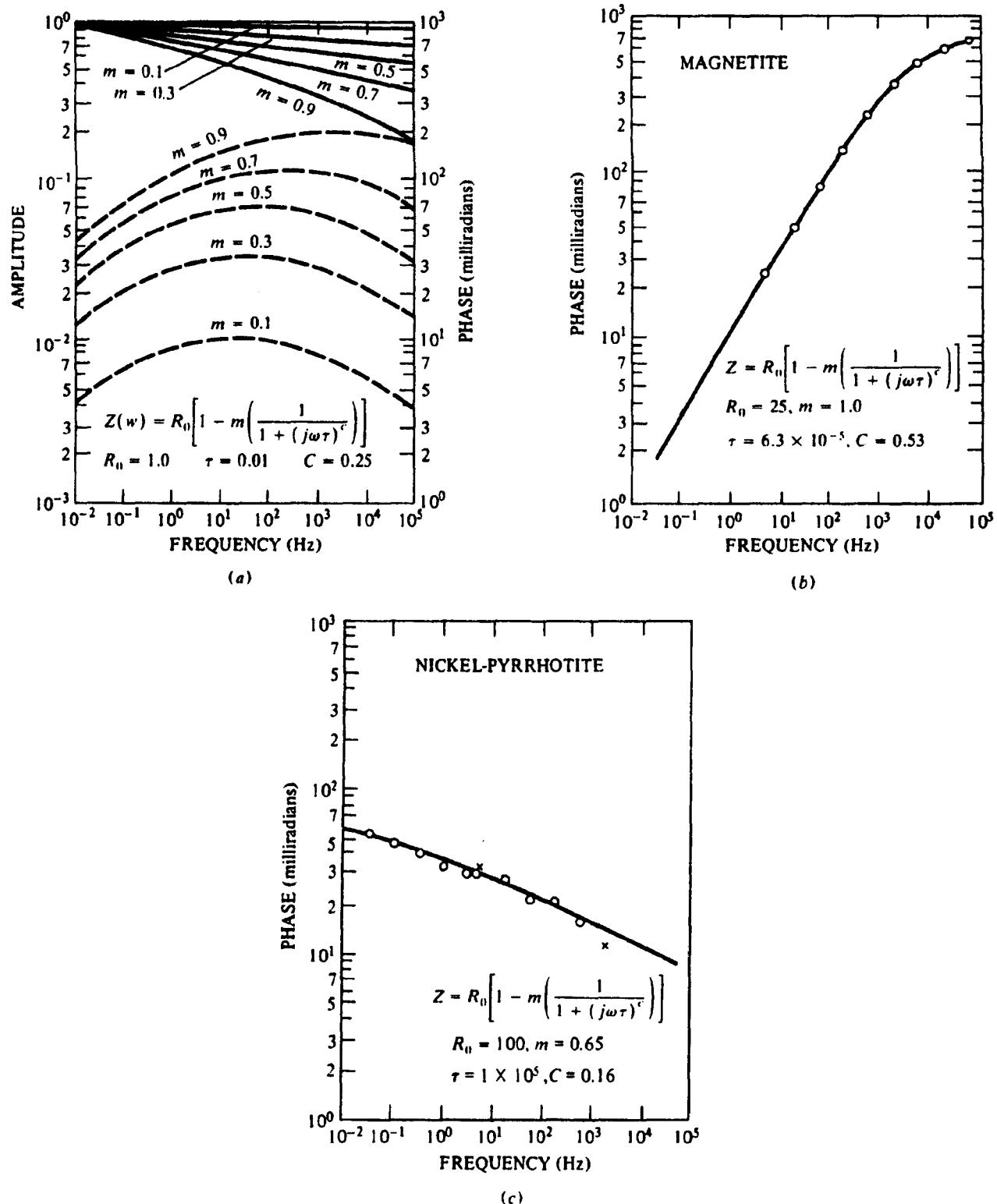


Figure 9.16. IP signatures for different types of minerals. (After Pelton et al., 1978.) (a) Amplitude (solid line) and phase (dashed) curves for a Cole-Cole relation model for various values of  $m$ ;  $R_0 = 1.0$ ,  $\tau = 0.01$ ,  $c = 0.25$ . (b) Magnetite signature, southern Utah. (c) Nickel-pyrrhotite, Sudbury, Ontario.

surements on various mineral samples it was found that the phase spectrum peaked at different frequencies for certain minerals, being much lower for graphite than most sulfides. Although this distinction was not nearly as clear in field tests, the possibilities have been pursued with more advanced equipment

and with the aid of the Cole-Cole model for interpretation.

Several examples of this work, taken from Pelton et al. (1978), are shown in Figure 9.16. Theoretical plots of amplitude and phase for the Cole-Cole relaxation model for various values of  $M$  are shown

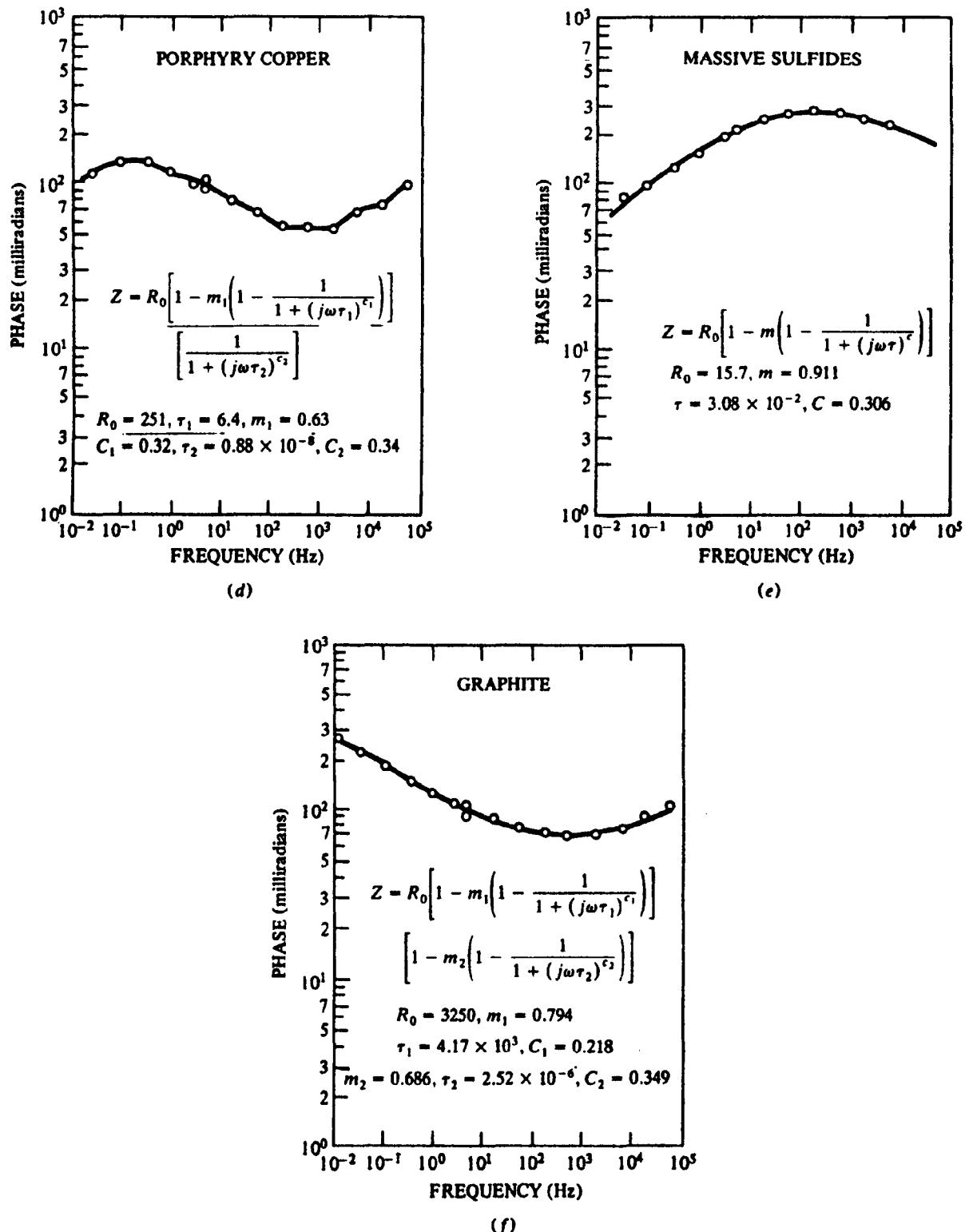


Figure 9.16. (Continued) (d) Porphyry copper, New Mexico. (e) Massive sulfides, Timmins, Ontario. (f) Graphite, Labelle, Quebec.

in Figure 9.16a. Obviously the phase curves are more diagnostic. Changes in  $M$  merely move both sets of curves vertically. If we vary  $R_0$ ,  $c$ , and  $\tau$ , we find that (i) changing  $R_0$  shifts the amplitude curves vertically but has no effect on the phase curves, (ii) increasing  $c$  makes the phase set more sharply peaked and increases the slopes of the amplitude curves, and (iii)  $\tau$  controls the horizontal positions of both sets

of curves and consequently is the most significant parameter in source determination.

The remaining diagrams in Figure 9.16 contain profiles from field surveys. Note that the frequency band extends from 0.01 Hz to 60 kHz. The unusually high frequencies required very small electrode spreads ( $\sim 1$  m) to minimize EM coupling effects, and this in turn necessitated extremely shallow tar-

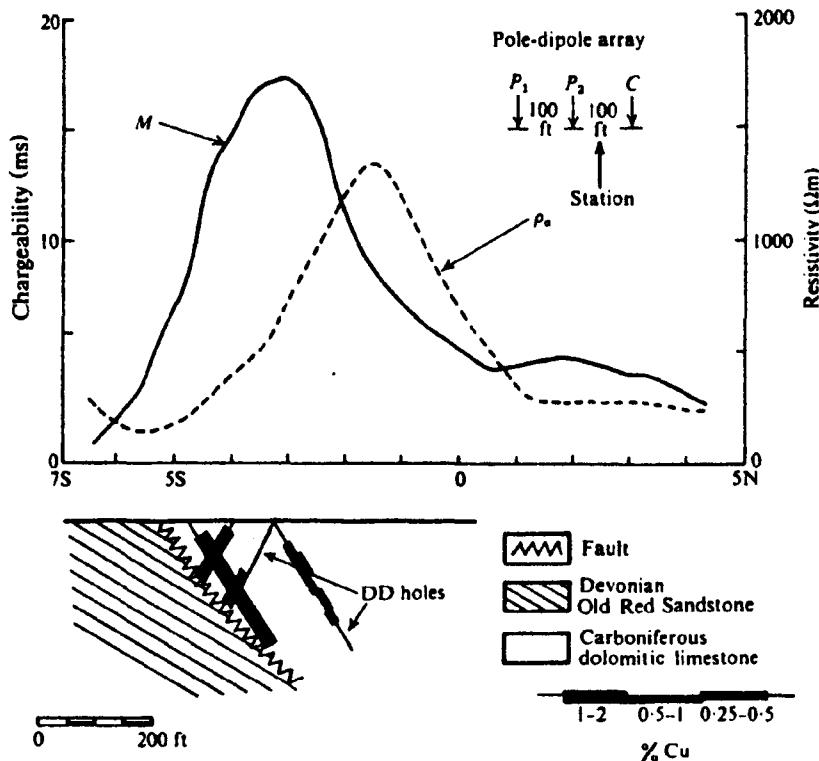


Figure 9.17. Time-domain IP over Cortdrum copper-silver body. (From Seigel, 1967.)

gets. Consequently the sites selected were mainly in open pit mines. Only the phase spectra are illustrated and best-fit Cole-Cole models have been matched to the data in all cases.

The examples in Figure 9.16b to f include a porphyry copper, massive sulfides, magnetite, nickel-pyrrhotite, and graphite. Profiles (b) and (c) were carried out to discriminate between two common sources in nickel sulfide areas. Although the magnetite was of ~ 76% concentration, the phase curve peaks at high frequency and requires a very small time constant to match the model. This is probably due to lack of continuity between very small mineral grains, because  $\tau$  values were larger at other sites with conventionally massive magnetite. The profile in Figure 9.16c indicates closely connected pyrrhotite mineralization of higher conductivity with a very low-frequency phase maximum requiring a large  $\tau$ .

The phase curve for the porphyry copper deposit in Figure 9.16d is not as simple as the previous examples. Sulfide concentration was high (~ 17%) and the mineralization was of vein type rather than highly disseminated as in true porphyries. Fitting this curve required two Cole-Cole factors as shown and the primary time constant  $\tau_1$  was much larger (to fit the low-frequency peak at 0.1 Hz) than at other porphyry sites surveyed.

Figure 9.16e from a volcanogenic massive sulfide is similar to spectra obtained from disseminated sulfides, requiring a small  $\tau_1$ -value, although the

chargeability is higher. The curves from Fig. 9.16b, e and from several porphyry sites are similar in this respect, suggesting that electrical continuity in massive sulfides is relatively poor.

Figure 9.16f shows phase spectra from a graphite deposit. Even in small concentrations graphite and pyrrhotite seem to be excellent conductors. The curve rises steadily as the frequency decreases; if there is a peak it occurs further to the left. Thus  $\tau_1$  is several orders larger than in the other examples (except for the nickeliferous pyrrhotite).

The possibilities in using IP equipment of this type to obtain a whole body of additional information in base-metal search seem promising. Certain reservations, however, remain concerning the blanket use of the Cole-Cole model; also the complex surveying equipment requires some expertise in operation, and the long "time constant" involved in carrying out measurements down to frequencies of 0.001 Hz increases the cost. The use of *T-D* instead of *F-D* techniques is potentially attractive with respect to the latter drawback (Johnson, 1984).

Spectral IP application in petroleum exploration has recently been considered. Resistivity and IP anomalies have been detected over oil and gas fields. The response is thought to be the result of geochemical alteration of overlying rock structures caused by transport of  $H_2S$  and  $CH_4$  upward to shallower levels from the reservoir. In the USSR IP surveys have been employed for this purpose since about 1978.

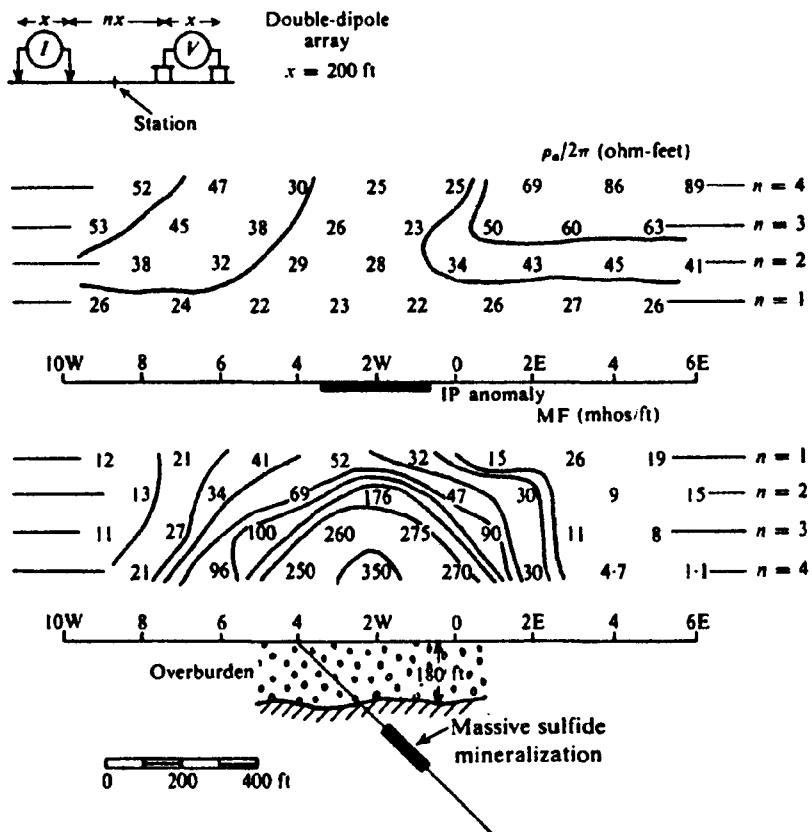


Figure 9.18. Frequency-domain IP results for massive sulfides overlain by thick conductive overburden.

## 9.6. FIELD EXAMPLES

Several examples of IP field results have already been given in Figures 9.11, 9.12, and 9.16. Three further illustrations are described in the following paragraphs.

1. Figure 9.17 is a profile of apparent resistivity and chargeability obtained during a time-domain IP survey on the Gortdrum copper-silver orebody in Ireland. This is a low-grade deposit, averaging only 1.2% by volume of copper and 0.75 oz. of silver per ton, that is, less than 2% metallic conducting minerals. With this type of mineralization, the conductivity is often enhanced by the presence of pyrite or pyrrhotite but this is not the case here. However, the chargeability anomaly is very strong and well located. The  $\rho_a$  profile shows a large resistivity contrast between the dolomitic limestone and sandstone with a minimum directly over the fault; there is no indication of the sulfide zones containing chalcocite, bornite, and chalcopyrite. The pole-dipole spread was used in this work, with spacing as shown in the diagram.

2. Pseudodepth plots from the results of a double-dipole traverse using frequency-domain IP are shown in Figure 9.18. This is in the Timmins area of northern Ontario where the glacial overbur-

den is frequently 100 to 200 ft thick and, being of low resistivity, effectively masks the response of conductors lying beneath it. Using 200 ft dipole spacing and separations of 200, 400, 600, and 800 ft, a good IP response was obtained. The shape of the metal-factor contours indicates a source at depth. The resistivity section shows low resistivity continuing to depth with a westward dip, as well as the effect of the conductive overburden. Subsequent drilling intersected massive sulfide mineralization over 100 ft wide at a depth of 240 ft. It is not surprising that EM methods failed to detect this zone.

3. Figure 9.19 displays curves of  $M$  and  $\rho_a$  for a traverse over the Lornex porphyry copper deposit in British Columbia. This is a type of mineralization for which the IP technique is particularly effective, because no other electrical method would be capable of detecting the main body, although there might be minor indications on the flanks. Moreover, it is unlikely that the gravity would produce any response.

The resistivity profiles for 400 and 800 ft electrode separations might be interpreted as showing a mild reflection of the mineralization, were it not for the fact that the apparent resistivity increases with depth. This tells us that the overburden, which is 200 ft thick on the east, has a higher conductivity than the ore zone below it. On the other hand, chargeability response increases with electrode separation and

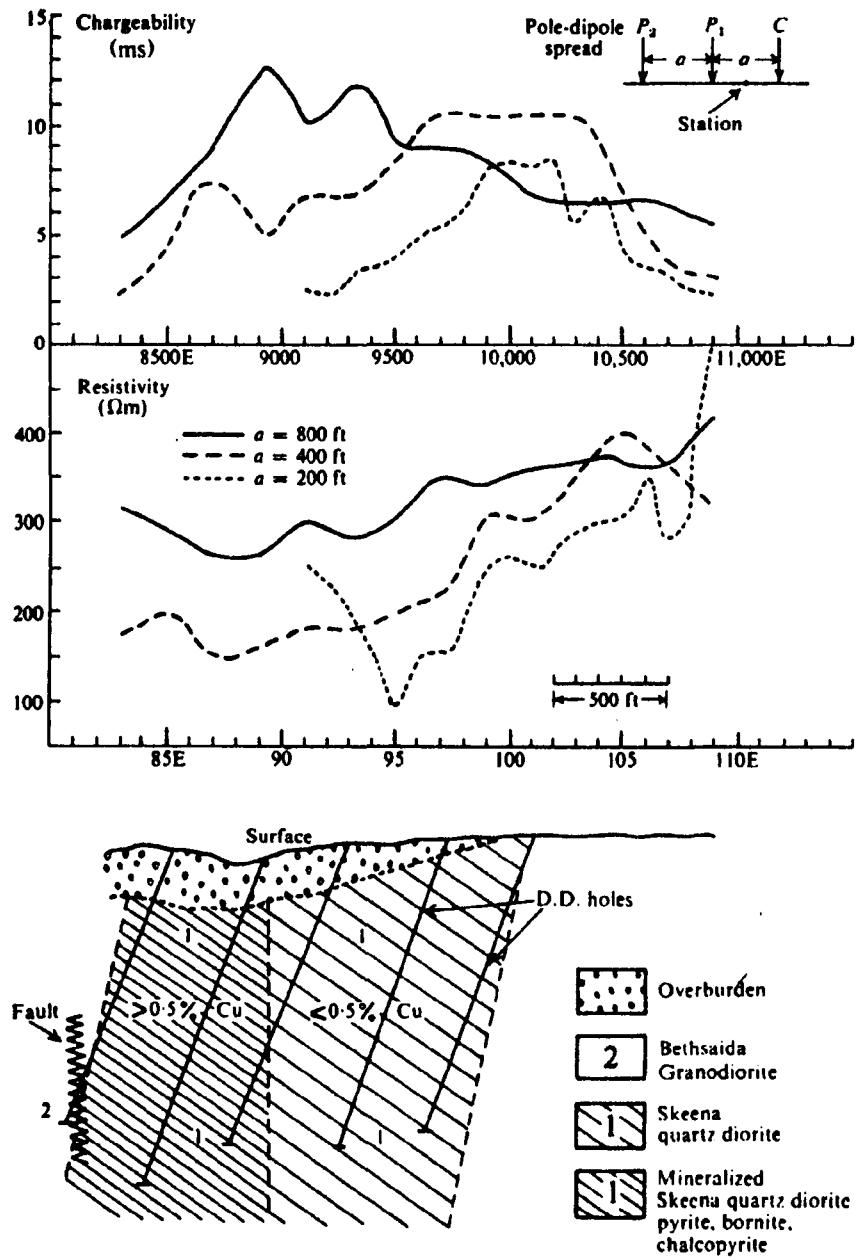


Figure 9.19. Time-domain IP results over porphyry-copper deposit. (After Seigel, 1967.)

Table 9.6.

Potential dipole	$n = 1$		$n = 2$		$n = 3$	
	$\rho_a/2\pi$	MF	$\rho_a/2\pi$	MF	$\rho_a/2\pi$	MF
10S-9S	—	—	—	—	280	27
9S-8S	180	28	190	24	270	33
8S-7S	210	31	275	36	290	60
7S-6S	270	42	280	35	72	219
6S-5S	315	39	80	172	70	175
5S-4S	480	40	220	17	675	99
4S-3S	330	88	1,120	41	1,751	61
3S-2S	1,091	46	1,130	29	1,830	31
2S-1S	1,200	31	1,510	27	1,710	28

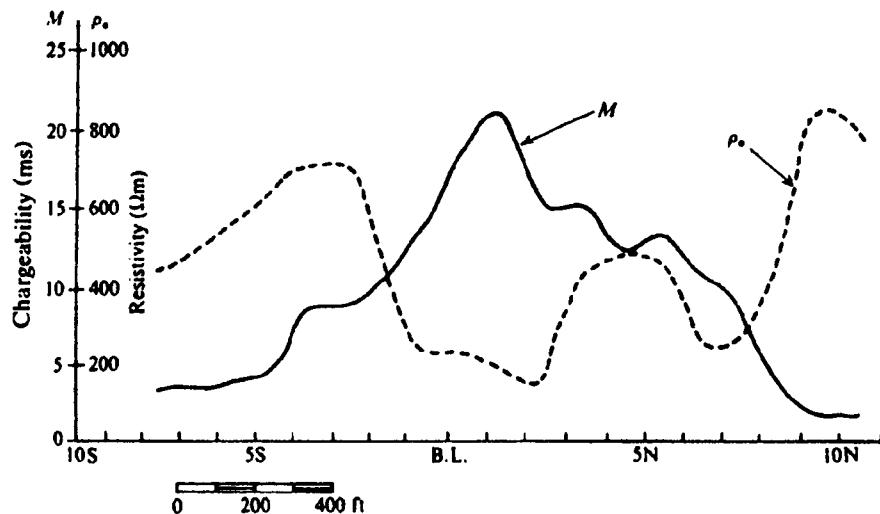


Figure 9.20. IP chargeability and apparent resistivity, Northwest Territories, Canada.  
(After Seigel, 1967.)

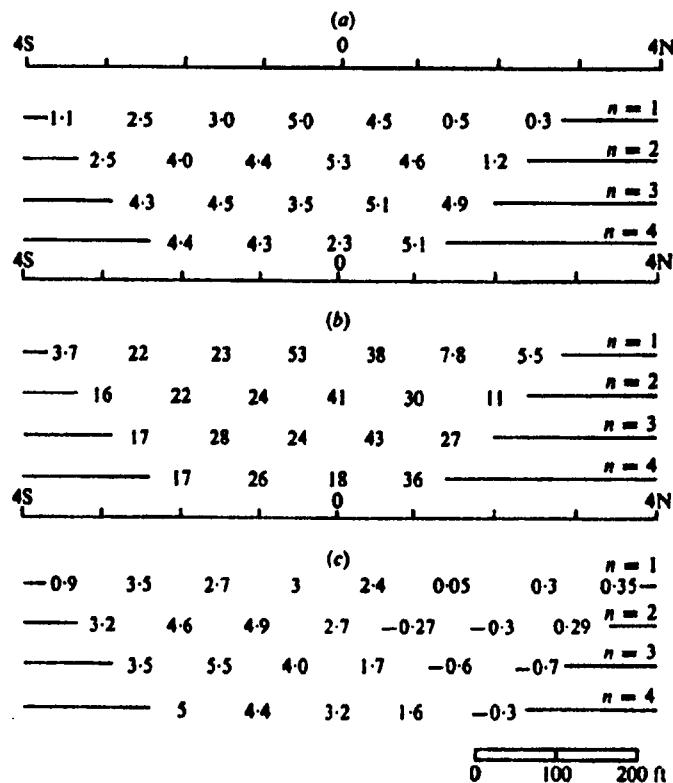


Figure 9.21. Time- and frequency-domain IP pseudodepth plots. Double-dipole array,  $x = 100$  ft. (a) Percent frequency effect. (b) Metal factor (mhos per foot). (c) Chargeability (milliseconds).

determines the lateral extent and depth of the zone quite well.

## 9.7. PROBLEMS

- The results in Table 9.6 were obtained using frequency-domain IP in a survey over suspected sulfide mineralization in northern New Brunswick. The double-dipole array was used

with dipole separations of 100 ft and  $n = 1, 2, 3$ . Resistivity values are in the form  $\rho_a/2\pi \Omega\text{-ft}$ . The grid line is roughly N-S with stations every 100 ft. In all cases the potential dipole was south of the current dipole.

- Prepare pseudodepth plots for  $\rho_a/2\pi$  and MF; draw contours and interpret the results.
- A time-domain IP profile of chargeability and apparent resistivity is shown in Figure 9.20. This is from the Pine Point sedimentary area of the

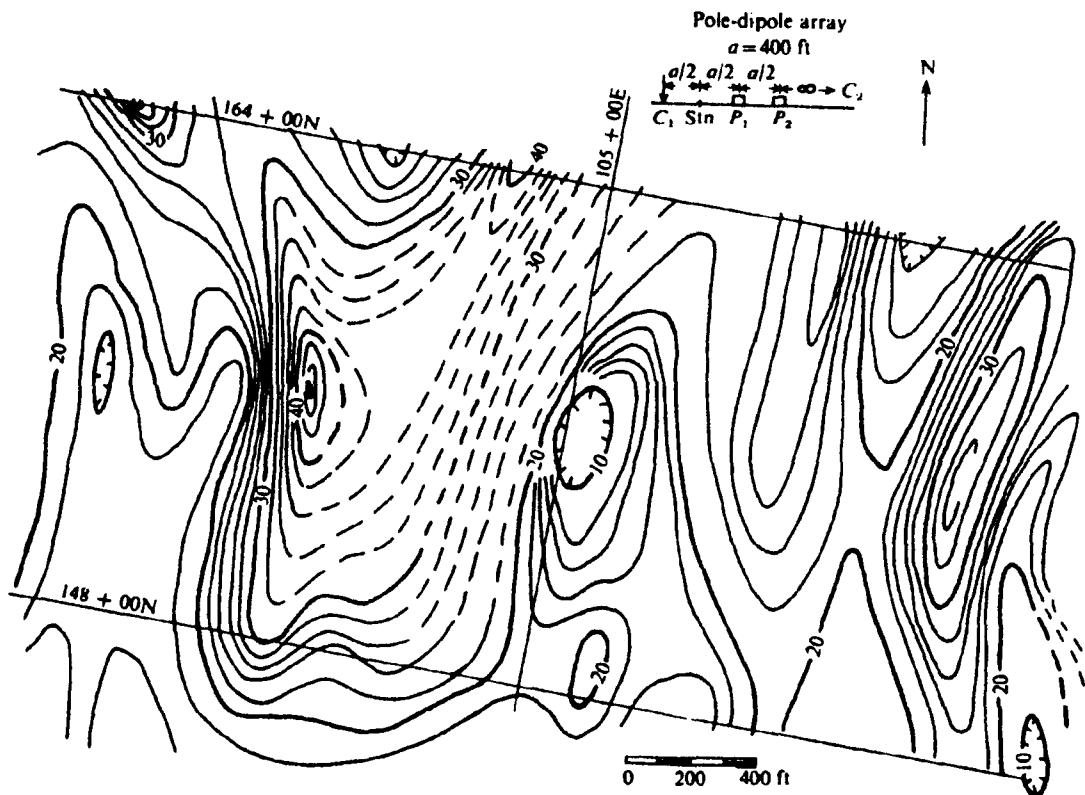


Figure 9.22. Time-domain IP survey, southern New Brunswick. Contour interval: 2 ms.

Canadian Northwest Territories, where IP methods have been successfully employed to locate large lead-zinc deposits. The host rocks are carbonates and the background IP is generally low and uniform. With no additional information, try to answer the following questions.

- (a) What type of electrode array was used?
  - (b) Was the electrode separation relatively large or small?
  - (c) Is the anomaly caused by electrode or membrane polarization?
  - (d) Is the anomalous source deep, shallow, wide, of great depth extent?
  - (e) Would you recommend further geophysical work, and if so, what?
  - (f) Would you drill this anomaly, and if so, where?
3. In the course of sulfide exploration in northwest Quebec, both frequency- and time-domain IP techniques were employed. Figure 9.21 shows pseudodepth plots for PFE, metal factor, and chargeability from a particular line traverse; as noted, the double-dipole array was used in both cases, with 100 ft separation. Compare the results obtained with the two methods and make whatever interpretation you can from all the data. What is the significance of the negative chargeability values?

4. Figure 9.22 shows chargeability contours from a time-domain IP survey carried out on a base-metal property in southern New Brunswick. During previous drilling, massive sulfide mineralization, striking N-S, had been found in the vicinity of line 105E, about the middle of the map; the zone was not very wide. Take off an E-W profile across the sheet around 156N. From this profile and the contours, make whatever interpretation you can of the data. Can you explain why the known mineral zone was not detected by IP?
5. Data for the metal-factor contours in Figure 9.23 were obtained from a survey in Nova Scotia, using the double-dipole array with  $x = 100$  ft and  $n = 1$ . Make an interpretation of the area based on these results. Can you match this map with the one from problem 10 in Chapter 8 and if so is the additional information an aid to the interpretation?
6. A frequency-domain survey, similar to that in problem 1, carried out over two lines on a property in Brazil, produced the results in Table 9.7. The dipole separation was 50 m, with  $n = 1, 2, 3, 4$ . Lines are E-W and separated by 400 m, with stations 50 m apart; the current dipole was to the west in all cases. Resistivities are in ohmmeters.

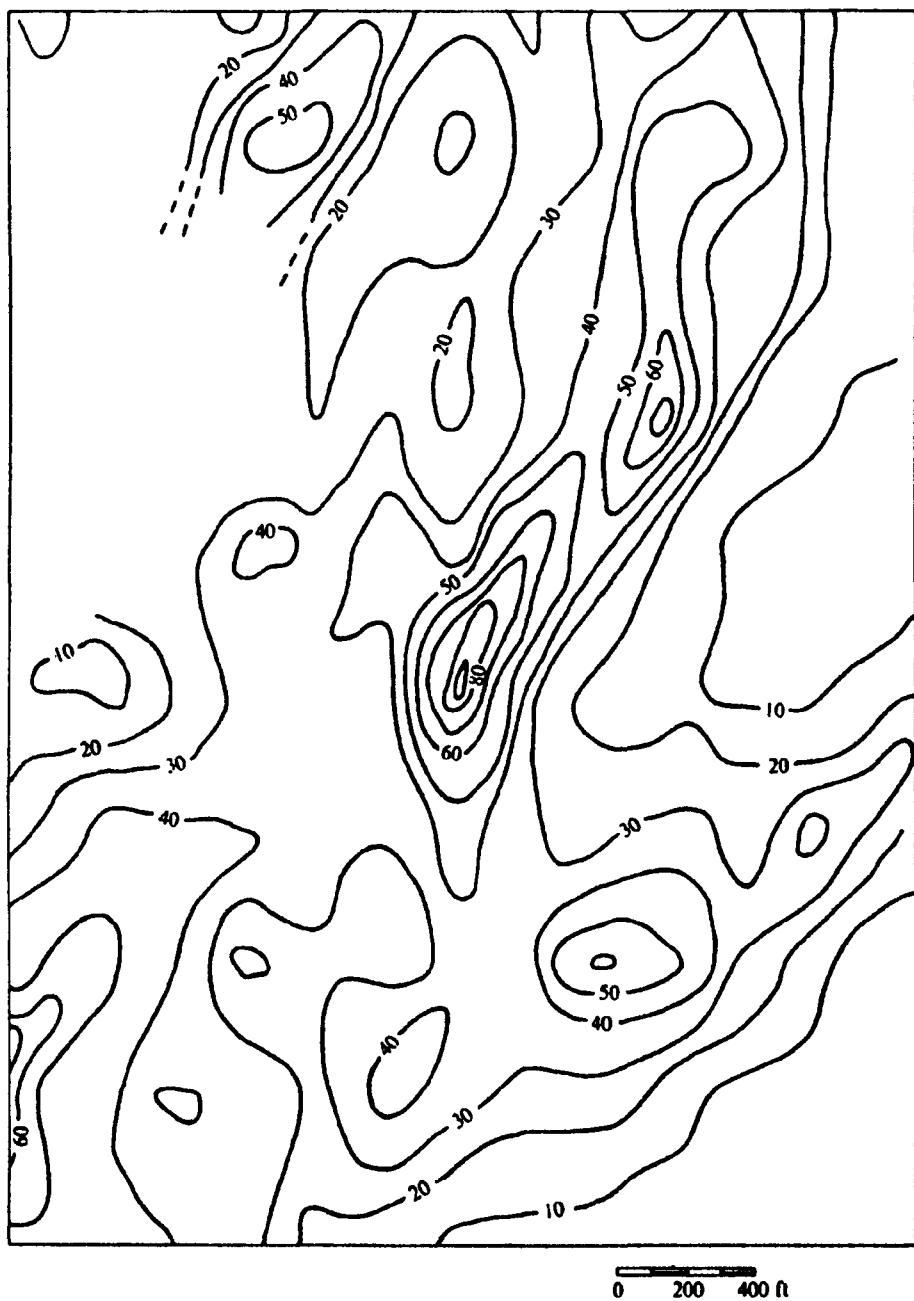


Figure 9.23. Metal-factor contours, double-dipole array:  $x = 100$  ft,  $n = 1$ .

Table 9.7.

Current dipole	$n = 1$			$n = 2$			$n = 3$			$n = 4$		
	$\rho_s$	PFE	MF	$\rho_s$	PFE	MF	$\rho_s$	PFE	MF	$\rho_s$	PFE	MF
<b>Line 0</b>												
44W–43W	228	1.6	13	390	1.8	9	637	1.6	5	250	4.8	37
43W–42W	248	1.7	13	520	1.5	5	217	4.5	40	71	14.5	390
42W–41W	220	1.2	10	128	3.0	45	44	14.5	630	29	11.5	740
41W–40W	76	2.5	62	34	13.5	750	22	11.5	1,000	29	9.5	630
40W–39W	30	11	760	17	11.5	1,330	19	9.8	980	34	8.4	470
39W–38W	36	3.7	195	38	3.5	175	59	4.0	130	65	4.2	124
38W–37W	114	1.5	25	217	1.5	13	275	2.2	15	340	1.5	8
37W–36W	190	0.2	2	305	0.7	4	410	1.0	5	650	1.2	3.5
<b>Line 2S</b>												
40W–39W	150	1.7	24	120	4.5	72	59	9.0	290	105	8.0	150
39W–38W	86	4.5	100	52	8.5	315	88	8.7	190	80	8.5	200
38W–37W	36	7.4	390	71	8.0	215	61	8.5	265	69	8.3	230
37W–36W	260	0.2	5	305	1.3	8	380	1.4	7	450	1.3	5.5
36W–35W	240	1.3	10	355	0.5	2.5	460	0.5	2	670	0.5	1

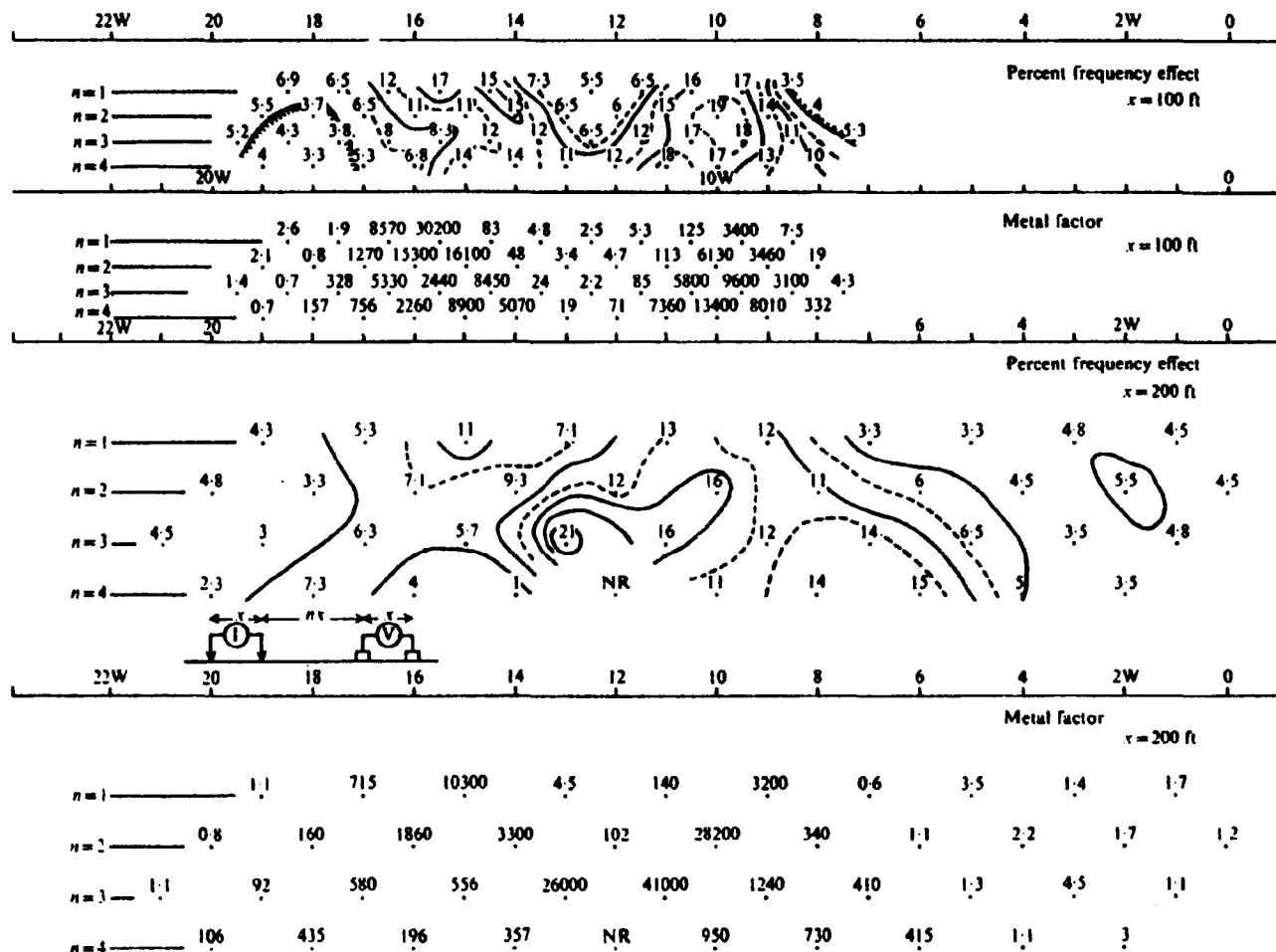
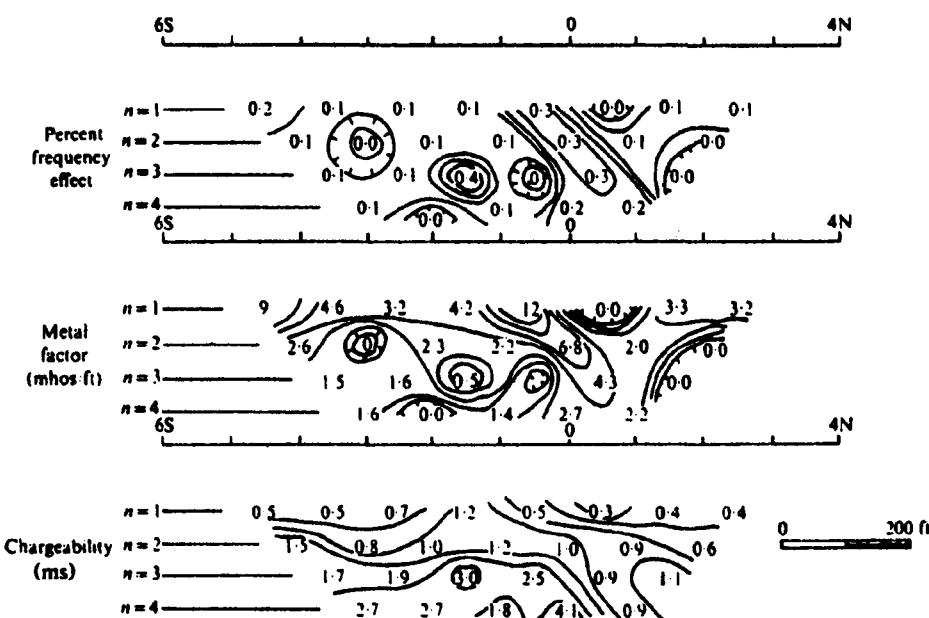


Figure 9.24. Pseudodepth plots for frequency-domain IP, western Ontario.

Figure 9.25. Time- and frequency-domain IP, double-dipole array,  $x = 100 \text{ ft}$ , Abitibi West, Quebec.

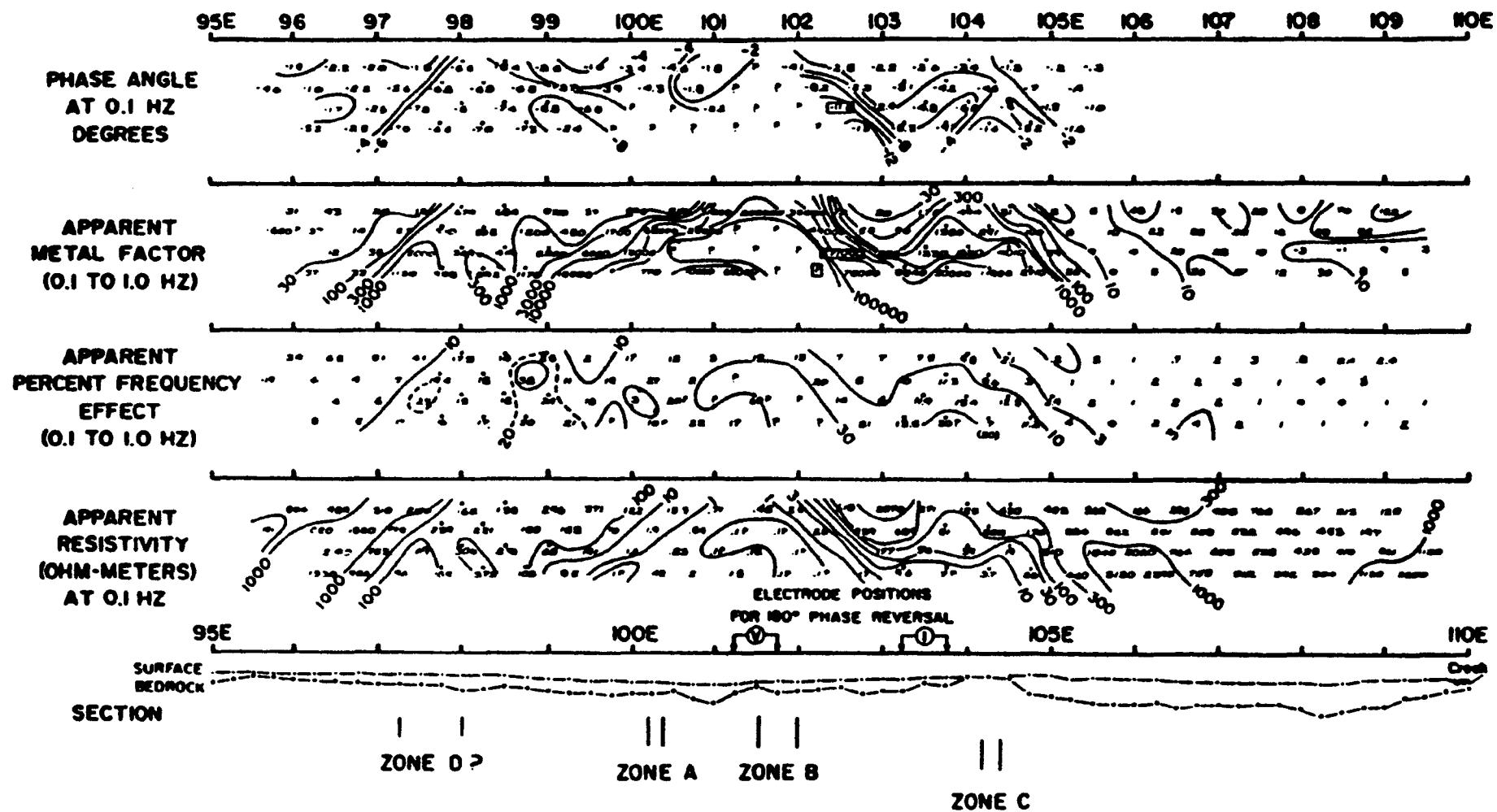


Figure 9.26. Results of an F-D survey in southern New Brunswick, using a double-dipole array:  $x = 50$  ft,  $n = 1, 2, 3, 4$ . (After Scott, 1971.)

Table 9.8.

Freq (Hz)	Phase (mrad)
0.01	340
0.0316	330
0.1	330
0.316	335
1.0	344
3.16	346
4.79	355
19.0	344
62.5	344
175	321
350	300
1,660	270
5,500	230
17,000	195

Make pseudodepth plots of  $\rho_a$ , PFE, and MF, and interpret the results.

7. Pseudodepth plots for frequency effect and metal factor, on a base-metal prospect in western Ontario are shown in Figure 9.24. Two spacings of double-dipole array were employed – 100 and 200 ft – as noted on the diagram. Contour the metal-factor data and compare the results with the PFE contours. Can you see any particular advantages in using two spreads? Is one more suitable for this particular job than the other? Interpret the data.
8. Figure 9.25 shows frequency- and time-domain contours in pseudodepth for an area in the Abitibi West region of Quebec. As noted in the diagram, the double-dipole array had a separation of 100 ft with  $n = 1, 2, 3, 4$ . The IP results are obviously not very promising, particularly in the frequency domain. There is, however, a base-metal orebody here of economic grade. Can you make any estimate of its location, depth, and width from the IP survey? Can you explain the poor response?
9. Figure 9.26 shows pseudodepth plots from a detailed frequency-domain IP survey performed at a base-metal property in southern New Brunswick. The short (50 ft ~ 15 m) double-dipole array was used because it was known that the mineralization occurred in several thin shallow zones contained in silicified wall rocks of high resistivity. Take off a couple of profiles from each of the  $\rho_a$ , PFE, and phase sections to check this. Compare these results with problem 4, particularly with regard to electrode spacing.
10. Using the Cole–Cole model of Figure 9.3, determine the real and imaginary components of impedance  $Z$  from the mathematical expression of this circuit in Equation (9.11), hence obtain the phase angle  $\phi$ . Check your result by numeri-

cal calculation of a few points in Figure 9.16a. [Hint: Eq. (A.46c) is useful here.]

11. The broad-band IP readings in Table 9.8 were obtained from a survey over mineralization containing both sulfides and graphite.

Plot these values on a log-log scale of phase versus frequency and attempt to match them with a best-fit Cole–Cole model of two terms. Assume plausible values for the parameters, the two  $M$  and  $c$  values being approximately the same and the time constants widely different.

## REFERENCES

- Bertin, J. 1968. Some aspects of induced polarization (time domain). *Geophys. Prosp.* 16, 401–26.
- Coggon, J. H. 1971. Electromagnetic and electric modelling by the finite element method. *Geophysics* 36, 132–55.
- Coggon, J. H. 1973. A comparison of IP electrode arrays. *Geophysics* 38, 737–61.
- Cole, K. S., and Cole, R. H. 1941. Dispersion and absorption in dielectrics. 1 Alternating current fields. *J. Chem. Phys.* 9, 341.
- Collett, L. S. 1959. Laboratory investigation of overvoltage. In *O vervoltage Research and Geophysical Applications*, J. R. Wait, ed., pp. 50–70. London: Pergamon.
- Dieter, K., Paterson, N. R., and Grant, F. S. 1969. IP and resistivity type curves for three-dimensional bodies. *Geophysics* 34, 615–32.
- Dolan, W. M., and McLaughlin, G. H. 1967. Considerations concerning measurement standards and design of pulsed IP equipment. In *Proc. Symp. on Induced Electrical Polarization*, pp. 2–31. Berkeley: Univ. Calif. Press.
- Edwards, R. N. 1974. The magnetometric resistivity method and its application to the mapping of a fault. *Can. J. Earth Sc.* 11, 1136–56.
- Edwards, R. N., and Howell, E. C. 1976. Field tests of magnetometric resistivity (MMR) method. *Geophysics* 41, 1170–83.
- Edwards, R. N., Lee, H., and Nabighian, M. N. 1978. On the theory of magnetometric resistivity (MMR) methods. *Geophysics* 43, 1176–1203.
- Fraser, D. C., Keevil, N. B., and Ward, S. H. 1964. Conductivity spectra of rocks from the Craigmont ore environment. *Geophysics* 29, 832–47.
- Hedstrom, H. 1940. Phase measurements in electrical prospecting. *Trans. A.I.M.E.* 138, 456–72.
- Inman, J. R. 1975. Resistivity inversion with ridge regression. *Geophysics* 40, 798–817.
- Inman, J. R., Ryu, J., and Ward, S. H. 1973. Resistivity inversion. *Geophysics* 38, 1088–1108.
- Johansen, H. K. 1975. Interactive computer-graphic-display-terminal system for interpretation of resistivity soundings. *Geophys. Prosp.* 23, 449–58.
- Johansen, H. K. 1977. A man/computer interpretation system for resistivity sounding over a horizontally stratified earth. *Geophys. Prosp.* 25, 667–91.
- Johnson, I. M. 1984. Spectral induced polarization parameters as determined through time-domain measurements. *Geophysics* 49, 1993–2003.
- Katsube, T. J., and Collett, L. S. 1973. Measuring techniques for rocks with high permittivity and high loss. *Geophysics* 38, 92–105.

- Lambert, R. 1974. Etude des paramètres affectant l'impédance électrique de certains métaux et minéraux. Ph.D. thesis, McGill Univ., Montreal.
- Major, J., and Silic, J. 1981. Restrictions on the use of Cole-Cole dispersion models in complex resistivity interpretation. *Geophysics* 46, 916-31.
- Marshall, D. J., and Madden, T. R. 1959. Induced polarization: A study of its causes. *Geophysics* 24, 790-816.
- Millett, F. B., Jr. 1967. Electromagnetic coupling of collinear dipoles on a uniform half-space. In *Mining Geophysics*, vol. II, pp. 401-19. Tulsa: Society of Exploration Geophysicists.
- Nabighian, M. N., and Elliot, C. L. 1976. Negative induced polarization effects from layered media. *Geophysics* 41, 1236-55.
- Pelton, W. H., Ward, S. H., Halloff, P. G., Sill, W. R., and Nelson, P. H. 1978. Mineral discrimination and removal of inductive coupling with multifrequency induced polarization. *Geophysics* 43, 588-609.
- Petrick, W. R., Pelton, W. H., and Ward, S. H. 1977. Ridge regression inversion applied to crustal resistivity sounding data from South Africa. *Geophysics* 42, 995-1005.
- Quick, D. H. 1974. Interpretation of gradient array chargeability anomalies. *Geophys. Prosp.* 22, 736-46.
- Scott, W. J. 1971. Phase angle measurements in the IP method of geophysical prospecting. Ph.D. thesis, McGill Univ., Montreal.
- Seigel, H. O. 1959a. A theory of induced polarization effects for step-function excitation. In *Overvoltage Research and Geophysical Applications*, J. R. Wait, ed., pp. 4-21. London: Pergamon.
- Seigel, H. O. 1959b. Mathematical formulation and type curves for induced polarization. *Geophysics* 24, 547-65.
- Seigel, H. O. 1967. The induced polarization method. In *Mining and groundwater geophysics*, L. W. Morley, ed., Econ. Geol. Report No. 26, Geol. Surv. Canada, pp. 123-37.
- Seigel, H. O. 1974. The magnetic induced polarization (MIP) method. *Geophysics* 39, 321-39.
- Seigel, H. O., and Howland-Rose, A. W. 1983. The magnetic induced polarization method. In *Developments in Geophysical Exploration Methods-4*, A. A. Fitch, ed., pp. 65-100. London and New York: Applied Science Publishers.
- Sumner, J. S. 1976. *Principles of Induced Polarization for Geophysical Exploration*. Amsterdam: Elsevier.
- Sumner, J. S. 1979. The induced polarization exploration method. In *Geophysics and geochemistry in the search for metallic ores*, P. J. Hood, ed., Econ. Geol. Report 31, Geol. Surv. Canada, pp. 123-33.
- Wynn, J. C., and Zonge, K. L. 1975. EM coupling, its intrinsic value, its removal, and the cultural coupling problem. *Geophysics* 40, 831-50.
- Zonge, K. L. 1972. Electrical parameters of rocks as applied to geophysics. Ph.D. dissertation, Univ. of Arizona, Tucson. (Microfilm at Univ. Michigan, Ann Arbor.)
- Zonge, K. L., and Wynn, J. C. 1975. Recent advances and applications in complex resistivity measurements. *Geophysics* 40, 851-64.

# Chapter 10

## *Radioactivity Method*

### 10.1. INTRODUCTION

The geophysical techniques described in previous chapters have depended on variations in the mechanical, chemical, electrical, or magnetic properties of rocks and minerals. Since about 1945 another property of certain elements has become of considerable economic importance. This property is known as *radioactivity*.

The original discovery was made by Becquerel in 1896, shortly after Röentgen had announced in 1895 the discovery of X-rays. Becquerel found that minerals containing uranium, as well as salts of uranium, emitted radiations that passed through material opaque to ordinary light, affected photographic emulsions in a manner similar to X-rays, and would ionize a gas.

The discovery of other radioactive elements soon followed. Mme. Curie, investigating minerals of uranium, extracted two new elements, polonium and radium, which were much more active than uranium. About the same time Schmidt discovered that thorium was radioactive and Debierne found the new radioactive element actinium.

Although at least 20 naturally occurring elements are now known to be radioactive, only uranium (U), thorium (Th), and an isotope of potassium (K) are of importance in exploration. One other, rubidium, is useful in determining ages of rocks, but the rest are either so rare or so weakly radioactive, or both, as to be of no significance in applied geophysics. A complete list, with characteristic radiations and other pertinent data, is given in Table 10.1.

The two elements, uranium and thorium, are important today as a source of fuel for the generation of heat and power in nuclear reactors. Large areas in all parts of the world have been surveyed on the ground and particularly by air in the search for uranium, using special detectors, which will be discussed later.

Surface work in radioactivity exploration is relatively a minor effort (see Table 1.2 for 1987 figures.) Airborne radiometric prospecting is still comparatively cheap and efficient from the point of view of

detecting gamma rays ( $\gamma$  rays) because the intensity of a 1 MeV beam is reduced by only 50% at 100 m above surface.

Considerable airborne work was done in the late 1950s using scintillation meters with large crystals. The results were not very useful owing to the lack of discrimination in total-count measurements (§10.3.4). When the demand for uranium fell off, the technique was almost abandoned. A revival of interest in uranium in the early 1970s, plus the availability of greatly improved  $\gamma$ -ray spectrometers (§10.3.4), made the method more attractive. A large-scale airborne radiometric program was initiated by the Geological Survey of Canada (GSC); this provided a stimulus for ground followup by private interests in various parts of Canada (Darnley, Cameron, and Richardson, 1975; Bristow et al., 1977).

The radioactive method is relatively unimportant in comparison with other geophysical techniques. It was first used in the late thirties for stratigraphic correlation in oil well logging (§11.1.2). Radioactivity prospecting became quite popular in the period 1945–57, fell off with the decrease in demand for uranium, and was revived again in the late sixties and early seventies. This sporadic progress, however, has not affected well-logging applications of the method, where several radiometric techniques have become standard. These will be discussed in Chapter 11.

### 10.2. PRINCIPLES OF RADIOACTIVITY

#### 10.2.1. Constituents of the Nucleus

(a) *Introduction.* Although much of the original work on emanations from radioactive substances was done by Rutherford and others nearly 80 years ago, their source – the nucleus of the atom – was not well understood at the time. We shall now consider this source and its elementary parts.

(b) *Atoms.* The *atom*, which is the fundamental part of all the elements, consists of a dense, small

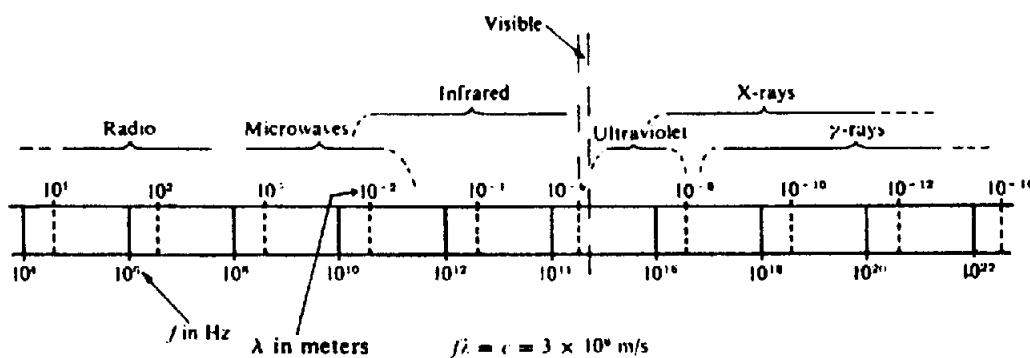


Figure 10.1. The electromagnetic spectrum showing relative frequency (wavelength) bands.

(~  $10^{-13}$  cm in radius), positively charged nucleus surrounded by negatively charged electrons, in number equal to the nuclear charge. The arrangement is quite analogous to a solar system, with planets moving about a central sun. Because there are never more than 92 electrons and because the atomic radii are of the order  $10^{-8}$  cm, most of the atom, like the solar system, is empty.

(c) **Protons.** The nucleus is composed of tightly packed protons and neutrons. The proton, carrying unit positive charge, has a mass 1.00812 on the physical scale ( $O = 16.0000\dots$ ), the actual mass being  $1.7 \times 10^{-24}$  g. The number of protons in a nucleus determines the element itself. For example, the first element in the Periodic Table, hydrogen, has 1 proton, oxygen has 8, cadmium 48, and so on, up to uranium, with 92 protons.

(d) **Neutrons.** The other nuclear particle, the neutron, has zero charge and a slightly greater mass than the proton (1.00893). The only element lacking neutrons is common hydrogen. As we proceed through the Periodic Table, the ratio of the number of neutrons to the number of protons increases from 1 to ~ 1.5. Thus helium has 2 neutrons and 2 protons, whereas thorium contains 142 neutrons and 90 protons.

(e) **Isotopes.** Most elements are composed of a mixture of nuclei having different numbers of neutrons, the number of protons, of course, being the same. These are called isotopes, that is, forms of the same element having different atomic weights. (Practically all the mass of an element is contained in the nucleus, hence is determined by the number of protons and neutrons called the atomic weight). For instance, hydrogen is a mixture of two isotopes:  ${}_1H^1$ , which is a single proton (99.985% abundance), and  ${}_1H^2$ , one proton and one neutron, familiarly known as deuterium (0.015% abundance). Titanium has 5 isotopes, tin has 10, tungsten 5, lead 4, and so on.

(f) **Alpha particles.** Actually these are the equivalent of a helium nucleus,  ${}^2p + {}^2n$ ; the name was attached in the pioneer days of radioactivity, before the nature of the particle was understood. It has a charge +2, mass 4.00389, and is frequently a tightly bound entity within nuclei heavier than helium. It may be ejected from the nucleus during a disintegration.

(g) **Electrons.** The outer atomic constituent, the electron, has a charge -1 (actual charge on the electron and proton is  $1.60 \times 10^{-19}$  C) and mass about  $1/1,840$  of the proton. Although the electron does not exist as a separate entity in the nucleus, it is ejected in certain nuclear disintegrations when a neutron splits into a proton and an electron, the proton remaining in the nucleus. This transmutation results in a gain of +1 unit of charge and practically zero mass change, that is to say, the element moves up one place in the Periodic Table. Electrons ejected from the nucleus were originally called beta ( $\beta$ ) particles or rays.

(h) **Gamma radiation.** During nuclear disintegrations, pure electromagnetic radiation representing excess energy is frequently emitted from the excited nucleus. The early name assigned, gamma ray ( $\gamma$  ray) is quite appropriate in this case ( $\alpha$  and  $\beta$  rays are really discrete particles). Gamma rays differ from X-rays only in name, although usually the latter term is used for radiation of lower energy. The relative location of  $\gamma$  rays in the electromagnetic spectrum is illustrated in Figure 10.1.

### 10.2.2. Nuclear Disintegrations

While carrying on pioneer work in nuclear physics, Sir Ernest Rutherford investigated the radiations from naturally occurring radioactive elements and showed that they consisted of the three distinct types mentioned above:  $\alpha$ ,  $\beta$ , and  $\gamma$  rays. Each of these rays produces three different effects in varying

Table 10.1. Naturally occurring radioactive isotopes.

Element	Isotope	Abundance (%)	Half-life (yr)	Type of radiation	Energy (MeV)
Potassium	$^{39}\text{K}^{40}$	0.012	$1.3 \times 10^9$	$\beta, K$ cap	1.46
Calcium	$^{40}\text{Ca}^{48}$	0.18	$> 2 \times 10^{16}$	$\beta$	0.12
Vanadium	$^{50}\text{V}^{50}$	0.24	$6 \times 10^{15}$	$\beta, K$ cap	0.71, 1.59
Rubidium	$^{87}\text{Rb}^{87}$	27.8	$4.7 \times 10^{10}$	$\beta$	0.27
Indium	$^{115}\text{In}^{115}$	95.72	$6 \times 10^{14}$	$\beta$	0.60
Lanthanum	$^{138}\text{La}^{138}$	0.089	$1.1 \times 10^{11}$	$\beta, K$ cap	0.54, 0.81, 1.43
Cerium	$^{142}\text{Ce}^{142}$	11.1		$\alpha$	1.5
Neodymium	$^{144}\text{Nd}^{144}$	23.8	$5 \times 10^{15}$	$\alpha$	1.8
Samarium	$^{147}\text{Sm}^{147}$	14.97	$10^{11}$	$\alpha$	2.32
Samarium	$^{148}\text{Sm}^{148}$	11.2	$1.2 \times 10^{13}$	$\alpha$	2.14
Samarium	$^{149}\text{Sm}^{149}$	13.8	$\sim 4 \times 10^{14}$	$\alpha$	1.84
Gadolinium	$^{152}\text{Gd}^{152}$	0.2	$1.1 \times 10^{14}$	$\alpha$	2.24
Lutecium	$^{176}\text{Lu}^{176}$	2.6	$3 \times 10^{10}$	$\beta, \gamma$	0.088, 0.20, 0.31
Hafnium	$^{174}\text{Hf}^{174}$	0.16	$2 \times 10^{15}$	$\alpha$	2.5
Rhenium	$^{187}\text{Re}^{187}$	62.9	$7 \times 10^{10}$	$\beta$	$\leq 0.008$
Platinum	$^{190}\text{Pt}^{190}$	0.013	$6 \times 10^{11}$	$\alpha$	3.11
Platinum	$^{192}\text{Pt}^{192}$	0.78	$\sim 10^{15}$	$\alpha$	2.6
Lead	$^{204}\text{Pb}^{204}$	1.48		$\alpha$	
Thorium*	$^{232}\text{Th}^{232}$	100	$1.39 \times 10^{10}$	$\alpha, \beta, \gamma$	0.03 – 2.62
Uranium*	$^{235}\text{U}^{235}$	0.72	$7.1 \times 10^8$	$\alpha, \beta, \gamma$	0.02 – 0.9
Uranium*	$^{238}\text{U}^{238}$	99.3	$4.5 \times 10^9$	$\alpha, \beta, \gamma$	0.4 – 2.5

\*Each of these undergoes a long series of disintegrations yielding lead isotopes 208, 207, 206, respectively. During these disintegrations numerous  $\gamma$  rays are emitted, in addition to the  $\alpha$ - and  $\beta$  particles.

degrees, namely:

1. They affect photographic emulsions in much the same way as light and X-rays.
2. They ionize gas, making it electrically conducting.
3. They produce scintillations or phosphorescence in certain minerals and chemical compounds.

All three effects have been used in geophysical prospecting by the radioactivity method.

The three "rays" characteristic of natural nuclear disintegrations have very different penetrating powers. Thus,  $\alpha$  rays are easily stopped by a sheet of paper,  $\beta$  rays by a few millimeters of aluminum, whereas  $\gamma$  radiation requires several centimeters of lead. Their equivalent range in overburden or rock is thus practically zero for the first two and not more than 50 to 75 cm of rock for  $\gamma$  rays.

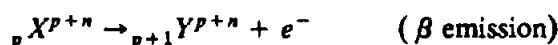
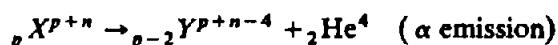
In fact, this range is a complicated function of the energy and character of the particles or radiation and of the density or atomic number of the medium through which they pass. It is clear that the range varies with initial energy and the rate of dissipation of energy. The latter is a complex process of scattering, collision, and absorption involving the atoms of the host material and resulting in ionization along the path. Charged particles ( $\alpha, \beta$ ) ionize strongly, uncharged electromagnetic radiations ( $\gamma$  rays, X-rays) do not.

Maximum energy in natural nuclear disintegrations is generally less than 3 MeV [1 MeV =  $10^6$

electron-volts (eV), the energy acquired by a particle of unit charge, falling through a potential of  $10^6$  V.] Even in air, the range of 3 MeV  $\alpha$  and  $\beta$  particles is only a few centimeters and meters, respectively. On the other hand,  $\gamma$  rays of this energy will travel a few hundred meters in air.

In addition to  $\alpha$ ,  $\beta$ , and  $\gamma$  emissions, there is one other type of nuclear transmutation, called *K capture* (see Table 10.1 and Fig. 10.2), which occurs in several of the natural radioelements. In this process, an electron from the innermost *K* orbit enters the nucleus, which then emits  $\gamma$  rays; as a result of the electron capture the atomic number decreases by one and a different element is created.

The equations representing transitions of element *X* to *Y* by  $\alpha$ - and  $\beta$ -ray emission and electron capture are



In this nomenclature, the number of protons in elements *X*, *Y*, and He is the lower left subscript, whereas the number of protons plus neutrons (atomic weight) is given by the upper right superscript. Because the *X*, *Y*, and He symbols define the number of protons uniquely, this notation has recently been changed by entering the nuclear mass (*p* + *n*) at the

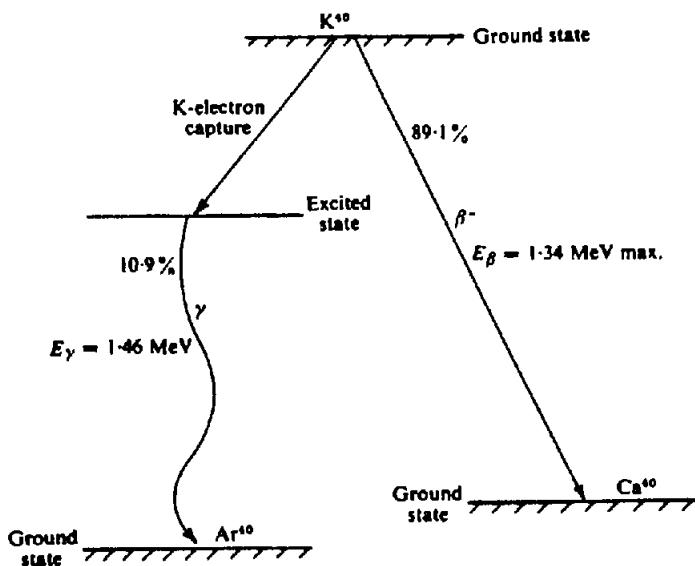


Figure 10.2. Energy-level diagram for radioactive potassium.

upper left and deleting the proton number altogether. Thus  ${}_{37}^{87}\text{Rb}$  becomes  ${}^{87}\text{Rb}$ .

### 10.2.3. Radioactive Decay Processes

In 1902 Rutherford and Soddy announced the theory of radioactive transformation, in which they stated that when an element emitted  $\alpha$  or  $\beta$  rays, it was transmuted into a new element, the rate of disintegration being a characteristic of each radioactive nucleus. They showed that the rate of change was proportional to the number of atoms present and was not affected by physical or chemical processes in the surroundings.

Thus, for any type of radioactive atom, we have the relation

$$dN/dt = -\lambda N$$

where  $N$  is the number of atoms present at time  $t$  and  $\lambda$  is a decay constant that is characteristic of each element. Therefore,

$$\int_{N_0}^N \frac{dN}{N} = -\lambda \int_0^t dt \quad \text{or} \quad N = N_0 e^{-\lambda t} \quad (10.1)$$

where  $N_0$  is the number of atoms at an arbitrary time  $t = 0$ . If  $T_{1/2}$  is the time required for half of the nuclei to disintegrate, we have

$$N/N_0 = \frac{1}{2} = e^{-\lambda T_{1/2}}$$

or

$$\lambda = (\ln 2)/T_{1/2} = 0.693/T_{1/2} \quad (10.2)$$

Half-life values of radioactive nuclei vary enormously, from  ${}^{212}\text{Po} \approx 10^{-7}$  s to  ${}^{204}\text{Pb} \approx 10^{19}$  y. Obviously a short half-life goes with a vigorous rate of disintegration, whereas the lead isotope 204 is, for all practical purposes, stable – the disintegration rate is three or four nuclei per week per gram.

As mentioned earlier, only three radioactive elements, U, Th, and K are of practical significance in prospecting. The potassium is mainly a nuisance when searching for the other two; although the  ${}^{40}\text{K}$  isotope is, apparently, no more plentiful than U or Th, the widespread occurrence of potassium-rich rocks and particularly the association of these with U and Th, for example, in pegmatites, creates a problem somewhat analogous to that of graphite versus metal sulfides in electrical prospecting.

As shown by Table 10.2 and Figure 10.3, there are three radioactive series for uranium and thorium, starting with  ${}_{90}\text{Th}^{232}$ ,  ${}_{92}\text{U}^{235}$  (the so-called actinium series), and  ${}_{92}\text{U}^{238}$ . All decay eventually to stable isotopes of lead, with 10, 15, and 17 intermediate radioactive stages, respectively.

It is useful to calculate the number of daughter atoms present at any time, given the number  $N_0$  of the parent at time  $t = 0$ . Then the number of parent atoms left at a later time  $t$  will be  $N_1 = N_0 e^{-\lambda_1 t}$ , where  $\lambda_1$  is its decay constant. But the rate of decay of the parent atoms,  $dN_1/dt = -\lambda_1 N_1$ , is just the rate of production of the daughter. At the same time the daughter atoms are disintegrating at a rate  $\lambda_2 N_2$ , where  $N_2$  is the number present at time  $t$  and  $\lambda_2$  is the decay constant. Hence the rate of accumulation of the daughter atoms is the difference between production and decay, or

$$dN_2/dt = \lambda_1 N_1 - \lambda_2 N_2 = \lambda_1 N_0 e^{-\lambda_1 t} - \lambda_2 N_2 \quad (10.3)$$

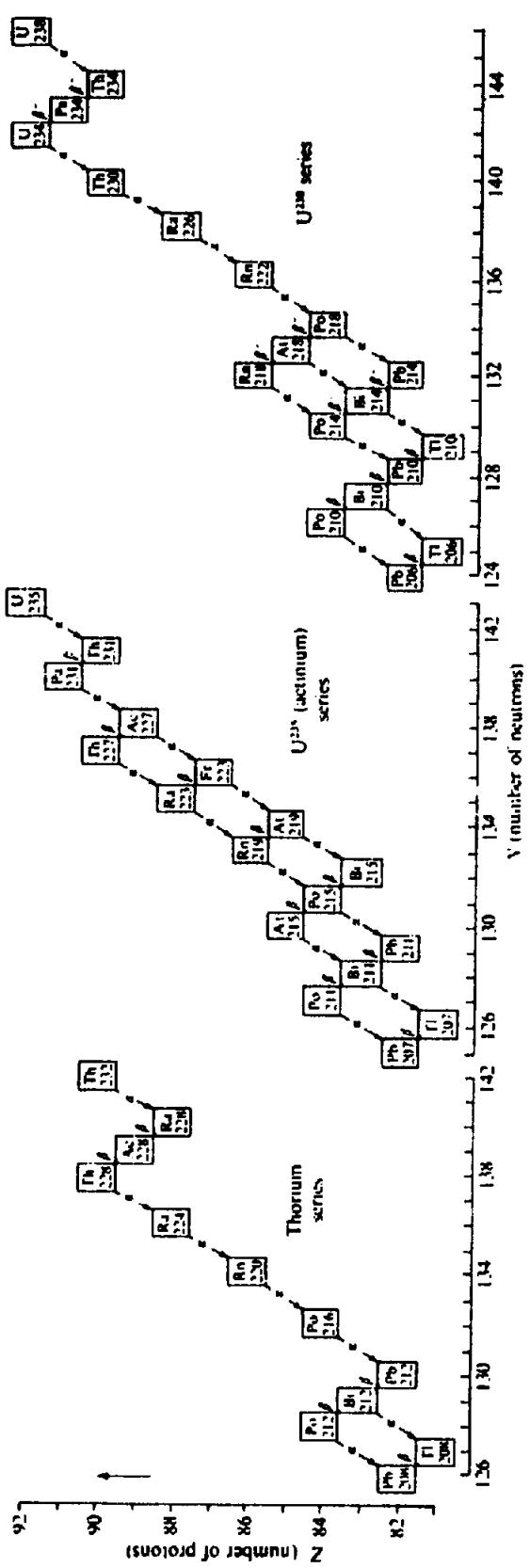


*Figure 10.3. Uranium and thorium radioactive series. Schematic showing decay processes.*

Table 10.2. Natural radioactive series of thorium and uranium.

Isotope	Half-life	Decay constant (s <sup>-1</sup> )	Radiation	γ-ray energies (MeV)	No. of γ-rays
<i>Thorium series</i>					
<sup>90</sup> Th <sup>232</sup>	$1.4 \times 10^{10}$ yr	$1.58 \times 10^{-18}$	α, SF*, γ	0.059	
<sup>88</sup> Ra <sup>228</sup>	6.7 yr	$3.3 \times 10^{-9}$	β, γ	0.03	
<sup>89</sup> Ac <sup>228</sup>	6.1 hr	$3.1 \times 10^{-4}$	β, γ	0.06 – 0.97	> 10
<sup>90</sup> Th <sup>228</sup>	1.91 yr	$1.15 \times 10^{-8}$	α, γ	0.085 – 0.214	5
<sup>88</sup> Ra <sup>224</sup>	3.64 day	$2.2 \times 10^{-6}$	α, γ	0.24, 0.29	
<sup>86</sup> Rn <sup>220</sup>	51 s	$1.3 \times 10^{-2}$	α, γ	0.54	
<sup>94</sup> Po <sup>216</sup>	0.16 s	4.3	α		
<sup>82</sup> Pb <sup>212</sup>	10.6 hr	$1.8 \times 10^{-5}$	β, γ	0.11 – 0.41	5
<sup>83</sup> Bi <sup>212</sup>	60.6 min	$1.9 \times 10^{-4}$	β, α, γ	0.04 – 2.2	> 10
<sup>84</sup> Po <sup>212</sup>	$0.3 \times 10^{-6}$ s	$2.3 \times 10^6$	α		
<sup>81</sup> Tl <sup>206</sup>	3.1 min	$3.7 \times 10^{-3}$	β, γ	0.28 – 2.62	5
<sup>82</sup> Pb <sup>208</sup>	Stable				
<i>Actinium Series</i>					
<sup>92</sup> U <sup>235</sup>	$7.1 \times 10^8$ yr	$3.1 \times 10^{-17}$	α, SF*, γ	0.07 – 0.38	10
<sup>90</sup> Th <sup>231</sup>	25.6 hr	$7.4 \times 10^{-6}$	β, γ	0.08 – 0.31	> 10
<sup>91</sup> Pa <sup>231</sup>	$3.4 \times 10^4$ yr	$6.5 \times 10^{-13}$	α, γ	0.29 – 0.36	> 10
<sup>89</sup> Ac <sup>227</sup>	21.6 yr	$10^{-9}$	β, α, γ	0.09 – 0.19	9
<sup>90</sup> Th <sup>227</sup>	18.2 day	$4.35 \times 10^{-7}$	α, γ	0.05 – 0.33	> 10
<sup>87</sup> Fr <sup>223</sup>	22 min	$5.2 \times 10^{-4}$	β, α, γ	0.05 – 0.31	4
<sup>88</sup> Ra <sup>223</sup>	11.7 day	$6.76 \times 10^{-7}$	α, γ	0.03 – 0.45	> 10
<sup>86</sup> Rn <sup>229</sup>	4 s	0.17	α, γ	0.27, 0.4	
<sup>85</sup> At <sup>229</sup>	54 s	$1.28 \times 10^{-2}$	α, β		
<sup>84</sup> Po <sup>215</sup>	$1.8 \times 10^{-3}$ s	$3.8 \times 10^2$	α, β		
<sup>85</sup> At <sup>215</sup>	$10^{-4}$ s	$6.9 \times 10^3$	α		
<sup>83</sup> Bi <sup>215</sup>	8 min	$1.44 \times 10^{-3}$	β		
<sup>83</sup> Bi <sup>211</sup>	2.15 min	$5.35 \times 10^{-3}$	α, β, γ	0.35	
<sup>84</sup> Po <sup>211</sup>	0.52 s	1.32	α, γ	0.56, 0.88	
<sup>82</sup> Pb <sup>211</sup>	36 min	$3.2 \times 10^{-4}$	β, γ	0.065 – 0.83	4
<sup>81</sup> Tl <sup>207</sup>	4.8 min	$2.4 \times 10^{-3}$	β, γ	0.89	
<sup>82</sup> Pb <sup>207</sup>	Stable				
<i>Uranium Series</i>					
<sup>92</sup> U <sup>238</sup>	$4.51 \times 10^9$ yr	$4.9 \times 10^{-18}$	α, SF*, γ	0.048	
<sup>90</sup> Th <sup>234</sup>	24.1 day	$3.3 \times 10^{-7}$	β, γ	0.03 – 0.09	3
<sup>91</sup> Pa <sup>234</sup>	6.7 hr	$2.84 \times 10^{-5}$	β, γ	0.044 – 1.85	> 10
<sup>92</sup> U <sup>234</sup>	$2.48 \times 10^5$ yr	$8.9 \times 10^{-14}$	α, SF*, γ	0.053, 0.118	
<sup>90</sup> Th <sup>230</sup>	$8 \times 10^4$ yr	$2.75 \times 10^{-10}$	α, γ	0.068 – 0.25	7
<sup>88</sup> Ra <sup>226</sup>	1622 yr	$1.35 \times 10^{-11}$	α, γ	0.19 – 0.64	4
<sup>86</sup> Rn <sup>222</sup>	3.82 day	$2.07 \times 10^{-6}$	α, γ	0.51	
<sup>84</sup> Po <sup>218</sup>	3.05 min	$3.8 \times 10^{-3}$	α, β		
<sup>85</sup> At <sup>218</sup>	1.35 s	0.51	α		
<sup>86</sup> Rn <sup>218</sup>	0.03 s	23.1	α	0.61	
<sup>83</sup> Bi <sup>214</sup>	19.7 min	$5.85 \times 10^{-4}$	β, α, γ	0.45 – 2.43	> 10
<sup>84</sup> Po <sup>214</sup>	$1.64 \times 10^{-4}$ s	$4.2 \times 10^3$	α		
<sup>82</sup> Pb <sup>214</sup>	26.8 min	$4.3 \times 10^{-4}$	β, γ	0.05 – 0.35	> 10
<sup>82</sup> Pb <sup>210</sup>	21 yr	$1.05 \times 10^{-9}$	β, γ	0.047	
<sup>83</sup> Bi <sup>210</sup>	5 day	$1.58 \times 10^{-6}$	β		
<sup>84</sup> Po <sup>210</sup>	138.4 day	$5.7 \times 10^{-8}$	α, γ	0.79	
<sup>81</sup> Tl <sup>210</sup>	1.3 min	$8.85 \times 10^{-3}$	β, γ	0.3, 0.78, 1.1	
<sup>81</sup> Tl <sup>206</sup>	4.2 min	$2.75 \times 10^{-3}$	β		
<sup>82</sup> Pb <sup>206</sup>	Stable				

SF\* = spontaneous fission.

We can solve this equation by assuming  $N_2 = Ae^{-\lambda_1 t} + Be^{-\lambda_2 t}$ , with the condition that, when  $t = 0$ ,  $N_2 = 0$ . The result is

$$N_2 = \frac{\lambda_1 N_0}{\lambda_2 - \lambda_1} (e^{-\lambda_1 t} - e^{-\lambda_2 t}) \quad (10.4a)$$

This calculation can be carried on for successive members of the series. The number of atoms of the  $n$ th product produced after time  $t$  is given by

$$N_n = C_1 e^{-\lambda_1 t} + C_2 e^{-\lambda_2 t} + \dots + C_n e^{-\lambda_n t} \quad (10.4b)$$

Table 10.3. Emission of  $\gamma$  rays by U and Th series and by K.

Energy (MeV)	Uranium series		Thorium series		Potassium	
	(Phot/s g)	%U	(Phot/s g)	%Th	(Phot/s g)	%K
0.2–0.5	$9.4 \times 10^3$	36	$3.9 \times 10^3$	34		
0.5–1.0	$8.0 \times 10^3$	31	$5.5 \times 10^3$	47		
1.0–1.5	$4.3 \times 10^3$	17	$0.4 \times 10^3$	3	3.4	100
1.5–2.0	$3.2 \times 10^3$	12	$0.3 \times 10^3$	3		
2.0–2.5	$1.1 \times 10^3$	4				
2.5–3.0			$1.5 \times 10^3$	13		
Total	$2.6 \times 10^4$	100	$1.2 \times 10^4$	100	3.4	100

where

$$\begin{aligned} C_1 &= \frac{\lambda_1 \lambda_2 \cdots \lambda_{n-1} N_0}{(\lambda_2 - \lambda_1)(\lambda_3 - \lambda_2) \cdots (\lambda_n - \lambda_1)} \\ &= KN_0/\delta_1 \\ C_2 &= \frac{\lambda_1 \lambda_2 \cdots \lambda_{n-1} N_0}{(\lambda_1 - \lambda_2)(\lambda_3 - \lambda_2) \cdots (\lambda_n - \lambda_2)} \\ &= KN_0/\delta_2 \\ &\vdots \\ C_n &= \frac{\lambda_1 \lambda_2 \cdots \lambda_{n-1} N_0}{(\lambda_1 - \lambda_n)(\lambda_2 - \lambda_n) \cdots (\lambda_{n-1} - \lambda_n)} \\ &= KN_0/\delta_n \end{aligned} \quad (10.4c)$$

where

$$K = \lambda_1 \lambda_2 \cdots \lambda_{n-1},$$

and

$$\delta_i = (\lambda_1 - \lambda_i)(\lambda_2 - \lambda_i) \cdots (\lambda_n - \lambda_i).$$

#### 10.2.4. Radioactive Equilibrium

From Equation (10.3) it follows that when a radioactive series is in equilibrium, we have

$$\lambda_1 N_1 = \lambda_2 N_2 = \lambda_3 N_3 = \cdots \lambda_n N_n. \quad (10.5)$$

That is to say, at equilibrium the number of daughter atoms disintegrating per second is the same as the number being created by disintegrations of the parent.

The state of radioactive equilibrium merits further explanation. Consider radium and radon, the successive intermediate products in the  $^{235}\text{U}$  series (see  $^{88}\text{Ra}^{223}$  and  $^{86}\text{Rn}^{219}$ , Table 10.2 and Fig. 10.3). Here the daughter product decays about  $10^5$  times faster than its parent. If we start with a sample of pure radium, we find that its decay rate is practically constant for the first day or two, because the half-life is about 12 days. During the same interval the supply of radon atoms is building up at the same rate, although the radon is decaying considerably faster

than the radium. From Equations (10.1) and (10.4a) we can get the ratio of the number of atoms of parent to daughter at any time

$$\frac{N_2}{N_1} = \frac{\lambda_1}{\lambda_2 - \lambda_1} \{1 - e^{(\lambda_1 - \lambda_2)t}\}.$$

When equilibrium has been reached, the rates of decay of parent and daughter are the same, that is,  $N_2/N_1 = \lambda_1/\lambda_2$ . Thus we have

$$\frac{\lambda_1}{\lambda_2} = \frac{\lambda_1}{\lambda_2 - \lambda_1} \{1 - e^{(\lambda_1 - \lambda_2)t_{eq}}\}$$

or

$$e^{(\lambda_1 - \lambda_2)t_{eq}} = \frac{\lambda_1}{\lambda_2}$$

hence,

$$t_{eq} = \left( \frac{1}{\lambda_1 - \lambda_2} \right) \ln \left( \frac{\lambda_1}{\lambda_2} \right) \quad (10.6a)$$

For this example the value of  $t_{eq}$  is about 1 min, after which the two will be in equilibrium, as long as the radium holds out.

In the case of a series with  $n$  products, the time to reach equilibrium can be found from Equation (10.4b). It is

$$\frac{N_n}{N_1} = K \left\{ \frac{1}{\delta_1} + \frac{e^{(\lambda_1 - \lambda_2)t_{eq}}}{\delta_2} + \frac{e^{(\lambda_1 - \lambda_3)t_{eq}}}{\delta_3} + \cdots + \frac{e^{(\lambda_1 - \lambda_n)t_{eq}}}{\delta_n} \right\} = \frac{\lambda_1}{\lambda_n} \quad (10.6b)$$

where  $K$  and  $\delta$  were defined in Equation (10.4c).

For thorium this time interval is less than 100 yr and for the two uranium chains, of the order  $10^6$  yr. Measurement of series products, in which the equilibrium situation is significant, will be discussed later; under these conditions it is possible to determine the amount of a parent product in a sample by measuring the amount of one of the succeeding members.

Table 10.2 and Figure 10.3 show the three radioactive series in detail, with the principal radiation accompanying each disintegration. There is in addition a wide spectrum of  $\gamma$  rays accompanying both  $\alpha$

Table 10.4. Radioactive minerals.

Potassium	Mineral Occurrence	(i) Orthoclase and microline feldspars [ $KAlSi_3O_8$ ]
		(ii) Muscovite [ $H_2KAl(SiO_4)_3$ ]
		(iii) Alunite [ $K_2Al_6(OH)_12SO_4$ ]
		(iv) Sylvite, carnallite [ $KCl, MgCl_2, 6H_2O$ ]
		(i) Main constituents in acid igneous rocks and pegmatites
		(ii) Same
		(iii) Alteration in acid volcanics
		(iv) Saline deposits in sediments
Thorium	Mineral Occurrence	(i) Monazite [ $ThO_2 + \text{rare earth phosphate}$ ]
		(ii) Thorianite [ $(Th, U)O_2$ ]
		(iii) Thorite, uranothorite [ $ThSiO_4 + U$ ]
		(i) Granites, pegmatites, gneiss
		(ii) Granites, pegmatites, placers
		(iii) Same
Uranium	Mineral Occurrence	(i) Uraninite [oxide of U, Pb, Ra + Th, rare earths]
		(ii) Carnotite [ $K_2O \cdot 2UO_3 \cdot V_2O_5 \cdot 2H_2O$ ]
		(iii) Gummite [uraninite alterations]
		(i) Granites, pegmatites, and with vein deposits of Ag, Pb, Cu, etc.
		(ii) Sandstones
		(iii) Associated with uraninite

Table 10.5. Background radioactivity in rocks and waters.

Rock	Ci/g ( $\times 10^{-12}$ )	K (ppm)	Th (ppm)	U (ppm)	Water (radium)	Ci/g ( $\times 10^{-12}$ )
Hornblende	1.2				Saratoga, NY	0.01–0.1
Granite	0.7–4.8	35,000	15	4	Bath, England	0.14
Basalts	0.5	9,000	2	0.6	Carlsbad, Czech.	0.04–0.1
Olivine	0.33				St Lawrence River	0.00025
Ultramafics		10	0.2	0.05	Valdemorillo, Spain	0.02
Marble	1.9				Aix-les-Bains, France	0.002
Quartzite	5.0				Manitou, CO	0.003
Sandstone	2–4				Hot Springs, AR	0.0009
Slates	3–8				Atlantic Ocean	0.014–0.034
Dolomites	8				Indian Ocean	0.007
Chalk	0.4					
Chondrites		850	0.08	0.02		
Iron meteor.			0.015	0.04		

and  $\beta$  emission, some of which are included in the table; also, Table 10.3 gives  $\gamma$ -ray emissions in units of photons per second per gram for various energy windows. The thorium series has an isolated  $\gamma$  ray from  $^{208}\text{Tl}$  at 2.62 MeV; the uranium series do not produce such distinctive radiations, although the 1.76 MeV  $\gamma$  ray from  $^{214}\text{Bi}$  is reasonably so.

#### 10.2.5. Units

The unit used for measuring the activity of a radioactive specimen is the *curie* (Ci) named for the discoverer of radium, Mme. Curie. It is the activity, that results in  $3.7 \times 10^{10}$  disintegrations per second, this being the number of  $\alpha$  particles emitted by 1 g of pure radium,  $^{226}\text{Ra}$ , in 1 s.

Because  $\gamma$  rays are similar in nature to X-rays, the strength or intensity of gamma radiation (as well as  $\alpha$  and  $\beta$  particles) is also measured in the X-ray unit, called the *röentgen*. This is the quantity of radiation that will produce one electrostatic unit of charge ( $2.08 \times 10^9$  ion pairs) per cubic centimeter in air at  $0^\circ\text{C}$  and 760 Torr (NTP). Subunits are the milliröentgen (mR) and microröentgen ( $\mu\text{R}$ ). This is the unit used in defining maximum dosage permissible to humans exposed to radioactivity, about 300 mR/week.

Some field instruments indicate radioactivity as counts per minute, generally marked on the scale of a microammeter in an integrating circuit that adds up pulses to measure total intensity. None of these units takes into account the energy of the radiation.

### 10.2.6. Radioactivity of Rocks and Minerals

Some of the common radioactive minerals of Th and U are listed in Table 10.4. The potassium minerals, as mentioned previously, are very widespread. Large deposits of monazite are found in Brazil, India, and South Africa. Thorite and uraninite (pitchblende) occur particularly in Canada (Great Bear Lake, northern Saskatchewan; Blind River, Ontario), in Zaïre, Central Europe (Saxony and Czechoslovakia), Malagasy, and so forth.

Trace quantities of radioactive material are found in all rocks. Along with minute amounts of cosmic radiation always present in the air, these trace amounts produce a continuous background reading, which may vary from place to place by as much as a factor of 5. Table 10.5 gives the activity and/or trace amounts of radioactivity of a number of typical rocks, as well as the amount of radium in waters.

In general the activity in sedimentary rocks and metamorphosed sediments is higher than that in igneous and other metamorphic types, with the exception of potassium-rich granites.

### 10.2.7. Age Determination Using Radioisotopes

Determining the age of rocks is often an important factor in developing an overall geological picture of an area and thus is indirectly relevant to applied geophysics. Isotope ratios that are useful for geological age dating include the natural disintegration reactions  $^{87}\text{Sr}/^{87}\text{Rb}$ ,  $^{40}\text{Ar}/^{40}\text{K}$ ,  $^{146}\text{Sm}/^{147}\text{Nd}$ ,  $^{14}\text{C}/^{12}\text{C}$ , various Pb/U and Pb/Th ratios, and others.

For the decay process  $^{87}\text{Rb} \rightarrow ^{87}\text{Sr} + \beta$ , taking the initial number of  $^{87}\text{Rb}$  atoms as  $N_0$  and assuming that no  $^{87}\text{Sr}$  atoms were present initially, Equation (10.1) shows that the numbers of rubidium and strontium atoms now present,  $N_{\text{Rb}}$  and  $N_{\text{Sr}}$ , are

$$N_{\text{Rb}} = N_0 e^{-\lambda t} \quad N_{\text{Sr}} = N_0 (1 - e^{-\lambda t})$$

so that

$$N_{\text{Sr}}/N_{\text{Rb}} = (1 - e^{-\lambda t})/e^{-\lambda t} = (e^{\lambda t} - 1)$$

Thus, knowing the decay constant  $\lambda$ , the time  $t$  can be determined by measuring the ratio of  $^{87}\text{Sr}$  to  $^{87}\text{Rb}$ . Because the half-life is  $4.9 \times 10^{10}$  years, the Sr/Rb method is useful in determining the age of Precambrian rocks. An advantage of the Sr/Rb method is that all products are solids and therefore unlikely to have been lost. Minerals suitable for analysis include mica, feldspar, granite, and gneiss.

The half-life of  $^{40}\text{K}$  is about  $1.4 \times 10^9$  years; thus the K/Ar method is useful in determining ages from about 50 thousand years to about 3.5 billion years. The reaction is complicated because  $^{40}\text{K}$  disintegrates in two ways: (i) capture of an electron from the innermost shell (K capture):  $^{40}\text{K} + e \rightarrow ^{40}\text{Ar}$ ; (ii) beta emission:  $^{40}\text{K} \rightarrow ^{40}\text{Ca} + \beta$ . Each reaction has its characteristic decay constant, so that the ratio of the rates of decay is constant; therefore the existence of the dual decay modes does not interfere with the use of  $^{40}\text{K}$  for dating. However,  $^{40}\text{Ca}$  also occurs naturally and this makes the second mode unsuitable for dating. Using the first mode, the  $^{40}\text{Ar}$  can be obtained by melting the specimen. An alternative method is to place the sample in the neutron flux of a nuclear reactor where stable  $^{39}\text{K}$  (which has a fixed abundance ratio relative to  $^{40}\text{K}$ ) undergoes the reaction  $^{39}\text{K} + e \rightarrow ^{39}\text{Ar}$ ; the age can then be determined from the ratio  $^{40}\text{Ar}/^{39}\text{Ar}$ , this ratio being found by mass spectrographic analysis. This method yields high accuracy because mass spectrographic ratios can be determined to better than 0.01%.

Argon diffuses rapidly above  $300^\circ\text{C}$ , hence  $^{40}\text{K}$  measurements determine the age since the temperature of the rock dropped below about  $200^\circ\text{C}$ .  $^{40}\text{Ar}$  is also present in the atmosphere and this sometimes results in contamination;  $^{40}\text{Ar}$  (presumably coming from trapped magmatic gases) is sometimes a contaminant in ocean-floor basalts. Minerals suitable for analysis by the  $^{40}\text{K}$  method include mica, hornblende, and plagioclase feldspars.

Several isotope ratios can be measured for the disintegration series  $^{238}\text{U} \rightarrow ^{206}\text{Pb}$ ,  $^{235}\text{U} \rightarrow ^{207}\text{Pb}$ , and  $^{232}\text{Th} \rightarrow ^{208}\text{Pb}$ . Having several different ratios to measure permits confirmation of determinations. Ratios sometimes measured include  $^{207}\text{Pb}/\text{U}$ ,  $^{206}\text{Pb}/\text{U}$ ,  $^{208}\text{Pb}/\text{Th}$ ,  $^{207}\text{Pb}/^{206}\text{Pb}$  (since the ratio of  $^{235}\text{U}/^{238}\text{U}$  is fixed). Zircon is especially suitable for such analyses.

$^{14}\text{C}$  has a half-life of 5,730 years and disintegrates according to the equation  $^{14}\text{C} \rightarrow ^{14}\text{N}$ ,  $^{14}\text{N}$  then disintegrating to give stable  $^{12}\text{C}$  finally. The reaction is used to date events during the last 30,000 years or so. The  $^{14}\text{C}$  is produced in the upper atmosphere by cosmic-ray bombardment of  $^{14}\text{N}$ . The carbon subsequently becomes incorporated in plants, animals, or other materials; the ratio of  $^{14}\text{C}$  to  $^{12}\text{C}$  (or other carbon isotopes) gives the time elapsed since the plant or animal was alive.

The  $^{18}\text{O}$  to  $^{16}\text{O}$  ratio in ocean waters changes during cool continental glacial periods and hence the  $^{18}\text{O}$  to  $^{16}\text{O}$  ratio is an indicator of paleo-temperatures. Although not useful for age determinations, the ratio of oxygen isotopes is a useful tool in the study of depositional temperature changes that are associated with the low-stand sea-level patterns sometimes seen in seismic data.

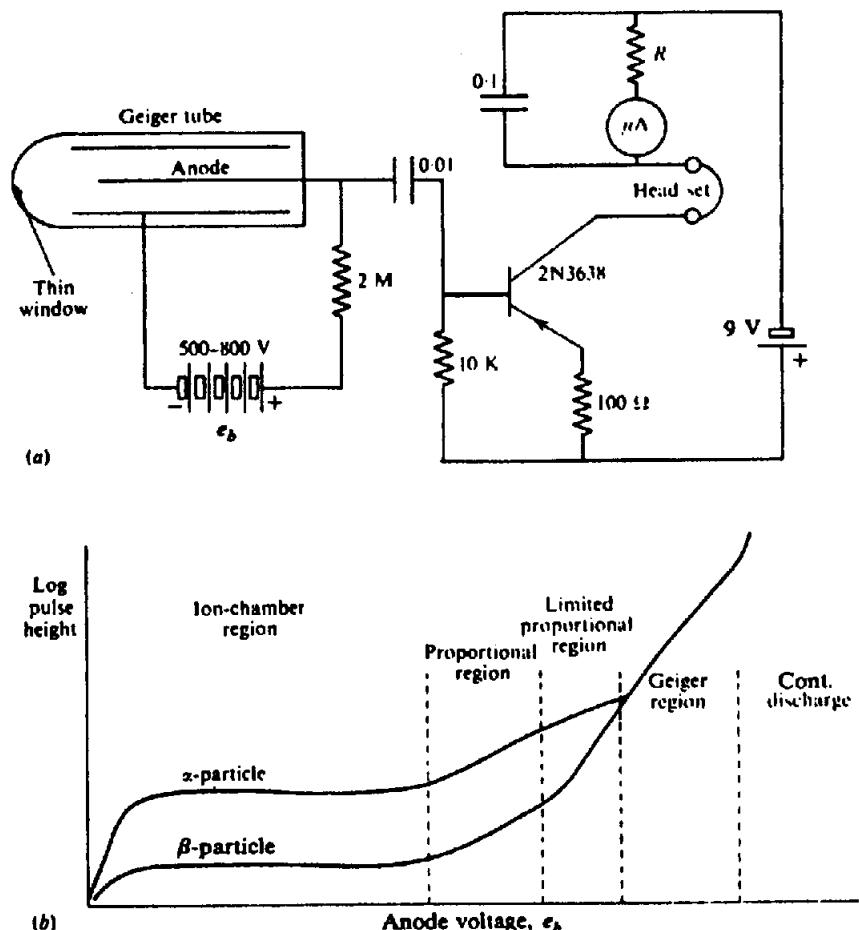


Figure 10.4. Geiger-Müller counter. (a) Simplified counter circuit. (b) Geiger-tube characteristics as a function of anode voltage.

The foregoing age determinations all assume that the system is closed, that is, no daughter isotopes were present at the beginning and none escaped from the system up to the time of measurement. If some daughter isotopes were lost in some manner, for example, by reheating above a critical temperature which resulted in the loss of the daughter isotopes, the radioisotope clock is "reset" and the abundance ratios give the time elapsed since the loss occurred. Zircon seems to be especially resistant to resetting so that analysis of zircons from granite overgrown rims using an ion microprobe gives ages different from those of zircons in the core (which presumably came from the original source of the granite). Thus, it is possible at times to date processes as well as rock samples.

### 10.3. INSTRUMENTS

#### 10.3.1. Introduction

Various devices have been used for the detection of radioactivity. One of the earliest was the *ionization chamber*. At present there are two principal instruments, the *Geiger counter* and the *scintillation meter*,

plus the *pulse-height analyzer* or  $\gamma$ -ray spectrometer, which is an extension of the scintillation meter. Both these detectors also were used very early in the course of radioactivity study. In their present prospecting form they are adaptations of laboratory instruments developed in the period 1944-50.

The heart of the radioactive detector is a device that will respond efficiently to  $\beta$  and  $\gamma$  radiation ( $\alpha$  particles have such short ranges that they need not be considered generally). As noted previously, natural  $\beta$  rays also have a short range, even in air; hence a  $\beta$  detector is effective only within a few meters of the source. Consequently gamma-radiation detection is most desirable.

#### 10.3.2. Geiger - Müller Counter

This is a very simple device that responds primarily to  $\beta$  radiation. Consequently it can be used only in ground traversing. A diagram showing the essential parts is given in Figure 10.4a. Like the ionization chamber, the detector is a thin-walled cylindrical tube, often with a very thin ( $\leq 0.025$  mm) mica window in the end, to permit the passage of  $\beta$  particles.

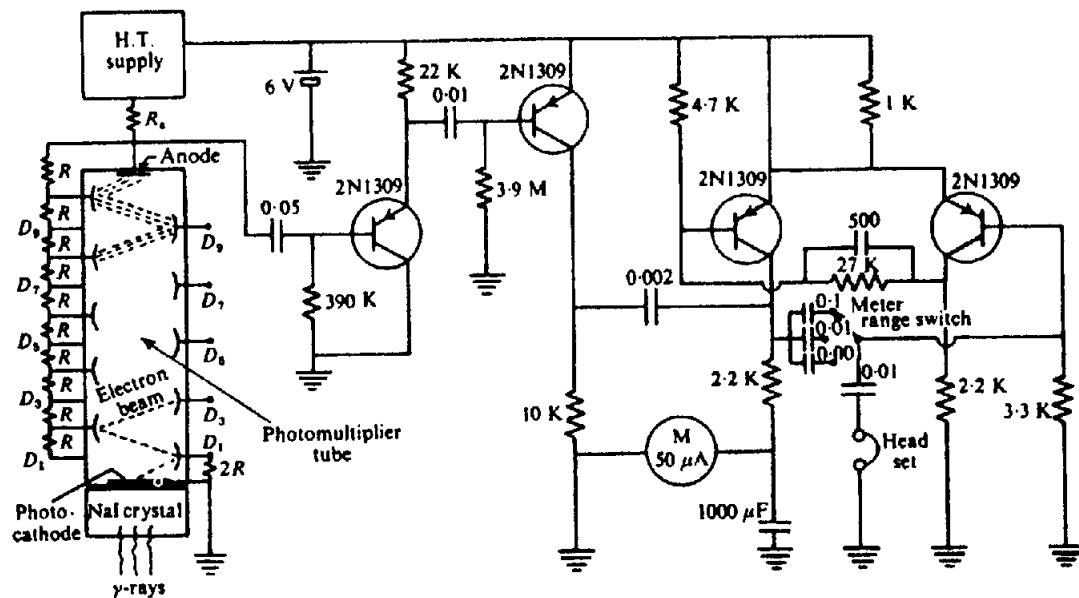


Figure 10.5. Scintillation-meter schematic.

The tube contains an axial anode wire with a coaxial cathode cylinder and is filled to a pressure of about 0.1 atm with an inert gas, such as argon, plus a trace of alcohol, methane, water vapor, or a combination of these. This gas mixture produces a quenching action. A dry cell or other low-current source supplies several hundred volts across the diode, as shown in the diagram.

Radiation entering the tube ionizes gas atoms and the positive ions and electrons are accelerated by the high voltage to the cathode and anode, respectively. These charges also ionize other gas atoms en route. The ionization is cumulative and the original ray produces a discharge pulse across the anode resistor, which is amplified in the transistor stage to produce a click in the headphones. Figure 10.4a also shows a simple integrating circuit in series with the headset. Successive pulses charge up the condenser which then leaks off slowly through the high resistance  $R$ , in series with the microammeter. The meter registers a current proportional to the integral of the charge entering the condenser.

The purpose of the quenching agent is to suppress secondary electron emission from the cathode, caused by positive ion bombardment. This effect tends to prolong the discharge. Fast quenching of the discharge allows the tube to return quickly to the non-conducting state and hence respond to succeeding rays entering the chamber shortly after the first. Although even in a good tube the clean-up time is still appreciable, it can be reduced to less than 100  $\mu$ s with a suitable quenching gas mixture.

The electronic section of Figure 10.4a is oversimplified. Normally the Geiger tube pulse drives a

multivibrator circuit which shapes the pulses as well as amplifying them.

Figure 10.4b shows the characteristics of the Geiger tube as a function of anode voltage. Normally the voltage is kept within the plateau (ion-chamber) region of the curve, where pulse height is independent of the voltage, thus reducing the effect of variations in battery voltage.

The prospecting Geiger counter has the virtue of being simple and cheap. However, it has little else to recommend it. It must be held close to the outcrop to detect  $\beta$  rays (because it is an extremely inefficient detector of  $\gamma$  rays, which are weak ionizers and tend to pass right through the tube without being registered). Lead fins have been mounted on the outside of the tube to degrade and convert the  $\gamma$  rays to  $\beta$  rays; however, this has not improved the efficiency enough to make the instrument competitive with the scintillation meter. Thus the Geiger counter remains a tool of limited application.

### 10.3.3. Scintillation Meter

(a) *General.* The counting of scintillations produced by radiation bombardment of a zinc sulfide screen was one of the earliest methods of detection. Other materials that have been used for this purpose include anthracene, stilbene, and scheelite. One of the best scintillation detectors is made by growing natural crystals of sodium iodide (NaI), treated with thallium (Tl). The NaI is transparent to its own fluorescent emission and all faces but one are coated with light reflecting material. If the crystal is large enough, its conversion efficiency for natural (< 3

MeV)  $\gamma$  rays is practically 100%. A portable device of this type became possible following the development of the photomultiplier tube.

(b) *Gamma-ray interactions.* As mentioned briefly in Section 10.2.2, the dissipation of energy as radiation passes through matter is a complex process. To explain the operation of the scintillation meter, it is necessary to discuss the sequence of events in which the radiation is absorbed. The interaction of  $\gamma$  radiation with matter takes place by the following processes (see also §11.8.1c).

(i) The *photoelectric effect*, in which the  $\gamma$  ray loses all of its energy to a bound atomic electron, part of the energy being used to overcome its binding to the atom, the remainder appearing as kinetic energy of the electron. This effect predominates at low energy ( $\leq 200$  keV) although it also varies greatly with the atomic number of the absorbing material.

(ii) *Compton scattering* by atomic electrons, in which the  $\gamma$  ray is deflected in its path. When the  $\gamma$ -ray energy is much larger than the electron binding energy (which varies from  $\sim 10^3$  eV for innermost K electrons of heavy elements to a few electron volts in light elements), the scattering takes place as though the electrons were unbound and at rest. This is the dominant interaction at intermediate energies (100 keV to 2 MeV), and the effect of atomic number is not so pronounced.

(iii) *Pair production*, in which the  $\gamma$  ray is annihilated near a nucleus or electron while creating an electron-positron (positive electron) pair. The energy required for this process must be greater than the rest energy (energy equivalent to the mass) of the pair; any excess appears as kinetic energy of the electron and positron. Because the electron rest energy is 0.51 MeV, pair production cannot take place unless the  $\gamma$ -ray energy originally was larger than 1.02 MeV. Hence it is essentially a high-energy phenomenon.

Of these three modes of interaction, the first is most desirable for  $\gamma$ -ray spectroscopy (see next section), because the original radiation is converted to a light photon, giving up all its energy in the process. For the ordinary scintillation meter, however, the only requirement is that the input  $\gamma$  rays be eventually converted to light, regardless of the mode of absorption.

(c) *Description of scintillation meter.* A schematic of the scintillation meter is shown in Figure 10.5. Light generated in the NaI crystal by  $\gamma$  conversion falls on the semitransparent photocathode of the photomultiplier tube, causing electron emission. The crystal and multiplier tube are mounted as a single

unit in a light-tight cylindrical can, the crystal face being in contact with the photocathode end.

The electrons emitted from the photocathode are accelerated toward the first electrode,  $D_1$ , operating at  $\sim 150$  V positive with respect to the grounded cathode. The intermediate electrodes,  $D_1$  to  $D_{10}$ , called dynodes and usually  $\sim 10$  in number, provide electron multiplication by secondary emission from surfaces coated with low work-function material, for example, Cs<sub>3</sub>Sb, the chain being so mounted that the electrons must proceed from  $D_1$  to  $D_2$ , and so forth, then finally to the anode. With a gain factor of  $\sim 4$  per stage, the total current amplification is roughly  $10^6$ . This produces a current pulse of about 0.5  $\mu$ A through the anode resistor,  $R_a$ , and the resulting voltage pulse of some 20 mV is amplified and integrated as in the Geiger counter circuit.

The great advantage of this instrument is in the efficiency of  $\gamma$ -ray detection. It will also detect  $\beta$  rays. The price is about 10 times that of a Geiger counter and the size and weight are somewhat greater than the Geiger. It can be used in completely portable form (frequently with detachable crystal-multiplier head for entering a confined space), or as a semi-portable unit in a car or aircraft. The airborne instrument is much more elaborate. Portable sets usually have crystals 40 to 75 mm diameter, 25 to 75 mm thick, with a multiplier photocathode to match the diameter. The earlier airborne versions used several crystals about 100 mm thick and 200 to 250 mm diameter, with a group of photomultipliers (three to seven) on each crystal; this was necessary to maximize the light collection, because the photocathode diameter was limited. Such an arrangement required manipulation of many gain adjustments to optimize the overall resolution. More recently arrays of four to six prismatic crystals 400 mm long and 100  $\times$  100 mm cross section with a single multiplier mounted on one end of each have resulted in a compact packaged-slab geometry and reduced the equalization time. Airborne units are equipped with analog and digital readouts.

Further improvements in scintillation meter detection may result from using (i) relatively huge organic plastics as scintillators, (ii) germanium solid-state detectors, (iii) combination NaI-CsI crystals, and (iv) silicon-diode "one-shot" photomultiplier tubes.

#### 10.3.4. Gamma-Ray Spectrometer

A logical extension of the scintillometer is a spectrometer that separates characteristic  $\gamma$  rays of  $^{40}\text{K}$ , U, and Th for identification of the source. Such instruments are widely used in airborne surveys and a couple of portable units are also available.

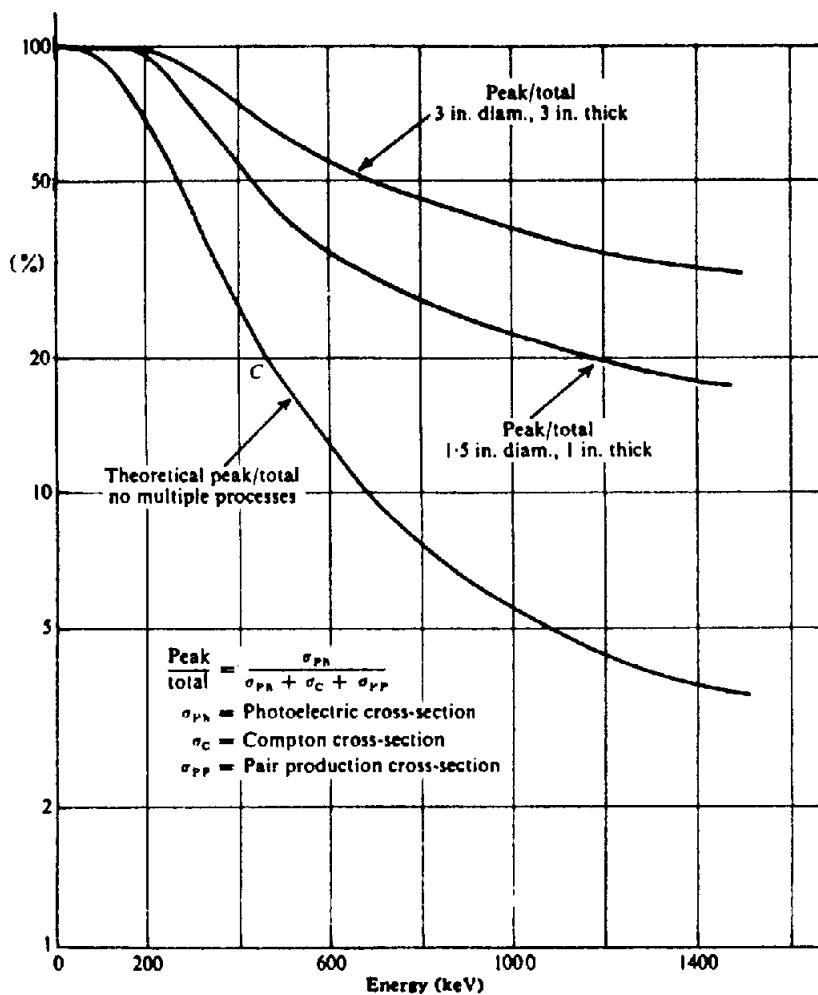


Figure 10.6.  $\gamma$ -ray absorption efficiency in NaI crystals.

Spectrometers of this type, known as *pulse-height analyzers* or "kick sorters," have been used for  $\gamma$ -ray analysis in nuclear physics laboratories for some 40 years. They make use of the fact that the intensity of the light pulse, and hence the amplitude of the voltage pulse from the multiplier, is proportional to the original  $\gamma$ -ray energy. Actually this is only partially true, due to the complex process of  $\gamma$ -ray absorption, and further explanation is necessary.

When the  $\gamma$ -ray loses all of its initial energy at once by photoconversion, the preceding statement is entirely correct. Even if it is first degraded by scattering and/or pair production, resulting eventually in photoelectrons of lower energy, these will still add up to a pulse of the same amplitude, *provided* the  $\gamma$  ray does not escape from the crystal, that is, it is completely absorbed. This is true because all the processes occur essentially simultaneously (because  $\gamma$  rays, being electromagnetic radiation, travel with the velocity of light). However, if the beam of  $\gamma$  rays entering the crystal were monochromatic, of energy  $E$ , and some rays escape with lower energy  $e$ , there is a contribution to the pulse-height spectrum corresponding to  $E - e$ .

Figure 10.6 illustrates the efficiency of NaI crystals in converting the  $\gamma$  rays into pulses of maximum amplitude by multiple processes. A theoretical curve C shows the ratio of cross section (effectively absorption) by photoconversion only, to total cross section, that is, all three conversion processes, for comparison. For energies between 1.5 MeV and 100 keV (below which the photoelectric effect predominates) the larger crystal is on average 35% more efficient, whereas the smaller loses an increasingly larger fraction of  $\gamma$  rays by scattering out of the crystal.

To obtain 100% efficiency in converting the  $\gamma$  rays, it would be necessary to mount the radioactive source, as a minute grain, inside the crystal, and in fact this is done in laboratory installations. In these circumstances – and provided the crystal is large enough – all the  $\gamma$  rays would be absorbed in the crystal and the original  $\gamma$ -ray spectrum of the source would be quite faithfully reproduced as a pulse-voltage spectrum in the analyzer. In a field measurement, however, the situation is more complicated. Some  $\gamma$  rays lose energy by scattering in escaping from the source and also during passage through the

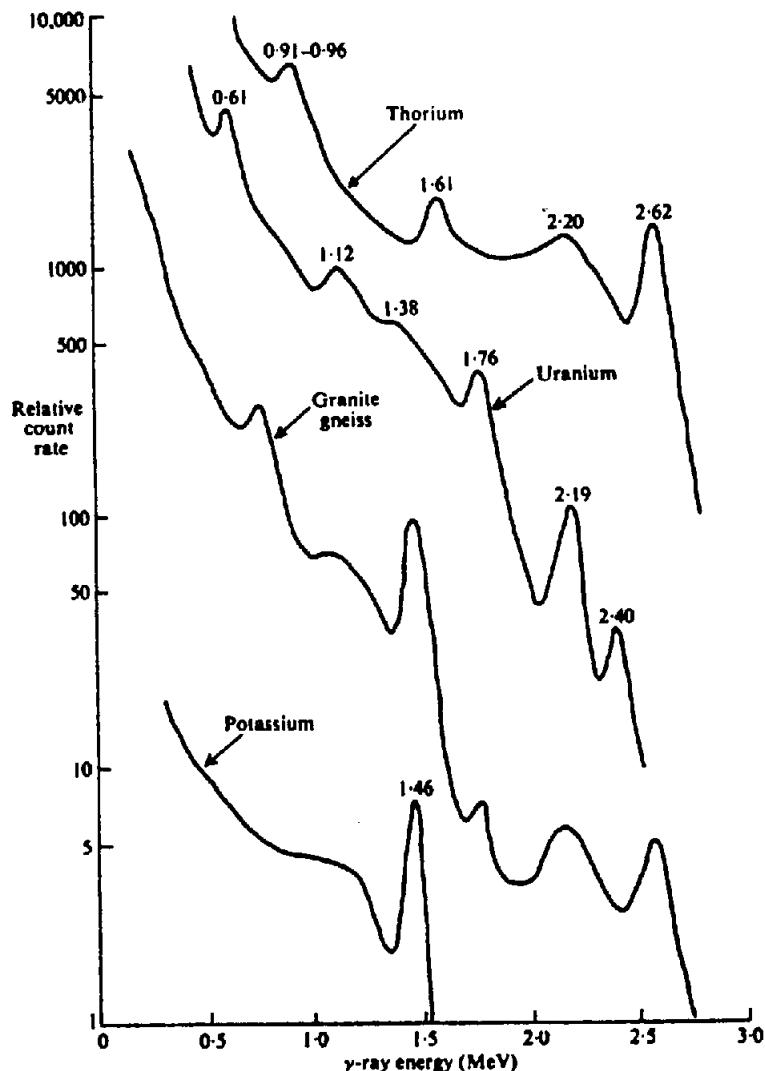


Figure 10.7.  $\gamma$ -ray spectra of K, U, and Th samples and granite-gneiss outcrop.

air to the crystal. This, coupled with the fact that the U and Th series emit numerous  $\gamma$  rays over a wide energy range, results in a complex pulse-height spectrum, as shown in Figure 10.7. All four curves have characteristic peaks and, in addition, an increasing continuum at low energies, due to Compton scattering. The pure potassium sample produces a relatively simple curve, having only the  $^{40}\text{K}$  peak at 1.46 MeV. Thorium is characterized by the strong 2.62 MeV peak of  $^{208}\text{Tl}$ . The uranium spectrum is most complex, although the peak at 1.76 MeV is reasonably distinctive. Potassium and thorium are clearly evident in the granite gneiss, as well as a smaller fraction of uranium.

A prospecting  $\gamma$ -ray spectrograph, then, should be capable of isolating the K, U, and Th peaks at 1.46, 1.76, and 2.62 MeV. This is accomplished by replacing the integrator-counter circuit in the scintillation meter with three electronic circuits to select the appropriate pulse heights that correspond to the preceding  $\gamma$ -ray energies. Considering channel 2 in

Figure 10.8a, the detail diagram at the upper right of the figure shows that the channel is actually two parallel channels. The discriminator 2A is biased so that it gives an output pulse only for  $\gamma$  rays with energy greater than 1.36 MeV, whereas discriminator 2B responds only to  $\gamma$  rays with energy in excess of 1.56 MeV. Thus neither discriminator registers  $\gamma$  rays whose energies are less than 1.36 MeV, whereas for values greater than 1.56 MeV the anticoincidence circuit adds the two outputs out of phase to give zero output as well.

The other two channels operate in the same manner for 1.76 and 2.26 MeV. Generally the channel centers and widths are adjustable. Clearly the window must be wide enough to accommodate the finite width of the peaks in Figure 10.7, but not so wide that the flanks of adjacent peaks may be accepted as well.

The pulses are counted and integrated separately and, in the airborne instrument, applied to a three-channel recorder. Because the radioactive sources

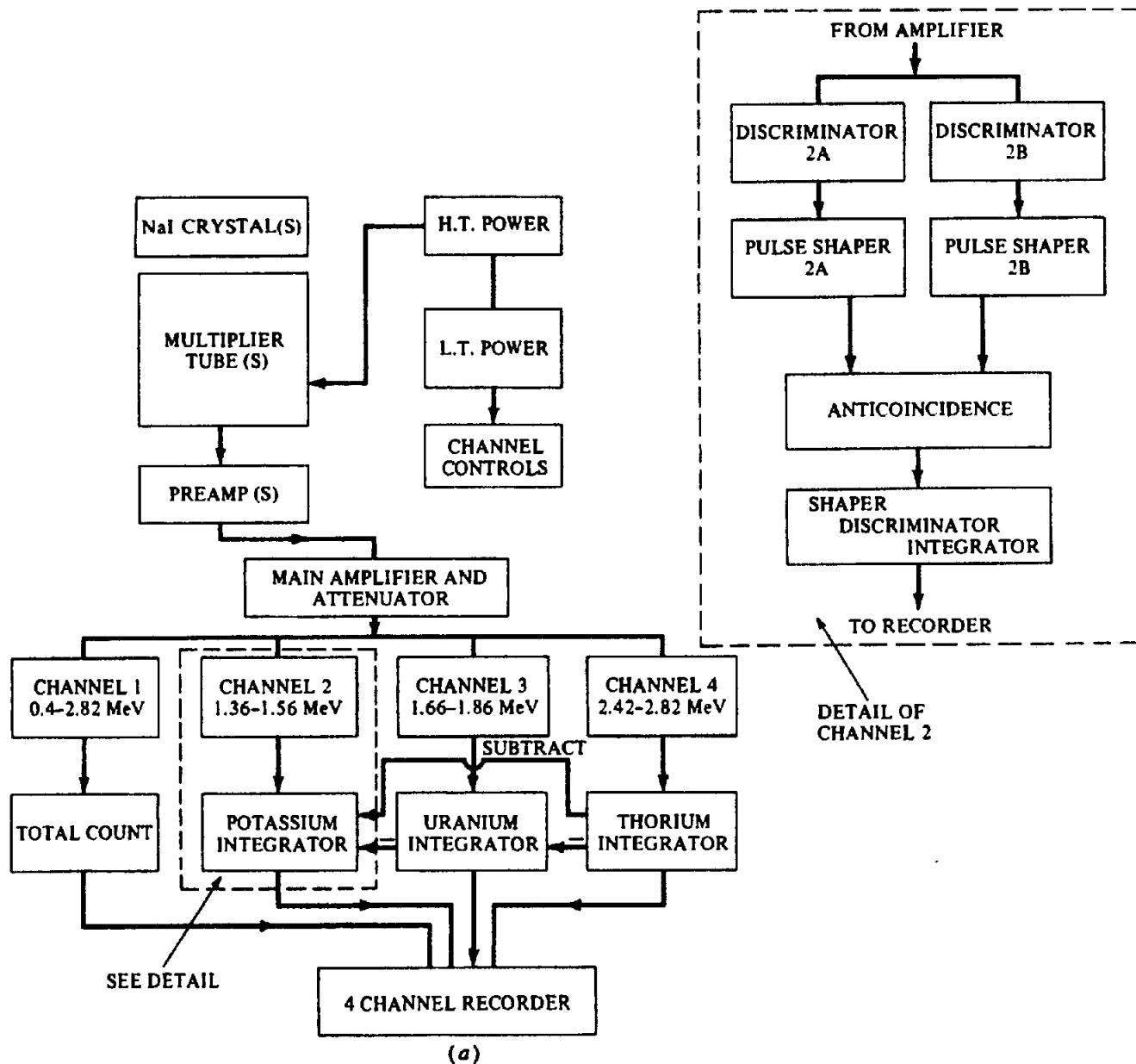


Figure 10.8. Four-channel  $\gamma$ -ray spectrometer. (a) Block diagram.

often contain both U and Th and even K as well, and because the count level may be considerably higher for one channel than the others (as in Fig. 10.7, where the count rate of the Th sample at 1.46 MeV, even in the absence of a peak, is more than 100 times larger than the potassium peak), some means of subtracting a predetermined fraction of the higher count rate, known as *spectral stripping*, is generally incorporated near the output end of the spectrometer, as shown by the subtract lines in Figure 10.8a. An early model of this type of instrument designed for airborne work is illustrated in Figure 10.8b. It employed twelve  $9 \times 4$  in. ( $23 \times 10$  cm) crystals; the correct position of the channels was monitored with a Cs standard  $\gamma$  source (661 keV). Note that this instrument has four channels (Fig.

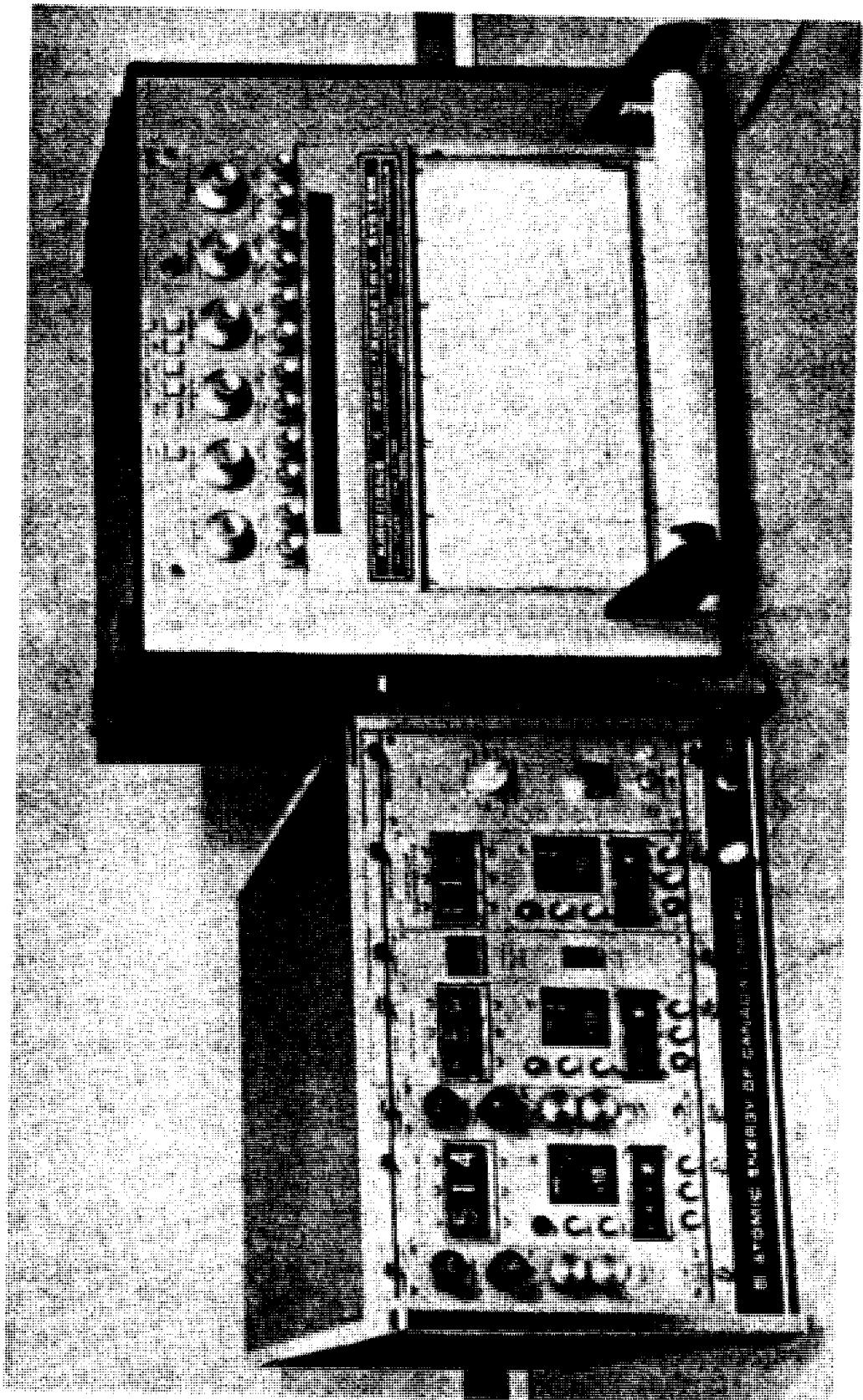
10.8a), channel 1 being for total count over the whole energy band from 0.4 to 2.8 MeV.

The block diagram in Figure 10.9 shows a more recent computer-controlled airborne system. Spectrometers with 256 and 512 channels have also been used in airborne surveys.

An inherent problem with the pulse-height analyzer is the effect of pulse shape, voltage drift, temperature changes, and so forth, on the instrument sensitivity and accuracy. Further improvements in instrumentation have resulted from using analog-to-digital (A/D) conversion and by incorporating a minicomputer to provide on-line data correction and ultimately interpretation during the survey. [For these and other developments in instrumentation, see Bristow (1979).] A glance at Figures 10.8 and 10.9,

(b)

Figure 10.8. (Continued) (b) Photo.



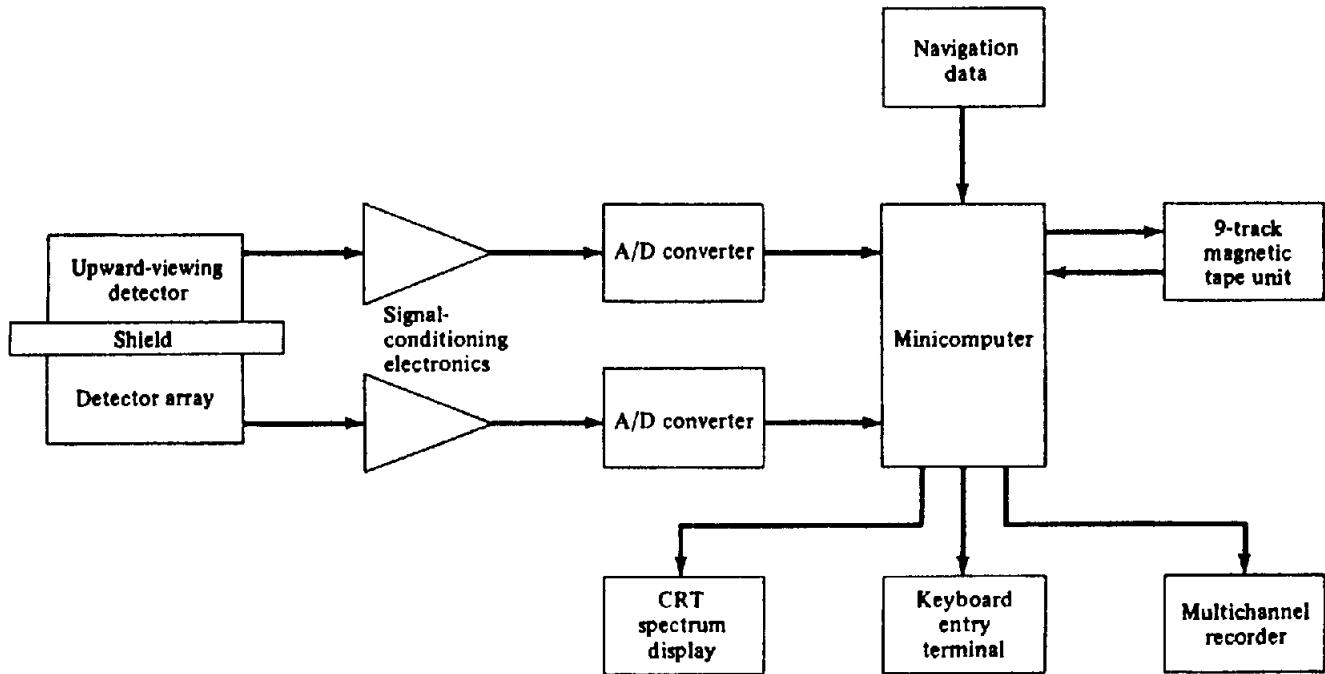


Figure 10.9. Modern  $\gamma$ -ray spectrometer. (After Bristow, 1979.)

the second displaying a block diagram of an up-to-date airborne installation, shows clearly that the present-day model is considerably more complex and sophisticated than the earlier one, employing as it does analog-to-digital conversion, a minicomputer, and consequent additional electronics, as well as an *upward-view detector*, shielded from ground radiation, to monitor atmospheric radiation. The computer is particularly attractive for storing useful control data to correct for background effect of atmospheric radon, which is erratic and often large.

### 10.3.5. Miscellaneous Instruments

Some portable scintillation meters have simple circuit modifications that permit rough discrimination between K, U, and Th, as well as measurement of total  $\gamma$ -ray count. A switch provides two bias levels on the pulse amplifier, equivalent to about 2.5 and 1.6 MeV, so that one can, in effect, introduce wide windows, one at a time, for Th and U + Th. Calibration of this type of equipment is discussed in Section 10.3.6.

An instrument known as the *emanometer*, or *radon sniffer*, has been used to measure the radon content of waters, oils, and soils. Because radon is a noble gas, it does not form chemical compounds. It moves freely through pore spaces, joints, and faults for distances up to several hundred meters. It will also dissolve in ground water and so move about in the subsurface.

Air samples are obtained from the soil by drilling a shallow hole (0.5 to 1 m) and pumping air from the hole through filters and a dryer into an ionization

chamber or thin ZnS scintillator. Water samples are degassed and the gas-air mixture goes to the detecting chamber. In one model the 4.8 MeV  $\alpha$  particles of  $^{222}\text{Rn}$  are counted, rather than the 0.51 MeV  $\gamma$  ray.

If the radon is in equilibrium with the other decay products in the vicinity, the amount of parent product may be determined from Equation (10.5),

$$N_u = N_{rn} \lambda_{rn} / \lambda_u \approx 2 \times 10^{-6} N_{rn} / 5 \times 10^{-18} \\ \approx 4 \times 10^{11} N_{rn}$$

assuming the radon originated from  $^{238}\text{U}$ . The numerical factor would be about  $4 \times 10^{15}$  for radon gas from  $^{235}\text{U}$  or  $^{232}\text{Th}$ . These have very short half-lives, however; hence it is much more likely that  $^{222}\text{Rn}$  is the isotope detected. If the series is not in equilibrium, for example, some member or members are reduced or missing because of weathering, and so forth, the count would be reduced and the preceding relation would not hold.

Two other integrating-type radon detectors, which collect and measure  $\alpha$  radiation over much longer periods than the sniffer, have been in limited use since about 1978. The first, known as the *Track Etch*, consists of a cellulose nitrate film (sensitive to  $\alpha$  particles) taped on the inside bottom of a plastic cup. The inverted cup is placed in a soil hole for about three weeks, accumulating  $\alpha$  radiation inside from soil gas (the cup wall is thick enough to exclude penetration from outside). The film is retrieved, chemically etched to expose the  $\alpha$  tracks, and the

amount of radiation is found from the track density viewed under a microscope.

The *Alpha Cup*, similar to the Track Etch in principle, uses a silicon semiconductor in place of the film. This detector is connected to an electronic unit outside the cup and the whole is buried for three days. After digging up the device, the  $\alpha$  counts stored in the electronic memory are transferred to a reader. A later modification called *Alpha Card* appears to have better counting geometry, which reduces the burial period to 12 hr. This reduction in integrating times compared to Track Etch is said to be possible because of higher collection efficiency. The alpha devices also have an advantage, because there is no need to flush out the collector (required for cleaning out the sniffer) or change the detector after each station.

Because the radon diffusion process is complex and sensitive to several external factors, such as temperature, pressure, and climate, generally, one might expect that the long integration time would produce more reliable results. However, there is little available evidence to establish a definite superiority of one instrument over the others (Warren, 1977; Wollenburg, 1977; Telford, 1983).

A variety of other instruments has been developed for radioactivity measurements in geophysics. Several are adaptations of nuclear physics laboratory equipment for assaying. Others, such as the *beryllium detector*, used for ground prospecting, and the *density logger*, contain their own radioactive sources to initiate artificial radioactive processes in nearby rock. Some of these are discussed in Sections 11.8.3 and 11.8.4.

#### 10.3.6. Calibration of Instruments

The calibration of instruments for reasonably quantitative measurements in radioactivity is a straightforward procedure in laboratory work, more complicated for field operations. For example, the scintillation meter described in Section 10.3.3c, may be adjusted to determine the relative amounts of uranium and thorium by means of a standard Th source and successive adjustments of the bias potentiometer control. When an instrument like the four-channel spectrometer is used in the field, however, a small standard source is quite unsuitable for overall calibration. Some of the difficulties encountered in stabilizing and calibrating multichannel spectrometers, particularly for airborne work, were mentioned briefly in Sections 10.3.3c and 10.3.4. Measures designed to resolve these difficulties included the stripping process and an upward view detector to correct for atmospheric radon background (see Fig. 10.9). An additional effect from cosmic-ray variations

caused by terrain relief may be reduced by providing an extra energy window (3 to 6 MeV).

Clearly these background sources are larger and have higher intensity than laboratory standards, even though the count rate in the uranium window is the main concern for good calibration of the instrument. Two empirical techniques have been used to measure uranium background. The simplest is to fly over a lake, where the measured activity will be the total from K, U, and Th, but several orders lower than from the ground surface. An alternative is air sampling with filters, using an upward-view detector as in Figure 10.9; although not as reliable, this may be a necessity where reasonably sized bodies of water are not available.

For a satisfactory and complete spectrometer calibration, however, it is necessary to employ concrete structures of appropriate size as secondary standards for static calibration of ground, airborne, and bore-hole instruments, plus larger ground strips for test flights of airborne systems. The Geological Survey of Canada has five concrete slabs ( $\sim 7.5 \times 7.5$  m, 0.5 m thick) at Uplands Airport near Ottawa. These contain varying fractions of radioactive material (for example 2.2% K, 3 ppm eU, 26 ppm eTh; see §10.5 for definition of eU and eTh) and are suitable for calibration of ground and airborne equipment. At the same location nine concrete test columns with standard size boreholes are available for calibrating logging instruments. Ground strips for flight tests are also installed near Ottawa. Similar installations exist in the United States and several other countries.

#### 10.4. FIELD OPERATIONS

Ground prospecting is readily carried out with any of the instruments described in Sections 10.3.2 to 10.3.5. The Geiger counter is used only for foot traverses; the scintillometer and  $\gamma$  ray spectrometer, especially the former, may also be used in vehicles. Radiometric surveys are comparatively cheap, whether airborne or on the ground (see §10.1); in surface work this is partly because the line cutting is often unnecessary and measurements are simple and rapid. No particular expertise is required for this work. It is sufficient to note the count rate (counts/s, mr/hr) of the instrument and compare it with a background reading. Ratios  $> 3:1$  over background would generally be of interest.

The background itself may vary considerably from place to place, depending on depth of soil cover and potassium content of the local rocks. Some notice must be taken of the geometry of outcropping formations in this regard, because the instrument response is influenced by source-detector separation

and the source dimensions. This is particularly true of the Geiger counter. Obviously the source-detector geometry will have a significant effect on the readings; compared to the usual position of the instrument over a flat surface ( $2\pi$  geometry), a wide ledge backed by a vertical wall ( $3\pi$ ) or a steep road cut ( $\sim 4\pi$ ) will increase response by 50 to 100%.

Background variation in different rocks has already been referred to in Table 10.5. In the early days of radioactive prospecting, erratic increases in background occurred occasionally as a result of atomic tests; this is no problem nowadays.

Two good reports on  $\gamma$ -ray spectrometric methods for uranium - airborne, ground, and well-logging - may be found in Grasty (1979) and Killeen (1979). Airborne radiometric reconnaissance has frequently been accompanied by aeromagnetics and occasionally EM. This stage is generally followed by detailed ground radiometric coverage of favorable areas, possibly with geochemical sampling, auxiliary geophysical methods, and finally trenching and drilling plus  $\gamma$ -ray logging. When the survey area is small or difficult for ground access, a detailed airborne helicopter survey may be warranted to reduce the ground followup.

Airborne radioactivity surveys have been carried out for minerals other than uranium and thorium, such as titanium and zirconium-bearing heavy minerals, including tantalum, niobium, and the rare earths. In this connection carbonatites (such as at Oka and other locations in the province of Quebec) are an intriguing target for  $\gamma$ -ray spectrometer exploration because they have a very low ratio of uranium to thorium. This distinctive signature applies to kimberlites as well; hence the method is useful in prospecting for diamonds.

Limited attempts have been made to use the radioactivity method in oil exploration. Surveys in known oil fields sometimes indicated a radioactive low directly over the oil-bearing structure with a halo slightly above the background surrounding it. Actually this pattern was reported about 1928 from crude ground surveys in Texas fields. The source of radioactivity appears to be radon gas, which moves upward through fractures in the perimeter rock to escape at surface; the suggestion has been made that the tight cap rock over the oil pool is relatively impervious to this migration.

Other indirect applications that may be worthwhile are in relation to phosphorites, whose host rocks often are anomalous in uranium content, and even for sulfides. Also, radiometrics occasionally have been used as an aid to geological mapping; a case history using airborne data is illustrated in Section 10.6, example 1. These indirect applications of radioactivity will be discussed further in Section 10.5.

## 10.5. INTERPRETATION

In spite of great improvements in instrumentation, the interpretation of radiometric survey data is still mainly qualitative. This is partly due to the extremely small depth of penetration possible with the method. It is also the result of the inherently complex nature of the  $\gamma$ -ray spectra.

Spectrometer profiles taken in a helicopter are illustrated in Figure 10.10a. Altitude in both cases was 150 m. The low air speed possible with the helicopter (40 km/hr) is a decided advantage both for amplitude of response and discrimination of anomalies. This was an early test of the four-channel spectrometer. Its superiority over instruments providing only total-count data is clearly demonstrated in Figure 10.10b where the strong U anomaly marked by the arrows is lost in the total-count (integral) profile because K and Th responses are low over the same 5 km stretch of the profile.

Both airborne and ground spectrometer data may be plotted as profiles or contoured as shown in various diagrams of Sections 10.6 and 10.7, in terms of U, Th, K, and total counts per second, ratios of U : Th, U : K, or in relation to some arbitrary background.

Uranium and thorium amplitudes may also be given as eU and eTh; that is, *equivalent uranium* and *thorium*. These designations arose because in  $\gamma$ -ray spectrometry the elements actually measured in the 1.76 and 2.62 MeV channels are  $^{214}\text{Bi}$  and  $^{208}\text{Tl}$ , respectively, rather than their U and Th parents. The distinction obviously is unnecessary for K because it is measured directly in the 1.46 MeV channel.

Some attempts have been made to obtain quantitative results in airborne work. By correlation of detailed ground data with airborne surveys over the same area, it is possible to get an approximate fit between the airborne profiles and upward continuation of the ground data, using an empirical expression for the  $\gamma$ -ray attenuation in air (Soonawala, 1968). This correlation is reasonably valid because of the high attenuation in solid material; that is, the source must outcrop to be detected in either survey. Characteristic curves for elementary shapes are then drawn up for the airborne interpretation in other areas. Three elementary geometries are considered:

1. A finite or elementary circular source.
2. An infinite plane source (outcrop) of great lateral extent.
3. The line source, having infinite exposed length along one axis, considered to be the strike direction.

Clearly the finite source is the most usual geometry encountered in the field, because either of the

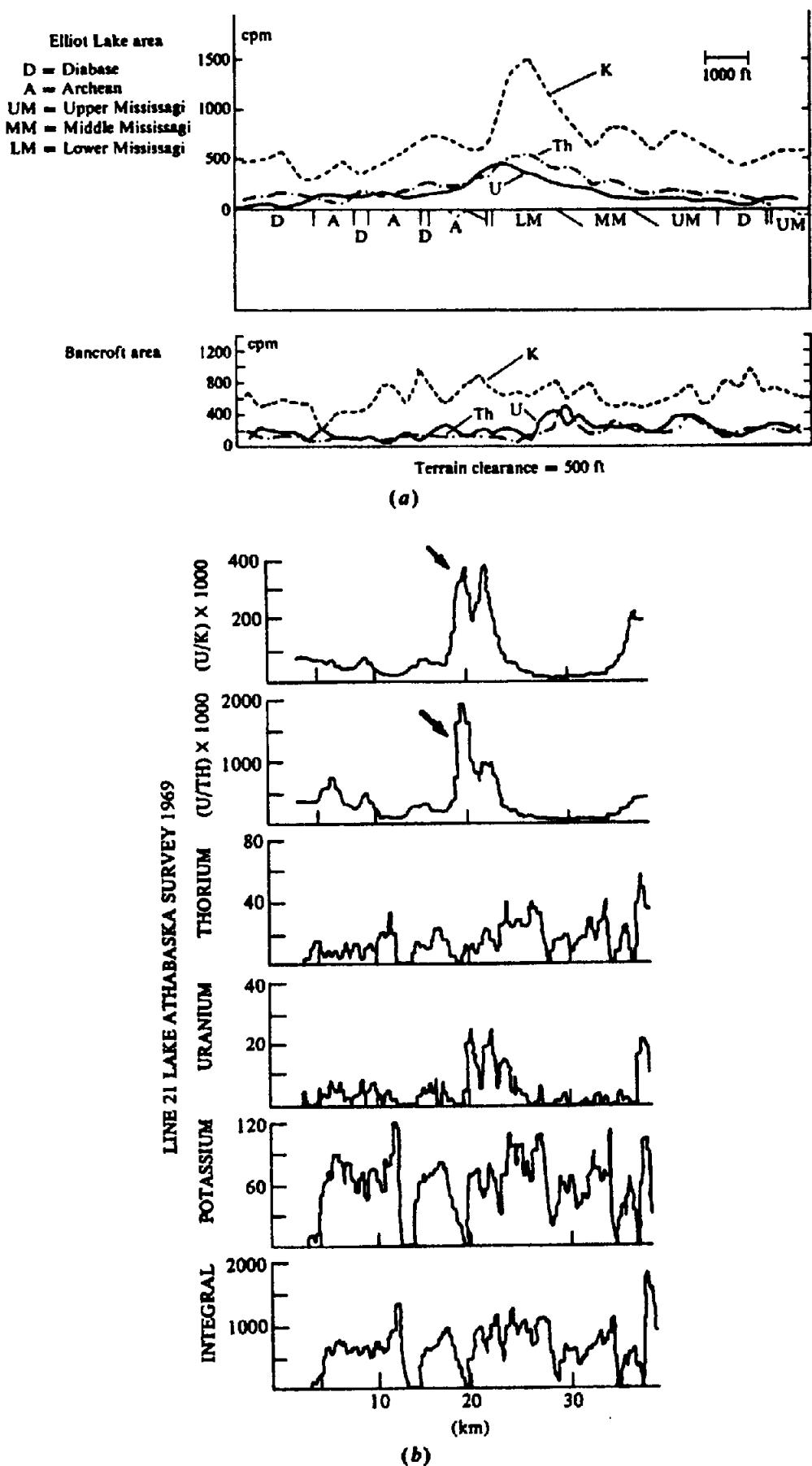


Figure 10.10. Airborne  $\gamma$ -ray spectrometer profiles. (a) Total-count profiles in the Elliot Lake and Bancroft areas, Ontario. (b) Four-channel results, Uranium City area, Saskatchewan. (After Damley, 1970.)

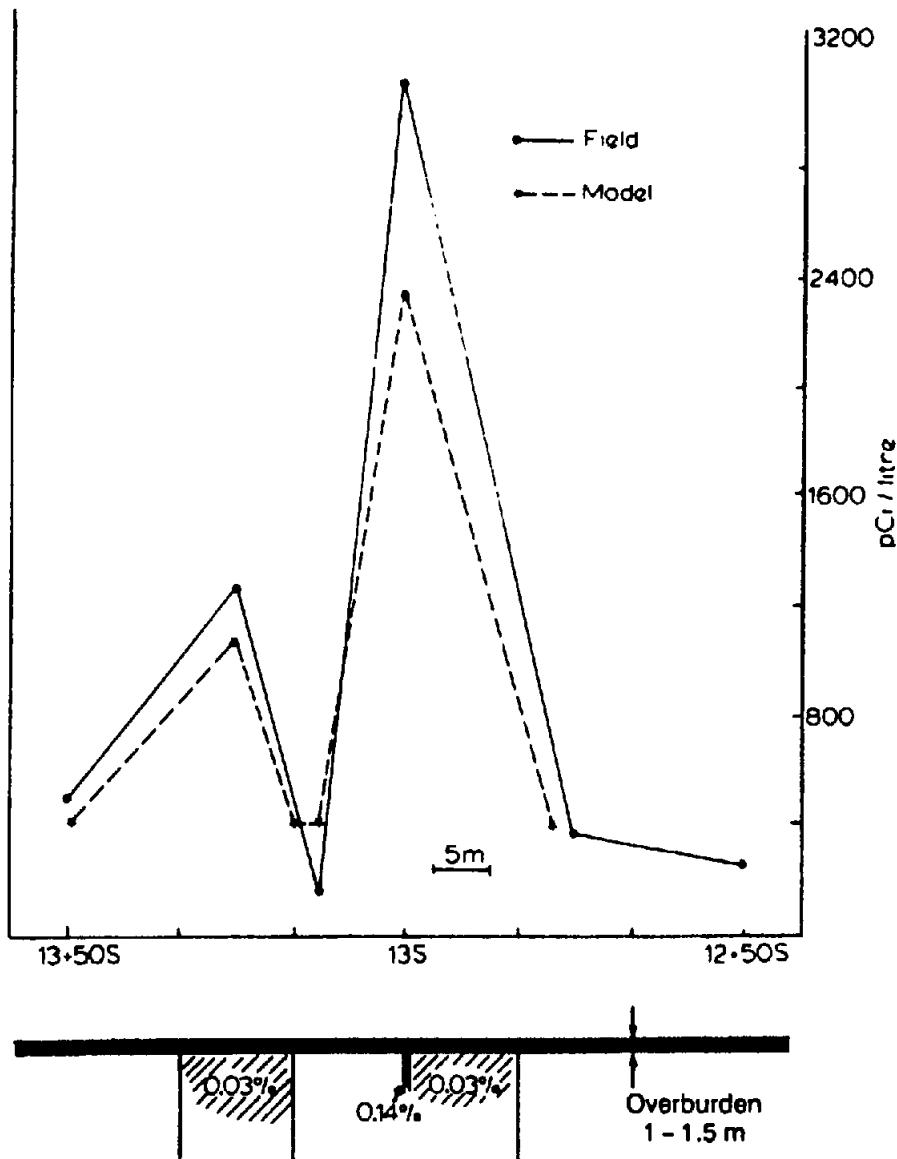


Figure 10.11. Radon profile and model results, Northern Saskatchewan. (From Soonawala, 1976.)

others will generally be covered with overburden at various places. Practically, the elementary source need not be circular, but its largest dimension should not greatly exceed the altitude of the aircraft.

The characteristic curves enable us to determine a parameter involving the product of surface area and source intensity; these quantities (as in gravity, EM, and other situations) cannot be resolved individually.

Measurement of the K, U, and Th  $\gamma$ -ray peaks in the 1.46, 1.76, and 2.62 MeV energy windows, together with U : K and U : Th ratios plus total count (using a four-channel spectrometer) is only a first approximation to a quantitative determination of relative ground abundance of the three elements. The numerous background variables, some of which have been mentioned already, include source-detector geometry, sampling rates, aircraft altitude, ra-

dioactive equilibrium, Compton scattering, and cosmic and atmospheric radon background.

Crossley and Reid (1982) used a matrix equation (see §A.2) to solve for the abundances

$$\mathcal{A}x = \mathcal{C}$$

where  $x$  is an  $(m \times 1)$  matrix of the abundances, the  $(n \times 1)$  matrix  $C$  gives the counts in the  $n$  channels, and  $A$  is an  $(n \times m)$  matrix of the calibration constants. For three-channel equipment the elements  $a_{ij}$  are stripping constants (see §10.3.4 and problem 4) for K, U, and Th.

To improve the accuracy, we must use more than three channels. Crossley and Reid (1982) used data from 63 channels in the range 0.78–2.98 MeV ( $n = 63$ ) to solve for K, U, Th, and cosmic background

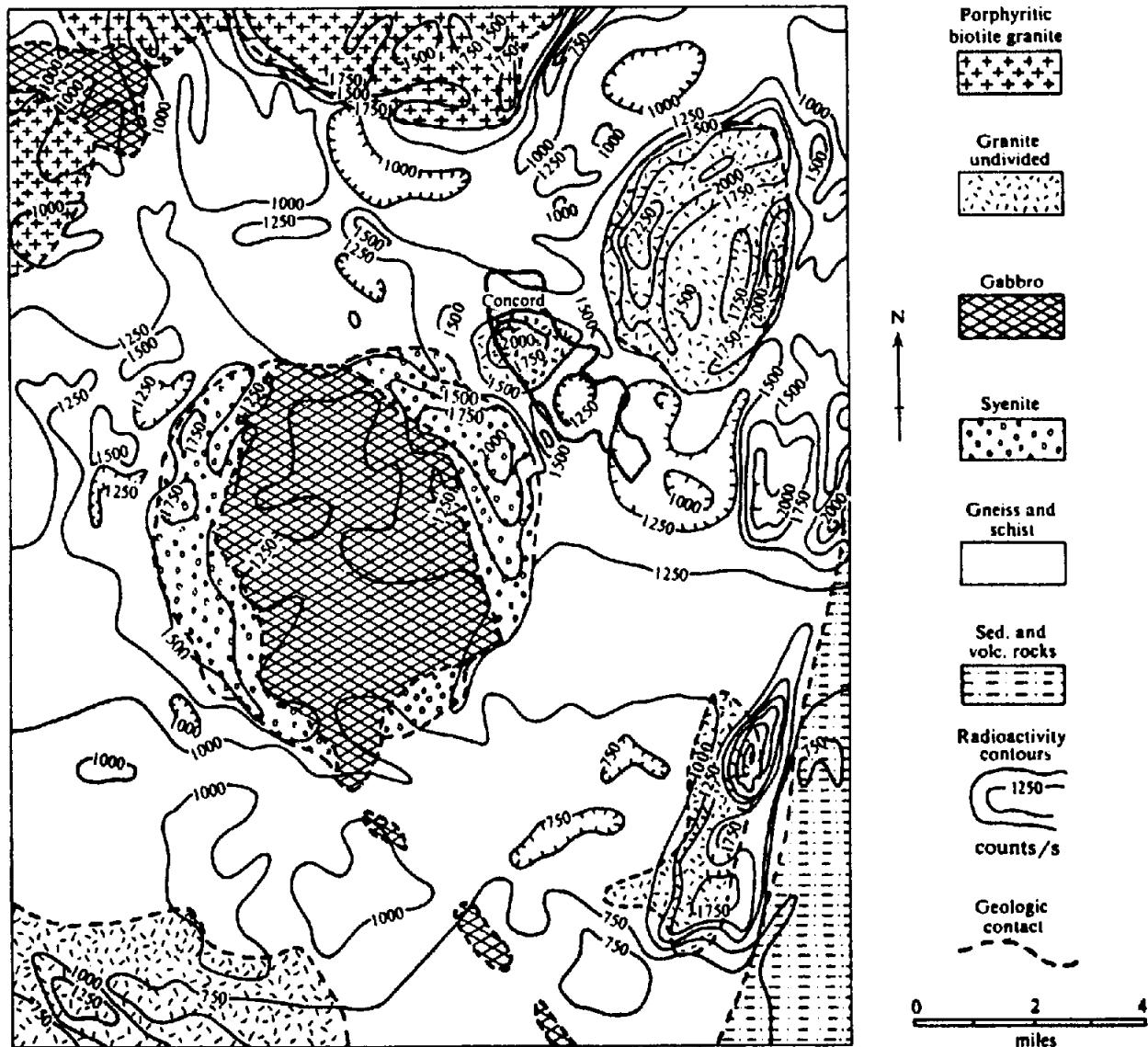


Figure 10.12. Airborne radiometrics as an aid to geological mapping, Concord Quadrangle, North Carolina. (After Bates, 1966.)

abundances ( $m = 4$ ); because  $n > m$ , they used a least-squares solution (§A.8). The results indicated that a full-spectrum multichannel matrix solution was desirable, particularly additional U and Th windows at 1.12 and 0.94 MeV, respectively, well below the usual 1.76 and 2.62 MeV windows. They also found that the cosmic background varied appreciably over periods of a few seconds; this might be significant in calibrating equipment by flying over lakes (although their assumed cosmic data might include other background effects not taken into account, that is,  $m > 4$ ).

Analytic work involving diffusion and convection of radon through overburden has led to numerical methods for modeling various geometries such as 2-D and 3-D blocks under overburden (Soonawala, 1976; Soonawala and Telford, 1980). The treatment is similar to that used in EM and MT analysis. Figure 10.11 shows an example in which a thin zone

of 0.14% U, 0.5 m wide, surrounded by a 0.03% halo, all under 1 m overburden, was used to match a field profile; the anomaly had been partly confirmed by previous drilling.

Use of the radioactivity method in exploration for petroleum and natural gas was mentioned briefly in Section 10.4, where the anomaly and its possible mechanism were described. An early reference to this technique is given by Sikka (1959), who analyzed radiometric contours from an airborne test survey over the Redwater oil field near Edmonton, Alberta. The area was flown twice, first in 1951 with a scintillometer measuring total count, and again in 1957 using a total-count  $\gamma$ -ray instrument that also recorded energies above 1.5 MeV, thus eliminating the effect of  $^{40}\text{K}$  (see problem 5).

Recent applications of this method are reported in Weart and Heimberg (1981). They measured total  $\gamma$ -ray count in a large ionization chamber from a

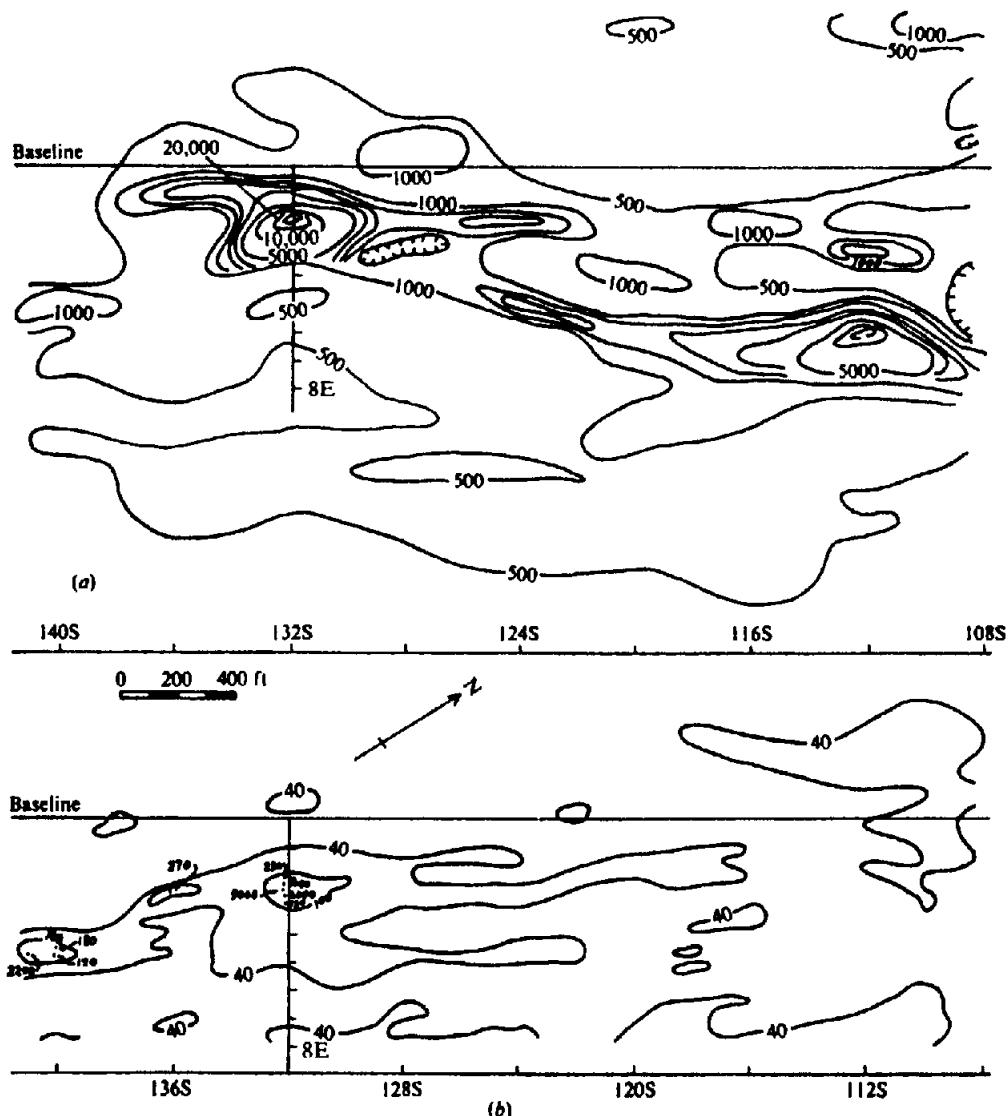


Figure 10.13. Uranium exploration using ground magnetics and radiometrics. (a) Magnetic contours (nT). (b) Radioactivity contours (total  $\gamma$ -ray flux in counts/s).

vehicle or on foot where access was difficult. Surveys were carried out in six states (United States) generally before, in some cases after, drilling. Of some 1,000 wells drilled, about 750 are reported to have been correctly predicted, either as producers or dry, by their location with respect to the radiometric survey data; this compares favorably with domestic drilling statistics for oil and gas. Curry (1984) gives somewhat similar results for about 500 wells in the Powder River Basin area of Wyoming.

Limited tests with ground radon detectors for shallow structural mapping have been reported. King (1978) measured  $^{222}\text{Rn}$  on the San Andreas fault in California. Soonawala (1976) obtained feeble radon anomalies across fault planes in the Eldorado area, northwestern Canada, about the magnitude expected from diffusion theory; the fault response, however, was contaminated by mining activity, because there are several major orebodies nearby. Abdoh-Reza

(1984) measured distinctive anomalies over faults in the vicinity of Ile Bizard, west of Montreal. The clarity of response here, compared to that obtained by Soonawala, is probably the result of much lower background radiation in this area.

Airborne radiometrics have occasionally been used as an aid in geological mapping; a case history is discussed in the next section. An attractive color map for this purpose was recently reported by the U.S. Geological Survey (Duval, 1983). A composite color image contour map is produced by combining any three K, U, Th parameters, or their ratios. Anomalous areas may be shown either as dark zones, known as *direct image displays*, or bright sections, called *inverse images*. This type of reproduction at both ends of the visible spectrum is said to offer more complete sensitivity to the eye for interpretation. Judging by an example of the color maps from an area in southeast Texas, the technique might have

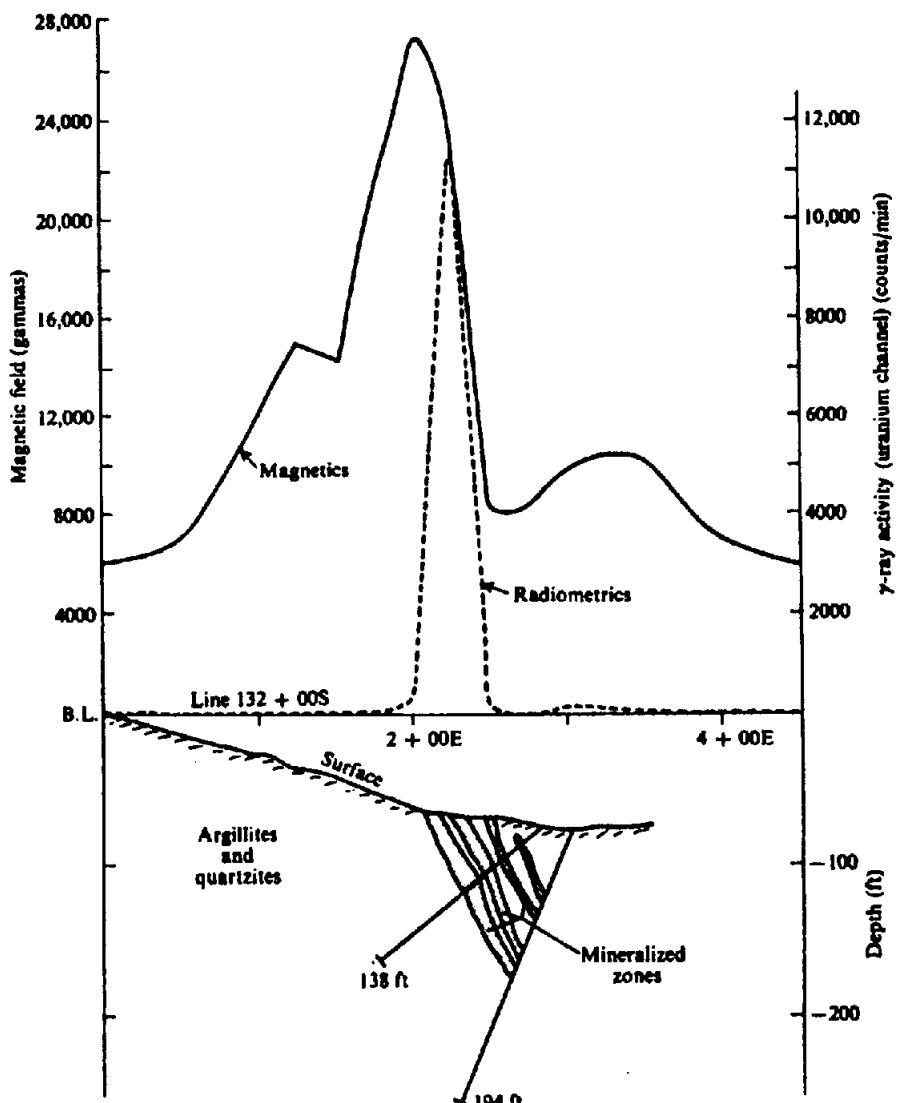


Figure 10.14. Radioactivity and magnetic profiles plus geologic section, line 132 + 00S, uranium survey.

limited application in mapping and qualitative interpretation of surface geology.

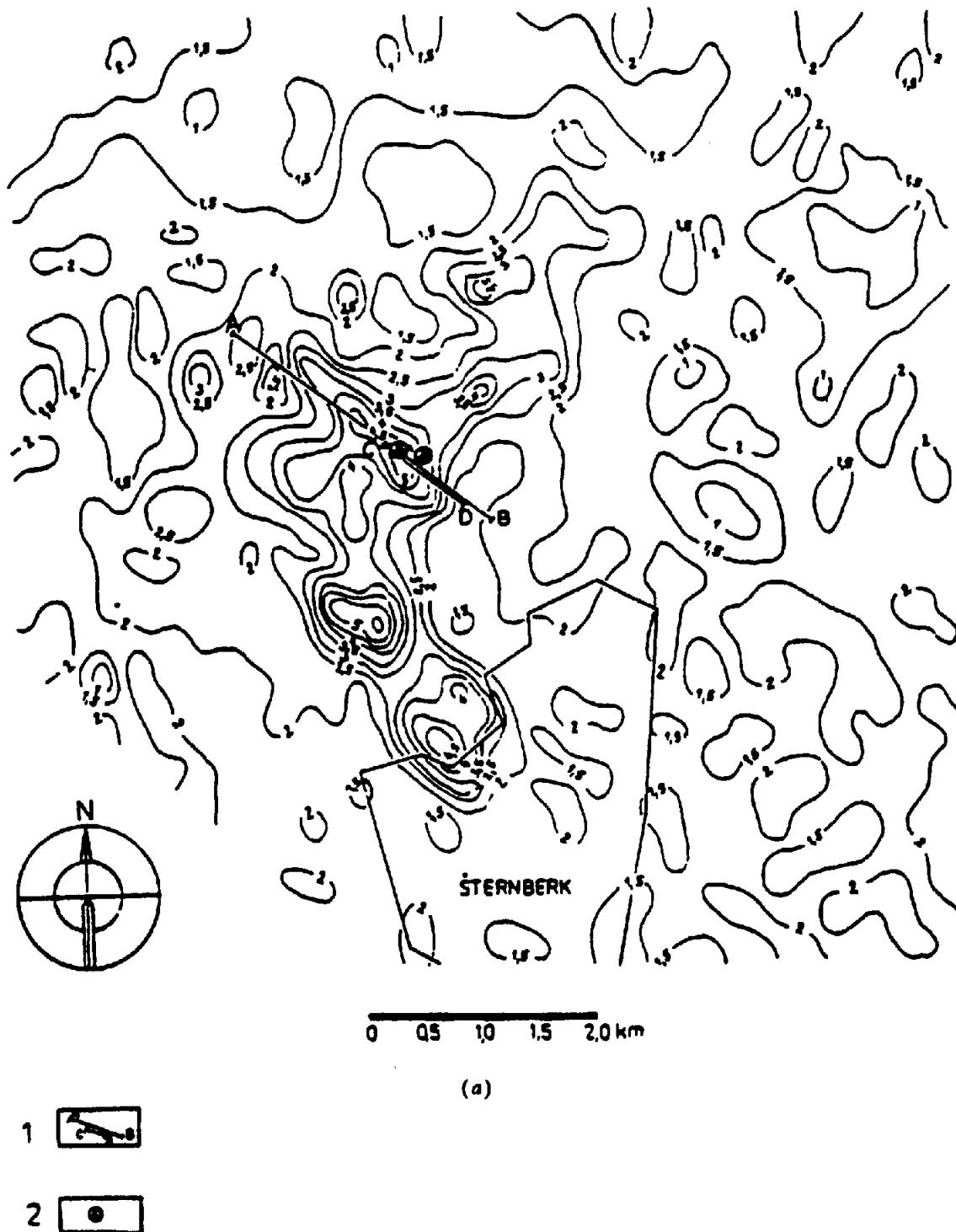
#### 10.6. FIELD EXAMPLES

1. Figure 10.12 illustrates the application of airborne radioactivity to geologic mapping. The area shown is the Concord quadrangle of North Carolina, where the U.S. Geological Survey carried out an airborne radiometric survey as an aid to detailed mapping of complex geology. Six NaI crystals, 10 cm diameter, 5 cm thick, and six photomultiplier tubes connected in parallel were used for the detector. Particular care was taken to correct the data for variations in aircraft altitude.

The compilation of geologic and radioactivity information in Figure 10.12 represents a progressive refinement of data; that is, the original geologic information was changed as a result of additional geologic mapping, which was to a considerable ex-

tent guided by the radioactivity results. For example, the radiometric survey outlined a granite stock, northeast of the town of Concord, whose borders could not be well defined by field geology; it also located the smaller granite body in the northwest part of the town.

The granitic zone in the southeast corner of the figure is marked by high radioactivity, whereas that on the southwest is not. A porphyritic biotite granite in the northern part of the quadrangle shows medium to high radioactivity, but in the vicinity of the gabbro mass in the northwest corner the response is lower. The anomalous high along the east border coincides with a considerable injection of granite into the surrounding gneiss and schist. Finally, the large gabbro-syenite mass in the center of the quadrangle is fairly well outlined by the radioactivity contours, because the syenite zones on the east and west flanks show higher response than either the gneiss-schist surroundings or the enclosed gabbro.



1

2

*Figure 10.15. Airborne survey for potassium used to locate associated Zn mineralization. (After Gnojek and Prichystal, 1985.) (a)  $^{40}\text{K}$  contours, contour interval 0.5%; • mark two drillholes.*

The variation in radioactivity response over different granitic zones is not definitely explained, although it is suggested that there may be different types of granite within the quadrangle. No mention is made of the depth of overburden; slight variations in the thickness or type of cover could account for the lows in the northwest and southwest corners.

Neither the airborne radiometrics nor the geologic mapping could have produced this inter-

pretation independently. It is the product of a combination of the two, plus some aeromagnetic data. Furthermore, the airborne survey, as mentioned previously, was useful in selecting areas for further detailed mapping, thus saving time and money.

2. An example of the direct method of radioactivity prospecting is shown in Figure 10.13 and 10.14 taken from an extensive survey for uranium in

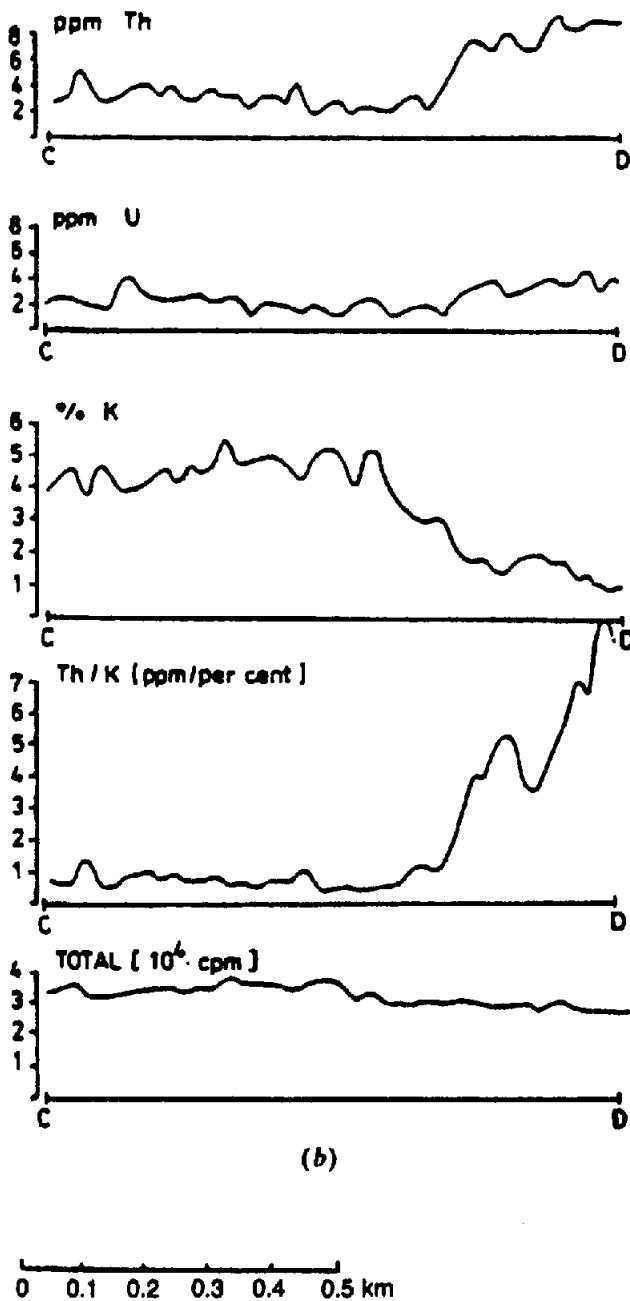


Figure 10.15. (Continued) (b) Th, U, K, Th/K, and total-count profiles on line CD [see part (a) for location].

Labrador. Following large-scale reconnaissance with airborne radiometrics and magnetics, a set of targets was selected for detailed ground followup. The latter operation proceeded in two steps. First, the airborne radioactivity anomalies were located and assessed roughly; then the more promising of these were examined in detail by scintillometer and magnetometer (in some cases ground EM was also employed, because there were sulfides associated with the radioactive minerals). Stations were 10 to 25 ft apart along cut lines spaced 100 ft apart.

Figure 10.13 shows the radioactivity and magnetic contours for a small area of the ground survey.

Strong anomalies of both types are coincident on L132S at 2E. These were indicated by the airborne survey, the location being almost exactly the same as the ground anomaly. At L112S, 6E, however, there is no abnormal radioactivity associated with the high magnetics.

Magnetic and radiometric profiles on L132S (the latter being obtained by using the uranium channel on the scintillometer), together with a vertical geologic section obtained from drilling, are displayed in Figure 10.14. The host rocks are argillites, quartzites, and amphibolites. The mineralization, consisting of magnetite and pitchblende with some chalcopyrite, sphalerite, and pyrrhotite, occurs in bands of ferruginous quartzites which alternate with diorite dikes. The overburden at the collars of the two drill holes is about 2 m thick and the huge magnetic and  $\gamma$ -ray peaks occur directly over exposed mineralization.

Although the  $U_3O_8$  mineralization is probably of economic grade, the volume is small. The maximum depth extent is 40 m, whereas additional drilling showed the zone width and strike length to be no greater than 3 m and 75 m, respectively. Although the contours of Figure 10.13a and b indicate the small lateral extent of the showing, this evidence is not conclusive in itself for two reasons: first, a meter of overburden would be sufficient to mask the presence of uranium; second, the association of  $Fe_3O_4$  and  $U_3O_8$  mineralization does not prevail throughout the area, as proved by drilling in the vicinity of the magnetic anomaly near 6E on L112S.

3. Gnojek and Prichystal (1985) report the detection of zinc mineralization in northern Moravia by potassium anomalies from airborne  $\gamma$ -ray spectroscopy. Hydrochemical and self-potential anomalies accompanied by tectonic considerations had shown that sulfides might be present in the area. The airborne survey was carried out with a four-channel spectrometer and a magnetometer in a helicopter at 80 m ground clearance with 250 m line spacing. Two distinct  $^{40}K$  anomalies of  $\geq 5\%$  were detected, accompanied by variable U and very low Th.

The anomalies were verified by ground followup using radiometrics, a variety of electrical methods, and geochemistry. Despite the presence of basic rocks, there were no magnetic anomalies. The  $^{40}K$  data provided locations for drilling, which encountered ZnS at 150 and 75 m depths in two holes. Figure 10.15a displays contours of  $^{40}K$  over the area and the borehole locations, and Figure 10.15b shows various concentrations from a profile along line CD. The latter again illustrates the superiority of separate K, U, and Th measurements over total count.

Unless this example is an isolated case, the use of radiometric surveys for base-metal and other mineral targets may be useful, particularly in areas where

Table 10.6.

Station	Lines							
	1	2	3	4	5	6	7	8
1	11	11	11	12	11	12	14	15
2	12	12	11	12	12	15	15	17
3	14	14	12	14	14	17	17	17
4	17	15	15	15	15	24	17	17
5	19	18	18	18	17	34	22	16
5½	—	30	21	24	22	—	—	—
6	16	25	24	23	28	47	27	18
7	17	23	25	28	34	47	30	24
8	16	17	30	36	46	66	47	38
8½	—	—	—	70	200	—	66	60
9	15	22	36	1,200	200	310	260	40
10	14	18	22	50	35	35	46	25
11	13	15	18	22	26	26	33	17
12	12	12	15	18	17	17	14	13

normal techniques are ruled out by high electrical noise.

## 10.7. PROBLEMS

1. Scintillometer readings were taken at station intervals of 8 m on a set of parallel lines 8 m apart over an area in Saskatchewan during the course of a uranium exploration program. The readings, in counts per minute, are given in Table 10.6.

Plot and contour these readings; estimate the strike and width of the anomalous zone. Are there indications of the depth of overburden and variations of the overburden thickness in these values?

2. A 2.5 kg rock sample was tested for radioactivity with a scintillometer, both being enclosed in a large shielded container. The average count rate was 540 cpm. The background count in the container was 35 cpm. Assuming the overall efficiency of the scintillometer to be 30%, and either that the radioactivity is approximately equally distributed between uranium, thorium, and potassium or that there is no potassium in the rock and the U : Th ratio (§10.5) is about 0.5, determine the content of each element in the sample for the two cases (see Table 10.2, §10.2.4).

3. Scintillometer and vertical-component magnetic contours, taken from a detailed ground survey for uranium in northern Canada are shown in Figure 10.16. An excerpt from the geological report on the region says: "Geologically these areas are quite featureless and consist of pink quartzites with dark bands of mafic minerals, the latter coinciding with the radioactivity and magnetic anomalies at a number of places."

Make an interpretation of this small section using the limited data available and keeping in mind possible coincidences of magnetic and radiometric anomalies, variations in depth of overburden, presence of granitic rock ( $^{40}\text{K}$  radioactivity), and so forth. As an aid to interpretation, it is suggested that the two contoured maps be overlaid and also that a few profiles be taken off each map.

4. As mentioned in Section 10.3.4, the present type of  $\gamma$ -ray spectrometer has three channels at 1.46, 1.76, and 2.62 MeV to isolate K, U, and Th peaks, respectively. Consequently it is possible to determine the individual amounts of potassium, uranium, and thorium contained in a rock sample when the spectrometer has been calibrated by using standard samples of known composition. We obtain the relative content of the three elements in terms of the count rates of the instrument as outlined in the following text.

None of the  $\gamma$  rays from uranium or potassium has sufficient energy to be recorded in the thorium (2.62 MeV) channel; hence

$$T = k_1 T_c$$

where  $T$  is the thorium content in parts per million,  $T_c$  is the 2.62 MeV channel count rate less background, and  $k_1$  is the constant for the thorium channel.

The 1.76 MeV uranium channel records  $\gamma$  radiation for uranium and thorium but none from potassium. Hence we have

$$U = k_2 (U_c - S_1 T_c)$$

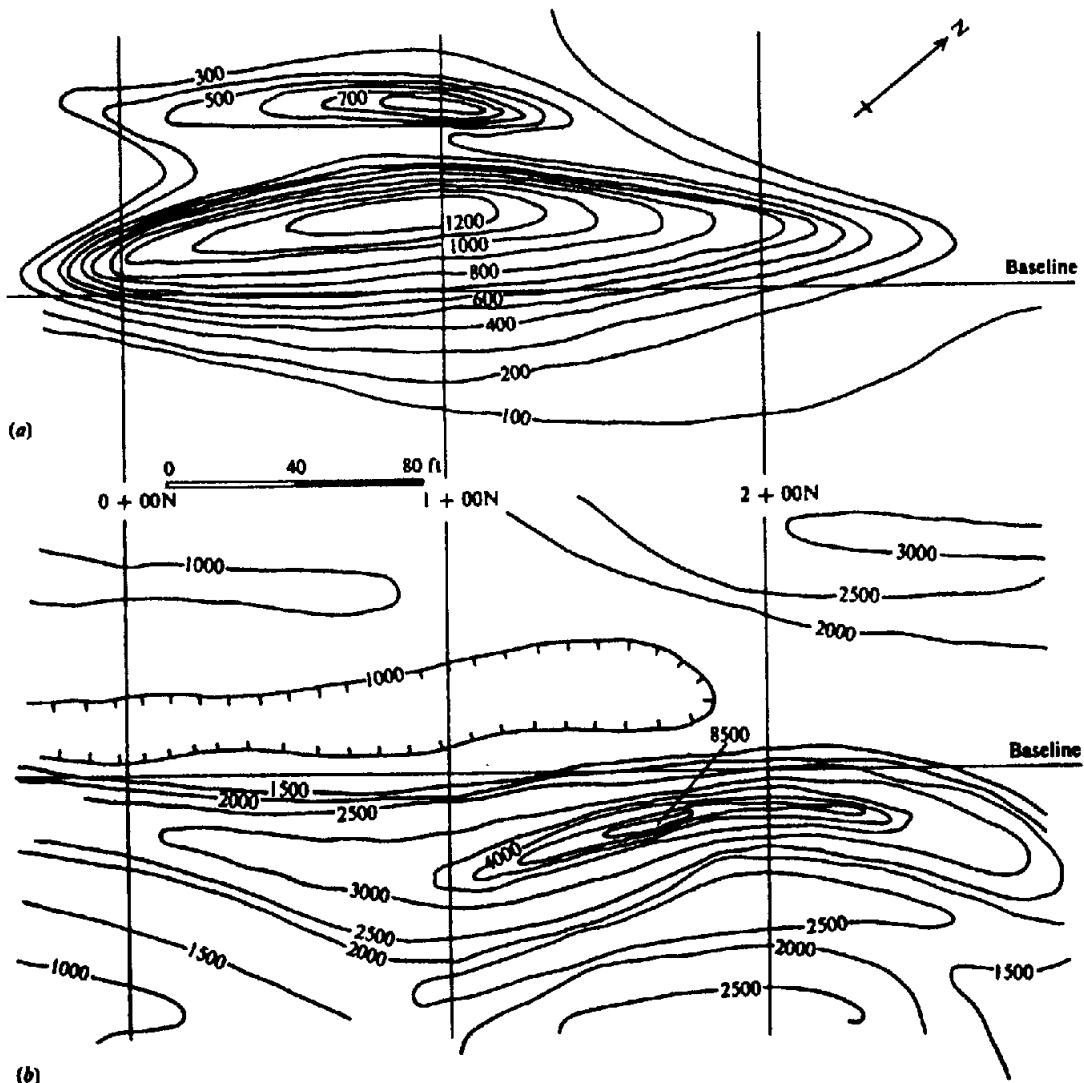


Figure 10.16. Radioactivity and magnetic contours, Northern Canada. (a) Wide-window  $\gamma$ -ray flux (counts/s), background 60 counts/s. (b) Vertical-component of the magnetic field (gammas).

where  $U$  is the uranium content in parts per million,  $k_2$  is the constant for the uranium channel,  $U_c$  is the 1.76 MeV channel count rate less background, and  $S_1$  is the stripping constant for thorium  $\gamma$  rays in the uranium channel (see next paragraph).

Finally, in the 1.46 MeV potassium channel we may have counts from uranium and thorium as well as potassium. The potassium content,  $K_{\text{g}}$  (expressed as a percentage because it is generally much larger than the amounts of U and Th), is given by

$$K_{\text{g}} = k_3 \{ K_c - S_2(U_c - S_1 T_c) - S_3 T_c \}$$

where  $k_3$  is the constant for the potassium channel,  $K_c$  is the 1.46 MeV channel count rate less background, and  $S_2, S_3$  are the stripping constants for U and Th  $\gamma$  rays in the K channel. Because the  $\gamma$ -ray spectrum of an element is in-

Table 10.7.

Station (ft)	Spectrometer readings (cpm)		
	$T_c$	$U_c$	$K_c$
0	13	28	195
100	8	27	243
170	22	34	265
200	25	36	218
210	18	30	135
230	10	24	223
300	15	27	193
400	15	30	197
425	12	20	242
500	8	21	233

variant, the stripping constant is merely the fixed ratio of the count rates for U or Th at the appropriate energy levels; thus,  $S_1$  is the ratio of the count rates for Th in two channels centered at 1.76 and 2.62 MeV; hence multiplying the observed count rate for the 2.62 MeV channel by  $S_1$

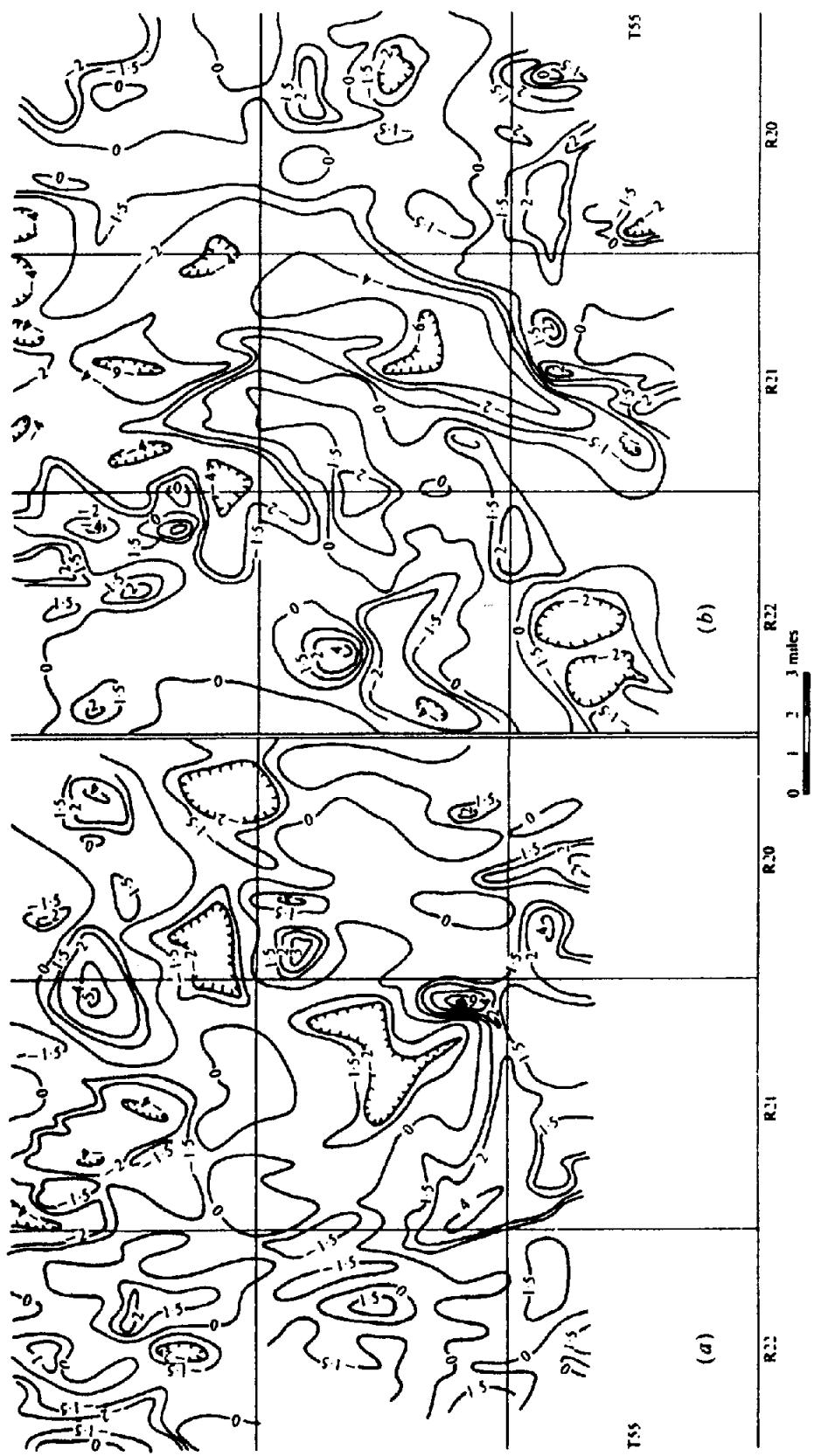


Figure 10.17. Aeroradiometric survey, Redwater Oilfield, Alberta. (a) Area flown east-west, winter of 1957; contours are total-count for energies above 1.5 MeV. (b) Area flown east-west, autumn of 1951; contours are for total count only.

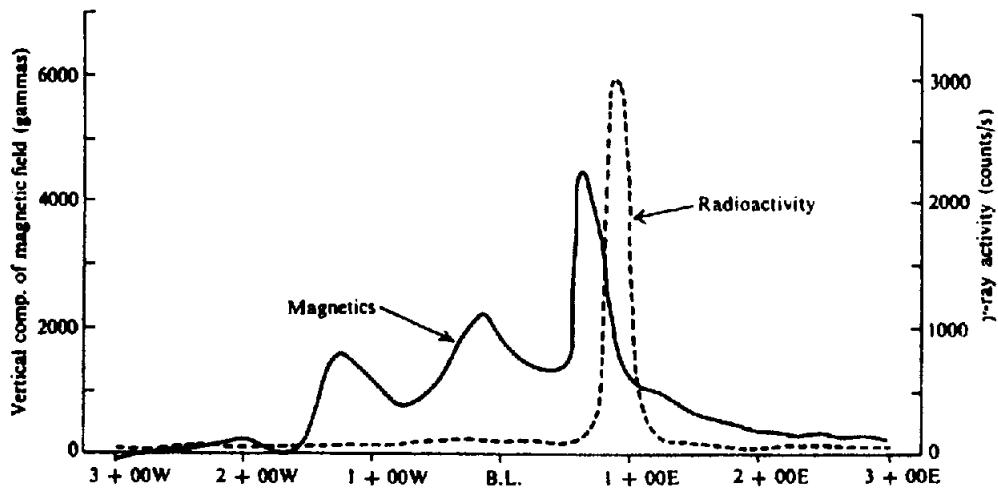


Figure 10.18. Radiometric and magnetic profiles from a survey for base-metals plus uranium.

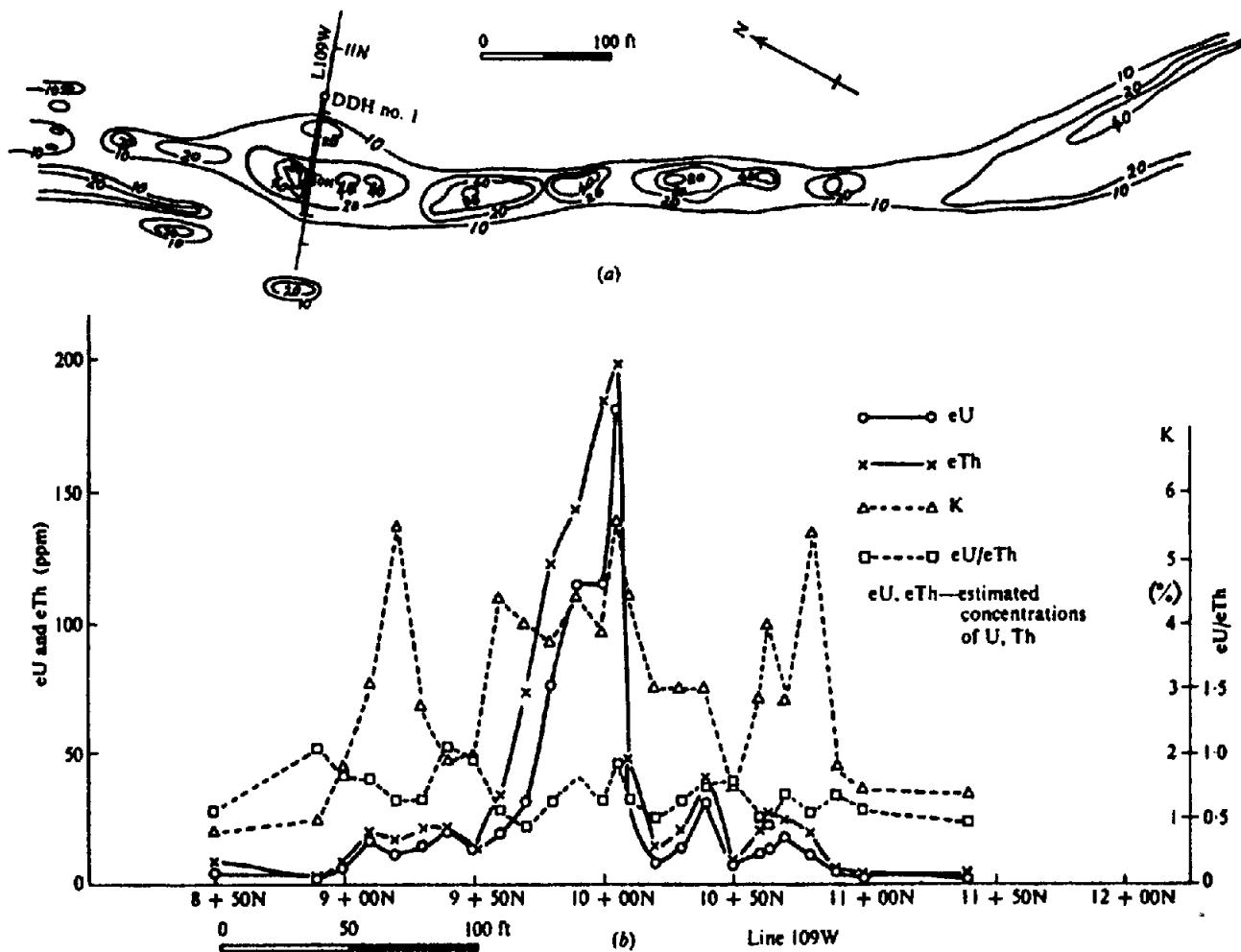


Figure 10.19. Results of radiometric survey over pegmatite, Portneuf, Quebec. (a) Isorad contours; contour interval 1,000 counts/min. (b) Radiometric profiles of  $eU$ ,  $eTh$ ,  $K$ , and  $eU/eTh$  ratio for line 109W.

336

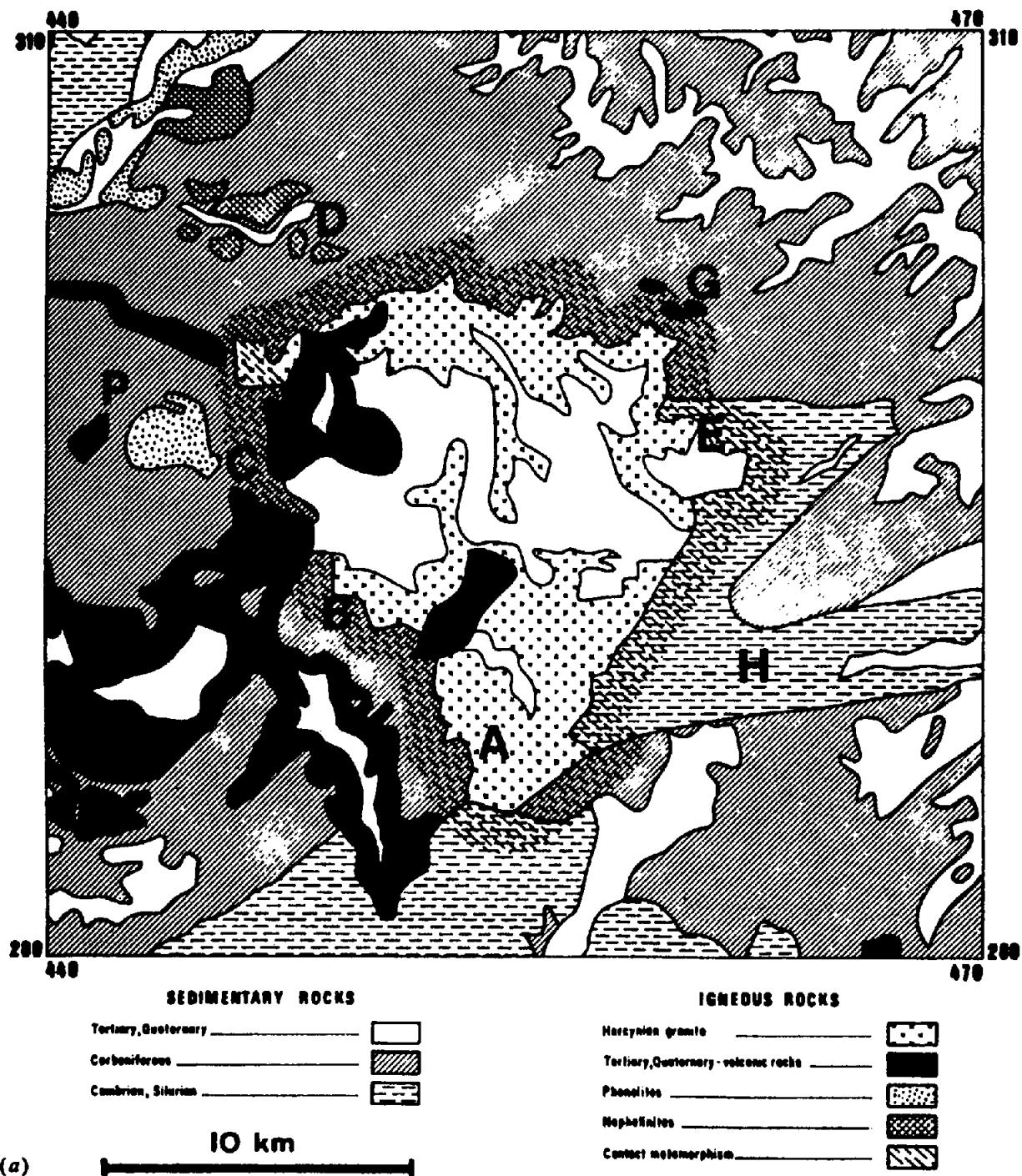


Figure 10.20. Airborne radiometric and magnetic surveys over granite zone, Morocco.  
(a) Detailed geology of the area.

yields the thorium count rate that would be observed at the same instant in the 1.76 MeV channel.

Theoretically only one thorium, two uranium, and three potassium standard samples are required to furnish the data to solve the three equations and determine the three constants,  $k_1$ ,  $k_2$ ,  $k_3$ . In practice it is best to use as many

standards as possible because of instrumental and sampling errors.

The readings in Table 10.7 were obtained with a  $\gamma$ -ray spectrometer in a traverse perpendicular to foliation across a granite-gneiss outcrop near St. Columban, Quebec.

Given that  $k_1 = 0.6$ ,  $k_2 = 0.13$ ,  $k_3 = 0.020$ ,  $S_1 = 1.0$ ,  $S_2 = 1.5$ , and  $S_3 = 1.7$ , determine the

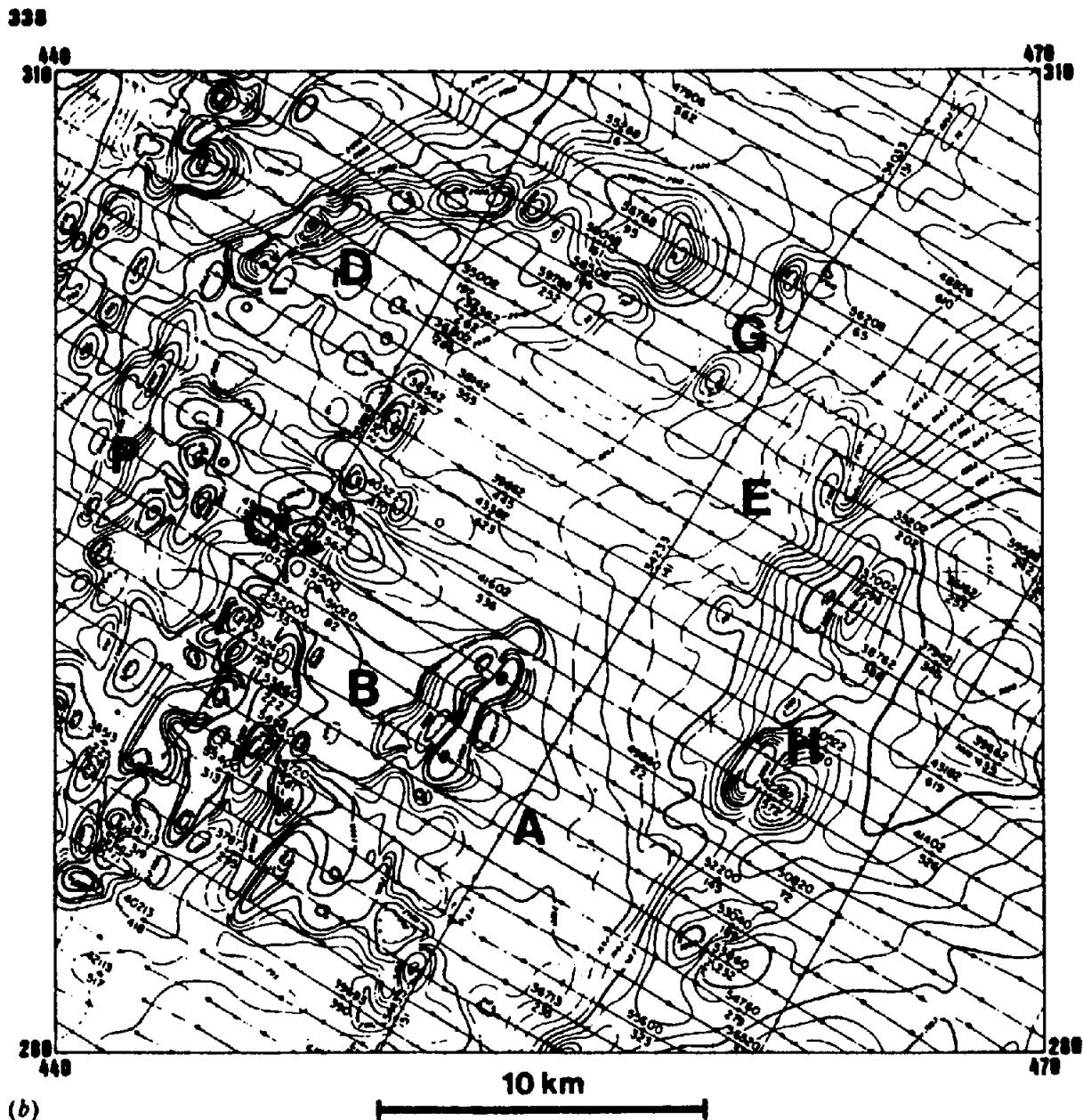


Figure 10.20. (Continued) (b) Total-field magnetic map; contour interval five gammas.

Th, U, and K content at each station and plot profiles for each element as well as a profile of the Th : U ratio.

The formation appears to be homogeneous, that is, completely granitized, except for remnants of sedimentary rocks at 35 and 215 ft. Do the profiles bear this out over the whole 500 ft traverse or any part of it? On the assumption that high Th : U ratios would be more characteristic of sediments than of the granite-gneiss intrusive, does the Th : U profile provide any additional information? Is the sampling density adequate for a petrogenetic study of the rocks?

- Figure 10.17 shows radiometric contours from an airborne test survey of Redwater oil field near Edmonton, Alberta. Figure 10.17a shows total count for  $\gamma$ -ray energies above 1.5 MeV, Figure

10.17b, total count only. The rocks of the area are mainly shales and sandstones, with some conglomerate, black quartzite, and argillaceous sandstone in the SW and SE corners of the survey area. Green shale forms a caprock over the oil pool.

The airborne data have been analyzed by Sikka (1959), who made corrections for variations in the radioactivity of the different soils in the area. The arithmetic mean and standard deviation were calculated for the area. The difference between each observed value and the arithmetic mean was divided by the standard deviation and the result plotted as the station value; thus, the contour interval is a multiple of the standard deviation. Sikka also measured the distribution of radon emission on the ground. In the course of this

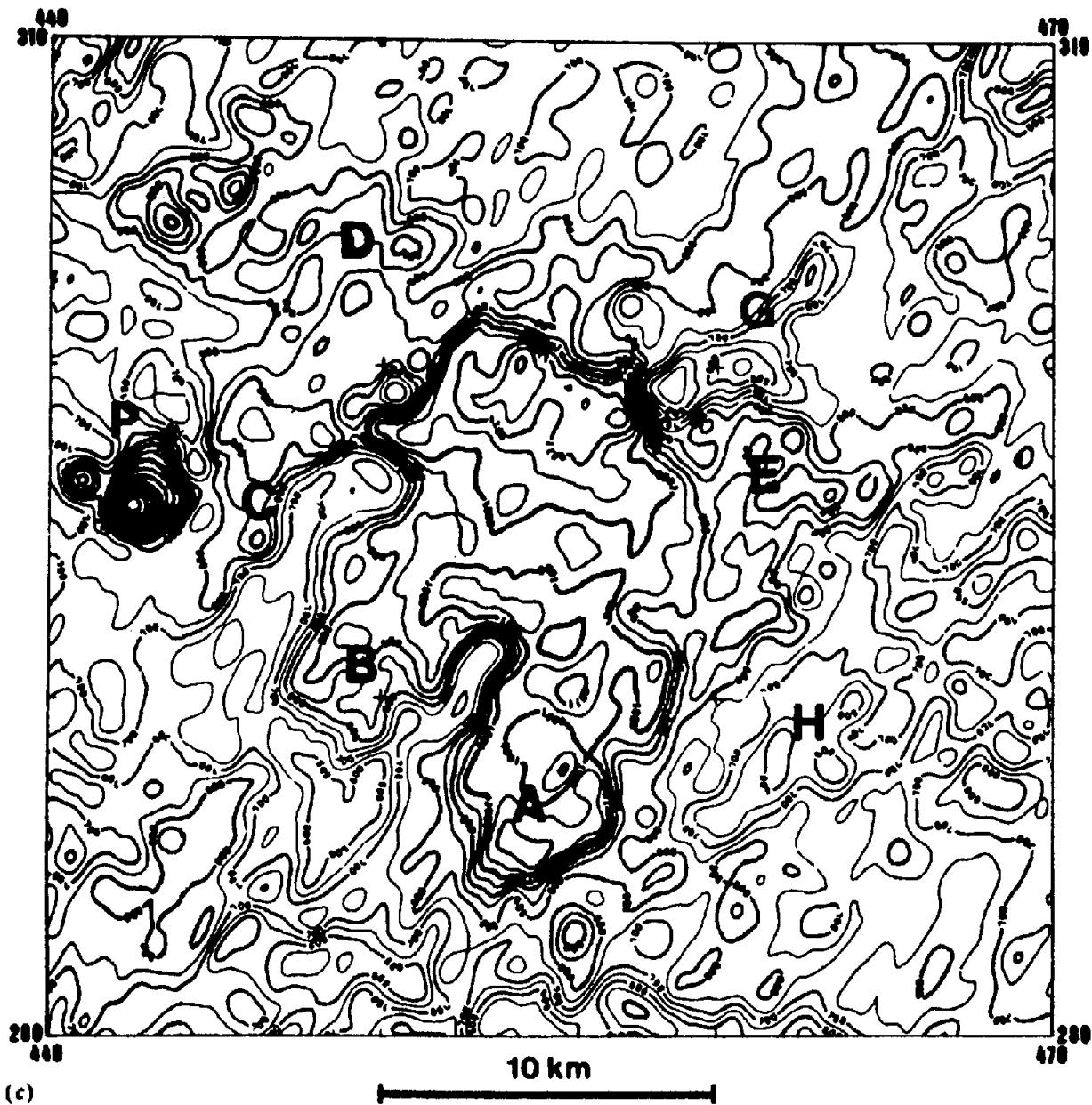


Figure 10.20. (Continued) (c) Total-count map; contour interval 50 counts/s.

work, he found that the type of soil, for example, sands, sandy loams, loams, and so forth, as well as the soil parent material, controlled the regional pattern of radioactivity to a considerable extent. Details may be found in the original work.

The airborne radiometric data from 1951 (Fig. 10.17b) were corrected only for the soil type. The contours of 1957 (Fig. 10.17a) were corrected for soil parent material as well. This was done to show the significance of both factors. Sikka states that the two maps would be similar if the complete corrections were made in both cases.

On the hypothesis that radioactivity lows reflect the relatively impervious caprock over the oil pool, try to outline its boundaries on each map. (Note: The survey covered only about 65% of the total area of the oilfield.) Can you spot muskeg

and swamps from anomalous high radioactivity? Apart from a possible halo of high radioactivity around the oilfield, are there any structures, such as faults, indicated by linear high-low contrasts striking in a preferred direction?

6. The profiles in Figure 10.18 are taken from a detailed survey for base metals and uranium. Station readings were made every 10 ft. The magnetic-radiometric correlation is similar to that of Figure 10.14, although the geology is different and this anomaly has a strike length of 1,600 ft. Locate the radioactive source, the boundaries of the magnetic anomaly, and the dip of the mineralized section. What is the likely source of the magnetic mineralization?
7. Some results from a radiometric survey over a pegmatite in Portneuf County, about 35 miles

west of the city of Quebec, are shown in Figure 10.19. This feature outcrops continually for a distance of about 1,100 ft. As can be seen in Figure 10.19a the strike is roughly N20°W over most of the length, the main width varying between 30 and 80 ft; there are narrower pegmatitic bands on the flanks. The host rocks are gneisses with some hornblende.

- The uranium, thorium, and potassium content of the rocks, shown in the profiles of Figure 10.19b, were determined with a multichannel  $\gamma$ -ray spectrometer by a method similar to that described in problem 4. Locate the main pegmatite section and any additional pegmatite bands with the aid of these data. Are these sections of shallow or steep dip? Can you determine the direction of dip? Does the uranium mineralization appear to be of economic grade? Compare the U : Th ratios with the actual uranium and thorium concentrations at various places along the profile. Do large ratios correlate with high uranium content?
8. The maps in Figure 10.20b and c are taken from a large-scale airborne magnetic and radiometric survey in Morocco, carried out in 1972. Geology of this  $30 \times 30$  km granitic zone is illustrated in Figure 10.20a. Flight lines were NW-SE, with 1 km spacing at 150 m ground clearance. Data compilation was by computer, corrected for altitude; radiometric background was obtained before and after each flight by means of a short pass at 600 m, whereas a fixed magnetic ground station provided a similar check for the magnetic data. Only total count radioactivity is shown here, although Th, K, Th/K, and U counts were also available from the three-channel spectrometer.

Make a sufficiently detailed tracing of the total count and magnetic contours for overlays on the original maps of Figure 10.20. Assess the correlation and complementary information obtained by the airborne data with respect to the geologic map; do the same for the two survey methods. Is there evidence of much overburden in the area? From the limited lists of rocks and minerals in Tables 10.4 and 10.5, can you suggest any further anomalies that might appear on the Th and K maps? Why was the U channel not reproduced?

## REFERENCES

- Abdoh, A. B., 1984. Field geophysical studies in the Pierrefonds-Ile Bizard region, Montreal. M.Sc. thesis, McGill Univ., Montreal.
- Bates, R. G. 1966. Airborne radioactivity surveys, an aid to geologic mapping. In *Mining Geophysics*, Vol. I, pp. 67-76. Tulsa: Society of Exploration Geophysicists.
- Bristow, Q. 1979. Gamma-ray spectrometric methods in uranium exploration - airborne instrumentation. In *Geophysics and geochemistry in the search for metallic ores*, P. J. Hood, ed., Econ. Geol. Report 31, Geol. Surv. Canada, pp. 135-46.
- Bristow, Q., Carson, J. M., Darnley, A. G., Holroyd, M. T., and Richardson, K. A. 1977. Specifications for federal-provincial uranium reconnaissance program 1976-1980 airborne radioactivity surveys. Geol. Surv. Canada Open File No. 335.
- Crossley, D. J., and Reid, A. B. 1982. Inversion of gamma-ray data for element abundances. *Geophysics* 47, 117-26.
- Curry, W. H., III 1984. Evaluations of surface gamma radiation surveys for petroleum exploration in the Deep Powder River Basin, Wyoming. In *Unconventional Methods in Exploration for Petroleum and Natural Gas III*, M. J. Davidson and B. M. Gottlieb, eds. pp. 25-40. Dallas: Southern Methodist University Press.
- Darnley, A. G. 1970. Airborne gamma-ray spectroscopy. *Can. Inst. Min. Bull.* 63, no. 694, 145-54.
- Darnley, A. G., Cameron, E. W., and Richardson, K. A. 1975. The federal-provincial uranium reconnaissance program. In *Uranium exploration '75*, Geol. Surv. Canada Paper 75-26, pp. 49-63.
- Duval, J. S. 1983. Composite color images of aerial gamma-ray spectrometric data. *Geophysics* 48, 722-35.
- Gnojek, I., and Prichystal, A. 1985. A new zinc mineralization detected by airborne gamma-ray spectrometry in northern Moravia (Czechoslovakia). *Geoexplor.* 23, 491-502.
- Grasty, R. L. 1979. Gamma-ray spectrometric methods in uranium exploration - theory and operating procedures. In *Geophysics and geochemistry in the search for metallic ores*, P. J. Hood, ed., Econ. Geol. Report 31, Geol. Surv. Canada, pp. 147-61.
- Killeen, P. G. 1979. Gamma-ray spectrometric methods - application and interpretation. In *Geophysics and geochemistry in the search for metallic ores*, P. J. Hood, ed., Econ. Geol. Report 31, Geol. Surv. Canada, pp. 163-229.
- King, C. Y. 1978. Radon emanation on San Andreas fault. *Nature* 271, 516-19.
- Sikka, D. A. 1959. A radiometric survey of Redwater oilfield, Alberta, Canada. Ph.D. thesis, McGill Univ., Montreal.
- Soonawala, N. M. 1968. Correlation of ground and airborne radiometrics. M.Sc. thesis, McGill Univ., Montreal.
- Soonawala, N. M. 1976. Diffusion of radon 222 in overburden and its application to uranium exploration. Ph.D. thesis, McGill Univ. Montreal.
- Soonawala, N. M., and Telford, W. M. 1980. Movement of radon in overburden. *Geophysics* 45, 1297-1315.
- Telford, W. M. 1983. Radon mapping in the search for uranium. In *Developments in Geophysical Exploration Methods - 4*, A. A. Fitch, ed., pp. 155-94. New York: Applied Science Publishers.
- Warren, R. K. 1977. Recent advances in uranium exploration with electronic alpha cups. *Geophysics* 42, 982-9.
- Weart, R. C., and Heimberg, G. 1981. Exploration radiometrics postsurvey drilling results. In *Unconventional Methods in Exploration for Petroleum and Natural Gas II*, B. M. Gottlieb, ed., pp. 116-23. Dallas: Southern Methodist University Press.
- Wollenberg, H. A. 1977. Radiometric methods. In *Nuclear Methods in Mineral Exploration*, J. Morse, ed., Ch. 2, pp. 5-36. Amsterdam: Elsevier.

# Chapter

# 11

## *Geophysical Well Logging*

### 11.1. INTRODUCTION

#### 11.1.1. Uses of Well Logging

Well logging involves measuring the physical properties of surrounding rocks with a sensor located in a borehole. The record of the measurements as a function of depth is called a *well log*.

Geophysical well logging has become a standard operation in petroleum exploration. Identification of geological formations and formation fluids, correlation between holes, and evaluation of the productive capabilities of reservoir formations are usually the principal objectives.

Except for the natural  $\gamma$ -ray log, which is used routinely in uranium exploration, well logging is still not used extensively in the search for metallic minerals. Some argue that the complete recovery of cores in diamond drilling eliminates the need for logging holes because the information is laid out in the core box. It is unfortunate that this attitude still prevails because well logging is cheap compared to drilling and would be valuable in correlation and identification of mineral-associated anomalies, particularly when core is lost or difficult to identify.

Geophysical well-logging methods include mechanical methods, passive and a number of active electrical methods (including self-potential, resistivity, induction, induced polarization), several nuclear methods (natural  $\gamma$ -ray detection and observations from induced nuclear reactions), acoustic logging, and measurement of magnetic and thermal properties. The emphasis in what follows will be on logging for petroleum (Pickett, 1970) because this is the major application.

#### 11.1.2. History of Well Logging

The first borehole log, run on September 5, 1927 by the Schlumberger brothers in the Pechelbron oil field in France (Segesman, 1980 and Snyder and Fleming, 1985, upon whom this history is mainly based), measured formation resistivity. The first log (called

*electric coring*) in the United States was in 1929 when Doll noted spontaneous potentials (SP) and that negative SP was associated with permeable formations. Beginning about 1932, two logs were usually run, resistivity and SP. Around this time Schlumberger also began using different electrode configurations and spacings to reduce distortions. About 1936 photographic recording of measurements replaced manual reading of meters and tabulating of data. The first efforts to measure dip in a borehole came in 1933, using an array of electrodes, and the first uses of a recording thermometer and teleclinometer (to measure borehole deviation and direction) were also about this time.

In 1941, Archie developed empirical equations relating resistivity measurements to porosity and water saturation and in 1945, Guyod published a discussion of well-log interpretation. In 1949, Wyllie related electrochemical SP effects to differences between the resistivities of mud filtrate and formation water and to chemical activities.

The induction log, developed in 1949, allowed the measurement of electrical resistivity (actually its reciprocal, conductivity) without requiring fresh water mud; it was an outgrowth of World War II research. A number of other electrical logs, such as microresistivity and focused logs, were developed in the 1950s.

Natural  $\gamma$ -ray logging, introduced about 1939, permitted distinguishing shales from other formations by their higher natural radioactivity. A neutron log was described in 1941; it utilized a downhole neutron source and measured the  $\gamma$  rays emitted upon the capture of the neutrons, a response depending mainly on a formation's hydrogen content. Logs depending on other nuclear reactions followed in the 1950s. Gamma-gamma (density) logs for determining density began about 1957. The first continuously recording dipmeter in 1950 utilized a three-arm mechanical scratcher for correlating irregularities in the borehole wall.

The measurement of seismic velocity in boreholes was first done in the 1930s and continuous velocity logging began about 1953. However, sonic logging

did not become used widely until Wyllie's time-average equation related seismic velocity to porosity (Wyllie, Gregory, and Gardner, 1958).

Although digital tape recording of log data became available about 1961, well-log processing did not progress much until the 1970s. Downhole digitizing of measurements, multiplexing of different measurements, and telemetering the data to the surface have increased greatly the number of measurements that are feasible. Processing made it practical to combine the readings of different logs so that the plotted values give the needed information more directly.

### 11.1.3. General Aspects of Well Logging

Well bores are generally drilled by circulating a fresh-water suspension (*drilling mud*) down through the drill pipe and back to the surface through the annular region between the drill pipe and the rock. Occasionally salt-water mud, oil, or air is the circulating medium. The circulating drilling fluid removes rock cuttings from the bottom of the borehole.

The fluids in a rock's pore spaces (*interstitial fluids*) are normally under a pressure about that of a column of water extending to the surface. Their pressure is roughly in balance with that of the borehole fluid. If the borehole pressure were less, the pressure differential would tend to expel the interstitial fluids into the borehole. Sufficient solids are added to the mud to make the pressure of the fluid column approximately equal to that of the formation fluids. Mud densities range between 1.1 and 2.0 g/cm<sup>3</sup>. Exact balance is rarely achieved, however, and the usual tendency is for the mud to be under slightly greater pressure. This causes the borehole fluid (*mud filtrate*) to enter porous formations and push the indigenous fluid back from the borehole, a process called *invasion*. In the invasion process the mud solids plaster the borehole wall to form a *mud cake* whereas the fluid portion (*mud filtrate*) enters the formation interstices. The mud cake quickly becomes sufficiently thick (up to 2 to 3 cm) to prevent further entry of borehole fluid into the formation. However, the mechanical aspects of drilling abrade the mud sheath, which is then repeatedly renewed by additional filtrate invasion.

Boreholes are ordinarily cased with steel pipe (*casing*) several times during drilling to provide permanent protection against collapse of the borehole, loss of borehole fluid into "thief" formations, or formation fluid entering the borehole. This is necessary because different formations have different interstitial fluid pressures relative to the borehole fluid

pressure, so that the borehole fluid density cannot be adjusted to be appropriate for all of them. *Open-hole logs* are usually run just before the setting of casing. Consequently, most well logs consist of portions run at different times. Some logs (*cased-hole logs*) measure through casing and cement.

The cable used to lower and raise the sonde in the borehole usually contains seven conductors. It is wrapped (*armored*) with a steel mesh to prevent abrasion. Ordinarily the well *tool* (the part containing the sensors being called the *sonde*) is lowered to the bottom of the borehole and logging is done as the sonde is pulled up the hole. Depths are determined more reliably coming out of the hole than if measured going into the hole because the sonde may not sink at a constant rate.

Borehole diameters are usually 6 to 10 in. (15 to 25 cm), occasionally up to 16 in. (40 cm), in petroleum exploration and 1 to 4 in. (2.5 to 10 cm) in mineral exploration. Boreholes are often not uniform (Fig. 11.1a) either along their axis or in cross section, tending to be slightly egg-shaped (Fig. 11.1b). Some formations, especially shales, absorb fresh water from the borehole, soften, and then slough off material to make enlarged portions called *caves*. Usually a sonde rests against the side of the borehole. Some logs employ an *eccentering arm* to press the sonde against the borehole wall and some employ a *centralizer* to keep it in the center of the borehole. Sondes have to be built to withstand the very high pressures (1,000 to 1,500 atm or 100 to 150 MPa) and temperatures (100 to 250°C) in a deep borehole.

Sonde depth is determined by an odometer counting the revolutions of a measuring wheel over which the cable passes. Depths are usually referred to the kelly bushing (KB) on the drilling rig floor. In addition, magnetic marks located every 100 ft (30 m) along the cable are sensed to check the odometer readings. The sonde is lowered to the bottom of the hole and then slowly raised until the sonde begins to move. The cable depth is then compared with the drill depth record; a cable stretch correction usually has to be made. Occasionally during logging the sonde may stick temporarily and then jerk free, producing a yo-yo motion. Usually several sensors are recorded on each log run and a  $\gamma$ -ray record is made on every logging run to correlate between recorded depths on different runs. Portions logged on previous runs are usually repeated on a subsequent run as a check. A *memorizer* in the recording cab corrects the depth differences between sensors located at different places on long sondes (which may be up to 30 m in length). Bottom-hole temperature is obtained by a maximum-reading thermometer attached to the sonde.

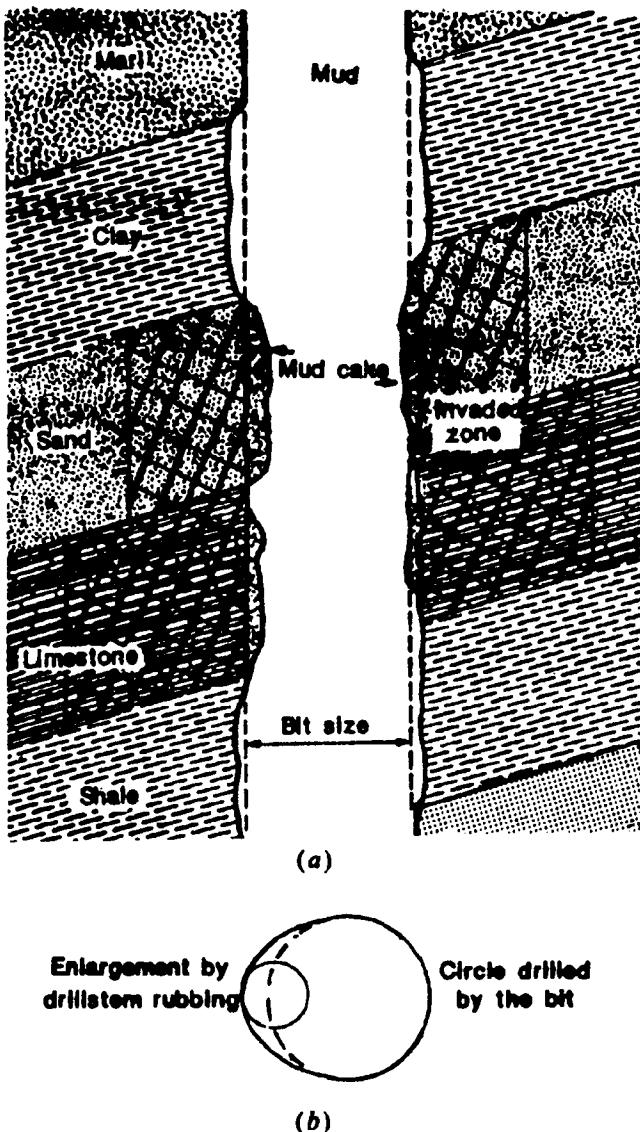


Figure 11.1. Borehole shape. (a) Conceptual vertical slice through a borehole showing caving and mud buildup on permeable formations. (From Tittman, 1986.) (b) Egg-shaped cross section of borehole showing most probable location of a sonde equipped with an "eccentering" arm.

#### 11.1.4. Rock Property Measurements

The objective of well logging is to measure *in situ* the properties of the undisturbed rocks and the fluids that they contain. However, the act of drilling a hole disturbs them. Appreciation of the invasion process is essential to interpreting well logs because the rock region that exerts the greatest effect on log readings is the portion nearest the logging sonde, the portion altered most by the drilling process.

The relative contribution of formations at various distances from the logging tools varies with different sensor configurations (Fig. 11.2). The effective *depth of penetration* (*investigation*), a qualitative term, is the distance from the borehole that contains the

material whose properties dominate the measurements (Roy and Dhar, 1971; Moran, 1972). *Deep penetration* implies that the dominant contribution is from formations that have not been disturbed by invasion. At the other extreme, *very shallow penetration* implies that the properties of the mud cake or of the borehole mud dominate the measurements, depending on whether the logging tool is pressed against the borehole wall or is centered in the borehole. *Intermediate penetration* implies domination by the area invaded by mud filtrate in porous formations. Electric log measurements using different electrode arrangements may give different results because the mud and filtrate are usually more resistive than the indigenous formation whose water is usually highly saline and conductive.

Well logging for petroleum usually has the primary objective of identifying potential reservoir rocks, determining their porosity and permeability, and determining the nature and proportions of the fluids present. *Porosity* is the fractional portion of rock volume occupied by pore space, often expressed as a percentage. Reservoir rocks usually have from 10 to 30% porosity although rocks of lesser porosity can also be hydrocarbon reservoirs. The product of porosity, area, and average thickness of a reservoir gives the volume of fluids that the reservoir contains. Porosity can be determined from resistivity, acoustic velocity (sonic), density, and neutron logs. Each may be subject to distortions and hence better determinations can be made from combinations of logs than from individual logs.

In most reservoirs hydrocarbons fill only part of the pore space, that fraction being the *hydrocarbon saturation*. Where water is the only other fluid present (the usual situation), the water saturation plus the hydrocarbon saturation equals 1. The water saturation is calculated from the Archie equations (11.1), (11.2), and (11.3) and porosity measurements, and it often provides the distinguishing trait of formations that are capable of commercial hydrocarbon production.

Besides porosity, an equally important property is the degree to which the pores are interconnected, that is, the *permeability*. Permeability is usually measured in darcys; a *darcy* is the permeability that will allow a flow of one milliliter per second of fluid of one centipoise viscosity through one square centimeter under a pressure gradient of one atmosphere per centimeter. Commercial reservoirs generally have permeabilities ranging from a darcy to a few millidarcys. Permeability is estimated from logs using empirical rules but only with order of magnitude accuracy. The SP curve is usually a reasonably good indicator of permeability.

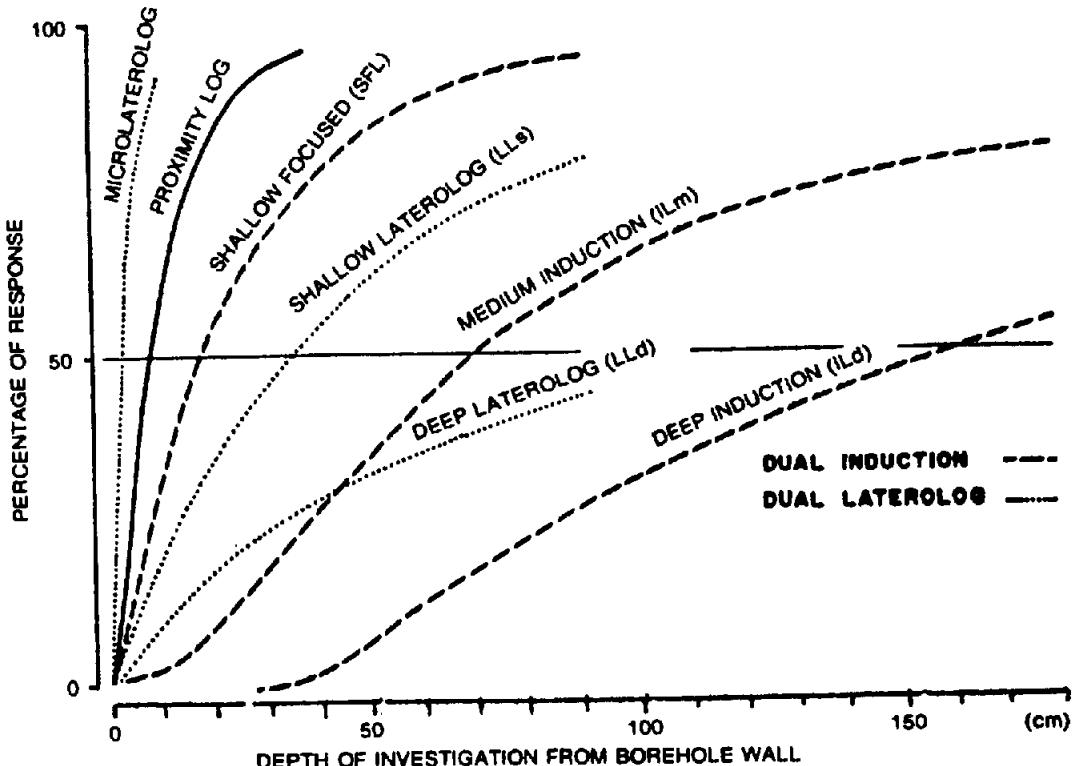


Figure 11.2. Percent of response attributable to rocks within different distances from the borehole for infinite homogeneous medium. (After Schlumberger, 1972).

Formation identification and correlation between wells is often as important as the determination of porosity and estimation of permeability. Particular formations may yield distinctive patterns making it possible to correlate not only major lithologic breaks but many points within formations themselves. Faults and unconformities often can be located fairly precisely by noting a missing section (or repeated section, in the case of reverse faults) in one well compared with others nearby. Stratigraphic details often can be worked out from log-shape patterns. As logs from more wells in an area become available, the amount of detail that can be extracted increases.

## 11.2. RESISTIVITY METHODS

### 11.2.1. Introduction to Resistivity Logging

The physical properties of rocks and minerals measured in electrical well logging are principally electrical resistivity and self-potential (SP). The induced-polarization effect has not yet developed as a routine logging technique in petroleum application (see however §11.6).

In most petroleum exploration logging, several logs are recorded on the same logging run (Fig. 11.3). Resistivity and SP logs are generally recorded as adjacent curves. Because most electrical measurements can be made only where the hole has not been cased, logs are commonly run over different parts of

the borehole at different times. Also, because the primary objective of logging usually is to evaluate the productive potential of reservoir sands, logging is often done soon after sands are drilled, before drilling deeper; otherwise the sands may change their log characteristics as a result of standing open to drilling fluid with the consequent invasion of mud filtrate.

Resistivities of various rocks and minerals are given in Tables 5.1 to 5.4 (§5.4.1). Sedimentary minerals normally encountered in oil wells are generally poor conductors, having resistivities in the range  $10^3$  to  $10^{10}$   $\Omega\text{m}$ . The minerals common in sedimentary rocks (silicates, oxides, and carbonates) are practically all nonconductors. However, most sedimentary rocks contain water in which various salts are dissolved; in solution these disassociate into cations ( $\text{Na}^+$ ,  $\text{Ca}^{++}$ ,  $\text{Mg}^{++}$ , and so on) and anions ( $\text{Cl}^-$ ,  $\text{SO}_4^{--}$ , and so on). The movement of ions in the interstitial fluid provides the formation's conductivity.

Metamorphic and igneous rocks may contain minerals (usually disseminated), such as pyrite, chalcopyrite, graphite, magnetite, galena, and so on, which contribute to their conductivity. As in sediments, however, interstitial water is often the controlling factor on resistivity.

Three equations used in petroleum work relate the resistivities of rocks and interstitial fluids, porosity, and the fraction of water filling the pore spaces. These are modifications of the empirical formula of

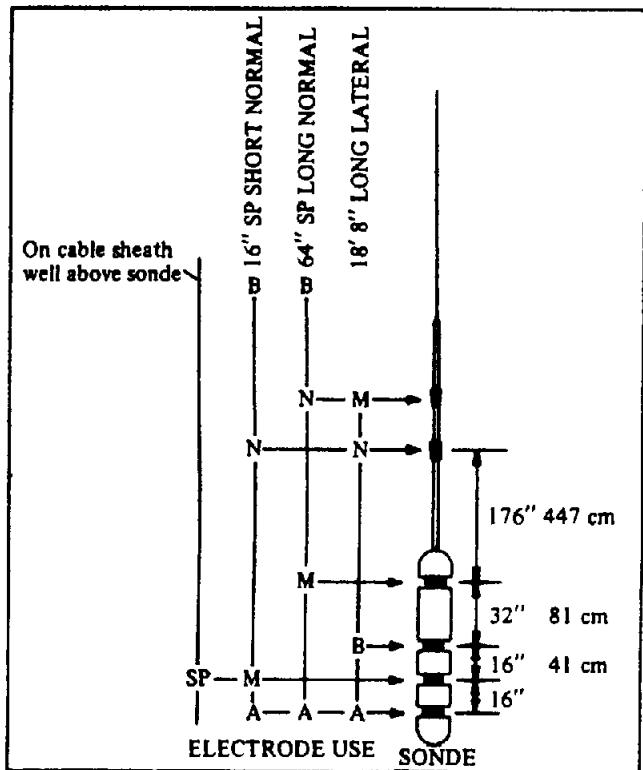


Figure 11.3. Showing how electrodes on a sonde can be used to record different electrical logs. A and B are current electrodes, M and N are potential electrodes. (After Labo, 1987.)

Archie (1942) [see Eq. (5.7)]. The first expresses the bulk water-wet resistivity of a rock sample,  $\rho_0$ , and the resistivity of the water contained in its pores,  $\rho_w$ , in terms of a *formation resistivity factor*  $F$ :

$$F = \rho_0 / \rho_w \quad (11.1)$$

(In formation evaluation the symbol  $R$  is usually used for resistivity; however, we shall use  $\rho$  to be consistent with Chapters 5 to 9.) Values of  $\rho_0$  can be determined from resistivity logs, those of  $\rho_w$  from prior experience in the area, formation water samples, SP logs, or resistivity log crossplots (Schlumberger, 1987, pp. 28–31).

Archie showed that the formation factor is a function of the porosity and, to a lesser degree, of the permeability of the sample. His second relation is

$$F = 1/\phi^m \quad (11.2a)$$

where  $\phi$  is the porosity of the material and  $m$  is a *cementation factor* whose value lies between 1.3 and 2.5. An alternative form of this expression, called the *Humble formula*, applicable to many granular rocks, is

$$F = 0.62 / \phi^{2.15} \quad (11.2b)$$

Another form, the *Shell formula*, is used for low-porosity carbonates:

$$F = 1 / \phi^{(1.87 + 0.019/\phi)} \quad (11.2c)$$

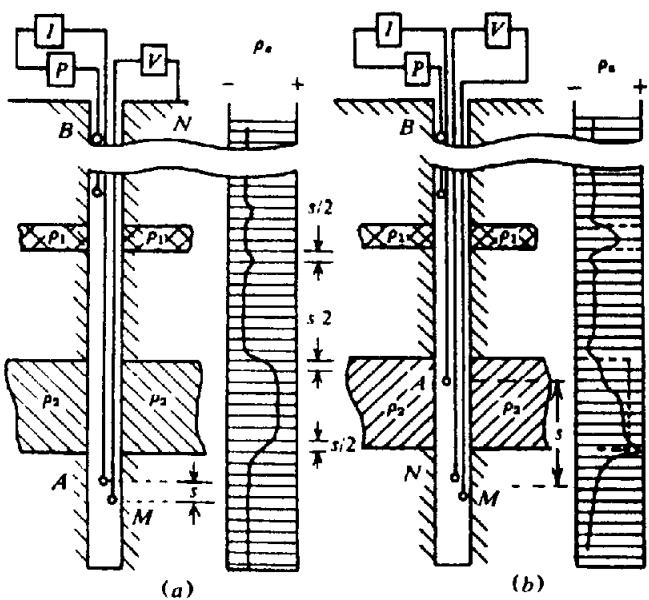


Figure 11.4. Electrode configurations and log curves;  $\rho_1$ ,  $\rho_2$  indicate resistive beds. P is the power source, I is the ammeter, V is the voltmeter, s is the spacing. (a) Two-electrode (normal) arrangement. (b) Three-electrode (lateral) arrangement; the upper B electrode is on the cable sheath well above the sonde.

If the rock pores are not completely filled with water but contain gas and/or oil also, the effective resistivity is larger than  $\rho_0$ . The third empirical equation of Archie accounts for partial *water saturation* of the rock. If  $S_w$  is the fraction of the pore volume filled with water,

$$S_w = (\rho_0 / \rho_r)^{1/n} \quad (11.3)$$

where  $\rho_r$  is the true resistivity of the sample, derived by applying corrections for logging tool dimensions and configuration, borehole diameter, mud resistivity, and so on, to the measured (or apparent) resistivity  $\rho_a$ , and  $n$  is the *saturation exponent* that lies between 1.5 and 3.0; it is usually assumed to be 2 where there is no evidence to the contrary. Determination of  $S_w$  under a variety of circumstances is discussed by Schlumberger (1987, pp. 95–125).

### 11.2.2. Normal Resistivity Logging

The basic methods of resistivity logging are similar to those used in surface resistivity prospecting. A low-frequency alternating current is applied between current electrodes and the potential is measured between two or more potential electrodes. The record is then a plot of potential variation (or its equivalent, apparent resistivity) versus depth.

Figure 11.4a shows a *normal* electrode configuration. One current electrode (A) and one potential electrode (M) on the logging sonde are closely spaced

downhole [16 in. (0.4 m) apart for the *short normal*, 64 in. (1.6 m) for the *long normal*] and the other two electrodes (*B*, *N*) are either fixed near the top of the hole or a long distance away in the borehole. From Equation (8.26) and Figure 8.3, we get for the apparent resistivity  $\rho_a$  in homogeneous ground,

$$\rho_a = (4\pi\Delta V/I)(1/AM - 1/BM - 1/AN + 1/BN)^{-1} \quad (11.4)$$

[The factor is  $4\pi$  here rather than  $2\pi$  as in Equation (8.26) because this equation holds in the interior of the medium rather than at the surface of a semiinfinite medium.] Because the distance *AM* is much smaller than any of the other three dimensions, this becomes

$$\rho_a \approx (4\pi\Delta V/I)(AM) \quad (11.5)$$

The measured apparent resistivity depends mainly on the resistivities of the beds in the vicinity of *A* and *M*. Measurements will also be affected by the mud in the borehole and by the penetration of the drilling fluid into formations.

The resistivity log of Figure 11.4a is symmetrical with respect to beds where the resistivity differs from that above and below. The interfaces are marked sharply (but not necessarily at their true locations), particularly in the short-normal curve. High resistivity beds appear thinner than their actual thickness whereas conductive beds appear thicker. The effective penetration into the formations is about twice the electrode spacing and varies inversely as the hole diameter.

The definition and sharpness of normal logs decreases with an increase in the hole diameter and with a decrease in mud resistivity. The effects of adjacent beds and the invasion of porous zones by drilling fluid are also significant. These effects used to be reduced by the use of correction charts called *departure curves*, but today corrections are generally made by computer algorithms.

The short-normal spread is sometimes suitable for measuring the resistivity of porous zones flushed by mud filtrate (flushed zone) and hence for determining formation porosity. It is most useful in geological correlation between wells, because the interfaces between beds are usually well defined. The long normal measures an intermediate resistivity, which, in theory at least, permits calculation of both the invaded-zone resistivity,  $\rho_i$ , and an estimate of the true formation resistivity,  $\rho_f$ . Old electrical logs provided poor measurements of  $\rho_f$  because of poor vertical resolution and hole effects.

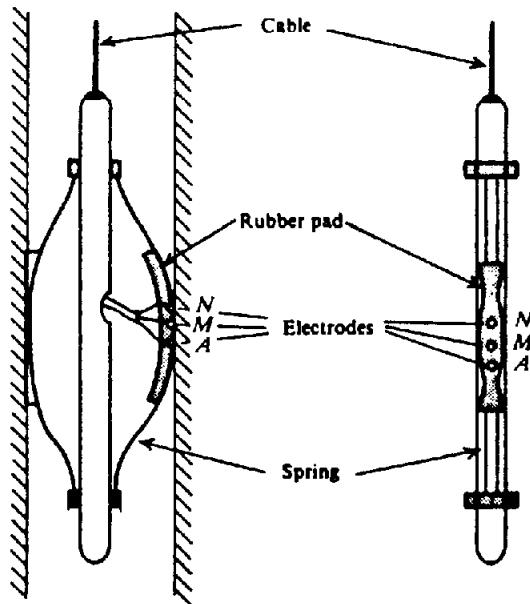


Figure 11.5. Microlog wall-resistivity arrangement.

### 11.2.3. Lateral Arrangement

A three-electrode sonde yields a *lateral curve*, illustrated in Figure 11.4b. The downhole potential electrodes are usually separated by 32 in. (81 cm) with their center 18 ft 8 in. (5.7 m) from the near current electrode; this latter distance is called the *spacing*. They measure a resistivity of the form

$$\rho_a = (4\pi\Delta V/I)(AM)(AN)/(MN) \quad (11.6)$$

where  $(AM)$ ,  $(AN)$ , and  $(MN)$  are distances between the respective electrodes.

The most striking feature of lateral curves is their asymmetry; in Figure 11.4b this is particularly apparent at the upper and lower boundaries of the thick bed. If the current and potential electrodes are interchanged, the asymmetry is reversed. Lateral curves are distorted by borehole effects similar to those described in the preceding section, as well as by the electrode geometry. The depth of investigation is large and is often taken as approximately equal to the spacing. For homogeneous beds of thickness greater than about 12 m, the lateral curve measures formation resistivity  $\rho_f$  unaffected by the invaded zone. A combination of lateral and normal logs permits approximate determination of  $\rho_i$  and  $\rho_f$ , as well as the extent of fluid invasion. Despite its deep investigation, the long lateral (now obsolete) was of little use except in thick beds.

### 11.2.4. Microlog

The *microlog* (wall resistivity log) is used as a detector of mud cake and for measuring mud resistivity. Mud cake is a qualitative indication that formations

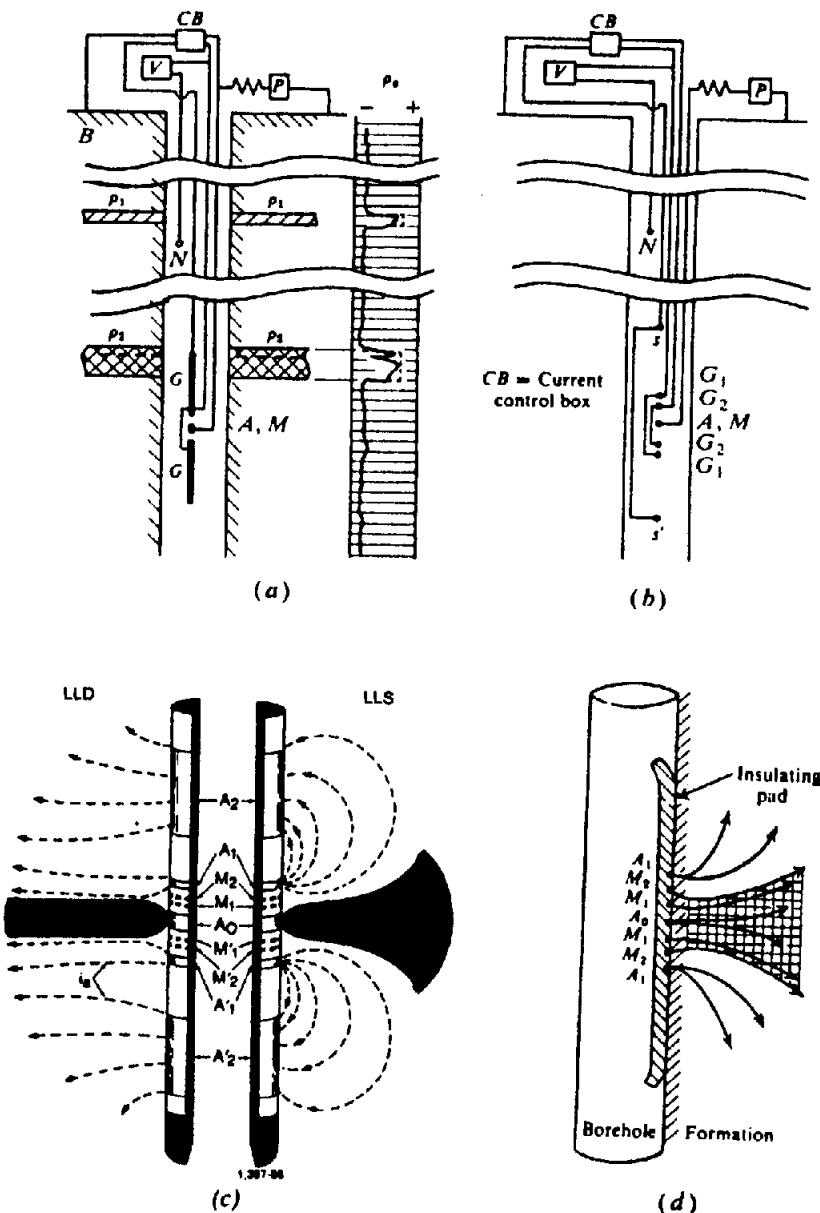


Figure 11.6. Focused current logs. (Courtesy Schlumberger.) (a) Guard log (Laterolog-3). (b) Laterolog-7. (c) Dual laterolog showing how deep and shallow penetration modes of operation can be achieved by reversing the polarity of the  $A_2$  electrodes. (d) Microlaterolog with schematic current flow lines. The shading in (c) and cross-hatching in (d) indicate the current concentration.

are permeable because mud cake forms only on formations that are invaded. However, it may not form in a carbonate section with vugular or fracture porosity. The microlog is illustrated in Figure 11.5. The button-size electrodes are imbedded in an insulating pad that is pressed against the borehole wall by means of an expansion device which is also used to measure hole diameter.

Because the electrodes are against the wall, the effects of hole diameter, mud resistivity, and adjacent beds are negligible. Because the electrodes are very closely spaced (1.5 and 2 in., that is, 38 and 51 mm, apart), very thin beds can be sharply defined, but the depth of penetration is small, less than 10 cm. Differences between resistivities measured with

different electrodes is called *separation*, which depends on the thickness of the mud cake. The microlog also measures mud resistivity when the electrode is not pressed against the borehole wall.

### 11.2.5. Focused-Current Logs

The normal and lateral resistivity devices are too large to measure thin beds, whereas the microlog is influenced by mud cake, and all are ineffective with saline muds. The possibility of using a sharply focused current was realized in the *guard log* or *Laterolog-3*, illustrated in Figure 11.6a (Doll, 1951; Moran and Chemali, 1979; Jackson, 1981).

To measure resistivity,  $\rho_r$ , with a vertical resolution of a few centimeters and in the vicinity of thin beds and conductive muds, the current is focused into a horizontal disk that penetrates the formation laterally instead of flowing up the walls. The focusing is achieved by maintaining electrodes  $G$  at the same potential as the  $A_1, M$  electrode.

Depth of penetration, taken as the distance at which the current begins to defocus appreciably, is approximately three times the length of the guards. Thus a long guard produces great penetration, but the lower guard prevents logging to the bottom of the hole.

The system known as *Laterolog-7* (Fig. 11.6b) achieves a focused current sheet about 80 cm thick by maintaining the  $G$  electrodes at the same potential. Depth of penetration is about 3 m if the spacing between  $A_1, M$  and the nearest guard point is 1.2 m. This arrangement gives essentially the same results as the guard log except that measurements can be made closer to the bottom of the hole.

Both shallow (LLs) and deep (LLd) measurements are made by a *dual laterolog* sonde (Fig. 11.6c); the figure is split to illustrate the two modes of operation. By reversing the polarity of the  $A_2$  electrodes, the focused current bends back after a short distance, producing a focused beam with shallow penetration.

The focusing principle is used with very small electrode spacing in the *microlaterolog*, or *trumpet log*, illustrated in Figure 11.6d (Doll, 1953). The electrodes are mounted like the microlog on a rubber pad that is pressed against the borehole wall. The electrodes are concentric rings 9/16 in. (1.4 cm) apart. Electrodes  $M_1$  and  $M_2$  are maintained at the same potential so that an essentially constant beam of current is produced. The depth of penetration is about 8 cm. This device is used to measure the resistivity of the flushed zone; it also calipers the hole diameter.

### 11.2.6. Induction Log

The induction log involves the same principle as FDEM prospecting. It is effective with high-resistivity oil-based muds, in an air-filled borehole, and in fresh muds. A schematic diagram is shown in Figure 11.7. A simplified explanation is that the EM field produced by a transmitter coil (with time factor  $e^{j\omega t}$ ) induces circular eddy currents in conductive formations; their time dependence is the time derivative of  $e^{j\omega t}$ , that is,  $j\omega e^{j\omega t}$ . These eddy currents in turn induce secondary voltages in the receiver coil proportional to  $-\sigma\omega^2 e^{j\omega t}$  where  $\sigma$  is the conductivity. The transmitter coil also induces directly into the receiver coil a voltage whose time dependence is  $90^\circ$

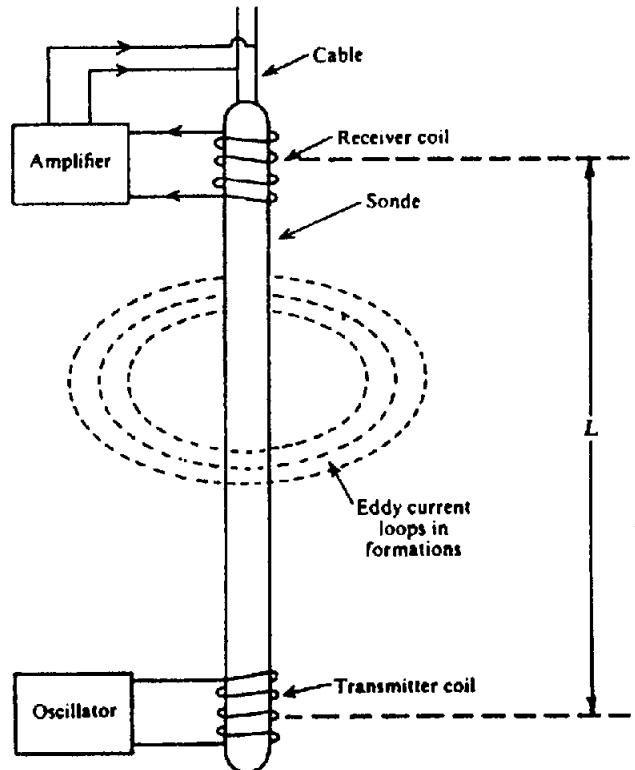


Figure 11.7. Induction log schematic. The tool itself is made of nonconducting material.

out-of-phase (in quadrature) with the secondary current. Most of this mutual-inductance voltage can be compensated (bucked out), or a phase-sensitive discriminator can be used, so that the secondary voltage can be detected by itself.

The induced secondary voltage is the sum of all the eddy-current loops  $s(r, z)$  weighted by geometrical factors to allow for their radial distance from the borehole  $g(r)$  and distance above or below the sonde  $g(z)$ ; this can be expressed approximately as

$$V \approx K \int \int g(r) g(z) dr dz \quad (11.7)$$

Graphs of  $g(r)$  and  $g(z)$  are shown in Figure 11.8; the radial dependence is greatest at a radius of about  $L/2$  where  $L$  is the distance between transmitter and receiver coils, and  $g(z)$  is nearly constant over the range  $|z/L| < 0.5$  but falls off rapidly beyond them. However, the conductivity of formations has such a broad range that a highly conductive bed well beyond the tool may still have a significant effect. Less conductive nearby beds have little effect.

The current in an additional coil midway between transmitter and receiver coils can be adjusted so that the secondary voltage in the receiver coil cancels out some of the contribution from the very shallow zone, producing the effect shown dashed in Figure 11.8a. Auxiliary coils are also used to focus the effective

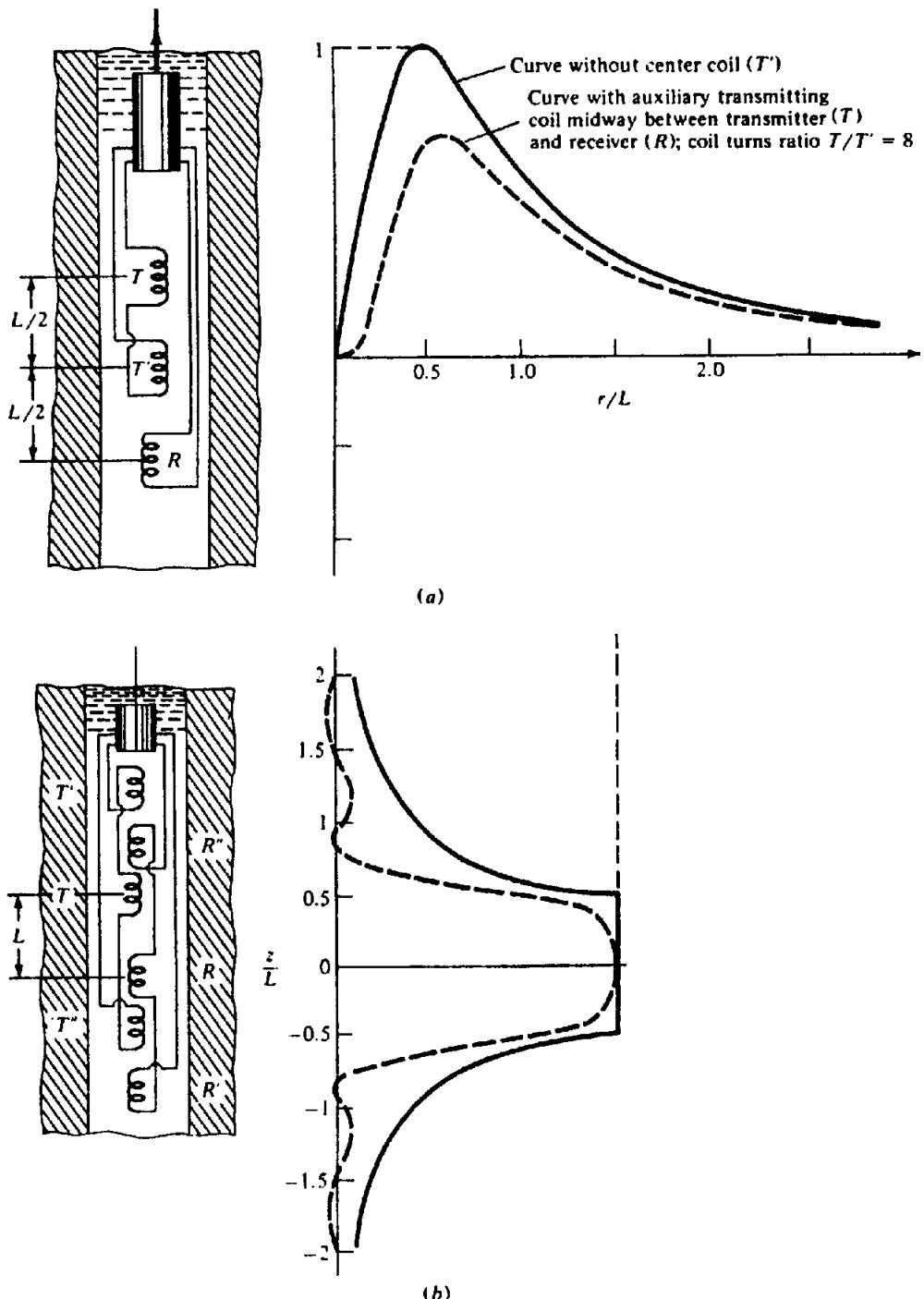


Figure 11.8. Geometric factors for induction sondes without (solid curves) and with (dashed curves) auxiliary coils ( $T'$ ,  $T''$ ,  $R'$ ,  $R''$ ). (After Doll, 1949.) (a) Radial factor  $g(r)$ . (b) Depth factor  $g(z)$ .

depth. The induction-log signal is proportional to the conductivity of the formations.

The *dual induction log* records separate responses that peak at different distances into the formation, a deep (40 in.) induction log (ILD) and an intermediate (27 in.) induction log (ILM). The induction logging tool usually also includes a shallow focused log (16 in.) so that it measures the resistivity at three distances. The three measurements with different

depths of penetration can be interpreted to indicate the invasion of filtrate, implying permeability.

Ground currents generated by atmospheric effects cause no problem because of the high frequency (20 kHz) of the transmitter. Although interfaces of low-resistivity beds are sharply marked, the log is automatically corrected for adjacent bed effects and it provides an accurate measure of the conductivity for formations more than 10 cm thick. Anomalous read-

ings may result from a low-resistivity ring called an *annulus* which is sometimes produced in oil-bearing formations by the-invasion process; because of their greater mobility, hydrocarbons are displaced farther beyond the invaded zone than formation water, resulting in a high proportion of conductive formation water in a ring around the borehole. Such an annulus may move with time.

A *phasor induction log* separately measures the quadrature and in-phase signals. The additional information allows a better correction for skin effects and improves the thin-bed response. The sonde can be operated at 10, 20, and 40 kHz, which give different effective penetrations. Measurements at 10 kHz also have less skin effect [Eq. (6.17)] and those at 40 kHz give more reliable readings in high-resistivity formations. (Correction is automatically made for the skin effect with standard induction logs operating at 20 kHz.)

### 11.2.7. Resistivity Logging in Mineral Search

Resistivity logging has not been used extensively in mineral areas except in connection with IP logging. Because the structure in mineral areas is usually complex, the interpretation may be only qualitative. Electric logging should locate high-conductivity zones and help in identifying and correlating them. The resistivity tools, employed mainly in experimental work, are single-point resistance, normal, and pole-dipole (similar to the lateral) arrays. These have been used for estimating borehole fluid and resistivities of the host rock (Glenn and Nelson, 1979). Glenn and Nelson also used a combination of resistivity and IP logs to discriminate between disseminated and vein-type sulfide mineralization and to estimate mineral content.

Directional resistivity and *mise-à-la-masse* (sometimes called *applied potential*) configurations are illustrated in Figure 11.9 (Roy, 1984). The first is designed to locate the azimuth of conductors with respect to the borehole, whereas the second is capable of tracing interconnecting anomalies (Mansinha and Mwenifumbo, 1983) and outlining their geometry (§8.5.4d). It is necessary to calculate the geometric factor for each location of the moving electrodes.

The expression for  $\rho_a$  is given in terms of  $\Delta V/I$  and a geometric factor whose general form for down-hole electrodes is

$$k = 4\pi / [\{1/r_1 + 1/r'_1\} - \{1/r_2 + 1/r'_2\} - \{1/r_3 + 1/r'_3\} + \{1/r_4 + 1/r'_4\}] \quad (11.8)$$

where  $r_1 = AM$ ,  $r_2 = BM$ ,  $r_3 = AN$ ,  $r_4 = BN$ , and

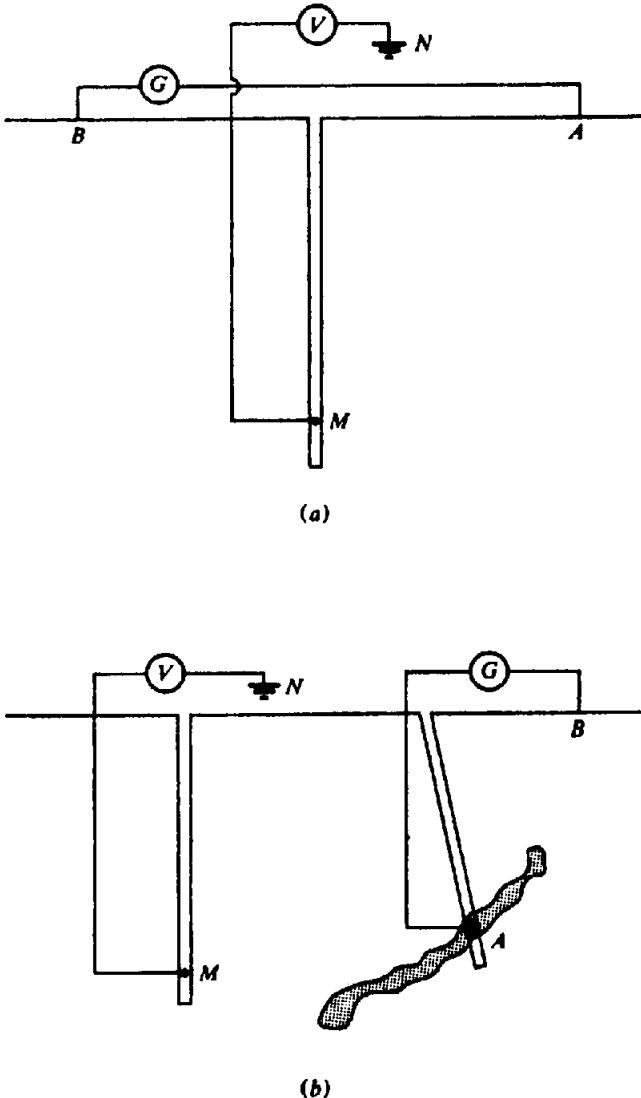


Figure 11.9. Resistivity log configurations for orebody definition. (After Roy, 1984.) (a) Directional resistivity method; the azimuthal direction of AB is changed 90° between measurements. (b) *Mise-à-la-masse* method with the A electrode embedded in conductive orebody and potential measured in nearby boreholes.

the  $r'$  values are the corresponding distances to the images of  $A$ ,  $B$ ,  $M$ ,  $N$  reflected in the air-earth interface. That is, an electrode located at  $+z$  below ground produces an image at  $-z$  above ground (see also §8.3.3 and §8.3.4). For electrodes on the surface the  $r'$  terms are zero and  $k$  is merely twice the  $p$  factor in Equation (8.26). For downhole arrays the  $k$  factor is approximately constant.

## 11.3. SELF-POTENTIAL (SP) LOGGING

### 11.3.1. Sources of SP

The principal sources of SP (shale potential, liquid-junction potential, streaming potential, and mineralization potential) have been described in Sections 5.2.1 and 6.1.1.

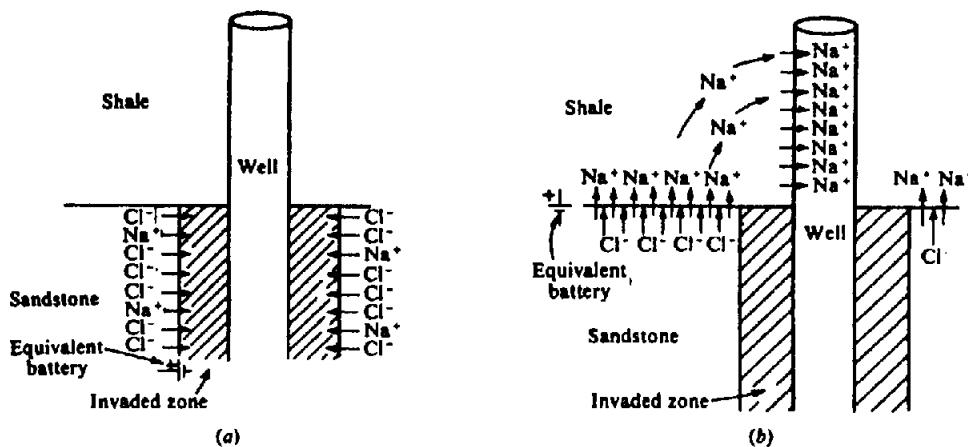


Figure 11.10. The self-potential effect in a sand-shale section. (Courtesy Schlumberger, Ltd.) (a) Liquid-junction (diffusion) potential. (b) Shale (Nernst) potential.

In oil-well logging the potentials involve principally the boundaries of the shale units, especially shale-sand interfaces, and the principal effect is the electrochemical (shale plus liquid-junction) potential, which is normally less than 75 mV. Shales are permeable to Na<sup>+</sup> cations but not to Cl<sup>-</sup> anions; as a result a *shale potential* is set up when Na<sup>+</sup> ions pass from saline formation water in sands into adjacent shale beds, then into the fresh water of the mud. In addition, a *liquid-junction potential* develops at the interface between the fresh-mud filtrate in the invaded zone and saline formation water beyond the invaded zone; as a result of the greater mobility of Cl<sup>-</sup> anions over Na<sup>+</sup> cations, there is a net flow of Cl<sup>-</sup> into the invaded zone. These effects are illustrated in Figure 11.10.

Equation (5.4) can be modified by replacing the ratio of concentrations with the resistivity ratio to give

$$E_c = -70.7 \{ (T + 273)/298 \} \ln(\rho_{mf}/\rho_w) \quad (11.9)$$

where  $E_c$  is in millivolts,  $T$  is the Celsius temperature,  $\rho_{mf}$  is the mud-filtrate resistivity, and  $\rho_w$  is the resistivity of the original formation water. The shale potential contributes 59.1 and the liquid-junction potential 11.6 to the factor 70.7 in Equation (11.9).

A *streaming potential* arises because of differences in pressure between fluids in the well and those in the surrounding formations. Equation (5.1) can be expressed in the form

$$E_k = 0.039 \Delta P (\rho_{mc} t_{mc})^{1/2} \quad (11.10)$$

where  $E_k$  is in millivolts,  $\rho_{mc}$  and  $t_{mc}$  are the resistivity and thickness of the mud-cake, respectively,  $f$  is a filter-loss factor, and  $\Delta P$  is the pressure difference between the borehole mud and the adjacent formation fluid.

The streaming potential usually is much smaller than the electrochemical potential, hence  $E_c$  in Equation (11.9) represents approximately the total SP anomaly in oil-well logging (Wyllie, 1949).

In mineral-zone logging a mineralization potential is usually dominant. In zones involving sulfides, graphite, and/or magnetite, the mineralization potential between the minerals and surrounding rock may be as much as 700 to 800 mV. Because this is generally much larger than the shale, liquid-junction, and streaming potentials, they can be ignored.

The principal uses of SP logs are in (1) identifying permeable zones, (2) correlation, (3) providing a measure of formation water resistivity  $\rho_w$ , and (4) providing a measure of the amount of dispersed shale in the formation pore spaces.

### 11.3.2. Instrumentation

Equipment for SP logging is fundamentally very simple. A recording potentiometer or dc voltmeter with high input impedance is connected across two nonpolarizable electrodes, short lead cylinders. The potential recorded is generally between a moving downhole electrode and a fixed electrode at the surface or in the borehole near the surface. In mineral logging the potential gradient between two downhole electrodes at a fixed small spacing is occasionally measured.

Errors may be caused by armor leakage, bimetalism, current leakage causing electrode polarization, or faulty design, especially when SP is run with a single-point resistance log (Keys and MacCarey, 1971; Roy, 1984). The first arises from cables with an external metal sheath in contact with the borehole fluid, which produces spurious potentials varying with cable depth. The second is the result of a voltaic cell between the probe casing (usually stainless steel) and the insulated lead electrode. Current leakage

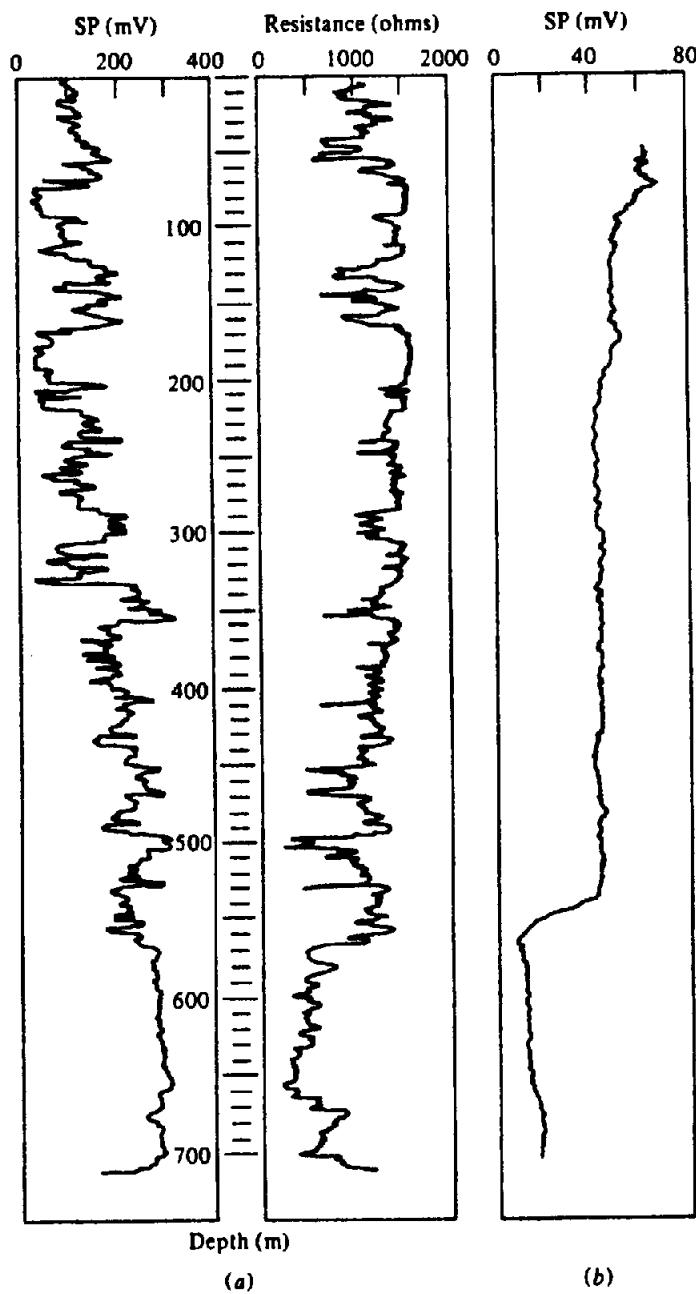


*Figure 11.11. SP log comparison. (Data courtesy Atomic Energy Canada, Ltd., Chalk River, Ont.) (a) Result of a carefully designed survey. (b) Commercial log in the same borehole.*

caused by large telluric transients or current injection through the SP electrode in single-point resistance logging may change the electrode polarization. Faulty instrument design usually means that the input impedance is too low. Errors tend to be more severe in mineral logging where resistivity is higher than in sediments. Errors can be reduced by using a cable with isolated external jacket, by isolating the instrument ground from the reference electrode, by insulating the SP circuit from the single-point resistance circuit, and by maintaining a high input resistance. Figure 11.11 compares an SP log produced in a carefully designed survey with a commercial log. The former shows much larger differences and more

complexity, the latter is nearly a greatly smoothed mirror image of the SP log to the left with a level shift around 540 m.

### 11.3.3. Uses of SP Curves in Oil-Well Logging

The main uses of SP logging are locating boundaries between shales and porous beds such as sandstones, determining the cleanliness of sands, correlating between wells, and determining formation water resistivity. The shape of the SP curve is often characteristic of particular depositional conditions and

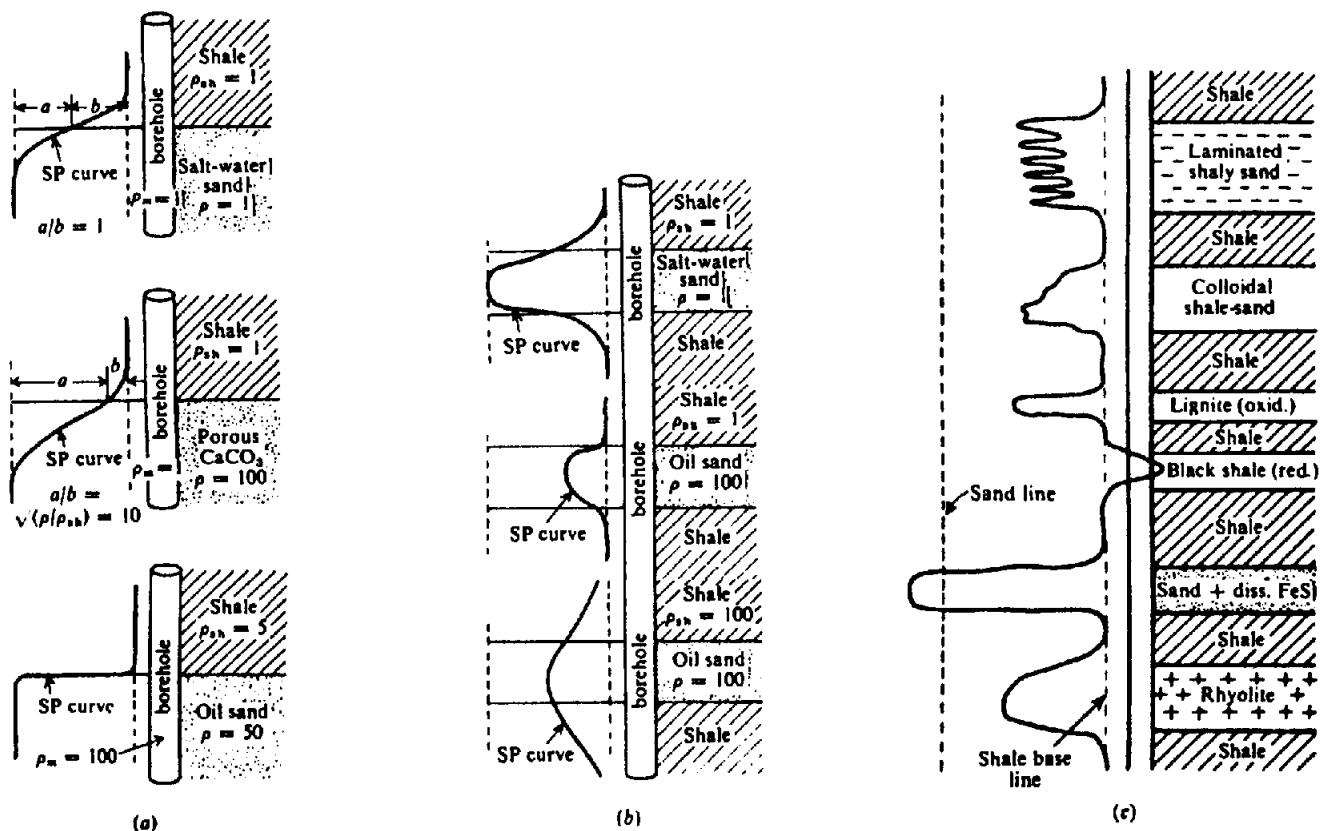


Figure 11.12. Characteristic SP curves for a sand-shale section. (After Pirson, 1970.)  
(a) Curves for thick beds. (b) Curves for thin beds. (c) Characteristic curves for various formations; the distance between the dashed lines is the static SP.

well-to-well correlation can be used to indicate thinning, pinching-out, and dip of formations.

Equation (11.9) is used to determine  $\rho_w$ ,  $\rho_{mf}$  being found by measurements on samples of mud. Having  $\rho_w$ , we can determine  $F$  in Equation (11.1) because we can measure  $\rho_0$  from a resistivity log.  $F$  is an important quantity in calculating water and hydrocarbon saturations.

If a thick shale is adjacent to a thick, clean, permeable sand, the maximum potential difference across the sand-shale boundary develops between two points in the well located some distance from the actual interface. The SP values at these respective points indicate the *shale-base-line value* and the *sand-line value*. The difference is called the *static SP* (SSP). The static SP depends on the difference in salinity between the mud and the formation water. If the formation water should change salinity, as might be the case between formations above and below an unconformity, the shale base line will shift. If the formation water should be fresher than the mud, the SP phenomena will be inverted and produce a *reverse SP*, sands being positive with respect to the shale base line rather than negative. When a sand is not clean but contains appreciable disseminated clay or shale, the full static SP may not develop and the SP value is called the *pseudostatic SP* (PSP).

Typical SP curves for thick beds are shown in Figure 11.12a. The interface between shales and porous beds can be located by the inflection point on the SP curve. In thin beds, as illustrated in Figure 11.12b, the maximum negative SP may be considerably less than the ideal static value.

Figure 11.12c shows an SP log through several different formations. Note the effect of the thin bedding in the laminated shale-sand, the asymmetric curves for colloidal shale-sand and rhyolite, the positive anomaly for a reducing bed, and the large anomaly associated with disseminated pyrite (FeS).

Although borehole and formation factors influence the SP curve, as with resistivity logs, most of these can be corrected. The effects of hole diameter, adjacent beds, and bed thickness can be eliminated by corrections from standard charts. The density and resistivity of the mud affect the curve greatly. Spurious effects due to streaming potentials depend on the mud density and can be removed by use of a correction chart based on Equation (11.10). The ratio of mud resistivity to formation-water resistivity,  $\rho_{mf}/\rho_w$ , is the main factor controlling the curve shape. The temperature is corrected for in Equation (11.9).

The effect of penetration of mud filtrate into porous zones is complicated. Generally the SP deflection decreases with depth of invasion, but occa-

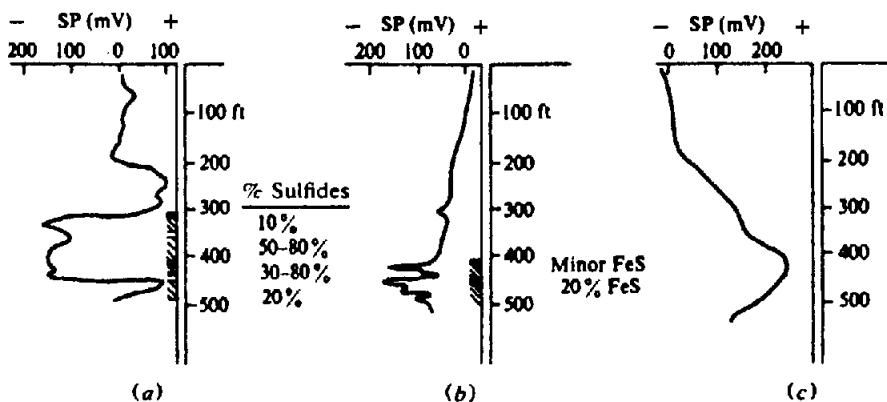


Figure 11.13. Characteristic SP curves in mineral zones. (a), (b) Logs through sulfide zones. (c) Log near a massive pyrite zone not intersected in the borehole.

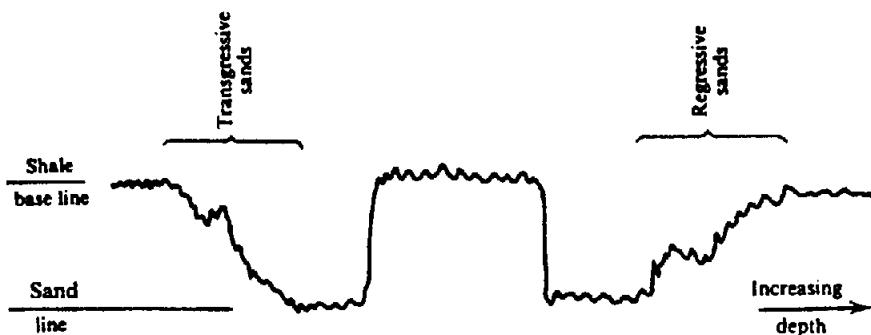


Figure 11.14. Characteristic SP curves for transgressive and regressive sands.

sionally the reverse is true. The potential may change with time as a result of invasion of zones containing water; the fact that the curve is not reproducible on successive logging runs may be diagnostic of this situation.

Polarization of electrodes, as in surface SP surveys (§6.1.2), affects SP measurement but usually the electrodes can be restored to equilibrium by leaving them in the mud for a time. Telluric currents, proximity to power lines, local electrical operations, large-scale electrolytic corrosion in the vicinity, and cathodic-protection devices affect SP readings.

#### 11.3.4. Uses of SP Curves in Mineral Logging

Potentials may be considerably larger in the presence of sulfides (Becker and Telford, 1965) and graphite than for sedimentary beds; consequently borehole effects are insignificant as long as the hole is filled with water. Three examples of SP logs run in 2 in. diamond-drill holes are shown in Figure 11.13. From the first two curves there appears to be no correlation between the deflection and the mineral content of the anomalous zones. The largest negative potentials occur at the interface between barren rock and disseminated mineralization, but this is not too significant because "massive sulfides" are usually inho-

mogeneous, being composed of many thin sections of high concentration interspersed with disseminated or barren zones.

Two other effects in these logs are worth noting. In the second curve there is a base-line drift with depth, which is not due to temperature. In the third example the broad positive anomaly is caused by a massive pyrite zone near the hole but not intersected by it. The current flow in the barren host rock is from depth to surface.

By having both electrodes downhole at small fixed spacing (15 cm), one can measure the potential gradient. The resultant curve shows sharp deflections at the edges of mineral zones. Except for this feature, the regular electrode arrangement provides more information.

#### 11.3.5. Geological Interpretation of SP

In addition to its use in identifying shales (and especially, distinguishing shales from sands in a clastic sequence) and for correlating corresponding points from well to well, other stratigraphic interpretation can sometimes be inferred from the SP curve. In a somewhat simplistic way, the SP value is read as the degree of shaliness (or the relative abundance of clay minerals) and as the inverse of the "energy" in the original depositional environment. For example,

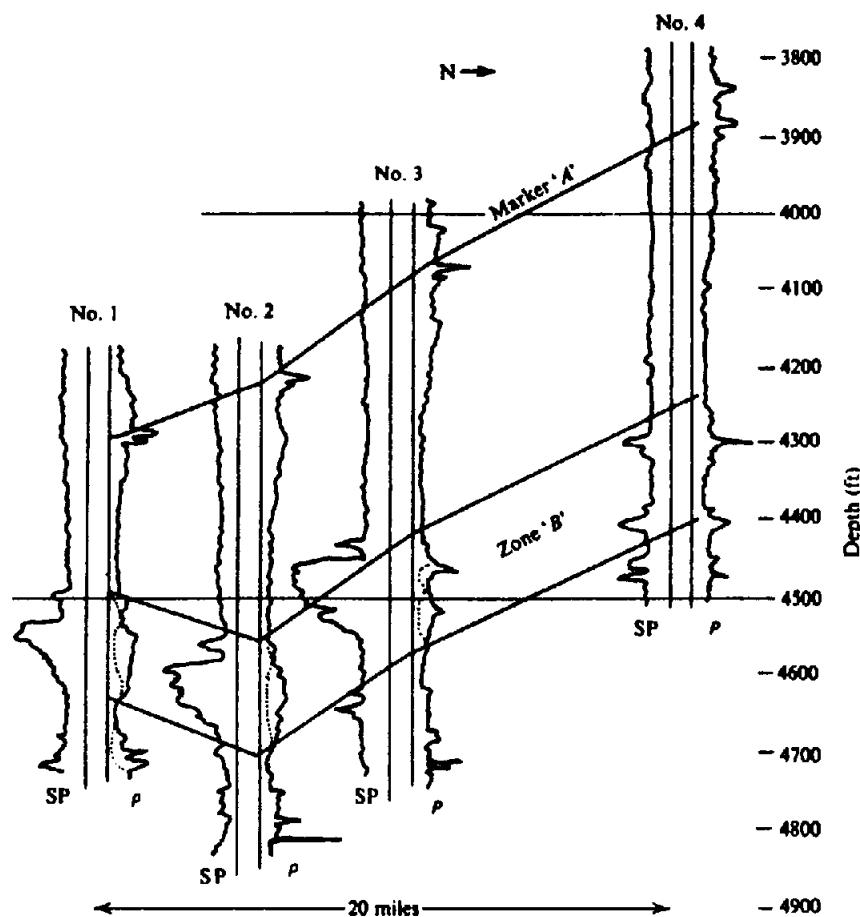


**Figure 11.15.** Well-log correlation. The convention for plotting well logs is to show an SP or  $\gamma$ -ray log to the left of the borehole and a resistivity log to the right. (After Pirson, 1970.)

proximity to a shoreline where there is wave action represents "high energy," with the consequent removal of clay minerals. Hence an SP curve that gradually increases in shaliness as we approach the surface indicates a receding shoreline and hence a transgressive sea. Conversely, increase in shaliness with depth is interpreted as a regressive sea. This concept is used to develop "theoretical" SP curve shapes such as in Figure 11.14. This concept can be expanded to many other types of sedimentation patterns (see Fig. 11.18). Correct recognition of such patterns, however, is often not very clear in practice.

Figure 11.15 shows short portions of SP and resistivity logs in four wells located approximately in a N-S line. The correlation of corresponding points on these curves is clear despite minor differences. The resistivity curve in the vicinity of the point *A* is characteristic of a marker bed that can be correlated over a fairly wide region. Obviously the formations dip south about 400 ft in 20 miles; this is a gentle slope of  $\frac{1}{4}^\circ$ . The SP curve deflection to the left in region *B* indicates sand in a predominantly shale environment. The shortened distance between marker

*A* and the top of this sand in well no. 1 indicates missing section – a normal fault with about 150 ft of throw. The lower portion of sand *B* indicates a regressive pattern as far as well no. 3. Sand *B* is not seen in well no. 4; correlations of points below the sand compared with those above indicate that the sand has not merely been faulted out but rather that shale was being deposited at the location of well no. 4 while sand was being deposited in the other three wells. Hence a sand-shale facies boundary must lie between wells no. 3 and no. 4. Such a pinchout, of course, represents a potential oil field.

#### 11.4. THE DIPMETER

In some cases formation dip can be estimated by correlation between holes where no structure intervenes, but often the determination is difficult or impossible. Early dipmeters employed EM response and later SP.

The modern dipmeter (Fig. 11.16a) employs four microresistivity pads in the same plane, pressed against the borehole wall at  $90^\circ$  intervals. The upper

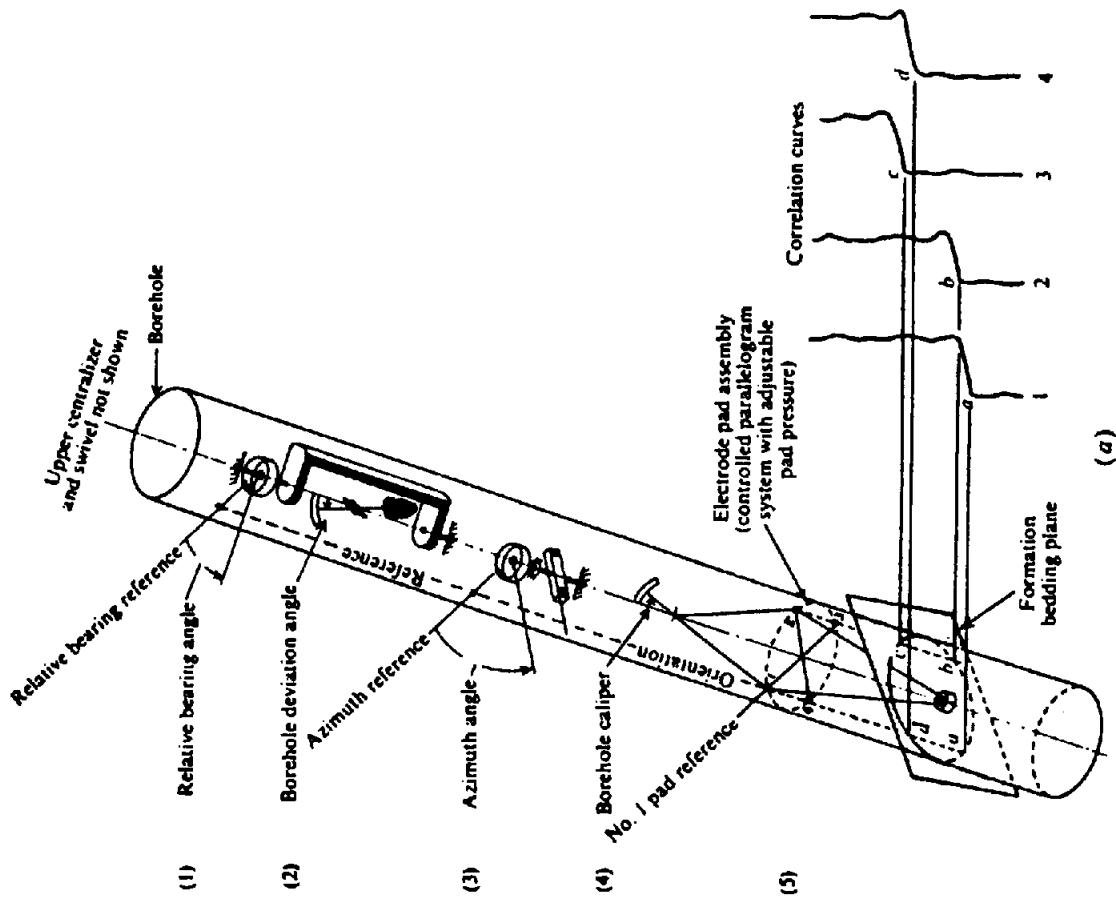


Figure 11.16. The dipmeter. (a) Schematic of diplog tool. (Courtesy Dresser Industries.) (b) Portion of a four-arm processed dipmeter log showing deviation of the hole, caliper log, smoothed resistivity, tadpole plot of dips, rosettes (each showing directions of all dips within a 10 ft. interval), and output of the four microresistivity pads with computer-drawn correlations. (Courtesy Schlumberger Ltd.)

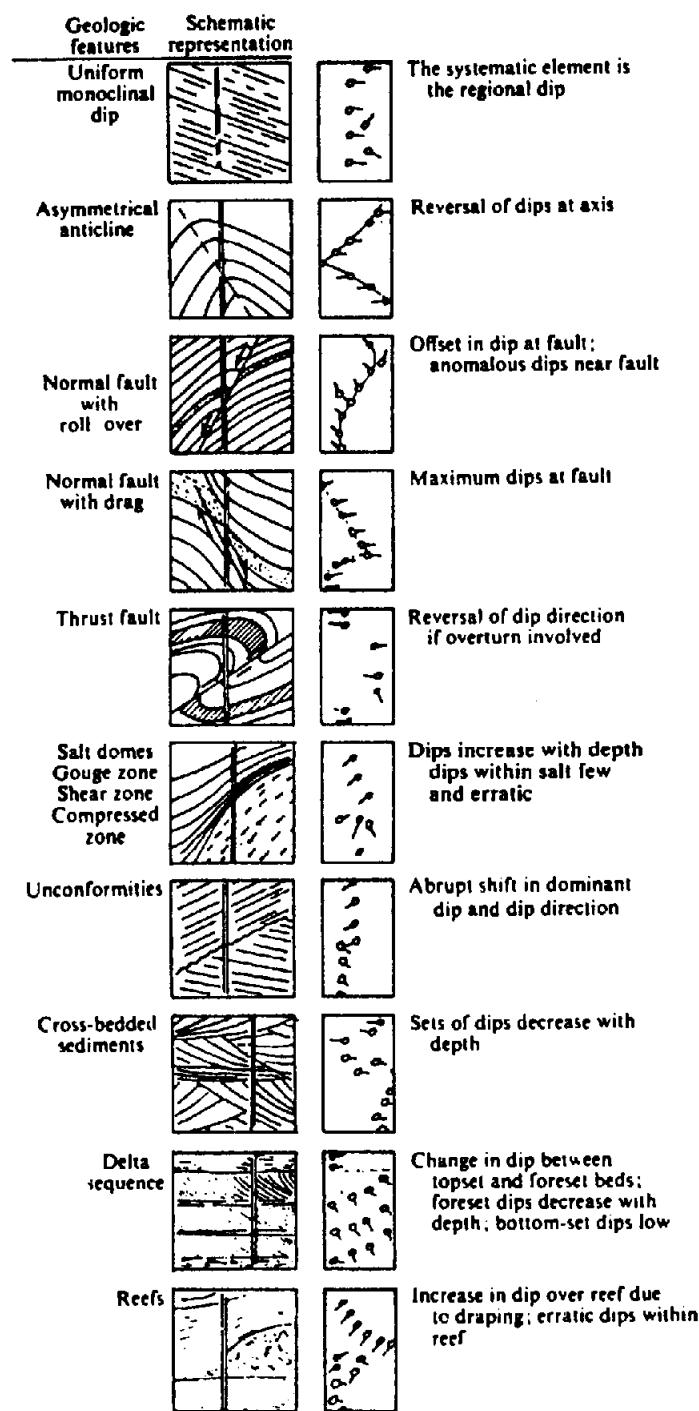


Figure 11.17. Idealized dipmeter patterns indicating structural and stratigraphic features. (After Pirson, 1970.)

part of the 16 ft (4.9 m) long sonde contains an inclinometer to record the drill-hole drift angle and bearing and a magnetometer to determine the azimuth of the reference pad. Two hole-caliper logs at right angles are also recorded. The log recorded in the field shows the azimuth of the no. 1 electrode, the relative bearing of hole drift, the deviation of the hole from the vertical, the resistivity curves from the four pads, and the caliper logs. A portion of such a log is shown in Figure 11.16b.

Formation boundaries are defined by the microresistivity curves and the dip and strike are determined from the slight differences in depth of the boundaries and the orientation data. Rough interpretation based on major features of the raw plots can be made fairly easily. The correlation of many closely spaced points, however, requires processing. The result is usually a "tadpole plot" such as shown in Figure 11.16b where the result of each correlation is shown as a small circle indicating the dip angle, with a short ray

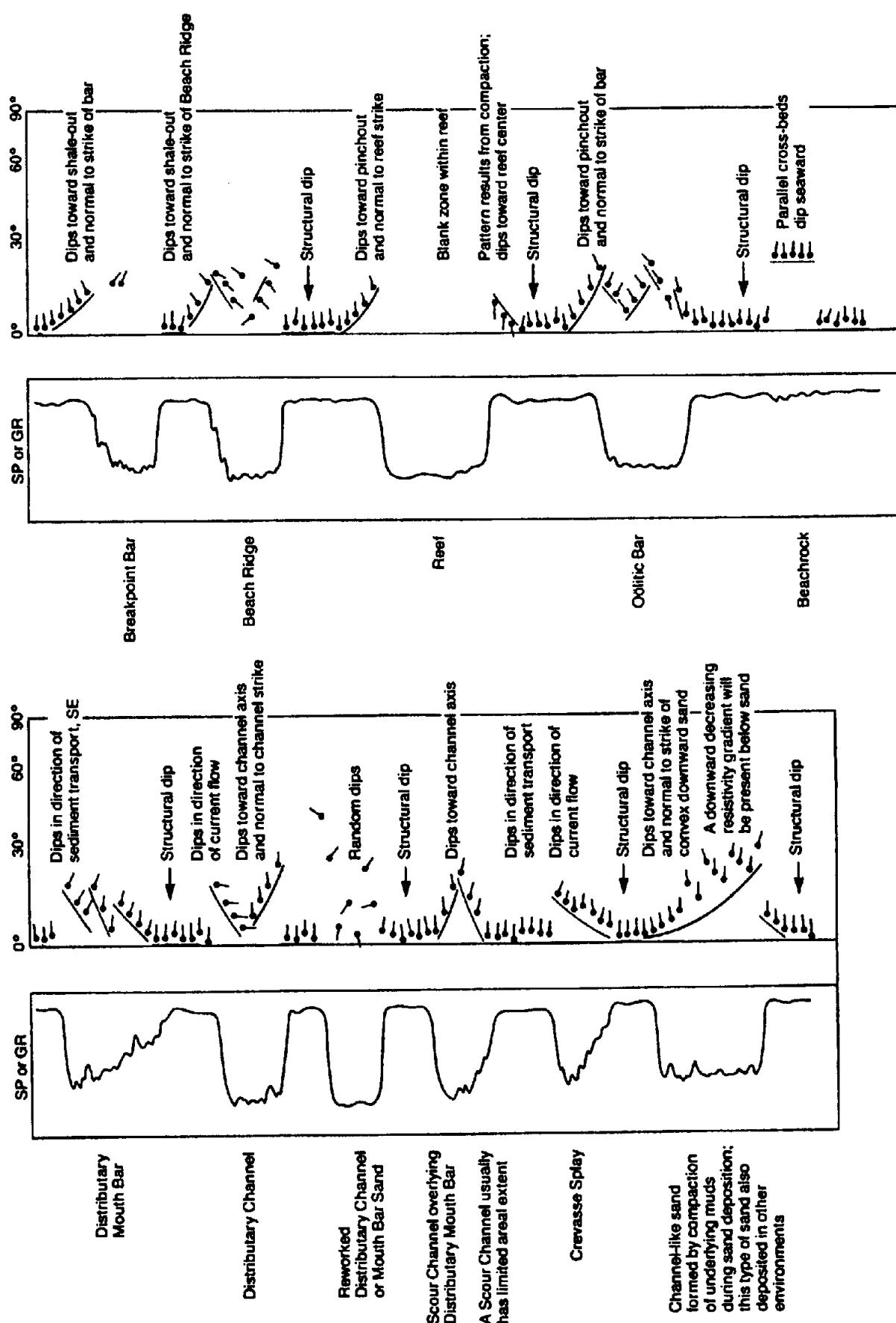


Figure 11.18. Stratigraphic patterns in SP (or  $\gamma$ -ray) and dipmeter data. (From Gilman, 1987.)

emerging from the circle indicating the down-dip direction, north being upward, east to the right, and so forth.

The variation of dip with depth often indicates geological structure, as shown in Figure 11.17. The dip distortions resulting from fault movement may not extend very far from the fault plane. Various types of sedimentation patterns sometimes may be distinguished when many detailed correlations exist (Fig. 11.18).

## 11.5. ELECTROMAGNETIC WAVE PROPAGATION METHOD

Although the induction log discussed in Section 11.2.6 is an electromagnetic method, this term is usually reserved for other devices.

The phase velocity of an electromagnetic wave at gigahertz frequency  $V$  is given by (Freedman and Vogiatzis, 1979; Pascal, 1983)

$$V = 1/\{\mu\epsilon + (\alpha/2\pi f)^2\}^{1/2} = 1/\tau \quad (11.11)$$

where  $\mu$  is the magnetic permeability,  $\epsilon$  is the dielectric permittivity,  $\alpha$  is the absorption coefficient,  $f$  is the frequency, and  $\tau$  is the time to travel a unit distance equal to *interval transit time*. Both the attenuation and the interval transit time can be measured. Because the dielectric permittivity of water is much larger than that of oil or rock (by a factor of 10 to 40), water dominates measurements with an electromagnetic log. The large contrast between the dielectric permittivity of water-saturated sediments and rock salt makes it possible to map a salt dome from a borehole in the dome.

Nickel et al. (1983) report a survey of this type using a pulse system operating at 20 and 40 MHz in a salt-dome borehole. With closely spaced Tx and Rx antennas they obtained good reflections from zones of anhydrite, clay, and basalt embedded in the highly resistive salt at distances of several hundred meters. They also measured absorption in these structures by moving the receiver to a second borehole. The results were compared with sonic log data from the same location.

By analogy with the time-average equation [Eq. (11.14b)] used in sonic log interpretation, we write for the porosity seen by the electromagnetic waves  $\phi_{EM}$ ,

$$\phi_{EM} = ((\tau - \tau_m)/(\tau_w - \tau_m)) \quad (11.12)$$

where  $\tau_m$  and  $\tau_w$  are the interval transit times for the rock matrix and for the water in the pore spaces.

Because the total porosity  $\phi$  can be obtained from neutron and density logs, we can solve for the water saturation  $S_w$ :

$$S_w = \phi_{EM}/\phi \quad (11.13)$$

The electromagnetic propagation log at 1.1 GHz defines interfaces sharply but has limited penetration and thus yields mainly the water saturation of the invaded zone. In conjunction with density and neutron logs, it also locates hydrocarbons, identifies the hydrocarbon type, indicates mobile oil, and provides residual oil values. The EM propagation log at 10 to 50 MHz ordinarily has a penetration of about 1 m and is useful where the salinity is small.

Modifications of EM surface-prospecting units (§7.4.2 and §7.4.3) have been employed to a minor extent in mineral-hole logging. Usually the aim is to locate mineralized (high-conductivity) zones nearby, rather than to evaluate the formations intersected by the drill hole (Worthington, Kuckes, and Oristaglio, 1981). An example is shown schematically in Figure 11.19a. The transmitting coil is a conventional vertical loop, set up near the hole and pointing toward it; connected in series with this loop is a small vertical vernier coil, which can be rotated about its vertical axis. The sonde lowered into the hole consists of a small receiver coil wound on a high-permeability core, amplifier, and battery. The received signal can be nulled by rotating the vernier transmitting coil and the azimuth angle is plotted against sonde depth. The measurement is repeated during the uphole passage, this time with the transmitter coil and vernier rotated 90°. The maximum azimuth angles of the two curves, when plotted as vector components parallel to the planes of the transmitter coils produce a resultant vector that points toward the conductor; the depth can be obtained from the curves. The amplitudes of the maximum azimuth angles are roughly indicative of the horizontal distance and/or the conductivity of the zone, and the distance between null points of the curve gives an indication of the vertical extent. The range of investigation is about 100 m.

A somewhat different drillhole EM log is illustrated in Figure 11.19b. The transmitter loop is a large square of one to four turns laid out on the surface. The vertical depth of penetration desired and the type of objective determine the required loop size; loop sides are usually 125 m or longer. A receiver coil with preamplifier is lowered into the hole, the gain being adjusted to maintain constant meter reading; gain is then plotted against depth. Alternately, two coils 15 m apart are connected in opposition to produce a difference signal, as with the Turam method. The transmitter square with the hole

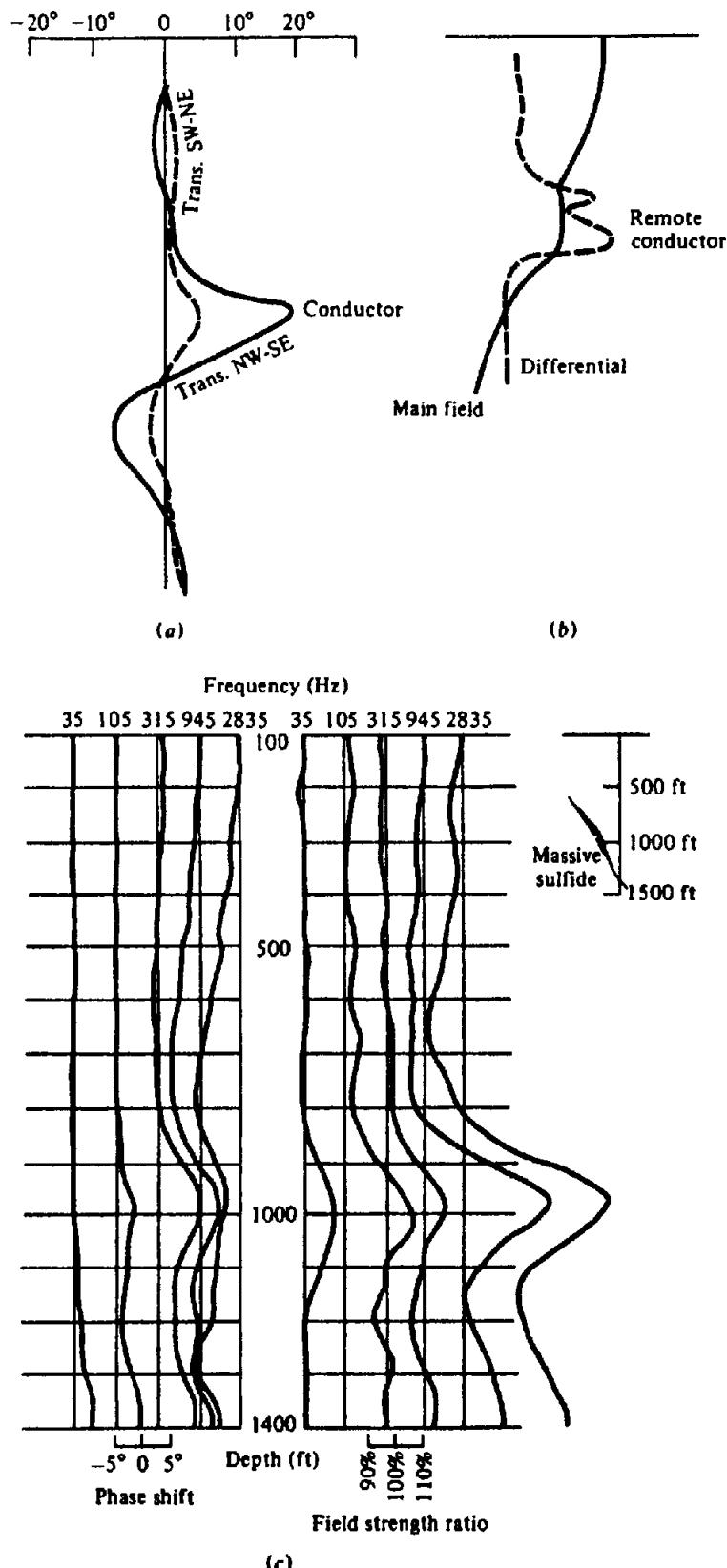


Figure 11.19. EM logging. (a) Logs for two orthogonal directions of the vertical transmitter loop. (b) Logs for a horizontal transmitter loop and one (solid line) or two (dashed line) receivers in the hole. (c) Multifrequency logs. (After Seigel, 1979.)

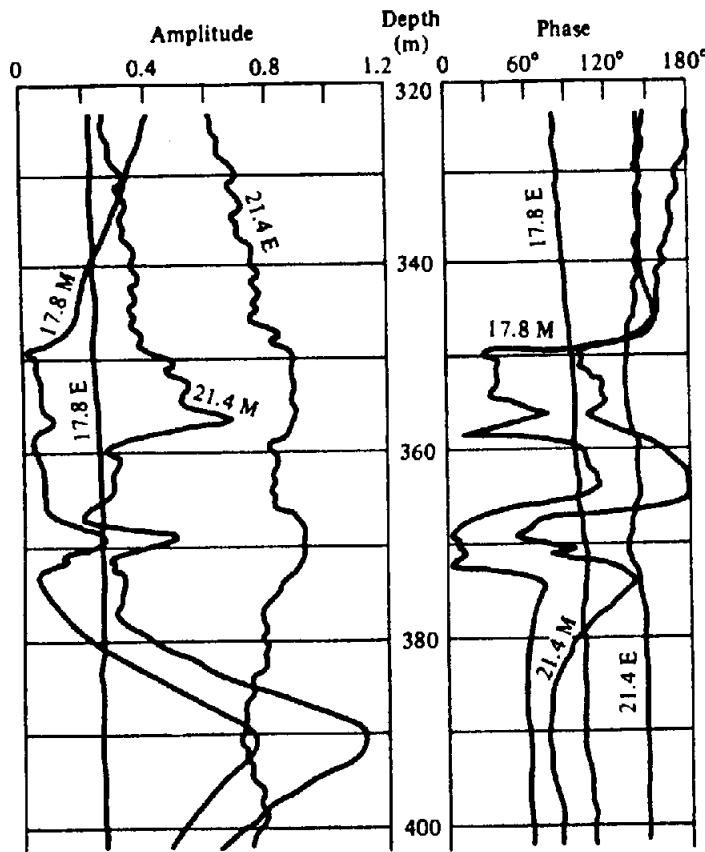


Figure 11.20. Amplitude and phase plots of VLF log past a conductor. E is the electric and M is the magnetic reading, each at 17.8 and 21.4 kHz.

located at one corner is rotated 90° for a successive logging run so that a rough estimate of conductor azimuth can be made. The interpretation is qualitative.

A recently developed EM log uses a large transmitter loop laid out on the ground to one side of the borehole. A moving detector coil coaxial with the hole compares the axial H-field amplitude and phase at five frequencies with those obtained from a similar near-surface coil. Logs from a drill hole near the Gertrude sulfide deposit west of Sudbury, Ontario, are displayed in Figure 11.19c.

The EM16 VLF receiver (§7.4.2f) has been adapted for borehole logging (Roy, 1984). The down-hole unit has magnetic and electrical sensors that detect in-phase and quadrature components of the axial magnetic field and electrical potential. A surface reference magnetic sensor is oriented for maximum coupling with the distant VLF transmitter and provides reference data for the downhole magnetic readings; the downhole potentials are measured with respect to surface potentials nearby (analogous to SP – see §11.3.2). The log (Fig. 11.20) shows the amplitudes and phases of the VLF magnetic and electrical vectors measured with respect to the surface values. Both vectors are determined at two frequencies: 17.8 and 24.1 kHz. The effects of two conductors are quite clearly seen.

## 11.6. INDUCED POLARIZATION LOGGING

IP can be measured simultaneously with resistivity, either in the frequency or time domain, to determine the frequency effect, phase shift, chargeability, and complex resistivity (Wagg and Seigel, 1963). The Kennecott IP-resistivity logging tool gives continuous measurement of IP amplitude and phase as well as resistivity to depths of 1,500 m. Glenn and Nelson (1979) suggest a relation between IP and sulfide percentages. For disseminated porphyry-type mineralization, the resistivity is independent of sulfide concentration whereas the phase shift is proportional to the sulfide surface area exposed to pore fluid. In vein-type mineralization, the phase is independent of sulfide content and the resistivity decreases inversely as the square of the sulfide percentage.

## 11.7. ELASTIC-WAVE (ACOUSTIC) METHODS

### 11.7.1. Elastic Waves in Boreholes

Elastic (seismic) wave travel was discussed in Chapter 4. The sonic log transmitter generates several wave modes (Paillet and White, 1982; Schmitt and Bouchon, 1985), which are subsequently picked up

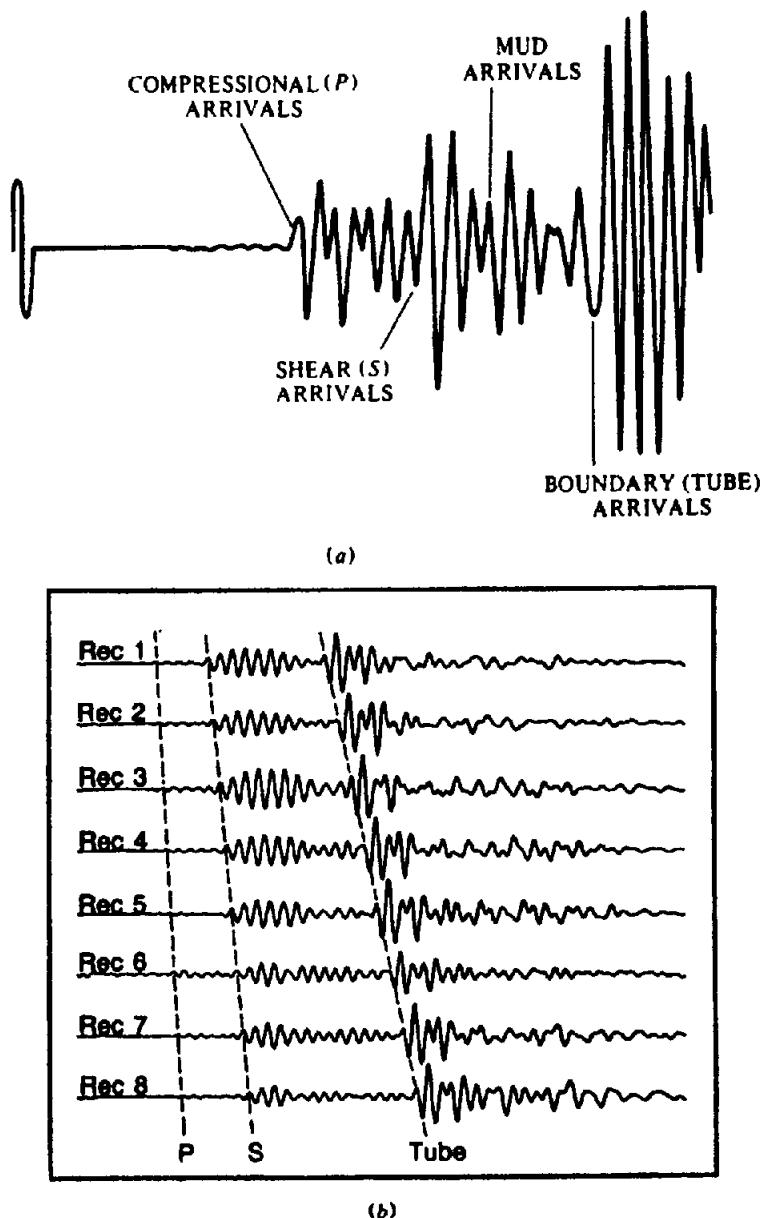


**Figure 11.21.** Waveforms recorded in a borehole. (a) Waveform showing formation arrivals (*P* and *S* waves), mud arrivals, and boundary (tube-wave) arrivals. (Courtesy Schlumberger.) (b) Waveforms from eight broad-band receivers spaced at intervals of 6 in. (15 cm). (After Morris, Little, and Letton, 1984.)

by the receivers (Fig. 11.21). The first energy to arrive is almost always a refracted *P* wave (headwave mode) in the rock wall. It has impinged on the borehole wall at the critical angle  $\theta_p = \sin^{-1}(V_f/V_p)$ , where  $V_f$  is the seismic (acoustic) velocity of a *P* wave in the borehole fluid and  $V_p$  that in the formation (Fig. 11.22). The sonic log records the transit time (reciprocal of velocity) of this wave. Some of the headwave energy "peels off" at various places along its travelpath, reflects at the sonde or opposite borehole wall, and rejoins the headwave; this adds tail to the headwave, which thus develops a "ringy" appearance.

The acoustic wave striking the borehole wall at the angle  $\theta_s = \sin^{-1}(V_f/V_s)$ , where  $V_s$  is the *S*-wave

velocity in the formation, generates a converted *S* wave (also a headwave mode) whenever  $V_s$  is larger than  $V_f$ . The *S*-headwave develops a ringy character by the same mechanism as the *P*-headwave. It is usually the second arrival and stronger than the *P*-headwave.

Much of the energy reflects at the borehole walls to reverberate in the borehole fluid. Energy striking the borehole walls at angles larger than  $\theta_s$  is totally reflected and bounces back and forth in the borehole as a trapped dispersive wave (*guided wave*; see §4.11.3). This energy constitutes a *mud wave* (whose onset may not be recognizable). Most of the reverberatory energy striking the borehole walls at angles between  $\theta_p$  and  $\theta_s$  is also reflected, except for small

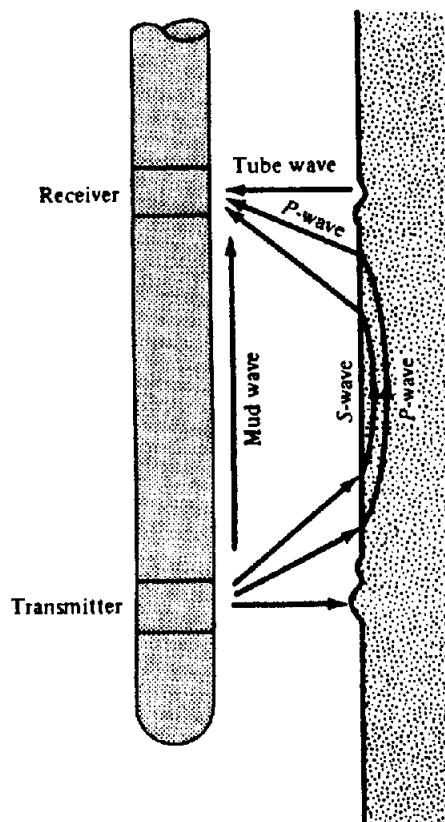


Figure 11.22. Propagation paths for  $P$ ,  $S$ , mud, and tube waves. (From Labo, 1987.)

portions which are lost by being converted to refracted  $S$  waves; this *leaky-mode* transmission is also part of the reverberatory trapped wave. The trapped mode is often the strongest in terms of energy density and sometimes obscures the  $S$ -wave arrival, especially in soft formations.

A tube wave, also called a *Stoneley wave*, travels as a surface wave on the borehole wall (see Sheriff and Geldart, 1982, pp. 51–52). This wave is only mildly dispersive and thus shows as a reasonably sharp arrival. The shear modulus can be calculated from the Stoneley-wave velocity. The Stoneley wave is often very strong and of relatively low frequency content.

All of the waves travel as  $P$  waves in the borehole fluid, and hence the terms *acoustic* and *sonic*; however, the major interest is usually in the seismic wave in the adjacent rock formations. Although it was introduced to determine seismic velocity as an aid in seismic prospecting, determining porosity, which correlates with seismic velocity, soon became the major application of this log. Sonic logs continue to be used for seismic velocity measurement and reflection (synthetic seismogram; see §4.10.2) analysis. Seismic detectors located in boreholes are also used for determining surface-to-depth traveltimes for velocity surveys (§4.5.5) and for vertical seismic profiling (VSP) studies (§4.11.4).

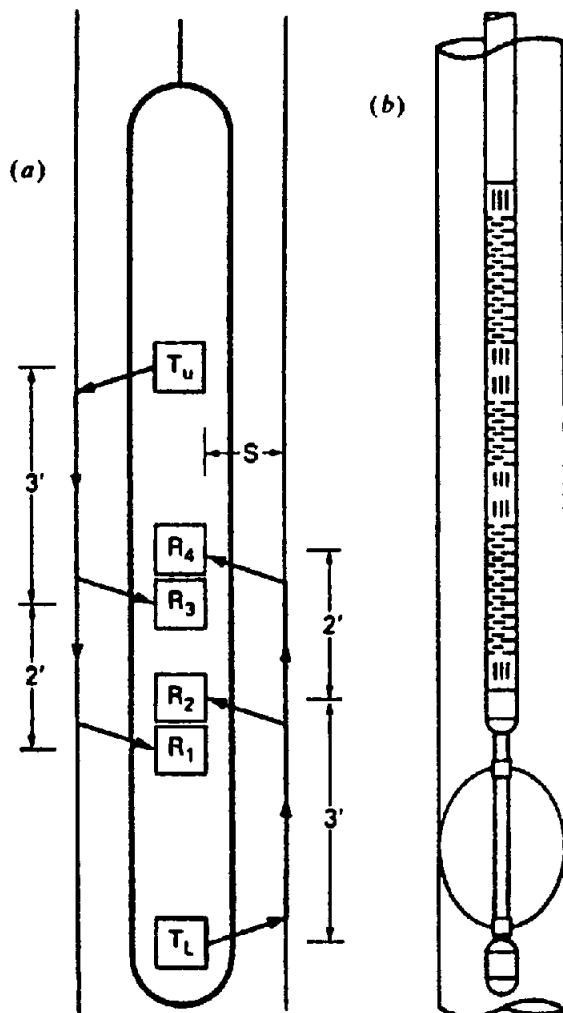


Figure 11.23. Sonic logging sonde. (a) Borehole-compensated sonde. (b) The sonde in a borehole. Vertical slits are openings to transmitters and receivers; horizontal slits prevent signal travel in the sonde itself.

### 11.7.2. Sonic Log

Early continuous velocity loggers consisted of a single receiver a few meters away from a transmitter that emitted pulses of acoustic energy. The travel-time of the first arrival was measured to determine the  $P$ -wave velocity in the adjacent rock. The design of the logging sonde prevents energy travel through the sonde from transmitter to receiver. The travel-time is determined by the time when the receiver output exceeds a threshold that is set higher than the noise but lower than the first cycle of energy. If the threshold should be too high, triggering may not occur until a later cycle, producing an error in measurement, called *cycle skip*. Cycle skipping is more likely when the signal has been attenuated by unconsolidated formations, fractures, gas in the pore spaces, aerated mud, or caved sections. Errors of this kind can usually be recognized and eliminated. However, with single transmitter-receiver sondes, errors also resulted when the axis of the sonde was not

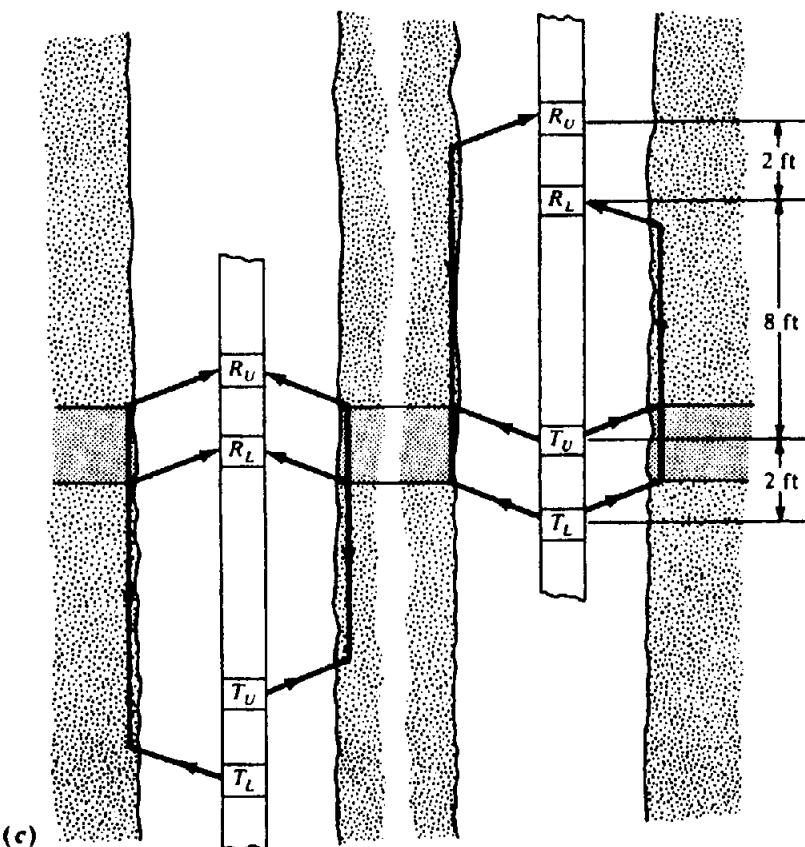


Figure 11.23. (Continued) (c) Long-spaced sonde in the two positions for borehole compensation.

Table 11.1. Fluid and matrix velocities.

Material	P waves		S waves	
	$V_f$ or $V_m$ (m/s)	$\Delta t$ ( $\mu\text{s}/\text{m}$ )	$V_f$ or $V_m$ (m/s)	$\Delta t$ ( $\mu\text{s}/\text{m}$ )
Water (20% salt to pure)	1,400 – 1,600	714 – 625	[870]*	[1,150]*
Salt	4,570	219		
Shale	4,875	205		
Iron casing	5,334	187		
Unconsolidated sands	5,180	193		
Sandstone	5,490 – 5,940	182 – 168	3,550	282
Anhydrite	6,100	164	3,030	330
Limestone	6,400 – 7,010	156 – 143	3,400	294
Dolomite	7,010 – 7,925	143 – 126	4,000	250

\*Although water does not carry S waves, use of this value in the time-average equations yields good results.

parallel to the borehole wall, from enlarged borehole, from mud buildup, and from inadequate penetration beyond the altered invaded zone.

Errors in transit-time measurements occur because of hole-size changes (caving) or tilt of the sonde in the borehole. These effects oppose the transmitter are largely eliminated by measuring the difference in the traveltimes to two receivers at different distances. Likewise, the use of two transmitters allows eliminating variable effects opposite the receivers. The borehole-compensated sonic-logging

sonde, illustrated in Figure 11.23a, employs two transmitters (which emit short 20 kHz pulses alternately about every 50 ms) and four receivers. About five measurements are averaged for each value recorded and the sonde is usually moved at about 15 cm/s, so that it moves about 3 cm during a measurement cycle. Centralizers keep the sonde in the center of the borehole.

The borehole-compensated sonde just described does not always correctly measure the velocity in the formation. Penetration may not extend beyond the

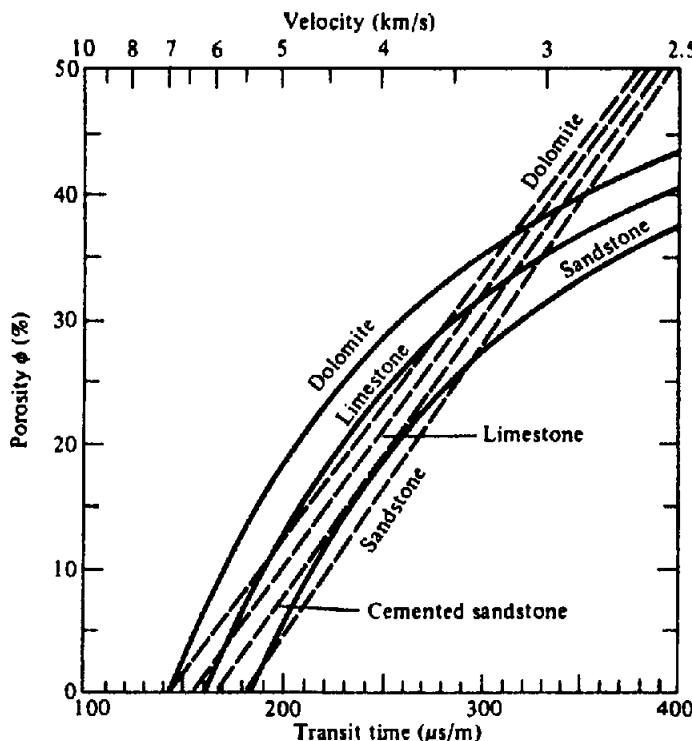


Figure 11.24. Porosity versus interval transit time. The curved lines are empirical, the straight lines give values from the time-average equation. (After Schlumberger, 1986.)

invaded zone, and shales at the borehole wall may have been altered so as to have lower velocity than those farther away from the borehole wall. Use of a long-spaced sonde, shown in Figure 11.23c, remedies these defects. Because the sonde moves, the transmitters are subsequently opposite the portion of the borehole that the receivers previously occupied (Fig. 11.23c); this permits averaging appropriate values to compensate for changes in borehole diameter and other abnormalities.

The sonic log displays the time interval for the sonic wave to travel one foot, usually expressed in microseconds per foot. Porosity usually is determined from the empirical *time-average equation* developed by Wyllie, Gregory, and Gardner (1958):

$$\Delta t = 1/V_p = (\phi/V_f) + (1 - \phi)/V_m \quad (11.14a)$$

or

$$\phi = (\Delta t - \Delta t_m) / (\Delta t_f - \Delta t_m) \quad (11.14b)$$

where  $\Delta t$  is the formation transit time (or *slowness*),  $V_p$  is the formation velocity,  $V_f = 1/\Delta t_f$  is the velocity in the fluid which fills the pore spaces,  $V_m = 1/\Delta t_m$  is the velocity in the rock matrix, and  $\phi$  is the porosity. Velocities used in this calculation, given in Table 11.1, involve ranges from which the velocity that gives the best porosity values is selected. Figure 11.24 indicates the dependence of matrix velocity on porosity and provides a way of getting better porosity values from Equation (11.14).

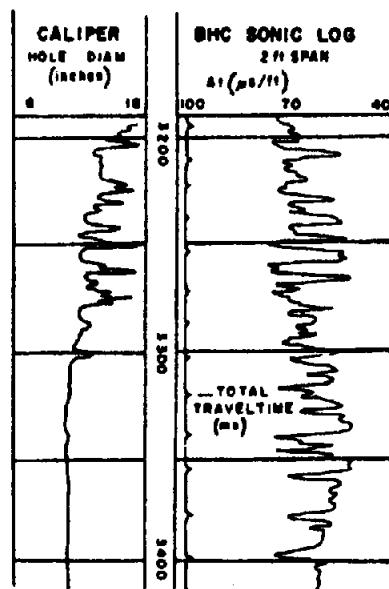
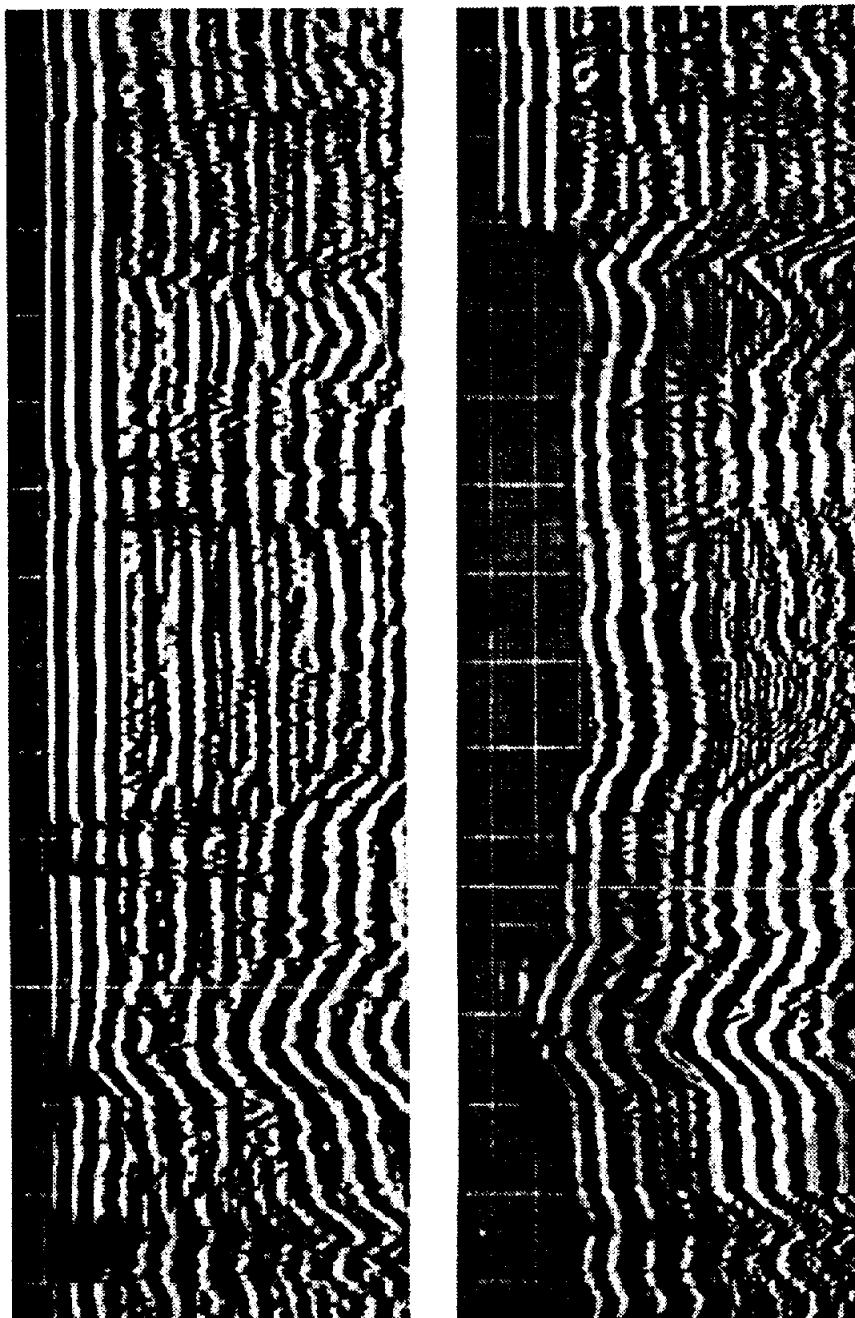


Figure 11.25. Portion of a sonic log. (From Schlumberger, 1987.)

For many formations, especially consolidated sandstones, the interval time in sands does not depend markedly on whether mud filtrate, formation water, or silt fills the pore spaces. Consequently the porosity calculated for shaly sands is too large. Where a sand is filled with oil or gas, especially with high porosity sandstones, the actual porosity is often 70 to 90% of the calculated porosity. In unconsolidated sands, porosities are sometimes corrected by dividing by 1/100th of the transit times (in microseconds per



*Figure 11.26. Microseismogram log used to indicate cement bonding. (Courtesy Welex.)  
 (a) The first arrival is a strong signal transmitted through the casing before cementing.  
 (b) After bonding the casing to the formation with cement, the first arrival is energy which travels through the formation.*

foot) of adjacent shales (when the shale transit time  $> 100 \mu\text{s}/\text{ft}$ ). The transit-time of shale normally increases rather steadily with depth, except where the shale is overpressured (§4.2.8a); a break in the shale transit-time curve provides an indication of an abnormal pressure situation. In carbonates the velocity is mainly determined by the primary porosity and vugular and fracture secondary porosity has relatively little effect. Correction is also accomplished from cross-plots with values determined from density and/or neutron logs (§11.10.2) and in other ways.

The sonic log is automatically integrated to give the total traveltime; this is shown on logs as ticks at intervals of 1 ms (track 2 in Fig. 11.25). However, small systematic errors tend to accumulate in integration. Traveltimes from check shots (from a source at the surface to a geophone in the well) can be used to remove accumulated errors.

#### 11.7.3. Amplitude and Full-Waveform Logs

Whereas the sonic log measures only the traveltime of the first arrival  $P$  wave, the amplitudes and

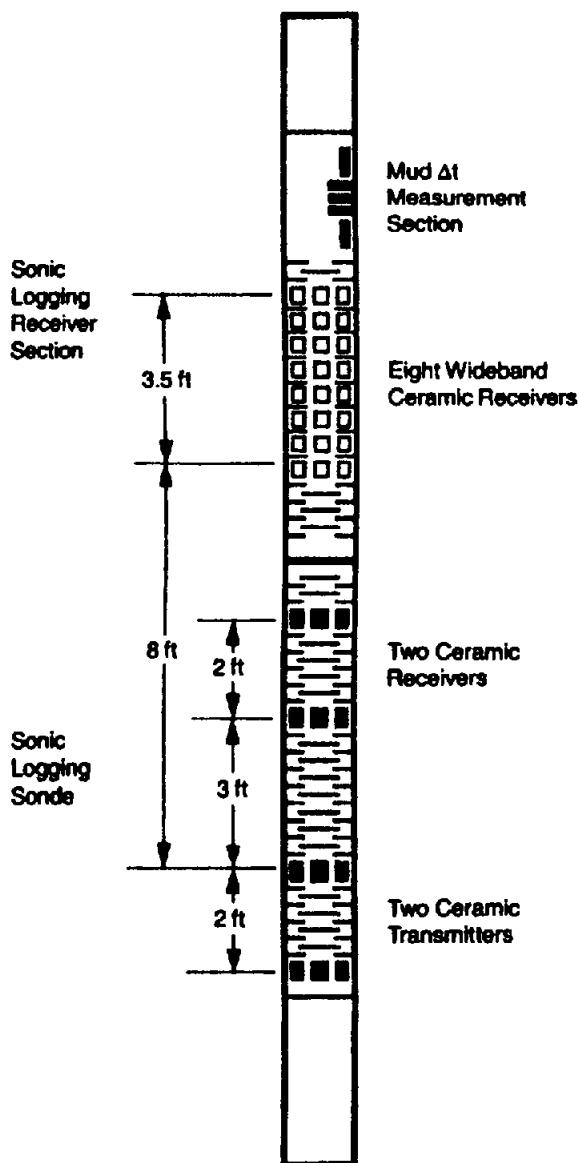


Figure 11.27. Array sonic sonde with two transmitters and 10 receivers. An example of the output of the upper 8 receivers is shown in Figure 11.21. (From Schlumberger, 1987.)

traveltimes of the various arrivals also convey information. The amplitude of arrivals is plotted in an acoustic amplitude log. The entire acoustic wavetrain is recorded on the microseismogram and variable density logs. Such a log is shown in Figure 11.26. These logs may use only a single transmitter and receiver separated by a greater distance than for sonic logging. Logs of this type are also made of the S-wave arrival.

An *array sonde* (shown in Figure 11.27) multiplexes (§4.5.3f) and transmits to the surface for computer analysis the measurements from a number of receivers. It yields the same measurements as the borehole-compensated and long-spaced sondes, plus additional ones. It determines the traveltimes, by searching for semblance maxima (§4.7.13) of P-, S-, and Stoneley-wave

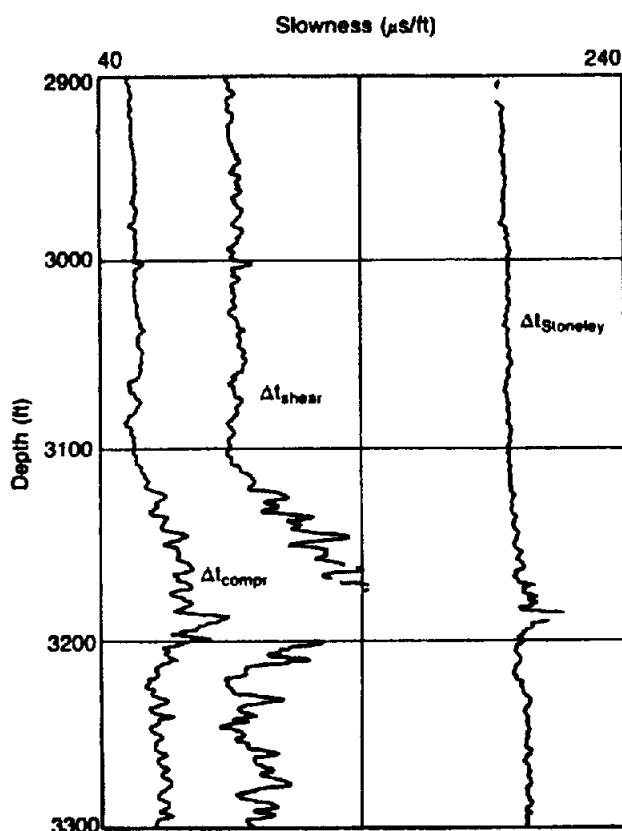
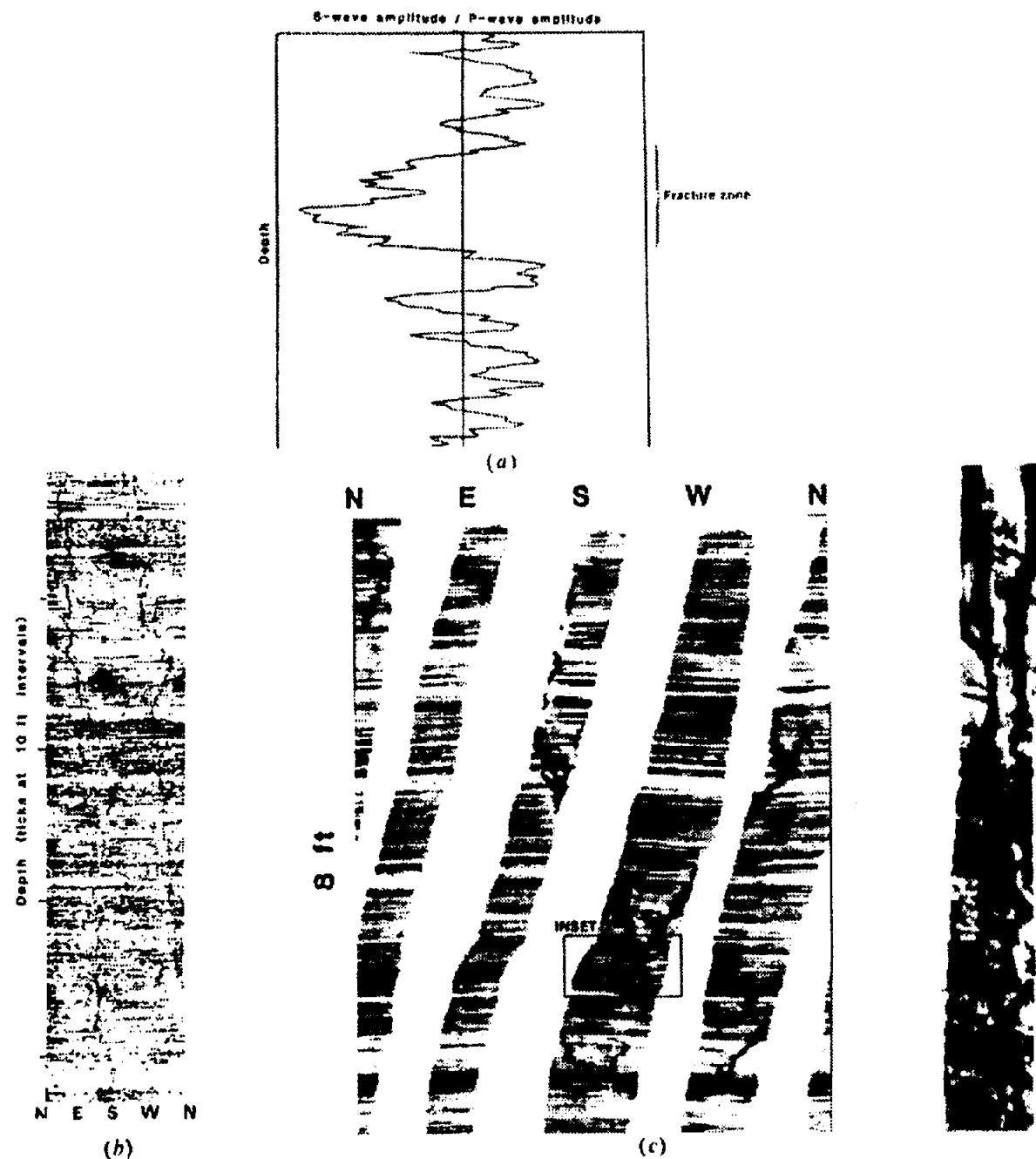


Figure 11.28. Log of P-, S-, and Stoneley-wave transit times. (From Schlumberger, 1987.)

arrivals among the full-waveform signals recorded by eight wideband receivers (Fig. 11.21b). These are displayed as shown in Figure 11.28. The mud transit time is also measured on fluid drawn through the upper part of the sonde. The S-wave transit time plotted against P-wave transit time helps identify lithologies, as discussed in Section 4.11.5. S-wave arrivals have appreciably higher amplitude than P-wave arrivals, so S-wave transit times can also be detected by setting the picking threshold high enough that the S-wave triggers the time counting. However, where the S-wave velocity is low, mud- and Stoneley-wave arrivals may override the S-wave arrivals.

Amplitudes are especially useful in determining the quality of the cement-to-casing and cement-to-formation bonding. Where the casing is not well cemented to the formation, the first-arrival headwave in the casing is especially strong, but when it is well cemented, the energy passes on through into the formation. Figure 11.26 shows a *cement-bond log*, a microseismogram log used to indicate the quality of cementing. High-velocity formations ( $\Delta t < 57 \mu\text{s}/\text{ft}$ ) can be logged behind casing when they are well cemented to the casing.

Sonic logs are used for fracture detection. Fractures cause a decrease in seismic amplitude, often by



**Figure 11.29. Fracture detection.** (a) Fracture finder log showing low S-wave/P-wave amplitudes in a fractured zone. (After Labo, 1987.) (b) Fracture seen by a borehole televiewer. (Courtesy Gearhart Industries.) (c) Formation microscanner showing fractures. The microscanner uses a number of electrodes on each of four pads pressed against the borehole walls to give four swaths of closely spaced electric log responses. The sonde was twisting somewhat during this log run. (Courtesy Schlumberger.)

a factor of 10. However, thin beds, thin shale streaks, and healed fractures often give much the same response. Fractures dipping up to 70° also may cause a 20 to 30% lowering of P-wave amplitude and a 60 to 80% lowering of S-wave amplitude (Labo, 1987). The fracture-finder log measures the peak amplitude within a gate that includes both P- and S-wave arrivals (Fig. 11.29a). Fractures also tend to show on full-waveform logs. Off-centering of the sonde in the borehole may also reduce amplitude due to waves from different azimuths not arriving simultaneously.

An amplitude decrease where  $\Delta t$  is constant may indicate fracturing.

#### 11.7.4. Borehole Televiewer

An ultrasonic transmitter-receiver is rotated in the borehole as the sonde is raised. The ultrasonic beam, which does not penetrate into the formation, traces a helix on the borehole wall. The receiver records the amplitude of the reflection from the borehole wall (Fig. 11.30). The display is as if the borehole wall

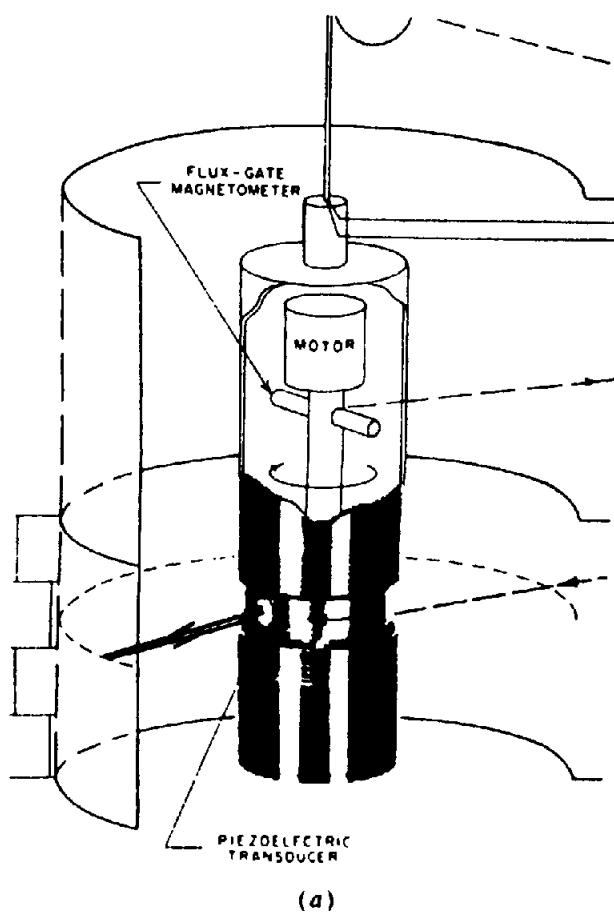


Figure 11.30. The borehole televiewer. (From Zemanek et al., 1970.) (a) Schematic view of the sonde; the magnetometer gives the sonde orientation.

were cut longitudinally and then laid out flat (Zemanek et al., 1970). The result is used to study fractures (see Fig. 11.29b).

## 11.8. NUCLEAR METHODS

### 11.8.1. Nuclear Processes

(a) *Introduction.* As discussed in Chapter 10, some atomic nuclei emit natural radiations and others can be induced to do so by bombardment. The nuclear radiations are in the form of  $\alpha$ ,  $\beta$ , or  $\gamma$  rays. Natural and induced  $\gamma$  radiation and neutrons possess appreciable penetrating power and are used in radioactivity logging.

Well-logging instruments that measure radioactivity of nearby formations may be considered under three headings: (i) those that detect  $\gamma$  radiation resulting from natural radioactivity, (ii) those that employ artificial  $\gamma$  rays, and (iii) those that use neutron sources to induce nuclear processes. Instruments employing  $\gamma$ -ray detectors are calibrated by measuring the detector response at various distances from a standard  $\gamma$ -ray source. Slow-neutron devices are calibrated by surrounding them with a standard volume of hydrogen-bearing material.

(b) *Natural radioactivity.* Natural radioactivity results from the presence of small amounts of U, Th, and  $^{40}\text{K}$ ; it is usually lowest in basic igneous rocks, intermediate in metamorphic rocks, and highest in some sedimentary rocks, especially shales. Although the  $\gamma$  radiation from either the U or Th series is much higher intensity than that of  $^{40}\text{K}$  (see Table 10.3, §10.2.4),  $^{40}\text{K}$  is far more common and the total background radiation is attributable more-or-less equally to the three elements.

Gamma-ray emissions of U, Th, and K are shown in Figure 11.31. The energy spectra of U and Th are broad and relatively complex, with characteristic  $\gamma$  rays: 1.76 MeV from U ( $^{214}\text{Bi}$ ) and 2.62 MeV from Th ( $^{208}\text{Tl}$ ). The  $\gamma$  ray from  $^{40}\text{K}$  is monoenergetic at 1.46 MeV. Radiation of different energies can be distinguished by using a  $\gamma$ -ray spectrometer (§10.3.4) sensitive only to narrow bands.

(c) *Interaction of  $\gamma$  rays.* An energetic  $\gamma$  ray may interact with the surrounding material by three distinct processes (see also §10.3.3b): (i) it may transfer its entire energy to a single atomic electron (*photoelectric conversion*), (ii) it may lose a fraction at a time to several electrons in successive collisions

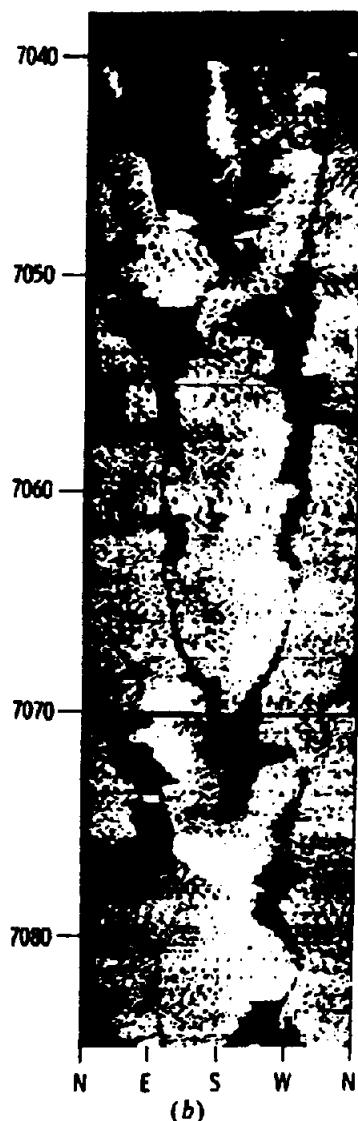


Figure 11.30. (Continued) (b) Portion of a log showing fractures.

(Compton scattering), or (iii) the  $\gamma$  ray may disappear in the creation of an electron-positron pair (*pair production*). The probability of each process occurring depends on the energy of the photon. The photoelectric effect occurs mainly at low energies ( $< 0.2$  MeV), whereas pair production can take place only if the  $\gamma$ -ray energy is sufficient to create two particles of 0.51 MeV each (that is,  $> 1.02$  MeV). The three processes are all related to the density of electrons in the medium, that is, to the atomic number  $Z$ . Photoconversion is proportional to  $Z^6$ , Compton scattering to  $Z$ , and pair production to  $Z^2$ . The attenuation of a  $\gamma$  ray is thus determined by the material through which it passes. Most logging sources do not emit  $\gamma$  rays of sufficient energy to cause pair production.

Table 11.2 shows the penetrating power of  $\gamma$  rays in various media. The attenuation is measured in terms of the material thickness, which reduces the

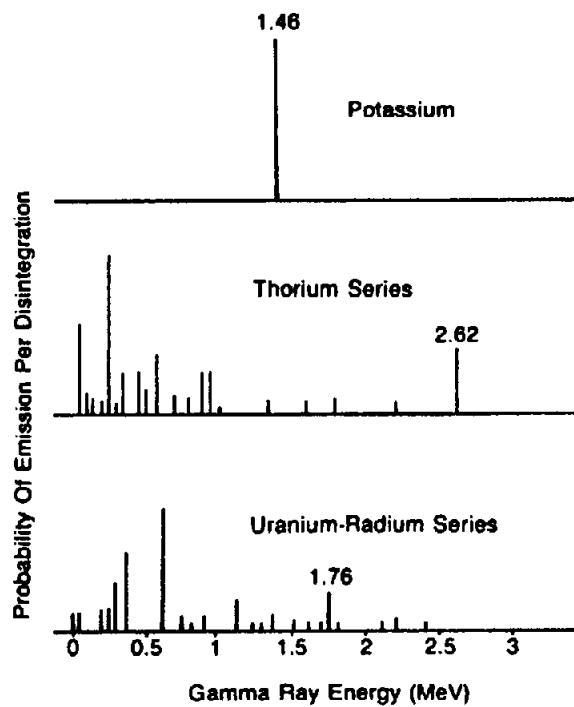


Figure 11.31. Gamma-ray spectra of potassium and the thorium and uranium series. (From Schlumberger, 1987.)

Table 11.2. Absorption of  $\gamma$  rays in various materials.

Energy (MeV)	Half-value layer (cm)			
	Water	Sandstone, $\text{CaCO}_3$	Iron	Lead
0.2	5	2	0.7	0.1
1.0	10	5	1.5	1.0
5.0	23	10	3.0	1.5

intensity to some fraction of the original. The relation is exponential, as for electromagnetic waves generally:

$$I = I_0 e^{-\mu x} \quad (11.15)$$

where  $\mu$  is the absorption coefficient. When  $I/I_0 = 1/2$ , the thickness of the half-value layer is  $x_{1/2} = (1/\mu) \ln 2 = 0.69/\mu$ . The average energy of natural  $\gamma$  rays is about 1 MeV and their range in sediments is roughly 30 cm. About half the  $\gamma$  rays detected in a borehole originate within 15 cm of the borehole walls. Casing reduces the intensity by about 30%.

(d) Interaction of neutrons. The interaction of neutrons with surrounding matter is also diagnostic of the medium. Fast neutrons (kinetic energy  $> 0.1$  MeV) are slowed down by elastic and inelastic collisions with nuclei. Inelastic collisions result in the nucleus (in addition to acquiring kinetic energy) being left in an excited state; it subsequently emits a characteristic  $\gamma$  ray. Elastic collisions result in a

Table 11.3. Neutron-capture and inelastic-scattering cross sections with characteristic  $\gamma$  rays emitted.

Element	Cross section (barns)		Characteristic $\gamma$ rays (MeV)
	Inelast. scatt. <sup>a</sup>	Capture	
Hydrogen		0.33	2.2
Beryllium	0.4	0.01	6.8
Boron		755	
Carbon	0.25	0.003	1.3, 4.9
Oxygen		0.0002	
Sodium	0.5	0.53	3.6, 3.9
Magnesium	0.7	0.27	2.8, 3.9
Aluminum	0.7	0.23	2.8, 7.7
Silicon	0.7	0.16	2.7, 4.9
Sulfur	0.8	0.52	3.0, 5.4
Chlorine	0.8	34	2.0, 6.1, 6.6
Potassium	1.0	2.1	4.4, 7.7
Calcium	1.0	0.43	1.9, 6.4
Manganese		13.3	1.8, 5.3, 7.2
Iron	1.2	2.6	5.5, 6.2
Cobalt	1.4	3.7	
Nickel	1.4	4.6	8.5
Copper	1.5	3.8	7.9
Zinc	1.5	1.1	
Molybdenum	2.0	2.7	
Silver	2.0	6.3	
Cadmium	1.9	2,500	1.0 – 7.0
Tin	1.6	0.63	
Tungsten	2.5	19	4.8
Gold	2.5	99	4.0 – 7.0
Mercury	2.5	360	3.8
Lead	1.8	0.7	6.7, 7.4
Uranium		7.7	1.0, 3.0

<sup>a</sup>Average value over the energy range 1 to 14 MeV.

partition of energy and the rate at which a neutron loses energy varies inversely with the mass of the target nucleus. When a neutron has been slowed to a velocity compatible with the temperature of the environment (kinetic energy < 0.025 eV), it is called a *thermal neutron* and can be captured by a nearby nucleus, which then emits a characteristic  $\gamma$  ray. The probability of neutron capture depends on the *capture cross section*, a quantity that is measured in barns ( $1 \text{ b} = 10^{-24} \text{ cm}^2$ ). Table 11.3 gives neutron capture cross sections and some of the characteristic  $\gamma$  rays emitted on capture.

### 11.8.2. Gamma-ray Logging

(a) *The gamma-ray log.* The  $\gamma$ -ray sonde consists of a detector and an amplifier. Early  $\gamma$ -ray logging used either an ionization chamber or a Geiger counter, but these have been replaced by the more efficient scintillation counter. The last two detectors are described in Section 10.3. A scintillation counter is only  $\sim 20 \text{ cm}$  in length so that resolution is good. Several measurement units have been employed, such as microroentgens per hour ( $\mu\text{R}/\text{hr}$ ), counts per

minute, and micrograms of Ra-equivalent per ton ( $\mu\text{g of Ra-eq/ton}$ ), but  $\gamma$ -ray logs are now calibrated in API units (American Petroleum Institute units, which are different from API neutron units; §11.8.4b). The difference between the high- and low-radioactivity sections of cement in the API calibration pit at the University of Houston is defined as 200 API units. Average shales have values around 100 API units.

In sediments the  $\gamma$ -ray log (Wahl, 1983) reflects mainly shale content because the radioactive elements tend to concentrate in clays and shales. Volcanic ash, granite wash, formation waters that contain radioactive salts, potash, and uranium ores may cause  $\gamma$ -ray anomalies. The  $\gamma$ -ray log responding to shale and clay is generally correlatable with the SP log. It now often replaces the SP log in general logging, especially where the SP is not diagnostic, as in very resistive formations where there is little difference between the salinities of the mud and formation water, or with oil-based muds, in empty holes, and in cased holes.

Figure 11.32 shows a schematic  $\gamma$ -ray log. Statistical variations, significant at low counting rates, are

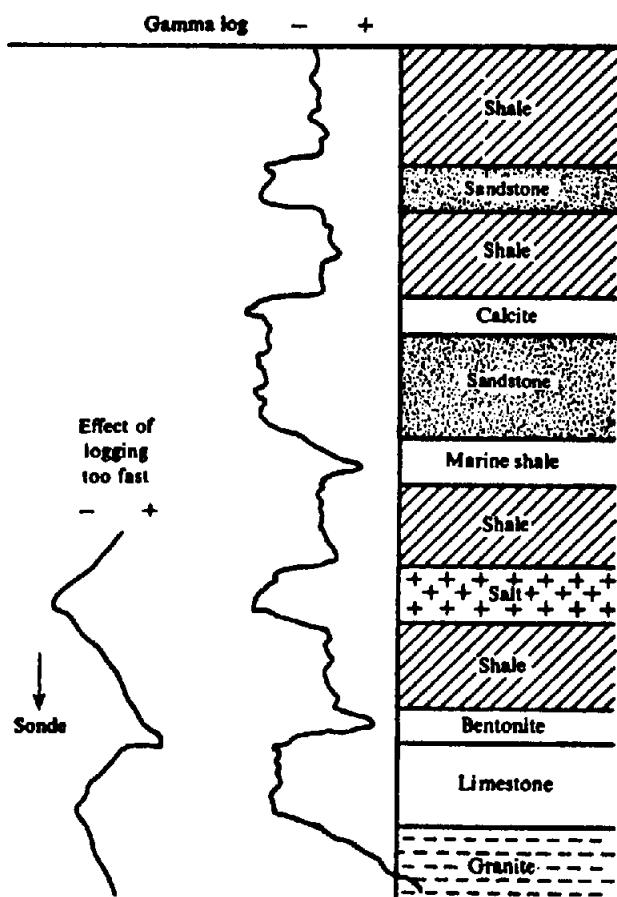


Figure 11.32. A  $\gamma$ -ray log.

smoothed out by integration over a time interval of several seconds. If the hole is logged too quickly, the smoothing effect causes barren zones to be apparently shifted in the direction of the logging, as illustrated in Figure 11.32, and thin beds to be missed. The logging speed is determined by the measurement time interval selected. It generally defines beds thicker than 1 m.

The interface between adjacent barren and radioactive beds is located fairly accurately at half the maximum deflection when the beds are thicker than 1 m. For thinner beds the bed center is taken as the peak deflection. Because the  $\gamma$ -ray log generally defines formation interfaces sharply in both open and cased holes, it is often run with other logs and production tools so that one can correlate the cased and open-hole logs and relate other logs to specific formations with greater certainty. The  $\gamma$ -ray log is used quantitatively to indicate shale percentage and to grade uranium deposits. It is the only logging tool used routinely in the mineral industry.

(b) *Natural gamma-ray spectroscopy.* The natural gamma-ray spectroscopy tool (§10.3.4) measures the energy level of  $\gamma$ -rays and permits determining the concentrations of K, U, and Th in rocks. The NaI scintillation detector is held against the borehole

wall as with the  $\gamma$ -ray log. The spectra of potassium, uranium, and thorium are smeared out (as shown in Fig. 11.33). Measurements in four or five windows permit solving for concentrations of K, U, and Th. A portion of a  $\gamma$ -ray spectrometer log is shown in Figure 11.34. This log is used to identify and evaluate radioactive minerals. It can also be used to identify clay types.

### 11.8.3. Density Log

(a) *Density log.* The *density log*, or *gamma-gamma log*, is used to determine porosity. Figure 11.35 is a schematic diagram of a density-logging sonde; the sonde is pressed against the borehole wall. The bottom of the sonde usually contains  $^{137}\text{Cs}$ , a concentrated source of 0.662 MeV  $\gamma$  rays; early sondes used a  $^{60}\text{Co}$  source. A scintillation meter is  $\sim 60$  cm above the source. Both source and detector are surrounded by lead shielding except for windows facing the wall, so that only  $\gamma$  rays that have traveled through the adjacent formation reach the detector. The spring force that presses the sonde against the borehole wall is considerable and the skid has a plow-shaped leading edge so that it cuts through soft mud cakes. The sonde occasionally sticks and then jerks free. The  $\gamma$  rays from the source interact with the elements in the rock mainly by Compton scattering, to a lesser extent by photoconversion (the sonde design excludes the portion of the spectrum affected by photoelectric absorption). The detected  $\gamma$ -ray intensity is an exponential function of the rock density. The maximum depth of investigation is about 15 cm, with most of the signal coming from the first 8 cm. Modern devices measure separately the Compton scattering and photoelectric absorption effects, the former depending mainly on formation density, the latter on lithology.

The instrument is calibrated for source intensity and detector sensitivity by clamping an aluminum, manganese, or sulfur block to it. Corrections for borehole size are small for hole diameters under 10 in. (25 cm) but amount to  $\sim 0.03 \text{ g/cm}^3$  for large holes. It may be used in empty holes as well as those filled with mud. Logging through casing is generally poor (accuracy  $\approx \pm 0.05 \text{ g/cm}^3$ ). A hole caliper log is an auxiliary output. Because the tool is short, adjacent beds or thin beds have little distorting effects. The logging speed must be adjusted in relation to the instrument time constant to avoid distortion of the curves and loss of sensitivity. Because count rate is high, fairly fast logging (2,000 m/hr) is permitted.

The compensated density-logging sonde employs two detectors at different distances from the source. The shorter spacing is more affected by mud buildup

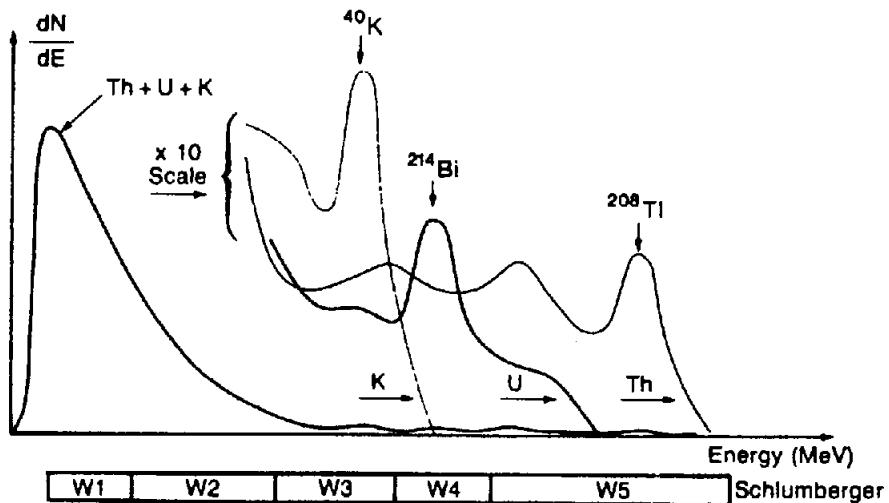


Figure 11.33. Gamma-ray spectra using a NaI crystal detector and energy windows for examining portions of the spectra. (From Schlumberger, 1987.)

and the difference between the readings from the two detectors is used to correct for the thickness and density of the mud cake.

Compton scattering cross sections per electron are nearly independent of the atom containing the electrons, and so the density log responds to the density of electrons (Table 11.4). Most atoms have nearly two electrons per atomic-weight unit; hydrogen is an exception and a few other elements also depart slightly from this ratio. The density log is usually calibrated for fresh-water saturated limestone, but it also gives quite accurately the bulk density in sandstone and dolomite. Corrections are needed to give the bulk density in salt, gypsum, anhydrite, coal, and gas, for which the ratio of electron density to atomic weight departs from that for limestone ( $Z/A = 0.5$ ).

Porosity  $\phi$  can be determined from the bulk density  $\rho_b$  by the exact relation

$$\phi = (\rho_{ma} - \rho_b) / (\rho_{ma} - \rho_f) \quad (11.16)$$

where  $\rho_f$  and  $\rho_{ma}$  are the densities of the formation fluid and the rock matrix. Density values are too low (up to  $0.08 \text{ g/cm}^3$ ) for formations that contain gas (because the pore fluid is assumed to be brine). The matrix density of most clay minerals is close enough to that of quartz that no difficulty is encountered in calculating the porosity of shaly sands. Disseminated shale often has a lower density than interbedded shale. Density logs are used to predict overpressure (Fig. 11.36) because shale density begins to decrease 100 m or so above high-pressure sands. The bulk porosity determined with this log includes secondary porosity and porosity that is not interconnected. If interpreted with other porosity-sensitive logs (§11.10.2), some of these complicating factors can be

sorted out.

(b) *Lithodensity log.* The lithodensity logging sonde employs a beryllium window that passes low-energy  $\gamma$  rays. By comparing counts at very low energies with those at higher energies (Fig. 11.37), this log measures a *photoelectric absorption index* (Tittman, 1986, pp. 33–6) which is related to lithology of the formation.

#### 11.8.4. Neutron Logging

(a) *Neutron reactions, sources, and detectors.* High-energy neutrons from a source in the sonde bombard the formations and lose energy mainly in elastic collisions with nuclei. The energy loss per collision is greater when the neutron and the nucleus with which it collides have comparable masses. Hence, the rate of energy loss (*moderation*) for fast neutrons is almost proportional to the density of protons (which have nearly the same mass as neutrons). Consequently, the response is primarily to hydrogen content, and neutron logs locate porous zones and determine the amount of liquid-filled porosity. The amount of hydrogen per unit volume is called the *hydrogen index*. After neutrons have been slowed to thermal energies, they may gain or lose energy in collisions because their energy is comparable to that of the colliding particle. Eventually they are captured by nuclei, which then emit capture  $\gamma$  rays. Where thermal neutrons or capture  $\gamma$  rays are measured, the nature and abundance of the capturing nucleus have a perturbing effect.

Several neutron sources have been used for the neutron log. These include combinations of beryllium with an  $\alpha$ -particle source such as radium, polonium, plutonium, or americium. Most logs today use

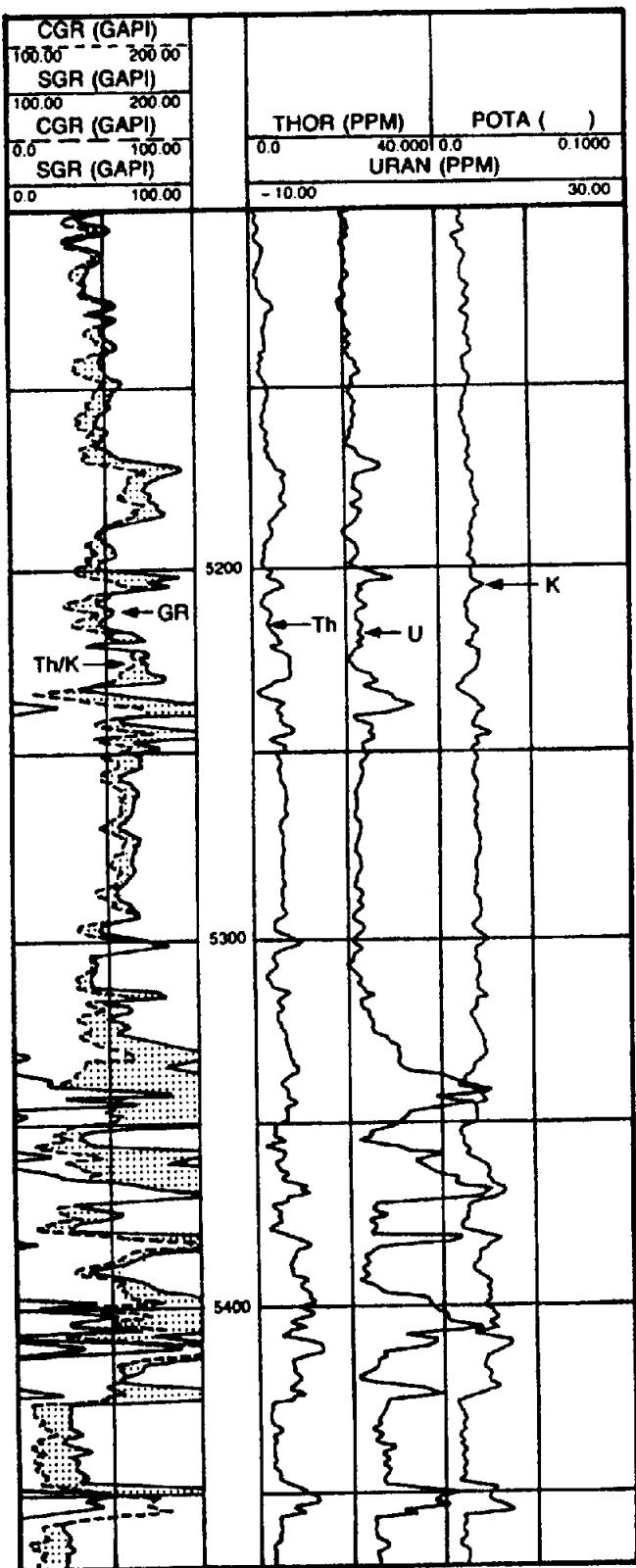
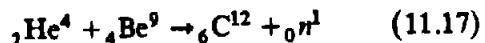


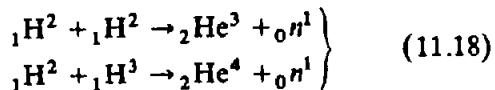
Figure 11.34. A natural  $\gamma$ -ray spectrometry log. (From Schlumberger, 1987.)

an americium-beryllium source with a 460 yr half-life. The reaction is



A 16 curie source produces about  $4 \times 10^7$  neutrons/s. Charged-particle accelerators have also

been used to produce neutrons by the reactions



The first reaction produces 2.3 MeV neutrons, the second 14.3 MeV neutrons. These neutron sources are monoenergetic and the source can be shut off.

Either the capture  $\gamma$  rays or the neutrons themselves may be counted. In porous formations saturated with water or oil, the neutrons lose energy rapidly so that the counting flux is high and most of the response is within 20 cm or so of the borehole. In low-porosity formations the neutrons penetrate farther, producing low counting flux, and the response range is of the order of 60 cm.

Several types of detectors are used. Some use a proportional counter shielded by a sheet of cadmium that absorbs thermal neutrons, so that only neutrons with energy above some threshold are detected.

(b) *Neutron log (hydrogen index log).* The neutron log indicates porosity by determining the amount of hydrogen and hence the amount of fluid filling the pore spaces. The first neutron logs were nondirectional and their detectors responded to both thermal neutrons and high-energy  $\gamma$  rays resulting from the neutron capture; however, these logs needed correction for salinity, mudcake, hole size, and casing. Best resolution was obtained when the hole was small, so that fewer neutrons were lost in the mud column. Sometimes the source-detector spacing was increased for operation in large diameter holes.

The *sidewall neutron log* is a sidewall device (like the density logging sonde); it was used in empty (but not cased) holes, but it is now obsolete. It employed a proportional counter so shielded that it measured only epithermal neutrons (energy  $\approx 0.4$  eV), whose energy is greater than that of the thermal neutrons involved with capture. Hence it was not perturbed by neutron absorbers, such as chlorine and boron, and was not sensitive to hole size. However, the count rate of epithermal neutrons was small so the detectors had to be close to the source and consequently depth of penetration was small and invasion effects large.

The *compensated neutron log* measures thermal neutrons. It employs two detectors spaced at different distances from the source, which makes it possible to correct for the effects of mud cake and hole roughness (*rugosity*). It has greater depth of penetration than the sidewall tool and can be run in either cased or uncased holes but not in empty holes. It is sensitive to shales, which often contain small amounts of boron and other elements with high capture cross section.

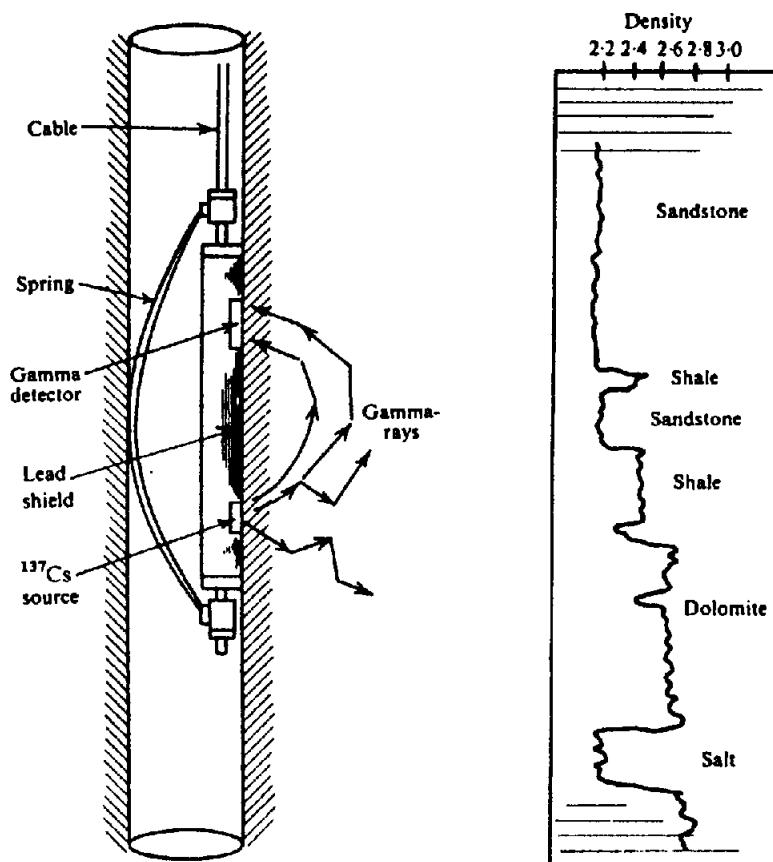


Figure 11.35. Density log schematic and typical log.

Table 11.4. Common elements encountered in hydrocarbon exploration.

	Z	A	Z/A
H	1	1.007	0.9921
C	6	12.011	0.4995
N	7	14.006	0.4998
O	8	15.999	0.5000
Na	11	22.989	0.4785
Mg	12	24.312	0.4934
Al	13	26.981	0.4818
Si	14	28.085	0.4984
Cl	17	35.453	0.4794
K	19	39.098	0.4859
Ca	20	40.08	0.4990

The dual porosity neutron log employs two detectors to measure thermal neutrons and two detectors to measure epithermal neutrons, neutrons of both energy classes being measured at different distances from the source (Fig. 11.38). The additional measurements permit corrections for shale content and salinity, and also yield improved gas detection in shaly reservoirs.

Neutron logs are usually plotted either in API neutron units or in "limestone porosity," which assumes that the matrix is limestone. API neutron units are based on measurement in a standard neu-

tron pit where 19%-porosity water-filled limestone is defined as 1,000 API neutron units. Correction is made for mud weight, temperature, hole-size variations, and salinity. The salinity is usually taken as that of the formation water except for invaded zones, where it is assumed to be that of the mud. A plot of a portion of a dual-porosity neutron log is shown in Figure 11.39.

Neutron logs are affected by all protons, including those in bound water associated with shales or water of crystallization, such as contained in gypsum. Consequently, shales and gypsum have distorting effects. Because neutron logs are affected by lithology, the best porosity values are obtained from the combined interpretation of neutron logs with other porosity-sensitive logs, especially with density logs (§11.10.2); this is particularly useful with a density log to indicate gas in the pore spaces.

(c) Pulsed-neutron logging. Pulsed-neutron logs, which include the *thermal-decay-time-log* and *neutron-lifetime log*, record the rate of decay of thermal neutrons. Chlorine, the most common element with high capture cross section (Table 11.3), is found in most formations and is the principal absorber of thermal neutrons. Consequently pulsed-neutron logs mainly determine the amount of chlorine, that is, the amount of saline water present. They thus accom-

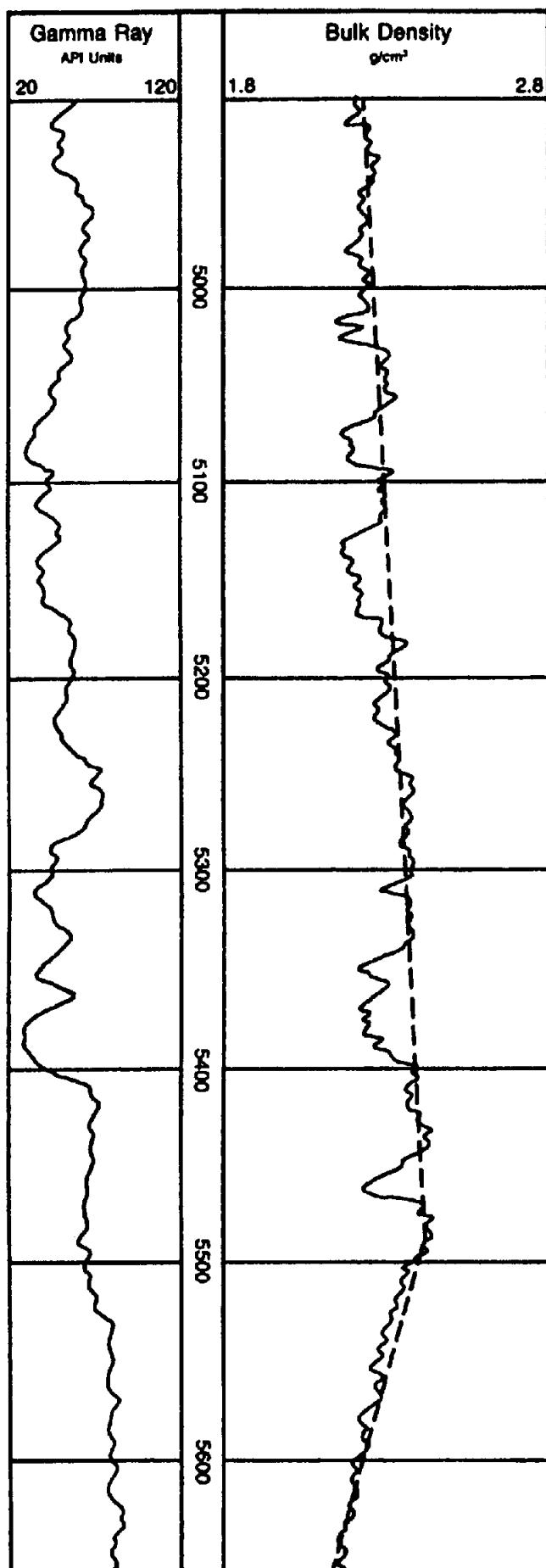


Figure 11.36. Density log, with overpressured shale below 5,490 ft. (From Schlumberger, 1987.)

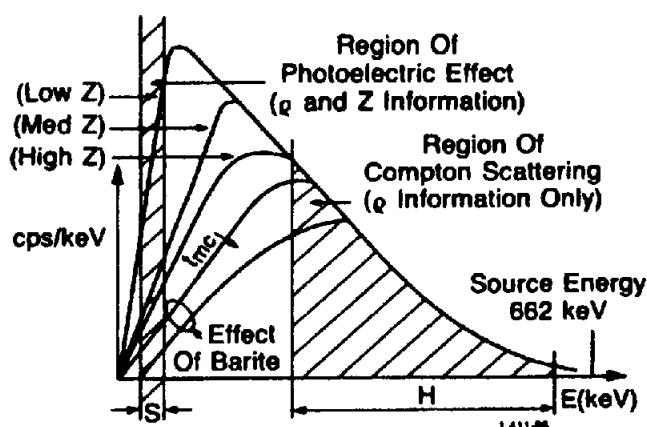


Figure 11.37. Gamma-ray energy spectrum showing the two windows in which measurements are made. The counts in the high-energy window H depend on density only, whereas those in the low-energy windows depend on both density and atomic number Z of the capturing atom. (From Snyder and Fleming, 1985.)

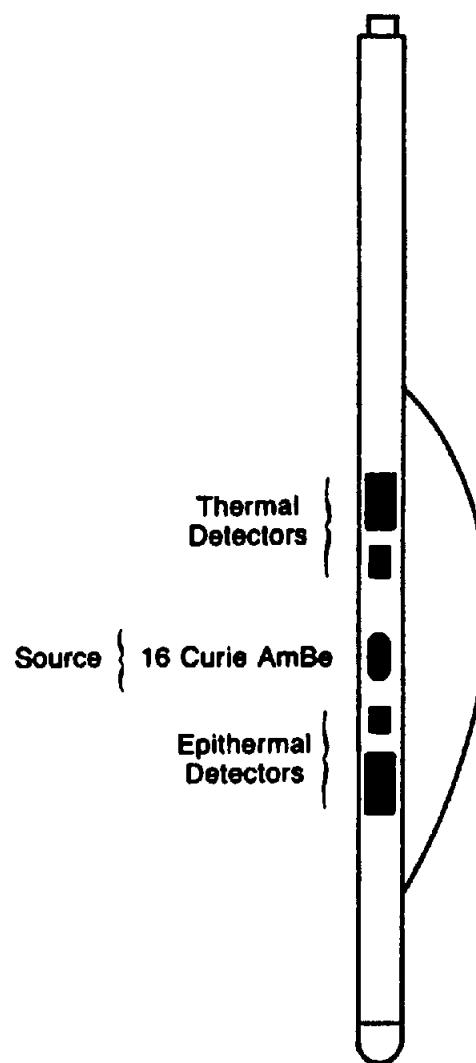


Figure 11.38. Schematic of dual-porosity neutron-logging sonde. (From Schlumberger, 1987.)

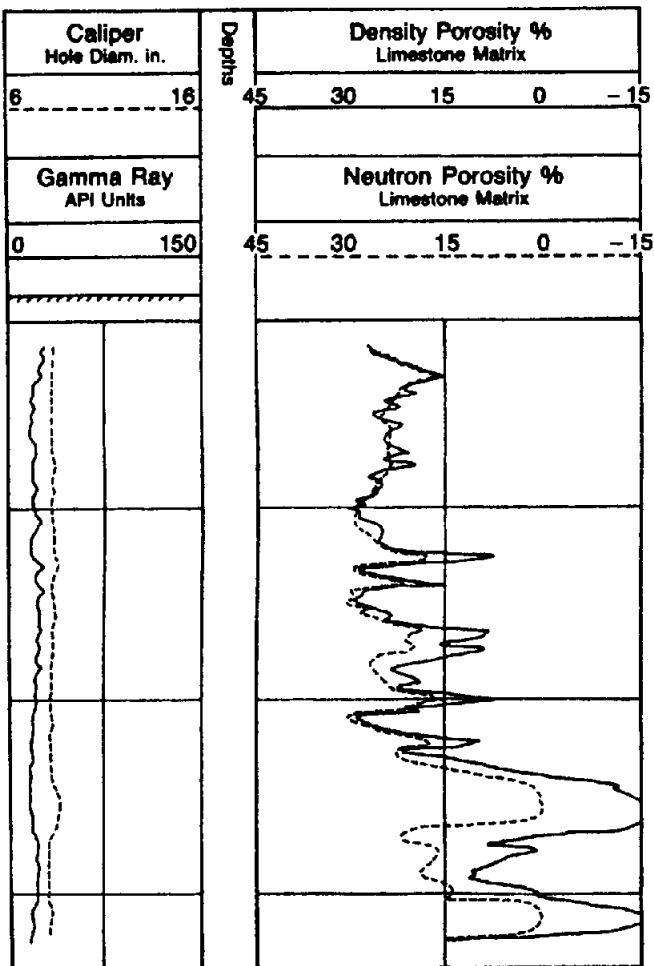


Figure 11.39. Portion of a dual-porosity neutron log. (From Schlumberger, 1987.)

plish essentially the same purpose as resistivity logs and can generally be correlated with them. Their advantage over resistivity logs is that they can be used in cased holes.

A neutron generator emits a burst of high-energy neutrons, as in Equation (11.18). These are rapidly

slowed to thermal energies and captured, whereupon capture  $\gamma$  rays are emitted. The  $\gamma$  rays arriving during a fixed time interval after the burst are detected a short distance away from the source. Measurements are made over two or more time intervals (Fig. 11.40) to determine the *die-away* time; this permits correcting for background effects and determining the rate of thermal-neutron capture. Absorption by the borehole fluid and casing primarily affects readings made soon after the burst; absorption effects can be largely eliminated by delaying the first measuring interval.

The *gamma-ray spectrometry log* involves a 256-channel spectral analysis of either elastic scattering or capture  $\gamma$  rays in two modes of operation. It gives water saturation independent of salinity and provides the data for determining the ratios of various elements, such as C/O and Si/Ca, by measuring their capture  $\gamma$  rays. This tool can also be used in analysis for coal, Cu, Fe, and U.

## 11.9. GRAVITY, MAGNETIC, AND THERMAL METHODS

### 11.9.1. Gravity and Magnetic Field Logging

Borehole gravity measurements were discussed in Section 2.3.4b. Borehole magnetic measurements (Silva and Hohmann, 1981) can be made with fluxgate or proton-precession instruments (§3.4.2 and §3.4.3). Vertical-gradient measurements can also be made in boreholes.

### 11.9.2. Susceptibility Log

Borehole instrumentation is similar to the field susceptibility meter (§3.3.8a). The solenoid is wound on

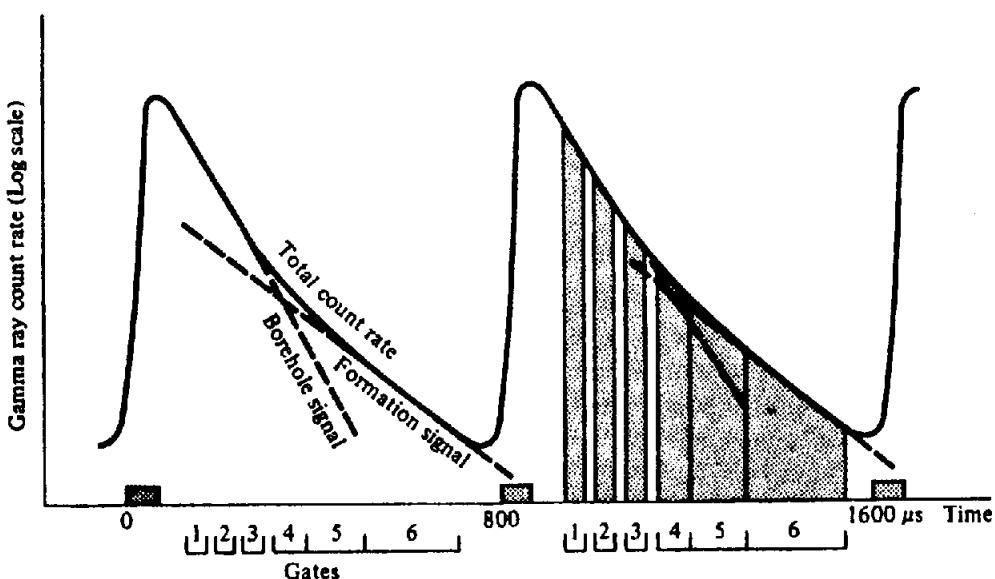


Figure 11.40. Pulsing and gating parameters for pulsed neutron log. A burst of neutrons occurs every 800  $\mu$ s. (From Snyder and Fleming, 1985.)

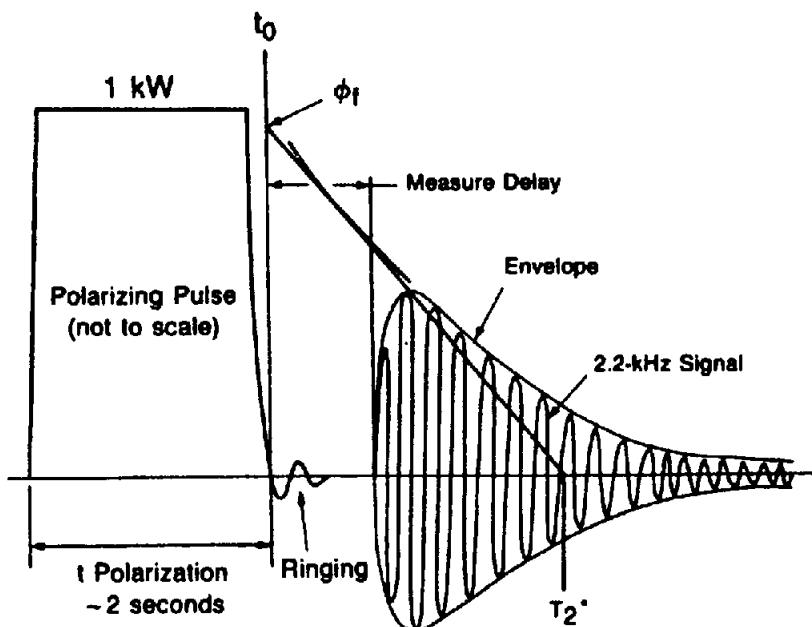


Figure 11.41. Nuclear-magnetic-resonance signal decay. Signals from resonances other than those of the free fluid decay before measurement begins. The signal decay is exponential so that the free-fluid index ( $\phi_f$ ) can be found by extrapolating the log of the decay back to zero time. (After Pinnington, 1981.)

a core of low-reluctance material and connected to one arm of a Wheatstone bridge. If the bridge is balanced in a barren environment, the presence of formations of anomalous susceptibility or conductivity unbalances it, because the susceptibility effect changes the reactance and produces a quadrature voltage whereas the conductivity produces an in-phase voltage. The effects can be separated by phase detectors and logs of susceptibility and conductivity displayed separately. The susceptibility log is not affected by mud resistivity and can be run in dry holes. The conductivity log compares favorably with resistivity logs for  $\rho_a > 2 \Omega\text{m}$ . Depth of penetration is about equal to the coil length.

Anomalous susceptibility may indicate the presence of magnetic materials, such as magnetite, ilmenite, and pyrrhotite. Good correspondence between SP and susceptibility logs indicate that porous zones have been enriched by ground-water deposition of magnetic minerals.

### 11.9.3. Nuclear Magnetic-Resonance Log

The proton-precession magnetometer was discussed in Section 3.4.3 as a device to determine the magnetic field strength, which is proportional to the measured Larmor frequency. [Eq. (3.30a)]. When, in the measurement cycle, the impressed field is removed, the protons with aligned spins gradually get misaligned (and the proton signal decays) as the protons are affected by somewhat random local magnetic fields. The time required for the proton reso-

nance signal to decay following the removal of an impressed field is a measure of the environment of the protons. The nuclear magnetic-resonance log measures the decay rate to determine this environment.

An impressed field at a large angle to the Earth's field is applied for about 2 s to orient the proton spins, and then the impressed field is cut off. The signal due to the residual oriented spins (Fig. 11.41) precessing about the Earth's field is measured beginning ~ 25 ms later (to allow transients to die out). The signal decay is affected by the protons in the borehole fluid, protons in moveable formation fluids, and protons bound to the lattice. The borehole fluid signal decays very rapidly because the drilling mud contains finely divided magnetite and the contribution of the borehole fluid is over before the measurement period begins. Protons in solids or bound to surfaces also have very short decay times. Thus the only significant contribution during the measurement period is that due to the protons in fluids that are free to move in the rock's pore spaces. The amplitude of the decaying signal is thus a measure of the amount of fluid (hydrogen) that is free to move. The measurement yields a *free-fluid index* (FFI), a measure of the porosity occupied by free fluids  $\phi_f$ . The rate of signal decay further indicates the type of fluid (water or hydrocarbons). Combining these measurements with data from other logs permits estimates of the *irreducible water saturation* (trapped water which is not free to flow), the permeability, and the *residual oil saturation* (the oil that can not be

flushed out by invading fluids) in the invaded zone (Tittman, 1986).

#### 11.9.4. Thermal Logging

Measurement of temperature has been employed mainly to determine large-scale terrestrial heat flow, but it can also be used to locate thermal anomalies caused by fluid flow, abnormal radioactivity, and oxidation regions. Various types of thermometers have been used, including resistance thermometers and thermisters.

### 11.10. WELL-LOG INTERPRETATION

#### 11.10.1. General

Interpretation of well logs for mineral objectives is usually qualitative, that is, locating and correlating anomalous zones. Interpretation for oil objectives, on the other hand, is highly developed. A variety of methods is employed and an enormous amount of data is accumulated. Oddly enough, geophysicists play a minor role in oil well-log interpretation. The logging contractor usually carries out routine interpretation, whereas detailed assessment is left to a specially trained oil-company geologist who has all the pertinent data (including classified data) at his disposal. Detailed log interpretation for the evaluation of porous and permeable formations for potential production is beyond the scope of this book.

Inspection of conventional electric logs (SP, normal, lateral, microlog, induction) often can locate, correlate, and identify formations of interest. When this information is combined with data obtained from additional logs (caliper, acoustic, radioactivity), the interpretation begins to be diagnostic and quantitative. Finally, in favorable situations, quantitative estimates of porosity, fluid content, water : oil ratio, and so on can be made. The results are controlled by the combination of logs available and borehole and drilling factors.

#### 11.10.2. Combining Measurements from Several Logs

Each log is affected by a number of parameters (Hoyle, 1986) of the rocks and borehole conditions, and different kinds of logs depend on the same parameters. By using combinations of logs, the interpreter hopes to separate these effects.

As an example, consider the measurement of porosity. Resistivity, sonic, density, and neutron log measurements all depend on both the porosity and the lithology, but in different ways. Cross-plots involve plotting results from different kinds of mea-

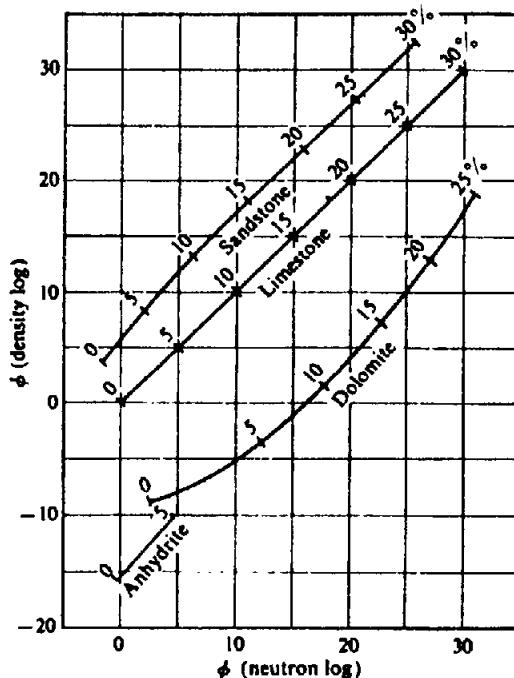


Figure 11.42. Porosity cross-plot. (Courtesy Schlumberger Ltd.)

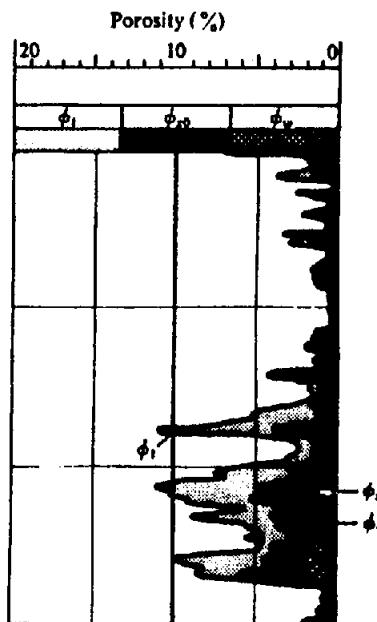


Figure 11.43. Moveable oil plot. (Courtesy Schlumberger Ltd.)

surements against each other. Figure 11.42 shows plots of the porosity calculated from density and from neutron logs. These calculations, in limestone porosity units, presumably give correct porosity values if the lithology is limestone (the limestone curve on this graph is linear with 45° slope). However, if the lithology is not limestone, the porosity is in error, but by different amounts depending on the nature of the lithology; thus the location of a plotted point on this graph gives both the lithology and the correct porosity. For mixed lithologies, interpolation be-

tween the curves gives the porosity and the average lithology, although the latter usually involves some ambiguity. Hopefully this can be further reduced by cross-plotting different log combinations.

The fact that the porosity determined from different logs is different is used in a moveable-oil plot (Fig. 11.43). Total porosity ( $\phi_t$ ) is calculated from a sonic log (§11.7.2), apparent water-filled porosity ( $\phi_w$ ) from a deep-investigation resistivity log such as a laterolog (§11.2.3), and flushed zone porosity ( $\phi_{xz}$ ) from a shallow resistivity log such as a micro-laterolog (§11.2.5). The difference between the latter two curves is interpreted as "moveable hydrocarbons" and the difference between the first two as "residual hydrocarbons."

The concept of cross-plotting two sets of measurements to separate the effects of two factors can be generalized to separate more than two factors. Extended analysis generally requires a computer with lookup tables of empirical relationships. Several analysis programs are now available. The Saraband\* sand-shale program utilizes five cross-plots and the Coriband\* complex lithology program utilizes many more. The "wild-card" in most analyses is clay content. Ions in the layer of water surrounding clay minerals contribute to the rock conductivity, requiring modification of relations, such as the Archie equations, which assume that the formation water is the only conductor present. A dual-water model allows for both the bound water and the formation water. It forms the basis for several computer-analysis programs (Volan\*, Cyberlook\*, and Global\*).

## 11.11. FIELD EXAMPLES

Although the detailed interpretation of well-log data is beyond the scope of this book, a few simple examples may indicate the possibilities. These are taken mainly from Pickett (1970). The variety of minerals encountered in these examples illustrates the versatility of logging techniques, especially combinations of logs.

### 11.11.1. Analysis of an Oil Sand

Figure 11.44 shows SP, resistivity, and acoustic-velocity logs for a Miocene sand section containing gas and oil. The SP log has a distinct break of 100 mV from positive to negative at 9,270 ft, indicating shale above and sand below this (compare with Fig. 11.12). Having found the mud filtrate resistivity by other means, we can use Equation (11.9) to get  $\rho_w$ ; it is about 0.06  $\Omega\text{m}$ . Using a combination of the lateral and normal curves with departure charts to correct

for borehole, invasion, and thin-bed effects, we obtain the formation resistivity  $\rho_f$ . It is about 30  $\Omega\text{m}$  from 9,272 to 9,308 ft and 0.6  $\Omega\text{m}$  between 9,308 and 9,350 ft. Finally, by means of Equation (11.3), the water saturation  $S_w$  is found to be about 15% between 9,272 and 9,308 ft and 100% below 9,308 ft.

Significant qualitative information may also be derived from these logs. Separation of the two microlog curves (note that the electrode spacing is different) indicates sections that are more permeable. The resistivity logs suggest which of these contain gas and oil (because of the resultant high resistivity).

In this rather simple example using only four logs, we can estimate a possible 15 ft of gas-bearing sand and 15 ft of oil-bearing sand, both having an average porosity of 30% [calculated from the sonic log and Eq. (11.14b)] and a water saturation of about 15%.

### 11.11.2. Analysis of Carbonate Section

The section in Figure 11.45 consists of dolomitic sands, evaporites, carbonates, and shaly carbonates. Gamma-ray, sonic, SP, and induction logs are shown at the left. The break in the SP curve is less definite than in the previous example so that an estimate of  $\rho_w$  would be unreliable. The induction log gives a reasonable value for  $\rho_f$  in the sands, but not for the higher-resistivity carbonates. The porosity estimate from the acoustic log was questionable because the values of  $V_f$  and  $V_m$  for Equation (11.14) were not well established. Thus an evaluation of the carbonates was not possible with this log combination.

Neutron and focused resistivity logs were added to aid in determining  $\phi$  and  $\rho_f$  in the carbonates. In both these devices the relative response between different zones was reliable but the absolute calibration was not. Sand porosities obtained from the acoustic log were used to calibrate the neutron-log response and the carbonate porosities were then determined. A similar calibration of the Laterolog-7, using the induction-log response in sands, permitted estimates of  $\rho_f$  in the carbonates. Values of  $\rho_w$  were obtained by measurements on cores. This interpretation does not seem as satisfactory as in the previous example; more logs would be required for a more reliable evaluation.

### 11.11.3. Coal Identification

Coal may be identified by high resistivity, low density, and low acoustic velocity. Electric logs were used as early as 1931 for this purpose. Figure 11.46 shows a section containing bituminous coal beds from a well in Colorado. The logging program included density, sonic, induction, 16 in. normal,  $\gamma$ -ray

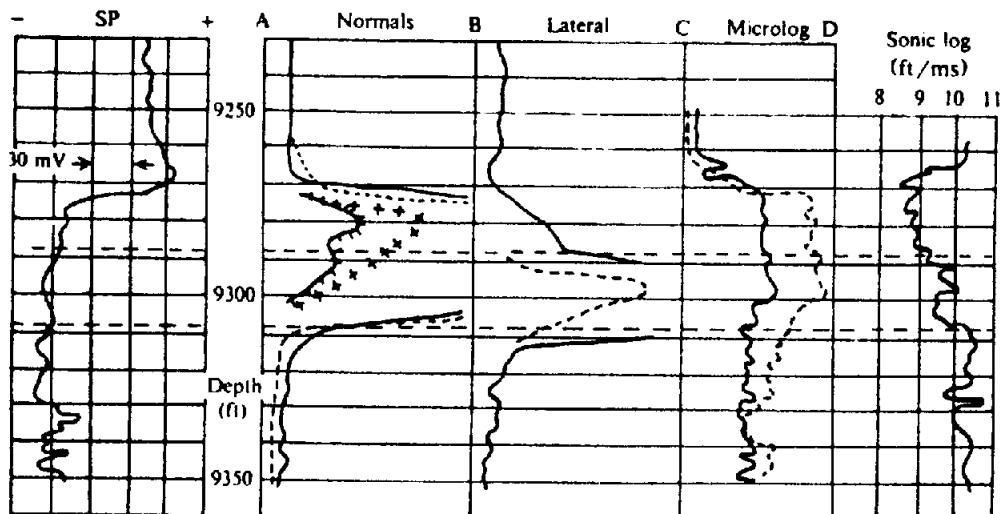


*Figure 11.44. Log suite in Miocene sand section containing oil and gas. Full scale for the 16 in. normal (solid curve) is 10  $\Omega\text{m}$ , for the amplified 16 in. normal (solid hachured) is 100  $\Omega\text{m}$ , for the 64 in. normal (dashed) is 10  $\Omega\text{m}$ , for the amplified 64 in. normal (crosses) is 1,000  $\Omega\text{m}$ , for the 18 ft 8 in. lateral (solid) is 10  $\Omega\text{m}$ , for the amplified 18 ft 8 in. lateral (dashed) is 100  $\Omega\text{m}$ , and for the microlog inverse (solid) and for the micronormal (dashed) is 10  $\Omega\text{m}$ .*

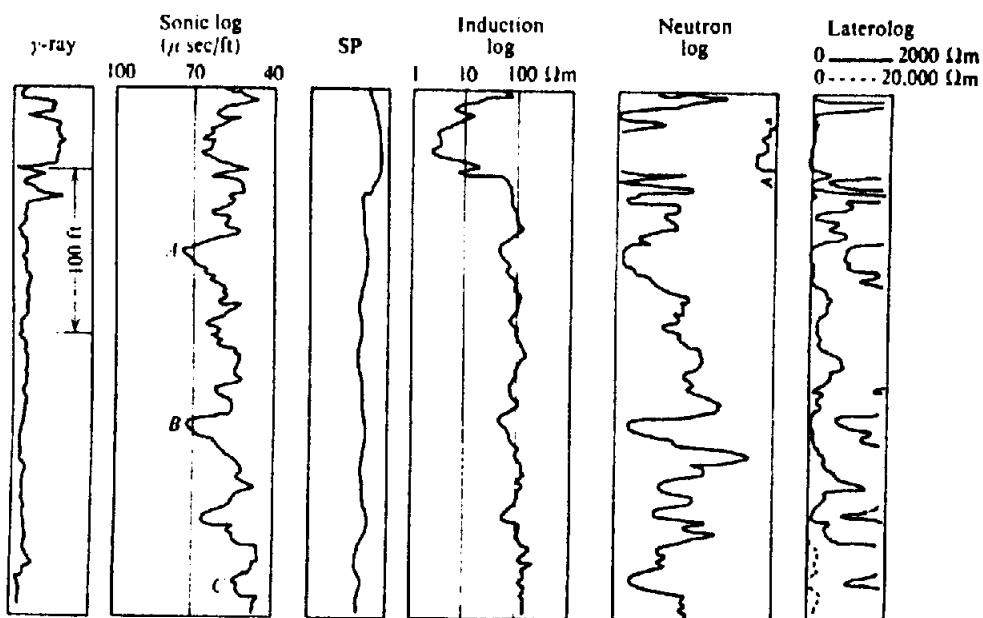


*Figure 11.45. Log suite in Minnelusa oil-bearing sand section. Zones A, B, and C contain oil.*

(not shown), and SP logs. The first three correlate particularly well with coal seams.

Generally the  $\Delta t$  values from the sonic log are larger for coal than in the adjacent shale beds, although the contrast depends on the coal grade and depth, both of which affect the compaction. For example, lignite produces a larger  $\Delta t$  excursion than anthracite, but increasing depth of burial will reduce the variation. The same factors affect the resistivity log, because higher grade coal and deeper beds contain less moisture and consequently have higher resistivity. The density log is probably the most reli-

able, because coal density is considerably lower than that of the adjacent beds, ranging from a maximum of 1.8 for anthracite to less than 1.0  $\text{g}/\text{cm}^3$  for lignite. The SP curve occasionally is anomalous opposite a coal seam.

#### 11.11.4. Evaporites

Caliper,  $\gamma$ -ray, and density curves through a section of interbedded shale, halite, and anhydrite are displayed in Figure 11.47. Halite and anhydrite are nonradioactive evaporites. The  $\gamma$ -ray log would be

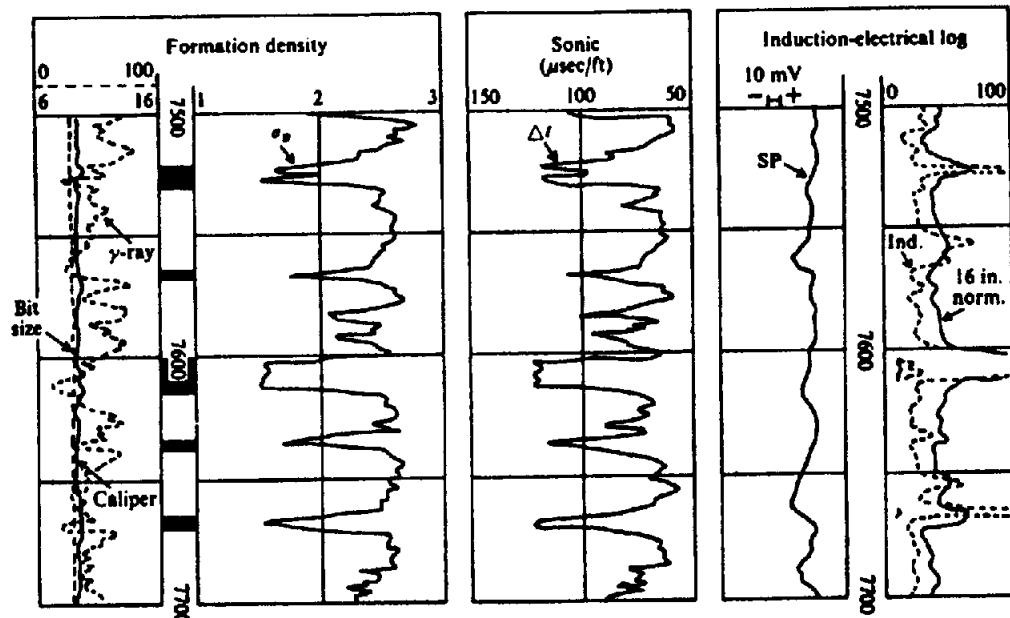


Figure 11.46. Identification of coal beds by density, sonic, and resistivity logs. (From Tixier and Alger, 1970.)

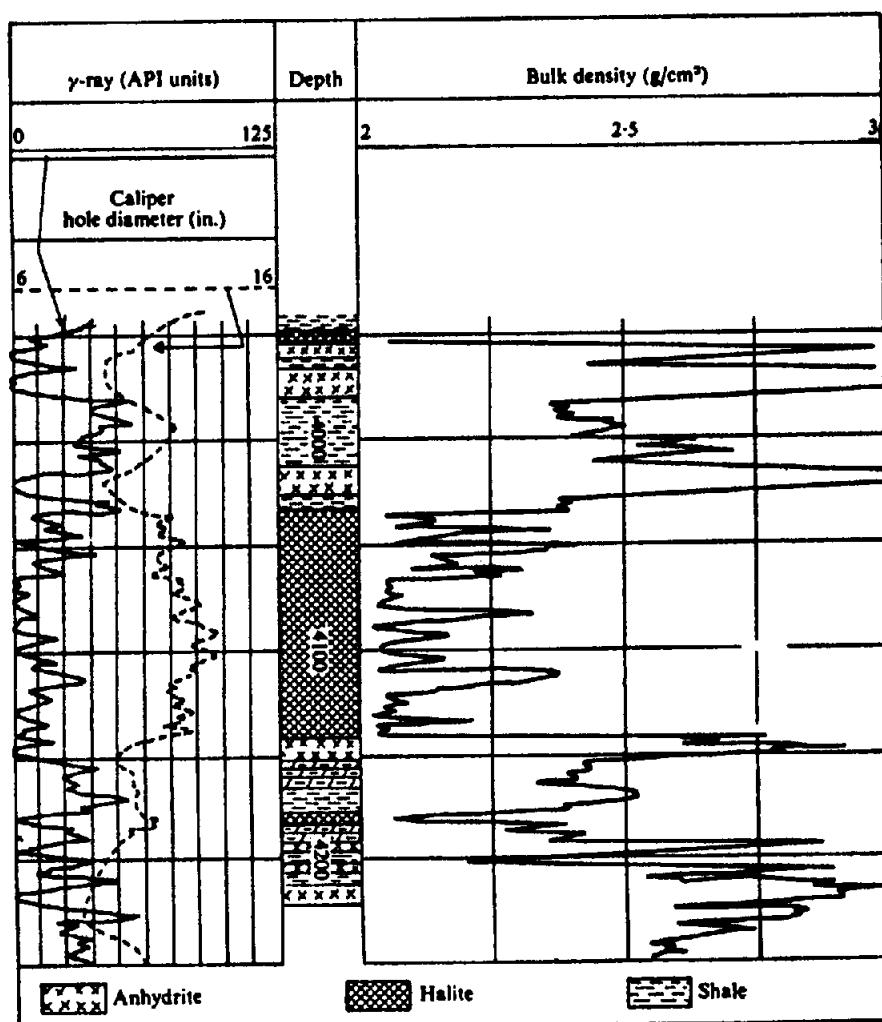


Figure 11.47. Identification of evaporites by density,  $\gamma$ -ray, and caliper logs. (From Tixier and Alger, 1970.)

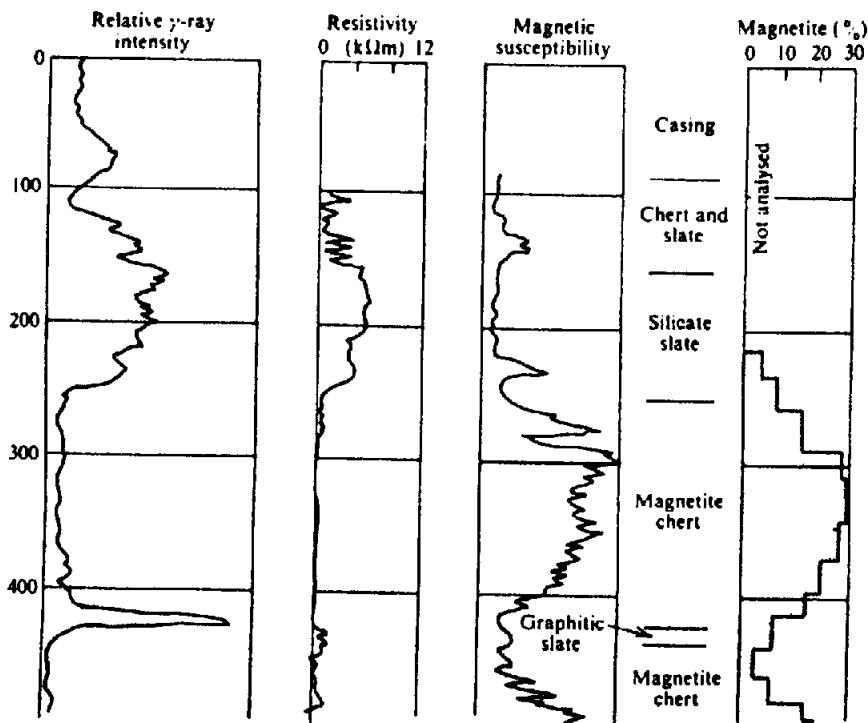


Figure 11.48. Gamma-ray, susceptibility, and resistivity logs in chert and slate beds.

more useful for potash, sylvite, and similar varieties containing potassium. The  $\gamma$ -ray log identifies the shale beds because of their higher radioactivity. The caliper log shows hole enlargement in the salt and shale zones. Anhydrite, with a density of nearly  $3 \text{ g/cm}^3$ , is clearly identified by the density log, whereas the intercalated shale is indicated by coincident highs and lows in the  $\gamma$ -ray and density curves.

#### 11.11.5. Sulfur

Sulfur, which occurs mainly in limestone, may be identified by the density or acoustic log because of its low density and low velocity ( $\Delta t$ ). The neutron log is also useful in sulfur detection. Occasionally the neutron log is replaced by a resistivity device for porosity determination.

In formations containing only limestone, sulfur, and water, two of these logs may suffice to provide a quantitative evaluation as well as identification. Where other rock minerals are also present, it may be necessary to employ all three logs.

#### 11.11.6. Slate and Chert

Figure 11.48 shows resistivity,  $\gamma$ -ray, and magnetic-susceptibility logs through a section of slate and chert beds. The  $\gamma$ -ray log clearly shows the slate because of its K content and the susceptibility curves show the chert because it is enriched with magnetite.

#### 11.11.7. Mineral Exploration

The Lac Dufault orebody northwest of Noranda, Quebec, is a classic example of the use of geophysical well logging in mining exploration where no other technique is feasible. Massive sulfides, pyrite, pyrrhotite, chalcopyrite, and sphalerite are found in gently dipping contacts between rhyolite and andesite at depths greater than 1,000 ft. Although the lateral extent of these ore zones is small, the high grade of chalcopyrite and sphalerite makes an attractive mining operation, provided they can be located. However, a deep-hole diamond drilling program on 200 ft centers is extremely costly.

Salt (1966) described a logging study that was carried out in 1962 using vertical-loop EM, horizontal-loop EM (large Turam-type transmitter loop), induced-polarization, and resistivity methods. The problem was to establish the existence of a nearby mineralized zone by logging a hole that missed it. It was found that any one of these methods would detect an orebody roughly  $400 \times 400$  ft in horizontal extent and 150 ft thick using a vertical drill hole within 125 ft of the edge of the orebody. However, it was difficult to determine the direction of the orebody with respect to the hole and to distinguish between massive sulfides and other conductors of unknown character. A plan of the orebody and diamond-drill-hole (DDH) locations can be seen in Figure 11.49a.

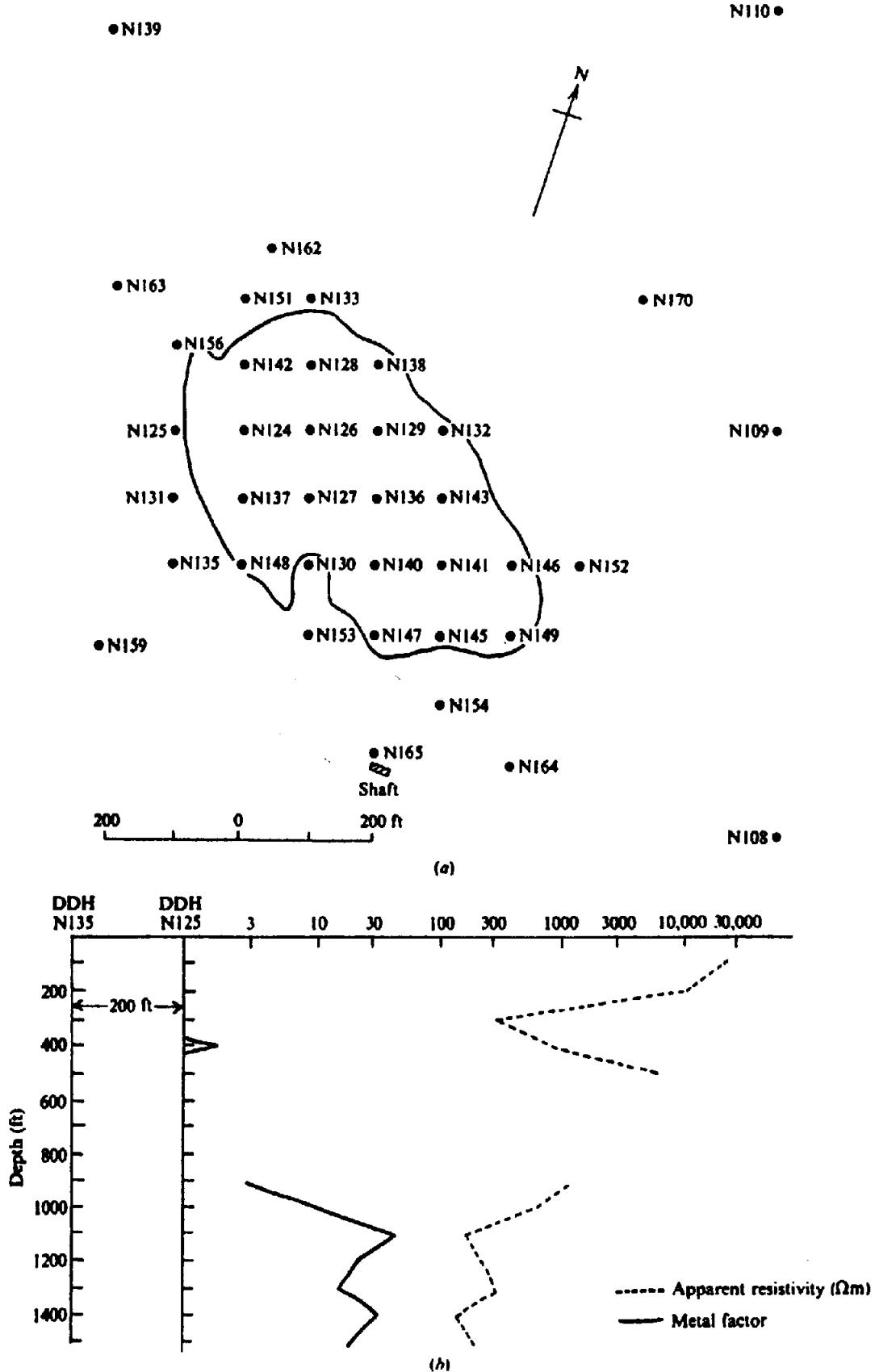


Figure 11.49. Combined IP-electrical survey to locate orebody at depth, Lac Dufault, Quebec. (From Salt, 1966.) (a) Plan of orebody and diamond-drill holes. (b) IP logs in DDH N125 and N135.

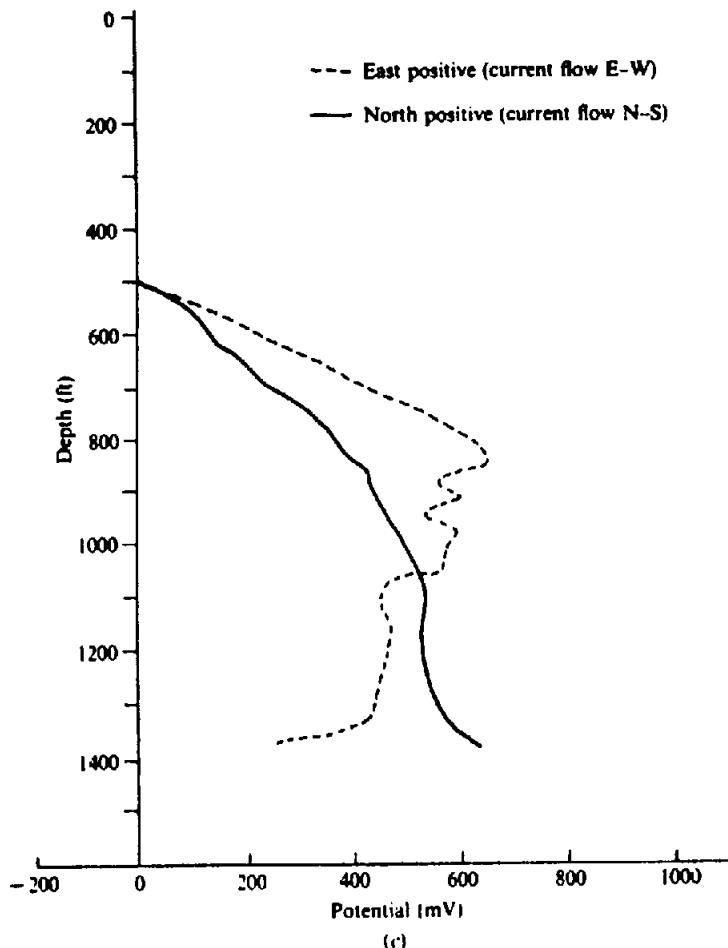


Figure 11.49. (Continued) (c) Log of potential in DDH N135.

Two logs from this study are shown in Figure 11.49b and c. Figure 11.49b shows metal factor and apparent resistivity measured with a frequency-domain IP unit. Large cable-coupling effects made it necessary to place the current and potential electrodes in separate drill holes (N125 and N135); with one current electrode at a distant point on the surface, a second current electrode was lowered down one hole and the two potential electrodes down the other at the same time. In Figure 11.49b the anomaly around 400 ft is not explained, but a definite peak at 1,100 ft corresponds to the massive sulfides east of the electrodes. Both the MF and  $\rho_a$  peaks decrease slowly to 1,300 ft, indicating that the sulfides lie mainly below 1,100 ft. The response at 1,400 ft is caused by disseminated sulfides below the main ore zone.

The second log, Figure 11.49c, is essentially the vertical potential distribution produced by current flow from two orthogonal pairs of current electrodes (connected alternately) at the surface. One potential electrode is fixed near the top of DDH N135 and the other is lowered in the hole, while direct current flows from north to south between surface electrodes 2,000 ft apart straddling the hole. Then the moveable

potential electrode is raised, with current flow E-W between similarly spaced current electrodes. In both curves the potential increases steadily downhole to about 850 ft. The E-W potential curve remains relatively constant between 850 and 1,050 ft and then falls off at greater depths. This effect is not apparent in the N-S curve, although the positive gradient is not so pronounced below 850 ft. From the differences between the two curves and the direction of current flow, one concludes that a conductor is located east of drill hole N135 and has a depth extent no greater than 200 ft.

Neither log is conclusive by itself, nor were the other techniques used in the survey. However, the reduction of drilling costs by allowing increased hole spacing would be significant and the possible control of future drilling programs by immediate logging is attractive.

#### 11.11.8. Borehole Methods in the USSR

Borehole geophysics apparently is essentially routine in the USSR (Zietz et al., 1976; Buselli, 1980). Well logging is carried out during detailed surveys with all types of mineralization; this is said to reduce by 50%

Table 11.5. Well-logging techniques used in USSR.

Borehole logging method	Purposes for which used
Various nuclear logs	Qualitative, quantitative mineral valuation
Gamma, gamma-spectroscopy	Locate U, Th, K, evaluate formations
Gamma-gamma	Determine density, porosity, clay content
Three-component magnetics and magnetic susceptibility	Dip, strike measurements, evaluate formations, locate and trace missed beds
IP, resistivity	Structure, continuity, sulfide evaluation
Three-component EM	Outline structures, locate missed conductors
SP	Determine depth extent of sulfide bodies

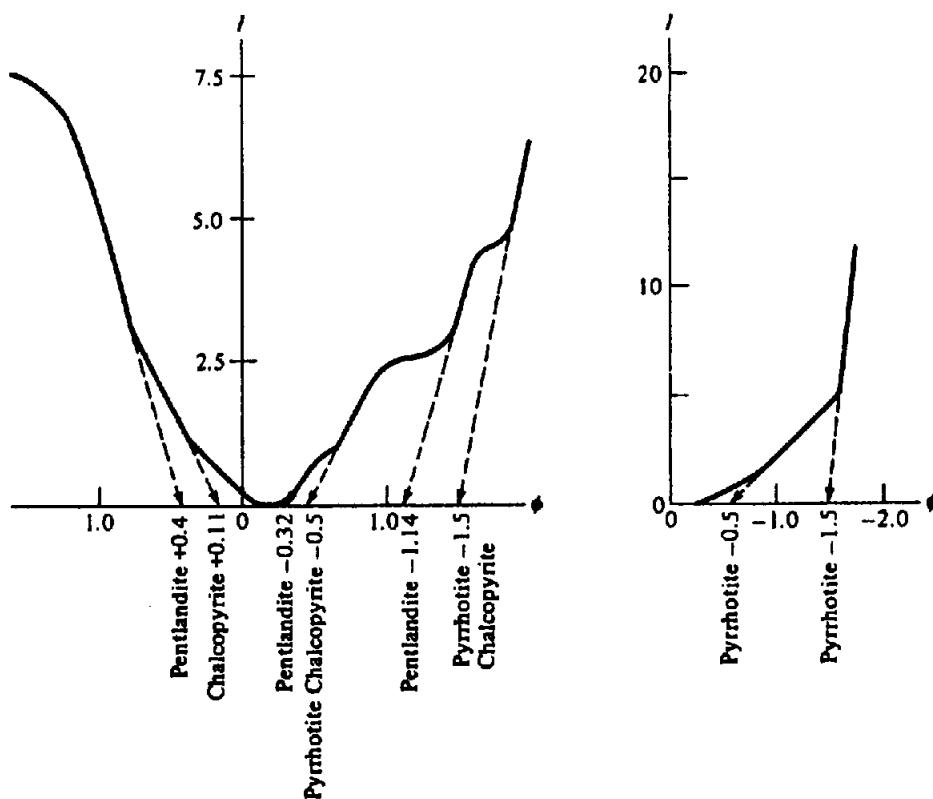


Figure 11.50. Polarization curves for a copper-nickel and pyrrhotite ore bodies. Current  $I$  is in amperes and contact potential  $\phi$  is in volts.

the drilling required to evaluate an orebody. Table 11.5 lists methods and applications; the last four methods in this table are used between holes and for *mise-à-la-masse* applications as well as in single holes.

An acoustic shadow technique uses an exploding wire source in one hole and receivers in another a few hundred meters distant. It is designed to outline faults, fractures, and anomalous beds. A radiowave shadow technique using frequencies in the range 150 kHz to 40 MHz is used to locate conductors in hole-to-hole measurements.

A piezoelectric method detects seismic and electric signals from a small explosive charge; it is used to trace quartz veins, sphalerite, and cassiterite mineralization between adjacent holes up to 120 m apart.

A contact method of polarization (somewhat analogous to *mise-à-la-masse*, see §8.5.4d) uses one

current electrode downhole in contact with mineralization and the other on the surface; voltage measurements are made on a surface grid as current is increased from 0 to  $\sim 250$  A. The breaks in a curve (Fig. 11.50) represent diagnostic contact potentials of various minerals; these are identified by extending the linear segments back to the  $\phi$  axis. The maximum current required to produce complete polarization curves indicates whether the mineralization is economic.

## 11.12. PROBLEMS

1. In the example in Section 11.11.7, is it possible to conclude from the IP log that the conductor is

definitely located east of drill holes N125 and N135 or merely that it is either east or west?

A direct-current source was used with the surface electrodes for the resistivity log in hole N135. By sketching the current lines and equipotentials, attempt to reproduce the curves in Figure 11.49c. How would you change either curve if the electrode polarization were reversed? Sketch the E-W potential curve if the drill holes were east of the orebody. What difference would it make if ac were used?

- The IP log shown in Figure 11.51 was obtained in a base-metal survey in northwestern Quebec. The mineralization consists of pyrite (up to 20%) and chalcopyrite (maximum 2.6% Cu) in a host rock of tuffs and agglomerates. One current and one potential electrode were lowered in the hole with

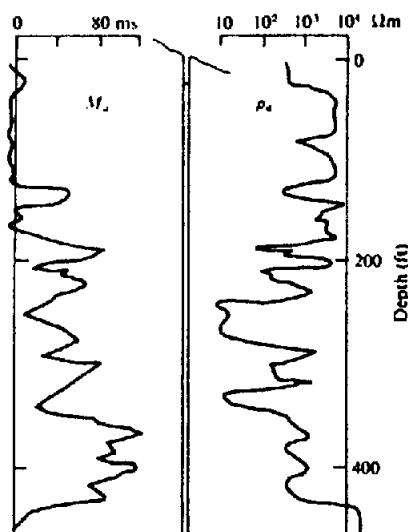


Figure 11.51. IP log in northwest Quebec.

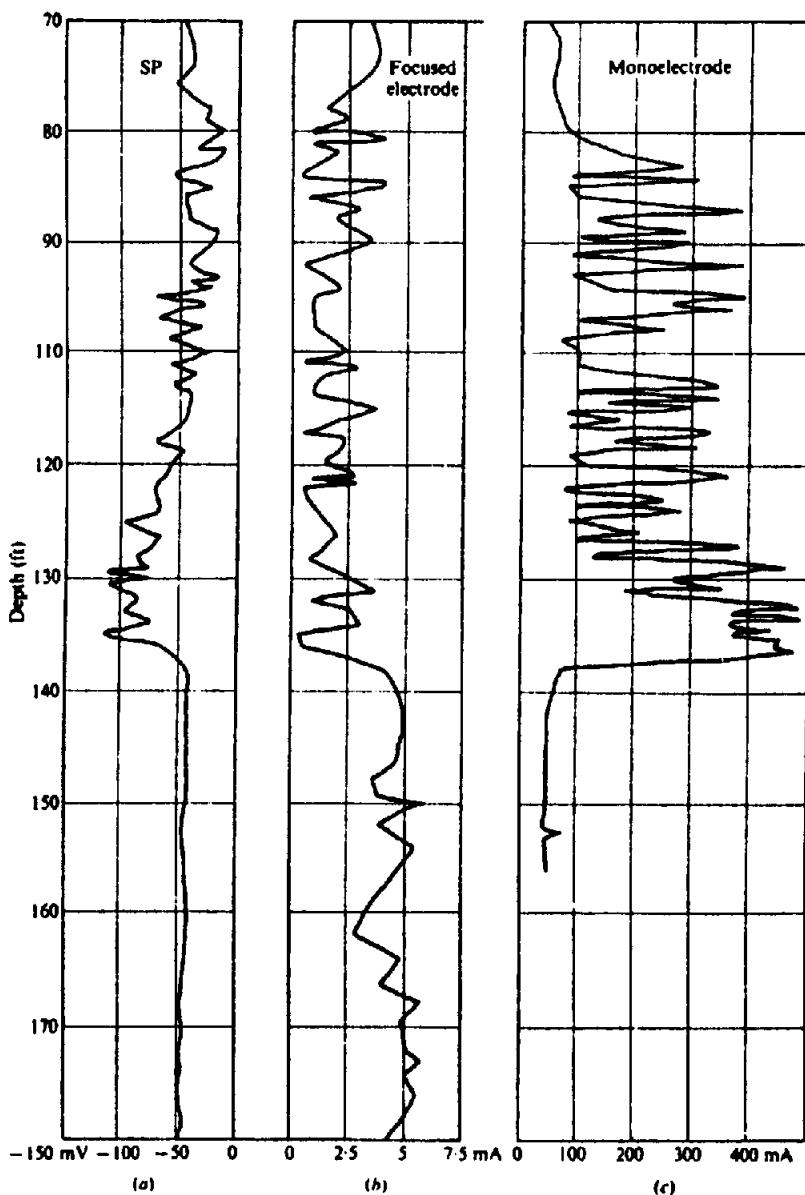


Figure 11.52. Experimental logs in base-metal area. (a) SP log. (b) Focused electrode sonde. (c) Monoelectrode survey using current-return electrode 80 to 110 ft deep in adjacent hole.

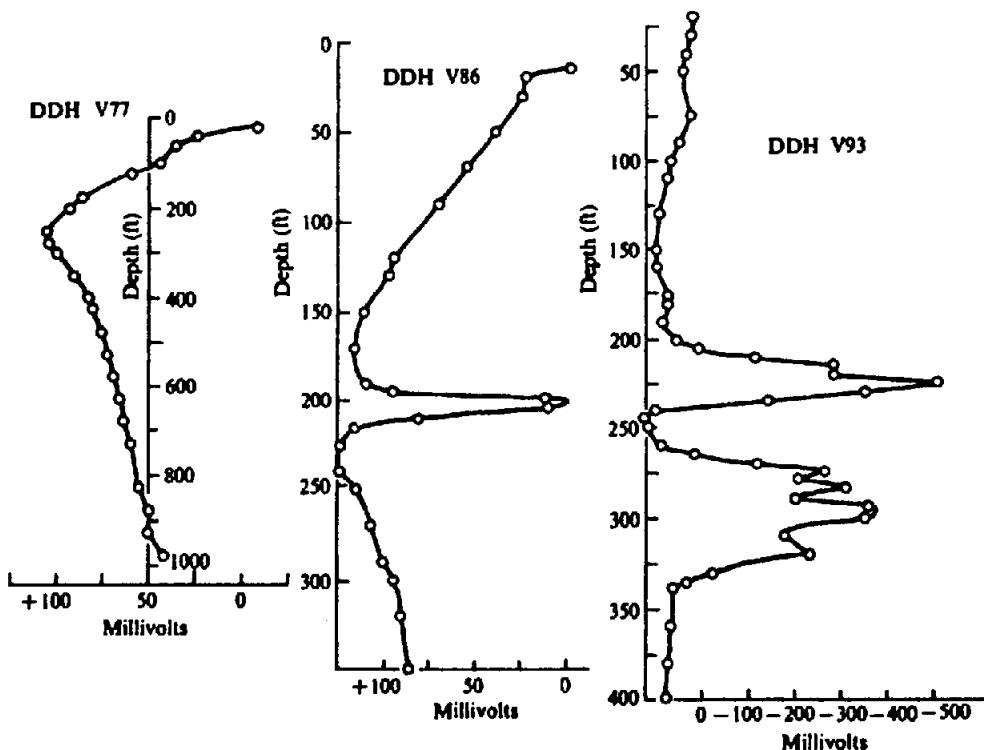


Figure 11.53. SP-logs in base-metal zones.

a fixed separation of 2 ft; the second current and potential electrodes were located on the surface at a considerable distance from the drill collar. Identify the mineral zones and if possible distinguish between chalcopyrite and pyrite sections.

3. Some results from an experimental logging study in base-metal areas are shown in Figure 11.52. The mineralization here occurs in two steeply dipping zones, one containing pyrite and chalcopyrite, the other mainly pyrite. The diamond-drill hole from which the logs were obtained was inclined approximately 60°.

The SP log is conventional with one fixed electrode in the hole just below the water level (and below the casing). The focused-electrode sonde, similar to Figure 11.6a, was made from 1 in. diameter lead-antimony pipe with PVC spacers, with 2 ft guard electrodes, 3 in. measuring electrode, and 2.5 in. spacers. Current return was through the uphole fixed SP electrode. The current source was a small 60 Hz motor generator.

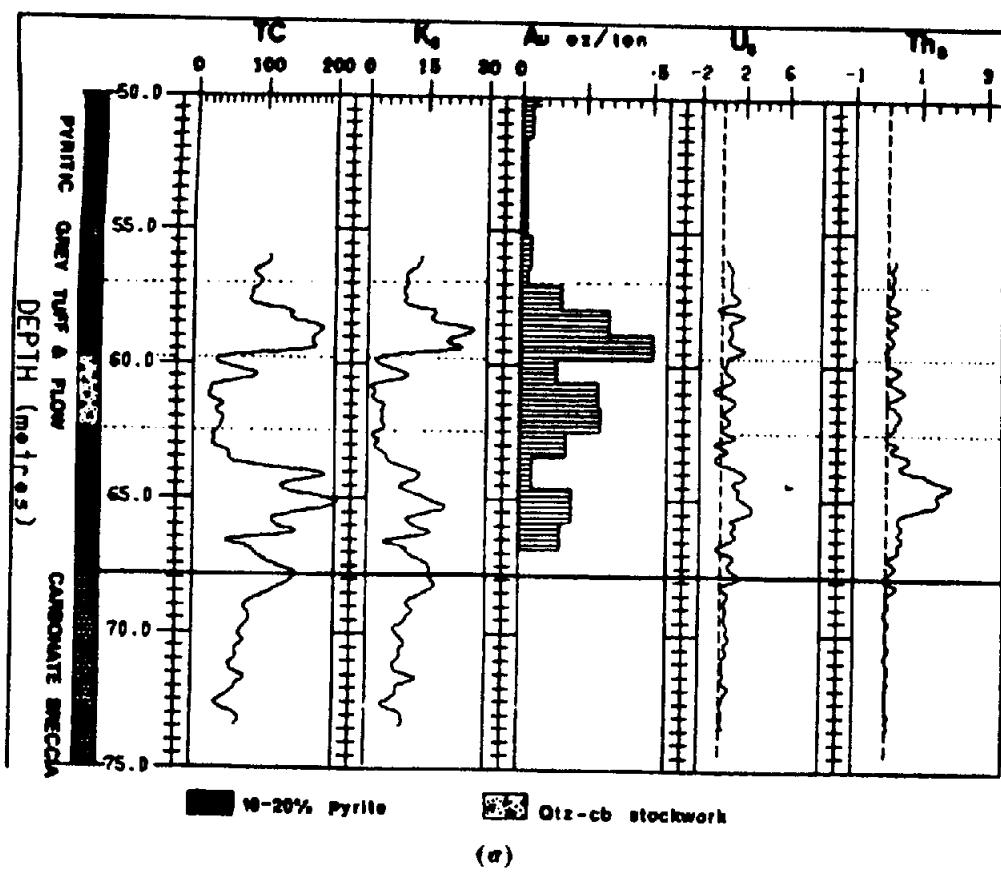
The *monoelectrode* curve in Figure 11.52 measured the current between the focused-electrode system and a second hole (previously logged and found to be essentially barren) in an attempt to establish mineralization continuity. The electrode in the second hole (an aluminum rod) was long enough to straddle the main mineral intersections; specifically, it extended from 80 to 110 ft. The two holes were about 100 ft apart. Identify the mineralization zone or zones. Is there any

indication of lateral extent? Calculate the effective resistivity at a few points on the focused resistivity curve from the formula of Dakhnov (1962),

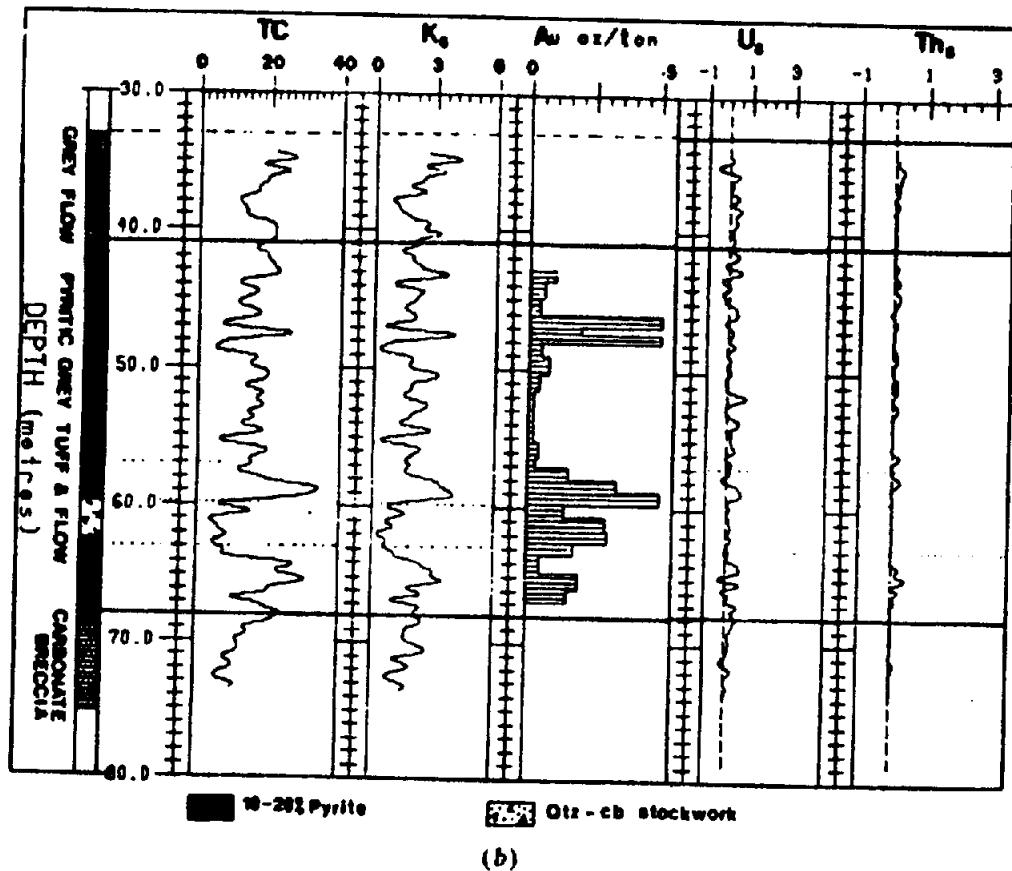
$$\rho_e = 2\pi \left( \frac{L_m}{L_r} \right) \left( \frac{V}{I} \right) \frac{(L_r^2 - 1)^{1/2}}{\log(L_r^2 - 1)}$$

where  $L_m$  is the length of the focused electrode,  $L_r$  is the ratio of length to diameter of the electrode assembly,  $V$  is the potential of the focused electrode (110 V), and  $I$  is the current in the focused electrode.

4. SP logs at a base-metal property in northwestern Quebec are shown in Figure 11.53. The host rocks are andesites, diorites, and rhyolites, the overburden is sand and clay. The mineralization consists of pyrite, pyrrhotite, sphalerite, chalcopyrite, and, in places, bands of magnetite. An earlier surface SP survey showed no anomaly. What is your explanation for the barren surface SP? Given the additional information that massive sulfides were found from 25 to 31 ft and from 65 to 89 ft in a fourth hole nearby, would you change your explanation? Can you account for the pronounced positive excursion in holes V77 and V86 between surface and 200 ft? Make as complete an interpretation as you can.
5. Use of airborne and ground radiometrics for gold exploration has been reported in Soviet journals since 1970; these indicate a strong association

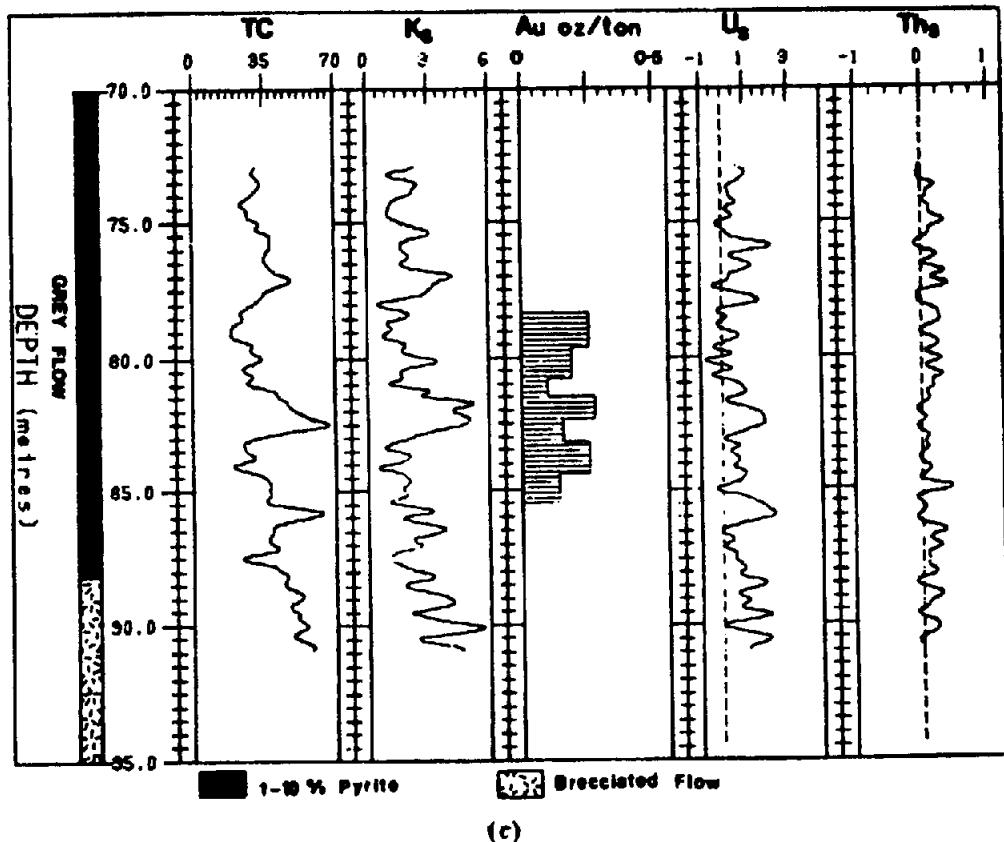


(a)

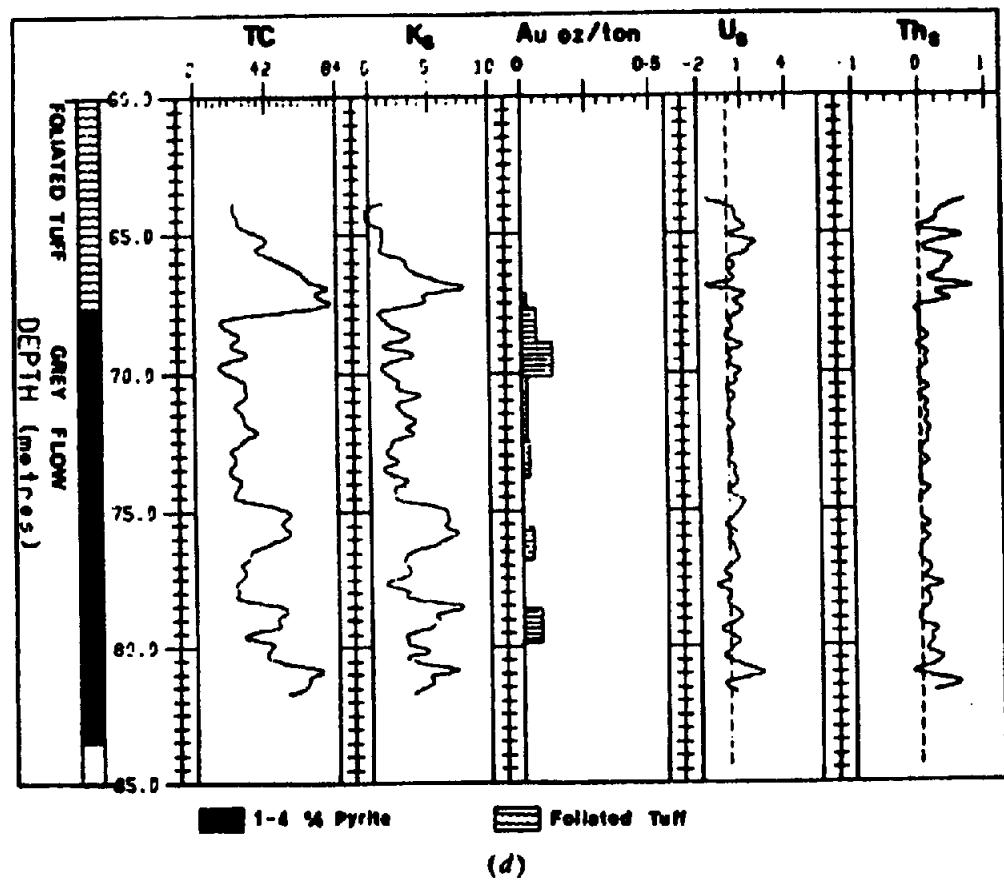


(b)

Figure 11.54. Gamma-ray spectral logs in four boreholes in the Larder Lake gold camp, northern Ontario. (a) Logs in boreholes BL-80-25, (b) BL-80-40.



(c)



(d)

Figure 11.54. (Continued) (c) BL-80-31. (d) BL-80-30. (From Mwenifumbo, Urbancic, and Killeen, 1983.)

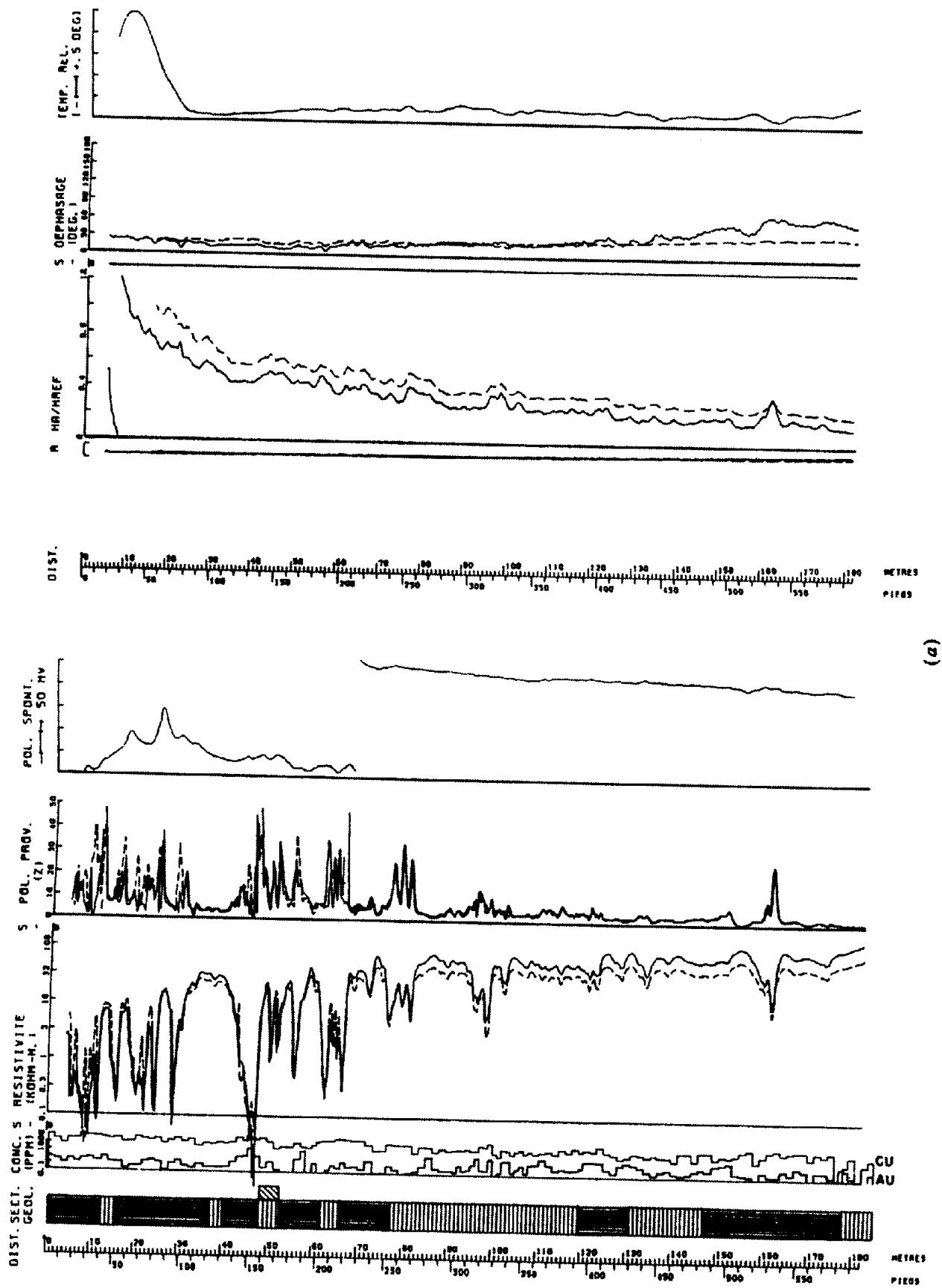


Figure 11.55. Logs from three holes in the Pascalis gold area near Val d'Or in northern Quebec. For the first hole, gold and copper assays are shown; for the second hole, gold assays are shown. (a) Logs in boreholes 83-22.

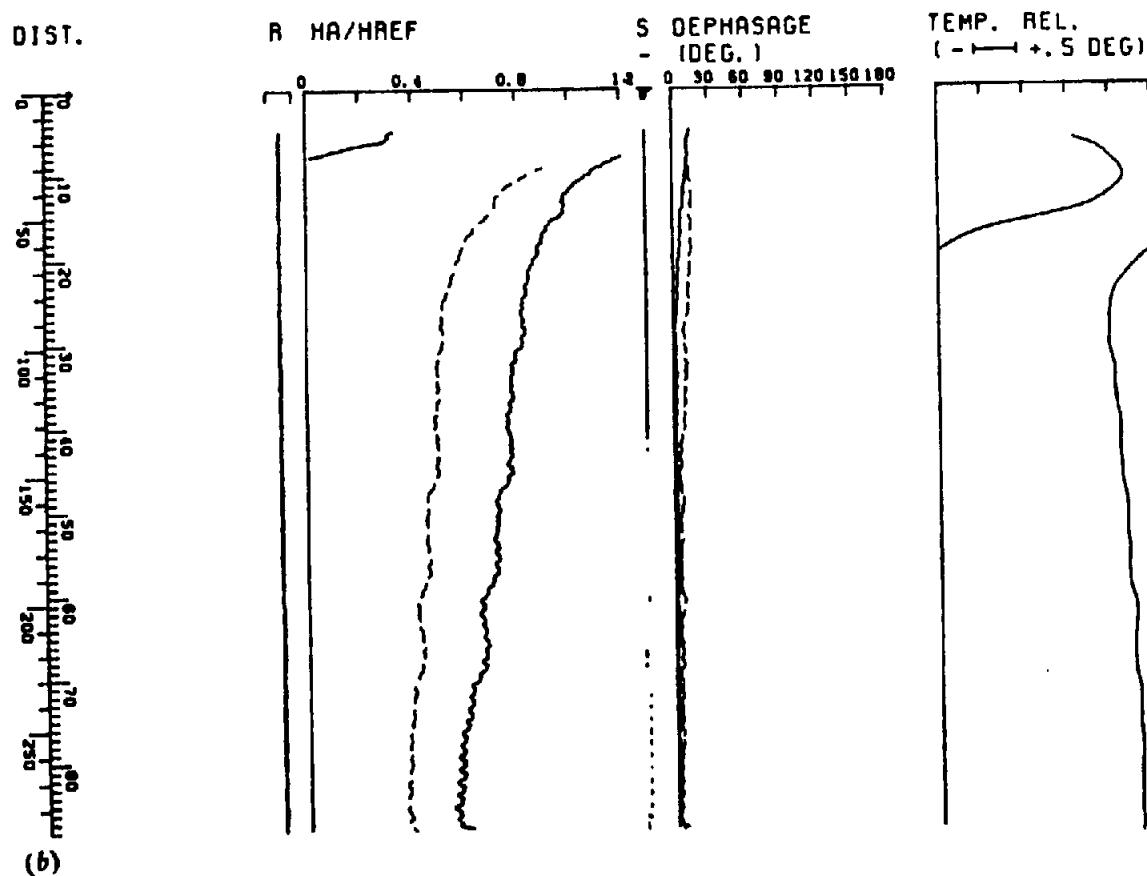
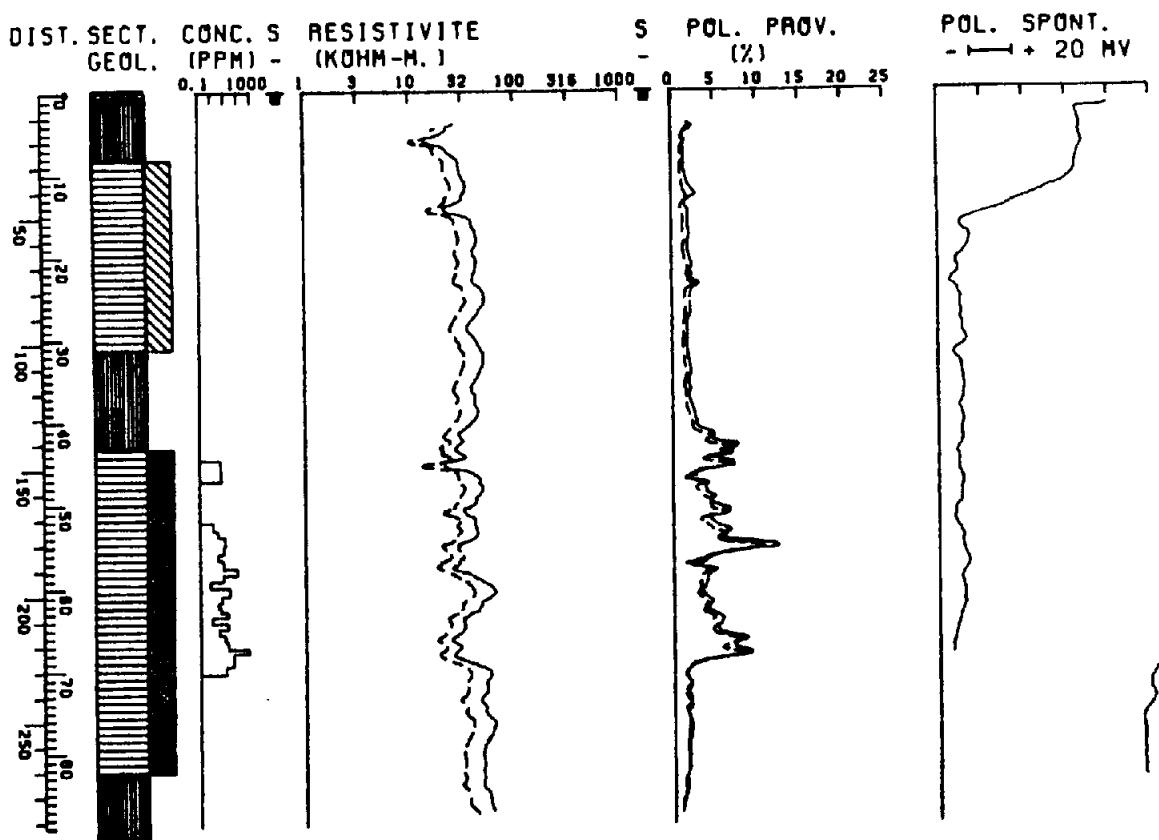


Figure 11.55. (Continued) (b) 83-102.

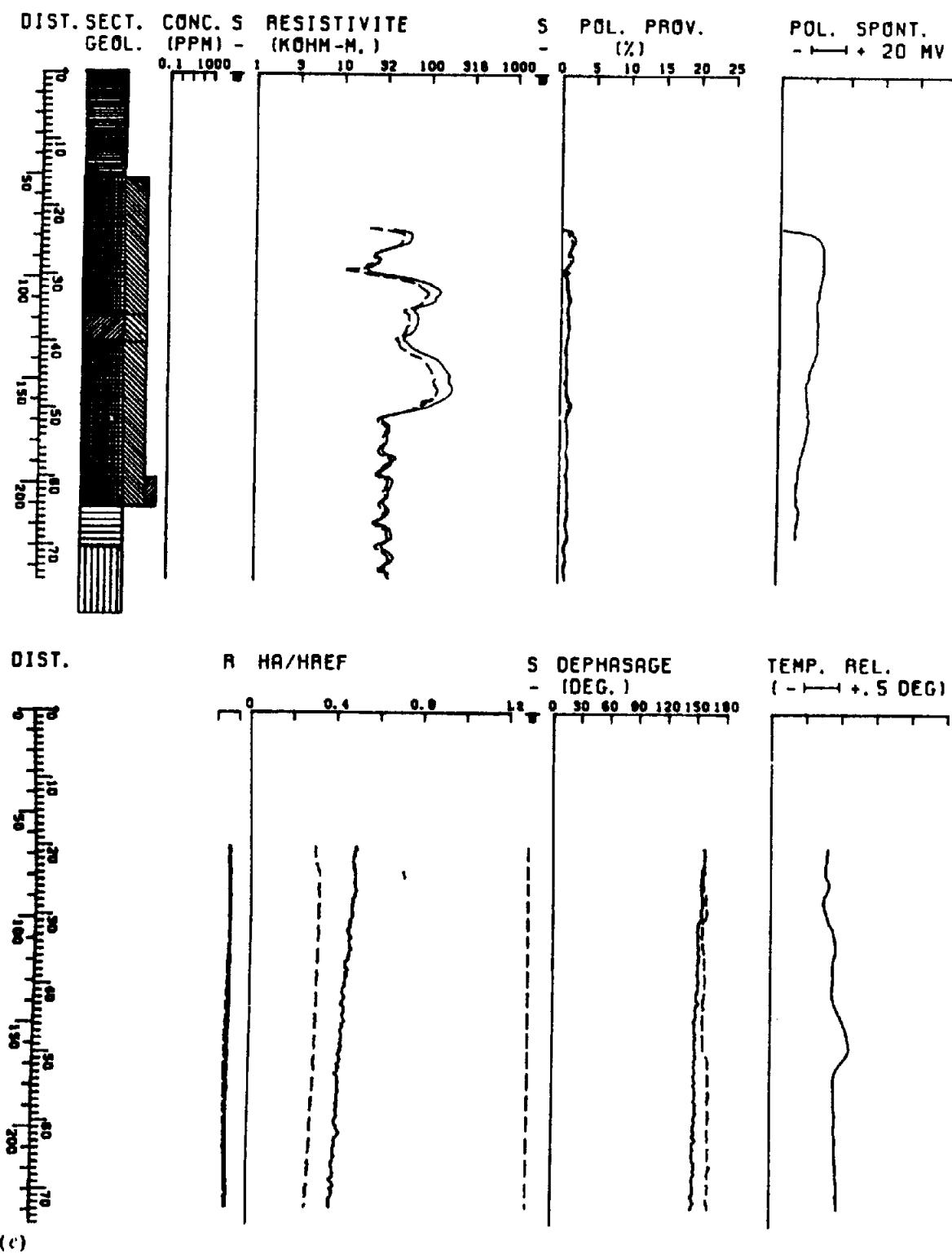


Figure 11.55. (Continued) (c) 83-116.

- between gold mineralization and potassium alteration zones. Mwenifumbo, Urbancic, and Killeen (1983) applied  $\gamma$ -ray spectral logging in the Larder Lake gold camp in northern Ontario. They used a Geological Survey of Canada logging unit described in Conaway, Bristow, and Killeen (1980). Results from four boreholes are displayed in Figure 11.54 which include total count (TC), stripped K, U, and Th ( $K_s$ ,  $U_s$ , and  $Th_s$ ) (§10.7, problem 4), gold assay (Au), and core logs showing pyrite mineralization. The geology consists of flow-type pyritized and silicified zones lying in altered volcanic flows and tuffs. Gold correlation with pyrite mineralization is very good. What can you say about gold association with  $^{40}\text{K}$ ? The ratios Th/K, U/K, and U/Th are used as halo indicators around mineral deposits; do they correlate with gold? What logging techniques are suited for detecting the pyrite zones? Some elementary statistical analysis should be useful.
6. Pyrite, after quartz, is the most abundant mineral associated with gold; a more general statement would link gold occurrences with a variety of sulfide mineralization. Examples are shown in Figure 11.55 from the Pascalis gold deposit near Val d'Or in northern Quebec (Roy, 1984). Three drill holes were logged with SP, IP, resistivity, and VLF EM tools. The SP is conventional with one electrode downhole, the other at surface. IP and resistivity, measured simultaneously, are identical either in the normal or pole-dipole configuration. Two spacings are available for each; for the normal,  $AM = 0.4$  or  $0.8$  m,  $MN = 7.5$  or  $2.2$  m, respectively, whereas for the pole-dipole,  $AM = MN = 7.5$  or  $15$  m. The VLF log measures two phase components of the downhole signal, with a maximum-coupled magnetic sensor at the surface for phase and amplitude reference. The VLF frequencies used were  $17.8$  kHz (NAA Cutler) and  $21.4$  kHz (NSS Annapolis). Figure 11.55 shows an uninteresting SP log, strong IP, and resistivity response at the two normal spacings, much less so for the pole-dipole. Figure 11.55a also shows gold and copper assays over the  $180$  m depth extent of DDH 83-22 and Figure 11.55b shows only gold. The VLF amplitude and phase variations have been normalized. Correlate these logs with gold and copper as completely as possible.

## REFERENCES

- Archie, G. E. 1942. The electrical resistivity log as an aid in determining some reservoir characteristics. *Trans. A.I.M.E.* 146, 54–64.
- Becker, A., and Telford, W. M. 1965. Spontaneous polarization studies. *Geophys. Prosp.* 13, 173–88.
- Buselli, G. 1980. Electrical geophysics in the U.S.S.R. *Geophysics* 45, 1551–62.
- Conaway, J. G., Bristow, Q., and Killeen, P. G. 1980. Optimization of gamma-ray logging techniques for uranium. *Geophysics* 45, 292–311.
- Dakhnov, V. N. 1962. Geophysical well logging. *Quarterly of Col. School of Mines* 57.
- Doll, H. G. 1949. Introduction to induction logging and applications to logging of wells drilled with oil-based mud. *Trans. A.I.M.E.* 186, 148–62.
- Doll, H. G. 1951. The laterolog, a new resistivity logging method with electrodes using an automatic focusing system. *Trans. A.I.M.E.* 192, 305–16.
- Doll, H. G. 1953. The microlaterolog. *Trans. A.I.M.E.* 198, 17–32.
- Freedman, R., and Vogatzis, K. P. 1979. Theory of microwave dielectric constant logging using the electromagnetic wave propagation method. *Geophysics* 44, 969–86.
- Gilreath, J. A. 1987. Dipmeter interpretation rules. In *The Technical Review*. Houston: Schlumberger Educational Services.
- Glenn, W. E., and Nelson, P. H. 1979. Borehole logging techniques applied to base-metal ore deposits. In *Geophysics and geochemistry in the search for metallic ores*, P. J. Hood, ed., Econ. Geol. Report 31, Geol. Surv. Canada, pp. 273–94.
- Hoyle, J. B. 1986. Computer techniques for the zoning and correlation of well-logs. *Geophys. Prosp.* 34, 648–64.
- Jackson, P. D. 1981. Focused electrical resistivity arrays: Some theoretical and practical experiments. *Geophys. Prosp.* 29, 601–26.
- Keys, W. S., and MacCarey, L. M. 1971. Applications of borehole geophysics to water resources investigations. In *Techniques of Water Resources Investigation*, Book 2, Ch. E1. Washington: U.S. Geol. Surv.
- Labo, J. 1987. *A Practical Introduction to Borehole Geophysics*. Tulsa: Society of Exploration Geophysicists.
- Mansinha, L., and Mwenifumbo, C. J. 1983. A mise-à-la-masse study of the Cavendish geophysical test site. *Geophysics* 48, 1252–7.
- Moran, J. H. 1972. Discussion on radius of investigation in dc resistivity well logging. *Geophysics* 37, 542–3.
- Moran, J. H., and Chermali, R. E. 1979. More on the Laterolog device. *Geophys. Prosp.* 27, 902–3.
- Morris, C. F., Little, T. M., and Letton, W. 1984. Soc. Petr. Eng. 59th Ann. Fall Tech. Conf., paper SPE 13285.
- Mwenifumbo, C. J., Urbancic, T. I., and Killeen, P. G. 1983. Preliminary studies on gamma-ray spectral logging in exploration for gold. In *Current research, Part A*, Geol. Surv. Can. Paper 83-1A, pp. 391–7.
- Nickel, H., Sender, R., Thierbach, R., and Weichert, H. 1983. Exploring the interior of salt domes from boreholes. *Geophys. Prosp.* 31, 131–48.
- Paillet, F. L., and White, J. E. 1982. Acoustic modes of propagation in the borehole and their relationship to rock properties. *Geophysics* 47, 1215–28.
- Pascal, H. 1983. Further discussion of attenuation and dispersion of electromagnetic wave propagation in fluid-saturated rocks and applications to dielectric constant well logging. *Geophysics* 48, 1373–80.
- Pickett, G. R. 1970. Applications for borehole geophysics in geophysical exploration. *Geophysics* 35, 81–92.
- Pinnington, D., ed. 1981. *Well Evaluation Conference, Abu Dhabi*. Ridgefield (CT): Schlumberger.
- Pirson, S. J. 1970. *Geologic Well Log Analysis*. Houston: Gulf Publishing.

- Roy, A., and Dhar, R. L. 1971. Radius of investigation in dc resistivity well logging. *Geophysics* 36, 754-60.
- Roy, J. 1984. Electrical methods in mineral well logging. Ph.D. thesis, McGill Univ., Montreal.
- Salt, D. J. 1966. Tests of drill-hole methods of geophysical prospecting on the property of Lac Dufault Mines Ltd., Dufresnoy Twp., Quebec. In *Mining Geophysics*, vol. I, pp. 206-26. Tulsa: Society of Exploration Geophysicists.
- Schlumberger 1972. *Log Interpretation I - Principles*. Houston: Schlumberger Ltd.
- Schlumberger 1986. *Log Interpretation Charts*. Houston: Schlumberger Educational Services.
- Schlumberger 1987. *Log Interpretation Principles / Applications*. Houston: Schlumberger Educational Services.
- Schmitt, D. P., and Bouchon, M. 1985. Full-wave acoustic logging: Synthetic microseismograms and frequency-wavenumber analysis. *Geophysics* 50, 1756-78.
- Segesman, F. F. 1980. History of geophysical exploration: Well logging method. *Geophysics* 45, 1667-84.
- Seigel, H. O. 1979. An overview of mining geophysics. In *Geophysics and geochemistry in the search for metallic ores*, P. J. Hood, ed., Econ. Geol. Report 31, Geol. Surv. Canada, pp. 7-24.
- Sheriff, R. E., and Geldart, L. P. 1982. *Exploration Seismology*, vol. I. Cambridge: Cambridge University Press.
- Silva, J. B. C., and Hohmann, G. W. 1981. Interpretation of three-component borehole magnetometer data. *Geophysics* 46, 1721-31.
- Snyder, D. D., and Fleming, D. B. 1985. Well logging - a 25 year perspective. *Geophysics* 50, 2504-29.
- Tittman, J. 1986. *Geophysical Well Logging*. New York: Academic Press.
- Tixier, M. P., and Alger, R. P. 1970. Log evaluation of non-metallic deposits. *Geophysics* 35, 124-42.
- Wagg, D. M., and Seigel, H. O. 1963. IP in drill holes. *Can. Mining Jour.* 84, 54-9.
- Wahl, J. S. 1983. Gamma-ray logging. *Geophysics* 48, 1536-50.
- Worthington, M. H., Kuckes, A., and Oristaglio, M. 1981. A borehole induction procedure for investigating electrical conductivity structure within the broad vicinity of a hole. *Geophysics* 46, 65-7.
- Wyllie, M. R. J. 1949. A quantitative analysis of the electrochemical component of the SP curve. *Trans. A.I.M.E.* 186, 17-26.
- Wyllie, M. R. J., Gregory, A. R., and Gardner, G. H. F. 1958. An experimental investigation of factors affecting elastic wave velocities in porous media. *Geophysics* 23, 459-93.
- Zeitz, I., Eaton, G. P., Frischknecht, F. C., Kane, M. F., and Moss, C. K. 1976. A Western view of mining geophysics in the USSR. *Geophysics* 41, 310-23.
- Zemanek, J., Caldwell, R. L., Glenn, E. E., Holcomb, S. V., Norton, L. J., and Strauss, A. J. D. 1970. The borehole televIEWER - a new logging concept for fracture location and other types of borehole investigation. *Jour. Petr. Tech.* 21, 762-74.

# Chapter 12

## *Integrated Geophysical Problems*

### 12.1. INTRODUCTION

The application of several disciplines – geology, geochemistry, geophysics – constitutes an integrated exploration program. In a more restricted sense we may consider the integrated geophysics program as the use of several geophysical techniques in the same area. The fact that this type of operation is so commonplace is because the exploration geophysicist, by a suitable selection of, say, four methods, may obtain much more than four times the information he would get from any one of them alone.

Before elaborating on this topic it is necessary to point out again the paramount importance of geology in exploration work. Every geological feature, from tectonic blocks of subcontinental size to the smallest rock fracture, may provide a clue in the search for economic minerals. Thus geologic information exerts a most significant influence on the whole exploration program, the choice of area, geophysical techniques, and, above all, the interpretation of results. Without this control the geophysicist figuratively is working in the dark.

The subject of integrated geophysical surveys has received considerable attention in the technical literature since about 1960. In petroleum exploration the combination of gravity and magnetic reconnaissance, plus seismic for both reconnaissance and detail (and, of course, various well-logging techniques during the course of drilling) is well established.

The best combination for an integrated mineral exploration program is not so definite because of the great variety of targets and detection methods available. Base-metal search is a case in point. If the area is large enough and the money available, the program normally would start with a combined airborne magnetic and EM survey. On a more modest scale, the work might proceed from a study of acquired airborne data or from a reconnaissance geochemical survey. In either case the ground followup would

include magnetics, one or more EM techniques, and possibly gravity. IP may replace EM or follow it, particularly where the mineralization appears to be diffuse or low grade. There are, of course, additional possibilities, for example, SP, tellurics, and magnetotellurics. In any event, the base-metal program, compared to the standard sequence in oil search, appears either pleasantly flexible or somewhat fuzzy, depending on the attitude and experience of the exploration manager.

There is another significant factor affecting exploration work in general and multiple geophysical surveys in particular, which is not sufficiently stressed. This is the time element. In an ideal situation the survey work would be carried out in a well-ordered sequence, proceeding from reconnaissance to detail and extracting all possible information from each survey before starting the next one. Practically this orderly, controlled procedure is impossible. Frequently there is pressure from the competition and from the equipment suppliers and contractors (several surveys must be done simultaneously, or in the wrong sequence, or one survey cannot be made until it is too late to be of much use). Time is money as well; the financial source may elect to start drilling or to abandon the operation entirely (for reasons which could be quite valid) before the survey is complete.

Finally it is wise to keep in mind that the exploration program should lead to elimination as well as acquisition of prospects. An overabundance of anomalies is, in the end, almost as unattractive as none at all.

The reader who has studied the field examples and problems in the various chapters with anything more than casual interest doubtless will have deduced that many of them are not isolated examples of a single geophysical method applied to a particular area. This is indeed the case and in the present chapter we will assemble some of these to make

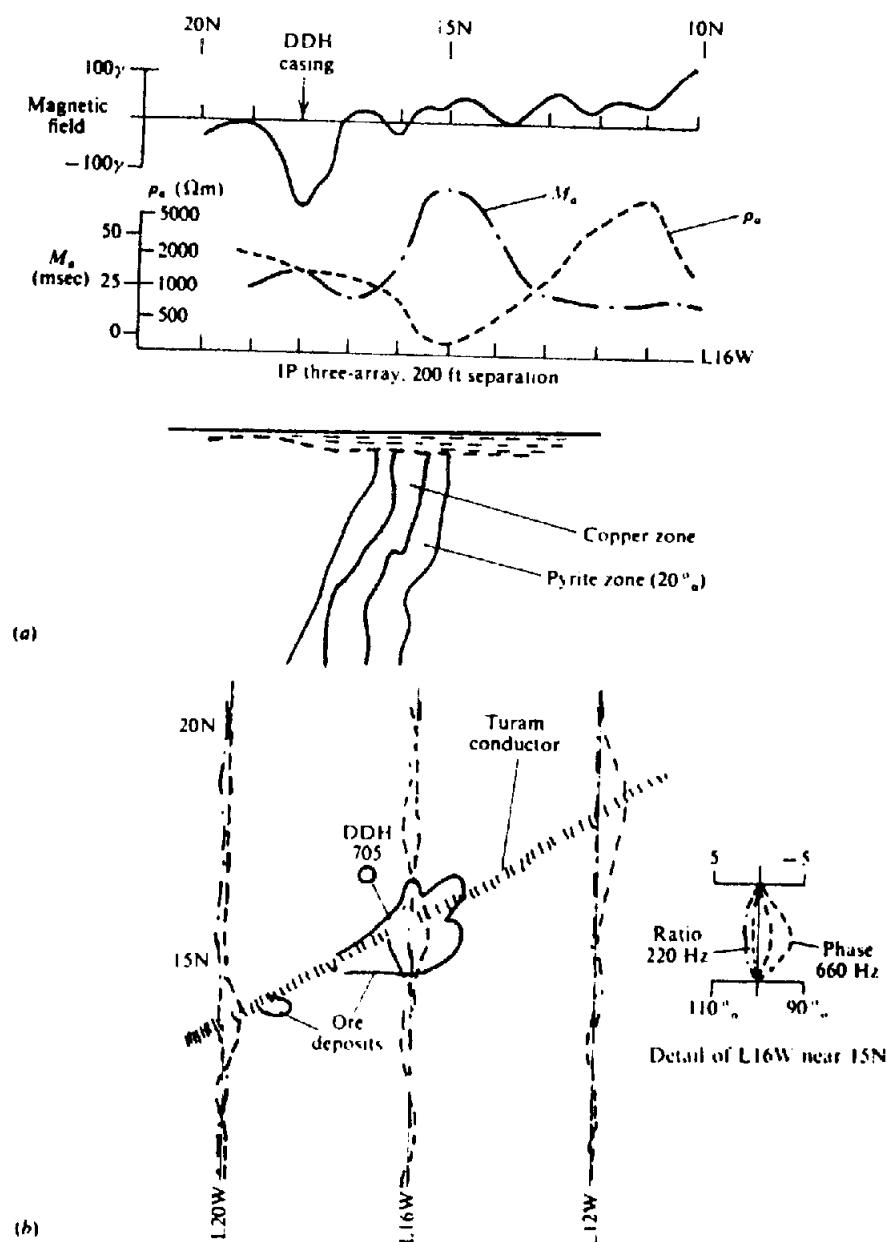


**Figure 12.1.** Magnetics, IP, and Turam results, Louvicourt area, Quebec. (a) Magnetic and IP profiles, L16W, and vertical section. (b) Turam results; loop located at 0 + 00N.

integrated surveys for further consideration. Analyses of the examples and problems given here should be made on the basis of several factors, including the following.

How much additional information is provided by the combination of techniques?

Is this information positive or negative, definite or indefinite in quality?

Is the procedural sequence reasonable (magnetics with EM, followed by gravity, or whatever) and, if not, why was it done in this way and how would you modify it?

Are the number and selection of methods necessary and sufficient to make a decision either to walk away from the prospect or develop it further?

Are any of the methods used in a particular example superfluous? Would the money be better spent on drilling?

## 12.2. EXAMPLES AND PROBLEMS

1. Compare the gravity interpretation of problem 17, Section 2.9, with the analysis of the magnetic feature near St. Bruno, Quebec, described in field example 1, Section 3.8.2. Presumably the same structure produces both anomalies. Are the results satisfactory and if not, is it possible to make reasonable adjustments of certain parameters to obtain better agreement?

2. The large gravity anomaly of field example 1 (Portland Creek Pond), Section 2.8, occurs within

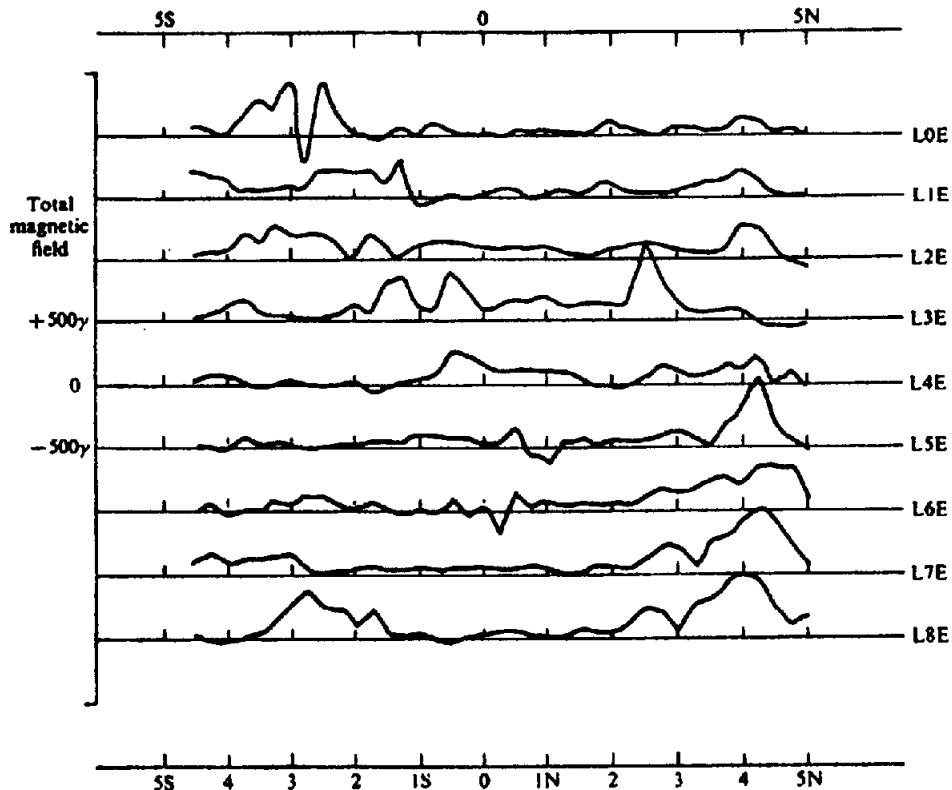


Figure 12.2. Total-field ground-magnetic profiles, Uchi Lake, northwestern Ontario.

the area shown in Figure 3.42, problem 13, Section 3.9. (It is difficult to locate it precisely because the aeromagnetic section is from a much larger map; certain topographic features, such as shorelines in Figure 2.36a, which were not reproduced in Figure 3.42, do not coincide. Furthermore it is surprising that there is no mention in the gravity work report of the 200 m scarp described in problem 13; such rugged topography would certainly require a terrain correction.) Unfortunately ground magnetics were not carried out during the gravity survey. In spite of these discrepancies, the positive gravity feature appears to correlate with a zone of low magnetics striking SW-NE.

Take off a SE-NW profile through the magnetic low and attempt to match it with the aid of the dolomite section of Figure 2.36c, using Equation (3.59b). Alternatively, because the inclination is about 75°, one might approximate  $F$  by  $Z$  and employ Equation (3.44a). The height of the aircraft was 300 m and one would expect the susceptibility contrast between the dolomite and adjacent sedimentary rocks to be small and negative.

3. The aeromagnetic contours in Figure 3.43, problem 15, Section 3.9, are from the same area (St. Lawrence Lowlands) as the gravity profile of Figure 2.38, field example 3, Section 2.8. The north end of the gravity profile terminates approximately at the cross on the north direction arrow shown in Figure 3.43. Take off a N-S total-field profile from this

Table 12.1.

Survey technique	Section	Problem or field example	Figure
Gravity	2.9	prob. 16	2.44
Magnetic	3.9	prob. 7	3.36
Seismic	4.12	prob. 21	4.122
EM16	7.8	Field ex. 3	7.96
Resistivity	8.8	prob. 11	8.50
IP	9.7	prob. 4	9.22

point for about 10 miles south and compare it with the gravity profile.

If the geologic section of Figure 2.38 is correct (there is considerable evidence to show that it is), the magnetic profile, like the gravity, should be a reflection of the Precambrian step, because the sedimentary beds have very low and uniform susceptibilities. Hence it should be possible to obtain a fair match to the magnetic profile, using a form of Equation (3.59b), Section 3.6.7, (or alternatively §3.6.9), given that the inclination and declination in the area are about 75° and 22°W, respectively, and that the aircraft altitude was 300 m.

If this interpretation is not satisfactory, can you establish some definite limits on the depth of the magnetic source? (See also §3.7.11) Would such a depth be satisfactory for the gravity profile? Are the gravity and magnetic results compatible at all?

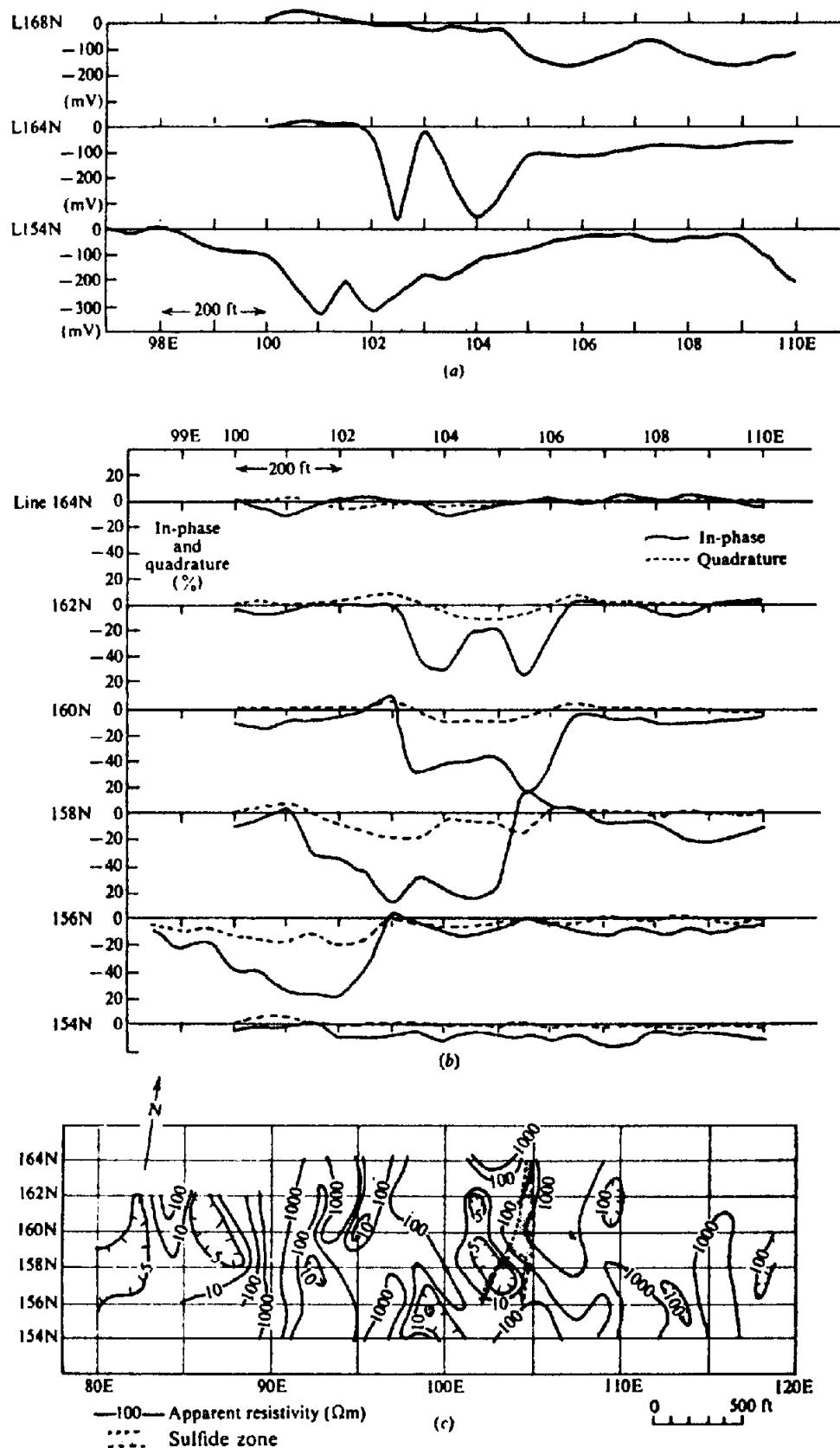


Figure 12.3. Results of different electrical surveys, Atlantic Nickel Property, southern New Brunswick. (a) SP profiles. (b) HLEM profiles; frequency 876 Hz, coil separation 200 ft. (c) Telluric contour map; frequency 8 Hz, electrode spacing 100 ft.

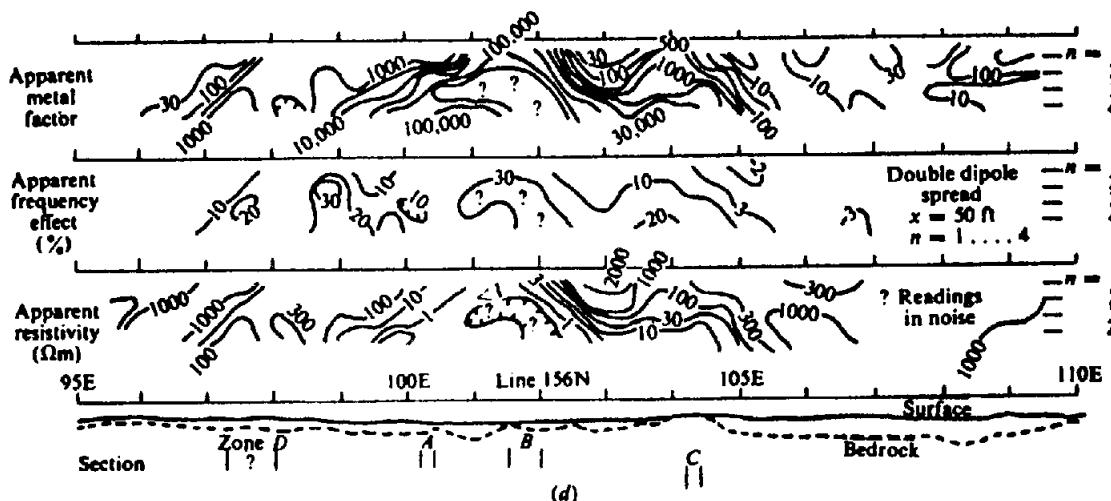


Figure 12.3. (Continued) (d) IP and resistivity pseudodepth plots, double-dipole spread,  $x = 50$  ft,  $n = 1, 2, 3, 4$ .

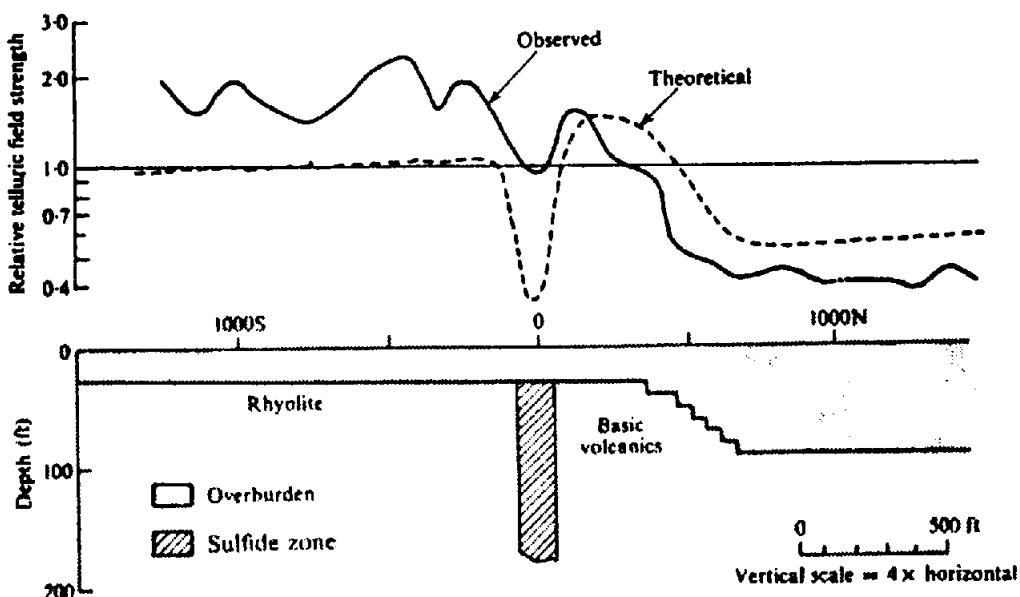


Figure 12.4. Telluric profile and geologic section, Mobrun Sulfide Deposit, northwest-Quebec. For theoretical model,  $\rho_{\text{Sul}} = 1 \Omega\text{m}$ ,  $\rho_{\text{over}} = 70 \Omega\text{m}$ , and  $\rho_{\text{host}} = 7,000 \Omega\text{m}$ .

4. The magnetic and IP profiles of Figure 12.1a and the Turam profiles of Figure 12.1b are from the Louvicourt copper deposit near Val d'Or, Quebec. Line 16W passes almost directly over the main copper mineralization, shown in vertical section below 15N. This zone has an oval cross section ~ 300 ft by 100 ft and is enclosed in a steeply dipping bed of disseminated pyrite (~ 20%) ~ 160 ft thick. The pyrite extends for more than a mile along strike, which is parallel to the bedding of acid tuffs and agglomerates. Consider these profiles individually:

- (i) Magnetic – note the strong negative anomaly caused by the drill-hole casing. Can you explain the lack of magnetic signature associated with the ore zone?

- (ii) Turam – the original discovery hole was drilled on the strength of the weak Turam anomaly at 15N. Would you consider this a good bet for drilling?  
 (iii) IP – this profile was obtained after drilling, using the three-electrode array with 200 ft separation. Chargeability and resistivity are both strongly anomalous over the ore zone. Is the former response due to pyrite, chalcopyrite, or both? Would you make a similar interpretation for the resistivity low?

The gravity profile of field example 2, Section 2.8, along with Figure 2.37 and the EM data given in problem 15, Section 7.9, are also from line 16W. In addition, the IP and resistivity logs shown in Figure

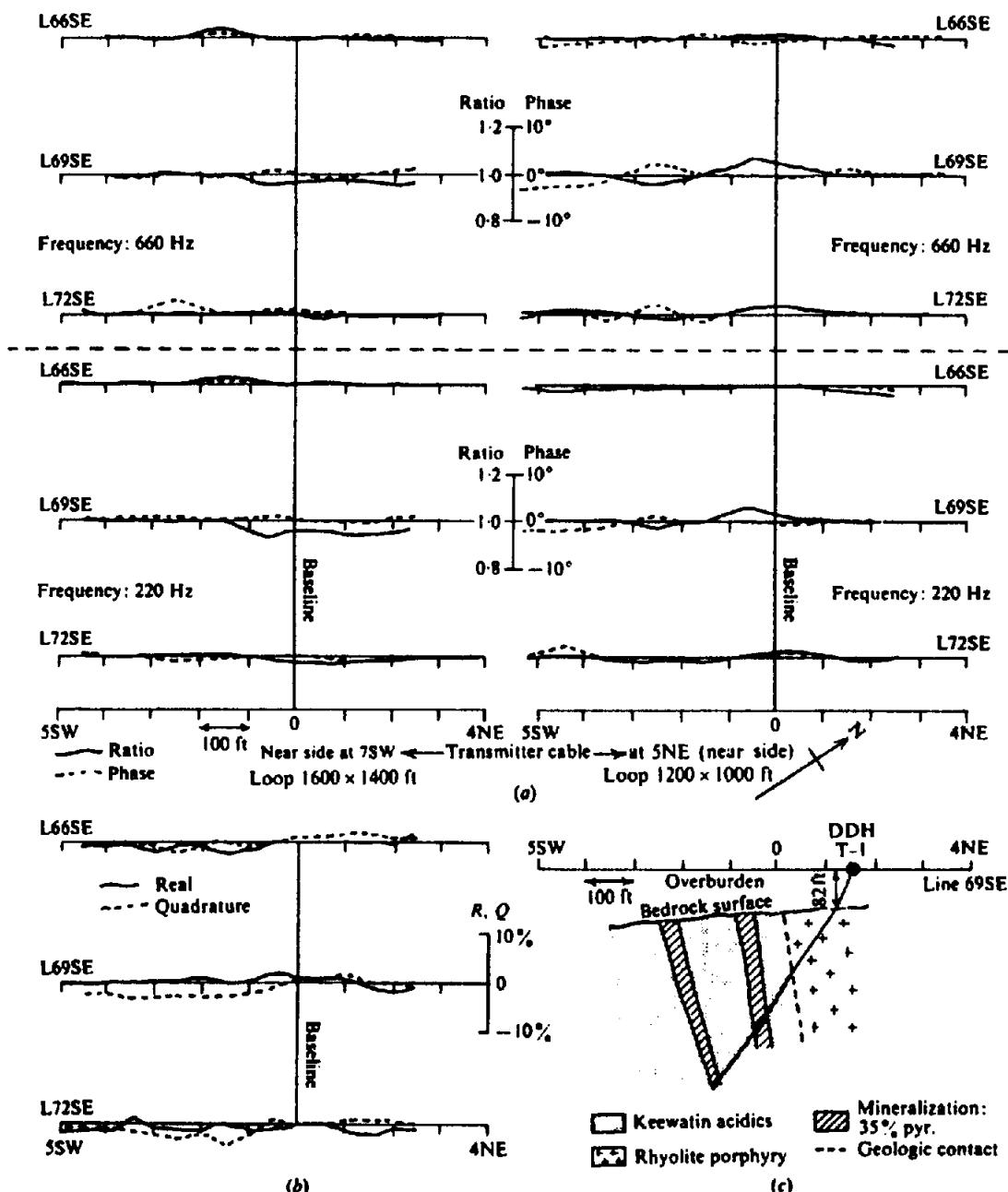


**Figure 12.5. Geophysical results and geologic section, Barraute, northwestern Quebec.**  
**(a)** Turam profiles; frequencies 660 Hz (upper three profiles) and 220 Hz (lower three profiles). **(b)** HLEM profiles; frequency 1,000 Hz, T-R spacing 300 ft. **(c)** Assumed geologic section.

11.51 (see problem 2, §11.12) were taken in a hole that intersected the ore zone. The geological log gave the following information.

- 0–25 ft: overburden.
- 25–175 ft: barren tuff, agglomerate.
- 175–240 ft: pyrite mineralization, 20% average.
- 240–300 ft: copper mineralization, 2.6%, pyrite ~ 5%.
- 300–330 ft: pyrite ~ 5%.
- 330–345 ft: pyrite ~ 5%, copper 1.3%.
- 345–435 ft: pyrite 10–15%.
- 435–480 ft: barren.

Although we have a great variety of geophysical results for this relatively small copper orebody, seven of the eight surveys were performed *after* drilling, to determine which of the methods were best suited for such a target. Assess the geophysical data and consider the results on the basis of the factors listed in Section 12.1.

5. Figure 12.2 shows a set of total-field ground-magnetic profiles from the Uchi Lake sulfide deposit in northwestern Ontario. Other geophysical results from this zone have already been displayed in Figure 7.95 (see field example 2 in §7.8), also Figures 7.116 and 7.122 of problems 14 and 21, Section 7.9.

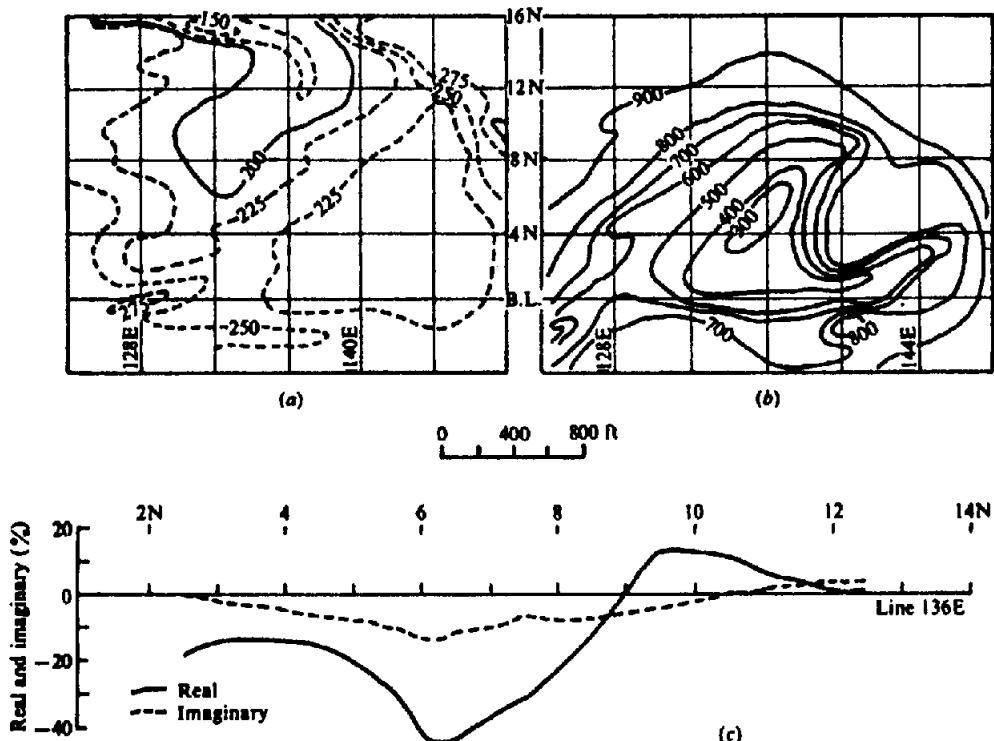


Figure 12.6. Magnetic and electrical data, Murray sulfide deposit, New Brunswick.  
 (a) Magnetic contours; contour interval 25 $\gamma$ . (b) SP contours; contour interval 100 mV.  
 (c) HLEM profile; frequency 440 Hz, T-R spacing 300 ft.

The original reconnaissance work was done by air, including the Input and nuclear-precession airborne magnetic profiles shown in Figure 7.122. The line spacing was  $\frac{1}{4}$  mile at an altitude of 380 ft. Although the Input anomaly is weak, it stands out clearly against a low background and persists through at least three channels.

Favorable geology, involving siliceous volcanic rocks surrounded by extensive granites, made it attractive to investigate this anomaly in detail with ground geophysics. The first ground followup included the vertical-loop broadside method, which located the conductor outlined in Figure 7.95a, and the magnetic profile of Figure 12.2, which indicated a possible weak anomaly associated with it.

The sulfide structures are described in field example 2, Section 7.8. Initial drilling gave good grades of copper (3–8%), zinc (9–12%), and silver (2–4 oz./ton). The zone near 1N between 5E and 7E (see Fig. 7.95a), is mainly sphalerite with very little iron mineralization, and is probably a poor target for EM and magnetics.

The horizontal-loop, Turam, and shootback EM profiles shown in Figure 7.116 were obtained in test surveys performed after the preliminary drilling. In this regard the procedure and sequence of events are similar to the previous example at Louvicourt, be-

cause the discovery was made on the basis of only part of the geophysics. As in example 4, the problem should be assessed by considering all the results, to establish a necessary and sufficient exploration procedure, if, in fact, one exists.

6. Numerous geophysical techniques have been tested over the Atlantic Nickel base-metal property in southern New Brunswick. Examples already included in the text are listed in Table 12.1.

In addition, the SP log of Figure 6.7a, Section 6.1.4, was made in a diamond-drill hole near line 156N. Self-potential, horizontal-loop EM, telluric, and further IP results from the same area are shown in Figure 12.3a to d.

Although the gravity data plus earlier magnetic and vertical-loop EM surveys were used directly to establish the ore zone on this property, much of the subsequent geophysics was done for test purposes, or to find possible extension of the mineralization. As a result there is an enormous amount of information here. In general, one can see that the gravity and EM anomalies are very strong and relatively simple, the magnetics are complex, whereas the original IP and the telluric data are poor. However, the IP and resistivity sections in Figure 12.3, obtained by using unusually small electrode spacing, show extremely small anomalies. What are the reasons for the

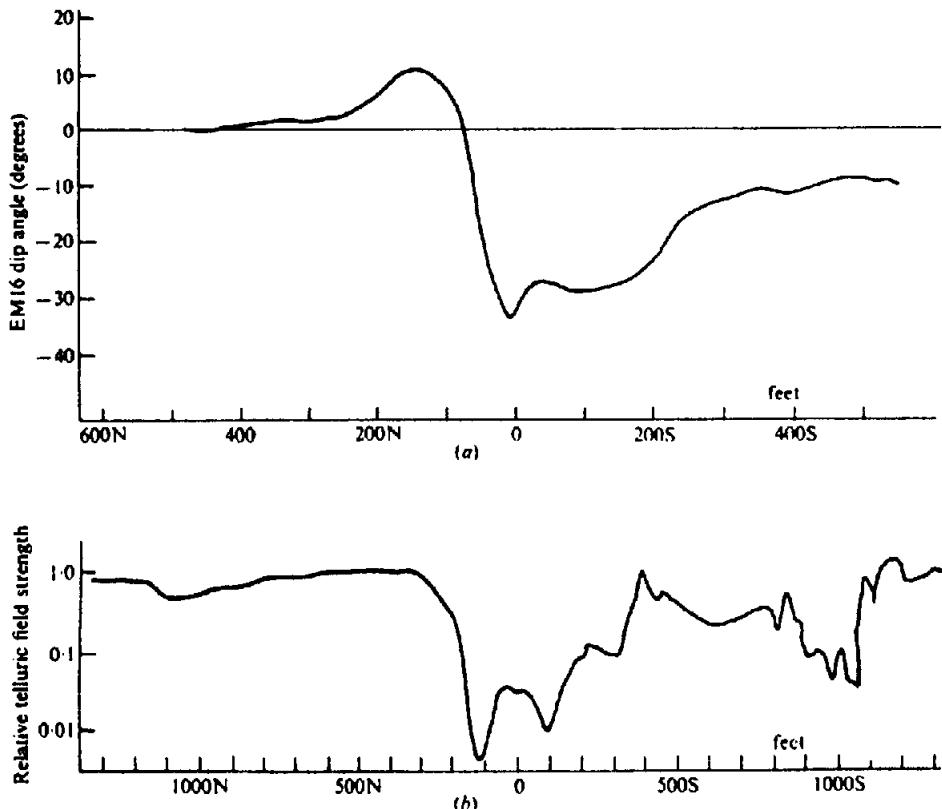


Figure 12.7. EM and telluric results, Bartouille, northwestern Quebec. (a) VLF-EM16 dip-angle profile. (b) Telluric profile, electrode spacing 25 ft.

tremendous difference between the results in the two IP surveys? Make as complete an interpretation as you can.

7. Gravity data of Figure 2.40, problem 10, Section 2.9, and magnetic contours in Figure 3.34 of problem 2, Section 3.9, are from the Mobrun sulfide deposit, which is also illustrated in example 1, Section 7.8, Figure 7.94. The dip angle and gravity profiles in Figures 7.94 and 2.40 are on the line marked N-S in Figure 2.40; the appropriate magnetic profile may be obtained on a line joining the two crosses in Figure 3.34.

A measured telluric profile is shown in Figure 12.4, accompanied by a rough vertical geologic section. This was a N-S traverse about 60 m west of the dotted line in Figure 3.34. Thus the sections of Figures 7.94 and 12.4 should be much the same.

The mild magnetic low indicates that the sulfides are nonmagnetic, but otherwise this survey is of little significance. High background noise from nearby power lines affected the telluric measurements somewhat. The telluric profile is interesting because it reflects a much lower resistivity north of the ore zone than south of it. This large effect partially masks the anomaly directly over the sulfides. It may be due to a considerable resistivity contrast between rhyolite and the volcanics to the north. However, the steep slope near 400N looks very much like an overburden

anomaly, as indicated in the theoretical profile obtained by numerical modeling. Would you expect to see this anomaly in the vertical-loop profile?

8. Figures 12.5a and b show two-frequency Taram and horizontal-loop EM profiles over zones of pyrite mineralization in Carpentier Township, near Barraute in northwestern Quebec. Magnetic and IP data from this area are found in Figure 3.28 of example 1, Section 3.8.1, and in Figure 9.21 of problem 3, Section 9.7.

The magnetic results have been discussed in some detail in Section 3.8.1, where it was concluded that the large magnetic anomalies could only be caused by magnetite or pyrrhotite zones near surface. IP and EM responses, on the other hand, are uniformly negative, which should eliminate the possibility of pyrrhotite.

The geologic section shown in Figure 12.5c is based mainly on information from diamond-drill hole T-1 (see Fig. 3.28) and to a lesser degree on the magnetic anomalies. Drilling results establish the depth of overburden to be 82 ft at the collar and the presence of two zones of 35% pyrite at ~300 and ~450 ft depth. There is some doubt of the bedrock surface outline shown in Figure 12.5c in view of the seismic results on line 75SE, mentioned in example 1, Section 3.8.1. However, even if this surface is correct, it is difficult to understand the lack of hori-

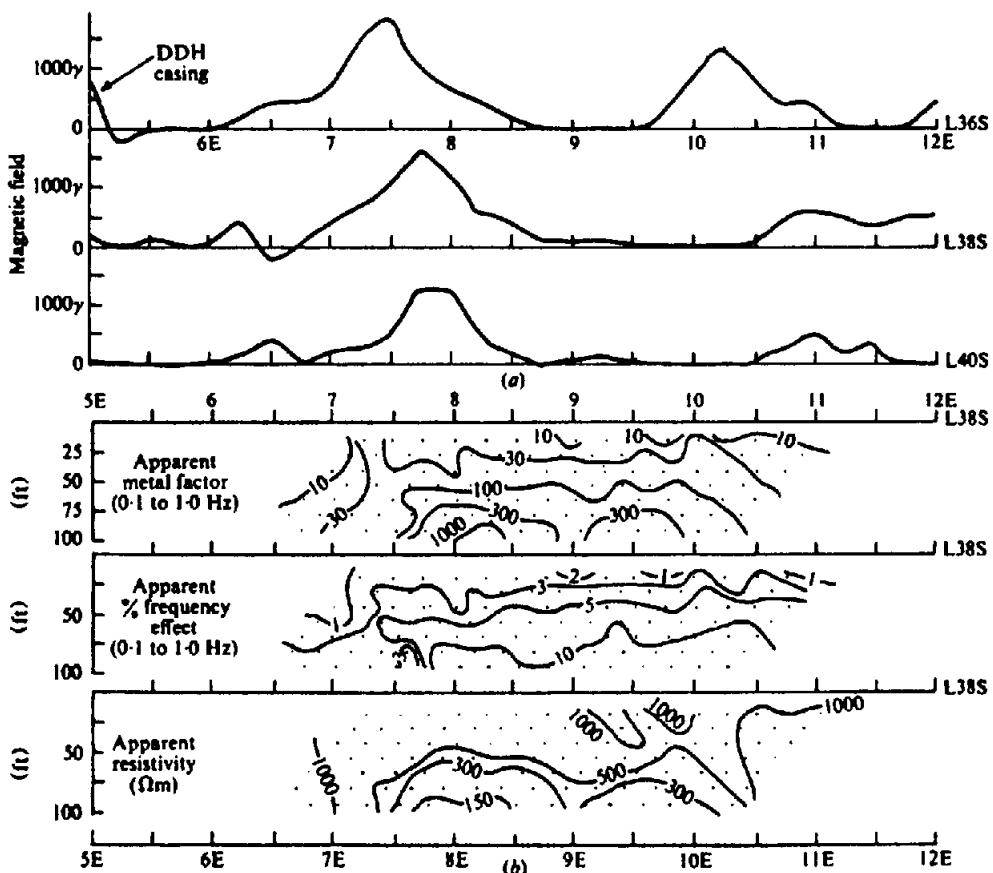


Figure 12.8. Magnetic and electrical results, Woburn, Quebec. (a) Vertical component (magnetic field) profiles. (b) IP and apparent-resistivity pseudodepth plots.

horizontal-loop EM and Turam response, especially the latter, because shallow resistivity values in the area would not normally be low enough to mask the presence of the 50 ft wide pyrite zones at a depth of 80 to 100 ft. One is forced to conclude either that the pyrite zones do not continue to bedrock surface or that the pyrite is not a good conductor. Try to make an interpretation of these results that is consistent with the magnetic and electrical data.

9. The Murray sulfide deposit in Restigouche County, northern New Brunswick, was used as an illustration of the Turam method in example 7, Section 7.8, Figure 7.100. Additional geophysical results are displayed in Figure 12.6 for magnetics, self-potential, and horizontal-loop EM.

Although there is no magnetic reflection of the sulfide mineralization (for a description, see §7.8), the SP and HLEM anomalies are very strong, possibly as a result of the gossan cover. In particular the horizontal-loop profile indicates a wide conductor dipping north, with the negative maxima falling between the Turam peaks. Make an estimate of the geometry and conductivity of the zone from horizontal-loop characteristic curves. Take off a SP profile from line 136E and interpret the SP results.

10. The VLF dip-angle and telluric profiles of Figure 12.7 were obtained from the same road tra-

verse that supplied the following data:

Self-potential, example 1(SP), Section 6.3.1, Figure 6.25.

Magnetotellurics, problem 9, Section 6.4, Figure 6.37.

This massive sulfide showing, in Bartouille Township, near Senneterre in northwest Quebec, is described in the SP example.

There is good correlation here between the various geophysical methods, although it is by no means exact. Both SP and EM16 profiles indicate the strongest anomaly to be a thin conductor dipping north, located at 40N (SP) and 70N (EM16). (The latter is measured from the zero crossover, which may be slightly downdip.) Both show a second conductor in the swampy area at 180S, although it cannot be located with any precision in the EM16 profile. There is a third smaller SP anomaly at 110N.

Magnetic anomalies are similarly sharp. The smaller positive is at 25N, whereas the main peak is at 125N. A definite magnetic low at 150S correlates with the swamp zone. These are not shown here.

The telluric and MT profiles of Figure 6.37 reflect a wide conductive zone extending at least 200 ft north and south of station 0; the MT profile also has a slight dip near 200S. When Figure 6.37 is com-

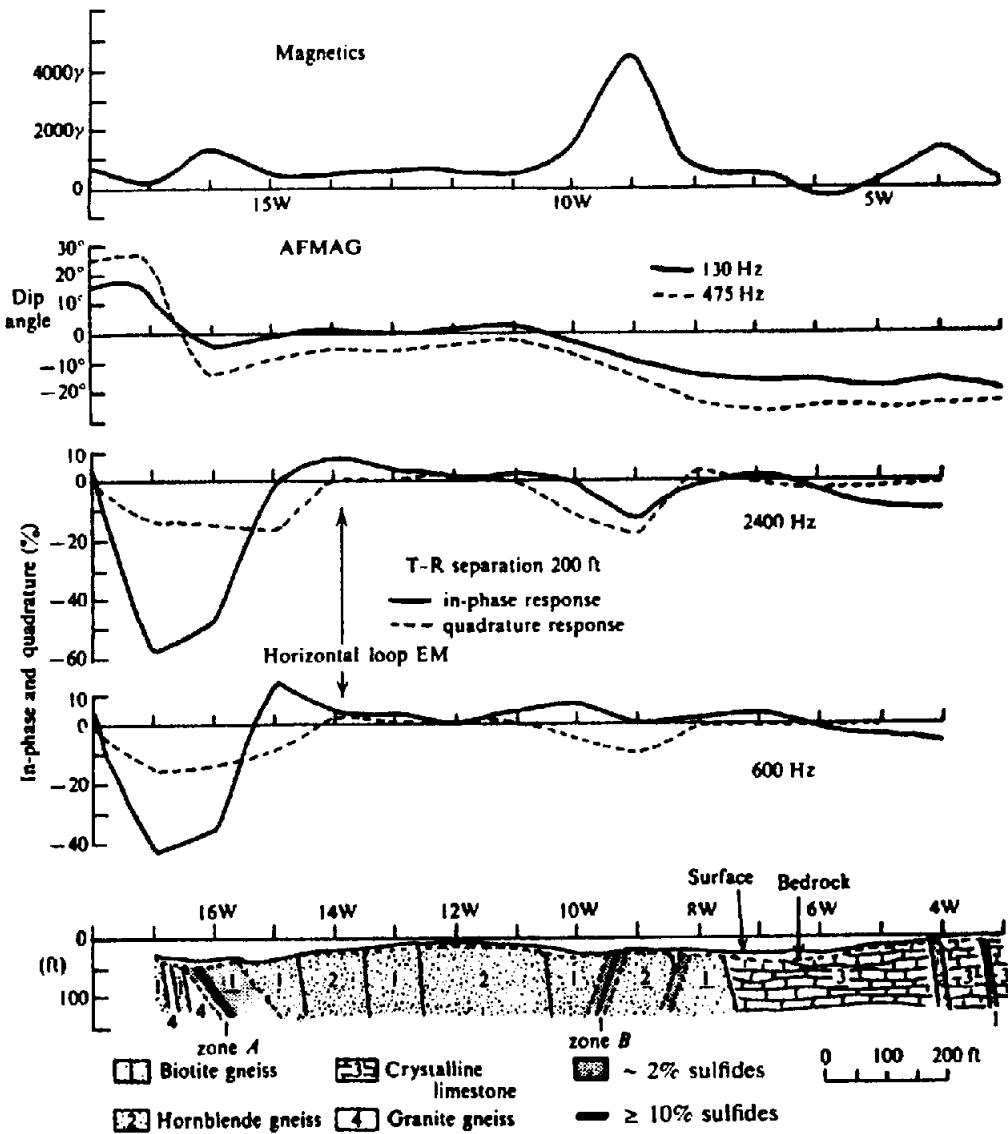


Figure 12.9. Geophysical results and geologic section, line C, Cavendish Township, Ontario.

pared with Figure 12.7b, there is clearly a lack of discrimination in the former. This is caused by the larger electrode spacing, 100 ft, rather than 25 ft as in Figure 12.7b. With the 25 ft spacing the wide conductor is resolved into two peaks, the main one being at 110N and the second at 100S. There is also a minor low at 350S, coinciding with a magnetic anomaly. The telluric low at 1000S, which was equally strong with 100 ft electrode spacing, has no correlation with the magnetics.

11. Induced polarization, resistivity, and magnetic data, shown in Figure 12.8, are taken from the same area discussed in (i) field example 6, for horizontal-loop EM, Section 7.8, Figure 7.99, (ii) the telluric profiles of problem 6, Section 6.4, Figure 6.34, (iii) drill-hole logs in problem 3, Section 11.12, Figure 11.52. The zones of mineralization, which are mainly pyrite, are shown in Figure 7.99. There is, in addition, a section of chlorite schist containing traces of

pyrite between 7 + 00E and 7 + 50E. All zones dip about 70° west.

Considering line 38S, the three-frequency telluric profiles in Figure 6.34 have two peaks, at 8 + 30E and 9 + 30E, which correlate very well with the two sulfide zones. The high-frequency response is most pronounced, whereas the 8 Hz profile indicates that the better conductor is at 8 + 30E. The horizontal-loop EM profile, on the other hand, reflects only the massive sulfides. Neither sulfide zone appears to have any magnetic contrast on line 38S, although there is a small tail on the west flank of the magnetic peak at 7 + 75E, which falls between the chlorite bed and the massive sulfide.

The IP traverse was made with a double-dipole array, with  $x = 25$  ft and  $n = 1, \dots, 7$ . The small spacing was used purposely in an attempt to discriminate between the conductors. Clearly this was only partly successful, because the frequency-effect con-

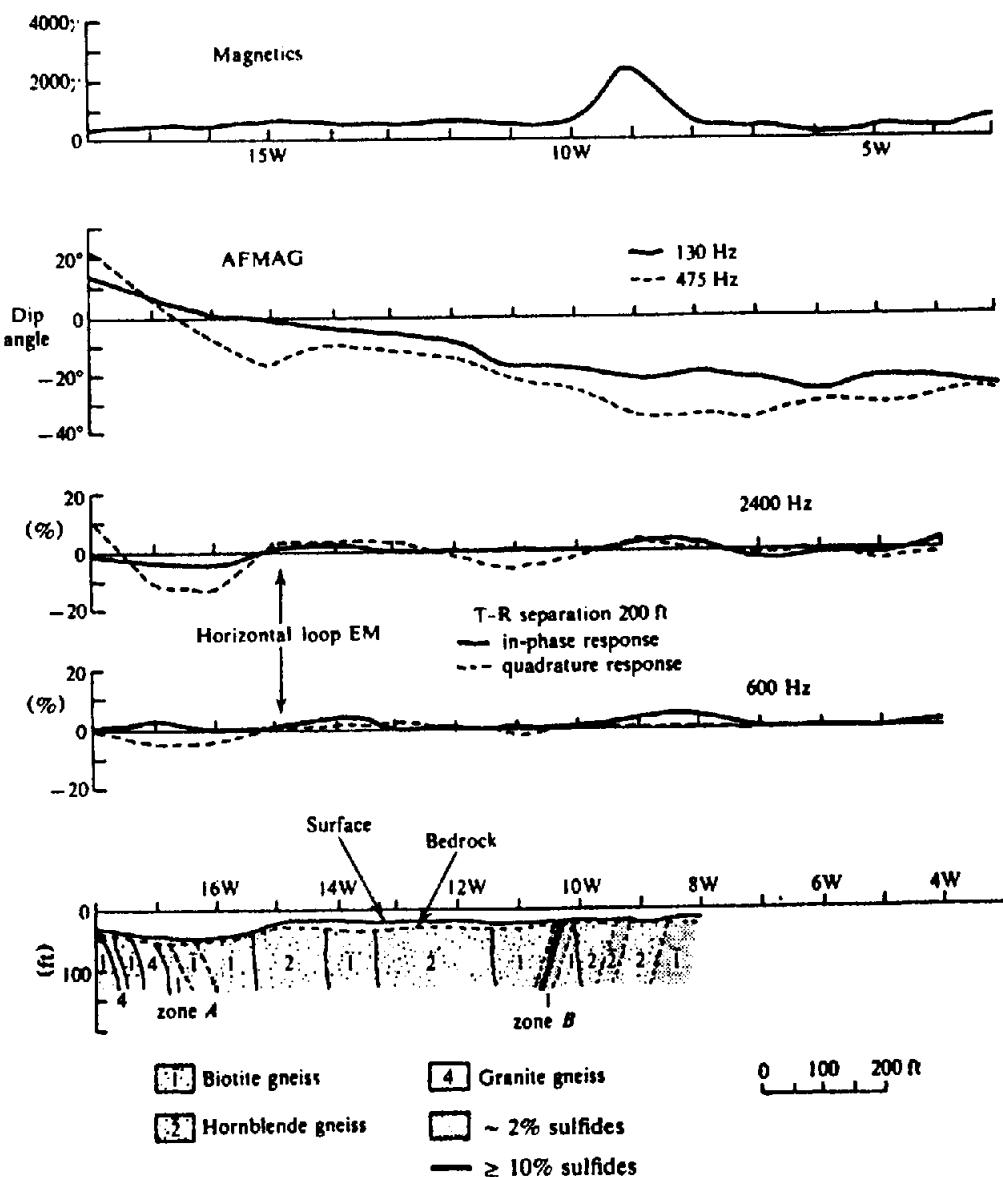


Figure 12.10. Geophysical results and geologic section, line D, Cavendish Township, Ontario.

tours show a single wide zone from 7 + 75E to 10 + 50E. Apparent-resistivity and metal-factor results are better in this regard, with the stronger response over the better conductor, but only for  $n = 6$  and 7, the largest dipole separations.

On lines 36S and 40S, the HLEM peaks again occur over the massive sulfide zone, whereas the telluric profiles (which, it should be noted, were made with 50 ft electrode separation) locate both zones. In addition, the strongest response in all three lines is at 145 Hz. However, this is not particularly significant, because the average resistivity is sufficiently high to make the skin depth at 145 Hz considerably greater than the depth extent of the conductive zones.

This is a relatively straightforward example of nonmagnetic sulfide conductors lying at shallow depth. The magnetic data are, at best, merely an

indicator of mildly anomalous susceptibility contrast on the flanks of the sulfides. All the electrical techniques responded to the anomalous zones in some fashion. The horizontal-loop survey located only the better conductor, indicated its dip, and provided an estimate of depth and conductivity-thickness product; these profiles also show that the zone is thin. As mentioned in the discussion of field example 6 (§ 7.8); it might have been possible to detect the two zones by using 100 ft spacing between the transmitter and receiver. The telluric measurement resolved the two conductors with 50 ft electrode spreads, but failed to do so when the separation was 100 ft; there is little evidence of dip on lines 38S and 40S, whereas the profile on 36S suggests a dip to the east. Finally, the IP survey successfully established the presence of two conductors by employing extremely small dipole spreads. Had the conventional 100 ft separation been

Table 12.2.

Section	Problem	Method	Figure	Correlation of lines
6.4	4	SP	6.33	Line 12N is line C, 8N is D
7.9	3	VL Broadside	—	Line 12N is line C, 8N is D
7.9	18	AEM Quadrature	7.119	
9.7	7	IP Freq. domain	9.24	Data obtained on line C

Table 12.3.

Conductor	Frequency (Hz)	$z/l$	$z$ (ft)	$\mu\omega t/l$	$\sigma t$ (S)	$t$ (ft)	$\sigma$ (S/m)
Zone A	600	0.1	40	45	140	70	7
	2400	0.05	20	60	55	100	2
Zone B	600	0.2	80	3	10	—	—
	2400	0.1	40	4	4	< 10	1

Table 12.4. Cavendish line C data

Method	Location		Dip	Depth (ft)		Depth ext. (ft)		Width (ft)		$\sigma t$ (S)	
	Zone A	Zone B		A	B	A	B	A	B	A	B
Magnetic	16W	9W	E W	100?	100?	—	—	—	—	—	—
SP	16W	9-11W	W W	—	—	—	—	—	—	—	—
VL Broad.	16 + 55	9 - 9 + 65	W W	120	$\geq 100$	—	—	—	—	?	5
AFMAG	16 + 50	?	E ?	—	—	—	—	—	—	—	—
HL	16 + 55	9	W W	20-40	40-80	—	—	70-100	$\leq 10$	55-140	4-10
IP	15 - 15 + 50	9-11	E W	$< 100$	$< 100$	400?	—	150?	100?	—	—
Drilling	16 + 30(conc.)	9 + 30	E W	$\approx 20$	$\approx 20$	$> 125$	$> 125$	10	0.3	—	—
	15 + 60	9 + 15						80	30		
	-16 + 40	-9 + 45									
	(disseminated)										

used, it is practically certain that this resolution would not have been achieved.

12. Vertical geologic sections obtained by drilling the Cavendish Township area in central Ontario are displayed in Figures 12.9 and 12.10. Lines C and D are 400 ft apart. This has been a favorite site for testing geophysical equipment since 1967, when a case history was prepared by McPhar Geophysics for the Canadian Centennial Conference on Mining and Groundwater Geophysics. Practically all the electrical techniques, plus magnetics, have been used here.

Magnetic, AFMAG, and horizontal-loop EM profiles are also shown in the same diagrams. Other examples from Cavendish already incorporated in this book are listed in Table 12.2.

A shallow drilling program, carried out by the Geological Survey of Canada, produced the sections of Figures 12.9 and 12.10. The rocks are Grenville mafic gneisses, crystalline limestones, and granite gneiss, which generally dip steeply to the east. Pyrrhotite is associated with calcite and pyrite with quartz in calcareous-silicate sulfide alteration zones

and there is a general background content of 0.1% sulfides in the rocks of the area. Both zones A and B strike approximately N30°E for more than 1,600 ft, the B zone apparently splitting into two or three zones, over a greater width, to the south. The sulfides, almost entirely pyrrhotite and pyrite, occur in widths up to 80 ft at concentrations of 1 or 2%. Within these zones there are narrower sections of 10% and higher grade; for example, in zone A, the 10 ft wide section on line C extends 100 ft north and south, whereas within zone B there appears to be a similar, but much narrower, section that is ~ 1,000 ft long. The mineralization occurs as stringers that are mainly parallel to the foliation, although zone B appears to dip west.

Neither the depth nor the depth extent of these zones has been established by the drilling to date. However, they seem to be no more than 25 ft deep and probably subcrop at bedrock surface in many places. The depth extent is at least 125 ft.

With such a wealth of geophysical data available here, it should be possible to make a fairly complete

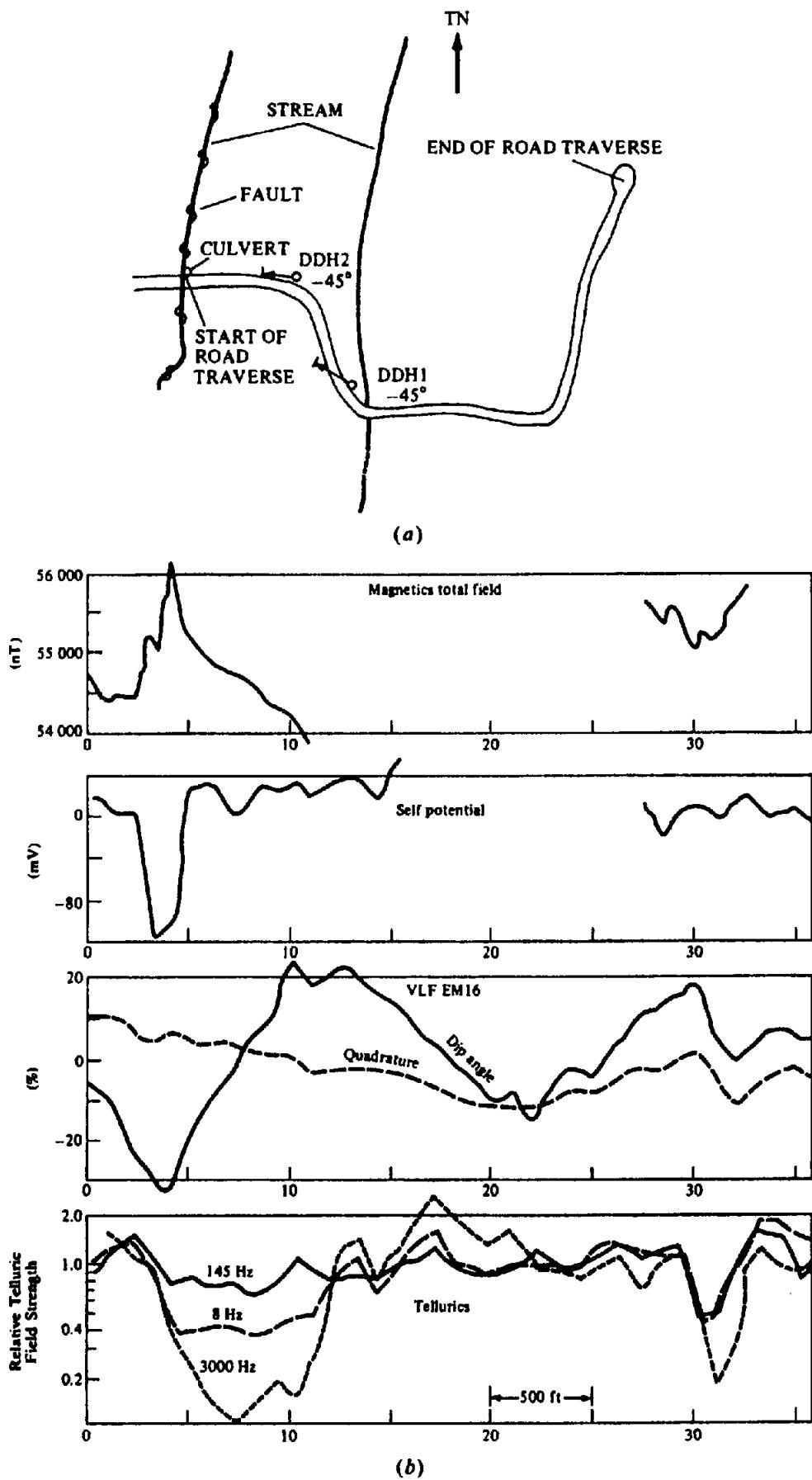


*Figure 12.11. Geophysical data from a base-metal prospect in eastern Nova Scotia. Data in (b) are from ground surveys, data in (c) to (f) are from helicopter airborne surveys, flight lines (light solid lines plotted at map positions) are E-W at nominal 200 m spacing. (a) Map of area and road traverse. (b) Total-field magnetics, SP, EM16, and three-frequency tellurics from road traverse.*

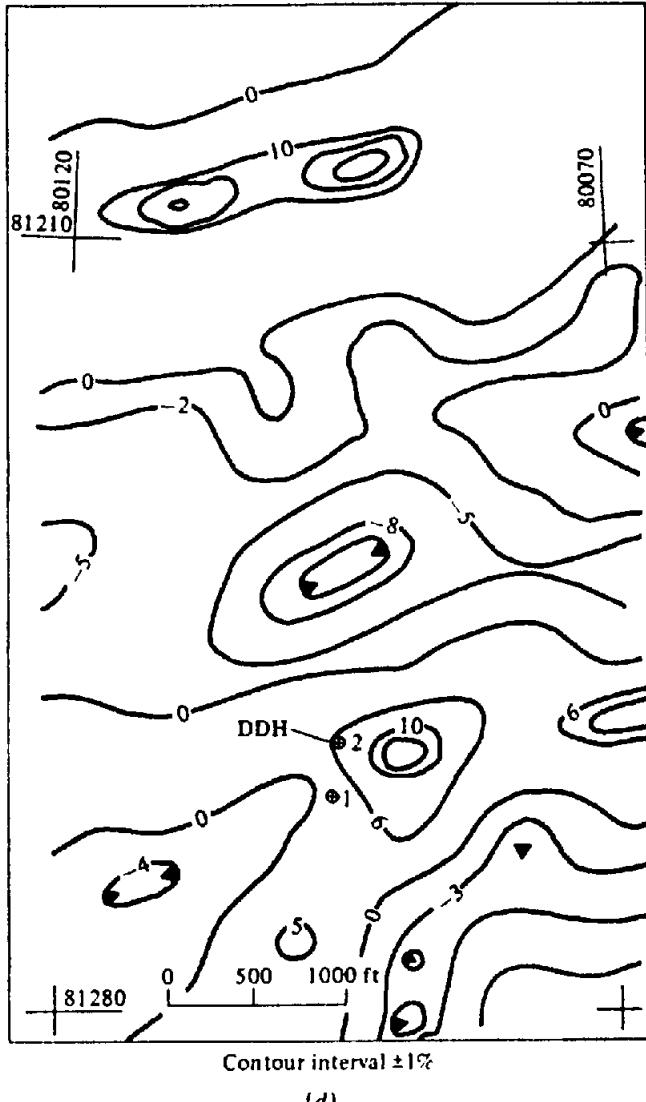
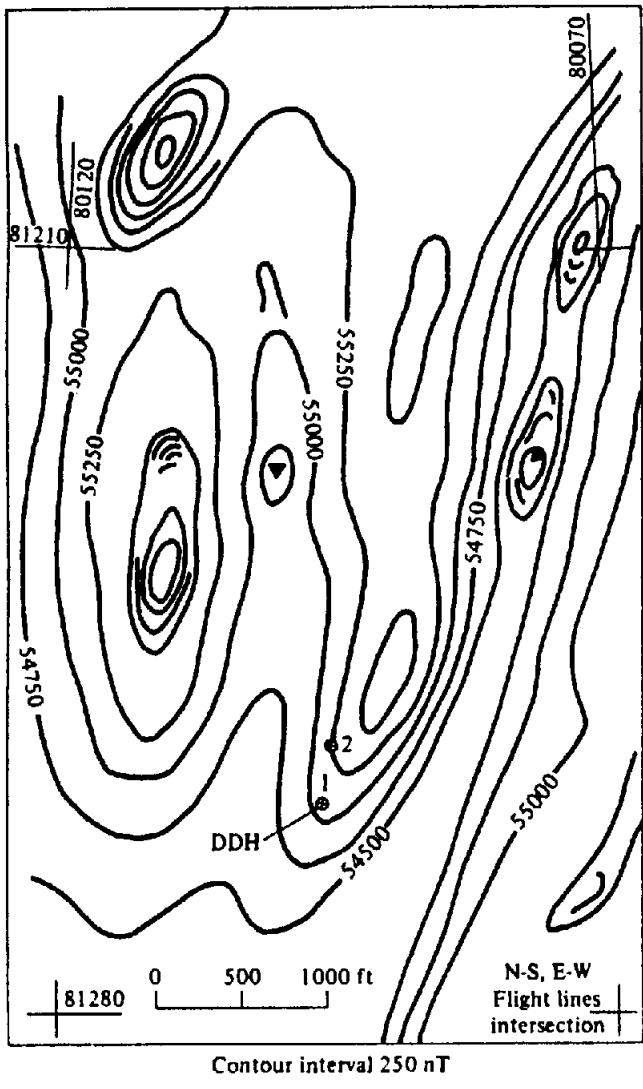


Figure 12.11. (Continued) (c) Total-field magnetic contours. (d) Total-field VLF contours.

interpretation of these zones. Considering line C, the magnetic profile shows a good peak at 16W and a much stronger one at 9W, correlating well with zone A, centered at 16W and reasonably well with the main section of B at about 9 + 25W. There is not much indication of the dips of these beds, although the peak at 16W has a slightly steeper slope on the west flank and the larger anomaly at 9W decreases more rapidly to the east, suggesting east and west dips, respectively. The two peaks, of course, are a reflection of the pyrrhotite that apparently is in greater concentration and/or closer to the surface at zone B. Depth estimates from the width at half-maximum indicate about 100 ft in both cases, but these are obviously unreliable because both zones are probably wider than the depth to the top.

If we take a SP profile from line 12N in Figure 6.33, Section 6.4, we find good correlation between the negative peak of 373 mV and zone A. The

broader minimum from 8W to 11W, however, indicates a second SP source at 11W, which is not apparent from the geologic section. The asymmetry of the SP anomalies suggests a general steep dip to the west. Clearly no valid depth estimates can be made from this profile.

On plotting the broadside vertical-loop profiles for 12N (line C) from the data in problem 3, Section 7.9, we find that zone A produces a good anomaly at all four frequencies. The crossovers lie between 16 + 50 and 16 + 60W, and the asymmetry of the 1,000 and 5,000 Hz profiles indicates a westward dip. Employing the characteristic curve of Figure 7.42a, Section 7.7.3i (admittedly this is a very crude approach, because the marked asymmetry of the profiles does not imply a steeply dipping sheet), we find that  $z/l \approx 0.3$ , or  $z \approx 120$  ft. This value appears to be much too large. Further evidence that it is unreliable is provided when we attempt to estimate the

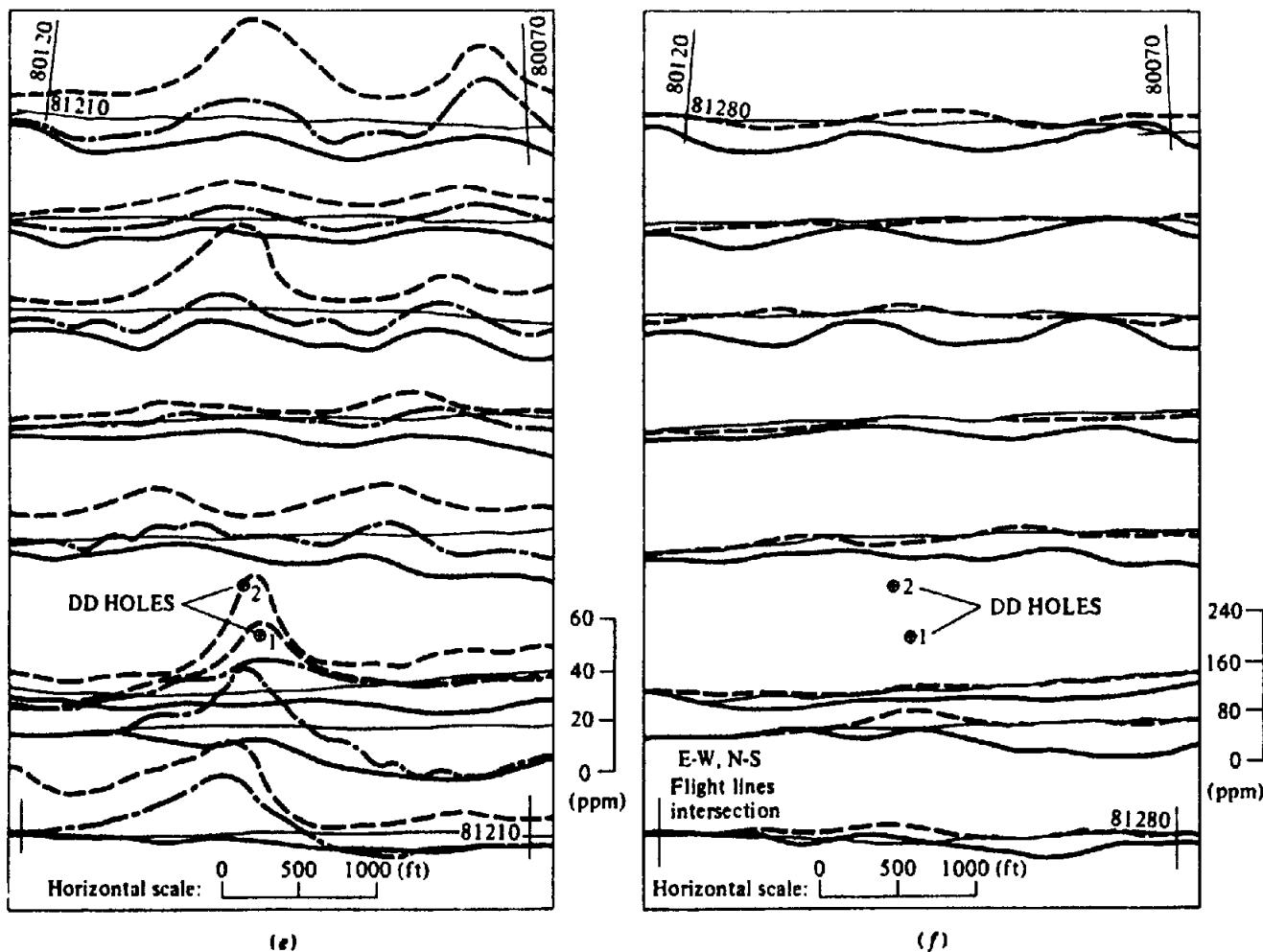


Figure 12.11. (Continued) (e) 935 Hz coaxial pair in-phase (—); 34 kHz coplanar pair in-phase (···) and quadrature (---) on line 81210. (f) 4,600 Hz coaxial pair (—); 4,775 Hz coplanar pair (---) (both in-phase) on line 81280.

response parameter from Figure 7.43b, Section 7.7.3i. The peak-to-peak response is much too large, at both frequencies, for a conductor 120 ft deep.

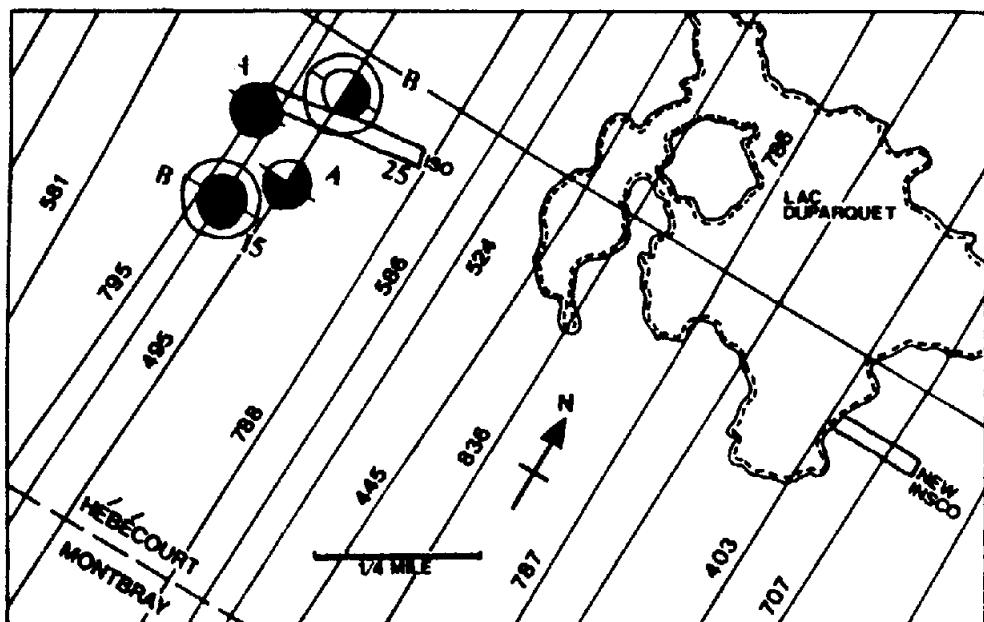
Using the same curves for zone *B*, we find that  $z \approx 100, 120$ , and  $340$  ft, for frequencies of 5,000, 2,400, and 1,000 Hz respectively. (There is no response at 600 Hz.) From Figure 7.43b, we then obtain values of  $\sigma t \approx 5$  at 5,000 and 2,400 Hz; the depth  $z$  corresponding to 1,000 Hz is again too large to fit the curves.

The AFMAG profiles in Figure 12.9 show a good crossover approximately at  $16 + 50W$ , corresponding to zone *A*, while the asymmetry indicates an eastward dip. There is little more than a suggestion of zone *B* on these profiles. It should be noted that in both the vertical-loop and AFMAG methods (and in the horizontal-loop results as well), the high-frequency response is the larger, which tells us that the conductors are shallow.

Figure 12.9 also shows a very strong response for the horizontal-loop EM, centered at  $16 + 50W$  over

zone *A* and a relatively weak anomaly at 9W for zone *B*. This type of EM equipment is not particularly sensitive to dip; one might guess that the profiles indicate a general dip to the west. Employing the characteristic curves of Figure 7.44b, Section 7.7.3i, we can estimate the parameters in Table 12.3. The values for  $t$  are obtained from the profiles in Figure 12.9, being the excess of the horizontal distance between zero crossovers over the transmitter-receiver separation.

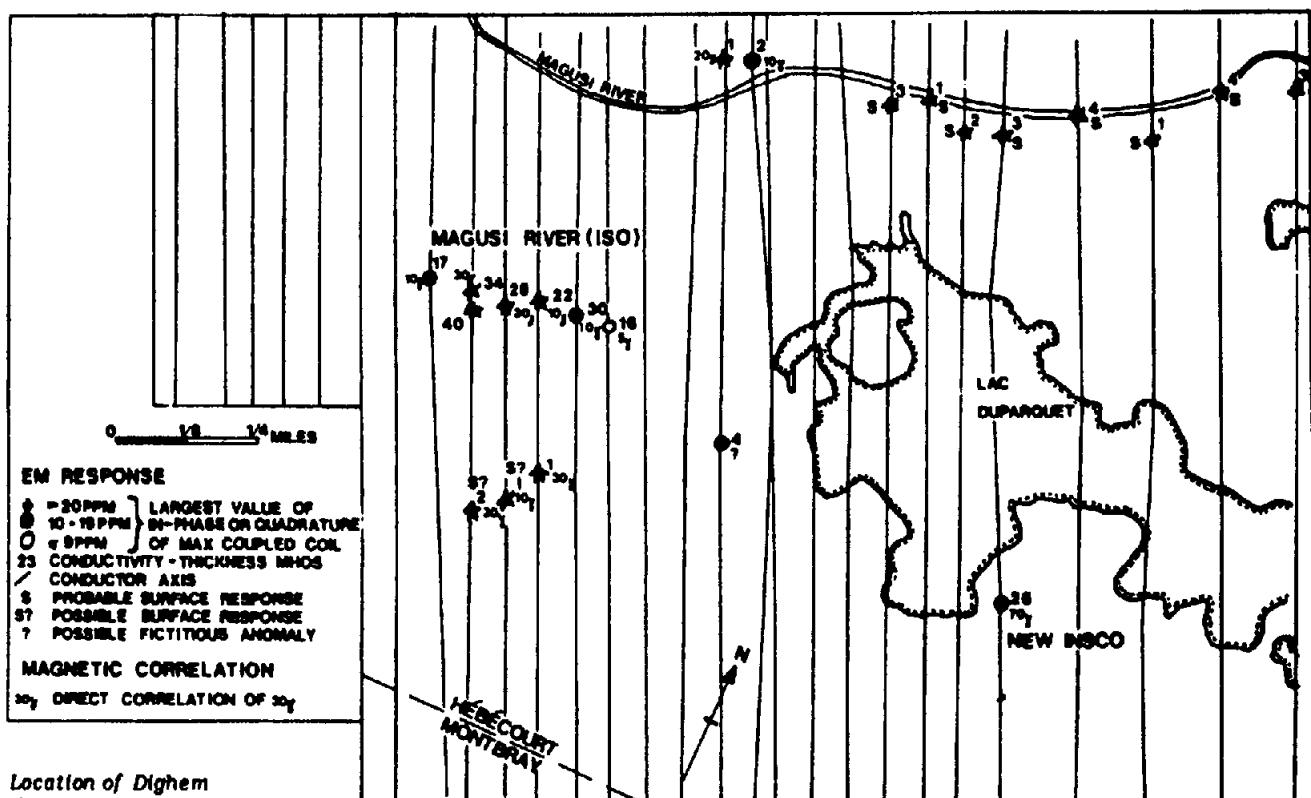
Finally, the IP data for line C (Fig. 9.24, §9.7) present a somewhat different picture. The top of zone *A* is located at least 100 ft east of its actual position. Both frequency-effect and metal factor contours suggest it to be a conductor of rather limited depth extent dipping east. Zone *B*, on the other hand, appears to be located in about the right place; it also appears to dip west and to increase in conductivity at depth. In the pseudodepth plots for  $x = 200$  ft there is an indication that the zones come together at  $n = 3$  (supposedly  $\sim 400$  ft). Although the fre-



● 6 CHANNELS  
○ 5 CHANNELS

● 4 CHANNELS  
○ 4 CHANNELS WITH  
MAGNETIC CORRELATION

(a)



(b)

Figure 12.12. Geophysical ground surveys over anomalies located by airborne Input and Dighem surveys. (a) Map showing locations of Input anomalies. (b) Map showing locations of Dighem anomalies. (c) to (e) VLEM, HLEM, and IP profiles over anomaly A along the N-S lines L800W, L0 + 00, L800E which straddle the rectangle marked NEW INSCO in (a).

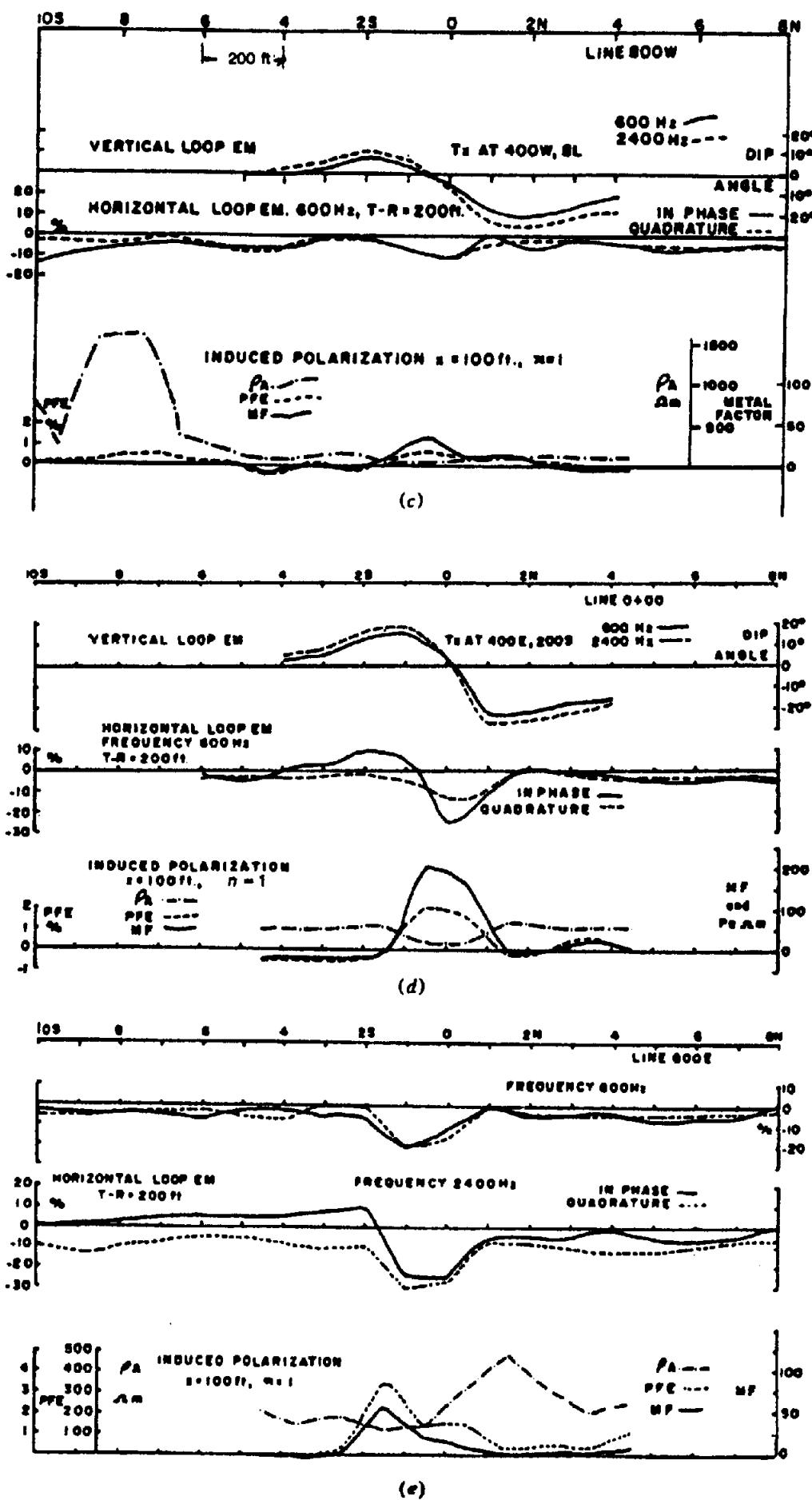


Figure 12.12. (Continued)

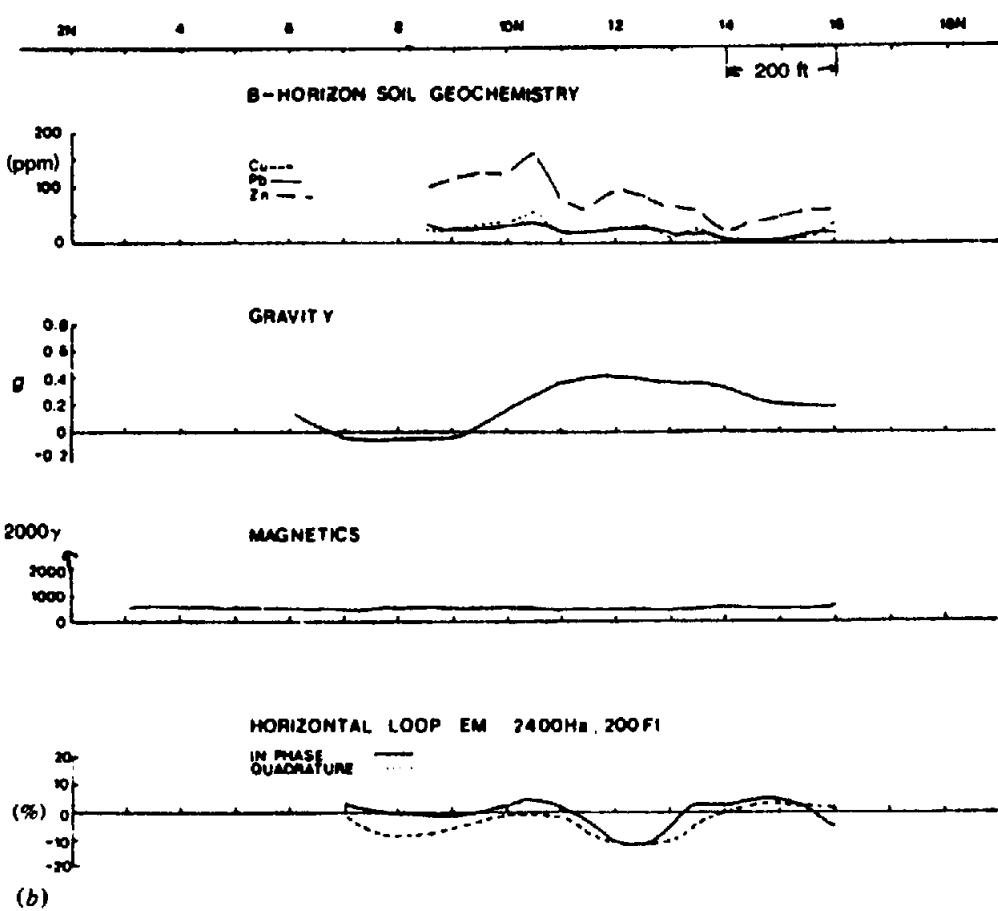
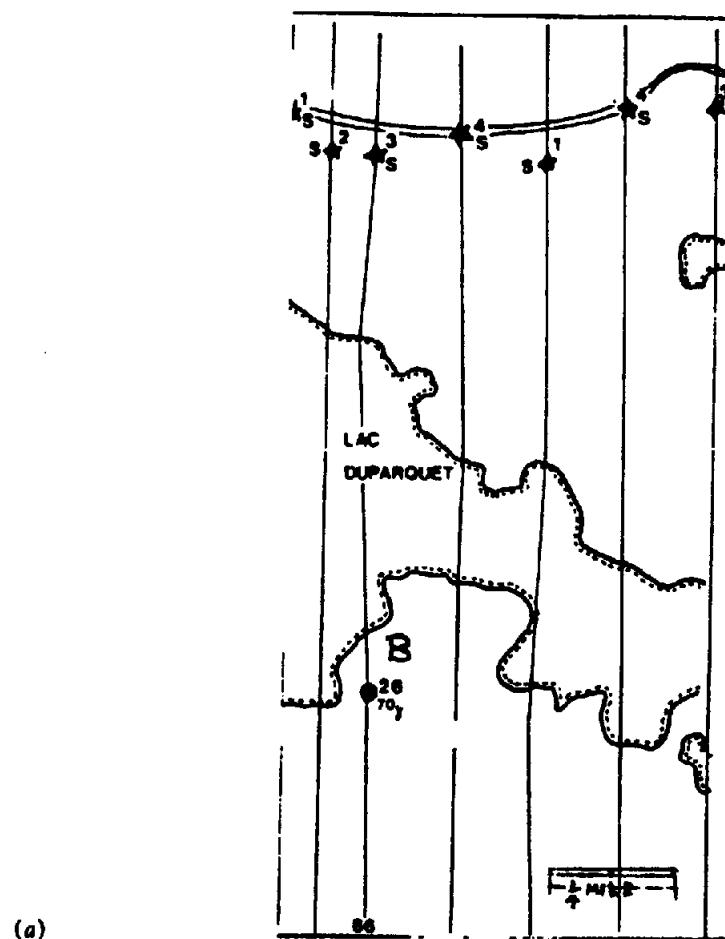


Figure 12.13. Geophysical and geochemical ground surveys over Dighem anomaly discovered during airborne surveys in Figure 12.12. (a) Map showing location of Dighem anomaly B. (b) to (d) Geochemical and geophysical profiles along lines 0 + OOE, 2 + OOE, and 4 + OOE, respectively.

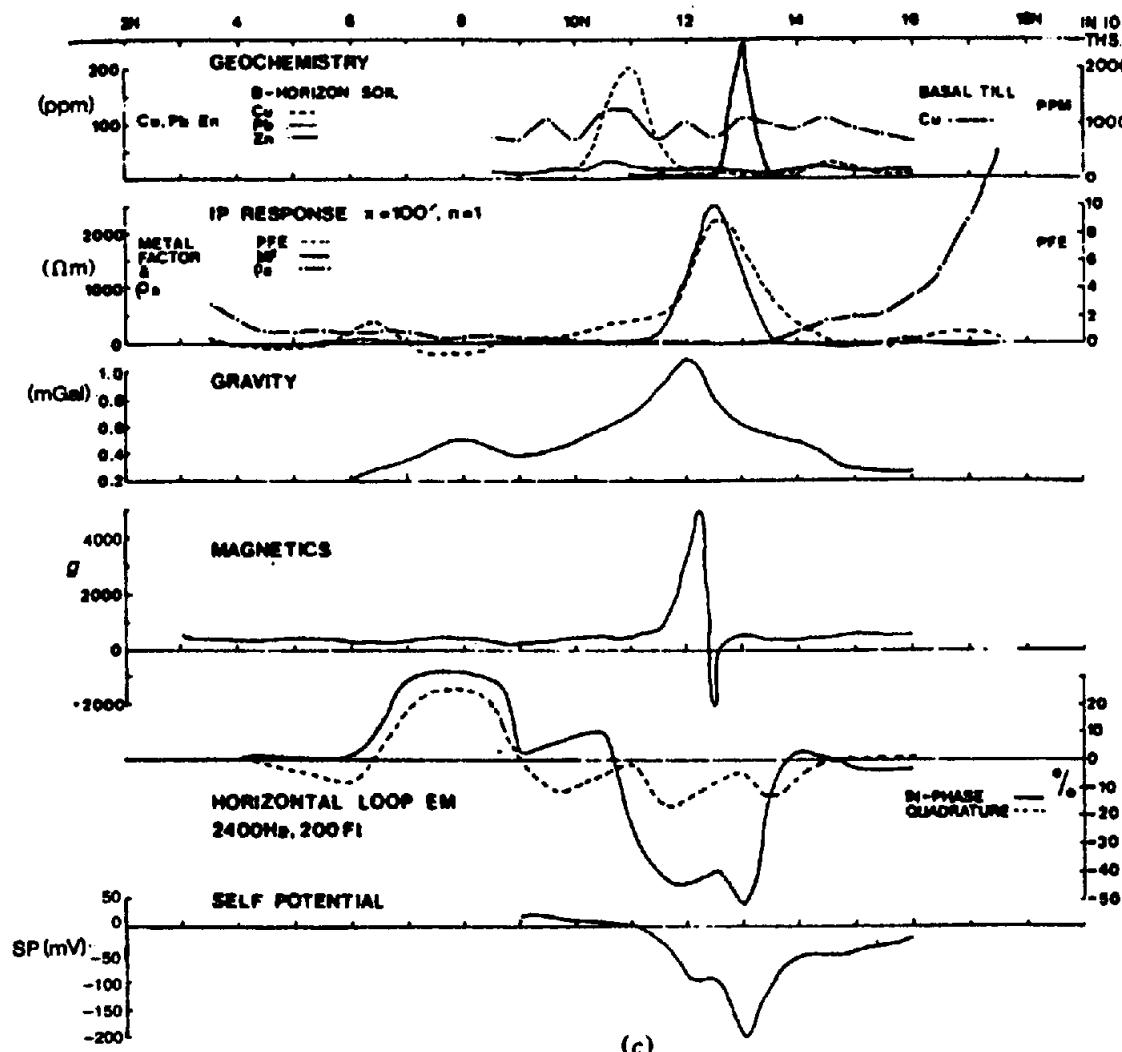


Figure 12.13. (Continued) (c) Same as (b) for line 2 + 00E

quency-effect values continue to  $n = 4$ , mainly below zone B, the metal-factor anomaly appears to pinch out at this depth.

Judging from the evidence presented by the shallow drilling program, this site is not a particularly good target for IP. However, a limited amount of deep drilling (say, 750 ft holes) would be very interesting, both to determine the depth extent of the two zones and to check the IP indication that they are joined at depth.

The information obtained from the various surveys on line C is summarized in Table 12.4.

We may conclude that all these methods locate the zones reasonably well, with the exception of the IP and possibly SP. The dip of zone B is established to be steep and to the west, whereas there is considerable doubt about the attitude of zone A. Only the horizontal-loop technique gives reasonable depth estimates; the SP and vertical-loop data, qualitatively at least, suggest that both zones are shallow and that B may lie somewhat deeper than A, although the magnetic profile does not necessarily bear this out.

Depth extent cannot properly be determined by any of these methods, whereas the width is roughly indicated only by the horizontal loop. Finally, conductivity or conductivity-width product, as estimated by horizontal loop and partially by vertical loop, tells us that zone A is a better conductor than zone B (probably because of the width of the 10%-sulfide section), but that neither zone is a very good conductor.

It is suggested that the interested reader carry out a similar interpretation of Line D.

13. The profiles in Figure 12.11b were obtained from a bush-road traverse (Fig. 12.11a) in eastern Nova Scotia during base-metal reconnaissance work. There is a strong electric and magnetic anomaly in the western part of the traverse. Interpret the four sets of profiles as completely as you can, estimating depth, geometry, and character of the anomaly source.

Is there evidence of conductive overburden varying in thickness? Consider as well the sharp telluric response around station 31, where the road has

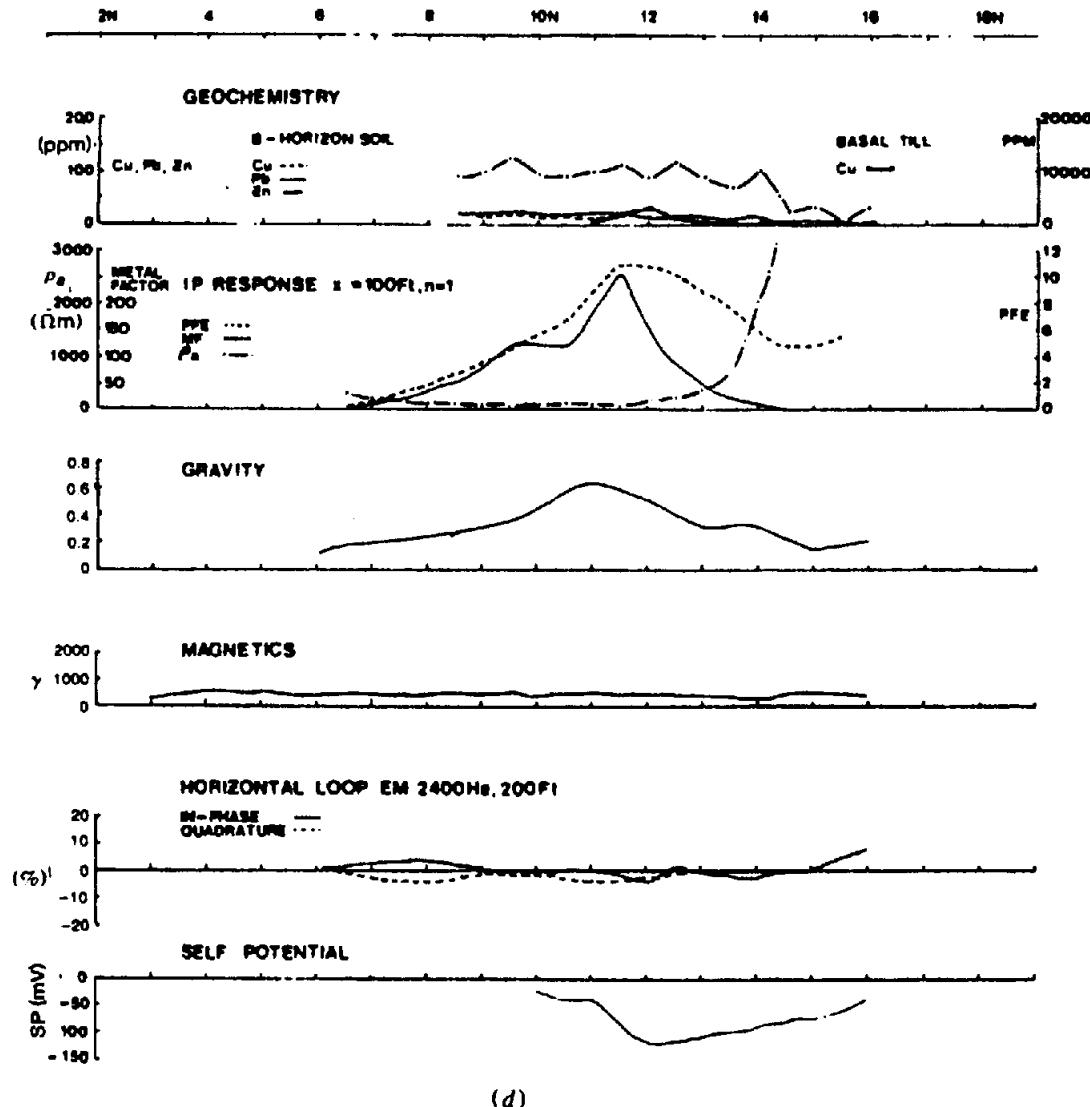


Figure 12.13. (Continued) (d) same as (b) for line 4 + 00E

turned north. Given that the VLF station was NAA Cutler, almost due west of the area, could the EM16 profiles be significant in this vicinity?

Later, a detailed helicopter survey was carried out in this region, producing multifrequency EM, VLF, and total-field magnetic data, which are displayed in Figure 12.11c to f over a larger portion of the same area. Try to locate the ground traverse from the airborne data and make use of any additional information derived from the combination (see §7.5.4, §7.5.5, §7.7.9, and §7.7.10).

The following detail will clarify the airborne data for correlation and further interpretation. The magnetometer is an optically pumped Cs type taking 5 samples/s; noise level is 0.1 nT. The Herz Totem 2A VLF unit measures total field and quadrature components for two stations. EM equipment consists of two vertical coaxial-coil pairs (935 and 4,600 Hz) and two horizontal coplanar-coil pairs (4,175 and 34,000 Hz). Coils are separated ~ 7 m in the boom mounting, which is carried ~ 30 m above ground level.

Lines were flown both N-S and E-W at nominal 200 m spacing. Clearly, E-W line 81260 was out of position by about 100 m most of the way between the E-W limits on Figure 12.11c to f; this figure is within the contract limit over 1 km. Quadrature data for 935, 4,600, and 4,175 Hz are not included here because they provide no additional information. The same is true for the data on the N-S flight lines which are barren. This fact is significant.

14. The discovery in 1972 of two small economic base-metal deposits near Rouyn, northwestern Quebec, was the direct result of a large-scale airborne Input (and subsequently other) EM surveys in the region. Both are located on the north slope of rhyolite, dacite, and andesite flows bounding the Dufault and Flavrian granodiorite intrusives of the area, about 30 km northwest of Rouyn. Only a limited ground followup with magnetics, VLEM, and HLEM was necessary to outline both mineral zones, although other geophysical techniques were carried out later. Preliminary drilling at the larger property in late 1972 encountered ore-grade sulfides, while the

Table 12.5.

Survey	Section	Problem	Figure	Lines surveyed	Stations
Gravity	2.9	4, 12	—	0, 2S	53W - 24W
Tellurics	6.4	7	6.35	0, 2S	55W - 23W
VLEM	7.9	1	—	0, 2S	42W - 34W, 43W - 37W
AFMAG	7.9	7	7.111	6(N), 4, 2, 0	52W - 0
Resistivity	8.8	8	8.47	0	42W - 35W
IP	9.7	6	—	0, 2S	44W - 36W, 40W - 35W

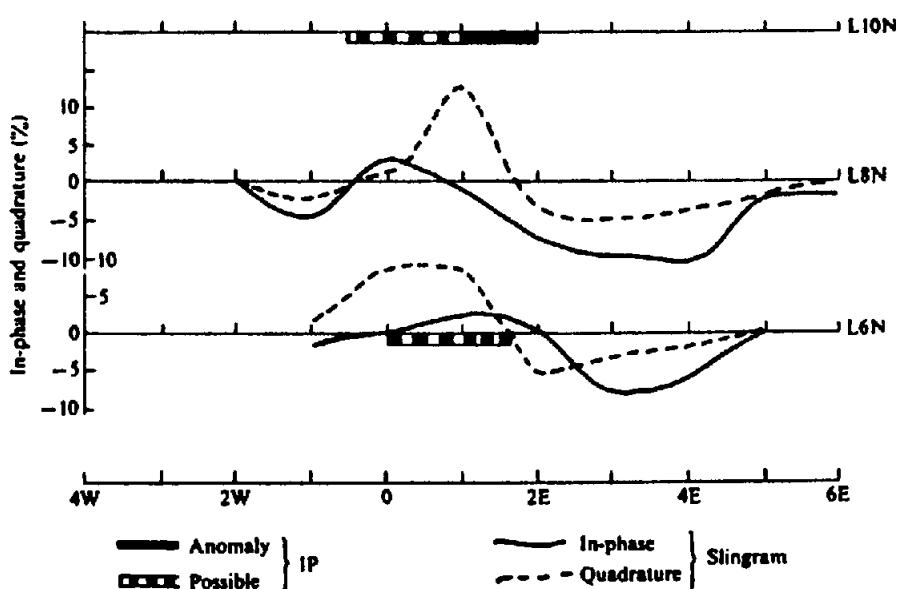


Figure 12.14. Slingram and IP results, northern New Brunswick. EM frequency 876 Hz, T-R separation 200 ft.

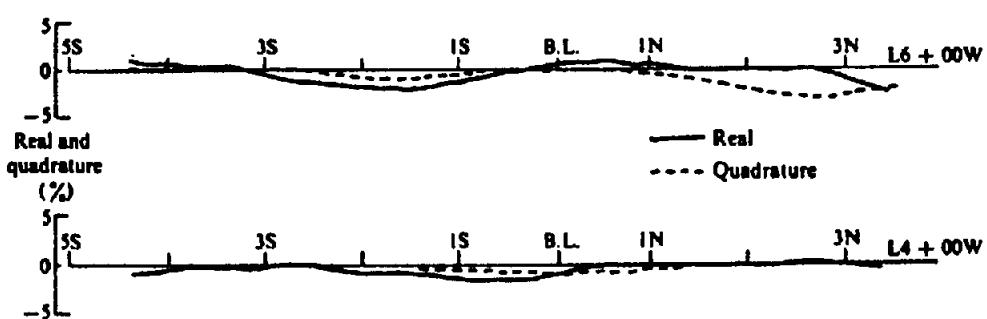


Figure 12.15. HLEM profiles, Abitibi West, Quebec. Frequency 1,000 Hz, T-R separation 300 ft.

other was brought in with a discovery hole in January 1973.

The original Input EM map of the area is displayed in Figure 12.12a, showing strong response from the larger deposit, marked A. Flight-line spacing varied between 300 and 1,000 ft (100 and 300 m), with the bird at about 300 ft. In Figure 12.12b, Dighem results at 100 m spacing and 150 ft (45 m) altitude, are illustrated for the same area. No men-

Table 12.6.

Type of survey	Section	Problem	Figure
Magnetic	3.9	5	—
Turam	7.9	13	—
Resistivity	8.8	9	8.48
IP	9.7	8	9.25

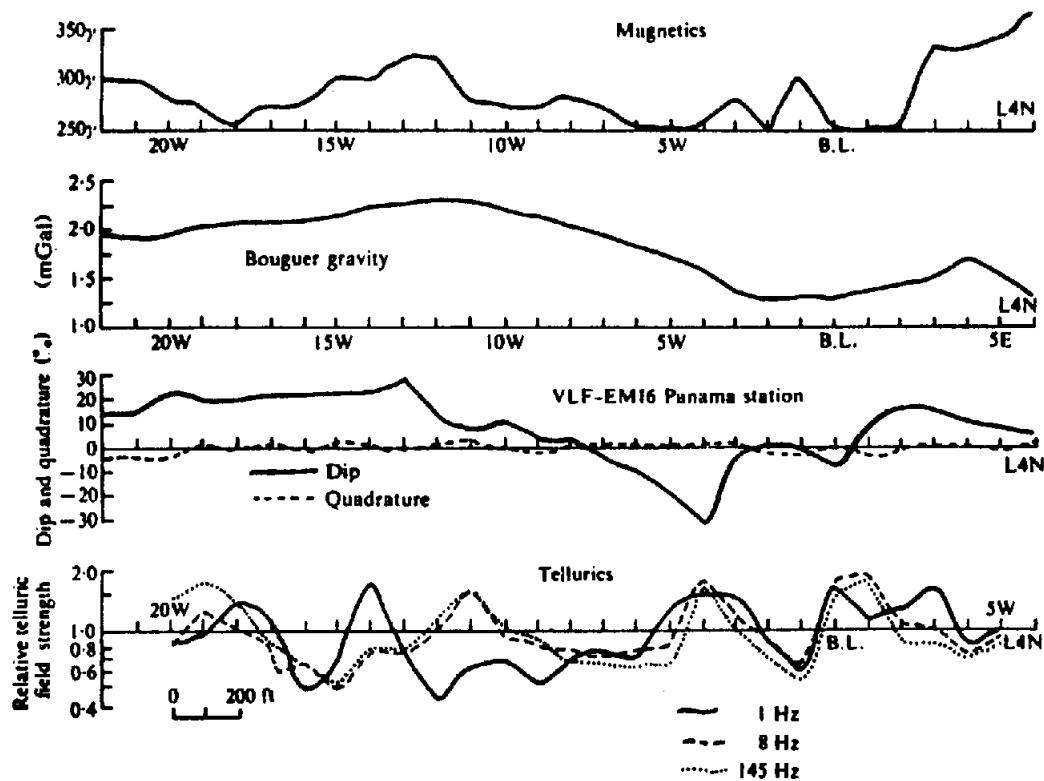


Figure 12.16. Magnetic, gravity, VLF, and telluric profiles, eastern Nova Scotia.

Table 12.7.

Type of Survey	Section	Problem	Figure	Type of display
Topographic	2.9	7	2.39	Terrain contours
Gravity	2.9	15	2.43	Bouguer gravity contours
Magnetic	3.9	11	3.40a	Terrain and magnetic contours
EM16	7.9	5	—	Profiles

Table 12.8.

Type of survey	Section	Problem	Figure	Type of display
Magnetic	3.9	11	3.40b	Terrain and magnetic contours
Telluric	6.4	5	—	Single profile
Resistivity	8.8	5	—	Three profiles

tion is made of the conductors along the Magus River or those south of anomaly A, which appears to strike E-W for ~ 2,000 ft (600 m).

Ground profiles from three N-S lines over the Dighem anomaly appear in Figures 12.12c, d, e. Although two of the Input conductors show magnetic correlation, this was weak as can be seen from the Dighem data. Consequently no ground magnetic measurements were made. The IP survey was carried out later to determine possible lateral and depth extensions of the mineral zone.

By selecting a suitable model, make use of all data in Figure 12.12 to estimate the depth and depth extent, dip, strike length, thickness, and/or product of the conductor. Is the lack of a magnetic signature significant with regard to mineralization? Are there evidences of conductive overburden of variable thickness?

15. The smaller sulfide deposit near Rouyn noted in problem 14 was not detected during the Input survey. However, the Dighem operation located it at B on line 66 in Figure 12.13a, where it obviously has

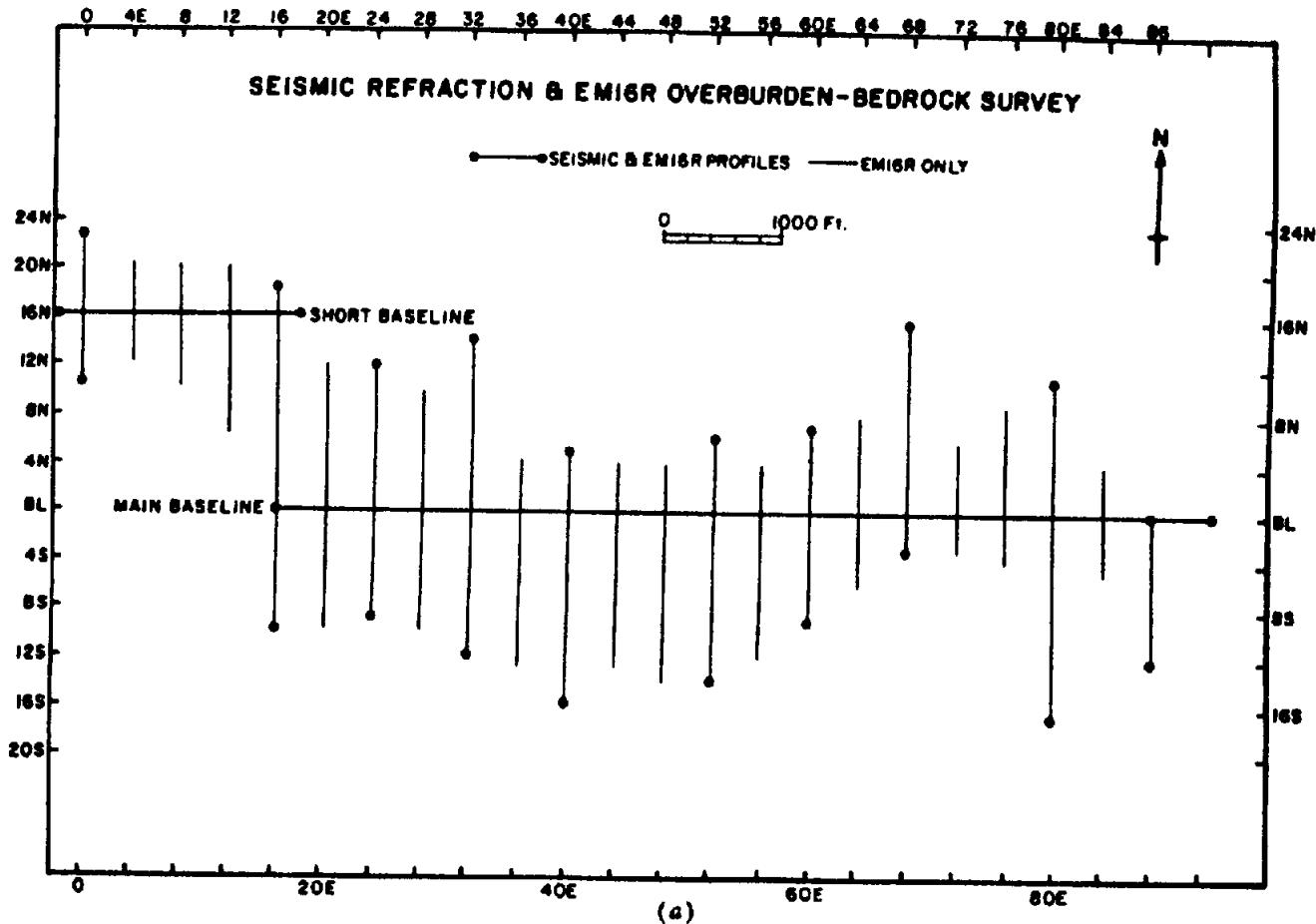


Figure 12.17. Groundwater survey, northeastern Ontario. (a) Survey grid system.

a limited strike length ( $\sim 200$  m). Again there is no reference to conductors along Magusi River to the north. Three sets of N-S ground profiles are shown in Figures 12.13b, c, d. They include B-horizon soil geochemistry, gravity, magnetics, and HLEM on all three lines, along with FD IP and SP in Figures 12.13c, d.

The sharp magnetic peak of 5,000 nT on line 2 + 00E does not appear to correlate with the gravity profiles; the latter are somewhat anomalous on all three lines, whereas the magnetic feature extends barely 200 ft (60 m) along strike.

Carry out an interpretation similar to that for anomaly A in problem 14, estimating the same parameters, but with emphasis on the gravity and magnetic data. Attempt to explain the differences between gravity and magnetic models in terms of the probable mineralization, as well as the geometry. Why was anomaly B not detected during the Input survey? Make an estimate of tonnage and type of mineralization for both these properties.

16. The problems listed in Table 12.5 are all from the same survey area in northeastern Brazil.

As noted in problem 12, Section 2.9, the base line for this survey, which is at station 0, strikes  $20^\circ$  east, making an angle of  $110^\circ$  with the traverse lines,

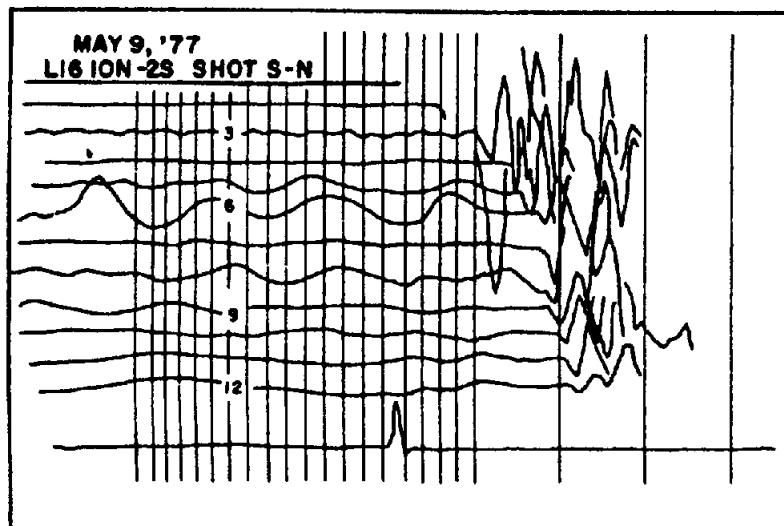
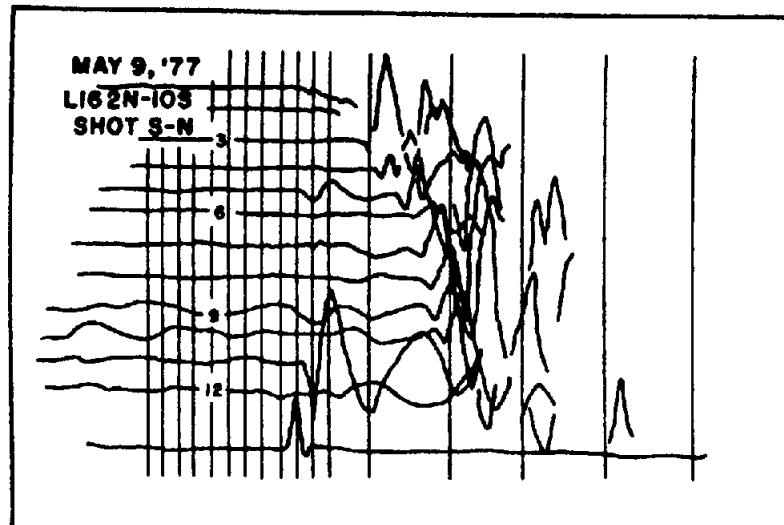
which are due E-W. Thus it is necessary to shift the AFMAG lines in Figure 7.111; that is to say, lines 2, 4, and 6 (lines are 200 m apart measured on the base line) should be moved 68, 137, and 205 m respectively, east of line 0.

17. The gravity and SP data, problem 11, Section 2.9, and problem 2, Section 6.4, Figure 6.31, are on the same grid. To these have been added the Slingram (horizontal-loop EM) and spot IP results shown in Figure 12.14.

18. Figure 12.15 displays horizontal-loop EM profiles on two lines taken from a survey in northwest Quebec. Further geophysical results, all from line 4 + 00W, are given in Table 12.6.

19. The profiles in Figure 12.16 are a compilation for a single traverse line from a survey carried out in eastern Nova Scotia. Other problems dealing with this area are listed in Table 12.7.

The contour map of Figure 3.41a may be located with respect to the other survey data by noting that the upper left-hand corner of the margin is station 22W, line 12N. As an aid to the assessment of this area, it should be explained that the original geological reconnaissance was a followup of a geochemical anomaly with EM16, SP, and magnetics. The first two methods located a weak anomaly just



(b)

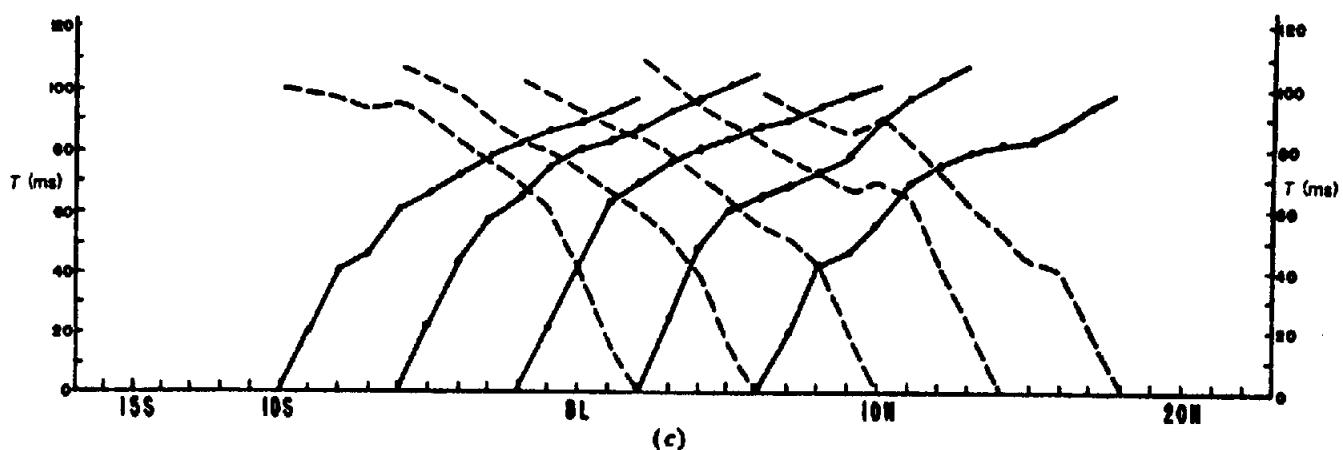


Figure 12.17. (Continued) (b) Typical reversed refraction profiles, line 16E. (c) Refraction time-distance plot, line 16E.

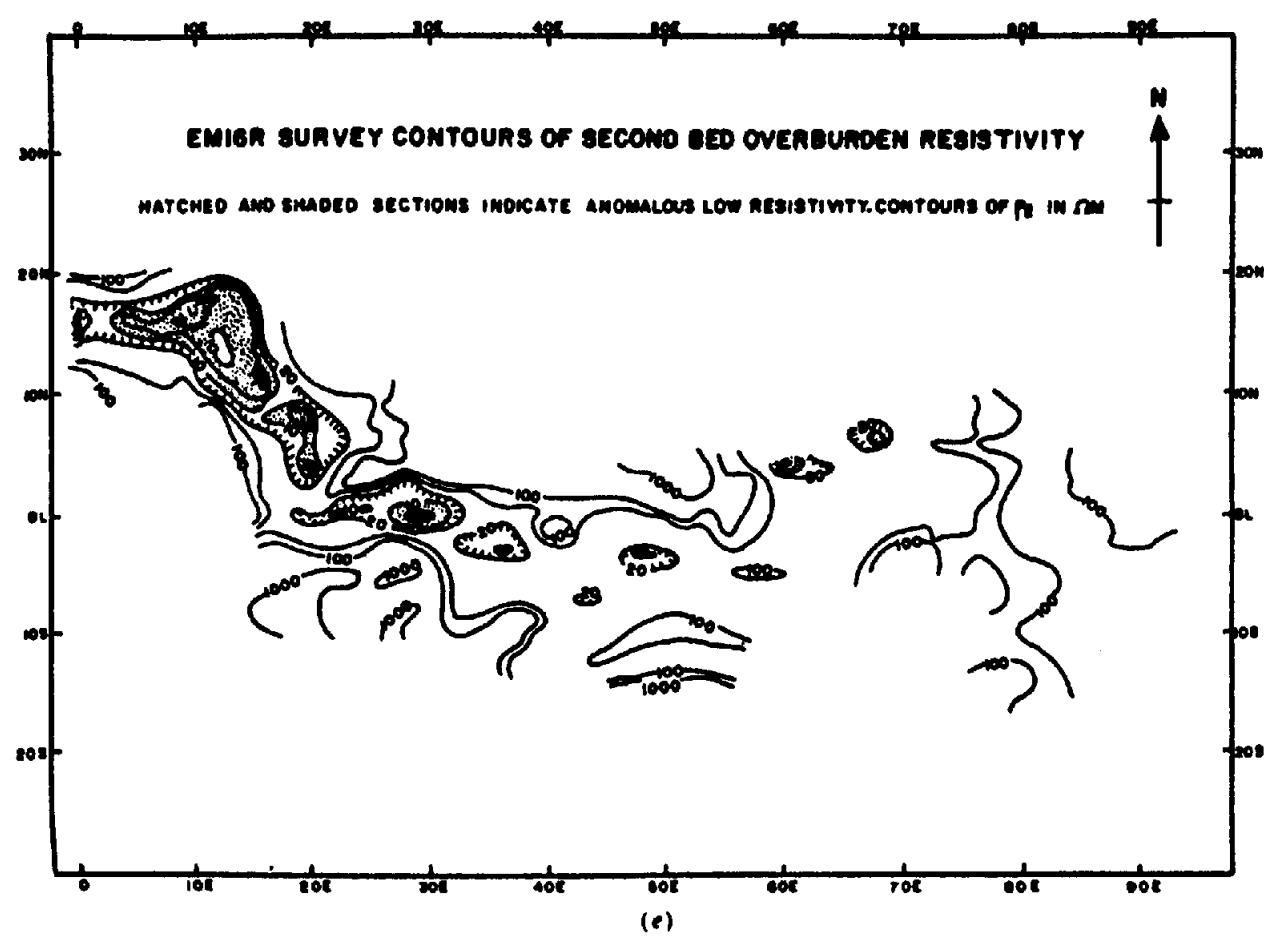
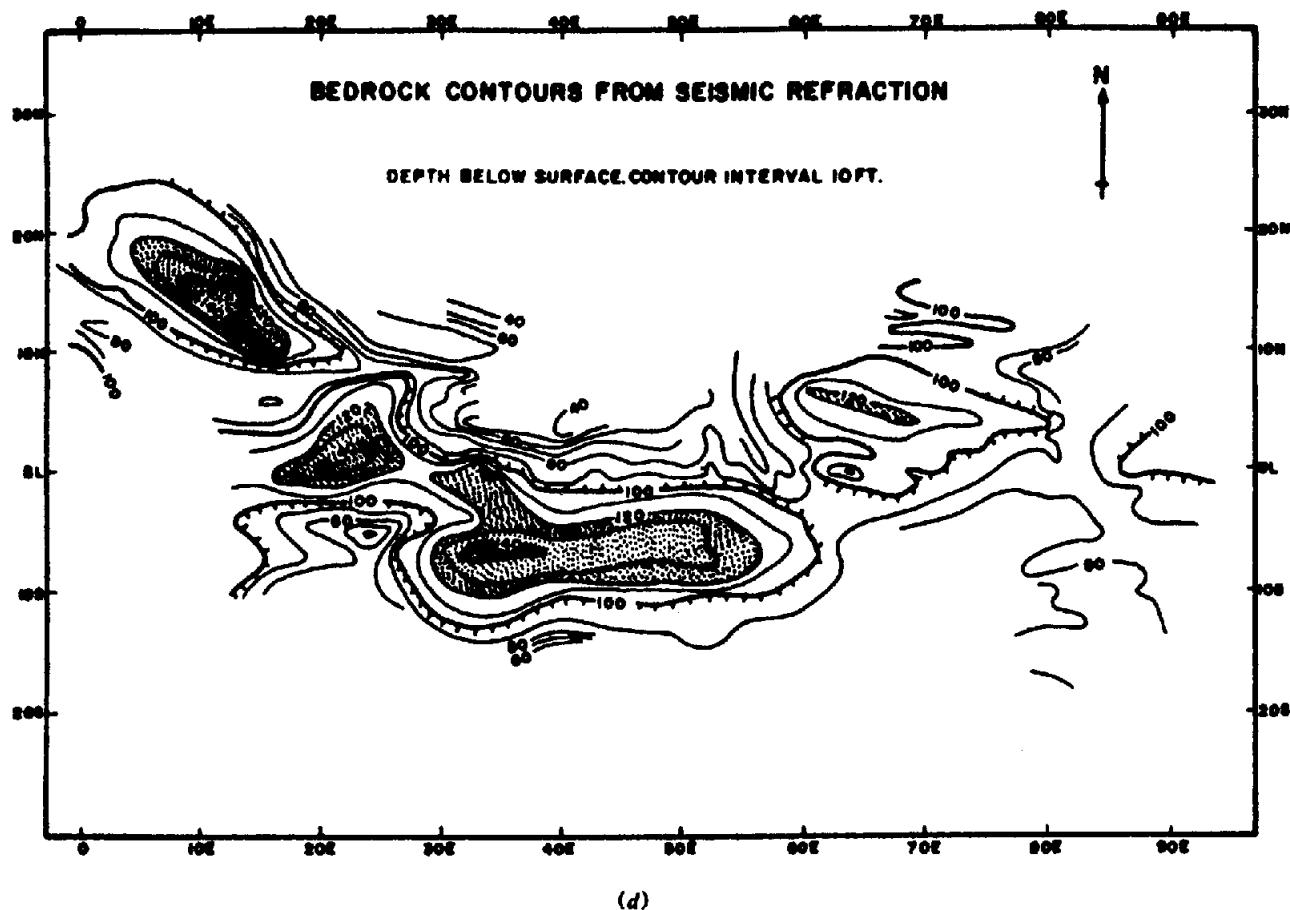


Figure 12.17. (Continued) (d) Bedrock contours from seismic refraction. (e) EM16 survey contours.

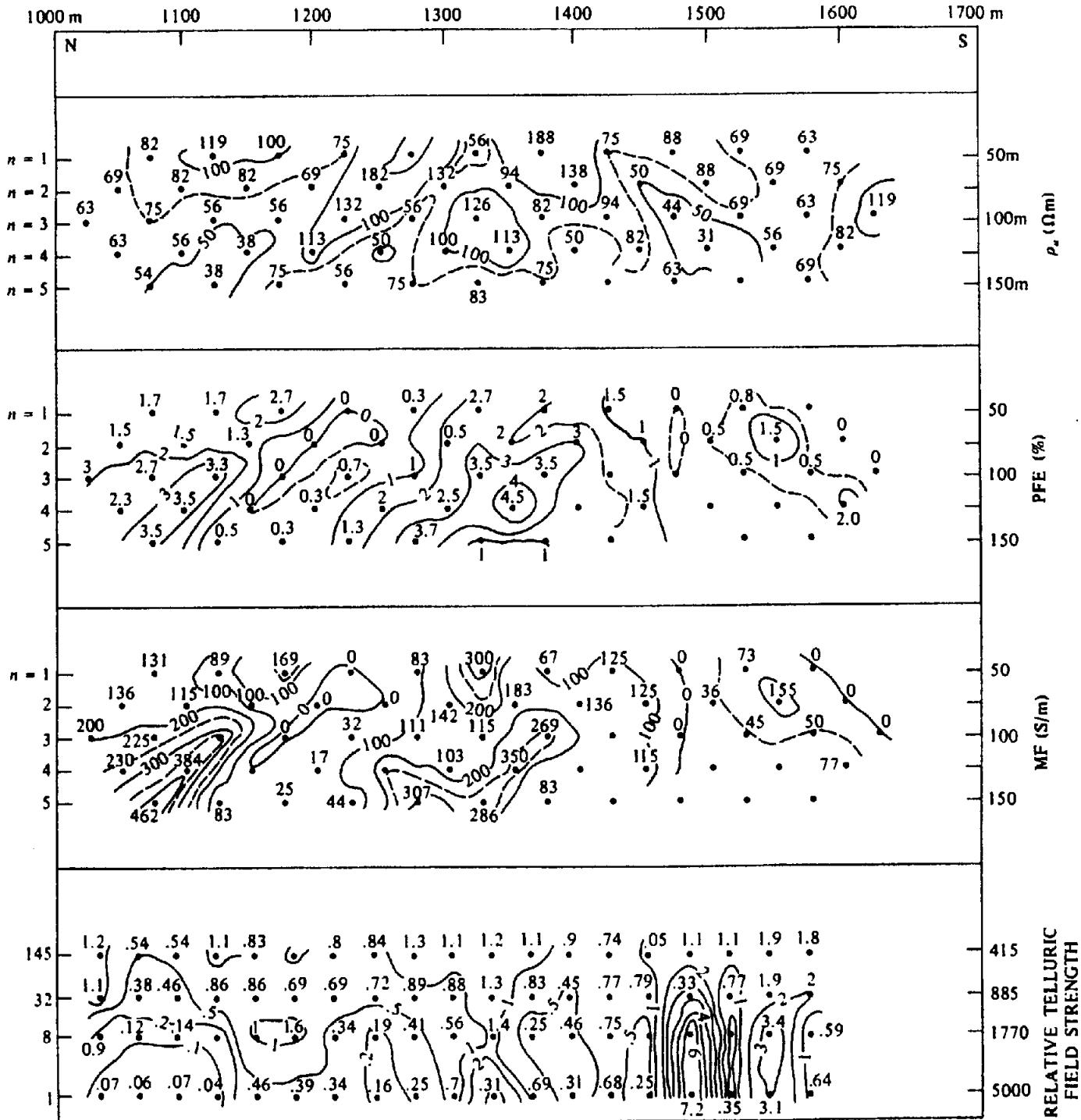


Figure 12.18. Resistivity, IP, and telluric pseudodepth plots, northern Chile.

west of the base line between lines 0 and 8N. Following the layout of a small grid, HLEM and limited gravity surveys produced promising results. The survey area then began to grow.

20. The data contained in Table 12.8 originated in the same area in eastern Nova Scotia.

21. A contract survey to map bedrock topography and character of overburden was carried out at a mining site in northeastern Ontario to determine the presence of groundwater and leakage paths into a nearby open pit. The site lies within the regional conductive clay belt extending across this part of

Ontario and Quebec, frequently underlain by sand-gravel beds immediately above bedrock. The area surveyed was about  $4,000 \times 9,000$  ft ( $\sim 1,200 \times 2,750$  m), over a practically flat surface; the NW corner was swampy.

Seismic refraction and EM16R surveys were carried out on N-S grid lines spaced 400 ft (120 m), the seismic lines generally 800 ft (240 m) apart, EM16R on all 23 lines; 10,000 ft ( $\sim 3,000$  m) of E-W base lines were done with both techniques. The grid is shown in Figure 12.17a. Time limitations made it impossible to employ resistivity sounding profiles.

Because of high attenuation in the clay, it was necessary to fire three or more sticks of Tovex high explosive to obtain reasonable bedrock returns at 100 ft (30 m) geophone intervals using a 12-channel seismic unit, and this ruled out measurement of velocity variations in the overburden with smaller spreads (because surface motion was too violent to give useable first breaks). Reverse profiles generally overlapped 400 ft to provide reasonable coverage. Figures 12.17b, c show a typical pair of reversed profiles on line 16E plus the time-distance plots for the same line.

Determine the velocities and depths along the profiles by analysis of Figure 12.17c, assuming a constant velocity throughout the clay and sand-gravel overburden, and hence plot the bedrock topography. Is there evidence that this assumption is incorrect? Check your result from the contours in Figure 12.17d. Locate possible faults.

From a few conventional soundings carried out to measure the resistivity of the clay and sand-gravel beds, the near-surface value of resistivity was found to be about  $20 \Omega\text{m}$ , increasing with the spread length. Results of the EM16R survey, shown in contoured form in Figure 12.17e, verified this over much of the grid where the phase angle was less than  $45^\circ$  and  $\rho_a$  frequently increased. In the NW portion, however,  $\phi > 45^\circ$  and  $\rho_a < 20 \Omega\text{m}$  at many stations, indicating a more conductive second layer. This is illustrated by the shaded areas. Do these zones reflect the sand-gravel, the bedrock, or some other possibility? Consider the skin depth in this connection, as well as the fact that EM16R measurements are incapable of resolving more than two beds.

22. Figure 12.18 shows a set of pseudodepth plots from frequency-domain IP and four-frequency telluric profiles over a porphyry copper prospect in northern Chile. The IP sections were obtained from a conventional double-dipole array expansion (see Figs. 9.8a, and 9.13) with  $x = 50$  m. Telluric depths were estimated from an assumed ground resistivity of  $100 \Omega\text{m}$  and by calculating skin depth for each of the four measured frequencies: 145, 32, 8, and 1 Hz. Of course, the skin depths, which are approximately 415, 885, 1,770, and 5,000 m, are much larger than the penetration of the double-dipole array, which ranges from 50 to 150 m. The tellurics are plotted on a compressed log scale of about the same dimensions as the IP and  $\rho_a$  sections.

The telluric survey was performed some months after the IP and there were difficulties in establishing the precise station locations of the latter, although both traversed the same N-S line. Telluric measurements were made at 30 m electrode spacing. Because of the regional aridity, the IP work (of which this example is only a part), took three weeks. The same coverage with tellurics was done in two days.

It is clear that the three pseudodepth plots from the IP survey have general similarities, becoming increasingly anomalous with increasing  $n$ . The  $\rho_a$  response, however, is weak compared to the IP sections, particularly the metal factor. What is the probable reason for this? Make a transparency of the telluric data and attempt a fit on each of the other plots. Which seems best? Which parameter is actually measured in a telluric survey? Is the skin depth a realistic figure?

# Appendix

## A

# *Mathematical Background*

### A.1. DETERMINANTS

A *determinant* is a square array of numbers or symbols, called *elements*, with a rule for finding the value of the array. Determinants are denoted in several ways, for example,

$$\det(a) = |a_{ij}|$$

$$= \begin{vmatrix} a_{11} & a_{12} & \cdots & a_{1n} \\ a_{21} & a_{22} & \cdots & a_{2n} \\ \vdots & \vdots & \ddots & \vdots \\ a_{n1} & a_{n2} & \cdots & a_{nn} \end{vmatrix} \quad (\text{A.1})$$

the element  $a_{ij}$  being in the  $i$ th row and  $j$ th column. The determinant obtained by deleting the  $i$ th row and  $j$ th column is the *minor*,  $M_{ij}$ , of the element  $a_{ij}$ . The quantity,  $(-1)^{i+j}M_{ij}$ , is the *cofactor* of  $a_{ij}$ ,  $A_{ij}$ .

One rule for finding the value of  $\det(a)$  can be stated thus (Pipes and Harvill, 1978, pp. 85–6):

$$\left. \begin{array}{l} \sum_j a_{ij} A_{ij} = \sum_i a_{ij} A_{ij} = \det(a) \\ \sum_j a_{ij} A_{kj} = 0 \quad i \neq k \\ \sum_i a_{ij} A_{ik} = 0 \quad j \neq k \end{array} \right\} \quad (\text{A.2})$$

This equation states that the value of  $\det(a)$  can be found by summing the products of each element of any row (or any column) and its cofactor. However, if we sum products of any row (or any column) by the cofactors of a different row (column), the sum is zero.

We illustrate Equation (A.2) by finding the value of the determinant

$$\begin{vmatrix} 2 & 4 \\ 3 & 5 \end{vmatrix}$$

Using the first row, the value is  $(2 \times 5 - 4 \times 3) = -2$ ; using the first column, we have  $(2 \times 5 - 3 \times 4)$

$= -2$ . Determinants are usually evaluated using the first row or column, but the rule is better illustrated by expanding the following determinant using the second column:

$$\begin{aligned} \begin{vmatrix} 4 & 2 & 7 \\ 3 & -8 & 8 \\ 9 & 6 & 5 \end{vmatrix} &= (-1)^{1+2}(2) \begin{vmatrix} 3 & 8 \\ 9 & 5 \end{vmatrix} \\ &\quad + (-1)^{2+2}(-8) \begin{vmatrix} 4 & 7 \\ 9 & 5 \end{vmatrix} \\ &\quad + (-1)^{3+2}(6) \begin{vmatrix} 4 & 7 \\ 3 & 8 \end{vmatrix} \\ &= -2(-57) - 8(-43) - 6(11) \\ &= 392. \end{aligned}$$

The same result is obtained regardless of which row or column is used.

If we expand the preceding determinant using the third row and cofactors of the first row, we obtain

$$\begin{aligned} &(-1)^{3+1}(9) \begin{vmatrix} -8 & 8 \\ 6 & 5 \end{vmatrix} + (-1)^{3+2}(6) \begin{vmatrix} 3 & 8 \\ 9 & 5 \end{vmatrix} \\ &\quad + (-1)^{3+3}(5) \begin{vmatrix} 3 & -8 \\ 9 & 6 \end{vmatrix} = 0 \end{aligned}$$

This illustrates the second result in Equation (A.2).

The solution of a set of simultaneous linear equations can be expressed in terms of determinants using *Cramér's rule* (Pipes and Harvill, 1970, p. 101). Given a set of  $n$  equations in the  $n$  unknowns  $x_1, x_2, \dots, x_n$ ,

$$\left. \begin{array}{l} a_{11}x_1 + a_{12}x_2 + \cdots + a_{1n}x_n = k_1 \\ a_{21}x_1 + a_{22}x_2 + \cdots + a_{2n}x_n = k_2 \\ \vdots \\ a_{n1}x_1 + a_{n2}x_2 + \cdots + a_{nn}x_n = k_n \end{array} \right\} \quad (\text{A.3a})$$

the solution is

$$x_j = \det(a_j)/\det(a) \quad (\text{A.3b})$$

where  $\det(a)$  is the determinant of the coefficients  $a_{ij}$ , and  $\det(a_j)$  is  $\det(a)$  with the  $j$ th column replaced by the column  $(k_1, k_2, \dots, k_n)$ . As an example, we solve the equations

$$\begin{aligned} 4x_1 + 2x_2 + 7x_3 &= -4 \\ 3x_1 - 8x_2 + 8x_3 &= -15 \\ 9x_1 + 6x_2 + 5x_3 &= 11 \end{aligned}$$

The value of  $\det(a)$  is found to be 392. Then,

$$\begin{aligned} \det(a_1) &= \begin{vmatrix} -4 & 2 & 7 \\ -15 & -8 & 8 \\ 11 & 6 & 5 \end{vmatrix} \\ &= -4 \begin{vmatrix} -8 & 8 \\ 6 & 5 \end{vmatrix} + 15 \begin{vmatrix} 2 & 7 \\ 6 & 5 \end{vmatrix} + 11 \begin{vmatrix} 2 & 7 \\ -8 & 8 \end{vmatrix} \\ &= 664 \end{aligned}$$

so that  $x_1 = 664/392 = 1.69$ . The values of  $x_2$  and  $x_3$  are found by substituting the  $k$  column for the second and third columns of  $\det(a)$ .

## A.2. MATRICES

A *matrix* is a rectangular array of numbers or symbols (elements) plus rules for their manipulation. Matrices are represented in several ways; for example, a matrix of order  $(m \times n)$  may be written

$$A = \left\| a_{ij} \right\| = \begin{array}{|c c c c|} \hline a_{11} & a_{12} & \cdots & a_{1n} \\ a_{21} & a_{22} & \cdots & a_{2n} \\ \vdots & \vdots & \ddots & \vdots \\ a_{m1} & a_{m2} & \cdots & a_{mn} \\ \hline \end{array} \quad (\text{A.4a})$$

Matrices of the same order  $(m \times n)$  can be added (or subtracted) by adding (subtracting) corresponding elements; thus, if  $A, B, C$  are matrices of the same order, then  $C = A \pm B$  has elements  $c_{ij} = a_{ij} \pm b_{ij}$ . To form the product  $AB$ , the orders of  $A$  and  $B$  must be  $(m \times p)$  and  $(p \times n)$ , the product  $C$  being of order  $(m \times n)$ . The elements  $c_{ij}$  are given by the formula

$$c_{ij} = \sum_k a_{ik} b_{kj} \quad (\text{A.4b})$$

that is,  $c_{ij}$  is the sum of the products, element by element, of the  $i$ th row of  $A$  and the  $j$ th column of  $B$ . In general,  $AB \neq BA$ . To illustrate,

$$\begin{aligned} &\left\| \begin{array}{ccc} 2 & -4 & 1 \\ 3 & 5 & -6 \end{array} \right\| \left\| \begin{array}{cccc} 6 & 2 & -8 & 1 \\ 5 & -3 & 9 & 0 \\ 2 & -7 & 3 & 2 \end{array} \right\| \\ &(2 \times 3) \quad (3 \times 4) \\ &= \left\| \begin{array}{cccc} -6 & 9 & -49 & 4 \\ 31 & 33 & 3 & -9 \end{array} \right\| \\ &(2 \times 4) \end{aligned}$$

The element  $c_{13}$  is, for example,  $2 \times (-8) + (-4) \times 9 + 1 \times 3 = -49$ .

The *transpose* of a matrix,  $A^T$ , is the matrix  $A$  with rows and columns interchanged. A matrix of order  $(n \times 1)$  is a *column matrix*, for example, the  $k$  column in Equation (A.3a). A matrix of order  $(1 \times n)$  is a *row matrix*. A *null matrix*  $\mathbf{0}$  has zeros for all elements; thus, if  $A = B$ , then  $A - B = \mathbf{0}$  and each element of  $A$  equals the corresponding element of  $B$ .

An  $(n \times n)$  matrix is a *square matrix* and has a determinant,  $\det(a)$ , whose elements are those of the matrix; elements  $a_{ii}$  form the *principal diagonal* of the matrix. A square matrix in which all elements off the principal diagonal are zero but at least one of the diagonal elements is not zero is a *diagonal matrix*. The *identity (unit) matrix* is a diagonal matrix with elements  $a_{ii} = 1$ . A *symmetric matrix* is a square matrix with  $a_{ij} = a_{ji}$ ; if  $a_{ij} = -a_{ji}$ , the matrix is *skew symmetric*.

If each element of a square matrix is replaced by its cofactor in  $\det(a)$  of the matrix and the result transposed, we get the *adjoint* of  $A$ ,  $\text{adj } A$ . The *reciprocal* of  $A$  is

$$A^{-1} = \{1/\det(a)\} \text{adj } A \quad (\text{A.5a})$$

[provided that  $\det(a) \neq 0$ ; this follows from Equation (A.2) because on using Equation (A.4b) to find the elements of the product  $AA^{-1}$ , all off-diagonal terms are zero whereas all diagonal terms equal  $\det(a)$ ].

The equivalent of division by a square matrix is multiplication by  $A^{-1}$ . If  $A$  is not square, we make it square by forming the product  $A^T A$ , which is always square. Thus, the solutions of the matrix equations  $M = AN$  and  $P = BN$ , where  $A$  and  $B$  are, respectively, square and nonsquare are

$$N = A^{-1}M \quad P = (B^T B)^{-1} B^T M \quad (\text{A.5b})$$

Matrices can be used to solve equations. Equation (A.3a) in matrix form is

$$AX = X \quad (\text{A.6a})$$

where  $A$  is a square matrix of the coefficients,  $X$  is a column matrix of the unknowns  $x_i$ , and  $\mathbf{x}$  is a column matrix of the  $k$ 's. The solution is

$$X = A^{-1}X \quad (\text{A.6b})$$

Equating the  $(n \times 1)$  column matrix on the left with the product, which is also a  $(n \times 1)$  column matrix, we get the  $n$  values of  $x_i$ .

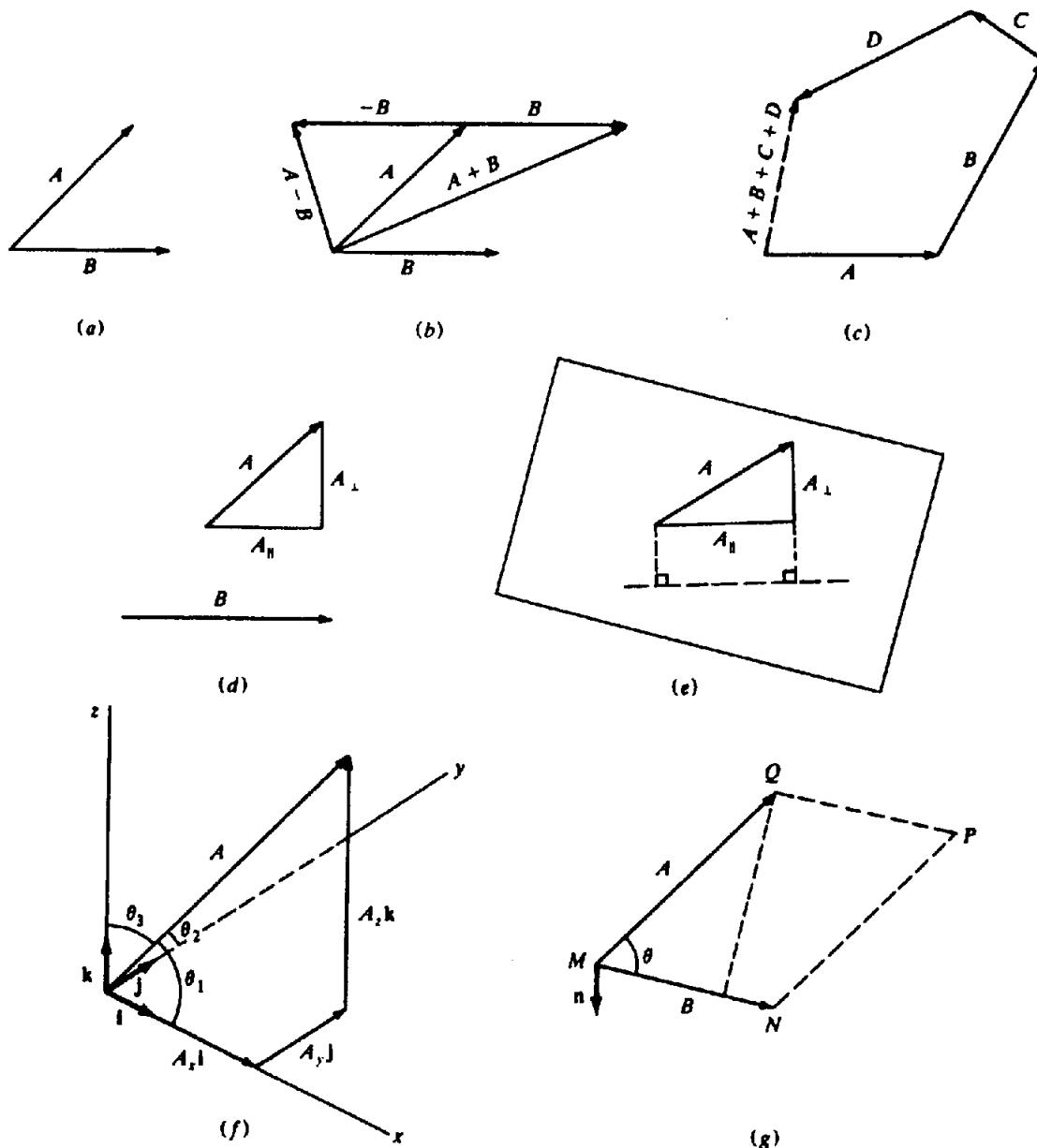


**Figure A.1.** Various operations on vectors. (a) Two vectors to be added or subtracted. (b) Addition and subtraction of vectors in (a). (c) Summing several vectors. (d) Resolving  $\mathbf{A}$  into components parallel to and perpendicular to  $\mathbf{B}$ . (e) Resolving  $\mathbf{A}$  into components parallel to and perpendicular to a plane. (f) Resolving  $\mathbf{A}$  into rectangular components. (g) Illustrating the products  $\mathbf{A} \cdot \mathbf{B}$  and  $\mathbf{A} \times \mathbf{B}$ .

### A.3. VECTOR ANALYSIS

#### A.3.1. Basic Theory

All measurable quantities can be divided into two classes: (i) *scalars*, which have magnitude only, hence can be completely specified by a single number, for example, temperature and density, and (ii) *vectors*, which have both magnitude and direction so that they are specified by giving a number (magnitude) and a direction, for example, force and velocity. Vectors will be denoted by boldface letters.

A vector can be represented by an arrow whose length is proportional to the magnitude and whose direction is that of the vector. To add two vectors,  $\mathbf{A}$  and  $\mathbf{B}$  (Fig. A.1a), we move one of them as in Figure A.1b, and the sum is the vector from the initial to the final point. The vector  $-\mathbf{B}$  is  $\mathbf{B}$  reversed in direction, so we subtract  $\mathbf{B}$  from  $\mathbf{A}$  by adding  $-\mathbf{B}$  to  $\mathbf{A}$  (Fig. A.1b). Several vectors can be added together as in Figure A.1c.

Calculations involving vectors are often facilitated by resolving them into *components*. Any vector can be regarded as the sum of several arbitrary

vectors; for example, in Figure A.1c the sum ( $\mathbf{A} + \mathbf{B} + \mathbf{C} + \mathbf{D}$ ) can be a given vector with arbitrary components  $\mathbf{A}$ ,  $\mathbf{B}$ ,  $\mathbf{C}$ , and  $\mathbf{D}$ . Sometimes we resolve a vector into components parallel to and perpendicular to another vector (Fig. A.1d) or to a plane (Fig. A.1e). More often we use components parallel to the axes of a coordinate system; for example, in Figure A.1f we take vectors of unit length,  $\mathbf{i}$ ,  $\mathbf{j}$ , and  $\mathbf{k}$ , along the  $x$ ,  $y$ , and  $z$  axes, and the components of  $\mathbf{A}$  are the scalar quantities  $a_x$ ,  $a_y$ ,  $a_z$ . Then

$$\mathbf{A} = a_x \mathbf{i} + a_y \mathbf{j} + a_z \mathbf{k} \quad (\text{A.7})$$

Also, from Figure A.1f, we get

$$\begin{aligned} a_x/A &= \cos \theta_1 = \ell \\ a_y/A &= \cos \theta_2 = m \\ a_z/A &= \cos \theta_3 = n \end{aligned}$$

where  $\theta_1$ ,  $\theta_2$ , and  $\theta_3$  are the angles between  $\mathbf{A}$  and the three axes,  $(\ell, m, n)$  are the *direction cosines* of  $\mathbf{A}$ , and  $A$  is the *magnitude* of  $\mathbf{A}$ . Because  $A^2 = a_x^2 + a_y^2 + a_z^2$ , on dividing by  $A^2$ , we have

$$\ell^2 + m^2 + n^2 = 1 \quad (\text{A.8})$$

We can add and subtract vectors by adding and subtracting components:

$$\begin{aligned} \text{if} \quad \mathbf{A} &= 2\mathbf{i} + 3\mathbf{j} - 4\mathbf{k} \\ \mathbf{B} &= 4\mathbf{i} - \mathbf{j} - 5\mathbf{k} \\ \mathbf{C} &= 2\mathbf{i} - 3\mathbf{j} + 3\mathbf{k} \end{aligned}$$

then

$$\begin{aligned} \mathbf{A} - \mathbf{B} + \mathbf{C} &= (2 - 4 + 2)\mathbf{i} + (3 + 1 - 3)\mathbf{j} \\ &\quad + (-4 + 5 + 3)\mathbf{k} \\ &= \mathbf{j} + 4\mathbf{k} \end{aligned}$$

### A.3.2. Vector Products

Products involving vectors are of three basic types. A vector can be multiplied by a scalar to give a new vector changed only in magnitude; this property is used to write a vector  $\mathbf{A}$  in the form  $A\mathbf{a}_1$ , where  $A = |\mathbf{A}|$  = magnitude of  $\mathbf{A}$  and  $\mathbf{a}_1$  is a unit vector parallel to  $\mathbf{A}$ . The other two basic products involve two vectors and are written  $\mathbf{A} \cdot \mathbf{B}$  and  $\mathbf{A} \times \mathbf{B}$ . The first, called the *dot product* or *scalar product*, is equal to the scalar quantity ( $\mathbf{AB} \cos \theta$ ) where  $\theta$  is the acute angle between  $\mathbf{A}$  and  $\mathbf{B}$  (Fig. A.1g); it is also equal to the magnitude of one of the vectors times the component of the other parallel to the first. The second product,  $\mathbf{A} \times \mathbf{B}$ , called the *cross product* or *vector product*, is defined as the vector ( $\mathbf{AB} \sin \theta$ ) $\mathbf{n}$ , where  $\mathbf{n}$  is a unit vector perpendicular to the plane containing  $\mathbf{A}$  and  $\mathbf{B}$  and in the direction of advance

of a right-handed screw rotated from  $\mathbf{A}$  to  $\mathbf{B}$  (Fig. A.1g).

The definition of the dot product shows that  $\mathbf{A} \cdot \mathbf{B} = \mathbf{B} \cdot \mathbf{A}$ , also

$$\mathbf{i} \cdot \mathbf{i} = \mathbf{j} \cdot \mathbf{j} = \mathbf{k} \cdot \mathbf{k} = 1$$

$$\mathbf{i} \cdot \mathbf{j} = \mathbf{j} \cdot \mathbf{k} = \mathbf{k} \cdot \mathbf{i} = 0$$

$$\begin{aligned} \mathbf{A} \cdot \mathbf{B} &= (a_x \mathbf{i} + a_y \mathbf{j} + a_z \mathbf{k}) \cdot (b_x \mathbf{i} + b_y \mathbf{j} + b_z \mathbf{k}) \\ &= (a_x b_x + a_y b_y + a_z b_z) \end{aligned} \quad (\text{A.9})$$

$$\mathbf{A} \cdot \mathbf{A} = A^2 = a_x^2 + a_y^2 + a_z^2 \quad (\text{A.10})$$

From the definition, we see that  $\mathbf{A} \times \mathbf{B} = -\mathbf{B} \times \mathbf{A}$ , also (for a right-handed set of orthogonal coordinate axes)

$$\mathbf{i} \times \mathbf{j} = \mathbf{k} \quad \mathbf{j} \times \mathbf{k} = \mathbf{i} \quad \mathbf{k} \times \mathbf{i} = \mathbf{j}$$

$$\mathbf{i} \times \mathbf{i} = \mathbf{j} \times \mathbf{j} = \mathbf{k} \times \mathbf{k} = 0$$

$$\begin{aligned} \mathbf{A} \times \mathbf{B} &= (a_x \mathbf{i} + a_y \mathbf{j} + a_z \mathbf{k}) \times (b_x \mathbf{i} + b_y \mathbf{j} + b_z \mathbf{k}) \\ &= (a_y b_z - a_z b_y) \mathbf{i} + (a_z b_x - a_x b_z) \mathbf{j} \\ &\quad + (a_x b_y - a_y b_x) \mathbf{k} \end{aligned} \quad (\text{A.11a})$$

$$= \begin{vmatrix} \mathbf{i} & \mathbf{j} & \mathbf{k} \\ a_x & a_y & a_z \\ b_x & b_y & b_z \end{vmatrix} \quad (\text{A.11b})$$

Figure A.1g shows that

$$|\mathbf{A} \times \mathbf{B}| = \frac{1}{2}(\text{area of parallelogram } MNPQ)$$

This means that a plane area can be considered as a vector with direction along the normal to the plane. Therefore we can resolve areas into components; in particular, an infinitesimal area  $ds$  can be written

$$ds = (dy dz) \mathbf{i} + (dz dx) \mathbf{j} + (dx dy) \mathbf{k} \quad (\text{A.12})$$

Vector products may involve more than two vectors. Because  $(\mathbf{B} \cdot \mathbf{C})$  is a scalar, it can only enter into a triple product in the form  $(\mathbf{B} \cdot \mathbf{C})\mathbf{A}$ . On the other hand,  $(\mathbf{B} \times \mathbf{C})$  is a vector, so we can have the products  $\mathbf{A} \cdot (\mathbf{B} \times \mathbf{C})$  and  $\mathbf{A} \times (\mathbf{B} \times \mathbf{C})$ . From Equations (A.9) and (A.11b) we find that

$$\mathbf{A} \cdot (\mathbf{B} \times \mathbf{C}) = \mathbf{B} \cdot (\mathbf{C} \times \mathbf{A}) = \mathbf{C} \cdot (\mathbf{A} \times \mathbf{B}) \quad (\text{A.13a})$$

$$= -\mathbf{A} \cdot (\mathbf{C} \times \mathbf{B}) = -\mathbf{B} \cdot (\mathbf{A} \times \mathbf{C})$$

$$= -\mathbf{C} \cdot (\mathbf{B} \times \mathbf{A}) \quad (\text{A.13b})$$

$$= \begin{vmatrix} a_x & a_y & a_z \\ b_x & b_y & b_z \\ c_x & c_y & c_z \end{vmatrix} \quad (\text{A.13c})$$

Thus, interchanging dot and cross does not change the value, but changing the cyclic order changes the sign. The triple product  $\mathbf{A} \times (\mathbf{B} \times \mathbf{C})$  can be expanded twice using Equation (A.11b), the result being

$$\mathbf{A} \times (\mathbf{B} \times \mathbf{C}) = (\mathbf{A} \cdot \mathbf{C})\mathbf{B} - (\mathbf{A} \cdot \mathbf{B})\mathbf{C} \quad (\text{A.14})$$

Although any number of vectors can be multiplied together, products of more than three are rare.

### A.3.3. The Vector Operator $\nabla$

If  $\phi(x, y, z)$  is the value of a scalar function at  $P(x, y, z)$ , then the value at a nearby point  $Q(x + dx, y + dy, z + dz)$  is  $\phi + d\phi$  where

$$d\phi = (\partial\phi/\partial x)dx + (\partial\phi/\partial y)dy + (\partial\phi/\partial z)dz \quad (\text{A.15})$$

Writing  $d\mathbf{r}$  for the vector displacement from  $P$  to  $Q$ , we have

$$d\mathbf{r} = dx\mathbf{i} + dy\mathbf{j} + dz\mathbf{k}$$

and Equation (A.15) can be written as

$$d\phi = (\nabla\phi) \cdot d\mathbf{r} \quad (\text{A.16})$$

where

$$\nabla\phi = (\partial\phi/\partial x)\mathbf{i} + (\partial\phi/\partial y)\mathbf{j} + (\partial\phi/\partial z)\mathbf{k} \quad (\text{A.17a})$$

= gradient of  $\phi(x, y, z)$  (A.17b)

= grad  $\phi$  (A.17c)

Dividing both sides of Equations (A.15) and (A.16) by  $d\mathbf{r}$  gives

$$\begin{aligned} d\phi/d\mathbf{r} &= (\nabla\phi) \cdot \{(dx/d\mathbf{r})\mathbf{i} + (dy/d\mathbf{r})\mathbf{j} \\ &\quad + (dz/d\mathbf{r})\mathbf{k}\} \end{aligned} \quad (\text{A.18a})$$

$$= (\nabla\phi) \cdot (l\mathbf{i} + m\mathbf{j} + n\mathbf{k}) \quad (\text{A.18b})$$

$$= (\nabla\phi) \cdot \mathbf{r}_1 \quad (\text{A.18c})$$

$\mathbf{r}_1$  being a unit vector along  $PQ$  with direction cosines  $(l, m, n)$ . Because  $(\nabla\phi) \cdot \mathbf{r}_1$  is the derivative of  $\phi(x, y, z)$  at  $P$  as we go in the direction  $\mathbf{r}_1$ , it is called the *directional derivative*.

The vector  $\nabla\phi$  is fixed at a given point but  $(\nabla\phi) \cdot \mathbf{r}_1$  varies as the direction  $\mathbf{r}_1$  is varied. When  $\mathbf{r}_1$  is parallel to  $\nabla\phi$ , the product will have its maximum value because  $|\mathbf{r}_1| = 1$  and  $\cos\theta$  is a maximum for  $\theta = 0$ . Therefore  $\nabla\phi$  is a vector in the direction of, and equal to, the maximum rate of increase of  $\phi(x, y, z)$ .

The expression  $((\partial/\partial x)\mathbf{i} + (\partial/\partial y)\mathbf{j} + (\partial/\partial z)\mathbf{k}$ ) is known as a *vector operator*; it is represented by the symbol  $\nabla$  (pronounced del). When we apply it to a scalar function  $\phi(x, y, z)$ , we get  $\nabla\phi$  or  $\text{grad } \phi$ . It can also be applied to a vector function of position,  $\mathbf{A}(x, y, z)$ , by taking either the dot or the cross product. In the first case we get

$$\begin{aligned} \nabla \cdot \mathbf{A} &= ((\partial/\partial x)\mathbf{i} + (\partial/\partial y)\mathbf{j} + (\partial/\partial z)\mathbf{k}) \\ &\quad \cdot (A_x\mathbf{i} + A_y\mathbf{j} + A_z\mathbf{k}) \\ &= (\partial A_x/\partial x) + (\partial A_y/\partial y) + (\partial A_z/\partial z) \end{aligned} \quad (\text{A.19a})$$

$$= \text{divergence of } \mathbf{A}(x, y, z) \quad (\text{A.19b})$$

$$= \text{div } \mathbf{A}(x, y, z) \quad (\text{A.19c})$$

In the second case, Equation (A.11b) gives

$$\nabla \times \mathbf{A} = \begin{vmatrix} \mathbf{i} & \mathbf{j} & \mathbf{k} \\ \partial/\partial x & \partial/\partial y & \partial/\partial z \\ A_x & A_y & A_z \end{vmatrix} \quad (\text{A.20a})$$

$$\begin{aligned} &= (\partial A_z/\partial y - \partial A_y/\partial z)\mathbf{i} \\ &\quad + (\partial A_x/\partial z - \partial A_z/\partial x)\mathbf{j} \\ &\quad + (\partial A_y/\partial x - \partial A_x/\partial y)\mathbf{k} \end{aligned} \quad (\text{A.20b})$$

$$= \text{curl } \mathbf{A} \quad (\text{A.20c})$$

The operator  $\nabla$  involves differentiation, and when it is applied to the product  $\phi\mathbf{A}$ ,  $\phi$  being a scalar function, we get two terms involving differentiation of  $\phi$  and  $\mathbf{A}$  separately. Therefore,

$$\nabla \cdot (\phi\mathbf{A}) = \nabla\phi \cdot \mathbf{A} + \phi\nabla \cdot \mathbf{A} \quad (\text{A.21})$$

$$\nabla \times (\phi\mathbf{A}) = \nabla\phi \times \mathbf{A} + \phi\nabla \times \mathbf{A} \quad (\text{A.22})$$

Treating  $\nabla$  as a true vector, we would have

$$\begin{aligned} \nabla \cdot \nabla &= \nabla^2 \\ &= \partial^2/\partial x^2 + \partial^2/\partial y^2 + \partial^2/\partial z^2 \\ &= \text{Laplacian} \end{aligned} \quad (\text{A.23})$$

$$\nabla \times \nabla\phi = 0 \quad \nabla \cdot (\nabla \times \mathbf{A}) = 0 \quad (\text{A.24})$$

$$\nabla \times (\nabla \times \mathbf{A}) = \nabla(\nabla \cdot \mathbf{A}) - \nabla^2\mathbf{A} \quad (\text{A.25})$$

Equations (A.21) to (A.25) can be verified by substituting the definition of  $\nabla$ . [Note that Equation (A.25) is valid only in rectangular cartesian coordinates.]

### A.3.4. Vector Theorems

The divergence of a vector has a geometrical interpretation that is often very useful. Let  $\mathbf{A}(x, y, z)$  be

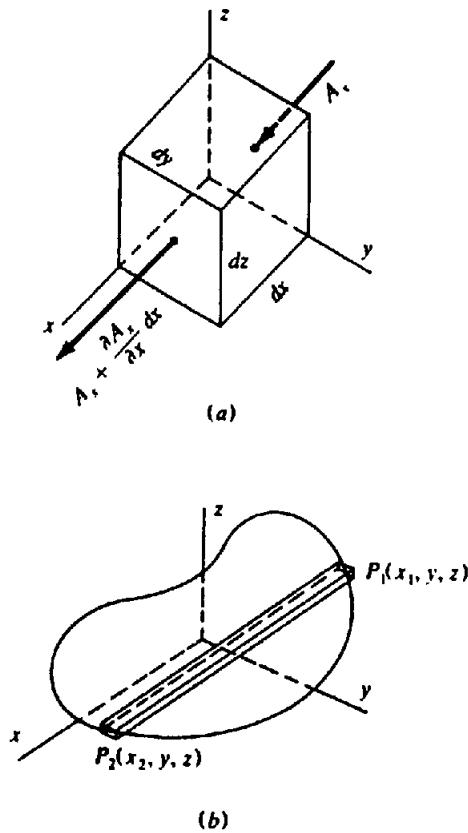


Figure A.2. Vector theorems. (a) Significance of  $\operatorname{div} \mathbf{A}$ . (b) Derivation of Gauss's theorem.

a vector equal to the velocity times density of a fluid. Referring to Figure A.2a, the quantity of fluid entering the element of volume ( $dx dy dz$ ) along the  $x$  axis per unit time is ( $A_x dy dz$ ) whereas that leaving the opposite face per unit time is  $\{A_x + (\partial A_x / \partial x) dx\} dy dz$ . Subtracting, the net outward flow is  $(\partial A_x / \partial x) dx dy dz$ . Adding terms for the outward flow along the  $y$  and  $z$  axes and dividing by the volume  $dx dy dz$ , we find that the net loss per unit volume per unit time is

$$\begin{aligned}\nabla \cdot \mathbf{A} &= \operatorname{div} \mathbf{A} \\ &= (\partial A_x / \partial x) + (\partial A_y / \partial y) + (\partial A_z / \partial z) \\ &= -(\partial \rho / \partial t)\end{aligned}\quad (\text{A.26})$$

where  $\rho$  is the density of the fluid.

The following theorems involve line, surface, and volume integrals. These are discussed in any advanced calculus text, for example, Wiley (1966, pp. 559–67), and so we shall give here only a very terse description.

A *line integral* is written in various ways:  $\int_C^B \mathbf{A} \cdot d\mathbf{l}$ ,  $\int_C \mathbf{A} \cdot d\mathbf{l}$ ,  $\oint_C \mathbf{A} \cdot d\mathbf{l}$ ,  $\oint \phi \mathbf{A} \cdot d\mathbf{l}$ ,  $C$  denoting a specific curve and  $\oint$  a closed curve; the line integral is the limit of the sum along the curve of products of the element of the curve  $d\mathbf{l}$  and the component of  $\mathbf{A}$  at  $d\mathbf{l}$  and parallel to it. A *surface integral*, usually

written  $\int_S \mathbf{A} \cdot d\mathbf{s}$ ,  $\iint \mathbf{A} \cdot d\mathbf{s}$ ,  $\int_S A_n ds$ , or  $\iint A_n ds$ , is the limit of the sum over the surface  $S$  of products of elements of the surface  $ds$  and the components of  $\mathbf{A}$  normal to the surface,  $A_n$ ; if the surface is closed,  $A_n$  is positive when it is in the direction of the outward-drawn normal. A *volume integral*,  $\int_V \phi(x, y, z) dv$ ,  $\iiint \phi(x, y, z) dx dy dz$ , and so on, is the limit of the sum of products of elements of volume  $dv$  and the values of a scalar function  $\phi(x, y, z)$  at the centers of  $dv$ .

Gauss's theorem, also known as the *divergence theorem*, states that

$$\int_V (\nabla \cdot \mathbf{A}) dv = \int_S \mathbf{A} \cdot d\mathbf{s} \quad (\text{A.27})$$

where the surface  $S$  encloses the volume  $V$ . To prove the theorem, we evaluate the first term of the volume integral,  $(\partial A_x / \partial x) dx dy dz$ , along a strip parallel to the  $x$  axis with cross section  $dy dz$  and extending from  $P_1(x_1, y, z)$  to  $P_2(x_2, y, z)$  (Fig. A.2b). Because  $y$  and  $z$  are fixed along the strip, the result is

$$\begin{aligned}\int_V \left( \frac{\partial A_x}{\partial x} dx \right) dy dz &= \{A_x(x_2, y, z) - A_x(x_1, y, z)\} dy dz \\ &= A_x ds_x|_{P_2} + A_x ds_x|_{P_1}\end{aligned}$$

because  $dy dz$  equals  $ds_x$  [Eq. (A.12)] at  $P_2(x_2, y, z)$  and  $-ds_x$  at  $P_1(x_1, y, z)$  (note that the outward-drawn normal is along the negative  $x$  axis here). Letting  $y$  and  $z$  vary, the right-hand side becomes the integral  $\int_S A_x ds_x$  over the surface  $S$ . Adding the integrals along the  $y$  and  $z$  axes, we obtain Equation (A.27).

Gauss's theorem has an important corollary known as *Green's theorem*. We let  $\mathbf{A}$  in Equation (A.27) be the vector  $w \nabla u$ ,  $u$  and  $w$  being scalar functions of position,  $u(x, y, z)$ , and  $w(x, y, z)$ . Replacing  $\mathbf{A}$  in Equation (A.21) with  $\nabla u$  and  $\phi$  with  $w$ , we see that

$$\nabla \cdot (w \nabla u) = w \nabla^2 u + (\nabla w) \cdot (\nabla u)$$

Equation (A.27) now becomes

$$\int_V \{ w \nabla^2 u + (\nabla w) \cdot (\nabla u) \} dv = \int_S (w \nabla u) \cdot d\mathbf{s}$$

Interchanging  $u$  and  $w$  and subtracting the two results gives Green's theorem:

$$\int_V (w \nabla^2 u - u \nabla^2 w) dv = \int_S (w \nabla u - u \nabla w) \cdot d\mathbf{s} \quad (\text{A.28})$$

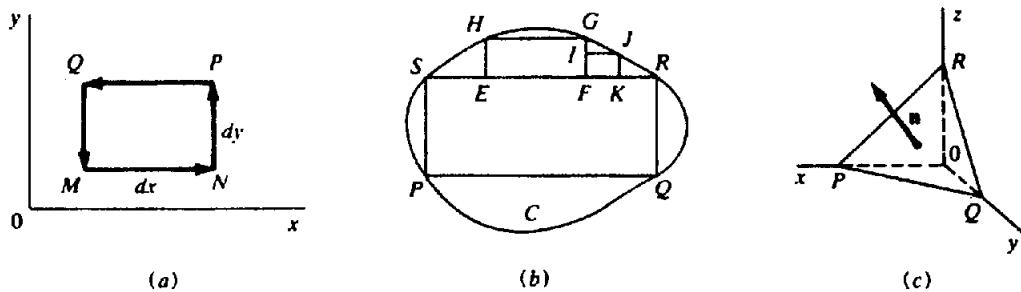


Figure A.3. Derivation of Stokes's theorem. (a) Evaluating a line integral around a rectangle. (b) Evaluating a line integral around an arbitrary closed planar curve  $C$ . (c) Resolving a surface integral over a plane triangle into components.

*Stokes's theorem* relates the line integral of a vector  $\mathbf{A}$  along a closed curve  $C$  to the surface integral of  $\text{curl } \mathbf{A}$  over any open surface that terminates on  $C$ . We establish the theorem first for the infinitesimal plane area  $dx dy$  in Figure A.3a. We take  $A_x$  and  $A_y$  as the values of the components at  $M(x, y)$ . Then the line integral around the rectangle is the sum of the line integrals along the sides  $MN$ ,  $NP$ ,  $PQ$ , and  $QM$ . Thus,

$$\begin{aligned} \int_C \mathbf{A} \cdot d\mathbf{l} &= A_x dx + \{ A_y + (\partial A_y / \partial x) dx \} dy \\ &\quad - \{ A_x + (\partial A_x / \partial y) dy \} dx - A_y dy \\ &= (\partial A_y / \partial x - \partial A_x / \partial y) dx dy \\ &= (z \text{ component of } \nabla \times \mathbf{A})(ds_z) \quad (\text{A.29a}) \end{aligned}$$

Next we generalize Equation (A.29a) for a plane surface of arbitrary shape (Fig. A.3b). We approximate the area inside  $C$  by a large rectangle, then add smaller and smaller rectangles until, in the limit, their sum equals the area inside  $C$ . The line integral around the perimeters of the first two rectangles in Figure A.3b is along  $PQRFGHESP$  (because  $EF$  is traversed twice in opposite directions), and in the limit the path of the line integral will be the curve  $C$  and Equation (A.29a) will become

$$\int_C \mathbf{A} \cdot d\mathbf{l} = \iint_S (\nabla \times \mathbf{A})_z ds_z, \quad (\text{A.29b})$$

Because Equation (A.29b) holds for a plane figure of any shape, it holds for a plane triangle. Any 3-D surface of arbitrary shape can be approximated as closely as desired by an infinite number of plane triangles. In Figure A.3c,  $\Delta PQR$  of area  $ds$  can be resolved into components [Eq. (A.12)]  $\Delta QRO$ ,  $\Delta RPO$ , and  $\Delta PQO$  with areas  $ds_x$ ,  $ds_y$ , and  $ds_z$ . The right-hand side of Equation (A.29b) then becomes three surface integrals over these triangles with integrands  $(\nabla \times \mathbf{A})_x ds_x$ ,  $(\nabla \times \mathbf{A})_y ds_y$ , and  $(\nabla \times \mathbf{A})_z ds_z$ . When we sum the contributions for all of the triangles making up  $S$ , the line integrals along

interior paths cancel in pairs leaving only the line integral along  $C$ ; the surface integrals over the triangles can be replaced by integrals over the component triangles perpendicular to the axes, which are then summed at each point and reconstituted into  $(\nabla \times \mathbf{A}) \cdot ds$  for each element of area  $ds$ . The result is Stokes's theorem:

$$\int_C \mathbf{A} \cdot d\mathbf{l} = \iint_S (\nabla \times \mathbf{A}) \cdot ds \quad (\text{A.29c})$$

The positive direction of traversing curve  $C$  is the one in which the area is on the left.

If we integrate Equation (A.16) along any curve  $C$  joining  $P_1$  and  $P_2$  we get

$$\Delta\phi = \phi_2 - \phi_1 = \int_C \nabla\phi \cdot d\mathbf{l} \quad (\text{A.30})$$

Obviously this result is independent of the path followed. If  $C$  is closed,  $\phi_2 - \phi_1$  and the integral vanishes. On the other hand, if  $\text{curl } \mathbf{A}$  vanishes at all points, the left-hand side of Equation (A.29c) vanishes; therefore  $\mathbf{A}$  must be the gradient of a scalar. Thus, if  $\text{curl } \mathbf{A} = 0$  everywhere,

$$\mathbf{A} = \nabla\phi \quad (\text{A.31})$$

In this case  $\mathbf{A}$  is said to be *irrotational*, or the field of  $\mathbf{A}$  is conservative.

#### A.4. CURVILINEAR COORDINATES

Often we require the functions div, grad, curl, and the Laplacian in cylindrical, spherical, or other coordinates. The first two systems, illustrated in Figure A.4a, b are related to rectangular cartesian coordi-

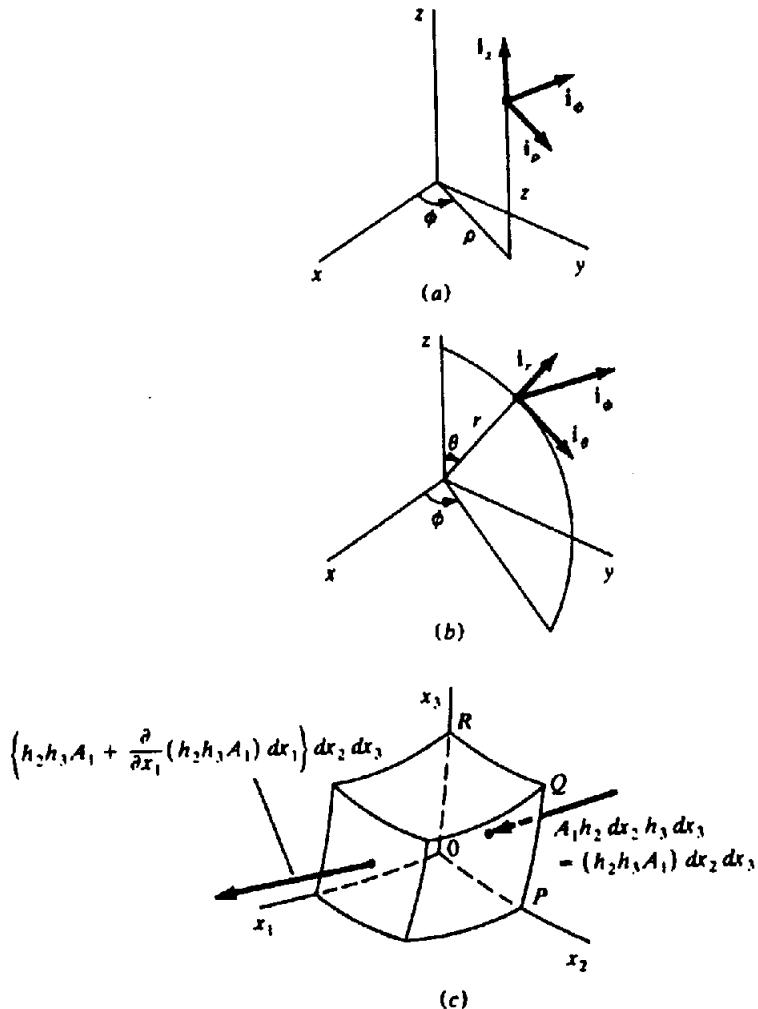


Figure A.4. Curvilinear coordinates. (a) Cylindrical coordinates. (b) Spherical coordinates. (c)  $\operatorname{div} \mathbf{A}$  in curvilinear coordinates.

nates as follows:

Cylindrical	Spherical	
$x = \rho \cos \phi$	$x = r \sin \theta \cos \phi$	(A.32)
$y = \rho \sin \phi$	$y = r \sin \theta \sin \phi$	
$z = z$	$z = r \cos \theta$	

In cylindrical coordinates we can draw unit vectors  $i_\rho, i_\phi, i_z$ , in the directions of increasing  $\rho, \phi, z$ , respectively; for spherical coordinates the unit vectors are  $i_r, i_\theta, i_\phi$ . In both cases, the three unit vectors are orthogonal.

If we write  $x_1, x_2, x_3$  for a set of *orthogonal curvilinear coordinates* in general, the coordinate surfaces  $x_i$  constant are curved; for example, in spherical coordinates,  $r$  constant is a spherical surface,  $\theta$  constant is a cone, and  $\phi$  constant is a plane. When the coordinate  $x_i$  increases by  $dx_i$ , a point moves a distance  $h_i dx_i$ , where  $h_i$  is a function of all the  $x_i$ 's in general. In cylindrical coordinates,  $h_\rho = 1 = h_z$ , and  $h_\phi = r$ ; in spherical coordinates,  $h_r = 1$ ,  $h_\theta = r$ , and  $h_\phi = r \sin \theta$  [because as  $\phi$  changes,  $r$  and  $\theta$  being fixed, a point moves on a circle of radius

$r \sin \theta$ , hence a change  $d\phi$  moves the point a distance  $(r \sin \theta) d\phi$ ].

The gradient in curvilinear coordinates is obtained by replacing  $\partial x, \partial y, \partial z$  in Equation (A.17) by  $h_1 \partial x_1, h_2 \partial x_2, h_3 \partial x_3$ ; the result is

$$\nabla \psi = (\partial \psi / h_1 \partial x_1) i_1 + (\partial \psi / h_2 \partial x_2) i_2 + (\partial \psi / h_3 \partial x_3) i_3 \quad (A.33)$$

To find  $\operatorname{div} \mathbf{A}$ , we use the same concept that we used to get Equation (A.26). Referring to Figure A.4c, the inward flow along the  $x_1$  axis is  $A_1(h_2 dx_2 h_3 dx_3) = (h_2 h_3 A_1) dx_2 dx_3$ . Subtracting this from the outward flow  $[(h_2 h_3 A_1) + (\partial / \partial x_1 (h_2 h_3 A_1)) dx_1] dx_2 dx_3$ , adding terms for the  $x_2$  and  $x_3$  axes, then dividing by the volume  $(h_1 h_2 h_3 dx_1 dx_2 dx_3)$  gives

$$\begin{aligned} \nabla \cdot \mathbf{A} = & (1/h_1 h_2 h_3) \\ & \times \{ \partial / \partial x_1 (h_2 h_3 A_1) + \partial / \partial x_2 (h_3 h_1 A_2) \\ & + \partial / \partial x_3 (h_1 h_2 A_3) \} \quad (A.34) \end{aligned}$$

To get the Laplacian, we find  $\nabla^2 = \nabla \cdot \nabla$ . Applying Equation (A.34) to Equation (A.33), we get the result

$$\nabla^2\psi = (1/h_1 h_2 h_3) [\partial/\partial x_1 \{ (h_2 h_3/h_1) \partial\psi/\partial x_1 \} + \partial/\partial x_2 \{ (h_3 h_1/h_2) \partial\psi/\partial x_2 \} + \partial/\partial x_3 \{ (h_1 h_2/h_3) \partial\psi/\partial x_3 \}] \quad (\text{A.35})$$

We get the expression for curl in the same way that we derived Equation (A.29a). Because the dimensions of face  $MNPQ$  in Figure A.4c are infinitesimal, we start with the components  $A_2$  and  $A_3$  at  $M$ , then apply Equation (A.29a) for a plane area. This gives

$$\begin{aligned} (\nabla \times \mathbf{A})_1 h_2 dx_2 h_3 dx_3 \\ = A_2 h_2 dx_2 + \{ A_3 h_3 + \partial/\partial x_2 (A_3 h_3) dx_2 \} dx_3 \\ - \{ A_2 h_2 + \partial/\partial x_3 (A_2 h_2) dx_3 \} dx_2 \\ - A_3 h_3 dx_3 \\ = \{ \partial/\partial x_2 (A_3 h_3) - \partial/\partial x_3 (A_2 h_2) \} dx_2 dx_3 \\ (\nabla \times \mathbf{A})_1 = (1/h_2 h_3) \{ \partial/\partial x_2 (A_3 h_3) \\ - \partial/\partial x_3 (A_2 h_2) \} \end{aligned}$$

When the other two components are found in the same way, the result can be written:

$$\nabla \times \mathbf{A} = (1/h_1 h_2 h_3) \begin{vmatrix} h_1 i_1 & h_2 i_2 & h_3 i_3 \\ \partial/\partial x_1 & \partial/\partial x_2 & \partial/\partial x_3 \\ h_1 A_1 & h_2 A_2 & h_3 A_3 \end{vmatrix} \quad (\text{A.36})$$

Equations (A.33) to (A.36) can be used to obtain grad, div, curl, and the Laplacian in cylindrical and spherical coordinates by inserting the appropriate values of  $h_i$ ; for example, the Laplacian in spherical coordinates is, from Equation (A.35),

$$\begin{aligned} \nabla^2\psi = \left( \frac{1}{r^2 \sin \theta} \right) \left\{ \frac{\partial}{\partial r} \left( r^2 \sin \theta \frac{\partial \psi}{\partial r} \right) \right. \\ + \frac{\partial}{\partial \theta} \left( \frac{r \sin \theta}{r} \frac{\partial \psi}{\partial \theta} \right) \\ \left. + \frac{\partial}{\partial \phi} \left( \frac{r}{r \sin \theta} \frac{\partial \psi}{\partial \phi} \right) \right\} \\ - \left( \frac{1}{r^2} \right) \left\{ \frac{\partial}{\partial r} \left( r^2 \frac{\partial \psi}{\partial r} \right) + \left( \frac{1}{\sin \theta} \right) \frac{\partial}{\partial \theta} \left( \sin \theta \frac{\partial \psi}{\partial \theta} \right) \right. \\ \left. + \left( \frac{1}{\sin^2 \theta} \right) \left( \frac{\partial^2 \psi}{\partial \phi^2} \right) \right\} \quad (\text{A.37}) \end{aligned}$$

Curl  $\mathbf{A}$  in spherical coordinates is given by Equation (A.36):

$$\begin{aligned} \nabla \times \mathbf{A} = (1/r \sin \theta) \{ \partial/\partial \theta (\sin \theta A_\phi) - \partial A_\theta / \partial \phi \} \mathbf{i}_r \\ + (1/r \sin \theta) \{ \partial A_r / \partial \phi \\ - \sin \theta \partial (r A_\phi) / \partial r \} \mathbf{i}_\theta \\ + (1/r) \{ \partial (r A_\theta) / \partial r - \partial A_r / \partial \theta \} \mathbf{i}_\phi \end{aligned} \quad (\text{A.38})$$

## A.5. TAYLOR'S SERIES; MACLAURIN'S SERIES

*Taylor's series* is discussed in most advanced calculus texts, for example, Wiley (1966). One form of the series is

$$\begin{aligned} f(x+h) = f(x) + hf'(x) + \frac{h^2}{2!} f''(x) \\ + \cdots + \frac{h^{n-1}}{(n-1)!} f^{n-1}(x) + R(\xi) \end{aligned} \quad (\text{A.39})$$

where  $f'(x), f''(x), \dots, f^{n-1}(x)$  are derivatives of order  $1, 2, \dots, (n-1)$ , respectively,  $\xi = kh$ ,  $0 < k < 1$ , and  $R(\xi)$  is the remainder after  $n$  terms. The series is valid for all values of  $h$  provided the  $n$  derivatives exist. Also,  $R(\xi) = (h^n/n!)f''(\xi)$  and approaches zero as  $n$  approaches infinity.

Taylor's series enables us to find the change in  $f(x)$  when  $x$  increases by  $h$  in terms of  $h$  and the derivatives of  $f(x)$ . The larger  $h$  is, the more terms that we must take to get an accurate value of  $f(x+h)$ . When  $h$  is small, often the first two or three terms are sufficient.

A special case of Taylor's series, called *Maclaurin's series*, is obtained by interchanging  $x$  and  $h$  in Equation (A.39), then setting  $h$  equal to zero. This gives Maclaurin's series:

$$\begin{aligned} f(x) = f(0) + xf'(0) + \frac{x^2}{2!} f''(0) \\ + \frac{x^3}{3!} f'''(0) + \cdots \end{aligned} \quad (\text{A.40})$$

where all derivatives are evaluated at  $x = 0$ . As an example, we calculate the series corresponding to  $\sin x$ . Because the derivatives of  $\sin x$  are either  $\pm \sin x$  or  $\pm \cos x$  and these equal 0,  $\pm 1$  at  $x = 0$ , the series is

$$\sin x = x - \frac{x^3}{3!} + \frac{x^5}{5!} - \cdots \quad (\text{A.41a})$$

In the same way, we get for  $\cos x$

$$\cos x = 1 - \frac{x^2}{2!} + \frac{x^4}{4!} - \dots \quad (\text{A.41b})$$

### A.6. BINOMIAL EXPANSION

If we set  $n$  equal to 2, 3, 4, and so on, we can show that the general *binomial expansion* of  $(a + b)^n$  is

$$\begin{aligned} (a + b)^n &= a^n + na^{n-1}b + \frac{n(n-1)}{2!}a^{n-2}b^2 + \dots \\ &\quad + \frac{n(n-1) \cdots (n-r+1)}{r!}a^{n-r}b^r + \dots \end{aligned} \quad (\text{A.42})$$

When  $n$  is a positive integer, the series ends with  $r = n$ , but otherwise the series is infinite. The infinite series is valid provided  $|a| > |b|$ . (Pipes and Harvill, 1970, p. 843).

We are interested mainly in using Equation (A.42) to find approximate values, so we divide through by  $a^n$  and then set  $x = b/a$  so that  $|x| < 1$ . Discarding the factor  $a^n$ , the series becomes

$$\begin{aligned} (1+x)^n &= 1 + nx + \frac{n(n-1)}{2!}x^2 \\ &\quad + \frac{n(n-1)(n-2)}{3!}x^3 + \dots \end{aligned} \quad (\text{A.43})$$

Note that the series converges (has a finite sum) for all values of  $n$  (Pipes and Harvill, 1970, p. 843).

The series for  $n = -1, -2$  are especially useful:

$$(1 \mp x)^{-1} = 1 \pm x + x^2 \pm x^3 + \dots \quad (\text{A.44a})$$

$$(1 \mp x)^{-2} = 1 \pm 2x + 3x^2 \pm 4x^3 + \dots \quad (\text{A.44b})$$

### A.7. COMPLEX NUMBERS

Because we cannot calculate the square root of a negative number, a quantity such as  $\sqrt{-7}$  is said to be *imaginary*. Writing  $j = \sqrt{(-1)}$  ( $i$  is also used), imaginary numbers can be written  $jy$  (or  $yj$ ),  $y$  being real; thus,  $\sqrt{-7} = j\sqrt{7}$ . The sum of a real number and an imaginary number is a *complex number*, for example,  $3 - 8j$ . The *conjugate complex* of  $z = (x + jy)$  is  $\bar{z} = (x - jy)$ .

A complex quantity  $f(z)$  can be represented geometrically in the *complex plane*; this is merely the  $xy$  plane with the real part,  $\text{Re}(f(z))$ , of a complex quantity plotted on the  $x$  axis, the imaginary part,  $\text{Im}(f(z))$ , on the  $y$  axis (Fig. A.5). Plotted thus,

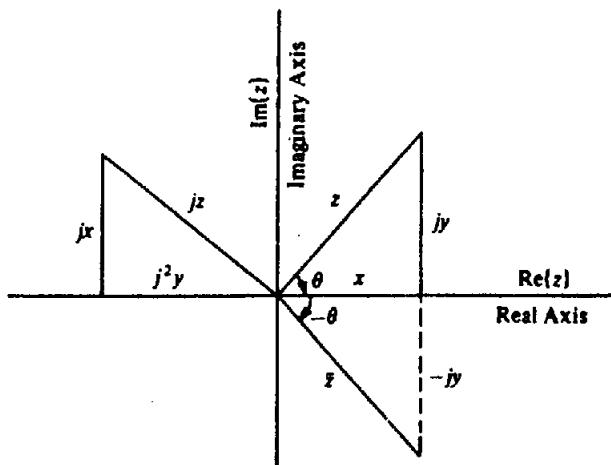


Figure A.5. Plotting complex quantities in the complex plane.

complex numbers are similar to 2-D vectors, real and imaginary parts corresponding to components. Complex numbers are added (or subtracted) by adding (subtracting) separately the real and imaginary parts; thus,

$$(4 - 7j) + (6 + 4j) - (18 - 12j) = (-8 + 9j)$$

Multiplication of complex numbers follows the usual rules of algebra, keeping in mind that  $j^2 = -1$ ,  $j^3 = -j$ ,  $j^4 = +1$ , and so on; thus,

$$\begin{aligned} (8 - 9j)(-4 - 6j) &= -32 + 36j - 48j + 54j^2 \\ &= -86 - 12j \end{aligned}$$

Multiplication by  $j$  rotates  $z$  and its real and imaginary components through  $90^\circ$  counterclockwise (Fig. A.5). Multiplication of  $z$  by  $\bar{z}$  gives  $(x^2 + y^2)$ ; the square root of this quantity is the magnitude of  $z$ ,  $|z|$ ; thus  $|z|$  is the length of the line representing  $z$  in Figure A.5.

Division is done by multiplying the numerator and denominator by the conjugate complex of the denominator (called *rationalization of the denominator*), then dividing; for example,

$$\begin{aligned} \frac{(7 - 2j)}{(-9 + 5j)} &= \frac{(7 - 2j)(-9 - 5j)}{(-9 + 5j)(-9 - 5j)} \\ &= \frac{-(73 + 17j)}{(9^2 + 5^2)} = \frac{-(73 + 17j)}{106} \end{aligned}$$

A complex quantity is zero only when its real and imaginary parts are zero. It follows that two complex quantities are equal only when their real parts are equal and their imaginary parts are also equal.

The base of the system of natural logarithms,  $e$ , is defined by the infinite series, valid for all values of  $x$ ,

$$e^x = 1 + \frac{x}{1!} + \frac{x^2}{2!} + \frac{x^3}{3!} + \dots \quad (\text{A.45a})$$

Setting  $x = 0$ , we get a series from which the value of  $e$  can be calculated. Replacing  $x$  with  $\pm jx$ , we get the following series:

$$e^{+jx} = 1 + jx - (x^2/2!) - j(x^3/3!) + \dots \quad (\text{A.45b})$$

$$e^{-jx} = 1 - jx - (x^2/2!) + j(x^3/3!) + \dots \quad (\text{A.45c})$$

Comparing these series with Equations (A.41), we find that

$$\begin{aligned} \cos x &= \frac{1}{2}(e^{jx} + e^{-jx}) \\ \sin x &= (1/2j)(e^{jx} - e^{-jx}) \end{aligned} \quad \left. \right\} \quad (\text{A.46a})$$

$$\begin{aligned} (\cos x + j \sin x) &= e^{jx} \\ (\cos x - j \sin x) &= e^{-jx} \end{aligned} \quad \left. \right\} \quad (\text{A.46b})$$

Replacing  $x$  by  $nx$ , we get *De Moivre's theorem*:

$$(\cos nx \pm j \sin nx) = e^{\pm jnx} = (\cos x \pm j \sin x)^n \quad (\text{A.46c})$$

When  $z = x + jy$ , we define  $\theta$  by the relation (Fig. A.5)

$$\theta = \tan^{-1}(y/x) = \tan^{-1}[\Im z / \Re z] \quad (\text{A.47a})$$

where  $\theta$  is the phase of  $z$ . Also,

$$z = |z|(\cos \theta + j \sin \theta) = |z|e^{j\theta} \quad (\text{A.47b})$$

using Equation (A.46b); this is known as the *polar form* of  $z$ . Changing the sign of  $j \sin \theta$  and using Equation (A.46b) again, we obtain

$$\bar{z} = |z|e^{-j\theta} \quad (\text{A.47c})$$

The polar form of  $z$  is convenient for multiplication, division, and finding powers and roots; for example, if  $z_1 = |z_1|e^{j\theta_1}$  and  $z_2 = |z_2|e^{j\theta_2}$ , then

$$\begin{aligned} z_1 z_2 &= |z_1||z_2|e^{j(\theta_1+\theta_2)} \\ z_1/z_2 &= (|z_1|/|z_2|)e^{j(\theta_1-\theta_2)} \\ z_1^3 &= |z_1|^3 e^{j3\theta_1} \\ z_1^{1/4} &= |z_1|^{1/4} e^{j(\theta_1+2rw)/4} \quad r = 0, 1, 2, 3 \end{aligned}$$

(In finding the fourth root of  $z$ , insertion of  $2rw$  gives four distinct roots; these repeat when  $r > 3$ .)

## A.8. METHOD OF LEAST SQUARES

Assume that we measure a quantity  $y$  for various values of  $x$  and end up with a set of values  $(y_i, x_i)$ ; often we wish to express  $y$  as a function of  $x$  in the form

$$y = a_0 + a_1 x + a_2 x^2 + \dots + a_m x^m \quad (\text{A.48})$$

In principle, we could solve for the  $(m+1)$  unknowns  $a_i$  if we had  $(m+1)$  sets of values  $(y_i, x_i)$ , but usually we have  $n$  sets,  $n > (m+1)$ , so the constants  $a_i$  are "overdetermined." In this case we look for the "best-fit" solution; the usual criterion for best fit is that the sums of the squares of the "errors" be a minimum, an error being the difference between a measured value of  $y_i$  and the value calculated from Equation (A.48) for the corresponding value  $x_i$  and the best-fit values of  $a_i$ . Squares of the errors are used to avoid cancellation of positive and negative errors.

The sum of the errors squared is

$$\begin{aligned} E &= \sum_i e_i^2 \\ &= \sum_i \{ y_i - (a_0 + a_1 x_i + a_2 x_i^2 + \dots + a_m x_i^m) \}^2 \end{aligned} \quad (\text{A.49})$$

To get the minimum of  $E$ , we vary the  $(m+1)$   $a_i$ 's; hence for each  $a_i$ ,

$$\begin{aligned} \partial E / \partial a_r &= 0 = \sum_i \{ y_i - (a_0 + a_1 x_i + a_2 x_i^2 + \dots + a_m x_i^m) \} (-2x_i^r) \end{aligned}$$

so that

$$\begin{aligned} a_0 \sum_i x_i^r + a_1 \sum_i x_i^{r+1} + a_2 \sum_i x_i^{r+2} \\ + \dots + a_m \sum_i x_i^{r+m} &= \sum_i y_i x_i^r \end{aligned} \quad (\text{A.50})$$

where  $r = 0, 1, 2, \dots, m$  (note that for  $r = 0$ ,  $\sum_i x_i^0 = n$  and  $\sum_i y_i x_i^0 = \sum_i y_i$ ). This set of  $(m+1)$  equations can be solved for the  $(m+1)$   $a_i$ 's.

For a more detailed discussion, including the matrix solution of Equation (A.50), see Sheriff and Geldart (1983, §10.1.5).

## A.9. FOURIER SERIES AND TRANSFORMS

### A.9.1. Fourier Series

A periodic function  $f(t)$ , which repeats itself exactly after each interval  $T$ , can (with few exceptions) be represented by a *Fourier series* of the form

$$\begin{aligned} g(t) = & a_0 + a_1 \cos \omega_0 t + a_2 \cos 2\omega_0 t \\ & + \cdots + a_n \cos n\omega_0 t + \cdots + b_1 \sin \omega_0 t \\ & + b_2 \sin 2\omega_0 t + \cdots + b_n \sin n\omega_0 t + \cdots \end{aligned} \quad (\text{A.51a})$$

where  $\omega_0 = 2\pi\nu_0 = 2\pi/T$  is the *fundamental angular frequency* and  $t$  is the independent variable (often time or distance). The frequency  $n\omega_0$  is the  $n$ th harmonic of the fundamental  $\omega_0$ , and so expressing a function as a Fourier series is called *harmonic analysis* (the same name is applied to transforming a function into its Fourier transform; see §A.9.2).

The integral over the interval  $T$  of the product of any two cosines, two sines, or sine and cosine in Equation (A.51a) is zero except for the integrals of  $\cos^2 n\omega_0 t$  and  $\sin^2 n\omega_0 t$ , and these both equal  $T/2$ . Thus, to find the values of  $a_n$  and  $b_n$  we multiply both sides of Equation (A.51a) by  $\cos n\omega_0 t$  to get  $a_n$ , then by  $\sin n\omega_0 t$  to get  $b_n$ . Integration over the interval  $T$  results in

$$\left. \begin{aligned} a_n &= (2/T) \int_{-T/2}^{T/2} g(t) \cos n\omega_0 t dt \\ b_n &= (2/T) \int_{-T/2}^{T/2} g(t) \sin n\omega_0 t dt \end{aligned} \right\} \quad (\text{A.51b})$$

In practice Fourier series are used to analyze a set of observations, such as gravity readings along a profile; the integrals become sums, the length of the profile is  $T$  (note that this means that we are assuming that the readings will be repeated exactly if the profile is extended), and the relative values of  $a_n$ ,  $b_n$  [more accurately,  $(a_n^2 + b_n^2)^{1/2}$ ] are interpreted as *magnitudes* of the  $n$ th harmonic.

Fourier series can be developed for more than one dimension. The 2-D form is

$$\begin{aligned} g(x, y) = & \sum_0^\infty \sum_0^\infty (a_{mn} \cos m\omega_x x \cos n\omega_y y \\ & + b_{mn} \cos m\omega_x x \sin n\omega_y y \\ & + c_{mn} \sin m\omega_x x \cos n\omega_y y \\ & + d_{mn} \sin m\omega_x x \sin n\omega_y y) \end{aligned} \quad (\text{A.52a})$$

where the coefficients are given by equations such as

$$\begin{aligned} b_{mn} &= (4/T_x T_y) \\ & \times \int_{-T/2}^{T/2} \int_{-T/2}^{T/2} g(x, y) \cos m\omega_x x \sin n\omega_y y dx dy \end{aligned} \quad (\text{A.52b})$$

Equation (A.52a) defines a *Fourier surface* that can be fitted to a two-dimensional set of data, for example, gravity readings over an area, by finding the four sets of coefficients using double sums equivalent to the integral in Equation (A.52b).

### A.9.2. Fourier Integral; Fourier Transforms

Equation (A.46a) can be used to write Equations (A.51) as

$$\begin{aligned} g(t) &= \sum_{-\infty}^{+\infty} a_n e^{jn\omega_0 t} \\ a_n &= (1/T) \int_{-T/2}^{T/2} g(t) e^{-jn\omega_0 t} dt \\ n &= 0, \pm 1, \pm 2, \dots, \pm \infty \end{aligned} \quad (\text{A.53})$$

Combining the two relations gives

$$g(t) = \sum_{-\infty}^{+\infty} (1/T) e^{jn\omega_0 t} \int_{-T/2}^{T/2} g(t) e^{-jn\omega_0 t} dt$$

If we let  $T$  approach infinity,  $g(t)$  repeats itself at longer and longer intervals; in the limit when  $T = \infty$ ,  $g(t)$  does not repeat, hence is aperiodic. The preceding expression then becomes the *Fourier integral*:

$$g(t) = (1/2\pi) \int_{-\infty}^{\infty} e^{j\omega t} \left\{ \int_{-\infty}^{\infty} g(t) e^{-j\omega t} dt \right\} d\omega \quad (\text{A.54})$$

(see Wiley, 1966, §6.7, for more details). If we evaluate the integral within the braces, we get a function of  $\omega$ ; then the integral with respect to  $\omega$  gives us  $g(t)$  again (except for the factor  $1/2\pi$ ).

The Fourier integral is easier to apply if we break Equation (A.54) down into two operations:

$$\begin{aligned} G(\omega) &= \int_{-\infty}^{\infty} g(t) e^{-j\omega t} dt \\ &= \text{Fourier transform of } g(t) \end{aligned} \quad (\text{A.55a})$$

$$\begin{aligned} g(t) &= (1/2\pi) \int_{-\infty}^{\infty} G(\omega) e^{j\omega t} d\omega \\ &= \text{inverse Fourier transform of } G(\omega) \end{aligned} \quad (\text{A.55b})$$

When  $t$  is time, application of Equation (A.55a)

transforms  $g(t)$  from the *time domain* into the *frequency domain* whereas Equation (A.55b) does the reverse. (The terms *time domain* and *frequency domain* are often used even when  $t$  and  $\omega$  are not time and frequency.) The distinction between *transform* and *inverse transform* is arbitrary and is due to our greater familiarity with the time domain.

The Fourier transform has several advantages in data processing. Equations (A.55) show that  $g(t)$  can be transformed into the frequency domain, then back to the time domain unchanged, that is, theoretically there is no error involved [in practice the integrals must be calculated numerically and so errors (loss of information) exist, but these can be made as small as we wish]. A major advantage is that we can do part of the processing in one domain and part in the other, taking advantage of the fact that some processes can be executed more economically in one domain than in the other.

The functions  $g(t)$  and  $G(\omega)$  [ $G(\nu)$  is sometimes used,  $\omega$  being replaced by  $2\pi\nu$  in the exponentials in Eqs. (A.55),  $d\omega/2\pi$  becoming  $d\nu$ ] are referred to as a *transform pair*. The relation between them can be expressed as  $g(t) \leftrightarrow G(\omega)$ . In general,  $G(\omega)$  is complex and can be written in the form [Eq. (A.47b)]

$$G(\omega) = A(\omega) e^{j\phi(\omega)} \quad (\text{A.56})$$

$A(\omega)$  is the *frequency spectrum* and  $\phi(\omega)$  is the *phase spectrum* of  $g(t)$ .

Like the Fourier series, Fourier transforms can be used with functions of several dimensions. In two dimensions, we have

$$G(\kappa_x, \kappa_y) = \int_{-\infty}^{\infty} \int_{-\infty}^{\infty} g(x, y) e^{-j(\kappa_x x + \kappa_y y)} dx dy, \quad (\text{A.57a})$$

$$\begin{aligned} g(x, y) &= (1/2\pi)^2 \\ &\times \int_{-\infty}^{\infty} \int_{-\infty}^{\infty} G(\kappa_x, \kappa_y) e^{j(\kappa_x x + \kappa_y y)} d\kappa_x d\kappa_y \end{aligned} \quad (\text{A.57b})$$

where  $\kappa_x = 2\pi/\lambda_x$  and  $\kappa_y = 2\pi/\lambda_y$ , (compare with  $\omega = 2\pi/T$ ).

Calculation of Fourier transforms of continuous functions is often quite difficult; however, in practice we use digital functions mainly (§A.9.3) and their transforms are easy to calculate. Calculation of both types is greatly facilitated by using several theorems regarding Fourier transforms; we list the most important of these in Equations (A.58) to (A.62) and give brief explanations of their applications. Other theorems plus proofs can be found in Sheriff and Geldart (1983, pp. 164–6).

### Shift theorems:

$$g(t - k) \leftrightarrow e^{-j\omega k} G(\omega) \quad (\text{A.58a})$$

$$e^{-jkt} g(t) \leftrightarrow G(\omega + k) \quad (\text{A.58b})$$

### Scaling theorem:

$$g(kt) \leftrightarrow (1/|k|) G(\omega/k) \quad (\text{A.59})$$

### Symmetry theorem:

$$G(t) \leftrightarrow 2\pi g(-\omega) \quad (\text{A.60})$$

### Derivative theorems:

$$\frac{d^n g(t)}{dt^n} \leftrightarrow (j\omega)^n G(\omega) \quad (\text{A.61a})$$

$$(-jt)^n g(t) \leftrightarrow \frac{d^n G(\omega)}{d\omega^n} \quad (\text{A.61b})$$

### Integral theorem:

$$\int_{-\infty}^t g(\tau) d\tau \leftrightarrow (1/j\omega) G(\omega) \quad (\text{A.62})$$

When we add a constant to the independent variable, functions of the variable are shifted along the horizontal axis; for example, the curve  $y = (x - 3)^2$  is the curve  $y = x^2$  shifted three units to the right;  $y = (x + 3)^2$  is  $y = x^2$  moved to the left three units. Equation (A.58a) states that shifting  $g(t)$   $k$  units to the right multiplies the transform by  $\exp(-j\omega k)$ ; shifting  $G(\omega)$   $k$  units to the left multiplies  $g(t)$  by  $\exp(-jk\omega)$ . Also, if we know  $G(\omega)$ , we can write down the transform of  $e^{-jkt} g(t)$  by inspection.

Equation (A.59) permits us to replace  $t$  with, for example,  $-7t/8$ , without having to recalculate the transform. Equation (A.60) is useful in obtaining new transforms; if we know a transform pair,  $g(t)$  and  $G(\omega)$ , we get a new transform pair by replacing  $\omega$  in  $G(\omega)$  with  $t$  and  $t$  in  $g(t)$  with  $-\omega$ .

The derivative theorems are probably the most important theorems. Equation (A.61a) enables us to replace transforms of derivatives of  $g(t)$  with  $(j\omega)^n$  times the transform of  $g(t)$ ; this is very useful in finding new transforms and in replacing differential equations with algebraic equations (§A.13). Equation (A.61b) is useful in getting transforms of  $t^n g(t)$ . Equation (A.62), although used infrequently, is nevertheless important; note that for causal functions (§A.9.3), the lower limit of the integral is zero.

### A.9.3. Digital Functions; z Transforms

A continuous function  $g(t)$  has a definite value for all values of  $t$  (disregarding discontinuities, infinite and multiple values), whereas a *digital function*, which we write as  $g_t$ , has values only at discrete values of  $t$ ; for example, a seismic trace (§4.1.3) may be sampled at intervals  $\Delta = 0.002$  s so that  $g_t$  is known only at the discrete times 0.000, 0.002, 0.004, ... s, or we might measure gravity values along a line at intervals of 100 m so that  $g_x$  is known only at points 100 m apart. (Whenever convenient, we take  $\Delta = 1$ , that is, we take it as the unit so that  $t = n$  or  $x = n$  instead of  $n\Delta$ .)

The *unit impulse* or *Dirac delta*,  $\delta(t)$  or  $\delta_t$ , is by definition zero for all values of  $t$  except  $t = 0$  where  $\delta(t)$  (or  $\delta_t$ ) equals +1 (for a more rigorous definition, see Papoulis, 1962, Appendix I). The product  $g(t)\delta(t) = g(0)$ , the value of  $g(t)$  at  $t = 0$ . The shifted impulse  $\delta(t - n)$  or  $\delta_{t-n}$  is zero except at  $t = n$ . A *comb* is an infinite series of unit impulses spaced at intervals  $\Delta$ ; thus,

$$\text{comb}(t) = \sum_{-\infty}^{\infty} \delta(t - n) \\ n = 0, \pm 1, \pm 2, \pm 3, \dots, \pm \infty$$

Multiplying  $g(t)$  by  $\text{comb}(t)$  gives  $g_t$ :

$$g_t = \sum_{-\infty}^{\infty} g(t) \delta(t - n) \\ = \dots, g_{-3}, g_{-2}, g_{-1}, g_0, g_1, g_2, g_3, \dots$$

Normally the digital functions that we encounter are *causal*, that is, they are zero for negative values of  $t$ ; in this case the first term is  $g_0$ .

If we substitute  $\delta(t)$  for  $g(t)$  in Equations (A.55a) and (A.58a), we find that

$$\left. \begin{aligned} \delta(t) &\leftrightarrow e^{-j\omega t}|_{t=0} = +1 \\ \delta(t - n) &\leftrightarrow e^{-jn\omega\Delta} \end{aligned} \right\} \quad (\text{A.63})$$

Accordingly, the transform of  $g_t$  is

$$\begin{aligned} g_t &\leftrightarrow g_0 + g_1 e^{-jn\omega\Delta} + g_2 e^{-jn2\omega\Delta} + \dots + g_n e^{-jn\omega\Delta} \\ &\leftrightarrow g_0 + g_1 z + g_2 z^2 + \dots + g_n z^n \end{aligned} \quad (\text{A.64})$$

where  $z = e^{-jn\omega\Delta}$ . The right-hand side of Equation (A.64) is  $G(z)$ , the *z transform* of  $g_t$ . Obviously, calculation of *z* transforms is trivial, for example, for a causal function  $g_t = 0.56, -1.24, -2.45, 0.67, 3.78$ , the *z* transform is  $0.56 - 1.24z - 2.45z^2 + 0.67z^3 + 3.78z^4$ .

In data processing,  $n$  in Equation (A.64) may be several hundred or thousand; at the same time we

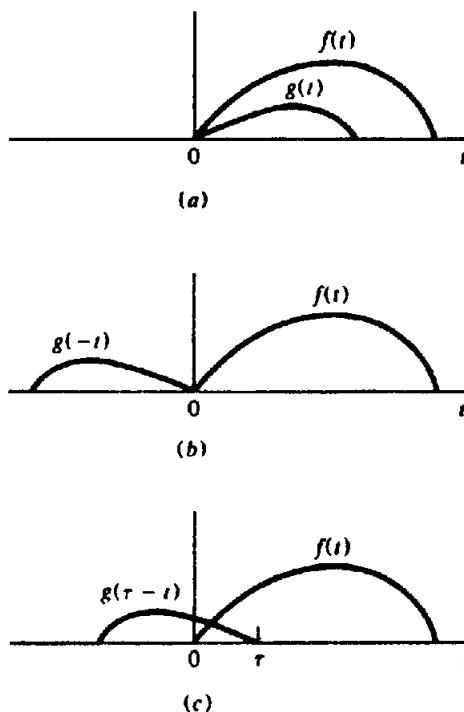


Figure A.6. Illustrating  $f(t) * g(t)$ . (a) Two functions,  $f(t)$  and  $g(t)$ . (b)  $g(t)$  reflected in the vertical axis. (c)  $g(t)$  reflected and displaced  $\tau$  units to the right.

often need values of  $G(z)$  for a large range of  $z$  values (that is,  $\omega$  values); if we adopt the straightforward approach, the calculations are extremely laborious. However, the method known as the *fast Fourier transform* (FFT) reduces the labor by a factor of  $10^3$  or more when  $n > 10^3$  [Sheriff and Geldart, 1983, §10.6.4].

### A.10. CONVOLUTION

The *convolution* of two functions,  $f(t)$  and  $g(t)$ , often written  $f(t) * g(t)$ , is defined by the integral

$$f(\tau) * g(\tau) = \int_{-\infty}^{\infty} f(t) g(\tau - t) dt \quad (\text{A.65a})$$

The curve  $g(-t)$  is  $g(t)$  reflected in the vertical axis (Fig. A.6a, b) and  $g(\tau - t)$  is  $g(-t)$  moved  $\tau$  units to the right (Fig. A.6c). Thus, geometrically, Equation (A.65a) means that we reflect  $g(t)$ , move it  $\tau$  units to the right, and then sum the products of the corresponding ordinates. The result depends on the displacement  $\tau$ , hence the argument  $\tau$  on the left side of Equation (A.65a). For causal functions of length  $m$  and  $n$ , it is obvious that  $0 \leq \tau \leq (m + n)$ . Also, we get the same result if we reflect and displace  $f(t)$  instead of  $g(t)$ , that is,

$$f(t) * g(t) = g(t) * f(t) \quad (\text{A.66})$$

The *convolution theorem* states that

$$f(\tau) * g(\tau) \leftrightarrow F(\omega)G(\omega) \quad (\text{A.67a})$$

To prove the theorem, we write

$$\begin{aligned} f(\tau) * g(\tau) \\ \leftrightarrow \int_{-\infty}^{\infty} \left\{ \int_{-\infty}^{\infty} f(t)g(\tau-t) dt \right\} e^{-j\omega\tau} d\tau \end{aligned}$$

using Equation (A.55a) with  $\tau$  in place of  $t$  [because  $f(\tau) * g(\tau)$  is a function of  $\tau$ ]. Interchanging the order of integration and writing  $s = \tau - t$  and  $ds = d\tau$  (because  $t$  is fixed in this integration), we obtain

$$\begin{aligned} f(\tau) * g(\tau) \\ \leftrightarrow \int_{-\infty}^{\infty} f(t) \left\{ \int_{-\infty}^{\infty} g(s) e^{-j\omega(s+t)} ds \right\} dt \\ \leftrightarrow \int_{-\infty}^{\infty} f(t) e^{-j\omega t} dt \int_{-\infty}^{\infty} g(s) e^{-j\omega s} ds \\ \leftrightarrow F(\omega)G(\omega) \end{aligned}$$

For digital functions, Equations (A.65a), (A.66), and (A.67a) are

$$f_r * g_r = \sum_k f_k g_{r-k} = \sum_k g_k f_{r-k} \quad (\text{A.65b})$$

$$f_r * g_r \leftrightarrow F(z)G(z) \quad (\text{A.67b})$$

where the sums in Equation (A.65b) are over the appropriate values of  $k$  [ $0 \leq k \leq (m+n)$ ].

In two dimensions the convolution of  $f(x, y)$  and  $g(x, y)$  becomes (Sheriff and Geldart, 1983, §10.3.9)

$$\begin{aligned} f(\tau, \sigma) * g(\tau, \sigma) \\ = \int_{-\infty}^{\infty} \int_{-\infty}^{\infty} f(x, y)g(\tau-x, \sigma-y) dx dy \end{aligned} \quad (\text{A.68})$$

and the convolution theorem states that

$$f(\tau, \sigma) * g(\tau, \sigma) \leftrightarrow F(\kappa_x, \kappa_y)G(\kappa_x, \kappa_y) \quad (\text{A.69})$$

## A.11. CORRELATION

### A.11.1. Cross-Correlation

The *cross-correlation* of  $f(t)$  and  $g(t)$ ,  $\phi_{fg}(\tau)$ , is defined as

$$\phi_{fg}(\tau) = \int_{-\infty}^{\infty} f(t)g(t+\tau) dt \quad (\text{A.70a})$$

If we find the convolution of  $f(t)$  and  $g(-t)$ , we change  $g(\tau-t)$  in Equation (A.65a) to  $g(\tau+t)$ ;

therefore

$$\begin{aligned} \phi_{fg}(\tau) &= \text{convolution of } f(t) \text{ with } g(-t) \\ &\quad (\text{A.71a}) \end{aligned}$$

$$\begin{aligned} \phi_{gf}(\tau) &= \text{convolution of } f(-t) \text{ with } g(t) \\ &\quad (\text{A.71b}) \end{aligned}$$

The *cross-correlation theorem* states that

$$\begin{aligned} \phi_{fg}(\tau) &\leftrightarrow \overline{F(\omega)G(\omega)} \\ \phi_{gf}(\tau) &\leftrightarrow F(\omega)\overline{G(\omega)} \end{aligned} \quad (\text{A.72a})$$

The proof follows directly from the proof of the convolution theorem on changing the sign of  $t$  in the argument of  $g(\tau-t)$  in the first step of the proof.

The digital forms of Equations (A.70a) and (A.72a) are

$$\phi_{fg} = \sum_k f_k g_{r+k} \quad \phi_{gf} = \sum_k f_{r+k} g_k \quad (\text{A.70b})$$

where  $-m < k < n$  or  $-n < k < m$ .

$$\begin{aligned} \phi_{fg} &\leftrightarrow F(\bar{z})G(z) \\ \phi_{gf} &\leftrightarrow F(z)G(\bar{z}) \end{aligned} \quad (\text{A.72b})$$

where  $\bar{z} = e^{+j\omega\Delta}$  and  $F(\bar{z}) = \overline{F(z)}$ .

### A.11.2. Autocorrelation

If  $f(t)$  is the same as  $g(t)$ , the cross-correlation becomes the *autocorrelation*. Replacing  $f(t)$  with  $g(t)$  in the preceding section, we get the following results.

$$\phi_{gg}(\tau) = \int_{-\infty}^{\infty} g(t)g(t+\tau) dt \leftrightarrow |G(\omega)|^2 \quad (\text{A.73})$$

$$\phi_{gg} = \sum_k g_k g_{r+k} \quad \phi_{gg} \leftrightarrow |G(z)|^2 \quad (\text{A.74})$$

## A.12. LAPLACE TRANSFORMS

### A.12.1. Basic Theory

Laplace transforms are closely related to Fourier transforms (Sheriff and Geldart, 1983, pp. 172–4). The commonly used *Laplace transform* is *one-sided*, that is, the transform integral has the lower limit  $t = 0$ , so that all functions are in effect causal. The transform pair  $g(t) \leftrightarrow G(s)$  is defined by the relations

$$G(s) = \int_0^{\infty} g(t) e^{-st} dt \quad (\text{A.75a})$$

$$g(t) = (1/2\pi j) \int_{\sigma-j\omega}^{\sigma+j\omega} G(s) e^{st} ds \quad (\text{A.75b})$$

where  $s = \sigma + j\omega$ ,  $\sigma$  is positive and large enough that  $\lim_{t \rightarrow \infty} g(t)e^{-\sigma t} = 0$  (in practice almost all functions satisfy this requirement). Generally  $G(s)$  is more easily calculated than  $G(\omega)$ , but the inverse transformation of Equation (A.75b) involves integration in the complex plane, which is usually difficult. Fortunately, many extensive tables of Laplace transforms are readily available (for example, Pipes and Harvill, 1970, Appendix A), so we get transform pairs from tables, just as in the case of integrals.

Most theorems for Fourier transforms have counterparts for Laplace transforms. The most useful are listed in the following equations (proofs can be found in Sheriff and Geldart, 1983, pp. 173–4):

*Shift theorems:*

$$g(t - a) \leftrightarrow e^{-as}G(s) \quad (\text{A.76a})$$

$$e^{-at}g(t) \leftrightarrow G(s + a) \quad (\text{A.76b})$$

*Scaling theorem:*

$$g(at) \leftrightarrow (1/a)G(s/a) \quad (\text{A.77})$$

*Derivative theorems:*

$$\begin{aligned} d^n g(t)/dt^n &\leftrightarrow s^n G(s) - s^{n-1}g(0+) \\ &\quad - s^{n-2}g'(0+) \\ &\quad - s^{n-3}g''(0+) - \dots - g^{n-1}(0+) \end{aligned} \quad (\text{A.78a})$$

$$(-t)^n g(t) \leftrightarrow d^n G(s)/ds^n \quad (\text{A.78b})$$

The notation  $g(0+)$  and  $g'(0+)$  denotes  $g(t)$  and  $d^r g(t)/dt^r$  evaluated at  $t = 0$  where  $t$  approaches zero from the positive side (this allows for discontinuities at  $t = 0$ ).

Fourier transforms are convenient for studying the frequency and phase characteristics of a function whereas the Laplace transform is more useful in studying the analytical properties of the transform (as in filter design). Both are useful in solving differential equations with constant coefficients, the choice depending mainly on the type of boundary conditions.

### A.12.2. Calculation of Laplace Transforms

Many transforms are easily found using Equation (A.75a); for example,

$$\cos at \leftrightarrow s/(s^2 + a^2)$$

$$\sin at \leftrightarrow a/(s^2 + a^2)$$

$$t^n \leftrightarrow n!/s^{n+1}$$

$$te^{at} \leftrightarrow 1/(s - a)^2$$

$$t \sin at \leftrightarrow 2as/(s^2 + a^2)^2$$

Many transforms can be found by using the theorems, for example, the transform of  $\sin at$  can be found by differentiating  $\cos at$ ;  $te^{at}$  can be found by applying Equation (A.76b) to the transform of  $t^n$  with  $n = 1$ ;  $t \sin at$  can be found using (A.78b).

Two useful “special” functions are the unit impulse,  $\delta(t)$ , introduced in Section A.9.3, and the *unit step function*,  $u(t)$ , defined as

$$u(t) = \begin{cases} 0 & t < 0 \\ +1 & t > 0 \end{cases} \quad (\text{A.79})$$

The step function is discontinuous at  $t = 0$ ; it is often used to “wipe out” a function for  $t < 0$ ; thus,

$$\begin{aligned} \cos at u(t) &= 0 & t < 0 \\ &= \cos at & t > 0 \end{aligned}$$

The transforms of  $\delta(t)$  and  $u(t)$  are easily found from Equation (A.75a):

$$\delta(t) \leftrightarrow +1 \quad u(t) \leftrightarrow 1/s \quad (\text{A.80})$$

### A.12.3. Transforms of the Error Function and its Derivatives

The *error function*,  $\text{erf}(x)$ , is defined as

$$\text{erf}(x) = (1/\pi^{1/2}) \int_0^x e^{-u^2} du \quad (\text{A.81})$$

We also use  $\text{erfc}(x) = 1 - \text{erf}(x)$  which is the *complementary error function*. From the definition,  $\text{erf}(0) = 0$ ,  $\text{erf}(+\infty) = 1$ . The error function is tabulated in many handbooks (for example, Gradshteyn and Ryzhik, 1965).

Derivatives of  $\text{erf}(x)$  can be obtained from Equation (A.81). Thus,

$$\text{erf}'(x) = d/dx \{ \text{erf}(x) \} = (2/\pi^{1/2}) e^{-x^2} \quad (\text{A.82a})$$

on using Leibnitz' rule (Wiley, 1966, p. 274; Kaplan, 1952, p. 218). If  $x$  is replaced by  $(a/2t^{1/2})$  [Eq. (7.31)] and we write  $\text{erf}'(a/2t^{1/2})$  for the derivative of  $\text{erf}(a/2t^{1/2})$  with respect to  $t$ , then on setting  $y = (a/2t^{1/2})$ , we find

$$\begin{aligned} \text{erf}'(a/2t^{1/2}) &= d/dy \{ \text{erf}(y) \} dy/dt \\ &= (2/\pi^{1/2}) e^{-y^2} (-a/4t^{3/2}) \\ &= (-a/2\pi^{1/2}t^{3/2}) e^{-a^2/4t} \quad (\text{A.82b}) \end{aligned}$$

We can expand  $\text{erf}(x)$  in a power series, one form being (Pipes and Harvill, 1970, p. 493)

$$\begin{aligned}\text{erf}(x) &= (2/\pi^{1/2}) \{ x - x^3/3 \times 1! \\ &\quad + x^5/5 \times 2! - \dots \\ &\quad + (-1)^n x^{2n+1} / (2n+1) \times n! + \dots \}\end{aligned}\quad (\text{A.83})$$

The Laplace transform of  $\text{erfc}(\alpha/2t^{1/2})$  is listed in most tables (Pipes and Harvill, 1970, p. 778):

$$\text{erfc}(\alpha/2t^{1/2}) u(t) \leftrightarrow e^{-\alpha t^{1/2}}/s \quad (\text{A.84a})$$

hence

$$\text{erf}(\alpha/2t^{1/2}) u(t) \leftrightarrow (1 - e^{-\alpha t^{1/2}})/s \quad (\text{A.84b})$$

on using Equation (A.80) [ $u(t)$  is usually omitted in tables].

Although  $\alpha$  is a constant in Equation (A.84), we can fix  $t$  and vary  $\alpha$ ; then

$$\partial/\partial\alpha = \partial/\partial y (\partial y/\partial\alpha) = (1/2t^{1/2}) \partial/\partial y$$

Writing Equation (A.84b) in the form of Equation (A.75) and differentiating with respect to  $\alpha$  under the integral sign, we obtain

$$\begin{aligned}\int_0^t (1/2t^{1/2}) \text{erf}'(\alpha/2t^{1/2}) e^{-st} dt \\ = d/d\alpha \left\{ (1 - e^{-\alpha t^{1/2}})/s \right\} = e^{-\alpha t^{1/2}}/s^{1/2}\end{aligned}$$

Comparing with Equation (A.75) we see that

$$(1/2t^{1/2}) \text{erf}'(\alpha/2t^{1/2}) \leftrightarrow e^{-\alpha t^{1/2}}/s^{1/2} \quad (\text{A.85a})$$

Using Equation (A.82a), Equation (A.85a) becomes

$$(1/\pi t)^{1/2} e^{-\alpha^2/4t} \leftrightarrow e^{-\alpha t^{1/2}}/s^{1/2}$$

Differentiating again with respect to  $\alpha$ , we get

$$(\alpha/2\pi^{1/2}t^{3/2}) e^{-\alpha^2/4t} \leftrightarrow e^{-\alpha t^{1/2}}$$

or, on using Equation (A.82a),

$$(\alpha/4t^{3/2}) \text{erf}'(\alpha/2t^{1/2}) \leftrightarrow e^{-\alpha t^{1/2}} \quad (\text{A.85b})$$

Equations (A.85) and (A.84) comprise a series of transform pairs with descending powers of  $s$ . The following two pairs, found in Abramowitz and

Stegun (1972) and Erdélyi (1954) respectively, extend this series:

$$e^{-\alpha s^{1/2}}/s^{3/2} \leftrightarrow 2(t/\pi)^{1/2} e^{-\alpha^2/4t} - \alpha \text{erfc}(\alpha/2t^{1/2}) \quad (\text{A.85c})$$

$$\begin{aligned}e^{-\alpha s^{1/2}}/s^2 \leftrightarrow t(1 + \alpha^2/2t) \text{erfc}(\alpha/2t^{1/2}) \\ - (2t/\pi^{1/2})(\alpha/2t^{1/2}) e^{-\alpha^2/4t}\end{aligned}\quad (\text{A.85d})$$

### A.13. LINEAR SYSTEMS

The term *system*, as used here, refers to a set of objects and/or concepts such that an input signal applied to the system results in an output signal. We concern ourselves solely with the relation between the input and output signals, and not with the inner workings of the system.

A system is *linear* if the output  $h(t)$  is proportional to the input signal of  $g(t)$ . If we were to study the inner workings of the system, we could, in principle, describe the relation between  $h(t)$  and  $g(t)$  by a linear differential equation with constant coefficients. Because the order of the equation is rarely more than 2, we take as a typical equation

$$\frac{d^2h(t)}{dt^2} + a_1 \frac{dh(t)}{dt} + a_2 h(t) = g(t) \quad (\text{A.86})$$

Taking Fourier transforms and using Equation (A.61a), we get

$$(j\omega)^2 H(\omega) + a_1(j\omega) H(\omega) + a_2 H(\omega) = G(\omega)$$

so

$$H(\omega) = F(\omega) G(\omega)$$

where

$$F(\omega) = \{(j\omega)^2 + (j\omega a_1) + a_2\}^{-1} \quad (\text{A.87a})$$

$F(\omega)$  being the *transfer function*. If we know  $F(\omega)$ , we can find  $H(\omega)$  for any input  $G(\omega)$ . If we apply a unit impulse  $\delta(t)$  to the input, then  $G(\omega) = 1$  from Equation (A.63) and the transform of  $F(\omega)$  gives the output, that is,

$$F(\omega) \leftrightarrow f(t) = \text{unit impulse response}$$

Thus, application of a unit impulse at the input of a

linear system gives us the data to calculate the output for any other input.

Equation (A.87a) can be written in terms of Laplace transforms, the only difference being that use of Equation (A.78a) adds terms in  $h(0+)$ ,  $h'(0+)$ , and  $h''(0+)$  to  $G(s)$  [which replaces  $G(\omega)$  in Eq. (A.87a)]; however, the usual assumption is that the system is *initially relaxed*, meaning that  $h(0+) = 0 = h'(0+) = h''(0+)$ , so that Equation (A.87a) becomes

$$\left. \begin{aligned} H(s) &= F(s)G(s) \\ \text{where } F(s) &= (s^2 + a_1s + a_2)^{-1} \end{aligned} \right\} \quad (\text{A.87b})$$

## REFERENCES

- Abramowitz, M. and Stegun, I. A. 1972. *Handbook of Mathematical Functions*, Nat. Bur. of Standards. Washington: U.S. Gov't Printing Office.
- Erdélyi, A. (ed.) 1954. *Tables of Integral Transforms, vol. I.* New York: McGraw-Hill.
- Gradshteyn, I. S. and Ryzhik, I. M. 1965. *Tables of Integrals, Series, and Products*. New York: Academic.
- Kaplan, W. 1952. *Advanced Calculus*. Reading, MA: Addison-Wesley.
- Papoulis, A. 1962. *The Fourier Integral and Its Applications*. New York: McGraw-Hill.
- Pipes, L. A., and Harvill, L. R. 1970. *Applied Mathematics for Engineers and Physicists*. New York: McGraw-Hill.
- Sheriff, R. E., and Geldart, L. P. 1983. *Exploration Seismology, Vol. 2*. New York: Cambridge University Press.
- Wiley, Jr., C. R. 1966. *Advanced Engineering Mathematics*. New York: McGraw-Hill.

# Mathematical Conventions

## A. General functions

$f(x, y, z)$	function of continuous variables ( $x, y, z$ )
$f_i$	function of the discrete variable $i = n\Delta$ , $n$ integral
$f(t) * g(t)$	convolution of $f(t)$ with $g(t)$
$G(v), G(\omega)$	Fourier transform of $g(t)$
$\phi_{fg}(\tau)$	correlation of $f(t)$ with $g(t)$ for a displacement $\tau$
$J_n(x)$	Bessel function of the first kind of order $n$
$I_n(x)$	Modified Bessel function of the first kind
$K_n(x)$	Modified Bessel function of the second kind

## B. Special functions

$u(t)$	unit step function; $u(t) = 0, t < 0; u(t) = +1, t > 0$
$\delta(t), \delta,$	unit impulse (Dirac delta), $\delta(t) = \delta_i = +1, t = 0; = 0$ for $t \neq 0$
$\text{boxcar}(t)$	$\text{boxcar}(t) = +1, -\omega_0 \leq \omega \leq +\omega_0; = 0$ outside this range
$\text{comb}(t)$	infinite series of equally spaced unit impulses
$\text{sinc}(t)$	$(\sin t)/t$

## C. Mathematical conventions

$>, <$	greater than, less than
$\geq, \leq$	greater than or equal to, less than or equal to
$\ll, \gg$	much greater than, much smaller than
$\sim$	of the order of
$\approx$	approximately equal to
$\leftrightarrow$	correspondence between a function and its transform
$\mathbf{A}$	vector of magnitude $A$
$\mathbf{A} \cdot \mathbf{B}$	scalar (dot) and vector (cross) products of vectors $\mathbf{A}$ and $\mathbf{B}$
$\mathbf{A} \times \mathbf{B}$	
$\nabla$	del, the vector operator $\mathbf{i} \partial/\partial x + \mathbf{j} \partial/\partial y + \mathbf{k} \partial/\partial z$
$\nabla^2$	Laplacian $\partial^2/\partial x^2 + \partial^2/\partial y^2 + \partial^2/\partial z^2$
$\nabla \phi$	gradient of $\phi(x, y, z) = \text{grad } \phi$ (see Eq. (A.17))
$\nabla \cdot \mathbf{A}$	divergence of $\mathbf{A}(x, y, z) = \text{div } \mathbf{A}$ (see Eq. (A.19))
$\nabla \times \mathbf{A}$	curl of $\mathbf{A}(x, y, z) = \text{curl } \mathbf{A}$ (see Eq. (A.20))
$\mathcal{A}$	matrix with elements $a_{ij}$
$\mathcal{A}^T$	transpose of $\mathcal{A}$ with elements $a_{ji}$
$\mathcal{A}^{-1}$	inverse of $\mathcal{A}$
$ x $	absolute value of $x$
$\det(a_{ij})$	determinant with elements $a_{ij}$

$\sum_0^n g_i$	$g_0 + g_1 + g_2 + \cdots + g_n$
$\sum_{k=0}^n$	$g_0 + g_1 + g_2 + \cdots + g_n$
$\sum_k g_k$	sum of $g_k$ for appropriate values of $k$
$\ln x$	$\log_e x$
$\log x$	$\log_{10} x$
$U_{xx}, U_{xy}, U_{xzz}$	partial derivatives of $U$ with respect to $x$ (twice), $x$ and $y, z$ (three times)
$j$	$\sqrt{-1}$
$\left. \begin{matrix} \operatorname{Re} \{ f(z) \} \\ \operatorname{Im} \{ f(z) \} \end{matrix} \right\}$	real and imaginary parts of a complex quantity $f(z)$

# APPLIED GEOPHYSICS

SECOND  
EDITION

Telford Geldart Sheriff

This is the completely revised and updated version of the popular and highly regarded textbook, *Applied Geophysics*. It describes the physical methods involved in exploration for hydrocarbons and minerals, which include gravity, magnetic, seismic, electrical, electromagnetic, radioactivity, and well-logging methods. All aspects of these methods are described, including basic theory, field equipment, techniques of data acquisition, data processing and interpretation, with the objective of locating commercial deposits of minerals oil, and gas and determining their extent.

In the fourteen years or so since the first edition of *Applied Geophysics*, many changes have taken place in this field, mainly as the result of new techniques, better instrumentation, and increased use of computers in the field and in the interpretation of data. The authors describe these changes in considerable detail, including improved methods of solving the inverse problem, specialized seismic methods, magnetotellurics as a practical exploration method, time-domain electromagnetic methods, increased use of gamma-ray spectrometers, and improved well-logging methods and interpretation.

As before, the intent is to be practical, and thus many field examples and problems are given. In this edition the authors have adopted SI (*Système Internationale*) units to a considerable extent, but other units are also used where SI units are still not in common use in exploration geophysics. The authors assume that the reader has at least a general background in geology, physics, and mathematics. While many of the derivations require more than an elementary knowledge of mathematics, readers may skip these if they are interested only in the results. An appendix gives a concise explanation of the more advanced mathematics used in the book.

This is the most complete book available on the subject. It is suitable as a text for an undergraduate geophysics course for geologists, geophysicists, and engineers, as well as for more advanced study at the graduate level. Its comprehensiveness makes it eminently suitable as a reference work for professional geologists, geophysicists, and mining and civil engineers.

Reviewer praise for the first edition of *Applied Geophysics*

"It is an excellent text book... it will serve well as a reference for practicing geophysicists and for other earth scientists who become closely involved with geophysical prospecting. I believe that it will be necessary for almost every practicing exploration geophysicist to have a copy available to him. The book is well produced."

G. V. Keller, *EOS: Transactions. American Geophysical Union*

"This book provides a thorough and comprehensive treatment of the various geophysical measurements used in the search for hydrocarbons and other minerals. An obvious effort has been made to describe pertinent geologic concepts in ways that make understanding easier for physicists, mathematicians, and electrical engineers."

Mahlon M. Ball, *American Association of Petroleum Geologists Bulletin*

"This particular volume is an excellent complete treatment of applied geophysics, useful both as a comprehensive textbook and as a basic reference. The knowledgeable economic geologist can be well prepared for a variety of important applications of geophysical methods. A total compilation in exploration geophysics." John A. Sumner, *Economic Geology*



AEEIZH

D.H. MOOQADAS

ISBN 0-521-33938-3



9 790521 339383 >